Regional Geology Reviews

Zakaria Hamimi · Ahmed El-Barkooky ·
Jesús Martínez Frías · Harald Fritz ·
Yasser Abd El-Rahman *Editors*

The Geology of Egypt

Springer

Regional Geology Reviews

The Geology of series seeks to systematically present the geology of each country, region and continent on Earth. Each book aims to provide the reader with the state-of-the-art understanding of a regions geology with subsequent updated editions appearing every 5 to 10 years and accompanied by an online "must read" reference list, which will be updated each year. The books should form the basis of understanding that students, researchers and professional geologists require when beginning investigations in a particular area and are encouraged to include as much information as possible such as: Maps and Cross-sections, Past and current models, Geophysical investigations, Geochemical Datasets, Economic Geology, Geotourism (Geoparks etc), Geo-environmental/ecological concerns, etc.

More information about this series at http://www.springer.com/series/8643

Zakaria Hamimi • Ahmed El-Barkooky •
Jesús Martínez Frías • Harald Fritz •
Yasser Abd El-Rahman
Editors

The Geology of Egypt

Springer

Editors
Zakaria Hamimi
Department of Geology
Benha University
Benha, Egypt

Jesús Martínez Frías
Institutes of Geosciences
Ciudad University
Madrid, Spain

Yasser Abd El-Rahman
Department of Geology
Cairo University
Giza, Egypt

Ahmed El-Barkooky
Department of Geology
Cairo University
Giza, Egypt

Harald Fritz
Department of Geology and Environment
Earth Science
University of Graz
Vienna, Austria

ISSN 2364-6438 ISSN 2364-6446 (electronic)
Regional Geology Reviews
ISBN 978-3-030-15264-2 ISBN 978-3-030-15265-9 (eBook)
https://doi.org/10.1007/978-3-030-15265-9

Book Cover Photo: Gravity-controlled east-vergent recumbent fold in the area north of Nuweiba' City, western side of Gulf of Aqaba, Sinai (Photo by: Prof. M.A. Abd El-Wahed, Tanta University, Egypt)

This Springer imprint is published by the registered company Springer Nature Switzerland AG
The registered company address is: Gewerbestrasse 11, 6330 Cham, Switzerland

Preface

Why This Book?

The passion to understand the Geology of Egypt could be traced back to 1150 BC. In this year, the oldest geological map in the world was prepared to illustrate the geology of the Hammamat-Fawakhir area in the central part of the Eastern Desert of Egypt. This beautifully colored papyrus map, which is preserved in the Egyptian Museum in Turin (Italy), describes the distribution of sedimentary and igneous, mostly granitic, rocks in black and red colors, respectively. The map shows also the siltstone and sandstone (Bekhen stone) quarry and the gold-bearing quartz veins and the settlements that are related to the gold exploitation from the igneous rocks at Bir Umm Fawakhir area.

In 1990 (A. A. Balkema, Rotterdam), Rushdi Said invited 40 scholars to participate in assembling the large amount of information that was accumulated since his earlier book on the Geology of Egypt, which was published by Elsevier in 1962. From 1990 to 2019, huge amount of data stemmed from advances in many techniques have been accumulated on diverse disciplines related to the geological evolution of Egypt. Thus, various ideas have been changed and many new models have been raised regarding our understanding of the geology of Egypt. In such circumstances, a new updated book on the Geology of Egypt becomes a must to integrate these new enormous data and to exhibit the revised thoughts and new models related to the geological evolution of Egypt. This is exactly the aim of our resurgent "*Geology of Egypt*" book, which presents the essence of data accumulated for almost 30 years since 1990 and their interpretation from the perspectives of the invited authors.

Content

This volume contains 18 chapters written by the following 58 contributors (arranged in alphabetical order): Abd El-Aziz Khairy Abd El-Aal, Abdel-Rahman Fowler, Adel R. Moustafa, Adel Surour, Ahmed El-Kammar, Ahmed Hassan Ahmed, Ahmed Madani, Ahmed N. El-Barkooky, Amr Abdelnasser, Baher El Kalioubi, Basem Zoheir, Bassem Abdellatif, Fathy Abdalla, Fekri A. Hassan, Hassan Khozyem, Hassan M. Helmy, John Dolson, K. R. McClay, Kamal Ali, Kamal Sakr, Karim Abdelmalik, L. Folco, M. Ligi, Marwah M. Kamal El-Din, Mohamed A. Hamdan, Mohamed Abd El-Wahed, Mohamed Ahmed, Mohamed El-Ahmadi Ibrahim, Mohamed El-Alfy, Mohamed El-Rawy, Mohamed El-Sharkawi, Mohamed Z. El-Bialy, Mona H. Darwish, Mortada El Aref, Nader A. Edress, Nagy Shawky Botros, Robert J. Stern, Samar Nour-El-Deen, Samir Khalil, Sultan Awad Sultan Araffa, W. Bosworth, W. U. Reimold, Wael Hagag, Wagieh E. El-Saadawi, Yasser Abdelrahman, Zainab M. El-Noamani, Zakaria Hamimi. We would like first to thank all of them for their valuable and impressive contributions to the Geology of Egypt.

Chapter 1 "History of the Geological Research in Egypt" comprises six separate sections. In the first section, Mohamed El-Sharkawi highlighted the stages of the geological research in

Egypt before the establishment of the Egyptian Geological Survey and Stages after. Hume's book and Said's '62 & '90 Books are dealt with in this part. In the second section, Nagy Shawky Botros shed much light on the History of geological mapping in Egypt since the Turin papyrus map that was drawn during the reign of Ramses IV (1156–1150 BC) and reveals the Bekhen stone quarries and the Fawakhir gold mines in the Wadi Hammamat in the Eastern Desert of Egypt. He addresses three episodes of mapping. In the third section, Ahmed A. Madani provides a noteworthy idea about the geological remote sensing publications in Egypt throughout some statistics on Satellite Sensors and techniques. In fourth section, Mohamed Ahmed and Bassam Abdellatif dealt with monitoring spatiotemporal variabilities in Egypt's groundwater resources using GRACE data. In fifth section, Yasser M. Abd El-Rahman gave a comprehensive idea about geochronological measurements of the Egyptian basement complex and associated mineralization. In the last section, Sultan Awad Sultan Araffa briefly described several airborne survey data which are mainly magnetic, electromagnetic and in several surveys, total count (TC) radiation for Thorium, Uranium, and Potassium elements data. These airborne surveys were carried out for some authorities and institutions in Egypt, such as the Egyptian Geological Survey and Mining Authority (EGSMA), the Nuclear Materials Corporation (NMC), the Desert Research Institute (DRI), and the Egyptian General Petroleum Corporation (EGPC).

Chapter 2 "Precambrian Basement Complex of Egypt, by Mohammed Z. El-Bialy" reviews different aspects of the Precambrian basement complex of Egypt based on the author's ~quarter-century research experience in the petrology and geochemistry of the different basement rocks both in Sinai and the Eastern Desert of Egypt. This chapter presents integrated digest of the up-to-date published information, data, and ideas on the various Precambrian basement rock units. Apart from the introduction section, this chapter discusses three main topics, namely, nature and evolution of the basement crust, review of the Egyptian basement classifications and the Precambrian basement succession. The last topic is the most voluminous and covers the major part of the chapter. This foremost section provides a comprehensive preview on these basement rock units in a geochronological order starting from the oldest Archean–Mesoproterozoic "Metacratonic Gneisses of Uweinat-Kamil inlier". With the exception of the Neoproterozoic "Alaskan-type mafic-ultramafic complexes" and "Katherina Volcanics" rock units, introduced herein for the first time, the rest of rock units dealt with have been formerly identified, although under different names, in earlier classifications.

Chapter 3 "Structural and Tectonic Framework of Neoproterozoic Basement of Egypt: From Gneiss Domes to Transpression Belts, by: Abdel-Rahman Fowler and Zakaria Hamimi" addresses the Neoproterozoic tectonic evolution of the Egyptian Eastern Desert basement which is documented, predominantly through its history of structural events, and to a lesser degree, important magmatic and sedimentation events. Main outline of this chapter includes (1) introductory statement, (2) regional context of the Egyptian Eastern Desert in the Arabian–Nubian Shield and East African Orogen, (3) major tectonic events from oldest to youngest, and the evidence for the latest Mesoproterozoic rifting of Rodinia in Sinai, and features of the oldest gneissic complexes (Feiran-Solaf and Sa'al complexes), (4) aspects of the intra-oceanic subduction stage and consequent arc–arc and arc–continent collisions, and suturing of terranes, (5) the orogenic extension stage, including appraisal of the evidence and scale of extension, its possible tectonic origins (rifting, tectonic escape and extrusion, orogenic collapse, mantle delamination, etc.), and its role in the exhumation of distinctive gneissic dome structure, best represented by the Meatiq complex, and (6) post-extension compressional events, primarily as recorded in the deformation of the extension-stage Hammamat molasse basins

Chapter 4 "Crustal Evolution of the Egyptian Precambrian Rocks, by: Robert J. Stern and Kamal Ali" summarizes what is known about the exposed continental crust of Egypt which is exposed in 10% of the country. Basement exposures are in three main areas: the southern Sinai, the Eastern Desert, and discontinuous exposures in the Western Desert, just north of the

border with Sudan. The overwhelming majority of basement rock exposures are of Neoproterozoic age, between ~850 Ma and 570 Ma in age. Significant similarities as well as differences are shown between three main subdivisions of the Eastern Desert: the Northern Eastern Desert, the Central Eastern Desert, and the South Eastern Desert. These three regions of Neoproterozoic crust also share similarities and differences with Neoproterozoic exposures in southern Sinai. A small proportion of exposed Egyptian crust is pre-Neoproterozoic in age. The oldest rocks, of Archean (3.3–25 Ga) and Paleoproterozoic (~2.1–1.9 Ga) age, are found in far southwestern Egypt. The next oldest rocks, a small exposure of Late Mesoproterozoic age (~1.1 Ga), are found in Sinai. We know almost nothing about crust buried beneath Phanerozoic sediments in the Western Desert and northern Sinai. The chapter summarizes what we know and also discusses work that needs to be done.

Chapter 5 "Suture(s) and Major Shear Zones in the Neoproterozoic Basement of Egypt, by: Zakaria Hamimi and Mohamed A. Abd El-Wahed" reviews major shear zones traversing the Egyptian–Nubian Shield, such as Hamisana, Hodein-Kharite, Nugrus, Atallah Mubarak-Barramiya, and Abu Dabbab Shear Zones. It addresses also the Allaqi–Heiani Suture which is regarded as the western segment of the enormous arc–arc Allaqi–Heiani-Oneib-Sol Hamid-Yanbu Suture Zone. The authors classified megashears encountered in the Egyptian–Nubian Shield into two main groups; syn-accretion and post-accretion shear zones; the first group resulted from the collision between E- and W- Gondwanalands. The predominantly Neoproterozoic basement complex outcropping in the Egyptian–Nubian Shield is traversed by map-scale semi-ductile–semi-brittle shear zones of variable orientations, dimensions, and ages. These shear zones are consistent and in complete harmony with those encountered elsewhere in the entire Arabian–Nubian Shield in terms of their extensions, widths, and degree and sense of shearing.

Chapter 6 "The Metamorphism and Deformation of the Basement Complex in Egypt, by: Baher El Kalioubi, Abdel-Rahman Fowler and Karim Abdelmalik" is the product of integrated efforts of these three scholars in their individual areas of specialization and experience, namely, metamorphic petrology, structural geology and remote sensing, and geological mapping. This voluminous chapter discusses, in somewhat depth, the metamorphic and structural evolution of the Precambrian basement complex in Egypt. Emphasis is given to providing comprehensive quintessential case examples for gneissic complexes, ophiolite sequences, syn-kinematic granitoids, and shear zones. One of the great assets of this chapter is the concentrated information it presents from the wealth of recent published data on the geochronology of various basement rock units in Egypt.

Chapter 7 "Mesozoic-Cenozoic Deformation History of Egypt, by Adel R. Moustafa" discusses the Mesozoic–Cenozoic deformation history of Egypt based on the author's ~35 years' experience of detailed surface structural mapping of different areas in northern Egypt as well as subsurface structural knowledge based on his work with different oil companies. The chapter also derives information from the wealth of published data on the Phanerozoic structures of Egypt. Four main phases of deformation discussed in this chapter have been attributed to the movements between the African Plate and the surrounding plates. These phases are Tethyan (NE-SW to ENE-WSW) rifting, Cretaceous–Early Tertiary (NW–SE to WNW–ESE) rifting, Late Cretaceous–Tertiary inversion of the Tethyan basins, and continued compressional deformation of other areas till present day. A fourth phase of Neogene–Recent deformation in the Gulf of Suez–Gulf of Aqaba–Red Sea area is referred to in this chapter but detailed in a separate chapter (Moustafa and Khalil, Chap. 8).

Chapter 8 "Structural Setting and Tectonic Evolution of the Gulf of Suez, NW Red Sea and Gulf of Aqaba Rift Systems, by Adel R. Moustafa and Samir M. Khalil" deals with the extensional deformation of the Gulf of Suez–Red Sea area that started in Late Oligocene and continues to the present time in the Red Sea. The structures of the Gulf of Aqaba area and its western onshore area as part of the Dead Sea Transform are also discussed in this chapter. The authors' long experience in field structural mapping of the exposed parts of the Gulf of Suez and Red Sea rifts represents the backbone of this chapter. The geometry of rift structures is

well explained based on subsurface structural data from hydrocarbon exploration in the Gulf of Suez rift. The chapter includes description of the pre-rift structures of the area, the tectonostratigraphy of the Gulf of Suez/Red Sea area, the geometry of the faults (their orientations, dip angles, pattern, etc.), the geometry of the accommodation zones between the different half grabens, the stages of rift evolution, and neotectonic activity.

Chapter 9 "Geology of Egypt: The Northern Red Sea by: W. Bosworth, S. M. Khalil, M. Ligi, D. F. Stockli and K. R. McClay" discusses the onshore and offshore margin of the Egyptian northern Red Sea. Authors Bosworth, Khalil, Ligi, Stockli, and McClay integrate results from fieldwork, petrological, geochemical and geochronometric studies, natural seismicity, industry reflection seismic surveys, and exploratory drilling to produce a synthetic view of the evolution of this young continental rift. The onset of rifting is represented by local, structurally controlled deposits of red beds, probably of latest Oligocene age. The first well-dated syn-rift event is the eruption of a regional dike swarm and local basalt flows centered at 23 Ma. This volcanism is synchronous with similar eruptions that extend through Saudi Arabia to Yemen and the Afar. Early Miocene extension resulted in the formation of a complex, discontinuous fault pattern, high rates of fault block rotation, and initiation of uplift of the Red Sea Hills rift shoulder. Through time the intra-rift fault networks coalesced into through-going structures and fault movement became progressively more focused along the rapidly extending rift axis. This reconfiguration of the rift structure resulted in more laterally continuous depositional facies, the preponderance of moderate-to-deep marine deposits, and eventually the formation of an axial trough with localized oceanic-style volcanism. Throughout the rifting process, gabbroic rocks were intruded into the sub-Red Sea crust at progressively shallower depths. These gabbros are now exposed at Zabargad and the Brothers Islands and have been penetrated in an offshore exploratory well. Initiation of the Gulf of Aqaba–Dead Sea transform margin in the Middle Miocene resulted in a change from NE–SW rift-orthogonal to NNE–SSW highly oblique Red Sea extension and abandonment of most opening of the Gulf of Suez. Despite the development of hyper-extended continental crust and the local presence of volcanism at axial deeps, laterally integrated seafloor spreading has not yet manifest itself in the northern Red Sea.

Chapter 10 " Seismicity, Seismotectonics and Neotectonics in Egypt" addresses four main topics: (1) historical earthquakes and seismotectonic zones in Egypt, by: Abd El-Aziz Khairy Abd El-Aal, (2) application of EMR Data in detecting seismotectonic zones in Egypt, by: Wael Hagag, (3) role of GPS measurements in seismological study in Egypt, by: Kamal Sakr, and (4) application of InSAR data in ground deformation monitoring, by: Mohamed Saleh.

Chapter 11 "Impact Craters and Meteorites: The Egyptian Record, by: L. Folco1, W. U. Reimold and A. El-Barkooky" offers a detailed account of the present Egyptian impact record and of the Egyptian meteorite collection. The authors provide an overview of the impact cratering process, with basic information for understanding its importance as a geological process and for identifying new impact structures and their ejecta. This is followed by a review of current knowledge on the 45-m-diameter Kamil Crater—the only confirmed impact structure in Egypt, and by a discussion of the nonimpact origin of several crater-like circular structures superficially resembling impact craters in the Western Desert of Egypt, as well as of the proposed impact origin of Libyan Desert Glass and Dakhleh Glass. Folco et al. subsequently provide a general introduction to meteorites that highlights their fundamental role in our understanding of the origin and evolution of the solar system. They then provide an overview of the Egyptian meteorite collection, which comprises 78 meteorites including the ~10 kg rare Martian meteorite fall of 1911—Nakhla, and discuss the potential of Egyptian deserts for systematic searches for meteorites. An account of the role of meteoritic iron in the Egyptian archeo-anthropological record and its bearing on the history of human civilization is also provided. The chapter ends with a discussion of future perspectives for meteoritics and planetary science in Egypt.

Chapter 12 "Quaternary of Egypt, by: Mohamed A. Hamdan and Fekri A. Hassan" introduces an up-to-date synthesis of recent research on high-resolution and well-dated paleo-environmental archives. This chapter provides proxy data to understand the emerging

picture of the impact of climate change on sediments, paleo environments, and landscapes in Egypt as a whole.

Chapter 13 "Fossil Flora of Egypt, by: Wagieh E. El-Saadawi, Samar Nour-El-Deen, Zainab M. El-Noamani, Mona H. Darwish and Marwah M. Kamal El-Din" summarizes the results of two centuries of laborious investigations. Emphasis was placed on fossil remains as elements of the biota in the geologic history of Egypt and as indicators of paleoclimate, paleoenvironment, and their significance with respect to biostratigraphy and dating. The paleoflora of Egypt is very rich and diverse consisted of a mixture of the major plant groups extended from the Devonian to the Quaternary. The discovered fossil plant remains include algae, pteridophytes, gymnosperms, angiosperms, and palynomorphs of all groups. Very little is known about fossil fungi. Fossil evidence of bacteria and bryophytes (except their spores) is generally lacking. Paleoclimate inferences of different geologic epochs are given based on the studied fossil plants. The provided illustrations of micro- and macrofossils and the map of the main fossiliferous sites add to the interest and value of the chapter.

Chapter 14 "Mineral Resources in Egypt (I): Metallic Ores" highlights nine metallic ore deposits: (1) iron ores of Egypt, by: Mortada El Aref, (2) Egyptian BIF: Glaciogenic versus Hydrothermal Origin?, by: Yasser Abd El-Rahman, (3) Orogenic Gold in the Eastern Desert, Egypt, by: Basem Zoheir, (4) Titanium-rich deposits (Titaniferous Iron Ore Deposits and black sand), by: Adel Surour, (5) Sulfide and Precious Metal Deposits in Egypt, by Hassan M. Helmy, (6) Industrial Metal Oxides (Sn, W, Ta, Nb, and Mo), by: Amr Abdelnasser, (7) Chromite Deposits in Egypt, by: Ahmed Hassan Ahmed, (8) Low Grade Uranium Occurrences in the Basement Rocks of Egypt, by: Mohamed El-Ahmadi Ibrahim, and (9) Egyptian Manganese Deposits, by: Mortada El Aref.

Chapter 15 "Mineral Resources in Egypt (II): Non-metallic Ore Deposits" reviews four main items: (1) phosphate deposits in Egypt, by: Ahmed El-Kammar, (2) white sand (glass sand or silica sand), by: Adel Surour, (3) argillic deposits, by: Mohamed El-Sharkawi, and (4) review on some evaporate deposits in Egypt, by: Hassan Khozyem. Egypt produces phosphate ore on a commercial scale since about a century where its share in 2015 is 2.5% of the total world production. Applying new mining methods especially in the Red Sea and Abu Tartur, exploration, and beneficiation of the medium and low-grade ore may drive the present 5.5 m tons annual production of Egypt to a prosperous frontier. Phosphate deposits in Egypt belong to the Late Cretaceous–Paleogene time interval where stratigraphic boundaries are strongly time-transgressive. They belong to the Late Cretaceous Tethyan phosphogenic Province that has regional extension in the Middle East and North Africa. They distributed in the Egyptian territories among seven main domains, some of them are not yet exploited. The main apatite variety in the marine sedimentary phosphorites including those of Egypt is the carbonate fluorapatite "francolite" that contains 3 to 5% F, with F/P_2O_5 ratio of about 0.12 in average. The francolite lattice has 9.335 ± 0.028 Å and 6.899 ± 0,018 Å for ao and co dimensions, respectively, whereas the lattice volume is 520 ± 4 Å3. The calculated empirical formulae are $Ca_{9.22}$ $(Sr,La,..)_{0.63}(OH)_{0.15}P_{5.12}(C,S,..)_{0.88}(F_{1.46}O_{22.71})OH_{0.83}$ and $Ca_{9.21}(Sr,La,..)_{0.75}(OH)_{0.04}P_{5.05}(C,S,..)_{0.95}(F_{1.52}O_{22.72})OH_{0.76}$ for the weathered and non-weathered francolite, respectively. In average, the abundance of the heavy metals in the Egyptian phosphorites follow the order: Zn > V > Co > Cu > Pb > Mo > Cd > Sn. However, the phosphorites of the Red Sea region accumulate higher quotient of the heavy metals compared with those of the Nile Valley and Abu Tartur. The later occurrence is a better accumulator of the terrestrial elements such as Th, Sc, Zr, Hf, Nb, Ta, and LREE. Consideration should be given to the peculiarities of the single beds in each geographic occurrence. The phosphorites that deposited at the beginning of the Late Cretaceous transgression event occur at the base of the Duwi Formation, or even intercalated within the uppermost Quseir (Variegated Shale) Formation. These beds represent the shallowest basin forming the southern limits of the Tethyan phosphogenic belt and can be encountered in Hammadat south Quseir, south Edfu (e.g., in Fawaza and Silwa villages), and the lower bed of Abu Tartur plateau. All

these phosphate beds are remarkably rich in REE+Y (>1000 ppm). The radioactivity of phosphate is essentially related to U-decay series and not Th-decay series.

Chapter 16 "The Petroleum Geology of Egypt and History of Exploration, by: John Dolson" approaches understanding the petroleum systems of Egypt from the eyes of the pioneering explorers who have developed Egypt's hydrocarbon resources. In the words of Wallace Pratt, and early founder of AAPG, "Where oil is first found, is in the minds of men (and women)". Although oil was known to Egyptians for thousands of years through seeps along the Sinai margin of the Gulf of Suez, real growth in reserves did not occur until the late 1950s and 1960s. Today, Egypt's petroleum resource continues to expand dramatically, with new giant trends discovered in deep waters offshore and to the east in the Levant Basin. Our current understanding of the basins and petroleum systems of Egypt continues to evolve. Big advances in finding rates and plays can occur from only three types of innovations. The first is the concepts themselves, pursued through creative and rigorous analysis of data and techniques available at any given time. While some people look back on historical explorers as 'old school', they fail to recognize that the technologies used for breakthrough exploration in those early periods were 'cutting edge' for the geoscientists of their time. Second, new technology, such as 3D seismic, horizontal drilling, or workstation integration tools provide additional ways to find new resources. But without proper fiscal terms and government regulations, great concepts and technology often sit idle for decades before being applied. This chapter illustrates the evolution of thought, technology, fiscal terms, and other innovations that has led to giant resources continuing to be found today in basins with stacked pays from Precambrian through Pliocene strata.

Chapter 17 "Other Fuel Resources" summarizes (1) the oil shale, by: Ahmed El-Kammar, and (2) coal, by: Nader A. A. Edress. The first section draws the attention to the critical importance of the indigenous oil shale resources in Egypt as a genuine replacement for the continuously depleting conventional resources. It is important to endorse environmentally friendly development and utilization of oil shale as a part of our energy security strategy. Detailed exploration of predictable prolific oil shale resources in Egypt is mandatory. The dry basis Fischer assay data suggest that the oil shale in Quseir-Safaga produces oil yield which ranges between 35 and 120 liters per ton. This oil shale has an immature nature, mostly of marine liptinite composition and shall be potential upon retorting. Because of the anoxic conditions of deposition it is markedly enriched in the multivalent redox-sensitive elements such as Cd, Mo, V, Zn, and U. Some of these metals are extractable on a commercial scale. The factor analysis of large volume of data (54 variable of 423 metric core samples containing more than 4% TOC) suggests four controlling factors, namely, marine, terrestrial, anoxic, and oxic influence during sedimentation. Acids generated from the breakdown of organic matter and sulfides enhance weathering even by dew, but mostly during the pluvial periods. Oil shale, in particular, is readily vulnerable to chemical weathering. The total mass loss of black shales upon chemical weathering under arid environments is estimated to be about 45%, on average. Oil shale spent shale (ash) is a by-product of retorting and it may cause a serious environmental hazard if not properly utilized. It is mainly applied as road mortar and to improve the stabilization of constructions. It is also used as additives for the Portland cement industry. The modern application of spent shale includes the production of heavy metals, polymers, and remediation of polluted and acid soil.

Chapter 18 "Water Resources in Egypt" includes two sections: (1) surface water resources in Egypt, by: Mustafa El-Rawy and Fathy Abdalla and (2) groundwater resources in Egypt, by: Mohamed El Alfy and Fathy Abdalla. From the late Eocene up to the late Middle Pleistocene, Egypt was a wet country due to the rainfall and rivers running through it. Recently, Egypt is experiencing a severe water shortage that is expected to worsen because of the increasing demand for water for domestic, agricultural, and industrial use. Water resources in Egypt include the river Nile, in addition to the renewable and nonrenewable groundwater, domestic wastewater, desalinated water, rainfall, and flash floods. The river Nile, which originates outside the country, is **considered to be the lifeblood of Egypt** contributing

about 97% of the renewable water resources with 55.5 BCM/y. The main groundwater resources in Egypt are the Nile Valley and Nile Delta and Nubian Sandstone aquifers in the Western Desert and Sinai Peninsula. Various minor aquifers are available locally in the coastal areas, and the eastern and western Nile Delta; however, new strategies for the development of these water resources must be implemented.

Benha, Egypt — Zakaria Hamimi
Giza, Egypt — Ahmed El-Barkooky
Madrid, Spain — Jesús Martínez Frías
Vienna, Austria — Harald Fritz
Giza, Egypt — Yasser Abd El-Rahman

Acknowledgements

The editors gratefully acknowledge the following reviewers (arranged in alphabetical order) for their great help, constructive criticism, and valuable comments: Abdalla Bamousa, Abdel-Rahman Fowler, Abbra Mogessie, Ahmed El Kammar, Alvaro P. Crósta, Baher El Kalioubi, Broder Merkel, Dave Blanchard, Dubravko Lučić, George A. Brook, Harald Fritz, Hassan Helmy, Hassan Harraz, Jean-Paul Liégeois, Jeremy Boak, Joe Versfelt, John Dolson, Karl Föllmi, László Kocsis, Mark Jessell, Mohamed Abd El-Wahed, Mohamed El Sharkawy, Mohamed Z. El-Bialy, Mohamed A. Rashed, Mortada El Aref, Moustafa El-Rawy, Mustapha Meghraoui, Peter Johnson, Pierre Rochette, Rakesh C. Mehrotra, Roger Flower, Said Maouche, Said Matbouly, Samir AbdelMoaty, Sebastian Lüning, Stanislav Opluštil, Steven R Manchester, Thierry Adatte, Timothy Jull, Thomas Grischek, Vasit Sagan, W. Bosworth, Walid Salama, Yasser Abdelrahman, Yehia Dawood, Younes Hamed, and Zakaria Hamimi.

Contents

About the Editors

Zakaria Hamimi is a structural geologist who spent majority of his academic career at Benha University (Egypt) along with some years at Sana'a University (Yemen) and King Abdulaziz University (Saudi Arabia). He has graduated (1984) from Assiut University (distinction with honor degree), and holds the M.Sc. (1988) from Zagazig University (Egypt) and the Ph.D. in Structural Geology and Tectonics (1992) from Cairo University. His research interests focus on Structural Geology, Microstructures, and Tectonics. He has worked in many field-related sub-disciplines of Earth Sciences including geologic mapping, microstructural analysis, strain analysis, paleostress reconstruction, active tectonics, tectonic geomorphology, crustal deformation, and image processing. He used all these fields to study key areas in the Arabian–Nubian Shield, and to decipher their deformation history. Zakaria Hamimi is the President, and one of the founding team, of the Arabian Geosciences Union since 2012. He has received the medal of the Egyptian Geological Society of Egypt in 2015, and also the medal of the Arab Mining and Petroleum Association in 2016. He has co-published 50 research articles in national and international indexed and refereed journals and authored several books. In 2016, Zakaria Hamimi (1) joined the AJGS as Associate Editor responsible for evaluating submissions in the fields of Structural Geology, Microstructures, and Tectonics, (2) selected as a Member of the Egyptian Universities Promotion Committee, the Supreme Council for Universities (SCU, Egypt), (3) nominated as a Secretary of the National Committee for Geological Sciences, Academy of Scientific Research and Technology, and (4) designated as the IUGS-Representative for Egypt. November 2017, he attended the Gondwana 16 International Conference held at Bangkok, Thailand, as the Representative of the National Committee for Geological Sciences, Academy of Scientific Research and Technology, Egypt.

Ahmed El-Barkooky is a Professor of applied sedimentary geology at Cairo University in Egypt, where he graduated with B.Sc. (Hons.) degree in geology in 1980. He obtained his M.Sc. and Ph.D. as well from the same university. He has been teaching several courses and supervising many M.Sc. and Ph.D. research programs at the Geology Department, Faculty of Science in Cairo University. In the meantime, he has been engaged in the petroleum industry as a geological advisor. He enjoys more than 35 years of experience in both academia and industry. He has led and been involved in several exploration projects and special studies regarding basin architecture and tectonostratigraphic controls of petroleum systems. His research arena involves various depositional environments (rift basins, fluvial facies, shallow and deep marine clastics), basin analysis, sequence stratigraphy, and tectonic control on sedimentation and stratigraphy. He conducts geological field seminars for both students of geology and professional geoscientists. Dr. El-Barkooky obtained broad regional experience in the geology of Egypt, North Africa, and Middle East through several consultation and research projects.

Jesús Martínez Frías born in Madrid, on October 3, 1960, is a Spanish geologist graduated at the Complutense University of Madrid in 1982, where he also obtained his Ph.D. degree in 1986. He has developed several stays of research in UK (University of Leeds), Canada (University of Toronto), Germany (University of Heidelberg), and the USA (University of California). He is Scientific Researcher at the Geosciences Institute, IGEO (CSIC-UCM), Head of the Research Group of Meteorites and Planetary Geosciences, and Founder and Director of the Spanish Planetology and Astrobiology Network. He is also Honorific Professor of the Department of BioEngineering and AeroSpace Engineering of the Carlos III University (Madrid). He has participated in more than 40 projects and scientific campaigns (e.g., Antarctica, Mauritania, Iceland, Costa Rica). In 2002, he participated in the NASA flight to study the Leonid Meteor Shower. He is co-I in NASA-MSL (rover Curiosity), ESA-ExoMars, and NASA-Mars2020 and in 2016 and 2017 he was an instructor of ESA astronauts in the PANGAEA program (Lanzarote and Chinijo Islands UNESCO Global Geopark). He has published 8 books and more than 200 articles (Science, Nature, Geology, etc). He was Former Member of the UN ECOSOC Committee on Natural Resources, Ex-ViceChair of the UNCSTD, and Ex-Chair of IUGS-COGE. He is Co-founder and President of the International Association for Geoethics (IAGETH), Committee Member of the IAU Astrobiology Commission, and Senior Advisory Board Member of the Arabian Geoscience Union (ArabGU). He is Editor-in-Chief of the journal Geosciences (MDPI) and Co-editor of the Springer Book Series: "Geoheritage, Geoparks and Geotourism" and "GeoGuides". He has received several awards and recognitions (i.e., NASA, ESA, GSAf (Goodwill Ambassador for Africa), ArabGU, Spanish Association of Scientists).

Harald Fritz Born 1956, started his scientific career at Department Earth Sciences, University of Graz, Austria where he is based since about 40 years. In his early times, he conducted projects on Variscan Europe and the evolution of the Alpine–Carpathian Belt. Somewhat accidentaly, he was invited for some weeks of teaching and fieldwork in Egypt which was starting point of 30 years of research on East African mobile belts. Since the early 90s of the last century, he conducted continuous projects on mountain building processes in East Africa with focus on Egypt, Kenya, and Tanzania. Rooted in Alpine tectonics he also led projects in the Alpine Himalayan Belt and the European Alps. His expertise is mountain building processes, in general, with focus on tectonics, structural geology, and isotope geology. Harald Fritz is married; father of three children and grandfather of growing amount of grandchildren. Teaching, administrative, and editorial work at University of Graz is continuously increasing but he kept curious and is open to new challenges in Earth Science.

Yasser Abd El-Rahman is Associate Professor at Cairo University. He earned his Ph.D. Degree from University of Windsor in 2009 and was appointed as a Lecturer in the Geology Department of Cairo University. He worked for 2 years in the Institut für Mineralogie, TU Freiberg as an Alexander von Humboldt postdoc fellow. Then he worked for 1 year in the Institute of Geology and Geophysics of the Chinese Academy of Science supported by the CAS President's International Fellowship Initiative (PIFI). He served also as an Assistant Minister in the Ministry of Petroleum and Mineral Resources Egypt.

History of the Geological Research in Egypt

1

Mohamed El-Sharkawi, Nagy Shawky Botros, Ahmed A. Madani, Mohamed Ahmed, Bassam Abdellatif, Yasser M. Abd El-Rahman, and Sultan Awad Sultan Araffa

Contents

M. El-Sharkawi · A. A. Madani · Y. M. Abd El-Rahman (✉)
Geology Department, Faculty of Science, Cairo University, Giza, Egypt
e-mail: yassermedhat@yahoo.com

M. El-Sharkawi
e-mail: maelsharkawim@yahoo.com

A. A. Madani
e-mail: aamadani18@hotmail.com

N. S. Botros
The Egyptian Geological Survey and Mining Authority, 3 Salah Salem Road, Abbassia, Cairo, Egypt
e-mail: nagyshawky35611@yahoo.com

M. Ahmed
Department of Physical and Environmental Sciences, Texas A&M University-Corpus Christi, Corpus Christi, TX, USA
e-mail: mohamed.ahmed@tamucc.edu

M. Ahmed
Department of Geology, Faculty of Science, Suez Canal University, 4.5 km the Ring Road, Ismailia, 41522, Egypt

B. Abdellatif
Division of Data Reception, Analysis and Receiving Station Affairs, Department of Digital Image Processing and its Applications, National Authority of Remote Sensing and Space Sciences, Cairo, New Nozha, Alf Maskan, 1564, Egypt

S. A. S. Araffa
National Research Institute of Astronomy and Geophysics, Helwan, Cairo, 11722, Egypt
e-mail: sultan_awad@yahoo.com

Z. Hamimi et al. (eds.), *The Geology of Egypt*, Regional Geology Reviews,
https://doi.org/10.1007/978-3-030-15265-9_1

Abstract

This chapter documented the history of the geological research in Egypt. It exhibits the ancient literature written and complied on the geology of Egypt including Hume's book and Geology of Egypt books of Rushdi Said that were issued in 1962 and 1990. In addition to literature, the chapter covers the history of geological mapping in Egypt and also a review on geological remote sensing publications including statistics on satellite sensors and techniques. Monitoring spatiotemporal variability in Egypt's Ground water resources using Grace data and the history of geochronological measurements are also considered.

1.1 Stages Before the Geological Survey and Stages After

Mohamed El-Sharkawi

It is fortunate that Geologist Samih Afia, the son of the famous Surveyor El Sayed Afia, to whom most of the survey triangulation points on top of the wild Eastern Desert mountains were planted, gave me old manuscript for reviewing. This manuscript mostly written by a typewriter and partly elegantly hand written with ink pen. The title is the Geological activities since 1609 till 1900. The last is actually the starting date of the newly established Geological Survey of Egypt in 1897, staffed with foreign geologists and engineers.

It is interesting to note that Egypt was visited by well known geologists, such as D.S. Dolomieu, who discovered the mineral dolomite during the French occupation of Egypt (1789–1802) and Napleon ordered him to leave the mission and return home, since he was a trouble maker. The other one is mineralogist Lord Hutchinson who was sent by King George of Great Britain to bring back to Britain the famous Rosetta Stone. He successfully managed to get it from the withdrawing French Army after failing trials to hide it away from the eyes of this specialized British mineralogist. Both Dolmuei and Hutchinson added nothing to our knowledge about the Egyptian geology. Contrary to these names foreign geologists such as W.F. Hume and O. Little inspired the activity of the following generations till present. Many recent discoveries relied on reading important accounts of the pioneer foreign geologists.

The reviewed Samih Afia-hold manuscript turned to be written by W.F. Hume and not O. Little as thought first. In parts in the manuscript Hume asked Little for revising or rewriting paragraphs. Due to the importance of this document and after being reviewed by myself, the Egyptian Geological Survey and the Geological Society of Egypt copied the worn yellow papers and loaded on CDs available at cost in the Geological Society of Egypt.

The British Museum announced in 1998 about a meeting to discuss the achievement of Joseph Hekekyan (1807–1875) the world first geomorphologist. The talk "Joseph Hekekyan at Heliopolis" was delivered by DG Jefferys in London in 1999. I attended the meeting and to my surprise to know that Hekekyan is an Armenian born in Turkey and lived in Egypt in the mid 1800s during the reign of Mohamed Ali who sent him to Great Britain to study Civil engineering for the purpose to construct a barrage in the Nile Delta named Alkanater Alkhayria. He was the chief Engineer for this ambitious project and was assigned by the ruler as the minister of Public Work.

After changing the ruler, Abbas I was not happy with Hekekyan and ordered him to resign from his post. He then contacted the president of the British Geological Survey seeking his advice for his future contributions to the science. His advice to Hekekyan is to explore the surface geology of Egypt. He roved the northern part of the country around Cairo and digged shallow hand wells in Heliopolis, describing in details the well log, with excellent colored illustrations. It is reputed that he discovered the famous statue of Ramses II in Memphis. His fancy drawings and his account on the geomorphological aspects of the studied parts in northern Egypt, hosted now in the British Museum, deserve ranking him as the pioneer geologist in the field of geomorphology. Egypt was visited by travelers, especially Sinai for the search for turquoise and visiting holy places, and the Eastern Desert for the search for gold in the ancient mines exploited by the Pharos. Wadi El Gimal in the southern part of the Eastern Desert is traversed by many pilgrims who stay at Zabara and Sikait on their way to Mecca digging for good emerald "Zomorod" to reimburse their expenditure for their pligrimage. Their adventures reached the hearing of interested audience in Cairo. The

news about the treasures are normally kept secret by the successive rulers of Egypt. Adventures kept pace by foreign and local travelers. They follow the Roman and Arab routes in the wild Eastern Desert. The geology of the crossed lands was naively explained. The Western Desert, featureless land covered by loose sand dunes, was crossed by travelers especially in upper Egypt to reach the border of the present day Libya to see the imaginary Zarzora Oasis. The northern part of the Western Desert is not risky to travel. Alexander the Great reached Siwa with minimum losses. Contrary to the Persian Cambyses who lost his army at El Fawakhir Hill in the Western Desert following severe sandy wind storms.

During the phase prior to the establishment of the Geological Survey of Egypt in 1897, talks concentrated on the Egyptian treasures were with Geological tarnish. Egyptian geology was left to the Germans, British, French and Italians. Foreigners living Egypt were planning adventures to extract gold and was much easier to dig the Pharos ruins to gain the ready made gold treasures. Non-Specialists, such as Professor E. Sicken Berger, of the Medical School wrote three lectures bearing the title the Geology of Egypt and published by the National Printing House in 1891 with fancy views unrelated to modern geology. These views were read before the students of the school of Ulema (Dar El Uloum). This is the first published book on the Geology of Egypt. Reports coming from Fayium Oasis during the 1880s about the presence among the fossil field of skeleton of unicorn-look alike Arsinoitherium, inspired a rush from the British counselor and French Counselor to compete to acquire the best to ship it back to their museums. The account written by Walter Granger published in 1907, is worth reading. The Fayium fossil bone field still alive in the mind of the vertebrate paleontologists heralded with the discovery of the walking whales in the nearby Wadi El Hitan during 1970s by D. Gingerich.

Early in the last Century, most of the mining companies were operated and staffed by foreign geologists and engineers. A call from the director of the phosphate company in Quseir to encourage young Egyptian graduate to work under desert conditions, was received with dismay. The Manganese Company at Um Bogma was directed by the British. The young geologist S.O. Ford, obtained his Ph.D. On the geology of Um Bogma as external student to the geology department of Durham University in 1956.

Hassan Sadek Pacha is the pioneer Egyptian Geologist, basically was an engineer but studied also geology and cooperated with the foreign geologists. He participated in joint reports published by the Egyptian Geological Survey.

The first geology graduate from present day Cairo University was in 1929. The number increased in the following years. The graduates were mostly employed by the Geological Survey of Egypt and encouraged to work in the Egyptian deserts.

During the 1950s geology departments in the Egyptian universities were headed by Egyptian staff. They cooperated with the Geological Survey geologists who surveyed most of the Egyptian deserts.

Geological projects were run jointly with foreign geologists. The outcome of these projects inspired further researches to understand the geology of Egypt. The Geological Society of Egypt was established in the 1950s and still active till now.

Geologic thoughts were regularly re-evaluated to cope with the new concepts in this science. The Egyptian geologists are well experienced and participated in fostering the geologic activities in other countries.

1.1.1 Hume's Book

William Fraser Hume (1867–1949) at the age of 30 joined the Geological Survey of Egypt. His book "Geology of Egypt" is the greatest contribution to understand the geology of the country based on his travels and keen observations. He published volume I in 1925 (Fig. 1.1a), which deals with the surface features of Egypt, their determining causes, and their relation to Geological structures, published by Cairo Government Press (408 pp). Volume II consists of three parts published during 1934–1937.

While walking along AlAzbakia Wall in Cairo, I spotted three books for sale, these were Hume parts of volume II on the Geology of Egypt, published by Cairo Government press.

The three parts of volume II bear the same title "the fundamental Precambrian rocks of Egypt and the Sudan, their distribution, age and character".

The first part of volume II is on the metamorphic rocks (pp. 1–300) published by Cairo Government Press in 1934 (Fig. 1.1b).

The second part of volume II deals with the late plutonic and minor intrusive rocks with a special chapter dealing with dynamic geology and the age of the Precambrian rocks in Egypt, (pp. 301–688) published by Government Press of Bulaq in 1935 (Fig. 1.1c).

The third part deals with the minerals of economic value associated with the intrusive Precambrian igneous rocks and ancient sediments (in collaboration with R.H. Greaves) and methods suggested for the dating of historical and geological times (pp. 689–990), published by Cairo Government Press in 1937 (Fig. 1.2a).

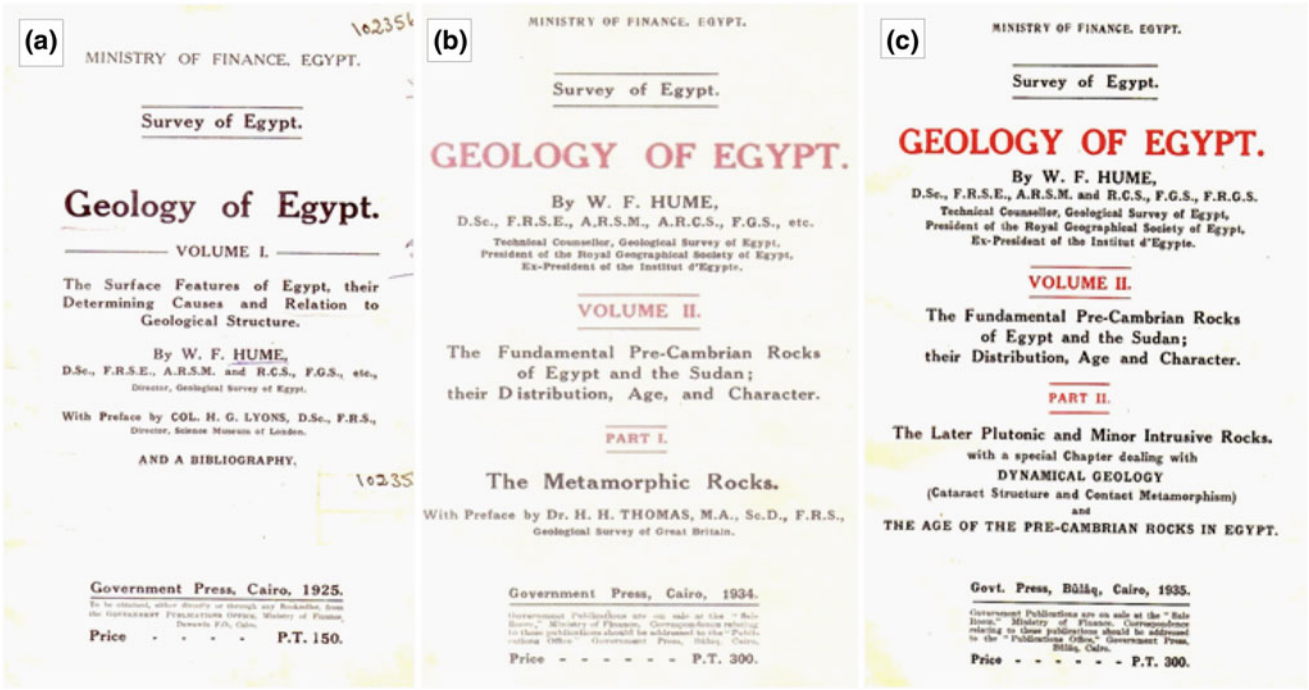

Fig. 1.1 Front page of volume I (**a**), volume II, part I (**b**) and volume II, part II (**c**)

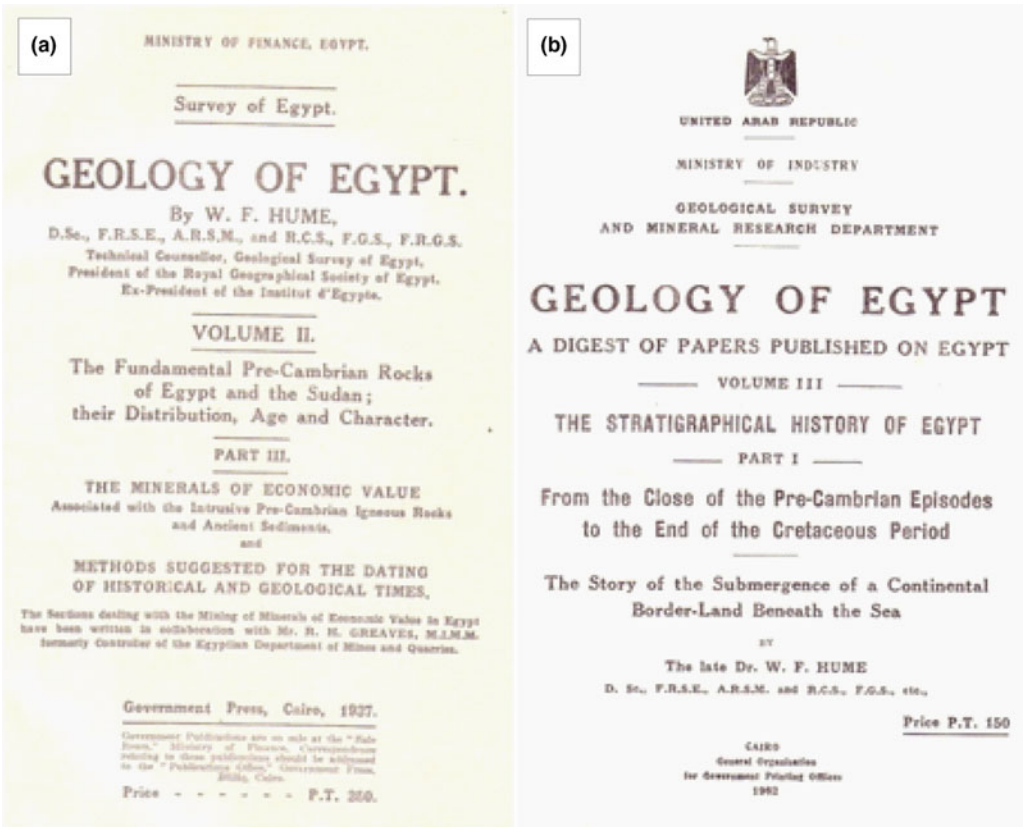

Fig. 1.2 Front page of volume II, part III (**a**) and volume III, part I (**b**)

The main theme of the three parts of Volume II is the Precambrian basement rocks, with field and lab photos in addition to folders housing coloured Geological maps.

It was a real treasure to acquire a copy of these publications who normally find their way to the libraries and not personal copies.

These books were written by an imminent geologist who travelled in the Egyptian desert riding camels in most cases. He wrote other books, but some were published later following his death on 1949.

The Geological Survey of Egypt published in 1962 part I (712 pp) of Volume III Geology of Egypt (Fig. 1.2b) with addition of the following phrase—"digest of papers published on Egypt" by the Editor Dr. Galal H. Awad. Volume III deals with the stratigraphical history of Egypt, and part I covers this history from a the close of the Precambrian episodes to the end of the Cretaceous Period. In other words the story of the submergence of a continental border-land beneath the sea. The Editor of part II of Volume III which was incomplete due to the death of W.F. Hume in 1949 is Dr. Rushdi Said.

1.1.2 Said's '62 & '90 Books

Rushdi Said was a graduate of Cairo University in 1941. He was granted a Ph.D. scholarship from the Egyptian Government to study abroad. Harvard University was his stop for a post graduate research in micro-paleontology. This degree granted in 1950 qualified him to teach at Cairo University, conducting research in the same field to be promoted to Associate professor during his service at Cairo University (1950–1968). Geology Department of Cairo University followed the British University system with only two Chair Professors. This means that Rushdi Said never to be promoted till the retirement or death of the relevant Chair Professors. He was an excellent university teacher. During 1959 I attended a course on the Geology of Egypt, with data gained from the oil business. These data were used only by Rushdi Said and printed and each student acquired these maps and illustrations. I graduated in 1960 and was a post-graduate student at the University of Newcastle Upon Tyne. One day in 1962, Professor Thomas Stanley Westoll the Chairman of the department, entered my room with a voluminous elegant hard bound and with colourful cover with attractive title "Geology of Egypt" by Rushdi Said, published by El Sevier, Amesterdam. He commented that it is a good production but we have to read to justify the scientific merit and admitted that it cost too much to buy it but he will order it to the department library. This was a good chance for the poor student "me" to go through the book in details. To my surprise, the book included all data we taught by Rushdi Said at Cairo University. The book

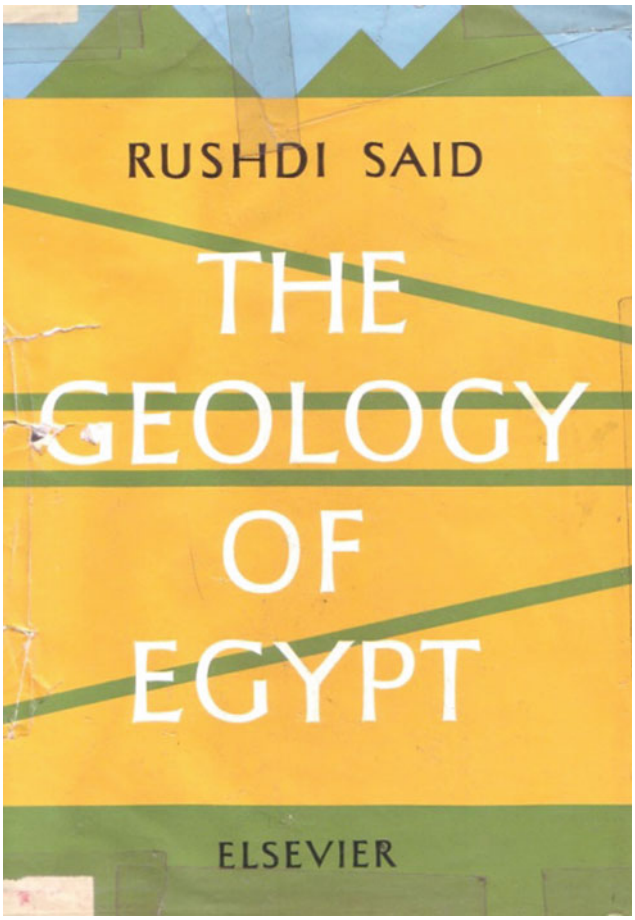

Fig. 1.3 Cover and front page of 1962 book

paper was heavy glossy and well prepared illustrations which characterized El Sevier as a leading publishing house. On my return to Egypt in 1965, I was informed that the Chair Professor Nasri Metri Shukri, who inspired Said to write a book on the Geology of Egypt (Fig. 1.3), did not write the chapter on the Precambrian of Egypt, on which Rushdi Said was expecting his support. That is why the weakest part of 1962 edition of Rushdi Said's Geology of Egypt is that dealing with the Precambrian rocks. No doubt this book written by an Egyptian was a beacon to Egyptian geologists and in general earth scientists. It was consulted by many oil companies and his author became a high rank consultant in the oil business. The Egyptian scientists refer to many geological aspects to Rushdi Said as he is the author of them, which are away from his speciality. Mineral resources in basement rocks were referred to be after Rushdi Said who was embarrassed to say no.

From 1962 till 1990, twenty eight years of feverish geological activities in all fields of geology, the Geological Survey was vibrant and Rushdi Said chaired the survey from 1968 till 1977, who directed the geological missions of the survey to solve certain problems. The Quaternary of Egypt

was his piece of cake. The junior staff gained much from his experience and he gained also much from the outcome of these studies. Our knowledge about the geology of Egypt was modified and polished by the research activities of the university staff in all aspects of geology. The joint projects with foreign universities contributed much and changed much taboos in our geologic thoughts. New theories entered in the geologic arena, challenged by some, acknowledged by others. Heated meetings were active. Within this pregnant situation, Rushdi Said with his piercing thoughts decided to update his 1962 book though grant offered from a leading oil company and to be published in another publishing house. He will act as editor to avoid the criticisms he received on his 1962 book. He carefully invited leading Egyptian and foreign geologists to write or share with others in chapters.. Unfortunately Rushdi Said in the early sixties got involved in politics, where he was assigned as a member of the Egyptian Parliament. I remember meeting him in London in 1965 as a member of delegates to the U.K. representing the Egyptian Parliament. This definitely affected his scientific career.

During 1988 he was preparing the pits and pieces of his new book and showed me a chapter on the geology of Cairo-Suez stretch he wrote while living in USA. This chapter could have been accepted if reviewed during the 1960s and I advised him not to include it in the new book and call a scientist aware of the new additions to our knowledge about this important stretch. He listened carefully with a hard feeling that he lost much when he was involved in politics and migrating to USA. He is really a person who listen carefully to others views, one of the characters of a real scientist.

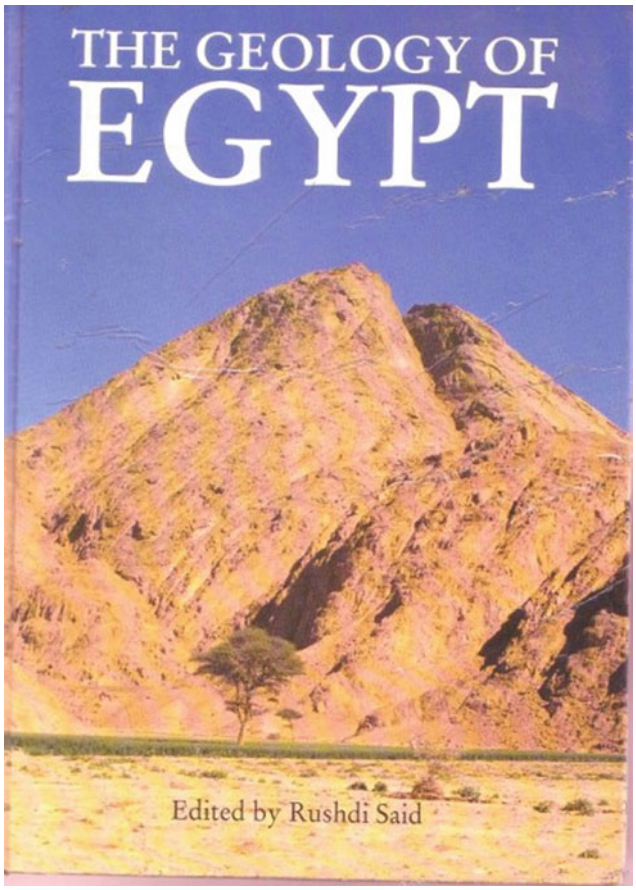

Fig. 1.4 Cover and front page of 1990 book

The 1990 book of Geology of Egypt (Fig. 1.4) is voluminous with many contributors, each in his speciality and responsible for what is included in his chapter. Reference should bear his name and not the editor. What was new in the science is included in this edition, published by Balkema, also in Amesterdam. The paper quality is not the heavy glossy of 1962 edition.

So, the plan to prepare a new book bearing the same title with the same policy followed by Rushdi Said in the 1990 book is welcome by all earth scientists.

It is not a coincidence that 28 years appears to be the reasonable lapse of time between publishing new data concerning the geology of Egypt. This new Geology of Egypt book published by Springer in 2020 followed (Said 1990a, b, 1962) and Hume main book Geology of Egypt Volume II published in 1934.

1.2 History of Geological Mapping in Egypt

Nagy Shawky Botros

1.2.1 Introduction

Egypt has an area of 1000 000 km^2. It is divided into four major physical regions: Nile Valley and Nile Delta, Western Desert, Eastern Desert and Sinai Peninsula.

In Pharaonic times, Egyptian roved the Eastern Desert looking for gold, copper and precious stones, and introduced the first geological map in history (the Turin papyrus map). The Papyrus (Fig. 1.5) was drawn during the reign of Ramses IV (1156–1150 BC) and reveals the bekhen stone quarries and the Fawakhir gold mines in the Wadi Hammamat (Harrell and Brown 1992). The papyrus map is now preserved in the Egizio Museum of Turin (Italy).

The Modern history of mapping in Egypt can be divided into three episodes. The first episode is extending from the French Expedition (1798–1801) to the establishment of the Egyptian Geological Survey, at 1896. The second episode extends from the establishment of geological survey until the revolution of 1952. The third episodes extends from 1952 to the present.

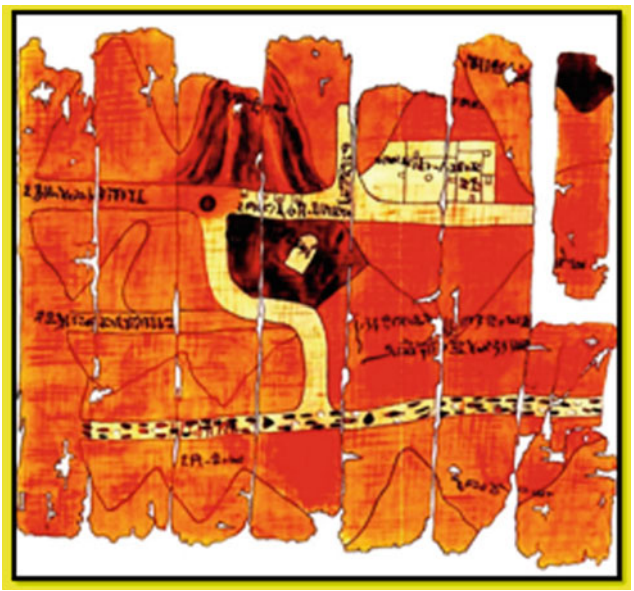

Fig. 1.5 Turin mining map showing Fawakhir gold mine and its surroundings

1.2.2 First Episode of Mapping

The first episode extending from the French Expedition (1798–1801) to the establishment of the Geological survey of Egypt was characterized by sporadic research carried out by individual naturalists and travellers and commissioned scientists. In this episode Napoleon Bonaparte's expedition and Rolf's Expedition (1874–1875) are of special importance (Said 1990a, b). In this episode, Egypt came to direct contact with Western scientific thinking and methodology.

Napoleon Bonaparte's expedition to Egypt in 1798 carried out the first multidisciplinary exploration mission and formed the Institute of Egypt, the first scientific organization in Egypt (Tawadros 2012). Napoleon's expedition was responsible for bringing Egypt to the attention of the scientists of Europe by the publication of the memorable "Description de l´ Egypte". This work included in many of its volumes, and specially the second volume (published in 1813) several chapters that are of interest to geologists and mineralogists and contain the first reliable map of the Eastern Desert of Egypt (Said 1990a, b). Several of the French scientists who accompanied the expedition, traversed the Egyptian Deserts and left their maps and scientific observations.

Rolf's Expedition (1874–1875) published the first reliable geological map of the extensive deserts of Egypt to the south of latitude of Fayum (scale 1:300 000). This map remained the standard geological map of the country up to the publication of the Survey map of 1910 (Said 1990a, b). Schweinfurth (1836–1925) visited Egypt and worked in Gabal Elba region in1864, and published detailed account on the Central Eastern Desert with a map which was published in ten sheets between 1899 and 1910 (Said 1990a, b). Fraas crossed the Eastern Desert at 1867 between Qift and Qusseir, and published a map and a geognostic profile of this area (Said 1990a, b).

The oldest scientific geological map of Africa originated from Egypt and was compiled by R. Russeger in 1842 (Fig. 1.6). The term Nubian Sandstone, which is sometimes still in use today, is mentioned for the first time in this map (Schluter 2008).

1.2.3 Second Episode of Mapping

The Egyptian Geological Survey was founded in the year 1896 as a result of a memorandum written by Captain H.G. Lyons (engineer, meteorologist, geomorphologist and museologist) to the ministry of Public Works in Cairo. The survey started as a small section in the ministry of Public Works with a humble annual budget of 730 Egyptian pounds a year and less than 2500 lb for field operations (Issawi 1979). By 1898, it was passed through various departments such as Topographic Survey, Mines and Quarries until 1945 when it was merged with the Ministry of Commerce and Industry (Issawi 1979).

Irrespective of the different titles and affiliations, the Egyptian Geological Survey has had from the beginning a specific role to play in exploring and mapping the Egyptian Deserts and in discovering and evaluating the country's mineral potential.

Shortly, after the turn of the nineteenth century, several eminent geologists collaborated to produce a geologic map. The scale was 1:1 000 000 in six sheets and 1:2 000 000 in one sheet. The map was accompanied by explanatory note by Hume. However, one third of the area of Egypt was not explored, so no information for this part was given in that map. In 1922, regional map by Gilbert Clayton (1875–1929) was carried out. This map was in one sheet, scale 1:2 000 000, and accompanied Hume's "Geology of Egypt: published in 1925. In 1928, map of Egypt was produced in Atlas of Egypt. The map was in four sheets, scale 1:1 000 000. A copy of this map appeared in the 14th International Geological Congress held in Madrid in 1926. The 1928 map included the results of mapping of Sinai and Gulf of Suez, and also included gneisses and granites recorded in the most south-west corner of Egypt.

In fact, much of the pioneering work in Egypt was undertaken between 1900 and 1940 when several eminent British geologists (Fig. 1.7) carried out field surveying on a systematic basis in both the Western and Eastern Deserts (O'Connor 1996). Important maps and explanatory memoirs of several classical areas of Egyptian geology were compiled in this time interval. For example, Ball and Beadnell worked

Fig. 1.6 Geological map of Egypt compiled by R. Russeger in 1842

Fig. 1.7 Photograph of members of the Geological Survey of Egypt in 1925. H.L. Beadnell (1), W.F. Hume (2), John Ball (3), George Murray (4), Patrick Clayton (5), O.H. Little (6), Hassan Sadek pasha, the first Egyptian geologist in the Egyptian Survey (7)

predominantly in the Western Desert of Egypt and produced descriptive accounts of the geology of Oasis districts including Kharga, Fayum, Kurkur, Farafra, Baharia and Dakhla Oasis (Ball 1900, 1939; Ball and Beadnell 1903). Beadnell was a specialist in Phanerozoic stratigraphy and contributed valuable scientific knowledge on the Cretaceous and Tertiary sequences around the Oases and also the Nile Valley around Aswan and part of the Red Sea Coast. His last published work in Egypt was a geographic and geological overview of the Sinai Peninsula (Beadnell 1927). Barron concentrated his work on the then little known topography and geology of the Sinai Peninsula and Cairo-Suez district (Barron 1907) and together with W. Hume compiled a report on the topography and geology of the Central Eastern Desert (Barron and Hume 1902). Hume was one of the most productive geological investigators in Egypt and his work includes the famous three –part treatise on "The Geology of Egypt", V.2 which was the first major scientific compilation on the metamorphic and igneous geology of the Eastern Desert and the minerals of economic value (Hume 1934, 1935, 1937).

During the late thirties and early forties, an extensive program for oil exploration in the northern part of the country led to the publication of a regional geological map (1:500 000) for the area north of latitude 27°30′N (Issawi 1979).

1.2.4 Third Episode of Mapping

From 1928 to the early 1940s geological activity was very limited, and geological mapping did not receive any attention from the state. After the discovery of some ore deposits like chromite in Barramiya district, Tin in Um Bissila and cassiterite in Igla (all in the Central Eastern Desert), in the late 1940s and early 1950s, the geological mapping of the basement rocks in the Central Eastern Desert on a scale of 1:100 000 became the main activity of the Egyptian Survey.

In 1956 the survey under the name "Geological and Mineral Research Department" appeared as part of the new Ministry of Industry. This situation remained until 1965 when the Survey was amalgamated with the General Egyptian Organisation for Mining and Geological Researchers founded largely to supervise the national mining industry. By 1970 the Egyptian Geological Survey became a separated body under the name of Egyptian Geological Survey and Mining Authority (EGSMA).

During the interval (1944–1957), 22 quadrangles constituting an area covering 10 275 km^2 between latitudes 24°30′ and 25°40′N were mapped in the Central Eastern Desert (CED) of Egypt (Akaad 1996). The compilation and fitting of the 22 quadrangles maps into a single map for the Central Eastern Desert was undertaken by El Ramly and Akaad during three field seasons (1957–1960). Adjacent quadrangles mapped by different field parties had to be reconciled with discrepancies judged, decided upon and amended (Akaad 1996). Crucial areas were remapped and alterations and amendments were undertaken by El Ramly and Akaad and the compiled map was then reduced to scale 1:250 000 to permit publication (El-Ramly and Akaad 1960). This map was the first reliable map for any part of the Egyptian Basement and was accompanied by the first realistic and applicable succession of rock units, derived from the systematic mapping of a virgin terrain of a representative part of the CED (Akaad 1996).

The mapping of the South Eastern Desert (SED) and North Eastern Desert (NED), S and N of the CED 1960 map was carried out in three phases. The first phase was undertaken by Assiut University team under the supervision of Akaad in both Qift-Qusseir and Qina-Safaga districts. Noweir (1965, 1968) mapped the Um Hombos area (85 km^2) and the Hammamat- Um Selimat district (1145 km^2), later extended to 5500 km^2 (Akaad and Noweir 1980). Shazly (1966, 1971) supervised by Akaad mapped 1200 km^2 around G. Meatiq and Wadi Abu Ziran, and

Habib (1968, 1970) mapped 1400 km^2 around G. Abu Furad, south of Qina- Safaga road.

The second phase of mapping the SED was carried out by EGSMA team (1955–1972) and Hunting Ltd. (1967). Hunting Geology and geophysics Ltd. (1967), financed by UNDP and assisted by six geologists from the Aswan Regional Planning Project, prepared a photo-geological map of a region 75 000 km^2 between latitudes 22° and 25°N using aerial photographs 1:40 000, and work was ended in the 1:500 000 map (Hunting Geology and geophysics 1967).

The third phase of mapping concentrated in the NED, started in 1968. This work included mapping of nine quadrangles, in addition to the works of Sabet (1961), El-Akkad and Dardir (1965), Ghobrial and Lotfi (1967).

In 1971, a new geological map, scale 1:2 000 000, black and white in one sheet was produced. The map was accompanied with an explanatory note. This was followed by the publication of the basement complex (scale 1:100 000) of the Eastern and Western Deserts (El Ramly 1972).

In 1979, EGSMA published the coloured geological map of Aswan sheet, scale 1:1 000 000, and in the same year EGSMA published the first mineral map of Egypt, scale 1:2 000 000 (Afia and Imam 1979). The mineral map recorded at that time all available knowledge of mineral deposits and occurrences. The map is divided into two sheets; one sheet gives the distribution of metallic mineral deposits and occurrences, the other gives the distribution of the non-metallic mineral deposits and occurrences. The two sheets were prepared in both Arabic and English and the map was printed in black and white. The number of mineral locations plotted on this map amounts to 268 locations for metallic mineral and 376 locations for non metallic minerals, a total of 644 locations. Once, the map was out of print, and due to its obligation towards geology students and those interested in the basic information concerning the natural resources of Egypt, EGSMA decided to reprint the same map as second edition in 1994.

In 1981, an improved, updated and coloured version of the 1971 geological map was published in one sheet, scale 1:2 000 000, and in 1982 EGSMA published the coloured Dakhla Sheet, scale 1:1 000 000.

In 1984 the Overseas Development Administration (ODA) of London sanctioned a new geological project in EGSMA. The emphasis of this pilot project was placed on training to EGSMA field staff of field mapping techniques assisted by high resolution aerial photography with the objective of producing a revised geological and mineral occurrence map at scale of 1:50 000. The course of training covered a variety of geological and related remote sensing topics which included development in Earth Observation satellites and their applications for resource mapping and management (O'Connor 1996).

Following the success of the pilot training exercise, the project moved forwards towards mapping training on a regional basis supported by enhanced imagery derived from both the Landsat TM sensor and the traditional aerial photography which used, in part, as topographic maps. The enhanced imagery highlighted several sites of alteration zones which carried mineral potential (O'Connor 1996). EGSMA field-mapping geologists soon adapted to the TM imagery technique and it became the standard planning tool of the strategic remapping projects in the CED and SED. During the interval 1986–1992 five quadrangle sheets had been remapped

In 1983, EGSMA published the metallogenic map of the Aswan Quadrangle, scale 1:500 000. The number of locations plotted on this map is 192 locations and the geological information of this metallogenic map was based on the geological map of Aswan Quadrangle, scale 1:500 000 published by EGSMA in 1978. In 1984, EGSMA published another metallogenic map for the Qena Quadrangle, scale 1:500 000. The number of locations plotted on Qena metallogenic map is 79 locations and the geological information of this metallogenic map was based on the geological map of Qena Quadrangle published by EGSMA in 1978.

In 1998 EGSMA, in cooperation with the Egyptian Academy for Scientific Research and Technology, published the Metallogenic Map of Egypt on the scale of 1:1 000 000 in 4 sheets covering 1 million km^2. Latitude 27°00′ and Longitude 30°00′E were the border lines separating these sheets. The sheets were given the numbers I, II, III and IV (Fig. 1.8). Owing to density of data, the map was published as two parts: part one for Metallic and Non-metallic ores, and part two for Building, Construction Materials and Ornamental Stones.

For a long time, the South Western Desert suffered from lacking enough information for the development programs, except for sporadic works carried out in Kharga, Dakhla and Farafra Oases which are accessible through roads from the Nile Valley. Consequently a join project between the Egyptian Government and the United Nations Development Program (UNDP) and UNESCO was launched in 1998 under the title "Capacity building of the Egyptian Geological Survey and Mining Authority (EGSMA) and the National Authority of Remote Sensing and Space Sciences (NARSS) for the sustainable development of the South Valley and Sinai".

One of the main achievements of this project was the Geological Map of the Western Desert. The map of the southern Western Desert was prepared in digital formats and produced in its original form in thirty sheets distributed according to the International map grid of scale 1:250 000 and updated according to the latest available geological information. The symbols and colours of the International

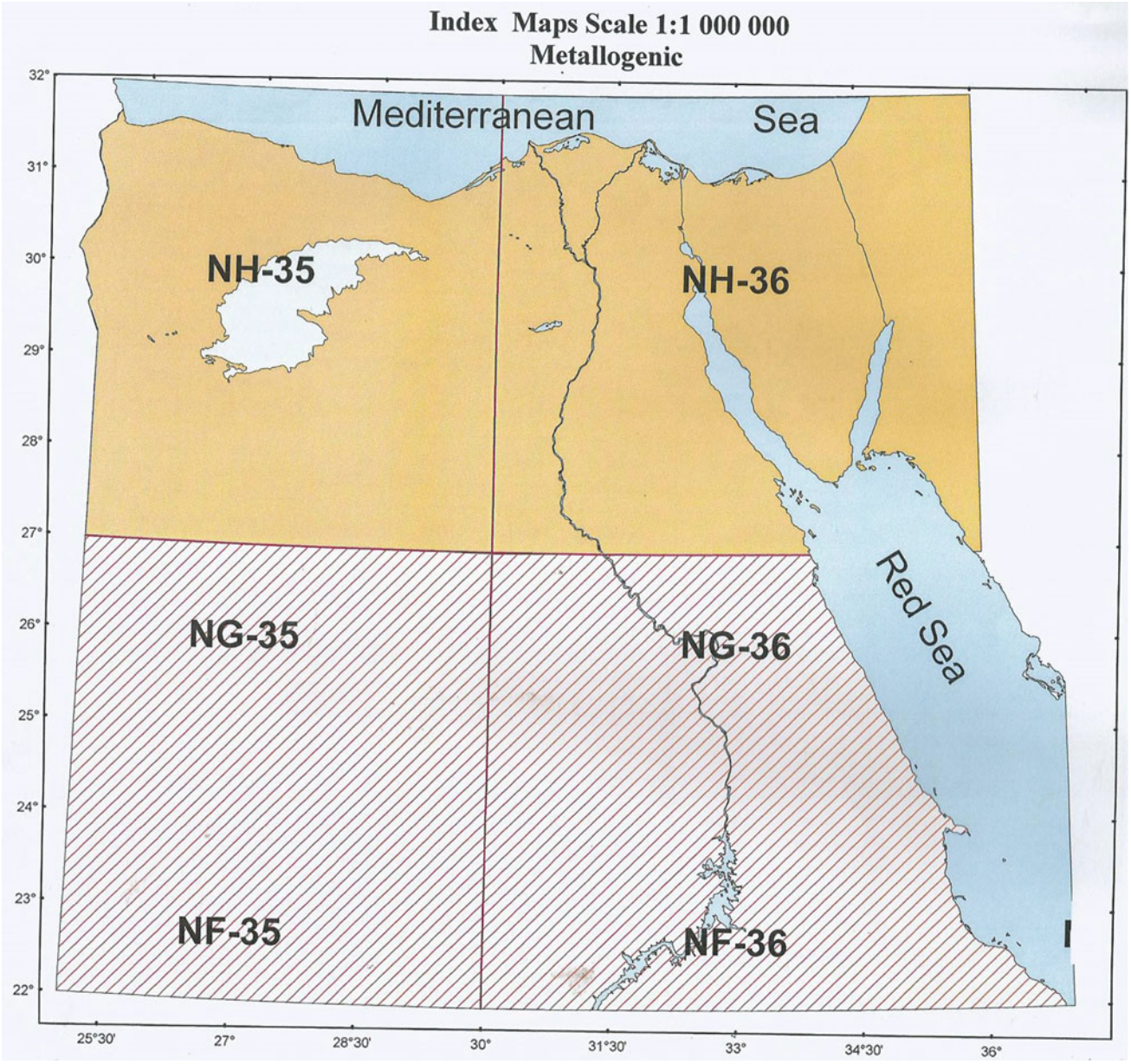

Fig. 1.8 The four sheets of the metallogenic map of Egypt, scale 1:1 000 000

Stratigraphic Chart issue in 2004 by the International Commission on Stratigraphy (ICS) of the International Union of Geological Sciences (IUGS) and the UNESCO for the World Map were applied in the Geological Map of the South Western Desert. Besides, digital geological mosaics for the South Western Desert on both the scale 1:1 000 000 and 1:2 000 000 were also produced during this project.

For the northern part of the Western Desert, 25 image maps covering the area north of Latitude 27°00′N as 1 × 1.5 degree quadrants were produced. These image maps were originally prepared at a scale of 1:250 000, matching the official map system of the country, but here printed at a scale 1:500 000. These image maps are useful in the identification of the different land use/land cover features, the selection of the suitable areas for development projects and enhancing the exploration activities for natural resources utilization and management. Moreover, image maps represent the base maps required for researchers, planners and decision makers to prepare their planes for investigating such vast area in the Western Desert.

Concerning Sinai, the geological map was also prepared in digital formats and produced in twelve sheets distributed

according to the international map grid of scale 1:250 000 updated according to the latest available geological information.

Also besides, digital geological mosaics for Sinai Peninsula of scale 1:250 000 and 1:500 000 were produced during this project.

In both the Western Desert, (south and north) and Sinai Peninsula, the produced maps and the accompanying sheets are incorporated in three geological atlases of reasonable scale. The three atlases are entitled as follows: "Geological Atlas of the South Western Desert (2005)", "Atlas of Space images of North Western Desert, Egypt (2005)" and "Geological Atlas of Sinai (2004).

Generally speaking, and according to Naim (1996), the available geological maps covering the surface area of the country are as follows: 1:2 million scale (100%), 1:1 million scale(100%), 1:500 000 scale (100%), 1:250 000 scale (40%) and 1:100 000 scale (20%). In addition, many local areas are covered by detailed maps of 1:50 000, 1:20 000, 1:10 000 and 1:5 000 specially around mineral deposits and areas mapped for geotechnical purposes.

1.3 Geological Remote Sensing Publications in Egypt: Some Statistics on Satellite Sensors and Techniques

Ahmed A. Madani

1.3.1 Introduction

The years 2007 and 2018 witnessed two significant events for Egyptian remote sensing and space sciences community. EgyptSat-1 is Egypt's first Earth observation remote sensing satellite launched on board a Dnepr rocket on 17 April 2007 from the Cosmodrome in Baikonur, Kazakhstan. It consists of two devices. Infrared imager has one band covers (1.55–1.7 μm) wavelength region with 39 m spatial resolution at nadir. And, multispectral imager has three visible bands and one panchromatic covers (0.50–0.89 μm) with spatial resolution of about 7.8 m at nadir. Unfortunately, only few published papers were utilized Egyptsat-1 in soil applications. Afify et al. (2010) produced physiographic soil map for the Nile alluvium in the middle Egypt using Egyptsat-1 data. Zaghloul et al. (2013) utilized Egyptsat-1 data for detection of ancient irrigation canals of Deir El-Hagar playa, Dakhla Oasis, Egypt. The year 2018 marked the establishment of the Egyptian Space Agency based on the Presidential Decree No. 3, for 2018. Establishment of the Egyptian Space Agency was the first recommendation of the road map prepared by the space and remote sensing council and accepted by Academy of Scientific Research and Technology (ASRT) in 1998. The dream of establishing Egyptian space agency was realized twenty years later.

Satellite remote sensing activities in Egypt started in 1971 as a joint research project based at the counterpart of (ASRT) with the American side and then developed to a Remote Sensing Center in 1972. Since the entrance of satellite remote sensing techniques Egypt and so far, there is no any statistical information about the types of satellites sensors and/or techniques used for geological applications. In the present article, we reviewed satellite data types and techniques used for geological applications especially mineral exploration and geological mapping by looking into more than 100 peer-reviewed papers published in Egyptian Journal of Remote Sensing and Space Sciences (EJRS) during the last two decades.

Remote sensing is an essential technique used for geological, hydrological and environmental applications. It can be defined as a technique of obtaining information about an object without touching it by means of capturing images either from the air using aircrafts or from space using satellites. Before launching earth observation satellites, aerial photographs are considered the most important source for image data used for geological applications. Several authors were utilized analog aerial photos "scale 1:40 000" and/or photo-mosaic "scale 1:50 000" for geological mapping (El-Etr 1976; El-Etr and Abdel-Rahman 1976; Mostafa 1977; Madani 1995; Youssif and El-Assy 1999 and others). After Launching Landsat satellite series in 1972, multispectral satellite imageries (MSS) become the most useful and they have more advantages in lithologic discrimination compared with aerial photographs. Several authors were utilized ERTS-1 data for geological applications. El-Shazly et al. (1974) and El-Shazly et al. (1979) were utilized ERTS-1 "Landsat-1" satellite data for geological interpretation and mapping of west Aswan area and Sinai Peninsula.

Utilization of satellite data for geological applications in Egypt was increased significantly after the establishment of National Authority for Remote Sensing and Space Sciences (NARSS) in 1991 (re-organized in 1994) and increased the interest of the Egyptian universities to teach undergraduate and post-graduate remote sensing courses. In 1998, The Egyptian Journal of Remote Sensing and Space Sciences (EJRS) published its first issue. The present review represents the first attempt that tried to present some statistics on satellite data types and techniques used for geological applications in Egypt, especially their applications in minerals exploration and geological mapping.

1.3.2 A Review on Geological Remote Sensing Publications in Egypt (from 1998 till 2017): Statistical Approach

This review is based on a comprehensive survey of about more than 100 peer-reviewed papers (Table 1.1) published during the period between 1998 and 2017 in EJRS. Some papers published in ISI journals are added to this review. In the present review, we included all papers that utilized remote sensing techniques for lithological discrimination, mineral exploration, surface hydrology, geomorphology in addition to some environmental application (e.g. change detection). And, we excluded: (a) all papers that utilized remote sensing techniques in the fields of agriculture and soil mapping, urban planning, air pollution and space sciences; (b) all papers applied in regions outside Egypt; and (c) all M. Sc. and Ph.D. theses that utilized remote sensing techniques in geological applications. Figure 1.9a shows numbers and years of geologic remote sensing papers published mainly in Egyptian Journal of Remote Sensing and Space Sciences. Figure 1.9b shows the percentages of satellite sensors used for geological applications. Landsat series recorded highest score of about 76% of the total published papers whereas ASTER, Radar and SPOT data scored 12%, 7% and 5% respectively.

Table 1.1 shows sensor resolutions and suitability of common satellites used for geological mapping and mineral exploration. For regional geological mapping (scale 1:1 000 000 up to 1:100 000) Landsat satellite series and ASTER data are the most suitable data due to their moderate spectral and spatial resolutions. For detailed geological mapping (1:10 000 or finer) both are not suitable because they lack detailed spatial data. SPOT data are suitable to some extent.

1.3.2.1 Publications on Utilization of Remote Sensing Techniques for Geological Mapping

Geological mapping is the process of preparing a 2D map for an area of interest that shows the spatial distribution of rock units in addition to the distribution of the structural elements. List et al. (1990) reviewed the activities for geological map production in Egypt. They presented the methodology for production of what is called "new geological map of Egypt", scale 1:500 000. Several geological maps of Egypt were produced by CONOCO and EMRA using the processed Landsat MSS & TM with aid of field data. About 20 geological maps (scale 1:500 000) covered entire Egypt produced by CONOCO in 1987 using the processed Landsat MSS data under the supervision of Egyptian General Petroleum Corporation. List et al. (1990) presented the digital image procedures for maps production.

The present review showed that, the most common used satellite sensors for geological applications are Landsat and ASTER data. Landsat sensors (MSS, TM, ETM+ & OLI) and ASTER data were utilized by many authors for lithologic discrimination and geological mapping. Sultan et al. (1986) utilized the processes Landsat TM data for mapping of serpentinites in the Eastern Desert of Egypt. Sultan et al. (1987) presented new Landsat band ratios imageries used for lithologic discrimination and mapping of Meatiq Dome area, Egypt. El Baz (1998) and Robinson (1998) studied the potential applications of Radar and Landsat data for mapping the buried radar rivers in the Western Desert, Egypt. Kusky and El-Baz (1999) revealed the presence of three main structural provinces characterized by different styles of deformation in the Sinai Peninsula using the processed Landsat imageries. Madani (2001) utilized Landsat data for mapping Wadi Natash volcanic field, SED, Egypt. Sadek and Khyamy (2003) applied band ratios 5/7, 5/1 & 4 of Landsat TM images to delineate the borders, lithologic units and structural features of low relief basement outcrops exposed in south Western Desert of Egypt between Long. 29°E and the River Nile. Sadek (2005) revealed that Landsat TM false color composite band ratio imagery (5/1, 5/7, 5/4 * 3/4) is the best discriminator for the different basement rocks and detected the mineralized alteration zones hosted within Wadi Beida sheared metavolcanics, Shalateen area, SED. Sadek (2006) revealed that the ETM+ image bands 7, 4 & 2 and FCC ratio image 5/7, 5/1 & 4 in RGB improved the lithological discrimination of basement rocks at Gabal Gerf area, SED as well as distinguishes the linear features (dyke swarms & faults). Gad and Kusky (2007) applied successfully new ASTER band ratio image 4/7, 4/6 & 4/10 for lithologic mapping in the Wadi Kid area, Sinai, Egypt. Aita and Bishta (2009) interpreted lithologic units, structural framework and high zones of radioactive anomalies of Gabal El-Minsherah-ElHasanah district, north Sinai using Landsat 7-ETM+ data and digital image processing techniques. Bishta and Aita (2009) applied the processed Landsat-7 data to discriminate structure and lithology for defining the horizons of radioactive anomalies at Gabal Halal, north Sinai, Egypt. Hassan et al. (2008) discriminated the Oligocene sands and gravels, Wadi Ghoweiba area, northwest Gulf of Suez, Egypt using FCC principal component color image PC2, PC6 and PC9 in RGB. Youssef et al. (2009) proposed and tested a new Landsat ETM+ band ratio 5/3, 3/1 & 7/5 in RGB for lithologic discrimination of basement rock units around Gabal Al Hadid, CED, Egypt. Wasfi et al. (2009) discriminated younger granitic masses at Gabal Qattar area NED, Egypt using DN values of Landsat ETM + band-5 imagery. Amer et al. (2010) presented a new method for using ASTER data for lithological mapping in

Table 1.1 Satellites suitability for geological applications and related references in Egypt

Applications	Common satellites used for geological applications					
	Landsat		ASTER		SPOT	
	Revisit 16 days		Revisit 16 days		Revisit 26 days	
	Spatial resolution 30–15 m	Spectral resolution Landsat-8 (11 bands)	Spatial resolution 30–15 m	Spectral resolution 14 bands	Spatial resolution 1.5 m	Spectral resolution 5 bands
(1) Geological mapping: (a) Regional mapping (1:1 000 000; 1:500 000; 1:250 000 & 1:100 000)	Suitable		Suitable		Suitable	Slightly suitable
(b) Detailed mapping 1:10 000 or fine scale	Not suitable		Not suitable		Suitable	Slightly suitable
Landsat references Kusky and El-Baz (1999), Hamdan and El-Etr (1998), Youssif and Aly (1998)*, Youssif and El-Assy (1998)*, Abdel-Motaal and Ramadan (1998), Yousif and Shedid (1999), Hegazy et al. (1999), El Baz et al. (2001),, Ramadan (2002)*[1], Wahbi et al. (2002), Abdeen et al. (2002), Bishta and El-Tarras (2002), Abdeen (2002), Sadek and Khayamy (2003), Ramadan (2003), Madani (2004)*[1], Sadek (2005), Madani et al. (2005), Assran et al. (2005) Wasfi (2007), Abdeen and AbdelGaffar (2008), Hassan et al. (2008), Sadek (2006), Youssef et al. (2009), Wasif et al. (2009), Aita and Bishta (2009), Bishta and Aita (2009), Abdeen et al. (2009), Salem et al. (2012), Kamel et al. (2016), Hassan and Sadek (2017), Hassan et al. (2017), Khamies and El-Tarras (2010), Masoud and Koike (2017)*[2] *ASTER references* Gad and Kusky (2007), Amer et al. (2010), Madani and Emam (2011), Madani (2012), Jakob et al. (2015), Madani (2015), Hassan and Sadek (2017), Hassan et al. (2017), Abdeen et al. (2003, 2009) *SPOT references* Wahbi et al. (2002), Abdeen et al. (2009)						
(a) Gold	Suitable		Suitable		Slightly suitable	
	Landsat references Ramadan (2002), Madani et al. (2003), El-Fouly and Salem (2003), Sdaek (2004), Salem (2007), Ramadan and Kontny (2004), Ramadan et al. (2005), Gabr et al. (2015), Amer et al. (2016) *ASTER references* Gabr et al. (2010), Amer et al. (2012)*[3], Gabr et al. (2015), Salem and Soliman (2015), Salem et al. (2016) *SPOT reference* Gabr et al. (2015)					
(b) Radioactive (Uranium) (Black sand), Heavy metals	Suitable		No reference		No reference	
	Landsat references Yehia et al. (1998), Ramadan et al. (1999), Ramadan and El-Lithy (2005), (El-Sadek and Mousa 2010a, b), Ramadan et al. (2013) and Shokr et al. (2016)*[2]					
(c) Iron Ore and BIF	Suitable				No reference	
	Landsat references Salem et al. (2013), Salem and El-Gammal (2015) *ASTER reference* El-Nagdy and Abdel Salam (2006)					

(continued)

Table 1.1 (continued)

Applications	Common satellites used for geological applications					
	Landsat		ASTER		SPOT	
	Revisit 16 days		Revisit 16 days		Revisit 26 days	
	Spatial resolution 30–15 m	Spectral resolution Landsat-8 (11 bands)	Spatial resolution 30–15 m	Spectral resolution 14 bands	Spatial resolution 1.5 m	Spectral resolution 5 bands
(d) Barite and Titanite	Suitable				No reference	
	Landsat reference Khalil et al. (2017) *ASTER reference* Madani and Emam (2011)					
(3) Environmental applications	References					
	Abdel Rahman et al. (1998), Nasr and Darwish (1998), El-Baz (1998)*[1], Robinson (1998)*[1], Ashmawy and Nassim (1998), El Gammal et al. (1998), Yehia et al. (1999a, b), c), Ahmed (1999), Hamdan (1999), El Gammal (1999a, b), Elewa et al. (2000), Ahmed (2000), El-Askary et al. (2000)*[4], Hassan (2000), Yehia et al. (2000), Hegazy (2001), El-Gamily (2001) Yehia et al. (2003), El Nahry (2003), Elewa (2003), Faid et al. (2003), El Gammal (2002), El Gammal (2003), El Gammal et al. (2003), Nasr et al. (2003), Hamdan et al. (2004), Hassan and El-Leithy (2004), Hassan et al. (2005a, b)*[5], El-Gammal (2005), El-Rakaiby and Ammar (2005), Eid et al. (2006), Elewa (2006), Abdou Azaz (2008), Youssef and Baroudy (2008), Azab (2009), Hegazy and Effet (2010), Abou El-Magd et al. (2010), El-Gammal et al. (2010), Rasmy et al. (2010), El-Gammal and El-Gammal (2010), Shokr (2011), El-beih et al. (2011), Belal and Moghanm (2011), Kato et al. (2012), El Asmar et al. (2013), Moawad (2013), Zaghloul et al. (2013), El-Gammal et al. (2013), Abou El-Magd and El-Zeiny (2014), Embabi and Moawad (2014), El-Hattab (2015), Gabr and El Baswawesy (2015), El-Hattab (2016)					

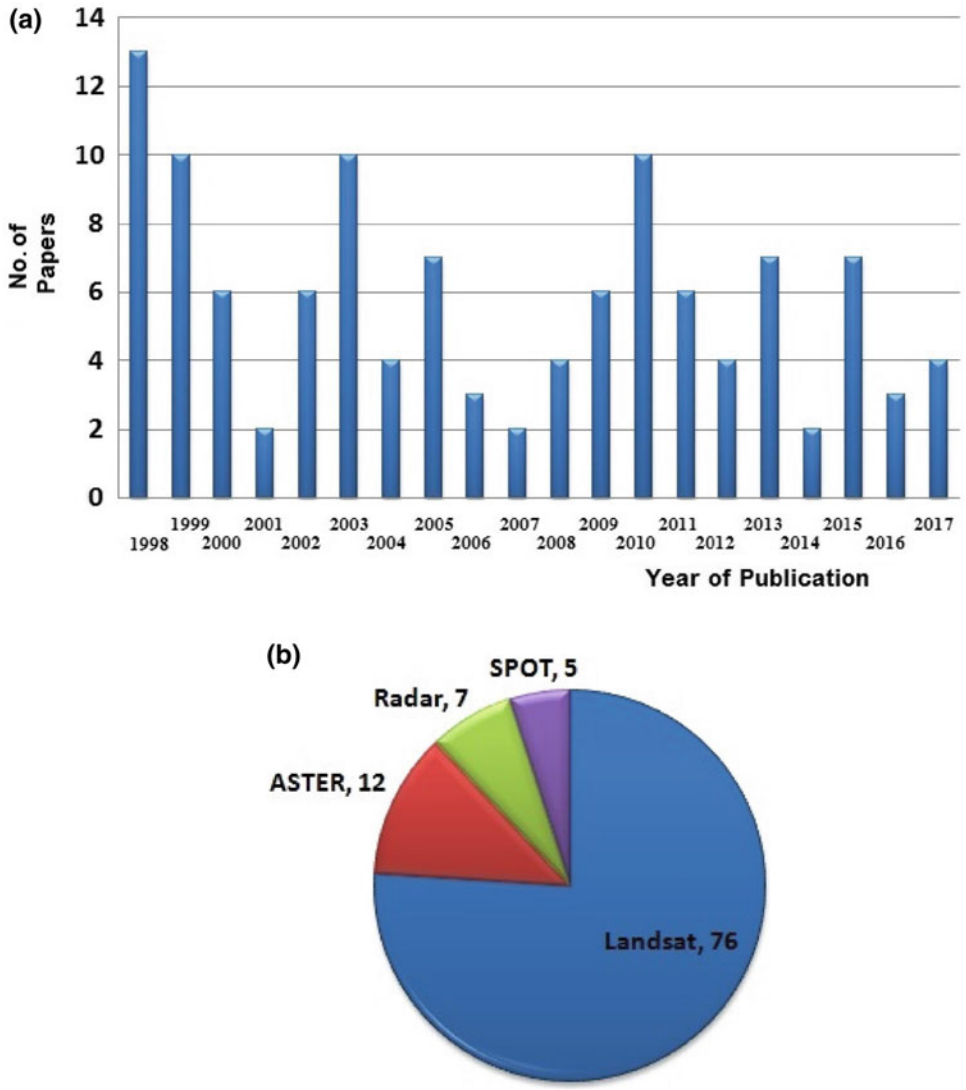

Fig. 1.9 **a** Numbers and years of publications of geological remote sensing papers. The publications included in the graph are cited in Table 1.1. **b** Satellite sensors percentages used for geological applications

arid environment. ASTER FCC band ratio image (2 + 4)/3, (5 + 7)/6, (7 + 9)/8 in RGB identified ophiolitic rocks much better than previously published ASTER ratios. PCA (5, 4 & 2) in RGB enabled the discrimination between ophiolitic rocks and grey and pink granites. Madani (2012) discriminated the Jurassic volcanicity at Jabal Al Maqtal area, SED, Egypt using ASTER PCA false color composite image. He delineated NW-SE strike-slip basin recorded at the study area using PC9 image. Salem et al. (2012) integrated remote sensing, geology and geochemistry data for lithologic discrimination of serpentinites and other rock units exposed at Um Salim-Um Salatit area CED, Egypt. Madani (2015) evaluated band ratios and fusion techniques for mapping Wadi Natash volcanic field, SED, Egypt. Also, he revealed the spectral properties of olivine basalts using ASD FieldSpec measurements. Jakob et al. (2015) improved the existing geological maps of Neoproterozoic Ras Gharib area, north ED, Egypt by including texture features in a classification scheme of ASTER and Landsat8 data. Kamel et al. (2016) stated that the products of Landsat ETM+ image processing procedures (FCC7, 4, 2, & FCC7, 5, 1 & PCA 1, 2, 4 & band ratios 5/1, 3/2, 7/2 & 5/3, 4/2, 3/1 & 3/1, 4/2, 5/7) are improved the lithologic discrimination between serpentinites, talc carbonates, and other rock units exposed at Wadi Ghadir—Gabal Zabara area, CED, Egypt. Hassan et al. (2017) proposed three Landsat-8 band ratio images (6/2, 6/7, 6/4 * 4/3; 6/7, 6/4, 4/2 & 7/5, 7/6, 5/3) for detailed mapping and lithologic discrimination of the rock units exposed in Meatiq dome area, CED, Egypt. They proposed fourteen spectral bands of ASTER data for the distribution of some rock forming minerals. These are; ASTER muscovite index (B7/B6), quartz index (B14/B12), ferrous iron index (B5/B3) ferrous silicate index (B5/B4), mafic index (B12/B13), hydroxyl-bearing minerals index (B7/B6 * B4/B6). Hassan and Sadek (2017) stated that the enhanced Landsat 8 band ratio (6/2, 6/7 & 6/5 * 4/5) and ASTER

principal component image (PC2, PC6 & PC5) were successfully discriminate most of the rock units and produced a detailed geologic map for Korbiai-Gerf nappe complex SED, Egypt.

1.3.2.2 Publications on Utilization of Remote Sensing Techniques for Mineral Exploration

Remote sensing is an effective technique for mineral exploration through many ways such as mapping geological structure and locating the hydrothermal alteration zones hosting mineralization in the Eastern Desert. Results of the present preview revealed that the processed Landsat ETM + and ASTER satellite imageries are the most suitable data for gold exploration in which they successfully identify and delineate gold-bearing hydrothermally alteration zones recorded at (Haimur gold mine area, Um Khasila district, Shalatein district, Um El Touyur El Fuqani area, Al Faw-Eqat belt, Um Rus area, El-Hoteib area, Abu Marawat, Fawakhir area, Dungash district and Wadi Allaqi) areas. Madani et al. (2003) utilized Landsat ETM$^+$ imageries and scanned aerial photograph for mapping hydrothermal alteration zones at Haimur gold mine area, SED, Egypt. They utilized PCA, band ratios and fusion techniques to delineate the hydrothermal alteration zones as well as listwaenite ridges exposed at the study area and produced 1:20 000 geologic image map. Ramadan (2003) applied TM–ratioing enhancement and supervised classification methods for gold bearing listwaenites exploration at Um Khasila district, CED, Egypt. He indicated that the listwaenites and associated veins are promising for gold and silver mineralizations. Ramadan and Kontny (2004) combined the processed Landsat data and fieldwork with mineralogical and geochemical investigations in order to detect and characterize the alteration zones exposed at Shalatein district, ED, Egypt. The processed Landsat ratio imagery (5/7, 4/5 & 3/1 in RGB) successfully discriminated two different types of alteration products. Ramadan et al. (2005) utilized processed Landsat ETM+ imageries to recognize the mineralized alteration zones at Um El Touyur El Fuqani area, SED, Egypt. Their study indicated that the alteration zones in the metavolcanics and listwaenites are promising and need detailed exploration for AU and Ag mineralizations. Salem (2008) utilized the processed Landsat ETM$^+$ ratio imageries to trace gold bearing alteration zones exposed at Al Faw-Eqat area, SED, Egypt. Gaber et al. (2010) detected areas around Abu Marawat of high potential gold mineralization using ASTER data. Amer et al. (2012) utilized the processed ASTER data (PCA & band ratios) for detection of gold related alteration zones in Um Rus area, CED, Egypt. Gabr et al. (2015) utilized band ratios ASTER imagery for prospecting new gold bearing alteration zones at El-Hoteib area, SED, Egypt. In addition, they produced the lineament map for the study area using SPOT data. Abu El-Magd et al. (2015) mapped the alteration zones of Fawakhir area using reference spectra of ASTER data based on two supervised classification techniques including the spectral angle mapper (SAM) and spectral information divergence (SID). Salem and Soliman (2015) utilized ASTER images of band ratios supported by field geology, mineralogical, and geochemical analyses enabled detection of two alteration zones as targets for gold exploration at Al Faw-Eqat belt (a case study in the eastern end of Wadi Allaqi). Salem et al. (2016) explored the new gold occurrences in the alteration zones at Dungash district using the processed ASTER band ratio technique.

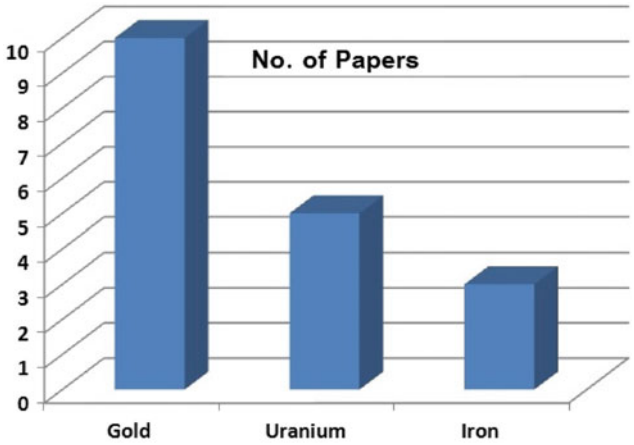

Fig. 1.10 **left** Numbers of published papers for each deposit in Egypt

Several studies (Yehia et al. 1998; Ramadan et al. 1999; Ramadan and El-Lithy 2005; Sadek and Mousa 2010 and Ramadan et al. 2013) proved the suitability of the processed Landsat images and airborne radiometric data for exploration of radioactive bearing minerals in several localities at the Eastern Desert (e.g. Gabal El Sela area, Wadi Araba area, El Qasia and Um Maggat granites, Um Greifat, Abu Gherban, Um Gheig, Essel, Kadabora granites, Gabal Um Naggat).

Salem et al. (2013); Salem and El-Gammal (2015) integrated remote sensing, geological and geochemical studies to locate the promising iron ore deposits around Aswan area and west of Lake Nasser, Egypt. El-Nagdy and Abdel Salam (2006) utilized hyperspectral analyses of ASTER data to discriminate Um Nar banded iron formation (BIF). They concluded that the interpretation driven from the hyperspectral analyses enhance the delineation of ductile and brittle geological structures as well as the lithologic discrimination. Figure 1.10 shows the number of published papers for each ore in Egypt. The percentage of the papers treated with gold is about 55.5% followed by 28% for uranium and ended by 16.5% for iron ore deposits. These percentages reflect the importance of gold as strategic mineral followed by uranium exploration and iron.

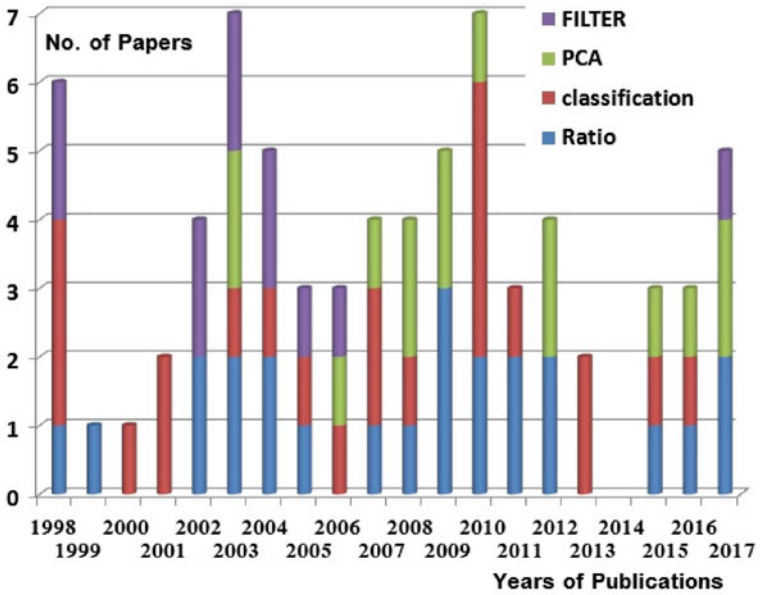

Fig. 1.11 The main remote sensing techniques used for geological and environmental applications

1.3.2.3 Remote Sensing Techniques

Analyses of satellite remote sensing data were performed either by visual and/or digital image processing. Digital image processing are grouped into three categories: pre-processing, main-processing and post-processing procedures. Figure 1.11 demonstrated the most frequently main image processing procedures used for geological applications. The present review revealed that: (1) band ratios and PCA are the most common techniques used for lithologic discrimination and geological mapping. To enhance lineament features in satellite images, filtering techniques are used. Band ratio can be simply generated by dividing the reflectance value of each pixel in one band by the reflectance value of the same pixel in another band (Drury 1993). It successfully delineated gold- bearing hydrothermally alteration zones which are mainly clay minerals, Fe-minerals and carbonate minerals exposed along major structure at several localities in the Eastern Desert. (2) classification and change detection are the most common techniques used for land-use mapping and other environmental applications.

1.3.3 Concluding Remarks

The present review is the first attempt that exhibits some statistics on satellite sensors and techniques and it recorded the most common ore deposits explored using remote sensing techniques in Egypt. Results of this short review revealed that: (1) Moderate spatial and spectral resolutions Landsat series are found to be the most common data used for geological applications followed by ASTER data. Little publications utilized high spatial resolution SPOT data for detailed structural mapping. (2) About 55% of published papers demonstrated methodologies successfully identified and delineated gold- bearing hydrothermally alteration zones whereas 28% of are treated with radioactive minerals especially uranium. (3) The most common techniques used for lithologic discrimination and hydrothermal alteration zones mapping are band ratios and PCA. For land-use mapping and change detection applications classification techniques are used. (4) Unfortunately, no record for papers utilized Egyptian satellite "Egyptsat-1" for geological applications.

1.4 Monitoring Spatiotemporal Variabilities in Egypt's Groundwater Resources Using GRACE Data

Mohamed Ahmed, Bassam Abdellatif

Temporal Gravity Recovery and Climate Experiment (GRACE) derived Terrestrial Water Storage (GRACE-TWS) data along with reservoirs, rainfall, and soil moisture datasets were used to monitor and quantify modern recharge and depletion rates of the Nubian aquifer in Egypt during the period from April 2002 through January 2017. Results indicate: (1) the Nubian aquifer in Egypt is receiving a total recharge of 18.46 $\pm$ 1.95 km^3 during 4/2002 − 2/2006 and 4/2008 − 1/2017 periods; recharge events occur only under excessive precipitation conditions over the Nubian recharge domains and/or under a significant rise in Lake Nasser levels, (2) the Nubian aquifer in Egypt is witnessing a groundwater depletion of −13.90 $\pm$ 0.82 km^3 during 3/2006 − 3/2008 period; the groundwater depletion is largely related to exceptional drought conditions and/or normal baseflow recession, and (3) a conjunctive surface

water and groundwater management plan needs to be adapted for sustainable management of water resources of the Nubian aquifer in Egypt.

1.4.1 Introduction

To pursue and sustain plans for modernization and development, Egypt needs to secure its freshwater resources. In Egypt, the sources of freshwater include the surface water of the Nile River and groundwater in addition to a minor contribution (<2%) from rainfall and sea water desalination. Both climatic (e.g., changes in rainfall patterns, duration, and magnitude) and anthropogenic (e.g., population growth, overexploitation, and pollution) factors affect these sources. For example, according to climate change studies there is a tendency toward higher extremes, where the arid or semiarid areas are becoming increasingly dry and the wetter areas will witness intensified precipitation and flooding (e.g., Hulme et al. 2001). In addition, Egypt's total population is on rise; it increased from 22 million in 1950 to 100 million in 2017 and is expected to continue increasing for decades to come.

Given these challenges, understanding of the geologic and hydrologic settings of, and the controlling factors affecting, freshwater resources in Egypt are gaining increasing importance. The Nile River has been a dynamic surface freshwater resource for Egypt's population. However, Egypt is currently using its total annual allocation of Nile River water, estimated at 55×10^9 m^3/yr. Given the scarcity of surface freshwater resources in Egypt, limited rainfall, and the difficulties and expenses entailed in sea water desalination, groundwater remains a viable alternative that could address Egypt's growing demands for freshwater resources.

Currently, Egypt is required to utilize more of its groundwater resources, at the expense of limited Nile River water, to support national reclamation projects. For example, a minimum of 1.5×10^6 acres (feddan) will be reclaimed during the coming five years in Egyptian deserts. These reclamation projects depend solely on groundwater resources. In Egypt, groundwater resources are found in one of five major aquifer systems namely, Nile, Moghra, coastal, fractured basement, and Nubian aquifers (RIGW/IWACO 1988). Most of the current and future Egyptian reclamation projects depend mainly on Nubian aquifer groundwater resources.

The Nubian aquifer (area: 2×10^6 km^2) is a transboundary aquifer system shared by four countries: Egypt (38%), Libya (34%), Sudan (17%), and Chad (11%). The aquifer contains three major tectonically-defined sub-basins: the Dakhla sub-basin in Egypt; the Kufra sub-basin in Libya, northeastern Chad, and northwestern Sudan; and the northern Sudan sub-basin in northern Sudan (Thorweihe and Heinl 2002). In Egypt, the health of the Nubian aquifer affects the success of the Egyptian reclamation and development projects as well as the livelihood of many people. Hence, the ability to routinely observe the water resources of that aquifer and make those observations publicly available to the decision makers is highly recommended. In situ observations of the Nubian aquifer in Egypt are difficult to obtain; the historically available observations, if any, usually suffer from gaps, discontinuities, inconsistency, and poor quality. In addition, the historical observations are local, sparse, and do not adequately represent the entire aquifer averaged estimates. In this regard, satellite remote sensing observations offer an alternative and/or complement to local in situ measurements and could be used to monitor the Nubian aquifer health and longevity. Most of these observations are globally distributed, publicly available, and temporally and spatially homogeneous. The Gravity Recovery and Climate Experiment (GRACE) provides significant practical strategies to routinely observe and monitor the water resources of the Nubian aquifer in Egypt.

GRACE is a joint satellite mission that is sponsored by the National Aeronautics and Space Administration (NASA) and the German Aerospace Center (DLR). GRACE is designed to map the temporal variations in Earth's global gravity field on a monthly basis as well as the Earth's static gravity field (Tapley et al. 2004a, b). The GRACE-derived variabilities in Earth's gravity field can be used to make global estimates of the spatiotemporal variations in the total vertically integrated components (e.g., surface water, groundwater, soil moisture and permafrost, snow and ice, wet biomass) of terrestrial water storage (TWS) (Wahr et al. 1998). GRACE-derived TWS (GRACE-TWS) data have been extensively used to quantify aquifers' recharge and depletion rates (Ahmed et al. 2011, 2014, 2016; Wouters et al. 2014; Ebead et al. 2017; Fallatah et al. 2017). In this study, temporal GRACE-TWS data that span the period from April 2002 through January 2017 along with the outputs of land surface models (LSMs) and other relevant remote sensing data were used to monitor the water resources of the Nubian aquifer in Egypt and provide improved estimates of recharge and depletion rates.

1.4.2 Data and Methods

GRACE-TWS data from the global mass concentration (mascons) solutions of the University of Texas Center for Space Research (UT-CSR; Release 05; version 1; 0.5° × 0.5° grid; available at: http://www.csr.utexas.edu/grace/RL05_mascons.html) was used in this study. The UT-CSR mascon approach utilizes the geodesic grid technique to model the surface of the Earth using equal area gridded representation of the Earth via 40,962 cells (40,950

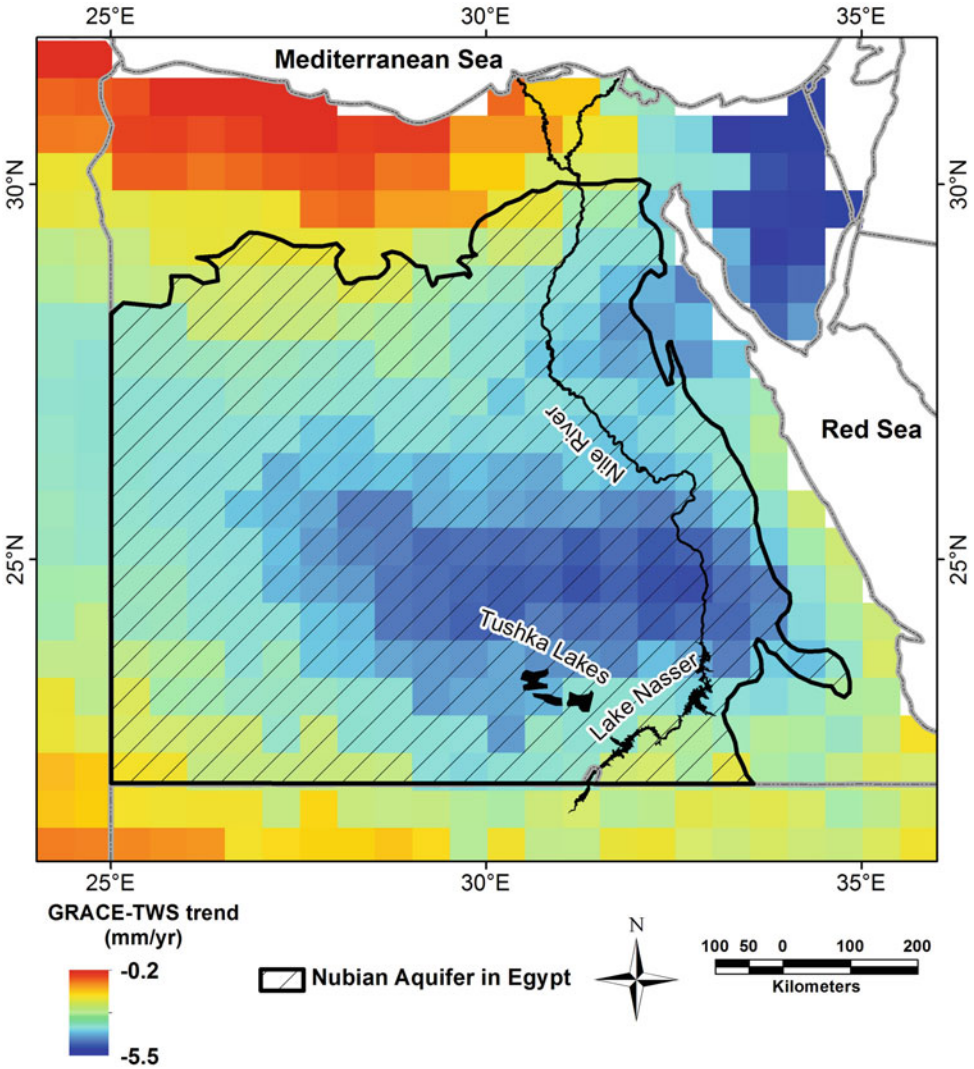

Fig. 1.12 Secular trend in monthly (April 2002–January 2017) GRACE-TWS estimates generated over the Nubian aquifer in Egypt (hatched area) and surroundings

hexagons + 12 pentagons) (Save et al. 2012, 2016). The secular trend in GRACE-TWS data was extracted by simultaneously fitting a trend and annual and semiannual terms to each GRACE-TWS time series (Fig. 1.12). GRACE-TWS time series over the Nubian aquifer in Egypt was generated by summing results for all grid points lying within the spatial domain of the Nubian aquifer in Egypt (black polygon; Fig. 1.12). Errors associated with monthly GRACE-TWS and trend values were then estimated using the approach advanced in Ahmed and Abdelmohsen (2018).

GRACE data cannot distinguish between anomalies resulting from different compartments of TWS (e.g., surface water [SW], soil moisture [SM], and groundwater [GW]). Therefore, the combined contributions of SW and SM need to be quantified and subtracted from GRACE-TWS time series to calculate GW time series over the Nubian aquifer in Egypt.

Two main SW reservoirs within the Nubian aquifer in Egypt were examined: Lake Nasser and the Tushka Lakes (Fig. 1.12). The Lake Nasser surface levels time series was extracted from the U.S. Department of Agriculture's Foreign Agricultural Service (USDA-FAS) global reservoir and lake monitoring database (GRLM; available at: https://www.pecad.fas.usda.gov/cropexplorer/global_reservoir/). The Lake Nasser monthly level anomalies, with respect to the temporal mean (April 2002–January 2017), were then generated, over the entire Nubian aquifer in Egypt. On the other hand, the temporal variability in the volume, area, and water height in the Tushka Lakes were quantified, in a geographic information system (GIS) environment, using Landsat images along with a digital elevation model that was acquired prior to the formation of the Tushka Lakes. The SM data over the Nubian aquifer in Egypt was extracted from the Global Land Data Assimilation System (GLDAS) model (version 1; available at: ftp://hydro1.sci.gsfc.nasa.gov). The

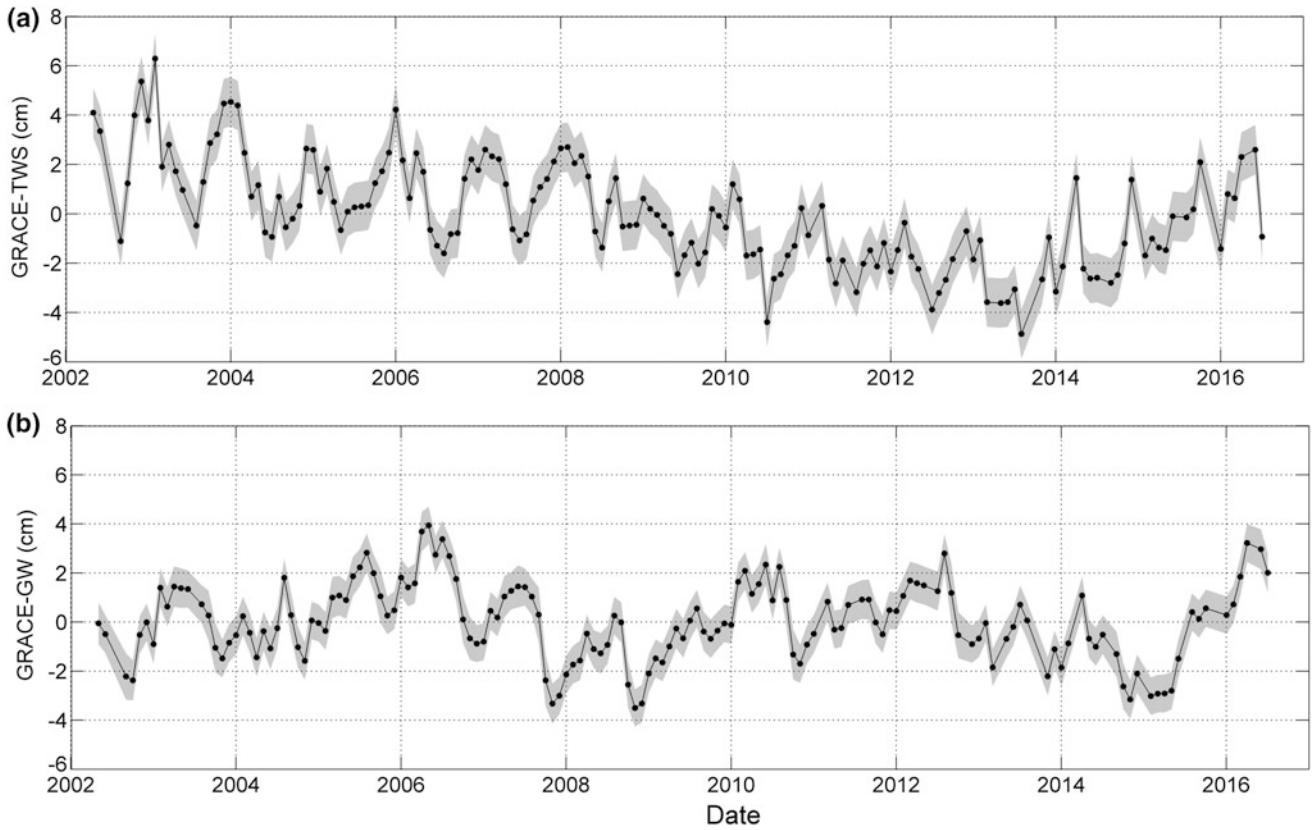

Fig. 1.13 Temporal variations in **a** GRACE-TWS and **b** GRACE-GW estimates, along with the associated uncertainties, extracted over the Nubian aquifer in Egypt

soil moisture time series was calculated by averaging the soil moisture estimates from four GLDAS model versions (Rodell et al. 2004). Trends in the SM and SW and associated trend errors were estimated using the procedures described in Ahmed and Abdelmohsen (2018).

1.4.3 Results and Discussion

Figure 1.12 shows the secular trend in GRACE-TWS generated over Egypt, northern parts of Sudan, and eastern parts of Libya. The outline of the Nubian aquifer in Egypt (black polygon) is also shown. Inspection of Fig. 1.12 indicates that the Nubian aquifer in Egypt is experiencing an overall negative GRACE-TWS trends during the investigated period (4/2002 − 1/2017). Higher GRACE-TWS depletion rates (< −5 mm/yr) are observed over the central parts of Nubian aquifer and the northeastern parts of Egypt. The northern coastal areas as well as the southern parts of the Nubian aquifer in Egypt, close to recharge areas in Sudan, are witnessing lower GRACE-TWS depletion rates (>−2 mm/yr). Figure 1.13a shows the temporal variations in GRACE-TWS time series averaged over the Nubian aquifer in Egypt. Examination of Fig. 1.13a shows an overall GRACE-TWS depletion of -3.26 ± 0.15 mm/yr that is equivalent to -2.15 ± 0.09 km^3/yr. The temporal variability in GRACE-TWS is related to temporal variations in one or more of the GRACE-TWS compartments (e.g., SW, SM, and GW).

Examination of temporal variations in Lake Nasser level anomalies over the Nubian Aquifer in Egypt shows that Lake Nasser is witnessing an overall height increase of 0.41 ± 0.05 mm/yr. However, piecewise trend analysis of Lake Nasser level anomalies indicates that Lake Nasser level anomalies are witnessing both decreasing and increasing trends during investigated period (4/2002 – 1/2017). Temporal fluctuations in Lake Nasser levels are mainly attributed to the seasonality in the Nile River. On the other hand, analysis of the temporal variations in the Tushka Lakes level anomalies indicates that they cumulatively lost 56, 80, and 98% of their volumes in 2006, 2010, and 2016, respectively, compared to their volume in 2002 that is estimated at 27.11 km^3. The loss in the Tushka Lakes' volumes, levels, and areas is believed to be an evaporation loss (e.g., Sultan et al. 2013). Trends in Tushka Lakes level anomalies over the Nubian Aquifer in Egypt indicate an overall systematic decrease in water levels of -2.29 ± 0.28 mm/yr. Finally, the temporal variations in GLDAS-derived SM time series

averaged over the Nubian Aquifer in Egypt indicates that, during investigated period (4/2002 – 1/2017), the SM is witnessing an overall depletion of −1.05 ± 0.05 mm/yr.

The GW time series extracted by subtracting the combined SM and SW from GRACE-TWS is shown in Fig. 1.13b. Inspection of Fig. 1.13b shows that the Nubian aquifer in Egypt is witnessing an overall GW decline of −0.42 ± 0.03 mm/yr that is equivalent to −0.27 ± 0.01 km^3/yr during investigated period (4/2002 – 1/2017). Close examination of Fig. 1.13b indicates that the GW time series exhibits temporal variability over four distinctive periods: April 2002–February 2006 (Period I), March 2006–March 2008 (Period II), April 2008–December 2012 (Period III), and January 2013–January 2017 (Period IV). Piecewise trend analysis results of GW time series shows that the Nubian aquifer in Egypt is experiencing a GW increase (5.00 ± 1.24 mm/yr; 3.30 ± 0.81 km^3/yr) during Period I followed by a sharp GW decrease (−21.07 ± 1.25 mm/yr; −13.90 ± 0.82 km^3/yr) during Period II, then a GW increase during periods III and IV (Period III: 6.52 ± 0.85 mm/yr, 4.30 ± 0.56 km^3/yr; Period IV: 3.50 ± 2.11 mm/yr, 2.31 ± 1.39 km^3/yr). Analysis of GW time series reveals that the Nubian aquifer in Egypt is receiving groundwater recharge during Periods I, III, and IV and witnessing groundwater depletion during Period II.

The sharp GW decline rate during Period II (−21.07 ± 1.25 mm/yr) is largely related to exceptional drought conditions in Period I compared to the previous periods. Examination of the average annual rainfall (AAR) and Lake Nasser levels indicates a decline during Period I (AAR: 120 mm; Lake Nasser level: 174.6 m) compared to the average of preceding years (1998 to 2002; AAR: 133 mm; Lake Nasser level: 178.2 m). Other common contributing factor, for the observed GW depletion, could be the baseflow recession. Normal baseflow recession occurs naturally during periods of extended drought and could cause extensive water level declines over time periods of weeks to months that result in volumetrically significant storage depletion (e.g., Alley and Konikow 2015).

To quantify the recharge rates of the Nubian aquifer in Egypt during Periods I, III, and IV, the discharge rates (natural discharge + anthropogenic groundwater extraction) was added to the GW trends. The sum of the average annual groundwater extraction and natural discharge for Nubian aquifer in Egypt was estimated at 2.85 km^3/yr (Mohamed et al. 2016). The total recharge for the Nubian aquifer in Egypt are estimated at 6.15 ± 0.81 km^3, 7.15 ± 0.56 km^3, and 5.16 ± 1.39 km^3 during Periods I, III, and IV, respectively. The total recharge during Periods I, III, and IV is estimated at 18.46 ± 1.95 km^3, however, approximate average annual recharge rate of 1.51 ± 0.15 km^3/yr is estimated during the three periods. The increase in average annual recharge of the Nubian aquifer in Egypt during Periods I, III, and IV is partially attributed to increasing the AAR during the investigated periods compared to the preceding periods as well as the increase in Lake Nasser levels.

Given the current overall GW depletion rate (−0.27 ± 0.01 km^3/yr) during the entire investigated period (April 2002–January 2017), the longevity of the Nubian aquifer in Egypt can be estimated. Based on modeled recoverable groundwater volumes (5180 km^3) (Bakhbakhi 2006) the Nubian aquifer in Egypt could last for more than 10,000 years assuming a constant GW depletion and recharge rates. Increasing depletion rates and/or decreasing the recharge rate would reduce the aquifer's longevity. For example, if the GW depletion is doubled, the groundwater resources of the Nubian aquifer in Egypt could last for 9,000 years, assuming constant recharge rate. Moreover, if the GW depletion are doubled every 50 years, the groundwater resources of the Nubian aquifer in Egypt could last for 400 years, assuming constant recharge rate.

1.4.4 Summary and Conclusions

Egypt is currently planning to use more of its groundwater resources, at the expenses of the limited Nile River surface water to support national development and reclamation projects. In this study, temporal (April 2002–January 2017) GRACE-TWS data along with reservoirs, rainfall, and soil moisture data were used to provide improved estimates of recharge and depletion rates of the Nubian aquifer in Egypt. Results indicate that during April 2002–February 2006 (Periods I) and April 2008–January 2017 (Periods III and IV) the Nubian aquifer in Egypt is receiving a total recharge of 18.46 ± 1.95 km^3. Recharge events of the Nubian aquifer in Egypt occur only under excessive precipitation conditions over the Nubian recharge domains and/or under a significant rise in Lake Nasser levels. The sharp groundwater depletion (−13.90 ± 0.82 km^3) during March 2006–March 2008 (Period II) is largely related to exceptional drought conditions in Period I compared to the previous periods as well as the normal baseflow recession.

Findings indicate that Egyptian decision makers are facing a real challenge to provide and maintain sustainable freshwater resource management for Egyptian population. However, they are highly recommended to use a conjunctive surface water and groundwater management plan. The results of this study demonstrate that global monthly GRACE-TWS solutions can provide a practical, informative, and cost-effective approach for monitoring aquifer systems located in any geologic or hydrologic setting across the globe.

Acknowledgments

This work was supported by the Global Environmental Facility/World Bank grant (number: P130801, title: Regional Coordination for Improved Water Resources Management and Capacity building program) to National Authority of Remote Sensing and Space Sciences.

1.5 Geochronological Measurements

Yasser M. Abd El-Rahman

The term "geochronology" was coined to distinguish between the geologic timescale, which is applicable to Earth processes from timescales related to humans (Williams 1893). After 1913, isotope geochronology emerged as a branch of science that uses the radioactive decay of isotopes in minerals to define the absolute age of most Earth materials and to quantify the geologic timescale (Condon and Schmitz 2013). Our understanding of evolution of the Egyptian basement is highly affected by the isotope geochronology as explained by Stern and Ali (This book) and El Bialy (This book).

The Egyptian basement is a complex of igneous and metamorphic rocks exposed in the Eastern Desert, Sinai, and limited areas in the southern part of the Western Desert. The earliest book of Hume (1934, 1935) on the geology of Egypt does not include radioactive measurements. Based on the petrographicaly and structural similarities between the basement rocks of Egypt and those rocks that are overlain by the Cambrian sandstone in Jordan, he assigned Precambrian age for the entire Egyptian basement complex. Moreover, Hume (1934, 1935) divided the basement complex into 9 groups that belong to Protarchaean, Metarchaean, Eparchean and Late Precambrian or Gattarian age. The details of the Hume's classification are given by El-Bialy (This book).

In 1962, Rushdi Said published his book "The Geology of Egypt". Until 1962, significant geochronological measurements on the Egyptian basement complex were absent. Using K-Ar technique, Gheith (1959) concluded that some crystalline basement rocks from the Eastern Desert of Egypt were formed during the upper Cambrian and lower Ordovician Periods (430–450 Ma). Applying the same K-Ar technique, Higazy and Ramly (1960) concluded also that the ages of the basement complex of the Eastern Desert range from Eo-Cambrian to Devonian. Said (1962) noted that these measurements were conducted on granites and other rock assemblages that belong to Hume's Gattarian episode. Although Said (1962) acknowledged the series argon loss caused by hydrothermal and later alteration, he considered that the only available radiogenic ages determined by Gheith (1959) and Higazy and Ramly (1960) substantial. Thus, Said (1962) concluded that the age of the Egyptian complex is Precambrian but the Hume's Gattarian episode could be as late as lower Paleozoic.

In early seventies, isotopic age determination of the basement rocks was accumulating using mainly the Rb-Sr technique (e.g. Hashad et al. 1972; El Shazly, et al. 1973). At the end of seventies, geochronology of the basement rocks in the Eastern Desert of Egypt was enriched by the Ph.D. work of Stern (1979a) and Dixon (1979), while geochronology of the basement rocks of Sinai was benefited from the Ph.D. work of Bielski (1982). Hashad (1980) compiled geochronological data in 1970s, but without robust analytical details. Another updated compilation for the geochronological data was considered during a trial to understand the evolution of the Arabo-Nubian massif by Bentor (1985). At the end of seventies and in eighties, the zircon U-Pb dating technique was applied to the Egyptian basement rocks (e.g. Abdel-Monem and Hurley 1979, 1980; Dixon 1981). The analytical procedure was based on the method of Krogh (1973), who used the technique of zircon hydrothermal-dissolution and Pb extraction taking the advantage of teflon^{TM} availability (Mattinson 2013). One of the comprehensive geochronological studies on the Egyptian basement rocks in eighties was conducted by Stern and Hedge (1985). They provided the ages for twenty-four rock units from the Eastern Desert of Egypt using combined Rb-Sr and U-Ph zircon techniques. In addition to the Rb-Sr technique, whole-rock Sm/Nd modal ages were defined for the basement inliers in the Western Desert of Egypt by Schandelmeier et al. (1987).

Rushdi Said was the editor of the updated version of the Geology of Egypt book that was published in 1990. The book included two chapters on the basement rocks in the Eastern Desert and Sinai that were written by El-Gaby et al. (1990), and Hassan and Hashad (1990). Moreover, there was a chapter on the basement inliers in the Western Desert of Egypt that was written by Richter and Schandelmeier (1990). The compiled geochronological data between 1962 and 1990 on the basement rocks from the Eastern Desert and Sinai supports the late Proterozoic age measured for these rocks and the occurrence of older aged for the basement inliers in the Western Desert. However, El-Gaby et al. (1990) and Hassan and Hashad (1990) suspected the reliability of some of these ages, which result in controversies over the origin of some of the rocks units in the Egyptian basement complex. El-Gaby et al. (1990) and Hassan and Hashad (1990) considered the gneiss domes in the Eastern Desert and Sinai as a structurally low reworked part of the older Sahara Craton exposed further to the west as inliers in the Western Desert of Egypt. Their conclusion was based mainly on the highly metamorphosed and deformed natured of these rocks and on their structurally lower position relative to the late Proterozoic ophiolitic and volcano-sedimentary assemblages without potent geochronological evidence. Another example to show how lithology surpassed the available geochronological

data was given by El Gaby et al. (1990) who suggested by the total absence of island arc metavolcanic rocks (the Younger Metavolcanics) from the Sinai. Shimron (1980) and Bentor (1985) affiliated the Sa'al and Kid metavolcanic rocks to the Younger Metavolcanics, which is consistent with the age given by Rb-Sr ischron age of 734 Ma given by Bielski (1982). Based on high proportion of acidic volcanic rocks, El Gaby et al. (1990) affiliated the Sa'al and Kid volcanic rocks with Dokhan Volcanic Group, which is younger group of Cordilleran volcanics in Egypt that was formed between 639 and 581 Ma.

Modern geochronology has evolved by reducing sample size from whole-rock and multigrain fraction to single mineral grains (Nemchin et al. 2013). After 1990, such approach was adopted and geochronological studies on the Egyptian basement were based mainly on zircon U-Th–Pb measurements using ID-TIMS (isotope dilution-thermal ionization mass spectroscopy), SIMS (secondary ion mass spectrometry), SHRIMP (sensitive high mass resolution ion microprobe), and recently LA-ICP-MS (laser ablation inductively coupled plasma mass spectrometry). In early 1990s, Alfred Kröner commonly used single zircon evaporation techniques to date different rock units from the Egyptian basement complex, such as gneisses from Sinai (Kröner et al. 1990), ophiolitic rocks and their associated gabbro-diorite complexes (Kröner et al. 1992), and granitoid gneisses from the CED and SED (Kröner et al. 1994). Wilde and Youssef (2000, 2002) used SHRIMP II ion microprobe at Curtain University to date zircon yielded from the Ediacaran Dokhan Volcanic Series and Hammamat Group from the NED. El-Gaby et al. (1990), and Hassan and Hashad (1990) were highly convinced that the volcanic rocks from Sinai and NED are affiliated with this Ediacaran Dokhan Volcanic Series. Sa'al volcano-sedimentary complex, which was a matter of debate as mentioned earlier, was assigned late Mesoproterozoic age by Be'eri-Shlevin et al. (2012) CAMECA IMS 1270 facility hosted by the Swedish Museum of Natural History (NORDSIM). This instrument was commonly used to date various rocks units from Sinai (e.g. Be'eri-Shlevin et al. 2009b, 2011; Samuel et al. 2011; Abu El-Enen and Whitehouse 2013; Eyal et al. 2014). Using U-Pb zircon LA-ICP-MS data support the presence of Pre-Ediacaran volcano-sedimentary rocks in Sinai (e.g. Moghazi et al. 2012; Andresen et al. 2014). Recently, another CAMECA IMS-1280HR SIMS facility hosted by the Institute of Geology and Geophysics, Chinese Academy of Science was used to date the Ediacaran Hammamat Group in thier type locality at Wadi Hammamat area in the CED (Abd El-Rahman et al., 2019). The same facility used in combination of Neptune multicollector ICP-MS hosted by the same institute were used to detect the recycled Hf isotoe signature from Cryogenian zircon yiekded from a felsic vlcanic fragment from the juvenile crust of the Eastern Desert of Egypt (Li et al., 2018).

Similar to Sinai, the volcano-sedimentary units in the NED are considered part of the Ediacaran Dokhan Volcanic Series and associated Hammamt Group by El-Gaby et al. (1990), and Hassan and Hashad (1990). Based on LA-ICP-MS U-Pb zircon dating, Tonian-Cryogenian volcanic rocks and volcano-sedimentary successions were identified from the Ras Gharib Segment (Bühler et al. 2014; Abd El-Rahman et al. 2017). Adopting modern geochronological approach enabled Eliwa et al. (2014) to define the Tonian age (741 ± 3 Ma) of the muscovite trondhjemite using the SIMS zircon U-Pb zircon dating. The same pluton was assigned six-point Rb-Sr isochron age of 516 ± 7 Ma by Abdel-Rahman and Doig (1987).

Regarding the CED, the ID-TIMS laboratory at the University of Oslo for U-Pb dating were commonly used to determined the ages of various rocks units from this segment of the Egyptian basement complex (Andresen et al. 2009; Augland et al. 2012; Lundmark et al. 2012). The geochronology of the Eastern Desert was greatly benefited from the work of Kamel Ali. Ali et al. (2009) recorded the common presence of the pre-Neoproterozoic zircon xenocrysts during the U-Pb SHRIMP zircon dating of the Neoproterozoic volcanic rocks for the CED. Stern et al. (2010) compiled the data on the pre-Neoproterozoic zircons to exhibit their distribution and significant in the juvenile Neoproterozoic igneous rocks. Ali et al. (2010a, b) integrated his work on zircon yielded from the metasedimentary rocks in the CED with the earlier study of Dixon (1981) to assume ~750 Ma glaciation, not only in the CED, but also in the ANS. The work of Kamel Ali includes dating the granitoids and granitoids gneisses from the CED using both SHRIMP and LA-ICP-MS U-Pb zircon techniques.

After Kröner et al. (1992), who dated the ophiolitic rocks and associated intrusive gabbro-diorite complexes using single zircon evaporation method, Ali et al. (2010a, b) reported SHRIMP U-Pb zircon ages for the ophiolitic layered gabbro, overlaying arc-type dacite and younger intrusive gabbro and diorite bodies to understand the ophiolite emplacement history in the Allaqi suture zone. Following the track of Kröner et al. (1994), who dated the granitoid gneisses from Hafafit area, Ali et al. (2015) yielded SHRIMP U-Pb zircon emplacement ages for the Wadi Beitan granitoid gneisses further towards the south in SED. In addition to the ophiolitic rocks and the granitoid gneisses, the SED are characterized by the presence of the bimodal Shadli Metavolcanics, which are poorly dated. The mafic and felsic lava yielded a Rb-Sr isochron age of 712 ± 24 Ma, which is considered to represent the time of volcanic eruption by Stern et al. (1991). Unfortunately, there is no study conducted on this rock unit using high-spatial-resolution technique to yield U-Pb zircon age.

The basement inliers in exposed in the southern part of the Western Desert are known to be older than the basement complex in the Eastern Desert and Sinai (Richter and Schandelmeier 1990). Based on zircon fraction dissolution

method of Krogh (1973), Sultan et al. (1994) confirmed the Archean and Paleoproterozoic emplacement age from Gebel Kamil and Gebel El Asr. Using a modern geochronological approach, Bea et al. (2011b) confirmed the Archean age of the Uweinat-Kamil inlier based on SHRIMP U-Pb zircon dating. However, Bea et al. (2011a) integrated both SHRIMP and Pb–Pb stepwise evaporation and obtained an Ediacaran age for one of the Bir Safsaf inlier, which is one of the four basement inliers located midway between the Neoproterozoic Eastern Desert and the Archean terranes of the Gebel Kamil.

Accessory minerals other than zircon were rarely used in geochronological studies on the Egyptian basement complex. Few studies used monazite were analyzed by electron microprobe (EMP) Th-U-Pb dating method. For examples, Finger and Helmy (1998) and Karmakar and Schenk (2015) used this in situ monazite EMP dating method to obtain the age of metamorphic events in high-grade rocks from the Egyptian complex and Abu Sharib et al. (2019) dated the metamorphism based on the monazite of the metasedimentary rocks of CED. It worth mention that Zoheir et al. (2015) considered for the first time Re–Os isotope systematic arsenopyrite to determine the timing of epigenetic gold mineralization in CED.

1.6 Airborne Geophysical Mapping

Sultan Awad Sultan Araffa

The airborne surveys in Egypt are acquired out at different times of different scales for a lot of purposes as mineral resources exploration, petroleum exploration, groundwater aquifer definition, and natural radiation mapping. The most airborne survey data is principally magnetic, electromagnetic and in several surveys, total count (TC) radiation for Thorium, Uranium and Potassium elements data were recorded (Fig. 1.14). The airborne surveys are carried out for different agencies such as: Geological Survey of Egyptian and Mining Authority (EGSMA), the Nuclear Materials Corporation (NMC), the Desert Research Institute (DRI), and the Egyptian General Petroleum Corporation (EGPC). According to the independent interests of the different agencies, some information of surveys that are including flight line spacing, flight direction, and flight elevation has been flown. The following is a brief description of the several airborne surveys.

1.6.1 Period from 1962–1978

Airborne magnetic surveys are an important geophysical tool for many junior mining and mineral exploration companies, and for many oil companies for detecting structures and depth of top surface of basement rocks to estimate the thickness of sedimentary succession. These surveys make it possible to gather detailed information about the presence of various magnetic and non-magnetic bodies in the Earth's crust over a large scale geographical area. This type of survey is cost-effective, safe and time efficient because of the large areas of land that can be surveyed. Magnetometers have been attached to a small machine of airplane or helicopter, which can be flied pre-planned survey lines over the survey area and take readings that show differences in earth magnetic fields. The improvement of technology in magnetometers and other magnetic sensors have made it possible to accurately acquire data relative to these magnetic fields from the height of the aircraft. The regional airborne surveys are acquired at different higher altitudes and at wider line spacing intervals. These airborne surveys give more general information about the magnetic fields over a larger survey area but provide clues about which areas may be of more interest. Detailed airborne surveys have been acquired at lower altitudes and narrower line spacing intervals in order to give higher resolution data for better processing of the area.

a. **Aswan Region**

This survey is acquired on Aswan Region by Lockwood of Canada, Ltd. (1968) for the United Nations Development Project (UNDP), this is one of the earlier airborne surveys, was done in 1968 over two large areas in the Aswan area of Eastern Desert, Egypt (Fig. 1.14). This survey aims to apply geophysical investigations for the assessment of mineral ore deposits. The main elements of the survey are shown in Table 1.2. The magnetic data were measured as total intensity magnetic anomaly maps at different scales: n such as 1:50 000, 1:100 000, and 1:1 000 000 (10 nT C.I). The processing and interpretation of magnetic data have been applied on map of scale 1:500 000. The constructed maps of total intensity magnetic maps have not been removed for IGRF from the data. The measured aeromagnetic data were adjusted to a datum of 34, 500 nT, which represents the mean values of total intensity of the earth's field in the area under consideration. The most magnetic anomalies over the parts of Nubian Shield, like those observed on the Red Sea region in the Arabian Shield, to delineate these features such as ring structure, plutons, dyke systems. The quantitative processing and interpretation of data in the northeastern part of study area, Huntec (1969) found two magnetic sources: (1) large and regional sources of deep depths at average depths of 1 km below observation level; and (2) shallow features at average depths of 300 m below observation level. Much remarks were given to the study of the systems of magnetic lineation caused by dykes, some of which were reversely polarized. The result of interpretation indicated that, none of the dyke systems are related to the development of the Red Sea rift zone.

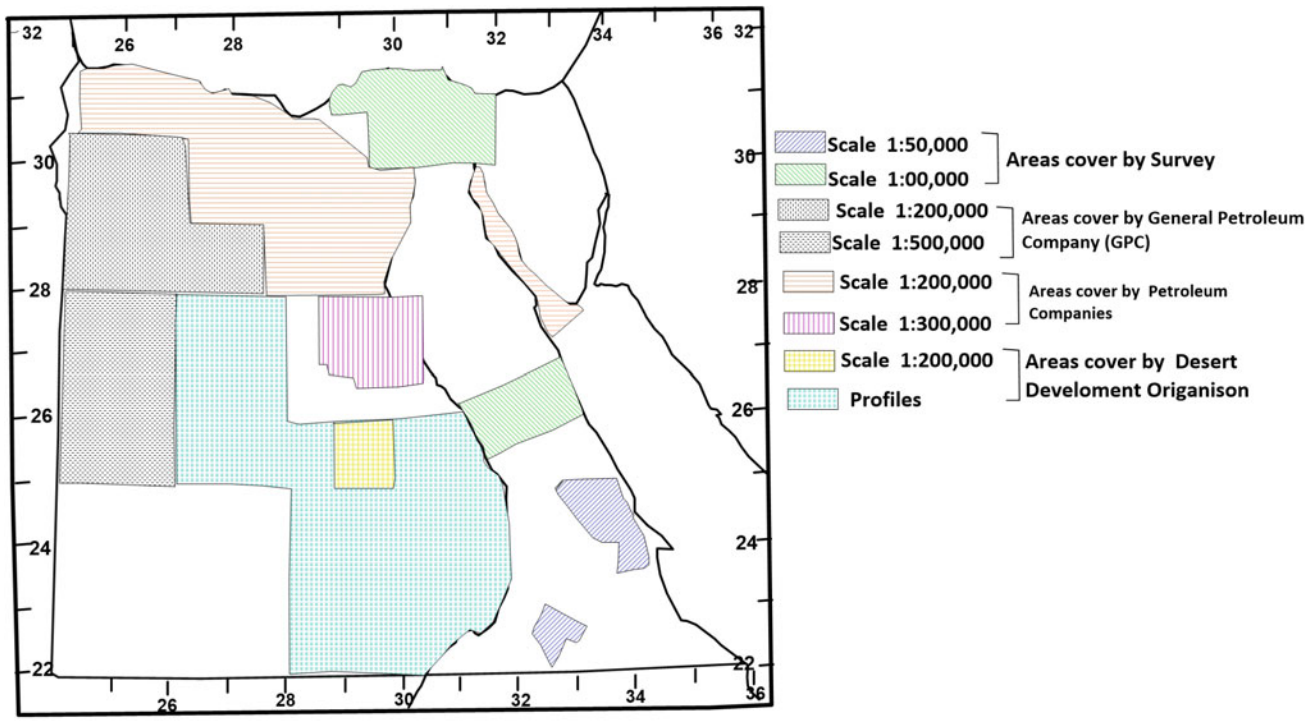

Fig. 1.14 Index map showing locations of airborne geophysical survey areas

b. **Delta Area**

The Delta Area was surveyed for Geological Survey of Egypt (EGSMA) during the period from 1962 to 1963, the EGSMA flew more than 20,000 line kilometers in Nile Delta area along N-S flight lines of line spacing of 1 km and 200 m above land surface (Fig. 1.14). Using a Russian AN2 (single engine) aircraft and an AM13 fluxgate magnetometer. The resulting data contoured for 10 nT interval for a map of scale 1:100 000. The main results of interpretation of the aeromagnetic data has been prepared by El Diasty (1969), where the result indicated that the southern part of the surveyed area is occupying by E-W trending, high frequency, short wave length anomalies which indicating shallow depths producing magnetic bodies. These high frequency anomalies lie adjacent to the low amplitude, long, wave length anomalies that occupying the northern part of the area. The Western Desert of Egypt was surveyed by Aero Service company where this survey was flown in 1961 under AID contract ICA c1775 for the Desert Research Institute (DRI) by in the Aero Service company (1961). The purpose of the survey to assist the definition of possible aquifer thickness by estimating depth to basement surface from magnetic interpretation. Most of this survey was regional, where the flight lines along which data were measured are too far apart to be contoured. The spaced flight lines were flown in the Kharga Oasis area to give greater magnetic detail. The main elements of the reconnaissance survey and the Kharga Oasis survey are given in Table 1.3. Flight line locations were represented on 1:500 000 scale topographic

Table 1.2 Main elements of UNDP airborne survey, Aswan Region, Egypt

	SW zone	NE zone
Survey area in sq. km.	5,000	15,000
Line -kilometers flow	10,000	15,000
Flight line direction	N 25°E	N 60°E
Flight line spacing (km)	0.5	1.12
Flight elevation (m)	130	150
Instrumentation: Magnetic Radiation (TC) Electromagnetic	Fluxgate (18) Yes None	Fluxgate (18) None (400 and 2300 Hz)

Table 1.3 Main elements of UNDP aeromagnetic survey of Western Desert, Egypt

	Reconnaissance survey	Kharga Oasis detail
Survey area in sq. km.	N.A.	12,000
Line -kilometers flow	11,500	5,000
Flight line direction	N–S	N–S
Flight line spacing	50 Pairs	3.3 km
Flight elevation	2000 Bars	2000 Bars
Instrumentation: Map scales	Gulf Mark III Fluxgate Mag. 1:10 000	Gulf Mark III Fluxgate Mag. 1:100 000 1:500 000

maps. The magnetic data were compiled at 1:100 000 (six sheets). 1:500 000 aeromagnetic compilation was also prepared. The datum for the magnetic data was chosen to be 3,700 nT. The main results of interpretation for airborne survey indicated that the magnetic tool could be give a depth to basement rocks, and, thus, aid in the estimation of thickness of the overlying sedimentary successions specially that contain ground water aquifers. (Table 1.3).

c. **Qena-Safaga sector**

Qena-Safaga sector was flown for magnetics from Safaga and Quseir, on the Red Sea, southwest to the Nile River (Fig. 1.14). This project was flown with the same aircraft and Instrumentation as the Delta Area (described above). The area of the par is about 20,000 square km. Flight line direction was normal to the axis of the Red Sea (about N. 60°E.), the spacing 2 km, and the altitude above ground, 150 m. The data for the northern half of this sector were processed and interpreted by El Hakim (1978). The magnetic data for the southern half of the sector were constructed at a scale of 1:100 000 and contoured at 10 nT intervals.

d. **Western Desert (Aeromagnetic surveys for oil exploration)**

Part of Aeromagnetic survey was acquired at different areas for oil companies (Fig. 1.14) a part of the contour map was available for the large area in northwestern part of Egypt (bounded, by the, River Nile on the East, the Libyan Desert on the West, the Mediterranean Sea on the north, and latitude 28° on the south). The direction of flight line was N-S and the line spacing of 2 km apart.

e. **Airborne radiometry surveys**

A major mineral resources survey of natural gamma radiations was made by the EGSMA (through UNDP) in 1968, as a part of the Lockwood aeromagnetic survey in the Aswan Region (see above). The data were acquired a flight altitude of 130 m, for cosmic radiation, and for instrument drift. The collected data were compiled as profiles and as contour maps (1:50 000 and 1:100 000 scales). The total count γ radiation data yielded much information useful in prospecting for most ore mineral elements. The data are represented as contour maps (same scale as the magnetic maps) that have been interpreted qualitatively, the maps have been especially useful in ground follow up geophysical and geochemical investigations. The total count of radiation was applied for both Qena-Safaga sector and for the Delta area. Some more additional information for radiation surveys was obtained from Nuclear Materials Corporation (NMC). The location map which indicates the areas which were applied by airborne radiometric surveys was prepared by NMC. This map indicate that it is not possible to determine which areas were flown by NMC, but certainly the areas in the Eastern Desert (Aswan Region), south of Idfu, were flown by Lockwood. According to the NMC plans a country wide aeromagnetic and gamma ray spectrometry survey, to be done with a twin engine Islander, equipped with Geometrics magnetometer and an Exploranium gamma ray Spectrometer. Surprisingly, no Doppler navigation is planned. And although on board recording equipment is both analog and digital, data reduction will be by manual methods.

f. **Airborne Electromagnetic Survey**

The main objective of Airborne Electromagnetic (AEM) surveys is to acquire a rapid and relatively low-cost technique for metallic ore bodies, such as massive sulphides which located in bed rock. This method can be applied for most geological environments except where the country rock is highly conductive. Also, this technique can be applied to general geologic mapping, geotechnical applications and groundwater exploration. This technique can be applied in some regions such as semi-arid areas, particularly with internal drainage patterns, can be usually poor AEM environments. The Weathered products of mafic flows can give

more conductive backgrounds, specially flows of Tertiary or Quaternary age. Some geological materials exhibit high range of conductivity over seven orders of magnitude, bodies of massive sulphides is the strongest electromagnetic responses, followed in decreasing order of intensity by graphite, unconsolidated sediments (clay, gravel and sand), and basement rocks. The consolidated sedimentary have range in conductivity from the level of graphite down to less than the most resistive igneous materials. The aquifers which contain fresh water is highly resistive than that contain salt water. The following examples can be suggested possible target types and they can be indicated the grade of the AEM response that can be expected from these targets. The alternating magnetic field is defined by passing a current

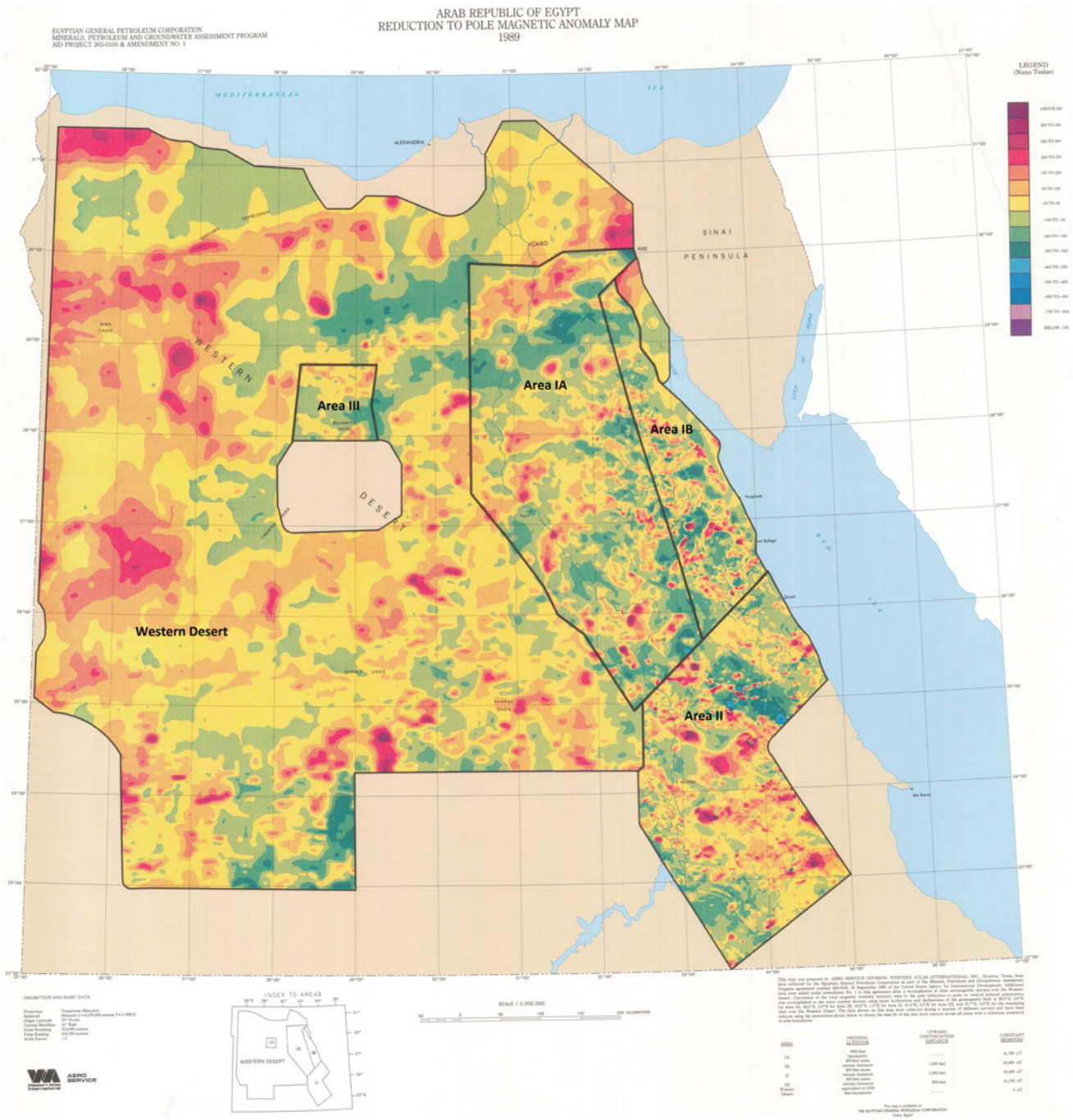

Fig. 1.15 Index map for Aero service survey for Egypt

through a coil. The resultant magnetic field is measured through the receiver of the instrument which is consisting of a sensitive amplifier and meter or potentiometer bridge.

By this way the airborne electromagnetic (AEM) technique was carried out at some areas in Egypt. The airborne electromagnetic (AEM) data were measured only in the southwest part of the Aswan Region in 1968 by Lockwood Survey. The direction of axis of the transmitting coil was vertical and the direction of axis of the receiving coil was horizontal, trailing 50 m below and 139 m aft of the DC 3 aircraft.

1.6.2 Period from 1980–1984

The Airborne survey for this period was carried out by Aero-service Western Atlas International, INC, Houston, Airborne data were collected for Egyptian General Petroleum Cooperation and Egyptian Geological Survey as apart of mineral, petroleum and groundwater assessment program through the agreement number 263–0105 November 1980 of the United State Agency for international development additional data were added under amendment No.1 to this agreement after recompilation of order aeromagnetic surveys over the Western Desert. Conversion of total magnetic intensity anomaly data to the pole (reduction to the pole) or vertical induced polarization was accomplished in wave number domain using mean inclination and declination of geomagnetic field of 39.5°N, and 2.0°E for area IA; 39.5°N, and 2.0°E for area IB: 32.8°N, and 1.9°E for area II; 40.5°N, and 2.0°E for area III; and 37.7°N, and 2.0°E for the remining data over the Western Desert. The maps of airborne survey which carried out by Aero service company are represented by different scales such as 1:50 000 for Eastern Desert and Bahariya Oasis; 1:100 000 for some parts of Eastern Desert; 1:500 000 for most areas of Egypt and 1:2 000 000 for all Egypt in one sheet. Also, different maps of aeromagnetic are constructed such reduced to pole, Interpreted maps for depths of magnetic sources. The airborne surveys include different geophysical data such as aeromagnetic, airborne radiation for total cont., Thorium, Potassium and Uranium elements in PPM and maps for ratios for U/K, K/Th (Fig. 1.15). The geologists of geological survey of Egypt used ratio maps of radioactive elements (U, Th and K) as results of interpretation for airborne data which acquired by aero service to detect the contacts between geologic units and then used for regional and detailed geologic mapping. In some areas in Eastern Desert the interpreted maps are used to detect and define the source of magnetic bodies which can be at shallow depths (near surface) or can be extended to deep depths. The aeromagnetic maps used by geophysicists of geological survey to planning for ground geophysical investigations specially for mineral exploration on some areas in Eastern Desert which are rich for metallic and none metallic ore minerals.

References

Abd El-Rahman Y, Seifert T, Gutzmer J, Said A, Hofmann M, Gärtner A, Linnemann U (2017) The South Um Mongol Cu-Mo-Au prospect in the Eastern Desert of Egypt: from a mid-Cryogenian continental arc to Ediacaran post-collisional appinite-high Ba–Sr monzogranite. Ore Geol Rev 80:250–266

Abdeen M (2002) Comparison between optical remote sensing and radar imagery for mapping fossil rivers in arid regions, Kom Ombo area, South Egypt. Egypt J Remote Sens Space Sci 5:99–108

Abdeen M, AbdelGaffar A (2008) Mapping Neoproterozoic structures along the central Allaqi-Heiani suture, South Eastern Egypt, using remote sensing and field data. Egypt J Remote Sens Space Sci 11:109–138

Abdeen M, Thurmond AK, Abdelsalam MG, Stern RJ (2003) Use of Terra Satelite ASTER band-ratio images for geological mapping in arid regions: the Neoproterozoic Allaqi Suture, Egypt. Egypt J Remote Sens Space Sci 5:19–40

Abdeen M, EL-Kazzaz YA, Attia GM, Yehia MA, Hassan SM (2009) Mapping geological structures in wadi Ghoweiba area, North West Gulf of Suez, Egypt, Using ASTER-SPOT Data Fusion and Aster DEM. Egypt J Remote Sens Space Sci 12:101–126

Abdel Motaal E, Ramadan T (1998) Morphotectonics of Gabal Zeit-EshMellaha Region (Eastern Desert, Egypt) using remotely-sensed data. Egypt J Remote Sens Space Sci 1:165–280

Abdel Rahman SI, EI-Asmar H, Yehia MA (1998) Remote sensing applications for change detection in the coastal region of the Nile Delta, Egypt. Egypt J Remote Sens Space Sci 1:57–68

Abdel-Monem AA, Hurley PM (1979) U-Pb dating of zircons from psammitic gneisses, Wadi Abu Rosheid-Wadi Sikait area, Egypt. In: A.M.S. A1-Shanti (ed), Evolution and Mineralization of the Arabian-Nubian Shield. Inst Appl Geol Jeddah Bull 3. Pergamon Press, 3:165–170

Abdel-Monem AA, Hurley PM (1980) Age of the Aswan monumental granite, Egypt, by U-Pb dating of zircons. In: A.M.S. A1-Shanti (ed) Evolution and Mineralization of the Arabian-Nubian Shield. Inst Appl Geol Jeddah Bull 3. Pergamon Press, 3:141–144

Abdel-Rahman AFM, Doig R (1987) The Rb–Srgeochronological evolution of the Ras Gharib segment of the northern Nubian Shield. J Geol Soc London 144:577–586

Abdou-Azaz LK (2008) Analysis and assessment of land use change in Alexandria, Egypt Using satellite images, GIS and modeling techniques. Egypt J Remote Sens Space Sci 11:17–26

Abou El-Magd I, El-Zeiny A (2014) Quantitative hyperspectral analysis for characterization of the coastal water from Damietta to Port Said, Egypt. Egypt J Remote Sens Space Sci 17(1):61–76

Abou El-Magd I, Hermas E, El Bastawesy M (2010) GIS-modeling of the spatial variability of flash flood hazard in Abu Dabbab catchment, Red Sea Region, Egypt. Egypt J Remote Sens Space Sci 13(1):81–88

Abou El-Magd I, Mohy H, Basta F (2015) Application of remote sensing for gold exploration in the Fawakhir area, Central Eastern Desert of Egypt. Arab J Geosci 8:3523–3536

Abu El-Enen MM, Whitehouse MJ (2013) The Feiran–Solaf metamorphic complex, Sinai, Egypt: geochronological and geochemical constraints on its evolution. Precambr Res 239:106–125

Afia MS, Imam I (1979) Mineral map of the Arab Republic of Egypt, scale 1: 2000 000, 1st edn. Egyptian Geological Survey

Afify AA, Arafat SS, AboelGhar M, Khader MH (2010) Physiographic soil map delineation for the Nile alluvium and Desert outskirts in middle Egypt using remote sensing data of EgyptSat-1. Egypt J Remote Sens Space Sci 13(2):129–135

Ahmed MH (1999) Environmental status of the coastal zone of Al Sukhna area, Gulf Of Suez, Red Sea, Egypt. Egypt J Remote Sens Space Sci 2:117–129

Ahmed MH (2000) Long-term changes along the Nile Delta coast: Rosetta Promontory. A case study. Egypt J Remote Sens Space Sci 3:125–134

Ahmed M, Abdelmohsen K (2018) Quantifying modern recharge and depletion rates of the Nubian Aquifer in Egypt. Surv Geophys. 39: 729-751 https://doi.org/10.1007/s10712-018-9465-3

Ahmed M, Sultan M, Wahr J, Yan E, Milewski A, Sauck W, Becker R, Welton B (2011) Integration of GRACE (Gravity Recovery and Climate Experiment) data with traditional data sets for a better understanding of the time-dependent water partitioning in African watersheds. Geology 39(5):479–482. https://doi.org/10.1130/G31812.1

Ahmed M, Sultan M, Wahr J, Yan E (2014) The use of GRACE data to monitor natural and anthropogenic induced variations in water availability across Africa. Earth Sci Rev 136:289–300. https://doi.org/10.1016/j.earscirev.2014.05.009

Ahmed M, Sultan M, Yan E, Wahr J (2016) Assessing and improving land surface model outputs over Africa using GRACE, field, and remote sensing data. Surv Geophys 37(3):529–556. https://doi.org/10.1007/s10712-016-9360-8

Aita SK, Bishta A (2009) Geology and radioactivity of Gabal El Minsherah—El Hasanah District, Northern Sinai, Egypt. Egypt. J Remote Sens Space Sci 12:149–164

Akaad MK (1996) Rock succession of the basement: an autobiography and assessment. Centennial of the Egyptian Geological Survey 1896–1996. Geol Surv Egypt Spec. Paper No. 71, 87 pp

Akaad MK, Noweir AM (1980) Geology and lithostratigraphy of the Arabian Desert orogenic belt of Egypt between latitudes 25°35′ and 26°30′N. Inst Appl Geol Bull 3:127–135

Ali KA, Stern RJ, Manton WI, Kimura J-I, Khamis HA (2009) Geochemistry, Nd isotopes, and U–Pb SHRIMP zircon dating of Neoproterozoic volcanic rocks from the Central Eastern Desert of Egypt: new Insights into the ~750 Ma crust-forming event. Precambr Res 171:1–22

Ali KA, Azer MK, Gahlan HA, Wilde SA, Samuel MD, Stern RJ (2010a) Age constraints on the formation and emplacement of Neoproterozoic ophiolites along the Allaqi-Heiani Suture, South Eastern Desert of Egypt. Gondwana Res 18:583–595

Ali KA, Stern RJ, Manton WI, Johnson PR, Mukherjee SK (2010b) Neoproterozoic diamictite in the Eastern Desert of Egypt and Northern Saudi Arabia: evidence of ~750 Ma glaciation in the Arabian-Nubian Shield. Int J Earth Sci 90:705–726

Ali KA, Kröner A, Hegner E, Wong J, Li S-Q, Gahlan HA, El Ela FF (2015) U-Pb zircon geochronology and Hf–Nd isotopic systematics of WadiBeitan granitoid gneisses, South Eastern Desert, Egypt. Gondwana Res 27:811–824

Alley WM, Konikow LF (2015) Bringing GRACE down to earth. Groundwater 53(6):826–829. https://doi.org/10.1111/gwat.12379

Amer R, Kusky T, Ghulam A (2010) Lithological mapping in the Central Eastern Desert of Egypt using ASTER data. J Afr Earth Sc 56(23):75–82

Amer R, Kusky T, ElMezayen A (2012) Remote sensing detection of gold related alteration zones in Um Rus area, Central Eastern Desert of Egypt. Adv Space Res 49(1):121–134

Amer R, EL Mezayen A, Hasanein M (2016) ASTER spectral analysis for alteration minerals associated with gold mineralization. Ore Geol Rev 75:239–251

Andresen A, Abu El-Rus MA, Myhre PI, Boghdady GY, Corfu F (2009) U-Pb TIMS age constraints on the evolution of the Neoproterozoic Meatiq Gneiss Dome, Eastern Desert of Egypt. Int J Earth Sci 98:481–497

Andresen A, El-Enen MM, Stern RJ, Wilde SA, Ali KA (2014) The Wadi Zaghra metasediments of Sinai, Egypt: new constraints on the late Cryogenian–Ediacaran evolution of the northernmost Arabian-Nubian Shield. Int Geol Rev 56:1020–1038

Ashmawy M, Nassim A (1998) Hydrological impact and assessment of morphometric aspects of Wadi Al-Asyuti basin, Eastern Desert, Egypt. Egypt J Remote Sens Space Sci 1:207–232

Assran AS, El-Tarras MM, Bishta AZ (2005) Remote sensing, aeroradiometric and aeromagnetic interpretation of Wadi Safaga-Wadi Saqia area, Central Eastern Desert of Egypt. J Remote Sens Space Sci 8:129–142

Atlas of Space images of North Western Desert, Egypt (2005) EGSMA, NARSS,UNESCO project of the Capacity building of the Egyptian Geological Survey and Mining Authority (EGSMA) and the National Authority of Remote Sensing and Space Sciences (NARSS) In Cooperation with UNDP and UNESCO, EGY/97/011 (executed by UNESCO Cairo Office)

Augland LE, Andresen A, Boghdady GY (2012) U-Pb ID-TIMS dating of igneous and metaigneous rocks from the El-Sibai area: time constraints on the tectonic evolution of the Central Eastern Desert. Egypt Int J Earth Sci 101:25–37

Azab MA (2009) Assessment and management of natural hazards and disasters along Qena-Safaga road, Central Eastern Desert, Egypt. Egypt J Remote Sens Space Sci 12:55–70

Bakhbakhi M (2006) Nubian Sandstone Aquifer System. In Nubian sandstone aquifer system. In: Foster S, Loucks DP (eds.) Non-renewable groundwater resources: a guidebook on socially sustainable management for water-policy makers. United Nations Educational, Scientific and Cultural Org, Paris 75–81

Ball J (1900) Kharga Oasis, its topography and geology. Egyptian Geological Survey, Cairo, 116 pp

Ball J (1939) Contributions to the geography of Egypt. Egyptian Geological Survey, Cairo, 300 pp

Ball J, Beadnell HJL (1903) Bahariya Oasis: its topography and geology. Egyptian Geological Survey, Cairo, 84 pp

Barron T (1907) The topography and geology of the Peninsula of Sinai (Western Portion). Egyptian Geological Survey, Cairo, 241 pp

Barron T, Hume WF (1902) Topography and geology of the Eastern Desert of Egypt (Central Portion). Egyptian Geological Survey, Cairo, 331 pp

Be'eri-Shlevin Y, Katzir Y, Whitehouse M (2009b) Post-collisional tectonomagmatic evolution in the northern Arabian-Nubian Shield (ANS): time constraints from ion-probe U-Pb dating of zircon. J Geol Soc (London) 166:71–85

Be'eri-Shlevin Y, Samuel MD, Azer MK, Rämö OT, Whitehouse MJ, Moussa HE (2011) The late Neoproterozoic Ferani and Rutig volcano-sedimentary successions of the northernmost Arabian-Nubian Shield (ANS): new insights from zircon U-Pb geochronology, geochemistry and O–Nd isotope ratios. Precambr Res 188:21–44

Be'eri-Shlevin Y, Eyal M, Eyal Y, Whitehouse MJ, Litvinovsky B (2012) The Sa'al volcano-sedimentary complex (Sinai, Egypt): a latest Mesoproterozoic volcanic arc in the northern Arabian Nubian Shield. Geology 40:403–406

Bea F, Montero P, Abu Anbar M, Molina JF, Scarrow JH (2011a) The BirSafsaf Precambrian inlier of South West Egypt revisited. A model for ~1.5 Ga TDM late Pan-African granite generation by crustal reworking. Lithos 125:897–914

Bea F, Montero P, Abu Anbar M, Talavera C (2011b) SHRIMP dating and Nd isotope geology of the Archean terranes of the Uweinat-Kamil inlier, Egypt-Sudan-Libya. Precambr Res 189:328–346

Beadnell HJL (1927) The wilderness of Sinai. Arnold, London, p 180

Belal AA, Moghanm FS (2011) Detecting urban growth using remote sensing and GIS techniques in Al Gharbiya governorate, Egypt Egypt. J Remote Sens Space Sci 14(2):73–79

Bentor YK (1985) The crustal evolution of the Arabo–Nubian massif with special reference to the Sinai peninsula. Precambr Res 28:1–74

Bielski M (1982) Stages in the evolution of the Arabian-Nubian Massif in Sinai. PhD thesis, Hebrew University, Jerusalem, 155 pp

Bishta AZ, Aita SK (2009) Geology and radioactivity of Gabal Halal, Northern Sinai, Egypt Egypt. J Remote Sens Space Sci 12:165–178

Bishta AZ, El Tarras MM (2002) Integration of Landsat-7 ETM+, aeroradiometric and aeromagnetic data to delineate the tectonic framework of Dihmit District, South Eastern Desert, Egypt. Egypt J Remote Sens Space Sci 5:41–62

Bühler B, Breitkreuz C, Pfänder JA, Hofmann M, Becker S, Linnemann U, Eliwa HA (2014) New insights into the accretion of the Arabian-Nubian Shield: Depositional setting, composition and geochronology of a Mid-Cryogenian arc succession (North Eastern Desert, Egypt). Precambr Res 243:149–167

Condon DJ, Schmitz MD (2013) One hundred years of isotope geochronology, and counting. Element 9:15–17

Dixon TH (1979) The evolution of continental crust in the Late Precambrian Egyptian Shield. PhD thesis, University of Cairo, San Diego, 231 pp

Dixon TH (1981) Age and chemical characteristics of some pre-Pan-African rocks in the Egyptian Shield. Precambr Res 14:119–133

Drury S (1993) Image interpretation in geology, 2nd edn. Chapman and Hall, London

Ebead B, Ahmed M, Niu Z, Huang N (2017) Quantifying the anthropogenic impact on groundwater resources of North China using Gravity Recovery and Climate Experiment data and land surface models. J Appl Remote Sens 11(2):26029. https://doi.org/10.1117/1.JRS.11.026029

EI-Baz F (1998) Groundwater concentration beneath sand fields in the Western Desert of Egypt: indications by Radar images from space, Egypt. J Remote Sens Space Sci 1:1–24

Eid MM, Abdel Rahman MT, Zaghloul EA, Elbeih SF (2006) Integrated remote sensing and GIS for proposing groundwater recharge locations: case study at West El-Nubariya Canal, Egypt. Egypt J Remote Sens Space Sci 9:113–134

El-Askary H, Kafatos M, Hegazy MN (2000) Environmental monitoring of dust storms over the Nile Delta, Egypt using Modis satellite data. Egypt J Remote Sens Space Sci 3:113–112

El Gaby S, List FK, Tehrani R (1990) The basement complex of the Eastern Desert and Sinai. In: Said R (ed) Geology of Egypt. A. A. Balkerna Publishers, Netherlands, pp 175–184

El Gammal EM, Salem SM, Greiling RO (2013) Applications of geomorphology, tectonics, geology and geophysical interpretation of, East Kom Ombo depression, Egypt, using Landsat images. Egypt J Remote Sens Space Sci 16(2):171–187

El Nahry A (2003) Integration of radar and thematic mapper imagery data for natural resources assessment at BirSafsaf Area, South Western Egypt. Egypt J Remote Sens Space Sci 6:61–72

El-Rahman YA, Anbar MA, Li X-H, Li J, Ling X-X, Wu L-G, Masoud AE (2019) The evolution of the Arabian-Nubian Shield and survival of its zircon U-Pb-Hf-O isotopic signature: a tale from the Um had conglomerate, central Eastern Desert, Egypt. Precambr Res 320:46–62

El Ramly MF (1972) A new Geological map for the basement rocks in the Eastern and South Western Deserts of Egypt, scale1:1 000 000. Ann Geol Surv Egypt 2:1–18

El Ramly MF, Akaad MK (1960) The basement complex in the Central Eastern Desert of Egypt between lat. 24°30′ and 25°40′. Geol. Surv. Egypt. Paper No. 8, 35 pp

El Shazly EM, Hashad AH, Sayyah TA, Bassyuni FA (1973) Geochronology of Abu Swayel area, South Eastern Desert. Egypt J Geol 17:1–18

El-Akkad S, Dardir AA (1965) Geological map of the coastal strip between Qena-Safaga road and Wadi Sharm El-Bahari, scale 1:100 000. Geol Surv Egypt

El-Asmar HM, Hereher ME, El Kafrawy SB (2013) Surface area change detection of the Burullus Lagoon, North of the Nile Delta, Egypt, using water indices: a remote sensing approach. Egypt J Remote Sens Space Sci 16(1)119–123

El-Baz F, Yehia MA, Ramadan T, Kusky T (2001) Notes on the structural and neotectonic evolution of El-Faiyum depression, Egypt: relationships to earthquake hazards. Egypt J Remote Sens Space Sci 3:1–12

El-beih SF, Belal AB, Zaghloul EA (2011) Hazards mitigation and natural resources evaluation around Sohag—Safaga highway, Eastern Desert, Egypt Egypt. J Remote Sens Space Sci 14(1):15–28

El-Diasty ME (1969) The aeromagnetic map of the Delta area and the interpretation of the geophysical data. MS thesis, Alexandria University, Faculty of Science, 89 pp

Elewa H (2003) Water resources and geomorphological characteristics of Tushka area, West of Lake Nasser, Egypt. Egypt J Remote Sens Space Sci 6:73–90

Elewa H (2006) Determining priority areas for the sustainable development of Wadi El Assiuti, Eastern Desert, Egypt, using hydrogeological, remote sensing and GIS criteria. Egypt J Remote Sens Space Sci 9:79–92

Elewa H, Fathy RG, Zaghloul EA (2000) Groundwater potential of the Southern Part of Wadi Qena basin, Eastern Desert of Egypt, using remote sensing techniques. Egypt J Remote Sens Space Sci 3:135–152

El-Fouly A, Salam H (2003) Mapping potential areas for gold and base metals mineralization In South Eastern Desert, Egypt: an approach by using remote sensing and GIS. Egypt J Remote Sens Space Sci 6:25–46

El-Gamily H (2001) Assessment of environmental deterioration due to landuse land cover changes in El Guna area using multi-dates Landsat data, Red Sea coast, Egypt. Egypt J Remote Sens Space Sci 4:45–60

El-Gammal EA (1999a) Impact of geomorphological features on sustainable development of the South Eastern Desert, Egypt, using Landsat images. Egypt J Remote Sens Space Sci 2:57–68

El-Gammal EA (1999a) Geomorphology of southern Sinai, Egypt, using Landsat images. Egypt. J Remote Sens Space Sci 2:35–56

El-Gammal EA (2003) Morphogenetic study of Wadi Araba Eastern Desert Egypt, using Landsat images. Egypt J Remote Sensing & Space Sciences 6:107–124

El-Gammal EA(2005) Impact of surface processes and lithology on drainage network functions and sustainable development in South Sinai, Egypt, using Landsat images. Egypt J Remote Sens Space Sci 8:65–82

El-Gammal EA, El Gammal AE (2010) Hazard impact and genetic development of sand dunes west of Samalut, Egypt. Egypt J Remote Sens Space Sci 13:137–151

El-Gammal EA, Morsy MA, El Rakaiby M (1998) Impact of geomorphological hazards on El-Mokattam area, Egypt. Egypt. J Remote Sensing & Space Sciences 1:281–297

El-Gammal EA, Kolkila AE, EL-Gammal AA (2002) Use of Landsat images for study the environmental impact of Lead–Zinc mines in Eastern Desert, Egypt. Egypt J Remote Sens Space Sci 5:109–126
El-Gammal EA, Salem SM, El Gammal AEA (2010) Change detection studies on the world's biggest artificial lake (Lake Nasser, Egypt). Egypt J Remote Sens Space Sci 13(2):89–99
El-Hakim BM (1978) Study of aeromagnetic survey for Qena-Safaga (A. R. E.): Alexandria University thesis for M.S. Lockwood Survey Co., Ltd., 1968, Airborne magnetometer, scintillation counter, deal frequency electromagnetic survey of a part of the Aswan Region, UAR: Report prepared for United Nations Development Program, 178 pp
El-Hattab MM (2015) Change detection and restoration alternatives for the Egyptian Lake Maryut. Egypt J Remote Sens Space Sci 8(1):9–16
El-Hattab MM (2016).Applying post classification change detection technique to monitor an Egyptian coastal zone (Abu Qir Bay). Egypt J Remote Sens Space Sci 19(1):23–36
Eliwa HA, Breitkreuz C, Murata M, Khalaf IM, Bühler B, Itaya T, Takahashi T, Hirahara Y, Miyazaki T, Kimura J-I, Shibata T, Koshi Y, Kato Y, Ozawa H, Daas MA, El Gameel Kh (2014) SIMS zircon U-Pb and mica K–Ar geochronology, and Sr–Nd isotope geochemistry of the north Eastern Desert, Egypt. Gondwana Res 25, 1570–1598
El-Nagdy AS, Abdelsalam MG (2006) Hyper-spectral analysis of the advanced spaceborne thermal emission and reflection radiometer (Aster) data: an example from the Neoproterozoic Um Nar Banded Iron Formation (BIF), Egypt. Egypt J Remote Sens Space Sci 9:53–78
El-Rakaiby ML, Ammar FA (2005) Spectral reflectance characteristics of igneous Rocks in the visible region of the electromagnetic spectrum. Egypt J Remote Sens Space Sci 8:83–108
El-Sadek MA, Mousa MI (2010a) Integration of space images and airborne radiometric data for discrimination of radioactive mineralizations at Wadi Araba area, North Eastern Desert, Egypt. Egypt J Remote Sens Space Sci 13(1):11–19
El-Sadek MA, Mousa MI (2010b) Integration of space images and airborne radiometric data for discrimination of radioactive mineralizations at Wadi Araba area, North Eastern Desert, Egypt. Egypt J Remote Sens Space Sci 13(1):11–19
Embabi N, Moawad MB (2014) A semi-automated approach for mapping geomorphology of El Bardawil Lake, Northern Sinai, Egypt, using integrated remote sensing and GIS techniques. Egypt J Remote Sens Space Sci 17(1):41–60
Eyal M, Be'eri-Shlevin Y, Eyal Y, Whitehouse MJ, Litvinovsky B (2014) Three successive Proterozoic island arcs in the Northern Arabian-Nubian Shield: evidence from SIMS U-Pb dating of zircon. Gondwana Res 25:338–357
Faid AM, Hinz EA, Montgomery H (2003) The effect of land cover/land use on groundwater resources in Southern Egypt (Luxor Area): remote sensing and field studies. Egypt J Remote Sens Space Sci 6:91–106
Fallatah OA, Ahmed M, Save H, Akanda AS (2017) Quantifying temporal variations in water resources of a vulnerable middle eastern transboundary aquifer system. Hydrol Process 31(23):4081–4091. https://doi.org/10.1002/hyp.11285
Finger F, Helmy HM (1998) Composition and total-Pb model ages of monazite from high-grade paragneisses in the Abu Swayel area, Southern Eastern Desert. Mineral Petrol 62:269–289
Gabr S, El Bastawesy M (2015) Estimating the flash flood quantitative parameters affecting the oil-fields infrastructures in Ras Sudr, Sinai, Egypt, during the January 2010 event. Egypt J Remote Sens Space Sci 18(2):137–149
Gabr S, Ghulam A, Kusky T (2010) Detecting areas of high potential gold mineralization using ASTER data. Ore Geol Rev 38(1–2):59–69
Gabr S, Hassan S, Sadek M (2015) Prospecting for new gold-bearing alteration zones at El-Hoteib area, South Eastern Desert, Egypt using remote sensing data analyses. Ore Geol Rev 71:1–13
Gad S, Kusky T (2007) ASTER spectral ratioing for lithological mapping in the Arabian-Nubian shield, the Neoproterozoic Wadi Kid area, Sinai. Egypt Gondwana Res 11:326–335
Geological Atlas of Sinai (2004) EGSMA, NARSS, UNESCO project of the capacity building of the Egyptian Geological Survey and Mining Authority (EGSMA) and the National Authority of Remote Sensing and Space Sciences (NARSS) In Cooperation with UNDP and UNESCO, EGY/97/011 (executed by UNESCO Cairo Office)
Geological Atlas of the South Western Desert (2005) EGSMA, NARSS, UNESCO project of the Capacity building of the Egyptian Geological Survey and Mining Authority (EGSMA) and the National Authority of Remote Sensing and Space Sciences (NARSS) In Cooperation with UNDP and UNESCO, EGY/97/011 (executed by UNESCO Cairo Office)
Gheith MA (1959) Program of measurements in the Middle East, South Eastern Desert of Egypt. USA EC. Contract At (30-1)-1381. Ann Progr Rept Dept Geol Geophys, M.I.T 7:195–206
Ghobrial MG, Lotfi M (1967) The geology of Gabal Gattar and Dokhan areas. Geol Surv Egypt. Paper No. 40, 26 pp
Habib ME (1968) Geology of the area around Gabal Abu Furad, Eastern Desert, near Safaga. MSc thesis, Assiut University
Habib ME (1970) Preliminary geological map of the area SW of Safaga, scale 1:100 000 (Lat. 26°20′–26°40′ and Long. 33°30′–33°50′E). Geol Surv Egypt Map accompanying internal report No. 39/70
Hamdan A (1999) Potential of flash flooding of the drainage basins of the East Cairo area and risk evaluation. Egypt J Remote Sens Space Sci 2:15–33
Hamdan A, El-Etr H (1998) Quantitative photolineation analysis and some geomorphic and structural aspects of the GilfKebir and Abu Ras Plateaus, South Western Desert. Egypt J Remote Sens Space Sci 1:101–144
Hamdan A, Abdel Rahman NM, Cherif OH (2004) Geomorphology of the area South East of Aswan, Egypt. Egypt J Remote Sens Space Sci 7:53–70
Harrell JA, Brown VM (1992) The world's oldest surviving geological map: the 1150 B.C. Turin Papyrus Egypt. J Geol 100:3–18
Hashad AH (1980) Present status of geochronological data on the Egyptian basement complex. In: A.M.S. A1-Shanti (ed) Evolution and mineralization of the Arabian-Nubian Shield. App Geol Jeddah Bull 3. Pergamon Press, 3:31–46
Hashad AH, Sayyah TA, El Kholy SB, Yousef A (1972) Rb/Sr isotopic age determination of some basement Egyptian granites. Egypt J Geol 16:269–281
Hassan OA (2000) Salient Geo-environmental parameters of Ras Malaab—Abu Zenima area, Gulf of Suez, Egypt, with an emphasis on flash flood potential and mitigative measures. Egypt J Remote Sens Space Sci 3:37–58
Hassan OA, El-Leithy BM (2004) Monitoring of sand dunes migration for developing mitigative measures in El-kharga depression, Western Desert, Egypt. Egypt. J Remote Sens Space Sci 7:71–88
Hassan MA, Hashad AH (1990) Precambrian of Egypt. In: Said R (ed) Geology of Egypt. A.A. Balkerna Publishers, Netherlands, pp 201–245
Hassan S, Sadek M (2017) Geological mapping and spectral based classification of basement rocks using remote sensing data analysis: the Korbiai-Gerf nappe complex, South Eastern Desert. Egypt J Afr Earth Sci 134:404–418
Hassan OA, Zaghloul EA, El-Etr HA (2005a) Pattern and hazard of sand dunes encroachment with their environmental impacts in the New Valley, Egypt. Egypt J Remote Sens Space Sci 8:51–64
Hassan OA, Ahmed MH, Arafat SM (2005b) Environmental land-cover/land-use change detection in the coastal zone of the Gulf of Aqaba, Egypt, using multi-temporal Landsat imagery. Egypt J Remote Sens Space Sci 8:21–38

Hassan S, Abdeen MM, Yehia MA, El-Kazzaz YA, Attia GM (2008) Characterization of Oligocene sands and gravels, Wadi Ghoweiba, Northwest Gulf of Suez, Egypt, using spectral signature and principal component analysis of Terra Aster images. Egypt J Remote Sens Space Sci 11:73–92

Hassan S, El Kazzaz Y, Taha M, Mohammad A (2017) Late Neoproterozoic basement rocks of Meatiq area, Central Eastern Desert, Egypt: petrography and remote sensing characterizations. J Afr Earth Sc 131:14–31

Hegazi M (2001) Land cover change detection in Regged Terrain using multi-temporal satellite imageries and elevation data. Egypt J Remote Sens Space Sci 4:3–18

Hegazy MN, Effat HA (2010) Monitoring some environmental impacts of oil industry on coastal zone using different remotely sensed data. Egypt J Remote Sens Space Sci 13(1):63–74

Hegazy AM, Khawasik SM, Seleem TA (1999) Using gis for locating the optimal sites of industrial granite at Wadi sanad area, South Sinai. Egypt J Remote Sens Space Sci

Higazy RA, Ramly MF (1960) Potassium-Argon ages of some rocks from the Eastern Desert of Egypt. Geol Survey Egypt, Cairo, paper 7, 18 pp

Hulme M, Doherty R, Ngara T, New M, Lister D (2001) African climate change: 1900–2100. Clim Res 17(2 SPECIAL 8):145–168 https://doi.org/10.3354/cr017145

Hume WF (1934) Geology of Egypt, vol II, part I. Cairo Government Press

Hume WF (1935) Geology of Egypt, vol II, part II. Bulaq Government Press

Hume WF (1937). Geology of Egypt, vol II, part III. Cairo Government Press

Huntec Ltd. (1969) Report of re-interpretation of aeromagnetic data, Red Block area, Aswan Region. Report prepared for United Nations Development Program, UAR, 37 pp

Hunting Geology and Geophysics (1967) Assessment of the mineral potentials of the Aswan Region, U.A.R. 138 pp

Issawi B (1979) Advancing Egyptian Geology. Episodes 1979(3):25–29

Jakob S, Buhler B, Gloaguen R, Breitkreuz G, Eliwa H, El Gameel K (2015) Remote sensing base improvement of the geological map of the Neoproterozoic Ras Gharib segment in the Eastern Desert (NE-Egypt) using texture features. J Afr Earth Sci 111:138–147

Kamel M, Youssef M, Hassan M, Bagash F (2016) Utilization of ETM + Landsat data in geologic mapping of wadiGhadir-Gabal Zabara area, Central Eastern Desert, Egypt. Egypt J Remote Sens Space Sci 19(2):343–360

Karmakar S, Schenk V (2015) Neoarchean UHT metamorphism and Paleoproterozoic UHT reworking at Uweinat in the East Sahara Ghost Craton, SW Egypt: evidence from petrology and texturally controlled in situ monazite dating. J Petrol 56:1703–1742

Kato H, Kimura R, Elbeih SF, Iwasaki E, Zaghloul EA (2012) Land use change and crop rotation analysis of a government well district in Rashda village—Dakhla Oasis, Egypt based on satellite data Egypt. J Remote Sens Space Sci 15(2):185–195

Khalil AE, El-Desoky H, Salem SM (2017) Contribution of remote sensing techniques to the recognition of titanite occurrences at Gabal El-Degheimi area, Central Eastern Desert, Egypt. Egypt J Remote Sens Space Sci 20(1):41–50

Khameis A, Nigm A (2010) Magnetic interpretation of north Gebel El Shallul area, central Eastern Desert, Egypt. Egypt J Remote Sens Space Sci 13(1):53–62

Krogh TE (1973) A low contamination method for hydrothermal decomposition of zircon and extraction of U and Pb for isotopic age determinations. Geochim Cosmochim Acta 37:485–494

Kröner A, Eyal M, Eyal Y (1990) Early Pan-African evolution of the basement around Elat, Israel, and the Sinai Peninsula revealed by single-zircon evaporation dating, and implications for crustal accretion rates. Geology 18:545–548

Kröner A, Todt W, Hussein IM, Mansour IM, Mansour M, Rashwan AA (1992) Dating of late Proterozoic ophiolites in Egypt and the Sudan using the single grain zircon evaporation technique. Precambr Res 59:15–32

Kröner A, Krüger J, Rashwan AAA (1994) Age and tectonic setting of granitoid gneisses in the Eastern Desert of Egypt and South-West Sinai. Geol Rundsch 83:502–513

Kusky T, El-Baz F (1999) Structural and tectonic evolution of the Sinai Peninsula, using Landsat Data: implications for ground water exploration. Egypt J Remote Sens Space Sci 1:69–100

Li X-H, El-Rahman YA, Anbar MA, Li J, Ling X-X, Wu L-G, Masoud AE (2018) Old continental crust underlying juvenile oceanic arc: evidence from northern Arabian-Nubian shield, Egypt Geophys Res Lett 45(7):3001–3008

Lundmark AM, Andresen A, Hassan MA, Augland LE, Abu El-Rus MA, Boghdady GY (2012) Repeated magmatic pulses in the East African Orogen of Central Eastern Desert, Egypt: an old idea supported by new evidence. Gondwana Res 22:227–237

Madani A (1995) The basaltic rocks of the northern part of Bahariya Oasis, Western Desert, Egypt. MSc thesis, Faculty of Science, Cairo University

Madani A (2001) Geological studies and remote sensing applications on Wadi Natash volcanic, Eastern Desert, Egypt. PhD thesis, Faculty of Science, Cairo University

Madani A (2004) Utilization of Landsat-7 ETM+ and SIR-C/X SAR data for mapping the basaltic rocks and their alteration products, Gebel Qatrani–6th October District, North Western Desert, Egypt. Egypt J Remote Sens Space Sci 7:99–108

Madani A (2012) Discrimination of Jurassic volcanicity in strike-slip basin, Jabal Al Maqtal area, South Eastern Desert, Egypt, using ASTER and field data JAKU. Earth Sci 23(2):1–18

Madani A (2015) Spectroscopy of olivine basalts using FieldSpec and ASTER data: a case study from Wadi Natash volcanic field, South Eastern Desert, Egypt. J Earth Syst Sci 124(7):1475–1486

Madani A, Emam A (2011) SWIR ASTER band ratios for lithological mapping and mineral exploration: a case study from El Hudi area, South Eastern Desert, Egypt. Arab J Geosci 4:45–52

Madani A, Abdel Rahman EM, Fawzy KM, Emam A (2003) Mapping of the hydrothermal alteration zones at Haimur gold mine area, South Eastern Desert, Egypt using remote sensing techniques. Egypt. J Remote Sens Space Sci 6:47–60

Madani A, Gamal M, AAshour (2005) Utilization of Landsat-7 ETM + imagery and seismic hazard assessment for the urban planning: a case study from El-Amal New City, East Cairo, Egypt. Egypt J Remote Sens Space Sci 8:3–20

Masoud A, Koike K (2017) Applicability of computer-aided comprehensive tool (LINDA: LINeament Detection and Analysis) and shaded digital elevation model for characterizing and interpreting morphotectonic features from lineaments, J Comp Geosci 106:89–100

Mattinson JM (2013) Revolution and evolution: 100 years of U-Pb geochronology. Element 8:53–57

Moawad MB (2013) Detection of the submerged topography along the Egyptian Red Sea Coast using bathymetry and GIS-based analysis. Egypt J Remote Sens Space Sci 16(1):35–52

Moghazi A-KM, Ali KA, Wilde SA, Zhou Q, Andersen T, Andresen A, Abu El-Enen MM, Stern RJ (2012) Geochemistry, geochronology, and Sr-Nd isotopes of the late Neoproterozoic Wadi Kid volcano-sedimentary rocks, Southern Sinai, Egypt: implications for tectonic setting and crustal evolution. Lithos 154:147–165

Mohamed A, Sultan M, Ahmed M, Yan E, Ahmed E (2016) Aquifer recharge, depletion, and connectivity: inferences from GRACE, land surface models, geochemical, and geophysical data. GSA Bull 1–13. https://doi.org/10.1130/b31460.1

Mostafa A (1977) Photogeology of the central Western Desert, Egypt (with special emphasis on Siwa and Bahariya Oases). MSc thesis, Ain Shams University

Naim GM (1996) The Egyptian geological survey: a century of achievements. In: Proceedin gs of the geological survey of Egypt center conference, pp 33–59
Nasr A, Darwish A (1998) Change detection of the western part of El-Fayoum area and El-Rayan Lakes using multitemporal TM data. J Remote Sens Space Sci 1:195–206
Nasr A, EI-Leithy BM, F I Khalaf (2003) Environmental modeling using remote sensing and Gis for sustainable ecotourism development of Ras Banas area, Red Sea coast, Egypt. Egypt J Remote Sens Space Sci 6:3–12
Nemchin AA, Horstwood MSA, Whitehouse MJ (2013) High-spatial-resolution geochronology. Element 9:31–37
Noweir AM (1965) Geology of Umm Hombos-Umm El Saneyat area, Eastern Desert. MSc thesis, Assiut University
Noweir AM (1968) Geology of Hammamat–Um Seleimat district, Eastern Desert. PhD thesis, Assiut University
O'Connor EO (1996) One hundred years of geological partnership: British-Egyptian geoscientific collaboration, 1896–1996. British Geol Surv, Keyworth
Ramadan TM (2002) Exploration For Gold-Bearing Listwaenites at Um Khasila District, Central Eastern Desert, Egypt, using Orbital Remote Sensing. Egypt J Remote Sens Space Sci 5:63–76
Ramadan T (2003) Exploration for gold-bearing listwaenites at um Khasila district, Central Eastern desert, Egypt, using orbital remote sensing. Egypt J Remote Sens Space Sci
Ramadan TM, El-Lithy BS (2005) Application of airborne radiometric data and Landsat-TM imagery in exploration for the mineralization in El-Qasia-Um-Naggat granites, Central Eastern Desert, Egypt. Egypt J Remote Sens Space Sci 8:143–160
Ramadan T, Kontny A (2004) Mineralogical and structural characterization of alteration zones detected by orbital remote sensing at Shalatein District, SE Desert. Egypt J Afr Earth Sci 40(1–2): 89–99
Ramadan TM, El-Leithy BS, Nada A, Hassaan MM (1999) Application of Remote Sensing and GIS In Prospecting for Radioactive Materials In the Central Eastern Desert of Egypt. Egypt J Remote Sens Space Sci 2:141–151
Ramadan T, Sadek MF, Abu El Leil I, Salem SM (2005) Um El Touyur El Fuqani gold mineralization, South Eastern Desert, Egypt. Ann Geol Surv Egypt V.XXVIII, 263–281
Ramadan TM, Ibrahim TM, Said AD, Baiumi M (2013) Application of remote sensing in exploration for uranium mineralization in Gabal El Sela area, South Eastern Desert, Egypt. Egypt J Afr Earth Sci 16 (2):199–210
Rasmy M, Gad A, Abdelsalam H, Siwailam M (2010) A dynamic simulation model of desertification in Egypt. Egypt J Remote Sens Space Sci 13(2):101–111
Richter A, Schandelmeier H (1990) Precambrian basement inliers of Western Desert: geology, petrology and structural evolution. In: Said R (ed) Geology of Egypt. A.A. Balkerna Publishers, Netherlands, pp 185–200
RIGW/IWACO (1988) Hydrogeological mapping of Egypt; scale 1:2 000 000. EMGR Project
Robinson C (1998) Potential and applications of radar data in Egypt. Egypt J Remote Sens & Space Sci 1:25–56
Rodell M, Houser PR, Jambor U, Gottschalck J, Mitchell K, Meng C-J, Arsenault K, Cosgrove B, Radakovich J, Bosilovich M et al (2004) The global land data assimilation system. Bull Am Meteor Soc 85 (3):381–394. https://doi.org/10.1175/BAMS-85-3-381
Sabet AH (1961) Geology and mineral deposits of Gebel El Sibai area, Red Sea hills, Egypt.U.A.R. PhD thesis, Leidan State University, Netherlands
Sadek MF (2004) Discrimination of basement rocks and alteration zones in Shalatein area, South Eastern Egypt, using Landsat TM imagery data. Egypt J Remote Sens Space Sci 7:89–98
Sadek MF (2005) Geology and spectral characterization of the basement rocks at Gabal Gerf Area, South Eastern Egypt. Egypt J Remote Sens Space Sci 8:109–128
Sadek MF, Khyamy AA (2003) Contribution to the geology of basement rocks in the south Western Desert of Egypt. Egypt J Remote Sens Space Sci 6:125–146
Said R (1962) The geology of Egypt. Elsevier, Amsterdam
Said R (1990a) The geology of Egypt. Balkema, Rotterdam
Said R (1990b) History of geologic research. In: Said R (ed) The Geol of Egypt. Balkema, Rotterdam
Salem (2007) Using remote sensing techniques in the geology and gold mineralization at al Faw—Eqat area, South Eastern Desert, Egypt. Egypt J Remote Sens Space Sci 10:137–150
Salem SM, El Gammal EA (2015) Iron ore prospection East Aswan, Egypt using remote sensing techniques. Egypt J Remote Sens Space Sci 16(2):195–206
Salem, SM Soliman, NM (2015) Exploration of gold at the east end of Wadi Allaqi, South Eastern Desert, Egypt, using remote sensing techniques. Arab J Geosci 8(11):9271–9282
Salem A, Khalil AE, Ramadan TM (2012) Geology, geochemistry and tectonic setting of Pan-African serpentinites of Um Salim-Um Salatit area central Eastern Desert, Egypt. Egypt J Remote Sens Space Sci 15(2):171–184
Salem SM, El Gammal EA, Soliman NM (2013) Morphostructural record of iron deposits in paleosols, cretaceous Nubia Sandstone of Lake Naser basin, Egypt, Western Desert, Egypt. Egypt J Remote Sens Space Sci 16(1):71–82
Salem SM, El Sharkawi M, El-Alfy Z, Soliman NM, Ahmed SE (2016) Exploration of gold occurrences in alteration at Dungash district, South Eastern Desert of Egypt using ASTER data and geochemical analyses. J Afr Earth Sci 117:389–400
Samuel MD, Be'eri-Shlevin Y, Azer MK, Whitehouse MJ, Moussa HE (2011) Provenance of conglomerate clasts from the volcani-sedimentary sequence at Wadi Rutig in Southern Sinai, Egypt as revealed by SIMS U-Pb dating of zircon. Gondwana Res 20:450–464
Save H, Bettadpur S, Tapley BD (2012) Reducing errors in the GRACE gravity solutions using regularization. J Geodesy 86(9):695–711. https://doi.org/10.1007/S00190-012-0548-5
Save H, Bettadpur S, Tapley B (2016) High resolution CSR GRACE RL05 mascons. J Geophys Res
Schandelmeier H, Richter A, Harms U (1987) Proterozoic deformation of the East Saharan Craton in Southeast Libya, South Egypt and North Sudan. Tectonophysics 140:233–246
Schluter T (2008) Geological Atlas of Africa, with notes on stratigraphy, tectonics, economic geology, geohazards, geosites and geoscientific education of each country, 2nd edn. Springer, Berlin, Germany
Sharib ASA, Maurice AE, El-Rahman YMA, Sanislav LV, Schulz B, Bakhit BR (2019) Neoproterozoic arc sedimentation, metamorphism and collision: evidence from the northern tip of the Arabian-Nubian Shield and implication for the terminal collision between East and West Gondwana. Gondwana Res 66:13–42
Shazly AG (1966) Geology of the area South of Gebel Meatiq, Eastern Desert. MSc thesis, Assiut University
Shazly AG (1971) Geology of Abu Ziran area, Eastern Desert. PhD thesis, Assiut University
Shimron AE (1980) Proterozoic island arc volcanism and sedimentation in Sinai. Precambr Res 12:437–458
Shokr M (2011) Potential directions for applications of satellite earth observations data in Egypt. Egypt J Remote Sens Space Sci 14 (1):1–13
Shokr M, ElBaroudy A, Fullen M, El-Beshbeshy T, Ramadan A, Abd EL, Halim A, Guerra A, Jorge M (2016) Spatial distribution of heavy metals in the middle Nile Delta of Egypt. Int Soil Water Conserv Res 4(4):293–303

Stern RJ (1979a) Late Precambrian ensimatic volcanism in the Central Eastern Desert of Egypt. PhD thesis, University of California, San Diego, 210 pp

Stern RJ, Hedge CE (1985) Geochronologic and isotopic constraints on late Precambrian crustal evolution in the Eastern Desert of Egypt. Am J Sci 285:97–127

Stern RJ, Kröner A, Rashwan AA (1991) A Late Precambrian (~710 Ma) high volcanicity rift in the Souther Eastern Desert of Egypt. Geol Rundsch 80(1):155–170

Stern RJ, Ali KA, Liégeois J-P, Johnson P, Wiescek F, Kattan F (2010) Distribution and significance of pre-Neoproterozoic zircons in juvenile Neoproterozoic igneous rocks of the Arabian-Nubian Shield. Am J Sci 310:791–811

Sultan M, Arvidson RE (1986) Mapping of serpentinites in the Eastern Desert of Egypt by using Landsat thematic mapper data. J Geol 14:995–999

Sultan M, Tucker RD, El Alfy Z, Attia R (1994) U-Pb (zircon) ages for the gneissic terrane west of the Nile, Southern Egypt. Geol Rundsch 83:514–522

Sultan M, Ahmed M, Sturchio N, Yan YE, Milewski A, Becker R, Wahr J, Chouinard K (2013) Assessment of the vulnerabilities of the Nubian sandstone fossil aquifer, North Africa. In: Pielke RA, Hossain F (eds) Climate vulnerability: understanding and addressing threats to essential resources. Elsevier Inc., Academic Press, pp 311–333

Tapley BD, Bettadpur S, Ries JC, Thompson PF, Watkins MM (2004a) GRACE measurements of mass variability in the Earth system. Science 305(5683):503–505 https://doi.org/10.1126/science.1099192

Tapley BD, Bettadpur S, Watkins M, Reigber C (2004b) The gravity recovery and climate experiment: mission overview and early results. Geophys Res Lett 31(9):1–4. https://doi.org/10.1029/2004GL019920

Tawadros E (2012) History of geology in Egypt. Earth Sci Hist 31 (1):50–75

Thorweihe U, Heinl M (2002) Groundwater resources of the Nubian aquifer system NE-Africa. Observatoire du Sahara et du Sahel, Paris, 23

Wahr J, Molenaar M, Bryan F (1998) Time variability of the Earth's gravity field: hydrological and oceanic effects and their possible detection using GRACE. J Geophys Res 103(B12):30205–30229. https://doi.org/10.1029/98JB02844

Wasfi (2007) Statistical analysis of surface structural lineaments and radioactivity of the alkaline rocks province, South Eastern Desert, Egypt. Egypt J Remote Sens Space Sci 10:119–136

Wasfi SA, Iliase EL, Mousa MI (2009) Discriminations of younger granitic masses at gabal Qattar area, North eastern desert, egypt, using remote sensing techniques. Egypt J Remote Sens Space Sci 12

Wilde SA, Youssef K (2000) Significance of SHRIMP U-Pb dating of the imperial prophyryabd associated Dokhan volcanics, Gabal Dokhan, northern Eastern Desert, Egypt. J Afr Earth Sci 3:403–413

Wilde SA, Youssef K (2002) A re-evaluation of the origin and setting of the late Precambrian Hammamat Group based on SHRIMP-U-Pb dating of detrital zircons from Gebel Umm Tawat, North Eastern Desert. Egypt J Geol Soc Lond 159:595–604

Williams HS (1893) The making of the geological time-scale. J Geol 1:180–197

Wouters B, Bonin JA, Chambers DP, Riva REM, Sasgen I, Wahr J (2014) GRACE, time-varying gravity, Earth system dynamics and climate change. Rep Prog Phys 116801. https://doi.org/10.1088/0034-4885/77/11/116801

Yehia MA, Cherif OH, Al-Leithy BM, Ramadan TM, Hassaan MM (1998) A note on the prospecting for radioactive material and black sands in the Central Eastern Desert of Egypt. J Remote Sens Space Sci 1:413–420

Yehia MA, Ashmawy MH, El-Etr HA (1999a) Flash flooding threat to the Red Sea coastal towns of Ras Gharib and Hurghada Egypt. J Remote Sens Space Sci 2:87–106

Yehia MA, Hassan OA, Hamdan AH, Ashmawy MH, Hermas EA, El-Etr HA (1999a) Geo-environmental study of the Sohag-Lake Nasser Stretch, Egypt. Egypt J Remote Sens Space Sci 2:1–14

Yehia MA, Ashmawy MH, EI-Etr HA, Abdel Monsef H, EI Shamy IZ, Hermas EA, Higazy MN, Hassan SM (1999b) Flash flooding threat to the Red Sea coastal towns of Safaga, Quseir and Marsa El Alam. Egypt J Remote Sens Space Sci 2:69–86

Yehia MA, Hamdan AH, Ashmawy MH, Hassan OA, Hermas EA, El-Etr HA (2000) Geo-environmental study of the central part of the western Desert, Egypt. Egypt J Remote Sens Space Sci 3:25–36

Yousif MS, Shedid GA (1999) Remote sensing signature of some selected basement rock units from the Central Eastern Desert of Egypt. Egypt J Remote Sens Space Sci 2:171–189

Youssef AM, El Baroudy AA (2008) Using remote sensing and Gis techniques for assessment the environmental changes in the area surrounding Suez Canal, Egypt. Egypt J Remote Sens & Space Sci 11:43–56

Youssef AM, Zaghloul EA, Moussa MF, Mahdi AM (2009) Lithological mapping using Landsat enhanced thematic mapper in the Central Eastern Desert, Egypt: case study: area surround Gabal Al Haded. Egypt J Remote Sens Space Sci 12:87–100

Youssif MS, Aly KG (1998) Use of space imagery and aeroradiometry for the delineation of some geologic aspects of the Wadi El-Allaqi area, South Eastern Desert, Egypt. Egypt J Remote Sens Space Sci 1:233–263

Youssif MS, El-Assy AT (1998) Quantitative study of the fracture pattern of the area around the western part of Wadi El-Kharit, South Eastern Desert, Egypt. J Remote Sens Space Sci 1:145–163

Zaghloul EA, Hassan SM, Bahy El-Dein AM, Elbeih SF (2013) Detection of ancient irrigation canals of Deir El-Hagar playa, Dakhla Oasis, Egypt, using Egyptsat-1 data. Egypt J Remote Sens Space Sci 16(2):153–161

Zoheir BA, Creaser RA, Lehmann B (2015) Re–Os geochronology of gold mineralization in the Fawakhir area, Eastern Desert. Egypt Int Geol Rev 57:1418–1432

Precambrian Basement Complex of Egypt

2

Mohammed Z. El-Bialy

Contents

M. Z. El-Bialy (✉)
Geology Department, Faculty of Science, Port Said University,
Port Said, 42522, Egypt
e-mail: mzbialy@yahoo.com

Z. Hamimi et al. (eds.), *The Geology of Egypt*, Regional Geology Reviews,
https://doi.org/10.1007/978-3-030-15265-9_2

Abstract

Surface exposure of the Egyptian Precambrian basement complex covers ca. 100 000 km^2. Outcrops of the basement rocks extend over extensive areas in southern Sinai, the Eastern Desert south of latitude 29°N and the Western Desert south of latitude 24°N between the Nile valley at Aswan in the east to Gabal Uweinat, near the Egyptian-Libyan-Sudanese border, in the west. Apart from the rejuvenated Paleoproterozoic to Archean rocks of Gabal Uweinat-Gabal Kamil inlier (charnockitic, TTG and gabbro-diorite gneisses), belonging to the Saharan Metacraton, the Precambrian basement complex of Egypt, in Sinai and the Eastern Desert, belongs to the juvenile Neoproterozoic (550–900 Ma) crust of the Arabian-Nubian Shield (ANS). The Uweinat-Kamil inlier rocks have been reworked by several events at 3.1–2.55 Ga ago and 2.0 Ga ago. In the southern Western Desert, midway between Aswan and Uweinat-Kamil inliers, there exist three Precambrian inliers; Gabal-Umm-Shagir, Gabal-El-Asr and Bir Safsaf that contain Neoproterozoic Pan-African granitoids and remnants of the pre-Pan-African crust, probably representing the eastern transition between the Paleoproterozoic to Archean terranes of the Sahara Metacraton (i.e. Uweinat-Kamil inlier) and the juvenile Neoproterozoic terranes of the Arabian-Nubian Shield. The evolution of the ANS juvenile crust took place during most of the Neoproterozoic time (900–600 Ma) throughout three major stages, namely: (1) accretion stage (~870–670 Ma) including the formation of island arc volcano-sedimentary sequences and plutonic rocks and amalgamation of these accreted terrains onto east Gondwana continental block; (2) collision (~650–640 Ma) between the juvenile accreted ANS crust with the older pre-Neoproterozoic continental margin of West Gondwana (Saharan Metacraton) along arc-arc and arc–continental sutures, which prompt crustal thickening, and (3) post-collisional stage (630–550 Ma), which commenced after termination of collision, and encompassed extensional collapse of the thickened lithosphere, inducing extension and thinning of the ANS crust, which lasted until about 550 Ma. The main lithologies of the Egyptian part of the ANS include low- to medium-grade metamorphosed volcanosedimentary successions, dismembered ophiolite sequences, metagabbro–diorite complexes and calc-alkaline granitoids formed during the island arc (i.e. subduction) stage. Also, a substantial volume of undeformed late-collisional more evolved calc-alkaline granitoids were emplaced, subsequent to crustal thickening phase and preceding the onset of crustal extensional phase (630–590 Ma). A major period of mafic to felsic, high-K, Dokhan volcanics (610–580 Ma) and high-silica A-type granites and rhyolites (610–560 Ma) is associated with escape tectonics and crustal extension in the post-collisional stage.

2.1 Introduction

Basement, basement rocks and basement complex, are terms that are commonly applied to igneous and metamorphic rocks, overlain unconformably by sedimentary strata. In this sense, basement rocks in Egypt are often considered Precambrian in age, although in some cases much younger unconformities exist (Paleozoic, Mesozoic, or even Cenozoic). Precambrian to early Cambrian surface exposure of the basement rocks in Egypt cover ca. 100 000 km^2 but around 90% of the basement is buried beneath the Phanerozoic sedimentary cover (Fig. 2.1).

The outcrops of the Egyptian basement rocks extend over extensive areas in southern Sinai and the Eastern Desert south of latitude 29°N. In the Western Desert south of latitude 24°N, exposures of basement rocks are scattered outcrops in an area extending from the Nile valley at Aswan in the east to Gabal Uweinat, near the Egyptian-Libyan-Sudanese border, in the west (Fig. 2.1).

Regarding the age of the Egyptian basement rocks, pioneer workers noted that in Sinai, they are unconformably overlain by Carboniferous rocks (e.g. Barron 1907; Ball 1916), which imply that they are undeniably Pre-Carboniferous in age. Further north in the Dead Sea region in Jordan, Blankenhorn (1910) found that granites, diorites etc., comparable to those outcropping in Sinai are overlain unconformably by sedimentary strata containing Middle Cambrian trilobite remains. Omara (1972) identified an Early Cambrian (based on archaeocyathids) sandstone section unconformably resting on the pink granites of Gabal Abu Durba, SW Sinai. These findings showed that the Egyptian basement rocks are fundamentally Precambrian in age. This was verified later through isotopic age dating.

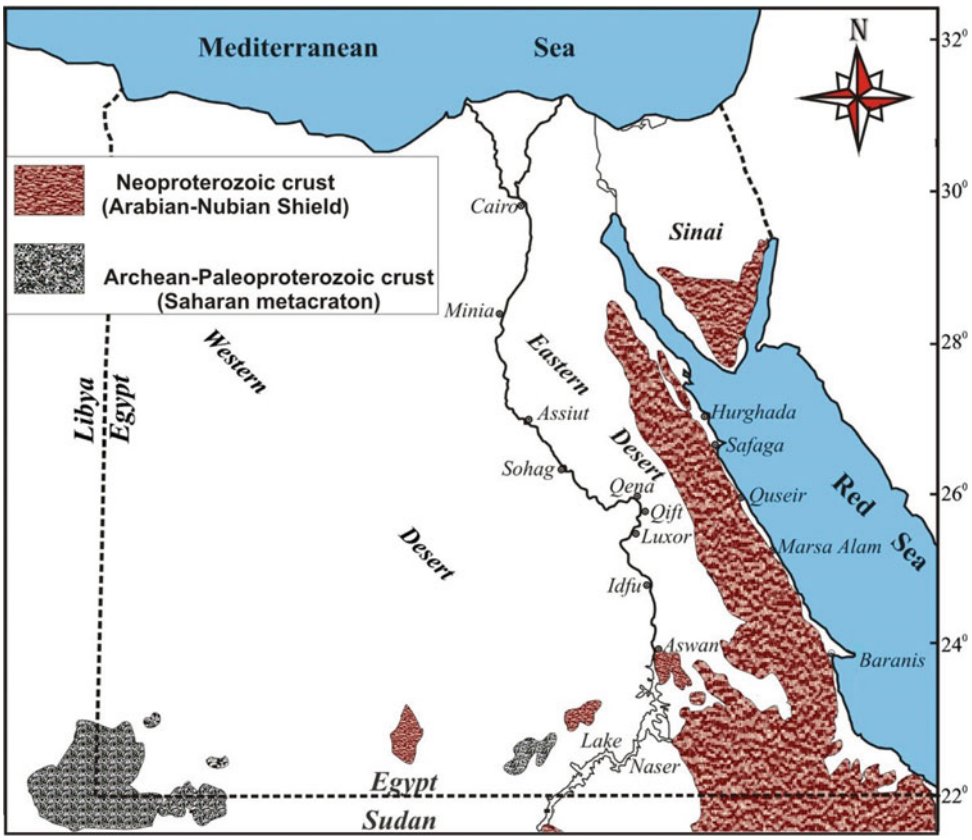

Fig. 2.1 Distribution of the Precambrian basement rocks in Egypt

2.2 Nature and Evolution of the Basement Crust

With the exception of the rejuvenated Paleoproterozoic to Archean (2600–3200 Ma; Klerkx 1980; Harris et al. 1984; Sultan et al. 1994; Bea et al. 2011a; Garfunkel 2015) rocks of Gabal Uweinat-Gabal Kamil inlier (charnockitic, TTG and gabbro-diorite gneisses) (Bea et al. 2011a; Karmakar and Schenk 2015) belonging to the Saharan Metacraton (Abdelsalam et al. 2002), the Precambrian basement complex of Egypt, in Sinai and the Eastern Desert, belongs to the juvenile Neoproterozoic (550–900 Ma) crust of the Arabian-Nubian Shield (ANS) (Stern 1994, 2002).

The Uweinat-Kamil inlier exposes Archean rocks (Rb–Sr isochron ages around 2.6 Ga; Klerkx 1980) and SHRIMP U-Pb ages peaking at 3.0 and 3.2 Ga (Bea et al. 2011a), that have been reworked by several events 3.1–2.55 Ga ago and 2.0 Ga ago (Bea et al. 2011a; Garfunkel 2015). In the southern Egyptian Western Desert, midway between Aswan and Uweinat-Kamil inliers, there exist three Precambrian inliers; Gabal-Umm-Shagir, Gabal-El-Asr and Bir Safsaf, which crop out irregularly underneath Nubian Paleozoic to Mesozoic sediments and are partially covered by the mobile sands of the Sahara. These inliers contain Neoproterozoic Pan-African granitoids and remnants of the pre-Pan-African crust, probably representing the eastern transition between the Paleoproterozoic to Archean terranes of the Sahara Metacraton (e.i. Uweinat-Kamil inlier) and the juvenile Neoproterozoic terranes of the Arabian-Nubian Shield (Harris et al. 1984; Sultan et al. 1994; Abdelsalam et al. 2002; Stern 2002; Bea et al. 2011b).

The ANS is considered the best-preserved and largest exposed tract of Neoproterozoic juvenile crust on Earth (Stern 1994, 2002; Hargrove et al. 2006; Be'eri-Shlevin et al. 2009a, 2012). The evolution of the ANS juvenile crust has occurred during most of the Neoproterozoic time (900–600 Ma; Stern 1994). The tectonomagmatic evolution of the ANS took place throughout three major stages, namely: (1) accretion stage (~870–670 Ma) including the formation of island arc volcano-sedimentary sequences and plutonic rocks and amalgamation of these accreted terrains onto east Gondwana continental block (Kröner et al. 1994; Stern 1994, 2002; Abdelsalam and Stern 1996; Johnson et al. 2011; Nasiri Benzenjani et al. 2014); (2) Collision (~650–640 Ma) between the juvenile accreted ANS crust with the older pre-Neoproterozoic continental margin of West Gondwana (Saharan Metacraton) along arc-arc and arc–continental sutures, which instigate immense crustal thickening (Stern 1994, 2002; Abdelsalam and Stern 1996; Hargrove et al. 2006; Stoeser and Frost 2006; Avigad and Gvirtzman 2009; Basta et al. 2017), and (3) post-collisional

stage (630–550 Ma), which commenced after termination of collision, and encompassed extensional collapse of the thickened lithosphere, inducing extension and thinning of the ANS crust, which lasted until about 550 Ma (Avigad et al. 2005; El-Bialy 2010; Eyal et al. 2010; Be'eri-Shlevin et al. 2011; Johnson et al. 2011; Cox et al. 2012; Fritz et al. 2013; Eliwa et al. 2014). The basement rocks of Sinai and the Eastern Desert along with those of NE Sudan, Somalia and Ethiopia constitute the Nubian Shield that had formed a contiguous part with the Arabian Shield (western Arabia) before the opening of the Red Sea less than 30 Ma ago.

The principal lithologies of the ANS comprise low- to medium-grade metamorphosed volcanosedimentary successions, dismembered ophiolite sequences, metagabbro–diorite complexes and calc-alkaline granitoids formed during the island arc (i.e. subduction) stage. Also, a substantial volume of undeformed late-collisional more evolved calc-alkaline granitoids were emplaced, subsequent to crustal thickening phase and preceding the onset of crustal extensional phase (630–590 Ma). A major period of mafic to felsic, high-K, Dokhan volcanics (610–580 Ma) and A-type granites (610–560 Ma) is associated with escape tectonics and crustal extension in the post-collisional stage.

In addition to their contrasting lithology and difference in absolute age, the Egyptian basement rocks east and west of the River Nile (i.e. ANS versus eastern Saharan Metacraton) are likewise different isotopically. Rocks of the west of the Nile have significantly older depleted mantle model ages (T_{DM}), whereas to the east young model ages are present (Harris et al. 1984; Sultan et al. 1994).

2.3 Review of the Egyptian Basement Classifications

The opinions, concepts and theories on the geological evolution of the Egyptian basement rocks have changed fundamentally since the early decades of the last century and several classifications have been adopted since then. Some of these classifications are based on the obsolete geosynclinal hypothesis (e.g. Hume 1934; Akaad and El Ramly 1960; El Shazly 1964; El Ramly 1972; Akaad and Noweir 1969, 1980). Somewhat recently, from the 1980s, classifications hinge on the plate tectonic theory are proposed to elucidate the crustal evolution of the Egyptian basement rocks (e.g. Ries et al. 1983; El Gaby et al. 1984, 1988; Bentor 1985).

2.3.1 Classification of Hume (1934)

Among the early and pioneer endeavors towards the classification of the Egyptian Precambrian basement rocks is that adopted by the Egyptian Survey geologist W.F. Hume who published several articles on these rocks since the beginning of the preceding century but of special interest is his 1934 volume II on the "Geology of Egypt" in which he gave a classification of these rocks.

Hume (1934) proposed an evolutionary model, a classification of the basement rocks and an age assessment mainly based on the concept of depth zones within the earth's crust. He arranged these rocks into ten units belonging to four chronologic divisions or cycles (Late Precambrian or Gattarian, Eparchaean, Metarchaean, Protarchaean) and assigned names to each (Table 2.1).

2.3.2 Classification of Schürmann (1953, 1966)

Schürmann (1953) adopted Hume's classification with some amendments and the simple addition of a new division/unit namely "Shaitian"/"Shaitian plutonism" after a granite well developed in Wadi Shait in the south Eastern Desert. He considered it as representative of a period of plutonic activity prior to the deposition of the Eparchaean sediments. Nevertheless, it was subsequently revealed that the Shaitian granite is sheared Older Granite and should not be regard as

Table 2.1 Hume (1934) classification of the Egyptian basement rocks (simplified)

Division	Unit
Late Precambrian (Gattarian)	1. Dolerite, felsite and porphyry dykes
	2. Acid granites (red pegmatitic and pink porphyritic)
	3. Biotite and hornblende granites and granodiorites
	4. Diorites and metagabbros
	5. Dacites, andesites and porphyrites invading the Eparchean sediments
Eparchaean	6. Slates, siliceous schists and conglomerates with fragments of earlier granites and andesites
	7. Schists
Metarchaean	8. Barramiya serpentinites and associated rocks
Protarchaean	9. Fundamental gneisses and crystalline schists of Egypt and Sudan

a new unit (Akaad and El Ramly 1963). Few years later in his book entitled "The Precambrian along the Gulf of Suez and the northern part of the Red Sea", Schürmann (1966) divided the Gattarian into Upper Gattarian and Lower Gattarian with the Hammamat series in between.

2.3.3 Classification of El Ramly and Akaad (1960)

El Ramly and Akaad (1960) set up a chronological sequence for the basement rocks appeared in a geological map scale 1:250 000 which they compiled for the central part of the Eastern Desert between lat. 24°30′ and 25°40′N. They arranged the basement rock units, appearing on this map, in a chronological order starting with the youngest as follows:

11. Alkaline volcanic rocks (Youngest).

10. Post granite dykes.
9. The younger granites.
8. The Igla Formation.
7. Old volcanics (Dokhan type).
6. The grey granites.
5. Epidiorite-diorite complex.
4. Serpentinites and related rocks.
3. Metavolcanic series.
2. Schist-mudstone-greywacke series.
1. The Migif-Hafafit gneisses (Oldest).

This classification has been followed in a way or another by most later workers, and in the geologic map of Egypt published by the Egyptian Geological Survey in 1981. Both authors then developed a model for the evolution of these rocks through successive episodes of sedimentation, plutonism, volcanism and tectonism based on a geosynclinal orogenic cycle (Akaad and El Ramly 1960).

2.3.4 Classification of El Shazly (1964)

In his paper entitled; "Precambrian and other rocks of magmatic affiliation in Egypt", El Shazly (1964) categorized the basement rocks of Egypt into three major stages of geological-structural evolution (geosynclinal main orogenic, post geosynclinal and late orogenic and foreland volcanic stages) which were further subdivided according to auxiliary criteria such as structural development, petrography, etc. An outline of his classification with the modifications he made in 1977 and 1980 is given in Table 2.2.

Table 2.2 El Shazly's (1964) classification of the Egyptian basement

Geological-structural stage	Representatives and Type locality
III. Foreland volcanic stage (Upper Cretaceous-Tertiary)	
III.2. Basic volcanics	Gabal Qatrani basalts
III.1. Alkaline volcanism with subordinate plutonism	Wadi Natash volcanics and Abu Khruq ring complex
Major unconformity	
II. Post geosynclinal and late orogenic stage (Late Precambrian passing through Early Paleozoic)	
II.4. Post orogenic volcanics	Dyke swarms of G. Kadabora
II.3. Post orogenic plutonites and associated pegmatites and aplites	Aswan granites and granodiorites
II.2. Late orogenic plutonites and associated pegmatites, aplites, felsites and quartz veins	G. Gattar, G. Um Shilman, Sheikh Salem granites
II.1. Post geosynclinal sediments and associated volcanics	Hammamat series of Wadi Hammamat
Major unconformity	
I. Geosynclinal main orogenic stage (Precambrian)	
I.5. Emerging geosynclinal volcanics	Gabal Dokhan volcanics
I.4. Synorogenic plutonites	Wadi Gerf granodiorite
I.3. Early orogenic plutonites	Wadi Shait plagiogranite
I.2. Main geosynclinal volcanics	Barramiya association (essentially serpentinites)
I.1. Geosynclinal sediments	Abu Swayel schist series

2.3.5 Classification of Akaad and Noweir (1969, 1980)

The comprehensive mapping of an area covering 5500 km^2, between latitudes 25°35′ and 26°30′N, crossed by the Qift–Quseir road by Akaad and Noweir and their co-workers which started in 1963, revealed a complete succession of the rock units forming the Egyptian basement. They arranged all the metasedimentary and metavolcanic rock units into Groups, Formations and Members and assigned them formal names in accordance with the Code of Stratigraphic Nomenclature. Akaad and Noweir (1969, 1980), also elucidated the evolution of the basement complex according to the geosynclinal theory.

However, this classification is unpopular and has not followed by most workers owing to the difficulty of correlation beyond the mapped area, and the impossibility of fitting their model with the plate tectonic models dominating the geologic literature at that time.

2.3.6 El Ramly's (1972) Classification

El Ramly (1972) compiled a geological map for the basement rocks in the Eastern and Western Deserts of Egypt (scale 1:1 000 000) and introduced a new classification for the Egyptian basement complex. A new younger gabbroic unit is included in this classification. The rock units forming the basement complex of Egypt in his classification are nearly the same as those appearing on the Geological map of the country scale 1:2 000 000 published by the Geological Survey of Egypt in 1981.

2.3.7 The Classification of Ries et al. (1983)

Ries et al. (1983) carried out a detailed structural traverse across the basement rocks of the Eastern Desert at latitude 26°N and between longitudes 33°30′, 34°30′E. This traverse showed that these rocks consist, apart from intrusions, of four broadly recumbent tectonic units. From base to top, these units are as follows:

1. A lowest unit, of arkosic metasediments of continental shelf facies, is exposed in the Meatiq dome.
2. This unit is overlain by allochthonous ophiolitic melange containing complete and dismembered ophiolitic masses in a matrix of deep-oceanic graphitic pelites and turbidites. The melange is locally overlain by calc-alkaline volcanics (the Dokhan Volcanics).
3. Unconformable on the ophiolitic melange and the Dokhan Volcanics is a locally strongly deformed molasse facies series (The Hammamat Group).
4. Late tectonic granites preceded, and locally post-date, the molasse-facies sediments (Older and Younger granites, respectively). Still later, diapiric peralkaline riebeckite granites locally up-domed the recumbent structures.

These authors emphasized that this succession is a structural rather than a stratigraphic one, since many of the contacts between the different rock units are tectonic.

2.3.8 Classification of Bentor (1985)

Bentor (1985) proposed four phases model for the evolution of the Precambrian basement rocks of the Arabian-Nubian Shield, including those exposed in Sinai and the Eastern Desert.

Phase I (the oceanic assemblage) is characterized by the emplacement of oceanic tholeiites, mainly pillow basalts, and their intrusive equivalents. These rocks overlie ophiolite sequences which are tectonically transported and often strongly disrupted. Phase II (the island arc stage; ~950–650 Ma ago) is represented by a thick sequence of mainly intermediate volcanics, their intrusive equivalents, and associated largely volcanogenic-clastic sediments. Most rocks of this sequence are metamorphosed, usually in the greenschist facies. The plutonic rocks of this phase are generally referred to as the "Older Granitoids" and include (quartz-) diorites, tonalites, (quartz-) monzonites, and trondhjemites. During the batholithic Phase III (~640–590 Ma ago), the ANS is cratonized. Magmatism is at its maximum, magmas are calc-alkaline and silica-rich. Plutons of Phase III span the entire spectrum from gabbro and diorite to granite, but the felsic types are definitely the largest volume present. Unlike those of phase II, gabbros of this phase are virtually unmetamorphosed. The volcanic rocks of the batholithic Phase III (Dokhan Volcanics) are largely correlative with the contemporaneous plutonics. The alkaline Phase IV (~590–550 Ma ago) is characterized by the dominance of alkaline to peralkaline high-level granites and their extrusive equivalents; alkali-feldspar rhyolites, comendites, and pantellerites. These rocks were emplaced during the anorogenic stage of the ANS evolution.

Table 2.3 shows the correlation of the four evolutionary phases of Bentor with the Precambrian rock units in the Eastern Desert according to the classification of El Ramly (1972), Akaad and Noweir (1969, 1980) and Ries et al. (1983).

Table 2.3 The Precambrian successions of Egypt according to El Ramly (1972), Akaad and Noweir (1969, 1980) and Ries et al. (1983). Correlated with the four evolutionary stages of the Arabian-Nubian Shield of Bentor (1985)

Bentor (1985)	El Ramly (1972)	Akaad and Noweir (1969, 1980)	Ries et al. (1983)
Alkaline phase IV (~590–550 Ma ago)	Alkali granites	Alkali granites	Alkali granites
Calc-alkaline Batholithic phase III (~640–590 Ma ago)	Younger granites	Younger granites	Younger granites (615–570 my)
	Gabbros (Fresh)		
	Post-Hammamat Felsites	Post-Hammamat Felsites	
		Qash volcanics	
	Hammamat Group	Hammamat Group	Hammamat Group
	Dokhan volcanics	Dokhan volcanics	Calc-alkaline volcanics (639–602 my) (including Dokhan volcanics)
Phase II (the island arc stage) ~950–650 Ma ago	Syntectonic-late tectonic granites, granodiorites and diorites	Older granites	Syntectonic-late tectonic granodiorites, tonalites, quartz diorites (987–700 my)
	Metagabbro-diorite complex	Rubshi Group	Eastern Desert
	Serpentinites		
Ovelap between phases I and II	Geosynclinal Shadli metavolcanic Group	Abu Ziran Group	Ophiolite melange
Phase I (the oceanic assemblage)	Geosynclinal metasediments		
		Abu Fannani schists	
	Gneisses and migmatites	Meatiq Group	Meatiq Group

2.3.9 The Classification of El Gaby et al. (1988, 1990)

El Gaby et al. (1988) identified three main groups of rock units within the Egyptian basement according to their space and time relationships:

I. Pre-Pan-African rocks: These are Archaean to early Proterozoic granites, gneisses and schists and their mylonitized and remobilized equivalents cropping out at Gabal Uweinat in the southwestern corner of Egypt. In a later work, the same authors (El Gaby et al. 1990) included other medium- to high-grade schist and gneiss outcrops in the Eastern Desert and Sinai to this old continental crust rocks (e.g. Gabal Meatiq, Hafafit area, Wadi Feiran).
II. Pan-African rock association: This association dominates the basement complex of the Eastern Desert and Sinai. These are formed in two successive stages namely:

    II-1. The ophiolites and island arc stage association: Ophiolites and rocks pertaining to an island arc constitute a highly deformed sequence of low-grade, regionally metamorphosed serpentinites, gabbros, volcanics and volcaniclastics.

    II-2. The cordilleran stage association: This stage is characterized by the prevalence of granite among plutonic rocks, and rhyodacite and rhyolite among volcanic rocks, a feature that prefigures the participation of continental crust in magma generation or modification. The lithology of magmatic and sedimentary rocks documents the end of the oceanic island-arc phase and the passage into the continental-margin Cordilleran stage.

III. Phanerozoic alkaline rocks: including alkaline A-type granite bodies and also volcanics (e.g. Katherina Volcanics in Sinai, and Wadi Natash volcanics in the Eastern Desert).

2.3.10 The Classification of Ragab and El Alfy (1996)

Ragab and El Alfy (1996) introduced an arc- arc collision plate tectonic model for the crustal evolution of the central Eastern Desert. They identified eleven petrotectonic assemblages, namely:

1. Ophiolitic mélange (e.g. Rubshi and Fawakhir ophiolites).

Table 2.4 The chronological sequence of the Precambrian basement rock units in Egypt, adopted in this chapter

Geologic province	Age	Rock unit
Arabian Nubian Shield	Neoproterozoic	Katherina A-type volcanics
		Post-collisional Younger granites
		Post-collisional layered and gabbro intrusions
		Post Hammamat Felsites.
		Hammamat Group
		Dokhan volcanics
		Island arc older granites
		Metagabbro-diorite complex
		Alaskan-type mafic-ultramafic complexes
		Metasediments (volcaniclastic wackes, BIF and diamictite)
		Island-arc metavolcanics
		Ophiolitic sequences
		Infrastructural gneissic complexes
Saharan Metacraton	Archean-Paleoproterozoic	Metacratonic Gniesses of Uweinat-Kamil inlier

2. The gneiss dome and associated schists (e.g. Meatiq gneiss dome).
3. Arc metavolcanics and associated pyroclastics.
4. Volcanogene metasediments.
5. Arc granitoids.
6. Foreland molasse type sediments.
7. Syncollision granites.
8. Allochthonous mélange.
9. Late collision granites.
10. Intermontane molasse-type sediments.
11. Acidic volcanics (e.g. Felsites known as Post Hammamat Felsites).

Accordingly, they recognized four stages of crustal evolution; pre-collision, ocean closure, syn- collision, late collision stages.

2.4 The Precambrian Basement Succession

In this chapter, the rock units forming the Precambrian complex of Egypt will be dealt with under the names shown in the succession given in Table 2.4. With the exception of the Archean "Metacratonic Gneisses of Uweinat-Kamil inlier" and the Neoproterzoic "Alaskan-type mafic-ultramafic complexes" and "Katherina Volcanics" units, introduced herein, the rest of rock units are somewhat comparable to those appearing on the geological map for the basement rocks in the Eastern and Western Deserts of Egypt (scale 1:1 000 000) compiled by El Ramly (1972) and the formal geological map of Egypt scale 1:2 000 000 published by the Geological Survey of Egypt in 1981.

The following sections represent a comprehensive preview on these basement rock units starting from the oldest. For the sake of convenience, the granitoid rock units will be treated together in one section in order to provide a sort of comparison between them.

2.4.1 Metacratonic Gniesses of Uweinat-Kamil Inlier

2.4.1.1 Geologic and Geochronologic Overview

Apart from the Eastern Desert and southern Sinai, Precambrian basement rocks occur also in southern Egypt where they occupy an area of some 40 000 km^2, west of the river Nile. From Lake Nasser towards the junction of the borders of Egypt, Sudan and Libya, there are four Precambrian Inliers; Gabal Umm-Shagir, Gabal El-Asr, Bir Safsaf, and Gabal Kamil–Gabal Uweinat (Fig. 2.1), cropping out intermittently underneath Nubian Mesozoic strata and are partially covered by the mobile sands of the Sahara (e.g. Richter 1986; Schandelmeier et al. 1988).

These four basement inliers were thought of being the eastern continental margin or as a minimum comprising parts of the pre-Pan-African (Archean/Early Proterozoic) Saharan Metacraton (Abdelsalam et al. 2002), hitherto known as East Saharan Craton or Nile Craton, onto which the volcanosedimentary-ophiolite and related granitoid assemblages of the Arabian-Nubian Shield were accreted in

the Neoproterozoic (Schandelmeier et al. 1988; Richter and Schandelmeier 1990).

The largest of those is the farthermost Gabal Kamil–Gabal Uweinat inlier (35 000 km^2), located at the Egypt–Sudan border near Libya, which is also evidenced to exclusively contain rocks that have yielded Rb–Sr ages around 2.6 Ga (Klerkx and Deutsch 1977; Klerkx 1980; Cahen et al. 1984), Nd T_{DM} model ages around 3.0–3.2 Ga (Harris et al. 1984), conventional U-Pb zircon and sphene ages slightly above 2.6 Ga (Sultan et al. 1994) and recently Archean ages as old as 3.3 Ga with SHRIMP U-pb zircon (Bea et al. 2011a). The oldest reported rocks in this twofold inlier, which are also the oldest rocks found so far in north east Africa, are the tonalite–trondhjemite–granite (TTG) gneisses of Gabal Kamil containing large magmatic zircons with SHRIMP U-pb crystallization ages peaking at 3.22 ± 0.04 Ga (Bea et al. 2011a).

The only other Pre-Pan-African rocks, but significantly younger, among these basement inliers were identified in Gabal El-Asr inlier with Paleoproterozoic Sm–Nd whole-rock model age 2399–1839 Ma for migmatites (Schandelmeier et al. 1988) and conventional U-Pb zircon age 1.9–2.1 Ga for an anorthosite (Sultan et al. 1994). In opposition to previous conviction, Bir Safsaf inlier is exclusively composed of late Pan-African granitoids, with Neoproterozoic U-Pb SHRIMP ages between 627 and 595 Ma (Bea et al. 2011b). In the same way, Sultan et al. (1994) indicated an emplacement age of 626 ± 4 Ma for granitic migmatite from Gabal Umm Shagir inlier using conventional U-Pb zircon dating.

The Precambrian high-grade metamorphic rocks cropping out in the eastern and southern slopes of Gabal Uweinat are quite different from those exposed in the neighboring Gabal Kamil area, hence each will be discussed separately in the following sections.

2.4.1.2 Gabal Uweinat Massif

Klerkx (1980), based on RblSr whole rock age data and petrography, categorized the Precambrian rocks of Gabal Uweinat into two metamorphic formations: (1) the granulitic 'Karkur Murr Series', at the eastern and southern slopes of Gabal Uweinat, and (b) the migmatitic 'Ayn Dua Series' which crops out along the northem and westem margin of the massive, mostly comprised of quite uniform, often strongly migmatized, granitic gneisses with minor intercalations of amphibolite and diopside-hornblende gneisses. Both series are separated by a clastic horizon, the 'II Passo mylonite' that was dated at 2637 ± 392 (K/Ar WR; Cahen et al. 1984).

In the Karkur Talh valley located in Egyptian territory, the granoblastitic gneisses of the Karkur Murr series are composed of biotite gneisses, hornblende-diopside gneisses, metaquartzites and granulitic gneisses with charnockitic affinities. They have suffered an intense low-temperature retrogression that preserved their mesoscopic structures, but almost totally transformed their original mineral assemblage to an aggregate of quartz, hematite and clays (Bea et al. 2011a). The Karkur Murr gneisses yielded a SHRIMP U-pb zircon crystallization age of around 3.0 Ga (Bea et al. 2011a). Previous determined Rb–Sr whole-rock (2.6–2.9 Ga; Klerkx and Deutsch 1977; Klerkx 1980; Cahen et al. 1984) and Sm–Nd model ages (3.0–3.2 Ga; Harris et al. 1984) of Karkur Murr charnockitic gneisses are consistent with the 3.0 Ga SHRIMP U-pb zircon c age of of Bea et al. (2011a).

The characteristic feature of the 'Ayn Dua Series' is the predominance of migmatized, granitic gneisses (i.e. diatexites, metatexites and metablastites), minor intercalations of amphibolite and diopside-hornblende gneisses. The mainstream of these migmatitic gneisses are of granodioritic composition, with a range from tonalite to granite. Geochemical characteristics of these gneisses include their low concentrations of Rb, Th, U and K, a low value of K/Rb, relative enrichment of Ba and Sr and a low BalSr ratio relative to modern upper continental crust (Richter and Schandelmeier 1990). The available geochronological data of migmatitic gniesses from Ayn Dua series are Paleoproterozoic Rb–Sr isochron ages (1836 ± 43 Ma: Klerkx and Deutsch 1977; 1784 ± 126: Cahen et al. 1984) suggesting their later formation after the Karkur Murr series gneisses.

2.4.1.3 Gabal Kamil Massif

In the eastward adjacent (∼100 km) Gabal Kamil area, Richter (1986) distinguished three metamorphic formations by their lithofacies: (1) the Granoblastite Formation, made of gneissic granulites and granoblastites with metaquartzites, serpentinites, and metagabbros, equivalent to Klerkx's Karkur Murr Series; (2) the Anatexite Formation, mostly composed of migmatites with minor marbles, calc-silicate rocks and (3) the Metasedimentary Formation, composed of paragneisses and schists. The latter is exclusive to Gabal Kamil and has no equivalent on the Libyan side. On the other hand, Sultan et al. (1994) argued that the Gabal Kamil massif comprised about 400 km^2 of gabbro-dominated layered igneous complexes, not depicted by early workers. However, the recent work of Bea et al. (2011a) does not agree with the latter authors but are consistent with Richter (1986). Instead, Bea and his coworkers found (Fig. 2.2) that the Egyptian part of the inlier nearby Gabal Kamil embraces: (i) a western variably metamorphosed metaigneous complex composed of dominant tonalite-trondhjemite-granodiorite (TTG gneisses), and subsidiary gabbro-diorite gneisses;

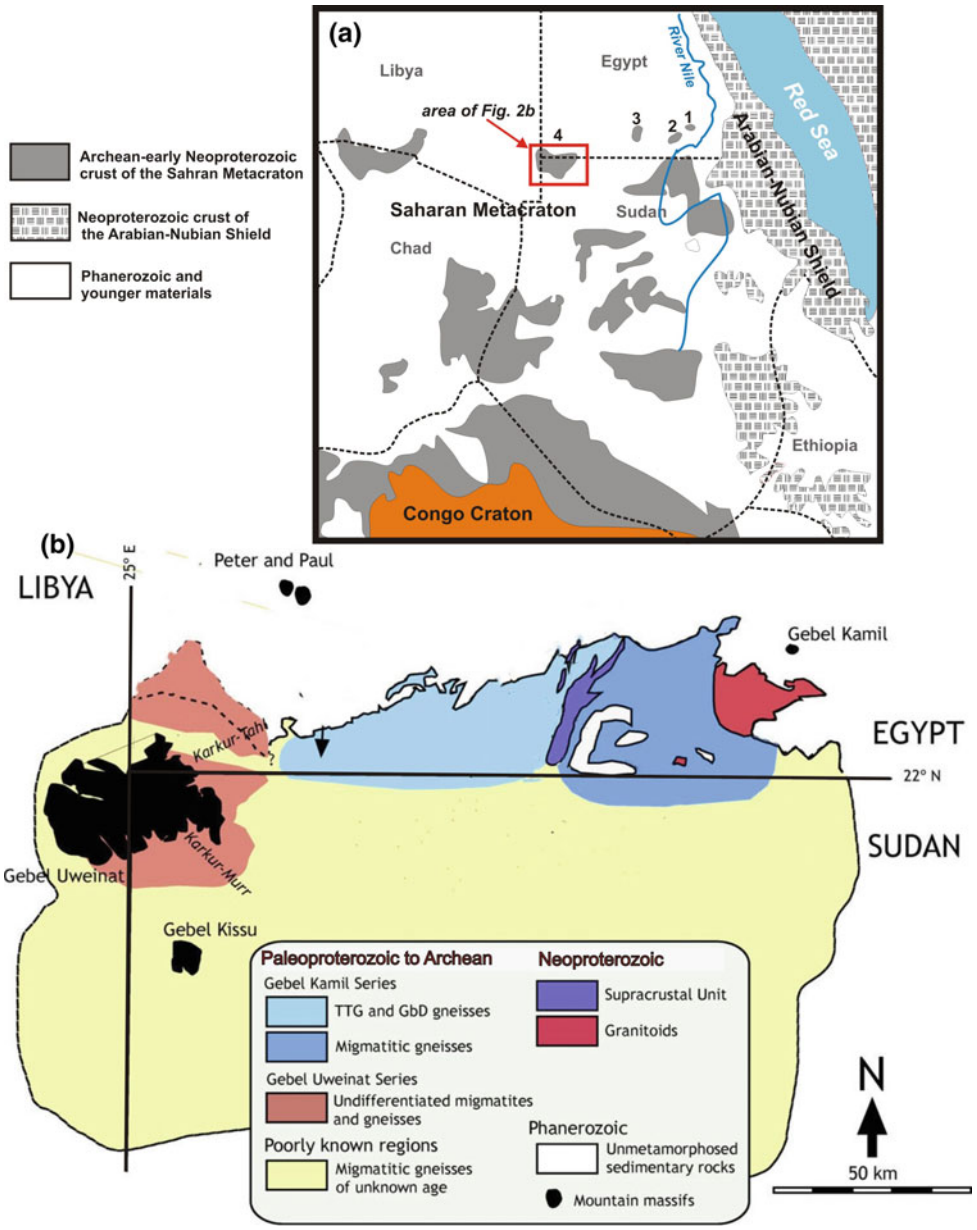

Fig. 2.2 **a** A generalized geological map of NE Africa showing the exposures of the Neoproterozoic juvenile Arabian-Nubian Shield and the dominantly Archean-Paleoproterozoic Sahran Metacraton (drawn largely after Abdelsalam et al. 2002). Numbers denote basement inliers in Egypt: 1, Gabal Umm Shagir; 2, Gabal el Asr; 3, Bir Safsaf; 4, Uweinat-Kamil. **b** Geological sketch of the Uweinat-Kamil Precambrian inlier (after, Bea et al. 2011a)

(ii) an eastern anatectic complex formed of strongly migmatized metasediments and orthogneisses with abundant Ediacaran granitoids (~590 Ma; unpublished data reported in Bea et al. 2011a), (iii) a central Neoproterozoic supracrustal unit composed of silicic sediments in addition to a banded iron formation (BIF) including ~600 Ma detrital zircons (unpublished data reported in Bea et al. op. cit.) that forms north–south lineaments and groups of small hills. These three units are, respectively, roughly equivalent to Richter's (1986) Granoblastite, Anatexite, and Metasedimentary formations, respectively.

Prior to the recent work of of Bea et al. (2011a), radiometric data for these metamorphic rocks were limited to a Rb–Sr age of 673 ± 56 Ma and a Nd model age of 2.0 Ga for a migmatite (Schandelmeier et al. 1988), as well as an ID-TIMS U-pb zircon upper intercept age of 2.7 Ga for an anorthositic gabbro (Sultan et al. 1994).

In contrast to the previous conception which affirms that the Karkur Murr gneisses, of Gabal Uweinat to be the oldest rocks in north east Africa (~3.0 Ga; see Sect. 2.4.1.2), Bea et al. (2011a) demonstrated that the metaigneous complex near Gabal Kamil (equivalent to the Granoblastite Formation of Richter 1986) contains much older rocks. They obtained a whole-rock Sm–Nd isochron age of 3.16 ± 0.16 Ga, and average Nd T_{CR} of 3.17 ± 0.04 Ga for the tonalite–trondhjemite–granite and gabbro-diorite gneisses belonging to the Gabal Kamil metaigneous complex. The oldest TTG gneisses, which are also the oldest rocks known in north east

Africa, contain large magmatic zircons with SHRIMP U-pb crystallization ages peaking at 3.22 ± 0.04 Ga, closely matching the Sm–Nd and the Nd T_{CR} model ages. These ages are interpreted to represent arc-magmas produced between 3.1 and 3.3 Ga.

2.4.2 Infrastructural Gneissic Complexes

2.4.2.1 Characteristics and Distribution

The basement complex in the Eastern Desert and the Sinai consists of a lower infrastructure that comprises medium- to high-grade gneiss-cored domes or gneiss complexes (including also amphibolites and migmatites) of variable parentage, overthrusting a suprastructural, low-grade, folded and imbricated ophiolitic nappes or mélange plus subsidiary island arc metavolcanics and volcaniclastics sequences with rare banded-iron formation (Fritz et al. 1996; Liégeois and Stern 2010; Abu El-Enen et al. 2016).

The low-grade assemblage of the suprastructural unit is widespread, while the infrastructural gneiss complexes are exposed within tectonic windows, constituting metamorphic core complexes (Fig. 2.3). For example, the Hafafit metamorphic complex (Khudeir et al. 2008; Liégeois and Stern 2010; Shalaby 2010), the Sibai Gneissic Complex (Bregar et al. 2002; Fritz et al. 2002; Fowler et al. 2007; Abd El-Wahed 2008), the Meatiq dome (Sturchio et al. 1983; Neumayr et al. 1996; Loizenbauer et al. 2001; Andresen et al. 2009, 2010; Hamdy et al. 2017), El-Shalul dome (Osman 1996; Ali et al. 2012a) and Um Had dome (Fowler et al. 2007; Andresen et al. 2010) in the Eastern Desert, and the Feiran–Solaf metamorphic complex (El-Shafei and Kusky 2003; Abu-Alam and Stuwe 2009; Abu El-Enen and Whitehouse 2013; Fowler et al. 2017) in Sinai (Fig. 2.3).

Apart from the aforementioned major gneissic complexes, small outcrops of gneisses and migmatites are recorded from several localities such as: Wadi Betan, Wadi El Hudi and Urf El Mahib (Eastern Desert), Wadi Qenaia (Sinai) and Bir Safsaf, Gabal Um Shagher (Western Desert). All in all, these infrastructural gneisses and migmatites cover limited areas of the Egyptian Basement (about 7% of the surface outcrops; M.F. El Ramly, personal communication).

In the Eastern Desert, the gneiss complexes are commonly bounded by sinistral strike-slip shear zones (Hamdy et al. 2017). The core complexes in the Eastern Desert are aligned NW–SE, roughly parallel to the general strike of the orogen and parallel to the strike of the Najd Fault System (Stern 1985; Fritz et al. 1996; Loizenbauer et al. 2001). Within in the Egyptian shield, the Hafafit metamorphic complex is the largest and is bordered by major shear zones and was exhumed between 593 and 580 Ma (Fritz et al. 2002; Abd El-Naby et al. 2008).

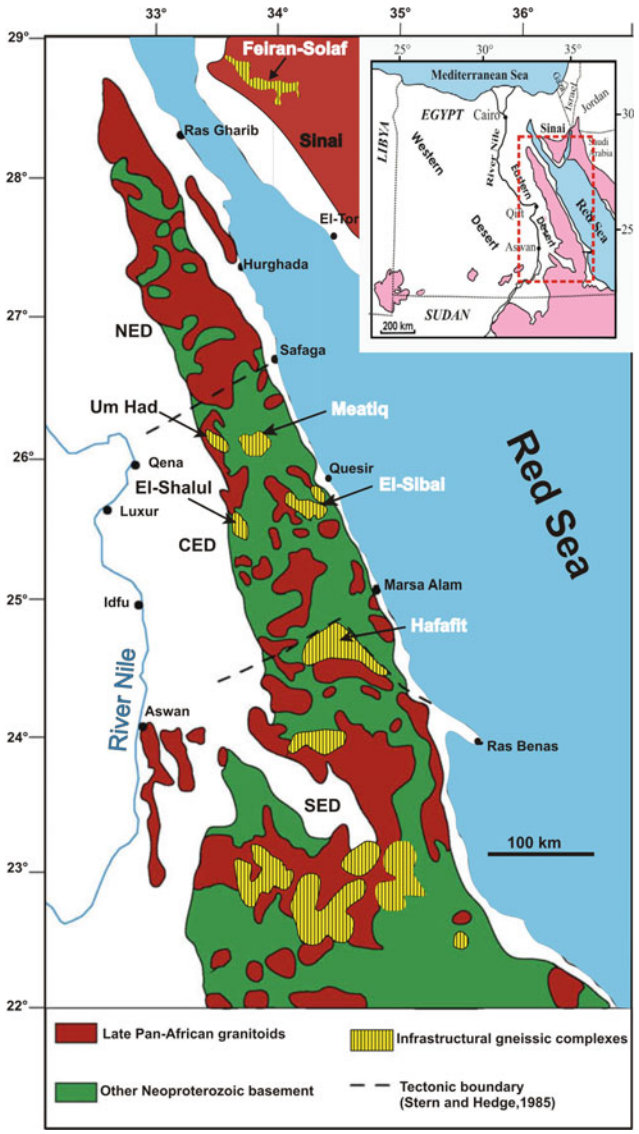

Fig. 2.3 Distribution of the major infrastructural gneiss complexes in the Eastern Desert of Egypt and Sinai (modified after Liégeois and Stern 2010). The three key complexes discussed in Sect. 2.4.2.3 as well as El-Sibai complex are further shown

A brief description of the three main occurrences of gneiss in the Eastern Desert and Sinai is given in following separate sections to show the variations in their lithology and genesis.

2.4.2.2 Age and Tectonic Evolution

Eastern Desert gneiss domes (e.g. Hafafit, Meatiq, El-Shaloul, and El-Sibai) are not pre-Neoproterozoic in age and yield radiometric ages of 800–600 Ma (Stern and Hedge 1985; Kröner et al. 1994; Loizenbauer et al. 2001; Bregar et al. 2002; Andresen et al. 2009; Liégeois and Stern 2010; Ali et al. 2012a, 2015; Augland et al. 2012; Lundmark et al. 2012; Fritz et al. 2013). On the other hand, the Sinai

metamorphic complexes are, although still of Neoproterozoic age, clearly older than the Eastern Desert crystalline basement, including these gneiss domes (Abu El-Enen et al. 2016). The gneisses and migmatites of Sinai metamorphic complexes evolved over a ca. 1004–630 Ma time period (Stern and Manton 1987; Kröner et al. 1990, 1994; Stern et al. 2010; Abu El-Enen and Whitehouse 2013; Eyal et al. 2014).

Different tectonic models have been suggested to explain the formation of the gneiss domes or complexes. The first model, by Sturchio et al. (1983), is dedicated only to Meatiq dome, in which these authors concluded that the Meatiq dome was the result of compressional tectonics and thrusting. The second model regards the gneiss domes as metamorphic core complexes and ascribes their formation and exhumation to E–W shortening coupled with NW–SE oriented crustal scale strike-slip faulting of the Najd Fault System and formation of pull-apart basins separating the gneiss domes (Fritz et al. 1996, 2002; Bregar et al. 2002; Abd El-Wahed 2008, 2010, 2014; Abd El-Wahed et al. 2016). The third model debated against the presence of core complexes in the CED and attributed the development of the gneiss domes to extensional tectonics in an environment of NW–SE complex folding and NW–SE extension (e.g. Fowler et al. 2007; Andresen et al. 2009, 2010).

2.4.2.3 Hafafit, Meatiq and Feiran-Solaf Metamorphic Complexes

Herein, a brief description of these three main occurrences of gneiss in the Eastern Desert and Sinai is given to show the variations in their lithology and genesis.

The Hafafit metamorphic complex (HMC) is an arcuate belt of orthogneisses, migmatites and other high-grade metamorphic rocks, which delineates the boundary between the CED and the SED of Egypt. It is a spectacular Precambrian structure that forms a huge doubly plunging anticline trending NW–SE direction and is traced for more than 55 km from Wadi Shait in the north to Wadi El Gemal in the south. The HMC consists of five granitoid-cored gneiss domes (dome A to dome E) (Fowler and El-Kalioubi 2002). The HMC is bordered to the north by a major, convex to the north low-angle sinistral thrust, called the Nugrus thrust, characterized by a thick mylonite shear zone. This complex is further bounded to the south by the folded Wadi El-Gemal thrust, which separates the infrastructure from the overlying Wadi El-Gemal unit (Greiling 1997). Kröner et al. (1994) reported Pb–Pb single zircon evaporation ages of 677 ± 9 and 700 ± 12 Ma for granitic gneisses from HMC that they related to subduction-related calc-alkaline magamtism during an early stage of the East African Orogen. Lundmark et al. (2012) acquired U-pb zircon ID-TIMS upper Concordia intercept ages of 630 ± 7 Ma on three zircon grains and 659 ± 5 Ma on five zircon grains and obtained an older Pb–Pb age of 680 ± 7 Ma for a single grain from a hornblende-bearing tonalitic neosome, taken from a gneiss in the core of the Hafafit dome. Abu El-Enen et al. (2016) presented U-pb data from magmatic zircons that yields protolith ages of 731 ± 3 Ma for the biotite–hornblende gneisses and 646 ± 12 Ma for the garnet–biotite gneisses from the southeastern sector of Hafafit complex.

The Meatiq Complex is a large (500 km^2) quartzofeldspathic gneiss dome surrounded by low-grade suprastructural rocks (ophiolites and island arc assemblages).The general structure of the Meatiq Dome is that of an asymmetric doubly plunging anticline with an axis trending NW–SE to NNW–SSE (Fig. 2.4). It is bounded in the east and west by two major sinistral faults (Fig. 2.4). The core of the dome consists of coarse-grained, foliated granitic to granodioritic gneisses (Um Ba'anib gneiss; Bregar et al. 2002) (Fig. 2.4). The Um Ba'anib gneiss is surrounded and overlain by a variably mylonitized suite of ortho- and paragneisses, predominantly garnet-mica schists and quartzofeldspathic-schists/gneisses, particularly in the west and south (Khudeir et al. 2008; Andresen et al. 2009; Stern 2017). These mylonites enclose large lenticular relicts of migmatites, kyanite- and cordierite-bearing gneisses and staurolite–almandine mica schists (Khudeir et al. 2008). These orthogneisses at their NE flank, enclose strongly folded migmatized amphibolite and dioritic enclaves or xenoliths, of several tens of meters in diameter, as well as mafic dykes (Neumayr et al. 1996). Sturchio et al. (1983) obtained a whole-rock Rb–Sr isochron age of 626 ± 2 Ma for five samples from Um Ba'anib gneissose granites and quartzofeldspathic mylonites. Loizenbauer et al. (2001) reported very different older age using Pb–Pb single zircon evaporation technique for Um Ba'anib granitic gneiss (779 ± 4 Ma) and a much older age of 819 ± 38 Ma for ortho-amphibolite xenolith from Meatiq dome. Recently, Andresen et al. (2009) obtained a U-pb zircon age of 663 ± 2 Ma (ID-TIMS) on a sample from Um Ba'anib granitic gneiss.

The Feiran–Solaf metamorphic complex (FSMC) is exposed over an area of about 35 km long and of variable width (5–11 km), trending NW–SE in the northwestern corner of the exposed basement in Sinai (Abu El-Enen and Whitehouse 2013) (Fig. 2.5). Structurally, it encompass a series of NW-trending anticlines overturned to the west and separated by NW-trending thrust faults (El-Shafei and Kusky 2003). The FSMC has been juxtaposed against granitoid country rock of various compositions by the sinistral NW–SE striking Najd transcurrent shear system in an oblique transpressive regime (Abu-Alam and Stüwe 2009). An undeformed elongated dioritic body trending northeast divides the FSMC into the Feiran zone and Solaf zone (El-Shafei and Kusky 2003) (Fig. 2.5).

The exposed succession of high-grade metamorphics in the Feiran and Solaf zones attains a total stratigraphic

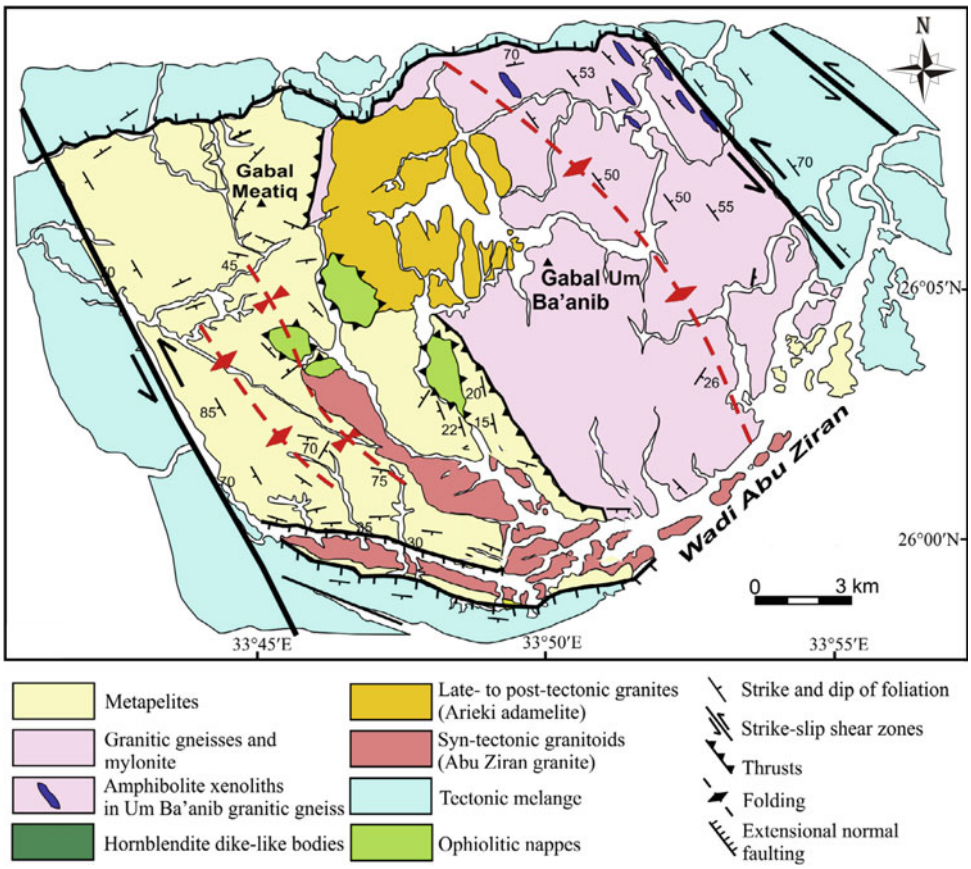

Fig. 2.4 Geological map of Meatiq Metamorphic Complex (MMC) (largely from Hamdy et al. 2017; after Fritz et al. 2002). Location of the MMC is indicated in Fig. 2.3

thickness of about 5000 m (Ahmed 1981). The FSMC includes gneisses of various parentage, calc-silicates and metapelites, which have undergone high-grade metamorphism (Abu-Alam et al. 2010; Abu El-Enen and Whitehouse 2013) and are locally migmatized, especially around the Feiran Oasis and in Wadi Tarr (Abu El-Enen et al. 2009). The predominant lithologies in the Feiran zone are hornblende-biotite gneiss and biotite gneiss, transitioning downwards into granitic and migmatitic gneiss, hosting amphibolite, hornblende gneiss, calc-silicate gneiss and copious pegmatite (Fowler et al. 2017). The major rock types in Solaf zone are gneissic diorite in the lower part, overlain by hornblende-biotite gneiss, quartzofeldspathic granulite (metapsammite), and likely silicic metapyroclastics, followed by a calc-silicate gneiss/marble sequence (Fowler et al. 2017). Detrital zircons dated at 1 Ga or older (Abu El-Enen and Whitehouse 2013) have generally been inferred as the provenance of the paragneisses (Fowler et al. 2017). Fowler et al. (2017) considered the depositional age of the sedimentary protoliths to predate 800 Ma, yet, Abu El-Enen and Whitehouse (2013) concluded that pelite deposition had taken place at 656 ± 6 Ma. An interpreted igneous origin for the biotite gneisses and biotite hornblende gneisses has also led to broad range of protolith crystallization ages from 1004 Ma to <625 Ma (Stern and Manton 1987; Kröner et al. 1994; Abu El-Enen and Whitehouse 2013). The most recent deciphered orthogneiss crystallization ages in the FSMC are in the 870–800 Ma range (Eyal et al. 2014). The age estimates for the high grade metamorphism and migmatization events fall within the 580–635 Ma time span (Eliwa et al. 2008; Abu El-Enen and Whitehouse 2013).

2.4.3 Ophiolite Sequences

2.4.3.1 Historic Perspective

Throughout the last four decades, various areas of the basement rocks of the Eastern Desert of Egypt have been studied and re-interpreted as ophiolitic rock assemblages. These ophiolite bodies were earlier mapped and interpreted as "serpentinites" (El Ramly 1972), and as the lithostratigraphic units of "Abu Ziran and El-Rubshi Groups" (Akaad and Noweir 1980). Also, components of these ophiolites were frequently merged within other stratigraphically different units such as the "geosynclinal metasediments", "geosynclinal Shadli metavolcanics Group", or "metagabbro-diorite complexes" on the geologic map of the Eastern Desert of El Ramly (1972). The ophiolites were first recorded in the Eastern Desert by Rittmann (1958) in Wadi

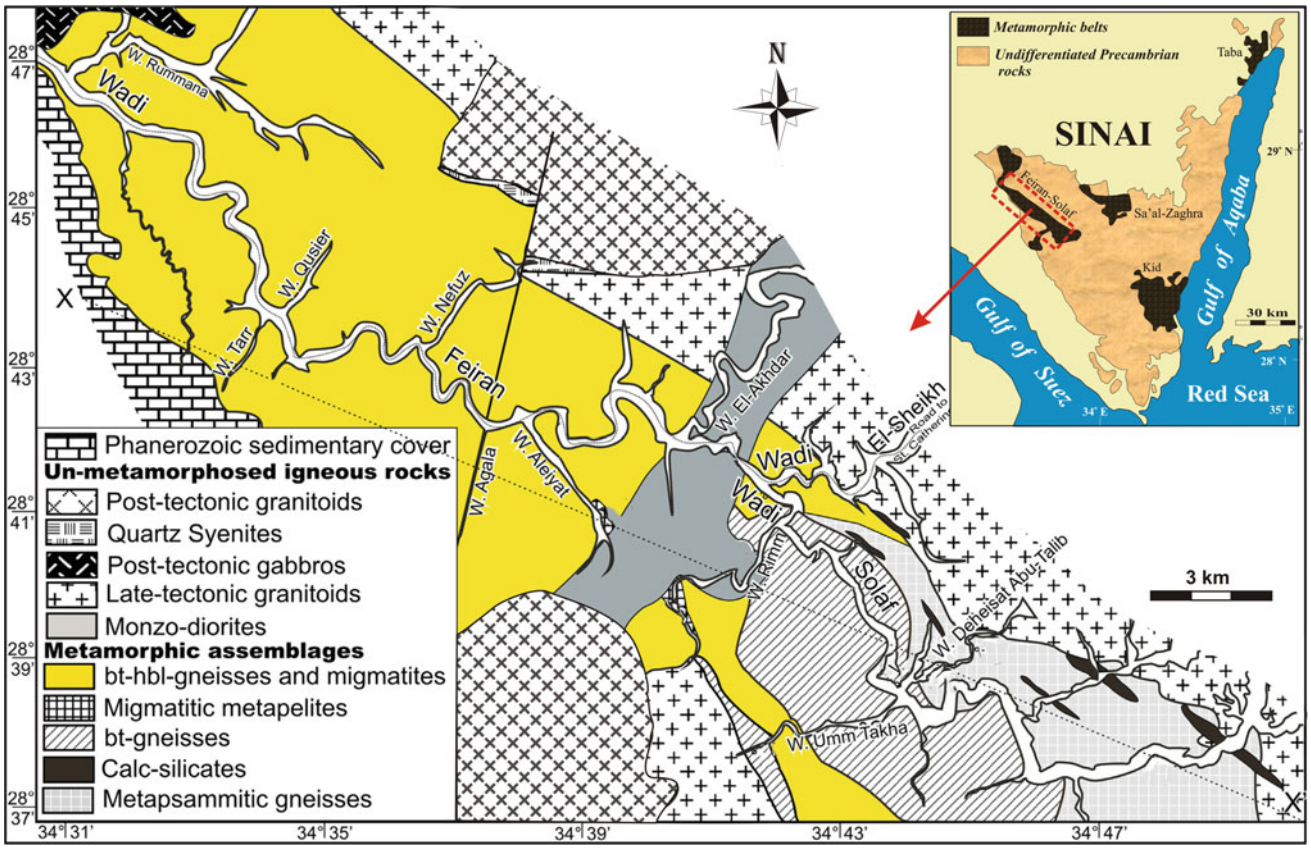

Fig. 2.5 Geological map of the Feiran–Solaf Metamorphic Complex (FSMC) (modified after Abu El-Enen and whitehouse 2013). The inset figure on the right is a sketch map of the Sinai Peninsula showing the regional extent of the Neoproterozoic basement rocks and indicates the mapped area. Dark grey areas represent the four metamorphic complexes of the southern Sinai

El-Barramiya. Two decades later, El-Sharkawy and El-Bayoumi (1979) were the first to identify and describe the occurrence of ophiolite as a mapable unit in the Wadi Ghadir area, 30 km SW of Marsa Alam (Fig. 2.6). Shortly after, Nasseef et al. (1980), Shackleton et al. (1980) and Ries et al. (1983) documented ophiolite components from many segments of the Precambrian basement between the Qift–Quseir and Idfu–Marsa Alam areas of theEastern Desert of Egypt.

2.4.3.2 Spatial Distribution

The Neoproterozoic ophiolites are widespread in the central (CED) and southern (SED) domains of the Eastern Desert of Egypt (Fig. 2.6), where they occur as tectonized masses and melanges of pillowed metabasalt, metagabbro, and variably altered predotites (El Sharkawy and El Bayoumi 1979; Shackleton et al. 1980). With the exception of a very small outcrop of serpentinite in the Esh-El Mellaha range, no ophiolitic rocks are found in the North Eastern Desert (i.e. north of latitude 26°20′N; M.F. El Ramly, personal communication).

Unlike the SED ophiolites that mostly occur as well-defined elongated belts along sutures, most CED ophiolites are essentially mélanges likely produced by tectonic disruption related to deformation by the post-accretionary Najd fault system, rather than representing a suture zone (Abdelsalam and Stern 1996; Farahat 2010, 2011; Abd El-Rahman et al. 2012a, b). Most of the SED ophiolitic sequences form parts of major suture zones: the Allaqi–Heiani-Gerf and Onib-Sol Hamed suture zones (Fig. 2.6). Located midway between these two sutures, the Gabal Gerf nappe represents the largest ophiolitic body in the whole Egyptian Eastern Desert. With the exception of Sol Hamid ophiolite, most of Onib-Sol Hamed suture ophiolites extend beyond the Egyptian borders into the Sudanese territories. The immense ophiolitic stretch of Allaqi-Heiani suture, Gerf nappe and Sol Hamid ophiolite can be traced for about 400 km from Lake Nasser to the Red Sea. This is the western part of a much extended ophiolite-decorated suture zone, the Ess-Yanbu-Onib-Sol Hamed-Gerf-Allaqi-Heiani belt (YOSHGAH suture of Stern et al. 1990) which trends from the western edge of the northern Arabian Shield to Lake Nasser.

Representative ophiolites of the CED region are described separately from more southerly ophiolites of the SED

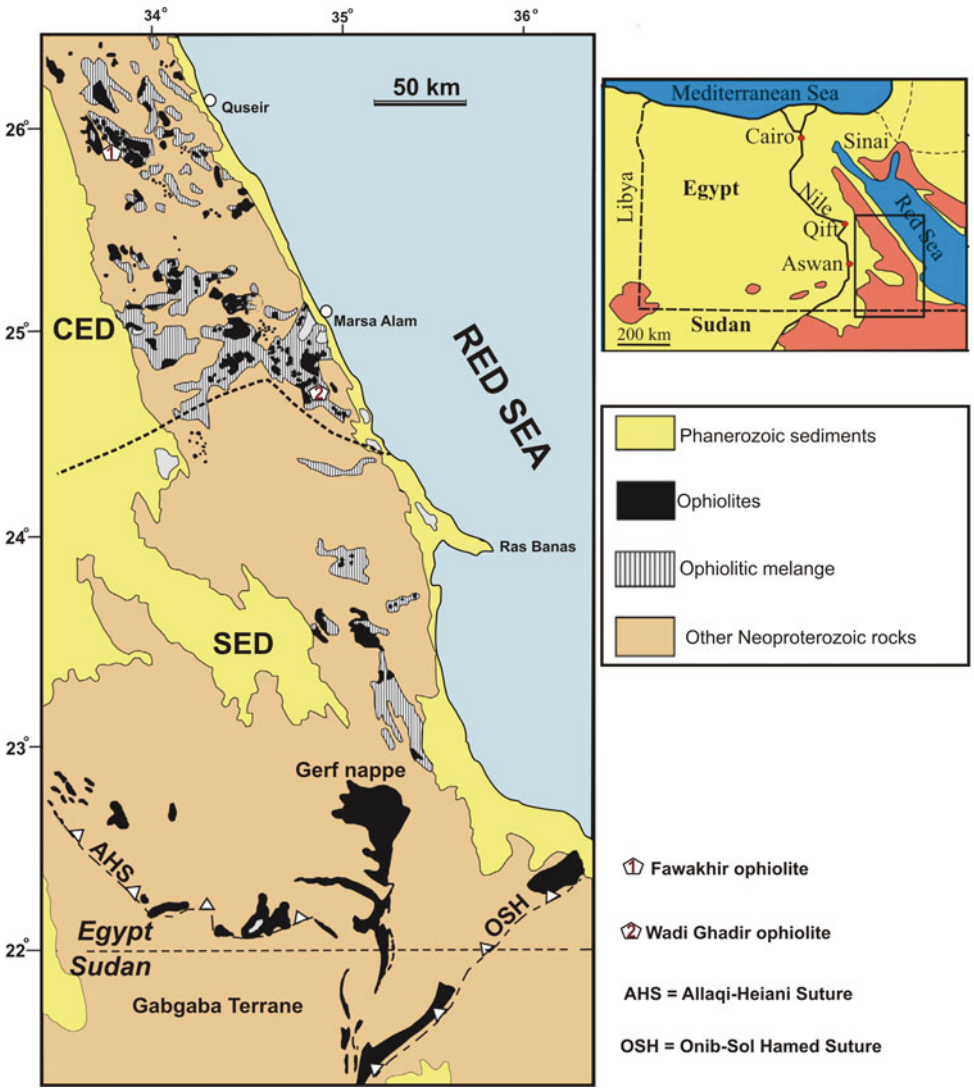

Fig. 2.6 Distribution of ophiolitic rocks in the Eastern Desert of Egypt (modified after Shackleton 1994). The general map of Egypt, to the right, shows the location of the mapped area. The five key ophiolite occurrences discussed in Sects. 2.4.3.5 and 2.4.3.6 are further indicated

region in consideration of their spatial distinction and certain other previously known attributes in a following two sections.

2.4.3.3 Ophiolite Components

In a few areas in the Eastern Desert, specifically Fawkhir, Ghadir and Gerf, a complete ophiolite sequence can be found (Abu El-Ela and Farahat 2010; Azer et al. 2013; Obeid et al. 2015). Moreover, sheeted dykes are rare in the CED ophiolites and are only found in the SED (Farahat 2010, 2011). Wherever found, complete ophiolitic sequences consist of a mantle unit of serpentinized ultramafic rocks and an upper crustal sequence of layered and isotropic gabbros, sheeted dykes and massive or pillow basalts (e.g. Abd El-Rahman et al. 2009a, b; Abdel-Karim and Ahmed 2010; Gahlan and Arai 2009; Basta et al. 2011; Abdel-Karim et al. 2016). Typically, the Eastern Desert ophiolites occur as tectonized masses and melanges of these ophiolitic lithologies (El Sharkawy and El Bayoumi 1979). Nevertheless, owing to folding and shearing, the largest part of the Egyptian ophiolites lack one or more of these distinctive lithologies (Stern et al. 2004). Ophiolites occur either as a nappe (intact thrust sheet) or as a melange (tectonic mixture of fragments). Ophiolitic melange is commonly inferred wherever abundant serpentinite is put together with metabasalt. The base of most Egyptian ophiolites consists of the mantle peridotite harzburgite, lherzolite being rarely reported, often with intensely deformed or transposed compositional layering, forming harzburgite tectonite. In most cases, the mantle harzburgites are mostly altered, with no silicate minerals survived alteration, to serpentinites and talc-carbonate rocks enclosing rare fresh relics of unaltered ultramafic protolith (Azer and Stern 2007; Ahmed et al. 2012, Ahmed 2013; Abu-Alam and Hamdy 2014).

2.4.3.4 Age and Tectonic Setting

The Eastern Desert ophiolites were emplaced on the continent during the ultimate collision between East and West Gondwana (850–620 Ma) and closure of the Mozambique Ocean (Stern et al. 2004; Fritz et al. 2013). They are not all the same age and there are progressive changes in age of ophiolites across the Eastern Desert. These ophiolites have an isotopic Neoproterozoic age extending between 890 and 690 Ma, recording a 200 Ma year stage of oceanic magmatism (e.g., Kröner et al. 1992; Stern et al. 2004; Ali et al. 2010a; Bühler et al. 2014), and are incorporated in ca. 780–680 Ma suture zones that document a 100 Ma year period of terrane convergence (Stern et al. 2004).

Consensus exists that most Eastern Desert ophiolites are formed in a suprasubduction zone (SSZ); that is, they developed by sea floor spreading above an active subduction zone e.g.; (Abu El-Ela 1996; El-Sayed et al. 1999; Stern et al. 2004; Azer and Khalil 2005; Ahmed et al. 2006; Azer and Stern 2007; Abd El-Rahman et al. 2009a, b). Nevertheless, there is a debate on whether these SSZ ophiolites were emplaced in a fore-arc or a back-arc setting.

It is often inferred, based on the geochemical characteristics (e.g. REE patterns and Ti/V ratios), that the Eastern Desert ophiolitic volcanics show transitional island arc-MORB character and a back-arc setting (e.g. El-Sayed et al. 1999; Ahmed et al. 2001; Abd El-Rahman et al. 2009a, b; Farahat 2010). Conversely, Azer and Stern (2007) and Khalil and Azer (2007) suggested that the Eastern Desert ophiolites were developed in a fore-arc setting based on the depleted nature and the high Cr# in the relict Cr-spinels of the serpentinized mantle peridotites. Analogous conclusion was reached for other Egyptian ophiolites (Abd El-Rahman et al. 2009a; Ahmed 2013; Azer et al. 2013; Hamdy et al. 2013; Obeid et al. 2015; Abdel-Karim et al. 2016; Khedr and Arai 2017).

Among the Egyptian ophiolites, the Gerf ophiolitic nappe is the only one with clear N-MORB chemistry (e.g., Ti/V ratios, REE patterns and Pb isotope), where the pillowed basalts and sheeted dikes originally formed in a mid-ocean ridge setting (Zimmer et al. 1995).

2.4.3.5 CED Ophiolites

The Wadi Ghadir ophiolite exposes an almost complete ophiolite sequence, which is one of the best preserved sections through Neoproterozoic upper oceanic crust anywhere in the world (Kröner et al. 1992). The Wadi Ghadir area is occupied by an ophiolitic melange composed essentially of dimensionally variable ophiolitic fragments embedded in a sheared serpentinite and pelitic matrix (Abd El-Rahman et al. 2009b). The ophiolitic fragments of Wadi Ghadir are mainly dismembered, and rarely occur as intact sequence (Basta et al. 2011). The ophiolite sequence consists of serpentinized peridotites, layered gabbro, massive rosette-structure gabbro, microgabbro, sheeted diabase dykes, and pillowed basalts (El-Sharkawy and El-Bayoumi 1979; Abdel-Karim and Ahmed 2010; Basta et al. 2011). It was concluded that the Wadi Ghadir ophiolite formed in a back-arc basin above a NE-dipping subduction zone (Abd El-Rahman et al. 2009b; Basta et al. 2011). For a plagiogranite sample from Wadi Ghadir ophiolite, Kröner et al. (1992) reported single zircon Pb–Pb evaporation age of 746 ± 19 Ma.

The Fawakhir ophiolitic sequence consists of, from the base to the top, ultramafic rocks (mainly serpentinized peridotite), gabbros and volcanic rocks, mainly basalt and basaltic andesite towards the east (El-Sayed et al. 1999; Abd El-Rahman et al. 2009a; Hamdy et al. 2013) (Fig. 2.7). All these ophiolite units are encountered from base to top successively from west to east. Regarding its geodynamic setting, Ries et al. (1983) regarded the Fawakhir ophiolite as a mid-ocean-generated oceanic crust that has been preserved in an olistostromal melange. El Gaby et al. (1988) interpreted the Fawakhir ophiolite as a segment of oceanic crust formed in a marginal (back-arc?) basin. El-Sayed et al. (1999) suggested that the Fawakhir ophiolite was formed in back-arc basin. Andresen et al. (2009) inferred that the Fawakhir ophiolite likely formed in a forearc setting. Recently, Abd El-rahman et al. (2009a) suggested that the Fawakhir ophiolite may have formed in an incipient arc–forearc setting during subduction initiation. Andresen et al. (2009) obtained a crystallization age of 736.5 ± 1.2 Ma for zircons from an ophiolitic gabbro of the Fawakhir area.

2.4.3.6 SED Ophiolites

The Allaqi-Heiani suture (AHS) is defined by an E-W curvilinear ophiolitic belt (e.g. Wadi Allaqi, Wadi Haimur, Wadi Murra; Gabal Felat; Gabal Heiani) that can be traced for more than 200 km across the southern Egyptian shield, near the border with Sudan (Fig. 2.6). This suture zone is broad and embraces gneiss, dismembered ophiolites, island arc volcanosedimentary-plutonic assemblages, and syn- to post-orogenic intrusions (e.g. Abd El-Naby and Frisch 2002; Abdelsalam et al. 2003; Zoheir and Klemm 2007; Ali et al. 2010a; Azer et al. 2013). The dismembered ophiolite assemblages comprise nappes composed chiefly of mafic-ultramafic rocks plus slices of serpentinite and talc-carbonate rocks (Gahlan and Arai 2009, Ali et al. 2010a). Ophiolitic gabbroic rocks are largely isotropic or layered metagabbros which are overlain by arc volcanic and volcaniclastic rocks and shelf metasediments (Ali et al. 2010a, b). An amphibolitic metamorphic sole at the bottom of the ophiolite is defined at Wadi Haimur (Abd El-Naby et al. 2000a, b). Kröner et al. (1992) obtained single zircon Pb–Pb evaporation ages of 729 ± 17 Ma and 736 ± 11 Ma for two samples from a single gabbro-diorite intrusion into sheared serpentinites in the Shilman area. Ali et al. (2010a) reported U-pb zircon SHRIMP ages of 730 ± 6 Ma and

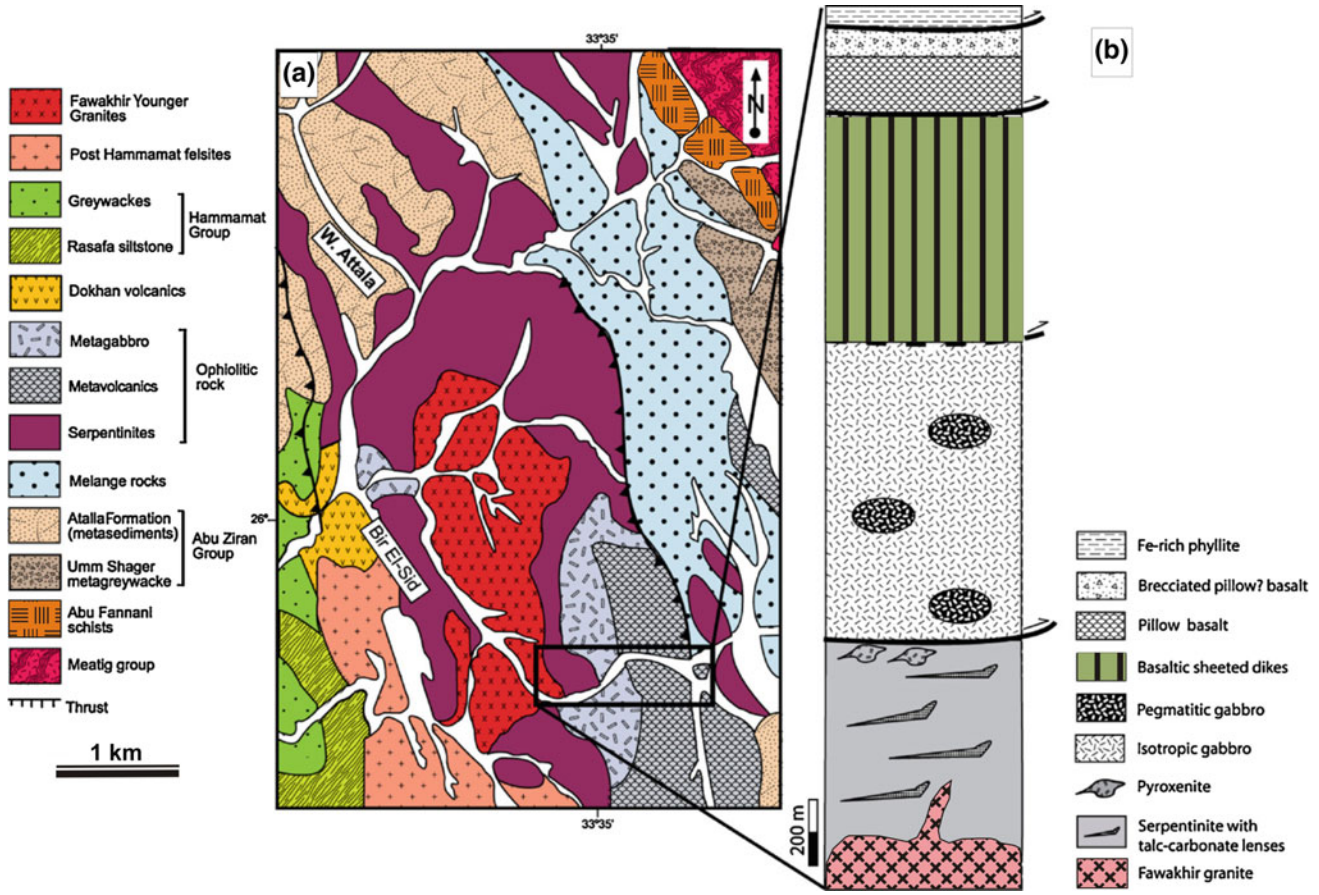

Fig. 2.7 **a** Geological map of the Fawakhir area (after El-Sayed et al. 1999; Abd El-Rahman et al. 2009a). **b** Symbolic stratigraphic section showing the main rocks units of the Fawakhir ophiolite (after Abd El-Rahman et al. 2009a)

697 ± 5 Ma for coarse-grained layered and isotropic gabbro samples, respectively, from the Gabal Moqsim area. They interpreted the 730 ± 6 Ma age as approximating the formation age of the Allaqi ophiolite in this area.

Sol Hamed ophiolite differs from other northward ophiolites in the Eastern Desert in being an elongated and intact belt defining a near-source tectonic facies (Abdelsalam and Stern 1996). To the north, ophiolites occur in tectonic melanges or as olistostromal debris, implying a distal tectonic facies (El Bahariya 2012). The ultramafic rocks of the Sol Hamed consist of serpentinites, chromite-bearing serpentinites and magnesite-bearing serpentinites, forming the base of a dismembered ophiolite (Abu-Alam and Hamdy 2014). The Sol Hamed ophiolitic sequence comprises also metagabbros, thin sheeted dykes, pillow lavas and pelagic sediments. Serpentinites occur as both melange and tectonized bodies. Tectonized serpentinites form ~20 km lengthened ridges of about 0.4–1.8 km width, elongated in NE–SW direction (Abu-Alam and Hamdy 2014). They are bordered and thrusted over arc metavolcanics from the NW (Fig. 2.8). Although no available radiometric age for the Sol Hamed ophiolite, a plagiogranite from the Onib ophiolite (the southern Sudanese segment of Onib-Sol Hamed suture) yielded a Pb–Pb evaporation age of 808 ± 14 Ma (Kröner et al. 1992), appreciably older than any other YOSHGAH suture ophiolite age.

The Gabal Gerf ophiolite complex exposes an ostensibly complete sequence from the mantle section at the base, passing through gabbroic crust, to the basaltic rocks at the top (e.g. Zimmer et al. 1995; Nasr and Beniamin 2001; Gahlan and Arai 2009). Collectively, it consists of basaltic pillow lavas, sheeted dykes, isotropic and layered gabbros and an ultramafic melange, all in tectonic contact along thrust sheets (Zimmer et al. 1995; Abdel-Karim and Ahmed 2010; Abdel-Karim et al. 2016). Gerf Ophiolite consists of the Gerf nappe which is comprised of serpentinized ultramafic melange with fragments of gabbro and basalt of dimensions reaching some tens of metres. As a first finding from the ANS ophiolites, Gahlan and Arai (2009) reported carbonate-orthopyroxenites bodies in the Gerf ophiolite. They form massive lenses (5–40 m long and 3–5 m wide) at the southern tip of the Gerf ophiolite nappe, along the contact between the Gabal Shinai granite and Gerf serpentinized peridotites. Northward at Gabal Gerf massif,

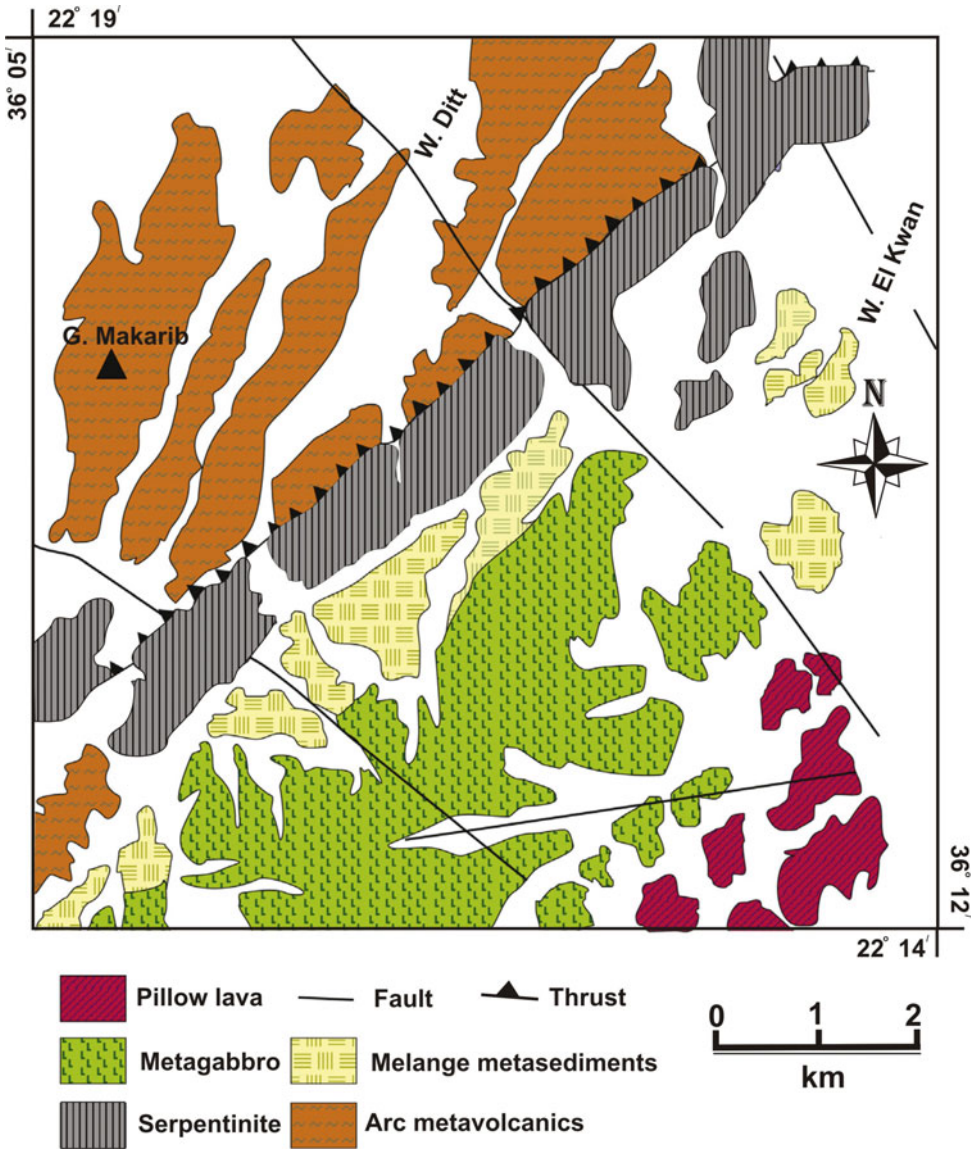

Fig. 2.8 Simplified geological map of Sol Hamed area (after Abu-Alam and Hamdy 2014)

Abdel-Karim et al. (2016) recoded somewhat similar but smaller pyroxenite bodies (thin sheets; ~50 cm thick and a few tens of meters long). The Gerf ophiolite has been dated by zircon Pb–Pb evaporation and Sm–Nd techniques. Kröner et al. (1992) obtained a Pb–Pb single zircon evaporation age of 741 ± 21 Ma for a coarse-grained, layered gabbro. Zimmer et al. (1995) reported three Sm–Nd isochron ages: (1) whole rock gabbros (720 ± 9 Ma); (2) gabbro mineral separates (771 ± 58 Ma); and (3) ophiolitic metabasalts (758 ± 24 Ma). According to these results, Zimmer et al. (1995) concluded that the Gerf ophiolite formed at ~750 Ma.

2.4.4 Arc Metavolcanics

2.4.4.1 Overview

The initial stage of Neoproterozoic crustal evolution in Egypt was typified by the extrusion of volcanic rocks known as the metavolcanics series (El Ramly and Akaad 1960), Shadli metavolcanics (Schürmann 1966), or Shadli geosynclinal metavolcanics (El-Ramly 1972). The name "Shadli" refers to their type locality nearby the Tomb of Sheikh Shadli in the SED. These metavolcanic rocks are exposed over vast areas in the CED and SED, but were considered almost absent the NED (Farahat 2006, 2010). However,

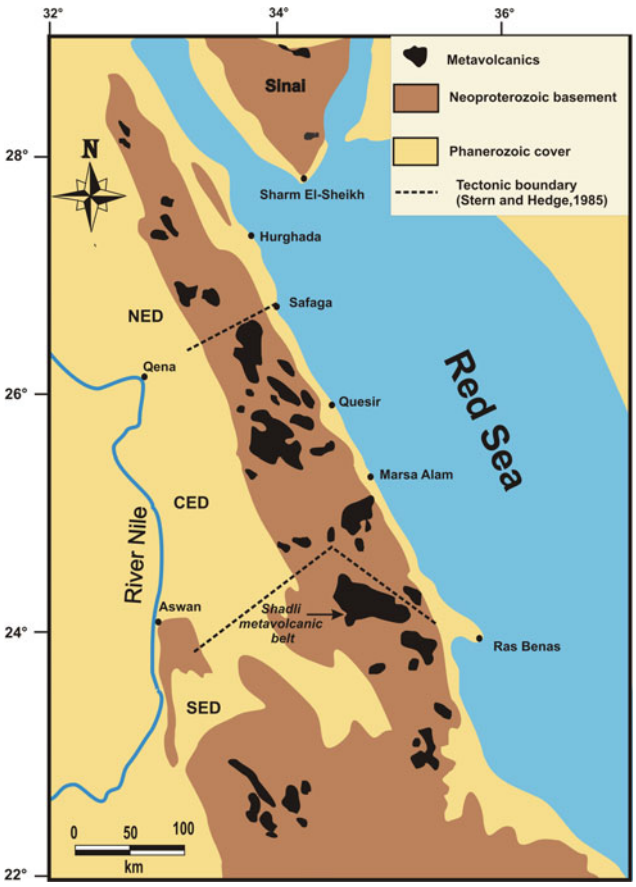

Fig. 2.9 Distribution of the metavolcanics in the Eastern Desert and Sinai, Egypt (modified after El-Ramly 1972)

recent studies revealed major occurrences of metavolcanics in the NED (e.g. El-Tokhy et al. 2010; Bühler et al. 2014) (Fig. 2.9). In Sinai, the metavolcanic rocks are almost restricted to definite formations in the Kid Metamorphic complex (Malhaq Formation; Shimron 1984, 1987; Furnes et al. 1985) and Sa'al Metamorphic complex (Agramyia Formation; Shimron et al. 1993).

They represent a group of regionally metamorphosed volcanic rocks closely associated and partly alternating with the metasediments. The metavolcanics range in composition from acidic to basic. The metavolcanics possess relict volcanic structures and textures, which are partly or largely preserved both in the outcrop and under the microscope and the rocks retain their original volcanic identity. Imprints of regional metamorphism are, however, superimposed upon the original volcanic forms but in most cases do not obliterate them. Metamorphic mineral assemblages indicate that the grade of metamorphism corresponds to the greenschist facies and rarely do they reach the epidote-amphibolite facies.

2.4.4.2 Metavolcanics of the SED

Among all the metavolcanic occurrences in the SED, Shadli metavolcanic belt (SMB) rocks are in some ways exceptional. They represent the largest metavolcanic outcrop (80 × 25 km) and attain a maximum thickness of 10 km (Stern et al. 1991, Farahat 2006) (Fig. 2.9). The Shadli metavolcanics constitute bimodal suites of tholeiites and low-K rhyolites and dacites.

The Shadli and other SED metavolcanics have been conventionally regarded as a bimodal island-arc metavolcanic rocks (e.g. Khudeir et al. 1988; Obeid 2006; Maurice et al. 2012). El Ramly et al. (1982) studied the Kulet Um Khari metavolcanic rocks (NW of SMB) and found it difficult to evaluate their tectonic setting but accepted an island-arc setting, in spite of the recognition of relatively high TiO_2 contents. Conversely, Farahat (2006) recognized the bimodal metavolcanics of Kulet Um Kharit as derived from an enriched mantle source reviving interest in models that involve enrichment from "plume" interaction during the evolution of the ANS. Based on some geological and geochemical arguments, Stern et al. (1991) rejected this model for the bimodal metavolcanic rocks from Um Samiuki area and suggested a continental rift origin for these rocks. From the forgoing it is evident that there exist a disagreement about whether or not the Shadli (and other SED) metavolcanics formed in subduction environment.

Available radiometric ages for the Shadli metavolcanics are limited. The earliest was from rhyodacitic metavolcanics at Wadi Kreiga in the SED yielded a Rb–Sr whole-rock age of 768 ± 31 Ma (Stern and Hedge 1985). The second comes from the work of Stern et al. (1991) who obtained a Rb–Sr whole-rock isochron age of 712 ± 24 Ma for metavolcanic rocks around Um Samiuki. Recently, Ali et al. (2010a) reported SHRIMP U-pb zircon age of 733 ± 7 Ma for a metadacite from arc-type metavolcanic rocks overlying ophiolitic rocks of the AHS (W. Shilman). These three ages together indicate that metavolcanics in the SED are 750 Ma old.

2.4.4.3 Metavolcanics of the CED

For the metavolcanic rocks in the CED, Stern (1981) presented a subdivision based on stratigraphic position and composition into "Older Metavolcanics" (OMV) demonstrating an oceanic crust association and non-ophiolitic arc-related "Younger Metavolcanics" (YMV). OMV have a tholeiitic character and are supposed to be parts of dismembered ophiolites, or form individual ophiolitic fragments in the ubiquitous Eastern Desert mélange. They were erupted in an oceanic rift and/or marginal sea setting, and are akin to mid-oceanic ridge basalts. Younger metavolcanics

(YMV) are mafic to felsic and evolved in an ensimatic island arc setting. The OMV defined by Stern (1981) as monotonous successions of aphyric pillow basalts with occasional sedimentary intercalations. Associations with mafic to ultramafic units such as gabbros and serpentinites are common. The OMV are conformably overlain by immature volcanogenic sedimentary rocks intercalated with banded iron formation, cherts and marls. Diamictites in this stratigraphic position have been studied by Ali et al. (2010b). The YMV are typified by the prevalence of porphyritic andesites and more felsic lithologies, volcaniclastic sediments along with the lack of pillow lava piles and serpentinites. The subdivision of metavolcanic rocks into OMV and YMV is generally utilized for the whole Eastern Desert, although recent studies suggest that this routine is improper. For example, Ali et al. (2009a, b) and Andresen et al. (2009) concluded that the OMV and the YMV overlap in time and are similar expressions of the ~750 Ma crust-forming event, and that in some areas OMV basalts may even be slightly younger than YMV lavas.

Andresen et al. (2009) sampled a felsic volcanic unit adjacent to the Meatiq gneiss dome in the CED, previously correlated with the Ediacaran Dokhan Volcanics (Ries et al. 1983), yielded a single zircon ID-TIMS age of 747.8 ± 3.0 Ma, implying that this unit might be affiliated to the Cryogenian metavolcanics. SHRIMP U-pb zircon analyses of some marine non-ophiolitic metavolcanics from Wadi Kareim and Wadi El Dabbah (CED) yielded ages ranging between 730 Ma and 769 Ma, and point to a formation around 750 Ma (Ali et al. 2009a, b), an assumption which is consistent with an age limitation to ~760 Ma for the overlying Atud diamictite (Ali et al. 2010b). Very recently, LA-ICP-MS analysis of magmatic zircons extracted from metavolcanics from three localities in the CED yield three distinct age populations with weighted averages of 827 ± 5, 772 ± 5, and 727 ± 4 Ma (El-Shazly and Khalil 2016). These ages likely represent the timing of major volcanic pulses and numerous sub-pulses (El-Shazly and Khalil, op. cit.).

2.4.4.4 Metavolcanics of Sinai

The metavolcanic rocks of Sinai are different from those of the Eastern Desert, particullarly in their age of formation. The late Mesoproterozoic Agramyia Formation metavolcanics (ca. 1.03–1.02 Ga; Be'eri-Shlevin et al. 2012; Eyal et al. 2014) predate the eruption of the ED metavolcanics, while those of Malhaq Formation appears much younger (detrital zircons from the interbedded Malhaq Formation metasediments yielded a U-pb age of ca.615 Ma; Moghazi et al. 2012).

The intermediate-silicic Sa'al complex metavolcanics (Agramyia Formation; Shimron et al. 1993) represents the deepest exposed stratigraphic levels of the Arabian-Nubian Shield (Ali-Bik et al. 2017). Shimron et al. (1993) identified virtually all of the northern parts of the complex as belonging to Agramiya Formation (Fig. 2.10). It is a ~2300 m thick interbedded sequence consists mainly of metabasaltic–metaandesitic flows and pyroclastics (~1300 m) and a metarhyolite–ignimbrite sequence (~1000 m). The base of the units is not exposed, hence these thicknesses are minimum approximations (Eyal et al. 2014). The Sa'al metavolcanics were thought as equivalent to the island arc YMV of the Eastern Desert of Egypt (Bentor 1985). Recent precise U-pb zircon dating of Sa'al metavolcanics (based on two meta-rhyolite and one meta-rhyodacite samples) yielded a late Mesoproterozoic age of 1031–1028 ±5 Ma (Be'eri-Shlevin et al. 2012).

The Malhaq Formation is the northernmost volcano-sedimentary unit of the Kid complex. It includes a series of massive to schistose metavolcanics interbedded and intercalated with fine- to medium-grained foliated metasediments (Abu El-Enen 2008; El-Bialy 2013). At the northern segment of this formation, the metasediments obviously dominate, whereas towards the central and southern parts the metavolcanics increase gradually, even still varyingly interbedded and intercalated with metasediments. The metavolcanics are mainly acidic to intermediate with subordinate basalts, consisting of fine to coarse pyroclastics such as breccias, lapillistone, lapilli tuff and finely bedded tuffs plus lesser lava (El-Bialy 2013; Khalaf and Obeid 2013; Sultan et al. 2017). The Malhaq metavolcanics have not been dated yet, although intercalated metapelitic schists have yielded Ediacaran U-Pb detrital zircon age of 615 ± 6 Ma (Moghazi et al. 2012).

2.4.5 Metasediments

This unit was first defined by El Ramly and Akaad (1960) as including a thick succession of mostly fine grained "geosynclinals" sediments mainly in a low grade metamorphism and occasionally reached medium grade. They named it "Schist-mudstone-greywacke series". It is later come to be known as geosynclinal metasediments on the geological map of El Ramly (1972). Metasediments are widely distributed in the Eastern Desert particularly south of latitude 26°N (i.e. CED and SED) and also in southeastern Sinai (within the Kid and Sa'al metamorphic complexes). They cover extensive areas and attain thicknesses measurable in kilometers.

The Eastern Deseret metasediments comprise mostly greenschist facies volcaniclastic wackes/pelites and diamictite, along with occasional banded iron formation (BIF) (Ali et al. 2010b, Stern et al. 2011; El-Shazly and Khalil 2016; Stern 2017; Khalil et al. 2018). The BIF and the diamictites

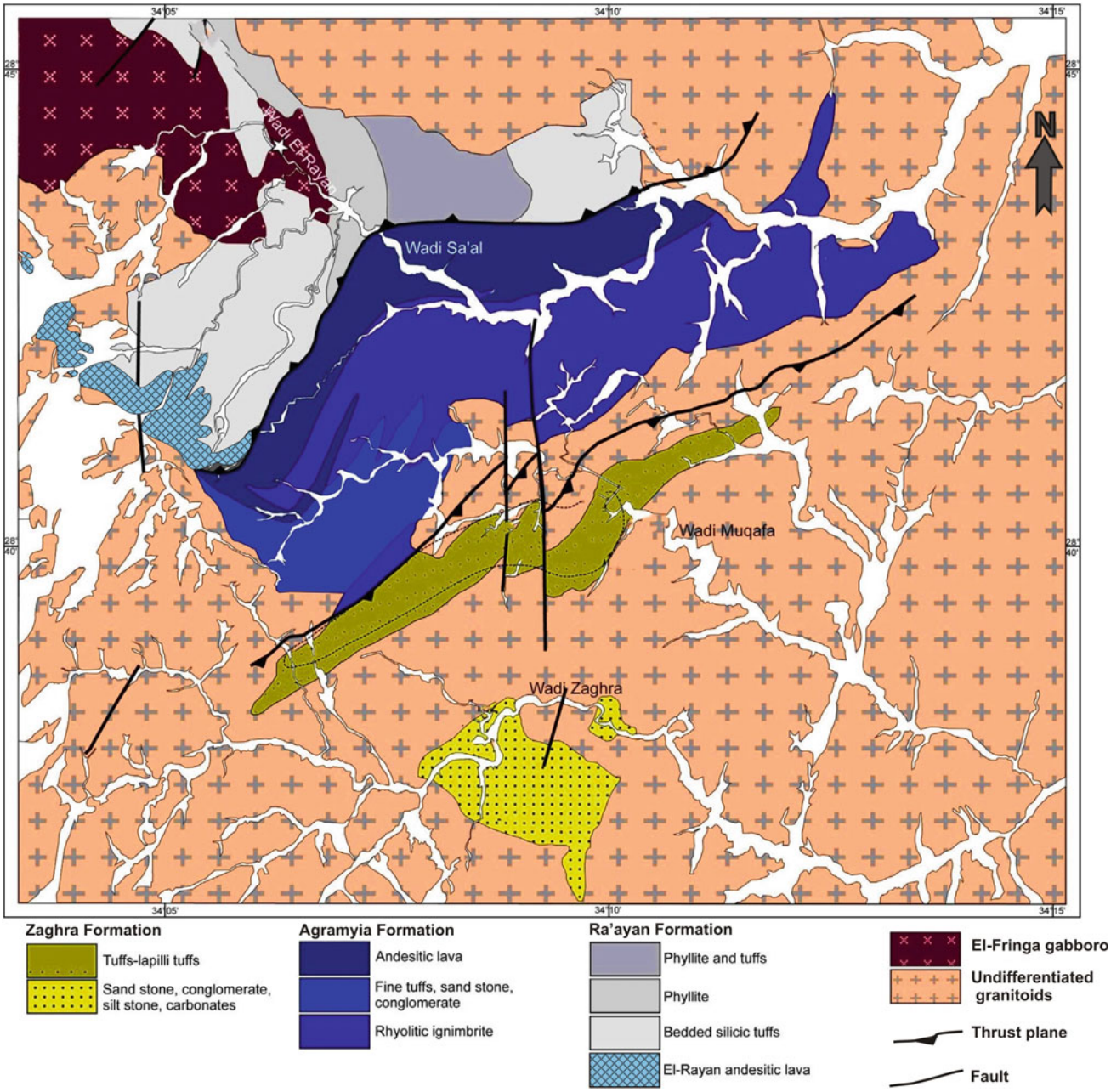

Fig. 2.10 Geological map of the Sa'al metamorphic complex (modified after Hassan et al. 2014)

are diagnostically restricted to the CED of Egypt (Ali et al. 2010b; Stern et al. 2011; El-Shazly and Khalil 2016; Stern 2017) (Fig. 2.11a). The CED diamictite (Atud diamictite; Ali et al. 2010b) and BIF are components of the broadly Cryogenian (~700 Ma) metasedimentary succession, and are found in regional association with Neoproterozoic ophiolites, a three-party association that denotes that both sedimentary units were deposited in a relatively deep ocean basin (Stern et al. 2006; Ali et al. 2010b; Stern et al. 2011). Although BIF and Atud diamictite are unknown from the NED (Stern 2017), diamictite deposits are well known from the Sa'al metamorphic complex, SE Sinai (Zaghra conglomerate/diamictite; Stern et al. 2010; Andresen et al. 2014; Hassan et al. 2014) (Fig. 2.11a).

With the exception of the exhaustive works of Ali et al. (2010b) on Atud diamictite and El-Shazly and Khalil (2016) on the CED BIF's, no recent studies of CED metasediments have been done. We know that the volcaniclastic

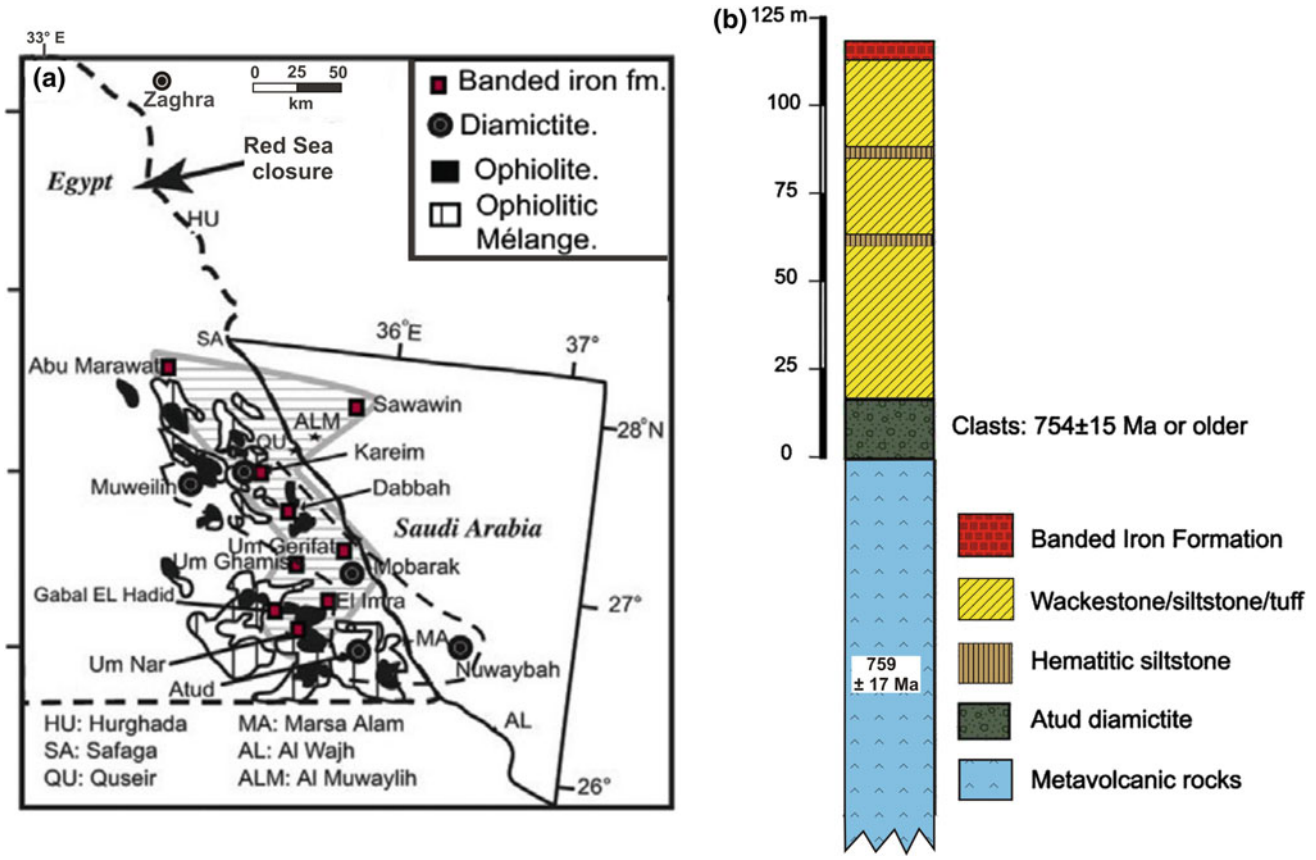

Fig. 2.11 **a** Location of the Egyptian diamictite, BIF, and ophiolitic rocks, with the Red Sea closed (modified after Ali et al. 2010c). **b** Simplified stratigraphic column for Atud diamictite and associated BIF in Wadi Kareim, CED of Egypt, from Stern et al. (2011)

wackes/pelites are related to the BIF and Atud diamictite are broadly andesitic in bulk composition, but not much more (Stern 2017).

2.4.5.1 Metasediments of the Eastern Desert

No generalized sequence is established for these metasediments which show great variations both in lithology and thickness from one locality to the other. Considerable lateral variations in the same outcrop are also observed. Besides, there is an intimate relation between these metasediments and the arc metavolcanics and both display an alternation or interfingering of sedimentation (flysch type) and volcanism. This led Akaad and Noweir (1969, 1980), while studying the Hammamat-Um Seleimat area, to group together the metasediments and metavolcanics in one group which they named Abu Ziran Group and subdivided it into eight formations.The original sediments were subjected to low grade metamorphism (greenschist facies) but the grade is usually higher the more south we go and the rocks are within the low amphibolite facies.

Atud Diamictite

The Atud diamictite has been reported from four localitiess in the CED of Egypt: Wadi Kareim, Wadi Mobarak, Wadi Muweilih, and the type locality east of Gabal Atud (Fig. 2.11a). The Atud diamictite consists of massive poorly sorted and rounded gravelly clasts, from pebble to boulder, set in a sheared grey matrix. Atud clasts include quartzite, highly altered granitoid, and a inimitable arkosic breccia (microdiamictite) (Ali et al. 2010b). The diamictite is part of a supracrustal succession in which metavolcanics (YMV of Stern 1981) are overlain by immature metasediments (c. 100 m thick of wackestone-sandstone, siltstone and diamictite), which are succeeded upwards by the BIF (Fig. 2.11b). The whole succession is thrust over younger Hammamat conglomerate to the south.

The age of Atud diamictite is confined to be younger than both the age of the underlying metavolcanics and the age of the youngest clast within the diamictite. Ali et al. (2009a, b) report a SHRIMP U-pb zircon age of c. 750 Ma for the metavolcanics that underlie the Atud diamictite at Wadi

Kareim. The Atud diamictite at Wadi Kareim is dominated by Cryogenian clasts (754 ± 15 Ma) and matrix material although includes abundant clasts of Palaeoproterozoic and Neoarchaean granitic rocks and pre-Neoproterozoic quartzite. Quite similarly, the diamictite matrix contains zircons that were derived from mixed Neoproterozoic and Paleoproterozoic sources (Ali et al. 2010b). Consequently, the pre-Neoproterozoic clasts and matrix in the Atud diamictite must have been derived from outside the CED and deposited in the marine basin that existed in the CED ~750 Ma (Stern et al. 2011; Stern 2017).

Banded Iron Formation

BIFs occur at thirteen occurrences distributed over ~30 000 km^2 in the CED (Fig. 2.11b). BIF occurs as rather regular bands interbedded with metasediments and occasionally metavolcanics in a zone that originally had a stratigraphic thickness of 100–200 m, within which the aggregate BIF thickness is about 10–20 m (Sims and James 1985). Egyptian BIF is typically an oxide facies, consisting of interlayered dense magnetite and hematite layers alternating with jasper, and containing 40–46% Fe (Sims and James 1985). BIFs and interbedded wackes are strongly deformed and metamorphosed to greenschist and sometimes amphibolite facies (El-Shazly and Khalil 2016). In many localities, BIF-bearing metasediments are intruded by metadiabase sills (Stern et al. 2011).

BIF age is best constrained from Wadi Kareim, where ages of conformably underlying diamictite and metavolcanics denote that it is younger than ca. 750 Ma (Ali et al. 2009a, b, 2010b), but perhaps not much younger. Therefore, these BIFs seem to have formed ~750 Ma (Fig. 2.11b).

With the popularity of a glaciogenic origin related to Snowball Earth hypothesis for most Neoproterozoic BIFs (deposited worldwide 850–700 Ma), Ali et al. (2010b) and Stern et al. (2011) ascribed BIF deposition in CED to concomitant melting of glacial ice ca. 750 Ma. Consequently, BIFs are evidently related to distal submarine igneous activity and may reflect re-oxygenation of the ocean associated with the Sturtian glaciation (Stern 2017).

2.4.5.2 Metasediments of the Sinai

Metasediments in Sinai are quite different from their counterparts of the Eastern Desert, particularly in their age and lack of BIFs. They occur as sedimentary successions within the volcanosedimentary sequences of the Kid metamorphic complex (Malhaq and Um Zariq formations) and Sa'al metamorphic complex (Ra'ayan and Zaghra formations).

The Sa'al complex is distinguished into the metavolcanic Agramiya Formation, bounded from north and south by the volcanosedimentary Ra'ayan and Zaghra formations, respectively (Shimron et al. 1993) (Fig. 2.10). The Ra'ayan Formation comprises metamorphosed clastics that were differentiated on mineralogical and grain-size bases into metagreywacke and semi-metapelite and metapelites (Ali-Bik et al. 2017). Detrital zircons from the Ra'ayan Formation metapelite give concordant U-Pb ages clustered between 1.12 and 0.95 Ga (Be'eri-Shlevin et al. 2009b, 2012), supporting their derivation from the Mesoproterozoic Sa'al volcanics (Agramyia Formation) as arc detritus.

The Zaghra Formation consists of a succession of interbedded feldspathic sandstones, conglomerate, diamictite, and schists (Hassan et al. 2014; Andresen et al. 2014). These sediments are folded and metamorphosed under greenschist facies conditions, locally converting the pelitic units into biotite-schists (Shimron et al. 1993). A steeply dipping, variably foliated matrix-supported metaconglomerate (diamictite) cropping out on both banks of Wadi Zaghra embraces most of the Zaghra Formation in this area (Stern et al. 2010; Andresen et al. 2014). Andresen et al. (2014) carried out extensive LA-ICP-MS dating of zircons from diamictite granitoid clasts, diamictite matrix, and biotite-schist. Three granitoid boulders from a metadiamictite of the Zaghra Formation give crystallization ages of 651 ± 3 Ma, 647 ± 3 Ma, and 640 ± 4 Ma. Detrital zircon age populations from laminated siltsones and conglomerate matrix vary somewhat with stratigraphic position The youngest detrital zircons indicate deposition after 630–625 Ma.

The Kid metamorphic complex comprises metamorphosed ENE-trending folded thick volcano-sedimentary sequence that has been divided by Shimron (1984, 1987) and Furnes et al. (1985) into the Malhaq and Um Zariq formations (northern Kid area), and the Heib and Tarr formations (southern Kid area).

The Um Zariq Formation is predominantly a metasedimentary sequence consisting mostly of well-bedded metapelitic schists with scarce graphitic phyllites. Non-foliated metapsammites and calcareous metapelites occur as minor intercalation within these foliated metasediments and constitute substantially thick beds (up to 10 m) in the lower horizons of this formation (Abu El-Enen et al. 2003; El-Bialy 2013; El-Bialy et al. 2015).

The Malhaq Formation is the northernmost volcanosedimentary unit of the Kid complex. At the northern part of this formation, the metasediments obviously dominate. These metasediments are, likely volcanogenic, derived from the associated volcanics and include conglomerates, pebbly graywackes and pelites. Metamorphism and deformation have converted these lithologies into folded schists and phyllites (Abu El-Enen 2008, El-Bialy 2013; Sultan et al. 2017).

K/Ar dating of biotite from schists from the Malhaq Formation yielded an age of 609 ± 12 Ma (Eliwa et al.

2004). Comparably, detrital zircons from the Malhaq Formation yield a weighted mean U-Pb age of 615 ± 6 Ma (Moghazi et al. 2012). In contrast, detrital zircons from the Um Zariq Formation give an older U-pb age of 813 ± 6 Ma (Cryogenian), which may represent the maximum depositional age of this unit (Moghazi et al. op. cit).

2.4.6 Alaskan-Type Mafic-Ultramafic Complexes

Mafic-ultramafic rocks constitute about 5% of the Precambrian basement cropping out in the Eastern Desert of Egypt (Abd El-Rahman et al. 2012a, b). Apart from the ophiolitic mafic–ultramafic rocks discussed earlier (Sect. 2.4.3), other two non-ophiolitic types are recognized; a post-collisional vertically-zoned layered intrusion (e.g., Motaghairat; Abdel Halim et al. 2016) and concentrically zoned Alaskan-type ultramafic–mafic complexes (Helmy and El Mahallawi 2003; Farahat and Helmy 2006; Ahmed et al. 2008; Helmy et al. 2008, 2014, 2015). The layered intrusions and Alaskan-type complexes have somewhat similar lithology, but the second shows concentrically zoned intrusions with ultramafic rocks in the core and mafic rocks at the margin of zonation. Furthermore, island arc gabbros and Alaskan-type complexes are distinguished from the post-collisional Younger Gabbros ((Abdel-Karim 2013; Abu Anbar 2009) and mafic-ultramafic layered intrusions (Abdel Halim et al. 2016; Azer et al. 2017) in being depleted in HFSE (Zr, Nb, Y, Ti) (Abd El-Rahman et al. 2012a, b; Helmy et al. 2014).

Alaskan-type complexes have been identified in different orogenic belts from the Archean to Phanerozoic ages. Neoproterozoic Alaskan-type complexes have only been recorded in three localities in the SED of Egypt, i.e., at Abu Hamamid (Farahat and Helmy 2006; Helmy et al. 2015), Gabbro Akarem (Helmy and El Mahallawi 2003; Abd El-Rahman et al. 2012a, b) and Genina Gharbia (Helmy et al. 2008, 2014) (Fig. 2.12). These zoned mafic-ultramafic complexes are not metamorphosed although weakly altered. Each intrusion is composed of a predotite core (dunite, wehrlite or lherzolite,) enveloped by pyroxenites and gabbros at the margin.

Alaskan-type complexes are considered as uplifted fragments of the deep levels or roots of Neoproterozoic island arcs in the Nubian Shield that exposed along deep fracture zones trending NE–SW (Farahat and Helmy 2006; Abd El-Rahman et al. 2012a, b; Helmy et al. 2014, 2015). Criteria for island arc setting of these complexes come from the overall geologic setting, field relations, mineralogy and mineral and whole-rock chemistry. For instance, Island arc signature is indicated by enrichment in large ion lithophile elements and low concentration of high field-strength elements (Helmy et al. 2014, 2015).

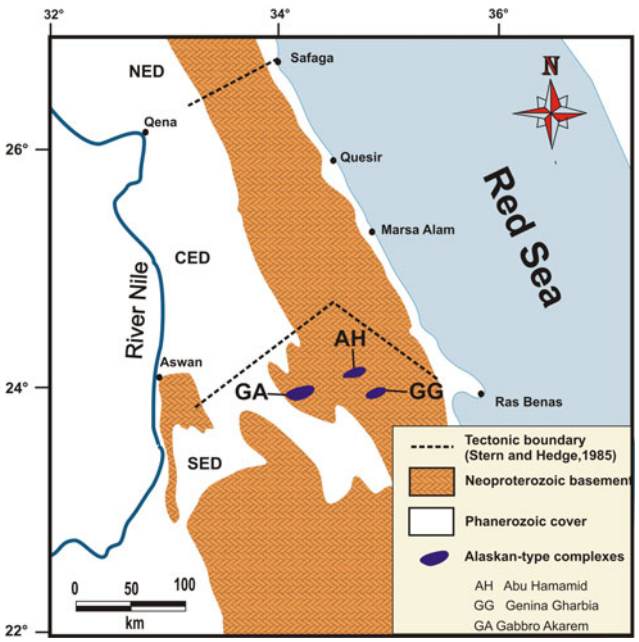

Fig. 2.12 Location map of the Alaskan-type mafic-ultramafic complexes in the Eastern Desert of Egypt (after Helmy and El Mahallawi 2003)

The available Sm/Nd model ages for the CED Alaskan-type complexes are controversial. Helmy et al. (2014) obtained an exceptionally old Tonian Nd model age of the Genina Gharbia complex (963 ± 81 Ma). On the other side, Ahmed et al. (2008) reported Sm/Nd and Rb/Sr ages of 673 ± 10 Ma of two of these complexes; Gabbro Akarem and Genina Gharbia. In between, Helmy et al. (2005) have assigned Sm/Nd model age of 773 ± 23 Ma to Abu Hamamid complex. However, the age of these intrusions can be better constrained through their field relations with the more precisely U-Pb zircon dated older and younger basement units. The rocks of Abu Hamamid and Genina Gharbia complexes intrude the arc Shadli metavolcanics and metasediments (~750 Ma; Ali et al. 2009a, b, 2010b) (e.g. Ahmed et al. 2008; Helmy et al. 2008, 2015). Conversely, island arc calc-alkaline granitoids (630–650 Ma; Moussa et al. 2008; Ali et al. 2016)) were found intruding the outer margins of the Abu Hamamid and Gabbro Akarem Alaskan-type complexes (Helmy and El Mahallawi 2003; Farahat and Helmy 2006; Abdel-Rahman et al. 2012a, b).

2.4.7 Metagabbro-Diorite Complex

The Egyptian gabbroic rocks belong to geochronologically and petrogenetically different types that constitute an integral part of the Neoproterozoic basement of Egypt. The gabbros of the Egyptian shield were earlier classified into two major

groups: older metagabbros and post-orogenic younger gabbros (Basta and Takla 1974; Takla et al. 1981). The older metagabbros were assigned different names; epidiorite (Hume 1934), epidiorite–diorite association (El Ramly and Akaad 1960), Metagabbro complex (Akaad and Noweir 1969), metagabbros–diorite complex (El Ramly 1972) and Sid metagabbros (Akaad and Noweir 1980). All of these names have been abandoned in favor of 'metagabbro-diorite complex'.

El Gaby et al. (1988, 1990) were the first to recognize that the older metagabbros are either a fundamental part of oceanic lithosphere (ophiolitic gabbros) or island-arc calc-alkaline gabbro–diorite complexes. Excluding whole-rock geochemistry, the distinction between the metagabbros pertaining to ophiolites and those formed in island arcs (metagabbros–diorite complex) is challenging because both are regionally deformed, sheared, metamorphosed up to greenschist or lower amphibolite facies and are petrographically identical (El Gaby et al. 1990). Ultimately, the Egyptian gabbros have been categorized into three major types (El Gaby et al. 1990; Khalil 2005; El Gaby 2005): (1) ophiolitic metagabbros with tholeiitic affinity, (2) intrusive arc-related calc-alkaline metagabbros (=metagabbro-diorite complexes) which intruded the island arc metavolcanics, metasediments, and (3) Cordilleran stage tholeiitic-calc-alkaline olivine gabbro and related rocks (post-collisional younger gabbros). Recent petrogenetic studies on the island-arc metagabbro-diorite complexes are scarce either in the Eastern Desert (e.g. Kharbish 2010; Obeid 2010; Khalil et al. 2017) or Sinai (e.g. Qaoud and Abdelnasser 2012; Samuel et al. 2015; Azer et al. 2016).

The outcrops of the metagabbro-diorite complexes are of limited extension and show uneven distribution all over the Egyptian basement. However, rocks of the metagabbro-diorite complex are of wider distribution in the Eastern Desert and Sinai compared with the younger post-collisional gabbros. They form relatively large outcrops which may follow the regional setting. Some of these outcrops cover substantial areas in the central and southern parts of the Eastern Desert, such as the mass outcroping west of Marsa Alam, which extends from Wadi Mubarak in the north to Gabal Atud in the south and covers about 1400 km^2. In the south Eastern Desert, huge masses of metagabbro are encountered in Ras Banas-Abu Dahr area (e.g. Gabal Um Gunud) and west of Halaib (e.g. G. Um Salim).

The complexes are typically variable in composition even some occurrences are exclusively gabbroidal (El-Aradiya; Abu El-Ela 1999). The gabbroic rocks include pyroxene-hornblende gabbro, hornblende gabbro, quartz-hornblende gabbro and amphibolite. In addition to the diorites and quartz diorites, as felsic members, occasional tonalites (Abdel-Rahman 1990; Abu El-Ela 1997) and pyroxene diorites (Basta et al. 2017) are reported.

In the Eastern Desert, these rocks intrude the ophiolitic rocks, arc metavolcanics and metasediments, and in opposition are intruded by the island arc Older Granites and the post-collisional younger gabbros and Younger Granitoids (e.g. Abu El-Ela 1997, 1999; Kharbish 2010; Abdelnasser and Kumral 2016; Basta et al. 2017). Their contacts with the older rocks are sharp and they do not cause any noticeable contact effects on these rocks.

Questionable exceedingly old and diverging K-Ar whole-rock and biotite and hornblende ages were reported for metagabbro-diorite complexes from the NED (881 ± 58 Ma; Abdel-Rahman 1990) and Sinai (794 ± 30 Ma; Abdel-Karim 1995), respectively. More precise and reliable comparable ages are obtained for metagabbro-diorite complexes only from Sinai; 632 ± 4 Ma (ion-microprobe zircon U-pb age; Be'eri-Shlevin et al. 2009a) and 640 ± 6 Ma (single zircon Pb/Pb evaporation age; Kröner et al. 1990).

2.4.8 Egyptian Granitoids

2.4.8.1 Overview

In the northern ANS, including the Eastern Desert of Egypt and Sudan, Sinai and northwestern Arabia, granitoids constitute about 50% of this Neoproterozoic tract (Moghazi et al. 2004; Farahat et al. 2007, 2011; El-Bialy and Omar 2015). Within the Egyptian shield, the predominance of grantoids increases northward (Fig. 2.13), where they reach the utmost abundance in Sinai, and even the entire ANS, constituting about 70% of the total basement area (Bentor 1985; El-Bialy and Streck 2009) (Fig. 2.13). The Egyptian granitoids have long been classified into two distinct groups:

(a) An older (750–610 Ma) group commonly referred to as the Older Granites, but several other terms are used in the literature [gray granites (Hume 1935; Akaad and Noweir 1980), syn-to late-orogenic granites, (El Ramly 1972; Ries et al. 1983), subduction-related G1-granites (Hussein et al. 1982), Gα granites (El Gaby et al. 1984)].
(b) A younger (610–580 Ma) granitoid group commonly referred to as the Younger Granites group, but again several other names have been in use [Gattarian Granites (Hume 1935), late orogenic plutonites (El Shazly 1964), suture-related G2 granites (Hussein et al. 1982) and Gβ granites (El Gaby et al. 1984)].

Throughout the ANS in Egypt, the relative abundance of the Older Granites to the Younger Granites decreases from 4

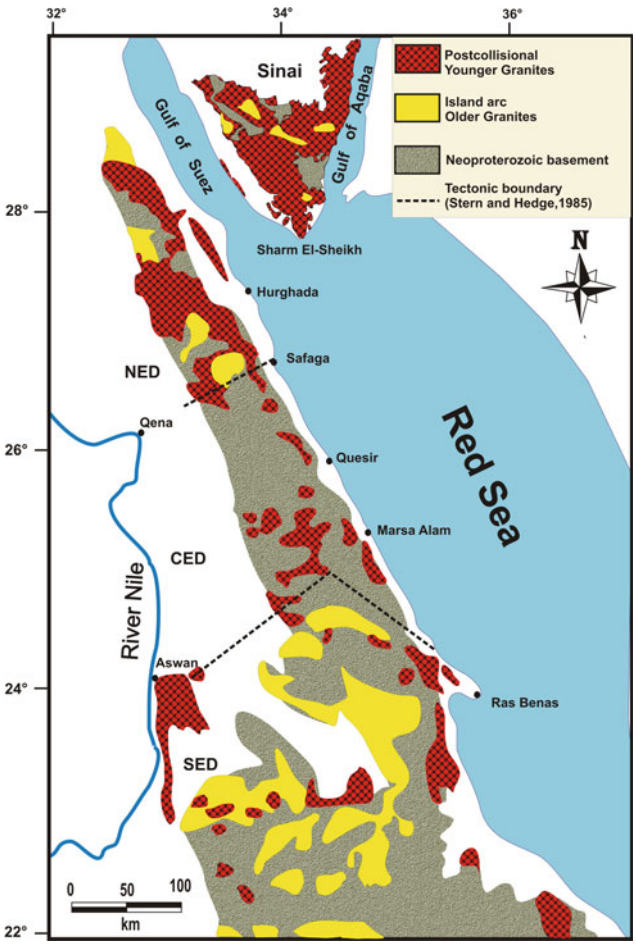

Fig. 2.13 Distribution map of the Egyptian Older and Younger Granites within the Neoproterozoic basement of the Eastern Desert and Sinai (modified after Farahat et al. 2011)

to 1 in the south of the ED to approximately 1–1 in the north (Stern 1979) and 1–12 in Sinai (Bentor 1985), notably concomitant with the general ANS trend of increasing granitoid abundance from south to north (Fig. 2.13).

2.4.8.2 Island Arc Older Granites

This group constitutes about 27% of the basement outcrop in the ED (Stern 1979). It includes calc-alkaline I-type granitoids that were emplaced during active subduction processes between 850 Ma (?) and 610 Ma (Hussein et al. 1982; Stern and Hedge 1985; Hassan and Hashad 1990; Stern 1994; Kröner et al. 1994; Moghazi 2002; Moussa et al. 2008; Be'eri-Shlevin et al. 2009a; Eliwa et al. 2014; Ali et al. 2016).

Hassan and Hashad (1990) recognized three possible events of igneous activity during which different plutons of the Older Granites suite were emplaced: The Shaitian event (850–800 Ma), Hafafit event (760–710 Ma) and Meatiq event (630–610 Ma). However, most U-Pb zircon ages recently obtained for Older Granites from the Eastern Desert are younger than 750 Ma (Loizenbauer et al. 2001; Andresen et al. 2009; Eliwa et al. 2014; El-Shazly and Khalil 2016) negating the early Shaitian event of Hassan and Hashad (1990). Early Cryogenian ages (780–850 Ma) are only reported for Older Granites from Sinai (Stern and Manton 1987; Bea et al. 2009; Be'eri-Shlevin et al. 2012).

Old Granites vary to some extent in their mineral composition even within the same hosting-area or pluton, and the varieties comprise such basic as quartz diorite, through the ultimately common granodiorites and tonalites to the less abundant but not uncommon monzogranites (El-Bialy 2004). The common mafics are either flaky biotite or prismatic amphiboles or variable proportions of both.

The contacts of these granitoids either with the older basement or the Younger Granites are often sharp non-reactive one. The shape of the contacts varies between straight, angular, broadly crenulated and much irregular shapes of intruding offshoots and apophyses. Contacts with the older rocks are sometimes characterized by the development of fine-grained chilled margin of usually several centimeters width. On the contrary, marginal zones with the Younger Granites, in many cases, exhibit prominent metasomatic K-feldspar overgrowth into larger megacrysts leading to formation of porphyritic granodiorites.

One of the most distinctive field characteristic of the Older Granites is their inclusion of rounded to subrounded microgranular mafic enclaves of amphibolite or melanocratic diorite composition (El-Metwally 1993; Surour and Kabesh 1998; El-Bialy 2004; Asran and Abdel Rahman 2012). Such enclaves are commonly ovoid, but elongated ribbons, lenticular and elliptical forms are not uncommon. The enclaves are variable in size from few centimeters up to a half meter across or more and have either sharp or reactive contacts with their granitoid host. These enclaves are quite impossible to separate from their hosts because they crystallized at the same time as their hosts, in contrast to other foreign enclaves (xenolithes). The distinction between these mafic enclaves and other fine-grained xenolithes of metagabbro-diorite complex rocks or biotite schists in the field is easily accomplished through the previous property, in addition to their almost rounded shape and the absence of the thermal metamorphism textural effects (El-Bialy 2004).

The available whole-rock data of the Egyptian Older Granites (e.g. El-Bialy 2004; Farahat et al. 2007; Bea et al. 2009; El Mahallawi and Ahmed 2012; Eliwa et al. 2014; El-Bialy and Omar 2015) show that they are medium-K calc-alkaline, metaluminous to slightly peraluminous, magnesian ($FeO^*/FeO^* + MgO < 0.8$) I-type granites that have a broad compositional spectrum from highly silicic to basic (75–50 wt% SiO_2), low K_2O and K_2O/Na_2O (less than 2.5 wt% and 0.7, respectively) and REE patterns with both delicate negative and positive Eu anomalies. Also, they are relatively enriched in the LILE Ba and Sr and conversely

significantly depleted in the HFSE (e.g. Nb, Zr, Y), Ga and ∑REE (commonly <100 ppm).

The prevalence of young juvenile crust in the ANS at the time when the Older Granites were generated does not easily allow geochemical and isotopic distinction between crustal- and mantle-derived sources. However, two contrasting petrogenetic models have been proposed for the origin of the Older Granites: (1) high fractional crystallization of lithospheric mantle-derived mafic magmas, with crustal modification through either assimilation or melt hybridization (e.g. El-Bialy 2004; Eliwa et al. 2014; El-Bialy and Omar 2015), (2) Fractional crystallization of mafic crustal melts generated by high degrees of partial melting of mafic lower crustal amphibolite protolith (Farahat et al. 2007; El Mahallawi and Ahmed 2012).

2.4.8.3 Postcollisional Younger Granites

The Younger Granites are extensively distributed across the Egyptian Shield, constituting approximately 16% of it and 30% of its plutonic assemblage (Stem 1979; Hassan and Hashad 1990). Their relative abundance to the Younger Granites increases northward; from 1 to 4 in the SED, to almost 1–1 in the NED (Stem 1979) and 12–1 in Sinai (Bentor 1985). In Sinai, Younger Granites reach their climax and constitute about 65% of the exposed basement (Fig. 2.13).

They occur mostly as roughly equidimensional plutons of diameters between 1 and 10 km, intruding virtually all the other Precambrian basement rock units with sharp non-reactive contacts. In turn, they are crosscut by younger very late Neoproterzoic and Phanerozoic anorogenic volcanics including for instance the post-granite dykes, Katherina Volcanics and Tertiary dykes (e.g. Friz-Töpfer 1991; El-Sayed 2006; El-Bialy and Hassen 2012). At some Younger Granite contacts, marginal facies are characterized by the development of a fine-grained chilled margin, few tens of centimeters width, whereas country rocks might be thermally metamorphosed with formation of contact aureoles of variable widths. Pegmatitic pockets and vien-like bodies occur sporadically in some Younger Granite plutons, whereas quartz veins and aplite dykes and veins are very widespread. Some Younger Granite outcrops enclose intermittent mafic xenoliths and/or microgranular enclaves. Within the same pluton, Younger Granites occasionally show marked variations in texture, grain size and modal mineralogy. The contact between the granitoid varieties within the same pluton is usually not evident, but the different varieties grade into each other over a distance of several tens of meters; nowhere can one observe a sharp intrusive contact between them.

Mineralogically, Younger Granites are predominantly syenogranites, monzogranites and alkali feldspar granites, even granodiorites and quartz monzonites are seldom reported. Alkali feldspar granites are typically hypersolvous in texture while other compositions are transsolvous to subsolvous. This variation in the type of granite texture is related to the water pressure during crystallization: hypersolvus granites crystallize from melts with low water fugacity, while for subsolvus granite to develop, magma ought to be enriched in water. A Transsolvus granitoid usually forms when dry hypersolvus crystallization (low P_{H2O}) is interrupted by the introduction of late fluids. The Younger Granites exhibit a distinctive red to pink color caused by the predominance of pink K-feldspars and/or deep impregnation of feldspars by hematitic dust. Color variations towards white and grey tints are f common. The Younger Granites are stereotypically biotite, muscovite or two-mica granitoids. However, hornblende may occur in association with biotite in the less evolved varieties, garnet (almandine-rich) occur in the strongly peraluminous granites (e.g. Moghazi et al. 2004; Emam et al. 2011) and riebeckite and arvedsonite in peralkaline grantoids.

This granitoid unit includes highly fractionated calc-alkaline I-type granites as well as A-type granites that are strongly peraluminous to slightly metaluminous. Some A-type plutons are alkaline and may be further peralkaline (e.g. Abdel-Rahman and El-Kibbi 2001; El-Bialy and Streck 2009; Azer 2013; Abd El Ghaffar and Ramadan 2017).

Younger Granites are believed to be generated during the post-collisional stage of the ANS evolution (Moghazi 2002; Farahat et al. 2007, 2011; Mohamed and El-Sayed 2008; Moussa et al. 2008; Eyal et al. 2010; Ali et al. 2012b, 2013). Hussein et al. (1982) have previously placed the alkaline/peralkaline Younger Granites in a separate group (G3) and considered them intraplate, anorogenic granites, which is ruled out later as all of these granitoids are proved to be generated in the postcollisional stage of the ANS evolution (e.g. El-Bialy and Streck 2009; Eyal et al. 2010; Farahat and Azer 2011; Ali et al. 2012b; Azer 2013; Moreno et al. 2012; El-Bialy and Shata 2017).

Recently published U-pb zircon geochronology (Moussa et al. 2008; Ali et al. 2009a, b; Be'eri-Shlevin et al. 2009a; Eyal et al. 2010; Ali et al. 2012b; Andresen et al. 2014; Eliwa et al. 2014; Ali 2015) revealed that the emplacement of the postcollisional Younger Granites had taken place throughout the prolonged 635–580 Ma period. They have been emplaced as two separate, but partially overlapping calc-alkaline and alkaline suites at 635–590 Ma and 608–580 Ma, respectively (Ali et al. 2009a, b; Be'eri-Shlevin et al. 2009c; Eyal et al. 2010, Morag et al. 2011).

These recent geochronological data prove that various granitoid types that were supposed to be evolved in different tectonic settings (i.e. late- to postorogenic vs. anorogenic), were indeed emplaced and crystallized almost contemporaneously within the northern ANS for 20 m.y. long period.

Based on the tremendous published geochemical data, Younger granites show SiO_2 range between 70 and 80 wt%, K_2O tend to be generally higher than 3.8 wt%, the K_2O/Na_2O ratios >1, the FeO*/MgO ratios >4, and the CaO varies widely between 0.1 and 1.6 wt%. On the other hand, they are enriched in the high field strength elements (HFSE; Nb, Ta, Zr, Hf, Y, U, Th) and total REEs and relatively depleted in Ba, Sr, and have high Rb/Sr and conversely low K/Rb ratios. Although their REE patterns vary between LREE-enriched to almost flat, they all exhibit only negative Eu anomaly regardless of its magnitude. The calc-alkaline suite granitoids (subsolvous to transsolvous fractionated I-type and A-type) are magnesian and peraluminous to metaluminous, whereas the alkaline suite ones (hypersolvous A-type) are ferroan to slightly magnesian and peralkaline (although aluminous and metaluminous rocks are not uncommon). The calc-alkaline Younger Granites are more enriched in Sr and Ba, but relatively depleted in Zr, Nb, Y, Zn and K in comparison with the alkaline suite granitoids. Limited overlap in trace element abundances of the two suites occurs at silica values of 74–76 wt%. The most distinctive feature of the calc-alkaline suite granitoids is their higher Eu/Eu* values (0.5–1), giving rise to shallow negative anomalies. Despite the marked multiplicity in REE patterns observed in Younger Granites from the alkaline suite, overall these granitoids are obviously differentiated from the calc-alkaline granitoids by higher ΣREE and much lower Eu/Eu* values. The previous trait accounts for the characteristic gull-wing shape of their REE patterns due to the pronouncedly large negative Eu anomalies.

There are two contrasting views on the source of magma from which the Younger Granites have crystallized. Many workers have argued magma derivation by high degree partial melting of crustal materials including mafic lower crustal rocks (e.g. Farahat et al. 2007), middle crust granodiorites-tonalites (e.g. Mohamed and El-Sayed 2008; Farahat and Azer 2011) and metasedimentary protolith (e.g. Moghazi et al. 2004; El-Bialy and Omar 2015). Alternatively, others maintained mixing/mingling of juvenile mantle-derived magma with felsic crustal melts (e.g. Farahat et al. 2011; Ali et al. 2016).

2.4.9 Dokhan Volcanics

The terminal post-collisional stage of the Neoproterozoic crustal evolution of the ANS in Egypt (Eastern Desert and Sinai) was commenced by a second major volcanic episode in which the calc-alkaline Dokhan Volcanics were erupted. This was immediately succeeded or in places synchronously accompanied by the deposition of molasse-type Hammamat Group of sediments (Akaad and Noweir 1980) and the emplacement of the postcollisional Younger Granite intrusions (Moghazi 2003; Be'eri-Shlevin et al. 2009b, c, 2011; Abd El-Rahman et al. 2010; El-Bialy 2010; Eyal et al. 2010; Johnson et al. 2011; Eliwa et al. 2014). Dokhan Volcanics differ from the preceding younger arc metavolcanics (YMV; Stern 1981) in their larger abundance of felsic varieties (e.g. dacite and rhyolite), higher content in potassium, and typical occurrence of welded tuffs and ignimbrites (El Gaby et al. 1991).

The Dokhan volcanics occupy a limited area of the Egyptian basement, and are best exposed north of latitude 26°N in the Eastern Desert (e.g. NED and northernmost CED) particularly at their type locality Gabal Dokhan from which they acquired their name and also in south Sinai (Fig. 2.14). In the south Eastern Desert, they are less common and reported from few areas such as Wadi Allaqi (e.g. El-Sayed et al. 2004) and Wadi Ranga (Gharib and Ahmed 2012). They are not recorded in the Western Desert. In south Sinai, the what's known as Rutig, Fierani, Kid-Malhak, Meknas and other late Neoproterozoic volcanics are believed to belong to the classical Dokhan volcanics of the Eastern Desert (e.g. Bentor 1985; Samuel et al. 2001; Moussa 2003; El-Bialy 2010; Azer and Farahat 2011; Be'eri-Shlevin et al. 2011).

Most studies have shown that Dokhan Volcanics have medium- to high-K calc-alkaline affinities and are unmetamorphosed with dominantly porphyritic texture and felsic to intermediate composition that have been formed in subaerial environment (El Gaby et al. 1989; Abdel-Rahman 1996; Mohamed et al. 2000; Moghazi 2003; El-Sayed et al. 2004; Eliwa et al. 2006, 2010, 2014a, b; Breitkreuz et al. 2010; El-Bialy 2010; Azer and Farahat 2011; Obeid and Azer 2015). The Dokhan volcanic successions vary with respect to their compositional spectrum, association and/or stratigraphic relationship with the Hammamat sediments and thickness from basin to basin.

The Dokhan Volcanics are frequently associated and/or interbedded with the immature Hammamat sediments, forming extensive Dokhan–Hammamat volcanosedimentary successions (e.g. Eliwa et al. 2010; Azer and Farhat 2011; Be'eri-Shlevin et al. 2011; Khalaf 2013). However, some Dokhan occurrences at the northernmost NED, for instance Gabal Samr El-Qaa, are represented merely by Dokhan Volcanic successions and lack the Hammamat sediment (e.g. Eliwa et al. 2014).

The most common and volumetrically important lava types among Dokhan Volcanics are andesites, dacites and rhyodacites with frequent rhyolites and less common andesitic basalt, basalt and trachyte intercalations. Ash fall tuffs

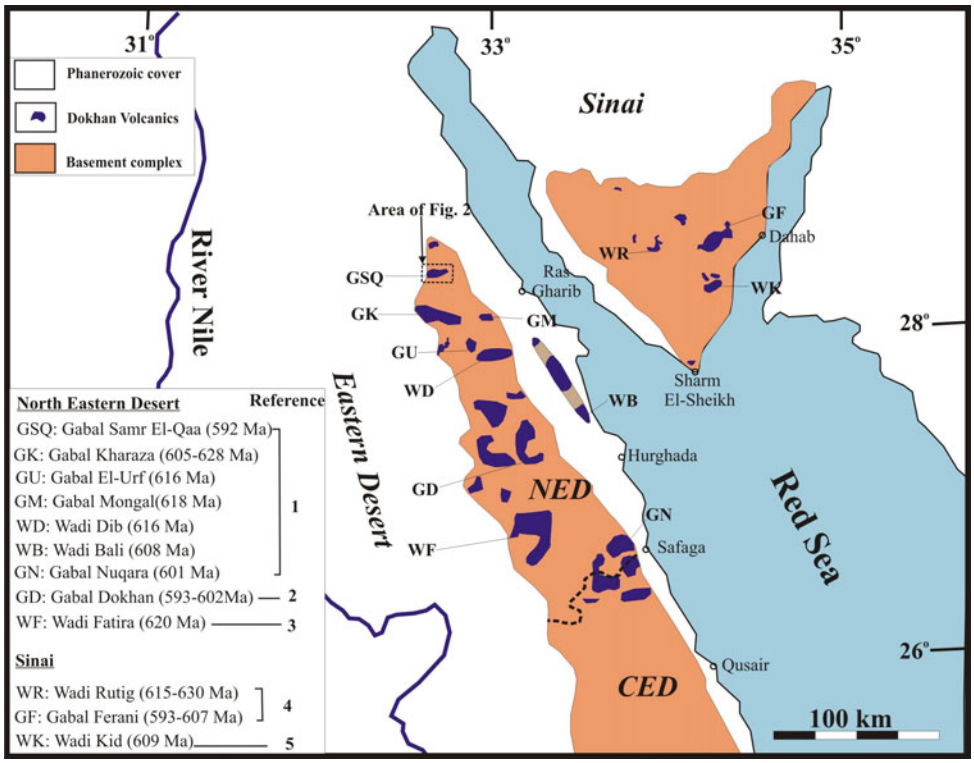

Fig. 2.14 Distribution and radiogenic ages of Dokhan Volcanics in the northern and central Eastern Desert and Sinai (after Eliwa et al. 2014). The boundary between NED and CED is after Greiling et al. (1994). References for the given isotopic ages are: (1) Breitkreuz et al. (2010); (2) Wilde and Youssef (2000); (3) Abdel-Rahman and Doig (1987); (4) Be'eri-Shlevin et al. (2011); (5) Bielski (1982)

and ignimbritic rocks are commonly interbedded with the lava succession. Although these volcanics are characteristically medium- to high-K calc-alkaline, occasional low-K tholeiitic basaltic and andesitic lavas have been recorded in some successions (e.g. Gharib and Ahmed 2012; Khalaf 2012; Alaabed and El Tokhy 2014; Azzaz et al. 2015). Successions containing basaltic lavas are argued to represent either continuums of basalt-rhyolite composition with no apparent compositional gaps (e.g. Abdel-Rahman 1996; El-Sayed et al. 2004; Eliwa et al. 2006; Obeid and Azer 2015), or bimodal suites (Stern and Gottfried 1986; Mohamed et al. 2000).

At their type locality, Gabal Dokhan (Basta et al. 1980), these volcanics constitute a thick sequence of stratified lava flows of intermediate to acid composition together with subordinate sheets of ignimbrite and few intercalations of pyroclastics. The maximum thickness of the sequence is 1200 m and the flows are 10–50 m thick each. The rocks are mostly porphyritic and amygdaloidal of different shades of grey, that frequently grade into the reddish to deep purple color of the "Imperial Porphyry". The base of each individual flow is usually chilled, being fine grained and almost non-porphyritic, the porphyritic crystals increase in size upwards. Alternation of intermediate (andesite and Imperial Porphyry) and acidic (rhyodacite) flows extend over the greater part of Gabal Dokhan area, but the andesites and the petrographically related Imperial Porphyry predominate near the top of the sequence.

As to the relative age of the Dokhan Volcanics, field relations signify that they crosscut the island arc Older Granites, intruded by the postcollisional Younger Granites and predate the Hammamat Group of sediments (El Ramly 1972; Akaad and Noweir 1980). The last relation is demonstrated by the abundance of locally derived Dokhan porphyritic pebbles in the Hammamat conglomerates. Moreover, in the area of Wadi Shait and Gabal Dokhan, these volcanics are unconformably overlain by the Hammamat sedimentaries. In some other localities, however (Wadi Dara, Wadi Dib and Gabal El Urf north of latitude 27°30′N), an interfingering relation between the two rock units can be observed indicating that the Dokhan volcanicity was still active when the basal parts of the Hammamat were being deposited (M.F. El Ramly, personal communication). Based upon precise U-pb zircon SHRIMP ages of twelve Dokhan Volcanic samples from different nine occurrences in the NED, Breitkreuzet al. (2010) have revealed that the Dokhan Volcanics were erupted during two main pulses of volcanic activity: 630–623 Ma and 618–592 Ma. Their obtained ages in company with the formerly published reliable U-Pb zircon ages for Dokhan Volcanics from the Eastern Desert (e.g. Stern and Hedge 1985; Wilde and Youssef 2000) and Sinai (Be'eri-Shlevin et al. 2011;

Moghazi et al. 2012; Moreno et al. 2012) indicate the eruption of the Dokhan Volcanics within the 590–630 Ma time frame (Fig. 2.14).

The characteristic geochemical features of the calc-alkaline Dokhan Volcanics are their strong enrichment in the large ion lithiophile elements (LILE) Rb, Ba, K and Th relative to the high field strength elements (HESF) Nb, Zr, Y, P and Ti, high LILE/HFSE ratios, and depletions of Nb relative to N-MORB. Subsidiary adakitic lavas are recorded in some Dokhan volcanic successions in the NED, and are geochemically distinguished by very low Y (<18 ppm) and HREE (Yb $\leq$ 2 ppm) contents, with high Al2O3 (>15 wt%), Sr (>650 ppm) and Sr/Y (>40) (Eliwa et al. 2006; Obeid and Azer 2015). They additionally have low Zr, Nb and Rb, and high Ni and Cr concentrations contrasted to the coexisting calc-alkaline lavas.

Until the opening years of this century, there was a considerable controversy about the tectonic environment in which the Dokhan magmas were generated. The debate hinged about whether Dokhan Volcanics have been evolved: (1) in a subduction environment (Ragab 1987; El Gaby et al. 1989, 1990; Hassan and Hashad 1990; Abdel-Rahman 1996; Samuel et al. 2001), (2) in an anorogenic extensional intra-continental rift after crustal thickening (Stern and Gottfried 1986; Stern 1994); or (3) during transition between subduction and extension (Ressetar and Monard 1983; Mohamed et al. 2000; Moghazi 2003). Based on the dual orogenic arc-type and anorogenic within-plate geochemical signatures coupled with the recently published U-Pb zircon ages (590–630) of Dokhan Volcanics, a consensus has been reached that these volcanics were erupted in a transitional post-collisional setting (El-Sayed et al. 2004; Eliwa et al. 2006; El-Bialy 2010; Azer and Farahat 2011; Be'eri-Shlevin et al. 2011; Khalaf 2012; Obeid and Azer 2015). The post-collision Dokhan Volcanism is demonstrated by the extensional collapse of the ANS following continental collision between the juvenile ANS crust and the pre-Neoproterozoic continental blocks of west Gondwana (Saharan Metacraton), which was controlled primarily by lithospheric delamination and slab breakoff (Moghazi 2003; El-Bialy 2010; Eliwa et al. 2014).

The parent magma of the Dokhan Volcanics was most likely produced by partial melting of more primitive crustal rocks belonging to older accreted arc terrains of the juvenile ANS crust (Breitkreuz et al. 2010; El-Bialy 2010, Azer and Farahat 2011; Eliwa et al. 2014). This conclusion is supported by the existence of older Cryogenian, inherited zircon component in some Dokhan volcanics (Wilde and Youssef 2000; Breitkreuz et al. 2010). Moreover, the record of considerably older Mesoproterozoic zircon xenocrysts in several Dokhan Volcanics in the NED (Breitkreuz et al. 2010) authenticates the contribution of pre-ANS crustal rocks to the Dokhan magmas. Nevertheless, some authors consider the generation of several Dokhan Volcanics through partial melting of lithospheric mantle source with varying contributions from either older crustal rocks or slab-derived melts (e.g. Mohamed et al. 2000; Eliwa et al. 2006; Khalaf 2012; Alaabed and El-Tokhi 2014; Makovicky et al. 2016).

2.4.10 Hammamat Group

The terms "Hammamat Series" (El Ramly and Akaad 1960) and "Hammamat Group" ((Akaad and Noweir 1969, 1980) are after the type locality at Wadi Hammamat, CED, Egypt (Fig. 2.15). Therein, they are represented by terrestrial thick clastic sedimentary succession reaching a thickness of about 4000 m (Akaad and Noweir 1980). In other areas for instance Wadi Kariem and Wadi Arak, Hammamat successions attain a thickness of 5000–6000 m (Eliwa et al. 2010). They consist of fluvial conglomerates and sandstones and lacustrine pelites, which are in part volcaniclastic in composition (Grothaus et al. 1979; Holail and Moghazi 1998; Eliwa et al. 2010).

The Hammamat Group sediments occur in numerous isolated basins in the NED and CED, and there are over twenty-five Hammamat basin relics there. The outcropped succession in Wadi Hammamat together with those of Wadi Kareim, Wadi Zeidun, Wadi Igla, Wadi El Miyah are the main occurrences of in the CED (Fig. 2.15). In the NED, a number of relatively small exposures are recorded in the areas of Wadi Dib, Wadi Dara, Esh El Mellaha range, Gabal El Urf and Gabal Um Tawat. In the SED four minor exposures were mapped at Wadi Shait, Wadi Ranga, Wadi Khashab and north east of Gabal Mansouri ring complex just north of Egypt-Sudan border line.

Numerous volcano-sedimentary successions from Sinai have been correlated with the Dokhan–Hammamat successions of the Eastern Desert (e.g., Ferani, Rutig, Kid-Malhaq; Fig. 2.15) (Schürmann 1966; Bentor 1985; El Gaby et al. 1991; Moussa 2003; El-Bialy 2010; Be'eri-Shlevin et al. 2011; Samuel et al. 2011; Andresen et al. 2014). Recent robust SIMS U-pb zircon ages have placed some of these sequences within the age limit of the Dokhan–Hammamat successions of the ED. Be'eri-Shlevin et al. (2011) reported SIMS zircon U-pb ages spanning ca. 620–595 Ma for the Rutig and Ferani volcanics, while Samuel et al. (2011) obtained U-pb deposition age confined to ca. 620–610 Ma and 600–590 Ma for Rutig conglomerates, implying that these volcanics and sediments were coeval with that of the Dokhan Volcanics and Hammamat Group from the ED, respectively. All in all, the Hammmamt sediments gave a late Ediacaran depositional age, in the time interval

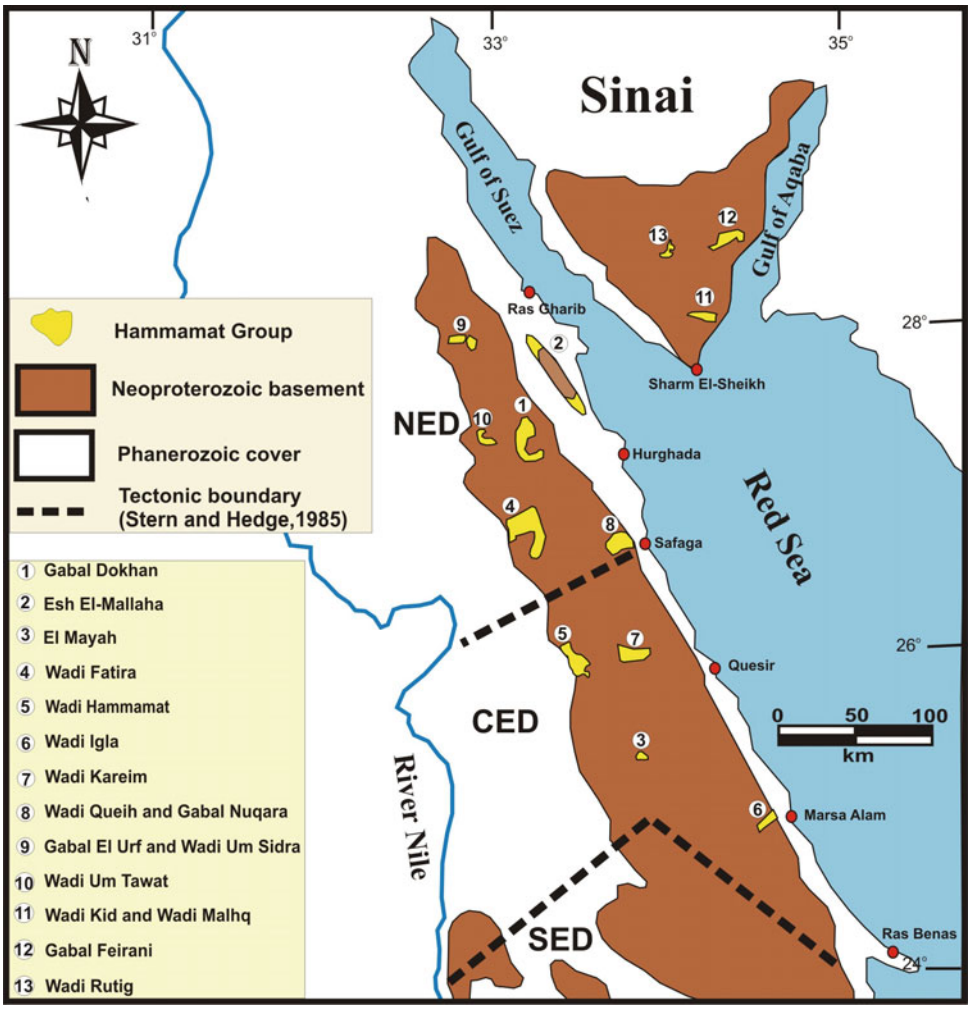

Fig. 2.15 A map showing the distribution of the major Hammamat basins in the Eastern Desert and Sinai (modified after Abd El-Wahed 2010 and Nasiri Benzenjani et al. 2014)

632–590 Ma, in both the Eastern Desert (Wilde and Youssef 2002; Nasiri Bezenjani et al. 2014) and Sinai (e.g. Samuel et al. 2011; Moreno et al. 2012; Eyal et al. 2014).

Akaad and Noweir (1969, 1980) divided The Hammamat Group into two formations; the lower Igla Formation at the base followed by the Shihimiya Formation above. The Igla Formation in the area of Wadi Hammamat comprises an interbedded and repeatedly alternating sequence of wholly clastic red to purple beds with minor greenish grey to grey coloured beds. They consist of sandstones, siltstones and minor fine conglomerates. Primary structures such as graded bedding, current bedding, banding and rhythmic alternation and sometimes asymmetrical current ripple marks and rain drops are still preserved. The Igla Formation gradually merges upward into the Shihimiya Formation with the development of the greenish and greyish beds and the gradual disappearance of the red beds. The latter is subdivided into three members including Um Had Conglomerates which is but the classic "Breccia Verde d'Egitto"; the characteristic rock type of the Hammamat Group, plus Um Hassa Greywack and Rasafa Siltstone members.

The Hammamat Group sediments have been diversely studied from different standpoints including their tectonic and structural controls (Fritz and Messner 1999; Shalaby et al. 2006; Abd El-Wahed 2010; Fowler and Osman 2013; Fowler and Abdeen 2014), depositional style (Grothaus et al. 1979; Eliwa et al. 2010, Khalaf 2012, 2013), petrography, geochemistry and provenance (Willis and Stern 1988; Holail and Moghazi 1998; Abd El-Rahman et al. 2010), lithostratigraphy (Akaad and Noweir 1969, 1980; Khalaf 2010) and detrital zircon provenance and geochronology (Wilde and Youssef 2002; Samuel et al. 2011; Nasiri Bezenjani et al. 2014).

The stratigraphic relationship between the Dokhan volcanics and Hammamat sediments seems to differ with locality. In some Hammamat basins the molasse sediments rest unconformably upon Dokhan Volcanics (Hassan and Hashad 1990; Akaad 1996; Holail and Moghazi 1998, Khalaf 2010, 2012). In others, they are interfingered with the Dokhan Volcanics (Ressetar and Monrad 1983; Ries et al. 1983; El Gaby et al. 1990, Abd El-Wahed 2010; Eliwa et al. 2010) and infrequently, the Hammamat sediments rest

conformably underneath the Dokhan (Stern and Hedge 1985; Willis et al. 1988). These different stratigraphic relations may be linked to locally diverse geodynamic controls on sedimentation and the volcanism (Johnson et al. 2011; Fowler and Osman 2013).

The Hammamat Group is generally accepted to have been deposited in post-amalgamation basins during the Ediacaran time (e.g. Johnson et al. 2011; Hamimi et al. 2013). Nevertheless, it has also been proposed that some sediments do not possess post-amalgamation molasse attributes, since they are folded, cleaved, and the pebbles are stretched at Wadi Hammamat and elsewhere (Ries et al. 1983). Whatever, the depositional tectonic setting of the Hammamat molasse basins is greatly disputed and various tectonic settings have been implied for them: deposition in fluvial systems of continental proportions (Wilde and Youssef 2002), isolated basins (Grothaus et al. 1979), intra-arc basins (Holaila nd Moghazi 1998), foreland basin (El Gaby et al. 1984; Fritz et al. 1996), intermontane basins (Abd El-Wahed 2010); piggy-back foreland basins (Andresen et al. 2009), fault-bounded basins (Abdeen and Greiling 2005; Fowler and Osman 2013), strike-slip basins (Fritz and Messner 1999), or strike-slip pull-apart basins (Shalaby et al. 2006).

2.4.11 Post Hammamat Felsites

This rock unit includes effusive felsite, felsite porphyry and quartz porphyry bodies, sheets, dykes and cone-like intrusions commonly associating the Hammamat Group in a number of localities in the Eastern Desert such as Gabal Atalla, Wadi Igla, Wadi Ranga, Wadi Shait and Wadi El Miyah. They are not known and no comparable rocks have been recorded in Sinai and the Western Desert.

The Atalla felsite intrusion, which is an elongate mass (almost 19.5 km long by 1–3 km wide), is definitely the largest felsite intrusion recorded in the basement complex of the Eastern Desert (Essawy and Abu Zeid 1972). Aside from this immense felsite intrusion, other felsites were recorded in several areas in the Eastern Desert. The majority of these felsites crosscuts the rocks of the Hammamat Group and are consequently known as Post-Hammamat felsites.

The first discovery of felsite intrusions were in Wadi Igla by Akaad (1957), where they are intruding the Igla Formation. Akaad and El Ramly (1958) detected analogous felsites intruding or intimately associated with the Igla Formation at Wadi Shait, Wadi Ranga, and Wadi El Miyah. Noweir (1968) mapped an elongate belt of felsites some 15 km long cutting the Igla and Shihimiya Formations, the serpentinites and the Dokhan Volcanics in the Hammamat-Um Seleimat district south of the Qena-Quseir road. Akaad and Noweir (1969) considered these felsites as a distinct unit in the succession of the Egyptian basement and gave them the name "Post-Hammamat Felsite" because of the intimate association of many of their outcrops with the Hammamat sediments. Essawy and Abu Zeid (1972) studied the felsite intrusion forming Gabal Atalla, north of Qena-Quseir road and the rhyolite tuffs and flows to its west. This huge felsite intrudes the rhyolite tuffs and flows which are overlain unconformably by sediments of the Hammamat Group. These two authors postulated that the felsites and rhyolite tuffs and flows pertain to the same parent magma which gave rise to the Dokhan volcanics and that the rhyolites predate the deposition of the Hammamat sediments but the felsites post-date them. According to Greenberg (1981), field evidence and chemistry indicate that the felsite might be directly related to or comagmatic with the Younger Granites.

These felsites have not been dated yet, but according to their stratigraphic position above the Dokhan volcanics, their cutting relation with the Hammamat sediments and their intrusion by the Younger Granites, they are probably intruded around 600 Ma.

2.4.12 Postcollisional Layered and Gabbro Intrusions

This rock unit comprises two distinct varieties of somewhat akin compositions that have the same relative age, lithostratigraphic position and had been intruded in postcollisional tectonic regime. The first of them is the mafic-ultramafic layered intrusions that have been just recently acknowledged (Azer and El-Gharabawy 2011; Abdel Halim et al. 2016; Azer et al. 2017). The second genre is represented by undifferentiated gabbroic intrusions, popularly known as "Younger Gabbros" (e.g. Basta and Takla 1974, Takla et al. 1981). Among other Precambrian basement units, these rocks are only intruded by the postcollisional Younger Granites, and in turn intrude and enclose xenoliths of Older Granites, Dokhan Volcanics, metagabbro-diorite complex and other older basement rock units (e.g. El-Metwally 1992; El-Metwally and Abdallah 2004; Azer and El-Gharabawy 2011, Khalil et al. 2015; Abdel Halim et al. 2016; Gahlan et al. 2017).

2.4.12.1 Layered Mafic-Ultramafic Intrusions

In the Egyptian shield, mafic-ultramafic intrusions are classified into four tectonomagmatic groups: obducted oceanic lithosphere (ophiolitic sequences; Sect. 2.4.1), island-arc intrusions (Alaskan-type complexes; Sect. 2.4.6), postcollisional layered intrusions and rift-related intrusions. Rift-related peridotites are limited to Zabargad Island ($\approx$4 km^2), and are concluded that they may be an asthenopheric mantle diapir which intruded the thinned ANS juvenile continental crust during opening of the Red Sea

(Boudier et al. 1988; Brueckner et al. 1995; Bosch and Bruguier 1998).

The postcollisional mafic-ultramafic layered intrusions are very infrequent in the Egyptian Precambrian basement. So far, the established of these layered intrusions are limited to those of Gabal Imleih (Azer and El-Gharabawy 2011) in Sinai and Gabal Motaghairat (Abdel Halim et al. 2016) and Gabal Dahanib (Azer et al. 2017) in the south Eastern Desert. The layered mafic-ultramafic intrusions show vertical zonation from ultramafic members at the bottom upwards into mafic rocks towards the superior parts of the intrusion. The layered intrusions and Alaskan-type complexes sometimes possess analogous lithologies, but the latter is distinguished by exhibiting concentrically zoned intrusions with ultramafic members in the center and mafic rocks at the margin of zonation as well as other mineralogical attributes (for more details see Azer et al. 2017). The magma type of these intrusions varies from tholeiitic to medium-K calc-alkaline (Azer and El-Gharabawy 2011; Abdel Halim et al. 2016; Azer et al. 2017). Until now, there are no available isotopic ages for the three aforementioned layered intrusions.

The Motaghairat intrusion occurrs few kilometrs southwest of Ras Benas as a NE–SW elongate dike-like body (3 km long and 1.5 km wide) at the frontiers between the Precambrian basement and Miocene sedimentary Rocks. It intrudes the surrounding metagabbro-diorite complex country rocks with sharp contact and the development of a contact aureole of 20–40 m width (Abdel Halim et al. 2016). The Motaghairat intrusion consists of unmetamorphosed layered sequence with ultramafic cumulates at the base changing upward into troctolite and gabbro. The ultramafic component includes peridotite and pyroxenite. Peridotite forms the substructure of the intrusion and consists mostly of lherzolite with lesser dunite. Pyroxenite forms a 5–8 m thick discontinuous layer topping the peridotite and as thin bands in the overlying troctolite The later passes upward to olivine gabbro, gabbro and anorthosite.

Further about 30 km southwest of the Gabal Motaghairat, the prominent layered mafic–ultramafic intrusion of Gabal Dahanib does exist. Dixon (1981) concluded that the Gabal Dahanib is a layered mafic–ultramafic 1.5 km thick sill consisting of dunites, harzburgites plus thin chromite layers at the base grade upward through pyroxenites to layered gabbros and occasional anorthosite at the top. Recently, based mainly on mineral chemistry of silicates and spinels and limited whole-rock geochemistry (6 samples), Khedr and Arai (2016) identified Gabal Dahanib intrusion as a concentrically zoned Alaskan-type complex. However, more recently, Azer et al. (2017) argued that the Dahanib mafic–ultramafic intrusion lacks any features that credibly identify it as a representative Alaskan-type complex and confirmed that it is more analogous in all aspects to layered mafic-ultramafic intrusions emplaced into stable cratons. The Gabal Dahanib covers about 7 km^2 and forms a N-S-trending elliptical lopolith-like layered intrusion (Azer et al. 2017). Dahanib intrusion is made up of a basal suite of ultramafic lithologies including dunite, lherzolite, wehrlite and pyroxenite and a superimposing mafic suite of olivine gabbronorite, gabbronorite and anorthosite. It exhibits obvious layering of modal content, discernable directly in outcrop, along with cryptic layering noticeable through variations in mineral compositions (Dixon 1981; Azer et al. 2017). The Dahanib intrusion lacks any evidence of metamorphism or deformation, with good preservation of textures and primary mineralogy. It shows sharp intrusive contacts against the Older Granites, metamorphic and gabbro/diorite gneissic country rocks, as well as enclosing xenoliths of the former (Azer et al. 2017).

The Gabal Imleih layered mafic–ultramafic intrusion sits in the northwestern segment of the exposed basement of Sinai, about 50 km to the northwest of Saint Katherina. The intrusion of Gabal Imleih occurs as an ovoid intrusive body covering an area of about 45 km^2. The country rocks include gneisses, Older Granites, Dokhan Volcanics and postcollisional Younger Granites. The field relationships indicate that the intrusion is older than other country rocks excepting the Younger Granites of Gabal Iqna (Azer and El-Gharbawy 2011). It intrudes into gneisses and Older Granites whereas it is intruded by the postcollisional Iqna granite. The contacts between this intrusion and these couple of older country rocks are sharp intrusive. Also, this layered intrusion is younger than the Iqna Sharaa volcanics (Dokhan Volcanics) since the marginal parts of the intrusions enclose volcanic xenoliths of the latter (Azer and El-Gharabawy 2011). The Imleih intrusion is normally undeformed, shows little or no indication of metamorphism, and exhibits distinct cumulate textures. This intrusion is typified by layering; starting with peridotite at the bottom to pyroxenite, gabbros and anorthosite at the top. Volumetrically, The main rock type of Gabal Imleih layered intrusion is the cumulus gabbro followed by lesser amounts of peridotite, pyroxenite and anorthosite (Fig. 2.2b in Azer and El-Gharabawy 2011).

2.4.12.2 Younger Gabbro Intrusions

Younger Gabbro intrusions are widespread in both the Eastern Desert and Sinai, even those of Sinai have received more attention during the last decade (e.g. Abu Anbar 2009; Azer et al. 2012; Abdel-Karim 2013; Khalil et al. 2015; Gahlan et al. 2017). As in the case of layered intrusions, Younger Gabbros are bracketed between the preceding Older Granites and the postdating Younger Granites. These intrusions are almost devoid of ultramafic members and undeformed and unmetamorphosed (e.g. El-Metwally 1992; Abu anbar 2009; Azer et al. 2012; Abdel-Karim 2013). The majority of these intrusions consist of pyroxene–hornblende

gabbro and hornblende gabbro, although other rock types are encountered including quartz diorite, anorthosite, hornblendite, appinitic gabbro and olivine pyroxene-, pyroxene gabbros (e.g. Azer et al. 2012; Abdel-Karim 2013; Gahlan et al. 2017).

The magma type of the postcollisional Younger Gabbros varies from tholeiitic to calc-alkaline and they are rarely alkaline (Azer et al. 2012; Abdel-Karim 2013; Gahlan et al. 2017). The two published isotopic ages of these gabbroic intrusions are limited to the Wadi Nesriyn gabbro intrusion in SW Sinai and point to their younger emplacement relative to the metagabbro-diorite and Alaskan-type complexes. They are a Rb–Sr whole-rock isochron age of 599 ± 5 Ma (Abu Anbar 2009) and an ion microprobe U-pb zircon age of 617 ± 19 Ma (Be'eri-Shlevin et al. 2009a).

2.4.13 Katherina A-Type Volcanics

Katherina Volcanics (Agron and Bentor 1981) represent the last chapter of magmatism in the Precambrian basement of Egypt, and mark the onset of the anorogenic period during which the Arabian-Nubian Shield was subjected to tensional stresses and intra-plate rifting (El-Bialy and Hassen 2012). This late Neoproterozoic intra-plate volcanism was mainly represented by alkaline rhyolitic flows and pyroclastics and subvolcanic porphyries. However, this unit is restricted in occurrence to Sinai and no equivalent rocks have been identified in the Eastern Desert yet.

The Katherina Volcanics outcrops in Sinai comprise those at Gabal Katherina (Eyal and Hezkiyahu 1980; Bielski 1982; Farahat and Azer 2011; Azer et al. 2014), Gabal Abu-Durba (El-Bialy 1999; Abu-El Leil and Abdel Razek 2001); W. Mahash, W. Khilifeya and Gabal Homra in NE Sinai (Agron and Bentor 1981; Samuel et al. 2007) and Gabal Ma'ain (El-Bialy and Hassen 2012) (Fig. 2.16).

Further northward, alkaline volcanics of quite similar age and nature are exposed in some localities such as Yotam Plain and Amram massive and Wadi Araba, Abu Khusheiba, Wadi, Feinan, Gharandal (Jordan). The previous Levantine alkaline volcanic suites have a typical "rift-related" bimodal character, with available isotopic ages in the 530–565 Ma range (Segev 1987; Mushkin et al. 2003).

Quite different whole-rock Rb–Sr isochron ages have been constrained for Katharina Volcanics in Sinai. Aegirine-riebeckite rhyolite porphyries from Gabal Katherina were dated at 578 ± 6 Ma and some alkaline rhyolites from the abovementioned three NE Sinai localities yielded

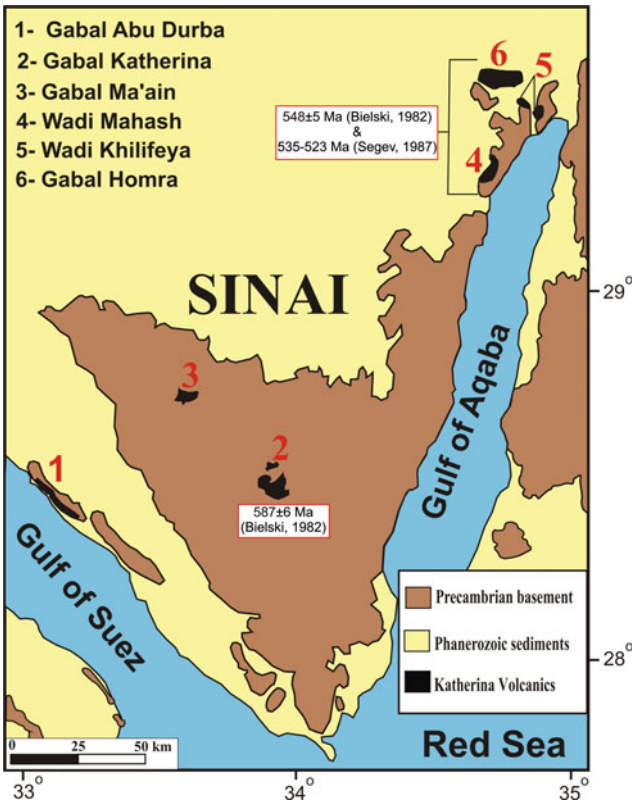

Fig. 2.16 Location of the main exposures of Katherina Volcanics in Sinai. Available Rb–Sr ages are also given for some of them

548 ± 5 Ma (Bielski 1982). Nevertheless, Segev (1987) obtained rather young er ages (523–535 Ma) for alkaline rhyolitic volcanics from two of the NE localities (Gabal Homra and W. Khilifeya).

Katherina Volcanics occur as stratified volcanic sequences of alkaline rhyolitic lavas and pyroclastics, associated with subvolcanic intrusions of rhyolite-granite porphyries and granophyres. However, those of Gabal Ma'ain lack the subvolcanic intrusions (El-Bialy and Hassen 2012). The recorded thicknesses of Katherina volcanic sequences vary between 200 m and 450 m and are dominated by pyroclastics (tuffs and ignimbrites) rather than lava flows (El-Bialy 1999; Samuel et al. 2007; El-Bialy and Hassen 2012).

The preceding postcollisional Younger Granites are unconformably overlain and/or crosscut by the Katherina volcanic successions and also intruded by the rhyolite-granite porphyry bodies (Fig. 2.17). The subvolcanic intrusions seem to be emplaced after the extrusion of the volcanics as they intrude them in Wadi El-Mahash and Gabal Katherina areas (Samuel et al. 2007; Azer et al. 2014).

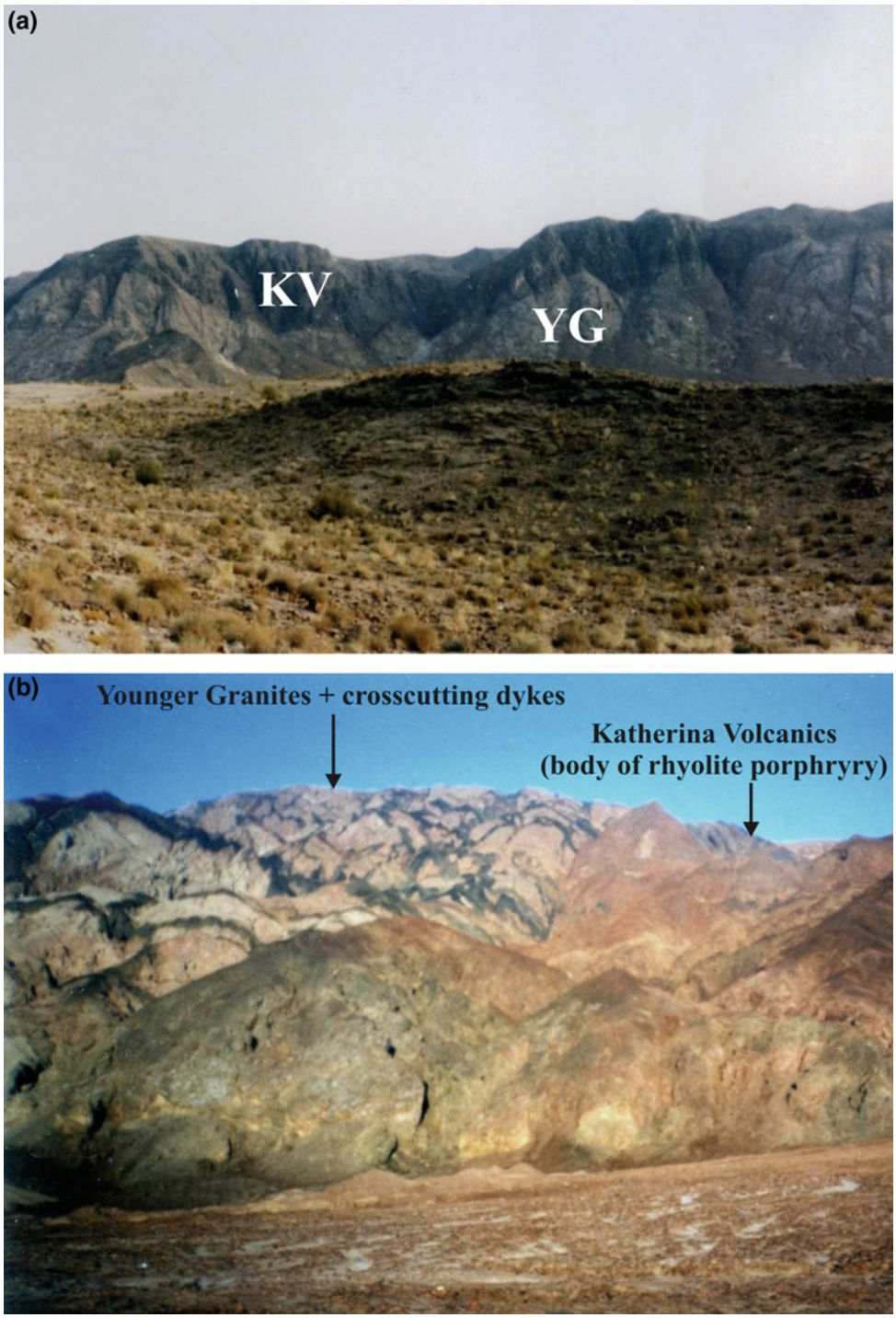

Fig. 2.17 **a** Distant view showing the Katherina volcanics (KV) unconformably overlying the Younger Granites along a sub-horizontal contact, Gabal Ma'ain. **b** A body of rhyolite porphyry intrudes both Younger Granites and a swarm of dykes crosscutting them, Gabal Abu Durba. Location of the two localities is indicated in Fig. 2.16

The Katherina volcanic rocks belong to the potassic to ultrapotassic alkaline magma series and are typically peralkaline, though some possesses peraluminous to slightly metaluminous character. These alkaline rhyolites show most of the classical geochemical features of A-type magmas, including their evident enrichment of the incompatible elements, Nb, Y, Ga, Zn, Ce and total REE, as well as high FeO*/(FeO* + MgO) and 10 000*Ga/Al_2O_3 ratios (Samuel et al. 2007, El-Bialy and Hassen; Azer et al. 2014).

Acknowledgements Thanks are due to Professor Dr. Zakaria Hamimi for the kind invitation to present this chapter in the 2018 version of "Geology of Egypt". I am indebted to Professor Dr. Harald Fritz for his constructive reviews which improved the chapterr considerably.

References

Abd El Ghaffar NI, Ramadan AA (2017) Geochemistry and origin of alkaline granites at Wadi Umm Adawi-Yahmid area, south Sinai, Egypt. J Afr Earth Sci http://dx.doi.org/10.1016/j.jafrearsci.2017.07.002

Abd El-Naby HH, Frisch W (2002) Origin of the Wadi Haimur-Abu Swayel gneiss belt, south Eastern Desert, Egypt: Petrological and geochronological constraints. Precambr Res 113:307–322

Abd El-Naby H, Frisch W, Hegner E (2000a) Evolution of the Pan-African Wadi Haimur metamorphic sole, Eastern Desert. Egypt J Metamorph Geol 18:639–651

Abd El-Naby HH, Dawood YH, Saleh GM (2000b) Pan-African Granitoids Magmatism in the Gabel Homr Akarem Area, south Eastern Desert, Egypt: geochemistry and petrogenetic implications. Chemie Erde******** 60:251–267

Abd El-Naby HH, Frisch W, Siebel W (2008) Tectonic–metamorphic evolution of the Wadi Hafafit culmination (central Eastern Desert, Egypt). Implication for Neoproterozoic core complex exhumation in NE Africa. Geol Acta 6:293–312

Abd El-Rahman Y, Polat A, Dilek Y, Fryer BJ, El-Sharkawy M, Sakran S (2009a) Geohemistry and tectonic evolution of the Neoproterozoic incipient arc-fore-arc crust in the Fawakhir area, Central Eastern Desert of Egypt. Precambrian Res 175:116–134

Abd El-Rahman Y, Polat A, Dilek Y, Fryer B, El-Sharkawy M, Sakran S (2009b) Geochemistry and tectonic evolution of the Neoproterozoic Wadi Ghadir ophiolite, Eastern Desert, Egypt. Lithos 113:158–178

Abd El-Rahman Y, Polat A, Fryer BJ, Dilek Y, El-Sharkawy M, Sakran S (2010) The provenance and tectonic setting of the Neoproterozoic Um Hassa Greywacke Member, Wadi Hammamat area, Egypt: evidence from petrography and geochemistry. J Afr Earth Sci 58:185–196

Abd El-Rahman Y, Helmy HM, Shibata T, Yoshikawa M, Arai S, Tamura A (2012a) Mineral chemistry of the Neoproterozoic Alaskan-type Akaremintrusion with special emphasis on amphibole: implications for the pluton origin and evolution of subduction-related magma. Lithos 155:410–425

Abd El-Rahman Y, Polat A, Dilek Y, Kusky TM, El-Sharqawi M, Said A (2012b) Cryogenian ophiolite tectonics and metallogeny of the central Eastern Desert of Egypt. Int Geol Rev 54:1870–1884

Abd El-Wahed MA (2008) Thrusting and transpressional shearing in the Pan-African nappe southwest El-Sibai core complex, Central Eastern Desert, Egypt. J Afr Earth Sci 50:16–36

Abd El-Wahed MA (2010) The role of the Najd fault system in the tectonic evolution of the Hammamat molasse sediments, Eastern Desert. Egypt. Arab J Geo Sci 3:1–26

Abd El-Wahed MA (2014) Oppositely dipping thrusts and transpressional imbricate zone in the Central Eastern Desert of Egypt. J Afr Earth Sci 100:42–59

Abd El-Wahed MA, Harraz HZ, El-Behairy MH (2016) Transpressional imbricate thrust zones controlling gold mineralization in the Central Eastern Desert of Egypt. Ore Geol Rev 78:424–446

Abdeen MM, Greiling RO (2005) A quantitative structural study of Late Pan-African compressional deformation in the Central Eastern Desert (Egypt) during Gondwana assembly. Gondwana Res 8:457–471

Abdel Halim AH, Helmy HM, Abd El-Rahman YM, Shibata T, El Mahallawi MM, YoshikawaM AS (2016) Petrology of the Motaghairatmafic–ultramafic complex, Eastern Desert, Egypt: a high-Mg post-collisional extension-related layered intrusion. J Asia Earth Sci 116:64–180

Abdel-Karim AM (1995) Late Precambrian metagabbro–diorite complex from southwest Sinai. Egypt. Egypt J Geol 39:715–738

Abdel-Karim AM (2013) Petrology, geochemistry and petrogenetic aspects of younger gabbros from south Sinai: A transition from arc to active continental margin. Chemie Erde 73:89–104

Abdel-Karim AM, Ahmed Z (2010) Possible origin of the ophiolites of Eastern Desert, Egypt, from geochemical perspectives. Arab J Sci Eng 35:115–143

Abdel-Karim AM, Ali S, Helmy HM, El-Shafei HM (2016) A fore-arc setting of the Gerf ophiolite, Eastern Desert, Egypt: evidence from mineral chemistry and geochemistry of ultramafites. Lithos 263:52–65

Abdelnasser M, Kumral M (2016) Mineral chemistry and geochemical behavior of hydrothermal alterations associated with mafic intrusive-related Au deposits at the Atud area, Central Eastern Desert, Egypt. Ore Geol Rev 77:1–24

Abdel-Rahman AM (1990) Petrogenesis of early-orogenic diorites, tonalites and post-orogenic trondhjemites in the Nubian Shield. J Petro 31:1285–1312

Abdel-Rahman AM (1996) Pan-African volcanism: petrology and geochemistry of the Dokhan volcanic suite in the northern Nubian Shield. Geol Mag 133:17–31

Abdel-Rahman AM, El-Kibbi MM (2001) Anorogenic magmatism: chemical evolution of the Mount El-Sibai A-type complex (Egypt), and implications for the origin of within-plate felsic magmas. Geol Mag 138:67–85

Abdelsalam MG, Stern RJ (1996) Sutures and shear zones in the Arabian-Nubian Shield. J Afr Earth Sci 23:289–310

Abdelsalam MG, Lie´geois JP, Stern RJ (2002) The Saharan Metacraton. J Afr Earth Sci 34:119–136

Abdelsalam MG, Abdeen MM, Dowaidar HM, Stern RJ, Abdelghaffar AA (2003) Structural evolution of the Neoproterozoic Western Allaqi-Heiani suture, southeastern Egypt. Precambr Res 124:87–104

Abu Anbar MM (2009) Petrogenesis of the Nesryin gabbroic intrusion in SW Sinai, Egypt: new contributions from mineralogy, geochemistry, Nd and Sr isotopes. Miner Pet 95:87–103

Abu El-Ela FF (1996) The petrology of the Abu Zawal gabbroic intrusion, Eastern Desert, Egypt: an example of an island arc setting. J Afr Earth Sci 22:147–157

Abu El-Ela FF (1997) Geochemistry of an island-arc plutonic suite: Wadi Dabr intrusive complex, Eastern Desert. Egypt. J Afr Earth Sci 24:473–496

Abu El-Ela FF (1999) Neoproterozoic tholeiitic arc plutonism: petrology of gabbroic intrusions in the El-Aradiya area, Eastern Desert. Egypt. J Afr Earth Sci 28:721–741

Abu El-Ela FF, Farahat ES (2010) Neoproterozoic podiform chromites in serpentinites of the Abu Meriewa-Hagar Dungash district, Eastern Desert, Egypt: Geotectonic implications and metamorphism. Island Arc 19:151–164

Abu El-Enen MM (2008) Geochemistry and metamorphism of the Pan-African back-arc Malhaq volcano-sedimentary Neoproterozoic association, W. Kid area, SE Sinai,Egypt. J Afr Earth Sci 51:189–206

Abu El-Enen MM, Whitehouse MJ (2013) The Feiran-Solaf metamorphic complex, Sinai, Egypt: Geochronological and geochemical constraints on its evolution. Precambr Res 239:106–125

Abu El-Enen MM, Okrusch M, Will TM (2003) Metapelitic assemblages in the Umm Zariq schists, central western Kid Belt, Sinai Peninsula. Egypt. Neu Jahrb Miner Abh 178:277–306

Abu El-Enen MM, Zalata AA, Abd El-Shakour ZA (2009) Subsolidus and anatectic migmatites: examples from the Pan African crystalline basement, Southern Sinai, Egypt. Egypt J Geol 53:63–86

Abu El-Enen MM, Abu-Alam TS, Whitehouse MJ, Ali KA, Okrusch M (2016) P-T path and timing of crustal thickening during amalgamation of East and West Gondwana: a case study from the Hafafit Metamorphic Complex, Eastern Desert of Egypt. Lithos 263:213–238

Abu-Alam TS, Stüwe K (2009) Exhumation during oblique transpression: the Feiran-Solaf region, Egypt. J Metamorph Geol 27:439–459

Abu-Alam TS, Stüwe K, Hauzenberger C (2010) Calc-silicates from Wadi Solaf, Sinai, Egypt. J Afr Earth Sci 58:475–488

Abu-Alam AT, Hamdy MM (2014) Thermodynamic modelling of Sol Hamed serpentinite, South Eastern Desert of Egypt: implication for fluid interaction in the Arabian-Nubian Shield ophiolites. J Afr Earth Sci 99:7–23

Abu-El Leil I, Abdel Razek M (2001) A geological study on the basement rocks of Abu Durba-Abu Haswa area, south Western Sinai, Egypt. Ann Geol Surv Egypt 24:219–232

Agron N, Bentor YK (1981) The volcanic massif of Biq'at Hayareah (Sinai-Negev): a case of potassium metasomatism. J Geol 89:479–495

Ahmed AA (1981) Reconsidered view on Feirane–solaf gneisses Southwest of Sinai, Egypt. Bull Fac Sci Assiut Univ 10:131–142

Ahmed AH (2013) Highly depleted harzburgite–dunite–chromitite complexes from the Neoproterozoic ophiolite, south Eastern Desert, Egypt: a possible recycled upper mantle lithosphere. Precambr Res 233:173–192

Ahmed AH, Arai S, Attia AK (2001) Petrological characteristics of podiform chromitites and associated peridotites of the Pan African ophiolite complexes of Egypt. Miner Depos 36:72–84

Ahmed AH, Hanghøj K, Kelemen PB, Hart SR, Arai S (2006) Osmium isotope systematics of the Proterozoic and Phanerozoic ophiolitic chromitites: In situ ion probe analysis of primary Os-rich PGM. Earth Planet Sci Lett 245:777–791

Ahmed AH, Helmy HM, Arai S, Yoshikawa M (2008) Magmatic unmixing in spinel from Late Precambrian concentrically-zoned mafic–ultramafic intrusions, Eastern Desert, Egypt. Lithos 104:85–98

Ahmed AH, Gharib M, Arai S (2012) Characterization of the thermally metamorphosed mantle–crust transition zone of the Neoproterozoic ophiolite at Gebel Mudarjaj, south Eastern Desert, Egypt. Lithos 142–143:67–83

Akaad MK (1957) Petrography, structure and time relations of the Igla formation. Egypt J Geol 1:93–102

Akaad MK (1996) Rock succession of the basement: an autobiography and assessment. Geol Surv Egypt. Paper No 71, 78 pp

Akaad MK, El Ramly MF (1958) Seven new occurrences of the Igla formation in the Eastern Desert of Egypt. Geol Surv Egypt. Paper No 3, 37 pp

Akaad MK, El Ramly MF (1960) Geological history and classification of the basement rocks of the central Eastern Desert of Egypt. Geol Surv Egypt. Paper No 9, 24 pp

Akaad MK, El Ramly MF (1963) The cataclastic mylonitic gneiss north of Gabal El Maiyit and the origin of the granite of Shaitian type. Geol Surv Egypt. Paper No 26:14 pp

Akaad MK, Noweir AM (1969) Lithostratigraphy of the Hammamat-Um Seleimat District, Eastern Desert. Egypt. Nature 223:284–285

Akaad MK, Noweir AM (1980) Geology and lithostatigraphy of the Arabian Desert orogenic belt of Egypt between latitudes25°35′ and 26°35′N. In: Cooray PG, Tahoun SA (eds) Evolution and mineralization of the Arabian-Nubian Shield. Inst Appl Geol Jeddah Bull, vol 3, Pergamon, Oxford, pp 127–135

Alaabed S, El-Tokhi M (2014) Mineralogical and geochemical aspects of the petrogenesis of Pan African Dokhan Volcanics at Esh El Mellaha Area-NE Desert. Egypt. Arab J Geo 7:5553–5568

Ali BH (2015) SHRIMP U-Pb zircon geochronology: evidence for emplacement time of some granitoids north Eastern Desert, Egypt. Arab J Geo sci 8:5465–5474

Ali BH, Wilde SA, Gaber MMA (2009a) Granitoid evolution in Sinai, Egypt, based on precise SHRIMP U-Pb zircon geochronology. Gondwana Res 15:38–48

Ali KA, Stern RJ, Manton WI, Kimura J-I, Khamees HA (2009b) Geochemistry, Nd isotopes and U-Pb SHRIMP dating of Neoproterozoic volcanic rocks from the Central Eastern Desert of Egypt: new insights into the ~750 Ma crust-forming event. Precambr Res 171:1–22

Ali KA, Azer MK, Gahlan HA, Wilde SA, Samuel MD, Stern RJ (2010a) Age constraints on the formation and emplacement of Neoproterozoic ophiolites along the Allaqi-Heiani Suture, south Eastern Desert of Egypt. Gondwana Res 18:583–595

Ali KA, Stern RJ, Manton WI, Johnson PR, Mukherjee SK (2010b) Neoproterozoic diamictite in the Eastern Desert of Egypt and Northern Saudi Arabia: evidence of ~750 Ma glaciation in the Arabian-Nubian Shield. Int J Earth Sci 99:705–726

Ali KA, Stern RJ, Manton WI, Kimura J-I, Whitehouse MJ, Mukherjee SK, Johnson PR, Griffin WR (2010c) Geochemical, U–Pb zircon, and Nd isotope investigations of the Neoproterozoic Ghawjah Metavolcanic rocks, Northwestern Saudi Arabia. Lithos 120:379–393

Ali KA, Andresen A, Stern RJ, Manton WI, Omar SA, Maurice AE (2012a) U-Pb zircon and Sr–Nd–Hf isotopic evidence for a juvenile origin of the c 634 Ma El-Shalul Granite, Central Eastern Desert, Egypt. Geol Mag 149:783–797

Ali KA et al (2012b) Composition, age, and origin of the ~620 Ma Humr Akarim and Humrat Mukbid A-type granites: no evidence for pre-Neoproterozoic basement in the Eastern Desert, Egypt. Int J Earth Sci 101:1705–1722

Ali KA, Wilde SA, Stern RJ, Moghazi AM, Ameen SMM (2013) Hf isotopic composition of single zircons from neoproterozoic arc volcanics and post-collision granites Eastern Desert of Egypt: implications for crustal growth and recycling in the Arabian-Nubian Shield. Precambr Res 239:42–55

Ali KA, Kröner A, Hegner E, Wong J, Li S-Q, Gahlan HA, Abu El Ela AA (2015) U-Pb zircon geochronology and Hf–Nd isotopic systematics of Wadi Beitan granitoid gneisses, south Eastern Desert, Egypt. Gondwana Res 27:811–824

Ali KA, Zoheir BA, Stern RJ, Andresen A, Whitehouse MJ, Bishara WW (2016) Lu–Hf and O isotopic compositions on single zircons from the North Eastern Desert of Egypt, Arabian-Nubian Shield: implications for crustal evolution. Gondwana Res 32:181–192

Ali-Bik MW, Abd El Rahim SH, Abdel Wahab W, Abayazeed SD, Hassan SM (2017) Geochemical constraints on the oldest arc rocks of the Arabian-Nubian Shield: the late Mesoproterozoic to late Neoproterozoic (?) Sa'al volcano-sedimentary complex, Sinai, Egypt. Lithos 284–285:310–326

Andresen A, Abu El-Rus MA, Myhre PI, Boghdady GY, Corfu F (2009) U-Pb TIMS age constraints on he evolution of the Neoproterozoic Meatiq Gneiss Dome, Eastern Desert of Egypt. Inter J Earth Sci 98:481–497

Andresen A, Augland LE, Boghdady GY, Lundmark AM, Elnady OM, Hassan MAA, Abu El-Rus MA (2010) Structural constraints on the evolution of the Meatiq Gneiss Dome (Egypt). East Afr Orog: J Afr Earth Sci 57:413–422

Andresen A, Abu El-Enen MM, Stern RJ, Wilde SA, Ali KA (2014) The Wadi Zaghra metasediments of Sinai, Egypt: new constraints on the late Cryogenian-Ediacaran tectonic evolution of the northernmost Arabian-Nubian Shield. Int Geol Rev 56:1020–1038

Asran AM, Abdel Rahman EM (2012) The Pan-African calc-alkaline granitoids and the associated mafic microgranular enclaves (MME) around Wadi Abu Zawal area, North Eastern Desert, Egypt: geology, geochemistry and petrogenesis. J Biol Earth Sci 2 (E1–E1):6

Augland LE, Andresen A, Boghdady GY (2012) U-Pb ID-TIMS dating of igneous and metaigneous rocks from the El-Sibai area: time constraints on the tectonic evolution of the Central Eastern Desert, Egypt. Int J Earth Sci 101:25–37

Avigad D, Gvirtzman Z (2009) Late Neoproterozoic rise and fall of the northern Arabian-Nubian shield: the role of lithospheric mantle delamination and subsequent thermal subsidence. Tectonophysics 477:217–228

Avigad D, Sandler A, Kolodner K, Stern TJ, McWilliams M, Miller N, Beyth M (2005) Mass-production of Cambro-Ordovician quartz-rich sandstone as a consequence of chemical weathering of Pan-African terranes: environmental implications. Earth Planet Sci Lett 240:818–826

Azer MK (2013) Late Ediacaran (605–580 Ma) post-collisional alkaline magmatismin the Arabian-Nubian Shield: a case study of Serbal ring-shaped intrusion, southern Sinai, Egypt. J Asia Earth Sci 77:203–223

Azer MK, El-Gharbawy RI (2011) Contribution to the Neoproterozoic layered mafic-ultramafic intrusion of Gabal Imleih, south Sinai, Egypt: implication of post-collisional magmatism in the north Arabian-Nubian Shield. J Afr Earth Sci 60:253–272

Azer MK, Farahat ES (2011) Late Neoproterozoic volcano-sedimentary successions of Wadi Rufaiyil, Southern Sinai, Egypt: a case of transition from late-to post-collisional magmatism. J Asia Earth Sci 42:1187–1203

Azer MK, Khalil AES (2005) Petrological and mineralogical studies of Pan-African serpentinites at Bir Al-Edeid area. Central Eastern Desert, Egypt. J Afr Earth Sci 43:525–536

Azer MK, Stern RJ (2007) Neoproterozoic (835–720 Ma) serpentinites in the Eastern Desert, Egypt: fragments of fore-arc mantle. J Geol 115:457–472

Azer MK, Abu El-Ela FF, Ren M (2012) The petrogenesis of late Neoproterozoic mafic dyke-like intrusion in south Sinai, Egypt. J Asia Earth Sci 54–55:91–109

Azer MK, Obeid MA, Ren M (2014) Geochemistry and petrogenesis of late Ediacaran (580–605 Ma) post-collisional alkaline rocks from the Katherina ring complex, south Sinai, Egypt. J Asia Earth Sci 93:229–252

Azer MK, Obeid MA, Gahlan HA (2016) Late Neoproterozoic layered mafic intrusion of arc-affinity in the Arabian-Nubian Shield: a case study from the Shahira layered mafic intrusion, southern Sinai, Egypt. Geol Acta 14:237–259

Azer MK, Gahlan HA, Asimow PD, Al-Kahtany KH (2017) The late Neoproterozoic Dahanib mafic-ultramafic intrusion, south Eastern Desert, Egypt: is it an Alaskan-type or layered intyrusion? Am J Sci 317:901–940

Azzaz SA, Blasy M, Moharem A, Amer O (2015) Late Neoproterozoic Dokhan volcanics, around G. Esh, North Eastern Desert, Egypt: geochemistry and relation of K2O and Nb abundances with crustal thickness. Arab J Geosci 8:3551–3564

Ball J (1916) Geography and geology of West Central Sinai. Egypt Surv Dept, Cairo

Barron T (1907) The topography and geology of the Peninsula of Sinai (Western portion). Egypt Surv Dept, Cairo

Basta EZ, Takla MA (1974) Distribution of opaque minerals and the origin of the gabbroic rocks of Egypt. Bull Fac Sci Cairo Univ 47:347–364

Basta EZ, Kotb H, Awadallah MF (1980) Petrochemical and geochemical characteristics of the Dokhan Formation at the type locality, Gabal Dokhan, Eastern Desert, Egypt. Inst Appl Geol Jeddah Bull, Vol 4, Pergamon, Oxford, pp 127–135

Basta FF, Maurice AE, Bakhit BR, Ali KA, Manton WI (2011) Neoproterozoic contaminated MORB of Wadi Ghadir Ophiolite, NE Africa: geochemical and Nd and Sr isotopic constraints. J Afr Earth Sci 59:227–242

Basta FF, Maurice AE, Bakhit BR, Azer MK, El-Sobky AF (2017) Intrusive rocks of the Wadi Hamad Area, North Eastern Desert, Egypt: change of magma composition with maturity of Neoproterozoic continental island arc and the role of collisional plutonism in the differentiation of arc crust. Lithos 288–289:248–263

Bea F, Abu-Anbar M, Montero P, Peres P, Talavera C (2009) The 844 Ma Moneiga quartz-diorites of the Sinai, Egypt: evidence for Andean-type arc or riftrelated magmatism in the Arabian–Nubian shield? Precambrian Research 175:161–168

Bea F, Montero P, Anbar MA, Talavera C (2011a) SHRIMP dating and Nd isotope geology of the Archean terranes of the Uweinat-Kamil inlier, Egypt–Sudan–Libya. Precambr Res 189:328–346

Bea F, Montero P, Anbar MA, Molina JF, Scarrow JH (2011b) The Bir Safsaf Precambrian inlier of south West Egypt revisited. A model for ~1.5 Ga TDM late Pan-African granite generation by crustal reworking. Lithos 125:897–914

Be'eri-Shlevin Y, Katzir Y, Valley JW (2009a) Crustal evolution and recycling in a juvenile continent: oxygen isotope ratio of zircon in the northern Arabian Nubian Shield. Lithos 107:169–184

Be'eri-Shlevin Y, Katzir Y, Whitehouse MJ, Kleinhanns IC (2009b) Contribution of pre Pan-African crust to formation of the Arabian Nubian Shield: new secondary ionization mass spectrometry U-Pb and O studies of zircon. Geology 37:899–902

Be'eri-Shlevin Y, Katzir Y, Whitehouse M (2009c) Post-collisional tectono-magmatic evolution in the northern Arabian-Nubian Shield (ANS): time constraints from ion probe U-Pb dating of zircon. J Geol Soc 166:71–85

Be'eri-Shlevin Y, Samuel MD, Azer MK, Rämö OT, Whitehouse MJ, Moussa HE (2011) The late Neoproterozoic Ferani and Rutig volcano-sedimentary successions of the northernmost Arabian-Nubian Shield (ANS): new insights from zircon U-Pb geochronology, geochemistry and O–Nd isotope ratios. Precambr Res 188: 21–44

Be'eri-Shlevin Y, Eyal M, Eyal Y, Whitehouse MJ, Litvinovsky B (2012) The Sa'al volcano-sedimentary complex (Sinai, Egypt), a latest Mesoproterozoic volcanic arc in the northern Arabian-Nubian Shield. Geology 40:403–406

Bentor YK (1985) The crustal evolution of the Arabo-Nubian Massif with special reference to the Sinai Peninsula. Precambr Res 28:1–74

Bielski M (1982) Stages in the evolution of the Arabian-Nubian massif in Sinai, Egypt. PhD thesis, Hebrew University, Jerusalem

Blankenhorn M (1910) Neues zur Geologie Palästinas und des ägyptischen Niltals. Zeitschrift der Deutschen Geologischen Gesellschaft 62:405–461

Bosch D, Bruguier O (1998) An early Miocene age for a high temperature event in gneisses from Zabargad Island (Red Sea, Egypt): mantle diapirism? Terra Nova 10:274–279

Boudier F, Nicolas A, Ji S, Kienast JR, Mevel C (1988) The gneiss of Zabargad Island—deep crust of a rift. Tectonophysics 150:209–227

Bregar M, Bauernhofer A, Pelz K, Kloetzli U, Fritz H, Neumayr P (2002) A late Neoproterozoic magmatic core complex in the Eastern Desert of Egypt: emplacement of granitoids in a wrench-tectonic setting. Precambr Res 118:59–82

Breitkreuz C, Eliwa HA, Khalaf IM, El Gameel K, Bühler B, Sergeev S, Larionov A, Murata M (2010) Neoproterozoic SHRIMP U-Pb zircon ages of silica-rich Dokhan Volcanics in the North Eastern Desert. Egypt. Precambrian Res 182:163–174

Brueckner HK, Elhaddad MA, Hamelin B, Hemming S, Kröner A, Reisberg L, Seyler MA (1995) Pan-African origin nand uplift for the gneisses and peridotites of Zabargad-Island, Red-Sea—a Nd, Sr, Pb, and Os isotope study. J Geophys Res 100:22283–22297

Bühler B, Breitkreuz C, Pfänder J, Hofmann M, Becker S, Linnemann U, Eliwa HA (2014) New insights into the accretion of the Arabian-Nubian shield: depositional setting, composition and

geochronology of a mid-cryogenian arc succession (north eastern desert, Egypt). Precambr Res 243:149–167
Cahen L, Snelling NJ, Delhal J, Vail JR (1984) The geochronology and evolution of Africa. Clarendon, Oxford
Cox GM, Lewis JC, Collins SA, Halverson PG, Jourdan F, Foden J, Nettle D, Kattan F (2012) Ediacaran terrane accretion within the Arabian-Nubian Shield. Gondwana Res 21:341–352
Dixon TH (1981) Gebel Dahanib, Egypt: a late Precambrian layered sill of komatiitic composition. Contrib Miner Petrol 76:42–52
E1-Tokhi M, Alaabed S, Amin BM (2010) Late Precambrian metavolcanics of Um Anab North Eastern Desert, Egypt, geochemistry and tectonic environment studies. Eur J Sci Res 42:507–524
El Bahariya GA (2012) Classification and origin of the Neoproterozoic ophiolitic mélanges in the Central Eastern Desert of Egypt. Tectonophysics 568–569:357–370
El Gaby S (2005) Integrated evolution and rock classification of the Pan-African belt in Egypt. 1st Symposium on the classification of the basement complex of Egypt, Assiut Univ, pp 1–9
El Gaby S, El Nady O, Khudeir A (1984) Tectonic evolution of the basement complex in the Central Eastern Desert of Egypt. Geol Rundsch 73:1019–1036
El Gaby S, List FK, Tehrani R (1988) Geology, evolution and metallogenesis of the Pan-African Belt in Egypt. In: El Gaby S, Greilling RO (eds) The Pan-African belt of Northeast Africa and adjacent areas. Vieweg & Sons, Braunschweig/Wiesbaden, pp 17–68
El Gaby S, Khudeir AA, El Taky M (1989) The Dokhan Volcanics of Wadi Queih Area, Central Eastern Desert, Egypt. In: Proceedings of the 1st Conference on Geochemistry. Alexandria University, Egypt, pp 42–62
El Gaby S, List FK, Tehrani R (1990) The basement complex of the Eastern Desert and Sinai. In: Said R (ed) The geology of Egypt. Balkema, Rotterdam, pp 75–184
El Gaby S, Khudeir AA, Abdel Tawab M, Atalla RF (1991) The metamorphosed volcano-sedimentary succession of Wadi Kid, southeastern Sinai, Egypt. Ann Geol Surv Egypt 17:19–35
El Mahallawi MM, Ahmed AF 92012) Late Proterozoic older granitoids from the North Eastern Desert of Egypt: petrogenesis and geodynamic implications. Arab J Geosci 5:15–27
El Ramly MF (1972) A new geological map for the basement rocks in the Eastern and Southwestern Deserts of Egypt. Ann Geol Surv Egypt 2:1–18
El Ramly MF, Akaad MK (1960): The basement complex in the central Eastern Desert of Egypt between latitudes 24°30′ and 25°40′N. Geol Surv Egypt. Paper No. 8. 35 pp
El Ramly MF, Hashad AH, Attawiya MY, Mansour MM (1982) Geochemistry of Kolet Um Kharit bimodal metavolcanics, South Eastern Desert. Egypt. Ann Geol Surv Egypt 12:103–120
El Sharkawy MA, El Bayoumi RM (1979) The ophiolites of Wadi Ghadir area, Eastern Desert, Egypt. Ann Geol Surv Egypt 9:125–135
El Shazly EM (1964) On the classification of the Precambrian and other rocks of magmatic affiliation in Egypt, U. A. R. In: Proceedings of 24th international geological congress, India. Part 5, pp 88–101
El-Bialy MZ (1999) Geology of the basement rocks of Abu Durba–Abu Haswa area, Southwestern Sinai, Egypt. MSc Thesis, Suez Canal University, Ismailia
El-Bialy MZ (2004) Petrologic, geochemical and petrogenetic characterization of the old granites of Sinai, Egypt. PhD thesis, Suez Canal University, Ismailia
El-Bialy MZ (2010) On the Pan-African transition of the Arabian-Nubian Shield from compression to extension: the post-collision Dokhan volcanic suite of Kid-Malhak region, Sinai, Egypt. Gondwana Res 17:26–43
El-Bialy MZ (2013) Geochemistry of the Neoproterozoic metasediments of Malhaq and Um Zariq formations, Kid Metamorphic Complex, Sinai, Egypt: implications for source-area weathering, provenance, recycling, and depositional tectonic setting. Lithos 175–176:68–86
El-Bialy MZ, Hassen IS (2012) The late Ediacaran (580–590 Ma) onset of anorogenic alkaline magmatism in the Arabian-Nubian Shield: Katherina A-type rhyolites of Gabal Ma'ain, Sinai, Egypt. Precambr Res 216–219:1–22
El-Bialy MZ, Omar MM (2015) Spatial association of Neoproterozoic continental arc I-type and post-collision A-type granitoids in the Arabian-Nubian Shield: the Wadi Al-Baroud Older and younger granites, North Eastern Desert. Egypt. J Afr Earth Sci 103:1–29
El-Bialy MZ, Shata AE (2017) Geochemistry, petrogenesis and radioactive mineralization of two coeval Neoproterozoic post-collisional calc-alkaline and alkaline granitoid suites from Sinai, Arabian Nubian Shield. Chemie Erde. https://doi.org/10.1016/j.chemer.2017.12.001
El-Bialy MZ, Streck MJ (2009) Late Neoproterozoic alkaline magmatism in the Arabian-Nubian Shield: the postcollisional A-type granite of Sahara-Umm Adawi pluton, Sinai, Egypt. Arab J Geo Sci 2:151–174
El-Bialy MZ, Ali KA, Abu El-Enen MM, Ahmed AH (2015) Provenance and metamorphic PT conditions of Cryogenian-Ediacaran metasediments from the Kid metamorphic complex, Sinai, NE Arabian-Nubian Shield: Insights from detrital zircon geochemistry and mineral chemistry. Tectonophysics 665:199–217
Eliwa HA, Abu El-Enen MM, Khalaf IM, Itaya T (2004) Metamorphic evolution of Sinai metapelites and gneisses: constraints from petrology and K/Ar dating. Egypt J Geol 48:169–185
Eliwa HA, Kimura J-I, Itaya T (2006) Late Neoproterozoic Dokhan Volcanics, North Eastern Desert, Egypt: geochemistry and petrogenesis. Precambrian Res 151:31–52
Eliwa HA, Abu El-Enen MM, Khalaf IM, Itaya T, Murata M (2008) Metamorphic evolution of Neoproterozoic metapelites and gneisses in the Sinai, Egypt: insights from petrology, mineral chemistry and K-Ar age dating. J Afr Earth Sci 51:107–122
Eliwa HA, Breitkreuz C, Khalaf I, El Gameel K (2010) Depositional styles of early Ediacaran terrestrial volcano-sedimentary succession in the Gebel El Urf area, North Eastern Desert, Egypt. J Afr Earth Sci 57:328–344
Eliwa HA et al (2014a) SIMS zircon U-Pb and mica K–Ar geochronology, and Sr–Nd isotope geochemistry of Neoproterozoic granitoids and their bearing on the evolution of the north Eastern Desert, Egypt. Gondwana Res 25:1570–1598
Eliwa HA, El-Bialy MZ, Murata M (2014b) Ediacaran post-collisional volcanism in the Arabian-Nubian Shield: the high-K calc-alkaline Dokhan Volcanics of Gabal Samr El-Qaa (592 ± 5 Ma), North Eastern Desert, Egypt. Precambr Res 246:180–207
El-Metwally (1992) Pan-African post-orogenic gabbro cumulates from Sinai massif, Egypt: geochemistry and mineral chemistry. J Afr Earth Sci 14:217–225
El-Metwally AA, Abdallah Sh (2004) Petrography and geochemistry of intrusive younger gabbros of Wadi Nisryin and Wadi El-Bida areas, South Sinai, Egypt. In: Proceedings of the 7th conference of Sinai for development, Ismailia, pp 93–109
El-Metwaly AA (1993) Microgranular enclaves in the Pan-African I-type granites from the Sinai Massif: petrology, mineralogy and geochemistry. J Afr Earth Sci 17:95–110
El-Sayed MM (2006) Geochemistry and petrogenesis of the postorogenic bimodal dyke swarms in NW Sinai, Egypt: constraints on the magmatic–tectonic processes during the late Precambrian. Chemie Erde 66:129–141
El-Sayed MM, Furnes H, Mohamed FH (1999) Geochemical constraints on the tectonomagmatic evolution of the late Precambrian Fawakhir ophiolite, Central Eastern Desert, Egypt. J Afr Earth Sci 29:515–533

El-Sayed MM, Obeid MA, Furnes H, Moghazi AM (2004) Late Neoproterozoic volcanism in the southern Eastern Desert, Egypt: petrological, structural and geochemical constraints on the tectonic–magmatic evolution of the Allaqi Dokhan Volcanic suite. Neu Jahrb Miner Abh 180(3):261–286

El-Shafei MK, Kusky TM (2003) Structural and tectonic evolution of the Neoproterozoic Feiran-Solaf metamorphic belt Sinai Peninsula: implications for the closure of the Mozambique ocean. Precambr Res 123:269–293

El-Shazly AK, Khalil KI (2016) Metamorphic and geochronologic constraints on the tectonic evolution of the Central Eastern Desert of Egypt. Precambr Res 283:144–168

Emam A, Moghazy NM, El-Sherif AM (2011) Geochemistry, petrogenesis and radioactivity of El Hudi I-type younger granites, South Eastern Desert, Egypt. Arab J Geosci (2011) 4:863–878

Essawy MA, Abu Zeid KM (1972) Atalla felsite intrusion and its neighbouring rhyolitic flows and tuffs, Eastern Desert. Ann Geol Surv Egypt 2:271–281

Eyal M, Hezkiyaku T (1980) Katherina pluton: the outlines of a petrological framework. Israel J Earth Sciences 29:41–52

Eyal M, Litvinovsky B, Jahn BM, Zanvilevich A, Katzir Y (2010) Origin and evolution of post-collisional magmatism: coeval Neoproterozoic calc-alkaline and alkaline suites of the Sinai Peninsula. Chem Geol 269:153–179

Eyal M, Zanvilevich AN, Litvinovsky BA, Jahn BM, Vapnik Y, Be'eri-Shlevin Y (2014) The Katherina ring complex (Sinai Peninsula, Egypt): sequence of emplacement and petrogenesis. Am J Sci 314:462–507

Farahat ES (2006) The Neoproterozoic Kolet Um Kharit bimodal metavolcanic rocks, south Eastern Desert, Egypt: a case of enrichment from plume interaction? Int J Earth Sci 95:275–287

Farahat ES (2010) Neoproterozoic arc-back-arc system in the central Eastern Desert of Egypt: evidence from supra-subduction zone ophiolites. Lithos 120:293–308

Farahat ES (2011) Geotectonic significance of Neoproterozoic amphibolites from the Central Eastern Desert of Egypt: a possible dismembered sub-ophiolitic metamorphic sole. Lithos 125:781–794

Farahat ES, Azer MK (2011) Post-collisional magmatism in the northern Arabian-Nubian Shield: the geotectonic evolution of the alkaline suite at Gebel Tarbush area, south Sinai. Egypt. Chemie Erde 71:247–266

Farahat ES, Helmy HM (2006) Abu Hamamid Neoproterozoic Alaskan-type complex, south Eastern Desert, Egypt: petrogenetic and geotectonic implications. J Afr Earth Sci 85:187–197

Farahat ES, Mohamed HA, Ahmed AF, El Mahallawi MM (2007) Origin of I- and Atype granitoids from the Eastern Desert of Egypt: implications for crustal growth in the northern Arabian-Nubian Shield. J Afr Earth Sci 49:43–58

Farahat ES, Zaki R, Hauzenberger C, Sami M (2011) Neoproterozoic calc-alkaline peraluminous granitoids of the Deleihimmi pluton, Central Eastern Desert, Egypt: implication for transition from late- to post-collisional tectonomagmatic evolution I the northern Arabian-Nubian Shield. Geol J46:544–560

Fowler A, El-Kalioubi B (2002) The Migif-Hafafit gneissic complex of the Egyptian Eastern Desert: fold interference patterns involving multiply deformed sheath folds. Tectonophyscis 346:247–275

Fowler A, Abdeen MM (2014) Reappraisal of strain estimations and measurement methods in the Hammamat group sediments: comparison of primary and secondary grain fabrics with new data from Wadi Zeidun and Wadi Arak basins, CED, Egypt. Precambr Res 247:1–32

Fowler A, Osman AF (2013) Sedimentation and inversion history of three molasses basins of the western Central Eastern Desert of Egypt: implications for the tectonic significance of Hammamat basins. Gondwana Res 23:1511–1534

Fowler A, Khamees H, Dowidar H (2007) El Sibai gneissic complex, Central Eastern Desert, Egypt: folded nappes and syn-Kinematic gneissic granitoid sheets—note a core complex. J Afr Earth Sci 49:119–135

Fowler A, Hassen IS, Hassan M (2017) The Feiran-Solaf metamorphic complex, Sinai, Egypt: evidence for orthogonal or oblique tectonic convergence? J Afr Earth Sci. http://dx.doi.org/10.1016/j.jafrearsci.2017.09.007

Fritz H, Messner M (1999) Intramontane basin formation during oblique convergence in the Eastern Desert of Egypt: magmatically versus tectonically induced subsidence. Tectonophysics 315:145–162

Fritz H, Wallbrecher E, Khudeir AA, Abu El Ela FF, Dallmeyer DR (1996) Formation of Neoproterozoic metamorphic core complexes during oblique convergence (Eastern Desert, Egypt). J Afr Earth Sci 23:311–329

Fritz H, Dallmeyer DR, Wallbrecher E, Loizenbauer J, Hoinkes G, Neumayr P, Khudeir AA (2002) Neoproterozoic tectonothermal evolution of the Central Eastern Desert, Egypt: a slow velocity tectonic process of core complex exhumation. J Afr Earth Sci 34:137–155

Fritz H et al (2013) Orogen styles in the East African Orogen: a review of the Neoproterozoic to Cambrian tectonic evolution. J Afr Earth Sci 86:65–106

Friz-Töpfer A (1991) Geochemical characterization of Pan-African dyke swarms in southern Sinai: from continental margin to intraplate magmatism. Precambr Res 49:281–300

Furnes H, Shimron AE, Roberts D (1985) Geochemistry of Pan-African volcanic arc sequences in southeastern Sinai Peninsula and plate tectonic implications. Precambr Res 29:359–382

Gahlan H, Arai S (2009) Carbonate-orthopyroxenite lenses from the Neoproterozoic Gerf ophiolite, South Eastern Desert, Egypt: the first record in the Arabian Nubian Shield ophiolites. J Afr Earth Sci 53:70–82

Gahlan HA, Obeid MA, Azer MK, Asimow PD (2017) An example of post-collisional appinitic magmatism with an arc-like signature: the Wadi Nasb mafic intrusion, North Arabian-Nubian Shield, South Sinai. Int Geol Rev, Egypt. https://doi.org/10.1080/00206814.2017.1360804

Garfunkel Z (2015) The relations between Gondwana and the adjacent peripheral Cadomian domain—constrains on the origin, history, and paleogeography of the peripheral domain. Gondwana Res 28:1257–1281

Gharib ME, Ahmed AH (2012) Late Neoproterozoic volcanics and associated granitoids at Wadi Ranga, South Eastern Desert, Egypt: a transition from subduction related to intra-arc magmatism. Lithos 155:236–255

Greenberg JK (1981) Characteristics and origin of Egyptian younger granites. Geol Soc Am Bull 92:224–232

Greiling RO, Abdeen MM, Dardir AA, El Akhal H, El-Ramly MF, Kamal El Din GM, Osman AF, Rashwan AA, Rice AH, Sadek MF (1994) A structural synthesis of the Proterozoic Arabian-Nubian Shield in Egypt. Geol Rundsch 83:484–501

Greiling RO (1997) Thrust tectonics in crystalline domains: the origin of a gneiss dome. Proc India Acad Sci 106:209–220

Grothaus B, Eppler D, Ehrlich R (1979) Depositional environments and structural implications of the Hammamat Formation, Egypt. Ann Geol Surv Egypt 9:564–590

Hamdy MM, Harraz HZ, Aly GA (2013) Pan-African (intraplate and subduction related?) metasomatism in the Fawakhir ophiolitic serpentinites, Central Eastern Desert of Egypt: mineralogical and geochemical evidences. Arab J Geosci 6:13–33

Hamdy MH, Abd El-Wahed MA, Gamal El Dien H, Morishita T (2017) Garnet hornblendite in the Meatiq Core Complex, Central Eastern Desert of Egypt: Implications for crustal thickening preceding the

~600 Ma extensional regime in the Arabian-Nubian Shield. Precambr Res 298:593–614

Hamimi Z, El-Fakharani A, Abdeen MM (2013) Polyphase deformation history and strain analyses of the post-amalgamation depositional basins in the Arabian-Nubian Shield: evidence from Fatima, Ablah and Hammamat Basins. J Afr Earth Sci 99:64–92

Hargrove US, Stern RJ, Kimura JI, MantonWI JP (2006) How juvenile is the Arabian-Nubian Shield? Evidence from Nd isotopes and pre-Neoproterozoic inherited zircon in Bi'r Umk suture zone, Saudi Arabia. Earth Planet Sci Lett 252:308–326

Harris NBW, Hawkesworth CJ, Ries AC (1984) Crustal evolution in North-East and East Africa from model Nd ages. Nature 309:773–776

Hassan MA, Hashad AH (1990) Precambrian of Egypt. In: Said R (ed) The geology of Egypt. Balkema, Rotterdam, pp 201–248

Hassan M, Abu-Alam TS, Stüwe K, Fowler A, Hassen I (2014) Metamorphic evolution of the Sa'al–Zaghra Complex in Sinai: evidence for Mesoproterozoic Rodinia break-up? Precambr Res 241:104–128

Helmy HM, El Mahallawi MM (2003) Gabbro Akarem mafic–ultramafic complex, Eastern Desert, Egypt: a Late Precambrian analogue of Alaskan-type complexes. Miner Petrol 77:85–108

Helmy HM, Ahmed AH, Kagami A, Arai S (2005) Sm/Nd and platinum-group element geochemistry of a late-Precambrian Alaskan-type complex from the Eastern Desert of Egypt. In: 10th Platinum Symp Oulu-Finland (Abstract)

Helmy HM, Yoshikawa M, Shibata T, Arai S, Tamura A (2008) Corona structure from arc mafic–ultramafic cumulates: the role and chemical characteristics of late-magmatic hydrous liquids. J Miner Petrol Sci 103:333–344

Helmy HM, Abd El-Rahman YM, Yoshikawa M, Shibata T, Arai S, Tamura A, Kagami H (2014) Petrology and Sm–Nd dating of the Genina Gharbia Alaskan-type complex (Egypt): insights into deep levels of Neoproterozoic island arcs. Lithos 198–199:263–280

Helmy HM, Yoshikawa M, Shibata T, Arai S, Kagami H (2015) Sm–Nd and Rb–Sr isotope geochemistry and petrology of Abu Hamamid intrusion, Eastern Desert, Egypt: an Alaskan-type complex in a back arc setting. Precambrian Res 258:234–246

Holail HM, Moghazi AKM (1998) Provenance, tectonic setting and geochemistry of greywackes and siltstones of the late Precambrian Hammamat Group, Egypt. Sed Geol 116:227–250

Hume WF (1934) Geology of Egypt 2, part 1: the metamorphic rocks. Geol Surv Egypt, 293 pp

Hume WF (1935) Geology of Egypt 2, part 2: the later plutonic and minor intrusive rocks. Geol Surv Egypt, 387 pp

Hussein AA, Aly MM, El Ramly MF (1982) A proposed new classification of the granites of Egypt. J Volc Geotherm Res 14:187–198

Johnson PR et al (2011) Late Cryogenian-Ediacaran history of the Arabian-Nubian Shield: a review of depositional, plutonic, structural, and tectonic event in the closing stages of the northern East African Orogen. J Afr Earth Sci 61:167–232

Karmakar S, Schenk V (2015) Paleoproterozoic UHT reworking at Uweinat in the East Sahara Ghost Craton, SW Egypt: evidence from petrology and texturally controlled in situ monazite dating. J Petro 56:1703–1742

Khalaf EA (2010) Stratigraphy, facies architecture, and palaeoenvironment of Neoproterozoic volcanics and volcaniclastic deposits in Fatira area, Central Eastern Desert, Egypt. J Afr Earth Sci 58:405–426

Khalaf EA (2012) Origin and evolution of post-collisional volcanism: an exam-ple from Neoproterozoic Dokhan volcanics at Gabal Nugara area, Northeastern Desert, Egypt. Arab J Geosci 5:663–695

Khalaf EA (2013) Variations in eruptive style and depositional processes of Neopro-terozoic terrestrial volcano-sedimentary successions in the Hamid area, North Eastern Desert, Egypt. J Afr Earth Sci 83:74–103

Khalaf EA, Obeid MA (2013) Tectonostratigraphy and depositional history of the Neoproterozoic volcano-sedimentary sequences in Kid area, Southeastern Sinai, Egypt: implications for intra-arc to foreland basin in the Northern Arabian-Nubian Shield. J Asia Earth Sci 73:473–503

Khalil SO (2005) The Egyptian gabbroic rocks. In: El-Gaby S (ed) First symposium on the classification of the basement complex of Egypt. Fac Sci Assuit Univ 49–51

Khalil AES, Azer MK (2007) Supra-subduction affinity in the Neoproterozoic serpentinites in the Eastern Desert, Egypt: Evidence from mineral composition. J Afr Earth Sci 49:136–152

Khalil AES, Obeid MA, Azer MK (2015) Late Neoproterozoic post-collisional mafic magmatism in the Arabian-Nubian Shield: a case study from Wadi El-Mahash gabbroic intrusion in southeast Sinai, Egypt. J Afr Earth Sci 105:29–46

Khalil AE, El-Desoky HM, Salem AA (2017) Geochemistry and petrogenesis of the Neoproterozoic island arc gabbro-diorite-tonalite complexes at Wadi Abu El-Lijam and Wadi Selilab area, Central Eastern Desert, Egypt. Egypt J Geol 61:1–11

Khalil AE, El-Desoky HM, Shahin TM, Abdelwahab W (2018) Late Cryogenian arc-related volcaniclastic metasediment successions at Wadi Hammuda, Central Eastern Desert, Egypt: geology and geochemistry. Arab J Geosci 11:74

Kharbish S (2010) Geochemistry and magmatic setting of Wadi El-Markh island-arc gabbro–diorite suite, central Eastern Desert, Egypt. Chemie Erde 70:257–266

Khedr MZ, Arai S (2016) Petrology of a Neoproterozoic Alaskan-type complex from the Eastern Desert of Egypt: implications for mantle heterogeneity. Litho 263:15–32

Khedr MZ, Arai S (2017) Peridotite-chromitite complexes in the Eastern Desert of Egypt: insight into Neoproterozoic sub-arc mantle processes. Gondwana Res 52:59–79

Khudeir AA, Ali MM, EL Habaak GH (1988) The metavolcanics at Um Samiuki area, Egypt. Bull Fac Sci Assiut Univ 17(2-F):73–101

Khudeir AA, Abu El-Rus MA, El-Gaby S, El-Nady O, Bishara WW (2008) Sr–Nd isotopes and geochemistry of the infrastructural rocks in Meatiq and Hafafit core complexes, Eastern Desert, Egypt: evidence for involvement of pre-Neoproterozoic crust in the growth of Arabian-Nubian Shield. Island arc 17:90–108

Klerkx J (1980) Age and metamorphic evolution of the basement complex around Jabal Al Awaynat. In: Salem MJ, Busrewil M (eds) The Geology of Libya, Academic Press, New York, Vol 3, pp 901–906

Klerkx J, Deutsch S (1977) Re´sultats pre´ liminaires obtenus par la me´thode Rb/Sr sur l'aˆge des formations Precambriennes de la region d'Uweinat (Libye). Rapp Ann (1976) Mus Roy Afr Centrale, Dep Geol Min, Tervuren 83–94

Kröner A, Eya M, Eyal Y (1990) Early Pan-African evolution of the basement around Elat, Israel, and Sinai Peninsula revealed by single-zircon evaporation dating, and implications for crustal accretion rates. Geology 18:545–548

Kröner A, Todt W, Hussein IM, Mansour M, Rashwan AA (1992) Dating of late Proterozoic ophiolites in Egypt and Sudan using the single grain zircon evaporation technique. Precambr Res 59:15–32

Kröner A, Kruger J, Rashwan AA (1994) Age and tectonic setting of granitoid gneisses in the Eastern Desert of Egypt and south-west Sinai. Geol Rundsch 83:502–513

Liégeois JP, Stern RJ (2010) Sr–Nd isotopes and geochemistry of granite–gneiss complexes from the Meatiq and Hafafit domes, Eastern Desert, Egypt: no evidence for pre-Neoproterozoic crust. J Afr Earth Sci 57:31–40

Loizenbauer J, Wallbrecher E, Fritz H, Neumayr P, Khudeir AA, Kloetzli U (2001) Structural geology, simple zircon ages and fluid

inclusion studies of the Meatiq metamorphic core complex: implications for Neoproterozoic tectonics in the Eastern Desert of Egypt. Precambrian Res 110:357–383

Lundmark AM, Andresen A, Hassan MA, Augland LE, Abu El-Rus MA, Boghdady GY (2012) Repeated magmatic pulses in the East African Orogen of Central Eastern Desert, Egypt: an old idea supported by new evidence. Gondwana Res 22:227–237

Makovicky E, Frei R, Bailey JC, Karup-Moller S (2016) Imperial Porphyry from Gebel Abu Dokhan, the Red Sea Mountains, Egypt: Part II. Geochemistry. N Jb Miner Abh 193:29–44

Maurice AE, Basta FF, Khiamy AA (2012) Neoproterozoic nascent island arc volcanism from the Nubian Shield of Egypt: magma genesis and generation of continental crust in intra-oceanic arcs. Lithos 132–133:1–20

Moghazi AM (2002) Petrology and geochemistry of pan-African granitoids, Kab Amiri area, Egypt—implications for tectonomagmatic stages of the Nubian Shield evolution. Miner Petrol 75:41–67

Moghazi AM (2003) Geochemistry and petrogenesis of a high-K calc–alkaline Dokhan volcanic suite, South Safaga area, Egypt: the role of late Neoproterozoic crustal extension. Precambrian Res 423:161–178

Moghazi AM, Hassanen MA, Mohamed FH, Ali S (2004) Late Neoproterozoic strongly peraluminous leucogranites, South Eastern Desert, Egypt: petrogenesis and geodynamic significance. Miner Petrol 81:19–41

Moghazi AM, Ali KA, Wilde SA, Zhou Q, Andersen T, Andresen A, Abu El-Enen MM, Stern RJ (2012) Geochemistry, geochronology, and Sr–Nd isotopes of the late Neoproterozoic Wadi Kid volcano-sedimentary rocks, Southern Sinai, Egypt: implications for tectonic setting and crustal evolution. Lithos 154:147–165

Mohamed FH, El-Sayed MM (2008) Post-orogenic and anorogenic A-type fluorite-bearing granitoids, Eastern Desert, Egypt: petrogenetic and geotectonic implications. Chemie Erde 68:431–450

Mohamed FH, Moghazi AM, Hassanen MA (2000) Geochemistry, petrogenesis and tectonic setting of late Neoproterozoic Dokhan type volcanic rocks in the Fatira area, eastern Egypt. Int J Earth Sci 88:764–777

Morag N, Avigad D, Gerdes A, Belousova E, Harlavan Y (2011) Crustal evolution and recycling in the northern Arabian-Nubian Shield: new perspectives from zircon Lu–Hf and U-Pb systematics. Precambr Res 186:101–116

Moreno JA, Montero P, Abu Anbar M, Molina JF, Scarrow JH, Talavera C, Cambeses A, Bea F (2012) SHRIMP U-Pb zircon dating of the Katerina ring complex: insights into the temporal sequence of Ediacaran calc-alkaline to peralkaline magmatism in southern Sinai, Egypt. Gondwana Res 12:887–900

Moussa HE (2003) Geologic setting, petrography and geochemistry of the volcano-sedimentary succession at Gebel Ferani area, Southeastern Sinai, Egypt. Egypt J Geol 47:153–173

Moussa EMM, Stern RJ, Manton WI, Ali KA (2008) SHRIMP zircon dating and Sm/Nd isotopic investigations of Neoproterozoic granitoids, Eastern Desert, Egypt. Precambr Res 160:341–356

Mushkin A, Navon O, Halicz L, Hartmann G, Stein M (2003) The petrogenesis of A-type magmas from Amram Massif, southern Israel. J Petrol 44:815–832

Nasiri Benzenjani R, Pease V, Whitehouse MJ, Shalaby MH, Kadi KA, Kozdroj W (2014) Detrital zircons geochronology and provenance of the Neoproterozoic Hammamat Group (Igla Basin), Egypt and the Thalbah Group, NW Saudi Arabia: Implications for regional collision tectonics. Precambr Res 245:225–243

Nasr BB, Beniamin NY (2001) Ophiolite sequence of Gerf-Hasium and Sol Hamed-Shiab areas, South Eastern Desert, Egypt. Ann Geol Surv Egypt 24:63–78

Nasseef AO, Bakor AR, Hashad AH (1980) Petrography of possible ophiolitic rocks along the Qift-Quseir road, Eastern Desert, Egypt. In: Cooray PG, Tahoun SA (eds) Evolution and mineralization of the Arabian-Nubian Shield. Inst Appl Geol Jeddah Bull, vol 3, Pergamon, Oxford, pp 157–168

Neumayr P, Mogessie A, Hoinkes G, Puhl J (1996) Geological setting of the Meatiq metamorphic core complex in the Eastern Desert of Egypt based on amphibolite geochemistry. J Afr Earth Sci 23:331–345

Noweir AM (1968) Geology of the Hammamat-Um Seleimat District, Eastern Desert, Egypt. PhD thesis, Assuit University, Assuit

Obeid MA (2006) The Pan -African arc-related volcanism of the wadi Hodein area, South Eastern Desert: petrological and geochemical constraints. J Afr Earth Sci 44:383–395

Obeid MA (2010) Petrogenesis of Bir Madi Gabbro-Diorite and Tonalite-Granodiorite Intrusions in Southeastern Desert, Egypt: implications for tectono-magmatic processes at the Neoproterozoic Shield. Int J Econ Env Geol 1:27–35

Obeid MA, Azer MK (2015) Pan-African adakitic rocks of the north Arabian-Nubian Shield: petrological and geochemical constraints on the evolution of the Dokhan volcanics in the north Eastern Desert of Egypt. Int J Earth Sci 104:541–563

Obeid MA, Khalil AES, Azer MK (2015) Mineralogy, geochemistry and geotectonic significance of the Neoproterozoic ophiolite of Wadi Arais area, South Eastern Desert, Egypt. Int Geol Rev 58:687–702

Omara S (1972) An Early Cambrian outcrop in southwestern Sinai, Egypt. Neu Jahrb Geol Pal Mh 5:306–314

Osman AFS (1996) Structural geological and geochemical studies on the Pan-African basement rocks, Wadi Zeidun, Central Eastern Desert, Egypt. Forschungszentrum J€ulich GmbH. Sci Ser Int Bur 39:262

Qaoud N, Abdelnasser A (2012) Geochemistry and petrogenesis of El-Fringa metagabbro-diorite rocks, Wadi Sa'al area, south Sinai, Egypt. J Azhar Univ-Gaza (Nat Sci) 14:111–138

Ragab AI (1987) On the petrogenesis of the Dokhan volcanics of the Northern Eastern Desert of Egypt. MERC Ain Shams Univ, Earth Sci Ser 1:151–158

Ragab AI, El-Alfy Z (1996) Arc-arc collision model and its implications on a proposed classification of the Pan-African rocks of the Eastern Desert of Egypt. MERC Ain Shams Univ, Earth Sci Ser 10:89–101

Ressetar R, Monard JR (1983) Chemical composition and tectonic setting of the Dokhan volcanic formation, Eastern Desert, Egypt. J Afr Earth Sci 1:103–112

Richter A (1986) Geologie der metamorphen und magmatischen Einheiten im Gebiet zwischen Gebel Uweinat und Gebel Kamil, SW Aegypten/NW Sudan. Berl Geowiss Abh (A) 73:201 pp

Richter A, Schandelmeier H (1990) Precambrian basement inliers of Western Desert geology, petrology and structural evolution. In: Said R (ed) The geology of Egypt. Balkema, Rotterdam, pp 185–200

Ries AC, Shackelton RM, Graham RH, Fitches WR (1983) Pan-African structures, ophiolites and melange in the Eastern Desert of Egypt: a traverse at 26°N. J Geol Soc London 140:75–95

Rittmann A (1958) Geosynclinal volcanism, ophiolites and Barramiya rocks. Egypt J Geol 2:61–66

Samuel MD, Moussa HE, Azer MK (2001) Geochemistry and petrogenesis of iqna shar'a volcanic rocks, central Sinai, Egypt. Egypt J Geol 45:921–940

Samuel MD, Moussa HE, Azer MK (2007) A-type volcanics in Central Eastern Sinai, Egypt. J Afr Earth Sci 47:203–226

Samuel MD, Be'eri-Shlevin Y, Azer MK, Whitehouse MJ, Moussa HE (2011) Provenance of conglomerate clasts from the volcanosedimentary sequence at Wadi Rutig in southern Sinai, Egypt as revealed by SIMS U-Pb dating of zircon. Gondwana Res 20:450–464

Samuel MD, Ghabrial DS, Moussa HE, Ali-Bik MW (2015) The petrogenesis of late Neoproterozoic gabbro/diorite intrusion at Sheikh El-Arab area, Central Sinai, Egypt: Arab J Geosci 8:5579–5599

Schandelmeier H, Darbyshire DPF, Harms U, Richter A (1988) The East Saharan Craton: evidence for pre-Pan-African crust in NE Africa west of the Nile. In: E1-Gaby S, Greiling RO (eds) The Pan African belt of Northeast Africa and adjacent areas. Friedr Vieweg, Braunschweig, pp 69–94

Schürmann HME (1953) The Precambrian of the Gulf of Suez area. In: 19th international geological congress Algiers, CR, Sec 1, pp 115–135

Schürmann HME (1966) The Precambrian along the Gulf of Suez and the northern part of the Red Sea. E.J. Brill, Leiden

Segev A (1987) The age of the latest Precambrian volcanism in southern Israel, northeastern Sinai and SW Jordan: a re-evaluation. Precambr Res 36:277–285

Shackleton RM, Ries AC, Graham RH, Fitches WR (1980) Late Precambrian ophiolite melange in the Eastern Desert of Egypt. Nature 285:472–474

Shackleton RM (1994) Review of Late Proterozoic sutures, ophiolite melanges and tectonics of eastern Egypt and NE Sudan. Geologische Rundschau 83:537–546

Shalaby A (2010) The northern dome of Wadi Hafafit culmination, Eastern Desert, Egypt: structural setting in tectonic framework of a scissor-like wrench corridor. J Afr Earth Sci 57:227–241

Shalaby A, Stüwe K, Fritz H, Makroum F (2006) The El Mayah molasses basin in the Eastern Desert of Egypt. J Afri Earth Sci 45:1–15

Shimron AE (1984) Evolution of the Kid Group, Southeast Sinai Peninsula: thrusts, mélanges, and implications for accretionary tectonics during the Proterozoic of the Arabian-Nubian Shield. Geology 12:242–247

Shimron AE (1987) Pan-African metamorphism and deformation in the Wadi Kid region, SE Sinai Peninsula: evidence from porphyroblasts in the Um Zariq Formation. Israel J Earth Sci 36:173–193

Shimron A, Bogoch R, Furnes H, Roberts D (1993) The Sa'al Group: An ensialic island arc sequence in Sinai. In: Thorweihe U, Schandelmeier H (eds) Geoscientific research in northeast Africa. Balkema, Rotterdam, pp 49–53

Sims RJ, James HL (1985) Banded iron-formations of late Proterozoic age in the Central Eastern Desert, Egypt: geology and tectonic setting. Econ Geol Bull 79:1777–1784

Stern RJ (1979) Late Precambrian crustal environments as reconstructed from relict igneous minerals, Central Eastern Desert of Egypt. Ann Geol Surv Egypt 9:9–13

Stern RJ (1981) Petrogenesis and tectonic setting of late Precambrian ensimatic volcanic rocks, Central Eastern Desert of Egypt. Precambr Res 16:195–230

Stern RJ (1985) The Najd fault system, Saudi Arabia and Egypt: a late Precambrian rift related transform system. Tectonics 4:497–511

Stern RJ (1994) Arc assembly and continental collision in the Neoproterozoic East African Orogen: implications for the consolidation of Gondwanaland. Ann Rev Earth Planet Sci 22:319–351

Stern RJ (2002) Crustal evolution in the East African Orogen: a neodymium isotopic perspective. J Afr Earth Sci 34:109–117

Stern RJ (2017) Neoproterozoic formation and evolution of Eastern Desert continental crust—the importance of the infrastructure-superstructure transition. J Afr Earth Sci. http://dx.doi.org/10.1016/j.jafrearsci.2017.01.001

Stern RJ, Gottfried D (1986) Petrogenesis of a Late Precambrian (575–600 Ma) bimodal suite in Northeast Africa. Contrib Miner Petrol 92:492–501

Stern RJ, Hedge CE (1985) Geochronological and isotopic constraints on late Precambrian crustal evolution in the Eastern Desert of Egypt. Am J Sci 285:97–127

Stern RJ, MantonWI, (1987) Age of Feiran basement rocks, Sinai: implications for late Precambrian crustal evolution in the northern Arabian-Nubian Shield. J Geol Soc London 144:569–575

Stern RJ, Nielsen KC, Best E, Sultan M, Arvidson RE, Kröner A (1990) Ophiolite orientation of late Precambrian sutures in the Arabian-Nubian Shield. Geology 18:1103–1106

Stern RJ, Kröner A, Rashwan AA (1991) A late Precambrian (~710 Ma) high vulcanicity rift in the south Eastern Desert of Egypt. Geol Rundsch 80:155–170

Stern RJ, Johnson PR, Kröner A, Yibas B (2004) Neoproterozoic ophiolites of the Arabian-Nubian Shield. In: Kusky TM (ed) Precambrian ophiolites and related rocks: developments in Precambrian geology, vol 13. Elsevier, Amsterdam, pp 95–128

Stern RJ, Avigad D, Miller NR, Beyth M (2006) Evidence for the snowball Earth hypothesis in the Arabian-Nubian Shield and the East African Orogen. J Afr Earth Sci 44:1–20

Stern R, Ali K, Andresen A, Wilde S, Abu-El-Enien M, Hassan I (2010) Results of geochronological investigations in Sinai undertaken as part of the 2008 JEBEL Fieldtrip. In: Pease V, Kadi K, Kozdroj W (eds) JEBEL project October 2009 field excursion to the Midyan terrane, Kingdom of Saudi Arabia, with reports on research by participants in the JEBEL Project: Saudi Geological Survey Technical Report SGS-TR-2010–2, pp 46–51

Stern RJ, Johnson PR, Ali KA, and Mukherjee SK (2011) Evidence for early and Mid-Cryogenian glaciation in the Northern Arabian-Nubian Shield (Egypt and western Arabia) In: Arnaud E, Halverson G, Shields-Zhou G (eds) The geological record of neoproterozoic glaciations. Geol Soc London Mem 36:277–284

Stoeser DB, Frost CD (2006) Nd, Pb, Sr, and O isotopic characterization of Saudi Arabian Shield terranes. Chem Geol 226:163–188

Sturchio NC, Sultan M, Batiza R (1983) Geology and origin of Meatiq dome, Egypt: a Precambrian metamorphic core complex. Geology 11:72–76

Sultan M, Tucker RD, El Alfy Z, Attia R, Ragab AG (1994) U-Pb (zircon) ages for the gneissic terrane west of the Nile, southern Egypt. Geol Rundsch 83:514–522

Sultan YM, El-Shafei MK, Arnous MO (2017) Tectonic evolution of kid metamorphic complex and the recognition of Najd fault system in South East Sinai. Egypt. Int J Earth Sci 106:2817–2836

Surour AA, Kabesh ML (1998) Calc-alkaline magmatism and associated mafic microgranular enclaves of Wadi Risasa area, Southeastern Sinai, Egypt. Ann Geol Surv Egypt 21:35–54

Takla MA, Basta EZ, Fawzi E (1981) Characterization of the older and younger gabbros of Egypt. Delta J Sci 5:279–314

Wilde SA, Youssef K (2000) Significance of SHRIMP U-Pb dating of the imperial prophyry and associated Dokhan volcanics, Gabal Dokhan, Northern Eastern Desert, Egypt. J Afr Earth Sci 3:403–413

Wilde SA, Youssef K (2002) A re-evaluation of the origin and setting of the late Precambrian Hammamat Group based on SHRIMP-U-Pb dating of detrital zircons from Gebel Umm Tawat, North Eastern Desert, Egypt. J Geol Soc Lond 159:595–604

Willis KM, Stern RJ, Clauer N (1988) Age and geochemistry of Late Precambrian sediments of the Hammamat sediments from the northeastern Desert of Egypt. Precambr Res 42:173–187

Zimmer M, Kröner A, Jochum KP, Reischmann T, Todt W (1995) The Gabal Gerf complex: a Precambrian N-MORB ophiolite in the Nubian Shield, NE Africa. Chem Geol 123:29–51

Zoheir BA, Klemm DD (2007) The tectono-metamorphic evolution of the central part of the Neoproterozoic Allaqi-Heiani suture, south Eastern Desert of Egypt. Gondwana Res 12:289–304

3 Structural and Tectonic Framework of Neoproterozoic Basement of Egypt: From Gneiss Domes to Transpression Belts

Abdel-Rahman Fowler and Zakaria Hamimi

Contents

A.-R. Fowler (✉)
Faculty of Science, Geology Department, United Arab Emirates University, Al Ain, United Arab Emirates
e-mail: afowler@uaeu.ac.ae

Z. Hamimi
Faulty of Science, Department of Geology, Benha University, Banha, 13518, Egypt
e-mail: zakariahamimi123@gmail.com; zakaria.hamimi@fsc.bu.edu.eg

Z. Hamimi et al. (eds.), *The Geology of Egypt*, Regional Geology Reviews,
https://doi.org/10.1007/978-3-030-15265-9_3

Abstract

The Neoproterozoic tectonic evolution of the Egyptian Eastern Desert (EED) basement is documented, principally through its history of structural events, and to a lesser degree, important magmatic and sedimentation events. The essential facts, range of opinions and outstanding problems associated with the key structural-tectonic events are presented. Following the introduction (Sect. 3.1), the regional context of the EED in the Arabian-Nubian Shield and East African Orogen is discussed in Sect. 3.2, including introduction to the popular tripartite division of the EED into the Northern, Central and Southern Eastern Deserts (NED, CED and SED, respectively). Major tectonic events are dealt with from oldest to youngest, so that the following sections, begin with Sect. 3.3: the evidence for the latest Mesoproterozoic rifting of Rodinia in the Sinai, and features of the oldest gneissic complexes (Feiran-Solaf and Sa'al complexes); followed by Sect. 3.4: aspects of the intra-oceanic subduction stage and consequent arc-arc and arc-continent collisions, and suturing of terranes (e.g. the Allaqi–Heiani–Onib–Sol Hamed suture), and with reference to earlier models based on proposed subduction zones within the CED; then Sect. 3.5: the orogenic extension stage, including appraisal of the evidence and scale of extension, its possible tectonic origins (rifting, tectonic escape and extrusion, orogenic collapse, mantle delamination, etc.), and its role in the exhumation of distinctive gneissic dome structure, best represented by the Meatiq complex; and finally, Sect. 3.6: post-extension compressional events, primarily as recorded in the deformation of the extension-stage Hammamat molasse basins, and divided into substages of NW-SE compression, NE-SW compression (both of which are marked by thrusting and folding), regional transpression (including strike-slip zones and flower structures), and high-strain N-S shortening zones represented by the Hamisana Zone and the Oko Shear Zone. The chapter concludes with a short list of comments highlighting key problems and opportunities, with recommendations for future work.

3.1 Introduction

Progress in understanding the structural configuration, deformation history, deformation style and tectonic setting of the ANS in the last few decades is partly due to rapid improvements in remote sensing techniques, a growing geochronological database, and the application of AMS (anisotropy of magnetic susceptibility) to reveal bulk strains in rocks, especially where suitable strain markers are absent (de Wall et al. 2001; Abdeen et al. 2014; Greiling et al. 2014; Hagag et al. 2018). Distinct stages in the development of the Arabian-Nubian Shield (ANS) are becoming clearer, and agreement on a framework of structural events is within reach, however, there remain numerous questions and divided opinions on several issues. These include problems with (1) the tectonic origin/significance of key lithostratigraphic elements (e.g. what tectonic processes were involved in the formation of the Hammamat basins? What is the tectonic setting of Dokhan volcanism?), (2) the regional extent of the deformation events (e.g. how far can post-collision extension in the Central Eastern Desert (CED) be traced to the N, S and E? What are the zonal boundaries of the Najd Fault system?), (3) the spatial and time relations between the events (e.g. are SW-ward thrusts coeval with Najd strike-slip faulting in the CED? Can deformation events be correlated between gneissic complexes of the Sinai?), and (4) the directions of the principal regional stresses and the intensities of strains associated with structural events.

Early attempts at deciphering the tectonic history of the ANS were based on geosynclinal theory and took a mainly stratigraphic approach that even considered the degree of deformation of rock units to have stratigraphic significance (El-Ramly and Akaad 1960; Akkad and Noweir 1969; El Ramly 1972). Establishing the early oceanic character of the ANS was a major achievement, as was the recognition of ophiolite-decorated belts as suture zones, and correlation of these sutures across the Red Sea rift (Bakor et al. 1976; Garson and Shalaby 1976; Frisch and Al-Shanti 1977; Gass 1977, 1981; Engel et al. 1980; Vail 1985; Stoeser and Camp 1985; Kröner et al. 1987; Stern et al. 1990; Shackleton 1994). Comparisons and correlations of EED events were made with other well-studied orogenic belts (e.g. the Cordillera models of El-Gaby et al. 1990; El-Gaby 1994), and with well-accepted generic studies of tectonic phenomena, such as Dewey's (1988) orogenic collapse model (Greiling et al. 1994).

Systematic structural-stratigraphic studies of particular areas have helped to shape a scheme of tectonic events that could be applied regionally (e.g. Ries et al.'s 1983 study of the Meatiq complex and its neighbourhood). A similar approach by Fritz et al. (1996, 2002) was to build a structural-tectonic-magmatic-metamorphic model of the Meatiq complex and apply this model to others in the EED, thereby identifying and dating the main regional events. Petrogenetic models have been combined with field data to explore tectonic events and settings via magmatic histories (Eliwa et al. 2006; Avigad and Gvirtzman 2009).

Some workers have suggested that a structural history consisting of events (D1, D2, D3, etc.) common to all of the ANS may exist. These events may have different characteristics despite being contemporary. One such scheme is described by Hamimi et al. (2019), who outlined three ANS-scale deformation events (D1 to D3). D1 resulted from

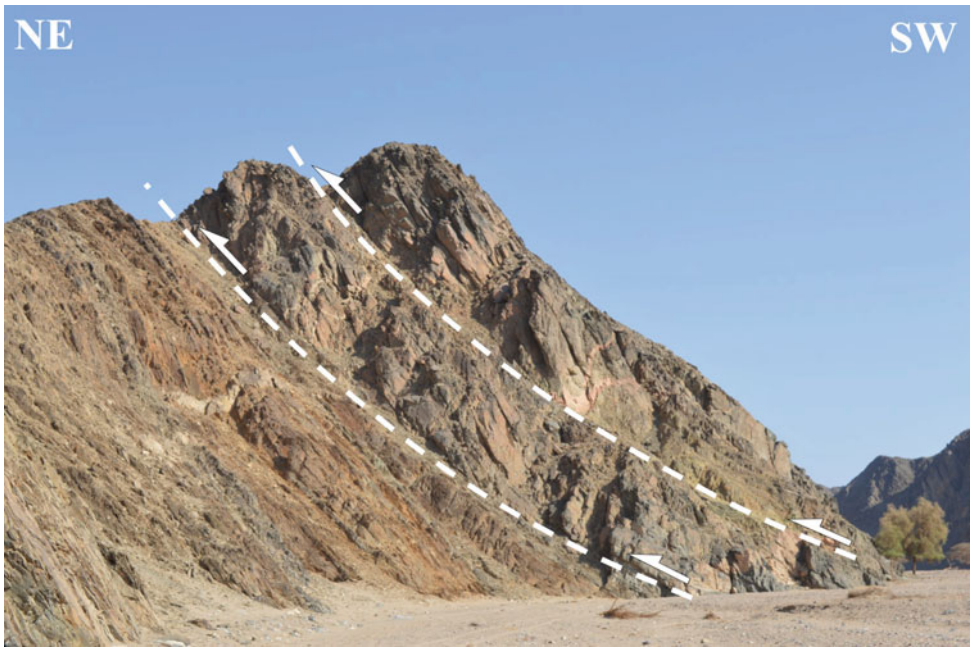

Fig. 3.1 Top-to-NE-propagated thrusting in highly sheared metaultramafics along the eastern flank of Nugrus Shear Zone, from Hamimi et al. (2018)

arc accretion, and was divided into two progressive stages, D1a and D1b. The D1a event was a shortening event, concurrent with the early assembly of east and west Gondwana, and led to the formation of S-, SE-, SW- and NE-directed thrusts (Figs. 3.1 and 3.2) (e.g. at Wadi Beitan, the Allaqi–Heiani suture zone and Nugrus; Abdelkhalek et al. 1992; Abdelsalam et al. 2003; Hagag et al. 2018; Hamimi et al. 2018). The following D1b event was associated with N-directed escape of the ANS, via N- to NNW-directed thrusts and thrust-propagation folds (e.g. at Wadi El-Mayet, Wadi Mubarak and Wadi El Umra in the CED; Shalaby et al. 2005; Abd El-Wahed and Kamh 2010). As in many areas in the ANS, propagation of thrusting carried out according the footwall-nucleating-footwall-vergent role (Fig. 3.3). The D2 deformation was a post-accretion shortening phase, that produced transpressive structures, including NNW-SSE

Fig. 3.2 Well-developed thrust duplexes in slightly sheared metaultramafics of Gabal Abu Dahr, SED, Egypt

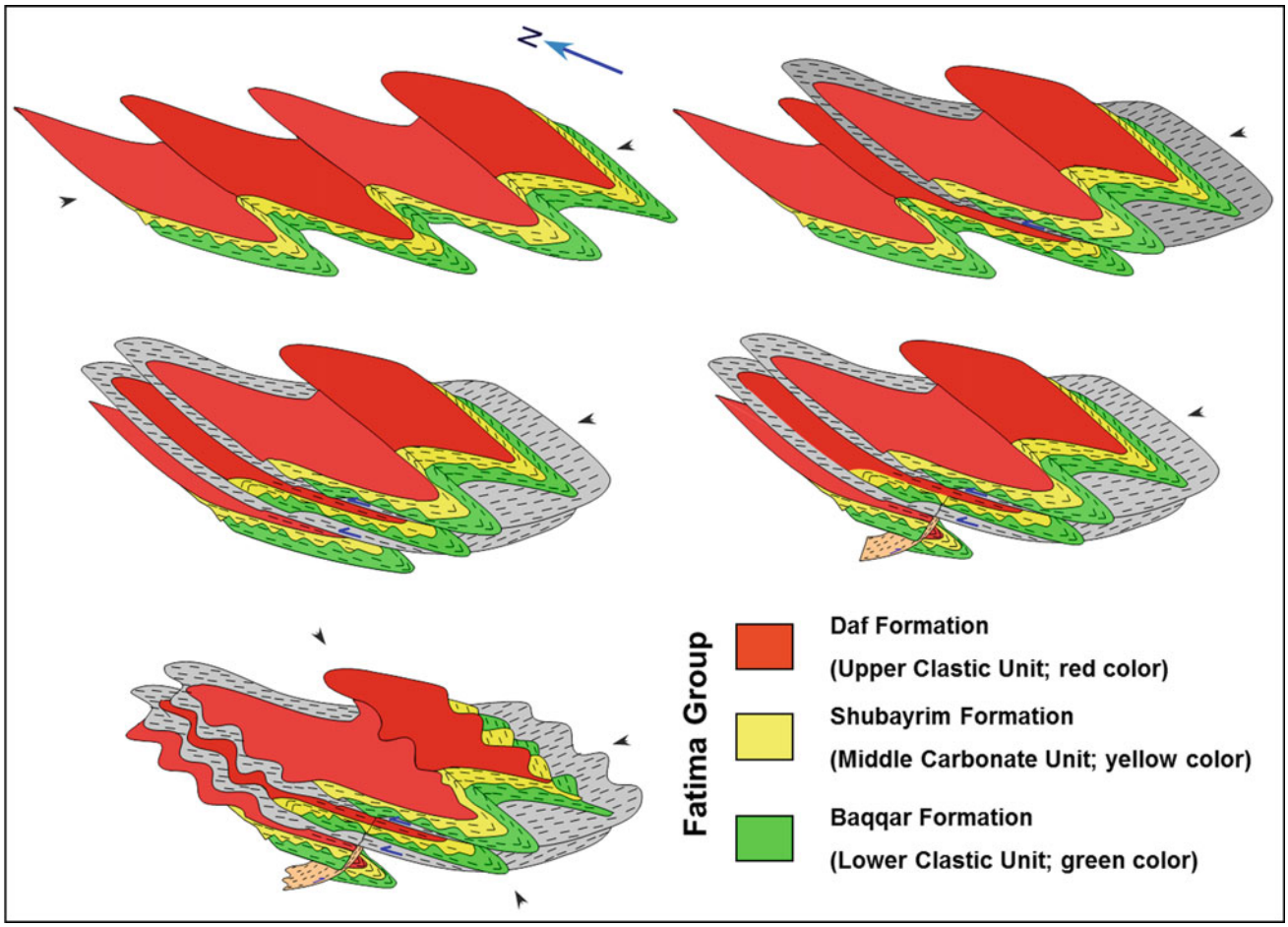

Fig. 3.3 Block model from Hamimi et al. (2012) showing propagation of thrusting according to footwall-nucleating-footwall-vergent rule in Fatima Group Volcanosedimentary Sequence of Western Arabia. In the EED and the entire ANS propagation of thrusting follows this rule

trending sinistral transcurrent shears (e.g. Nugrus and Atalla Shear Zones) (Fig. 3.4), the dextral transcurrent shearing along NE-directed mega shears (e.g. Idfu-Mersa Alam and Qena Safaga Shear Zones), and the post-accretionary shear zone-related gneiss domes (e.g. Meatiq, Sibai, Shalul, Fig. 3.5, and Hafafit gneiss domes) (Fritz et al. 1996, 2002, 2013; Loizenbauer et al. 2001; Ibrahim and Cosgrove 2001; Abd El-Wahed 2008, 2014; Abdeen et al. 2014; Fowler and Osman 2009; Abd El-Wahed et al. 2016; Hamimi and Hagag 2017; Stern 2017; Hagag et al. 2018). The D3 deformation, was an extensional long-lasting phase, associated the crustal relaxation following the Gondwana assembly.

For this chapter, the broadly accepted tectonic stages in the formation of the ANS form the basis of subsections, in each of which the structural characteristics of these stages are described. The stages include Rodinia rifting and oceanic spreading (Sect. 3.3), subduction and arc-collision (Sect. 3.4), post-collision extension (Sect. 3.5) and post-extension deformation (Sect. 3.6).

3.2 Egyptian Precambrian Basement in the Context of NE African Geology

There is a growing consensus (e.g. Li et al. 2008) that the late Mesoproterozoic and most of the Neoproterozoic were dominated by the assembly, amalgamation and break-up of the supercontinent Rodinia (Murphy et al. 2013). There is also general agreement that Gondwana was amalgamated through the closure of a number of large ocean basins and the collision of a series of separate Australia-scale continents, that occurred during the late Neoproterozoic Ediacaran period (635–542 Ma) (e.g. Collins and Pisarevsky 2005; Meert and Torsvik 2003; Pisarevsky et al. 2008). This stage was a turning point in the Earth's history, in terms of profound climate changes and rapidly evolving life (e.g. Squire et al. 2006; Maruyama and Santosh 2008; Halverson et al. 2009; Meert 2012; Maruyama et al. 2013; Abu-Alam et al. 2013). Rodinia supposedly formed by ca., 1,000 Ma

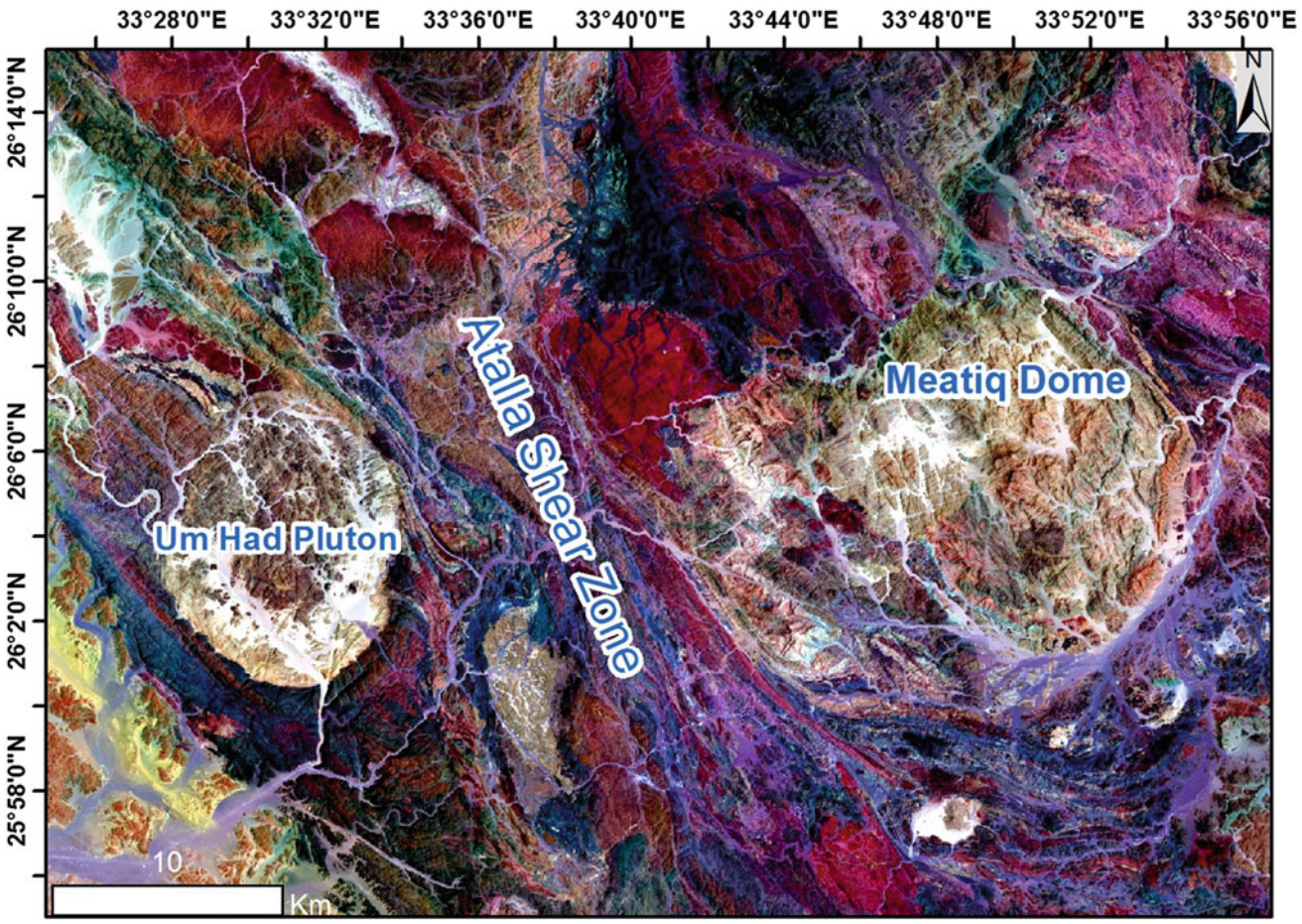

Fig. 3.4 Landsat image showing the NNW-trending Atalla Shear Zone and the related Meatiq Dome, CED, Egypt

and broke apart in the interval 800–700 Ma (Meert and Torsvik 2003)—broadly synchronously with the beginning of the assembly of Gondwana (Meert 2003; Powell and Pisarevsky 2002; Boger et al. 2002; Meert 2001; Torsvik et al. 1996; Meert and Torsvik 2003). The assembly of Gondwana in the Ediacaran (e.g., Meert and Lieberman 2004) was a long and complex process that may have lasted well over 50 million years, and involved several different orogenic events (Rapalini 2018). Gondwana was formed by closure of several major Neoproterozoic oceans (Kröner and Stern 2004) and suturing between continents during the Brasiliano, Pan-African, Adelaidean and Beardmore orogenies. It represents around 64% of today's continental crust (Torsvik and Cocks 2013), composed of the continents of Africa, South America, India, Australia and Antarctica, including several smaller fragments now incorporated into Asia, Europe and North America (Schmitt et al. 2018).

Two main periods of orogenic activity are identified in Gondwana; (1) the first at c. 750 Ma includes some, 15 orogens (Saharan, West African Sao Francisco-Congo and Paranapanama paleocontinents, along with the ANS) that were accreted to form the proto-Gondwana core; (2) the second stage, at 575–480 Ma, incorporated about 40 orogens that were combined to form the Amazonia, Rio de La Plata, Kalahari, Dhawar, East Antarctica and Australian paleocontinents (Schmitt et al. 2018). The assembly of the Gondwana involved large-scale orogenesis, forming the extensive Pan-African mountain ranges, exceeding in size the Cenozoic Alpine-Himalayan chain (Collins and Pisarevsky 2005; Meert and Lieberman 2004; Abu-Alam and Stüwe 2009). These orogenies are collectively known by the name of 'Pan-African events' and their geological record is the traceable evidence of the tectonic processes that assembled the supercontinent Gondwana at this time (Abu-Alam et al. 2013). The Mozambique Ocean separated Neoproterozoic India from the Congo–Tanzania–Bangweulu Block; the Adamastor Ocean separated Africa and South America; Damara Ocean lay between the Kalahari and Congo Cratons; and the Trans- Sahara Ocean divided the West Africa Craton from the pre-Pan-African terrane in north-central Africa.

Fig. 3.5 Field photograph showing the southeastern part of Shalul Dome. The Pan-African thrusting between the hanging wall ophiolitic mélange and the footwall gneissose granite is remarkably observed

These are the main oceans that closed during this period (e.g. Klerkx and Deutsch 1977; Toteu et al. 1990; Black and Liégeois 1993).

3.2.1 The East African Orogen (EAO)

The closure of the Mozambique Ocean ultimately led to one of the most extensive of the Gondwana-forming orogens (Collins and Windley 2002; Dalziel 1997; Jacobs and Thomas 2004), forming the East African Orogen (EAO) (Stern 1994). The EAO constitutes a global scale Neoproterozoic orogenic belt, considered to be one of greatest collision zones on the Earth (Stern 1994; Kusky et al. 2003; Fritz et al. 2013). Closure of the Mozambique Ocean and ANS consolidation occurred by a protracted ~250 My long period of subduction and island arc accretion, arc-arc collision and finally collision of the previously amalgamated arc terranes with the Saharan and Indian cratons (Johnson et al. 2011; Fritz et al. 2013). Such closure led to the formation the EAO which is an accretionary-type orogeny in its northern parts (Fritz et al. 2013), extending over 6000 km in the present-day N-S direction from the Sinai and Jordan to Madagascar. The preserved relics of the EAO range from exhumed high-grade metamorphic belts in Southern India, Madagascar and East Africa (the Mozambique Belt; MB) to greenschist and sub-greenschist facies volcanic, plutonic and sedimentary belts in NE Africa and Arabia (the Arabian-Nubian Shield, ANS) (Cox et al. 2012). The EAO records a full supercontinental cycle from the break-up of Rodinia at the end of an orogeny of Grenvillian age (~950 Ma), through opening and spreading of the Mozambique Ocean and subduction, to collision and amalgamation of East and West Gondwana during the Brasiliano-Pan-African Orogeny (Stern 1994; Collins and Pisarevsky 2005; Johnson et al. 2011; Fritz et al. 2013). It resulted from multiphase convergence and amalgamation of crustal blocks during the Late Neoproterozoic-early Cambrian (Johnson et al. 2013). Granulites within the EAO, which are a first order indicator of continental collision and crustal thickening, are found predominantly along the western margin (Sudan, Ethiopia, Madagascar, and Tanzania), while the northeastern margin, represented by the ANS, lacks such high metamorphic grades (Cox et al. 2012).

This implies that either metamorphic conditions were lower in the ANS (i.e. less crustal thickening) or that deeper crustal sections are simply not exposed (Cox et al. 2012).

3.2.2 The Arabian-Nubian Shield (ANS)

The ANS covers most of NE Africa and the Arabian Peninsula, with a total area of about 3 million km^2. It occupies the northern continuation of the EAO and represents the upper crustal equivalent of the MB. It is regarded as the largest tract of juvenile continental crust of Neoproterozoic age on Earth (Patchett and Chase 2002; Stern et al. 2004), and is bounded to the east and west by pre-Neoproterozoic crust (e.g. Johnson and Woldehaimanot 2003; Whitehouse et al. 2001a, b). The broad range of geological ages of the ANS rocks, ranging from Archean (in the Yemeni part) to lowest Paleozoic, imply a long history of assembly and dispersal of the earlier supercontinents, in general (Unrug 1996), and Rodinia, in particular (Yoshida et al. 1983; Dalziel 1991; Dalziel et al. 2000; Hoffman 1991). Several lines of evidence attest to the idea that the ANS is juvenile Neoproterozoic crust, including non-radiogenic initial Sr and radiogenic initial Nd isotopic compositions for a wide range of igneous rocks (Stern et al. 2004). The ANS was stable continental crust by early Cambrian time at 530 Ma. It was the result of diverse and polycyclic geodynamic events and consists of a collage of volcanic arcs, Tonian to Ediacaran terranes and ophiolite remnants that evolved during most of Neoproterozoic time (870–540 Ma). These terranes were amalgamated within and around the margins of the Pacific-sized Mozambique Ocean, the ocean basin that opened during the Middle Neoproterozoic break-up of Rodinia ~800–900 Ma (Stern 1994). The ANS ophiolitic mantle was mostly harzburgitic, containing magnesian olivines and spinels with compositions consistent with extensive melting (Stern et al. 2004). Cr# for spinels in ANS harzburgites are mostly >60, comparable to spinels from modern forearcs, and distinctly higher than spinels from mid-ocean ridges and backarc basin peridotites (Stern et al. 2004).

Four evolutionary events or phases have been proposed by Bentor (1985) to frame the tectonic setting of the ANS: (1) an oceanic phase (1100–900 Ma), characterized by the emplacement of oceanic tholeiites (including ophiolites) and their plutonic equivalents; (2) an island arc phase (950–650 Ma), mainly represented by andesitic volcanism and dioritic plutonism; (3) a calc-alkaline batholithic phase (650–590 Ma); and (4) an alkaline batholithic phase (590–550 Ma). Stern (1994), Abdelsalam et al. (2002) and Johnson and Woldehaimanot (2003) proposed three main stages for the evolution of the ANS; (1) subduction stage (~870–635 Ma) resulting in the formation of island arc volcanosedimentary sequences; (2) continental collision stage (~630–580 Ma) resulting in the formation of the EAO, due to the ongoing convergence between East and West Gondwana; and (3) post-collision stage (580–540 Ma) during which the ANS crust stabilized. Development of sedimentary basins in fault-controlled down sags and pull-aparts, and intrusion of calc-alkaline and alkaline magmatism took place during the last two stages. Proposed models discussing the tectonic evolution the ANS include (Hamimi et al. 2013); (1) infracrustal orogenic model, whereby ophiolites and island-arc volcanics and volcaniclastics were thrusted over an old craton consisting of high-grade gneisses, migmatites and remobilized equivalents during Neoproterozoic time (e.g. Akaad and Noweir 1980; El-Gaby et al. 1988; Abdel Khalek et al. 1992; Khudeir and Asran 1992); (2) Turkic-type orogenic model, whereby much of the ANS formed in broad fore-arc complexes (Şengor and Natal'in 1996); (3) hot-spot model, in which much of the ANS formed by accretion of oceanic plateaux generated by upwelling mantle plumes (Stein and Goldstein 1996); and (4) arc assembly (arc accretion) model, in which EAO juvenile crust was generated around and within the previously mentioned Mozambique Ocean (Vail 1985; Stoeser and Camp 1985; Stern 1994).

3.2.2.1 Egyptian Eastern Desert Terrane, The North, Central and South Eastern Deserts, and The Southern Sinai

The Precambrian basement rocks in Egypt crop out over an area of ~100,000 km^2 in the Eastern Desert (between River Nile and Red Sea) and southern Sinai, as well as exposures in the southwestern corner of the Western Desert at the Gabal Uweinat—Gabal Kamil inlier. The crystalline basement complex of the Eastern Desert and Southern Sinai is of Neoproterozoic age and occupies the northwestern part of the ANS. The Uweinat—Kamil inlier lies in the East Sahara 'ghost' Craton (or Metacraton) in NE Africa, and is the only inlier in the craton containing rocks of Archean age. These rocks consist of an association of dominantly basic meta-igneous rocks that are overlain by a metamorphosed sequence of shallow-marine sediments, comprising banded-iron formations (BIFs), quartzites, marbles, calc-silicates and some rare meta-pelites (Wulff 2001; Karmakar and Schenk 2015).

The Eastern Desert of Egypt represents a complete succession of the Neoproterozoic basement encountered elsewhere in the ANS. Several attempts have been made to classify and categorize these rocks (e.g. Hume 1934; Schürmann 1953, 1966; El Ramly and Akaad 1960; El Shazly 1964; Akaad and Noweir 1969, 1980; El Ramly 1972; Ries et al. 1983; Bentor 1985; El-Gaby et al. 1988, 1990; Abdelkhalek et al. 1992; Rajab and El Alfy 1996). Some of these attempts are based on classical geosynclinal

models, in which the geosynclines were considered to be ensialic (oceanic) and various lithologies were formed during successive stages of evolution. However, these classifications are the subject of vigorous discussion in a previous chapter in this book. Recently, the Neoproterozoic rocks of the Eastern Desert have been interpreted as a series of Neoproterozoic intra-oceanic arcs amalgamated during the climax of the Pan-African Orogeny c. 630 Ma (e.g. Kröner and Stern 2004). The Neoproterozoic volcanosedimentary succession in the Eastern Desert is classified into a Cryogenian island arc association and an Ediacaran post-collision Dokhan volcanic–Hammamat clastic sediment association (Akaad and Noweir 1969; El-Gaby et al. 1990; Mogazi et al. 2012). At their type locality in Gabal Dokhan, the Dokhan volcanics were erupted between 600 and 590 Ma (Wilde and Youssef 2000). The Neoproterozoic Hammamat basins of the central Eastern Desert of Egypt (CED) contain typically several-kilometre thick accumulations of pebble, cobble and boulder conglomerates and sandstones that were deposited unconformably upon accreted arcs in the late stages of the assembly of the ANS (Fowler and Abdeen 2014). The lower part of the Hammamat Group contains zirons as young as 585 ± 13 Ma, reflecting contemporaneous development of Dokhan and Hammamat successions (Wilde and Youssef 2002; Ali et al. 2009a, b).

The Eastern Desert of Egypt is traditionally subdivided into three main provinces (Stern and Hedge 1985; El-Gaby et al. 1988)—the **North Eastern Desert** (NED), **Central Eastern Desert** (CED) and **South Eastern Desert** (SED).

The **North Eastern Desert** is dominated by voluminous granitoids, together with slightly deformed- unmetamorphosed Dokhan Volcanics and post-amalgamation Hammamat volcanosedimentary sequences. There are three principal schools of thoughts regarding the tectonic setting of the Dokhan Volcanics; (1) in a subduction environment (e.g. Hassan and Hashad 1990; Abdel-Rahman 1996; Abdel Wahed et al. 2012) (2) in an environment of crustal extension following crustal thickening (Stern et al. 1984; Stern and Gottfried 1986), or (3) during transition between subduction and extension (Ressetar and Monard 1983; Moghazi 2003; El-Sayed et al. 2004; Eliwa et al. 2006; El-Bialy 2010; Azer and Farahat 2011; Khalaf 2012).

The **Central Eastern Desert** incorporates gneisses, migmatites and sheared granitoids, and remobilized equivalents outcropping as elliptical domal-like structures, in addition to a volcanosedimentary succession (mainly volcanogenic metagreywackes and metamudstones) and ophiolitic meta-ultramafites.

The **South Eastern Desert** is dominated by the same lithologic units as the CED, with the exception of a higher proportion of gneisses and migmatitic gneisses, as well as the ophiolitic meta-ultramafites that existed as tectonically emplaced nappes. Gneissic and migmatitic rocks of the SED occupy much larger, more complexly shaped areas associated with batholiths of foliated granodiorites (Fowler and Osman 2009). Moreover, the typical greenschist facies of volcanogenic metagreywackes and metamudstones of the CED are also comparable with the high-grade schistose-metasediments of the SED (El-Gaby et al. 1988; Hermina et al. 1989; Hassan and Hashad 1990). Apart from the lithologic differences, the previously mentioned provinces of the Egyptian Eastern Desert show remarkable differences in structural architecture (Hamimi et al. 2015). The NED is dominated by fault/joint systems, while thrusts appear to be subordinate. Most of this province is masked by younger granitoid intrusions. Fold-related faults are dominant in the CED, and are commonly associated with pull-apart basins linked to the Najd Fault System. In the SED, fold-thrust belts prevail and thrusts are first-order kinematics that were later overprinted by regional-scale transpression.

The Neoproterozoic basement complex in **southern Sinai** resembles in many respects those encountered in the Eastern Desert with the exception of the absence of ophiolites and the existence of Katherina Volcanics. The Katherina Volcanics (Agron and Bentor 1981) is represented mainly by alkaline rhyolitic flows and pyroclastics and subvolcanic porphyries outcropping at Gabal Katherina (e.g. Bielski 1982; Farahat and Azer 2011; Azer et al. 2014), Gabal Abu-Durba (El-Bialy 1999), Wadi Mahash, Wadi Khilifeya and Gabal Homra in NE Sinai (Agron and Bentor 1981; Samuel et al. 2007) and Gabal Ma'ain (El-Bialy and Hassen 2012). It is regarded as the latest magmatism in the Egyptian basement and marks the onset of the anorogenic period, during which the ANS tectonic regime switched to tensional and intra-plate rifting (El-Bialy and Hassan 2012). The metamorphic complexes in Sinai exist in Taba, Feiran-Solaf, Sa'al and Kid, and are represented by infracrustal amphibolite-facies orthogneisses and supracrustal greenschist-facies metasedimentary and volcanic sequences (e.g. Abu El-Enen 2011; Abu-Alam and Stüwe 2009; Eliwa et al. 2008; El-Shafei and Kusky 2003). U-Pb zircon ages for the gneisses are mainly 850–740 Ma, but older metasediments of ~1 Ga and younger gneisses of 660–630 Ma have also been found (Mogazi et al. 2012, and references therein). Whether these complexes were dominated by extensional or compressional deformations is a matter of controversy. For instance, Blasband et al. (1997, 2000) and Brooijmans et al. (2003) proposed that the Kid area was an example of an extension-related metamorphic and igneous core complex, while Fowler et al. (2010a, b) argued that this area evolved in a compressional tectonic setting.

The boundaries between the three segments of the EED lie along sheared zones that remain controversial in their interpretation. The **Qena-Safaga Shear Zone** (QSSZ) is usually taken to represent the boundary between the NED

from CED. El-Gaby et al. (1988) described the QSSZ as a major dextral strike-slip shear. Alternatively, it is considered to be a major steep extensional shear zone by Fowler et al. (2006), or a low angle thrust overprinted by strike slip shears with complex orientations by Kamal El-Din and Abdelkareem (2018). The boundary between the CED and SED was identified as the **Idfu-Mersa Alam Shear Zone** by El-Gaby et al. (1988), and as the **Sha'it–Nugrus Shear Zone** (SNSZ) by Fowler and Osman (2009). The SNSZ is also diversely interpreted, as the roof thrust of a duplex structure (Greiling et al. 1988), or a low-angle extensional shear zone (Fowler and Osman 2009), or a combination of normal fault and strike-slip shear zone (Fritz et al. 1996; Hagag et al. 2018).

3.3 Earliest Neoproterozoic Deformation Events

Field relations and geochronological data published since the middle, 1990's (Kröner et al. 1994; Liegeois and Stern 2010; Ali et al. 2012a; Johnson et al. 2011; Johnson 2014) have consistently challenged the erstwhile view that the infracrustal metamorphic complexes (high-grade gneisses, migmatites and re-mobilized equivalents, comprising the Meatiq, El-Sibai and Hafafit gneissic complexes) were the oldest lithologic units in the Arabian-Nubian Shield. In the Egyptian ED these high-grade rocks were exhumed from beneath the supracrustal rocks (ophiolites, ophiolitic mélange and island arc assemblages) along major low-angle shear zones (e.g. Wadi Sha'it—Nugrus and Eastern Desert Shear Zones) and thrust faults. The infracrustal-suprastructure shear zones and thrusts were long regarded by many workers (e.g. El-Gaby et al. 1988; Abdelkhalek et al. 1992) as the first deformation phase in the ED and Sinai. However, latest Mesoproterozoic deformations have recently been documented in the Sa'al complex in the basement rocks of southern Sinai by Be-eri-Shlevin et al. (2012). In the nearby Feiran-Solaf gneissic complex, Abu-Alam and Stüwe (2009) described remnants of an early fabric preserved only as inclusion trails in garnet porphyroblasts, and referred this palimpsest fabric to the early metamorphic phase (M1) in this metamorphic belt. The regional principal strains during the M1 metamorphic event in the Feiran -Solaf belt were found to be vertical flattening with stretching in the NW–SE direction (and minor NE–SW stretching—Fowler and Hassan 2008). This early deformation event was suggested to reflect a larger-scale extension related to the break-up of Rodinia (Fowler and Hassen 2008).

3.3.1 Feiran-Solaf Metamorphic Complex

Based on SHRIMP U–Pb zircon age data, Ali et al. (2009a, b) interpreted the granitoid evolution in Sinai, and concluded that: (1) both calc-alkaline monzogranites/syenogranites and alkali granites were emplaced over a restricted time span between ~580 and 595 Ma (2) contrary to the view generally held with respect to the Eastern Desert of Egypt (Bentor 1985), the alkali granites were not emplaced during a separate later stage of magmatism, and (3) the rather imprecise $^{207}Pb/^{206}Pb$ age of 1789 ± 56 Ma for an inherited grain in the syenogranite from Wadi Nasb (north of Wadi Kid) indicates that older material is present within the basement in the northeastern Sinai. Samuel et al. (2011) reported an age of age ca. 900–1100 Ma for rock fragments in the volcano-sedimentary succession intermediate to silicic volcanics of mainly high-K calc-alkaline affinity, interbedded with immature sediments at Wadi Rutig, Sinai. Another noteworthy Mesoproterozoic age was reported by Abu El-Enen and Whitehouse (2013) from Wadi Solaf metapsammitic gneisses (Feiran–Solaf complex). These latter authors found ~1.0 Ga zircons that they believed represented an acid igneous provenance for the metapsammites, which they regarded as originally arkoses, deposited sometime after ~975 ± 10 Ma. A similar ~1.0 Ga age from granodioritic biotite gneisses was given by the same authors, and could also be xenocrystic, but was interpreted as the protolith crystallization age. These Mesoproterozoic ages contrast with the earlier estimates of 630 to 610–615 Ma for the possible age range of high temperature metamorphism of the Feiran-Solaf complex given by Stern and Manton (1987), and an age of 590–600 Ma by Eliwa et al. (2008) for the probable metamorphic cooling age of the Feiran gneisses.

Hassan et al. (2014) attributed such differences in radiogenic age estimates at Feiran–Solaf complex to isotopic disturbances during the Pan-African metamorphism or during the exhumation. Nevertheless, the Mesoproterozoic ages recorded in both Sa'al–Zaghra and Solaf complexes hint that the oldest lithologic units in the Egyptian basement are not the EED gneisses as once claimed.

3.3.2 Sa'al-Zaghra Metamorphic Complex

Recently published zircon U-Pb age data and geochemistry for the Sa'al-Zaghra volcano-sedimentary sequence (Sa'al--Zaghra metamorphic complex) in Sinai provide the first robust evidence of latest Mesoproterozoic island arc rocks at the northernmost ANS (Be'eri-Shlevin et al. 2012).

The complex is subdivided tectono- stratigraphically into two superimposed metavolcanic formations (Agramiya and post-Ra'ayan), separated by the metasedimentary Ra'ayan Formation (metagreywacke, semi-metapelite and metapelite), and encompasses a wide variety of non-consanguineous, late Mesoproterozoic to late Neoproterozoic rock units that preserve a complicated and protracted record of orogenic and tectonic assembly (Fowler et al. 2015; Ali-Bik et al. 2017). Such data show that this area contains the oldest lithologies so far found in the northernmost ANS, preserving evidence for a 1110–1030 Ma rift-related volcanic system formed during Rodinia break-up.

Hassan et al. (2014) carried out detailed petrographic, mineral chemistry and thermodynamic modeling, in combination with structural data from the field (Fowler et al. 2015), to derive a P–T–D–t path for the Sa'al-Zaghra metamorphic complex. Hassan et al. (2014) found that these conditions corresponded to a geothermal gradient of 38–41 °C/km which is much higher than that documented elsewhere in the metamorphic complexes of Sinai (i.e. 25–27 °C/km). The majority of the metavolcanic–metasedimentary associations of the Sa'al–Zaghra Complex show good preservation of primary volcanic and sedimentary microstructures (e.g. porphyritic and eutaxitic textures) and have been affected by only low-strain typically involving a weakly developed foliation parallel to layering and bedding planes. The authors suggest that the flat lying D1 fabric in association with the metamorphic conditions around 400 °C and 3 kbar indicate metamorphism during a crustal thinning event that occurred during an extension regime. The peak metamorphism of the M1 in the study area occurred at a depth of 9–11.5 km.

The 38–41 °C/km geothermal gradient at Sa'al is much higher than the geothermal gradients for the 630 Ma M1 event at Feiran–Solaf (25–27 °C/km) (Abu-Alam and Stüwe 2009), or for the Gabal Samra metapelites from the same general region (27 °C/km; Abu El-Enen 2011). Hassan et al. (2014) and Fowler et al. (2015) came to the conclusion that the complex records an earlier stage of metamorphism and deformation during break-up of Rodinia. Such conclusion is in harmony with that given by Fowler and Hassen (2008) concerning a larger-scale extension-related to the breakup of Rodinia. The lower gradients documented elsewhere are thought to be related to the Gondwana collision. During the subsequent East -West Gondwana collision, the Sa'al–Zaghra complex remained at shallow crustal levels (<9 km), and therefore escaped the deep crustal metamorphism of the Pan-African event as indicated by the existence of a single metamorphic event (M1) in the Sa'al complex in the time interval, 1030–1017 Ma (Hassan et al. 2014).

On the other hand, it must be noted that, based on the youngest concordant zircon ages in the matrix of the Zaghra metaconglomerate and the emplacement age of 614 Ma for a dioritic pluton intruding the metaconglomerate, Andresen et al. (2014) concluded that: (1) the Zaghra Formation (interbedded feldspathic sandstones, conglomerates and pelites) was deposited and deformed after 622 ± 6 Ma, but before 614 ± 4 Ma (2) the late Mesoproterozoic age for the deformation and metamorphism of the Zaghra Formation, as postulated by Hassan et al., (2014), is in direct conflict with Anderson's et al.'s (2014) data (3) detrital zircons from the Zaghra have ages indicating magmatic/volcanic activity in northern Sinai at ca. 630–650, 770, 800, and, 1000 Ma, and (4) the ~1.0 Ga detrital zircons present in the Zaghra Formation indicate the presence of a late Mesoproterozoic source area in the northern part of ANS.

3.4 Arc Accretion Stage

The oceanic volcanic arc and subduction stage in the northern ANS is dated as 850–650 Ma, with subduction terminated by arc-arc collisions and suturing between 760 and 690 Ma (Stern 1994), though compressional deformation and 'subduction-related' plutonism persisted until about 625 Ma (Johnson and Woldehaimanot 2003, Fritz et al. 2013). The volcanic and plutonic rocks and sediments of this stage have been metamorphosed to mainly greenschist facies grade during deformation.

In the CED, the arc products have been divided into the Older Metavolcanics (OMV), consisting of ultramafic to mafic rocks of ophiolitic affinity (serpentinites, gabbros, basalts), and the Younger Metavolcanics (YMV) of the mature arc stage (mainly andesites, rhyodacites, pyroclastics), with BIF-bearing deep water immature sediments (greywackes, and mudstones, rarer cherts, carbonates and conglomerates) between the OMV and YMV (Stern 1981; Stern et al. 2013). THE YMV has been recognized also in the NED (Bühler et al. 2014). The OMV and YMV have largely overlapping ages in the range 750–700 Ma (Ali et al. 2009a, b; Bühler et al. 2014). In the SED the ~715–765 Ma Shadli metavolcanics and equivalents represent the arc volcanic stage (Stern and Hedge 1985; Stern et al. 1991).

3.4.1 Arc-Arc Sutures: Timing and Kinematics of the Arc Collisions

Arc-arc collision zones are represented by ophiolite-decorated sutures (Figs. 3.6 and 3.7) that have been correlated across the Red Sea rift from southern Egypt and Sudan into the western arc terranes of Saudi Arabia. These include the Allaqi–Heiani–Onib–Sol Hamed (Egypt)–Yanbu (Arabia) suture [AHOSHY], and the Amur–Nakasib (Sudan)–B'ir Umq (Arabia) suture–ANBU] (Stoeser and Camp 1985; Vail 1985; Shackleton 1986; Kröner et al. 1987; Stern et al. 1990; Shackleton 1994; Johnson and

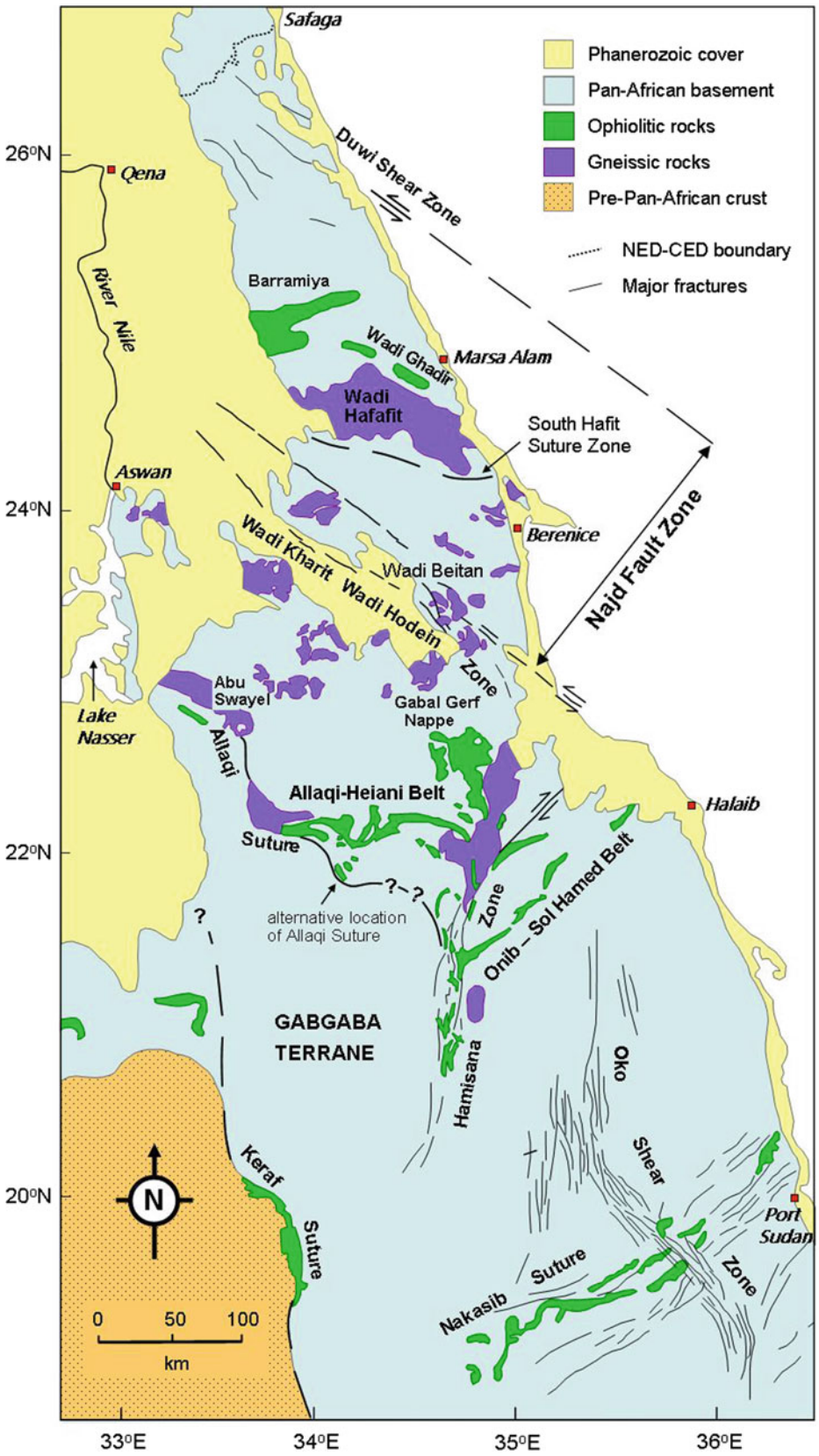

Fig. 3.6 The Nubian Shield of northern Sudan and Egypt, modified from de Wall et al. (2001). The locations of the N–S Hamisana Zone and Oko Shear Zone are shown. Also shown are the major suture zones, the Allaqi–Heiani, Onib–Sol Hamed, Naskasib and Keraf; and the South Hafafit Suture Zone of Greiling et al. (1994). The extent of the Najd Fault Zone in the CED and SED is also shown

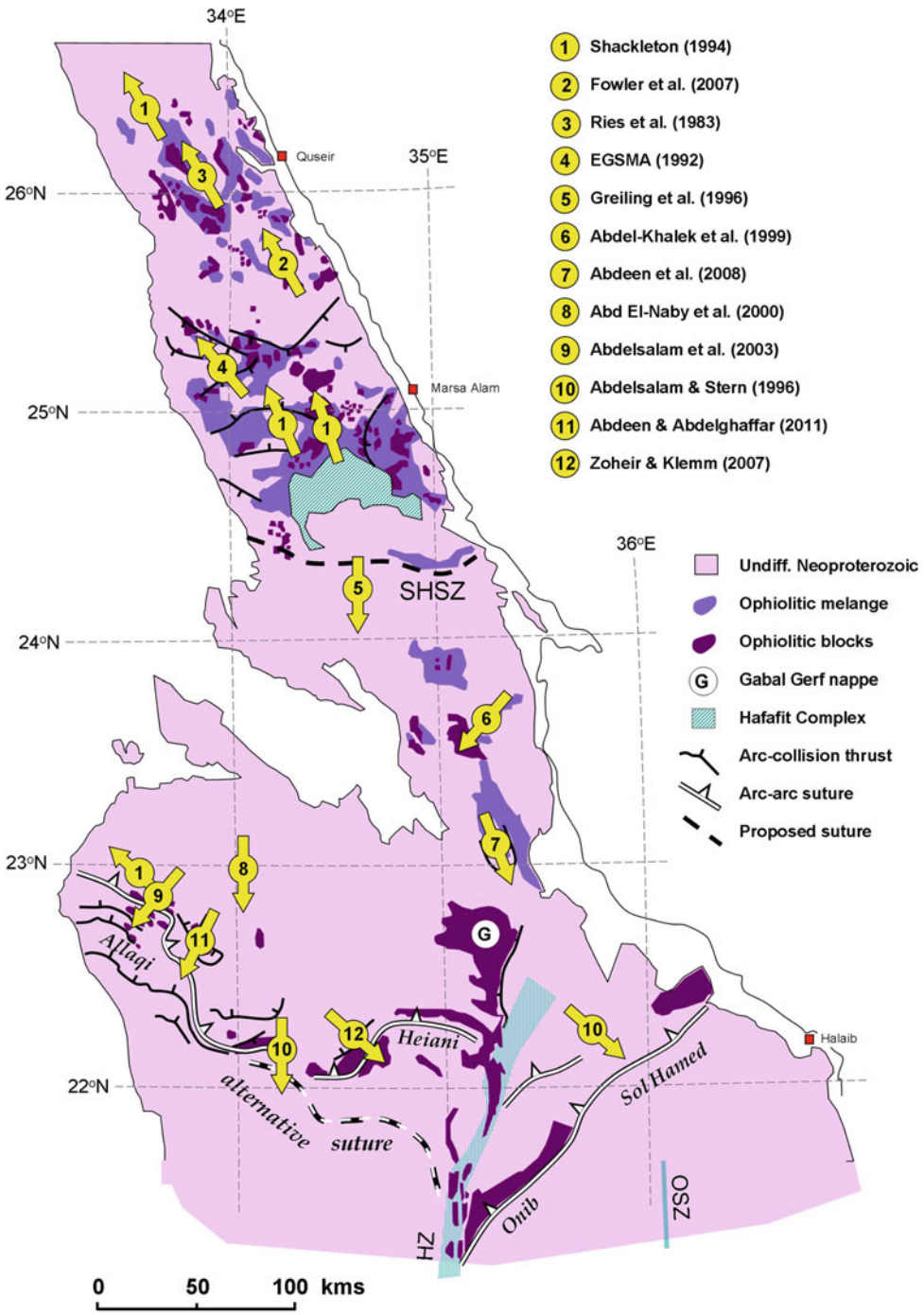

Fig. 3.7 Distribution of ophiolitic rocks in the EED, divide into massive (relatively intact blocks) and mélange ophiolite assemblages, modified from Shackleton (1994). Thrusting directions are referenced by numbers to published works. Note the dominance of mélange and NW-ward thrusting directions north of 24°30′N (i.e. north of either the South Hafafit Suture Zone or Hafafit Complex), compared to dominantly intact ophiolitic masses and S-, SE- and SW-ward thrusting directions south of this latitude. The alternative location of the Allaqi–Heiani suture was proposed by de Wall et al. (2001). The existence of the South Hafafit Suture Zone (SHSZ) was suggested by Greiling et al. (1994)

Woldehaimanot 2003; Johnson et al. 2011). Both are identified as arc-arc sutures with NW-SE convergence directions, though some transpression resulting in strike-slip component along the sutures is also indicated. The ANBU is dated at 780–750 Ma, while the AHOSHY suture zone to the north is dated at 740–700 Ma (Abdelsalam and Stern 1996; Ali et al. 2010; Johnson et al. 2011).

The collision along the AHOSHY is characterized by folding, and thrusting and steeper imbricate reverse faulting of the Gerf arc southwards (or to the SE or SW) over the 830–720 Ma Gabgaba terrane arc (Abdelsalam and Stern 1996; Abdelsalam et al. 2003; Kusky and Ramadan 2002; Zoheir and Klemm 2007; Abdeen and Abdelghaffar 2011) (Figs. 3.7 and 3.8a, b). Approximately southwards thrusting of arc metavolcanics and ophiolites has also been reported in a number of SED locations between AHOSHY and the Hafafit complex (Fig. 3.7). Sadek (2008) and Abdeen et al. (2008) reported SSE-wards thrusting and associated tight folding in

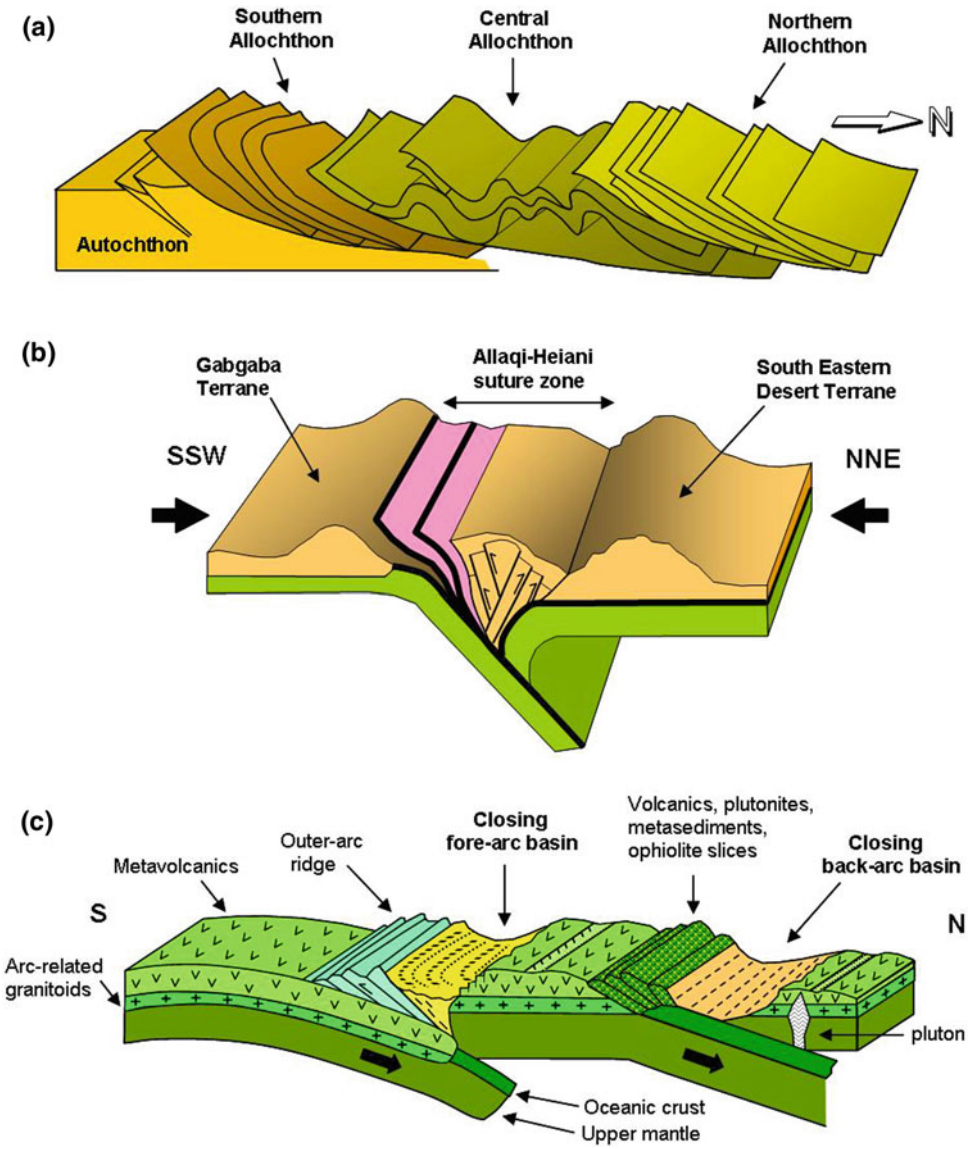

Fig. 3.8 Structural styles of the Allaqi–Heiani Suture Zone. **a** Western part of the suture from Abdelsalam et al. (2003). The suture zone is divided into northern allochthon (low-dipping SW-vergent thrusts), central allochthon (NW-trending folds affecting earlier thrusts, and southern allochthon (SW-verging thrusts folded about N-trending folds). The suture zone is about 20 km wide (N-S). **b** Model of the central part of the suture zone from Abdeen and Abdelghaffar (2011) showing their D1 structures, including steep reverse faults with displacement towards and away from the collision zone. **c** Model of the Wadi Haimur—Abu Swayel gneiss belt tectonic setting (630 Ma) from Abd El-Naby and Frisch (2002). The gneiss belt is interpreted by the latter authors as a back arc basin sequence that was metamorphosed during deformation associated with the central Allaqi–Heiani suture

the Wadi Hodein area, while Abdel Khalek et al. (1999) showed thrusting to the SW in this area. Abd El-Naby et al. (2000) and Abd El-Naby and Frisch (2002) described southwards thrusting during arc collision, involving closing of a back-arc basin at Abu Swayel (Fig. 3.8c). Greiling et al. (1994, 1996) recognized SSW-wards thrusting immediately to the south of the Hafafit complex and proposed the existence of an offset segment of the AHOSHY south of Hafafit, which they referred to as the 'South Hafafit Suture' (Fig. 3.6).

Descriptions of the ophiolitic rocks along the AHOSHY and the Jabal Gerf klippe indicate that they are mainly massive almost intact ophiolite blocks and steeply dipping thrust slices, with only minor mélange (Kusky and Ramadan 2002; Abdeen and Abdelghaffar 2011; Abdel-Karim et al. 2016) (Fig. 3.7). This is consistent with the ophiolite having been transported only a short distance from its source (Abdelsalam and Stern 1996). However, Shackleton (1986, his Fig. 3.3b) hypothesized that there was a continuous thrusted sheet of ophiolitic mélange extending in a NNW-SSE direction from Onib–Sol Hamed nearly to the river Nile (Fig. 3.7).

In the remainder of the SED, and throughout the CED, the ophiolite is widespread but discontinuous (Sultan et al. 1986), being represented by a series of, 1–2 km thick low-dipping sheets of ophiolitic mélange (Shackleton et al. 1980). The mélange contains chaotically assembled smaller blocks of ophiolitic (but not arc) lithologies set in a foliated matrix of graphitic pelites and greywackes. Some large thrust dissected ophiolite successions are found within the mélange, e.g. Wadi Ghadir (El-Sharkawy and El-Bayoumi 1979; Elbayoumi and Greiling 1984), El-Barramiya Range

(Gad and Kusky 2006), Wadi Mubarak (El-Bayoumi and Hassanein 1983; Farahat et al. 2004; Abdel-Karim et al. 2008), El Fawakhir–Wadi Atalla (El-Sayed et al. 1999; Abd El-Rahman et al. 2009) and Jabal El Rubshi (Amstutz et al. 1984; Habib 1987; El-Desoky et al. 2015) (Fig. 3.7).

In contrast to the SED, the mélange in the CED has experienced top-to-the-NW displacement on low dipping shears (Bennett and Mosley 1987; Greiling 1987; Greiling et al. 1993, 1994; Abdelsalam and Stern 1996; Abd El-Wahed 2014) (Fig. 3.7). The mélange sheets may overlay arc volcanics with sheared contact or be interleaved with them.

3.4.2 Tectonic Environment of the Ophiolitic Material

Nearly all geochemical studies of the mélange serpentinites, especially the chromitites bodies within them, have shown that the ophiolites are not oceanic in affinity, but are either forearc (suprasubduction zone) (Azer and Stern 2007; Salem et al. 2012; Azer 2014; Obeid et al. 2015) or back-arc in origin (Shackleton 1994; Khudeir and Asran 1992; Abd El-Naby and Frisch 2006; El-Sayed et al. 1999; Abdel-Karim and Ahmed 2010; Abdel-Karim et al. 1996; Farahat 2010; Abd El-Rahman et al. 2009), or in forearc and back-arc or other arc positions (Stern 1994; Khalil and Azer 2007; Abd El-Rahman et al. 2012; Gamal El Dien et al. 2016). There are differences of opinion on the recognition of forearc from back arc environments, e.g. Jabal Gerf serpentinites were regarded as forearc by Abdel-Karim et al. (2016) and Abu Anbar (2015), but as mid-oceanic by Zimmer et al. (1995). Gabal El-Rubshi ophiolites were regarded as forearc by Abdel-Karim and El-Shafei (2018), but as back-arc by Amstutz et al. (1984). According to Abdel-Karim et al. (2016) these different conclusions are based on the evidence of different materials of the ophiolite (volcanics versus ultramafics) being analyzed.

3.4.3 Mechanisms of Emplacement of the Ophiolitic Mélange

The thrusting and folding mechanisms of emplacement of the ophiolitic thrust complexes along the AHOSHY are fairly clear (Fig. 3.8), though the relative importance of nappe folding versus thrusting may be debated. There is much less certainty about the mechanism(s) of emplacement of the mélange of the CED, and its relation to arc collision. Some more intact mélange bodies in the CED do show evidence of thrust stacking and thrust dissection, e.g. Wadi Ghadir (Elbayoumi and Greiling 1984), and the Barramiya Range. However, the CED mélange generally shows only minor internal deformation, expressed commonly as a scaly foliation anastomosing around stretched blocks, with high strains localized in mylonitized contacts.

Shackleton (1994) noted that the semi-continuous coverage of a huge area of the CED by mélange may be due to the typically large extent of back-arc basins from which the mélange was derived. El-Sharkawy and El-Bayoumi (1979) found that the mélange exhibited facies variations. A proximal facies consisted of giant angular blocks, mainly of serpentinite, while the distal facies was a deep water pelitic sequence with lenses of ophiolite debris and pebbly sections. It is likely that primary fragmentation of the mélange occurred before tectonic displacement. Shackleton et al. (1980) and Ries et al. (1983) described parts of the mélange as olistostromal, implying gravity sliding and disaggregation of ophiolitic material in a subduction trench before later thrusting to the NW. A gravity gliding mechanism for initial formation of the mélange may account for some displacement of the mélange away from the arc suture zone, providing a possible explanation for the change in directions from S-wards thrusting at the suture to NW-wards displacement in the back-arc areas (Fig. 3.7).

3.4.4 Calc-Alkaline ‘Subduction’-Related (‘Older’) Granitoids of the Arc and Arc-Collision Stage

Timing of tectonic displacement of the ophiolitic mélange slices and sheets can be revealed by dating of the calc-alkaline granitoid intrusions that have been, (1) overthrusted by the ophiolites and arc rocks, (2) intruded during thrusting of the ophiolites and arc rocks, and (3) intruded through the ophiolites and arc rocks after thrusting. These ‘grey’ or ‘Older’ granitoids (Akaad and Noweir 1969; El Ramly 1972) are usually large trondhjemite, tonalite and granodiorite plutons with chemical characteristics similar to subduction zone magmas, and commonly showing xenolithic, gneissic, reactive or sheared margins and concordant wallrock contacts (Hassan and Hashad 1990). The Older granites are abundant throughout the NED, CED and SED, while the NED has only scant exposures of arc metavolcanics and ophiolites. This has been explained as being due to a deeper erosion level in the NED removing the upper volcanic and ophiolitic units (El-Gaby et al. 1988).

3.4.4.1 Arc Plutons

A broad range of radiometric dates has been determined for the Older granites (850–615 Ma), coinciding with the dates for the arc and arc collision stage (Hassan and Hashad 1990). The latter authors and others have regarded this long age range as a series of magmatic pulses (described as ‘cycles’ by some) rather than a continuum of magmatic activity

(Stern and Hedge 1985; Moussa et al. 2008; Lundmark et al. 2012; Robinson et al. 2014). The first pulse of magmatism is represented mainly by quartz diorite–tonalite intrusions in the 850–800 Ma range that are representative of arc magmatism. Somewhat younger arc magmatism dated as 770–730 Ma has been described at Abu Swayel, just north of the AHOSHY (Abd El-Naby and Frisch 2002).

3.4.4.2 Syn-Collision Plutons

A second magmatic pulse in the 710–670 Ma range corresponds to the arc collision stage (Hassan and Hashad 1990). This pulse correlates with two of Stern and Hedge's magmatic groups (715–700 Ma and 685–665 Ma) and maybe two of Moussa et al.'s (2008) groups (710–690 Ma and 675–650 Ma), also Lundmark et al. (2012) (their 705–680 Ma pulse) and Robinson et al. (2014) (their ~710 Ma 'syn-collision' magmatic pulse). The granitoids of this stage are trondhjemites, tonalites and granodiorites that intruded syn-kinematically with respect to arc- related thrusting and folding, and show locally strong deformation including mylonitization and migmatitic/gneissic structure. Important examples are the granitoid gneisses of the **Hafafit** complex (zircon 677–700 Ma ages for magmatic emplacement, Kröner et al. 1994, 682 Ma zircon age, Stern and Hedge 1985, and 700 Ma Nd model ages, Liegeois and Stern 2010, though Abu El-Enen et al. 2016 gave a zircon 730 Ma gneissic protolith age) and the **El-Sibai** complex (zircon 670–690 Ma ages for magmatic emplacement, Bregar et al. 2002, and TIMS zircon 680–685 Ma emplacement ages, Augland et al. 2012). Other somewhat older ages are represented at **Wadi Beitan** (zircon 704 Ma, Kröner et al. 1994, zircon 720–745 Ma age, Ali et al. 2015), **Wadi Sha'it** (El Kalioubi and El Ramly 1991, 730 Ma).

The syn-kinematic granitoids near the AHOSHY, intruded along S-ward directed arc collision-related reverse faults, have gneissic foliations concordant with the foliations in the wallrocks and show complex folding of migmatitic banding. These granitoids have intrude during the top to S (or SSE) shearing of the arc metavolcanics. NNW-SSE trending stretching lineations are preserved in the wallrocks (Abdeen et al. 2008; Ali et al. 2015). A cluster of gneissic granitoids of this group have intruded into amphibolite facies mafic rocks in the Hafafit complex, and have adopted early sheath fold geometry that developed during N-wards extension and top-to-N shearing on low angle mylonite zones (Fowler and El Kalioubi 2002), perhaps reflecting a N-wards gliding mechanism at the time of emplacement. The El-Sibai gneisses have intruded during NW-wards displacement on reverse faults (Fowler et al. 2007; Augland et al. 2012). Both the Hafafit and El-Sibai complexes (and indeed most of the gneisses in the Eastern Desert) are controversial, and other structural/tectonic interpretations of these complexes are discussed ahead.

3.4.4.3 Late- to Post-Collision Plutons

A third well-represented magmatic pulse occurred within the range 630–610 Ma (625–610 Ma of Stern and Hedge 1985; 635–610 Ma of Moussa et al. 2008; ~620 Ma of Robinson et al. 2014, and possibly the 610–604 Ma of Lundmark et al. 2012). These plutons are typically post-arc-collision granodiorites with sharp discordant contacts and flow banded enclave rich margins. They show little, if any, internal deformation, e.g. the ~630 Ma Barud, Um Tagher and El Bula intrusions (NED) (Helmy et al. 2004; Fowler et al. 2006; Farahat et al. 2007), post-collision granodiorite at Kab Amiri (NED) (Moghazi 2002), and the 620–615 Ma undeformed Wadi Dib and Wadi Hawashiya granodiorites (NED) (Stern and Hedge 1985).

An important representative of this group in the CED is the Um Ba'anib composite granodiorite—alkali granite of the Meatiq complex. The intrusion of the Um Ba'anib is dated at 625 Ma (Sturchio et al. 1983; Andresen et al. 2009). However, unlike its correlatives in the post-kinematic group, this intrusion is quite strongly deformed and metamorphosed (Ries et al. 1983; Habib et al. 1985a, b; Fritz et al. 1996; Neumayr et al. 1996, 1998; Andresen et al. 2010). Deformation effects are mainly associated with an impressive ~1.5 km thick mylonitized zone that separates the Um Ba'anib intrusion from top-to-the-NW displaced (Abu Ziran Group) ophiolites and arc volcanics tectonically emplaced over the intrusion. The originally gently dipping mylonite zone (also known as the Eastern Desert Shear Zone EDSZ) may have been an extensional detachment structure, or a compressional (lo- angle thrust) structure related to the late phases of arc collision, and was subsequently deformed into a domed geometry. The somewhat younger Abu Ziran granodiorite (615–605 Ma, Stern and Hedge 1985; Andresen et al. 2009) along the southern margin of the Meatiq complex appears also to have been deformed mainly by extension shearing (Fritz and Puhl 1996; Fritz et al. 1996, 2014). Further discussion of the Meatiq is provided in Sect. 3.5. On the *Orogenic Extension Stage* and briefly also below in the context of alternative views and interpretations of the structure and tectonics of the arc collision stage of the ANS.

3.4.5 Further Models for the Arc-Collision Stage of the ANS

3.4.5.1 Models Preferring Additional Suture Zones Within the CED

The extreme distance (nearly 800 km) from the AHOSHY suture to the northern limits of the NED strains credibility that this suture could be the source for all of the transported arc rocks and ophiolitic mélange in the Eastern Desert. The popular solution to this problem (as noted above) is that there are several back-arc basins north of the AHOSHY

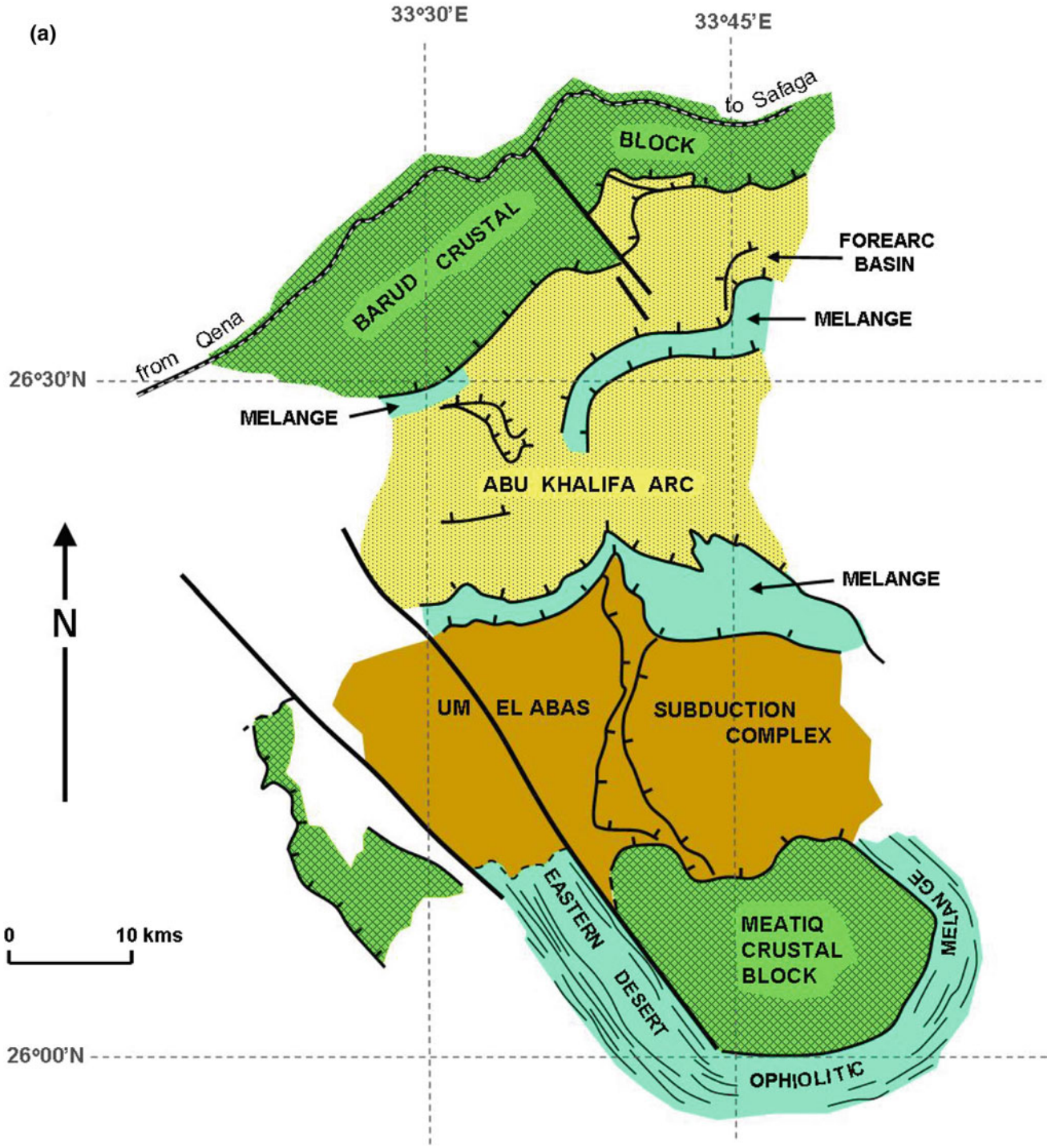

Fig. 3.9 Other proposed subduction zone models for the arc collision stage in the EED. **a** a N-dipping subduction zone between the Meatiq and Barud continental crustal blocks, proposed by Habib (1987). **b** a SE-dipping subduction zone, located south of Meatiq continental margin. The figure shows the formation of mélange in the trench, and thrusting of arc volcanics NW-wards over the Meatiq complex. **c** a NE-dipping subduction zone in the CED, proposed by Ragab and El-Alfy (1996). Subduction of an island arc beneath the forearc sited on the overlying plate is illustrated as the origin of the Meatiq gneissic complex

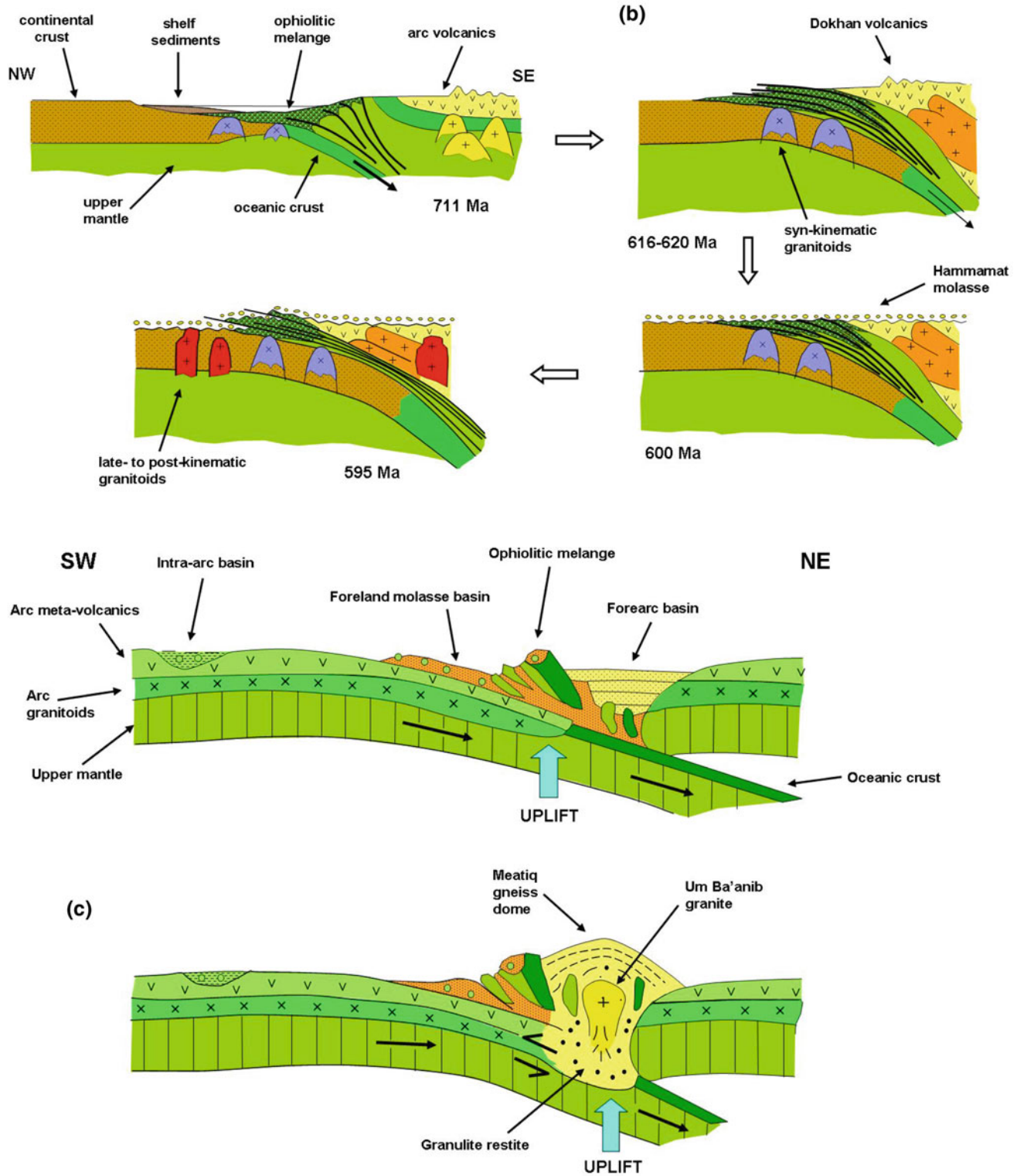

Fig. 3.9 (continued)

which provided arc rock and ophiolitic mélange with much shorter transport distances. However, another proposal has been the existence of an arc-arc collision suture zone within the CED (Fig. 3.9b). This suture was proposed by Ries et al. (1983) to lie SE of the Meatiq complex and to result from obduction of mélange NW-wards over a SE dipping subduction zone, and onto the sedimentary protoliths of the Meatiq gneisses. Habib (1987) and earlier Amstutz et al. (1984) also considered the possibility of a subduction zone in this area. The first authors placed it north of the Meatiq complex and showed it dipping to the N (Fig. 3.9a). The configuration preferred by Habib (1987) therefore required southwards thrusting during collision. The large ophiolitic mass of Gabal El-Rubshi northwest of Meatiq, was explained in this model as being a remnant of the ocean basin between the Meatiq and Barud crustal blocks (Fig. 3.9a).

A sophisticated model of arc-arc suture zones in the CED was devised in 1987 by Ragab and others (Ragab 1987; Ragab et al. 1993a, b; Ragab 1993; Ragab et al. 1995; Ragab and El-Alfy 1996) (Fig. 3.9c). In this ensimatic arc collision model, two belts of ophiolitic mélange, one adjacent to the Meatiq complex, and the other adjacent to the Hafafit complex were interpreted as approximately WSW-ESE trending arc-arc sutures in the CED. The first suture was termed the 'Wadi Atalla–Wadi Hammuda suture' and was located SW of Meatiq. The second was referred to as the 'Wadi Ghadir–Barramiya suture' and was located N and NE of the Hafafit complex (Ragab et al. 1993a). The proposed suture at Meatiq received most attention. There, the subduction zone was illustrated as dipping to the northeast (Ragab et al. 1993b). The present site of Meatiq was identified as a former forearc basin (Fig. 3.9c). Ophiolitic mélange was not thrusted over the Meatiq complex but was collected in a trench complex adjacent to it. The mélange was also derived by tectonic erosion of the forearc ophiolitic crust. A distinctive feature of the model was the continuation of the ensimatic arc-arc collision event in the CED into the 630–620 Ma range or even later, in order to account for the ~625 Ma Ba'anib gneiss. The consequence of this is that Dokhan volcanism and Hammamat sedimentation were also interpreted in this arc-collision setting, rather than the more commonly accepted post-collision setting for these successions.

Abd El-Naby and Frisch (2006) modelled the Hafafit complex as occupying a back-arc basin above a NW-dipping zone (Fig. 3.8c). Abd El-Rahman et al. (2009) suggested that the Wadi Ghadir ophiolite formed in a back-arc setting above a NE-dipping subduction zone during the active arc stage. After collision at ~630 Ma, subduction direction reversed, so that the subduction zone dipped to the SW beneath the Hafafit complex. This latter configuration is similar that proposed by El Ramly et al. (1984). Abd El-Rahman et al. (2012) suggested on the basis of patterns of fore-arc and back-arc ophiolite belts that the CED lay above an E dipping subduction zone during the arc stage.

3.4.5.2 Two-Tier Models of Infrastructure-Suprastructure (Westward Obduction)

The tectonic setting and kinematics of the arc collision stage have long been popularly viewed in a classic model of obduction over a continental margin. This is a two-tiered model in which the lower tier is old continental crustal infrastructure (>1000 Ma, i.e. pre-Neoproterozoic), and the upper tier is juvenile arc and associated rocks of Neoproterozoic age that formed to the east of the continental margin. The boundary between the two tiers is marked by a major shear zone accommodating east to west obduction direction (El-Gaby 1983, 1994; El-Gaby et al. 1984, 1988, 1990; Khudeir et al. 2008), in accord with early models for the ANS that invoked N-S trending arc axes (Gass 1977, 1982). This model also harmonized with the dominant NNW structural trends, at least in the CED. The EED gneissic complexes (Hafafit, Meatiq, El-Sibai, etc.) were regarded as windows cored by old infrastructure. Each window represented a macroscopic dome associated with giant antiforms that buckled the ophiolite cover and the underlying 'rejuvenated' or 'remobilized' (i.e. mylonitized or migmatized) basement gneisses (El-Gaby et al. 1988). According to the model the basement extended eastwards from the Saharan shield under the present-day EED. The obduction resulted in a NNW-trending foreland fold and thrust belt with westerly vergence. The principal problem for the model lies in the growing database of precision zircon dating from the gneissic complexes that have consistently refuted the claims of ancient crystalline basement beneath the EED, at least as a continuous substrate (Liegeois and Stern 2010), however, the presence of ancient xenocrystic zircons in the gneissic protoliths has complicated the debate (Kröner et al. 1994; Moussa et al. 2008; Ali et al. 2009a, b; Andresen et al. 2009; Johnson 2014). Stern and Hedge (1985) found that $^{87}Sr/^{86}Sr$ isotopic ratios were low in samples throughout the EED, which also supports a juvenile character for the gneissic protoliths.

3.4.5.3 Two-Tier Model (Thin-Skin Thrusting)

The two-tier model described above has been adapted to include SW-wards (instead of westward) thrusting of arc and ophiolite rocks over the infrastructure (El Ramly et al. 1984; Kröner et al. 1987; Greiling et al. 1988). This model was inspired by the SW-ward thrusts and associated folds in the Wadi Ghadir ophiolites NE of the Hafafit complex (Elbayoumi and Greiling 1984). Models of imbricate thrusts and thrust duplexes also included fault bend folding to explain the gneissic domal structures of the Hafafit Complex. An alternative model in which the thrusting direction of the

upper tier over the lower was to the NW, in the style of an antiformal stacking duplex structure, was suggested by Greiling et al. (1993, 1996) and Greiling and Rashwan (1994).

3.4.5.4 Two-Tier Model—Partitioned Strain in Strike-Slip Corridor

A structural model presented by Wallbrecher et al. (1993) and Fritz et al. (1996) for the Meatiq complex included NW-ward translation of ophiolitic mélange over the gneissic domes by a transpression mechanism, in which E-W convergence could be expressed as NW-wards thrusting within a strike slip corridor, and SW-wards thrusting outside of the corridor (Fig. 3.10). The partitioning into these displacement components was made possible by the activity of NW-trending strike slip faults. Within the corridor NW-SE extension and normal faulting could develop, which led to the rise of the Meatiq as a core complex. This model of NW-SE sinistral strike-slip corridors (equivalent to the Najd fault system—see Sect. 6.3 ahead) was later applied to other gneissic complexes (El-Sibai, El-Shalul, Hafafit) extending the core complex model to all of the gneissic complexes of

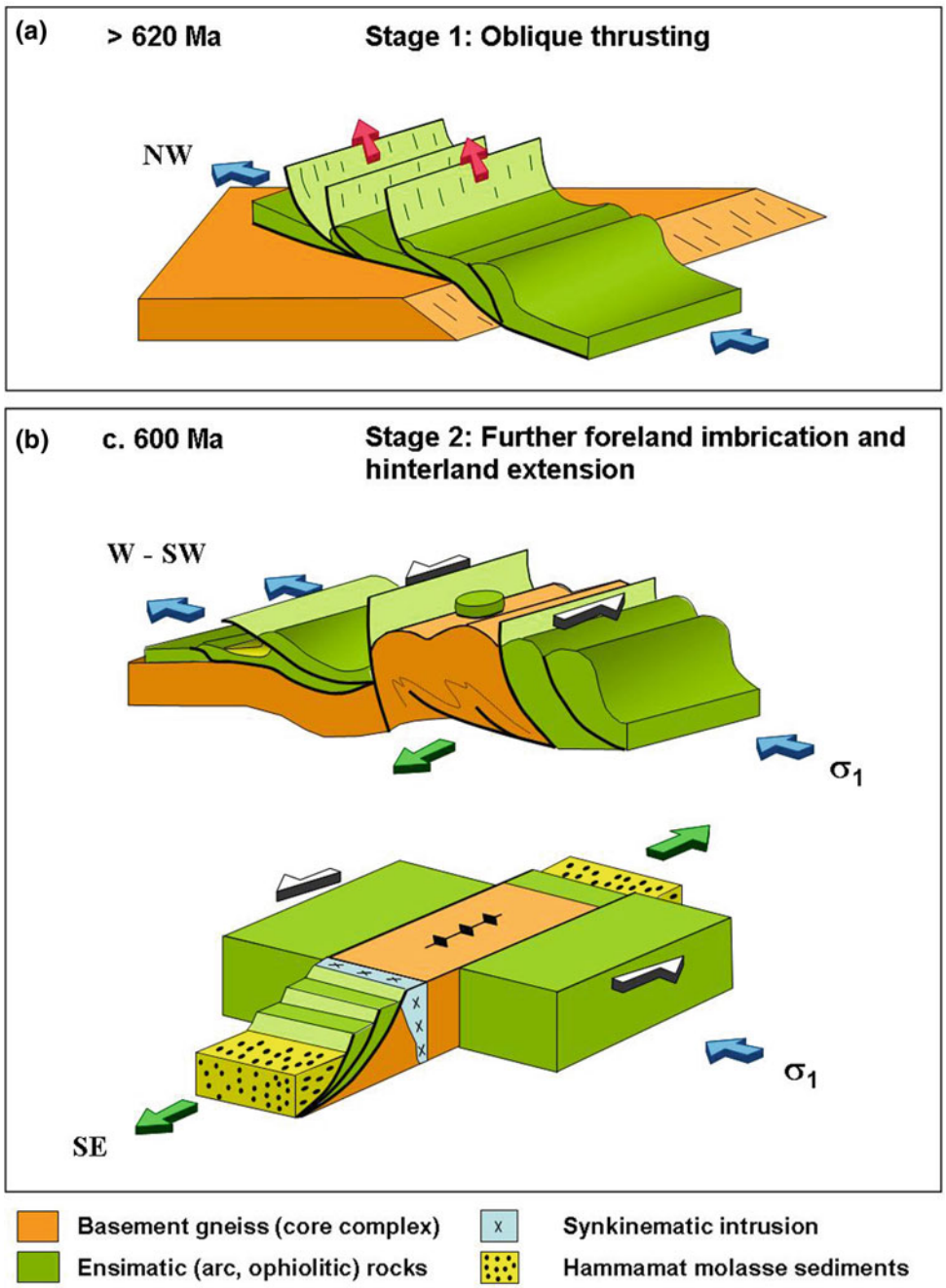

Fig. 3.10 Block model from Fritz et al. (1996) demonstrating the sequence of events in the transpression-assisted rise of CED core complexes. **a** NW-ward thrusting of ophiolitic rocks over continental crustal basement >620 Ma. **b** partitioned displacement at ~600 Ma, involving NW-SE strike-slip faulting and NW-SE extension in the inner parts of the orogen, and SW-wards thrusting in the external parts of the orogen. This is followed by normal faulting and exhumation of the Meatiq core complex

the CED (Fritz and Messner 1999) (see Fig. 3.18b). Fritz et al. (2002) noted that the event involving NW-wards translation of arc and ophiolitic materials did not result in crustal thickening, perhaps due to lateral extrusion during the E-W shortening. Rise and exhumation of the Meatiq and other gneissic complexes was thought to have been assisted by the buoyancy of rising magmas.

3.5 Orogenic Extension Stage

3.5.1 Early Recognition and Interpretation of Extensional Tectonism in the NED

Stern et al.'s (1984) study of the NED identified four main crustal components that were presented as evidence for an extensional tectonic setting. These were: (a) Hammamat molasse sediments, (b) Dokhan volcanics, (c) dykes and (d) granitoids. The Hammamat sedimentary basins were found to be comparable to rift basins in the Basin and Range. The Dokhan volcanics were described as locally bimodal in chemistry (a characteristic of continental extensional terrains) (Stern and Gottfried 1986). The dykes were close-spaced and parallel, forming regional dyke swarms with similar bimodal chemistry to the Dokhan, and dykes were found to be feeders for the Dokhan in some localities (Stern and Voegeli 1987; Stern et al. 1988; Stern and Gottfried 1986) (Fig. 3.11b, c). The grey (Older) granitoids showed no association with compressional tectonics, and the pink (Younger) granitoids were thought to have been fed by felsic dykes. The above phenomena and the lack of compressional features, apart from broad open folds, led Stern et al. (1984) to conclude that the NED had largely developed in an extensional setting, that lasted from 600 Ma to 575 Ma. Stern et al. (1984) drew attention to the fact that the Najd strike slip faults from Saudi Arabia did not continue into the NED. Stern (1985) proposed that the displacements of the Najd fault system in Saudi Arabia (active from 620–540 Ma) functioned in a transform mode for continental rifts in the NED (Fig. 3.11a).

3.5.2 Tectonic Extension in the Areas South of the NED

3.5.2.1 Central Eastern Desert

Stern (1985) thought that the ~600 Ma extension event did not continue into the CED or SED. Stern and Hedge (1985) suggested that the younger granites in the CED were intruded into crustal weaknesses, rather than into an extensional setting. No dyke swarms have been reported from the CED. However, the northern half of the CED has been identified as a ~600 Ma extensional domain by Greiling et al. (1993, 1994) and Greiling and Rashwan (1995). Regional low-angle shear zones within this zone were regarded as extensional detachments. The Meatiq gneissic dome and other CED metamorphic core complexes have also been posited as evidence of substantial extension in the CED in the 600 ± 20 Ma range (Sturchio et al. 1983; Fritz et al. 1996; Neumayr et al. 1998; Loizenbauer et al. 2001). The Wadi Sha'it—Nugrus shear zone at the CED-SED boundary has also been described as a ~600 Ma regional scale extensional shear zone (Fowler and Osman 2009).

Throughout the northern parts of the CED there are locally strong NW-SE trending stretching lineations associated with the low-angle shear zones. These are best represented by the stretched pebbles in Hammamat basin conglomerates (deposited 615–580 Ma) (Ries et al. 1983; Sturchio et al. 1983; Abdel-Meguid 1992; Abdeen and Warr 1998; Hamimi 2000; Fowler and Osman 2001; Fowler and El Kalioubi 2004; Abd El-Wahed 2007), though Greiling (1987) demonstrated that the NW-trending stretching lineations were widespread throughout the CED. These regionally developed stretching lineations may be cited as evidence for tectonic extension in the CED though some workers are of the view that the lineations are related to NW-SE transcurrent shear zones (Stern 1985; Abd El-Wahed 2007). However, Fowler and Osman (2001) and Fowler and El Kalioubi (2004) pointed out that the lineations are found on low-dipping foliations, the stretching strains vary in intensity vertically, not so much laterally (Fowler and Abdeen 2014), and Shackleton (1994) noted that the lineations show no spatial association with strike-slip shear zones. Still other workers have interpreted the CED low-angle shear zones as thrust-related, and the associated stretching lineations as thrust transport direction indicators, suggesting a compressional tectonic setting for these structures (Ries et al. 1983; Shackleton and Ries 1984; Habib et al. 1985a; Greiling 1987; Greiling et al. 1994; Greiling and Rashwan 1994; Fowler and Osman 2001; Andresen et al. 2010). Other extensional setting indicators from the NED, the Dokhan volcanics, Hammamat basins and A-type granites are also present in the CED. Dokhan volcanics (630–590 Ma) and Hammamat basins (615–580 Ma) also lie dominantly in the CED northern half. Younger granites with A-type geochemistry are very common throughout the CED.

Altogether, there appears to be a reasonable case for some form of extensional tectonic event at ~600 Ma in the CED, at least in its northern half, though the connections between shear zones, stretching lineations, molasse basins, etc. on the one hand and extension tectonic processes on the other, remain unclear.

3.5.2.2 South Eastern Desert

In the SED, stretching lineations have been reported by Abdel-Meguid (1992), but with northeasterly trends. Dyke

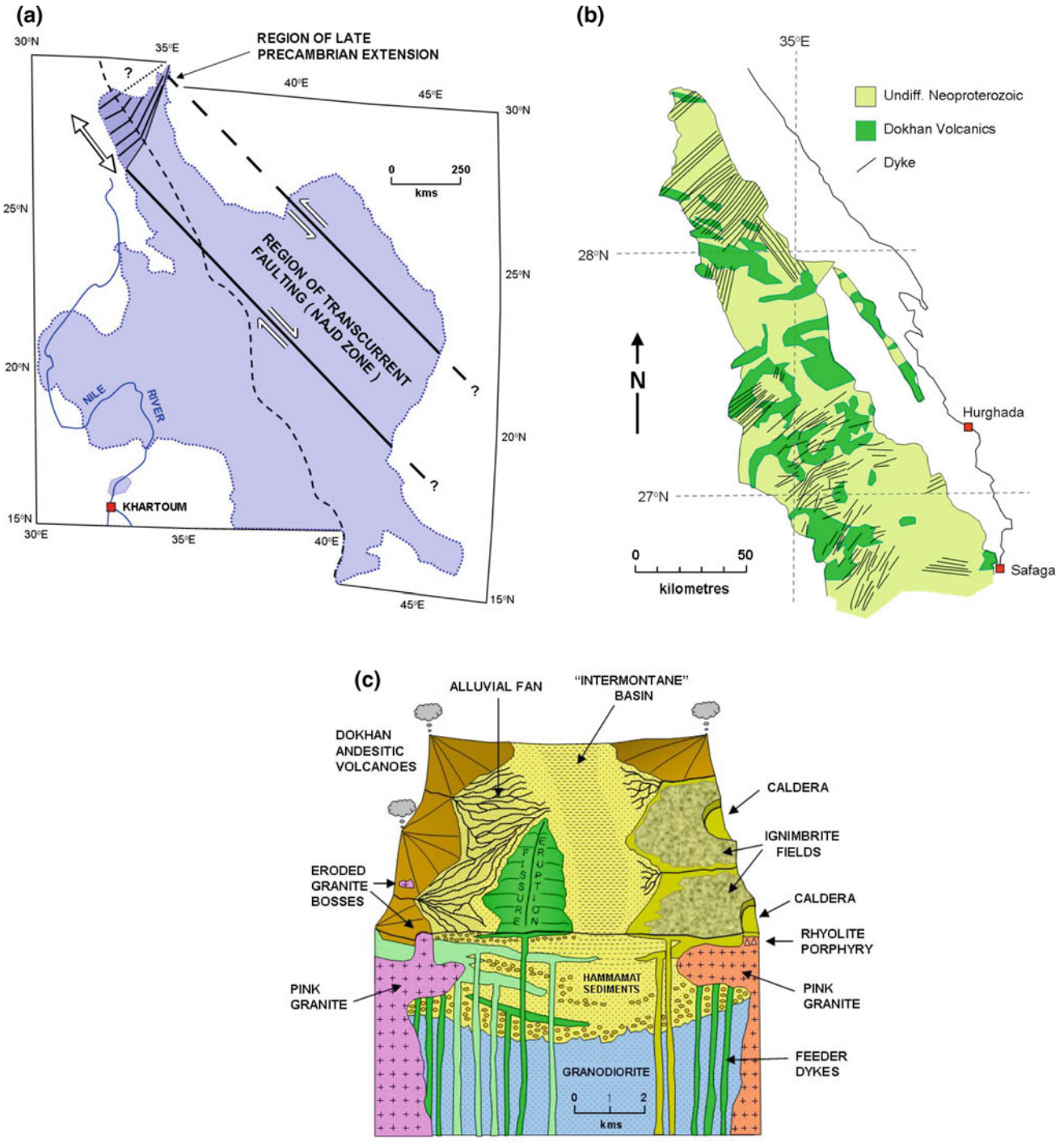

Fig. 3.11 Distribution of Dokhan Volcanics, Hammamat molasse basins and late- to post-collision (Younger) granites in the EED. Note the predominance of Dokhan Volcanics in the NED, the concentration of Hammamat basins in the northern half of the CED, and the abundance of the Younger granites in the NED and Sinai. Modified from Johnson et al. (2011)

swarms have also been claimed (Hamdy et al. 2017). Younger granites with A-type geochemistry are exemplified by Gabal Hamata, Sikait-Nugrus, Homr Akarim and Aswan granites (Noweir et al. 1990; Hassaan and El-Desoki 2016; Moghazi et al. 2004; Mohamed and El-Sayed 2008; Finger et al. 2008), though their ages vary greatly from >620 Ma to <540 Ma. There are very few examples of Hammamat basins or Dokhan volcanic successions in the SED. Thus the evidence for the ~600 Ma extension event in the SED is much weaker than for the CED.

3.5.3 Geological Features that Have Been Attributed to the Tectonic Extension Stage

In this section, each of the features attributed to the ~600 Ma extensional tectonic stage is briefly described, with particular reference to its value as evidence of extension. The features include dyke swarms, bimodal(?) Dokhan volcanics, Hammamat rift(?) basins, A-type Younger granites, extensional shear zones, stretching lineations and metamorphic core complexes.

3.5.3.1 Dyke Swarms

Dyke swarms of andesitic and rhyolitic composition, with dominantly NE-SW to NNE-SSW trend are very well developed in the NED (Stern et al. 1984; Stern and Voegeli 1987; Stern et al. 1988; Dawoud et al. 2006), and Sinai (Stern and Manton 1987; Abdel-Karim and Azzaz 1995; Iacumin et al. 1998; El-Sayed 2006; El-Nisr et al. 2014) (Fig. 3.11b). The dykes have been dated at 590–545 Ma. Similar dykes (but not forming swarms) are present in the CED. The NED dykes have been described as calc-alkaline and of bimodal chemistry, characteristic of continental extensional settings (Stern and Voegeli 1987; Stern and Gottfried 1986; El-Sayed 2006). There is some doubt about the bimodal character of the dykes, as Dawoud et al. (2006) found the felsic dykes to be consistently older than the mafic dykes. Reversed time relations were found for Sinai dykes by Abdel-Karim (1993), who described the mafic dykes as relatively older than the felsic dykes. The youngest felsic dykes (550–545 Ma) in Sinai were described as subalkaline or alkaline, rather than calc-alkaline, by Abdel-Karim and El-Baroudy (1995), Jarrar (2001) and Dawoud et al. (2006).

3.5.3.2 Dokhan Volcanics

This 1200 m thick sequence of terrestrial andesitic and rhyolitic lavas and pyroclastics sits unconformably on Older granites or arc metavolcanics, and either predates or interfingers with Hammamat clastics. These are calc-alkaline or medium- to high-K calc-alkaline volcanics. Dokhan is widespread in the NED, especially at El Kharaza, Gabal Dokhan and Wadi Fatira (Abdel-Rahman 1996; Mohamed et al. 2000; Eliwa et al. 2006; Khalaf 2010), and they also exist in the CED, especially near Safaga (Moghazi 2003). The Dokhan continues at least as far south as Wadi Sodmein, west of Quseir (Ries et al. 1983; Asran et al. 2005) (Fig. 3.12). Dokhan has been reported by Noweir et al. (2005) near Wadi Kareim, southwest of Quseir. Traces of Dokhan in the SED, near the Allaqi suture, have also been reported (El-Sayed et al. 2004). Ressetar and Monrad (1983) and Stern et al. (1984) considered that the Dokhan volcanics had bimodal chemistry, indicative of extensional setting. However, Abdel-Rahman (1996), Eliwa (2000), Mohamed et al. (2000) and Moghazi (2003) noted a continuous chemical range for Dokhan from basalt/andesite to dacite/rhyolite, with the exception of Dokhan at south Safaga, which showed bimodal chemistry (Eliwa et al. 2006).

Dokhan has been dated between 620 and 560 Ma (Stern 1979; Stern and Hedge 1985; Abdel-Rahman and Doig 1987), with narrower range, 630–590 Ma, more consistent with the later geochronological results of Wilde and Youssef (2000) and Breitkreuz et al. (2010). The latter authors suggested two volcanic stages, 630–623 Ma and 618–592 Ma. The first volcanic stage predated the extension stage. The second lies within the extension stage.

The principal problem of Dokhan has been lack of agreement on the tectonic setting of these volcanics. Based on geochemistry, most workers have described the Dokhan as having erupted in a transitional setting between compressional (Andean setting) and anorogenic (within-plate setting) (Mohamed et al. 2000; Moghazi 2003; El-Desoky et al. 2014). Others have preferred an entirely Andean setting (Dardir et al. 1982; Abdel-Rahman 1995; Hassan et al. 2001; Eliwa et al. 2006; Abdel Wahed et al. 2012; Azzaz et al. 2015). More recently, the role of mantle or mafic lower crust delamination has been suggested (Moghazi 2003; Khalaf 2012; Eliwa et al. 2014b; Obeid and Azer 2015), partly in recognition of adakite compositions amongst the volcanics.

3.5.3.3 Hammamat Molasse Basins

These post-collision basins are mostly found in the northern half of the Eastern Desert (NED, but particularly in the CED) (Fig. 3.12). They are filled with conglomerates, lithic sandstones and minor mudstones (Abd El-Rahman et al. 2010). The sediments are derived by erosion of mainly Dokhan volcanics, arc metavolcanics and related plutons, metasediments and pink granites. A small proportion of clasts are recycled basin sediments. The Hammamat basins are generally regarded as terrestrial intermontane ('intramontane' of some authors) alluvial fan, braided stream and minor lacustrine deposits.

Present exposures of the Hammamat basins are deformed residuals, and the original extent of the basins is uncertain. The four largest examples occur within a small area of the CED. These are the larger Hammamat basins: El Qash basin (380 km^2), Kareim basin (240 km^2), Wadi Hammamat basin (135 km^2), and Zeidun basin (125 km^2). The preserved fill in these larger basins varies from 7500 m (Kareim) to 3500 m (Zeidun). Smaller basins in the CED include the Queih, Igla, Arak, Um Seleimat, Atawi and El-Mayah basins (Naim et al. 1996; Abdeen and Warr 1998; Khalaf 2012; Bezenjani et al. 2014; Rice et al. 1993a, b; Fowler and Osman 2013; Akaad

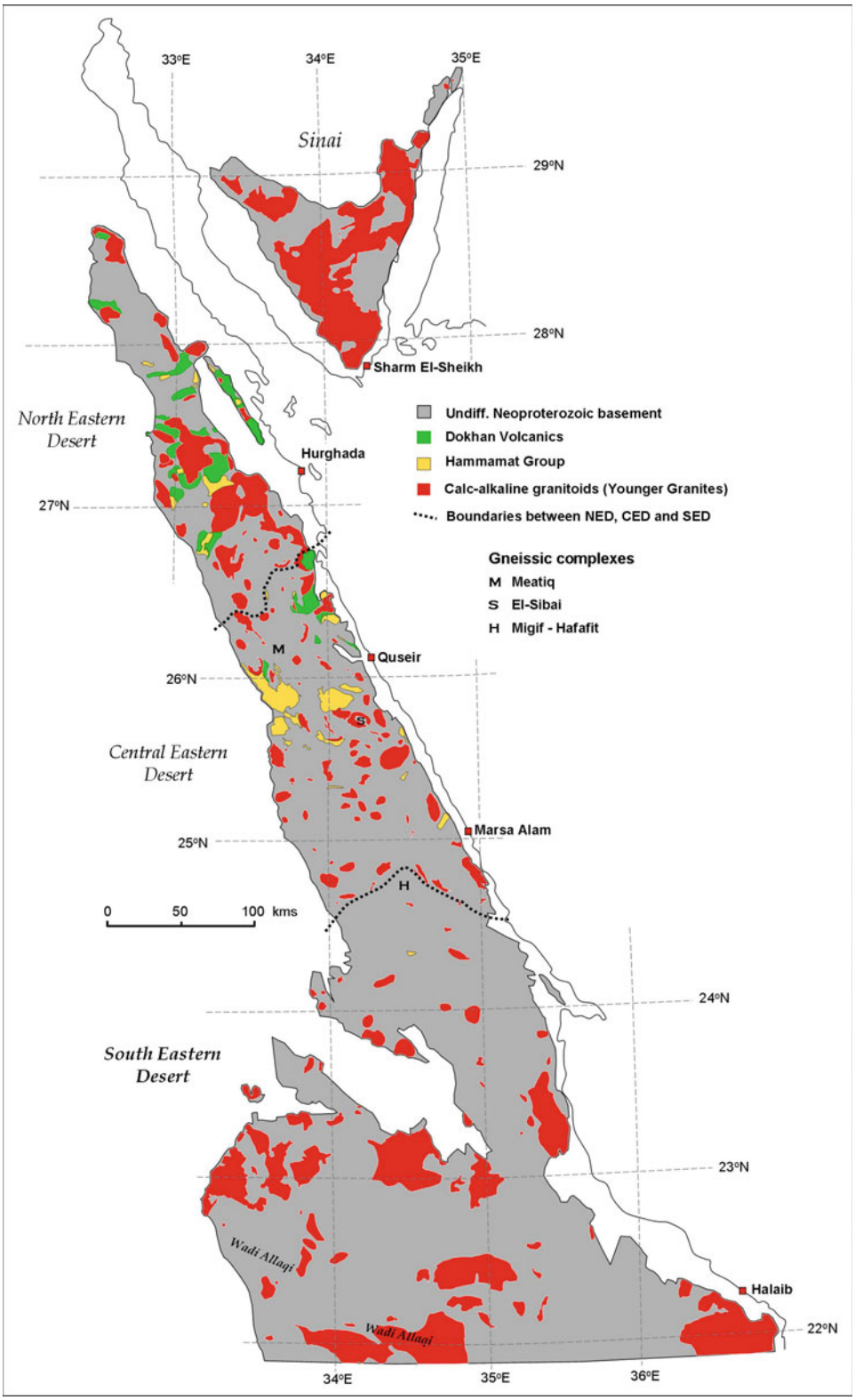

Fig. 3.12 The rift model for NED post-collision extension. **a** Tectonic model explaining the relations between the rifting mechanism and the Najd transcurrent fault system, from Stern (1985). Coloured area represent the Arabian-Nubian Shield restored to pre-Red Sea spreading. Note that the most southwesterly shear is expected to be dextral shear sense. **b** Pattern of dyke swarms in the NED. Map is assembled from Stern et al. (1984) and Stern and Voegeli (1987). **c** Block diagram of a volcanic rift environment for the NED, from Stern et al. (1984). Direction of viewing is towards the E or W, looking along a Hammamat filled rift basin flanked by volcanic highlands

et al. 1996; Fowler and El Kalioubi 2004; Shalaby et al. 2006; Abd El-Wahed 2010), and in the NED, the Um Tawat, Gebel El Urf and Wadi Bali basins (Willis et al. 1988; Holail and Moghazi 1998; Wilde and Youssef 2001, 2002; Osman et al. 2001; Eliwa et al. 2010; Abd El-Wahed 2010).

NED Hammamat basins such as Gebel El Urf and Um Tawat, are commonly narrow NE-SW to E-W elongated structures, with NE-SW to E-W striking beds and sedimentary lithofacies trends. Geochemical and modal studies show a narrow range of components for the sediments of the NED basins, the main sources being local Dokhan volcanics, and an increasing contribution of pink granite detritus in the higher beds (Willis et al. 1988). These features are consistent with the basins being small NE-SW or E-W trending grabens, similar to the western US Basin and Range (Grothaus et al. 1979; Stern et al. 1984) (Fig. 3.11c).

The CED Hammamat basins are a more diverse group, with a greater range of proposed origins and tectonic settings, from extensional (orthogonal rift, pull-apart basin) to compressional (foreland basin, basins of active continental margin settings). The basins vary markedly in areal extent and thickness of the preserved sediment fill. They include examples which are elongate NE-SW (El-Mayah, Igla, Queih), or equant (Zeidun, Kareim, El Qash) or elongate NW-SE (Wadi Hammamat, Um Seleimat). The variety of provenance lithologies is complex, though the trend of upwardly increasing component derived from pink granites, found in the NED basins, is also evident in some CED basins (Zeidun, Kareim, El-Mayah), and in the same basins there is usually one or more cycles of upward coarsening of the sediments, leading to boulder conglomerates in the higher stratigraphic sections (El Shazly 1977; Grothaus et al. 1979; Messner 1996; Fritz and Messner 1999; Shalaby et al. 2006; Fowler and Osman 2013). Other basins (Igla, Queih) show the opposite trend, with pink granite boulders in the lowest stratigraphic units and the basin sequence fining upwards (Samuel 1977; Rice et al. 1993a; Abdeen and Greiling 2005; Abd El-Wahed 2007, 2010). These broad grain-size and modal trends point to common factors in the formation of groups of basins (timing of formation, geological setting, structural origin, subsidence history, relations to magmatism). Unfortunately, the key features that allow recognition of the mechanisms controlling individual basin histories (nature and rate of slip on original boundary faults, total extension involved, duration of sedimentation, sedimentation rate, and three-dimensional form of the basin) remain poorly known. Furthermore, the original basin marginal and syn-depositional faults have been obscured during later basin inversion and granite intrusions. It appears that much more needs to be known about each of the CED Hammamat basins, before any firm conclusions can be made about the relations between the Hammamat basin histories and the extension stage, at least in the CED.

3.5.3.4 A-Type Granites

The pink (or Younger) granites are the most abundant plutons in the ANS (Fig. 3.12). They have been described as post-collision or intruded in a tensional tectonic setting. They have been dated to between 630 and 530 Ma, though the majority range from 600 to 560 Ma. These granites form characteristically equant, isolated undeformed plutons with subsolvus, transsolvus or hypersolvus textures, and with well-defined thermal aureoles, marginal pegmatites, shallow dipping apophyses and intrusion geometry (ring dyke, phacolith, cone sheet) consistent with epizonal emplacement (Greenberg 1981; El Ramly et al. 1982; Rogers and Greenberg 1983; Hassan and Hashad 1990; Fowler 2001). The Younger Granites have been divided geochemically into two groups: calc-alkaline, peraluminous to metaluminous monzogranites/syenogranites intruded mainly in the range 630–570 Ma; and alkaline or peralkaline alkali feldspar granites intruded mainly during 570–530 Ma (Hussein et al. 1982; Abdel-Rahman and Martin 1987; Hassan and Hashad 1990; Abdel-Rahman 1995; Moghazi 2002; El-Sayed et al. 2002; Azer 2007; Farahat et al. 2011).

A late-orogenic intrusive compressional environment (Andean subduction-related) has been interpreted for the calc-alkaline I-type Younger granites (Hussein et al. 1982; Abdel-Rahman 1995; El-Sayed et al. 1999, 2002; Moghazi 2002; Hassaan and El-Desoky 2016), while the A-type mildly alkaline to peralkaline Younger granites have been recognized as post-collision to anorogenic (tensional) tectonic settings (Stern and Gottfried 1986). The A-types are further subdivided into A1 and A2 (Eby 1992), with A2 being representative of post-collisional environment (10–20 My after collision), and A1 representing a truly anorogenic setting (intrusion 50–100 My after collision). Both A1 and A2 types have been recognized in the EED, with A2 intruding earlier than A1 (El-Sayed et al. 2003; Mohamed and El-Sayed 2008; Ali et al. 2012a; El-Bialy and Omar 2015; Fawzy 2017).

The presence of A-type granites from NED and Sinai to CED and SED indicates that crustal tension affected all of the EED within 100 My of the collision event (Hassanen 1997; Moghazi et al. 2004; Farahat et al. 2007; Azer 2013; Fawzy 2017; Khalil et al. 2017).

3.5.3.5 Regional Low-Angle Normal Shear Zones and Metamorphic Core Complexes

Regional scale low-angle shear zones enclosing gneissic domes are well-recognized in the CED, but are very controversial features. Opinion is divided on whether the shear zones are compressional or extensional in origin. Independently, the gneissic domes are popularly, regarded as metamorphic core complexes, with exhumation of the complexes in an extensional regime.

The regional low-angle shear zones are 1–2 km thick originally low-dipping mylonitic or schistose shears with

NW-SE trending stretching lineations on the shear foliations. In the hanging wall of the shear zones are ophiolitic mélange, arc metavolcanics and related rocks. Beneath the shear zones are high temperature gneisses, gneissic granitoids and migmatites. The shear zone includes commonly mylonitized footwall lithol ogies in its lower parts and schistose sheared hangingwall lithologies in its upper parts, and also encloses foliated small syn-shearing intrusions, usually tonalites and granites. The strain softening effects of hydrous and carbonate alterations and their role in controlling the location of these shear zones has been explored recently by Stern (2017). The best studied example of shear zone-outlined gneissic domes is the Meatiq complex of the CED. Other claimed examples include the El-Sibai complex and the Gabal El-Shalul complex of the CED, the Hafafit complex of the SED, and the Wadi Kid complex of the Sinai.

The mylonitic shear zone overlying the Meatiq gneissic complex was originally identified as a stratigraphic formation (Abu Fannani Formation) of metapsammites or silicic metavolcanics by Akaad and Noweir (1969, 1980). This view was overturned by three separate studies published in 1983 (Ries et al. 1983; Sturchio et al. 1983; El-Gaby and El-Nady 1983). Ries et al. (1983) regarded the shear zone as a low-angle thrust structure transporting trench mélange and arc volcanics NW-wards over gneissic shelf metasediments (Fig. 3.9b). Sturchio et al. (1983) described Meatiq as a core complex, with the shear zone forming a carapace. They also regarded the shear as a NW-vergent thrust. El-Gaby and El-Nady (1983) saw the shear zone as a W-vergent thrust accommodating the obduction of ophiolitic mélange and arc volcanics over old continental basement gneisses. Subsequent studies of Meatiq have been consistent in finding a top-to-NW transport direction on the shear zone, and most have concluded that the shear was a product of compressive tectonism, i.e. thrusting (Habib et al. 1985a, b; Habib 1987; Bennett and Mosley 1987; Fritz et al. 1996; Neumayr et al. 1998; Loizenbauer et al. 2001; Fritz et al. 2014). Andresen et al. (2010), however, presented two possibilities: the shear zone (their Eastern Desert Shear Zone EDSZ) was thrust related, or it was a regional extensional shear system. The regional scale of CED extensional low-angle shear zones with NW-SE subhorizontal stretching direction has been suggested before by Greiling et al. (1993, 1994) and Greiling and Rashwan (1995). The extensional domain of the northern CED proposed by Greiling included the EDSZ of the Meatiq complex, and also the shear zones overlying the gneissic rocks in the El-Sibai and El-Shalul gneissic complexes (Fig. 3.13). Interestingly, the transport direction on

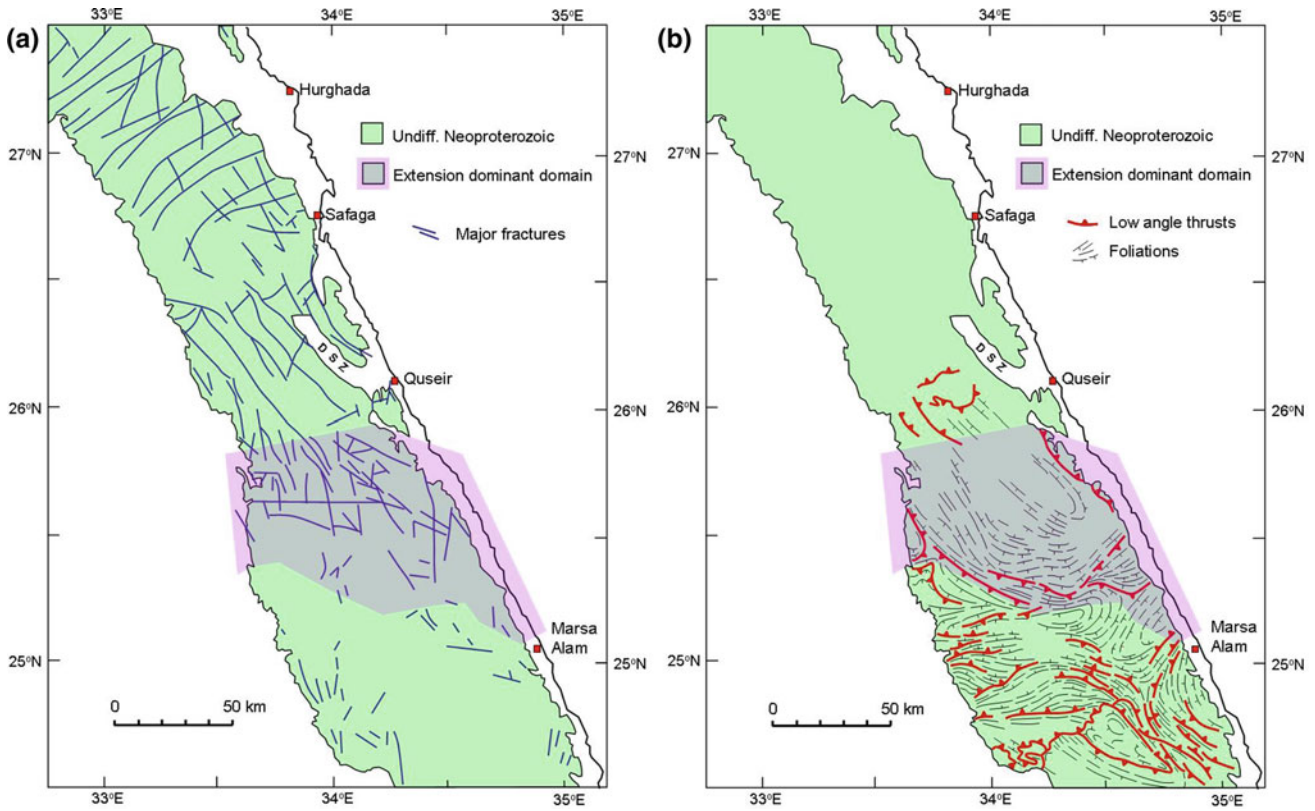

Fig. 3.13 Structural map of the NED and CED, modified from Greiling et al. (1988). **a** The NED is dominated by NE-SW trending normal faults. These pass into the mainly NW-SE trending strike-slip faults of the CED. **b** foliated supracrustal rocks and low-angle thrusting are dominant features of the southern CED and areas south. In both (**a**) and (**b**) DSZ represents Duwi Shear Zone, and the pink shaded area was designated by Greiling et al. (1988) as an extensional zone, where the low angle shear zones are extensional

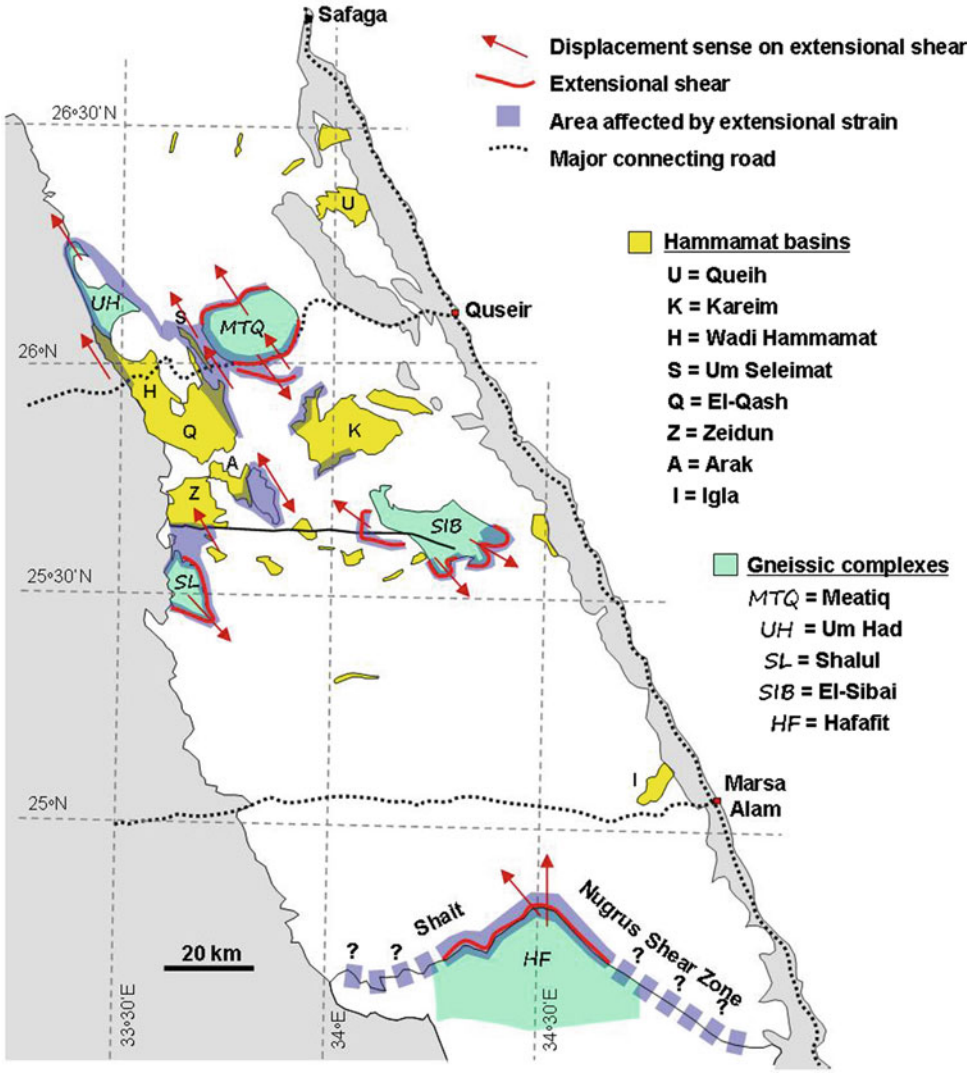

Fig. 3.14 Map of the CED showing the location of regional scale extensional shear zones. Displacement sense of the hangingwall of the extensional shears shows both top-to-NW and top-to-SE. Compiled from Greiling et al. (2014) and Fowler and Osman (2009, 2013)

the low-angle extensional mylonite zones at El-Sibai and El-Shalul is top-to-the-SE, i.e. opposite and perhaps conjugate to the NW-ward transport direction of the Meatiq EDSZ (Kamal El-Din et al. 1992; Greiling et al. 1993; Khudeir et al. 1995; Osman 1996; Youssef et al. 2001; Fowler et al. 2007) (Fig. 3.14). This is consistent with regional NW-SE extension. Ali et al. (2012b) speculated that the shear zone covering the El- Shalul complex may be a correlative of the EDSZ. Fowler and El-Kalioubi (2004) traced the EDSZ to the west of Meatiq through the Um Seleimat molasse basin, and extending from there to cover the gneissic metamorphic rocks forming the Um Had complex (Fowler and Osman 2001). A likely extensional origin of this shear zone was suggested by Fowler and El-Kalioubi (2004) for affected parts of the Um Seleimat basin and by Fowler and Osman (2013) and Fowler and Abdeen (2014) for similar shear zones at the base of the Arak basin. The Wadi Sha'it—Wadi Nugrus shear zone at the northern boundary of the Hafafit complex was thought by Fowler and Osman (2009) to be a low-angle extensional shear zone (Fig. 3.14).

An important aspect of the low-angle shear zones is the time range during which they were active. Evidence points to an overlap between shear zone activity and the time range for the extension stage. The gently dipping foliations in the Hammamat conglomerates and NW-SE stretching of pebbles in these molasse basins have been identified as extension tectonic-related (Fowler and El-Kalioubi 2004; Fowler and Osman 2013; Fowler and Abdeen 2014) consistent with low-angle shear activity during or after Hammamat basin sedimentation (615–595 Ma). Ali et al. (2012b) found that the top-to-SE shear zone affecting the El-Shalul granitoid was <630 Ma and probably ceased activity by about 600 Ma. The timing of shear activity on the EDSZ is constrained at Meatiq to the interval <630 Ma to >590 Ma. EDSZ shearing must have been active following the ~630 Ma intrusion of the Um Ba'anib gneiss (which lies beneath

the shears and is affected by them) (Sturchio et al. 1983; Stern and Hedge 1985). Shearing also affected syn-shearing diorites and granodiorites dated at 615–605 Ma (Sturchio et al. 1983; Stern and Hedge 1985; Andresen et al. 2009). EDSZ shearing must have ceased by the ~590 Ma intrusion of the Arieki granite (which pierces the mylonites in the Meatiq dome and is not deformed) (Sturchio et al. 1983; Andresen et al. 2009). Andresen et al. (2009) concluded that the EDSZ shearing occurred <630 Ma, and the shear zone was inactive and deformed into a dome by 600 Ma. These data constrain the activity of the EDSZ at Meatiq to 630–600 Ma. Fritz et al. (1996) found that normal fault and strike slip shears associated with exhumation of the Meatiq gneisses were active at 595–590 Ma. Stern (2017) suggested that the EDSZ (his Eastern Desert Decollement, EDD) may have been related to Najd faulting at about 600 Ma. In summary, the low-angle shear zones of the CED were active sometime between 630 and 600 Ma, and may constitute extensional detachments, though a more popular view is that these shears are products of a NW-SE compressional thrusting environment.

3.5.4 Proposed Mechanisms of the ~600 Ma Extension Tectonic Event

There have been various proposed structural/tectonic mechanisms for the regional extension in the Eastern Desert of Egypt. Six of the most popular extension tectonic models (continental rifting, gravitational collapse, delamination, transpression, tectonic extrusion/escape, and gravity uplift) that have been applied to the EED are described below.

3.5.4.1 Continental Rifting

This model was proposed for the NED by Stern et al. (1984) and Stern (1985) to explain the rapid formation of continental crust in the NED within a short period of time (670–550 Ma), and the apparent absence of the older lithotectonic units in the NED (i.e. ophiolites, gneisses, etc. of the CED and SED). The NED was seen as a volcanic rift, within which the Dokhan erupted from dyke feeders, Hammamat molasse was deposited in graben structures and anorogenic Younger granites were emplaced high in the crust, fed by dykes (Fig. 3.11c). Both Dokhan and dykes were found to be bimodal chemistry (Stern and Gottfried 1986; Stern and Voegeli 1987; Stern et al. 1988). The greater contribution of young magmas and volcanics to the NED compared to the CED (Fig. 3.12) could be explained in terms of the greater extension in the NED. Similar extensional setting for the Younger granites and Hammamat was suggested by Greenberg (1981). The principal extension direction was approximately NW-SE based on the NE-SW trending dyke swarm trends in the NED. The zone of extension was fan shaped with apex sited at Aqaba (Fig. 3.11a). The actual amount of extension has never been estimated though the extension was described as "strong" (Stern 1985; Willis et al. 1988), and Stern (1985) referred to work by Davies (1981) who found that dyke-accommodated extension effects in the Arabian Shield amounted to 100% extension. NW-SE rift extension was accommodated on NW-SE trending Najd transform faults.

The nature of the pre-rifting crust is a question for this model, though there are Older granodiorites dating to 670 Ma (Stern and Gottfried 1986) in the NED, and older basement units in the Sinai. Supporting the model is the strong time overlap of Najd activity (620–540 Ma) with main age range of NED lithologies (625–575 Ma) (Stern and Hedge 1985). Also the lack of Najd fault penetration into the NED from the CED was a point in favour of the model. An important point to emphasize in this rift model was that the ~600 Ma extension in the NED *caused* the Najd faulting, not vice versa. The Najd was a set of transform faults, rather than strike-slip structures arising from continent-continent collision.

Challenges to Stern's NED continental rift model include later findings that (1) there are substantially older intrusive rocks in the NED than the rifting event (Abdel-Rahman and Doig 1987, 1989; Abdel-Rahman 1995); (2) the chemistry of dykes and Dokhan volcanics have been suggested to be continuous in composition, not bimodal (Abdel-Rahman 1995, 1996; Mohamed et al. 2000; Eliwa et al. 2006, 2014a); (3) the NED Younger granites have been claimed to be continental volcanic arc-related, and not of extensional tectonic setting (Abdel-Rahman and Martin 1987, 1989; Abdel-Rahman and Doig 1987; Abdel-Rahman 1995); (4) the dyke swarms were much younger (<500 Ma) than Stern's time range estimate of the extension stage (Abdel-Rahman and Doig 1987); (5) the NED Hammamat basins are not post-tectonic (Abdel-Rahman 1995); and (6) the dextral slip required on the SE representative of the Najd fault system (i.e. the Duwi shear zone) has been found to be sinistral in shear sense (Sultan et al. 1988) (compare Fig. 3.6, with dextral sense on the Duwi Shear Zone, and Fig. 3.11a in which the shear sense is found to be sinistral). These challenges have been discussed by Stern and Manton (1988) and Stern and Gottfried (1989).

3.5.4.2 Extensional Collapse

The extensional event in the EED has popularly been regarded as an orogenic/gravitational collapse that followed the lithospheric thickening effects of compressional tectonism. Numerous references have been made to extensional collapse in recent works, with differences between models relating to, (1) the mechanism of crustal thickening (arc accretion; continental collision; continent-arc collision;

transpression), (2) the trigger mechanism of collapse (slab break-off; delamination; convectional erosion of lithospheric root); (3) the timing of collapse (syn- orogenic; post-orogenic); and (4) the scale of the collapse (CED and NED; entire ANS or even larger).

Unquestionable crustal thickening due to the collision of west Gondwana and elements of east Gondwana exist in the EAO, south of the ANS, where thrust stacked granulites can be traced from Tanzania to Sudan (Stern 1993). In these southern areas subsequent gravitational collapse has been accommodated by low and normal ductile shear detachments, but with variable directions of mass translation (NW, SE and E -W) (Ghebreab 1999; Tsige and Abdelsalam 2005; Fritz et al. 2009, 2013; Sommer et al. 2017). As the east-west Gondwana convergence migrated northwards the deformation appears to have been confined to N-S and NW-SE folding and thrusting and Najd transcurrent faulting, yielding a zone of gentler collision effects (Stern 1993, 2002; Greiling et al. 1994), with little if any evidence for lithospheric thickening (Fritz et al. 1996, 2002; Johnson et al. 2011). In fact, the extension stage features in the EED are notably dominant in its northern parts, and are not obvious south of Hafafit (Greiling et al. 1994; Avigad and Gvirtzman 2009), suggesting that the northern ANS extensional event may be a separate entity.

Slab break-off and mantle lithosphere delamination are preferred by most workers as the immediate causes of collapse (Moghazi 2003; Farahat et al. 2007, 2011; Finger et al. 2008; Avigad and Gvirtzman 2009; El Bialy 2010; Moghazi et al. 2012; Sami et al. 2018). Black and Liegeois (1993) commented that the Moho under continents is stronger than the Moho beneath an arc assemblage, as the latter had been thermally softened by long magmatism. This focused lithospheric mantle delamination under the arc assemblage. Convective removal of a thickened lithospheric root has also been suggested as a trigger for extensional collapse by Black and Liegeois (1993), Greiling et al. (1994), Blasband et al. (1997, 2000), Avigad and Gvirtzman (2009).

Post-collision uplift or subsidence, erosional denudation and crustal ductile thinning are events that commonly attend gravitational collapse. Dewey (1988) showed that topographic uplift will occur during phase 3 of extensional collapse if the lithospheric mantle is thinned, however, subsidence will occur if crustal thinning dominates. The discriminant between uplift and subsidence is the ratio Cz/lz (crustal thickness/lithospheric mantle thickness), which signals uplift if it is <0.16, else subsidence if it is >0.16. Rapid uplift will reduce crustal thickness by erosional denudation. Avigad and Gvirtzman (2009) attempted to quantify uplift and erosion in the northern ANS and found that uplift to elevations >3 km had occurred during extensional collapse, leading ultimately to 10 km of erosional unroofing of the orogen. However, in the CED, the common presence of major low angle probable extensional detachment shears, such as the EDSZ, may have yielded ductile crustal thinning by crustal delamination, avoiding consequences of major uplift (Fowler and Osman 2013). This may explain the preservation of supracrustal sequences in the CED that are missing in the NED, as recognized early by El-Gaby (1983), and post- amalgamation subsidence of parts of the Arabian Shield to sea level allowing marine incursions in the Jibalah basins (Genna et al. 2002; Johnson 2003).

3.5.4.3 Tectonic Escape and Rigid Indenters

The extension event in the ANS has also been modeled as an example of tectonic extrusion or tectonic escape. These models feature mainly lateral, more than vertical displacement of orogenic material, assisted by the Najd transcurrent faults that were active during extension. Tectonic extrusion in the CED has been suggested by Fowler and Osman (2001), and in the Hafafit complex by Abd El-Naby et al. (2008). Abu El-Enen and Makroum (2003) and Abu El-Enen (2008) included NW-ward tectonic escape prior to extensional collapse in the Kid complex. Escape tectonic mechanism has also been suggested recently by Greiling et al. (2014).

Burke and Sengor (1986) and Hoffman (1991) considered the entire ANS as having experienced N-wards tectonic escape as a result of a rigid indenter producing crustal thickening in the Mozambique Belt to the south (Fig. 3.15). Abdelsalam et al. (1998) found sinistral motion on the Keraf suture consistent with N-wards escape of the ANS. Bonavia and Chorowicz (1992) and Stern (1994) also concluded that the ANS had escaped N-wards from a rigid indenter identified as the Tanzanian craton. Stern dated the onset of escape to sometime between 660 and 610 Ma, continuing to

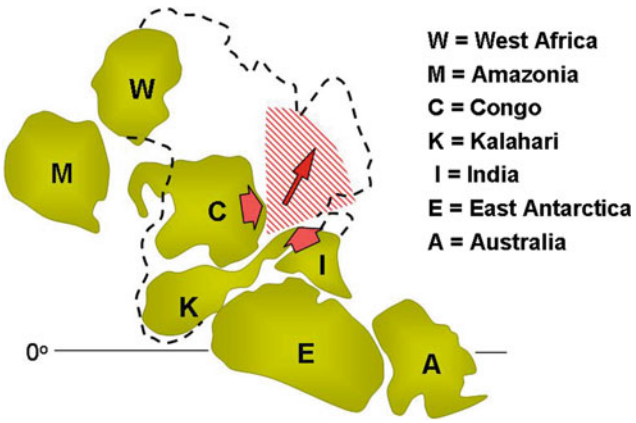

Fig. 3.15 Configuration of microcontinents at the time of assembly of Gondwanaland at about 500 Ma, according to Hoffman (1991). A scissor-like convergence with pivotal point somewhere in the Mozambique belt resulted in expulsion of orogenic material in the direction of the slender red arrow (present-day NW). The Arabian-Nubian Shield is shown as a striped area

530 Ma. This was comparable to the time of activity of the Najd strike slip system (630–530 Ma) which was regarded as the mechanisms accommodating escape. Other models of escape have invoked a phase of transpression before escape (Ibrahim et al. 2015; Abu Alam et al. 2014) or initial dextral slip on the Najd that was later changed to sinistral during tectonic escape.

3.5.4.4 Thermal/Gravity Assisted Rise of Gneiss Domes

Gravitational uplift (buoyant rise) was a final stage in the generation of gneissic domes in the Hafafit complex according to models derived by Greiling et al. (1984) and El Ramly et al. (1984). Shalaby (2010) thought that buoyancy may have been a later minor component of the rise of these gneissic domes but preferred a combined extensional—extrusion model for the Hafafit complex. Transpression assisted rise of magmatic material is also regarded by Fritz et al. (2002) as an important component in the exhumation of CED gneissic domes.

3.6 Post-extensional Compressional Deformation Events

It is generally agreed that the extension stage in the ANS was not the terminal tectonic event, as it was followed by later compressional tectonism that produced folding, thrusting and strike-slip faulting (Abdeen and Greiling 2005). The effects of these late compressive events are most obvious in the Hammamat basins of the extension stage (Fig. 3.16). The molasse sediments of the basins show folding and faulting along several trends. The post-extension deformation in these basins was recognized early by Ries

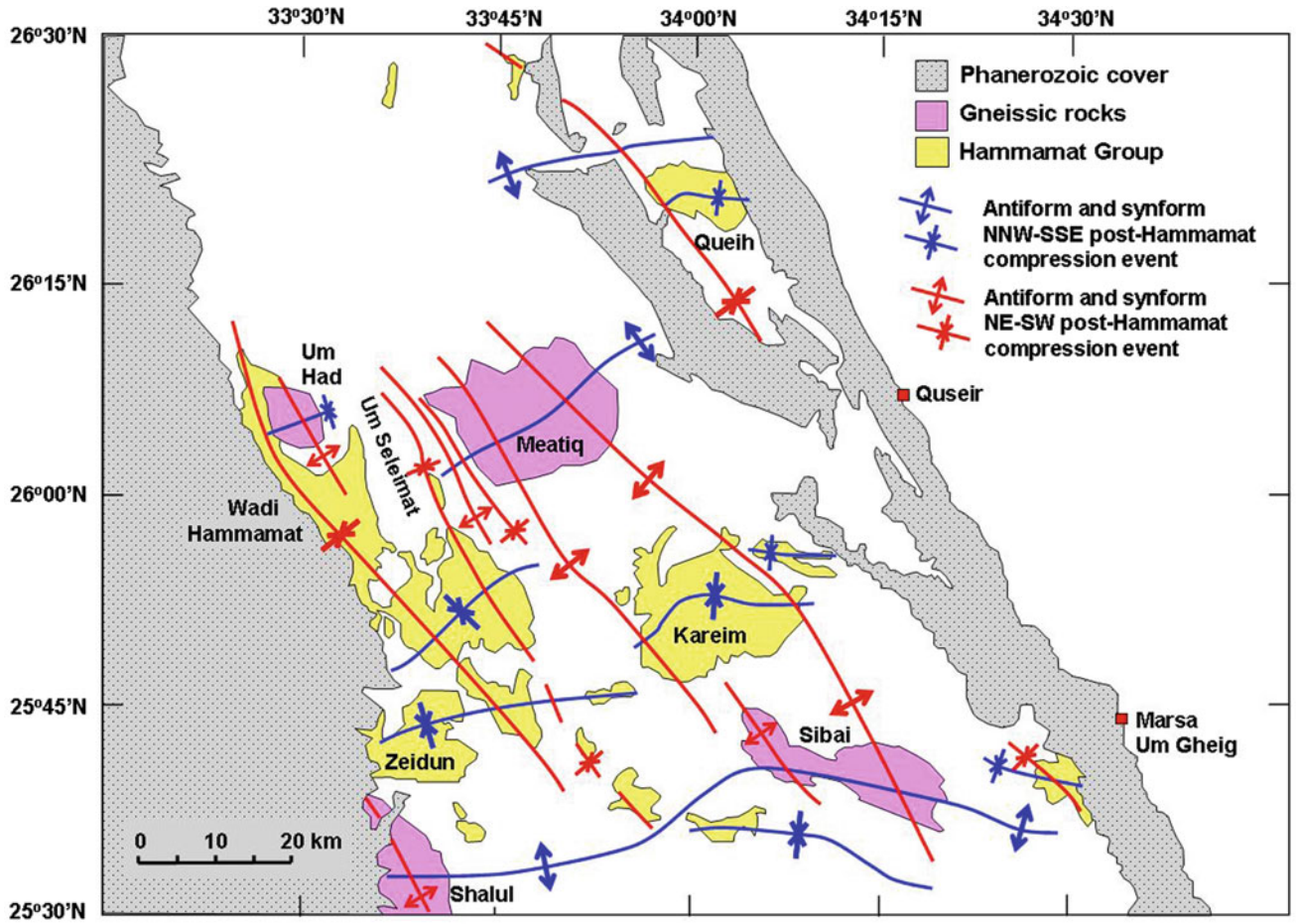

Fig. 3.16 Map of the northern part of the CED, modified from Abdeen and Greiling (2005), presenting a model to explain the pattern of gneissic domal structures and Hammamat filled basinal structures in terms of a type-1 (dome-and-basin) fold interference pattern. According to the model, the folds marked in blue are the product of the post-Hammamat NNW-SSE compression event, while the folds marked in red relate to the later NE-SW compression event. One implication of the model is that the Hammamat sedimentation could have been continuous over a much larger area than presently exposed, and the gneissic rocks of the domes could extend beneath the Hammamat basins

et al. (1983) and Greiling et al. (1994). Hammamat basins that have been studied, with the aim of investigating the events that deformed them or quantifying those effects, include: the **Wadi Hammamat** basin (Kamal El-Din et al. 1996; Fowler and Osman 2001), **Um Seleimat** basin (Ries et al. 1983; Fowler and El Kalioubi 2004; Greiling et al. 2014), **Zeidun and Arak** basins (Osman 1996; Youssef et al. 2001; Fowler and Osman 2013; Fowler and Abdeen 2014) (Fig. 3.17a), **El-Mayah** basin (Kamal El-Din and Asran 1995; Shalaby et al. 2006), **Quieh** basin (Naim et al. 1996; Abdeen and Warr 1998; Abdeen and Greiling 2005) (Fig. 3.17b), **Qash basin** (Abd El-Wahed 2004), **Kareim** basin (Fritz and Messner 1999; Akawy and Zaky 2008; Ibrahim et al. 2013; Hamimi et al. 2014), and **Igla** basin (Rice et al. 1993a; Abd El-Wahed 2007). Broader surveys reviewing the deformation of these basins have also been conducted by Rice et al. (1993b), Hamimi (2000), Abdeen and Greiling (2005), and in detail by Abd El-Wahed (2007, 2010).

From the earliest to the youngest the post-Hammamat deformations include E-W to NE-SW trending folds and thrusts; NW-SE trending folds and thrusts; and NW-SE trending sinistral (Najd) shear zones. A series of N-S tight upright folds exists in the southern parts of the EED beyond the Hammamat basins. A further transpressional regional deformation is also identified as a precursor to Najd. Each of these events is described below.

3.6.1 E-W to NE-SW Trending Folds and Thrusts (Post-Hammamat NW-SE Compression Event)

A post-extension (post-Hammamat) NNW-SSE (or NW-SE) compression event producing folds and thrusts with E-W, ENE-WSW or NE-SW trends and dated around 605–600 Ma is accepted in several versions of the late structural development of the ANS (Greiling et al. 1994, 2014; Abdeen and Greiling 2005; Abd El-Wahed 2010; Johnson et al. 2011; Hamimi et al. 2014) (Fig. 3.16). The event has been described as widespread but variable in intensity. Abdeen and Greiling (2005) estimated a minimum, 25% bulk horizontal shortening in the NW-SE direction at Wadi Queih due to this event. Ries et al. (1983) suggested that this post-Hammamat NW-SE compression may have been a resumption of subduction.

The folds and thrusts of this event are found in most of the Hammamat basins. Abd El-Wahed (2004) mapped NE-trending folds in the Qash basin. The Zeidun basin also shows an E-W fold near its southern faulted boundary, and some NE-trending folds in its northern part, while the nearby Arak basin has an ENE trending syncline dominating the basin centre (Osman 1996; Fowler and Osman 2013) (Fig. 3.17a). Kareim basin has a well- known E-W syncline at its centre (Fritz and Messner 1999). Abdeen and Greiling (2005) figured this syncline as curvilinear. Queih basin has N-vergent and S-vergent thrusts and associated E-W trending folds (Naim et al. 1996; Abdeen and Warr 1998) (Fig. 3.17b). The nearby Abu Sheqeili basin also has well-developed NE-trending folds (Khudeir and Ahmed 1996). Igla basin was shown as having NE-trending folds and thrusts by Akaad et al. (1993) and Abd El-Wahed (2010). There are NE-trending folds in the Um Tawat basin in the NED (Abd El-Wahed 2010). The beds in the El Mayah basin in the CED are steep to vertical with ENE trends (Shalaby et al. 2006). Significantly, the NW-trending Wadi Hammamat and Um Seleimat basins have much less developed NE-trending structures. Fowler and Osman (2001) described NW-vergent thrusts and NE-trending minor folds in the Hammamat basin, but related them to tectonic extrusion. The NW-vergent structures in the Um Seleimat basin are related to the tectonic extension stage (Fowler and El Kalioubi 2004).

The above are clear evidence for post-extension compressional deformation, however, the general view that these folds and thrusts automatically imply a NNW-SSE or NW-SE regional compression direction (Greiling et al. 1994; Abdeen and Greiling 2005) must be balanced against the following points: (1) the folds described appear mostly confined to the Hammamat basins, with surrounding basement rocks unaffected except at thrusted margins of the basins; (2) with previous NW-SE regional extension it is likely that many of the Hammamat basins had some NE-SW or ENE-WSW trending normal faulted boundaries, indeed the NE-trend is still evident in several of these basins; and (3) it is the orientation of compartmental faults in the northern part of the Zeidun basin that has controlled the local fold orientations (Fowler and Osman 2013). Based on points, (1) to (3) it is likely that the NE-SW trending folds and thrusts in the Hammamat basins are the results of basin inversion, in which earlier normal faulted margins become reverse or oblique reverse reactivated faults with the same trends as the original normal faults. Experimental inversion of normal fault bounded basins, shows almost the same results for oblique and orthogonal inversion (Dubois et al. 2002; Panien et al. 2005), meaning that the direction of the regional applied stresses during inversion could be very different to the NW-SE estimations that assume orthogonal inversion (Abdeen and Warr 1998; Abdeen and Greiling 2005). From this, it is possible that the maximum compressional direction during inversion of NE-trending normal fault controlled Hammamat basins could vary to N-S or even NNE-SSW. Fowler and Osman (2013) found that a NNE-SSW maximum compression was best suited to explain the early stage of inversion of the Zeidun and Arak basins (Fig. 3.17a).

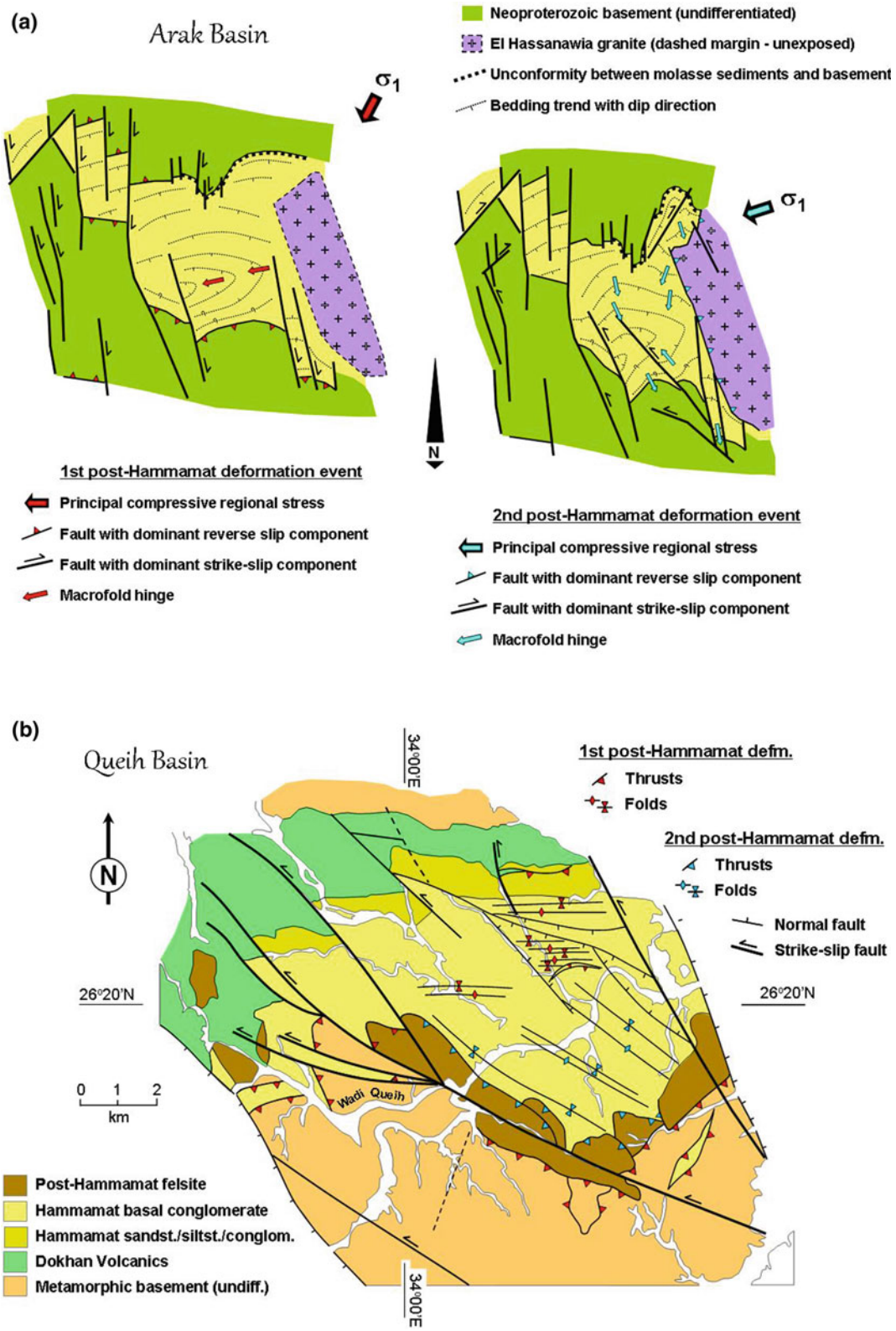

Fig. 3.17 Structures associated with the inversion of CED Hammamat basins. In **a** and **b** the structures belonging to two post-Hammamat deformation events are recorded. The first event produced E-W to ENE-WSW trending folds in the basin sediments. The second event generated N-S to NW-SE trending folds, SW- or NE directed thrusts, strike- slip faults and flower structures. **a** Arak basin inversion history, from Fowler and Osman (2013), involving an early NNE-SSW compression, followed by ENE-WSW compression. **b** Queih basin, from Abdeen and Greiling (2005), involving early N-S shortening, followed by NE-SW compression and transpression

There remains a possibility that other parts of the EED could have experienced post-extension NW-SE directed compression, if models involving NW-ward thrust stacking to explain the rise of the Meatiq and Um Had gneissic complexes are correct (Bennett and Mosley 1987; Fowler and Osman 2001; Abdeen and Greiling 2005; Andresen et al. 2010). Ultimately, the problem may be solved by more comprehensive studies of fault histories in the EED, especially those faults that can be shown to have been active after Hammamat basin deposition.

3.6.2 NW-SE Trending Folds and Thrusts (NE-SW Compression Event)

Following the NE-trending folds and thrusts was an episode of thrusting towards the SW (and to a lesser degree towards the NE), accompanied by NW-SE folding. This structural episode is also widely accepted as regional, at least in the CED, though again its intensity is variable (Figs. 3.16, 3.17 and 3.18). Equivalent structures in the NED are not obvious. The deformation is regarded as being due to NE-SW compression that is estimated to have occurred between 600 and 590 Ma (Greiling et al. 1994; Abdeen and Greiling 2005; Abd El-Wahed 2010; Fowler and Osman 2013) (Fig. 3.17). One of the best studied areas of this folding and thrusting is centred on the NW-SE trending Wadi Hammamat and Um Seleimat basins (Akaad and Noweir 1980; Ries et al. 1983; Kamal El-Din et al. 1996; Fritz et al. 1996; Fowler and Osman 2001; Fowler and El Kalioubi 2004). In the Wadi Hammamat basin NW- trending folds are dominant (Akaad and Noweir 1980) (Figs. 3.16, 3.18 and 3.19). The eastern margin of this basin is marked by SW-ward directed thrusting of ophiolitic rocks, arc volcanics and Dokhan along the Atalla shear zone (El-Gaby et al. 1984; Fritz et al. 1996; Kamal El-Din et al. 1996). Northeastward directed thrusts lie along the western margin of the basin near the Nubia Sandstone cover (Fig. 3.19). The thrusting predates the intrusion of the ~595 Ma Um Had granite (Greiling et al. 2014).

Northwest-trending folds deform originally low-dipping extension stage foliations in the nearby Um Seleimat basin. Fowler and El Kalioubi (2004) considered that the NW-trending folds overlapped in time with the extensional foliations, suggesting that the extension event was ongoing during the regional NE-SW compression. Andresen et al. (2009) suggested that the NW-trending Hammamat basins west of Meatiq may be piggy-back foreland basins associated with westwards thrusting, rather than upper crustal grabens. Other Hammamat basins showing NW-SE trending folds and/or thrusts include the Qash and Queih basins (Figs. 3.16 and 3.17b). There are minor NW-SE trending folds within the Kareim basin, and thrusts are well developed in the NW-trending smaller outlying basin northeast of Kareim. NW-trending folding are weakly developed in the Zeidun and Arak basins (Fig. 3.17a) but are dominant in the Meesar basin to their south (Osman 1996; Fowler and Osman 2013). WNW-trending folds are reported in the Igla basin by Abd El-Wahed (2010).

Abdeen and Greiling (2005) estimated NE-SW bulk shortening in the CED to be about, 15–17%, similar to, 20% shortening based on Fowler and El Kalioubi's (2004) cross-section of the Um Had—Meatiq area (Fig. 3.19). The ~20% shortening must be considered as a minimum value, as the contribution of the thrusts to shortening is unknown. Unlike the earlier NE-SW trending folds and thrusts, the NW-SE trending folds and thrusts are well represented outside of the Hammamat basins throughout the northern part of the CED, and are largely responsible for the NW-SE tectonic "grain" in that region. The common NW-SE trending pencil structures in the same area are a result of the interference of weak to moderate strains associated with the NE-SW compression and the earlier extension stage low-lying foliations (Osman 1996; Fowler 2015).

One of the proposed mechanisms for the doming of gneissic infrastructure in the CED (Meatiq, Um Had, El Shalul, El-Sibai) is type-1 fold interference between NW-SE trending antiforms and NE-trending antiforms of the previous deformation event. This concept is illustrated in Abdeen and Greiling (2005) (Fig. 3.16) and has support from other studies of these complexes (Fowler and Osman 2001; Habib et al. 1985a, b; Hamimi et al. 1994; Andresen et al. 2010; Ali et al. 2012b).

3.6.3 NW-SE Sinistral Najd Faulting and E-W Transpression

Transpression zones are steep strike-slip influenced deformation zones that deviate from simple shear by an additional component of shortening across the zone (Fossen and Tikoff 1998). Fossen and Tikoff (1998) described a spectrum of transpression zones, of which the commonest involve no extension or shortening along strike of the zone (Sanderson and Marchini 1984). Transpression may also be described as 'oblique' if displacements are not parallel to any of the three principal geometric axes of the transpression zone (x axis along the strike of the zone, y axis horizontal and normal to the zone, z axis vertical) (Jones and Holdsworth 1998). Transpressional structures (both sinistral and dextral) have been reported from nearly all of the suture zones in the ANS, including those associated with oblique arc-arc collisions at 780–650 Ma (Quick 1991; Greiling et al. 1994; Abdelsalam and Stern 1996; Wipfler 1996; Johnson and Kattan 2001; Johnson and Woldehaimanot 2003; Zoheir and Klemm 2007; Fritz et al. 2013; Johnson 2014), and the oblique

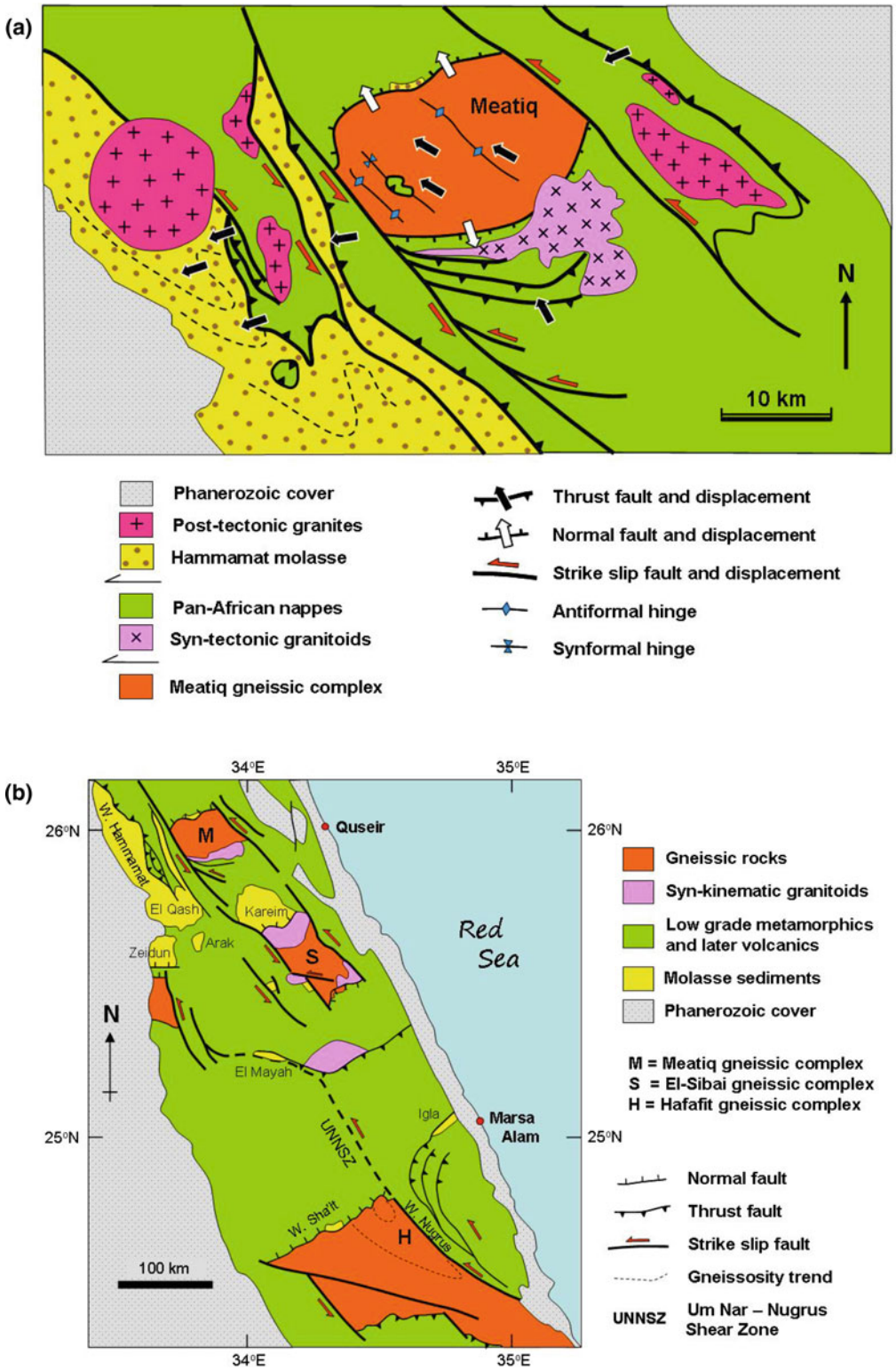

Fig. 3.18 Transpression-assisted core complex exhumation model showing partitioning of displacement directions. **a** Map of Meatiq dome area, modified from Fritz et al. (1996). According to the model, the Meatiq dome is enclosed by NW-SE trending Najd strike-slip faults and represents the internal part of the orogen. Areas to the west of Meatiq are described as external parts of the orogen. The internal parts record top-to-NW translation on subhorizontal shears and NW-SE extensional strains, associated with normal faults that assisted exhumation of the Meatiq gneisses. The external parts record NW-SE trending folding and top-to-SW (or W) displacement on thrusts. **b** Map of the CED, modified from Shalaby et al. (2006) showing application of the model in **a** to other gneissic complexes in the CED and the Hafafit Complex of the northernmost SED

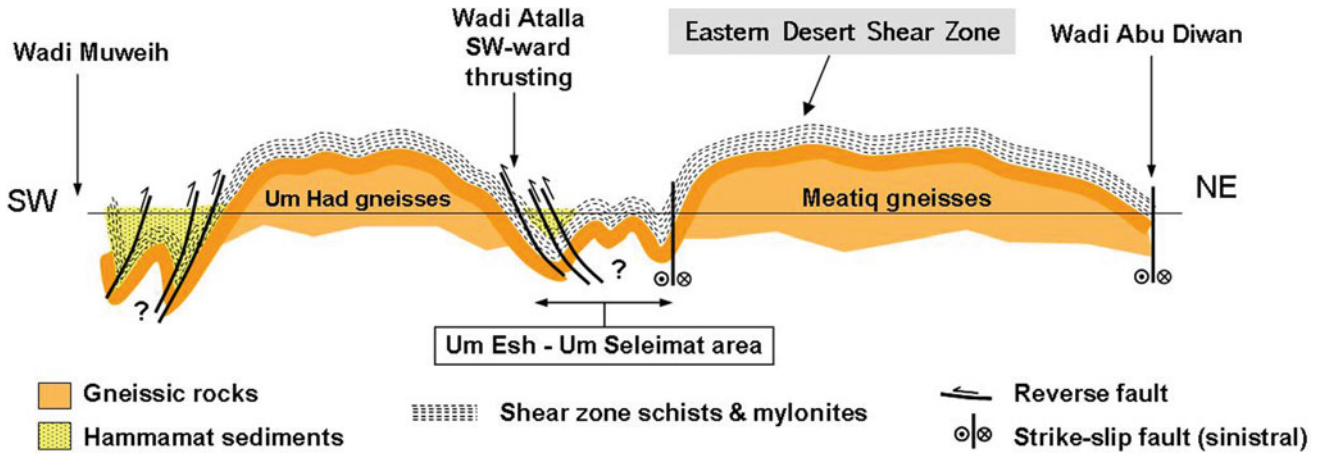

Fig. 3.19 NE-SW oriented cross-section through Meatiq and the Um Had gneissic complex, from Fowler and El Kalioubi (2004). The estimated shortening (based on arc length measurement) in the NE-SW direction is 20%. This shortening is the result of the NE-SW post-Hammamat compression event

arc-continent collision at 640–580 Ma along the Keraf suture (Abdelsalam et al. 1998).

The popular view is that sinistral transpression *followed* the extension stage, and occurred during the period 620–580 Ma, i.e. during the late stage E-W convergence of east and west Gondwana. Some workers, however, consider transpression to have been a long-lived event, dating as far back as 660 Ma, during the early stage of collision of east and west Gondwana (650–600 Ma) (Abd El-Wahed 2014). This 'early' onset of transpression would include the oblique convergence that yielded the Allaqi–Heiani suture, as noted above. Unzog and Kurz (2000) have suggested that transpression progressed in time from south to north in the CED. The model for post-extension transpression proposed by Greiling et al. (1994) and Abdeen and Greiling (2005) envisaged sinistral transpression immediately following the NNW-SSE compression stage, with SW-ward thrusting and NW-SE trending folds as part of the transpression event. A more recent model by Abd El-Wahed (2007, 2010) invokes two phases of thrusting (the first to the NNW and the second to the SW) followed by sinistral transpression. In this latter model the sinistral transpression is associated with tectonic escape, extrusion and strike-slip faulting.

Transpression plays a greater role in models that include nearly all of the CED and large parts of the SED (from the Duwi Shear Zone to the Wadi Kharit—Wadi Hodein shear zone) within the Najd Fault Zone (Abd El-Wahed 2007) (Figs. 3.6 and 3.20). The Wadi Kharit—Wadi Hodein shear zone is suspected to have accommodated up to 300 km of sinistral displacement during late stages of transpression. Transpression has also been described as being confined to identifiable discrete shear zones (Greiling et al. 1994; Zoheir 2011; Hagag et al. 2018). Post- extension transpression is most commonly referenced to the CED, though there are transpression models from the NED (Abd El-Wahed and Abu Anbar 2009), and the SED (Zoheir 2011; Abdeen and Abdelghaffar 2011).

Sinistral transpression is seen as important in the exhumation of ANS gneissic domes (Bregar et al. 2002; Fritz et al. 2002; Abd El-Wahed 2008; Abu Alam and Stüwe 2009; Johnson et al. 2011; Abu Alam et al. 2014; Makroum 2017; Hagag et al. 2018). The transpression model supported by Wallbrecher et al. (1993), Fritz et al. (1996) and Loizenbauer et al. (2001) describes partitioning of transpression between NW-SE displacement/extension associated with gneiss dome exhumation, and westward or SW-ward thrusting and NW-SE oriented folding (Fig. 3.18a). This transpression-assisted rise of the gneissic complexes has formed the basis for later popular models for all of the gneissic complexes in the CED, and also for the northernmost SED (in the Hafafit complex) (Neumayr et al. 1998; Loizenbauer et al. 2001; Bregar et al. 2002; Shalaby et al. 2005, 2006; Abd El-Wahed 2008, 2010, 2014) (Fig. 3.18b). Transpression effects can also clearly be seen in several Hammamat basins, especially the Queih basin (Greiling et al. 1994; Abdeen and Greiling 2005; Abd El-Wahed 2010; Johnson et al. 2013) (Fig. 3.17b).

The evidence presented by workers for transpression may be as simple as observation of parallel trends of strike-slip faults and coeval thrusts and folds. However, the most convincing evidence given for transpression is the existence of positive flower structures (Abd El-Wahed and Kamh 2010; Abd El-Wahed 2014), and stretching lineations that progressive change from steeply pitching at depth to subhorizontal in higher crustal levels on the same steeply dipping foliation planes (Johnson and Kattan 2001; Loizenbauer et al. 2001; Fritz et al. 2002; Genna et al. 2002; Zoheir 2011; Johnson et al. 2011). The steeply pitching

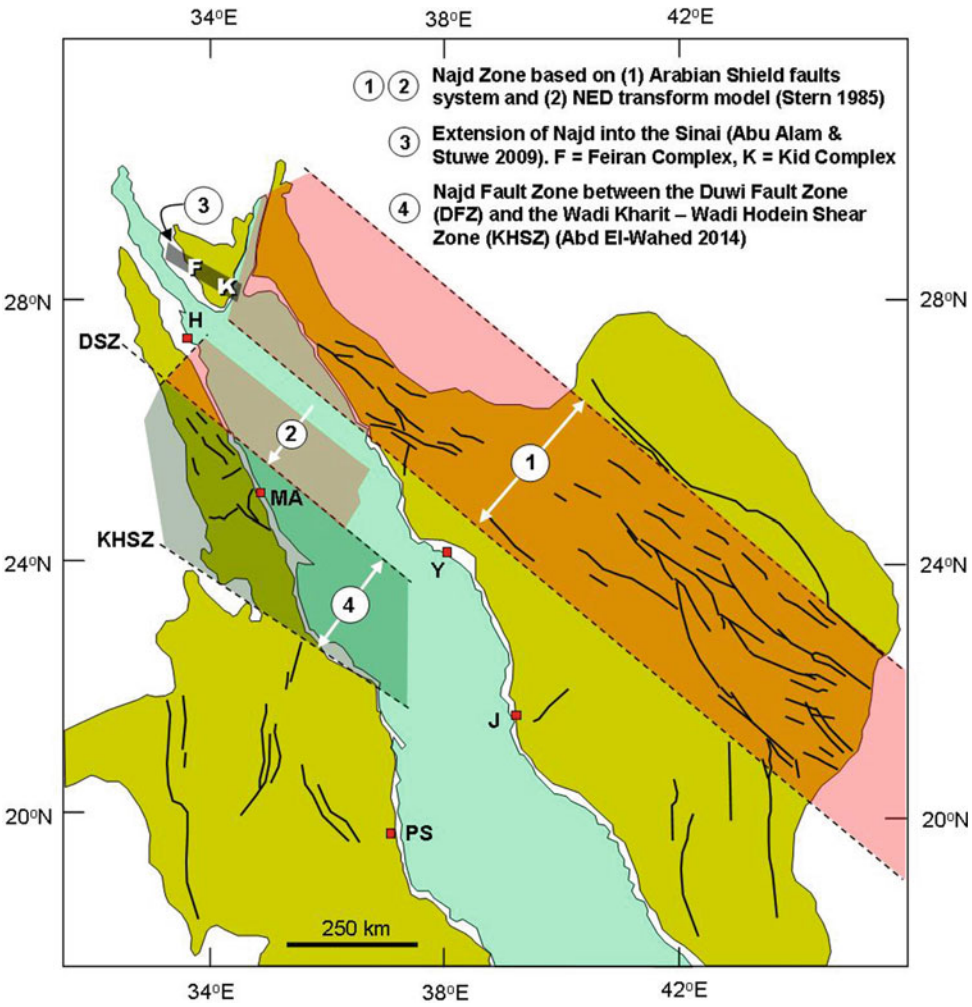

Fig. 3.20 Different views on the regional scale and zone of influence of the Najd Fault System. Closure of the Red Sea would bring zones (circled numbers) 1 and 2 into closer alignment. A more detailed map of the Najd Zone between the Duwi and Wadi Kharit-Wadi Hodein Shear zones is presented in Fig. 3.19. H = Hurghada, MA = Marsa Alam, Y = Yanbu, J = Jiddah, PS = Port Sudan

versus subhorizontal stretching lineations are correlated with transpression with flower structures, and transpression with lateral extrusion, respectively (Abd El-Wahed and Abu Anbar 2009; Abd El-Wahed 2014), and by others with pure shear dominated transpression and simple shear dominated transpression, respectively (Fritz et al. 2013, 2014). Smith et al. (1999) and Fritz et al. (2013) further noted that flower structures and pure shear dominated transpression characterized the southern parts of the ANS, while Najd strike slip movement and simple shear dominated transpression characterized the northern parts.

The existence of both dextral and sinistral post-extension transpression has been reported in the CED, involving early NW-trending sinistral transpression overprinted by later ENE-trending dextral transpression (Shalaby et al. 2005; Abd El-Wahed and Kamh 2010; Abd El-Wahed 2014). The sinistral-dextral transpressional pair have been thought of as conjugates of bulk E-W shortening, or as R and R′ Riedel shears of a NW-striking sinistral Najd shear system (Abdeen and Abdelghaffar 2011; Abd El-Wahed 2014; Hamimi et al. 2013, 2014; Abd El-Wahed et al. 2016), or as being due to a change in direction of the principal compressive stress (Shalaby et al. 2005). Transpression models have been used to explain the geometry and kinematics of gold-bearing quartz veins in the Eastern Desert of Egypt (Hassaan et al. 2009; Zoheir 2008, 2011; Zoheir and Lehmann 2011; Abd El-Wahed 2014).

3.6.4 N-S Shortening Zones

The convergence of east and west Gondwana culminated in simple shear dominated transpression effects in the northern parts of the ANS, characteristically expressed as the impressive NW-trending sinistral strike slip Najd fault system (active between 630 and 530 Ma). In the southern parts of the ANS this E-W convergence is expressed ultimately as typically N-S trending belts of intensely foliated and isoclinally upright folded rock cross-cutting and displacing the earlier arc-arc sutures (Johnson et al. 2011; Fritz et al. 2013). These N-S trending belts (actually varying in strike from NW to NNE), measuring hundreds of kms in length and tens

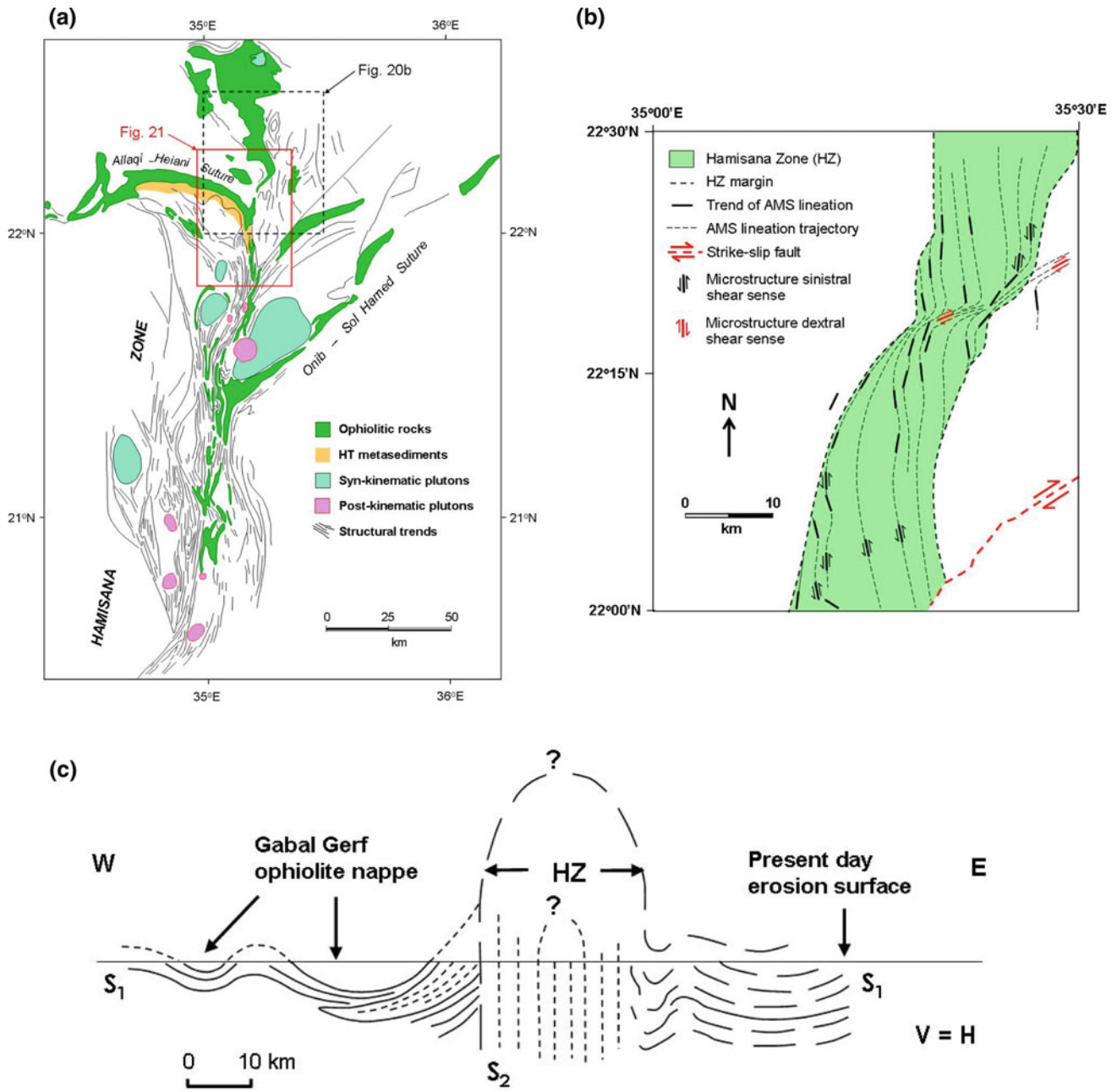

Fig. 3.21 The geology and structure of the Hamisana Zone. **a** Map of the structural trends and distribution of ophiolite bodies of the Hamisana Zone, modified from Stern et al. (1990). **b** detail of the northern part of the Hamisana Zone, from de Wall et al. (2001), showing shear foliations and the orientation of magnetic fabrics. Late stage dextral shear zones are shown. See location of this figure in Fig. 3.20a. **c** idealized E-W cross-section of the Hamisana Zone, modified from de Wall et al. (2001), showing the antiformal structure of the zone

of km in width, are referred to as shortening zones, of which the most important are the Hamisana Zone (HZ) and the Oko Shear Zone (OSZ) (Fig. 3.6). Duncan et al. (1990) suggested that the HZ may extend northwards as far as the Midian terrane as the Hanabiq shear zone.

The HZ (or Hamisana Shear Zone HSZ of some authors) is an ophiolite-decorated high strain zone (Figs. 3.21a and 3.22) that was viewed originally as an arc-arc suture (Vail 1983, 1985; Shackleton 1986), or as a transcurrent or transpressive shear zone formed either during or after arc accretion (Almond and Ahmed 1987; Kröner et al. 1987; Greiling et al. 1994; O'Connor et al. 1994; Wipfler 1996; Smith et al. 1999; Khudeir et al. 2003; Ibrahim et al. 2015), but has also been described as a post-accretionary mainly

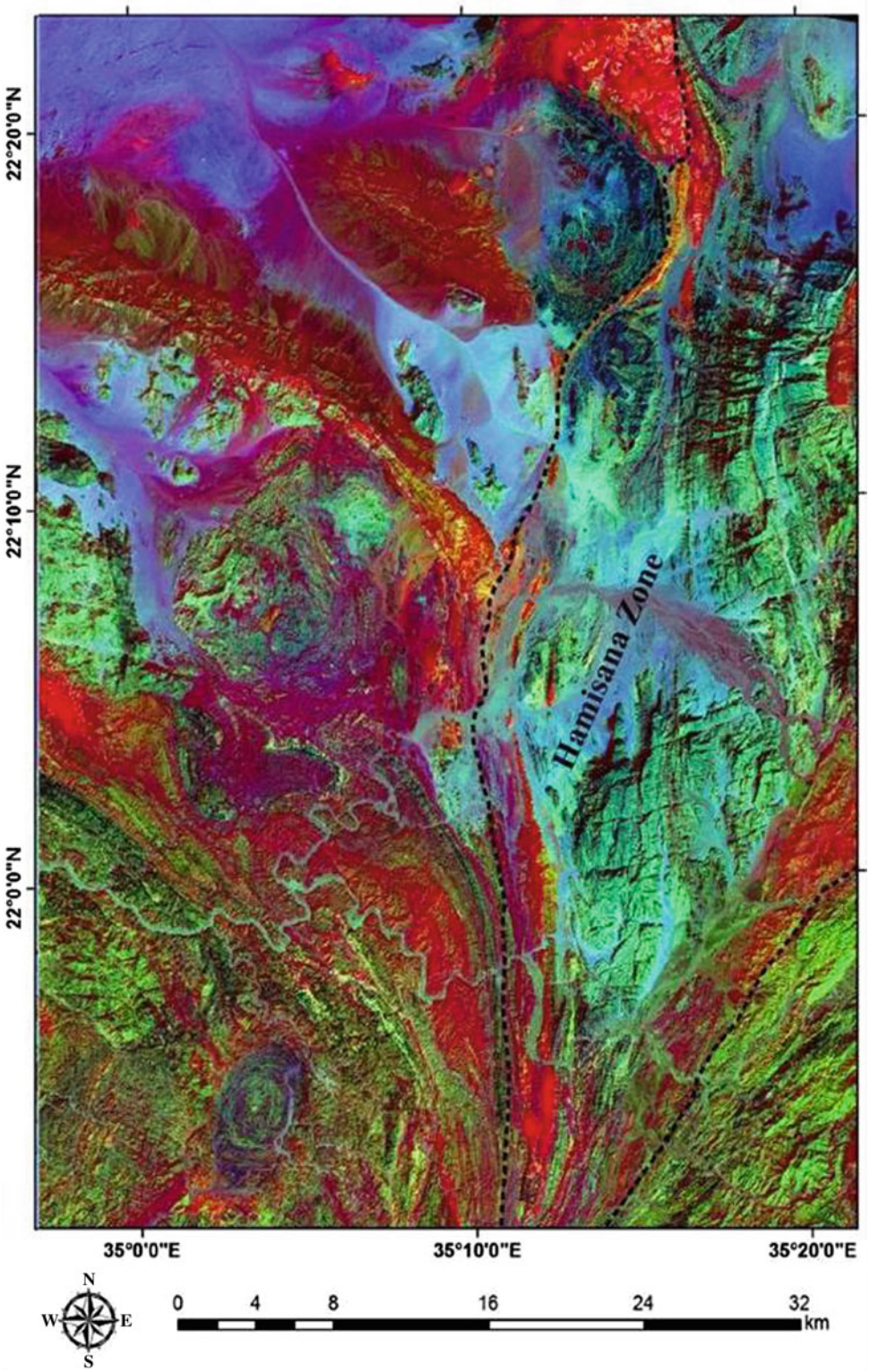

Fig. 3.22 Remote sensing image of the northern part of the Hamisana Zone, from Ali-Bik et al. (2014). Location of this image is shown in Fig. 3.20a

pure shear dominated high strain zone with subordinate parallel or cross-cutting ductile shears (Fig. 3.21b). The last is supported by recent strain studies (Stern et al. 1989, 1990; Miller and Dixon 1992; Abdelsalam and Stern 1993b, 1996; de Wall et al. 2001; Johnson and Woldehaimanot 2003). The HZ consists of gneissic and schistose rocks, and isoclinally folded slivers of ophiolite derived from the Allaqi–Heiani and Onib–Sol Hamed sutures (Fig. 3.21a).

HZ deformation commenced sometime after 660 Ma, with intense E-W shortening and N-S extension

accompanied by greenschist to amphibolite facies metamorphism and development of upright isoclinal folds and vertical foliations (Stern et al. 1989; Ali-Bik et al. 2014) (Fig. 3.21c). Deformation probably ceased by 550 Ma (Stern et al. 1989). Latest deformation effects are minor dextral NE-striking shears, especially at the northern end of the HZ.

The apparent dextral displacement between the Allaqi–Heiani and Onib–Sol Hamed sutures was refuted by Abdelsalam and Stern (1996) and de Wall et al. (2001), eliminating the main evidence for major shearing along the HZ. In addition, de Wall et al.'s (2001) AMS studies confirmed a pure shear dominated constrictional strain for the HZ, inconsistent with transpression or tectonic escape along this structure. Spaced mylonitic shears within the HZ and parallel to it, are found to have sinistral shear sense (Fig. 3.21b). The late NE trending dextral shears were accompanied by a greenschist facies metamorphism (Ali-Bik et al. 2014).

The Oko Shear Zone (OSZ) lies SSE of the Hamisana Zone, and cross-cuts the Nakasib suture (Fig. 3.6). Both the HZ and OKZ lie within an area outlined by Fritz et al. (2013), referred to as the "central compression zone", which occupied the region south of the Allaqi–Heiani and Onib–Sol Hamed sutures, and extended west to the Keraf suture and east into the Asir terrane. The OKZ has a complex deformation history under greenschist facies conditions, and its activity commenced around 700–670 Ma and continued until 560 Ma (Almond and Ahmed 1987; Almond et al. 1989; Abdelsalam and Stern 1993a; Johnson and Woldehaimanot 2003; Abdelsalam 2010). It displaces the Nakasib suture in a sinistral sense by 10 km (Fig. 3.6). North-south strands of the OZ continue northwards to meet the Onib–Sol Hamed suture (Almond and Ahmed 1987). The OZ experienced early E-W shortening forming tight N-S trending folds, followed by NW-SE sinistral and minor NE-SW dextral conjugate strike-slip shearing, before development of positive flower structure (Abdelsalam 1994, 2010). Strain along the OZ has also been shown to be constrictional (Abdelsalam 2010), however, Wipfler (1996) described the OZ as a transpressional zone associated with oblique collision, rather than a dominantly pure shear strain event.

3.7 Commentary on Major Points Covered in This Chapter

The account of progress in this study on the structural and tectonic evolution of the ANS includes the following important highlights, with comments:

1. There has been a major reassessment of the significance and setting of the Sinai metamorphic complexes (Feiran-Solaf, Sa'al-Zaghara, Kid and Taba-Elat) in the light of recent results from SHRIMP U-Pb zircon isotopic analyses that yielded late Mesoproterozoic (Stenian) dates for the metavolcanics in the Sa'al complex. A new narrative on the break-up of Rodinia at 1100–900 Ma may be forthcoming.
2. However, the immense value of precision zircon dating of the Sinai complexes is still being compromised by lack of understanding of the protoliths of some of the dated rocks, e.g. the persistent problem of whether the Feiran-Solaf gneisses are metasedimentary, metavolcanic or gneissic intrusives (or all of the above). Another related problem for the zircon geochronology (Sinai and elsewhere in the ANS) is the presence of xenocrystic zircons, possible lead loss events and other questions about isotopic systematics that complicate the interpretations of the U-Pb zircon and previous Rb-Sr data.
3. The opportunity to locate, map and synthesize data from small dispersed gneissic xenolithic blocks between the Sinai complexes should not be lost, and should provide better understanding of the extent and structural relations between these complexes, as well as assist in correlating the metamorphic and structural events recorded in them. Remote sensing should play a major role in this effort.
4. There is a clear reversal of arc collision-related thrusting/transport directions of ophiolitic rocks, from S- or SW- wards transport (south of the Hafafit complex) to N- or NW-wards transport (north of the Hafafit complex). Other aspects correlate with this directional change: steep thrusts dissecting largely intact blocks of ophiolitic rocks between Hafafit and the Allaqi-Heiani-Onib-Sol Hamed-Yanbu 'AHOSHY' suture; compared with gently dipping long-displaced thin ophiolitic mélange-dominated nappes (with occasional intact megablocks) and with abundant sedimentary component showing only minor internal deformation, in the CED. This change may reflect profound deformation style differences between SED areas near to the suture, and CED back-arc(?) areas distant from the sutures.
5. Also within the arc amalgamation stage (760–690 Ma), the voluminous intrusions of calc-alkaline plutons into active thrust-affected zones (e.g. Hafafit, El-Sibai) well north of the AHOSHY suture raises the question of what processes delivered such volumes of magmas so far from the subduction-zone at that time.
6. There is growing recognition of a distinct phase of late- to post-collision calc-alkaline magmatism and volcanism in the 630–610 Ma range (undeformed granodiorites of late subduction or primitive Younger Granite affinity, and early stages of Dokhan volcanism) provide potential evidence for the mechanism of transition from the compressional arc collision stage to the later orogenic extensional stage. The fact that the Um Ba'anib pluton in

the Meatiq complex is a representative of this phase is particularly interesting for studies aiming to understand the origin and significance of this complex.

7. With respect to the orogenic extensional stage of the ANS, there is an embarrassment of riches in models and themes for this event (or group of events). The popularity of mantle lithospheric delamination is growing as an explanation for the triggering of upper crustal brittle extension, volcanism and widespread granitic intrusion. What is not yet clear, though, is whether, and to what extent the proposed mantle delamination was accompanied by crustal delamination and thinning, perhaps accommodated by the regional low-angle extensional ductile shear zones (such as the EDSZ and the Sha'it--Nugrus shear zone). Dewey's (1988) stages of orogenic collapse considered uplift and subsidence as equally possible outcomes of mantle delamination, depending on whether crustal thinning was operative or not. The possible role of crustal thinning, in partnership with mantle delamination is a topic well worth investigating in the EED.
8. The culminating extensional event in the ANS raises further major questions. How should the delamination models be reconciled with the equally popular Najd Shear System models that also describe many aspects of the extension event in terms of tectonic escape? To what extent are strike-slip fault systems in the EED significantly transpressive? The study of the origin of the gneissic domes in the CED lies at the forefront of such debates.
9. The post-amalgamation Hammamat molasse basins have yet to yield the full measure of information contained in them. These basins have still not received comprehensive stratigraphic studies, and basin evolution defining parameters such as sedimentation rates, boundary fault subsidence rates, bulk extensional strains, etc., are still unavailable. This results in continuing uncertainty about their evolution and subsidence mechanisms. The inversion of the basins provides a range of structures useful for measuring the post-Hammamat deformation effects and assessing their style differences across the CED, however, more detailed studies are needed on fault rejuvenation before regional stresses can be reliably reconstructed.

References

Abdeen MM, Abdelghaffar AA (2011) Syn- and post-accretionary structures in the Neoproterozoic Central Allaqi-Heiani suture zone, Southeastern Egypt. Precambr Res 185:95–108

Abdeen MM, Greiling RO (2005) A quantitative structural study of Late Pan-African compressional deformation in the Central Eastern Desert (Egypt) during Gondwana assembly. Gondwana Res 8:457–471

Abdeen MM, Warr LN (1998) Late orogenic basin evolution, deformation and metamorphism in the Pan-African basement, Wadi Queih, Eastern Desert of Egypt. Forschungszentrum Jülich, Sci. Ser. Int. Bureau v. 42, 272 pp

Abdeen MM, Sadek MF, Greiling RO (2008) Thrusting and multiple folding in the Neoproterozoic Pan-African basement of Wadi Hodein area, south Eastern Desert, Egypt. J Afr Earth Sci 52:21–29

Abdeen MM, Greiling RO, Sadek MF, Hamad SS (2014) Magnetic fabrics and Pan-African structural evolution in the Najd Fault corridor in the Eastern Desert of Egypt. J Afr Earth Sci 99:93–108

Abdel-Karim AM, Azzaz SA (1995) On the age dating of the dyke swarms of southwestern Sinai, Egypt. Arab Gulf J Sci Res 13:41–53

Abdel-Karim AM (1993) Petrology and geochemistry of Late Precambrian mafic dyke swarms in southwestern Sinai, Egypt. Acta Miner Petrograph Szeged 34:61–69

Abdel-Karim AM, Ahmed Z (2010) Possible origin of the ophiolites of Eastern Desert, Egypt, from geochemical perspectives. Arab J Sci Eng 35:115–143

Abdel-Karim AM, El-Baroudy AF (1995) Petrology and geochemistry of felsic dyke swarms in southwest Sinai, Egypt. Arab Gulf J Sci Res 13:239–257

Abdel-Karim AM, El Shafei SA (2018) Mineralogy and chemical aspects of some ophiolitic metaultramafics, central Eastern Desert, Egypt: evidences from chromites, sulphides and gangues. Geol J 53:580–599

Abdel-Karim AM, El-Mahallawy MM, Finger F (1996) The ophiolitic mélange of Wadi Dunqash and Arayis, Eastern Desert Egypt: petrogenesis and tectonic evolution. Acta Miner Petrograph Szeged 37:129–141

Abdel-Karim AM, Azzaz SA, Moharem AF, El-Alfy HM (2008) Petrological and geochemical studies on the ophiolite and island arc association of Wadi Hammariya, Central Eastern Desert, Egypt. Arab J Sci Eng 33:117–138

Abdel-Karim AM, Ali S, Helmy HM, El-Shafei SA (2016) A fore-arc setting of the Gerf ophiolite, Eastern Desert, Egypt: evidence from mineral chemistry and geochemistry of ultramafites. Lithos 263:52–65

Abdel Khalek ML, Takla MA, Sehim A, Hamimi Z, El Manawi AW (1992) Geology and tectonic evolution of Wadi Beitan area, south Eastern Desert, Egypt. GAW, Cairo Univ, Egypt 1:369–393

Abdel Khalek ML, Takla MA, Sehim AA, Abdel Wahed M, Hamimi Z, Sakran SM (1999) Tectonic evolution of the shield rocks, east Wadi Beitan area, Southeastern Desert, Egypt. Egypt J Geol 43:1–25

Abdel-Meguid AA (1992) Late Proterozoic Pan-African tectonic evolution of the Egyptian part of the Arabian-Nubian Shield. MERC Ain Shams Univ Earth Sci Ser 6:13–28

Abd El-Naby HH, Frisch W (2002) Origin of the Wadi Haimur–Abu Swayel gneiss belt, south Eastern Desert, Egypt: petrological and geochronological constraints. Precambr Res 113:307–322

Abd El-Naby H, Frisch W (2006) Geochemical constraints from the Hafafit Metamorphic Complex (HMC): evidence of Neoproterozoic back-arc basin development in the central Eastern Desert of Egypt. J Afr Earth Sci 45:173–186

Abd El-Naby H, Frisch W, Hegner E (2000) Evolution of the Pan-African Wadi Haimur metamorphic sole, Eastern Desert, Egypt. J Metam Geol 18:639–651

Abd El-Naby H, Frisch W, Siebel W (2008) Tectono-metamorphic evolution of the Wadi Hafafit Culmination (central Eastern Desert, Egypt). Implication for Neoproterozoic core complex exhumation in NE Africa. Geol Acta 6:293–312

Abd El-Rahman Y, Polat A, Dilek Y, Fryer B, El-Sharkawy M, Sakran S (2009) Geochemistry and tectonic evolution of the Neoproterozoic Wadi Ghadir ophiolite, Eastern Desert, Egypt. Lithos 113:158–178

Abd El-Rahman Y, Polat A, Fryer BJ, Dilek Y, El-Sharkawy M, Sakran S (2010) The provenance and tectonic setting of the Neoproterozoic Um Hassa Greywacke Member, Wadi Hammamat area, Egypt: evidence from petrography and geochemistry. J Afr Earth Sci 58:185–196

Abd El-Rahman Y, Polat A, Dilek Y, Kusky TM, El-Sharkawi M, Said A (2012) Cryogenian ophiolite tectonics and metallogeny of the Central Eastern Desert of Egypt. Int Geol Rev 54(16):1870–1884

Abdel-Rahman AM (1995) Tectonic-magmatic stages of shield evolution: the Pan-African belt in northeastern Egypt. Tectonophysics 242:223–240

Abdel-Rahman AM (1996) Pan-African volcanism: petrology and geochemistry of the Dokhan Volcanic Suite in the northern Nubian shield. Geol Mag 133:17–31

Abdel-Rahman AM, Doig R (1987) The Rb-Sr geochronological evolution of the Ras Gharib segment of the northern Nubian Shield. J Geol Soc Lond 144:577–586

Abdel-Rahman AM, Doig R (1989) Discussion on the age of Feiran basement rocks, Sinai: implications for late Precambrian evolution in the northern Arabian-Nubian Shield. J Geol Soc Lond 146:883–884

Abdel-Rahman AM, Martin RF (1987) Late Pan-African magmatism and crustal development in northeastern Egypt. Geol J 22:281–301

Abdel-Rahman AM, Martin RF (1989) Late Pan-African magmatism and crustal development in northeastern Egypt: reply. Geol J 24:375–381

Abdelsalam MG (1994) The Oko shear zone: post-accretionary deformations in the Arabian-Nubian Shield. J Geol Soc Lond 151:767–776

Abdelsalam MG (2010) Quantifying 3D post-accretionary tectonic strain in the Arabian-Nubian Shield: superimposition of the Oko Shear Zone on the Nakasib Suture, Red Sea Hills, Sudan. J Afr Earth Sci 56:167–178

Abdelsalam MG, Stern RJ (1993a) Timing of events along the Nakasib suture and the Oko shear zone, Sudan. In: Thorweihe U, Schandelmeier H (eds) Geoscientific research in northeast Africa. Balkema, Rotterdam, pp 99–103

Abdelsalam MG, Stern RJ (1993b) Structure of the Late Proterozoic Nakasib suture, Sudan. J Geol Soc Lond 150:1065–1074

Abdelsalam MG, Stern RJ (1996) Sutures and shear zones of the Arabian-Nubian Shield. J Afr Earth Sci 23:289–310

Abdelsalam MG, Stern RJ, Copeland P, Elfaki EM, Elhur B, Ibrahim FM (1998) The Neoproterozoic Keraf Suture in NE Sudan: sinistral transpression along the eastern margin of West Gondwana. J Geol 106:133–147

Abdelsalam MG, Liegeois JP, Stern RJ (2002) The Saharan Metacraton. J Afr Earth Sci 34:119–136

Abdelsalam MG, Abdeen MM, Dowaidar HM, Stern RJ, Abdelghaffar AA (2003) Structural evolution of the Neoproterozoic Western Allaqi-Heiani suture, southeastern Egypt. Precambr Res 124:87–104

Abd El-Wahed MA (2004) Structural analysis of Wadi El Qash area, Central Eastern Desert, Egypt. Ann Geol Surv Egypt 27:79–108

Abd El-Wahed MA (2007) Late Pan-African tectonic evolution and strain determinations in the Late Neoproterozoic molasse sediments, Eastern Desert, Egypt: evidence for post-Hammamat compression and transpression. Egypt J Geol 51:1–39

Abd El-Wahed MA (2008) Thrusting and transpressional shearing in the Pan-African nappe southwest El-Sibai core complex, Central Eastern Desert, Egypt. J Afr Earth Sci 50:16–36

Abd El-Wahed MA (2010) The role of the Najd Fault System in the tectonic evolution of the Hammamat molasse sediments, Eastern Desert, Egypt. Arab J Geosci 3:1–26

Abd El-Wahed MA (2014) Oppositely dipping thrusts and transpressional imbricate zone in the Central Eastern Desert of Egypt. J Afr Earth Sci 100:42–59

Abd El-Wahed M, Abu Anbar M (2009) Synoblique convergent and extensional deformation and metamorphism in the Neoproterozoic rocks along Wadi Fatira shear zone, Northern Eastern Desert, Egypt. Arab J Geosci 2:29–52

Abd El-Wahed MA, Kamh SZ (2010) Pan-African dextral transpressive duplex and flower structure in the Central Eastern Desert of Egypt. Gondwana Res 18:315–336

Abd El-Wahed MA, Harraz H, El-Behairy MH (2016) Transpressional imbricate thrust zones controlling gold mineralization in the Central Eastern Desert of Egypt. Ore Geol Rev 78:424–446

Abdel Wahed AAA, Ali KG, Khalil MMA, Abdel Gawad AE (2012) Dokhan volcanics of Gabal Monqul area, North Eastern Desert, Egypt: geochemistry and petrogenesis. Arab J Geosci 5:29–44

Abu-Alam TS, Stüwe K (2009) Exhumation during oblique transpression: the Feiran-Solaf region, Egypt. J Metam Geol 27:439–459

Abu-Alam TS, Santosh M, Brown M, Stüwe K (2013) Gondwana collision. Miner Petrol

Abu-Alam TS, Hassan M, Stüwe K, Meyer SE, Passchier CW (2014) Multistage tectonism and metamorphism during Gondwana collision: Baladiyah complex, Saudi Arabia. J Petrol 55:1941–1964

Abu Anbar MM (2015) The Pan-African ophiolites and related mineralization in Egypt. Acta Geol Sin 89(supp. 2):65–68

Abu El-Enen MM (2008) Geochemistry and metamorphism of the Pan-African back-arc Malhaq volcano-sedimentary Neoproterozoic association, W. Kid area, SE Sinai, Egypt. J Afr Earth Sci 51:189–206

Abu El-Enen MM (2011) Geochemistry, provenance, and metamorphic evolution of Gabal Samra Neoproterozoic metapelites, Sinai, Egypt. J Afr Earth Sci 59:269–282

Abu El-Enen MM, Makroum FM (2003) Tectonometamorphic evolution of the northeastern Kid Belt, southeastern Sinai, Egypt. Ann Geol Surv Egypt 26:19–37

Abu El-Enen MM, Whitehouse MJ (2013) The Feiran-Solaf metamorphic complex, Sinai, Egypt: geochronological and geochemical constraints on its evolution. Precambr Res 239:106–125

Abu El-Enen MM, Abu-Alam TS, Whitehouse MJ, Ali KA, Okrusch M (2016) P-T path and timing of crustal thickening during amalgamation of East and West Gondwana: a case study from the Hafafit Metamorphic Complex, Eastern Desert of Egypt. Lithos 263:213–238

Agron N, Bentor YK (1981) The volcanic massif of Biq'at Hayareah (Sinai-Negev): a case of potassium metasomatism. J Geol 89:479–485

Akaad MK, Noweir AM (1969) Lithostratigraphy of the Hammamat-Um Seleimat District, Eastern Desert, Egypt. Nature 223:284–285

Akaad MK, Noweir A (1980) Geology and lithostratigraphy of the Arabian Desert Orogenic Belt of Egypt between Lat. 25°35′ and 26° 30′. Bull Inst Appl Geol King Abdulaziz Univ 3:127–135

Akaad MK, Abu El Ela AM, El Kamshoshy HI (1993) Geology of the region west of Mersa Alam, Eastern Desert, Egypt. Ann Geol Surv Egypt 19:1–18

Akaad MK, Noweir AM, Abu El Ela AM, El-Bahariya GA (1996) The Muweilih Conglomerate; Qift-Quseir road region, and the problem of the Atud Formation. In: Proceedings of the Geological Survey of Egypt Centennial Conference (1996). pp 23–45

Akawy A, Zaky K (2008) Structural analysis of the tectonically inverted Kareim Basin, Eastern Desert, Egypt. N Jb Geol Palaont Abh 250:9–30

Ali BH, Wilde SA, Gabr MMA (2009a) Granitoid evolution in Sinai, Egypt, based on precise SHRIMP U-Pb zircon geochronology. Gondwana Res 18:38–48

Ali KA, Stern RJ, Manton WI, Kimurab J-I, Khamees HA (2009b) Geochemistry, Nd isotopes and U-Pb SHRIMP zircon dating of Neoproterozoic volcanic rocks from the Central Eastern Desert of Egypt: new insights into the ~750 Ma crust-forming event. Precambr Res 171:1–22

Ali KA, Azer MK, Gahlan HA, Wilde SA, Samuel MD, Stern RJ (2010) Age constraints on the formation of Neoproterozoic ophiolites along the Allaqi–Heiani Suture, South Eastern Desert of Egypt. Gondwana Res 18:583–595

Ali KA, Moghazi AM, Maurice AE, Omar SA, Wang Q, Wilde SA, Moussa EM, Manton WI, Stern RJ (2012a) Composition, age, and origin of the ~620 Ma Humr Akarim and Humrat Mukbid A-type granites: no evidence for pre-Neoproterozoic basement in the Eastern Desert, Egypt. Int J Earth Sci 101:1705–1722

Ali KA, Andresen A, Manton WI, Stern RJ, Omar SA, Maurice AE (2012b) U-Pb zircon dating and Sr-Nd-Hf isotopic evidence to support a juvenile origin of the ~634 Ma El Shalul granitic gneiss dome, Arabian-Nubian Shield. Geol Mag 149:783–797

Ali KA, Kröner A, Hegner E, Wong J, Li S-Q, Gahlan HA, Abu El Ela FF (2015) U-Pb zircon geochronology and Hf-Nd isotopic systematics of Wadi Beitan granitoid gneisses, South Eastern Desert, Egypt. Gondwana Res 27:811–824

Ali-Bik MW, Sadek MF, Sadek Ghabrial D (2014) Late Neoproterozoic metamorphic assemblages along the Pan-African Hamisana Shear Zone, southeastern Egypt: metamorphism, geochemistry and petrogenesis. J Afr Earth Sci 99:24–38

Ali-Bik MW, Abd El Rahim SH, Abdel Wahab W, Abayazeed SD, Hassan SM (2017) Geochemical constraints on the oldest arc rocks of the Arabian-Nubian Shield: the late Mesoproterozoic to late Neoproterozoic (?) Sa'al volcano-sedimentary complex, Sinai, Egypt. Lithos 284–285:310–326

Almond DC, Ahmed F (1987) Ductile shear zones on north Red Sea Hills, Sudan and their implication for crustal collision. Geol J 22:175–184

Almond DC, Darbyshire DPF, Ahmed F (1989) Age limit for major shearing episodes in the Nubian Shield of northeast Sudan. J Afr Earth Sci 9:489–496

Amstutz GC, El-Gaby S, Ahmed AA, Habib ME, Khudeir AA (1984) Back-arc ophiolite association, Central Eastern Desert, Egypt. Bull Fac Sci Assiut Univ 13:95–136

Andresen A, Abu El-Rus MA, Myhre PI, Boghdady GY, Corfu F (2009) U-Pb TIMS age constraints on the evolution of the Neoproterozoic Meatiq Gneiss Dome, Eastern Desert, Egypt. Int J Earth Sci 98:481–497

Andresen A, Augland LE, Boghdady GY, Lundmark AM, El Nady OM, Hassan MA, Abu El-Rus MA (2010) Structural constraints on the evolution of the Meatiq Gneiss Dome (Egypt), East-African Orogen. J Afr Earth Sci 57:413–422

Andresen A, Abu El-Enen MM, Stern RJ, Wilde SA, Ali KA (2014) The Wadi Zaghra metasediments of Sinai, Egypt: new constraints on the late Cryogenian–Ediacaran tectonic evolution of the northernmost Arabian-Nubian Shield. Int Geol Rev 56 (8):1020–1038

Asran AMH, Azer MK, Aboazom AS (2005) Petrological and geochemical investigations on Dokhan volcanics and felsites in Wadi Sodmein area, Central Eastern Desert, Egypt. Egypt J Geol 49:1–20

Augland LE, Andresen A, Boghdady GY (2012) U-Pb ID-TIMS dating of igneous and metaigneous rocks from the El-Sibai area: time constraints on the tectonic evolution of the Central Eastern Desert, Egypt. Int J Earth Sci 101:25–37

Avigad D, Gvirtzman Z (2009) Late Neoproterozoic rise and fall of the northern Arabian-Nubian shield: the role of lithospheric mantle delamination and subsequent thermal subsidence. Tectonophysics 477:217–228

Azer MK (2007) Tectonic significance of Late Precambrian calc-alkaline and alkaline magmatism in Saint Katherina area, Southern Sinai, Egypt. Geol Acta 5:255–272

Azer MK (2013) Late Ediacaran (605–580 Ma) post-collisional alkaline magmatism in the Arabian-Nubian Shield: a case study of Serbal ring-shaped intrusion, southern Sinai, Egypt. J Asian Earth Sci 77:203–223

Azer MK (2014) Petrological studies of Neoproterozoic serpentinized ultramafics of the Nubian Shield: spinel compositions as evidence of the tectonic evolution of Egyptian ophiolites. Acta Geol Polon 64:113–127

Azer MK, Farahat ES (2011) Late Neoproterozoic volcano-sedimentary successions of Wadi Rufaiyil, southern Sinai, Egypt: a case of transition from late to post-collisional magmatism. J Asian Earth Sci 42:1187–1203

Azer MK, Stern RJ (2007) Neoproterozoic (835–720 Ma) serpentinites in the Eastern Desert, Egypt: fragments of fore-arc mantle. J Geol 115:457–472

Azer MK, Obeid MA, Ren M (2014) Geochemistry and petrogenesis of late Ediacaran (580–605 Ma) post-collisional alkaline rocks from the Katherina ring complex, south Sinai, Egypt. J Asian Earth Sci 93:229–252

Azzaz SA, Blasy M, Moharem A, Amer O (2015) Late Neoproterozoic Dokhan volcanics, around G. Esh, North Eastern Desert, Egypt: geochemistry and relation of K_2O and Nb abundances with crustal thickness. Arab J Geosci 8:3551–3564

Bakor AR, Gass IG, Neary CR (1976) Jabal Al Wask, northwest Saudi Arabia: an Eocambrian back-arc ophiolite. Earth Planet Sci Lett 30:1–9

Be'eri-Shlevin Y, Eyal M, Eyal Y, Whitehouse MJ, Litvinovsky B (2012) The Sa'al volcano-sedimentary complex (Sinai, Egypt). A latest Mesoproterozoic volcanic arc in the northern Arabian Nubian Shield. Geology 40:403–406

Bennett JD, Mosley PN (1987) Tiered-tectonics and evolution, Eastern Desert and Sinai, Egypt. In: Matheis G, Schandelmeier H (eds) Current research in African Earth sciences. Balkema, Rotterdam, pp 79–82

Bentor YK (1985) The crustal evolution of the Arabian-Nubian Massif with special reference to the Sinai Peninsula. Precambr Res 28:1–74

Bezenjani RN, Pease V, Whitehouse MJ, Shalaby MH, Kadi KA, Kozdroj W (2014) Detrital zircon geochronology and provenance of the Neoproterozoic Hammamat Group (Igla Basin), Egypt and the Thalbah Group, NW Saudi Arabia: implications for regional collision tectonics. Precambr Res 245:225–243

Bielski M (1982) Stages in the evolution of the Sinai Peninsula. Unpublished PhD thesis, The Hebrew University of Jerusalem

Black R, Liegeois J-P (1993) Cratons, mobile belts, alkaline rocks and continental lithospheric mantle: the Pan-African testimony. J Geol Soc Lond 150:89–98

Blasband B, Brooijmans P, Dirks P, Visser W, White S (1997) A Pan-African core complex in the Sinai, Egypt. Geol Mijnb 76:247–266

Blasband B, White P, Brooijmans H, de Boorder H, Visser W (2000) Late Proterozoic extensional collapse in the Arabian-Nubian Shield. J Geol Soc Lond 157:615–628

Boger SD, Carson CJ, Fanning CM, Hergt JM, Wilson CJL, Woodhead JD (2002) Pan-African intraplate deformation in the northern Prince Charles Mountains, East Antarctica. Earth Planet Sci Lett 195:195–210

Bonavia FF, Chorowicz J (1992) Northward expulsion of the Pan-African of northeast Africa guided by a reentrant zone of the Tanzania Craton. Geology 20:1023–1026

Bregar M, Bauernhofer A, Pelz K, Kloetzli U, Fritz H, Neumayr P (2002) A Late Neoproterozoic magmatic core complex in the Eastern Desert of Egypt: emplacement of granitoids in a wrench-tectonic setting. Precambr Res 118:59–82

Breitkreuz C, Eliwa H, Khalaf I, El Gameel K, Bühler B, Sergeev S, Larionov A, Murata M (2010) Neoproterozoic SHRIMP U-Pb zircon ages of silica-rich Dokhan Volcanics in the North Eastern Desert, Egypt. Precambr Res 182:163–174

Brooijmans P, Blasband B, White SH, Visser WJ, Dirks P (2003) Geothermobarometric evidence for a metamorphic core complex in Sinai, Egypt. Precambr Res 123:249–268

Bühler B, Breitkreuz C, Pfänder JA, Hofmann M, Becker S, Linnemann U, Eliwa HA (2014) New insights into the accretion of the Arabian-Nubian Shield: depositional setting, composition and geochronology of a Mid-Cryogenian arc succession (North Eastern Desert, Egypt). Precambr Res 243:149–167

Burke K, Sengor C (1986) Tectonic escape in the evolution of the continental crust, vol 14. American Geophysical Union, Geodynamic Series, pp 41–53

Collins AS, Pisarevsky SA (2005) Amalgamating eastern Gondwana: the evolution of the Circum-Indian Orogens. Earth-Sci Rev 71(3–4):229–270

Collins AS, Windley BF (2002) The tectonic evolution of central and northern Madagascar and its place in the final assembly of Gondwana. J Geol 110:325–339

Cox GM, Lewis JC, Collins SA, Halverson PG, Jourdan F, Foden J, Nettle D, Kattan F (2012) Ediacaran terrane accretion within the Arabian-Nubian Shield. Gondwana Res 21:341–352

Dalziel IW (1991) Pacific margins of Laurentia and East Antarctica-Australia as a conjugate rift pair: evidence and implications for an Eocambrian supercontinent. Geology 19(6):598–601

Dalziel IWD (1997) Neoproterozoic-paleozoic geography and tectonics: review, hypothesis, environmental speculation. Geol Soc Am Bull 109:16–42

Dalziel IWD, Mosher S, Gahagan LM (2000) Laurentia-Kalahari collision and the assembly of Rodinia. J Geol 108:499–513

Dardir AA, Awadallah MF, Abu Zeid KM (1982) A new contribution to the geology of Gebel Dokhan Volcanics, Eastern Desert, Egypt. Ann Geol Surv Egypt 12:19–27

Davies FB (1981) Reconnaissance geologic map of the Wadi Thalbah Quadrangle, sheet 26/36A, Kingdom of Saudi Arabia, scale 1:100,000 Geol. Map GM Saudi Arabia Dir. Gen. Miner. Resour., 32 pp

Dawoud M, Eliwa HA, Traversa G, Attia MS, Itaya T (2006) Geochemistry, mineral chemistry and petrogenesis of a Neoproterozoic dyke swarm in the north Eastern Desert, Egypt. Geol Mag 143:115–135

de Wall H, Greiling RO, Sadek MF (2001) Post-collisional shortening in the Late Pan-African Hamisana high strain zone, SE Egypt: field and magnetic fabric evidence. Precambr Res 107:179–194

Dewey JF (1988) Extensional collapse of orogens. Tectonics 7:1123–1139

Dubois A, Odonne F, Massonnat G, Lebourg T, Fabre R (2002) Analogue modelling of fault reactivation: tectonic inversion and oblique remobilization of grabens. J Struct Geol 24:1741–1752

Duncan IJ, Rivard B, Arvidson RE, Sultan M (1990) Structural interpretation and tectonic evolution of a part of the Najd Shear Zone (Saudi Arabia) using Landsat thematic-mapper data. Tectonophysics 178:309–335

Eby N (1992) Chemical subdivision of the A-type granitoids: petrogenetic and tectonic implications. Geology 20:641–644

El Bayoumi RM, Hassanein SM (1983) Ophiolite mélange complex, Wadi Mubarak area, Eastern Desert. Int Basement Tect Assoc Publ 5:45–52

El Bayoumi RMA, Greiling RO (1984) Tectonic evolution of a Pan-African plate margin in southeastern Egypt—a suture zone overprinted by low angle thrusting? In: Klerkx J, Michot J (eds) African geology. Tervuren, pp 47–56

El-Bialy MZ (1999) Geology of the basement rocks of Abu Durba–Abu Haswa area, southwestern Sinai, Egypt. MSc thesis, Suez Canal University, Ismailia

El-Bialy MZ (2010) On the Pan-African transition of the Arabian-Nubian Shield from compression to extension: the post-collision Dokhan volcanic suite of Kid-Malhak region, Sinai, Egypt. Gondwana Res 17:26–43

El-Bialy MZ, Hassen IS (2012) The Late Ediacaran (580–590 Ma) onset of anorogenic alkaline magmatism in the Arabian-Nubian Shield: Katherina A type rhyolites of Gabal Ma'ain, Sinai, Egypt. Precambr Res 216–219:1–22

El-Bialy MZ, Omar MM (2015) Spatial association of Neoproterozoic continental arc I-type and post-collision A-type granitoids in the Arabian-Nubian Shield: the Wadi Al-Baroud Older and Younger Granites, North Eastern Desert, Egypt. J Afr Earth Sci 103:1–29

El-Desoky HM, Khalil AE, Salem AA (2015) Ultramafic rocks in Gabal El-Rubshi, Central Eastern Desert, Egypt: petrography, mineral chemistry, and geochemistry constraints. Arab J Geosci 8:2607–2631

El Desoky HM, Mezayen AM, Serag AE (2014) Petrology, geochemistry and petrogenetic aspects of Ediacaran Dokhan Volcanics at Wadi Zareib, Central Eastern Desert, Egypt. Stand Global J Geol Explor Res 1:53–73

El-Gaby S (1983) Architecture of the Egyptian basement complex. Int Basement Tect Assoc Publ 5:1–8

El-Gaby S (1994) Geologic and tectonic framework of the Pan-African orogenic belt in Egypt. In: 2nd international conference geology of the Arab World. Cairo University, pp 3–17

El-Gaby S, El-Nady O (1983) Meatiq mantled gneiss dome, Eastern Desert, Egypt. Int Basement Tect Assoc Publ 5:131–135

El-Gaby S, El-Nady O, Khudeir A (1984) Tectonic evolution of the basement complex in the Central Eastern Desert of Egypt. Geol Rundsch 73:1019–1036

El-Gaby S, List FK, Tehrani R (1988) Geology, evolution and metallogenesis of the Pan-African belt in Egypt. In: El-Gaby S, Greiling RO (eds) The Pan-African belt of NE Africa and adjacent areas. Earth Evolution Sciences Vieweg and Sohn, Wiesbaden, pp 17–68

El-Gaby S, List FK, Tehrani R (1990) The basement complex of the Eastern Desert and Sinai. In: Rushdi S (ed) The geology of Egypt. Balkema, Rotterdam, pp 175–184

Eliwa HA (2000) Petrology, geochemistry, mineral chemistry and petrogenesis of Samr El-Qaa Volcanics, North Eastern Desert, Egypt. Sci J Fac Sci Minufiya Univ 14:1–45

Eliwa HA, Kimura J-I, Itaya T (2006) Late Proterozoic Dokhan Volcanics, North Eastern Desert, Egypt: geochemistry and petrogenesis. Precambr Res 151:31–52

Eliwa HA, Abu El-Enen MM, Khalaf IM, Itaya T, Murata M (2008) Metamorphic evolution of Neoproterozoic metapelites and gneisses in Sinai, Egypt: insights from petrology, mineral chemistry and K-Ar age dating. J Afr Earth Sci 51:107–122

Eliwa H, Breitkreuz C, Khalaf I, El Gameel K (2010) Depositional styles of Early Ediacaran terrestrial volcano-sedimentary succession in Gebel El Urf area, North Eastern Desert, Egypt. J Afr Earth Sci 57:328–344

Eliwa HA, El-Bialy MZ, Murata M (2014a) Ediacaran post-collisional volcanism in the Arabian-Nubian Shield: the high-K calc-alkaline

Dokhan Volcanics of Gabal Samr El-Qaa (592 ± 5 Ma), North Eastern Desert, Egypt. Precambr Res 246:180–207

Eliwa HA, Breitkreuz C, Murata M, Khalaf IM, Bühler B, Itaya T, Takahashi T, Hirahara Y, Miyazaki T, Kimu ra J-I, Shibata T, Koshi Y, Kato Y, Ozawa H, Daas MA, El Gameel K (2014b) SIMS zircon U-Pb and mica K-Ar geochronology, and Sr-Nd isotope geochemistry of Neoproterozoic granitoids and their bearing on the evolution of the north Eastern Desert, Egypt. Gondwana Res 25:1570–1598

El Kalioubi BA, El Ramly MF (1991) Nomenclature, origin and tectonic setup of the "granite" suite at Wadi Shait, South Eastern Desert, Egypt. Ann Geol Surv Egypt 17:1–17

El-Nisr SA, Surour AA, Moufti AMB (2014) Geochemistry and petrogenesis of dyke swarms in NW Sinai, Egypt: a case of transition from compressional to extensional regimes during the late Neoproterozoic. J Tethys 2:160–177

El Ramly MF, Akaad MK (1960) The basement complex in the Central-Eastern Desert of Egypt between latitudes 24°30′ and 25° 40′N. Geological Survey Egypt, paper No. 8, pp 35

El Ramly MF (1972) A new geological map the basement rocks in the Eastern and South-Western Deserts of Egypt. Scale 1:1,000,000. Ann Geol Surv Egypt 2:1–18

El Ramly MF, Hilmy ME, Ali MM, Hassan OA (1982) Petrological and petrochemical studies on some Young Granite masses in the South Eastern Desert of Egypt. Ann Geol Surv Egypt 12:73–102

El Ramly MF, Greiling R, Kröner A, Rashwan AAA (1984) On the tectonic evolution of the Wadi Hafafit area and environs, Eastern Desert of Egypt. Bull Fac Earth Sci King Abdulaziz Univ 6:113–126

El-Sayed MM (2006) Geochemistry and petrogenesis of the post-orogenic bimodal dyke swarms in NW Sinai, Egypt: constraints on the magmatic–tectonic processes during the late Precambrian. Chem Erde 66:129–141

El-Sayed MM, Hassanen MA, Obeid MA (1999) Geochemistry and petrogenesis of Late Precambrian tonalite-granodiorite-syenogranite series at Umm Shaddad district (Egypt). N Jb Miner Abh 175:29–51

El-Sayed MM, Mohamed FH, Furnes H, Kanisawa S (2002) Geochemistry and petrogenesis of the Neoproterozoic granitoids in the Central Eastern Desert, Egypt. Chem Erde 62:317–346

El-Sayed MM, Shalaby MH, Hassanen MA (2003) Petrological and geochemical constraints on the tectonomagmatic evolution of the Late Neoproterozoic granitoid suites in the Gattar area, North Eastern Desert, Egypt. N Jb Miner Abh 178:239–275

El-Sayed MM, Obeid MA, Furnes H, Moghazi AM (2004) Late Neoproterozoic volcanism in the southern Eastern Desert, Egypt: petrological, structural and geochemical constraints on the tectonic-magmatic evolution of the Allaqi Dokhan volcanic suite. N Jb Miner Abh 180:261–286

El-Shafei MK, Kusky TM (2003) Structural and tectonic evolution of the Neoproterozoic Feiran–Solaf metamorphic belt Sinai Peninsula: implications for the closure of the Mozambique Ocean. Precambr Res 123:269–293

El-Sharkawy MA, El-Bayoumi RM (1979) The ophiolites of Wadi Ghadir area, Eastern Desert, Egypt. Ann Geol Surv Egypt 9:125–135

El-Shazly EM (1964) On the classification of the Precambrian and other rocks of magmatic affiliation in Egypt. In: UAR Int. Geol. Congr. XVII, Sec. 10

El-Shazly EM (1977) The geology of the Egyptian region. In: Nairn AEM, Kanes WH, Stehli FG (eds) The ocean basins and margins. Plenum Press, pp 379–444

Engel AEJ, Dixon TH, Stern RJ (1980) Late Precambrian evolution of Afro-Arabian crust from ocean arc to craton. Geol Soc Am Bull 91:699–706

Farahat ES (2010) Neoproterozoic arc–back-arc system in the Central Eastern Desert of Egypt: evidence from supra-subduction zone ophiolites. Lithos 120:293–308

Farahat ES, Azer MK (2011) Post-collisional magmatism in the northern Arabian-Nubian Shield: the geotectonic evolution of the alkaline suite at Gebel Tarbush area, south Sinai, Egypt. Chem Erde 71:247–266

Farahat ES, El Mahallawi MM, Hoinkes G, Abdel Aal AY (2004) Continental back-arc basin origin of some ophiolites from the Eastern Desert of Egypt. Miner Petrol 82:81–104

Farahat ES, Mohamed HA, Ahmed AF, El Mahallawi MM (2007) Origin of I- and A-type granitoids from the Eastern Desert of Egypt: implications for crustal growth in the northern Arabian-Nubian Shield. J Afr Earth Sci 49:43–58

Farahat ES, Zaki R, Hauzenberger C, Sami M (2011) Neoproterozoic calc-alkaline peraluminous granitoids of the Deleihimmi pluton, Central Eastern Desert, Egypt: implications for transition from late- to post-collisional tectonomagmatic evolution in the northern Arabian-Nubian Shield. Geol J 46:544–560

Fawzy KM (2017) Characterization of a post orogenic A-type granite, Gabal El Atawi, Central Eastern Desert, Egypt: geochemical and radioactive perspectives. Open J Geol 7:93–117

Finger F, Dorr W, Gerdes A, Gharib M, Dawoud M (2008) U-Pb zircon ages and geochemical data for the Monumental Granite and other granitoid rocks from Aswan, Egypt: implications for the geological evolution of the western margin of the Arabian Nubian Shield. Miner Petrol 93:153–183

Fossen H, Tikoff B (1998) Extended models of transpression/transtension and application to tectonic settings. In: Holdsworth RE, Strachan RA, Dewey JF (eds) Continental transpressional and transtensional tectonics. J Geol Soc Lond, Special Pub 135, pp 15–33

Fowler TJ (2001) Pan-African granite emplacement mechanisms in the Eastern Desert, Egypt. J Afr Earth Sci 32:61–86

Fowler A (2015) Pencil structures in the Central Eastern Desert, Egypt: what can they tell us? In: World Multidisciplinary Earth Sciences Symposium (WMESS), Prague, Czech Republic, September, 2015. WMESS Abstracts, p 15

Fowler A, Abdeen MM (2014) Reappraisal of strain estimations and measurement methods in the Hammamat Group sediments: comparison of primary and secondary grain fabrics with new data from Wadi Zeidun and Wadi Arak basins, CED, Egypt. Precambr Res 247:1–32

Fowler A, El Kalioubi B (2002) The Migif-Hafafit gneissic complex of the Egyptian Eastern Desert: fold interference patterns involving multiply deformed sheath folds. Tectonophysics 346:247–275

Fowler A, El Kalioubi B (2004) Gravitational collapse origin of shear zones, foliations and linear structures in the Neoproterozoic cover nappes, Eastern Desert, Egypt. J Afr Earth Sci 38:23–40

Fowler TJ, Osman AF (2001) Gneiss-cored interference dome associated with two phases of late Pan-African thrusting in the Central Eastern Desert, Egypt. Precambr Res 108:17–43

Fowler A, Hassen IS (2008) Extensional tectonic origin of gneissosity and related structures of the Feiran-Solaf metamorphic belt, Sinai, Egypt. Precambr Res 164:119–136

Fowler A, Osman AF (2009) The Sha'it-Nugrus shear zone separating central and south eastern deserts, Egypt: a post-arc collision low-angle normal ductile shear zone. J Afr Earth Sci 53:16–32

Fowler A, Osman AF (2013) Sedimentation and inversion history of three molasse basins of the western Central Eastern Desert of Egypt: implications for the tectonic significance of Hammamat basins. Gondwana Res 23:1511–1534

Fowler A, Ali KG, Omar SM, Eliwa H (2006) The significance of gneissic rocks and synmagmatic extensional ductile shear zones of the Barud area for the tectonics of the North Eastern Desert, Egypt. J Afr Earth Sci 46:201–220

Fowler A, Khamees H, Dowidar H (2007) El Sibai gneissic complex, Central Eastern Desert, Egypt: folded nappes and syn-kinematic

gneissic granitoid sheets -not a core complex. J Afr Earth Sci 49:119–135
Fowler A, Hassen IS, Osman AF (2010a) Neoproterozoic structural evolution of SE Sinai, Egypt: I. Re-investigation of the structures and deformation kinematics of the Um Zariq and Malhaq Formations, northern Wadi Kid area. J Afr Earth Sci 58:507–525. https://doi.org/10.1016/j.jafrearsci.2010.05.009
Fowler A, Hassen IS, Osman AF (2010b) Neoproterozoic structural evolution of SE Sinai, Egypt: II. Convergent tectonic history of the continental arc Kid Group. J Afr Earth Sci 58:526–546. https://doi.org/10.1016/j.jafrearsci.2010.05.011
Fowler A, Hassen I, Hassan M (2015) Tectonic evolution and setting of the Sa'al complex, southern Sinai, Egypt: a Proterozoic continental back-arc rift model. J Afr Earth Sci 104:103–131
Frisch W, Al-Shanti A (1977) Ophiolite belts and the collision of island arcs in the Arabian Shield. Tectonophysics 43:293–306
Fritz H, Messner M (1999) Intramontane basin formation during oblique convergence in the Eastern Desert of Egypt: magmatically versus tectonically induced subsidence. Tectonophysics 315:145–162
Fritz H, Puhl J (1996) Granitoid emplacement in a shear-extensional setting: a semiquantitative approach from physical parameters (Eastern Desert, Egypt). Zbl Geol Palaont Teil 1:257–276
Fritz H, Wallbrecher E, Khudier AA, Abu El Ela F, Dallmeyer RD (1996) Formation of Neoproterozoic metamorphic core complexes during oblique convergence, Eastern Desert, Egypt. J Afr Earth Sci 23:311–329
Fritz H, Dalmeyer DR, Wallbrecher E, Loizenbauer J, Hoinkes G, Neumayr P, Khudeir AA (2002) Neoproterozoic tectonothermal evolution of the Central Eastern Desert, Egypt: a slow velocity tectonic process of core complex exhumation. J Afr Earth Sci 34:543–576
Fritz H, Tenczer V, Hauzenberger C, Wallbrecher E, Muhongo S (2009) Hot granulite nappes—Tectonic styles and thermal evolution of the Proterozoic granulite belts in East Africa. Tectonophysics 477:160–173
Fritz H, Abdelsalam M, Ali KA, Bingen B, Collins AS, Fowler AR, Ghebreab W, Hauzenberger CA, Johnson PR, Kusky TM, Macey P, Muhongo S, Stern RJ, Viola G (2013) Orogen styles in the East African Orogen: a review of the Neoproterozoic to Cambrian tectonic evolution. J Afr Earth Sci 86:65–106
Fritz H, Loizenbauer J, Wallbrecher E (2014) Magmatic and solid state structures of the Abu Ziran pluton: deciphering transition from thrusting to extension in the Eastern Desert of Egypt. J Afr Earth Sci 99:122–135
Gad S, Kusky T (2006) Lithological mapping in the Eastern Desert of Egypt, the Barramiya area, using Landsat thematic mapper (TM). J Afr Earth Sci 44:196–202
Gamal El Dien H, Hamdy M, Abu El-Ela A, Abu-Alam T, Hassan A, Kil Y, Mizukami T, Soda Y (2016) Neoproterozoic serpentinites from the Eastern Desert of Egypt: insights into Neoproterozoic mantle geodynamics and processes beneath the Arabian-Nubian Shield. Precambr Res 286:213–233
Garson MS, Shalaby IM (1976) Precambrian-Lower Paleozoic plate tectonics and metallogenesis in the Red Sea region. Geol Assoc Canada Spec 14:573–596
Gass IG (1977) The evolution of the Pan-African crystalline basement in NE Africa and Arabia. J Geol Soc Lond 134:129–138
Gass IG (1981) Pan-African (Upper Proterozoic) plate tectonics of the Arabian-Nubian Shield. In: Kröner A (ed) Precambrian plate tectonics. Elsevier, Amsterdam, pp 388–405
Gass IG (1982) Upper Proterozoic (Pan-African) calc-alkaline magmatism in north-eastern Africa and Arabia. In: Thorpe RS (ed) Andesites. Wiley & Sons, pp 591–609
Genna A, Nehlig P, Le Goff E, Guerrot C, Shanti M (2002) Proterozoic tectonism of the Arabian Shield. Precambr Res 117:21–40
Ghebreab W (1999) Tectono-metamorphic history of Neoproterozoic rocks in eastern Eritrea. Precambr Res 98:83–105
Greenberg JK (1981) Characteristics and origin of Egyptian Younger Granites: summary. Geol Soc Am Bull 2:749–840
Greiling RO (1987) Directions of Pan-African thrusting in the Eastern Desert of Egypt derived from lineation and strain data. In: Matheis G, Schandelmeier H (eds) Current research in African Earth sciences. Balkema, Rotterdam, pp 83–86
Greiling RO, Rashwan AA (1994) Large-scale shear-zones and related mineral deposits: examples from the Nubian Shield (Proterozoic, Egypt). Afr Geosci Rev 1:503–514
Greiling RO, Rashwan, AA (1995) The structure of the Nubian Shield in Egypt and its importance for the geometry and distribution of mineral deposits. Egyptian Geological Survey Paper No. 69:199–209
Greiling RO, Kröner A, El-Ramly MF, Rashwan AA, El-Gaby S, Greiling RO (1988) Structural relationships between the southern and central parts of the Eastern Desert of Egypt: details of a Fold and Thrust Belt. In: El-Gaby S, Greiling RO (eds) The Pan-African Belt of NE Africa and adjacent areas. Vieweg & Sohn, pp 121–145
Greiling RO, Rashwan AA, El Ramly MF, Kamal El Din GM (1993) Towards acomprehensive structural synthesis of the (Proterozoic) Arabian-Nubian Shield in E. Egypt. In: Thorweihe U, Schandelmeier H (eds) Geoscientific research in Northeast Africa. Balkema, Rotterdam, pp 15–19
Greiling RO, Abdeen MM, Dardir AA, El Akhal H, El Ramly MF, Kamal El Din GM, Osman AF, Rashwan AA, Rice AH, Sadek MF (1994) A structural synthesis of the Proteorozoic Arabian-Nubian Shield in Egypt. Geol Rundsch 83:484–501
Greiling RO, de Wall H, Warr LN, Naim GM, Hussein AA, Sadek MF, Abdeen MM, El Kady MF, Makhlouf A (1996) Basement structure in eastern Egypt: quantitative perspectives for the second century. In: Proceedings of the geological survey of Egypt Centennial conference (1996), pp 289–302
Greiling RO, de Wall H, Sadek MF, Dietl C (2014) Late Pan-African granite emplacement during regional deformation, evidence from magnetic fabric and structural studies in the Hammamat-Atalla area, Central Eastern Desert of Egypt. J Afr Earth Sci 99:109–121
Greiling RO, Kröner A, El Ramly MF (1984) Structural interference patterns and their origin in the Pan-African basement of the southeastern desert of Egypt. In: Kro¨ner A, Greiling R (eds), Precambrian Tectonics Illustrated. E. Schweizerbart'sche Verlagsbuchhandlung, Stuttgart, pp. 401–412
Grothaus B, Eppler D, Ehrlich R (1979) Depositional environment and structural implication of the Hammamat formation, Egypt. Ann Geol Surv Egypt 9:564–590
Habib ME (1987) Microplate accretion model for the Pan-African basement between Qena-Safaga and Qift-Quseir roads, Egypt. Bull Fac Sci Assiut Univ 16:199–239
Habib ME, Ahmed AA, El Nady OM (1985a) Two orogenies in the Meatiq area of the Central Eastern Desert, Egypt. Precambr Res 30:83–111
Habib ME, Ahmed AA, El Nady OM (1985b) Tectonic evolution of the Meatiq infrastructure, Central Eastern Desert, Egypt. Tectonics 4:613–627
Hagag W, Moustafa R, Hamimi Z (2018) Neoproterozoic evolution and Najd-related transpressive shear deformations along Nugrus Shear Zone, South Eastern Desert, Egypt (implications from field—structural data and AMS-technique). Geotectonics 52:114–133
Halverson GP, Hurtgen MT, Porter SM, Collins AS (2009) Neoproterozoic-Cambrian Biogeochemical Evolution. In: Gaucher C, Sial AN, Halverson GP, Frimmel HE (eds) Neoproterozoic-Cambrian tectonics, global change and evolution: a focus on Southwestern Gondwana. Developments in Precambrian Geology, vol 16. Elsevier, pp 351–365

Hamdy MM, Abd El-Wahed MA, Thabet IA (2017) Origin of dyke swarms in Wadi El Redi-Wadi Lahami area, southern Eastern Desert of Egypt. Arab J Geosci 10:414

Hamimi Z (2000) Quantitative strain analyses of some late-tectonic Hammamat sediments, Eastern Desert, Egypt. Egypt J Geol 44:85–107

Hamimi Z, Abd El-Wahed M, Gahlan HA, Kamh SZ (2019) Tectonics of the Eastern Desert of Egypt: key to understanding the Neoproterozoic evolution of the Arabian-Nubian Shield (East African Orogen). In: Bendaoud A, Hamimi Z, Hamoudi M, Djemai S, Zoheir B (eds) Geology of the Arab world—an overview. Springer Geology, pp 1–81. https://doi.org/10.1007/978-3-319-96794-3_1

Hamimi Z, El Amawy MA, Wetait M (1994) Geology and structural evolution of El Shalul dome and environs, Central Eastern Desert, Egypt. Egypt J Geol 38:575–595

Hamimi Z, El-Fakharani A, Abdeen M (2014) Polyphase deformation history and strain analysis of the post-amalgamation depositional basins in the Arabian-Nubian Shield: evidence from Fatima, Ablah and Hammamat basins. In special issue: Arabian-Nubian Precambrian basement geology—progress and developments (eds AR Fowler, RO Greiling and MM Abdeen). J Afr Earth Sci 99(1):64–92

Hamimi Z, El-Fakharani A, Emam A, Barreiro JG, Abdelrahman E, Abo-Soliman MY (2018) Reappraisal of the kinematic history of Nugrus Shear Zone using PALSAR and Microstructural data: implications for the tectonic evolution of the Eastern Desert Tectonic Terrane, Northern Nubian Shield. Arab J Geosci (in press)

Hamimi Z, El-Shafei M, Kattu G, Matsah M (2013) Transpressional regime in southern Arabian Shield: insights from Wadi Yiba Area, Saudi Arabia. Miner Petrol 107:849–860

Hamimi Z, Hagag W (2017) A new tectonic model for Abu-Dabbab seismogenic zone (Eastern Desert, Egypt): evidence from field-structural, EMR and seismic data. Arab J Geosci 10:11. https://doi.org/10.1007/s12517-016-2786-y

Hamimi Z, Matsah M, El-Shafei M, El-Fakharani A, Shujoon A, Al-Jabali M (2012) Wadi Fatima thin-skinned Foreland FAT Belt: a post Amalgamation Marine Basin in the Arabian Shield. Open J Geol 2:271–293

Hamimi Z, Zoheir BA, Younis MH (2015) Polyphase deformation history of the Eastern Desert tectonic terrane in northeastern Africa. In: XII International Conference "New Ideas in Earth Sciences". Moscow, April 2015 (Abstract)

Hassaan MM, El-Desoky H (2016) Granites in the tectonic environs of the Nubian Shield, Egypt: geochemical characterizations and new contributions. Curr Res 10:59–103

Hassaan MM, Ramadan TM, Abu El Leil I, Sakr SM (2009) Lithochemical surveys for ore metals in arid region, Central Eastern Desert, Egypt: using Landsat ETM+imagery. Aust J Basic Appl Sci 3:512–528

Hassan IS, Khalifa IH, Ibrahim SK (2001) Petrogenesis of late Precambrian Dokhan Volcanic Suite at Wadi Meknas, southeastern Sinai, Egypt. Egypt J Geol 45:309–323

Hassan M, Abu-Alam TS, Stüwe K, Fowler A, Hassan I (2014) Metamorphic evolution of the Sa'al–Zaghra Complex in Sinai: evidence for Mesoproterozoic Rodinia break-up? Precambr Res 241:104–128

Hassan MA, Hashad AH (1990) Precambrian of Egypt. In: Said R (ed) The geology of Egypt. Balkema, Rotterdam, pp 201–245

Hassanen MA (1997) Post-collision, A-type granites of Homrit Waggat Complex, Egypt: petrological and geochemical constraints on its origin. Precambr Res 82:211–236

Helmy HM, Ahmed AF, El Mahallawi MM, Ali SM (2004) Pressure, temperature and oxygen fugacity conditions of calc-alkaline granitoids, Eastern Desert of Egypt, and tectonic implications. J Afr Earth Sci 38:255–268

Hermina M, Klitzsch E, List FK (1989) Stratigraphic lexicon and explanatory notes to the geological map of Egypt 1:500,000. Conoco Inc., Cairo, Egypt

Hoffman PF (1991) Did the breakout of Laurentia turn Gondwanaland inside-out? Science 252:1409–1412

Holail HM, Moghazi AM (1998) Provenance, tectonic setting and geochemistry of greywackes and siltstones of the Late Precambrian Hammamat Group, Egypt. Sed Geol 116:227–250

Hume WF (1934) Geology of Egypt 2, part 1: the Metamorphic Rocks. Geol Surv Egypt, 293 pp

Hussein AA, Ali MM, El Ramly MF (1982) A proposed new classification of the granites of Egypt. J Volc Geotherm Res 14:187–198

Iacumin M, Marzoli A, El-Metwally AA, Piccirillo EM (1998) Neoproterozoic dyke swarms from southern Sinai (Egypt): geochemistry and petrogenetic aspects. J Afr Earth Sci 26:49–64

Ibrahim S, Cosgrove J (2001) Structural and tectonic evolution of the Umm Gheig/El-Shush region, central Eastern Desert of Egypt. J Afr Earth Sci 33:199–209

Ibrahim SK, Abdel Ghani IM, El-Sawey EH, Dessouky OK (2013) Suture zone molasse-type Hammamat sedimentary rocks of Wadi El Kareim, Central Eastern Desert, Egypt: a re-evolution of setting and origin. Egypt J Geol 57:233–246

Ibrahim WS, Watanabe K, Ibrahim ME, Yonezu K (2015) Neoproterozoic tectonic evolution of Gabal Abu Houdied Area, South Eastern Desert, Egypt: as a part of Arabian-Nubian Shield Tectonics. Arab J Sci Eng 40:1947–1966

Jacobs J, Thomas RJ (2004) Himalayan-type indenter-escape tectonics model for the southern part of the late Neoproterozoic-early Paleozoic East-African-Antarctic Orogen. Geology 32:721–724

Jarrar G (2001) The youngest Neoproterozoic mafic dyke suite in the Arabian Shield: mildly alkaline dolerites from South Jordan—their geochemistry and petrogenesis. Geol Mag 138:309–323

Johnson PR (2003) Post-amalgamation basins of the NE Arabian Shield and implications for Neoproterozoic tectonism in the northern East African Orogen. Precambr Res 123:321–337

Johnson PR (2014) An expanding Arabian-Nubian Shield geochronologic and isotopic dataset: defining limits and confirming the tectonic setting of a Neoproterozoic accretionary orogen. Open Geol J 8:3–33

Johnson PR, Kattan F (2001) Oblique sinistral transpression in the Arabian shield: the timing and kinematics of a Neoproterozoic suture zone. Precambr Res 107:117–138

Johnson PR, Woldehaimanot B (2003) Development of the Arabian-Nubian shield: perspectives on accretion and deformation in the northern East African Orogen and the assembly of Gondwana. In: Yoshida M, Windley BF, Dasgupta S (eds) Proterozoic East Gondwana: supercontinent assembly and breakup. Geological Society, London, Special Publications 206, pp 290–325

Johnson PR, Andresen A, Collins AS, Fowler AR, Fritz H, Ghebreab W, Kusky T, Stern RJ (2011) Late Cryogenian–Ediacaran history of the Arabian-Nubian Shield: a review of depositional, plutonic, structural, and tectonic events in the closing stages of the northern East African Orogen. J Afr Earth Sci 61:167–232

Johnson PR, Halverson GP, Kusky TM, Stern RJ, Pease V (2013) Volcanosedimentary basins in the Arabian-Nubian Shield: markers of repeated exhumation and denudation in a Neoproterozoic accretionary orogen. Geosciences 3:389–445

Jones RR, Holdsworth RE (1998) Oblique simple shear in transpression zones. In: Holdsworth RE, Strachan RA, Dewey JF (eds) Continental transpression and transtension tectonics. Geological Society, London, Special Publications 135, pp 35–40

Kamal El-Din GM, Asran AM (1995) Structural elements and metamorphism controlling the Late Pan-African Hammamat

sediments at the up-stream of Wadi El-Miyah, Central Eastern desert of Egypt. In: Proceedings of the International Conference on 30 years cooperation on the geology of Egypt and related sciences (April 1993). pp 213–228

Kamal El Din GM, Khudeir AA, Greiling RO (1992) Tectonic evolution of a Pan-African gneiss culmination, Gabal El Sibai area, Central Eastern Desert, Egypt. Zbl Geol Paläont Teil 1 1991:2637–2640

Kamal El-Din GM, Rashwan AA, Greiling RO (1996) Structure and magmatism in a molasse-type basin Wadi Hammamat–Wadi Atalla areas. In: Greiling RO, Naim GM, Hussein AA (eds) Excursion across the Pan-African Neoproterozoic basement Qena-Quseir guide book. Egypt Geol Surv Min. Authority, Cairo, Egypt, pp 11–18

Kamal El-Din G, Abdelkareem M (2018) Integration of remote sensing, geochemiocal and field data in the Qena-Safaga shear zone: implications for structural evolution of the Eastern Desert, Egypt. J Afr Earth Sci 141:179–193

Karmakar S, Schenk V (2015) Neoarchean UHT metamorphism and Paleoproterozoic UHT Reworking at Uweinat in the East Sahara Ghost Craton, SW Egypt: evidence from petrology and texturally controlled in situ Monazit e Dating. J Petrol 56(9):1703–1742

Khalaf EA (2010) Stratigraphy, facies architecture, and palaeoenvironment of Neoproterozoic volcanics and volcaniclastic deposits in Fatira area, Central Eastern Desert, Egypt. J Afr Earth Sci 58:405–426

Khalaf EA (2012) Origin and evolution of post-collisional volcanism: an example from Neoproterozoic Dokhan volcanics at Gabal Nugara area, Northeastern Desert, Egypt. Arab J Geosci 5:663–695

Khalil AES, Azer MK (2007) Supra-subduction affinity in the Neoproterozoic serpentinites in the Eastern Desert, Egypt: evidence from mineral composition. J Afr Earth Sci 49:136–152

Khalil AES, Obeid MA, Azer MK, Asimow PD (2017) Geochemistry and petrogenesis of post-collisional alkaline and peralkaline granites of the Arabian-Nubian Shield: a case study from the southern tip of Sinai Peninsula, Egypt. Int Geol Rev 60:998–1018

Khudeir AA, Ahmed EAS (1996) Tectono-sedimentary framework of the molasse sediments, Wadi Abu Shiqieli, Egypt. Egypt J Geol 40:197–226

Khudeir AA, Asran AH (1992) Back-arc Wizr ophiolites at Wadi Um Gheig district, Eastern Desert, Egypt. Bull Fac Sci Assiut Univ 21:1–22

Khudeir AA, El-Gaby S, Kamal El Din GM, Asran AMH, Greiling RO (1995) The pre-Pan-African deformed granite cycle of the Gabal El-Sibai swell, Eastern Desert, Egypt. J Afr Earth Sci 21:395–406

Khudeir A, El Gaby S, El Habaak G, Gahlan H (2003) Metamorphic and tectonic history of Wadi Fiqo area, south Southeastern Desert, Egypt. In: 3rd international conference on the geology of Africa (Assiut, Egypt), vol 2. pp 249–264

Khudeir AA, Abu El-Rus MA, El-Gaby S, El-Nady O, Bishara WW (2008) Sr-Nd isotopes and geochemistry of the infrastructural rocks in the Meatiq and Hafafit core complexes, Eastern Desert, Egypt: evidence for involvement of pre-Neoproterozoic crust in the growth of Arabian-Nubian Shield. Island Arc 17:90–108

Klerkx J, Deutsch S (1977) Resultats preliminaires obtenus par la method Rb/Sr sur l'age des formations Precamhriennes de la region d'Uweinat (Libye). Mus R Afr Centr, Tervuren (Belg), Dep Geol Min Rapp Ann 1976:83–94

Kröner A, Stern RJ (2004) Pan-African orogeny. In: Selley RC, Cocks LRM, Plimer IR (eds) Encyclopedia of Geology, 1. Elsevier, Amsterdam, pp 1–12

Kröner A, Greiling R, Reischmann T, Hussein IM, Stern RJ, Durr S, Krüger J, Zimmer M (1987) Pan-African crustal evolution in the Nubian segment of Northeast Africa. Am Geophys Union Geodyn Ser 17:235–257

Kröner A, Krüger J, Rashwan AAA (1994) Age and tectonic setting of granitoid gneisses in the Eastern Desert of Egypt and south-west Sinai. Geol Rundsch 83:502–513

Kusky TM, Ramadan TM (2002) Structural controls on Neoproterozoic mineralization in the South Eastern Desert, Egypt: an integrated field, Landsat TM, and SIR-C/X SAR approach. J Afr Earth Sci 35:107–121

Kusky TM, Abdelsalam M, Tucker R, Stern RJ (2003) Evolution of the East African and related Orogens, and the assembly of Gondwana. Spec Issue Precambr Res 123:81–344

Li ZX, Bogdanova SV, Collins AS, Davidson A, De Waele B, Ernst RE, Fitzsimons ICW, Fuck RA, Gladkochub DP, Jacobs J, Karlstrom KE, Lu S, Natapov LM, Pease V, Pisarevsky SA, Thrane K, Vernikovsky V (2008) Assembly, configuration, and break-up history of Rodinia: a synthesis. Precambr Res 160:179–210

Liegeois J-P, Stern RJ (2010) Sr–Nd isotopes and geochemistry of granite-gneiss complexes from the Meatiq and Hafafit domes, Eastern Desert, Egypt: no evidence for pre-Neoproterozoic crust. J Afr Earth Sci 57:31–40

Loizenbauer J, Wallbrecher E, Fritz H, Neumayr P, Khudeir AA, Kloetzli U (2001) Structural geology, single zircon ages and fluid inclusion studies of the Meatiq metamorphic core complex: implications for Neoproterozoic tectonics in the Eastern Desert of Egypt. Precambr Res 110:357–383

Lundmark AM, Andresen A, Hassan M, Augland LE, Boghdady GY (2012) Repeated magmatic pulses in the East African Orogen in the Eastern Desert, Egypt: an old idea supported by new evidence. Gondwana Res 22:227–237

Makroum F (2017) Structural interpretation of the Wadi Hafafit culmination: a Pan-African gneissic dome in the central Eastern Desert, Egypt. Lithosphere 9:759–773

Maruyama S, Ikoma M, Genda H, Hirose K, Yokoyama T, Santosh M (2013) The naked planet Earth: most essential pre-requisite for the origin and evolution of life. Geosci Front 4:141–165

Maruyama S, Santosh M (2008) Models on snowball Earth and Cambrian explosion: a synopsis. Gondwana Res 14(1):22–32

Meert JG (2001) Growing Gondwana and rethinking Rodinia. Gondwana Res 4:279–288

Meert JG (2003) A synopsis of events related to the assembly of eastern Gondwana. Tectonophysics 362:1–40

Meert JG (2012) What's in a name? The Columbia (Paleopangea/Nuna) supercontinent. Gondwana Res 21:987–993

Meert JG, Lieberman BS (2004) A palaeomagnetic and palaeobiogeographical perspective on latest Neoproterozoic and Early Cambrian tectonic events. J Geol Soc Lond 161:1–11

Meert JG, Torsvik TH (2003) The making and unmaking of a super-continent: Rodinia revisited. Tectonophysics 375:261–288

Messner M (1996) The Hammamat formation: preliminary comparison of the Wadi Hammamat—Wadi El Qash and Wadi Kareim basins, Pan-African molasse basins, Eastern Desert, Egypt. In: Proceedings of the Geological Survey Egypt Centennial Conference, Cairo. pp 529–545

Miller MM, Dixon TH (1992) Late Proterozoic evolution of the north part of the Hamisana zone, northeast Sudan: constraints on Pan-African accretionary tectonics. J Geol Soc Lond 149:743–750

Moghazi AM (2002) Petrology and geochemistry of Pan-African granitoids, Kab Amiri area, Egypt: implications for tectono-magmatic stages in the Arabian-Nubian Shield evolution. Miner Petrol 75:41–67

Moghazi AM (2003) Geochemistry and petrogenesis of a high-K calc-alkaline Dokhan Volcanic suite, South Safaga area, Egypt: the role of late Neoproterozoic crustal extension. Precambr Res 125:161–178

Moghazi AM, Hassanen MA, Mohamed FH, Ali S (2004) Late Neoproterozoic strongly peraluminous leucogranites, South Eastern Desert, Egypt—petrogenesis and geodynamic significance. Miner Petrol 81:19–41

Moghazi AM, Ali KA, Wilde SA, Zhou Q, Andersen T, Andresen A, Abu El-Enen MM, Stern RJ (2012) Geochemistry, geochronology, and Sr-Nd isotopes of the Late Neoproterozoic Wadi Kid volcano-sedimentary rocks, Southern Sinai, Egypt: implications for tectonic setting and crustal evolution. Lithos 154:147–165

Mohamed FH, El-Sayed MM (2008) Post-orogenic and anorogenic A-type fluorite-bearing granitoids, Eastern Desert, Egypt: petrogenetic and geotectonic implications. Chem Erde 68:431–450

Mohamed FH, Moghazi AM, Hassanen MA (2000) Geochemistry, petrogenesis and tectonic setting of late Neoproterozoic Dokhan-type volcanic rocks in the Fatira area, eastern Egypt. Int J Earth Sci 88:764–777

Moussa EMM, Stern RJ, Manton WI, Ali KA (2008) SHRIMP zircon dating and Sm/Nd isotopic investigations of Neoproterozoic granitoids, Eastern Desert, Egypt. Precambr Res 160:341–356

Murphy JB, Pisarevsky S, Nance RD (2013) Potential geodynamic relationships between the development of peripheral orogens along the northern margin of Gondwana and the amalgamation of West Gondwana. Miner Petrol 107(5)

Naim GM, Hussein AA, Dardir AA, Abdeen MM, Greiling RO, Warr LN (1996) The Wadi Queih area. Lithology and structure in a Molasse-type Basin. In: Greiling RO, Naim GM, Hussein AA (eds) Excursion across the Pan-African, Neoproterozoic basement Qena-Quseir guide book. Egypt Geol Surv Min. Authority, Cairo, Egypt. pp 65–85

Neumayr P, Mogessie A, Hoinkes G, Puhl J (1996) Geological setting of the Meatiq metamorphic core complex in the Eastern Desert of Egypt based on amphibolite geochemistry. J Afr Earth Sci 23:331–345

Neumayr P, Hoinkes G, Puhl J, Mogessie A, Khudeir AA (1998) The Meatiq dome (Eastern Desert, Egypt) a Precambrian metamorphic core complex: petrological and geological evidence. J Metam Geol 16:259–279

Noweir AM, Sewifi BM, Abu El Ela AM (1990) Geology, petrography, geochemistry and petrogenesis of the Egyptian Younger Granites. Qatar Univ Sci Bull 10:363–393

Noweir MA, Ghoneim MF, Abu Alam TS (2005) Deformation phases and tectonic evolution of the Neoproterozoic rocks of Wadi Kareim area, Central Eastern Desert, Egypt. Ann Geol Surv Egypt 28:81–109

Obeid MA, Azer MK (2015) Pan-African adakitic rocks of the north Arabian-Nubian Shield: petrological and geochemical constraints on the evolution of the Dokhan volcanics in the north Eastern Desert of Egypt. Int J Earth Sci 104:541–563

Obeid MA, Khalil AES, Azer MK (2015) Mineralogy, geochemistry, and geotectonic significance of the Neoproterozoic ophiolite of Wadi Arais area, south Eastern Desert, Egypt. Int Geol Rev 58:687–702

O'Connor EA, Bennett JD, Rashwan AA, Nasr BB, Mansour MM, Romani RF, Sadek MF (1994) Crustal growth in the Nubian Shield of south eastern Egypt. In: Proceedings of the International Conference on 30 years cooperation on the geology of Egypt and related sciences (April 1993). pp 189–195

Osman AF (1996) Structural geological and geochemical studies on the Pan-African basement rocks, Wadi Zeidan, Central Eastern Desert, Egypt. Scientific Series of the International Bureau. Forschungszentrum Julich GmbH, vol. 39, 262 pp

Osman AF, El Kalioubi B, Gaafar AS, El Ramly MF (2001) Provenance, geochemistry and tectonic setting of Neoproterozoic molasse-type sediments, North Eastern Desert, Egypt. Ann Geol Surv Egypt 24:93–114

Panien M, Schreurs G, Pfiffner A (2005) Sandbox experiments on basin inversion: testing the influence of basin orientation and basin fill. J Struct Geol 27:433–445

Patchett PJ, Chase CG (2002) Role of transform continental margins in major crustal growth episodes. Geology 30:39–42

Pisarevsky SA, Murphy JB, Cawood PA, Collins AS (2008) Late Neoproterozoic and early Cambrian palaeogeography: models and problems. In: Pankhurst RJ, Trouw RAJ, Brito Neves BB, de Wit MJ (eds) West Gondwana: pre-Cenozoic correlations across the South Atlantic Region. Geological Society, London Special Publications 294, pp 9–31. https://doi.org/10.1144/sp294.20305-8719/08

Powell CMA, Pisarevsky SA (2002) Late Neoproterozoic assembly of East Gondwanaland. Geology 30:3–6

Quick JE (1991) Late Proterozoic transpression on the Nabitah fault system: implications for the assembly of the Arabian shield. Precamb Res 53:119–147

Ragab AI (1987) The Pan-African basement of the northern segment of the Eastern Desert of Egypt: a crustal evolution model and its implications on tectono-stratigraphy and granite types. MERC Ain Shams Univ Earth Sci Ser 1:1–18

Ragab AI (1993) A geodynamic model for the distribution of the oceanic plate slivers within a Pan-African orogenic belt, Eastern Desert, Egypt. J Geodyn 17:21–26

Ragab AI, El Alfy Z (1996) Arc-arc collision model and its implications on a proposed classification of the Pan-African rocks of the Eastern Desert of Egypt. MERC Ain Shams Univ Earth Sci Ser 10:89–101

Ragab AI, El-Kalioubi B, El-Alfy Z (1993a) Petrotectonic assemblages and crustal evolution of the area north of Abu El-Tiyur, central Eastern Desert, Egypt. MERC Ain Shams Univ Earth Sci Ser 7:1–16

Ragab AI, El-Gharbawi RI, El-Alfy Z (1993b) Pan-African tectonostratigraphic assemblages of Gabal Meatiq—Wadi Atalla area, Eastern Desert, Egypt: evidence for arc-arc suturing. MERC Ain Shams Univ Earth Sci Ser 7:131–145

Ragab AI, Osman AF, Hilmy ME, Greiling RO, El Ramly MF (1995) Pan-African sedimentary basement assemblages in Wadi Zeidoun arc terrain, central Eastern Desert, Egypt. MERC Ain Shams Univ Earth Sci Ser 9:27–41

Ramberg H (1975) Superposition of homogeneous strain and progressive deformation in rocks. Bull Geol Inst Univ Uppsala 6:35–67

Ramsay JG (1980) Shear zone geometry: a review. J Struct Geol 2(1–2):83–99

Ramsay JG, Graham RH (1970) Strain variation in shear belts. Can J Earth Sci 7(3):786–813

Rapalini AE (2018) The assembly of Western Gondwana: reconstruction Based on Paleomagnetic Data. In: Geology of Southwest Gondwana. Springer, Cham, pp 3–18

Ressetar R, Monrad JR (1983) Chemical composition and tectonic setting of the Dokhan Volcanic Formation, Eastern Desert, Egypt. J Afr Earth Sci 1:103–112

Rice AHN, Sadek MF, Rashwan AA (1993a) Igneous and structural relations in the Pan-African Hammamat Group, Igla Basin, Egypt. In: Thorweihe U, Schandelmeier H (eds) Geoscientific research in Northeast Africa. Balkema, Rotterdam, pp 35–39

Rice AHN, Osman AF, Abdeen MM, Sadek MF, Ragab AI (1993b) Preliminary comparison of six late- to post-Pan-African molasse basins, E. Desert, Egypt. In: Thorweihe U, Schandelmeier H (eds) Geoscientific research in Northeast Africa. Balkema, Rotterdam, pp 41–45

Ries AC, Shackleton RM, Graham RH, Fitches WR (1983) Pan-African structures, ophiolites and melanges in the east Desert of Egypt: a traverse at 26 North. J Geol Soc Lond 140:75–95

Robin PYF, Cruden AR (1994) Strain and vorticity patterns in ideally ductile transpression zones. J Struct Geol 16(4):447–466

Robinson FA, Foden JD, Collins AS, Payne JL (2014) Arabian Shield magmatic cycles and their relationship with Gondwana assembly:

insights from zircon U-Pb and Hf isotopes. Earth Planet Sci Lett 408:207–225
Rogers JJW, Greenberg JK (1983) Summary of recent work on Egyptian Younger Granites. Ann Geol Surv Egypt 13:185–191
Sadek MF (2008) Geological and structural setting of Wadi Hodein area southeast Egypt with remote sensing applications. Int Archiv Photogramm Rem Sens Spatial Inform Sci 37(B8):1245–1249
Salem AKA, Khalil AE, Ramadan TM (2012) Geology, geochemistry and tectonic setting of Pan-African serpentinites of Um Salim-Um Salatit area, Central Eastern Desert, Egypt. Egypt J Rem Sens Space Sci 15:171–184
Sami M, Ntaflos T, Farahat ES, Mohamed HA, Hauzenberger C, Ahmed AF (2018) Petrogenesis and geodynamic implications of Ediacaran highly fractionated A-type granitoids in the north Arabian-Nubian Shield (Egypt): constraints from whole-rock geochemistry and Sr-Nd isotopes. Lithos 304–307:329–346
Samuel MD (1977) Lithological and sedimentological studies on the red beds of Wadi Igla, Eastern Desert, Egypt. Bull Nat Res Centre Egypt 2:287–297
Samuel MD, Be'eri-Shlevin Y, Azer MK, Whitehouse MJ, Moussa HE (2011) Provenance of conglomerate clasts from the volcano-sedimentary sequence at Wadi Rutig in southern Sinai, Egypt as revealed by SIMS U–Pb dating of zircon. Gondwana Res 20:450–464
Samuel MD, Moussa HE, Azer MK (2007) A-type volcanics in Central Eastern Sinai, Egypt. J Afr Earth Sci 47:203–226. https://doi.org/10.1016/j.jafrearsci.2007.02.006
Sanderson DJ, Marchini WRD (1984) Transpression. J Str Geol 6:449–458
Sarkarinejad K, Azizi A (2008) Slip partitioning and inclined dextral transpression along the Zagros thrust system. Iran J Str Geol 30:116–136
Schmitt AK, Konrad K, Andrews GD, Horie K, Brown SR, Koppers AA, Tamura Y (2018) 40Ar/39Ar ages and zircon petrochronology for the rear arc of the Izu-Bonin-Marianas intra-oceanic subduction zone. Int Geol Rev 60(8):956–976
Schreurs G, Colletta B (1998) Analogue modelling of faulting in zones of continental transpression and transtension. Geol Soc Lond Spec Publ 135(1):59–79
Schürmann HME (1953) The Precambrian of the Gulf of Suez area. In: 19th Int. Geol. Congr. Algiers, CR, Sec. 1:115–135
Schürmann HME (1966) The Precambrian Along the Gulf of Suez and the Northern Part of the Red Sea. E.J. Brill, Leiden. 404 p
Sengör AMC, Natal'in BA (1996) Turkic-type Orogeny and its role in the making of the continental crust. Ann Rev Earth Planet Sci 24:263–337
Shackleton RM (1986) Precambrian collision tectonics in Africa. In: Coward MP, Ries AC (eds) Collision tectonics. Geol Soc Lond Spec Publ 19. pp 329–349
Shackleton RM (1994) Review of Late Proterozoic sutures, ophiolitic melanges and tectonics of eastern Egypt and northeast Sudan. Geol Rundsch 83:537–546
Shackleton RM, Ries AC (1984) The relation between regionally consistent stretching lineations and plate motions. J Struct Geol 6:111–117
Shackleton RM, Ries AC, Graham RH, Fitches WR (1980) Late Precambrian ophiolitic melange in the east Desert of Egypt. Nature 285:472–474
Shafiei Bafti S, Mohajjel M (2015) Structural evidence for slip partitioning and inclined dextral transpression along the SE San-andaj–Sirjan zone, Iran. Int J Earth Sci 104:587–601
Shalaby A (2010) The northern dome of Wadi Hafafit culmination, Eastern Desert, Egypt: structural setting in tectonic framework of a scissor-like wrench corridor. J Afr Earth Sci 57:227–241
Shalaby A, Stüwe K, Makroum F, Fritz H, Kebede T, Klotzli U (2005) The Wadi Mubarak belt, Eastern Desert of Egypt: a Neoproterozoic conjugate shear system in the Arabian-Nubian Shield. Precambr Res 136:27–50
Shalaby A, Stüwe K, Fritz H, Makroum F (2006) The El Mayah molasse basin in the Eastern Desert of Egypt. J Afr Earth Sci 45:1–15
Smith M, O'Connor E, Nasr BB (1999) Transpressional flower structures and escape tectonics: a new look at the Pan-African collision in the Eastern Desert, Egypt. In: de Wall H, Greiling RO (eds) Aspects of Pan-African Tectonics. Bilateral Seminars of the International Bureau 32 Forschungszentrum Julich, Germany. pp 81–82
Sommer H, Kröner A, Lowry J (2017) Neoproterozoic eclogite- to high-pressure granulite-facies metamorphism in the Mozambique belt of east-central Tanzania: a petrological, geochemical and geochronological approach. Lithos 284–285:666–690
Squire RJ, Campbell IH, Allen CM, Wilson CJL (2006) Did the Transgondwanan Supermountain trigger the explosive radiation of animals on Earth? Earth Planet Sci Lett 250:116–133
Stein M, Goldstein SL (1996) From plume head to continental lithosphere in the Arabian Nubian Shield. Nature 382:773–778
Stern RJ (1979) Late Precambrian ensimatic volcanism in the central eastern desert of Egypt. PhD thesis, University of California, San Diego, CA, 210 pp
Stern RJ (1981) Petrogenesis and tectonic setting of Late Precambrian ensimatic volcanic rocks, Central Eastern Desert of Egypt. Precambr Res 16:195–230
Stern RJ (1985) The Najd fault system, Saudi Arabia and Egypt: a Late Precambrian rift related transform system. Tectonics 4:497–511
Stern RJ (1993) Tectonic evolution of the Late Proterozoic East African Orogen: constraints from crustal evolution in the Arabian-Nubian Shield and the Mozambique Belt. In: Thorweihe U, Scandelmeier H (eds) Geoscientific research in Northeast Africa. Balkema, Rotterdam, pp 73–74
Stern RJ (1994) Arc assembly and continental collision in the Neoproterozoic East African Orogen implications for the consolidation of Gondwanaland. Ann Rev Earth Planet Sci 22:319–351
Stern RJ (2002) Crustal evolution in the East African Orogen: a neodymium isotopic perspective. J Afr Earth Sci 34:109–117
Stern RJ (2017) Neoproterozoic formation and evolution of Eastern Desert continental crust—the importance of the infrastructure-superstructure transition. J Afr Earth Sci (in press). http://dx.doi.org/10.1016/j.jafrearsci.2017.01.001
Stern RJ, Gottfried D (1986) Petrogenesis of a Late Precambrian (575–600 Ma) bimodal suite in Northeast Africa. Miner Petrol 92:492–501
Stern RJ, Gottfried D (1989) Late Pan-African magmatism and crustal development in northeastern Egypt. Discuss Geol J 24:371–374
Stern RJ, Hedge CE (1985) Geochronologic and isotopic constraints on Late Precambrian crustal evolution in the Eastern Desert of Egypt. Am J Sci 285:97–127
Stern RJ, Manton WI (1987) Age of Feiran basement rocks, Sinai: implications for late Precambrian evolution in the northern Arabian-Nubian Shield. J Geol Soc Lond 144:569–575
Stern RJ, Manton WI (1988) Discussion on the age of Feiran basement rocks Sinai: implications for late Precambrian crustal evolution in the northern Arabian-Nubian Shield. J Geol Soc Lond 145:1034–1035
Stern RJ, Voegeli DA (1987) Geochemistry, geochronology, and petrogenesis of a Late Precambrian (~590 Ma) composite dike from the North Eastern Desert of Egypt. Geol Rundsch 76:325–341
Stern RJ, Gottfried D, Hedge CE (1984) Late Precambrian rifting and crustal evolution in the Northeastern Desert of Egypt. Geology 12:168–172

Stern RJ, Sellers G, Gottfried D (1988) Bimodal dyke swarms in the North Eastern Desert of Egypt: significance for the origin of late Precambrian "A-type" granites in northern Afro-Arabia. In: El-Gaby S, Greiling RO (eds) The Pan-African Belt of NE Africa and Adjacent Areas. Vieweg & Sohn, pp 147–179

Stern RJ, Kröner A, Manton WI, Reischmann T, Mansour M, Hussein IM (1989) Geochronology of the late Precambrian Hamisana shear zone, Red Sea Hills, Sudan and Egypt. J Geol Soc Lond 146:1017–1030

Stern RJ, Nielsen KC, Best E, Sultan M, Arvidson RE, Kröner A (1990) Orientation of Late Precambrian sutures in the Arabian-Nubian Shield. Geology 18:1103–1106

Stern RJ, Kröner A, Rashwan AA (1991) A Late Precambrian (~710 Ma) high vulcanicity rift in the south Eastern Desert of Egypt. Geol Rundsch 80:155–170

Stern RJ, Johnson PR, Kröner A, Yibas B (2004) Neoproterozoic ophiolites of the Arabian-Nubian Shield. In: Kusky TM (ed) Precambrian ophiolites and related rocks. Developments in Precambrian Geology, vol 13. Elsevier, Amsterdam, pp 95–128

Stern RJ, Mukherjee SK, Miller NR, Ali K, Johnson PR (2013) ~750 Ma banded iron formation from the Arabian-Nubian Shield—implications for understanding Neoproterozoic tectonics, volcanism, and climate change. Precambr Res 239:79–94

Stoeser DB, Camp VE (1985) Pan-African microplate accretion of the Arabian Shield. Geol Soc Am Bull 96:817–826

Sturchio NC, Sultan M, Batiza R (1983) Geology and origin of Meatiq Dome, Egypt: a Precambrian metamorphic core complex? Geology 11:72–76

Sultan M, Arvidson R, Sturchio NC (1986) Mapping of serpentinites in the Eastern Desert of Egypt by using Landsat thematic mapper data. Geology 14:995–999

Sultan M, Arvidson RE, Duncan IJ (1988) Extension of the Najd shear system from Saudi Arabia to the Central Eastern Desert of Egypt based on integrated field and Landsat observations. Tectonics 7:1291–1306

Tavarnelli E, Holdsworth RE, Clegg P, Jones RR, McCaffrey KJW (2004) The anatomy and evolution of a transpressional imbricate zone, Southern Uplands, Scotland. J Str Geol 26:1341–1360

Teyssier C, Tikoff B (1998) Strike-slip partitioned transpression of the San Andreas fault system: a lithospheric-scale approach. Geol Soc Lond Spec Publ 135(1):143–158

Tikoff B, Teyssier C (1994) Strain modeling of displacement-field partitioning in transpressional orogens. J Struct Geol 16:1575–1588

Torsvik TH, Smethurst MA, Meert JG, Van der Voo R, McKerrow WS, Brasier MD, Sturt BA, Walderhaug HJ (1996) Continental break-up and collision in the Neoproterozoic—a tale of Baltica and Laurentia. Earth Sci Rev 40:229–258

Torsvik TH, Cocks LRM (2013) New global palaeogeographical reconstructions for the Early Palaeozoic and their generation. Geol Soc 38(1):5–24. London, Memoirs

Toteu SF, Bertrand JB, Penaye J, Macaudière J, Angoua S, Barbey P (1990) Cameroon: a tectonic keystone in the Pan-African network. In: Lewry JL, Stauffer MR (eds) The early Proterozoic Trans-Hudson Orogen of North America. Geological Association of Canada Special Paper, vol 37. pp 483–496

Tsige L, Abdelsalam MG (2005) Neoproterozoic-Early Paleozoic gravitational tectonic collapse in the southern part of the Arabian-Nubian Shield: the Bulbul Belt of southern Ethiopia. Precambr Res 138:297–318

Unrug R (1996) The assembly of Gondwanaland. Episodes 19:11–20

Unzog W, Kurz W (2000) Progressive development of lattice preferred orientations (LPOs) of naturally deformed quartz within a transpressional collision zone (Panafrican orogen in the Eastern Desert of Egypt). J Struct Geol 22:1827–1835

Vail JR (1983) Pan-African crustal accretion in northeast Africa. J Afr Earth Sci 1:285–294

Vail JR (1985) Pan-African (late Precambrian) tectonic terranes and reconstruction of the Arabian-Nubian Shield. Geology 13:839–842

Wallbrecher E, Fritz H, Khudeir AA, Farahad F (1993) Kinematics of Pan-African thrusting and extension in Egypt. In: Thorweihe U, Schandelmeier H (eds) Geoscientific research in northeast Africa. Balkema, Rotterdam, pp 27–30

Whitehouse MJ, Stoeser DB, Stacey JS (2001a) The Khida terrane geochronological and isotopic evidence for Paleoproterozoic and Archean crust in the eastern Arabian Shield of Saudi Arabia. Gondwana Res 4:200–202

Whitehouse MJ, Windley BF, Stoeser DB, Al-Khirbash S, Ba-Bttat MAO, Haider A (2001b) Precambrian basement character of Yemen and correlations with Saudi Araba and Somalia. Precambr Res 105:357–369

Wilde SA, Youssef K (2000) Significance of SHRIMP U-Pb dating of the Imperial Porphyry and associated Dokhan Volcanics, Gebel Dokhan, north Eastern Desert, Egypt. J Afr Earth Sci 31:403–413

Wilde SA, Youssef K (2001) SHRIMP U–Pb dating of detrital zircons from the Hammamat Group at Gebel Umm Tawat, North-Eastern Desert, Egypt. In: Divi, R.S. & Yoshida, M. Tectonics and Mineralization in the Arabian Shield and its Extensions. IGCP 368 International Conference Abstracts, Jeddah, Saudi Arabia. Gondw Res 4:202–206

Wilde SA, Youssef K (2002) A re-evaluation of the origin and setting of the Late Precambrian Hammamat Group based on SHRIMP U-Pb dating of detrital zircons from Gebel Umm Tawat, North Eastern Desert, Egypt. J Geol Soc Lond 159:595–604

Willis KM, Stern RJ, Clauer N (1988) Age and geochemistry of Late Precambrian sediments of the Hammamat series from the Northeastern Desert of Egypt. Precambr Res 42:173–187

Wipfler EL (1996) Transpressive structures in the Neoproterozoic Ariab-Nakasib Belt, northeast Sudan: evidence for suturing by oblique collision. J Afr Earth Sci 23:347–362

Wulff K (2001) Clockwise P–T-path of granulites at Jebel Uweinat (SW Egypt): Eburnian reworking of Archean crust. Diploma Thesis, University of Kiel

Yoshida M, Suzuki M, Shirahata H, Kojima H, Kizaki K (1983) A review of the tectonic and metamorphic history of the Lützow-Holm Bay region, East Antarctica. In: Oliver RL, James RR, Jago JB (eds) Antarctic earth science. Australian Academy of Science Canberra, pp 44–47

Youssef MM, Zaky KS, Khudeir AA (2001) Finite strain determination in deformed conglomerates of south Wadi Zeidun, Central Eastern Desert, Egypt. Bull Fac Sci Assiut Univ 30:133–145

Zimmer M, Kröner A, Jochum KP, Reischmann T, Todt W (1995) The Gabal Gerf complex: a Precambrian N-MORB ophiolite in the Nubian Shield, NE Africa. Chem Geol 123:29–51

Zoheir BA (2008) Characteristics and genesis of shear zone-related gold mineralization in Egypt: a case study from the Um El Tuyor mine, south Eastern Desert. Ore Geol Rev 34:445–470

Zoheir BA (2011) Transpressional zones in ophiolitic mélange terranes: potential exploration targets for gold in the South Eastern Desert, Egypt. J Geochem Explor 111:23–38

Zoheir BA, Klemm DD (2007) The tectono-metamorphic evolution of the central part of the Neoproterozoic Allaqi-Heiani suture, south Eastern Desert of Egypt. Gondwana Res 12:289–304

Zoheir BA, Lehmann B (2011) Listvenite-lode association at the Barramiya gold mine, Eastern Desert, Egypt. Ore Geol Rev 39:101–115

4 Crustal Evolution of the Egyptian Precambrian Rocks

Robert J. Stern and Kamal Ali

Contents

Abstract

Precambrian basement of the Egyptian sector of the Arabian-Nubian Shield are well exposed on the flanks of the Red Sea and along the border with Sudan, making it an excellent place to study Neoproterozoic processes of crustal growth, obduction–accretion tectonics, and post collisional escape tectonics. We review the published field observations, structural geological analyses, and geochemical and isotopic data to provide an up-to-date overview Neoproterozoic and pre-Neoproterozoic crustal formation in Egypt. Egyptian basement exposures are distributed in three major places: southern Sinai, the Eastern Desert and in the southernmost Western Desert. Neoproterozoic igneous rocks dominate basement exposures in southern Sinai, the Eastern Desert, and the eastern part of the SW Desert, although ~1.0 Ga crust is documented from northernmost basement exposures in southern Sinai. Neoproterozoic basement rocks mainly consist of ophiolite associations, calc-alkaline and alkaline, and immature sediments; these rocks are especially well exposed in the Central Eastern Desert. Older Neoproterozoic basement rocks represent juvenile arc terranes that formed during Upper Tonian–Cryogenian time at ~650–750 Ma around the margins of the Mozambique Ocean. Accretion of juvenile arc and backarc basin systems ended by Late Neoproterozoic time (~620 Ma) when large fragments of east and west Gondwana collided, closing the Mozambique Ocean and forming the East African-Antarctic Orogen. Orogenic collapse and escape tectonics to form NW-SE trending "Najd" shear zones was associated with intense igneous activity in Ediacaran time; these igneous rocks are especially abundant in Sinai and the NE Desert. Exposures along the E-W Nubian Swell from Aswan to Uweinat provide a glimpse of the transition from juvenile Neoproterozoic rocks of the Arabian-Nubian Shield westward into Archean and Paleoproterozoic rocks of the Saharan Metacraton. We have much to learn about the formation of Egypt's crust; the SE Desert is especially poorly known, and there are surprises to be discovered in the NE Desert basement. Future efforts to understand the crust of Egypt will require seismic refraction profiles to resolve its crustal structure; aeromagnetic mapping to resolve its crustal fabric; and drilling to sample basement buried beneath sediments of the vast Western Desert and Mediterranean coast.

R. J. Stern (✉)
Geosciences Department, The University of Texas at Dallas, Richardson, TX 75080, USA
e-mail: rjstern@utdallas.edu

K. Ali
Faculty of Earth Sciences, King Abdulaziz University, Jeddah, 21589, Saudi Arabia

Z. Hamimi et al. (eds.), *The Geology of Egypt*, Regional Geology Reviews,
https://doi.org/10.1007/978-3-030-15265-9_4

4.1 Introduction

Egypt is a large country, the 30th largest nation in area, covering over 1,000,000 km^2. Continental crust (also called "basement") underlies all of Egypt but is only exposed in ~10% of this area. Even though only a small fraction of Egypt exposes basement, these exposures span 800 km N-S and 1000 km E-W (Fig. 4.1). These extensive exposures provide a very useful if incomplete snapshot of Egypt's crust. Egyptian basement is exposed in 3 places: southern Sinai, the Eastern Desert, and in the southernmost Western Desert along the crest of the Nubian Swell.

In this chapter, the basement of Egypt is briefly summarized. These exposures can be subdivided into 5 smaller regions, from NE to SW: (1) Sinai; (2) Northeastern Desert; (3) Central Eastern Desert; (4) South Eastern Desert; and (5) Aswan and the Southwestern Desert subdivisions of the Eastern Desert are briefly reviewed. The first 4 subdivisions are dominated by Neoproterozoic rocks but the last subdivision contains basement of much greater age. In this chapter, we will conclude that the SE Desert and buried crust of the Western Desert are the new frontiers for future research. Our continuing dissection of Sinai strongly suggests that a similar level of effort in these two Eastern Desert terranes would resolve a similarly complex and interesting geologic history in these poorly studied regions.

Another important point is that our knowledge of Egyptian basement is incomplete, most importantly because most of it is hidden. Because ~90% of Egyptian crust is buried beneath sediments, we do not know whether or not the proportion of exposed basement is indicative of the buried crust. Future efforts to map this buried basement using geophysical techniques and sampling via drilling are needed to obtain a less-biased record of Egyptian crust, including both basement exposures and buried crust. Oil companies working in the Western Desert and N. Sinai may have such information. This chapter focuses only on exposed basement rocks.

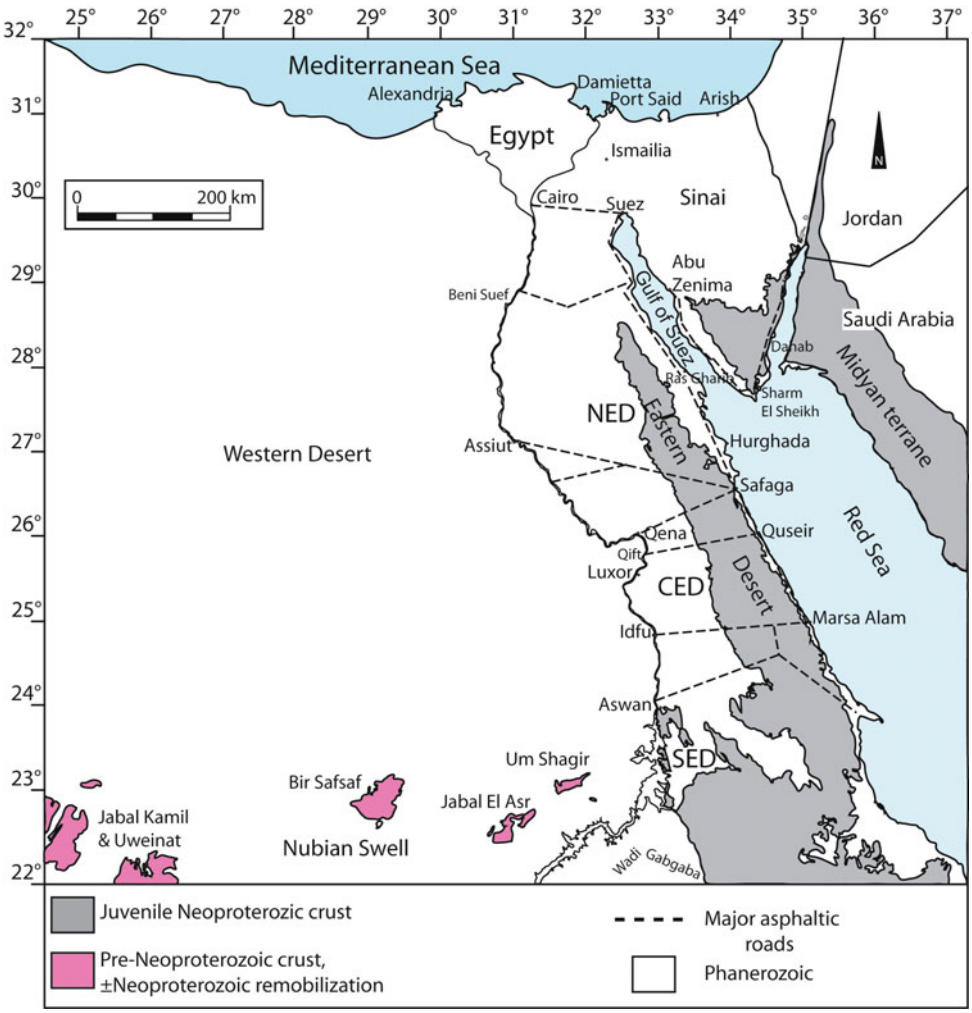

Fig. 4.1 Simplified geologic map of Egypt showing exposed Precambrian basement. NED = Northeastern Desert, CED = Central Eastern Desert, SED = Southeastern Desert

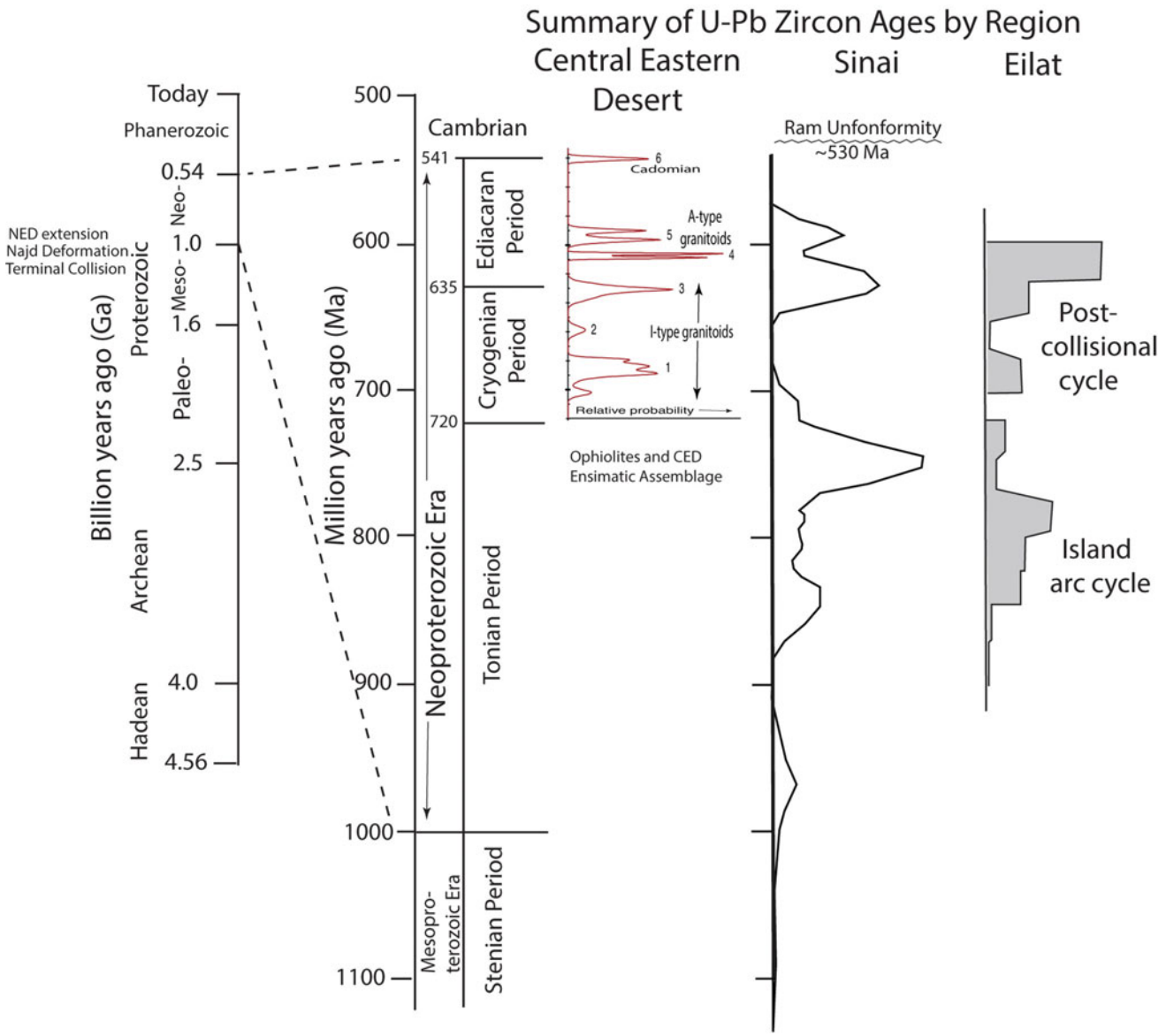

Fig. 4.2 Late Proterozoic temporal evolution of Egypt. Left: Geologic time, from Walker et al. 2012. Neoproterozoic time, showing time subdivisions used here. Also shown are the six magmatic pulses identified by Augland et al. (2012) for the Central Eastern Desert and relative crustal proportions as reflected by detrital zircons in Ediacaran terrestrial sediments (Samuel et al. 2011). The Rum unconformity—which signals cratonization of the ANS—is best exposed in Jordan and Israel but also eastern Sinai (Powell et al. 2014). This unconformity marks when the ANS—including the Eastern Desert—cooled and cratonized. "Cadomian" pulse ~540 Ma may be a far-field expression of Cadomian igneous activity as recently identified on the northern margin of the Arabian Plate (Stern et al. 2016a, b). Modified after Stern (2018) by adding summary curves for Sinai crust (Samuel et al. 2011) and exposures near Eilat (Morag et al. 2011)

When describing the basement of Egypt, it is essential to use the internationally-accepted subdivision of Precambrian time. This is shown in simplified form on the left side of Fig. 4.2, modified from Walker et al. (2012). The Neoproterozoic era is emphasized because the vast majority of exposed Egyptian basement rocks formed during this time period.

The crust of Egypt stabilized at the end of Ediacaran time. In general, stabilization of the crust follows cessation of igneous activity, which allows the crust to cool and strengthen. Further strength is gained from cooling and thickening of the underlying mantle lithosphere, which also happens after igneous activity stops. This strengthening of the continental crust and lithospheric mantle is often referred to as "cratonization". The great pulse of Neoproterozoic igneous activity in Egypt was over by ~580 Ma, although a minor "Cadomian" pulse occurred ~540 Ma (Augland et al. 2012). The clearest evidence of Egyptian cratonization is

cutting of the Rum Unconformity, which was completed by ~530 Ma. This unconformity is beautifully preserved in Jordan, Israel, and Saudi Arabia (Powell et al. 2014) but is only observed in Egypt in Sinai and in the far NE Desert. Elsewhere in Egypt, evidence of the Rum unconformity was obliterated by especially Cretaceous uplift, erosion, and deposition of the Nubian Sandstone.

4.2 Sinai

Precambrian basement in Sinai is exposed as a "V" with two arms, a short western arm extending NW along the eastern margin of the Gulf of Suez to ~29°N and a longer eastern arm extending to the border with Israel and beyond (Fig. 4.3). Sinai basement exposures encompass ~10,000 km^2 and consist of ~80% granite and ~20% volcanics and sediments (Stern and Hedge 1985). Exposed basement can be further subdivided into 3 groups, from oldest to youngest: (1) metamorphic complexes; (2) calc-alkaline; and (3) within-plate granitoids. Ediacaran rocks dominate over Cryogenian, Tonian, and Stenian rocks. These rocks are further discussed below.

The basement geology of Sinai can be simply described as islands of Tonian–Cryogenian metamorphic rocks floating in a sea of Ediacaran granites, all cut by Ediacaran dykes. From N to S, the four main metamorphic complexes exposed in Sinai are Taba, Sa'al, Feiran-Solaf, and Kid. Each of these metamorphic belts tells a different story about what existed in the region before the Ediacaran granite flood. Taba lies in the

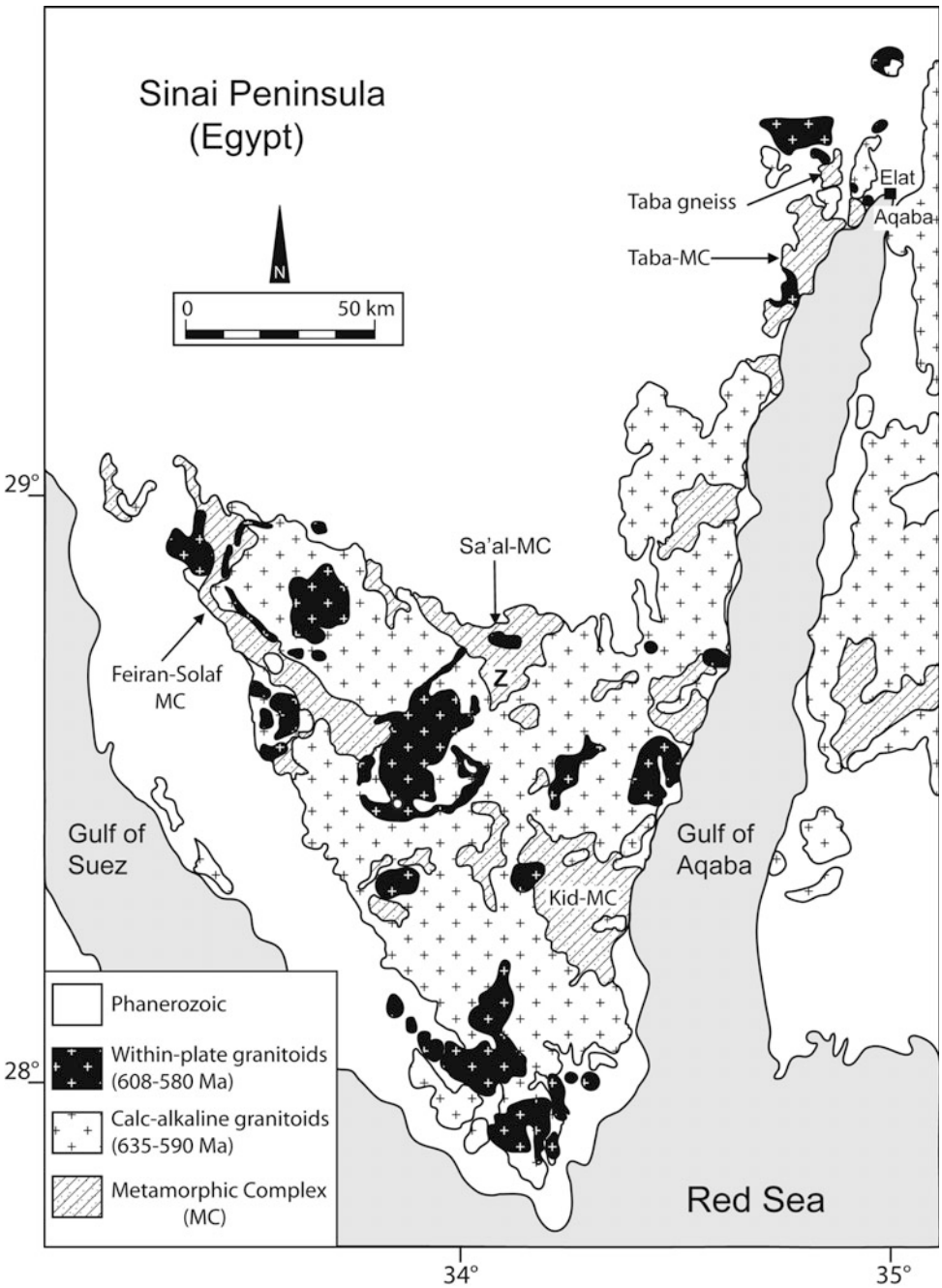

Fig. 4.3 Geological map of Sinai, showing the distribution of the main rock units and the main metamorphic complexes (MC) (after Eyal et al. 1980; Be'eri-Shlevin et al. 2009a, b). Z = location of Wadi Zaghra

far north, near the border with Israel. Basement exposures of the Taba complex extend for ~20 km along the northernmost western margin of the Gulf of Aqaba. This basement was uplifted associated with Late Neogene transtension along the Dead Sea Transform fault and broken up into the three small blocks, from S to N: Taba (Egypt), Elat, and Roded (Israel). Exposures of Tonian–Cryogenian metamorphic rocks are dominated by narrow E-W trending belts of metapelite separated by orthogneiss, all intruded by Ediacaran granites and dykes (Abu El-Enen et al. 2004). Amphibolite-facies metamorphism to ~640 °C and 6 kbar is documented (Abu El-Enen et al. 2004). Basement rock exposures in ED and Sinai are very similar to that exposed in the Elat Block and Roded Block in southernmost Israel (Morag et al. 2011). Basement exposures in this region preserve a remarkable variety of Neoproterozoic lithologies and ages (Abu El-Enen et al. 2004; Morag et al. 2011), in part because basement structure trends (E-W) are perpendicular to the uplift trend (N-S). Taba-Elat-Roded Complex metapelites contain detrital zircons dated at 800–820 Ma (Kröner et al. 1990) and its northern extensions in Israel (Elat Schist) and Jordan. More recent studies of metasediments near Elat (Elat association and Roded association) give detrital zircon ages of ~760 to ~850, with a few grains dating back to ~930 Ma (Morag et al. 2011). Dioritic to granitic orthogneisses intrude Elat complex metapelite and these intrusions are dated at 782–744 Ma (Kröner et al. 1990; Morag et al. 2011). Amphibolite bodies in the complex give ages of 670–612 Ma (Kröner et al. 1990; Morag et al. 2011). Similar rocks are also found in the Abu Barqa suite of SW Jordan, which has been displaced by ~80 km northwards due to Dead Sea Transform sinistral movements (Jarrar et al. 2013).

The Sa'al Metamorphic Complex in the north-central basement exposures of the Sinai peninsula provides a unique exposure of 1.12–0.95 Ga crust and sediments (Fig. 4.3) (Be'eri-Shlevin et al. 2012). This small belt strikes E-W and is dominated by two or three volcanosedimentary formations that were metamorphosed in greenschist to amphibolite facies (Eyal et al. 2014; Ali-Bik et al. 2017). Sa'al metavolcanics may have formed at a convergent plate margin (island arc). Crust of this age is recognized nowhere else in the Arabian-Nubian Shield. The influence of the ~1.0 Ga crust extends southward into Wadi Zaghra (Fig. 4.3) where deformed Ediacaran conglomerates (deposited ~615 Ma) contain ~1.0 Ga detritus as well as more abundant 750–850 Ma and 630–670 Ma detritus (Andresen et al. 2014). Sinai basement also preserves evidence of pre-Ediacaran crust near the Katherina complex where ~1.05 Ga inherited zircons are found in the 844 ± 4 Ma Moneiga quartz diorite (Bea et al. 2009).

The Feiran-Solaf Metamorphic Complex (Fig. 4.3) differs from Taba, Elat, and Sa'al complexes by covering a larger area (~100 km^2) and by having a strong NW-SE trending structure, 35 km long and 5–11 km wide (Fig. 4.3). Metamorphic rocks include ortho- and paragneisses and some calc-silicates, all flanked and intruded by granitic rocks. Its structure is dominated by a NW-trending anticlinorium cut by NW-trending thrust faults (Abu-Alam and Stüwe 2009). U-Pb zircon dating of Feiran-Solaf metamorphic complex rocks reveal a succession of magmatic and metamorphic events from ~1 Ga to <600 Ma (Abu El-Enen and Whitehouse 2013). Ages of ~1 Ga are found for zircons in meta-sandstones and from orthogneiss. Ages of 785–800 Ma are obtained from other orthogneisses (Abu El-Enen and Whitehouse 2013; Eyal et al. 2014). Metamorphism occurred between ~630 and ~590 Ma (Abu El-Enen and Whitehouse 2013). Abu-Alam and Stüwe (2009) concluded that Feiran-Solaf metamorphic rocks experienced peak metamorphism at ~700–750 °C and 7–8 kbar (~21.5–26 km deep in the crust) and subsequent isothermal decompression to ~4–5 kbar (~13–16.5 km deep in the crust). They argued that this was associated with shortening and concluded that ductile deformation associated with Najd shearing partly exhumed the gneisses during oblique transpression, but that the final ~15 km of exhumation happened later in Ediacaran time, perhaps associated with cutting of the Ediacaran unconformity ~600 Ma (associated with deposition of Hammamat and related sediments). An alternate tectonic interpretation, that the Feiran-Solaf metamorphic complex deformation reflects collision with the Sa'al Metamorphic Complex, is offered by Fowler et al. (in press).

The Kid complex is a volcano-sedimentary sequence occupying ~600 km^2 in southernmost Sinai (Fig. 4.3). It is similar to the other 3 metamorphic complexes in preserving pre-Ediacaran crustal remnants but differs in also preserving thick volcanic sections that formed at the beginning of the Ediacaran episode of igneous activity affecting Egypt. The Kid Metamorphic Complex consists of 4 major units: the mostly volcanic Heib and Tarr formations in the south and the volcaniclastic Melhaq and siliciclastic Um Zariq formations in the north, all separated by shear zones that formed at ~615–605 Ma (Moghazi et al. 2012). Qenaia migmatites and quartz diorite gneisses on the SW margin of the Kid complex, next to the Heib Formation, give a U-Pb zircon age ~768 ± 5 Ma (Eyal et al. 2014). The Heib, Tarr, and Melhaq formations reflect an intense episode of volcanism associated with Ediacaran core complex formation (Moghazi et al. 2012). The Heib Formation is a volcano-sedimentary succession and metarhyolites was dated by U-Pb zircon ages at 609 ± 5 Ma (Moghazi et al. 2012) and ~630–635 Ma (Eyal et al. 2014). The Um Zariq Formation consists of amphibolite-facies metapelites; detrital zircons give ages that mostly range between 895 and 730 Ma but a few are as young as ~647 Ma (Moghazi et al. 2012). Eyal et al. (2014) considered that these young ages reflect Pb-loss and that the Um Zariq Formation was deposited ~730 Ma.

Overall, the four metamorphic complexes of Sinai show evidence of having formed first as a 1000–700 Ma E-W belt that was disrupted in Early Ediacaran times by strong extension and exhumation in a marine environment (Azer et al. 2010) and followed by intense Najd shearing. The overall E-W trending fabric that defines Sinai and NE Desert crust was established in Stenian-Tonian time.

Calc-alkaline (CA) and alkaline-peralkaline (Alk) suites occupy ~80% of the Sinai basement exposures (Eyal et al. 2010). CA suite spans a wide range of mafic to felsic plutons (SiO_2 = 45–77 wt%). U-Pb zircon geochronology indicates prolonged and partially contemporary CA and Alk magmatism at 635–590 Ma and 608–580 Ma, respectively. Igneous rocks of the CA suite are further subdivided into deformed CA1 (650–625 Ma) and undeformed CA2 subsuites (Be'eri-Shlevin et al. 2009b). CA and Alk have distinct chemical compositions but mafic and felsic components have similar Nd, Sr, and O isotopic composition. Both suites have similar $\varepsilon_{Nd(t)}$ = +1.5 to +6.0 and indistinguishable, mantle-like mean zircon $\delta^{18}O$ = +5.8 and +5.9 (Be'eri-Shlevin et al. 2009a). Many have the characteristics of A-type granite. CA and Alk granitoids are probably related to mafic lower crust as inferred from analogous crust identified beneath western Arabia (Stern and Johnson 2010). Magmatic evolution of CA and Alk suites reflects mantle melting, mafic magmatism, and silicate melt fractionation into mafic lower and felsic upper crust. Distinct mantle sources are envisioned for CA and Alk suites, metasomatized lithospheric mantle for the former, upwelling asthenosphere due to delamination for the latter (Avigad and Gvirtzman 2009). Alk suites are associated with dense NE-trending dike swarms. These dike swarms are regionally bimodal and locally composite (Katzir et al. 2007), testifying to the coexistence of mafic and felsic magmas; similar dyke swarms are found in the NE Desert (Stern and Vogeli 1987; Stern et al. 1988). Volcanics also occur, especially in association with epizonal alkaline plutons (Azer et al. 2014).

It is worth noting that not all of the granitic intrusions in Sinai are part of the huge Ediacaran episode. There are also Tonian intrusions such as 782 ± 7 Ma El Sheikh granodiorite on the east flank of the Feiran-Solaf Complex (Stern and Manton 1987) and the 844 ± 4 Ma Moneiga quartz diorite along the southern extension of Feiran-Solaf, adjacent to the Katherina Ring Complex (Bea et al. 2009). These older plutons do not stand out in the field, and more likely await discovery in the Sinai basement. A similar conclusion that there is a significant proportion of pre-Ediacaran crust in the Sinai was reached on the basis of the abundant detritus in Ediacaran conglomerates (Samuel et al. 2011; Andresen et al. 2014).

Finally, remnants of Ediacaran terrigenous volcano-sedimentary successions are locally preserved in the Sinai basement. A good example is the ~620–590 Ma Rutig succession near Gebel Katherina. This is >2 km thick sequence of intermediate to felsic lavas and pyroclastics along with sandstones and conglomerates (Samuel et al. 2011). The Elat conglomerate is similar but may be younger (~580 Ma; Morag et al. 2012). These rocks reveal the Sinai in Ediacaran time as a magmatically active rift, with several terrestrial basins with rivers winding through desolate lava plains. An intriguing insight into what might lie at depth beneath northern Sinai and Egypt is provided by the Zenafim formation in the subsurface of Israel, which has been sampled by 4 drillholes along a ~150 km N-S transect (Avigad et al. 2015). This seems to mark an Ediacaran passive margin on the north side of Africa. The Zenafim formation thickens northward from thin alluvial fans in the south to >2 km thick marine sediments in the north; these sedimentary rocks testify to the encroachment of the proto-Tethys onto the margins of the subsiding Neoproterozoic orogen. U-Pb dating of detrital zircons from the alluvial fan facies reveal a concentration of 0.6–0.7 Ga ages, with a peak ~0.63 Ga; there is little evidence of older crust in these sediments (Avigad et al. 2015). In contrast, the marine facies is younger, ~0.58 Ga and contains abundant evidence of older crust.

4.3 Eastern Desert

Basement exposures in Egypt east of the Nile are found in the Eastern Desert (Fig. 4.4). These exposures encompass ~60,000 km^2 and reflect rift-flank uplift on the NW margin of the Red Sea. These can be subdivided along strike into Northeastern Desert (NED), Central Eastern Desert (CED) and Southeastern Desert (SED). These are discussed in this order below.

4.3.1 The North Eastern Desert

The NED lies north of a NE-trending boundary drawn south of the Qena-Safaga road and is the smallest (~10,000 km^2) of the three ED subdivisons. Like the Sinai, exposed NED crust is dominated by Ediacaran igneous rocks and associated sediments (Fig. 4.5). NED basement exposures are ~75% granite and gneiss and ~25% volcanics and sediments (Stern and Hedge 1985). Also similar to the geology of Sinai, there is strong evidence for extension in the form of abundant ~600 Ma bimodal dike swarms (including composite dikes) that trend E-W to NE-SW, indicating ~N-S oriented extension about the same time that Najd strike-slip deformation was affecting the CED (Stern et al. 1984). Abundant epizonal A-type granites require passive emplacement and indirectly demonstrate strong extension. The Ediacaran development of NED crust thus is very similar to that of Sinai, leading Stern et al.

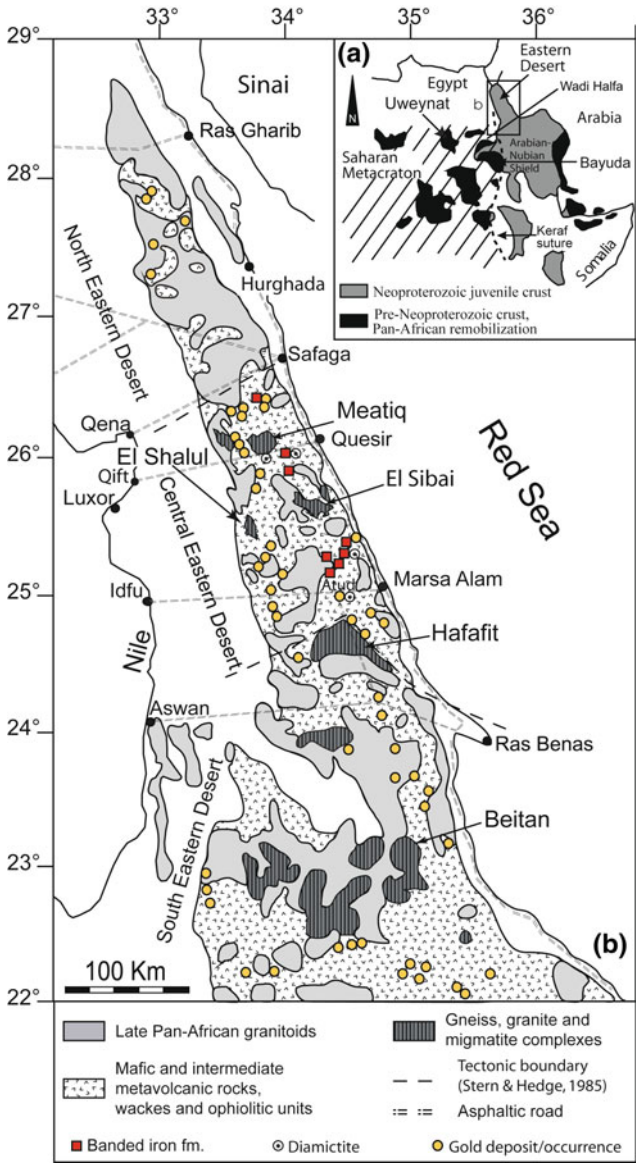

Fig. 4.4 **a**, *inset* Geological sketch map of NE Africa showing the Arabian-Nubian Shield, the Saharan Metacraton, and Archaean and Palaeoproterozoic crust that was remobilized during the Neoproterozoic. **b** Simplified geological map of the Eastern Desert of Egypt (modified from Stern and Hedge 1985) showing the BIF-diamictite sequences and gold deposits occurrences

(1984) and Stern (1985) to identify this region as the site of major NW-SE directed extension during Ediacaran time.

The geology of the NED is very different than the terranes to the south, especially the CED to its immediate south. The well-developed Cryogenian and Late Tonian sequences that are spectacularly exposed in the CED are missing. Ophiolites are absent and gneisses are rare. Distinctive Late Tonian–Ediacaran sediments especially banded iron formation (BIF) and Atud diamictite (Fig. 4.4b) are unknown from the NED (ophioites, BIF, and Atud diamictite are also missing from the Sinai). Evidence for Najd deformation—which affects the CED as well as western Arabia—is also missing. The Dokhan Volcanics were erupted during the Ediacaran "magmatic flare-up" (Stern and Hedge 1985; Wilde and Youssef 2000). There is disagreement as to whether Dokhan volcanism was associated with a continental arc or magmatic rift (Stern et al. 1984; Eliwa et al. 2006). It was thought up to recently that the overwhelming majority of NE Desert igneous rocks and associated Hammamat sediments were ~600 Ma, but recent investigations show that it is not quite this simple. Breitkreuz et al. (2010) reported U-Pb zircon SHRIMP ages for 10 Dokhan silica-rich ignimbrites and two subvolcanic dacitic bodies from the NED. These ages range between 592 and 630 Ma, indicating that Dokhan volcanism occurred over a 40 M.y. timespan.

In spite of the fact that NED and Sinai share a similar Ediacaran magmatic history, the NED contrasts with Sinai in having fewer documented examples of Cryogenian and Tonian crust. One of the most exciting recent developments in studies of the NED is that we are starting to identify small tracts of pre-Ediacaran crust. There have been hints of pre-Ediacaran crustal remnants in the NED for some time. One is the 666 Ma Mons Claudianus granodiorite (Stern and Hedge 1985); the 652 ± 3 Ma Um Taghir granodiorite collected along the Qena-Safaga road (Moussa et al. 2008) may be part of the Mons Claudianus batholith. Another is from SW of Gebel Dara near 27°50′N where Abdel-Rahman and Doig (1987) used whole-rock Rb-Sr geochronology to identify a Tonian muscovite tonalite. This is by far the oldest age reported for rocks of the NED and has yet to be confirmed by U-Pb zircon dating. Eliwa et al. (2014) used SIMS U-Pb zircon techniques to document the presence of ~740 Ma muscovite trondhjemite and ~720 Ma granodiorite from this area. Larger tracts of Tonian crust have recently been identified in the far NE Desert around 27°53′N where Bühler et al. (2014) studied the ~550 m thick Wadi Malaak succession of lavas, volcaniclastics, and clastic sedimentary rocks and documented the presence of ~720 Ma ignimbrites unconformably overlying ~740 Ma granitoids. Working in this general region but 15 km to the ESE, Abd El-Rahman et al. (2017) documented ~780 Ma dacite associated with Cu mineralization. Further efforts to identify and study slivers of Cryogenian–Tonian crust hidden in the NED are called for.

Ediacaran granitic rocks in the NED show remarkable mantle-like isotopic characteristics. Ali et al. (2016) studied 4 examples of these intrusions: the 653 Ma Um Taghir granodiorite, the 595 Ma Abu Harba intrusion, the 605 Ma Gattar syenogranite, and the 597 Ma Missikat syenogranite. All of these intrusions show strongly positive whole rock εNd(t) and zircon εHf(t), and zircon $\delta^{18}O$ ~ +3.6 to 6.7 per mill. The origin of the large volumes of enriched granite with such mantle-like isotopic compositions remains a mystery.

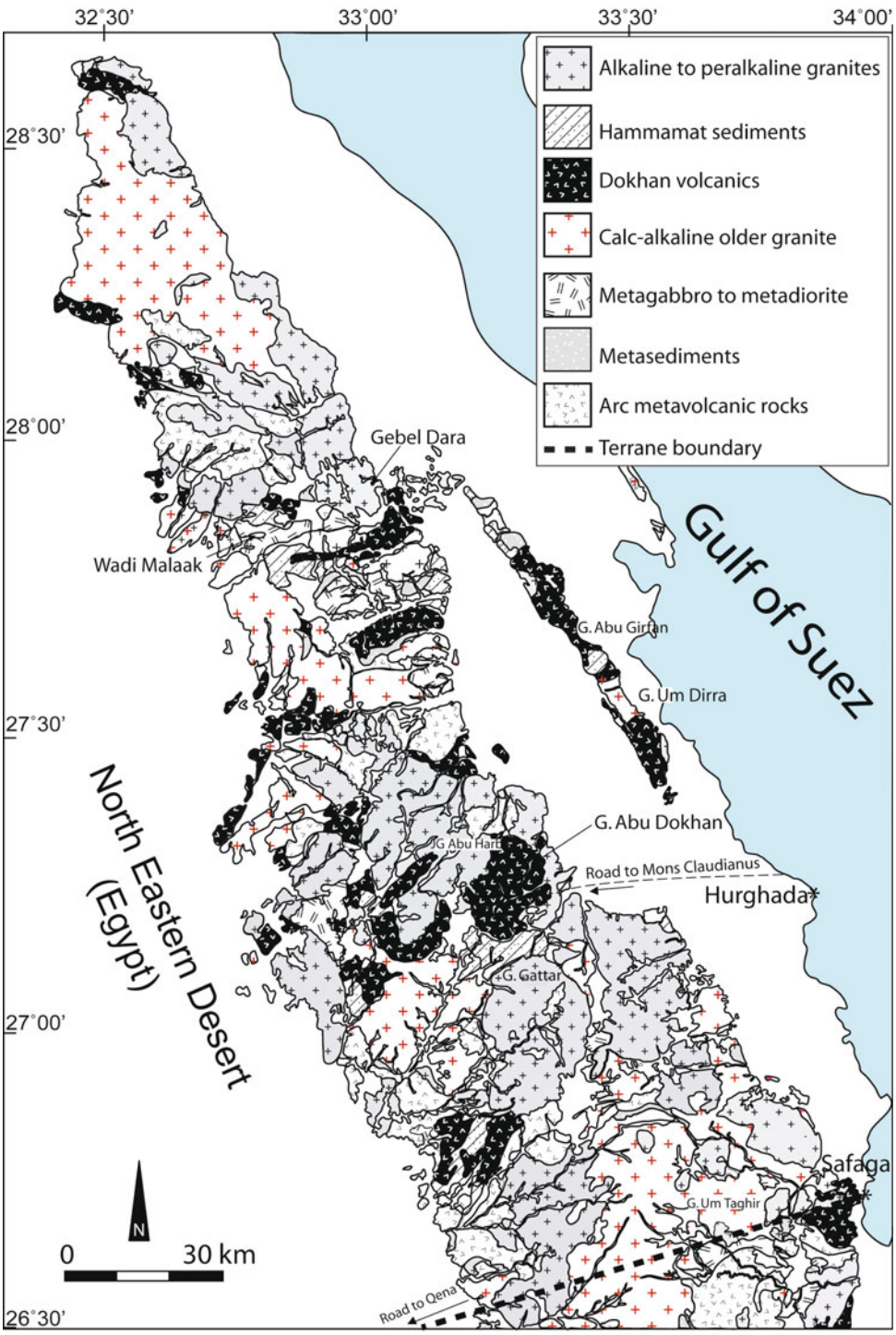

Fig. 4.5 Geological map for the North Eastern Desert of Egypt showing the Neoproterozoic basement rocks (modified from CONOCO map 1:500 000 and compiled from three quadrangle maps: Quseir quadrangle NG 36NE, Assuit quadrangle NG 36NW and Beni Suef quadrangle NH 36SW). General Petroleum Corporation, 1987, editors: Eberhard Klitzsch, Frank List, Gerhard Pöhlmann and associate editors: Robert Handley, Maurice Hermina and Bernard Meisner

4.3.2 The Central Eastern Desert

The CED lies south of the NED and north of an irregular boundary ~24°30′N where the SED begins (Fig. 4.6). CED exposures cover ~20,000 km^2 and consist of ~40% granite and gneiss, 55% sediments and volcanics, and ~5% serpentinites and related rocks (Stern and Hedge 1985). Much of the following information about the CED is adapted from Stern (2018). The CED best preserves the oldest (Tonian–Cryogenian) history of Egypt and also preserves Ediacaran deformation (Najd), volcanism (Dokhan) and sedimentation (Hammamat), all associated with intense igneous activity. The CED is by far the best known of the three Eastern Desert subdivisions. This is partly due to its

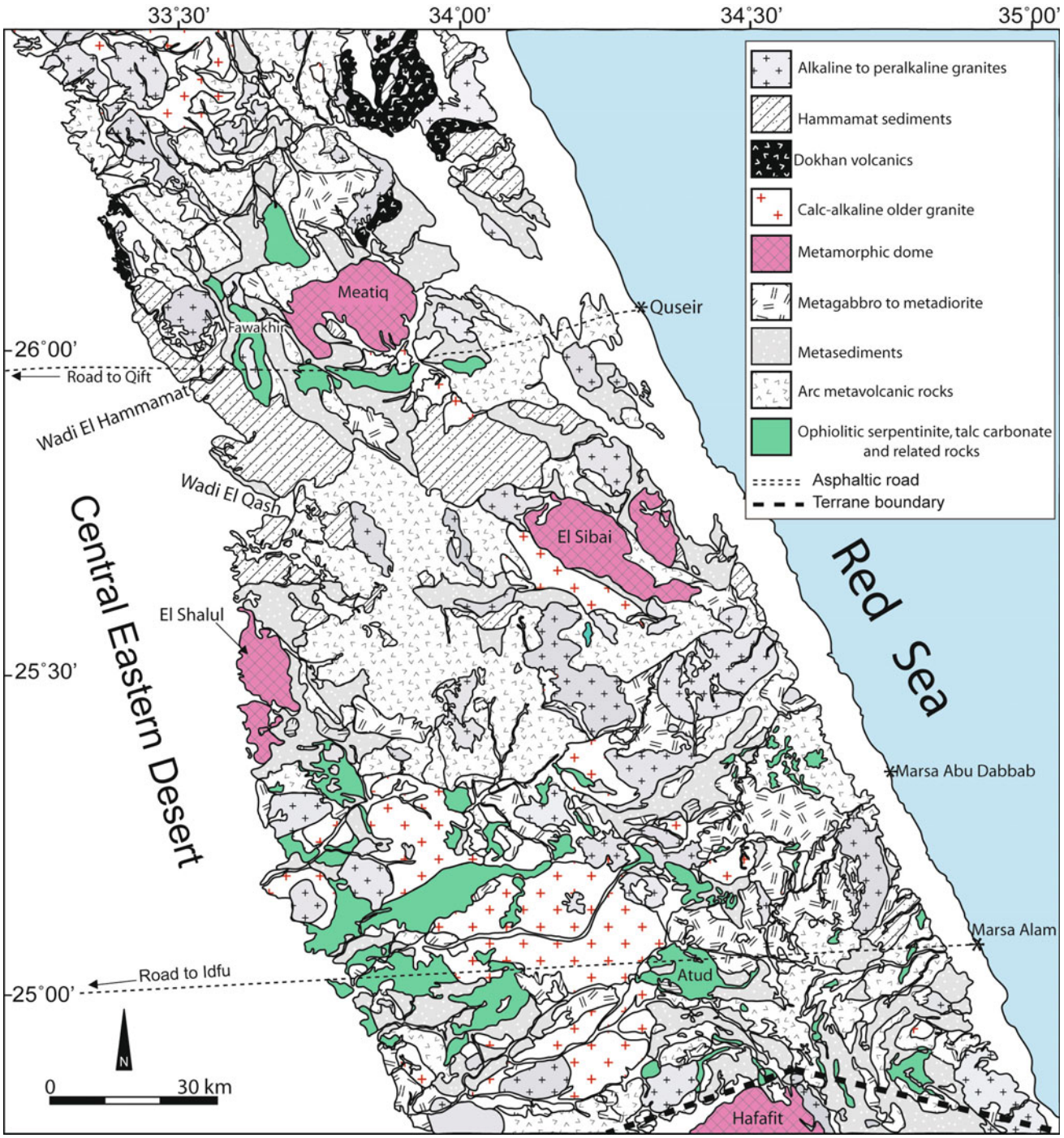

Fig. 4.6 Geological map for the Central Eastern Desert of Egypt showing the Neoproterozoic basement rocks (modified from CONOCO map 1:500 000 and compiled from two quadrangle maps: Quseir quadrangle NG 36 NE and Gabal Hamata quadrangle NG 36 SE). General Petroleum Corporation, 1987, editors: Eberhard Klitzsch, Frank List, Gerhard Pöhlmann and associate editors: Robert Handley, Maurice Hermina and Bernard Meisner

accessibility (it is traversed by two asphalt highways) and because it is a region of relatively subdued relief, but also because its supracrustal sequences are especially interesting and informative and because gold mineralization is concentrated here (Fig. 4.4).

The northern limit of the CED is a diffuse boundary marked by intrusions of granitic plutons of the southern NED. This transition is marked by a metamorphic gradient that increases northwards—from greenschist to amphibolite facies as the NED batholith is approached. It is more of a

broad transition zone than a sharp boundary and lies south of the Qena-Safaga road. The NED-CED transition zone has not yet been studied in any detail but may mark where the infrastructure-superstructure boundary intersects the surface. This transition is worthy of future research, including the extent to which it is metamorphic or structural (Qena-Safaga Shear Zone of Hamimi et al. 2019).

CED supracrustal sequences comprise an ensimatic (oceanic) assemblage characterized by a wide range of mostly greenschist-facies ophiolitic rocks and arc volcanics, along with volcaniclastic wackes, banded iron formation (BIF), and diamictite (Fig. 4.4b). The ensimatic assemblage comprises the oldest documented CED units, with ~750 Ma U-Pb zircon ages (Kröner et al. 1992; Andresen et al. 2009; Ali et al. 2009). The supercrustal ensimatic assemblage is punctured by Cryogenian I-type granitoids and Ediacaran I- and A-type granites (Fig. 4.6) and are further disrupted by several Ediacaran magmatic-metamorphic core complexes. These core complexes are locations where infracrustal "Tier 1" of Bennett and Mosely 1987) poke through lower-grade rocks of the superstructure ("Tier 2" of Bennett and Mosely 1987). CED supercrustal sequences are locally overlain by Ediacaran (~600 Ma) successor basins of the Hammamat Group. Hammamat basins formed in response to differential relief between higher regions in the NED and lower regions in the CED that accompanied Najd deformation in the CED and magmatic rifting in the NED. Possible links by one or more rivers between Ediacaran terrigeneous sediments in Jordan, Israel, Sinai, NED, and Hammamat sedimentary basins in the northern part of the CED warrant future focused investigations.

Eastern Desert infrastructure consists of upper amphibolite-facies quartzofeldspathic (granitic) gneisses and amphibolites exposed in several places in the CED, including the Meatiq, Abu Had, El Shalul, and El Sibai domes as well as the Migif-Hafafit and Beitan domes in the SED. These gneisses are intruded by dioritic, granodioritic, and granitic plutons, which formed in the infrastructure and differentially rose up through weak crustal shear zones. Infrastructure gneisses and intrusives are often mistakenly thought to be pre-Neoproterozoic "fundamental basement" but these clearly represent juvenile middle crust that formed in Neoproterozoic time, as shown by repeated radiometric and isotopic investigations (Liégeois and Stern 2010). The contact between superstructure and infrastructure is sometimes an intrusive contact and sometimes a high-strain mylonitic zone (see Stern 2018 for further details).

The CED is well known for its ophiolites, which comprise the base of the superstructure. We have two ages for CED ophiolites: (1) zircon evaporation $^{207}Pb/^{206}Pb$ ages of 745 ± 23 Ma for plagiogranite of the Wadi Ghadir ophiolite (Kröner et al. 1992) and U-Pb zircon TIMS age of 736.5 ± 1.2 Ma for gabbro from the Fawakhir ophiolite (Andresen et al. 2009). CED ophiolites are mostly highly disrupted and carbonated, although complete if abbreviated sequences of peridotites, gabbros, and pillow basalts are broadly exposed throughout the CED, for example along the Qena-Quseir road near Fawakhir and at Wadi Ghadir. Abdel-Karim and Ahmed (2010) summarized what is known about 38 different ophiolitic occurrences in the CED and SED. The volcanic section of these ophiolitic occurrences shows clear evidence of forming over a subduction zone, although it is controversial whether these formed in a backarc basin or in a forearc during subduction initiation (Abd El-Rahman et al. 2009a, b; Farahat 2010; El Bahariya 2018).

Understanding the significance of Eastern Desert ophiolitic ultramafic rocks is complicated because these are intensely altered by carbonate and sheared (Boskabadi et al. 2016; Hamimi et al. 2019). It is controversial how many episodes of deformation occurred but it is clear that ~600 Ma Najd deformation strongly affected the CED (Abdeen and Greiling 2005). Serpentinites and related talc-carbonates are weak, easily deformed and serve to localize major faults and shear zones. As a result, they form mélange that is easily mylonitized; some of carbonated ultramafics are so intensely sheared as to appear in the field to be bedded metasediments. Fortunately, modern orbital remote sensing technology allows us to identify the distinct spectral characteristics of serpentinite and carbonate from space (Sultan et al. 1986). Studies of CED ophiolitic ultramafics show that, before serpentinization and carbonation, these were highly depleted harzburgites (Azer and Stern 2007; Khalil and Azer 2007); such depleted peridotites are only found in forearc environments today.

Sedimentary rocks are important supracrustal components of the CED above the ophiolites. These are thick sequences of greenschist-facies arc volcanics and associated wackes and volcaniclastics. Early ideas that CED arc volcanic sequences stratigraphically overlie ophiolites and metasediments (Stern 1981) are not supported by U-Pb zircon geochronology. No discernible difference in age is found for ophiolites and arc sequences; both range from ~730 to ~750 Ma. One of the most interesting features of CED arc metavolcanics is that they sometimes contain abundant pre-Neoproterozoic zircon; these are especially common in mafic lavas (Ali et al. 2009; Stern et al. 2010a, b). These volcanics have mantle-like whole-rock Nd isotopic compositions and show no isotopic evidence for involvement of pre-Neoproterozoic crust, suggesting that the old zircons were inherited from the mantle (Stern et al. 2010a, b).

Metasediments occupy a significant proportion of CED outcrops. These are dominated by immature clastic sediments such as greywacke, siltstone and shale; many contain volcaniclastics and sometimes are interbedded with lava flows. These metasediments are broadly andesitic in bulk composition, but not much more is known about them. Future efforts to extract detrital zircon ages from

metawackes should provide useful insights into the geologic history of the CED.

Banded Iron Formation (BIF) and Atud diamictite are minor but very interesting components of the CED metasedimentary sequence (Fig. 4.4b). Atud diamictite is a poorly sorted, polymictic breccia, with clasts up to 1 m of granitoid, quartz porphyry, basalt, quartzite, greywacke, marble, arkose, and microconglomerate in fine-grained matrix (Ali et al. 2010a). The Atud diamictite is only documented from the CED, although a correlative unit, the Nuwaybah diamictite, is found in coastal Saudi Arabia (Ali et al. 2010a). Ali et al. (2010a) dated zircons from eight Atud diamictite clasts (five granitoids, 1 quartzite, 1 quartz porphyry, and 1 arkose) and a sample of diamictite matrix. The clasts gave a variety of ages. Two granitic clasts contained only Neoproterozoic (~750 Ma) zircons; another granitoid clast yielded mostly Neoproterozoic (0.75–0.79 Ga) zircons along with abundant 2.1–2.4 Ga zircons; a fourth granitoid also yielded Paleoproterozoic (2.0 Ga) ages, which were partially reset in Neoproterozoic time; the fifth granitic clast yielded only Paleoproterozoic–Archean ages. The quartz porphyry clast yielded mostly Neoproterozoic ages (697–778 Ma) along with one Early Paleoproterozoic and one Archean zircon. The quartzite clast yielded Paleoproterozoic to Archean (2.1–2.7 Ga) zircons. The arkose clast contained Neoproterozoic (0.72–0.77 Ga) and older Paleoproterozoic zircons (1.8–2.5 Ga). The diamictite matrix contains zircons with mixed Neoproterozoic and Paleoproterozoic ages (Ali et al. 2010a). There are no reliable pre-Neoproterozoic radiometric ages for in situ units in the CED or anywhere else in the Eastern Desert, so Atud diamicite pre-Neoproterozoic clasts and matrix components must have been derived from outside the CED and deposited in the oceanic basin that existed ~750 Ma in the CED. Ali et al. (2010a) inferred that Atud diamictite components may have been glacially eroded from the Saharan Metacraton to the west (Abdelsalam et al. 2002), where pre-Neoproterozoic and Neoproterozoic crust are both abundant (Sultan et al. 1994) during the Sturtian (~730 Ma) "Snowball Earth" episode.

Banded Iron Formation (BIF) is another diagnostic component of the CED metasedimentary sequence (Sims and James 1984; El-Shazly and Khalil 2014). There are thirteen different BIF localities in the CED (Fig. 4.4b). There is a correlative BIF occurrence in NW Saudi Arabia, the Sawawin deposit (Stern et al. 2013). Limited age constraints suggest that these BIFs formed ~750 Ma. CED BIFs consist of interlayered dense magnetite and hematite layers alternating with jasper. BIFs and interbedded wackes are strongly deformed and metamorphosed to greenschist and occasionally amphibolite facies. CED BIFs are related to distal submarine igneous activity and may reflect re-oxygenation of the ocean during or after the Sturtian glaciation (Stern et al. 2013).

The above overview indicates that the CED ~730–750 Ma was an ensimatic basin with an oceanic crustal structure. By analogy with modern oceanic crust, this would have been ~6 km thick. CED crust at this time may have been somewhat thicker because of associated arc volcanics and sediments. It is not clear when and how this region attained its present thickness of ~30 km (Hosny and Nyblade 2016). Some insight comes from the distribution of ~600 Ma Hammamat sediments, which define terrestrial basins that are especially well-developed in the northern CED, adjacent to the NED. These sediments were deposited on top of the Cryogenian sequences above an angular unconformity. Thicknesses of these sequences can reach several thousand meters (Fowler and Osman 2013). The Hammamat basins show that the much of the northern CED was low relative to the NED in Ediacaran time (Fowler and Osman 2013). Hammamat basins are filled with coarse clastic sediment that was largely eroded from the NED and carried by one or more rivers south and deposited in terrestrial basins that are now best preserved in the northern CED. The course of the Ediacaran river can be traced along the western flank of the Meatiq Dome (strongly deformed conglomerates of Wadi Um Esh; Ries et al. 1983) which opens up southward into a broad expanse of Hammamat NW of Wadis Hammamat, El Qash, and Arak (Fowler and Osman 2013). The crust that supported Hammamat Basins was somewhat above sea-level and so must have reached approximately its present thickness by that time. Hammamat basins formed in the CED formed without any evidence of Najd shearing and about the same time as Dokhan volcanism and intrusion of pink A-type granites, ~600 Ma. Fowler and Osman (2013) concluded that Hammamat sequences were deposited in basins formed by N-S extension.

Ediacaran granitic bodies were intruded in the CED but these are significantly less abundant than in the NED or Sinai. Early Ediacaran granitic rocks are mostly I-type whereas Late Ediacaran intrusions are mostly A-type (Fig. 4.2). There are also Cryogenian intrusions in the CED, although these are more poorly known.

There are significant gold deposits in the CED (Fig. 4.4b), including volcanogenic massive sulphide (VMS) deposits like Wadi Hamama (Abd El-Rahman et al. 2015) and gold mineralized quartz veins like El-Sid (Helmy and Zoheir 2015).

The southern limit of the CED is a sharp, structural boundary that follows the northern flank of the Migif-Hafafit dome (Shalaby 2010) and its continuation to the SW and SE. The Migif-Hafafit complex represents an excellent window into the infrastructure-superstructure transition and the nature of the infrastructure, which repeated geochronologic and isotopic measurements indicate is a juvenile Neoproterozoic crustal addition (Liégeois and Stern 2010). The boundary is a complex fault system that can be traced for several tens of kilometers NW along Wadi Nugrus and Gebel Hafafit, then

turns abruptly SW along Gebel Migif and Wadi Shait to mark the boundary between superstructure and the CED to the north and infrastructure and the SED to the south.

4.3.3 The South Eastern Desert

Precambrian basement exposed in the SED covers a much larger area (~30,000 km^2) and is much less studied than the basement exposures of Sinai, the NED or the CED. In many ways, the SED represents the "last frontier" for future studies of the Precambrian basement of Egypt; this reflects its remote location and lack of asphalt roads.

The SED can be partially defined by its geologic boundaries (Fig. 4.7). In the north is the mostly tectonic boundary with the CED, described in the previous section. The eastern boundary is defined by the Red Sea coastal plain. Before the Red Sea opened in mid-Cenozoic time, the SED was contiguous with the Midyan terrane of NW Arabia (Johnson and Woldhaimanot 2003), which is also poorly known. The southern boundary of the SED is marked by the Nubian portion of the Yanbu-Sol Hamed-Onib-Gerf-Allaqi-Heiani (YOSHGAH) suture; Stern et al. 1990). The western boundary is poorly defined but seems to trend ~N-S along ~33°E just east of the Nile, where abundant Ediacaran granitic rocks outcrop discontinuously around Aswan and farther south; these have Nd isotopic compositions and inherited zircons that indicate involvement of older crust (Sultan et al. 1990; Finger et al. 2008).

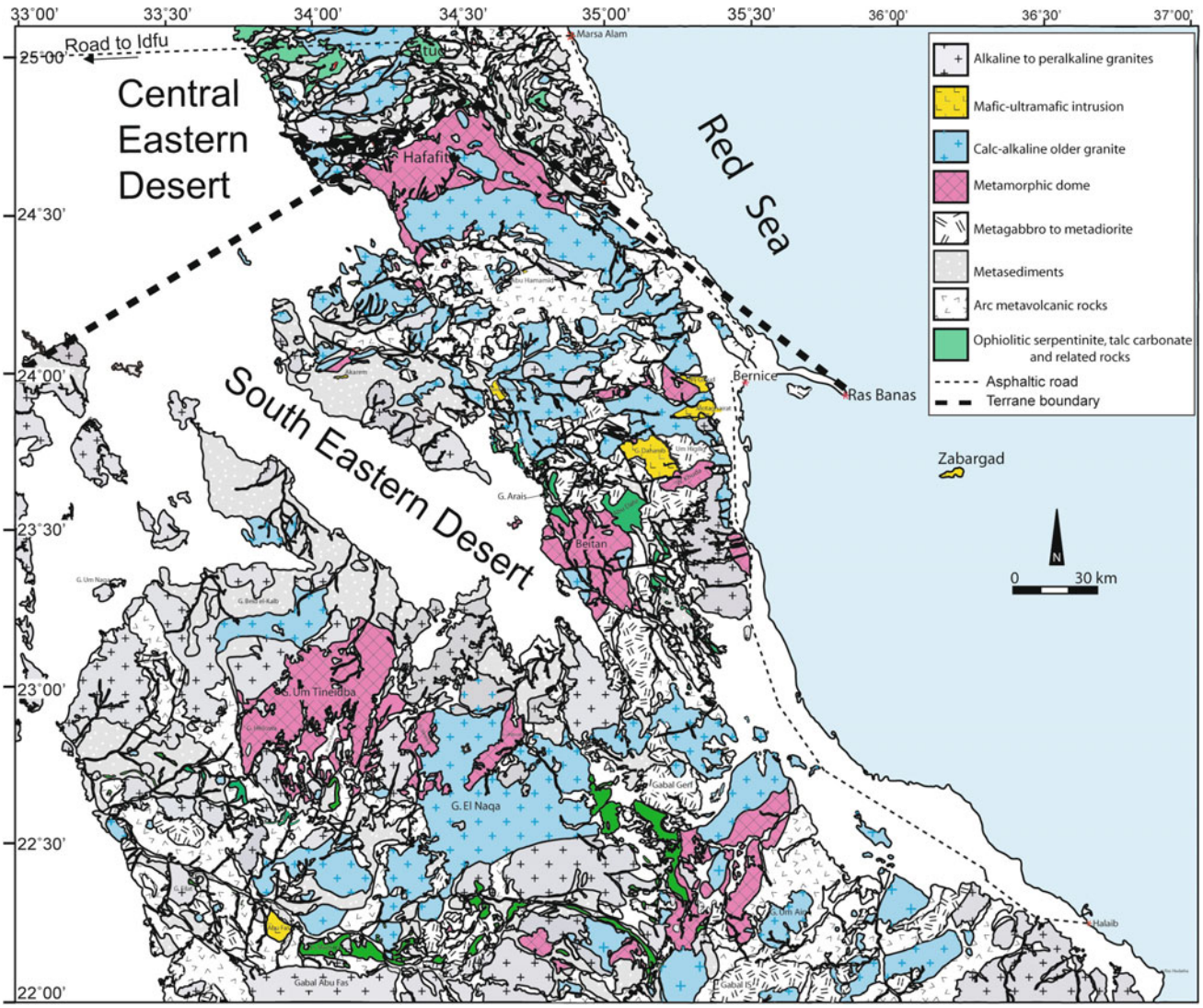

Fig. 4.7 Geological map for the Southern Eastern Desert of Egypt showing the Neoproterozoic basement rocks (modified from CONOCO map 1:500 000 and compiled from two quadrangle maps: Gabal Hamata quadrangle NG 36 SE and Bernice quadrangle NF 36 NE). General Petroleum Corporation, 1987, editors: Eberhard Klitzsch, Frank List, Gerhard Pöhlmann and associate editors: Robert Handley, Maurice Hermina and Bernard Meisner

The SED contrasts with the CED by lacking BIF deposits. It may also lack possible glaciogenic deposits comparable to the Atud diamictite, although these have not been actively searched for. The SED also lacks significant Ediacaran sedimentary or volcanic successions such as the Hammamat Group and Dokhan Volcanics found in the NED and CED, although SED volcanic successions have been mistakenly assigned to the Dokhan. The SED and CED contain similar proportions of serpentinites but these are scarcely studied except for ophiolites along the E-W trending Allaqi-Heiani-Gerf suture in the far south SED YOSHGAH suture and at Abu Dahr (Gahlan et al. 2015). The SED seems to also show infrastructure-superstructure relationships like those of the CED, but the units in the SED are somewhat older (Stern 2018). The SED in general seems to represent a deeper level of exposure than the CED and is much less affected by Najd shearing. Because the SED is less studied than the CED, there is less geochronologic data; what is available suggests that it is generally slightly older than the CED (Stern and Hedge 1985), but more geochronological studies are needed in order to better outline the main features of SED crust.

The northernmost SED is dominated by gneiss, migmatite, and granitic rocks of the Migif-Hafafit region, a belt that trends ~E-W. This complex metamorphic dome represents an unusually large exposure of infrastructure (Bennett and Mosely 1987) and is separated from the southernmost CED by a broad mylonitic shear zone, the Nugrus thrust. Gneissic metagabbros define large scale fold interference patterns cored by foliated meta-tonalites (Fowler and El Kalioubi 2002). Three of these intrusions give zircon Pb evaporation ages of 675–700 Ma (Kröner et al. 1994) and have Nd and Sr isotopic compositions indicating that these are juvenile crustal additions (Liégeois and Stern 2010).

South of the Migif-Hafafit gneissic terrane is a large and poorly known granitic batholith. South of the great, poorly studied E-W trending batholith there is a great E-W volcanic belt ~25 km wide, the Shadli metavolcanics. This name is sometimes mistakenly applied to CED metavolcanic rocks but the two sequences are different. Near the Umm Samiuki mine, the Shadli metavolcanics consist of the older Um Samiuki and the younger Hamamid groups, both comprising mafic to felsic successions of slightly metamorphosed lavas. They both comprise bimodal suites with modes at 48–53 and 69–75 wt% SiO_2. Basalts can be further subdivided into a fractionated low K, high-Ti (~0.3 wt% K_2O; >2 wt% TiO_2) and a primitive med.- K, low-Ti (~1 wt% K_2O; ~1 wt% TiO_2) suites. These are both fairly depleted suites, with flat or LREE-depleted REE patterns (Stern et al. 1991). A composite Rb-Sr whole rock isochron age of 711 ± 24 Ma and εNd(t) = +6.3 to +7.8 was also reported by Stern et al. (1991); U-Pb zircon ages for these volcanics are needed. On trace element discrimination diagrams, these volcanics plot outside the field of arc lavas; formation in a magmatic rift was suggested by Stern et al. (1991). This metavolcanic belt is associated with polymetallic massive Zn-Cu-Pb-Ag sulfides, such as El Atshan, Egat, Derhib, Abu Gurdi, Helgate, Maqaal, and Um Samiuki (Helmy 1999). These deposits probably reflect submarine hydrothermal deposits.

On the southern margin of the Shadli metavolcanic belt there are several mafic-ultramafic Alaska-type and layered intrusions aligned ~E-W around 24°N. From W to E these are: (1) Gabbro Akarem (24°00′N, 34°08′E, ~12 km^2); (2) Gabbro Gharbia (23°56′N, 34°38′E ~12 km^2); (3) Abu Hamamid (24°19.5′N, 34°44′E, ~0.5 km^2); Dahanib (23°46′N, 35°10′E, ~9 km^2); El Motaghairat (23°52′N, 35°23′E, ~8 km^2); and Zabargad in the Red Sea (23°37′N, 36°11′E, ~7.5 km^2). We do not know if these are different manifestations of a single igneous event because we only have radiometric ages for a quartz diorite near Dahanib (U-Pb zircon age of 711 ± 7 Ma; Dixon 1981a, b), approximate Rb-Sr and Sm–Nd ages of 650–700 Ma for Zabargad peridotites (Brueckner et al. 1995), Sm–Nd errorchron of 963 ± 81 Ma for Genina Gharbia (Helmy et al. 2014).

Gabbro Akarem is a concentrically-zoned mafic-ultramafic intrusion (dunite core, then hornblende lherzolite, olivine–plagioclase hornblendite, and plagioclase hornblendite (Helmy and El Mahallawi 2003). It is elongated ~80°E–260°W, ~10 km long and ~2 km wide, intruded into metasediments. All lithologies have essentially flat REE patterns. Genina Gharbia is an elongated NW-SE (~3 × 6 km) cumulate intrusion into metasediments. It consists of a core of pyroxenite and peridotite surrounded by norite and gabbro (Helmy 2004), all with Nd isotopic compositions indicating derivation from depleted mantle. Abu Hamamid is elongated and intruded into Shadli volcanics (see below) on the north and granodiorite on the south (Helmy et al. 2015). It is zoned from dunite through clinopyroxenite to gabbro. A Sm–Nd isochron suggests an age of 963 ± 81 Ma (Helmy et al. 2014). Dahanib is a tilted layered intrusion oriented N-S, ~6 km × 2 km, composed of peridotite (dunite, wehrlite, lherzolite, pyroxenite, and gabbronorite/norite (Dixon 1981a, b; Azer et al. 2017). Trace elements of Dahanib igneous rocks indicate a convergent margin tectonic environment (Azer et al. 2017). El Motghairat consists of a NE-elongated ~4 × 1 km layered intrusion of basal dunite, lherzolite, and pyroxenite; dominant troctolite; and upper gabbro and anorthosite intruded into metagabbro (Abdel-Halim et al. 2016). The Zabargad intrusion consists of scattered exposures of amphibole-bearing plagioclase peridotites on a small (~3 km across) island (Agrinier et al. 1993). Zabargad peridotites are emplaced into HP-HT metamorphic rocks (850 °C, 10 kbar or ~33 km deep in the crust; Boudier et al. 1988) these gneisses give Rb-Sr and Sm–Nd ages of 655 ± 8 Ma and 699 ± 34 Ma, interpreted as dating peak metamorphism (Lancelot and Bosch 1991).

SED mafic-ultramafic intrusions are associated with potentially economic deposits of Cu-Ni-PGE (Helmy 2004). Gabbro Akarem and Genina complexes contain Cu-Ni-PGE ores, but these are currently deemed sub-economic (700,000 tons of ore at Gabbro Akarem with ~2 wt% Cu and Ni; Genina Gharbia contains hundreds of thousands of tons of ore with <1 ppm PGE).We have much to learn about the age and significance of these and similar deposits further south ~22°N at Abu Fas and Gerf-Khobani, most importantly whether they are the same age or not. Remote sensing studies would be useful for mapping these intrusions and to help search for more of these spectrally-distinctive bodies.

The region between the Shadli Metavolcanics ~24°30′N and the YOSHGAH suture near 22°N is especially poorly known. There are two key pieces of age information for this poorly-known region, both indicating an age of ~710–750 Ma. One is a U-Pb zircon age of 711 ± 7 Ma for a tonalite from Wadi Shut (23°45′N, 35°12′E; Dixon 1981b) and the is for hornblende-bearing orthogneisses along Wadi Beitan (~23°20′N, 35°E), where U-Pb zircon ages of 719 ± 10 Ma, 725 ± 9 Ma, and 744 ± 10 Ma are reported (Ali et al. 2015). Zircon εHf(t) values of −4.8 to +12.5 in the Beitan gneisses hint that pre-Neoproterozoic crustal remnants might exist in the SED although whole-rock εNd(t) values of +5.1 to +6.6 indicate this is an overwhelmingly juvenile crustal addition (Ali et al. 2015).

The southernmost geologic feature of interest in the SED is the Yanbu-Sol Hamed-Onib-Gerf-Allaqi-Heiani (YOSHGAH) suture. The YOSHGAH suture is decorated with abundant ophiolites and can be traced for ~600 km across SE Egypt, NE Sudan, and NW Saudi Arabia (Stern et al. 1990). The YOSHGAH suture in Egypt trends approximately E-W just N of the Egypt-Sudan border until it intersects the N-S trending Hamasana Shear Zone ~34°40′ E. YOSGAH ophiolites and surrounding rocks in the SED are studied in the east (Gerf; east of 35°E) and the west (Allaqi; west of 34°E), with few studies in between.

The Gerf complex is the largest ophiolite in Egypt (~1–5 km wide, ~17 km long) and consists of basaltic pillow lavas, sheeted dykes, isotropic and layered gabbros and ultramafic mélange, all in thrust contact. Zimmer et al. (1995) concluded from major and trace element data that pillow lavas and sheeted dykes are indistinguishable from modern high-Ti N-MORB whereas Abdel-Karim et al. (2016) concluded from analyses of peridotites and pyroxenites that Gerf formed in a fore-arc supra-subduction zone (SSZ) environment. Kröner et al. (1992) analyzed single zircons from a coarse leucogabbro within the layered sequence using the evaporation method. They obtained a mean $^{207}Pb/^{206}Pb$ age of 741 + 42 Ma (2σ error) for four grains and interpreted this as the crystallization age of the gabbro and thus the ophiolite. εNd(t) values of +6.5 to +7.9 indicate derivation from depleted mantle (Zimmer et al. 1995).

Within the Halaib area is found the northernmost part of the N-S Hamisana shear zone (HSZ) and the Onib segment of the YOSHGAH suture. The HSZ formed after collision formed the YOSHGAH suture and consists of amphibolite-facies meta-igneous and metasedimentary rocks intruded by deformed granitic plutons. The HSZ stands out because it trends N-S encompassing about 1500 km^2 of southeastern Egypt and northeastern Sudan and disrupts the older, ~E-W trending YOSHGAH. de Wall et al. (2001) used anisotropy of magnetic susceptibility along with field and microstructural studies to demonstrate that HSZ deformation was dominated by pure shear, producing E–W shortening with a strong N–S-extensional component. This deformation also led to folding of regional-scale thrusts (including the YOSHGAH ophiolite and related structures). Metamorphism to amphibolite facies (up to 600 ± 50 °C and 5–6.5 kbar, or 15–20 km deep in the crust; Ali-Bik et al. 2014). Three zircon Pb–Pb evaporation and two U-Pb conventional zircon ages range from 663 ± 29 Ma to 844 ± 10 Ma ± 5 Ma; Rb-Sr whole rock isochron and errorchron ages for 7 deformed granitic and gneissic bodies range from 551 ± 28 Ma to 665 ± 62 Ma; these ages reflect a protracted episode of Neoproterozoic crust formation and deformation. Two mineral isochrons and one undeformed granite give ages of 510 ± 40 Ma to 573 ± 15 Ma, indicating that exhumation and cooling encompassed a significant amount of Late Ediacaran and perhaps Cambrian time (Stern et al. 1989). The northern HSZ thus provides a remarkable exposure of exhumed ANS middle crust, worthy of further integrated study involving structural, metamorphic, and geochronological studies.

The western YOSHGAH suture has been studied around Wadi Allaqi west of 34°E. Abdelsalam et al. (2003) carried out structural studies supported by remote sensing to show that this part of the suture zone constitutes three S-to SW verging low-angle thrust sheets and folds, forming a 10 km wide imbrication fan. Similar conclusions were reached by Hamimi et al. (2019). Volcanic rocks including rhyolites and felsic tuffs above metasedimentary rocks dominate the upper allochthon. This overrides the central allochthon dominated by arc and ophiolitic assemblages. The structurally lowest nappe (southern allochthon) is dominated by amphibolite facies schistose metavolcanic and metavolcanoclastic rocks. Serpentinized ophiolitic peridotites are very depleted and interpreted as fragments of forearc mantle on the basis of major element and spinel compositions (Azer et al. 2013). Mafic to felsic metavolcanics mapped as Dokhan volcanics are exposed along Wadi Allaqi south of the southern allochthon (El-Nisr 1997).

There is some robust geochronological control for rocks around the Allaqi segment of YOSHGAH. Kröner et al. (1992) obtained single zircon Pb–Pb evaporation ages of 729 ± 17 Ma and 736 ± 11 Ma for gabbro and diorite

samples, respectively, from a single intrusion into sheared serpentinites; they were uncertain whether the dated gabbrodiorite was part of the ophiolite or intruded it, but finally interpreted it as a post-obduction intrusion. Ali et al. (2010b reported five SHRIMP U-Pb zircon ages. Ophiolitic layered gabbro gave a concordia age of 730 ± 6 Ma, and a metadacite from overlying arc-type metavolcanic rocks yielded a weighted mean $^{206}Pb/^{238}U$ age of 733 ± 7 Ma. Taken together—and considering the results of Kröner et al. (1992)—this indicates ophiolite formation at ~ 730 Ma. The Allaqi ophiolite is thus similar in age to Gerf and CED ophiolites. Ophiolite emplacement in Wadi Allaqi is constrained by U-Pb zircon concordia ages for intrusive gabbro (697 ± 5 Ma) and quartz diorite (709 ± 4 Ma) indicating <30 million years between ophiolite formation by seafloor spreading and terrane accretion.

4.4 Aswan and the Southwestern Desert

Crust of the Western Desert of Egypt (Fig. 4.8) is mostly buried beneath Phanerozoic sediments. Some oil companies have drilled to basement but information about the basement they encountered is not yet available to the public. Maps of the magnetic field over this huge region would also be useful for understanding basement lithologies and trends but these are not available as of this writing in early 2018. Fortunately, the Nubian Swell—an E-W trending uplift extending ~800 km to the border of Libya (Thurmond et al. 2004)—allows glimpses of this buried basement. We know that crust on the buried northern flank of Arabia is mostly younger than ANS crust and suspect that this is also true for adjacent parts of Egypt, but the E-W transect provided by Nubian Swell exposures are nevertheless extremely informative about the nature of Egyptian crust buried beneath the Western Desert.

It is not easy to define the boundary between juvenile Neoproterozoic crust of the Eastern Desert and older crust of the northwestern Saharan Metacraton in the Western Desert of Egypt. This is sometimes interpreted as a tectonic boundary, with Eastern Desert ensimatic assemblages thrust over the Metacraton (e.g., Hamimi et al. 2019), but the boundary is obscured by Ediacaran granitic intrusions. There are extensive outcrops of Archean and Paleoproterozoic rocks in the far west along the Nubian Swell around Gebel Kamil and Gebel Oweinat but farther east these disappear and are replaced by mostly Ediacaran igneous rocks that preserve isotopic evidence that pre-Neoproterozoic crust once existed here. Previous workers take the granitic exposures around Aswan to mark the boundary between the Saharan Metacraton and juvenile Neoproterozoic crust of the SED (Harris et al. 1984; Sultan et al. 1990). These exposures include several varieties of granite along with tonalite, pegmatite, and metamorphic rocks (Gindy and Tamish 1998). U-Pb zircon ages by TIMS and LA-ICP-MS give ages of 595 ± 11 Ma to 622 ± 11 Ma for Aswan plutonic rocks (Finger et al. 2008) and 634 ± 4 Ma for granitic gneiss from Aswan (Sultan et al. 1994). These granitic rocks show isotopic evidence for the involvement of pre-Neoproterozoic crust, especially in terms of whole rock εNd(t) = +1.0 to +2.3 (Harris et al. 1984; Sultan et al. 1990).

Basement exposures SW of Aswan and Gebel Umm Shagir are the next important basement exposures west of Aswan and the Nile. These outcrops are dominated by migmatite, gneiss, post-tectonic granite, dikes, and sills (Bernau et al. 1987; Sultan et al. 1994). Biotite granite gneiss from 160 km SW of Aswan along the road to Abu Simbel gave a U-Pb zircon TIMS age of 741 ± 5 Ma whereas a granitic migmatite from Gebel Umm Shaghir gave a U-Pb zircon TIMS age of 626 ± 4 Ma (Sultan et al. 1994).

The next important outcrop to the west of Gebel Umm Shaghir is around Gebel El Asr, where amphibolite- to granulite-facies quartzo-feldspathic gneiss and other metamorphic rocks (including BIF) dominate and intrusive rocks are subordinant (Bernau et al. 1987). Anorthosite from Gebel El Asr contain an unusually complex zircon population, with 2 fractions that give a TIMS U-Pb zircon concordia age of

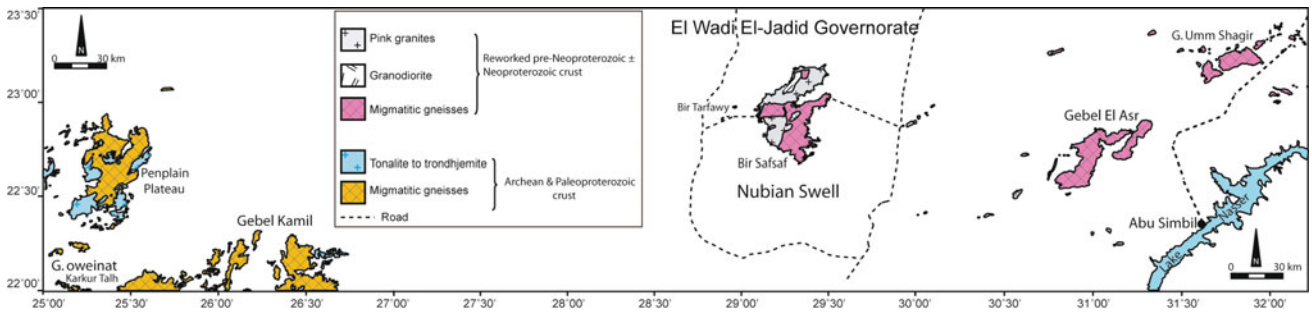

Fig. 4.8 Geological map for the Southern Western Desert of Egypt showing the pre-Neoproterozoic and Neoproterozoic remobilization basement rocks (modified from CONOCO map 1:500 000 and compiled from two quadrangle maps: Gilf Kebir Plateau quadrangle NF 35 NW, Bir Misaha quadrangle NF 35 NE and El-Saad El-Ali quadrangle NF 36 NW). General Petroleum Corporation, 1987, editors: Eberhard Klitzsch, Frank List, Gerhard Pöhlmann and associate editors: Robert Handley, Maurice Hermina and Bernard Meisner

604 ± 5 Ma and a discordia with a lower intercept age of ~689 Ma and upper intercepts of 1922–2141 Ma (Sultan et al. 1994). These ages give clear evidence that pre-Neoproterozoic crust was intensively reworked in Neoproterozoic time.

Bernau et al. (1987) identified three metamorphic stages for rocks of Gebel Umm Shaghir and Gebel El Asr. The first stage is reflected in scapolite formation in calc-silicates, indicating lower T limits of ~800 °C and P ~8–9 kb (~25–30 km deep in the crust). The second stage is shown by the breakdown of scapolite into anorthite and calcite and occurred at T ~750–800 °C and P < 6 kbar (<~20 km deep in the crust). The third stage was retrogression under greenschist-facies conditions. E-W trending mylonite zones are common in basement outcrops around Umm Shaghir and El Asr (Bernau et al. 1987).

The next major outcrop of basement to the west along the Nubian Swell is around Bir Safsaf. This is a very large exposure, encompassing ~1000 km^2. Bernau et al. (1987) show this large region as consisting of subequal proportions of metamorphic and plutonic rocks (granite and granodiorite), all cut by dikes, but Bea et al. (2011a) depict it as consisting entirely of various granitic rocks. Some of the granites contain muscovite and show affinities with S-type granites (Bernau et al. 1987). The dominant igneous rock at Bir Safsaf is coarse red biotite granite (Bernau et al. 1987) or pink granite, syenogranite, and granodiorite (Bea et al. 2011a); this intrudes granodiorite and sometimes contains abundant xenoliths of the older granodiorite (Bea et al. 2011a). Bea et al. (2011a) carried out U-Pb SHRIMP dating of zircons from 9 samples of Safsaf gneissic and granitic rocks. Their results indicate that all Safsaf granitoids and migmatitic gneisses formed during an Ediacaran magmatic event that lasted from 627 to 595 Ma. They also noted that some zircon cores and xenocrysts show ages of 2.1 and 2.7 Ga. They also analyzed 28 whole-rock samples for Sr isotopic compositions and found that these defined an errorchron with an age of ~616 Ma and an initial $^{87}Sr/^{86}Sr$ ~0.7050. Twenty-eight analyses of whole-rock Nd isotopic compositions yielded a narrow range of εNd(t), between −5 and −6, clearly indicating the presence of pre-Neoproterozoic crust. Bea et al. (2011a) obtained Nd model ages of ~1.5 Ga but interpreted this as having no age significance but as an artifact of mixing between 2.1 and 2.7 Ga old crust and juvenile Neoproterozoic melts.

Gebel Kamil is the next exposure to the west of Bir Safsaf. The area around Gebel Kamil is the easternmost part of the ~200 km wide basement outcrop that continues all the way to Gebel Oweinat at the border with Libya and Sudan, and here the oldest rocks in Egypt are exposed. Sultan et al. (1994) dated five grains from a gabbroic anorthosite from Gebel Kamil using TIMS U-Pb zircon techniques. Two single-grain analyses yielded identical $^{207}Pb/^{206}Pb$ ages of 2629 ± 3 Ma whereas three multigrain fractions and two single grains define a discordia with an upper intercept age of 2063 ± 8 Ma and a poorly defined Neoproterozoic lower intercept age. Sultan et al. (1994) interpreted these results as reflecting an Archean igneous rock that was metamorphosed in Paleoproterozoic time. Bea et al. (2011b) confirmed the presence of Archean crust in the Gebel Kamil—Gebel Oweinat uplift and a Paleoproterozoic (~2.1 Ga) overprint. Bea et al. (2011b) also documented a meta-igneous complex that they called the Gebel Kamil complex, composed of low- to medium-K calcic to calc-alkaline tonalitic to trondhjemitic, rarely granitic, gneisses (TTG) associated with subordinate gabbro-dioritic gneisses. These TTGs yield a Sm–Nd whole-rock isochron age of 3.16 ± 0.16 Ga and have a range of U-Pb zircon ages from 2.55 to 3.1 Ga. The most primitive TTG gneisses contain zircons with crystallization ages between 3.1 Ga and 3.3 Ga peaking at 3.22 ± 0.04 Ga, almost identical, within error, to the Sm–Nd isochron. These are by far the oldest rocks in Egypt and some of the oldest rocks in Africa.

Karmakar and Schenk (2015) studied textural and compositional relationships in metapelites and metabasites from all over the Gebel Kamil—Gebel Oweinat area. Metapelitic granulites show a two-stage metamorphic evolution; the first stage occurred at ~1050 °C and P ~10 kbar (~33 km deep in the crust), and the second stage involved near-isothermal decompression to ~6 kbar at T of 900–1000 °C followed by near-isobaric cooling to temperatures of ~700 °C at 5.5–6 kbar (17–20 km deep in the crust). Karmakar and Schenk (2015) also documented the second metamorphic stage in the associated metabasic granulites. Karmakar and Schenk (2015) conducted texturally-controlled in situ Th–U–total Pb monazite dating of the metapelites and concluded that metamorphism first occurred at ~2.6 Ga during an episode of Neoarchean ultrahigh-temperature metamorphism. The second stage occurred ~1.9 Ga during a Paleoproterozoic ultra-high temperature isothermal decompression event. Karmakar and Schenk (2015) found no evidence of significant Neoproterozoic metamorphism.

4.5 Buried Crust of the Western Desert

No summary of the Precambrian basement of Egypt would be complete without mention of crust buried beneath Phanerozoic sediments west of the Eastern Desert and north of the Nubian Swell. We know nothing about this crust. Aeromagnetic and gravity maps would be useful, but these

are not readily available. Oil and gas drilling in this vast region may have sampled this basement, but if so we know nothing about where these penetrations occurred or what was found. Nor can we extrapolate from the buried basement of Libya, this crust is also unknown. What we do know is that buried crust north of the Arabian Shield is surprisingly heterogeneous. We know that 1.2–0.95 Ga crust is exposed in Sinai. There is evidence of a Late Ediacaran (~580 Ma) passive margin developed on the NW flank of Arabia (Zenafim Formation; Avigad et al. 2015) buried beneath younger sediments in Israel, and a similar passive margin sequence might lie beneath the Phanerozoic sediments of the Western Desert. We also know that Cadomian crust ~560 Ma lies beneath sediments in northern Jordan (Stern et al. 2016a, b) and that Carboniferous crust ~357 Ma lies beneath sediments in southern Syria (Stern et al. 2014). It will be for the next generation to explore the buried crust of Egypt. Who knows what they will find?

4.6 Conclusions

Our overview of Egyptian basement rocks can be summarized in the following 10 points:

1. Only a small fraction (~10%) of Egyptian crust is exposed and available for study. Most of this exposed crust is Neoproterozoic in age.
2. Exposures around the Red Sea mark the NW extent of the Arabian-Nubian Shield. These are readily subdivided into 4 basement provinces: Sinai, NE Desert, Central E Desert, and SE Desert. Basement exposures from Aswan westwards along the Sudan border to the border with Libya represent a fifth basement province, the SW Desert.
3. Sinai basement exposures include small remnants of Cryogenian, Tonian, and Late Mesoproterozoic crust that are engulfed in a sea of Ediacaran granites and related dikes and volcanic rocks.
4. In the NE Desert, remnants of Cryogenian and Tonian crust are engulfed in a sea of Ediacaran granites and related dikes and volcanic rocks.
5. Cryogenian and Late Tonian sequences are spectacularly exposed in the Central ED. Relationships between infracrustal gneisses and mesozonal granitic rocks structurally overlain by Late Tonian–Cryogenian ophiolites and distinctive sediments especially banded iron formation and Atud diamictite are locally preserved where they are not disrupted by Ediacaran shear zones of the Najd system, cut by abundant Ediacaran granites, or buried beneath Ediacaran terrestrial sediments of the Hammamat Group. Widespread carbonatization and gold mineralization also characterize the CED.
6. Infrastructure gneisses and intrusives in CED and SED are mistakenly thought to be pre-Neoproterozoic "fundamental basement" but these are clearly represent juvenile middle crust that formed in Neoproterozoic time, as shown by radiometric and isotopic investigations.
7. Basement exposed in the SED covers a much larger area and is much less studied than the basement exposures of Sinai, the NED or the CED. SED basement shares many petrologic characteristics like that of the CED including abundance of ophiolites and gneisses. Limited geochronologic data suggests that it is generally slightly older than the CED; the SED is less affected by Najd shearing than is the CED. Much more work is needed to better understand SED crustal evolution, especially zircon geochronology and related studies. The SED represents one frontier of Egyptian basement geology.
8. The only well-preserved suture in Egypt is the E-W trending Allaqi-Heiani-Gerf-Onib ophiolite belt. ~730 Ma ophiolites were emplaced during terrane collision ~700 Ma.
9. A glimpse of older basement is provided by scattered outcrops along the E-W trending Nubian Swell, just N of the Sudan border. The boundary between juvenile crust of the Arabian-Nubian Shield in the east and the Saharan Metacraton in the west is marked by a broad zone of Neoproterozoic granites and gneisses with isotopic compositions indicating reworking of older crust. West of this transition zone are extensive outcrops of Archean and Paleoproterozoic rocks in the far SW of the Western Desert.
10. We need to find ways to obtain and study samples of Precambrian basement buried beneath Phanerozoic sediments west of the Eastern Desert and north of the Nubian Swell. Future efforts to understand this crust will require co-operation between industrial and academic geophysicists and geologists. Geophysical studies will be very useful for understanding the large scale crustal structure of this region. Exploration of this "last frontier" is likely to reveal some surprising results.

Acknowledgements Thanks to Ghaleb Jarrar (U. Jordan) for help understanding the basement of SW Jordan, to Dov Avigad (Hebrew U.) for help understanding the basement of southernmost Israel, Hassan Helmy (El Minia U.) for help understanding SE Desert mafic-ultramafic intrusions. We appreciate critical comments and suggestions of two anonymous referees. This is UTD Geosciences contribution # 1339.

References

Abdeen MM, Greiling RO (2005) A quantitative structural study of late Pan-African compressional deformation in the central eastern desert (Egypt) during Gondwana assembly. Gondwana Res 8:457–471

Abdel Halim AH, Helmy HM, Abd El-Rahman YM, Shibata T (2016) Petrology of the motaghairat mafic-ultramafic complex, Eastern Desert, Egypt: a high-Mg post-collisional extension-related layered intrusion. J Asian Earth Sci 116:164–180

Abdel-Karim A-AM, Ahmed Z (2010) Possible origin of the ophiolites of Eastern Desert, Egypt, from geochemical perspectives. Arab J Sci Eng 35:115–143

Abdel-Karim AAM, Ali S, Helmy HA, El-Shafei SA (2016) A fore-arc setting of the Gerf ophiolite, Eastern Desert, Egypt: evidence from mineral chemistry and geochemistry of ultramafites. Lithos 263:52–65

Abdelsalam MG, Abdeen MM, Dowaidar HM, Stern RJ, Abdelghaffar AA (2003) Structural evolution of the Neoproterozoic Western Allaqi–Heiani suture, southeastern Egypt. Precambr Res 124:87–104

Abdelsalam MG, Liégeois JP, Stern RJ (2002) The Saharan Metacraton. J Afr Earth Sci 34:119–136

Abdel-Rahman AFM, Doig R (1987) The Rb-Sr geochronological evolution of the Ras Gharib segment of the Northern Nubian Shield. J Geol Soc Lond 144:577–586

Abd El-Rahman Y, Polat A, Dilek Y, Fryer BJ, El-Sharkawy M, Sakran S (2009a) Geochemistry and tectonic evolution of the Neoproterozoic incipient arc–forearc crust in the Fawakhir area, Central Eastern Desert of Egypt. Precambr Res 175:116–134

Abd El-Rahman Y, Polat A, Dilek Y, Fryer BJ, El-Sharkawy M, Sakran S (2009b) Geochemistry and tectonic evolution of the Neoproterozoic Wadi Ghadir ophiolite, Eastern Desert, Egypt. Lithos 113:158–178

Abd El-Rahman Y, Seifert T, Gutzmer J, Said A, Hofmann M, Gärtner A, Linnemann U (2017) The south Um Mongol Cu-Mo-Au prospect in the Eastern Desert of Egypt: from a mid-Cryogenian continental arc to Ediacaran post-collisional appinite-high Ba-Sr monzogranite. Ore Geol Rev 80:250–266

Abd El-Rahman Y, Surour AA, El-Manawi AHW, El-Dougdoug A-MA, Omar S (2015) Regional setting and characteristics of the Neoproterozoic Wadi Hamama Zn-Cu-Ag-Au prospect: evidence for an intra-oceanic island arc-hosted volcanogenic hydrothermal system. Int J Earth Sci 104:625–644

Abu-Alam TS, Stüwe K (2009) Exhumation during oblique transpression: the Feiran-Solaf region. Egypt J Metamorph Geol 27:439–459

Abu El-Enen MM, Whitehouse MJ (2013) The Feiran-Solaf metamorphic complex, Sinai, Egypt: geochronological and geochemical constraints on its evolution. Precambr Res 239:106–125

Abu El-Enen M, Will TM, Okrusch M (2004) P–T evolution of the Pan-African Taba metamorphic belt, Sinai, Egypt: constraints from metapelitic mineral assemblages. J Afr Earth Sci 38:59–78

Agrinier P, Mével C, Bosch D, Javoy M (1993) Metasomatic hydrous fluids in amphibole peridotites. Earth Planet Sci Lett 120:187–205

Ali KA, Azer MK, Gahlan HA, Wilde SA, Samuel MD, Stern RJ (2010a) Age constraints on the formation and emplacement of Neoproterozoic ophiolites along the Allaqi–Heiani Suture, South Eastern Desert of Egypt. Gondwana Res 18:583–595

Ali KA, Stern RJ, Manton WI, Kimura J-I, Khamis HA (2009) Geochemistry, Nd isotopes, and U-Pb SHRIMP zircon dating of Neoproterozoic volcanic rocks from the Central Eastern Desert of Egypt: new insights into the ~750 Ma crust-forming event. Precambr Res 171:1–22

Ali KA, Stern RJ, Manton WI, Johnson PR, Mukherjee SK (2010b) Neoproterozoic diamictite in the Eastern Desert of Egypt and Northern Saudi Arabia: evidence of ~750 Ma glaciation in the Arabian-Nubian Shield. Int J Earth Sci 90:705–726

Ali KA, Kröner A, Hegner E, Wong J, Li S-Q, Gahlan HA, El Ela FF (2015) U-Pb zircon geochronology and Hf–Nd isotopic systematics of Wadi Beitan granitoid gneisses, South Eastern Desert, Egypt. Gondwana Res 27:811–824

Ali KA, Zoheir BA, Stern RJ, Andresen A, Whitehouse MJ, Bishara WW (2016) Lu-Hf and O isotopic compositions on single zircons from the North Eastern Desert of Egypt, Arabian-Nubian Shield: implications for crustal evolution. Gondwana Res 32:181–192

Ali-Bik MW, Sadek MF, Ghabrial DS (2014) Late Neoproterozoic metamorphic assemblages along the Pan-African Hamisana Shear Zone, southeastern Egypt: metamorphism, geochemistry and petrogenesis. J Afr Earth Sci 99:24–38

Ali-Bik MW, Abd El Rahim SH, Abdel Wahab W, Abayazeed SD, Hassan SM (2017) Geochemical constraints on the oldest arc rocks of the Arabian-Nubian Shield: the late Mesoproterozoic to Late Neoproterozoic (?) Sa'al volcano-sedimentary complex, Sinai, Egypt. Lithos 284–285:310–326

Andresen A, El-Enen MM, Stern RJ, Wilde SA, Ali KA (2014) The Wadi Zaghra metasediments of Sinai, Egypt: new constraints on the late Cryogenian–Ediacaran evolution of the northernmost Arabian-Nubian Shield. Int Geol Rev 56:1020–1038

Andresen A, Abu El-Rus MA, Myhre PI, Boghdady GY, Corfu F (2009) U-Pb TIMS age constraints on the evolution of the Neoproterozoic Meatiq Gneiss Dome, Eastern Desert of Egypt. Int J Earth Sci 98:481–497

Augland LE, Andresen A, Boghdady GY (2012) U-Pb ID-TIMS dating of igneous and metaigneous rocks from the El-Sibai area: time constraints on the tectonic evolution of the Central Eastern Desert, Egypt. Int J Earth Sci 101:25–37

Avigad D, Gvirtzman Z (2009) Late Neoproterozoic rise and fall of the northern Arabian-Nubian Shield: the role of lithospheric mantle delamination and subsequent thermal subsidence. Tectonophysics 477:217–228

Avigad D, Weissbrod T, Gerdes A, Zlatkin O, Ireland TR, Morag N (2015) The detrital zircon U-Pb-Hf fingerprint of the northern Arabian-Nubian Shield as reflected by a Late Ediacaran arkosic wedge (Zenifim Formation; subsurface Israel). Precambr Res 266:1–11

Azer MK, Gahlan HA, Asimow PD, Al-Kahtany K (2017) The Late Neoproterozoic Dahanib Mafic-ultramafic intrusion, south-eastern desert, Egypt: is it an Alaskan-type or layered intrusion? Am J Sci 317:91–940

Azer M, Obeid MA, Ren M (2014) Geochemistry and petrogenesis of late Ediacaran (605–580 Ma) post-collisional alkaline rocks from the Katherina ring complex, south Sinai, Egypt. J Asian Earth Sci 93:229–252

Azer MK, Samuel MD, Ali KA, Gahlan HA, Stern RJ, Ren M, Moussa HE (2013) Neoproterozoic ophiolitic peridotites along the Allaqi–Heiani suture, South Eastern Desert, Egypt. Mineral Petrol 107:829–848

Azer MK, Stern RJ (2007) Neoproterozoic (835–720 Ma) serpentinites in the Eastern Desert, Egypt: fragments of forearc mantle. J Geol 115:457–472

Azer MK, Stern RJ, Kimura JI (2010) Origin of a Late Neoproterozoic (605 ± 13 Ma) intrusive carbonate–albitite complex in southern Sinai, Egypt. Int J Earth Sci 99:245–267

Bea F, Abu-Anbar M, Montero P, Peres P, Talavera C (2009) The ~844 Ma Moneiga quartz-diorites of the Sinai, Egypt: evidence for

Andean-type arc or rift-related magmatism in the Arabian-Nubian Shield? Precambr Res 175:161–168
Bea F, Montero P, Abu Anbar M, Molina JF, Scarrow JH (2011a) The Bir Safsaf Precambrian inlier of South West Egypt revisited. A model for ~1.5 Ga T_{DM} late Pan-African granite generation by crustal reworking. Lithos 125:897–914
Bea F, Montero P, Abu Anbar M, Talavera C (2011b) SHRIMP dating and Nd isotope geology of the Archean terranes of the Uweinat-Kamil inlier, Egypt–Sudan–Libya. Precambr Res 189:328–346
Be'eri-Shlevin Y, Katzir Y, Valley JW (2009a) Crustal evolution and recycling in a juvenile continent: oxygen isotope ratio of zircon in the northern Arabian-Nubian Shield. Lithos 107:169–184
Be'eri-Shlevin Y, Katzir Y, Whitehouse M (2009b) Post-collisional tectonomagmatic evolution in the northern Arabian-Nubian Shield (ANS): time constraints from ion-probe U-Pb dating of zircon. J Geol Soc Lond 166:71–85
Be'eri-Shlevin Y, Eyal M, Eyal Y, Whitehouse MJ, Litvinovsky B (2012) The Sa'al volcano-sedimentary complex (Sinai, Egypt): a latest Mesoproterozoic volcanic arc in the northern Arabian Nubian Shield. Geology 40:403–406
Bennett GD, Mosely P (1987) Tiered tectonics and evolution, Eastern Desert and Sinai, Egypt. In: Matheis G, Schandelmeier H (eds) Current research in African Earth sciences. Balkema, Rotterdam, The Netherlands, pp 79–82
Bernau R, Darbyshire DPF, Franz G, Harms U, Huth A, Mansour N, Pasteels P, Schandelmeier H (1987) Petrology, geochemistry, and structural development of the Bir Safsaf-Aswan uplift, Southern Egypt. J Afr Earth Sci 6:79–90
Boskabadi A, Pitcairn IK, Broman C, Boyce A, Teagle DAH, Cooper MJ, Azer MK, Mohamed FH, Stern RJ (2016) Carbonate alteration of ophiolitic rocks in the Arabian Nubian Shield of Egypt: sources and compositions of the carbonating fluid and implications for the formation of Au deposits. Int Geol Rev 59:391–419
Boudier F, Nicolas A, Kienast JR, Mevel C (1988) The gneiss of Zabargad island: deep crust of rift. Tectonophysics 150:209–227
Breitkreuz C, Eliwa H, Khalaf I, El Gameel K, Bühler B, Sergeev S, Larionov A (2010) Neoproterozoic SHRIMP U-Pb zircon ages of silica-rich Dokhan Volcanics in the northeastern Desert, Egypt. Precambr Res 182:163–174
Brueckner HK, Elhaddad MA, Hamelin B, Hemmings S, Kröner A, Reisberg L, Seyler M (1995) A Pan African origin and uplift for the gneisses and peridotites of Zabargad Island, Red Sea: a Nd, Sr, Pb, and Os isotope study. J Geophys Res Solid Earth 100:22283–22297
Bühler B, Breitkreuz C, Pfänder JA, Hofmann M, Becker S, Linnemann U, Eliwa HA (2014) New insights into the accretion of the Arabian-Nubian Shield: depositional setting, composition and geochronology of a mid-Cryogenian arc succession (North Eastern Desert, Egypt). Precambr Res 243:149–167
de Wall H, Greiling RO, Sadek MF (2001) Post-collisional shortening in the late Pan-African Hamisana high strain zone, SE Egypt: field and magnetic fabric evidences. Precambr Res 107:179–194
Dixon TH (1981a) Gebel Dahanib, Egypt: a late Precambrian layered sill of komatiitic composition. Contrib Miner Petrol 76:42–53
Dixon TH (1981b) Age and chemical characteristics of some pre-Pan-African rocks in the Egyptian Shield. Precambr Res 14:119–133
El Bahariya GA (2018) Classification of the Neoproterozoic ophiolites of the Central Eastern Desert, Egypt based on field geological characteristics and mode of occurrence. Arab J Geosci 11:313. https://doi.org/10.1007/s12517-018-3677-1
El-Nisr SA (1997) Late Precambrian volcanism at Wadi Allaqi, south Eastern Desert, Egypt: evidence for transitional continental arc/margin environment. J Afr Earth Sci 24:301–312
El-Shazly AK, Khalil KI (2014) Banded iron formations of Um Nar, Eastern Desert of Egypt: P-T-X conditions of metamorphism and tectonic implications. Lithos 196–197:356–375
Eliwa HA, Breitkreuz C, Murata M, Khalaf IM, Bühler B, Itaya T, Takahashi T, Hirahara Y, Miyazaki T, Kimura J-I, Shibata T, Koshi Y, Kato Y, Ozawa H, Daas MA, El Gameel KH (2014) SIMS zircon U-Pb and mica K–Ar geochronology, and Sr–Nd isotope geochemistry of the north Eastern Desert, Egypt. Gondwana Res 25:1570–1598
Eliwa H, Kimura J-I, Itaya T (2006) Late Neoproterozoic Dokhan Volcanics, North Eastern Desert, Egypt: geochemistry and petrogenesis. Precambr Res 151:31–52
Eyal M, Bartov Y, Shimron AE, Bentor YK (1980) Sinai geological map, aeromagnetic map. Survey of Israel, Scale: 1:500 000, 1 sheet
Eyal M, Be'eri-Shlevin Y, Eyal Y, Whitehouse MJ, Litvinovsky B (2014) Three successive Proterozoic island arcs in the Northern Arabian-Nubian Shield: evidence from SIMS U-Pb dating of zircon. Gondwana Res 25:338–357
Eyal M, Livinovsky B, Jahn BM, Zanvillevich A, Katzir Y (2010) Origin and evolution of post-collisional magmatism: coeval calc-alkaline and alkaline suites of the sinai Peninsula. Chem Geo 269:153–179
Farahat ES (2010) Neoproterozoic arc–back-arc system in the Central Eastern Desert of Egypt: evidence from supra-subduction zone ophiolites. Lithos 120:293–308
Finger F, Dörr W, Gerdes A, Gharib M, Dawoud M (2008) U-Pb zircon ages and geochemical data for the Monumental Granite and other granitoid rocks from Aswan, Egypt: implications for the geological evolution of the western margin of the Arabian-Nubian Shield. Miner Petrol 93:153–183
Fowler A, Hassan IS, Hassan M (2018) The Feiran-Solaf metamorphic complex, Sinai, Egypt: evidence for orthogonal or oblique tectonic convergence? J Afr Earth Sci 46:48–65
Fowler A-R, El Kalioubi B (2002) The Migif-Hafafit gneissic complex of the Egyptian Eastern Desert: fold interference patterns involving multiply deformed sheath folds. Tectonophysics 346:247–275
Fowler A, Osman AF (2013) Sedimentation and inversion history of three molasse basins of the western Central Eastern Desert of Egypt: implications for the tectonic significance of Hammamat basins. Gondwana Res 23:1511–1534
Gahlan HA, Azer MK, Khalil AES (2015) The Neoproterozoic Abu Dahr ophiolite, South Eastern Desert, Egypt: petrological characteristics and tectonomagmatic evolution. Mineral Petrol 109:611–630
Gindy AR, Tamish MM (1998) Petrogenetic revision of the basement rocks in the environs of Aswan, southern Egypt. Egypt J Geol 42:1–14
Hamimi Z, Abd El-Wahed MA, Gahlan HA, Kamh SZ (2019) Tectonics of the Eastern Desert of Egypt: key to understanding the Neoproterozoic evolution of the Arabian-Nubian Shield. In: Bendaoud A et al (eds) The geology of the Arab world—an overview. Springer Geology. https://doi.org/10.1007/978-3-319-96794-3_1
Harris NBW, Hawkesworth CJ, Ries AC (1984) Crustal evolution in north-east and east Africa from model Nd ages. Nature 309:773–776
Helmy HM (1999) The Um Samiuki volcanogenic Zn-Cu-Pb-Ag deposit, Eastern Desert: a possible new occurrence of Cervelleite. Can Mineral 37:143–158
Helmy HM (2004) Cu-Ni-PGE mineralization in the Genina Gharbia mafic-ultramafic intrusion, Eastern Desert, Egypt. Can Mineral 42:351–370
Helmy HM, Abd El-Rahman YM, Yoshikawa M, Shibata T, Arai S, Tamura A, Kagami H (2014) Petrology and Sm-Nd dating of the Genina Gharbia Alaskan-type complex (Egypt): insights into deep levels of Neoproterozoic island arcs. Lithos 198–199:263–280

Helmy HM, El Mahallawi MM (2003) Gabbro Akarem mafic-ultramafic complex, Eastern Desert, Egypt: a Late Precambrian analogues of Alaskan-type complexes. Miner Petrol 77:85–108

Hosny A, Nyblade A (2016) Crustal structure of Egypt from Egyptian National Seismic Network data. Tectonophysics 687:257–267

Helmy HM, Yoshikawa M, Shibata T, Arai S, Kagami H (2015) Sm-Nd and Rb-Sr isotope geochemistry and petrology of Abu Hamamid intrusion, Eastern Desert of Egypt: an Alaskan-type complex in a backarc setting. Precambr Res 258:234–246

Helmy H, Zoheir B (2015) Metal and fluid sources in a potential world-class gold deposit: El-Sid mine, Egypt. Int J Earth Sci 104:645–661

Jarrar GH, Theye T, Yaseen N, Whitehouse M, Pease V, Passchier C (2013) Geochemistry and P-T-t evolution of the Abu-Barqa Metamorphic Suite, SW Jordan, and implications for the tectonics of the northern Arabian-Nubian Shield. Precambr Res 239:56–78

Johnson PR, Woldhaimanot B (2003) Development of the Arabian-Nubian Shield: perspectives on accretion and deformation in the northern East African Orogen and the assembly of Gondwana. In: Yoshida M, Dasgupta S, Windley B (eds) Proterozoic East Gondwana: supercontinent assembly and breakup. Special Pub. 206. Geological Society of London, pp 289–325

Karmakar S, Schenk V (2015) Neoarchean UHT metamorphism and Paleoproterozoic UHT Reworking at Uweinat in the East Sahara Ghost Craton, SW Egypt: evidence from petrology and texturally controlled in situ Monazite dating. J Petrol 56:1703–1742

Katzir Y, Litvinovsky BA, Jahn BM, Eyal M, Zanvilevich AN, Valley JW, Vapnik Y, Beeri Y, Spicuzza MJ (2007) Interrelationships between coeval mafic and A-type silicic magmas from composite dykes in a bimodal suite of southern Israel, northernmost Arabian-Nubian Shield: geochemical and isotope constraints. Lithos 97:335–364

Khalil AES, Azer MK (2007) Supra-subduction affinity in the Neoproterozoic serpentinites in the Eastern Desert, Egypt: evidence from mineral composition. J. Afr Earth Sci 49:136–152

Kröner A, Eyal M, Eyal Y (1990) Early Pan-African evolution of the basement around Elat, Israel, and the Sinai Peninsula revealed by single-zircon evaporation dating, and implications for crustal accretion rates. Geology 18:545–548

Kröner A, Krüger J, Rashwan AAA (1994) Age and tectonic setting of granitoid gneisses in the Eastern Desert of Egypt and south-west Sinai. Geol Rundsch 83:502–513

Kröner A, Todt W, Hussein IM, Mansour IM, Mansour M, Rashwan AA (1992) Dating of late Proterozoic ophiolites in Egypt and the Sudan using the single grain zircon evaporation technique. Precambr Res 59:15–32

Lancelot JR, Bosch D (1991) A Pan African age for the HP-HT granulite gneisses of Zabargad island: implications for the early stages of the Red Sea rifting. Earth Planet Sci Lett 107:539–549

Liégeois J-P, Stern RJ (2010) Sr-Nd isotopes and geochemistry of granite-gneiss complexes from the Meatiq and Hafafit domes, Eastern Desert, Egypt: no evidence for pre-Neoproterozoic crust. J Afr Earth Sci 57:31–40

Morag N, Avigad D, Gerdes A, Belousova E, Harlavan Y (2011) Crustal evolution and recycling in the northern Arabian-Nubian Shield: new perspectives from Late Neoproterozoic sediments (Elat area, Israel). Precambr Res 186:101–116

Morag N, Avigad D, Gerdes A, Harlavan Y (2012) 1000–580 Ma crustal evolution in the northern Arabian-Nubian Shield revealed by U-Pb-Hf of detrital zircons from Late Neoproterozoic sediments (Elat area, Israel). Precambr Res 208–211:197–212

Moghazi A-KM, Ali KA, Wilde SA, Zhou Q, Andersen T, Andresen A, Abu El-Enen MM, Stern RJ (2012) Geochemistry, geochronology, and Sr-Nd isotopes of the Late Neoproterozoic Wadi Kid volcano-sedimentary rocks, southern Sinai, Egypt: implications for tectonic setting and crustal evolution. Lithos 154:147–165

Moussa EMM, Stern RJ, Manton WI, Ali KA (2008) SHRIMP zircon dating and Sm/Nd isotopic investigations of Neoproterozoic granitoids, Eastern Desert, Egypt. Precambr Res 160: 341–356

Powell JH, Abed AA, Le Nidre Y-M (2014) Cambrian stratigraphy of Jordan. GeoArabia 19:81–134

Ries AC, Shackleton RM, Graham RH, Fitches WR (1983) Pan-African structures, opiolites and mélange in the Eastern Desert of Egypt: a traverse at 26°N. J Geol Soc London 140:75–95

Samuel MD, Be'eri-Shlevin Y, Azer MK, Whitehouse MJ, Moussa HE (2011) Provenance of conglomerate clasts from the volcani-sedimentary sequence at Wadi Rutig in southern Sinai, Egypt as revealed by SIMS U-Pb dating of zircon. Gondwana Res 20:450–464

Shalaby A (2010) The northern dome of Wadi Hafafit culmination, Eastern Desert, Egypt: structural setting in tectonic framework of a scissor-like wrench corridor. J Afr Earth Sci 57:227–241

Sims PK, James HL (1984) Banded iron-formation of Late Proterozoic age in the Central Eastern Desert, Egypt: geology and tectonic setting. Econ Geol 79:1777–1784

Stern RJ (1981) Petrogenesis and tectonic setting of late Precambrian ensimatic volcanic rocks, Central Eastern Desert of Egypt. Precambr Res 16:195–230

Stern RJ (1985) The Najd fault system, Saudi Arabia and Egypt: a Late Precambrian rift–related transform system. Tectonics 4:497–511

Stern RJ (2018) Neoproterozoic formation and evolution of Eastern Desert Continental Crust—the importance of the infrastructure-superstructure transition. J Afr Earth Sci 18:15–27

Stern RJ, Ali KA, Liégeois J-P, Johnson P, Wiescek F, Kattan F (2010a) Distribution and significance of pre-Neoproterozoic Zircons in Juvenile Neoproterozoic igneous rocks of the Arabian-Nubian Shield. Am J Sci 310:791–811

Stern RJ, Ali K, Ren M, Jarrar GH, Romer RL, Leybourne M, Whitehouse MJ (2016a) Cadomian (~560 Ma) crust buried beneath the Northern Arabian Peninsula: mineral, chemical, geochronological, and isotopic constraints from NE Jordan xenoliths. Earth Planet Sci 436:31–42

Stern RJ, Ali K, Ren M, Jarrar GH, Romer RL, Leybourne M, Whitehouse MJ (2016b) Cadomian (~560 Ma) crust buried beneath the Northern Arabian Peninsula: mineral, chemical, geochronological, and isotopic constraints from NE Jordan xenoliths. Earth Planet Sci 436:31–42

Stern RJ, Gottfried D, Hedge CE (1984) Late Precambrian rifting and crustal evolution in the Northeastern Desert of Egypt. Geology 12:168–171

Stern RJ, Hedge CE (1985) Geochronologic constraints on late Precambrian crustal evolution in the Eastern Desert of Egypt. Am J Sci 285:97–127

Stern RJ, Ali KA, Liégeois J-P, Johnson P, Wiescek F, Kattan F (2010b) Distribution and Significance of pre-Neoproterozoic Zircons in Juvenile Neoproterozoic Igneous Rocks of the Arabian-Nubian Shield. Am J Sci 310:791–811

Stern RJ, Johnson P (2010) Continental lithosphere of the Arabian plate: a geologic, petrologic, and geophysical synthesis. Earth Sci Rev 101:29–67

Stern RJ, Kröner A, Manton WI, Reischmann T, Mansour M, Hussein IM (1989) Geochronology of the late Precambrian Hamisana shear zone, Red Sea Hills, Sudan and Egypt. J Geol Soc 146:1017–1029

Stern RJ, Kröner A, Rashwan AA (1991) A Late Precambrian (~710 Ma) high volcanicity rift in the souther Eastern Desert of Egypt. Geol Rundsch 80(1):155–170

Stern RJ, Manton WI (1987) Age of Feiran basement rocks, Sinai: implications for late Precambrian evolution in the northern Arabian-Nubian Shield. J Geol Soc Lond 144:569–575

Stern RJ, Mukherjee SK, Miller NR, Ali K, Johnson PR (2013) banded iron formation from the Arabian-Nubian Shield—implications for understanding Neoproterozoic climate change. Precambr Res 239:79–94

Stern RJ, Nielsen KC, Best E, Sultan M, Arvidson RE, Kröner A (1990) Orientation of late Precambrian sutures in the Arabian-Nubian Shield. Geology 18:1103–1106

Stern RJ, Ren M, Ali K, Förster H-J, Al Safarjalani A, Nasir S, Whitehouse MJ, Leybourne MI (2014) Early Carboniferous (~357 Ma) crust beneath northern Arabia: tales from Tell Thannoun (southern Syria). Earth Planet Sci Lett 393:83–93

Stern RJ, Sellers G, Gottfried D (1988) Bimodal dike swarms in the Northeastern Desert of Egypt: significance for the origin of late Precambrian 'A-Type' granites in northern Afro–Arabia. In: Greiling R, El Gaby S (eds) The Pan-African belt of NE Africa and Adjacent Areas: tectonic evolution and economic aspects, pp 147–179

Stern RJ, Voegeli DA (1987) Geochemistry, geochronology, and petrogenesis of a late Precambrian (~590 Ma) composite dike from the North Eastern Desert of Egypt. Geol Rundsch 76:325–341

Sultan M, Arvidson RE, Sturchio NC (1986) Mapping of serpentinites in the Eastern Desert of Egypt by using Landsat thematic mapper data. Geology 14:995–999

Sultan M, Chamberlain KC, Bowring SA, Arvidson RE, Abuzeid H, El Kaliouby B (1990) Geochronologic and isotopic evidence for involvement of pre-Pan-African crust in the Nubian shield, Egypt. Geology 18:761–764

Sultan M, Tucker RD, El Alfy Z, Attia R (1994) U-Pb (zircon) ages for the gneissic terrane west of the Nile, southern Egypt. Geol Rundsch 83:514–522

Thurmond AK, Stern RJ, Abdelsalam MG, Nielsen KC, Abdeen MM, Hinz E (2004) The Nubian Swell. J Afr Earth Sci 39:401–407

Walker JD, Geissman JW, Bowring SA, Babcock LE (2012) Geologic Time Scale v. 4.0, Geological Society of America

Wilde, SA, Youssef, K (2000) Significance of SHRIMP U–Pb dating of the Imperial Porphyry and associated Dokhan Volcanics, Gabal Dokhan, North Eastern Desert, Egypt. J Afr Earth Sci 31:403–413

Zimmer M, Kröner A, Jochum KP, Reischmann T, Todt W (1995) The Gabal Gerf: a precambrian N-MORB ophiolite in the Nubian Shield, NE Africa. Chem Geol 123:29–51

Suture(s) and Major Shear Zones in the Neoproterozoic Basement of Egypt

5

Zakaria Hamimi and Mohamed A. Abd El-Wahed

Contents

Abstract

The Arabian-Nubian Shield (ANS), the northern extension of the East African Orogen (EAO), consists of a number of amalgamated island-arc tectonic terranes, separated along suture zones, major shear zones and cryptic major high strain zones. The Allaqi-Heiani-Oneib-Sol Hamid-Yanbu Suture separates the Eastern Desert-Midyan terrane from the Gabgaba-Gebeit-Hijaz terrane. The latter terrane juxtaposes Haya-Jiddah terrane along the Nakasib-Bir Umq Suture which is the longest ophiolite-decorated shear zone allover the ANS. The Haya-Jiddah terrane is separated from the Nakfa-Asir terrane along Baraka-Al-Damm Fault Zone. The previously mentioned Hijaz-Jiddah-Asir borders the continental Afif terrane through the Hulaifa-Ad-Dafinah-Ruwah sinistral transpressional zone. Ad-Dawadimi and Ar-Rayan terranes occupy the eastern part of the Arabian Shield, being separated from the Afif terrane and from each others along the Halaban and Al-Amar Sutures. The smallest terrane in the ANS is the Ha'il terrane. This chapter reviews some of the major shear zones existed inside the Eastern Desert of Egypt (The Egyptian Nubian Shield; ENS). It addresses also the Allaqi-Heiani Suture which is regarded as the western segment of the enormous arc-arc Allaqi-Heiani-Oneib-Sol Hamid-Yanbu Suture Zone. The shear zones are dealt with through two main groups; syn-accretion- and post-accretion shear zones. The first group is manifested by the NNE-oriented Hamisana Shear Zone, whereas the second group is typified by the Najd-related NW-trending Shear Zones, such as Hodein-Karite-, Nugrus- and Atallah-Shear Zones, as well as by the relatively younger ENE- (to E-) trending shear zones and shear belts, such as

Z. Hamimi
Faculty of Science, Department of Geology, Benha University, Benha, 13518, Egypt
e-mail: zakariahamimi123@gmail.com; zakaria.hamimi@fsc.bu.edu.eg

M. A. Abd El-Wahed (✉)
Faculty of Science, Geology Department, Tanta University, Tanta, 31527, Egypt
e-mail: mohamed.abdelwahad@science.tanta.edu.eg

Z. Hamimi et al. (eds.), *The Geology of Egypt*, Regional Geology Reviews,
https://doi.org/10.1007/978-3-030-15265-9_5

Mubarak-Barramiya Shear Belt and Abu Dabbab Shear Zone. The shear zone-related mineralizations (particularly gold) is dealt in the last section.

5.1 Introduction

Sutures are sites delineating closure of ocean basins and back-arc basins, and therefore the obliteration of oceanic lithosphere by subduction and the consequent intracontinental welding of continental blocks. These sites provide the only record for the ancient sea-floor spreading and the subsequent continental collision. Sutures are widely distributed in the orogenic belts all over the globe (e.g. the Pan-African Sutures around North Africa, Arabia, West Congo, Damara and Zambesi, the Alpine Sutures, the Caledonides and Sveco-Norwegian Sutures, the Ural Sutures, the Cordilleran Sutures, the Northern and Southern Appalachian Sutures, the Grenville Sutures). Linear arrangement of ophiolitic belts and nappes is the solid evidence confirming the sutures. Likewise, shear zones are zones accommodating deformation and relative movement of crustal or lithospheric blocks. They are frequently planar zones of concentrated deformation help to accommodate imposed regional or local strain rates beyond the strength of the country rocks. These high strain zones are also widely distributed worldwide. However, the study of both sutures and shear zones in the Arabian-Nubian Shield (ANS) (Fig. 5.1), and probably in the entire East African Orogen (EAO) has given much more attention since the leading works of Abdelsalam and Stern (1996) who subdivided the deformational belts in the ANS (Fig. 5.1) into: (1) those associated arc-arc- and arc-continental-sutures; and (2) post-accretionary structures which include N-trending shortening zones and NW-trending strike-slip faults. According to these authors, the arc-arc sutures manifest collision between arc terranes at 800–700 Ma. The arc-continental sutures define the eastern and western boundaries of the ANS and are marked by N-trending deformational belts which accompanied collision of the ANS with E- and W-Gondwanalands at ~750–650 Ma. The

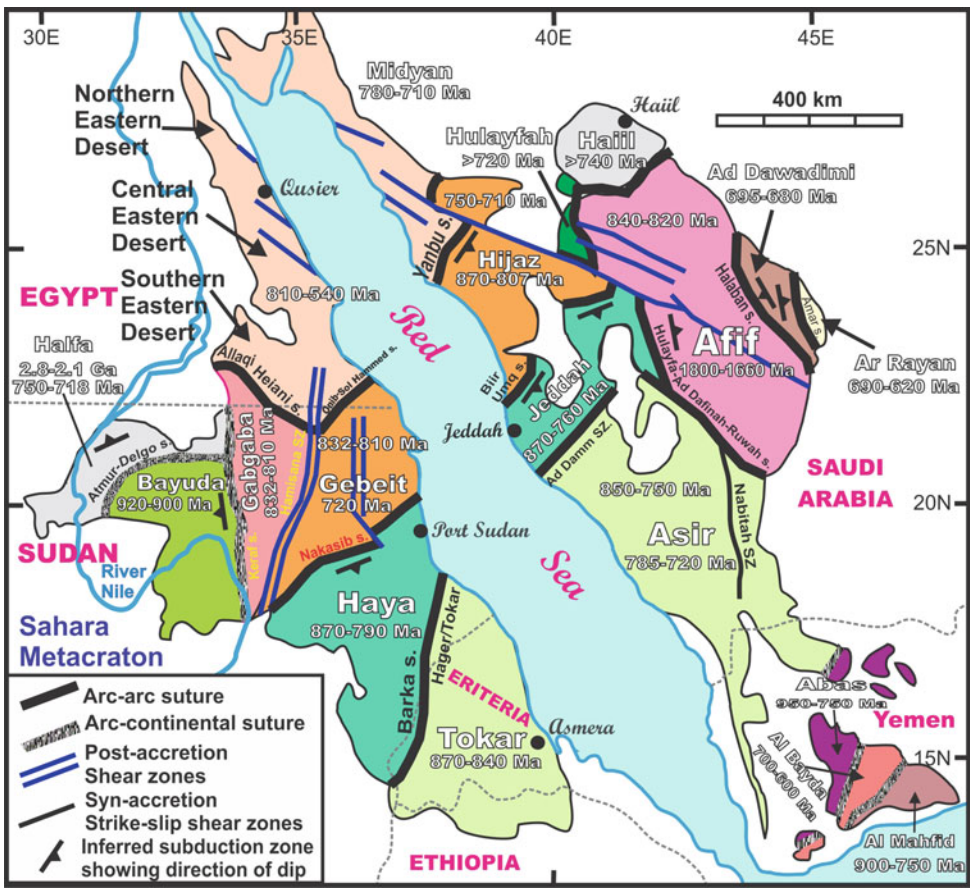

Fig. 5.1 Tectonic map of the Arabian–Nubian Shield showing the locations and extents of terranes, sutures and post-accretionary structures. Modified after Johnson and Woldehaimanot (2003), Hargrove et al. (2006a, b) and Abdelsalam (2010). Terrane ages from Stern et al. (1994), Stern et al. (1989), Kröner et al. (1992), Kröner et al. (1991), Pallister et al. (1988), Agar et al. (1992), Whitehouse et al. (2001), Hargrove et al. (2006a, b), Andresen et al. (2009), Küster et al. (2008)

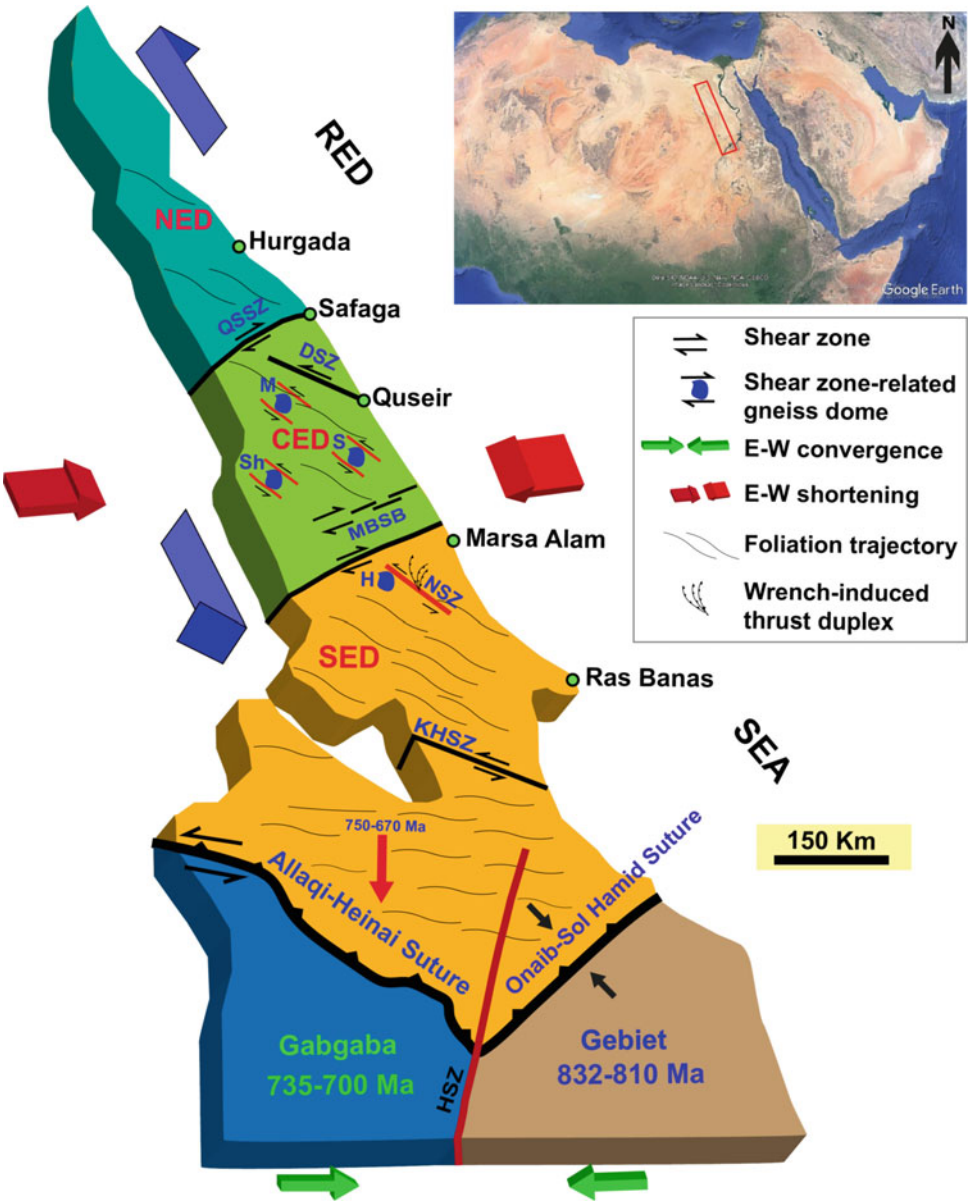

Fig. 5.2 The major shear zones in the Egyptian Nubian Shield

post-accretionary structures were developed between ~650 and 550 Ma due to continued shortening of the ANS.

The ENS outcrops mainly in the Eastern Desert and southern Sinai. The Eastern Desert is traditionally subdivided into Northern Eastern Desert (NED), Central Eastern Desert (CED) and Southern Eastern Desert (SED) (Fig. 5.2). In the ENS, major shear zones plays significant role in the structural shaping of the Neoproterozoic Pan-African belt. El-Gaby et al. (1988, 1990) considered Qena-Safaga Shear Zone as a conspicuous right-lateral shear zone juxtaposing remobilized older continental crust and infolded, locally metamorphosed, Dokhan Volcanics and molasse Hammamat sediments to the north, and ophiolites, island arc metavolcanics and metavolcanogenics to the south. The obvious shear trend in the ENS is the Najd-related NW- (to NNW-) trend. This trend is exemplified by Wadi Kharit-Wadi Hodein-, Nugrus- and Atallah-Shear Zones (Fig. 5.2). Other remarkable shearing trend is the NE (to ENE), such as Qena-Safaga- and Idfu-Mersa Alam-Shear Zones (Fig. 5.2). Whether the Najd-related NW- (to NNW-) and the NE (to ENE) trends are conjugate or not was and still is a matter of controversy.

5.2 Arc-Arc Sutures

In the northern ANS, the subduction stage in the northern ANS is dated as 850–650 Ma, with subduction terminated by arc-arc collisions and suturing between 760 and 690 Ma

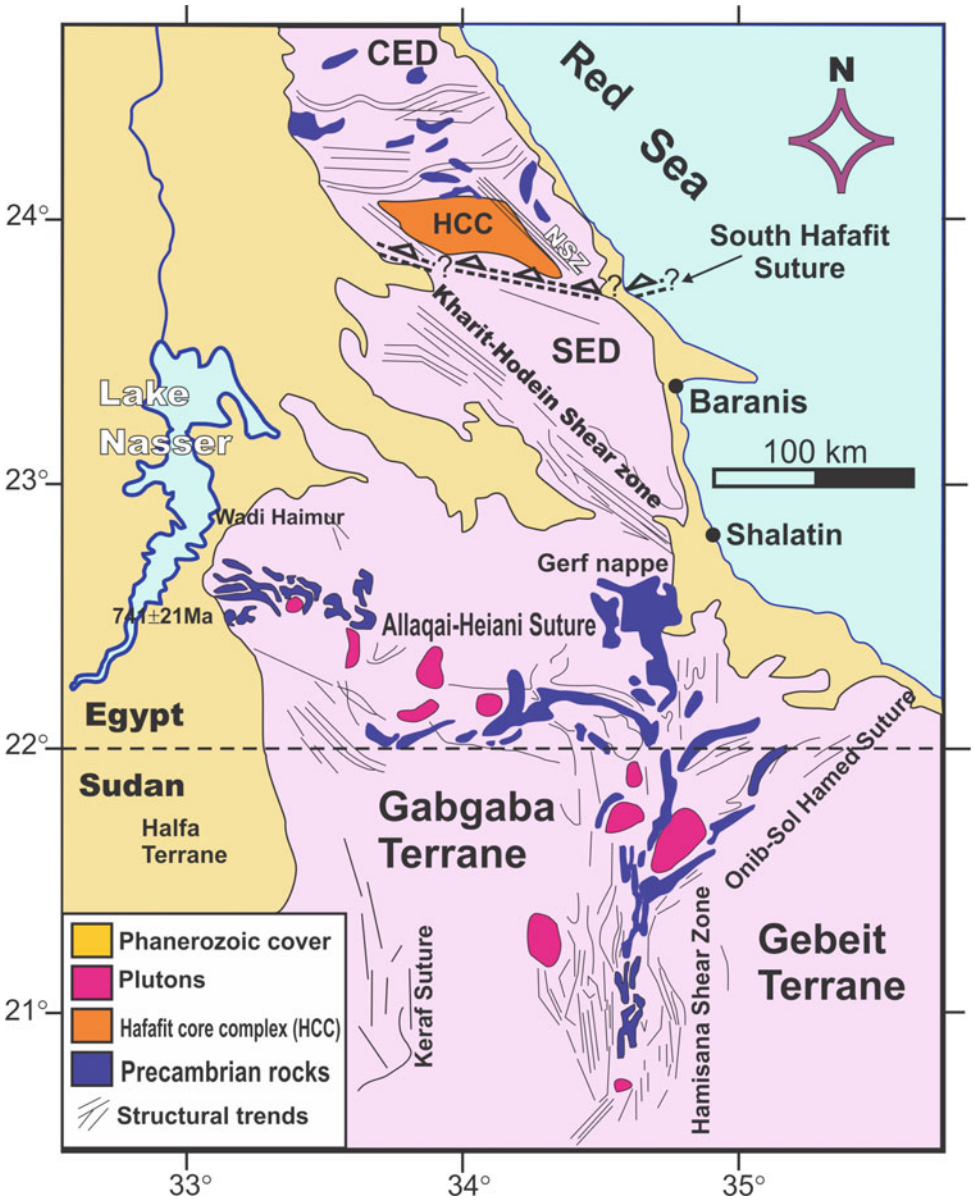

Fig. 5.3 Tectonic map of the Allaqi-Heiani-Gerf suture, South-Eastern Desert of Egypt (modified after Abdelsalam et al. 2003), showing location of ophiolites along the suture

(Stern 1994), but compressional deformation and subduction-related plutonism persisted until about 625 Ma (Johnson and Woldehaimanot 2003; Stern et al. 2010; Fritz et al. 2013). During deformation, lithologic volcanic, plutonic and sedimentary rocks belonging to this stage have been metamorphosed to greenschist facies. The ~715–765 Ma Shadli metavolcanics and equivalents of the SED are affiliated to the volcanic arc stage by many workers (e.g. Stern and Hedge 1985a, b; Stern et al. 1991). The arc-arc collisional zones are represented by ophiolite-decorated sutures that extend on both sides of the Red Sea. These zones include the Allaqi-Heiani-Onib-Sol Hamed-Yanbu Suture (AHOSHY) (Fig. 5.3), the Amur-Nakasib-B'ir Umq Suture (ANBU) (Stoeser and Camp 1985; Vail 1985; Shackleton 1986, 1994; Kröner et al. 1987; Stern et al. 1990; Johnson and Woldehaimanot 2003; Johnson et al. 2011). The AHOSHY is dated at 740–700 Ma, while the ANBU is dated at 780–750 Ma (Abdelsalam and Stern 1996; Ali et al. 2010; Johnson et al. 2011), and both zones are regarded as arc-arc sutures with NW-SE convergence directions, with some transpression resulting in strike-slip component.

5.2.1 Allaqi-Heiani Suture

The Allaqi-Heiani-Onib-Sol Hamed Zone (AHOSH) is the western continuation of the previously mentioned AHOSHY Suture (Fig. 5.3). The western segment of AHOSH is known

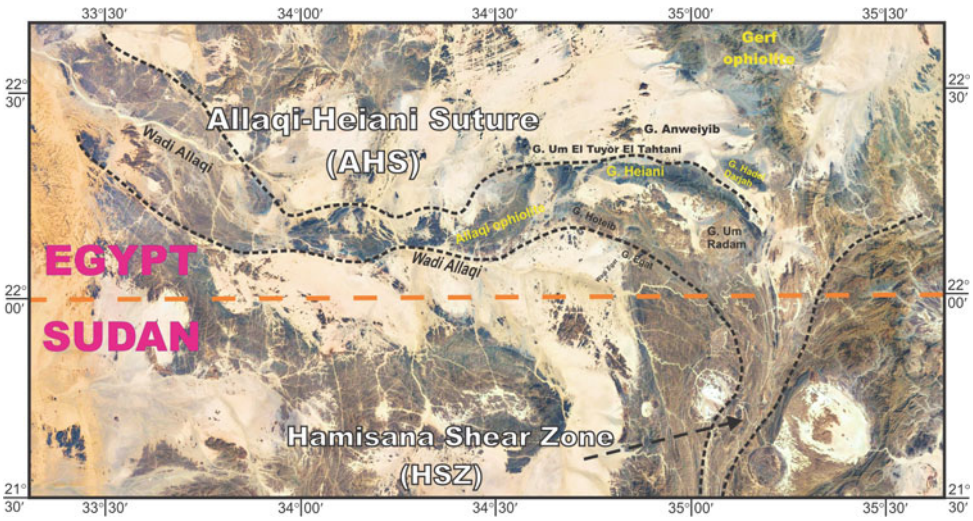

Fig. 5.4 The AHS extends over 200 km (average width 3 km) from Gabal Um Shilman and probably to Nasser Lake in the west to the NNE-trending Hamisana Shear Zone in the east

as Allaqi-Heiani Suture (AHS). Abdelsalam et al. (2003) believed that the Neoproterozic AHS is the western extension of the AHOSHY that represents one of arc-arc sutures in the ANS. From the authors opinion, this suture is worthy to understand Neoproterozoic evolution of the ANS because: (1) It is the northernmost linear ophiolitic belt that defines an arc-arc suture in the ANS (Kröner et al. 1987; Stern 1994; Abdelsalam and Stern 1996); (2) It is the only suture in the ANS where a complete ophiolite is preserved at Gabal Gerf (Zimmer et al. 1995); (3) The suture extends in a general east-west direction and its western end is at a high angle to the proposed N-trending western margin of the ANS; and (4) Recent tectonic models have resulted in conflicting views about the continuity of the AHS, its structural style, and the overall tectonic transport direction involved. However, the AHS was described as a major shear zone for the first time by Taylor et al. (1993), Greiling et al. (1994) and EGSMA (1996). Abdelsalam et al. (2003) and others indicate that this zone is not a high strain zone, but an ophiolitic decorated shear zone (i.e. a suture zone). Kusky and Ramadan (2002) carried out integrated remote sensing and field work to distinguish exposed lithologic units, and to investigate overprinting relations between geologic structures along AHS in the vicinity of Gabal Um Shilman. These authors considered the AHS as an arc/arc collision suture zone (750–720 Ma) formed when the Gerf terrane (Eastern Desert or Aswan terrane) in the north overrode the Gabgaba terrane in the south, prior to the closure of the Mozambique Ocean (830–720 Ma).

The AHS extends over 200 km (average width ≈ 3–4 km) from Gabal Um Shilman probably to Nasser Lake (Figs. 5.3 and 5.4) in the west to the NNE-trending Hamisana Shear Zone in the east (Hamimi et al. 2019). It can be traced easily on the satellite imagery and aerial photomosaics (scale 1:50.000) covering Gabgaba-Elba Topographic Sheets (scale 1:250.000). The strike of this zone is remarkably variable from E-W, NW-SE and N-S. Such strike variation makes this suture to be perpendicular to the main Wadi Allaqi to the west (Fig. 5.4) and align the southern flank of the same wadi to the east, where it is apparently cut by the NE-oriented Hamisana Shear Zone (Greiling et al. 1994). The collision along the AHS is characterized by folding, and thrusting and the S- (to SE- or SW-) steeper imbrication of Gabal Gerf Nappe (Gabal Gerf Klippe) over the 830–720 Ma Gabgaba arc terrane (Abdelsalam and Stern 1996; Abdelsalam et al. 2003; Kusky and Ramadan 2002). Investigations of the ophiolitic rocks in the Gerf Nappe or klippe indicate that they are mainly massive almost intact ophiolite blocks and steeply dipping thrust slices (Fig. 5.5), with only minor mélange (Kusky and Ramadan 2002, Abdel-Karim et al. 2016) This is in complete harmony with opinion that the ophiolites having been transported only a short distance from its source (Abdelsalam and Stern 1996) and a long distance as suggested by Greiling et al. (2014). In this context, Abdelsalam et al. (2003) considered the AHS as an E-W to NW-SE trending fold/thrust belt forming three allochthons and one autochthonous block.

Abdelsalam and Stern (1996) proposed four Neoproterozoic deformations ($D_1 \rightarrow D_4$) for the development of the AHS. D_1 and D_2 are associated with early collisional stages between the Gerf terrane in the north, and Haya and Gabgaba terranes in the south, whereas D_3 and D_4 are associated with later stages of collision. Such conclusion is inconsistent with that given by El-Kazzaz and Taylor (2000) who used facing direction and folded thrust patterns to demonstrate north-verging and top-to-north transport direction. The AHS

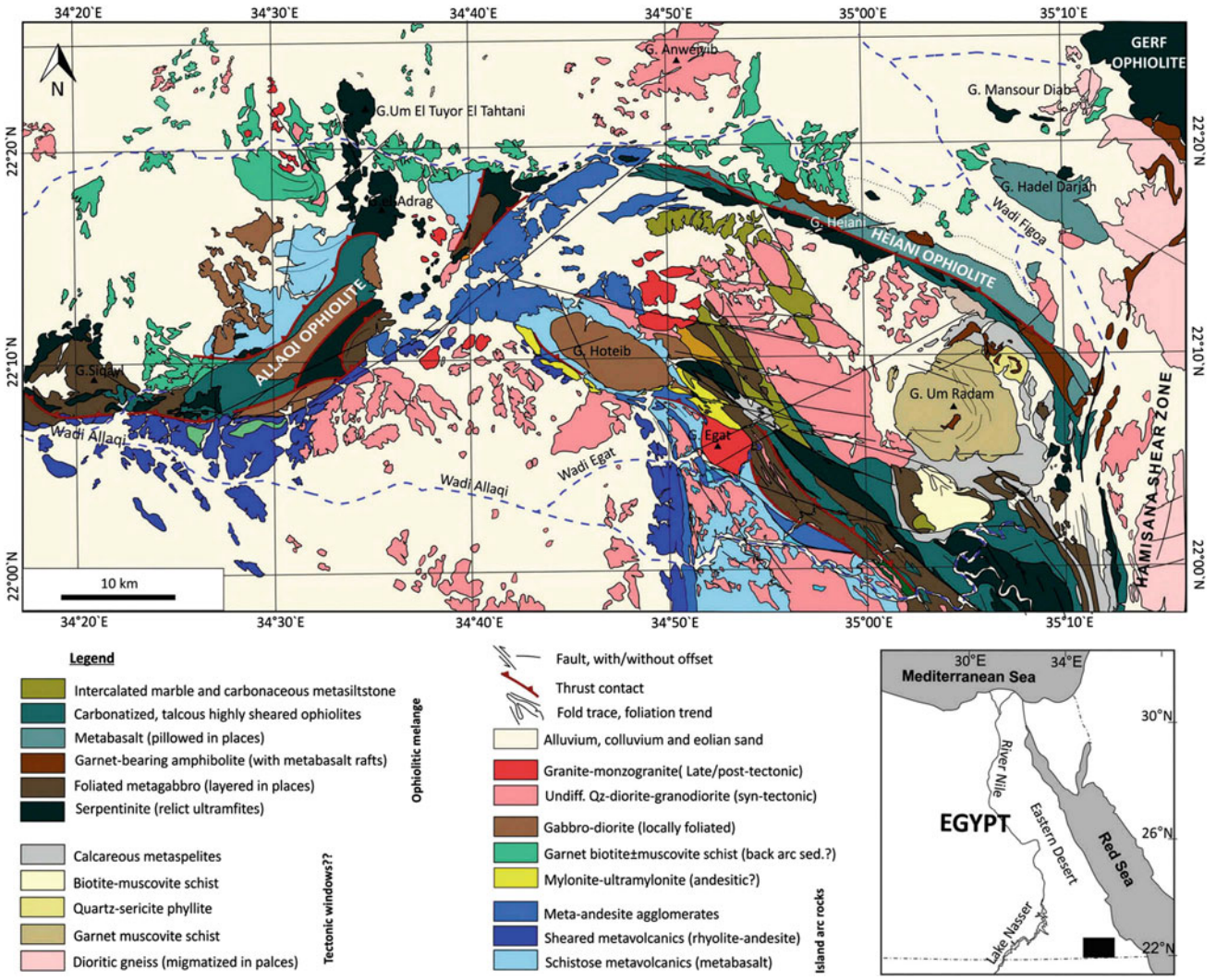

Fig. 5.5 Geologic map of the Allaqi-Heiani suture, related ophiolites, and structures (after Emam et al. 2015)

shows sinistral sense of shear indicated by shear band mylonitic foliation, mineral and mica fish, and S-C fabrics. Progressive shearing produced a complex history of folding with development of planar and non-planar refolded sheath folds. Abdeen and Abdelghaffar (2011) subdivided the Allaqi-Heiani belt into three structural domains. The western domain (I) is characterized by NNE dipping thrusts and SSW-vergent folds. The central domain (II) includes upright tight to isoclinal NNW–SSE oriented folds and transpressional faults. The eastern domain (III) shows NNW–SSE oriented open folds. Structural analysis indicates that the area has a polyphase deformation history involving at least two events. Event D_1 was a N–S to NNE–SSW regional shortening generating the SSW-verging folds and the NNE dipping thrusts. Event D_2 was an ENE–WSW shortening producing NNW–SSE oriented folds in the central and eastern parts of the Allaqi-Heiani belt and reactivating older thrusts with oblique-slip reverse fault movement.

5.2.2 South Hafafit Suture (?)

The South Hafafit Suture (SHS) (Fig. 5.3) was proposed by Greiling et al. (1994, 1996) who recognized SSW-wards thrusting immediately to the south of the Hafafit complex and proposed the existence of an offset segment of the AHS south of Hafafit. The proposed SHS juxtaposes Hafafit terrane to the north and Aswan terrane to the south, and restores for a lateral transport distance of at least 300 km to the SE to form the eastward continuation of the previously mentioned AHS. The Aswan terrane is considered to be the equivalent and westward continuation of the Hafafit terrane, and the terrane to the south of the South Hafafit suture is regarded to extend as far south as the Onib-Sol Hamed belt is an equivalent of the Gabgaba terrane (Fig. 5.3). However, such hypothesized restoration is not documented in the field either in the CED and SED of Egypt.

5.3 Shear Zones in the Egyptian Nubian Shield

5.3.1 Syn-accretion Shear Zones

In central and southern ANS, the collision between E- and W-Gondwana is expressed ultimately as typically N–S trending belts of intensely foliated and isoclinally upright folded rock cross-cutting and displacing the earlier arc-arc sutures (Johnson et al. 2011; Fritz et al. 2013). Typical example of these belts is the Hamisana Shear Zone (HSZ; Stern et al. 1989, 1990; Miller and Dixon 1992; Abdelsalam and Stern 1996; De Wall et al. 2001) and Oko Shear Zone (OSZ; Abdelsalam 1994). The major HSZ (Figs. 5.1, 5.2 and 5.6) covers an area of about 15,000 km^2 (300 × 50 km) in southeastern Egypt and northeastern Sudan (e.g. Stern et al. 1989; Miller and Dixon 1992; De Wall et al. 2001; Sakran et al. 2001; Takla et al. 2002). It consists of gneissic and schistose rocks (Fig. 5.6), and isoclinally folded slivers of ophiolite derived from the Allaqi-Heiani and Onib-Sol Hamed sutures. Because of its sinistral sense of shear, the HSZ causes remarkable dragging of the AHS and goes further north bounding the Gerf Nappe from the east, then continues to meet the Red Sea Coast. Abdelsalam and Stern (1996) proposed dextral sense of shear along the HSZ based on the dextral offsetting of the Yoshgah Suture (Stern et al. 1989, 1990). According to Stern et al. (1989), the HSZ deformation began after 660 Ma, with intense E–W shortening and N–S extension accompanied by greenschist to amphibolite facies metamorphism and development of upright isoclinal folds and vertical foliations. Deformation probably ceased by 550 Ma. Latest deformation effects are minor dextral NE-striking shears, especially at the northern end of the HSZ. The apparent dextral displacement between the Allaqi-Heiani and Onib-Sol Hamed sutures was disproved by Abdelsalam and Stern (1996) and De Wall et al. (2001) eliminating the main evidence for major shearing along the HSZ.

The geometric aspect and kinematic history of the HSZ have been the subject matter of controversy where it was

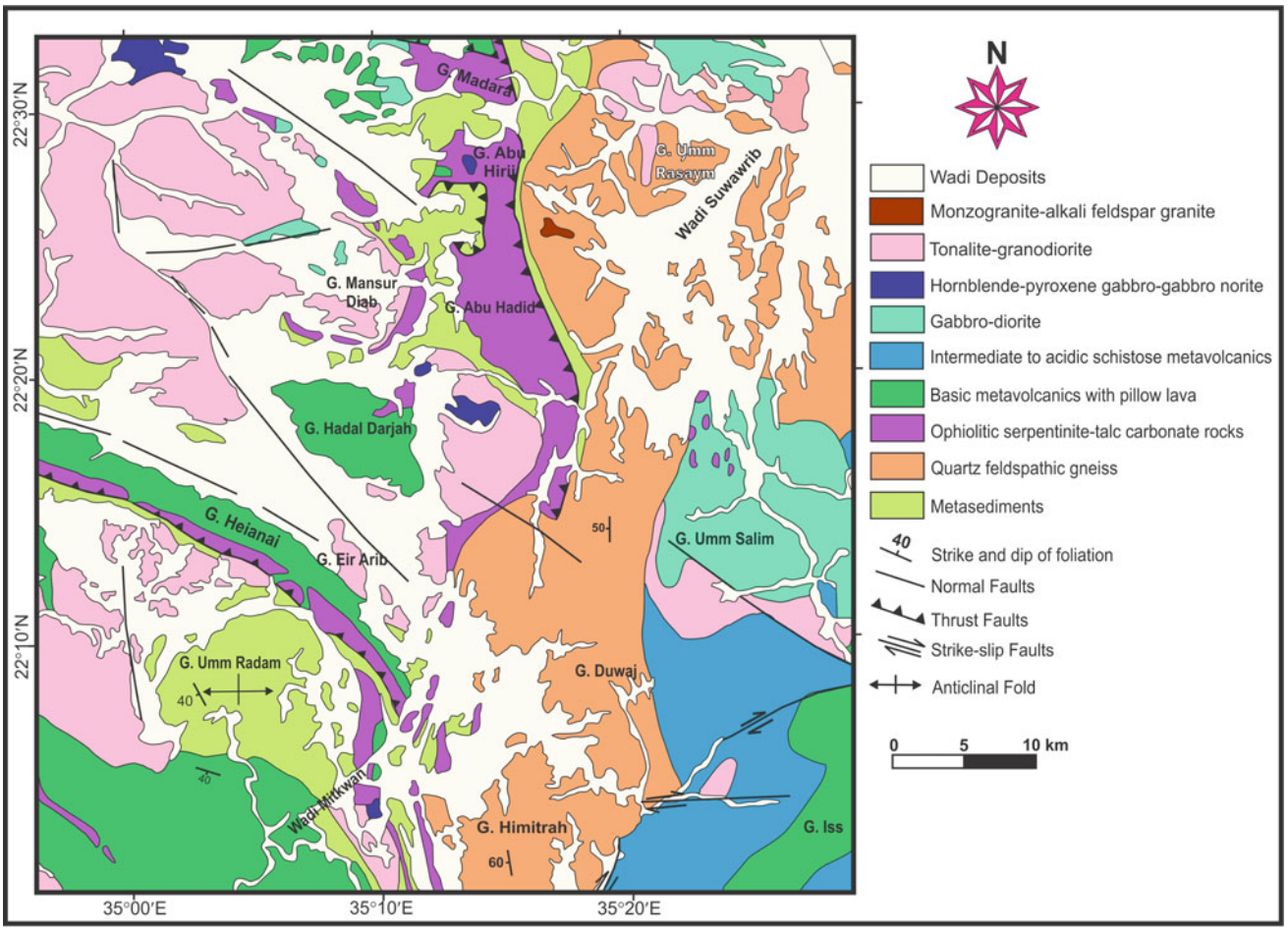

Fig. 5.6 Geologic map of the northern part of Hamisana Shear Zone (HSZ), southern Egypt, slightly modified after EGSMA (2002) and Ali-Bik et al. (2014)

regarded as (1) an arc-arc suture (e.g. Vail 1985, Shackleton 1986), (2) as a transcurrent or transpressive shear zone formed just after the arc accretion stage (e.g. Almond and Ahmed 1987; Kröner et al. 1987; Greiling et al. 1994; Smith et al. 1999; Ibrahim et al. 2016), or as (3) post accretion mainly dominated high strain zone with subordinate parallel or cross-cutting ductile shears (e.g. Stern et al. 1989,1990; Miller and Dixon 1992; Abdelsalam and Stern 1996; De Wall et al. 2001; Johnson and Woldehaimanot 2003). Miller and Dixon (1992) argued that transpression in itself is polyphase and this is consistent with the geometric relationship between the eastern extension of the AHS and the HSZ. De Wall et al. (2001) carried out integrated field and AMS studies, and demonstrated that deformation in the HSZ is dominated by pure shear under upper greenschist/amphibolite grade metamorphic conditions, producing E–W shortening, but with a strong N–S-extensional component. The authors demonstrated that deformation was responsible for folding of regional-scale thrusts (including the base of Gerf and Onib ophiolitic nappes) and indicate that high strain deformation is younger than ophiolite emplacement and suturing of arc-arc terranes. The obtained data led these authors to conclude that the HSZ is dominated by late orogenic compressional deformation and cannot be related to either large-scale transpressional orogeny or major escape tectonics. Stern et al. (1990) proposed four deformation phases in the vicinity of the HSZ. The oldest phase (D_1) records emplacement of the ophiolitic rocks. This produced a complex imbrication of ophiolitic and metavolcanic sequences. D_2 folding around north-trending axes produced a regional cleavage (S_2), subhorizontal intersection lineation (L_2), and tight, upright to inclined folds (F_2). D_3 is coaxial with D_2 and refolds S_2, locally producing pencil structures and crenulations in the western Hamisana. The resultant pervasive northsouth fabric is truncated by narrow, NNE-trending D_3 dextral shear zones. These become more dominant in the extreme south as the HSZ turns southwest. Later kinks (D_4) and brittle faults have variable movement sense and account for limited regional strain. Thus, the principal ductile deformation in the HSZ is characterized by nearly coaxial folding about a north-south axis, indicating shortening normal to the zone, i.e. east-west.

5.3.2 Post-accretion Shear Zones

Hamimi et al. (2019) outlined three ANS-scale deformation events (D_1 to D_3). Among this scheme, the D_2 deformation was considered to be a post-accretion shortening phase, that produced transpressive structures, including NNW-SSE trending sinistral transcurrent shears (Fig. 5.7) (e.g. Nugrus, and Atalla Shear Zones), the dextral transcurrent shearing along NE-directed mega shears (e.g. Idfu-Mersa Alam and Qena Safaga Shear Zones), and the post-accretionary shear zone-related gneiss domes (Fig. 5.7) (e.g. Meatiq, Sibai, Shalul, and Hafafit gneiss domes) (Fritz et al. 1996, 2002, 2013; Loizenbauer et al. 2001; Abd El-Wahed 2008, 2014; Abdeen et al. 2014; Fowler and Osman 2009; Abd El-Wahed et al. 2016; Hamimi and Hagag 2017; Stern 2017; Hagag et al. 2018).

5.3.2.1 Najd-Related NW-Trending Shear Zones

It is widely accepted that there are significant effects of Najd Fault System (NFS) on the ANS and the CED of Egypt. Stern (1985) considered the NFS as the largest Proterozoic Shear System on Earth, representing the youngest major structural element in the Eastern Desert of Egypt. The NFS has a great importance due to its major extension, role in the exhumation of metamorphic core complexes and prominence in Gondwana cratonization. Moore (1979) studied primary and secondary faulting in the NFS of the Arabian Shield and defined the NFS as a major transcurrent (strike-slip) fault system of Proterozoic age in the Arabian Shield. He suggested a similarity of NFS to many of the world's major transcurrent fault systems, including the San Andreas (USA) and Alpine (New Zealand) faults in terms of its length (possible length of more than 2000 km). He added that the system is a braided complex of parallel and curved en echelon faults. For the NFS and especially close to the terminations of some major faults, a complex association of secondary structures including strike-slip-, oblique-slip-, thrust- and normal-faults, in addition to folds and dike swarms are usually present forming an intricate array. Therefore, the importance and complexity of NFS is augmented by this array of secondary structures that give an allusion to synchronous compressional, extensional and dilational conditions in various parts of the fault zone.

The NFS was identified originally as a NW-trending brittle–ductile shear zone with 300 km width and length over 1100 km extending across the northern part of the ANS (Brown and Jackson 1960; Delfour 1970). Stern (1985) and Johnson et al. (2011) defined the NFS as a huge shear zone system striking NW–SE and has more than 1000 km extension across the shield. So, how was it evolved or formed? Brown and Jackson (1960) earlier interpreted the NFS in the Arabian Shield as late Neoproterozoic and early Phanerozoic strike-slip faulting dislocation associated with the culmination of the Hijaz Orogenic Cycle (multiple episodes of sedimentation, volcanism and intrusive activity accompanied by deformation (Brown and Coleman 1972). Moore (1979) elucidates that the NFS formation is a result of simple shear that allowed the Nubian Shield and southern Arabian Shield to move several hundred kilometers sinistrally with respect to northern Arabia. Originally, the NFS and the other NW-trending strike-slip faults in the ANS are considered post-accretionary structures and were interpreted

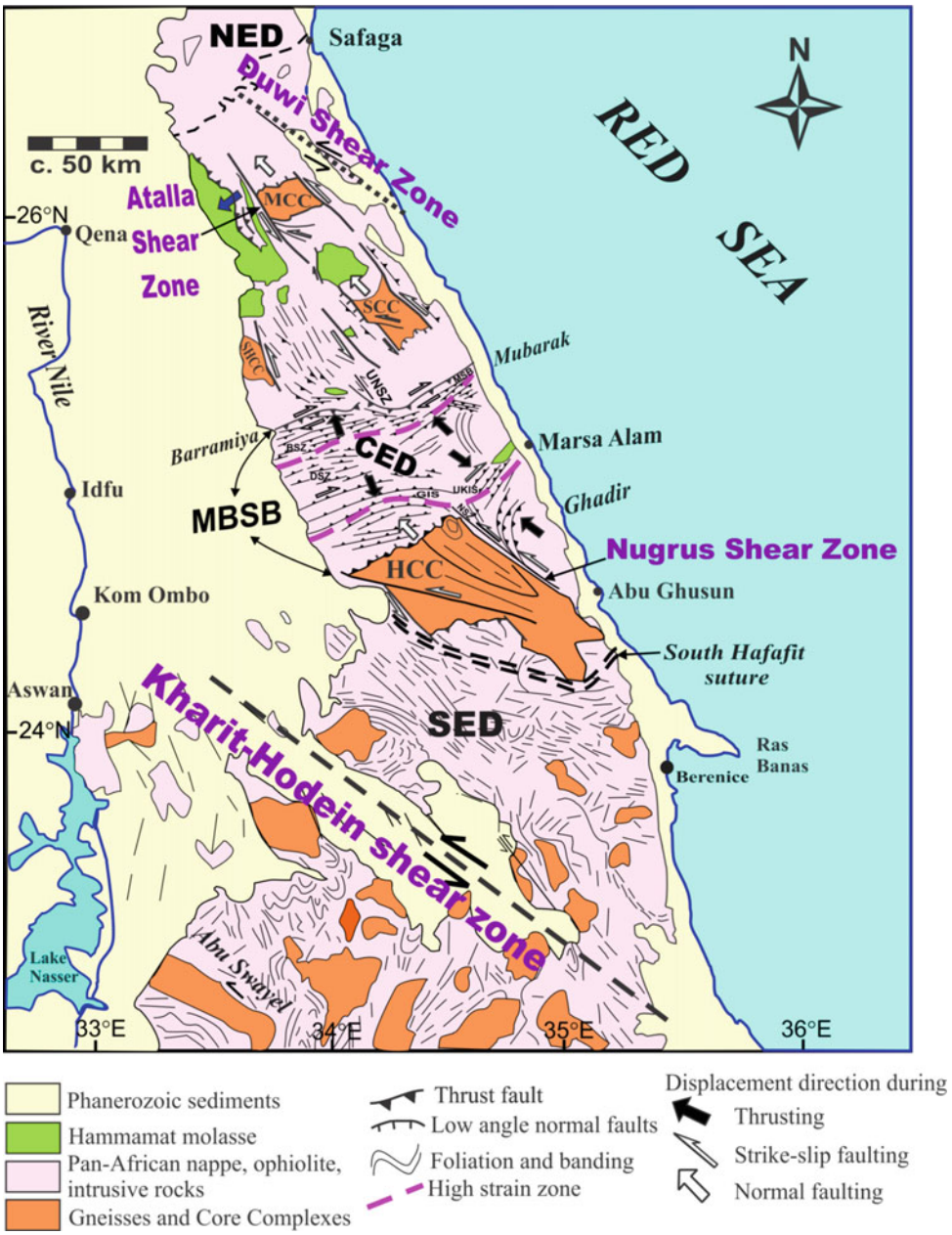

Fig. 5.7 Major structures in the Central Eastern Desert (CED). The Najd Fault Zone in the Eastern Desert is enclosed between Kharit-Hodein shear zone in the south and Duwi Shear Zone to the north. SED; South Eastern Desert, CED; Central Eastern Desert, NED; Northern Eastern Desert, NSZ, Nugrus shear zone, UNSZ, Um Nar shear zone, HCC; Hafafit Core Complex, SCC; Sibai Core Complex; MCC; Meatiq Core Complex; MBSB, Mubarak-Barramiya shear belt. This map is compiled from Greiling et al. (1994), Fritz et al. (1996), De Wall et al. (2001) and (Abd El-Wahed 2014)

to be the result of the squeezing of the ANS between E- and W-Gondwana (Berhe 1990; Stern 1994; Abdelsalam 1994; Abdelsalam and Stern 1996; Abdelsalam et al. 2003). The same mechanism is adopted also for N-trending shortening zones, such as the HSZ (Stern et al. 1989; De Wall et al. 2001) and supported also this mechanism for the formation of subordinate NE–SW trending ones.

The structures in the NFS were developed in response to a sinistral transpressive tectonic regime, with the axis of maximum compressional stress oriented at oblique angles to the NW-trending orogenic front (Abd El-Wahed 2014). The first requirement for any fault is the displacement. The displacement along the strike of the Najd shear zone was reported by Brown (1972) as 240 km cumulative displacement but field displacements can be demonstrated as only tens of kilometers for particular faults (Johnson et al. 2011). From the Arabian shield, the northwestern extensions are probably in the Eastern Desert of Egypt and to the southeast, the line of faulting coincides with structures in the south Yemen coast and in the bed of the Arabian Sea (Brown 1972). In southern Jordan rocks, the NFS is inferred to be present and disrupted by much younger Cenozoic slip on the Dead Sea Transform (El-Rabaa et al. 2001). In the Mozambique Belt in Kenya and Madagascar, similar NW-trending shear zones were identified (Raharimahefa and Kusky 2010). The influence of the NFS also continued to

southeast into parts of India and the Lut block of Iran as s reported by Al-Husseini (2000) from Magnetic and gravity data.

Geochronologically, the absolute radiometric ages obtained from small intrusions denoted that the Najd-related shear zones were active from late Neoproterozoic into early Phanerozoic times, 580–530 Ma (Fleck et al. 1979). The late stages (630–535 Ma) of the Pan-African event witnessed the NFS development in the form of huge shear zone system striking NW–SE (Stern 1985; Johnson et al. 2011). Geophysically, subsurface aeromagnetic maps interpretation denoted a continuity of the NFS beneath the surface faults arrays concluding that NFS is broader at depth than the outcropping fault complex (Moore 1979). At depth and under amphibolite facies prevailing conditions, an early shear ductile activity of the NFS is prevailing which is turned into brittle shearing at the shallower levels (Johnson et al. 2011; Fritz et al. 2013). Hydrothermal activity, in turn was pervasive indicating abnormally high heat transfer in the time of faulting. The hydrothermal alteration is probably also a reflection of the mechanical importance of fluid pressure in the mechanism of faulting at this structural level (Phillips 1972).

Master faults of the NFS is constituted of parallel and en echelon major faults attaining more than 300 km in length. These faults or other major fractures are preferentially susceptible to weathering and form Wadi valleys shown clearly in aerial photographs and satellite images. Minor secondary structures are associated with the NFS and are simply classified according to their relation to the major structures into pre-date or independent of major faults, and those which are directly interrelated to master structures (Moore 1979).

Deformation analysis and field studies gave evidence that the ductile deformation was followed by brittle failure during the main faulting episodes. Strictly speaking, the NFS is dominated by northwest striking faults. On the other hand, the theoretical complements (Major northeast striking dextral faults) to the main system are rare (Moore 1979). It is worth mentioning to denote that the NFS is a coherent structure that can be explained by a single regional event (Moore 1979). The sinistral strike–slip shearing along the NFS was accompanied by transpressional and transtensional tectonic regimes (Fritz et al. 1996). Abu-Alam et al. (2014) assigned all of the structural events that occurred in the northern Arabian–Nubian Shield during the last 90 Myr of the Pan African orogeny as a part of the NFS, which start in a compressional tectonic setting, with strike-slip function that ultimately assisted escape tectonics.

Hassan et al. (2016) stated that the Najd-related Shear Zones are responsible for re-configuring the structure of the lithosphere, especially in active tectonic regions and also concluded that the timing of the Ajjaj Shear Zone (in the Arabian Shield) is younger than the exhumation history of the rest of the domes in Arabian Nubian Shield, perhaps correlating with differences in exhumation mechanism. In the Arabian part of the shield, the Ajjaj Shear Zone is one of strands of the NFS (Hassan et al. 2016) that is considered to be extended into the Eastern Desert of Egypt (Sultan et al. 1988). The CED and the northern parts of the SED are characterized mainly by the prevalence of a NW-trending tectonic fabric marking the NW–SE sinistral shear zone of the NFS (Fig. 5.7) (Fritz et al. 1996, 2002; Abd El-Wahed and Kamh 2010; Abd El-Wahed et al. 2016; Makroum 2017; Abd El-Wahed and Thabet 2017). Other comprehensive structural studies in the basement areas west of Quseir established time relationships between stages of Pan-African folding and thrusting and subsequent Najd wrench faulting (Abdeen et al. 1992; Fowler and El Kalioubi 2004; Greiling et al. 1994; Fritz et al. 1996; Abdeen and Greiling 2005). The CED deformation events (Loizenbauer et al. 2001; Makroum 2001; Fritz et al. 2002; Shalaby et al. 2005; Abd El-Wahed 2008, 2014; Abd El-Wahed and Abu Anbar 2009; Abdeen et al. 2008; Abd El-Wahed et al. 2016) might have started with an early phase preserved in amphibolite enclaves in the gneiss-cored domes. What is followed by thrust-related structures associated with oblique convergence of the arc and back-arc assemblage onto the Saharan Metacraton around 620–640 Ma (Loizenbauer et al. 2001). Subsequently, NW-trending sinistral shear zones of NFS were developed (Fritz et al. 2002; Abd El-Wahed 2007, 2008; Abd El-Wahed et al. 2016). This phase of deformation was associated with transpression and lateral extrusion and was followed by exhumation of core complexes in orogen parallel extension around 620–580 Ma (Fritz et al. 1996; Makroum 2001; Fritz et al. 2002; Bregar et al. 2002; Abd El-Wahed 2008; Abd El-Wahed et al. 2016; Makroum 2017; Abd El-Wahed and Thabet 2017).

In the CED, several lines of evidence indicate that the exhumation of the core complexes is related to the sinistral shearing along the NFS, which bound them from the SW and NE (Fig. 5.7). Not only core complexes of the CED, but also its Hammamat molasse sediments which are tectonically affected by the NFS (Abd El-Wahed 2010).

To sum up, the NFS consists of brittle–ductile shearing in a zone as much as 300 km wide and more than 1100 km long, extending across the northern part of the Arabian Shield. Its relation to the CED could be epitomized in the following three points:

- The role of sinistral shearing and transpression related to the NFS in the exhumation of the gneiss domes and in deformation styles,
- The tectonic history of the CED is recently explained through NW-trending sinistral shear zones of the NFS (Fritz et al. 1996, 2002, 2013; Bregar et al. 2002; Shalaby

et al. 2005; Abd El-Wahed 2008, 2010; Abd El-Wahed and Kamh 2010; Abd El-Wahed et al. 2016).

- The genetic relationship of the NFS deformation either with deposition and deformation of Hammamat sediments (Abd El-Wahed 2010) or with syntectonic granitoids emplacement (Fritz et al. 2013; Hamdy et al. 2017b).

Kharit-Hodein Shear Zone

Kharit-Wadi Hodein Shear Zone (KHSZ) (Fig. 5.8) is a distinctive high angle NW-oriented transcurrent shear zone extending for about 186 km in the SED of Egypt, and exhibiting sinistral sense of shear confirmed by various kinematic indicators such as veins, deflected markers, S-C structures, microscale foliations, porphyroclasts, mica fish and mineral fish (Hamimi et al. 2019). The KHSZ is suspected to have accommodated up to 300 km of sinistral displacement during late stages of transpression. Transpression has also been described as being confined to identifiable discrete shear zones (Greiling et al. 1994; Zoheir 2011; Hagag et al. 2018). Opinions differ about the tectonic affinity of this shear zone, where some workers (e.g. El Gaby et al. 1988; Stern et al. 1990) proved that it is a Najd-related shear system (analog of the 655–540 Ma NFS in the Egyptian Eastern Desert), others (e.g. Fritz et al. 1996; Fowler and El Kalioubi 2004) considered it as a youngest major structural element in the Egyptian Eastern Desert, or a transpressional corridor (Greiling et al. 1994; Nano et al. 2002). Ramadan and Kontny (2004) reported gold mineralization in listwaenite-type wallrock alteration at Gabal El-Anbat (Fig. 5.9) in the vicinity of this shear zone. Greiling et al. (1994) supposed that the KHSZ has connected the perhaps once continuous-previously mentioned Allaqi- and South Hafafit-Sutures (before being overprinted by the HSZ). Hamimi et al. (2016) reported a dextral sense of shear along the main Wadi Kharit overprinting the main sinistral shearing, which may demonstrate switching in tectonic regime from sinistral to dextral along the Najd Shear Corridor in the Egyptian Eastern Desert.

Nugrus Shear Zone

Nugrus Shear Zone (NSZ) represents one of the conspicuous Najd-related shears to the southwest of Mersa Alam Costal City, between Wadi Ghadir to the east and Hafafit Gneiss Complex to the west (Figs. 5.10, 5.11 and 5.12). The NSZ trends in a NW direction as a NE-steeply dipping high strain zone, with approximately 750 m maximum width. It separates hanging wall low-grade ophiolitic metaultramafic nappes and volcanogenic metasediments from Hafafit high grade gneisses in its footwall which is thought to be of high temperature–low pressure amphibolite facies (El-Ramly et al. 1984, 1993). The metamorphic conditions were estimated by Asran and Kabesh (2003) at 720–740 °C for Migif-Hafafit amphibolites and at 800–820 °C for associated migmatites, both under pressures of 6–7 kbar. The pressure

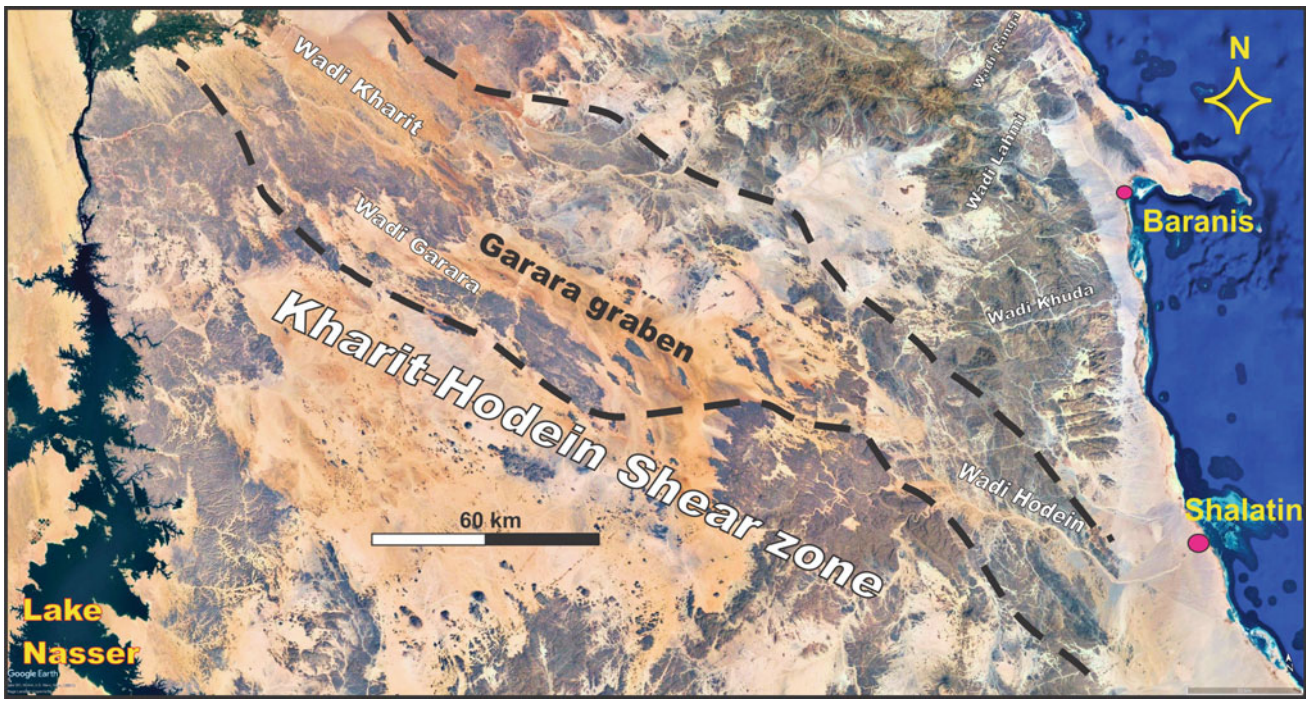

Fig. 5.8 Kharit-Wadi Hodein Shear Zone (KHSZ) is NW-oriented transcurrent shear zone extending for about 186 km in the SED of Egypt

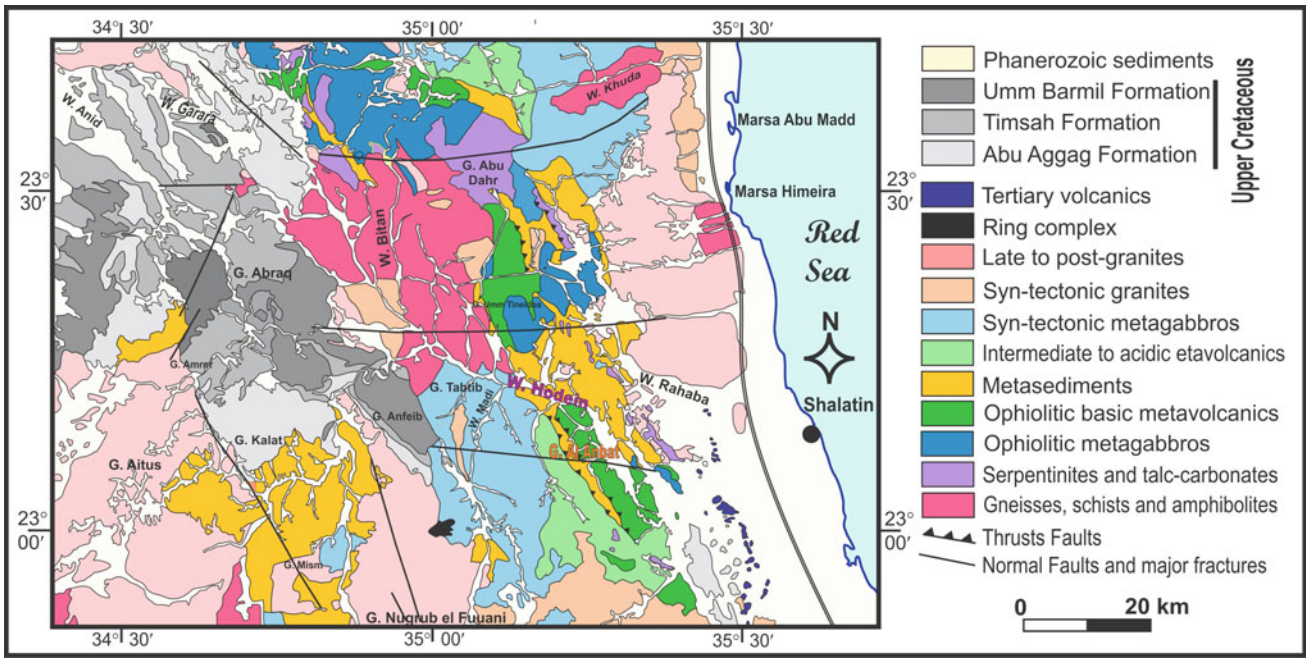

Fig. 5.9 Geological map of the eastern part of Kharit-Hodein Shear Zone (modified after Conoco 1987)

conditions were confirmed as 6–8 kbar by Abd El-Naby and Frisch (2006).

Emplacement of the low-grade meta-ultramafic nappes over the high-grade Hafafit gneisses taken place at c. 680 Ma (Greiling et al. 1988; Liégeois and Stern 2010). The NSZ was interpreted in terms of (a) thrust duplexes (Greiling et al. 1988; El-Ramly et al. 1993), (b) Najd-related Shear Zone with sinistral sense of shear (Fritz et al. 1996; Makroum 2003; Abd El-Wahed et al. 2016), and (c) as part of a northerly dipping Sha'it–Nugrus Shear Zone which is a post-arc collision low-angle normal ductile shear zone separating CED from SED (Fowler and Osman 2009). Various kinds of kinematic indicators reflect the sinistral sense of shearing along the NSZ, including mylonitic foliation, shear bands, S-C foliations and deformed objects with monoclinic symmetry. The sense of shearing is also confirmed at the microscopic scale by sigmoidal structure and mineral fish that are remarkably observed in the oriented thin sections. In the field, these structures overprint arc collision-related nappe structures (≈680 Ma) and are therefore post-arc collision (Fowler and Osman 2009).

The timing of shearing of the NSZ is also debatable. Fowler and Osman (2009) argued that the timing of the NSZ shearing is a distinctly younger shearing event at around 600 Ma. This idea is supported by the conclusion of Greiling et al. (1994) that extensional collapse in the region began at about 600 Ma, and accelerated during the period 595–575 Ma. Greiling (1985) stated that NSZ age is bracketed between 680 Ma (the age of sheared trondhjemite) to 595 Ma (age of post-tectonic granite), relatively. On the other hand, Mohamed (1993) showed that the activity time on the NSZ was bracketed between the intrusion of the older granitoids and the younger granitoids. Rb/Sr whole rock ages of 610 ± 20 Ma and 594 ± 12 Ma for leucogranites intruded into the schists bordering the Sha'it-Nugrus Shear Zone was given by Moghazi et al. (2004).

The Hafafit-Nugrus area (Figs. 5.11 and 5.12) has attracted the attention of many authors through displaying an apparent contrast not only in metamorphic grade but also in the deformation intricateness which leads El Ramly et al. (1993) to disaggregate the area into two main groups disaffiliated mainly by a low angle Nugrus thrust tracing along the upper part of Wadi Sikait in a NW direction and intruded by the late granitoids. The Nugrus-Sikait belt was defined as structural contact represented by a regional NW-SE trending thrust belt dipping due NE direction and featured remarkably by ductile deformational fabrics including folding, mineral lineation and foliation (Fig. 5.13a, b) in the metamorphic exposure rocks. The NSZ is considered as a Najd-related ductile strike-slip shear (Fritz et al. 1996; Hassan 1998; Shalaby et al. 2005) considered the NSZ as a Najd-related ductile strike-slip shear. Shalaby et al. (2006) argued about the NSZ being a strike-slip shear zone as the NW trending, along strike, schistose shear foliations is ceased at the intersection of Wadi Nugrus with Wadi Sha'it. The NSZ is described as an example of a low-angle normal ductile shear (LANF) as its approximately E–W strike, low-angle N-dip and a normal shear sense.

Various interpretations were introduced for the NSZ formation. El-Gaby et al. (1988), El-Bayoumi and Greiling

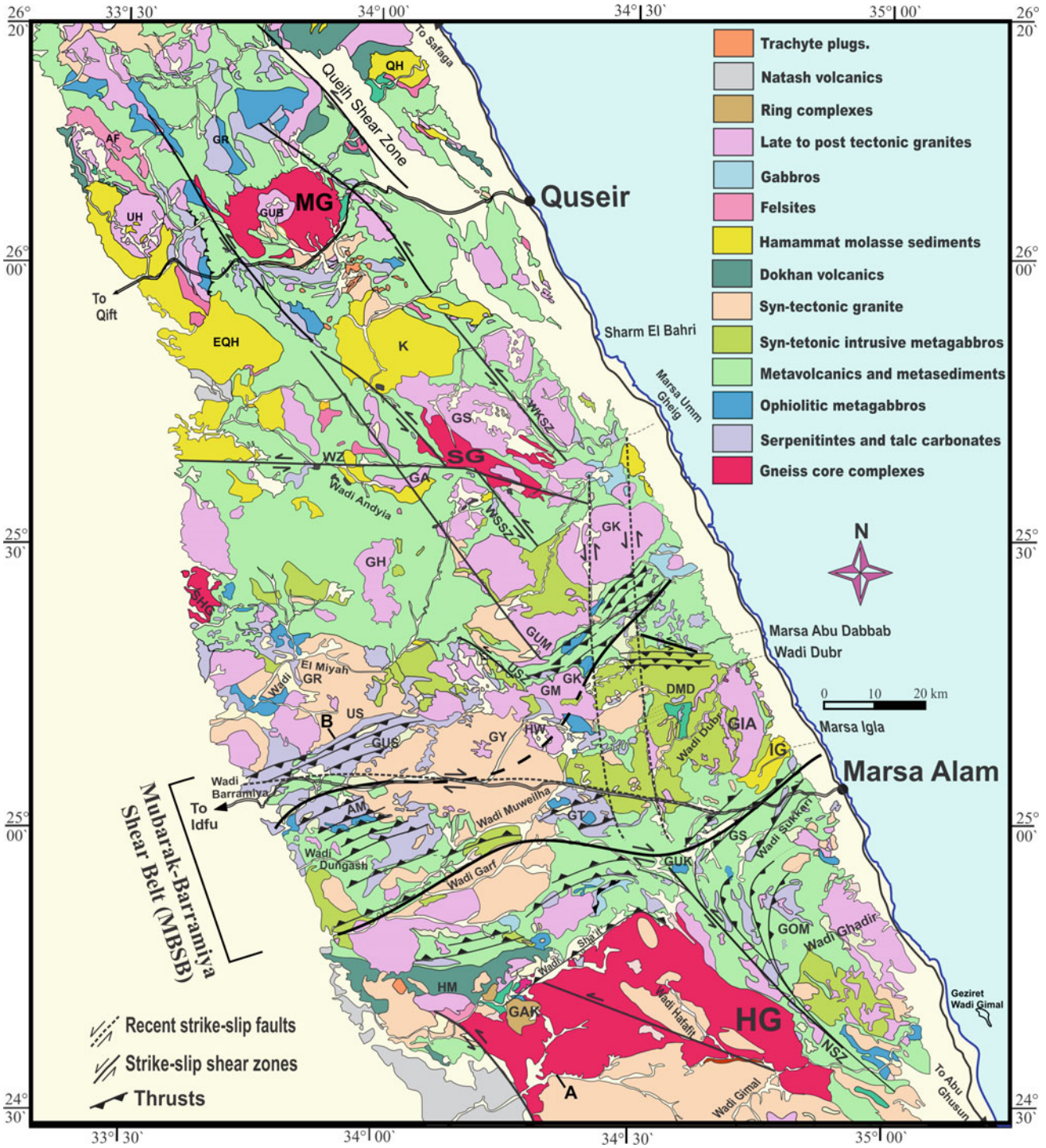

Fig. 5.10 Geological map of the southern part of the Central Eastern Desert of Egypt (modified after Conoco 1987). GAK; Gebel Abu Khruq, HG; Hafafit gneiss, GOM; Wadi Ghadir ophiolitic mèlange, HM; Hamash gold mine, NSZ; Wadi Nugrus shear zone, GS; Gebel Sukkari and Sukkari gold mine, GUK; Gebel Um Khariga, IG; Igla molasse basin, DMD; Dubr metagabbro-diorite complex, GIA; Gebel Igl Al-Ahmar, HW, Gebel Homrat Waggad, GY, Gebel El-Yatima, GUS; Gebel Umm Salim, US, Gebel Umm Saltit, GK; Gebel Abu Karanish, GM, Gebel Al Miyyat, USZ; Um Nar shear zone, GUM; Gebel El-Umra, GK; Gebel Kadabora, GA; GH; Gebel El-Hidilawi, GU; Gebel Umm Atawi, SHG; El Shalul gneiss, GR; Gebel El Rukham; SG; Sibai gneiss, GS; Gebel Sibai, WZ; Wadi Zeidon, WSSZ; Wadi Sitra shear zone, WKSZ; Wadi Kab Ahmed shear zone, K; Kareim molasse basin, MG; Meatiq gniess, AF: Gabal Atalla Felsites, QH, Quieh Hamammat sediments, EQH, El-Qash Hamammat sediments, UH; Um Had granite, GR; Gabal Rabshi, GUB; Gabal Um Ba'anib. The major structures are after Akaad et al. (1993), Fritz et al. (1996), Shalaby et al. (2005), Abd El-Wahed (2008) and Abd El-Wahed and Kamh (2010), Abd El-Wahed et al. 2016; Hamdy et al. (2017b) and Hamimi et al. (2019)

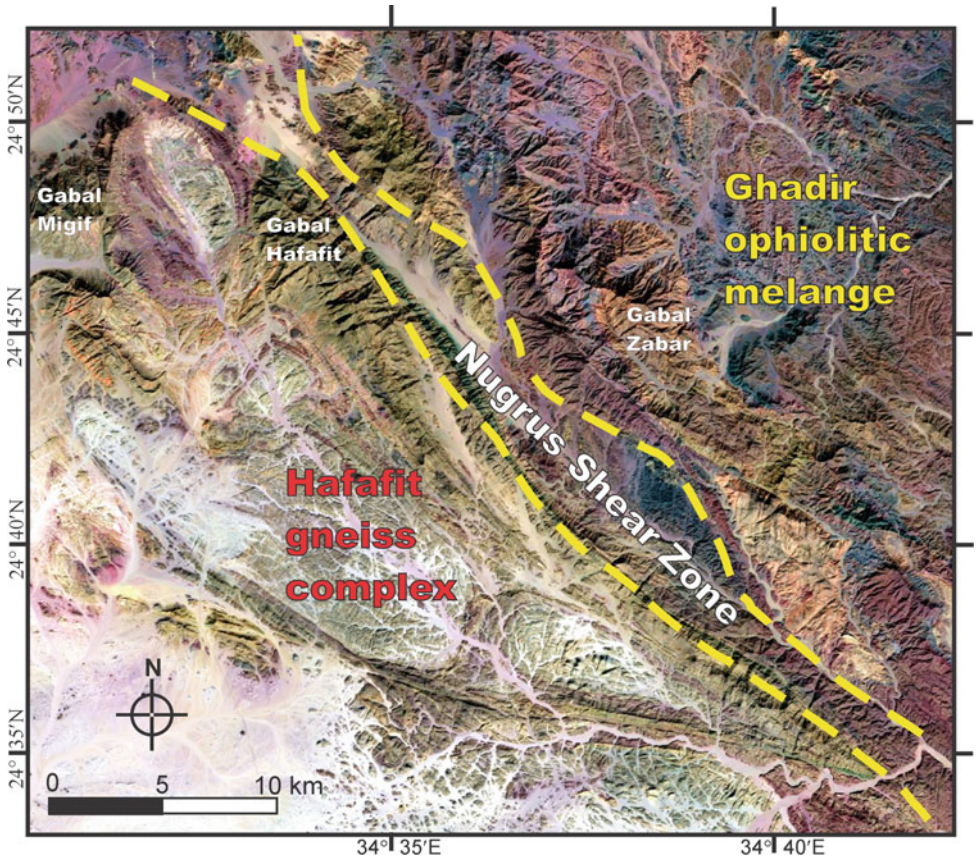

Fig. 5.11 Location of Nugrus Shear Zone

(1984), and El-Ramly et al. (1984) envisaged it as thrust accommodating westward or SW-ward ophiolitic material transport over the continental margin. In full awareness of that the NSZ shows top to-NW kinematic indicators, Greiling et al. (1994) and Greiling (1997) elucidated it as a roof thrust linked up NW-dipping thrust imbricates of gneissic rocks and allowing NW-ward displacement of low-grade CED metavolcanics over the latter gneisses. Let us remark that the gneisses are younger than the metavolcanics (Andresen et al. 2009).

A significant point of view was introduced by Fritz et al. (1996) and Unzog and Kurz (2000) who interpreted the NSZ as a sinistral strike-slip fault (along Wadi Nugrus) and also interpreted the remaining part of the CED and SED boundary as low-angle normal fault (along Wadi Sha'it). A dramatic hypothesis was claimed by Shalaby et al. (2006) denoting a continued extension of the sinistral strike-slip NSZ more northerly till the latitude of the Meatiq gneissic complex. The field evidence for this continuation are absent beyond the meeting point of Wadi Sha'it and Wadi Nugrus. Fowler and Osman, (2009) concluded that the NSZ was originally a gently N or NNW dipping shear structure with top-to-NW or NNW displacement. Such a fault has a normal sense of displacement supported by the juxtaposition of low-grade rocks in the hangingwall against high-grade footwall gneisses.

The metamorphic grade contrast along NSZ constitutes the main estimated displacement along it. The footwall of NSZ is Migif-Hafafit gneisses seemed to be of high temperature—low pressure amphibolite facies (El-Ramly et al. 1984, 1993). Numerically, the metamorphic conditions were estimated by Asran and Kabesh (2003) as 720–740 °C for Migif-Hafafit amphibolites and 800–820 °C for associated migmatites, both under pressures of 6–7 kbars. The pressure conditions were confirmed as 6–8 kbars by Abd El-Naby and Frisch (2006).

On the other hand, numerical estimations of the greenschist facies CED metamorphics show about 450 °C at 4 kbars pressure (Fritz et al. 2002). This gives a 3 ± 1 kbar pressure difference across the SNSZ corresponding to a loss of section measuring 10 ± 3.5 km. Assuming the 25° dip of the NSZ, an estimated displacement of 15–30 km is considered. Geochronologically, the data suggests that the emplacement of low-grade nappes above gneisses occurred at around 630 Ma (Andresen et al. 2009). The timing of the NSZ shearing is a distinctly younger shearing event at around 600 Ma (Fowler and Osman 2009). This corroborates the conclusion by Greiling et al. (1994) that extensional collapse in the region began at about 600 Ma, and

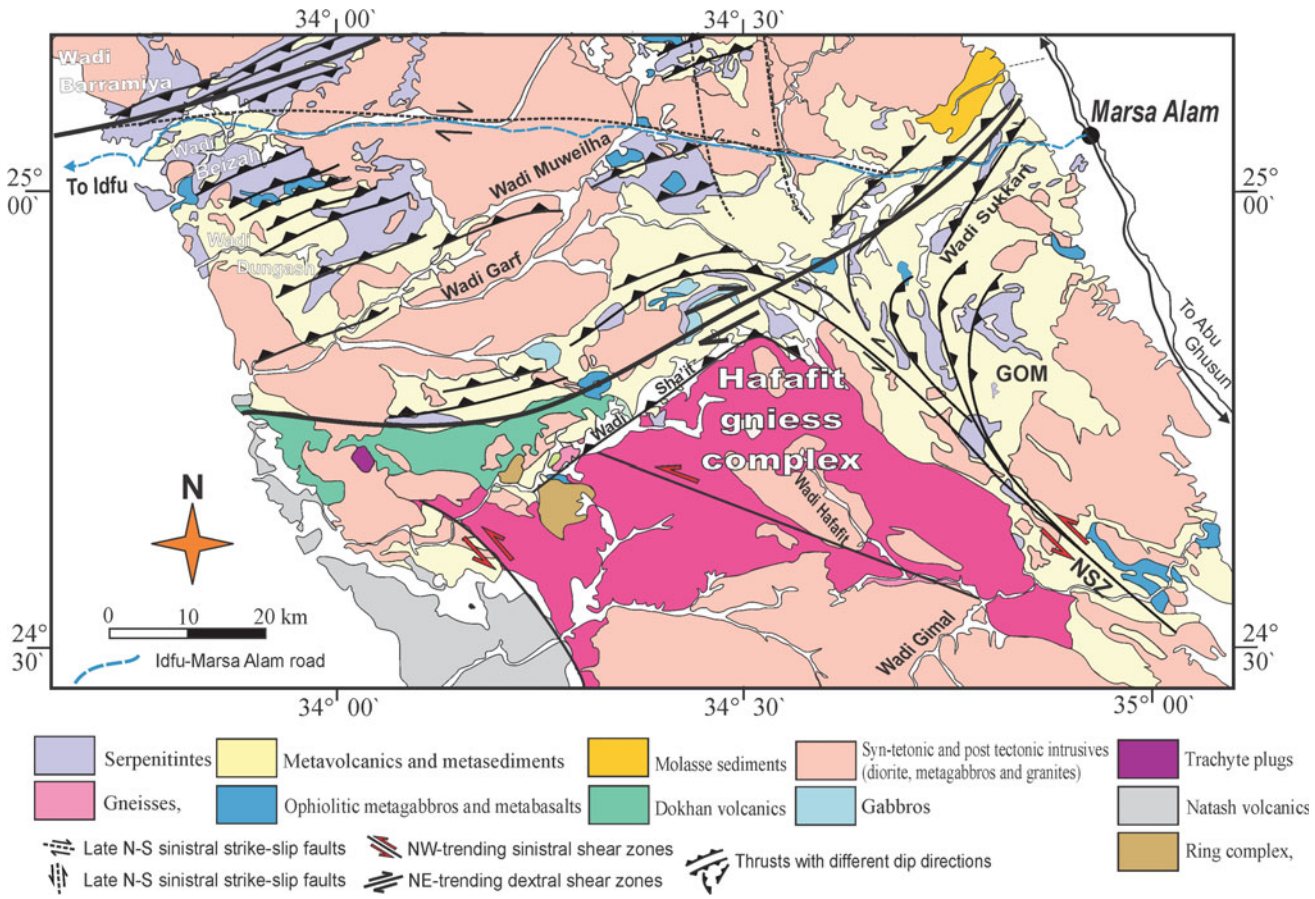

Fig. 5.12 Geological map of the southern part of the Central Eastern Desert of Egypt showing Nugrus Shear Zone and Hafafit gneiss complex (modified after Conoco 1987)

accelerated during the period 595–575 Ma. Greiling (1985) stated that NSZ age is bracketed between 680 Ma (the age of sheared trondhjemite) to 595 Ma (age of post-tectonic granite). Relatively, Mohamed (1993) mentioned the activity time on the NSZ was bracketed between the intrusion of the older granitoids and the younger granitoids. Rb/Sr whole rock ages of 610 ± 20 and 594 ± 12 Ma for leucogranites intruded into the schists bordering the SNSZ was given by Moghazi et al. (2004).

Atalla Shear Zones

Atalla Shear Zone (ASZ) (Fig. 5.14) is a NW-oriented steeply dipping high strain zone encompassing several map- to centimeter-scales kinematic indicators with monoclinic symmetries reflecting sinistral sense of shearing (Zoheir et al. 2018). The ASZ is marked by Atalla felsite mass (28.4 km long by 7.2 maximum width) (Akaad and Noweir 1977; Akaad 1996). Opinions differ about the tectonic setting of the Atalla felsite. Some authors (e.g. Noweir 1968) defined this unique lithologic unit as "a post Hammamat felsite", whereas others (e.g. Essawy and Abu Zeid 1972) considered the Atalla felsite and the associated siliceous metatuffs and acidic flows as rocks belonging to ummetamorphosed old volcanics of the Dokhan type. On the other hand, Akaad and Noweir (1977) and Akaad et al. (1979) considered the Atalla felsite as older than Um Had granite pluton, and this is proved in the field where the felsite extruded the mélange rocks (serpentinites, metasediments metavolcanics and acidic tuffs) and both of them are intruded by Um Had granite. Mélange in Wadi Atalla contains chaotically assembled smaller blocks of ophiolitic (but not arc) lithologies set in a foliated matrix of graphitic pelites and greywackes (Fig. 5.15). These blocks and matrix are encountered in many other areas in the CED and SED, such as Wadi Ghadir (El-Sharkawy and El-Bayoumi 1979; Elbayoumi and Greiling 1984), El-Barramiya Range (Gad and Kusky 2006), Wadi Mubarak (El-Bayoumi and Hassanein 1983; Farahat et al. 2004; Abdel-Karim et al. 2008), and Gabal El Rubshi (Amstutz et al. 1984; Habib 1987; El-Desoky et al. 2015). In this context, two belts of ophiolitic mélange were identified adjoining with both Meatiq and Hafafit complexes (Liégeois and Stern 2010). Both belts were interpreted in terms of an arc collision model as defining arc-arc sutures known as Wadi Atalla-Wadi

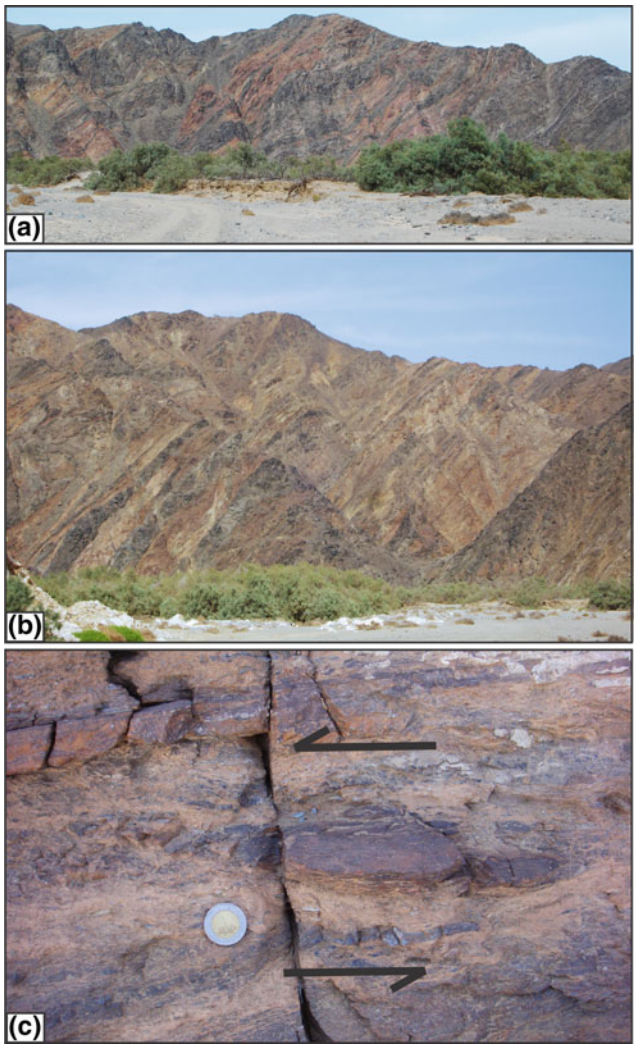

Fig. 5.13 **a**, **b** Banded gneisses within Nugrus Shear Zone, Wadi Nugrus, looking SE. **c** σ-type serpentinite porphyroclasts indicating sinistral sense of shear, northern part of Nugrus shear zone, looking NE

Hammuda- and Wadi Ghadir-Barramiya-sutures (e.g. Ragab 1993; Ragab et al. 1993). The so called Atalla-Wadi Hammud Suture was identified as a former forearc basin. Because of the effect of ASZ, both felsite and mélange are intensively sheared, cataclased and exhibiting stretching lineations and slickenlines particularly at their margins.

The NNW–SSE structural trend is related to marginal shear zones and steeply dipping mylonitic foliation. Strike-slip faults juxtapose the ophiolitic mélange nappe to the Dokhan Volcanics and Atalla felsites. Gold mineralization is related to milky and smoky quartz veins in NE-trending faults cutting a small monzogranite body, the Atalla intrusion. The mine area is underlain mainly by a NW–SE elongate belt of ophiolitic rocks, cut by felsic dyke swarms and the Atalla intrusion (Fig. 5.14). Fragments of metabasalt (Zoheir et al. 2018), serpentinite and metagabbro are embedded in a matrix of metasiltstone form large exposures west and north of the mine area. To the east, mafic and intermediate island arc metavolcanic/volcanogenic rocks include foliated metabasalt intercalated with andesite tuffs and breccias (Zoheir et al. 2018). Successions of purple metagreywacke, siltstone and conglomerate (Hammamat Sediments) unconformably overlie the arc metavolcanic rocks (Zoheir et al. 2018). These sediments are generally characterized by NW-SE bedding. Post-Hammamat felsite porphyries (Rb/Sr isochron age of 588 ± 12 Ma; Hassan 1998) form a NNW elongate body cutting the ophiolitic and island arc rocks. In the mine area, these rocks are intensely jointed, finegrained porphyritic rhyodacites. Monzo-syenogranite rocks occur as small intrusions orientated parallel to the NNW–SSE ASZ. The Atalla intrusion ($\sim$0.35 km^2) cuts ophiolitic serpentinites and the post-Hammamat felsite intrusion, and is composed of medium- to coarse-grained, pale pink monzogranite with abundant xenoliths of older rocks (Zoheir et al. 2018).

5.3.2.2 ENE- (to E-) Trending Shear Zones

The ENE- (to E-) trending Shear Zones are eye-catching high strain zones in the entire ANS. These megashear are typified by Fatima- and Ad-Damm-Shear Zones in the Arabian Shield, and Qena-Safaga-, Idfu-Mersa Alam-Shear Zones, along with Mubarak–Barramiya Shear Belt and Abu Dabbab seismotectonic Zone in northern Nubian Shield.

Idfu-Mersa Alam Shear Zone

Idfu-Mersa Alam Shear Zone (IMASZ) is an ENE-oriented dextral transcurrent megashear regarded by some authors (e.g. El Gaby et al. 1988) to represent the boundary between the CED and the SED. Greiling et al. (1994) considered the ENE-trending Idfu-Mersa Alam road a shear zone originated as extension collapse during a post collisional event. The effect of the IMASZ could be traced easily either in the field, or on the Landsat and ASTER imagery, for a distance over 110 km from the area to the west of Barramiya Gold Mine to Mersa Alam Coastal City. The IMASZ deforms the ophiolite-dominated supracrustal successions as well as the structures associated with the older Najd-related NW-trending shear fabrics. Sense of shearing along this shear zone is dextral and well observed at Sheikh Salem area where a huge leucocratic granitic intrusion is remarkably affected by right lateral shearing.

Mubarak–Barramiya Shear Belt

Mubarak-Barramiya Shear Belt (MBSB) is first named by Abd El-Wahed and Kamh (2010) for enormous NE- (to ENE-) trending high strain belt extends from Wadi Mubarak

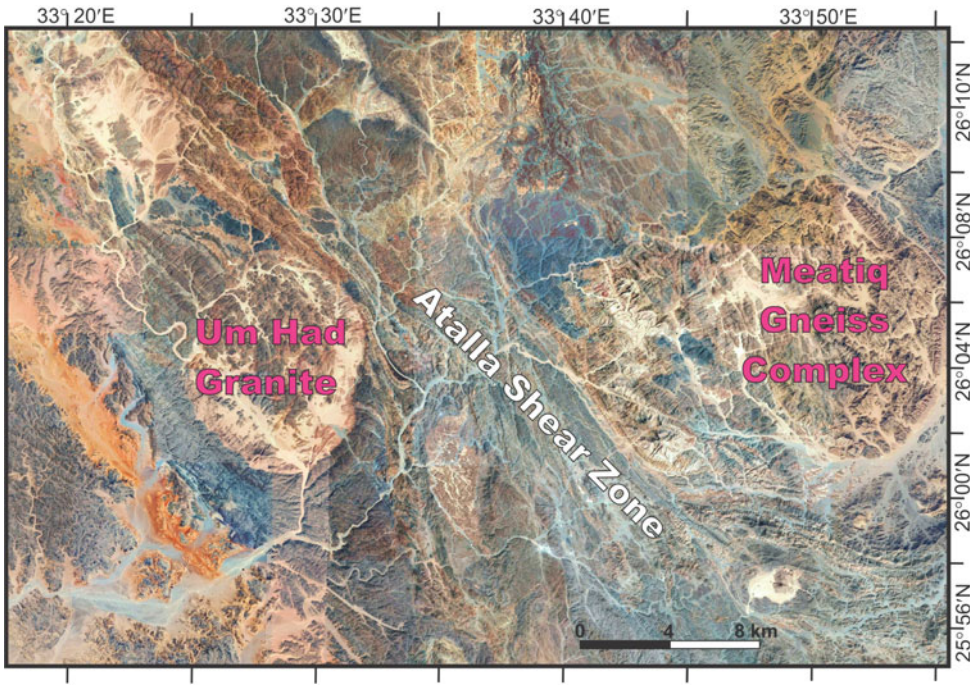

Fig. 5.14 Location of Atalla Shear Zone

on the Red Sea Coast to the area west of Barramiya. Abd El-Wahed and Kamh (2010) and Abd El-Wahed (2014) and reference therein considered this belt as being extending from Wadi Mubarak and Wadi Ghadir on the Red Sea to Wadi Barramiya and Wadi Sha'it to the west. Therefore, the previously mentioned IMASZ represents an elongated sector of the MBSB (Figs. 5.10, 5.16 and 5.17a). The NE-trending MBSB is marked by sheared ophiolites slices scattered in schistose mélange (El Bahariya 2012; 2018). This shear zone separates the low-grade volcanogenic metasediments and metavolcanics in the north from the medium-grade gneissic, migmatites of Hafafit dome. Various structures in this shear belt indicate highly oblique convergence leading to wrench-dominated transpression and development of a major flower structure between Wadi Mubarak and Hafafit dome (Fig. 5.17b) occupying the whole width of the CED (Abd El-Wahed and Kamh 2010).

Three major lithotectonic units were described in the MBSB (e.g. Shalaby et al. 2005; Abd El-Wahed and Kamh 2010; Abd El-Wahed 2014; Abd El-Wahed et al. 2016; Hamdy et al. 2018) namely (i) ophiolite slices and ophiolitic mélange (El Bahariya 2012, 2018), (ii) island arc metavolcanic and metasedimentary successions and (iii) syn- to post-orogenic gabbroic to granitic intrusions. The structural succession and tectonic evolution of the MBSB have been the subject matter of detailed investigations by many workers. Abd El-Wahed (2014) proposed the following sequence of tectonic events (1) Early NW–SE shortening (D_1) associated with accretion of island arcs and obduction of ophiolites over old continent. D_1 produced NNW-directed thrusts and ENE–WSW oriented folds in the CED. (2) an E–W-directed shortening deformation was superimposed due to oblique collision between the Arabian–Nubian Shield and the Nile Craton (D_2) this produced NW-trending upright folds, NE-dipping and SW-dipping thrusts and discreet NW–SE tending shear zones in the CED. NNW-directed thrusts belonging to D_1 were folded around NNW–SSE trending fold axes. Continuing E–W shortening rotated the folded thrust to steeply dipping orientations and initiation of major NW-trending sinistral shear zones and culminated in the initiation of major dextral strike–slip shear zones (D_3) as conjugate sets with the NW-trending sinistral shear zones at c. 640–540 Ma ago. The structures associated with the NW-sinistral shear zones are strongly superimposed by the NE-trending transpressional deformation of the MBSB.

Abu Dabbab Seismotectonic Zone

Abu Dabbab Zone (ADZ) is a Najd-related ENE-oriented high strain zone, located at about 30 km to north of the eastern segment of the previously mentioned IMASZ (Fig. 5.17a). The mouth of Wadi Abu Dabbab can be reached easily through the Marsa Alam-Quseir asphaltic road. ADZ represents one of five seismotectonic zones in Egypt (Hamimi and Hagag 2017), showing daily recorded microearthquakes with local magnitudes (ML < 2.0). In November 12, 1955 and July 2, 1984, two giant earthquakes were recorded with magnitudes 5.6 and 5.2, respectively (Fairhead and Girdler 1970; Badawy et al. 2008). The recorded seismic activity from Abu-Dabbab region by the Egyptian National Seismic Network (ENSN) ranges from 10

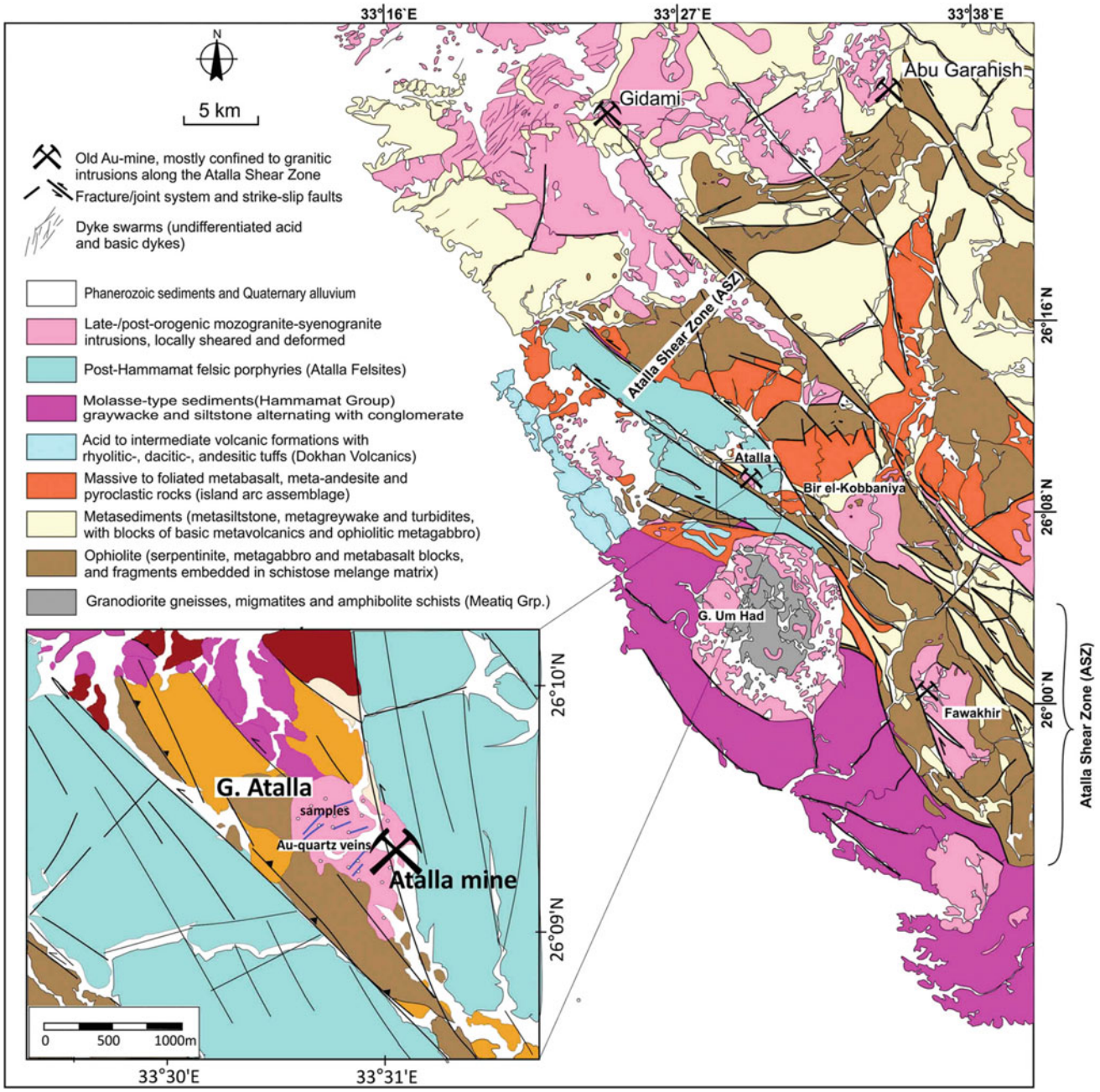

Fig. 5.15 Geological setting of the Atalla shear zone (ASZ) and associated granitic intrusions and gold mineralization (Zoheir et al. 2018)

to 15 events/day to more than 60 events/day, and sometimes attained 100 events/day during swarms (Badawy et al. 2008; Mohamed et al. 2013). Such enigmatic seismic record has attracted the attention of many workers (e.g. Fairhead and Girdler 1970; Daggett et al. 1986; Hassoup 1987; Kebeasy 1990; El-Hady 1993; Ibrahim and Yokoyama 1998; Badawy et al. 2008; Hosny et al. 2009, 2012; Azza et al. 2012; Mohamed et al. 2013) to decipher origin of the earthquakes. The magmatic origin of the seismicity and associated shallow and deep earthquakes is promoting most of the publications dealt with the tectonic setting and seismic activity of Abu Dabbab area (Hamimi et al. 2019). Sabet et al. (1976) suggested that the tectonic evolution of the area was associated with volcanic activity, whereas Daggett et al. (1986) attributed Abu Dabbab seismicity to the subsurface volcanic environment of a cooling pluton. Meanwhile, Hassoup (1987) interpreted this seismicity in the light of the subsurface structural heterogeneity. Hosny et al. (2009) proposed a structural model for the area based on seismic velocity tomography, and related the P and S-wave velocity

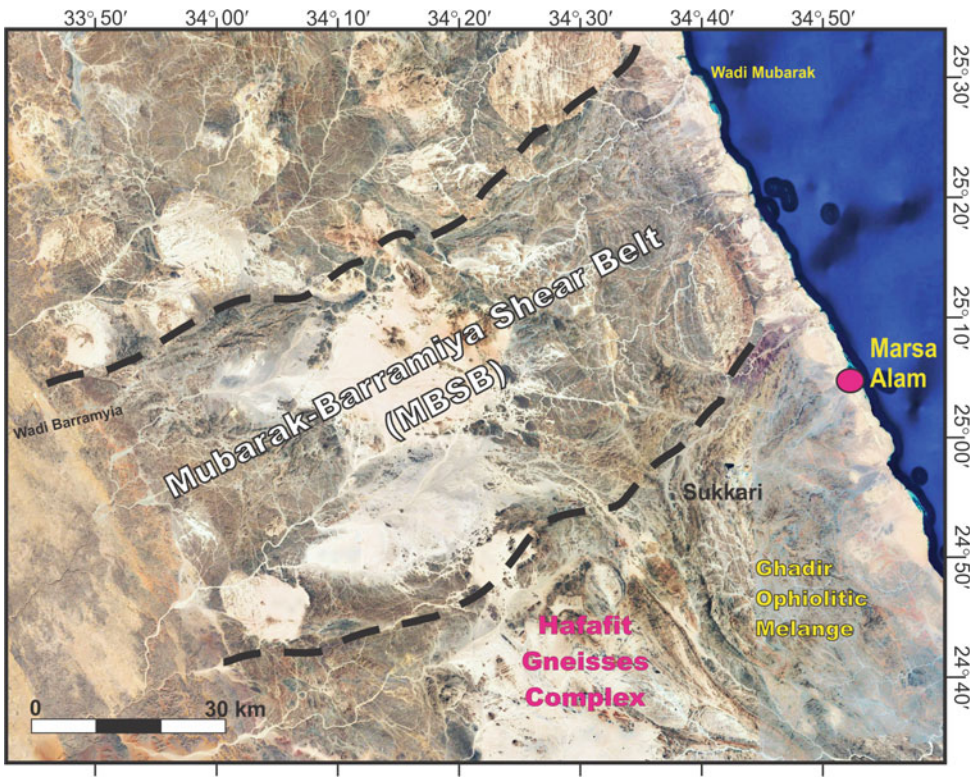

Fig. 5.16 Location of Mubarak-Barramiya Sher Belt (MBSB)

anomaly to magmatic intrusion. Recently, El Khrepy et al. (2015) reveal strong arguments for the tectonic origin of the seismicity of Abu Dabbab area despite of the prevalent magmatic origin. Hamimi and Hagag (2017) proposed a new tectonic model for Abu-Dabbab seismogenic zone based on integrated field-structural investigations, and EMR/seismic data. The obtained results led the authors to indicate a present-day faulting activity in the area and to determine the depth of the brittle-ductile transition zone underlies the Abu-Dabbab area. The transition zone is estimated to be existed at a relatively shallow depth (10–12 km) depending upon the following main criteria: (1) the absence of a large seismic main shock, (2) the periodically recorded swarm's hypocenters of focal depths not deeper than 16 km, (3) the high Vp/Vs ratio (from seismic tomography) until 12 km depth, (4) the occurring of tensile earthquakes of high compensated linear-vector dipole (CLVD) ratios, and (5) the high heat flow rates (about 92 mW/m^2 ± 10, which is more than twice the average value of Egyptian Eastern Desert; 47 mW/m^2). The authors came to the conclusion that there is a mechanical decoupling between the shallow and deep crustal-levels of Abu-Dabbab Neoproterozoic basement succession, where the maximum principal stress axis ($\sigma 1$) rotates from a sub-horizontal position at the uppermost crustal-levels practicing transpressional deformation to a near vertical attitude in the deeper levels, where the transtensional deformation predominated.

5.3.3 Shear Zone-Related Gneiss Domes

The gneiss domes (Fig. 5.10) in the Eastern Desert terrane (e.g., Meatiq, Sibai, El-Shalul and Hafafit) have been interpreted as metamorphic core complexes exhumed in extensional settings. The origin and mode of deformation and exhumation of these gneissic domes and their relation to the Najd Fault System have been the subjects of many publications (e.g. Fritz et al. 1996, 2002, 2013; Loizenbauer et al. 2001; Bregar et al. 2002; Shalaby et al. 2005; Fowler et al. 2007; Abd El-Wahed 2008, 2014; Andresen et al. 2010; Fowler and Osman 2009; Abd El-Wahed and Abu Anbar 2009; Abu Alam and Stüwe 2009; Abd El-Wahed and Kamh 2010; Shalaby 2010; Johnson et al. 2011; Abu Alam et al. 2014; Abd El-Wahed et al. 2016; Makroum 2017; Stern 2017; Hassan et al. 2016). Gneiss domes in Egypt are mostly bordered by NW-striking sinistral shear zones and low angle normal-faults (Fritz et al. 1996). Geochronology suggests that extension and exhumation of gneiss domes commenced around 620–606 Ma (Fritz et al. 2002; Andresen et al. 2009), contemporaneously with the metamorphism itself (Andresen et al. 2009), all the lithologies being juvenile Neoproterozoic rocks (Liégeois and Stern 2010; Stern et al. 2010).

Some points support the role of the Najd shear zones in the evolution and exhumation of core complexes in the Eastern Desert: (i) The large scale, oblique transpressive shear zones of the Najd Fault System in the Eastern Desert and Sinai was developed during the second

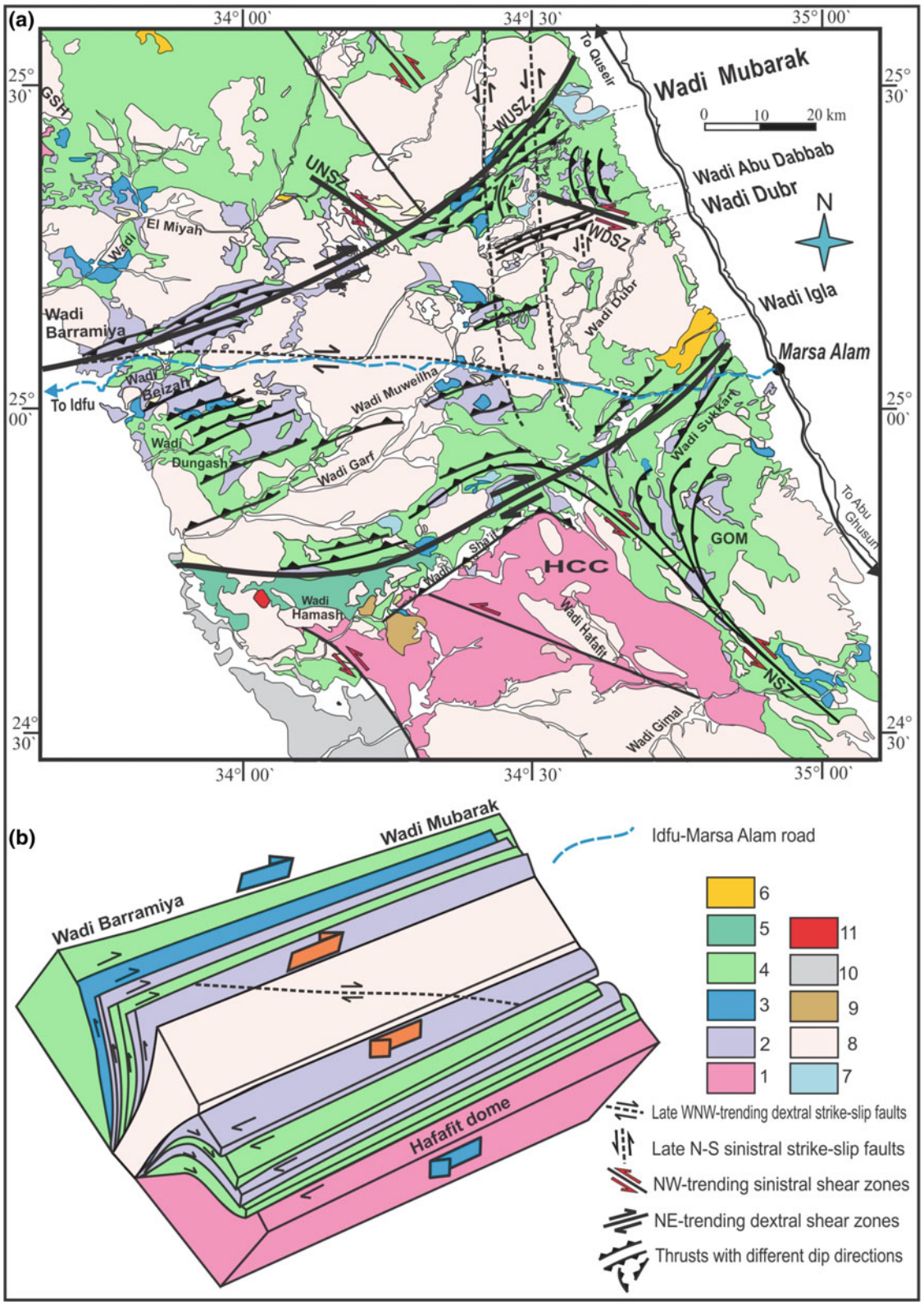

Fig. 5.17 **a** Geological map of the southern part of the Central Eastern Desert of Egypt (after Abd El-Wahed and Kamh 2010, modified from Conoco 1987). 1; gneisses, 2; serpenitintes, 3; ophiolitic metagabbros and metabasalts, 4; metavolcanics and metasediments, 5; Dokhan volcanics, 6; molasse sediments, 7; gabbros, 8; syn-tetonic and post tectonic intrusives (diorite, metagabbros and granites), 9; ring complex, 10; Natash volcanics and 11; trachyte plugs, **b** block diagram showing flower structure constituting Mubarak-Baramiya shear belt. HCC; Hafafit core complex, GOM; Wadi Ghadir ophiolitic mèlange, NSZ; Wadi Nugrus shear zone, UNSZ; Um Nar shear zone, WDSZ; Wadi Abu Dabbab shear zone, WUSZ; Wadi El-Umra shear zone

tectonometamorphic event (D_2) occurred between 680 and 640 Ma (Johnson et al. 2011). During D_2 the ANS collided with the Sahara Metacraton (Liégeois et al. 2013) and moved towards the paleo-Tethys ocean (Stern 1994), (ii) the gneiss domes is bounded by transtensional marginal shears linked by low angle normal faults (Fritz et al. 1996, 2002, 2013), (iii) The oblique setting of the gneiss domes to the main NW-trending shear zones (Abd El-Wahed and Kamh 2010; Abu Alam et al. 2014), (iv) Exhumation history of the core complexes is accompanied by crustal thickening, development of molasse sedimentary basins (e.g. Kareim Basin to the north of Sibai core complex; Abd El-Wahed 2010), (v) There is a relationship between change of the Najd shear kinematics from transpressive to transtension through time and emplacement of transpressive and transtension related granitoids (655 and 645 Ma respectively, Bregar et al. 2002; Abu Enen et al. 2016).

The main constituents of the infrastructural sequence in the Eastern Desert are gneisses and amphibolites which are found in core complexes (e.g., Meatiq, Sibai, El-Shalul and Hafafit). The Meatiq Core Complex is located ~40–60 km west of Quseir, north of the Quseir-Qift road, forming the most prominent gneisscored dome in the Central Eastern Desert of Egypt. The core of the dome consists of coarse-grained, foliated granitic gneisses (Um Ba'anib gneiss; c. 640 Ma; Andresen et al. 2009, the whole gneissic sequence being late Neoproterozoic lithologies; Liégeois and Stern 2010) structurally overlain by metasedimentary succession of quartz-rich schists which are locally intercalated with metapelitic rocks (Fig. 5.18). The Um Ba'anib gneiss is granitic to granodioritic gneiss which is mylonitized close to high strain shear zones. These orthogneisses at their NE side, contain strongly folded migmatized amphibolite xenoliths of several tens of meters in size (Neumayr et al. 1996, 1998; Hamdy et al. 2017a). On the other hand, the metapelitic rocks at the western flank of the MCC are intercalated with weakly foliated, gabbroic and amphibolitic bodies of several hundred meters in size (Loizenbauer et al. 2001). These bodies were interpreted as klippen or outliers of the eugeoclinal allochthon (Loizenbauer et al. 2001; Fritz et al. 2002; Hamdy et al. 2017a). The MCC lies within a NW–SE oriented corridor bordered by two sub-parallel left-lateral NW–SE oriented strike-slip shear zones (Wallbrecher et al. 1993; Fritz et al. 1996; Loizenbauer et al. 2001; Hamdy et al. 2017a). These shear zones separate the medium- to high grade granitic gneisses in the core of the dome from the low grade metamorphosed rocks and consist of steeply dipping biotite, muscovite schists, garnet-mica schists and quartzofeldspathic-schists/gneisses, and mica-rich mylonites. The main segment of the shear zone is principally composed of steeply E- and W-dipping porphyroclastic and ribbon mylonites carrying plunging lineations (Hamdy et al. 2017a). A well-developed mylonitic fabric formed under amphibolite grade conditions dominates the Abu Fannani mylonitic schist where slightly deformed granitic gneiss lenses occur (Hamdy et al. 2017a). Both the granitic gneisses and mylonitic schists are characterized by well-developed stretching lineation that together with shear sense indicators, indicate top-to-NW displacement (Sturchio et al. 1983; Fritz et al. 1996; Loizenbauer et al. 2001). During oblique island arc convergence, deformation in MCC partitioned into NW-SE sinistral strike-slip shear zones marking the eastern and western borders of the core complex and constraining orogen-parallel extension including NE-SW normal faults (Fig. 5.19). Top-to-NNW ductile shearing in the Meatiq Core Complex resulted from the transpression combined with lateral extrusion dynamics (Hamdy et al. 2017a). Oblique extrusion of the deep crust during oblique convergence together with magma generation and extensional structures supports a transpression–extrusion kinematics model (Robin and Cruden 1994; Teyssier and Tikoff 1999) for evolution and exhumation of Meatiq Core Complex (Fritz et al. 1996, 2002) that occurred after 630 Ma (Andresen et al. 2009). NW-SE directed orogen parallel extension leads to formation of strike-slip shear zone bordering the MCC, emplacement of the Abu Ziran granite (606 ± 1 Ma; Andresen et al. 2009), formation of the low angle normal ductile shear zones and final exhumation of MCC. This followed by intrusion of the post-tectonic granites (598–590 Ma; Andresen et al. 2009; Hamdy et al. 2017a).

Hafafit is one of the famous core complexes in the Nubian Shield and represents one of the important suture zones occupying the southern part of the Central Eastern Desert of Egypt. It represents the largest antiformal structures in the Nubian Shield and considered as one of the prodigious structures in the Eastern Desert. El Ramly et al. (1993) studied the tectonic evolution of Wadi Hafafit area and environs and called it Wadi Hafafit culmination (WHC). The Hafafit gneiss complex (Figs. 5.10, 5.11, 5.12, 5.16 and 5.20) attracted the attention of many authors. Not only its controversial formation mechanism, but also the closeness of the area from Ghadir ophiolitic mélange and Nugrus-Sikait belt (very rich in various economic mineralization such as U, Th, Nb, Ta, Zn, Be, Sn, Cu, Ga and REEs) makes this area as one of the most significant areas in the Egyptian Eastern Desert. A major feature is that all lithologies are Neoproterozoic juvenile rocks (Liégeois and Stern 2010; Stern et al. 2010). Petrographically, it has a wide range in composition from orthogneiss to paragneiss (Shalaby 2010). Hafafit gneiss complex comprises five granitoid-cored domes constituted of medium grade gneisses, detached from the overlying low grade metamorphic rocks by low angle thrust zones (Fig. 5.20). The main composition of the overlying unit (Nugrus unit) is low grade mica schists and metavolcanics associated with serpentinites and metagabbros

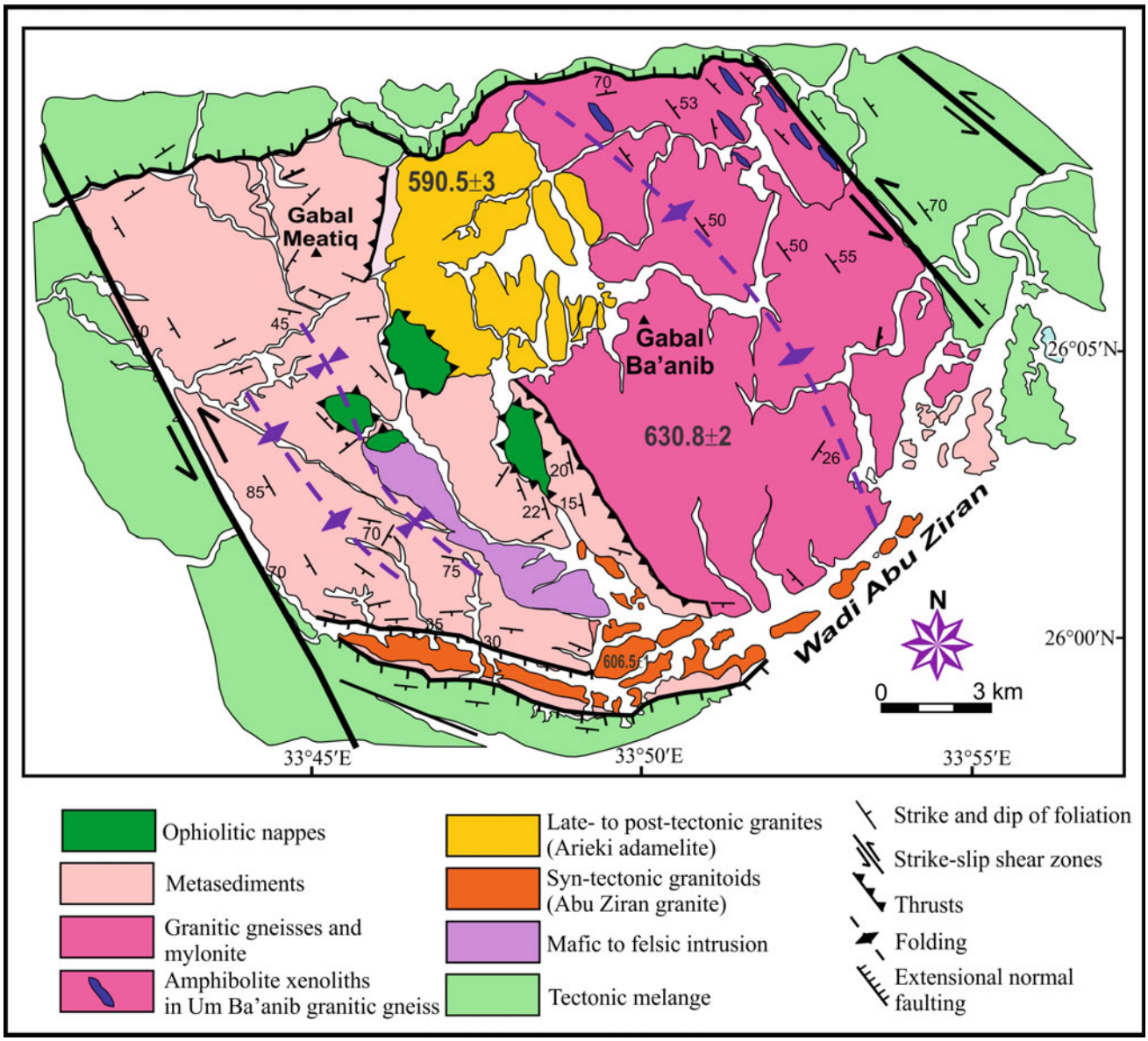

Fig. 5.18 Geological map of Meatiq Core Complex (MCC) (modified after Fritz et al. 2002) and Hamdy et al. (2017b)

outcropping in the eastern and northern part of the Hafafit gneiss complex. On the other hand, the underlying unit (Hafafit unit) is represented mainly by the Hafafit domes and consists of (from core to rim): granitic gneiss of tonalitic and trondhjemitic composition, metagabbro and banded amphibolite, altered ultramafic rocks, biotite- and hornblende-gneiss and psammitic gneiss at the rim of the domal structure (Fig. 5.21a–c). Both units have well developed folds (Fig. 5.22) and have been intruded by leucogranites, especially along thrust zones (Gharib 2012). Strictly speaking and from structural point of view, the entire structural history for core complexes formation is still not fully understood and the formation process is controversial and still a matter of debate.

The most common and generic mechanism for Hafafit gneiss complex exhumation is believed to be regional-scale extension and crustal thinning, where higher grade rocks are brought up in the footwalls of gently dipping shear zone systems oblique to the regional extension direction (often termed 'low-angle detachments') forming so called core complexes (Lister et al. 1984; Tirel et al. 2008; Huet et al. 2010). Meyer et al. (2014) stated that core complexes can also be locally exhumed along major vertical strike-slip shear zones in areas of crustal shortening without regional-scale crustal thinning using an example from the Najd shear-zone system in Saudi Arabia (Abdelsalam and Stern 1996). Although recent studies have dealt in a considerable detail with the gneissic domes of CED; their origin

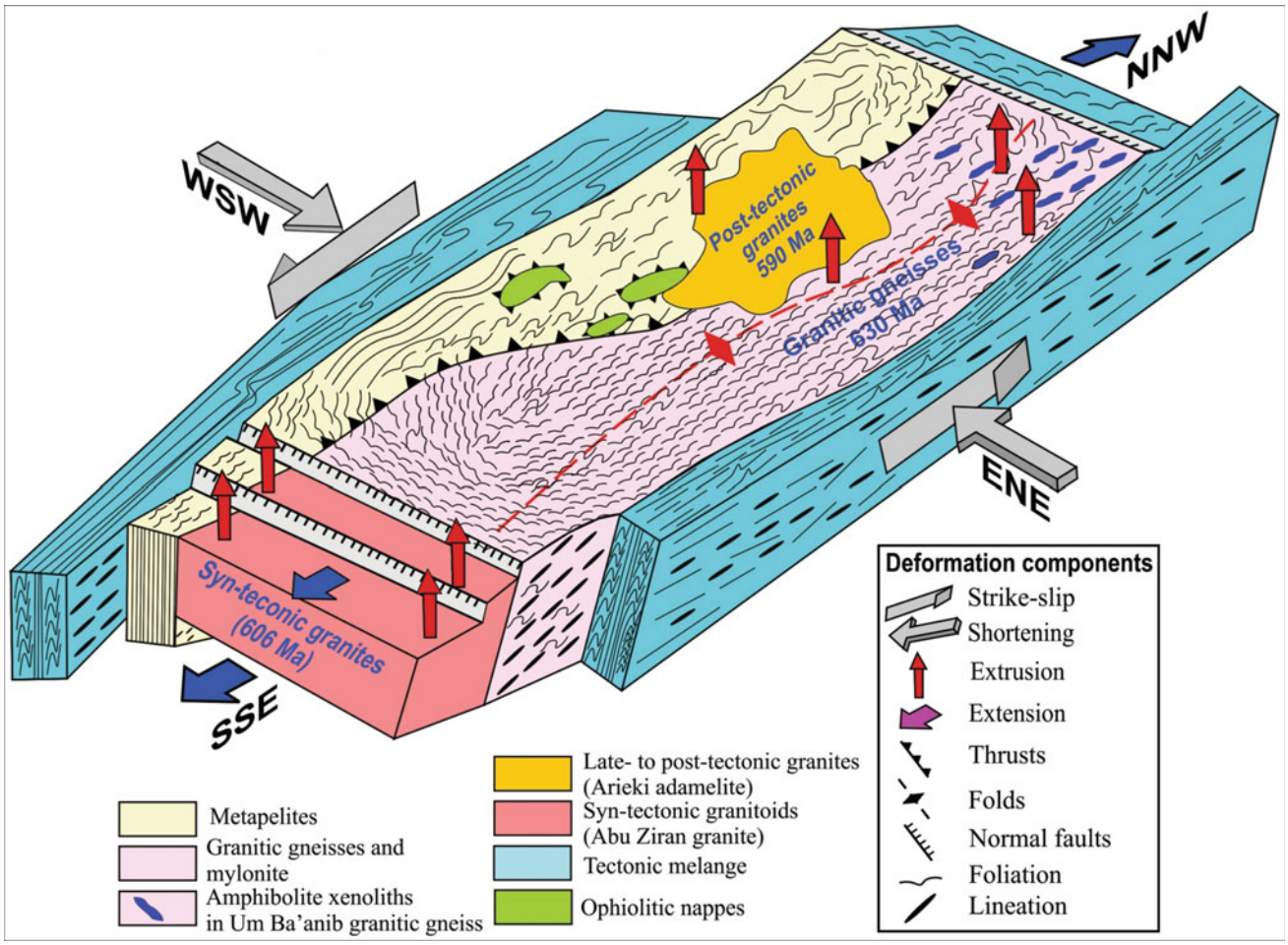

Fig. 5.19 Cartoon explaining evolution of the Meatiq gneiss complex during orogen parallel extension in the Central Eastern Desert (After Hamdy et al. 2017b)

remains controversial. Intrinsically, four scenarios are posited. The first scenario considered a parallel crustal extension origin, the second argues for emplacement within antiformal stacks, the third conceptualize a young emplacement within a core of a sheath fold origin and the final scenario envisages that the emplacement is due to overlap of regional folds and extension parallel to the fold axes (Shalaby 2010). The involvement of a significant extension within NW-trending zones bounded by sinistral strike-slip shears of the Najd Fault System is adopted by Stern (1985) that was accompanied by NW- and SE-dipping normal faults that created intramontane molasse basins (Wallbrecher et al. 1993; Fritz et al. 1996, 2002; Neumayr et al. 1998; Fritz and Messner 1999; Loizenbauer et al. 2001; Bregar et al. 2002; Abd El-Wahed 2007, 2008).

Strike-slip shear zones of Najd Fault System and the accompanied subsidiary shear arrays postdate emplacement of the dome (Shalaby 2010). The gneisses contiguously underlie the Pan-African nappe assemblages through discrete low-angle left-lateral thrust-dominated shear zones from the East. Ceaseless and continued nappe assemblages accretion on the gneisses augments the density disparity and contrast between the overlying denser intensified nappe and the underlying lighter quartz-rich gneisses, resulting in squeezing the gneissic components in oblique convergence regime. Subsequently, the gneisses are thought to have up-domed vertically through the rock units of the nappe.

The Sibai gneissic complex (Figs. 5.23 and 5.24) occur within the core of Gabal-El Sibai that located in Umm Ghieg area. Nearly, 90% of the Sibai core complex is consist of Neoproterozoic granitoid rocks of calcalkaline to alkaline chemical affinity (Kamal El Din 1993; Khudeir et al. 1995; Bregar et al. 2002). The gneisses of Sibai have been considered as pre-Neoproterozoic continental crust by El Gaby et al. (1984) and Khudeir et al. (1992, 1995), but are actually all late Neoproterozoic in age as the other core gneisses in the Eastern Desert (Johnson et al. 2011 and references therein). Sibai gneissic complex consist of two major lithological associations. The first unit include arc metavolcanics, metavolcanogenics, ophiolitic masses and mélange

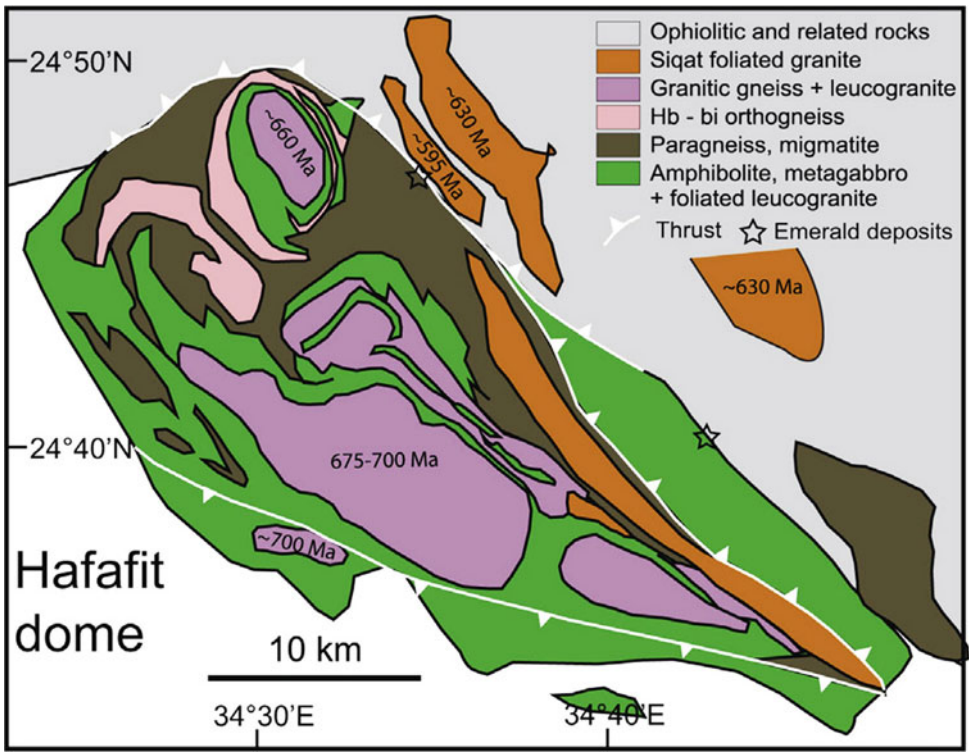

Fig. 5.20 Simplified geological map for the Hafafit gneiss complex (after Stern 2017). Also shown are approximate U-Pb zircon ages for Hafafit from Lundmark et al. (2012) and Kröner et al. (1994). Approximate emerald deposit localities are from Grundmann and Morteani (2008)

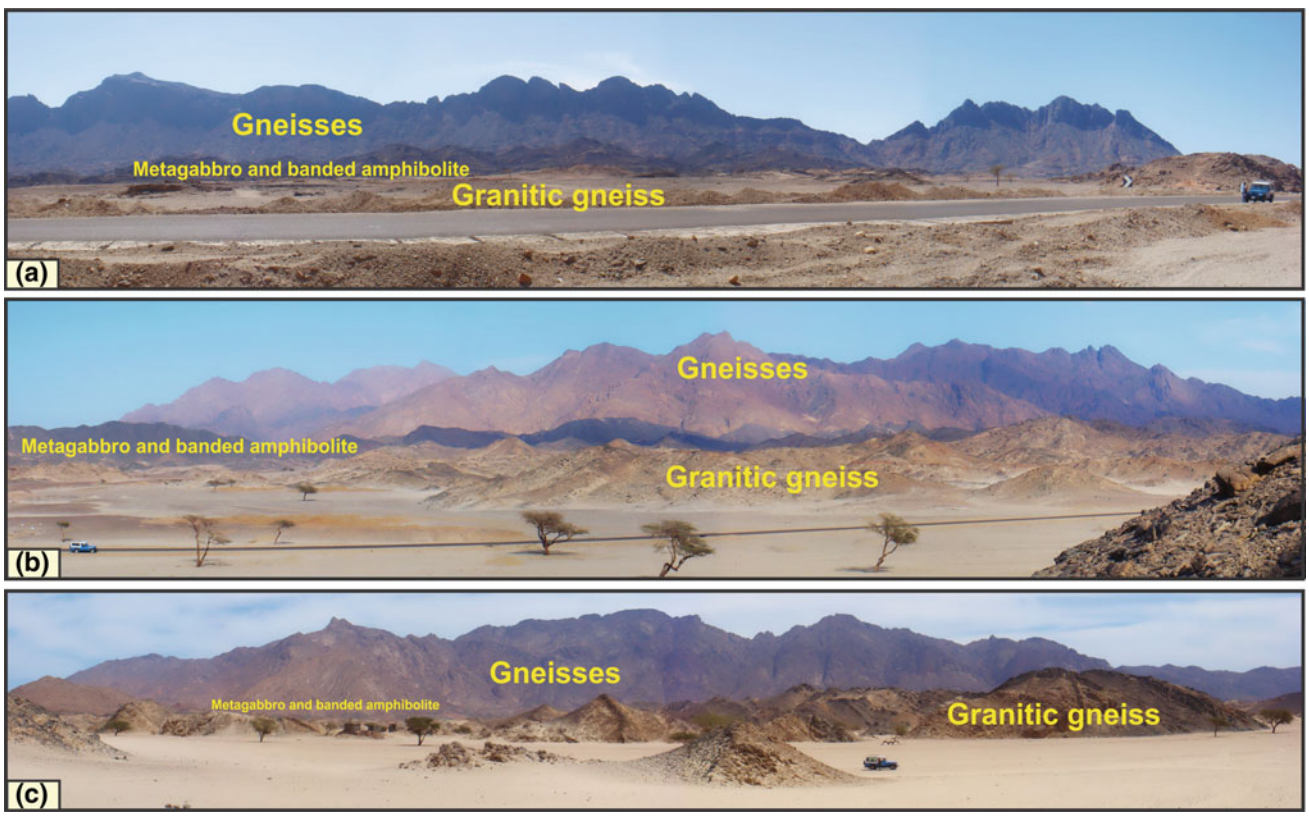

Fig. 5.21 Panoramic views showing hafafit domes consisting of granitic gneiss of tonalitic and trondhjemitic composition, metagabbro and banded amphibolite, altered ultramafic rocks, biotite- and hornblende-gneiss and psammitic gneiss at the rim of the domal structure

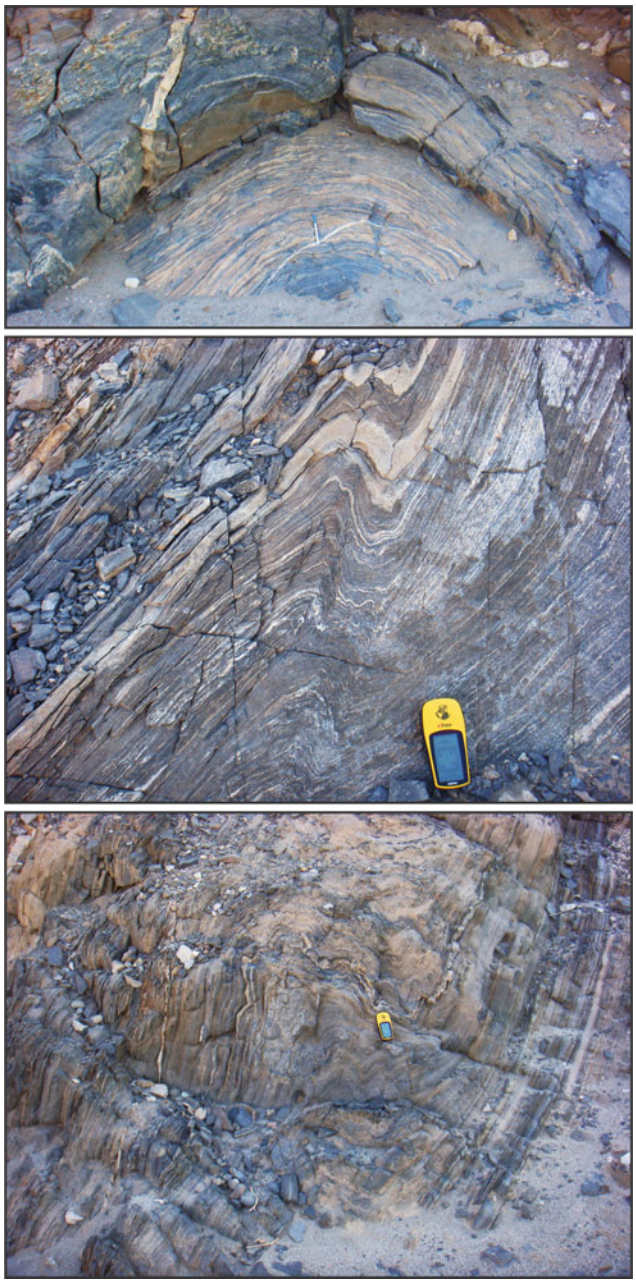

Fig. 5.22 Different types of folds from Hafafit dome

(ophiolitic association) that known by pan-African nappes. Some rocks of these associations metamorphosed to greenschist facies and some reaching amphibolites Facies. While the other unit that form the gneissic domes or Sibai core complex consist of a gneissic association of amphibolite, gneissic diorite, tonalite, granodiorite, schists and granite, As well as minor mafic intrusions. Pan-African nappe separated from the Sibai gneissic complex by strike slip shear zones (Fowler et al. 2007).

Bregar et al. (2002) and Abd El-Wahed (2008) divided the Sibai Core Complex into four groups of variably deformed granitoids related to different tectonic events and magmatic depending on petrography, geochemical composition, structural setting and age: Group (I), syntectonic granitoids (El-Shush gneissic tonalites), Group (II) Central Gneisses or first extension stage granitoids (El-Shush gneissic granodiorites), Group (III), exhumation-related granites or orogen parallel-extension or second extension stage granitoids (Abu Markhat syenogranites, Umm Shaddad syenogranites, Al Miyah granodiroite-monzogranite, Al-Andiya syenogranites and El-Sibai alkali granites), Group (IV), late tectonic granitoids (Umm Luseifa porphyritic granodiorites).

The Sibai Core Complex and their enveloping Pan-African nappe have been evolved through four main phases, namely, Oceanic stage (900–740 Ma), compressional arc-accretion and lithospheric thickening (740–660 Ma), gravitational collapse and core complex formation (660–645 Ma), transtension and core complex exhumation (645–560 Ma) (Abd El-Wahed 2008).

Two stage models have been suggested by Bregar et al. (2002) for the evolution of the Sibai Core Complex. (a) Formation of the sinistral wrench corridor associated with NE–SE directed extension and synkinematic intrusion of group (II) granitoids (central block). (b) Ongoing northwest–southeast directed extension triggered the intrusion of group (III) granitoids and the formation of detachment shear zones. Continuous activity of strike-slip and normal shear zones leads to the exhumation of the core complex and the formation of the Kareim molasse basin in the northwest.

Gabal El Shalul (Figs. 5.25 and 5.26) represents one of the westernmost deformed plutons (El Shalul granitoid) in the Central Eastern Desert forming a NW–SE-trending antiform (Fig. 5.26). The core of the variably deformed granitoid is dominated by monzogranite, whereas granitic gneisses are more common structurally upwards and away from the core (Ali et al. 2012). Enclaves of monzogranite in the deformed granites show the granite to be the younger of the two (Hamimi et al. 1994). The dominant structural feature within the gneiss dome is a NW–SE-trending mineral lineation. Isoclinal folds with hinge-lines trending NW–SE are also observed. A high-strain zone separates the El Shalul granitoid from the structurally overlying ophiolitic mélange, composed of tectonic blocks of meta-ultramafite, pyroxenite and metagabbro (Ali et al. 2012). The mélange is overlain tectonostratigraphically by basic to intermediate volcanic rocks, including pillowed basalts and andesites. The ophiolitic mélange and volcanic rocks are succeeded by volcanogenic metasediments, including deformed flat pebble conglomerates interbedded with grey phyllite, mudstone and graded greywackes (Ali et al. 2012). Hamimi et al. (1994) interpreted the high-strain zone (El Shalul Shear Zone) separating the eugeoclinal rocks (= ophiolite mélange + island arc sequence) from the underlying orthogneisses to

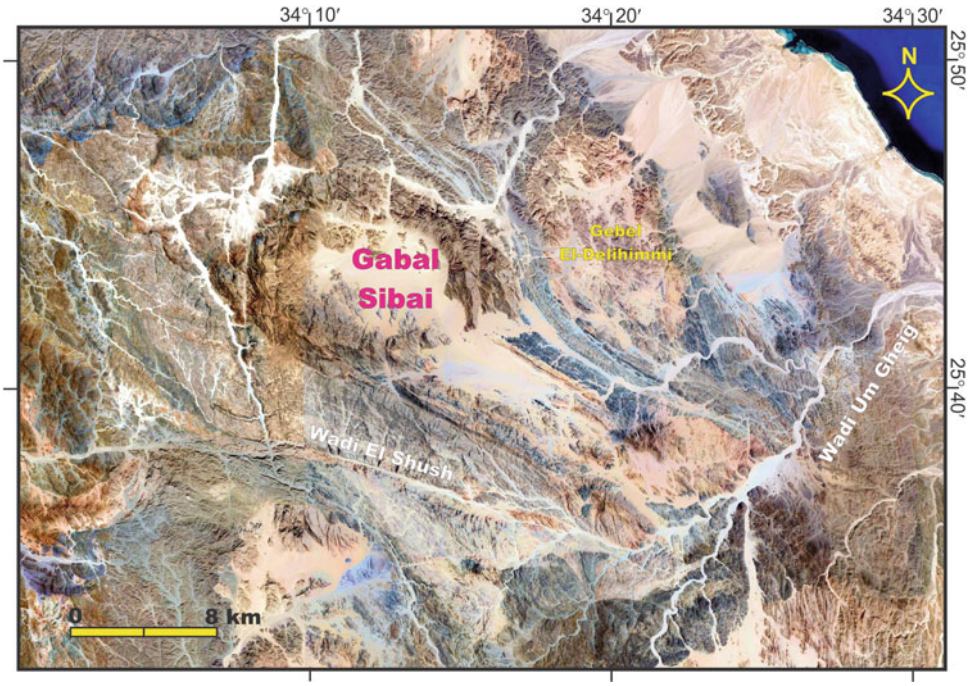

Fig. 5.23 Geological map of the El Sibai study area showing the main gneissic and ophiolitic association units. Planar structural data and macroscopic fold axial traces are also shown. DA = Delihimmi Antiform; HA = Higlig Antiform; KASZ = Kab Ahmed shear zone; ESSZ = El Shush shear zone. Faults are strike-slip. A–A0 and B–B0 are cross-sections presented in (b). Wadis: WA = Wadi Al Hamra; WG = Wadi Um Gheig; WL = Wadi Um Luseifa; WT = Wadi Talat Salah; WM = Wadi Abu Markhat; WH = Wadi Higlig; WD = Wadi El Dabbah; WS = Wadi El Shush; WR = Wadi Sitra; WW = Wadi Wizr; WB = Wadi Sharm El Bahari; WI = Wadi Abu Garadi; WK = Wadi Kareim

have developed during NW to WNW thrusting of the former (Ali et al. 2012). The El Shalul shear zone is c. 10 m wide and characterized by a mix of foliated metasediments and lenses of mylonitic granite, and it post-dates folding and cleavage development on the structurally overlying eugeoclinal rocks (Ali et al. 2012).

5.4 Shear Zone-Related Mineralizations

Most significant gold deposits throughout the world are controlled by major and subsidiary shear zones (e.g., Bonnemaison and Marcoux 1990; Hodgson 1989; Roberts 1987). Syn-deformational ore deposition played an important role in many Au deposits according to field and laboratory evidence, which indicates that flow of Au-bearing fluids was synchronous with regional-scale deformation events. Gold-related deformation events linked to ore genesis were distinct from high-level, brittle deformation that is typical of many epithermal deposits. Many Au deposits, with brittle–ductile features, most likely formed during tectonic events that were accompanied by significant fluid flow. Interactive deformation-fluid processes involved brittle–ductile folding, faulting, shearing, and gouge development that were focused along illite–clay and dissolution zones caused by hydrothermal alteration (Peters 2004). Alteration along these deformation zones resulted in increased porosity and enhancement of fluid flow, which resulted in decarbonated, significant dissolution, collapse, and volume and mass reduction. On the other hand, intrusion-related systems of the TGB exhibit intermediate structural styles of mineralization that provide a useful bridge in understanding the diversity of mechanically controlled structural styles in otherwise mostly unrelated gold deposit types (Stephens et al. 2004).

The Eastern Desert was a gold-mining province in ancient Egypt since the pre-dynastic times (Zoheir et al. 2018). Despite the several thousand years mining history, the large number of gold deposits (Fig. 5.27), and considerable recent research, the age of Au mineralization in the Eastern Desert is poorly known. The area is considered to be highly prospective for undiscovered gold deposits that occur as shear zone-hosted, disseminated sulfide mineralization or as quartzcarbonate veins along major structures in ophiolitic and island arc metasediments. Gold mineralization is closely associated with the granitic rocks that can be grouped into three categories i.e. syn-late tectonic calc-alkaline granites, calc-alkaline to mildly alkaline granites of the transitional stage and post-tectonic alkaline granites (Botros 2015). Tectonically, gold mineralization is linked with the

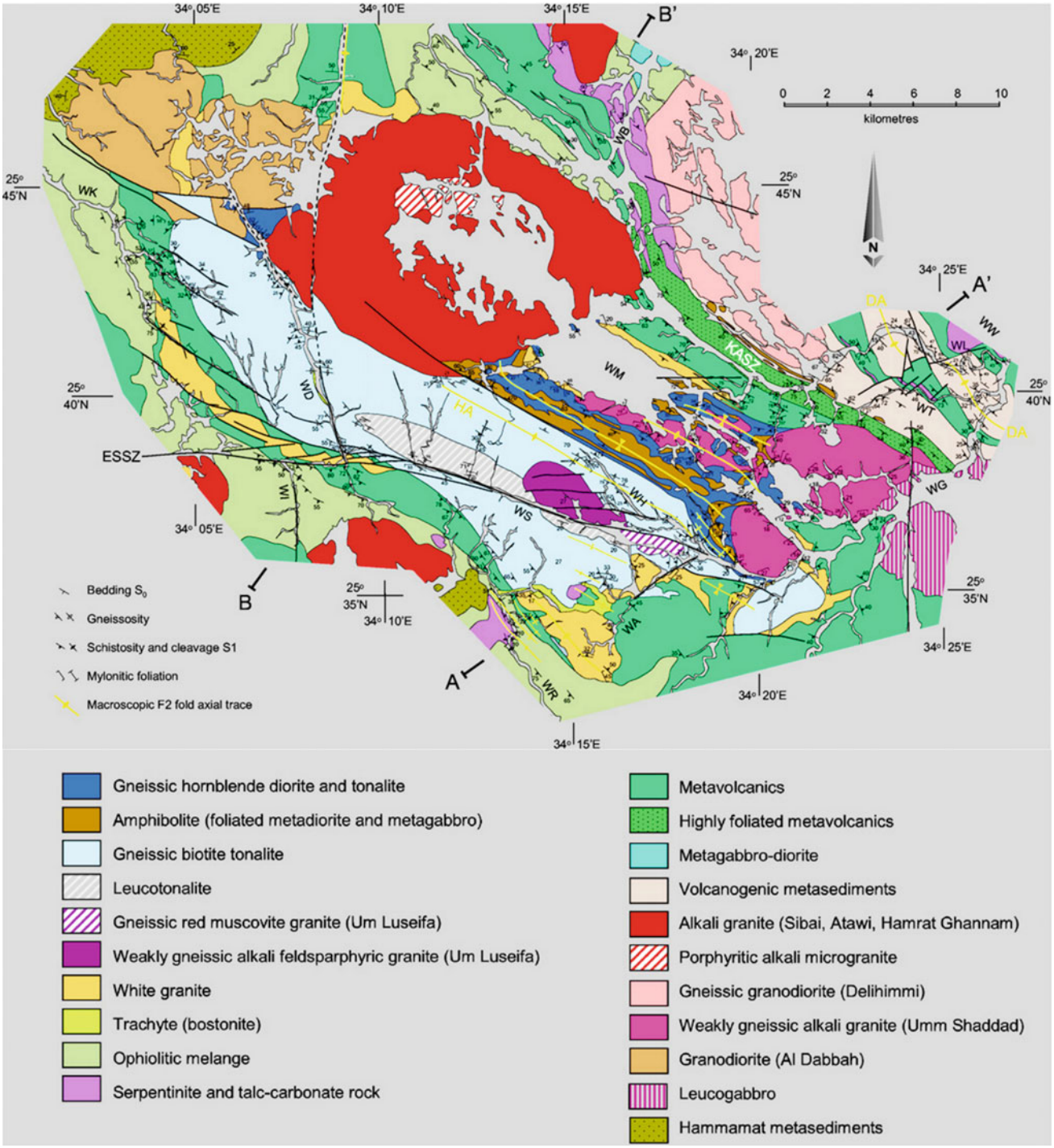

Fig. 5.24 Geological map of the Gabel El Shalul area (after Ali et al. 2012)

deformational tectonothermal events that were active during the evolution of the ANS. During the primitive stages of the island-arc formation, pre-orogenic gold mineralization was formed by hot brines accompanying submarine volcanic activity (Botros 2015).

Wrench-dominated transpression, a characteristic feature of obliquely convergent mobile belts, has been suggested to explain the complex deformation kinematics in the Eastern Desert of Egypt (e.g., Wallbrecher et al. 1993; Greiling et al. 1994; Loizenbauer et al. 2001; Makroum 2001; Fritz et al.

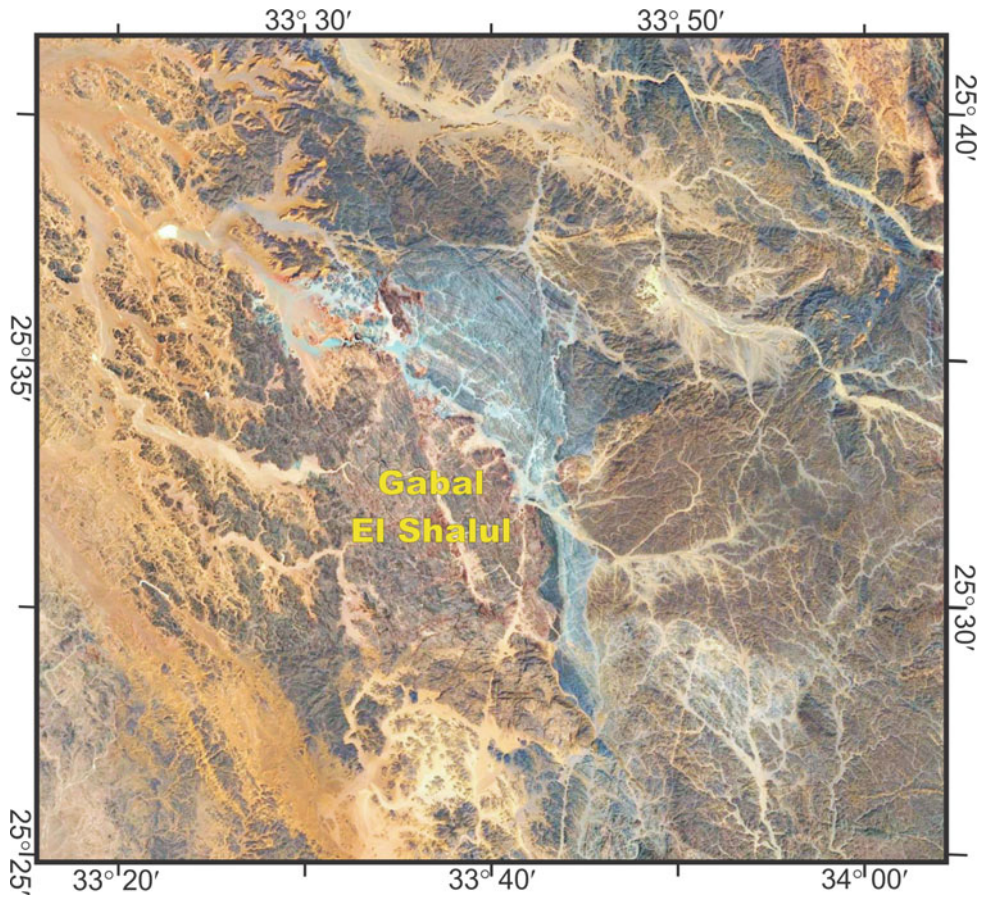

Fig. 5.25 Location of El-Shalul gneiss complex

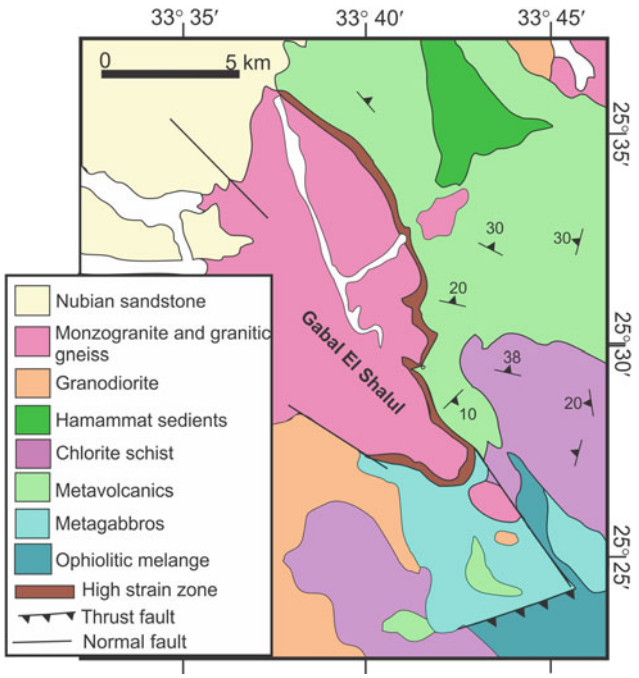

Fig. 5.26 Geological map of the Gabel El Shalul area (after Ali et al. 2012)

1996, 2002; Shalaby et al. 2005; Abd El-Wahed 2008; Abdeen et al. 2008; Abd El-Wahed and Kamh 2010; Abd El-Wahed et al. 2016) and to explain the geometry and kinematics of gold-bearing quartz veins (Hassaan et al. 2009; Zoheir 2008, 2011; Zoheir and Lehmann 2011; Abd El-Wahed 2014; Zoheir et al. 2017, 2018). Gold mineralization occurs mainly in fault-fill quartz veins, and appears to be confined to zones of strike-slip fault/shear structures cutting ophiolites and molasse-type sediments (Fig. 5.10). At least 70% of the auriferous quartz veins in this area is associated with late-orogenic, I-type granitic intrusions (e.g. Murr 1999; Zoheir et al. 2011; Harraz 1999, 2000; Helmy et al. 2004; Zoheir and Moritz 2014; Helmy and Zoheir 2015; Zoheir et al. 2017, 2018). These intrusions are commonly small in size and their emplacement was most likely subsequent to northeast-southwest transpressional regime rather than in an extensional tectonic environment (Fowler 2001).

Botros (2015) classified the gold mines in the CED as follows: (i) Veins hosted in volcanogenic metasediments and/or the syn-orogenic granites surrounding them (e.g. Sukari, Dungash, Kurdeman), (ii) Veins localized at the

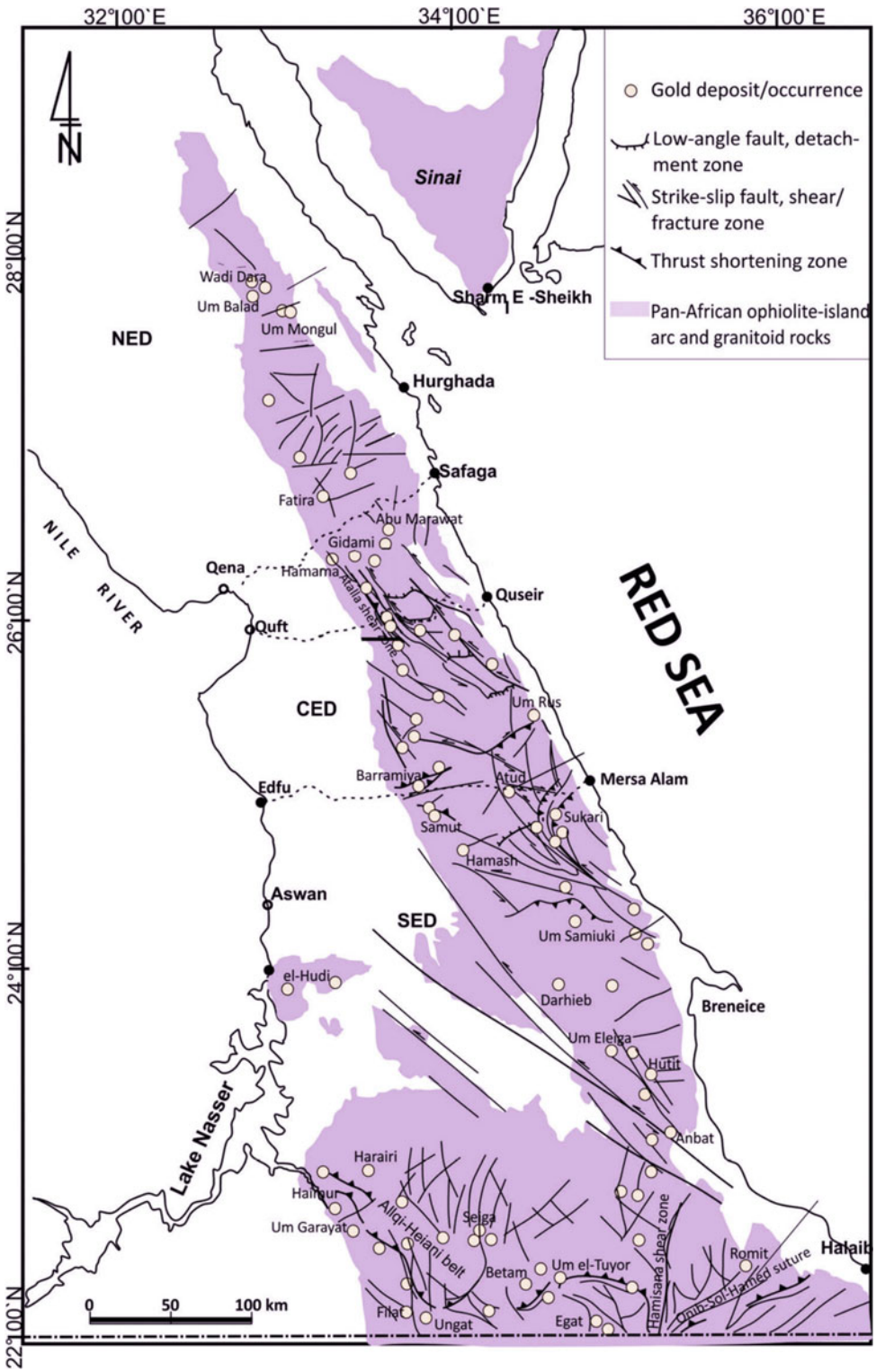

Fig. 5.27 Distribution of gold occurrences in the Eastern Desert of Egypt in relation to the main lithological units and major faults/shear zones (after Zoheir et al. 2018). Gold mines and occurrences names and locations are verified by Basem Zoheir, through field work and Global Positioning System (GPS) readings based on Bing Maps

contacts between younger gabbros and younger granites (e.g. Atud gold mines, Harraz and Hamdy 2015; Abdel-nasser and Kumral 2016), (iii) Quartz veins traversing calc-alkaline to mildly alkaline younger granites (e.g. Hangalia gold mine), (iv) Gold hosted in altered ophiolitic serpentinites along thrust faults (e.g. Barramiya gold mines). Gold mineralization in the Barramiya, Dungash, Sukari and Kurdeman gold mines are mainly controlled by the regional,

NNW- and NE-trending zones of transpression. The Hangalia gold deposit (Khalil and Helba 2000) and the Hamash Au–Cu deposit (Hilmy and Osman 1989; Helmy and Kaindl 1999) occur within post tectonic granites of Egypt. Gold mineralization at Um Rus is in quartz veins along NE-SW trending fractures in granitoid-gabbroic rocks (Harraz and EI-Dahhar 1993).

In the Atalla mine area, gold-bearing sulfide-quartz veins cutting mainly through the Atalla monzogranite intrusion in the Eastern Desert of Egypt are controlled by subparallel NE-trending brittle shear zones. These veins are associated with pervasive sericite-altered, silicified and ferruginated rocks (Zoheir et al. 2017, 2018). The new geochronological data demonstrate that the post-intrusion Au-mineralization that formed during the ~600 Ma period, controlled by wrench tectonics along Najd-related structures in the region (620–585 Ma) (Zoheir et al. 2017, 2018).

The Fawakhir–El Sid district is part of a regional NNW-trending shear corridor (15 km wide) that hosts several other historic gold mines associated with left-lateral wrench structures and related granite intrusions. Vein-style gold mineralization is hosted within and at the margin of an I-type and magnetite-series monzogranite, the Fawakhir granite intrusion (Zoheir et al. 2015), and a Pan-African (~740 Ma) ophiolite sequence (El Bahariya 2018).

At the Barramiya gold mine, the mineralized zone is composed of mylonitized graphite schist, talc–carbonate rocks containing bodies of listwaenite and quartz veins and veinlets (Zoheir and Lehmann 2011; Harraz et al. 2012; Botros 2015). The Au-bearing main lode is flanked by listwaenite on one side and talc–carbonate on the other side. The mineralized and folded quartz and quartz–carbonate veins are associated with ENE-WSW dextral shear zones (Abd El-Wahed et al. 2016), whereas some barren and unfolded milky quartz veins are accommodated in steeply dipping NW–SE extensional fractures (Zoheir and Lehmann 2011; Abd El-Wahed et al. 2016). The Barramiya shear belt consists of two conjugate sets of shear zones, namely a NW-SE-trending sinistral and NESW-trending dextral (Abd El-Wahed 2014; Abd El-Wahed et al. 2016).

In the Dungash mine area, Dungash mélange composed of remnants of imbricate ophiolitic slices tectonically intermixed with island arc metavolcanic/volcanogenics and metasedimentary rocks. The transpressive character of deformation in the Dungash mine area is shown by the coexistence of strike-slip and dip-slip shear zones. The gold deposits at Dungash mine area occur in an EW-trending quartz vein along post-metamorphic brittle–ductile shear zones in metavolcanic and metasedimentary host rocks (Helba et al. 2001; Abd El-Wahed and Abu Anbar 2009; Zoheir and Weihed 2014; Abd El-Wahed 2014). The sigmoidal geometry of a zone of quartz pods along the Dungash shear zone defines E–W dextral shear system between foliated metavolcanic and volcanogenic metasediments (Abd El-Wahed et al. 2016).

The Hamash gold mine area is mainly occupied by metamudstones, phyllites, chlorite–quartz–epidote schists and actinolite–epidote schists. Serpentinite and talc–carbonate rocks are enclosed in metasediments (Hilmy and Osman 1989; Helmy and Kaindl 1999). The gold mineralization in Hamashmine initiated during D_2 dextral shearing and continued until D_3 which an extensional phase related to intrusion of post tectonic granites (Abd El-Wahed et al. 2016).

The highest Au contents in Sukari gold mine (e.g. Main Zone and Hapi Zone) are principally SSE-dipping back-thrusts branching from the major Sukari Thrust. Gold mineralization at Quartz Ridge, V-Shear and North Sukari are largely controlled by NE-trending strike-slip shear zones and transpressional imbricate thrust zones in the East Sukari Thrust belt. From the structural point of view, Quartz Ridge, North Sukari and V Shear are most suitable sites for gold exploration in Sukari mine area (Abd El-Wahed et al. 2016).

Gold-bearing quartz veins are widespread in south Eastern Desert of Egypt, commonly showing spatial and temporal association with shear zones (e.g., Kusky and Ramadan 2002; Zoheir 2008, 2011). Au-quartz lodes in the Wadi El Beida–Wadi Khashab area are associated with NNW-trending shear zones in pervasively silicified, ferruginated volcanic/volcanogenic rocks, or along steeply dipping thrust segments bounding allochthonous ophiolitic blocks. Development of the mineralized shear zones is attributed to a wrench-dominated transpression (Zoheir 2012a, b). Structural analysis of the shear fabrics along the ore zones in El-Anbat mine area indicate that geometry of the mineralized quartz veins and alteration patterns are controlled by the regional, NNW-trending zone of transpression, known as the Wadi Kharit–Wadi Hodein shear system, which is related to the 655–540 Ma, Najd strike–slip fault system in the Eastern Desert of Egypt (Zoheir 2011).

Finally, many of the mineralized quartz veins and alteration patterns in the Central Eastern Desert and the Southern Eastern Desert are controlled by the regional, NW to NNW-trending zones of transpressional strike slip shear zone associated with Najd Fault System.

5.5 Discussion

Progress in understanding the tectonic setting, deformation history and structural architecture of the ENS, the northwestern continuation of the ANS, is attributed to intensive field-structural mapping since the establishment of the Egyptian Geological Survey (1896), wealth of remote

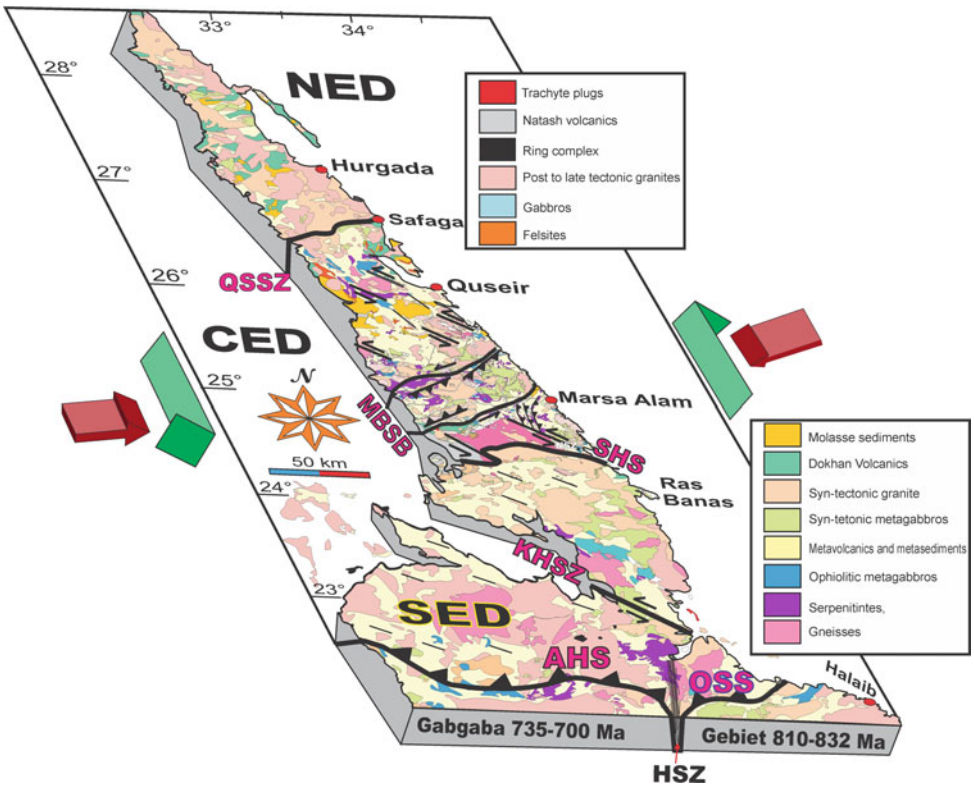

Fig. 5.28 Major shear zones and sutures in the Egyptian Nubian Shield

sensing data and a growing geochronological database. Recently, application of anisotropy of magnetic susceptibility (AMS) technique and quantitative strain analysis play also a crucial role in unraveling strain in rocks, especially in the absence of potential strain markers (De Wall et al. 2001; Abdeen et al. 2014; Greiling et al. 2014; Hagag et al. 2018). The predominantly Neoproterozoic basement complex outcropping in the ENS is traversed by map-scale semi ductile-semi brittle shear zones of variable orientations, dimensions and ages. These shear zones are consistent and in complete harmony with those encountered elsewhere in the entire ANS in terms of their extensions, widths, and degree and sense of shearing. Among these high strain zones, Qena-Safaga- and Idfu-Mersa Alam-Zones split the Eastern Desert of Egypt into three main provinces; NED, CED and SED (Fig. 5.28). Such traditional subdivision is based mainly on the lithologic variations recorded in the three provinces, where voluminous granitoids, Dokhan Volcanis and post-amalgamation Hammamat volcanosedimentary Sequence are dominated in the NED, and infracrustal units (gneisses, migmatites, gneissose granites and remobilized equivalents) and ophiolite- and island arc-dominated supracrustal units occupy both the CED and the SED with variable proportions. In the CED and SED, low angle shear zones separate hanging walls low grade ophiolite- and island arc-dominated supracrustal lithologies from high grade infracrustal rocks in their footwalls. Such detachment surfaces are marked by zones of intensive mylonitization and cataclasis, and are best represented in Beitan, Hafafit, Meatiq and Shalul areas (Fig. 5.28). Because of the absence of gneisses and ophiolites, it is not easy to deal with these two tiers in the NED or in Sinai.

However, based on our own field investigations and studies, along with reviewing previous literature, it can be stated with reasonable confidence that AHS is the only confirmed suture zone in the extreme SED. This suture forms a segment of the greater AHOSHY that separates the Eastern Desert-Midyan terrane to the north from the Gabgaba-Gebeit-Hijaz terrane to the south. Elongation of ophiolitic nappes in the vicinity of Wadi Allaqi is rather evidence demonstrating suturing in this zone.

In the ENS, shear zones could be subdivided into two main categories; syn-accretion- and post-accretion-shear zones. From our opinion, the syn-accretion shear zones are typified by the HSZ that juxstaposes Gabgaba and Gebeit terranes located just to the south of the AHS (Fig. 5.28). As mentioned before, the HSZ was considered as an arc-arc suture, a transcurrent, or a transpressive shear zone formed just after the arc accretion stage. The HSZ deformation began after 660 Ma, with intense E–W shortening and N–S extension accompanied by greenschist to amphibolite facies metamorphism and development of upright isoclinal folds and vertical foliations. Whether the sense of shearing along the HSZ is sinistral or dextral was and still is a matter of

much debate. Abdelsalam and Stern (1996) proposed dextral sense of shearing depending on the dextral offsetting of the Yoshgah Suture (Stern et al. 1989, 1990). The post-accretion shear zones are manifested by the NW- and ENE- (to E-) oriented high strain zones. Both shearing trends are affiliated to the D_2 deformation in the proposed ANS-scale deformation scheme of Hamimi et al. (2019). The NW trend is evidently Najd-related exhibiting sinistral sense of movement. This trend is exemplified by KHSZ, NSZ and ASZ. The ENE- (to E-) trend shows dextral sense of shearing and is obviously younger than the former trend. Such conclusion indicates that both trends are not conjugate pairs as mentioned in some previous publications.

Also, the major shear zones bounding the gneiss domes have been interpreted as sinistral strike-slip shear zones combined with extensional shears that formed during exhumation of domes (e.g., Fritz et al. 1996, 2002; Abd El-Wahed 2008, 2014) or as remnants of NW-directed thrusts (Andresen et al. 2010). Nowadays, sinistral shearing along the NW-trending shear zones of the Najd Fault System is genetically linked with deposition of sediments, exhumation of gneiss domains, and emplacement of syn-tectonic granitoids (e.g. Fritz et al. 1996, 2002, 2013; Bregar et al. 2002; Shalaby et al. 2005; Abd El-Wahed 2008, 2010; Abd El-Wahed and Kamh 2010; Abdeen et al. 2014; Abd El-Wahed et al. 2016: Makroum 2017).

In general, the syn-orogenic gold mineralization in the Eastern Desert of Egypt is connected with oblique transpression associated with conjugate NW-sinistral strike slip shear zones related to the Najd fault system and hosted by volcanogenic metasediments and altered ophiolitic serpentinites. The NW-sinistral and NE-dextral shear zones (620–540 Ma) and extensional NW-trending fractures play a great role in the development of gold bearing quartz veins in the CED and SED.

References

Abd El-Naby H, Frisch W (2006) Geochemical constraints from the Hafafit Metamorphic Complex (HMC): evidence of Neoproterozoic back-arc basin development in the central Eastern Desert of Egypt. J Afr Earth Sci 45:173–186

Abd El-Wahed MA (2007) Pan-African strike-slip tectonics of Wadi El-Dabbah area, north Sibai Core Complex, Central Eastern Desert, Egypt. Ann Egypt Geol Surv 29:1–36

Abd El-Wahed MA (2008) Thrusting and transpressional shearing in the Pan-African nappe southwest El-Sibai core complex, Central Eastern Desert, Egypt. J Afr Earth Sci 50:16–36

Abd El-Wahed MA (2010) The role of the Najd Fault System in the tectonic evolution of the Hammamat molasse sediments, Eastern Desert, Egypt. Arab J Geosci 3:1–26

Abd El-Wahed MA (2014) Oppositely dipping thrusts and transpressional imbricate zone in the Central Eastern Desert of Egypt. J Afr Earth Sci 100(2014):42–59

Abd El-Wahed MA, Abu Anbar MM (2009) Syn-oblique convergent and extensional deformation and metamorphism in the Neoproterozoic rocks along Wadi Fatira shear zone, Northern Eastern Desert, Egypt. Arab J Geosci 2:29–52

Abd El-Wahed MA, Kamh SZ (2010) Pan-African dextral transpressive duplex and flower structure in the Central Eastern Desert of Egypt. Gondwana Res 18:315–336

Abd El-Wahed MA, Thabet IA (2017) Strain geometry, microstructure and metamorphism in the dextral transpressional Mubarak Shear Belt, Central Eastern Desert, Egypt. Geotectonics 51(4):438–462

Abd El-Wahed MA, Harraz HZ, El-Behairy MH (2016) Transpressional imbricate thrust zones controlling gold mineralization in the Central Eastern Desert of Egypt. Ore Geol Rev 78:424–446

Abdeen MM, Abdelghaffar AA (2011) Syn- and post-accretionary structures in the Neoproterozoic Central Allaqi-Heiani suture zone, Southeastern Egypt. Precambr Res 185:95–108

Abdeen MM, Greiling RO (2005) A quantitative structural study of late Pan-African compressional deformation in the Central Eastern Desert (Egypt) during Gondwana assembly. Gondwana Res 8 (4):457–471

Abdeen MM, Dardir AA, Greiling RO (1992) Geological and structural evolution of the Wadi Queih Area (N Quseir), Pan-African Basement of the Eastern Desert of Egypt. Zbl Geol Palfiontol Teil I:2653–2659

Abdeen MM, Sadek MF, Greiling RO (2008) Thrusting and multiple folding in the Neoproterozoic Pan-African basement of Wadi Hodein area, south Eastern Desert, Egypt. J Afr Earth Sci 52:21–29

Abdeen MM, Greiling RO, Sadek MF, Hamad SS (2014) Magnetic fabrics and Pan-African structural evolution in the Najd Fault corridor in the Eastern Desert of Egypt. J Afr Earth Sci 99:93–108

Abdel-Karim AM, Azzaz SA, Moharem AF, El-Alfy H (2008) Petrological and geochemical studies on the ophiolite and island arc association of Wadi Hammaryia, Egypt. Arab J Sci Eng 33 (1C):117–138

Abdel-Karim A-AM, Ali S, Helmy HM, El-Shafei SA (2016) A fore-arc setting of the Gerf ophiolite, Eastern Desert, Egypt: Evidence from mineral chemistry and geochemistry of ultramafites. Lithos 263:52–65

Abdelnasser A, Kumral M (2016) Mineral chemistry and geochemical behavior of hydrothermal alterations associated with mafic intrusive-related Au deposits at the Atud area, Central Eastern Desert, Egypt. Ore Geol Rev 77:1–24. https://doi.org/10.1016/j.oregeorev.2016.01.011

Abdelsalam MG (1994) The Oko Shear Zone: post-accretionary deformation in the Arabian-Nubian Shield. J Geol Soc Lond 151:767–776

Abdelsalam MG (2010) Quantifying 3D post-accretionary tectonic strain in the Arabian-Nubian Shield: Superimposition of the Oko Shear Zone on the Nakasib Suture, Red Sea Hills, Sudan. J Afr Earth Sci 56(4–5):167–178

Abdelsalam MG, Stern RJ (1996) Sutures and shear zones in the Arabian-Nubian Shield. J Afr Earth Sci 23:289–310

Abdelsalam MG, Abdeen MM, Dowaidar HM, Stern RJ, Abddelghaffar AA (2003) Structural evolution of the Neoproterozoic western Allaqi-Heiani structure, southeastern Egypt. Precambr Res 124:87–104

Abu-Alam TS, Hassan M, Stüwe K, Meyer S, Passchier C (2014) Multistage tectonism during Gondwana collision: Baladiyah Complex, Saudi Arabia. J Petrol 55:1941–1964

Abu-Alam TS, Stüwe K (2009) Exhumation during oblique transpression: The Feiran-Solaf region, Egypt. J Metamorph Geol 27:439–459

Abu El-Enen MM, Abu-Alam TS, Whitehouse MJ, Ali K, Okrusch M (2016) P-T path and timing of crustal thickening during amalgamation of East and West Gondwana: a case study from the Hafafit

Metamorphic Complex, Eastern Desert of Egypt. Lithos 263:213–238
Agar RA, Stacey JS, Whitehouse MJ (1992) Evolution of the southern Afif terrane—a geochronologic study. Saudi Arabian Deputy Ministry for Mineral Resource Open File Report DGMR-OF-10-15, 41 pp
Akaad MK (1996) Rock succession of the basement: an autobiography and assessment. In: The Egyptian Geological Survey, Centennial Conference, Paper No. 71, p 87
Akaad MK, Noweir AM (1977) The post Hammamat felsites and their age relation with the younger granites of Egypt. Proc Acad Sci 30:163–168
Akaad MK, Noweir AM, Kotb H (1979) Geology and petrochemistry of the granite association of the Arabian Desert Orogenic Belt of Egypt between 25°35′ and 26°30′. Delta J Sci 3:107–151
Akaad MK, El Ela AM Abu, El Kamshoshy HI (1993) Geology of the region West of Marsa Alam, Eastern Desert, Egypt. Ann Egypt Geol Survey 19:1–18
Al-Husseini M (2000) Origin of the Arabian plate structures: Amar collision and Najd rift. Geo Arabia 5:527–542
Ali KA, Azer MK, Gahlan HA, Wilde SA, Samuel MD, Stern RJ (2010) Age constraints on the formation and emplacement of Neoproterozoic ophiolites along the Allaqi-Heiani Suture, South Eastern Desert of Egypt. Gondwana Res 18:583–595
Ali KA, Andresen A, Stern RJ, Manton WI, Omar SA, Maurice AE (2012) U-Pb zircon and Sr-Nd-Hf isotopic evidence for a juvenile origin of the c 634 Ma El-Shalul Granite, Central Eastern Desert, Egypt. Geol Mag 149:783–797
Ali-Bik MW, Sadek MF, Ghabrial DS (2014) Late Neoproterozoic metamorphic assemblages along the Pan-African Hamisana Shear Zone, Southeastern Egypt: Metamorphism, geochemistry and petrogenesis. J Afr Earth Sci 99:24–38
Almond DC, Ahmed F (1987) Ductile shear zones in the northern Red Sea Hills of Sudan and their implications for crustal collision. In: Bowden P, Kinnaird JA (eds) African geology reviews. Geol J 22:175–184
Amstutz GC, El-Gaby S, Ahmed AA, Habib ME, Khudeir AA (1984) Back-arc ophiolite association, central Eastern Desert, Egypt. Bull Fac Sci Assiut Univ 13:95–136
Andresen A, Abu El-Rus MA, Myhre PI, Boghdady GY, Corfu F (2009) U-Pb TIMS age constraints on the evolution of the Neoproterozoic Meatiq Gneiss Dome, Eastern Desert, Egypt. Int J Earth Sci (Geol Rundsch) 98:481–497
Andresen A, Augland LE, Boghdady GY, Lundmark AM, El Nady OM, Hassan MA, El Rus MA (2010) Structural constraints on the evolution of the Meatiq gneiss dome (Egypt), east-African orogen. J Afr Earth Sci 57:413–422
Asran AM, Kabesh M (2003) Evolution and geochemical studies on a stromatic migmatite-amphibolite association in Hafafit area CED Egypt. Egypt J Geol 47:1–24
Azza M, Hosny A, Gharib A (2012) Rupture process of Shallow Earthquakes of Abou-Dabbab Area, South East of Egypt. Egypt J Appl Geophys 11(1):85–100
Badawy A, El-Hady S, Abdel-Fattah AK (2008) Microearthquakes and neotectonics of Abu-Dabbab, Eastern Desert of Egypt. Seismol Res Lett 79(1):55–67
Berhe SM (1990) Ophiolites in northeast and east Africa: implications for Proterozoic crustal growth. J Geol Soc Lond 147:41–57
Bonnemaison M, Marcoux E (1990) Auriferous mineralization in some shear zones. A three stage model of metallogenesis. Miner Deposita 25:96–104
Botros NS (2015) The role of the granite emplacement and structural setting on the genesis of gold mineralization in Egypt. Ore Geol Rev 70:173–187
Bregar M, Bauernhofer A, Pelz K, Kloetzli U, Fritz H, Neumayr P (2002) A late Neoproterozoic magmatic core complex in the Eastern Desert of Egypt; emplacement of granitoids in a wrench-tectonic setting. Precambr Res 118:59–82
Brown GB (1972) Tectonic map of the Arabian Peninsula. Saudi Arabian Directorate General of Mineral Resources Map AP-2, Scale 1:4,000,000
Brown GF, Jackson RO (1960) The Arabian Shield. In: XIX international geological congress, Pt 9, pp 69–77
Cononco (1987) Egyptian General Petroleum Corporation-Conoco Coral, 1987. Geological map of Egypt, Scale 1:500,000, Cairo
Daggett PH, Morgan P, Boulos FK, Hennin SF, El-Sherif AA, El Sayed AA, Basta NZ, Melek YS (1986) Seismicity and active tectonics of the Egyptian Red Sea margin and the northern Red Sea. Tectonophysics 125:313–324
De Wall H, Greiling RO, Sadek MF (2001) Post-collisional shortening in the late Pan-African Hamisana high strain zone, SE Egypt: field and magnetic fabric evidence. Precambr Res 107:179–194
Delfour J (1970) Le Group de J'balah, une nouvelle unite de Bouclier Arabe. BRGM Bull 2:19–32
EGSMA (1996) Egyptian Geological Survey and Mining Authority, Geological map of Wadi Jabjahah Quadrangle, Egypt, Scale 1:250.000
EGSMA (2002) Geological Map of Marsa Shaab Quadrangle, Egypt at Scale 1:250,000. Egyptian Geological Survey and Mining Authority, Cairo, Egypt
Emam A, Zoheir B, Johnson P (2015) ASTER-based mapping of ophiolitic rocks: examples from the Allaqi–Heiani suture, SE Egypt. Int Geol Rev 1–15. https://doi.org/10.1080/00206814.2015.1094382
El Bahariya G (2012) Classification and origin of the Neoproterozoic ophiolitic mélanges in the Central Eastern Desert of Egypt. Tectonophysics 568–569:357–370
El Bahariya G (2018) Classification of the Neoproterozoic ophiolites of the Central Eastern Desert, Egypt based on field geological characteristics and mode of occurrence. Arab J Geosci 11(12). https://doi.org/10.1007/s12517-018-3677-1
El-Bayoumi RM, Greiling R (1984) Tectonic evolution of a Pan-African plate margin in southeastern Egypt—a suture zone overprinted by low angle thrusting? In: Klerkx J, Michot J (eds) African geology. Tervuren, pp 47–56
El-Desoky HM, Khalil AE, Salem AKA (2015) Ultramafic rocks in Gabal El-Rubshi, Central Eastern Desert, Egypt: petrography, mineral chemistry, and geochemistry constraints. Arab J Geosci 8 (5):2607–2631. https://doi.org/10.1007/s12517-014-1407-x
El-Gaby S, List FK, Tehrani R (1988) Geology, evolution and metallogenesis of the Pan-African Belt in Egypt. In: El-Gaby S, Greiling RO (eds) The Pan-African Belt of Northeast Africa and Adjacent Areas. Vieweg & Sohn, Weisbaden, pp 17–68
El-Gaby S, El Nady O, Khudeir A (1984) Tectonic evolution of the basement complex in the central Eastern Desert of Egypt. Geol Rundsch 73:1019–1036
El-Gaby S, List FK, Tehrani R (1990) The basement complex of the Eastern Desert and Sinai. In: Said R (ed) The geology of Egypt. Balkema, Rotterdam, pp 175–184
El-Hady ShM (1993) Geothermal evolution of the Red Sea margin and its relation to earthquake activity. MSc thesis, Cairo University, Cairo, Egypt
El-Kazzaz YA, Taylor WE (2000) Tectonic evolution of the Allaqi Shear Zone and implications for the Pan-African terrain amalgamation in the South Eastern Desert of Egypt. J Afr Earth Sci 33 (2):177–197
El Khrepy S, Koulakov I, Al-Arifi N (2015) Crustal structure in the area of the cannon earthquakes of Abu Dabbab (Northern Red Sea, Egypt), from seismic tomography inversion. Bull Seismo Soc Am 105(4):13. http://dx.doi.org/10.1785/0120140333

El-Rabaa SM, Al-Shumaimri MS, Al-Mishwat AT (2001) Fate of the Najd fault system in northwestern Saudi Arabia and southwestern Jordan. Gondwana Res 4:164–165

El-Ramly MF, Greiling R, Kröner A, Rashwan AA (1984) On the tectonic evolution of the Wadi Hafafit area and environs, Eastern Desert of Egypt. Bull Fac Earth Sci 6:114–126

El-Ramly MF, Greiling RO, Rashwan AA, Ramsy AH (1993) Explanatory note to accompany the geological and structural maps of Wadi Hafafit area, Eastern Desert of Egypt. Ann Geol Surv Egypt 9:1–53

El-Ramly MF, Hussein AAA (1983) The ring complexes of the Eastern Desert of Egypt. J Afr Earth Sci 3(1/2):77–82

El-Sharkawy MA, El-Bayoumi RM (1979) The ophiolites of Wadi Ghadir area Eastern Desert, Egypt. Ann Geol Survey Egypt 9:125–135

Essawy MA, Abu Zeid KM (1972) Atalla felsite intrusion and its neighbouring rhylitic flows and tuffs, Eastern Desert, Egypt. Ann Geol Surv Egypt 2:271–280

Fairhead JD, Girdler RW (1970) The seismicity of the Red Sea, Gulf of Aden and Afar triangle. Philos Trans R Soc A 267:49–74

Farahat ES, El Mahalawi MM, Hoinkes G, Abdel Aal AY (2004) Continental back-arc basin origin of some ophiolites from the Eastern Desert of Egypt. Mineral Petrol 82:81–104

Fleck RJ, Greenwood WR, Hadley DG, Anderson RE, Schmidt DL (1979) Rubidium-Strontium geochronology and plate-tectonic evolution of the southern part of the Arabian Shield. US Geological Survey Saudi Arabian Mission Report 245, p 105

Fowler AR, El-Kalioubi B (2004) Gravitational collapse origin of shear zones, foliations and linear structures in the Neoproterozoic cover nappes, Eastern Desert, Egypt. J Afr Earth Sci 38:23–40

Fowler TJ, Osman AF (2001) Gneiss-cored interference dome associated with two phases of late Pan-African thrusting in the Central Eastern Desert, Egypt. Precambr Res 108:17–43

Fowler AR, Osman AF (2009) The Sha'it-Nugrus shear zone separating Central and South Eastern Deserts, Egypt: a post-arc collision low-angle normal ductile shear zone. J Afr Earth Sci 53:16–32

Fowler A, Khamees H, Dowidar H (2007) El Sibai gneissic complex, Central Eastern Desert, Egypt: folded nappes and syn-kinematic gneissic granitoid sheets-not a core complex. J Afr Earth Sci 49 (4):119–135

Fritz H, Messner M (1999) Intramontane basin formation during oblique convergence in the Eastern Desert of Egypt: magmatically versus tectonically induced subsidence. Tectonophysics 315:145–162

Fritz H, Abdelsalam M, Ali KA, Bingen B, Collins AS, Fowler AR, Ghebreab W, Hauzenberger CA, Johnson PR, Kusky TM, Mace P, Muhongo S, Stern RG, Viola G (2013) Orogen styles in the East African Orogen: a review of the Neoproterozoic to Cambrian tectonic evolution. J Afr Earth Sci 86:65–106

Fritz H, Dalmeyer DR, Wallbrecher E, Loizenbauer J, Hoinkes G, Neumayr P, Khudeir AA (2002) Neoproterozoic tectonothermal evolution of the Central Eastern Desert, Egypt: a slow velocity tectonic process of core complex exhumation. J Afr Earth Sci 34:543–576

Fritz H, Wallbrecher E, Khudeir AA, Abu El Ela F, Dallmeyer DR (1996) Formation of Neoproterozoic core complexes during oblique convergence (Eastern Desert, Egypt). J Afr Earth Sci 23:311–329

Gad S, Kusky TM (2006) Lithological mapping in the Eastern Desert of Egypt, the Barramiya area using Landsat thematic mapper (TM). J Afr Earth Sci 44:196–202

Gharib ME (2012) Origin and evolution history of magmatic garnet-bearing pegmatites and associated granitoids, Abu Had area, south Eastern Desert, Egypt: inference from petrology and geochemistry. J Amer sci 8(10):536–554

Greiling RO (1985) Thrust tectonics in Pan-African rocks of SE Egypt. Terra Cognita 5

Greiling RO (1997) Thrust tectonics in crystalline domains: the origin of a gneiss dome. Proc Ind Acad Sci (Earth Planet Sci) 106:209–220

Greiling RO, Kröner A, El-Ramly MF, Rashwan AA (1988) Structural relationship between the southern and central parts of the Eastern desert of Egypt: details of a fold and thrust belt. In: El-Gaby S, Greiling RO (eds) The Pan-African Belt of Northeast Africa and adjacent areas. Vieweg & Sohn, Weisbaden, Germany, pp 121–146

Greiling RO, De Wall H, Sadek MF, Dietl C (2014) Late Pan-African granite emplacement during regional deformation, evidence from magnetic fabric and structural studies in the Hammamat-Atalla area, Central Eastern Desert of Egypt. J Afr Earth Sci 99:109–121

Greiling RO, Abdeen MM, Dardir AA, El Akhal H, El Ramly MF, Kamal El Din GM, Osman AF, Rashwan AA, Rice AH, Sadek MF (1994) A structural synthesis of the Proteorozoic Arabian-Nubian Shield in Egypt. Geol Rundsch 83:484–501

Greiling RO, de Wall H, Warr LN, Naim GM, Hussein AA, Sadek MF, Abdeen MM, El Kady MF, Makhlouf A (1996) Basement structure in Eastern Egypt: quantitative perspectives for the second century. Proc Geol Surv Egypt Cenn Conf 289–302

Grundmann G, Morteani G (2008) Multi-stage emerald formation during Pan-African regional metamorphism: The Zabara, Sikait, Umm Kabo deposits, South Eastern desert of Egypt. J Afr Earth Sci 50(2–4):168–187. https://doi.org/10.1016/j.jafrearsci.2007.09.009

Habib ME (1987) Arc ophiolites in the Pan-African basement between Meatiq and Abu Furad, Eastern Desert, Egypt. Bull Fac Sci Assiut Univ 16:241–283

Hagag W, Moustafa R, Hamimi Z (2018) Neoproterozoic evolution and Najd-related transpressive shear deformations along Nugrus Shear Zone, South Eastern Desert, Egypt (Implications from field-structural data and AMS-technique). Geotectonics 52(1):114–133

Hargrove US, Stern RJ, Kimura JI, Manton WI, Johnson PR (2006a) How juvenile is the Arabian-Nubian Shield? Evidence from Nd isotopes and pre-Neoproterozoic inherited zircon in the Bi'r Umq suture zone, Saudi Arabia. Earth Planet Sci Lett 252:308–326

Hargrove US, Stern RJ, Griffin WR, Johnson PR, Abdelsalam MG (2006b) From island arc to craton: timescales of crustal formation along the Neoproterozoic Bi'r Umq Suture zone, Kingdom of Saudi Arabia. Saudi Geological Survey Technical Report SGS-TR-2006-6, 69 pp

Hamdy M Abd, El-Wahed MA, Thabet E (2017a) Origin of dyke swarms in Wadi El Redi area, south Eastern Desert Egypt. Arab J Geosci 10(18):414

Hamdy MM, Abd El-Wahed MA, Gamal El Dien H, Morishita T (2017b) Garnet hornblendite in the Meatiq core Complex, Central Eastern Desert of Egypt: Implications for crustal thickening preceding the ~600 Ma extensional regime in the Arabian-Nubian Shield. Precambr Res 298:593–614

Hamdy M, Gamal El-Dien H, Abd El-Wahed MA, Morishita T (2018) Garnierite-bearing serpentinite from the Central Eastern Desert of Egypt: a signature of paleo-weathering in the Arabian Nubian Shield? J Afr Earth Sci 146:95–117

Hamimi Z, Ghazaly MK, Mohamed EA, Younis AM (2016) Structural history of Wadi Kharit transpressional Shear Zone, Eastern Desert tectonic terrane, Northern Nubian Shield. Ann Meeting of the Egyptian Geological Society (Abstract)

Hamimi Z, Hagag W (2017) A new tectonic model for Abu-Dabbab seismogenic zone (Eastern Desert, Egypt): evidence from field-structural, EMR and seismic data. Arab J Geosci 10:11. https://doi.org/10.1007/s12517-016-2786-y

Hamimi Z, Abd El-Wahed MA, Gahlan HA, Kamh SZ (2019) Tectonics of the Eastern Desert of Egypt: key to understanding the Neoproterozoic evolution of the Arabian-Nubian Shield (East African Orogen). In: Bendaoud A, Hamimi Z, Hamoudi M, Djemai S, Zoheir B (eds) Geology of the Arab world—an overview,

Springer Geology, pp 1–81. https://doi.org/10.1007/978-3-319-96794-3_1
Hamimi Z, El Amawy MA, Wetait M (1994) Geology and structural evolution of El Shalul Dome and environs, Central Eastern Desert, Egypt. Egypt J Geol 38–2:575–959
Harraz HZ (1999) Wall rock alteration, Atud gold mine, Eastern Desert, Egypt: processes and P-T-XCO2 conditions of metasomatism: J Afr Earth Sci 28(3):527–551. https://doi.org/10.1016/s0899-5362(99)00031-7harraz
Harraz HZ (2000) A genetic model for a mesothermal Au deposit: evidence from fluid inclusions and stable isotopic studies at El Sid gold mine, Eastern Desert, Egypt. J Afr Earth Sci 30:267–282. https://doi.org/10.1016/s0899-5362(00)00019-1
Harraz HZ, EI-Dahhar MA (1993) Nature and composition of gold-forming fluids at Umm Rus area, Eastern Desert, Egypt: evidence from fluid inclusions in vein materials. J Afr Earth Sci 16:341–353
Harraz HZ, Hamdy MM (2015) Zonation of primary haloes of Atud auriferous quartz vein deposit, Central Eastern Desert of Egypt: A potential exploration model targeting for hidden mesothermal gold deposits. J Afr Earth Sc 101:1–18. https://doi.org/10.1016/j.jafrearsci.2014.09.001
Harraz HZ, Hamdy MM, El-Mamoney MH (2012) Multi-element association analysis of stream sediment geochemistry data for predicting gold deposits in Barramiya gold mine, Eastern Desert, Egypt. J Afr Earth Sci 68:1–14
Hassaan MM, Ramadan TM, Abu El Leil I, Sakr SM (2009) Lithochemical surveys for ore metals in arid region, Central Eastern Desert, Egypt: using Landsat ETM+ imagery. Aust J Basic Appl Sci 3:512–528
Hassan M, Stüwe K, Abu-Alam TS, Klötzli U, Tiepolo M (2016) Time constraints on deformation of the Ajjaj branch of one of the largest Proterozoic shear zones on Earth: The Najd Fault System. Gondwana Res 34:346–362
Hassan AM (1998) Geochemistry, Rb-Sr geochronology and petrogenesis of the Late Pan-African Atalla Felsite, central Eastern Desert, Egypt. In: Geology of the Arab world, 4th international conference, Cairo University. Cairo University Press, Giza, pp 89–90
Hassoup A (1987) Microearthquakes and magnitude studies on earthquake activity at Abu Dabbab region, Eastern Desert Egypt. MSc thesis, Fac. Sci., Cairo Univ., pp 1–169
Helba HA, Khalil KI, Abdou NM (2001) Alteration patterns related to hydrothermal gold mineralization in meta-andesites at Dungash area, Eastern Desert Egypt. Resour Geol 51:19–30
Helmy HM, Kaindl R (1999) Mineralogy and fluid inclusion studies of the Au–Cu quartz veins in the Hamash area, South-Eastern Desert, Egypt. Mineral Petrol 65:69–86
Helmy H, Zoheir B (2014) Metal and fluid sources in a potential world-class gold deposit: El-Sid mine, Egypt. Int J Earth Sci 104 (3):645–661. https://doi.org/10.1007/s00531-014-1094-6
Helmy H, Kaindl R, Fritz H, Loizenbauer J (2004) The Sukari Gold Mine, Eastern Desert, Egypt: structural setting, mineralogy and fluid inclusion study. Mineral Deposita 39:495–511
Hilmy ME, Osman A (1989) Remobilization of gold from a chalcopyrite–pyrite mineralization Hamash gold mine, Southeastern Desert, Egypt. Mineral Deposita 24:244–249
Hodgson CJ (1989) The structure of shear-related, vein-type gold deposits: a review. Ore Geol Rev 4:635–678
Hosny A, El Hady SM, Mohamed AA, Panza GF, Tealeb A, El Rahman MA (2009) Magma intrusion in the upper crust of Abu Dabbab area, south east of Egypt, from Vp and Vp/Vs tomography. Rend Fis Acc Lincei 20:1–19. http://dx.doi.org/ https://doi.org/10.1007/s12210-009-0001-8
Hosny A, El-Hady SM, Guidarelli M, Panza GF (2012) Source moment tensors of the earthquake Swarm in Abu-Dabbab area, South-East Egypt. Rend Fis Acc Lincei 23:149–163
Huet B, Le Pourhiet L, Labrousse L, Burov E, Jolivet L (2010) Post-orogenic extension and metamorphic core complexes in a heterogeneous crust: the role of crustal layering inherited from collision, Application to the Cyclades (Aegean domain). Geophys J Int 184:611–625
Ibrahim ME, Yokoyama I (1998) Probable origin of the Abu Dabbab earthquakes swarms in the Eastern Desert of Egypt. Bull IISEE 32
Ibrahim WS, Watanabe K, Yonezu K (2016) Structural and litho-tectonic controls on Neoproterozoic base metal sulfide and gold mineralization in North Hamisana shear zone, South Eastern Desert, Egypt: the integrated field, structural, Landsat 7 ETM+ and ASTER data approach. Ore Geol Rev 79:62–77
Johnson PR, Andresen A, Collins AS, Fowler AR, Fritz H, Ghebreab W, Kusky T, Stern RJ (2011) Late Cryogenian-Ediacaran history of the Arabian-Nubian Shield: a review of depositional, plutonic, structural, and tectonic events in the closing stages of the northern East African Orogen. J Afr Earth Sci 61:167–232
Johnson PR, Woldehaimanot B (2003) Development of the Arabian-Nubian Shield: perspectives on accretion and deformation in the northern East African Orogen and the assembly of Gondwana. Geol Soc Lond Spec Publ 206:289–325
Kamal El Din GM (1993) Geochemistry and tectonic significance of the Pan-African El Sibai Window, Central Eastern Desert, Egypt. Unpublished PhD thesis, Forschungzentrum Julich GmbH, 19, p 154
Kebeasy RM (1990) Seismicity. In: Said R (ed) Geology of Egypt. Balkema, Rotterdam, pp 51–59
Khalil KI, Helba A (2000) Gold mineralization and its alteration zones at the Hangalia Gold Mine area, Eastern Desert, Egypt. Egypt Mineral 12:65–92.
Khudeir AA, El-Gaby S, Greiling RO, Kamal El Din GW (1992) Geochemistry and tectonic significance of polymetamorphosed amphibolites in the Gebel Sibai window, Central Eastern Desert, Egypt. Geology of the Arab world conference. Cairo University, Egypt, pp 461–476
Khudeir AA, Kamal El-Gaby S, El Din GM, Asran AMH, Greiling RO (1995) The pre-Pan-African deformed granite cycle of the Gabal El-Sibai swell, Eastern Desert, Egypt. J Afr Earth Sci 21:395–406
Kröner A, Greiling RO, Reischmann T, Hussein IM, Stern RJ, Durr St, Kruger J, Zimmer M (1987) Pan-African crustal evolution in northeast Africa. In: Kröner A (eds) Proterozoic lithospheric evolution. American Geophysical Union, Geodynamic Series 17, pp 235–257
Kröner A, Krüger J, Rashwan AA (1994) Age and tectonic setting of granitoid gneisses in the Eastern Desert of Egypt and south-west Sinai. Geol Rundsch 83:502–513
Kröner A, Linnebacher P, Stern RJ, Reischmann T, Manton WI, Hussein IM (1991) Evolution of Pan-African island arc assemblages in the southern Red Sea Hills, Sudan and in southwestern Arabia as exemplified by geochemistry and geochronology. Precambr Res 53:99–118
Kröner A, Todt W, Hussein IM, Mansour M, Rashwan AA (1992) Dating of late Proterozoic ophiolites in Egypt and the Sudan using the single grain zircon evaporation technique. Precambr Res 59:15–32
Kusky TM, Ramadan TM (2002) Structural controls on Neoproterozoic mineralization in the South Eastern Desert, Egypt: an integrated field, Landsat TM, and SIRC/ X SAR approach. J Afr Earth Sci 35:107–121
Küster D, Liégeois J-P, Matukov D, Sergeev S, Lucassen F (2008) Zircon geochronology and Sr, Nd, Pb isotope geochemistry of granitoids from Bayuda Desert and Sabaloka (Sudan): Evidence for a Bayudian event (920–900 Ma) preceding the Pan-African orogenic cycle (860–590 Ma) at the eastern boundary of the Saharan Metacraton. Precambr Res 164(1–2):16–39

Liégeois J-P, Abdelsalam MG, Ennih N, Ouabadi A (2013) Metacraton: nature, genesis and behavior. Gondwana Res 23(1):220–237

Liégeois JP, Stern RJ (2010) Sr–Nd isotopes and geochemistry of granite-gneiss complexes from the Meatiq and Hafafit domes, Eastern Desert, Egypt: no evidence for pre-Neoproterozoic crust. J Afr Earth Sci 57:31–40

Lister GS, Banga G, Feenstra A (1984) Metamorphic core complexes of Cordilleran type in the Cyclades, Aegean Sea, Greece. Geology 12:221–225

Loizenbauer J, Wallbrecher E, Fritz H, Neymayr P, Khudeir AA, Kloetzli U (2001) Structural geology, single zircon ages and fluid inclusion studies of the Meatiq metamorphic core complex: implications for Neoproterozoic tectonics in the Eastern Desert of Egypt. Precambr Res 110:357–383

Lundmark AM, Andresen A, Hassan MA, Augland LE, Abu El-Ru MA, Boghdady GY (2012) Repeated magmatic pulses in the East African Orogen of Central Eastern Desert, Egypt: an old idea supported by new evidence. Gondwana Res 22:227–237

Makroum FM (2001) Pan-African tectonic evolution of the Wadi El Mayit Area and its environs, Central Eastern Desert, Egypt. In: The second international conference on the geology of Africa, Assiut University, Egypt, 2, pp 219–233

Makroum FM (2003) Lattice preferred orientation (LPO) study of the orogen-parallel Wadi Nugrus and Wadi Um Nar shears, Eastern Desert-Egypt, using EBSD-technique. In: The third international conference on the geology of Africa 1, pp 213–232

Makroum F (2017) Structural interpretation of the Wadi Hafafit culmination: a Pan African gneissic dome in the central Eastern Desert, Egypt. Lithosphere (in press)

Meyer SE, Passchier C, Abu-Alam T, Stüwe K (2014) A strike-slip core complex from the Najd fault system, Arabian shield. Terra Nova 26(5):387–394. https://doi.org/10.1111/ter.12111

Miller MM, Dixon TH (1992) Late Proterozoic evolution of the north part of the Hamisana zone, northeast Sudan: constraints on Pan-African accretionary tectonics. J Geol Soc Lond 149:743–750

Moghazi AM, Hassanen MA, Mohammed FH, Ali S (2004) Late Neoproterozoic strongly peraluminous leucogranites, South Eastern Desert, Egypt—petrogenesis and geodynamic significance. Mineral Petrol 81:19–41

Mohamed AS, Hosny A, Abou-Aly N, Saleh M, Rayan A (2013) Preliminary crustal deformation model deduced from GPS and earthquakes' data at Abu-Dabbab area, Eastern Desert, Egypt. NRIAG J Astronomy and Geophysics 2(1):-67–76

Mohamed FH (1993) Rare metal-bearing and barren granites, Eastern Desert of Egypt: geochemical characterization and metallogenetic aspects. J Afr Earth Sci 17:525–539

Moore JM (1979) Tectonics of the Najd transcurrent fault system, Saudi Arabia. J Geol Soc Lond 136:441–454

Murr, A., 1999, Genesis of gold mineralization of Fatria, Gidami, Atalla and Hangaliya, Eastern Desert of Egypt. Münchner Geological Hefte A 27:202 (in German)

Nano L, Kontny A, Sadek MF, Greiling RO (2002) Structural evolution of metavolcanics in the surrounding of the gold mineralization at El Beida, South Eastern Desert, Egypt. Ann Geol Surv Egypt 25:11–22

Neumayr P, Hoinkes G, Puhl J, Mogessie A, Khudeir AA (1998) The Meatiq dome (Eastern Desert, Egypt) a Precambrian metamorphic core complex: petrological and geological evidence. J Metamorph Geol 16:259–279

Neumayr P, Mogessie P, Hoinkes G, Puhl J (1996) Geological setting of the Meatiq metamorphic core complex in the Eastern Desert of Egypt based on amphibolite geochemistry. J Afr Earth Sci 23 (3):331–345

Noweir AM (1968) Geology of the Hammamat-Um Seleimat District, Eastern Desert, Egypt. PhD Thesis, Assiut Univ, Egypt

Pallister JS, Stacey JS, Fischer LB, Premo WR (1988) Precambrian ophiolites of Arabia; geologic setting, U-Pb geochronology, Pb-isotope characteristics, and implications for continental accretion. Precambr Res 38:1–54

Peters SG (2004) Syn-deformational features of Carlin-type Au deposits. J Struct Geol 26(6–7):1007–1023

Phillips WJ (1972) Hydraulic fracturing and mineralization. Geol Soc Lond 128:337–361

Ragab A (1993) A geodynamic model for the distribution of the oceanic plate slivers within a Pan-African orogenic belt, Eastern Desert, Egypt. J Geodyn 17(1–2):21–26. https://doi.org/10.1016/0264-3707(93)90014-w

Ragab Al, EI-Gharabawi RI, El-Ally Z (1993) Pan-African tectonostratigraphic assemblages of Gabal Meatiq-Wadi AtaUa area, Eastern Desert, Egypt: evidence for arc-arc suturing. MERC Ain Shams University. Earth Sci Ser 7:131–145

Raharimahefa T, Kusky TM (2010) Structural and remote sending analysis of the Betsimisaraka Suture in northeastern Madagascar. Gondwana Res 15:14–27

Ramadan TM, Kontny A (2004) Mineralogical and structural characterization of alteration zones detected by orbital remote sensing at Shalatin District area, SE Desert, Egypt. J Afr Earth Sci 40: 89–99

Roberts RG (1987) Archean lode gold deposits. Geosci Can 14:1–19

Robin PYF, Cruden AR (1994) Strain and vorticity patterns in ideal transpression zones. J Struct, Geol

Sabet AH, Tsogoev V, Sarin LP, Azazi SA, Bedewi MA, Ghobrial GA (1976) Tin Tantalum deposits of Abu Dabbab. Ann Geol Survey Egypt 6:93–117

Sakran ShM, Hussein AA, Takla MA, Makhlouf AA (2001) Structural evolution of Um Radam area, south Eastern desert, Egypt. Ann Geol Survey Egypt XXIII(2):1–14

Shackleton RM (1986) Precambrian collision tectonics in Africa. Geol Soc Lond Spec Publ 19(1):329–349. https://doi.org/10.1144/gsl.sp.1986.019.01.19

Shackleton RM (1994) Review of late Proterozoic sutures, ophiolitic mélanges and tectonics of eastern Egypt and north Sudan. Geol Rundsch 83:537–546

Shalaby A (2010) The northern dome of Wadi Hafafit culmination, Eastern Desert, Egypt: structural setting in tectonic framework of a scissor-like wrench corridor. J Afr Earth Sci 57:227–241

Shalaby A, Stüwe K, Fritz H, Makroum F (2006) The El Mayah molasse basin in the Eastern Desert of Egypt. J Afr Earth Sci 45:1–15

Shalaby A, Stüwe K, Makroum F, Fritz H, Kebede T, Klotzli U (2005) The Wadi Mubarak belt, Eastern Desert of Egypt: a Neoproterozoic conjugate shear system in the Arabian-Nubian Shield. Precambr Res 136:27–50

Smith M, O'Connor E, Nasr BB (1999) Transpressional flower structures and escape tectonics: a new look at the Pan-African collision in the Eastern Desert, Egypt. In: De Wall H, Greiling RO (eds) Aspects of Pan-African Tectonics. International Cooperation, Bilateral Seminars Int Bureau, Germany, Forschungszentrum Jülich, pp 81–82

Stephens JR, Mair JL, Oliver NH, Hart CJ, Baker T (2004) Structural and mechanical controls on intrusion-related deposits of the Tombstone Gold Belt, Yukon, Canada, with comparisons to other vein-hosted ore-deposit types. J Struct Geol 26(6–7):1025–1041

Stern RJ (1985) The Najd fault system, Saudi Arabia and Egypt: a late Precambrian rift-related transform system. Tectonics 4:497–511

Stern RJ (1994) Arc assembly and continental collision in the Neoproterozoic East African Orogen: implications for the consolidation of Gondwanaland. Ann Rev Earth Planet Sci 22:319–351

Stern RJ, Hedge CE (1985a) Geochronologic and isotopic constraints on late Precambrian crustal evolution in the Eastern Desert of Egypt. Am J Sci 258:97–127

Stern RJ, Hedge CE (1985b) Geochronologic constraints on late Precambrian crustal evolution in the Eastern Desert of Egypt. Am J Sci 285:97–127

Stern RJ, Kröner A, Manton WI, Reischmann T, Mansour M, Hussein IM (1989) Geochronology of the late Precambrian Hamisana shear zone, Red Sea Hills, Sudan and Egypt. J Geol Soc Lond 146:1017–1030

Stern RJ, Nielsen KC, Best E, Sultan M, Arvidson RE, Kroner A (1990) Orientation of late Precambrian sutures in the Arabian-Nubian Shield. Geology 18:1103–1106

Stern RJ (2017) Neoproterozoic formation and evolution of Eastern Desert continental crust—the importance of the infrastructure-superstructure transition. J Afr Earth Sci 146:15–27

Stern RJ, Ali KA, Liegeois JP, Johnson PR, Kozdroj W, Kattan FH (2010) Distribution and significance of pre-Neoproterozoic zircons in juvenile Neoproterozoic igneous rocks of the Arabian-Nubian Shield. Am J Sci 310(9):791–811

Stern RJ, Kröner A, Rashwan AA (1991) A late Precambrian (~710 Ma) high volcanicity rift in the southern Eastern Desert of Egypt. Geol Rundsch 80:155–170

Stoeser DB, Camp VE (1985) Pan-African microplate accretion of the Arabian Shield. Geol Soc Am Bull 96:817–826

Sturchio NC, Sultan M, Batiza R (1983) Geology and origin of Meatiq Dome, Egypt: a Precambrian metamorphic core complex? Geology 11:72–76

Sultan M, Arvidson RE, Duncan IJ, Stern RJ, El Kalioubi B (1988) Extension of the Najd Shear System from Saudi Arabia to the central Eastern Desert of Egypt based on integrated field and Landsat observations. Tectonics 7:1291–1306

Takla MA, Hussein AA, Sakran ShM, Makhlouf AA (2002) Tectonometamorphic history of Um Radam area, south Eastern Desert, Egypt. Ann Geol Surv Egypt XXIV:41–61

Taylor WEG, El Hamad YA, El-Kazzaz YA, Rashwan AA (1993) An outline of the tectonic framework for the Pan-African orogeny in the vicinity of Wadi Um Relan, SE Desert, Egypt. In: Thorweihe U, Shandelmeier H (eds) Geoscientific research in NE Africa. Balkema, Rotterdam, pp 31–34

Teyssier Ch, Tikoff B (1999) Fabric stability in oblique convergence and divergence. J Struct Geol 21:969–974

Tirel C, Brun J-P, Burov E (2008) Dynamics and structural development of metamorphic core complexes. J Geophys Res 113:B04403

Unzog W, Kurz W (2000) Progressive development of lattice preferred orientations (LPOs) of naturally deformed quartz within a transpressional collision zone (Panafrican orogen in the Eastern Desert of Egypt). J Struct Geol 22:1827–1835

Vail JR (1985) Pan-African (late Precambrian) tectonic terrains and the reconstruction of the Arabian-Nubian Shield. Geology 13:839–842

Wallbrecher E, Fritz H, Khudeir AA, Farahad F (1993) Kinematics of Pan-african thrusting and extension in Egypt. In: Thorweih U, Shandelmeister H (eds) Geoscientific research in Northeast Africa. Balkema, Rotterdam, pp 27–30

Whitehouse MJ, Stoeser D, Stacey JS (2001) The Khida Terrane—geochronological and isotopic evidence for paleoproterozoic and Archean Crust in the Eastern Arabian Shield of Saudi Arabia. Gondwana Res 4:200–202

Zimmer M, Kröner A, Jochum KP, Reischmann T, Todt W (1995) The Gabal Gerf complex: a Precambrian N-MORB ophiolite in the Nubian Shield, NE Africa. Chem Geol 123:29–51

Zoheir B (2012) Lode-gold mineralization in convergent wrench structures: examples from South Eastern Desert, Egypt. J Geochem Explor 114:82–97

Zoheir B, Moritz R (2014) Fluid evolution in the El-Sid gold deposit, Eastern Desert, Egypt. In Garofalo PS, Ridley JR (eds) Gold-transporting hydrothermal fluids in the Earth's crust. Geological Society, London, Special Publications, 402. https://doi.org/10.1144/sp402.3

Zoheir B, Deshesh F, Broman C, Pitcairn I, El-Metwally A, Mashaal S (2017) Granitoid-associated gold mineralization in Egypt: a case study from the Atalla mine. Miner Deposita 53(5):701–720

Zoheir B, Feigenson M, Zi J-W, Turrin B, Deshesh F, El-Metwally A (2018) Ediacaran (~600 Ma) orogenic gold in Egypt: age of the Atalla gold mineralization and its geological significance. Int Geol Rev 1–16

Zoheir BA (2008) Characteristics and genesis of shear zone-related goldmineralization in Egypt: a case study from the Um El Tuyor mine, south Eastern Desert. Ore Geol Rev 34:445–470

Zoheir BA (2011) Transpressional zones in ophiolitic mélange terranes: potential exploration targets for gold in the South Eastern Desert, Egypt. J Geochem Explor 111:23–38

Zoheir BA (2012) Lode-gold mineralization in convergent wrench structures: Examples from South Eastern Desert, Egypt. J Geochem Explor 114:82–97. https://doi.org/10.1016/j.gexplo.2011.12.005

Zoheir BA, Creaser RA, Lehmann B (2015) Re-Os geochronology of gold mineralization in the Fawakhir area, Eastern Desert, Egypt. Int Geol Rev 57:1418–1432. https://doi.org/10.1080/00206814.2014.935964

Zoheir BA, Goldfarb RJ, Weihed P (2011) Granitoidassociated lode gold deposits in the central Eastern Desert of Egypt. In: Geological Society of America (GSA) annual meeting. Minneapolis, MN, 470 pp

Zoheir BA, Lehmann B (2011) Listvenite-lode association at the Barramiya gold mine, Eastern Desert, Egypt. Ore Geol Rev 39:101–115

Zoheir BA, Weihed P (2014) Greenstone-hosted lode-gold mineralization at Dungash mine, Eastern Desert, Egypt. J Afr Earth Sci 99(1):165–187

The Metamorphism and Deformation of the Basement Complex in Egypt

6

Baher El Kalioubi, Abdel-Rahman Fowler, and Karim Abdelmalik

Contents

B. El Kalioubi (✉) · K. Abdelmalik
Faulty of Science, Department of Geology, Ain Shams University, Cairo, Egypt
e-mail: belkaliouby@yahoo.com

A.-R. Fowler
Faculty of Science, Geology Department, United Arab Emirates University, Al Ain, United Arab Emirates

Z. Hamimi et al. (eds.), *The Geology of Egypt*, Regional Geology Reviews,
https://doi.org/10.1007/978-3-030-15265-9_6

Abstract

The Precambrian crust of Africa comprises large remnants of Archaean massifs, which are parts of even larger units, some of which were subjected to tectonic reactivation in Proterozoic time. The youngest of these tectonic events is the 'Pan-African' episode, which led to the cratonization of ocean arc complexes following their collision with the older African craton during the period 1200–450 Ma.

The Arabian-Nubian-Shield (ANS) evolved during the evolution of the East African Orogen (EAO), after break-up of the ~1000–800 Ma Rodinia supercontinent. The break-up and subsequent divergence of the Rodinia fragments led to the formation of the Mozambique Ocean. The Mozambique Ocean began to close about 870–800 Ma ago, by intra-oceanic subduction and accretion of island arc terranes. Dismembered ophiolite suites, juvenile island arc meta-volcanosedimentary assemblages, and island arc gabbro-diorite complexes were formed during the pre-collision arc stage. The stacking of arcs occurred during the middle to late Cryogenian (790–640 Ma). An early stage of arc collision in the eastern part of the shield led to the formation of the proto-ANS. The final collision between East and West Gondwana incorporated the ANS as a unit within the EAO. The East-West Gondwana continent-continent collision involved the proto-ANS Neoproterozoic terranes colliding with the East Sahara Metacraton in the late Cryogenian to early Ediacaran (650–580 Ma). A post-amalgamation extensional stage in the late Cryogenian to early Ediacaran accompanied the formation of the supercontinent Gondwana. This stage was characterized by tectonic escape, strike-slip faulting, probable mantle and/or crustal delamination, and regional extension (630–550 Ma) of the newly formed continental crust. During this late stage, volcanic eruptives and molasse basins formed, typically followed by high-level granitoid and gabbroic intrusions during the period 610–550 Ma.

This chapter reviews the various settings and conditions of metamorphism in the Precambrian basement rocks of Egypt, which represent the southwestern side of the ANS. The rocks of Egyptian basement are widely exposed in the Eastern Desert, southern Sinai and Western Desert in the extreme southwestern corner of Egypt.

The chapter deals with the distribution, composition, origin, tectonic setting, age and geodynamic environment of the low- to high-grade metamorphosed sedimentary, volcanic and plutonic rocks and their geothermobarometric evolution. It aims to draw conclusions by integrating data on the age, lithology, metamorphic grade and origins of the metamorphic rocks in the basement complex of Egypt. To this end, the main Precambrian rocks exposed in Egypt will be reviewed as successive tectonostratigraphic units. These units are traditionally subdivided into major tiers based on their lithology, structural and stratigraphic position, and metamorphic grade. These include:

Tier 1: A striking feature of the basement rocks of Egypt, representing a structurally lower unit of highly metamorphosed gneissic massifs exhibiting multiple deformation, polyphase metamorphism and partial migmatization.
Tier 2: A composite structurally higher unit characteristically separated from tier 1 in the Central Eastern Desert by a major low-angle shear zone consisting of dismembered ophiolite nappes, ophiolitic mélange, island arc volcanics and associated plutonites, all of which have experienced mainly low-grade metamorphism (greenschist to exceptionally amphibolite facies).

The most complete examples of ophiolite sequence in the EED, and the main occurrences of serpentinite bodies, ophiolitic mélange and talc carbonate-altered ultramafic rocks are described. Following this, the metagabbros, the ophiolitic Older Metavolcanics (OMV) and metasediments are considered. The (OMV) are typically thick massive to pillowed tholeiitic basalts that may represented the simatic crustal floor of marginal basins. The Younger Metavolcanics (YMVs) represent the surface products of the island arc stage. Magmatic rocks of the island arc stage include tholeiitic and calc-alkaline suites of gabbros, diorites, granodiorite and granites that have been emplaced during all stages of subduction, and also during arc collision. They show varying degrees of deformation and metamorphism. Two popularly distinguished magmatic groups of the island arc stage are the metagabbro-diorite complex, followed immediately by the 'Older' or 'grey' granites.

Ductile shears zones and equivalent brittle faults are essential structural features of all stages in the evolution of the Egyptian Basement. An outline of the major shear zones and their settings in relation to surrounding areas are given, with emphasis on their metamorphic and strain features.

The youngest successions showing metamorphic effects are the post-collision volcanics (Dokhan) and molasse basins (Hammamat), showing only localized metamorphic effects. They represent one of the most important features marking the extensional tectonic stage in the ED. We briefly introduce the Hammamat basins in the light of their stratigraphy, petrology, age and basin deformation, then concentrate on the metamorphic aspects of the Hammamat basins.

6.1 Introduction

The Precambrian crust of Africa is typical of shield areas. It comprises large remnants of Archaean massifs, which are parts of even larger units, some having been subjected to tectonic reactivation in Proterozoic time. The youngest of these tectonic activities is referred to as the 'Pan-African' (Kennedy 1964), which is a thermo-tectonic episode that led to the assembly of ~2000 Ma cratons separated by Cryogenian-Ediacaran fold belts. Kröner (1984) assigned a period (950–450 Ma) for this episode. Gass (1977) used the term Pan-African to describe the whole process of cratonization of ocean arc complexes and their collision and welding to the older African craton during the period 1200–450 Ma. Abdel-Rahman (1996) used the term Pan-African to describe the geodynamic and geochemical differentiation of East Africa and Arabia into mobile zones and tectonic provinces, which occurred in a tectonothermal orogenic event at 950–550 Ma. During this interval, breakup of the supercontinent Rodinia occurred at ~800–850 Ma, leading to the opening of the Mozambique ocean. Intra-oceanic subduction commenced soon after, with consequent development of immature volcanic island arcs and associated sedimentation. Arc collisions at 600–680 Ma yielded a number of allochthonous terranes, separated by ophiolite-decorated sutures (Johnson 1998; Nehlig et al. 2002; Stern et al. 2004).

The Arabian-Nubian-Shield (ANS) is one of several Pan-African orogenic belts, which evolved during the evolution of the East African Orogen (EAO). The EAO is considered one of the largest exposures of juvenile Neoproterozoic continental crust on Earth, formed by plate tectonic processes. It extends from south to north for about 6000 km and more than 1500 km east-west (Stern 1994).

The history of ANS began after break-up of the ~1000–800 Ma Rodinia supercontinent in the interval 800–700 Ma ago (Meert and Torsvik 2003). The break-up and subsequent divergence led to the formation of the Mozambique Ocean (Abdelsalam and Stern 1996; Johnson 2000; Johnson et al. 2004; Stern and Johnson 2010). The Mozambique Ocean began to close about 870–800 Ma ago, by intra-oceanic subduction and accretion of island arc terranes (Gass 1982; Jacobs et al. 1998; Kröner et al. 1994, 2000; Stern 2002). Dismembered ophiolite suites, juvenile island arc meta-volcano sedimentary assemblages, and island arc gabbro-diorite complexes were formed during the pre-collision arc stage. The stacking of arcs occurred during the middle to late Cryogenian (790–640 Ma). Collisions of arcs and oceanic lithosphere fragments are marked by suture zones. A proto-ANS was formed by amalgamation of terranes that composed the Arabian Shield (Stern 1994; Johnson and Woldehaimanot 2003; Johnson et al. 2004; Collins and Pisarevsky 2005; Stern and Johnson 2010; Johnson et al. 2011; Johnson 2014). The final collision between East and West Gondwana incorporated the ANS as a unit within the EAO. The East-West Gondwana continent-continent collision involved the proto-ANS Neoproterozoic terranes colliding with the East Sahara Metacraton in the late

Cryogenian to early Ediacaran (650–580 Ma) (Finger and Helmy 1998; Kusky et al. 2003; Stern and Johnson 2010; Johnson et al. 2011). The collision of the southerly parts of East Gondwana with the African craton led to crustal thickening in the Mozambique Belt, characterized by granulite facies metamorphism at lower crustal levels and migmatization at higher levels.

A post-amalgamation extensional stage in the late Cryogenian to early Ediacaran accompanied the formation of the supercontinent Gondwana (Stern 1994; Meert 2001; Powell and Pisarevsky 2002; Boger et al. 2002; Katz et al. 2004; Meert and Torsvik 2003; Abu-Alam et al. 2013; Fritz et al. 2013). Tectonic escape, strike-slip faulting, delamination, and crustal extension (630–550 Ma) of the newly formed continental crust characterize this stage (Kröner 1985; Stoeser and Camp 1985; Genna et al. 2002; Hargrove et al. 2006; Avigad and Gvirtzman 2009; Johnson et al. 2011). During this late stage, effusions of volcanic rocks and post-amalgamation depositional basins formed. Finally, voluminous granitoid and gabbroic plutons intruded this crust during the period 610–550 Ma.

6.2 The Precambrian Basement Rocks of Egypt

The Precambrian basement rocks of Egypt represent one of the world's most impressive examples of Neoproterozoic fold and thrust belts. They cover about one-tenth of the total land surface of Egypt (about 93,000 km^2) and are widely exposed in the Eastern Desert that separates the Nile valley from the Red Sea coast for a distance of about 800 km. A considerable part also constitutes the southern Sinai. Another large exposure is found east of Gabal (G.) Uweinat and G. Kamil in the extreme southwestern corner of Egypt. These latter rocks are the oldest dated basement rocks, ranging in age from Archaean to Neoproterozoic (Klerx 1980; Harris et al. 1984; List et al. 1989; Bea et al. 2011a; Karmakar and Schenk 2015. They are regarded as part of the East Sahara Craton (Bertrand and Caby 1978; El-Gaby et al. 1984, 1988a, 1990). Further scattered outcrops appear at G. Al-Asr, and in the area between the Nile valley and the cataract region of Aswan, in the southern part of the Western Desert (Fig. 6.1). Similar basement rocks are exposed along the Saudi Arabian side of the Red Sea, forming the Arabian Shield.

Most of the Precambrian basement rocks of Egypt consist of belts of low- to high-grade metamorphosed sedimentary, volcanic and plutonic rocks. This chapter presents a brief summary of various aspects of these metamorphic belts. It focuses on the distribution, composition, origin, tectonic setting, age and geodynamic environment of the metamorphic rock types and their geothermobarometric evolution. The geologic history of the metamorphic and igneous rocks in Egypt has been investigated for more than two centuries. During this long span, models to explain the basement rocks have radically changed. Nevertheless, we intend to show that some older ideas may promote new interpretations when examined to the light of cumulative information.

6.2.1 Tier 1 and Tier 2 Crustal Levels

A thorough knowledge of the metamorphic belts in the Egyptian basement is key to understanding the Neoproterozoic tectonic framework of the ANS. Another aim of this chapter is to draw conclusions by integrating data on the age, lithology, metamorphic grade and origin of the different metamorphic rocks in the basement complex of Egypt. To this end, the main Precambrian rocks exposed in Egypt will be treated as successive tectonostratigraphic units. These units are traditionally subdivided into major tiers based on their lithology, structural and stratigraphic position, and metamorphic grade. These include:

Tier 1: A structurally lower unit of highly metamorphosed gneissic massifs exhibiting multiple deformation, polyphase metamorphism and partial migmatisation. They occupy the lowermost structural level, and consist of amphibolite facies and high-grade granulite facies metasediments and metavolcanics, etc., now represented by granite gneiss, amphibolite, and schists. They were typically metamorphosed between 6 and 12 kbar and at 650–700 °C (Neumayr et al. 1998; Abd El-Naby et al. 2008; Abu-Alam and Stüwe 2009).

The gneisses and allied rock units are differentiated according to age into Archaean to early Proterozoic crust (infracrustal province) remobilized during the accretion of Pan-African island arcs onto the passive continental margin of the old Nile Craton (Rocci 1965; Gass 1977) or East Sahara Craton (Kröner 1979). The individual tier 1 complexes are detailed in Sect. 6.3, and further discussed in Sect. 6.4.

Tier 2: A composite structurally higher unit separated from tier 1 by a low-angle shear zone. This tier is also referred to as the Pan-African nappes. Tier 2 consists of obducted dismembered ophiolite nappes, ophiolitic mélange, island-arc-type volcanics and associated plutonites, all of which have experienced low-grade metamorphism (greenschist facies). Successively younger than these are post-collision volcanics and molasses basins with only localized metamorphic effects, leaving primary textures commonly still preserved. The characteristics of tier 2 subunits are described in Sects. 6.5–6.8 and 6.10. The shear separating the two tiers is described in Sect. 6.9, along with other major shear zones in the EED.

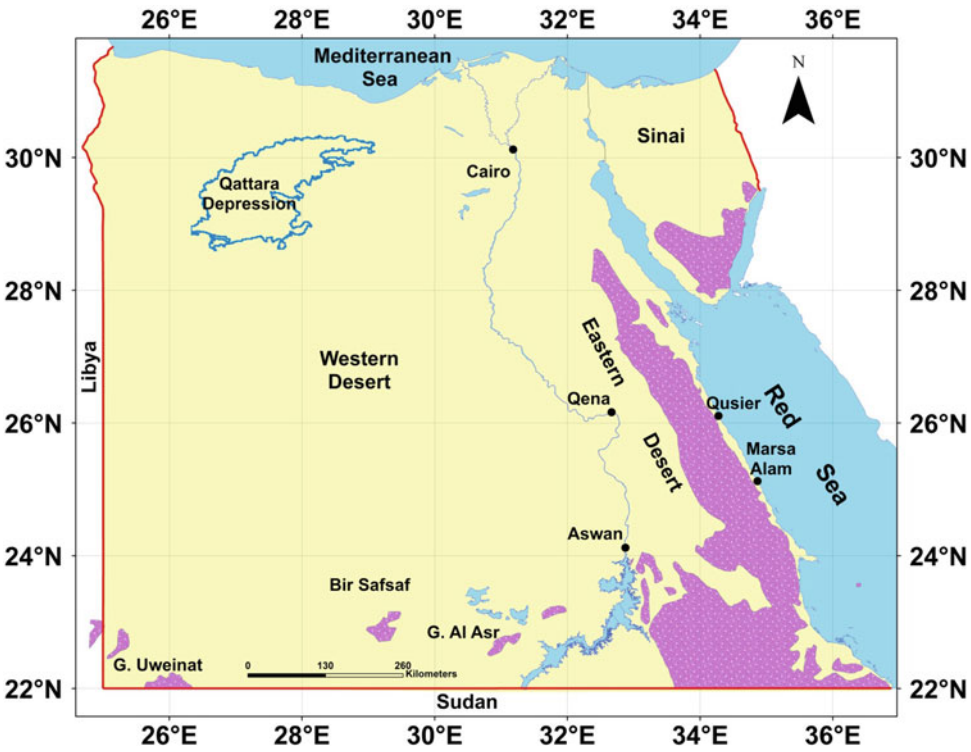

Fig. 6.1 Distribution of the Basement rocks in Egypt

6.2.2 Opposing Interpretations of Tier 1 and Tier 2

There are two opposing schools of thought regarding the significance of tier 1 and tier 2 rocks and their interrelations. At the present time both schools have adherents amongst the researchers in ANS geology.

The first school of thought is the earlier of the two, and may be described as a classical geosynclinal or infrastructural-superstructural model, stemming from the original observations by Hume (1934), and modified by geosynclinal theory (El Ramly and Akaad 1960), which regards the highly metamorphosed paragneisses, forming the base of geosynclinal sediments as pre-geosynclinal (i.e. Pre-Pan-African) continental basement rocks, the so-called 'fundamental gneisses'. Supporters of this model maintain that tier 1 rocks are the oldest rocks in Egypt (Archaean to early Proterozoic) forming an infracrustal province, and that they were remobilized during the Pan-African (Hume 1935; El Ramly and Akaad 1960; Schürmann 1966; EI Ramly 1972; El-Gaby and Ahmed 1980; El-Gaby 1983; El-Gaby et al. 1984, 1988a; Habib et al. 1985a).

This model considers that the tier 2 ophiolite and island-arc assemblages were thrusted during the Pan-African orogeny over an old craton consisting of tier 1 gneisses, migmatites and remobilized equivalents, which are exposed in a number of tectonic windows. The windows are dome-like structures or 'swells' exposed in the Eastern Desert and Sinai (the Beitan, Hafafit, Meatiq, El-Sibai, El-Shalul, Ras Barud and Feiran gneissic complexes). The tier 2 back-arc ophiolites and island arc assemblages (collectively referred to as the ophiolitic mélange) were thrusted over the attenuated eastern margin of the East Saharan Craton that extended nearly to the Red Sea coast (Abdel Monem and Hurley 1979; Dixon 1981; Habib et al. 1985a; El-Gaby et al. 1984, 1988a, 1990; Khudeir et al. 1995, 2008; El-Gaby 1983). The obducted ophiolitic mélange and underlying ancient continental crust were later transformed during the Pan-African Orogen into an active continental margin (El-Gaby's cordillera model).

The second, more recent, popular school of thought opines that both tiers originated by amalgamation and cratonization of Neoproterozoic juvenile rocks (Engel et al. 1980; Kröner et al. 1988; Bregar et al. 2002; Andresen et al. 2009; Liégeois and Stern 2010; Lundmark et al. 2012). Accretion resulted in the formation of a nappe assembly, which includes ophiolites, arc volcanics and sedimentary rocks (Frisch and El Shanti 1977; Engel et al. 1980; Gass 1982; Ries et al. 1983; Kröner 1984; Kröner et al. 1994) emplaced over polymetamorphosed and polydeformed deeper rocks of island arc origin. This concept may be referred to as an ensimatic accretionary or island arc model. In this model the ANS is considered to result from nappe stacking and folding during oblique (transpressional) convergence of boundary plates. The lines of collision between arcs are delineated by sutures (Bakor et al. 1976; Gass 1979;

Shackleton 1979). These stacked island arcs were later accreted to the passive continental margin of the old East Sahara Craton west of the present River Nile (Stern 1994; Unrug 1996; Johnson and Woldehaimanot 2003; Abdeen and Greiling 2005). Recently, some authors have argued that formation of the gneiss domes is strongly controlled by diapiric emplacement of Late Neoproterozoic plutons located at depth below the domes (Bregar et al. 2002; Fritz et al. 2002 and Neumayr et al. 1998).

Kröner (1985) and Kröner et al. (1987) offered a compromise model whereby the disputed pre-Pan-African continental crust in the Central Eastern Desert was proposed to exist as small continental fragments within the Mozambique ocean.

The two popular models differ from each other in the relative importance of ensialic and ensimatic contributions (Greenwood and Brown 1973; Greenwood et al. 1976, 1980, 1983; Bakor et al. 1976; Frisch and Al Shanti 1977; Gass 1977, 1979, 1981; Rogers et al. 1978; Engel et al. 1980; Shackleton et al. 1980; Stern 1981; Church 1982, 1983; Ries et al. 1983; Vail 1983; Kröner 1983, 1985; Stacey and Stoeser 1983; Cahen et al. 1984; Bentor 1985; Stoeser and Camp 1985, El-Gaby et al. 1988a; Ragab and El-Alfy 1996).

6.2.3 The ANS and the Mozambique Belt

The ANS narrows southwards and passes into the relatively older pre-Neoproterozoic crust of higher metamorphic grade forming the Mozambique Belt (MB) of Eritrea and Ethiopia. In contrast to the Archaean to Proterozoic high-grade gneisses in the Mozambique Belt, the ANS, is an accretionary orogeny of mostly Neoproterozoic age (~870–550 Ma), consisting predominantly of juvenile arc assemblages of low metamorphic grade, formed from partial melting of Earth's mantle. The ANS tectonic evolution is characterized by compressional tectonics represented by folded thrust sheets. This collision represents a multi-stage accretion of various continental fragments and arc terranes as the result of several orogenies (Ries et al. 1983; Stern 1994; Shackleton 1996; Kusky et al. 2003; Kröner et al. 2003; Stern and Johnson 2010; Johnson et al. 2011; Abu-Alam et al. 2013). The most intense part of the collision occurred in southern Africa, where older crust in Tanzania, Mozambique, and Madagascar was remobilized to form the Mozambique Belt.

Some authors (e.g. Reymer and Schubert 1986; Stein and Hofmann 1994; Teklay et al. 2002; Stein 2003) have warned that the crustal growth rate of the ANS was implausibly high for a simple arc-arc accretion model. They proposed that mantle plume magmatism could play an important role in the formation of juvenile ANS crust.

6.3 Gneissic Complexes of the Eastern and Western Deserts and Sinai

A striking feature of the basement rocks of Egypt, particularly in the Central Eastern Desert, is the presence of highly metamorphosed gneiss-cored dome structures. Their most popular interpretation is as metamorphic core complexes (Sturchio et al. 1983a, b; Fritz et al. 1996; Loizenbauer et al. 2001); or as gneiss domes (El Ramly et al. 1984; Habib et al. 1985a, b; Bennett and Mosley 1987; El-Gaby et al. 1990, 1991; Greiling et al. 1993; Wallbrecher et al. 1993; Kröner et al. 1994; Neumayr et al. 1998; Blasband et al. 1997,2000; Fowler and Osman 2001; Fritz et al. 2002; Bregar et al. 2002). Diverse mechanisms have been proposed to explain their origin and distribution relative to major structural lineaments and sutures (Blasband et al. 2000; Genna et al. 2002). The gneissic complexes are grouped as follows:

(1) **Central Eastern Desert complexes**:
These include the Meatiq, El-Sibai, El-Shalul and Um Had complexes.
(2) **South Eastern Desert complexes**:
These include the Migif-Hafafit, and Wadis El-Hudi, Haimur-Abu Swayel, Beitan, Kharit and Khuda complexes.
(3) **Western Desert complexes**:
These include the Gabal Uweinat, Gabal Kamel, Bir Safsaf and Gabal El-Asr complexes.
(4) **Southern Sinai complexes**:
These include the Feiran-Solaf, Sa'al-Zaghara, Taba-Elat and Kid complexes.

A brief description of these metamorphic complexes in the Egyptian Basement is given below.

6.3.1 Gabal Meatiq Complex

Meatiq Dome is the best known of the gneissic dome structures in the Central Eastern Desert of Egypt. It is located north of the main Qift-Quseir road, about 45 km west of Quseir city. The gneisses of this complex cover an area of about 300 km^2 (Fig. 6.2a, b). Meatiq has featured in the early geological reports in Egypt as the type example of the gneissic rocks (Andrew 1931; Hume 1934; Schürmann 1953; Shazly 1966; Noweir 1968; Shazly 1971; Akaad and Shazli 1972; Akaad et al. 1976). Since the 1980's the Meatiq has been interpreted in terms of modern plate tectonic theory (Ries et al. 1983; Sturchio et al. 1983a, b; Habib et al. 1985a, b; Sultan et al. 1987; El-Gaby et al. 1988a; EGSMA 1992a, b; Wallbrecher et al. 1993; Neumayr et al. 1996; Fritz et al.

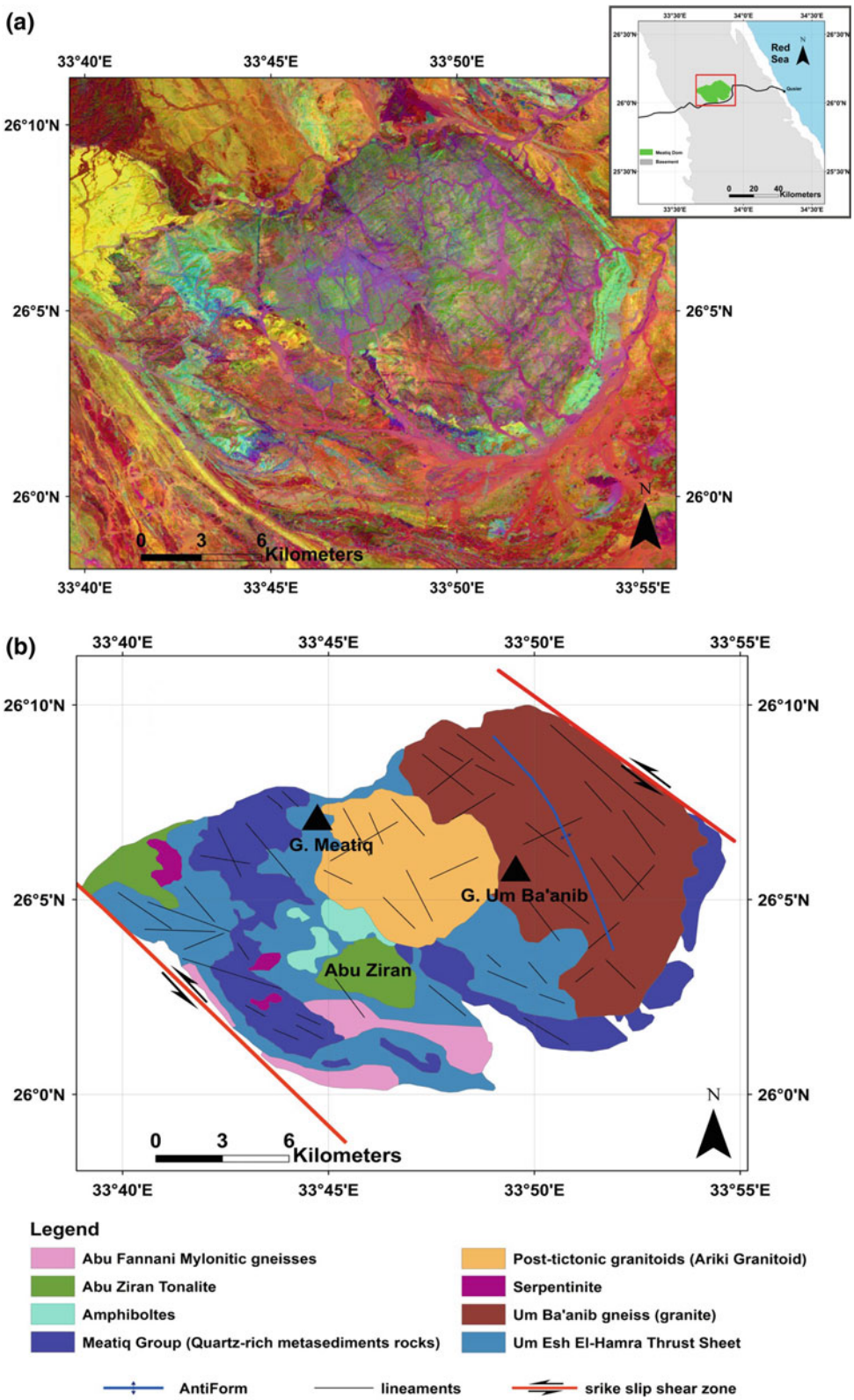

Fig. 6.2 **a** False color Principal Component Image of Landsat8 satellite image (PC5, PC4, PC2 in RGB) for the Meatiq dome area and **b** Geological map of the Meatiq dome (modified after Hassan et al 2017)

1996, 2002; Fowler and Osman 2001; Loizenbauer et al. 2001; Andresen et al. 2009, 2010; Hamdy et al 2017; Hassan et al 2017).

Structural and metamorphic similarities between the Meatiq and the North American Cordilleran metamorphic core complexes led Sturchio et al. (1983a) to conclude that

the Meatiq was a metamorphic core complex with a granite protolith, which they dated at 626 ± 2 Ma. Following Akaad and Noweir (1980), some workers thought that the Meatiq was a metasedimentary sequence (Meatiq Group). Habib et al. (1985a) and El-Gaby et al. (1990) thought that the Meatiq was metamorphosed in the Meatiqian Orogeny before the Pan-African, and represented a deeper infrastructure over which nappes of ophiolitic and arc volcanic assemblages (Abu Ziran Group) were thrusted from the east and low-grade metamorphosed during the Pan-African orogeny (Habib et al. 1985a; El-Gaby et al. 1984, 1988a, 1990; Neumayr et al. 1996, 1998). However, Ries et al. (1983) considered the Meatiq gneisses and greenschist facies overthrusted nappes as having formed during one orogeny without a significant metamorphic break between the gneissic basement and the cover sequence. Ragab (1987) considered the Meatiq mantled gneiss dome as an outer arc magmatic belt formed during the initial stage of arc-arc collision.

The gneissic rocks in the Meatiq complex consist of medium to high-grade amphibolite facies (estimated conditions 610–690 °C at P 6–8 kbars—Neumayr et al. 1998) metasediments and plutonic rocks that were later dissected by lower-temperature low-dipping mylonite zones at the time of overthrusting of the low-grade cover nappes. The gneisses, mylonites and cover nappes were subsequently folded into a domal geometry (Sturchio et al. 1983a, b; Habib et al. 1985a). Internally, the dome may be divided into the Um Ba'anib granite-gneiss on the eastern side of the dome, and the mylonite dissected metasediment units that overlie the Um Ba'anib and crop out on the western side of the dome. The Um Ba'anib gneisses describe an antiformal structure with a distinctly curved trend. The gneisses consist of coarse-grained quartzofeldspathic gneiss, characterized by well-developed foliation defined by feldspar augen, locally intercalated with migmatites, hornblende-biotite gneisses and amphibolites, and intruded by fine- to medium-grained gneissic alkali granite. The sheared upper parts of the Um Ba'anib gneiss are locally mylonitic to schistose and garnet-bearing (Andresen et al. 2009). The metasediments to the west of the Um Ba'anib have been described as meta-arkoses by Ries et al. (1983) but as semipelites by Habib et al. (1985a), who noted the presence of kyanite and garnet in the structural lower levels and sillimanite and staurolite in the upper levels. Habib et al. (1985a) also noted that there were sheared amphibolite (metagabbro) and serpentinite lenses in the upper parts and that shear strain increased rapidly towards the sheared boundary with the cover nappes. The uppermost sheared Um Ba'anib gneisses and metasediments are represented by a micaceous schist/phyllonite referred to as the Abu Fannani Schist by Akaad and Noweir (1980).

The lower grade cover nappes surround the Meatiq gneissic dome. These greenschist facies rocks (estimated conditions 320–480 °C at P 3 kbars—Neumayr et al. 1998) are referred to as the Abu Ziran Group, and consist of ophiolitic rocks (serpentinites, melanges and amphibolites of metagabbro and metabasalt origins) and island arc assemblages (intermediate and silicic metavolcanics, foliated diorites, granodiorites and arc-related metasediments). These nappes have been referred to as supracrustal cover by Habib et al. (1985b), and Neumayr et al. (1996, 1998); and as the Pan-African nappe complex (El-Gaby et al. 1988a; Fritz et al. 1996; Bregar et al. 2002); or eugeoclinal allochthon (Andresen et al. 2009, 2010). They are characterized by greenschist to lower amphibolite facies assemblages (Neumayr et al. 1998).

Important constraints on the evolution of Meatiq are provided by radiometrically dated syn-kinematic granodiorites (the Abu Ziran tonalite) near the southern margin of the dome, and the post-kinematic Arieki monzogranite pluton in the northern part of the dome. The Abu Ziran tonalite has a U-Pb zircon upper intercept age ranging from 614 to 609 Ma (Sturchio et al. 1983b; Stern and Hedge 1985; Andresen et al. 2009), which is regarded as a crystallization age. The post-kinematic Arieki monzogranite has produced a U-Pb zircon age of 585 ± 14 Ma (Sturchio et al. 1983b) and 590 ± 3.1 Ma (Andresen et al. 2009). Andresen et al. (2009) gave an age of 626 ± 2 Ma with an initial $^{87}Sr/^{86}Sr$ ratio of 0.7030 ± 0.0001 for the Um Ba'anib granite-gneiss, which coincides with the age for the Um Ba'anib given by Sturchio et al. (1983a, b). The significantly older $^{207}Pb/^{206}Pb$ zircon ages averaging 819 Ma for an amphibolite xenolith within the Um Ba'anib gneiss, and 779 Ma for the Um Ba'anib itself, reported by Loizenbauer et al. (2001) were not reproduced in the later investigations by Andresen et al. (2009). Andresen et al. (2009) reported a crystallization age of 736.5 ± 1.2 Ma for ophiolitic gabbro recovered from the ophiolites of the cover. This is younger than the average 788 Ma age given by Loizenbauer et al. (2001) for the ophiolitic nappes surrounding Meatiq. In view of the most recent radiometric data, many authors believe that the Meatiq gneiss protoliths must be younger than the surrounding ophiolitic mélange. Furthermore, the 609–604 Ma dates given by Andresen et al. (2009) for syn-kinematic dioritic bodies intruding both the amphibolite facies gneisses, and the greenschist facies cover; and the 614–609 Ma age of the Abu Ziran syn-kinematic pluton, suggest that thrusting of the cover nappes NW-wards over the Meatiq gneisses occurred between 605 and 615 Ma. Doming of the complex was complete before the intrusion of the ~590 Ma Arieki monzogranite.

The above radiometric data also constrain the age of the high temperature metamorphism of the Meatiq gneisses. This must not have been complete earlier than Um Ba'anib intrusion at 626 Ma and has been overprinted by the lower grade metamorphism during thrusting at 605–615 Ma. Thus

the high-grade metamorphism may have begun sometime before 625 Ma and was complete by about 615 Ma. The thrusting of cover nappes over the Meatiq gneisses between 605–615 Ma also corresponds to a time when some Hammamat molasses basin formation was taking place. For example, the sedimentation in the Wadi Hammamat basin to the near west must have been terminated by basin inversion before intrusion of the Um Had granite at 590 ± 11 Ma (Ries et al. 1983) or 596 ± 1.7 Ma (Andresen et al. 2009). It appears that the essential events in the formation of Meatiq date to the later stages of ANS shield development.

6.3.2 Gabal El-Sibai Complex

The El-Sibai gneissic complex lies south of Meatiq in the Central Eastern Desert. The El-Sibai complex is somewhat elongate in a NW-SE direction and is limited at its NW end by the El-Sibai granite, and at its southern end by normal faulting (Fig. 6.3a, b). It may be considered as consisting of two major lithological associations. The first association defines the inner parts of the complex and consists of gneissic textured granitoids (diorites, tonalites, granodiorites, and granites), amphibolites and schists. The second association surrounds the complex and comprises a series of low-dipping greenschist to amphibolite facies ophiolitic mélange and arc metavolcanic and metasedimentary nappes, with NW-ward translation kinematic indicators (Khudeir et al. 1992; Kamal El Din 1993; El-Gaby et al. 1994; Ibrahim and Cosgrove 2001; Bregar et al. 2002; Fowler et al. 2007; Augland et al. 2012).

As with the Meatiq, the El-Sibai complex has been the subject of studies over several decades. Hume (1934) and Schürmann (1966) described the El-Sibai as orthogneisses of the same or younger age than the enclosing rocks, and distinguished them from what they regarded as old crystalline basement elsewhere in Egypt. Sabet (1961) and El Ramly (1972) attributed the amphibolites and hornblende schists in the El-Sibai area to metasedimentary origin. Thus at this early stage, neither the amphibolites nor the granite gneisses at El-Sibai were considered to represent old infrastructure. Later authors identified the high temperature rocks as a pre-Neoproterozoic lower continental infrastructure remobilized during the Pan-African thrusting of ensimatic suprastructure cover nappes (El-Gaby 1983; El-Gaby et al. 1984, 1988a; Kamal El Din et al. 1992; Khudeir et al. 1992, 1995). Beginning in the 1990's, the El-Sibai was proposed to represent a metamorphic core complex, similar in origin to Meatiq (Greiling et al. 1993; Bregar et al. 1996; Fritz et al. 1996; Fritz and Messner 1999; Fritz et al. 2002; and Bregar et al. 2002). A recent study by Fowler et al. (2007) found that El-Sibai gneisses were granitoid bodies syn-kinematically intruded into the ophiolite—arc metavolcanic nappes. They noted that the gneisses were not infrastructural, with gneissic, migmatitic and amphibolite facies rocks being reported beyond the perimeter of the complex, as had been noticed earlier by Sabet (1961) and El-Gaby et al. (1994). Fowler et al. (2007) also concluded that the El-Sibai complex did not have a domal structure.

The main gneissic association rocks are tabular intrusions roughly concordant with the shears dividing the ophiolitic association into nappes. The intrusions are syn-kinematic with respect to the nappe-stacking event (700–650 Ma). Bregar et al. (1996, 2002) recognized four magmatic suites (I–IV) constituting the El-Sibai orthogneisses. Group I were exemplified by the El Shush gneissic tonalite (680–695 Ma) with intra-oceanic subduction affinities. Group I were intruded by Group II mid-crustal granitoids (e.g. the Abu Markhat gneissic granodiorite or Central Gneisses, foliated parallel to strike slip shears) at 660 Ma. Group III were described as exhumation-related (and locally foliated parallel to normal sense shears) intruded at 645–660 Ma, including the Um Shaddad and El-Sibai red granites. Group IV were late tectonic post-Hammamat intrusions that included the El Dabbah granodiorite, the slightly gneissic Um Luseifa granite and the El-Mirifiya leucogranite.

Fritz et al. (1996), Bregar et al. (1996), Fritz and Messner (1999) and Bregar et al. (2002) interpreted the El-Sibai history as a metamorphic core complex that was exhumed in two stages. The first stage was associated with the rise of Group I granites (and complementary slow subsidence of the nearby Wadi Kareim Basin). The second stage was transpression-controlled and involved extension in a strike-slip corridor (as envisaged for the Meatiq complex), which correlated with rapid subsidence of the nearby Wadi Kareim Basin. At this stage, Group II and III granitoids were intruded. The gneissic rocks were thought to have been exhumed rapidly in the second stage along normal faults. The core complex model has remained popular, though Fowler et al.'s (2007) data places the gneissic granites within a compressional environment (arc metavolcanic nappe stacking, during the arc collision stage). In this latter model, the heat of metamorphism was derived from intrusion of massive granitoids along thrusts in metabasic rocks, yielding contact amphibolites and composite magmatic-solid state gneissic foliations in the granitoids. El Shush Gneiss was intruded at approximately, 680–10 Ma ago (Bregar et al. 2002). Recent U-Pb ID-TIMS radiometric data by Augland et al. (2012) confirm the ~680 Ma age for the El Shush gneiss and give an age of about 682 Ma for the Um Luseifa gneiss. Augland et al. (2012) also noted that the El Shush gneissosity was syn-emplacement, not a later imposed HT metamorphic feature, and that the adjacent amphibolites show textures of static metamorphism. El-Gaby et al. (1994) earlier recognized this static thermal metamorphism, which produced an almandine-hornblende zone, and distinguished

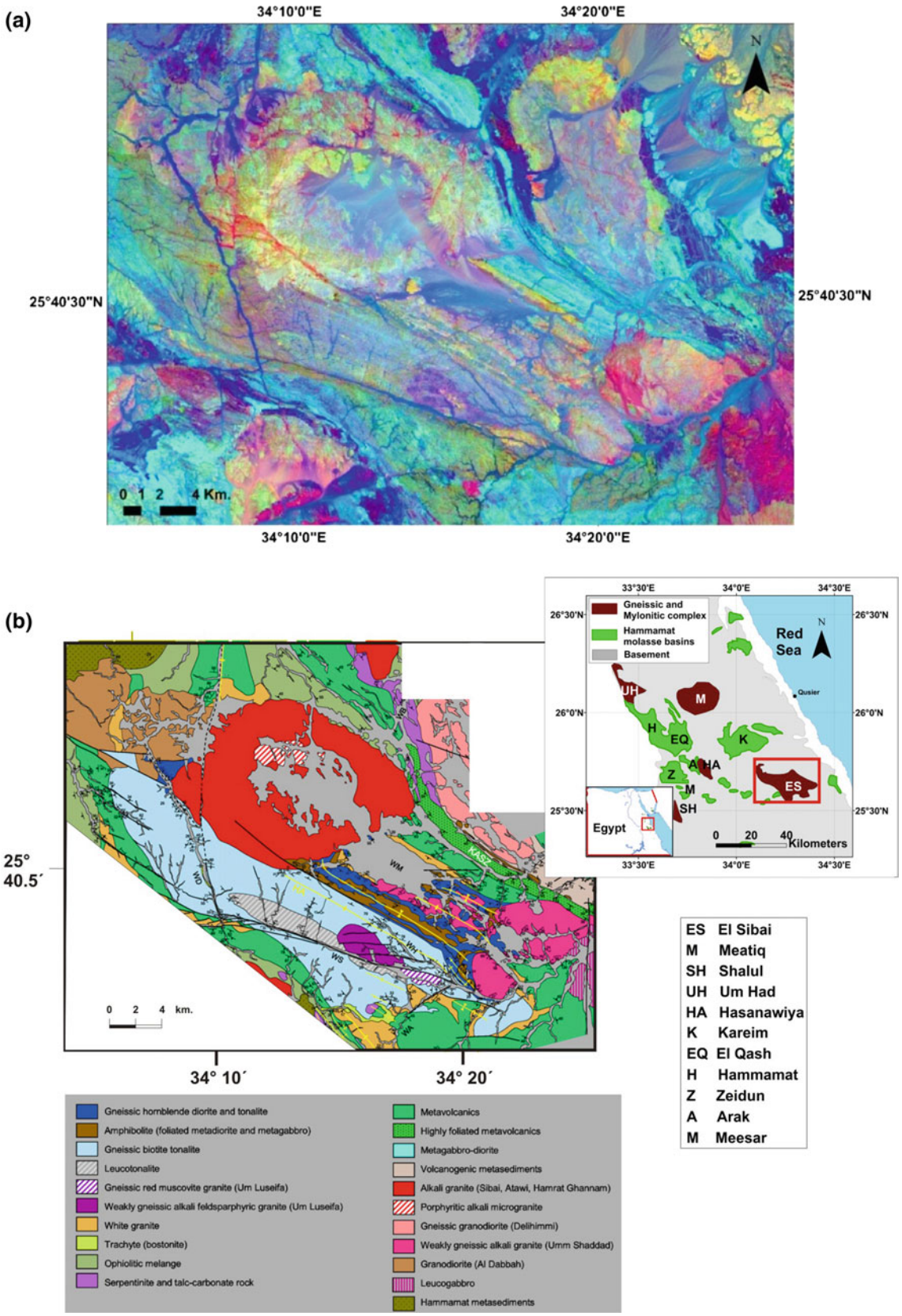

Fig. 6.3 Gabal Sibai area. **a** False color Principal Component Image of Landsat8 satellite image (PC8, PC4, PC5 in RGB) for the Meatiq dome area and **b** Geological map of Gabal Sibai (after Fowler et al. 2007)

it from the earlier regional greenschist facies event that affected the ophiolitic and arc-related rocks.

The El-Sibai gneisses and low- to medium-grade ophiolitic, and arc metavolcanic/metasedimentary host rocks were later folded about upright NW-SE trending mainly open folds during a NE-SW directed shortening event (625–590 Ma). Subsequently, NW-SE regional extension was responsible for low-angle normal ductile shear zones and mylonites with top-to-the-SE sense (Greiling et al. 1993). The latest gneissic red granites are syn-kinematic with respect to these normal-sense shear zones. WNW-ESE and N-S trending transcurrent faults (590–570 Ma) have later affected the El-Sibai complex.

6.3.3 El-Shalul Complex

The El-Shalul gneissic granite lies along the western margin of the Central Eastern Desert. It forms an open domal structure with NNW-SSE to NW-SE trend. It is partly covered by Phanerozoic sediments on its western flank. The gneissic core is monzogranite in composition, with progressively greater granitic component in the upper parts. Enclaves of monzogranite in the deformed granites show the granite to be the younger of the two (Hamimi et al. 1994). The gneisses are roofed by a major shear zone marked by chlorite schist, which separates the gneisses from overlying ophiolitic mélange, arc-related plutons, volcanics and volcanogenic pebbly sediments, phyllites and metagreywackes (Ragab et al. 1995). These overlying units show greenschist facies metamorphism that occurred before emplacement of the Shalul granitoid gneisses (Ries et al. 1983; Osman 1996). The overlying rocks are strongly foliated especially towards the El-Shalul gneisses and show NW-SE trending stretching lineations. Osman et al. (1992) and Osman (1996) showed that the shear zone separating gneisses and cover rocks has a top-to-the-SE shear sense, though Hamimi et al. (1994) earlier proposed that this shear zone was a result of NW- to WNW-ward thrusting.

Hume (1934) mapped the El-Shalul area as schist. Later studies continued with Sabet and Zatout (1955), Sabet (1961), El Ghawabi (1973), and Hashad (1980). El-Maharawy (1977) reported pre-Pan-African Rb-Sr whole rock ages of c. 1200 Ma from El-Shalul and its environs. El-Gaby (1983) considered El-Shalul as old continental crust of pre-Pan-African age that had been mylonitized during the Pan-African orogeny. This interpretation was consistent with the El-Shalul being an extension of the Sahara metacraton. Fritz et al.'s (1996) regional map compares El-Shalul to the Meatiq, in regarding it as a core complex, exhumed within a N-S strike slip corridor. Recent radiometric dating by Ali et al. (2012) supports the possibility that the El-Shalul gneisses represent melts derived from the underlying metacraton. Ali et al.'s (2012) U-Pb zircon dating and Sr-Nd-Hf isotopic evidence support a juvenile origin for the ~634 Ma El-Shalul gneisses.

Hammamat sediments of the Wadi Meesar basin unconformably overlie the ophiolite-arc volcanic/sedimentary cover of the El-Shalul complex (Osman 1996). The foliations in the shear zone carapace of the complex can be traced upwards into the base of this Hammamat basin, suggesting that the shear was active up to at least the beginning of the Hammamat deposition. Ali et al. (2012) have correlated this major shear zone with the shears defining the top of the Meatiq Complex, referred to as the Eastern Desert Shear Zone (EDSZ) by Andresen et al. (2009). These features, and the comparable age of the El-Shalul granitoid gneisses and the Um Ba'anib gneiss at Meatiq, are striking similarities between these complexes.

6.3.4 Wadi Um Had Complex

A commonly neglected occurrence of gneissic rocks and schists is exposed along Wadi Um Had, along the western margin of the CED. The gneisses and schists are enclosed in a NW-SE elongate dome structure (Fowler and Osman 2001; Osman and El-Kalioubi 2014), and have similar lithology to schists and gneisses of Meatiq. The high temperature metamorphic rocks consist of deeper poorly foliated garnet quartzofeldspathic rock with upper sections of quartz-rich garnet-cordierite-sillimanite schist cut by retrograde shear zones of mica-chlorite-staurolite schist (Noweir and El Sharkawy 1988). Northerly parts of the Um Had complex are composed of garnet amphibolite and garnet muscovite-biotite schist of apparent metavolcanic origin (Fowler and Osman 2001).

Original studies of these rocks by Essawy and Abu Zeid (1972), El Ramly and Hermina (1978) and El-Gaby et al. (1984) recognized their status as infrastructural gneisses. However, Noweir and El Sharkawy (1988) regarded the metamorphism at Um Had as a hornblende hornfels facies contact effect of the Um Effein and Um Had granites. The latter authors and El-Gaby et al. (1988b) interpreted the protoliths of the Um Had gneisses as Hammamat Group sediments, despite the phases andalusite, sillimanite, cordierite, garnet, staurolite being indicative of semi-pelitic composition, quite distinct from the average andesitic composition of nearby Hammamat sediments. A NW-elongated staurolite zone and overlying garnet zone, north of the Um Had granite, mapped by El-Gaby et al. (1988b), was interpreted to be due to a buried pluton, and not the Um Had or Um Effein granites. The garnet zone and staurolite zone were also mapped by El Kalioubi (1988), though his map showed the staurolite zone bordering the Um Had granite, along Wadi Um Sheqila. El-Sayed et al. (2000) gave P-T

conditions of 510 °C for the garnet zone, 590 °C for the staurolite zone, and 850 °C for the cordierite zone at P 4–5 kbars for the rocks along Wadi Um Sheqila. El Kalioubi (1988) also concluded that the pressure of metamorphism was about 4 kbar, but that peak metamorphic temperatures were 650 °C. Fowler (2001) pointed out that garnet, sillimanite and cordierite porphyroblasts in the Wadi Um Sheqila schists are deformed by the foliation, while the Um Had granite is clearly post-foliation. This rules out the Um Had as a heat source for the metamorphism that produced these phases. All metamorphism and shearing activity in the Um Had complex, including thrusting of Hammamat sediments over the gneisses, must have ceased before the intrusion of the Um Had granite at 595 Ma.

6.3.5 Ras Barud Complex

The Ras Barud gneiss belt lies at the southern border of the North Eastern Desert and approximately parallels the Qena–Safaga Road. The term "Barud Gneiss" (El-Gaby 1983; El-Gaby et al. 1988a) includes the NE-trending gneissic southern margin of the giant Barud tonalite intrusion, plus thin discontinuous bodies of amphibolite, schist and gneissic diorites intruded or engulfed by it. The Barud gneiss marks El-Gaby's (1983) Qena-Safaga Line or Qena-Safaga Shear Zone, which is supposed to separate the partly remobilized old continental crust that dominates the NED, from the ophiolite and Abu Ziran Group island arc lithologies that constitute the CED.

The Ras Barud area has been investigated by many authors (El-Akkad and Dardir 1965; Habib 1972; Akaad et al. 1973; Abu EI-Ela 1979; EI-Gaby and Habib 1982; Kamal El Din and Asran 1994; Masoud 1997; Hassan 1999; Abd El-Wahed and Abdeldayem 2002; Kamal El Din 2003; Fowler et al. 2006). Near Safaga, the Barud gneisses include the Abu Furad amphibolite, a highly foliated body of amphibolite and hornblende schist that has been intensively intruded by thin, boudinaged and isoclinally folded granite dykes. The hornblende schists may be the intensely shear-strained equivalents of the metagabbro-diorite complex to their south (Abd EI-Wahed and Abdeldayem 2002). The Abu Maya hornblende diorite gneiss lie along strike from the amphibolites. It is richly xenolithic in amphibolite blocks and shows magma contamination and magmatic foliation structures. Some of the magmatic foliations and streaky contamination zones have been described as "migmatites", though these structures are dominantly magmatic. The Barud tonalite intrusive contact is discordant to the foliations in the amphibolites. The margin of the tonalite contains flow extended enclave swarms and schlieren giving it a gneissic appearance (Fowler et al. 2006). These primary foliations follow the margins of apophyses as they discordantly penetrate the wallrocks. The core of the Barud tonalite is isotropic, and shows no deformation effects at all.

The characteristics of the Barud gneiss are distinctly different to those of the CED gneiss domes. The tectonic setting of the Barud gneiss is not yet clear. Fowler et al. (2006) tentatively proposed that the shear foliations in the amphibolite were related to arc rifting at 700 ± 20 Ma. The extensional shears intersected metagabbro-diorite beneath the arc, where they tapped arc granitoids, which thermally softened the sheared rocks and kept them at amphibolite facies temperatures. Shear foliation may correspond to Abd El-Wahed and Abdeldayem's (2002) S1, which formed during HT metamorphism. The shears were rotated to steeper orientation on later SE-vergent listric thrusts during the arc collision stage (~650 Ma). This may correlate with Abd El-Wahed and Abdeldayem's (2002) D2 NE-SW folding event. El-Bialy and Omar (2015) have concluded that the Barud tonalite was a pre-collision mature continental arc intrusion.

6.3.6 Migif-Hafafit Complex

The Migif-Hafafit gneiss complex is located about 60 km southwest of Marsa Alam, and is one of the largest gneiss complexes in the Eastern Desert, covering about 1500 km^2 (Fig. 6.4a, b) It spans almost the width of the Eastern Desert, yet the only well-studied part is the eastern portion, drained by Wadi Hafafit and bordered by Wadi Nugrus. First mapped in detail by El Ramly between 1955–1957, and reported in El Ramly and Akaad (1960), this complex was described as a doubly plunging antiform, consisting of >4000 m of migmatites, biotite hornblende gneisses, psammitic gneisses and biotite gneisses. Psammitic and biotite paragneisses (with lenses of serpentinite/anthophyllite schist) dominate the northern part of the complex while mafic orthogneisses (metagabbros) dominate in the south, and immediately enclose tonalite-trondhjemite gneiss-cored domes.

The Migif-Hafafit gneissic rocks are separated from low-grade greenschist ophiolitic mélange and volcanic arc assemblages of the CED by shear zones. The eastern boundary shear is the Wadi Nugrus Shear Zone. The northern boundary is the Wadi Sha'it Shear Zone. These two shear zones are taken to be the boundary between the CED and the SED. The nature of these shear zones is controversial, especially the Nugrus, which has been viewed as a basal thrust, a strike-slip shear zone, or a folded extensional shear zone (Greiling et al. 1988; Fritz et al. 1996; Fowler and Osman 2009; Makroum 2017; Hagag et al. 2018). Further details of these shear zones are presented in Sect. 6.9.

Estimated P-T conditions for the Migif-Hafafit complex migmatites are provided by El Bahariya (2008) as >700 °C at 5 kbar. Abd El-Naby and Frisch (2006) and Abd El-Naby et al. (2008) raised pressure estimates for the gneisses to 6–

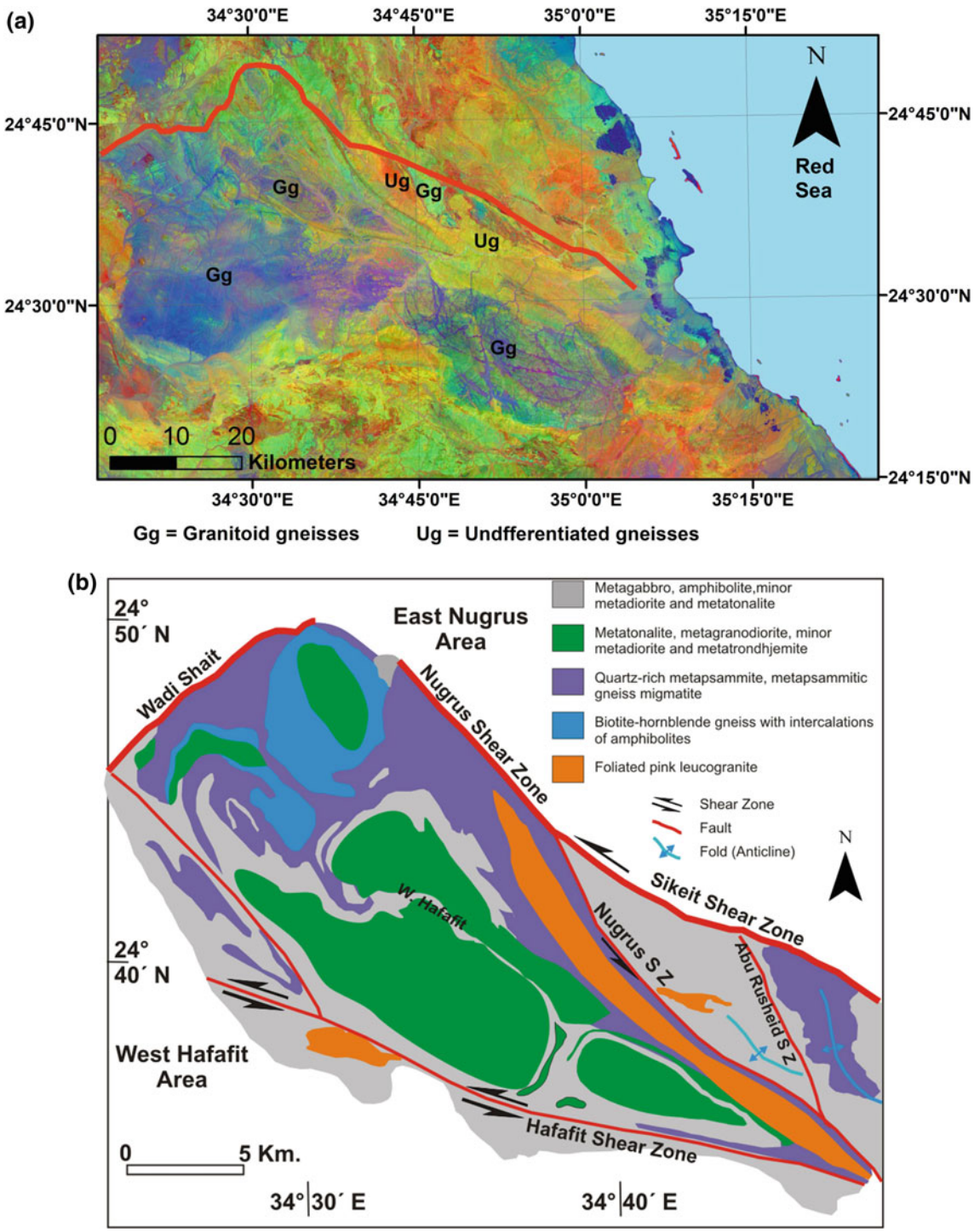

Fig. 6.4 Hafafit gneissic Dome. **a** False color Principal Component Image of Landsat8 satellite image (PC5, PC4, PC2 in RGB) for Hafafit gneissic Dome and **b** Geological map of the Hafafit gneissic Dome (after Hassan et al 2017)

8 kbar and temperatures 600–750 °C. Abu El-Enen et al. (2016) gave even higher pressure estimate of P 9–13 kbars and temperatures 570–675 °C (upper amphibolite facies).

Abdel-Khalek and Abdel-Wahed (1983) recognized a polydeformation history with a strong NW trend. El Ramly et al. (1984) devised a polydeformation history involving gneissosity development during amphibolite facies metamorphism then intrusion of Older Granites, followed by overthrusting from the east. This structural model was maintained and evolved by Greiling et al. (1984, 1988),

Greiling and El Ramly (1990), Rashwan (1991) and El Ramly et al. (1993). The dome structures have been viewed by Greiling et al. (1988) and Shalaby (2010) as due to buoyancy of granitoid beneath overthrusted mafic orthogneisses. Fowler and El Kalioubi (2002) interpreted the domes as refolded sheath fold structures.

The concept of Migif-Hafafit gneisses being older (pre-Pan-African) continental crust dates from Hume (1934), and was held also by Abdel-Khalek and Abdel-Wahed (1983), El-Gaby (1983), El-Gaby et al. (1988a), El-Gaby (1994) and recently by Khudeir et al. (2008). However, geochronology and isotopic studies do not support this interpretation. The age of Migif-Hafafit tonalite magmatism is represented by U-Pb zircon age of 682 Ma (Stern and Hedge 1985), $^{207}Pb/^{206}Pb$ zircon emplacement ages of 677 ± 9 Ma and 700 ± 12 Ma (Kröner et al. 1994), Rb-Sr age 609 ± 17 Ma (Liégeois and Stern 2010), U-Pb ID-TIMS ages of 660 Ma and 680–705 Ma for migmatites (Lundmark et al. 2012), and the U-Pb zircon age range of 646 ± 12 Ma to 731 ± 3 Ma by Abu El-Enen et al. (2016). Nd and Sr isotopes indicate juvenile origin for the tonalites (Liégeois and Stern 2010).

The original tectonic setting of this complex is contested. The abundance of psammitic gneiss implies that a continental source of sediment was nearby. The geochemistry of ultramafic lenses and mafic orthogneisses has been found to be similar to MOR tholeiites (Rashwan 1991), and the tonalitic gneisses are calc-alkaline and consistent with subduction-related magmatism. Kröner et al. (1994) noted that the tonalites were not derived by melting of continental crust, but were subduction-related. Subduction models for the Migif-Hafafit are given by Abd El-Naby and Frisch (2006), Abd El-Naby et al. (2008) and Abd El-Rahman et al. (2009b). These authors along with Kröner et al. (1987) and Greiling et al. (1988) proposed that SW-ward thrusting of the Wadi Ghadir ophiolite complex over the Migif-Hafafit protoliths occurred during high temperature metamorphism and tonalite magmatism. A core complex setting for Migif-Hafafit is also a popular element of proposed histories of this complex, explaining the exhumation of this complex from depths pertaining to upper amphibolite facies metamorphism (>5 kbars, i.e. >20 km depths) by transpression involving strong extension and uplift (Fritz et al. 1996, 2002).

6.3.7 Wadi El-Hudi Complex

The W. El-Hudi area lies approximately 30 km southeast of Aswan in the South Eastern Desert. The El-Hudi gneisses lie close to the boundary between the juvenile crust of the ANS and the Eastern Sahara Craton (Abdelsalam and Dawoud 1991; Schandelmeier et al. 1988; Sultan et al. 1993; Greiling et al. 1994). This complex comprises a high-grade metamorphic body of gneisses, migmatite, hornblende and biotite schists and minor amphibolites, cored by an adamellite intrusion.

The Wadi El-Hudi area has been studied by Nakhla and El Hinnawi (1960), Hilmy and Awad (1969), Saleeb-Roufaiel et al. (1976), El-Gharabawi (1981), Soliman (1983), Ragab and El-Gharabawi (1989) and Moghazi et al. (2001). Ragab and El-Gharabawi (1989) describe the complex as a small dome cored by adamellite, enclosed in a migmatized envelope derived from biotite gneiss of metasedimentary origin. The migmatites contain sheets of garnetiferous leucogranite and pegmatite as mobilizates during partial anataxis. The leucogranites form prominent lenses in the schists (Madani and Emam 2011). The migmatites showed transition from metatexite to diatexite with increasing component of leucosome.

Moghazi et al. (2001) described a larger garnet leucogranite mass within the migmatite zone. The leucogranite is S-type and contains numerous xenoliths of metasediment. They concluded that the leucogranite formed by dehydration partial fusion of chemically immature pelitic materials, and suggested that 800 °C and 5 kbar pressure would result in the degrees of partial melting and mobility shown by the leucogranite. Despite the small size of the El-Hudi migmatites, Moghazi et al. (2001) pointed out the significance of the presence of an S-type granite in this complex. The S-type granite could have implications for the debate on the presence and role of old continental crust in the magmatism. However, Ragab and El-Gharabawi's (1989) preferred model was an arc-arc collision where the volcanics and plutons of one arc were subducted beneath the accretionary prism of another arc. The complete melting at depth of the subducted arc rocks generated the adamellite core. The partial melting of the upper parts of the arc resulted in the migmatite carapace.

6.3.8 Wadi Haimur–Abu Swayel Complex

The W. Haimur–Abu Swayel gneisses lie about 185 km southeast of Aswan, covering an area of about 470 km^2. The area was previously studied by Hathout (1963), Bassyuni (1973), Omar (1978), El Ramly et al. (1980), Finger and Helmy (1998), Abd El-Naby et al. (2000) and Abd El-Naby and Frisch (2002).

The area is characterized by ophiolitic rocks overthrusted by paragneisses, with later granite intrusions, especially north of the complex (Fig. 6.5). The gneisses of the W. Haimur area are considered to be of sedimentary origin (Abd El-Naby and Frisch 2002; Finger and Helmy 1998). A Neoproterozoic age for the paragneisses was obtained

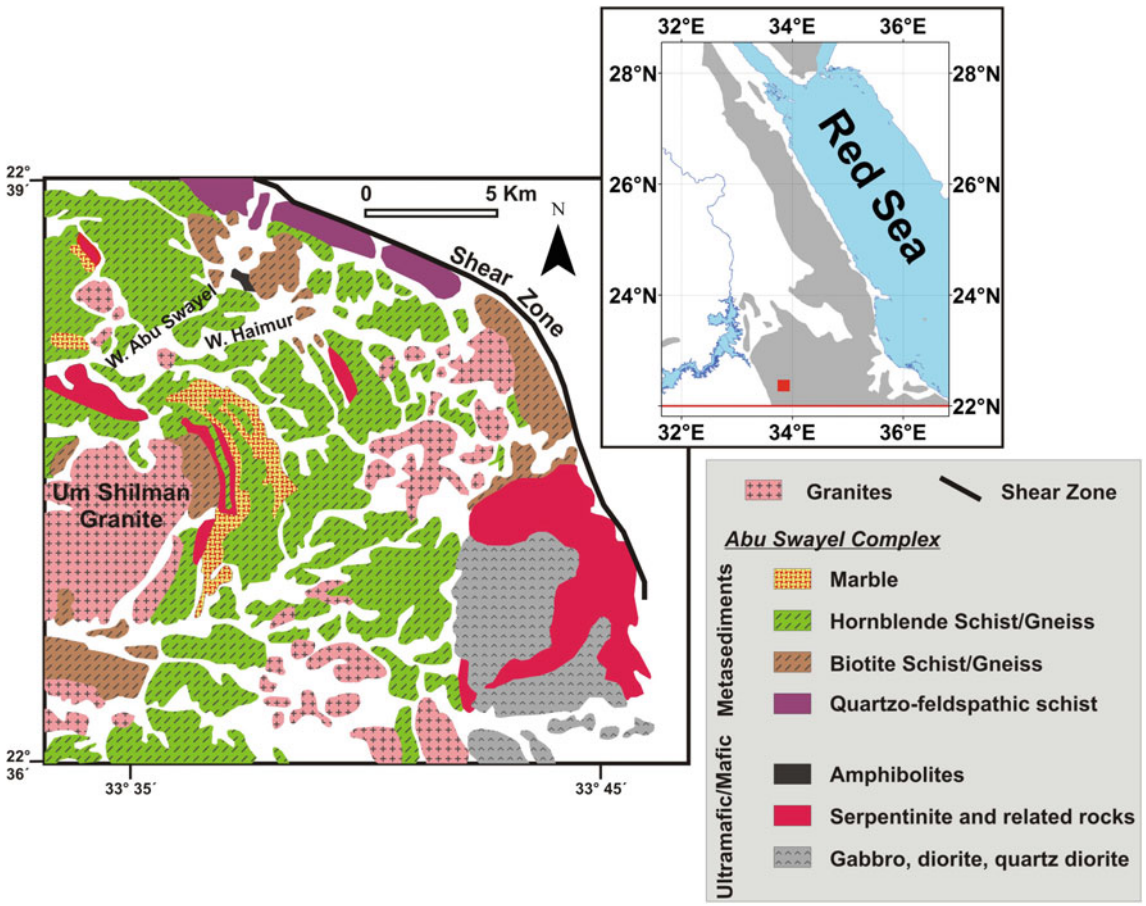

Fig. 6.5 Geological sketch map of the Abu Swayel area, compiled by Helmy (1996), mainly according to mapping results of El Shazly et al. (1977)

from monazites by Th(U)-Pb dating, giving ages of about 635 ± 10 Ma.

Abd El-Naby and Frisch (2002) concluded that the Wadi Haimur–Abu Swayel gneisses formed during an arc collision event between 580 and 630 Ma, which involved medium grade metamorphism under conditions 495–550 °C at 3.4–6.5 kbars pressure. The arc collision involved southwards thrusting at the Wadi Allaqi suture zone. Thrusting of back-arc ophiolites and back-arc sediments occurred at about 630 Ma leading to the medium grade gneiss-forming metamorphism in the back-arc sediments. Ophiolitic serpentinites were thrusted over amphibolites (metagabbros), which Abd El-Naby et al. (2000) suspected to be a metamorphic sole. Thrusting was followed by intrusion of collision-related granites at 600–580 Ma.

6.3.9 Wadi Beitan Complex

The Wadi Beitan gneisses lie in the South Eastern Desert, about 60 km southwest of Ras Banas. The gneisses are exposed in the cores of NW-trending antiforms, and are overlain by ophioliolitic rocks. The geology of the area has been studied previously by Ashmawy (1987), El Amawy (1991), Abdel-Khalek et al. (1992, 1999), Hamimi (1992), Ghoneim et al. (1993, 2002), Kröner et al. (1994), Khudeir et al. (2006a, b), Obeid et al. (2015) and Ali et al. (2015).

The gneisses are divided into three concordant tabular bodies consisting of tonalitic orthogneiss and hornblende paragneiss in the lower division, hornblende biotite paragneiss in the middle division and garnet biotite paragneiss in the upper division (Khudeir et al. 2006a, b). Amphibolites and silicic porphyry sheets separate the divisions. Migmatization is a feature of the deeper gneisses and amphibolites. The grade of metamorphism is almandine amphibolite facies, with P-T conditions estimated by Khudeir et al. (2006a, b) varying according to the geothermometer chosen, but ranged from 725 to 870 °C at pressures also varying according to method, ranging from 4.5 to 8 kbars. Temperature and pressure estimates were lowest in the amphibolites.

The gneisses are separated from SW-wards overthrusted ophiolitic rocks (serpentinites and metagabbros) and mafic to silicic arc metavolcanics, by a mylonitized retrograde shear zone. Abdel-Khalek et al. (1999) described complex antiformal stacked duplex structures in the gneisses and ophiolites. Thrusting probably occurred between 550 and 660 Ma (Ghoneim et al. 2002). Obeid et al. (2015) found the ophiolites to have formed in a suprasubduction zone setting.

Ghoneim et al. (1993) estimated a Sm-Nd age for the gneisses of 889 ± 8 Ma and Rb-Sr age of 863 ± 15 Ma ie early Pan-African. Kröner et al. (1994) Pb-Pb dated zircons from the tonalitic gneiss at Beitan, which yielded a 704 ± 8 Ma age, regarded as the age of magmatic emplacement of the protolith. Ali et al. (2015) gave Sm-Nd ages for the tonalitic gneiss at 744 ± 9 and 719 ± 10 Ma. Magmatic zircons from the migmatites produced $^{206}Pb/^{238}U$ ages of 744 ± 10, 725 ± 9 and 719 ± 10 Ma. These data clearly indicate that gneiss formation was Neoproterozoic and that the gneisses do not themselves represent old continental crust as originally thought by Abdel-Khalek et al. (1999). Nevertheless, Ali et al. (2015) found that both juvenile and old continental crust had contributed to the gneissic protoliths, and suggested that the Wadi Beitan gneisses may have formed in an active continental margin. Ghoneim et al. (1993) calculated that there was between 35 and 50% crustal contamination in the gneissic protolith.

6.3.10 Wadi Kharit and Wadi Khuda Complexes

The Wadi Kharit gneisses are located midway between Berenice and Aswan. They were briefly described by Hassan and Hashad (1990) as resulting from the "infolding of geosynclinal sediments and volcanics with syn-tectonic granitoids, and the imposition of gneissic structures upon them". El Kazzaz (2010) described high grade psammitic and pelitic biotite mica schists with large syn-kinematic staurolite porphyroblasts and intercalations of intermediate metavolcanics in Wadi Kharit area. He suggested that the timing of the high grade metamorphism was 630–600 Ma.

The Wadi Khuda gneisses are located immediately south of Berenice. They were referred to by El-Gaby et al. (1990) as examples of reworked pre-Pan-African crust. El Ramly (1972) and Hashad (1980) regarded these rocks as gneissified Shadli metavolcanics, though Dixon (1979, mentioned by Hassan and Hashad 1990) and El-Gaby et al. (1990) thought that the Khuda gneisses were paragneisses representing old sialic material.

Asran et al. (2000) described the Khuda gneisses as defining a NE-SW trending doubly plunging dome representing a metamorphic core complex. They described the metamorphic rocks as amphibolite facies hornblende paragneisses, psammitic gneisses and migmatites with amphibolite lenses deeper in the core of the dome. The paragneiss protoliths were thought to be impure marls and feldspathic sandstones, while the amphibolites were metabasalts. Foliated diorites were thrusted NW-wards over the gneissic rocks before formation of the dome structure.

6.3.11 Western Desert Complexes

Low-lying outcrops of gneissic and migmatitic rocks of the Sahara Metacraton extend from Gabal El Asr, 190 km westward of the southern end of Lake Nasser, through Bir Safsaf and Gabal Kamil, to Gabal Uweinat in the far SW corner of Egyptian Western Desert, in region referred to as the Uweinat-Bir Safsaf-Aswan Uplift (Richter and Schandelmeier 1990; Abdelsalam et al. 2002). The gneisses of the Egyptian Western Desert are known to include the oldest rocks in NE Africa, with early Mesoarchaean ages being recorded at Gabals Uweinat by Harris et al. (1984). These Archaean rocks were remobilized a number of times via partial melting during the early Proterozoic, and therefore represent an excellent example of crustal reworking that is a major theme of the EAO south of the ANS. The geology and geochronology of Gabal Uweinat and areas to its east have been reported by Klerkx (1980), Schandelmeier et al. (1983), Schandelmeier and Darbyshire (1984), Cahen et al. (1984), Richter (1986, summary given by Bea et al. 2011a), Richter and Schandelmeier (1990), Harms et al. (1990), Sultan et al. (1994) and Bea et al. (2011a, b).

Klerkx (1980) defined two main units at Uweinat, the Karkur Murr Formation (including granulitic charnockites) and the Ayn Daw (or Ayn Dua) Formation (migmatitic granites), separated by mylonites. Detailed mapping at Gabal Kamil was later completed by Richter (1986) who defined three units beginning with the Granoblastite Formation (gneissic granulites and minor meta-ultramafites), the Anatexite Formation (migmatites, quartzites and calc-silicates) and the Metasediment Formation (paragneiss and schist). In the area between Uweinat and Kamil, Bea et al. (2011a) described tonalite/ gabbro-diorite gneisses (magmatic zircons 3.22 ± 0.04 Ga) and migmatitic gneisses, which they correlated with the Karkur Murr and Ayn Daw Formations, respectively. The tonalite gneisses and migmatites were separated by a Neoproterozoic metasedimentary series including famous banded iron formations (Naim et al. 1998; Elkady 2003) with similar BIF's described from Uweinat by Khattab et al. (2002).

Evidence for crustal remobilization events includes the presence of migmatites and zircons within them with rims dating to late Archaean and early Proterozoic times. Harris et al. in (1984) thought that Gabal Uweinat was an Archaean nucleus rimmed by a Middle Proterozoic fold belt. Harms et al. (1990) presented evidence of isotopic resetting of

nearby gneisses of northern Sudan, which showed 560–920 Ma Rb-Sr dates but Nd model ages of 1.6–2.6 Ga. They regarded this as evidence for Pan-African reworking of old crust. Sultan et al. (1994) reported U-Pb ages of 2.14 Ga and 1.92 Ga for anorthosite at Gabal El Asr, and 2.63 and 2.06 Ga for anorthosites at Gabal Kamil. Bea et al. (2011b) regarded the Bir Safsaf 2.1 and 2.7 Ga zircons as inherited and included all of the Safsaf gneisses as Pan-African granitoids. Bea et al. (2011a) found that Mesoarchaean crustal formation occurred between 3.3 and 3.0 Ga, followed by crustal reworking at 2.97, 2.85 and 2.73 Ga. This was followed by stability between 2.5 and 2.1 Ga, then a major metamorphic event at 2.1 Ga. Pan-African granites were intruded at 0.75–0.60 Ga.

6.3.12 Gneisses Belts in Southern Sinai

Southern Sinai represents the northernmost corner of the ANS. The metamorphic rocks in southern Sinai embraces four main metamorphic complexes, separated from each other by large tracts of syn-to post-collision granitoid intrusions. These include the Feiran-Solaf, Sa'al-Zaghara, Taba-Elat and Kid complexes (Fig. 6.6).

6.3.12.1 Wadi Feiran-Solaf Complex

The Wadi Feiran–Solaf metamorphic complex in the southern Sinai, has been studied since the earliest scientific investigations of Egyptian geology (e.g. Hume 1906, 1934; Barron 1907; Ball 1916; Schürmann 1953, 1966), and is one of the best examples of Egyptian gneissic complexes. It is a narrow, 6–10 km wide, 40 km long NW-SE elongate belt bordered to the NE by younger gneissic granitoids and to the SW by post-kinematic granites (Fig. 6.7).

The main lithological units are quartzofeldspathic gneiss, biotite-hornblende gneiss, biotite gneiss, and local intercalations of amphibolite, calc-silicate gneiss and biotite schist. In the northwestern part of the complex migmatized quartzofeldspathic gneisses and syn-kinematic pegmatites are abundant. Orthogneisses of diorite, tonalite and granodiorite composition with deformed enclaves are also present (Eyal et al. 2015). The complex is usually divided into two parts—the Feiran segment and the Solaf segment, separated by a distinctive NE trending meladiorite dyke. El-Gaby and

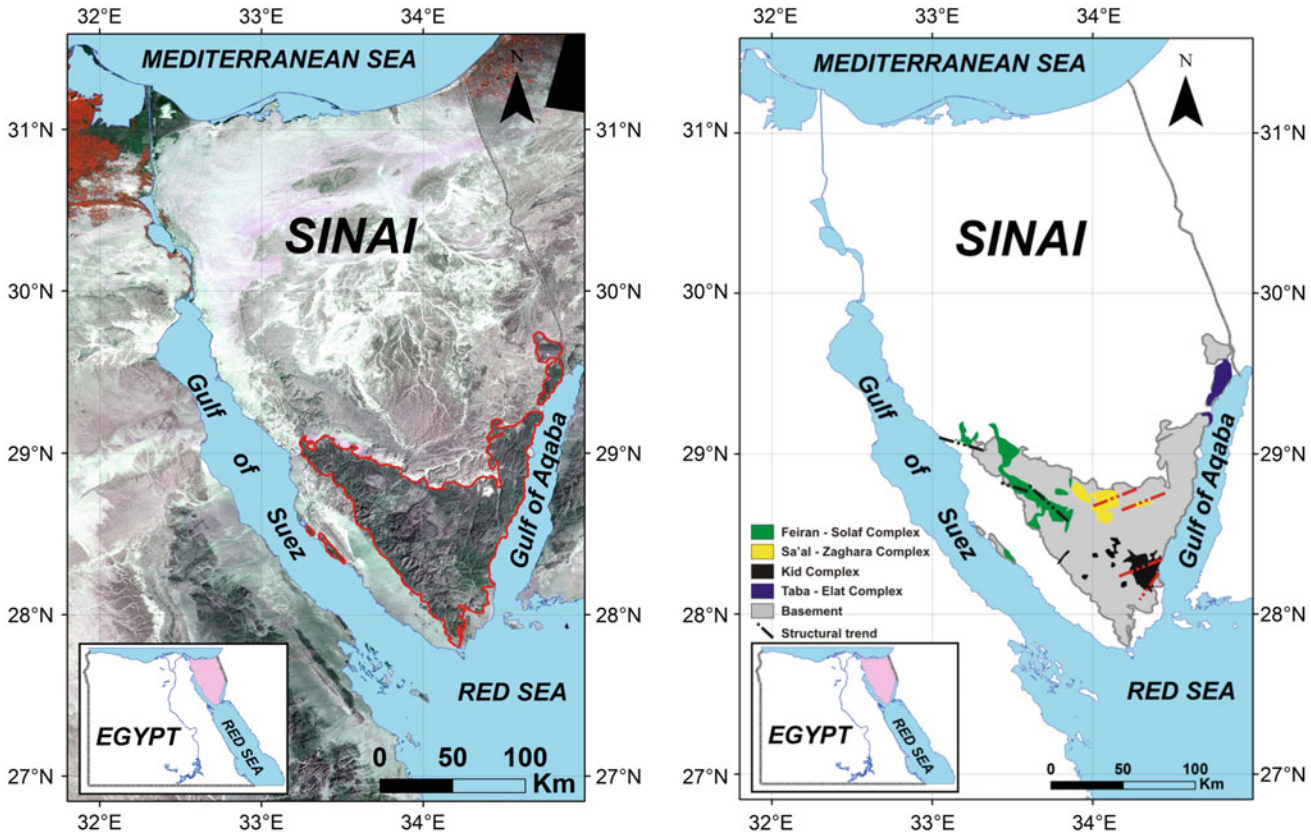

Fig. 6.6 The gneisses belts in southern Sinai

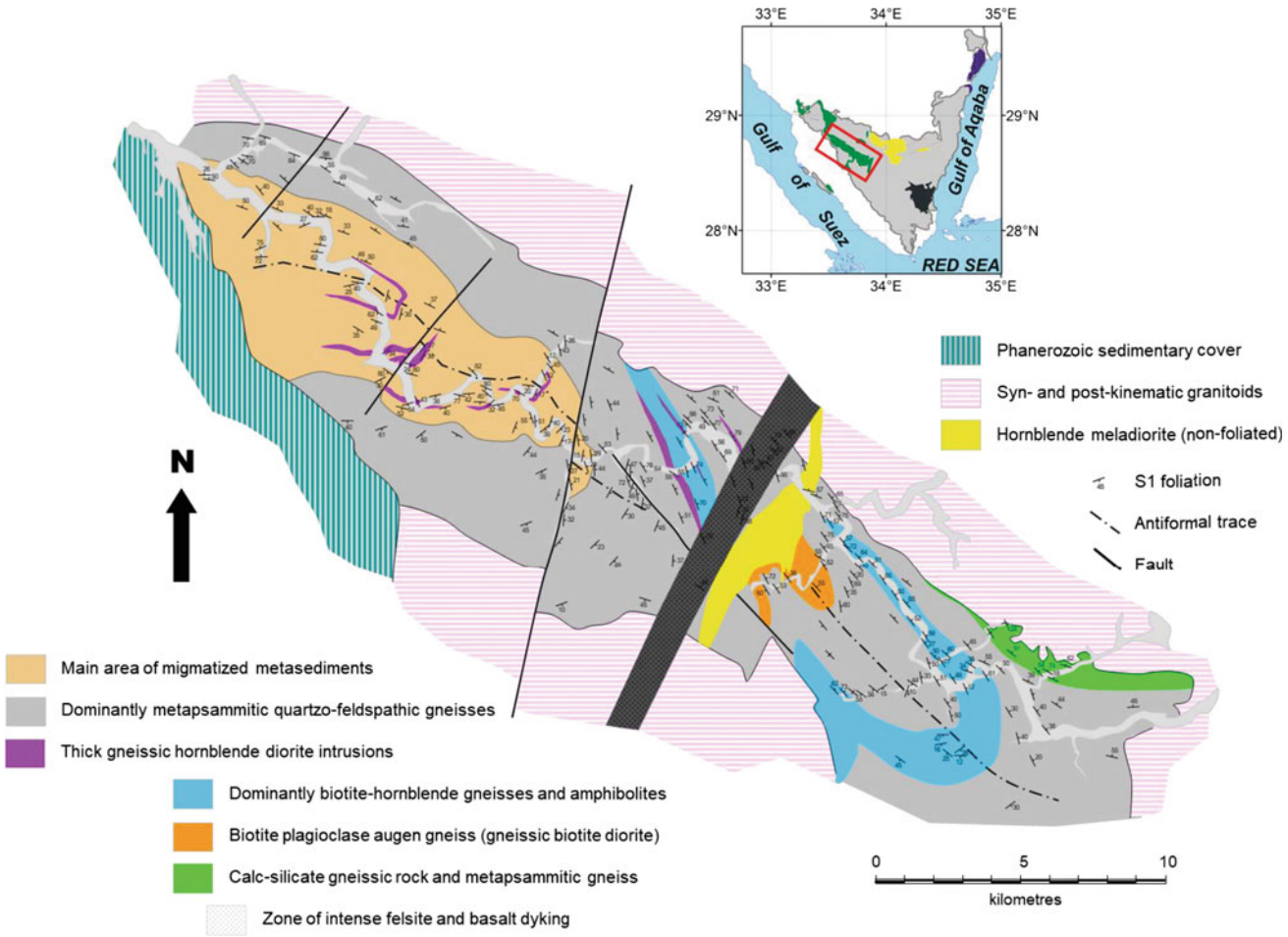

Fig. 6.7 Feiran-Solaf gneisses (after Fowler and Hassan 2008)

Ahmed (1980) defined and correlated metasedimentary formations in the Feiran and Solaf segments.

The protoliths of the quartzofeldspathic gneisses and migmatites, and calc-silicate gneisses have generally been accepted as metasedimentary. The amphibolites have been viewed as mainly metabasaltic, though some thin amphibolite layers may have been calc-pelites. However, the hornblende biotite rich gneisses are controversial, being regarded as calcareous metapelites by Akaad (1959), El-Gaby and Ahmed (1980) and El-Shafei and Kusky (2003), but as calc-alkaline volcanic or volcanogenic metasediments by Stern and Manton (1987), Abu Anbar et al. (2004) and Abu El-Enen and Whitehouse (2013); and as including both metasediments and metavolcanics by others. Thus, the setting for the protoliths of these gneisses has been thought of as a sedimentary or volcanic rift.

The metamorphic history has also been disputed. Early studies preferred an amphibolite facies event followed by K metasomatism (Akaad et al. 1967). El-Shafei and Kusky (2003) referred to two metamorphisms, amphibolite facies followed by migmatization. Most of the recent studies have described a single metamorphism (600–700 °C with $P < 5$ kbars) (El-Tokhi 2003; Eliwa et al. 2008; Abu El-Enen et al. 2009). Low pressure of metamorphism is consistent with Ahmed's (1981) observation that a sillimanite-muscovite zone was present, while kyanite was absent. A clockwise P-T-t path with substantially higher P of 7–8 kbars and isothermal decompression to 4–5 kbars was reported by Abu-Alam and Stüwe (2009) and Abu El-Enen (2011).

The narrow width of the complex and its limited vertical exposure make structural analysis difficult. Perhaps for this reason there are several competing models for the structural history of this complex. The most comprehensive structural studies have been provided by El-Shafei (1998), El-Shafei and Kusky (2003), Hegazi et al. (2004), Fowler and Hassan (2008), Sultan (2011) and Fowler et al. (2018). A distinct feature of the Feiran-Solaf complex is its NW-SE structural trend (expressed in the NW-SE trending Feiran and Solaf Antiforms), compared to the nearly E-W dominant trends of

other Sinai metamorphic complexes. The proposed structural histories for the Feiran-Solaf complex have attempted to explain this NW-SE trend in terms of (1) multiple folding with a dominant NW-SE trend (El-Shafei and Kusky 2003); (2) extension followed by NW-SE trending folding or fault-bend folding (Fowler and Hassan 2008; Fowler et al. 2018); and (3) extension followed by NW-SE trending sinistral transpression folding and shearing (Abu-Alam and Stüwe 2009; Arnous and Sultan 2014).

Perhaps the most controversial aspect of the Wadi Feiran-Solaf gneisses is the estimated ages of key events in the complex. Tonian ages for deposition of sedimentary protolith (U-Pb zircon 800–960 Ma) were reported by Shimron (1988) and Eyal et al. (2015), whereas Stern and Manton (1987) concluded that if the gneiss protoliths were sedimentary, then they were deposited soon after 632 Ma. Abu El-Enen and Whitehouse (2013) have suggested that pelites may have been deposited as late as 656 ± 6 Ma. Dates for crystallization of igneous protoliths vary from about 630 Ma (U-Pb zircon—Stern and Manton 1987: Abu El-Enen and Whitehouse 2013) to a >1400 Ma Sm-Nd age by Abu Anbar et al. (2004). Similarly, for the high temperature metamorphism, age estimates have varied widely from 592 ± 10 Ma (U-Pb zircon—Abu El-Enen and Whitehouse 2013) to 1150 ± 7 Ma (U-Pb zircon—El-Shafei 1998). Eyal et al. (2013) gave a U-Pb zircon age of 785 ± 7 Ma for a tonalitic gneiss that intruded the Feiran migmatite. The foliated granodiorite intruding the Feiran-Solaf complex on its NE has been more consistently dated as ~780–800 Ma (U-Pb zircon) (El-Shafei and Kusky 2003; Stern and Manton 1987; Eyal et al. 2013, 2014, 2015), with the implication that the ages of protolith formation and metamorphism probably lie in the 800–1000 Ma range, with younger ages resulting from isotopic resetting or xenocrystic zircon populations. Large masses of undeformed granite dated at 610–550 Ma postdate the structural and metamorphic evolution of this complex (Stern and Hedge 1985; Beyth et al. 1994).

On the matter of the tectonic setting of the Wadi Feiran-Solaf complex, Hume (1934) and El-Gaby et al. (1988a) regarded the gneisses as representatives of very old continental crust. Akaad et al (1967) concluded that the gneissic protoliths were mainly geosynclinal sedimentary fill. Fowler and Hassan (2008) preferred an extensional intracratonic basin representing an early stage of Rodinia rifting.

6.3.12.2 Wadi Sa'al-Zaghara Complex

The Sa'al-Zaghara Complex lies in the central northern part of the Precambrian basement of Sinai, about 25 km NE of the town of St Catherine. The Sa'al-Zaghara Complex incorporates a terrestrial sequence of mainly greenschist facies metamorphosed andesitic lavas, rhyolitic pyroclastics, ignimbrites, sandstones and conglomerates. El-Gaby et al. (2002) regarded these volcanics and sediments as equivalents of the Eastern Desert Dokhan Volcanics and Hammamat Group molasse, respectively, however, recent geochronology has demonstrated that the volcanics, at least, are latest Mesoproterozoic in age.

The complex has an ENE-WSW trend and can be divided into a northern belt of phyllitic metapyroclastics (Ra'ayan Formation) and silicic metatuffs (Agramiya Fm); a central belt of steeply dipping metamorphosed andesitic lavas and rhyolitic ignimbrites (Agramiya Formation) and a southern area of silicic metatuffs and quartzofeldspathic glacigene metasandstones and metaconglomerates (Zaghara Formation) (Shimron 1993a, b; Hassan et al. 2014; Fowler et al. 2015; Ali-Bik et al. 2017). In Wadi Mughafa, the southern area includes a section of migmatized and gneissified metapyroclastics, intensively intruded by red granite sheets. These high temperature rocks were earlier regarded as old sialic granulites by Hussein et al. (1993) but are more recently believed to be due to local contact heating effects (Hassan et al. 2014). The Agramiya Formation volcanics have the calc-alkaline chemistry of island active continental margin eruptives (Ali-Bik et al. 2002, 2017) or continental back-arc rift volcanics (Fowler et al. 2015). The Ra'ayan sediments were freshwater deposits (Ali-Bik et al. 2002).

Structural studies were initiated by Soliman (1986), followed by El-Shafei (1991) and El-Shafei et al. (1992), and Shimron et al. (1993a, b). Most recent work has been presented by Hegazi (2006), Hassen et al. (2007) and Fowler et al. (2015). Nearly all workers have recognized three phases of deformation: an early bedding-parallel foliation producing event (D1); a NE-SW to ENE-WSW trending folding or faulting event (D2); and a latest NW-SE trending fold event (D3). D1 was initially thought to involve thrusting but has been argued by Fowler et al. (2015) to be an extensional event, as at Feiran. The D2 event was a NNW-wards thrusting and folding event responsible for the ENE-WSW main trend of the complex.

Low-pressure greenschist facies metamorphic conditions (340–370 °C at 3.4–4 kbars: Hassen et al. 2007, or hotter at 450–560 °C and P ~3 kbars: Abu Anbar et al. 2009) have generated biotite, chloritoid and andalusite in the phyllites. Contact effects are responsible for metamorphic hornblende in some andesite metavolcanics, and cordierite and garnet in some metasediments. Hassan et al. (2014) estimated the Wadi Mughafa migmatites to have formed at 630–650 °C and P ~3 kbars.

The Sa'al-Zaghara Complex is intensively intruded, obscuring stratigraphic relations. Red granites have intruded D1 shear zones, triggering local HT metamorphism. The Ra'ayan and Agramiya formations were intruded in the NW by a syn-D2 hornblende gabbro (the Firinga Gabbro—Ali-Bik 1999; Qaoud and Abdelnasser 2012).

A syn-kinematic (probably syn-D2) foliated diorite (the Murad Diorite) intruded the NE part of the complex. The entire central part of the complex is engulfed in a locally mylonitized intra-D2/D3 hornblende biotite diorite (Khalaf et al. 1999). This diorite is enclosed in post-kinematic pink monzogranites.

Initial dating of volcanics at Sa'al-Zaghara suggested a 750–710 Ma range (Shimron 1987) based on Rb-Sr 734 ± 17 Ma for Sa'al volcanics (Bielski 1982) and U-Pb zircon 757 ± 28 Ma for pebbles in the Zaghara metaconglomerate (Priem et al. 1984). Precise radiometric dating of zircon populations by Be'eri-Shlevin et al. (2012) has cast a different perspective on this complex. These workers obtained a concordia age of 1110 ± 6 Ma (Stenian) for Agramiya volcanics, similar to their previous results of 1.03 and 1.11 Ga for detrital zircons from Ra'ayan phyllites (Be'eri-Shlevin et al. 2009a, b). Eyal et al. (2013) gave slightly younger U-Pb zircon date for Agramiya metarhyolite of 962 ± 10 Ma. Titanite in the Murad diorite was U-Pb dated by Eyal et al. (2013) as 720 ± 8 Ma, significantly younger than the U-Pb zircon age of 819 ± 4 Ma for this intrusion given by Be'eri-Shlevin et al. (2012). Stern et al. (2010) found zircons as young as 606 ± 10 Ma in the Zaghara metaconglomerates. Andresen et al. (2014) obtained zircon ages 640–650 Ma from clasts of this metaconglomerate and matrix zircons as young as 630 Ma. The central diorite that intrudes the Zaghara and incorporates blocks of it as xenoliths, is thought to be <615 Ma in age by Be'eri-Shlevin et al. (2012). The 768 ± 8 Ma zircons recovered from it were regarded as xenocrysts. If the given dates for the central diorite and the Zaghara are correct, then there is a large time difference between the Agramiya and Zaghara Formations.

6.3.12.3 Taba-Elat Complex

The Taba-Elat complex is a relatively small exposure of gneisses, migmatites and schists along the western side of the Gulf of Aqaba, spanning the border between Egypt and Israel. The complex is dominantly composed of a range of tonalitic to granitic orthogneisses, which have intruded a metapelitic series referred to as the Elat Schists (Cosca et al. 1999). This complex has been investigated in detail by Shimron (1972), Eyal (1980), Kröner et al. (1990), Eyal et al. (1991), Katz et al. (1998), Cosca et al. (1999), and Abu El-Enen et al. (1999,2004).

The 820–800 Ma Elat Schist is the oldest rock unit in the area. It has a pelitic protolith derived from weathering of an island arc source rather than pre-existing continental crust (Morag et al. 2011), and is represented by biotite schists and garnet biotite schists (Kröner et al. 1990; Eyal et al. 1992; Beyth et al. 2011). The first (D1) deformation of the metapelites involved E-W trending foliation development and HT metamorphism. This was followed by Taba Gneiss intrusion (~780 Ma), then D2 folding and spaced cleavage, then Fjord Gneiss intrusion (760–765 Ma) and Elat Granite Gneiss intrusion (740–745 Ma). A third intrusive event involving mafic to granitic melts occurred at ~640 Ma (Eyal et al. 1991). A collision-related metamorphism (~620 Ma) later affected the complex (Cosca et al. 1999).

The metapelitic schists permit the mapping of several NE-SW trending metamorphic zones, including a garnet zone, staurolite zone, staurolite-sillimanite zone and staurolite-cordierite zone (Abu El-Enen et al. 2004). The presence of andalusite and sillimanite indicates a low-pressure metamorphic history, while the abundance of staurolite is consistent with Al_2O_3–FeO_t rich metasediment compositions. Abu El-Enen et al. (2004) described a single metamorphic event with estimated peak conditions at 550–590 °C and P 4 ± 1 kbar, at which the peak assemblage garnet-staurolite-sillimanite-biotite-muscovite formed. Andalusite and cordierite formed after the peak. The peak metamorphic gradient was estimated at 50–60 °C/km consistent with a magmatic arc environment. The metasediment compositions also point towards an active continental margin or island arc environment. Eliwa et al. (2008) provided similar peak P-T conditions of 560–578 °C and 3–4.5 kbar, rising to 685 °C and 5.3 kbar for the migmatites, and a 30–50 °C/km thermal gradient. Somewhat higher temperatures and pressures of 650–700 °C at 7 ± 1 kbar were found by Cosca et al. (1999) for the Elat area.

Two groups of granitoid gneisses can be distinguished in the Taba-Elat complex: an older (780–760 Ma) series of quartz-dioritic to tonalitic gneisses in the north, giving P-T conditions 620–660 °C and P 4.6–6.2 kbars, including the Fjord and Taba Gneisses; and a younger (~745 Ma) series of quartz-monzonitic to alkali granitic gneisses in the south, giving P-T conditions 755–815 °C and P 3.9–4.5 kbars, including the Elat Granite Gneiss. Both granitoid groups are metamorphosed subduction-related arc granitoids belonging to an active continental margin setting (Kröner et al. 1990; Abu El-Enen et al. 1999).

6.3.12.4 Wadi Kid Complex

The Wadi Kid complex is one of the largest areas (~435 km^2) of metamorphic rocks in the southern Sinai. It is located on the Gulf of Aqaba coast between Sharm El-Sheikh and Dahab. It has similarities to the Taba-Elat Complex, but with a much larger proportion of metavolcanics. The Wadi Kid Complex has a dominant ENE-WSW trend that permits division into three parts: a northern half, comprising amphibolite facies rocks; a central belt of low-grade metavolcanics; and a small southeastern area of low-grade metasediments and metavolcanics (Fig. 6.8).

This complex has been rigorously studied from structural, petrological, geochronological and remote sensing points of interest, however, consensus has not yet been reached on the

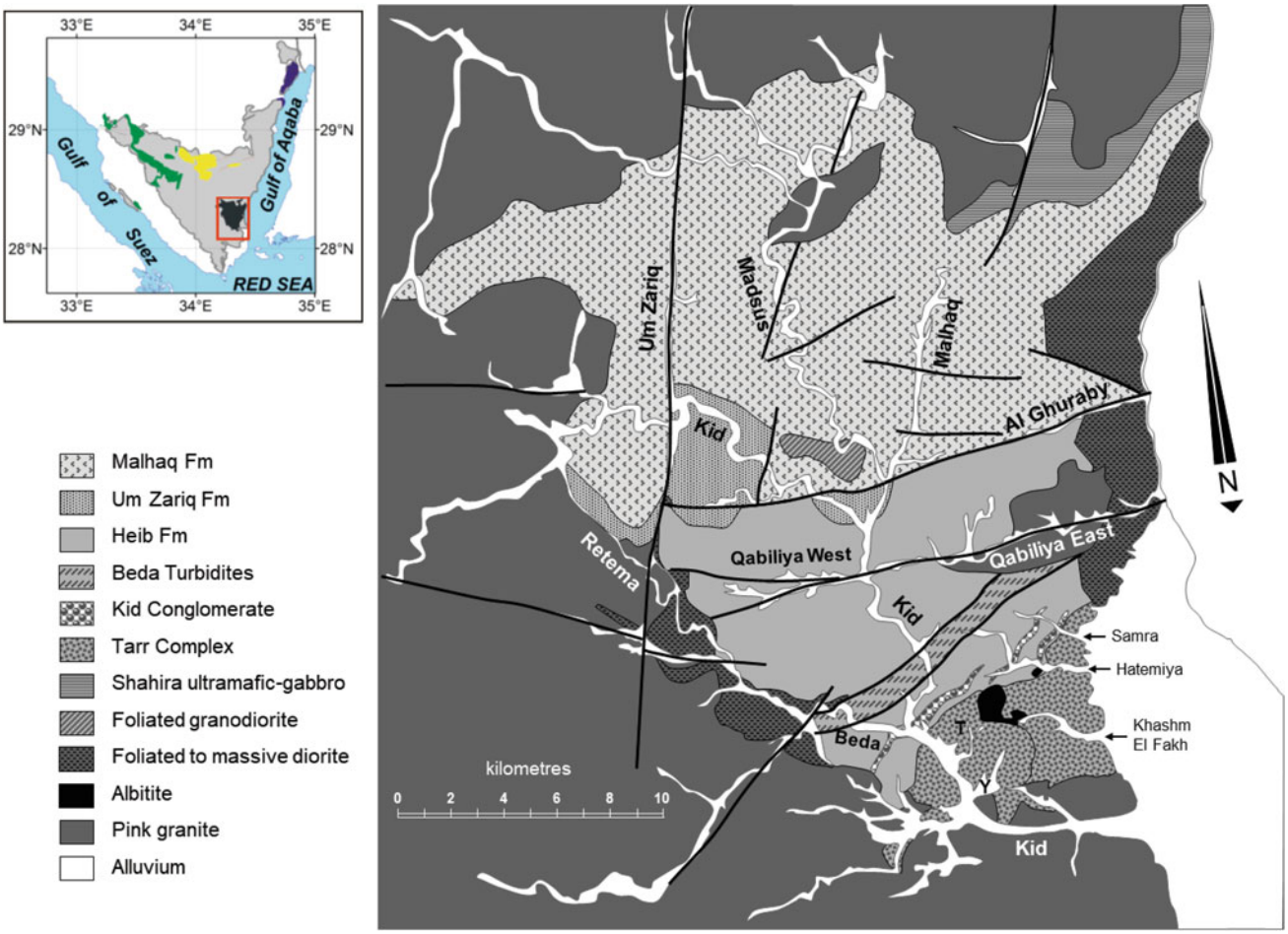

Fig. 6.8 Wadi Kid gneisses (after Fowler et al. 2010b)

structure, its relations to the high temperature metamorphism, the source of metamorphic heat and the tectonic setting.

Mapping of the Wadi Kid Complex and stratigraphic division of the sequence were achieved early by Bentor et al. (1974) and Shimron and Arkin (1978). In the northern half of the complex, the Um Zariq Formation is composed of quartz-rich, aluminous graphitic metapelites with interbeds of metagreywacke. The overlying Malhaq Formation consists of metamorphosed silicic and intermediate lavas, breccias, pyroclastics, volcanogenic sediments and minor impure carbonates. The Um Zariq and Malhaq Formations are metamorphosed to amphibolite facies grade. The central Kid area is dominated by the low-grade metamorphosed Heib Formation andesitic to rhyolitic flows and pyroclastics, which host turbiditic mudstones (Beda Turbidites) and volcanogenic cobble conglomerates (Kid Conglomerate). The SE part of the Kid complex consists of the variable lithologies of the Tarr Complex. These include low-grade metamorphosed dacitic to andesitic lavas, ignimbrites, volcanic breccias and tuffs, pebbly mudstones and impure carbonate sediments.

There are at least three structural events D1–D3 that have affected the Kid complex. The first, D1, involved thrusting to the NNW or SSE, leading to steepening of beds and development of ENE-SWS trending F1 folds (Shimron 1980a, b; Reymer 1983; Reymer and Yogev 1983; Fowler et al. 2010a, b). The D2 event produced SE-vergent recumbent F2 folds and mylonitic shear zones that dominate in the northern part of the complex, and in the SW part of the Tarr Complex (Shimron 1980b, 1984a, b; Abu El-Enen and Makroum 2003; Fowler et al. 2010a). The D3 deformation generated NW-SE trending upright folds, mostly apparent in the SW part of the Tarr Complex (Abdel Wahed et al. 2006; Fowler et al. 2010b).

Textural studies indicate two metamorphic events, M1 and M2, in the Kid Complex (Brooijmans et al. 2003). M1 was a syn-D1 greenschist facies event, with conditions 300–400 °C

and P 3–4 kbars (Shimron 1987; Eliwa et al. 2008). M2 was an amphibolite facies event that was syn-D2 (Brooijmans et al. 2003), or inter-D1/D2 (Shimron 1987). M2 has been investigated in the Um Zariq and Malhaq Formations. In the Um Zariq, Navon and Reymer (1984) outlined a staurolite-andalusite zone, flanked north and south by a garnet zone. Reymer et al. (1984) gave P-T conditions of 520–565 °C at P 2.35–3.2 kbars. Abu El-Enen et al. (2003) identified differently trending zones including a garnet zone, a garnet-staurolite-andalusite zone, and a garnet-cordierite-andalusite zone, with T range 560–580 °C and P ~3 kbar. Eliwa et al. (2008) and Brooijmans et al. (2003) gave comparable P-T conditions. The Malhaq Formation shows higher P-T conditions than the Um Zariq (645 °C and 4.5–5.5 kbars: Abu El-Enen 2008), and a migmatitic zone (andalusite-sillimanite-Kspar zone) forming diapiric masses, with estimated P-T conditions >620 °C and P 3.2 kbars (Reymer 1983; Abu El-Enen et al. 2003). Similar P-T estimates for the Malhaq were given by Abu El-Enen and Makroum (2003). Metamorphic conditions for the Heib Formation are mostly low greenschist facies in the Biotite Zone. For the Tarr Complex Shimron (1981b, 1983) estimated greenschist facies conditions of 300 °C and P 2 kbars, but up to 550 °C producing cordierite porphyroblasts in local thermal aureoles.

Restricted exposures of gneissic migmatitic metasediment (Qenaia migmatite) exist in Wadi Beda in sheared contact with Heib volcanics. These gneisses have detrital zircons with ages ranging from 840 to 790 Ma, and an interpreted metamorphic age of 768 ± 5 Ma, and have been correlated with Taba gneisses and Elat Schist by Eyal et al. (2013). The Um Zariq, similarly, probably predates the Kid arc volcanic activity, having detrital zircons ranging from 895 to 730 Ma (Eyal et al. 2013) and zircon clusters at 813 and 647 Ma (Moghazi et al. 2012; El-Bialy et al. 2015), and no zircons dated at ~630 Ma. Geochemistry of the Um Zariq indicates a deeply weathered continental arc provenance (El-Bialy 2013). The preferred age range for the Kid Group has varied from high estimates of 770–650 Ma (Navon and Reymer 1984; Blasband et al. 1997) to low estimates of 615 ± 15 Ma (Bielski 1982). Eyal et al. (2013) gave 634 ± 4 Ma and 630 ± 3 Ma ages for zircons from the Heib Formation. The Malhaq is apparently older than the Heib as it is intruded by the 632 Ma Shahira metagabbros and the 628 Ma Ghurabi diorite pluton. The Tarr Complex is also constrained to be in the range 628–634 Ma. Stern et al. (2010) found 609 ± 5 Ma and 598 ± 8 Ma zircons in clasts in the Kid Conglomerate, raising questions about its relations to the Heib volcanics. The D1 deformation was thought by Shimron (1984b) to be ~640 Ma, or 720–650 Ma (Blasband et al. 2000). The D2 deformation and M2 HT metamorphism were estimated at 620–600 Ma (Shimron 1985, 1987; Reymer and Oertel 1985; Blasband et al. 1997). All deformation was completed before the intrusion of post-kinematic granites at 607 ± 4 Ma (Be'eri-Shlevin et al. 2009a) or 580–595 Ma (Ali et al. 2009a); and before an undeformed granite vein in the Um Zariq dated 611 ± 4 Ma (Eyal et al. 2013); and before the Tarr Albitite intrusion (605 ± 13 Ma: Azer et al. 2010).

The tectonic setting of the Wadi Kid Complex is diversely interpreted. There is a '**continental arc—thrusting model**' (Shimron 1981a, b, 1983, 1984a, b, 1987; Furnes et al. 1985; Fowler et al. 2010a, b) in which Malhaq is back-arc, Heib is arc axis, and Tarr is forearc or accretionary wedge. D2 is thrust-related and the heat source for metamorphism is syn-thrusting intrusions. There is an '**ascending diapir model**' (Reymer 1983, 1984; Reymer and Yogev 1983; Navon and Reymer 1984; Reymer et al. 1984; Reymer and Oertel 1985) in which the Heib is subaerial volcanics of continental affinity, lying unconformably on earlier Zariq and Tarr. D2 is associated with a rising magma diapir, above which horizontal flattening foliation developed as a domed carapace. There is a '**Dokhan-Hammamat ensialic model**' (El-Gaby et al. 1991; Hassanen 1992; Soliman et al. 1996; El-Metwally et al. 1999; El-Bialy 2010; El-Bialy and Ali 2013; Moghazi et al. 2012) where the volcanics are post-collisional, rift or continental arc related, and the heat source is unexposed granites. There is a '**core complex model**' (Blasband 1995; Blasband et al. 1997, 2000; Brooijmans et al. 2003) in which D1 is an arc-continent crustal thickening event followed by the D2 gravitational collapse extension event, involving a mid-crustal shear detachment. The heat source for metamorphism was intrusions of extension related granites. Extension models have also been preferred by Eliwa et al. (2004, 2008). Abu El-Enen and Makroum's (2003) and Abu El-Enen's (2008) model accepted compressional D1 and D2 but suggested that escape and core complex formation followed. Khalaf and Obeid (2013) adopted a similar model of arc collision (D1 and D2), followed by extension, rifting and volcanism. There is a '**Najd-involvement model**' (Stern 1985; Abu-Alam and Stüwe 2009; Arnous and Sultan 2014; Sultan et al. 2017) in which NW-trending stretching lineations are suspected to be Najd fault-related, or WNW D3 trends in Kid are correlated with WNW trends in Feiran, and the two are considered to lie along the trend of the (Najd) Qazaz Shear Zone in the Arabian Shield.

6.4 The Question of Pre-Pan-African Crustal Beneath the Eastern Desert and Sinai

A persistent and controversial question regarding the ANS gneisses is the contribution (if any) of older Pre-Pan-African (>1 Ga) crust to the gneissic rocks or granitoids of the ANS. Early surveyors of the Eastern Desert (1900s–1950s) were impressed with the gneissic complexes, especially the Meatiq,

El-Sibai, Shalul and Migif-Hafafit complexes of the Eastern Desert and the Feiran complex in the Sinai. Based on these complexes, Hume (1934) identified the 'Mitiq Series' as a Protarchaean 'fundamental basement' of old continental crust, separated by an unconformity from younger series. This fundamental basement extended beneath the entire Eastern Desert and Sinai. Schürmann (1974) thought that migmatites formed by granite injections, while Akaad et al. (1967) thought the migmatites were stages of granitization. Schürmann (1966) regarded the CED gneissic domes as examples of Eskola's mantled gneiss domes. In this model, the gneisses formed from early geosynclinal sediments, followed by uplift and erosion, then were covered by late geosynclinal mafic igneous volcanics, before being rejuvenated as a gneissic dome by late Precambrian granite intrusions. In Schürmann's model, the contact between gneisses and low-grade cover rocks is an unconformity. Features of the gneissic domes that vindicated a view of extreme age for these rocks included their deep structural setting, the sharp contact between the basement gneisses and greenschist facies cover, and the absence of contact effects in the cover attributable to the gneisses. An ensialic setting was most popular up to the 1970s (e.g. El Ramly and Akaad 1960; El Ramly 1972) and regained popularity the 1980s–1990s (El-Gaby 1983; El-Gaby et al. 1984, 1988a, b, 1990; Hassan and Hashad 1990).

Following the Penrose Conference (1972), ophiolites became a recognized component of the ANS (Garson and Shalaby 1976; Bakor et al. 1976; Stern 1979; Naseef et al. 1980; Shackleton et al. 1980), and the concept of an essentially ensimatic original setting for the ANS became popular (e.g. Al-Shanti and Mitchell 1976; Frisch and Al Shanti 1977; Gass 1977; Fleck et al. 1980; Engel et al. 1980; Stern 1981; and many others since). Proponents of an ensialic setting for the Eastern Desert viewed the ophiolites as having formed either (1) in local rifts, within otherwise continuous continental crust (Hashad and Hassan 1979; Church 1983), or (2) in the Mozambique Ocean east of the present Eastern Desert, and later obducted westwards over the EED continental basement, with the basement-cover contact now represented by a major shear zone, or sheared unconformity (El-Gaby et al. 1984, 1988a, 1990). Later support for and against the two models (ensialic and ensimatic) was provided by radiometric dating of whole-rocks and mineral separates, particularly zircon. This data is now discussed in the following section.

6.4.1 Radiometric Dating (Rb-Sr, U-Pb, Pb-Pb, Sm-Nd)

The age of the gneissic rocks in the ANS was early investigated by Rb-Sr whole-rock dating (Bielski 1982; Bentor 1985; Stern and Hedge 1985). Shimron (1978) dated Feiran diorite gneiss at 1013 ± 35 Ma, similar to Siedner et al.'s (1974) estimate of 1035 ± 11 Ma, but very different to Bielski's (1982) 643 ± 41 Ma date for the gneisses, and Stern and Manton's (1987) date of 610 ± 44 Ma for Feiran paragneiss and 614 to 610 Ma for migmatites. In turn, these Rb-Sr ages have differed much from U-Pb zircon ages for the same rocks. A similar theme has been repeated across the Sinai basement where Rb-Sr dates for gneisses are commonly variable and in disagreement with other dating techniques. Thus, a 734 Ma Rb-Sr date for Sa'al metavolcanics by Bielski (1982), and 736 ± 27 Ma by Abu Anbar et al. (2009) for the same rocks are very different to subsequent U-Pb zircon dates of 1.1–0.9 Ga for these rocks by Be'eri-Shlevin et al. (2012). This discordance has been explained as Rb-Sr dates perhaps representing phases of metamorphism and cooling ages, not protolith ages (Stern and Manton 1987; Abu Anbar et al. 2004), or Rb-Sr disturbances due to a major regional thermal event (Shimron 1980a, b; Kröner et al. 1990; El-Gaby et al. 2002). In contrast, the late stage Sinai granitoids have been Rb-Sr dated at 620–585 Ma (calc-alkaline, Phase III) and 580–550 Ma (alkaline granites, Phase IV) (Bentor 1985), in good agreement with U-Pb zircon dates for the same granitoids at 635–590 Ma (calc-alkaline CA2) and 610–570 Ma (alkali granites AL) by Be'eri-Shlevin et al. (2009a) and Ali et al. (2009a). If a regional thermal event disturbed the Rb-Sr in the gneisses, it was probably before (or identical with) the intrusion of these voluminous granitoids. In the Eastern Desert, a Rb-Sr date of 626 ± 2 Ma has been obtained for Meatiq Um Ba'anib gneiss (Sturchio et al. 1983a, b), consistent with the TIMS U-Pb (zircon) 631 ± 2 Ma age of the gneisses (Andresen et al. 2009). A composite Rb-Sr isochron (619 ± 25 Ma) was obtained from combined data of Meatiq and Hafafit gneisses by Khudeir et al. (2008), who thought that this date represented the nappe thrusting event in the EED. Liégeois and Stern (2010) also obtained a composite isochron for these two complexes (596 ± 15 Ma), but ascribed it to resetting of Rb-Sr in a ~600 Ma thermal event.

Dating of rocks via U-Pb or Pb-Pb isotopic analysis of zircon extracts represents by far the largest geochronological database in the ANS. Compilations of this data for the ANS are provided by Stern et al. (2010, their Table A1) and Johnson et al. (2011, their Appendix A). For each of the gneissic complexes the details of zircon dating have been provided above in Sects. 6.3.1–6.3.12 and will not be repeated here. In this section only some points on the significance of these dates are made. In Feiran, the zircons extracted from gneisses may be dating the crystallization age of orthogneiss protoliths, suggested to be 870–740 Ma. Other zircon ages are thought to date a metamorphic event (632–627 Ma), perhaps the HT metamorphism. Still others date the protolith, which was the source of the paragneisses

(~1.0 Ga). At Sa'al, unexpected Mesoproterozoic (1.1 Ga) U-Pb zircon dates for the metavolcanics were discovered by Be'eri-Shlevin et al. (2012). The Zaghara metasediments returned a population of zircons ranging in age from 931 to 606 Ma, suggesting a much younger age for the Zaghara, however the data could also describe a discordia with upper intercept 1.045 Ga and a lead loss event at 570 Ma (Stern et al. 2010). Taba-Elat gneisses and schists gave coherent dates for pelitic schist provenance at 820 Ma, with intrusions at 780, 765 and 745 Ma. At Wadi Kid, the Qenaia gneisses were dated at 840–790 Ma, supporting the idea that they were rifted from the older Feiran-Elat arc (Eyal et al. 2014). Malhaq (635–630 Ma) followed by Heib and Tarr volcanics (~630 Ma) were metamorphosed between 630 and 610 Ma. The Kid arc is therefore the youngest in the Sinai.

In the Eastern Desert, at Meatiq, Loizenbauer et al.'s (2001) Pb-Pb zircon dates for the Um Ba'anib gneiss (779 ± 4 Ma) contrasted with Andresen et al.'s (2009) TIMS U-Pb zircon dates (631 ± 2 Ma). Andresen et al.'s dates require the gneissification event at Meatiq to be a young (<631 Ma) event, similar to previous Rb-Sr age estimates. At Hafafit, early attempts to date this complex by Abdel Monem and Hurley (1979) suggested a pre-Pan-African age (1770 Ma), however, this date has not been replicated by later workers (Kröner et al. 1994; Stern and Hedge 1985; Lundmark et al. 2012) who found Pb-Pb and U-Pb zircon emplacement ages of migmatitic orthogneiss protoliths that cluster around a 687 Ma mean of best estimates. This places Hafafit gneiss formation well within the Pan-African. Zircons from the El-Sibai Complex El Shush gneiss have been dated by Bregar et al. (2002) and Augland et al. (2012) at 680 Ma with remarkable consistency, demonstrating the Pan-African age of these gneisses. Ali et al.'s (2012) U-Pb zircon dates for the El-Shalul gneissic granite varied between 630–637 Ma, comparable to the Um Ba'anib gneiss.

Sm and Nd isotopic ratios are most valuable in distinguishing mantle source from crustal source for igneous rocks and rocks derived from them via ε_{Nd} values and Nd model ages, which are reported for ANS gneisses in a following section. The use of the ^{147}Sm to ^{143}Nd decay series for isochron dating of ANS rocks is less common than Rb-Sr or U-Pb and Pb-Pb methods, as Sm-Nd dating is mostly restricted to initially Sm-rich mafic rocks and mineral separates (garnet, biotite, pyroxenes, hornblende). A notable example is the Sm-Nd dating of mantle xenoliths in ANS orthogneisses at 800 Ma (Stein and Goldstein 1996), as an indicator of the age of melting of the orthogneiss protoliths. Abu Anbar et al. (2004) dated Feiran gneisses and amphibolites at 1.4 and 1.1 Ga (considered protolith ages). Abd El-Naby et al. (2008) Sm-Nd dated Hafafit hornblende gneiss (593 ± 4 Ma) and amphibolite (585 ± 8 Ma). They considered these ages to mark the end of peak metamorphic temperatures. Helmy et al. (2014) Sm-Nd dated SED ultramafic cumulates that they believed were formed at a deep arc level.

6.4.2 Pb Isotope Studies

The hypothesis of continental crust underlying Pan-African cover was tested early by Pb isotope studies of potassium feldspar and galena samples from granitoids collected across the Nubian and Arabian Shields. Stacey et al. (1980), Stacey and Stoeser (1983) and Stacey and Hedge (1984) discovered two groups of Pb isotopic compositions. Group I leads had oceanic (mantle) characteristics, while Group II leads had a continental-crustal component of at least early Proterozoic age. The distribution of these groups suggested that the ANS was dominantly an ensimatic domain with continental crustal contributions evident only in the SE part of the Arabian Shield (Afif, Asir and Al Amal terranes) and at Aswan and areas west. Sultan et al. (1992) allowed for the possibility that some continental Pb may have contributed to samples with intermediate Group I/II characters but that the likely source within the Eastern Desert was continent-derived sediments that were subducted. Gillespie and Dixon (1983), Stoeser and Stacey (1988) found basically three Pb isotopic composition types (I to III) so that Type I represented primitive oceanic character, Type II was oceanic but with contamination by more evolved Pb, and Type III was continental Pb. Hargrove et al.'s (2006) compilation of Pb isotopic data shows the Eastern Desert to be overwhelmingly in the Type I (primitive oceanic) Pb domain.

6.4.3 Initial Sr Isotope Ratios

A huge database on initial Sr isotopic ratios ($^{87}Sr/^{86}Sr$ or Sr_i) for igneous and metamorphic rocks of the ANS has been collected since Hashad et al. (1972). Engel et al. (1980) found that the modal value of initial $^{87}Sr/^{86}Sr$ ratio for volcanics and intrusives from sampling across Egypt, Saudia Arabia and Jordan was 0.7028. Stern and Hedge's (1985) broad sampling of Eastern Desert rocks led them to conclude that all of the igneous rocks had low initial $^{87}Sr/^{86}Sr$ ratios in the range 0.702–0.704, precluding any reworking of older crustal material in their formation. They found that the igneous rocks formed by melting of metasomatically enriched mantle or by recycling of immature geosynclinal materials. Subsequent Sr isotopic analyses have confirmed

this range, leaving little room for continental crustal reworking. For the Egyptian gneissic complexes, published initial Sr isotopic signatures are as follows. Initial Sr isotopic ratios for Feiran gneiss are 0.7032 ± 0.0007 (Bielski 1982), 0.7034–0.7039 (Stern and Manton 1987), and 0.7037 for gneiss and 0.7024–0.7027 for amphibolite (Abu Anbar et al. 2004). For the Elat Schist the Sr_i value is 0.7035 ± 0.0005 (Bielski 1982). For Meatiq gneisses the initial Sr isotopic ratios have been estimated at 0.7030 ± 0.0001 (Sturchio et al. 1983a, b), 0.7024–0.7027 (Khudeir et al. 2008), and 0.7026 ± 0.0011 (Liégeois and Stern 2010). For the Hafafit gneisses the Sr_i values are 0.7024 (Stern and Hedge 1985), 0.7021 ± 0.001 (Liégeois and Stern 2010), and 0.7039–0.7046 (Abd El-Naby et al. 2008). For the Abu Swayel metarhyolite the Sr_i value is 0.7019 ± 0.0003 (Stern and Hedge 1985), while Shalul gneiss Sr_i values are 0.7025–0.7149 (Ali et al. 2012).

6.4.4 Initial ε_{Nd} Values and Nd τ_{DM} Model Ages

Stern's (2002) comprehensive Nd isotopic database for the EAO showed that Egyptian basement rocks, east of the Nile had Nd model ages 0.74 ± 0.17 Ga (mode 0.7–0.8 Ga), indicating Neoproterozoic crustal residence age. Slightly older Neoproterozoic model ages (0.84–0.85 Ga) were given for the Sinai and Arabian Shield areas (excluding the Afif terrane), comparable to Stoeser and Frost's (2006) Nd τ_{DM} range.

Near the northern margin of the ANS at Sa'al-Zaghara, Be'eri-Shlevin et al. (2009b) found that Kibaran aged schists (1.0–1.1 Ga) had whole-rock $\varepsilon_{Nd}(T)$ of +2, significantly lower than for juvenile crust in the region. Abu Anbar et al. (2004) gave $\varepsilon_{Nd}(T)$ +0.9 to +3.4 for Feiran gneisses, suggesting contribution from depleted mantle, contaminated by some crustal material. For the Feiran amphibolites the $\varepsilon_{Nd}(T)$ was +2.9 to +5.5, and τ_{DM} was considerably older than the Pan-African. Moghazi et al. (1998) showed that pre-Pan-African sialic crust was not evident under the Kid Complex, as the Kid granitoids gave initial ε_{Nd} values between +1.5 to +4.5 and initial $^{87}Sr/^{86}Sr$ ratios of 0.703 to 0.7044, with average τ_{DM} 0.79 Ga. Sinai basement calc-alkaline granites (τ_{DM} 0.86–1.2 Ga) and alkaline granites (τ_{DM} 0.8–1.1 Ga) have indistinguishable $\varepsilon_{Nd}(T)$ of +1.5 to +6.0 suggesting a significant mantle-derived component in these silicic magmas (Eyal et al. 2010).

In the Eastern Desert, at Meatiq, the Ba'anib gneiss and paragneiss gave $\varepsilon_{Nd}(T)$ values of +5.45 to +6.96 (Liégeois and Stern 2010), with average τ_{DM} age 0.71 ± 0.06 Ga. For the Hafafit Complex, the same authors gave $\varepsilon_{Nd}(T)$ +4.94 and +7.05 for gneisses; +6.69 to +10.21 for amphibolites; and +7.01 for migmatite. The average τ_{DM} age was 0.69 ± 0.07 Ga, i.e. indistinguishable from the Meatiq τ_{DM} values and similar to the average for the EED. These data are consistent with Meatiq and Hafafit being 750–600 Ma juvenile crust with no contribution from pre-Neoproterozoic crust. Abd El-Naby et al.'s (2008) analysis of Hafafit hornblende gneiss and amphibolite gave $\varepsilon_{Nd}(T)$ whole-rock values of +6.0 and +4.9, respectively, and τ_{DM} ages 0.78–0.80 Ga, and 0.87–0.90 Ga, respectively. Ali et al. (2012) estimated $\varepsilon_{Nd}(T)$ for El-Shalul gneissic granite samples of +6.62 to +7.52 with no indication of pre-Pan-African crust contribution. Ali et al. (2015) found that migmatitic gneiss from Wadi Beitan showed no evidence of old continental crust contribution in whole-rock $\varepsilon_{Nd}(T)$ (+5.1 to +6.6), with protolith extracted from the mantle at τ_{DM} average 0.76 Ga, though one sample had lower values than expected for its age. They also found that $\varepsilon_{Hf}(T)$ values in the zircons indicated both mantle and old continental crustal contributions. Moussa et al (2008) studied NED and SED older granodiorite and younger granites. The initial ε_{Nd} for the older granodiorite was +6.74; while it was between +3.97 and +5.75 for the younger granites, indicating magma sources were dominated by juvenile crust and mantle. Estimated τ_{DM} ages varied from 0.65 to 0.76 Ga.

6.4.5 Tectonic Significance of the "Gneissic Complexes"

From the above summaries of the characteristics and age of the gneissic and metamorphic complexes in the Sinai and the EED, two conclusion seems inescapable: (1) there is no firm evidence for any significant role for pre-Pan-African continental crust in the evolution of these complexes, though some continent-derived sediment containing old zircons has made its way into the ANS oceanic setting; and (2) there are so many differences in style and age between the complexes, that an all-inclusive category of "gneissic complexes" will not be helpful in understanding their origins, though some grouping may be possible. In the past there have been several attempts to group sets of these complexes in broadly shared histories, e.g. the model of transpression, magmatic uplift and core complex formation linking Meatiq, El-Shalul, El-Sibai and Hafafit (Fritz et al. 1996, 2002); or the linking of Meatiq, Um Had, El-Shalul and El-Sibai via interference folding (Abdeen and Greiling 2005); the possibility of some shared history between Meatiq, Um Had and El-Shalul gneissic complexes and the Eastern Desert Shear Zone (Fowler and El Kaliouby 2004; Andresen et al. 2010; Ali et al. 2012); and the concept of the Feiran-Elat arc and its relations with the Kid arc (Eyal et al. 2014).

An interesting shared characteristic of the Feiran, Meatiq, Hafafit and maybe Sa'al-Zaghara complexes is the

abundance of quartz-rich metapsammites and local metaconglomerates, with pre-Pan-African zircons in the matrix and/or clasts. It has been suggested that these sediments may be an indicator of the proximity to an ancient continental margin (Abdel Monem and Hurley 1979; Hashad and Hassan 1979; Dixon et al. 1979; Dixon 1981; Ries et al. 1983; El Ramly et al. 1984; El-Gaby et al. 1994). El-Gaby et al. (1994) considered the metapsammites to have been deposited on a continental shelf, while El Ramly et al. (1993) viewed them as being underlain by oceanic crust. Rashwan (1991) found the metapsammites to have been deposited in an active continental margin environment. An active continental margin setting has also been suggested overall for Hafafit (Kröner et al. 1994; Abd El-Naby and Frisch 2006; Abd El-Rahman et al. 2009a, b) and Meatiq (Ries et al. 1983; Habib 1987) complexes, though Hafafit magmatism is 690–685 Ma, within the subduction stage, while Meatiq Um Ba'anib magmatism is dated at 630–625 Ma, at the end of the arc collision stage.

Some metamorphic and structural aspects of the Meatiq Complex remain puzzling. Pressure estimates for the amphibolite facies metamorphism of the metasediments of the complex are 6–8 kbar (Neumayr et al. 1998), i.e. 24–32 km depth. The depth of the active Eastern Desert Shear Zone (EDSZ) is not known but its upper parts affect the lower exposed sections of Hammamat sediments in Um Seleimat, Wadi Hammamat and Arak basins (Fowler and Osman 2001; Fowler and El Kaliouby 2004; Fowler and Osman 2013) with the ~5 km thick basin sediments showing anchizonal to epizonal metamorphism (Osman et al. 1993). The EDSZ was therefore probably active at depths of 5–7 km (~2 kbars). If the metamorphism of the Meatiq metasediments is coeval with the gneissification of the Um Ba'anib, then this metamorphism occurred between 625 and 615 Ma (Andresen et al. 2009). This allows little time for a substantial rise of the gneiss core (by 14 to 25 km) to the levels of the EDSZ, and this within the small area of the complex. An alternative is that the Meatiq metasediment metamorphism is an earlier, deeper event than the Um Ba'anib intrusion. This could be resolved by separate dating of the metasediment HT phases and by determination of the depth of crystallization of the Um Ba'anib protolith. If the Um Ba'anib crystallized at 6–8 kbars, then massive rapid uplift of the gneissic core must have occurred. If it crystallized at much lower pressure, then it belongs to a later stage in the history of the complex. If the metasediments were metamorphosed earlier, at deeper levels, they may have been raised by thrust stacking to higher levels (Andresen et al. 2010) in the late stages of arc collision, before the intrusion of the Um Ba'anib. That proposed thrust stacking would have the same kinematics as the EDSZ (top-to-the-NW) and may be difficult to distinguish from the EDSZ.

6.5 Ophiolite Sequences and Ophiolitic Melange

The term 'ophiolite' refers to a distinctive assemblage of ultramafic and mafic volcanics and intrusives that were formed at a spreading centre above extended mantle, and have subsequently been tectonically transported over continental, microcontinental or island arc crust (Dilek 2003). The ophiolite sequence, in its simplest and most complete form, consists of upper mantle ultramafic rocks, typically serpentinized, in its deepest parts, overlain by layered and isotropic gabbroids, sheeted dolerite dykes, and pillow lavas of basalt, often capped by layers of deep-sea sediments (mudstones, siliciclastic turbidites, carbonates and cherts). Fragments of ophiolite sequences in the ANS are widespread, particularly in the Central Eastern Desert (CED) and South Eastern Desert (SED), but are nearly absent in the North Eastern Desert (NED) and Sinai. They exist as belts of well-preserved sequences marking arc-arc, arc-continent and terrane collision suture zones; extensive thrust dissected nappes and massifs; dismembered sequences, serpentinite lenses and sheets; and blocks within mélanges. According to Stern et al. (2004) they range in age from 890 to 690 Ma. In other studies of ophiolites from around the world, the vast majority of ophiolites have been found to have formed in spreading centres adjacent to oceanic and continental margin island arcs, particularly in back-arc and forearc settings, rather than in mid-ocean spreading ridges. Recent geochemical studies confirm that this is also true for the ANS Neoproterozoic ophiolites (Azer and Stern 2007 Abdel-Rahman et al. 2012).

In early studies of the Egyptian basement the allochthonous nature of these rocks was not recognized, despite the sheared contacts between the ophiolites rocks and underlying rocks. Their concordant discontinuous tabular to lens-like shape, and variable setting were interpreted to indicate an intrusive or submarine effusive origin (Rittman 1958; El Ramly and Akaad 1960). Akaad and Noweir (1969) placed the intrusive serpentinites and metagabbros at the end of the eugeosynclinal stage, and Akaad and Noweir (1980) referred to them as the Rubshi Group (Barramiya Serpentinites and Sid Metagabbro). Garson and Shalaby (1976) were the first to consider the ANS serpentinites and related rocks as ophiolitic suites. A complete and highly preserved sequence of ophiolite was first recognized in the Eastern Desert by El-Sharkawi and EI Bayoumi (1979) in the Wadi Ghadir area in the SED. The ophiolitic mélange of the

Eastern Desert was described by Shackleton et al. (1980) and Ries et al. (1983) as olistostromes that were thrusted NW and were in sheared contact with underlying rocks.

In the following section, the most complete examples of ophiolite sequence in the EED are described first. Following this, the main occurrences of serpentinite bodies, ophiolitic mélange and talc-carbonate altered ultramafites rocks are considered. The last sections give details of the metagabbros, the ophiolitic metavolcanics and metasediments.

6.5.1 Complete Ophiolite Sequences in the EED

There are several localities in the EED where complete ophiolite successions are exposed. These are found in the CED and SED at Gabal El Rubshi, Qift-Quseir road, Wadi Ghadir, Gabal Gerf and Sol Hamed. The geology of each will briefly described below.

6.5.1.1 Gabal El Rubshi

Studied by Amstutz et al. (1984) and Habib (1987), the ~790 Ma Gabal El Rubshi ophiolite represents the most northerly significant serpentinite occurrence in the EED. The ophiolite is greenschist facies metamorphosed and was thrusted westwards over distal turbidites. From base to top it consists of serpentinites, structurally overlain by metagabbro complex and metadolerite, overthrusted by the Kab Amiri ophiolitic mélange. The ultramafics are mainly serpentinite (originally harzburgite and dunite) but contain some amphibolite bodies and substantial lenses of chromite (El-Taher 2010). The mafic rocks are metagabbro-diorite, metadolerite and pillow metabasalts. The metagabbros are cumulate at the base and massive hornblende metagabbro in higher sections, and have been intruded by younger pyroxenites and troctolites. The metagabbros pass upwards into tholeiitic metadolerite dykes and pillow metabasalts. Dacitic tuffs are interbedded with the basalts indicating proximity to an island arc. Recent studies of the chromites from this ophiolite have concluded a supra-subduction zone (SSZ) environment for the serpentinites, either in a forearc (Abdel-Karim and El-Shafei 2017) or back-arc (El-Desoky et al. 2015) setting.

6.5.1.2 Qift-Quseir Road

The ultramafic-mafic sequence along the Qift-Quseir road, particularly the exposures surrounding the El Fawakhir granite, is one of the best studied ophiolites in Egypt. It was recognized as an ophiolite succession by Shackleton et al. (1980) and Nasseef et al. (1980). Enclosing the El Fawakir granite is a massive body of serpentinized harzburgite with local cumulate textures, disseminations and bands of chromite, and veins of pyroxenite. These ultramafics are thrusted eastwards over the isotropic El Sid Metagabbro, which has ophitic to sub-ophitic texture and is locally pegmatoidal and leucocratic to trondhjemitic. Amer et al. (2009, 2010), however, found that a body of metabasalts separates the serpentinites from the metagabbros. The metagabbro is commonly (magmatic) hornblende bearing. The metagabbros are in thrusted contact with a narrow zone of basaltic sheeted dykes that are thrusted over amygdaloidal, porphyritic pillowed metabasalts and basalt breccias. Abd El-Rahman et al. (2009a) found that the ophiolite geochemistry was comparable to forearc oceanic crust, with magmas derived from a depleted N-MORB-like mantle source. The chemistry of the pillowed basalts was closer to back-arc volcanics. Hamdy et al. (2013) also suggested a forearc setting based on spinel chemistry. El-Sayed et al. (1999) preferred a back-arc environment for these ophiolites. A tholeiitic chemistry with arc affinity and SSZ setting was found for the El Sid metagabbro by El Bahariya (2006), who also described upper greenschist facies conditions as 300–550 °C and 1–3 kbars. A zircon age of 736 Ma, has been obtained for the El Sid metagabbro (Andresen et al. 2009).

6.5.1.3 Wadi Ghadir

The Wadi Ghadir ophiolite, located south of Marsa Alam, is one of the most complete ophiolite sequences in Egypt. El Sharkawy and El Bayoumi (1979) and El Bayoumi (1983) described Wadi Ghadir as consisting of serpentinized peridotite (lherzolite, cumulate dunite and harzburgite), a gabbro complex (layered at the base passing up into massive gabbro, with local pegmatitic textures and pyroxenite cumulates), sheeted diabase dykes and associated pillowed basalts covered by deep-water sediments. Basta et al. (1983) distinguished between the low-Ti, high-Ni, Cr MORB-like sheeted diabases of depleted mantle origin, and the high-Ti, low-Ni, Cr ocean floor tholeiitic composition of the pillowed basalts of undepleted mantle origin. El Bayoumi and Greiling (1984) thought that the Wadi Ghadir ophiolite formed either as ocean floor or in a back-arc basin. A forearc environment was preferred by El Akhal and Greiling (1987). Farahat et al. (2004) found that the geochemistry of the ophiolite was between within-plate and island arc, and suggested a back-arc environment, whereas Khalil (2007) suggested a mid-ocean ridge environment based on chemistry of chromite deposits within the ultramafics. Abd El-Rahman et al.'s (2009b) geochemical investigation of Wadi Ghadir ophiolite again pointed out differences between the ophiolitic intrusives and volcanics. They found that the gabbros were LREE-depleted while the pillow basalts were LREE-enriched. The gabbros were thought to have formed in a back-arc environment while the basalts erupted in a transitional setting between back-arc and active continental margin following arc-continent collision. Recently, Basta et al. (2011) re-investigated the ophiolites and confirmed a

difference in the chemistry between the sheeted dykes and pillow basalts that could be accounted for by contamination of MORB magmas by older oceanic arc crust (giving a C-MORB chemistry). Involvement of the older crust resulted in relatively lower $\varepsilon_{Nd}(t)$ values than for DM ($\sim$+6.5) at 750 Ma (cf. Kröner et al.'s 1992 Pb-Pb zircon date for Ghadir plagiogranite of 746 $\pm$ 19 Ma). Contamination also produced the observed LREE-enrichment of the basalts, giving them intermediate MORB/IAT chemical characteristics.

6.5.1.4 Gabal Gerf

Gabal Gerf ophiolite lies in the far SED at the northern end of the Hamisana Zone, between Ras Banas and Halaib. It is a N-S elongate mass described by Kröner et al. (1987) as a ophiolitic nappe complex, perhaps part of a single nappe including the Allaqi-Heiani and Onib-Sol Hamed ophiolites (Stern et al. 1990). The ophiolite was thrusted S or SW over forearc metasediments and sheared volcanics. The ophiolite has been metamorphosed to greenschist facies (Abdel-Karim et al. 2001). Kröner et al. (1992) obtained a 741 $\pm$ 42 Ma Pb-Pb zircon date from a leucogabbro at Gerf, while Zimmer et al. (1995) presented Sm-Nd isotopes data and dated zircons giving an $\sim$750 Ma age for the Gerf ophiolite. Zimmer et al. (1995) described the ophiolite as consisting of basaltic pillow lavas, sheeted dykes, isotropic and layered gabbros in low-angle thrust contact with a serpentinized ultramafic mélange. They found that it was distinguished from other ophiolites in having a normal MORB (high-Ti N-MORB) chemical affinity indicating its origin as part of an ocean basin, rather than a volcanic arc setting. Similar conclusions were expressed by Abdel-Karim and Ahmed (2010). Pb isotopic composition and lack of Nb depletion for the sheeted dykes and basalts were consistent with the N-MORB affinity, however, the Pb isotopic composition of the gabbros pointed to island arc character, with contamination of the gabbroic parent magma by pelagic sediments in a subduction zone. The basalts had ε_{Nd} initial values (for an age of 750 Ma) of +6.5 and + 8.8 in the basaltic rocks, which were similar to DM values of that age. The gabbros showed somewhat lower ε_{Nd} values, perhaps reflecting a subduction component. Abdel-Karim et al. (2016) noted that the high-Cr spinels in the ultramafics at Gerf suggest that they are highly depleted mantle residues. They described LREE-enriched serpentinites and LREE-depleted serpentinized peridotites at Gerf. The first were interpreted to result from crustal contamination or interaction of their mantle source with subduction-related fluid in a SSZ forearc setting; the second formed by mantle interaction with MORB melt.

6.5.1.5 Sol Hamed

The Sol Hamed ophiolite lies near Halaib and is the most northeasterly segment of the NE-trending suture that includes the ophiolite at Wadi Onib to the SW (Kröner 1985; Kröner et al. 1987; Hussein et al. 2004). This Onib-Sol Hamed suture is itself an extension of the Wadi Allaqi-Heiani Suture of the SED (Abdelsalam and Stern 1996; Abdelsalam et al. 2003). The age of the Sol Hamed is taken to be the same as the Onib ophiolites, which were dated as 808 $\pm$ 14 Ma via Pb-Pb method applied to zircons from a plagiogranite (Kröner et al. 1992). The Sol Hamed ophiolite is greenschist facies metamorphosed and consists of a nearly vertically dipping thin ultramafic body, bordered to its SE by thicker gabbro that passes to the SE into a poorly developed sheeted dyke zone then pillowed basalts (Fitches et al. 1983). The ultramafic rocks include intensely serpentinized dunite and peridotites, and pyroxenites. The dunites contain bands and pods of chromitite. Gabbros share a sheared contact with the ultramafics. The lowermost gabbros are coarse-grained but become finer grained and more leucocratic in higher sections. Magmatic banding is present. Textures in the sheeted dykes are obscured by recrystallization. The pillow lavas are vesicular and brecciated and overlain by shales and reportedly cherts. The ultramafic rocks were studied recently by Abu-Alam and Hamdy (2014) who concluded that these rocks were originally depleted harburgites that interacted with Ti-rich boninite melts in a SSZ forearc environment. However, Berhe (1990) thought that the trace element chemistry of Sol Hamed ophiolitic basalts indicated a back-arc environment.

6.5.2 Serpentinites, Ophiolitic Mélange and Talc-Carbonate Rocks

6.5.2.1 Serpentinites

The serpentinites constitute one of the most distinctive rock units in the basement complex of Egypt. They have been studied by many authors, especially as they are hosts for the magnesite, chromite and some gold deposits in Egypt. They are usually composed of antigorite, chrysotile, lizardite, minor carbonate, chromite, magnetite, magnesite and chlorite (Azer and Stern 2007). Sultan et al. (1986) used Landsat TM images to test the previously mapped distribution of serpentinites in the CED and found that they were more widespread, but more fragmentary, than expected. The serpentinite masses were also shown to be typically NW-trending in the northern half of the CED and ENE-trending in the southern half. With the exception of minor outcrops in the Esh-El Mellaha range, no serpentinite

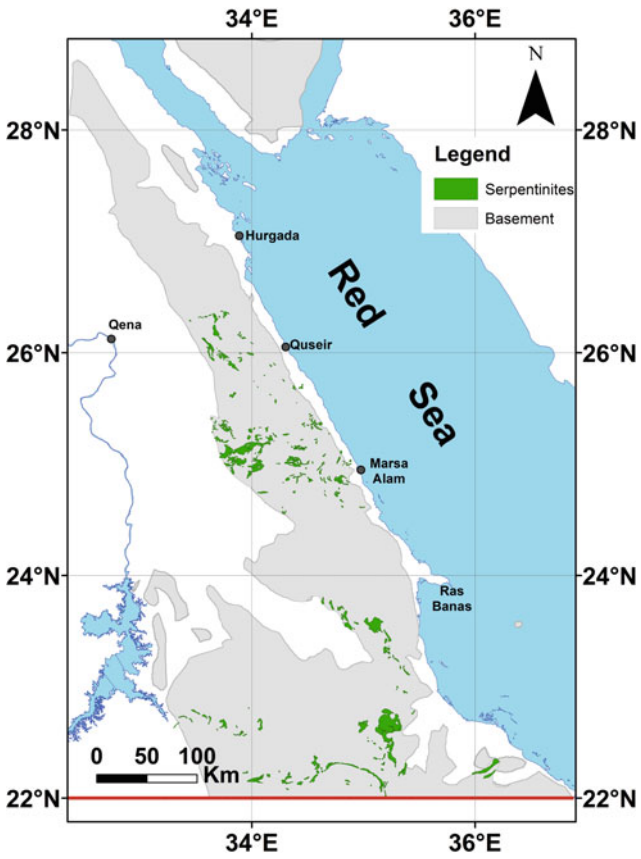

Fig. 6.9 Distribution map of Serpentinites, in the Eastern Desert

bodies are found in NED or Sinai. Apart from the complete ophiolite occurrences described above, and the disrupted serpentinized peridotites in the ophiolitic mélange, described in the next section, there are massifs of serpentinite in the CED and SED as large as mountains (Fig. 6.9). These massifs may be thrust nappes or megablocks enclosed within ophiolitic mélange. The largest of these serpentinite bodies in the CED are found at Wadi Atalla (El Kassas 1974; Ries et al. 1983; Abou El-Maaty et al. 2012), Barramiya Range (Ali-Bik et al. 2012), Wadi Mubarak (El Bahariya 2008), Wadi Dungash (Zoheir and Weihed 2014), Gabal Mudargag (Ahmed et al. 2012), Wadi Ghadir (Khalil and Azer 2007) and Gabal Ras Shait (Khudeir et al. 1992). SED serpentinite masses are represented at Gabals Abu Dahr (Gahlan et al. 2015), Gerf, Moqsim (Ali et al. 2010a), and Sol Hamed (Abu-Alam and Hamdy 2014).

Gamal El Dien et al. (2016) studied serpentinite masses at from Wadi Mubarak, Gabal El-Maiyit, Wadi Um El Saneyat and Wadi Atalla. Based on relict olivine and orthopyroxene they were found to be originally harzburgites. The harzburgite was a residue from up to 24% previous partial melting, but were enriched in incompatible elements due to interaction with Ti-rich fluids. The chromites collected from the serpentinites showed distinct fields based on Cr# and Mg# for each area, but all plotted in the forearc field. The parent peridotites probably formed at a spreading ridge in a forearc basin and were contaminated by rising subduction related fluids. Azer and Khalil (2005) examined serpentinites along Wadi Sodmein, east of Meatiq, and found that the original ultramafics were mainly harzburgite and lesser dunite and wehrlite that formed in a SSZ back-arc environment. Chrysotile veinlets probably formed late in the history of the serpentinites. Khalil and Azer (2007) studied serpentinites derived from harzburgites and dunites at Um Khariga and Gabal Ghadir, and found them to be originally forearc depleted peridotites. Azer and Stern (2007) studied the northernmost serpentinites of the CED at Wadi Semna and also concluded a depleted peridotite parent in a forearc setting. Azer (2014) also found a forearc setting for the serpentinites at El-Degheimi near the El-Sibai complex.

The Barramiya Range including Gabal Um Salatit represents some of the largest bodies of ophiolitic serpentinite in the CED, with continuous exposures of these rocks for ~25 km in the E-W direction. The extensive ophiolite exposures in this range have been useful for refinements in remote sensing methods for discrimination between ultramafic and mafic lithologies (Gad and Kusky 2006; Amer et al. 2010). The serpentinites are mainly composed of antigorite with rare chrysotile and very rare lizardite (Surour 2017), and are derived from dunites and harzburgites. Surour (2017) also deduced that the Barramiya serpentinites had higher metamorphic grade than those at Fawakhir or Ghadir, being estimated by Abdel-Karim and El-Shafei (2017) as transitional greenschist to amphibolite facies. A ~790 Ma age for the Barramiya was suggested by Abdel-Karim and El-Shafei (2017). They found that the chromites of the parent ultramafics indicated a boninitic affinity and a forearc suprasubduction setting.

Ras Shait serpentinites lie immediately north of the Hafafit complex and consist of mainly peridotites (harzburgite and lherzolite) and foliated gabbros, with serpentinites hosting important podiform chromite deposits (Khudeir et al. 1992; Saad 1996). The SED Gabal Abu Dahr serpentinites border the Wadi Beitan complex to its northeast. The mantle section consists of serpentinized harzburgite with bodies of dunite containing cumulate wehrlite and pyroxenite as sills and layers (Gahlan et al. 2015). The geochemistry of the ultramafics is consistent with a highly refractory mantle origin in a forearc setting.

6.5.2.2 Ophiolitic Mélange

The ophiolitic mélange represents an important map unit in the Eastern Desert. Ries et al. (1983) described the mélange as containing mainly angular fragments of all sizes up to the scale of mountains of all of the lithologies of the complete ophiolites (serpentinites, peridotites, gabbros, diabase,

pillow basalts) plus rare metamorphic (amphibolite of metagabbroic parentage and marble), sedimentary fragments (cherts, graphitic pelites and greywackes) and non-ophiolitic volcanics or plutonites (silicic tuff and other pyroclastics, and rare granite). The matrix is an unstratified grey pelite. Clasts are randomly distributed but with a tendency for large blocks to occur on certain horizons, with roughly parallel tabular shapes. Ries et al. (1983) warned that neither the absence of stratification nor the presence of ophiolite fragments can be used as a criterion for recognizing the boundaries of the mélange. The mélange was formed by sedimentary processes, with later deformation (most commonly a poor cleavage, rarely mylonitic, with a common NW-SE elongation lineation or local pencil structure) heterogeneously imposed on this unit. The mélange is weakly greenschist (rarely amphibolite facies) metamorphosed. Ries et al. (1983) viewed the mélange as having formed by sliding of forearc (accretionary prism) slices into a trench to form olistostromes. Shackleton et al. (1980) suggested that the mélange sheets were only 1–2 km thick but of very wide areal extent. Shackleton (1994) supposed that there was a transition from ophiolitic thrust complexes to typical ophiolitic mélange to olistostromic mélange. These different stages of mélange formation could be distinguished on Landsat TM images (Sultan et al. 1986).

Probably because of the difficulty in defining mélange boundaries, some workers have avoided using the term 'mélange' altogether and have mapped the mélange areas shown by Ries et al. (1983) and Shackleton (1994) as 'mafic metavolcanics' (arc or ophiolite-related) or 'metasediments' (e.g. on the Conoco 1:500,000 geological maps, 1987). Amer et al. (2010), however, have spectrally distinguished mélange in remote sensing studies of Fawakhir. Gad and Kusky (2006) readily distinguished serpentinite from metavolcanics and assessed the degree of mixing of these two lithologies in mélange areas in the Barramiya Ranges. The best examples of ophiolitic mélange in the CED include the NW-SE trending foliated mélange west of Meatiq in the Um Seleimat area (Ries et al. 1983; Akaad et al. 1996; Fowler and El Kalioubi 2004), mélange bordering the Sibai complex to its SW and forming a NW-SE trending foliated belt at its NE margin (El-Alfy 1992; Ragab et al. 1993a), mélange in the Barramiya Range (Zoheir and Lehmann 2011; Ali-Bik et al. 2012), Wadi Dungash (Abdel-Karim et al. 1996; Zoheir and Weihed 2014), Wadi Mubarak (El Bayoumi and Hassanein 1983; El Bahariya 2008) and particularly at Wadi Ghadir (Basta et al. 1983; El Akhal 1993; Abd El-Rahman et al. 2009b; Kamel et al. 2016).

A geochemical study of the Dungash and Arayis mélanges by Abdel-Karim et al. (1996) found that the ultramafics in the mélange were comparable to SSZ ophiolites, while the gabbro and basalt of the mélange had high-Ti tholeiitic to minor calc-alkaline chemistry, consistent with oceanic floor MORB or back-arc environment. Arc volcaniclastic material was abundant in the mélange matrix, as would be expected for an arc-proximal environment. El Bahariya (2008) found three compositional groups of peridotites in mélanges from Wadis Esel and Mubarak. The three groups included one with MORB chemistry, and two groups with SSZ chemistry. The MORB affinity peridotite was thought to have formed in a back-arc fast spreading ridge, while the other two formed when subduction began. El Bahariya (2008, 2012) classified mélanges as olistostromes (formed by gravity collapse); tectonic mélange (formed by thrusting and tectonic mixing); and olistostromal melanges (partly sedimentary and partly tectonic), reflecting a similar classification by Shackleton (1994). An earlier classification of mélange by Ragab et al. (1993b) and Ragab and El-Alfy (1996) identified two types: subduction ophiolitic mélange (formed during the subduction stage in an accretionary wedge as scraped slices of oceanic crust and sediment), and allochthonous ophiolitic mélange (thrusted over volcano-sedimentary/plutonic arc assemblages at the close of subduction). The subduction mélanges were exemplified by those along the Qift-Quseir road and at Wadi Ghadir, and showed locally higher than greenschist metamorphism. Allochthonous mélange was found NE and SW of El-Sibai and elsewhere in the CED and showed greenschist facies metamorphism.

6.5.2.3 Talc-Carbonate Deposits

Talc-carbonate alterations of ultramafic rocks are widespread in the EED. They are economically and environmentally significant as (1) industrial sources of MgO, (2) refractory materials, (3) components of ceramics, (4) hosts to gold deposits, and (5) as models for the future sequestration of atmospheric carbon dioxide. These alterations are mainly developed along thrusts and shear zones, which are most permeable to the metasomatic fluids responsible for the alterations. The talc-carbonate rocks are one of a spectrum of carbonatization alterations of peridotites, dunites and serpentinites. The low Al_2O_3 content of the ultramafic rocks permits the Al-free phase talc to form by reaction of Mg-rich minerals with CO_2. Byproducts of this reaction are quartz, brucite, chlorite, amphibole (tremolite, cummingtonite, etc.) and/or magnesite (rarely dolomite) (Basta and Abdel-Kader 1969), depending on ultramafic rock chemistry, particularly MgO%. Other factors exerting a control on the mineralogy of the alterations include fluid temperature and XCO_2, and the presence of minor elements in the metasomatic fluids, e.g. K and Ca. The popular research on these rock alterations is aimed at deciphering the geological controls, finding the origin of the fluids, and clarifying the timing of the alteration event.

The carbonatization alterations have been classified by several authors. 'True' listwaenite alteration is distinguished

from carbonate-rich alterations by its high SiO_2 and low carbonate contents, and especially by the presence of the green Cr-mica, fuchsite (Azer 2013). Quartz-rich listwaenites commonly stand out as weathering resistant reddish brown ridges. According to Botros (2004) and Emam and Zoheir (2012), gold mineralization is more commonly associated with SiO_2-rich listwaenites than talc-carbonate alterations.

Many authors have considered the origin of the fluids and the carbon source for the carbonatization alteration. Zoheir and Lehmann (2011) examined listwaenites at Barramiya and found that graphitic schist in contact with serpentinites played some role in the evolution of the metasomatizing fluids and gold deposition. Ghoneim et al. (2003) thought that the magnesite alterations of ultramafics at Gabal El Rubshi occurred at 300 °C. Calcite and dolomite were also found but were later stage precipitates. The carbon source of the CO_2 was suggested to be the nearby organic shales. Ali-Bik et al. (2012) noted that at Barramiya, the alterations within serpentinites were magnesite-rich while alterations were talc-rich at the contact of serpentinite with SiO_2-rich rocks. They estimated the conditions of alteration were ~490 °C and XCO_2 no more than 0.13. Gahlan and Arai (2009) described magnesite-orthopyroxene alterations of Gabal Gerf serpentinized peridotites that occurred at high temperatures (520–560 °C) related to granite intrusion and high CO_2 ($XCO_2 > 0.87$) probably derived from nearby impure sedimentary carbonate layers. Hamdy's (2007) study of magnesite alterations at Umm Salatit, Barramiya area, found that the carbon source was magmatic. Hamdy and Gamal El Dien (2017) found that the carbon for the H_2O-CO_2 metasomatizing fluids that produced talc-carbonate alterations at Wadi Atalla, Wadi Maiyit and Wadi Ghadir was mantle derived. A dissenting view on the origin of talc-carbonate rocks was provided by Schandl et al. (2002) who described talc-serpentine and talc-tremolite rocks near the contact of Shadli metavolcanics with serpentinites as metamorphed siliceous carbonate sediments.

Remote sensing methods have been applied to the search for talc-carbonate alterations in EED peridotites. Abou El-Maaty et al. (2012) characterized the talc-carbonates at Wadi Atalla using TEM band ratio images. Kamel et al. (2016) were able to distinguish Wadi Ghadir talc-carbonate rocks on ETM+ Landsat images.

6.6 Metasediments

A range of metapsammites, metaconglomerates, metamudstones of diverse characteristics and settings, with the common property of being metamorphosed, usually to greenschist facies (locally amphibolite facies) have been traditionally grouped together as 'geosynclinal metasediments' (El Ramly 1972), or simply as 'metasediments' (Hassan and Hashad 1990), and in early studies as 'schist-mudstone-greywacke series' in part (El Ramly and Akaad 1960). The commonest metasediment lithologies include quartzofeldspathic meta-arenite and quartz pebble metaconglomerate; marble and other calc-silicate rocks; feldspathic metagreywacke; slate and phyllite; schists composed of biotite, chlorite and hornblende; and pebbly to cobbly metaconglomerates with arc volcanic clasts. The diversity of this category is represented in Hassan and Hashad (1990), who subdivided the metasediments into (1) mature quartzites with metacarbonates; (2) immature flysch-type metavolcaniclastics, metagreywackes and metamudstones (including metaconglomerates); (3) metacherts and banded iron formations (BIFs); and (4) (ophiolitic) mélange. Of these, (1) has been previously mentioned as a component of the gneissic complexes, but exists mainly outside of these complexes, covering large areas of the SED. Here we will emphasize the exposures lying outside of the complexes. Group (4) ophiolitic mélange has also been discussed in Sect. 6.5.1, however, it must be noted that groups (2) and (4) may be cogenetic, with (4) having sediments of (2) as matrix for the mélange blocks. Each of the groups (1) to (3) will be described below as Sects. 6.6.1, 6.6.2 and 6.6.3, respectively.

6.6.1 Mature Quartzites and Metacarbonates

In Akaad and Noweir's (1969) lithostratigraphy, these quartzofeldspathic sandstones and calcareous sediments were 'pre-orogenic mature sediments' forming the Meatiq Group, and were therefore protoliths of the basement gneisses. The sediments were later placed in the Abu Fannani Schist of Akaad and Noweir (1980). Ries et al. (1983) also regarded them as protoliths, at least of the Meatiq gneisses. The largest exposures of these sediments were suggested to be the Abu Swayel area by Hassan and Hashad (1990), where they noted the existence of rare cross-bedding and graded bedding, and considered the sediments to be shallow water deposits. They reported that Hunting (1967) found these mature sediments to pass north of latitude 24°N into the immature greywacke sediments (of group 2), with the two sediment types possibly separated by a structural break. El-Gaby et al. (1988a, 1990) identified the lower sections of these metasediments as deposits on an attenuated or rifted pre-Pan-African basement, and distinguished them from the upper sections which they believed were foreland basin deposits (similar to the Hammamat molasse) produced during the arc-collision stage.

In the areas outside of the metamorphic complexes, the main lithologies of this group are quartzites, quartz-rich and quartzofeldspathic schists, biotite schists, quartz pebble metaconglomerates and marbles. Kröner et al. (1987) has

noted that these sediments are also partly aluminous, as well as being SiO_2-rich. Intervening volcanics or sills have been reported in these sediments (e.g. Kröner et al. 1987; El-Gaby et al. 1990; Surour 1995; Abdelsalam et al. 2003), perhaps associated with rift related volcanicity or early island arc stage, while there are also arc volcanic slices in tectonic contact with the sediments (Abdeen and Abdelghaffar 2011). Within the complexes are higher grade (up to HT amphibolite facies equivalents) including metapsammitic migmatites and paragneisses, staurolite schist, garnet-biotite schist, garnet-sillimanite-biotite gneiss, hornblende-biotite gneiss (Finger and Helmy 1998; Abd El-Naby et al. 2000; Khudeir et al. 2006a; El Kazzaz 2010). The presence of riebeckite in the psammitic gneisses at Hafafit has been explained as due to later soda metasomatism (El Ramly and Saleeb-Roufaeil 1974; Rashwan 1991).

Dating of these sediments is difficult. Extracted zircons produced 1.1–2.3 Ga ages that probably indicate a pre-Pan-African provenance to the west (Dixon 1981). Whole rock Rb-Sr analyses have returned ages in the range 1200–750 Ma, and relatively higher initial $^{87}Sr/^{86}Sr$ ratios in the southern areas than further north (Hashad 1980). Khudeir et al. (2006b) attempted to date Hafafit paragneisses (hornblende gneiss, biotite gneiss) using Rb-Sr and Nd isotopes, however the large errors in the Rb-Sr date (588 ± 110 Ma) and the large ranges for ε_{Nd} (+6.64 to +10.28) and τ_{DM} ages (375–749 Ma), were indicators of diverse sediment provenances with different initial isotopic compositions, rather than actual ages.

The environment of deposition of these mature quartzose sediments is generally accepted as shelf/passive margin, rifted or attenuated older crustal basement (Kröner et al. 1987; El-Gaby et al. 1990; El-Gaby 1994). The proximity of the ANS to this shelf environment is demonstrated by the large size of some conglomerate clasts, e.g. the 5 kg granite boulders collected by Dixon (1981) from these sediments at Wadi Mubarak. The sediments may have been transported beyond the shelf and into the Mozambique Ocean, so the substrate of the sediments is not necessarily pre-Pan-African. The mechanism by which these shallow-water sediments were incorporated into the Hafafit, Meatiq and other CED gneissic complexes is either primary (complex built on top of sediments) or tectonic (thrusts assembled sediments with other elements of the complex, before HT metamorphism).

6.6.2 Immature Metagreywackes and Metamudstones

This group of immature metasediments is also known as the schist-mudstone-greywacke series (El Ramly and Akaad 1960). It is widespread in the EED and is the dominant metasediment type north of latitude 24°N (Hassan and Hashad 1990). The main lithologies are greenschist facies metamorphosed greywacke, mudstone, slate, chlorite and biotite schist, phyllite, and pyroclastics, with less common conglomerates, containing clasts of granite, sedimentary rocks and arc volcanics (felsite, basalt, andesite and quartz porphyry).

The stratigraphic position of these sediments according to Akaad and Noweir (1969) was at the base of the Abu Ziran Group, i.e. overlying the mature sediments described in the previous section. Akaad and Noweir (1980) regarded these sediments as alternating with volcanic formations of the Abu Ziran Group. In this sense they regarded these sediments as approximate time equivalents of the Shadli Metavolcanics. The Abu Ziran Group marked Akaad and Noweir's eugeosynclinal (or subsidence) stage of EED history.

The sedimentary facies of these sediments has been described as flysch-like, emphasizing the rapid alternation of sand and mud, with sedimentary structures characteristic of deep-water deposition (thin lamination in mudstones, graded bedding, slumps, rare cross-bedding). As with classic flysch, a turbidity current deposition mechanism is likely. The greywackes are lithic and contain quartz and feldspar grains. The lithic particles are of arc volcanics and ultramafics. Carbonate beds are very rare. The chemistry of the wackes and mudstones may reflect the tholeiitic and calc-alkaline character of the associated metavolcanic rocks (Khalil et al. 2018).

This metasediment group is well developed at Gabal Atud where the type area of the Atud Conglomerates is located. The Atud Conglomerate is rich in mafic igneous and ultramafic clasts. A similar conglomerate at Dungash is rich in calc-alkaline arc volcanic clasts (Abu El-Ela 1985). Stern et al. (2006) renamed these conglomerates as Atud Diamictite, based on the clastic textures and poor sorting. Ali et al. (2010b) later studied this diamictite at Wadi Kareim and Wadi Mubarak. Dixon (1981) found pre-Neoproterozoic zircons in arkose cobbles from the Atud conglomerate in Wadi Mubarak. Dixon believed that the cobbles could not have been derived from within the EED and must have been transported long distances from their source into the Mozambique Ocean. Ali et al. (2010b) interpreted this evidence for long transport to support a glacial origin for the diamictites. Based on zircons collected from the diamictite clasts they estimated deposition of the diamictite not long after 750 Ma supported by the 752 Ma age of youngest clasts in the diamictite. This corresponded in time to the Sturtian glaciation.

The deep-water turbiditic greywackes and mudstones of this immature series form the sedimentary matrix of the ophiolitic mélanges, which are believed to have formed by sedimentary processes of collapse in a trench or back-arc basin setting (Ries et al. 1983; El Bahariya 2012). Shackleton et al. (1980) described alternation of ophiolitic mélange bodies and graphitic pelites, turbidites and cherts at

Barramiya. Ries et al. (1983) described the mélange at Sodmein as underlain by sediments. They found that graphitic pelite and greywacke also formed sedimentary clasts within the mélange, and described the mélange matrix as finely laminated dark siliceous sediment of probable tuffaceous origin, cherty mudstone, graphitic mudstone and Fe rich mudstone. The matrix contained arc-derived sediments. El Sharkawy and El Bayoumi (1979) noted that the significance of the ophiolitic mélange was not recognized in early studies, and as a result, the mélange was included in the schist-mudstone-greywacke series. They described a proximal and distal mélange facies at Wadi Ghadir. El Bayoumi and Hassanein (1983) provided details of these mélange facies. The proximal facies consisted of variable sized ophiolite fragments in muddy matrix. The distal facies consisted of mudstones and greywackes with minor pebbles. Basta et al. (1983) suggested a turbidite origin of the metasediments at Wadi Ghadir, and also found that there were clasts of the earlier continent-derived shelf sedimentary rocks (quartzite and marble pebbles) in the mélange. Takla et al. (1990) studied the mélange exposed between Ras Shait and Gabal Atud. They found a gradation from mélange with ophiolitic blocks, to a sedimentary mélange, passing into pebbly muddy sediments lacking blocks. Their chemical analysis of these sediments indicated oceanic island arc setting.

6.6.3 Banded Iron Formations

Banded Iron Formations (BIFs) are found in the CED and NED as typically <100 m thick packages of finely laminated beds of Fe oxide and jasper (or chert) alternating with arc metavolcanics and metapyroclastics (metabasalt, meta-andesite) or quartz-rich sandy/muddy and carbonate shelf sediments. The ANS BIFs are Neoproterozoic (~750 Ma) examples of Algoma-type iron formations. The Algoma type are globally normally confined to 3.2–1.8 Ga, and are associated with greenstone belts in which mafic volcanic hydrothermal activity is believed to have released Fe^{2+} that was precipitated as hematite-magnetite BIFs as the ocean surface waters became oxygenated. Neoproterozoic BIFs on other continents are usually found to be glacigene (Rapitan-type) sediments deposited between the Sturtian and Marinoan glacial periods (Ilyin 2009). Research on Egyptian BIFs has focused on about 15 significant examples, of which the best studied are Um Anab in the NED, and Wadi Semna, Abu Marawat, Wadi Kareim, Wadi El Dabbah, Gabal Um Nar, and Gabal El Hadid in the CED.

Eastern Desert BIF facies consist dominantly of oxide facies (hematite and magnetite), silicate facies (quartz, chlorite, stilpnomelane, greenalite) and carbonate facies (ankerite, calcite, dolomite), while sulphide facies is rare. In the oxide facies, Fe was first precipitated as an oxyhydroxide (e.g. goethite), then dehydrated during early diagenesis to form hematite dust. This was recrystallized to form magnetite (Khalil et al. 2015).

The similarity of the BIFs at Kareim, El-Hadid and Um Nar to Algoma types was early identified by Sims and James (1984). El Aref et al. (1993) also studied Um Nar and conclude that the BIFs were associated with shelf metasediments (amphibole schists, marbles and quartzites) and were likely to be of the passive margin Lake Superior type BIFs. El-Shazly and Khalil (2014) also noted that Um Nar BIF was hosted by graphitic chlorite schists and marbles, overlain by pebbly amphibole schists of volcaniclastic origin. They also disputed the volcanogenic origin of these BIFs. They pointed to low Ni and Cr levels as evidence for a sedimentary origin. Stern et al. (2013) proposed that a Snowball Earth hypothesis could explain the Kareim BIFs and reported the existence of the glacial Atud Diamictite beneath the BIFs. They accepted that Rodinia rifting could also have been a factor in the development of these BIFs (Eyles and Januszczak 2004). El-Shazly and Khalil (2014) regarded the Atud Diamictite as a volcanic agglomerate.

The favoured mechanism of precipitation of Fe and silica in the Egyptian BIFs is similar to that of the Algoma types in involving mixing of deeper reduced Fe rich hydrothermal waters derived from mafic volcanics with shallow oxygenated surface waters. The BIF deposition must have been rapid, as the BIFs contain <20% detrital content, despite being deposited in a regime with high volcaniclastic sedimentation rate (Stern et al. 2013). In addition to chemical processes, there are possibilities of biological activity in the deposition of silica, and spherulitic possibly biomorphic textures have been preserved in the cherts (Sims and James 1984). El Habaak and Mahmoud (1994) thought that bacteria may also have been involved in Fe oxide precipitation and formation of stilpnomelane. Al Boghdady (2003) suggested two models for Egyptian BIF formation (1) chemical precipitates from fumaroles, and (2) hydrothermal interaction with host rocks. Stern et al. (2013) suggested that hydrogenous precipitation of BIF sediment involved dilution of hydrothermal fluid, some distance from vents. El Habaak (2012) observed that the jasper lenses at Um Anab were not true BIFs but formed by hydrothermal alteration of volcanics.

An environment below wave base has been suggested based on the lack of ripples in these BIFs, however, there are preserved carbonate oolitic textures (Sims and James 1984). El Ramly et al. (1963) described oolitic iron ore at Gabal El Hadid. Taman et al. (2005) found oolites in the carbonate facies of the Abu Marawat BIF and thought that it was

deposited in shallower waters than Semna. The close association of the BIFs with calc-alkaline amygdaloidal lavas and pyroclastics has been used as evidence for a back-arc, forearc or inter-arc environment (Taman et al. 2005; Khalil and El-Shazly 2012; Stern et al. 2013). Enhanced hydrothermal fluid activity due to arc rifting has also been suggested as a factor in the formation of the Egyptian BIFs (Gaucher et al. 2015). The rift themselves may have provided local anoxic seafloor conditions suitable for Fe to accumulate in solution.

The BIFs have been greenschist facies metamorphosed, and silicate phases such as chlorite and stilpnomelane are metamorphic in origin. Higher temperature metamorphism was experienced in the more southerly BIFs at Um Nar (El Shimi and Soliman 2002). At Um Nar the temperatures of metamorphism were 520 ± 30 °C and P 5 ± 2 kbar, characterized by andradite garnet in the BIF. The metacarbonate layers at Um Nar contain andradite, diopside, amphibole and epidote and have been modeled as an Fe skarn formed by later diorite intrusion (El Habaak 2004). A similar pyrometasomatic origin was attributed to the El Imra BIF (Salem et al. 1994).

The age of the Egyptian BIFs is partly constrained by the dating of volcanics beneath them. These volcanics have been dated at 759 Ma (Gaucher et al. 2015). Khalil et al. (2015) dated a zircon in the volcaniclastics at El-Hadid BIF at 717 ± 8 Ma. Stern et al. (2013) estimated the age of ANS BIFs as ~750 Ma, i.e. before Sturtian glaciation (which began ~716 Ma). The underlying Atud Diamictite has zircons as young as 754 ± 15 Ma (Ali et al. 2010b). There are Archaean to Early Proterozoic rocks BIFs in the Southwestern Desert reported by Richter (1986), Richter and Schandelmeier (1990), Said et al. (1998) and Khattab et al. (2002). Naim et al. (1996) described BIF in the form of small beds and lenses within the Precambrian rocks of Gabal Kamel.

6.7 Metavolcanics and Metapyroclastics

The metavolcanics and metapyroclastics in Egypt are most extensively developed in the CED and SED, with fewer exposures present in NED (Fig. 6.10). On the basis of their associations and age they have been divided into two groups: (1) tholeiitic metabasalts associated with ophiolites; and (2) tholeiitic to calc-alkaline metamorphosed andesites, dacites, rhyolites, minor basalts and abundant pyroclastics of oceanic island arc setting. Stern (1981) referred to (1) as 'Older Metavolcanics' (OMV) and to (2) as 'Younger Metavolcanics' (YMV). The OMV and YMV are the topic of this section. In the Sinai, metavolcanics are also major components of the metamorphic complexes at Sa'al-Zaghara and Kid. The Mesoproterozoic metavolcanics in the

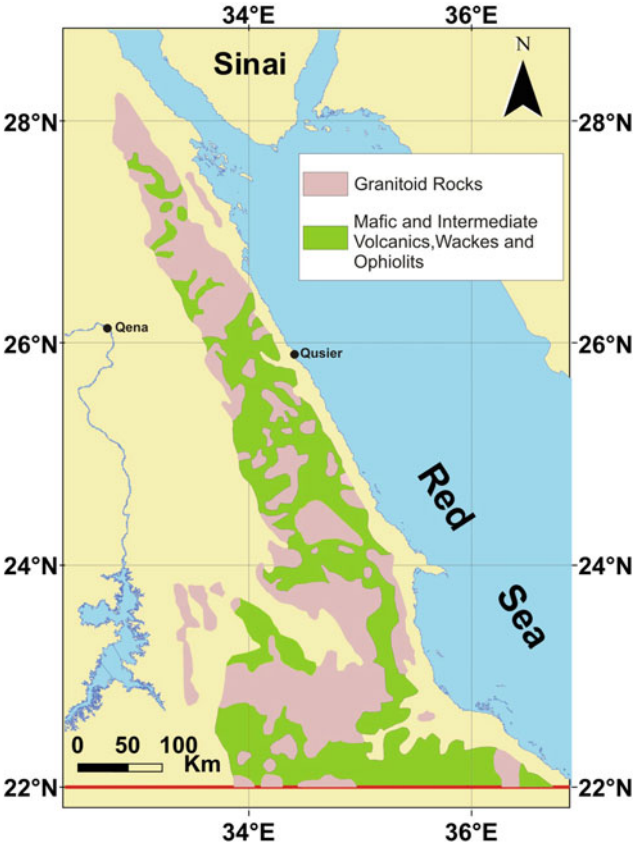

Fig. 6.10 Distribution of the metavolcanic belts in the Eastern Desert of Egypt (modified after EI Ramly 1972)

Sa'al-Zaghara complex have already been covered in the section on the gneissic complexes above, and will not be further discussed. The metavolcanics in the Kid Complex have also been mentioned in the gneissic complexes. They are younger than most YMVs and have a controversial setting. They have similar age and character to the post-collision Dokhan volcanics, which are mentioned in Sect. 6.10 of this chapter, which deals mainly with metamorphic aspects of the Hammamat sediments.

Early work by El Ramly and Akaad (1960) did not subdivide these rocks, referring to them simply as 'Metavolcanics'. They were described as basic to intermediate metavolcanics, followed by acidic metavolcanics and metapyroclastics, and were recognized as partly contemporary and partly younger than the nearby immature metasediments. The still-popular term 'Shadli Metavolcanics' was employed by El Ramly (1972) to denote these rocks. He regarded them as surface or submarine fissure eruptions. Their type area was set as the Sheikh El Shadli area in the SED. Akaad and Noweir (1969) placed the metavolcanics in their eugeosynclinal Abu Ziran Group, and recognized that they alternated with metasedimentary formations. In this classification and the later revised scheme of

Akaad and Noweir (1980) the metavolcanics formed two units separated by the Atud Formation metasediments. The lower volcanics (Muweilih Fm) were spilitized basalts, comparable to Stern's OMV, while the upper volcanics (Atalla and Um Seleimat Formations, Sukkari Metabasalts and Eraddia Formation) were much thicker accumulations of basalts, andesites, rhyolites and tuffs, comparable to Stern's YMV. Stern (1981) clarified the tectonic settings of the OMV and YMV. He mapped broad areas of both in the CED, with the OMV characteristically associated with large bodies of mafic-ultramafic ophiolitic rock. A good example is the belt of OMV along Wadi Atalla that incorporates the Fawakhir serpentinites and gabbros at its southern end. Subsequent work, however, has mainly represented these areas of OMV as ophiolitic mélange (e.g. Ragab et al. 1993b), and consequently as facies of the metasediments. On the Conoco geological maps, the OMV are distinguished as small bodies within the ophiolitic mélange. Recent dating of OMV and YMV has raised some doubts about the validity of the OMV-YMV division (Bühler et al. 2014) as some OMV examples have proved to be younger than YMV.

6.7.1 Older Metavolcanics

The most complete description of the OMV was provided by Stern (1979, 1981). They are typically thick massive to pillowed tholeiitic basalts lying directly above the sheeted dykes, though this relationship is found in only a few places within the mélange. There are locally thick metagabbroic sills in the OMV. The OMV represented the oceanic floor above a spreading centre, with the sheeted dykes as feeders for the basalts. Conformably overlying the OMV are metamorphosed volcanogenic greywackes, mudstones, BIFs and conglomerates (including the Atud conglomerate). The chemistry of the OMV is much like abyssal tholeiites in showing low K_2O, Rb (typically 1–2 ppm) and Ba (typically 20–40 ppm), and high K/Rb ratio of 450–1800. By comparison YMVs have higher Rb (typically 15–60 ppm) and Ba (typically 40–400 ppm) and K/Rb ratio of 400–600. The basalts of the YMV show characteristics of island arc tholeiitic, with chemistry similar to the OMV, but can be distinguished from MORB basalts on Ti versus Cr, and Ti/1000 versus Zr plots. Andesitic and dacitic YMVs describe calc-alkaline chemical trends. The OMV and YMV can also be discriminated by their normalized REE patterns, in that OMV shows LREE depletion, whereas the YMV shows LREE enrichment and clear HREE depletion.

Dating for the OMV is limited. Kröner et al. (1992) found 746 ± 19 Ma for plagiogranite from OMV exposures in Wadi Ghadir, while Andresen et al.'s (2009) date of 738–735 Ma for Fawakhir gabbro may also be considered as the age of OMV in that area. From these data, Ali et al. (2009b) concluded that the OMV was around 740 Ma.

The OMV environment was identified by Stern (1981) as a restricted back-arc basin or small oceanic rift. He concluded that the OMVs probably formed by 20–25% partial melting of previously depleted mantle, while the YMVs were thought to be 2–10% melting of hydrous undepleted mantle.

The outcrops of OMVs are typically in contact with ophiolitic metagabbro, e.g. along the Wadi Allaqi suture, and between Gabal Eraddia and Gabal El Rubshi; or form inclusions within serpentinite massifs e.g. in the Barramiya range and at Gabal Umm Salim. Some large OMV exposures lie within metasediment exposures e.g. between Kadabora intrusion and Wadi El Imra, and along Wadi Sukkari.

6.7.2 Younger Metavolcanics

The YMVs occupy larger more continuous areas of the Eastern Desert than the OMV, and were erupted over a much longer period, from 850 to 620 Ma, during which they represented a large portion of the surface products of the island arc stage. The YMVs typically vary in composition from mafic (basalts, andesites) to felsic (dacites, rhyodacites, rhyolites, felsites, pyroclastics), and were metamorphosed during the arc collision stage to grades ranging from lower greenschist to amphibolite facies. Primary features are commonly well preserved and include porphyritic, ophiolitic, vesicular, amygdaloidal, fluxional and pyroclastic textures. YMV metabasalts characteristically have plagioclase and/or pyroxene phenocrysts, while OMV metabasalts are usually aphyric.

The best studied YMVs are in the CED. Abu El Ela (1992) found bimodal metavolcanic compositions at Igla El-Iswid, west of Marsa Alam, that he believed were island arc tholeiites with felsic melts derived by fractional crystallization. The metavolcanics at Wadi Kareim and Wadi El Dabbah (Ali et al. 2009b) consist of tholeiitic to calc-alkaline low-grade metamorphosed basalts, andesites and minor dacites, overlain by metasediments, including BIFs. While geochemically similar in many respects, the Kareim metavolcanics leaned towards a more tholeiitic MORB affinity and were thought to have formed in a back-arc basin, while the El Dabbah with more calc-alkaline character formed in an arc environment. Both formed by melting of depleted mantle. The Kareim and El Dabbah YMVs were U-Pb zircon dated at ~750 Ma but contained many pre-Neoproterozoic zircons (up to 2.7 Ga), perhaps derived from underlying metasediments or continental crust. Ali et al. (2009b) gave a U-Pb zircon date of 769 ± 29 Ma for a Kareim felsic tuff lacking xenocrystic zircons. An El Dabbah andesite contained zircons as young as 734 ± 7 Ma.

Altogether, the age of the Kareim and El Dabbah YMV is ~750 Ma. This age is probably representative for CED metavolcanics, and is further supported by U-Pb TIMS 748 ± 3 Ma age for zircons from felsic metavolcanics of the area (Andresen et al. 2009). Ali et al. (2009b) found ε_{Nd} values (at 750 Ma) to be +6.7 to +8.9 for Wadi Kareim metavolcanics, and +5.1 to +7.5 for Wadi El Dabbah. These are close to DM model values, though the slightly lower values for El Dabbah suggest some crustal contamination. Analysis of discordant zircons from Kareim and El Dabbah yielded negative values of $\varepsilon_{Hf}(t)$ confirming the possibility of contamination from pre-Pan-African materials. Filtered τ_{DM} ages averaged 0.72 Ga, close to the eruption age of 0.75 Ga.

There are disagreements between the recent U-Pb zircon dates and some previous Rb-Sr whole rock dates given by earlier workers (Stern 1981; Stern and Hedge 1985) for CED YMVs, e.g. Rb-Sr dates for Wadi El Mahdaf YMV at 622 ± 6 Ma, and Wadi Arak and Wadi Massar YMVs at 632 ± 28 Ma. With these dates may also be added Stern's (1981) 618–612 Ma estimate for YMVs. These younger dates may be a result of disturbances to the Rb-Sr isotopic system, though they are matched by a 639 ± 40 Ma U-Pb zircon age for metavolcanics from Wadi Arak by Dixon (1979). Hashad (1980) provided a Rb-Sr whole rock date of 890 Ma for metavolcanics from Wadi El-Miyah.

As noted above, the Shadli Metavolcanics, defined from a type section in the SED (El Ramly 1972), is taken to include the YMVs. El Ramly (1972) also highlighted other belts of metavolcanics—e.g. at Abu Swayel–Um Geriat in the SED, and Weiera-Samna in the CED. However, studies of the metavolcanics in the SED, including the type section, show that correlation between SED and CED metavolcanics along the lines of the OMV-YMV division may not be simple, or even possible. This may be partly due to the fact that the metavolcanics are found to be progressively younger northwards from 850 to 750 Ma common ages in the SED to 750–650 Ma or younger in the CED (Stern and Hedge 1985). Attempts to correlate the SED and CED sequences may obscure the changes in magmatic trends with time and the distinct environments in which the metavolcanics have formed.

The Shadli Metavolcanics were investigated at Wadi Um Samiuki near the type area in the SED by Searle et al. (1976), who divided the weakly metamorphosed volcanic sequence into two units. The lower unit was the Wadi Um Samiuki Volcanics, composed of basic and intermediate lavas and rhyolitic volcanics. The upper unit constituted the Hamamid Group, containing two cycles, each beginning with pillow basalts followed by acidic lavas. Kotb (1983) found the Hamamid Group to be a tholeiitic immature island arc series. A metarhyolite from Um Samiuki was K-Ar dated as 825 Ma by El Shazly et al. (1973). An immature island arc environment was preferred for the Shadli Metavolcanics by Noweir and Abu El Ela (1992). Stern et al. (1991) found the Hamamid Group to be bimodal, and distinguished the first cycle basalts as N-MORB tholeiites, and the second cycle as E-MORB tholeiites. Both were thought to be derived from strongly depleted mantle source. The environment, however, was suggested to be a high-volcanicity intra-continental rift, not an arc or back-arc basin. El-Shazly and El-Sayed (2000) thought that the Shadli Metavolcanics may be coeval OMV (back-arc) and YMV (arc) assemblages.

To the NW of Um Samiuki in the SED is the Kolet Um Kharit area of transitional greenschist to amphibolite facies metavolcanics, studied by El Ramly et al. (1982). It was described as a bimodal series of island arc tholeiitic to calc-alkaline basalt-andesite lavas, overlain by pyroclastics, then calc-alkaline rhyolites. Farahat (2003, 2006) also investigated Kolet Um Kharit and noted that the mafic and felsic metavolcanics appeared to be bimodal, and had similar trace element ratios (Zr/Nb; K/Rb; Ba/La, etc) and parallel LREE enriched patterns. The original setting of these rocks was suggested to be an oceanic plateau or an LIP (large igneous province) of the break-up stage, with plume-enriched mantle. The mafics were compared to within-plate basalts and contrasted with island arc basalts.

El-Shazly and Hegazy (2000) investigated metavolcanics at Magal Gebriel, northwest of Abu Swayel in the SED, and considered them to be equivalent to the YMVs. The metavolcanics were described as arc volcanics of transitional tholeiite to calc-alkaline basalt, andesite and dacite, metamorphosed to greenschist to lower amphibolite facies. The suite formed by fractional crystallization of melt derived by 5–8% partial melting of depleted mantle. The nearby Abu Swayel metavolcanics were Rb-Sr (whole rock) dated by Stern and Hedge (1985) as 768 ± 31 Ma, by El Shazly et al. (1973) as 842 ± 22 Ma, and by Hashad (1980) as 856 Ma. Obeid (2006) studied lower greenschist facies metavolcanics along Wadi Hodein. These included metamorphosed basalts, andesites and dacites of island arc environment. The basalts were transitional tholeiitic to calc-alkaline, and the andesites and dacites were calc-alkaline. Obeid preferred a fractional crystallization of mantle-derived magma to explain chemical variations in the suite.

Examples of YMVs are far fewer and smaller in the NED than those further south. Asran et al. (2008) described the metabasalts, meta-andesites and metadacites of the El Atrash area as calcalkaline island arc eruptives, equivalent to the YMV. El-Tokhi et al. (2010) studied the metavolcanics at Um Anab. These are greenschist to amphibolite facies tholeiitic amphibolites, and calc-alkaline meta-andesites, metafelsites and metarhyolites identified as YMV. El-Tokhi et al. observed that the range of compositions was not bimodal, and was probably a result of fractional

crystallization. The volcanics were erupted in an island arc environment at an active continental margin. Bühler et al (2014) reported metavolcanics near Gabal El Kharaza, and found them to be partly terrestrial lavas and tuffs of continental arc affinity. They recovered zircons, which provided dates of 717 ± 8 Ma and 725 ± 7 Ma for this sequence. A problem for identifying YMVs in the NED is their similarity to abundant Dokhan and Hammamat in the same area (Osman et al. (2001).

6.8 Metamorphosed Plutonic Association

Magmatic rocks of the island arc stage include tholeiitic and calc-alkaline suites of gabbros, diorites, granodiorite and granites within the range 980–620 Ma (Bentor 1985). These plutonites have been emplaced during all stages of subduction, and also during arc collision. They show varying degrees of deformation and metamorphism. Two popularly distinguished magmatic groups of the island arc stage are the metagabbro-diorite complex, followed immediately by the 'Older' or 'grey' granites.

6.8.1 Metagabbro-Diorite Complex

The metagabbro-diorite complex is a highly heterogeneous assemblage of deuterically altered (uralitized and saussuritized) gabbros, norites, minor hornblendites, dolerites and basalts that have been pervasively intruded by granitic veinlets. The granites show contamination by the mafic rocks or hybridization by interaction of granite with incompletely consolidated gabbro (Hassan and Essawy 1976), leading to hornblende diorite hybrid magmas found as veins, dykes, xenolith zones and pods with typically gradational contacts (Hassan and Hashad 1990). Rapid grain-size variations and minor secondary foliations are also characteristic of this complex. The rocks of the complex were later greenschist to amphibolite facies metamorphosed and mildly deformed. The metagabbro-diorite is dated between 980–870 Ma and is found to intrude metasediments, arc metavolcanics and serpentinites. It is intruded by Older Granites, with melanocratic diorite contamination zones at the contact of metagabbro-diorite wallrock and Older granites.

El Ramly and Akaad (1960) referred to these rocks as 'epidiorite-diorite association', though the term 'epidiorite' was dropped by Akaad and Essawy (1964), who introduced the name 'metagabbro-diorite' in their study of the best known example of this unit at Gabal Atud. The largest exposures of metagabbro-diorite complex in Egypt are found west of Marsa Alam (at Gabal Atud) and along Wadi Umm Gheig west of the Kadabora granite. Substantial exposures are found between 23° and 24°N, east of Wadi Kharit. The metagabbro-diorite complex is represented by smaller scattered exposures in the northern part of the CED and in the NED (e.g. at Wadi Atalla—Abd El-Rahman et al. 2009a; and Wadi El Bula—Fowler et al. 2006). Small examples of metagabbro-diorite in the Sinai were described from Wadi Baba (Abdel-Karim 1995) and the Shahira ultramafic-gabbro intrusion in the Wadi Kid Complex (El-Gharabawi and Hassen 2001), however, 632 Ma dated zircons from the Shahira intrusion indicate that it is too young for metagabbro-diorite, and is probably part of the younger Kid arc (Be'eri-Shlevin et al. 2009b; Azer et al. 2016).

Geochemical study by Hassan and Essawy (1976) established that the metagabbro-diorites were calc-alkaline. Akaad and Noweir (1980) grouped them with the Sid Metagabbro. Furnes et al. (1996) confirmed that the metagabbro-diorite complex members were calc-alkaline and formed in an oceanic island arc setting during subduction. They gave ε_{Nd} values of +5.9 to +7.9 (850 Ma) indicating their derivation from depleted mantle. Abdel-Rahman (1995) referred to this association in the NED as 'gabbro-diorite-tonalite complex', dated it at ~880 Ma (Rb-Sr) and found it to be tholeiitic in chemistry. Ghoneim et al. (1992) identified three chemically distinct metagabbro groups, of which the metagabbro-diorites were calc-alkaline to tholeiitic and formed in a back-arc environment. Hassan and Hashad (1990) thought that the metagabbro-diorite was a "border facies for the huge batholithic (Older Granite) intrusions" produced by interaction of these batholithic melts with older ocean floor sequences. Mohamed and Hassanen's (1996) study indicated a mild tholeiitic to calc-alkaline continuum of compositions, and identified them as the earliest manifestations of island arc activity (~980–870 Ma). The evolution from primitive tholeiite to calc-alkaline chemistry reflected the progressive incorporation of subduction zone components. Derivation of the metagabbro-diorite by melting of a metasomatized upper mantle wedge was confirmed by Moghazi et al. (1999). They contrasted this magmatic origin with that of the following Older Granites, which were derived from melting of lower crust.

Fowler et al. (2006) described Ras Barud hornblende schists defining extension ductile shear zones that intersected an island arc core, tapping mafic and felsic magmas that intruded the shears, making the shear zones very hot. The parent of the amphibolites was thought to be metagabbro-diorite and mafic arc volcanics. Zoheir et al.

(2008) noted that metagabbro-diorite complexes are normally compositionally zoned, e.g. in the Um Eleiga complex, which intrudes the Abu Dahr ophiolitic serpentinites. The Um Eleiga complex has a core of gabbro surrounded in turn by diorite, tonalite and granodiorite. The zoning was due to fractional crystallization and assimilation of parent calc-alkaline magma. They concluded that the intrusion formed at 4–5 kbars in an early subduction zone setting.

6.8.2 Older or Synkinematic Granitoids

The 'Older Granites' (Akaad and El Ramly 1960), also known as 'Grey Granites', 'Synorogenic Granites' or 'Shaitian Granites' are typically giant intrusions of white to light grey tonalite, granodiorite and trondhjemite. The petrography of these granitoids is simple, being combinations of quartz, oligoclase-andesine, green hornblende and brown biotite, with minor orthoclase, and accessory apatite, sphene, allanite, epidote, chlorite and magnetite. The intrusions commonly have margins concordant to wallrock structure, and may be flow foliated, gneissic or schistose at their margins. They intrude the metavolcanics, metasediments and metagabbro-diorite complex. Any of these units may appear as xenoliths of various sizes and degrees of interaction with the magma.

The Older Granites are particularly abundant in the SED and NED, less so in the CED. These calc-alkaline plutons were intruded over a very long period of time from >850 to 615 Ma. This is a similar time range to the metavolcanics, though in any locality where a primary contact between the two is preserved, the Older Granite intrudes the metavolcanics. With such an extended age range (>220 My) there are likely to be several stages of Older Granite magmatism, and probably a number of different tectonic associations for these intrusives (Hassan and Hashad 1990). The latter authors recognized three such magmatic events: the Shaitian event (850–800 Ma), the Hafafit event (710–670 Ma) and the Meatiq event (630–610 Ma). Stern and Hedge's (1985) compilation of radiometric data led them to suggest three igneous events that include Older Granites. These were a 715–700 Ma event (Dhahanib intrusion in the SED); a 685–665 Ma event (similar to Hafafit event above, and including SED Hafafit, CED Wadi Mia, and NED Mons Claudianus intrusions); and a 625–610 Ma event (similar to the Meatiq event, and including CED Abu Ziran and NED granodiorite intrusions). Lundmark et al. (2012) used a radiometric database of samples within and near to the Hafafit complex to define three syn-orogenic (compressional tectonic) igneous events, namely, a 705–680 Ma event (Hafafit and El-Sibai gneissic tonalites); c. 660 Ma event (a tentative event with examples from Hafafit and perhaps El-Sibai); and a 635–630 Ma event (Meatiq Abu Ziran gneissic intrusion). Their fourth and fifth events at 610–604 Ma and 500–590 Ma, respectively, were thought to be associated with activity of the Eastern Desert Shear Zone (EDSZ). The work of Lundmark et al. (2012) is significant in confirming links between magmatic events and tectonic stages—compressional arc-collision stage first, and extensional, perhaps delamination stage second. In the following text we provide description of examples of deformed Older granites from three tectonic settings: (a) subduction-zone granitoids (deformed after intrusion, e.g. granitoids of Wadi Shait and Gabal El-Maiyit); (b) syn-collision granitoids (deformed during intrusion into active tectonic structures or compressional deformation zones, e.g. Hafafit and El-Sibai tonalites); and (c) syn-extensional(?) shear zone granitoids (e.g. Abu Ziran intrusion at Meatiq).

6.8.2.1 'Shaitian' Granites

This group of older granitoids was separated from the more abundant Grey Granites by Schürmann (1953), as he thought they were pre-metasediment, while Grey Granites were post-metasediments. This claim was challenged by El Ramly and Akaad (1960) and refuted by Moustafa and Akaad (1962), who showed that the Wadi Shait granitoid was intruded into the metasediments. El Ramly (1972) included Shaitian granites with the rest of the Grey Granites, and Hussein et al. (1982) included Shaitian granites with other subduction-related G1 granites. El-Gaby et al. (1983, 1988a), however, continued to regard the Shaitian granites as ancient continental basement. The Shaitian "granites" are I-type calc-alkaline intrusions of mainly tonalite-trondhjemite (and minor granodiorite) composition, typical of immature ensimatic island arc (VAG) (El Kalioubi and El Ramly 1991). The Wadi Shait intrusion has been metamorphosed to greenschist facies during cataclasis and mylonitization in a low angle shear zone, resulting in augen gneiss (with characteristic blue quartz porphyroclasts), protomylonite, mylonite and schists indicating high plastic and brittle strain. Greiling et al. (1993) identified that shear zone as the floor thrust for the Hafafit thrust complex. The age of the Wadi Shait intrusion has been reported as 876 Ma (Rb-Sr, whole rock) (Hashad et al. (1972). Kröner et al. (1994) report a lower age of 730 Ma (U-Pb, Pb-Pb zircon) for the Wadi Shait intrusion. El Ramly and Akaad (1960) discovered that Gabal El-Maiyit (CED) was identical to the Wadi Shait granite. Gabal El-Maiyit has been dated at 883 Ma (Rb-Sr, whole rock) by El Manharawy (1977).

6.8.2.2 Hafafit Tonalites

The most striking feature of the Migif-Hafafit Complex is its intriguingly shaped dome structures, cored by gneissic tonalite and associated rocks. Hafafit was originally viewed as an example of pre-Pan-African gneissic basement (Hume 1935), and this view remained popular into the 1990s (El-Gaby 1983, 1994; Abdel-Khalek and Abdel Wahed 1983; El-Gaby et al. 1988a; Abdel-Khalek et al. 1992; Khudeir et al. 2008), though support has diminished as more geochemical, isotopic, geochronological and structural work has accumulated, pointing to a juvenile origin for the components of the complex.

Early studies by El Ramly et al. (1984) and Greiling et al. (1984,1988) identified the granitoid in the domes as intrusives into the psammitic and biotite paragneisses and hornblende orthogneisses, during intense isoclinal folding (D2 deformation) and high temperature (M2) metamorphism (M1 being a preceding syn-D2 migmatization event). The tectonic setting was described as Andean subduction. Radiometric dating of single zircons from the gneissic domes by Stern and Hedge (1985) (Pb-Pb date, 682 Ma), Kröner et al. (1994) (Pb-Pb date range, 700 ± 12 to 677 ± 9 Ma) and Lundmark et al. (2012) (U-Pb data, range 680–705 Ma) confirm that they are identical to other Older Granite intrusions surrounding the complex. Rashwan (1991) and El Ramly et al. (1993) noted that strain is most intense at the margins of the domes, where it is characterized by isoclinally folded gneissic foliations, deformed pegmatitic vein networks and digested xenolith zones. There are blocks of serpentinite and concordant lenses of foliated metagabbro at the margins of some domes. Strain is minimal in the cores of the domes, where magmatic textures are commonly preserved. The northernmost dome (referred to as dome A) is tonalite cored (intruded 698 ± 14 Ma), while domes B and C to the south are cored by granodiorite, and the largest dome D, and dome E, farthest south, are cored by trondhjemite (intruded 677 ± 9 Ma). Mineralogical variations exist from the margin to the core of dome A, in that there is a higher percentage of quartz and hornblende at the margin, but more biotite in the core.

The Hafafit tonalites are I-type calc-alkaline, LREE-enriched and HREE-depleted, with evidence for crystal fractionation (Rashwan 1991; Kröner et al. 1994). Hafafit granitoid compositions plot in the field of volcanic arc granitoids (VAG). They were intruded in an active continental margin setting, and have similar chemistry to other Older Granites in the EED, including the Shaitian granites and the Older Granites of the NED. An initial $^{87}Sr/^{86}Sr$ ratio of 0.7024 (Stern and Hedge 1985) is inconsistent with these magmas being derived from a pre-Neoproterozoic source. Low initial $^{87}Sr/^{86}Sr$ and ε_{Nd} between +5 and +7 are indicative of a depleted mantle source for these magmas (Liégeois and Stern 2010). The τ_{DM} Nd model ages for Hafafit tonalites are 0.69 ± 0.007 Ga, close to their emplacement age, indicating no contribution from pre-Pan-African crust.

The (M2) metamorphic P-T conditions affecting the Hafafit complex during intrusion of the tonalites have been estimated by Abd El-Naby and Frisch (2006), Abd El-Naby et al. (2008), El Bahariya (2008) and Abu El-Enen et al. (2016) to be from lower T estimate of 570–675 °C to >700 °C, though the greater difference is in the pressure estimates that range from 5 kbars (18 km depth) to 9–13 kbars (33–47 km depth). These pressure (depth) values give geothermal gradients of 39 °C km^{-1} (5 kbars) to 21 °C km^{-1} (9 kbars) to 15 °C km^{-1} (13 kbars), whereas the normal range for a magmatic arc is 25–50 °C km^{-1}, favouring values closer to the lower pressure estimate. The stability of sillimanite in the metapsammitic gneisses also places a limit on the pressure at peak metamorphic temperatures of 700 °C at about 8 kbars.

The ~600 Ma regional extensional event in the EED led to uplift and cooling of the Hafafit complex. The cooling may be recorded in the $^{40}Ar/^{39}Ar$ cooling ages for hornblende of 584 and 586 Ma, provided by Fritz et al. (2002). Liégeois and Stern (2010) also noted that their Rb-Sr dates for Hafafit gneisses (609 ± 17 Ma), probably reflected resetting of the Rb-Sr system during this extension event.

6.8.2.3 El-Sibai El Shush Tonalite

Unlike the Meatiq and Hafafit gneissic complexes, the El-Sibai complex was not regarded by early workers as ancient continental (fundamental) basement (Hume 1934; Schürmann 1966; El Ramly 1972). However, following El-Gaby's (1983) model of ensimatic nappes thrusted westwards over infrastructural gneisses, the El-Sibai was regarded by many workers as a pre-Pan-African basement dome surrounded by low-grade ensimatic nappes of mainly arc metavolcanics and ophiolitic material (El-Gaby et al. 1988a; Kamal El Din et al. 1992; Khudeir et al. 1992). The orthoamphibolites and schists of the El-Sibai complex have been intruded by gneissic diorites, tonalites and granodiorites on its western flank. At its northwestern end it has been intruded by the alkaline El-Sibai granite, and at its southeastern end it is intruded by the mylonitized Um Shaddad granite. The structure of the El-Sibai complex was revised by Fowler et al. (2007) who found that there were ensimatic nappes structurally below, as well as above the high temperature gneisses and amphibolites of the complex. In the latter authors' model the gneissic granitoids intruded the ensimatic nappes during their NW-wards translation at the stage of arc collision, and acquired their deformation characteristics as syn-kinematic intrusions.

The largest of the gneissic intrusions is the El Shush tonalite, which extends in a NW direction for about 36 km at the western margin of the complex and is about 6 km wide.

The El Shush tonalite has a moderately dipping lens-like geometry with an estimated thickness of 2 km. The El Shush is a biotite tonalite in its higher levels and diorite in its lower levels. The diorite and tonalite appear to have been separate contemporary melt phases that meet in a zone of enclaves indicating magma mingling. Another lens-shaped syn-magmatic intrusion of biotite-muscovite granodiorite is located in the core of the El Shush (Fowler et al. 2007). Primary fabrics include schlieren and flow-oriented phenocrysts, locally defining a linear fabric. Secondary strain effects are represented by a weak gneissosity or schistosity at a low angle to the primary fabrics. Fowler et al. (2007) found submagmatic textures (relocation of residual melt during deformation of a semiconsolidated crystal mush) indicating intrusion during deformation of the wallrocks. The El Shush tonalite is cut by a major ENE trending sinistral strike-slip fault—the El Shush shear zone—along which high strain mylonitic shears are found (Ibrahim and Cosgrove 2001; Abd El-Wahed 2008). Ibrahim and Cosgrove (2001) thought that the El Shush had intruded along this strike-slip fault, however the trend and geometry of the El Shush is not compatible with this model. Fritz et al. (1996), Bregar et al. (1996, 2002) and Fritz and Messner (1999) regarded the intrusion of the El Shush as contributing to the slow exhumation of the complex by magma rise.

Bregar et al. (1996, 2002) dated the El Shush to 695–680 Ma. This age was confirmed by Augland et al.'s (2012) U-Pb TIMS zircon ages of 682 Ma for the El Shush. These dates place the El Shush tonalite within the Older Granite group. Khudeir et al. (1995) and Bregar et al. (2002) described the El Shush tonalite as an I-type calc-alkaline intrusion of island arc setting. Bregar et al. also concluded that there was no contribution from pre-Pan-African crust. They recognized fractional crystallization in the evolution of El Shush magma.

6.8.2.4 Abu Ziran Tonalite

The Meatiq complex consists of structurally lower gneissic granitoids and high temperature metasediments (referred to by some as infrastructure or tier 1) and an overlying NW-transported nappe sequence of greenschist facies ensimatic arc lithologies and ophiolitic mélange (superstructure or tier 2). These two structural levels are separated by a ~2 km thick mylonitic zone containing intensively sheared components of both levels (Ries et al. 1983; Sturchio et al. 1983a, b; Habib et al. 1985a, b). The sheared zone is folded into a dome shape carapace enclosing the high grade rocks in the core of the complex. The sheared zone forms part of a much larger structure—the Eastern Desert Shear Zone (EDSZ—Andresen et al. 2010), which will be described in the next section. This sheared zone has been intruded synkinematically by numerous, mainly small bodies of diorite to trondhjemite (the diorite slightly older and more deformed than the trondhjemite), with affinities to the Older Granites. The smallest of these are preserved as amphibolitized lenses within the protomylonites, mylonites and schists of the shear zone. The largest intrusion of this group is the Abu Ziran tonalite (also referred to as the Abu Fannani tonalite by Habib et al. 1985a, and Neumayr et al. 1998).

The Abu Ziran synkinematic intrusion is composed of hornblende-biotite tonalite (Sturchio et al. 1983b), though this intrusion is inhomogeneous, with the western, narrower, more deformed, earlier part having diorite-tonalite composition; and the eastern, wider, less deformed, later SiO_2-richer, eastern part having granodiorite composition (Fritz et al. 1996, 2014). The intrusion has abundant xenoliths of amphibolite and serpentinite. Initial $^{87}Sr/^{86}Sr$ ratios for the Abu Ziran are 0.7030 (Stern and Hedge 1985). It shows LREE enrichment and is calc-alkaline with subduction-related chemistry (Sturchio et al. 1983b). Fritz et al. (2014) showed that the Abu Ziran was a high-K calc-alkaline magma with composition plotting in the VAG field. The Abu Ziran magma evolved at 20 km depth (5.5 kbars) at >900 °C giving a high geothermal gradient of 45 °C km^{-1}, probably due to lithospheric thinning during extension (Fritz and Puhl 1996).

The Abu Ziran tonalite was intruded into a zone of top-to-the-S tensional shearing, which is a characteristic of the southern margin of the Meatiq complex (Wallbrecher et al. 1993). Fritz et al. (1996) explained the role of these normal sense shear zones in terms of the rise of the Meatiq as a core complex, and the complementary subsidence of nearby Hammamat basins. Time of activity on the normal shears was estimated at 595 Ma by $^{40}Ar/^{39}Ar$ of synkinematic micas in the shears (Fritz et al. 1996). The Abu Ziran was intruded into a growing tension gash structure association with transpression at this southern margin. The intrusion was associated with W to E magmatic flow and a decrease in strain to the E, with change in the shape of the strain ellipsoid from oblate to prolate from W to E (Fritz et al. 2014). The Abu Ziran intruded during the extensional D3 deformation event (Loizenbauer et al. 2001) and M3 greenschist facies metamorphism (Neumayr et al. 1998). Pressure at the time of crystallization is estimated as 4–5 kbars (Fritz et al. 1996).

This synkinematic intrusion is significant in providing a date for shear activity on the mylonitic carapace, which in turn constrains models for the evolution of the Meatiq complex. Single zircon U-Pb dating of the Abu Ziran by Stern and Hedge (1985) gave 614 ± 8 Ma crystallization age for this intrusion. However, the NW-displacement of ophiolitic nappes over the gneissic rocks (the Abu Ziran 'Orogeny' of Habib et al. 1985a), took place a little before the development of the extensional shears accommodating the

Abu Ziran tonalite. The U-Pb TIMS zircon dating of Abu Ziran zircons at 606 ± 1 Ma by Andresen et al. (2009), along with similar dates for other synkinematic diorite lenses in the mylonite zone (crystallization ages 606 ± 1 Ma and 609 ± 1 Ma), indicate late top-to-the-S extensional shearing at the southern margin of the Meatiq complex related to the ~600 Ma tectonic extension stage.

6.9 Shear Zones

Ductile shears zones and equivalent brittle faults are essential structural features of all stages in the evolution of the ANS. They must have existed in the early rifting and oceanic development stage, though there is little chance of recognizing structures of this age. Ductile extensional shears in the Feiran-Solaf complex may belong to this stage, but dating of this complex is still controversial. Major shear zones formed in the subduction stage in spreading forearcs, back-arcs, and in compressional settings, such as accretionary prisms and trench complexes. The amphibolite facies ductile normal shears near the NED-CED boundary in the Ras Barud area, which are interpreted as related to arc rifting by Fowler et al. (2006), may date from this stage. Ductile thrusts and reverse faults accompanied the arc collision stage in all parts of the ANS, and are represented in suture zones and in deformed forearc, arc and back-arc regions. These are typically the earliest stuctures to be confidently correlated with tectonic events. The south-vergent steep reverse faults north of the Allaqi–Heiani suture, the NW-ward vergent mylonites in the Hafafit complex and El-Sibai complex are also good examples. The tectonic extension stage at ~600 Ma generated a set of regional low dipping (?)normal sense shear zones, for example the Eastern Desert Shear Zone. These were followed by widespread mainly W- and SW-directed thrust faulting during the East and West Gondwana collision. Late E-W shortening produced major NW-SE trending sinistral ductile shears and wrench faults of the Najd Fault System, accompanied by ENE- to NE-trending dextral shear conjugates, and N-S trending high strain shortening zones, which some have identified as possessing a shear component. Metamorphic conditions during shearing are typically greenschist to amphibolite facies, with some shears being hotter than their wallrocks due to synkinematic intrusions along the active shears. In this section we have chosen three important shear zones to describe. These are the Nugrus Shear Zone and Shait Shear Zone at the CED-SED boundary, and the Eastern Desert Shear Zone in the northern half of the CED. These were chosen due to their tectonic significance, their size, their economic importance (Nugrus), and the history of lively debate surrounding them (Fig. 6.11a, b).

6.9.1 Nugrus Shear Zone

The Nugrus Shear Zone (NSZ) is a NW-trending zone of mylonites, schists and minor gneissic granitoids, extending from the junction of Wadi Nugrus with Wadi Shait at the tip of the Hafafit complex, and continuing along Wadi Nugrus to Wadi Gemal, a distance of 45 km. On most regional geological maps, the NSZ is shown continuing to the Red Sea coast at Wadi Ranga, giving an 85 km overall length. The section from Wadi Shait to Wadi Gemal is the best studied segment of this structure. In this segment the shear zone has a steep dip (70°NE), and maintains a thickness of ~700 m (Harraz and El-Sharkawy 2001; Fowler and Osman 2009). This segment also hosts an abundance of exotic mineral and ore deposits, including tourmaline, beryl, zircon, cassiterite, monazite, wolframite, fluorite, topaz, and Li, Nb, Ta, Th and U ore minerals (El Gemmizi 1984; Abdalla and Mohamed 1999; Harraz and El-Sharkawy 2001; Harraz et al. 2005; Grundmann and Morteani 2008; Saleh et al. 2012), which attest to diverse hydrothermal fluid activity along this shear zone.

The sheared rocks in the NSZ include metasediments, metabasites and ophiolitic materials represented by garnet mica schists, tourmaline chlorite schists, chlorite graphite schists, quartzites, amphibolites, hornblende biotite schists, serpentinite, actinolite schists and talc schists. These were derived from both the high T rocks of the Hafafit complex and the ophiolitic mélange of the Wadi Ghadir complex, which are juxtaposed against the shear zone. The NSZ is intruded by leucogranites and pegmatites, commonly boudinaged and foliated, with intrusions mostly concordant to the shear zone mylonitic foliations. The foliations have stretching lineations (assumed to represent displacement vectors), typically gently plunging to the NW or SE (El Bahariya and Abd El-Wahed 2003; Fowler and Osman 2009). Sense of slip indicators consistently show a dominant *apparently* sinistral sense of shear on the NSZ (Unzog and Kurz 2000). Metamorphic conditions in the NSZ reached the amphibolite facies, with 550 °C and 3–4 kbars estimated by El Bahariya and Abd El-Wahed (2003). This is hotter than the conditions experienced by the hangingwall ophiolitic rocks, presumably due to the synkinematic granitoid intrusions along the shear zone. Kyanite has been reported (Awad 1994; El Rahmany et al. 2015), perhaps representing cooler (<450 °C) parts of the shear zone. Shearing on the NSZ continued as temperatures dropped, allowing overprint of high temperature foliations by brittle deformation with same kinematics, and retrogression of the earlier higher T phases.

The tectonic significance of the NSZ is its most controversial aspect. While the apparent sinistral slip sense on this zone is not disputed, the structural and tectonic significance of it is. There are three models:

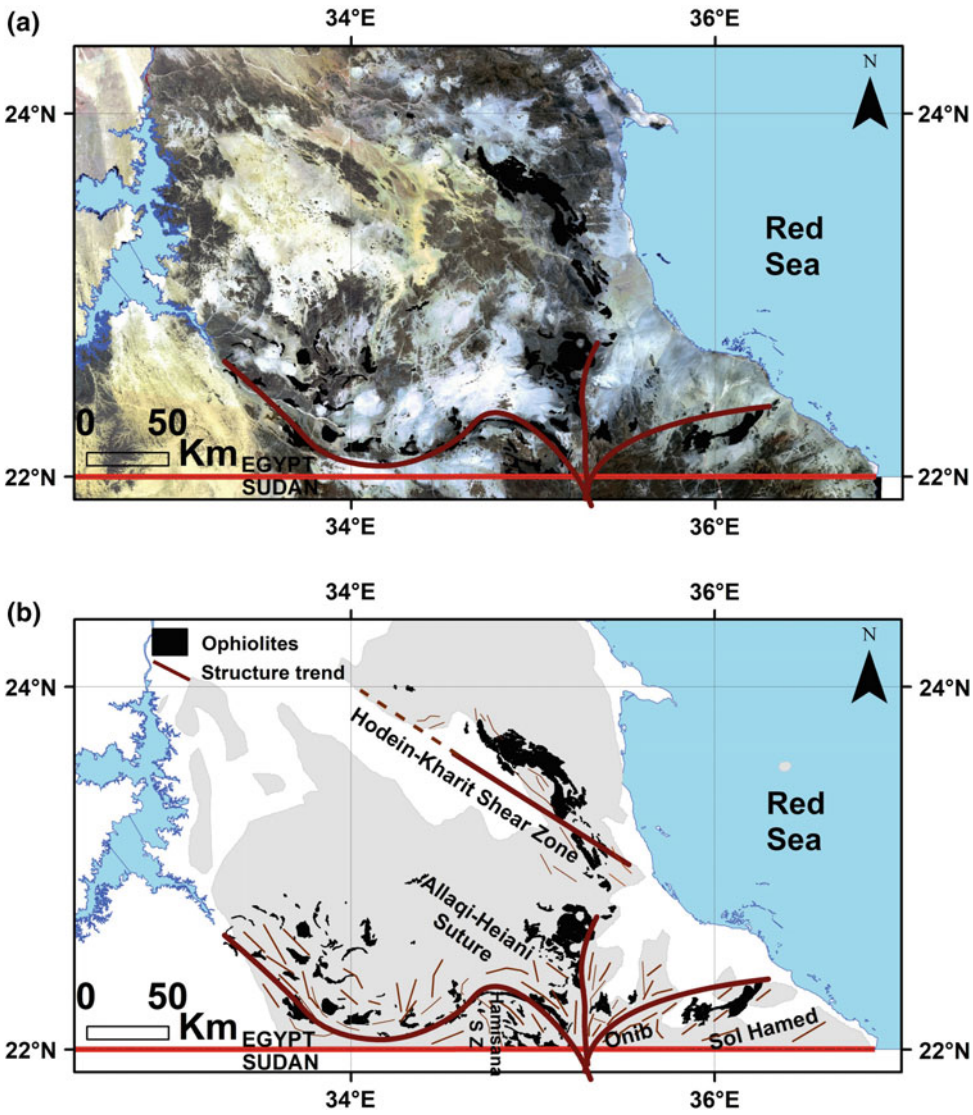

Fig. 6.11 **a** False color Landsat8 satellite image (7, 5, and 3 in RGB) for the SED and Northern Sudan overlaid by the ophiolites occurrences and **b** Simplified regional geological map showing the major deformational zones as well as structural trends in the SED and Northern Sudan

(1) the earliest structural work by Greiling and El Ramly (1985) and Greiling et al. (1988) regarded the NW-striking NGS as initially a lateral ramp for NW-wards thrusting of low grade arc assemblages over the Hafafit gneisses. This accounted for the sinistral sense of slip on the NGZ. With a change in tectonic convergence direction, the NGZ later became a frontal ramp for rethrusting of Wadi Ghadir ophiolites SW-wards over the Hafafit complex.

(2) the core complex evolution model for CED gneissic complexes by Fritz et al. (1996) re-interpreted the NGZ as fundamentally a sinistral strike-slip structure. It was viewed as an element of the Najd Fault System. In this model, the NGZ links with the normal faults along Wadi Shait to assist the rise of the Hafafit gneissic complex.

(3) the recognition of continuity of the Wadi Shait and Wadi Nugrus thrust belts at the northern tip of the Hafafit complex led Fowler and Osman (2009) to suggest that the two shear zones were part of one original low angle normal shear that was later macrofolded about a N to NW striking axial plane. This folding more or less preserved the orientation of the Shait segment, but rotated the Nugrus segment to a steep orientation with subhorizontal slip lineations and an *apparent* sinistral shear sense.

Model (2) remains the most popular, with strain and AMS fabric studies (Hagag et al. 2018) developing the model

further as a transpression zone, with flower structure. A variant on model (2) recognizes the lateral ramp aspect of (1) followed by the strike-slip function of (2) (Makroum 2003; Helmy et al. 2004). Shalaby (2010) thought that the strike-slip NSZ overprinted earlier SW-ward thrust duplexes of Wadi Ghadir ophiolites. The main problem for model (2) is the sudden termination of the NSZ at Wadi Shait. This is not expected for a major strike-slip shear zone. Some authors have extended the NSZ beyond Wadi Shait and farther into the CED where it is shown to link with the Um Nar Fault near Wadi Mubarak (Shalaby et al. 2005; Johnson et al. 2011; Hagag et al. 2018; Hamimi et al. 2019). While this is a popular hypothesis, there is no field or remote sensing evidence for this proposed extension of the NSZ (Fowler and Osman 2009; Abd El-Wahed 2014). Abd El-Wahed (2014) and Abd El-Wahed and Thabet (2017) mapped the Mubarak Barramiya Shear Belt (MBSB), a broad ENE-trending belt of thrusts and dextral ductile shears that interrupts the proposed extension of the NSZ to Wadi Mubarak. Other workers have tentatively extended the Wadi Shait fault across the termination of the NSZ (Makroum 2017). A problem for model (3) is the requirement that macroscopic folding produced a very long (85 km) rotated eastern fold limb (represented by the NSZ). This model can be modified in the light of studies of detachment megafaults that have not been disturbed by later deformation. Detachment fault geometry is usually "corrugated", giving a sinusoidal strike trace of the fault, with corrugations showing wavelengths of 10–30 km and amplitudes 1–2 km (Friedmann and Burbank 1995; Ersoy et al. 2011; Oner and Dilek 2011). If this is applicable, the λ-shaped northern end of the Hafafit complex could be an antiformal corrugation in a detachment shear.

6.9.2 Sha'it Shear Zone

The Shai't Shear Zone (SSZ) along Wadi Sha'it has many features in common with the Nugrus Shear Zone described above. The SSZ extends about 42 km in the NE-SW direction along Wadi Sha'it, from the northern tip of the Hafafit complex to Gabal Sufra. The footwall of the SSZ is represented by metapsammitic gneisses and migmatites, while the hangingwall consists of arc metavolcanics and ophiolites, however, the exposure of the SSZ along Wadi Sha'it is rather poor compared to the NSZ along Wadi Nugrus. There are only a few places of continuous exposure from footwall to hangingwall. In addition, the most northeasterly 5 km of the SSZ shows thinning of the shear zone due to loss on a later steeper normal fault along Wadi Sha'it. The preserved parts of the SSZ are nowhere more than 500 m thick.

The SSZ dips 15–35°NW and is defined by foliations that overprint the high temperature gneissic and migmatitic foliations of the metapsammites and biotite schists of the footwall (Rashwan 1991). Shear foliations in the footwall are muscovite schists and mylonites. Oddly, riebeckite is also a foliation-defining phase taking the place of hornblende and biotite locally. The riebeckite is due to syn-kinematic Na metasomatic effects (El Ramly and Saleeb Roufaiel 1974). Other metasomatic phases are fluorite, zircon and sphene, suggesting Na, Zr, Ti, F hydrothermal fluids, similar to those inferred for the Nugrus Shear Zone. Thin mylonitized red granite sheets intruded along the shear foliations of the footwall (Fowler and Osman 2009). The stretching lineations on the shear zone foliations plunge nearly downdip. Shear sense indicators in the mylonites (Fowler and Osman 2009) and quartz crystallographic fabrics (Unzog and Kurz 2000) indicate a top-to-the-NW shear sense on the mylonitic foliations, giving a low-angle normal fault (LANF) slip sense.

Slip lineations for the SSZ and NSZ are parallel. There are also F3 folds that are parallel to these slip lineations allowing the possibility that the SSZ and NSZ were once parts of one continuous LANF shear zone as described above for the NSZ. This is the interpretation of the SSZ by Fowler and Osman (2009). Based on differences of metamorphic pressure recorded in the assemblages of the hangingwall and footwall, these authors estimated displacement on the SSZ of 15–30 km. As with the NSZ there are other interpretations of this shear. Fritz et al.'s (1996) model for the rise of the Hafafit complex considered the SSZ as a steeper normal fault zone. Greiling et al. (1996, 1988) and Greiling and Rashwan (1994) regarded the SSZ as the NW dipping roof thrust of the thrust duplexes, which were transported to the NW over the Hafafit complex.

6.9.3 Eastern Desert Shear Zone

The Eastern Desert Shear Zone (EDSZ) is potentially the largest shear structure in the EED, however, its low dip and the limited depth of exposure in the EED make tracking and correlating this structure a difficult task. There are very few studies that have targeted the EDSZ, and as a result, the data on this structure are incomplete in most aspects, including its extensional or compressional nature and therefore its relations to tectonic events. In the following text we will attempt to build a picture of this structure based on the best studied exposures.

The largest continuous exposure and amongst the earliest recognized occurrences of the EDSZ is at Meatiq, where the EDSZ forms the highly sheared 1800 m thick carapace separating the Meatiq gneisses from the overlying

greenschist facies arc metavolcanics and ophiolitic mélange (Ries et al. 1983; Sturchio et al. 1983a, b; Habib et al. 1985a, b). Sturchio et al. (1983a, b) thought that this shear zone was related to compressional tectonism. The EDSZ at Meatiq consists of sheared ensimatic cover rocks in its upper part (mafic mylonites with slivers of serpentinite) and sheared high temperature metasediments and gneisses in its lower parts (quartzofeldspathic mylonites and phyllonites). The shear zone foliations are protomylonites, mylonites and schists enclosing lenses and boudins of more resistant rock, including syn-shearing diorites and tonalites dated at 606–609 Ma (Andresen et al. 2009). The metamorphic temperatures in the shear zone are lower than those sufficient for phases hornblende, garnet, sillimanite and staurolite to be stable (Habib et al. 1985a; Neumayr et al. 1998). The youngest unit affected by this shear zone in Meatiq is the ~630 Ma Um Ba'anib gneissic granite. This constrains shear activity on the EDSZ to later than 630 Ma and active at 606 Ma (Andresen et al. 2010). A well-developed stretching lineation on these foliations trends NW-SE and shows kinematic indicators for top-to-the-NW shear sense.

The mylonitic foliations enclosing the Meatiq dome can be traced to the west into the Um Esh-Um Seleimat molasse basin, where the deeper mylonites show temperatures of shearing at which hornblende is stable. The foliations are strongly folded about NW-SE trending axial planes (Fowler and El Kalioubi 2004). In the Um Esh-Um Seleimat area the EDSZ has affected Hammamat conglomerates and the metabasalts of the unconformably underlying mélange. The shear sense is again top-to-the-NW. Farther west, the EDSZ shear foliations are dissected by SW-vergent thrusts along Wadi Atalla. The shear foliations can be traced around the Um Had dome. On opposite sides of this dome the EDSZ shows a reversal of apparent sinistral (eastern limb of the dome) to dextral (western limb of the dome) interpreted by Fowler and Osman (2001) as folding of an originally gently dipping top-to-the-NW shear zone. The EDSZ on both limbs of the Um Had dome is affected by thrusting, making its thickness estimate very approximate, though the EDSZ is probably not more than 1000 m thick on the western limb, while on the eastern limb it has affected the ~2 km thick post-Hammamat Atalla Felsite. The Um Had granite (596.3 ± 1.7 Ma, Andresen et al. 2009) and the Atalla monzogranite (615 ± 9 Ma, Zoheir et al. 2018) are unaffected by the EDSZ shearing. This indicates that EDSZ shearing ceased before 606 Ma. The total restored (unfolded) NE-SW dimension of the EDSZ, based on a constructed cross-section from Meatiq to Um Had is about 65 km (Fowler and El Kalioubi 2004).

Top-to-the-NW shear on low dipping planes is evident in the Wadi Hammamat basin sediments south of Um Had granite (Fowler and Osman 2001). The ESDZ foliations or equivalents have not been reported in the El Qash basin or the Wadi Zeidun basin, but are evident in the nearby Wadi Arak basin and Wadi Meesar basin, where the unconformable base of the Hammamat on basement metavolcanics is exposed (Osman 1996; Fowler and Osman 2013; Fowler and Abdeen 2014). The foliations here do not show evidence for shear displacement on them. The pebble stretching lineations at Meesar are NW-trending (Fowler and Osman 2013), whereas the W plunging pebble long axes at Arak are likely to represent a primary pebble fabric (Fowler and Abdeen 2014). The temperature at time of foliation development in these southern examples is quite low, no more than Chlorite Zone and locally anchizonal. If these foliated lower Hammamat sections can be included as an upper weak strain part of the EDSZ, then the NW-SE dimension of the ESDZ is at least 55 km.

Other structures, which may be related to the EDSZ, are the 20 m thick extensional mylonite carapace to the El-Shalul granite (Osman 1996; Hamimi et al. 1994; Ali et al. 2012). This shear is gently domed and shows NW-SE stretching lineations and top-to-the-SE shear sense indicators (Osman et al. 1992; Osman 1996). Ali et al. (2012) have suggested that this shear may be a correlative of the EDSZ, though with its top-to-the-SE shear sense it may be a parallel shear to the EDSZ. The Kab Ahmed Shear Zone (KASZ), to the northeast of the El-Sibai complex, is a NW-SE trending ~1000 m thick foliated and mylonitic sheared zone of metavolcanics with bodies of serpentinite. It dips SW beneath the gneissic granitoids of the El-Sibai complex and shows top-to-the-NW shear sense after unfolding. The KASZ separates high T hornblende garnet mica schists below from low grade metavolcanics above. At El-Sibai, top-to-the-SE shear sense mylonite zones dip gently SE at the southeastern end of the complex, and affect the red granitic Um Shaddad intrusion, roughly estimated at 590–600 Ma by Fowler et al. (2007).

The shear zones identified here as the EDSZ were previously thought to have formed during (a) SW-wards thrusting (El-Gaby et al. 1984,1988a), (b) NW-wards thrusting (Ries et al. 1983; Sturchio et al. 1983a, b; Fritz et al. 1996), (c) NW-wards tectonic extrusion (Fowler and Osman 2001), and (d) extensional collapse by gliding spreading (Fowler and El Kalioubi 2004). Top-to-the-NW shear sense indicators argue against (a). The gentle original dip of the EDSZ makes it problematic to describe as compressional or tensional in origin. The activity of the EDSZ in the 610–600 Ma time frame, at the outset of the tectonic extension stage, does however point towards a tensional environment. Fowler and Osman (2013) have suggested that the EDSZ and associated shears may have provided a mechanism for crustal thinning during the extension tectonic stage, by crustal delamination. Ring et al. (1999) noted that extension-related low-dipping foliations are common indicators of crustal ductile thinning.

6.10 Hammamat Sequences

One of the most important features marking the extensional tectonic stage in the EED is the array of Hammamat molasse basins, and associated post-collision Dokhan Volcanics, which are best developed in the CED, but also have important representatives in the NED. Many aspects of these basins continue to be investigated due to their value in constraining the timing, mechanics and tectonic setting of the extension event. Active topics of research on the Hammamat basins include (1) the stratigraphic subdivisions, correlation and thickness of basin fill; (2) sedimentary environment of deposition; (3) geochemistry, petrography and provenance studies of the sediments; (4) subsidence mechanisms and sedimentation rates; (5) the age of the sediments and zircon population studies; (6) basin deformation and inversion, and relations of basin deformation structures to those in the surrounding areas; and (7) metamorphic aspects of the basins. Topics (1)–(6) could easily occupy a major independent work, but are not core issues for a chapter on metamorphism. Therefore, we will very briefly introduce the Hammamat basins in the light of those topics, then concentrate on (7), the metamorphic aspects of the Hammamat basins.

6.10.1 Features of the Hammamat Basins

The Hammamat basins are generally equant to ENE-elongate (rarely NW-elongate) Ediacaran molasse basins filled mainly with lithic volcanogenic arenites and pebble to cobble conglomerates with clasts of Dokhan volcanics, arc metavolcanics, metasediments and granitoids, Younger Granite and rarer ophiolitic lithologies. The largest examples are all found in the northern half of the CED and include El Qash (380 km^2), Kareim (240 km^2), Wadi Hammamat (135 km^2) and Zeidun (125 km^2) basins (Figs. 6.12 and 6.13). Stratigraphic studies have been hindered by basin deformation, marked discontinuity of sedimentary units and lack of marker horizons. A stratigraphic scheme was proposed by Akaad and Noweir (1980) introducing the reddish Igla and greenish Shihimiya Formations, which have subsequently proved to be coeval facies (Khudeir and Ahmed 1996). Rice et al (1993) concluded that correlations between the basins was unlikely to succeed. The preserved sequences measure up to 7500 m (Kareim basin–Messner 1996b), but are only a few hundreds of metres thick in the smaller basins. The molasse sediments were immature terrestrial sediments deposited on intramontane alluvial fans and in braided streams, with minor lacustrine deposits (Grothaus et al. 1979). Geochemistry studies indicate a poorly weathered volcanic, metavolcanic and granite provenance (Willis et al. 1988; Abd El-Rahman et al. 2010), and QFL modal studies show a transitional to dissected arc and recycled orogen as the provenance type (Messner 1996a). Hammamat deposition has been bracketed to 639–602 Ma by postdating Dokhan Volcanics and predating Younger Granite (Ries et al. 1983). NED Hammamat appears to be younger with age range 597–568 Ma (Stern et al. 1988) or 593–579 Ma (Wilde and Youssef 2002) estimates by dating of detrital zircon populations.

The basin subsidence mechanism has been a controversial issue, with continental rifting, pull-apart or sagging mechanisms proposed (Stern et al. 1984; Fritz and Messner 1999;

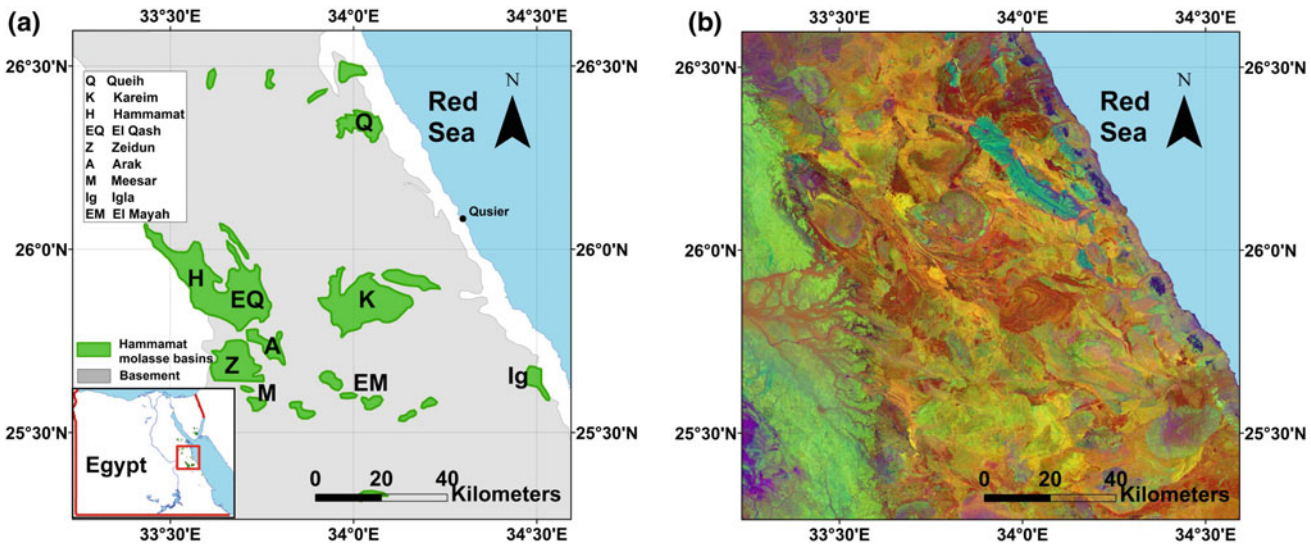

Fig. 6.12 **a** Regional distribution map of within the Central Eastern Desert of Egypt (CED), and **b** Principal Component Image of Landsat8 satellite image (PC5, PC4, PC2 in RGB) illustrates the Hammamat basins with brownish to yellowish brown colors

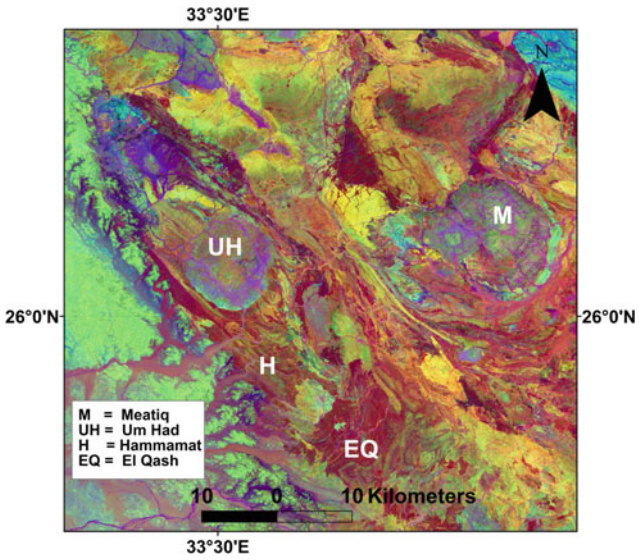

Fig. 6.13 Landsat8 Principal Component Image (PC5, PC4, PC2 in RGB) for Hammamat basins area illustrates the Hammamat Group sediments with brownish to yellowish brown colors

Shalaby et al. 2006). Overall coarsening upwards of basin fill has been interpreted in terms of early slow and late rapid subsidence phases (Fritz and Messner 1999). Appearance of pink granite pebbles in higher stratigraphic levels may indicate deepening erosion in the source areas (Ragab et al. 1993b). Andresen et al. (2009) estimated the time of deformation of the CED Hammamat basins at 605–600 Ma. The SW-wards thrusting of basement rocks over Hammamat in the CED must predate the 595 Ma Younger Granite intrusions, which are undeformed. The EDSZ shear zone has affected the basal sections of some Hammamat basins (e.g. Um Esh-Um Seleimat basin) and there are indications that activity of the EDSZ overlapped with NW-SE folding in this basin (Fowler and El Kalioubi 2004). NW-SE extension has resulted in stretched pebble conglomerates in some basins (Hamimi 2000; Abd El-Wahed 2007; Fowler and Abdeen 2014) Two stages of thrusting have been reported in these basins (Fowler and Osman 2001; Abd El-Wahed 2010; Abdeen and Greiling 2005). The original basin margins may have been normal faults, but have been reactivated as steep oblique reverse faults and transcurrent faults, and are overprinted by lower dipping thrusts, obscuring their original nature (Fowler and Osman 2013).

6.10.2 Metamorphic Aspects of the Hammamat Basins

Three reported scenarios have led to metamorphism of the Hammamat sediments. The first is contact metamorphism around Younger Granite intrusions, producing well-defined indurated zones of hornfels, usually reaching temperatures of the hornblende hornfels facies. The second case has been already mentioned above in connection with the EDSZ shearing effects on the lower sequences of some Hammamat basins. The EDSZ affected rocks have a schistose to mylonitic appearance and can reach epidote-amphibolite facies grade. The third situation was described by El-Gaby et al. (1988a, 1991) and involved low-pressure Buchan-style metamorphism in thermal domes affecting sediments and volcanics that they identified as Hammamat and Dokhan at Um Had and Wadi Kid. These metamorphic grades reached temperatures of anatexis. Each of the three metamorphic scenarios will be described below.

6.10.2.1 Contact Metamorphism Due to Younger Granite Intrusions

An excellent example of this is found at the southern margin of the Um Had pluton in the western CED (El Kalioubi 1988; Fowler 2001). The Um Had granite has intruded Hammamat sandstones, siltstones and conglomerates, producing a well-defined 1.5 km wide inner aureole, characterized by induration and darkening of sandstones, siltstones and conglomerate matrix, due to thermal metamorphic biotite crystallization. White spotted hornfels are also found in this zone, with spots of retrogressed andalusite or cordierite. Thermal metamorphic hornblende is also present in mafic hornfels. The innermost parts of the aureole have abundant pegmatite-aplite intrusions, quartz-epidote veins and hydrothermal alterations. A zone extending a further 2.5 km represents a transitional outer aureole (El Kalioubi 1988). Contact metamorphic effects are also clear in the Kareim basin molasse where it has been intruded by the El Dabbah granodiorite.

6.10.2.2 Dynamic Metamorphism Associated with the EDSZ

The setting and structure of the EDSZ has been described above in Sect. 6.9. The maximum temperatures reached during EDSZ shearing correlate with high extensional strains, mylonitic foliations and evidence for syn-shearing diorite and tonalite intrusions. Such conditions are documented for the EDSZ affected metasediments at Meatiq, where Habib et al. (1985a) and Neumayr et al. (1998) described greenschist to lower amphibolite (epidote-amphibolite) facies conditions accompanying mylonitization. In metabasalts beneath the Hammamat at Um Esh-Um Seleimat, the EDSZ sheared zone is responsible for amphibolite facies mafic mylonites with stable hornblende defining mineral lineations (Fowler and El Kalioubi 2004). In the Hammamat sediments, the hottest shearing has resulted in foliated metasandstones, with metamorphic muscovite and green biotite, or brownish biotite and chlorite defining the foliation (Andrew 1939; Ries et al. 1983; Fowler and El Kalioubi 2004). Clastic grains were deformed

and commonly sericitized along with the detrital lithic particles. This led to strain softening and development of mica schists. Metaconglomerates at these temperatures begin to show ductile behavior expressed as pebble elongation fabric. At lower temperatures, pebbles show brittle deformation (microfaulting) and low temperature layer silicates fill cracks giving a fracture cleavage appearance in the sandstones (Fowler and Abdeen 2014).

6.10.2.3 'Buchan Type' Low-Pressure Metamorphism

El-Gaby et al.'s (1988a) comprehensive description of the Pan-African belt projected a much broader picture of molasse sedimentation in the EED than the discrete Hammamat basins of the CED and NED. They described two major sedimentary sequences in the Allaqi 'swell' of the SED that contrasted with the mainly immature greywacke-mudstone sediments of the CED. The older of the SED sequences was a shelf/rifted margin series of mature clastics and carbonate rocks. The younger was described as poorly sorted arenites, siltstones and fine pebble conglomerates with intercalations of rhyolitic and rhyodacitic volcanics. El-Gaby et al. (1988a) regarded this younger series as molasse deposits in a foreland basin that developed during their Cordilleran stage. They compared (and later equated) this foreland sequence to the Hammamat, and the intercalated volcanics to the Dokhan. The metamorphism of these "Hammamat" foreland sediments to high temperature schists and gneisses with a characteristically low-pressure progression of zones from biotite to cordierite to andalusite to sillimanite, was identified as a Buchan (Abukuma) metamorphic series, distinct from the medium-pressure Barrovian series associated with the Cordilleran stage. The low-pressure metamorphic zones in the SED were considered as defining large thermal domes associated with Older Granite diapirs. Peak metamorphic pressures were estimated to be 3–4 kbars, locally higher in the SED due to greater sediment thicknesses. This model of Buchan series metamorphism in the Hammamat sediments was applied to several areas, including the Um Had metasediments, north of the Um Had Granite (El-Gaby et al. 1988b), the Wadi Kid complex (El-Gaby et al. 1991), the Um Gheig area east of El-Sibai complex (El-Gaby et al. 1994) and the Sa'al-Zaghra complex (El-Gaby et al. 2002).

The metamorphic rocks of the area north of the Um Had Granite were regarded as Hammamat by Akaad and Noweir (1980) and many workers since. Metamorphic zones of biotite, garnet, staurolite have been mapped and found to be elongate in a NW-SE direction. El-Gaby pointed out that this argues against the Um Had as the heat source, Noweir and El-Sharkawi (1988) thought that the Um Had and Um Effein granites were connected beneath these zones. A NE-SW trending zone of cordierite-sillimanite or migmatite or staurolite was included by El-Gaby et al. (1988b), El Kalioubi (1988), Hegazy (1999) and El-Sayed et al. (2000) along Wadi Sheqila—roughly conforming to the Um Had granite. The zone lying along Um Sheqila follows a later shear zone that cuts through the older metamorphic zones and deforms the high T porphyroblasts (Fowler and Osman 2001). Metamorphic conditions were estimated to be 650 °C and 4 kbars (El Kalioubi 1988), or 850 °C at 4–5 kbars (El-Sayed et al. 2000). El Kalioubi (1988) thought that the Um Had granite was katazonal and responsible for the metamorphism. Fowler and Osman (2001), Osman and Gadoo (2007) and recently, Abu Sharib et al. (2018), did not regard these rocks as Hammamat. Abu Sharib et al. obtained monazite dates for the metamorphism at 625 ± 5 Ma, similar to the age of the Um Ba'anib gneiss, and found the Um Had HT rocks were distinct chemically from Hammamat in being derived from a weathered terrain.

The Um Gheig aureole, east of El-Sibai was described by El-Gaby et al. (1994). They described it as a folded thrust stacked sequence of arc metavolcanics and slices of Hammamat calc-pelites. The Hammamat was represented by amphibolite facies hornblende biotite micaschists, and higher temperature migmatites in the inner aureole. Fowler et al. (2007) regarded these rocks as volcanoclastic metasediments.

The Kid complex and Sa'al-Zaghara complex were thought to be Hammamat-Dokhan sequences by El-Gaby et al. (1991, 2002). The cordierite, staurolite, andalusite, sillimanite, garnet zones in the Um Zariq metasediments at Kid were viewed as developed in thermal domes above a diapir. This model was suggested earlier by Reymer et al. (1984) and Reymer and Oertel (1985) to explain the subhorizontal foliations produced by 50–70% vertical shortening in the Kid complex. The P-T conditions for the Um Zariq metamorphism of >620 °C and 3.2 kbars (Reymer et al. 1984) were consistent with the Buchan series. Migmatites were also found in other thermal aureoles in the Kid complex (Reymer 1985). The Kid volcanics were divided into older Dokhan (andesitic) and younger Dokhan (acidic sub-volcanic dyke). Dating of the Kid sequence at 630+ Ma (Eyal et al. 2013) is within the age range for Dokhan, though the Um Zariq is probably >645 Ma (Moghazi et al. 2012) raising doubts about its identification as Hammamat. Subsequent workers on the geochemistry of the Kid have accepted these volcanics as Dokhan (Moghazi et al. 2012; El-Bialy 2010, 2013). The Sa'al-Zaghara complex volcanics, identified as Dokhan on the basis of their high K calc-alkaline chemistry and active continental margin affinities (El-Gaby et al. 2002) have recently been dated at 1.1 Ga (Be'eri-Shlevin et al. 2012), discounting completely this correlation. El-Gaby et al.'s 'younger' Hammamat along Wadi Zaghara have been dated by Stern et al. (2010) to be no

older than 606 ± 10 Ma, or a little older (>630 Ma) by Andresen et al. (2014). The younger date is similar to the Kid Conglomerate and if correct could permit correlation of the Zaghara conglomerates with Hammamat.

References

Abdalla HM, Mohamed FH (1999) Mineralogical and geochemical investigation of emerald and beryl mineralization, Pan-African Belt of Egypt: genetic and exploration aspects. J Afr Earth Sci 28:581–598

Abdeen MM, Abdelghaffar AA (2011) Syn- and post-accretionary structures in the Neproterozoic Central Allaqi-Heiani suture zone, Southeastern Egypt. Precambr Res 185:95–108

Abdeen MM, Greiling RO (2005) A quantitative structural study of late Pan-African compressional deformation in the Central Eastern Desert (Egypt) during Gondwana assembly. Gondwana Res 8:457–471

Abdel-Karim AM (1995) Late Precambrian metagabbro-diorite complex from southwest Sinai, Egypt. J Geol 39:715–738

Abdel-Karim AM, Ahmed Z (2010) Possible origin of ophiolites of Eastern Desert, Egypt, from geochemical perspectives. Arab J Sci Eng 35:115–143

Abdel-Karim AM, El-Shafei SA (2017) Mineralogy and chemical aspects of some ophiolitic metaultramafics, central Eastern Desert, Egypt: evidences from chromites, sulphides and gangues. Geol J. https://doi.org/10.1002/gj.2914

Abdel-Karim AM, El-Mahallawy MM, Finger F (1996) The ophiolite mélange of Wadi Dunqash and Arayis, eastern Desert of Egypt: petrogenesis and tectonic evolution. Acta Mineral Petrog 37:129–141

Abdel-Karim AM, Soliman MM, El Kazzaz YA, Mazhar AA, Abdel Gawad GM (2001) Geological and geochemical characteristics of the mafic–ultramafic rocks of Gabal Gerf area, South Eastern Desert of Egypt. Ann Geol Surv Egypt 24:193–218

Abdel-Karim AM, Ali S, Helmy HM, El-Shafei SA (2016) Fore-arc setting of the Gerf ophiolite, Eastern Desert, Egypt: evidence from mineral chemistry and geochemistry of ultramafites. Lithos 263:52–65

Abdel-Khalek ML, Abdel-Wahed M (1983) Structural setting of the Hafafit gneisses, Eastern Desert, Egypt. In: Riad S, Baars DL (eds) Proceedings of 5th international conference on basement tectonics, Cairo, pp 85–104

Abdel-Khalek ML, Takla MA, Sehim A, Hamimi Z, El Manawi AW (1992) Geology and tectonic evolution of Wadi Beitan area, SE Desert, Egypt. In: Sadek A (ed) Proceedings of 1st conference on geology of the Arab World, pp 369–394

Abdel-Khalek ML, Takla MA, Sehim A, Abdel Wahed M, Hamimi Z, Sakran SM (1999) Tectonic evolution of the Shield rocks, east Wadi Beitan area, southeastern Desert, Egypt. Egypt J Geol 43:1–25

Abdel Monem AA, Hurley PM (1979) U-Pb dating of zircons from psammitic gneisses, Wadi Abu Rusheid-Wadi Sikait area, Egypt. Inst Appl Geol Jeddah Bull 3:165–170

Abd El-Naby H, Frisch W (2002) Origin of the Wadi Haimur-Abu Swayel Gneiss belt, South Eastern Desert, Egypt: petrological and geochronological constraints. Precambr Res 113:307–322

Abd El-Naby H, Frisch W (2006) Geochemical constraints from the Hafafit Metamorphic Complex (HMC): evidence of Neoproterozoic back-arc basin development in the central Eastern Desert, Egypt. J Afr Earth Sci 45:173–186

Abd El-Naby H, Frisch W, Hegner E (2000) Evolution of Pan-African Wadi Haimur metamorphic sole, Eastern Desert, Egypt. J Metam Geol 18:639–651

Abd El-Naby H, Frisch W, Siebel W (2008) Tectono-metamorphic evolution of the Wadi Hafafit Culmination (central Eastern Desert, Egypt): implication for Neoproterozoic core complex exhumation in NE Africa. Geol Acta 6:293–312

Abdel-Rahman AM (1995) Tectonic-magmatic stages of shield evolution: the Pan-African belt in northeastern Egypt. Tectonophysics 242:223–240

Abdel-Rahman AM (1996) Pan-African volcanism: petrology and geochemistry of the Dokhan Volcanic suite in the northern Nubian Shield. Geol Mag 133:17–31

Abd El-Rahman Y, Polat A, Dilek Y, Fryer BJ, El-Sharkawy M, Sakran S (2009a) Geochemistry and tectonic evolution of the Neoproterozoic incipient arc–forearc crust in the Fawakhir area, Central Eastern Desert of Egypt. Precambr Res 175:116–134

Abd El-Rahman Y, Polat A, Dilek Y, Fryer B, El-Sharkawy M, Sakran S (2009b) Geochemistry and tectonic evolution of the Neoproterozoic Wadi Ghadir ophiolite, Eastern Desert. Egypt. Lithos 113:158–178

Abd El-Rahman Y, Polat A, Fryer BJ, Dilek Y, El-Sharkawy M, Sakran S (2010) The provenance and tectonic setting of the Neoproterozoic Um Hassa Greywacke Member, Wadi Hammamat area, Egypt: evidence from petrography and geochemistry. J Afr Earth Sci 58:185–196

Abd El-Rahman Y, Polat A, Dilek Y, Kusky TM, El-Sharkawi M, Said A (2012) Cryogenian ophiolitic tectonics and metallogeny of the Central Eastern Desert of Egypt. Int Geol Rev 54(16):1870–1884. https://doi.org/10.1080/00206814.2012.682777

Abdelsalam MG, Dawoud AS (1991) The Kabus ophiolitic melange, Sudan, and its bearing on the W boundary of the Nubian Shield. J Geol Soc Lond 148:83–92

Abdelsalam MG, Stern RJ (1996) Sutures and shear zones in the Arabian-Nubian shield. J Afr Earth Sci 23:289–310

Abdelsalam MG, Liegeois JP, Stern RJ (2002) The Saharan Metacraton. J Afr Earth Sci 34:119–136

Abdelsalam MG, Abdeen MM, Dowaidar HM, Stern RJ, Abdelghaffar AA (2003) Structural evolution of the Neoproterozoic Western Allaqi-Heiani suture, southeastern Egypt. Precambr Res 124:87–104

Abdel Wahed M, Hafez AMA, Shahin MG, Abu Sharib A (2006) Structural framework of Wadi Samra area, SE Sinai, Egypt. In: Abstract, 8th International conference on geology of the Arab World, Cairo, Egypt, pp 94–95

Abd El-Wahed MA (2007) Late Pan-African tectonic evolution and strain determinations in the late Neoproterozoic molasse sediments, Eastern Desert, Egypt: evidence for post-Hammamat compression and transpression. Egypt J Geol 51:1–39

Abd El-Wahed MA (2008) Thrusting and transpressional shearing in the Pan-African nappe southwest El-Sibai core complex, Central Eastern Desert, Egypt. J Afr Earth Sci 50:16–36

Abd El-Wahed M (2010) The role of the Najd Fault System in the tectonic evolution of the Hammamat molasse sediments, Eastern Desert, Egypt. Arab J Geosci 3:1–26

Abd El-Wahed MA (2014) Oppositely dipping thrusts and transpressional imbricate zone in the Central Eastern Desert of Egypt. J Afr Earth Sci 100:42–59

Abd EI-Wahed M, Abdeldayem AL (2002) Evolution of the Ras Barud gneisses, South northern Eastern Desert, Egypt: a magneto-structural study. In: 6th Internaional conference on the geology of the Arab World, Cairo Univ., pp 311–326

Abd El-Wahed MA (2017) Thabet IA (2017) Strain geometry, microstructure and metamorphism in the dextral transpressional Mubarak Shear Belt, Central Eastern Desert, Egypt. Geotectonics 51:438–462

Abou El-Maaty MA, Taman ZI, Abdel Wahab W (2012) Characterization of the Atalla talc-carbonate rocks, Central Eastern Desert, Egypt. Egypt J Geol 56:67–83

Abu-Alam TS, Hamdy MM (2014) Thermodynamic modelling of Sol Hamed serpentinite, South Eastern Desert of Egypt: implications for fluid interaction in the Arabian-Nubian Shield ophiolites. J Afr Earth Sci 99:7–23

Abu-Alam TS, Stüwe K (2009) Exhumation during oblique transpression: an example from the Feiran-Solaf region, Egypt. J Metam Geol 27:439–459

Abu-Alam TS, Santosh M, Brown M, Stüwe K (2013) Gondwana collision. Miner Petrol 107:631–634

Abu Anbar M, Solís Pichardo G, Hernández Bernal MS, Morales Contreras J, Hernández Treviño T (2004) Sm-Nd and Rb-Sr isotopes of Feiran gneisses and amphibolites: evidences of Pre-Pan-African continental crust in Sinai, Egypt

Abu Anbar M, Finger F, Solís Picharo G (2009) Evolution of the metamorphosed volcano-sedimentary rocks in Sa'al area, southern Sinai, Egypt: implications from lithology, geochemistry, mineralogy, P-T conditions and age dating. Egypt J Geol 53:1–35

Abu El-Ela AMR (1979) Geology of the Ras Barud area, Eastern Desert, Egypt. Unpublished MSc thesis, Assiut Univ., 193 pp

Abu El-Ela AM (1985) Geology of Wadi Mubarak district Eastern Desert, Egypt. Unpublished PhD thesis, Tanta Univ., 359 pp

Abu El Ela FA (1992) Bimodal volcanism of the Igla Eliswid-Um Khariga metavolcanics, Eastern Desert, Egypt. J Afr Earth Sci 14:477–491

Abu El-Enen MM (2008) Geochemistry and metamorphism of the Pan-African back-arc Malhaq volcano-sedimentary Neoproterozoic association, W. Kid area, SE Sinai, Egypt. J Afr Earth Sci 51:189–206

Abu El-Enen MM (2011) Geochemistry, provenance, and metamorphic evolution of Gabal Samra Neoproterozoic metapelites, Sinai, Egypt. J Afr Earth Sci 59:269–282

Abu El-Enen MM, Makroum FM (2003) Tectonometamorphic evolution of the northeastern Kid Belt, SE Sinai, Egypt. Ann Geol Surv Egypt 26:19–37

Abu El-Enen MM, Zalata AA, El-Metwally AA, Okrusch M (1999) Orthogneisses from the Taba metamorphic belt, SE Sinai, Egypt: witnesses for granitoid magmatism at an active continental margin. Neues Jahrb Mineral Abh 175:53–81

Abu El-Enen MM, Whitehouse MJ (2013) The Feiran-Solaf metamorphic complex, Sinai, Egypt: geochronological and geochemical constraints on its evolution. Precambr Res 239:106–125

Abu El-Enen MM, Okrusch M, Will TM (2003) Metapelitic assemblages in the Umm Zariq schists, central western Kid belt, Sinai Peninsula, Egypt. Neues Jahrb Mineral Abh 178:277–306

Abu El-Enen MM, Okrusch M, Will TM (2004) P-T evolution of the Taba Metamorphic belt, Egypt: constraints from the metapelite assemblages. J Earth Sci 38:59–78

Abu El-Enen MM, Zalata AA, Abd El-Shakour ZA (2009) Subsolidus and anatectic migmatites: examples from the Panafrican crystalline basement, Southern Sinai, Egypt. Egypt J Geol 53:63–86

Abu El-Enen MM, Abu-Alam TS, Whitehouse MJ, Ali KA, Okrusch M (2016) P-T path and timing of crustal thickening during amalgamation of East andWest Gondwana: a case study from the Hafafit Metamorphic Complex, Eastern Desert of Egypt. Lithos 263:213–238

Abu Sharib ASAA, Maurice AE, Abd El-Rahman YM, Sanislav IV, Schulz, Bakhit BR (2018) Neoproterozoic arc sedimentation, metamorphism and collision: evidence from the northern tip of the Arabian-Nubian Shield and implication for the terminal collision between East and West Gondwana. Gond Res. https://doi.org/10.1016/j.gr.2018.09.004

Ahmed AA (1981) Reconsidered view on Feiran-Solaf Gneisses Southwest of Sinai, Egypt. Bull Fac Sci Assiut Univ 10:131–142

Ahmed AH, Gharib ME, Arai S (2012) Characterization of the thermally metamorphosed mantle-crust transition zone of the Neoproterozoic ophiolite at Gabal Mudarjaj, south Eastern Desert, Egypt. Lithos 142:67–83

Akaad MK (1959) The migmatitic gneisses of Wadi Feiran, Sinai, Egypt. Assiut Bull Sci Technol 2:211–237

Akaad MK, El Ramly MF (1960) Geological history and classification of the basement rocks of the Central Eastern Desert of Egypt. Geol. Surv. Egypt, Pap. No. 9, 24 pp

Akaad MK, Noweir AM (1969) Lithostratigraphy of the Hammamat-Um Seleimat District, Eastern Desert, Egypt. Nature 223:284–285

Akaad MK, Noweir AM (1980) Geology and lithostratigraphy of the Arabian Desert Orogenic Belt of Egypt between Lat. 25°35′ and 26° 30′. Bull Inst Appl Geol King Abdulaziz Univ 3:127–135

Akaad MK, Shazli MG (1972) Description and petrography of the Meatiq Group. Ann Geol Surv Egypt 2:215–238

Akaad MK, Essawi MA (1964) The metagabbro-diorite complex northeast of Gabal Atud, Eastern Desert, and the term Epidiorite. Bull Sci Tech Assiut Univ Egypt 7:63–108

Akaad MK, El-Gaby S, Abbas AA (1967) On the evolution of Feiran migmatites, Sinai. J Geol U.A.R. 11:49–58

Akaad MK, El-Gaby S, Habib M (1973) The Barud gneisses and the origin of grey granite. Bull Fac Sci Assiut Univ 2:55–70

Akaad MK, Shazly AG, Noweir AM (1976) The Abu Fannani schist and the problem of the gneiss-schist contact in the Qift-Quseir road district, Eastern Desert, Egypt. In: Proceedings of 3rd Conference on Geological Society Africa, Khartoum

Akaad MK, Noweir AM, Abu El-Ela AM, El-Bahariya GA (1996) The Muweilih Conglomerate', Qift-Quseir Road region, and the problem of the Atud Formation. In: Proceedings of geological survey Egypt centennial conference, 1996, pp 23–45

Al Boghdady AA (2003) Association of apatite with magnetite in some banded iron-formations of Central Eastern Desert Egypt: comparative mineralogical and geochemical studies. Ann Geol Surv Egypt 26:183–197

Ali BH, Wilde SA, Gabr MMA (2009a) Granitoid evolution in Sinai, Egypt, based on precise SHRIMP U-Pb zircon geochronology. Gond Res 18:38–48

Ali KA, Stern RJ, Manton WI, Kimurab J-I, Khamees HA (2009b) Geochemistry, Nd isotopes and U-Pb SHRIMP zircon dating of Neoproterozoic volcanic rocks from the Central Eastern Desert of Egypt: new insights into the ~750 Ma crust-forming event. Precambr Res 171:1–22

Ali KA, Azer MK, Gahlan HA, Wilde SA, Samuel MD, Stern RJ (2010a) Age constraints on the formation of Neoproterozoic ophiolites along the Allaqi-Heiani Suture, South Eastern Desert of Egypt. Gond Res 18:583–595

Ali KA, Stern RJ, Manton WI, Johnson PR, Mukherjee SK (2010b) Neoproterozoic diamictite in the Eastern Desert of Egypt and Northern Saudi Arabia: evidence of ~750 Ma glaciation in the Arabian Nubian Shield? Int J Earth Sci 99:705–726

Ali K, Andresen A, Manton WI, Stern RJ, Somar A, Maurice AE (2012) U-Pb zircon dating and Sr-Nd-Hf isotopic evidence to support a juvenile origin of the ~634 Ma El Shalul granitic gneiss dome, Arabian-Nubian Shield. Geol Mag 149:783–797

Ali KA, Kröner A, Hegner E, Wong J, Li S-Q, Gahlan HA, Abu El Ela FF (2015) U-Pb zircon geochronology and Hf-Nd isotopic systematics of Wadi Beitan granitoid gneisses, South Eastern Desert, Egypt. Gond Res 27:811–824

Ali-Bik MW (1999) Mineralogy and mineral chemistry of amphibolitized gabbroic rocks at Wadi Sa'al El Rayan, south central Sinai. Egypt Mineral 11:1–21

Ali-Bik MW, Moussa HE, Akarish AIM, Sadek Ghabrial D (2002) Wadi Sa'al metamorphosed sediments and tuffs, south central Sinai: geological setting, metamorphism and geochemistry. Egypt J Geol 46:1–19

Ali-Bik MW, Taman Z, El Kalioubi B, Abdel Wahab W (2012) Serpentinite-hosted talc-magnesite deposits of Wadi Barramiya

area, Eastern Desert, Egypt: characteristics, petrogenesis and evolution. J Afr Earth Sci 64:77–89

Ali-Bik MW, Abd El Rahim SH, Abdel Wahab W, Abayazeed SD, Hassan SM (2017) Geochemical constraints on the oldest arc rocks of the Arabian-Nubian Shield: the late Mesoproterozoic to late Neoproterozoic (?) Sa'al volcano-sedimentary complex, Sinai, Egypt. Lithos 284–285:310–326

Al Shanti AMS, Mitchell AHG (1976) Late Precambrian subduction and collision in the Al-Amar-Idsas region, Arabian Shield, Kingdom of Saudi Arabia. Tectonophysics 30:41–47

Amer R, Kusky T, Reinert PC, Ghulam A (2009) Image processing and analysis using Landsat ETM+ Imagery for lithological mapping at Fawakhir, Central Eastern Desert of Egypt. ASPRS 2009 Annual Conference Baltimore, Maryland, 9–13 Mar 2009

Amer R, Kusky T, Ghulam A (2010) Lithological mapping in the Central Eastern Desert of Egypt using ASTER data. J Afr Earth Sci 56:75–82

Amstutz GC, El-Gaby S, Ahmed AA, Habib ME, Khudeir AA (1984) Back-arc ophiolite association, Central Eastern Desert, Egypt. Bull Fac Sci Assiut Univ 13:95–136

Andresen A, El-Rus MA, Myhre PI, Boghdady GY (2009) U-Pb TIMS age constraints on the evolution of the Neoproterozoic Meatiq Gneiss Dome, Eastern Desert, Egypt. Int J Earth Sci 98:481–497

Andresen A, Augland LE, Boghdady GY, Lundmark AM, Elnady OM, Hassan MA, Abu El-Rus MA (2010) Structural constraints on the evolution of the Meatiq Gneiss Dome (Egypt), East-African Orogen. J Afr Earth Sci 57:413–422

Andresen A, Abu El-Enen MM, Stern RJ, Wilde SA, Ali KA (2014) The Wadi Zaghra metasediments of Sinai, Egypt: new constraints on the late Cryogenian-Ediacaran tectonic evolution of the northernmost Arabian-Nubian Shield. Int Geol Rev 56:1020–1038

Andrew G (1931) Note on the geology of Gabal Mitiq. In: Hume WF (ed) Geology of Egypt, vol. 2 (part 1). Geol. Surv. Egypt, Cairo, pp 295–296

Andrew G (1939) The greywackes of the Eastern Desert of Egypt. Bull Inst Egypte 21:153–190

Arnous MO, Sultan YM (2014) Geospatial technology and structural analysis for geological mapping and tectonic evolution of Feiran-Solaf metamorphic complex, South Sinai, Egypt. Arab J Geosci 7:3023–3049

Ashmawy MH (1987) The ophiolitic mélange of the south Eastern Desert of Egypt, remote sensing, field work and petrographic investigations. PhD thesis, Berlin, Berliner Geowiss. Abh, 84, p 134

Asran AMH, Kamal El Din GM, Akawy A (2000) Petrochemistry and tectonic significance of gneiss-amphibolite-migmatite association of Khuda metamorphic core complex, Southeastern Desert, Egypt. In: 5th International conference on geology of the Arab World, pp 15–34

Asran AMH, Hassan MA, Ali BH, Embaby AI (2008) Geological and geochemical investigations of the Pan-African rocks along Wadi El-Atrash area, North Eastern Desert, Egypt. In: 8th International conference on geochemistry, vol 1. Alex. Univ., pp 89–113

Augland LE, Andresen A, Boghdady GY (2012) U-Pb ID-TIMS dating of igneous and metaigneous rocks from the El-Sibai area: time constraints on the tectonic evolution of the Central Eastern Desert, Egypt. Int J Earth Sci 101:25–37

Avigad D, Gvirtzman Z (2009) Late Neoproterozoic rise and fall of the northern Arabian-Nubian shield: the role of lithospheric mantle delamination and subsequent thermal subsidence. Tectonophysics 477:217–228

Awad NT (1994) Kyanite in quartz segregations in the central Eastern Desert, Egypt. Egypt Mineral 6:77–94

Azer MK (2013) Late Ediacaran (605–580 Ma) post-collisional alkaline magmatism in the Arabian-Nubian Shield: a case study of Serbal ring-shaped intrusion, southern Sinai, Egypt. J Asian Earth Sci 77:203–223

Azer MK (2014) Petrological studies of Neoproterozoic serpentinized ultramafics of the Nubian Shield: spinel compositions as evidence of the tectonic evolution of Egyptian ophiolites. Acta Geol Polon 64:113–127

Azer MK, Khalil AES (2005) Petrological and mineralogical studies of Pan-African serpentinites at Bir Al-Edeid area, central Eastern Desert, Egypt. J Afr Earth Sci 43:525–536

Azer MK, Stern RJ (2007) Neoproterozoic (835–720 Ma) serpentinites in the Eastern Desert, Egypt: fragments of fore-arc mantle. J Geol 115:457–472

Azer MK, Stern RJ, Kimura J-I (2010) Origin of a late Neoproterozoic (605 ± 13 Ma) intrusive carbonate-albitite complex in Southern Sinai, Egypt. Int J Earth Sci 99:245–267

Azer MK, Obeid MA, Gahlan HA (2016) Late Neoproterozoic layered mafic intrusion of arc-affinity in the Arabian-Nubian Shield: a case study from the Shahira layered mafic intrusion, southern Sinai, Egypt. Geol Acta 14:237–259

Bakor AR, Gass JG, Neary CR (1976) Jabal al Wask, Northwest Saudi Arabia: An Eocambrian back-arc ophiolite. Earth Planet Sci Lett 30:1–9

Ball J (1916) Geography and geology of West Central Sinai. Egypt Surv. Dept., Cairo, p 219

Barron T (1907) The topography and geology of the Peninsula of Sinai (Western portion). Egypt Surv. Dept., Cairo, p 241

Bassyuni TFW (1973): Contribution to the geology of Abu Swayel Cu-Ni mine area, Eastern Desert. PhD thesis, Cairo Univ.

Basta EZ, Church WR, Hafez AMA, Basta FF (1983) Proterozoic ophiolitic mélange and associated rocks of Gabal Ghadir area, Eastern Desert, Egypt. Internat Basement Tect Assoc 5:115–124

Basta EZ, Abdel Kader Z (1969) The mineralogy of the Egyptian serpentinites and talc-carbonate. Min Mag 37:394–408

Basta FF, Maurice AE, Bakhit BR, Ali KA, Manton WI (2011) Neoproterozoic contaminated MORB of Wadi Ghadir ophiolite, NE Africa: geochemical and Nd and Sr isotopic constraints. J Afr Earth Sci 59:227–242

Bea F, Montero P, Abu Anbar M, Talavera C (2011a) SHRIMP dating and Nd isotope geology of the Archean terranes of the Uweinat-Kamil inlier, Egypt-Sudan-Libya. Precambr Res 189:328–346

Bea F, Montero P, Abu Anbar M, Molina JF, Scarrow JH (2011b) The Bir Safsaf Precambrian inlier of South West Egypt revisited. A model for ~1.5 Ga T_{DM} late Pan-African granite generation by crustal reworking. Lithos 125:897–914

Be'eri-Shlevin Y, Katzir Y, Whitehouse MJ (2009a) Post-collisional tectonomagmatic evolution in the northern Arabian-Nubian Shield: time constraints from ion-probe U-Pb dating of zircon. J Geol Soc Lond 166:71–85

Be'eri-Shlevin Y, Katzir Y, Whitehouse MJ, Kleinhanns IC (2009b) Contribution of pre Pan-African crust to formation of the Arabian-Nubian Shield: new secondary ionization mass spectrometry U-Pb and O studies of zircon. Geology 37:899–902

Be'eri-Shlevin Y, Eyal M, Eyal Y, Whitehouse MJ, Litvinovsky B (2012) The Sa'al volcano-sedimentary complex (Sinai, Egypt). A latest Mesoproterozoic volcanic arc in the northern Arabian Nubian Shield. Geology 40:403–406

Bennett JD, Mosley PN (1987) Tiered-tectonics and evolution, E. Desert and Sinai, Egypt. In: Matheis G, Schandelmeier H (eds) Current research in African earth sciences. Balkema, Rotterdam, pp 79–82

Bentor YK (1985) The crustal evolution of the Arabo-Nubian massif with special reference to the Sinai peninsula. Precambr Res 28:1–74

Bentor YK, Bogoch R, Eyal M, Garfunkel Z, Shimron A (1974) Geological Map of Sinai: Jebel Sabbagh Sheet (1:100,000). Isr Acad Sci Hum, Jerusalem

Berhe SM (1990) Ophiolites in Northeast and East Africa: implications for Proterozoic crustal growth. J Geol Soc Lond 147:41–57

Bertrand JML, Caby R (1978) Geodynamic evolution of the Pan-African orogenic belt: a new interpretation of the Hoggar Shield (Algerian Sahara). Geol Rundsch 67:357–388

Beyth M, Stern RJ, Altherr R, Kröner A (1994) The late Precambrian Timna igneous complex, Southern Israel: evidence of comagmatic-type sanukitoid monzodiorite and alkali granite magma. Lithos 31:103–124

Beyth M, Eyal Y, Garfunkel Z (2011) The geology of the elat sheet. Explanatory notes. Geological Survey of Israel, Report No. GSI/22/2011, 27 pp

Bielski M (1982) Stages in the Arabian-Nubian Massif in Sinai. Unpublished PhD thesis, Hebrew Univ., Jerusalem, 155 pp

Blasband B (1995) Structural geology and tectonics of Precambrian metamorphic rocks in the Sinai, Egypt. Unpublished MSc thesis, Utrecht University

Blasband BB, Brooijmans P, Dirks P, Visser W, White S (1997) Pan-African core complex in the Sinai, Egypt. Geol Mijnb 73:247–266

Blasband B, White SH, Brooijmans P, de Boorder H, Visser W (2000) Late Proterozoic extensional collapse in the Arabian-Nubian Shield. J Geol Soc Lond 157:615–628

Boger SD, Carson CJ, Fanning CM, Hergt JM, Wilson CJL, Woodhead JD (2002) Pan-African intra plat e deformation in the northern Prince Charles Mountains, east Antarctica. Earth Planet Sci Lett 195:195–210

Botros NS (2004) A new classification of gold deposits of Egypt. Ore Geol Rev 25:1–37

Bregar M, Fritz H, Unzog W (1996) Structural evolution of low-angle normal faults SE of the Gabal El-Sibai Crystalline Dome, Eastern Desert, Egypt: evidence from paleopiezometry and vorticity analysis. Zbl. Geol. Palaont. Teil I, H. 3/4, pp 243–256

Bregar M, Bauernhofer A, Pelz K, Kloetzli U, Fritz H, Neumayr P (2002) A late Neoproterozoic magmatic core complex in the Eastern Desert of Egypt: emplacement of granitoids in a wrench-tectonic setting. Precambr Res 118:59–82

Brooijmans P, Blasband B, White SH, Visser WJ, Dirks P (2003) Geothermobarometric evidence for a metamorphic core complex in Sinai, Egypt. Precambr Res 123:249–268

Bühler B, Breitkreuz C, Pfänder JA, Hofmann M, Becker S, Linnemann U, Eliwa HA (2014) New insights into the accretion of the Arabian-Nubian Shield: Depositional setting, composition and geochronology of a Mid-Cryogenian arc succession (North Eastern Desert, Egypt). Precambr Res 243:149–167

Cahen L, Snelling NJ, Delhal J, Vail JR (1984) The geochronology and evolution of Africa. Clarendon Press, Oxford, p 512

Church WR (1982) The Northern Appalachians and the Eastern Desert of Egypt. Precambr Res 16:13

Church WR (1983) Precambrian evolution of Afro-Arabian crust from ocean arc to craton. Discuss Geol Soc Am Bull 94:679–681

Collins AS, Pisarevsky SA (2005) Amalgamating eastern Gondwana; the evolution of the Circum-Indian Orogens. Earth Sci Rev 71:229–270

Cosca MA, Shimron A, Caby R (1999) Late Precambrian metamorphism and cooling in the Arabian-Nubian Shield: petrology and $^{40}Ar/^{39}Ar$ geochronology of metamorphic rocks of the Elat area (southern Israel). Precambr Res 98:107–127

Dilek Y (2003) Ophiolite concept and its evolution. In: Dilek Y and Newcomb S (Eds.) Ophiolite concept and the evolution of geological thought. Geol. Soc Am. Spec. Pap. 373, pp 1–16

Dixon TH (1979) The evolution of continental crust in the Late Precambrian Egyptian Shield. Unpublished PhD thesis, Univ. Calif. at San Diego

Dixon TH (1981) Age and chemical characteristics of some pre-Pan-African rocks in the Egyptian Shield. Precambr Res 14:119–133

Dixon TH, Abdel Meguid AA, Gillespie JG (1979) Age, chemical and isotopic characteristics of some pre-Pan African rocks in the Egyptian Shield. Ann Geol Surv Egypt 9:591–610

EGSMA (1992a) Wadi Al Barramiya Quadrangle Map, at Scale, 1: 250,000. Egyptian Geological Survey, Cairo

EGSMA (1992b) Al Qusayr Quadrangle Map, at Scale, 1: 250,000. Egyptian Geological Survey, Cairo, Egypt

El Akhal H (1993) A transect from a tectonic mélange to an island-arc in the Pan-African of SE Egypt (Wadi Ghadir area). Sci Ser Int Bur 20:1–244

El Akhal H, Greiling RO (1987) A section through a Late Proterozoic fore-arc domain from the Eastern Desert of Egypt. Terra Cognita 7:150

El-Akkad S, Dardir AA (1965) Geological map of the coastal strip between Qena–Safaga road and Wadi Sharm El Bahari, scale 1:100,000 (latitudes 25°45′–26°45′N and longitudes 34°10′–34°20′ E). Unpubl. Geol. Surv. Egypt map

El-Alfy Z (1992) Geological studies on the area north of Gabal Abu Tiyur, Central Eastern Desert, Egypt. Unpublished PhD thesis, Ain Shams Univ., Cairo

El Amawy MA (1991) Structural and tectonic development of Wadi Bitan—Wadi Rahaba area, South Eastern Desert. Sci J Fac Sci Menoufia Univ 5:293–334

El Aref MM, El Dougdoug A, Abd El-Wahed M, El Manawi AW (1993) Diagenetic and metamorphic history of the Umm Nar BIF, Eastern Desert, Egypt. Mineral Deposita 28:264–278

El Bahariya GA (2006) Petrology, mineral chemistry and metamorphism of two Pan-African ophiolitic metagabbro occurrences, Central Eastern Desert, Egypt. Egypt J Geol 50:183–202

El Bahariya GA (2008) Geology, mineral chemistry and petrogenesis of Neoproterozoic metamorphosed ophiolitic ultramafics, Central Eastern Desert, Egypt: implications for the classification and origin of the ophiolitic mélange. Egypt J Geol 52:55–82

El Bahariya GA (2012) Classification and origin of the Neoproterozoic ophiolitic mélanges in the Central Eastern Desert of Egypt. Tectonophysics 568–569:357–370

El Bahariya GA, Abd El-Wahed MA (2003) Petrology, mineral chemistry and tectonic evolution of the northern part of Wadi Hafafit area, Eastern Desert, Egypt. In: 3rd International conference on geology of Africa, vol 2, pp 201–231

El Bayoumi RMA (1983) Ophiolite and mélange complex of Wadi Ghadir area, Eastern Desert, Egypt. Bull Fac Sci King Abdulaziz Univ 6:329–342

El Bayoumi RM, Greiling RO (1984) Tectonic evolution of Pan-African plate margin in Southeastern Egypt—a suture zone overprinted by low angle thrusting? In: Klerkx J, Michot J (eds) African geology, Tervuren, pp 47–56

El Bayoumi RM, Hassanein SM (1983) Ophiolite mélange complex, Wadi Mubarak area, Eastern Desert, vol 5. Int. Basement Tect. Assoc. Publ., pp 45–52

El-Bialy MZ (2010) On the Pan-African transition of the Arabian-Nubian Shield from compression to extension: the post-collision Dokhan volcanic suite of Kid-Malhak region, Sinai, Egypt. Gond Res 17:26–43

El-Bialy MZ (2013) Geochemistry of the Neoproterozoic metasediments of Malhaq and Um Zariq formations, Kid metamorphic complex, Sinai, Egypt: implications for source-area weathering, provenance, recycling, and depositional tectonic setting. Lithos 175–176:68–85

El-Bialy MZ, Ali KA (2013) Zircon trace element geochemical constraints on the evolution of the Ediacaran (600–614 Ma) post-collisional Dokhan Volcanics and Younger Granites of SE Sinai, NE Arabian-Nubian Shield. Chem Geol 360–361:54–73

El-Bialy MZ, Omar MM (2015) Spatial association of Neoproterozoic continental arc I-type and post-collision A-type granitoids in the

Arabian-Nubian Shield: the Wadi Al-Baroud Older and Younger Granites, North Eastern Desert, Egypt. J Afr Earth Sci 103:1–29

El-Bialy MZ, Ali KA, Abu El-Enen MM, Ahmed AH (2015) Provenance and metamorphic PT conditions of Cryogenian-Ediacaran metasediments from the Kid metamorphic complex, Sinai, NE Arabian-Nubian Shield: insights from detrital zircon geochemistry and mineral chemistry. Tectonophysics 665:199–217

El-Desoky HM, Khalil AE, Salem AA (2015) Ultramafic rocks in Gabal El-Rubshi, Central Eastern Desert, Egypt: petrography, mineral chemistry, and geochemistry constraints. Arab J Geosci 8:2607–2631

El-Gaby S (1983) Architecture of the Egyptian basement complex, Inter. Basement Tectonics Assoc., Publ. No. 5, pp 1–18

El-Gaby S (1994) Geologic and tectonic framework of the Pan-African orogenic belt in Egypt. In: 2nd International conference geology of the Arab World, Cairo University, pp 3–17

El-Gaby S, Habib MS (1982) Geology of the area southwest of Port Safaga, with special emphasis on the granitic rocks, Eastern Desert, Egypt. Ann Geol Surv Egypt 12:47–71

El-Gaby S, Ahmed AA (1980) The Feiran–Solaf gneiss belt, S. W. of Sinai, Egypt. I.A.G. Bull. No. 3 "Evolution Mineralization Arabian-Nubian Shield" 4:95–105

El-Gaby S, El Nady OM, Khudeir AA (1984) Tectonic evolution of the basement complex in the Central Eastern Desert of Egypt. Geol Rundsch 73:1019–1036

El-Gaby S, List F, Tehrani R (1988a) Geology, evolution and metallogenesis of the Pan-African belt in Egypt. In: El-Gaby S, Greiling RO (eds) The Pan-African Belt of Northeast Africa and Adjacent Areas. Vieweg and Sohn, Weisbaden, pp 17–68

El-Gaby S, Khudeir AA, Youssef M, Kamal El Din G (1988b) Low pressure metamorphism in Hammamat sediments at Wadi Um Had area, central Eastern Desert, Egypt. Bull Fac Sci Assuit Univ 17: 51–71

El-Gaby S, List F, Tehrani R (1990) The basement complex of the Eastern Desert and Sinai. In: Said R (ed) The geology of Egypt. Balkema, Rotterdam, pp 175–200

El-Gaby S, Khudeir AA, Abd El-Tawab M, Atalla RF (1991) The metamorphosed volcanosedimentary succession of Wadi Kid, southeastern Sinai, Egypt. Ann Geol Surv Egypt 17:19–35

El-Gaby S, Khudeir AA, Asran AM (1994) Geology and geochemistry of the Pan-African volcanosedimentary belt at Wadi Um Gheig, Eastern Desert, Egypt. Bull Fac Sci Assiut Univ 23:185–219

El-Gaby S, Khalaf IM, Eliwa HA, El-Miligy A, Gomaa RM (2002) Volcanosedimentary successions of the Wadi Sa'al-Wadi Zaghra area, southeastern Sinai, Egypt. In: 6th International conference on geology of the Arab World, Cairo Univ., pp 25–44

El-Gemmizi MA (1984) On the occurrence and genesis of mud zircon in the radioactive psammitic gneiss of Wadi Nugrus, Eastern Desert, Egypt. J Univ Kuwait (Sci) 11:285–294

El-Gharabawi RI (1981) Petrological studies on the metamorphic rocks of Gabal El Hudi area, East of Aswan. Unpublished MSc thesis, Ain Shams Univ., Cairo

El-Gharabawi RIA, Hassen IS (2001) The Late Precambrian metagabbro-diorite complex, Wadi Melheg area, southeastern Sinai, Egypt: an active continental margin setting. Ann Geol Surv Egypt 24:131–158

El Ghawabi MA (1973) Structural geology and radioactive mineralization of Wadi Zeidun area, Eastern Desert, Egypt. Unpublished PhD thesis, Ain Shams Univ. Cairo, Egypt

El Habaak GH (2004) Pan-African skarn deposits related to banded iron formation, Um Nar area, central Eastern Desert, Egypt. J Afr Earth Sci 38:199–221

El Habaak GH (2012) Ferruginous jasper and chert deposits associated with island-arc metavolcanics, Eastern Desert, Egypt. Acad J Sci 1:347–381

El Habaak GH, Mahmoud MS (1994) Carbonaceous bodies of debatable organic provenance in the Banded Iron Formation of the Wadi Kareim area, Eastern Desert, Egypt. J Afr Earth Sci 19:125–133

Eliwa HA, Abu El-Enen MM, Khalaf IM, Itaya T (2004) Metamorphic evolution of Sinai metapelites and gneisses: constraints from petrology and K/Ar dating. Egypt J Geol 48:169–185

Eliwa HA, Abu El-Enen MM, Khalaf IM, Itaya T, Murata M (2008) Metamorphic evolution of Neoproterozoic metapelites and gneisses in Sinai, Egypt: insights from petrology, mineral chemistry and K-Ar age dating. J Afr Earth Sci 51:107–122

El Kady MFM (2003) Structural evolution in the palaeoproterozoic basement (banded iron formation and related rocks) of SW Egypt. Unpublished PhD thesis, Ruprecht-Karls Univ., Heidelberg

El Kalioubi B (1988) Deformation events, mineral facies and metamorphic conditions in the contact aureoles of the Hammamat Group around Um Had pluton, central Eastern Desert, Egypt. M.E. R.C. Ain Shams Univ Earth Sci Ser 2:172–190

El Kalioubi BA, El Ramly MF (1991) Nomenclature, origin and tectonic setup of the "granite" suite at Wadi Shait, South Eastern Desert, Egypt. Ann Geol Surv Egypt 17:1–17

El Kassas IA (1974) Radioactivity and geology of Wadi Atalla area, Eastern Desert of Egypt. Unpublished PhD thesis, Fac. Sci., Ain Shams Univ., Cairo, 502 pp

El Kazzaz YA (2010) Geometry of fold interference patterns in Wadi Kharit area, South Eastern Desert, Egypt. J Rem Sens Space Sci 13:113–120

El-Manharawy MA (1977) Geochronological investigations of some basement rocks in the central Eastern Desert, Egypt, between lat. 25° and 26°N. Unpublished PhD thesis, Cairo Univ., 211 pp

El-Metwally AA, El-Aasy IE, Ibrahim ME, Essawy MA, El-Mowafy AA (1999) Petrological, structural and geochemical studies on the basement rocks of Gabal Um Zariq-Wadi Kid area, South-eastern Sinai. Egypt J Geol 43:147–180

El-Rahmany MM, Saleh GM, El-Desoky HM, El-Awny HM (2015) Wadi El-Gemal tourmaline-bearing deposits, Southern Eastern Desert, Egypt: constraints on petrology and geochemistry. Int J Sci Eng Appl Sci 1:88–119

El Ramly MF (1972) A new geological map for the basement rocks in the Eastern and Southwestern Deserts of Egypt. Ann Geol Surv Egypt 2:1–18

El Ramly MF, Akaad MK (1960) The basement complex in the central Eastern Desert of Egypt between lat. 24°30′ and 25°40′N. Geol. Surv. Egypt, Paper No. 8, pp 1–35

El Ramly MF, Hermina M (1978) Geologic map of the Qena Quadrangle, Egypt, scale 1:500000. Egypt. Geol. Surv. Min. Authority, Cairo, Egypt

El Ramly MF, Saleeb-Roufaiel GS (1974) Sodic-silica metasomatism and introduced zircon in the Migif-Hafafit gneisses, Eastern Desert. Egypt J Geol 18:119–126

El Ramly MF, Akaad MK, Shaaban AS (1963) Geology and structure of the iron ore deposit of Gabal El Hadid, Eastern Desert of Egypt. Geol. Surv. Egypt. Paper No. 16, 31 pp

El Ramly MF, Meneisy MY, Ragab AI, Aly MM, Rashwan AA (1980) Petrology and age of Um Shilman granite rocks, south Eastern Desert. Ann Geol Surv Egypt 10:783–796

El Ramly MF, Hashad AH, Attawyia MY, Mansour MM (1982) Geochemistry of Kolet Umm Kharit bimodal metavolcanics, south Eastern Desert, Egypt. Ann Geol Surv Egypt 12:103–120

El Ramly MF, Greiling RO, Kröner A, Rashwan A (1984) On the tectonic evolution of Wadi Hafafit area and environs, Eastern Desert of Egypt. In: Al Shanti AM (ed) Proceedings of a symposium on Pan African crustal evolution in the Arabian Shield, vol 6. I.G.C. P. No. 164. Fac. Earth Sci., King Abdulaziz Univ., Jeddah, Bull., pp 113–126

El Ramly MF, Greiling RO, Rashwan AA, Rasmy AH (1993) Explanatory note to accompany the geological and structural maps of the Wadi Hafafit area, Eastern Desert of Egypt. Geol. Surv. Egypt, Paper No. 68, 53 pp

El-Sayed MM, Furnes H, Mohamed FH (1999) Chemical constraints on the tectonomagmatic evolution of the late Precambrian Fawakhir ophiolite, Central Eastern Desert, Egypt. J Afr Earth Sci 29:515–533

El-Sayed GM, Hassan MA, El-Nady O (2000) Geothermobarometry of garnet-biotite-staurolite and cordierite from Wadi Um Sheqila, Central Eastern Desert, Egypt. Bull Fac Sci Assiut Univ 29:11–28

El-Shafei MK (1998) Structural evolution of Feiran-Solaf Metamorphic Belt, SW Sinai, Egypt. Unpubl. Ph.D. thesis. Suez Canal Univ., Ismailia, Egypt, 172 pp

El-Shafei MK (1991) Deformational system in the tectonics of Wadi Sa'al Area, Southeastern Sinai, Egypt. Unpublished MSc thesis. Suez Canal Univ., Egypt, 168 pp

El-Shafei MK, Kusky TM (2003) Structural and tectonic evolution of the Neoproterozoic Feiran-Solaf metamorphic belt Sinai Peninsula: implications for the closure of the Mozambique ocean. Precambr Res 123:269–293

El-Shafei MK, Khawasik, SM, El-Ghawaby MA (1992) Deformational styles in the tectonites of Wadi Sa'al area, central-south Sinai. In: Proceedings of 3rd conference on geology and Sinai development, Ismailia, pp 1–8

El-Sharkawy MA, El-Bayoumi RM (1979) The ophiolites of Wadi Ghadir area, Eastern Desert, Egypt. Ann Geol Surv Egypt 9:125–135

El Shazley EM, Bassyoumi FA, Abdel Khalek ML (1977) Geology of the Greater Abu Swayel Area, Eastern Desert, Egypt. Egypt J Geol 19:1–41

El-Shazly SM, El-Sayed MM (2000) Petrogenesis of the Pan-African El-Bula Igneous Suite, Central Eastern Desert, Egypt. J Afr Earth Sci 31:317–336

El-Shazly SM, Hegazy HA (2000) Geochemistry and petrogenesis of a Late Proterozoic volcanic sequence in the Magal Gebriel area, South Eastern Desert, Egypt. Qatar Univ Sci J 20:181–195

El-Shazly AK, Khalil KJ (2014) Banded iron formations of Um Nar, Eastern Desert of Egypt: P-T-X conditions of metamorphism and tectonic implications. Lithos 196–197:356–375

El Shazly EM, Hashad AH, Sayyah TA, Bassyuni FA (1973) Geochronology of Abu Swayel area, South Eastern Desert. Egypt J Geol 17:1–18

El Shimi KAM, Soliman AA (2002) Gold mineralization associated the banded iron formations in the Central Eastern Desert of Egypt: first record. Ann Geol Surv Egypt 25:281–299

El-Taher A (2010) Determination of chromium and trace elements in El-Rubshi chromite from Eastern Desert, Egypt by neutron activation analysis. Appl Rad Isotop 68:1864–1868

El-Tokhi M (2003) Petrogenesis, geochemistry and origin of the Precambrian gneisses of Feiran Complex, south western Sinai, Egypt. Ann Geol Surv Egypt 26:1–17

El-Tokhi M, Alaabed S, Amin BM (2010) Late Precambrian metavolcanics of Um Anab North Eastern Desert, Egypt, geochemistry and tectonic environment studies. Eur J Sci Res 42:507–524

Emam A, Zoheir B (2012) Au and Cr mobilization through metasomatism: Microchemical evidence from ore-bearing listvenite, South Eastern Desert of Egypt. J Geochem Explor 125:34–45

Engel AEJ, Dixon TH, Stern RJ (1980) Late Precambrian evolution of Afro-Arabian crust from ocean arc to craton. Geol Soc Am Bull 91:699–706

Ersoy YE, Halvaci C, Palmer MR (2011) Stratigraphic, structural and geochemical features of the NE–SW trending Neogene volcano-sedimentary basins in western Anatolia: implications for associations of supra-detachment and transtensional strike-slip basin formation in extensional tectonic setting. J Asian Earth Sci 41:159–183

Essawy MA, Abu Zeid KM (1972) Atalla felsite intrusion and its neighbouring rhyolitic flows and tuffs, Eastern Desert. Ann Geol Surv Egypt 2:271–280

Eyal Y (1980) The geological history of the Precambrian metamorphic rocks between Wadi Twaiba and Wadi Um Mara, NE Sinai. Isr J Earth Sci 29:53–66

Eyal Y, Eyal M, Kröner A (1991) Geochronology of the Elat Terrain, metamorphic basement, and its implication for crustal evolution of the NE part of the Arabian-Nubian Shield. Isr J Earth Sci 40:5–16

Eyal M, Litvinovsky B, Jahn BM, Zanvilevich A, Katzir Y (2010) Origin and evolution of post-collisional magmatism: Coeval Neoproterozoic calc-alkaline and alkaline suites of the Sinai Peninsula. Chem Geol 269:153–179

Eyal M, Bentor YK, Eyal Y, Calvo R, Hall JK, Rosensaft M (2013) Geological Map of Precambrian Rocks of South-West Sinai, Egypt, Scale 1:75,000. Geol. Surv., Israel

Eyal M, Be'eri-Shlevin Y, Eyal Y, Whitehouse MJ, Litvinovsky B (2014) Three successive Proterozoic island arcs in the northern Arabian-Nubian shield: evidence from SIMS U-Pb dating of zircon. Gond Res 25:338–357

Eyal M, Bentor YK, Shimron AE, Eyal Y, Calvo R, Hall JK (2015) Geological map of Feiran Metamorphic Belt, Sinai, Egypt. Scale 1:75,000. Geological Survey of Israel

Eyles N, Januszczak N (2004) 'Zipper-rift': a tectonic model for Neoproterozoic glaciations during the breakup of Rodinia after 750 Ma. Earth Sci Rev 65:1–73

Farahat ES (2003) Metamorphism of Kolet Um Kharit metavolcanics, south Eastern Desert, Egypt: a case of transitional greenschist-amphibolite facies. Egypt J Geol 47:67–85

Farahat ES (2006) The Neoproterozoic Kolet Um Kharit bimodal metavolcanic rocks, south Eastern Desert, Egypt: a case of enrichment from plume interaction? Int J Earth Sci 95:275–287

Farahat ES, El Mahallawi MM, Hoinkes G, Abdel Aal AY (2004) Continental back-arc basin origin of some ophiolites from the Eastern Desert of Egypt. Mineral Petrol 82:81–104

Finger E, Helmy H (1998) Composition and total-Pb model ages of monazite from high-grade paragneisses in the Abu Swayel area, southern Eastern Desert, Egypt. Mineral Petrol 62:269–289

Fitches WR, Graham RH, Hussein IM, Ries AC, Shackleton RM, Rice RC (1983) The Late Proterozoic ophiolite of Sol Hamed, NE Sudan. Precambr Res 19:385–441

Fleck RJ, Greenwood WR, Hadley DG, Anderson RE, Schmidt DL (1980) Rubidium-Strontium geochronology and plate-tectonic evolution of the southern part of the Arabian Shield. U.S. Geol. Surv. Prof. Pap. No. 1131, 38 pp

Fowler TJ (2001) Pan-African granite emplacement mechanisms in the Eastern Desert, Egypt. J Afr Earth Sci 32:61–86

Fowler A, Abdeen MM (2014) Reappraisal of strain estimations and measurement methods in the Hammamat Group sediments: comparison of primary and secondary grain fabrics with new data from Wadi Zeidun and Wadi Arak basins, CED, Egypt. Precambr Res 247:1–32

Fowler A, El-Kalioubi B (2002) The Migif-Hafafit gneissic complex of the Egyptian Eastern Desert: fold interference patterns involving multiply deformed sheath folds. Tectonophysics 346:247–275

Fowler A, El-Kalioubi B (2004) Gravitational collapse origin of shear zones, foliations and linear structures in the Neoproterozoic cover nappes, Eastern Desert, Egypt. J Afr Earth Sci 38:23–40

Fowler A, Hassen IS (2008) Extensional tectonic origin of gneissosity and related structures of the Feiran-Solaf metamorphic belt, Sinai, Egypt. Precambr Res 164:119–136

Fowler TJ, Osman AF (2001) Gneiss-cored interference dome associated with two phases of late Pan-African thrusting in the Central Eastern Desert, Egypt. Precambr Res 108:17–43

Fowler A, Osman AF (2009) The Sha'it-Nugrus shear zone separating central and south eastern deserts, Egypt: a post-arc collision low-angle normal ductile shear zone. J Afr Earth Sci 53:16–32

Fowler A, Osman AF (2013) Sedimentation and inversion history of three molasse basins of the western Central Eastern Desert of Egypt: implications for the tectonic significance of Hammamat basins. Gond Res 23:1511–1534

Fowler A, Ali KG, Omar SM, Eliwa H (2006) The significance of gneissic rocks and synmagmatic extensional ductile shear zones of the Barud area for the tectonics of the North Eastern Desert, Egypt. J Afr Earth Sci 46:201–220

Fowler A, Khamees H, Dowidar H (2007) El-Sibai gneissic complex, Central Eastern Desert, Egypt: folded nappes and syn-kinematic gneissic granitoid sheets—not a core complex. J Afr Earth Sci 49:119–135

Fowler A, Hassen IS, Osman AF (2010a) Neoproterozoic structural evolution of SE Sinai, Egypt: I. Re-investigation of the structures and deformation kine-matics of the Um Zariq and Malhaq Formations, northern Wadi Kid area. J Afr Earth Sci 58:507–525

Fowler A, Hassen IS, Osman AF (2010b) Neoproterozoic structural evolution of SE Sinai, Egypt: II. Convergent tectonic history of the continental arc Kid Group. J Afr Earth Sci 58:526–546

Fowler A, Hassen I, Hassan M (2015) Tectonic evolution and setting of the Sa'al Complex, southern Sinai, Egypt: a Proterozoic continental back-arc rift model. J Afr Earth Sci 104:103–131

Fowler A, Hassen IS, Hassan M (2018) The Feiran-Solaf metamorphic complex, Sinai, Egypt: evidence for orthogonal or oblique tectonic convergence? J Afr Earth Sci 146:48–65

Friedmann SJ, Burbank DW (1995) Rift basins and supradetachment basins: intracontinental extensional end-members. Basin Res 7:109–127

Frisch W, Al-Shanti A (1977) Ophiolite belts and the collision of island arcs in the Arabian Shield. Tectonophysics 43:293–306

Fritz H, Messner M (1999) Intramontane basin formation during oblique convergence in the Eastern Desert of Egypt: magmatically versus tectonically induced subsidence. Tectonophysics 315:145–162

Fritz H, Puhl J (1996) Granitoid emplacement in a shear-extensional setting: a semiquantitative approach from physical parameters (Eastern Desert, Egypt). Zbl Geol Palaont Teil 1:257–276

Fritz H, Wallbrecher E, Khudier AA, Abu El-Ela F, Dallmeyer RD (1996) Formation of Neoproterozoic metamorphic core complexes during oblique convergence, Eastern Desert, Egypt. J Afr Earth Sci 23:311–329

Fritz H, Dalmeyer DR, Wallbrecher E, Loizenbauer J, Hoinkes G, Neumayr P, Khudeir AA (2002) Neoproterozoic tectonothermal evolution of the Central Eastern Desert, Egypt: a slow velocity tectonic process of core complex exhumation. J Afr Earth Sci 34:543–576

Fritz H, Abdelsalam M, Ali KA, Bingen B, Collins AS, Fowler AR, Ghebreab W, Hauzenberger CA, Johnson PR, Kusky TM, Macey P, Muhongo S, Stern RJ, Viola G (2013) Orogen styles in the East African Orogen: a review of the Neoproterozoic to Cambrian tectonic evolution. J Afr Earth Sci 86:65–106

Fritz H, Loizenbauer J, Wallbrecher E (2014) Magmatic and solid state structures of the Abu Ziran pluton: deciphering transition from thrusting to extension in the Eastern Desert of Egypt. J Afr Earth Sci 99:122–135

Furnes H, Shimron AE, Roberts D (1985) Geochemistry of Pan-African volcanic arc sequences in southeastern Sinai Peninsula and plate tectonic implications. Precambr Res 29:359–382

Furnes H, El-Sayed MM, Khalil SO, Hassanen MA (1996) Pan-African magmatism in the Wadi El-Imra district, Central Eastern Desert, Egypt: geochemistry and tectonic environment. J Geol Soc Lond 153:705–718

Gad S, Kusky T (2006) Lithological mapping in the Eastern Desert of Egypt, the Barramiya area, using Landsat thematic mapper (TM). J Afr Earth Sci 44:196–202

Gahlan HA, Azer MK, Khalil AES (2015) The Neoproterozoic Abu Dahr ophiolite, South Eastern Desert, Egypt: petrological characteristics and tectonomagmatic evolution. Miner Petrol 109: 611–630

Gahlan H, Arai S (2009) Carbonate-orthopyroxenite lenses from the Neoproterozoic Gerf ophiolite, South Eastern Desert, Egypt: the first record in the Arabian Nubian Shield ophiolites. J Afr Earth Sci 53:70–82

Gamal El Dien H, Hamdy M, Abu El-Ela A, Abu-Alam T, Hassan A, Kil Y, Mizukami T, Soda Y (2016) Neoproterozoic serpentinites from the Eastern Desert of Egypt: insights into Neoproterozoic mantle geodynamics and processes beneath the Arabian-Nubian Shield. Precambr Res 286:213–233

Garson MS, Shalaby IM (1976) Precambrian - Lower Paleozoic plate tectonics and metallogenesis in the Red Sea region. Geol. Assoc. Canada Spec. Pap. No. 14, pp 573–596

Gass IG (1977) The evolution of the Pan-African crystalline basement in NE Africa and Arabia. J Geol Soc Lond 134:129–138

Gass IG (1979) Evolution model for the Pan-African crystalline basement. I.A.G. 3(1), Jeddah, pp 11–20

Gass IG (1981) Pan-African (Upper Proterozoic) plate tectonics of the Arabian-Nubian Shield. In: Kröner A (ed) Precambrian plate tectonics. Elsevier, Amsterdam, pp 388–405

Gass IG (1982) Upper Proterozoic (Pan-African) calc-alkaline magmatism in north-eastern Africa and Arabia. In: Thorpe RS (ed) Andesites. Wiley, pp 591–609

Gaucher C, Sial AN, Frei R (2015) Chemostratigraphy of Neoproterozoic Banded Iron Formation (BIF): types, age and origin. In: Ramkumar M (ed) Chemostratigraphy, concepts, techniques and applications. Elsevier, pp 433–449

Genna A, Nehlig P, Le Goff E, Guerrot C, Shanti M (2002) Proterozoic tectonism of the Arabian Shield. Precambr Res 117:21–40

Ghoneim MF, Takla MA, Lebda EM (1992) The gabbroic rocks of the central Eastern Desert, Egypt: a geochernical approach. Ann Geol Surv Egypt 18:1–21

Ghoneim MF, Aly SM, El-Baraga MH (1993) Age of Beitan Gneiss: implication for Late Precambrian crustal evolution in South Eastern Desert, Egypt. Acta Mineral Petrogr 34:41–50

Ghoneim MF, Lebda EM, Nasr BB, Khedr MZ (2002) Geology and tectonic evolution of the area around Wadi Arais, Southeastern Desert, Egypt. In: 6th International conference on geology of the Arab World, Cairo Univ., pp 45–66

Ghoneim MF, Salem IA, Hamdy MM (2003) Origin of magnesite veins in serpentinites from Mount El-Rubshi and Mount El-Maiyit, Eastern Desert, Egypt. Archiwum Mineralogiczne 2001–2002:41–63

Gillespie JG, Dixon TH (1983) Lead isotope systematics of some igneous rocks from the Egyptian Shield. Precambr Res 20:63–77

Greenwood WR, Brown GF (1973) Petrology and chemical analysis of selected plutonic rocks from the Arabian Shield, Kingdom of Saudi Arabia: Saudi Arab, vol 9. Direct. Gen. Miner. Res. Bull., 9 pp

Greenwood WR, Hadley DG, Anderson RE, Fleck RJ, Schmidt DL (1976) Late Proterozoic cratonization in Southwestern Saudi Arabia. Philos Trans R Soc Lond A-280:517–527

Greenwood WR, Anderson RE, Fleck RJ, Roberts RJ (1980) Precambrian geologic history and plate tectonic evolution of the Arabian shield: Saudi Arab, vol 24. Direct. Gen. Miner. Res. Bull., 35 pp

Greenwood WR, Stoeser DB, Fleck RJ, Stacey JS (1983) Late Proterozoic island-arc complexes and tectonic belts in the southern part of the Arabian Shield, Kingdom of Saudi Arabia. U.S. Geol. Surv. Open File Rep. 83-296, 46 pp

Greiling RO, El Ramly MF (1985) Thrust tectonics in the Pan-African basement of SE Egypt. CIFEG, Publ. Occ. 1985/3, pp 73–74

Greiling RO, El Ramly MF (1990) Wadi Hafafit area. Map, structural geology, 1:100.000. TFH

Greiling RO, Rashwan AA (1994) Large-scale shear-zones and related mineral deposits: examples from the Nubian Shield (Proterozoic, Egypt). Africa Geosci Rev 1:503–514
Greiling RO, Kröner A, El Ramly MF (1984) Structural interference patterns and their origin in the Pan-African basement of the southeastern desert of Egypt. In: Kröner A, Greiling R (eds) Precambrian tectonics illustrated. E. Schweizerb. Verlagsb, Stuttgart, pp 401–412
Greiling RO, Kröner A, El Ramly MF, Rashwan AA (1988) Structural relationships between the Southern and Central Parts of the Eastern Desert of Egypt: details of a fold and thrust belt. In: El-Gaby S, Greiling RO (eds) The Pan-African Belt of NE Africa and Adjacent Areas. Vieweg & Sohn, pp 121–145
Greiling RO, Rashwan AA, El Ramly MF, Kamal El Din GM (1993) Towards a comprehensive structural synthesis of the (Proterozoic) Arabian-Nubian Shield in E. Egypt. In: Thorweihe U, Schandelmeier H (eds) Geoscientific research in Northeast Africa. Balkema, Rotterdam, pp 15–19
Greiling RO, Abdeen MM, Dardir AA, El Akhal H, El Ramly MF, Kamal El Din GM, Osman AF, Rashwan AA, Rice AH, Sadek MF (1994) A structural synthesis of the Proteorozoic Arabian-Nubian Shield in Egypt. Geol Rundsch 83:484–501
Greiling RO, de Wall H, Warr LN, Naim GM, Hussein AA, Sadek MF, Abdeen MM, El Kady MF, Makhlouf A (1996) Basement structures in Eastern Egypt: quantitiative perspectives for the second century. In: Proceedings of geological survey Egypt centennial conference, pp 289–302
Grothaus B, Eppler D, Ehrlich R (1979) Depositional environment and structural implication of the Hammamat Formation, Egypt. Ann Geol Surv Egypt 9:564–590
Grundmann G, Morteani G (2008) Multi-stage emerald formation during Pan-African regional metamorphism: The Zabara, Sikait, Umm Kabo deposits, South Eastern desert of Egypt. J Afr Earth Sci 50:168–187
Habib ME (1972) Geology of the area west of Safaga, Eastern Desert. Unpublished PhD thesis, Assiut Univ.
Habib ME (1987) Arc ophiolites in the Pan-African basement between Meatiq and Abu Furad, Eastern Desert, Egypt. Bull Fac Sci Assiut Univ 16:241–283
Habib ME, Ahmed AA, El Nady OM (1985a) Two orogenies in the Meatiq area of the Central Eastern Desert, Egypt. Precambr Res 30:83–111
Habib ME, Ahmed AA, El Nady OM (1985b) Tectonic evolution of the Meatiq infrastructure, Central Eastern Desert, Egypt. Tectonics 4:613–627
Hagag W, Moustafa R, Hamimi Z (2018) Neoproterozoic evolution and Najd-related transpressive shear deformations along Nugrus Shear Zone, South Eastern Desert, Egypt (implications from field—structural data and AMS-technique). Geotectonics 52:114–133
Hamdy MM (2007) Stable isotope and trace element characteristics of some serpentinite-hosted vein magnesite deposits from the Eastern Desert of Egypt: arguments for magmatism and metamorphism-related mineralizing fluids. M.E.R.C. Ain Shams Univ Earth Sci Ser 21:29–50
Hamdy MM, Gamal El Dien HM (2017) Nature of serpentinization and carbonation of ophiolitic peridotites (Eastern Desert, Egypt): constraints from stable isotopes and whole-rock geochemistry. Arab J Geosci 10:429. https://doi.org/10.1007/s12517-017-3215-6
Hamdy MM, Abd El-Wahed MA, Gamal El Dien H, Morishita T (2017) Garnet hornblendite in the Meatiq Core Complex, Central Eastern Desert of Egypt: implications for crustal thickening preceding the ~600 Ma extensional regime in the Arabian-Nubian Shield. Precambr Res 298:593–614
Hamdy MM, Harraz HZ, Aly GA (2013) Pan-African (intraplate and subduction-related?) metasomatism in the Fawakhir ophiolitic serpentinites, Central Eastern Desert of Egypt: mineralogical and geochemical evidences. Arab J Geosci 6:13–33
Hamimi ZEA (1992) Geological and structural studies on Wadi Beitan area, South Eastern Desert, Egypt. Unpublished PhD thesis, Cairo Univ., 161 pp
Hamimi Z (2000) Quantitative strain analyses of some late-tectonic Hammamat sediments, Eastern Desert, Egypt. Egypt J Geol 44:85–107
Hamimi Z, El Amawy MA, Wetait M (1994) Geology and structural evolution of El Shalul dome and environs, Central Eastern Desert, Egypt. Egypt J Geol 38:575–595
Hamimi Z, Abd El-Wahed M, Gahlan HA, Kamh SZ (2019) Tectonics of the Eastern Desert of Egypt: key to understanding the Neoproterozoic evolution of the Arabian-Nubian Shield (East African Orogen). In Bendaoud A et al (eds) Geology of the Arab Region. Springer, pp 1–81
Hargrove US, Stern RJ, Kimura J-I, Manton WI, Johnson PR (2006) How juvenile is the Arabian-Nubian shield? Evidence from Nd isotopes and pre-Neoproterozoic inherited zircon in the Bi'r Umq suture zone, Saudi Arabia. Earth Planet Sci Lett 252: 308–326
Harms U, Schandelmeier H, Darbyshire DPF (1990) Pan-African reworked early/middle Proterozoic crust in NE Africa west of the Nile: Sr and Nd isotope evidence. J Geol Soc Lond 147:859–872
Harraz HZ, El-Sharkawy MF (2001) Origin of tourmaline in the metamorphosed Sikait pelitic belt, south Eastern Desert. J Afr Earth Sci 33:391–416
Harraz HZ, Hassan AM, Furuyama K (2005) The Wadi Sikait Complex: a fertile post-collisional granite-pegmatite suite, Eastern Desert, Egypt. Ann Geol Surv Egypt 28:1–35
Harris NBW, Hawkesworth CJ, Ries AC (1984) Crustal evolution in northeast and East Africa from model Nd ages. Nature 309:773–776
Hashad AH (1980) Present status of geochronological data on the Egyptian basement complex. In Al-Shanti A (ed) Evolution and mineralization of the Arabian-Nubian Shield, vol 3. Bull. Inst. Appl. Geol. King Abdulaziz Univ., Jeddah, Saudi Arabia, pp 31–46
Hashad AH, Hassan MA (1979) On the validity of an Ensimatic Island, arc cratonization model to the evolution of the Egyptian Shield. Ann Geol Surv Egypt, IX, pp 70–80
Hashad AH, Sayyah TA, El Kholy SB, Youssef A (1972) Rb-Sr isotopic age determination of some basement Egyptian granites. Egypt J Geol 16:169–181
Hassan MA (1999) Petrochemistry and petrogenesis of granitoids and granitic gneisses from Ras Barud area, Central Eastern Desert, Egypt. Egypt J Geol 43:109–130
Hassan MA, Essawy MA (1976) Petrography of the metagabbro-diorite complex of Wadi Mubarak-Gabal Atud area, Eastern Desert, Egypt. J Univ Kuwait (Sci) 4:203–213
Hassan MA, Hashad AH (1990) Precambrian of Egypt. In: Said R (ed) The geology of Egypt. Balkema, Rotterdam, pp 201–245
Hassan M, Abu-Alam TS, Stüwe K, Fowler A, Hassan I (2014) Metamorphic evolution of the Sa'al–Zaghra Complex in Sinai: evidence for Mesoproterozoic Rodinia break-up? Precambr Res 241:104–128
Hassen IS, El-Shafei MK, Stüwe K (2007) Late Proterozoic crustal evolution in the Arabian-Nubian Shield of Wadi Zaghra tectonites, south Sinai, Egypt. Ann Geol Surv Egypt 29:77–93
Hassan SM, El kazzaz YA, Taha MN, Mohammad AT (2017) Late Neoproterozoic basement rocks of Meatiq area, Central Eastern Desert, Egypt: petrography and remote sensing characterizations. J Afr Earth Sci 131:14–31
Hassanen MA (1992) Geochemistry and petrogenesis of the Late Proterozoic Kid volcanics: evidence relevant to arc-intra-arc rifting volcanism in Southern Sinai, Egypt. J Afr Earth Sci 14:131–145

Hathout MH (1963) Geology and geochemistry of some serpentinites in the Eastern Desert. Unpublished MSc thesis, Ain Shams Univ. Cairo

Hegazi AM (2006) Tectonic evolution of the polydeformed Sa'al Belt, South Sinai, Egypt. Acta Geol Hung 49:271–284

Hegazy HA (1999) Metamorphic conditions based on garnet-biotite compositions in some areas of the Eastern Desert, Egypt. In: 1st International conference on geology of Africa, Assiut, vol 1, pp 265–280

Hegazi AM, El-Shafei MK, Sultan YM (2004) Multiple deformation phases of Solaf Gneiss Belt, South Sinai Egypt. In: Proceedings of 7th international conference on geology of the Arab World, Cairo, pp 313–320

Helmy HM (1996) Precious metal and base metal mineralization at Abu Swayel and Um Samiuki, Eastern Desert, Egypt. Unpublished PhD thesis, El Minia Univ., Egypt, 238 pp

Helmy HM, Ahmed AF, El Mahallawi MM, Ali SM (2004) Pressure, temperature and oxygen fugacity conditions of calc-alkaline granitoids, Eastern Desert of Egypt, and tectonic implications. J Afr Earth Sci 38:255–268

Helmy HM, Abd El-Rahman YM, Yoshikawa M, Shibata T, Arai S Tamura A, Kagami H (2014) Petrology and Sm-Nd dating of the Genina Gharbia Alaskan-type complex (Egypt): insights into deep levels of Neoproterozoic island arcs. Lithos 198–199:263–280

Hilmy ME, Awad NT (1969) Barite mineralization at Aswan. In: Proceedings of 6th Arab Science Congress, Damascus, 4B, pp 797–816

Hume WF (1906) The topography and geology of the Peninsula of Sinai (South Eastern portion). Survey of Egypt, Cairo

Hume WF (1934) Geology of Egypt 2, Part 1: The metamorphic rocks. Geol Surv Egypt, 293 pp

Hume WF (1935): Geology of Egypt 2, Part 2: The later plutonic and intrusive rocks, with a special chapter dealing with dynamical geology and the age of the Pre-Cambrian rocks in Egypt. Surv. Egypt, Cairo, 294 pp

Hunting Geology and Geophysics Ltd (1967) Assessment of the mineral potential of the Aswan region, U.A.R.: Photogeological survey. U.N. Develop. Prog. U.A.R. Regional Planning of Aswan, 138 pp

Hussein AA, Ali MM, El Ramly MF (1982) A proposed new classification of the granites of Egypt. J Volc Geotherm Res 14:187–198

Hussein HA, Zalata AA, El-Aassy IE, El-Metwally AA, Ibrahim ME (1993) Structural pattern of Wadi Zaghra area, southeast Sinai. Egypt J Geol 37:1–19

Hussein IM, Kröner A, Reischmann T (2004) The Wadi Onib Mafic-Ultramafic complex: a neoproterozoic supra-subduction zone ophiolite in the Northern Red Sea Hills of the Sudan. Dev Precambr Geol 13:163–206

Ibrahim S, Cosgrove J (2001) Structural and tectonic evolution of the Umm Gheig/El-Shush region, central Eastern Desert of Egypt. J Afr Earth Sci 33:199–209

Ilyin AV (2009) Neoproterozoic banded iron formation. Lithol Mineral Res 44:78–86

Jacobs J, Fanning CM, Henjes-Kunst F, Olesch M, Paech H-J (1998) Continuation of the Mozambique into East Antarctica: Grenville-age metamorphism and polyphase Pan-African high grade events in central Dronning Maud Land. J Geol 106:385–406

Johnson PR (1998) The structural geology of the Samran-Shayban area, Kingdom of Saudi Arabia. Saudi Arabian Deputy Ministry for Mineral Resources, Tech. Rep. USGS-TR-98-2

Johnson PR (2000) Proterozoic geology of Western Saudi Arabia - Southern sheet. Saudi Geol. Surv. Open-File Rep USGS-OF-99-7

Johnson PR (2014) An expanding Arabian-Nubian shield geochronologic and isotopic dataset: defining limits and confirming the tectonic setting of a neoproterozoic accretionary orogen. Open Geol J 8:3–33

Johnson PR, Woldehaimanot B (2003) Development of the Arabian–Nubian shield: perspectives on accretion and deformation in the northern East African Orogen and the assembly of Gondwana. In: Yoshida M, Windley BF, Dasgupta S (eds) Proterozoic East Gondwana: supercontinent assembly and breakup, vol 206. Geol. Soc. Lond. Spec. Publ., pp 290–325

Johnson PR, Kattan FH, Al-Saleh AM (2004) Neoproterozoic ophiolites in the Arabian Shield: field relations and structure. In: Kusky TM (ed) Precambrian ophiolites and related rocks, vol 13. Develop. Precam. Geol., pp 129–162

Johnson PR, Andresen A, Collins AS, Fowler AR, Fritz H, Ghebreab W, Kusky T, Stern RJ (2011) Late Cryogenian-Ediacaran history of the Arabian-Nubian Shield: a review of depositional, plutonic, structural, and tectonic events in the closing stages of the northern East African Orogen. J Afr Earth Sci 61:167–232

Kamal El Din GM (1993) Geochemistry and tectonic significance of the Pan-African El-Sibai Window, Central Eastern Desert, Egypt. Unpublished PhD thesis, Forschung. Julich GmbH, vol 19, 154 pp

Kamal El Din GM (2003) Emplacement mechanisms of the Pan-African late-orogenic granites: an example from Um Taghir el Fogani pluton, Qena-Safaga road, Eastern Desert, Egypt. M.E.R.C. Ain Shams Univ Earth Sci Ser 17:138–156

Kamal El Din GM, Asran AM (1994) Highlight on the petrology, geochemistry and structural evolution of the amphibolite facies terrain at Wadi um Taghir along Qena - Safaga Road, Central Eastern Desert, Egypt. In: 2nd International Conference on Geology of the Arab World, Cairo, pp 91–108

Kamal El Din GM, Khudeir AA, Greiling RO (1992) Tectonic evolution of a Pan-African gneiss culmination, Gabal El-Sibai area, Central Eastern Desert, Egypt. Zbl. Geol. Paläont. Teil 1, v. 1991, pp 2637–2640

Kamel M, Youssef M, Hassan M, Bagash F (2016) Utilization of ETM + Landsat data in geologic mapping of wadi Ghadir-Gabal Zabara area, Central Eastern Desert, Egypt. Egypt J Rem Sens Space Sci 19:343–360

Karmakar S, Schenk V (2015) Neoarchean UHT metamorphism and paleoproterozoic UHT reworking at Uweinat in the East Sahara Ghost Craton, SW Egypt: evidence from petrology and texturally controlled in situ monazite dating. J Petrol 56(9):703–1742

Katz O, Avigad D, Matthews A, Heimann A (1998) Precambrian metamorphic evolution of the Arabian-Nubian Shield in the Roded area, southern Israel. Isr J Earth Sci 47:93–110

Katz O, Beyth M, Miller N, Stern R, Avigad D, Basu A, Anbar A (2004) A Late Neoproterozoic (630 Ma) boninitic suite from southern Israel: implications for the consolidation of Gondwana-land. Earth Planet Sci Lett 218:475–490

Kennedy WO (1964) The structural differentiation of Africa in the Pan-African tectonic episode. In: 8th Ann. Rep., Res. Inst. Afr. Geol., Leeds Univ., pp 48–49

Khalaf EA, Obeid MA (2013) Tectonostratigraphy and depositional history of the Neoproterozoic volcano-sedimentary sequences in Kid area, southeastern Sinai, Egypt: implications for intra-arc to fopreland basin in the northern Arabian-Nubian Shield. J Asian Earth Sci 73:473–503

Khalaf IM, Eliwa HA, Dawoud M, Negendank JFW (1999) The Granitoids of Wadi Zaghra area, southeastern Sinai, Egypt. In: 4th International conference on geochemistry, Alexandria Univ., Egypt, pp 389–399

Khalil KI (2007) Chromite mineralization in ultramafic rocks of the Wadi Ghadir area, Eastern Desert, Egypt: mineralogical, microchemical and genetic studies. Neues Jahrb Mineral Abhandl (J Mineral Geochem) 183(3):283–296

Khalil AES, Azer MK (2007) Supra-subduction affinity in the Neoproterozoic serpentinites in the Eastern Desert, Egypt: evidence from mineral composition. J Afr Earth Sci 49:136–152

Khalil KI, El-Shazly AK (2012) Petrological and geochemical characteristics of Egyptian banded iron formations: review and new data from Wadi Kareim. Geochem Explor Environ Anal 12:105–126

Khalil KI, El-Shazly AE, Lehmann B (2015) Late Neoproterozoic banded iron formation (BIF) in the central Eastern Desert of Egypt: mineralogical and geochemical implications for the origin of the Gabal El Hadid iron ore deposit. Ore Geol Rev 69:380–399

Khalil AE, El-Desoky HM, Shahin TM, Abdelwahab W (2018) Late Cryogenian arc-related volcaniclastic metasediment successions at Wadi Hammuda, Central Eastern Desert, Egypt: geology and geochemistry. Arab J Geosci 11:74. https://doi.org/10.1007/s12517-017-3370-9

Khattab MM, Greiling OR, Khalid AM, Said MM, Kontny A, Abu Salem AO, El Kady MF, Attia MN, Shaaban GM (2002) Al Awaynat Banded Iron Formation (SW Egypt) distribution and related gold mineralization. Ann Geol Surv Egypt 25:343–364

Khudeir AA, Ahmed EAS (1996) Tectono-sedimentary framework of the molasse sediments, Wadi Abu Shiqieli, Egypt. Egypt J Geol 40:197–226

Khudeir AA, El-Gaby S, Greiling RO, Kamal El Din GM (1992) Geochemistry and tectonic significance of polymetamorphosed amphibolites in the Gabal Sibai window, Central Eastern Desert, Egypt. In: 1st International conference on geology of the Arab World, Cairo Univ., pp 461–476

Khudeir AA, El-Gaby S, Kamal El Din GM, Asran AMH, Greiling RO (1995) The pre-Pan-African deformed granite cycle of the Gabal El-Sibai swell, Eastern Desert, Egypt. J Afr Earth Sci 21: 395–406

Khudeir AA, Bishara WW, El Tahlawi MR, Abu El-Rus MA, Boghdady GY (2006a) Wadi Beitan window in the Southeastern Desert of Egypt: petrography, mineral chemistry and Intensive properties of the Beitan gneisses. In: 7th International conference on geochemistry, Alexandria Univ., Egypt, vol 1, pp 17–37

Khudeir AA, Abu El-Rus MA, El-Gaby S, El-Nady O (2006b) Geochemical and geochronological studies on the infrastructural rocks of Meatiq and Hafafit core complexes, Eastern Desert, Egypt. Egypt J Geol 50:190–214

Khudeir AA, Abu El-Rus MA, El-Gaby S, El-Nady O, Bishara WW (2008) Sr-Nd isotopes and geochemistry of the infrastructural rocks in the Meatiq and Hafafit core complexes, Eastern Desert, Egypt: evidence for involvement of pre-Neoproterozoic crust in the growth of Arabian-Nubian Shield. Island Arc 17:90–108

Klerkx J (1980) Age and metamorphic evolution of the basement complex around Jabal al'Awaynat. In: Salim MJ, Busrewil MT (eds) The Geology of Libya 2. Academic Press, London, pp 901–906

Kotb NH (1983) Geochemistry of old metavolcanics at Sheikh El Shadli area, Eastern Desert, Egypt. Unpublished MSc thesis, Azhar Univ., Cairo

Kröner A (1979) Pan-African plate tectonics and its repercussions on the crust of northeast Africa. Geol Rundsch 68:565–583

Kröner A (1983) Evolution of tectonic boundaries in the Late Proterozoic Arabian-Nubian shield of northeast Africa and Arabia. Abstracts, International symposium on Precambrian crustal evolution, Beijing, China, pp 24–25

Kröner A (1984) Late Precambrian plate tectonics and orogeny: a need to redefine the term Pan-African. In: Klerkx J, Michot J (eds) African Geology. Tervuren, Belgium, pp 23–28

Kröner A (1985) Ophiolites and the evolution of tectonic boundaries in the late Proterozoic Arabian-Nubian shield of northeastern Africa and Arabia. Precambr Res 27:277–300

Kröner A, Greiling R, Reischmann T, Hussein IM, Stern RJ, Dürr S, Krüger J, Zimmer M (1987) Pan-African crustal evolution in the Nubian segment of Northeast Africa. Am Geophys Union Geodyn Ser 17:235–257

Kröner A, Reischmann T, Wust HJ, Rashwan AA (1988) Is there any Pre-Pan-African (>950 Ma) basement in the Eastern Desert of Egypt? In: El-Gaby S, Greiling RO (eds) The Pan-African Belt of Northeast Africa and adjacent areas. Vieweg and Sohn, Wiesbaden, pp 95–119

Kröner A, Eyal M, Eyal Y (1990) Early Pan-African evolution of the basement around Elat, Israel, and the Sinai Peninsula revealed by single-zircon evaporation dating, and implications for crustal accretion rates. Geology 18:545–548

Kröner A, Todt W, Hussein IM, Mansour M, Rashwan A (1992) Dating of Late Proterozoic ophiolites in Egypt and Sudan using the single grain zircon evaporation technique. Precambr Res 59:15–32

Kröner A, Krüger J, Rashwan AAA (1994) Age and tectonic setting of granitoid gneisses in the Eastern Desert of Egypt and south-west Sinai. Geol Rundsch 83:502–513

Kröner A, Hegner E, Collins AS, Windley BF, Brewer TS, Razakamanana T, Pidgeon RT (2000) Age and magmatic history of the Antananarivo Block, central Madagascar, as derived from zircon geochronology and Nd isotopic systematics. Am J Sci 300:251–288

Kröner A, Kehelpannala KVW, Hegner E (2003) Ca. 750-1100 Ma magmatic events and Grenville-age deformation in Sri Lanka: relevance for Rodinia supercontinent formation and dispersal, and Gondwana amalgamation. J Asian Earth Sci 22:279–300

Kusky TM, Abdelsalam M, Tucker R, Stern RJ (2003) Evolution of the East African and related Orogens, and the assembly of Gondwana. Spec Issue Precambr Res 123:81–85

Liegeois J-P, Stern RJ (2010) Sr–Nd isotopes and geochemistry of granite-gneiss complexes from the Meatiq and Hafafit domes, Eastern Desert, Egypt: no evidence for pre-Neoproterozoic crust. J Afr Earth Sci 57:31–40

List F, El-Gaby S, Tehrani R (1989) The basement rocks in the Eastern and Western Deserts and Sinai. In: Hermina M, Klitzsch E, List F (eds) Stratigraphic Lexicon and explanatory notes to the geological map of Egypt 1:500,000. Conoco Inc, Cairo, pp 33–56

Loizenbauer J, Wallbrecher E, Fritz H, Neumayr P, Khudeir AA, Kloetzli U (2001) Structural geology, single zircon ages and fluid inclusion studies of the Meatiq metamorphic core complex: implications for Neoproterozoic tectonics in the Eastern Desert of Egypt. Precambr Res 110:357–383

Lundmark AM, Andresen A, Hassan M, Augland LE, Boghdady GY (2012) Repeated magmatic pulses in the East African Orogen in the Eastern Desert, Egypt: an old idea supported by new evidence. Gond Res 22:227–237

Madani AA, Emam AA (2011) SWIR ASTER band ratios for lithological mapping and mineral exploration: a case study from El Hudi area, southeastern desert, Egypt. Arab J Geosci 4:45–52

Makroum F (2003) Lattice preferred orientation (LPO) study of the orogeny parallel Wadi Nugrus and Wadi Um Nar shears, Eastern Desert, Egypt, using EBSD technique. In: 2nd International conference on geology of Africa, Assiut Univ., vol 1, pp 213–232

Makroum F (2017) Structural interpretation of the Wadi Hafafit culmination: a Pan-African gneissic dome in the central Eastern Desert, Egypt. Lithosphere 9:759–773

Masoud AA (1997) Geology and tectonic evolution of the area around Gabal Abu Furad, Northern Eastern Desert of Egypt. Unpublished MSc thesis, Tanta Univ., Egypt, 88 pp

Meert JG (2001) Growing Gondwana and rethinking Rodinia. Gondwana Res 4:279–288

Meert JG, Torsvik TH (2003) The making and unmaking of a super-continent: Rodinia revisited. Tectonophys 375:261–288

Messner M (1996a) The Hammamat formation: preliminary comparison of the Wadi Hammamat—Wadi El Qash and Wadi Kareim basins, Pan-African molasse basins, Eastern Desert, Egypt. In: Proceedings of geological survey Egypt centennial conference, Cairo, pp 529–545

Messner M (1996b) Dynamics of sedimentation in Hammamat basins in the Qift-Quseir section. In: Greiling RO, Naim GM, Hussein AA (eds) Excursion across the Pan-African, neoproterozoic basement Qena-Quseir guide book. Egypt. Geol. Surv. Min. Auth., Cairo, pp 39–44

Moghazi AM, Andersen T, Oweiss GA, El Bouseily AM (1998) Geochemical and Sr-Nd-Pb isotopic data bearing on the origin of Pan-African granitoids in the Kid area, southeast Sinai, Egypt. J Geol Soc 155:697–710

Moghazi AM, Mohamed FH, Kanisawa S (1999) Geochemical and petrological evidence of calc-alkaline and A-type magmatism in the Homrit Waggat and EI-Yatima areas of eastern Egypt. J Afr Earth Sci 29:535–549

Moghazi AM, Hassanen MA, Hashad MH, Mohamed FH (2001) Garnet-bearing leucogranite in the EI-Hudi area, southern Egypt: evidence of crustal anatexis during Pan-African low pressure regional metamorphism. J Afr Earth Sci 33:245–259

Moghazi AM, Ali KA, Wilde SA, Zhou Q, Andersen T, Andresen A, Abu El-Enen MM, Stern RJ (2012) Geochemistry, geochronology, and Sr-Nd isotopes of the Late Neoproterozoic Wadi Kid volcano-sedimentary rocks, Southern Sinai, Egypt: implications for tectonic setting and crustal evolution. Lithos 154:147–165

Mohamed FH, Hassanen MA (1996) Geochemical evolution of arc-related mafic plutonism in the Umm Naggat district, Eastern Desert of Egypt. J Afr Earth Sci 22:269–283

Morag N, Avigad D, Gerdes A, Belousova E, Harlavan Y (2011) Crustal evolution and recycling in the northern Arabian-Nubian Shield: new perspectives from zircon Lu-Hf and U-Pb systematics. Precambr Res 186:101–116

Moussa EMM, Stern RJ, Manton WI, Ali KA (2008) SHRIMP zircon dating and Sm/Nd isotopic investigations of Neoproterozoic granitoids, Eastern Desert, Egypt. Precambr Res 160:341–356

Moustafa GA, Akaad MK (1962) Geology of Hamash Sufra district. Egypt. Geol. Surv. Pap. No. 12

Naim GM, Oweiss KA, Khalil A, Shabaan G, Sweisy S, Diaf A (1996) Regional geological and geochemical exploration at El Uwaynat area. In: Proceedings of geological survey Egypt centennial conference, pp 623–634

Naim GM, Khalid AM, Said MM, Shaaban GM, Hussein AM, El Kady MF (1998) Banded iron formation discovery at west of Gabal Kamel, and its gold potential, Western Desert, Egypt. Ann Geol Surv Egypt 21:303–330

Nakhla FM, El Hinnawi EE (1960) Contributions to the study of Egyptian barites. Proc Egypt Acad Sci 15:11–16

Nasseef AO, Bakor AR, Hashad AH (1980) Petrography of possible ophiolitic rocks along the Qift-Qusier Road, Eastern Desert, Egypt. Bull King Abdelaziz Univ 3:157–168

Navon O, Reymer APS (1984) Stratigraphy, structures and metamorphism of Pan-African age in central Kid, southeastern Sinai. Isr J Earth Sci 33:135–149

Nehlig P, Genna A, Asfirane F (2002) Review of the Pan-African evolution of the Arabian Shield. GeoArabia 7:103–124

Neumayr P, Mogessie A, Hoinkes G, Puhl J (1996) Geological setting of the Meatiq metamorphic core complex in the Eastern Desert of Egypt based on amphibolite geochemistry. J Afr Earth Sci 23:331–345

Neumayr P, Hoinkes G, Puhl J, Mogessie A, Khudeir AA (1998) The Meatiq dome (Eastern Desert, Egypt) a Precambrian metamorphic core complex: petrological and geological evidence. J Metam Geol 16:259–279

Noweir AM (1968) Geology of the Hammamat-Um Seleimat District, Eastern Desert. Unpublished PhD thesis, Assuit Univ. U.A.R.

Noweir AM, El Sharkawy MA (1988) The Um Had—Um Effein metamorphic aureole, Central Eastern Desert, Egypt. Bull. Fac. Sci. Cairo Univ., pp 63–93

Obeid MA (2006) The Pan-African arc-related volcanism of the Wadi Hodein area, south Eastern Desert, Egypt: petrological and geochemical constraints. J Afr Earth Sci 44:383–395

Obeid MA, Khalil AES, Azer MK (2015) Mineralogy, geochemistry, and geotectonic significance of the Neoproterozoic ophiolite of Wadi Arais area, south Eastern Desert, Egypt. Int Geol Rev 58:687–702

Omar HA (1978) Petrological studies on the carbonates and associated rocks of Abu Swayel area, South Eastern Desert, Egypt. Unpublished MSc thesis, Ain Shams Univ., Cairo

Oner Z, Dilek Y (2011) Supradetachment basin evolution during continental extension: the Aegean province of western Anatolia, Turkey. Geol Soc Am Bull 123:2115–2141

Osman AF (1996) Structural geological and geochemical studies on the Pan-African basement rocks, Wadi Zeidun, Central Eastern Desert, Egypt. Scientific Series of the International Bureau. Forschung. Julich GmbH, vol 39, 262 pp

Osman AF, Gadoo H (2007) Evolution of the Pan-African metamorphic sequence in Wadi Um Sheqila area, Central Eastern Desert, Egypt. M.E.R.C. Ain Shams Univ Earth Sci Ser 21:1–28

Osman AF, El Kalioubi BA (2014) Neoproterozoic post-collisional granitoids in the Central Eastern Desert of Egypt: petrological and geochemical constraints. J Afr Earth Sci 99:39–50

Osman AF, Greiling RO, Ragab AI (1992) Late Pan-African tectonic evolution in Wadi Zeidoun, Central Eastern Desert, Egypt. Frankf Geowiss Arb A 11:273

Osman AF, Greiling RO, Warr LN, Hilmy ME, Ragab AI, El Ramly MF (1993) Distinction of different syn- and late orogenic Pan-African sedimentary sequences by metamorphic grade and illite crystallinity (W Zeidun, Central Eastern Desert, Egypt). In: Thorweihe U, Schandelmeier H (eds) Geoscientific research in NE Africa. Balkema, Rotterdam, pp 21–25

Osman AF, El Kalioubi B, Gaafar AS, El Ramly MF (2001) Provenance, geochemistry and tectonic setting of Neoproterozoic molasse-type sediments, North Eastern Desert, Egypt. Ann Geol Surv Egypt 24:93–114

Powell CMA, Pisarevsky SA (2002) Late Neoproterozoic assembly of East Gondwanaland. Geology 30:3–6

Priem HNA, Eyal M, Hebeda EH, Verdurmen EAT (1984) U-Pb zircon dating in the Precambrian basement of the Arabo-Nubian Shield of the Sinai Peninsula—a progress report: ECOG VIII. Terra Cognita 4:30–33

Qaoud N, Abdelnasser A (2012) Geochemistry and petrogenesis of El-Fringa metagabbro-diorite rocks, Wadi Sa'al area, south Sinai, Egypt. J Al Azhar Uni-Gaza 14:111–138

Ragab AI (1987) The Pan-African basement of the northern segment of the Eastern Desert of Egypt: a crustal evolution model and its implications on tectono-stratigraphy and granite types. M.E.R.C. Ain Shams Univ Earth Sci Ser 1:1–18

Ragab AI, El-Alfy Z (1996) Arc-arc collision model and its implications on a proposed classification of the Pan-African rocks of the Eastern Desert of Egypt. M.E.R.C. Ain Shams Univ Earth Sci Ser 10:89–101

Ragab AI, El-Gharabawi RI (1989) Wadi El-Hudi migmatites, east of Aswan, Egypt: a geological study and some geotectonic implications for the Eastern Desert of Egypt. Precambr Res 44:67–79

Ragab AI, El-Kalioubi B, El-Alfy Z (1993a) Petrotectonic assemblages and crustal evolution of the area north of Abu El-Tiyur, central Eastern Desert, Egypt. M.E.R.C. Ain Shams Univ Earth Sci Ser 7:1–16

Ragab AI, El-Gharbawi RI, El-Alfy Z (1993b) Pan-African tectonostratigraphic assemblages of Gabal Meatiq—Wadi Atalla area, Eastern Desert, Egypt: evidence for arc-arc suturing. M.E.R.C. Ain Shams Univ Earth Sci Ser 7:131–145

Ragab AI, Osman AF, Hilmy ME, Greiling RO, El Ramly MF (1995) Pan-African sedimentary basement assemblages in Wadi Zeidoun arc terrain, central Eastern Desert, Egypt. MERC Ain ShamsUniv Earth Sci Ser 7:27–41

Rashwan AA (1991) Petrography, geochemistry and petrogenesis of the Migif-Hafafit Gneisses at Hafafit Mine Area, Egypt. Forschung. Julich GmbH. Sci. Ser. Internat. Bur. vol 5, 359 pp

Reymer APS (1983) Metamorphism and tectonics of a Pan-African terrain in southeastern Sinai. Precambr Res 19:225–238

Reymer APS (1984) Metamorphism and tectonism of a Pan-African terrain in southeastern Sinai—a reply. Precambr Res 24:189–197

Reymer APS (1985) The origin and microstructures of metamorphic felsic dykes emplaced during brittle-ductile extension (southeast Sinai). Geol Mag 122:27–38

Reymer APS, Oertel G (1985) Horizontal cleavage in southeastern Sinai: the case for a coaxial strain history. J Struct Geol 7:623–636

Reymer A, Schubert G (1986) Rapid growth of some segments of continental crust. Geology 14:299–302

Reymer APS, Yogev A (1983) Stratigraphy and tectonic history of the southern Wadi Kid metamorphic complex, southeastern Sinai. Isr J Earth Sci 32:105–116

Reymer APS, Matthews A, Navon O (1984) Pressure–temperature conditions in the Wadi Kid metamorphic complex: implications for the Pan-African event in SE Sinai. Contrib Min Petrol 85: 336–345

Rice AHN, Osman AF, Abdeen MM, Sadek MF, Ragab AI (1993) Preliminary comparison of six late- to post-Pan-African molasse basins, E. Desert, Egypt. In: Thorweihe U, Schandelmeier H (eds) Geoscientific research in Northeast Africa. Balkema, Rotterdam, pp 41–45

Richter A (1986) Geologie der metamorphen und magmatischen Einheiten im Gebiet zwischen Gabal Uweinat und Gabal Kamil-SW Aegypten/NW Sudan. Berlin. Geowiss Abteil (A) 73:201 pp

Richter A, Schandelmieir H (1990) Precambrian basement inliers of Western Desert, geology, petrology and structural evolution. In: Said R (ed) The geology of Egypt. Balkema, pp 185–200

Ries AC, Shackleton RM, Graham RH, Fitches WR (1983) Pan-African structures, ophiolites and mélanges in the east Desert of Egypt: a traverse at 26° north. J Geol Soc Lond 140:75–95

Ring U, Brandon MT, Willett SD, Lister GS (1999) Exhumation processes. In: Ring U, Brandon MT, Lister GS, Willett SD (eds) Exhumation processes: normal faulting, ductile flow and erosion, vol 154. Geol. Soc. Lond., Spec. Publ., pp 1–27

Rittman A (1958) Geosynclinal volcanism, ophiolites and Barramiya rocks. Egypt J Geol 2:61–65

Rocci G (1965) Essai d'interprétation des mésures géochronologiques. La structure de l'ouest africain. Sci Terre 10:461–479

Rogers J, Ghuma R, Nagy J, Greenberg JK, Fullager P (1978) Plutonism in Pan-African belts and the geological evolution of northeast Africa. Earth Planet Sci Lett 39:109–117

Saad N (1996) Tectonic setting and characters of Ras Shait podiform chromite, Eastern Desert, Egypt. Bull Fac Sci Alex Univ 36:207–229

Sabet AH (1961) Geology and mineral deposits of Gabal El-Sibai Area, Red Sea Hills, Egypt, U.A.R. Unpublished PhD thesis, Leiden State Univ., The Netherlands, 189 pp

Sabet AH, Zatout MA (1955) Geology of El-Shalul—El Bakriya District. Geol. Surv., Egypt, p 75

Said M, Khalid AM, El Kady M, Abu Salem A, Ibrahim S (1998) On the structural evolution of banded iron formation of Gabal Kamel and its role in the gold mineralization. Ann Geol Surv Egypt 21:345–352

Saleeb-Roufaiel GS, Hilmy ME, Awad MT (1976) Mineralization and geochemical features of the Hudi barite deposit, Egypt. Bulletin of the National Research Council, Cairo, p 1

Saleh GM, Abdallah SA, Abbas AA, Dawood NA, Rashed MA (2012) Uranium mineralizations of Wadi Sikait mylonites, Southeastern Desert, Egypt. J Geol Min Res 3:86–104

Salem AK, Niazy EA, Kamel OA (1994) New occurrence of contact metasomatic iron ores in El Imra area Eastern Desert, Egypt, its mineralogy and origin. Egypt Mineral 6:53–75

Schandelmeier H, Darbyshire F (1984) Metamorphic and magmatic events in the Uweinat—Bir Safsaf Uplift (Western Desert/Egypt). Geol Rundsch 73:819–831

Schandelmeier H, Richter A, Franz G (1983) Outline of the geology of magmatic and metamorphic units between Gabal Uweinat and Bir Safsaf (SW Egypt/NW Sudan). J Afr Earth Sci 1:275–283

Schandelmeier H, Darbyshire DPF, Harms U, Richter A (1988) The east Saharan Craton: evidence for pre-Pan-African crust in NE Africa west of the Nile. In: El-Gaby S, Greiling RO (eds) The Pan-African belts of Northeast Africa and adjacent areas. Vieweg & Sohn, Wiesbaden, pp 69–94

Schandl ES, Gorton MP, Sharara NA (2002) The origin of major talc deposits in the Eastern Desert of Egypt: relict fragments of a metamorphosed carbonate horizon? J Afr Earth Sci 34:259–273

Schürmann HM (1953) The Precambrian of the Gulf of Suez area. In: 19th International geological congress, Algiers, 1, pp 115–135

Schürmann HM (1966) The Precambrian along the Gulf of Suez and the Northern Part of the Red Sea. E. J. Brill, Leiden, Netherlands, 404 pp

Schurmann HME (1974) The Precambrian in North Africa. Brill, Leiden, p 404

Searle DL, Carter GS, Shalaby IM, Hussein AA (1976) Ancient volcanism of island-arc type in the Eastern Desert of Egypt (Abs.). In: 25th International geological congress Sydney, 1 Sec 1, pp 62–63

Shackleton RM (1979) Precambrian tectonics of northeast Africa. Inst Appl Geol Bull King Abdulaziz Univ Jeddah 3:1–6

Shackleton RM (1994) Review of late Proterozoic sutures, ophiolitic melanges and tectonics of eastern Egypt and northeast Sudan. Geol Rundsch 83:537–546

Shackleton RM (1996) The final collision zone between East and West Gondwana: where is it? J Afr Earth Sci 23:271–287

Shackleton RM, Ries AC, Graham RH, Fitches WR (1980) Late Precambrian ophiolitic melange in the east Desert of Egypt. Nature 285:472–474

Shalaby A (2010) The northern dome of Wadi Hafafit culmination, Eastern Desert, Egypt: structural setting in tectonic framework of a scissor-like wrench corridor. J Afr Earth Sci 57:227–241

Shalaby A, Stüwe K, Makroum F, Fritz H, Kebede T, Klotzli U (2005) The Wadi Mubarak belt, Eastern Desert of Egypt: a Neoproterozoic conjugate shear system in the Arabian-Nubian Shield. Precambr Res 136:27–50

Shalaby A, Stüwe K, Fritz H, Makroum F (2006) The El Mayah molasse basin in the Eastern Desert of Egypt. J Afr Earth Sci 45:1–15

Shazly AG (1966) Geology of the area north of Gabal Meatiq, Eastern Desert. Unpublished MSc thesis, Assiut Univ.

Shazly AG (1971) Geology of Abu Ziran area, Eastern Desert. Unpublished PhD thesis, Assiut Univ.

Shimron A (1972) The Precambrian structural and metamorphic history of the elat area. Unbublished PhD thesis, Hebrew Univ., Jerusalem, 244 pp

Shimron A (1978) Some Proterozoic events in the Sinai Peninsula: a case for plate tectonics. Geological Society Israel annual meeting, pp 36–38

Shimron AE (1980a) Proterozoic island arc volcanism and sedimentation in Sinai. Precambr Res 12:437–458
Shimron AE (1980b) Late phase deformation and mylonite belts in Sinai: Pan African thrust fault tectonics. Geol Surv Isr Curr Res 1980:75–80
Shimron AE (1981a) The Dahab mafic–ultramafic complex, southern Sinai Peninsula—a probable ophiolite of Late Proterozoic (Pan-African) age. Ofioliti 6:161–164
Shimron AE (1981b) Geology and tectonics of the Tarr Complex, SE Sinai Peninsula. Geol Surv Isr Curr Res 1981:73–82
Shimron AE (1983) The Tarr Complex revisited—folding, thrusts and mélanges in the southern Wadi Kid region, Sinai Peninsula. Isr J Earth Sci 32:123–148
Shimron AE (1984a) Metamorphism and tectonism of a Pan-African terrain in southeastern Sinai—a discussion. Precambr Res 24:173–188
Shimron AE (1984b) Evolution of the Kid Group, southeast Sinai Peninsula: thrusts, mélanges, and implications for accretionary tectonics during the late Proterozoic of the Arabian-Nubian Shield. Geology 12:242–247
Shimron AE (1985) Evolution of the Kid Group, southeast Sinai Peninsula: thrusts, mélanges, and implications for accretionary tectonics during the late Proterozoic of the Arabian-Nubian Shield—reply to comments. Geology 13:156–157
Shimron AE (1987) Pan-African metamorphism and deformation in the Wadi Kid region, SE Sinai Peninsula: evidence from porphyroblasts in the Um Zariq Formation. Isr J Earth Sci 36:173–193
Shimron AE (1988) Discussion on the age of Feiran basement rocks Sinai: implications for late Precambrian crustal evolution in the northern Arabian-Nubian Shield. J Geol Soc Lond 145:1033–1034
Shimron AE, Furnes H, Roberts D, Bogoch R (1993a) Petrogenesis of the Late Proterozoic Sa'al Group—southern Sinai Peninsula. Geol Surv Israel Curr Res 8:24–29
Shimron AE, Bogoch R, Furnes H, Roberts D (1993b) The Sa'al Group: an ensialic island arc sequence in Sinai. In: Thorweihe U, Schandelmeier H (eds) Scientific research in Northeast Africa. Balkema, Rotterdam, pp 49–53
Shimron AE, Arkin Y (1978) Precambrian geology of the Wadi Kid-Wadi Umm Adawi area, eastern Sinai. Reconnaissance map 1:25,000 and explanatory notes. Rep. No. MM/1/78. Geol. Surv. Isr. Mapp. Div.
Siedner G, Shimron A, Pringle JR (1974) Age relationships in basement rocks of the Sinai Peninsula: Internat. Meet., Geochron. Cosmo. Isotop. Geol., Paris (Abstract)
Sims PK, James HL (1984) Banded iron formations of late Proterozoic age in the Central Eastern Desert, Egypt: geology and tectonic setting. Econ Geol 79:1777–1784
Soliman MM (1983) Petrogenesis of the El Hudi batholith and related metamorphic rocks in the district east of Aswan, Egypt. J Univ Kuwait (Sci) 10:267–277
Soliman FAM (1986) Geology of Wadi Sa'al area with special emphasis of metamorphism and tectonics, Central Sinai of Egypt. Unpublished PhD thesis, Suez Canal Univ., Egypt, 240 pp
Soliman FA, Khalifa IH, Matheis G, Hassaan MM (1996) Geochemical characteristics of the metavolcanic rocks hosted sulphide mineralization at Wadi Kid area, South Sinai. Al-Azhar Bull Sci 7:1755–1775
Stacey JS, Hedge CE (1984) Geochronologic and isotopic evidence for early Proterozoic crust in the eastern Arabian shield. Geology 12:310–313
Stacey JS, Stoeser D (1983) Distribution of oceanic and continental leads in the Arabian-Nubian Shield. Contrib Mineral Petrol 84:91–105
Stacey JS, Doe BR, Roberts RJ, Delevaux MH, Gramlich JW (1980) A lead isotope study of mineralization in the Saudi Arabian Shield. Contrib Min Petrol 74:175–188
Stein M (2003) Tracing the plume material in the Arabian-Nubian Shield. Precambr Res 123:223–234
Stein M, Goldstein SL (1996) From plume-head to continental lithosphere in the Arabian-Nubian shield. Nature 382:773–778
Stein M, Hofmann AW (1994) Mantle plumes and episodic crustal growth. Nature 372:63–68
Stern RJ (1979) Late Precambrian ensimatic volcanism in the central eastern desert of Egypt. PhD Thesis, University of California, San Diego, CA, 210 pp
Stern RJ (1981) Petrogenesis and tectonic setting of Late Precambrian ensimatic volcanic rocks, Central Eastern Desert of Egypt. Precambr Res 16:195–230
Stern RJ (1985) The Najd fault system, Saudi Arabia and Egypt: a Late Precambrian rift related transform system. Tectonics 4:497–511
Stern RJ (1994) Arc assembly and continental collision in the Neoproterozoic East African Orogen implications for the consolidation of Gondwanaland. Annu Rev Earth Planet Sci 22:319–351
Stern RJ (2002) Crustal evolution in the East African Orogen: a neodymium isotopic perspective. J Afr Earth Sci 34:109–117
Stern RJ, Hedge CE (1985) Geochronologic and isotopic constraints on late Precambrian crustal evolution in the Eastern Desert of Egypt. Am J Sci 285:97–127
Stern RJ, Johnson PR (2010) Continental lithosphere of the Arabian Plate: a geologic, petrologic, and geophysical synthesis. Earth Sci Rev 101:29–67
Stern RJ, Manton WI (1987) Age of Feiran basement rocks, Sinai: implications for late Precambrian evolution in the northern Arabian-Nubian Shield. J Geol Soc Lond 144:569–575
Stern RJ, Gottfried D, Hedge CE (1984) Late Precambrian rifting and crustal evolution in the Northeastern Desert of Egypt. Geology 12:168–172
Stern RJ, Sellers G, Gottfried D (1988) Bimodal dyke swarms in the NE Desert of Egypt: significance for the origin of Late Precambrian "A-type" granites in northern Afro-Arabia. In: El-Gaby S, Greiling RO (eds) The Pan-African Belt of NE Africa and adjacent areas. Vieweg, Braunschweig, pp 147–179
Stern RJ, Nielsen KC, Best E, Sultan M, Arvidson RE, Kroner A (1990) Orientation of late Precambrian sutures in the Arabian-Nubian Shield. Geology 18:1103–1106
Stern RJ, Kroner A, Rashwan AA (1991) A Late Precambrian (~710 Ma) high vulcanicity rift in the south Eastern Desert of Egypt. Geol Rundsch 80:155–170
Stern RJ, Johnson PR, Kröner A, Yibas B (2004) Neoproterozoic ophiolites of the Arabian-Nubian Shield. In: Kusky TM (ed) Precambrian ophiolites and related rocks. Developments in Precambrian geology, vol 13. Elsevier, Amsterdam, pp 95–128
Stern RJ, Avigad D, Miller NR, Beyth M (2006) Evidence for the Snowball Earth hypothesis in the Arabian-Nubian Shield and the East African Orogen. J Afr Earth Sci 44:1–20
Stern R, Ali K, Andresen A, Wilde S, Abu El-Enen M, Hassen I (2010) Results of geochronological investigations in Sinai undertaken as part of the 2008 JEBEL field trip. In: Pease V et al (eds) JEBEL Project October 2009 field excursion to the Midyan Terrane, Kingdom of Saudi Arabia, with reports on research by participants in the JEBEL Project: Saudi Geological Survey Technical Report SGSTR-2010-2, pp 46–51
Stern RJ, Mukherjee SK, Miller NR, Ali K, Johnson PR (2013) ~750 Ma banded iron formation from the Arabian-Nubian Shield—implications for understanding Neoproterozoic tectonics, volcanism, and climate change. Precambr Res 239:79–94
Stoeser DB, Camp VE (1985) Pan-African microplate accretion of the Arabian Shield. Geol Soc Am Bull 96:817–826
Stoeser DB, Frost CD (2006) Nd, Pb, Sr, and O isotopic characterization of Saudi Arabian Shield terranes. Chem Geol 226:163–188

Stoeser DB, Stacey JS (1988) Evolution, U-Pb geochronology, and isotope geology of the Pan-African Nabitah orogenic belt of the Saudi Arabian Shield. In: El-Gaby S, Greiling RO (eds) The Pan-African Belt of NE Africa and adjacent areas: tectonic evolution and economic aspects of a late proterozoic orogen. Vieweg & Sohn, Wiesbaden, pp 227–228

Sturchio NC, Sultan M, Batiza R (1983a) Geology and origin of Meatiq dome, Egypt: a Precambrian metamorphic core complex? Geology 11:72–76

Sturchio NC, Sultan M, Sylvester P, Batiza R, Hedge C, El Shazly EM, Abdel-Maguid A (1983b) Geology, age, and origin of the Meatiq Dome: implications for the Precambrian stratigraphy and tectonic evolution of the Eastern Desert of Egypt. Bull Fac Earth Sci King Abdulaziz Univ 6:127–143

Sultan M, Arvidson RE, Sturchio NC (1986) Mapping of serpentinites in the Eastern Desert of Egypt by using Landsat thematic mapper data. Geology 14:995–999

Sultan M, Arvidson RE, Sturchio NC, Guinness EA (1987) Lithologic mapping in arid regions with Landsat thematic mapper data: Meatiq dome, Egypt. Geol Soc Am Bull 99:748–762

Sultan M, Bickford ME, El-Kaliouby B, Arvidson RE (1992) Common Pb systematics of Precambrian granitic rocks of the Nubian Shield (Egypt) and tectonic implications. Geol Soc Am Bull 104: 456–470

Sultan M, Tucker RD, Gharbawi RI, Ragab AI, El Alfy Z (1993) On the location of the boundary between the Nubian Shield and the old African continent: inferences from U-Pb (zircon) and common Pb data. In: Thorweihe U, Schandelmeier H (eds) Geoscientific research in NE Africa. Balkema, Rotterdam, pp 75–77

Sultan M, Tucker RD, El Alfy Z, Attia R, Ragab A (1994) U-Pb (zircon) ages for the gneissic terrane west of the Nile, Southern Egypt. Geol Rundsch 83:514–522

Sultan YMH (2011) Tectonic setting of South Sinai metamorphic belts based on remote sensing, structural analysis and GIS. Unpublished PhD thesis. Suez Canal Univ., Egypt, 226 pp

Sultan YM, El-Shafei MK, Arnous MO (2017) Tectonic evolution of Kid metamorphic complex and the recognition of Najd fault system in South East Sinai, Egypt. Int J Earth Sci 106:2817–2836

Surour AA (1995) Medium- to high-pressure garnet-amphibolites from Gabal Zabara and Wadi Sikait, south Eastern Desert, Egypt. J Afr Earth Sci 21:443–457

Surour AA (2017) Chemistry of serpentine "polymorphs" in the Pan-African serpentinites from the Eastern Desert of Egypt, with an emphasis on the effect of superimposed thermal metamorphism. Miner Pterol 111:99–119

Takla M, Hassanien S, Sakran S (1990) Geochemistry of the ophiolitic mélange between Idfu-Mersa Alam Road and Wadi Shait, Eastern Desert, Egypt. Egypt Mineral 2:31–50

Tamam ZI, Osman AM, Scott PW, Hilmy ME (2005) Mineralogy and geochemistry of the Banded Iron Formations (BIFs) of Semna and Abu Marawat areas—northern Eastern Desert—Egypt. M.E.R.C. Ain Shams Univ Earth Sci Ser 19:1–17

Teklay M, Kroner A, Mezger K (2002) Enrichment from plume interaction in the generation of Neoproterozoic arc rocks in northern Eritrea: implications for crustal accretion in the southern Arabian-Nubian Shield. Chem Geol 184:167–184

Unrug R (1996) The assembly of Gondwanaland. Episodes 19:11–20

Unzog W, Kurz W (2000) Progressive development of lattice preferred orientations (LPOs) of naturally deformed quartz within a trans-pressional collision zone (Panafrican orogen in the Eastern Desert of Egypt). J Struct Geol 22:1827–1835

Vail JR (1983) Pan-African crustal accretion in northeast Africa. J Afr Earth Sci 1:285–294

Wallbrecher E, Fritz H, Khudeir AA, Farahad F (1993) Kinematics of Pan-African thrusting and extension in Egypt. In: Thorweihe U, Schandelmeier H (eds) Geoscientific research in northeast Africa. Balkema, Rotterdam, pp 27–30

Wilde SA, Youssef K (2002) A re-evaluation of the origin and setting of the Late Precambrian Hammamat Group based on SHRIMP U-Pb dating of detrital zircons from Gabal Umm Tawat, North Eastern Desert, Egypt. J Geol Soc Lond 159:595–604

Willis KM, Stern RJ, Clauer N (1988) Age and geochemistry of Late Precambrian sediments of the Hammamat series from the North-eastern Desert of Egypt. Precambr Res 42:173–187

Zimmer M, Kroner A, Jochum KP, Reischmann T, Todt W (1995) The Gabal Gerf complex: a Precambrian N-MORB ophiolite in the Nubian Shield, NE Africa. Chem Geol 123:29–51

Zoheir BA, Lehmann B (2011) Listvenite-lode association at the Barramiya gold mine, Eastern Desert, Egypt. Ore Geol Rev 39:101–115

Zoheir B, Weihed P (2014) Greenstone-hosted lode-gold mineralization at Dungash mine, eastern Desert, Egypt. J Afr Earth Sci 99: 165–187

Zoheir BA, Mehanna AM, Qaoud NN (2008) Geochemistry and geothermobarometry of the Um Eleiga Neoproterozoic island arc intrusive complex, SE Egypt: genesis of a potential gold-hosting intrusion. Appl Earth Sci (Trans Inst Min Metall B) 117:89–111

Zoheir B, Feigenson M, Zi J-W, Turrin B, Deshesh F, El-Metwally A (2018) Ediacaran (~600 Ma) orogenic gold in Egypt: age of the Atalla gold mineralization and its geological significance. Int Geol Rev. https://doi.org/10.1080/00206814.2018.1463180

Mesozoic-Cenozoic Deformation History of Egypt

7

Adel R. Moustafa

Contents

Abstract

Detailed surface and subsurface structural data indicate that the Mesozoic-Cenozoic deformation history of Egypt witnessed four main phases of deformation related to the movements between the African Plate and the surrounding plates. The first phase (Tethyan rifting) started in Middle-Late Triassic almost to the end of Early Cretaceous due to the divergent movement between the Afro-Arabian Plate and Eurasian Plate and led to the formation of NE-SW to ENE-WSW oriented extensional basins in northern Egypt as well as normal faults of the same orientation in the central and southern areas. The second phase was also extensional and led to opening of NW-SE to WNW-ESE oriented rift basins during the Cretaceous-Early Tertiary time. This phase of deformation is probably related to the opening of the South Atlantic and the divergence between the Afro-Arabian and South American Plates. The third phase is compressional and resulted from the convergence between the Afro-Arabian and Eurasian Plates leading to inversion of the Tethyan extensional basins. Onshore data indicate that basin inversion was transpressive, started at Santonian time and continued to the Miocene. Offshore areas in the Herodotus Basin and eastern part of the Nile Cone indicate continued convergence and folding till present time. The fourth phase is related to divergence between the African and Arabian Plates in Late Oligocene-Miocene time forming the Gulf of Suez-Ancestral Red Sea rift. Both rifts were separated from each other by the left-lateral Dead Sea Transform at Late Miocene time leading to continued opening of the Red Sea Basin. This chapter deals with the first three phases whereas the fourth phase is dealt with in a separate chapter in this book.

7.1 Introduction

A wealth of data and new concepts has accumulated in the last three decades since the publication of Said's (1990) book on the Geology of Egypt. These data include detailed surface structural mapping of different areas of Egypt as well as subsurface geological information from industry 3D seismic and boreholes especially for the northern Western Desert and onshore/offshore Nile Delta. All of these new geological data and information have led to better understanding of the deformation history of Egypt.

The Phanerozoic structures of Egypt have gone through several stages of study. The earliest stage includes works that concentrated mainly on studying the stratigraphy of certain area(s) with little attention to the structures that appeared as single lines on the geological map(s) accompanying these studies (e.g. Ball 1900; Ball and Beadnell

A. R. Moustafa (✉)
Department of Geology, Ain Shams University, Cairo, 11566, Egypt
e-mail: armoustafa@sci.asu.edu.eg; ; armoustafa@hotmail.com

Z. Hamimi et al. (eds.), *The Geology of Egypt*, Regional Geology Reviews,
https://doi.org/10.1007/978-3-030-15265-9_7

1903; Beadnell 1909; Moon and Sadek 1921; among others). In these studies, the structures were not the main objective and represented only minor parts of the works. Among these studies, Sadek's 1926 geological map of the area between Gebel Ataqa and the North Galala Plateau is different due to the amount of structural details shown on the map. A later stage during the forties of the last century by geologists of Standard Oil Company of Egypt involved surface geological mapping of several areas in northern Egypt in search of suitable drilling sites for hydrocarbon exploration (e.g. Foley 1942; Bowles 1945; Iskandar 1946; Jones 1946; Shata and Sourial 1946; among others). These studies concentrated on the geometries and age of the mapped structures which form hydrocarbon traps. Mapping efforts increased in the fifties and early-mid 1960s, when structural symbols appeared on the maps instead of the simple lines on the maps of the earliest stage (e.g. Faris 1948; Shukri and Akmal 1953; Farag and Ismail 1955; Shukri and Ayouty 1956; Al-Far 1966; among others). A notable gap in the Egyptian surface structural studies accompanied the Israeli occupation of Sinai in 1967, lasting until the mid 1980s. During this stage, Israeli geologists carried out several detailed studies on Sinai (e.g. Garfunkel and Bartov 1977; Hildebrand et al. 1974; Bartov 1974; Bartov et al. 1980; Eyal et al. 1981; among others). A flourishing stage of detailed structural studies started in the mid 1980s and involved detailed surface structural studies of different areas of Egypt (e.g. studies of the present author and his colleagues since 1985; Abdel Khalek et al. 1993; Khalil and McClay 2002; Abd-Allah et al. 2004; Dupuis et al. 2011; Noweir and Fawwaz 2011; Sakran and Said 2018; among others). Subsurface studies on the other hand started with the exploration of hydrocarbons and the availability of new technology for better imaging of the subsurface. Reliable subsurface structural studies used 3D seismic data since the mid 1980s. Although detailed and regional subsurface structural mapping was achieved by oil companies, most of these maps are confidential and only small areas were released for publication (e.g. Deibis 1982; Karaaly et al. 1994; Nemec 1996; Matresu et al. 2016; among others).

The data and information presented in this chapter concern mainly the Mesozoic and Cenozoic rocks whereas older (Paleozoic) sequences are still less well understood due to the few Paleozoic outcrops and insufficient subsurface data. The latter is related to the low resolution of seismic reflection data at the depth of these rocks as well as insufficient (and non-released) deep borehole penetrations. A fairly good number of Paleozoic penetrations by operating oil companies in the area west and southwest of Shoushan Basin is not released yet.

The new geological data and information has been used for reaching a reasonable understanding of the Mesozoic-Cenozoic deformation history of Egypt as detailed in this chapter. The information presented in this chapter depends mainly on the author's own work as well as published works of other investigators that are cited. Published works relying on detailed structural studies and/or reliable data have been used whereas works providing concepts that are not supported by reliable data have been ignored. The stratigraphic sections of the discussed areas are shown in the Fig. 7.33.

7.2 Phases of Deformation

The Mesozoic-Cenozoic deformation of Egypt is a result of the movement of the African Plate and the surrounding (Eurasian, Arabian, and South American) Plates. Surface and subsurface geological data have helped recognition of several phases of deformation including extensional deformation leading to opening of rift basins and compressional deformation leading to closure of some of these basins. The extensional deformations were associated with volcanic events which have been dated with reasonable accuracy.

Four main deformations have been recognized in the Mesozoic-Cenozoic rock record as follows (Fig. 7.1):

1. Early Mesozoic (Tethyan) rifting phase formed rift basins/sub-basins oriented NE-SW to ENE-WSW affecting mainly the northern part of Egypt due to opening of the Neotethys and divergence between the Afro-Arabian and Eurasian Plates. Basin opening in the Jurassic most probably started also at Middle/Late Triassic based on local data. Extension continued also during the Early Cretaceous. Extensional basins related to this phase of deformation are well recognized in the northern Western Desert (Kattaniya, Mubarak, Alamein-Razzak, Matruh, and Shoushan Basins as well as small sub-basins within the area of the later Abu Gharadig Basin); northern Eastern Desert (Wadi Araba and Shabraweet area); and northern Sinai (Maghara, Yelleg and Halal Basins as well as other similar basins in the northern offshore area). Extension generally decreases to the south creating NE and ENE oriented normal faults with small slip, as in the central Western Desert (Bahariya Oases and northern Farafra) and southern Western Desert (Nubia Fault System).
2. Cretaceous rifting phase created extensional basins oriented NW-SE to WNW-ESE in different areas of Egypt such as Upper Egypt (Kom Ombo Basin), Nile Valley (Asyut and Beni Sueif Basins), as well as the northern Western Desert (e.g. Abu Gharadig Basin). This extensional phase may be attributed to the far field stress associated with the opening of the South Atlantic leading to reactivation of NW-SE and WNW-ESE oriented Precambrian faults and shear zones in the mentioned areas, among other areas in Africa. In addition to the mentioned

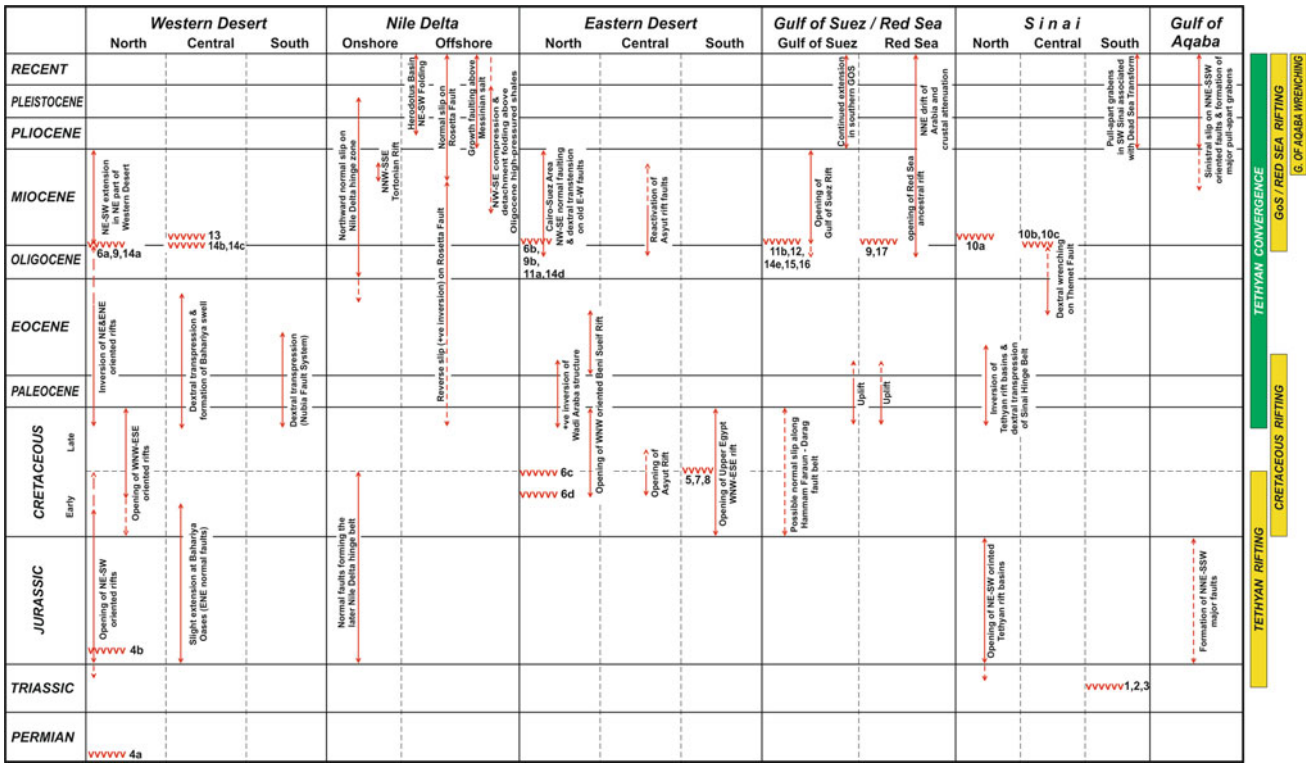

Fig. 7.1 Mesozoic-Cenozoic deformation events of Egypt and their associated volcanicity (represented by v-symbols with their cited references). Cited References are: 1: Moussa (1987); Um Bogma olivine basalt sill (233–243 Ma). 2: Roufaiel et al. (1989); Um Bogma olivine basalt sill (233–243 Ma). 3: Meneisy (1986); Um Bogma olivine basalt sill (233–243 Ma). 4: El Shazly (1977); a—Rabat-1 well olivine basalt (293 ± 12 Ma), b—Kattaniya well olivine basalt (191 ± 19 Ma). 5: Hashad and El Reedy (1979); Wadi Natash olivine basalt (104 ± 7 Ma). 6: Meneisy and Kreuzer (1974a), a—W. Samalut basalt (23 ± 2 Ma), b—Abu Zaabal basalt (23 ± 1 Ma), c—Wadi Abu Darag olivine basalt (113–115 Ma), d—Wadi Araba olivine basalt (125 ± 4 Ma). 7: Meneisy and Kreuzer (1974b); SED nepheline Syenite and alkali syenite (88–96 Ma). 8: Serencsits et al. (1979); SED nepheline Syenite and alkali syenite (88–96 Ma). 9: Meneisy and Abdel Aal (1983); a—G. Qatrani basalt (23–24 Ma), b—Qattamia basalt (22 ± 2 Ma). 10: Steinitz et al. (1978); a—G. Iktefa basalt (20 ± 1 Ma), b—Raqabet El Naam basalt (25 ± 2 Ma), c—Themed basalt (20 ± 1 Ma). 11: Meneisy (1990); a—El Gafra basalt (22 ± 2 Ma), b—G. Matulla basalt (24 ± 1 Ma). 12: Steen (1982); G. Araba, W. Tayiba, & W. Nukhul basalt (18–22 ± 1 Ma). 13: Meneisy and El Kalioubi (1975); Bahariya Oases basalt (18–20 Ma). 14: Bosworth et al. (2015b); a—G. Qattrani & West Faiyum basalt (22–24 Ma), b—Bahariya Oases basalts (23–25 Ma), c—Qaret Dab'a basalt (SW Beni Sueif) (23 Ma), d—Qattamia graben basalt (21 Ma), e—W. Tayiba, W. Nukhul, & W. Araba (S. Sinai) (22–23 Ma). 15: Bosworth and McClay (2001); S. side of G. Ataqa basalt dike (25.7 ± 1.7 Ma). 16: Ott d'Estevou et al. (1986); G. Monsill (Gharamul) basalt dike (24.7 ± 0.6 Ma). 17: Roussel et al. (1986); Sharm El Bahari basalt flow (24.9 ± 0.6 Ma)

Cretaceous basins, the northern part of the Gulf of Suez area is believed to have suffered similar extension leading to reactivation of a NW-SE oriented shear zone extending from the Darag Fault that bounds the eastern side of the North Galala Plateau at present time to the Hammam Faraun Fault on the other side of the gulf and the Rihba Shear Zone of Younes and McClay (2002).

3. Late Cretaceous to Recent Tethyan convergence of the African and Eurasian Plates affected the Egyptian territories by compressive stress since Late Cretaceous time. The direction of compression changed with time and space depending on the convergence direction of the two plates and the irregular shape of the Africa-Eurasia plate boundary. Compression started intensively during Santonian time in the ESE to SE direction (Smith 1971; Eyal and Reches 1983; Letouzey 1986) perhaps allover the Egyptian territories and continued to present time with slight clockwise rotation to the SE and SSE and local change to the SW direction at the eastern part of the Nile Cone. Focal mechanisms of the 1955 and the 2012 Nile Delta earthquakes by Costantinescu et al. (1966) and Abu El-Nader et al. (2013), respectively indicate that the present-day compressive stress affecting the northern and western outer parts of the Nile Cone is NNW to NW (N333–346°). Plate convergence led to inversion of the Jurassic extensional basins/sub-basins in northern Egypt. Detailed surface geological mapping indicates that inversion was probably transpressive with small dextral slip. Further south, convergence led to uplift of different areas above sea level with marked hiatuses in the rock

record, e.g. the southern part of the Gulf of Suez and northern part of the Red Sea region. Compressive stress also affected other areas farther south (in central and southern Egypt), such as the Bahariya-Farafra area as well as the southern Western Desert where ENE oriented faults of the Nubia Fault System were reactivated by dextral slip (Issawi 1968 and 1971; El Etr et al. 1982; Sakran and Said 2018; Hamimi et al. 2018). Continued convergence in the Neogene affected mainly the northernmost areas of Egypt such as the offshore Mediterranean areas due to subduction of the African Plate underneath the Eurasian Plate. This led to detachment folding in the central and eastern parts of the Nile Cone above Lower Oligocene ductile shales and was followed by gravity movement of the uppermost Miocene-Recent sediments above the Messinian salt, reactivation of main faults such as the Rosetta Fault by oblique extension, and NE-SW oriented folds of the Herodotus Basin.

4. NNW-SSE oriented Neogene rifting phase led to opening of the Gulf of Suez—ancestral Red Sea rift in Late Oligocene and Miocene times followed by continued opening and crustal thinning of the northern Red Sea area and separation from the Gulf of Suez rift by the Dead Sea transform fault since Late Miocene time. This rifting phase was triggered by the divergence of the Afro-Arabian Plate signaling the early phases of separation of Arabia from Africa. It also involved reactivation of a possibly Early Mesozoic NNE-SSW oriented fault belt forming the Dead Sea Transform at Late Miocene-Present time. Reactivation of nearby NW-SE oriented Cretaceous rift faults lying close to the Neogene rifts occurred in some areas such as Asyut Basin, Beni Sueif Basin, and the Abu Darag-Hammam Faraun-Rihba Shear Zone. The Gulf of Suez/Red Sea rift system and the Dead Sea transform are dealt with in a separate chapter (Moustafa and Khalil, this book).

7.2.1 Early Mesozoic Tethyan Rifting

Tethyan rifting affected the northern onshore and offshore areas of Egypt and led to opening of NE to ENE oriented basins/sub-basins in the northern areas and formation of normal faults of the same orientation in the central and southern areas of Egypt. Tethyan rifting is attributed to the divergent movement between the Afro-Arabian and Eurasian Plates. Detailed subsurface mapping of the northern Western Desert using 3D seismic and borehole data helped identification of several Tethyan extensional basins such as Kattaniya, Mubarak, Alamein-Razzak, Matruh and Shoushan Basins (Fig. 7.2). The Faghur Basin (Bosworth et al. 2015a) is considered here to be part of the Shoushan Basin. These extensional basins are oriented NE to ENE except Matruh Basin which is oriented NNE perhaps due to reactivation of old structural fabric (Moustafa et al. 2002). The NE to ENE oriented basins had half graben geometry with NNW tilt and are bounded by major normal faults on their northwestern sides. The easternmost one of these basins (Kattaniya Basin) seems to slightly extend further east into the Eastern Desert. In the Eastern Desert itself, as well as in northern Sinai, similar NE to ENE oriented extensional basins were also formed but with opposite polarity where the major basin-bounding faults lie on the southeastern sides of the basins. An accommodation zone between the northern Western Desert basins and the northern Eastern Desert—northern Sinai basins has not been mapped yet but is expected to be in vicinity of the present course of the Nile close to the longitude of Cairo. Continuation of the Tethyan basins further north in the Mediterranean offshore area is obvious in offshore northern Sinai but is difficult to map further west due to the large thickness of Neogene sediments of the Nile deep sea fan (Nile Cone) overlying such basins. The Rosetta Fault bounding the western side of the Nile Cone shows structural features at the top Mesozoic-Tortonian rocks that may indicate that it formed the boundary of one of these Tethyan extensional basins (Abd El-Fattah et al. 2018).

The stratigraphic sections in the Tethyan basins record extension during the Jurassic and Early Cretaceous times but local areas show evidence of onset of basin opening at Middle/Late Triassic time as follows:

1. The Triassic Qiseib Formation (Abdallah et al. 1963) or its synonym the Budra Formation (Weissbrod 1969) is made up of brick-red, purple to varicolored siltstone with some shale and sandstone beds of fluvial origin and is 327 m thick in Wadi Budra (Weissbrod 1969). The Budra Formation is underlain by a 20 m thick olivine basalt sill of Middle Triassic age (233–243 Ma based on K-Ar dating; Meneisy 1986; Moussa 1987; Roufaiel et al. 1989) at Wadi Sidri-Wadi Budra area (west-central Sinai). The sill is well exposed in the Um Bogma-Wadi Budra-Wadi Sidri area in the form of isolated patches that extend southward to Wadi Feiran (Moustafa 1992, 2004). These red clastics and the underlying basalt are perhaps related to the early stages of opening of the NeoTethys and its associated extensional basins in northern Egypt.
2. The lowermost unit of the syn-rift section in Matruh and Shoushan Basins is made up of red beds deposited on the top Paleozoic unconformity surface. Local deposition of these red beds changes from one area to another due to the irregular nature of the unconformity surface as well as the onlap of syn-rift deposits on the top Paleozoic unconformity. These red beds include the Ras Qattara (or

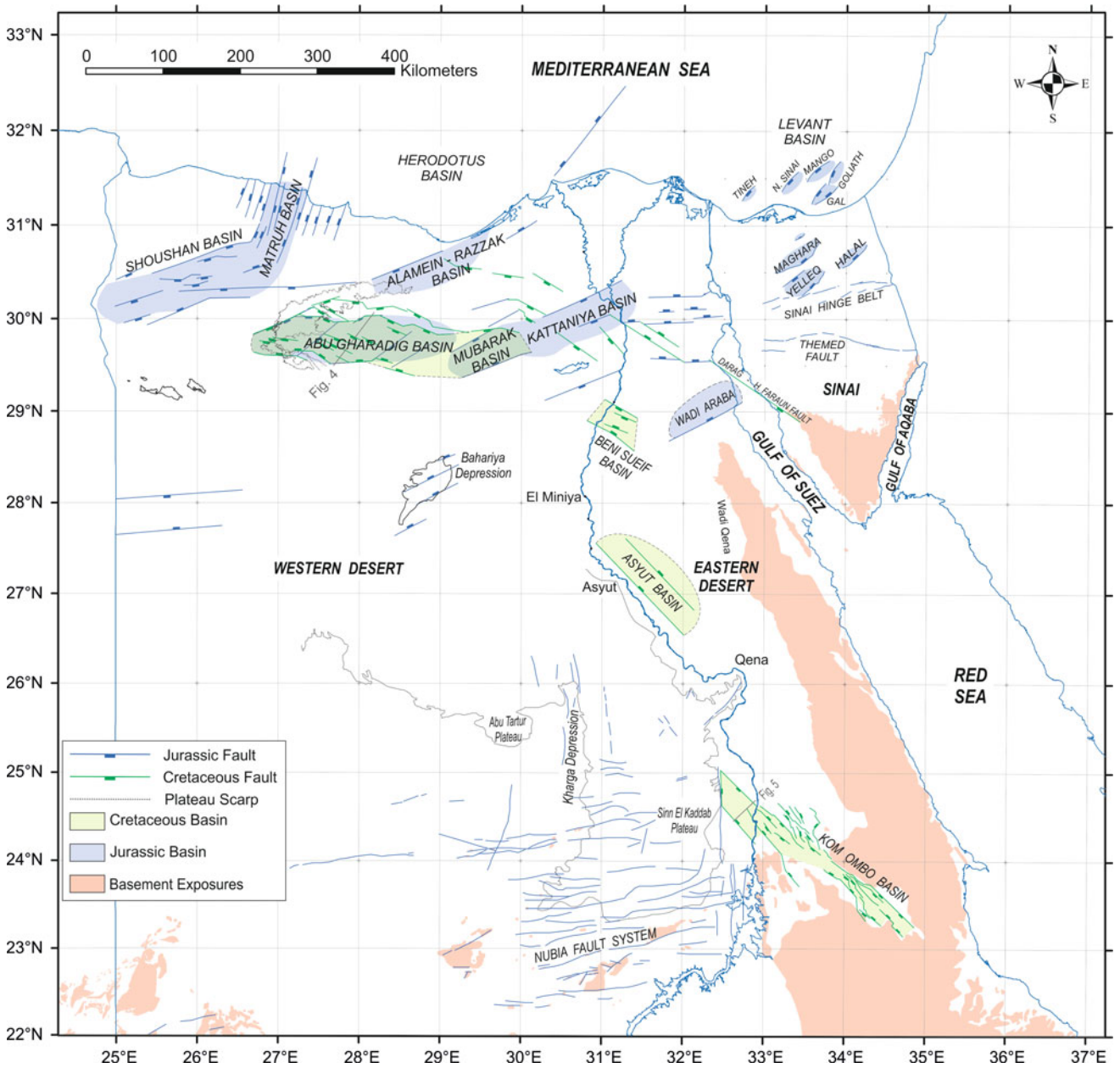

Fig. 7.2 Mesozoic extensional basins and faults of Egypt

Bahrein) and Yakout Formations. The Ras Qattara (Bahrein) Formation shows widespread reddening (Keeley et al. 1990; Hantar 1990). Red clastics with thin coal beds are also reported in the Shoushan and Matruh Basins at the base of the Jurassic section. In the Hazem-1 well (Shoushan Basin), these red beds are exceptionally thick and are associated with weathered basalt (Keeley et al. 1990). The Ras Qattara section includes Middle to Late Triassic and Lower Jurassic sandstones whereas the Yakout Formation is made up of Middle Jurassic shales. Core data of the Jc 17-2 well (Matruh Basin) indicate that the Yakout Formation is made up of red clastics with rounded to sub-rounded pebbles and granules of volcanic origin in polymictic conglomerates (Moustafa et al. 2002). Also, basalt was recorded in the Ras Qattara section in the J4 well (north of the Kattaniya Basin) and dated Late Triassic-Early Jurassic (K-Ar); Abdel Hakim (2017) and Fahmy et al. (2018).

The Triassic-Jurassic syn-rift units of the northern Western Desert basins clearly show thickening toward the basin-bounding faults and the lowermost units clearly show onlap on pre-rift Paleozoic rocks. The Jurassic syn-rift section in the Kattaniya Basin has wedge shape showing

northward thickening towards the main basin-bounding fault with maximum thickness of about 9000′ (~2750 m); Abd El-Aziz et al. (1998).

The Mubarak Basin includes several northwestward thickening Jurassic and Early Cretaceous sequences (Bevan and Moustafa 2012), Fig. 7.3. Other similar sub-basins lie to the west in the Abu Gharadig Basin area. These sub-basins as well as the Mubarak and Kattaniya Basins form a series of right-stepping troughs (Fig. 7.2).

The northern Sinai Tethyan basins include three main onshore basins at Gebel (= mountain) Maghara, Gebel Yelleg, and Gebel Halal. The syn-rift section is well exposed in the core of Gebel Maghara structure due to later inversion. About 2 km thick surface Jurassic section was described by Al-Far (1966) with the base unexposed. It includes six interbedded carbonate and clastic units. The topmost Jurassic unit is the Masajid carbonates and is overlain by Upper Jurassic-Lower Cretaceous shales of the Gifgafa Formation that are always eroded and/or covered by Quaternary alluvial deposits. The Gifgafa Formation was penetrated by two boreholes in Gebel Falig at the northwestern side of Gebel Yelleg with 220 m thickness (Moustafa and Fouda 2014).

A thicker Jurassic section equal to 3234 m was penetrated by Halal-1 well in the core of Gebel Halal inverted basin. In fact the lack of seismic data and dipmeter log for this well makes it difficult to consider the drilled thickness representative of the true stratigraphic thickness of the Jurassic rocks of Gebel Halal extensional basin. The true stratigraphic thickness is not expected to be less than that of Gebel Maghara Basin. 2D seismic section extending from Gebel Maghara Basin to the northeastern part of Gebel Yelleg Basin clearly shows the southward thickening Jurassic wedge of Gebel Maghara Basin toward the main basin-bounding fault (Moustafa 2010 and 2014). The seismic section also shows that the Jurassic section of Gebel Yelleg Basin is smaller than that of Gebel Maghara and was deposited in a southeast tilted half graben basin.

Detailed structural mapping of offshore northern Sinai clearly shows other NE-SW oriented Jurassic-Early Cretaceous extensional basins such as Mango and Goliath Basins, among others (Ayyad et al. 1998; Yousef et al. 2010), Fig. 7.2.

7.2.2 Cretaceous Rifting

The early indication of Cretaceous rifting is the presence of Cretaceous alkaline igneous rocks in the Eastern Desert. Olivine basalts at Wadi Natash were dated 104 ± 7 Ma by Hashad and El Reedy (1979), nepheline syenite and alkali

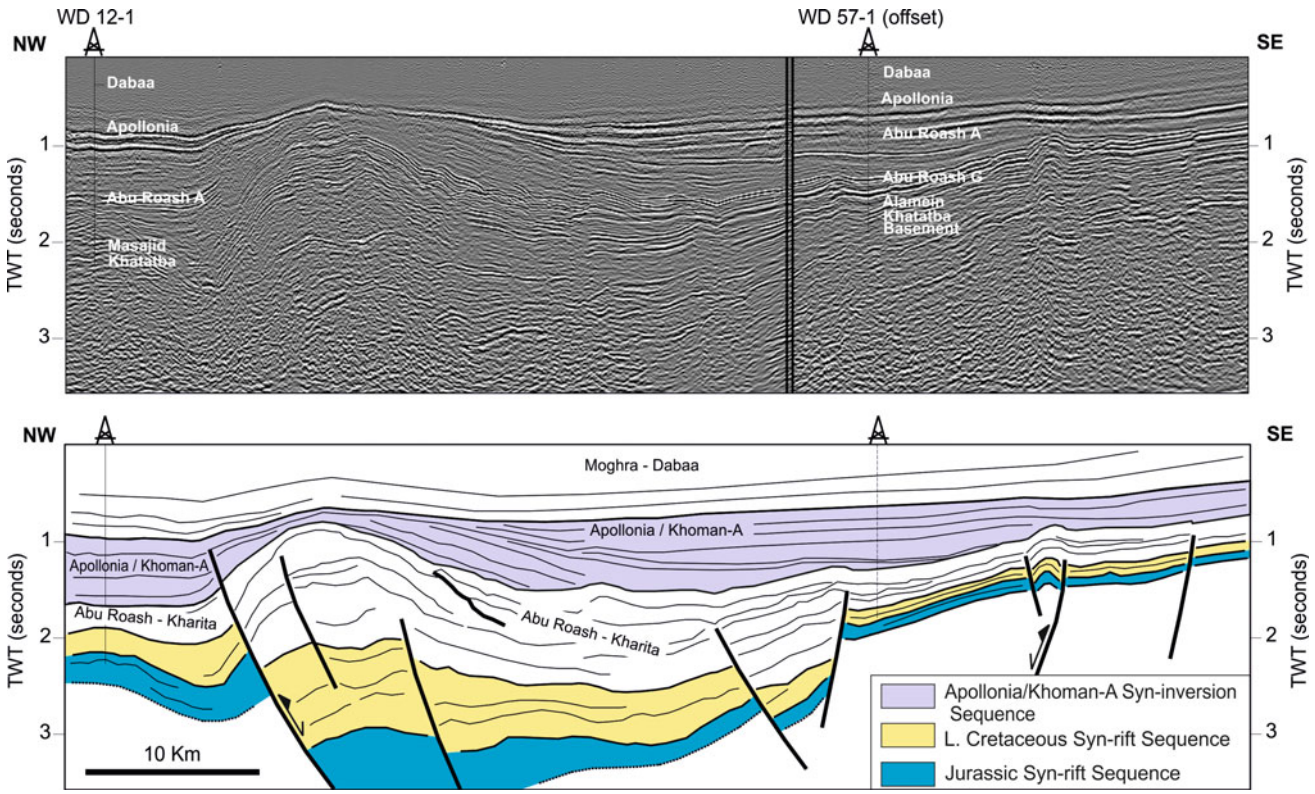

Fig. 7.3 Seismic section and line drawing of Mubarak inverted basin (northern Western Desert) modified after Bevan and Moustafa (2012). See Fig. 7.6 for location

syenite ring complexes in the south Eastern Desert were dated 88–96 Ma by Meneisy and Kreuzer (1974b) and Serencsits et al. (1979), and olivine basalts at Wadi Araba and Wadi Abu Darag were dated 125 ± 4 Ma and 113–115 Ma respectively by Meneisy and Kreuzer (1974a). Subsurface mapping for hydrocarbon exploration led to the recognition of several Cretaceous rift basins in the northern Western Desert as well as in the Eastern Desert and perhaps the Gulf of Suez area. These basins include the prolific Abu Gharadig Basin, Beni Sueif Basin, Asyut Basin, Kom Ombo Basin, and probably the Hammam Faraun-Abu Darag-Rihba Shear Zone area (Fig. 7.2). These basins clearly show Cretaceous syn-rift rocks thickening toward NW-SE to WNW-ESE oriented normal faults (Figs. 7.4 and 7.5). Tilted fault blocks in these half-graben basins dip toward the NE (e.g. Abu Gharadig and Kom Ombo Basins) or SW (Beni Sueif and Asyut Basins). As calculated in the present study, β values of these extensional basins are relatively small reaching a maximum value of 125% in the Abu Gharadig Basin.

7.2.2.1 Abu Gharadig Basin

The Abu Gharadig Basin is an oblique rift extending for about 300 km in the E-W direction. The main faults active during Cretaceous time within the basin are oriented WNW-ESE but the northern basin-bounding fault has a general E-W orientation that clearly shows the effect of pre-existing E-W faults on the general orientation of the basin. This basin-bounding fault is made up of several segments oriented E-W, NE-SW, and WNW-ESE (El Saadany 2008). Consistent NE and NNE tilting of the Cretaceous and older rocks in the rift is obvious at an angle of about 9–12° (Fig. 7.4). Average stretch (β) is locally about 112% in the eastern part of the basin at BED-1 field area (El Saadany and Mahmoud 2008) but β value of the whole basin has been estimated from a regional section across the whole rift to be about 125% during the Cretaceous time. Detailed structural mapping of the basin indicates NE-SW oriented faults of Jurassic age within the basin and were later inverted in Late Cretaceous-Early Tertiary time (e.g. Mid-Basin Arch as well as Mubarak Basin faults at the eastern edge of the Abu Gharadig Basin, among other faults). Deep erosion affected the northern shoulder of the basin being the footwall of the main basin-bounding fault where the Upper Cretaceous rocks are deeply eroded and are overlain by a relatively thin section of Maastrichtian chalk. Deeper erosion in other parts of the shoulder like the Rabat high led to deposition of Eocene sediments directly above the Paleozoic

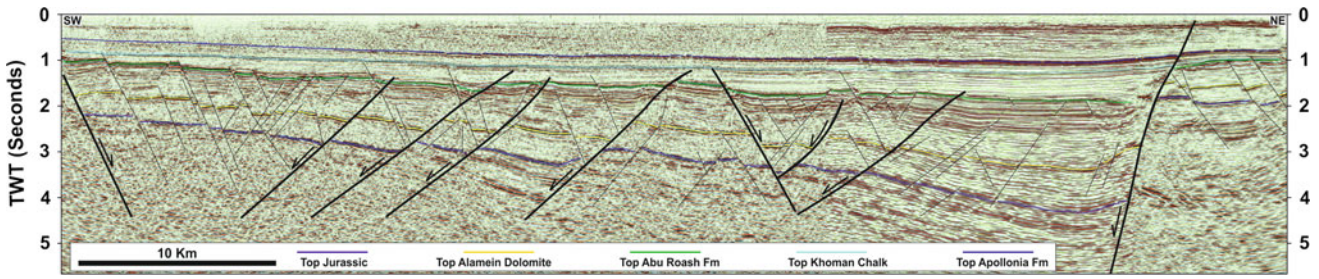

Fig. 7.4 Seismic section across the Abu Gharadig Basin, northern Western Desert showing Cretaceous syn-rift sequences (enclosed between the top Jurassic and top Khoman Chalk reflectors) thickening toward WNW-ESE oriented normal faults. See Fig. 7.2 for location

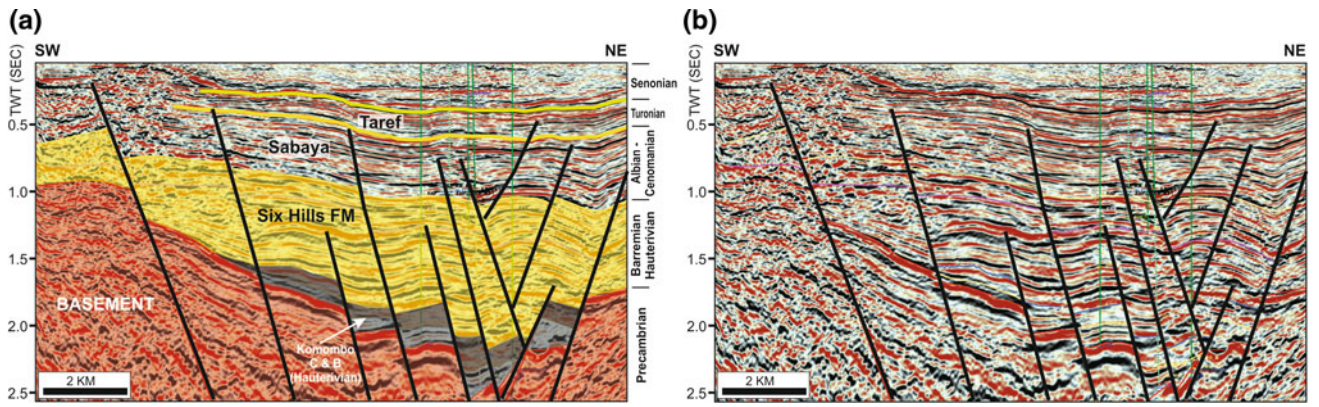

Fig. 7.5 Seismic section (with and without interpretation) across the Kom Ombo Basin at Al Baraka oil field (modified after Dolson et al. 2014) showing wedge-shaped Cretaceous syn-rift section thickening toward the main WNW-ESE basin-bounding fault and onlapping the Precambrian basement rocks. See Fig. 7.2 for location

rocks (Abdel Aal and Moustafa 1988). Early interpretation of the origin of the Abu Gharadig Basin as a series of pull-apart basins (Abdel Aal and Moustafa 1988) has proven incorrect by detailed mapping of high resolution 3D seismic data acquired during the last 20 years.

7.2.2.2 Beni Sueif Basin

The Beni Sueif Basin has WNW-ESE orientation and is crossed by the present-day Nile Valley at Beni Sueif and Maghagha towns (Zahran et al. 2011). Although this basin seems to be a whole graben (bounded by normal faults on both sides) at the Precambrian basement level, main subsidence is along the southwestern basin-bounding fault (Salem and Sehim 2017), indicating a SW dipping half-graben at Cretaceous time. Normal slip of the top basement on this fault is about 1 km. Basin initiation was at Albian time involving about one half of the total extension. Extension ceased at the end of Cretaceous time but was resumed during the Eocene resulting in the deposition of more than 1500 m thick carbonate rocks (Salem and Sehim 2017). Several ENE-WSW and E-W oriented pre-existing basement faults in the basin area were reactivated by dextral transtension into en echelon normal fault belts during Cretaceous and Eocene extension.

7.2.2.3 Asyut Basin

Asyut Basin lies to the south of Beni Sueif Basin and extends east of the Nile Valley from Miniya to the north of Qena in the NW-SE direction. Normal faults of the basin extend up to the surface through the Eocene rocks and also control the course of the Nile River. Seismic reflection data show NW-SE orientation of the normal faults of the basin. Like Beni Sueif Basin, the Asyut Basin was opened in Early Cretaceous time. The basin has half graben geometry with SW tilt and major-bounding fault on the southwestern side with throw of about 1–1.5 km at top Precambrian basement level. The exposed Precambrian basement rocks on the east side of Wadi Qena might represent the updip continuation of the basement rocks of the basin. Surface geological data at Wadi Qena (Klitzsch et al. 1990) indicate that the Precambrian basement is stratigraphically overlain by Albian cross-bedded sandstone, similar to the subsurface setting of Beni Sueif Basin. The presence of Oligo-Miocene basalts along some of the faults of Asyut Basin (e.g. in the area east of Miniya; EGSMA 1981) might indicate reactivation of the Asyut Basin faults at Oligo-Miocene time.

7.2.2.4 Kom Ombo Basin

Kom Ombo Basin extends for about 300 km in the southern Eastern Desert and extends northwestward across the Nile Valley to the eastern edge of Sin El Kaddab Plateau (Fig. 7.2). This NW-SE oriented rift basin was first recognized by gravity and magnetic data with estimated depth to Precambrian basement of about 4.5 km (Nagati 1988). NW-SE oriented normal faults of the rift dissect the exposed Upper Cretaceous rocks of the area. The southeastern part of the basin shows up as a structural low (trough) within the Precambrian exposures of the southern Eastern Desert (Fig. 7.2). Seismic reflection data indicate the half graben geometry of the basin with predominant NE dipping Cretaceous rocks (Dolson et al. 2000, 2001, and 2014; Selim 2016). Seismic and borehole data from El Baraka Oil Field in the extreme northwestern part of the basin indicate that the oldest syn-rift sediments in the half graben basins are Hauterivian clastics. Up to 4 km thick Lower and Upper Cretaceous syn-rift sediments onlap the Precambrian basement rocks in the half graben basins and thicken northeastward toward the main basin-bounding faults (Fig. 7.5). These features indicate continuous subsidence during the Cretaceous time. The basin fill of Kom Ombo Basin includes Lower Cretaceous (Hauterivian, Neocomian to Barremian) non-marine sediments followed by marine deposition during the Albian/Cenomanian (sandstone and shale) and Upper Cretaceous-Early Tertiary (carbonates); Abdelhady et al. (2016). Alkaline volcanics at Wadi Natash (El Ramly 1972), dated 104 Ma old by Hashad and El Reedy (1979), were probably associated (in time and place) with opening of Kom Ombo Basin. The NW-SE trend of the basin is probably controlled by reactivated Precambrian shear zones of the Najd Fault System.

7.2.3 Late Cretaceous to Recent Tethyan Convergence

During the Late Cretaceous-Recent times a change in the direction of movement of the African and Eurasian Plates led to convergent movement of the two plates and the development of compressional structures (Fig. 7.6). The earliest record of convergence is obvious in the Late Cretaceous-Early Tertiary folds affecting the Mesozoic exposures in northern Egypt; already considered as part of the Syrian Arc System of Krenkel (1925). Folded Mesozoic rocks exposed in northern Sinai, the northern Eastern Desert, as well as the folds of Abu Roash area and the Bahariya Oases in the Western Desert attracted the attention of geologists for a long period of time. Hydrocarbon exploration in the northern Western Desert and offshore Sinai also led to recognition of similar folding of the Mesozoic and older rocks. Surface and subsurface folds in northern Egypt are oriented NE-SW and are associated with faults of different orientations and types. The onset of folding was in the Late Cretaceous specifically in the Santonian-Campanian time and is considered to have been of maximum magnitude at that time but continued mildly during the Tertiary. Younger convergence structures are more obvious in the northernmost areas as if deformation

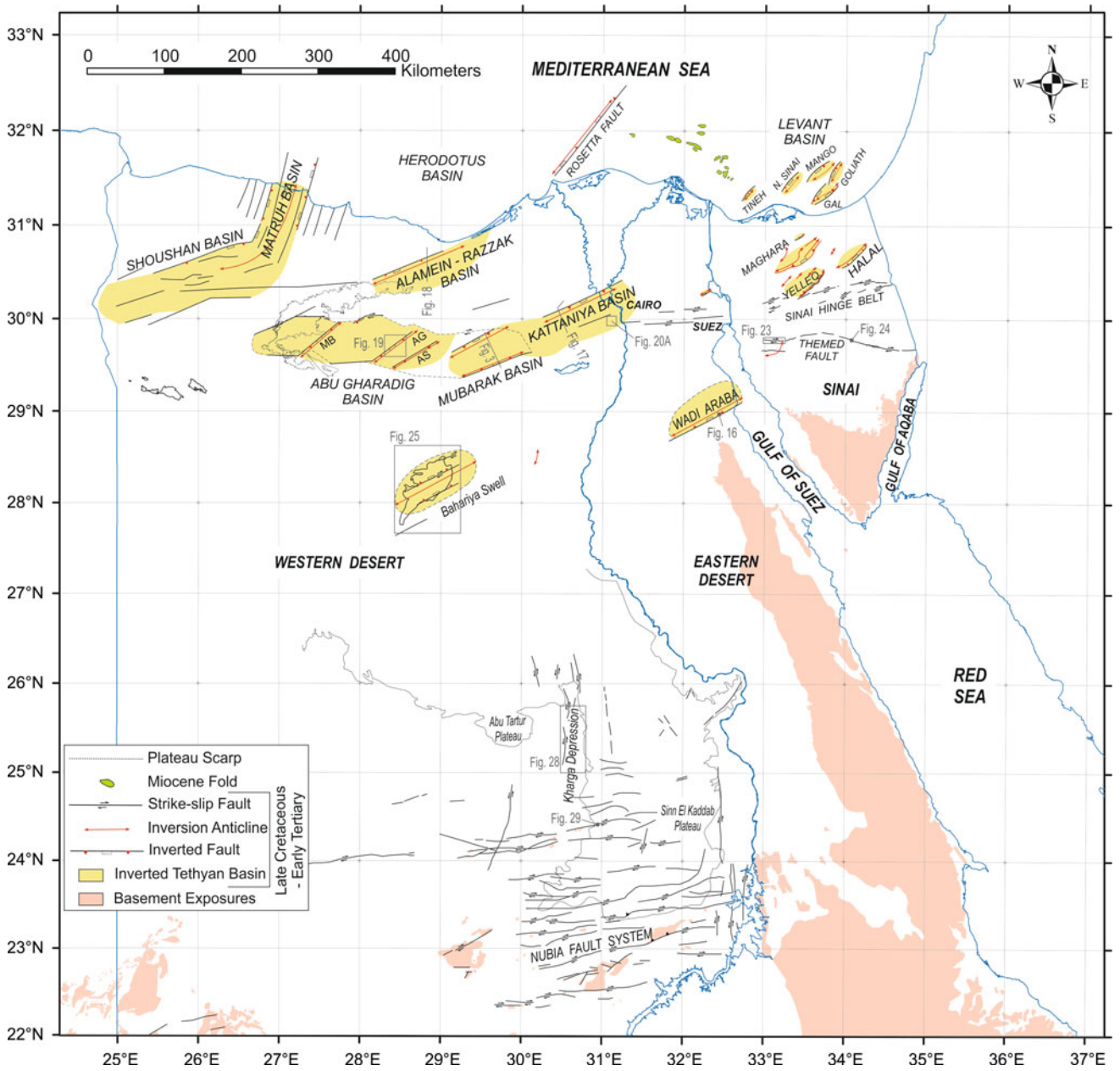

Fig. 7.6 Late Cretaceous-Recent compressive structures of Egypt. Abbreviations in the Abu Gharadig Basin stand for Mid-Basin Arch (MB), Abu Gharadig Anticline (AG), and Abu Sennan Anticline (AS)

affected the southern areas first and migrated northward to the northernmost part of the plate. This may be attributed to the fact that the Late Cretaceous-Tertiary convergent structures represent reactivation (inversion) of the Jurassic rift structures where these inverted faults were the first to respond to the compressive stress resulting from plate convergence. After a relatively long period of reactivation, the compressive stress formed younger structures in the younger rocks lying at the northern part of the plate.

7.2.3.1 Late Cretaceous-Tertiary Inversion Folds of Northern Egypt

Late Cretaceous-Tertiary inversion affected the Jurassic rift basins of northern Egypt. Inversion folds are several tens of kilometers long and about 20 km wide and have NE-SW orientation. They are also asymmetric with very steep, vertical, or overturned flanks at the side of the inverted main basin-bounding faults. Inversion structures are exposed in the following areas (Fig. 7.6):

1. Northern Sinai (Gebel Maghara, Gebel Yelleg, and Gebel Halal).
2. Northern Eastern Desert (Wadi Araba and Gebel Shabrawet).
3. Western Desert (Abu Roash area and Bahariya Oases).

Inversion structures were also recognized in the subsurface (during exploration for hydrocarbons) in the following areas:

1. Northern Western Desert (Kattaniya, Alamein-Razzak, Mubarak, Abu Gharadig, and Matruh-Shoushan Basins).
2. Offshore northern Sinai (e.g. Mango and Goliath folds, among others).
3. Rosetta fault area on the western side of the Nile Cone.

It is obvious that the inverted main basin-bounding faults change polarity from northern Sinai to the northern Western Desert (Fig. 7.6). For this reason, the steep flanks of the inversion folds also follow this polarity change.

A. Northern Sinai Inversion Structures

A belt of NE-SW oriented doubly-plunging, SE vergent anticlines is well exposed in northern Sinai (Moon and Sadek 1921; Sadek 1928; Shata 1959; Youssef 1968; Moustafa and Khalil 1990). This belt includes three major highly asymmetric folds at Gebel Maghara, Gebel Yelleg, and Gebel Halal; each with length of about 40–60 km and average width of about 15 km (Fig. 7.7). These highly asymmetric folds have gently dipping northwestern flanks and very steep southeastern flanks that are in places vertical or even overturned.

Gebel Maghara Structure

Gebel Maghara structure is about 60 km long and 15 km wide deforming the exposed Jurassic and Cretaceous rocks. It has the highest structural relief among the northern Sinai folds with about 2-km thick Jurassic section exposed in its breached core. Detailed structural mapping (Moustafa 2014) shows that this structure is made up of four main NE-SW oriented, asymmetric anticlines bounded on their southeastern sides by reverse faults dipping at 50–73° NW (Fig. 7.8). The amount of reverse slip of these faults reaches 1250 m. The Gebel Maghara anticlines are dissected by transverse, steeply dipping (>65°) normal faults with relatively small amounts of throw (few tens of meters), Moustafa (2013). Seismic reflection section shows that the Gebel Maghara reverse faults are positively inverted and had normal slip in Jurassic time (Fig. 7.9). The southernmost fault bounding the outer side of Gebel Maghara structure (Um Asagil Fault) is 55 km long and is the main bounding fault of an inverted Jurassic half graben basin. Surface geological mapping indicates that this fault is made up of six right-stepped en echelon segments (Fig. 7.8); perhaps indicating that inversion was transpressive. The middle reverse fault of Gebel Maghara area (Mizeraa Fault) is made up of several segments oriented NE-SW, N-S, and E-W to WNW-ESE. The NE-SW oriented fault segments show pure reverse slip whereas the N-S and E-W to WNW-ESE oriented fault segments show oblique-slip. These differently oriented fault segments reflect the early zigzag linkage of normal fault segments during the Jurassic extensional phase and were reactivated during the inversion stage where the NE-SW segments were reactivated by almost pure reverse slip and the other two fault trends were reactivated by oblique slip and form oblique ramps (Moustafa 2014).

Surface geological data (Moustafa 2014) indicate that inversion started in the Santonian and continued into the Middle Eocene. Breaching of the inversion anticlines started at Paleocene time as indicated by syn-tectonic debris flow derived from Jurassic rocks and deposited in the lower part of the Paleocene sediments on the southern side of Gebel Maghara (Fig. 7.10). Most of the Maghara inverted structure stood high above the Paleocene and Eocene sea levels, allowing deposition of the Lower Tertiary sediments on the outer margins of the inverted structure. Lower Eocene rocks on the southern side of the Maghara inverted structure contain syn-depositional carbonate boulders and also dip gentler than the nearby Cretaceous rocks due to continued folding during the Eocene time.

Gebel Yelleg Structure

The Gebel Yelleg NE-SW oriented anticline deforms the exposed Upper Cretaceous rocks and is 45 km long and 18 km wide. Detailed structural mapping (Moustafa and Fouda 2014) indicates that the Gebel Yelleg anticline is doubly plunging with SE vergence; the northwestern flank has average NW dip of 5° and the southeastern flank has steep dip up to 56° SE (Fig. 7.11). This anticline is pervasively dissected by steep (up to 79°) NW-SE oriented normal faults with 5 km average length and tens of meters throws (Moustafa 2013). The Yelleg anticline is bounded on the NW side by a number of NE-SW oriented right-stepped en echelon folds (Falig, Meneidret Abu Quroun, and Meneidret El Etheili) that are 5–14 km long and 4–2 km wide. The Falig Anticline is asymmetric with the northwestern flank dipping up to 70° NW (Fig. 7.12a). Seismic reflection data shows that this steep flank is bounded by a high-angle reverse fault covered by the Quaternary alluvium (Fig. 7.12b). Another seismic section at the northeastern downplunge area of the Yelleg Anticline (Fig. 7.9) indicates that the Gebel Yelleg folds overlie an asymmetric graben. This graben contains thicker Jurassic rocks than the areas to

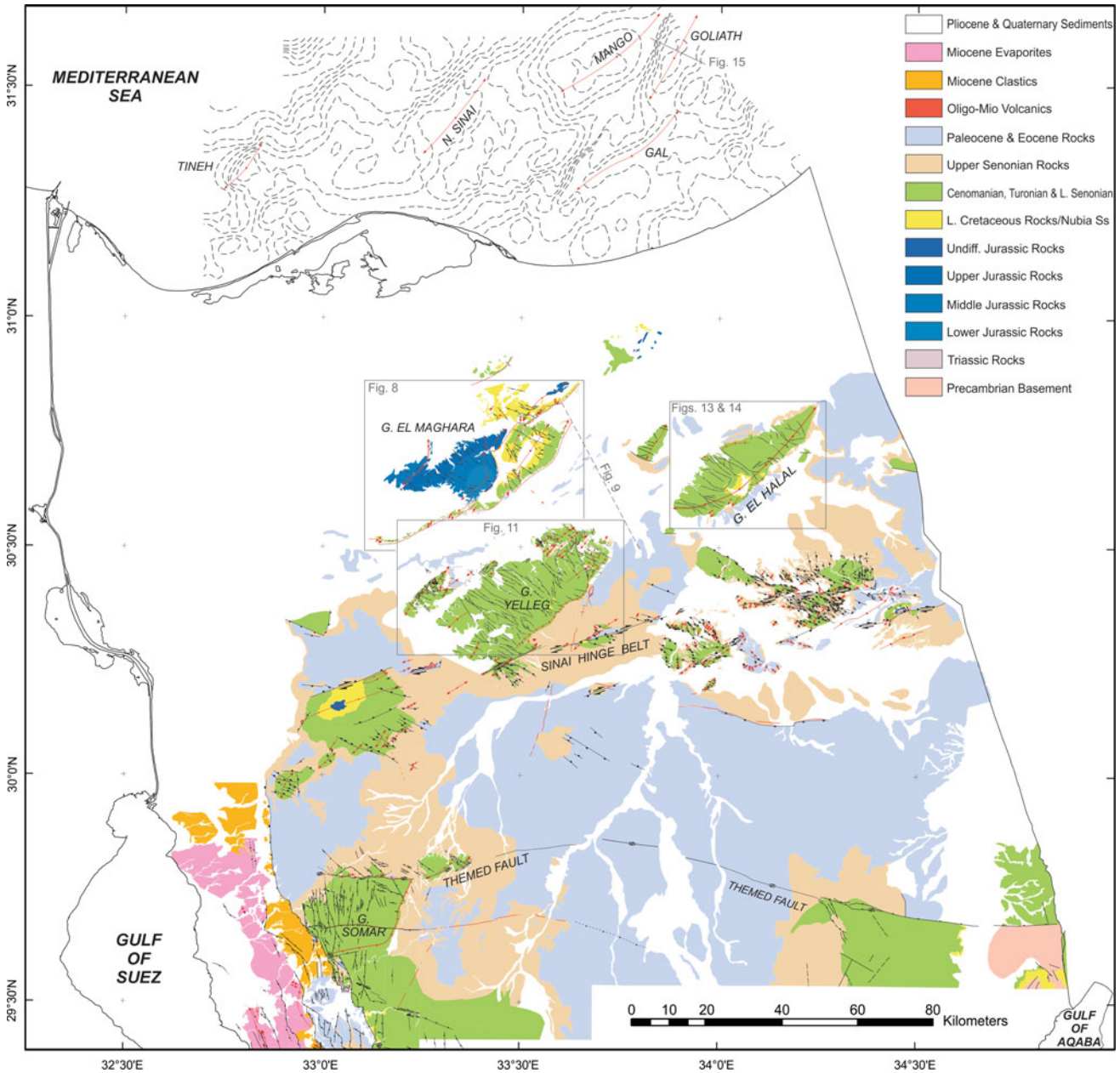

Fig. 7.7 Geological map of northern Sinai (compiled from Moustafa 2004, 2014; Abd-Allah et al. 2004; Moustafa and Khalil 1994; Moustafa and Fouda 2014, and Moustafa et al. 2014) showing the inversion structures of Gebel Maghara, Gebel Yelleg, and Gebel Halal as well as the Sinai Hinge Belt and Themed Fault. Structure contours in offshore northern Sinai are top Coniacian two-way-time structure contours (after Yousef et al. 2010) representing the offshore inversion folds

the NW and SE. The steep SE flank of Gebel Yelleg Anticline overlies the main SE-bounding fault of the graben and represents a fault-propagation fold above this inverted fault. On the other hand, the NW Falig reverse fault (Fig. 7.12b) coincides with the NW-bounding fault of the Jurassic graben. The Upper Cretaceous, Paleocene, and Eocene rocks are folded in the Gebel Falig area with the dip angles of the folded Eocene rocks gentler than those of the Cenomanian and Turonian rocks which indicate growth of the folding from Late Cretaceous to Early Tertiary time.

The surface and subsurface structures of Gebel Yelleg area indicate three phases of deformation; a Jurassic extensional phase, a Late Cretaceous-Early Tertiary compressional phase, and an Early Miocene extensional phase associated with volcanicity. The Jurassic extensional phase led to the development of NE-SW oriented asymmetric

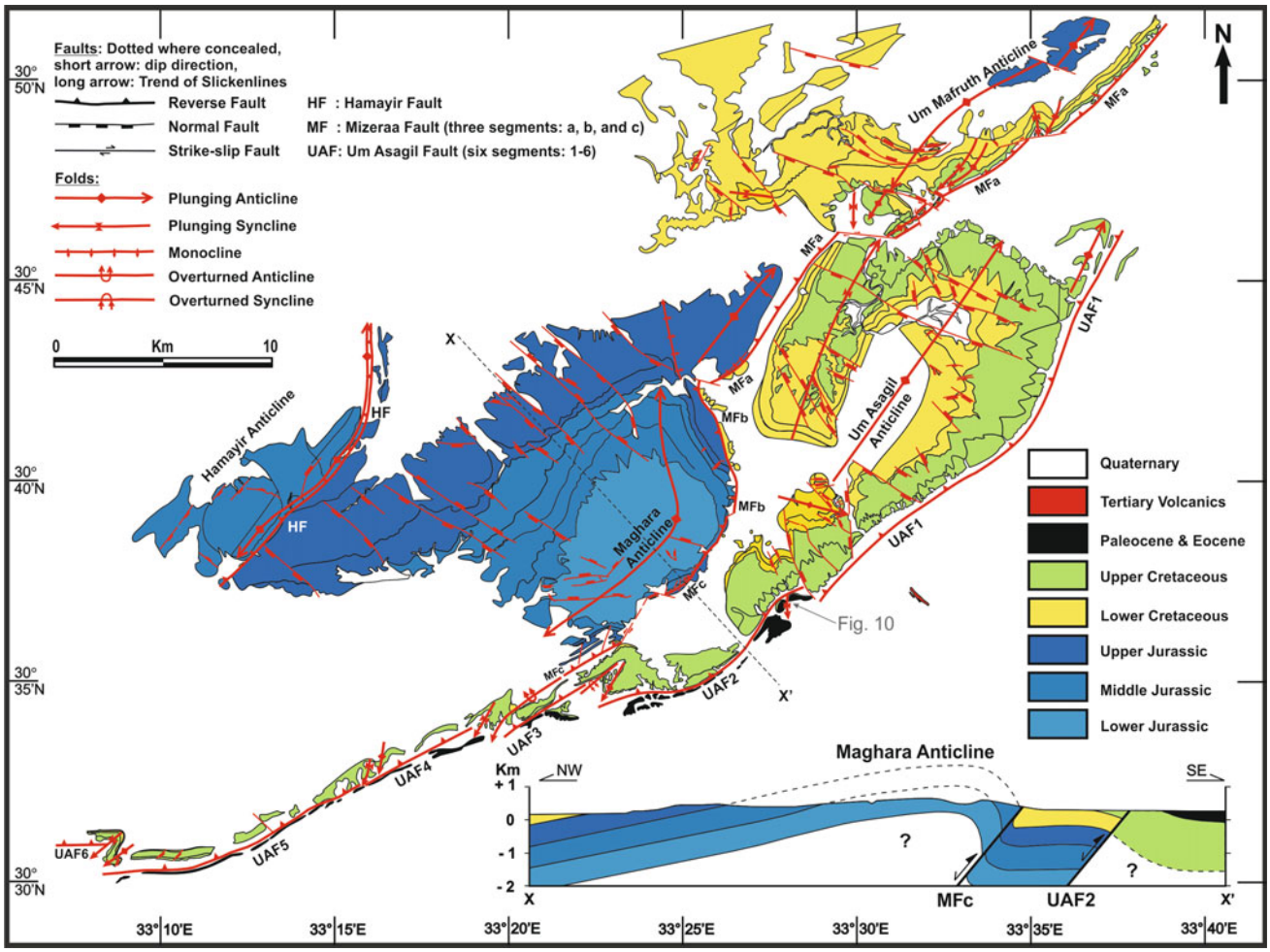

Fig. 7.8 Detailed geological map and structural cross section of Gebel Maghara area after Moustafa (2014)

graben with thicker Jurassic section. The compressional phase led to positive inversion of the graben and development of the surface-mapped folds and associated faults.

Gebel Halal Structure

The Gebel Halal NE-SW oriented doubly plunging anticline deforms the exposed Cretaceous rocks and is 43 km long and 14 km wide. Detailed structural mapping (Abd-Allah et al. 2004) indicates the SE vergence of the anticline (Fig. 7.13). The northwestern flank has an average dip of 15° NW and the southeastern flank is mostly vertical to overturned, especially in the central part of the fold at Wadi El Hazira. This flank is believed to overlie a NE-SW oriented reverse fault. The geometry of the steep fold flank indicates that the underlying reverse fault is made up of several right-stepping en echelon segments (Fig. 7.14); similar to the reverse faults bounding the southeastern side of Gebel Maghara structure. Like Gebel Maghara and Gebel Yelleg folds, the Gebel Halal Anticline is pervasively dissected by a large number of transverse NW-SE oriented normal faults that have steep dip (average 74°), long length (average 5 km), and relatively small throws of few tens of meters (Moustafa 2013). The Lower Senonian rocks are missing in the southern flank of Gebel Halal Anticline where the Turonian rocks are directly overlain by Upper Senonian chalk (Said 1962; Abd-Allah et al. 2004), indicating onset of folding before deposition of these chalks.

The Halal-1 well was drilled in the core of Gebel Halal Anticline and penetrated the thickest Jurassic and Triassic sections in Sinai (3234 m and 914 m, respectively); perhaps indicating that Gebel Halal area represents a NE-SW oriented Triassic-Jurassic extensional sub-basin positively inverted at Late Cretaceous time to form the folds mapped at the surface. The right-stepping en echelon segments of the inverted fault may indicate that inversion was transpressive.

Offshore Sinai Folds

The offshore north Sinai area includes inversion anticlines similar to the exposed folds discussed above (Ayyad et al. 1998 and Yousef et al. 2010). Yousef et al. (2010) mapped

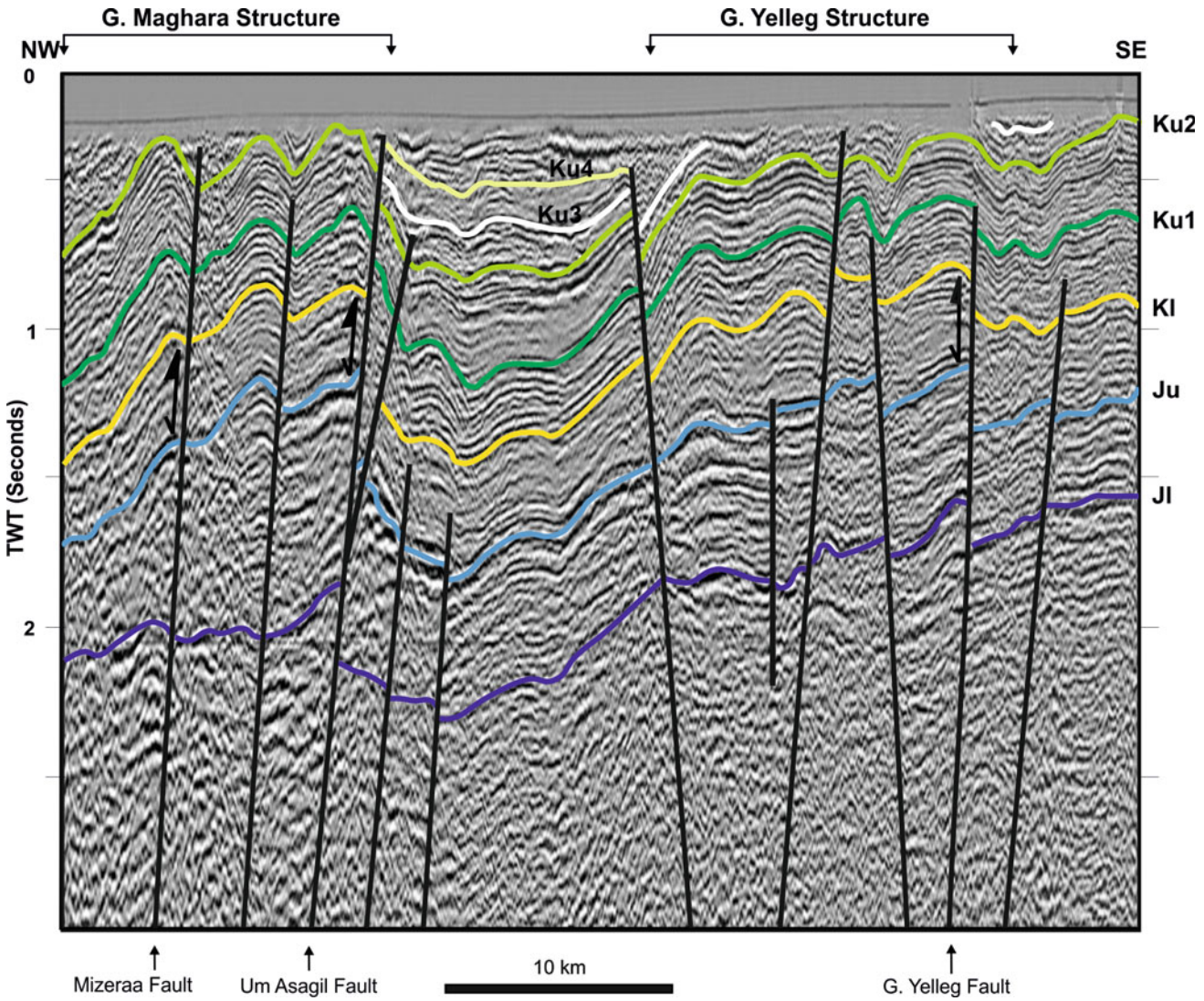

Fig. 7.9 Seismic section extending from the eastern part of Gebel Maghara Anticline to the eastern nose of Gebel Yelleg Anticline after Moustafa (2010). Symbols designate the following reflectors: top intra-Lower Jurassic Rajabiah Formation (Jl), top of the Upper Jurassic Masajid Formation (Ju), top of the Lower Cretaceous (Kl), tops of the Intra-Upper Cretaceous units (Ku1 and Ku2), top of Santonian (Ku3) and top of Maastrichtian chalk (Ku4). Note the sedimentary wedge between Jl and Ju reflectors that thickens southeastward against Um Asagil inverted fault. Note also SE-vergent folds affecting most of the rocks. See Fig. 7.7 for location

five doubly plunging inversion anticlines in the offshore area (Mango, Goliath, NS-21, Gal, and Tineh, Fig. 7.7) using seismic and borehole data. The Mango Anticline is 32-km long, NE-oriented, asymmetric with steeper northwestern flank and breached crest. The Goliath Anticline is 26-km long, NNE-oriented, and asymmetric with steeper northwestern flank bounded by a NNE-oriented inverted fault (Fig. 7.15). The North Sinai 21 Anticline is 25-km long, NE-oriented, and has steeper northwestern flank. The Gal Anticline is 35-km long, NNE-oriented, and has a relatively steep SE flank. The Tineh structure is 15-km long and NE-oriented. Borehole and seismic data indicate that the Top Jurassic to Top Santonian succession represents the syn-rift section. Inversion took place in post-Santonian time as the Campanian-Maastrichtian and Paleogene sequences are progressively onlapping the underlying folded units. Campanian–Maastrichtian sediments have minimum thicknesses over the crests of the inversion anticlines (Fig. 7.15). Basin inversion in offshore northern Sinai continued to the Middle Miocene time (Yousef et al. 2010) or even post-Miocene (Fig. 7.15).

B. Northern Eastern Desert Inversion Structures

Wadi Araba Structure

Wadi Araba Anticline is a prominent structure in the northern Eastern Desert (Fig. 7.6). It is oriented ENE-WSW

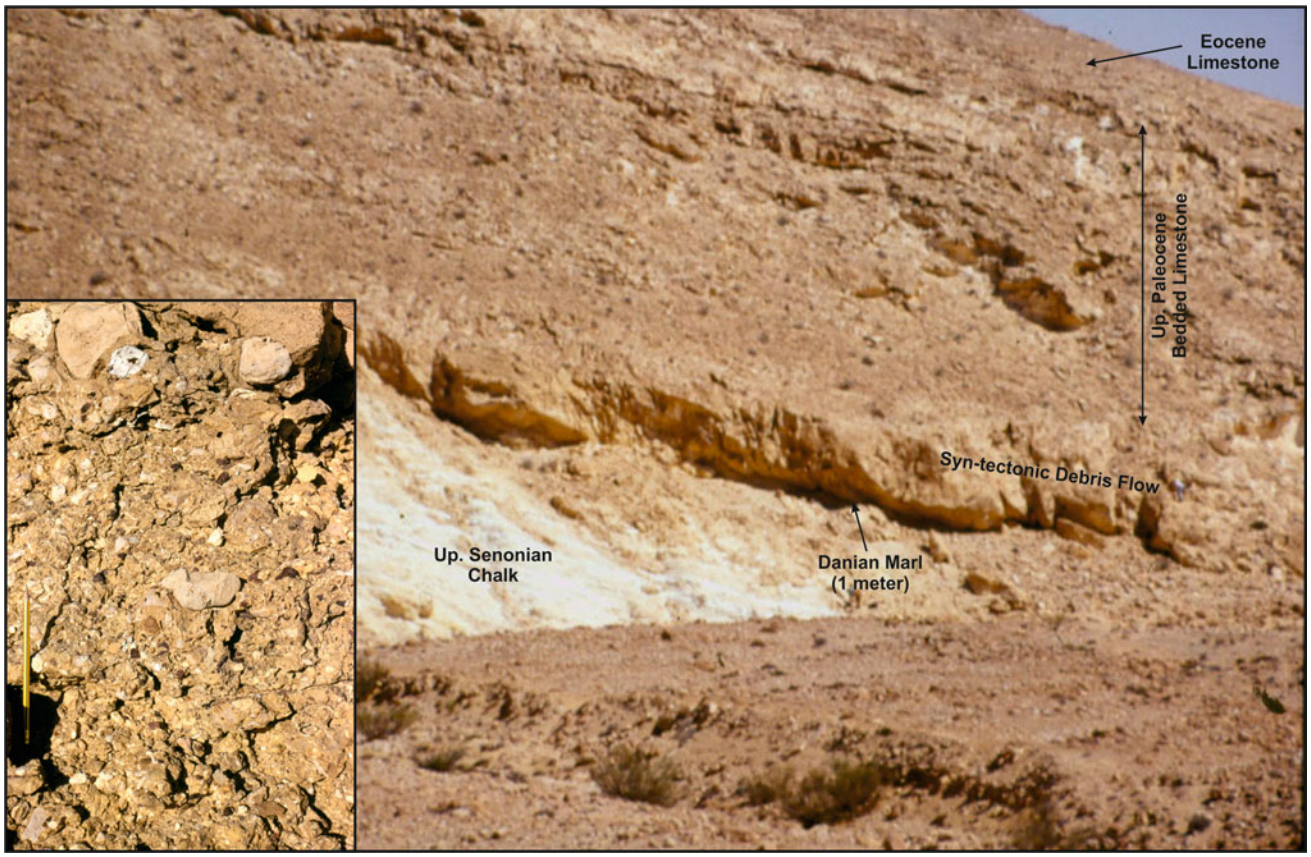

Fig. 7.10 Field photograph of the southern flank of Gebel Maghara Anticline showing debris flow unit in the lower part of the Paleocene rocks. Inset photo is a close-up view of the debris flow showing clasts derived from the Jurassic rocks. See Fig. 7.8 for location

with breached core occupied by Wadi Araba where the oldest (Carboniferous) rocks are exposed. The northern flank of Wadi Araba Anticline dips very gently (few degrees) toward the NNW whereas the southern flank has very steep SE dip represented by nearly vertical Upper Cretaceous rocks at the northern scarp of the South Galala Plateau with excellent exposure at St. Anthony Monastery (Fig. 7.16). Nearly vertical Turonian and Lower Senonian rocks at this locality are unconformably overlain by nearly flat Campanian and younger carbonate rocks indicating Santonian age folding. The Wadi Araba Anticline continues further east into the offshore area of the Gulf of Suez (Moustafa and Khalil 1995). The steep flank of the fold was interpreted to overlie a steep NW dipping reverse fault and the Wadi Araba Anticline is a fault-propagation fold. Although there is no direct evidence to show that the reverse fault of Wadi Araba structure had an earlier phase or normal slip, the structure is considered a positive inversion structure by comparison with similar structures of the same trend, geometry, and time of folding in other areas of northern Egypt. The development of Wadi Araba Anticline affected the facies of the Eocene sediments in vicinity of its steep southeastern flank indicating that Eocene sediments are part of the syn-inversion sequence. Eocene slope deposits were reported to the south and southeast of the Wadi Araba Anticline at St. Paul Monastery area and Wadi Thal (west-central Sinai) respectively (Abul-Nasr 1986; Abul-Nasr and Thunell 1987; Abou-Khadrah et al. 1994).

Gebel Shabrawet Structure

About 150 km to the north of Wadi Araba, Cretaceous rocks exposed at Gebel Shabrawet are folded by an ENE-WSW oriented anticline (Faris and Abbass 1961; Al-Ahwani 1982) with an overturned southeastern flank bounded by a northward dipping reverse fault (Moustafa and Khalil 1995). These folded rocks are unconformably overlain by gently dipping Middle Eocene rocks with a hiatus represented by Campanian-Maastrichtian, Paleocene, and Lower Eocene rocks (Al-Ahwani 1982) indicating post-Santonian to pre-Middle Eocene folding time. This anticline marks the southern side of an inverted basin most of which is now in the subsurface to the north of Gebel Shabrawet. Selim et al. (2014) showed that the Middle Eocene (syn-inversion) sediments on the southern side of the Gebel Shabrawet

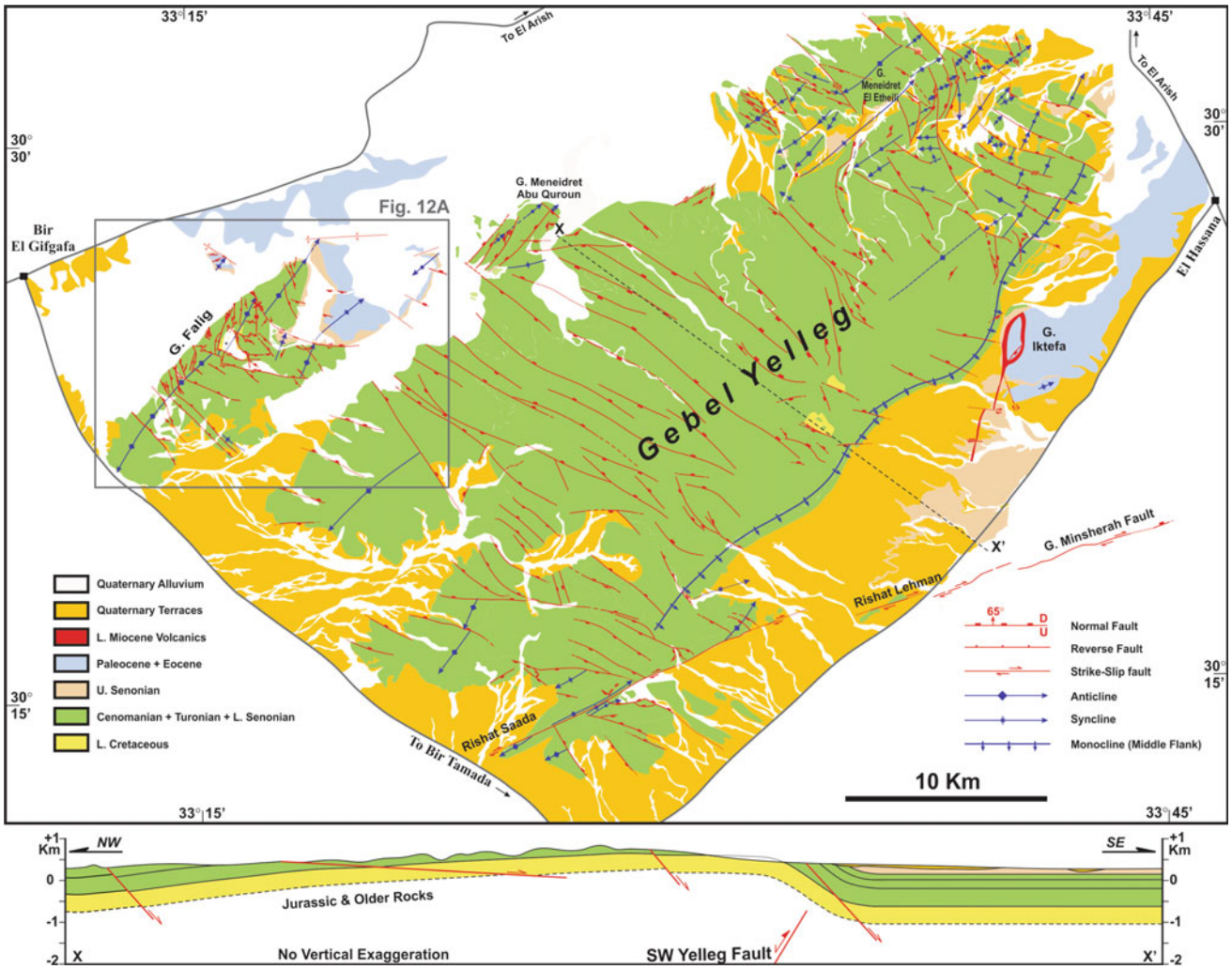

Fig. 7.11 Detailed geological map and structural cross section of Gebel Yelleg area (after Moustafa and Fouda 2014). See Fig. 7.7 for location

Anticline form a red clastic wedge made up of stacked alluvial fan to lagoonal sequences with cross beds showing southeastward paleocurrent direction (parallel to the vergence of the anticline).

C. Northern Western Desert Inversion Structures

Inverted structures in the northern Western Desert are located at Kattaniya, Mubarak, Alamein-Razzak, Abu Gharadig, and Matruh-Shoushan Basins.

Kattaniya Inverted Basin

The Kattaniya inverted basin is about 120 km long and 40 km wide and extends for some distance east of the Nile River. Syn-rift rocks in the Kattaniya Basin include about 2750 m Jurassic sediments in the depocenter of the basin (Abd El-Aziz et al. 1998), Fig. 7.17. Basin inversion at Late Cretaceous—Early Tertiary time led to the development of a very large NE-SW oriented asymmetric anticline with high structural relief comparable to that of Gebel Maghara area (Fig. 7.17a). Deep erosion of the crest of the anticline took place in the Campanian-Maastrichtian, Paleocene, and Eocene times leading to exposure of the Lower Cretaceous rocks in the eroded core of the anticline where they were covered later by Oligocene shales of the Dabaa Formation (area of T57-1 well in Fig. 7.17a). The syn-inversion sediments of the Campanian-Maastrichtian Khoman Chalk and the Paleocene-Middle Eocene Apollonia Formation were not deposited at the crest of the anticline that stood as an island in the Late Cretaceous-Middle Eocene seas (Salem 1976), Fig. 7.17. Thick syn-inversion sediments of the Khoman and Apollonia Formations were deposited on both sides of the inversion anticline in foredeep basins. The Apollonia Formation has a maximum thickness of about 2450 m in the Gindi Basin to the south of the Kattaniya inversion (area of Qarun E-1x well in Fig. 7.17a). Like Gebel Maghara inverted basin, the Kattaniya Basin is fully inverted and

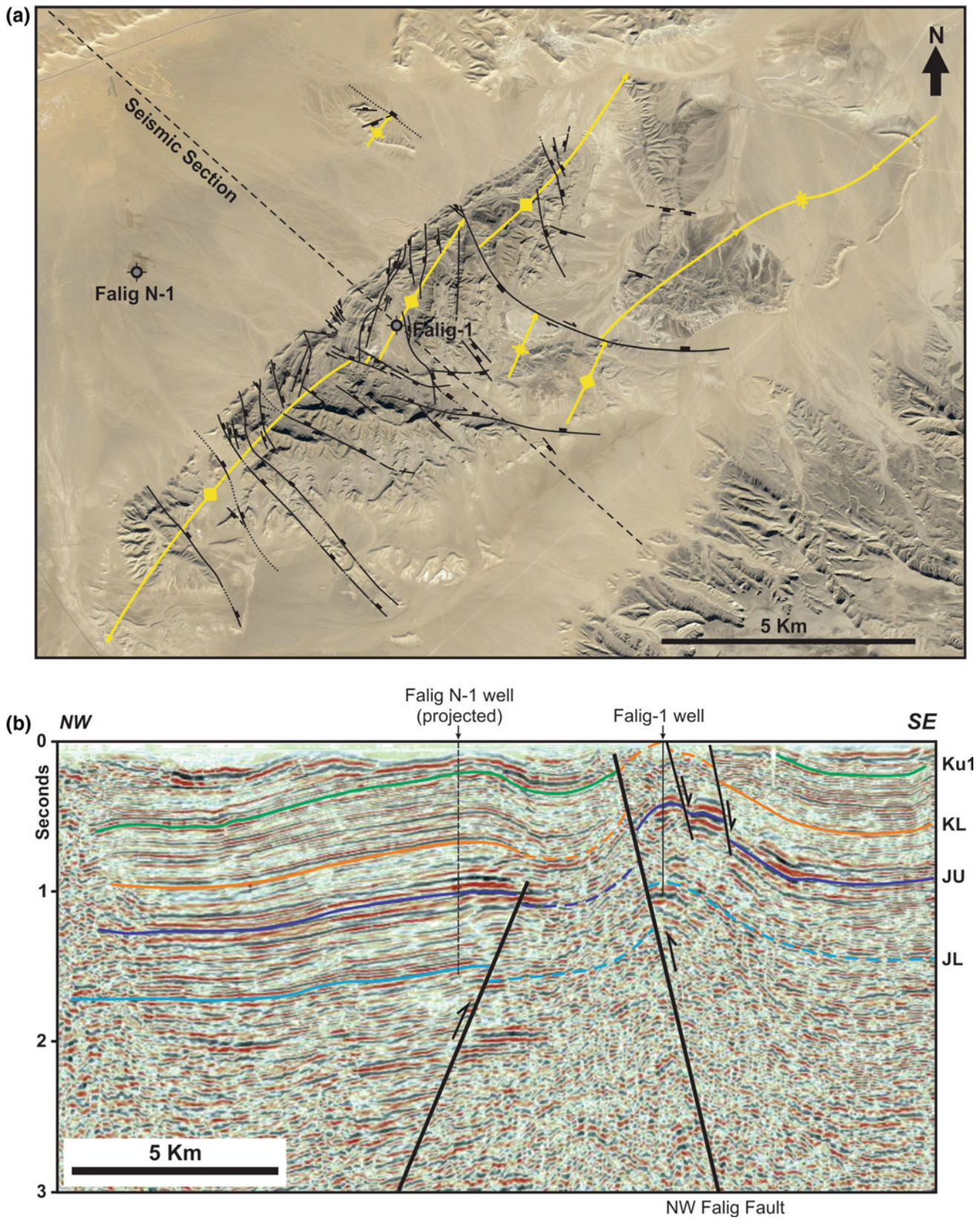

Fig. 7.12 **a** Google Earth image (©2013 DigitalGlobe) of the Gebel Falig Anticline showing its steep NW flank and the main structural features, See Fig. 7.11 for location. **b** Seismic section across the Falig Anticline showing a reverse fault bounding the steep NW flank (NW Falig Fault), after Moustafa and Fouda (2014)

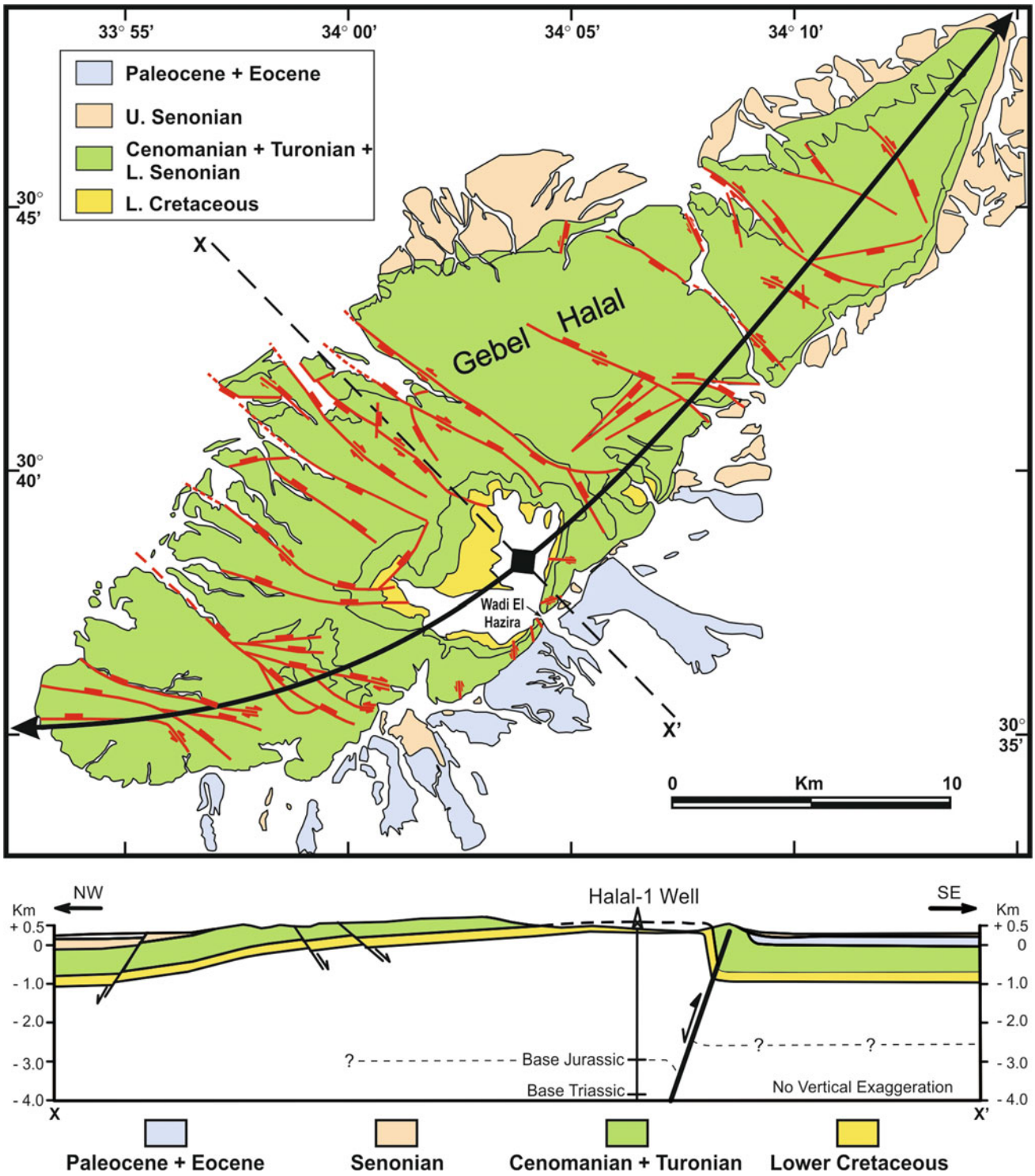

Fig. 7.13 Detailed geological map of Gebel Halal area (after Abd-Allah et al. 2004) and structural cross section (after Moustafa 2010). See Fig. 7.7 for location

seismic reflection data indicate reverse slip of all rock units (down to the Precambrian basement) on the Kattaniya inverted fault (Fig. 7.17a). Also, a clear truncation unconformity marks the boundary between the syn-rift/post-rift rocks and the syn-inversion rocks especially at the two flanks of the inversion anticline (Fig. 7.17b).

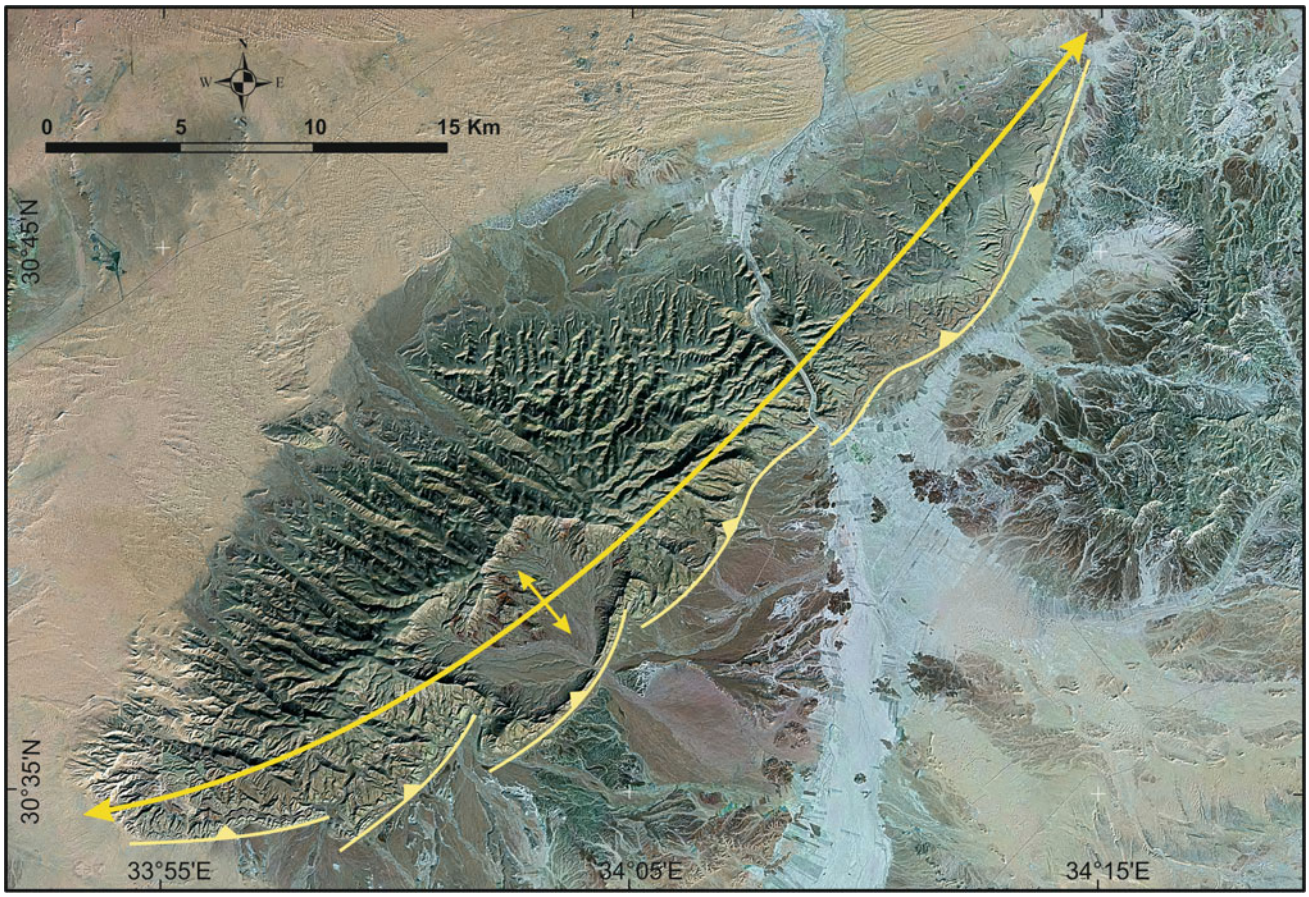

Fig. 7.14 Landsat image of Gebel Halal Anticline showing right-stepped en echelon faults bounding its southeastern asymmetric flank. See Fig. 7.7 for location

Mubarak Inverted Basin

Mubarak inverted basin lies at a short distance to the southwest of the Kattaniya Basin. It has NE-SW orientation and the main inversion anticline is located at the northwestern side of the basin (Figs. 7.3 and 7.6). The magnitude of inversion is less than that of the Kattaniya Basin as normal fault separation is obvious at the lower part of the inverted main basin-bounding fault. The southeastern bounding fault of Mubarak Basin was also inverted forming a small-relief anticline at this side of the basin (Fig. 7.3). Syn-rift sediments in the Mubarak Basin are represented by Jurassic as well as Cretaceous rocks as young as the Coniacian. Syn-inversion rocks include mainly the Campanian-Maastrichtian and Eocene rocks. Borehole data indicate a very thin Eocene section at the crest of the inversion anticline. Seismic reflection data also indicate that inversion continued mildly during Late Eocene and post-Oligocene times leading to gentle folding of the Dabaa Formation (Fig. 7.3).

Alamein-Razzak Inverted Basin

The Alamein-Razzak inverted basin has consistent NE-SW orientation and is 120 km long (Fig. 7.6). Syn-rift rocks in the basin probably include the Triassic in addition to the Jurassic and Lower Cretaceous (Fig. 7.18). Recent high-resolution 3D seismic reflection data indicate that not all of the Lower Cretaceous section (Alam El Bueib Formation) belongs to the syn-rift sequence but only its lower part as the upper part and the overlying Aptian to Coniacian section belong to the post-rift sequence showing no change in thickness across the basin-bounding fault (Fig. 7.18). Reverse slip on the main basin-bounding fault during basin inversion was not large enough to allow upward propagation of the fault through the post-rift sequence but a large NE-SW oriented fault-propagation anticline was formed above the inverted fault. The inversion anticline has several culminations that were mis-interpreted by some investigators (e.g. El-Shaarawy et al. 1992) to be en echelon folds formed by pure dextral strike-slip movement on the fault. Basin

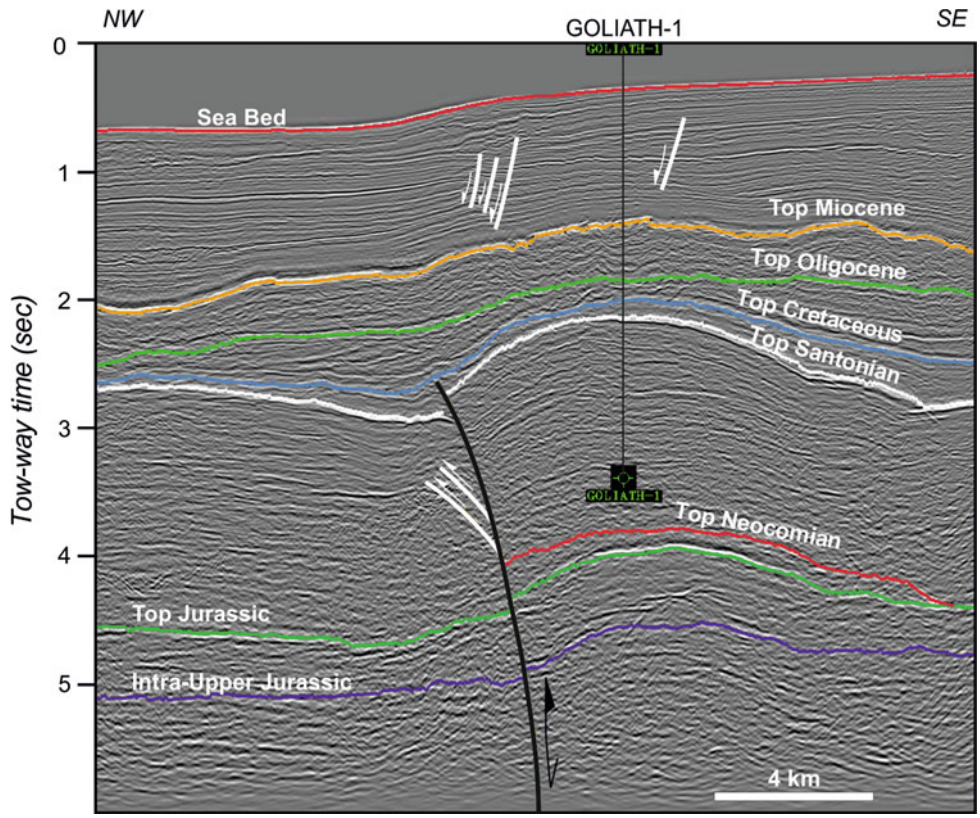

Fig. 7.15 Seismic section showing the Goliath inversion anticline, offshore northern Sinai (after Yousef et al. 2010). See Fig. 7.7 for location

Fig. 7.16 Field photograph of the southern steep flank of Wadi Araba Anticline at St. Anthony Monastery showing nearly vertical Turonian and Lower Senonian rocks unconformably overlain by flat-lying Campanian limestone beds. See Fig. 7.6 for location

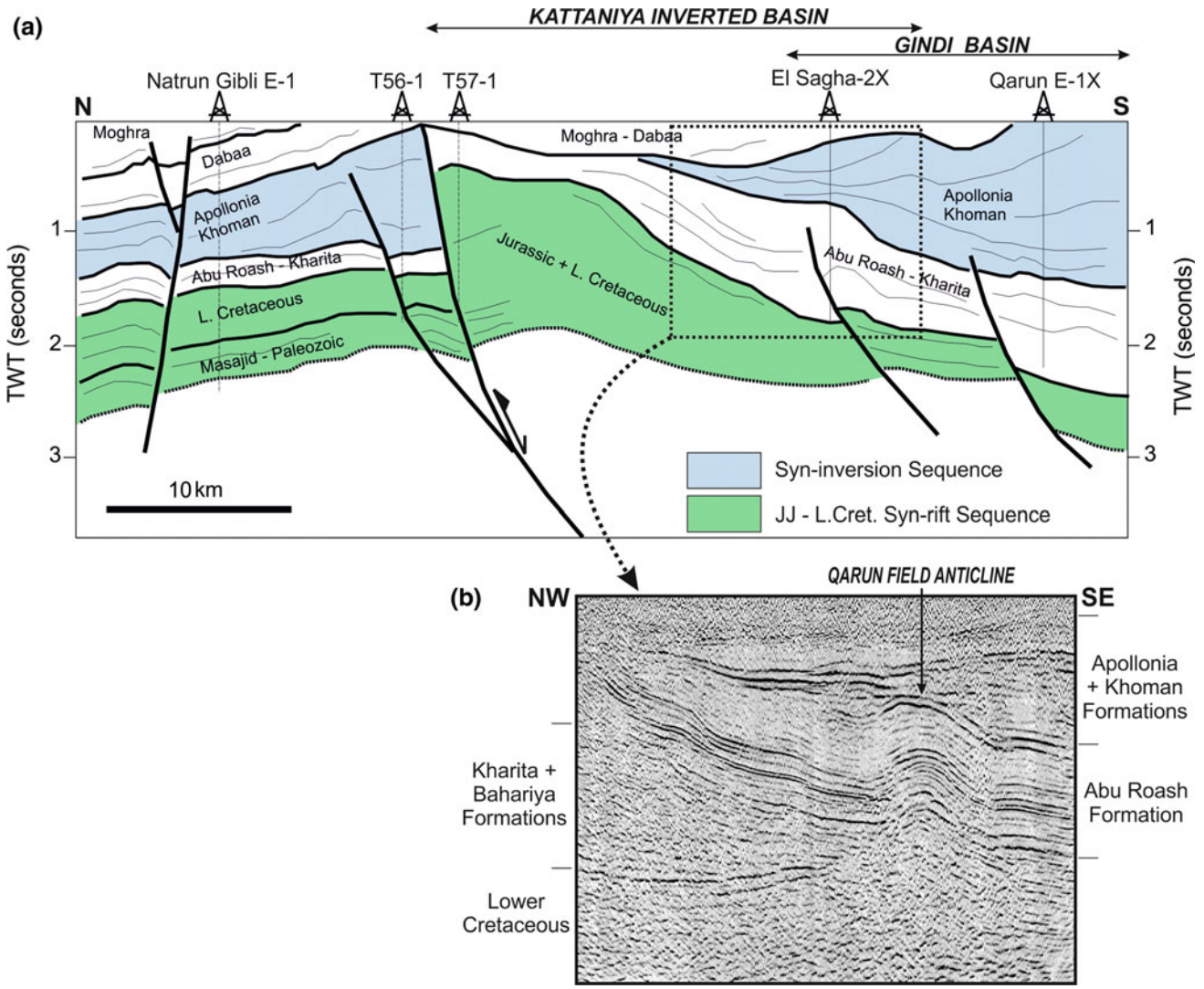

Fig. 7.17 **a** Geoseismic section of the Kattaniya inverted basin slightly modified after Bevan and Moustafa (2012). **b** Seismic section of a portion of the Kattaniya-Gindi Basins at Qarun Field Anticline (after Bakr 2010) showing the wedge shape of the Cretaceous Kharita-Bahariya sediments (that represent a portion of the syn-rift section) and erosion at the high area of the inverted basin. Note also onlap of the syn-inversion units of the Khoman and Apollonia Formations on the Abu Roash Formation at the Qarun Field Anticline and truncation unconformity of the top Abu Roash Formation NW of the anticline. See Fig. 7.6 for location

inversion took place during deposition of the Campanian-Maastrichtian Khoman Formation and affected its thickness at the crest of the inversion anticline. Inversion continued till the Miocene time (Fig. 7.18 and Yousef et al. 2015).

Inverted Structures within Abu Gharadig Basin

Although Abu Gharadig Basin is a Cretaceous rift basin, some NE-SW oriented structures were recognized inside the basin (Fig. 7.6) related to Jurassic NE-SW oriented normal faults reactivated by Late Cretaceous inversion. These inverted structures include the Mid-Basin Arch, Abu Gharadig Field Anticline, and the Abu Sennan structure.

The Mid-Basin Arch of Abu Gharadig Basin is a NE-SW oriented anticline extending diagonally for ~40 km within the basin. This anticline is dissected by NW-SE oriented normal faults into several compartments, one of which forms the BED-2 gas field. At the Cretaceous level of this field, the anticline is obviously asymmetric with steeper SE flank (EGPC 1992).

The Abu Gharadig Anticline is 18–20 km long NE-SW oriented doubly plunging anticline. It is bounded by two oppositely dipping en echelon inverted faults showing reverse slip and fault propagation folding in the Upper Cretaceous rocks (Fig. 7.19). Detailed subsurface mapping using 3D seismic and borehole data (El Gazzar et al. 2016)

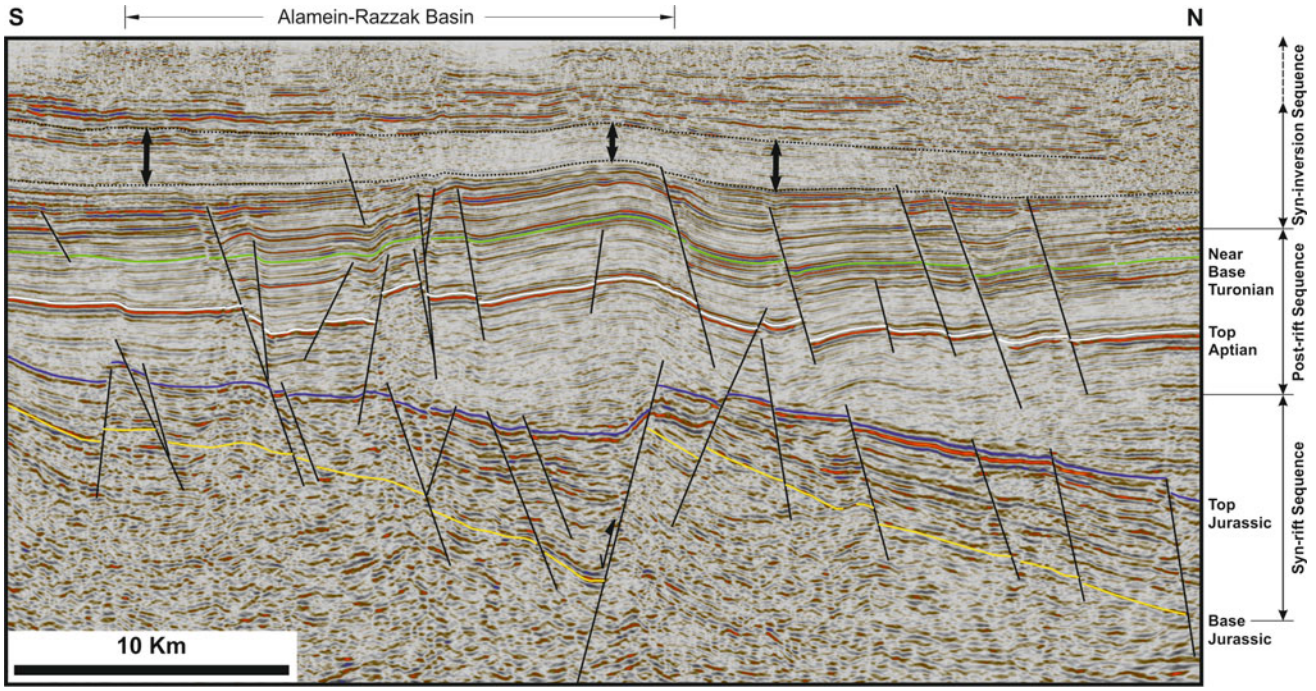

Fig. 7.18 Seismic section across Alamein-Razzak Basin (after Bakr 2010) showing the asymmetric inversion anticline. Note the syn-rift sequences (Jurassic and L. Cretaceous), onlap of the basal part of L. Cretaceous section on top Jurassic, and the thin section of syn-inversion sequence at the anticline crest compared to the flanks (areas marked by vertical lines with double-head arrows). Faults dissecting the post-rift sequence have NW-SE orientation whereas faults dissecting the pre-rift and syn-rift sequences are mostly oriented NE-SW. See Fig. 7.6 for location

indicates that inversion started during the Santonian time and continued to the Oligocene.

The Abu Sennan structure is a 45 km long NE-SW oriented asymmetric anticline lying some 15 km to the SE of the Abu Gharadig Anticline. This structure has several culminations named Southwest Sennan, GPT, GPX, GPY, and GPZ (EGPC 1992). A NW vergent positively inverted fault dissects the Cretaceous rocks underlying the Campanian-Maastrichtian Khoman Chalk of the inversion anticline. The Khoman Chalk and the overlying Eocene rocks are folded by a fault-propagation fold. Reduced thickness of the Khoman Chalk at the crest of the anticline indicates onset of the inversion and folding before its deposition. Folding continued mildly afterwards till end of the Eocene.

Other compressional structures of smaller dimensions also exist in the Abu Gharadig Basin. Although the basin has a general E-W orientation its northern main-bounding fault is made up of several segments oriented E-W, NE-SW, and NW-SE (El Saadany 2008). Late Cretaceous reactivation of these fault segments is represented by reverse slip on the NE-SW oriented fault segments and normal slip on the NW-SE fault segments. These synchronous opposite senses of slip led some investigators to infer dextral strike-slip movement on the E-W fault segments. Reverse slip on the NE-SW fault segments is either due to: (1) positive inversion of these fault segments, or (2) dextral strike- (or oblique-) slip movement on the E-W fault segments where the NE-SW faults form push-up structures between left-stepping E-W faults, as proposed by Said et al. (2014) and Salah et al. (2014) in the BED-17 oil field area.

Another NE-SW oriented push-up structure with similar geometry is located 160 km to the east of the BED-17 structure on the northern side of Abu Gharadig Basin. This push-up structure shows up very well on seismic reflection data and proves that the E-W segments of the main northern-bounding fault of Abu Gharadig Basin had dextral slip at Late Cretaceous time.

Abu Roash Area Push-Up Structures

Another push-up structure similar to that on the northern side of the Abu Gharadig Basin is exposed at Abu Roash area, SW of Cairo (Fig. 7.20). At that locality, the Upper Cretaceous rocks represent the only Cretaceous exposure in the northern Western Desert. Surface geological mapping (Faris 1948; Jux 1954) clearly shows NE-SW oriented folds. Detailed structural mapping led Moustafa (1988) and Abdel Khalek et al. (1989) to recognize strike-slip deformation of this area. The structure of Abu Roash area is made up of three main NE-SW oriented folds, the most prominent of which is dissected by WNW-ESE oriented en echelon, right-lateral, strike-slip faults that represent left-stepping

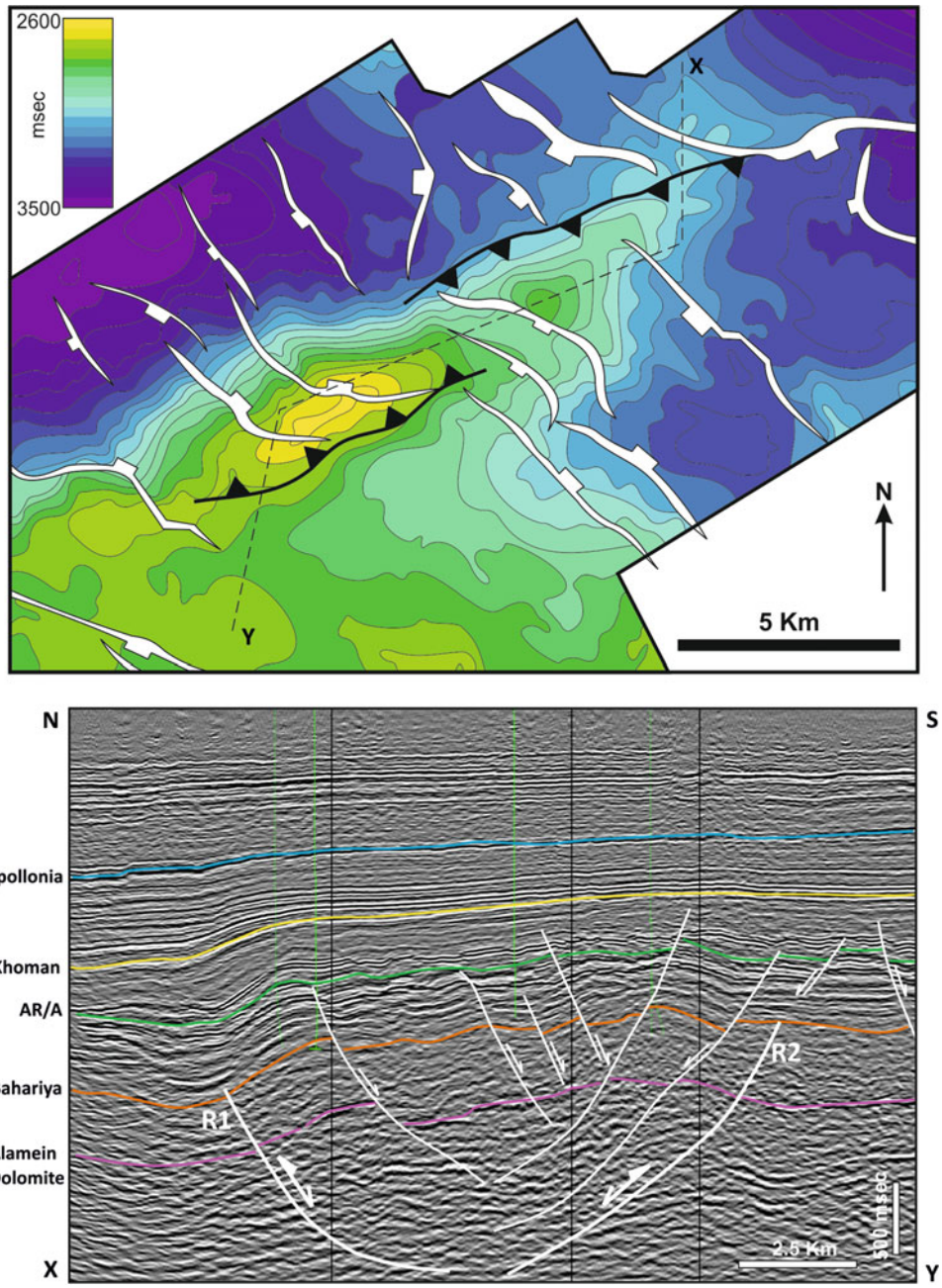

Fig. 7.19 Top Alamein Dolomite time-structural map and seismic section of Abu Gharadig Anticline showing the two en echelon inverted faults (R1 and R2) bounding the NE and SW sides of the anticline (slightly modified after El Gazzar et al. 2016). See Fig. 7.6 for location

Riedel shears (Moustafa 1988; Fig. 7.20). Smaller plunging anticlines lying between these en echelon faults are push-up structures that collectively form the large NE-SW oriented anticline extending from Abu Roash Village to Gebel El Ghighiga passing with the famous Hasana Anticline on the Cairo-Alexandria desert road (Fig. 7.20). A NE-SW oriented positive flower structure is well exposed at Gebel Abu Roash in the NE part of the area and is bounded by oppositely dipping NE-SW oriented reverse faults. Moustafa (1988) interpreted the Abu Roash structures to be the result of E-W dextral shear couple affecting the area. Integration of surface and subsurface structural data indicates that the structures of Abu Roash area represent a large push-up structure formed between the ends of E-W oriented, left-stepping, en echelon, right-lateral strike-slip faults; similar to the push-up areas at the northern-bounding fault of Abu Gharadig Basin.

An angular unconformity was mapped between the Coniacian-Santonian rocks (Plicatula Series) and the Campanian-Maastrichtian chalk on the NW side of Gebel Abu Roash (Moustafa 1988) indicating the onset of compressive deformation of the area. Neither Paleocene nor Lower Eocene rocks were deposited in Abu Roash area indicating that it stood as an island above the Early Tertiary sea level. The outer areas of the folded Upper Cretaceous

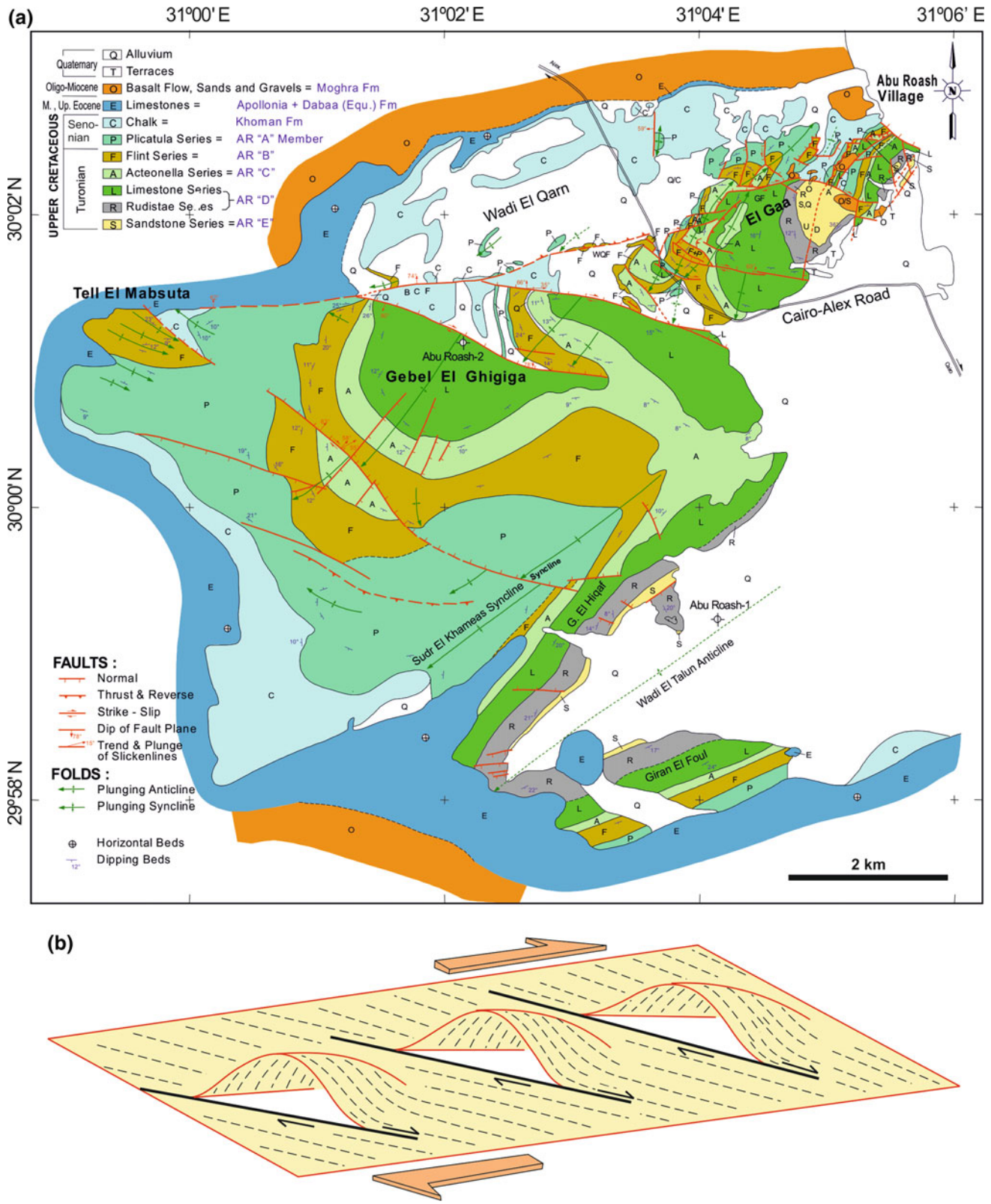

Fig. 7.20 **a** Geological map of Abu Roash area (southwest of Cairo) after Moustafa (1988) and 3D model (**b**) explaining the development of push-up folds between left-stepping en echelon right-lateral strike-slip faults. See Fig. 7.6 for location

outcrops are unconformably overlain by a condensed section of Middle and Upper Eocene rocks indicating continued growth of the structure in the Early Tertiary.

Matruh-Shoushan Inverted Basin

The Matruh-Shoushan inverted basin extends for about 220 km and is unique in showing a new inverted fault trend compared to the above-mentioned basins (Moustafa et al. 2002; Metwalli and Pigott 2005; Tari et al. 2012). NNE oriented faults in the basin show two phases of slip, a Triassic to Early Cretaceous phase of normal slip and a Late Cretaceous phase of reverse slip where the resulting inversion anticlines are oriented NNE-SSW. The Matruh Basin NNE-SSW oriented faults are connected to ENE-WSW and NE-SW oriented normal faults of the Shoushan Basin (Fig. 7.2). Inversion of the Matruh Basin formed a structural high above the Late Eocene-Oligocene sea level leading to non-deposition of the Dabaa Formation.

7.2.3.2 Late Cretaceous-Tertiary Deformation of Areas Lying South of the Inverted Basins

Platform areas lying south of the northern Egypt inverted basins are characterized by nearly horizontal to gently dipping Phanerozoic sedimentary rocks of relatively small uniform thickness compared to the basinal areas to the north. These areas were affected by the compressive stresses resulting from convergence of Afro-Arabia and Eurasia leading to uplift of these areas and/or the reactivation of deep-seated faults. Compressional structures in these areas are contemporaneous with the inversion of the northern basins. These areas include the Sinai Hinge Belt and the Themed Fault in Sinai, the southern Gulf of Suez and northern Red Sea area, the Bahariya Oases in the central Western Desert, and the Nubia Fault System in the southernmost part of the Western Desert.

A. Sinai Hinge Belt

The Sinai Hinge Belt (Fig. 7.7) was first recognized by Shata (1959) as a 250 km long and 20-km wide fractured area at the boundary between the northern Sinai strongly folded area (area where the inverted Mesozoic basins are located) and the north-central Sinai gently folded area. Detailed structural mapping (Moustafa et al. 2014) indicates that this belt includes several ENE-WSW oriented right-stepping en echelon faults associated with folds (Fig. 7.21). Most of the folds of the belt expose Upper Cretaceous (mostly Cenomanian and Turonian) rocks in their cores but a few of them also expose Triassic, Jurassic, or Lower Cretaceous rocks.

Each fault segment of the Sinai Hinge Belt shows right-lateral strike-slip deformation indicated by slickenlines and/or right-stepped en echelon folds (e.g. Mitla Pass, Fig. 7.22). Some lozenge-shaped compressional structures are formed between the ends and stepover areas of some of the right-lateral strike-slip faults (e.g. Um Hosaira Fold) or at restraining bends in the fault segments (e.g. Araif El Naqa Anticline), Fig. 7.21. The early stage of strike-slip deformation of the Sinai Hinge Belt led to popping up of the rocks before they were longitudinally dissected by the faults (Moustafa et al. 2014). The magnitude of horizontal slip on each fault segment is small and horizontal slip is accommodated by folding at the fault ends. NW-SE oriented normal faults dissect the rocks on both sides of the right-lateral strike-slip faults and are abutted by the strike-slip faults. Strike-slip movement in the Sinai Hinge Belt took place in two phases: (1) During the Late Cretaceous-Early Tertiary time. The Late Cretaceous deformation is displayed by the unconformity in the lower part of the Campanian-Maastrichtian chalk at Gebel El Minsherah area (Moustafa and Yousif 1990) and by the syn-tectonic sandstone deposited in the middle of the Campanian-Maastrichtian chalk of Araif El Naqa Anticline (Luning et al. 1998) whereas the Early Tertiary deformation is displayed by the absence of Paleocene sediments in Gebel El Hamra Anticline at the southwestern side of Mitla Pass (Hassan et al. 2015) as well as folding of Eocene rocks at Gebel Araif El Naqa. (2) In post-Early Miocene (leading to dextral offset of Lower Miocene igneous dikes). The Late Cretaceous phase of deformation resulting from the Tethyan convergence continued till the Eocene time in some areas, e.g. Gebel Araif El Naqa.

Moustafa et al. (2014) indicated that the ENE-WSW oriented en echelon strike-slip faults of the Sinai Hinge Belt exist in two sub-belts and reflect the reactivation of two deeper faults underneath these sub-belts. The deep-seated faults are thought to be Jurassic normal faults formed at the boundary between the southern platformal area and the northern basinal area during Tethyan rifting. Later shortening of the area due to the convergence of Afro-Arabia and Eurasia reactivated these faults by dextral transpression expressed by the strike-slip fault segments of the hinge belt and their associated folds. Moustafa et al. (2014) also attributed the post-Early Miocene slip on the Sinai Hinge Belt to the Neogene extensional deformation of the region associated with the NE drift of Arabia away from Africa and Miocene opening of the Gulf of Suez and ancestral Red Sea rift. The Sinai Hinge Belt terminated the Gulf of Suez rift at the latitude of Suez city that caused reactivation of the belt by dextral slip.

B. Themed Fault Area

The Themed Fault (Fig. 7.7) is a narrow 200 km long structural belt extending in north-central Sinai from the eastern margin of the Suez rift to the Dead Sea Transform. This narrow structural belt shows up as a number of en

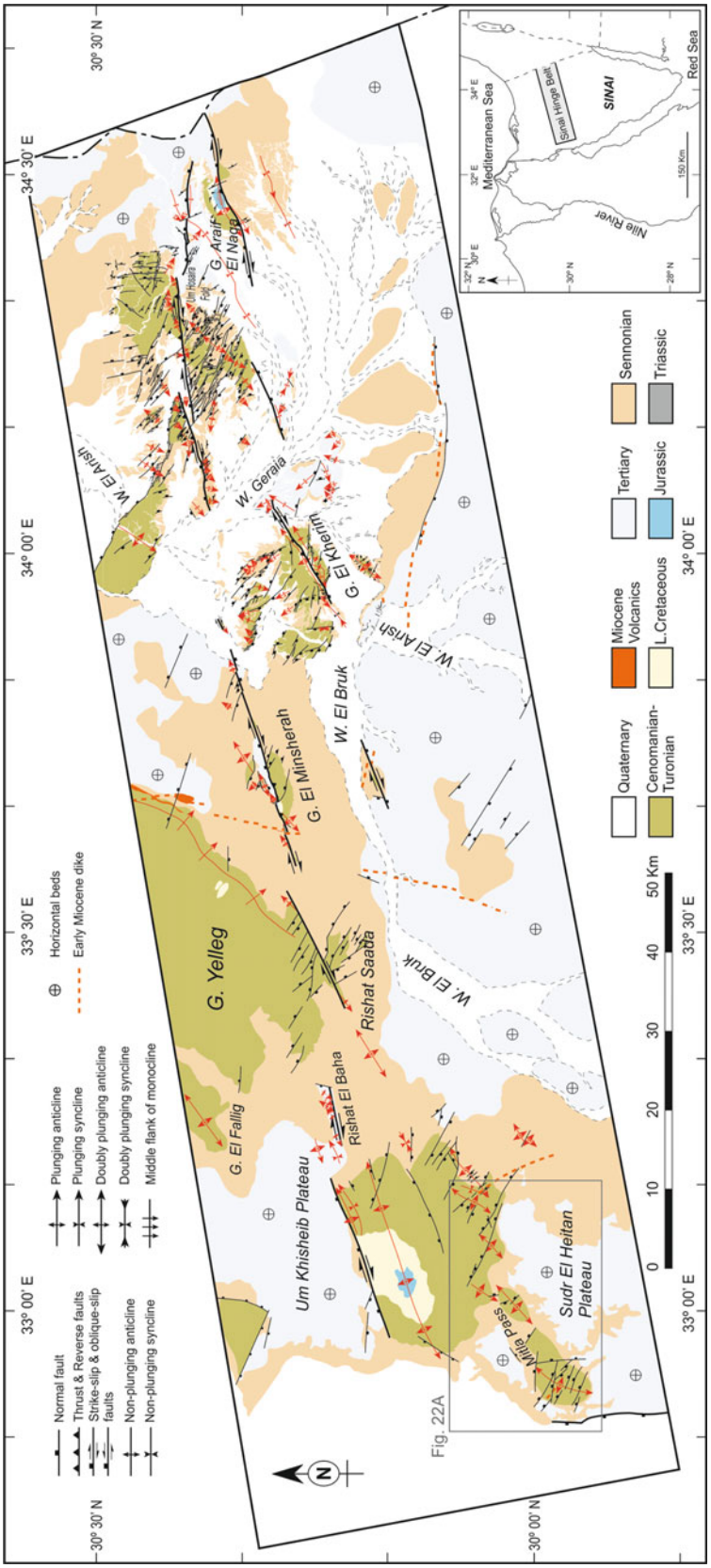

Fig. 7.21 Simplified geological map of the Sinai Hinge Belt after Moustafa et al. (2014)

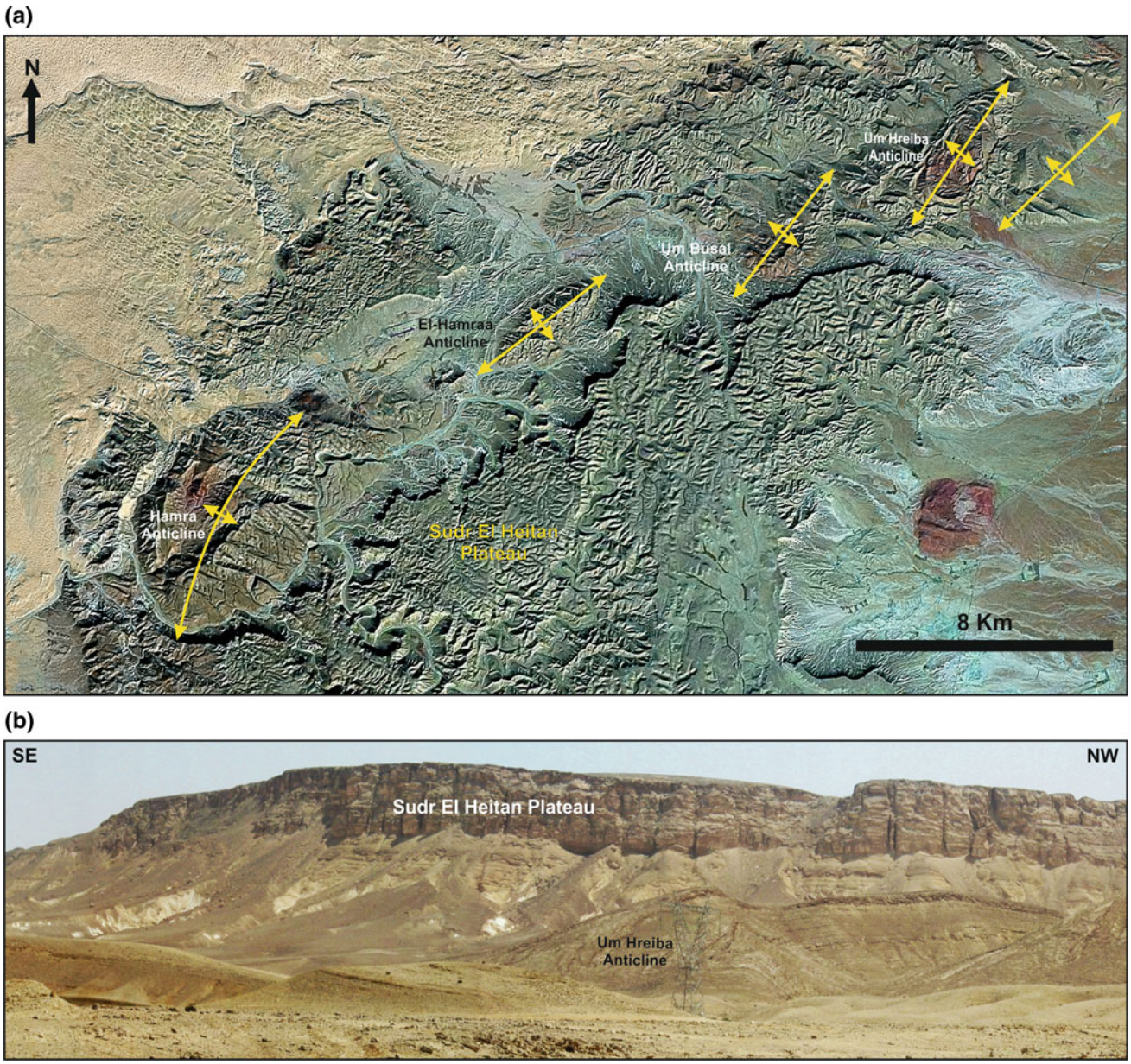

Fig. 7.22 **a** Landsat image of the en echelon anticlines affecting the Upper Cretaceous rocks of Mitla Pass area (northern Sinai). **b** Field photograph of the NE nose of Um Hreiba Anticline and the nearby flat-lying Sudr Chalk and Eocene limestones of Sudr El Heitan Plateau. See Fig. 7.21 for location

echelon faults associated with relatively small plunging and doubly plunging folds through the flat-lying rocks of the Tih Plateau (Fig. 7.23). It shows reactivation of one of the pre-existing faults dissecting the tectonically stable area south of the Sinai Hinge Belt.

Detailed field mapping of the Themed Fault (Moustafa and Khalil 1994) indicates that the eastern and western parts of the fault are very clear, whereas the central part is discontinuous. The western part of the Themed Fault consists of four steeply dipping (50–90°), E-W and ENE-WSW oriented, right-stepping en echelon segments with right-lateral strike-slip displacement. These fault segments are associated by E-W to NE-SW oriented, doubly plunging folds that make acute angles with the Themed Fault (Fig. 7.23). The time of slip on these fault segments is pre-Miocene as they die out before reaching the Suez rift and one of them is intruded by an Early Miocene basaltic dike. The age of folded rocks is Late Cretaceous to Early Eocene, indicating post-Early Eocene movement on the faults.

The eastern part of the Themed Fault dissects Precambrian to Lower Eocene exposures and has E-W orientation and steep northward dip (62–90°). Slickenside lineations and

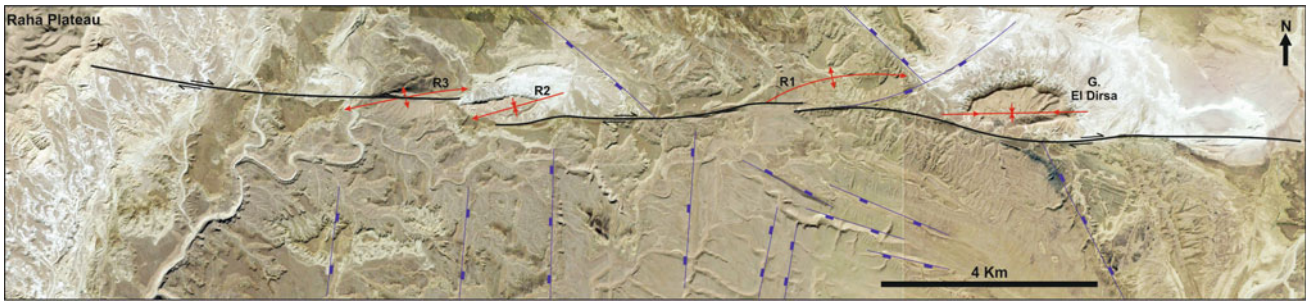

Fig. 7.23 Google Earth image (©2018DigitalGlobe) showing three E-W en echelon segments of the western part of the Themed Fault and the associated folds (R1, R2, R3, and Gebel El Dirsa folds). See Fig. 7.6 for location

chatter marks indicate right-lateral slip on the fault. Also, the Rishat El Themed doubly plunging anticline is dextrally offset by the fault for about 300 m (Fig. 7.24).

The en echelon arrangement of the Themed Fault segments as well as the field-recorded right-lateral slip indicate that it is a narrow dextral wrench zone. Further evidence for dextral wrenching is seen in the right-stepping, en echelon arrangement of the folds and the acute angle between the folds and the Themed Fault.

C. Southern Gulf of Suez Area

Afifi et al. (2016) carried out detailed subsurface study of the southernmost part of the Gulf of Suez rift using 3D seismic and borehole data. Some of the studied boreholes indicate an unconformity between the Cenomanian-Lower Senonian Mixed Facies Unit (Nezzazat Group) and the overlying Campanian-Maastrichtian Brown Limestone/Sudr Chalk unit. They believe the unconformity is Santonian-Campanian and correlates with the unconformity identified in the Syrian Arc folds of northern Egypt. As the nature of this unconformity in the southern Gulf of Suez is not angular, the missing rock units may indicate uplift of this region leading to erosion of the uppermost part of the Mixed Facies Unit at the same time inversion folds were developed further north. This uplifted area in the southern Gulf of Suez rift is referred to as the Ras Mohamed Arch by Peijs et al. (2012). Bosworth et al. (1999) suggested Late Santonian compressional deformation of Gebel El Zeit and Esh El Mellaha areas leading to reactivation of basement fabrics and development of small-scale folds in the sedimentary section.

Fig. 7.24 Vertical aerial photograph of Gebel Rishat El Themed Anticline showing dextral offset by the Themed fault (after Moustafa and Khalil 1994). Outlined area represents the outcrop of Cenomanian rocks in the core of the anticline. See Fig. 7.6 for location

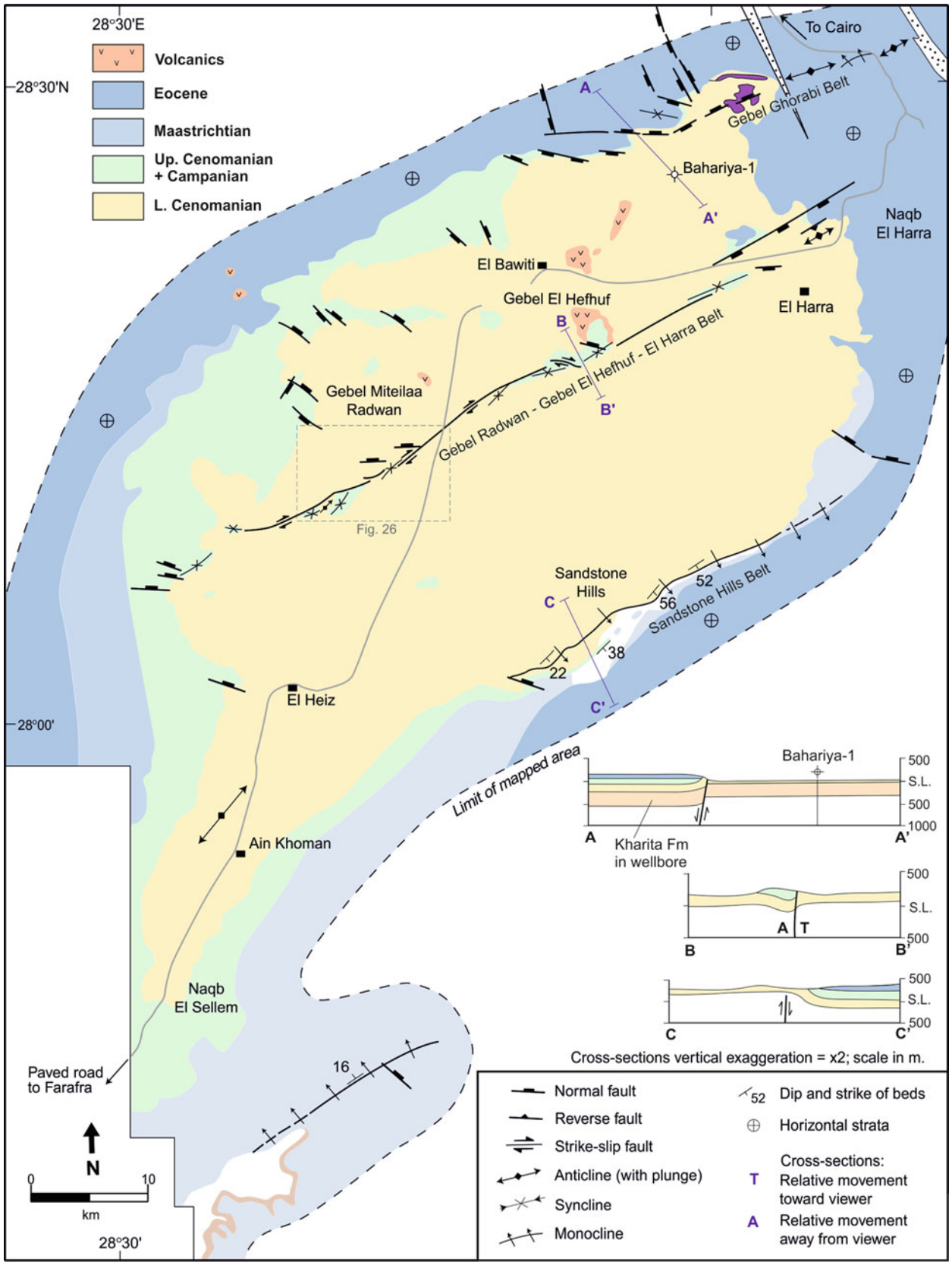

Fig. 7.25 Simplified geological map of the Bahariya Oases' area showing the ENE-WSW oriented structural belts, after Moustafa et al. (2003). See Fig. 7.6 for location

D. Bahariya Oases

The Bahariya Oases area (central part of the Western Desert) also shows the base Campanian parallel unconformity where Cenomanian marine sediments of El Heiz Formation are directly overlain by Campanian marine sediments of El Hefhuf Formation with a notable hiatus represented by the Turonian-Santonian rocks. This unconformity is perhaps related to uplift of the central Western Desert and non-deposition and/or erosion of the missing rocks coeval with the onset of Late Cretaceous inversion of the northern basins. Although the Bahariya Oases area lies in a platform area characterized by thin Phanerozoic sedimentary section (1400–2000 m; Moustafa et al. 2003), it displays folded Upper Cretaceous rocks due to Late Cretaceous-Early Tertiary deformation. The deformation is attributed to reactivation of pre-existing ENE-WSW oriented faults by NW compressive stress (Moustafa et al. 2003). Three well-defined ENE-WSW oriented structural belts were mapped in the area; Gebel Ghorabi Belt, Gebel Radwan–Gebel El Hefhuf–El Harra Belt, and the Sandstone Hills Belt (Moustafa et al. 2003), Fig. 7.25. In each of these three belts, Late Cretaceous deformation led to reactivation of deep-seated faults and folding of the exposed Upper Cretaceous rocks.

The Gebel Ghorabi Structural Belt extends for about 36 km in the northernmost part of the Bahariya depression and shows two phases of right-lateral strike-slip movement. The first phase was post-Cenomanian to pre-Middle Eocene and the second phase was post-Middle Eocene. The second phase deformed the Middle Eocene rocks at the eastern side of the belt by relatively small, right-stepping en echelon folds.

The Gebel Radwan–Gebel El Hefhuf–El Harra Structural Belt is 65 km long and extends across the oases depression from the western plateau to the eastern plateau. It includes four main left stepping, en echelon, ENE-oriented, steeply dipping faults associated with fault-drag or fault-propagation folds that change their orientation at the fault tips where they make acute angles with the faults. The fault segments show horizontal to oblique slickenside lineations indicating right-lateral strike-slip displacement and are also associated with right-stepped en echelon folds (Fig. 7.26). Two phases of deformation affected these fault segments; an earlier (stronger) phase of post-Campanian and pre-Middle Eocene age and a second phase of post-Middle Eocene age. The earlier phase involved right-lateral strike-slip movement indicated by the nearly horizontal slickenside lineations on some faults in the belt and by the right-stepped en echelon folds that make acute angles with the fault segments whereas the sense of slip of the second phase is not easy to determine.

The Sandstone Hills Structural Belt is a 32-km-long fault-propagation fold represented by ENE-oriented monocline with steep (30–56°) SE dip on the southeastern side of the Bahariya Depression. The monocline affects Upper Cretaceous rocks unconformably overlain by Lower Eocene rocks, indicating post-Campanian-pre-Early Eocene folding.

The subsurface geology of the Bahariya area is shown by a NW-SE oriented 2D seismic section located at a short distance to the northeast of the Bahariya Depression. This section clearly shows that the top Precambrian basement to top Paleozoic rocks are dissected by four normal faults (Fig. 7.27). The same faults have reverse slip at the top Cenomanian Bahariya Formation. Moustafa et al. (2003) attributed the normal slip of these faults to Early Mesozoic extension, perhaps related to the Tethyan rifting phase. Two of these faults represent the along-strike projection of Gebel Ghorabi Structural Belt and Gebel Radwan–Gebel El Hefhuf–El Harra Structural Belt. The seismic section indicates that two phases of movement took place; an early phase of normal slip and a later phase of reverse slip representing positive structural inversion of the Bahariya area. The section also shows that the Mesozoic rocks are folded by an anticline with broad crestal area which was named the Bahariya Swell by Moustafa et al. (2003) and is a result of the positive inversion. The Maastrichtian chalk (Khoman Formation) onlaps the southern side of the Bahariya Swell indicating that inversion was pre-Maastrichtian in age. The reverse slip shown by the seismic and dextral strike-slip movement shown by surface geological data indicate that inversion was transpressive. The seismic section also shows the eroded crest of the Bahariya Swell and the unconformable relationship between the eroded Upper Cretaceous rocks and the overlying Eocene rocks of the Apollonia Formation. As the top Apollonia reflector also shows the anticlinal structure of the Bahariya Swell, the inversion continued into the post-Middle Eocene and was contemporaneous with the second phase of deformation identified by the surface geological mapping.

E. Nubia Fault System

The Nubia Fault System is a belt of pervasive E-W to ENE-WSW oriented faults affecting the southernmost part of the Western Desert (Fig. 7.2). It extends for about 600 km west of the Nile and may extend further west for a longer distance underneath the Quaternary sand dunes. Bahy Issawi was probably the first geologist to map these prominent E-W faults in the Sinn El Kaddab (Issawi 1968) and Darb El Arbain (Issawi 1971) areas. The E-W faults of Issawi are accompanied by N-S faults especially at the eastern scarp of Sinn El Kaddab Plateau overlooking the Nile Valley. In fact, it was Ghobrial (1967) who identified and mapped such N-S faults further north in the Kharga Depression and mentioned that they are associated with N-S belts of left-stepped en echelon doubly plunging folds (Fig. 7.28). Similarly, the E-W faults are also associated with relatively small-scale folds (Fig. 7.29) that are mostly en echelon. Both of the E-W

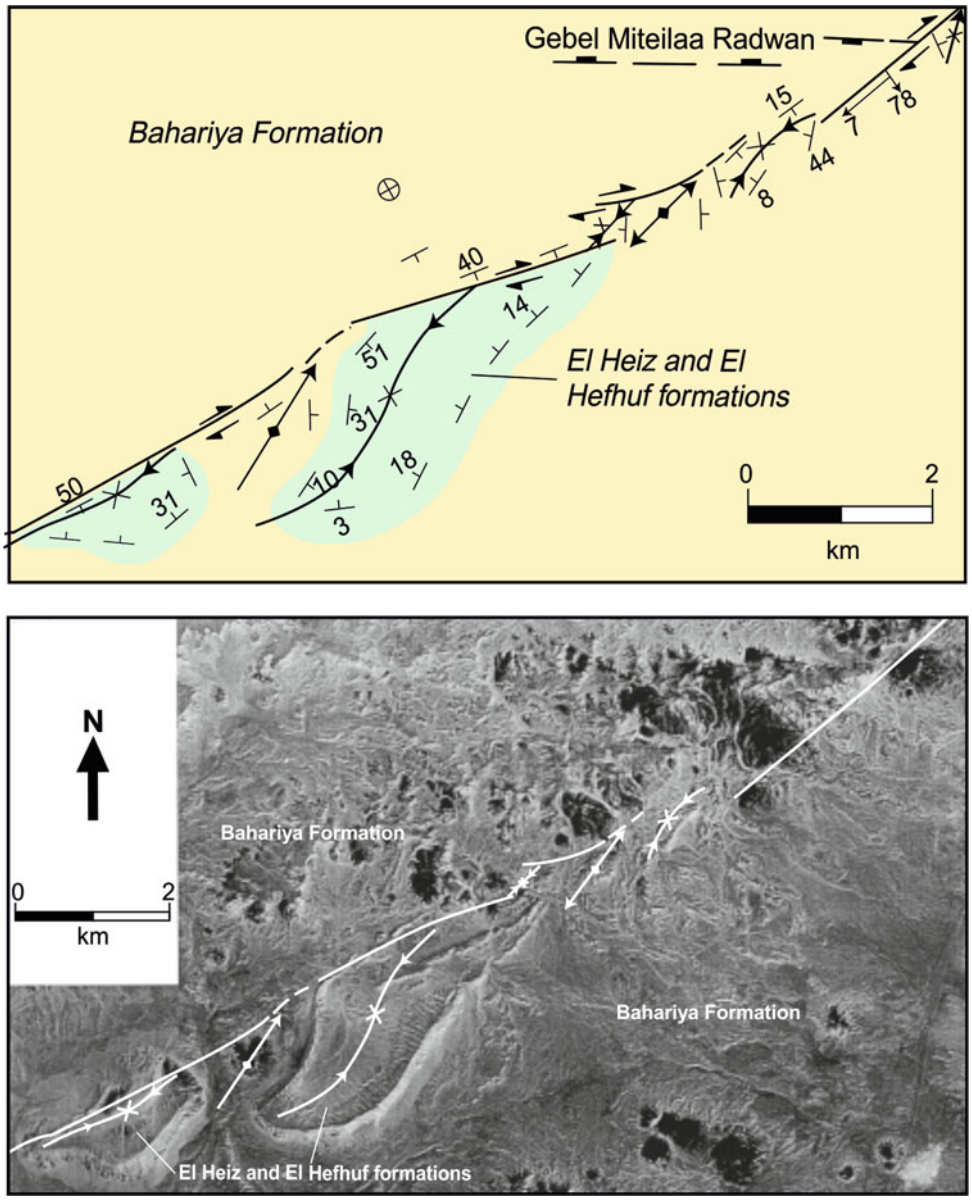

Fig. 7.26 Simplified geological map and vertical aerial photograph of Gebel Radwan segment of the Gebel Radwan–El Hefhuf–El Harra Structural Belt showing the NE-oriented, right-stepping en echelon folds associated with the right-lateral strike-slip faults, after Moustafa et al. (2003). See Fig. 7.25 for location

to ENE-WSW and N-S faults of Issawi and Ghobrial were assigned normal slip at these times. It was not until the 1981 Aswan earthquake that horizontal slip was noticed on these faults by Woodward-Clyde Consultants (1985); right-lateral slip on the E-W faults and left-lateral slip on the N-S faults. Guiraud et al. (1985) considered the E-W faults to be part of their Guinean–Nubian E-W trending lineaments that extend across Africa. Guiraud and Bosworth (1999) stated that these faults were deformed by dextral transpression in Late Santonian and Late Eocene times. Detailed structural studies of the E-W faults by El Etr et al. (1982), Abdeen (2001), Sakran and Said (2018), and Hamimi et al. (2018) also confirm right-lateral slip. Seismicity network in Aswan region indicates recent activity on these faults (Mekkawi et al. 2005; Telesca et al. 2012; Hussein et al. 2013; Meghraoui et al. 2016; and Abdelazim et al. 2016).

Perhaps the most detailed structural study of the E-W and N-S faults of the south Western Desert is that of Sakran and Said (2018). They studied three of the E-W faults (Kalabsha, Seyial and Abu Bayan) and indicated that they are characterized by horizontal slickenside lineations, ENE to NE oriented folds making acute angles with the faults, horizontally-offset folds, and releasing and restraining bends. They also studied the N-S faults of the eastern part of Sinn El Kaddab Plateau and noted that they have narrow widths and are less complex compared to the E-W right-lateral faults. These N-S faults consist of right stepping en-echelon segments with contractional step-overs in between. They are

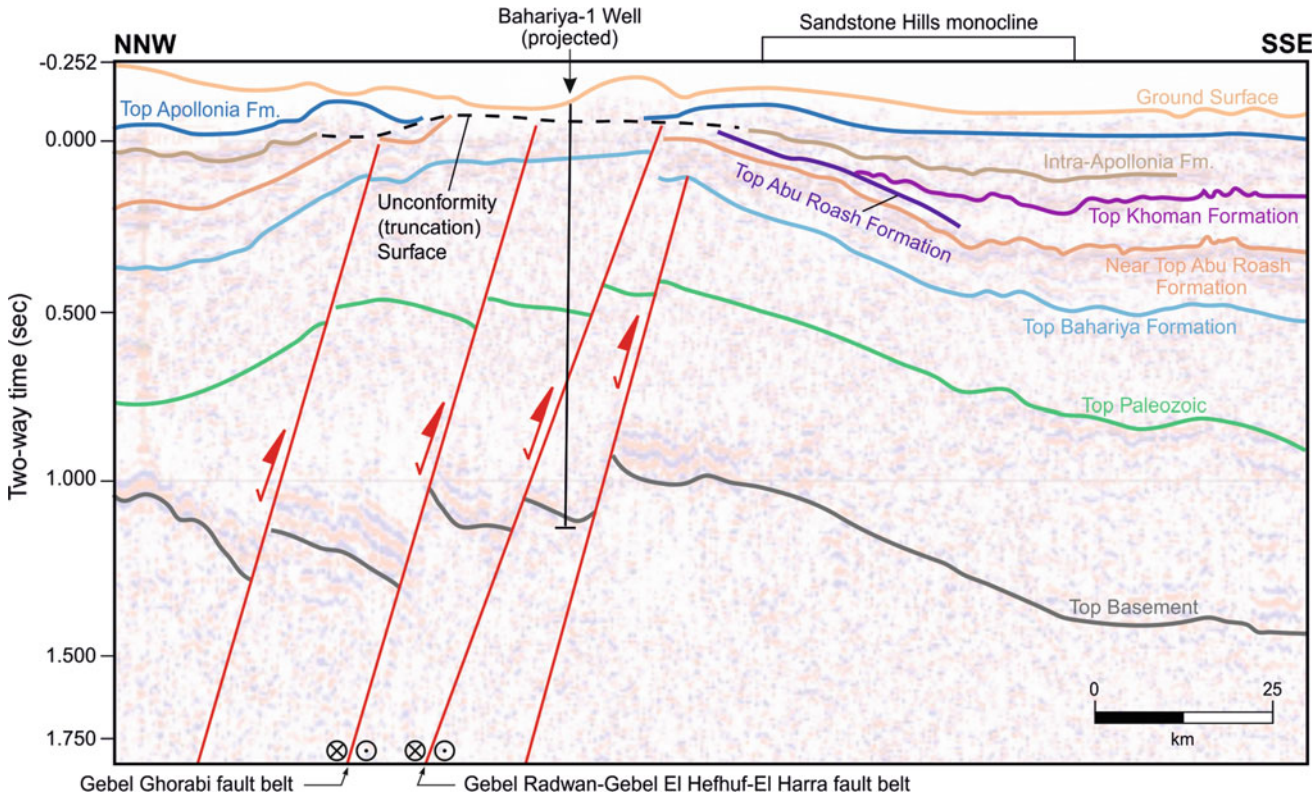

Fig. 7.27 Seismic section east of the Bahariya depression showing Jurassic-Early Cretaceous normal slip on the main faults of the Bahariya depression and reactivation by oblique-slip reverse movement during the Late Cretaceous-Early Tertiary basin inversion, after Moustafa et al. (2003)

also associated with NE to NNE oriented en echelon folds that are mostly dissected and horizontally displaced by the fault segments. Integration of surface geological and subsurface (seismic reflection and borehole) data by Sakran and Said (2018) indicated that the strike-slip faults of Sinn El Kaddab area show up on the seismic reflection data with nearly vertical attitude as well as negative and positive flower structures. The Upper Cretaceous rocks at the crestal areas of the positive flower structures are unconformably overlain by Upper Paleocene rocks while the Lower Paleocene rocks onlap the flanks of the flower structure indicating that the deformation took place by dextral transpression on the E-W faults and sinistral simple shearing on the N-S faults during the Late Cretaceous—Middle Eocene time.

7.2.3.3 Tethyan Convergence Affecting the Northernmost Areas of Egypt

Continued convergence of the African and Eurasian Plates exerted compression on the northernmost (offshore) areas of Egypt in Miocene to Recent times. This is evident in several areas as follows.

A. Reactivation of the Rosetta Fault

Tethyan convergence leading to positive structural inversion is evident in the areas lying north of the inverted basins of the northern Western Desert and onshore and offshore northern Sinai. The Rosetta Fault, on the western side of the Nile Cone, shows Tertiary convergent deformation represented by reverse slip and formation of a hanging wall anticline. Rosetta Fault is a major NE-SW oriented fault extending for ~160 km on the western side of the Nile Cone with steep NW dip (Fig. 7.2). Abd El-Fattah et al. (2018) mapped the fault at different stratigraphic levels on 3D seismic data and recognized a hanging wall asymmetric anticline affecting the top Serravallian and older rocks (Fig. 7.30). By restoring post-Messinian normal slip on the Rosetta Fault it displays reverse slip and the anticline is a hanging wall anticline related to the reverse movement. The crest of this anticline was breached during the Messinian Salinity Crisis that led to dramatic fall of the Mediterranean sea level. Abd El-Fattah et al. (2018) attributed the reverse slip and associated asymmetric hanging wall anticline to Late Cretaceous-Tertiary compressive deformation resulting from convergence of the African and Eurasian Plates.

As the Rosetta Fault is sub-parallel to other inverted faults in northern Egypt and shows similar structural style, it

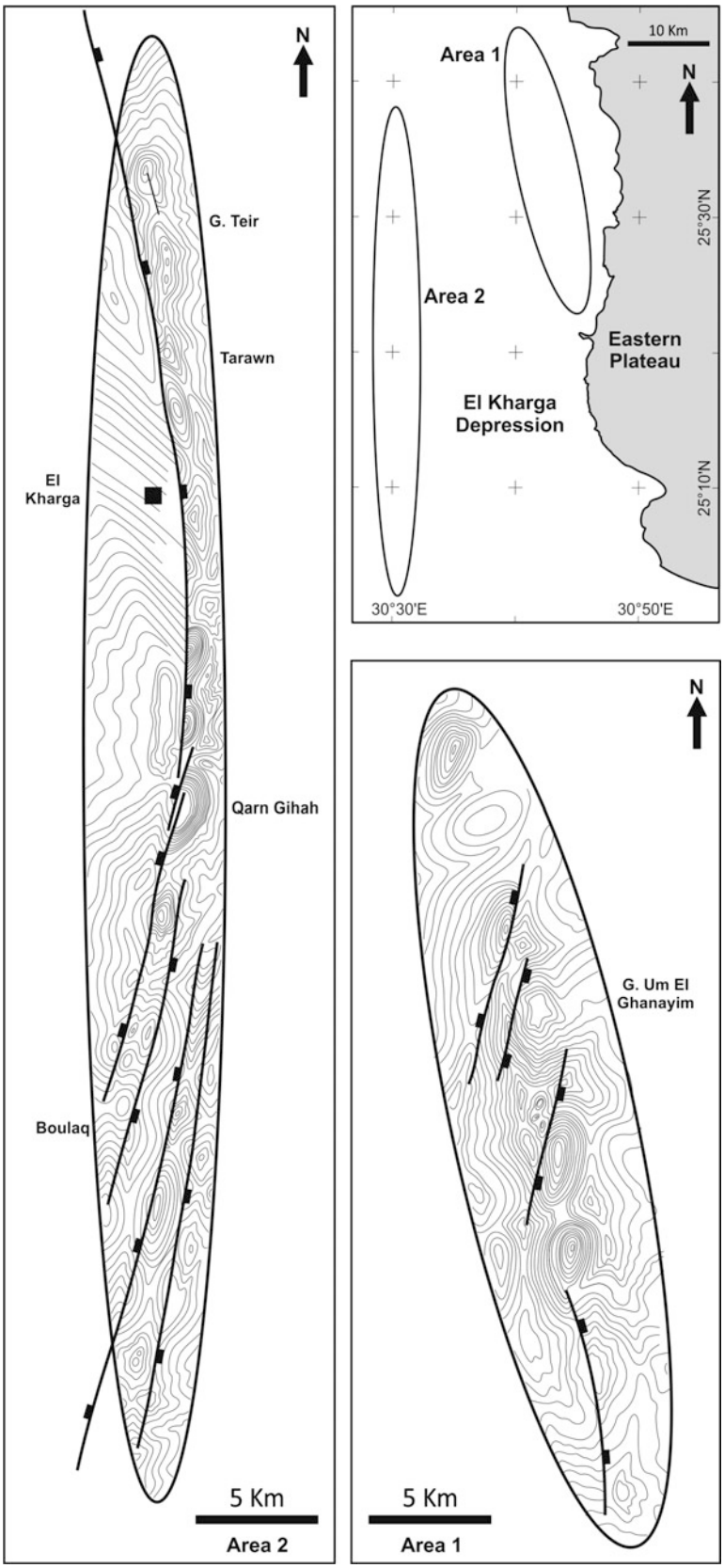

Fig. 7.28 Top Upper Cretaceous phosphate Formation structure contour maps of two areas in the northern part of El Kharga Depression (after Ghobrial 1967). Note the N-S to NNE-SSW oriented left-stepping en echelon folds and faults. See Fig. 7.6 for location

Fig. 7.29 Google Earth Image (©2013 DigitalGlobe) showing small-scale folds associated with an ENE-WSW oriented right-lateral strike-slip fault in the southern Western Desert. See Fig. 7.6 for location

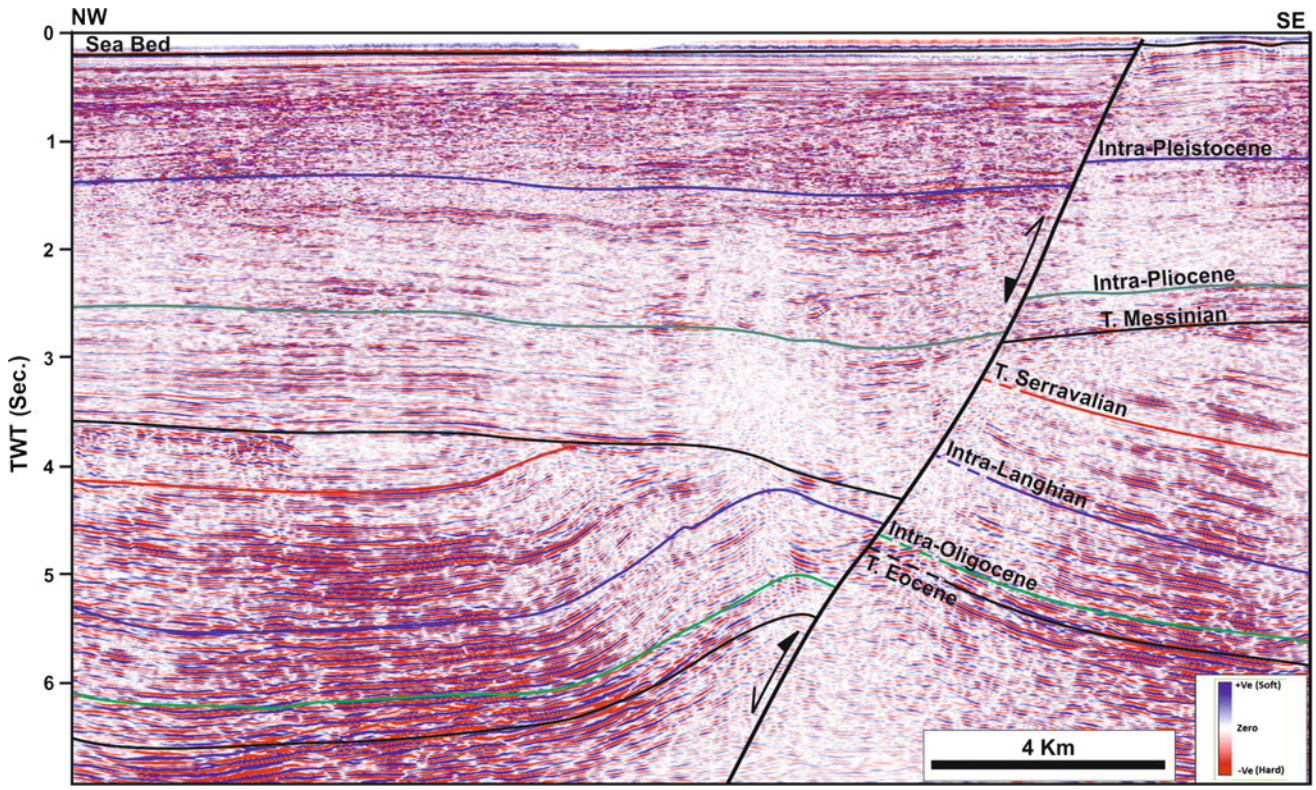

Fig. 7.30 Seismic section across the southern part of Rosetta Fault showing a hanging wall asymmetric anticline affecting the Tortonian and older rocks (after Abd El-Fattah et al. 2018). See Fig. 7.31 for location

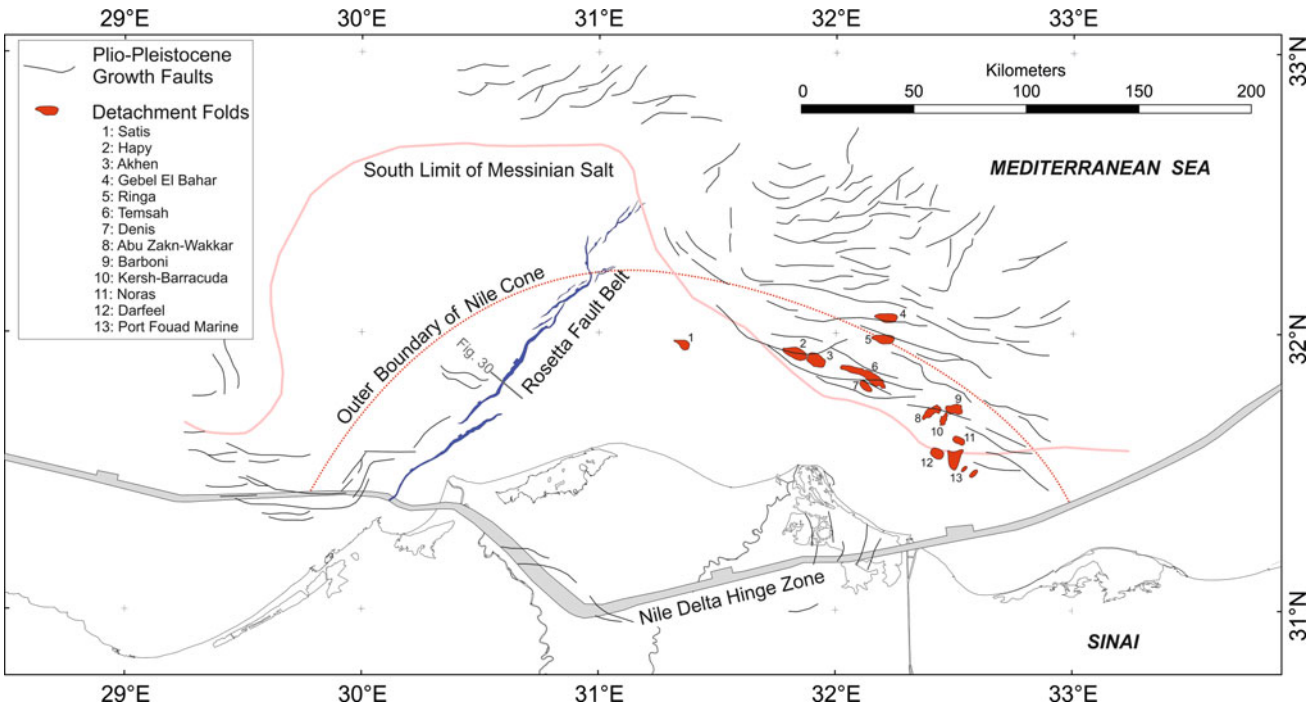

Fig. 7.31 Simplified structural map of the offshore Nile Delta area showing the Rosetta Fault (after Abd El-Fattah et al. 2018), Miocene detachment folds (after EGPC 1994; Kamel et al. 1998; Abdel Aal et al. 2001), and Plio-Pleistocene growth faults (after Tingay et al. 2011)

is believed that it probably had the same history of the inverted Jurassic faults of the onshore area. It is quite probable that the Rosetta Fault was formed as a normal fault during the Tethyan rifting phase before it was later affected by reverse slip and positive inversion at post-Serravallian time. It is unfortunate that Jurassic rocks lie deep below the resolution of the seismic data. Based on detailed integration and modeling of the gravity, magnetic, seismic refraction and seismic reflection data, as well as onshore fault trends, and regional arguments for plate tectonic reconstructions; Longacre et al. (2007) considered that the Rosetta Fault lies perpendicular to the Triassic extension direction and represents one of the rift-parallel faults of the East Mediterranean Basin.

Continued convergence of the African and Eurasian Plates led to left-lateral slip on the Rosetta fault at pre-Tortonian (Sehim et al. 2002) or Messinian time (Abd El-Fattah 2018). Abd El-Fattah (2018) mapped a swarm of NNW-SSE oriented normal faults affecting the Messinian sediments close to a fault bend at the northern portion of the Rosetta fault (Fig. 7.31), perhaps indicating that it is a releasing bend associated with left-lateral slip on the Rosetta Fault at Messinian time. Later (Pliocene and younger) movement of the Rosetta Fault shows predominantly normal slip.

B. Detachment Folds in the Outer Part of the Nile Cone

A number of NW to WNW oriented folds affect the Oligo-Miocene sedimentary section underlying the Messinian salt in the eastern part of the Nile Cone (Fig. 7.31). These folds have large dimensions (up to 25 km long) and are relatively tight and separated from each other by wider synclinal areas. Seismic reflection data indicate that the anticlines and synclines have rather box shapes in some cases and are believed to have been formed by detachment on the underlying Lower Oligocene shales. The detachment anticlines include Hapy, Akhen, Temsah, Gebel El Bahar, Ringa, Denis, Abu Zakn-Wakkar, Barboni, Kersh-Barracuda, Noras, Darfeel, and Port Fouad Marine Anticlines (Fig. 7.31). They indicate shortening direction different from the Late Cretaceous-Early Tertiary NW-SE Tethyan compressive stress. This might either reflect a local change in the stress direction in that area at Miocene (Messinian) time, or the effect of a deep-seated structure controlling the direction of detachment of the Oligocene-Miocene sediments. Several studies refer to an old WNW fault trend (referred to as the Misqaf or Temsah Fault) underneath the area affected by these folds although seismic reflection data do not show this fault. Despite that, compression leading to reactivation of older faults was reported by Dolson et al.

(2014) who show that the Habbar Anticline is a hanging-wall anticline of a reverse fault in the Oligocene section and Hussein (2013) proves that this fault is a positively inverted Oligocene-age normal fault.

C. Pliocene-Holocene Growth Faults

Growth faults dissecting the Pliocene-Holocene sediments in the outer part of the Nile Cone are well recognized on seismic reflection data. These structures are limited to the areal distribution of the Messinian salt and have WNW, E-W, and ENE orientations and northward slip (Fig. 7.31). It is worth mentioning that growth faults dissect the sediments overlying the Messinian salt in the area affected by the Miocene detachment folds. High-resolution seismic reflection data show that the Pliocene-Recent sediments overlying the northeastern flanks of the detachment folds are affected by growth faults. Continued detachment of the sedimentary section overlying the Lower Oligocene shales leads to increase in the fold amplitude allowing the Pliocene-Recent sediments overlying the Messinian salt in these flanks to detach northward by growth faulting. At the nose of each Oligo-Miocene detachment fold, the overlying growth faults change orientation to N-S.

7.3 Tectonic Evolution

The three phases of Mesozoic-Cenozoic deformation discussed in the previous sections are related to the movement of the Afro-Arabian Plate (later split into African and Arabian Plates) with respect to the surrounding (Eurasian and South American) plates. Pre-existing structures also played a role in the structural deformation where they controlled the structural trends or caused local changes in the stress directions.

The Tethyan rifting phase is attributed to the divergent movement between the Afro-Arabian and Eurasian Plates leading to opening of the Neotethys. This divergent movement started at the Late Triassic (Robertson and Dixon 1984; Dercourt et al. 1986; May 1991). Borehole and seismic data indicate that deposition of syn-rift sequences in the resulting basins continued almost to the end of the Early Cretaceous. Some small continental blocks were separated from the Afro-Arabian Plate during this extensional phase and started drifting to the north or northwest. The closest block to the African margin at present time is the Eratosthenes continental block (Ben Avraham et al. 2006). Onshore extensional basins formed during this phase in the southern passive margin of Neotethys are oriented NE to ENE indicating NW divergence of the major plates. Integration of gravity, magnetic, seismic refraction, and seismic reflection data from the Mediterranean offshore area of Egypt led Longacre et al. (2007) to propose NW extension direction of the East Mediterranean Basin during the Triassic, consistent with the Levant margin and offshore northern Sinai. According to those authors, rift-parallel fault in the East Mediterranean are oriented NE-SW to NNE-SSW whereas NW-SE oriented faults represent the transform boundaries. To these transforms belongs the NW-SE oriented fault bounding the offshore area of the northern Western Desert. This transform fault forms the boundary between the oceanic crust of the southern Tethys (in the offshore area) and the mildly-extended continental crust of northern Egypt (Fig. 7.32a). According to Cowie and Kusznir (2012), continental extension and seafloor spreading resulted in the formation of oceanic crust in the Herodotus Basin whereas the Levant Basin and areas underneath the Nile Cone and the Egyptian onshore areas have thinned continental crust. Mesozoic isopach maps of the Palmyride Trough in Syria (Brew et al. 2001) show similarity to the Tethyan extensional basins of northern Egypt.

Another rifting phase formed NW-SE oriented basins during the Cretaceous Period. The Kom Ombo, Asyut, Beni Sueif and Abu Gharadig Basins (Fig. 7.2) belong to this extensional phase. Basin fill indicates that extension continued almost during all of the Cretaceous and extended to the Early Tertiary. Pre-existing faults locally changed the general trend of some of these basins such as the Abu Gharadig Basin that is controlled by pre-existing E-W faults and dominated by NW-SE oriented normal faults making it an oblique rift. Other NW-SE oriented Cretaceous-Early Tertiary rift basins were also formed in the Afro-Arabian Plate. These include the Sirte Basin in Libya (Rusk 2001), the Sudan Rift System (Bahr El Arab, Abu Gabra/Muglad, White Nile, Blue Nile, and Atbara rift basins; Bosworth 1992; McHargue et al. 1992), the Azrag Basin in Jordan (Beydoun et al. 1994), and the Euphrates Graben in Syria (Brew et al. 2001). The NW-SE orientation of these basins reflects NE-SW extension which may have resulted from opening of the South Atlantic and the divergent movement between Afro-Arabia and South America during the breakup of Gondwana.

The third phase of deformation was compressional leading to closure of the Neotethys due to convergence of the Afro-Arabian and Eurasian Plates. Surface and subsurface data indicate that this phase started at Late Santonian time in Egypt where a marked angular unconformity is obvious between the Campanian and Santonian sediments especially at the structural highs (Moustafa 1988, 2002). This phase of deformation led to inversion of the Tethyan extensional basins of northern Egypt as well as reactivation of Tethyan faults in southern Egypt. The direction of compression during this compressional phase was NW or WNW (Smith 1971; Eyal and Reches 1983). As shown in the previous

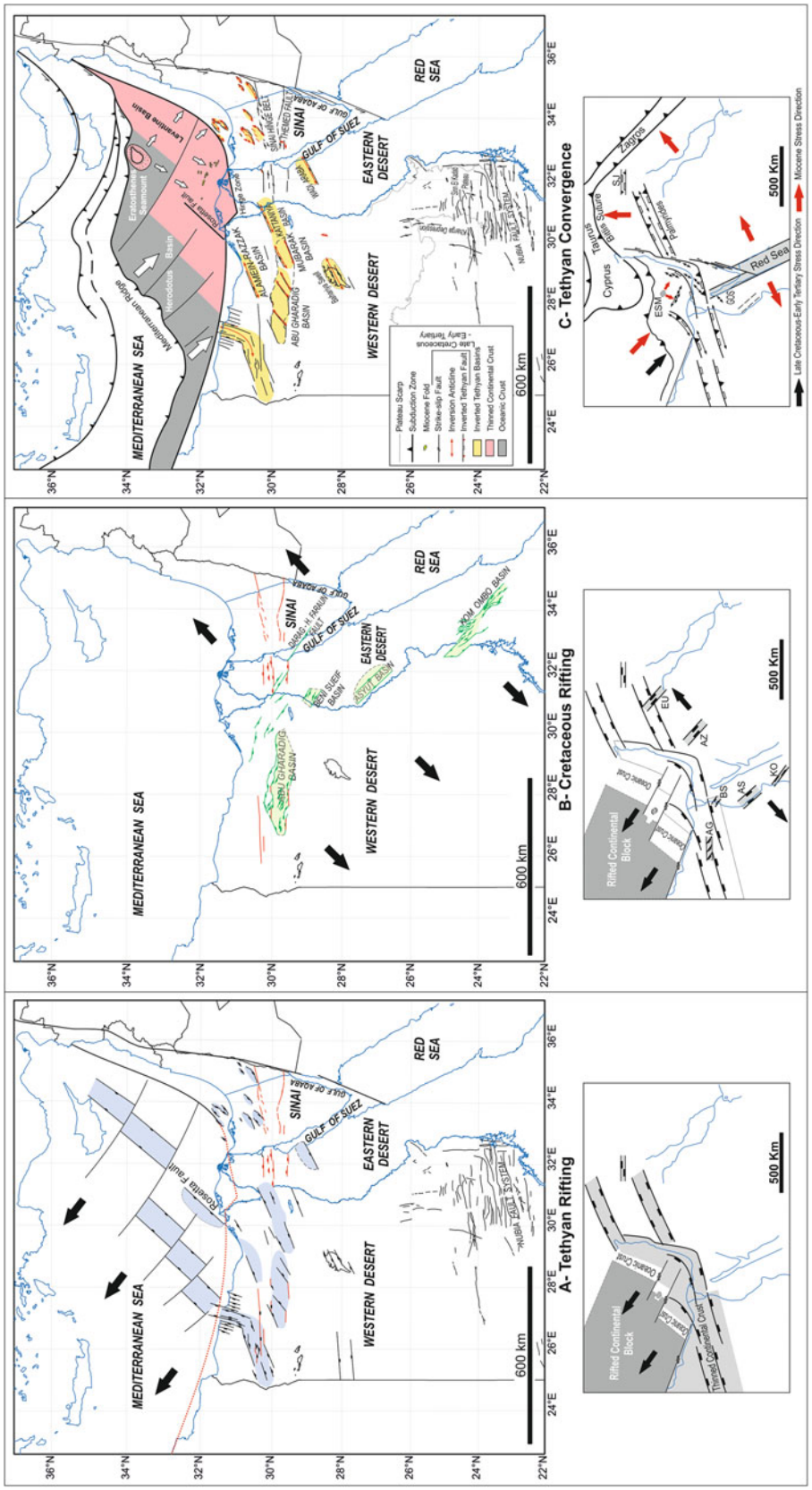

Fig. 7.32 Mesozoic-Cenozoic tectonic evolution of Egypt. Cartoons showing relative plate movements are shown below each map. **a** Tethyan rifting phase (Middle/Late Triassic—end of Early Cretaceous) related to NW drift of Eurasia and continental blocks fragmented from Afro-Arabia. This phase also included reactivation of old structural fabrics represented by red lines. **b** Cretaceous-Early Tertiary rifting phase leading to opening of NW-SE oriented rifts, probably related to opening of the South Atlantic. **c** Tethyan convergence phase (Late Cretaceous-Recent) related to convergent movement between Afro-Arabia and Eurasia and closure of the Neotethys. Stress directions change with time and location, Late Cretaceous compressive stress in the NW-SE direction changed in Miocene time to N-S at the north Arabian promontory due to collision with Eurasia at the Bitlis suture. Local changes in the stress directions are clear in the East Mediterranean due to southward movement of the Eratosthenes Seamount as it resists subduction underneath Eurasia. Abbreviations stand for: Abu Gharadig Basin (AG), Asyut Basin (AS), Azrag Basin (AZ), Beni Sueif Basin (BS), Euphrates Basin (EU), Kom Ombo Basin (KO), Eratosthenes Seamount (ESM), Gulf of Suez rift (GOS), and Sinjar Trough (SJ)

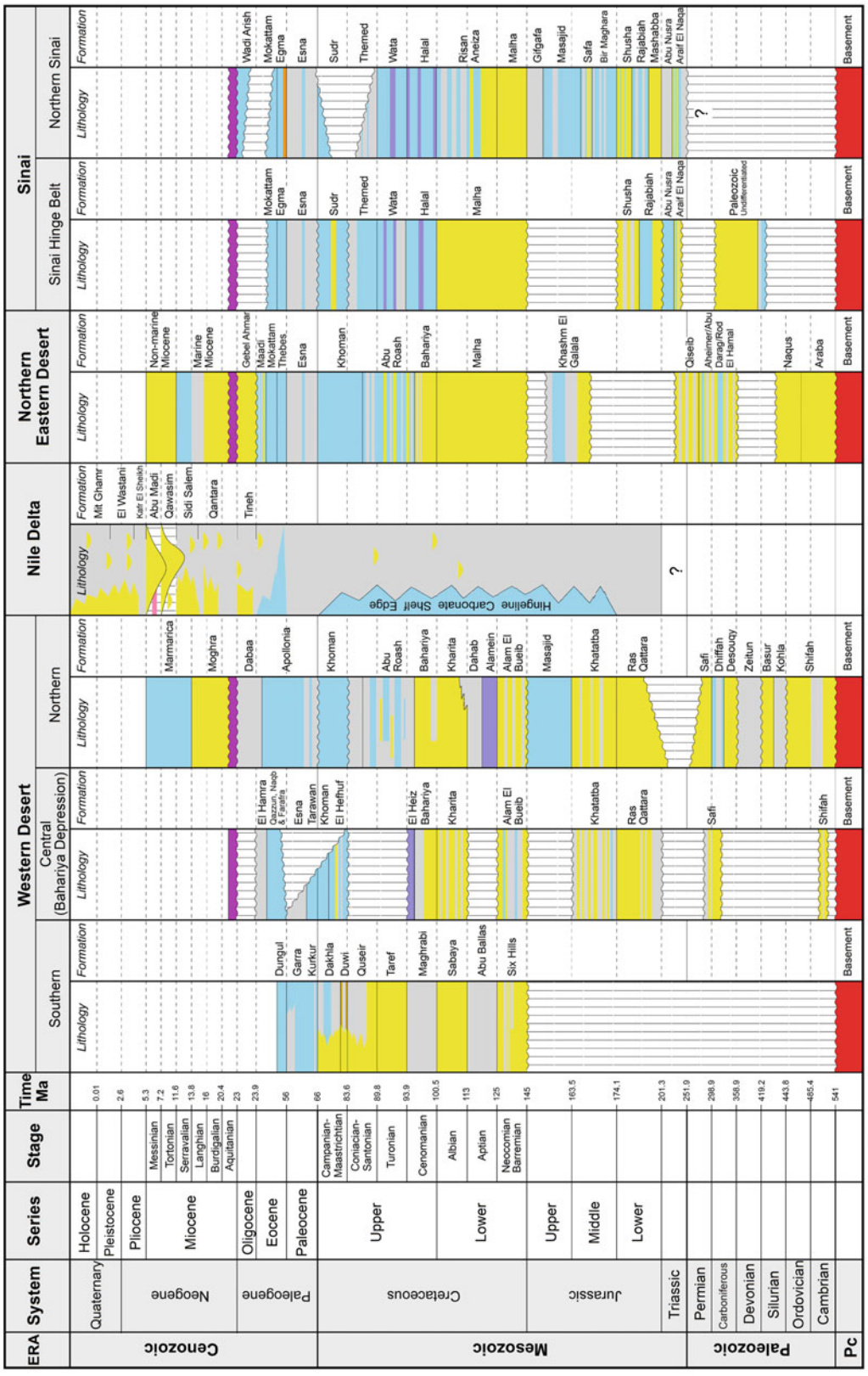

Fig. 7.33 Stratigraphic sections of the areas discussed in this chapter compiled from different sources as follows: southern Western Desert (Sakran and Said 2018); Bahariya depression (Moustafa et al. 2003); northern Western Desert (Moustafa 2008; Bosworth et al. 2015a); Nile Delta (Dolson et al. 2014; Abd El-Fattah 2018); northern Eastern Desert (Sadek 1926; Said 1962; Abdallah and Adindani 1963; Abdallah et al. 1963; Abdallah 1992; Salem and Sehim 2017); Sinai Hinge belt (Moustafa et al. 2014); northern Sinai (Jenkins 1990; Moustafa 2014). Time scale is from Cohen et al. 2013

sections, detailed mapping of the inversion structures (e.g. Halal and Maghara inverted basins) indicates that the deformation was transpressive with a minor component of dextral slip, perhaps providing evidence that the direction of convergence was WNW-ESE.

Onshore inverted structures in Egypt show strong evidence of continued convergence during the Tertiary up to the Miocene. The effect of Miocene and younger plate convergence can be seen in the offshore areas leading to pronounced Miocene-Recent NW-SE oriented folds in the NE side of the Nile Cone and NE-SW oriented folds in the Herodotus Basin (Loncke et al. 2006). Present-day folding of the seafloor sediments is obvious in the area between the Rosetta fault and the Mediterranean Ridge (see Ross and Uchupi 1977; Huguen et al. 2001) where the folds are oriented NE-SW and show SE vergence indicating SE compression. The change in the direction of compression (and hence the fold orientations) in the eastern part of the Nile Cone and west of it (Fig. 7.32c) is perhaps related to the presence of rifted continental fragments resisting subduction (e.g. Eratosthenes Seamount) causing local shortening and change in the stress directions. The northern and western areas of the Nile Cone as well as the Herodotus Basin show the effect of present-day SE compression. Also, the area east of the Eratosthenes Seamount (Levant Basin) is deformed by NE-SW oriented folds (Tari et al. 2012). On the other hand, the area south of Eratosthenes Seamount was affected by SW oriented compression forming NW-SE oriented folds (Fig. 7.32c). Such local change in the direction of the compressive stress is related to the local effect of the Eratosthenes Seamount and the presence of ductile units in the stratigraphic section causing detachment, e.g. the Lower Oligocene shales and the Messinian evaporites. The present-day stress orientations deduced from borehole breakouts and drilling induced fractures are different in the rock sections overlying and underlying the Messinian evaporites in the eastern Nile Delta area (Tingay et al. 2011). σHmax in the sediments underlying the Messinian evaporites or with no evaporites is oriented WNW-ESE in the eastern Nile Delta. However, σHmax in the sediments overlying the evaporites is oriented NNE-SSW. This 90° variation in the present-day σHmax above and below the Messinian evaporites indicates that the evaporites act as a major mechanical detachment zone. Present-day σHmax in the western Nile Delta as indicated by earthquakes is oriented NW-SE (Korrat et al. 2005; Costantinescu et al. 1966; and Abu El Nader et al. 2013). On a regional scale, present-day stress directions change due to the irregular shape of the convergent plate boundary, e.g. N-S compression at the north Arabian promontory due to collision with Eurasia at the Bitlis Suture compared to NW-SE compression of the SE Mediterranean (Fig. 7.32c).

Acknowledgements I would like to thank Shell Egypt for giving permission to use the seismic section of Abu Gharadig Basin (Fig. 7.4), John Dolson for providing me with the seismic section in Fig. 7.5, and Ali Bakr for providing me with the seismic sections in Figs. 7.17 and 7.18. Mediterra Energy Corporation and Kom Ombo Petroleum Company (KOPCO) are also thanked for giving permission to use seismic section of Al Baraka oil field (Kom Ombo Basin). Peer-review by Zakaria Hamimi and constructive comments by Sebastian Luening and John Dolson helped improve the manuscript.

References

Abdallah AM (1992) Paleozoic rocks in Egypt. Technika Poszukiwan Geologicznych Geosynoptyka i Geotermia 3/92:1–12

Abdallah AM, Adindani A (1963) Stratigraphy of upper Paleozoic rocks, western side of Gulf of Suez, Geol. Surv. Egypt, Paper 25, 18 pp

Abdallah AM, El-Adindani A, Fahmi N (1963) Stratigraphy of the Lower Mesozoic rocks, western side of the Gulf of Suez, Geol. Surv. Egypt, Paper 27, 23 pp

Abd-Allah MA, Moustafa AR, Hashem WA (2004) Structural characteristics and analysis of the Gebel El Halal fold, Northeast Sinai, Egypt. MERC, Ain Shams Univ Earth Sci Ser 18:1–26

Abdeen MM (2001) Active dextral wrenching on Kalabsha fault, Southern Egypt. Egypt J Remote Sens Space Sci 4:79–92

Abdel Aal A, Moustafa AR (1988) Structural framework of the Abu Gharadig basin, Western Desert, Egypt. In: Proceedings of 9th EGPC exploration and production conference (Cairo), vol 2, pp 23–50

Abdel Aal A, El Barkooky A, Gerrits M, Meyer H, Schwander M, Zaki H (2001) Tectonic evolution of the Eastern Mediterranean Basin and its significance for the hydrocarbon prospectivity of the Nile Delta deepwater area, vol 6. GeoArabia, pp 363–384

Abdelazim M, Samir A, Abu El-Nader I, Badawy A, Hussein H (2016) Seismicity and focal mechanisms of earthquakes in Egypt from 2004–2011. Natl Res Inst Astron Geophys (NRIAG) J Astron Geophys 5:393–402

Abd El-Aziz M, Moustafa AR, Said SE (1998) Impact of basin inversion on hydrocarbon habitat in the Qarun Concession, Western Desert, Egypt. In: Proceedings of 14th EGPC exploration and production conference, Cairo, vol 1, pp 139–155

Abd El-Fattah BK (2018) Structural analysis of the Rosetta Fault, offshore Nile Delta, Egypt. Unpublished MSc thesis, Ain Shams University, 155 pp

Abd El-Fattah BK, Yousef M, Moustafa AR (2018) 2D Structural restoration of the Rosetta fault system, offshore western Nile Delta, Mediterranean basin, Egypt. Egypt J Appl Geophys 17:83–98

Abdelhady A, Darwish M, El Araby A, Hassouba A (2016) Geochemical characterization of Al Baraka oil in Komombo rift basin, Egypt. Egypt J Geol 60:191–205

Abdel Hakim MMF (2017) Geological modeling of the Middle Jurassic reservoirs in East Tiba basin, northern Western Desert, Egypt. MSc thesis, Cairo University, 100 pp

Abou-Khadrah AM, Darwish M, El-Azabi M (1994) Contribution to the faulted-down Eocene limestones of the southern Galala Plateau "St. Paul area", Gulf of Suez, Egypt. In: Proceedings of 2nd international conference on the geology of the Arab World, Cairo University, pp 505–527

Abdel Khalek ML, El Sharkawi MA, Darwish M, Hagras M, Sehim A (1989) Structural history of Abu Roash district, Western Desert, Egypt. J Afr Earth Sci 9:435–443

Abdel Khalek ML, Abdel Wahed N, Sehim AA (1993) Wrench deformation and tectonic setting of the northwestern part of the Gulf of Aqaba. Geol Soc Egypt Spec Publ 1:409–444

Abu El-Nader IF, El Gabry MN, Hussein HM, Hassan HM, Elshrkawy A (2013) Source characteristics of the Egyptian continental margin earthquake, 19 October 2012. Seismol Res Lett 84:1062–1065

Abul-Nasr RA (1986) Syntectonic slope deposit at Gebel Hammam Faraun, Sinai (Egypt) (abs). In: Proceedings of 59th annual meeting of the South Carolina Academy of Science, vol 48. Bull. South Carolina Academy of Science, pp 100–101

Abul-Nasr RA, Thunell RC (1987) Eocene eustatic sea level changes: evidence from western Sinai, Egypt. Paleogeogr Paleoclimatol Paleoecol 58:1–9

Afifi AS, Moustafa AR, Helmy HM (2016) Fault block rotation and footwall erosion in the southern Suez Rift: Implications for hydrocarbon exploration. J Marine Pet Geol 76:377–396

Al-Ahwani MM (1982) Geological and sedimentological studies of Gebel Shabrawet area, Suez Canal district—Egypt. Ann Geol Survey Egypt 12:305–381

Al-Far DA (1966) Geology and coal deposits of Gebel El Maghara (north Sinai). Geological Survey of Egypt, Paper no. 37, 59 pp

Ayyad MH, Darwish M, Sehim A (1998) Introducing a new structural model for north Sinai with its significance to petroleum exploration. In: Proceedings of the 14th petroleum conference, Cairo, Egypt, vol 1. Egyptian General Petroleum Corporation, Cairo, pp 101–117

Bakr A (2010) Messages from the deepest oil discovered in the WD of Egypt. AAPG Western Desert Geotechnology Workshop (Cairo)

Ball J (1900) Kharga oasis, its topography and geology. Egyptian Survey Department, Cairo, 116 pp

Ball J, Beadnell HJL (1903) Bahariya oasis: its topography and geology. Egyptian Survey Department, Cairo, 84 pp

Bartov Y (1974) A structural and paleogeographical study of the central Sinai faults and domes. PhD thesis, Hebrew University, Jerusalem (in Hebrew)

Bartov Y, Lewy Z, Steinitz G, Zak I (1980) Mesozoic and Tertiary stratigraphy, paleogeography and structural history of the Gebel Areif en Naqa area, eastern Sinai. Isr J Earth Sci 29:114–139

Beadnell HJL (1909) An Egyptian oasis: an account of the oasis of Kharga in the Libyan Desert. Murray, London, 248 pp

Ben-Avraham Z, Woodside J, Lodolo E, Gardosh M, Grasso M, Camerlenghi A, Vai GB (2006) Eastern Mediterranean basin systems. In: Gee DG, Stephenson RA (eds) European lithosphere dynamics, vol 32. Geological Society, London, Memoirs, pp 263–279

Bevan TG, Moustafa AR (2012) Inverted rift-basins of Northern Egypt. In: Roberts DG, Bally AW (eds) Regional geology and tectonics: phanerozoic rift systems and sedimentary basins, vol 1B. Elsevier, pp 483–507

Beydoun ZR, Futyan ARI, Jawzi AH (1994) Jordan revisited: hydrocarbons habitat and potential. J Pet Geol 17:177–194

Bosworth W (1992) Mesozoic and early Tertiary rift tectonics in East Africa. In: Ebinger CJ, Gupta HK, Nyambok IO (eds) Seismology and related sciences in Africa. Tectonophysics, vol 209, pp 115–137

Bosworth W, McClay K (2001) Structural and stratigraphic evolution of the Gulf of Suez rift, Egypt: A synthesis. In: Zeigler PA, Cavazza W, Robertson AHF, Crasquin-Soleau S (eds) Peri-Tethyan rift/wrench basins and passive margins: peri-tethys memoir 6, vol 186. Memoires du Museum National d'Histoire Naturelle de Paris, pp 567–606

Bosworth W, Guiraud R, Kessler LG (1999) Late Cretaceous (Ca. 84 Ma) compressive deformation of the stable platform of northeast Africa (Egypt): Far-field stress effects of the "Santonian event" and origin of the Syrian arc deformation belt. Geology 27:633–636

Bosworth W, Drummond M, Abrams M, Thompson M (2015a) Jurassic rift initiation source rock in the Western Desert, Egypt—relevance to exploration in other continental rift systems. In: Petroleum systems in rift basins, pp 615–650

Bosworth W, Stockli DF, Helgeson DE (2015b) Integrated outcrop, 3D seismic, and geochronologic interpretation of Red Sea dike-related deformation in the Western Desert, Egypt—the role of the 23 Ma Cairo "mini-plume". J Afr Earth Sci 109:107–119

Bowles EO (1945) Geological report on the south west Gebel Yelleg anticline, central Sinai. Standard Oil Co., Egypt Internal Report

Brew G, Barazangi M, Al-Maleh AK, Sawaf T (2001) Tectonic and geologic evolution of Syria. GeoArabia 6:573–616

Cohen KM, Finney SM, Gibbard PL, Fan JX (2013) The ICS International Chronostratigraphic Chart. Episodes 36:199–204. http://www.episodes.org

Costantinescu L, Ruprecrtova L, Enescu D (1966) Mediterranean-Alpine earthquake mechanisms and their seismotectonic implications. Geophys J R Astron Soc 10:347–368

Cowie L, Kusznir N (2012) Mapping crustal thickness and oceanic lithosphere distribution in the Eastern Mediterranean using gravity inversion. Pet Geosci 18:373–380

Deibis S (1982) Abu Qir Bay, a potential gas province area, offshore Mediterranean, Egypt. In: Proceedings of EGPC 6th exploration seminar, vol 1, pp 50–65

Dercourt J, Zonenshain LP, Ricou LE, Kazmin VG, Le Pichon X, Knipper AL, Grandjacquet C, Sbortshikov IM, Geyssant J, Lepverier C, Pechersky DV, Boulin J, Sibuet JC, Savostin LP, Sorokhtin D, Westphal M, Bazhenov ML, Laurer JP, Bijou-Duval B (1986) Geological evolution of the Tethys belt from the Atlantic to the Pamirs since the Lias. Tectonophysics 123:241–315

Dolson JC, Shann MV, Hammouda H, Rashed R, Matbouly S (2000) The petroleum potential of Egypt. In: Second Wallace E. Pratt memorial conference "Petroleum provinces of the 21st century", 12–15 Jan 2000, San Diego, California, 37 pp

Dolson JC, Shann MV, Matbouly S, Harwood C, Rashed R, Hammouda H (2001) The petroleum potential of Egypt. In: Downey MW, Threet JC, Morgan WA (eds) Petroleum provinces of the twenty-first century. AAPG Memoir 74, pp 453–482

Dolson JC, Atta M, Blanchard D, Sehim A, Villinski J, Loutit T, Romine K (2014) Egypt's future petroleum resources: a revised look into the 21st century. In: Marlow L, Kendall C, Yose L (eds) Petroleum systems of the Tethyan region. AAPG Memoir 106, pp 143–178

Dupuis C, Aubry M, King C, Knox RW, Berggren WA, Youssef M, Galal WF, Roche M (2011) Genesis and geometry of tilted blocks in the Theban Hills, near Luxor (Upper Egypt). J Afr Earth Sci 61:245–267

EGPC (1992) Western Desert oil and gas fields (A comprehensive overview). Egyptian General Petroleum Corporation, 431 pp

EGPC (1994) Nile Delta & North Sinai fields, discoveries and hydrocarbon potentials (A comprehensive overview). Egyptian General Petroleum Corporation, 387 pp

EGSMA (The Egyptian Geological Survey and Mining Authority) (1981) Geologic map of Egypt, Scale 1:2,000,000

El Etr HA, Yehia MA, Dowidar H (1982) Fault pattern in the south Western Desert of Egypt. Ain Shams Univ Sci Res Ser 2:123–152

El Gazzar AM, Moustafa AR, Bentham P (2016) Structural evolution of the Abu Gharadig field area, Northern Western Desert, Egypt. J Afr Earth Sci 124:340–354

El Ramly MF (1972) A new geological map for the basement rocks in the Eastern and South-Western Deserts of Egypt scale 1:1,000,000. Ann Geol Survey Egypt 2:1–18

El Saadany M (2008) Structural style and tectonic evolution of the central part of the northern Western Desert, Egypt. PhD dissertation, Ain Shams University, 267 pp

El Saadany M, Mahmoud A (2008) Sequential structural restoration of the BED1 field area, Abu Gharadig basin, Western Desert, Egypt. MERC Ain Shams Univ Earth Sci Ser 22:25–46

El-Shaarawy OA, Abdel Aal A, Papazis P (1992) Tectonic setting of the Razzak oil field, northern Western Desert of Egypt. In: Proceedings of 11th EGPC petroleum exploration and production conference, vol 3, pp 310–323

El Shazly EM (1977) The geology of the Egyptian region, In: Nairn AEM, Kanes WH, Stehli FG (eds) The ocean basins and margins, vol 4(A). Plenum Press, pp 379–444

Eyal Y, Reches Z (1983) Tectonic analysis of the Dead Sea rift region since the Late Cretaceous based on mesostructures. Tectonics 2:167–185

Eyal M, Eyal Y, Bartov Y, Steinitz G (1981) The tectonic evolution of the western margin of the Gulf of Elat (Aqaba) rift. Tectonophysics 80:39–66

Fahmy M, Mostafa MM, Darwish M, Saber S (2018) Geological framework of Jurassic sequences, East Tiba sub-basin, North Western Desert, Egypt. Egypt J Geol 62:53–69

Farag IAM, Ismail MM (1955) On the structure of the Wadi Hof area (north-east of Helwan). Bull Inst Desert Egypte 5:179–192

Faris MI (1948) Contribution to the stratigraphy of Abu Rauwash and the history of the Upper Cretaceous in Egypt. Bull Fac Sci Cairo Univ 27:221–239

Faris MI, Abbass HL (1961) The geology of Shabrawet area. Ain Shams Univ Sci Bull 7:37–61

Foley EJ (1942) Geological survey of the west coast of the Gulf of Suez. Standard Oil Co., Egypt Internal Report

Garfunkel Z, Bartov Y (1977) The tectonics of the Suez rift. Geol. Surv. Israel Bull. No. 71, 44 pp

Ghobrial MG (1967) The structural geology of the Kharga Oasis. Geological Survey of Egypt paper no. 43, 39 pp

Guiraud R, Bosworth W (1999) Phanerozoic geodynamic evolution of northeastern Africa and the northwestern Arabian platform. Tectonophysics 315:73–108

Guiraud R, Issawi B, Bellion Y (1985) Les lineaments guineo-nubiens: un trait structural majeur a l'echelle de la plaque africaine. CR Acad Sci Paris 300:17–20

Hamimi Z, Hagag W, Osman R, El-Bialy M, Abu El-Nadr I, Fadel M (2018) The active Kalabsha Fault Zone in Southern Egypt: detecting faulting activity using field-structural data and EMR-technique, and implications for seismic hazard assessment. Arab J Geosci 20 pp

Hantar G (1990) North Western Desert. In: Said R (ed) The geology of Egypt. A.A. Balkema, Rotterdam, pp 293–319

Hashad AH, El Reedy MWM (1979) Geochronology of the anorogenic alkalic rocks, south Eastern Desert, Egypt. Ann Geol Surv Egypt 9:81–101

Hassan AM, Osman RA, Ahmed SM, Afify AM (2015) Sedimentological characteristics of the Late Jurassic-Early Eocene formations at Mitla Pass and its environs, east of Suez city, Egypt. Ann Geol Surv Egypt 32:19–61

Hildebrand N, Shirav M, Freund Z (1974) Structure of the western margin of the Gulf of Elat (Aqaba) in the Wadi El Quseib-Wadi Himur area, Sinai. Isr J Earth Sci 23:117–130

Huguen C, Mascle J, Chaumillon E, Woodside JM, Benkhelil J, Kopf A, Volkonskaia A (2001) Deformational styles of the eastern Mediterranean Ridge and surroundings from combined swath mapping and seismic reflection profiling. Tectonophysics 343:21–47

Hussein HM, Abou Elenean KM, Marzouk IA, Korrat IM, Abu El-Nader IF, Ghazala H, ElGabry MN (2013) Present-day tectonic stress regime in Egypt and surrounding area based on inversion of earthquake focal mechanisms. J Afr Earth Sci 81:1–15

Hussein MAE (2013) 3D Seismic reflection and well log data analysis for reservoir characterization at Oligocene sands, Nile Delta, Egypt. MSc thesis, Ain Shams University, 208 pp

Iskandar F (1946) Geological survey east coast Gulf of Suez, north of latitude 29°00′ north. Standard Oil Co. Egypt Internal Report, 41 pp

Issawi B (1968) The geology of Kurkur Dungul area. Geological Survey of Egypt, paper no. 46, 102 pp

Issawi B (1971) Geology of Darb El-Arbain, Western Desert. In: Said R, Meneisy MY (eds) Annales of the geological survey of Egypt, vol 1, pp 53–92

Jenkins DA (1990) North and Central Sinai. In: Said R (ed) The geology of Egypt. A.A. Balkema, Rotterdam, pp 361–380

Jones TH (1946) Geological survey of the east coast of the Gulf of Suez south of latitude 29°00′ north. Standard Oil Co., Egypt Internal Report, 37 pp

Jux U (1954) Zur Geologie des Kreidegebietes von Abu Roash bei Kairo. Neues Jb Geol Palaontol 100:159–207

Kamel H, Eita T, Sarhan M (1998) Nile Delta hydrocarbon potentiality. In: Proceedings of 14th EGPC petroleum conference, vol 2, pp 485–503

Karaaly H, Fahmy B, Wahdan M, Fahmy M (1994) Structure interpretation of Gemsa SE oil field and its impact on future development. In: Proceedings of 12th EGPC petroleum exploration and production conference, vol 1, pp 189–205

Keeley ML, Dungworth G, Floyd CS, Forbes GA, King C, McGarva RM, Shaw D (1990) The Jurassic System in northern Egypt: I. Regional stratigraphy and implications for hydrocarbon prospectivity. J Petrol Geol 13:397–420

Khalil SM, McClay KR (2002) Extensional fault-related folding, northwestern Red Sea, Egypt. J Struct Geol 24:743–762

Klitzsch E, Groeschke M, Herrmann-Degen W (1990) Wadi Qena: Paleozoic and pre-Campanian Cretaceous strata. In: Said R (ed) The geology of Egypt. A.A. Balkema, Rotterdam, pp 321–327

Korrat IM, El Agami NL, Hussein HM, El-Gabry MN (2005) Seismotectonics of the passive continental margin of Egypt. J Afr Earth Sci 41:145–150

Krenkel E (1925) Geologie Afrikas. Verlag von Gebruder, Berlin, p 461

Letouzey J (1986) Cenozoic paleo-stress pattern in the Alpine Foreland and structural interpretation in a platform basin. Tectonophysics 132:215–231

Loncke L, Gaullier V, Mascle J, Vendeville B, Camera L (2006) The Nile deep-sea fan: an example of interacting sedimentation, salt tectonics, and inherited subsalt paleotopographic features. Marine Pet Geol 23:297–315

Longacre M, Bentham P, Hanbal I, Cotton J, Edwards R (2007) New crustal structure of the Eastern Mediterranean Basin: detailed integration and modeling of gravity, magnetic, seismic refraction, and seismic reflection data. In: EGM 2007 international workshop: innovation in EM, Grav and Mag methods: a new perspective for exploration, Capri, Italy, 15–18 Apr 2007, 4 pp

Luning S, Kuss J, Bachmann M, Marzouk AM, Morsi AM (1998) Sedimentary response to basin inversion: Mid Cretaceous—Early Tertiary pre- to syndeformational deposition at Areif El Naqa anticline (Sinai, Egypt). Facies 38:103–136

Matresu J, Bettazzoli P, Bertello F, Nassar M, Bricchi G, Talaat A, Elsayed A (2016) The Nooros Discovery—offshore Central Nile Delta basin, Egypt; Geological framework and hydrocarbons implications. In: 8th Mediterranean offshore conference and exhibition (MOC 2016), 18 pp

May PR (1991) The Eastern Mediterranean Mesozoic basin: evolution and oil habitat. AAPG Bull 75:1215–32

McHargue TR, Heidrick TL, Livingston JE (1992) Tectonostratigraphic development of the Interior Sudan rifts, Central Africa. In: Ziegler PA (ed) Geodynamics of rifting, vol II. Case history studies on rifts. North and South America and Africa. Tectonophysics 213:187–202

Meghraoui M, Amponsah P, Ayadi A, Ayele A, Ateba B, Bensuleman A, Delvaux D, El Gabry M, Fernandes R, Midzi V, Roos M, Timoulali Y (2016) The seismotectonic map of Africa. Episodes 39:9–18

Mekkawi M, Schnegg P, Arafa-Hamed T, Elathy E (2005) Electrical structure of the tectonically active Kalabsha Fault, Aswan, Egypt. Earth Planet Sci Lett 240:764–773

Meneisy MY (1986) Mesozoic igneous activity in Egypt: Qatar Univ. Bull., v, Sci, p 6

Meneisy MY (1990) Vulcanicity. In: Said R (ed) The geology of Egypt. A.A. Balkema, Rotterdam, pp 157–172

Meneisy MY, Abdel Aal AY (1983) Geochronology of Phanerozoic volcanic rocks in Egypt. Bull Fac Sci Ain Shams Univ 25:163–176

Meneisy MY, El Kalioubi B (1975) Isotopic ages of the volcanic rocks of the Bahariya Oasis. Ann Geol Surv Egypt 5:119–122

Meneisy MY, Kreuzer H (1974a) Potassium-argon ages of Egyptian basaltic rocks. Geol Jb D9:21–31

Meneisy MY, Kreuzer H (1974b) Potassium-argon ages of nepheline syenite ring complexes in Egypt. Geol Jb D9:33–39

Metwalli FI, Pigott JD (2005) Analysis of petroleum system criticals of the Matruh-Shushan Basin, Western Desert, Egypt. Pet Geosci 11:157–178

Moon FW, Sadek H (1921) Topography and geology of north Sinai, Egypt. Petroleum Research Bulletin, Cairo, no. 10, 154 pp

Moussa HE (1987) Geologic studies and genetic correlation of basaltic rocks in west central Sinai. PhD dissertation, Ain Shams University, Egypt, 308 pp

Moustafa AR (1988) Wrench tectonics in the north Western Desert of Egypt (Abu Roash area, Southwest of Cairo). MERC Ain Shams Univ Earth Sci Ser 2:1–16

Moustafa AR (1992) Structural setting of the Sidri-Feiran area, Eastern side of the Suez rift. MERC Ain Shams Univ Earth Sci Ser 6:44–54

Moustafa AR (2002) Structural style and timing of Syrian arc deformation in northern Egypt. AAPG International meeting, Cairo, Oct 2002

Moustafa AR (2004) Geologic maps of the Eastern side of the Suez rift (western Sinai Peninsula), Egypt. AAPG/Datapages, Inc. GIS Series (Geologic maps and cross sections in digital format on CD)

Moustafa AR (2008) Mesozoic-Cenozoic basin evolution in the northern Western Desert of Egypt. In: Salem M, El-Arnauti A, Saleh A (eds) 3rd Symposium on the Sedimentary Basins of Libya (The Geology of East Libya), 3, pp 29–46

Moustafa AR (2010) Structural setting and tectonic evolution of north Sinai folds, Egypt. In: Homberg C, Bachmann M (eds) Evolution of the Levant Margin and Western Arabia Platform since the Mesozoic. Geological Society of London Special Publication 341, pp 37–63

Moustafa AR (2013) Fold-related faults in the Syrian Arc belt of northern Egypt. Marine Pet Geol 48:441–454

Moustafa AR (2014) Structural architecture and tectonic evolution of the Maghara inverted basin, Northern Sinai, Egypt. J Struct Geol 60:80–96

Moustafa AR, Fouda HGA (2014) Structural architecture and tectonic evolution of the Yelleg inverted half graben, northern Sinai, Egypt. Marine Pet Geol 51:286–297

Moustafa AR, Khalil MH (1990) Structural characteristics and tectonic evolution of north Sinai fold belts. In: Said R (ed) The geology of Egypt, Chapter 20. Balkema Publishers, Rotterdam, Netherlands, pp 381–389

Moustafa AR, Khalil MH (1994) Rejuvenation of the Eastern Mediterranean passive continental margin in northern and central Sinai: new data from the Themed Fault. Geol Mag 131:435–448

Moustafa AR, Khalil MH (1995) Superposed deformation in the northern Suez rift, Egypt: relevance to hydrocarbon exploration. J Pet Geol 18:245–266

Moustafa AR, Khalil SM (this book) Structural setting of the gulf of Suez-Northern Red Sea-Gulf of Aqaba region

Moustafa AR, Yousif MS (1990) Two-stage deformation at Gebel El Minsherah, north Sinai. MERC Ain Shams Univ Earth Sci Ser 4:112–122

Moustafa AR, El-Barkooky AN, Mahmoud A, Badran AM, Helal MA, Nour El Din M, Fathy H (2002) Matruh basin: hydrocarbon plays in an inverted Jurassic-Cretaceous rift basin in the northern Western Desert of Egypt. AAPG International meeting, Cairo, Oct 2002, abstract

Moustafa AR, Salama ME, Khalil SM, Fouda HG (2014) Sinai Hinge Zone: a major crustal boundary in NE Africa. J Geol Soc Lond 171:239–254

Moustafa AR, Saoudi A, Moubasher A, Ibrahim IM, Molokhia H, Schwartz B (2003) Structural setting and tectonic evolution of the Bahariya Oasis, Western Desert, Egypt. GeoArabia 8:87–120

Nagati M (1988) Possible Mesozoic rifts in Upper Egypt: an analog with the geology of Yemen-Somalia rift basins. In: Proceedings of the 8th EGPC exploration conference, Cairo, 1986, vol 2, pp 205–231

Nemec MC (1996) Qarun oil field, Western Desert, Egypt. In: Proceedings of 13th EGPC petroleum conference, Cairo, vol 1, pp 140–164

Noweir MA, Fawwaz EM (2011) The origin of minor folds associated with the Themed fault zone in west central Sinai, Egypt: a Tertiary dextral wrenching. Egypt J Geol 55:213–232

Ott d'Estevou P, Bolze J, Montenat C (1986) Etude géologique de la marge occidentale du Golfe de Suez: le Massif des Gharamul e le Gebel Dara. Documents et Travaux, Institut Géologique Albert de Lapparent, no. 10, pp 19–44

Peijs JAMM, Bevan TG, Piombino JT (2012) The Gulf of Suez rift basin. In: Roberts DG, Bally AW (eds) Regional geology and tectonics: phanerozoic rift systems and sedimentary basins, vol 1B. Elsevier, pp 165–194

Robertson AHF, Dixon JE (1984) Introduction: aspects of the geological evolution of the Eastern Mediterranean. In: Robertson AHF, Dixon JE (eds) The geological evolution of the Eastern Mediterranean. Geological Society, London, Special Publications, no. 17, pp 1–74

Ross D, Uchupi E (1977) Structure and sedimentary history of southeastern Mediterranean Sea—Nile Cone area. AAPG Bull 61:872–902

Roufaiel GS, Samuel MD, Meneisy MY, Moussa HE (1989) K-Ar age determinations of Phanerozoic basaltic rocks in west central Sinai. N Jb Geol Palaont Mh Stuttgart 11:683–691

Roussel N, Purser BH, Orszag-Sperber F, Plaziat JC, Soliman M, Al Haddad AA (1986) Géologie de la région de Qusier, Egypte. Documents et Travaux de l'Institut Géologique Albert de Lapparent, Paris, no. 10, pp 129–144

Rusk DC (2001) Libya: petroleum potential of the underexplored basin centers—a twenty-first-century challenge. In: Downey MW, Threet JC, Morgan WA (eds) Petroleum provinces of the twenty-first century. AAPG Memoir 74, pp 429–452

Sadek H (1926) The geography and geology of the district between Gebel Ataqa and El-Galala El-Bahariya (Gulf of Suez). Geol. Survey Egypt, 120 pp

Sadek H (1928) The principal structural features of the Peninsula of Sinai. In: 14th International geological congress, Madrid, 1926, vol 3, pp 895–900

Said R (1962) The geology of Egypt. Elseveir Pub Co., Amsterdam, p 377

Said R (ed) (1990) The geology of Egypt. A.A. Balkema, Rotterdam, 729 pp

Said WS, Yousef M, El-Mowafy HZ, Abdel-Halim A (2014) Structural geometry and evolution of BED 17 field, Abu El Gharadig basin, northern Western Desert of Egypt: an example of restraining stepovers in strike-slip fault systems. AAPG Search & Discovery Article # 20266, 22 pp

Sakran S, Said SM (2018) Structural setting and kinematics of Nubian fault system, SE Western Desert, Egypt: an example of multi-reactivated intraplate strike-slip faults. J Struct Geol 107:93–108

Salah W, Yousef M, Abdel-Halim A, El-Mowafy HZ, Kamel D (2014) Structural setting and hydrocarbon potential of BED-17 field, Abu Gharadig Basin, northern Western Desert, Egypt. Egypt J Geol 58:121–136

Salem E, Sehim A (2017) Structural imaging of the East Beni Sueif basin, north Eastern Desert, Egypt. J Afr Earth Sci 136:109–118

Salem R (1976) Evolution of Eocene-Miocene sedimentation patterns in parts of northern Egypt. AAPG Bull 60:34–64

Sehim A, Hussein M, Kasem A, Shaker A, Swidan N (2002) Structural architecture and tectonic synthesis, Rosetta Province, West Nile Delta, Mediterranean—Egypt. In: Mediterranean offshore conference, Alexandria, 18 pp

Selim SS (2016) A new tectono sedimentary model for Cretaceous mixed nonmarine–marine oil prone Komombo Rift, South Egypt. Int J Earth Sci (Geol Rundsch) 105:1387–1415

Selim SS, El Araby AA, Darwish M, Abu Khadrah AM (2014) Anatomy and development of tectonically-induced Middle Eocene clastic wedge on the southern Tethyan shelf, north Eastern Desert, Egypt. AAPG Search & Discovery article # 50939, 9 pp

Serencsits CM, Faul H, Roland KA, El Ramly MF, Hussein AA (1979) Alkaline ring complexes in Egypt: their ages and relationship to tectonic development of the Red Sea. Ann Geol Surv Egypt 9:102–116

Shata A (1959) Structural development of the Sinai Peninsula (Egypt). In: Proceedings of the 20th international geological congress, Mexico, 1956, pp 225–249

Shata A, Sourial G (1946) Geological report on the Gebel Halal structure, northern Sinai. Standard Oil Co., Egypt Internal Report, 12 pp

Shukri NM, Akmal MG (1953) The geology of Gebel El-Nasuri and Gebel El-Anqabia district. Bull Soc Geograph Egypte 26:243–276

Shukri NM, Ayouty MK (1956) The geology of Gebel Iweibid-Gafra area, Cairo-Suez district. Bull Soc Geograph Egypte 29:67–109

Smith AG (1971) Alpine deformation and the oceanic areas of the Tethys, Mediterranean and Atlantic. Geol Soc Am Bull 82:2039–2070

Steen G (1982) Radiometric age dating and tectonic significance of some Gulf of Suez igneous rocks. In: Proceedings of 6th EGPC exploration seminar, Cairo, vol 1, pp 199–211

Steinitz G, Bartov Y, Hunziker JC (1978) K-Ar age determinations of some Miocene-Pliocene basalts in Israel: their significance to the tectonics of the rift valley. Geol Mag 115:329–340

Tari G, Hussein H, Novotny B, Hannke K, Kohazy R (2012) Play types of the deep-water Matruh and Herodotus basins, NW Egypt. Pet Geosci 18:443–455

Telesca L, Mohamed AA, El Gabry M, El-Hady S, Abou Elenean KM (2012) Time dynamics in the point process modeling of seismicity of Aswan area (Egypt). Chaos Solitons Fractals 45:47–55

Tingay M, Bentham P, De Feyter A, Kellner A (2011) Present-day stress-field rotations associated with evaporites in the offshore Nile Delta. Geol Soc Am Bull 123:1171–1180

Weissbrod T (1969) The Paleozoic of Israel and adjacent countries: Part II, The Paleozoic outcrops in southwestern Sinai and their correlation with those of southern Israel. Bull Geol Surv Israel 48:32 pp

Woodward Clyde Consultants (1985) Seismic geology and tectonics studies of the Aswan region: Earthquake activity and dam stability evaluations for the Aswan High Dam, Egypt for the High and Aswan Dams Authority, Ministry of Irrigation, Arab Republic of Egypt, vol 3

Younes AI, McClay K (2002) Development of accommodation zones in the Gulf of Suez–Red Sea rift, Egypt. AAPG Bull 86:1003–1026

Yousef M, Moustafa AR, Shann M (2010) Structural setting and tectonic evolution of offshore north Sinai, Egypt. In: Homberg C, Bachmann M (eds) Evolution of the Levant Margin and Western Arabia Platform since the Mesozoic. Geological Society of London Special Publication 341, pp 65–84

Yousef MY, Sehim A, Yousef M (2015) Structural style and evolution of inversion structures, Horus oil field, Alamein basin, north Western Desert, Egypt. In: 8th International conference on the geology of the Middle East, Cairo, Egypt (abs)

Youssef MI (1968) Structural pattern of Egypt and its interpretation. AAPG Bull 52:601–614

Zahran H, Abu Elyazid K, Mohamad M (2011) Beni Suef Basin the key for exploration future success in Upper Egypt. AAPG Search & Discovery article # 10351, 45 pp

8 Structural Setting and Tectonic Evolution of the Gulf of Suez, NW Red Sea and Gulf of Aqaba Rift Systems

Adel R. Moustafa and Samir M. Khalil

Contents

Abstract

Crustal separation of Arabia from Africa formed a NNW-SSE oriented continental rift in the Gulf of Suez and Red Sea and a NNE-SSW oriented transform in the Gulf of Aqaba. The three regions typically form triple junction at the southern tip of Sinai Peninsula, with the Gulf of Suez form the failed arm. Continental rifting started in the late Oligocene and continued afterwards. Four mega-half grabens of opposite tilt directions are recognized in the Suez Rift and the northwestern part of the Red Sea. Pre-rift structures controlled the locations and orientations of the accommodation zones between these mega-half grabens. The onset of rifting is marked by the deposition of Oligocene red beds followed by Early Miocene basaltic volcanicity in the form of dikes (mostly oriented NNW-SSE) as well as sills and flows. Deposition

A. R. Moustafa (✉)
Faculty of Science, Department of Geology, Ain Shams University, Cairo, 11566, Egypt
e-mail: armoustafa@sci.asu.edu.eg; armoustafa@hotmail.com

S. M. Khalil
Faculty of Science, Department of Geology, Suez Canal University, Ismailia, 41522, Egypt
e-mail: s.khalil@science.suez.edu.eg; s_khalil3@yahoo.co.uk

Z. Hamimi et al. (eds.), *The Geology of Egypt*, Regional Geology Reviews,
https://doi.org/10.1007/978-3-030-15265-9_8

of the proper syn-rift sediments started in the Aquitanian with a phase of slow tectonic subsidence followed by a phase of rapid subsidence at ~20 Ma. This phase was followed by another phase of slow tectonic subsidence at ~17 Ma that lasted to the Recent time in the Suez Rift marking its abandonment and onset of movement on the Dead Sea Transform. Movement on the Dead Sea Transform aborted extension in the Suez Rift and led to continued opening of the Red Sea Basin. Being close to the Red Sea and the Dead Sea Transform, the southernmost part of the Suez rift witnessed another phase of rapid tectonic subsidence during the last 10 million years. Continued rotation of tilted fault blocks in the southern part of the Suez rift and in the NW Red Sea led to decrease in the dip angles of the main-bounding faults where they got locked and dissected by younger (second-generation) faults. The total slip on the Dead Sea Transform is 105–107 km leading to increase in the width of the Red Sea. The northern part of the Red Sea has highly attenuated continental crust as far south as the Zabargad Fracture Zone whereas seafloor spreading took place in the central and southern parts of the Red Sea. Left lateral slip on the Dead Sea Transform led to opening of the Gulf of Aqaba as a series of connected pull-apart grabens between the overlapping ends of left-lateral strike-slip faults. Total subsidence of these pull-apart basins is in the order of 4–5 km.

8.1 Introduction

Although the Gulf of Suez-Red Sea basin is a world class rift basin and an area showing the evolutionary stages of continental breakup and transition from continental rifting to seafloor spreading and formation of new ocean basins, it was not given the importance it deserves in previous books on the Geology of Egypt. The Gulf of Suez was dealt with briefly in Said's (1962) book and was almost ignored in Said's (1990) book. An integrated and detailed study of the structures of both the Gulf of Suez and Red Sea and the evolution from rift stage to drift and seafloor spreading stage has not been satisfactorily considered so far. Some papers have generally dealt with all the Gulf of Suez rift or with a large portion of it (e.g. Robson 1971; Garfunkel and Bartov 1977; Patton et al. 1994; Bosworth 1995; Bosworth and McClay 2001; Farhoud 2009; Peijs et al. 2012). Also, many studies have already been done and published on the Red Sea (Cochran 1983, 2005; Bosworth 2015 among many others) but integrated detailed structural studies on the two basins are few and perhaps concentrate more on the Red Sea (e.g. Khalil and McClay 2001, 2002, 2009, 2016, 2018). In this chapter, we try to show the structural geometry of the Gulf of Suez and NW Red Sea based on our own field mapping of these areas since 1984 as well as our own knowledge of the subsurface structural setting of the Gulf of Suez based on data acquired for petroleum exploration. Unfortunately, the subsurface structural setting of the Red Sea offshore area is still unclear due to insufficient subsurface data represented by very few drilled wells as well as the inadequate resolution of seismic data. A new seismic acquisition is being done in the Egyptian offshore part of the Red Sea at present time and when completed and becomes available it will definitely enhance our knowledge of the structural setting of this region.

This chapter also deals with the Gulf of Aqaba structures as part of the Dead Sea Transform that separates the Gulf of Suez from the Red Sea.

8.2 Plate Tectonic Setting

The Gulf of Suez-Red Sea basin is an excellent example of continental breakup and opening of new oceans. Both of the Gulf of Suez and Red Sea started as continental rifts at the initial phases of separation of Arabia from Africa. After a certain period of continental extension, they were separated from each other by the Dead Sea Transform that allowed continued extension in the Red Sea and abortion of the Suez Rift. Continued extension of the Red Sea led to increased crustal attenuation and seafloor spreading. The Gulf of Suez and Red Sea show different evolutionary stages represented by a failed continental rift in the Gulf of Suez area, a rift in the latest stage of continental rifting in the northern Red Sea, a transitional stage in the central Red Sea and seafloor spreading since 5 Ma in the southern Red Sea (Ehrhardt and Hübscher 2015), Fig. 8.1. Rift opening in the Gulf of Suez-Red Sea area started at Late Oligocene-Early Miocene (Robson 1971; Garfunkel and Bartov 1977; Moustafa 1993; Patton et al. 1994; Bosworth and McClay 2001; Cochran 2005) and activity of the Dead Sea Transform took place later; offsetting Early Neogene (20–22 Ma) igneous dikes intruded in Sinai and NW Arabia (Eyal et al. 1981) or at 7–12 Ma ago (Freund et al. 1968, 1970). Initial phases of extension took place orthogonal to the rift axis in the N65° E–S65°W direction (Lyberis 1988; Moustafa 1993; Khalil 1998; Khalil and McClay 2001) and switched into oblique extension in the NNE direction after the Dead Sea Transform has become active. The present-day movement of Arabia relative to Africa is in the NNE direction (ArRajehi et al. 2010). As a result of oblique extension, NNE-SSW oriented transform faults were formed in the Red Sea, the northernmost of them (Zabargad Transform or Zabargad Fracture Zone) passes through Zabargad Island. The average rate of sinistral slip on the Dead Sea Transform is 4.5–4.7 ± 0.2 mm/yr based on GPS observations (Mahmoud

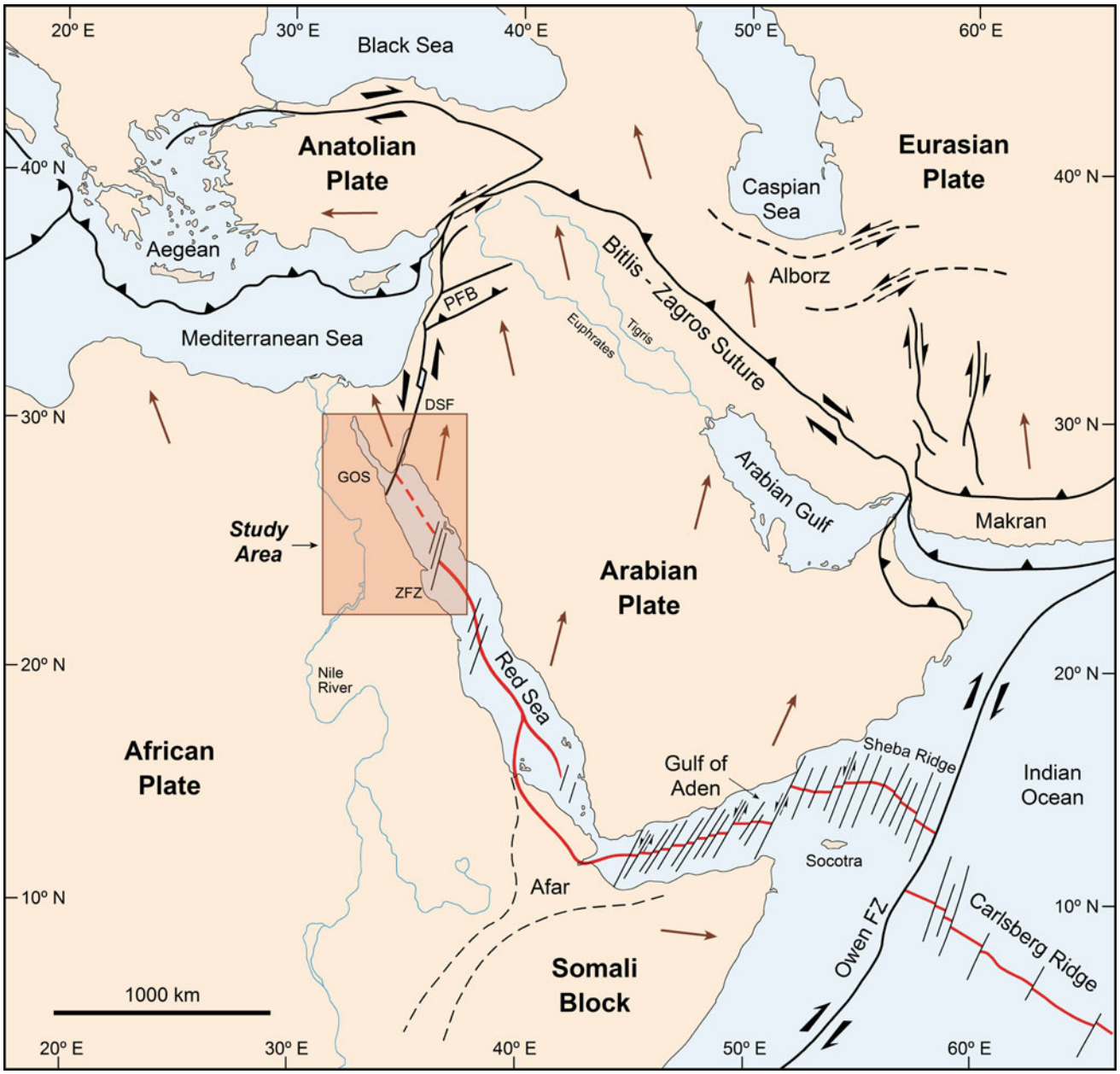

Fig. 8.1 Plate tectonic setting of the Gulf of Suez, Gulf of Aqaba, and Red Sea areas modified after Hempton (1987), Khalil and McClay (2002) and Bosworth et al. (2005). ZFZ is Zabargad Fracture Zone, DSF is Dead Sea Fault, and PFB is Palmyra Fold Belt. Thin arrows represent the plate movement directions after ArRajehi et al. (2010) and movement direction of Sinai is after Mahmoud et al. (2005)

et al. 2005; ArRajehi et al. 2010) and the total rate of opening of the northern Red Sea is currently 7.5–9.5 mm/yr (Joffe and Garfukel 1987; Jestin et al. 1994; Chu and Gordon 1988) or exactly 6.8–7 ± 1 mm/yr based on GPS observations (ArRajehi et al. 2010; Reilinger et al. 2015; respectively).

The crust of the northern part of the Red Sea as far south as the Zabargad Fracture Zone is still continental and highly attenuated where crustal thickness in the main trough is 5–8.5 km (Cochran 2005). Satellite gravity data (Saleh et al. in manuscript) indicates rise of the asthenosphere beneath the northern Red Sea with local centers of future magmatic activity at depths of 10–40 km. Some places in the northern Red Sea show the formation of basic igneous rocks at local centers. Gabbroic rocks cut by doleritic dykes exist at the Brothers Islands (Shukri 1945; Ligi et al. 2018; Fig. 8.2a) that represent the summit of a NW-SE oriented tilted fault block (Ligi et al. 2018) and have normal magnetization (Cochran 2005). The gabbro of the Brothers Islands crystallized at relatively shallow depth (~10–13 km) from melts

derived from a MORB-type primary magma and were intruded in sub-rift continental crust and then exhumed by footwall uplift during extension and block rotation (Ligi et al. 2018). Gabbro is also found at Zabargad Island and was derived from an alkali basalt magma (Ligi et al. 2018) that crystallized at depth of 30–35 km (Ligi et al. 2018; Bonatti et al. 1983) and was brought to its position near sea level by subsequent deformation related to the Zabargad Fracture Zone. Nicolas et al. (1985) determined a K–Ar age of 23 ± 7 Ma for amphiboles from an amphibolite adjacent to the peridotites.

Seafloor spreading in the Red Sea and Gulf of Aden allows north-northeastward movement of the Arabian Plate and its collision with the Eurasian Plate at the Bitlis-Zagros Suture (Fig. 8.1). The Dead Sea Transform and Owen Transform/Fracture Zone bound the NW and SE sides of the Arabian Plate as it moves toward Eurasia.

8.3 Bathymetry of the Gulf of Suez, Northen Red Sea, and Gulf of Aqaba

The bathymetry of the Gulf of Suez, northern Red Sea, and Gulf of Aqaba show remarkably different depths (Fig. 8.2a). The bathymetry of almost all of the Gulf of Suez indicates very shallow water depth that has an average of about 50–70 m. Being close to the Red Sea, only the southernmost part of the gulf is deep and reaches a depth close to 1000 m in the area between Shadwan Island and the Sinai coast (Fig. 8.2b). Several islands characterize the southern part of the Gulf of Suez and represent structural highs at the updip edges of tilted fault blocks bounded by major rift-parallel normal faults. The orientation of these faults accounts for the fact that almost all of these islands are elongated in the NW direction. The largest and structurally highest island is Shadwan Island (Fig. 8.2b) that is about 15 km long and has Precambrian basement exposures in addition to Miocene and post-Miocene sedimentary rocks (Shukri 1954). The other islands (Ashrafi, Ranim, Geisum, Tawila, and Gubal) are mostly covered by post-Miocene sediments.

The northern Red Sea has almost constant width remarkably larger than the width of the southern Gulf of Suez (Fig. 8.2a). The width of the Red Sea is constant as far south as latitude 24°N and reaches about 200 km with coastlines oriented NW-SE. South of this latitude the Red Sea has winding coasts and larger width of about 250 km in the area between latitudes 24° and 22°N (Fig. 8.2a). The northern Red Sea has narrow shelves and coastal plains and a broad main trough that is 400–1200 m deep. A deeper axial trough less than 60 km wide with depths more than 2000 m exists to the south in the central and southern parts of the Red Sea. The axial trough of the northern Red Sea lies in the middle of the Red Sea at a small angle to the coasts from Ras Mohammed to latitude 25.5° (Figs. 8.2a, b). South of latitude 25.5° to latitude 23.5°, the axial trough is oriented N-S and is controlled by the Zabargad Fracture Zone (Figs. 8.2a). Further south, the axial trough is occupied by the Red Sea spreading axis (Roeser 1975; Cochran 1983; Miller et al. 1985; Garfunkel et al. 1987; Ehrhardt and Hübscher 2015).

Oceanic deeps characterize the seafloor of the Red Sea and are considered to accompany the change from

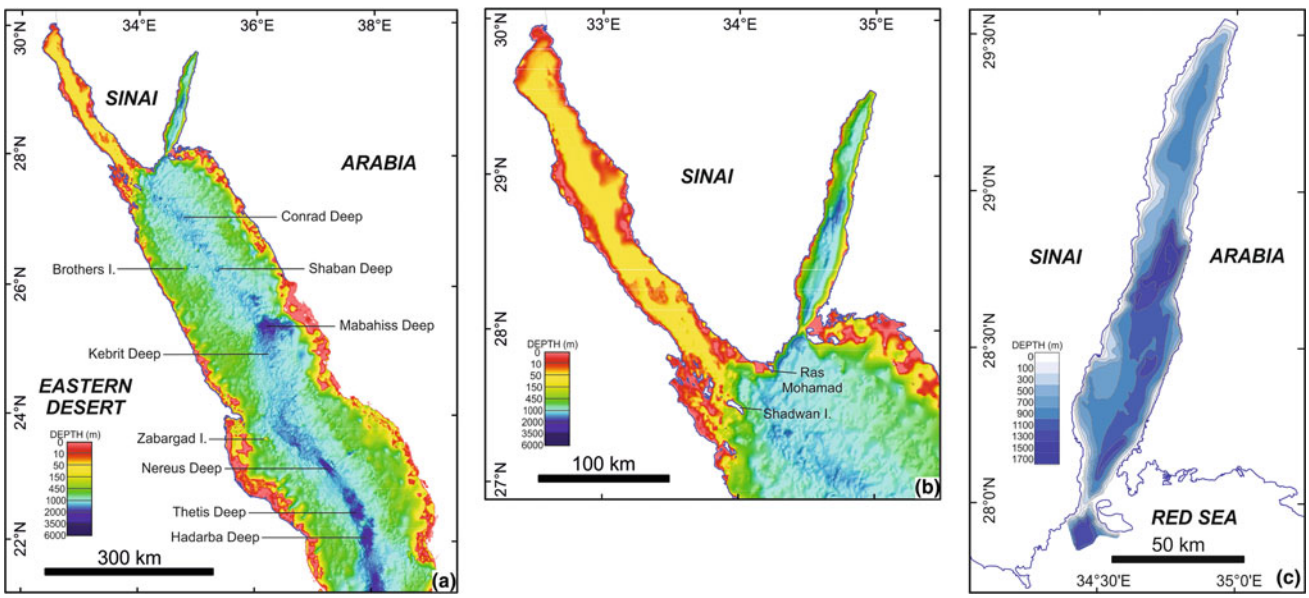

Fig. 8.2 Bathymetry maps of the northern Red Sea (**a**) and Gulf of Suez (**b**) from EMODnet (2016). **c** Gulf of Aqaba bathymetry after Ben-Avraham et al. (1979b)

continental rifting characterizing the northern Red Sea to seafloor spreading characterizing the southern Red Sea (Bonatti 1985; Cochran and Martinez 1988; Martinez and Cochran 1988). Several oceanic deeps were discovered along the axis of the Red Sea (Degens and Ross 1969) and many of them are associated with magmatism (Bicknell et al. 1986) and perhaps represent the initial seafloor spreading cells (Bonatti 1985; Martinez and Cochran 1988). Some deeps contain bottom-water brines and metalliferous sediments pointing to hydrothermal circulation of seawater (Botz et al. 2011). Compared to the central Red Sea deeps which are floored by young basaltic crust, the northern Red Sea deeps are smaller and form only isolated deeps within the axial depression. Some of them are accompanied by volcanic activity. The study of ocean deeps through using multichannel seismic reflection profiling, high-resolution bathymetric surveys, magnetic surveys as well as bottom rock sampling helps identify their structure and the nature of their rocks. According to Ehrhardt and Hübscher (2015), the deeps of the northern Red Sea where the main and axial troughs are oriented NW-SE are of two types: a- volcanic and tectonically impacted deeps (e.g. the Conrad and Shaban Deeps, Fig. 8.2a; Bonatti et al. 1984; Pautot et al. 1984) that opened by lateral tear of the Miocene evaporites (salt) and Plio-Quaternary overburden, and b—non-volcanic deeps that developed as collapse structures built by subsidence of Plio-Quaternary sediments due to evaporite sub-erosion processes. The Mabahiss Deep (Fig. 8.2a) also exists in the NW-SE area of the northern Red Sea and has evidence of oceanic crust (Cochran 2005). The Conrad and Shaban Deeps are ~1300–1500 m deep whereas the Mabahiss Deep is about 2400 m deep. Oceanic deeps in the area lying between latitude 25.5° to latitude 23.5° where the axial trough is oriented N-S (e.g. Kebrit Deep, Fig. 8.2a) are non-volcanic and are collapse-related structures. Oceanic deeps in the northern Red Sea south of the Zabargad Fracture Zone include the Nereus, Thetis, and Hadarba Deeps (Fig. 8.2a). Ligi et al. (2012) carried out a detailed study of the Nereus and Thetis Deeps and concluded that the Thetis Deep (Fig. 8.2a) is 65-km long, ~2200 m deep and has a linear axial volcanic ridge associated with a strong magnetic anomaly and scattered small central volcanoes. The floor of the Thetis Deep is almost sediment-free or with very thin sediment thickness whereas the walls are >1 km high and show step-like morphology and normal faults. The southern and central parts of the Thetis Deep have axial neo-volcanic ridges that are sharp-crested, few tens of km long, 2–4 km wide, and 300–400 m high and are covered by hummocky terrains made up of coalescence of several volcanic centers. The valley floor flanking these neo-volcanic ridges shows smooth terrains representing flat-lying lava fields, probably basaltic sheet flows. The northern part of the Thetis Deep lacks linear neo-volcanic zone although it displays strong central magnetization suggesting recent emplacement of oceanic crust. These features imply a south to north progression of the initial emplacement of oceanic crust within the Thetis Deep. The Nereus Deep (Fig. 8.2a) is ~50 km long, ~2500 m deep, and is flanked by >1 km asymmetric walls with step-like morphology due to normal faults partly masked by salt tectonics. A ~250 m high neo-volcanic axial ridge exposes fresh oceanic-type basalts dissects the 12 km wide valley floor. A ~35 km long, broad and gentle depression, carpeted by sediments and devoid of volcanism and linear magnetic anomalies separates the Thetis and Nereus Deeps. This inter-trough area is higher than the two deeps and has surface morphology indicative of evaporite flow toward the rift axis. It is speculated to consist of stretched-thinned continental crust injected by diffuse basaltic intrusions capped by Miocene evaporites and Plio-Pleistocene biogenic deposits. Ligi et al. (2012) proposed that the initial emplacement of oceanic crust in the Red Sea occurs in regularly spaced discrete cells that serve as nuclei for axial propagation of oceanic accretion that evolve then in linear segments of spreading. The Thetis cell is made by coalescence of three sub-cells that become shallower and narrower from south to north. The inter-trough zones that separate the Thetis oceanic cell from the Nereus oceanic cell to the north and from the Hadarba cell (Fig. 8.2a) to the south lack magnetic anomalies and contain thick sediments and relics of continental crust. Geochemistry of the Thetis and Nereus basaltic glass suggest rift-to-drift transition marked by magmatic activity with typical MORB signature.

Two islands (Brothers Islands; Fig. 8.2a) exist in the northern Red Sea at latitude 26°8′N and 26°15′N as mentioned in the previous section. Zabargad (St. John) Island is another island located at latitude 23°30′ N. Other islands also exist close to the Egyptian coast of the Red Sea at Hurghada, Safaga, and between Ras Banas and Halaib and are all covered by post-Miocene sediments.

The bathymetry of the Gulf of Aqaba (Fig. 8.2c) shows three linear NNE-SSW oriented fault-controlled depressions with water depth reaching 1700 m in the middle one. These depressions are pull-apart grabens formed between overstepping left-lateral strike-slip fault segments of the Dead Sea Transform as will be discussed in another section.

8.4 Tectonostratigraphy of the Gulf of Suez and Northern Red Sea

The stratigraphic section of the Gulf of Suez and northern Red Sea includes three tectonostratigraphic sequences. These are pre-rift, syn-rift, and post-rift (Fig. 8.3). Post-rift rocks exist only in the Suez Rift whereas the Red Sea is still extending.

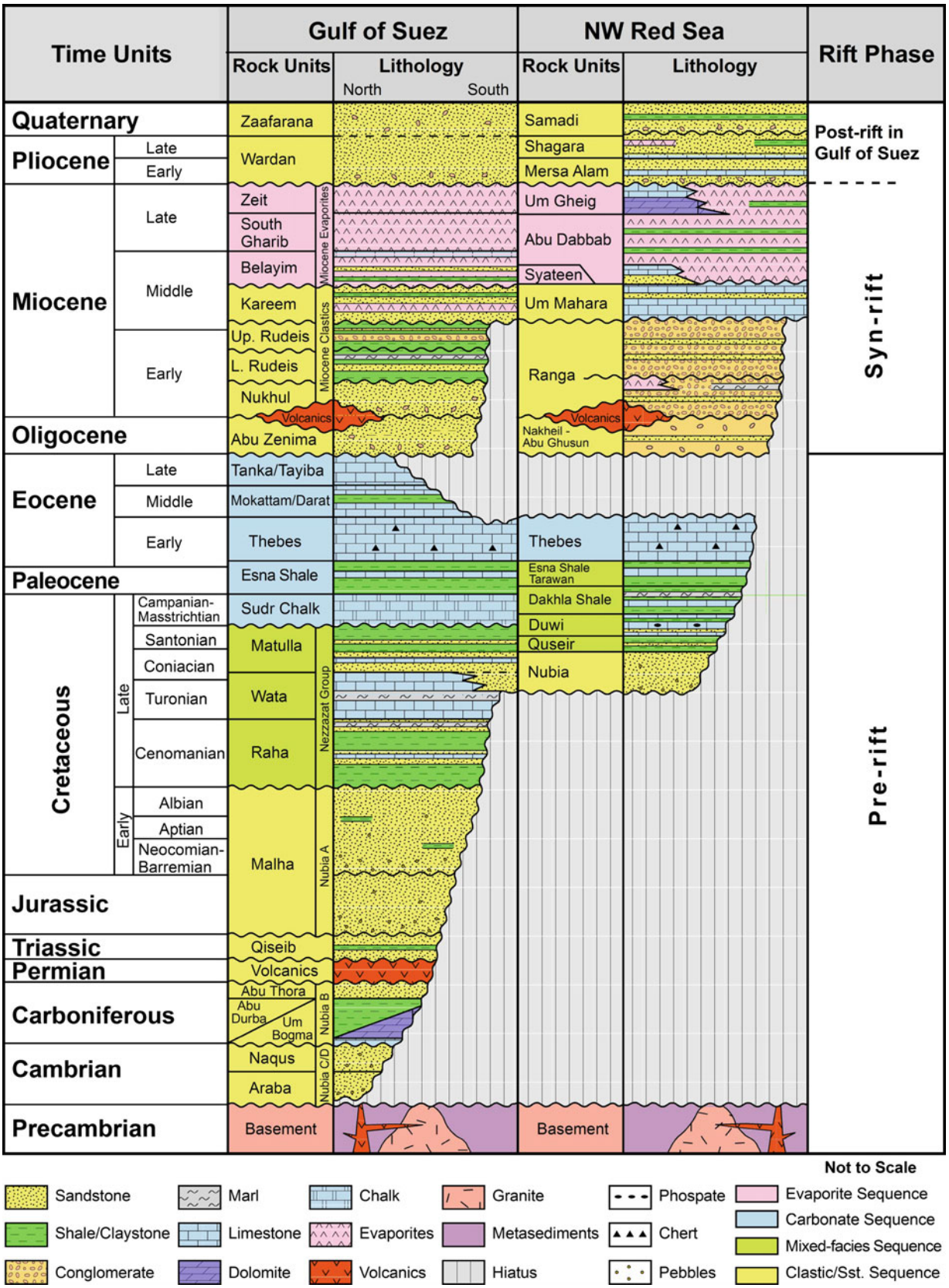

Fig. 8.3 Stratigraphic sections of the Gulf of Suez (after Moustafa and Khalil 2017) and NW Red Sea rifts (after Khalil and McClay 2016, 2018)

8.4.1 Pre-rift Sequences

The pre-rift rocks of the Gulf of Suez and northern Red Sea include platform sedimentary units unconformably overlying the Precambrian crystalline basement rocks (Fig. 8.3).

8.4.1.1 Precambrian Basement

The Precambrian basement rocks of the Gulf of Suez and northern Red Sea are Proterozoic in age and are exposed on the rift shoulders as well as at the eroded updip areas of tilted fault blocks inside the rift such as Gebel Abu Durba, Gebel Araba, and Ras Kenisa area on the eastern side of the Suez Rift; Gebel El Zeit and Esh El Mellaha on the western side of the Suez Rift, and almost all rift blocks in the northwestern onshore Red Sea area.

These Precambrian basement rocks are made up of metasediments, metavolcanics, metagabbros, and serpentinites associated with gneisses in structural highs and are unconformably overlain by non-metamorphosed to slightly metamorphosed intermediate to silicic volcanics (Dokhan volcanics) and clastic sediments of the Hammamat Group (El Gaby et al. 1990). These rocks are intruded by granites that become the dominant rocks further north and in the two shoulders of the Suez Rift. The basement rocks of the Gulf of Suez and northern Red Sea are dissected by a swarm of NE to ENE oriented felsic and mafic dikes (Schurmann 1966).

8.4.1.2 Pre-rift Sedimentary Rocks

The pre-rift sedimentary rocks overlying the Precambrian basement in the Gulf of Suez and Red Sea areas include three main rock sequences (Fig. 8.3). These are a predominantly sandstone sequence overlying the Precambrian basement (Nubia Sandstone) overlain by a mixed facies sequence and a carbonate sequence. Although these three sequences exist in the Suez and Red Sea rifts, they do not have equivalent ages. They represent platform deposits and show gradual northwestward thickening. Structural cross sections (shown in the next sections) indicate that these rock units have similar dip angle and are parallel to each other indicating almost no structural control during their deposition.

Nubia Sandstone

The Nubia Sandstone is a predominantly sandstone sequence with a few shale and carbonate intervals (Fig. 8.3). It is of Paleozoic to Early Cretaceous age in the northern and central parts of the Gulf of Suez but it is only of Cretaceous age in the southernmost area of the Suez Rift and northwestern Red Sea. The thickness of the Nubia Sandstone in the Suez Rift ranges from almost zero at the Ras Mohamed Arch at the extreme southern end of the gulf to 1800 m at the northern end of the gulf. The Nubia thickness increases in the northwestern Red Sea south of the Ras Mohamed arch and is up to 200 m at Quseir.

Mixed-Facies Sequence

The mixed-facies sequence is a predominantly marine sequence of Late Cretaceous age in the Gulf of Suez and includes three different rock units; Cenomanian Raha Formation, Turonian Wata Formation, and Lower Senonian Matulla Formation (Fig. 8.3; Ghorab 1961). These three rock units also form what is referred to as the Nezzazat Group which is a mechanically ductile layer between the predominantly brittle Nubia Sandstone sequence below and the competent carbonate sequence above. The Raha Formation is made up of fine-grained glauconitic and pyritic sandstone, grey calcareous shale, and thin limestone intercalations. The Wata Formation is made up of a thick sequence of massive yellowish brown to grey, hard, fossiliferous dolomite and limestone with sandstone and shale beds. Locally, the Abu Qaada Formation is another unit of Turonian age described at the base of the Wata Formation with an average thickness of 35 m. The Matulla Formation comprises two units: a lower predominantly fluvial sandstone unit and an upper predominantly shale unit. In the northwestern Red Sea, the mixed facies sequence includes the Quseir Variegated Shale (Santonian-Campanian), Duwi Formation (Campanian-Maastrichtian), Dakhla Formation (Late Maastrichtian-Paleocene), and Esna Shale (Paleocene); Figs. 8.3 and 8.4a.

Carbonate Sequence

The carbonate sequence represents the youngest pre-rift rocks and is made up mainly of uppermost Cretaceous chalk and Eocene limestones in the Suez Rift or only Eocene limestones in the NW Red Sea (Fig. 8.3). The Campanian-Maastrichtian Sudr Chalk represents the basal part of the carbonate sequence in the Gulf of Suez area (Fig. 8.3). It is overlain by the Paleocene to Early Eocene Esna Shale that has maximum thickness of about 50 m in the Suez Rift but changes in thickness due to Late Cretaceous-Early Cenozoic deformation caused by closure of the NeoTethys. The Esna Shale is overlain by the Thebes Formation (Early-Middle Eocene age); Said (1960) which is made up of limestone interbedded with thin chert bands (Fig. 8.3). This unit has a consistent facies throughout the Gulf of Suez and northern Red Sea except for Gebel Hammam Faraun-Gebel Thal area (Abul-Nasr 1986) on the eastern side of the Suez Rift and St. Paul area on the western side (Ismail and Abdallah 1966; Travis 1984) where it is

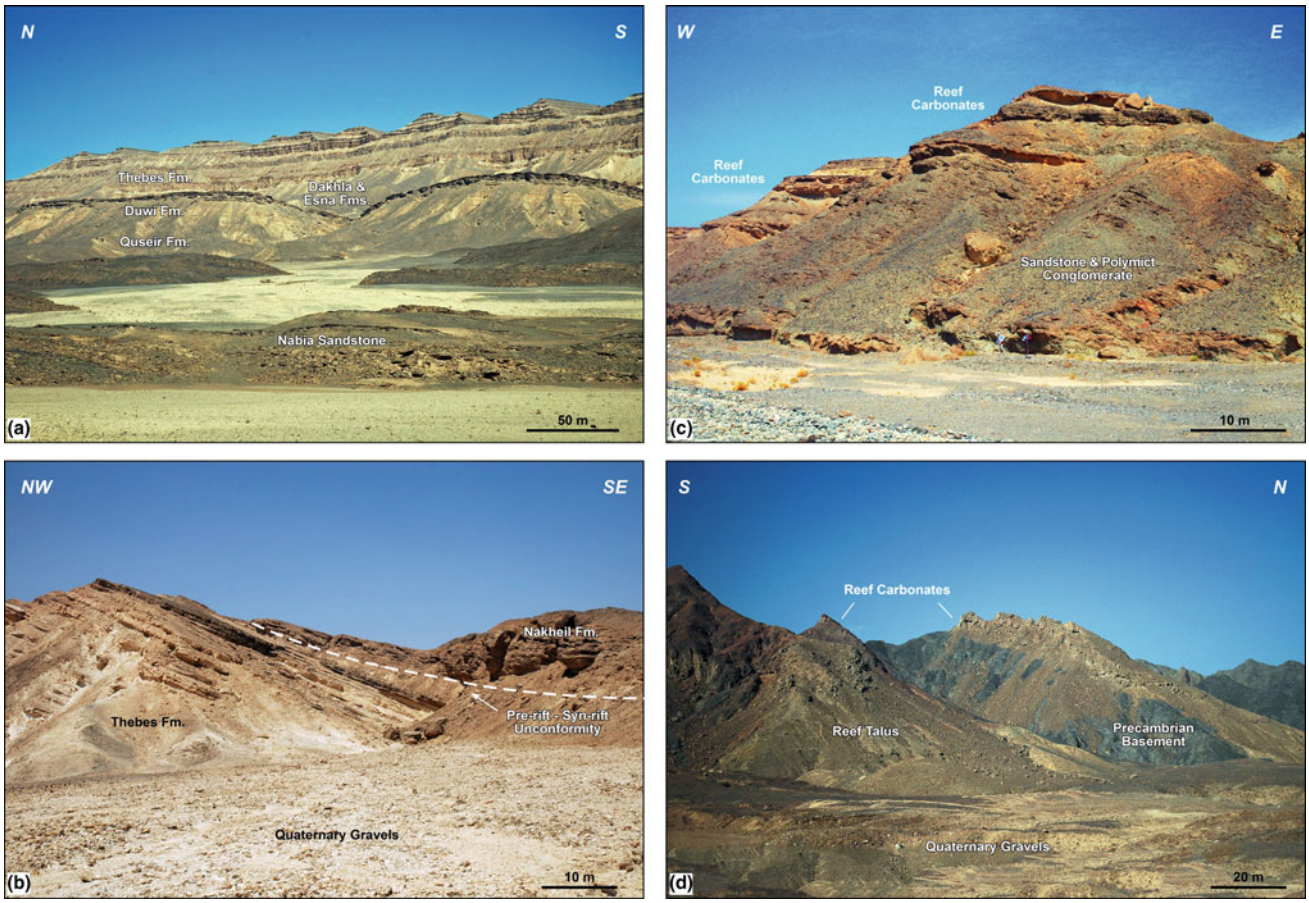

Fig. 8.4 Field views showing outcrop examples of the pre-rift and syn-rift stratigraphy in the NW margin of the Red Sea. **a** Cretaceous–Eocene, clastic and carbonate section in Gebel Duwi. **b** Angular discordance between the Oligocene Nakheil conglomerates and the Eocene Thebes cherty limestone in Quseir area. **c** Cruddy-bedded sandstone and conglomerate of the Lower Miocene Ranga Formation, north Quseir area. Note gently-dipping reef carbonate thin beds at the upper part of the section. **d** Middle Miocene reef carbonates and reef talus onlapping rotated basement blocks in Safaga area

represented by slope breccia and slump deposits (Abul-Nasr 1986; Abul-Nasr and Thunell 1987) related to Syrian Arc, Cretaceous-aged transpressional deformation.

The Thebes Formation is overlain by several Middle Eocene carbonate rock units in the Gulf of Suez area (Fig. 8.3). These include the Darat, Khaboba (Viotti and El-Demerdash 1969), Samalut and Mokattam (Said 1962) Formations but generally these formations are eroded from the crests of tilted fault blocks and are only preserved in down-dip areas. The Middle Eocene rocks are locally covered by the Upper Eocene Tanka (Hume et al. 1920) and Maadi (Said 1962) Formations. The Maadi Formation exist only in the northernmost part of the Suez Rift and is equivalent to the Tayiba Formation of Youssef and Abdelmalik (1972) and Abul-Nasr (1990) or "Red Beds" of Hume et al. (1920) and Moon and Sadek (1923, 1925). This section has a characteristic brown to reddish brown color and is made up of claystone with several limestone beds as well as friable, fine-grained sandstone beds. Eocene rocks in the northwestern Red Sea area include only the Thebes Formation (Fig. 8.3).

8.4.2 Syn-rift Sequences

The syn-rift sequence of the Gulf of Suez and northern Red Sea includes an early rift sequence unconformably overlain by proper syn-rift sequences (Fig. 8.3). The early rift sequence includes red beds (Abu Zenima Formation in the Suez Rift and Nakheil Formation in the NW Red Sea rift; Fig. 8.4b) overlain by Early Miocene volcanics (Fig. 8.5). Miocene sediments represent the proper syn-rift sequence in the Suez Rift and northwestern Red Sea. In both rifts, the syn-rift sequence includes a lower predominantly clastic sequence and an upper predominantly evaporitic sequence (Fig. 8.3). A carbonate unit is locally developed between the two sequences in the southern part of the Suez Rift and NW Red Sea. In the Suez Rift, the Miocene clastic sequence

Fig. 8.5 Field view at the mouth of Wadi Tayiba (Gulf of Suez) showing early rift red beds (Abu Zenima Formation) overlying pre-rift Eocene limestone/marl section. Early Miocene lava (basalt) flow and lower Miocene Nukhul Formation overlie the red beds. Note the angular discordance between the pre-rift Eocene and early rift and syn-rift rocks. Photo by Gamal Ammar

(Gharandal Group) includes the Nukhul, Rudeis, and Kareem Formations whereas in the NW Red Sea the clastic sequence includes the Ranga and Um Mahara Formations (Fig. 8.3). The Miocene evaporites in the Suez Rift include the Belayim, South Gharib, and Zeit Formations and in the NW Red Sea they belong to the Abu Dabbab Formation. The evaporites in the NW Red Sea area are overlain by the Upper Miocene carbonate rocks of the Um Gheig Formation (Fig. 8.3). Post-Miocene sediments in the Red Sea area are predominantly clastic and are related to the syn-rift sequence as the basin is a still extending.

8.4.2.1 Early Rift Sequence

Abu Zenima Formation

The Abu Zenima Formation (Hantar 1965) is a red clastic section with local geographic distribution on the east side of the Suez Rift in vicinity of Abu Zenima area (Fig. 8.5). It is 20–110 m thick and consists of red, purple, and varicolored siltstone, mudstone and coarse-grained, cross-bedded ferruginous sandstone with some polymictic conglomerate beds and plant remains. The age of the Abu Zenima Formation was controversial (Abul-Nasr 1990) until it was assigned an Oligocene age by Refaat and Imam (1999) based on the identification of well-preserved charophyte microfossils in the Wadi Nukhul section. According to Refaat and Imam, these red beds are of Late Eocene to Late Oligocene age. The presence of weathered basalt pebbles near the middle (Garfunkel and Bartov 1977) or the base (Montenat et al. 1988) of the Abu Zenima Formation at Wadi Nukhul perhaps indicates that the age of the red beds is Late Oligocene, contemporaneous with the time of volcanicity as indicated in the next section.

The Abu Zenima Formation marks the earliest phase of rifting in the Suez Rift (Patton et al. 1994). Gawthorpe et al. (2003), and Jackson et al. (2002) have shown that the Abu Zenima Formation was deposited in small depocenters formed on the downthrown sides of short-length, small-displacement normal faults during earliest rifting.

Nakheil Formation

The Nakheil Formation (Akkad and Dardir 1966a) is an early-rift lacustrine red beds marking the transition from pre-rift to syn-rift facies in the northwestern Red Sea area. The Nakheil Formation is 26–120 m thick (Khalil and McClay 2009), and it consists of chert and limestone conglomerate and breccia as well as yellow-brown iron-stained limestone and red sandstone. It is locally preserved in hanging-wall sub-basins and rests on the Eocene Thebes Formation with 8–10° of angular discordance (Fig. 8.4b). According to Khalil and McClay (2001, 2009), this angular discordance, together with the chert and carbonate clasts which were derived from the underlying Thebes Formation, indicate that the amount of fault block rotation and the uplift and erosion were relatively minor during the early stage of rifting in the Red Sea.

Early Rift Volcanics

An early rift magmatic phase characterizes the onset of rifting in the Gulf of Suez and northern Red Sea. Well exposed subalkaline (tholeiitic) to alkaline basaltic dikes, sills, and flows were mapped in the northeastern part of the Suez Rift especially around Abu Zenima and the nearby offshore area (Fig. 8.5; see Patton et al. 1994; Moustafa 2004 for details). K/Ar radiometric dates point to latest Oligocene-earliest Miocene age (22–24 Ma; Steen 1984; Montenat et al. 1986; Moussa 1987). Whole rock $^{40}Ar/^{39}Ar$ dates are also 22–24 Ma and centered at 23 Ma (Bosworth et al. 2015 and Bosworth and Stockli 2016). The dikes have two consistent trends, NW-SE and NE-SW.

Early rift volcanics are rare in the northwestern Red Sea onshore area. A small basalt dike is exposed on the northern side of Wadi Naqara (near Safaga), Bosworth et al. (1998) and thin basalt flows are interbedded with sediments of the

Nakheil Formation at Sharm el Qibli and Sharm el Bahari (south of Quseir). The Sharm el Bahari basalt was dated 24.9 ± 0.6 Ma by Roussel et al. (1986).

Peridotite and mafic dikes and sills were reported at Zabargad Island in the northern Red Sea (El Shazly and Saleeb Roufaiel 1977; Bonatti et al. 1983). Amphiboles from an amphibolite adjacent to the peridotites were dated 23 ± 7 Ma by Nicolas et al. (1985).

8.4.2.2 Syn-rift Sequence of the Suez Rift

Nukhul Formation

The Nukhul Formation (Figs. 8.3 and 8.5) was deposited above older pre-rift and early rift rock units in marginal-marine to shelf environments. It has relatively small thickness in outcrops but borehole data indicate large thickness in the downdip areas of tilted fault blocks up to 500 m in the West Zeit Trough (Peijs et al. 2012). Subsurface data (e.g. Youssef 2011; Afifi et al. 2013, 2016) also indicate that the Nukhul Formation may be absent at the crests of tilted fault blocks due to non-deposition. The Nukhul deposition was controlled by relatively short, unlinked fault segments, characteristic of early rifting (Khalil 1998; McClay et al. 1998; Carr et al. 2003; Gawthorpe et al. 2003; Jackson et al. 2002). The age of the Nukhul Formation is Early Burdigalian (El Heiny and Martini 1981) or Aquitanian-Early Burdigalian (Evans 1990).

The earliest Nukhul sediments (Shoab Ali Member of Saoudi and Khalil 1986) are fluvial to estuarine sandstones located in the southern areas of the rift. This led Patton et al. (1994) to consider that rifting started in the south and propagated northward but Peijs et al. (2012) are of the opinion that rifting was coeval along the whole rift as the Nukhul was deposited in separate small isolated sub-basins controlled by the main faults of the rift. Sea level rise after deposition of the Shoab Ali Member led to deposition of shallow water carbonates and anhydrites over most of the gulf and they are overlain by shales and sands.

Rudeis Formation

The Rudeis Formation (Fig. 8.3) includes the Lower Rudeis (Burdigalian) and Upper Rudeis (Langhian) units. Both units were deposited in fault-controlled sub-basins defined by the major faults of the rift. In these sub-basins, the two units have wedge shapes thickening toward the nearby faults. The Lower Rudeis (Mheiherrat Formation) was deposited during the main period of rifting when subsidence rates increased following the slow subsidence during deposition of the Nukhul Formation. Large accommodation space was formed on the downthrown sides of the main faults of the rift allowing deposition of a large thickness of deep marine marls (Globigerina Marls) with minor sands from local entry points (Moustafa and Khalil 2017). The thickness of the Lower Rudeis exceeds 1500 m in the northernmost part of the rift (Darag Basin), Peijs et al. (2012). Paleobathymetric interpretation from well cuttings suggests outer neritic to bathyal environments over the entire Gulf of Suez with the exception of shelf conditions in the extreme North Darag basin (Peijs et al. 2012).

The Upper Rudeis unit is thinner than the Lower Rudeis in all sub-basins and was also deposited in outer neritic to bathyal water depths, with the exception of some proximal environments landward of the coastal faults (Peijs et al. 2012). The absence of evaporites in the Lower and Upper Rudeis suggests that a relative rise in sea level permitted open marine circulation across the intervening basinal sills.

The boundary between the Lower and Upper Rudeis is an angular unconformity (Fig. 8.3) that marks a tectonic event (mid-rift, mid-Rudeis, or mid-Clysmic event; Garfunkel and Bartov 1977; Beleity 1984) at 17 Ma. This event led to tectonic reorganization of the rift when motion slowed or stopped on many faults. After this initial cessation of fault displacement, fault activity continued episodically along the major block-bounding faults, creating accommodation space marked by thick accumulations of conglomerate. These chert- and limestone-boulder conglomerates are spectacularly exposed as downlapping or prograding fan-deltas in west Sinai at Wadi Sudr (Patton et al. 1994; Moustafa 1997b), the southeastern part of Gebel Gushiya (Moustafa 1996b; Young et al. 2000), Gebel El Iseila (Moustafa and Abdeen 1992), Wadi Baba (Moustafa 1987; Khalil 1998; Sharp et al. 2000; Khalil and McClay 2006), and Wadi Sidri (Gawthorpe et al. 1990; McClay et al. 1998). According to Patton et al. (1994), the mid-Rudeis event occurred at or immediately prior to the transition from the phase of rapid tectonic subsidence found in the Lower Rudeis and the phase of relatively slow subsidence characteristic of the post-Middle Miocene history of the Suez Rift.

Kareem Formation

The Kareem Formation (Fig. 8.3) is Langhian in age and includes the Markha anhydrite at its base indicating a fall in sea level after deposition of the Upper Rudeis. Paleontologic data of off-structure wells in the Gulf of Suez indicate a hiatus between the Kareem and the Rudeis Formations. Sands of the Kareem Formation record uplift and exhumation of the rift shoulders due to the presence of basement-derived debris (Evans 1990) in the central and southern gulf.

Ras Malaab Group

Subsidence history (Peijs et al. 2012) indicates that deposition of the Belayim Formation and younger sediments marks another syn-rift megasequence contemporaneous with the

onset of movement on the Dead Sea Transform at approximately 14 Ma (Serravallian time). Extension during the later stages of rifting was confined to the coastal fault system that defines the present marine gulf, and rifting became oblique. A dramatic increase in the subsidence rate happened at approximately 10 Ma (Peijs et al. 2012) that extended to the present time (Moretti and Colletta 1987; Richardson and Arthur 1988) and is attributed to a shift of the Sinai-Africa plate boundary to the Dead Sea Transform (Bosworth et al. 1998; Evans 1988; Garfunkel and Bartov 1977; Richardson and Arthur 1988; Steckler et al. 1988). Major basin evaporation began during the Serravallian due to compression between Sinai and Africa accompanying the movement on the Dead Sea Transform (Patton et al. 1994; Bosworth and McClay 2001) and restriction of the connection between the Gulf of Suez and the Mediterranean in addition to global fall of sea level. Patton et al. (1994) believe that restriction of the Gulf from the Mediterranean during deposition of the Ras Malaab evaporites was by the Wadi Araba Anticline, in addition to the eustatic fall in sea level.

The Belayim Formation (Fig. 8.3) includes two evaporites members (Baba and Feiran Members) alternating with calstic/carbonate members (Sidri and Hammam Faraun Members). The Hammam Faraun Member is made up of reefal carbonate rocks (Nullipore Limestone of Moon and Sadek 1923) in the eastern onshore part of the Suez Rift (Moustafa 2004) as well as in the southern part of Esh El Mellaha Block on the western side of the rift. Carbonate rocks of the same age were deposited on the crests of some tilted rift blocks in the western offshore area of the rift at Gharib, Shoab Gharib, Al-Hamd, and Ras Fanar oil fields.

A significant fall in sea level during the Tortonian caused the restricted gulf to deposit halite in the South Gharib and Zeit Formations instead of the alternating evaporites and marls of the Belayim Formation (Patton et al. 1994).

8.4.2.3 Syn-rift Sequence of the Northwestern Red Sea

Ranga Formation

The coarse-grained sandstones and conglomerates of the Aquitanian-Burdigalian Ranga Formation (El Bassyony 1982) form a distinct syn-rift unit unconformably overlying the pre-rift Precambrian to Eocene units and in places also overlies the Late Oligocene-Miocene red clastics (Fig. 8.3). The Ranga Formation varies in thickness from 100 to 186 m (Khalil and McClay 2009). Its lower part consists of continental red sandstones and conglomerates locally interbedded up-section with a few gypsum thin beds and marls which contain Late Aquitanian-Burdigalian fauna (referred to as Rosa Member, Philobbos et al. 1993). The upper part of the Ranga Formation consists of shallow marine conglomerates and sandstones containing oyster shell fragments and patch reefs (Fig. 8.4c). The conglomerates are generally polymictic, dominated by pebble- and boulder-size basement clasts, indicating significant uplift and erosion of the rift margin at the time of deposition of the Ranga Formation (Khalil and McClay 2009). Along the coastal area between Safaga and Quseir, the conglomerates and sandstones of the Ranga Formation develop structurally-controlled, coarse-grained fan delta systems prograding basin-ward (see Khalil and McClay 2009, 2012 for details).

Um Mahara Formation

Um Mahara Formation (Samuel and Saleeb-Roufaiel 1977) consists of reef carbonates and fine grained clastics of Late Burdigalian-Langhian age (e.g. El Bassyony 1982; Said 1990). It unconformably overlies older syn-rift units and its thickness decreases from ~180 m at Wadi Abu Ghusun in the south to ~20–30 m in Quseir area in the north (Issawi et al. 1971; El Bassyouny 1982; Said 1990). Along the Red Sea coast, between Safaga and Quseir, the reef carbonates of the Um Mahara Formation onlap rotated basement blocks and form reef talus on subdued fault scarps facing basin-ward (Fig. 8.4d).

Abu Dabbab and Um Gheig Formations

The Abu Dabbab Formation (Samuel and Saleeb-Roufaiel 1977) is a massive to poorly bedded evaporite sequence consisting of gypsum interbedded with a few shale units (Fig. 8.3). It unconformably overlies older syn-rift or pre-rift strata and its lower contact is marked by thin conglomerate beds. In the onshore area between Safaga and Quseir, the Abu Dabbab evaporites occur in isolated outcrops gently dipping basin-ward, with thickness varying from 90 to 400 m (Said 1990). In the offshore area, well data indicate that the evaporites thickness increases to ~3 km of halite and anhydrite equivalent to the onshore evaporites sequence (Tewfik and Ayyad 1984). Although the Abu Dabbab Formation is non-fossiliferous, its age is considered Middle to Late Miocene based on its similarity with the Miocene evaporites in the Gulf of Suez (e.g. Said 1990). In general, deposition of the Abu Dabbab evaporites reflects a marked change in the depositional environment in the Red Sea basin when the clastic and carbonate facies of the underlying units changed into evaporites deposition in restricted marine conditions.

The Abu Dabbab Formation is overlain by the Um Gheig Formation (Samuel and Saleeb-Roufaiel 1977) which is ~10–20 m thick and is made up of hard crystalline

limestone and dolostone. The Um Gheig Formation is late Miocene in age and locally forms prominent ledges on top of the evaporites along the Red Sea coasal area.

Mersa Alam, Shagara and Samadi Formations

Overlying the Abu Dabbab evaporites and the Um Gheig dolomites is ~200-m-thick section of marine, mixed clastics and carbonates, comprising sandstones, marls, conglomerates and a few evaporites. The rock units of this post-evaporite section include the Mersa Alam Formation (Late Miocene–Pliocene age; Philobbos et al. 1989), the Pliocene Shagara Formation (Akkad and Dardir 1966b) and the Plio-Pleistocene Samadi Formation (Philobbos et al. 1989) (Fig. 8.3). Marine fauna with Indo-Pacific origin encountered in the Pliocene Shagara Formation, indicate connection of the Red Sea to the Indian Ocean via the Strait of Bab El Mandab during the Early Pliocene (Said 1990). Along the coastal plain between Safaga and Quseir, Plio-Pleistocene deposits form gently-dipping terraces uplifted a few meters above the present-day sea level.

8.4.3 Post-rift Sequence of the Suez Rift

The Pliocene-Recent sediments represent a post-rift sequence in the Suez Rift. Although it has been common to refer to these sediments as "post-rift", there is evidence to suggest that extension continued mildly during their deposition. Subsurface (seismic and borehole) data show thickening of Pliocene and younger rocks on the downthrown sides of many faults in the rift, indicating Pliocene and younger displacement on those faults. Awney et al. (1990) show remarkable thickening of post-Miocene sediments in the area of Belayim Land and Belayim Marine oil fields compared to the nearby onshore area of the Gulf of Suez, giving a strong evidence for post-Miocene activity of the coastal faults of the Gulf of Suez Rift. Also, Pliocene sediments in the downdip area of the Araba Block (eastern onshore area of the Suez Rift) are tilted at an angle of 4° (Moustafa 2004).

The Pliocene witnessed deposition of thick clastics and evaporites in the main basin depocenters, in addition to mobilization of halite in the southern Gulf of Suez due to sediment loading (Orszag-Sperber et al. 1998).

8.5 Structural Geometry of the Gulf of Suez and Northwestern Red Sea

Compilation of the geological map of the Gulf of Suez, northwestern Red Sea, and surrounding areas (Fig. 8.6) has been done in this study making use of the authors' field mapping combined with data from several publications including Sadek (1926), Shukri (1953), Shukri and Akmal (1953), Shukri and Ayouty (1956), Abdallah and Adindani (1963), Sadek (1968), Moustafa et al. (1985), Abdel Tawab (1986), Halim et al. (1986), Aboul Karamat (1987), Moustafa (1987, 1992a, b, 1993, 1996a, b, 1997a, b, 2002, 2004), Moustafa and Khalil (1987), Moustafa and Fouda (1988), Abd-Allah (1988, 1993), Moustafa and Abd-Allah (1991 and 1992), Moustafa and Abdeen (1992), Darwish and El-Azabi (1993), Moustafa and El-Raey (1993), Moustafa and Yousif (1993), Moustafa and Khalil (1995), Khalil (1998), Khalil and McClay (1998, 2001, 2002, 2006, 2009, 2012, 2016, 2018), Khafagy (2001), Youssef and Abd-Allah (2003), Henaish (2012), Moustafa et al. (2014), Maqbool et al. (2014), Sakran et al. (2016), and Moustafa and Khalil (2017). This map shows the structural geometry of the region.

The Suez Rift extends for about 330 km in the NNW-SSE direction between Sinai Peninsula and the Eastern Desert of Egypt (Fig. 8.6). The middle part of the rift is occupied by the Gulf of Suez itself whereas the northeastern and southwestern parts are well exposed in west Sinai and the Eastern Desert respectively, offering excellent opportunities to study the rift structures. The width of the Suez Rift reaches its maximum in the south where it is about 105 km and decreases to the north with a minimum width of about 55 km (Fig. 8.6). The rift shoulders show exposed Precambrian crystalline basement rocks in the south and non-rotated Phanerozoic sedimentary rocks of Paleozoic to Eocene age in the central and northern parts indicating significant uplift of the southern areas and striping of the pre-rift sedimentary cover (Fig. 8.6). Present-day average heights of the rift shoulders range from about 2000 m in SW Sinai to 600 m at the Raha Plateau and range from about 1000 m at the Red Sea Hills west of Esh El Mellaha area to 1100 m at the N. Galala Plateau (Fig. 8.6).

The northern Red Sea shows an abrupt change in the width of the rift compared to the Suez Rift. The width of the northern Red Sea is about 200 km. The onshore Egyptian part of the Red Sea includes excellent exposures of tilted Cretaceous and Cenozoic strata bounded on the west by Precambrian basement rocks of the rift shoulder at the Red Sea Hills (Fig. 8.6). The average height of the western Red Sea shoulder is about 1000 m with highest peaks at Gebel Shayib El Banat (2187 m).

Structurally, the Gulf of Suez and northwestern Red Sea include several kilometer-scale tilted fault blocks bounded by NW-SE oriented major normal faults (Fig. 8.6). The tilted fault blocks in the Suez Rift belong to three main provinces of different dip polarities defining three mega-half grabens; two SW dipping mega-half grabens at the northern and southern parts of the rift and an intervening NE dipping

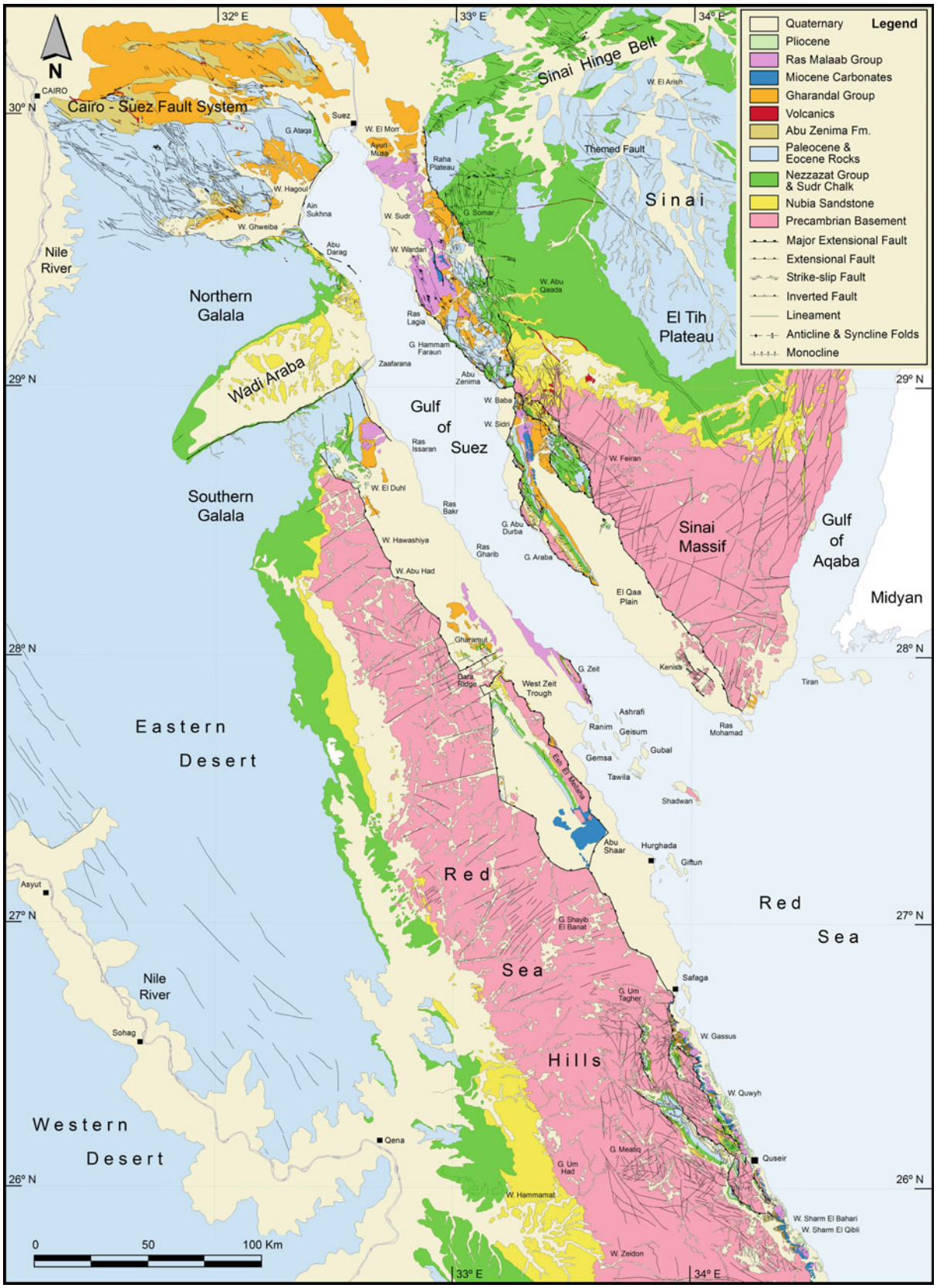

Fig. 8.6 Simplified geological map of the Suez Rift and northwestern Red Sea area based on the authors' field mapping and data from references cited in the text

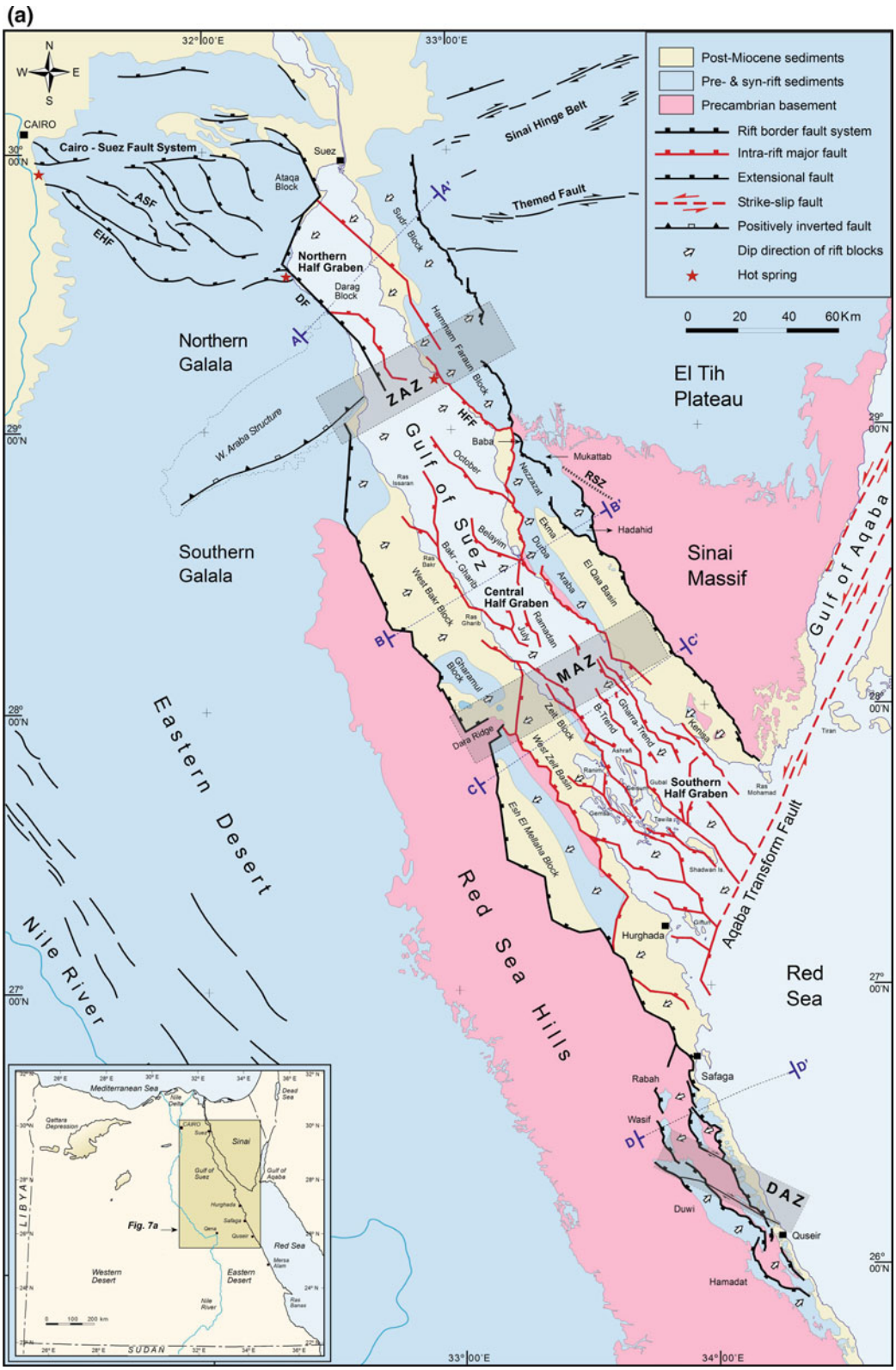

Fig. 8.7 **a** Simplified structural map showing the rift blocks of the Gulf of Suez and northwestern Red Sea and the accommodation zones between the meg-half grabens (Zaafarana (ZAZ), Morgan (MAZ) and Duwi (DAZ) accommodation zones). Offshore faults of the Gulf of Suez (after Patton et al. 1994) represent major faults with throw ≥ 1 km. Main faults of the Cairo-Suez area at the northwestern side of the Suez Rift are also shown. Abbreviations designate: Rihba Shear Zone (RSZ), Hammam Faraun Fault (HFF), Darag Fault (DF), Abu Shama Fault (ASF), and El Hai Fault (EHF). **b** Structural cross sections AA′, BB′, and CC′ after Patton et al. (1994) and DD′ after Thiriet et al. (1986). See Fig. 8.7a for locations of these cross sections

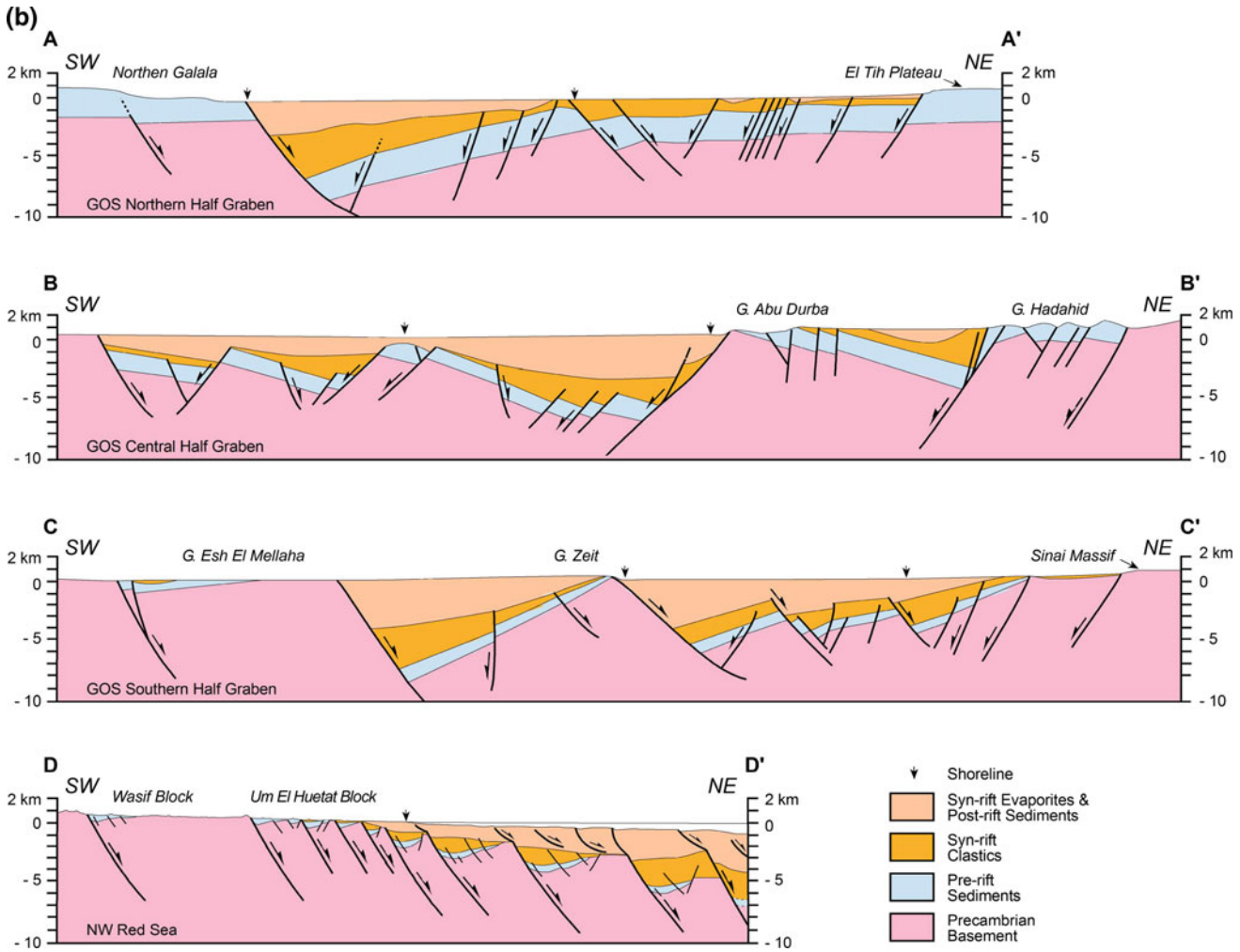

Fig. 8.7 (continued)

mega-half graben (Figs. 8.6 and 8.7). Moustafa (1976) was the first to observe the differently dipping half grabens and referred to them as "dip provinces".

The Egyptian onshore area of the Red Sea basin also includes several exposed tilted fault blocks (Figs. 8.6 and 8.7). SW dipping fault blocks in the northern part of the area indicate southward continuation of the SW dipping mega-half graben of the Suez Rift. At the latitude of El Quwyh and further south, NE tilted fault blocks of Gebel Duwi and Gebel Hamadat show a fourth mega-half graben (Fig. 8.8). Each of the four meg-half grabens of the Gulf of Suez-northern Red Sea area includes a number of tilted fault blocks (Fig. 8.7). The term rift block was defined by Moustafa (1993) as an area several tens of kilometers in length and width that includes a number of second-order (relatively small, several kilometers wide) fault blocks and is separated from adjacent rift blocks by major faults that have throws on the order of several hundreds of meters to few kilometers. The northern mega-half graben of the Suez Rift has SW dip and includes three main rift blocks; namely Sudr Block in the eastern onshore area, Darag Block in the offshore area and Ataqa Block in the western onshore area (Fig. 8.7). The central mega-half graben of the Suez Rift has NE dip and includes the Hammam Faraun, Baba, Hadahid, Nezzazat, Ekma, Durba, and Araba Blocks in the eastern onshore area; October, Belayim, Amer-Bakr-Gharib, July, and Ramadan Blocks in the offshore area; and West Bakr (in the subsurface) and Gharamul Blocks in the western onshore area (Fig. 8.7). The southern mega-half graben of the Suez Rift has SW dip and includes the Ras Kenisa Block in the eastern onshore area; Ghara Block, B-Trend Block, and the southeastern extension of G. El Zeit Block in the offshore area; and G. El Zeit and Esh El Mellaha Blocks in the western onshore area (Fig. 8.7). The southern mega-half graben of the Suez Rift extends southeastward into the northernmost part of the Red Sea and includes the G. Um Tagher, Mohamad Rabah, Wasif, Um El Huetat, and Gasus Blocks in the western onshore area (Fig. 8.9a). The fourth

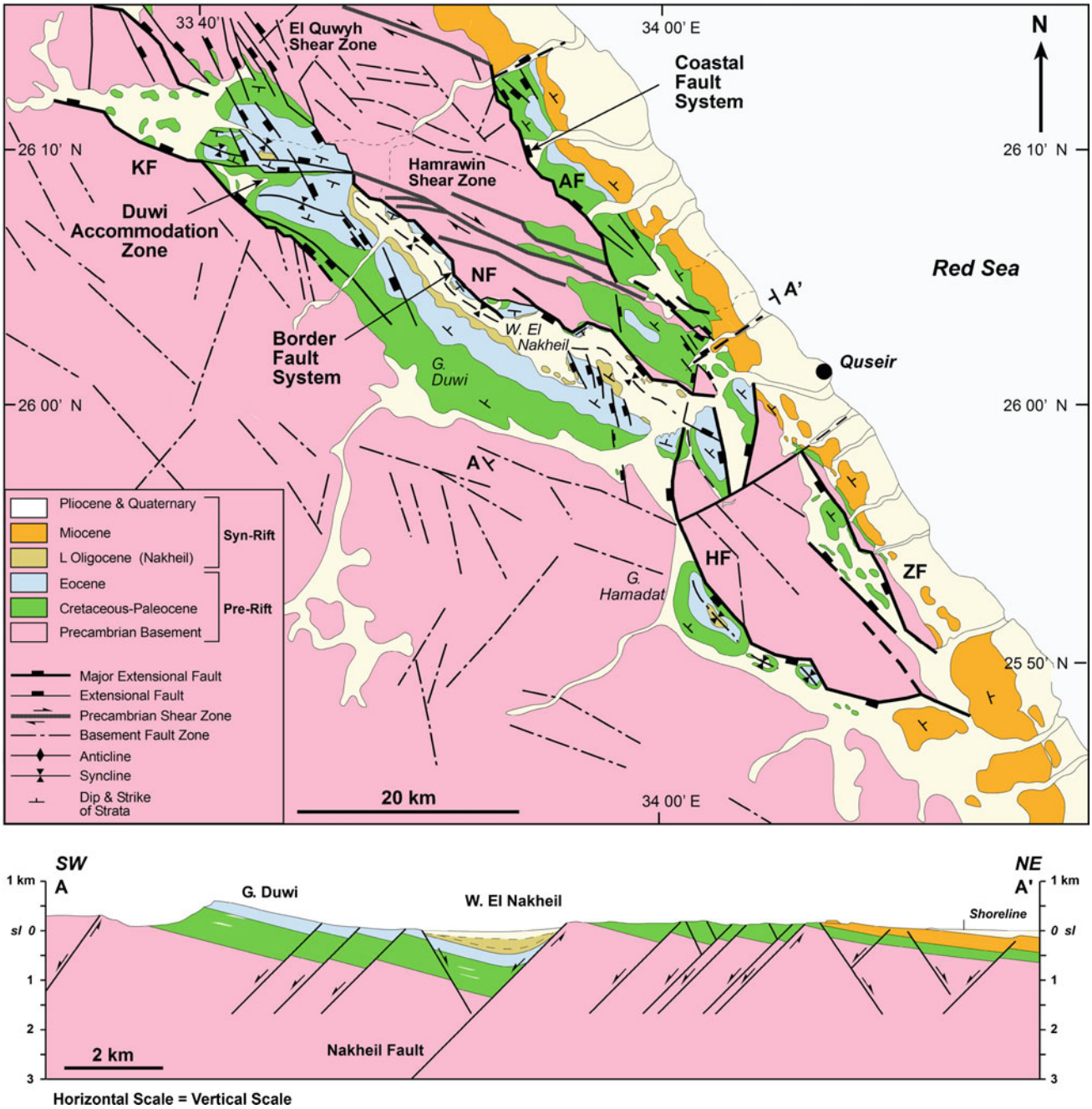

Fig. 8.8 Geological map and cross-section of the Quseir area (after Khalil and McClay 2002, 2018) showing the fault pattern and fault block geometries in the mega-half grabens of the NW Red Sea. Labels KF, NF and HF indicate the Kallahin, Nakheil and Hamadat segments of the border fault system, respectively. AF and ZF indicate the Anz and Zug El Bahar segments of the coastal fault system, respectively

mega-half graben (in the northwestern Red Sea) has NE dip and includes G. Um Hamad-G. Duwi, Anz-Ambaghi, Gihania, G. Atshan, G. Hamadat, and Zug El Bahar Blocks in the western onshore area (Figs. 8.7 and 8.8). Subsurface mapping of the Red Sea offshore area extending from Abu Ghussun to the south of Ras Banas (Tewfik and Ayyad 1984) indicates the southward continuation of the fourth (NE-dipping) mega-half graben perhaps to the southern border of Egypt.

Three accommodation zones separate the four mega-half grabens of the Suez Rift and northern Red Sea (Fig. 8.7). Two of these accommodation zones are located in the Suez

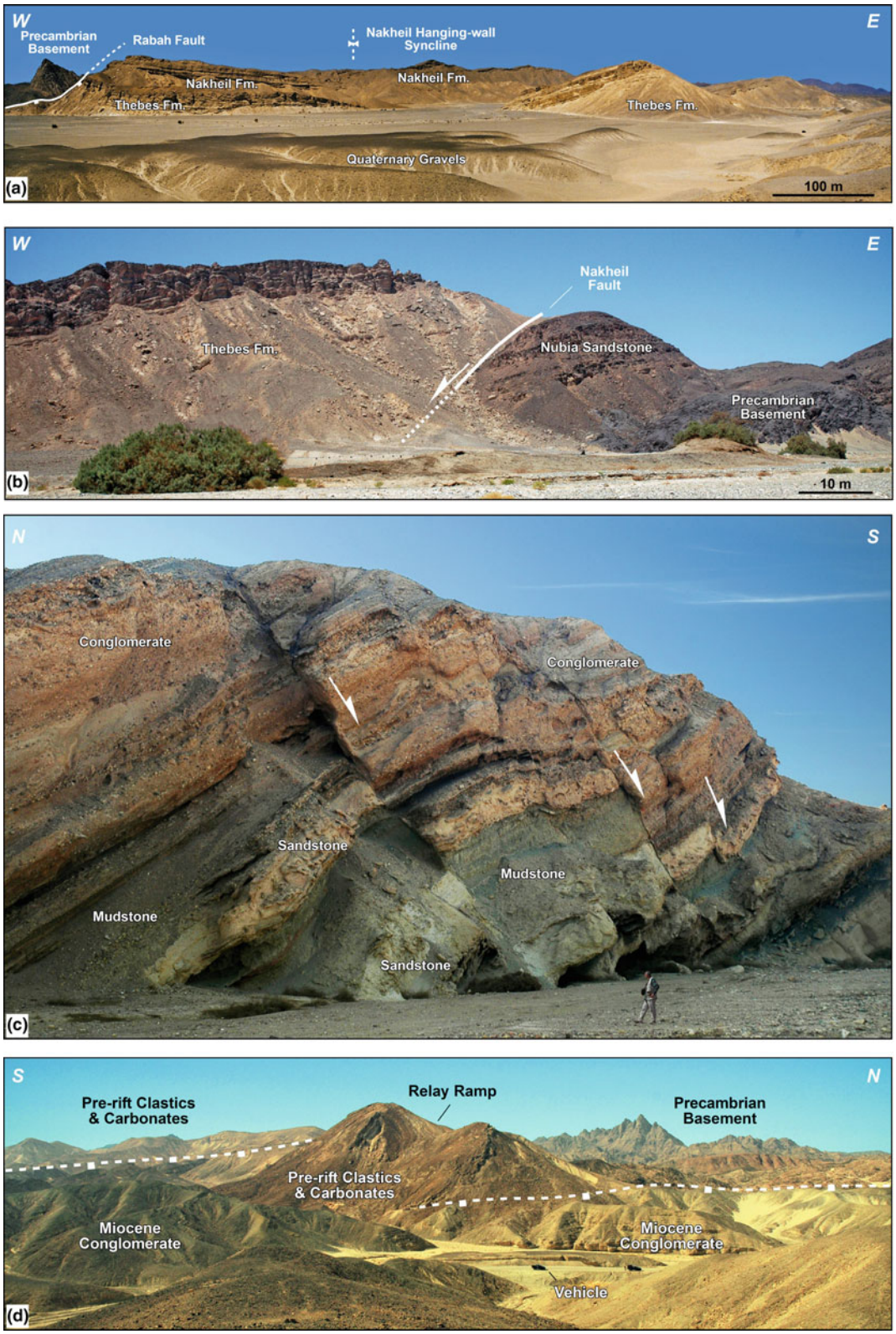

Fig. 8.9 Field views showing outcrop examples of major structural features in the NW margin of the Red Sea. **a** Basin-like hanging-wall syncline in Rabah fault block (after Khalil and McClay 2016). The Rabah Block is generally tilted to the SW and forms part of SW-dipping mega-half graben. **b** The Nakheil border fault near its northern termination. The fault surface is planar, dips 56° WSW and juxtaposes the Eocene Thebes Formation against the Cretaceous Nubia Sandstone. **c** Meso-scale extensional faults affecting Pliocene clastics and develop rotated domino-style fault blocks. **d** A steeply-dipping relay ramp between two segments of the coastal fault system in the area south of Safaga. This relay is part of a relay system controlling deposition of the Miocene coarse-grained clastics

Rift and the third is present in the northern Red Sea. Moustafa (1976) recognized the accommodation zones of the Gulf of Suez Rift and called them hinge zones instead of the later term "accommodation zones" of Bosworth (1985). Moustafa named the Gulf of Suez accommodation zones the Galala-Zenima and Morgan zones. The Galala-Zenima Accommodation Zone lies between the northern and central mega-half grabens whereas the Morgan Accommodation Zone separates the central and southern mega-half grabens (Fig. 8.7). The Galala-Zenima Accommodation Zone is also called Zaafarana Accommodation Zone in some studies (e.g. Khalil 1998) or Gharandal Accommodation Zone (Moustafa 1996a, b). Also, the western onshore part of the Morgan Accommodation Zone was named Sufr El Dara Accommodation Zone by Moustafa and Fouda (1988). The third accommodation zone is located in the northern Red Sea and was first recognized by Jarrige et al. (1990) and mapped in the northwestern onshore area. It was named the Brothers (Bosworth 1994), Sudmain (Moustafa 1997a) or Duwi Accommodation Zone (Khalil and McClay 2001; Younes and McClay 2002). We shall use the names Zaafarana, Morgan, and Duwi for the three accommodation zones.

The dip angles of the tilted blocks in the Suez Rift increase from NW to SE. The average dip of the pre-rift rocks is 12° in the northern mega-half graben, 14–15° in the central mega-half graben, and 30° in the southern mega-half graben in the southern part of the Suez Rift. On the other hand, the average dip angle of pre-rift rocks in the western onshore area of the NW Red Sea is 20–30°. No data is available for the pre-Miocene dip in the offshore Red Sea area. These dip angles show transition from steep SW dip in the southern part of the Suez Rift to relatively shallower SW dip in the northwestern part of the Red Sea. Such transition happens across the Dead Sea Transform which seems to have affected the structural deformation of the nearby areas of the Gulf of Suez/NW Red Sea rift as will be discussed in another section.

8.5.1 Pre-rift Structures of the Gulf of Suez and Northwestern Red Sea

Several pre-rift structures exist in the Gulf of Suez and Northwestern Red Sea and affected the structural geometry of the rift. These are:

1. The Sinai Hinge Belt at the northern end of the Gulf of Suez.
2. Wadi Araba inversion anticline.
3. Rihba Shear Zone.
4. Dara Ridge.
5. Ras Mohamed Arch.
6. Hamrawin and Quwyh Shear Zones.

8.5.1.1 Sinai Hinge Belt

The Sinai Hinge Belt (Moustafa et al. 2014) is a major ENE-WSW oriented structural belt in northern Sinai forming a crustal boundary between a platform area with a relatively thin Mesozoic section and shallow depth of Precambrian crystalline basement to the south (in central and southern Sinai) and an area with thicker Mesozoic sedimentary section and deeper basement to the north (Figs. 8.6 and 8.7a). This hinge belt extends from western Sinai to the Dead Sea Transform through a 250 km long and 20–25 km wide area in northern Sinai and the Naqb Desert. It started in the Precambrian or Paleozoic time as a narrow belt of ENE–WSW-oriented faults and was reactivated by normal faulting during Early Mesozoic opening of Neotethys, by dextral transpression during Late Cretaceous–Early Cenozoic closure of Neotethys, and by dextral transtension in the Miocene (Moustafa et al. 2014). Westward continuation of the Sinai Hinge Belt is obvious in the northern part of the Cairo-Suez district at the latitude of Suez city (Fig. 8.6). As the NW-SE oriented normal faults of the Suez Rift approached the Sinai Hinge Belt they were abutted by the deep-seated faults of the belt leading to abrupt termination of the rift at the latitude of Suez city (Moustafa et al. 2014). Rift structures are absent to the north of the Sinai Hinge Belt as no major faults like those of the northernmost part of the rift are present north of the Hinge Belt. Abrupt termination of the Suez Rift at the Sinai Hinge Belt led to transfer of throw and partitioning of the rift extension to the west in the Cairo-Suez area (Nelson 1987; Moustafa and Abd-Allah 1992).

8.5.1.2 Wadi Araba Inversion Anticline

The Wadi Araba structure is a major Late Cretaceous inversion anticline that extends for about 80 km between the North and South Galala Plateaus (Figs. 8.6, 8.7a and 8.10). This ENE plunging anticline has steep southern flank where nearly vertical Upper Cretaceous strata are exposed at the northern scarp of the South Galala Plateau. The northeastern nose of the Wadi Araba Anticline extends into the western part of the Gulf of Suez (Moustafa and Khalil 1995) (Fig. 8.10). The Wadi Araba Anticline controlled the northern propagation of the Suez Rift by defining the location of the Zaafarana Accommodation Zone between the northern and central mega-half grabens of the rift (Moustafa 1996a, b, 2002). The listric rift-bounding faults of the northern and central mega-half grabens of the Suez Rift gradually transferred throw to each other as they approached the Wadi Araba structure (Figs. 8.7a). These two faults overlap each other in the area of Wadi Araba Anticline indicating its effect on the propagation of these faults during rift opening and controlling the boundaries of the two mega-half grabens.

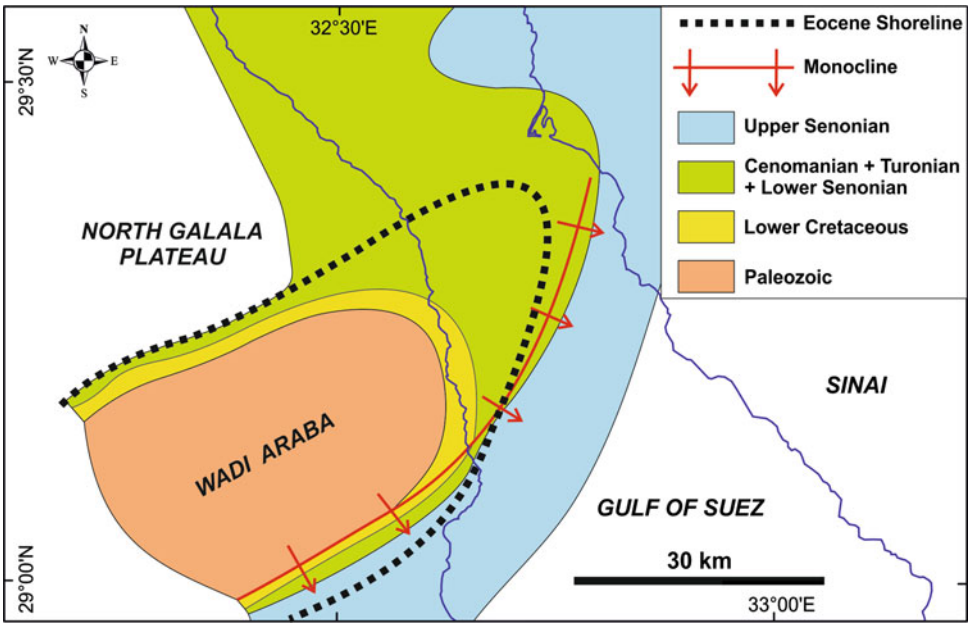

Fig. 8.10 Eocene subcrop map of the Wadi Araba Anticline and nearby areas of the Suez Rift after Moustafa and Khalil (1995)

8.5.1.3 Rihba Shear Zone

The Rihba Shear Zone (Fig. 8.7a) is a NW-SE oriented Precambrian shear zone that is perhaps a segment of the Najd Shear System (Khalil 1998; Khalil and McClay 2001; Younes and McClay 2002). It extends in the eastern shoulder of the Suez Rift for about 40 km to the southeast of the Hammam Faraun Block where it is well exposed along one of the tributaries of Wadi Feiran. The shear zone is more than 200 m wide and consists mainly of cataclasite with granite, diorite, andesite, and quartz clasts embedded in a fine grained crushed-rock matrix (Younes and McClay 2002). Two major faults (namely Hammam Faraun and Darag Faults; Fig. 8.7a) lie within the rift along strike with the Rihba Shear Zone and have large throws ranging from 4 to 7 km. Both of the Hammam Faraun and Darag Faults follow the NW extension of the Rihba Shear Zone (Moustafa and El Shaarawy 1987) indicating the control of the shear zone on the fault trends at rift opening. The relatively abundant early rift volcanicity in the vicinity of Abu Zenima area as well as the existence of the hot springs at Hammam Faraun and Ain Sukhna seem to be controlled by the Rihba Shear Zone. The Abu Shama and El Hai Faults (Fig. 8.7a) are two NW to WNW oriented major normal faults dissecting the Eocene rocks on the western shoulder of the rift and lie along strike with the Hammam Faraun and Darag Faults, perhaps representing the continuation of the Rihba Shear Zone. Hot mineral (sulfur) springs in Helwan are probably associated with the northwestern segment of El Hai Fault.

8.5.1.4 Dara Ridge

The Dara Ridge is an ENE-WSW oriented Precambrian basement ridge located at the west-central part of the Suez Rift (Fig. 8.7a). This ridge is controlled by ENE-WSW oriented faults parallel to a swarm of similar faults dissecting the Precambrian basement rocks at the western rift shoulder (Fig. 8.6). These faults have pre-Cenomanian (Moustafa and Fouda 1988) or specifically Late Proterozoic age (Ott d'Estevou et al. 1986). As a pre-rift discontinuity, the Dara Ridge controlled and defined the location and orientation of the Morgan Accommodation Zone in the western onshore area of the Suez Rift between the central and southern mega-half grabens (Fig. 8.7a).

8.5.1.5 Ras Mohamed Arch

The Ras Mohamed Arch is a pre-rift feature in the southernmost part of the Suez Rift in the form of a NE-SW oriented basement high across the present-day gulf. The evidence cited for the presence of this arch is the gradual decrease in thickness of the Nubia Sandstone from north to south along the axis of the rift and complete absence of Paleozoic Nubia at and south of this arch (Peijs et al. 2012). According to those authors, it is not known whether the absence of Paleozoic Nubia at the arch is due to erosion or non-deposition. Comparison of the total thickness of Nubia Sandstone in the Gulf of Suez and the Red Sea area indicates gradual increase in the Nubia thickness to the south of the arch where it is up to 200 m at Quseir (Khalil and McClay 2001). Detailed field mapping of the Gebel Araba Block (Moustafa 2004) indicates southward pinching out of some of the Paleozoic Nubia units, perhaps supporting the existence of the arch as a high area in the south. On the western side of the rift, El-Dawoody and Aboul Karamat (1997) showed southward truncation of Paleozoic to Turonian rock units in a NW-SE cross section along Esh El Mellaha Block due to an uplift at the southern

side of Esh El Mellaha area. They also showed the truncated units covered by the Coniacian sandstones, implying that the uplift and erosion took place at pre-Coniacian time. Data from both of the Araba and Esh El Mellaha Blocks support the presence of a pre-rift high (Ras Mohamed Arch) in the southern Gulf of Suez that affected the thickness and distribution of some of the pre-rift units.

8.5.1.6 Hamrawin and El Quwyh Shear Zones

The Hamrawin and El Quwyh Shear Zones were defined by Khalil and McClay (2001) and Younes and McClay (2002) at the northern side of Gebel Duwi (Fig. 8.8). The Hamrawin Shear Zone is a basement fabric defined by two main faults oriented N55°W and dipping steeply to the NE. Second-order structural features indicate that this shear zone had left-lateral slip in the Precambrian. The El Quwyh Shear Zone is parallel to the Hamrawin Zone and is located 20 km to the north and it also shows left-lateral slip as it displaces a granitic intrusion for about 2.5 km. Conjugate fault sets, intense fracturing, and mylonitization of the granite suggest reactivation of this shear zone. Both of the Hamrawin and El Quwyh Shear Zones represent segments of the Najd Fault System of Moore (1979). They were dextrally reactivated during the Oligo-Miocene rifting of the Red Sea where they controlled the Duwi Accommodation Zone that separates the two mega-half grabens of the northwestern Red Sea (Moustafa 1997a; Khalil and McClay 2001; Younes and McClay 2002).

8.5.2 Rift Geometry

8.5.2.1 Fault Orientations

Although the Gulf of Suez and northwestern Red Sea faults have predominant NNW-SSE orientation, the individual faults also have other trends (Fig. 8.11a, b). The population of these faults includes four sets:

- A predominant rift-parallel set oriented NNW-SSE usually referred to as the Gulf of Suez or Clysmic trend,
- Two sets oriented oblique to the rift axis (NW-SE and NNE-SSW) referred to as W-oblique and N-oblique fault sets (Patton et al. 1994), and
- A transverse fault set oriented NE-SW referred to as the cross fault set.

These four fault sets share in forming the boundaries of the rift blocks and the rift shoulders leading to a characteristic zigzag fault geometry. The cross faults are parallel to old faults and fractures dissecting the Precambrian basement

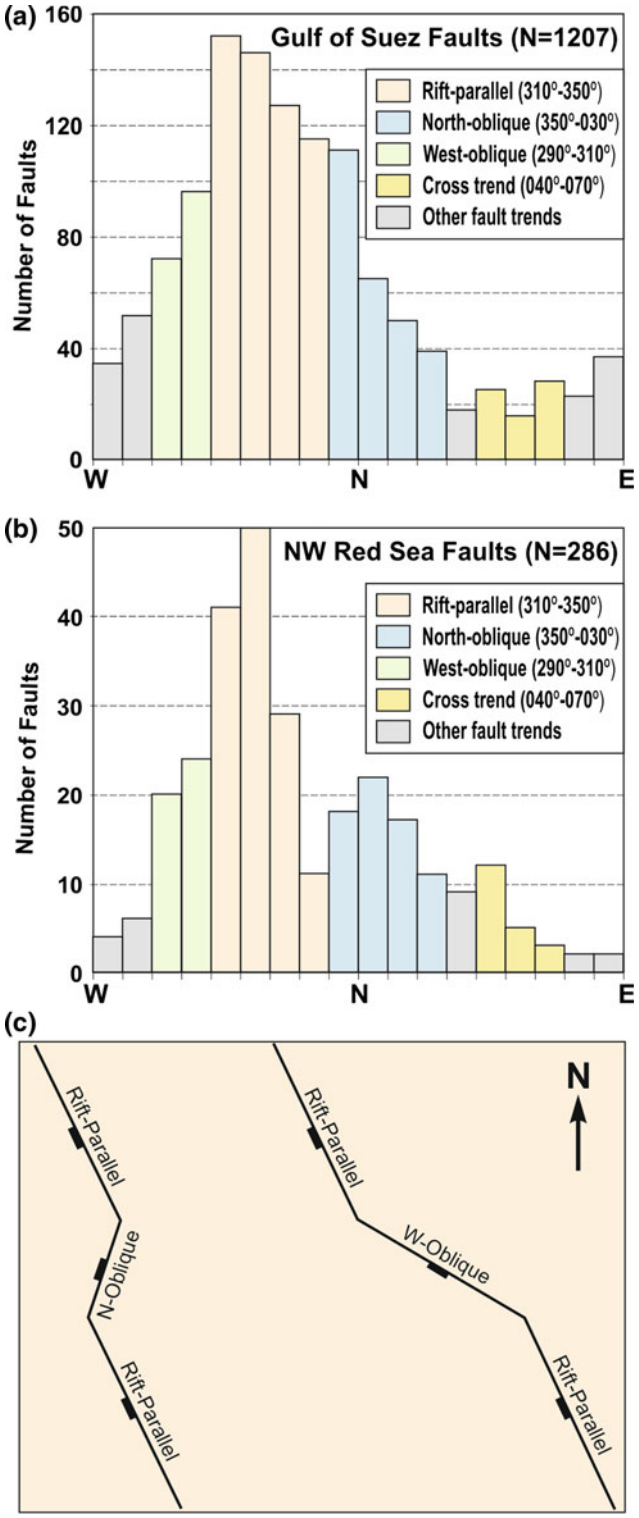

Fig. 8.11 Histograms of the faults in the onshore areas of the Gulf of Suez Rift (**a**) and the northwestern Red Sea (**b**). **c** Cartoon showing the development of north-oblique and west-oblique faults as transfer faults between rift-parallel faults, after Moustafa (2002)

rocks on the western shoulder of the rift (Fig. 8.6) and therefore represent reactivated pre-rift fabrics. Also, a few of the rift-oblique faults are reactivated old fabrics. The rift-parallel and the majority of the rift-oblique faults were formed during rift opening at Oligo-Miocene time where the rift-oblique faults acted as transfer faults between the rift-parallel faults (Patton et al. 1994; Moustafa 2002), Fig. 8.11c. Figures 8.6 and 8.7a show several clear examples of the zigzag linkage of rift-parallel and rift-oblique faults, not only in the offshore area but also in the two exposed portions of the rift as well as the rift-bounding faults.

The evidence for the pre-rift (Precambrian) age of the cross faults is based on the following facts:

- Cross faults dissect the lowermost part of the pre-rift sedimentary section where they were formed by upward propagation of the underlying basement faults.
- Sercombe et al. (1997, 2012) mapped small-throw NE and ENE oriented normal faults in the Nubia Sandstone of October oil field from borehole dipmeter logs and indicated that some of these faults do not extend upward through the overlying pre-rift rocks.
- Cross faults were mapped in the basement outcrops and Nubia Sandstone of the Araba Block (Moustafa 2004). Some of these faults extend upward and dissect the overlying rocks of the Nezzazat Group but they generally do not dissect the overlying uppermost Cretaceous and Cenozoic rocks (Fig. 8.12a). Figure 8.13 also shows ENE-WSW oriented (cross) fractures dissecting the Nubia Sandstone of the Gharamul Block (western onshore area of the Suez Rift). The overlying pre-rift rocks of Gharamul Block are not dissected by similar fracture trends.
- Mayhoub et al. (2017) proved on seismic reflection sections that cross faults in the area of Al Amir and Geyad oil fields (area between Gebel El Zeit and Esh El Mellaha) do not propagate upward though all the syn-rift section but stop in the Belayim Formation compared to the rift-parallel faults that propagate upward through all syn-rift section.

8.5.2.2 Fault Dip Angles

In each of the four mega-half grabens of the Gulf of Suez and NW Red Sea, the major faults bounding the rift blocks dip opposite to the tilt directions of the blocks (see maps and cross-sections of Figs. 8.7 and 8.8). For this reason, major faults in the northern and southern mega-half grabens of the Suez Rift dip toward the NE whereas in the central mega-half graben and the Duwi mega-half graben the major faults dip toward the SW.

The dip angles of the faults in the rift change according to the fault age, whether it is an early rift fault and affected by more rotation or it is a younger fault formed sometime after the onset of rift opening and affected by less rotation. Another factor controlling the faults dip angles is their orientation relative to the direction of block rotation. Cross faults are oriented nearly parallel to the direction of block rotation and are the least affected by this rotation. On the other hand, rift-parallel faults and the west-oblique faults are the most affected by block rotation. The faults' dip angles also depend on the amount of rotation of the block they dissect. For this reason, early rift (Clysmic) faults bounding the main blocks in the southern Gulf of Suez have the shallowest dip as some of them dip at 27° at Ranim-Tawila area (Bosworth 1995; his Fig. 10) or as low as 23°. Fault dip angle also depends on whether the fault is dipping opposite to or in the same direction of the dip of the strata. Faults dipping in the same direction of the tilted strata will attain steeper dip with continued block rotation. For this reason, some Clysmic faults may increase their dip angles with continued block rotation and may reach a vertical attitude or even exceed vertical attitude and flip their dip direction and show apparent reverse slip. This case is encountered in the southernmost part of the Suez Rift at Geisum oil field where a nearly vertical well encountered two reverse faults in the pre-rift rocks. These reverse faults are in fact rotated normal faults which were dipping in the same direction of the strata that dip 45°SW at present time.

A survey of the dip angles of the normal faults mapped on the eastern side of the Suez Rift (Moustafa 2004) has been done and these faults were restored to their original dip angles by restoring the amount of rotation of the rocks they dissect in order to determine the original dip angles. This methodology indicates that the rift-parallel faults started with average dip angles equal to 67° whereas the north-oblique and cross faults started with dip angles equal to 70° and 83° respectively. Few data for the west-oblique faults did not allow determining their original dip angles at the initial opening of the rift. This survey also indicates that the rift-parallel faults are the most affected by block rotation, being aligned orthogonal to the tilting direction of the rift blocks. It also indicates that the cross faults have the steepest dip among other faults in the rift, which might add further evidence that they represent upward propagating basement faults.

Surface mapping of the northwestern margin of the Red Sea by Khalil and McClay (2002, 2016, 2018) has shown that the faults are dominantly planar, with the NW- and WNW-trending faults dip ~55–65° (Figs. 8.8 and 8.9b) whereas the N-S and NE-trending faults have steeper dip of ~70–78° (Figs. 8.8 and 8.9c).

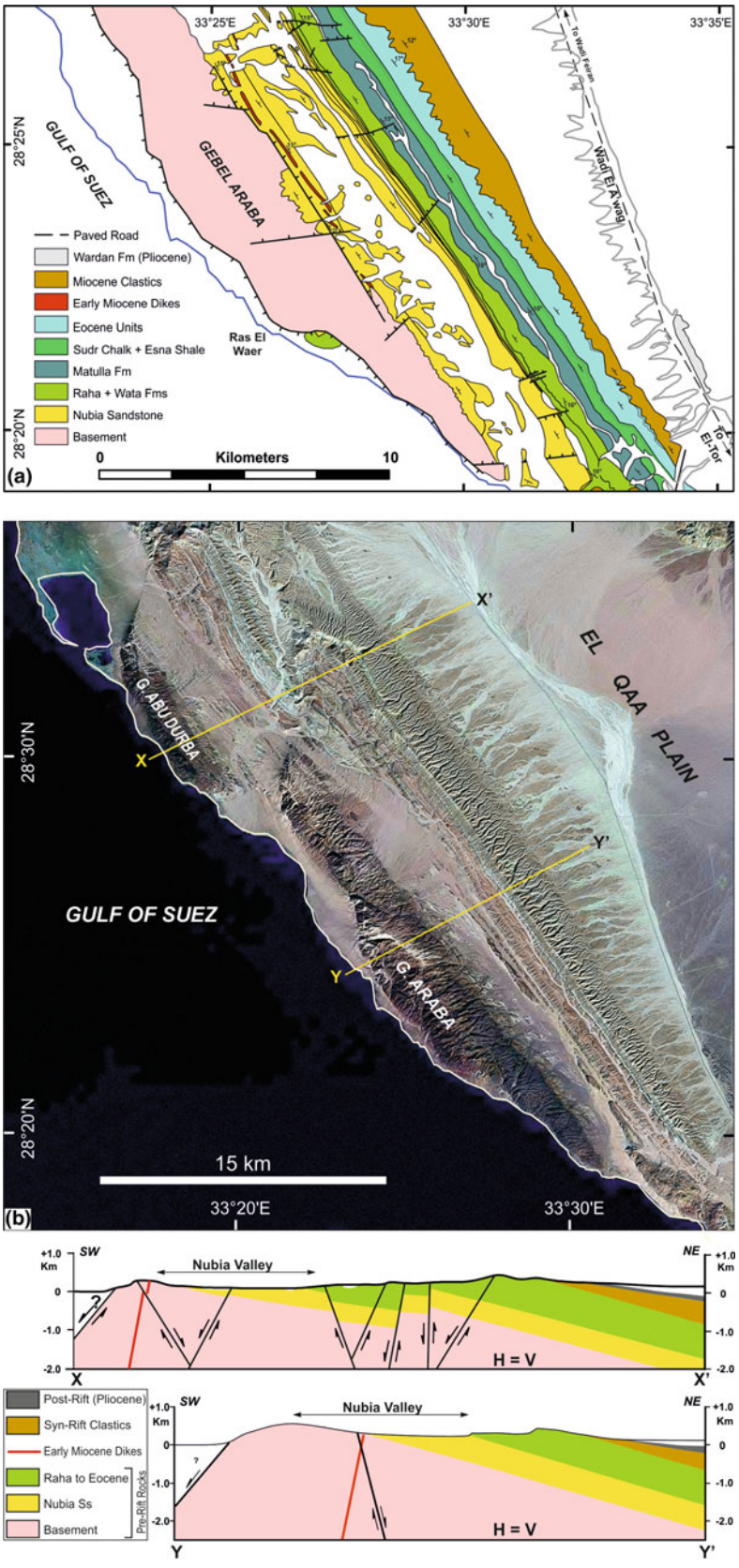

Fig. 8.12 **a** Detailed geological map of the southern part of Gebel Araba Block (after Moustafa 2004) showing E-W to ENE-WSW oriented normal faults dissecting mainly the Precambrian basement rocks and Nubia Sandstone and some of them extend upsection to the Nezzazat Group. All of these faults do not dissect the uppermost Cretaceous and Cenozoic pre-rift rocks. **b** Landsat image of the Durba and Araba blocks and structural cross sections after Moustafa (2004) showing deep erosion at the updip areas of the two blocks

Fig. 8.13 Field photograph showing ENE oriented (cross) fractures parallel to the dip direction of tilted beds of the Nubia Sandstone in Gebel East Gharamul (western side of the Suez Rift). These fractures do not dissect pre-rift rocks overlying the Nubia Sandstone of this area

8.5.2.3 Fault Geometries in Cross Sections

The fault geometries as seen on cross sections differ from the pre-rift to the syn-rift stratigraphy. In the pre-rift section, faults are mostly planar and have domino-style in addition to horsts and grabens in some cases. Some of the faults are listric, especially the major rift-bounding faults that are responsible for rotation of the mega-half grabens. Borehole and seismic data show that the North Nezzazat Fault (north-oblique trend) has listric shape (Bosworth et al. 2014; their Fig. 6).

The main faults bounding the rift blocks show a different pattern within the syn-rift stratigraphic section where they form several upward branching fault splays, e.g. the main faults bounding the October Block (Peijs et al. 2012; Lelek et al. 1992), Bakr Block (Youssef et al. 2002), Belayim Marine Block (Sobhy and Moustafa 2012), July Block (Pivnik et al. 2003), and Ramadan Block (Abdine et al. 1992), Fig. 8.14. These upward branching fault splays are probably associated with the drape (fault-propagation) folding of the syn-rift sediments above the main block-bounding faults.

In some cases, listric normal faults dipping in the same direction of stratal dip dissect the shallow syn-rift and post-rift sediments and sole down (detach) at or near the base of the Miocene evaporites, e.g. the central offshore area of the Suez Rift. Such faults may have been formed by downdip gravity gliding. The sediments in the hanging walls of these listric faults are folded by rollover anticlines (Fig. 8.15a).

Structural cross-sections of the NW Red Sea margin (Khalil and McClay 2002, 2018) indicate that the major faults are planar and bound domino-style fault blocks in the pre-rift section (Fig. 8.8). Meso-scale normal faults (with a few meters' displacement) also show planar geometries (Fig. 8.9c).

8.5.2.4 Extensional Fault-Propagation Folding

Excellent exposures on both sides of the Suez Rift and in the northwestern Red Sea area in addition to good imaging of the Miocene and post-Miocene rocks on seismic reflection sections have indicated fault-propagation folding associated with Miocene and post-Miocene reactivation of the main faults bounding the rift blocks. Large, rift-parallel monoclinal folds are obvious in the syn-rift and post-rift sediments as well as the upper part of the pre-rift sedimentary section. As the fault blocks are tilted, the monoclines show up as a steep common flank between a rift-parallel anticline and an adjacent syncline. Extensional fault-propagation folding was recognized in the syn-rift and post-rift section above the main bounding faults of several rift blocks like October Block (Fig. 8.15b; Abdo 2003) and Belayim Marine Block (Sobhy 2011); among many other blocks. In outcrop, fault-propagation folding is dominant at the rift-bounding fault east of the Baba Block (Moustafa 1987), Figs. 8.16

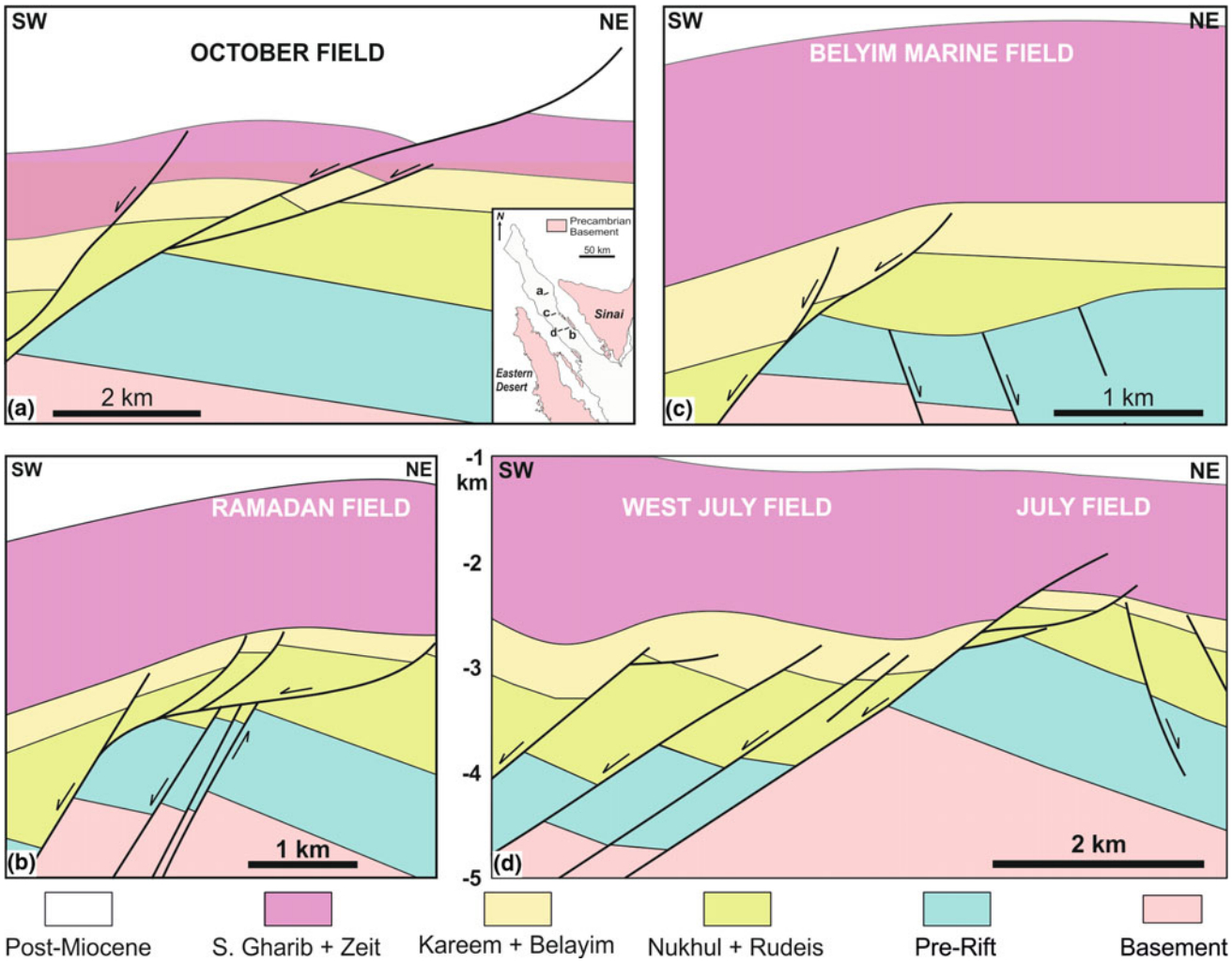

Fig. 8.14 Structural cross sections of different oil fields in the Gulf of Suez showing upward splaying of the main faults as they dissect the syn-rift section. **a** October oil field (modified after Lelek et al. 1992), **b** Ramadan oil field (modified after Abdine et al. 1992), **c** Belayim Marine oil field (modified after Sobhy and Moustafa 2012), and **d** July oil field (modified after Pivnik et al. 2003). Inset map shows the locations of the cross sections

and 8.17 as well as the west-bounding fault of Hadahid Block (Patton 1982; Moustafa and El Raey 1993; Khalil 1998; Khalil and McClay 2006), Fig. 8.18. In these two areas, large monoclines have been mapped in the pre-rift and syn-rift sections with very steep flanks reaching vertical attitudes in places. Increased folding and rotation of the steep monoclinal flank is sometimes associated with the local development of reverse faults as in the Baba Block. Such local reverse faults were interpreted to have either been formed due to space problem in the steep flank of the monocline or due to rigid-body rotation of early normal faults (Moustafa 1987). Fault-propagation folding is also well documented in the NW Red Sea onshore area (Khalil and McClay 2002, 2016, 2018). Almost each major fault bounding the downdip parts of rift blocks in the NW Red Sea area is associated with a fault-propagation fold that shows up as an asymmetric syncline due to erosion of the upper portion of the footwall block (Figs. 8.8 and 8.9a). The presence of mechanically ductile units within the pre-rift section (e.g. Nezzazat Group in the Suez Rift or Quseir Variegated Shale, Dakhla Fomration, and Esna Shale in the NW Red Sea area) sandwitched between the Nubia Sandstone and crystalline basement below and the competent pre-rift carbonate sequence above helped the development of such folds in the pre-rift and syn-rift rocks (Patton 1982; Moustafa 1987; Moustafa and El-Raey 1993; Khalil 1998; Khalil and McClay 2002, 2006). Ductile units within the syn-rift section (e.g. Rudeis Formation in the Suez Rift) also help development of these folds in the younger rocks.

Detailed studies of the geometries and kinematics of fault-related folds in the northwestern Red Sea margin (cf. Khalil and McClay 2002, 2016 and 2018) revealed that they

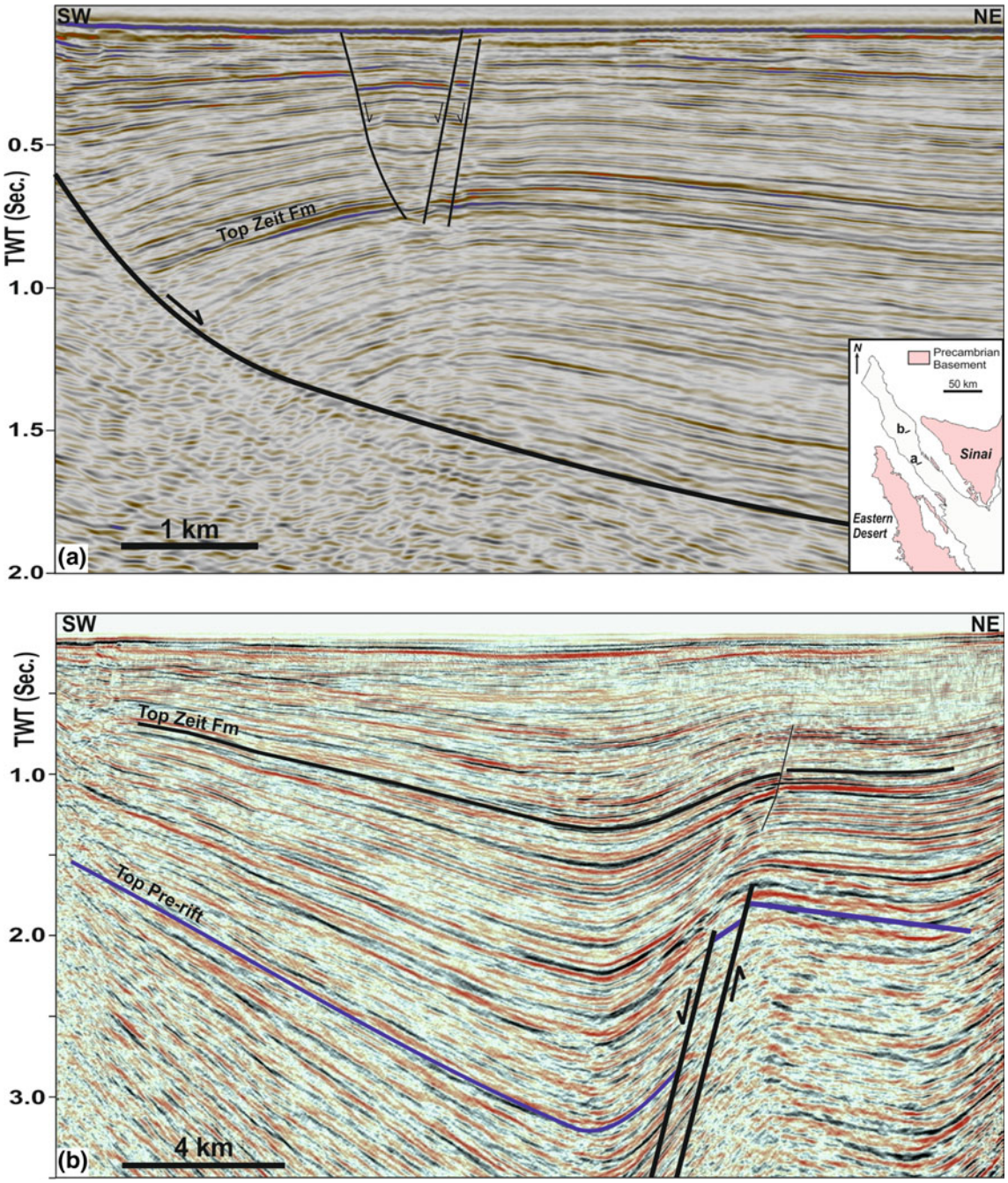

Fig. 8.15 Seismic sections from the Gulf of Suez. **a** Section showing listric normal fault (associated with a rollover anticline) dissecting the upper stratigraphic section in the Suez Rift and detaching near the base Miocene evaporites. **b** Section showing an extensional fault-propagation fold above the October Block (After Abdo 2003). Note the monoclinal structure of the syn-rift and post-rift rocks. Inset map shows the locations of these sections

are asymmetric, doubly plunging synclines developed on the hanging-walls of the major faults with the steeper limbs adjacent to the faults. Figure 8.8 shows example for the hanging-wall syncline basins (Nakheil and Hamadat synclines) in the Quseir-Duwi area. These synclines are dominated by pre-rift Cretaceous–Eocene strata, with syn-rift Nakheil sediments locally preserved in their troughs. The axial traces of these synclines trend sub-parallel to their bounding faults and bend or are offset at relay ramp zones and fault-link points (Fig. 8.8), indicating that the

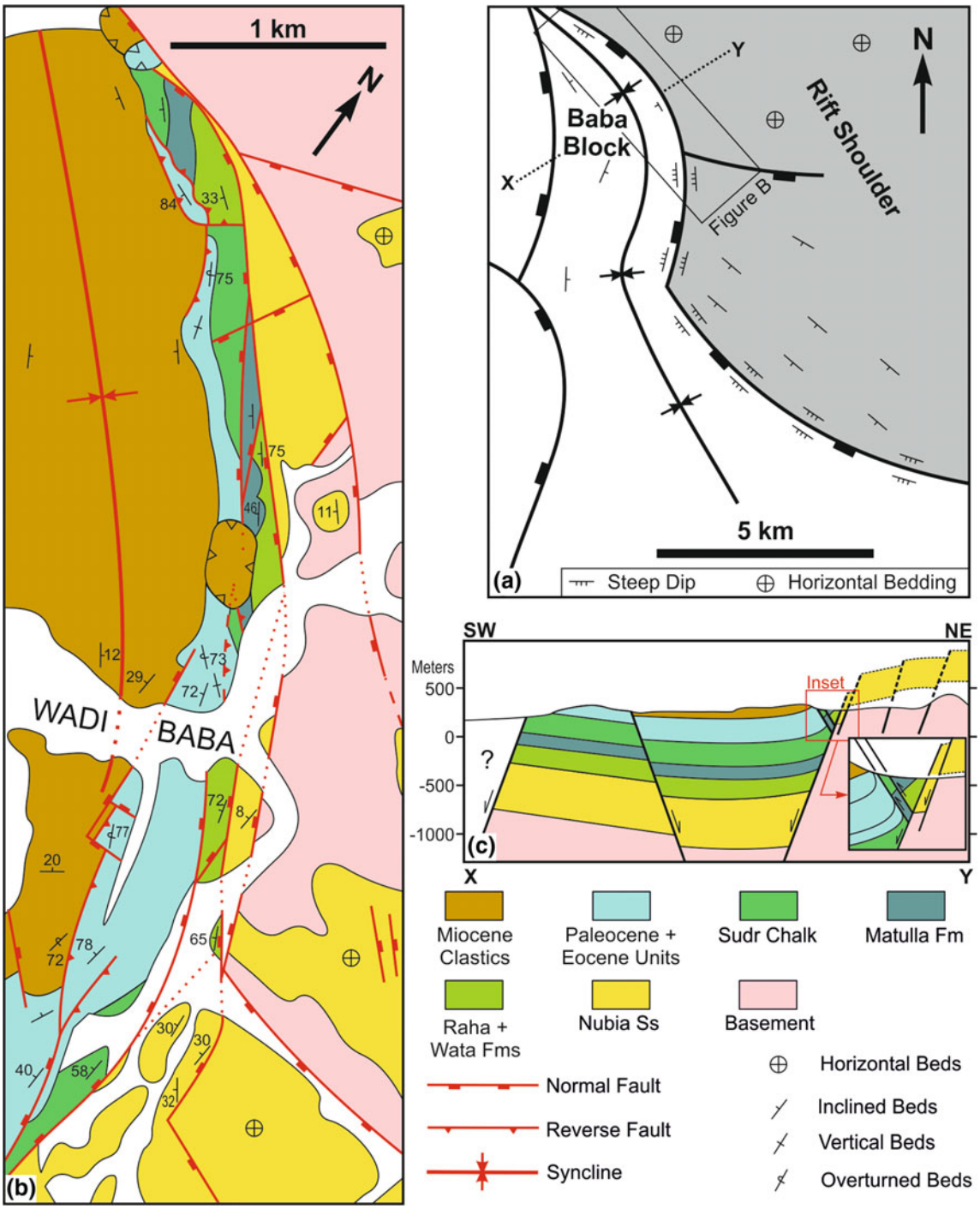

Fig. 8.16 Simplified (**a**) and detailed (**b**) geological maps and structural cross section (**c**) of the Baba fault-propagation fold, eastern onshore area of the Suez Rift (after Moustafa 1987)

geometries of the folds are pertinent to the orientation and segmented nature of their bounding faults (Khalil and McClay 2002, 2018).

8.5.2.5 Low-Angle Normal Faults

Abundant surface and subsurface data of the Suez Rift helped identify some low-angle normal faults with gentle dip

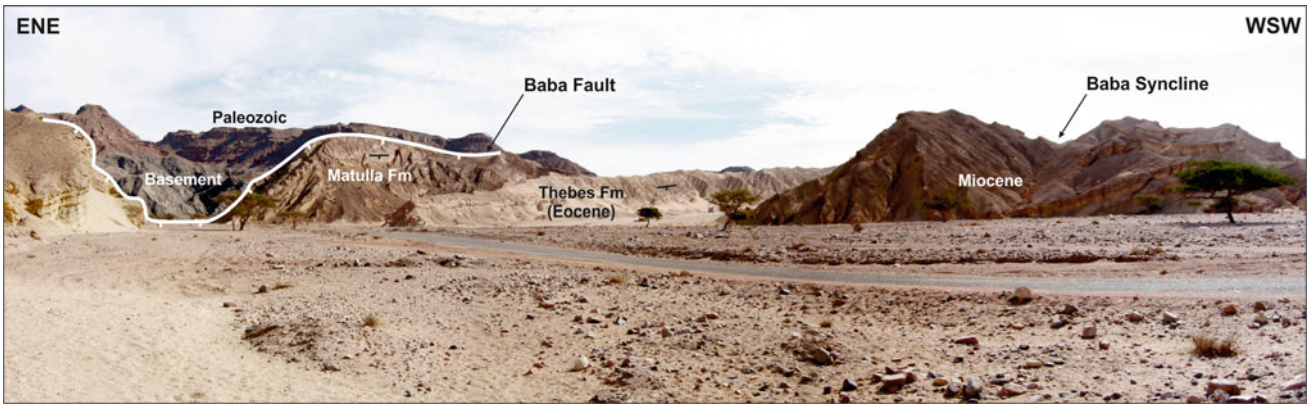

Fig. 8.17 Field panorama (looking SE) showing the steep flank of the Baba fault-propagation fold

as low as 23°. Three specific areas with low-angle normal faults are discussed here. These are the north Nezzazat Fault in the northeastern onshore area of the Suez Rift, Gebel El Zeit Fault and its southern offshore segment (Ranim-Tawila Fault), and Ashrafi-Shadwan Fault in the southern part of the Gulf of Suez.

Boreholes in the Markha Plain (north of the Nezzazat Block) penetrated the main fault bounding the northern side of the Nezzazat Block at different stratigraphic levels (see Bosworth et al. 2014; their Fig. 6). This fault (named herein the North Nezzazat Fault) is a north-oblique fault oriented N25°E-S25°W and has west-northwestward dip direction. The structural cross section of Bosworth et al. (2014) is oriented oblique to the fault and shows an apparent dip angle of the fault equal to 30°. By correcting for the direction of the cross section relative to the strike of the fault, the true dip angle of the fault is about 45°, which is low compared to other north-oblique faults in the rift. The North Nezzazat Fault, the eastern rift-bounding fault at Gebel El Samra, and the ENE-WSW oriented cross fault bounding the southern side of Hammam Faraun Block form the boundaries of the Markha Plain. Perhaps the three faults join at depth below the Markha Plain into the low-angle fault identified by the well data, giving the three linked faults a scoop shape. Seismic reflection data of the Markha Plain show recent movement on these faults leading to deformation and folding of the post-Miocene to Recent sediments.

The Gebel El Zeit Fault is another example of low-angle normal faults in the Suez Rift (Fig. 8.19a). This rift-parallel fault defines the eastern boundary of Gebel El Zeit Block and controls the coastline in this part of the Gulf of Suez. In the footwall of the fault, Precambrian basement is exposed at the crest of Gebel El Zeit Block and is overlain (downdip) by pre-rift and syn-rift sedimentary rocks on the western side of Wadi Kabrit (Fig. 8.19). The top basement surface and the overlying pre-Miocene sedimentary units dip at an average angle of 35–42° SW (Fig. 8.19c and Sakran et al. 2016). This amount of rotation of the Gebel El Zeit Block would decrease the dip angle of its east-bounding fault (Gebel El Zeit Fault). The east-facing scarp of the basement outcrop of Gebel El Zeit has consistent slope angle of about 25° (Fig. 8.19a) and seems to be controlled by Gebel El Zeit Fault reflecting its present-day dip angle. The Ranim-Tawila Fault represents the southern offshore continuation of Gebel El Zeit Fault. Borehole data indicate that the dip of this fault is 27° (Bosworth 1995), Fig. 8.20. The pre-Miocene rocks in the footwall of the Ranim-Tawila Fault dip very steeply at about 45° SW indicating high rotation of the block and its east-bounding fault.

The Ashrafi-Shadwan Fault lies to the east of the Ranim-Tawila Fault and represents the southern segment of the B-Trend Fault. Structure contour map of the Ashrafi-Shadwan Fault surface as constructed from borehole data indicates gentle dip of the fault as low as 23° (Bosworth 1995).

8.5.2.6 Accommodation Zones Between the Mega-Half Grabens

The three accommodation zones of the Gulf of Suez and northwestern Red Sea; namely the Zaafarana, Morgan, and Duwi Accommodation Zones (Fig. 8.7a) are discussed in this section. The study of these accommodation zones indicates the impact of pre-rift structures on controlling their locations.

Zaafarana Accommodation Zone

The Zaafarana Accommodation Zone is about 40 km wide and extends across the northern part of the Suez Rift between the northern and central mega-half grabens. This accommodation zone is exposed in the eastern onshore part of the rift as it lies between the SW dipping Sudr Block and the NE dipping Hammam Faraun Block (Fig. 8.7a). The location of this accommodation zone was controlled by the Late Cretaceous-Early Cenozoic Wadi Araba inversion

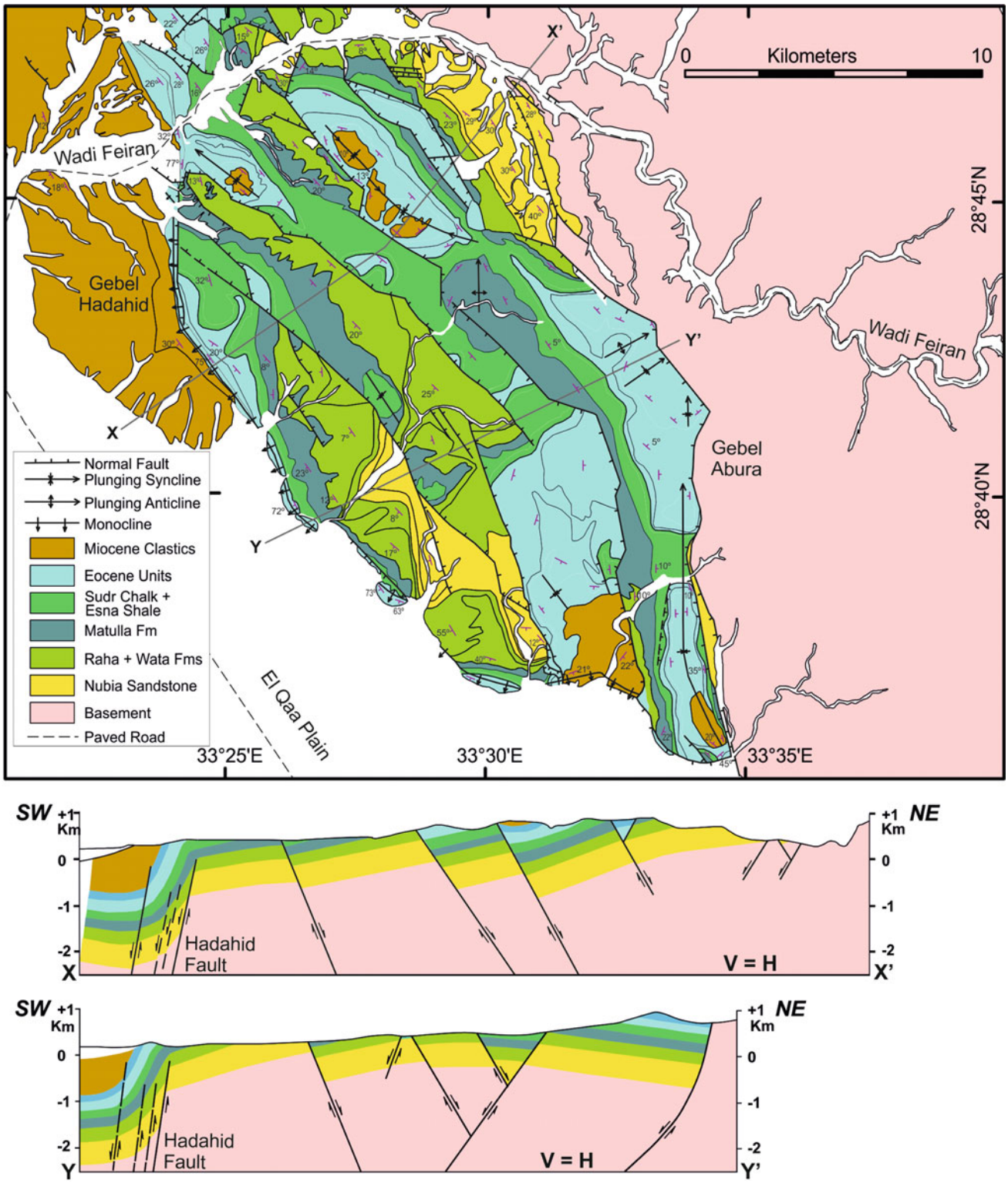

Fig. 8.18 Simplified geological map and structural cross sections of Hadahid Block showing the fault-propagation fold overlying the Hadahid Fault, after Moustafa and El-Raey (1993) and Moustafa (2004)

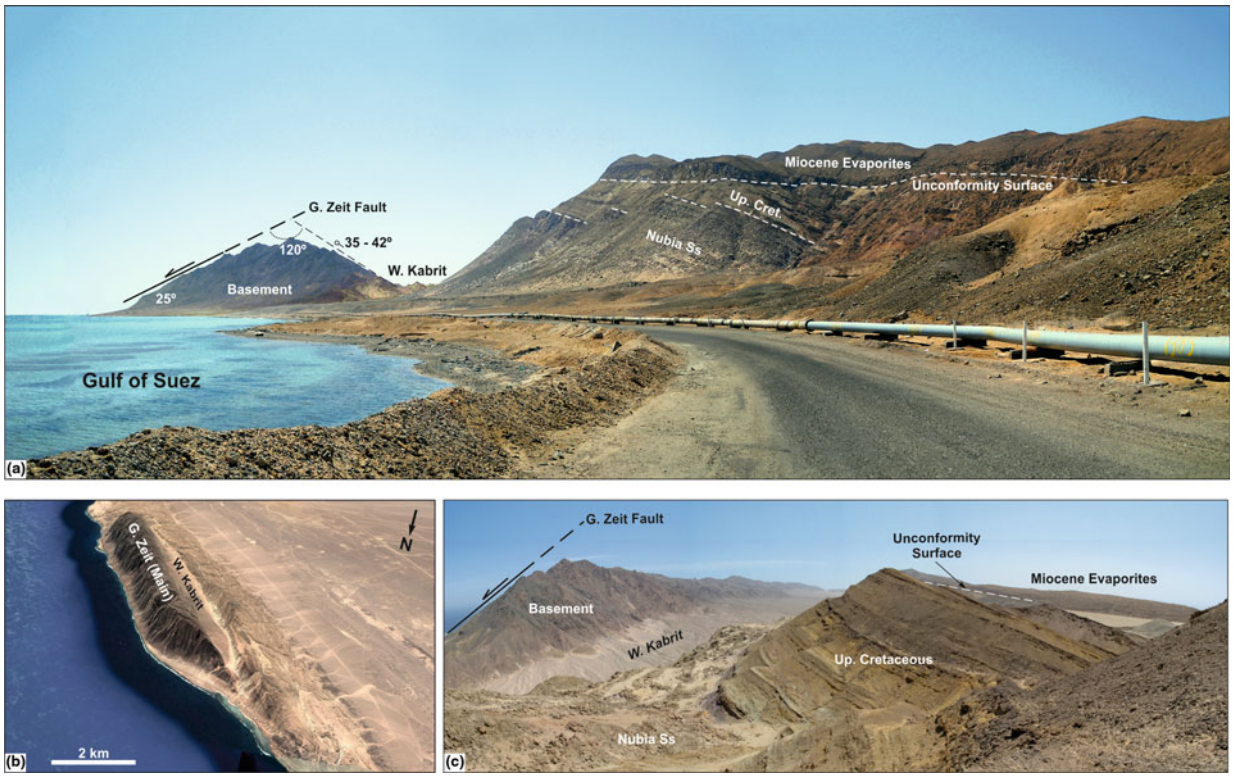

Fig. 8.19 **a** Field photograph of the northern part of Gebel El Zeit Block showing the basement outcrop with tilted upper (stratigraphic) surface and east-facing slope coinciding with a major low-angle fault (Gebel El Zeit coastal fault). Note also the rift breakup unconformity between the Raha–Matulla section and the Miocene evaporites. **b** Google Earth 3D view of the same area showing Gebel El Zeit coastal fault and change in its orientation from NNW to west-oblique (foreground). **c** Field photograph (looking SE) showing the SW dipping pre-Miocene sedimentary units overlying the Precambrian basement of Gebel El Zeit (photo by Gamal Ammar)

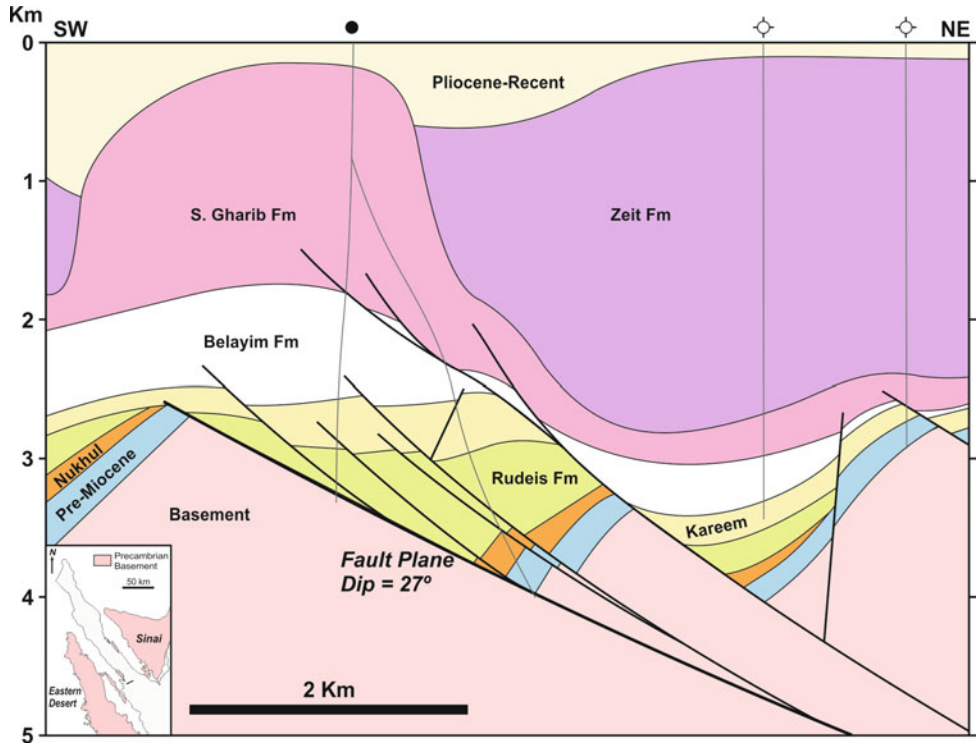

Fig. 8.20 Structural cross section showing the gentle (27°) dip of the Ranim-Tawila Fault, after Bosworth (1995). Note also the obtuse angle (~110°) between the fault and pre-Miocene beds

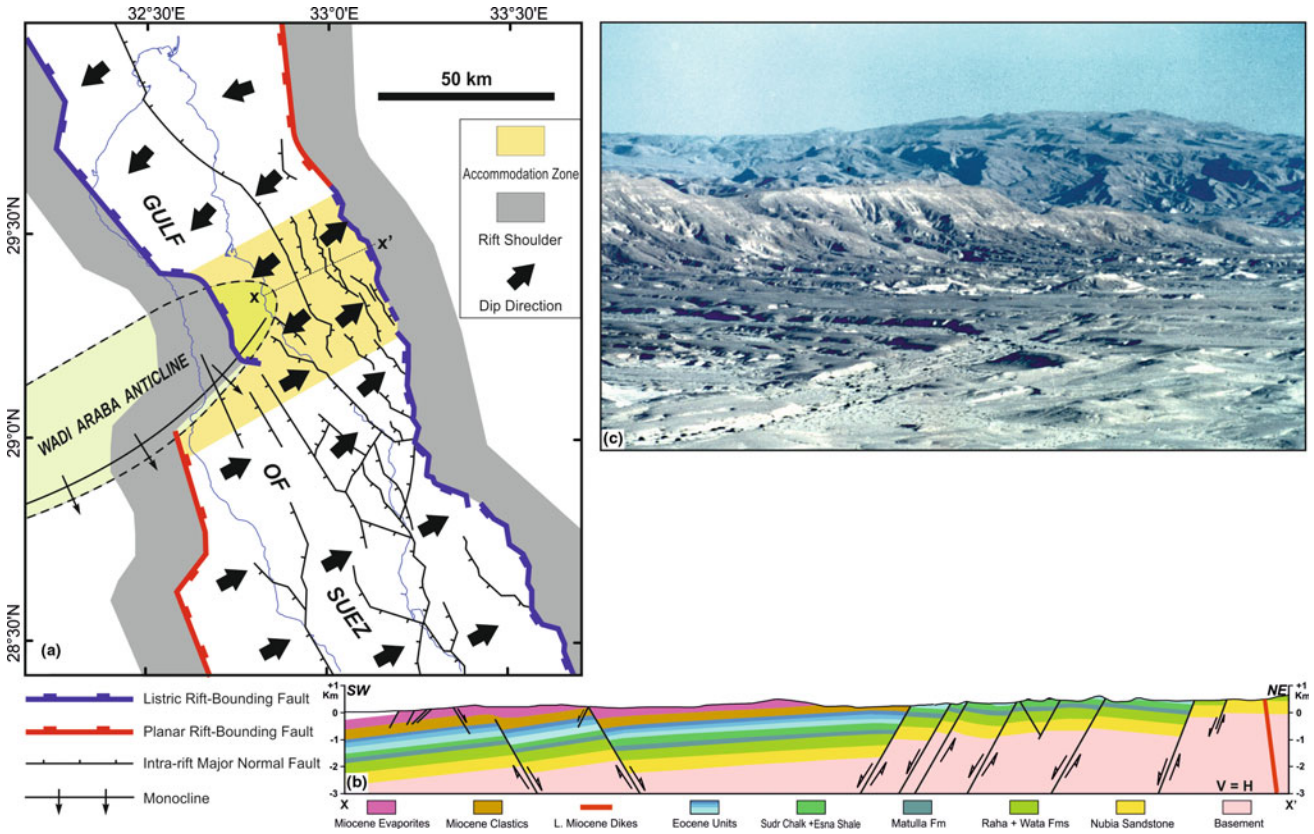

Fig. 8.21 **a** Simplified structural map showing the location of the Zaafarana Accommodation Zone relative to the Wadi Araba inversion anticline. **b** Structural cross section of the eastern onshore part of the accommodation zone after Moustafa (1996b). **c** Field photograph showing oppositely dipping fault blocks within the accommodation zone, blocks in the foreground dip NE and those in the background dip SW

anticline (Lambiase and Bosworth 1995; Moustafa 1996a, b) indicating the influence of pre-rift structures on the geometry of the rift. Detailed field mapping of the eastern onshore part of the accommodation zone (Moustafa 1996a, b) indicates that the deformation proceeded by dip-slip normal faulting. The listric rift-bounding faults of the northern and central mega-half grabens overlap each other at the area of the Wadi Araba Anticline (Fig. 8.21) and gradually transferred their throws to each other as they approached the anticline.

The overall structure of the accommodation zone is a large twist zone or antiform (Fig. 8.21b) lying between the overlapping ends of the two conjugate rift-bounding listric faults. This large antiform is dissected by several rift-parallel normal faults dipping NE (parallel to those of the northern mega-half graben) and SW (parallel to those of the central mega-half graben). These oppositely dipping faults interfinger with each other forming several horsts and grabens in the accommodation zone. One of these grabens lies in the offshore area between the ends of the Darag Fault and Hammam Faraun Fault. Seismic reflection profiles indicate that pre-rift and syn-rift rocks within this graben show gradual change in dip from NE to SW (Moustafa and El Shaarawy 1987).

Morgan Accommodation Zone

The Morgan Accommodation Zone separates the central and southern mega-half grabens of the Suez Rift (Fig. 8.7a). The NE dipping Araba, Ramadam, July, and Gharamul Blocks lie on the northern side of this accommodation zone whereas the SW dipping Esh El Mellaha, Zeit, B-Trend, Ghara, and Kenisa Blocks lie on the southern side (Figs. 8.6 and 8.7a). The western onshore segment of this accommodation zone is well exposed at the vicinity of Gebel Sufr El Dara (Moustafa and Fouda 1988; Coffield and Schamel 1989). Detailed field mapping of this area indicates that this 20-km wide accommodation zone was controlled by pre-rift cross faults of the Dara Ridge (Fig. 8.22a). Moustafa and Fouda (1988) believe that the cross faults of the Dara Ridge have pre-Cenomanian age whereas Ott d'Estevou et al. (1986) considered them of Late Proterozoic age. These faults dissect the Precambrian basement rocks of the western shoulder of the rift but do not dissect Cenomanian rocks

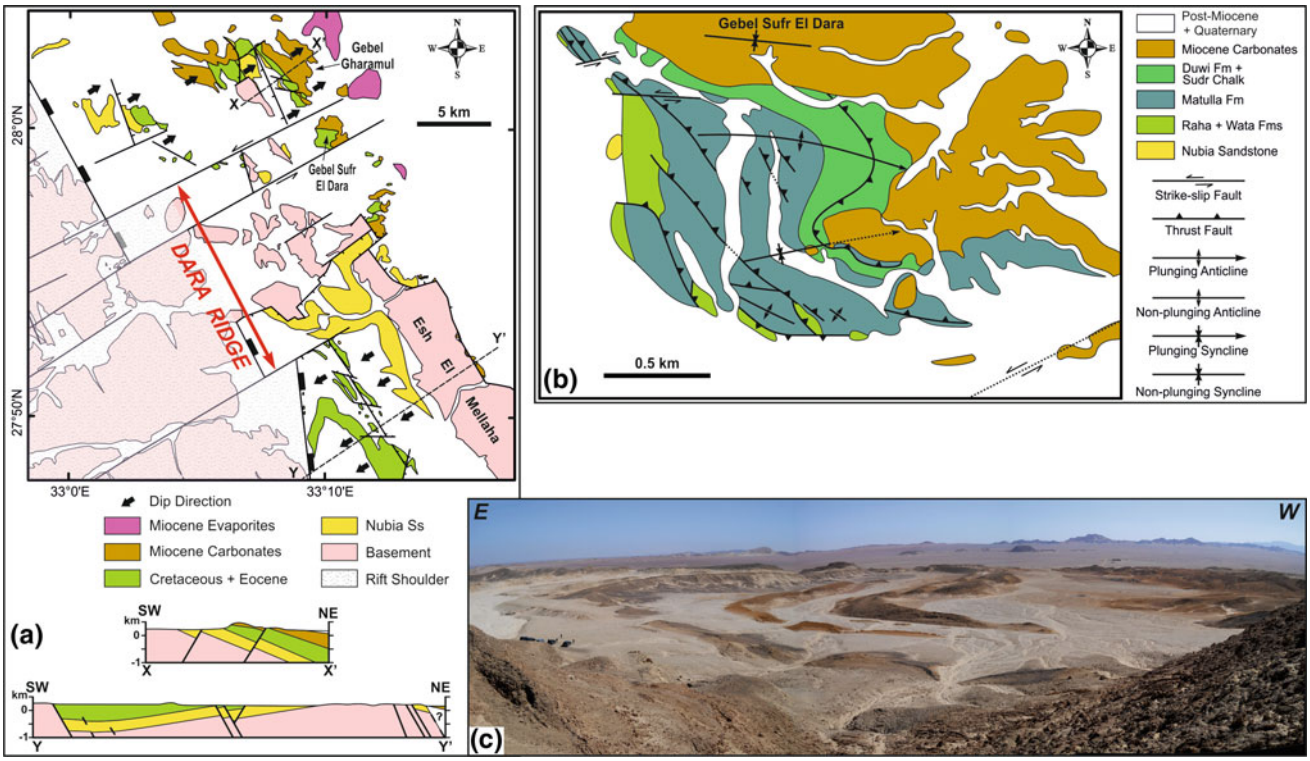

Fig. 8.22 Simplified geological maps of the western onshore segment of the Morgan Accommodation Zone (**a**) and Gebel Sufr El Dara (**b**), after Moustafa and Fouda (1988). Gebel Sufr El Dara lies within the accommodation zone between ENE-WSW oriented cross faults. **c** Field photograph showing the folded Upper Cretaceous rocks of Gebel Sufr El Dara

lying west of these Precambrian outcrops. The deformation in Sufr El Dara area is believed to have proceeded by transpression as a result of the opposite directions of tilting of the central and southern half grabens of the rift. Transpressional deformation led to folding of the pre-rift rocks of Gebel Sufr El Dara (Figs. 8.22b and 8.22c). Relatively small (km-scale) eastward and southeastward plunging folds in addition to NW-SE oriented reverse faults affect the pre-rift sedimentary rocks of Gebel Sufr El Dara and are bounded by large cross faults (Fig. 8.22a). Reverse faults affect the relatively more competent Raha, Wata, and the sandstones of the lower part of the Matulla Formation whereas folding affects the upper shale unit of the Matulla Formation and the overlying argillaceous chalk of the Sudr Formation. A detachment surface is expected to exist within the shales of the upper part of the Matulla Formation between the overlying folded rocks and the underlying reverse-faulted rocks. Peijs et al. (2012) considered these compressional structures to be related to the Late Cretaceous-Early Cenozoic Syrian-Arc structures resulting from Neotethyan deformation although the orientations of these compressional structures is different from the Syrian Arc structures of northern Egypt.

Duwi Accommodation Zone

The Duwi Accommodation Zone is located in the northwestern Red Sea area and has relatively narrow width compared to the Zaafarana and Morgan Accommodation Zones (Figs. 8.7a, 8.8, and 8.23). SW dipping rocks lie to the north of this accommodation zone and NE dipping rocks lie to the south. The location and orientation of the Duwi Accommodation Zone are controlled by a pre-rift, WNW-ESE oriented fault that belongs to the Late Proterozoic Najd Fault System (Moustafa 1997a) in the area of the Hamrawin and El Quwyh Shear Zones (Khalil and McClay 2001; Younes and McClay 2002). Excellent outcrops in the northwestern Red Sea onshore area show oppositely tilted fault blocks on both sides of the accommodation zone (Fig. 8.23). The pre-rift fault controlling the accommodation zone extends for about 60 km through the Precambrian basement rocks beyond the limits of the oppositely dipping fault blocks. This fault seems to continue southeastward into the offshore area as indicated on regional magnetic anomaly maps (Meshref 1990). Slickenside lineations show right-lateral slip on this fault to the east of Gebel Duwi (Abdeen 1995). This right-lateral slip was attributed to

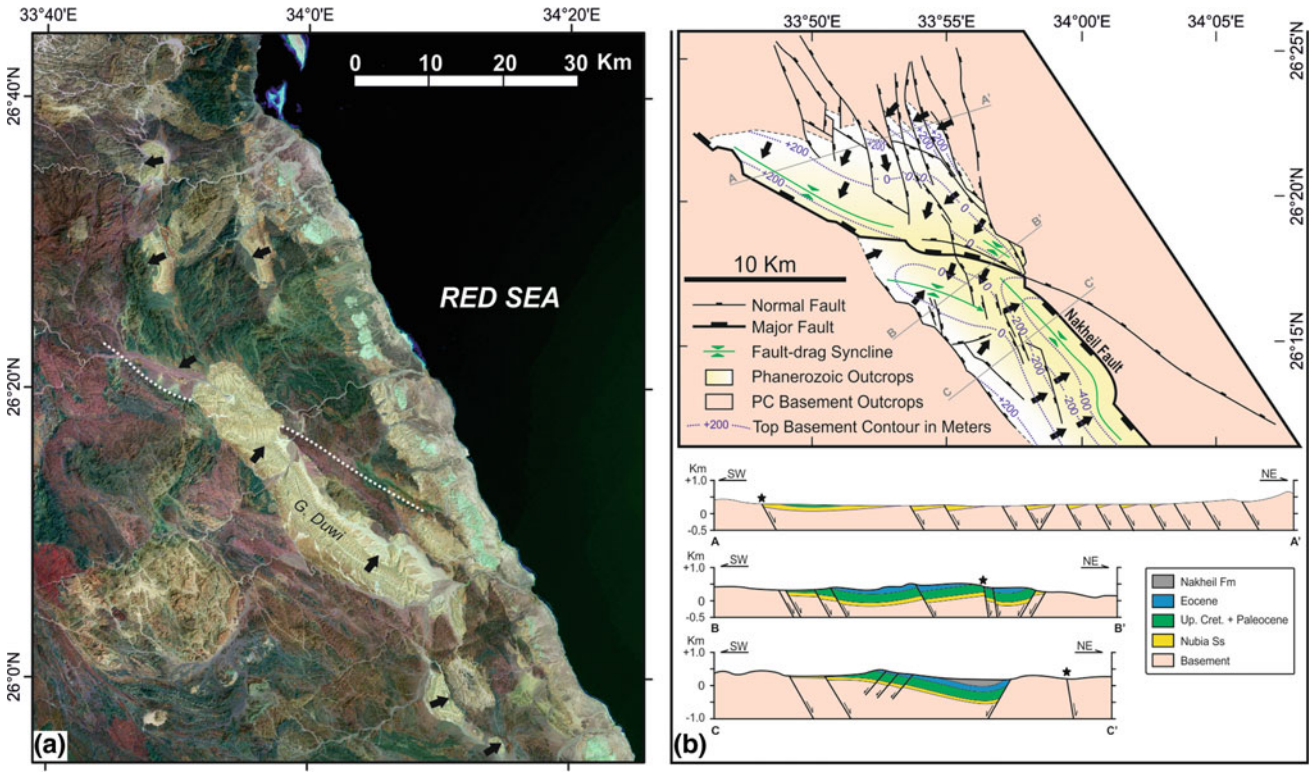

Fig. 8.23 **a** Landsat image showing the WNW-ESE oriented fault controlling the Duwi Accommodation Zone between SW dipping and NE dipping rift blocks. **b** Simplified structural map and structural cross sections of the accommodation zone after Moustafa (1997a)

reactivation of the Precambrian fault during the initial phases of rifting in the northern Red Sea (Moustafa 1997a). Other faults of the same orientation were also mapped in the Precambrian basement rocks of the area by Abdeen et al. (1992) and were also attributed to the Najd Fault System. The Nakheil Fault and other rift-parallel faults affecting the Duwi Block are abutted by the accommodation zone. Similarly, NNW-SSE oriented rift-parallel faults affecting the SW dipping rocks on the northern side of the accommodation zone are abutted by the major WNW-ESE oriented fault of the accommodation zone (Fig. 8.23b).

8.6 Impact of Tectonics on Sedimentation in the Gulf of Suez and Northwestern Red Sea

The deposition and distribution of syn-rift sediments in the Gulf of Suez and Red Sea rifts show excellent examples of the effect of tectonics on deposition of these sediments. Syn-rift rocks were deposited in half-graben basins bounded by major normal faults and have wedge shapes with largest thickness close to the bounding faults (see cross-sections of Figs. 8.7b and 8.24). The distribution of individual syn-rift units in these wedge-shaped packages depends on the rate of subsidence as well as the amount of block rotation. Not all syn-rift units are deposited in every part of the half-graben basin. The oldest syn-rift units are deposited in the downdip areas of these basins close to the main fault bounding this block. These units wedge out in the updip direction and may pinch out completely before reaching the highest (updip) area of the tilted fault block (Fig. 8.24a). Such highest areas of the tilted block may get covered by younger syn-rift units at relatively late time. On the other hand, pre-rift rocks in the updip areas of the tilted blocks may experience erosion and a big hiatus can be identified in this case which includes missing pre-rift units due to erosion and missing syn-rift units due to non-deposition (Fig. 8.24). In other cases, the facies change from the updip areas to the downdip areas of the half-graben basins where the updip areas always have shallower water depths that may be suitable for deposition of reefal carbonate rocks (Fig. 8.4d), when other environmental conditions are met. We cite some examples in the following paragraphs showing the impact of tectonics on sedimentation.

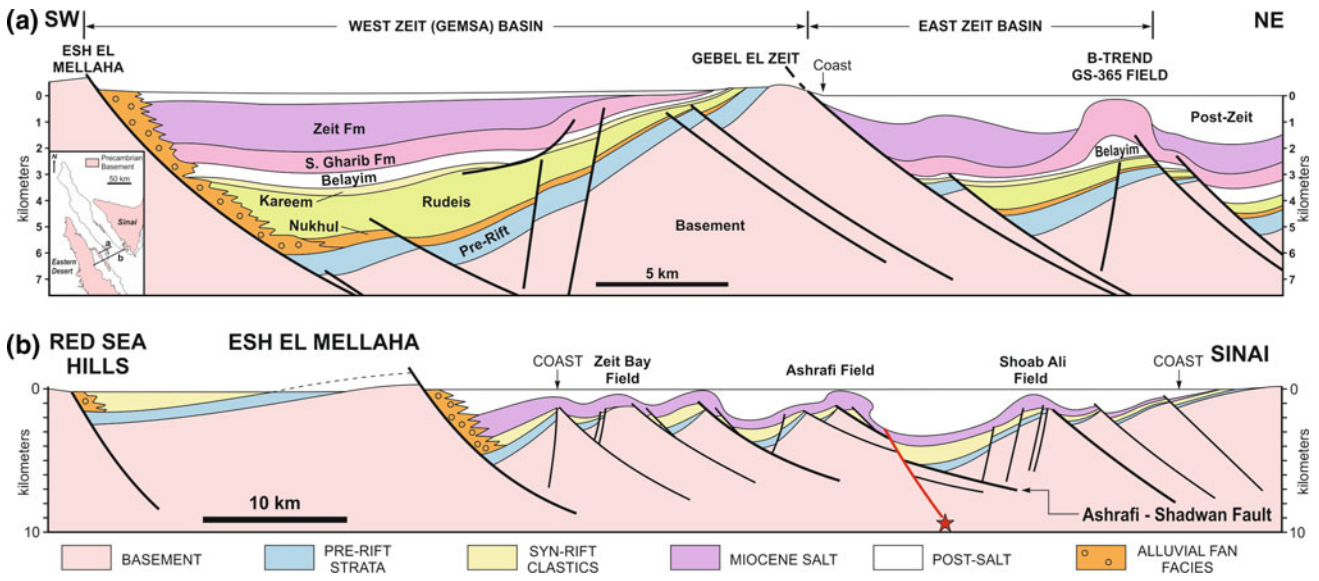

Fig. 8.24 Regional structural cross sections of the southern Gulf of Suez after Bosworth (1995). **a** Across the East Zeit and West Zeit (Gemsa) Basins showing the wedge-shaped syn-rift units. **b** Section showing a second-generation fault (red color and marked by star) dissecting the Ashrafi-Shadwan early rift fault. Inset map shows the locations of the cross sections

8.6.1 Wedge-Shaped Syn-rift Units

The West Zeit (also called Gemsa) and East Zeit Basins in the southwestern portion of the Suez Rift show the wedge-shaped geometries of the syn-rift units in the Suez Rift (Fig. 8.24a). The West Zeit Basin represents the downdip area of the Zeit Block and it lies between the exposures of Gebel El Zeit and Esh El Mellaha Range. This basin is about 20–25 km wide and about 45 km long. It is asymmetric as it occupies the tilted Zeit Block and is bounded on the SW by Esh El Mellaha Fault. Seismic and borehole data indicate that the depocenter of this basin lies in the southwestern area, close to the Esh El Mellaha Fault. The basin fill of syn-rift and post-rift sediments is about 6 km at the depocenter compared to only 0.5 km at the updip area (Fig. 8.24a). All of the Miocene and post-Miocene rock units in the West Zeit Basin have wedge shapes indicating tectonic subsidence during deposition of these units. A similar setting is also clear in the East Zeit Basin, which lies between the Gebel El Zeit outcrop and the B-Trend (Fig. 8.24a). The East Zeit Basin also has wedge shape with largest thicknesses deposited close to Gebel El Zeit Fault at the western side of the basin. The largest thickness of Miocene and post-Miocene sediments in the East Zeit Basin is ~4.5 km compared to ~1.7 km thickness (excluding the later salt flow) at the updip area (Fig. 8.24a).

The wedge shapes of the individual syn-rift units are associated with change in facies from deeper-water facies in the downdip area to shallower-water facies in the up-dip area, with the coarse clastics derived from erosion of pre-rift rocks at the updip areas are dumped down the fault scarp into the adjacent basin. For this reason, the facies of the thick parts of the wedge-shaped syn-rift units are dominated by such eroded and reworked material. In order to avoid correlation problems due to lateral facies changes, biostratigraphic correlation of the syn-rift units within these half-graben basins is more accurate. Figure 8.25 shows an example of biostratigraphic correlation of part of the syn-rift section in the October Basin (northern part of the Gulf of Suez Rift). It clearly shows the wedge shape of individual syn-rift units and updip pinchout of some of them.

8.6.2 Erosion of Updip Areas of Tilted Fault Blocks

The updip areas of tilted fault blocks in the Gulf of Suez and Red Sea rifts were affected by erosion at the same time syn-rift rock units were being deposited in the downdip areas. Of course not every tilted fault block will be affected by such erosion but only those that have their crests exposed above sea level. A good example of such erosion is the updip area of Gebel El Zeit Block (Fig. 8.19). Erosion led to the present-day exposure of the Precambrian basement at the updip area of the block but during deposition of the syn-rift units, erosion affected the uppermost part of pre-rift section and eroded the Eocene, Paleocene, and part of the Upper Cretaceous section. Figure 8.19a shows the Miocene evaporites unconformably overlying the Matulla Formation. The hiatus includes the lower part of the syn-rift section (Nukhul, Rudeis, and Kareem) and the upper part of the pre-rift section (Eocene, Paleocene, and Upper Cretaceous chalk). The

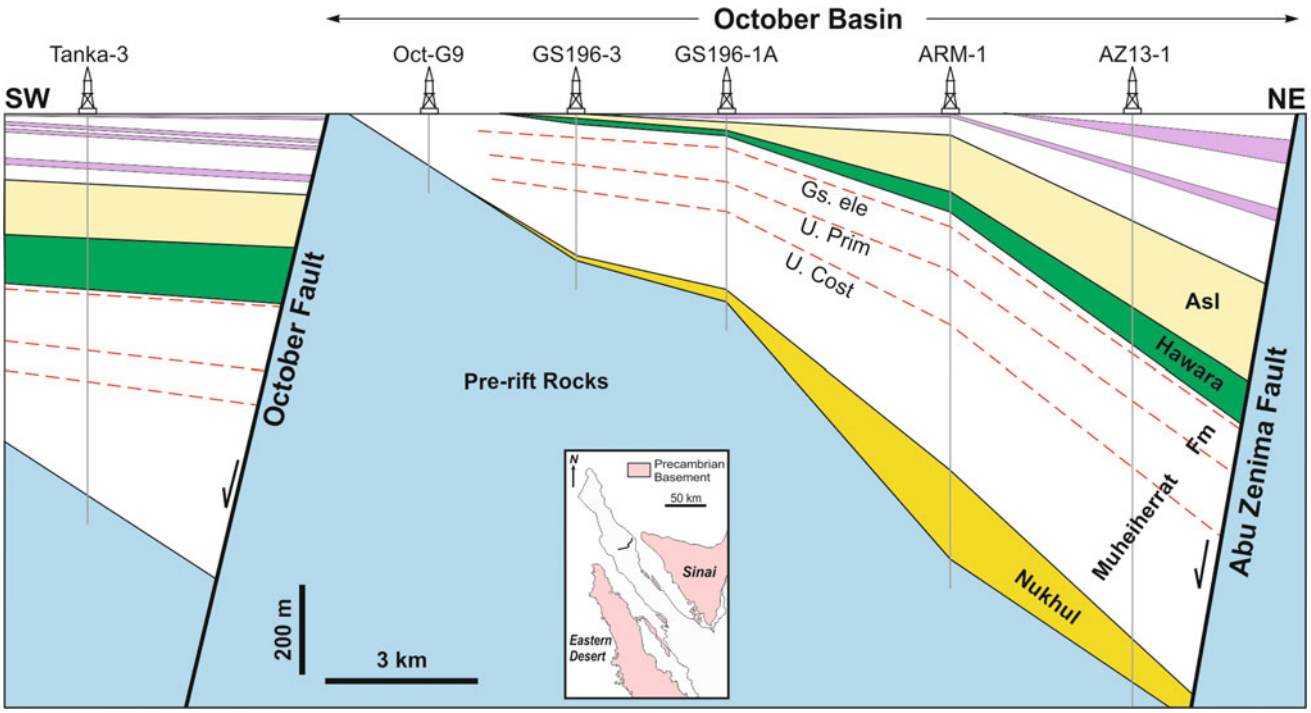

Fig. 8.25 Biostratigraphic correlation of syn-rift section (up to top Langhian (top Lagia Member)) in the wells in October Basin, redrawn after Youssef (2011)

missing part of the syn-rift section is attributed to non-deposition at the updip area of the Zeit Block as shown in Fig. 8.24a but the missing part of the pre-rift section is attributed to erosion of the updip area of the Zeit Block which was exposed above the Miocene sea level during rift history.

The Gharib oil field is another example of erosion of updip areas of tilted fault blocks during deposition of syn-rift units in the downdip areas (Fig. 8.26a). The Gharib Block is tilted toward the NE and is bounded by a major down-to-the-SW normal fault on its updip side. Deep erosion of the pre-rift rocks at the updip area of the block is evident form the correlation of a large number of borehole data. The pre-rift units in this area supposedly include, from base to top, the Precambrian basement, Nubia Sandstone (units C-D to unit A at the top), Upper Cretaceous Nezzazat Group, Upper Cretaceous Sudr Chalk, Paleocene Esna Shale, Lower Eocene Thebes Formation, and Middle Eocene Mokattam Formation. The oldest pre-rift sedimentary unit (Nubia/C-D) was exposed at the updip edge of the block with an erosional scarp due to deep erosion at the updip area of the block. Younger pre-rift rocks are found downdip from this Nubia/C-D subcrop as shown in Fig. 8.26a. The Eocene, Paleocene, Upper Cretaceous Chalk, and the upper part of the Nezzazat Group were completely eroded from the updip area of the block. The erosional surface at the top of the pre-rift units was covered by undifferentiated Miocene marl, limestone, and sandstone followed by reefal carbonate rocks of the Hammam Faraun Member (Belayim Formation) and Miocene evaporties. The eroded updip area of the Gharib Block is similar to the present-day exposures of Gebel Abu Durba and Gebel Araba (Fig. 8.12b) except for the timing of erosion which lasted to present-day in Gebel Abu Durba and Gebel Araba and led to exposure of the Precambrian basement rocks.

A topographically low area forming a strike valley can be seen in Fig. 8.12b. This valley is located at the outcrop of the Nubia Sandstone and is therefore referred to as the Nubia Valley. Subsurface data (e.g. Fig. 8.26b) indicate that such valley may be filled by reworked sands derived from the Nubia Sandstone and other units during Miocene time. In the cross section of Fig. 8.26b, the Nubia Valley was filled by the Lower Rudeis Sand.

8.6.3 Syn-rift Carbonate Build-Ups

Reefal carbonate rocks may be deposited on the updip areas of tilted fault blocks if they are covered by seawater and lie at shallow depth. This case is clear in several areas of the Gulf of Suez and NW Red Sea rifts. The belt extending southeastward from Gharib oil field is a good example and includes the Gharib Field (Fig. 8.26a), Shoab Gharib Field, Ras Fanar Field, Ras Bakr Field and Al-Hamd Field. This

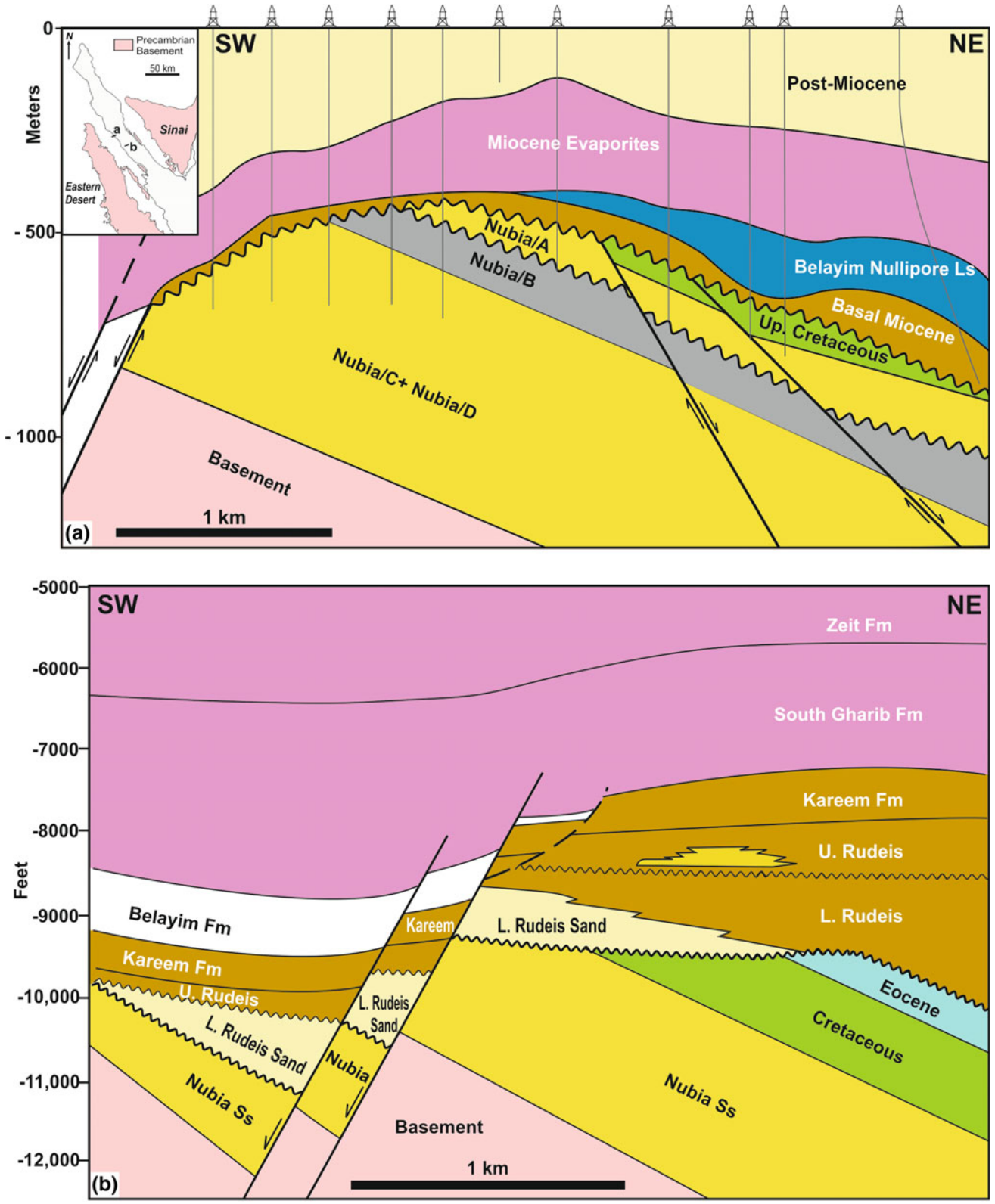

Fig. 8.26 **a** Structural cross-section of Gharib oil field after EGPC (1996) showing deep erosion of the pre-rift section at the updip part of the Gharib tilted fault block. **b** Structural cross-section of July Field slightly modified after Brown (1980) showing deposition of syn-rift sands of the lower Rudeis Formation in the Nubia Valley formed by erosion at the updip area of the tilted fault block. Inset map shows the locations of the cross sections

NW-SE oriented stretch contains reefal limestone in the Hammam Faraun Member of the Belayim Formation.

Another excellent example is the exposure at Gebel Abu Shaar El Qibli in the southernmost part of Esh El Mellaha Block (Fig. 8.27a, b). In this area, the Precambrian basement rocks were exposed by erosion at the updip edge of Esh El Mellaha Block in the early history of the rift. At Late Serravallian time, this portion of the fault block was submerged by seawater to a shallow depth favorable for the development of a reefal build-up. A similar subsurface example is present in Gemsa oil field (Fig. 8.27c). The Gemsa field is producing oil from a Late Miocene reefal limestone reservoir (Hammam Faraun Nullipore Limestone) that is 60 m (200 feet) thick overlying eroded basement rocks and lies at present time at an average depth of about −400 m below the Miocene evaporites.

8.6.4 Structural Control on Deposition of Syn-rift Coarse Clastics

Syn-rift coarse clastics deposited as alluvial fans and fan deltas within finer grained sediments are controlled by the geometry of the rift faults. Two types of entry points of coarse clastics derived from structurally high areas into nearby basinal areas were highlighted by Moustafa and Khalil (2017). These entry points are located at soft-linkage (relay ramps) and hard-linkage transfer zones between individual normal faults in the rift. Relay ramps between overlapping normal faults represent the entry points of coarse clastics from the footwall blocks into the basin (cf. Fig. 8.9d).

In hard-linkage transfer zones, the kinks between rift-parallel and transfer faults represent the entry points of coarse clastics from footwall blocks into the basinal areas of the hanging wall blocks. Several examples of these coarse clastics entry points in the Suez rift and northwestern Red Sea are presented by Moustafa and Khalil (2017).

8.7 Gulf of Aqaba

The Gulf of Aqaba is a relatively narrow (average 17 km wide) and elongated (~195 km long) depression extending in the NNE direction from the northern end of the Red Sea (Fig. 8.1). This depression is bounded on the eastern and western sides by high mountainous areas made up mainly of Precambrian basement rocks (Fig. 8.28a) leaving very narrow coastal areas. The shorelines of the gulf are almost straight and controlled by faults (Figs. 8.28a and 8.29a). The gulf has very steep side slopes representing the scarps of the bounding faults (Figs. 8.2c and 8.28b). The Gulf of Aqaba is significantly deeper than the Gulf of Suez with water depth exceeding 1700 m in its central area (Ben-Avraham et al. 1979b), Fig. 8.2b, c. The relief between the mountainous onshore areas and the seafloor of the gulf is up to 3500 m (Fig. 8.28b).

NNE-SSW to N-S oriented faults with exceptionally large lengths dissect the rocks on both sides of the Gulf of Aqaba (Fig. 8.29a). These faults dissect a 40-km wide swath of land on the Sinai side of the gulf and show evidence of left-lateral slip (Eyal et al. 1981; Abdel Khalek et al. 1993). They belong to the zone of the Dead Sea Transform, which extends north-northeastward from the northern end of the Red Sea to Taurus Mountains in south Turkey. Left-lateral slip on the Dead Sea Transform is related to the NNE drift of Arabia away from Africa and opening of the Red Sea rift. The transform connects the Red Sea extensional basin with the Taurus-Zagros collision zone (Fig. 8.1). The total amount of slip was estimated to be 105–107 km (Quennell 1959; Freund et al. 1970) indicated by the offset of the eastern bounding fault of the Gulf of Suez—Red Sea rift system (Fig. 8.29a). Eyal et al. (1981) studied the faults of the Dead Sea Transform in the western onshore area of the Gulf of Aqaba. They estimated a cumulative horizontal slip of 24 km on these faults and assumed a similar amount of slip for the faults on the Arabian side of the gulf, leaving about 60 km slip by the faults in the gulf itself. They indicated that the sinistral slip post-dates the intrusion of Early Neogene (20–22 Ma) NW-SE oriented basalt and dolerite dikes in southern Sinai and NW Arabia. Eyal et al. (1981) proposed that the total slip on the faults of the Dead Sea Transform post-dates the intrusion of these early Neogene igneous dikes and so is the time of opening of the Red Sea. On the other hand, previous investigators believe that the Dead Sea Transform witnessed two stages of slip separated by a quiet period during the Miocene. These are 60–67 km slip in the pre-Miocene (Freund et al. 1968, 1970) or in the Early Miocene (Quennel 1959) and 40–45 km in the last 7–12 Ma (Freund et al. 1968, 1970) or in the Late Pleistocene (Quennel 1959). The average rate of sinistral slip on the Dead Sea Fault is 4.5–4.7 ± 0.2 mm/yr based on GPS observations (Mahmoud et al. 2005; ArRajehi et al. 2010).

A number of pull-apart grabens were formed between the ends of overstepping left-lateral faults on the western side of the Gulf of Aqaba. At least three pull-apart grabens exist in this area (Fig. 8.29a) and contain Phanerozoic sedimentary units down-faulted against Precambrian basement rocks outside the grabens. This indicates that the basement rocks of the Sinai Massif were once covered by similar Phanerozoic sedimentary rock units that range in age from Paleozoic to Eocene. Figure 8.29b, c show one of these onshore pull-apart grabens that contains Cambrian to Senonian sedimentary units. Three larger pull-apart basins (rhombochasms) form the Gulf of Aqaba itself and lie between left-stepping en echelon left-lateral faults (Fig. 8.29a). These

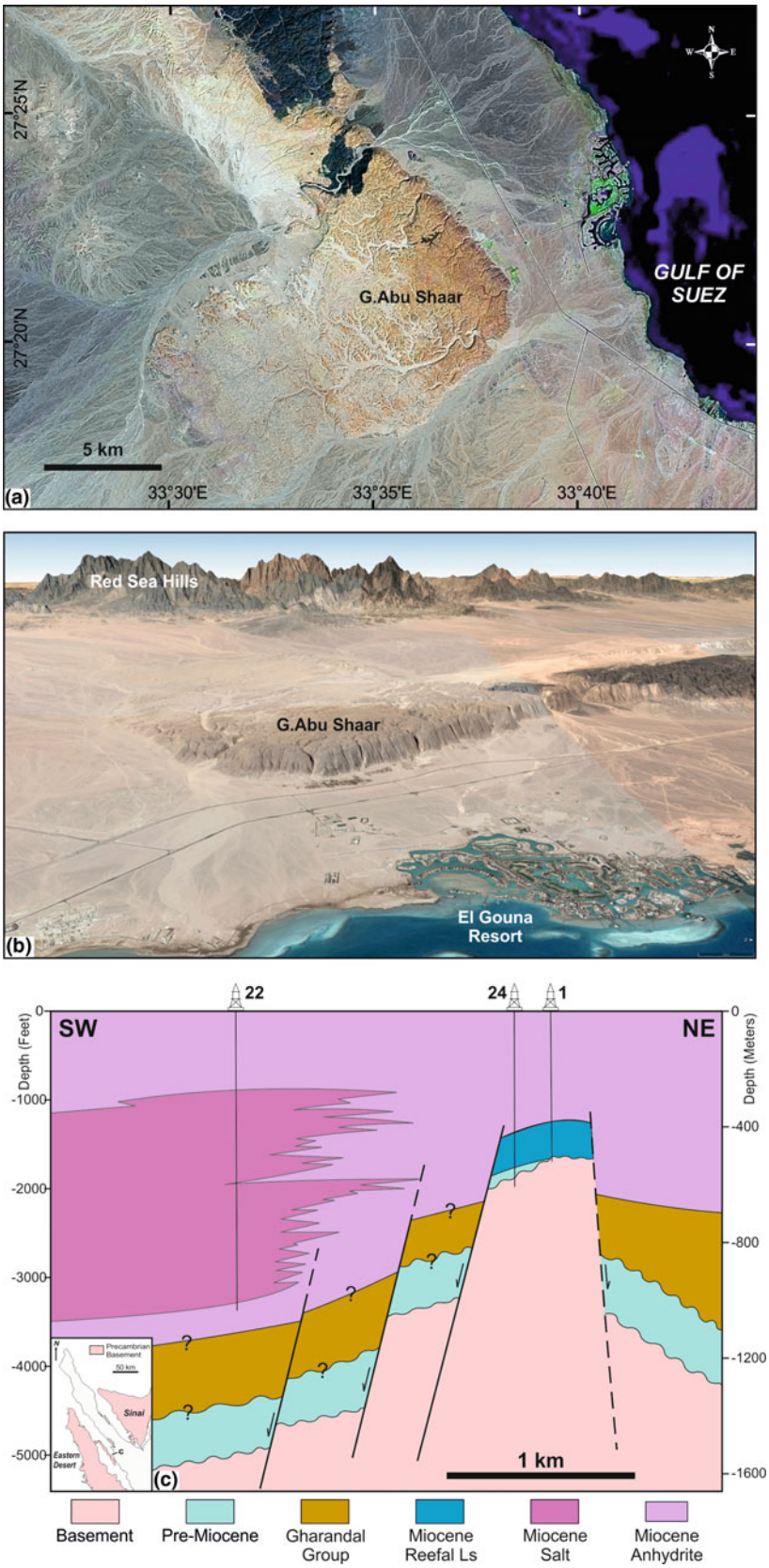

Fig. 8.27 Landsat image (**a**) and Google Earth 3D view (**b**) of Gebel Abu Shaar El Qibli (southern edge of Esh El Mellaha Block) showing Miocene reefal carbonate buildup deposited above Precambrian basement rocks. **c** Cross section of Gemsa oil field (modified after Hagras 1976) showing Miocene reefal limestone above eroded Precambrian basement rocks at the updip edge of a tilted fault block

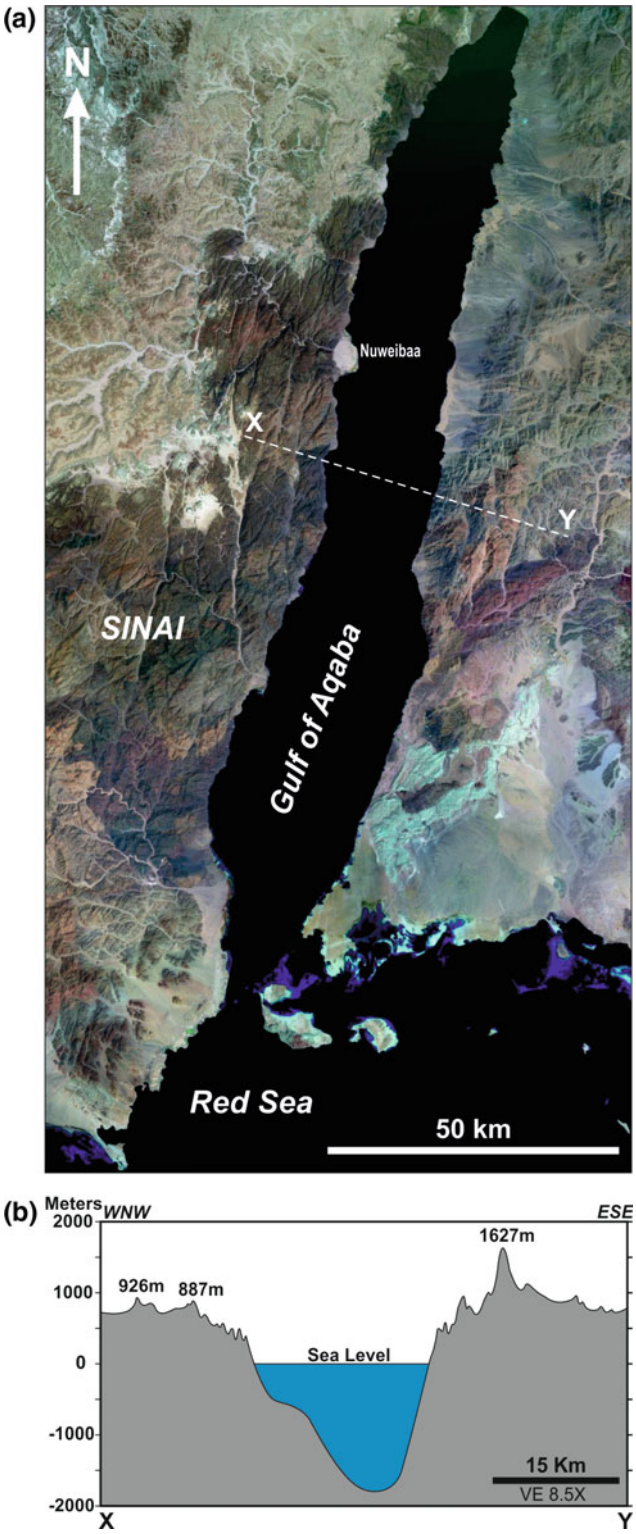

Fig. 8.28 **a** Landsat image of the Gulf of Aqaba and surrounding areas showing its nearly linear, fault-controlled shorelines. **b** Cross section showing the bathymetry of the deepest part of the Gulf of Aqaba and topography of the surrounding areas

basins are elongated parallel to the faults and are linked together into one large depression leading to the deep water nature of the gulf. The water depth in the middle one of these grabens exceeds 1700 m. Although the topographic relief between the mountainous onshore areas and the seafloor of this graben is about 3500 m (Fig. 8.28b), the structural relief is greater than this figure since the grabens contain a large thickness of sedimentary rocks estimated to exceed 2–3 km (Ben-Avraham et al. 1979a; Ben-Avraham and Tibor 1993). Seismic reflection profiles indicate the presence of active NW-SE oriented normal faults dissecting the floors of these pull-apart grabens (Ben Avraham and Garfunkel 1986). Continuous drift of Arabia away from Africa and associated opening of the Red Sea basin makes the Dead Sea Transform an active fault zone. This is reflected by the seismicity associated with the faults in the Gulf of Aqaba as well as other parts of the Transform. Bosworth et al. (2017) indicated that seismicity in the Gulf of Aqaba area is concentrated in the central sub-basin and decreases both to the north and south. They also found that the faulted margins of the gulf display largely dip-slip extensional movement accompanied by footwall uplift although the transform is principally a strike-slip plate boundary. They estimated the rate of tectonic uplift via measurements of elevated Pleistocene coral terraces and indicated a maximum total uplift value of $\sim$19 m adjacent to the central sub-basin and also decreases to the north and south.

Gravity sliding of Cretaceous sediments from the shoulders of the Gulf of Aqaba toward the down-faulted area is obvious in the area north of Nuweibaa leading to the formation of overturned and recumbent folds parallel to the Gulf of Aqaba faults (Fig. 8.30a, b); Hildebrand et al. (1974) and Abdel-Khalek et al. (1993). Detachment surfaces in the incompetent Upper Cretaceous shales facilitated the sliding of the overlying carbonate rocks.

8.8 Tectonic Evolution of the Gulf of Suez—NW Red Sea and Gulf of Aqaba Area

The onset of rifting in the Gulf of Suez and northwestern Red Sea is marked by the deposition of Late Oligocene red fluvial deposits of the Abu Zenima and Nakheil Formations above marine Eocene rocks. The rift-breakup unconformity shows clear angular discordance between the pre-rift rocks and the overlying syn-rift units (Fig. 8.5). The hiatus represented by this unconformity (Fig. 8.3) differs from one area to the other in the rift and also within each fault block. The hiatus is larger at the updip areas of the tilted fault blocks compared to the downdip areas. The distribution of

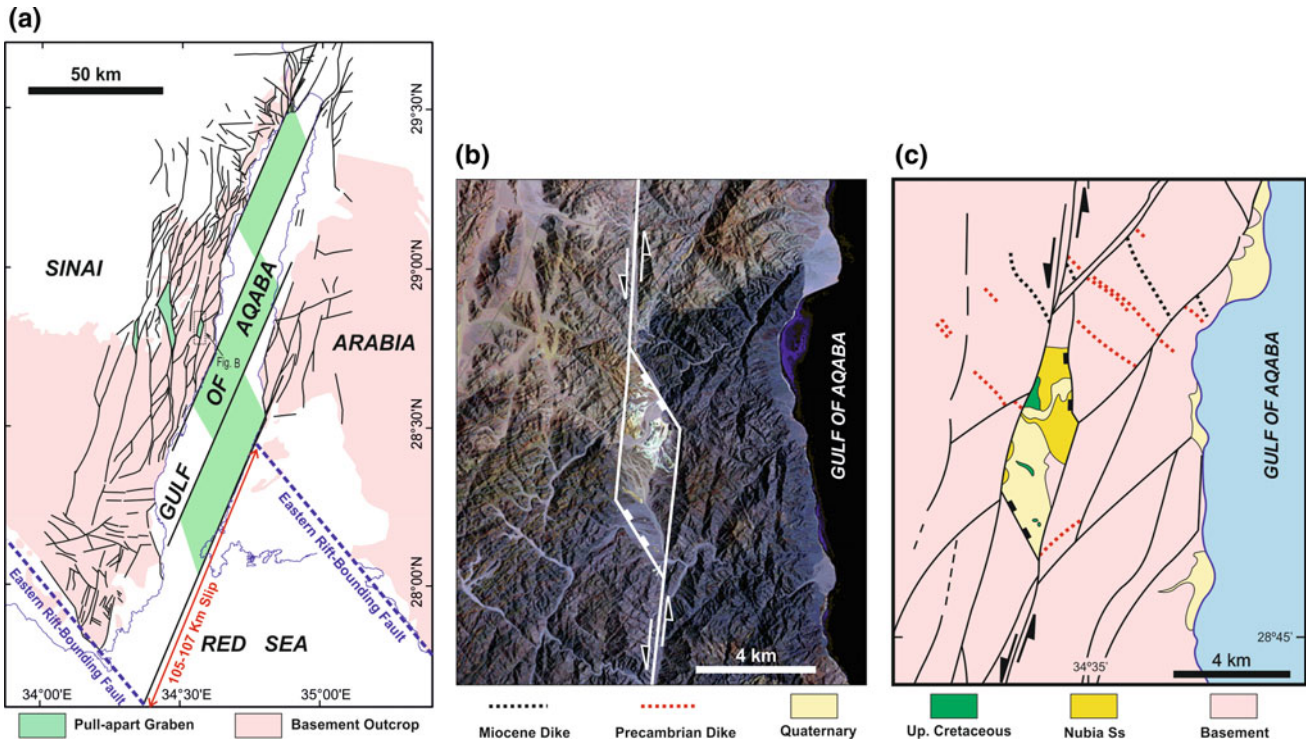

Fig. 8.29 **a** Structural map of the two margins of the Gulf of Aqaba modified after Eyal et al. (1981) and EGSMA (1994). Heavy dashed lines show the eastern bounding faults of the Suez Rift and Red Sea indicating 105–107 km offset by the Dead Sea Transform. **b** Landsat image and **c** geological map (slightly modified after Eyal et al. 1981) showing a small pull-apart graben in the area SW of Dahab

the red beds is controlled by early rift faults which accounts for their limited aerial distribution within the rift. Basic volcanics with $^{40}Ar/^{39}Ar$ ages centered at ~23 Ma in the form of dikes (mostly oriented NNW-SSE), sills and flows followed the deposition of the red beds in some areas of the rift (Fig. 8.5). Extrusion of the lava flows was subaerial (Patton et al. 1994) indicating that the early rift basin was not invaded by seawater at that time.

Deposition of Miocene syn-rift sediments followed the igneous activity as these Miocene sediments are never affected by the early rift volcanics. Basalt boulders are locally present in the basal part of the Lower Miocene Nukhul Formation. The earliest Miocene sediments in the Suez Rift (Nukhul Formation) were deposited in shallow marine environment. The distribution of the Nukhul Formation through the whole width of the rift till the present-day rift shoulders indicates that the rift shape was established at that time. Basin subsidence started slow during deposition of the Nukhul Formation in the Aquitanian-Early Burdigalian time (Fig. 8.31).

The Nukhul Formation is followed by deep-marine sediments of the Rudeis Formation. Tectonic subsidence curves of the Gulf of Suez (Scott and Govean 1986; Moretti and Colletta 1987; Richardson and Arthur 1988; Evans 1988; Steckler et al. 1988) show increased subsidence rate during deposition of the Lower Rudeis Formation. The Lower Rudeis is made up of Globigerina marls and is separated from the coarser clastics of the Upper Rudeis by an unconformity surface that marks a major tectonic event (mid-clysmic or mid-Rudeis event). This event occurred at or immediately prior to the transition from rapid subsidence during the deposition of the Lower Rudeis and slower subsidence of the Upper Rudeis (Patton et al. 1994 and Fig. 8.31). Seismic data show that the number of faults dissecting the Lower Rudeis and older rocks exceeds the number of faults dissecting the Upper Rudeis. This is what some investigators point to as re-organization of the rift at the Mid-clysmic event (e.g. Garfunkel and Bartov 1977). Major block-bounding faults continued movement during deposition of the Upper Rudeis whereas most of the small-throw faults died out at the mid-Rudeis unconformity. Bayer et al. (1988) and Voggenreitter et al. (1988) proposed a change in the direction of movement of the Arabian Plate from NE to NNE at about the time of the mid-Rudeis event, which is in fact related to the onset of movement on the Dead Sea Transform and oblique opening of the Red Sea.

The transition from slow to rapid tectonic subsidence started earlier in the southern part of the Suez Rift than in the

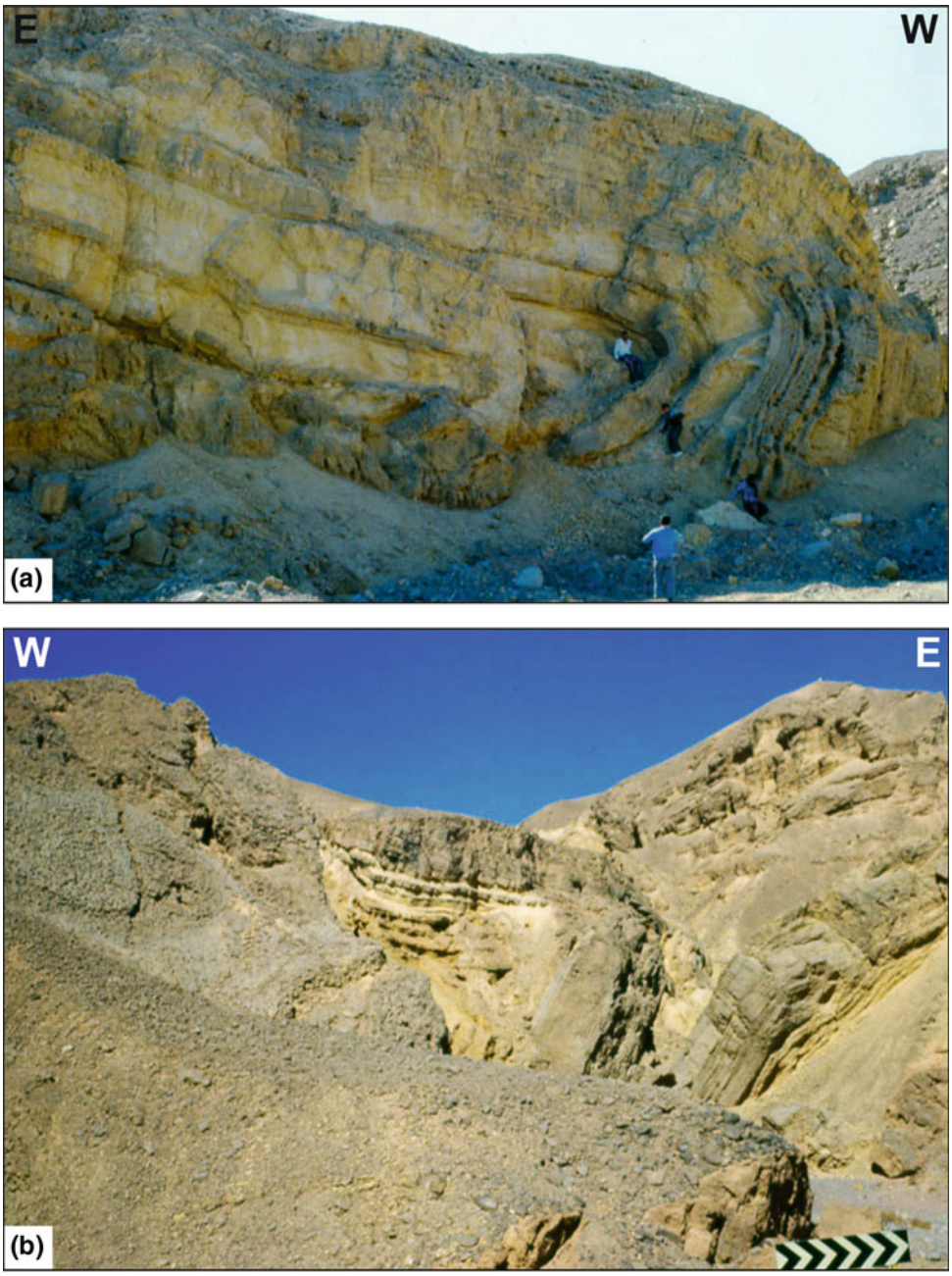

Fig. 8.30 Field photographs of east-vergent recumbent (**a**) and overturned (**b**) anticlines in the area north of Nuweibaa (western side of the Gulf of Aqaba) representing gravity sliding blocks toward the Gulf of Aqaba basin

northern and central parts of the rift (Fig. 8.31) and the deposition of the upper part of the Nukhul Formation witnessed rapid tectonic subsidence like the Lower Rudeis. In fact, the large thickness of the Nukhul Formation (up to 700 m; Richardson and Arthur 1988; Peijs et al. 2012) in the southern part of the Suez Rift confirms that the subsidence rate in the south (in vicinity of the northern Red Sea) exceeded that in the central and northern areas.

Slow subsidence during deposition of the Upper Rudeis continued in the northern and central parts of the Suez Rift during the rest of the Miocene (during deposition of the evaporties of the Belayim, South Gharib, and Zeit Formations) and post-Miocene times, indicating the beginning of abandonment of the Suez Rift. The development of the evaporite basin was attributed to restriction of the Suez Rift from the Mediterranean Sea by a structural high in the northern gulf. This high was either related to the Suez Sill of Said and Basiouni (1958) that occupied the Ayun Musa area and silled (blocked) the Gulf of Suez depression at the time of deposition of the Miocene evaporites or to the Wadi Araba Anticline (Patton et al. 1994).

The southern part of the Suez rift differs from the northern and central parts as the slow tectonic subsidence during deposition of the Upper Rudeis, Kareem, and

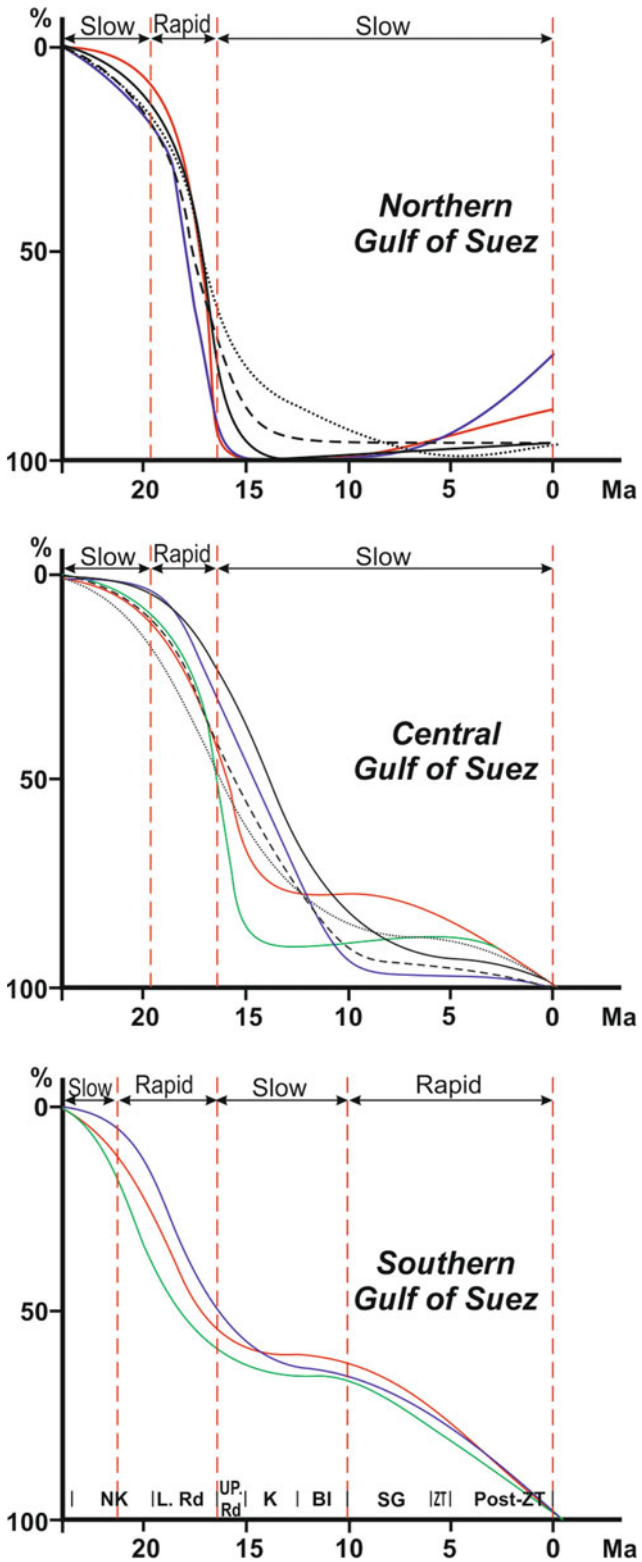

Fig. 8.31 Tectonic subsidence curves of the Gulf of Suez Rift after Moretti and Colletta (1987) with additional annotations by the present authors. Note the rapid subsidence in the last 10 Ma in the southern part of the gulf compared to the northern and central areas. Abbreviations designate Nukhul (NK), Lower Rudeis (L. Rd), Upper Rudeis (Up. Rd), Kareem (K), Belayim (Bl), South Gharib (SG), Zeit (ZT), and post-Zeit (Post-Zt) Formations. Tectonic subsidence is marked as rapid and slow

Belayim Formations was followed by another phase of rapid subsidence during the last 10 million years (Moretti and Colletta 1987; Fig. 8.31), during the deposition of the South Gharib, Zeit and Post-Miocene sediments, perhaps indicating reactivation of the faults in the southern gulf associated with the slip on the Dead Sea Transform. Indeed, subsidence in the southern part of the Suez Rift is related to the activity of the Dead Sea Transform as clearly seen in the southernmost offshore area lying between Shadwan Island and the Sinai coast. This area has large water depth (up to 1000 m). It probably represents a pull-apart area between one of the faults of the Dead Sea Transform and another (cross or N-oblique) fault of the Suez Rift (Fig. 8.32). Seismic reflection data of this deep-water area show recent faults dissecting the seabed, indicating recent deformation. Also, earthquake activity characterizes the southern part of the Suez Rift (Hussein et al. 2006) more than the northern and central areas, Fig. 8.32. In addition to earthquake activity, recent tectonic activity in the southernmost part of the Gulf of Suez is also indicated by raised Pleistocene reef terraces (Bosworth and Taviani 1996).

Post-Miocene extension in the Suez Rift is also obvious in several places especially the main faults bounding the coastal ranges and bounding most of the rift blocks (e.g. Esh El Mellaha Fault, Fig. 8.24a). Some onshore areas also display post-Pliocene fault activity such as the area close to Ras Sudr (Moustafa 1997b) and the western onshore area lying between Ras Issaran and Ras Bakr, also reported by Bosworth et al. (2019).

Generally, it can be stated that most of the post-Miocene extension in the Suez Rift affects mainly the central (offshore) part more than other parts of the rift due to reactivation of the main coastal faults leading to narrowing of the rift since that time.

Estimates of the amount of extension (β value) of the Suez Rift indicate that β values equal to 133% characterize the northern part of the rift compared to 155% in the southern part (Patton et al. 1994). Several studies also show the southward increase in the amount of extension in the Suez Rift but with different magnitudes (Colletta et al. 1988; Moretti and Colletta 1988; Richardson and Arthur 1988; Steckler et al. 1988; Afifi et al. 2013; among others). Southward increase in the amount of extension is also coupled with increase in the amount of block rotation where the average dip of pre-rift rocks is about 12° in the northern part of the Suez Rift, 14–15° in the central part of the rift, and 25–30° in the southern part of the rift. Some areas in the southern part of the Suez Rift also show steeper dip of the pre-Miocene rocks, reaching up to 45° in places (Bosworth 1995; Afifi et al. 2016). Increased block rotation leads to decrease in the dip angles of the early rift faults bounding these blocks. The shallowest recorded dip of the main faults bounding the rift blocks is 23° (Bosworth 1995).

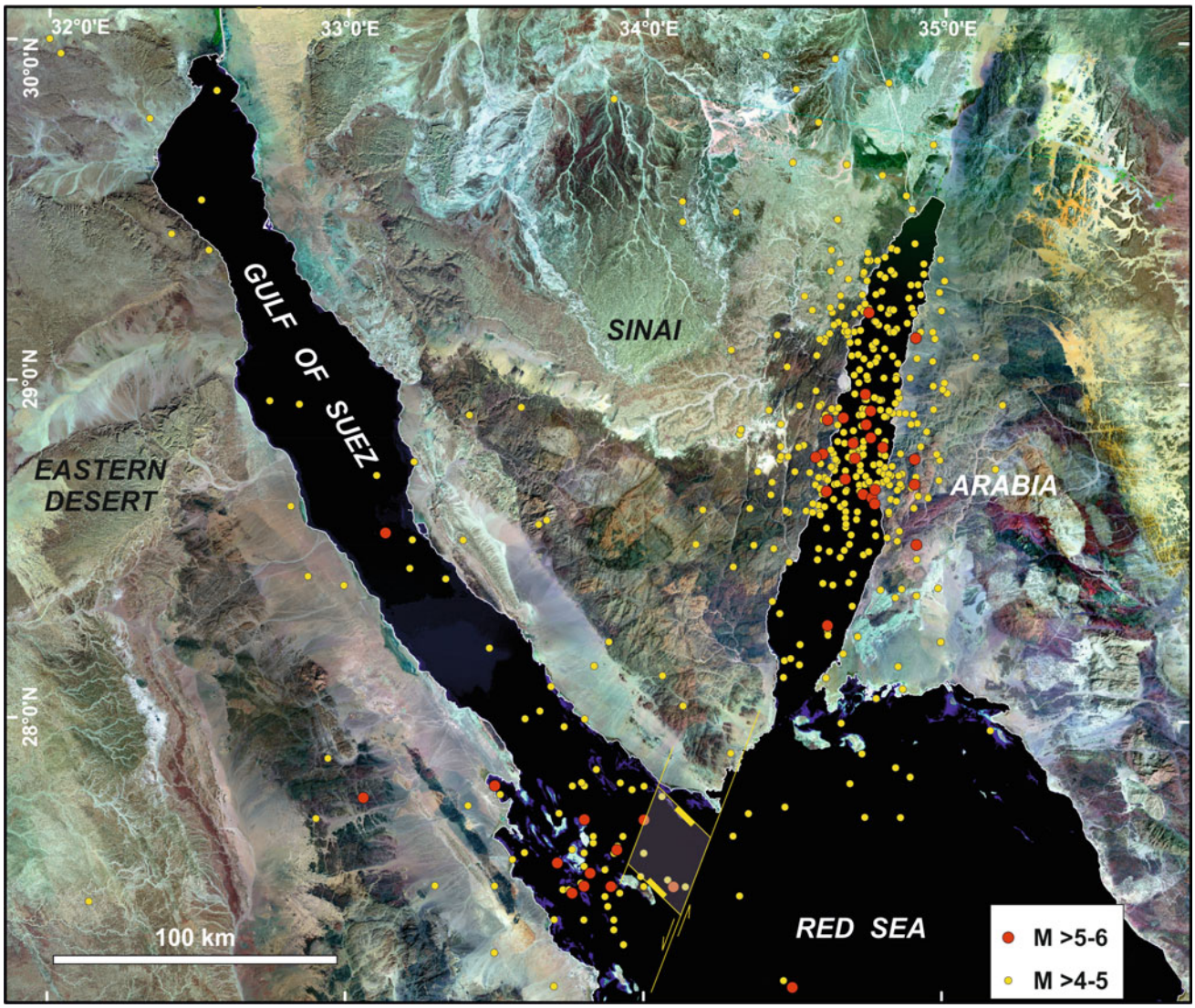

Fig. 8.32 Instrumentally recorded earthquakes (M $\geq$ 4) in the Gulf of Suez and Gulf of Aqaba since 1960 and relationship to the deep water area in the southeastern part of the Gulf of Suez

Continued rotation of the main block-bounding faults decreases their dip angles and as the faults decrease in dip they get locked at a certain stage and cannot continue slipping (Reston 2009). Continued extension of the basin leads to the formation of a new (second-generation) set of faults that dissects the older (locked) faults. This process can take place several times and at increased rates of extension higher generation faults are formed. The large amount of extension of the southern part of the Suez Rift has actually formed second generation faults. This is obvious at the main fault bounding the titled fault block of Ashrafi oil field. The Ashrafi-Shadwan Fault that bounds the Ashrafi oil field and represents the southern part of the B-trend fault is currently dipping at shallow angle as low as 23° and is dissected by a steeper normal fault (Bosworth 1995; Fig. 8.24b) representing a second-generation fault that was formed as the Ashrafi-Shadwan Fault became locked. Other major early rift faults in the southern part of the Suez Rift are also expected to have been locked and became dissected by second-generation faults. Gebel El Zeit Fault is expected to be among those faults. As the amount of extension of the northern Red Sea is higher than that of the Suez Rift, second- (and probably higher-) generation faults are also expected to exist.

Sinistral slip on the Dead Sea Transform led to the formation of the Gulf of Aqaba as a series of pull-apart grabens. It also led to separation of the Suez Rift from the northern Red Sea, allowing more extension of the Red Sea Basin (Fig. 8.33c). The northern part of the Red Sea is floored by highly attenuated continental crust as far south as the

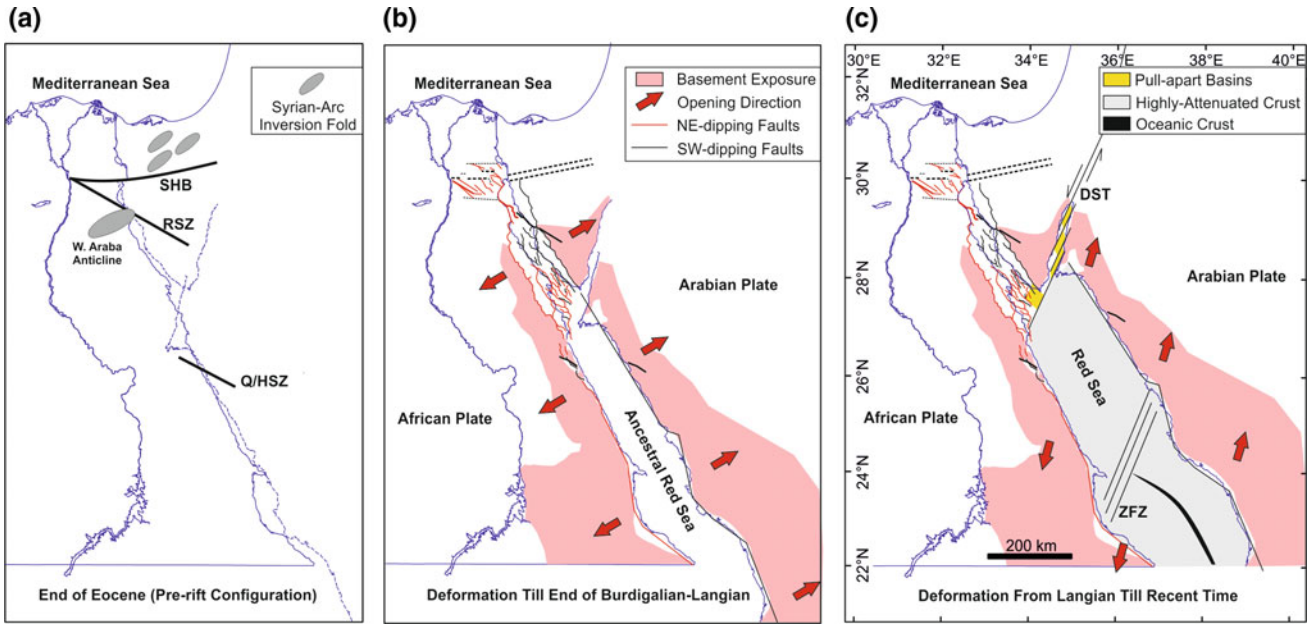

Fig. 8.33 Reconstruction of the Gulf of Suez-northern Red Sea-Gulf of Aqaba margins showing the rift evolution stages. **a** Pre-rifting, **b** end of Burdigalian-Langhian, and **c** Langhian to Recent time. The Nile River and Mediterranean coastline are shown for reference. Abbreviations designate Sinai Hinge Belt (SHB), Rihba Shear Zone (RSZ), El Quwyh-Hamrawin Shear Zone (Q/HSZ), Dead Sea Transform (DST), and Zabargad Fracture Zone (ZFZ). Bold arrows in (**b**) and (**c**) represent the opening directions of the two rift basins

Zabargad Fracture Zone and represents the latest stage of continental rifting. The presence of local centers of shallow magmatic activity at 10–40 km depths (Saleh et al. in manuscript) as well as the presence of oceanic crust in some of its oceanic deeps like Conrad, Shaban, and Mabahiss Deeps indicate that the northern Red Sea is in the last phases of continental extension and is close to start seafloor spreading.

Acknowledgements Constructive comments by William Bosworth and Dubravko Lučić helped improve the manuscript.

References

Abd-Allah AMA (1988) Structural setting of the area west and southwest of Gebel Qattamia: MSc thesis, Ain Shams University, 117 pp

Abd-Allah AMA (1993) Structural geology of the area between El Galala El Bahariya and Gebel Okheider. PhD dissertation, Ain Shams University, 199 pp

Abdallah AM, Adindani A (1963) Stratigraphy of upper Paleozoic rocks, western side of Gulf of Suez, Egypt. Egyptian Geol Surv 25:18 pp

Abdeen MM (1995) Late orogenic basin evolution and deformation in the Pan-African basement, Wadi Queih, Eastern Desert of Egypt. PhD dissertation, Heidelberg University, Germany, 272 pp

Abdeen MM, Dardir AA, Greiling RO (1992) Geological and structural evolution of the Wadi Queih area (N Quseir), Pan-African basement of the Eastern Desert of Egypt (extended abstract). Zbl Geol Palaont Teil I (1991) (11):2653–2659

Abdel Khalek ML, Abdel Wahed N, Sehim AA (1993) Wrenching deformation and tectonic setting of the northwestern part of the Gulf of Aqaba. Geol Soc Egypt Spec Pub 1:409–444

Abdel Tawab SM (1986) Structural analysis of the area around Gebel Mokattam. MSc thesis, Ain Shams University, 121 pp

Abdine AS, Meshref W, Shahin AN, Garossino P, Shazly S (1992) Ramadan field. In: Foster NH, Beaumont EA (eds) Structural traps VI, treatise of petroleum geology. AAPG, Tulsa, pp 113–140

Abdo TR (2003) Fault geometry and structural history of the October field, Gulf of Suez, Egypt. MSc thesis, Ain Shams University, 152 pp

Aboul Karamat MS (1987) Geology of the sedimentary succession of Esh El Mellaha range, Eastern Desert, Egypt. MSc thesis, Cairo University, 111p

Abul-Nasr RA (1986) Syntectonic slope deposit at Gebel Hammam Faraun, Sinai (Egypt). In: Proceedings of 59th annual meeting of the South Carolina academy of science. Bull S Carol Acad Sci 48: 100–101

Abul-Nasr RA (1990) Re-evaluation of the Upper Eocene rock units in west central Sinai, Egypt: Middle East Research Center, Ain Shams University. Earth Sci Ser 4:234–247

Abul-Nasr RA, Thunell RC (1987) Eocene eustatic sea level changes: evidence from western Sinai, Egypt. Paleogeogr Paleoclimatology Paleoecology 58:1–9

Afifi A, Moustafa AR, Helmy H (2013) Structural evolution of the southern Gulf of Seuz rift: implications for hydrocarbon exploration in a mature basin. Egypt Geophys Soc 10:12–31

Afifi AS, Moustafa AR, Helmy HM (2016) Fault block rotation and footwall erosion in the southern Suez Rift: implications for hydrocarbon exploration. J Mar Pet Geol 76:377–396

Akkad SE, Dardir AA (1966a) Geology and phosphate deposits of Wasif, Safaga area. Geol Surv Egypt. Paper no. 36, 35 pp

Akkad SE, Dardir AA (1966b) Geology of the Red Sea Coast between Ras Shagra and Marsa Alam with short note on exploratory work at Gebel El Rusas lead-zink deposits. Geol Surv Egypt. Paper no. 35, 67 pp

ArRajehi A, McClusky S, Reilinger R, Daoud M, Alchalbi A, Ergintav S, Gomez F, Sholan J, Bou-Rabee F, Ogubazghi G, Haileab B, Fisseha S, Asfaw L, Mahmoud S, Rayan A, Bendik R, Kogan L (2010) Geodetic constraints on present-day motion of the Arabian plate: implications for Red Sea and Gulf of Aden rifting. Tectonics 29:1–10

Awney F, Hussein R, Nakhla A (1990) Blayim Marine and Land oil fields structural styles. In: Proceedings of 10th EGPC petroleum exploration and production conference, vol 1, pp 400–430

Bayer HJ, Hotzl H, Jado AR, Roscher B, Voggenreiter W (1988) Sedimentary and structural evolution of the northwest Arabian Red Sea margin. Tectonophysics 153:137–151

Beleity AM (1984) The composite standard and definition of paleo events in the Gulf of Suez. In: Proceedings of 6th exploration seminar (Cairo, 1982), Egyptian general petroleum exploration conference, vol 1, pp 181–198

Ben Avraham Z, Garfunkel Z (1986) Character of transverse faults in the Elat pull-apart basin. Tectonics 5:1161–1169

Ben-Avraham Z, Tibor G (1993) The northern edge of the Gulf of Elat. Tectonophysics 226:319–331

Ben-Avraham Z, Almagor G, Garfunkel Z (1979a) Sediments and structure of the Gulf of Elat (Aqaba)—Northern Red Sea. Sediment Geol 23:239–267

Ben-Avraham Z, Garfunkel Z, Almagor G, Hall JK (1979b) Continental breakup by a leaky transform: the Gulf of Elat (Aqaba). Science 206:214–216

Bicknell JD, Macdonald KC, Miller SP, Lonsdale PF, Becker K (1986) Tectonics of the Nereus Deep, RedSea: A deep tow investigation of a site of initial rifting. Mar Geophys Res 8:131–148

Bonatti E, Clocchiatti R, Colantoni P, Gelmini R, Marinelli G, Ottonello G, Santacroce R, Taviani M, Abdel-Meguid AA, Assaf HS, El Tahir MA (1983) Zabargad (St. John's) Island: an uplifted fragment of sub-Red Sea lithosphere. J Geol Soc Lond 140:677–690

Bonatti E, Colantoni P, Della Vedova B, Taviani M (1984) Geology of the Red Sea transitional zone (22°N–25°N). Oceanol Acta 7:385–398

Bonatti E (1985) Punctiform initiation of seafloor spreading in the Red Sea during transition from a continental to an oceanic rift. Nature 316(6023):33–37

Bosworth W (1985) Geometry of propagating continental rifts. Nature 316:625–627

Bosworth W (1994) A model for the three-dimensional evolution of continental rift basins, north-east Africa. Geol Rundsch 83:671–688

Bosworth W (1995) A high-strain rift model for the southern Gulf of Suez (Egypt). In: Lambiase JJ (ed) Hydrocarbon habitat in rift basins. Geol Soc Lond Special Pub 80:75–102

Bosworth W (2015) Geological evolution of the Red Sea: historical background, review, and synthesis. In: Rasul NMA, Stewart ICF (eds) The Red Sea. Springer Earth System Sciences, pp 45–78

Bosworth W, Taviani M (1996) Late Quaternary reorientation of stress field and extension direction in the southern Gulf of Suez, Egypt: evidence from uplifted coral terraces, mesoscopic fault arrays, and borehole breakouts. Tectonics 15:791–802

Bosworth W, McClay KR (2001) Structural and stratigraphic evolution of the Suez rift, Egypt: a synthesis. In: Zeigler PA, Cavazza, W, Robertson AHF, Crasquin-Soleau S (eds) Peri-Tethyan rift-wrench basins and passive margins. Musee Nationale Hist Nat, pp 567–606

Bosworth W, Stockli DF (2016) Early magmatism in the greater Red Sea rift: timing and significance. Can J Earth Sci 53:1158–1176

Bosworth W, Crevello P, Winn RD Jr, Steinmetz J (1998) Structure, sedimentation, and basin dynamics during rifting of the Gulf of Suez and northwestern Red Sea. In: Purser BH, Bosence DWJ (eds) Sedimentation and tectonics of rift basins: Red Sea-Gulf of Aden. Chapman and Hall, London, pp 77–96

Bosworth W, Huchon P, McClay K (2005) The Red Sea and Gulf of Aden basins. J Afr Earth Sci 43:334–378

Bosworth W, Khalil S, Clare S, Comisky J, Abdelal H, Reed T, Kokkoros G (2014) Integration of outcrop and subsurface data during the development of a naturally fractured Eocene carbonate reservoir at the East Ras Budran concession, Gulf of Suez, Egypt. In: Spence GH, Redfern J, Aguilera R, Bevan TG, Cosgrove JW, Couples GD, Daniel J-M (eds) Advances in the study of fractured reservoirs: geological society, London, Special Publication 374, pp 333–359

Bosworth W, Stockli DF, Helgeson DE (2015) Integrated outcrop, 3D seismic, and geochronologic interpretation of Red Sea dike-related deformation in the Western Desert, Egypt—the role of the 23 Ma Cairo "mini-plume". J Afr Earth Sci 109:107–119

Bosworth W, Montagna P, Pons-Branchu E, Rasul N, Taviani M (2017) Seismic hazards implications of uplifted Pleistocene coral terraces in the Gulf of Aqaba. Sci Rep 7:1–13

Bosworth W, Taviani M, Rasul NMA (2019) Neotectonics of the Red Sea, Gulf of Suez and Gulf of Aqaba, In: Rasul NMA, Stewart ICF (eds) Geological setting, palaeoenvironment and archaeology of the Red Sea. Springer Nature, pp 11–35

Botz R, Schmidt M, Kus J, Ostertag-Henning C, Ehrhardt A, Olgun N, Garbe-Schonberg D, Scholten J (2011) Carbonate recrystallization and organic matter maturation in heat-affected sediments from the Shaban Deep, Red Sea. Chem Geol 280(1–2):126–143

Brown RN (1980) History of exploration and discovery of Morgan, Ramadan and July oilfields, Gulf of Suez, Egypt. Can Soc Pet Geol Mem 6:733–764

Carr ID, Gawthorpe RL, Jackson CAL, Sharp IR, Sadek A (2003) Sedimentology and sequence stratigraphy of early syn-rift tidal sediments: the Nukhul Formation, Suez rift, Egypt. J Sediment Res 73:407–420

Chu D, Gordon RG (1988) Current plate motions across the Red Sea. Geophys J Int 135:313–328

Cochran JR (1983) A model for the development of the Red Sea. AAPG Bull 67:41–69

Cochran JR (2005) Northern Red Sea: nucleation of an oceanic spreading center within a continental rift. Geochem Geophys Geosyst 6:Q03006. https://doi.org/10.1029/2004gc000826

Cochran JR, Martinez F (1988) Evidence from the northern Red Sea on the transition from continental to oceanic rifting. Tectonophysics 153:25–53

Coffield DQ, Schamel S (1989) Surface expression of an accommodation zone within the Gulf of Suez rift, Egypt. Geology 17:76–79

Colletta B, Le Quellec P, Letouzey J, Moretti I (1988) Longitudinal variation of the Suez rift structure (Egypt). Tectonophysics 153:221–233

Darwish M, El-Azabi M (1993) Contributions to the Miocene sequences along the western coast of the Gulf of Suez, Egypt. Egypt J Geol 37(1):21–47

Degens ET, Ross DA (1969) Hot brines and recent heavy metal deposits in the Red Sea. Springer, New York, p 600

EGPC (1996) Gulf of Suez oil fields (A comprehensive overview). Egyptian General Petroleum Corporation, 736 pp

EGSMA (1994) Geological map of Sinai, Arab Republic of Egypt (Sheets No. 1 and 2), scale 1: 250,000. Geol Surv Egypt

Ehrhardt A, Hübscher C (2015) The Northern Red Sea in transition from rifting to drifting-lessons learned from ocean deeps. In: Rasul NMA, Stewart ICF (eds) The Red Sea: the formation, morphology, oceanography and environment of a young ocean basin. Springer Earth System Sciences, Heidelberg, pp 99–121

El Bassyony AA (1982) Stratigraphical studies on Miocene and younger exposures between Quseir and Berenice Red Sea coast, Egypt. PhD theism, Ain Shams University, Cairo

El-Dawoody AS, Aboul Karamat MS (1997) Geologic studies on the sedimentary succession of Esh El Mellaha range, Eastern Desert, Egypt. Bull Fac Sci Cairo Univ 65:117–150
El Gaby S, List FK, Tehrani R (1990) The basement complex of the Eastern Desert and Sinai. In: Said R (ed) The geology of Egypt. Balkema, Rotterdam, pp 175–184
El-Heiny I, Martini E (1981) Miocene foraminiferal and nannoplankton assemblages from the Gulf of Suez region and correlations. Geol Medit 8:101–108
El Shazly EM, Saleeb Roufaiel GS (1977) Metasomatism of Miocene sediments in St. John's Island and its bearing on the history of the Red Sea. Egypt J Geol 21:103–108
EMODnet (2016) The European marine observation and data network. http://ows.emodnet-bathymetry.eu
Evans AL (1988) Neogene tectonic and stratigraphic events in the Suez rift area, Egypt. Tectonophysics 153:235–247
Evans AL (1990) Miocene sandstone provenance relations in the Gulf of Suez: insights into synrift unroofing and uplift history. AAPG Bull 74:1386–1400
Eyal M, Eyal Y, Bartov Y, Steinitz G (1981) The tectonic development of the western margin of the Gulf of Elat (Aqaba) rift. Tectonophysics 80:39–66
Farhoud K (2009) Accommodation zones and tectono-stratigraphy of the Gulf of Suez, Egypt: a contribution from aeromagnetic analysis. GeoArabia 14:139–162
Freund R, Zak I, Garfunkel Z (1968) Age and rate of the sinistral movement along the Dead Sea rift. Nature 220:253–255
Freund R, Garfunkel Z, Zak I, Goldgerg M, Weissbrod T, Derin B (1970) The shear along the Dead Sea rift. Philos Trans R Soc Lond A 267:107–130
Garfunkel Z, Bartov Y (1977) The tectonics of the Suez rift. Geol Surv Israel Bull 71:44 pp
Garfunkel Z, Ginzburg A, Searle RC (1987) Fault pattern and mechanism of crustal separation along the axis of the Red Sea from side scan sonar (GLORIA) data. Ann Geophys 5B:187–200
Gawthorpe RL, Hurst JM, Sladen CP (1990) Evolution of Miocene footwall-derived coarse-grained deltas, Gulf of Suez, Egypt: implications for exploration. AAPG 74:1077–1086
Gawthorpe RL, Jackson CAL, Young MJ, Sharp IR, Moustafa AR, Leppard CW (2003) Normal fault growth, displacement localisation and the evolution of normal fault populations; the Hammam Faraun fault block, Suez Rift, Egypt. J Struct Geol 25:883–895
Ghorab MA (1961) Abnormal stratigraphic features in Ras Gharib oilfield. In: Proceedings of the 3rd Arab petroleum congress, Cairo, Egypt, 10 pp
Hagras M (1976) The distribution and nature of the Miocene sediments in the Gulf of Suez. In: 5th exploration seminar (Cairo, Nov. 1976). Egyptian General Petroleum Corporation, 12 pp
Halim MA, Brady MJ, Harms JC (1986) Miocene platform carbonates in Hurghada area, south Western Gulf of Suez, Egypt. In: Proceedings of 8th EGPC exploration conference, vol 1, pp 74–95
Hantar G (1965) Remarks on the distribution of the Miocene sediments in the Gulf of Suez region. In: Proceedings of the 5th Arab petroleum congress, Cairo, Egypt, 13 pp
Hempton MR (1987) Constraints on Arabian plate motion and extensional history of the Red Sea. Tectonics 6:687–705
Henaish AA (2012) The structural studies of the southwestern side of the Gulf of Suez, Egypt. MSc thesis, Zagazig University, 155 pp
Hildebrand N, Shirav M, Freund R (1974) Structure of the western margin of the Gulf of Elat (Aqaba) in the Wadi El Quseib-Wadi Himur area, Sinai. Israel J Earth Sci 23:117–130
Hume WF, Madgwick TG, Moon FW, Sadek H (1920) Preliminary geological report on Gebel Tanka area. Pet Res Bull (Cairo) 4:16 pp
Hussein HM, Marzouk I, Moustafa AR, Hurukawa N (2006) Preliminary seismicity and focal mechanisms in the southern Gulf of Suez: August 1994 through December 1997. J Afr Earth Sci 45:48–60
Ismail M, Abdallah AM (1966) Contribution to the stratigraphy of St. Paul's Monastery area by microfacies. Bull Fac Sci Alexandria Univ 2:325–334
Issawi B, Francis M, El Hinnawi M, El Deftar T (1971) Geology of Safaga-Quseir coastal plain and of Mohamed Rabah area. Ann Geol Surv Egypt 1:1–19
Jackson CAL, Gawthorpe RL, Sharp IR (2002) Growth and linkage of the East Tanka fault zone, Suez Rift: structural style and syn-rift stratigraphic response. J Geol Soc Lond 159:175–187
Jarrige JJ, Ott d'Estevou P, Burollet PF, Montenat C, Prat P, Richert JP, Thiriet JP (1990) The multistage tectonic evolution of the Gulf of Suez and northern Red Sea continental rift from field observations. Tectonics 9:441–465
Jestin F, Huchon P, Gaulier JM (1994) The Somalia plate and the East African Rift system: present-day kinematics. Geophys J Int 116:637–654
Joffe S, Garfukel A (1987) Plate kinematics of the circum Red Sea—a re-evaluation. Tectonophysics 141:5–23
Khafagy AA (2001) Surface and subsurface structural setting of the area east and southeast of the South Galala Plateau. MSc thesis, Ain Shams University, 138 pp
Khalil SM (1998) Tectonic evolution of the eastern margin of the Gulf of Suez, Egypt. PhD thesis, Royal Holloway, University of London, 349 pp
Khalil S, McClay K (1998) Structural architecture of the eastern margin of the Gulf of Suez: field studies and analogue modelling results. In: Proceedings of the 14th exploration conference. Egyptian General Petroleum Corporation, Cairo, vol 1, pp 201–211
Khalil SM, McClay KR (2001) Tectonic evolution of the NW Red Sea–Suez rift system. In: Wilson RCL, Whitmarsh RB, Taylor B, Froitzheim N (eds) Non-volcanic rifting of continental margins: a comparison of evidence from land and sea. Geol Soc Lond Special Pub 187:453–473
Khalil SM, McClay KR (2002) Extensional fault-related folding, northwestern Red Sea, Egypt. J Struct Geol 24:743–762
Khalil SM, McClay KR (2006) Extensional fault-related folding, Gulf of Suez, Egypt. Middle East Research Centre, Ain Shams University, Earth Science Series, vol 20, pp 1–16
Khalil SM, McClay KR (2009) Structural control on syn-rift sedimentation, northwestern Red Sea margin, Egypt. Mar Pet Geol 26:1018–1034
Khalil SM, McClay KR (2012) Structural control on syn-rift sedimentation, northwestern Red Sea, Egypt. In: Roberts DG, Bally AW (eds) Regional geology and tectonics: phanerozoic rift systems and sedimentary basins. Elsevier, pp 73–103
Khalil S, McClay K (2016) 3D geometry and kinematic evolution of extensional fault-related folds, NW Red Sea, Egypt. In: Childs C, Holdsworth RE, Jackson CA-L, Manzocchi T, Walsh JJ, Yielding G (eds) The geometry and growth of normal faults. Geological Society, London, Special Publications 439, First published online March 30, 2016
Khalil SM, McClay KR (2018) Extensional fault-related folding in the northwestern Red Sea Egypt: segmented fault growth, fault linkages, corner folds and basin evolution. In McClay KR, Hammerstein JA (eds) Passive margins: tectonics, sedimentation and magmatism. Geological Society of London Special Publications. https://doi.org/10.1144/SP476.12
Lambiase JJ, Bosworth W (1995) Structural controls on sedimentation in continental rifts. In: Lambiase JJ (ed) Hydrocarbon habitat in rift basins. Geological Society Special Publication no. 80, pp 117–144

Lelek JJ, Shepherd DB, Stone DM, Abdine AS (1992) October field—the latest giant under development in Egypt's Gulf of Suez. In Halbouty MT (ed) Giant oil and gas fields of the decade 1978–1988. AAPG Memoir (54):231–249

Ligi M, Bonatti E, Bortoluzzi G, Cipriani A, Cocchi L, Tontini FC, Carminati E, Ottolini L, Schettino A (2012) Birth of an ocean in the Red Sea: initial pangs. Geochem Geophys Geosyst 13:1–29

Ligi M, Bonatti E, Bosworth W, Cai Y, Cipriani A, Palmiotto C, Ronca S, Seyler M (2018) Birth of an ocean in the Red Sea: oceanic-type basaltic melt intrusions precede continental rupture. Gondwana Res 54:150–160

Lyberis N (1988) Tectonic evolution of the Gulf of Suez and the Gulf of Aqaba. In: Le Pichon X, Cochran JR (eds) The Gulf of Suez and Red Sea Rifting. Tectonophysics 153:209–220

Mahmoud S, Reilinger R, McClusky S, Vernant P, Tealeb A (2005) GPS evidence for northward motion of the Sinai block: implications for E Mediterranean tectonics. Earth Planet Sci Lett 238:217–224

Maqbool A, Moustafa AR, Dowidar H, Yousef M (2014) Structural setting of Gebel Ataqa area, Gulf of Suez, Egypt: implications for rift-related fault array. Egypt J Geol 58:205–221

Martinez F, Cochran JR (1988) Structure and tectonics of the northern Red Sea: catching a continental margin between rifting and drifting. Tectonophysics 150:1–32

Mayhoub AA, Moustafa AR, Yousef M, Zalat SM (2017) Subsurface structural setting of Al Amir and Geyad fields, southwestern part of the Suez rift, Egypt. Bull Fac Sci Zagazig Univ 39:15 pp

McClay KR, Nicols GJ, Khalil SM, Darwish M, Bosworth W (1998) Extensional tectonics and sedimentation, eastern Gulf of Suez, Egypt. In: Purser BH, Bosence DWJ (eds) Sedimentation and Tectonics of Rift Basins: Red Sea-Gulf of Aden. Chapman and Hall, London, pp 223–238

Meshref WM (1990) Tectonic framework. In: Said R (ed) The geology of Egypt. Chapter 8. A. A. Balkema, Rotterdam, pp 112–155

Miller SP, Macdonald KC, Lonsdale P (1985) Nearbottom magnetic profile across the Red Sea. Mar Geophys Res 7:401–418

Montenat C, Ott D'Estevou P, Purser, B (1986) Tectonic and sedimentary evolution of the Gulf of Suez and the northwestern Red Sea: a review. In: Montenat C (ed) Geological Studies of the Gulf of Suez, the Northwestern Red Sea Coasts, Tectonic and Sedimentary Evolution of a Neogene Rift. Documents et Travaux Institut Geologique Albert de Lapparent, 10, pp 7–18

Montenat C, Ott D'Estevou P, Purser B, Burollet P, Jarrige J, Sperber F, Philobbos E, Plaziat J-C, Prat P, Richert J. Roussel N, Theiriet J (1988) Tectonic and sedimentary evolution of the Gulf of Suez and the northwestern Red Sea. Tectonophysics 153:166–177

Moon F, Sadek H (1923) Preliminary geological report on wadi Gharandal area. Pet Res Bull (Cairo) 12:42 pp

Moon F, Sadek H (1925) Preliminary geological report on Gebel Khoshera area. Pet Res Bull (Cairo) 9:40 pp

Moore JM (1979) Tectonics of the Najd transcurrent fault system, Saudi Arabia. J Geol Soc Lond 136:441–454

Moretti I, Colletta B (1987) Spatial and temporal evolution of the Suez Rift subsidence. J Geodyn 7:151–168

Moretti I, Colletta B (1988) Fault-block tilting: the Gebel Zeit example, Gulf of Suez. J Struct Geol 10:9–19

Moussa HE (1987) Geologic studies and genetic correlation of basaltic rocks in west central Sinai. PhD dissertation, Ain Shams University, Cairo, 308 pp

Moustafa AM (1976) Block faulting in the Gulf of Suez. In: Proceedings of 5th Egyptian general petroleum corporation exploration seminar, Cairo, 35 pp

Moustafa AR (1987) Drape folding in the Baba-Sidri area, Eastern Side of the Suez rift: Egypt. J Geol 31:15–27

Moustafa AR (1992a) Structural setting of the Sidri-Feiran area, Eastern side of the Suez rift: MERC, Ain Shams University. Earth Sci Ser 6:44–54

Moustafa AR (1992b) The Feiran tilted blocks: an example of a synthetic transfer zone, Eastern side of the Suez rift. Ann Tecton 6 (2):193–201

Moustafa AR (1993) Structural characteristics and tectonic evolution of the east margin blocks of the Suez rift. Tectonophysics 223:381–399

Moustafa AR (1996a) Internal structure and deformation of an accommodation zone in the northern part of the Suez rift. J Struct Geol 18:93–107

Moustafa AR (1996b) Structural setting and tectonic evolution of the northern Hammam Faraun Block (Wadi Wasit-Wadi Wardan area), eastern side of the Suez rift. Kuwait J Sci Eng 23:105–132

Moustafa AR (1997a) Controls on the development and evolution of transfer zones: the influence of basement structure and sedimentary thickness in the Suez rift and Red Sea. J Struct Geol 19:755–768

Moustafa AR (1997b) Structural characteristics of updip sides of half grabens and effect of pre-rift structures on rift geometry: northeastern part of the Suez rift. Ann Tecton 11(1–2):58–74

Moustafa AR (2002) Controls on the geometry of transfer zones in the Suez Rift and NW Red Sea: implications for the structural geometry of rift systems. AAPG Bull 86:979–1002

Moustafa AR (2004) Geologic maps of the Eastern side of the Suez rift (western Sinai Peninsula), Egypt. AAPG/Datapages, Inc. GIS Series (Geologic maps and cross sections in digital format on CD)

Moustafa AR, Abd-Allah AM (1991) Structural setting of the central part of the Cairo-Suez District: MERC, Ain Shams University. Earth Sci Ser 5:133–145

Moustafa AR, Abd-Allah AM (1992) Transfer zones with en echelon faulting at the northern end of the Suez rift. Tectonics 11:499–506

Moustafa AR, Abdeen M (1992) Structural setting of the Hammam Faraun Block, Eastern side of the Suez rift. J Univ Kuwait (Science) 19:291–309

Moustafa AR, El-Raey AK (1993) Structural character-istics of the Suez rift margins. Geol Rundsch 82:101–109

Moustafa AR, El Shaarawy OA (1987) Tectonic setting of the northern Gulf of Suez. In: Proceedings of 5th annual meeting, Egypt. Geophys Soc 339–368

Moustafa AR, Fouda HG (1988) Gebel Sufr El Dara accommodation zone, southwestern part of the Suez rift: Middle East Research Center, Ain Shams University. Earth Sci Ser 2:227–239

Moustafa AR, Khalil MH (1987) The Durba-Araba fault, southwest Sinai: Egypt. J Geol 31:1–13

Moustafa AR, Khalil MH (1995) Superposed deformation in the northern Suez rift, Egypt: relevance to hydrocarbon exploration. J Pet Geol 18:245–266

Moustafa A, Khalil S (2017) Control of extensional transfer zones on syntectonic and posttectonic sedimentation: implications for hydrocarbon exploration. J Geol Soc (London) 174:318–335. https://doi.org/10.1144/jgs2015-138

Moustafa AR, Yousif MS (1993) Structural evolution of the eastern shoulder of the Suez rift: Um Bogma area. N Jb Geol Palaont Mh 1993(11):655–668

Moustafa AR, Yehia MA, Abdel Tawab S (1985) Structural setting of the area east of Cairo, Maadi and Helwan. Mid East Res Cent Ain Shams Univ Sci Res Ser 5:40–64

Moustafa AR, Salama ME, Khalil SM, Fouda HG (2014) Sinai Hinge zone: a major crustal boundary in NE Africa. J Geol Soc Lond 171:239–254

Nelson RA (1987) Notes on the northern termination of the Gulf of Suez rift into a pre-existing east-west fault system. Al-Petrol, Nov-Dec 1987, Cairo, pp 57–62

Nicolas A, Boudier F, Lyberis N, Montigny R, Guennoc P (1985) L'île de Zabargad (Saint-Jean): témoin clé de l'expansion précoce en Mer Rouge: Comptes Rendus de l'Academie des Sciences. Serie 2 301:1063–1068

Orszag-Sperber F, Harwood G, Kendall A, Purser BH (1998) A review of the evaporites of the Red Sea-Suez rift. In: Purser BH, Bosence DWJ (eds) Sedimentation and Tectonics in Rift Basins: Red Sea—Gulf of Aden. Chapman Hall, London, pp 409–426

Ott d'Estevou P, Polze J, Montenat C (1986) Etude geologique de la marge occidentale du Golfe de Suez: Le massif des Gharamul et le Gebel Dara. Doc Trav Inst Geol Albert de Lapparent 10:19–43

Patton TL (1982) Surface studies of normal fault geometries in the Pre-Miocene stratigraphy, west central Sinai Peninsula. In: Proceedings of 6th EGPC exploration seminar, Cairo, vol 1, pp 437–452

Patton TL, Moustafa AR, Nelson RA, Abdine AS (1994) Tectonic evolution and structural setting of the Suez rift. In: Landon SM (ed) Interior rift basins. AAPG Memoir 59:9–55

Pautot G, Guennoc P, Coutelle A, Lyberis N (1984) Discovery of a large brine deep in the northern Red Sea. Nature 310:133–136

Peijs JA, Bevan TG, Piombino JT (2012) The Suez rift basin. In: Roberts DG, Bally AW (eds) Regional geology and tectonics: phanerozoic rift systems and sedimentary basins, vol 1B. Elsevier, pp 165–194

Reston TJ (2009) The extension discrepancy and syn-rift subsidence deficit at rifted margins. Pet Geosci 15:217–237

Philobbos ER, El-Haddad AA, Mahran TM (1989) Sedimentology of syn-rift Upper Miocene (?)-Pliocene sediments of the Red Sea area: a model from the environs of Marsa Alam, Egypt. Egypt J Geol 33:201–227

Philobbos ER, El Haddad AA, Luger P, Bekir R, Mahran T (1993) Syn-rift Miocen sedimentation around fault blocks in the Abu Ghusun-Wadi el Gemal area, Red Sea, Egypt. In: Philobbos ER, Purser BH (eds) Geodynamics and sedimentation of the Red Sea-Gulf of Aden rift system. Geological Society of Egypt, Special Publication, vol 1, pp 115–142

Pivnik DA, Ramzy M, Steer B, Thorseth J, El Sisi Z, Gaafar I, Garing J, Tucker R (2003) Episodic growth of normal faults as recorded by syntectonic sediments, July oil field, Suez rift, Egypt. AAPG Bull 87:1015–1030

Quennell AM (1959) Tectonics of the Dead Sea rift. In: 20th international geology congress, Mexico 1956. Asociacion de Servicios Geologicos Africanos, pp 385–408

Refaat AA, Imam MM (1999) The Tayiba Red Beds: transitional marine-continental deposits in the precursor Suez Rift, Sinai, Egypt. J Afr Earth Sci 28:487–506

Reilinger R, McClusky S, ArRajehi A (2015) Geodetic constraints on the geodynamic evolution of the Red sea. In: Rasul NMA, Stewart ICF (eds) The Red Sea: the formation, morphology, oceanography and environment of a young ocean basin. Springer Earth System Sciences, Berlin, Heidelberg, pp 135–149

Richardson M, Arthur MA (1988) The Gulf of Suez-northern Red Sea Neogene rift: a quantitative basin analysis. Mar Pet Geol 5:247–270

Robson DA (1971) The structure of the Gulf of Suez (clysmic) rift, with special reference to the eastern side. J Geol Soc Lond 127:242–276

Roeser HA (1975) A detailed magnetic survey of the southern Red Sea. Geol Jahrb 13:131–153

Roussel N, Purser BH, Orszag-Sperber F, Plaziat J-C, Soliman M, Al Haddad AA (1986) Géologie de la région de Qusier, Egypte. Documents et Travaux de l'Institut Géologique Albert de Lapparent, Paris 10:129–144

Sadek A (1968) Stratigraphy and structure studies on the Cairo-Suez district with special reference to Gebel Homeyera area. PhD dissertation, Cairo University

Sadek H (1926) The geography and geology of the district between Gebel Ataqa and El Galala El Bahariya (Gulf of Suez). Geol Surv Egypt. Paper no. 40, 120 pp

Said R (1960) Planktonic foraminifera from Thebes Formation, Luxor. Micropaleontology 6:277–286

Said R (1962) The geology of Egypt. Amsterdam, Elsevier Publishing Company, 377 pp

Said R (1990) The geology of Egypt. A.A. Balkema, Rotterdam, 729 pp

Said R, Basiouni MA (1958) Miocene foraminifera of Gulf of Suez region. AAPG Bull 42:1958–1977

Sakran SM, Nabih M, Henaish A, Ziko AO (2016) Structural regime and its impact on the mechanism and migration pathways of hydrocarbon seepage in the southern Suez rift: an approach for finding new unexplored fault blocks. Mar Pet Geol 71:55–75

Saleh S, Moustafa AR, Pohánka V (in manuscript) Impact of inherited structures on present-day tectonics of the central Eastern Desert and northern Red Sea, Egypt: evidence from 3-D gravity inversion and seismicity

Samuel MD, Saleeb-Roufaiel GS (1977) Lithostratigraphy and petrography of the Neogene sediments at Abu Ghusun, Um Mahara, Red Sea coast, Egypt. Beitrage zur Lithologi, Freiburg Forsch 323:47–56

Saoudi A, Khalil B (1986) Distribution and hydrocarbon potential of Nukhul sediments in the Gulf of Suez. In: 7th EGPC exploration seminar, 1984, pp 75–96

Schurmann HME (1966) The pre-Cambrian along the Gulf of Suez and the northern part of the Red Sea. Leiden, E.V. Brill, 405 pp

Scott R, Govean F (1986) Early depositional history of a rift basin: Miocene in the western Sinai. In: 7th EGPC exploration seminar, 1984, pp 37–48

Sercombe WJ, Golob BR, Kamel M, Stewart JW, Smith GW, Morse JD (1997) Significant structural reinterpretation of the subsalt, giant October Field, Gulf of Suez, Egypt, using SCAT, isogon-based sections and maps, and 3-D seismic. Lead Edge 1143–1150

Sercombe WJ, Thurmon L, Morse J (2012) Advanced reservoir modeling in poor seismic, October Field, northern Gulf of Suez, Egypt. AAPG Search Discov Article # 40872, 35 pp

Sharp I, Gawthorpe R, Underhill J, Gupta S (2000) Fault-propagation folding in extensional settings: examples of structural style and syn-rift sedimentary response from the Suez Rift, Sinai, Egypt. Geol Soc Am Bull 112:1877–1899

Shukri NM (1945) On the geology of the Brothers' Islets, Northern Red Sea. Bull Fac Sci Fouad I Univ (Cairo) 25:173–200

Shukri NM (1953) The geology of the area east of Cairo. Bull Inst Desert Egypte 3:89–105

Shukri NM (1954) The geology of Shadwan Island, northern Red Sea. Bull Soc Geogr Egypte 27:83–92

Shukri NM, Akmal MG (1953) The geology of Gebel El-Nasuri and Gebel El Anqabiya district. Bull Soc Geogr Egypte 26:243–276

Shukri NM, Ayouty MK (1956) The geology of Gebel Iweibid-Gafra area, Cairo-Suez district. Bull Soc Geogr Egypte 29:67–109

Sobhy H (2011) Structural setting of the northwestern part of Belayim Marine oil field and its impact on the hydrocarbon potential. MSc thesis, Ain Shams University, 160 pp

Sobhy H, Moustafa AR (2012) Tectonic evolution of the Belayim Marine oil field. Ann Geol Surv Egypt 31:99–107

Steckler MS, Bertholot F, Lyberis N, Le Pichon X (1988) Subsidence in the Gulf of Suez: implications for rifting and plate kinematics. Tectonophysics 153:249–270

Steen G (1984) Radiometric age dating and tectonic significance of some Gulf of Suez igneous rocks. In: Proceedings of the 6th Egyptian general petroleum corporation exploration seminar, Cairo, Egypt (1982), pp 199–211

Tewfik N, Ayyad M (1984) Petroleum exploration in the Red Sea shelf of Egypt. In: Proceedings of 6th exploration seminar (Cairo, 1982), Egyptian general petroleum exploration conference, vol 1, pp 159–180

Thiriet J, Burollet P, Montenat C, Ott d'Estevou P (1986) Evolution tectonique et sedimentaire Neogene a la transition du Golfe de Suez et de la Mer Rouge: La secteur de Port-Safaga (Egypte). Dot et Trav IGAL 10:93–116

Travis CJ (1984) Upper cretaceous stratigraphy of eastern Galala, Egypt. MSc Thesis, University of South Carolina, Columbia, South Carolina, 89 pp

Viotti C, El-Demerdash G (1969) Studies in Eocene sediments of Wadi Nukhul area, east coast-Gulf of Suez. In: Proceedings of the 3rd African micropaleontological colloquium, Cairo, Egypt, pp 403–423

Voggenreitter W, Hotzl H, Jado AR (1988) Red Sea related history of extension and magmatism in the Jizan area (SW Saudi Arabia): indication of simple-shear during early Red Sea rifting. Geologische Rundschau 77:257–274

Younes AI, McClay KC (2002) Development of accommodation zones in the Gulf of Suez–Red Sea rift, Egypt. AAPG Bull 86:1003–1026

Young MJ, Gawthorpe RL, Sharp IR (2000) Sedimentology and sequence stratigraphy of a transfer zone coarse-grained delta, Miocene Suez Rift, Egypt. Sedimentology 47:1081–1104

Youssef A (2011) Early–Middle Miocene Suez Syn-rift-Basin, Egypt: a sequence stratigraphy framework. GeoArabia 16:113–134

Youssef MI, Abd-Allah AM (2003) Structural geology of the southern part of the Cairo-Suez district, Egypt. In: Proceedings of 5th international conference on the geology of the Middle East (Cairo, Egypt), pp 559–569

Youssef MI, Abdelmalik WM (1972) Micropaleontological zonation of the tertiary rocks of Taiyba-Feiran area, west-central Sinai, Egypt. In: Proceedings of the 6th Arab science congress, Damascus, Syria (1969), vol 4-B, pp 675–684

Youssef S, Moustafa A, Fahmy I, El-Banbi A, Aly A, Emara M, El-Homosany A (2002) An integrated approach to optimizing a large asset—static modeling. In: AAPG annual meeting, Cairo

Geology of Egypt: The Northern Red Sea

9

W. Bosworth, S. M. Khalil, M. Ligi, D. F. Stockli, and K. R. McClay

Contents

W. Bosworth (✉)
Apache Egypt Companies, 11 Street 281, New Maadi, Cairo, Egypt
e-mail: bill.bosworth@apacheegypt.com

S. M. Khalil
Faculty of Science, Department of Geology, Suez Canal University, Ismailia, 41522, Egypt

M. Ligi
Istituto di Scienze Marine, CNR, Via Gobetti 101, 40129 Bologna, Italy

D. F. Stockli
Department of Geological Sciences, Jackson School of Geosciences, University of Texas at Austin, 1 University Station C9000, Austin, TX 78712-0254, USA

K. R. McClay
Department of Earth Sciences, Royal Holloway, University of London, Egham, Surrey TW20 0EX, UK

Abstract

The Red Sea and Gulf of Aden constitute parts of the Afro-Arabian rift system that are in the most advanced stages of continental break-up. These basins have therefore received extensive scrutiny in the geoscientific literature, but several aspects of their evolution remain enigmatic. Many of their most important features lie beneath several kilometers of water, in places covered by several kilometers of evaporite deposits, and along international political boundaries. All these factors greatly complicate the acquisition and interpretation of both subsurface wellbore and geophysical datasets. Much of our understanding of the evolution of the Red Sea has therefore relied on the integration of outcrop geology and land-based analytical studies with these more difficult to obtain marine

Z. Hamimi et al. (eds.), *The Geology of Egypt*, Regional Geology Reviews,
https://doi.org/10.1007/978-3-030-15265-9_9

observations. While stratigraphic, radiometric and structural data indicate that extension and rifting initiated in the southern Red Sea during the Late Oligocene (~28–25 Ma), the start of rifting in the northern Red Sea is more difficult to constrain due to paucity of rift-related volcanism and reliable biostratigraphy of the oldest syn-kinematic sedimentary strata. A regional NW-SE trending alkali basalt dike swarm, with associated extensive basalt flows in the vicinity of Cairo, appears to mark the onset of crustal-scale extension and continental rifting. These dikes and scarce local flows, erupted at the Oligocene-Miocene transition (~23 Ma) and coeval with similar trending dikes along the Yemen and Saudi Arabian Red Sea margin, are interbedded with the oldest part of the paleontologically dated siliciclastic syn-rift stratigraphic section (Aquitanian Nukhul Fm.), and are associated with the oldest recognized extensional faulting in the Red Sea. Bedrock thermochronometric results from the Gulf of Suez and both margins of the Red Sea also point to a latest Oligocene onset of major normal faulting and rift flank exhumation and large-magnitude early Miocene extension along the entire length of the Red Sea rift. This early phase of rifting along the Egyptian Red Sea margin and in the Gulf of Suez resulted in the formation of a complex, discontinuous fault pattern with very high rates of fault block rotation. The rift was segmented into distinct sub-basins with alternating regional dip domains separated by well-defined accommodation zones. Sedimentary facies were laterally and vertically complex and dominated by marginal to shallow marine siliciclastics of the Abu Zenima, Nukhul and Nakheil Formations. Neotethyan faunas appeared throughout all of the sub-basins at this time. During the Early Burdigalian (~20 Ma) tectonically-driven subsidence accelerated and was accompanied by a concordant increase in the denudation and uplift of the rift shoulders. The intra-rift fault networks coalesced into through-going structures and fault movement became progressively more focused along the rift axis. This reconfiguration of the rift structure resulted in more laterally continuous depositional facies and the preponderance of moderate-to-deep marine deposits of the Rudeis, Kareem and Ranga Formations. The early part of the Middle Miocene (~14 Ma) was marked by dramatic changes in rift kinematics and sedimentary depositional environments in the Red Sea and Gulf of Suez. The onset of the left-lateral Gulf of Aqaba transform fault system, isolating the Gulf of Suez from the active northern Red Sea rift, resulted in a switch from orthogonal to oblique rifting and to hyperextension in the northern Red Sea. The open marine seaway was replaced by an extensive evaporitic basin along the entire length of the rift from the central Gulf of Suez to Yemen/Eritrea. In Egypt these evaporites are ascribed to the Belayim, South Gharib, Zeit and Abu Dabbab Formations. Evaporite deposition continued to dominate in the Red Sea until the end of the Miocene (~5 Ma) when a subaerial unconformity developed across most of the basin. With the onset of seafloor spreading in the southern Red Sea, Indian Ocean marine waters re-entered through the Bab el Mandab in the earliest Pliocene and re-established open marine conditions. During the Pleistocene, glacial-isostatic driven sea-level changes resulted in the formation of numerous coral terraces and wave-cut benches around the margins of the Red Sea, Gulf of Suez and Gulf of Aqaba. Their present elevations suggest that the Egyptian Red Sea margin has been relatively vertically stable since the Late Pleistocene. While there is general agreement that full seafloor spreading, producing well-defined magnetic stripes, has been occurring in the southern Red Sea since ~5 Ma, there is ongoing debate whether and when lithospheric break-up has occurred in the northern Red Sea. Industry wellbore and seismic data demonstrate that continental crust extends at least several tens of kilometers offshore from the present-day coastline, and that the northern Red Sea is a non-volcanic rifted margin. On the basis of integrated geophysical, petrological, geochemical and geological datasets, we contend that true, laterally integrated sea-floor spreading is not yet manifest in the northern Red Sea.

9.1 Introduction

The Red Sea presents a collection of just about everything of interest to scientists studying the rifting of our planet's lithosphere. The curvilinear margins of Africa and Arabia restore together as first envisioned for the Atlantic except for overlap in the Afar, where one of the Earth's great volcanic provinces happens to sit (Fig. 9.1). A pronounced, submerged rift valley runs along its southern and central axis, giving way to more discrete deeps hosting brine pools and volcanos in the north. Large, uplifted, rotated fault blocks decorate its coastlines and similar structures have been imaged offshore with industry reflection seismic data. Much of the rift axis is seismically active, particularly at its junction with the Gulf of Aqaba transform fault. Exposures of the sub-rift lower crust and mantle are present at the Brothers and Zabargad Islands offshore Egypt. And there appears to be a progression of rift phases from well-organized oceanic seafloor spreading in the south, through some kind of continental-to-oceanic rift transition in the north, to an abandoned and largely exposed continental rift in the Gulf of Suez. There is something for everyone.

The Red Sea has therefore rightly become a model to compare with more poorly exposed, or less accessible, rifts around the world and across geologic time. Of particular recent interest has been its usefulness for understanding the evolution of hydrocarbon-rich passive continental margins

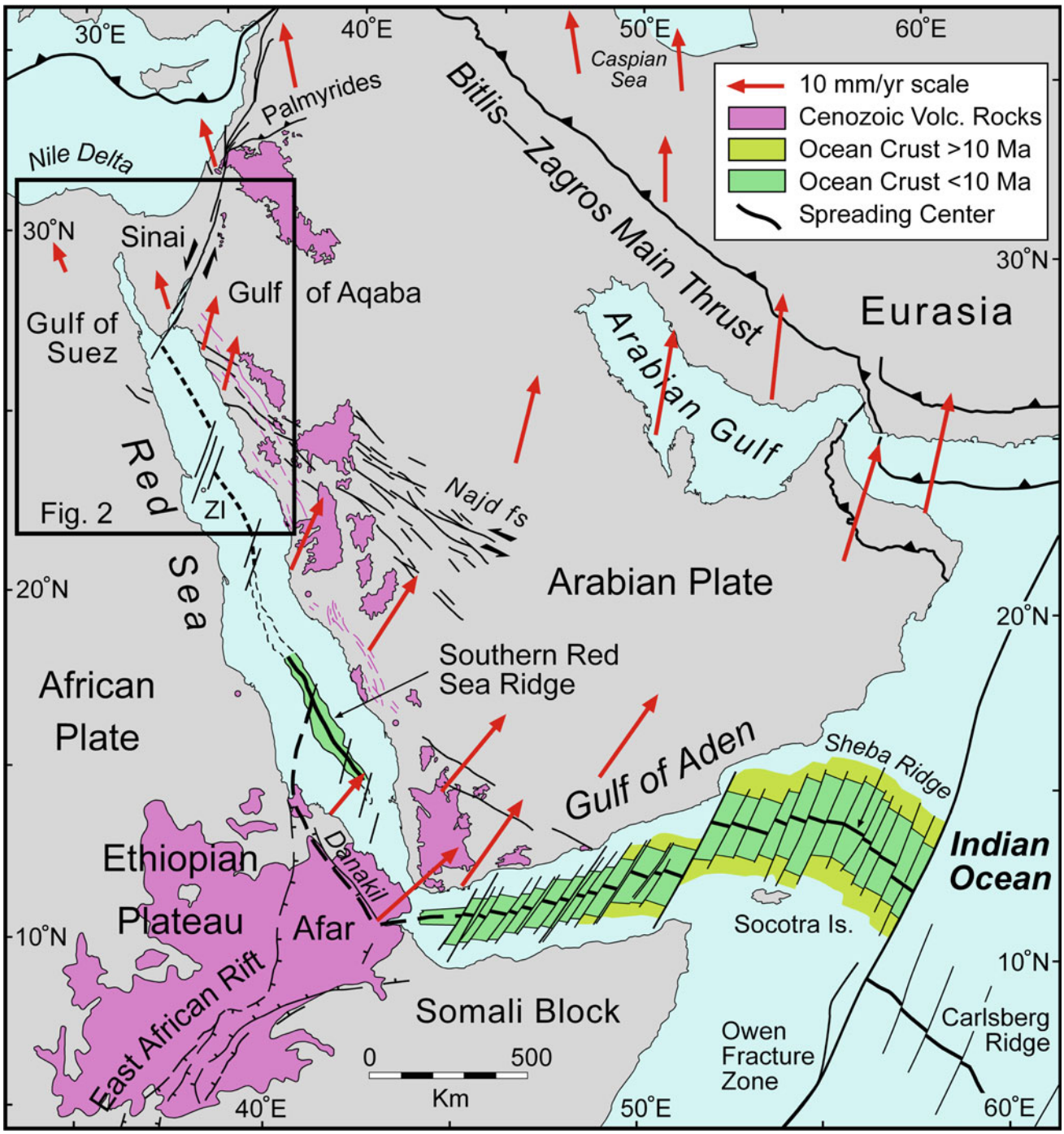

Fig. 9.1 Tectonic setting of the Red Sea. Modified from Bosworth et al. (2005) and references therein. Red arrows are GPS-derived velocities from ArRajehi et al. (2010). The location of Fig. 9.2 is indicated by the box

(Mohriak and Leroy 2013; Mohriak 2015). The position of the Red Sea within a much grander, multi-continent-scale rift system was recognized more than a century ago (Suess 1891; Gregory 1896; Du Toit 1937). The "Afro-Arabian rift system" reaches from transform fault and associated pull-apart basins of Syria, Jordan and Israel, continuing along the Gulf of Aqaba to the junction with the Red Sea, joining at Afar with the Gulf of Aden and the Ethiopian rift that further links the system to the complex East African rift system (Baker 1970; Khan 1975; Kaz'min 1977; Girdler 1991). Spanning ~7,500 km, this is the largest predominantly continental rift system in the world. The only

segments of the Afro-Arabian rift system that are experiencing "seafloor" spreading are parts of the Red Sea, Afar, and the Gulf of Aden.

Given the Red Sea's preeminence as a model for rifting, several fundamental questions have dominated discussions of its origin and evolution (reviewed in Stockli and Bosworth 2019): (1) was the Red Sea initiated by an active or passive mechanism, i.e. due to mantle upwelling or plate boundary forces (Sengör and Burke 1978)? (2) does the Red Sea represent a magma-rich or magma-poor rift system? (3) did the rift open orthogonally or was strike-slip movement and oblique opening involved? (4) was lithospheric extension distributed symmetrically both vertically and laterally, or was it asymmetric and characterized by large-scale, low-angle extensional faults? (5) what was the timing of the onset of seafloor spreading and what segments of the Red Sea are now oceanic rifts? and (6) do the complex geological and geophysical variations observed along the length of the Red Sea represent snapshots of the evolution of a rift through time, or are they perhaps unique to each rift segment, controlled by local geologic forces that define their character?

The Egyptian margin of the Red Sea covers ~650 km or about one third of the total length of the basin, and therefore discussion of this region alone cannot address completely all of these important questions. But some of the best-exposed Red Sea-related stratigraphy and structures are seen along the Egyptian margin, and the offshore has been explored with aeromagnetics, refraction and reflection seismics, and several wellbores that extend to crystalline basement. Abundant seismicity occurs in the northern Red Sea and Gulfs of Suez and Aqaba, and regional seismic network coverage is good. Global Positioning System (GPS) permanent stations have operated for several years to decades and provide important constraints concerning present-day plate movement. In this Chapter we integrate these diverse datasets to produce a view of how the Egyptian Red Sea margin helps to constrain understanding of the greater Red Sea rift. We start by summarizing geophysical and geochemical interpretations of the northern Red Sea crust and lithosphere, and how these relate to the Red Sea–Suez–Aqaba triple junction. This is followed by descriptions of Red Sea stratigraphy present along the coastal margin and in the offshore. The stratigraphy provides a framework in which to view the structural evolution of the margin, where we present both surface and subsurface observations. Available geochronologic and thermochronologic data are presented to constrain and refine our tectonostratigraphic interpretation. Our final step is to compare this northern Red Sea perspective with models proposed for other rifted margins to produce a reasonable 'best-fit' picture of this intriguing basin.

9.2 Geophysics of the Northern Red Sea and Environs

9.2.1 Seismicity

Most parts of northern Red Sea, Gulf of Suez and Gulf of Aqaba display low to moderate levels of seismic activity if compared to other active plate boundaries. In order to explore possible causes we carried out a quantitative analysis based on instrumental recorded seismicity in the region which we divided into three sectors (Fig. 9.2). Earthquake parameters occurring from January 1967 to December 2016 were obtained from the International Seismological Centre (ISC). This included data from both the ISC Bulletin and Reviewed ISC Bulletin. The Reviewed Bulletin contains events manually checked and relocated, but it lacks many low magnitude events from local networks. Thus, the two catalogues were merged and duplicate data were removed with priority to the Reviewed Bulletin events. A total of 31,829 events were analyzed after converting different magnitude types (M_b, M_s, M_d and M_L) to momentum magnitude M_w adopting strategies and magnitude conversion formulas suggested by Babiker et al. (2015).

Seismicity in the northern Red Sea is dominated by a large number of earthquakes with low and moderate magnitudes (Fig. 9.3). This contrasts with the southern Red Sea and Afar where several moderate to large magnitude events are focused along the rift axis (Al-Ahmadi et al. 2014). Since recording began, the ISC catalogue reports just 4 events with magnitude $M_w \geq 5$ that occurred in the northern Red Sea. The largest with $M_w = 5.3$ took place on July 2nd 1984, in the Abu-Dabbab region of the western Red Sea coastal plain. The focal mechanism from the global Centroid Moment Tensor (CMT) catalogue shows a normal dip-slip on approximately Red Sea (NW-SE) trending faults (Fig. 9.3a) with a focal depth in the proximity of the brittle-ductile transition (9–10 km). The Abu-Dabbab area is seismically very active: Fairhead and Girdler (1970) reported on an event of $M_b = 6$ on 12 November 1955, and several earthquake swarms have been recorded during 1976, 1984, 1993, 2003 and 2004 with epicenters aligned along a NE-SW direction perpendicular to the Red Sea axis. It has been suggested that these occurrences of earthquakes may be due to stress perturbation associated with either repeated magmatic intrusions in the lower crust beneath Abu-Dabbab (Hosny et al. 2012) or migration of magmatic or hydrothermal fluids through pre-existing crustal heterogeneities or fractures (Waite and Smith 2002).

The second largest event with $M_w = 5$ in the northern Red Sea occurred in the Mabahiss Deep on 12 January 2015. Fault plane solutions from the CMT database suggest normal

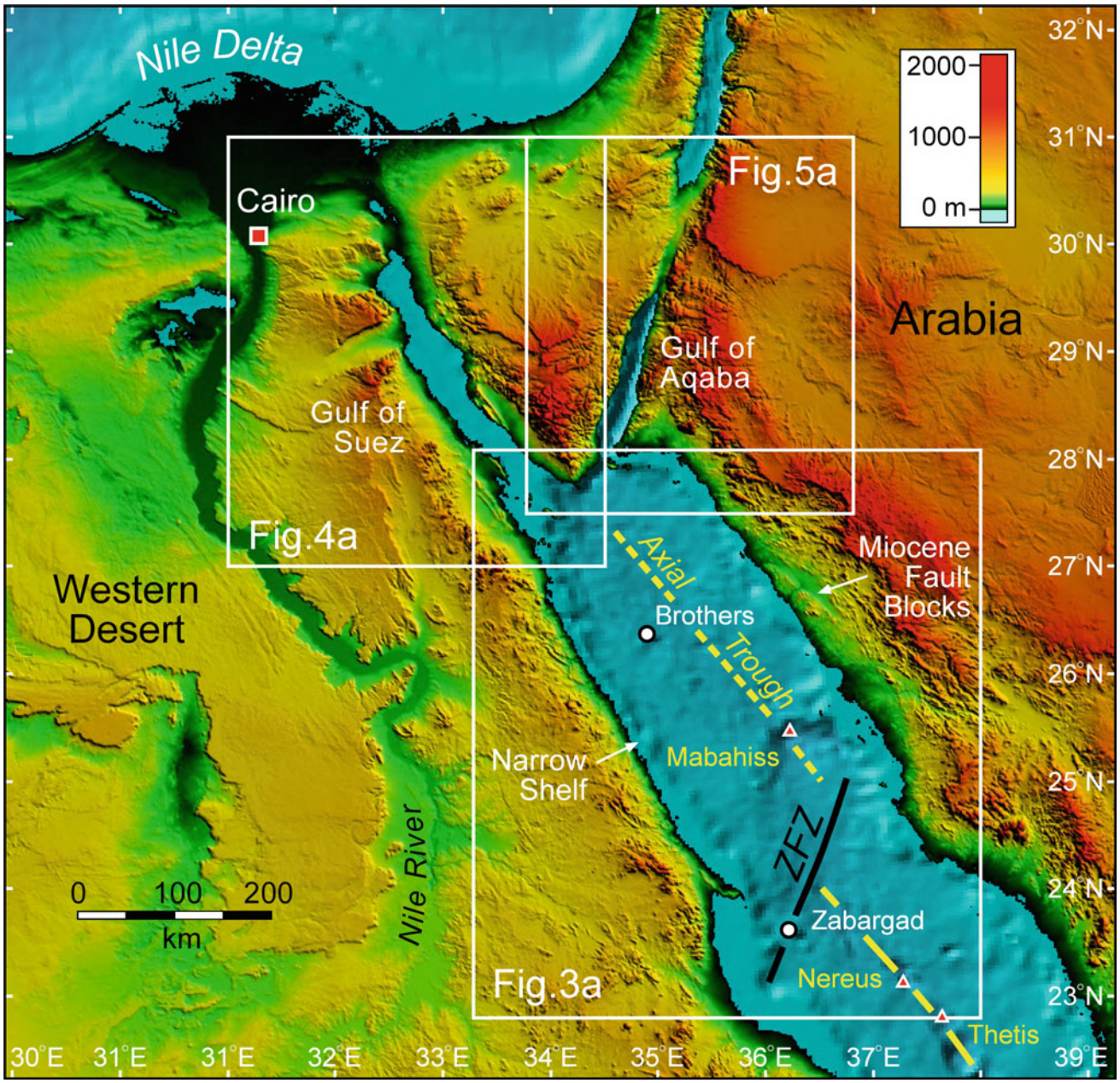

Fig. 9.2 Digital elevation and bathymetric model of the northern Red Sea, Gulf of Suez, and Gulf of Aqaba region (NOAA 2016). Locations of Figs. 9.3a, 9.4a, and 9.5a are shown by boxes. ZFZ = Zabargad fracture zone

faulting trending parallel to the Red Sea axis (Fig. 9.3a). Mabahiss Deep reaches a depth of 2200 m and displays a NW-SE-trending neo-volcanic zone with a wide central volcano at its northern tip (Guennoc et al. 1990). The Mabahiss depression has been interpreted as a pull-apart basin (Guennoc et al. 1988) and lies at the NE end of the Zabargad fracture zone (FZ) that marks the southern limit of the northern Red Sea and runs from Mabahiss to Zabargad Island (Figs. 9.2 and 9.3a). The Zabargad FZ is a major oblique, depressed morphotectonic feature striking almost parallel to the Dead Sea transform (~NNE-SSW) offsetting the Red Sea axis northward by ~100 km. Earthquake spatial distribution reveals two clearly separated clusters of epicenters: one centered in the Mabahiss Deep and the other along the Zabargad FZ to the south (Fig. 9.3a).

Moving northward, a seismic gap characterizes the Red Sea axial region for about 30 km up to the Shaban Deep located ~40 km east of Brothers Islands (Fig. 9.3a). In the center of this Deep an elongated NW-SE 6 km-long volcanic ridge rises to a depth of 900 m from a nearby maximum of 1600 m (Ehrhardt and Hubscher 2015). North of Shaban the seismicity becomes more scattered across the basin. The

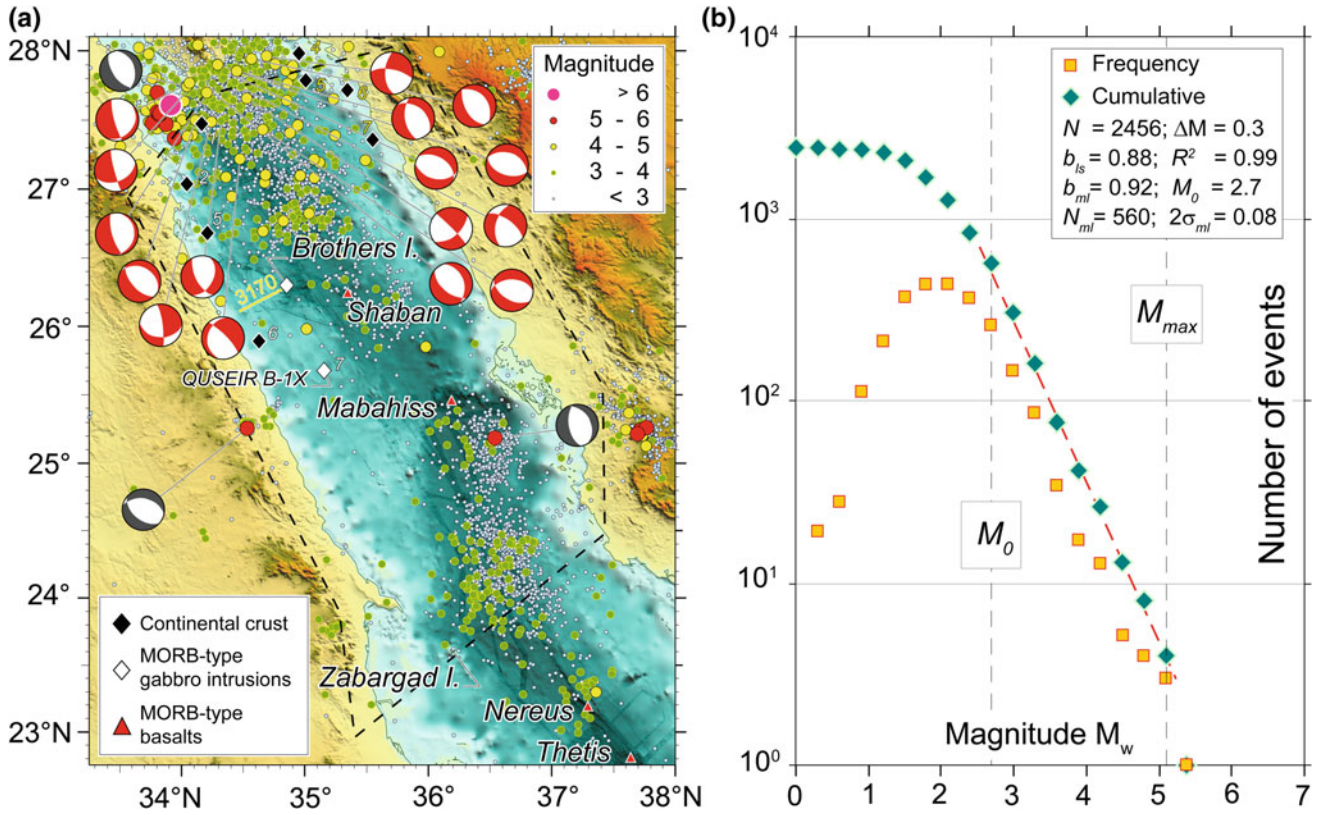

Fig. 9.3 Seismicity of the northern Red Sea. **a** Spatial distribution of earthquake epicenters. Seismic event locations are color-coded by magnitude. Events recorded during 1967–2017 are from ISC Bulletin (OnLine Bulletin: http://www.isc.ac.uk). Black dashed line polygon outlines the region that includes all the seismic events (northern Red Sea ISC sub-catalogue) considered in the magnitude distribution analysis shown in (**b**). Fault plane solutions from the Global CMT catalogue (E. Larson, G. Ekström, M. Nettles, http://www.globalcmt.org), Mohamed et al. (2015), and Abdel-Aal and Yagi (2017) are indicated as focal mechanisms (CMT: grey, others: red). Black filled diamonds show offshore wells where Nubian shield basement rocks have been encountered at total depth. White filled diamonds indicate locations where off axis MORB-type gabbroic intrusions have been sampled (Brothers islets and at total depth of Phillips exploratory well QUSEIR B-1X; Ligi et al. 2018, 2019). Axial major depressions are floored by oceanic crust as suggested by MORB-type basalts sampled along axis (red filled triangles). Yellow solid line southwest of Brothers Islands shows location of seismic line 3170 in Fig. 9.7b. **b** Cumulative (blue diamonds) and differential (yellow squares) frequency–magnitude distribution of estimated momentum magnitude M_w from the ISC northern Red Sea sub-catalogue. Red dashed line is the least-square regression (angular coefficient = b_{ls}-value) calculated through counts of events equal to or larger than a given M_0 and equal to or less than a given M_1 (completeness magnitudes). The vertical dashed lines indicate the assumed completeness thresholds (M_0 = 2.4 and M_1 = 5.1). Same range of magnitudes were used to estimate b_{ml}-value by the maximum likelihood method (Aki 1965; Utsu 1965)

number of larger events and the seismic event rate gradually increase reaching their maxima at the Sinai triple junction (Nubia–Sinai–Arabia), where normal faulting mechanisms on NNW-SSE and NW-SE trending faults are suggested by local network recordings (Badawy et al. 2008; Abdel-Aal and Yagi 2017).

Seismicity in the Gulf of Suez is locally much greater than in most segments of the northern Red Sea, although Suez is extending at a very slow rate (Fig. 9.4). Seismic events are clustered in three areas: the mouth of the Gulf adjacent to the Sinai triple junction; the central sub-basin; and the northern sub-basin including the adjacent land area as far west as the river Nile. The largest Suez event occurred on 31 March 1969 (M_w = 6.8) in the southern part of the Gulf next to the triple junction. Fault plane solutions indicate normal faulting along NW-SE striking faults (Fig. 9.4a; McKenzie et al. 1970; Ben-Menahem and Aboodi 1971; Huang and Solomon 1987). In this part of the Gulf, 15 other events with magnitudes in the range of 5–6 have been recorded. Earthquake focal mechanisms (Badawy et al. 2008; Mohamed et al. 2015) based on local recorded data are dominated by normal faulting with a left lateral strike-slip component on NW-striking preferred fault planes (Fig. 9.4a). The strike slip component gradually increases northward, accompanied by a general decrease in seismic activity.

In the Gulf of Aqaba-Dead Sea transform, larger earthquakes and in particular those with magnitude ≥ 5 are clustered in the Aragonese-Arnona deep (Fig. 9.5; Hofstetter

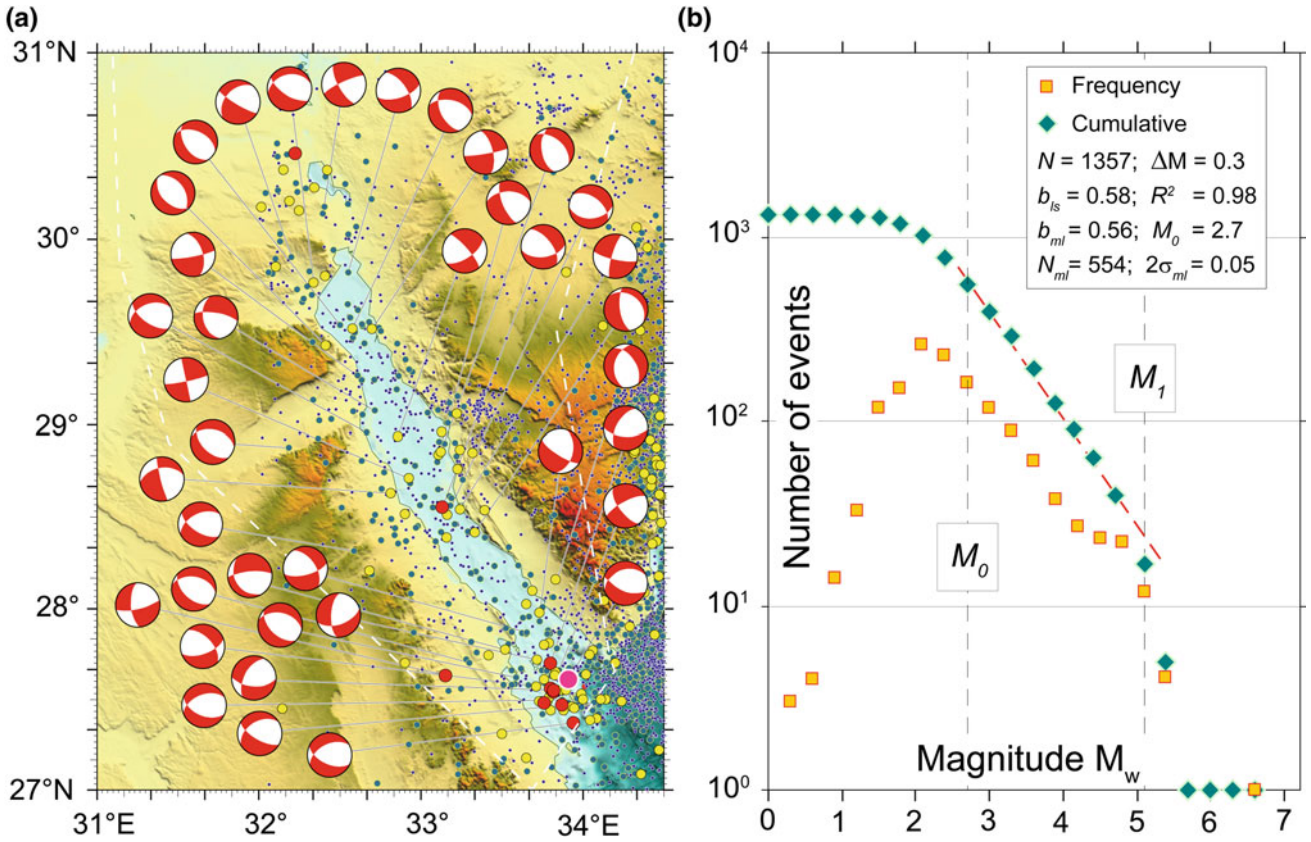

Fig. 9.4 Seismicity of the Gulf of Suez. **a** Spatial distribution of earthquake epicenters. White dashed line marks the region including all the earthquakes (Gulf of Suez sub-catalogue) considered in the frequency-magnitude distribution analysis shown in (**b**). Fault plane solutions from Badawy et al. (2008) and Mohamed et al. (2015) are shown as focal mechanisms. **b** Cumulative and differential frequency–magnitude distribution of estimated momentum magnitude M_w from the ISC Gulf of Suez sub-catalogue. Symbols as in Fig. 9.3

2003; Bosworth et al. 2017) and then in an elongated belt along and north of the Dead Sea (Salamon et al. 1996, 2003). Two events with magnitude ≥ 6 and 21 events with magnitudes between 5 and 6 have been recorded in the Gulf of Aqaba. The largest earthquake, with M_w = 7.2, occurred on 22 November 1995 (*Nuweiba* event) within the Aragonese-Arnona deep (Al-Tarazi 2000; Hofstetter 2003). It strongly shocked the whole area surrounding the Gulf, including the city of Cairo, and seismic shaking caused considerable damage in Nuweiba City on the western coast of the Gulf. CMT fault plane solutions show left-lateral strike-slip movement on a vertical NNE-SSW striking fault plane (Fig. 9.5a; Hofstetter 2003). Most teleseismic events in the CMT database have strike-slip fault solutions, but normal fault mechanisms are also commonly observed in local network recordings (Al-Amri et al. 1991; Mohamed et al. 2015). Composite focal mechanisms from events that occurred in the northern Aragonese and eastern Elat Deeps from 1985 to 1989 and with M_L from 2.6 to 3.8 indicate normal dip-slip on approximately north-south striking faults (Al-Amri et al. 1991). Although most of the larger aftershocks following the Nuweiba event displayed strike-slip mechanisms, one large normal fault event occurred in the offshore north of the main epicenter. From August 1993 to February 1994 a large swarm of 983 earthquakes occurred within and nearby the central Gulf of Aqaba deeps (Abdel-Aal and Badreldin 2016). The two largest events of the swarm (M_L = 5.8 and 5.6) were principally dip-slip (Hofstetter 2003). The epicenters of both of these earthquakes were located on NNE-SSW striking segments of the Arabia coastline documenting an east-west extensional component in addition to the left lateral strike-slip motion commonly observed along the Dead Sea transform (Bosworth et al. 2017).

The northern Red Sea, southern Gulf of Suez, and Gulf of Aqaba each display different levels of seismicity in terms of number of large events and seismic rate. In order to investigate the underlying controls on regional seismicity we define sub-catalogues of ISC events occurring within each of these regions (Figs. 10.3, 10.4 and 10.5). Distribution of earthquakes with respect to magnitude exhibits scale invariability, appears to be self-similar and obeys a power

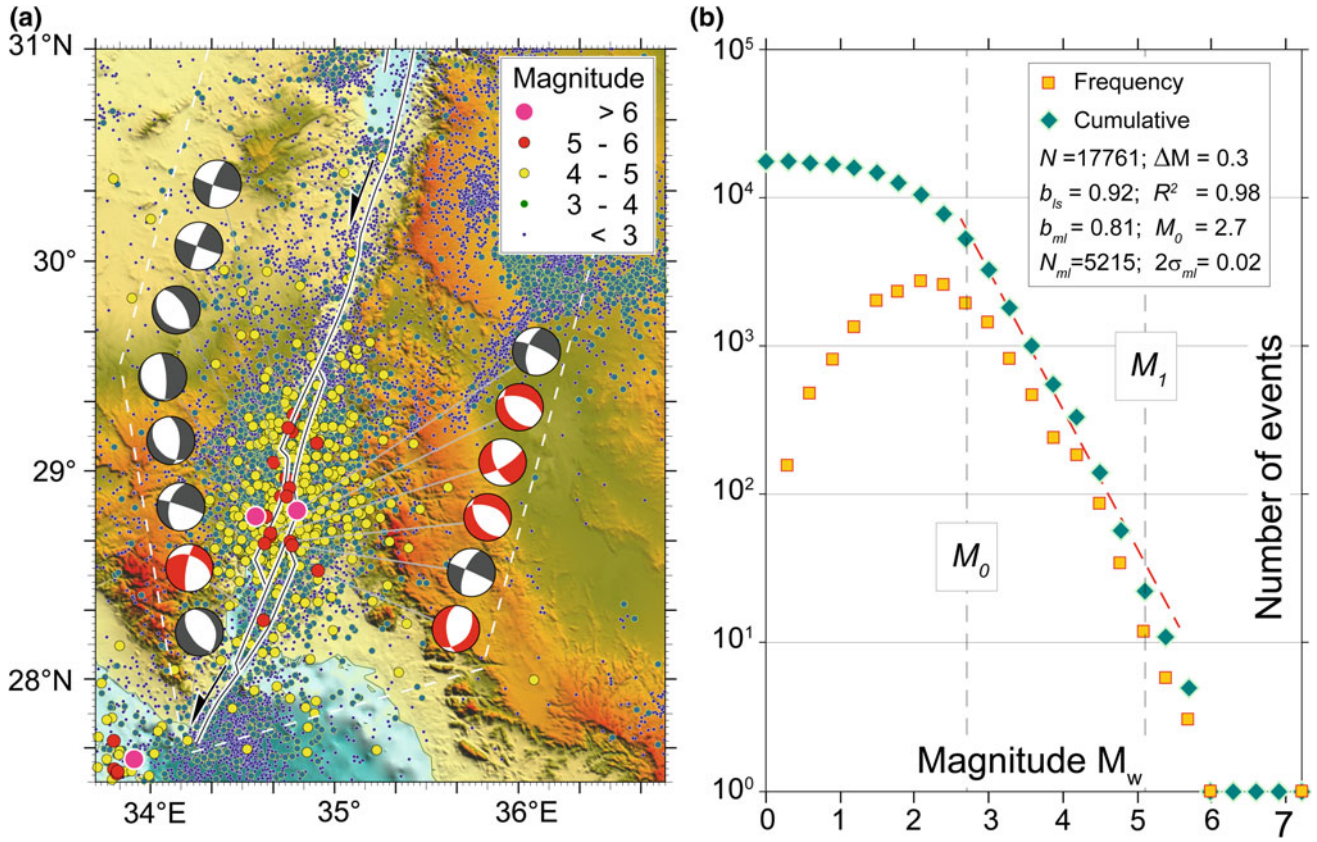

Fig. 9.5 Seismicity of the Gulf of Aqaba. **a** Spatial distribution of earthquake epicenters. Sub-basins and main faults are shown with black lines (Ben-Avraham et al. 1979). Focal mechanisms are from the CMT catalogue (grey) and Mohamed et al. (2015) (red). White dashed line marks the region including events (Gulf of Aqaba ISC sub-catalogue) considered in the magnitude-frequency distribution analysis shown in (**b**). **b** Cumulative and differential frequency–magnitude distribution of estimated momentum magnitude M_w from the ISC Gulf of Aqaba sub-catalogue. Symbols as in Fig. 9.3

law. On average over the long term, seismicity generally follows the empirical Gutenberg–Richter law (Ishimoto and Iida 1939; Gutenberg and Richter 1942):

$$\log(N) = a - b\,M \tag{1}$$

where N is the number of events with magnitude $\geq M$, and a and b are positive, real constants. The parameter a depends on the level of seismic activity, and b largely on the stress, the strain rate and the homogeneity of the rocks in the focal area and the average depth of the earthquakes considered. Comparison of the parameter b can yield very useful insights into the geodynamics of each of our sub-regions. Observational data are generally well described through Eq. (1) in a certain range of magnitudes ($M_0 \leq M \leq M_1$) and several methods have been proposed to estimate b in Eq. (1) in order to take into account the unavoidable problems with the binning of magnitudes and the original estimation of magnitude in any earthquake catalogue (Aki 1965; Utsu 1965; Shi and Bolt 1982; Bender 1983; Tinti and Mulargia 1987; Han et al. 2015). We have adopted the unbiased Maximum Likelihood method (Aki 1965) including influence of grouped magnitudes at intervals of ΔM (Utsu 1965), which yields b_{ml}. Selection of proper ΔM (0.3) was achieved to properly approximate continuous magnitude and at the same time to maximize the number of events in each magnitude group. The minimum magnitude for complete recording M_0 affects significantly the b_{ml} estimation. A b-value (b_{ls}) may also be evaluated by performing least-squares linear regression on the logarithmic plot of the cumulative distribution. Although it shows significant bias under relatively common conditions, it offers more stable results when M_0 changes. Thus, in order to guarantee the completeness of data, we selected as threshold magnitude M_0, the value that minimized the difference between estimates of b_{ml} and b_{ls}.

Frequency-magnitude distribution results are shown in Figs. 9.3b, 9.4b and 9.5b. Estimated b-values for the three regions are less than 1 (Gulf of Suez $b_{ml} = 0.54$, Gulf of Aqaba $b_{ml} = 0.70$, northern Red Sea $b_{ml} = 0.93$) suggesting that faulting is not associated with magmatism. The estimated Gulf of Suez b-value (Fig. 9.4b) is always lower than that of Gulf of Aqaba (Fig. 9.5b) and northern Red Sea (Fig. 9.3b) regardless of the magnitude range used in the calculation. This suggests

that in the Gulf of Suez, the level of stress accumulated in and around fault planes (Sholtz 1968; Wyss 1973) is larger than the stress level in the other two regions. In contrast, the northern Red Sea displays the highest *b*-value, despite extending at a total slip rate about four times that of the Gulf of Suez (Fig. 9.1; Mahmoud et al. 2005; ArRajehi et al. 2010). One possible explanation for the high Red Sea *b*-value is that extension is being accommodated over a broad area with elastic energy being released via smaller faults experiencing a large number of low-magnitude earthquakes.

The highest estimated *a*-value is found in the Gulf of Aqaba implying the highest earthquake activity (Gulf of Suez $a = 2.64$, Gulf of Aqaba $a = 4.56$, northern Red Sea $a = 3.37$, when N = number of events per year). The maximum probable maximum magnitude expected for the next 50 years (the time period spanned by the ISC catalogue) and the earthquake return period of a given magnitude may also be evaluated using the *a* and *b* parameters (Yadav et al. 2011). Adopting the estimated *a*- and *b*-values for the three regions, we obtain a probable maximum magnitude of 5.7, 7.5 and 7.7 for the northern Red Sea, Gulf of Suez and Gulf of Aqaba, respectively. Earthquakes with the largest magnitude recorded in the three regions (i.e., M_w of 5.3, 6.8 and 7.2) would have a return period of 19.5, 20.1 and 18.5 years. The southern Gulf of Suez is therefore long overdue for the occurrence of a large earthquake.

9.2.2 Crustal Structure and Depth to Moho

Crustal thickness patterns based on P-wave receiver functions in southeastern Egypt (Hosny and Nyblade 2014, 2016) and on S-wave receiver functions (Hansen et al. 2007) together with S-wave velocity–depth profiles by jointly modeling P-wave receiver functions and surface wave dispersion in western Saudi Arabia (Tang et al. 2016) reveal a symmetric lithospheric mantle necking across the northern Red Sea. Crustal thickness along the rifted margins of the Red Sea ranges from 22 to 30 km, whereas beneath northern and central Egypt and northern Saudi Arabia it ranges from 32 to 38 km (Nyblade et al. 2006; Hansen et al. 2007; Hosny and Nyblade 2016; Tang et al. 2016). Thus, the 35–40 km pre-rift crustal thickness implies a 5–10 km crustal thinning during rifting beneath the rifted margins near the coast (Hosny and Nyblade 2016). STEFAN E project refraction profiles (Voggenreiter et al. 1988) show a good agreement with these results, with a thickness of ~20 km near the coast decreasing to ~10 km at the rift axis.

Seismic data from two-ship 'expanded-spread-profiles' (ESP) gathered along the Gulf of Suez and parallel to the Egyptian Red Sea coast (Gaulier et al. 1988; Le Pichon and Gaulier 1988) indicated the presence of thinned crust (14 km) beneath the Gulf of Suez and very thin crust (12–6 km) underlying the evaporites in the northern Red Sea with a Moho surface that shoals toward the rift axis (Gaulier et al. 1988). Two ESP's crossed the axial trough near the Conrad Deep (~27° N) and Shaban Deep (~26° N) (Fig. 9.3a). The profiles show different crustal velocities, with relatively low crustal velocities (5–6.4 km/s) to the north and higher velocities to the south (5–6.8 km/s). Gaulier et al. (1988) interpreted the higher velocities in the southern transect as being diagnostic of oceanic crust. However, a comparison of crustal velocities below evaporites from ESP profiles with compilations of velocity-depth profiles corresponding to continental crust, thinned continental crust, young oceanic crust and exhumed mantle, shows a good match with the continental crust compilation from Arabia for the northern profiles and with thinned continental crust for the southern set (Ligi et al. 2018, 2019). High lower-crust seismic velocities (7.0–7.6 km/s) recorded in poorly evolved rifts such as Baikal and the southern Kenya rifts have been interpreted as due to magmatic intrusions that have compensated the amount of crustal thinning by the addition of new material (Birt et al. 1997; Thybo and Nielsen 2009). The southern ESP profile with the highest velocity gradient is the nearest to the coast, suggesting that the difference in the velocity structure between the northern and the southern transects may also correspond to a north-south change in the nature of the basement rocks observed onshore in Egypt (Stern et al. 1984; Stern and Hedge 1985; Greiling et al. 1988; Cochran 2005). The northern Egyptian basement is mainly composed of granite, granodiorite and weakly deformed plutonic rocks. In contrast, the southern basement consists of mafic metavolcanics, gabbros, ultramafic rocks and associated metasedimentary rocks, with the boundary between the two provinces located near Safaga (Stern et al. 1984; Cochran 2005). These observations suggest that the north-to-south change in the basement velocity structure in the northern Red Sea, interpreted by Le Pichon and Gaulier (1988) as a change from continental to oceanic crust, may actually represent a change between two very different, although both continental, types of pre-rift basement (Cochran 2005).

An air gun seismic experiment in conjunction with an onshore survey was carried out in 2011 by Saudi Aramco in the eastern part of the northern Red Sea extending for over 50 km from the shoreline toward the rift axis (Sinadinovski et al. 2017). The resulting detailed map of Moho discontinuity (assuming P-wave velocity of 8 km/s) shows variations in depth from 17 to 27 km offshore increasing from ~22 km up to 35 km onshore. Results reveal an eastern side of the northern Red Sea affected by a complex velocity structure suggesting rifting localization within a heterogeneous lithosphere and a present-day mantle necking domain largely located onshore to the north (next to the Gulf of Aqaba), and offshore to the south (Sinadinovski et al. 2017).

Marine magnetics data played a critical role in demonstrating that an organized mid-ocean spreading center is functioning in the southern Red Sea (Phillips 1970; Girdler and Styles 1974; Röser 1975; Searle and Ross 1975; Hall et al. 1977; Cochran 1983). Gravity and magnetics datasets for the northern Red Sea have been reviewed and synthesized by Cochran (2005) and Cochran and Karner (2007). They interpret these data in combination with bathymetric, heat flow and seismic observations to show that the northern Red Sea is largely amagmatic and though possessing discrete axial deeps and individual volcanoes, it has not yet developed true sea-floor spreading. The central Red Sea has often been described as transitional between the north and the south. However a recent interpretation of the marine gravity field suggests that lineaments similar to oceanic fracture zones are present around the Thetis Deep, indicative of oceanic rather than continental crust (Mitchell and Park 2014).

The seismicity scattered across the northern Red Sea basin (Hosny et al. 2012), Moho depth patterns (Hosny and Nyblade 2014, 2016; Sinadinovski et al. 2017), low crustal seismic velocity gradients (Gaulier et al. 1988; Ligi et al. 2018, 2019), the lack of organised magnetic anomalies (Cochran 1983, 2005; Cochran et al. 1986; Cochran and Karner 2007), the high-density crustal layers just beneath evaporites (El-Bohoty et al. 2012), and the presence of Precambrian shield rocks in boreholes near the coasts (Bosworth 1993; Almalki et al. 2015), all support the hypothesis that the northern Red Sea is underlain by stretched and thinned continental crust, with a few isolated sites of basaltic injection (Cochran 1983; Bonatti 1985; Cochran et al. 1986; Cochran and Martinez 1988; Guennoc et al. 1988; Bosworth 1993; Cochran 2005; Ligi et al. 2018, 2019).

9.2.3 Present-Day Plate Motions

Global Positioning System (GPS) observations indicate that the northern Red Sea is not opening perpendicular to its margins. Rather its present-day opening direction is parallel to the trend of the Gulf of Aqaba transform boundary at a rate of $\sim 0.7 \pm 0.1$ cm/yr (ArRajehi et al. 2010; Reilinger et al. 2015). At the Red Sea-Aqaba-Suez triple junction this movement is partitioned into ~ 0.15 cm/yr of NNW separation across the Suez rift and ~ 0.44 cm/yr left-lateral shear along the Aqaba transform (Mahmoud et al. 2005; ArRajehi et al. 2010). The GPS data also confirm the additional complexity of ~ 0.2 cm/yr of E-W extension between Sinai and Arabia (Reilinger et al. 2015) as suggested by the Gulf of Aqaba normal fault earthquake solutions.

The 0.15 cm/yr NNW movement of Sinai relative to Africa can be resolved into 0.05 cm/yr of Gulf of Suez rift-normal extension and 0.14 cm/yr of left lateral shear (Bosworth and Durocher 2017). On-going oblique opening in the Gulf of Suez is supported by earthquake data discussed above and other present-day shallow crustal stress field indicators such as borehole breakouts and young fracture systems (Bosworth and Taviani 1996; Badawy 2001).

9.3 Petrology and Geochemistry of Red Sea Magmatism

Along the Egyptian Red Sea margin, basement lies beneath a stratigraphic section very similar to that encountered in the southern Gulf of Suez, consisting of several hundred meters or more of syn-rift siliciclastics overlain by several kilometers of Miocene evaporite and/or mixed evaporite-shale (Tewfik and Ayyad 1984; Miller and Barakat 1988; discussed below). Further offshore, the siliciclastics are locally absent and a thick layer of evaporite directly overlies basement. However, at the bottom of major depressions along the axial trough, basement is exposed at the sea floor. Fresh glassy basalts have been dredged from the axial neo-volcanic ridges of Thetis, Nereus, Mabahiss and Shaban (Fig. 9.3a). Along axis chemical variability of major and trace elements of these basalts, after taking into account magmatic differentiation and geochemical characteristics of parental magmas, show mid-ocean ridge basalt compositions with N–S compositional variations indicating changes in the mantle sources as well as the degree and depth of mantle melting (Altherr et al. 1988; Volker et al. 1993; Haase et al. 2000; Ligi et al. 2012, 2015). Differences both in major elements (higher Na_2O, lower FeO_T in Shaban/Mabahiss compared to Nereus/Thetis lavas) and incompatible elements (higher La/Sm in Shaban/Mabahiss than in Nereus/Thetis basalts) indicate that the degree of melting decreases from south to north along the Red Sea rift and melting occurs at progressively shallower depths with northern magmas generated from a relatively cold shallow mantle (Fig. 9.6b).

During continental rifting and rupturing, contamination and assimilation processes may be an important factor in determining variations in major and trace element composition. Figure 9.6a shows the mean values of $^{143}Nd/^{144}Nd$ and $^{87}Sr/^{86}Sr$ of basaltic glasses from the northern Red Sea. Nd-Sr isotopic systematics indicate an absence of continental lithospheric components in the genesis of Thetis and Nereus basalts and suggests a source with slightly enriched "Depleted Mid-ocean-ridge Mantle" (DMM) composition (Workman and Hart 2005). No contamination by continental lithosphere is indicated by Nb/U values between 33 and 69 (Altherr et al. 1990), close to the average MORB value of 47 and significantly different from a continental crustal value of 10 (Hofmann et al. 1986). The mantle source affinity is also suggested by highly incompatible trace element ratios such as Ba/Nb and La/Nb shown in Fig. 9.6c, and by REE

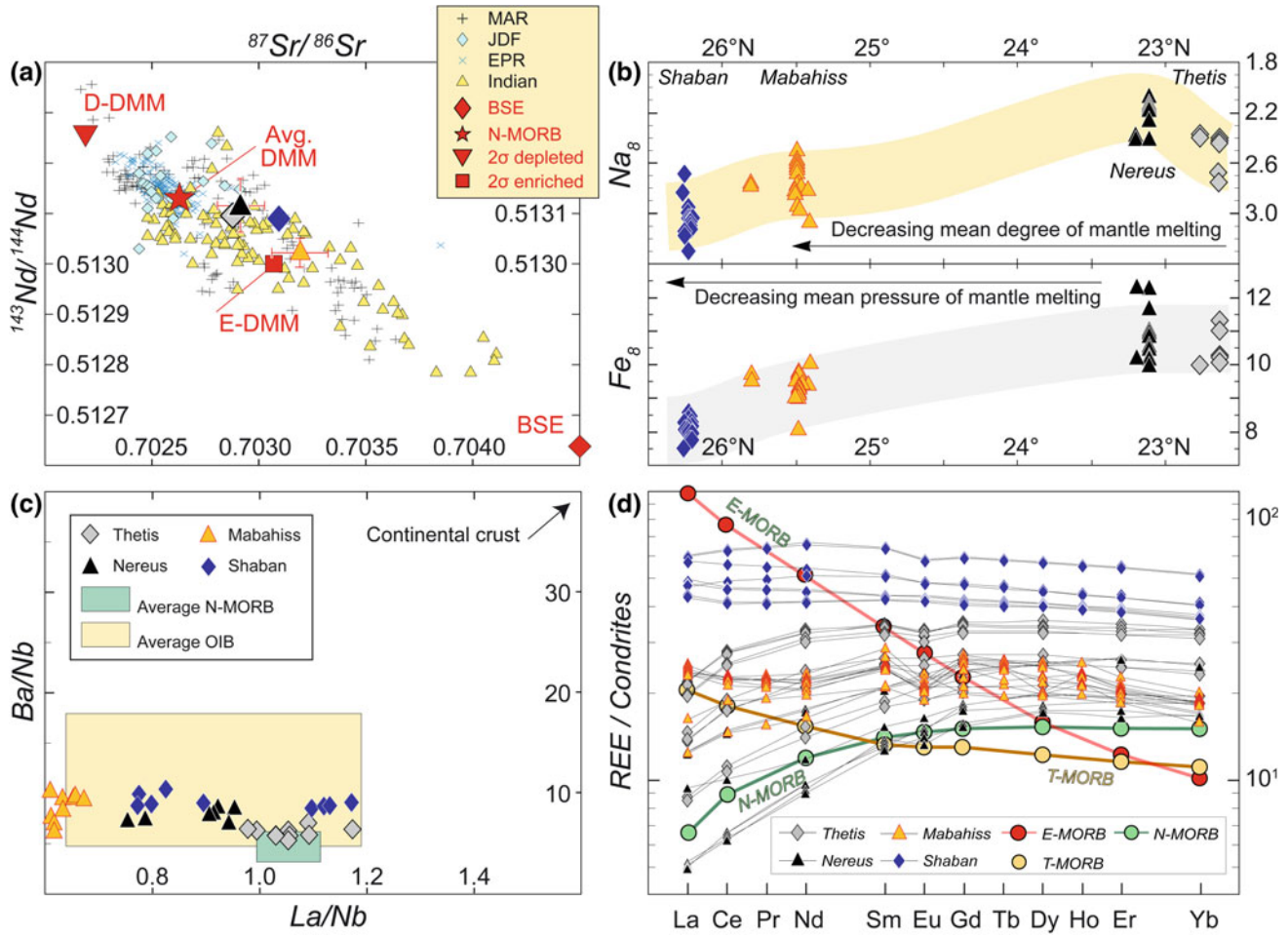

Fig. 9.6 Geochemistry of northern Red Sea axial oceanic rocks. **a** Source heterogeneity. Average Sr-Nd isotopic compositions of basalts from Thetis (gray diamond; data from Altherr et al. 1988, 1990), Nereus (black triangle; data from Volker and McCulloch 1993; Antonini et al. 1998), Mabahiss (yellow square; data from Altherr et al. 1988, 1990; Melson et al. 2002), and Shaban (blue diamond; data from Altherr et al. 1990; Haase et al. 2000) deeps. Error bars (2σ) are indicated by red lines. Axial northern Red Sea data are superimposed on Sr-Nd isotopic global MORB data (yellow triangles: Indian Ocean mid-ocean ridges; cyan diamonds: Juan De Fuca Ridge; plus symbol: Mid Atlantic Ridge; cross symbol: East Pacific Rise) of Workman and Hart (2005). Red filled diamond and star indicate isotopic composition of the bulk silicate Earth (BSE) and of the average depleted mantle (DMM), respectively. D-DMM: 2σ depleted DMM, and E-DMM: 2σ enriched DMM. **b** Fractionation corrected (8% MgO) major element Na_2O and FeO basalt compositions versus latitude along the northern Red Sea axis. Symbols as in 'a'. Data from PetDB (Lehnert et al. 2000) and Ligi et al. (2012). **c** Crustal contamination. Ba/Nb versus La/Nb plot. OIB and N-MORB fields are from Weaver (1991). **d** REE patterns for Thetis, Nereus, Mabahiss and Shaban deeps. Normalization to chondritic values is from Anders and Grevesse (1989). Enriched E-MORB, transitional T-MORB, and normal N-MORB are from Langmuir et al. (1992)

variability that can be explained by varying the mean degree and mean pressure of melting within the spinel stability field from a source having DMM composition (Fig. 9.6d). Axial basalt geochemistry suggests a sharp rift-to-drift transition marked by magmatic activity with typical MORB signature and no contamination by continental lithosphere. Most of the observed geochemical variability of northern Red Sea axial basaltic glasses can be explained by varying the mean degree and mean pressure of melting from a source having DMM composition (Haase et al. 2000; Ligi et al. 2012).

Direct observation of exhumed deep lithosphere in the Red Sea, along with the structures and the petrology associated with the formation of conjugate passive margins, is possible only on the island of Zabargad and on the Brothers Islets (Figs. 9.2 and 9.3). Zabargad represents an emerged sliver of sub-Red Sea lithosphere, probably uplifted by wrench tectonics along the Zabargad Fracture Zone, and provides a sample of continent-ocean transitional lithosphere (Bonatti et al. 1981, 1983, 1986; Nicolas et al. 1987). Zabargad exposes mantle-derived peridotites of sub-continental affinity in faulted contact with mafic-felsic granulitic gneisses of lower crustal origin, intruded by basaltic dykes. The gabbroic rocks were suggested to be originally part of a basic layered complex which crystallized

at relatively high pressure (Bonatti and Seyler 1987; Ligi et al. 2018). The Brothers are two islets located off-axis in the northern Red Sea. Previous work has shown that below a thin carbonate cap, the islets consist of MORB-like gabbroic rocks that crystallized at relatively low-P, cut by doleritic dykes (Shukri 1944; Hoang and Taviani 1991; Bosworth and Stockli 2016; Ligi et al. 2018). Gabbros were also sampled beneath a ~4 km thick sedimentary sequence, dominated by evaporites, at the base of the Quseir B-1X (QUSEIR) drill hole, ~80 km south of the Brothers (Fig. 9.3a). Brothers and QUSEIR gabbros have petrologic and geochemical signatures similar to those of MORB-type gabbroic cumulates (Ligi et al. 2018, 2019) and are compatible with their having been emplaced either in a continental or in an oceanic context. A QUSEIR gabbro yielded an $^{40}Ar/^{39}Ar$ age of 25 ± 6 Ma, suggesting intrusion during early rifting (Ligi et al. 2018). In addition, reflection seismic sections, running perpendicular to the rift axis from near the cost to the Brothers islets, reveal that the northern Red Sea has experienced significant footwall uplift during rifting which has ultimately brought early syn-rift deep crustal rocks to a suitable depth for sampling (Fig. 9.7). Thus, Brothers and QUSEIR gabbros represent thinned-continental lower-crust intrusions of asthenospheric melt that were later exposed at the seafloor during rifting. Geochronology and isotopic composition of these gabbros indicate that they may be related to the early syn-rift intense magmatic event ~23 Ma that gave rise to the dyke swarm running along the entire Arabian Red Sea coast (Bosworth et al. 2005; Bosworth and Stockli 2016). The offshore gabbros support the hypothesis that continental breakup in the northern Red Sea, a relatively non-volcanic narrow rift, is preceded by intrusions of basaltic melts that crystallize at progressively shallower crustal depths as rifting progresses toward continental break-up (Ligi et al. 2018).

9.4 Stratigraphy

9.4.1 Basement Complex

The crystalline basement complex of the Egyptian Red Sea margin and Eastern Desert is of Neoproterozoic age and displays strong effects of deformation during the various Pan-African orogenies (further discussed in this volume Chaps. 3 and 4). It is part of the greater Arabian-Nubian Shield (ANS) that evolved from ~870 to 550 Ma (Johnson 2014). The Egyptian ANS can be grossly divided into two general terranes, separated by a structural discontinuity that approximately follows the position of the younger Gulf of Aqaba and projects across the Eastern Desert through the area of Safaga (Stern et al. 1984). North of this boundary the basement is represented principally by granite, granodiorite, lesser metasediments and metavolcanics, and both basaltic and rhyolitic dikes. The units are generally only lightly to moderately deformed. The granodiorites are 670–610 Ma old and are syn-tectonic in origin, probably related to subduction processes (Stern et al. 1984). These were followed by the eruption of the Dokhan volcanics, associated dikes, a younger episode of granite pluton emplacement, and deposition of Hammamat siliciclastics from ~600 to 575 Ma. The volcanics and siliciclastics are thought to be an expression of a phase of rifting and north-south oriented extension (Stern et al. 1984), while the youngest granites appear to be post-tectonic (Rogers et al. 1978).

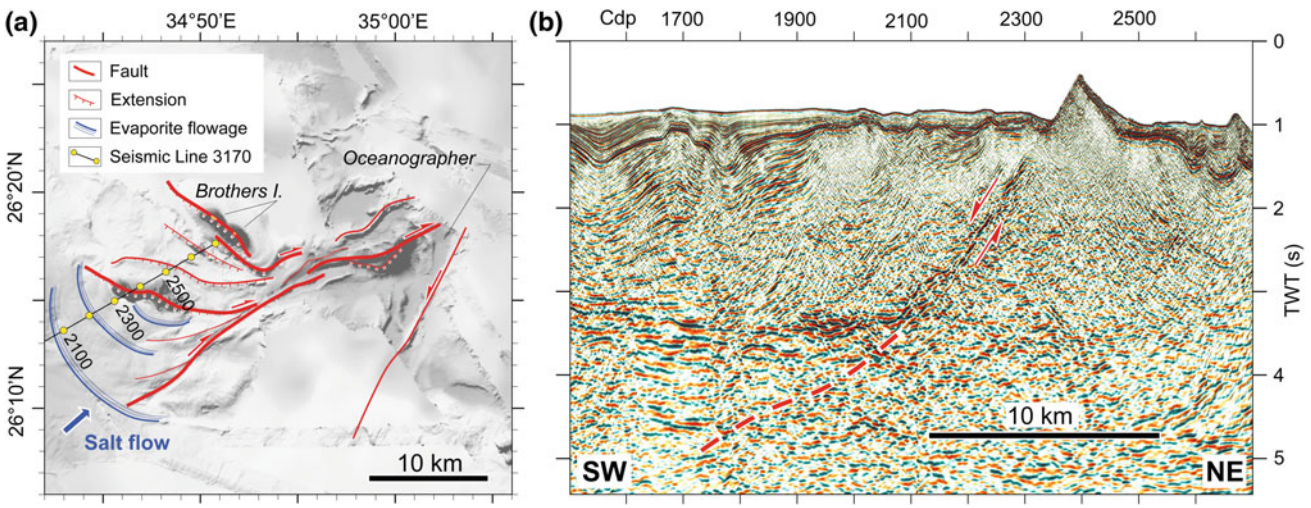

Fig. 9.7 Morphotectonic setting of the Brothers Islets region (after Ligi et al. 2018). **a** Shaded relief image showing tectonics of the Oceanographer Deep and of crustal blocks culminating in the two Brothers islets and the submarine structural high located SW of the islets. Illuminated from NE, grid resolution 25 m. **b** Time migrated seismic line 3170 extracted from 3D survey and running perpendicular to the axis of the northern Red Sea and across the crustal block lying to the SW of the Brothers Islets. Full profile location is shown in Fig. 9.3a

South of Safaga the basement composition is very different. Lithologies include ultramafics and pillowed tholeiites with ophiolitic affinities, banded iron-formation metasediments, and serpentinitic melanges in addition to a variety of plutonic rocks (Stern 1979; Sturchio et al. 1983; Ries et al. 1983). This part of the Eastern Desert therefore more closely resembles the ensimatic terranes of the Arabian shield and is cut by several major NW-SE trending shear zones that are continuations of the Najd fault system from the eastern margin of the Red Sea (Abdel Gawad 1969; Stern et al. 1984). In general the extent of deformation is much higher in the southern domain and this has been attributed to shortening in arc-back arc basins, the closing of small oceanic basins, and continental collisions: the full suite of Pan-African orogenesis (Bakor et al. 1976; Gass 1977; Frisch and Al-Shanti 1977; Rogers et al. 1978; Engel et al. 1980; Fleck et al. 1980; Stern 1981).

Several exploratory wells have reached the basement complex in Egyptian Red Sea waters. Four wells have encountered granite and granodiorite (RSO-X 94-1; RSO-B 96-1; Ra West-1; Mikawa-1) that are petrographically similar to the granitic rocks found in the Red Sea Hills (Tewfik and Ayyad 1984; Barakat and Miller 1986; Miller and Barakat 1988; Bosworth 1993). None of the plutonic rocks yield reliable age dates. Volcanic rocks (altered dacite and pyroclastics) lie beneath the Miocene sedimentary section at RSO-T 95-1 and tuffaceous material was dated as 583 ± 38 Ma (K-Ar; Barakat and Miller 1986). Quseir A-1X and Quseir B-1X penetrated metamorphic rocks, including serpentinite. These drilling results demonstrate that Pan-African-affiliated basement extends several tens of kilometers offshore from the Egyptian coastline, though it may not be a continuous substratum. Only at Quseir B-1X was gabbro encountered and cored. Geochemical and geochronological data indicate that this gabbro is much younger than Pan-African ($^{40}Ar/^{39}Ar$ 25 ± 6 Ma) and associated with an early phase of under-plating/intrusion during Red Sea-rift initiation (Ligi et al. 2018; discussed above).

9.4.2 Pre-rift Strata

The pre-rift sedimentary section of the Egyptian Red Sea margin and the southern Gulf of Suez are very similar (Figs. 9.8 and 9.9). In both areas the base of the section begins with thick, quartz-rich sandstones that are traditionally referred to the "Nubia sandstone" or its correlatives (Fig. 9.10a; Said 1962). In outcrop this section is not paleontologically dated, but numerous southern Gulf of Suez wellbores have recovered Aptian-Albian palynomorphs from these continental siliciclastics and therefore much of this section is equivalent to the Malha Formation of Sinai. (U-Th)/He thermochronology demonstrates the presence of Permian, Triassic and occasional Aptian detrital zircons in the Nubia sandstone immediately above the basement contact at Gebel Duwi (Fig. 9.10a; authors' unpublished data). Paleozoic strata are therefore absent and the chronometric data are compatible with this section also being equivalent in age to the Malha Formation. In the Gulf of Suez the massive Nubia facies are capped by a pronounced weathering surface/unconformity and overlain by a mix of shallow-marine siliciclastics and limestones (Raha, Wata, Matulla Formations; Fig. 9.8) that are well-dated and span from the Cenomanian to the Santonian (Kerdany and Cherif 1990; Darwish 1994). Along the Red Sea margin the top of the Nubia appears more conformable and gradational, with upward increasing shale content (Figs. 9.8 and 9.10a; Quseir Formation; "Kosseir" of Youssef 1957).

At the end of the Santonian, carbonate and shale deposition covered the entire Gulf of Suez–northern Red Sea region. The Campanian is marked by organic- and phosphate-rich shales of the Duwi Formation (Youssef 1957), which is informally referred to the "Brown Limestone" in the Gulf of Suez. This is the region's most important hydrocarbon source rock. The Duwi/Brown Limestone is capped by further marine carbonate and shale (Dakhla, Tarawan, Esna and Thebes Red Sea formations and their Gulf of Suez equivalents; Fig. 9.9a, b; Said 1961, 1962) that persisted through the Eocene. The upper part of the Eocene and early part of the Oligocene are missing in the southern Gulf of Suez and along the Red Sea margin.

No pre-rift strata have been encountered in the existing Egyptian Red Sea offshore wells (Fig. 9.9), although a 200 m thick interbedded sandstone-shale-carbonate section of probable Early Cretaceous age is preserved on Zabargad Island (Bosworth et al. 1996). Across the basin at its mirror margin in Midyan, the only pre-rift section observed is the Late Cretaceous Adaffa Formation (Clark 1986; Hughes et al. 1999). The Adaffa is constrained to be Albian to Maastrichtian in age, and consists of a thin basal conglomerate overlain by 100–200 m of quartz arenite and shale. It is probably correlative to the upper Nubia facies and/or Quseir Formation of the Egyptian margin.

9.4.3 Syn-rift Strata

The base of the Egyptian Red Sea syn-rift or "syn-kinematic" stratigraphic section is generally easily recognized but not generally easy to date. Strata are dominated by unfossiliferous, poorly sorted conglomerates and conglomeratic sandstones in the onshore exposures. Much of the section is described as "redbeds". Many of the included pebbles and cobbles are chert derived from the immediately underlying Thebes Formation. These rocks are assigned to the Nakheil Formation (Fig. 9.10c; El-Akkad and Dardir 1966) in the region of Quseir and Safaga and to the Abu Ghusun Formation further south (Fig. 9.8). As discussed below, these basal conglomerates are confined to

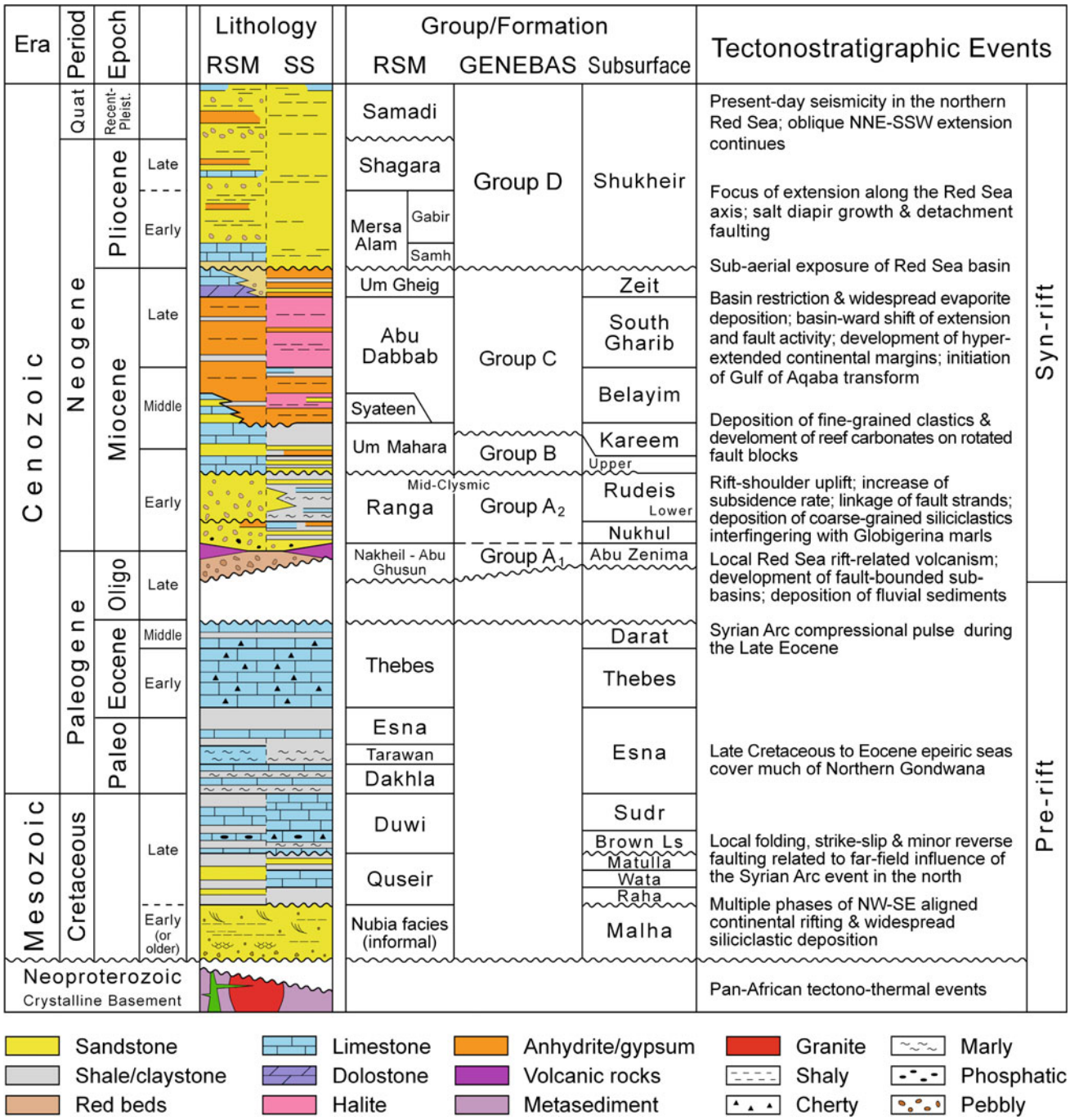

Fig. 9.8 Comparison of the stratigraphic terminology commonly used along the Egyptian Red Sea margin (RSM) and in the subsurface (SS) of the Red Sea and Gulf of Suez. GENEBAS Group terms are from Plaziat et al. (1998)

fault-bounded basins and display angular unconformity with the pre-rift section.

Nakheil Formation red siltstones and sandstones are interbedded with thin basaltic flows south of Quseir at Sharm el Qibli and Sharm el Bahari. The only radiometric age date for these volcanic units is a K-Ar value of 24.9 ± 0.6 Ma (Roussel et al. 1986). This makes this flow generally equivalent in age to the "Oligo-Miocene" flows and dikes of the Gulf of Suez, Cairo district and Bahariya oasis regions. More recent $^{40}Ar/^{39}Ar$ dating has shown that the K-Ar ages obtained in the past must be viewed cautiously, as has been observed throughout the Red Sea rift system (e.g. Baker et al. 1996). For comparison, published K-Ar and $^{40}Ar/^{39}Ar$ data for Egyptian Oligo-Miocene basalts are plotted in

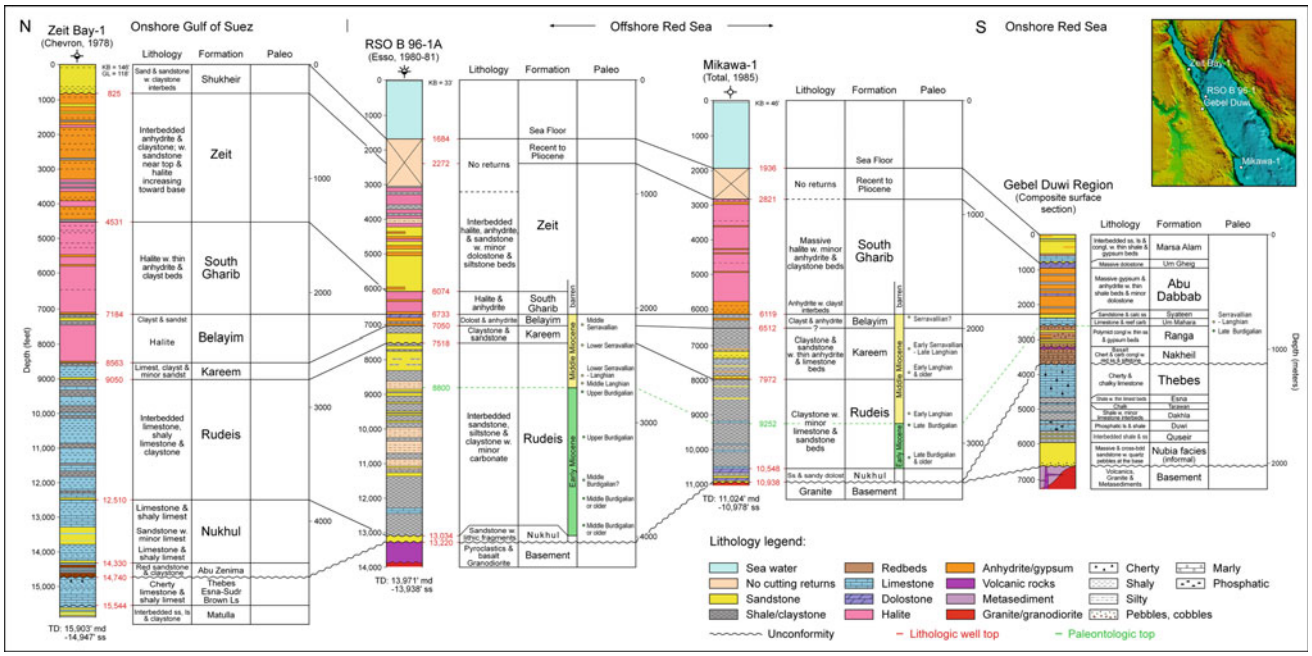

Fig. 9.9 Stratigraphic correlations from the southern Gulf of Suez to the offshore Red Sea and a composite measured section of the Gebel Duwi region. Gebel Duwi section is modified from Khalil and McClay (2001, 2009). Vertical axis is depth/thickness. Where available micropaleontologic age constraints are indicated (green = Early Miocene; yellow = Middle Miocene). Inset map shows locations of wells and Gebel Duwi. TD = well total depth; md = well measured depth; ss = well subsea depth

Fig. 9.11. The analyses come from the Red Sea margin, the Gulf of Suez, Sinai, the Eastern Desert, and the Cairo-Suez and Faiyum-Bahariya districts. Many of the analyses are from the same specific outcrops (details and references in Bosworth and Stockli 2016). Both datasets indicate a mean age of ~23 Ma, coincidentally at the Oligocene-Miocene chronostratigraphic boundary. But the $^{40}Ar/^{39}Ar$ data demonstrate that this basaltic eruption was extremely short lived and essentially synchronous throughout the region.

In Egyptian Red Sea offshore wells the basal syn-rift section includes a mixture of sandstone, shale and occasional sandy dolostone (Fig. 9.9). Some of the sandstone contains lithic fragments but massive conglomerates similar to those of the Nakheil Formation have not been identified. Following stratigraphic convention of the Gulf of Suez (EGPC 1964), these rocks are assigned to the Nukhul Formation (Tewfik and Ayyad 1984; Barakat and Miller 1986). They are not dated paleontologically but sit below Burdigalian strata. In the southern Gulf of Suez the stratigraphically equivalent units are Aquitanian in age (Winn et al. 2001). No Oligo-Miocene basalts have yet been identified in the offshore wells. In the central Gulf of Suez the syn-kinematic strata that immediately underlie the basalts are referred to the Abu Zenima Formation (Fig. 9.8). Without better age constraints it is possible that the Red Sea "Nukhul" units may actually be younger than any of the onshore Nakheil Formation.

Along the coast the ~23 Ma basalts and Nakheil Formation are overlain by more siliciclastics that locally include one or two thin gypsum beds as at north Wadi Um Affeen and Wadi Gassus (Figs. 9.10d and 9.12; Bosworth et al. 1998; Khalil and McClay 2009). This section is assigned to the Ranga Formation (Samuel and Saleeb-Roufaiel 1977) and locally has yielded Burdigalian microfossils (Figs. 9.8 and 9.9). Offshore the correlative units contain much more shale, siltstone and occasionally limestone and belong to the Rudeis Formation.

During the latter part of the Burdigalian a regional unconformity developed in many parts of the Gulf of Suez and along the Egyptian Red Sea margin. This is referred to as the "intra-Rudeis" or "mid-Clysmic" event (Evans 1988; Richardson and Arthur 1988; Patton et al. 1994) that, in the Quseir-Safaga region, was followed by the deposition of Um Mahara Formation limestone and reefal carbonates (Samuel and Saleeb-Roufaiel 1977). The Um Mahara locally directly onlaps rotated Precambrian basement blocks in the coastal plain near Quseir (Fig. 9.10e). In the offshore realm lithologic changes across this event were not pronounced (Fig. 9.9). Rudeis Formation deposition continued into the Middle Miocene, when thin evaporite beds were deposited in many sectors of the Red Sea and Gulf of Suez. This has resulted in the use of the term Kareem Formation for the strata overlying the evaporites, though otherwise the two units are generally indistinguishable (Figs. 9.8 and 9.9).

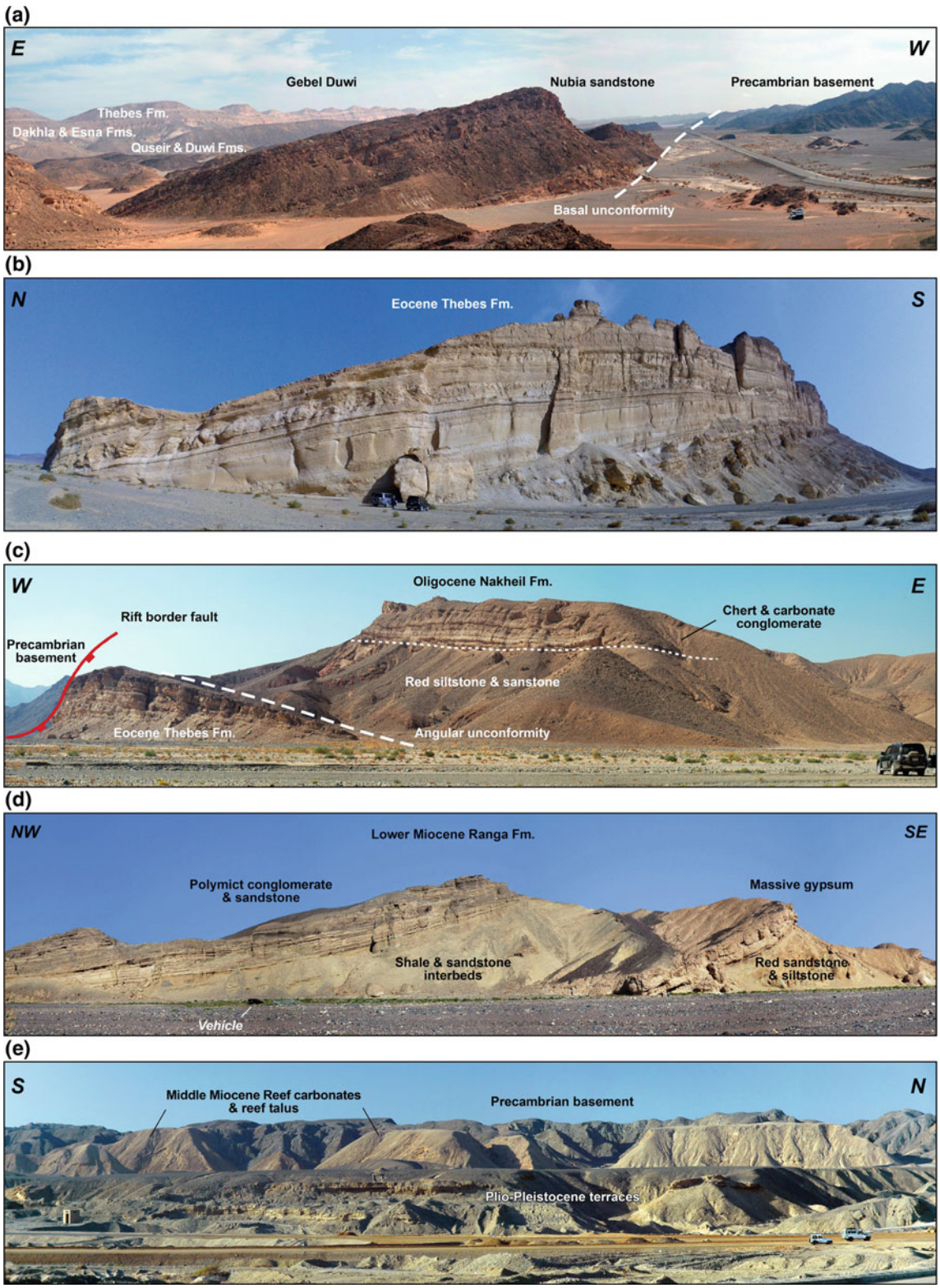

Fig. 9.10 Field views showing outcrop examples of the pre- and syn-rift strata in the Egyptian Red Sea margin. Named locations are shown in Fig. 9.12. **a** View looking SE showing the pre-rift Cretaceous–Eocene section unconformably overlying basement in Gebel Duwi block. **b** View looking east showing chalky and chert limestone of the Eocene Thebes Formation in the southern part of Gebel Duwi. **c** View looking north showing the angular unconformity between the Eocene Thebes limestones and the red sandstones and conglomerates of the Oligocene(?) early syn-rift Nakheil Formation in the Rabah block. **d** View looking NE showing the clastics and evaporites of the Lower Miocene Ranga Formation in Wadi Gassus. **e** View looking west showing Middle Miocene carbonates and reef talus onlapping the rotated basement blocks and the near horizontal uplifted Plio-Pleistocene terraces developed along the coastal area near Quseir

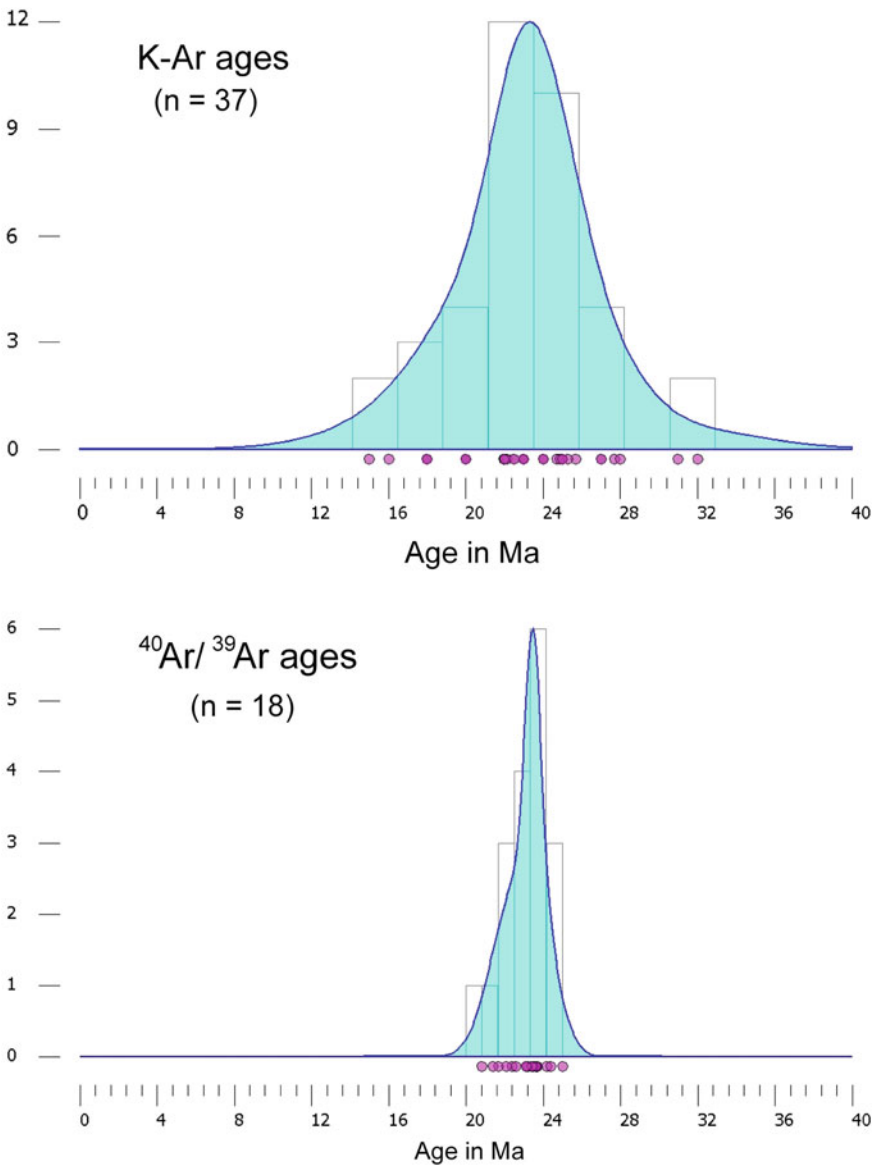

Fig. 9.11 Probability distribution plots of published radiometric ages for the Oligo-Miocene basaltic dikes and flows of the greater Gulf of Suez and Egyptian Red Sea region. The K-Ar and ^{40}Ar/^{39}Ar data are from same or similar exposures and the broader K-Ar distribution simply represents Ar loss. This volcanism occurred as a single, very short-lived event centered at ~23 Ma. Details of sample locations and references are in Bosworth and Stockli (2016). Plots were prepared using *DensityPlotter* software (Vermeesch 2012)

A drastic change in depositional environments occurred throughout the Red Sea and Gulf of Suez in the Serravalian, in which siliciclastic and carbonate deposition was nearly everywhere replaced with the formation of massive anhydrite and halite beds. Along the onshore Red Sea margin these are referred to the Abu Dabbab Formation (Samuel and Saleeb-Roufaiel 1977) and offshore to the Belayim and South Gharib Formations (Figs. 9.8 and 9.9). In the offshore, evaporite deposition continued to the end of the Late Miocene but generally included the cyclical inclusion of sandstone and shale and these interbedded strata are assigned to the Zeit Formation. The onshore equivalents are dolostones of the Um Gheig Formation (Samuel and Saleeb-Roufaiel 1977).

There is abundant discussion and disagreement concerning how much of the Middle to Late Miocene evaporite section was deposited in deep water versus sabkha environments (Orszag-Sperber et al. 1998) but strong evidence indicates that the entire basin dried up and was sub-aerially exposed at the end of the Miocene, forming the major "post-Zeit unconformity." In the Red Sea this laterally extensive event is referred to in seismic reflection profiles as the "S-reflector" (Girdler and Whitmarsh 1974; Mitchell et al. 2010, 2017, 2019).

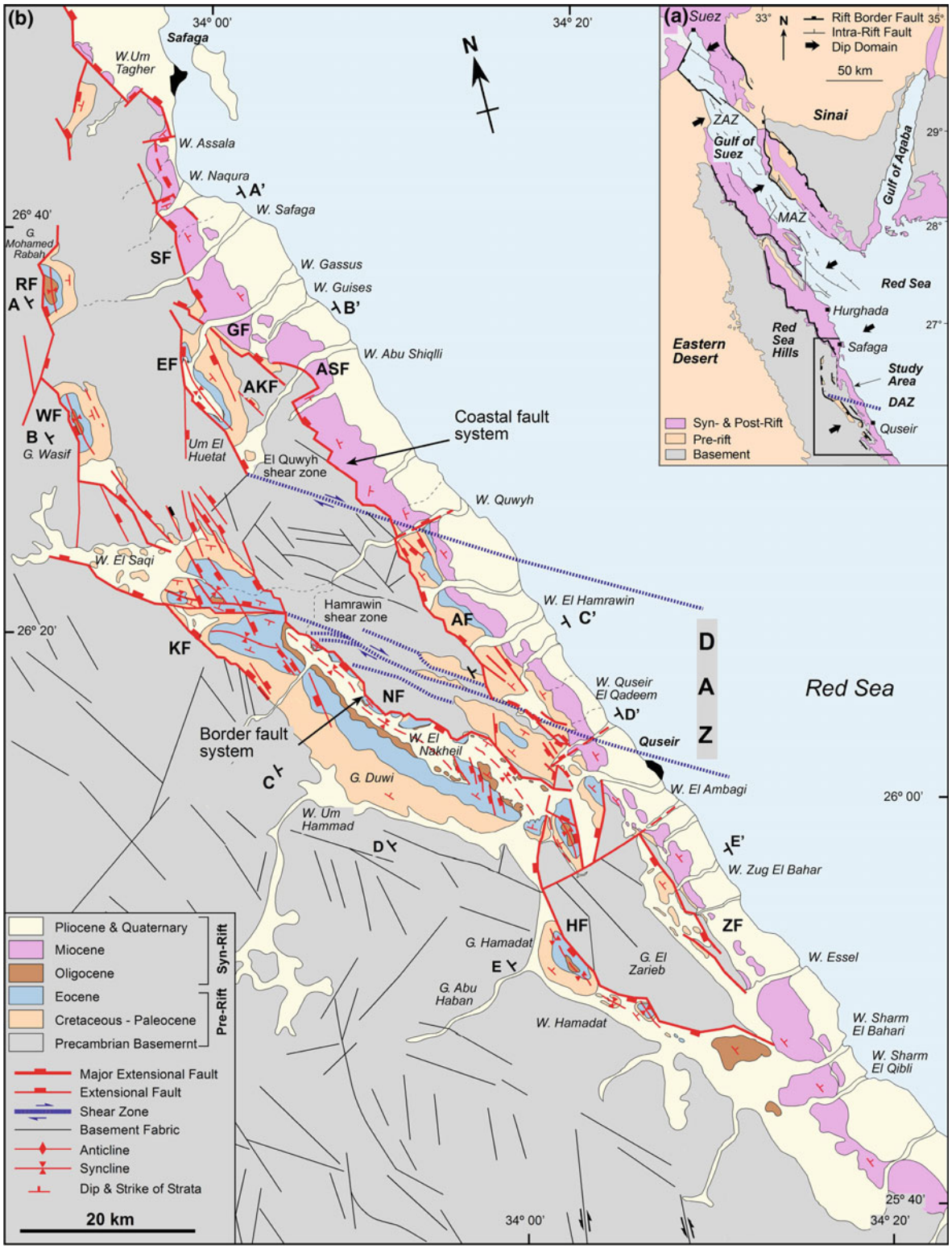

Fig. 9.12 Geology of the Safaga and Qusier region of the Egyptian Red Sea margin (after Khalil and McClay 2009). **a** Regional distribution of basement, pre-rift, and syn-rift to post-rift strata and the location of the study area. **b** Outcrop geologic map with faults differentiated according to type. Locations of cross-sections of Fig. 9.14 are labelled as A-A′ to E-E′. ZAZ, MAZ and DAZ indicate the Zaafarana, Morgan and Duwi accommodation zones. RF, WF, KF, NF and HF indicate the Rabah, Wasif, Kallahin, Nakheil and Hamadat segments of the border fault system. SF, EF, GF, AKF, ASF, AF and ZF indicate the Safaga, Um El Huetat, Gassus, Abu Kherfan, Abu Shiqlli, Anz and Zug El Bahar segments of the coastal fault system

In the early Pliocene open marine waters again reached most of the Red Sea and Gulf of Suez. Their source was the Indian Ocean via Bab el Mandeb (Said 1990). Pliocene strata include limestone, sandstone, claystone and occasional gypsum that are assigned to a variety of formations along the Red Sea coast (Figs. 9.8 and 9.10e). Onshore an unconformity is recognized at the end of the Pliocene. Offshore the entire Pliocene to Recent section is sand dominated and generally assigned to the Shukheir Formation or simply not described (Figs. 9.8 and 9.9).

Of tectonostratigraphic interest the Pleistocene depositional environment included numerous fringing coral reefs and associated wave-cut benches (Taviani 1998; Plaziat et al. 2008). Sea level fluctuated rapidly during this time period, and the coral terraces therefore lie at a variety of elevations both above and below present-day sea level (Fig. 9.10e). Measurements of the elevations of the terraces that formed during the last interglacial at ~125 ka suggest that the Egyptian Red Sea margin has been relatively stable over this time frame. The last interglacial corals are now found at about 6–7 m above present-day sea level (El Moursi 1993), and the eustatic sea level at 125 ka is estimated to also have been 6–7 m higher than today (Kopp et al. 2009). However recent field measurements indicate that a few meters of uplift has occurred in at least some specific coastal areas (Bosworth and Taviani 1996).

9.5 Structure

9.5.1 Onshore Fault Geometry

The structural architecture of the onshore area of the northern Egyptian Red Sea margin is dominated by two complex extensional linked fault systems that form a series of NW- to N-S-trending half-graben basins (Fig. 9.12). The western border fault system defines the western margin of the Red Sea basin, in part striking oblique to the rift trend, and consists of WNW, NW, N-S and NNE-trending segments that link in a prominent zigzag pattern (Fig. 9.12; Khalil and McClay 2001, 2002). The footwall of the border fault system consists of uplifted and eroded Neoproterozoic basement and the hanging wall includes pre-rift Cretaceous–Eocene strata and early syn-rift late(?) Oligocene Nakheil Formation (Figs. 9.10c, 9.12 and 9.13a). The eastern coastal fault system generally strikes NW, approximately parallel to the Red Sea. It consists of NW, NNW and N-S-trending segments that link by a series of breached relay ramps (Khalil and McClay 2009). The hanging wall of the coastal fault system is dominated by NE-dipping pre-rift and syn-rift Miocene strata that are juxtaposed against Neoproterozoic basement in the footwall (Figs. 9.12 and 9.13b). Throw along the fault systems ranges from 0.5 to greater than 2 km (minimum values as in most places the footwall stratigraphy and some basement have been removed by erosion).

The strong segmentation and zigzag pattern of the border and coastal fault systems clearly reflect the inherited basement fabrics which comprise NW, NNW, N-S, and NE-trending faults, dykes and Pan-African shear zones and fractures (Fig. 9.12; Jarrige et al. 1990; Bosworth et al. 1998; Khalil and McClay 2001, 2002). The Hamrawin and Quwyh shear zones (Fig. 9.12) are most likely part of the Late Neoproterozoic NW-trending Najd shear system that extends from the eastern margin of the Red Sea to the Egyptian Eastern Desert (e.g. Abdel Gawad 1969; Stern and Hedge 1985; Sultan et al. 1988).

NE-SW-trending cross-sections reveal that extensional faults in the northwest Red Sea are moderately dipping and crustal blocks are commonly arranged in domino style (Fig. 9.14). The hanging walls of many of the major faults display well-developed synclines (Fig. 9.13c) that are interpreted as fault-related folds, formed in response to the vertical and lateral propagation of the extensional faults (Khalil and McClay 2002, 2016, 2018).

At a regional scale, the northwestern margin of the Red Sea is characterized by two structural provinces or dip domains comprised of several, kilometer-scale half-graben basins (Fig. 9.12; Jarrige et al. 1990; Bosworth 1994; Khalil and McClay 2001, 2002). The northern (Safaga) province has a number of SW-dipping half-graben bounded by NE-dipping major faults (e.g. Rabah, Wasif and Um El Huetat fault blocks, Fig. 9.12). This province is the southward continuation of the SW-dipping Amal-Zeit province of the southern Gulf of Suez. The southern (Quseir) province consists of NE-dipping half-grabens bounded by SW-dipping faults (e.g. Duwi, Hamadat and Zug El Bahar fault blocks, Figs. 9.12 and 9.14). The change of fault polarity and switch of half-graben asymmetry occurs across the Duwi-Quseir-Brothers accommodation zone (Jarrige et al. 1990; Bosworth 1994; Moustafa 1997; Khalil and McClay 2001, 2009; Younes and McClay 2002). The Duwi accommodation zone is a complex zone of tilted fault blocks that dip in different directions and is deformed by intra-block faults, folds and fractures. The location of the Duwi accommodation zone in the north of Gebel Duwi (DAZ, Fig. 9.12) appears to be controlled by the Hamrawin shear zone that trends oblique to the rift axis (Khalil and McClay 2001, 2002, 2009; Younes and McClay 2002). Projections across the Red Sea to the conjugate Arabian margin indicate that the Duwi accommodation zone would have been linked to the Duba accommodation zone in an early-rift configuration (Bosworth 1994; Bosworth and Burke 2005).

Field investigations of the structural, stratigraphic and sedimentological relationships in the northwest margin of the Red Sea show that early syn-rift Nakheil strata are locally preserved in the hanging wall of the border fault

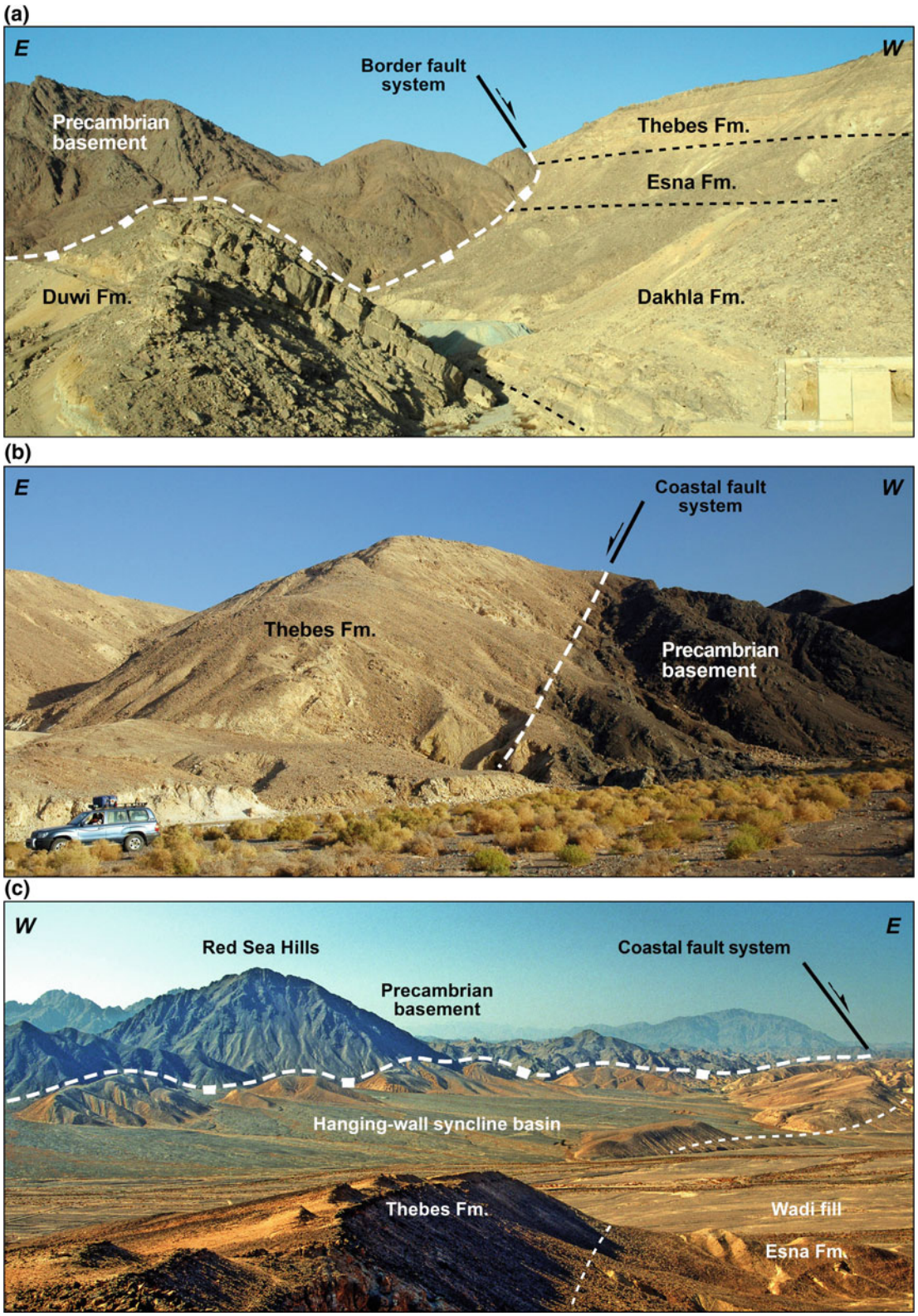

Fig. 9.13 Field views showing outcrop examples of major structural features in the Egyptian Red Sea margin. Named locations are shown in Fig. 9.12. **a** View looking south showing the border fault (Nakheil segment) juxtaposing west-dipping pre-rift strata in the hanging wall against Precambrian basement in the footwall. **b** View looking south showing the coastal fault (Anz segment) juxtaposing east-dipping Eocene Thebes limestone in the hanging wall against Precambrian basement in the footwall. **c** View looking north showing an example of a hanging wall syncline basin (fault-related folding) that formed during extension at the coastal fault system

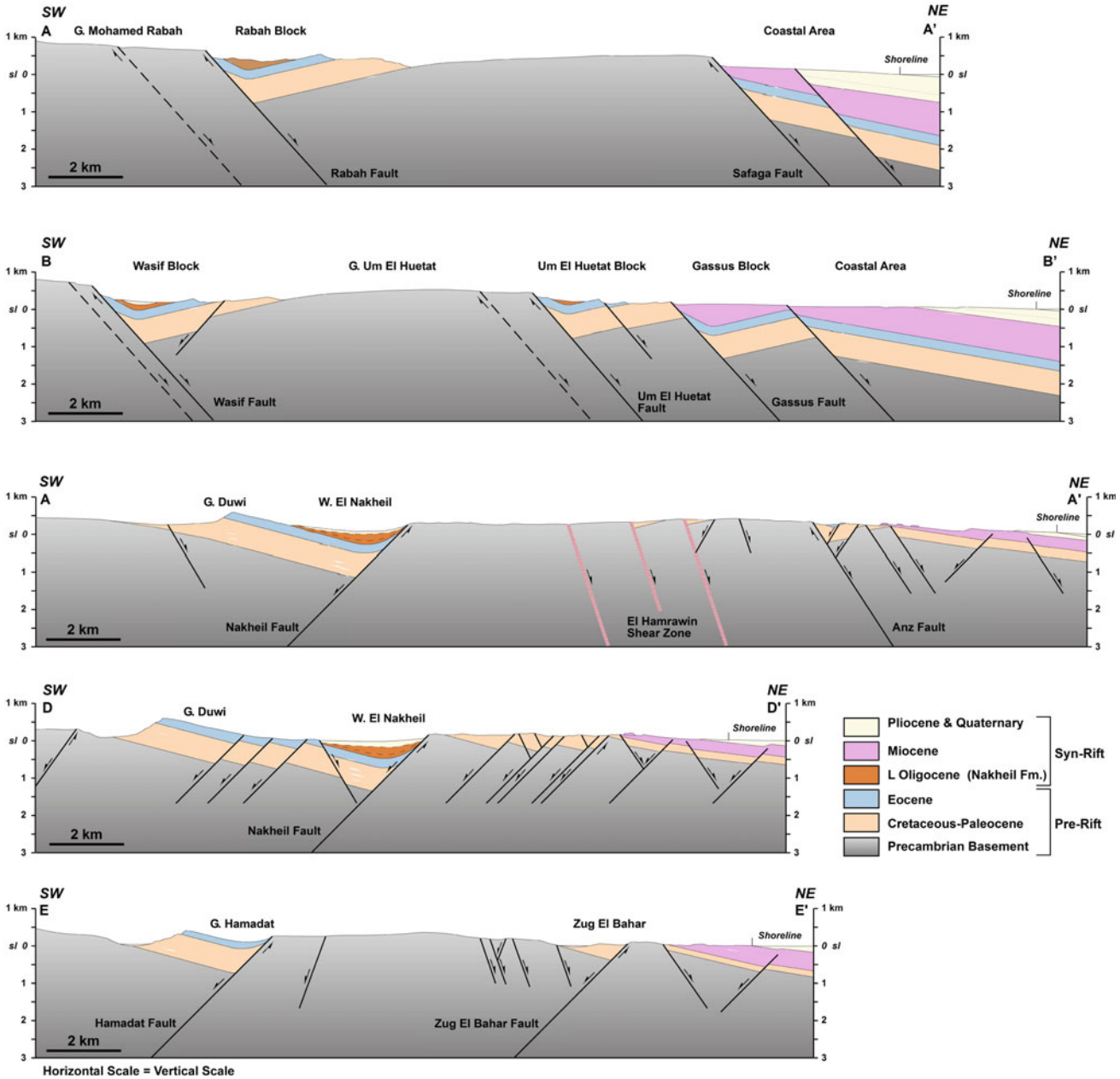

Fig. 9.14 Structural cross-sections through the Egyptian Red Sea margin (after Khalil and McClay 2002, 2016, 2018). Locations are shown in Fig. 9.12. Between profiles B-B′ and C-C′ the regional sense of stratal rotation reverses across the intervening Duwi accommodation zone. This large-scale change in fault block geometry coincides with the location of the El Hamrawin shear zone, a part of the Neoproterozoic Najd fault system

system but not in the hanging wall of the coastal fault system (Khalil and McClay 2002, 2009, 2012, 2016). This observation implies that the border fault system probably formed earlier, during the first stages of rift evolution, with the basal syn-rift sediments deposited in isolated hanging wall sub-basins. The sub-basins formed in the hanging wall of the border fault system do not contain the younger syn-rift strata (Khalil and McClay 2016, 2018), and appear to have ceased subsidence earlier than the depocenters of the coastal fault system. This resulted in early abandonment of the most in-board basins of the rift similar to the patterns in the Gulf of Suez and Saudi Red Sea margin (Moretti and Colleta 1987; Perry and Schamel 1990; Bosworth 1994, 1995; Bosworth and McClay 2001; Stockli and Bosworth 2019).

In the hanging wall of the coastal fault system, the Early to Middle Miocene sediments were deposited in coarse-grained fan deltas that prograded eastward (basin-ward). These fan deltas were localized at

sediment-input sites controlled by breached relay ramps that linked segments of the coastal fault system in the area between Safaga and Quseir (Khalil and McClay 2009).

In the area South of Quseir, the Precambrian basement in the footwall of the border and coastal fault systems (Gebels Zarieb and Zug El Bahar respectively; Fig. 9.12) plunges to the southeast as a result of the along-strike variations of fault displacement. The SE plunge of these basement footwall blocks appears to have controlled sediment dispersal during the Early Miocene and the deposition of coarse-grained fan deltas in Wadis Sharm El Bahari and Sharm El Qibli (Khalil and McClay 2009; Fig. 9.12). The absence of pre-rift strata in the southeastern part of the map area (south of Sharm El Bahari and Sharm El Qibli), together with the dominance of basement clasts within the Oligocene(?) Abu Ghusun Formation to the south of Wadi Hamadat, indicate that uplift and erosion of the rift shoulder was greater in the south than in the north. Erosion of the basement fault blocks probably occurred earlier and possibly faster in the southern part of the Egyptian rift margin compared to the basement blocks to the north (Khalil and McClay 2002, 2009).

9.5.2 Offshore Fault Geometry

Many structural details of the offshore Red Sea Egyptian margin have been studied since hydrocarbon exploration began in the 1970s. It was recognized that the structural style closely resembles that of the southern Gulf of Suez, with numerous rift-parallel fault trends cut or linked by complex cross-fault geometries (Fig. 9.15; Tewfik and Ayyad 1984; Barakat and Miller 1984). Several prominent salt walls and more irregular domes are associated with this structural domain, complicating the imaging of fault blocks at depth. Early 2-D reflection seismic profiling was followed by the acquisition of several 3-D surveys from 1999 to 2008 (Gordon et al. 2010). Comparison of limited published seismic data suggests that the structural style of the Egyptian and Saudi Arabian near-shore margins are very similar, though differences due to the early rift asymmetries are locally present (Stockli and Bosworth 2019).

All of the Egyptian offshore margin north of Quseir is included in the west-dipping mega-half graben that is recognized onshore and described above (Fig. 9.15). A major NE-side down fault trend parallels the coastline and the onshore Coastal Fault System. The details of this coastline fault are unknown because seismic acquisition in the environmentally sensitive nearshore region is not possible and a large-scale shallow detachment system within the Late Miocene evaporite section decapitates many of the deeper structures (Bosworth and Burke 2005; Stockli and Bosworth 2019). This shallow detachment is also observed in the Midyan region of Saudi Arabia (Mougenot and Al-Shakhis 1999).

Similar to the onshore domain, the internal structure of the offshore basin consists of nested extensional faults predominantly down-thrown to the northeast. These faults can generally be recognized where they cut the upper Rudeis, Kareem and Belayim Formations. The deeper structure is usually not resolvable in existing seismic data. Our interpretation of the offshore fault pattern is therefore a projection of shallow structure to the basement interface (Fig. 9.15). Offshore from Hurghada the faulting cuts completely through the Late Miocene Zeit Formation and overlying Plio-Pleistocene strata. This is probably due to young movement associated with the Red Sea–Aqaba transform junction.

9.6 Bedrock Exhumation and Thermal History

In addition to stratigraphic and magmatic constraints on the temporal evolution of the Gulf of Suez and Red Sea rift, thermochronometric data document the thermal evolution of the basement along the rift flanks. These studies have mainly leveraged zircon and apatite fission track and (U-Th)/He dating to determine the low-temperature cooling histories and the timing of unroofing of basement and pre-rift sedimentary rocks in the footwalls of normal faults and the proximal and distal rift flanks—an approach that is limited only by the magnitude of displacement required to expose rocks that resided above the closure temperatures prior to faulting and the suitability of the rocks for thermochronometric analysis (e.g., Stockli 2005).

Zircon fission track and (U-Th)/He data as well as apatite fission track data inboard from the Red Sea rift margins in Egypt and Saudi Arabia provide only limited information on the timing of late Cenozoic rifting, but shed light on the earlier Phanerozoic tectono-thermal evolution of the Arabian-Nubian shield. While much of the interior of the Arabian-Nubian shield records earliest Paleozoic exhumation in response to transtension and collapse tectonics following the East African Orogeny as documented by late Neoproterozoic and earliest Paleozoic cooling ages (Kohn et al. 1992; Vermeesch et al. 2009; Szymanski et al. 2016; Stockli and Bosworth 2019), there is ample evidence for a major Devonian to early Carboniferous (Hercynian) thermotectonic event, affecting much of the Arabian-Nubian shield from the Western Desert of Egypt to the Arabian margin in the Zagros (Kohn et al. 1992; Frizon de Lamotte et al. 2013; Stockli et al. 2009; Stockli and Bosworth 2019). Along the Red Sea margins both in Egypt and Saudi Arabia, this middle Paleozoic tectono-thermal event is documented by extensive basement domains characterized by Carboniferous zircon fission track and (U-Th)/He cooling ages (Kohn et al. 1992; Bojar et al. 2002; Szymanski et al. 2016; Stockli and

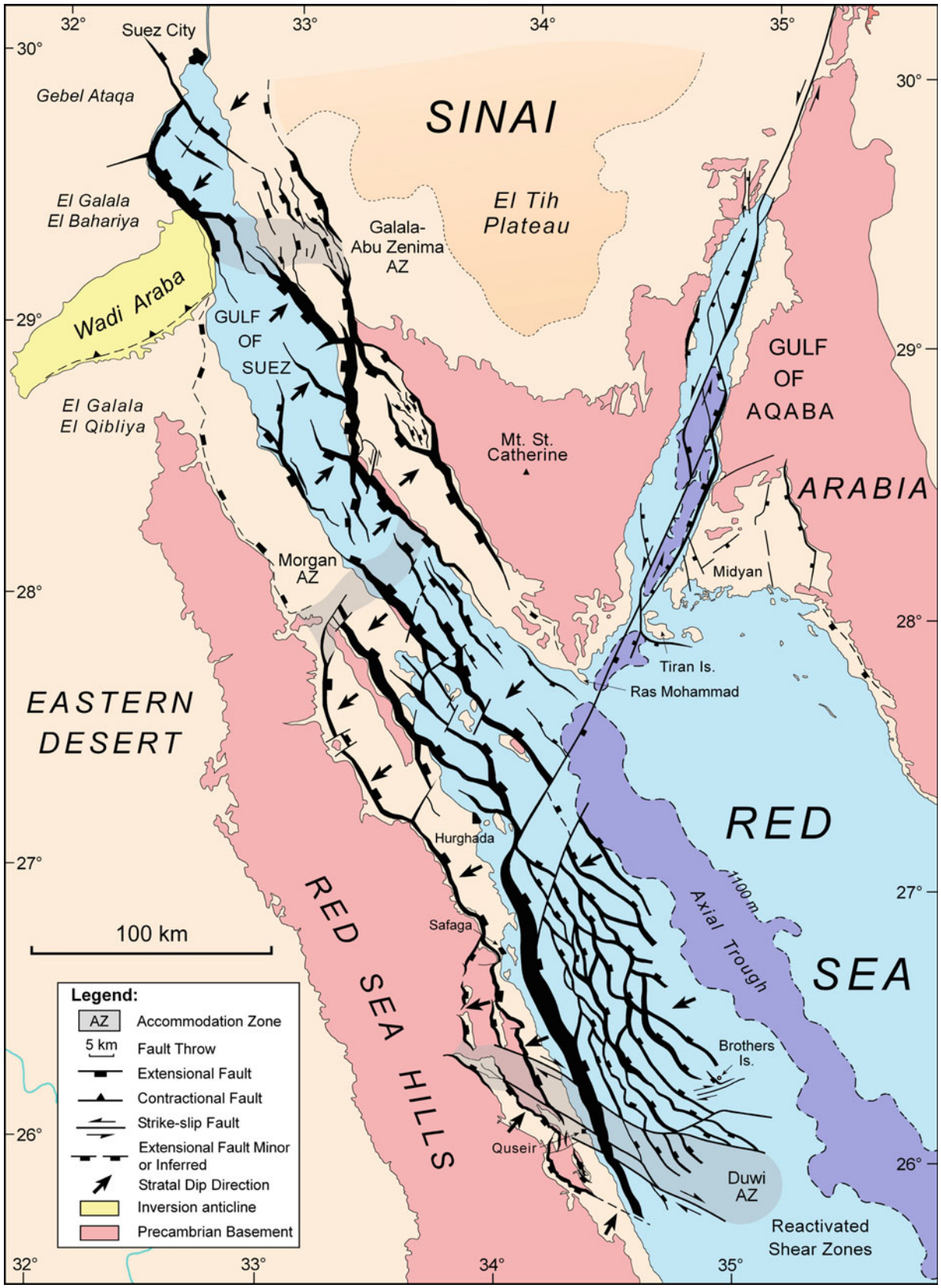

Fig. 9.15 Compilation of fault patterns for the Gulf of Suez (Khalil 1998; Bosworth and McClay 2001), Gulf of Aqaba (Ben-Avraham 1985; Ehrhardt et al. 2005; Bosworth et al. 2017), Midyan region of NW Saudi Arabia (Hughes et al. 2000), the northern part of the Egyptian Red Sea margin (Khalil and McClay 2001, 2009) and the Egyptian offshore Red Sea. Generalized bathymetric deeps (purple) are from Ben-Avraham et al. (1979; Gulf of Aqaba) and Cochran (2005; Red Sea)

Bosworth 2019). These Carboniferous cooling age domains tend to be juxtaposed against earliest Paleozoic cooling age domains along sub-vertical north-trending basement fault zones that appear to accommodate Hercynian block faulting (e.g., Stockli and Bosworth 2019).

With respect to the Cenozoic tectonic and thermal evolution of the Red Sea-Gulf of Suez rift system, Omar et al. (1989) presented extensive apatite fission track data from the entire western margin of the Gulf of Suez and demonstrated that rift flank exhumation and tectonic unroofing started at ~23–21 Ma. Similarly, apatite fission track data from both the Gulf of Suez and the Gulf of Aqaba sides of the Sinai Peninsula (Kohn and Eyal 1981) documented latest Oligocene and Miocene cooling related Red Sea rifting. These data are also supported by apatite (U-Th)/He dating on basement rocks and pre-rift strata from the Sinai rift margin border fault complex and fault blocks clustering between 24 and 19 Ma (Pujols 2011; Morag et al. 2019). Overall, these thermochronometric data from the Gulf of Suez document rapid Oligo-Miocene syn-rift cooling and exhumation followed by slower exhumation in post-Middle Miocene times. These constraints on the temporal evolution of the Gulf of Suez rift are in excellent agreement with the timing of syn-rift magmatism and rapid basin subsidence and syn-rift sedimentation (Evans 1988; Richardson and Arthur 1988; Steckler et al. 1988; Bosworth et al. 2005, 2015).

Unfortunately, low-temperature thermochronometric data for the Egyptian Red Sea margin south of Safaga are scarce and/or collected too far inboard from the rift margin to shed light on the cooling history of the Red Sea rift system (Omar et al. 1987; Omar and Steckler 1995; Bojar et al. 2002). Apatite fission track data from Cretaceous alkaline ring complexes in the Eastern Desert of Egypt indicate exhumation <32 Ma, but do not accurately provide information on the timing of rift initiation (Omar et al. 1987). Additional extensive apatite FT ages from the southern Eastern Desert of Egypt (Omar and Steckler 1995) are difficult to evaluate, but appear to be mostly collected >100 km from the rift border fault system and show old (>100 Ma) and/or partially reset ages. Their youngest apatite fission track ages with long mean-track lengths, indicative of rapid cooling, appear to be concentrated <100 km from the Red Sea coast and show both Eocene-Oligocene and Oligo-Miocene clusters. On the basis of these data, Omar and Steckler (1995) argued for a two stage-rift evolution with commencement of rift-related cooling ~34 Ma and the onset of a major rift-related unroofing between 25 and 21 Ma. However, while they stated that the magnitude of pre-Miocene extension was relatively minor, the geological evidence and thermochronometric evidence for latest Eocene to earliest Oligocene cooling and rift inception remain enigmatic and largely unsubstantiated. Bojar et al. (2002) presented limited zircon and apatite fission track data from the Quseir area with a single apatite fission track analysis yielding an age of ~23 Ma interpreted as rapid earliest Miocene extensional unroofing. Their zircon fission track ages, in contrast, mainly yielded Carboniferous cooling ages (366–315 Ma) related to a Hercynian tectono-thermal event. All in all, the paucity of structurally-integrated thermochronometric data along most of the Egyptian Red Sea margin, as well as along the Sudanese margin, make it difficult to evaluate the timing, magnitude, and spatial extent of Red Sea rifting along a large part of the western rift margin on the basis of thermochronometric data alone.

Along the northern and central Saudi Red Sea margin, zircon (U-Th)/He ages retain a record of both latest Neoproterozoic and Carboniferous cooling, while apatite (U-Th)/He data elucidate the Miocene cooling history of the Red Sea rift system. Along the northern Saudi margin, from the Midyan to Al Wajh area, apatite (U-Th)/He data show elevation invariant cooling ages clustering around 25–23 Ma, suggesting very rapid exhumation of these fault blocks at the very onset of Red Sea normal faulting (Stockli and Bosworth 2019). For the central Saudi Red Sea margin, Szymanski et al. (2016) documented a two-stage Cenozoic syn-rift thermal evolution. Their AHe ages record wide-spread rapid cooling and extensional unroofing starting ~23 Ma, simultaneous with dike emplacement and syn-rift sedimentation along the rift margin. They also documented a second phase of accelerated extension and cooling starting at ~14 Ma, focused along the coastal border fault system, marking a pronounced narrowing of the rift and the transition to coupled hyperextension in the northern Red Sea (Stockli and Bosworth 2019). This second pulse temporally coincides with a regional plate reorganization and establishment of the Dead Sea-Gulf of Aqaba transform. Apatite fission track ages from a large suite of samples from southern Saudi Arabia yielded a broad range of apparent ages as old as ~568 Ma (Bohannon et al. 1989). While their oldest ages from the Arabian Shield to the east of the rift flank escarpment imply little erosional denudation, their youngest ages (~14 Ma) indicate 2.5–5 km of exhumation due to extensional unroofing and escarpment retreat since the Oligocene. While only loosely constrained, they suggested that rift flank exhumation likely began at ~20 Ma.

The Red Sea margin in Eritrea exhibits a very similar temporal and spatial evolution of rifting (Abbate et al. 2002; Balestrieri et al. 2005). These studies documented an onset of rapid exhumation of coastal samples at ~20 Ma and accelerated exhumation starting at ~15 Ma. The youngest cooling ages along the coast also show rapid Pliocene apatite (U-Th)/He cooling ages that coincide with oceanic breakup and onset of seafloor spreading. Their data strongly argue against a late Eocene to early Oligocene onset of cooling and exhumation.

In summary, the available thermochronometric data from the Egyptian, Saudi, and Eritrean Red Sea rift margins

suggest a near simultaneous onset of extensional faulting and fault block exhumation along-strike and across-strike during the rift stretching phase and strongly argue against early rift propagation from south to north (Omar and Steckler 1995; Szymanski et al. 2016; Stockli and Bosworth 2019). This non-propagational, synchronous onset of large-magnitude rifting is also supported by the timing and spatial distribution of early syn-rift magmatism (e.g., Bosworth et al. 2015; Bosworth and Stockli 2016) and the simultaneous along-strike inception of syn-rift subsidence and sedimentation in the Gulf of Suez and Red sea. While the thermochronometric data illustrate the along-strike synchroneity of rift inception, they also document the profound differences in rift evolution, exhumation, and strain-localization between the Gulf of Suez and the northern and central Red Sea after the inception of Gulf of Aqaba transform and the transition from orthogonal to oblique rifting in the Middle Miocene (~14 Ma).

In addition to constraining the timing of Cenozoic Red Sea rift margin exhumation, the thermochronometric data also shed light on the pre-Cenozoic thermal history of the Arabian-Nubian shield. The data clearly show the importance of Hercynian exhumation and block faulting that likely influenced Cenozoic extensional fault patterns and linkages, similar to the documented role of late Neoproterozoic fault zones (e.g., Khalil and McClay 2001; Younes and McClay 2002). Lastly, while Triassic and Jurassic Tethyan rifting and Late Cretaceous inversion tectonics undoubtedly affected the tectono-thermal evolution of parts of the Gulf of Suez, the Mesozoic thermal evolution of the Red Sea region remains largely unconstrained, although there is evidence for possible kilometer-scale Cretaceous denudation (e.g., Vermeesch et al. 2009).

9.7 Synthesis and Discussion

We have attempted to integrate onshore and offshore, surface and subsurface geological and geophysical datasets to provide a reasonable model for the geological evolution of the Egyptian Red Sea margin. Some key points follow:

- The ~23 Ma regional NW-SE Red Sea parallel alkali basalt dike swarm, with associated extensive basalt flows in the vicinity of Cairo, represents the first upper-crustal expression of initial lithospheric-scale extension in the northern Red Sea. These dikes and local flows are interbedded with the oldest part of the paleontologically dated siliciclastic syn-rift stratigraphic section (Aquitanian Nukhul Fm.) and are cut by normal faults associated with the oldest recognized phase of northern Red Sea extension. Localized thin accumulations of conglomerate and sandstone that underlie the basalts (Nakheil and Abu Ghusun Fms.) suggest that only minor extension likely preceded eruption. The nature and duration of limited pre-dike subsidence and faulting is presently only poorly understood. High-pressure gabbros, such as those observed at Zabargad Island, were underplated beneath the continental crust contemporaneously with upper-crustal Oligo-Miocene magmatism.
- Initial Oligo-Miocene rifting resulted in the formation of a complex, discontinuous fault pattern with very high local rates of fault block rotation. Progressive uplift of the rift shoulders, increasing in magnitude to the far south, lead to local basement exposure. The incipient rift was separated into distinct sub-basins with alternating regional dip domains separated by well-defined accommodation zones. This segmentation resulted in laterally and vertically complex sedimentary facies distributions, dominated by marginal to shallow marine siliciclastics.
- During the early Burdigalian (~20 Ma) tectonically-driven subsidence accelerated and was accompanied by a concomitant rapid exhumation and unroofing of the rift shoulders. The intra-rift fault networks coalesced into more through-going structures, and fault movement became progressively more focused along the rift axis. This reconfiguration of the rift structure resulted in generally more laterally continuous depositional facies and the preponderance of moderate to deep marine deposits of the Rudeis, Kareem and Ranga Formations.
- The Middle Miocene (~14 Ma) was marked by dramatic changes in rift kinematics with the onset of the left-lateral Gulf of Aqaba transform fault system, a switch from orthogonal to oblique rifting, and hyperextension in the northern Red Sea. This also resulted in the abandonment of the Gulf of Suez as a strongly active rift and its separation from the northern Red Sea rift.
- This Middle Miocene tectonic reconfiguration also manifested itself in dramatic change in the sedimentary environments of the Red Sea and Gulf of Suez. The open marine seaway was replaced by an extensive evaporitic basin that reached from the central Gulf of Suez to offshore Yemen/Eritrea (Belayim, South Gharib, Zeit and Abu Dabbab Fms.).
- At the end of the Miocene (~5 Ma) a subaerial unconformity developed across most of the Red Sea basin. With the onset of seafloor spreading in the southern Red Sea, marine waters again gained access to the Red Sea through Bab el Mandeb establishing open marine conditions throughout the Pliocene. During the Pleistocene, numerous coral terraces and wave-cut benches formed as a result of sea-level changes induced by glacial cycles and associated isostatic and eustatic effects. The present elevations of these features suggest that at least during the Late Pleistocene to Recent the Egyptian Red Sea margin has been vertically relatively stable.

- Moderately high levels of seismicity are present in the northern Red Sea, Gulf of Aqaba and southern Gulf of Suez. Focal mechanisms are compatible with accumulating GPS datasets that show Arabia moving NNE away from Africa parallel to the Gulf of Aqaba, and Sinai moving to the NNW. This results in small components of E-W opening across the Gulf of Aqaba and left lateral transtensional opening of the Gulf of Suez.
- Industry exploratory wellbores and seismic data demonstrate that continental crust extends at least several tens of kilometers offshore from the present-day Egyptian and Saudi Red Sea coastlines. The well and geophysical data indicate that the northern Red Sea throughout its evolution represented mostly a magma-poor, non-volcanic rift system. Available geophysical, petrological, geochemical and geological datasets support the contention that laterally integrated sea-floor spreading has not yet manifest itself and that lithospheric break-up has not yet occurred in the northern Red Sea.

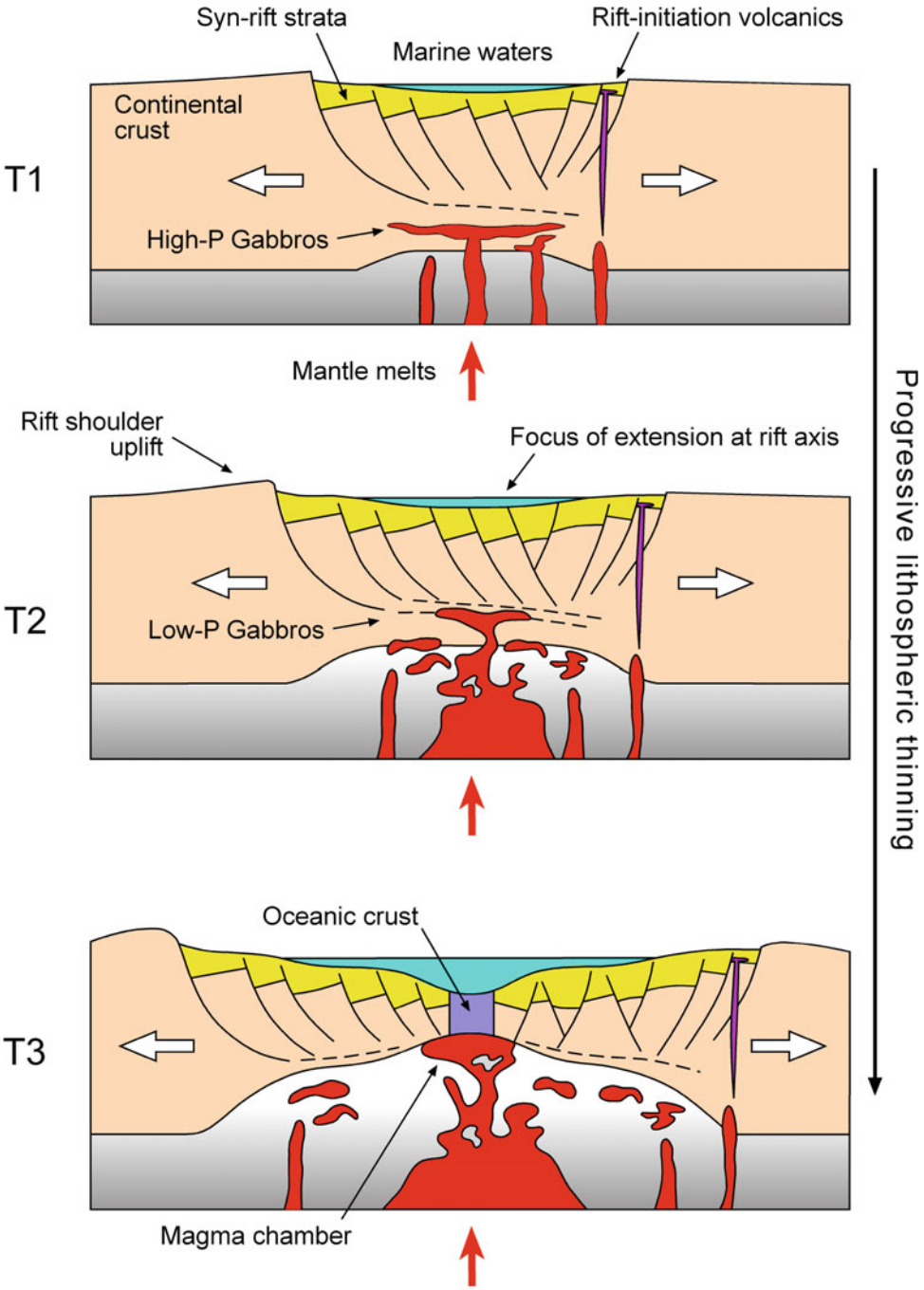

Fig. 9.16 A model of continental rift evolution based on the Red Sea. Rift initiation (T1) is accompanied by underplating of high-pressure gabbros (now exposed at Zabargad Island) and localized intrusion of basaltic dikes. As lithospheric thinning progresses (T2), lower-pressure gabbros (now exposed at the Brothers Islands) are intruded and extensional faulting focuses along the rift axis. Accretion of oceanic crust follows at a later time (T3; southern/central Red Sea). Inherent in this model are the corollaries that the age of the oceanic crust must be significantly younger than the age of the high-pressure gabbros, significant areas of thinned continental crust must be present within the basin and, in the case of the Red Sea, plate restorations cannot be "coastline-to-coastline". Aquamarine = water; beige = pre-rift continental crust; gray = lithospheric mantle; red = magmatic intrusions; violet = basaltic dikes; yellow = syn-rift strata; purple = oceanic crust (modified after Ligi and others 2018)

- Many gaps exist in our understanding of how the Red Sea rifted, and what its implications for other rift systems may be. However, a general model compatible with the observations presented in this review can be discussed (Fig. 9.16). Syn-rift magmatism in the northern Red Sea is limited to a small number of onshore basaltic dikes and very minor flows, a few offshore occurrences of underplated gabbros, and localized oceanic-style volcanism in isolated axial deeps. It is most accurately described as a magma-poor, non-volcanic rift (Ligi et al. 2018; Stockli and Bosworth 2019). High-pressure gabbros such as those now exposed at Zabargad Island suggest that mafic underplating of the continental crust occurred during very early stages of rifting. As crustal thinning continued, gabbros were intruded at progressively lower pressures (Ligi et al. 2018). Wellbore and geophysical datasets indicate that a well-defined oceanic spreading center has not yet been established along the northern Red Sea rift axis. Therefore, the continental margins of the northern Red Sea must have undergone large amounts of extension and crustal attenuation in order to accommodate the known separation of Arabia from Africa (Stockli and Bosworth 2019). Glimpses of this extension, in particular its early phases, are observed along the Egyptian coastal plain and easternmost Red Sea Hills.

Acknowledgements We appreciate the Editors' interest and proposal that initiated this review of the Egyptian Red Sea basin. Many colleagues have helped improve our understanding of this complex setting. We particularly thank Enrico Bonatti, the late Kevin Burke, Kenneth Carlson, René Guiraud, the late Giff Kessler II, Edgardo Pujols, Dave Smith, and Marco Taviani for fruitful discussions. Eugene Szymanski provided a very helpful review that assisted us in clarifying many points.

References

Abbate E, Balestrieri ML, Bigazzi G (2002) Morphostructural development of the Eritrean rift flank (southern Red Sea) inferred from apatite fission track analysis. J Geophys Res 107(B11)

Abdel Gawad M (1969) New evidence of transcurrent movements in Red Sea area and petroleum implications. AAPG Bull 53:1466–1479

Abdel-Aal AK, Yagi Y (2017) Earthquake source characterization, moment tensor solutions, and stress field of small-moderate earthquakes occurred in the northern Red Sea Triple Junction. Geosci J 21:235–251

Abdel-Aal AK, Badreldin H (2016) Seismological aspects of the 27 June 2015 Gulf of Aqaba earthquake and its sequence of aftershocks. J Seismol 20:935–952

Aki K (1965) Maximum likelihood estimate of b in the formula logN = a-bM and its confidence limits. Bull Earthq Res Inst Tokyo Univ 43:237–239

Al-Ahmadi K, Al-Amri A, See L (2014) A spatial statistical analysis of the occurrence of earthquakes along the Red Sea floor spreading: clusters of seismicity. Arab J Geosci 7:2893–2904

Al-Amri AM, Schult FR, Bufe CG (1991) Seismicity and aeromagnetic features of the Gulf of Aqaba (Elat) region. J Geophys Res 96:20179–20185

Almalki KA, Betts PG, Ailleres L (2015) The Red Sea—50 years of geological and geophysical research. Earth Sci Rev 147:109–140

Al-Tarazi E (2000) The Major Gulf of the Aqaba earthquake, 22 November 1995—maximum intensity distribution. Nat Hazards 22:17–27

Altherr R, Henjes-Kunst F, Puchelt H, Baumann A (1988) Volcanic activity in the Red Sea axial trough: evidence for a large mantle diapir? Tectonophysics 150:121–133

Altherr R, Henjes-Kunst F, Baumann A (1990) Asthenosphere versus lithosphere as possible sources for basaltic magmas erupted during formation of the Red Sea: constraints from Sr, Pb, and Nd isotopes. Earth Planet. Sci. Lett. 96:269–286

Anders E, Grevesse N (1989) Abundances of the elements: meteoritic and solar. Geochim Cosmochim Acta 53:197–214

Antonini P, Petrini R, Contin G (1998) A segment of sea-floor spreading in the central Red Sea: basalts from the Nereus Deep (23 degrees 00′-23 degrees 20′ N). J Afr Earth Sci 27:107–114

ArRajehi A, McClusky S, Reilinger R, Daoud M, Alchalbi A, Ergintav S, Gomez F, Sholan J, Bou-Rabee F, Ogubazghi G, Haileab B, Fisseha S, Asfaw L, Mahmoud S, Rayan A, Bendik R, Kogan L (2010) Geodetic constraints on present-day motion of the Arabian Plate: Implications for Red Sea and Gulf of Aden rifting. Tectonics 29(3)

Babiker N, Mula AHG, El-Hadidy S (2015) A unified Mw-based earthquake catalogue and seismic source zones for the Red Sea region. J Afr Earth Sci 109:168–176

Badawy A (2001) Status of the crustal stress in Egypt as inferred from earthquake focal mechanisms and borehole breakouts. Tectonophysics 343(1–2):49–61

Badawy A, Mohamed AMS, Abu-Ali N (2008) Seismological and GPS constraints on Sinai sub-plate motion along the Suez Rift. Stud Geophys Geod 52:397–412

Baker BH (1970) The structural pattern of the Afro-Arabian rift system in relation to plate tectonics. Philos Trans R Soc Lond Ser A Math Phys Sci 267:383–391

Baker J, Snee L, Menzies M (1996) A brief Oligocene period of flood volcanism in Yemen: implications for the duration and rate of continental flood volcanism at the Afro-Arabian triple junction. Earth Planet Sci Lett 138:39–55

Bakor AR, Gass IG, Neary CR (1976) Jabal al Wask, northwest Saudi Arabia: an Eocambrian back-arc ophiolite. Earth Planet Sci Lett 30 (1):1–9

Balestrieri ML, Stuart FM, Persano C, Abbate E, Bigazzi G (2005) Geomorphic development of the escarpment of the Eritrean margin, southern Red Sea from combined apatite fission-track and (U–Th)/He thermochronometry. Earth Planet Sci Lett 231:97–110

Barakat H, Miller P (1984) Geology and petroleum exploration, Safaga Concession, northern Red Sea, Egypt. In: Proceedings of the 7th exploration seminar, Egyptian General Petroleum Corporation, Cairo, pp 191–214

Barakat H, Miller P (1986) Geology and petroleum exploration, Safaga Concession, Northern Red Sea, Egypt. In: Proceedings of the seventh exploration seminar. Egyptian General Petroleum Corporation and Egypt Petroleum Exploration Society, Mar 1984, Cairo, pp 191–214

Ben-Avraham Z (1985) Structural framework of the Gulf of Elat (Aqaba) northern Red Sea. J Geophys Res 90:703–726

Ben-Avraham Z, Garfunkel Z, Almagor G, Hall JK (1979) Continental breakup by a leaky transform: the Gulf of Elat (Aqaba). Science 206:214–216

Ben-Menahem A, Aboodi E (1971) Tectonic patterns in the northern Red Sea region. J Geophys Res 76(11):2674–2689

Bender B (1983) Maximum likelihood estimation of *b*-values for magnitude grouped data. Bull Seismol Soc Am 73:831–851

Birt CS, Maguire PKH, Khan MA, Thybo H, Keller GR, Patel J (1997) The influence of pre-existing structures on the evolution of the southern Kenya Rift Valley—evidence from seismic and gravity studies. Tectonophysics 278:211–242

Bohannon RG, Naeser CW, Schmidt DL, Zimmermann RA (1989) The timing of uplift, volcanism, and rifting peripheral to the Red Sea: a case for passive rifting? J Geophys Res 94:1683–1701

Bojar AV, Fritz H, Kargl S, Unzog W (2002) Phanerozoic tectonothermal history of the Arabian-Nubian shield in the Eastern Desert of Egypt: evidence from fission track and paleostress data. J Afr Earth Sci 34:191–202

Bonatti E (1985) Punctiform initiation of seafloor spreading in the Red Sea during transition from continental to an oceanic rift. Nature 316:33–37

Bonatti E, Hamlyn P, Ottonello G (1981) Upper mantle beneath a young oceanic rift—peridotites from the island of Zabargad (Red-Sea). Geology 9:474–479

Bonatti E, Clocchiatti R, Colantoni P, Gelmini R, Marinelli G, Ottonello G, Santacroce R, Taviani M, Abdel-Meguid AA, Assaf HS, El Tahir MA (1983) Zabargad (St. John) Island: an uplifted fragment of sub-Red Sea lithosphere. J Geol Soc Lond 14D:667–690

Bonatti E, Ottonello G, Hamlyn PR (1986) Peridotites from the island of Zabargad (Red Sea). J Geophys Res 91:599–631

Bonatti E, Seyler M (1987) Crustal underplating and evolution in the Red Sea rift. J Geophys Res 92:12083–12821

Bosworth W (1993) Nature of the Red Sea crust. A controversy revisited: comment and reply. Geology 21:574–575

Bosworth W (1994) A model for the three-dimensional evolution of continental rift basins, north-east Africa. In: Schandelmeier H, Stern RJ (eds) Geology of Northeast Africa (Part 2). Geol Rundsch 83:671–688

Bosworth W, Burke K (2005) Evolution of the Red Sea—Gulf of Aden rift system. In: Post PJ, Rosen NC, Olson DL, Palmes SL, Lyons KT, Newton GB (eds) Petroleum systems of divergent continental margin basin. 2005 Gulf Coast Section SEPM Foundation 25th Bob F. Perkins Annual Research Conference, Houston, 4–7 Dec 2005, CD-ROM, pp 342–372

Bosworth W, Durocher S (2017) Present-day stress fields of the Gulf of Suez (Egypt) based on exploratory well data: non-uniform regional extension and its relation to inherited structures and local plate motion. J Afr Earth Sci 136:136–147

Bosworth W, McClay K (2001) Structural and stratigraphic evolution of the Gulf of Suez rift, Egypt: a synthesis. In: Ziegler PA, Cavazza W, Robertson AHF, Crasquin-Soleau S (eds) Peri-Tethys Memoir 6: Peri-Tethyan Rift/Wrench Basins and Passive Margins, Mémoires du Muséum National d'Histoire Naturelle de Paris, vol 186, pp 567–606

Bosworth W, Stockli D (2016) Early magmatism in the greater Red Sea rift: timing and significance. Can J Earth Sci 53:1158–1176

Bosworth W, Taviani M (1996) Late quaternary reorientation of stress field and extension direction in the southern Gulf of Suez, Egypt: evidence from uplifted coral terraces, mesoscopic fault arrays, and borehole breakouts. Tectonics 15(4):791-802

Bosworth W, Crevello P, Winn RD Jr, Steinmetz J (1998) Structure, sedimentation, and basin dynamics during rifting of the Gulf of Suez and northwestern Red Sea. In: Purser BH, Bosence DWJ (eds) Sedimentation and Tectonics of Rift basins: Red Sea-Gulf of Aden. Chapman and Hall, London, pp 77–96

Bosworth W, Darwish M, Crevello P, Taviani M, Marshak S (1996) Stratigraphic and structural evolution of Zabargad Island (Red Sea, Egypt) since the Early Cretaceous. In: Youssef El SA (ed) Proceedings of the 3rd international conference on geology of the Arab World, vol 1, pp 161–190

Bosworth W, Huchon P, McClay K (2005) The Red Sea and Gulf of Aden basins. J Afr Earth Sci 43:334–378

Bosworth W, Stockli DF, Helgeson DE (2015) Integrated outcrop, 3D seismic, and geochronologic interpretation of Red Sea dike-related deformation in the Western Desert, Egypt—the role of the 23 Ma Cairo "mini-plume". J Afr Earth Sci 109:107–119

Bosworth W, Montagna P, Pons-Branchu P, Rasul N, Taviani M (2017) Seismic hazards implications of uplifted Pleistocene coral terraces in the Gulf of Aqaba. Sci Rep 7:1–13

Clark MD (1986) Explanatory notes to the geologic map of the Al Bad' quadrangle, sheet 28A, Kingdom of Saudi Arabia. Saudi Arabian Deputy Ministry for Mineral Resources Geoscience Map Series GM-81A, C, scale 1:250,000, with text, 46 pp

Cochran JR (1983) A model for the development of the Red Sea. AAPG Bull 67:41–69

Cochran JR (2005) Northern Red Sea: nucleation of an oceanic spreading center within a continental rift. Geochem Geophys Geosyst 6:Q03006

Cochran JR, Martinez F (1988) Evidence from the northern Red Sea on the transition from continental to oceanic rifting. Tectonophysics 153:25–53

Cochran JR, Karner GD (2007) Constraints on the deformation and rupturing of continental lithosphere of the Red Sea: the transition from rifting to drifting. In: Karner GD, Manatschal G, Pinheiro LM (eds) Imaging, mapping and modelling continental lithosphere extension and breakup. Geological Society, London, Special Publications, vol 282, pp 265–289

Cochran JR, Martinez F, Steckler MS, Hobart MS (1986) Conrad Deep: a new Northern Red Sea Deep. Origin and implications for continental rifting. Earth Planet Sci Lett 78:18–32

Darwish M (1994) Cenomanian–Turonian sequence stratigraphy, basin evolution and hydrocarbon potentialities of Northern Egypt. In: Proceedings of the 2nd international conference on geology of the Arab world, vol 3. Cairo University, Cairo, Egypt, pp 315–362

Du Toit AL (1937) Our wandering continents. Oliver and Boyd, Edinburgh, xiii +366 pp

EGPC (1964) Oligocene and Miocene rock-stratigraphy of the Gulf of Suez region. Consultative Stratigraphic Committee of the Egyptian General Petroleum Corporation, Cairo, Report E.R. 575, 142 pp

Ehrhardt A, Hubscher C (2015) The northern Red Sea in transition from rifting to drifting—lessons learned from ocean deeps. In: Rasul NMA, Stewart ICF (eds) The Red Sea: the formation, morphology, oceanography and environment of a young ocean basin. Springer Earth System Sciences, Berlin, Heidelberg, pp 121–135

Ehrhardt A, Hübscher C, Ben-Avraham Z, Gajewski D (2005) Seismic study of pull-apart-induced sedimentation and deformation in the Northern Gulf of Aqaba (Elat). Tectonophys 396:59–79

El-Akkad SE, Dardir A (1966) Geology of the Red Sea coast between Ras Shagra and Mersa Alam with short note on exploratory work at Gebel El Rusas lead-zinc deposits. Geol Surv Egypt, 67 pp. Paper 35

El-Bohoty M, Brimich L, Saleh A, Saleh S (2012) Comparative study between the structural and tectonic situation of the Southern Sinai and the Red Sea, Egypt, as deduced from magnetic, gravity and seismic data. Contrib Geophys Geod 42:357–388

El Moursi MEE (1993) Pleistocene evolution of the reef terraces of the Red Sea coastal plain between Hurghada and Marsa Alam, Egypt. J Afr Earth Sci 17:125–127
Engel AEJ, Dixon TH, Stern RJ (1980) Late precambrian evolution of Afro-Arabian crust from ocean arc to craton. Geol Soc Am Bull 91 (12):699
Evans AL (1988) Neogene tectonic and stratigraphic events in the Gulf of Suez rift area, Egypt. Tectonophysics 153:235–247
Fairhead JD, Girdler RW (1970) The seismicity of the Red Sea, Gulf of Aden and Afar triangle. Philos Trans Roy Soc A 267:49–74
Fleck RJ, Greenwood WR, Hadley DG, Anderson RE, Schmidt DL (1980) Rubidium-strontium geochronology and platetectonic evolution of the southern part of the Arabian Shield: U.S. Geological Survey Professional Paper 1131, 38 p
Frisch W, Al-Shanti A (1977) Ophiolite belts and the collision of island arcs in the Arabian Shield. Tectonophysics 43(3–4):293–306
Frizon de Lamotte DF, Tavakoli-Shirazi S, Leturmy P, Averbuch O, Mouchot N, Raulin C, Leparmentier F, Blanpied C, Ringenbach JC (2013) Evidence for Late Devonian vertical movements and extensional deformation in northern Africa and Arabia: integration in the geodynamics of the Devonian world. Tectonics 32:107–122
Gass IG (1977) The evolution of the Pan African crystalline basement in NE Africa and Arabia. J Geol Soc 134(2):129–138
Gaulier J-M, Le Pichon X, Lyberis N, Avedik F, Geli L, Moretti I, Deschamps A, Hafez S (1988) Seismic study of the crustal thickness, northern Red Sea and Gulf of Suez. Tectonophysics 153:55–88
Girdler RW (1991) The Afro-Arabian rift system; an overview. Tectonophysics 197:139–153
Girdler RW, Styles P (1974) Two-stage Red Sea floor spreading. Nature 247:7–11
Girdler RW, Whitmarsh RB (1974) Miocene evaporites in Red Sea cores, their relevance to the problem of the width and age of oceanic crust beneath the Red Sea. In: Whitmarsh RB, Weser OE, Ross DA et al (eds) Initial reports of the Deep Sea drilling project, vol 2. U.S. Government Printing Office, Washington, D.C., pp 913–921
Gordon G, Hansen B, Scott J, Hirst C, Graham R, Grow T, Spedding A, Fairhead S, Fullarton L, Griffin D (2010) The hydrocarbon prospectivity of the Egyptian North Red Sea basin. In: Vining BA, Pickering SC (eds) Proceedings of the 7th petroleum geology conference, petroleum geology: from mature basins to new frontiers. Geological Society, London, pp 783–789
Gregory JW (1896) The Great Rift Valley. John Murray, London, p 422
Greiling RO, El Ramly MF, El Arhal H, Stern RJ (1988) Tectonic evolution of the northwestern Red Sea margin as related to basement structure. Tectonophysics 153:179–191
Guennoc P, Pautot G, Coutelle A (1988) Surficial structures of the northern Red Sea axial vally from 23° N to 28° N: time and space evolution of neo-oceanic structures. Tectonophysics 153:1–23
Guennoc P, Pautot G, Leqentrec MF, Coutelle A (1990) Structure of an early oceanic rift in the northern Red-Sea, Ocean. Acta 13:145–157
Gutemberg B, Richter CF (1942) Earthquake magnitude, intensity, energy and acceleration. Bull Seismol Soc Am 32:163–191
Haase KM, Muhe R, Stoffers P (2000) Magmatism during extension of the lithosphere: geochemical constraints from lavas of the Shaban Deep, northern Red Sea. Chem Geol 166:225–239
Hall SA, Andreason GE, Girdler RW (1977) Total intensity magnetic anomaly map of the Red Sea and adjacent coastal areas, a description and preliminary interpretation, vol 22. Saudi Arabia Directorate General Mineral Resources Bulletin, Red Sea Research 1970–1975, F1–F15
Han Q, Wang L, Xua J, Carpinteri A, Lacidogna G (2015) A robust method to estimate the b-value of the magnitude-frequency distribution of earthquakes. Chaos Solitons Fractals 81:103–110
Hansen SE, Rodgers AJ, Schwartz SY, Al-Amri AMS (2007) Imaging ruptured lithosphere beneath the Red Sea and Arabian Peninsula. Earth Planet Sci Lett 259:256–265
Hoang CT, Taviani M (1991) Stratigraphic and tectonic implications of uranium-series dated coral reefs from uplifted Red Sea islands. Quat Res 35:264–273
Hofmann AW, Jochum KP, Seufert M, White WM (1986) Nb and Pb in oceanic basalts: new constraints on mantle evolution. Earth Planet Sci Lett 79:33–45
Hofstetter A (2003) Seismic observations of the 22/11/1995 Gulf of Aqaba earthquake sequence. Tectonophys 369:21–36
Hosny A, El-Hady SM, Guidarelli M, Panza GF (2012) Source moment tensors of the earthquake Swarm in Abu-Dabbab area, South-East Egypt. Rend Fis Acc Lincei 23:149–163
Hosny A, Nyblade A (2014) Crustal structure in southeastern Egypt: symmetric thinning of the northern Red Sea rifted margins. Geology 42:219–222
Hosny A, Nyblade A (2016) The crustal structure of Egypt and the northern Red Sea region. Tectonophysics 687:257–267
Huang PY, Solomon SC (1987) Centroid depths and mechanisms of mid-ocean ridge earthquakes in the Indian Ocean. Gulf of Aden, and Red Sea. J Geophys Res 92(B2):1361
Hughes GW, Perincek D, Grainger DJ, Abu-Bshait A-J, Jarad A-RM (1999) Lithostratigraphy and depositional history of part of the Midyan region, northwestern Saudi Arabia. GeoArabia 4:503–541
Hughes GW, Perincek D, Abu-Bshait A-J, Jarad A-RM (2000) Aspects of Midyan geology, Saudi Arabian Red Sea, Saudi Aramco. J Technol Winter 1999(2000):12–42
Ishimoto M, Iida K (1939) Observations sur les seismes enregistres par le microsismographe construit dernierement (1). Bull Earthq Res Inst Tokyo Univ 17:443–478
Jarrige J-J, Ott d'Estevou P, Burollet PF, Montenat C, Prat P, Richert J-P, Thiriet J-P (1990) The multistage tectonic evolution of the Gulf of Suez and northern Red Sea continental rift from field observations. Tectonics 9:441–465
Johnson PR (2014) An expanding Arabian-Nubian Shield geochronologic and isotopic dataset: defining limits and confirming the tectonic setting of a Neoproterozoic accretionary orogeny. Open Geol J 8:3–33
Kaz'min VG (1977) Characteristics of geodynamic evolution of the Afro-Arabian rift system. Izd Nauka Sib Otd Novosibirsk [In Russian]
Kerdany MT, Cherif OH (1990) Mesozoic. In: Said R (ed) The geology of Egypt (Chapter 22). A.A. Balkema, Rotterdam, pp 407–438
Khalil SM (1998) Tectonic evolution of the eastern margin of the Gulf of Suez, Egypt. PhD thesis, Royal Holloway, University of London, 349 pp
Khalil SM, McClay KR (2001) Tectonic evolution of the northwestern Red Sea–Gulf of Suez rift system. In: Wilson RCL, Whitmarsh RB, Taylor B, Froitzheim N (eds) Non-volcanic rifting of continental margins: a comparison of evidence from land and sea. Geological Society, London, Special Publications, vol 187, pp 453–473. https://doi.org/10.1144/GSL.SP.2001.187.01.22
Khalil SM, McClay KR (2002) Extensional fault-related folding, northwestern Red Sea, Egypt. J Struct Geol 24:743–762
Khalil SM, McClay KR (2009) Structural control on syn-rift sedimentation, northwestern Red Sea margin, Egypt. Mar Pet Geol 26:1018–1034
Khalil SM, McClay KR (2012) Structural control on syn-rift sedimentation, northwestern Red Sea, Egypt (Chapter 5). In: Roberts DG, Bally AW (eds) Regional geology and tectonics: phanerozoic rift systems and sedimentary basins. Elsevier, pp 73–103
Khalil SM, McClay KR (2016) 3D geometry and kinematic evolution of extensional fault-related folds, NW Red Sea, Egypt. In: Childs C, Holdsworth RE, Jackson CA-L, Manzocchi T, Walsh JJ, Yielding G

(eds) The geometry and growth of normal faults. Geological Society, London, Special Publications, vol 439, pp 109–130. https://doi.org/10.1144/SP439.11

Khalil SM, McClay KR (2018) Extensional fault-related folding in the northwestern Red Sea Egypt: segmented fault growth, fault linkages, corner folds and basin evolution. In: McClay KR, Hammerstein JA (eds) Passive margins: tectonics, sedimentation and magmatism. Geological Society of London Special Publications. https://doi.org/10.1144/SP476.12

Khan MA (1975) The Afro–Arabian rift system. Sci Prog (1916) 62:207–236

Kohn BP, Eyal M (1981) History of uplift of the crystalline basement of Sinai and its relation to opening of the Red Sea as revealed by fission track dating of apatites. Earth Planet Sci Lett 52:129–141

Kohn BP, Eyal M, Feinstein S (1992) A major late Devonian-early Carboniferous (Hercynian) thermotectonic event at the NW margin of the Arabian-Nubian shield: evidence from zircon fission track dating. Tectonics 11:1018–1027

Kopp RE, Simons FJ, Mitrovica JX, Maloof AC, Oppenheimer M (2009) Probabilistic assessment of sea level during the last interglacial stage. Nature 462:863–868

Langmuir CH, Klein EM, Plank T (1992) Petrological systematics of mid-ocean ridge basalts: constraints on melt generation beneath ocean ridges. In: Morgan JP, Blackman DK, Sinton JK (eds) Mantle flow and melt generation at Mid-Ocean ridges. Geophysical monograph 71. American Geophysical Union, Washington DC, pp 183–280

Lehnert K, Su Y, Langmuir CH, Sarbas B, Nohl U (2000) A global geo-chemical database structure for rocks. Geochem Geophys Geosyst 1:1012

Le Pichon X, Gaulier J-M (1988) The rotation of Arabia and the Levant fault system. Tectonophysics 153:271–294

Ligi M, Bonatti E, Bortoluzzi G, Cipriani A, Cocchi L, Caratori Tontini F, Carminati E, Ottolini L, Schettino A (2012) Birth of an ocean in the Red Sea: initial pangs. Geochem Geophys Geosyst 13: Q08009

Ligi M, Bonatti E, Bosworth W, Cai Y, Cipriani A, Palmiotto C, Ronca S, Seyler M (2018) Birth of an ocean in the Red Sea: oceanic-type basaltic melt intrusions precede continental rupture. Gondwana Res 54:150–160

Ligi M, Bonatti E, Rasul NMA (2015) Seafloor spreading initiation: geophysical and geochemical constraints from the Thetis and Nereus Deeps, Central Red Sea. In: Rasul NMA, Stewart ICF (eds) The Red Sea: the formation, morphology, oceanography and environment of a Young Ocean Basin. Springer, Berlin, Heidelberg, pp 79–98

Ligi M, Bonatti E, Bosworth W, Ronca S (2019) Oceanization starts at depth during continental rupturing in the northern Red Sea. In: Rasul NM, Stewart ICF (eds) Geological setting, palaeoenvironment and archaeology of the Red Sea. Springer, Berlin, pp 131–157

Mahmoud S, Reilinger R, McClusky S, Vernant P, Tealeb A (2005) GPS evidence for northward motion of the Sinai Block: implications for E, Mediterranean tectonics. Earth Planet Sci Lett 238:217–224

Melson WG, O'Hearn T, Jarosewich E (2002) A data brief on the Smithsonian Abyssal Volcanic Glass Data File. Geochem Geophys Geosyst 3:1525–2027

Mckenzie DP, Davies D, Molnar P (1970) Plate tectonics of the Red Sea and east Africa. Nature 226 (5242):243–248

Miller PM, Barakat H (1988) Geology of the Safaga Concession, northern Red Sea, Egypt. Tectonophysics 153:123–136

Mitchell NC, Park Y (2014) Nature of crust in the central Red Sea. Tectonophysics 628:123–139

Mitchell NC, Ligi M, Ferrante V, Bonatti E, Rutter E (2010) Submarine salt flows in the central Red Sea. Geol Soc Am Bull 122:701–713

Mitchell NC, Ligi M, Feldens P, Hubscher C (2017) Deformation of a young salt giant: regional topography of the Red Sea Miocene evaporates. Basin Res 29:352–369

Mitchell NC, Ligi M, Rasul NMA (2019) Variations in Plio-Pleistocene deposition in the Red Sea. In: Rasul NMA, Stewart ICF (eds) Geological setting, palaeoenvironment and archaeology of the Red Sea. Springer, Berlin, pp 323–339

Mohamed EK, Hassoup A, Elenean AKM, Othman AAA, Hamed DMK (2015) Earthquakes focal mechanism and stress field pattern in the northeastern part of Egypt. NRIAG J Astron Geophys 4:205–221

Mohriak WU (2015) Rift basins in the Red Sea and Gulf of Aden: analogies with the Southern South Atlantic. In: Post PJ, Coleman JL Jr, Rosen NC, Brown DE, Roberts-Ashby T, Kahn P, Rowan M (eds) 34th annual GCSSEPM foundation Perkins-Rosen research conference petroleum systems in "Rift" basins, 13–16 Dec 2015, Houston, CD-ROM, pp 789–826

Mohriak WU, Leroy S (2013) Architecture of rifted continental margins and break-up evolution: insights from the South Atlantic, North Atlantic and Red Sea–Gulf of Aden conjugate margins. In: Mohriak WU, Danforth A, Post PJ, Brown DE, Tari GC, Nemčok M, Sinha ST (eds) Conjugate divergent margins. Geological Society, London, Special Publications, vol 369, pp 497–535

Morag N, Haviv I, Eyal M, Kohn BP, Feinstein S (2019) Early flank uplift along the Suez Rift: implications for the role of mantle plumes and the onset of the Dead Sea transform. Earth Planet Sci Lett (in press)

Moretti I, Colletta B (1987) Spatial and temporal evolution of the Suez Rift subsidence. J Geodyn 7:151–168

Mougenot D, Al-Shakhis AA (1999) Depth imaging sub-salt structures: a case study in the Midyan Peninsula (Red Sea). GeoArabia 4:335–463

Moustafa AR (1997) Controls on the development and evolution of transfer zones: the influence of basement structure and sedimentary thickness in the Suez rift and Red Sea. J Struct Geol 19: 755–768

Nicolas A, Boudier F, Montigny R (1987) Structure of Zabargad Island and early rifting of the Red Sea. J Geophys Res 92:461–474

NOAA (2016) National Oceanic and Atmospheric Administration, National Centers for Environmental Information. World data service for geophysics—bathymetry and global relief grid extract. Grid extract. https://www.ngdc.noaa.gov/mgg/bathymetry/relief.html

Nyblade A, Park Y, Rodgers A, Al-Amri A (2006) Seismic structure of the Arabian Shield lithosphere and Red Sea margin. Mar Newsl 17:13–15

Omar GI, Steckler MS (1995) Fission track evidence on the initial rifting of the Red Sea: two pulses, no propagation. Science 270:1341–1344

Omar GI, Kohn BP, Lutz TM, Faul H (1987) The cooling history of Silurian to Cretaceous alkaline ring complexes, south Eastern Desert, Egypt, as revealed by fission-track analysis. Earth Planet Sci Lett 83:94–108

Omar GI, Steckler MS, Buck WR, Kohn BP (1989) Fission-track analysis of basement apatites at the western margin of the Gulf of Suez rift, Egypt: evidence for synchroneity of uplift and subsidence. Earth Planet Sci Lett 94:316–328

Orszag-Sperber F, Harwood G, Kendall A, Purser BH (1998) A review of the evaporites of the Red Sea-Gulf of Suez rift. In: Purser BH, Bosence DWJ (eds) Sedimentation and tectonics of rift basins: Red Sea-Gulf of Aden. Chapman and Hall, London, pp 409–426

Patton TL, Moustafa, AR, Nelson RA, Abdine SA (1994) Tectonic evolution and structural setting of the Suez Rift. In: Landon SM (ed) Interior rift basins, vol 59. American Association Petroleum Geologists Memoir, pp 7–55

Perry SK, Schamel S (1990) The role of low-angle normal faulting and isostatic response in the evolution of the Suez rift, Egypt. Tectonophysics 174:159–173

Phillips JD (1970) Magnetic anomalies in the Red Sea. Philos Trans R Soc Lond Ser A Math Phys Sci 267:205–217

Plaziat J-C, Montenat C, Barrier P, Janin M-C, Orszag-Sperber F, Philobbos E (1998) Stratigraphy of the Egyptian syn-rift deposits: correlations between axial and peripheral sequences of the north-western Red Sea and Gulf of Suez and their relations with tectonics and eustacy. In: Purser BH, Bosence DWJ (eds) Sedimentation and tectonics in rift basins–Red Sea–Gulf of Aden. Chapman and Hall, London, pp 211–222

Plaziat J-C, Reyss J-L, Choukri A, Cazala C (2008) Diagenetic rejuvenation of raised coral reefs and precision of dating. The contribution of the Red Sea reefs to the question of reliability of the Uranium-series datings of middle to late Pleistocene key reef-terraces of the world. Carnets de Géologie/Notebooks on Geology, Brest, Article 2008/04 (CG2008_A04)

Pujols EJ (2011) Temporal and thermal evolution of extensional faulting in the central Gulf of Suez and detrital zircon (U-Th)/He constraints on the thermo-tectonic Paleozoic and Mesozoic history of the Sinai, Egypt. University of Kansas, Master of Science Thesis, 247 p

Reilinger R, McClusky S, ArRajehi A (2015) Geodetic constraints on the geodynamic evolution of the Red sea. In: Rasul NMA, Stewart ICF (eds) The Red Sea: the formation, morphology, oceanography and environment of a young ocean basin. Springer Earth System Sciences, Berlin Heidelberg, pp 135–149

Richardson M, Arthur MA (1988) The Gulf of Suez–northern Red Sea Neogene rift: a quantitive basin analysis. Mar Pet Geol 5:247–270

Ries AC, Shackleton RM, Graham RH, Fitches WR (1983) Pan-African structures, ophiolites and mélange in the Eastem Desert of Egypt: a traverse at 26°N. J Geol Soc 140(1):75–95

Rogers JJW, Ghuma MA, Nagy RM, Greenberg JK, Fullagar PD (1978) Plutonism in Pan-African belts and the geologic evolution of northeastern Africa. Earth Planet Sci Lett 39(1):109–117

Röser HA (1975) A detailed magnetic survey of the southern Red Sea. Geol Jahrb 13:131–153

Roussel N, Purser BH, Orszag-Sperber F, Plaziat J-C, Soliman M, Al Haddad AA (1986) Géologie de la région de Qusier, Egypte. Documents et Travaux de l'Institut Géologique Albert de Lapparent, Paris 10:129–144

Said R (1961) Tectonic framework of Egypt and its influence on distribution of foraminifera. AAPG Bull 45:198–218

Said R (1962) The geology of Egypt. Elsevier, Amsterdam, p 377

Said R (1990) Chapter 24. Cenozoic. In: Said R (ed) The geology of Egypt. A.A. Balkema, Rotterdam, pp 451–486

Salamon A, Hofstetter A, Garfunkel Z, Ron H (2003) Seismotectonics of the Sinai Subplate; the eastern Mediterranean region. Geophys J Int 155:149–173

Samuel MD, Saleeb-Roufaiel GS (1977) Lithostratigraphy and petrography of the Neogene sediments at Abu Ghusun, Um Mahara, Red Sea coast, Egypt. Beitrage zur Lithologi, Freiburg Forsch 323:47–56

Scholz CH (1968) The frequency-magnitude relation of microfracturing in rock and its relation to earthquakes. Bull Seismol Soc Am 58:399–415

Searle RC, Ross DA (1975) A geophysical study of the Red Sea axial trough between 20.5° and 22°N. Geophys J Roy Astron Soc 43:555–572

Şengör AMC, Burke K (1978) Relative timing of rifting on earth and its tectonic implications. Geophys Res Lett 5:419–421

Shi Y, Bolt BA (1982) The standard error of the magnitude-frequency b value. Bull Seismol Soc Am 72:1677–1687

Shukri NM (1944) On the geology of the Brothers Islets-Northern Red Sea. Bull Fac Sci Cairo Univ 25:175–196

Sinadinovski C, Aldamegh K, Ball P, Janoubi E, Afifi AK, Ion D, Nayak G, Borsato R (2017) Passive seismic experiment to understand the basement and crustal structure, Northern Red Sea. EGU General Assembly 2017. Geophys Res 19. EGU2017–5986 (Abstracts)

Steckler MS, Berthelot F, Lyberis N, Le Pichon X (1988) Subsidence in the Gulf of Suez: implications for rifting and plate kinematics. Tectonophysics 153:249–270

Stern RJ (1979) Late precambrian ensimatic volcanism in the central eastern desert of Egypt [Ph.D. thesis]. San Diego, University of California, 210 p

Stern RJ (1981) Petrogenesis and tectonic setting of late Precambrian ensimatic volcanic rocks, central eastern desert of Egypt. Precambr Res 16(3):195–230

Stern RJ, Gottfried D, Hedge CE (1984) Late Precambrian rifting and crustal evolution in the Northeastern Desert of Egypt. Geology 12:168–172

Stern RJ, Hedge CE (1985) Geochronologic and isotopic constraints on Late Precambrian crustal evolution in the Eastern Desert of Egypt. Am J Sci 285:97–127

Stockli DF (2005) Application of low-temperature thermochronometry to extensional tectonic settings. Rev Mineral Geochem 58(1):411–448

Stockli DF (2009) Tectonic evolution of the Tethyan margin of Gondwana from NE Africa to the Zagros and its ramifications for the Zagros collision-a detrital zircon (U-Th)/He thermochronometry perspective. Geol Soc Am Annu Mtg. Portland (abstracts)

Stockli DF, Bosworth W (2019) Timing of extensional faulting along the magma-poor central and northern Red Sea rift margin—transition from regional extension to necking along a hyperextended rifted margin. In: Rasul NM, Stewart ICF (eds) Geological setting, palaeoenvironment and archaeology of the Red Sea. Springer, Berlin, pp 81–111

Sturchio NC, Sultan M, Batiza R (1983) Geology and origin of Meatiq Dome, Egypt: a precambrian metamorphic core complex? Geology 11(2):72

Suess E (1891) Die Brüche des östlichen Afrika. In: Beitrage zur geologischen Kentniss des östlichen Afrika. Denkscri*f*ten Kaiserlichen Akademie der Wissensha*f*ten, Wien, Mathematisch-Naturwiseen Klasse 58:555–584

Sultan M, Arvidson RE, Duncan IJ, Stern RJ, El Kaliouby B (1988) Extension of the Najd shear system from Saudi Arabia to the central eastern desert of Egypt based on integrated field and LANDSAT observations. Tectonics 7(6):1291–1306

Szymanski E, Stockli DF, Johnson PR, Hager C (2016) Thermochronometric evidence for diffuse extension and two-phase rifting within the Central Arabian Margin of the Red Sea Rift. Tectonics 35:2863–2895

Tang Z, Julià J, Zahran H, Mai PM (2016) The lithospheric shear-wave velocity structure of Saudi Arabia: young volcanism in an old shield. Tectonophysics 680:8–27

Taviani M (1998) Post-Miocene reef faunas of the Red Sea: glacio-eustatic controls. In: Purser BH, Bosence DWJ (eds) Sedimentation and tectonics in rift basins: Red Sea-Gulf of Aden. Chapman and Hall, London, pp 574–582

Tewfik N, Ayyad M (1984) Petroleum exploration in the Red Sea shelf of Egypt. In: Proceedings of the 6th exploration seminar. Egyptian General Petroleum Corporation and Egypt Petroleum Exploration Society, Mar 1982, Cairo, vol 1, pp 159–180

Thybo H, Nielsen CA (2009) Magma-compensated crustal thinning in continental rift zones. Nature 457:873–876

Tinti S, Mulargia F (1987) Confidence intervals of *b*-values for grouped magnitudes. Bull Seismol Soc Am 77:2125–2134

Utsu T (1965) A method for determining the value of *b* in the formula log*N* = *a*-*bM* showing the magnitude-frequency relation for earthquakes. Geophys Bull Hokkaido Univ 13:99–103

Vermeesch P (2012) On the visualization of detrital age distributions, pp 1–6. http://www.ucl.ac.uk/∼ucfbpve/papers/VermeeschChemGeol2012/

Vermeesch P, Avigad D, McWilliams MO (2009) 500 my of thermal history elucidated by multi-method detrital thermochronology of North Gondwana Cambrian sandstone (Eilat area, Israel). Geol Soc Am Bull 121:1204–1216

Voggenreiter W, Hötzl H, Mechie J (1988) Low-angle detachment origin for the Red Sea Rift system? Tectonophysics 150:51–75

Volker F, McCulloch MT (1993) Submarine basalts from the Red Sea: New Pb, Sr, and Nd isotopic data. Geophys Res Lett 20:927–930

Volker F, McCulloch MT, Altherr R (1993) Submarine basalts from the Red Sea: New Pb, Sr, and Nd isotopic data. Geophys Res Lett 20 (10):927–930

Waite GP, Smith RB (2002) Seismic evidence for fluid migration accompanying subsidence of the Yellowstone caldera. J Geophys Res 107(2177):1–15

Weaver BL (1991) The origin of ocean island end-member compositions: trace element and isotopic constraints. Earth Planet Sci Lett 104:381–397

Winn RD Jr, Crevello PD, Bosworth W (2001) Lower Miocene Nukhul Formation of Gebel el Zeit, Egypt: sedimentation and structural movement during early Gulf of Suez rifting. AAPG Bull 85:1871–1890

Workman RK, Hart SR (2005) Major and trace element composition of the depleted MORB mantle (DMM). Earth Planet Sci Lett 231: 53–72

Wyss M (1973) Towards a physical understanding of the earthquake frequency distribution. Geophys J R Astr Soc 31:341–359

Yadav RBS, Tripathi JN, Shanker D, Rastogi BK, Das MC, Kumar V (2011) Probabilities for the occurrences of medium to large earthquakes in northeast India and adjoining region. Nat Hazards 56:145–167

Younes AI, McClay KR (2002) Development of accommodation zones in the Gulf of Suez-Red Sea rift, Egypt. Am Assoc Pet Geol Bull 86:1003–1026

Youssef MI (1957) Upper Cretaceous rocks in Kosseir area. Bull Inst Desert Egypte 7:35–54

Seismicity, Seismotectonics and Neotectonics in Egypt

10

Abd El-Aziz Khairy Abd El-Aal, Wael Hagag, Kamal Sakr, and Mohamed Saleh

Contents

Abstract

This chapter included four parts, which cover seismicity, seismotectonic and neotectonics in Egypt. The first part includes a historical review in earthquakes and a survey the seismotectonic zones in Egypt. The second parts considered the application of EMR data in detecting seismotectonic zones in Egypt. The third part describes the role of GPS measurements in seismological study in Egypt. The last part of the chapter considers the applications of InSAR data in ground deformation monitoring in Egypt.

A. E.-A. K. Abd El-Aal (✉)
Kuwait Institute for Scientific Research, Safat, Kuwait
e-mail: deawky@nriag.sci.eg; dewaky@yahoo.com

A. E.-A. K. Abd El-Aal · K. Sakr · M. Saleh
National Research Institute of Astronomy and Geophysics, Cairo, Egypt
e-mail: sakr_kamal@yahoo.com

W. Hagag
Faculty of Science, Geology Department, Benha University, 13518 Benha, Egypt

Z. Hamimi et al. (eds.), *The Geology of Egypt*, Regional Geology Reviews,
https://doi.org/10.1007/978-3-030-15265-9_10

10.1 Historical Earthquakes and Seismotectonic Zones in Egypt

Abd El-Aziz Khairy Abd El-Aal

10.1.1 Introduction

Egypt is situated in the north eastern corner of Africa within a sensitive seismotectonic location. Earthquakes are concentrated along the active tectonic boundaries of African, Eurasian and Arabian plates. It is bounded by three active tectonic plate margins: the African Eurasian plate margin; the Red Sea plate margin; the Levant transform fault (Fig. 10.1). The present day tectonic deformation within Egypt is related to the regional tectonic forces and its local tectonics. The African plate converges with the Eurasian plate along the subduction zone, while it diverges from the Arabian plate along the Red Sea floor spreading system. The northern Red Sea is branching into the Gulfs of Suez and Aqaba at the triple junction point. These gulfs are characterized by a complex structural pattern and the presence of earthquake swarms. Local inland seismic sources are also affecting the seismicity of Egypt.

With the beginning of the last century, the earthquake activity and seismic hazard in and around Egypt were mainly studied by many authors, (Sieberg 1932; Ismail 1960; Gergawi and El-Khashab 1968; Maamoun and Ibrahim 1978; Maamoun and Allam 1980; Maamoun et al. 1984; Albert 1987; Kebeasy 1990; Abou Elenean 1997; Deif 1998; Abd El-Aal 2010a, b) to delineate the seismotectonic zones. In these studies, the seismicity maps are approached based on the regional geological structures. They detected many seismic trends in and around Egypt are characterized by high seismic activities, which are reported to be concentrated mainly in six seismotectonic zones or trends. These seismic zones are documented as follow:

1. Mediterranean Coastal Dislocation.
2. Northern Red Sea-Gulf of Suez-Cairo.
3. Gulf of Aqaba-Dead Sea.
4. Red Sea Rifting.
5. Induced seismicity around Nasr Lake (Aswan).

In this section, the light will be thrown in details in the seismicity, seismotectonic zones and seismic trends affecting Egypt.

10.1.2 Historical Seismicity

Many authors along the entire history of the seismic recording studied historical seismicity of Egypt. So, Egypt is considered one of the few regions in the world where evidence for historical earthquake activity have been recorded during the past 4800 years. Figure 10.2 shows the spatial distribution of the historical events (before 1900). The historical seismic data are collected from Ambraseys (1961), Ambraseys et al. (1961, 1994), Kebeasy (1990), Maamoun et al. (1984), Poirier and Taher (1980) and list in Table 1. The historical earthquake distribution reflects to some extent the seismic sources that might affect Egypt. According to Ambraseys et al. (1994), the historical events were classified into three categories according to their intensities. Felt to strong earthquakes up to VI MSK, strong to damaging earthquakes from VI to VII MSK, and damaging to destructive from VII to IX MSK.

The information on historical earthquakes is documented in the annals of ancient Egyptian history and Arabic literature. The scientist As-Souty's work which so-called "Kashf El-Salsala fi wasf El-Zalzala" contains a list of earthquakes for the period between 712AD to 1499AD that was translated into English by Springer in 1843 from Arabic manuscript of the National Library at Paris. According to Sieberg (1932), Ambraseys (1961), Ambraseys et al. (1994), Karnik (1969), Maamoun (1979), Ibrahim and Marzouk (1979), Poirier and Taher (1980), Savage (1984) and Kebeasy 1990) many events were reported to have occurred in and around Egypt (Fig. 10.2). The description of a few major earthquakes will be given in the following paragraphs.

2000 BC Sharquia Province Earthquake

Tokuji (1989) postulated that this earthquake is located at 30.75 N and 31.50 E. It caused deep fissures and soil cracks in Tell Basta. The maximum intensity was VII near Tell Basta and Abu Hammad, about 16-km east-south of Zagazig City.

19 April 995 BC Cairo

According to Ambraseys et al. (1961), this earthquake was felt in Cairo and Alexandria. This earthquake shook Egypt for three hours and caused great damage. The intensity of this shock reached to VII in Alexandria.

14 October 520

A strong earthquake was felt in Egypt shaking buildings for a long time, (Ambraseys 1961). The correct identification of this earthquake is problematic. A later report mentions that many cities and villages were swallowed up.

7 April 857

Ambraseys (1961) pointed that a damaging earthquake occurred in Egypt. The shock was widely felt shacking walls of mosques and destroying mosques and houses. There are no further details on this event.

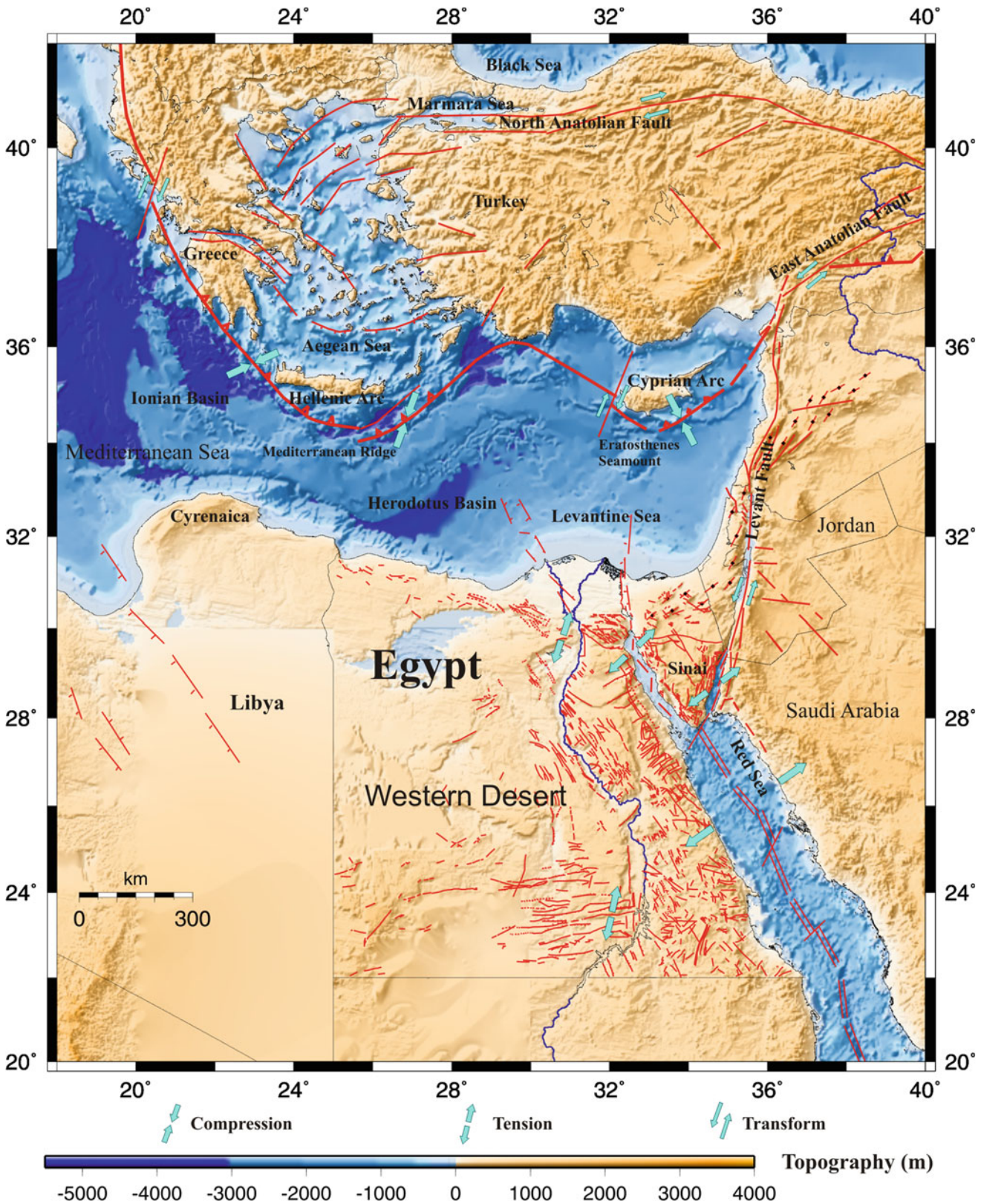

Fig. 10.1 Regional tectonic setting of the East Mediterranean region (map compiled from Abou Elenean 1997; Reilinger et al. 2000; Egyptian Geological Survey Authority 1981; and Salamon et al. 1996)

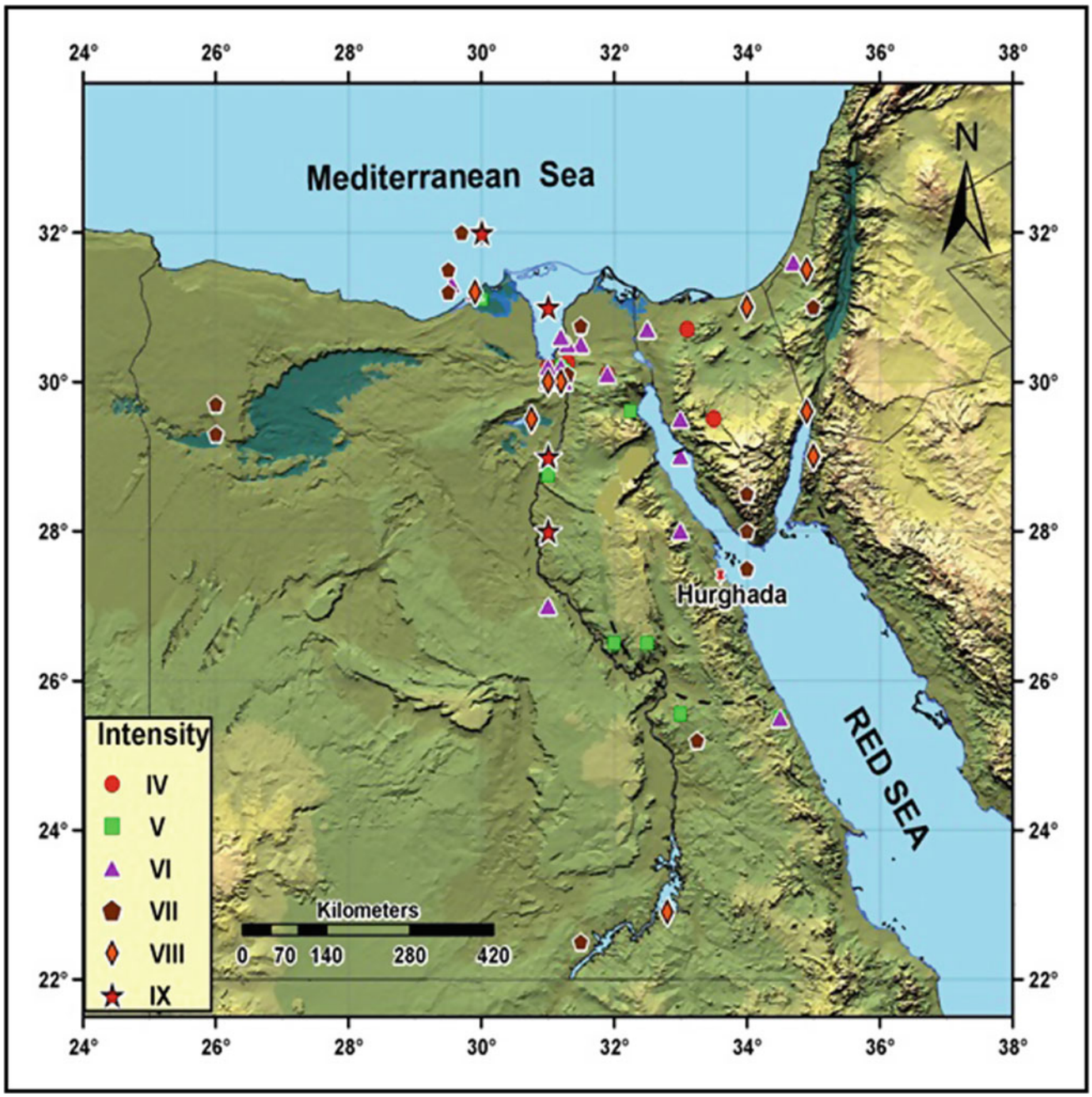

Fig. 10.2 The historical earthquakes in Egypt which occurred before the advent of the seismograph, in the period from 2200 B.C. till A.D. 1899 and compiled by Maamoun et al. (1984) and Ambraseys et al. (1994)

November–December 885

A strong earthquake in Egypt destroyed houses and the Friday mosque (i.e. the Mosque of Amr) in Misr Fustat, (Ambraseys et al. 1994). At least 1000 people were killed. The epicenter of this earthquake occurred near Lower Egypt.

4 October 935

According to Poirier and Taher (1980), a destructive earthquake with an epicenter located near Egypt was occurred. The shock was damaging in Old Cairo specifically or Egypt generally.

Table 1 Historical earthquakes and their parameters

long	lat	year	date	I MMI	Mag	Qe	Qd	Ql	Referance
21.6	23.7	262		7		Good	Good	Fair	Sieberg (1932); Ambraseys et al. (1994)
30	31.5	320		7		Good	Good	Good	Ambraseys et al. (1994)
23.6	35.25	365	12 July		7.5-8	Good	Good	Good	Ambraseys et al. (1994); Papadimetrio (2008)
31	31	520	14 Oct	7		Fair	Poor	Poor	Sieberg (1932); Ambraseys et al. (1994)
26	36	796	14 April	7		Good	Poor	Poor	Ambraseys et al. (1994); Guidoboni et al. (1994)
31	30	857	April	4		Good	Good	Fair	Ambraseys et al. (1994); Guidoboni et al. (1994)
31.2	30.1	885	Nov	7		Good	Good	Good	Ambraseys et al. (1994); Guidoboni et al. (1994)
31	30	912		7		Good	Good	Good	Ambraseys et al. (1994); Guidoboni et al. (1994)
31.2	30.5	935	4 Oct	8		Good	Good	Good	Ambraseys et al. (1994); Guidoboni et al. (1994)
31.2	30.2	950	25 July	6		Good	Good	Good	Ambraseys et al. (1994); Guidoboni et al. (1994)
30	32	951	15 Sept	7		Good	Good	Good	Ambraseys et al. (1994); Guidoboni et al. (1994)
32	34	956	1 Jan	8		Good	Good	Good	Ambraseys et al. (1994); Guidoboni et al. (1994)
26	35	963	12 May			Good	Good	Fair	Ambraseys et al. (1994); Guidoboni et al. (1994)
35	29.5	1068	18 March	8		Good	Good	Fair	Ambraseys et al. (1994)
34	28	1091	12 Feb	4		Good	Good	Good	Ambraseys et al. (1994)
31.15	30.03	1111	31 Aug	7		Good	Good	Good	Ambraseys et al. (1994)
32.5	34.5	1222	11 May			Fair	Fair	Fair	Ambraseys et al. (1994)
31	30	1259	6 Jun	8		Good	Fair	Good	Ambraseys et al. (1994)
31	30	1264	20 Feb	7		Good	Good	Fair	Ambraseys et al. (1994)
30.5	29.5	1299	8 Jan	7		Fair	Fair	Fair	Ambraseys et al. (1994)
28.5	34.5	1303	8 Aug	8	Mw=7.3	Good	Good	Good	Ambraseys et al. (1994)
31	30.2	1307	10 Aug	6		Good	Good	Good	Ambraseys et al. (1994)
31.2	30.5	1313	27 Feb	5		Good	Good	Good	Ambraseys et al. (1994)
31	30	1335	29 May	6		Good	Good	Good	Ambraseys et al. (1994)
31.2	30	1347	8 Dec			Good	Good	Good	Ambraseys et al. (1994); Poirier and Taher (1980)
28	35	1353	16 Oct	6		Good	Good	Fair	Ambraseys et al. (1994); Poirier and Taher (1980)
31.5	30.2	1373	19 Oct	6		Good	Good	Good	Ambraseys et al. (1994)
31	30.5	1385	19 Sept	7		Good	Good	Good	Ambraseys et al. (1994)
31.2	30.2	1386	17 July	4		Good	Good	Good	Ambraseys et al. (1994)
31.2	30	1422	28 Jan	4		Good	Good	Good	Ambraseys et al. (1994)
33.5	29.5	1425	23 Jun	6		Good	Good	Fair	Ambraseys et al. (1994)
31	30	1433	14 Dec	4		Good	Good	Good	Ambraseys et al. (1994)
31.2	30	1434	6 Nov	7		Good	Good	Good	Ambraseys et al. (1994)
28	35	1438	25 Feb			Good	Good	Good	Ambraseys et al. (1994)
31.2	30.5	1455	5 March	5		Good	Good	Good	Ambraseys et al. (1994)
31	30	1467	15 Dec	5		Good	Good	Good	Ambraseys et al. (1994)
31.2	30.2	1476	1 Nov	5		Good	Good	Good	Ambraseys et al. (1994)
30	35	1481	18 Mar			Good	Good	Fair	Ambraseys et al. (1994); Poirier and Taher (1980)
31.2	30.1	1483	15 Jun	5		Good	Good	Good	Ambraseys et al. (1994)
31.2	30.5	1486	11 Oct	5		Good	Good	Good	Ambraseys et al. (1994)
32	35	1491	24 Apr			Good	Good	Fair	Ambraseys et al. (1994)
31.2	30	1498	16 Oct	5		Good	Good	Good	Ambraseys et al. (1994)

(continued)

Table 1 (continued)

long	lat	year	date	I MMI	Mag	Qe	Qd	Ql	Referance
23	36	1500	24 July			Good	Good	Poor	Ambraseys et al. (1994); Poirier and Taher (1980)
31.25	30.15	1502	17 Nov	6		Fair	Fair	Fair	Ambraseys et al. (1994)
27	35	1508	29 May			Fair	Fair	Fair	Ambraseys et al. (1994)
27	35	1509	April			Fair	Fair	Fair	Ambraseys et al. (1994)
31.2	30	1513	28 March	5		Good	Good	Good	Ambraseys et al. (1994)
31.3	30.25	1523	4 April	5		Good	Good	Good	Ambraseys et al. (1994)
31.2	30.15	1525	9 March	5		Good	Good	Good	Ambraseys et al. (1994)
31.2	30	1527	14 July	5		Good	Good	Good	Ambraseys et al. (1994)
31.5	30.15	1529	12 Nov	5		Good	Good	Good	Ambraseys et al. (1994)
31.25	30.2	1532	10 July	4		Good	Good	Good	Ambraseys et al. (1994)
31.2	30.1	1534	23 March	5		Good	Good	Good	Ambraseys et al. (1994)
24	32	1537	8 Jan			Good	Good	Poor	Ambraseys et al. (1994)
32	32	1537				Good	Poor	Fair	Ambraseys et al. (1994)
25.5	36.5	1573	4 Feb			Good	Good	Fair	Ambraseys et al. (1994); Poirier and Taher (1980)
31.5	30	1576	1 Apr	7		Good	Good	Good	Ambraseys et al. (1994)
31.5	29.5	1588	7 April	5	Mf=4.7	Good	Good	Good	Ambraseys et al. (1994); Poirier and Taher (1980); Badawy (1998)
21	37	1592	May			Good	Good	Fair	Ambraseys et al. (1994)
28	35	1609				Good	Good	Fair	Ambraseys et al. (1994)
27	35	1613	Jun			Good	Good	Fair	Ambraseys et al. (1994); Poirier and Taher (1980)
21	37	1633	5 Nov			Good	Good	Fair	Ambraseys et al. (1994)
25	35	1664	20 Nov			Good	Good	Fair	Ambraseys et al. (1994)
31	29	1694	12 Dec			Good	Good	Fair	Ambraseys et al. (1994)
30	32	1698	2 Oct	6	Mf=6	Good	Good	Good	Ambraseys et al. (1994); Poirier and Taher (1980)
33.25	29.3	1710	27 Aug	6		Good	Good	Fair	Ambraseys et al. (1994)
28	35	1741	31 Jan			Good	Good	Fair	Ambraseys et al. (1994)
32.25	29.6	1754	18 Oct	5	Ms=5.4	Good	Good	Good	Ambraseys et al. (1994); Poirier and Taher (1980)
23	36	1756	13 Feb			Good	Good	Fair	Ambraseys et al. (1994)
32.1	26.2	1778	22 Jun	5	Ms=5.4	Good	Good	Good	Ambraseys et al. (1994); Poirier and Taher (1980)
25	35	1790	26 May			Good	Good	Fair	Ambraseys et al. (1994)
31.2	30	1801	10 Oct	5		Good	Good	Good	Ambraseys et al. (1994)
24	36	1805	3 July			Good	Good	Good	Ambraseys et al. (1994)
23	36	1810	17 Feb			Good	Good	Good	Ambraseys et al. (1994)
33	29	1814	27 Jun	7		Good	Good	Good	Ambraseys et al. (1994)
31	30.15	1825	21 Jun	5		Good	Good	Good	Ambraseys et al. (1994)
34	28.5	1839				Fair	Fair	Fair	Ambraseys et al. (1994)
25	35	1846	28 March	5		Good	Good	Good	Ambraseys et al. (1994)
31	30	1846	15 Jun	5		Good	Good	Good	Ambraseys et al. (1994)
30.75	29.5	1847	7 Aug	8	Mf=5.8	Good	Good	Good	Ambraseys et al. (1994)
31.25	30.15	1849	23 July	5		Good	Good	Good	Ambraseys et al. (1994)
31	27	1850	27 Oct	6		Good	Good	Good	Ambraseys et al. (1994)

(continued)

Table 1 (continued)

long	lat	year	date	I MMI	Mag	Qe	Qd	Ql	Referance
28	36	1851	3 April			Good	Good	Good	Ambraseys et al. (1994)
26	35.5	1856	12 Oct			Good	Good	Good	Ambraseys et al. (1994)
31.2	30	1858	30 Dec	5		Good	Good	Good	Ambraseys et al. (1994)
28	36.5	1863	22 April			Good	Good	Fair	Ambraseys et al. (1994)
30	31.1	1865	11 April	5		Good	Good	Fair	Ambraseys et al. (1994)
33	32	1868	20 Feb	5		Good	Good	Good	Ambraseys et al. (1994)
29.5	34.5	1870	24 Jun	7		Good	Good	Good	Ambraseys et al. (1994)
33	32.5	1873	12 Jan	7		Good	Good	Fair	Ambraseys et al. (1994)
33	29	1879	11 July	6	Mf=5.9	Good	Good	Good	Ambraseys et al. (1994)
23.5	36	1886	27 Aug	6		Good	Good	Fair	Ambraseys et al. (1994)
31.2	30.15	1886	17 Nov	5		Good	Good	Good	Ambraseys et al. (1994)
26	36	1887	17 July			Good	Good	Good	Ambraseys et al. (1994)
31.25	30.1	1895	7 Dec	5		Good	Good	Good	Ambraseys et al. (1994)

5 January 956

Ambraseys et al. (1994) postulated that a large offshore earthquake that was felt in Syria and Egypt, where the shock was of long duration and caused the collapse of the upper 22 meters of the lighthouse in Alexandria.

31 August 1111

According to Ambraseys et al. (1994), a damaging earthquake in Lower Egypt affected Cairo and Fustat was happened. It was felt throughout the country.

20 February 1264

Few reports of the event are available. Al-Suyuti stated that the earthquake occurred in Egypt. Ambraseys et al. (1994) suggested that the event destroyed houses in a number of places.

8 August 1303

This earthquake was located in the Hellenic Arc. Damage extended along the eastern Mediterranean coast from Cyprus to Palestine and Lower Egypt and it was strongly felt in North Africa. According to Ambraseys et al. (1994), the earthquake was strongest in Alexandria where many houses were ruined and much of the city walls were destroyed, killing a number of people. The shock destroyed two villages in the Sharqiyya. The shock was felt throughout Lower Egypt. In Cairo all the houses were damaged, the earthquake caused panic and women ran into the streets without their veils.

On the other hand, Sieberg (1932) located the epicentral region of this earthquake in Fayoum; area associates the event with faulting in the region. In the Nile valley, ground movements were so severe that boats sailing on the river were cast on dry land.

7 April 1588

This earthquake was felt in Cairo. The epicenter of the shock was located at Batnun to the east of Atfih. In the Muqattam hills, three fissures opened.

September or October 1754

Ambraseys et al. (1994) suggested that this destructive earthquake occurred in Egypt. It was affected Cairo particularly Qarafa, Bulaq and part of new Cairo. But according to Maamoun (1979), this destructive earthquake had the maximum intensity was VIII at Gharbiya province and VII in the Nile Delta and Cairo.

7 August 1847

A strong earthquake shook Lower Egypt causing widespread damage to local houses and a number of public buildings. This shock is very strong and was felt as far as Asyiut in the south and Gaza and Jerusalem in the northeast. The epicenter of this shock was located at El-Fayoum area. In Cairo, the event continued for about a minute, causing panic and considerable damage (Ambraseys et al. 1994).

The shock affected the whole buildings in the area surrounding the epicenter. In Al-Azbakiyya, 14 houses partly collapsed and in the Bab Al-Shariyya, 7 houses and one mosque were damaged. In Al-Jamaliyya, three walls collapsed but in the Bab Al-Khalq, 8 columns of the mosque of Al-Muayyad were destroyed.

Outside Cairo, damages extended from Ashmun in the north to Faiyum and Beni Suef in the south. The total damage was recorded from Cairo to Beni Suef due to this shock was 2987 houses, 42 mosques, and 45 pigeon towers damaged or destroyed, and 37 men, 48 women and 56 animals killed. Minor sporadic damage was occurred in

Madinat El-Fayoum and Beni Suef. The event was strongly felt throughout the Nile Delta where in Alexandria the shock stayed about 35 s.

According to Kebeasy et al. (1981), the epicenter of the shock was near El-Fayoum and its intensity was VIII. An aftershock was strongly felt in Cairo and Alexandria on the morning of 10 August 1847, but it caused no damage. Sieberg (1932) provided a little evidence support that the aftershocks of this earthquake causes damage and he reported that in the area between Cairo and Assuit another 1000 houses and 27 mosques were destroyed and 25 people killed.

10.1.3 Instrumental Seismicity

Concerning recent seismic activity in Egypt, the earthquakes recording started since 1899 with Helwan Station. Since this time Helwan Seismological Station is in active operation. In late 1975 three other stations were added at Aswan, Abu-Simbil and Mersa Matrouh. On the other hand, a radio-telemetry network of nine vertical short period stations was operated in July 1982 for recording microearthquake activity in and around the northern part of Nasser Lake. The stations of this network were increased to thirteen stations in 1983. Sometime errors in the epicenter location of moderate and large earthquakes may be occurred due to the non-uniform distribution of teleseismic stations, as well as local heterogeneity (Kebeasy 1990). The homogeneity of earthquake data is investigated by Maamoun et al. (1984) who found that information of all earthquakes of magnitude equal to or larger than 5.0 are complete during the period from 1906 to 1981. After 12 October 1992 earthquake, the Egyptian Government commissioned the National Research Institute of Astronomy and Geophysics to organize and construct Egyptian National Seismological Network (ENSN) in an attempt to minimize earthquake damages and anticipate the future safe development of big strategic projects.

10.1.3.1 Egyptian National Seismological Network

As a result of the damage caused by 12 October 1992 earthquake which led to 561 deaths, injured 9832 and left a damage of more than 35 million U$, the Egyptian Government gave order to National Research Institute of Astronomy and Geophysics to install the seismological network and strong motion network. The targets of these networks are protecting strategic buildings, new cities, and high dams and monitoring local and regional seismic activity. The ENSN includes 71 seismic stations distributed in the surface area of Egypt and also involve one main center at Helwan City and five sub-center at Burg El-Arab, Hurghada, Mersa Alam, Aswan and Kharga, (Fig. 10.3). The sub-centers are connected recently to the main center using satellite communication.

The digital data are extracted online from the remote stations telemetry, and via satellite stations by seismic data analysis software (Atlas program). The received data are analyzed to calculate the earthquake parameters and the location of epicenter. Since 1996, the National Research Institute of Astronomy and Geophysics has installed strong motion instruments model IDS-3602A-16 Bit-Digital Accelerographs and Nanometrics Titan Accelerograph at different sites distributed all over Egypt.

10.1.3.2 Plate Margins Around Egypt

The African-Eurasian Plate Margin

The African and Eurasian plates are converging across a wide zone in the northern Mediterranean Sea. The effects of the plate interaction are mainly north and remote from the Egyptian coastal margin. Some secondary deformation appears to be occurring along the northern Egyptian coast as represented by moderate earthquake activity. The earthquake activity (Fig. 10.4) is contained in a belt parallel to the Hellenic and Cyprean arcs. Some of the largest events that located to the south of Crete and Cyprus islands were felt and caused few damages on the northern part of Egypt (e.g. August 8, 1303; February 13, 1756; June 26, 1926, and October 9, 1996).

Red Sea Plate Margin

The earthquake activity in that region is related to plutonic activity, Red Sea rifting and the intersection points of the NW (Gulf of Suez-Red Sea faults) with the NE Levant-Aqaba faults. The extension of this deformation zone toward the north (Suez-Cairo shear zone) considered as the most active part on northern Egypt. Recently, some evidence of an extension of Suez-Cairo-Alexandria shear zone to the north towards Mediterranean Sea were appeared (Kebeasy et al. 1981; Ben-Avraham 1978, 1985; and Abou Elenean 1997). The larger earthquakes along this zone caused some damage to the northern part of Egypt (such as July 11, 1879; and March 6, 1900 “Gulf of Suez”; and March 31, 1969 “Shadwan island”).

Levant Transform Fault

The seismic activity of this region is relatively high and appeared to be clustered on some places at which there is intersection of two or more tectonic faults (NE-SW and NW-SE) or attributed to upwelling of magma. The larger events, which were reported and caused damage in northern Egypt, are March 18, 1068; May 20, 1202; and November

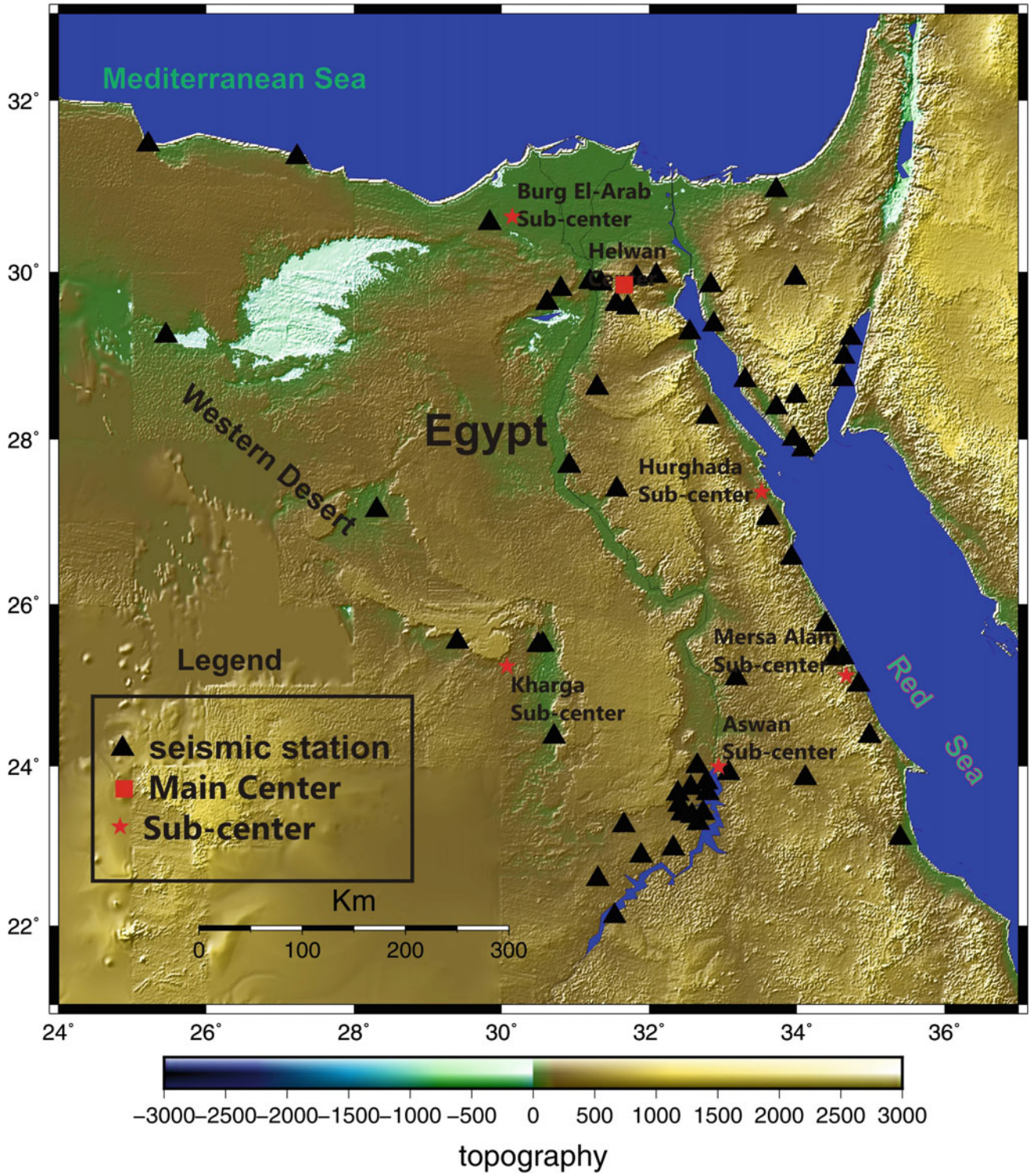

Fig. 10.3 Distribution of Egyptian national seismic network

22, 1995. The distribution of epicenters of instrumentally recorded earthquakes shows that all the earthquakes were occurred along main seismic trends. The earthquake data are collected from Gergawi and El-Khashab (1968), Maamoun and Ibrahim (1978), Maamoun (1979), Maamoun and Allam (1980), Maamoun et al. (1984), Kebeasy (1990), Ambraseys et al. (1994), International Seismological Center (ISC), and ENSN.

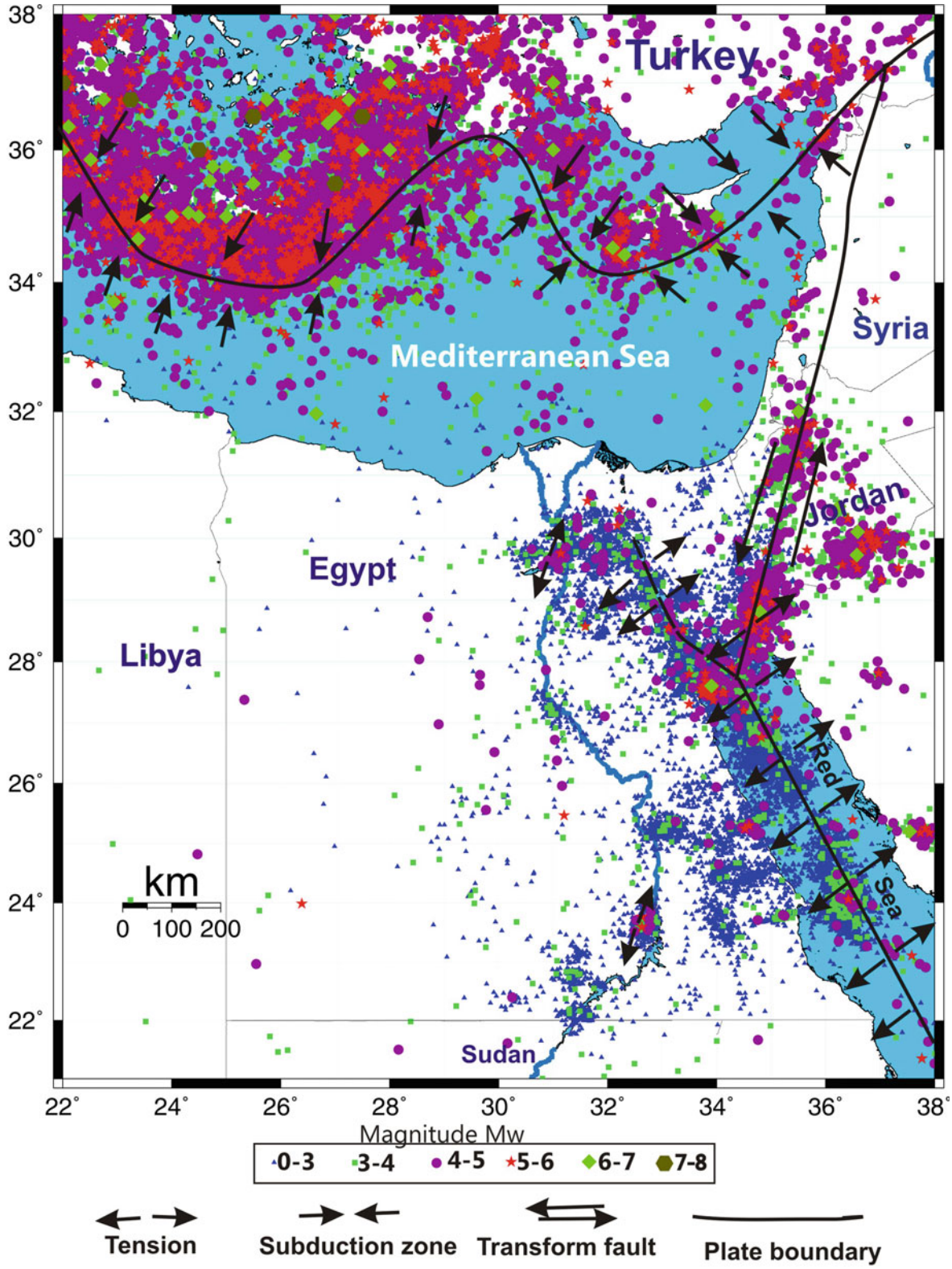

Fig. 10.4 The figure shows main tectonic boundaries around Egypt. Distribution of seismic activity from 1900 to 2014. The earthquakes data used in this map includes an update earthquake catalogue compiles from many sources, Egyptian National Seismological Network bulletins (www.nriag.sci.eg), Mamoun et al. 1984, International Seismological Center Bulletin (ISC) (http://www.isc.ac.uk/), European Mediterranean Seismological center (EMSC) (http://www.emsc-csem.org), Preliminary Determination of Epicenters, online bulletin provided by the National Earthquake Information Center (NEIC) (http://earthquake.usgs.gov/earthquakes/)

10.1.3.3 Seismic Sources in and Around Egypt

Mediterranean Coastal Dislocation Trend

This zone includes the seismic active region of the Egyptian Mediterranean coast. The activity of this trend is attributed to the continental shelf and the deep faults parallel to the coast. This trend begins from Cyrenacia (Libya) in the west to Alexandria and then northeastward to Beirut Bay. It is parallel to the continental margin. Ben-Avraham (1978) suggested that the crustal structure played an important role in controlling the slip rate at trenches, causing an active faulting at the passive margins and affecting the seismic pattern at the subduction zones. On the other hand, the author indicated that the disturbance of the subduction process causes some motion between the African plate and the plates to the north. This is taken as intra-deformation within the African plate in the form of active faulting along its northern continental margin. Also, the author supposed that this faulting could absorb some of the motion between the plates.

The region of this belt is distinguished by a various number of earthquakes recording systems. The information about the tectonics and geological structures of this offshore area are very few, thus no seismogenic source delineation could be made, based on the geological or seismological evidences.

Northern Red Sea-Gulf of Suez-Cairo Trend

Kebeasy (1990) stated that this trend is the major active trend in Egypt and extends along the northern Red Sea, Gulf of Suez, Cairo and Alexandria and extends along the northwest in the Mediterranean Sea. This Trend is characterized by the occurrences of shallow, micro, small, moderate and large earthquakes. The activity along this trend is mainly attributed to the Red Sea rifting, as well as several active faults. So, the seismic activity of this rift is associated with the deep axial trough in its central and southern parts. The seismic activity is migrated northerly toward the region of Jubal island at the entrance of the Gulf of Suez, where the activity tends to follow the two different structural trends of the Aqaba-Levant zone and the Gulf of Suez zone. It is clear that the high rate of seismicity in the southern end of the Gulf of Suez is related to the crustal movements among the Arabian plate, African plate and the Sinai subplate, as a result of the opening of the Red Sea extension in the Gulf of Suez and the left-lateral strike-slip motion of the Gulf of Aqaba (Fig. 10.6) (Fig. 10.5).

Daggett et al. (1986) indicated that although the southern end of the Gulf of Suez is seismically active, the activity does not extend along the length of the gulf. So there is a seismic gab in the Gulf of Suez. Maamoun and Allam (1980) stated that the distribution of earthquake epicenters in Nile, just in the front of the mouth of Alexandria Canyon may indicate that the course of the canyon is mainly affected by faulting extends in NW-SE direction. Sofratome Group (1984) demonstrated the possibility that the Cairo-Alexandria fault zone absorbs the main effects of internal deformation in the northeastern corner of Africa. This fault zone separates two different tectonic regimes, particularly in the Pliocene-Quaternary of the eastern and western Nile Delta. This suggestion was supported by field observations, Landsat images, aerial photographs, seismicity and seismic profiles indicating the active tectonism in the Eastern Desert between Cairo and Suez. The active spots lie on this belt at Wadi Hagul and Abu Hammad.

Gulf of Aqaba-Dead Sea Trend

Ben-Avraham (1985) stated that the mid-oceanic ridge of the Red Sea–Gulf of Aqaba system changes to transform fault and runs into continent. The horizontal motion along the Gulf of Aqaba –Dead Sea rift is left lateral. Joffe and Garfunkel (1987) pointed that the Dead Sea transform fault accommodates the relative motion between Sinai and Arabia. Kebeasy (1990) considered that the Gulf of Aqaba is a continuation of the active Levant fault, and pointed that earthquake occurrence are found mainly in both ends of the Gulf. Significantly this idea was completely changed after the occurrence of earthquake swarm of November 1995.

In 1983 more than 500 earthquakes were recorded in the Gulf of Aqaba, and these were strongly felt in the villages everywhere in the gulf. Another swarm of small-moderate earthquakes included about 1200 earthquakes was occurred to the south of the area. Again a swarm of 983 events from August 1993 up to February 1994 were recorded. In November 1995, a big earthquake swarm started with the largest earthquake in the Gulf of Aqaba with magnitude Ms 7.2 shocked strongly whole the area surrounding the Gulf. The impact of this earthquake has reached many places inside and outside Egypt. Serious damage was observed in Nuweba City on the western coast of the gulf. Recently on 27th June 2015, a swarm of 96 earthquakes with local magnitudes ranging from 0.7 to 5.2 were recorded by the ENSN. On 16th May 2016 another swarm started and continued for several consecutive days, and approximately 95 events with local magnitudes ranging from 1.6 to 5.5 were instrumentally recorded in the gulf south of 27th June 2015 swarm (Abd El-Aal and Badreldin 2016). The rift system in the Gulf of Aqaba-Dead Sea can be categorized, into the main basic segments: (1) the Gulf of Aqaba–Arava Valley; (2) the Dead Sea Rift and (3) Lebanon Mountains and around Gharb Fault. The earthquake activity in the Gulf of Aqaba segment indicates that this segment is the most active part of the transform system.

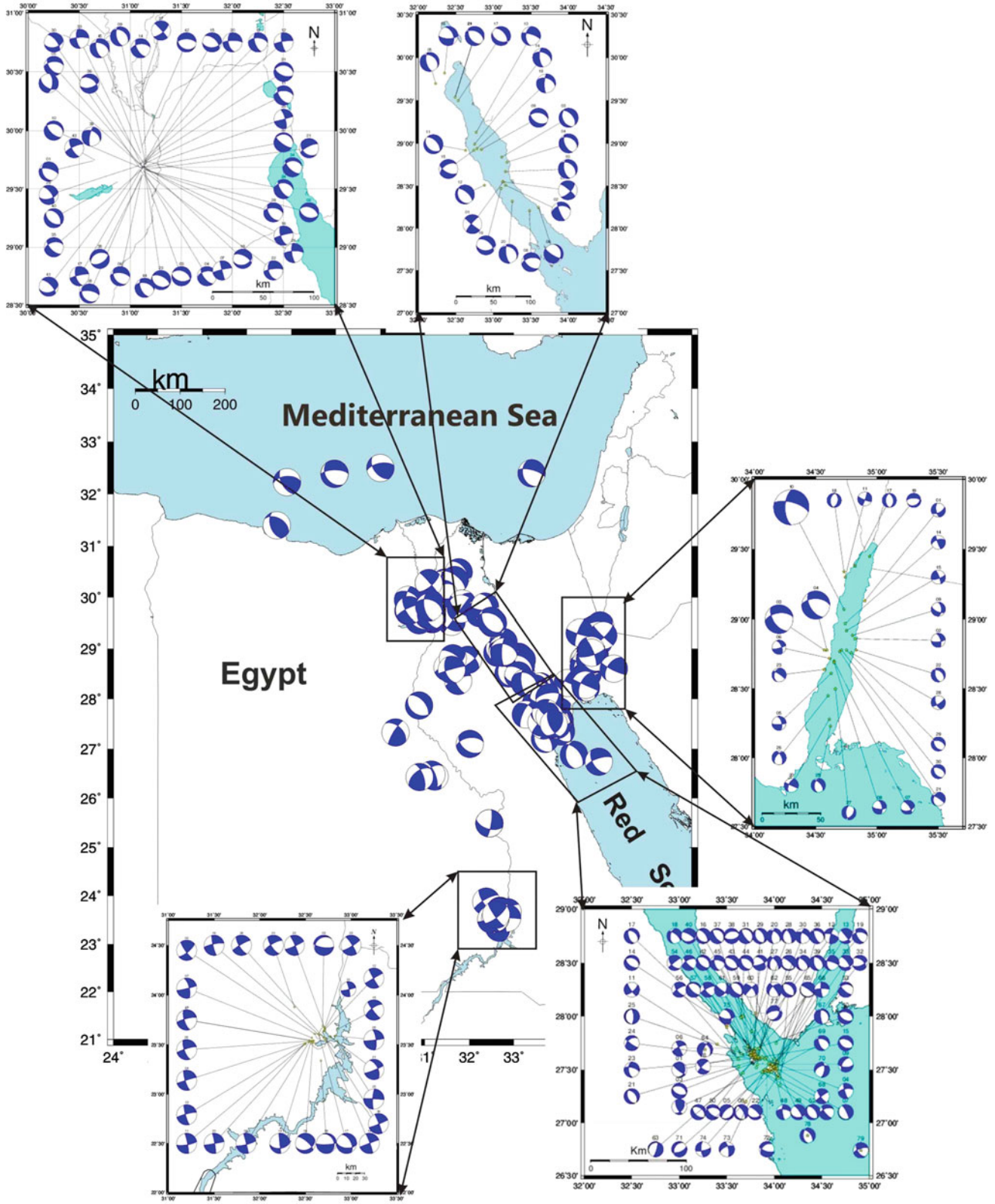

Fig. 10.5 The focal mechanism solutions of significant earthquakes which took place in and around Egypt

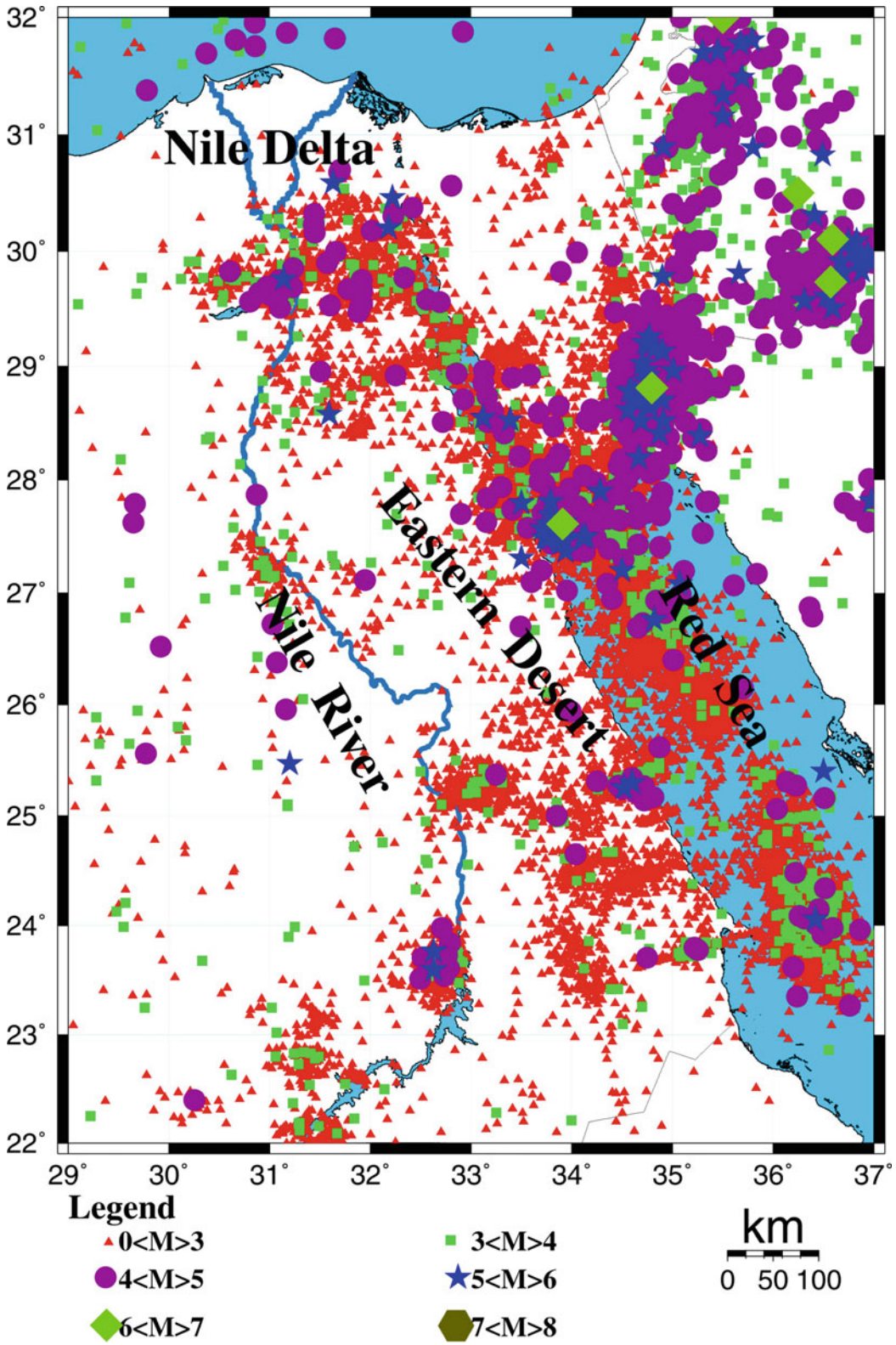

Fig. 10.6 Instrumental seismicity in and around northern Red Sea, Gulf of Suez, Gulf of Aqaba from 1900 to 2014.. Seismicity data are compiled after Egyptian National Seismological Network; ENSN, NEIC and ISC

Dahshour Seismic Source

The area of the epicenter of Dahshour earthquake, 1992, southwest of Cairo is considered as a separate seismic zone, depending on the epicentral distribution, seismicity level, and focal mechanisms (Abou Elenean 1997). Large numbers of historical earthquakes, as well as recent earthquakes were recorded from this area. A significant earthquake (Mb = 5.8) has been recorded southwest of Cairo in Dahshour region on 12 October 1992, at the coordinates 29.77 N, 31.07 E and focal depth of 23 km. This earthquake is the largest recorded earthquake in Dahshour region. Approximately 561 people were killed, and 12,192 injuries were reported, more than 20,000 people became homeless and 8300 buildings were completely or partially damaged or destroyed in the Cairo area alone. The economic casualties or losses of this event reached near 4 billion US dollars. The distribution of seismicity, focal mechanism of recent earthquakes (Fig. 10.5) and the surface and subsurface faults trends in this area demonstrate faults system either take northwest–southeast, parallel to the Gulf of Suez trend or trending east- west, parallel to the Mediterranean trend.

10.2 Application of EMR Data in Detecting Seismotectonic Zones in Egypt

Wael Hagag

10.2.1 Introduction

The effective role of the natural Electromagnetic Radiation (EMR) in the field of geosciences has been increased. As it is preceded the processes of rock failure during most of the laboratory experiments, it has been considered for determining of the crustal stress directions and also for detection of active faults. Although the source mechanisms of natural EMR are various, micro-cracking has been indicated by laboratorial studies as one of the most possible mechanisms generating EMR (Frid et al. 2003; Bahat et al. 2005; Rabinovitch et al. 2007). EMR emissions related to such process are characterized by directional properties, where the direction of growth of any micro-crack is parallel to their maximum intensities. As a consequence, the measurement of the main directions of EMR in the field enabled identification of the maximum horizontal stress direction. That is because the directions of micro-cracking are highly controlled by the applied stress field. The tool or method that is applied during the detection of active faults and related stress field is the Electromagnetic Radiation Technique (EMR-Technique). This method is apparently relying on that mechanical stresses when deforming the brittle rocks they emitted EMR energy. Testing the processes generating EMR phenomenon in laboratorial studies (Misra and Gosh 1980; Slifkin 1993; Frid et al. 2003; Bahat et al. 2005; Rabinovitch et al. 2007) had greater attention than testing the applicability of the EMR-Technique in the field of structural geology. The other possible processes considered as the main source of EMR are a transfer of charge during micro-cracking (O'Keefe and Thiel 1995; Gershenzon et al. 1986; Koktavy et al. 2004) and the surface vibrational wave model (SVW; Frid et al. 2003; Rabinovitch et al. 2007). Moreover, the SVW model is able to relate the EMR wave-properties with the dimensions of the crack generated EMR and the deformed material. The application of EMR-Technique in the structural geology and investigation of neotectonics is better outlined in the pioneer works of Lichtenberger (2006a, b) and Greiling and Obermeyer (2010). Furthermore, several structural and tectonic studies have been mainly achieved based on the EMR-Technique (Reuther et al. 2002; Lichtenberger 2005, 2006a, b; Mallik et al. 2008; Reuther and Moser 2007; Hagag and Obermeyer 2016, 2017; Hamimi and Hagag 2017; Hamimi et al. 2018)

10.2.2 Methodology

Electromagnetic Radiations are measured by a device called Cerescope (Fig. 10.7), a device developed and manufactured by cooperation between the Karlsruhe Institute of Technology (KIT) and Company of Exploration and Radiolocation (GE&O) in Karlsruhe, Germany. The device is made up of rod antenna and sensitive receiver recording frequencies ranging from 5 to 50 kHz. The antenna is more sensitive to the magnetic component of the Applied Electromagnetic Field and to a definite frequency of 12.8 kHz that enables it to distinguish between signals of geological origin (active fractures and stress localizations) from the artificial ones. For further information on the hardware of the device and also the adjustment steps, see the manual guide of the Cerescope (Obermeyer 2001). The Cerescope transfer the detected radiation into calculated values, Parameters A to E. Number of peaks, number of bursts, average amplitude of the bursts, energy of the bursts and average frequency of the bursts are the calculated parameters from A to E, respectively (Obermeyer 2001, 2005).

Linear measurements (Obermeyer et al. 2001) are performed along longitudinal profiles for detection of faulting activity, landslides and the location of other stress concentrations. Measurements along each profile should be taken using a triggered mode of time with a regular speed movement, to get a homogeneous distribution of measured points. In rugged areas (mountain chains and a like), these profiles attain kilometers in length and so measuring could be achieved by vehicles. The direction of the antenna during

Fig. 10.7 The Cerescope device

the measurement process in linear profiles should be perpendicular to the ground surface, and oscillation during the movement should be avoided. The information resulted from linear measurements provide us with predictions about the trend and dip direction of the detected faults. It is favorable to make a grid of linear EMR profiles crossing the faults to get data on their strike, whereas the dip direction could be estimated from the asymmetry in the intensity curves of the recorded EMR waves. The intensity of radiation increasing close to the fault surface and gradually decreased in the direction of dip, where the damping materials in the hanging wall reduce the strength of the emitted radiation.

The main direction of the EMR is possibly measured with horizontal measurements (Lichtenberger 2006a, b; Greiling and Obermeyer 2010). The main direction of radiation is coinciding with the crack orientation, when assuming tensile micro to nano-cracks are the main source of radiation or EMR. This assumption allows the identification of the direction of maximum horizontal stress axis (σ_1). Reuther et al. (2002) described the horizontal measurements and correlate between the results of horizontal EMR measurements and the classical techniques of stress determination such as borehole breakouts. They concluded that the horizontal EMR measurements could be safely used as an alternative tool for determination of the main direction of a horizontal stress (σH). Recently, it is a matter of fact that the directions of EMR are mutually related to the opening direction of micro- and nano-fractures and the resultant stress field (Bahat et al. 2005; Lichtenberger 2006a, b; Greiling and Obermeyer 2010). The horizontal measurements on contrary to the linear measurements are taken along a horizontal circle, either by using a template or through rotating the antenna each 5° and hence recording 72 measurements, in a complete circle, at each measured point. Multiple measuring are recommended at each location to enhance the recorded data. Parameters A and D are representing the recorded measurements on polar diagrams.

10.2.3 Investigation of Some Seismotectonic Source Zones in Egypt Applying EMR-Technique

So far, few attempts have been achieved for detection and investigation of ongoing faulting activity and related stress field using EMR-Technique, along the seismotectonic source zones in Egypt. In the last few years little work carried out using such technique on the Cairo-Suez district, Abu Dabbab area and Kalabsha Fault. All of them are considered as seismic source zones within the Egyptian Territory (Abdelazim et al. 2016). The collected data, results and how these

studies succeed in identification of activity along such zones will be addressed during the following paragraphs.

10.2.3.1 EMR Data from the Cairo-Suez District

The Cairo-Suez district is an accommodation zone transfers the rifting deformation from the northern tip of the Gulf of Suez in the east to the Nile Delta and north Western Desert to the west (Hagag 2016). Seismotectonically, the district considered as a seismic source zone (Dahy 2010; Abdelazim et al. 2016). Along the Cairo-Suez district, 23 linear EMR-profiles were measured and to some extent covered the different areas within the district, whereas about 20 locations were selected for horizontal measurements and stress field analysis (Hagag and Obermeyer 2016) (Fig. 10.8). The recently established settlements (New Cairo, Madinaty, El-Shirouk, El Salam-El Obour, Badr and 10th of Ramadan) and the New Administrative Capital of Egypt give the district much importance and make this study a pilot one. The sites of EMR anomaly were recorded along the linear profiles as a segment of active fault or a minor active fracture. The documented fault trends are arranged in two major categories, E-W (060°-110°, including ENE-WSW and WNW-ESE oriented faults) and NW-SE (130°-170°, including NNW-SSE oriented faults). On the measured profiles, the detected fault segments show graben and horst structural style along with fault surfaces of opposite dips and apparent normal sense of movement. As the detection process is a near surface one, the great number of shallow dipping fractures may indicate a listric shape of the detected fault segments with depth. It seems that the EMR linear profiling succeeded in determination of the structural style inherited in the Cairo-Suez district and reported in the subsurface by Hussein and Abdallah (2001) and assured on the surface mapping in Hagag (2016) from a field-structural study. Furthermore, the extensional origin of the Cairo-Suez faults (predominant normal dip-slip movements with minor strike-slip component) was discussed in Moustafa et al. (1985), Moustafa and Abdel Tawab (1985), and Moustafa and Abdallah (1991).

Interpretation of the analyzed EMR horizontal measurements indicated that the maximum horizontal stress (σ_1) is perturbed between NW-SE (130°-155°) and NNW-SSE (160°-180°). This result is supported by different seismic and seismotectonic studies such as Dahy (2010) and Abdelazim et al. (2016). Moreover, based on the EMR horizontal measurements a secondary stress direction (E-W, 070°-110°) and another minor direction (NE-SW, 030°-046°) but of less importance were estimated. As a concept (Heidbach et al. 2010), the intraplate tectonic stress field shall include first-order (powered by plate motion), second-order (originated by intraplate lateral contrasts like continental rifting) and third-order (due to local stress source) stress fields. Consequently, the NW to NNW directed horizontal stress is attributed to the present-day tectonics along the Africa-Eurasia convergent plate boundary. In the same context, the E-W and NE-SW oriented stresses are resulted from the intraplate tectonic setting currently deforming the northeastern Egypt, i.e. reactivation of the E-W oriented deep-seated faults along the Cairo-Suez district and the faulting activity on the Gulf of Aqaba-Dead Sea transform, respectively. Meanwhile, the detected stress orientations recorded at each location have projected on a simplified geological map of the Cairo-Suez district in a new attempt to construct a surface stress map for the district (Fig. 10.9). Overall, the results of the EMR data from the Cairo-Suez district suggest an active fault system binding the main and major fault trends dissecting the district, NW to NNW and E-W oriented faults. In addition, the aforementioned neotectonic implications and geodynamic considerations appreciate the role of EMR-Technique in detection of activity along any seismotectonic source zone.

10.2.3.2 EMR Data from Abu Dabbab Area

The Abu-Dabbab area is considered as one of the major seismic source zones in Egypt, located at the central Eastern Desert. In the Abu Dabbab area, 6 EMR linear profiles (Fig. 10.10a) were surveyed (Hamimi and Hagag 2017). The main aim of that study was to detect faulting activity along a major E-W oriented shear zone, characterized by strong seismic activity recorded daily in the form of earthquake swarms. Based on the EMR linear profiles, two sets of active fractures oriented ENE-WSW and NNW-SSE were proposed. EMR horizontal measurements were performed at 12 locations for identification of the main direction horizontal stress (Fig. 10.10b). The data of horizontal measurements indicate a primary direction of stress oriented E to NE (058°-110°) and also a secondary direction follow the NW to NNW (130°-170°) orientation. These information, however, refer to a complicated stress field, where the local tectonics characterizing the Abu Dabbab area interact with the regional stress field along the Egyptian Eastern Desert. It means that the stress field induced from the E-W oriented Abu Dabbab Shear Zone may interfere with the regional extensional stress field originated from the spreading along the NW oriented axis of the Red Sea-Gulf of Suez Rift. In the subsurface, the situation is somewhat different where the shallow brittle-ductile transition and the seismotectonic setting of the Abu Dabbab area suggest a mechanical decoupling between the lower and upper crustal levels and hence a complex seismic cycle and earthquake activity within such zone. These implications led the authors to construct a seismotectoic model for the Abu Dabbab area (Fig. 10.11).

10.2.3.3 EMR Data from Kalabsha Area

The Kalabsha Fault Zone is a seismotectonic source zone located at the south Western Desert of Egypt, immediately

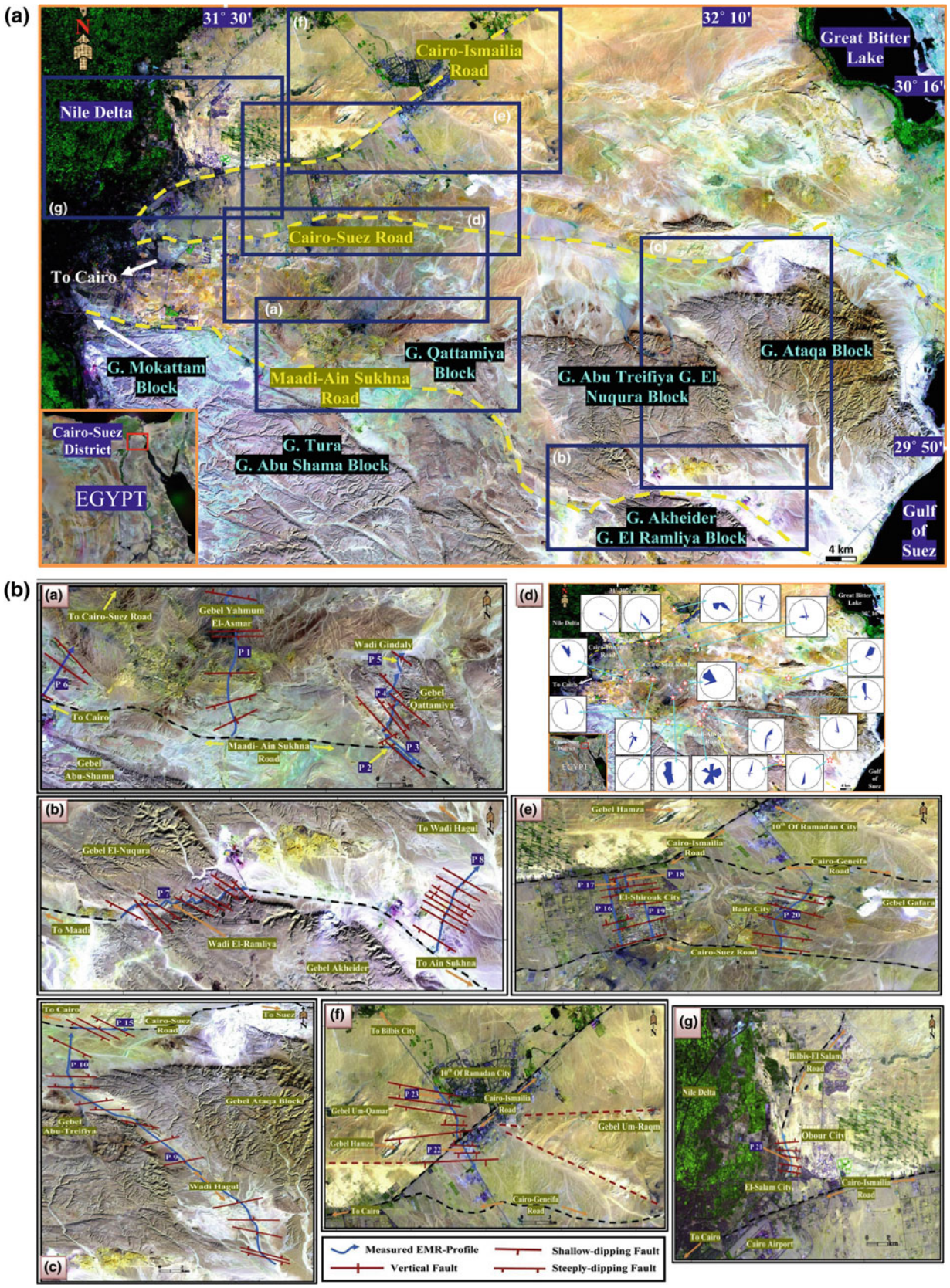

Fig. 10.8 **a** The localities investigated by Hagag and Obermeyer (2016) along the Cairo-Suez district. **b** The measured profiles and detected fault segments documented in Hagag and Obermeyer (2016). **c1–c6** Intensity curves of the linear EMR-profiles recorded in the study of Hagag and Obermeyer (2016), along the Cairo-Suez district. **d** The polar diagrams of the different horizontal EMR-measurements distributed along the Cairo-Suez district (from Hagag and Obermeyer 2016)

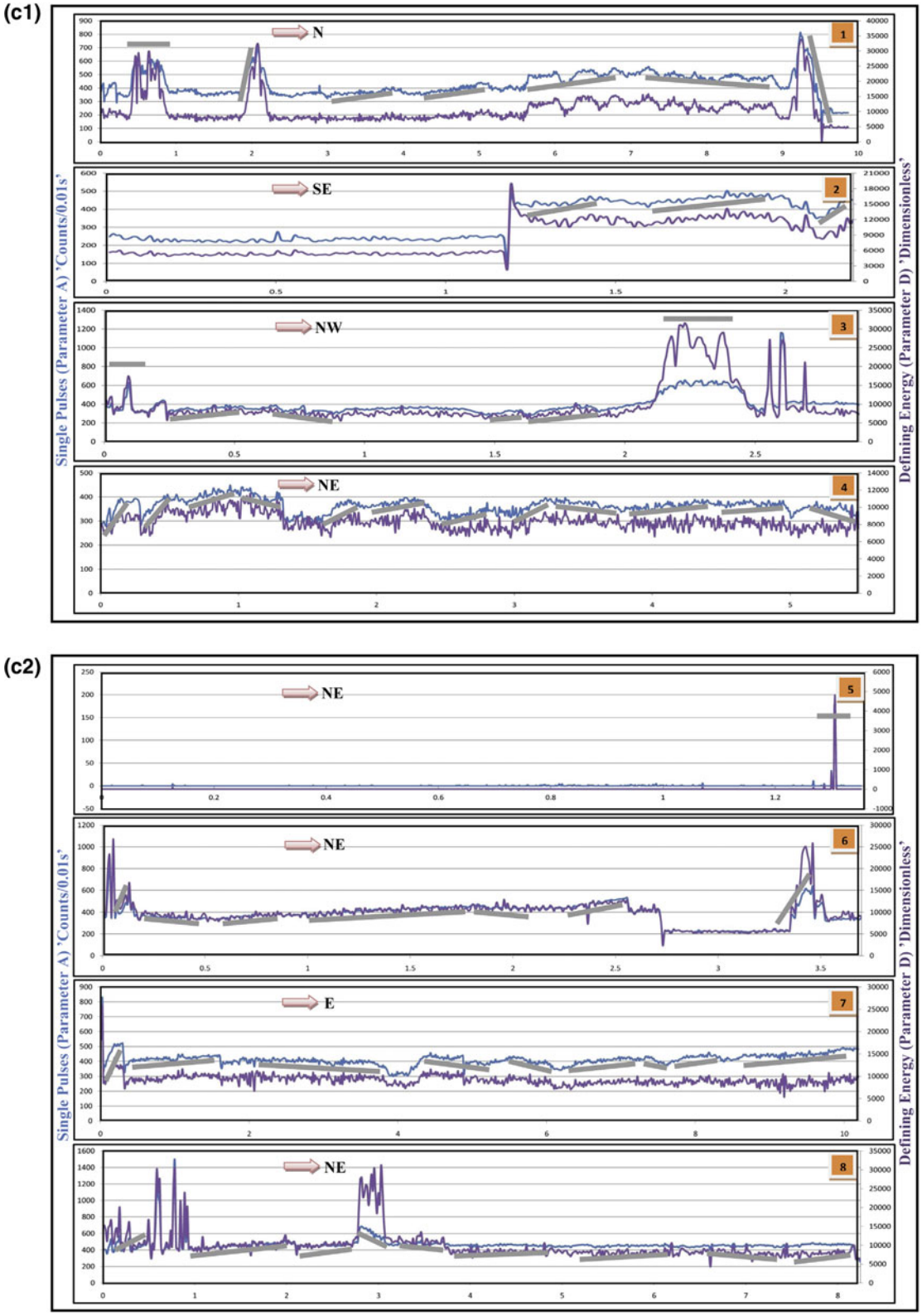

Fig. 10.8 (continued)

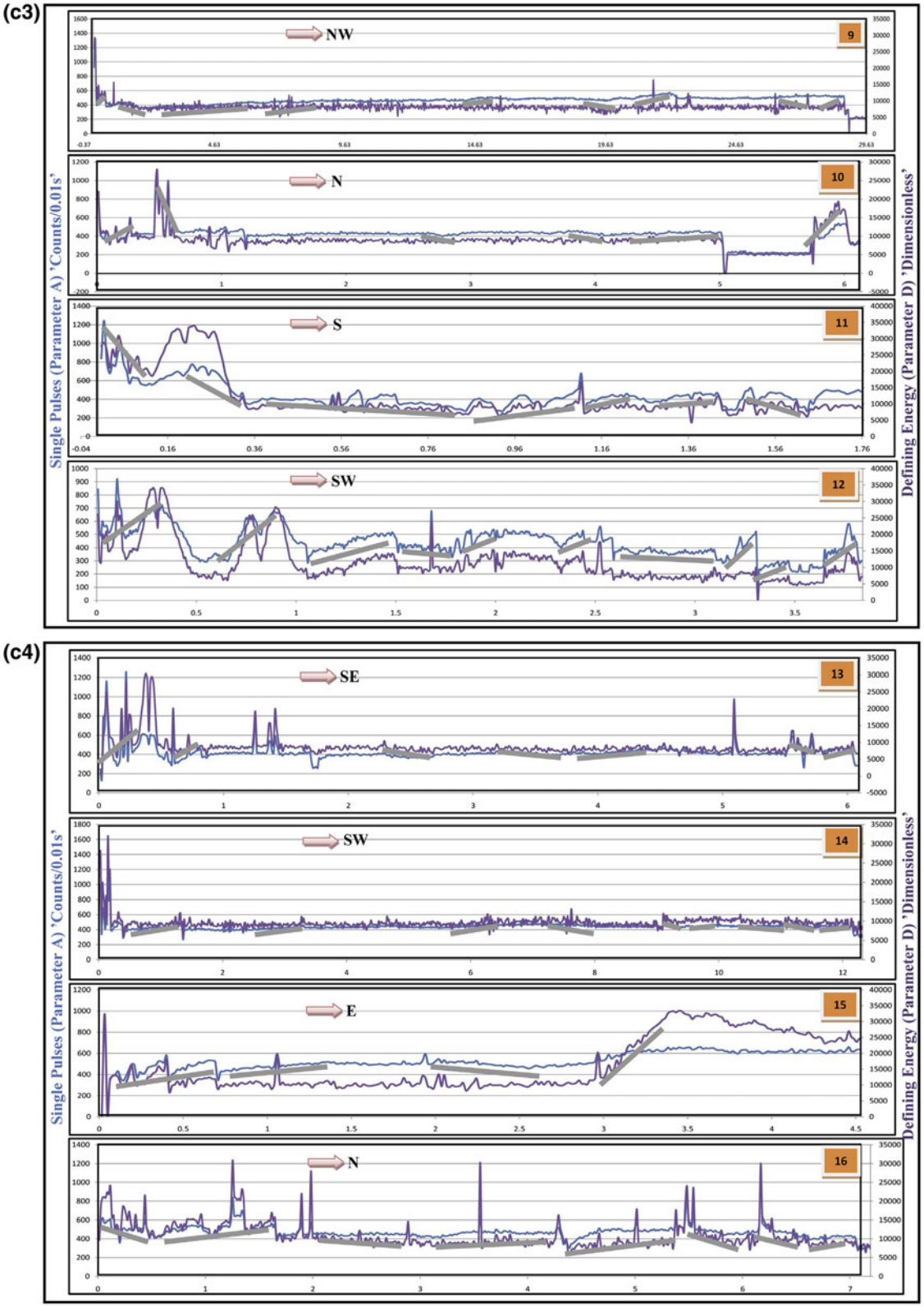

Fig. 10.8 (continued)

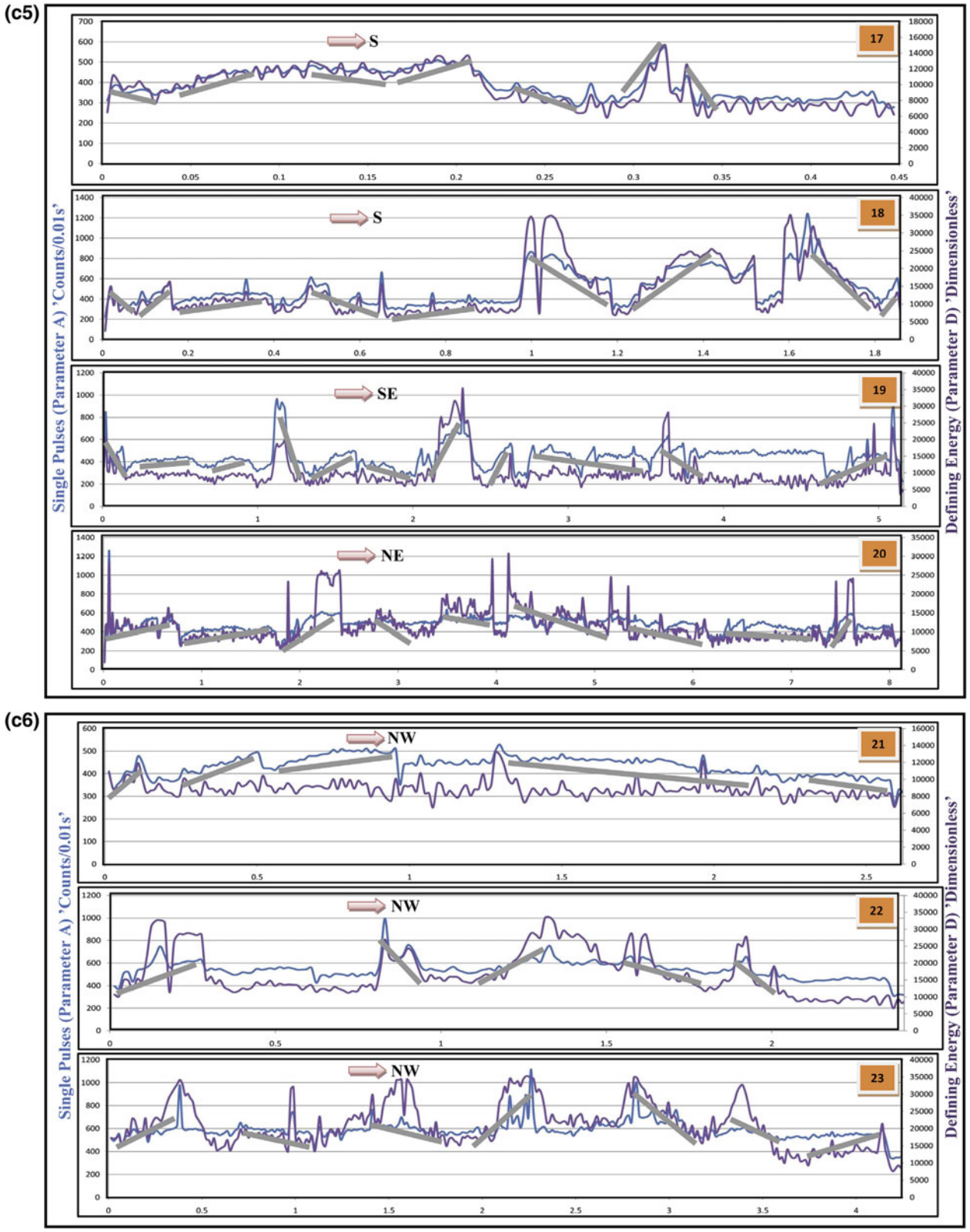

Fig. 10.8 (continued)

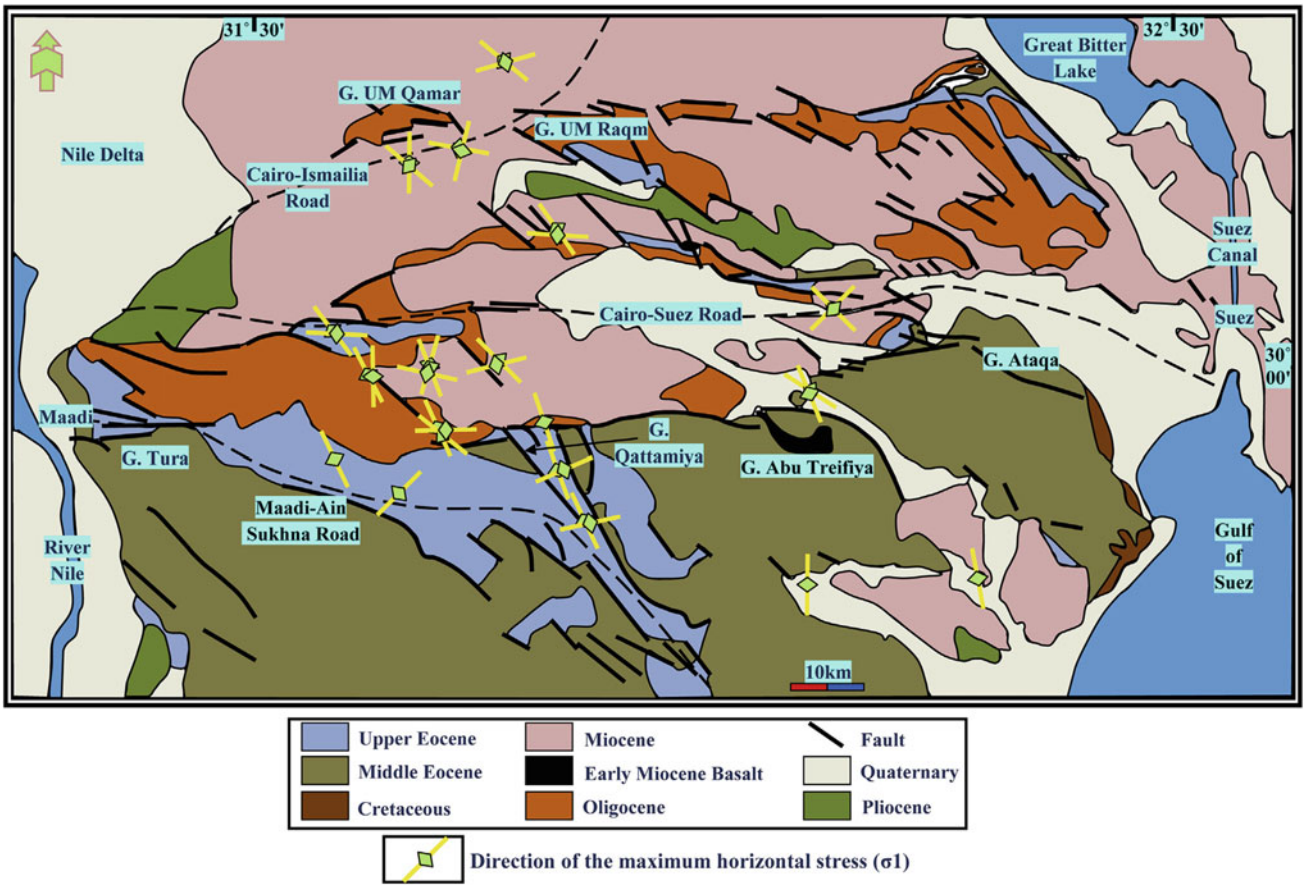

Fig. 10.9 The stress map proposed by Hagag and Obermeyer (2016) for the Cairo-Suez district based on the horizontal EMR-measurements

southwest of Aswan. Two EMR linear profiles were measured along the Kalabsha Fault Zone, besides several horizontal measurements recorded at four locations along the zone (Fig. 10.12) (Hamimi et al. 2018). The EMR data there confirmed an active set of fractures trending ENE-WSW. EMR horizontal data suggest a dominant ENE (065-085) direction of maximum horizontal stress. Moreover, a secondary direction follow NW to NNW (125-160) trend was also detected. Activity detected on the Kalabsha Fault Zone at the upper crustal levels is most probably affecting the seismic cycle (including the lower crustal levels) and the seismotectonic setting of the zone that reaches the western margin of the Lake Nasser, immediately south of the Aswan High Dam.

10.2.4 Conclusions and Evaluation of the Applied Technique

EMR-Technique is a modern tool for detection of ongoing activity on faults and fault zones. Application of such technique in the seismotectonic source zones in Egypt is still under evaluation and development. However, the achieved studies represent a first attempt or an initial stage of applicability of the EMR-Technique. Nowadays, EMR-Technology is increasingly used in the field of geology and material science for various purposes. Electromagnetic Radiation used in detection of the direction of maximum horizontal stress and in finding locations of landslides, along underground tunnels during mining processes. Furthermore, several systems of detection are mainly depending on Electromagnetic Radiation in mineral, petroleum and gas exploration. Concerning its application in Egypt, the data collected from the investigated areas indicate that both local and regional tectonics and related stress fields are effectively contributed to the seimotectonic activity in such regions. The primary stress field along the Cairo-Suez district and also the secondary stress fields along the Abu Dabbab and Kalabsha shear zones reflecting the present day NW to NNW directed maximum horizontal stress induced from a regional extensional stress field affecting most of the Egyptian Territory. Such stress field is attributed to the spreading along the rifting axis of the Red Sea, the accompanying counterclockwise rotation of the African-Arabian plate relative to the Eurasian plate, and the formation of African-Eurasian convergent plate boundary (DeMets et al. 1990; Gripp and

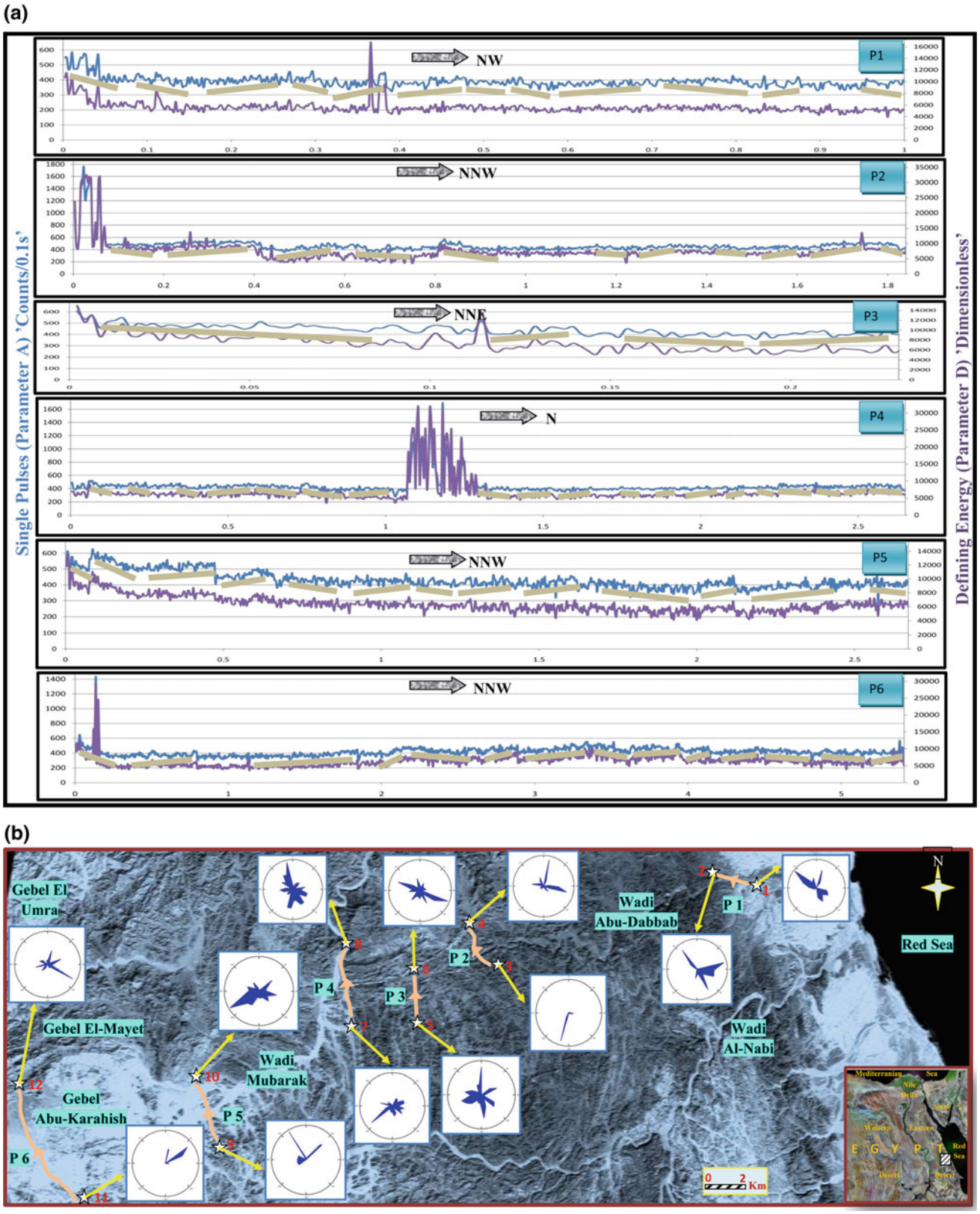

Fig. 10.10 **a** Intensity curves of the linear EMR-profiles recorded along the Abu Dabbab area (from Hamimi and Hagag 2017). **b** Polar diagrams of the horizontal EMR-measurements recorded along the Abu Dabbab area. See also the location of the measured linear EMR-profiles represented in Fig. (21-10A) (from Hamimi and Hagag 2017)

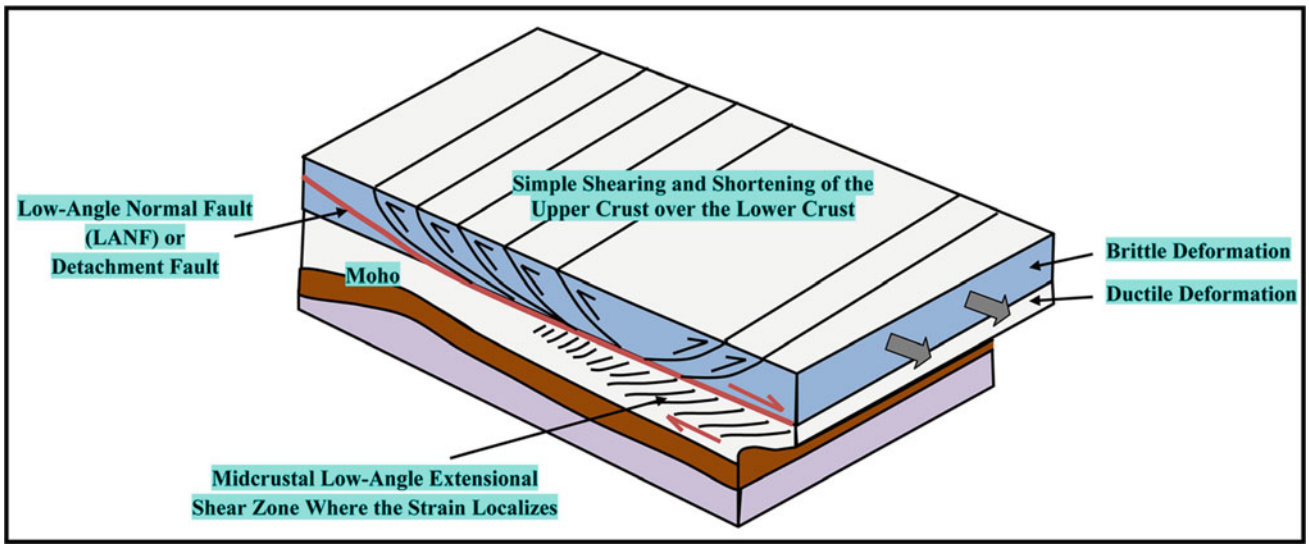

Fig. 10.11 The seismotectonic model proposed in Hamimi and Hagag (2017) based on field, EMR and seismic studies

Gordon 1990). However, the primary directions of horizontal stress along the Abu Dabbab and Kalabsha areas (E-W) could be attributed to the local tectonic setting of these areas as they represent major active shear zones following an old inherited trends along the Egyptian Eastern Desert.

10.3 Role of GPS Measurements in Seismological Study in Egypt

Kamal Sakr

10.3.1 Introduction

Recent crustal movements studies have a great role for evaluating the geodynamics of the seismo-active regions in any country. The crustal deformation must be put in mind where it connects significantly with the human life and its resources. There is a variety of geodetic and other techniques that are currently in use for monitoring such deformation on all local, regional and global scales. The recent precise geodetic tool which apply in crustal deformation is the Global Positioning System (GPS). There are other auxiliary data that could be relevant to the geodetic network's behavior, such as seismicity. Surface deformation and their directions can be measured by repeated accurate geodetic observations.

Study of recent crustal deformations in territory of Egypt is very important nowadays because of increasing tendency of erecting huge engineering structures like dams, bridges, factories, roads, railways, towers, tunnels and pipe lines. The safety of these structures is essential for both economic purposes and human security. The program for monitoring recent crustal movements in Egypt was primary established in Aswan region around Nasser Lake and High Dam using traditional geodetic techniques in 1983. Repeated geodetic measurements using GPS system have been carried out since 1996, which cover different regions in Egypt as Greater Cairo, Sinai Peninsula and Gulf of Suez, Nile Valley area, and Nile Delta Region. Results GPS observations from different networks in Egypt are to determine the following:

1. Determination of the stress orientation within the areas under research work to know the main major axes of Compressions or Extensions using the available GPS Observations and Seismic data of the considered areas.
2. Computing the strain parameters of deformation (extension, compression and shear) and its rate, as well as the rate of horizontal and vertical movements.
3. Establishing a more realistic model for some specified regions using the results achieved in the previous two items.

10.3.2 Distribution of Geodetic Networks in Egypt

10.3.2.1 Egyptian Permanent GPS Network (EPGN)

In 2006, the National Research Institute for Astronomy and Geophysics (NRIAG) started the establishment of the Egyptian Permeant GPS Network (EPGN). Basically, the site selection was aimed to cover geographically all the Egyptian territory but also considering the tectonic setting of Egypt.

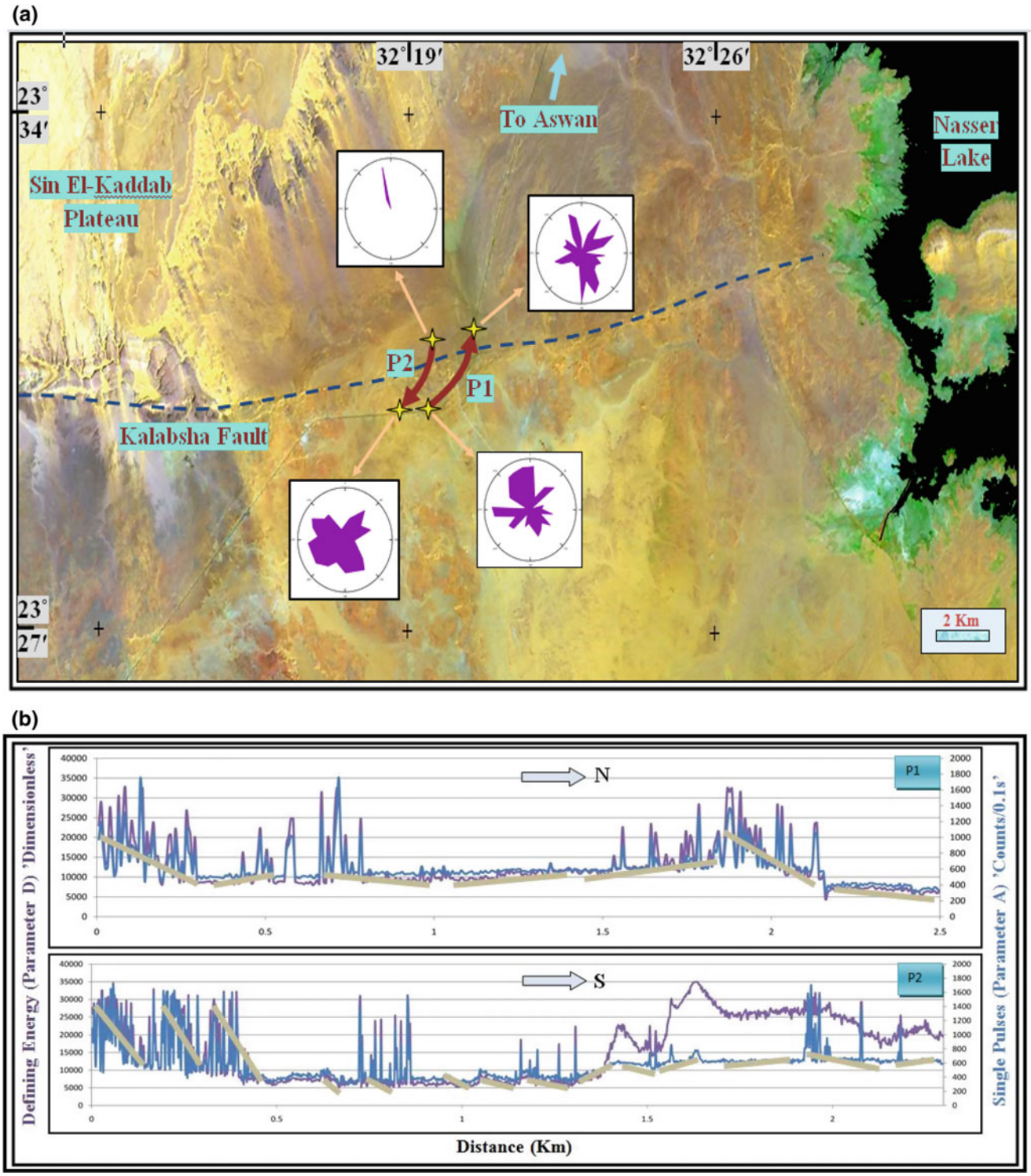

Fig. 10.12 **a** The location of the two linear profiles measured across the Kalabsha Fault Zone (KFZ), and the Polar diagrams of the horizontal EMR-measurements recorded at the ends of the two profiles (from Hamimi et al. 2018). **b** The intensity curves of the two linear EMR-profiles recorded across the Kalabsha Fault Zone (KFZ) by Hamimi et al. (2018)

The chosen places for constructing these stations fulfilled the required criteria such as clear view without any obstructions, away from any electromagnetic sources and accessibility. Three stations were situated in the Eastern Desert at the Red Sea coast, two stations in Sinai Peninsula, three stations in the Western Desert, two stations at the Nile Valley, and six

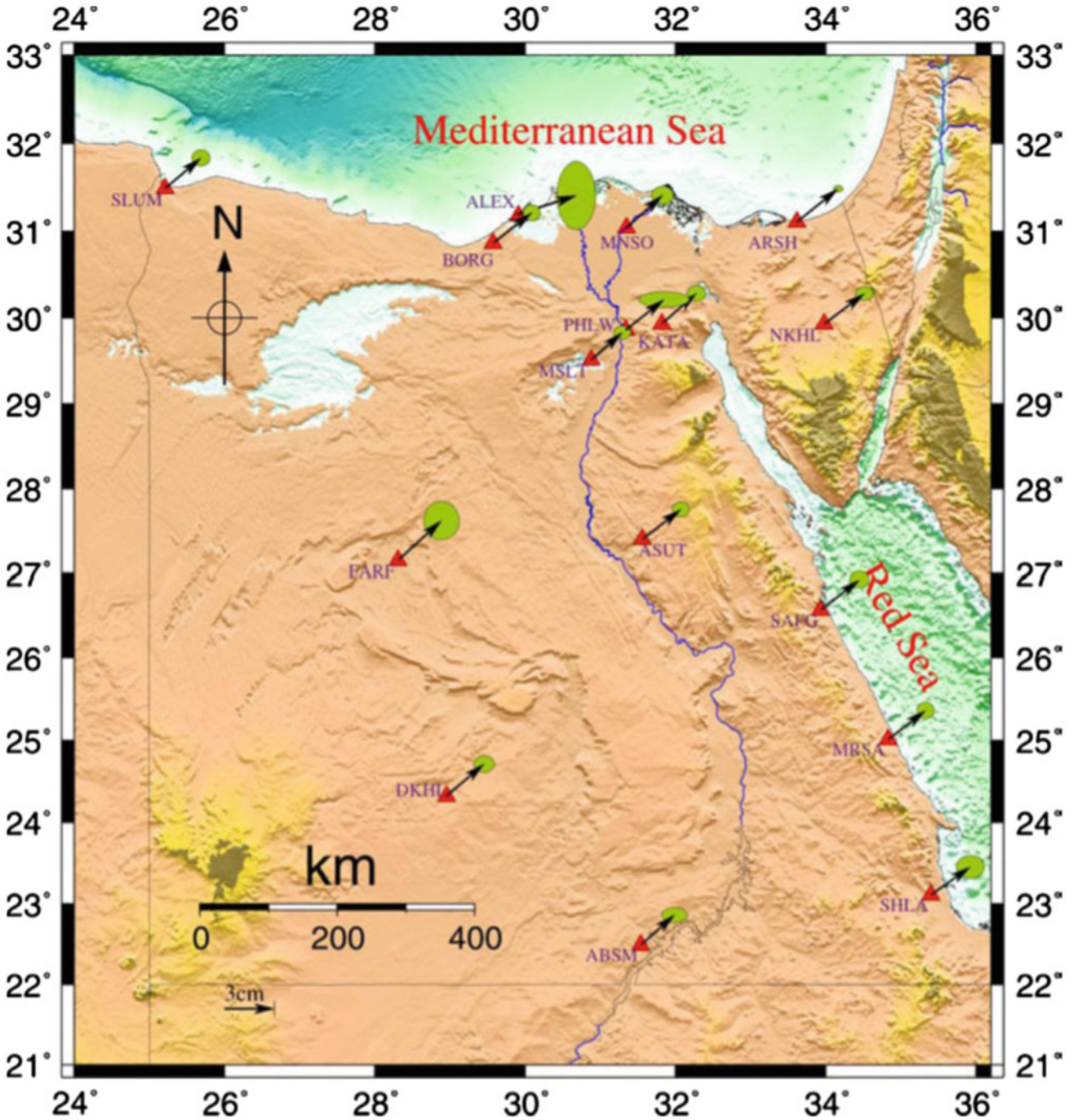

Fig. 10.13 The estimated horizontal velocity field derived from the Bernese software, with 95% confidence regions from the scaled standard deviation (σe) for EPGN (Saleh and Becker 2014)

stations around Cairo and the Nile Delta. Due to the importance of the monumentation type and its quality, which affects directly the stability of these stations, the majority of EPGN stations were installed on concrete pillars; but in a few cases, some stations were installed on a roof of building such as the case in Helwan (PHLW), and Marsa-Alam (MRSA) for safety considerations. Starting from 4 stations in 2007 to 15 stations were achievable at the end of 2011 (4 in 2007, 2 in 2008, 3 in 2010, and 6 stations in 2011).

Daily solutions, with residuals larger than 3-sigma, were rejected. Seventy-eight days out of 2,463 were rejected during the process of outlier rejection representing 3.2% of

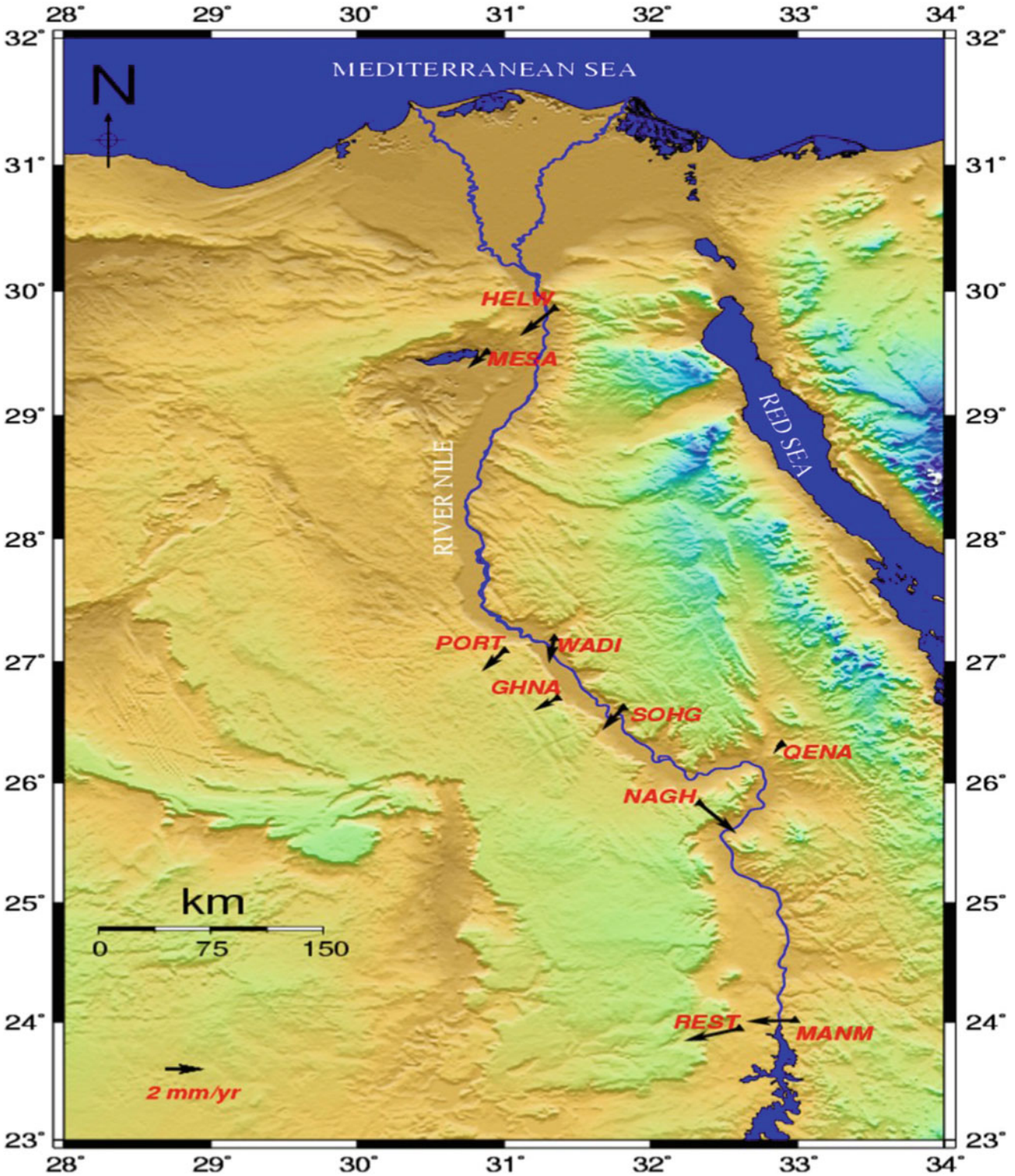

Fig. 10.14 The local horizontal displacement of Nile Valley network from May 2007 to September 2012 relative to ITRF 2008 (Kamal Sakr et al. 2015)

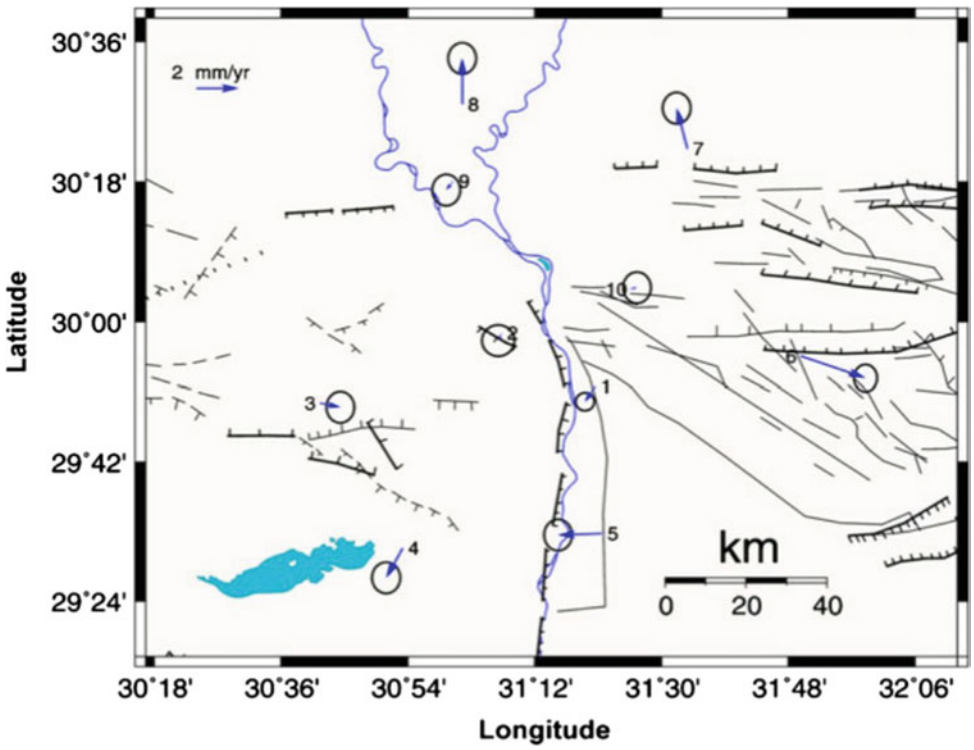

Fig. 10.15 Rate of horizontal movements of the period 2005 to 2010 for greater cairo geodetic network (Abdel-Monem S. M. et al. 2013)

the daily solutions. The annual velocity of the EPGN stations is presented in Fig. 10.13. It is clear that the repeatability for the EPGN stations in average is about 3 mm in the horizontal components, East and North, and 5.6 mm in the Up component (Saleh and Becker 2014).

10.3.2.2 Nile Valley Geodetic Network

In 2006, the GPS geodetic network which was established around the middle part of the Nile Valley in 1999 has been extended to cover the whole area of the Nile Valley. Processing of baselines analyses were performed using Bernese (V.5.0) software packages and other programs for adjustment. The IGS precise ephemeris applied in the calculation of the baselines and the displacement vectors at each GPS station were determined. Horizontal components at each station were computed from the difference of adjusted coordinates of the stations from one epoch to another and from the last epoch to the first. The displacement vectors between each two epochs of observations were calculated from the coordinate changes. Considering the confidence limit, most of these displacement vectors can be mainly attributed to the crustal movement within the study area during the campaigns of measurements. Analysis of the geodetic data in the region along the Nile Valley in Egypt indicated that the regional velocities of the GPS stations with respect to the regional tectonic plate were calculated with value between 18 mm/yr in the north direction to 23 mm/yr to the east direction. The local horizontal velocity vectors of the stations with respect to each others are small magnitude and in the range of 1–4 mm/yr in East direction and 1–3 mm/yr in North direction as shown in Fig. 10.14, (Sakr et al. 2015).

10.3.2.3 Greater Cairo Geodetic Network

Recent crustal movement monitoring was carried out in Cairo region after the earthquake of 12th October 1992 in Dahshour area, 35 km southwest of the center of Cairo, with a magnitude of 5.9. This earthquake was strongly felt over the whole area of Egypt. It caused a widespread damage in Cairo, Giza, and El-Faiyum provinces. Many aftershocks followed the main shock. The focal mechanisms of earthquakes located on the west bank of the Nile represent reverse faulting mechanism with strike-slip component, while normal faulting occurs in the eastern bank. A GPS network consisting of ten benchmarks covering Cairo City and the southern part of the Nile Delta was established. The horizontal and vertical components of displacement vectors with 95% confidence error ellipses were calculated. The horizontal displacement vectors show small magnitude and in the range of 2–5 mm/year. Some stations of the network indicated significant changes, while others recorded negligible changes through the period of observations (Fig. 10.15), (Abdel-Monem et al. 2013).

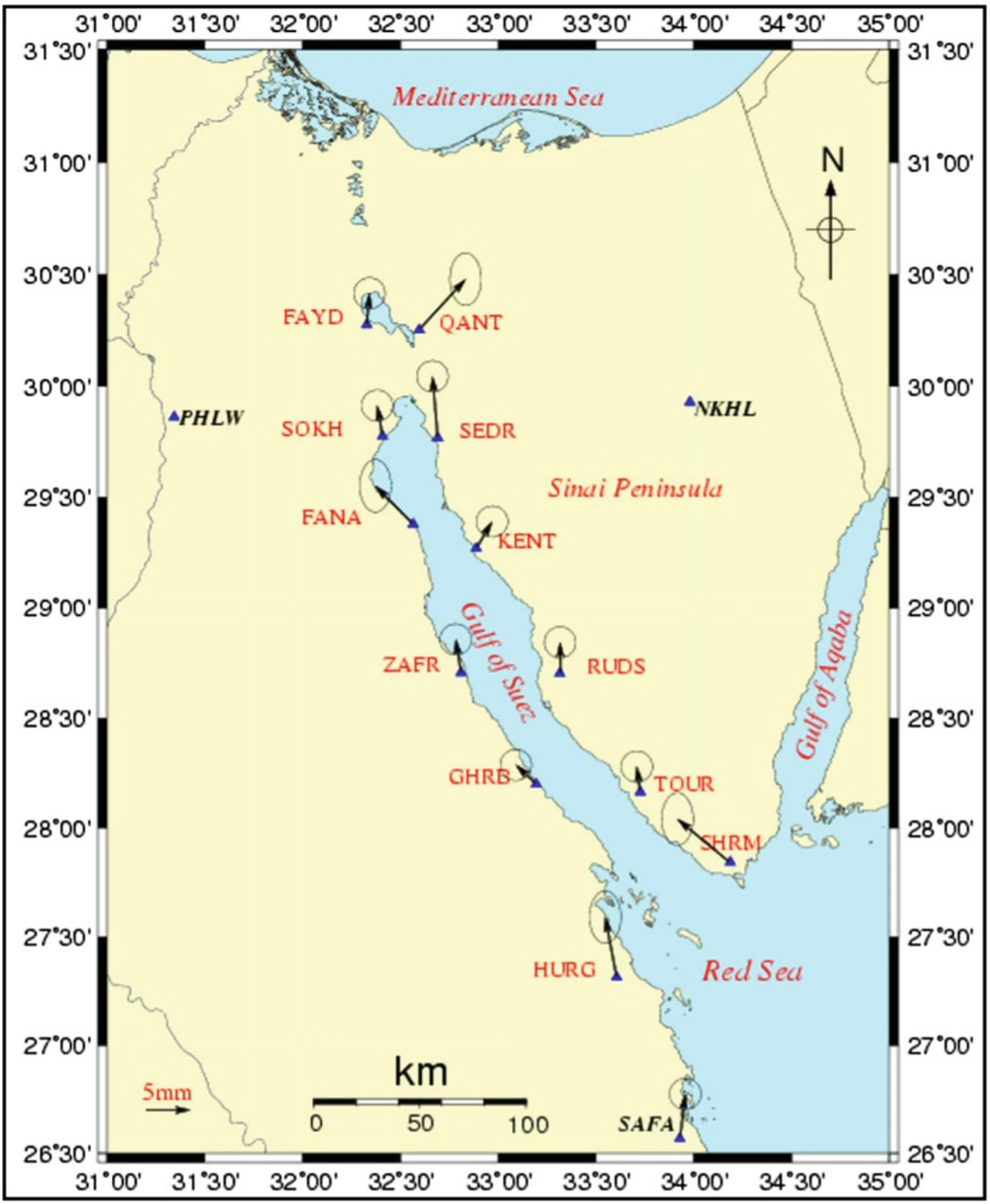

Fig. 10.16 The local horizontal velocity of the Gulf of Suez geodetic network (Abou-Aly et al. 2011)

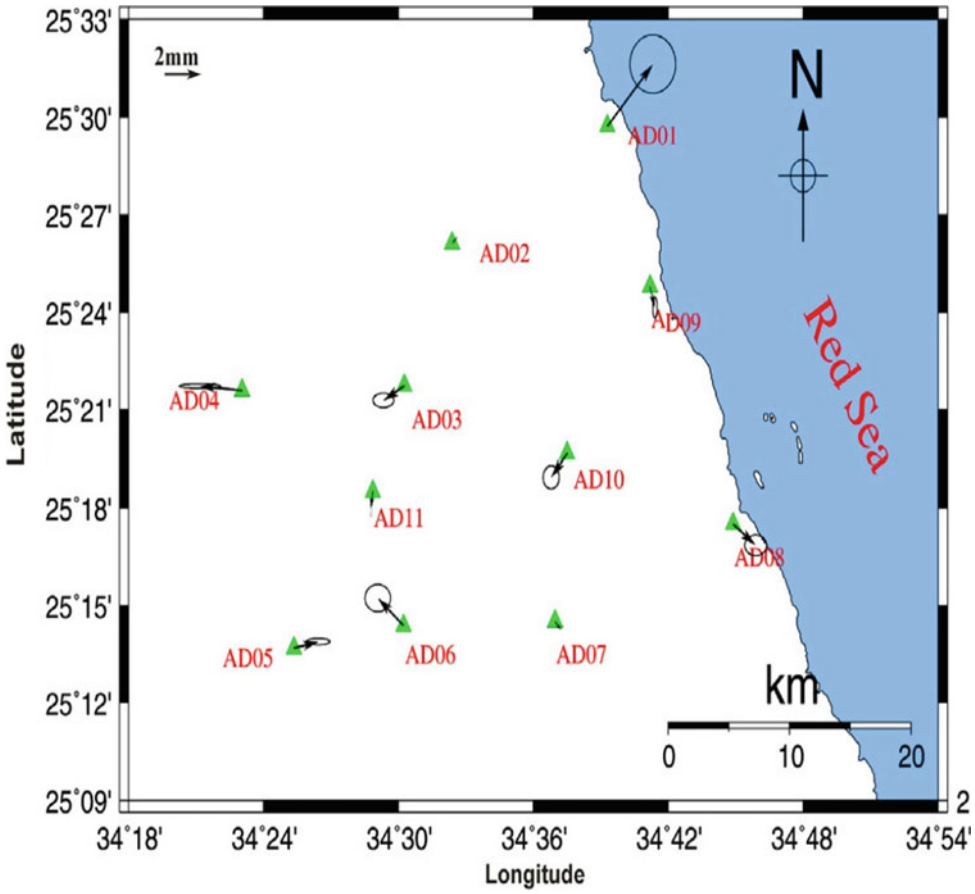

Fig. 10.17 The annual local horizontal velocity of Abu-Dabbab geodetic network (Abdel-Monem S. M. et al. 2012)

10.3.2.4 Gulf of Suez Geodetic Network

For monitoring the horizontal movements at the Gulf of Suez region, a geodetic network with special configurations has been designed and periodically observed using GPS technique. Geologic maps, topographic maps, and the available geologic information are used to select the possible ideal locations of the geodetic network stations. Station selection has also considered the geodynamical behavior of the selected region. A GPS network consisting of 12 observation stations was established early in 2007 to detect the crustal deformation around the Gulf of Suez and to monitor the relative plate motions. The stations found on the eastern side of the Gulf move in the direction of north to northeast direction with an average rate of 5 mm ± 1.17 mm per year, while the stations on the western side of the Gulf move in the direction of north to northwest with an average rate of 4.5 mm ± 1.15 mm per year (Fig. 10.16), (Abou-Aly et al. 2011).

10.3.2.5 Abu Dabbab Geodetic Network

In August 2008, a GPS network consisting of eleven stations was established in the area of Abu-Dabbab (Fig. 10.17). Five GPS campaigns were carried out from October 2008 to April 2010. The first campaign was in 2008 from 7 to 11October; the second campaign was in 31 December 2008 to 4 January 2009; the third one was from 6 June to 10 June 2009; the fourth campaign was in 2009, from 6 to 10 October; and finally the fifth and last one was in 2010, from 4 to 8 April. Some stations of the network indicate significant changes while other stations indicate no significant changes through the period of observations (Fig. 10.17), (Abdel-Monem et al. 2012).

10.3.2.6 Aswan Geodetic Networks

On November 14, 1981, a moderate earthquake with a local magnitude of 5.5 on Richter scale has occurred along Kalabsha fault, 100 km from the High Dam. This earthquake was followed by a tremendous number of smaller events that continue till now. The Kalabsha and Kurkur areas lies on the largest western embayment of the Nasser Lake (High Dam Lake). Since then, seismicity continued in the area, but with different magnitudes. The earthquakes were estimated to have occurred near the epicenter of the main earthquake of 1981, which was located along the eastern part of the Kalabsha fault (about 300 km length) near the wide area of the

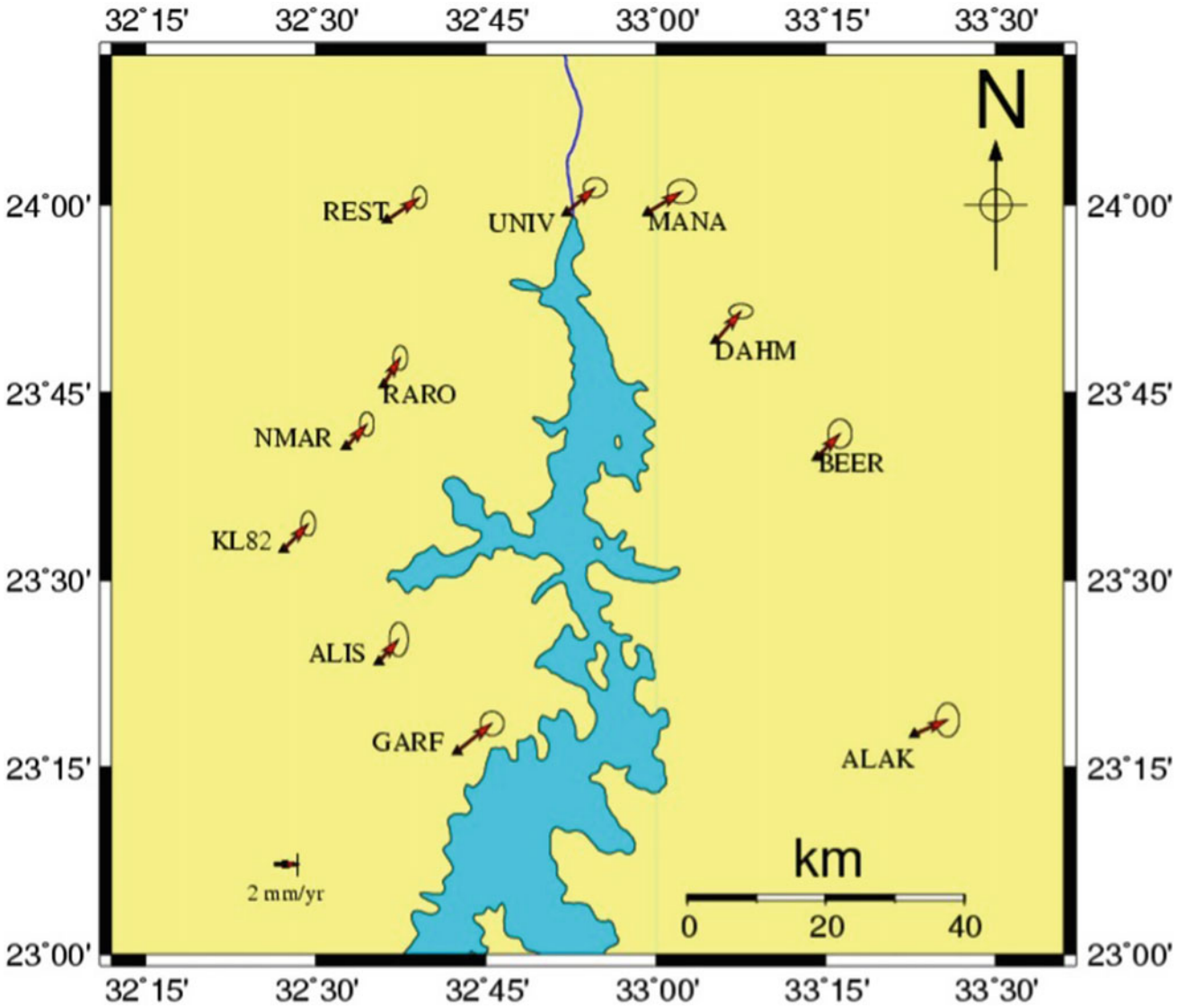

Fig. 10.18 Annual local Horizontal velocity during the period from 2004 to 2014, (Radwan et al. 2015)

lake. Analysis of the repeated last 10-years GPS campaigns revealed regional and local horizontal movements at the level from [20 to 28 (±1.5)] and [(2 to 4 (±0.5)] mm/a, respectively. The estimated strain tensor rate shows compression and tension components which are approximately consistent with the P- and T-axes derived from earthquake fault plane solutions, respectively (Fig. 10.18), (Radwan et al. 2015).

10.4 Application Of InSAR Data in Ground Deformation Monitoring in Egypt

Mohamed Saleh

10.4.1 Introduction

Generally, Egypt's crustal deformation is mainly controlled by the subduction of the Nubian plate under the Eurasian plate and activities along the Red Sea, Gulf of Suez and Gulf of Aqaba. Most of the seismic activity of Egypt is concentrated along the Red Sea-Gulf of Aqaba and Gulf of Suez. Moreover, some seismicity clusters are recorded in Egypt, such as clusters at Dahshour area close to the epicenter of October 12, 1992 Dahshour earthquake, Aswan area, South of Egypt, close to lake Nasser, and Abu-Dabbab area in the Eastern Desert at the Red Sea coast. Such areas of seismicity clusters could be associated with local ground deformation.

Ground deformation studies have been started after the Kalabsha earthquake in 1981. Previous studies were used

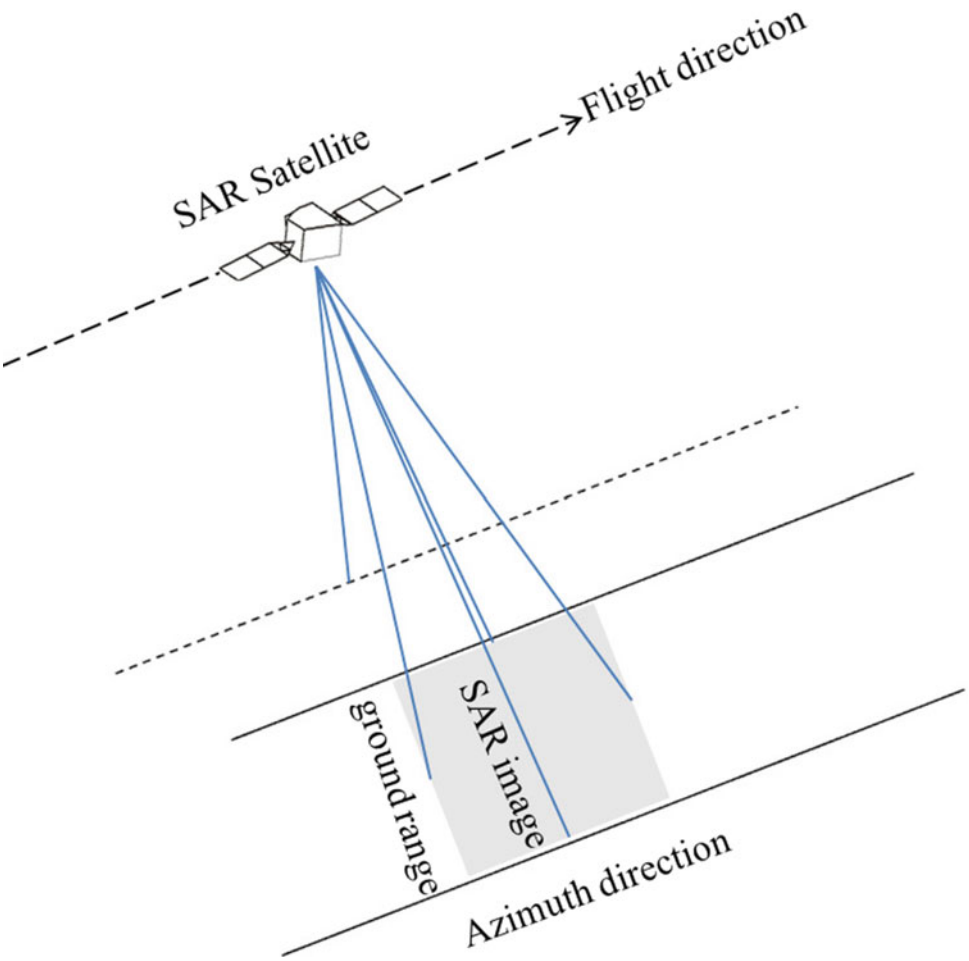

Fig. 10.19 SAR imaging geometry

terrestrial geodetic techniques such as precise leveling. Later, the space geodetic techniques were used instead, such as GPS. Recently, InSAR (Interferometric Synthetic Aperture Radar) has been applied to estimate the recent ground deformation of some active regions in Egypt. In this section, a small introduction on the concept and basics of InSAR will be given, followed by the discussion of the application of InSAR data in Egypt with some examples from published results. Two regions in Egypt will be dealt with, Aswan and Nile Delta.

10.4.2 InSAR

The InSAR is an active side looking remote sensing satellite technique which has the ability to map the terrain surface with a few meters accuracy and the surface deformation within millimeter level. InSAR has the capability of large-scale imaging in all weather conditions over days to years. It is widely used for the estimation of ground deformation including, but not limited to, crustal movements along active faults, co-seismic deformation, monitoring the active volcanoes, glacier dynamics and land subsidence. SAR systems have a side looking antenna that illuminates the Earth, with radar in the microwave range, in swath or track parallel to the sensor's flight direction. Three bands of the electromagnetic spectrum are commonly used in InSAR applications, L-band with 23.6 cm wavelength, C-band with 5.6 cm wavelength, and X-band with 3.1 cm wavelength. The imaging geometry presented in Fig. 10.19 is named the strip mapping mode. Even with new modern modes of collecting the SAR data like ScanSAR or spotlight SAR, the strip mapping mode still the most common mode in the current satellites. The two fundamental components of the SAR image are amplitude and phase. Amplitude reflects the amount of the backscattered energy. The second element in the SAR image is the phase that is considered as the key information in the interferometric measurements.

The values of pixels phase of one single scene is not very useful. But, in case of a second scene acquired over the same area, in the same time of the first one or in another time by the same sensor, the second scene can be interfered with the first one. The result of this interference process is the interferometric phase or the interferogram. The interferometric phase due to change in the path length will be:

$$\Delta\varphi = \frac{-4\pi}{\lambda} \cdot \Delta\rho$$

where $\Delta\varphi$ is the interferometric phase, $\Delta\rho$ is the change in the path length and λ is the radar wavelength. The minus sign is because of the measured phase defined as phase delay. The phase difference can be equal to the sum of all contributors:

$$\Delta\varphi = \varphi_{base} + \varphi_{topo} + \varphi_{defo} + \varphi_{atm} + \varphi_{noise}$$

where φ_{base} is the phase difference caused by the different positions of the satellite during the two images, φ_{topo} is the topography signal, φ_{defo} is the ground deformation contribution, φ_{atm} is the phase contribution due to the atmospheric delay and φ_{noise} is the contribution from other terms like system noise.

10.4.2.1 Differential InSAR

Figure 10.20 shows the interferometric configuration of two SAR antennas imaging the same area separated by a baseline B for either a repeat pass mode or two antennas mounted on one SAR satellite. In case of non-zero baseline between the two antennas, which is the most common case, the topography signal will be included in the interferogram. The signal due to topography can be estimated and removed from the interferogram using an external Digital Elevation Model (DEM) or from InSAR (Gabriel et al. 1989). The procedure of removing the signal due to topography from the interferogram is called Differential InSAR (DInSAR). Such an approach used by (Massonnet et al. 1993; Zebker and Rosen 1994) to image the co-seismic deformation associated with Landers earthquake, (Zebker and Goldstein 1986) to map the earth's topography, (Amelung et al. 2000; Pritchard and Simon 2002) for active volcanism, (Wright et al. 2001) for co- and post-seismic motions, (Amelung et al. 1999; Hoffmann et al. 2001) to estimate the ground subsidence from underground water withdrawal and (Ryder and Bürgmann 2008) to map active faults. The quality of results from the DInSAR approach is based on the degree of similarity between the SAR images or the Correlation. Changes in the imaging geometry and/or the nature of the surface being imaged may be lead to the decorrelation (Zebker and Villasenor 1992).

10.4.2.2 Multi-temporal InSAR

Simultaneous processing of multiple SAR scenes acquired over the same area gives the chance to correct the uncorrelated phase noise and consequently reduce the error in the deformation estimates. The multi-temporal (time series) InSAR algorithms can be broadly categorized into two classes: Persistent Scatterer InSAR (PSI) (Ferretti et al. 2001) and Small Baseline (SBAS) (Berardino et al. 2002; Schmidt and Bürgmann 2003; Hooper et al. 2012) algorithm.

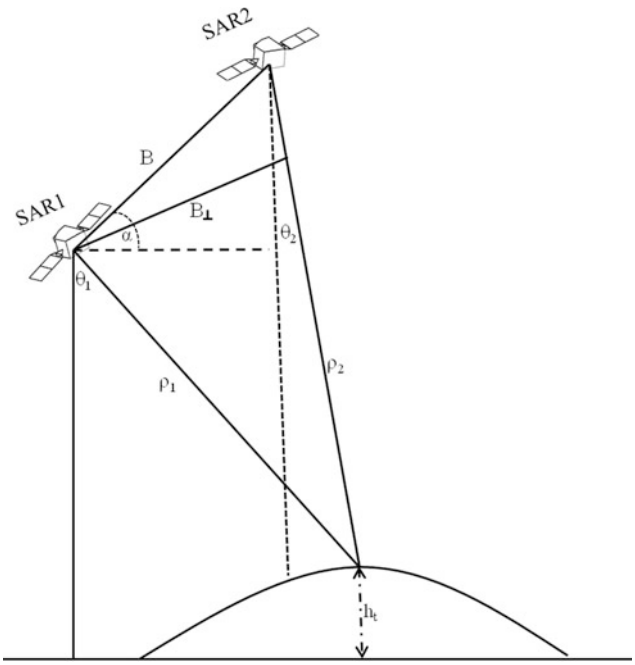

Fig. 10.20 Interferometeric configuration of two SAR antennas separated by a baseline B, $B_\perp$ is the perpendicular baseline, θ_1 and θ_2 are the look angles of SAR1 and SAR2, ρ_1 and ρ_2 are the range (slant range) for SAR1 and SAR2, respectively, and h_t is the point's height

10.4.3 Application of SAR Data in Egypt

Since InSAR offers a cheaper geodetic data source with respect to other geodetic tools, like GPS, it is more convenient to use it with large areas. SAR scenes have been used to map the ground deformation around the northern part of lake Nasser (Saleh et al. 2018) and the land subsidence of the Nile Delta (Saleh and Becker 2019).

10.4.3.1 Lake Nasser

Saleh et al. (2018) used 35 Envisat SAR scenes from the descending track number 350 covering the period 2003-2010 (Fig. 10.21) to estimate the ground deformation around lake Nasser by applying the PSI analysis (Hooper et al. 2012). The InSAR derived deformation field shows a slow deformation field around the lake. PS pixels in Fig. 10.22a which are moving away from the satellite are showed in warm colors, and pixels move toward the satellite are in cool colors as satellite is flying in the descending pass (heading southward). A general trend of negative LOS

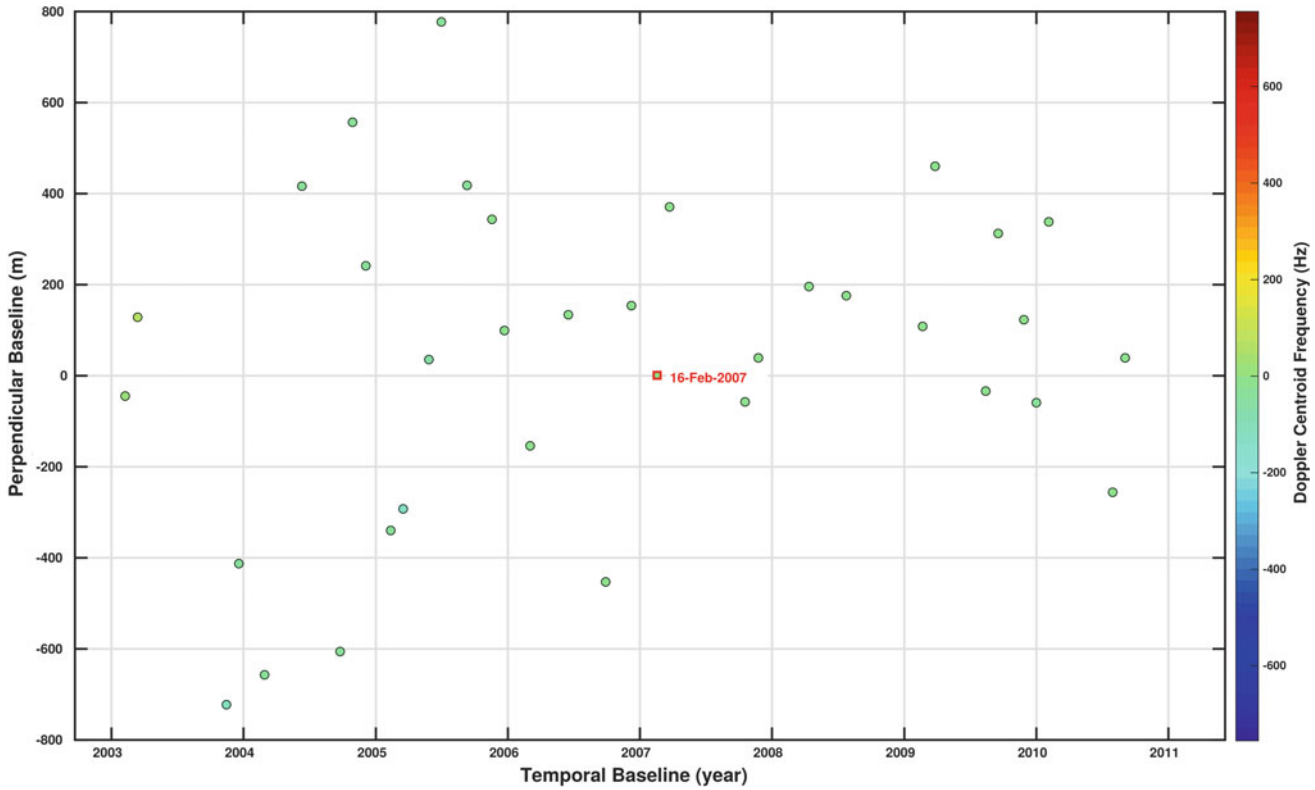

Fig. 10.21 Envisat SAR images of track 350 over Aswan area (Saleh et al. 2018)

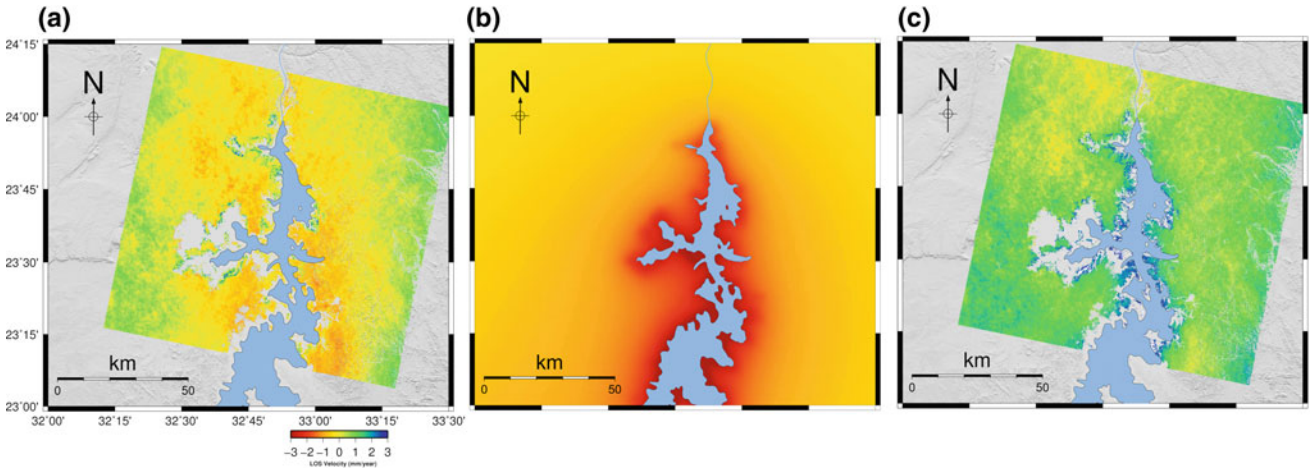

Fig. 10.22 **a** InSAR line-of-sight (LOS) velocity (left), **b** modeled visco-elastic deformation due to lake Nasser water level variations, assuming a viscosity of 10^{19} Pa s of the upper mantle (middle) and **c** residuals (right), (Saleh et al. 2018)

velocity is surrounding the lake ranging from 1 to 2 mm/yr. There are a gradual change in LOS velocity from negative values to positive values in areas away from the lake eastward and westward. Areas away 20–30 km from the lake showed a stable ground deformation which represented in Fig. 10.22a as yellow color. Further away from the lake, PS pixels are moving toward the Satellite (positive LOS values).

As lake Nasser water level variation induces transient deformation of the Earth crust as shown by the InSAR velocity, Saleh et al. (2018) model the Earth's response to water level changes, assuming a spherically symmetric,

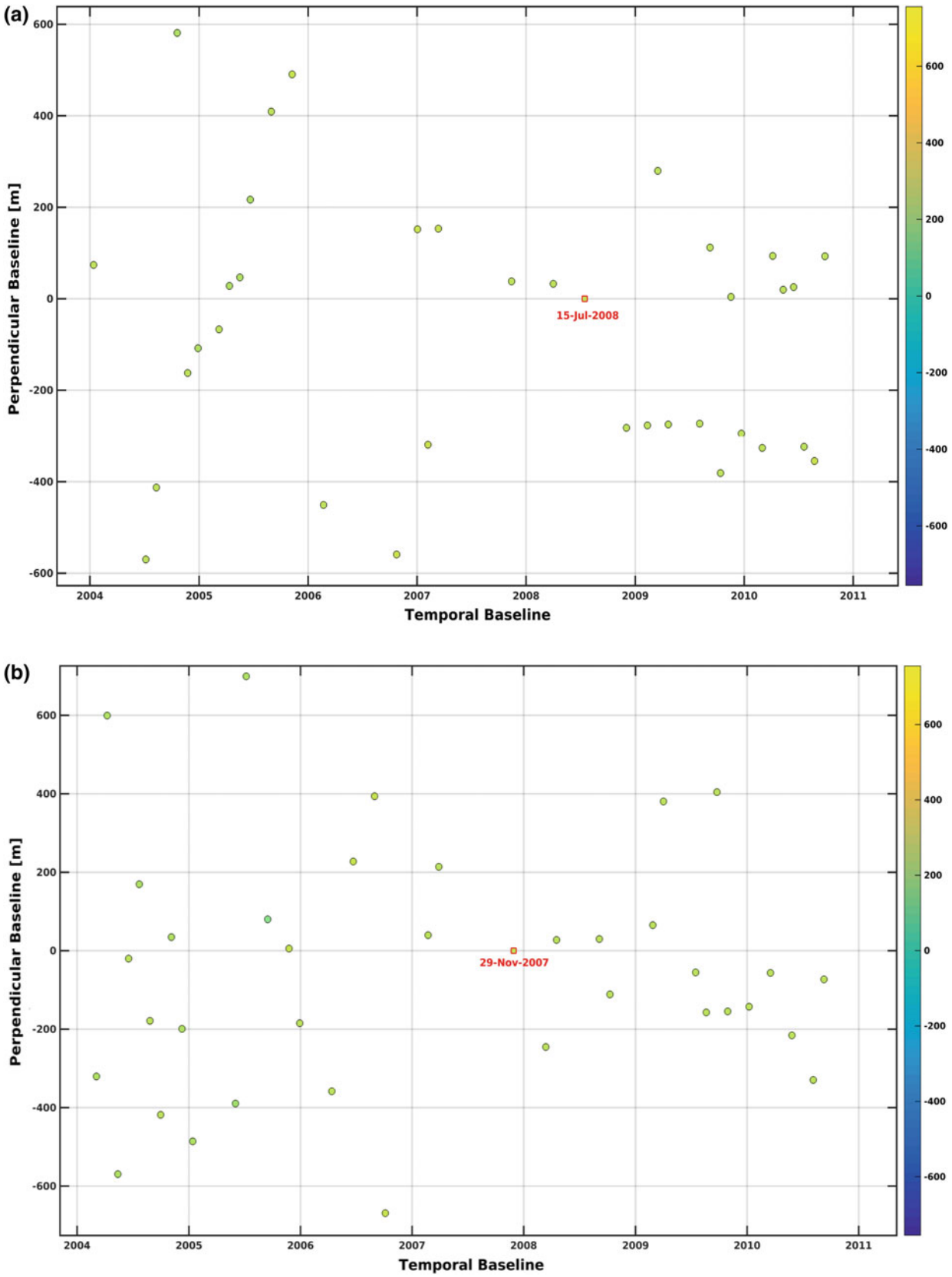

Fig. 10.23 **a** SAR images of track 207 and **b** SAR images of track 436 from Envisat satellite mission. Circles are the SAR dates. Red squares indicate the master scenes chosen for each track, (Saleh and Becker 2019)

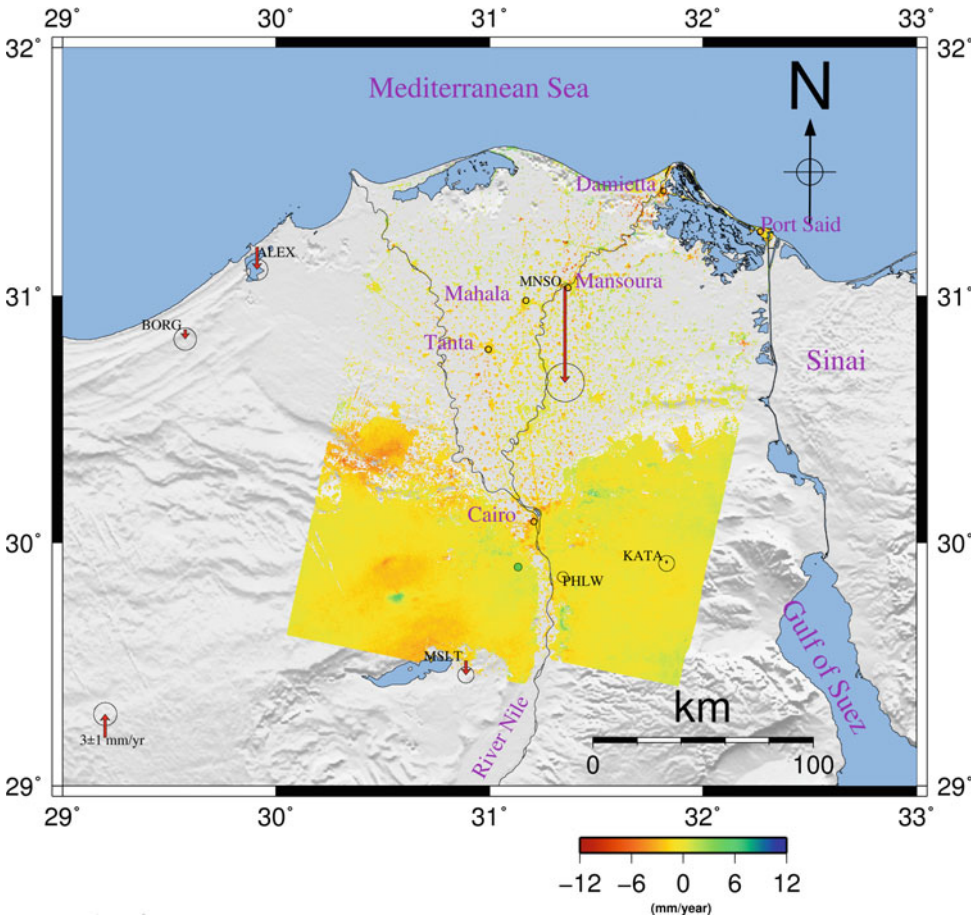

Fig. 10.24 LOS velocities of the Nile Delta. The green circle represents the reference location. Hollow circles represent the selected PS from each city for the time series plot, (Saleh and Becker 2019)

non-rotating, incompressible and self-gravitating Earth model, assuming a Maxwell visco-elastic rheology for the upper mantle (30–300 km) with a viscosity of 10^{19} Pa s (Spada et al. 2004) and elastic for other layers using PREM parameters (Dziewonski and Anderson 1981). Using the full daily water level records starting from 1982 to 2016, they computed the 2003 to 2010 vertical velocity. Figure 10.22 shows the InSAR line-of-sight (LOS) velocity (4a), the modeled visco-elastic deformation (4b) and the corresponding residuals (4c). The loading model captures the deformation features near the lake with similar amplitudes (up to 3 mm/yr). The modeled far field is close to zero, unlike the observations which may be affected by other geophysical contributions such as hydrological loading.

Based on the achieved InSAR velocities, Saleh et al. (2018) concluded that the area around the Lake is suffering from land subsidence ranging 1–2 mm/yr. The loading model confirms that the long-term subsidence around the lake is mainly due to the long-term water level changes in the Lake. Horizontally, the northern part of Nasser Lake shows a negligible motion of less 1 mm/yr toward North to Northeast direction. Moreover, no significant velocity changes recorded along Kalabsha and Sayal faults, west of the lake, which could be an indication that the main driving force in this area is the water level changes in the lake.

10.4.3.2 Nile Delta

As the Nile Delta is considered as one of the most vulnerable zones in Egypt, Saleh and Becker (2019) estimated the subsidence rate of the Nile Delta by applying the PSI processing for all the ESA archived Envisat SAR data from the descending tracks 207 and 436 for the period 2003–2010. They processed 37 and 36 SAR scenes from tracks 436 and 207, respectively, (Fig. 10.23). Figure 10.24 shows the LOS velocity field deduced from the Envisat descending tracks 207 and 436 over the Nile Delta. The LOS velocity field that covers a presumably undeforming part, represented as a green circle south of Cairo, is subtracted from the entire InSAR velocity field, producing a LOS velocity field in the Nubia fixed reference frame. As shown in Fig. 10.24, the majority of the Nile Delta looks quite stable, represented by yellow dots, where the LOS velocity is around zero. However, there are some areas of negative LOS velocities that are represented by orange-red dots, moving away from the satellite. From this figure, it is clear that the negative velocities are highly localized at the big cities in the Nile

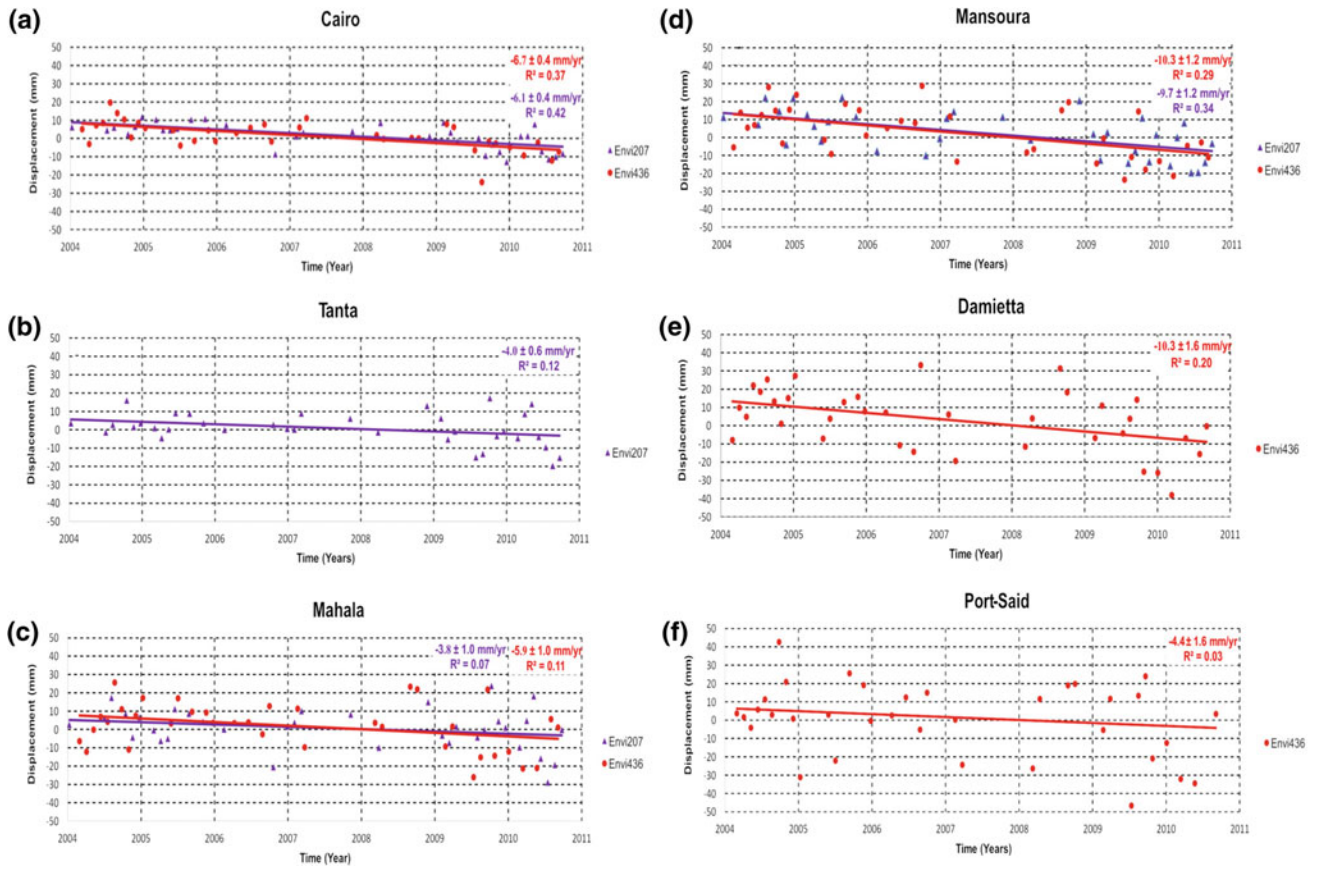

Fig. 10.25 Displacement versus time for **a** Cairo, **b** Tanta, **c** Mahala, **d** Mansoura, **e** Damietta and **f** Port-Said from Envisat descending scenes. Red dots are the results of track 436 with the velocity trend (the red line) and mauve triangles for track 207 results with trend line, (Saleh and Becker 2019)

Delta (Cairo, Tanta, Mahala, Mansoura, Damietta, and Port-Said). The LOS velocities for these cities are ranging from −3.6 to −9.3 mm/yr. The lowest velocity is estimated for Tanta and Port-Said as −3.6 mm/yr and −4.4 mm/yr, respectively. While the highest estimated velocity is found in Damietta and Mansoura as −9.3 mm/yr.

Based on the InSAR velocity of the Nile Delta, the ground movement is mainly concentrated at large cities which represented as hollow circles in Fig. 10.24, time series for selected PS pixels from these cities is constructed in order to estimate the rate of displacement for each city and the differences between the estimated rates from each track for the same PS. Figure 10.7a shows the time series for PS selected from Cairo from both tracks, 207 and 436. The estimated rates are −6.0 ± 0.4 mm/yr and −5.5 ± 0.4 mm/yr from tracks 436 and 207, respectively. The estimated rates from the two tracks are in good agreement as the difference in rates is 0.5 mm which is a small value. North of Cairo, cities Tanta, Mahala, and Mansoura are all exhibiting negative LOS velocities. Figures 10.25b, c, and d show the time series of the selected PS pixels from Tanta, Mahala, and Mansoura, respectively. Tanta is covered only by track 207. Figure 10.25b shows that the estimated LOS velocity for Tanta is −3.6 ± 0.6 mm/yr. Mahala and Mansoura are covered by both tracks 436 and 207. The LOS velocities for Mahala are −5.3 ± 1.0 mm/yr and −3.4 ± 1.0 mm/yr resulting from tracks 436 and 207, respectively. Along the Mediterranean coastline, also Damietta and Port-Said show negative LOS velocities. Both cities are covered only by track 436. Figure 10.25e shows the time series of the PS pixel selected from Damietta. The estimated velocity is −9.3 ± 1.6 mm/yr. It is obvious that the results are more scattered around the trend line than for the other cities in the Nile Delta. The LOS velocity of Port-Said is presented in Fig. 10.25f. The measured rate is −4.4 ± 1.6 mm/yr and a similar situation of scattering the results along the trend line like Damietta is seen.

The above two examples of the application of InSAR data in mapping the ground deformation in Egypt show that InSAR data are an ideal tool to derive and densify the information on the ground deformation in areas where the number of available GPS stations is rather small and sparse, which is the case of Egypt. From the Envisat results of both selected case studies, the deformation around the northern

part of lake Nasser is mainly controlled by the water level changes of the lake, while the Nile Delta is almost stable and the estimated ground deformation is highly localized at the big cities Cairo, Tanta, Mahala, Mansoura, Damietta, and Port-Said. The localization of the subsidence rates at the big cities imply that the detected signals are mainly due to human activities, such as underground water pumping and not due to a regional tectonic activity.

References

Abd El-Aal AK (2010a) Modeling of seismic hazard at the northeastern part of greater Cairo metropolitan area, Egypt. J Geophys Eng 7:75–90. https://doi.org/10.1088/1742-2132/7/1/007

Abd El-Aal AK (2010b) Ground motion prediction from nearest seismogenic zones in and around Greater Cairo Area, Egypt. Nat Hazards Earth Syst Sci 10:1495–1511. https://doi.org/10.5194/nhess-10-1495-2010

Abd El-Aal AK, Badreldin H (2016) Seismological aspects of the 27 June 2015 Gulf of Aqaba earthquake and its sequence of aftershocks. J Seismol. https://doi.org/10.1007/s10950-016-9572-x

Abdelazim M, Samir A, El-Nader IA, Badawy A, Hussein H (2016) Seismicity and focal mechanisms of earthquakes in Egypt from 2004 to 2011. NRIAG J Astron Geophys 5(2):393–402

Abdel-Monem SM, Zahran KH, Saleh M, Yossef MM, Omran AA, Radwan AM (2013) Gavity observation and crustal deformation at Cairo Region and its geodynamical implications. World Appl Sci J 21(12): 1721–1728. ISSN 1818-4952. IDOSI Publications. https://doi.org/10.5829/idosi.wasj.2013.21.12.721

Abdel-Monem SM, Becker M, Saleh M (2012) Comparative deformation analysis for Abu Dabab area, Egypt. Acta Geod Geoph Hung 47(3): 1–18 (2012). https://doi.org/10.1556/ageod.47.2012.3.3

Abou-Aly N, Abdel-Monem SM, Salah M, Saleh M, Sherif M, Khalil H, Hassib G, Rayan A (2011) Gps measurements of current crustal movements along the Gulf of Suez. Nriag J Geophys Special issue: 45–66

Abou Elenean K (1997) A study on the seismotectonics of Egypt in relation to the Mediterranean and Red Seas tectonics. PhD thesis, Ain Shams Univ., Cairo, Egypt

Albert RNH (1987) Earthquake activity in Cairo Suez district compared with the fault pattern from satellite photographs considering Egyptian large scale construction plans. Bull Intern Seismol Earthq Eng (IISEE), Tskuba, Japan, pp 27–40

Ambraseys NN (1961) On the seismicity of southwest Asia (data from XV century Arabic manuscript), Revue Pour L'etude des calamites, no 34, Geneve, pp 18–30

Ambraseys NN, Melville CP, Adams RD (1961) The seismicity of Egypt, Arabia and the Red Sea. A historical review. Cambridge Univ. Press, 181 pp

Ambraseys NN, Melville CP, Adams RD (1994) The seismicity of Egypt, Arabia and the Red Sea. A historical review. Cambridge Univ. Press, 181 pp

Amelung F, Jonsson S, Zebker H, Segall P (2000) Widespread uplift and 'trapdoor' faulting on galapagos volcanoes observed with radar interferometry. Nature 407:993–996

Bahat D, Rabinovitch A, Frid V (2005) Tensile fracturing in rocks-tectonofractographic and electromagnetic radiation methods. Springer, vol 16, 570 pp

Ben-Avraham Z (1985) Structural framework of the Gulf of Aqaba, northern Red Sea. J Geophys Res 90:703–726

Ben-Avraham Z (1978) The structure and tectonic setting of the levant continental margine, eastern Mediterranean. Tectonophysics 46 (313):331

Berardino P, Fornaro G, Lanari R, Sansosti E (2002) A new algorithm for surface deformation monitoring based on small baseline differential sar interferograms. IEEE Trans Geosci Remote Sens 40(11):2375–2383

Daggett PH, Morgan P, Boulos FK, Hennin SF, El Sherif AA, El Sayed AA, Basta NZ, Melek YS (1986) Seismicity and active tectonics of the egyptian red sea margine and the northern red Sea. Tectonophysics 125:313–324

Dahy SA (2010) A study on seismicity and tectonic setting in the northeastern part of Egypt. Res J Earth Sci 2(1):8–13

Deif A (1998) Seismic hazard assessment in and around Egypt in relation to plate tectonics. PhD thesis, Ain Shams Univ., Cairo, Egypt

DeMets C, Gordon RG, Argus DF, Stein S (1990) Current plate motions. Geophys J Int 101:425–478

Dziewonski AM, Anderson DL (1981) Preliminary reference Earth model. Phys Earth Planet Inter 25(4):297–356. https://doi.org/10.1016/0031-9201(81)90046-7

Egyptian Geological Survey Authority (1981) Geological map of Egypt

Ferretti A, Prati C, Rocca F (2001) Permanent scatterers in SAR interferometry. IEEE Trans Geosci Remote Sens 39(1):8–20

Frid V, Rabinovitch A, Bahat D (2003) Fracture induced electromagnetic radiation. J Phys D Appl Phys 36:1620–1628

Gabriel AK, Goldstein RM, Zebker HA (1989) Mapping small elevation changes over large areas: Differential radar interferometry. J Geophys Res Solid Earth 94(B7):9183–9191

Gergawi A, El-Kashab HMA (1968) Seismicity of U.A.R. Acad of Se Res and Tech Helwan Inst of Astro and Geoph Bull 76, 7–17

Gershenzon NI, Zilpimiani D, Mandzhgaladze PV, Pokhotelov OA, Chelidze ZT (1986) Electromagnetic emission of the crack top during rupture of ionic crystals. Dokladi Akademii Nauk SSSR 288:75–78

Greiling RO, Obermeyer H (2010) Natural electromagnetic radiation (EMR) and its application in structural geology and neotectonics. J Geol Soc India 75(1):278–288

Gripp AE, Gordon RG (1990) Current plate velocities relative to hot spots incorporating the Nuvel-1 global plate motion model. Geophys Res Lett 17:1109–1112

Guidoboni E, Comastri A, Traina G (1994) Catalogue of ancient earthquakes in the mediterranean area up to the 10th century. Istituto nazionale di geofisica, Rome

Hagag W (2016) Structural evolution and Cenozoic tectonostratigraphy of the Cairo-Suez district, north Eastern Desert of Egypt: Field-structural data from Gebel Qattamiya-Gebel Um Reheiat area. J Afr Earth Sci 118:174–191

Hagag W, Obermeyer H (2016) Rift-related active fault-system and a direction of maximum horizontal stress in the Cairo-Suez district, northeastern Egypt: a new approach from EMR-Technique and Cerescope data. J Afr Earth Sci 121:136–153

Hagag W, Obermeyer H (2017) Active structures in central Upper Rhine Graben, SW Germany: new data from Landau area using Electromagnetic Radiation (EMR) Technique and Cerescope. J Geol Geophys (6:5). https://doi.org/10.4172/2381-8719.1000303

Hamimi Z, Hagag W, Osman R, El Bialy M, Abu El Nadr I, Fadel M (2018) The active Kalabsha Fault Zone (KFZ) in Southern Egypt: detecting faulting activity using new field-structural data and EMR-technique, and implications for seismic hazard assessment. Arabian J Geosci, ARABGU2016 11:42. https://doi.org/10.1007/s12517-018-3774-1

Hamimi Z, Hagag W (2017) A new tectonic model for Abu-Dabbab seismogenic zone (Eastern Desert, Egypt): evidence from field-structural, EMR and seismic data. Arab J Geosci ARABGU2016. https://doi.org/10.1007/s12517-016-2786-y

Heidbach O, Tingay M, Barth A, Reinecker J, Kurfeß D, Müller B (2010) Global crustal stress pattern based on the world stress map database release 2008. Tectonophysics 482(1):3–15
Hoffmann J, Zebker HA, Galloway DL, Amelung F (2001) Seasonal subsidence and rebound in Las Vegas Valley, Nevada, observed by Synthetic Aperture Radar Interferometry. Water Resour Res 37 (6):1551–1566
Hooper A, Bekaert D, Spaans K, Arikan M (2012) Recent advances in SAR interferometry time series analysis for measuring crustal deformation. Tectonophysics 514–517:1–13
Hussein IM, Abdallah AMA (2001) Tectonic evolution of the northeastern part of the African continental margin, Egypt. J Afr Earth Sci 33(1):49–68
Ibrahim EM, Marzouk I (1979) Seismotectonic study of Egypt. Bull Helwan Inst Astronom Geophys 191
Ismail A (1960) Near and local earthquakes at Helwan from 1903–1950. Helwan Observatory Bull. no 49
Joffe S, Garfunkel Z (1987) Plate kinematics of the circum Red Sea—a re-evaluation, Tectonophysics, vol 141, 5–22
Sakr K, Radwan AM, Rashwan M, Gomaa M (2015) Estimation of crustal movements using the global positioning system (GPS) measurements along The Nile Valley Area, Egypt from 2007 to 2012, Nriag J Astron Geophys 4:55–63
Karnik V (1969) Seismicity of Europe, parts I and II. Academic Publishing House, Czechoslovakia Acad. Sci., Prague
Kebeasy RM (1990) Seismicity of Egypt. In: Said R (ed) Geology of Egypt. A. A. Balkema, Rotterdam, pp 51–59
Kebeasy RM, Maamoun M, Albert RNH, Megahed M (1981) Earthquakes activity and earthquakes risk around Alexandria, Egypt. Bull of IISEE, 19
Koktavy P, Pavelka J, Sikula J (2004) Characterization of acoustic and electromagnetic emission sources. Meas Sci Technol 15:973–977
Lichtenberger M (2005) Regional stress field as determined from electromagnetic radiation in a tunnel. J Struct Geol 27:2150–2158
Lichtenberger M (2006a) Bestimmen von Spannungen in der Lithosphäre aus geogener elektromagnetischer Strahlung. PhD thesis, University of Heidelberg, 140 pp
Lichtenberger M (2006b) Underground measurements of electromagnetic radiation related to stress-induced fractures in the Odenwald Mountains (Germany). Pure Appl Geophys 163:1661–1677
Maamoun M (1979) Macroseismic observations of principal earthquakes in Egypt. Bull of Helwan Inst of Ast and Geoph No 183
Maamoun M, Allam A (1980) A study of the seismicity of the east Mediterranean region. 7th Ann Meet, EGS-ESC, Budapest
Maamoun M, Ibrahim E (1978) Tectonic activity of Egypt as indicated by earthquakes. Bull. of Helwan Inst. of Ast. and Geoph. no. 170
Maamoun M, Megahed A, Allam A (1984) Seismicity of Egypt, HIAG Bull., v. IV, Ser B
Mallik J, Mathew G, Angerer T, Greiling RO (2008) Determination of directions of horizontal principal stress and identification of active faults in Kachchh (India) by electromagnetic radiation (EMR). J Geodyn 45:234–245
Massonnet D, Rossi M, Carmona C, Adragna F, Peltzer G, Feigl K, Rabaute T (1993) The displacement field of the Landers earthquake mapped by radar interferometry. Nature 364:138–142
Misra A, Gosh S (1980) Electromagnetic radiation characteristics during fatigue crack propagation and failure. Appl Phys 23:387–390
Moustafa AR, Abdallah AM (1991) Structural setting of the central part of the Cairo-Suez district. M.E.R.C. Ain Shams Univ. Earth Sc. Ser. 5, pp 133–145
Moustafa AR, Abdel Tawab SM (1985) Morphostructures and non-tectonic structures of Gebel Mokattam. MERC Ain Shams Univ Earth Sci Ser 5, pp 65–78
Moustafa AR, Yehia MA, Abdel Tawab S (1985) Structural setting of the area east of Cairo, Maadi and Helwan. MERC Ain Shams Univ Earth Sci Ser 5:40–64
O´Keefe SO, Thiel DV (1995) A mechanism for the production of electromagnetic radiation during fracture of brittle materials. Phys Earth Planet Interi 89:127–135
Obermeyer H (2001) Handbuch zur Anwendung der NPEMFE-Methode mittels des Cereskops. Ceres GmbH, Staffort, p 32
Obermeyer H (2005) Measurement of natural pulsed electromagnetic radiation (EMR) with the Cerescope. Ceres GmbH, Staffort
Obermeyer H, Lauterbach M, Krauter E (2001) Monitoring landslides with natural electromagnetic pulse radiation. In: international conference on landslides, 297–304.
Poirier IP, Taher MA (1980) Historical seismicity in the near and middle east, north Africa and Spain from Arabic documents (VIIIth–XVIIth century). Bull Seis Soc Amer 70:2185–2201
Rabinovitch A, Frid V, Bahat D (2007) Surface oscillations-a possible source of fracture induced electromagnetic radiation. Tectonophysics 431:15–21
Radwan AM, Hosney A, Kotb A, Khalil Ahmed, Abed A, Rayan A (2015) Assesment of the geodynamical setting around the main active faults at Aswan area, Egypt. Arab J Geosci 8:4317–4327
Reilinger R, Toksöz N, McClusky S, Barka A (2000) 1999 Izmit, Turkey earthquake was no surprise. GSA Today, vol 10, no 1, January 2000
Reuther C, Moser E (2007) Orientation and nature of active crustal stresses determined by electromagnetic measurements in the Patagonian segment of the South America Plate. Intern J Earth Sci 98:585–599
Reuther C, Obermeyer H, Reicherter K, Reiss S, Kaiser A, Buchmann T, Adam J, Lohrmann J, Grasso M (2002) Neotektonik und aktive Krustenspannung in Südost-Sizilien und ihre Beziehung zur regionalen Tektonik im Zentralen Mittelmeer. Mitteilungen Geologisches Paläontologisches Institut, Universität Hamburg 86:1–24
Ryder I, Bürgmann R (2008) Spatial variations in slip deficit on the central San Andreas Fault from InSAR. Geophys J Int 175(3): 837–852
Salamon A, Hofstetter A, Garfunkel Z, Ron H (1996) Seismicity of the Eastern Mediterranean region: Perspective from the Sinai subplate. Tectonophysics 263:293–305
Saleh M, Becker M (2014) A new velocity field from the analysis of the Egyptian permanent GPS Network EPGN. Arab J Geosci 7 (11):4665–4682
Saleh M, Becker M (2019) Mohamed Saleh and Matthias Becker, New estimation of Nile Delta subsidence rates from InSAR and GPS analysis. Environ Earth Sci 78:6. https://doi.org/10.1007/s12665-018-8001-6
Saleh M, Masson F, Mohamed A-MS, Boy J-P, Abou-Aly N, Rayan A (2018) Recent ground deformation around Lake Nasser Using GPS and InSAR, Aswan. Tectonophysics (Under publication), Egypt
Savage W (1984) Evaluation of regional seismicity. Woodward and Clyde Consultants, Internal Report to Aswan High Dam Authority (unpublished)
Schmidt DA, Bürgmann R (2003) Time-dependent land uplift and subsidence in the Santa Clara valley, California, from a large interferometric synthetic aperture radar data set. J Geophys Res Solid Earth 108(B9)
Sieberg A (1932) Untersuchungen ueber Erdbeben und Bruchschollenbau im Oestlichen Mittelrmeergebiet, Denkschriften der med., naturw., Ges. Zu Jena, 18-band, 2.Lief
Slifkin L (1993) Seismic electric signals from displacement of charged dislocations. Tectonophysics 224:149–152
Sofratome Group (1984) Report on El-Dabaa nuclear power plant. Ministry of Electricity, Egypt

Spada G et al (2004) Modeling Earth's post-glacial rebound. EOS Trans AGU 85(6):62–64. https://doi.org/10.1029/2004EO060007

Tokuji U (1989) Catalogue of damaging earthquakes of the world (Preliminary Compilation). Earthq Res Inst, Tokyo University, Japan

Zebker HA, Goldstein RM (1986) Topographic mapping from interferometric synthetic aperture radar observations. J Geophys Res Solid Earth 91(B5):4993–4999

Zebker H, Rosen P (1994) On the derivation of coseismic displacement fields using differential radar interferometry: the Landers earthquake. In Geoscience and remote sensing symposium, 1994. IGARSS 94. Surface and atmospheric remote sensing: technologies, data analysis and interpretation, International, volume 1, pp 286–288

Zebker H, Villasenor J (1992) Decorrelation in interferometric radar echoes. IEEE Trans Geosci Remote Sens 30(5):950–959

Impact Craters and Meteorites: The Egyptian Record

11

L. Folco, W. U. Reimold, and A. El-Barkooky

Contents

Abstract

This chapter provides an account of the present Egyptian impact cratering record as well as an overview of the Egyptian meteorite collection. The 45-m-diameter Kamil crater in the East Uweinat District in southwestern Egypt is so far the only confirmed impact crater in Egypt. Due to its exceptional state of preservation Kamil can be considered a type-structure for small-scale impacts on Earth. Enigmatic types of natural glasses including the Libyan Desert glass found in the Great Sand Sea and the Dakhleh glass found near Dakhla Oasis (note that Dakhla, Dakhleh and Dakhlah are transliterations) may be products of low-altitude airbursts of large and fragile cometary or asteroidal impactors. A number of circular, crater-shaped geological structures superficially resembling impact craters are discussed. To date the Egyptian meteorite collection totals 2 falls, including the ~10 kg Martian meteorite Nakhla that has served as a keystone for the understanding of magmatic differentiation processes on Mars, and 76 finds. With the exception of a minority of incidental findings, most Egyptian meteorite finds (~75%) were recovered over the last ~30 years from three dense meteorite collection areas, namely the El-Shaik Fedl, Great Sand Sea and Marsa Alam fields. The exceptional exposures of the Precambrian basement and Paleozoic to Cenozoic sedimentary covers in Egypt offer a good opportunity for the identification of new impact structures. Likewise, Egypt's vast rocky desert surfaces are of great potential for the collection of meteorites through systematic searches. These prospects are

L. Folco (✉)
Dipartimento di Scienze della Terra, Università di Pisa,
Via S. Maria 53, 56126 Pisa, Italy
e-mail: luigi.folco@unipi.it

W. U. Reimold
Laboratory of Geochronology, Instituto de Geociências,
Universidade de Brasília, 70910 900 Brasília, DF, Brazil

A. El-Barkooky
Department of Geology, Faculty of Sciences, Cairo University,
Giza, Egypt

Z. Hamimi et al. (eds.), *The Geology of Egypt*, Regional Geology Reviews,
https://doi.org/10.1007/978-3-030-15265-9_11

fundamental ingredients for fostering the ongoing development of meteoritics and planetary science in Egypt as disciplines for future scientific endeavor in Africa.

11.1 Introduction

The cosmochemical and mineralogical study of meteorites (cm-to-m-sized interplanetary rock debris fallen from space) and the geoscientific study of impact craters produced by the hypervelocity impacts of much larger bodies are of fundamental importance for understanding the geology of the Earth system in a planetary perspective. Impact cratering is one of the most important processes forming and modifying geological surfaces in the solar system. Impact crater structures are—or have been—the main landform on all solid bodies, from asteroids to comets, and from planets to their satellites. Over 50 years of study of the ~200 impact structures recognized to date on the surface of our planet has documented the important role of impacts throughout the history of the Earth, from their local to their global catastrophic effects. Meteorites are rock fragments of a large variety of planetary bodies in the solar system. The great petrologic diversity of meteorites provides a nearly continuous record of planetary evolution, from the early formation of primordial accretional aggregates (chondrites) in the protoplanetary disk to the differentiation of asteroids and terrestrial planets, including the proto-Earth, into metallic cores (iron meteorites) and silicate mantles (achondrites).

In this chapter we provide a detailed account of the present Egyptian impact record and an overview of the Egyptian meteorite collection (Fig. 11.1). Section 11.2 is an overview of the impact cratering process, giving basic information for understanding its importance as a geological process, and for the identification of new impact structures and their ejecta. Section 11.3 first presents the geology of the only impact crater in Egypt confirmed thus far—Kamil Crater (45 m in diameter)—a unique type-structure for investigating the processes and products associated with the impact of small impactors; this is followed by a discussion of the non-impact origin of several crater-like circular structures superficially resembling impact craters in the Western Desert of Egypt, as well as the proposed impact origin of the Libyan Desert Glass and Dakhleh Glass. Section 11.4 is a general introduction to meteorites that highlights their fundamental role in our understanding of the origin and evolution of the solar system. Section 11.5 reports on the 78 meteorites from Egypt to date (September 2018)—including the ~10 kg rare Martian meteorite fall of 1911—Nakhla, their role in the advancement of meteorite studies, and on the potential of the Egyptian deserts for systematic searches for meteorites. Section 11.6 provides an account of the role of meteoritic iron in the Egyptian archeo-anthropological record and its bearing on the history of human civilization. In the last section 11.7 we discuss a number of perspectives for the future of meteoritics and planetary science in Egypt.

11.2 Impact Cratering: An Overview

Large bolide impact cratering is one the most important geologic processes in the solar system (e.g., Melosh 1989; Reimold and Jourdan 2012; Hargitai et al. 2015)—and undoubtedly beyond. Impact crater structures are found on the surfaces of all solid bodies in the solar system, from planets to satellites, from asteroids to comets. On many of these bodies, like the Moon or Mercury, impact craters are the dominant landform. On Earth active geodynamics (mainly plate tectonics, erosion and sedimentation) tends to rapidly erase impact structures from the geological record. To date only ~200 impact structures have been confirmed on Earth (http://www.passc.net/EarthImpactDatabase/), with the largest and one of the oldest, the 2,020 million year old Vredefort impact structure (South Africa) having originally been ~250–300 km in diameter (Reimold and Koeberl 2014). Evidence of early impact events is rare and recorded only in a small number of impact deposits (so-called spherule layers) with ages of ~2.5 and ~3.5 billion years (Glass and Simonson 2012), many samples of which carry distinctive chemical signatures from the meteoritic impactors. Despite this relatively limited record, interdisciplinary research over the last 50 years has documented the important role of impacts throughout the history of the Earth, from their local to their global catastrophic effects (e.g., Osinski 2008; Reimold and Jourdan 2012; Pierazzo and Artemieva 2012). Catastrophic impact events have had a role in the development of life and have been implicated widely in the debates about the causes of mass extinctions and major evolutionary radiation events. Impact events are indeed destructive, but they may also provide certain economic benefits, including the formation of metalliferous ore deposits, convenient traps for fossil fuel reserves, and locations for water reservoirs (e.g., Reimold et al. 2005). Impact structures can also form new biological niches, which can provide favorable conditions for the survival and evolution of life (Cockell 2006). They can also reveal subsurface stratigraphic information. One of the most outstanding examples is the deeply eroded Vredefort structure, which has provided insight into the nature of the mid-crust and the geological evolution of the Kaapvaal craton over ~3.4

Fig. 11.1 Map of Egypt showing locations of the geological features discussed in this chapter: (i) Kamil crater, the only confirmed impact crater in Egypt (e.g., Folco et al. 2010). (ii) The geological circular features of non-impact origin: El Baz, the Gilf Kebir crater field (GKCF) and Kebira (Reimold and Koeberl 2014). (iii) The strewn field of the Libyan Desert Glass (LDG; green color area). (iv) The collection area of Dakhleh Glass (DG; yellow color area). (v) The find/fall locations of the 78 Egyptian meteorites (orange circles with and without central black dots for falls and finds, respectively) known to date (June 2018) and the boundaries (orange dashed lines) of the three official dense (meteorite) collection areas, as given in the Meteoritical Bulletin database (accessed September 2018, i.e. Great Sand Sea (GSS), Marsa Alam (MA), and El-Shaikh Fedl (ESF). Background image based on Bing and Google Map imagery (see http://www.google.com)

billion years (Gibson and Reimold 2008). Finally, many impact structures are sites of great educational value. It is for all these reasons that impact cratering studies have moved into the geological mainstream.

The effective intertwining between geological studies of impact structures on Earth and numerical modeling of the physical processes involved with impacts (Melosh 1989; Collins et al. 2012) has been instrumental in fostering better understanding of the impact cratering process—a unique, highly dynamic geological process. Extraterrestrial impactors approach Earth at hypervelocity speeds (on average, 18 km/s for asteroids and at least twice this speed for comets). The considerable kinetic energy of such bolides is transferred via a shock front into the target rock, generating

pressures and temperatures that are orders of magnitude greater than those produced by conventional endogenic processes. Rocks are broken, deformed, heated and transformed in unique and irreversible ways. Impact-generated strain rates surpass those of any other geological process by orders of magnitude. Kilometer-scale craters are excavated and collapse gravitationally in minutes, ejecting impact debris on scales that may be continental or global for kilometer-sized impactors. Released gases may cause relatively long-term climate perturbations and elevated temperatures in the crust may persist for thousands of years.

"Impactites" is the collective name for a series of distinct rock types generated by the passage of shock waves (i.e., a compression wave propagating faster than sound) associated with hypervelocity impacts. These impactite types range from purely clastic breccias, composed of fragments of target rock, to impact melt rocks, composed of a groundmass of melt that typically contains clasts of target rock and minerals. A transitional rock type is known as suevite and comprises small bodies of impact melt entrained in a clast-dominated groundmass. Stöffler and Grieve (2007) and Stöffler et al. (2018) have given detailed descriptions of the known impactite types and their recommended nomenclature. The passage of a shock wave first produces compression of the target rock, followed by decompression from peak shock pressures, with concomitant heat generation. Its irreversible effects on rocks and minerals are generally referred to as "shock metamorphism" (or as "impact metamorphism"; e.g. Gillet and El Goresy 2013; Ferrière and Osinsky 2013; Deutsch et al. 2015; Stöffler et al. 2018).

On the Moon and other solid planetary bodies in the solar system that are characterized by the lack of an atmosphere and of plate tectonics, impact craters are well preserved features, and can be recognized from their characteristic morphologies and structures. These vary progressively with increasing energy of the impact from relatively small simple bowl-shaped craters to relatively large (up to hundreds or thousands of km in diameter) complex crater structures, including the morphologies of central peak craters, peak-ring craters, and multi-ring basins (e.g., Reimold and Koeberl 2014; Hargitai et al., 2016).

On Earth identification of impact structures is often difficult, mainly due to the destructive effects of weathering, erosion, tectonic deformation, or burial of impact craters and possible remnants of the impactors. Fresh impact structures typically are characterized by a raised rim with overturned stratigraphy; extensive fracturing and brecciation are additional characteristic features but those alone are not diagnostic. In the interest of improving Earth's impact cratering record, diagnostic criteria for accurate identification and confirmation of impact structures and their deposits on Earth have been developed to overcome these problems (e.g., French and Koeberl 2010; Reimold and Koeberl 2014). Diagnostic evidence for impact events may be present in the target rocks that were affected by the impact—either in exposed target rock of the crater floor or, when present, a central stratigraphically uplifted terrain known as "central uplift"—and in breccia occurrences that may be found within a suspicious structure or perhaps outside. Circular structures that are anomalous in the regional geologic context, or circular or annular geophysical anomalies are possible indicators of impact crater structures. However, neither is diagnostic and an impact origin must be confirmed by the presence of any of the following key features (Fig. 11.2):

i. Shatter cones: a conical-to-subconical fracture phenomenon in rock, with narrow striae emanating from a small apex area. The formation process of shatter cones is still debated (Baratoux and Reimold 2016). However, this distinctive fracturing phenomenon to date has only been described from impact structures (and nuclear explosion sites), where they are formed in the shock pressure range from ~2 to 30 GPa. They occur at scales from centimeters to meters and are the only known meso- to macroscopic impact-diagnostic criterion.
ii. Diagnostic shock-metamorphic effects, including planar deformation features, deformation twins in zircon; diaplectic glass after silicate minerals; high-pressure mineral polymorphs such as diamond (after graphite), coesite and stishovite (after quartz), reidite (after zircon)—all mineral polymorphs that are not formed by other geological processes in rocks of the upper crust), or ringwoodite or wadsleyite (after olivine)—and many other high-pressure minerals discovered in meteorites (e.g., Langenhorst and Deutsch 2012; Ferrière and Osinsky 2013; Deutsch et al. 2015; Cavosie et al. 2018).
iii. It may also be possible to identify, admittedly rarely, remnants of the extraterrestrial impactors in the form of fragments of a meteorite, or traces of projectiles in impact breccias through detection of their chemical or isotopic extraterrestrial signatures (e.g., Koeberl et al. 2012; Goderis et al. 2013; Koeberl 2014).

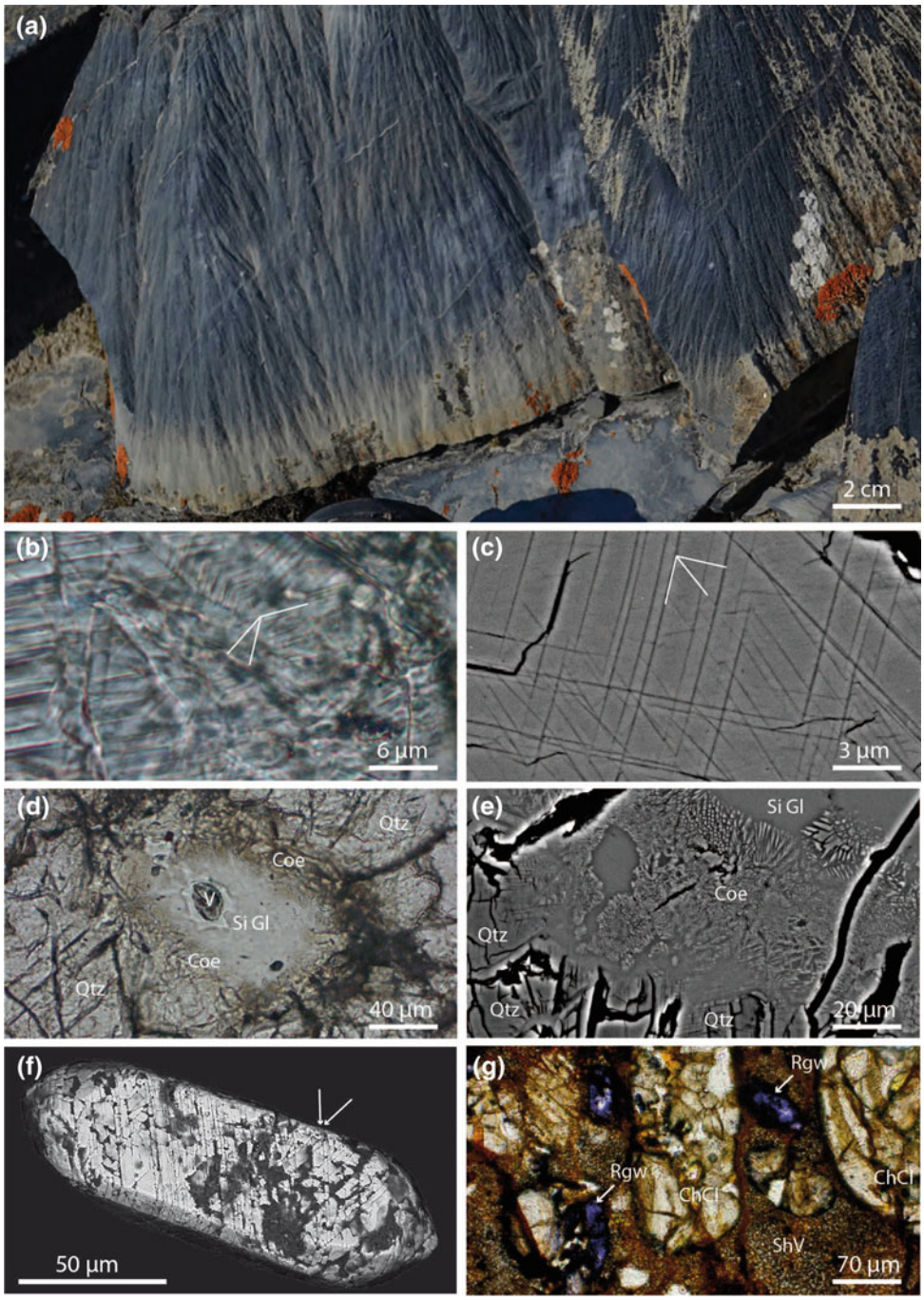

Fig. 11.2 A selection of key shock metamorphic features. **a** Shatter cones in fine-grained Neoproterozoic limestone in an outcrop at the center of the ~25-km-diameter Tunnunik crater (Canada). Image courtesy of Pierre Rochette (CEREGE, France). **b** Optical micrograph of planar deformation features (PDF) in a quartz crystal from a shocked sandstone found in the ejecta deposit around the 45-m-diameter Kamil Crater (Egypt, Fig. 11.1). The orientations of three sets of PDF are indicated. **c** Back-scattered electron image of PDF (three sets are indicated) in a quartz crystal from the same rock. Image courtesy of Agnese Fazio (Friedrich-Schiller—Universitat Jena). **d** Optical micrograph showing an intergranular assemblage of microcrystalline coesite (brown) set in silica glass in a shocked sandstone from Kamil Crater. **e** Back-scattered electron image of the same feature. **f** Back-scattered electron image of a detrital shocked zircon found in the Vaal River of South Africa (after Erickson et al. 2013). The zircon grain was eroded from shocked bedrock of the ~2.0 Gyr-old Vredefort impact structure. Planar microstructures visible on the surface of the grain (see arrows) are a manifestation of shock damage of zircon. These features were shown to be {112} deformation twins which form in zircon at ~20 GPa, conditions only created in Earth's crust during meteorite impacts. Image courtesy of Aaron Cavosie, Curtin University, Western Australia). **g** Optical micrograph of ringwoodite crystals (purple) set a in dark, clast laden, microcrystalline shock vein of a highly shocked chondritic (DaG 528) meteorite. Image courtesy of Fabrizio Campanale (Universita di Pisa, Italy). Abbreviations: Coe = coesite; Qtz = quartz; SiGl = Silica glass; V = vesicle; Rgw = ringwoodite; ChCl = chondritic clast; ShV = shock vein

11.3 The Impact Record of Egypt

11.3.1 Kamil Crater: The Only Confirmed Impact Crater in Egypt

Kamil Crater in the East Uweinat District, southwestern Egypt (22°01′06″ N, 26°05′15″ E Fig. 11.1), is a 45-m-diameter impact crater with a pristine ejecta ray structure in its environs (Fig. 11.3; Folco et al. 2010). Formed less than 5,000 years ago by the hypervelocity impact of an iron meteorite named Gebel Kamil, it is the only confirmed impact structure in Egypt so far. The structure was identified in 2008 by V. De Michele (former curator of the Natural History Museum in Milan, Italy) during a Google Earth™ survey. Two years later, field work carried out as part of the 2010 Italian-Egyptian geophysical investigation confirmed the impact origin of the structure (Folco et al. 2010).

Folco et al. (2011) and Urbini et al. (2012) reported that the crater occurs on exposed pale sandstones (mainly quartz arenites) of the Gilf Kebir Formation (Early Cretaceous) that are locally overlain by a few centimeters of loose soil. The sandstones have subhorizontal bedding and constitute part of the sedimentary cover uncomformably overlying the Precambrian crystalline basement. The crater has all the characteristic features of simple craters including a bowl shape and a raised rim (raised up to ~3 m above the presumed pre-impact surface). The true crater floor, at an average depth of 16 m below rim crest, is overlain by an ~6-m-thick crater-fill consisting of displaced blocks and stratified fallout debris. At crater walls, bedding of the bedrock is upturned (up to 40°) and dips radially outward. An overturned flap of ejected material is locally present at the rim crest. The bulk of the debris ejected from the impact crater consists of sandstone fragments ranging from large boulders, with masses up to 4 tons, to dust. Their pale color sharply contrasts with the darker color of the weathered bedrock (Fig. 11.3). A continuous ejecta blanket extends radially for ~50 m from the crater rim in a northward, eastward, and southward direction. Three ejecta rays extend for as much as 350 m from the crater rim and trend to the north, southeast, and southwest. Such well-preserved structures have been previously observed only on airless extraterrestrial rocky or icy planetary bodies and attest to the exceptional freshness of the structure.

Through systematic visual searches, over 5000 iron meteorite specimens amounting to a total of 1.7 tons were identified within the crater and in its vicinity (Fig. 11.4; Folco et al. 2010, 2011; D'Orazio et al. 2011). They all have the characteristics of shrapnel produced by fragmentation of the impactor upon impact with masses ranging up to ~34 kg (Fig. 11.4a, b), except for one regmaglypted, partly fusion-crusted individual of ~90 kg mass (Fig. 11.4c) that likely detached from the main impact body during atmospheric flight. This led Folco et al. (2010, 2011) to suggest that Kamil Crater was generated by an impactor that hit the ground nearly intact without significant fragmentation in the atmosphere. Meteoritic debris (shrapnel) is concentrated in terms of mass and number towards the southeast of the crater, whereas it is virtually absent in the northwestern quadrant (Fig. 11.4d). This asymmetric distribution defines the downrange jet of impactor debris produced by an oblique impact from the northwestern quadrant. Putting together the total mass of meteorite specimens found during systematic visual searches (D'Orazio et al. 2011), of specimens buried in the ejecta that could be detected through a magnetic survey (Urbini et al. 2012), and of microscopic impactor debris found in the soil around the crater, the projectile mass was estimated at about 10 tons (Folco et al. 2015). Noble gas and radionuclide analyses of the Gebel Kamil iron meteorite by Ott et al. (2014) point to a pre-atmospheric mass > 20 tons, but it may have been as much as 50–60 tons.

D'Orazio et al. (2011) provided a detailed account of the petrography and geochemistry of the Gebel Kamil meteorite. The meteorite is classified as an ungrouped Ni-rich ataxite (Ni = 19.8 weight% [wt%], Co = 0.75 wt%, Ga = 49.5 μg g^{-1}, Ge = 121 μg g^{-1}, Ir = 0.39 μg g^{-1}).

Fazio et al. (2014, 2016) carried out petrographic studies of samples from the crater wall and from ejecta deposits collected during the 2010 geophysical campaign in order to investigate shock effects recorded by small impact craters on Earth. They reported a wide range of shock metamorphic features indicative of a range of high pressures (locally up to ~60 GPa) and temperatures (even in excess of ~1700 °C) typical of hypervelocity impacts. These features include:

(i) Ill-developed shatter cones, pseudotachylitic breccia veinlets in sandstone specimens found in the ejecta, planar deformation features in quartz (Fig. 11.2b, c), the high-pressure silica polymorphs coesite (Fig. 11.2d, f) and stishovite, lechatelierite (silica glass), baddeleyite as decomposition product after zircon in shocked target sandstone.
(ii) Impact melt lapilli, bombs and microscopic impact spherules found scattered around the crater (Fig. 11.5). The impact velocity was estimated to have been at least some 3.5 km s^{-1}. Later, Fazio et al. (2016) and Hamann et al. (2018) conducted a detailed petrographic and geochemical investigation of impact melt glasses to improve our understanding of the projectile-target interaction during impact melting.

Based on geo-archeological reasoning, namely the chronological relationship between the impact structure and

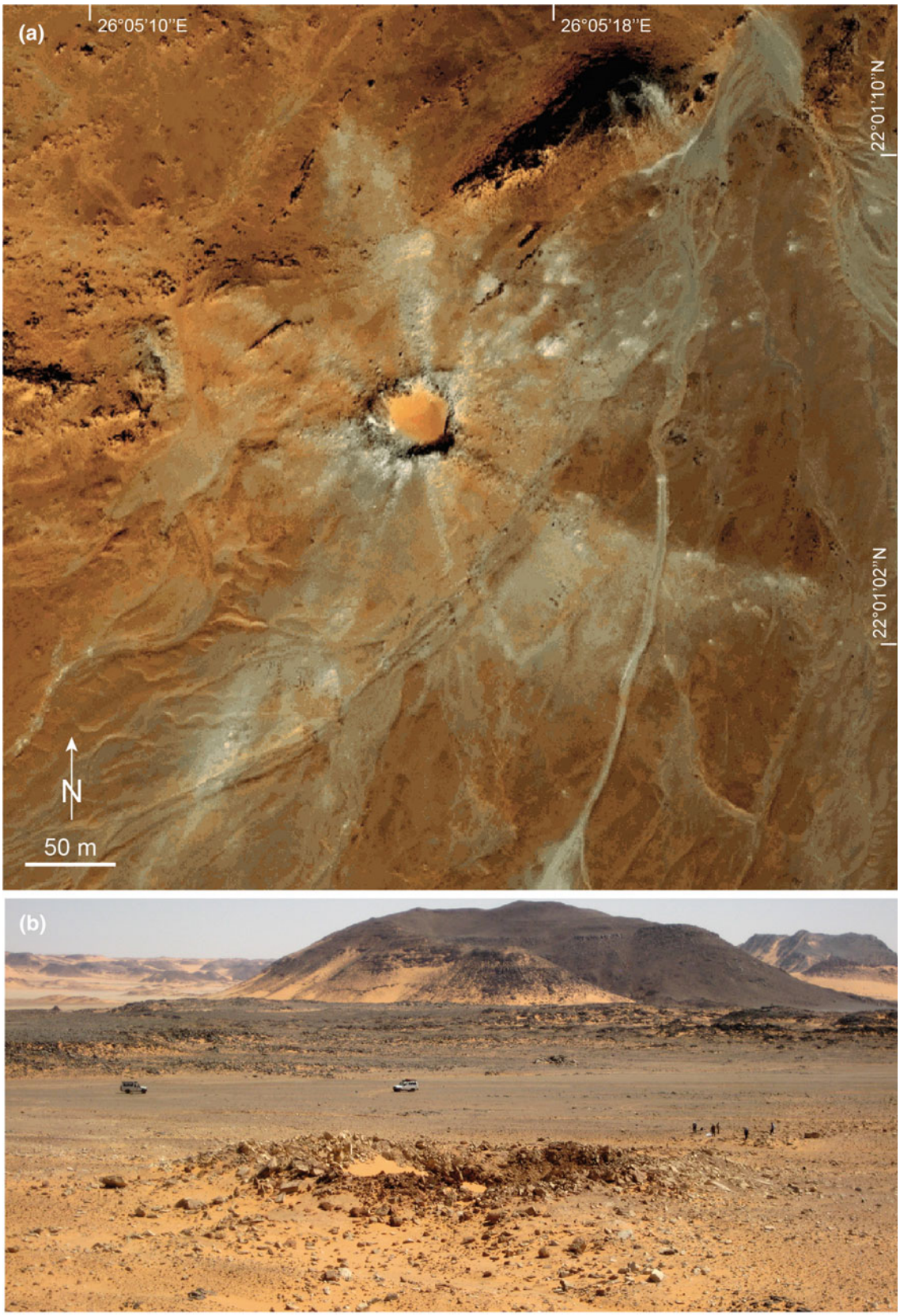

Fig. 11.3 The 45-m-diameter Kamil Crater, southwestern Egypt (22°01′06″ N, 26°05′15″ E; location map in Fig. 11.1) (after Folco et al. 2010, 2011). QuickBird satellite image (22 October 2005; courtesy of Telespazio); note simple crater structure and prominent ejecta ray pattern indicative of an exceptional state of preservation. Inset: Location map. B) View of the crater from the west

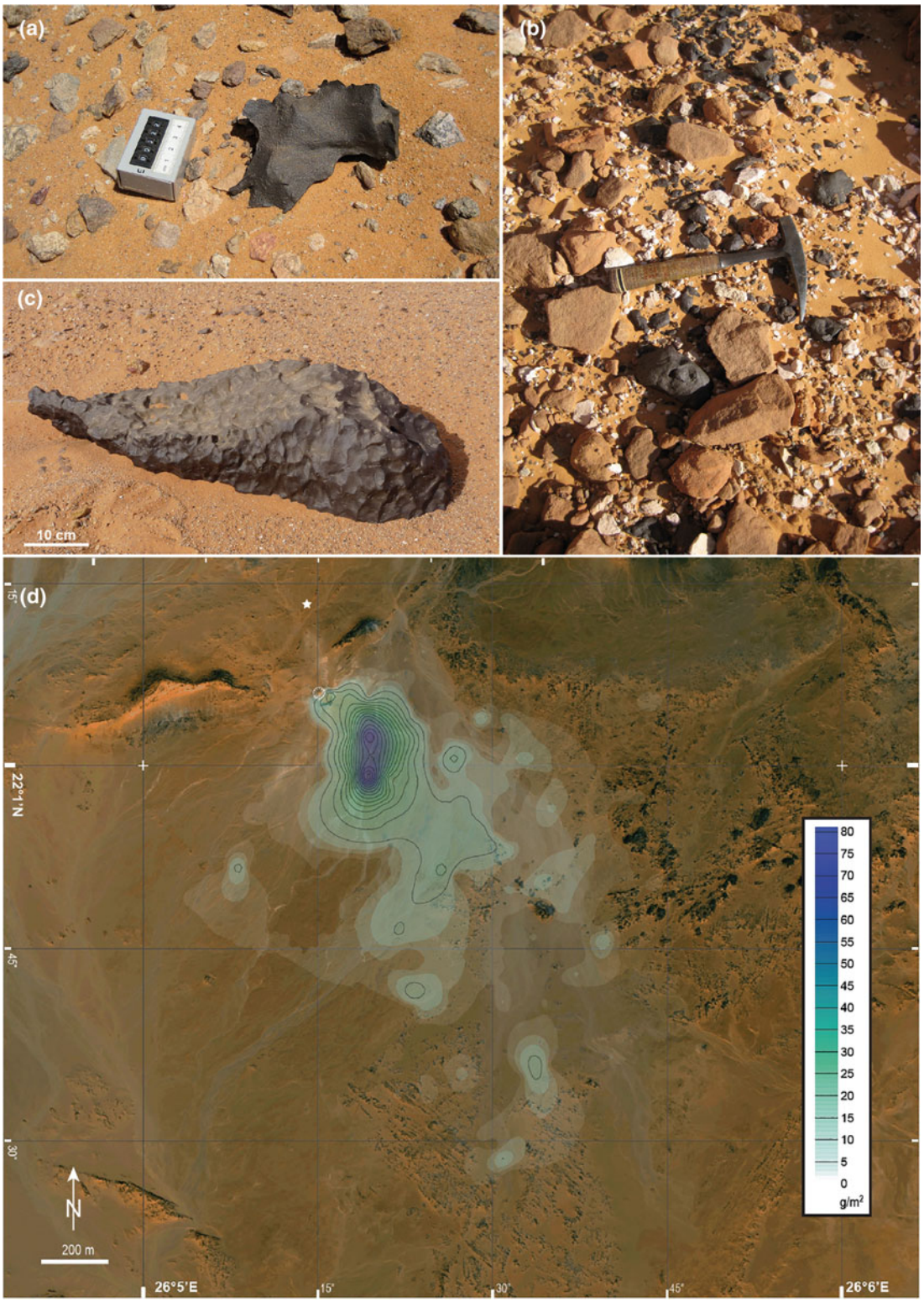

Fig. 11.4 The iron meteorite named Gebel Kamil (after Folco et al. 2011; D'Orazio et al. 2011). **a** Field photograph of one of the thousands of meteorite fragments (shrapnel) found scattered in the crater and surrounding area. **b** Local concentration of tens of iron meteorite shrapnel occurring close to the southeast rim of the crater. **c** Field photograph of the ~83 kg meteorite specimen with regmaglypts found ~230 m due north of the crater. **d** Gebel Kamil meteorite distribution map (g/m^2) obtained through linear interpolation of average meteorite density values for 50 m × 50 m cells, with values positioned at their centers. Contour lines are shown at 5 g/m2 intervals. The white star shows the original location of the 83 kg individual (D'Orazio et al. 2011). Image courtesy of Massimo D'Orazio (Universita di Pisa, Italy)

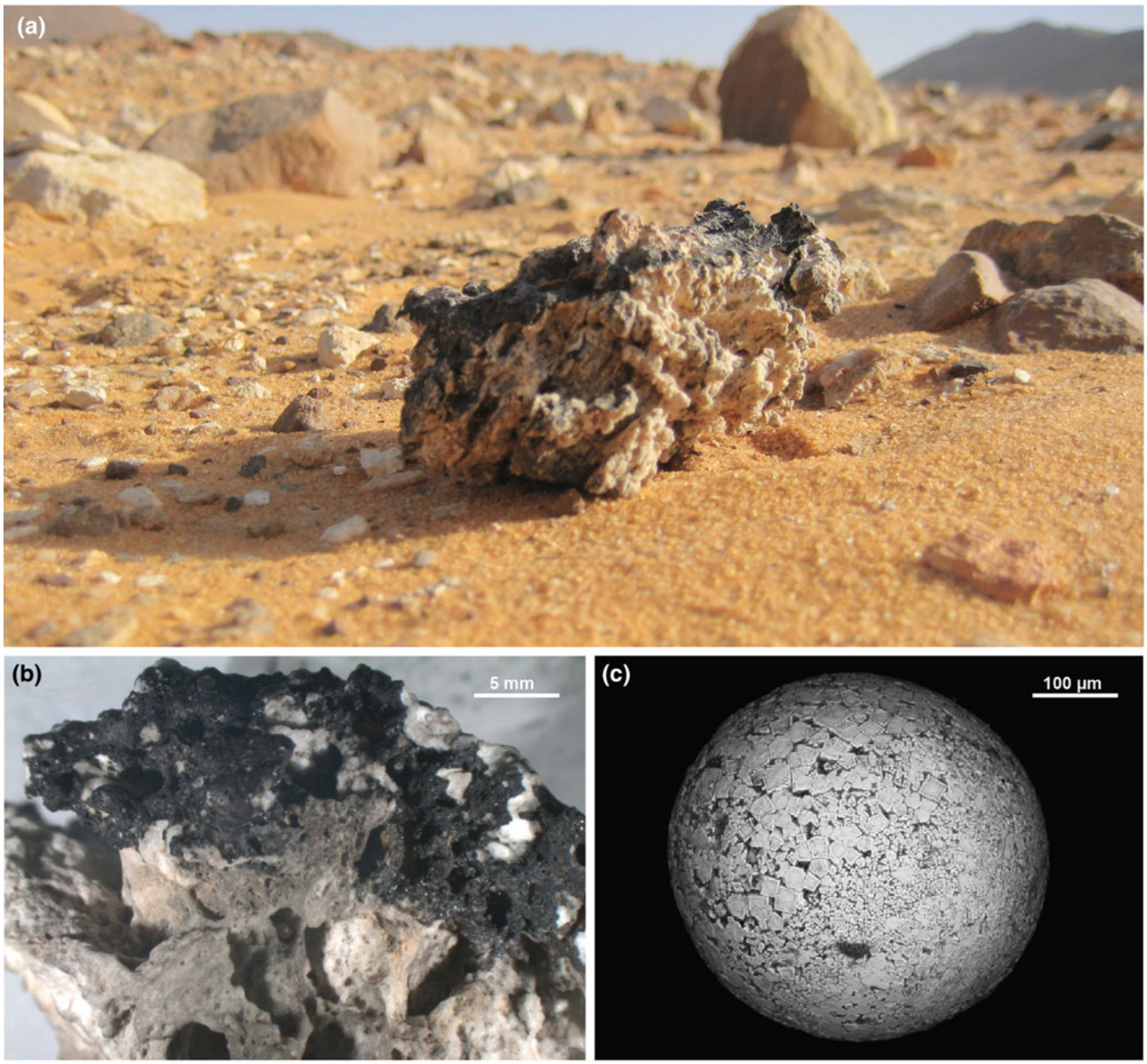

Fig. 11.5 Impact melt glass and spherules from Kamil Crater. **a** A fist-sized pumiceous impact glass specimen found scattered in the ejecta blanket. The white part of the specimen consists of silica-rich glass derived from the melting of the target sandstone. The darker parts are enriched in Fe and Ni as a result of mixing with projectile melt. **b** A section of the same specimen showing increasing darker colors with increasing projectile versus target components. **c** Back-scattered electron image of a microscopic impact melt spherule consisting mainly of Fe-Ni oxides and traces of interstitial silica-rich glass

a number of features (trails, settlements) attesting to pre-historic human occupation of the area, Folco et al. (2011) suggested that the impact event occurred less than 5000 years ago. This young age was later confirmed by thermoluminescence dating of quartz in the shocked target rocks, which yielded a formation age constrained between 2000 BCE and 500 CE, with a favored age interval between 1600 and 400 BCE (Sighinolfi et al. 2015).

Small impact craters (<300 m in diameter) are rare on Earth, and those known are mostly deeply eroded. A number of features attest to the extraordinary state of preservation of Kamil Crater: the bright ejecta rays, the large inventory of shock metamorphic features, and the remnants of fusion crust on a specimen of the iron projectile. Kamil can be considered a type-structure for small-impact craters on Earth and as such, as a natural laboratory to investigate the

processes and products associated with the impact of small projectiles (Folco et al. 2011).

11.3.2 Proposed and Discarded Impact-Crater Candidates

A number of crater-shaped geological structures in Egyptian territory, mainly identified remotely through satellite image analysis, were eventually proven to be of non-impact origin, mainly based on subsequent field work. They are the thousands of circular to elliptical structures in the Gilf Kebir region known in the literature as El Baz (El-Baz 1981), the Gilf Kebir Crater Field (e.g., Paillou et al. 2004) and Kebira (El-Baz and Ghoneim 2007).

11.3.2.1 El-Baz

Through Landsat satellite image analysis, El-Baz (1981) identified a circular structure ~4 km in diameter, located at 24°12′ N, 26°24′ E (Figs. 11.1 and 11.6), among the linear dunes of the Great Sand Sea of Egypt. The structure, denominated El-Baz Crater, occurs in sandstones of the Nubia Formation (note that this is a term traditionally used in a broad range of stratigraphical and sedimentological connotations to designate a thick series of quartzose sandstones overlying the igneous and metamorphic Archean to Lower Paleozoic basement rocks). The structure is characterized by a flat floor, terraced walls, crenulated rim, and subdued remains of a central feature ~1.6 km in diameter. The alleged crater is surrounded by a rough-textured deposit containing large bocks and extending up to 2 km from the crater rim. El-Baz (1981) interpreted the structure as an impact crater based on its overall morphology, similar to that of the bowl-shaped Barringer Crater (aka Meteor Crater) in Arizona, USA. He also noted, however, that the structure could also have been formed by a circular diorite intrusion. The site was visited in 2005 by an Italian geological expedition: Orti et al. (2008) concluded that the El-Baz Crater was one of the many volcanic circular features in the region that are defined by basaltic dikes intruded into the quartz-arenitic bedrock.

11.3.2.2 The Gilf Kebir Crater Field

In 2004, Paillou et al. identified numerous roughly elliptical to circular structures up to several kilometers in diameter through space-borne radar imaging analysis in an area of 4500 km^2 due east of the Gilf Kebir plateau (Figs. 11.1 and 11.7). Field work conducted on 13 structures from 20 m to 1 km in diameter led the research team to propose that they had discovered the largest impact crater field on Earth, possibly created by several meteorites that broke up when entering the atmosphere. Shock deformation in the form of planar deformation features in breccias and shatter cone-like features were alleged as positive evidence for an impact origin of these structures.

Two years later, Paillou et al. (2006) reported the results of an extended satellite imagery analysis of the Gilf Kebir region. Over an area of 40,000 km^2, more than 1300 circular crater-like structures with a typical size of 150 m had been identified. The size and number of the structures, coupled with geological data obtained from field work on a selection of 62 structures, led the team to discuss the alternative hypothesis of a hydrothermal vent complex for the origin of these structures.

In 2005, an Italian expedition (Orti et al. 2008) visited this region and carried out structural geological analysis and geophysical surveys, followed by petrographic and geochemical investigations on samples. They also presented a detailed geological account of the geology of the region surrounding the Gilf Kebir plateau. Extending for ~8000 km^2, the Gilf Kebir Plateau is ~1100 m high and ~300 m above the desert floor. It comprises Paleozoic-Mesozoic clastic Cretaceous to Lower Tertiary sedimentary units of the "Nubia Sandstone", locally covered by Quaternary sand dunes and sheets (Issawi 1982; Klitzsch et al. 1987).

Orti et al. (2008) found that of the 62 structures previously investigated by Paillou et al. (2006) ten structures could be directly associated with basalt dikes. Geophysical data acquired at selected structures did not show the bowl-shaped geometries characteristic of small impact craters. Oblique sandstone layers at the rims of some crater structures dip toward the center of the crater, in contrast to what is expected at small impact craters where uplifted bedding at the crater walls radially dips outwards. Breccias with no characteristic shock deformation features were interpreted as intraformational sedimentary breccias or tectonic breccias. Striations on sandstone and basaltic rocks previously interpreted as shatter cones were recognized as wind-abrasion features.

Orti et al. (2008), thus, determined that the earlier observations were inconsistent with an impact origin for these crater-like structures in the Gilf Kebir area. They concluded that these features are likely related to endogenic processes typical of hydrothermal vent complexes in volcanic areas, which may reflect the emplacement of subvolcanic rocks.

11.3.2.3 Kebira

The name Kebira is an Arabic word, which means "large". It is a circular topographic feature identified by El-Baz and Ghoneim (2007) using satellite imagery, Radarsat-1, and Shuttle Radar Topography Mission (SRTM) data. This feature lies to the west of the Gilf Kebir Plateau straddling the border between Egypt and Libya (~24°39′ N, 24°58′ E; Figs. 11.1 and 11.8). Based solely on the remote sensing data, El-Baz and

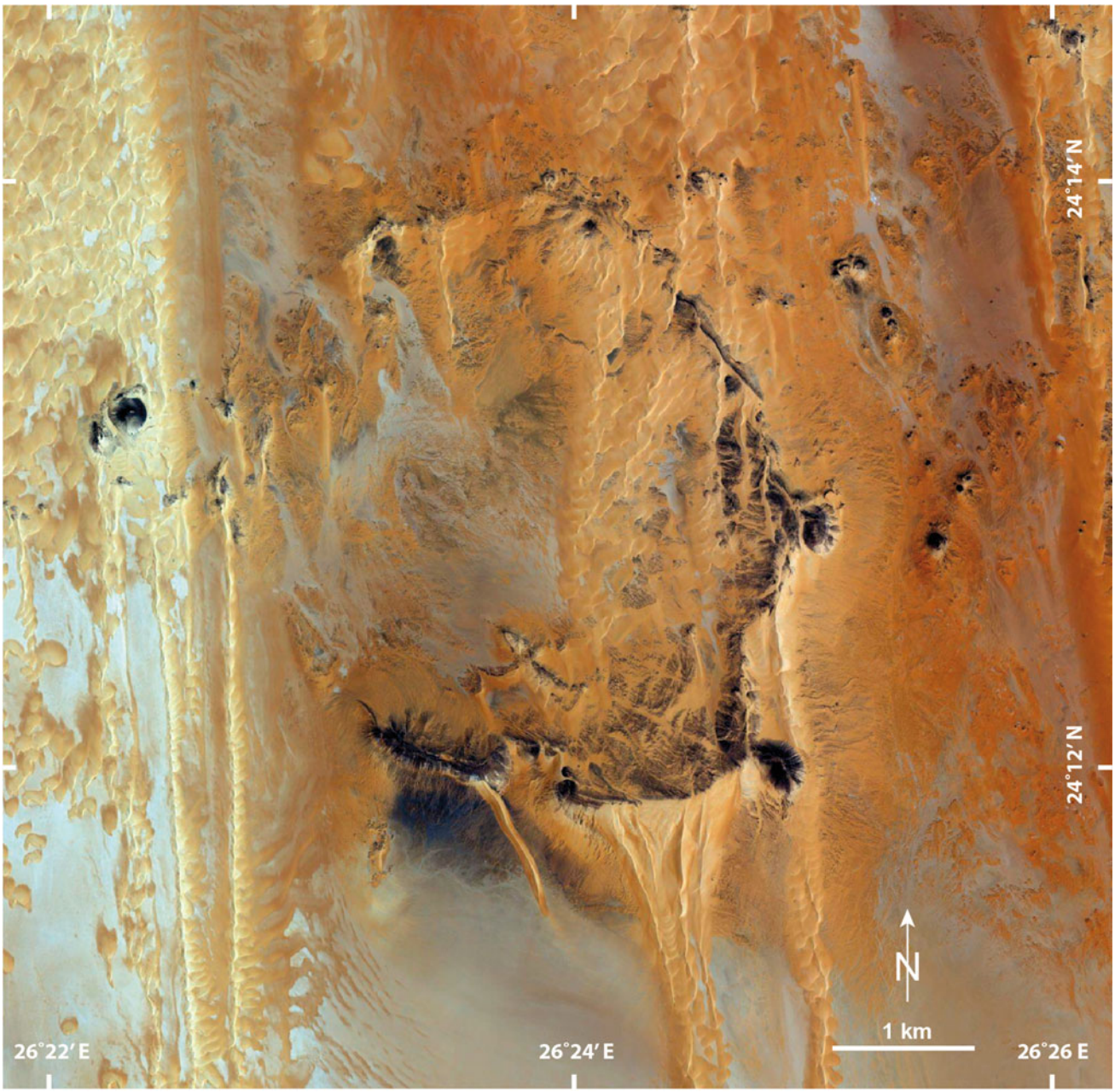

Fig. 11.6 The El-Baz circular (~4 km in diameter), crater-like feature listed amongst the discredited impact proposals (location map in Fig. 11.1). The feature is delimited by basaltic dikes intruded into the quartz-arenitic bedrock and is of volcanic origin (Orti et al. 2008)

Ghoneim (2007) argued that this feature is an exceptionally large (31 km in diameter), double-ringed, impact crater. They suggested that the crater's original morphology had been obscured by wind and water erosion over time. They neither conducted any fieldwork at this feature nor studied any samples collected from it. The alleged "central uplift" retains the horizontal bedding of the surrounding sandstone plateau without indication of stratigraphic uplift, providing clear evidence against a possible impact origin.

11.3.3 Libyan Desert Glass

Libyan Desert Glass (LDG) is an enigmatic, high-silica, natural glass found along the southwestern margin of the Great Sand Sea (Fig. 11.1). The origin of this glass has been a matter of debate since its first scientific investigation in 1932 (Clayton and Spencer 1933). Hundreds of scientific papers have been published about the physical-chemical properties of the LDG, and the vast majority of these agree

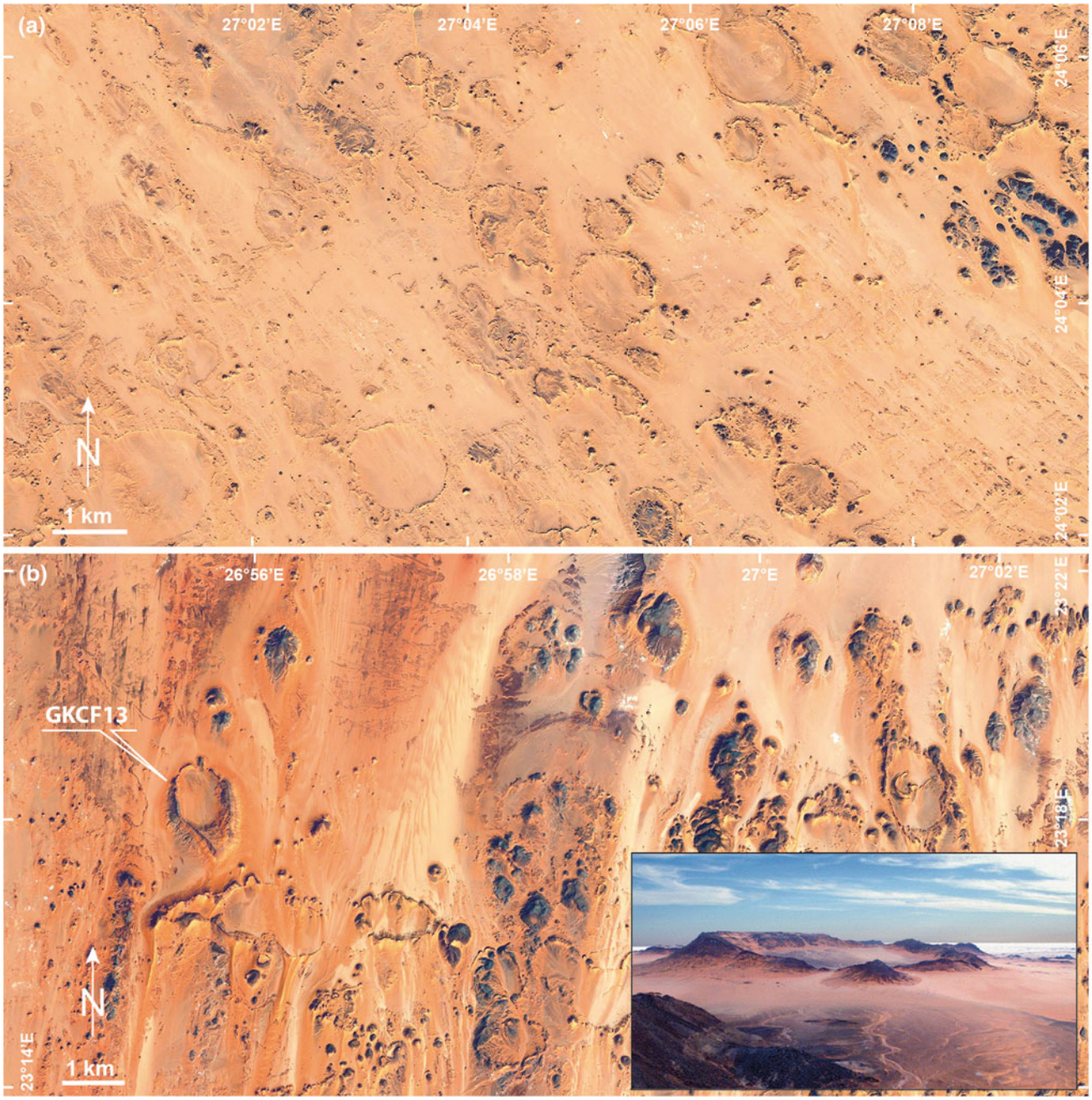

Fig. 11.7 Google Earth images of crater shaped geological features of non-impact origin in the Gilf Kebir region (location map in Fig. 11.1. **a** A portion of the study site 2a investigated by Paillou et al. (2006). **b** A portion of the study site "3a" investigated by Paillou et al. (2006). The inset shows a view from the north-northeast of the ~950-m-diameter crater-like structure denominated GKCF13 by Paillou et al. (2006). All these circular features are seemingly of volcanic origin(Orti et al. 2008)

that it is an impact glass; yet no source crater has been identified so far.

LDG occurs in the form of irregularly-shaped masses up to a few tens of cm in size (Fig. 11.9) that are found strewn across the exposed surface of sandstone bedrock (Cretaceous Nubia Formation) in the linear corridors between the ~100 m high and 3–5 km apart, ~N-S—trending seif sand dunes of the Great Sand Sea. The glass is found discontinuously over a nearly oval area of ~95 × 30 km^2 (Weeks et al. 1984), with a major concentration around ~25°25′ N, 25°30′ E (Barakat et al. 1997). Existing estimates of the amount of glass present on the surface are in

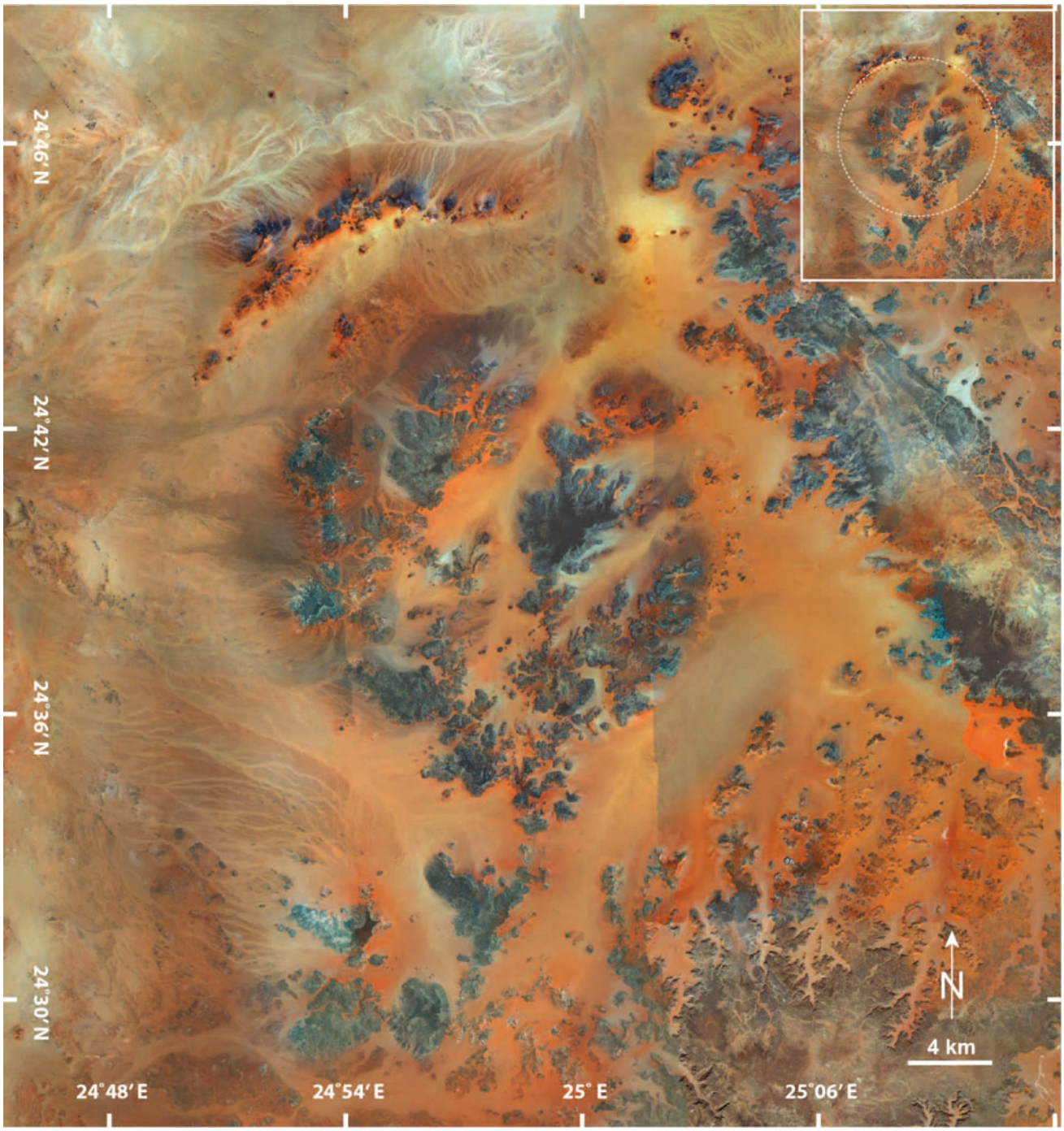

Fig. 11.8 The Kebira morphological feature. El-Baz and Ghoneim (2007) proposed that Kebira was an impact crater based on the analysis of satellite imagery (location map in Fig. 11.1). No crater is actually visible and no evidence of an impact origin has been found. Inset: the white dashed line traces the supposed crater outline (~31 km in diameter) according to El-Baz and Ghoneim (2007)

the order of 106 kg (Weeks et al. 1984) or 105 kg (Barakat et al. 1997). Accounting for the loss of material due to weathering, burial in the soil, and removal by primitive man who used LDG to make tools, the estimate of the original mass is 104 times greater (Weeks et al. 1984).

LDG specimens range in size from 30 cm to <1 cm across —biased by the limit of easy detection in the field. The largest specimen so far found has a mass of ~26 kg and is kept in the Museum National d'Histoire Naturelle in Paris, France (Diemer 1997). Although most specimens have irregular

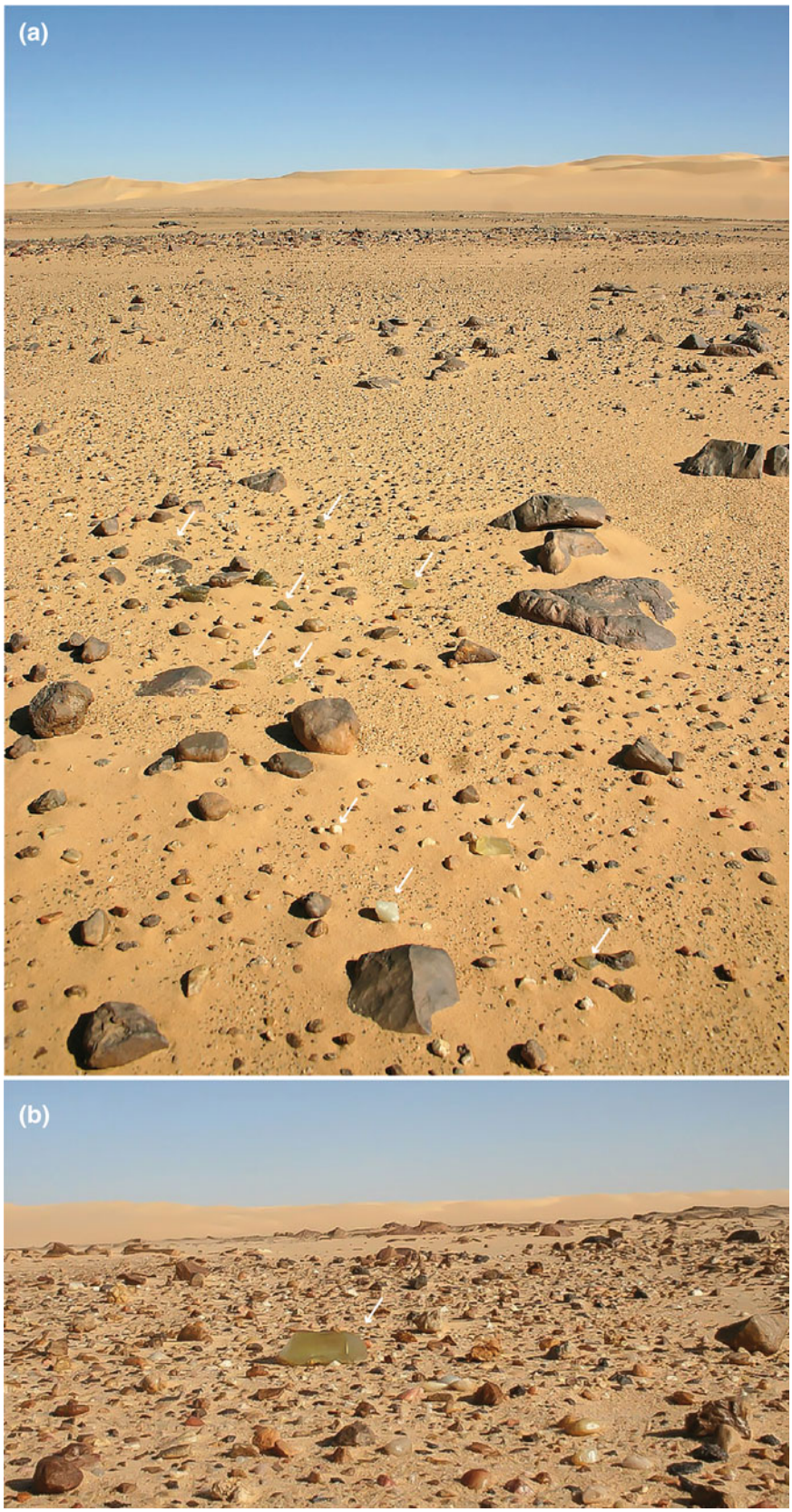

Fig. 11.9 Libyan Desert Glass: Field occurrence. **a** Centimeter-sized specimens of Libyan Desert Glass (arrowed) are found scattered in inter-dune corridors at the southern extension of the Great Sand Sea, Libyan Desert, southwestern Egypt (see Fig. 11.1 for location map). The surface of the inter-dune corridors consists of exposed sandstone bedrock (Cretaceous Nubia Formation), discontinuously covered by a colluvium-alluvium veneer of quartzose silt, sand and gravel (serir). **b** A closer view of one specimen in the field

shapes, many LDG samples are tabular reflecting the stratified character of the glass (Weeks et al. 1984). The dominant color of LDG is bright yellow–green, although varieties ranging from nearly colorless, to pale yellow, to grey-green are common too (Fig. 11.10). Most specimens are transparent to translucent, and some of them exhibit dark bands and schlieren. Some other specimens are opaque to milky white, with a cloudy appearance due to the conspicuous presence of vesicles. Clear and cloudy glass are arranged in layers in the largest tabular specimens. Oriented elongated vesicles and schlieren parallel to layering define flow textures. Scattered pale and dark millimeter-sized inclusions are visible to the naked eye in some specimens. The exposed surfaces are smooth, wind-polished with a glassy luster, whereas buried surfaces are irregular, rough and corroded by the dissolving action of soil moisture and ground water. Some pieces, namely flakes and hand-axes, show evidence of working by prehistoric man (Oakley 1952; Roe et al. 1982; Negro and Damiano-Appia 1992). LDG was also used in dynastic times as a valuable material; the scarab-shaped central motif of Tutankhamun's pectoral (14th C. BCE) was carved from LDG, according to the non-destructive refractive index analysis of De Michele (1998).

A number of mineralogical and petrographic studies (e.g. Kleinmann 1969; Barnes and Underwood 1976; Greshake et al. 2010, 2018; Swaenen et al. 2010; Cavosie and Koeberl 2019) have shown that LDG, although dominated by a glassy groundmass, does contain a variety of microscopic mineral inclusions including quartz, cristobalite, lechatelierite (pure silica glass), zircon and the thermal decomposition product of this latter mineral—baddeleyite, anatase, rutile, corundum, Al-rich orthopyroxene, and mullite (Figs. 11.10c, d). The occurrence, in particular, of lechatelierite, cristobalite, baddeleyite, decomposed Ti-magnetite and mullite testify to melting at temperatures in excess of 1670 °C. Such high formation temperatures are consistent with the emulsion textures observed under the transmission electron microscope (TEM) by Pratesi et al. (2002) in the dark bands, namely nanometer-scale spherules of glass enriched in Al, Fe and Mg indicative of liquid immiscibility with the surrounding silica glass. Granular zircons preserving evidence of reversion from former reidite were recently found in seven LDG specimens through electron back-scatter diffraction (EBSD) analysis (Cavosie and Koeberl 2019). This indicates the local attainment of pressure as high as 30 GPa.

The LDG is characterized by an extremely silica-rich composition. The SiO_2 content ranges from 96.5 to 99 wt%, with an average value of 98 wt% (Barnes and Underwood 1976; Fudali 1981; Koeberl 1997). Lithophile elements show inverse correlation with silica content, and the REE pattern is typical of upper continental crust materials (Koeberl 1997), consistent with a dominant quartz-rich sedimentary source. Further major and trace element analyses (Barrat et al. 1997), Sr and Nd isotopic abundances (Schaaf and Müller-Sohnius 2002), and oxygen isotopic composition (Longinelli et al. 2011) indicate that the dominant parent material of LDG was a mature Cretaceous sandstone (or sands) most likely derived from the erosion of intrusive rocks of Pan African age (Neoproterozoic). Magna et al. (2011) noted that Libyan Desert Glass is characterized by a heavy Li signature (d 7Li > 24.7‰) and suggested that the LDG parent materials formed as alluvial-plain deposits in lacustrine and/or coastal marine environment during the Cretaceous. Fröhlich et al. (2013) studied LDG samples and locally occurring sediments collected during an archeological expedition in January 2006 by combined Fourier transform infrared spectroscopy and scanning e (SEM) microscopy. Their results suggested that the source rock of LDG was most probably quartz sand that had resulted from the weathering (loss of the cementing microquartz) of the Cretaceous sandstones of the Gilf Kebir Plateau with subsequent deposition in a high-energy, fluviatile environment.

The composition of the dark bands is enriched in Cr (up to ~85 μg/g), Co (up to ~4 μg/g), Ni (up to ~55 μg/g), and Ir (up to ~6 ng/g), and their contents are also positively correlated with those of Fe and Mg (Murali et al. 1989; Rocchia et al. 1997; Koeberl 1997). This has been interpreted as a signature of a meteoritic component (Murali et al. 1989; Rocchia et al. 1997). In addition, Murali et al. (1997) showed that the siderophile element ratios in the dark bands of the LDG are consistent with a chondritic meteoritic component. Likewise, the significant PGE abundances detected in the dark bands by Barrat et al. (1997) and their CI normalized patterns revealed the presence of a chondritic component. Further evidence of the presence of a meteoritic component was provided by Re–Os isotope systematics of the dark bands (published in abstract form) by Koeberl (2000), a result later supported by the detection of crustal Sr and Nd abundances in LDG by Schaaf and Müller-Sohnius (2002) that are typical of intrusive rocks of Pan-African age and indicative of a negligible mantle component only.

Giuli et al. (2003) studied the iron oxidation state and coordination number in a LDG sample by means of iron K-edge high resolution X-ray absorption near-edge structure (XANES) spectroscopy. They found that iron is in the trivalent state in the pale silica glass, whereas it occurs in a more reduced state (bivalent) in the more Fe-rich dark bands. They suggested that some or most of the iron in these layers could be directly derived from the meteoritic projectile and that the LDG was not of terrestrial origin.

The age of the LDG was determined by the fission-track method. Storzer and Wagner (1977) obtained an Oligocene age of 29.4 ± 0.5 Ma, which was later confirmed by Bigazzi and de Michele (1997) with a result of 28.5 ± 0.8 Ma. Attempts to date LDG by means of the K–

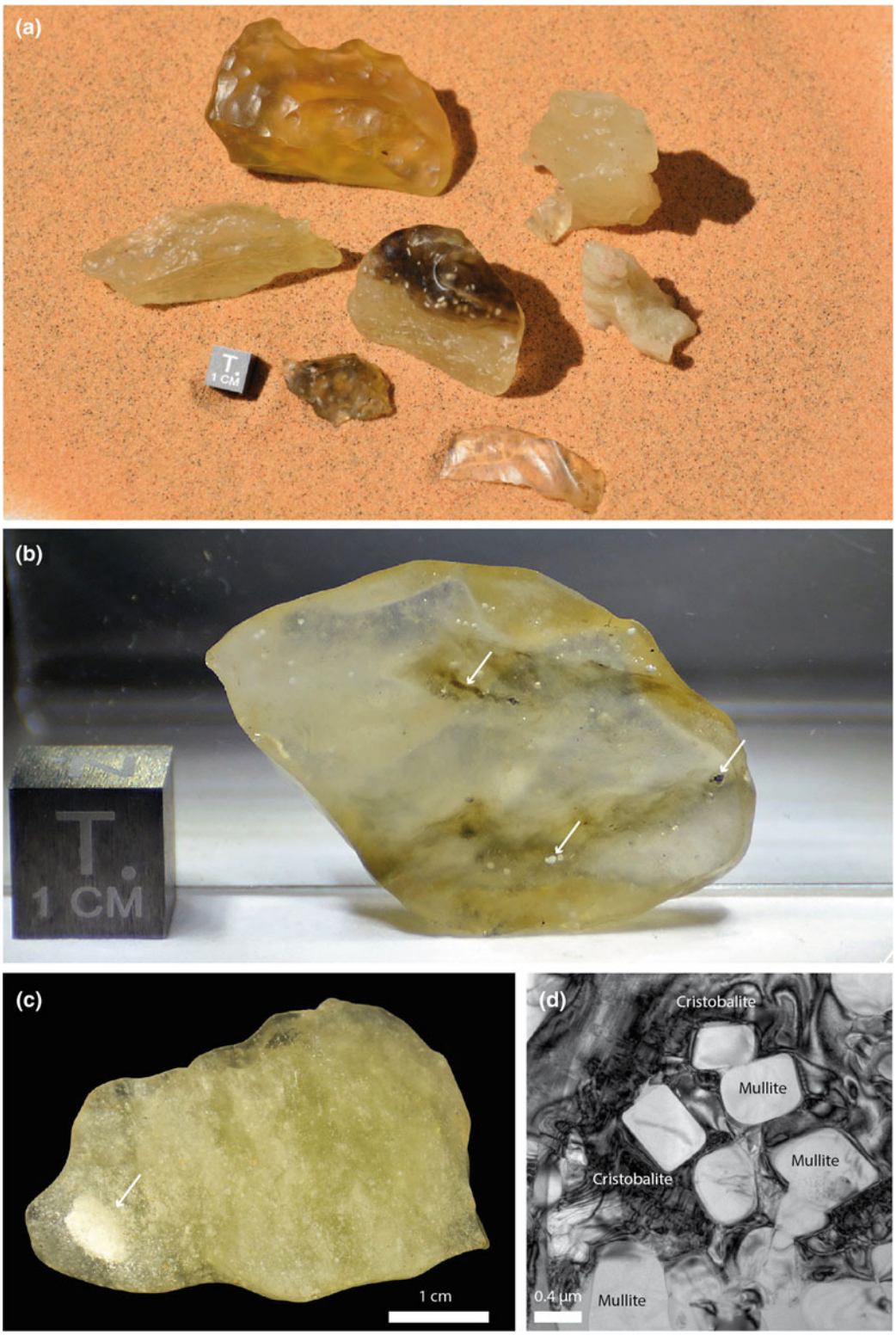

Fig. 11.10 Libyan Desert Glass: petrographic features. **a** A selection of Libyan Desert Glass specimens with varying color, transparency, amount of brown schlieren and degree of wind¬blown polishing, including a flaked artifact of prehistoric age in the foreground (1 cm metal cube for scale). **b** An end-cut specimen of transparent to translucent glass bearing dark schlieren, and microscopic white and dark inclusions (arrowed). **c** A translucent to transparent specimen of Libyan Desert Glass with a large whitish inclusion (arrowed) bearing high-temperature assemblages of mullite plus cristobalite. **d** Transmission electron microscope image of a mullite-cristobalite bearing region in a whitish inclusion in Libyan Desert Glass (bright field image). Field images of Libyan Desert Glass specimens were kindly provided by Romano Serra (University of Bologna, Italy). The images of the whitish inclusions are courtesy of A. Greshake (Museum fur Naturkunde, Berlin, Germany)

Ar method failed to provide reliable age data (Zahringer 1963; Horn et al., 1997; Matsubara et al. 1991).

There are several lines of evidence that LDG is an impact generated glass, although no source crater has been recognized so far. These include:

i. The very high formation temperatures (in excess of ~1700 °C) and pressures (up to 30 GPa; Cavosie and Koeberl 2019) documented by the occurrence of mineral inclusions like lechatelierite, cristobalite, mullite, baddeleyite, Ti-magnetite decomposition products, and evidence for former reidite, respectively.
ii. The presence of a chondritic geochemical signature in the dark bands.

In the past two possible source craters have been proposed: the 2-km-diameter BP impact crater and the 15 to 18-km-diameter Oasis impact structure, both located in southeastern Libya (Martin 1969; Underwood and Fisk 1980; Murali et al., 1988; Koeberl 1997; for detail about these structures: Reimold and Koeberl 2014). These structures are located ~150 km due W-SW of the LDG strewn field. The ages of these structures are essentially not known, as no datable materials have been identified at these structures. Based on a petrographic, geochemical, and Sr–Nd isotopic studies on a suite of target rock samples belonging to the Lower Cretaceous sandstone of the Nubian Sandstone from the BP and Oasis impact structures, Abate et al. (1999) concluded that the target rocks of the Libyan structures could represent the parent material for LDG. Later Schaaf and Müller-Sohnius (2002) determined Rb–Sr and Sm–Nd isotopic ratios from seven LDG samples and five associated sandstones from the LDG strewn field. They found Sr and Nd isotopic values for LDG similar to those of granitoid rocks from northeast Africa west of the Nile. They, thus, concluded that the LDG precursor material was a sandy matrix target material derived from a Precambrian crystalline basement, ruling out the Cretaceous sandstones of the Nubian Group as possible precursors for LDG.

To explain the lack of a source crater for LDG, some researchers have proposed that LDG was formed locally by the radiative heating/melting produced by the low-altitude airburst of a cometary or asteroidal object(s)—a process that might have been frequent in the collisional history of Earth (Wasson 2003; Boslough and Crawford 2008a, b). Indeed microscopic analysis of one of the five bedrock sandstone samples from the LDG strewn field studied by Kleinmann et al. (2001) and one out of a dozen studied by Koeberl and Ferrière (2019) revealed a wide range of deformation features in some of the constituent quartz grains, including crushing and fracturing, undulatory extinction, mosaicism, oriented cleavage, partial isotropization and multiple sets of planar deformation features. However, no trace of an impact structure was found at or around this location, and the other studied rocks showed undisturbed textures without evidence of brecciation or shock features typical of impactites. This poses the question whether these rocks were actually the target rock in a hypervelocity impact, or whether the observed shock metamorphic features could predate the formation of these clastic sediments. In any case, evidence of former reidite precludes an origin of LDG by airburst alone (Cavosie and Koeberl 2019).

The definition of the formation mechanism of LDG is further complicated by two poorly constrained processes that might have significantly affected the spatial distribution of LDG and the survival of an impact structure, if there ever was one, since LDG formation in the Oligocene: mass-transport and erosion. Based on the variability of ^{10}Be and ^{26}Al exposure ages in twelve samples collected from representative sites of the LDG strewn field, Klein et al. (1986) concluded that individual fragments of glass had experienced different exposure histories, implying several major stages of redistribution of the glass within the past million years. According to the stratigraphic considerations by Giegengack and Underwood (1997), the area where LDG is found has undergone ~400 m of erosion since the formation of LDG ~28.5 million years ago.

Although nearly 85 years of geochemical studies have provided a wealth of information on the LDG glass and the nature of the source material, and an impact origin has been debated for essentially the same time, the actual impact scenario is still a matter of debate. In any case, the confirmation of the lack of substantial evidence for high shock pressure involved in the formation of LDG and having affected the country rocks, which would be a diagnostic feature of hypervelocity impacts, lends strong support to the low-altitude airburst model for the formation of LDG (Wasson 2003; Boslough and Crawford 2008a, b).

Kramers et al. (2013) reported on a dark, centimeter sized (3.5 × 3.2 × 2.1 cm), carbon-dominated, diamond-bearing rock fragment named "Hypatia" that had been found in the vicinity of the LDG strewn field at 25°30′ E, 25°20′ N in 1996 (Barakat 2012). Based on Ar isotopic composition and non-terrestrial ∂ ^{13}C values, these authors concluded that the fragment was most likely of extraterrestrial origin, and they hypothesized that it could be a remnant of a comet nucleus that exploded in air. Building on this hypothesis, Kramers et al. (2013) further speculated that Hypatia was a remnant of the airburst that generated the LDG. Through a comprehensive study of noble gases and nitrogen in several mg-sized samples, Avice et al. (2015) later confirmed the extraterrestrial nature of Hypatia. In particular, they:

i. detected primordial noble gases (i.e., Q component) typical of various types of meteorites;

ii. found a N isotopic composition consistent with C-components in meteorites, indicating that diamonds in Hypatia formed in space;
iii. could not confirm detection of a noble gas presolar signature (i.e., the G component) that led Kramers et al. (2013) to speculate on a cometary origin of Hypatia;
iv. determined a low concentration of cosmogenic 21Ne, hinting at a parent object of at least a few meters in diameter but not necessarily large enough to have been able to create the LDG.

Recently, Belanyn et al. (2018) performed a mineralogical-petrographic study of a 4 g sample of Hypatia. They reported D and G bands in Raman spectra of disordered carbon with features similar to those observed in primitive solar system carbon materials, yet unlike any known cometary material. Therefore, although there is some evidence for an extraterrestrial origin of this anomalous and unique carbonaceous rock fragment, there is no evidence for a connection between Hypatia and the LDG—except that both these materials are derived from the same region. Hypatia, once its meteoritic origin is confirmed, would be one of the many meteorites found in the inter-dune corridors in the LDG strewn field (Fig. 11.1). Note also that Hypatia is not an official meteorite name. As reported by Belanyn et al. (2018), there is no type specimen curated in an acknowledged museum collection that would enable distribution of samples for research. This has thus far prevented proper classification of Hypatia as a meteorite, according to guidelines of the Nomenclature Committee of the Meteoritical Society.

11.3.4 Dakhleh Glass

In the Western Desert of Egypt, due south of the Libyan Plateau, the Dakhleh Oasis region (Figs. 11.1 and 11.11) preserves a rich history of habitation stretching back to over 400,000 years before the emergence of Homo sapiens. For this reason, this region has been the focus of intense (DOP) geo-archeological investigations by the Dakhleh Oasis Project since 1978 (Churcher and Mills 1999; Churcher et al. 1999). It was during the course of the Dakhleh Oasis Project field work in the 1980s and 1990s that a lag deposit of dark, glassy material on surface and within Pleistocene lacustrine deposits was discovered (Osinski et al. 2007): the so-called Dakhleh Glass—another unusual glass of proposed impact origin.

Subsequent reports of extensive field work and laboratory-based petrographic and geochemical analyses (Osinski et al. 2007, 2008) showed that the Dakhleh Glass lag deposit is composed of irregular and flattened masses of up to ~50 cm in size of vesicular glassy material. It occurs over an area of ~40 × ~10 km, with ~140 individual locations having been documented. Specimens of Dakhleh Glass are typically black in color when fresh, and greenish-grey when weathered (Fig. 11.11). Many specimens show impressions of leaves or plant stems. Petrographic analysis has shown that Dakhleh Glass consists of a highly vesicular, siliceous, glassy groundmass with variable contents of primary crystallites of clinopyroxene, with minor plagioclase, pyrrothite microspherules, and calcite globules, as well as lithic and mineral clasts. Groundmass glass shows a variety of quench and flow textures: from transparent hypohyaline glass with compositional schlieren to opaque hypocrystalline varieties. The glass composition (as determined by energy dispersive X-ray spectrometric system [EDS] and wavelength dispersive spectrometric system [WDS] analysis) is also variable, with silica contents ranging from ~50 to 70 wt%, and high concentrations of Ca and Al (CaO up to ~25 wt%, Al_2O_3 up to ~18 wt%), unlike any known volcanic glass. Clasts include rounded to sub-rounded quartz grains ~0.1–0.8 mm in diameter; pieces of silicified and/or fossilized plant matter; and angular fragments of fine-grained calcareous sedimentary rocks up to ~2 cm in size. In places, enclaves of silica-rich (90–100 wt% SiO_2) glass surround the quartz clasts. No evidence of shock metamorphism has been documented so far.

Based on archeological evidence from the DOP and preliminary ^{40}Ar–^{39}Ar data, Osinski et al. (2007) suggested that the glass formed during the Middle Stone Age time of occupation. Subsequently, Renne et al. (2010) reported the results of several argon step-heating experiments, which yielded a preferred isochron age of 145 ± 19 ka, in keeping with the archeological constraints.

The origin of the Dakhleh Glass is debated. Osinski et al. (2007, 2008) suggested an impact melting origin, based on the non-volcanic chemical composition of the glass (particularly the high Al and Ca contents for a given silica content) and the absence of evidence of volcanism in that area are ruling out a volcanic origin. The high silica glass enclaves are interpreted as the products of melting of quartz clasts and related to lechatelierite inclusions in high temperature (>1700 °C) impact glasses, thus ruling out an origin through burning of vegetation or sediments rich in organic matter. Finally, the ~150 thousand year age of the glass excludes an anthropogenic origin. The lack of evidence of shock metamorphism and of an associated impact crater led Osinski et al. (2007, 2008) to speculate that Dakhleh Glass could have formed through radiative/convective heating of the surface during a large aerial burst in an event similar to that described by Wasson (2003) and Boslough and Crawford (2008a, b) and assumed for the origin of the LDG. In this view, the effects ~150 thousands years ago on the environment and inhabitants of the Dakhleh Oasis region would have been catastrophic. Recently, Roperch et al. (2017) proposed that natural fires were responsible for the formation of surface layers of silica glass in the Atacama

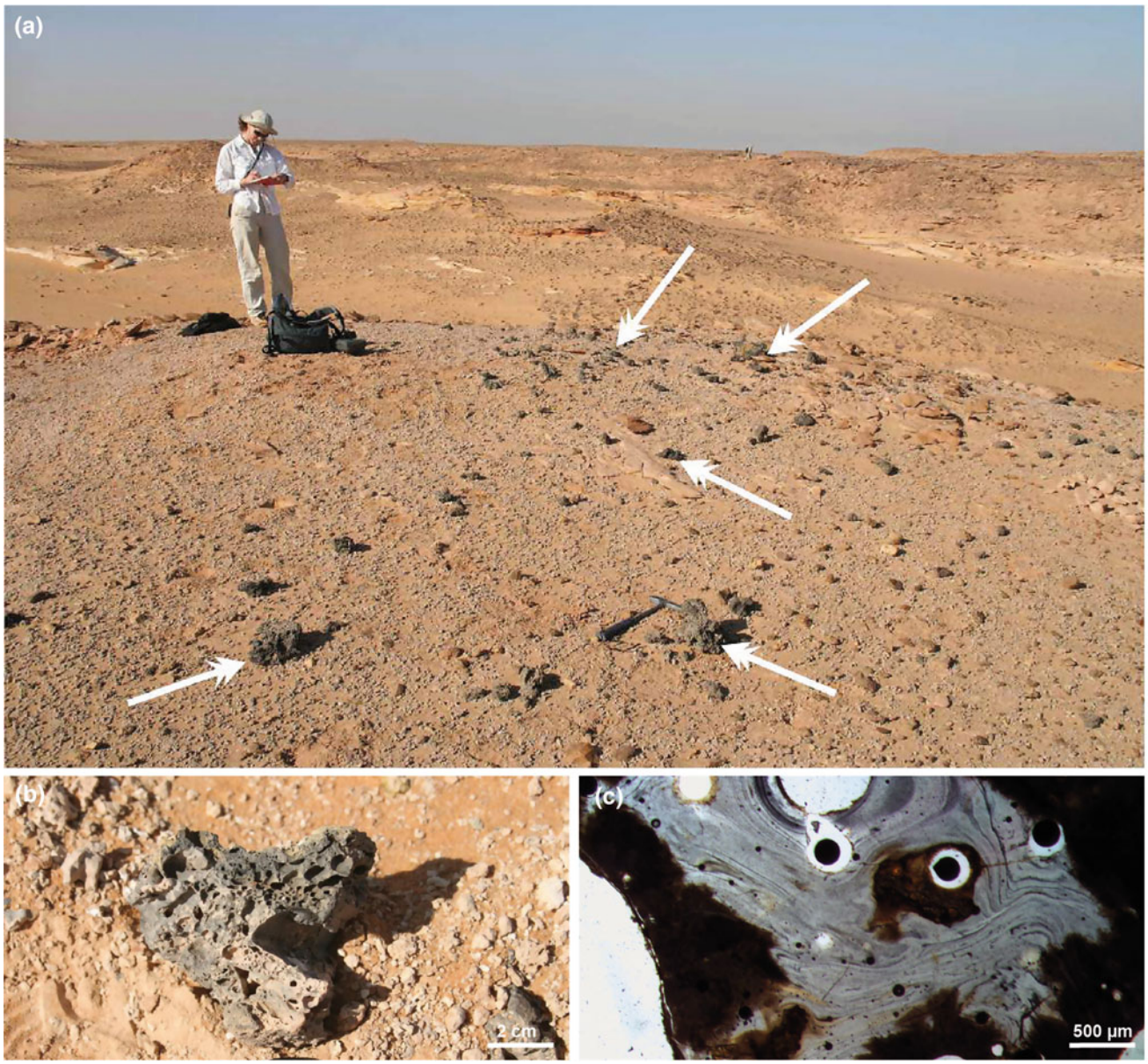

Fig. 11.11 The Dakhleh Glass (see Fig. 11.1 for location map). **a** Area of abundant masses of Dakhleh Glass lagged on the surface of Pleistocene lacustrine sediments; some large specimens are arrowed; hammer for scale. **b** Highly vesicular pumice-like Dakhleh Glass specimen. **c** Photomicrograph of a thin section of Dakhleh Glass showing an enclave of transparent, crystallite-free glass, within crystallite-rich darker glass. Images courtesy of G. Osinski (University of Western Ontario, Canada)

Desert (Chile), the so-called "Pica Glass". In particular, they suggested that Pica Glass formed through the burning of organic-rich soils in dried-out grassy wetlands during climate oscillations between wet and dry periods. Although they did not find evidence of high temperature melting, they observed that Pica Glass and DG shared a number of structural and paleo-geographic features. They both have abundant plant imprints and they are confined to areas around oases. Roperch et al. (2017), thus, speculated that Pica Glass and Dakhleh Glass could share a similar origin by natural fires.

11.4 Meteorites: An Overview

Meteorites are interplanetary rock debris captured by Earth's gravitational field and recovered at the Earth's surface. Their size ranges from millimeters to few meters, i.e., large enough to survive atmospheric entry heating and small enough to be decelerated from their cosmic velocities (in excess of the Earth's escape velocity of 11.2 km s^{-1}) through the Earth's atmosphere and, therefore, survive impact against the Earth's surface (e.g., Rubin and Grossman 2010). Their

hypervelocity passage through the upper Earth's atmosphere generates bright fireballs, explosions, detonations, and rumblings that have made them known since early human history (e.g., D'Orazio 2007). Object of veneration and popular superstition and recurring element in myths up until the 18th century CE, meteorites are for modern science a natural laboratory to investigate the origin and evolution of the solar system. Meteorites are in fact rock samples of a large variety derived from a range of solar system bodies, with a large variety of geological histories: from primitive minor bodies like the asteroids, to more evolved planetary bodies like Mars and the Moon (e.g., Chambers 2006). The cosmochemical and geochemical study of their physico-chemical properties thus allows investigation of the ~4.6 billion year long sequence of processes through which an interstellar molecular cloud of gas and dust became a system of planets and other minor bodies orbiting around the Sun (e.g., McSween et al. 2006; Russell et al. 2006).

Meteorites have traditionally been distinguished into three broad categories—stones, irons, and stony-irons based on the relative proportions of silicate minerals and metallic iron–nickel. Modern classification schemes group meteorites into homogeneous classes according to their structure, chemical and isotopic composition, and mineralogy (e.g., Krot et al. 2014). The most abundant meteorites in our collection (>99% of the total) are impact debris from collisions between asteroids orbiting between Mars and Jupiter. Asteroids are "fossil bodies" of the planet building era. Unlike the geologically more evolved terrestrial, Martian, and lunar rocks, asteroidal meteorites uniquely contain minerals that formed before the solar system, and during the growth and differentiation of planetesimals and planets from the disk of dust and gas around the Sun (known as the 'solar nebula') within the first few tens of million years of solar system evolution. Amongst asteroidal meteorites, ~85% are chondrites, primitive rocks that have elemental compositions similar to that of the Sun (e.g., Scott and Krot 2014). They sample asteroids that did not experience melting, although evidence of thermal metamorphism and aqueous alteration in some chondrite classes attests to some heating in bodies with anhydrous and hydrous compositions, respectively. About 14% of meteorites arriving on Earth consist of differentiated materials (McCoy et al. 2006). These are meteorites known under the names of achondrites, irons, and stony-irons, which derive from asteroids that underwent melting and differentiation into metallic iron cores and silicate mantles, like the ~500-km-diameter asteroid 4Vesta which can be associated with one group of achondrites denominated HED (the howardite-eucrite-diogenite group). Rare stony meteorites blasted off the surfaces of the Moon and Mars by impact events comprise less than 1% of the total known meteorites. The 340 lunar meteorites, or lunaites, to date present in our collections represent a valuable extension to the Apollo and Luna sampling of the Moon's surface debris, providing additional clues into the geological evolution of the lunar crust, the formation of the Earth-Moon system, and the intense cosmic bombardment that affected the inner solar system bodies during the first few hundred million years of its evolution (e.g., Warren and Taylor 2014). The 290 Martian meteorites are the only rock samples from planet Mars available in our laboratories (e.g., McSween and McLennan 2014). They include basalts and cumulates formed from basaltic magmas, and which have revealed that planetary differentiation on Mars occurred ~4.5 billion years ago, probably during accretion, and that magmatism extended through the period from 1.3 Ga to 180 Ma. These meteorites have also provided insight into the geological history of the planet, including the composition of its Fe-rich mantle, as well as atmosphere composition and subsurface water circulation in response to changes in the climatic evolution of Mars (e.g., Bridges et al. 2001; Chennaoui Aoudjehane et al. 2012).

Over 59,000 meteorites, of up to 60 t in mass, with many in the 10–100 g range, are listed in The Meteoritical Bulletin Database (https://www.lpi.usra.edu/meteor/metbull.php), the authoritative source of information on approved meteorites, which is provided by the Meteoritical Society. Of these, 1310 meteorites were seen to fall (and are known as 'falls').

The oldest meteorite fall, for which material is still available for science, is the meteorite of Ensisheim (Alsace, France, 1492). Since the late 1950s, the fall of a few meteorites have been detected through networks of camera stations (e.g., the European Camera Network in central Europe, Oberst et al. 1998; Prairie Meteorite Network in the mid-western United States, McCrosky et al. 1971; The Meteorite Observation and Recovery Project in western Canada, Halliday et al. 1978; the Australian Desert Fireball Network in Western Australia, Bland, 2004) designed to track meteoroids entering the atmosphere, determine pre-entry orbits, and recover meteorites. By far most of the others are the tens of thousands of 'finds' recovered from hot and cold deserts over the last 50 years. Hamada (nearly bare bedrock-desert) and serir (gravel/pebble-desert) type hot desert surfaces in the Sahara, Atacama, and Nullarbor Plain, and the many blue ice fields on the Antarctic plateau are the most productive terrains for the collection of meteorites on Earth—a treasure-trove for planetary science.

11.5 The Meteorite Record of Egypt

The Meteoritical Bulletin Database to date (June 2018) lists 78 meteorites from Egypt (Table 11.1). Seventy-six are finds and two are observed falls: Nakhla (1911) and Sinai (1916). With the exception of the iron meteorite Gebel Kamil from Kamil Crater with a total recovered mass of ~1.7 t,

Table 11.1 Egyptian meteorites (listed alphabetically; Meteoritical Bulletin Database; accessed September 2018)

Name	Abbreviation	Fall	Year	Place	Type	Mass	Name	Abbreviation	Fall	Year	Place	Type	Mass
Abu Moharek			1997	Al Wadi al Jadid, Egypt	Ordinary chondrite H4	4.5 kg	Great Sand Sea 033	GSS 033		2006	Al Wadi al Jadid, Egypt	Ordinary chondrite L5	80.1 g
Al Alamayn			2005	Marsa Matruh, Egypt	Ordinary chondrite H5	13.3 g	Great Sand Sea 034	GSS 034		2006	Al Wadi al Jadid, Egypt	Ordinary chondrite L5/6	7.7 g
Aswan			1955	Al Wadi al Jadid, Egypt	Iron, IAB-ung	12 kg	Great Sand Sea 035	GSS 035		2007	Al Wadi al Jadid, Egypt	Ordinary chondrite H5/6	40.9 g
Birkat Aghurmi 001			2012	Marsa Matruh, Egypt	Ordinary chondrite L6	1666 g	Great Sand Sea 036	GSS 036		2007	Al Wadi al Jadid, Egypt	Ordinary chondrite H5	128.9 g
El Bahrain			1983	Marsa Matruh, Egypt	Ordinary chondrite L6	14 kg	Great Sand Sea 037	GSS 037		2007	Al Wadi al Jadid, Egypt	Ordinary chondrite H4	66.9 g
El Faiyum			1993	Al Fayyum, Egypt	Ordinary chondrite H5	73.5 g	Great Sand Sea 038	GSS 038		2007	Al Wadi al Jadid, Egypt	Ordinary chondrite H5	146 g
El Qoseir			1921	Al Bahr al Ahmar, Egypt	Iron, ungrouped	2.41 kg	Great Sand Sea 039	GSS 039		2007	Al Wadi al Jadid, Egypt	Ordinary chondrite H5	128.6 g
El-Quss Abu Said			1999	Al Wadi al Jadid, Egypt	CM2	53.1 g	Great Sand Sea 040	GSS 040		2010	Al Wadi al Jadid, Egypt	Ordinary chondrite LL5	15 g
El-Shaikh Fadl 001	ESF 001		2010	Al Bahr al Ahmar, Egypt	Ordinary chondrite H5	476 g	Great Sand Sea 041	GSS 041		2010	Al Wadi al Jadid, Egypt	Ordinary chondrite H5	6.5 g
El-Shaikh Fadl 002	ESF 002		2010	Al Bahr al Ahmar, Egypt	Ordinary chondrite H5	806 g	Isna			1970	Al Wadi al Jadid, Egypt	CO3.8	23 kg
El-Shaikh Fadl 003	ESF 003		2009	Al Bahr al Ahmar, Egypt	Ordinary chondrite H4	73 g	Kharga			2000	Marsa Matruh, Egypt	Iron, IVA	1040 g
El-Shaikh Fadl 004	ESF 004		2009	Al Bahr al Ahmar, Egypt	Ordinary chondrite L5	8.01 kg	Marsa Alam			2012	Al Bahr al Ahmar, Egypt	Ordinary chondrite H5	69 g
El-Shaikh Fadl 005	ESF 005		2010	Al Bahr al Ahmar, Egypt	Ordinary chondrite L-mr*	538 g	Marsa Alam 002	MA 002		2013	Al Bahr al Ahmar, Egypt	Ordinary chondrite H5	336 g
El-Shaikh Fadl 006	ESF 006		2010	Al Bahr al Ahmar, Egypt	Ordinary chondrite H5	52.2 g	Marsa Alam 003	MA 003		2014	Al Bahr al Ahmar, Egypt	Ordinary chondrite H5	10.7 g
El-Shaikh Fadl 007	ESF 007		2010	Al Bahr al Ahmar, Egypt	Ordinary chondrite L5	8.2 kg	Marsa Alam 004	MA 004		2014	Al Bahr al Ahmar, Egypt	Ordinary chondrite L5-6	37.6 g
El-Shaikh Fadl 008	ESF 008		2010	Al Bahr al Ahmar, Egypt	Ordinary chondrite H5	66.5 g	Marsa Alam 005	MA 005		2014	Al Bahr al Ahmar, Egypt	Ordinary chondrite L5	314 g
El-Shaikh Fadl 009	ESF 009		2010	Al Bahr al Ahmar, Egypt	Ordinary chondrite H5	56.3 g	Marsa Alam 006	MA 006		2013	Al Bahr al Ahmar, Egypt	Ordinary chondrite H3-5	97 g
El-Shaikh Fadl 010	ESF 010		2010	Al Bahr al Ahmar, Egypt	Ordinary chondrite H5	75.7 g	Marsa Alam 007	MA 007		2013	Al Bahr al Ahmar, Egypt	Ordinary chondrite H3.6-4	90.5 g
Gebel Kamil			2009	Al Wadi al Jadid, Egypt	Iron, ungrouped	1.6 t	Marsa Alam 008	MA 008		2015	Al Bahr al Ahmar, Egypt	Ordinary chondrite L6	4.45 kg
Great Sand Sea 001	GSS 001		1991	Al Wadi al Jadid, Egypt	Ordinary chondrite L6	130 g	Marsa Alam 009	MA 009		2015	Al Bahr al Ahmar, Egypt	Ordinary chondrite H6	4.33 kg
Great Sand Sea 002	GSS 002		1991	Al Wadi al Jadid, Egypt	Ordinary chondrite L6	135 g	Marsa Alam 010	MA 010		2015	Al Bahr al Ahmar, Egypt	Ordinary chondrite H5	165.3 g

(continued)

Table 11.1 (continued)

Name	Abbreviation	Fall	Year	Place	Type	Mass	Name	Abbreviation	Fall	Year	Place	Type	Mass
Great Sand Sea 003	GSS 003		1991	Al Wadi al Jadid, Egypt	Iron	110 g	Marsa Alam 011	MA 011		2015	Al Bahr al Ahmar, Egypt	Ordinary chondrite L5	75.6 g
Great Sand Sea 004	GSS 004		1994	Al Wadi al Jadid, Egypt	Ordinary chondrite LL6	580 g	Marsa Alam 012	MA 012		2014	Al Bahr al Ahmar, Egypt	Ordinary chondrite H4	3.3 g
Great Sand Sea 005	GSS 005		1995	Al Wadi al Jadid, Egypt	Ordinary chondrite L6	80 g	Marsa Alam 013	MA 013		2015	Al Bahr al Ahmar, Egypt	Ordinary chondrite H6	168 g
Great Sand Sea 006	GSS 006		1995	Al Wadi al Jadid, Egypt	Ordinary chondrite L6	45 g	Marsa Alam 014	MA 014		2015	Al Bahr al Ahmar, Egypt	Ordinary chondrite L5	2.48 g
Great Sand Sea 007	GSS 007		1996	Al Wadi al Jadid, Egypt	Ordinary chondrite H6	1450 g	Marsa Alam 015	MA 015		2015	Al Bahr al Ahmar, Egypt	Ordinary chondrite H4	30.6 g
Great Sand Sea 008	GSS 008		1996	Al Wadi al Jadid, Egypt	Ordinary chondrite LL3-6	450 g	Marsa Alam 016	MA 016		2015	Al Bahr al Ahmar, Egypt	Ordinary chondrite H4	53.9 g
Great Sand Sea 009	GSS 009		1996	Al Wadi al Jadid, Egypt	Ordinary chondrite H5	414 g	Marsa Alam 017	MA 017		2015	Al Bahr al Ahmar, Egypt	Ordinary chondrite H6	115.1 g
Great Sand Sea 019	GSS 019		1999	Al Wadi al Jadid, Egypt	Ordinary chondrite LL6	12 kg	Marsa Alam 018	MA 018		2015	Al Bahr al Ahmar, Egypt	Ordinary chondrite H5	3.78 g
Great Sand Sea 020	GSS 020		2000	Al Wadi al Jadid, Egypt	Ordinary chondrite H	5.42 kg	Marsa Alam 019	MA 019		2015	Al Bahr al Ahmar, Egypt	Ordinary chondrite H6	291 g
Great Sand Sea 021	GSS 021		2002	Marsa Matruh, Egypt	Ordinary chondrite L5	1416 g	Minqar Abd el Nabi			1992	Marsa Matruh, Egypt	Ordinary chondrite H6	362 g
Great Sand Sea 022	GSS 022		1994	Al Wadi al Jadid, Egypt	Ordinary chondrite H6	0.9 g	Mut			2003	Al Wadi al Jadid, Egypt	Ordinary chondrite H5	1800 g
Great Sand Sea 023	GSS 023		1996	Al Wadi al Jadid, Egypt	Ordinary chondrite H5	1.5 g	Nakhla		Y	1911	Al Buhayrah, Egypt	Martian (nakhlite)	10 kg
Great Sand Sea 024	GSS 024		1996	Al Wadi al Jadid, Egypt	Ordinary chondrite H5	7.8 g	Nova 012			2010	Egypt	Ordinary chondrite H5	266 g
Great Sand Sea 025	GSS 025		2005	Al Wadi al Jadid, Egypt	Ordinary chondrite L5	10.9 g	Quarat al Hanish			1979	Al Wadi al Jadid, Egypt	Iron, IAB-sHL	593 g
Great Sand Sea 026	GSS 026		2007	Marsa Matruh, Egypt	Ordinary chondrite H6	100 g	Sinai		Y	1916	Al Isma'iliyah, Egypt	Ordinary chondrite L6	1455 g
Great Sand Sea 030	GSS 030		2006	Al Wadi al Jadid, Egypt	Ordinary chondrite H6	51.3 g	Siwa			1994	Marsa Matruh, Egypt	Ordinary chondrite L5-6	36 g
Great Sand Sea 031	GSS 031		2006	Al Wadi al Jadid, Egypt	Ordinary chondrite H5	62.3 g	Thamaniyat Ajras			2016	Al Wadi al Jadid, Egypt	Ordinary chondrite L6	866 g
Great Sand Sea 032	GSS 032		2006	Al Wadi al Jadid, Egypt	Acapulcoite	8.3 g							

Egyptian meteorites range in mass from just a few grams to less than 10 kg, for a total recovered mass of ~1725 kg. Besides 67 ordinary chondrites, the most abundant group of meteorites in the world's collection, there are a number of rare meteorites amongst the Egyptian collection. They include one Martian meteorite, two carbonaceous chondrites, one acapulcoite, and seven iron meteorites. The Martian meteorite is named Nakhla (Fig. 11.12), and it is surely a most remarkable specimen as it is one of the rare samples in the world's collections from the surface of planet Mars. As reported by the Meteoritical Bulletin Database, on 28 June 1911, at 9:00 a.m., a shower of multiple fragments of the

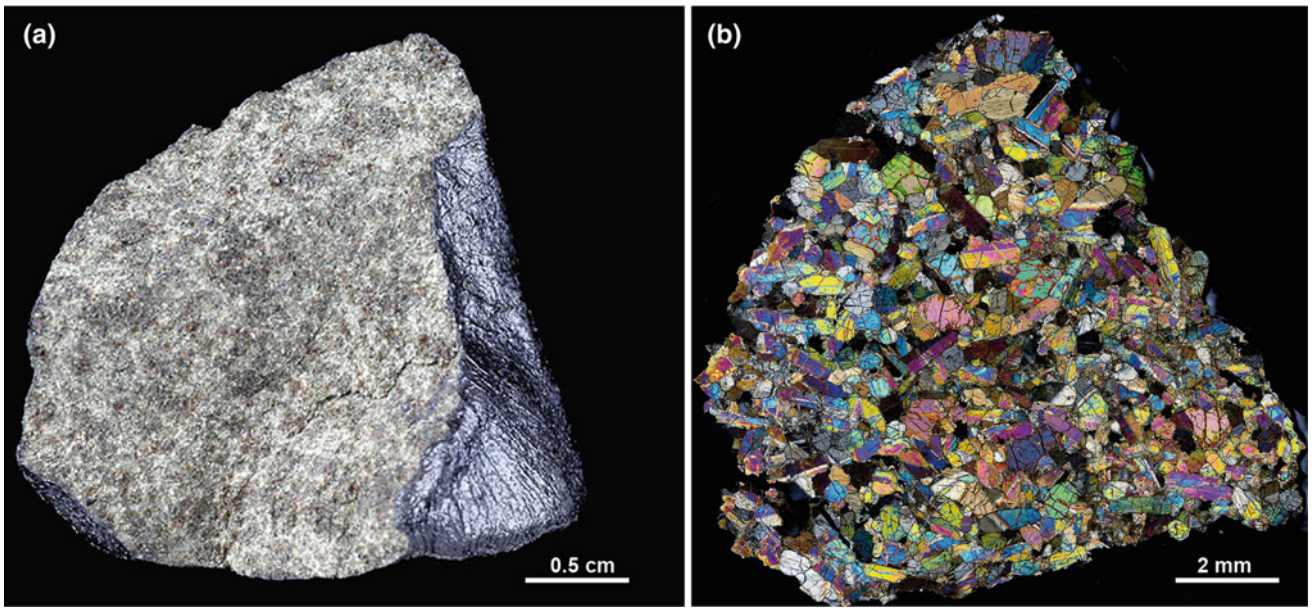

Fig. 11.12 The Nakhla martian meteorite. **a** A specimen of the Nakhla meteorite shower that fell in Egypt on June 28th, 1911 near the village of El Nakhla. The specimen, broken off for curatorial purposes, shows a shiny black fusion crust and a crystalline igneous textured interior. **b** Optical micrograph (crossed polars) of a petrographic thin section of the same specimen showing that Nakhla is a clinopyroxenite, dominated by augite with less abundant Fe-rich olivine, plagioclase, K-feldspars, Fe–Ti oxides, FeS, chalcopyrite and a hydrated alteration phase. Images courtesy of Sara Russell and Natashia Almeida (Natural History Museum, London, UK). Photo credit: © The Trustees of the Natural History Museum, London

Nakhla meteorite was seen to fall in the hamlets surrounding the village of El-Nakhla, El-Bahariya in Egypt, near Alexandria. Dr. W. F. Hume, at the time Director of the Geological Survey of Egypt, personally visited the site and collected both the evidence of eyewitnesses of the fall and about a dozen specimens varying in weight from 1813 to 20 g, for a total recovered mass of ~10 kg. Nakhla is a clinopyroxenite with a crystallization age of ~1.3 billion years before present (Treiman 2005)—a cornerstone specimen for understanding the igneous process on Mars (Bridges and Warren 2006; McSween and McLennan 2014).

With the exception of a minority of incidental finds (n = 18; ~25% of the total number of finds), the majority of the Egyptian finds (n = 58; ~75%) were recovered over the last 30 years from three regions defined as dense collection areas (DCAs; i.e., stable geological surfaces with the potential of yielding large accumulations of meteorites, namely ~0.01 to ~10 meteorites per square kilometer; Abu Aghreb et al. 2003; Gattacceca et al. 2011) in The Meteoritical Bulletin, namely the El-Shaik Fedl, Great Sand Sea and Marsa Alam fields (Figs. 11.1 and 11.13). The great majority of these meteorites were recovered by private collectors. As a consequence, little information is available on the geological characteristics of the collection surfaces and, thus, on the actual potential yield of those. Only few meteorites from the Great Sand Sea dense collection area were recovered during scientific expeditions carried out by Italian-Egyptian parties involved in the study of the Libyan Desert Glass during the early 1990s (e.g., Barakat et al. 1996; Barakat 1991). Even in this case, little information on the circumstances of the finds and on the meteorite collection surfaces has been reported, except that they were found in the inter-dune deflation corridors dominated by quartzose gravel, like the specimens of Libyan Desert Glass. The number of meteorites found in these three dense collection areas is, however, a small fraction of the hundreds-to-thousands of meteorites found in other desert areas in the Libyan and Algerian Sahara (e.g., the Acfer, Dar al Gani and Hamadah al Hamra DCAs; e.g., Schlüter et al. 2002), in the Atacama (e.g., the San Juan and El Medano DCAs; e.g., Gattacceca et al. 2011; Hutzler et al. 2016), and in Oman and Saudi Arabia (e.g., Dhofar; Al-Kathiri et al. 2005), and the actual meteorite accumulation potential of these Egyptian sites should be properly assessed.

11.6 Meteorites in the Archeological Record of Ancient Egypt

Amongst the earliest iron artifacts of human history, there are a number of Ancient Egyptian iron artifacts that predate the iron age, and for which a meteoritic origin has been recently documented through non-destructive geochemical analysis. These artifacts include nine small iron beads dated

Fig. 11.13 Meteorite finds from the Dense Collection Area denominated Great Sand Sea (GSS). See Fig. 11.1 for the location of the GSS area. A) Field photo of meteorite GSS 026 (28°11′21″ N, 25°37′18″ E), a H6 ordinary chondrite with a fairly oxidized (weathered) fusion crust sitting on the pale surface of an interdune deflation corridor dominated by well-sorted quartzose gravel (serir). B) A close-up view of the same meteorite in the field. C) Field photo of the relatively fresh GSS 004 LL6 ordinary chondrite (25°35′35″ N, 25°31′40″ E) showing some erosion of the black fusion crust. The black fusion crust, resulting from surface ablation during atmospheric entry heating, is a macroscopic diagnostic feature for the identification of meteorites in the field. Meteorites were collected during the Italian-Egyptian expeditions for the study of the Libyan Desert Glass carried out in between 1991 and 1996. Images courtesy of R. Serra (Universita di Bologna, Italy)

Fig. 11.14 Meteoritic iron in the history of Ancient Egypt. **a** Optical image (left) of a bead from a tomb in Gerzeh (Egypt) and dated about 3200 BCE made of meteoritic iron, and a Computer Tomography cross-section view (right) revealing how the bead was carefully hammered into thin sheets (Johnson et al. 2013; Rehren et al. 2013). The bead is ~2 cm in length and 3–8 mm in diameter. Images courtesy of Diane Johnson (Open University, UK). **b** The iron dagger of King Tutankhamun (14th C. BCE) with its gold sheath (Carter no. 256K, JE 61585). The full length of the dagger is 34.2 cm (modified after Comelli et al. 2016)

to ~3200 BC from two prehistoric burials discovered in Gerzeh, 70 km south of Cairo, northern Egypt, by British archeologist Gerald Wainwright in 1911 (Johnson et al. 2013; Rehren et al. 2013), and the iron blade of one of the two daggers found in the wrappings of King Tutankhamun (14th C. BCE) by British archeologist Howard Carter in 1925 (Comelli et al. 2016; Fig. 11.14).

Through a combination of scanning electron microscopy and micro X-ray microcomputer tomography, Johnson et al. (2013) showed that the microstructural and chemical analysis of a Gerzeh iron bead strung on a necklace from tomb 67 is consistent with a cold-worked iron meteorite. This finding was later confirmed by Rehren et al. (2013) by neutron and X-ray methods, which revealed substantial amounts of Ge (30–100 μg/g), 6–9 wt% Ni and 0.4–0.5 wt% Co. These results reveal the status of meteoritic iron as a valuable material for the production of precious objects, and document that already in the fourth millennium BC metalworkers had mastered the smithing of meteoritic iron.

The composition of the iron blade of King Tutankhamun's dagger (Fe plus 10.8 wt% Ni and 0.58 wt% Co), determined through portable X-ray fluorescence spectrometry, strongly supports its meteoritic origin (Comelli et al. 2016). In order to investigate whether known iron meteorites within the ancient Egyptian trade sphere could be linked to the studied blade, Comelli et al. (2016) compared this composition with those of the twenty known meteorites found in the region from the central-eastern Sahara to the Arabic Peninsula, Mesopotamia, Iran, and Eastern Mediterranean area, but no good match was found. This work confirmed that ancient Egyptians attributed great value to meteoritic iron for the production of fine ornamental or ceremonial objects. Furthermore, the high manufacturing quality of Tutankhamun's dagger blade, in comparison with other simple-shaped meteoritic iron artifacts, documents a significant mastery of ironworking in Tutankhamun's time.

11.7 Outlook

The work carried out at Kamil Crater (e.g., Folco et al. 2010, 2011) and in the so-called Gilf Kebir Crater Field (Paillou et al. 2006; Orti et al. 2008) has shown the importance of satellite image analysis in the identification of potential new impact craters, particularly in desert areas characterized by exceptional rock exposures. It has also shown the importance of field work in confirming the impact origin, through the identification of diagnostic features including traces of the impactor, and meso-to-microscopic shock metamorphic features (e.g., French and Koeberl 2010). The combination

of these two methodological approaches is a fundamental prerequisite for the identification of new impact structures.

Due to its extraordinary state of preservation, the 45-m-diameter, less than 5,000 years old Kamil Crater (Fig. 11.3) is a type-structure for small-scale meteorite impacts on Earth (Folco et al. 2011). Field and laboratory work has documented that Kamil is a natural laboratory for investigating processes and products generated by the hypervelocity impact of small meteoritic bodies. Advancements in the field of small-scale impact cratering are expected from the integration of ground truth, numerical models, and laboratory hypervelocity impact experiments (e.g., Kenkmann et al. 2013; Folco et al., 2018; Hamann et al. 2018; Wilk et al., 2018; Cavosie and Folco, 2018).

The large number of specimens of Gebel Kamil (the meteorite that formed Kamil Crater) which were smuggled out of Egypt and put on the worldwide market by private collectors document that the integrity of Kamil Crater is at serious risk. Egyptian geosocieties and legislative bodies should devise strategies for the conservation of this unique location and consider this structure as a resource not just for science, but also for tourism and education. Kamil is indeed located in a remote area of the Egyptian desert, yet it is close to the Gilf Kebir National Park, which is an extraordinary tourist attraction. Virtuous examples around the world of protected impact structures utilized for geotourism and educational purposes include—for instance—the Barringer crater (Arizona) or the Ries crater in the GeoPark Ries (Germany). The latter also features a unique museum in the City of Nordlingen, dedicated to the education about the Ries impact and impact cratering in general.

Although the Libyan Desert Glass and the Dakhleh Glass are silicate glasses of suggested impact origin (e.g., Barrat et al. 1997; Koeberl 2000; Osinski et al. 2007), no associated impact craters have been found yet. The study of these glasses has, thus, been instrumental for developing models for the formation of extended surface layers of unusual silicate glass by processes other than impact cratering, including a low-altitude airburst for the Libyan Desert Glass (Wasson 2003: Boslough and Crawford 2008a, b) and natural fires for the Dakhleh Glass (Roperch et al. 2017). The recent finding of evidence for high-pressures in some LDG specimens (Cavosie and Koberel 2019) requires a crater-forming event and that airburst alone could not be responsible for the formation of LDG.

Our knowledge of the origin and evolution of the solar system stems from the effective synergy between astronomical observations, space missions, astrophysical modeling and the cosmochemical study of thousands of meteorites (Russell, 2018). The larger the number of meteorites in our collections, the larger the chance of identifying new extraterrestrial rock types carrying new information about the processes that led to the formation of the solar system. This motivates the interest of the planetary science community in continuing the search for, and collection of, meteorites. The vast extensions of the hamada and serir type surfaces of the Egyptian desert plateaus are thus of great interest for systematic search for meteorites (Fig. 11.13). About 75% of the meteorites in the Egyptian collection were found in three dense collection areas (DCAs) mainly by private collectors, with little information on the characteristics of the collection surfaces being recorded. Therefore, the potential of these areas to yield high concentrations of meteorites should be investigated properly through field and laboratory work, taking advantage of the experience of other research groups in other desert areas in the Sahara, Atacama, Oman deserts, etc. (e.g., Schlüter et al. 2002; Hutzler et al. 2016). Data about terrestrial ages (i.e., the time since the fall) of the meteorites found in these DCAs and weathering style/rates would be relevant to assess the survival time of meteorites in these environments and the collection time window, and thus the local evolution of the climate (e.g., Bland et al. 1996; Jull 2006).

Fireball camera network projects are designed to track meteoroids entering the atmosphere, determine pre-entry orbits, and pinpoint fall positions for recovery (e.g., Oberst et al. 1998; Bland, 2004). These networks provide a wealth of information to the astronomical and planetary science community by linking pristine planetary materials to their source regions in the solar system (e.g., Bland et al. 2009). The vast desert lands of the Egyptian territory (~1 million square km), with virtually no vegetation for over 95% of their entire extension, should be assessed for the installation of fireball camera networks.

The Geological Museum in Cairo hosts a small yet valuable collection of meteorites, including a specimen of the Martian meteorite Nakhla (Fig. 11.12) and ~700 kg of the iron meteorite Gebel Kamil (~600 kg of shrapnel and the main mass of the regmaglypted individual featured in Fig. 11.4c). Systematic search for meteorites should be conducted by Egyptian research institutes in the Egyptian deserts to enrich this collection. All this would make great material for public exhibits. The scientific value and the societal impact of the study and curation of meteorites are widely accepted in today's scientific community (Baratoux et al. 2017).

Non-destructive compositional analyses of the Gerzeh iron beads (~3000 BCE; Johnson et al. 2013; Rehren et al. 2013) and of Tutankhamun's dagger blade (XIV C. BCE; Comelli et al. 2016) (Fig. 11.14) revealed that two pre-iron age Ancient Egyptian iron artifacts are made of meteoritic iron. The implications of such studies extend beyond this specific pre-iron age Egyptian use of iron, if we consider that the working of metal has played a crucial role in the evolution of human civilization. Non-destructive compositional analysis of other time-constrained ancient iron artifacts present in world collections are, thus, expected to provide significant insight into the use of meteoritic iron and into the

reconstruction of the evolution of metalworking technologies in the Mediterranean area.

Acknowledgements Natasha Almeida, Fabrizio Campanale, Aaron Cavosie, Massimo D'Orazio, Agnese Fazio, Gordon Osinski, Pierre Rochette, Sara Russell, and Romano Serra, made images available for this chapter. Massimo D'Orazio is thanked for helpful comments on an earlier version of the manuscript. LF's research on Kamil Crater has been supported over the last decade by the Italian Ministero degli Affari Esteri e Cooperazione Internazionale—Progetti di Grande Rilevanza.

References

Abate B, Koeberl C, Kruger FJ, Underwood JR Jr (1999) BP and Oasis impact structures, Libya, and their relation to Libyan Desert Glass. In: Dressler BO, Sharpton VL (eds) *Large meteorite impacts and planetary evolution II*, Geological Society of America Special Paper 339, pp 177–192

Abu Aghreb AE, Ghadi AM, Schlüter J, Schultz L, Thiedig F (2003) Hamadah al Hamra and Dar al Gani: a comparison of two meteorite fields in the Libyan Sahara. In: 66th annual meteoritical society meeting (2003), abstract no. 5081

Al-Kathiri A, Hofmann BA, Jull AJT, Gnos E (2005) Weathering of meteorites from Oman: correlation of chemical and mineralogical weathering proxies with ^{14}C terrestrial ages and the influence of soil chemistry. Meteorit Planet Sci 40:1215–1240

Avice G, Meier MMM, Marty B, Wieler R, Kramers JD, Langenhorst F, Cartigny P, Maden C, Zimmermann L, Andreoli MAG (2015) A comprehensive study of noble gases and nitrogen in "Hypatia", a diamond-rich pebble from SW Egypt. Earth Planet Sci Lett 432:243–253

Barakat AA (1991) Meteoritic iron from the Libyan glass area, southwestern Egypt. Meteorit Planet Sci 33:A173–A175

Barakat AA (2012) The precious gift of meteorites and meteorite impact processes. Nova Sciences Publishers Inc, New York, p 166

Barakat AA, De Michele V, Levi-Donati GR, Negro G, Serra R (1996) The desert of Great Sand Sea (GSS): an interesting reservoir of meteorite finds. Meteorit Planet Sci 31, A12 (abstract)

Barakat AA, de Michele V, Negro G, Piacenza B, Serra R (1997) Some new data on the distribution of Libyan Desert Glass (Great Sand Sea, Egypt). In: de Michele V (ed) Silica'96, Proceedings of the meeting on Libyan Desert Glass and related Desert Events, Milan, Italy, Pyramids, pp 29–36

Baratoux D, Chennaoui-Aoudjehane H, Gibson R, Lamali A, Reimold WU, Sapah SM, Chabou MC, Habarulema JB, Jessell MW, Mogessie A, Benkhaldoun Z, Nkhonjera E, Mukosi NC, Kaire M, Rochette P, Sickafoose A, Martínez-Frías J, Hofmann A, Folco L, Rossi AP, Faye G, Kolenberg K, Tekle K, Belhai D, Elyajouri M, Koeberl C, Abdeen MM (2017) The state of planetary and space sciences in Africa. Eos 98:16–23

Baratoux D, Reimold WU (2016) The current state of knowledge about shatter cones: introduction to the special issue. Meteorit Planet Sci 51:1389–1434

Barnes V, Underwood JR Jr (1976) New investigation of the strewn field of Libyan Desert Glass and its petrography. Earth Planet Sci Lett 30:117–122

Barrat JA, Jahn BM, Amosse J, Rocchia R, Keller F, Poupeau GR, Diemer E (1997) Geochemistry and origin of Libyan Desert Glasses. Geochim Cosmochim Acta 61:1953–1959

Bigazzi G, de Michele V (1997) New fission-track age determination on impact glasses. Meteorit Planet Sci 31:234–236

Bland PA, Berry FJ, Smith TB, Skinner S, Pillinger CT (1996) Flux of meteorites to the Earth and weathering in hot desert ordinary chondrite finds. Geochim Cosmochim Acta 60:2053–2059

Bland PA, Spurný P, Towner Martin C, Bevan AWR, Singleton AT, Bottke WF, Greenwood RC, Chesley SR, Shrbený L, Borovička J, Ceplecha Z, McClafferty TP, Vaughan D, Benedix GK, Deacon G, Howard KT, Franchi IA, Hough RM (2009) An anomalous basaltic meteorite from the innermost main belt. Science 325:1525–1527

Boslough MBE, Crawford DA (2008a) Low-altitude airbursts and the impact threat. Int J Impact Eng 35:1441–1448

Boslough MBE, Crawford DA (2008b) Low-altitude airbursts and the impact threat. Int J Impact Eng 35:1441–1448

Bridges JC, Warren PH (2006) The SNC meteorites: Basaltic igneous processes on Mars. J Geol Soc London 163:229–251

Bridges JC, Catling DC, Saxton JM, Swindle TD, Lyon IC, Grady MM (2001) Alteration assemblages in martian meteorites: implications for near-surface processes. Space Sci Rev 96:365–392

Cavosie AJ, Koeberl C (2019) Overestimation of threat from 100 Mt–class airbursts? High pressure evidence from zircon in Libyan Desert Glass. Geology 47:609–612

Cavosie AJ, Timms NE, Erickson TM, Koeberl C (2018) New clues from Earth's most elusive impact crater: evidence of reidite in Australasian tektites from Thailand. Geology 46:203–206

Chambers (2006) Meteoritic diversity and planetesimal formation. In: Lauretta DS, McSween HY Jr (eds) Meteorites and the early solar system II, pp 487–497

Chennaoui Aoudjehane H et al (2012) Tissint Martian meteorite: a fresh look at the interior, surface and atmosphere of Mars. Science 338 (6108):785–788

Churcher CS, Mills AJ (1999) Reports from the Survey of Dakhleh Oasis, Western Desert of Egypt, 1977–1987. Oxbow Press, Oxford, p 271

Churcher CS, Kleindienst MR, Schwarcz HP (1999) Faunal remains from a Middle Pleistocene lacustrine marl in Dakhleh Oasis, Egypt: palaeoenvironmental reconstructions. Palaeogeogr Palaeoclimatol Palaeoecol 154:301–312

Clayton PA, Spencer LJ (1933) Lecture on the Libyan Desert Glass presented on the 9 November 1933 at the Annual Meeting of the Mineralogical Society. Nature, 501–508

Cockell CS (2006) The origin and emergence of life under impact bombardment. Philos Trans R Soc Lond B Biol Sci 361(1474): 1845–1856

Collins GS, Melosh HJ, Osinski GS (2012) The impact-cratering process. Elements 8:25–30

Comelli D, D'Orazio M, Folco L, El Halwagy M, Frizzi T, Alberti R, Capogrosso V, Elnaggar A, Hassan H, Nevin A, Porcelli F, Rashed MG, Valentini G (2016) The meteoritic origin of Tutankhamoun's iron dagger blade. Meteorit Planet Sci 51:1301–1309

De Michele V (1998) The "Libyan Desert Glass" scarab in Tutankhamen's pectoral. Sahara 10:107–109

Deutsch A, Poelchau MH, Kenkmann T (2015) Impact metamorphism in terrestrial and experimental cratering events. In: Lee MR, Leroux H (eds) Planetary mineralogy. European Mineralogical Union, Notes in Mineralogy 15, Chapter 4, pp 89–127

Diemer E (1997) Libyan Desert Glass: an impactite. State of the art in July 1996. In: de Michele V (ed) Silica'96, Proceedings of meeting on Libyan Desert Glass and related desert events, Milan, Italy, Pyramids, pp 29–36

D'Orazio (2007) Meteorite records in the ancient Greek and Latin literature: between history and myth. In: Piccardi L, Masse WB (eds) Myth and geology. Geological Society London Special Publications 273, pp 215–225

D'Orazio M, Folco L, Zeoli A, Cordier C (2011) Gebel Kamil: the iron meteorite that formed the Kamil Crater (Egypt). Meteorit Planet Sci 46:1179–1196

El-Baz F (1981) Circular feature among dunes of the Great Sand Sea, Egypt. Science 213:439–440

El-Baz F, Ghoneim E (2007) Largest crater shape in the Great Sahara revealed by multi-spectral images and radar data. Int J Remote Sens 28(2):451–458

Erickson TM, Cavosie AJ, Moser DE, Barker IR, Radovan HA, Wooden J (2013) Identification and provenance determination of distally transported, Vredefort-derived shocked minerals in the Vaal River, South Africa using SEM and SHRIMP-RG techniques. Geochim Cosmochim Acta 107:170–188

Fazio A, Folco L, D'Orazio M, Frezzotti ML, Cordier C (2014) Shock metamorphism and impact melting in small impact craters on Earth: evidence from Kamil Crater, Egypt. Meteoritics and Planetary Science 49:2175–2200

Fazio A, D'Orazio M, Cordier C, Folco L (2016) Target-projectile interaction during impact melting at Kamil Crater, Egypt. Geochimica et Cosmochimica Acta 18:33–50

Ferrière L, Osinski G (2013) Shock metamprphism. In: Osinski GR, Pierazzo E (eds) Impact cratering—processes and products. Wiley-Blackwell, Oxford

Folco L, Di Martino M, El Barkooky A, D'Orazio M, Lethy A, Urbini S, Nicolosi I, Hafez M, Cordier C, van Ginneken M, Zeoli A, Radwan AM, El Khrepy S, El Gabry M, Gomaa M, Barakat AA, Serra R, El Sharkawi M (2010) The Kamil Crater in Egypt. Science 329:804

Folco L, Di Martino M, El Barkooky A, D'Orazio M, Lethy A, Urbini S, Nicolosi I, Hafez M, Cordier C, van Ginneken M, Zeoli A, Radwan AM, El Khrepy S, El Gabry M, Gomaa M, Barakat AA, Serra R, El Sharkawi M (2011) Kamil Crater (Egypt): ground truth for small scale meteorite impact on earth. Geology 39:179–182

Folco L, D'Orazio M, Fazio A, Cordier C, Zeoli A, van Ginneken M, Barkooky A (2015) Microscopic impactor debris in the soil around Kamil Crater (Egypt): inventory, distribution, total mass and implications for the impact scenario. Meteorit Planet Sci 50:382–400

French BM, Koeberl C (2010) The convincing identification of terrestrial meteorite impact structures: What works, what doesn't, and why? Earth Sci Rev 98:123–170

Fröhlich F, Poupeau G, Badou A, Le Bourdonnec FX, Sacquin Y, Dubernet JM, Bardintzeff M, Véran M, Smith DC, Diemer E (2013) Libyan Desert Glass: new field and Fourier transform infrared data. Meteorit Planet Sci 48, 2517–2530

Fudali RF (1981) The major element chemistry of Libyan Desert Glass and the mineralogy of its precursor. Meteoritics 16:247–259

Gattacceca J, Valenzuela M, Uehara M, Jull AJ, Giscard M, Rochette P, Braucher R, Suavet C, Gounelle M, Morata D, Munayco P, Bourot-Denise M, Bourles D, Demory F (2011) The densest meteorite collection area in hot deserts: the San Juan meteorite field (Atacama Desert, Chile). Meteorit Planet Sci 46:1276–1287

Gibson RL, Reimold WU (2008) The geology of the Vredefort impact structure. Memoir 97, Council for Geoscience, Pretoria, South Africa, 181 pp

Gillet P, El Goresy A (2013) Shock events in the solar system: the message from minerals in terrestrial planets and asteroids. Ann Rev Earth Planet Sci 41, 12.1–12.29

Giuli G, Paris E, Pratesi G, Koeberl C, Cipriani C (2003) Iron oxidation state in Fe-rich layer and silica matrix of Libyan Desert Glass: a high-resolution XANES study. Meteorit Planet Sci 38:1181–1186

Glass BP, Simonson BM (2012) Distal impact ejecta layers: Spherules and more. Elements 8:43–48

Goderis S, Paquay F, Claeys P (2013) Projectile identification in terrestrial impact structures and ejecta material. In: Osinski GR, Pierazzo E (eds) Impact cratering—processes and products. Wiley-Blackwell, Oxford, pp 1–20

Greshake A, Koeberl C, Fritz J, Reimold WU (2010) Brownish inclusions and dark streaks in Libyan Desert Glass: evidence for high-temperature melting of the target rock. Meteorit Planet Sci 45:973–989

Greshake A, Wirth R, Fritz J, Jakubowsky T, Böttger U (2018) Mullite in Libyan Desert Glass: evidence for high-temperature/low-pressure formation. Meteorit Planet Sci 53:467–481

Halliday I, Blackwell AT, Griffin AA (1978) The Innisfree meteorite and the Canadian camera network. J R Astron Soc Canada 72:15–39

Hamann C, Fazio A, Ebert M, Hecht L, Folco L, Deutsch A, Wirth R, Reimold WU (2018) Silicate liquid immiscibility in impact melts. Meteorit Planet Sci (in press) 53:1594–1632

Hargitai H, Reimold WU, Bray VJ (2015) Impact structure. In: Hargitai H, Kereszturi Á (eds) Encyclopedia of planetary landforms, vol. 2. Springer Science + Business Media LLC, New York, pp 988–1023

Horn P, Müller-Sohnius D, Schaaf P, Kleinmann B, Storzer D (1997) Potassium-argon and fission-track dating of Libyan Desert Glass, and strontium- and neodymium isotope constraints on its source rock. In: de Michele V (ed) Proceedings of the silica '96 meeting on Libyan Desert Glass and related desert events, Bologna, Segrate, Italy: Pyramids. pp 59–73

Hutzler A, Gattacceca J, Rochette P, Braucher R, Carro B, Christensen EJ, Cournede C, Gounelle M, Laridhi Ouazaa N, Martinez R, Valenzuela M, Warner M, Bourles D (2016) Description of a very dense meteorite collection area in western Atacama: insight into the long-term composition of the meteorite flux to Earth. Meteorit Planet Sci 51:468–482

Issawi B (1982) Geology of the southwestern desert of Egypt. In: El-Baz F, Maxwell TA (eds) Desert landforms of Southwest Egypt: a basis for comparison with Mars. National Air and Space Museum, Washington, DC, pp 57–66

Johnson D, Tyldesley J, Lowe T, Withers PJ, Grady MM (2013) Analysis of a prehistoric Egyptian iron bead with implications for the use and perception of meteorite iron in ancient Egypt. Meteorit Planet Sci 48:997–1006

Jull AJT (2006) Terrestrial ages of meteorites. In: Lauretta DS, McSween HY Jr (eds) Meteorites and the early solar system II, pp 889–905

Kenkmann T, Deutsch A, Thoma K, Poelchau M (2013) The MEMIN experimental impact cratering. Meteorit Planet Sci 48(1):164 (Special Issue)

Klein J, Giegengack R, Middleton R, Sharma P, Underwood JR Jr, Weeksi RA (1986) Revealing histories of exposure using in situ produced ^{26}Al and ^{10}Be in Libyan Desert Glass. Radiocarbon 28:547–555

Kleinmann B (1969) The breakdown of zircon observed in the Libyan Desert Glass as evidence of its impact origin. Earth Planet Sci Lett 5:497–501

Kleinmann B, Horn P, Langenhorst F (2001) Evidence for shock metamorphism in sandstones from the Libyan Desert Glass strewn field. Meteorit Planet Sci 36:1277–1282

Klitzsch E, List FK, Pöhlmann G (1987) Geologic map of Egypt 1:500000. The Egyptian General Petroleum Corporation, Cairo, Egypt, 20 sheets

Koeberl C (1997) Libyan Desert Glass: geochemical composition and origin. In: de Michele V (ed) Proceedings of the Silica '96 meeting on Libyan Desert Glass and related desert events, Bologna, Pyramids, Segrate, Milano, pp 121–131

Koeberl C (2000) Confirmation of a meteoritic component in Libyan Desert Glass from osmium isotopic data. Meteorit Planet Science 35. A89–A90 (abstract)

Koeberl C (2014) The geochemistry and cosmochemistry of impacts. In: Holland HD, Turekian KK (eds) Treatise on geochemistry, vol 2, 2nd edn. Elsevier, Oxford, pp 73–118

Koeberl C, Claeys Ph, Hecht L, McDonald I (2012) Geochemistry of impactites. Elements 8:37–42

Koeberl C, Ferrière L (2019) Libyan Desert Glass area in western Egypt: shocked quartz in bedrock points to a possible deeply eroded impact structure in the region. Meteorit Planet Sci (in press). https://doi.org/10.1111/maps.13250

Kramers JD, Andreoli MAG, Atanasova M, Belyanin GA, Block D, Franklyn C, Harris C, Lekgoathi M, Montross CS, Ntsoane T, Pischedda V, Segonyane P, Viljoen KS, Westraadt JE (2013) Unique chemistry of a diamond-bearing pebble from the Libyan Desert Glass strewnfield, SW Egypt: evidence for a shocked comet fragment. Earth Planet Sci Lett 382:21–31

Krot AN, Keil K, Scott ERD, Goodrich CA, Weisberg MK (2014) Classification of meteorites and their genetic relationships. In; Davis AM (ed) Meteorites and cosmochemical processes, volume 1 of treatise on geochemistry, 2nd edn, pp 1–63

Langenhorst F, Deutsch A (2012) Shock metamorphism of minerals. Elements 8:31–36

Longinelli A, Sighinolfi G, De Michele V, Selmo E (2011) $\partial^{18}O$ and chemical composition of Libyan Desert Glass, country rocks, and sands: new considerations on target material. Meteorit Planet Sci 46:218–227

Magna T, Deutsch A, Mezger K, Skála R, Seitz H-M, Mizera J, Řanda Z, Adolph L (2011) Lithium in tektites and impact glasses: implications for sources, histories and large impacts. Geochimica et Cosmochimica Acta 75, 2137–2158

Martin AJ (1969) Possible impact structure in Southern Cyrenaica, Libya. Nature 223:940–941

Matsubara K, Matsuda J, Koeberl C (1991) Noble gases and K–Ar ages in Aouelloul, Zhamanshin, and Libyan Desert impact glasses. Geochim Cosmochim Acta 55:2951–2955

McCoy TJ, Mittlefehldt DW, Wilson L (2006) Asteroid differentiation. In: Lauretta DS, McSween HY Jr (eds) Meteorites and the early solar system II, pp 733–745

McCrosky RE, Posen A, Schwartz G, Shao C-Y (1971) Lost City meteorite—its recovery and a comparison with other fireballs. J Geophys Res 76:4090–4108

McSween HY, McLennan SM (2014) Mars. In: Davis AM (ed) Planets, asteriods, comets and the solar system, volume 2 of treatise on geochemistry, 2nd edn. Elsevier, pp. 251–300

McSween HY, Lauretta DS, Lexhin LA (2006) Recent advances in meteoritics and cosmochemistry. In: Lauretta DS, McSween HY Jr (eds) Meteorites and the early solar system II, pp. 53–66

Melosh HJ (1989) Impact cratering: a geologic process: Oxford monographs on geology and geophysics. Oxford University Press, Oxford, p 245

Murali AV, Linstrom EJ, Zolensky ME, Underwood JR Jr, Giegengack RF (1989) Evidence of extraterrestrial components in the Libyan Desert Glass (abstract). EOS Trans AGU 70:1178

Murali AV, Zolensky ME, Underwood JR Jr, Giegengack RF (1997) Chondritic debris in Libyan Desert Glass. In: de Michele V (ed.) Proceedings of Silica'96 meeting on Libyan Desert Glass and related desert events, Milan, Italy, Pyramids, pp 133–142

Negro G, Damiano-Appia M (1992) II "Silica Park": un centro di lavorazione del LDSG nel Great Sand Sea. Sahara 5:105–108

Oakley KP (1952) Dating the Libyan Desert Silica Glass. Nature 170:447–449

Oberst J, Molau S, Heinlein D, Gritzner C, Schindler M, Spurny P, Ceplecha Z, Rendtel J, Betlem H (1998) The "European Fireball Network": current status and future prospects. Meteorit Planet Sci 33:49–56

Orti L, Di Martino M, Morelli M, Cigolini C, Pandeli E, Buzzigoli A (2008) Nonimpact origin of the crater-like structures in the Gilf Kebir area (Egypt): implications for the geology of eastern Sahara. Meteorit Planet Sci 43:1629–1639

Osinski GR (2008) Meteorite impact structures: the good and the bad. Geol Today 24:13–19

Osinski GR, Schwarcz HP, Smith JR, Kleindienst MR, Haldemann AFC, Churcher CS (2007) Evidence for a ~200–100 ka meteorite impact in the Western Desert of Egypt. Earth Planet Sci Lett 253:378–388

Osinski GR, Kieniewicz J, Smith JR, Boslough MBE, Eccleston M, Schwarcz HP, Kleindienst MR, Haldemann AFC, Churcher CS (2008) The Dakhleh Glass: product of an airburst or cratering event in the Western Desert of Egypt? Meteorit Planet Sci 43:2089–2107

Ott U, Merchel S, Herrman S, Pavetich S, Rugel G, Faestermann T, Fimiani L, Gomez-Guzman JM, Hain K, Korschinek G, Ludwig P, D'Orazio M, Folco L (2014) Cosmic ray exposure and pre-atmospheric size of the Gebel Kamil iron meteorite. Meteorit Planet Sci 49:1365–1374

Paillou P, El-Barkooky A, Barakat A, Melezieux JM, Reynard B, Dejax J, Heggy E (2004) Discovery of the largest impact crater field on Earth in the Gilf Kebir region, Egypt. Compte Rendus Géoscience de l'Académie de Sciences 336:1491–1500

Paillou P, Reynard B, Malezieux JM, Dejax J, Heggy E, Rochette P, Reimold WU, Michel P, Baratoux D, Razin P, Colin JP (2006) An extended field of crater-shaped structures in the Gilf Kebir region, Egypt: observations and hypotheses about their origin. J Afr Earth Sci 46:281–299

Pierazzo E, Artemieva NA (2012) Local and global environmental effects of impacts on Earth. Elements 8:55–60

Pratesi G, Viti C, Cipriani C, Mellini M (2002) Silicate-Silicate liquid immiscibility and graphite ribbons in Libyan Desert Glass. Geochim Cosmochim Acta 66:903–911

Rehren T, Belgya T, Jambon A, Káli G, Kasztovszky Z, Kis Z, Kovács I, Maróti B, Martinón-Torres M, Miniaci G, Pigott VC, Radivojević M, Rosta L, Szentmiklósi L, Szokefalvi-Nagy Z (2013) 5,000 years old Egyptian iron beads made from hammered meteoritic iron. J Archaeol Sci 40:4785–4792

Reimold U, Jourdan F (2012) Impact!—Bolides, craters and catastrophes. Elements 8:19–24

Reimold U, Koeberl C (2014) Impact structures in Africa: a review. J Afr Earth Sci 93:57–175

Reimold WU, Koeberl C, Gibson RL, Dressler BO (2005) Economic mineral deposits in impact structures: a review. In: Koeberl C, Henkel H (eds) Impact tectonics, impact studies series, vol 6, Springer, pp 479–552

Renne PR, Schwarcz HP, Kleindienst MR, Osinski GR, Donovan JJ (2010) Age of the Dakhleh impact event and implications for Middle Stone Age archeology in the Western Desert of Egypt. Earth Planet Sci Lett 291:201–206

Rocchia R, Robin E, Fröhlich F, Amosse J, Barrat J-A, Méon H, Froget L, Diemer E (1997) The impact origin of Libyan Desert Glass. In: de Michele V (ed) Proceedings of Silica'96 meeting on Libyan Desert Glass and related desert events, Milan, Italy, Pyramids, pp 143–149

Roe DA, Olsen JW, Underwood Jr, Giegengack RF (1982) A handaxe of Libyan Desert Glass. Antiquity LVI, 88–92

Roperch P, Gattacceca J, Valenzuela M, Devouard B, Lorand J-P, Arriagada C, Rochette P, Latorre C, Beck P (2017) Surface vitrification caused by natural fires in Late Pleistocene wetlands of the Atacama Desert. Earth Planet Sci Lett 469:15–26

Rubin AE, Grossman JN (2010) Meteorite and meteoroid: new comprehensive definitions. Meteorit Planet Sci 45:114–122

Russell SS, Hartman L, Cuzzi J, Krot AN, Gounelle M, Weidenschilling S (2006) Timescales of the solar protoplanetary disk. In: Lauretta DS, McSween HY Jr (eds) Meteorites and the early solar system II, pp 233–251

Schaaf P, Müller-Sohnius D (2002) Strontium and neodymium isotopic study of Libyan Desert Glass: inherited Pan-African age signatures and new evidence for target material. Meteorit Planet Sci 37:565–576

Schlüter J, Schultz L, Thiedig F, Al-Mahdi BO, Abu Aghreb AE (2002) The Dar al Gani meteorite field (Libyan Sahara): geological setting, pairing of meteorites, and recovery density. Meteorit Planet Sci 37, 1079–1093

Scott ERD, Krot AN (2014) Chondrites and their components. In: Davis AM (ed) Meteorites and cosmochemical processes, volume 1 of Treatise on geochemistry, 2nd edn, pp 65–137

Sighinolfi GP, Sibilia E, Contini G, Martini M (2015) Thermoluminescence dating of the Kamil impact crater (Egypt). Meteorit Planet Sci 50:204–213

Stöffler D, Grieve RAF (2007) Impactites. In: Fettes D, Desmons J (eds) Metamorphic rocks: a classification and glossary of terms, recommendations of the international union of geological sciences. Cambridge University Press, Cambridge, UK, pp 82–92, 111–125, and 126–242 (Chapter 2.11)

Stöffler D, Hamann C, Metzler K (2018) Shock metamorphism of planetary silicate rocks and sediments: proposal for an updated classification system. Meteorit Planet Sci 53:5–49

Storzer D, Koeberl C (1991) Uranium and zirconium enrichments in Libyan Desert Glass. Zircon, baddeleyite and high temperature history of the glass. Lunar Planet Sci XXII, 1345–1346

Storzer D, Wagner GA (1977) Fission-track dating of meteorite impacts. Meteoritics 12:368–369

Swaenen M, Stefaniak EA, Frost R, Worobiec A, Grieken RV (2010) Investigation of inclusions trapped inside Libyan Desert Glass by Raman microscopy. Analyt Bioanalyt Chem 397:2659–2665

Treiman AH (2005) The nakhlite meteorites: Augite-rich igneous rocks from Mars. Chemie Erde 65:203–270

Underwood JR Jr, Fisk EP (1980) Meteorite impact structures, Southeast Libya. In: Salem MJ, Busrewil MT (eds) The geology of Libya 3, 2. Symposium on the Geology of Libya 1978, London, pp 893–900

Urbini S, Nicolosi I, Zeoli A, El Khrepy S, Lethy A, Hafez M, El Gabry M, El Barkooky A, Barakat A, Gomaa M, Radwan A, El Sharkawi M, D'Orazio M, Folco L (2012) Geological and geophysical investigation of Kamil Crater, Egypt. Meteorit Planet Sci 47:1842–1868

Warren PH, Taylor GJ (2014) The moon. In: Davis AM (ed) Planets, asteriods, comets and the solar system, Volume 2 of Treatise on geochemistry, 2nd edn. Elsevier, pp 213–250

Wasson JT (2003) Large aerial bursts: an important class of terrestrial accretionary events. Astrobiology 3:163–179

Weeks RA, Underwood JR Jr, Giegengack R (1984) Libyan Desert glass: a review. J Non-Cryst Solids 67, 593–619

Quaternary of Egypt

12

Mohamed A. Hamdan and Fekri A. Hassan

Contents

Abstract

More than 100 years of continuing research into the Quaternary of Egypt has produced numerous publications. In the last twenty years, Quaternary studies have witnessed great advances in both theories and methodologies, and the pace of archaeological research has accelerated as a new generation of researchers joined in expounding the different dimensions of the Quaternary period of Egypt. We aim in this contribution to provide an up-to-date synthesis of recent research on high-resolution and well-dated paleo-environmental archives of proxy data to understand the emerging picture of the impact of climate change on sediments, paleoenvironments and landscapes in Egypt as a whole.

M. A. Hamdan (✉)
Geology Department, Cairo University, Giza, Egypt
e-mail: hamdanmohamed@hotmail.com

F. A. Hassan
Cultural Heritage Program, French University, Cairo, Egypt

12.1 Introduction

The Quaternary is youngest in a four-cycle division of earth history proposed by G. Arduino in 1759 (Arduino 1760). The term "Quaternary" first used by Raboul (1833), has continued to the present day. Until now, the official status of the Quaternary was that of period/system with a base at 1.8 Ma. The lower boundary of the Quaternary period (i.e. Pliocene-Pleistocene boundary) is varies between 2.5 Ma, based on studies of continental glacial deposits and 1.8 Ma

Z. Hamimi et al. (eds.), *The Geology of Egypt*, Regional Geology Reviews,
https://doi.org/10.1007/978-3-030-15265-9_12

on basis of oceanic oxygen isotope records. The latter age (i.e. 1.8 Ma) is most accepted by Quaternary scientists. The Quaternary Period, originally referred to as the "Ice Age", is now characterized as the geological interval during which the climate of the Earth witnessed spectacular alternations of cold and warm phases, which in Africa corresponded to the interpluvial and pluvial periods, respectively.

More recently, the Anthropocene is a proposed epoch dating from the beginning of significant human impact on the Earth's geology and ecosystems (Waters et al. 2016). As of August 2016, neither the International Commission on Stratigraphy nor the International Union of Geological Sciences has yet officially approved the term as a recognized subdivision of geological time, although the Anthropocene Working Group (AWG) of the Subcommission on Quaternary Stratigraphy (SQS) of the International Commission on Stratigraphy (ICS), voted to proceed towards a formal golden spike (GSSP) proposal to define the Anthropocene epoch in the Geologic Time Scale and presented the recommendation to the International Geological Congress on 29 August 2016. Various different start dates for the Anthropocene have been proposed, ranging from the beginning of the Agricultural Revolution 12–15 kyr BP, to recent.

The most important phenomenon, from a cultural perspective, in the Quaternary is the appearance of humans and from both ecological and anthropological perspectivesit is a period of frequent and often intense climatic fluctuations. Different proxies have therefore been deployed to reconstruct paleoclimatic conditions, paleoenvironmental changes, palaeosols, cultural geography and human evolutionary trajectories. The study of the Quaternary is therefore multidisciplinary par excellence and requires integration of data from different disciplines. One of the most productive developments in the Quaternary studies was the rise of geoarchaeology bringing geology closer to human affairs in the past with its implications for the present and future, especially in the domain of climate change on contemporary societies (see Gladfelter 1977; Hassan 1979a; Rapp and Hill 2006).

Study of Quaternary deposits in Egypt passed through several stages since the beginning of the Twentieth Century (named the foundation, collaboration and integration stages). The foundation stage (first half of the Twentieth Century) includes the seminal work of Blankenhorn (1900) on the Nile Valley; Caton-Thompson and Gardner (1934) in Faiyum and Kharga; Sandford and Arkell (e.g. 1929, 1939) on the Nile-Faiyum divide, Upper Egypt and Red Sea Coast (Sandford 1934) and the work of Ball (1927) and Beadnell (1909) in the Faiyum and Kharga, respectively.

Renewed investigations of the Quaternary in Egypt accompanied the archaeological salvage, exploration and research triggered by the Nubian Salvage campaign. Numerous archaeological expeditions included geologists and geographers. Karl Butzer, who continued to make significant contributions to the Quaternary geology and geography of Egypt, and became one of the leading authorities on ecological study of the Quaternary of Egypt. Butzer (1964, 1982), studied the Pleistocene and Holocene geology of the Nile Valley from Sudanese border to Kom Ombo plain (Butzer and Hansen 1968). De Heinzelin (1968) examined the Quaternary sediment in Sudanese Nile Valley, while that of the prehistory and Holocene geology of Lower Nubia were examined by Combined Prehistroic Expedition led by Fred Wendorf. The Combined Prehistoric Expedition was by far the most dedicated to the continuation of prehistoric and geoarchaeological studies in Egypt after the building of the Aswan High Dam. They began their investigations immediately after the completion of work in Nubia on the prehistory and geoarchaeology of Esna, Dandara, and Dishna sectors of Upper Egypt (Wendorf and Schild 1976). During these investigations, they closely collaborated with Egyptian geologists of the caliber of Rushdi Said and Bahay Issawi then associated with the Geological Survey of Egypt. As such they engaged numerous young Egyptian geologists from the Geological Survey in their geological investigations. Fekri Hassan, at the time a teaching assistant in the Department of Geology at Ain Shams University, joined the Prehistoric Combined Expedition in the archaeological and geological survey of the area between Dandara and Sohag. Combining his academic training both as a geologist and an archaeologist, he obtained his Ph.D. with Fred Wendorf at Southern Methodist University, USA. He led numerous expeditions as a Principal Investigators in Siwa, Bahariya, Naqada, East Delta and undertook geoarchaeological work in the Faiyum, Farafra and other sites during the next stage of Quaternary studies in Egypt, beginning in the 1980s. Over the long years of working first along the Nile and later in the Eastern Sahara, significant contributions to the Quaternary geology of Egypt were made by Vance Haynes as a collaborator with the Prehistoric Combined Expedition (Wendorf and Schild 1976) and with fellow geologists and geochronology specialists.

The integration stage is characterized by the application of chronometry to archaeological sites and sediments. Detailed paleoenvironmental studies using paleontological (pollen, ostracods, diatoms…etc.) and geochemical (trace metals, rare earth elements and stable isotope) proxies and associated detailed investigations of archaeological and bioarcheological materials (lithic artifacts, pottery, and charcoal) were made. Integration of dating technologies (^{14}C, OSL, TL and recently ESR) with paleoenvironmental proxies draw a clearer picture of paleoclimatic variation during the Quaternary that correlate well with the global climatic framework. Finally, the integration stage is

represented by the work of Wendorf and Schild in Nabta playa, Bir Tarfawi and in Wadi Kubbaniya (Wendorf and Schild 1986, 1989) and by Daniel Stanley and his coworkers (Stanley 1988; 1990) by their intensive coring programs in the Nile Delta. It also includes work by Fekri Hassan and his coworkers in the Nile Valley, Farafra and the Faiyum (Hassan 1986, 2007a, b, 2010; Hassan et al. 2001, 2012, 2017; Flower et al. 2012, 2013; Hamdan et al. 2016a; 2019). Hassan also initiated a research trend modeling the link between climate change and origins of agriculture in Egypt (Hassan 1986) and the relationships between Nile floods and the course of Egyptian civilization (e.g. Hassan 1997). This work extended research into the relevance of geoarchaeology to contemporary social affairs including the impact of climate change on food security and droughts in Africa. During this period, Rudolf Kuper and his coworkers began their survey of the Eastern Sahara from Siwa to Gilf Kebir (e.g. Kuper and Kröpelein 2006). At this time research in the Egyptian Sahara included studies of Kharga and Dakhla Oases (Smith et al. 2004).

12.2 Nile Sediments in the Nile Valley, Nile Delta and Faiyum

The Main Nile in Egypt is the northern extension of the course of the Nile starting in the Sudan as a result of the confluence of the Ethiopian tributaries, mainly the Blue Nile, and the White Nile draining a large area in Equatorial Africa (Fig. 12.1a). The river basin spans 35° of latitude (4° S to 31° N) encompassing a wide variety of climates, river regimes, biomes and terrains from the Equatorial lakes plateau of the White Nile headwaters to the delta complex in the Eastern Mediterranean Sea. It is unique among the large rivers of the world in that it flows for ca. 2700 km through the Sahara Desert without any significant perennial tributary inputs. Of all the world's rivers with catchments greater than 1 million km^2, the Nile has the lowest specific discharge, 0.98 L s^{-1} km^2 at Aswan (Shahin 1985). Geologic evolution of River Nile during Quaternary is controlled by major tectonic phenomena-including the rifting of East Africa—climatic changes and other factors (Said 1981, 1993; Butzer 1997; Woodward et al. 2007). According to Said (1981), the Nile Basin includes five major regions that differ from one another in structure and geological history (Fig. 12.1b). These are: (1) The Equatorial lake plateau, (2) The Sudd region and central Sudan with low gradient floodplains and extensive swamplands, (3) The Ethiopian Highlands forming the headwaters of the Blue Nile and the Atbara, (4) The great bends and cataracts of the desert Nile and (5) The Egyptian region including the low gradient delta complex.

12.2.1 The Nile Valley

12.2.1.1 Nile Early Origins (Pre-quaternary)

There is a substantial literature debating the geological history of the River Nile, based on different geological and geomorphological proxies (Macgregor 2012). There are two main theories about the early origin of the Nile River in Egypt: the Egyptian ancestor Nile and the African ancestor Nile.

The Egyptian ancestor Nile theory (Butzer and Hansen 1968; De Heinzelin 1968; Wendorf and Schild 1976; Said 1981; Issawi and McCauley 1993) proposes that the early ancestors of River Nile were Egyptian Rivers that drained from Egyptian territories. Evidence of this theory includes landform, radar and mineralogical data indicating a diminishing contribution from Ethiopian volcanic sources with increased age. The second theory, the African ancestor Nile (McDougall et al. 1975; Pik et al. 2003; Ebinger 2005; Underwood et al. 2013, Fielding et al. 2017, 2018) indicates that the Egyptian Nile was fed by waters originating from the Blue Nile and other Ethiopian tributaries during the Oligocene onward. Abdelkareem et al. (2012) proposed that the Nile formed during subsequent stages and lengthened as Africa drifted northward relative to the Earth's equator; i.e. it is probable that during the late Eocene or Oligocene, the Earth's Equator was located at the present-day latitudes of Chad and Sudan. That paleogeographic position of the Equator would have produced pluvial conditions throughout North Africa. They also suggest an easterly river course in Egypt during the Oligo-Miocene along the Qena Valley but others favored a more westerly course. Evidence presented by the second theory includes the large sediment volumes in the Nile which are proposed to be inconsistent with a purely Egyptian hinterland. More recently, Fielding et al. (2018) demonstrated the presence of Ethiopian Cenozoic Continental Flood Basalt (CFB) detritus in the Nile delta beginning ca. 31 Ma. They show that the Nile River was established as a river of continental proportions by Oligocene times with there was no significant input from Archaean cratons, supplied directly via the White Nile to the Nile Delta. Whilst there are subtle differences between the Nile delta samples from the Oligocene and Pliocene compared to those from the Miocene and Pleistocene, the overall stability of the Ethiopian signal throughout the delta record and its similarity to the modern Nile signature, indicates no major change in the Nile's drainage from Oligocene to the present day (Fielding et al. 2017, 2018).

The Egyptian ancestor Nile theory comprises two hypotheses: a single-master-stream and a multi master stream hypotheses. The former is based on the study of drill cores in the Nile Valley and the delta, which suggest that the Nile Valley started as a single-master-stream initiated since the late Miocene (Said 1981). This hypothesis does not take

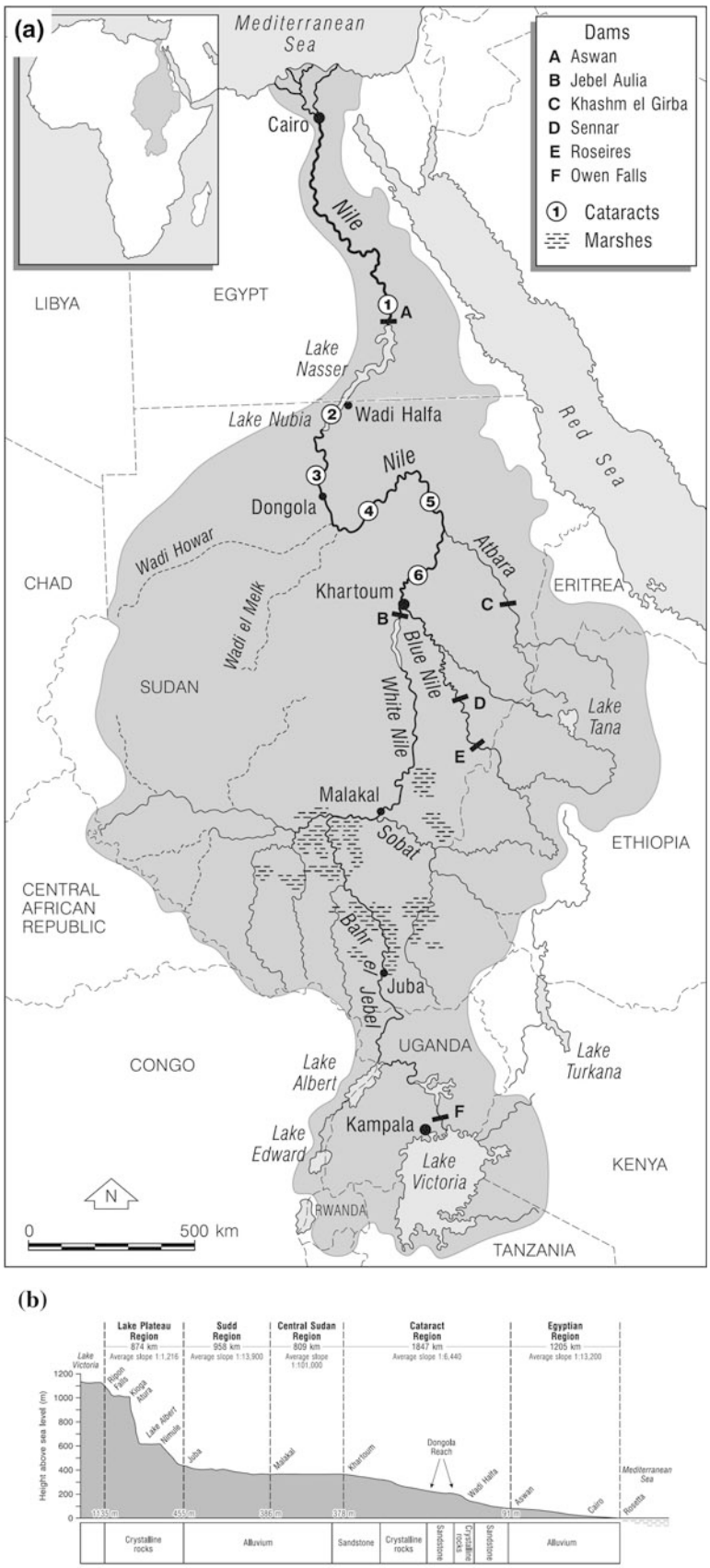

Fig. 12.1 **a** Map of the Nile Basin showing the drainage network, basin states, and major dams (*Source* Woodward et al. 2007). **b** Long profile of the Nile from the White Nile headwaters to the Mediterranean Sea (*Source* Said 1993)

into account any fluvial activity during the widespread northward regression of the Tethys Sea over Egypt (late Eocene-Oligocene). Five successive units of fluvial sediments were distinguished (Said 1993). Each one of these units has characteristic features referring to deposition by different rivers. These are from oldest to youngest: Eonile, Paleonile, Protonile, Prenile and Neonile. The last three river systems are dated to the Quaternary and are discussed in detail in following sections.

The second hypothesis is based on extensive field geological and geoarchaeological proxies as well as remote sensing technology (e.g. Issawi and McCauley 1993; Issawi and Osman 2008; Abotalib and Mohamed 2013). It attempts to avoid the major problems caused by the single-master-stream concept and described the evolution of river systems in Egypt from the late Eocene regression of the Tethys Sea to the Recent (Fig. 12.2). During the Cenozoic, Egypt was drained not only by a single master stream, but by several major drainage systems (Issawi and McCauley 1993). The first stage, called the Gilf system (ca. 40 to 24 million years), consisted of a northward flowing consequent stream river that followed aretreating Tethys Sea, creating newly emergent land in Egypt (Fig. 12.2a). It also includes streams that formed on the flanks of the Red Sea region towards the end of the Eocene.

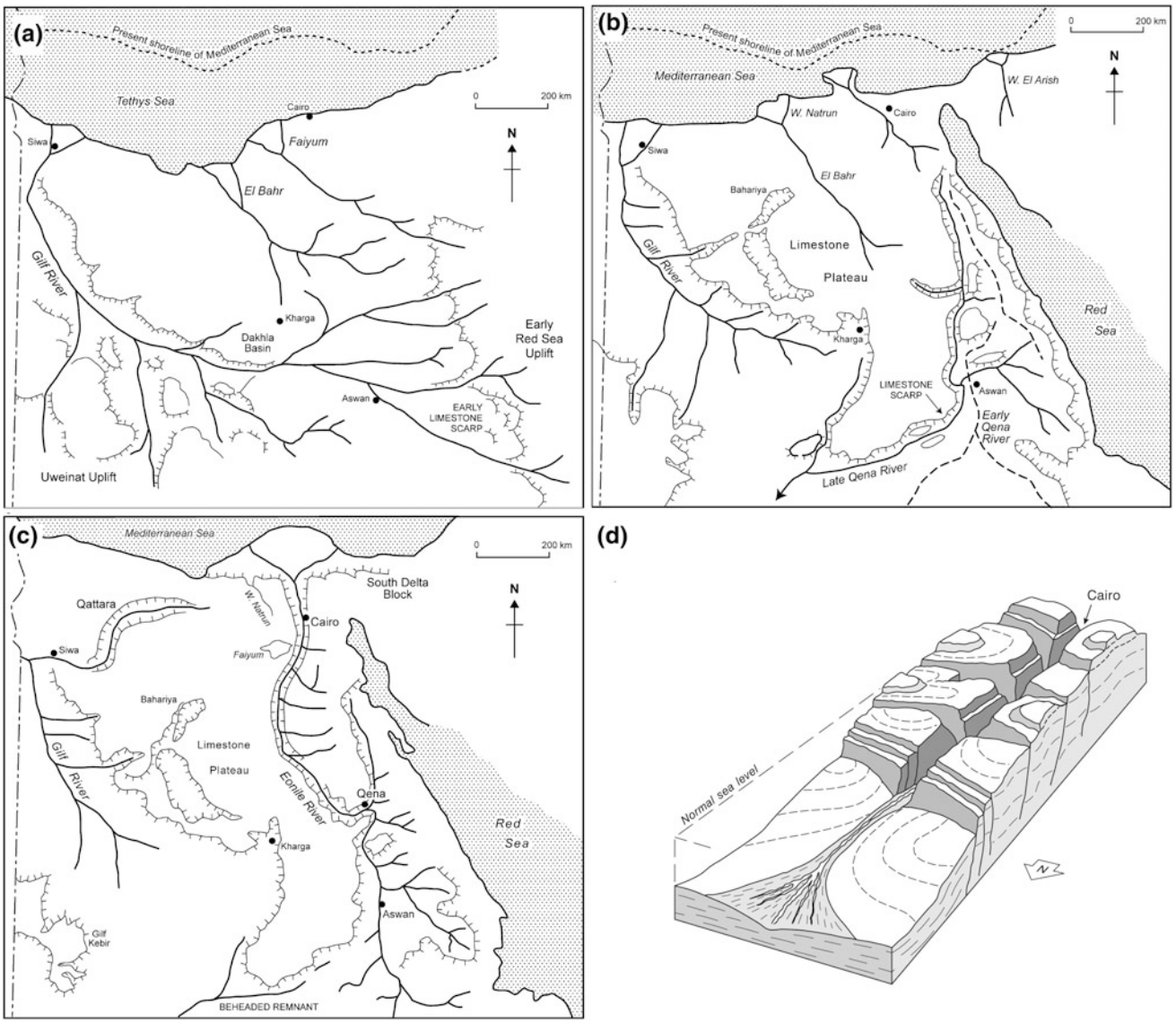

Fig. 12.2 **a** Sketch showing the Gilf system (System I) at the approximate end of the Oligocene; **b** Sketch showing the Qena system (System II) in approximately the middle Miocene; **c** Sketch showing the Nile system (System III), which resulted from a major drop in Mediterranean sea level in the Messinian (about 6 Ma) (*Source* Goudie 2005, modified from Issawi and McCauley 1992). **d** Schematic reconstruction of the Nile Canyon showing the main channel and tributary gorges cut by the Egyptian Nile drainage during the late Miocene (Messinian) salinity crisis (*Source* Said 1981)

The Gilf System involves three major rivers: the Gilf River, the Ur-Nil River and the Bown-Kraus River (Issawi and McCauley 1993). These rivers deposited their sediment load in delta systems along the shore of the late Eocene- Oligocene seas, located on what is known today as the Western Eocene Limestone Plateau. It seems that before the formation of the Nile Canyon, this plateau was continuous with its extension in the Eastern Desert (Abotalib and Mohamed 2013). The Bown Kraus River was a major river running NW and fanning in the northern part of Faiyum Depression. The Ur-Nile ran parallel to the Bown-Kraus River and built its delta in Bahariya Depression (Issawi and Osman 2008). The Gilf River ran northward from the Gilf Kebir Plateau to Siwa Depression. This river system is represented by deltaic deposits of the Gebel Qatrani Formation, which crops out in the Faiyum Depression and elsewhere in north-central Egypt. However, Underwood et al. (2013), believe that these delta sediments were deposited by a continental-scale, northerly drainage pattern draining waters from the Turkana region of East Africa during late Eocene-Oligocene.

The second stage, termed the Qena system (Miocene times), was caused by major tectonic activity in the Red Sea area (Fig. 12.2b). This caused a reversal of drainage to occur with a large river flowing southwards towards Aswan and the Sudan. Qena system consists of two major rivers: the Qena River and the Allaqi River. The Qena River flowed southward from the Red Sea Hills, while the Allaqi River flowed northward from southernmost hills as Gebel Gerf and Gebel Elba. These two rivers likely met along the present course of the Nile south of Aswan. Subsequently, the Qena River captured the Allaqi River and continued to flow southwestward at the foot slope of Gebel Kalabsha (Issawi and Osman 2008). On the other hand, Abdelkareem and El-Baz (2015) belief that the earlier Wadi Qena probably hosted the master river course prior to the present Nile River and had followed the general northward slope of Egypt prior to the Red Sea tectonics. It was at this time that catastrophic flooding may have created some major erosional flutes and gravel spreads in the Western Desert (Brookes 2001).

Abotalib and Mohamed (2013) introduced a new concept to river systems evolution in Egypt. It involves the existence of a new river system which flowed northward during late Miocene times: the North Egypt River. This river was separated from the oldest southern Qena System by a natural dam (E-W faulted block) between Nag Hammadi and Wadi El-Assuiti. The North Egypt River flowed first from the mouth of Wadi El-Assuiti and then, flowed northward to join the waters drained from the Tarfa and Sannur drainage basins befor terminating in the Miocene Wadi Natrun Delta.

The third stage, termed the Nile system (Fig. 12.2c), was associated with base level changes in the Mediterranean basin. In Messinian time (ca. 6 Ma.), the Mediterranean dried up for about 600,000 years (Hsu et al. 1973) because of closure of the Straits of Gibraltar. Base level dropped by 1000 m or more. Down cutting and headward erosion became dominant processes forming the Eonile Canyon (Fig. 12.2d), an incised deep gorge four times larger than the Grand Canyon of the Colorado in the USA. Because of its gradient advantage, it captured the south-flowing Qena system and became the first north-flowing river system that extended the length of Egypt to the Mediterranean. Further downstream, the late Miocene Nile created a series of fans in the region of the North Delta Embayment (Nile Cone) and evaporites accumulated in the distal areas of these fan complexes under arid climatic conditions.

Higher sea levels during the Pliocene resulted in the creation of a long narrow marine gulf in the Nile Valley that reached as far south as Aswan (Pliocene Gulf; Said 1981). The marine gulf is represented by a fossil cliff-line of an early Pliocene transgression on the escarpments bordering the Giza Pyramids Plateau (Aigner 1983). Moreover, the plateau formed a "peninsula" within the Pliocene gulf invading the "Eonile canyon". Marine Pliocene sediment is represented by the Kom el Shullul Formation exposed in the eastern foot slope of the Giza Pyramid Plateau and in the Shakhlouf area, north east of the Faiyum Depression (Said 1981; Hamdan 1993). The marine sediments of the early Pliocene filled about one third of the depth of the Messinian canyon. The late Pliocene Nile saw a shift from marine to brackish conditions with a load of fine-grained sediments derived from local wadi systems (Paleonile; Said 1981). This period saw the complete infilling of the Eonile canyon (Said 1981) as the freshwater zone moved northwards towards the modern Mediterranean coastline. These late Pliocene sediments are represented by the Helwan Formation exposed in the mouth of Wadi Garawi and contain brackish water microfossils (Said 1981; Hamdan 1993). The Paleonile sediments are also represented by the Qaret El-Muluk Formation; these are composed of friable sands, mudstones, shale and minor limestone with combined total thickness of approximately 50 m (El-Shahat et al. 1997). The fossil content consists of fresh and brackish water elements: charophytes, ostracods, gastropods, oysters and benthonic foraminifera. Planktonic forams which suggest marine influence have been also recorded. The terrestrial and aquatic continental vertebrate fauna includes mammals, reptiles, fish and aves (El-Shahat et al. 1997).

12.2.1.2 Early Pleistocene Nile

In Egypt, the early Pleistocene was generally arid, however, there were two short humid episodes (i.e. the Edfu and Armant formations; Said 1981) (Fig. 12.3). The Armant Formation is made up of alternating beds of locally derived gravels and fine-grained clastic rocks. The gravels are cemented by tufaceous material and the pebbles are subangular and poorly sorted. The formation abuts the sides of wadis draining into the Nile.

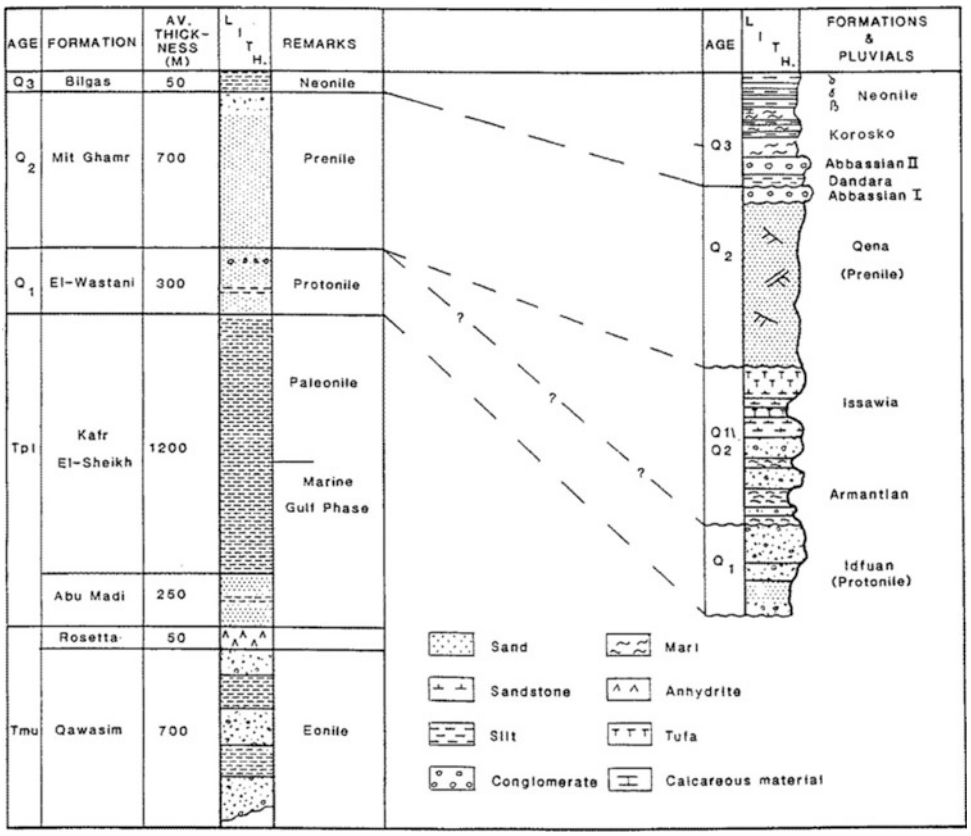

Fig. 12.3 Nile sediments in the Nile Valley and Nile Delta (*Source* Said 1993)

In the area between Esna and Manfalut, the Issawia Formation (Said 1981) is made up of 16 m of chocolate brown clays, followed by a 7 m thick tufaceous hard limestone bed below 22 m of red limestone breccia. The breccia contains a hard cemented bed in the higher levels known as brocatelli limestone (see Butzer 1980; Ahmed 1993). The Idfu Formation (Said 1981) is composed of more than 15 m of fluviatile gravels and sands embedded in red-brown silt matrix. The coarse sands and gravels consist mostly of rounded flint and are covered with a red-brown soil.

The early Pleistocene is well developed in a sand quarry near Mena House hotel on the Giza Pyramid Plateau and attains ca. 30 m in thickness, consisting of cross bedded gravelly quartzose sand. These deposits were deposited by a low sinuosity braided river. The early Pleistocene sediments are also exposed in a sand quarry at Qasr el Basil area, west Nile-Faiyum Divide (Hamdan 1993). They form a long, narrow and highly desiccated terrace ca. 70–80 above sea level, consisting of cross bedded pebbly coarse to medium grain quartzose sand occupying a channel 10–15 km west of the modern Nile floodplain.

12.2.1.3 Middle Pleistocene Nile

During middle Pleistocene, a powerful river with a distant source reached Egypt. This river, the Prenile, drew its waters from Ethiopia when the Atbara and possibly the Blue Nile pushed their way into Egypt across the Nubian swell by a series of cataracts (Said 1981, 1993). The Prenile (Qena Formation) is composed of alternating, cross-bedded, occasionally consolidated, coarse-grained sands and thin beds of grits, and gravels, with casts of fresh water shells and attains a thickness of 20 m (Fig. 12.3). The oldest Nile aggregation- also called "Alpha" aggregation (Said 1993) consists of two gravel formation (Abbasia "I" and Abbasia "II"), in between there is thick floodplain silt (Dandara Formation; Said 1993). The Dandara Formation is approximately 15 m in thickness and is composed of a grey, loose and fine sandy silt bed at the base, followed by brown silts with thin carbonate interbeds and occasional lenses of gravel and capped by a distinct red soil. It was dated more than 39–40 kyr B.P (Wendorf and Schild 1976). However, recent work shows that the Dandara silt is dated to late Acheulean ($\geq$ 200 kyr BP, see Deino et al. 2018).

The Abbasia Formation (Said 1981) is composed of massive, loosely consolidated gravels of polygenetic origin. The pebbles are rounded to subround. They were derived from the uncovered basement of the Eastern Desert. The Abbassia "I" gravels are archeologically sterile while as Abbasia "II" gravels are rich in archeological material of early Paleolithic (late Acheulean) tradition. These sediments are dated to 600–350 kyr BP (see Deino et al. 2018). According to the recent dates of artifacts in the Abbasia/Dandara complex, we consider these river systems

are dated to middle Pleistocene rather than late Pleistocene as mentioned previously by Said (1993).

12.2.1.4 Late Pleistocene Nile

The late Pleistocene history of River Nile is very complex and mainly controlled by different geological and climatic factors. Both local climatic conditions and those in the Nile headwaters have played an important role in late Pleistocene history of the River Nile. Local climatic conditions add more water to the river through run off from local wadis during wetter climate and accumulate dune sand on the western bank of the river during arid conditions. Indeed, the study of late Pleistocene Nile sediments is crucial not only for understanding the Nile behavior and paleoclimatic variation but also for understanding the early *Homo* species migrations out of Africa. It is now accepted that during late Pleistocene, the Nile Valley was a vegetated corridor through which the exodus of *Homo sapiens* out of Africa and into Eurasia occurred between ~50 and 120 kyr BP (see Timmermann and Friedrich 2016). Early Human migrated from northeastern Africa into the Arabian Peninsula and the Levant and expanding further into Eurasia and beyond.

Based on ^{14}C dating and associated archaeology, two late Pleistocene aggradations (i.e. "Beta" and "Gama" aggradations; Said 1993) are distinguished, i.e. middle and late Paleolithic floodplains. Middle Paleolithic silt is represented by the Dibeira-Jer Formation (De Heinzelin 1968). The Dibeira-Jer Formation forms terraces about 36 m above the modern flood plain in Nubia and about 8 m above the modern flood plain in Upper Egypt (Said 1981). It has been divided into several aggradations episodes (floodplain silt) separated by periods of regression (dune sands). It has an estimated thickness of more than 8 m. These silts include no archaeology at Kom Ombo, but in Nubia they include sites with middle Paleolithic artifacts (Wendorf et al. 1989). Another middle Paleolithic aggregation is recorded, the Makhadma Formation which consists of sheet wash gravels, pebbles, and boulders with middle Paleolithic artifacts (Wendorf and Schild 1976). They rest unconformable over Dandara Formation or Prenile sands (Said 1993) and overlain by sediments carrying fresh, late Paleolithic artifacts. In Wadi Kubbaniya (west Aswan), two overbank silts are interbedded with dune sands; the lowest and oldest parts of the silts lie beyond the range of radiocarbon dating; they could well be as old as 70 kyr BP (Butzer 1997). The topmost and youngest parts, on the other hand, ended well before 30 kyr BP (Wendorf et al. 1989).

Another middle Paleolithic silt is represented by the Ikhtiariya Formation (Said 1981), which is made up of well-sorted, massive, dune sands, with a thickness of 4–6 m. It contains middle Paleolithic artifacts and a few mammal bones. The Formation overlies eroded bedrock, the Dandara Formation, and is conformably overlain by the Masmas-Ballana Formation and fluvial sands. The Formation is assumed to represent aeolian deposits contemporaneous with the Mousterian-Aterian pluvial dated at 80–40 kyr BP (Said 1993). More recently, the age of the Aterian has dated to ca. 150–40 kyr BP (Campmas 2017). The middle/late Paleolithic boundary is characterized by deep cracking vertisols and the Nile entrenched its channel by at least 20–25 m and middle Paleolithic silts were deflated (Butzer 1997). Renewed aggradations ("Gamma" Neonile floodplain silt; Said 1993) within a more restricted valley is primarily recorded near Kom Ombo by channel complexes that range from channel beds and point-bar sequences to levee and overbank silts (Butzer 1997).

Late Paleolithic floodplain silt is represented by the Masmas-Ballana Formation which composed of dune sands intercalated with silts and capped by a podzol soil (Said 1981). The top of the dune deposits is rich in late Paleolithic artifacts. Butzer and Hansen (1968) introduced the name Masmas Formation for silts and channel beds in the Kom Ombo area in Upper Egypt with thickness more than 43 m and contain a mollusk fauna. De Heinzelin (1968) applied the name Ballana Formation to dune sands which interfinger the upper part of the Dibeira-Jer silts in the Egyptian Nubia. The Deir El-Fakhuri Formation (Wendorf and Schild 1976) is represented by diatomite and pond sediments interrupted by silt units, which overlie the Ballana Formation, and underlie the Sahaba Formation. This Formation has an estimated thickness of more than 6 m at Esna and Toshkka in Egyptian Nubia. Pollen and diatom analyses of the sediments of the Ballana and Deir El-Fakhuri Formations suggest an arid grassland environment (Wendorf and Schild 1976).

The Sahaba-Darau Formation (Said 1981) consists mainly of floodplain silts. It has a thickness of more than 6 m. The formation overlies the recessional pond deposits of the Deir El-Fakhuri Formation. The Sahaba-Darau Formation is equivalent to the Gebel Silsila Formation of Butzer and Hansen (1968) in the Kom Ombo area. The Sahaba Formation as described by De Heinzelin (1968) was divided into two aggradation units separated by an episode of down-cutting (Deir El-Fakhuri Formation). The Sahaba Formation yielded typical Sebilian assemblages characterized by abundant Levallois artifacts.

12.2.1.5 Holocene Nile

The Holocene aggragation in the Egyption Nile Valley floodplain (delta Neonile; Said (1993) is subdivided into several formations, i.e. Dishna-Ineiba, Arkin and El-Kab formations. The Dishna Formation, dated to 10–9 kyr BP, is represented by a succession of playa deposits and Nile silt with interbeds of gravels and pebble sheets. It is coeval with the Malki Member of Butzer and Hansen (1968), and slope-wash debris of the Birbet Formation of De Heizenlin (1968). This Formation overlies the Sahaba Formation which

is overlain by the Arkin Formation. The Ineiba Formation, 9–7 kyr BP, was introduced by Butzer and Hansen (1968) as a widespread wadi accumulation with a lower conglomeratic bed (Malki Member) and brown clays in the upper part (Sinqari Member). The Dishna-Ineiba Formation represents deposits which formed during the recession following the Sahaba-Darau aggradation. The playa deposits accumulated behind the natural levees and abandoned channels of the Sahaba-Darau aggradation (Said 1981).

The Arkin Formation (Said 1981) is made up of ca. 6 m of silts and fine-grained micaceous sands. It overlies the Dishna Formation and underlies post- Arkin sediments. Its age is assumed to be 9.2–7.2 kyr BP, based on radiocarbon dates (Said 1981). The Arkin Formation is coeval with the Arminna Member of the Gebel Silsila Formation of Butzer and Hansen (1968) in the Kom Ombo area. The El-Kab Formation is made up of a series of Nile sediments, now under cultivation, on the east bank of the Nile River, from El-Kilh (about 15 km north of Idfu) at the Old Kingdom fortress of El-Kab. Radiocarbon dates on charcoals yielded ages between 6.4 and 5.98 kyr BP.

Recent subsurface studies in Saqqara-Memphis floodplain (Fig. 12.4a) reveals a complex fluvial history of both aggradation and degradation events corresponding to magnitudes of Nile floods and paleoclimatic conditions in the African Nile headwaters (Hamdan 2000a; Hassan et al. 2017, Hamdan et al. 2016a, 2019). The sequence began with a unit of late Pleistocene fluvial sand and gravel and relics of early Holocene fluvial sediments (Fig. 13.4b). Middle Holocene is represented by period of high Nile flows associated with steep sea level rises and the floodplain occupied by swamps and anastomosing channels. After the Old Kingdom, the River Nile changed to a more stable meandering channel with well-developed levees and flood basins. Middle Kingdom is represented by a widespread layer of alluvial silt and sand, indicating high Nile floods, which agrees with historical records. Normal floods with several lows and highs prevailed during the last two thousand years. The Holocene floodplain sequence exhibits several discontinuities in sedimentation, particularly at 8.2 cal kyr BP between early Holocene and Predynastic period, at 5.4 cal kyr cal BP; between Predynastic and Old kingdom; at 4.2 cal kyr BP corresponding to First Intermediate Period; at 2.4 cal kyr BP between late Period and Ptolemaic, and at 0.8 cal kyr BP (Fig. 12.4c). These are extremely significant in linking major changes in Nile floods to global climatic events. These five events are recognized as events of global cooling, often abrupt, and associated with areas directly or indirectly affected by monsoonal rain and changes in the ITCZ. They are also evident in the drop of African lake levels in the Nile headwaters and a reduction in the level of the nearby Faiyum Lake (Hamdan et al. 2019).

12.2.1.6 Dramatic Events in the Geologic History of River Nile

The sedimentary history of the Nile River in Egypt bears witness to a number of dramatic events that occurred during the late Pleistocene-Holocene due to severe changes in global climatic conditions. The late Glacial Maximum (LGM), the Wild Nile pluvial period and several climatic events during the Holocene (e.g. the 4.2 dry event) all had great impacts on the hydrology and sedimentology of the river. In turn these events affected or interacted in a variety of ways with human activities.

Blocking of the Nile Valley During the LGM

Behavior of the Nile during the late Pleistocene was a matter of debate between the scientists working in the Egyptian Nile Valley. A model of the river during LGM indicates that the Nile Valley was occupied by series of braided channels with total discharge much less than today, at 10–20% of its modern volume (Wendorf and Schild 1976; Schild and Wendorf 1989; Hassan et al. 2017). The lack of vertical accretion of braided coarse siliciclastic sedimentation in Upper Egypt and lack of late Paleolithic sites in Lower Egypt, make a braided model unlikely. Another model of the LGM Nile Valley environments was proposed by Vermeersch and Van Neer (2015). These authors believe that a series of lakes occupied Nile Valley due to sand dunes blocking the Nile Valley at Naga Hammadi and other places in Upper Egypt during the LGM. The presence of lakes in the Nile Valley during the LGM could offer humans excellent possibilities for food exploitation in otherwise very harsh climatic and environmentally challenging conditions (Vermeersch, and Van Neer 2015). The damming of lakes occurred at different elevations above the present floodplain and in turn there is little correlation with cultural identities. Indeed, the existence of lakes within Nile Valley of upper Egypt was previously mentioned by Vignard (1923), who discovered sequence of late Paleolithic sites on the shores of a progressively shrinking lake fed by local wadi systems, which had been dammed up behind Gebel Silsila. The model of Vermeersch and Van Neer (2015) is plausible but needs to be supported by description of proper lacustrine sediment facies with diatom analysis.

The Wild Nile

The onset of post-glacial warming (after LGM) was marked by an upsurge of exceptionally high Nile floods at 13–11 cal kyr BP, an event labeled as the “Wild Nile”. The event indicates increased rainfall in the source areas of the Nile in Equatorial Africa and Ethiopia (Williams et al. 2010, 2015) and heralds the initial step in the establishment of the current Nile regime, which was well established by 11.5 cal kyr BP following a recessional episode from 13 to 11.5 cal kyr BP. In Wadi Kubbaniya wild Nile event was identified a

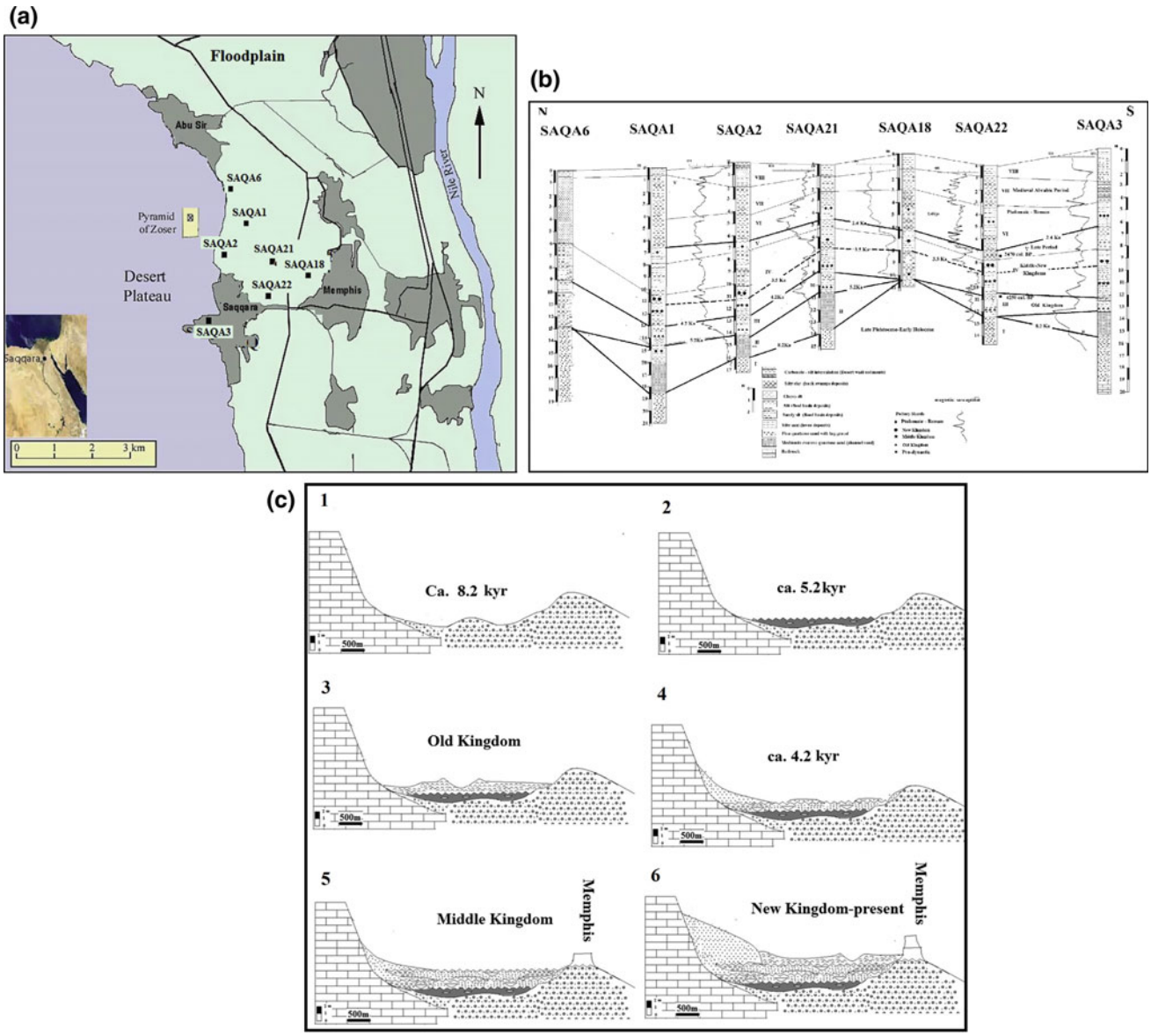

Fig. 12.4 Alluvial history of the Saqqara-Memphis Floodplain during the middle Holocene; **a** Google Earth image of the Saqqara-Memphis floodplain with core locations; **b** Lithostratigraphy of Holocene sediment in the Saqqara-Memphis floodplain; **c** Evolution of Saqqara-Memphis floodplain through the Holocene; (1) degradation of the floodplain during the 8.2 cal kyr BP arid event; (2) degradation of the floodplain during 5.2 cal kyr BP; (3) aggradation of the floodplain during the early Dynastic-Old Kingdom (5–4.2 cal kyr BP); (4) degradation of the floodplain during the First Intermediate Period (4.2 cal kyr BP); (5) aggradation of the floodplain during the extremely high middle Kingdom floods; (6) aggradation of the floodplain from New Kingdom to present (*Source* Hassan et al. 2017)

comparably rapid rise of Nile flood deposits from 111 to 118 m between about 12.6 and 12.3 cal kyr BP; exceptionally high flood waters entered far up the wadi but left only 50 cm of thin-bedded silts and marls (+25 to 26 m) (Schild and Wendorf 1989).

12.2.2 Dry Event (Collapse of Old Kingdom)

The collapse of the Egyptian Old Kingdom was triggered by low Nile floods, combined with a decentralization of political power and weakening of the central administration (Hassan 1997, 2007b; Hamdan et al. 2016b, 2019). The 4.2 cal kyr BP climatic event is clearly manifested in the geological record at Saqqara as an erosional event, recorded at the top Old Kingdom sediments. Hamdan et al. (2016b, 2019) used sedimentological, mineralogical, and geochemical proxies as well as pollen analysis to study sediments coeval to this event through drilled cores in Faiyum and Saqqara regions. The pollen diagram of these sediments shows that Asteraceae tubuliflorae pollen exceeded 50% and Amaranthaceae, Liguliflorae, small quantities of *Rumex* and

other ruderals as well as *Acacia* were present (Hamdan et al. 2019). These pollens indicate onset of desert conditions during the 4.2 dry event. This period spanned a 100 years or less, and Nile floodplain converted to dry desert conditions. The heavy minerals assemblage reflects mixing of Nile floodplain and desert wind-blown environments (Hamdan 2000a). The high zirconium content of these sediments also indicates high aridity and sand storms, which led to sand encroachment from the Western Desert to the Nile Valley (Hamdan et al. 2018). The latter is supported by an ancient eye witness account: "Ipuwer" who mentioned to his son Lo that "the desert claims the land and the lands are injured" (Hassan 2007b). XRF data for the 4.2 cal kyr BP event shows low ratios of both diagnostic Blue and White Nile elements (Fe/Al; Ti/Al; Sr/Al) and together with the high content of zirconium (Hamdan et al. 2019), which indicates reduced effects of Ethiopian flood water. Contemporary with this dry event, several lakes in the Nile catchment record water level declines at this time (Adamson 1982).

12.2.2.1 Shifting of Nile channel

Shifting of the Nile channels in the Nile floodplain has been substantial in the alluvial landscape, which fundamentally affected the structural and functional development of the ancient Egyptian civilization (Hassan et al. 2017). Detection of river shift in the Nile Valley is based on the relationship between the elevations above sea level of ancient settlements along the older courses of the Nile (Jeffreys 2008; Jeffreys and Tavares 1994; Bunbury et al. 2008, 2017). Hassan et al. (2017) proposed a model of channel shifting based on geoarchaeological investigations using drill core data to consider the relationship between settlement depths and sedimentological characteristics and the interpretation of Landsat and Google imagery (Fig. 12.5). The model supposes that there was a main Nile (on the eastern side of the Nile Valley) and secondary Nile distributary channels closer to the western plateau. During Old Kingdom there was an eastwards shift of the western Nile branch and a westward shift of the main Nile channel. In fact, these secondary branches migrated much faster than the main channel because they were situated at a relatively higher elevation and would have dried out in mid-winter during low Nile water flow. There are different estimates for the rate of Nile channel movement during the Old Kingdom; Hillier et al. (2006), measured a rate of eastwards shifting in some areas of the Nile floodplain to be about 9 km per 1000 years, mainly by island production and capture. Lutley and Bunbury (2008) also claimed that the River Nile had moved at a rate of 9 m/yr. Hawass (1997) estimated the migratin rate of the Bahr el-Lebeini, an Old Kingdom secondary channel near the Giza Plateau, to be about 3.58 m per year. Hassan et al. (2017) calculated a rate of 3.2 m per year for the eastern movement of the secondary channel (1.64 km the distance between the early Old settlement and late Old Kingdom settlement, over 500 years).

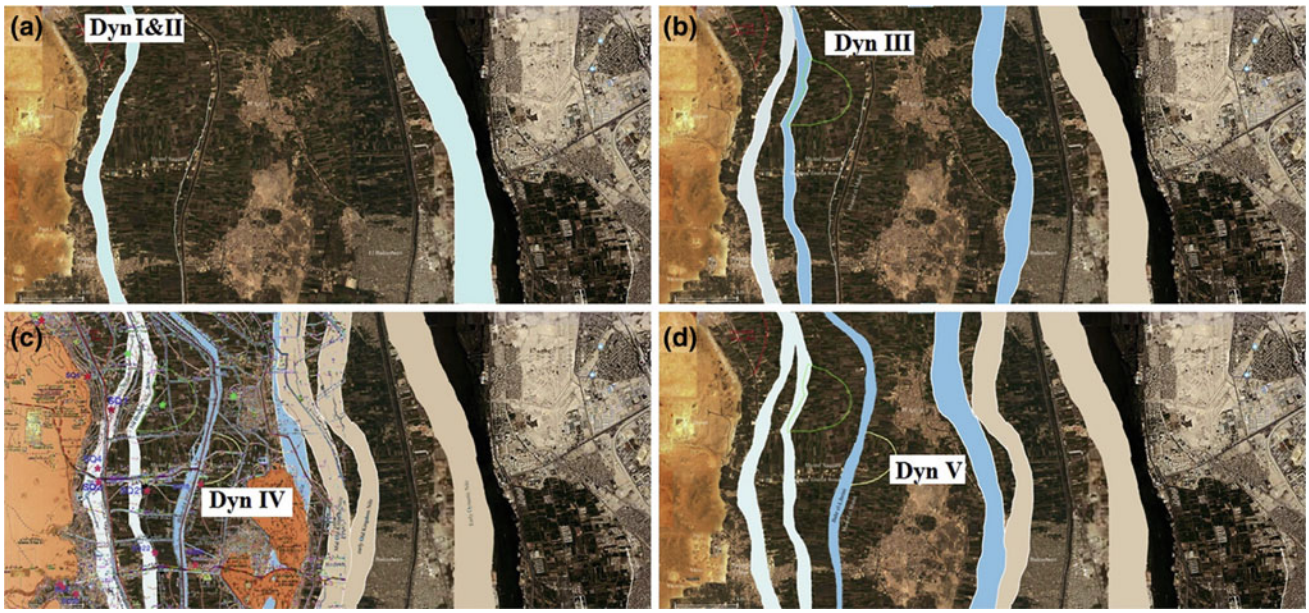

Fig. 12.5 Interpretive model of the Saqqara-Memphis floodplain: **a** location of a principal lateral channel running close to the escarpment of the Western plateau with the main branch of the Nile running along the eastern side of the modern floodplain; **b** during the Dynasty III, when the Djoser pyramid was built, the early Dynastic channel migrated eastward to the location now occupied by the Shebrament Canal; **c** continuous westward and eastward migration of the main channel and western channel, respectively and emergence of Memphis as a island between these two channels; **d** at the time of Unas (end of Dynasty V, 4.356–4.323 kyr BP) the ancient western channel in this location is currently occupied by the Bahr Libeini which parallels the Miheit Drain (*Source* Hassan 2017)

12.2.3 Nile Delta

The Nile Delta, one of the largest deltas in the world, occupies an area of ca. 25,000 km^2 and is bounded by desert to both the east and west. Its apex is located at Cairo, where the river divides into two main distributaries: the Rosetta and Damietta; these discharge over the triangular-shaped alluvial plain and flow north into the Mediterranean. The sedimentary succession in the Nile Delta attains thickness of ca. 4000 m and composed of sand and gravel overlain by a thin layer of alluvial clay. The geologic history of Nile Delta is complex, goes back to late Miocene, and includes five delta phases; Eonile Delta; Paleonile Delta; Protonile Delta; Prenile Delta and NeoNile Delta (Fig. 12.3). A large amount of research has been undertaken on the Pleistocene and earlier history of the Nile Delta, mainly as a result of oil exploration (e.g. Rizzini et al. 1978).

Eonile Delta was formed during the late Miocene and represented by the Quasiam Formation (Fig. 12.3). This Formation attains ca. 700 m in thickness and represented by coarse sand and gravel intercalated with thick shale beds. It is evident that the Quasiam formation has been deposited in the form of coalescing fans in front of an E-W active fault scarp. Quasiam Formation is overlain by ca. 50 m thick unit of evaporite rocks (Rosetta Formation). The Paleonile Delta phase (Pliocene Gulf) is represented by two formations; Abu Madi and Kafr el Sheikh. Abu Madi Formation attains about ca. 250 m of sand with a thin shale unit in the middle part of the section. Kafr el Sheikh Formation (late Pliocene), attains ca. 1200 m in thickness and consists of shale with marine fossils in the lower part and brackish and freshwater fossils in the upper part. Protonile Delta (early Pleistocene) is represented by El Wastani Formation (ca. 300 m) composed of coarse sand with few shale and gravel interbeds. The Prenile delta (middle Pleistocene) is represented by the Mit Ghamr Formation (ca. 700 m) and consists of coarse sand and gravel from Ethiopian sources. Finaly, Neonile delta phase (late Pleistocene-Holocene) is represented by the Bilqass Formation, which is made up of alternating fine and medium-grained sands, interbedded with clays rich in pelecypod, gastropod and ostracod fragments, plant material, and peat layers.

Late Quaternary sediments of Nile Delta were intensively investigated in the last three decades, based on archaeological excavations, drilling of shallow cores and radiocarbon dating. A survey of the published literature provided 1640 relevant core records within the fluvial zone of the delta (Pennington et al. 2017). These studies provide much evidence for the changing patterns of Nile behavior as well as for global sea level changes. In the coastal region of Nile Delta, late Quaternary sediments comprise three sedimentary sequences (Stanley and Warne 1993a). Sequence "I" (late Pleistocene—ca. 38–12 kyr BP), is represented by iron-stained quartz-rich sands and stiff mud, deposited by braided channels associate with a drop in sea level and the coastline was located further north of its modern position. Sequence "II" is represented by transgressive sand with a shallow marine fauna dated to mid-Holocene (ca. 8 cal kyr BP; Stanley and Warne 1993a). Sequence "III" (ca. 7.5 cal kyr BP onwards), is represented by a variety of lithologies of marine, semi-terrestrial, coastal, estuarine, lagoonal and in some cases fluvial deltaic environments.

In the fluvial-dominated region of the Nile Delta, late Quaternary succession is subdivided into three Sequences; Sequence "I", Transgressive Sand and Sequence "II" from older to younger. Indeed, for simplicity and preventing confusion with previous nomenclature, we used "Sequence" rather than "Formation" as originally used by Pennington et al. (2017). Figure 12.6 shows summary cross-sections of previous studied geoarchaeological/geological areas in the Nile Delta, reinterpreted within the stratigraphic divisions of the synthesis of Pennington et al. (2017). The Sequence "I" comprises medium-coarse quartzose sands, with pebbles of quartzite, chert and dolomite and is subdivided into two units; Zagazig and Minuf units, from older to younger, respectively. The Zagazig unit is generally, massive to laminated or cross-stratified; yellow fine to medium grained sands (De Wit and van Stralen 1988; Hamdan 2003a; Rowland and Hamdan 2012). Mineral composition includes iron oxides (magnetite, hematite and ilmenite), hornblende, augite and epidote (Hamdan 2003a; Pennington et al. 2017). Minuf unit consists of fine grained micaceous sand with stiff or compact clayey lenses (Butzer 1997; Sandford and Arkell 1939). The Transgressive Sand Sequence (early Holocene), is composed of coarse, poorly-sorted, olive-grey to yellowish-brown quartzose sands which contain a high percentage of heavy minerals, as well as mollusk and echinoderm fragments (Chen et al. 1992; Coutellier and Stanley 1987; Stanley et al. 1992). These deposits are probably originally fluvial sediments that incorporated a littoral signature during retrogradation of the shoreline and major reworking by waves and other coastal processes between ca. 15 and 8 cal kyr BP.

Sequence "II" is made up the "alluvial mud" of the delta plain and is divided into three units from base to top; Sequence "IIa", Sequence "IIb" and aeolian sand (Pennington et al. 2017). Sequence "IIa", is made up of bluish-black silty-clay to clayey silt containing a high percentage of organic matter and peat layers. Sequence "IIb" is generally brown-grey in color, less rich in organic material, and very predictable in the lateral variation of its grain size. This later unit represents overtopping of levees and the development of a wide floodplain during the late Holocene. The sequence of the fluvial-dominated delta is ended by a modern aeolian Member (Pennington et al. 2017).

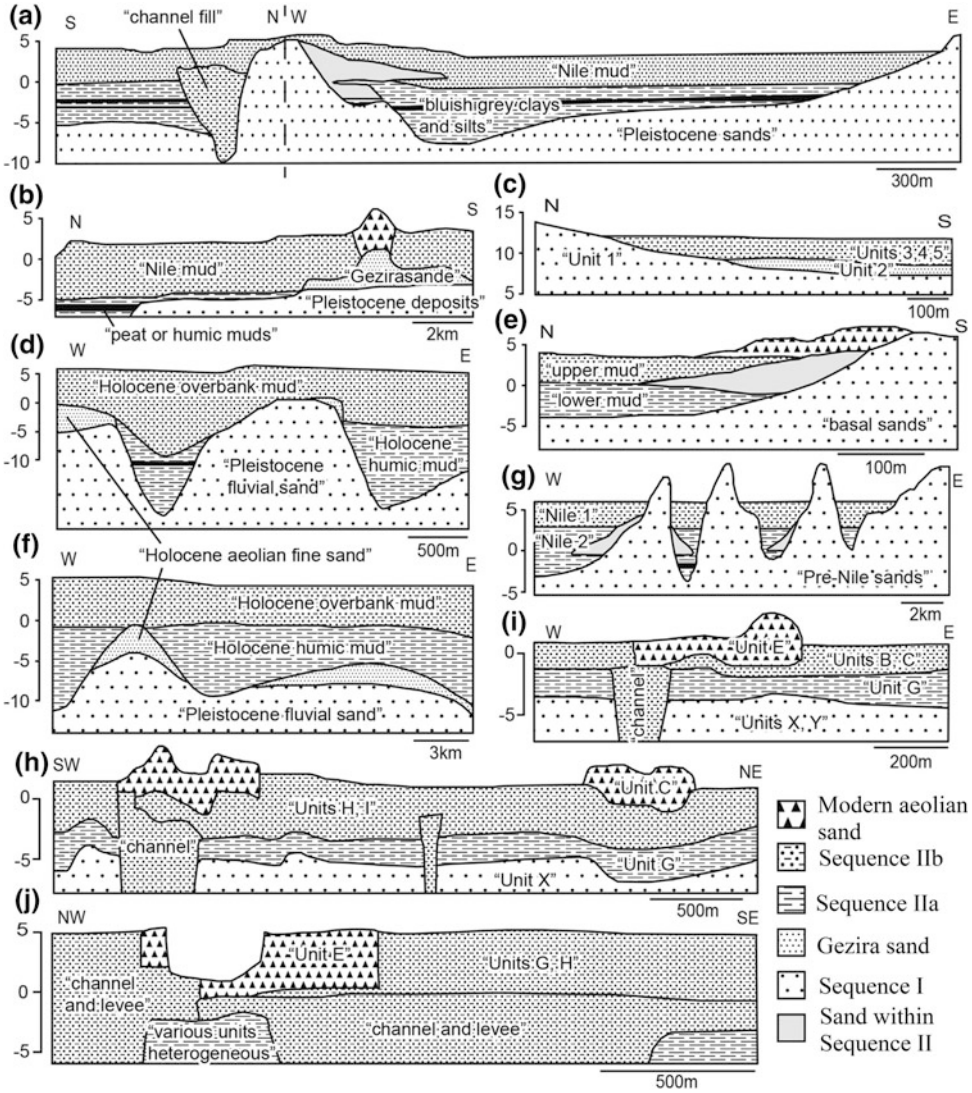

Fig. 12.6 Summary cross-sections of previously published geoarchaeological/geological works in the Nile Delta: **a** Minshat Abu Omar, adapted from Andres and Wunderlich (1992); **b** Kafr Hassan Dawood (Hamdan 2003a); **c** Quesna, adapted from Rowland and Hamdan (2012); **d** Sais, adapted from El-Shahat et al. (2005); **e** Kafr Hassan Dawood, adapted from Hamdan (2003a); **f** MUWDS, adapted from El-Awady (2009). **g** AUSE, adapted from Andres and Wunderlich (1992); **h** Kom al-Ahmer/Kom Wasit; **i** Tell Mutubis; **j** Kom Geif (Pennington et al. 2017). The names of the units given in quotation marks are those from the published literature; the key shows their reinterpretation within the framework of the current synthesis (*Source* Pennington et al. 2017)

12.2.4 Significant Geological Features in the Nile Delta

12.2.4.1 Nile Cone

Nile Cone is a largest Mediterranean deep sea fan and has a complex history related to large scale tectonics in the East Mediterranean basin and evolution of the Nile River which has served as its major sediment source (Stanley and Maldonado 1977). The cyclic nature of Nile Cone sediments record modifications of eustatic sea level and paleoclimatic conditions at the Nile headwaters. It also reflects changes in the physical oceanography of the coastal area, including current patterns and stratification, and biogenic productivity. The cone consists of six sediments types; turbidite sand and silt, turbiditic mud, hemiplegic mud, calcareous ooze, organic ooze and sapropels.

12.2.4.2 Sapropels

Sapropel is a dark-colored organogenic sediments that is rich in organic matter intercalated with the offshore Nile cone sediments since mid-Miocene times (Mourik et al. 2010). Their formation in the Mediterranean is relate to increasing amounts of freshwater reaching the basin by a combination of various factors including increased precipitation versus evaporation, discharge from the Nile and other bordering rivers. The large amounts of fresh water delivered by the Nile have led to increased nutrient supply and anoxia promoted by stratification of the water column (Krom et al. 2002; Fielding et al. 2018). Sapropels occur (quasi-) periodically in sedimentary sequences of the last 13.5 million years, and exist both in the eastern and western Mediterranean sub-basins (Rohling et al. 2015). Extensive study, based on records from both short (conventional) and long

(Ocean Drilling Program) sediment cores, and from a wide variety of uplifted marine sediment sequences on the basin margins and islands. The sapropels are important in paleo-climatic studies, especially monsoon intensity in the Nile headwaters.

12.2.4.3 Sea Level Change in the Nile Delta coast

Intensive coring programs in the delta plain have reveal that the Mediterranean Sea was some 100 m lower than the present level during late Pleistocene and fluvial and deltaic environments extended out 40–50 km beyond the modern coast (Butzer 1997). In response, the Nile channel and distributaries were entrenched up to 30 m below the present surface into older Pleistocene sands and gravels. During post-glacial warming, global temperature rise melted the ice-caps causing sea level to rise and, at the same time, rainfall increased in the catchment area of the Blue Nile (Woodward et al. 2007). The sea level rose rapidly by several meters per millennium at the shelf-edge of the Nile Delta between 10–7 cal kyr BP (Stanley and Warne 1994). Moreover, Fairbanks (1989) noted that the ending of the last ice age led to a global sea-level rise of 120 m. Assuming that the current floodplain gradient of ca. 1 m/km, this sea-level rise could potentially produce a marine transgression of a similar extent (Bunbury and Jeffreys 2011). Due to high rates of sea-level rise and river sediment loads high rates of flood basin aggradation took place. Subsequently, the delta plain was dominated by a swampy, wetland landscape with the formation of anastomosing rivers and crevasse splays (Pennington et al. 2017).

During the late Holocene period, a gentle sea level rise of 1.0 m per millennium occurred until the present lower rates. Subsequently, the in-channel aggradation rates decreased and the crevassing and avulsion became relatively less dominant processes in landscape formation. The channels would have migrated across their floodplain primarily via lateral channel migration and point bar deposition. The resulting landscape has been referred to as a "meandering" deltaic environment (Pennington et al. 2016).

12.2.4.4 Ancient Delta Branches

Since the end of the last ice age, global temperature rise melted the ice-caps causing sea level to rise and, at the same time, increased rainfall in the Nile Headwaters (Woodward et al. 2007). Rising sea level and increasing Nile flow both push the river towards the production of more distributaries and will also shift the delta head southward. According to Stanley and Warne (1993b), the number of distributaries reached a maximum around 6000 years ago and since then has gradually declined. In the present time, there are only two Nile channels bifurcates ca. 20 km north of Cairo; Rosetta and Damietta branches. However, there were seven branches during the pre-dynastic period that were reduced to five branches during the Paranoiac times (Tousson 1922). There were two branches in west delta as sub-branches of current Rosetta Branch, i.e. Canopic and Bolebetic. In west delta, there were five branches; Sebennitic, Bucolic, sub-branches of Damietta Branch; Mendesian, Tanitic and Peluciac. During early Holocene, probably the branches are more and mainly in the form of anastomosic channels associated with rapid sea level rise (Pennington et al. 2017). The concentration of former distributaries (Four major ones) in the northeastern part of the delta was partly due to the rapid subsidence (Stanley 1988). According to Said (1990), the disappearance of the ancient branches occurred during low-flood years, when deposition exceeded erosion. On the other hand, Sneh et al. (1986) concluded that the degeneration of the lower reaches of the Pelusaic Branch was due to the silting up of the mouth of the distributary by the prevailing W-E long-shore current.

12.2.4.5 Delta Subsidence

The subsidence of the Nile Delta received much attention from the scientific community and extensive coverage by the media in the last decades (Becker and Sultan 2009). Numerous studies have attempted to measure rate of subsidence along Nile Delta. The techniques used have included in situ observations (Marriner et al. 2012; Stanley and Warne 1993a; Warne and Stanley 1993) as well as remote sensing techniques (Aly et al. 2009, 2012; Becker and Sultan 2009). These studies have recorded differential subsidence velocities on the Nile Delta that range from slightly emergent to subsidence rates as high as approximately 10 mm/yr.

Early studies provided estimates of vertical motion from slightly emergent to subsidence of just over 4 mm a year. The maximum rates of subsidence occur east of the Damietta promontory. A zone containing the highest rate of subsidence was attributed to the major eastern Mediterranean fault system with accelerated velocities attributed to the thick belt of Holocene sediments in the north. The thick Holocene sediment layer is presumed to form a hinge line marking its southern edge (Stanley and Warne 1993a). A later study reported subsidence velocities ranging from 0.0 to 5.0 mm/yr across the northern Nile Delta (Marriner et al. 2012). Buried and submerged archaeological sites have also been used to date subsurface horizons (Warne and Stanley 1993). This information was then used to calculate rates of subsidence that range from 0.9 to 5 mm/yr (Stanley 2012; Stanley and Toscano 2009; Warne and Stanley 1993).

An alternative approach to sediment core studies has been to use radar satellite data to measure subsidence on the Nile Delta. One study used 34 descending ERS-1 and ERS-2 satellite data images spanning 8 years and beginning from 1993 to 2000 to measure average subsidence rates of 7 mm/yr. The study proposed that subsidence within the study area was influenced by groundwater extraction, tectonics, and possibly the subway system running under the

city (Aly et al. 2009). Another study conducted by Becker and Sultan (2009) used 14 ascending ERS-1 and ERS-2 satellite radar images spanning just over 7 years from 1992 to 1999. The maximum subsidence velocities measured by the study range from 6 to 8 mm/yr on the north-western portion of the delta.

Generally, all studies concluded that a combination of factors have been responsible for the Delta subsidence, including tectonic readjustment of strata at depth, sediment compaction, growth faulting and soft sediment deformations under large anthropogenic structures, possibly triggered by earthquakes, tsunamis. These studies show very clearly that the delta has ceased to increase in altitude relative to sea level. Although, tsunamis are relatively rare in the Mediterranean Sea, their potential risk cannot be neglected. Alexandria City was not affected by a major earthquake or tsunami in recent years (Jelínek et al. 2009). However, historical events show that approximately 5,000 people died and 50,000 houses were destroyed in the city after the earthquake in 21 July 365 AD. The Roman historian Ammianus Marcellinus wrote about the impact of this event in Alexandria: "*The solidity of the whole earth was made to shake and shudder, and the sea was driven away. The huge mass of waters was return when least expected killed many thousands by drowning. Huge ships perched on the roofs of houses and others were hurled nearly 3 km from the shore*". The last tsunami to hit the eastern Mediterranean occurred on August 8, 1303 AD. It destroyed the great lighthouse of Alexandria, one of the seven wonders of the ancient world (Jelínek et al. 2009).

12.2.4.6 Turtle-Backs

In the eastern Delta, geoarchaeological investigations showed the existence of scattered small or large ridges of Pleistocene coarse sand (turtle backs) (De Wit 1993; De Wit and Van Straten 1988; Andres and Wunderlich 1992; Hamdan 2003a; Rowland and Hamdan 2012). Turtle-backs are deposits of sand, sandy clay, and impure silt, yellow in color and forming higher longitudinal hummocks over the Delta surface. They appear as yellowish islands in the green fields of the Delta, rising some 10–12 m above the surface; some may rise only one meter above the surface. Four of these turtle-backs are found near Quweisna (see Rowland and Hamdan 2012), two between Banha and Qalyub, one near Fagus, and five near Manzala, occupying an average area of 2 km^2 each. Sandford and Arkell (1939) consider these turtle-backs as relics of middle Paleolithic silts analogous to deposits on the lateral margins of the delta.

12.2.5 Faiyum

The Faiyum Depression is encircled by a northern escarpment and for much of its past it contained a large lake (Lake Moeris) fed by Nile run-off through the Bar Yussef (Fig. 12.7a). Fluctuations in Nile flooding directly controlled the levels of the lake which, in turn affected ancient settlement patterns in the Faiyum (Hassan 1986). A series of ridges along the western edge of the depression define paleo-shorelines at 44–42, 34–39, 28–32, and 23–24 m ASL equivalent to heights of 71, 61–66, 55–59, and 50–51 m of the floodplain at Beni Suef in the Nile Valley (Hamdan 1993).

The Faiyum region has been widely investigated as early as the 19th and early 20th centuries by several geologists (Schweinfurth 1886; Brown 1892; Ball 1939). This interest arose due to the abundance of rich archaeological sites and extensive documentary records (see Brown 1892). However, these early archaeological investigations were inconsistent concerning the role of the lake and the first systematic investigation, performed by Caton–Thompson and Gardner (1929, 1934), confirmed that modern Lake Qarun is a remnant of the former great lake, Lake Moeris. Further studies were carried out by Sandford and Arkell (1929); Little (1936) and Wendorf and Schild (1976). Reviews by Hassan (1986) and Butzer (1997) have shown that past fluctuations in water availability, due to climate and human changes, caused major variations in the level of Lake Qarun during the Holocene. From the early Holocene until the Greece-Roman period, the basin received Nile water principally controlled by climate with lake levels fluctuating according to Blue Nile flow from monsoonal rainfall in Ethiopia and, to a lesser degree, to central east African rainfall via the White Nile. Since the middle Kingdom, Nile inflow has been more or less regulated by hydrological modifications

The Holocene Faiyum sedimentary sequence was investigated in surface exposures of ancient beaches, archaeological sites (Wendorf and Schild 1976; Hassan 1986; Butzer 1997, 1982; Hassan et al. 2012) and more recently in cores from modern Lake Qarun (Flower et al. 2006, 2012, 2013; Hamdan et al. 2016b; Marks et al. 2018). The early Holocene sediments of the former great lake are well known from subsurface and surface sections in the northern part of the lake (Wendorf and Schild 1976). They are related to several successive lakes called Paleomoeris (13 m ASL), Premoeris (19–24 m ASL) and Protomoeris (19–24 m ASL). Each of these lake units are separated by episodes of low stand lakes. The sediments of Paleomoeris stage are recorded only in the northern Faiyum and are represented by fluvial sands, shore facies and shallow lake bed facies of diatomite and diatomite marls, ca. 13 m ASL (Kozlowski 1983). These sediments are dated to 9948–10233 cal BP. The upper diatomite unit possesses deep fossil desiccation cracks, indicating episodes of low lake level. The deposits represent the Premoeris stage of Wendorf and Schild (1976) and consist of sand intercalated with dark grayish brown friable sediments. They obtained a date of

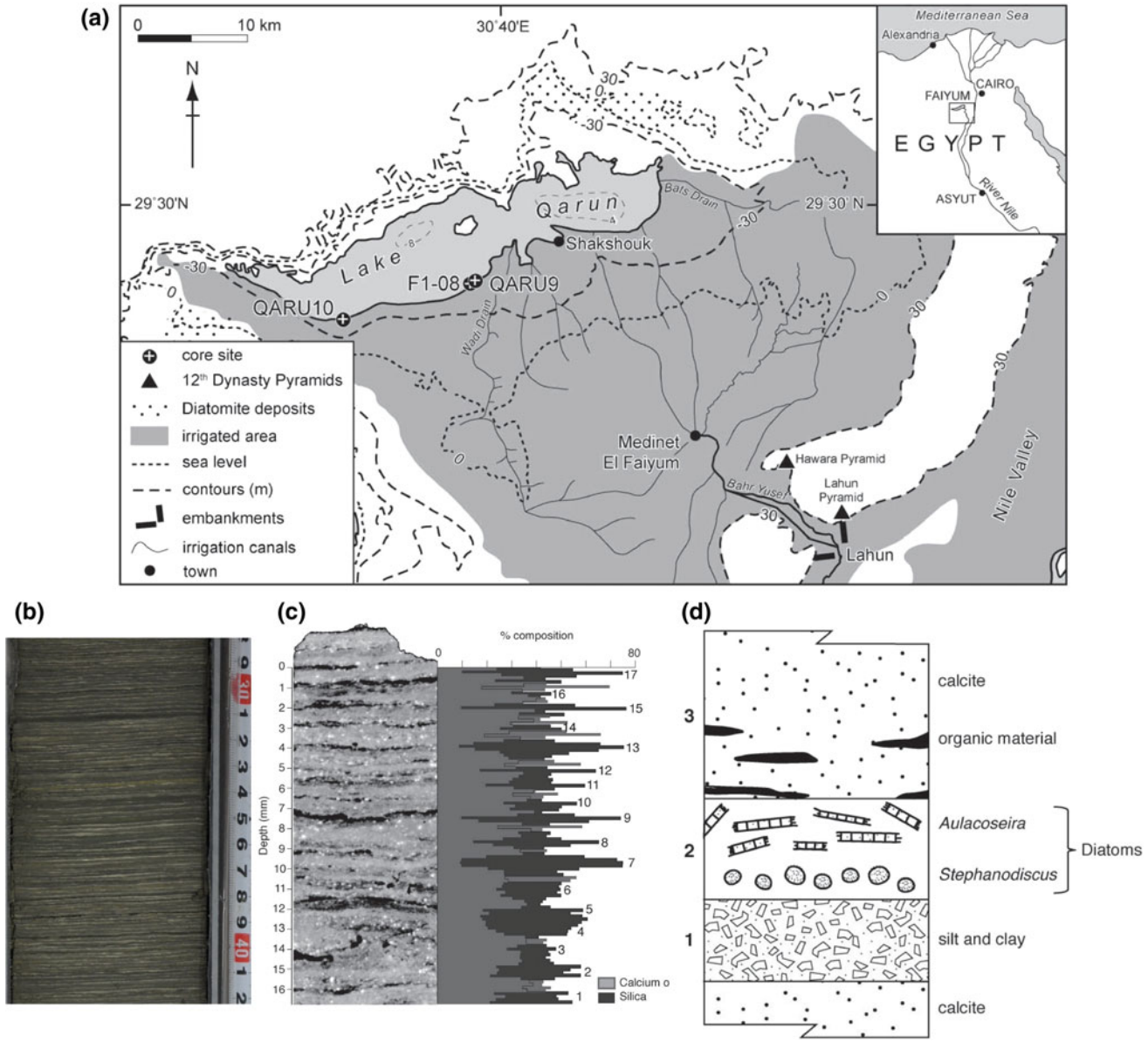

Fig. 12.7 **a** Faiyum Depression; **b** Early Holocene, non-glacial varves sub-sectionfrom a sediment core; **c** Microprobe elemental analysis of a thin section of Faiyum varve sediments showing the correspondence between the proportions of Si and Ca; **d** Diagrammatic representation of a typical varve structure in finely laminated sediment of Faiyum. See text for detail (*Source* Flower et al. 2013)

9450–8634 cal BP from charcoal obtained at an elevation of 19 m ASL, contemporaneous with a mat of swamp deposits. In Western Faiyum, deposits of Premoeris stage are banked against the eastern face of the Gisr el Hadid storm beach ridge and represented by of intercalations of beach sand and gravel with freshwater shells (Hassan 1986, Hassan et al. 2012). Terminal Paleolithic artifacts (Qarunian) were found in association with the Premoeris deposits and dated to 9064–9355 cal BP and 8445–8572 cal. BP. The sediments of Protomoeries stage consist of sand and sandy silt intercalated with dark swamp layers (19–24 m ASL) and dated to 8188–7699 cal BP.

In cores drilled at the margin and within Lake Qarun (Fig. 12.7a), the early Holocene sediments (ca. 10–8.2 cal kyr BP) is represented by varved sediments (Fig. 12.7b) corresponding to seasonal Nile flood water influx to Faiyum Lake via Howara channel (Flower et al. 2012, 2013; Hamdan et al. 2016b; Marks et al. 2018). The early Holocene varves (non-glacial) were formed in a deep lake with an absence of benthic bioturbation and with deep water anoxia (Flower et al. 2012). The varves consist of mm and sub-mm laminated sediment of calcareous clay with dark allogenic clayey silt (deposited during late summer Nile floods) time (Flower et al. 2012; Hamdan et al. 2016b). Elemental

analysis of the thin section in the varve sediments using microprobe techniques demonstrated clear geochemical differences between the laminae (Fig. 12.7c). Detailed microscopic, geochemical and micropaleontology reveal that the Faiyum varves generally consist of three laminae (Fig. 12.7d); (1) terrigenous laminae composed of angular clastic silt grains and clays indicate material of fluvial origin and could mark the effects of Nile flood (late summer); (2) a white authogenic diatom layer usually comprised of *Stephanodiscus* and then *Aulacoseira* valves formed late August or September after flood time, and (3) an endogenic calcite (micrite) layer deposited during the following summer season and ofteninter-calated with organic matter. Diatom and pollen data of early Holocene sediments in a long core from Tersa (middle of Faiyum Depression) also show abundant planktonic taxa, (e.g. *Cyclostephanos, Aulacoseira*) and high aquatic/terrestrial pollen ratios also indicating deep, open lake conditions (Hamdan et al. 2016b).

Hassan et al. (2012) studied stable isotopes of oxygen and carbon in freshwater mollusk shells from a sequence of dated paleolake deposits in the Faiyum Depression and provided an outline record of lake development during the Holocene. During early Holocene, the freshwater shells yielded more negative $\delta^{18}O$ and $\delta^{13}C$ ratios than did middle and late Holocene shells, suggesting high Faiyum lake levels and less evaporation compatible with high Nile discharge. The he isotopic composition of accretionary layers in the single *Unio* shell indicated two periods of low $\delta^{18}O$ values corresponding to two periods of water supply to the lake; Nile waters during summer flood and other due to runoff from local sources during winter rainy periods (Hassan et al. 2012). Study of the isotope composition of the accretionary layers of one *Unio* shell, indicated the existence of a short rainy season during winter time.

The middle-Holocene sediments represent the lower part of the Lake Moeris stage and are represented, in northern Faiyum, by pale brown sands, unconformably overlying older lacustrine sediments (e.g., Neolithic site Kom "W"; Caton-Thompson and Gardner 1929, 1934; Wendorf and Schild 1976). The dates associated with the Neolithic sites occupations are: 6897–6324 cal BP at 17 m ASL and 6957–6407 cal BP at 15 m ASL (Hassan et al. 2012). In southeast and southwest Faiyum, a middle Holocene beach forms a curved elongated ridge c. 20 km long from Edwa Village (16 m ASL) to Ezbet el Gebel Village in the southwest of the Faiyum (14 m ASL). The Edwa ridge dates to the Neolithic i.e. ca. 7150–5950 cal BP and extends in an E-W direction rising up to 18–14 m ASL; (Caton-Thompson and Gardner 1934; Hassan 1986; Hassan and Hamdan 2008, Hassan et al. 2012). In subsurface, middle Holocene lacustrine sediments are represented mainly by two different facies. The early middle Holocene (ca. 8–6.2 cal kyr BP) is represented by alternating homogenites layers and varve packets. The homogenite layers consist of a massive mud layer up to one cm in thickness resting on the eroded top of a laminated packet. The latter are generally thicker than the homogenite layers (several cm in thickness) and consist of horizontal mm-scale white and dark grey laminae. Subtle seismicity layers are recorded in the varve layers with clear microfolds and microfaults (Hamdan et al. 2016a). These sedimentological characteristics reflect a large deep lake. Late middle Holocene sediments (ca. 6.2–4.2 cal kyr BP), are represented by massive stiff clay with white carbonate and iron oxide layers, indicating drop in lake level. Isotope data show increasing ^{18}O enrichment and increasing benthic diatoms at end of the Holocene indicate lowering in lake level and increase aridity (Hassan et al. 2012).

Late Holocene lacustrine deposits occur at 35 m below sea level (Hassan et al. 2012). Based on the elevation, stratigraphic position and archaeological context, it is likely that lacustrine sediments in this area date to a time interval from the pharonic late Period to the Roman period; i.e. from ca. 3000 to 1600 cal BP (Caton-Thompson and Gardner 1934; Wendorf and Schild 1976; Hassan et al. 2012). Late Holocene sediments consist of 9 m of beach sand intercalated with scattered diatomaceous deposits. In subsurface, late Holocene lacustrine sediments (4-0 cal kyr BP), are represented by massive highly bioturbated, semi-soft silty clay, few diatoms, and becoming more sandy upwards with red potsherds near the top.

The analyses of the Faiyum cores reveal intersecting results about fluctuations in lake level, which reflect variation in the Nile floods and the climatic conditions on the African Nile headwaters. The lake was high large fresh water lake during early Holocene and then subjected to an abrupt drop the level at 8.2 cal kyr BP. before rising again from 8 to 6.2 cal kyr BP. From 6.2 to 6 cal kyr BP, the lake level dropped markedly and thin laminate sedimentation ended permanently. During 6–4.5 cal kyr BP, the lake became small and its level oscillated between 10 and 0 m ASL. At 4.5–4.2 cal kyr BP, the lake show great drop in lake and most parts of the lake were almost desiccated. Ancient modifications to regulate inflow to the Faiyum basin were notably introduced during the 12th Dynasty to compensate for fluctuations in water availability caused by variations in the Nile floods (Hassan and Hamdan 2008). Later, more hydrological modifications were introduced during Ptolamic time, to extend and regulate agricultural lands in the Faiyum (Hassan 1986).

12.3 Quaternary Sediments and Landforms Related to Humid Climate

Sediments related to humid periods commonly occur in the present day hyper-arid Egyptian deserts; they are represented by lacustrine, alluvial, solution and karstic features

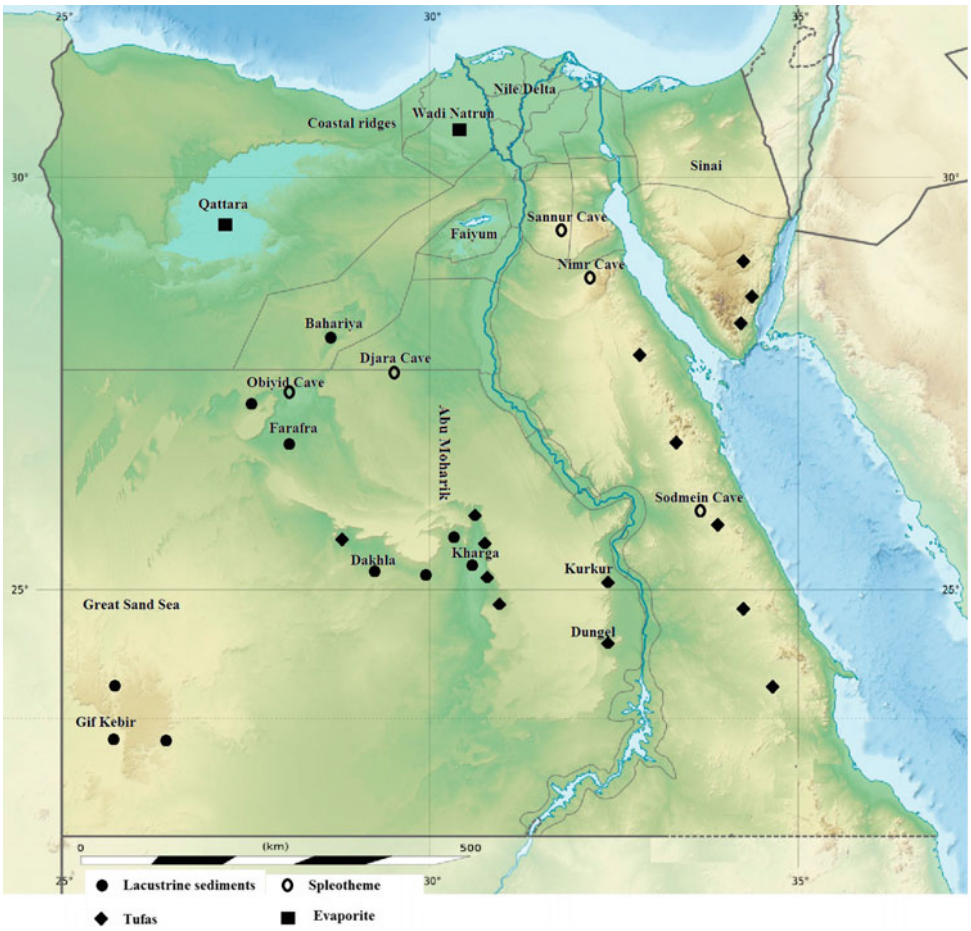

Fig. 12.8 Distribution of Quaternary sediments in the Western Desert of Egypt

(tufa and speleothem deposits) (Fig. 12.8). These deposits are well dated and associated with archaeological material indicate wetter conditions during Quaternary. Some of these landforms (i.e. karst, caves and alluvial) are inherited from a previous wetter climate but in many areas still dominate despite a major drying of climate. The hyperaridity has preserved these landforms and landscapes, which in wetter areas would have been totally eroded.

12.3.1 Lacustrine (Playa) Sediments

A playa is a Spanish term meaning a shore or beach; it is typically a dry, vegetation-free, flat area at the lowest part of an internally drained desert basin where ephemeral lakes form during wet periods. They are underlain by stratified clay, silt, and sand, and commonly, by soluble salts. Playas occur in intermontane basins throughout the arid lands. Indeed, these are many confusing definition in terms playa, playa lake and sabkha. To eliminate these confusions, Briere (2000) proposed that: (1) playa is a discharging intercontinental basin with a negative water balance, remaining dry 75% of the year, and often associated with evaporates; (2) Playa lake: a transitional category between playas and lakes, essentially a flooded playa; (3) Sabkha: a shallow basin limited to marginal marine settings and associated with several percent gypsum or gypsum, partly laminae due to preferential halite dissolution during flooding. Generally, playas have four characteristics (Motts 1969): (1) an area occupying a basin or topographic valley of interior drainage; (2) a smooth barren surface that is extremely flat and has a low gradient; (3) an area infrequently containing water that occurs in a region of low rainfall where evaporation exceeds precipitation, and (4) is an area of fairly large size (generally more than 600–1000 m in diameter).

The term playa was first used in Egypt to describe certain Quaternary sediments in Kharga and Dakhla Depressions (Beadnell 1909). Investigations of playa deposits intensified since the 1970s in conjunction with archaeological investigations of the middle Pleistocene and Holocene prehistory of the eastern Sahara. The playas occur as basin-fill deposits ranging in size from a few hundred m^2 to over a hundred km^2. The depth of the playa basin does not exceed several meters; 2.5–8 m deep in Farafra (Hassan et al. 2001); about 3–4 m in south Farafra (Embabi 1999); up to >10 in Nabta playa (Wendorf and Schild 1980). The playa basins have

five origins; (1) karstic e.g. Farafra Depression (Hassan et al. 2001; Hamdan and Lucarini 2013; (2) wind deflation e.g. Bir Kesiba playa (Wendorf and Schild 1980); (3) damming blockage of the wadis by sand dunes e.g. Gilf Kebir Plateau (Kröpelein 1987); (4) interdunal troughs e.g. Nabta playa (Wendorf and Schild 1980) and (5) ponding of irrigation waters, e.g. Kharga and Dakhla (Caton-Thompson 1952). Playa sediments consist of several meters of stratified, fine-grained silt intercalated with sand and occasionally gravel that either appear as flat areas with scarce or no vegetation or as fields of yardangs. They exhibit several sedimentary structures of fluvial environments, e.g. normal grading, mud drapes and cut and fill structures. Past lacustrine environments are indicated by e.g. flat laminated sand silt intercalation and beach gravels. Aeolian sand is often intercalated with the playa silt.

The playas are distributed from Siwa in the north to the southern limits of Egypt, as at Nabta, and lie mostly at the foot slopes of escarpments at the edge of depressions in the Western Desert. Here there are more than 100 playas whose areas exceed 2 km^2 (Embabi 1999). Of these, there are 25 in Dakhla Depression (Brookes 1989 and 1993), 21 in Kharga Depression (Hamdan 1987) and 24 in Farafra Depression (Hassan et al. 2001; Hamdan and Lucarini 2013). Other playas smaller than 2 km^2 are spread. Occur not only in the large depressions, but also in small ones on the plateaus and in the southern plains.

The current amount of rainfall in the southern part of Egypt is insufficient to sustain playas. However, occasional heavy rainstorm in the depressions of the Western Desert can create small pools and puddles. In the northern part of the Egypt, where rainfall is limited to 50–100 mm/year, winter rains over the El-Diffa (Marmarica) Plateau along the Mediterranean Coast create shallow pools in small karstic depressions. Some of those pools often last for about a month. The saline lakes in the Siwa Depression today are not playas in the sense used to describe the Holocene playas of the Western Desert. The Siwa lakes, such as Siwa, Aghourmi, Zaytoun, and Maa'ser are fed by limited groundwater discharges from along fault lines. With very limited influx of rainwater and a high rate of evaporation the lakes are saline. Accordingly, their influx salts levels fluctuate seasonally depending on the seasonal differences in evaporation rates. Salt deposits are found both at the bottom of these lakes and along their shorelines. The Holocene playas of the Western Desert are also different from the Wadi el-Naturn lakes (see below), which are fed by seepage from Nile water, and are enriched in sodium carbonate, bicarbonates and chloride. Playas are also distinguished from Birket Qarun in the Faiyum Depression, which is now fed, like the newly created Wadi Rayan Lake, by irrigation drainage water.

The playas were favorable places for human habitation during Holocene as attested by the abundance of artifacts in association with playa sediments compared to their paucity or total absence elsewhere. Those playas fed by surface runoff and/or by spring water would have been hospitable places for people, especially during episodes of dry climate and dry seasons of the year. Moreover, playas are a main target of modern national agriculture reclamation projects in the western Desert because of their lithological characterizes and low salinity soils. Subsequently, however, these projects represent great threats to the prehistoric archaeological sites. Indeed, the threats are very high in Bahariya, Dakhla and Kharga areas where almost all playas are disappearing.

Chronologically, there are two playa generations in Egypt, based on dating techniques and associated archaeological materials. The first is Pleistocene and lakes are mainly large, permanent and mainly fed by ground water with little surface water. In contrast, Holocene playas are typically smaller, temporary and mainly formed by surface discharge (few were fed by ground water).

12.3.1.1 Pleistocene Lacustrine Sediments

During the middle Pleistocene, several large lakes existed in central and southern Egypt. The Bir Tarfawi/Bir Sahara region contains sediments recording a series of discrete lake phases ca. 230–60 kyr BP (Wendorf et al. 1993). In the Bir Tarfawi Depression, Pleistocene sediment records significant climatic and environmental changes during the last half million years (Blackwell et al. 2017) with distinct three playa generations. The older existed at the periphery of the depression at an elevation of 247 m ASL associated with Acheulean artifacts. The second playa (White Lake), existed in the north-central part of the depression, and dated to 248 ± 28 and 218 ± 27 kyr BP (Hill and Schild 2017). The third generation (Grey-Green Lake) at an elevation of 242 m ASL and dated to 105 ± 15 to 141 ± 3 kyr BP (Blackwell et al. 2017).

In the last two decades, there are several hypotheses connecting the depressions of southwestern Egypt with several mega-lakes. Maxwell et al. (2010) used digital elevation models- but did not take into account deflation during arid periods- to assume the existence of intensive middle Pleistocene lakes in the Tarfawi-Kiseiba-Toshka region of southern Egypt. Moreover, another mega-lake would have covered an area extending from the Sudanese border north to the Kharga and Dakhla Oases during the late Pleistocene (Issawi and Osman 2008; Maxwell et al. 2010). Detailed investigations of exposed sections of these mega-lakes show different lithological characteristics which may indicate local lakes rather than one mega-lake (see Hill and Schild 2017). The only evidence supporting a late Pleistocene mega-lake is represented by bones of Nilotic fish (Van Neer 1993). These fossils are also used as an indication of an ancient channel transporting Nile waters to Tarfawi-Kiseiba Depression (Van Neer 1993; Issawi and Osman 2008).

Dakhla Depression also hosted several large Pleistocene lakes (and perhaps, at times, one very large lake; Smith 2012), with a potential combined area of ca. 1700 km^2 (Brookes 1993; Ashour et al. 2005; Kieniewicz and Smith 2009; Smith 2012). They are preserved in two basins in the Dakhla Piedmont and represented by two facies: Facies A and Facies B (Brookes 1993). Facies A comprises horizontal, parallel-stratified turbidite beds; more sandy in lower part and more muddy in the upper bed. Most of the sediments were reworked mainly from Dakhla shale. Facies B comprises two sub-facies; sub-Facies B1, comprises thin couplets of large-crystal gypsum and clastics and includes 10–20 cm beds of biogenic lacustrine marl, which indicate deposited in saline lakes (Brookes 1993). Sub-Facies B2 consist of massive, pale-brown muddy sand. An exceptional event associated with the Dakhla playa, is a mid-Pleistocene catastrophic meteoritic impact event which scattered 'Dakhla Glass' around the depression surface (Osinski et al. 2007, 2008). The Dakhla Glass has been found embedded in the pale lake beds and in lags on eroded outcrops around the depression. The ages of Dakhla Glass average at 145 ± 19 kyr BP by 39Ar/40Ar so constraining the age for deposition of the lacustrine units bearing the glass (Renne et al. 2010).

At Um Dabadib, in the north Kharga Depression, remnants playa sediments are heavily dissected and associated with middle Paleolithic artifacts. They are represented by a 11.5 m thick section filling a trough eroded into the lower pediment (Hamdan 1987). The section begins with layer of about 80 cm of very pale brown aeolian sand; then overlain by about 200 cm of thin laminated playa silt with abundant shale flake and brown aeolian sand. The rest of the section (about 8 m) is represented by thick layers of brown massive playa silt and clayey silt with abundant shale flakes and desiccation cracks and Dikika structure. The top part of the playa sediments may be eroded and shows the development of a brown palaeosol which has been truncated and is now overlain by a gypseous crust with dark patinated sandstone slabs. The formation of gypseous deposits suggests high ground water and an arid climate during the late Pleistocene (Hamdan 1987). At Abu el Agl playa, three OSL dates were given for middle Paleolithic playa sediments; 79 ± 20; 67.6 ± 10.7 and 110 ± 18 kyr BP. One ^{14}C date on aostrich eggshell at the top of the middle Paleolithic playa sediments yielded a date of 20,580 + 280 BP (Ashour et al. 2005; Donner et al. 2015).

In the Eastern Desert, the Sodmein Playa (ca. 40 km north-northwest of the Quseir) is one of the rare Pleistocene playas with Pleistocene human occupation (Kindermann et al. 2018). Based on the associated artifacts, the playa is dated to early phases of MIS 5 (i.e. 118 ± 8 kyr BP). The playa sequence consists of the following units from base to top: (1) thick aeolian sandy unit with very thin silt laminae and lag gravels, indicating slight water events; (2) laminated sandy silts with gravel layers, indicating fluvio-lacustrine sedimentation during wetter climate conditions; (3) thick and massive, calcareous silts, representing an ephemeral lake; (4) miixture of gravels, sand and some silt accumulations. Small mollusks were found in several sections of the entire profile. Similar playa was described by Hamdan (2000b) at Esh Malaha area, north Eastern Desert, with sequence of intercalated calcareous silt, sand and gravel and dated by U/Th dating to 45–65 kyr BP.

In Sinai, thick section of Pleistocene fresh water lake sediments was recorded in environs of Wadi Feiran and Tarfat (Gladfelter 1988, 1990). The lakes were developed at different levels, impounded by dykes who formed barriers across the major wadi system and also acted as aquicludes (Issar and Bruins 1983). The lacustrine sediments of Wadi Feiran consist of interbedded alluvial, palustrine and colluvial sediments. A major portion of the original sequence has been eroded away and badland terrain occurs where extensive remnants of the beds are found. A complete stratigraphic section of aggragation is not preserved at a single location, but within Wadi Abu Nashre, an unusually thick occurrence of these deposits is preserved and associated with the Upper Paleolithic sites (Gladfelter 1990). Marl in the Pleistocene contains mollusk, ostracods and charophytes, species from habitats of freshwater ponds that existed in shallow depressions on alluvial bottoms (Gladfelter 1992). The mollusk assemblages as well as fish bones recovered archaeologically indicate that the ponds were perennial features. Radiocarbon assays obtained from certain marl units establish the late Pleistocene age of these deposits (i.e. 29,100 ± 460 BP (SMU 1845); 18,910 ± 200 BP).

Pleistocene playa sediments are also recorded at Northern Sinai (Sneh 1982; Goldberg 1984; Kusky and El-Baz 2000; Embabi 2017). The Pleistocene lakes occur in wadis and low areas between hills and mountains (Kusky and El-Baz 2000) and sometimes formed behind sand dune dams (Sneh 1982). In the Quseima area, one of the tributaries of Wadi El Arish, the sediment begins with early middle Paleolithic gravels (90–65 kyr BP), overlain by unit of sands, clays and silts dated to ca. 33.8 kyr BP (Embabi 2017). Some of the fine-grained sediments are interpreted as lake deposits, although many of them probably existed for a short period only. Other lakes may have persisted for longer periods, as indicated by the presence of clays with ostracods, inter-bedded with horizontal silt and sand layers of Upper Paleolithic (Kusky and El-Baz 2000).

Abu-Bakr et al. (2013) summarize the geomorphic evolution of the paleodrainge and paleolakes in North Sinai. They mapped the ancestral course of Wadi El-Arish by integrating a Radarsat-1 image with SRTM data in synergy with optical images and field investigations. A segment of the former drainage course with a length of 109 km and a width of 0.5–3 km was discovered beneath the sand dunes

west of Gabel Halal. The former course of Wadi El-Arish was dammed as a result of recent structural uplifting (anticlinal fold) at Wadi Abu Suwera. This structural high blocked the NW pathway, and forced the flow direction to deviate to the NE through the gorges of Talet El-Badan and Gabel Halal, respectively. Three major paleolakes have been identified along the main course of Wadi El-Arish within structurally controlled depressions formed due to the anticlinal ridges of the Syrian Arc System in North Sinai. These paleolakes were most likely developed behind the folded hills in two main stages, interrupted by the deviation of the river course. During the first stage, the southern paleolake developed from excess rainfall in the upper reaches of Wadi El-Arish, where the river was probably blocked and failed to reach the Mediterranean Sea. The central and northern paleolakes were formed in the post-deviation stage and the latter are estimated to be the largest of the three paleolakes (about 337 km^2).

Another controversial playa called "armored playas" (Said 1990), are extensive sheets of playa deposits which are veneered by a layer of white nodular chalcedony cobbles up to 15 cm in diameter embedded in a reddish brown matrix. Issawi (1971) considered that these playas were related to doming movements and structure lines. Other studies (e.g. Haynes 1980), however, has shown that the chalcedony cobbles seem to have been formed in standing bodies of water, rich in sodium carbonate and silica having a pH of 9.5 or higher (Said 1990). The age of these playas is not known, but they are certainly older than Neolithic (i.e. Pleistocene).

12.3.1.2 Holocene Playas

Holocene playas are the most widespread landforms in the lowland of the Western Desert of Egypt and primarily associated with Neolithic sites. Generally, from the early to mid-Holocene (ca. 11,500–5000 calBP), playa sediments of the Western Desert indicate a vivid climatic change, from hyperaridity to semi-aridity and back to its present hyperarid state (Hoelzmann 2002). It seems that, playa deposition started in mountainous areas much earlier than in the lowlands and stable conditions were established soon after the regional rise in groundwater. By 8 cal kyr BP, optimum conditions prevailed throughout Western Desert as documented by playa sediments which prove the existence of stable freshwater lakes. The decline of the wet phase started earlier in the north (ca. 7.5 cal kyr BP) and later in the south (ca. 6 cal kyr BP). The end of playa sedimentation in Western Desert can only be placed tentatively around 5 cal kyr BP.

The lacustrine deposits at Nabta Playa have a direct stratigraphic relationship with many archaeological sites associated with the early Neolithic and range in age from ca. 9.3 to 7.3 cal kyr BP. These are El Adam, El Ghorab, El Nabta, and Al Jerar (Wendorf and Schild 1980). The base of the playa sequence is represented by phytogenic dunes which developed before the formation of the earliest lacustrine silts. The dune sands are overlain by beach sands containing freshwater gastropods which, in turn, are overlain by reddish brown playa silts with blocky structure. Based on pollen, diatom, and geochemical data, the lakes water level began to rise at ca. 8.4 cal kyr BP, reaching a maximum at ca. 8 cal kyr BP and persisted until ca. 7 kyr BP, around 6.2 kyr BP, the modern phase of hyperaridity began in the Eastern Sahara and the area was abandoned.

In Dakhla Depression, Brookes (1989) identified three sets of Holocene playa deposits. The first consists of playa sand, in places with redeposited carbonate sand and overlying gravelly slope wash andthen with reddish brown aeolian sand. This section identified from Locality A, is dated to $\geq$8.7 cal kyr BP. In another locality (Area B), 8 m thick playa sandy silt, capped by a halite-rich crust and overlain by massive, angular limestone gravel. The playa deposits of this setion are dated to => 8270 BP. In another area (Locality C), playa deposits consist of pale brown silty sand with gypsum encrustations dated to 7.8–7.1 cal kyr BP, or younger. The top of Area C shows inactive springs. Brookes attributed much of the variability to local differences within the depression.

Two generations of playa exist at Um Dabadib; early and middle Holocene playas (Hamdan 1987). The early Holocene playa is ca.7 m section of massive playa silt at the base with a thick unit of aeolian sand-thin playa silt intercalation in the middle and thick scree of large limestone boulders and reddish brown palaeosol at the top. It is associated with terminal Paleolithic artifacts which date to the early Holocene. In the Abu Tartur basin, playa sediments yield OSL dates ca. 9.4 cal kyr BP to about >ca. 7.93 cal kyr BP and associated with several temporary occupations of hunter gatherers associated (Bubenzer et al. 2007). One OSL date yielded 9.1 + 1.6 cal kyr BP in the Abu el Agl playa basin (Ashour et al. 2005; Donner et al. 2015). Middle Holocene playa exposures in the center of the Umm el Dabadib basin are represented by a massive homogeneous lacustrine deposit and associated Neolithic artifacts. One ^{14}C dating on ostrich eggshell associated with younger playa sediment at Umm el Dabadib yielded 7220 $\pm$ 150 cal BP (Hamdan 1987); a corresponding playa deposit in the Abu Tartur basin is dated to about 7200–6300 cal BP (Bubenzer et al. 2007). Playa dates of 6230 $\pm$ 90 BP and 5980 $\pm$ 90 BP were recorded at Abu el Agl playa (Ashour et al. 2005; Donner et al. 2015).

Several Holocene playa generations are evident in Farafra Depression (Barich and Hassan 1987; Hassan et al. 2001; Hamdan and Lucarini 2013). Early Holocene playa deposits are represented by massive mud with thin, gypsum crusts and iron oxide stains, suggesting deposition under warm, arid conditions and short wet periods sufficient to form shallow temporary lakes (Hassan et al. 2014). The deposits from the next moist episode in Farafra are recorded at Ain Raml where

they are dated to 9650 ± 190 cal BP. At Wadi Obeiyid, the playa deposits are exposed in a series of yardangs, consisting of a sequence of mostly white to very pale brown playa mud interbedded with cross-bedded sand and fluvial gravel in the lower unit (8080 ± 60 cal BP). The middle unit of this sequence is dated on in situ charcoal 7725 ± 60 to 7320 ± 110 cal BP. (Hamdan and Lucarini 2013; Hamdan 2014a, b). The youngest deposits at Wadi Obeiyid Playa are preserved at a rock shelter and consist of a intercalation of white, angular, chalk rubble in a friable, calcareous loam yielding a radiocarbon age of 6050 ± 75 cal BP (Hamdan and Lucarini 2013; Hamdan 2014a, b).

In Bir Obeiyid, Farafra Depression (Fig. 12.9a), three Holocene playa generations were described by Hamdan and Lucarini (2013), P_I, P_{II}, P_{III} (Fig. 12.9b). The early Holocene playa (P_I) sediments occupy a closed basin in the higher reaches of the Bir El-Obeiyid Depression (ca. 90 m ASL). One ^{14}C dating of 10,721 ± 325 cal BP is given to this basal Playa "P_I" (Hamdan and Lucarini 2013). The playa sequence begins with aeolian sand and then intercalates upward with thin laminae of white calcareous playa mud with desiccation cracks. The topmost of playa "P_I" sequence is represented by thick limestone rubbles mixed with gypsum and aeolian sand. The early Holocene playa is truncated by white subangular chalk rubble, grading vertically into the underlying bedrock chalk and horizontally to the playa deposits, probably indicating severe mechanical weathering under subaerial conditions during deposition. Temperature variations coupled with freezing of moisture trapped in fissures would have been sufficient to produce angular clasts and limestone blocks. The white color of the deposits indicates that temperature and rainfall were sufficiently low to mobilize iron oxides (Hassan et al. 2001). This phase of rubble formation is dated to 8079 ± 107 cal. BP and therefore related to the global 8.2 cal kyr BP cold phase (Hamdan and Lucarini 2013).

The middle Holocene playa "P_{II}" occupies the deepest part of the Bir El-Obeiyid Depression (ca.75 m ASL) and is mainly eroded into yardangs (up to 3.0 m above the surrounding depression). The sediments of playa "P_{II}" overlythe deflated surface of the limestone rubble of Playa "P_I" and are dated to 7510 ± 107–6407 ± 84 cal. BP. They consist of mainly of fine sand, silty sand and silt, deposited

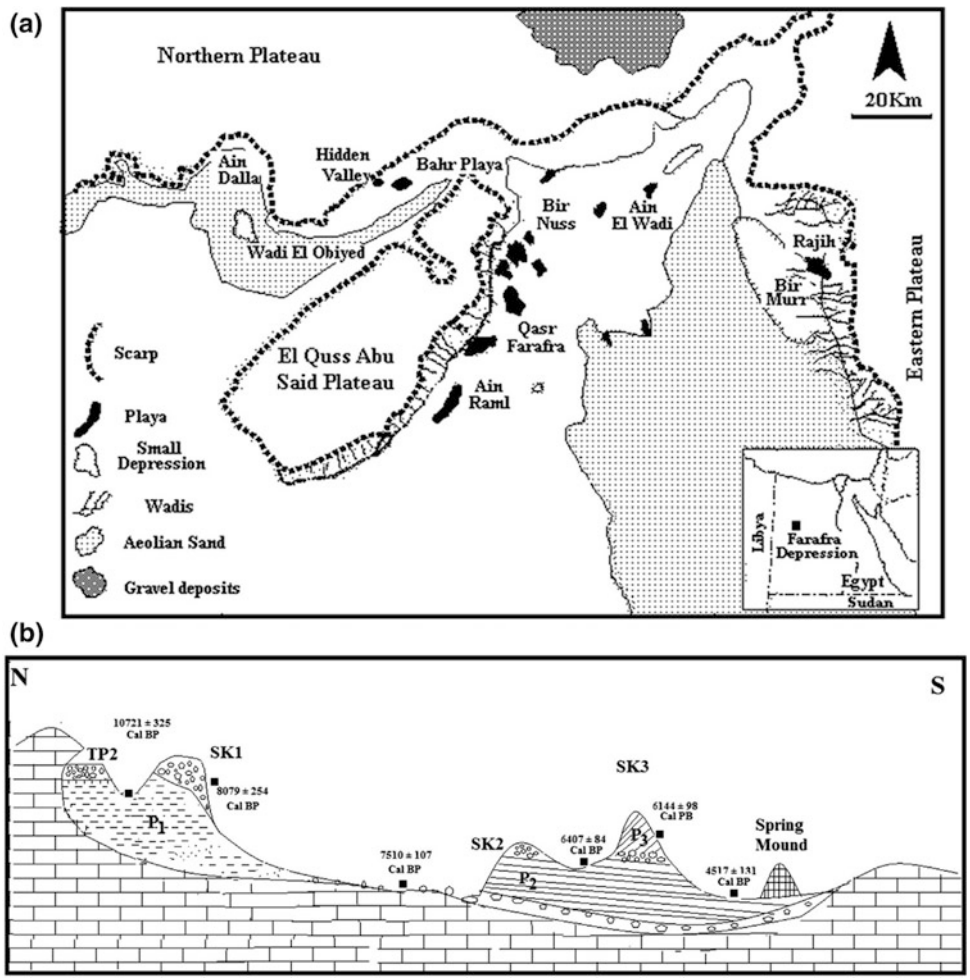

Fig. 12.9 **a** A map of the Farafra Depression showing locations of Sheikh El-Obeiyid area and other playa deposits in the Farafra Depression: **b** N-S geological cross section at the Bir El-Obeiyid Playa, showing that early Holocene; **c** middle Holocene playas "PII" and "PIII" (*Source* Hamdan and Lucarini 2013)

by two water sources. The calcareous playa sand and silt are cemented by freshwater carbonate and contains thin laminae of algal tufa, indicating a groundwatersource. The continuous sedimentation and absence of aeolian sand layers probably reflect stable, wetter conditions. The last phase of "P_{II}" is marked by a layer of grain-supported angular limestone rubble, indicative of a short dry and cold episode.

Late middle Holocene playa "P_{III}" is separated from "P_{II}" by thin limestone rubbles and consists of thin layers of playa silt intercalated with thick aeolian sand. One ^{14}C date of 6144 ± 98 cal. BP. is given for playa "P_{III}". The existence of several aeolian sand layers and a highly desiccated playa silt layer indicate that the climate was highly episodic during the deposition of playa "P_{III}". The last stage of the evolution of the Bir El-Obeiyid playa basin is represented by spring activity. The spring mounds exist in the deepest part of the basin and attain a height of about 10.0 m above the deflated level of the Holocene playa. This spring fed water to the playa in the late Holocene (4517 ± 131 cal BP).

Holocene playa deposits in Siwa consist of yellow and brownish yellow sand to loamy sand followed upward by very pale brown to yellow loamy silt. Granulometric analysis and X-ray diffraction analysis of the clays reveal a change through time toward greater surface runoff under gentle rainfall as suggested by an increase in the silt-clay content and kaolinite (Hassan 1976). This phase is dated to ca. 8.6–8.1 cal kyr BP and is correlated with the Nabta Phase I (8.6–8.2 cal kyr BP). In Bahariya Oasis, investigations at El-Heiz reveal mud pan deposits dated to c. 6.9–6.3 cal kyr BP (Hassan 1979b). They consist of a basal unit of aeolian sand with salt crusts followed by playa silt topped by aeolian sand.

Holocene playa sediments existed around Djara Cave region (see below), with a maximum thickness of 2 m (Kindermann et al. 2006). They consist of reddish sand and silt and capped with limestone scree and burned stones from hearth mounds (Bubenzer and Hilgers 2003). Luminescence dates of the playa sediments range between 6.8 ± 0.5 and 8.67 ± 0.5 cal kyr BP (OSL) and show that the entire playa sediments accumulated during the early and mid-Holocene (Bubenzer and Hilgers 2003).

In Gilf Kebir, Holocene playas are developed by blockage of wadis by sand dunes (Maxwell 1980; Pachur and Röper 1984; Kröpelein 1987). In Wadi Bakht, more than 10 m of inter-layered lake and aeolian deposits were deposited upstream from a dune dam (Maxwell 1980; Kröpelein 1987). The age of these playa sediments varies between 8200 ± 500 and 6080 ± 420 cal BP (Kröpelein 1987). Based on sedimentary analyses and archaeological context, the Gilf Kebir experienced wet climate between 9.5 and 6 cal kyr BP; between 6 and 5 cal kyr BP, the climatic conditions shift toward moderate aridity with the maximum rainfall of 100–150 mm (Kröpelein 1993).

12.3.2 Alluvial Deposits

Gravel terraces along wadi margins in the Egyptian deserts record relatively short distance fluvial transport of sediments off the high plateaus and mountainous areas (Caton-Thompson 1952; Brookes 1993). External drainage of many desert wadis is covered with Holocene alluvial and aeolian sand dunes which seem to have accumulated in response to the rising sea leve. Records of earlier deposits and terraces are known along many of wadis. In Western Desert, fluvial sediments are difficult to recognize, they either eroded away or modified and hidden by dune sands. In the present review, two types of Quaternary alluvial sediment are describe these are buried radar rivers and inverted wadis.

12.3.2.1 Radar Rivers

The term "Radar Rivers" refers to almost fully aggraded Tertiary basins and valleys that lie beneath the sand sheet in southern Egypt and northern Sudan. These features were first recognized when radar images produced by the imaging radar (SIR-A) experiment aboard the November, 1981 flight of the space shuttle Columbia (McCauley et al. 1982). Radar Rivers have been described under different synonymy; e.g. Radar Rivers and Subsurface Valleys (McCauley et al. 1982, 1986; Ghoneim et al. 2007); Paleo-rivers (McHugh et al. 1988); Paleo-drainages (McCauley et al. 1986; Schaber et al. 1997) and Paleo-channels (El-Baz et al. 1998).

Three types of "Radar Rivers" have been recognized in the SIR-coverage of the Eastern Sahara (McCauley et al. 1986): (1) a Radar River (RR-1) is a broad, aggraded valley or basin with stubby tributaries, 10 to 30 km wide and up to hundreds of kilometers long. Wadi Arid is the type area in Egypt. The RR-1 valleys as seen on SIR-A images are strikingly similar in scale and overall appearance to the Nile River Valley some 300 km to the east (McCauley et al. 1982). These broad valleys are now almost completely aggraded with fluvial deposits that underlie regional aeolian sand sheets; (2) Radar River RR-2 type (braided channels inset in the RR-1 valleys), consists of groups of narrow, 0.5- to 2-km-wide. The type area for these braided stream complexes is Wadi Safsaf. The islands are formed of RR-1 valley fill, which consists of sand and fine pebble alluvium cemented by secondary calcium carbonate. Nodules of $CaCO_3$ are commonly disseminated in the upper 2 to 3 m of the valley fill; (3) Radar River (RR-3) (narrow, long, bedrock-incised channels), are partly visible on the ground and on Landsat in areas where the sand sheet is patchy. They are conspicuous on SIR because the dark response of their unconsolidated channel fills contrasts with the brighter response of surrounding bedrock.

The Radar Rivers are relics of a Tertiary system that drained the Eastern Sahara before the onset of general aridity in the early Quaternary and again by intermittent running

water during the Quaternary pluvial episodes (McCauley et al. 1986). Red Sea Mountains are the main source of water for these valleys (Issawi and McCauley 1993). Three major paleo-drainage systems developed in response to tectonic uplift and sea level changes from late Eocene to late Pleistocene. They represent a part of a regional Tertiary system called "the Trans-African Drainage System" (Issawi and McCauley 1993). These systems are named as the Gilf system, the Qena system, and the Nile system (See Sect. 2.1.1). McHugh et al. (1988) have shown that at least the upper 40 m of these ancient valleys (which are hundreds of meters deep) are now filled with late Pleistocene alluvium, mainly sand and fine gravels. These sediments became cemented by calcium carbonate deposited under fluctuating groundwater conditions. The widespread alluvium and ubiquitous carbonated deposits imply climatic conditions with annual rainfall approaching 400–600 mm (McHugh et al. 1988). The last stages of aggradation are archaeologically dated by the Acheulean remains incorporated within the alluvium. Uranium-series age determinations on 25 carbonates samples have yielded modal dates for episodes of carbonate formation: >300, 212, 141 kyr BP and 45 kyr BP.

SIR-C data in the southern part of the Western Desert and Northern Sudan reveal the existence of four major drainage lines formed by the Toshka Hydro-System and drained internally in a basin into the Selima Sand Sheet (El-Baz et al. 1998). Ghoneim et al. (2007) used SRTM data to reveal wide paleo-river courses emerging from the Gilf Kebir plateau to the south, and draining towards the east (Fig. 12.10). These channels represent the upper stream area of a large paleo-drainage system and are believed to be responsible for the groundwater resources that supply productive agricultural farms in East Uweinat area of south-western Egypt. The shape of the derived SRTM contour lines around the exits of these channels along the mountain front suggests the existence of a broad, sloping depositional landscape caused by the coalescing of a number of alluvial fans to form a large Bajada (Ghoneim et al. 2007).

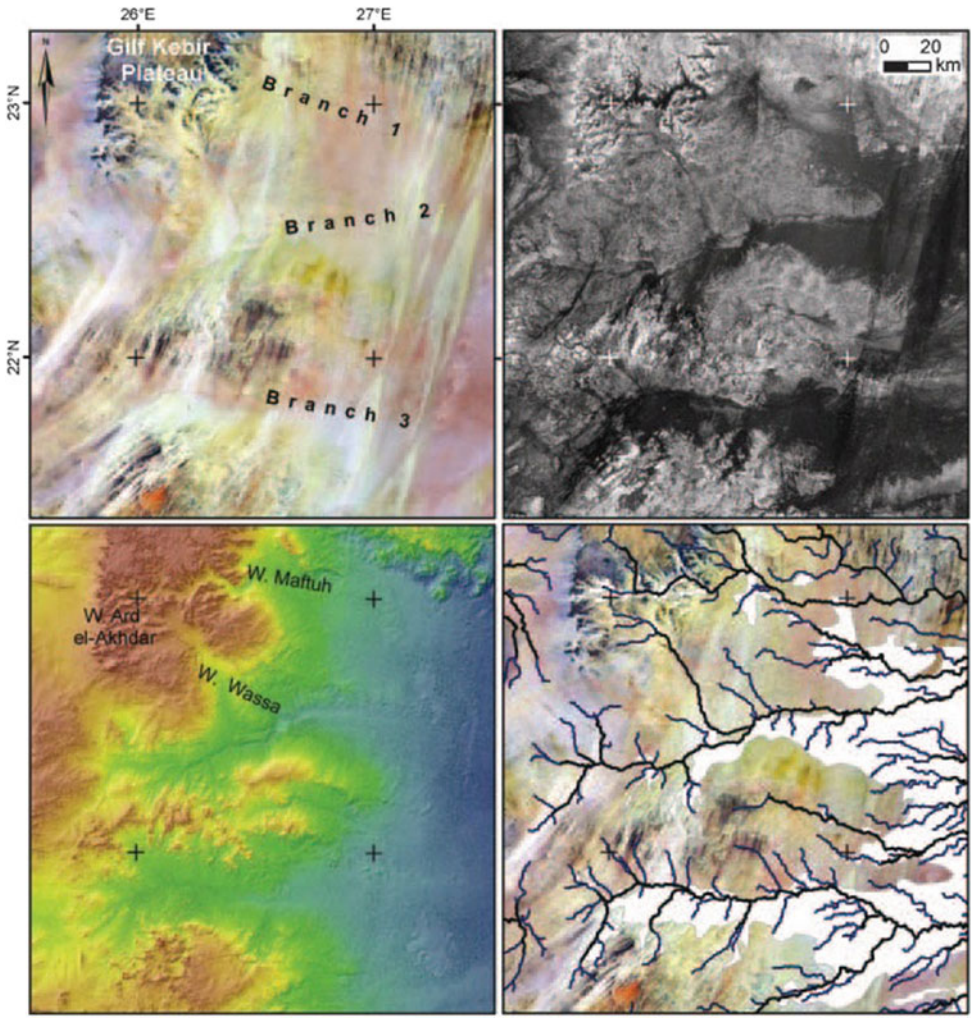

Fig. 12.10 **a** the ETM + image of the three wadi branches of the Gilf Kebir area; **b** Radarsat-1 image of these drainage networks; **c** SRTM data of Gilf Kiber area; **d** The digitized radar-dark feature (white spaces) with the SRTM-derived channels (dark lines) overlain (*Source* Ghoneim et al. 2007)

12.3.2.2 Inverted Wadis

Inverted wadis are elongated, sinuous and sometimes branching gravel ridges which stand out above the rock cut surfaces (Giegengack 1968). They were first noted by Knetsch (1954), who described one gravel-capped sinuous ridge in Egyptian Nubia and called it as a "pseudo-esker", by analogy with glacial deposits on the plains of northern Europe (Zaki and Giegengack 2016). Inverted wadis in SE Egypt form a rectangular pattern, with an average length extending for about 10 km, maximum width not exceeding 300 m, and height of as much as 20 m (Fig. 12.11). Inverted wadis developed via cementation of minerals causing surface armoring (Giegengack 1968). The minerals, which cause the cementation, are calcium carbonate, hematite, silicon dioxide, and iron oxide.

Inverted wadis occur throughout the Lake Nasser region area, on both sides of the Nile. Because blown sand covers much of the ground surface in the Western Desert, inverted wadis appear on air photos as dark traces in a sea of pale sand. Inverted wadis in the Eastern Desert, east of the Nile, are also abundant, but, since they represent dark traces on dark bedrock, they are not as easily identified from air photos as those in the Western Desert (Zaki and Giegengack 2016). Sediments of inverted wadis consist of indurated poorly sorted gravel and coarse sand deposits with abundant rolled Acheulean artifacts (Giegengack 1968). The gravels are mostly dark brown limestone and chert. They range in size from pebbles, poorly sorted, rounded to sub-rounded and sometimes discodial in shape embedded in pale brown sandy matrix. The stratigraphic framework of the formation of thse inverted wadis include three gravel units; (1) Early Nile Gravel deposited in Nile flood-plain gravel with Acheulean artifacts; (2) Wadi Conglomerate topographically inverted to form sinuous ridges after deposition of early Nile gravel; and (3) Late Nile Sediments (ca. 27–5 kyr BP) with late Paleolithic artifacts (Giegengack and Zaki 2017).

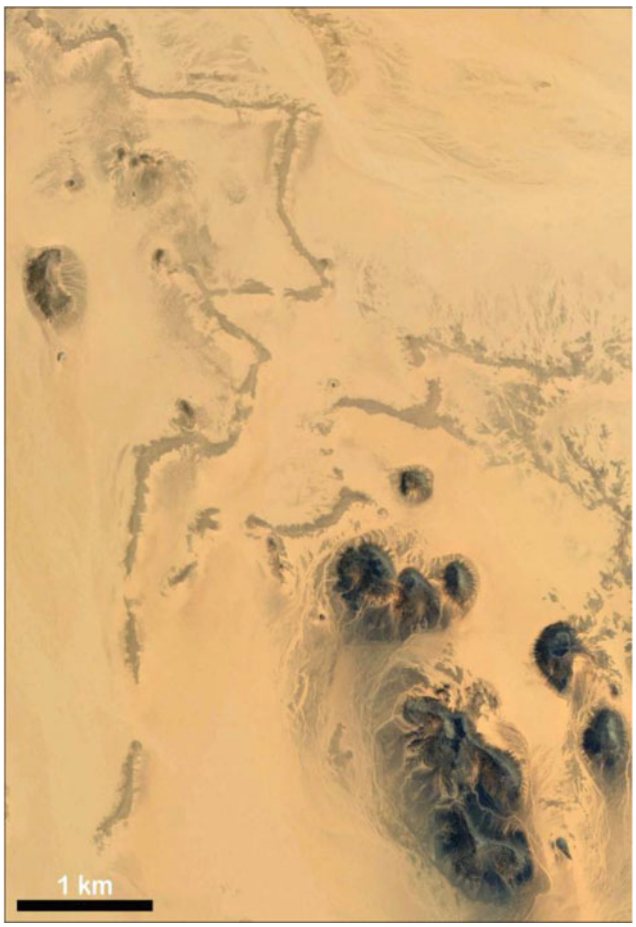

Fig. 12.11 Rectangular pattern of an inverted channel at 22°56′ N, 32°07′ E, 7 km in length, maximum width is about 80 m, and the height is about 7 m (*Source* Zaki et al. 2018)

More recently, Zaki et al. (2018) studied inverted wadis in seven sites in the Western Desert and compared them with similar features in Mars. East of the Bahariya Depression, fifty-nine bodies of mostly dendritic inverted channel features have been described with 761 m; 60 m; 7 m average length, width and height, respectively. 53 spell out sinuous inverted-channel bodies have been delineated in the area west of Ghard Abu Moharik with, with average length, width and height as 1.896 km, 91 m and 13 m, respectively. In the plateau east of Kharga Depression, fifty-nine inverted channel bodies are described, with 2.184 km, 104 m and 12 m asaverage length, width and length respectively. In the Nile Valley, west of Esna city, fifty-five inverted channels were recorded with average length width and height of 1.324 km; 49 m and 17 m, respectively. In addition, Zaki et al. (2018) mentioned poorly define inverted forms in the Nile-Faiyum Divide, previously described by Sandford and Arkell (1929) and dated them to Pliocene age. Another abnormal inverted features in Dakhla Depression, was described by Brookes (2003) as meander scrolls in the sandstone of the Taref Formation (Turonian). Indeed, most of these inverted channels are likely related to ancient river systems described by Issawi and McCauley (1993). However, some features relate to middle Pleistocene Nile hydrology, especially, those of Lake Nasser (Giegengack and Zaki 2017).

The formation of inverted wadis is essentially based on two criteria. Most of the channel fill is represented by bed-load gravel, sometimes of boulder size, such as those in the south-eastern part of the Western Desert. These materials exhibit high porosity and most likely are filled by secondary minerals e.g. iron oxides calcium carbonate and silica. The cemented bed load sediments become more resistant to erosion relative to the soft bedrock. A Few inverted features consist of sand and silt armored by lag gravel and caliche was recorded in the Sheikh Obeiyid playa, Farafra Depression (Hamdan and Lucarini 2013). These inverted features represent fluvial channels that fed the middle Paleolithic lakes.

The nature of inverted wadis reflects the different climatic conditions prevailing in the Western Desert, probably since the Oligocene. During wetter climatic conditions, rivers deposited their sediments, especially bed load gravels and successive wetter periods not only fed water to new channels but were also responsible for depositing secondary cementing materials in the older fluvial bed load gravels. This led to lithification of the ancient fluvial sediments and made them more resistant to erosion. We believe that most inverted topography is related to the hyperarid climatic conditions of the middle and late Pleistocene and late Holocene.

12.3.3 Solution and Karstic Features (Tufa and Spleothem Deposits)

12.3.3.1 Karstic Landforms

Karst is terrain with distinctive hydrology and landforms arising from the combination of high rock solubility and well-developed solution channel (secondary) porosity and permeability underground. Aqueous dissolution is the key process. It creates the secondary porosity and permeability may be largely or wholly responsible for a given surface landform (Gunn 2004). Karst landforms are inherited from past humid climates and have been exposed to modifications during their long history of development (El-Aref et al. 1987). Karst is a dominant feature in the limestone plateaus of Egypt and is represented by different landforms such as doline and uvala depressions, rock-towers, cone-karst, and blind valleys (El-Aref et al. 1987; Embabi 2017). It is important to note that the karstic activity in Egypt took place under wet tropical to subtropical conditions and are somewhat different from those of seasonally wet Mediterranean highlands karst region. The tropical karst regions are characterized by higher surface limestone solution than temperate karst because of the great amounts of surface runoff aided by vegetal and biological activity. The initial corrosive action of tropical waters occurs close to the surface where they become rapidly saturated. This may explain the typical temperate karst features such as large cave systems. Caves in tropical karst tend to be a network of tunnels and of solution dolines. Moreover, temperate karsts of dolines, uvalas and poljes form where solution is evenly spaced over the area. The depressions of tropical environments, the "cockpits" form because water goes rapidly underground without being saturated, thus promoting depth.

The most famous karstic features of the Western Desert are extraordinary chalk pillars, towers and rounded blocks in the "White Desert" artistic chalk of the Farafra Depression. The White Desert National protected area was declared in 1983 to protect the spectacular karst landscapes and associated erosional features. Among the 52 potential sites in the Bahariya—Farafra territory, about nineteen have been selected as potential geomorphosites (El-Aref et al. 2017a). These geomorphosites reveal great geodiversity reflecting high scientific, aesthetic and management values for various activities, not least geotourism (El-Aref et al. 2017a).

About sixteen fields of various karst landforms in the Bahariya-Farafra Plateau were described and mapped for first time by El-Aref et al. (2017b). Among these, karst fields, karst wadi, karst depressions, polygonal karst landforms and Qaret El Sheikh Abdalla Uvala (Denuded and Rejuvenated Karst Landforms). The latter explain well stages of karstication process since post Eocene major paleokarst formation until the final stage of denudation and paneplantion. The Eocene limestone plateau northwest of Assiut also contains karstic shafts infilled with solution breccias and reddish terra rossa (Mostafa 2013). The morphology of these shafts and their infillings suggest that they developed in vadose zones at the base of epi-karst limits. The Giza Pyramid Plateau contains surface karstic features (e.g. karrens, rain pits, rounded rims and solution basins) as well as subsurface features (e.g. karst ridges, shallow holes and dolines) (El-Aref and Refai 1987).

El-Aref et al. (1987) believe that karst and karstification processes were initiated since the late Cretaceous and adapted term "paleokarst" for the older landforms and attributed the Quaternary age to the last stage of karst landforms. A paleokarst is an inert landform and should be distinguished from fossil karst and relict karst. Fossil karst is used to describe karst features that are not in equilibrium with modern landscape process, but is not inert from a karst perspective. Relict karst is isolated from the karst excavation processes that formed it, but still is subject to modification for example by weathering, breakdown, and spleothem deposition. However, the terms paleokarst and fossil karst are often used interchangeably (Gunn 2004). In Egypt, the current hyperarid climate is not suitable for formation of karst landforms; therefore terms paleokarst and fossil karst are adequate.

The karst landforms of the Western Desert exist on three erosion surfaces. Each is characterized by its geomorphic, lithological and archaeological characteristics (El-Aref et al. 1987; Hamdan and Lucarini 2013): (a) Erosion surface "S_1" at the Paleocene/lower Eocene contact in the Farafra formation is characterized by low relief, eroded shallow karst depressions of different sizes; there are also abundant Egyptian alabaster and silcrete deposits and including a sharp pedestal-like hill rising about 40 m above the level of the surrounding plateau (Hamdan and Lucarini 2013); (b) Erosion surface "S_2" at the contact between the Tarawan and Ain Dalla formations is characterized by a rough surface and abundant silcrete duricrust and caverns; (c) Erosion surface "S_3" form the main depressions of the Western Desert.

Three erosional surfaces were also described by Philip et al. (1991) in the Nile Valley at Gebel Homret Shibun. The oldest (highest, "S_1") attains an elevation of 340 m ASL and

is represented by convex top hills with a free face of duricrust and debris slope of 30°. Duricrust profile consists, from base to top: (a) a lower horizon of cavernous and brecciated bedrock; (b) a middle horizon of limestone breccia fragments either cemented by gravitational and blocky calcite or embedded in residual terra rossa; (c) an upper hard cap calcrete, cementing highly subdued and fragmented limestone. The intermediate erosional surface "S_2" attains an elevation of 200–300 m ASL and is covered by terra rossa mixed with calcrete and a thin veneer of silcrete. The surfacial silcrete grades downward into highly cavernous and silicified limestone. The karst profile of surface "S_2" is subdivided into three horizons: (1) An upper horizon corresponding to the infiltration upper vadose zone covered by a thick terra rose and calcrete, (2) A subsoil horizon, where the rock horizon has been affected by intensive karstification resulting in sculpturing, dissolution, alteration of the limestone bedrock, and the formation of surface and subsurface solution features, subsurface caves and inter-karstic deposits. Solution features includes sinkholes and tabular and or funnel dolines. Subsurface solution features includes vertical or inclined solution cavities and horizontal solution cavities formed along bedding planes. Intra-karstic deposits are represented by dolines and cave fill. The lower horizon is represented by partially altered bedrock. The third erosion surface, at an elevation of 70–160 m ASL, is a plain surface characterized by undulating relief interrupted by residual duricrust of the cone-hills and ridges. The "S_3" surface is usually truncated by small and very small drainage basins with dendritic to subdendiritic patterns.

Absolute dating of the karstification in Egypt is not possible. U/Th dating of spleothem deposits in the caves (see below) gives only the age of last stage of karstic processes. However, the age of initial karst stages are given from terrestrial fossils associated with terra rossa in solution cavities in both the Western and Eastern Deserts. The karstic shafts in the limestone of Bahariya-Farafra Depressions contain small vertebrate fossils dated back to late Miocene (Pickford et al. 2006; Mein and Pickford 2010). In Khasm El-Raqaba limestone quarry (Eastern Desert), small fossil vertebrates representing snakes, rodents and bats, have been recovered from karst fissure-fill deposits intrusive into the Eocene limestone (Gunnell et al. 2016). These fossil assemblages indicate mixed subtropical and more arid microhabitats and dated to late middle Miocene.

Evaporite karst

The term "evaporite karst" is normally employed to denote karst in more soluble salts, most commonly in gypsum and halite. Under normal conditions, the solubility of gypsum is up to three orders of magnitude greater than that of calcite, but the solubility of rock salt is roughly 140 times greater than the solubility of gypsum (Gunn 2004). In the Red Sea Coast, the carbonates and the evaporites have been subjected to intensive karstification processes, dominated by surface and subsurface solution features (El-Aref et al. 1986). Isolated cone hills and karst ridges with surface depressions and subsurface caves characterize the carbonate rocks while cone-karst and cockpits characterize the evaporites. Formation of alabastrine gypsum, silicification, dolomitization and dedolomitization are the main wall rock alterations affecting bedrocks during karstification. The development of hard capping duricrusts is certainly the result of precipitation and evaporation during arid to semiarid climatic periods. Brecciation, collapsing and recementation of the duricrust indicate effectively drier and wetter oscillations condition during karstification. El-Aref et al. (1986) concluded that the karstification probably prevailed during the Pliocene or Pleistocene. In addition to paleoclimate, the tectonic setting of the Red Sea coastal zone and the lithology of the country rocks are considered to be the fundamental factors controlling the formation and the distribution of the Red Sea karst landforms.

Economic Importants and Geohazards of Karst Landforms

Several studies reveal that karstification processes were responsible for the formation of many economic ores. Oxides and sulphides of iron, lead and zinc and barite are also found in association with the Red Sea karst (El-Aref 1993; El-Aref et al. 1986). The types of ore minerals and their distributions are controlled by the physico-chemical conditions of the karst water induced during evolution of the karst. The barite and the oxide minerals, together with the final deposition of $CaCO_3$ and the silicification processes, characterize the percolation zone of the mature karst system. The sulphides must be deposited under reducing conditions which characterize the general inhibition zone of the karst system (El-Aref 1993). Iron and manganese ores in Bahariya and Umm Bogma, Sinai, respectively, are most likely related to paleokarst processes (e.g. El-Aref and Lotfy 1985; El-Sharkawi et al. 1990).

Several geohazard problems are associated with karst landforms since they are often underlain by cavernous carbonate and/or evaporite rocks. Impacts and problems associated with karst are rapidly increasing as development expands upon the karst landforms. This has led to an escalation of karst-related environmental and engineering problems such as landslides developed on rock cuts/slopes weakened by karstification features. Youssef et al. (2018) studied the effects of karstification and sinkholes on the stability of the rock cuts/slopes along some desert highways in middle Egypt. They concluded that there is a crucial impact of the karst features on slope instability; many sections of the rock cuts along these highways are not stable and

may endanger the traffic safety. Different karst features contribute to slope stability problems such as differential erosions, open joints, empty cavities, filled sinkholes, and weathering effect along discontinuities.

12.3.3.2 Speleothem (Cave) Deposits

Caves are the most important karstic feature that exists along the limestone plateaus of Eastern and Western Deserts as well as Sinai. Caves can be subdivided into different types according to their geological, geomorphological, archaeological significance, e.g. caves with speleothems, paleontology caves, historical and archaeological caves.

(1) **Caves with Speleothem deposits**

The largest known caves, with speleothem deposits in Egypt are represented by the Sannur and Djara caves, which are characterized by their internal speleothems and flow-stones (Embabi 2017). The Djara cave is an important site in Egypt, located in hyperarid terrain between Assiut and Farafra Oasis. It is a dissolution cave, consisting mostly of a single large chamber approximately 19 × 10 m, and is typically 6 m high (Brook et al. 2002). The main entrance leads to a steep slope initially on rock, and past a series of wall flow stones, stalactites and columns. The floor of the large chamber is covered by ca. 6 m of aeolian sand (Kuper 1996). The cave contains numerous large stalactites, columns (>15 m in diameter and >6 m high), flowstones and sporadic stalagmites (Brook et al. 2002). Helictites have grown from the roof and walls in several parts of the cave, and locally are present as smaller deposits on larger stalactites and columns. Collapse blocks of limestone and broken formations are common near the entrance. Younger speleothem of Djara cave yielded U/Th ages of 140 ± 16, 201 ± 2 and 233 ± 24, 221 ± 34, and 283 ± 56 cal kyr BP (Brook et al. 2002).

Sannur cave is the most important and beautiful Egyptian cave- assigned as a National Protected Area in 1998. It is found in low rolling hills of middle Eocene limestone (Philip et al. 1991). Its entrance is located near the bottom of a pit-like quarry 50 m deep where Egyptian alabaster (calcareous thermal spring deposits) is quarried. Basically, the cave consists of a flat-floored curving chamber, crescentic in plan-view and 275 m long and ca. 20 m high. Massive speleothems and curving walls characterize the eastern and western galleries (Günay et al. 1997). The roof of the cave is almost horizontal at the inner wall, it then curves downward to meet the cave floor by as much as 12 m (Halliday 2003). The speleothem deposits of Sannur Cave have a very fresh, glistening appearance and may have been deposited or enlarged very recently (Halliday 2003). They range from towering stalactitic columns and subaqueous mammillaries to glistening thickets of intricate crystalline "popcorn" and tiny glassy helictites. Stalactites vary from soda-straw forms to large tapered types (Philip et al. 1991). The dates of the speleothem of Wadi Sannur range between 140 ± 16 cal kyr BP and 283 ± 56 cal kyr BP (Dabous and Osmond 2000). However, these dates represent the U mobilization and the last phase in speleothem deposition. Rifai (2007) dated six laminae in the Wadi Sannur stalactite; they range from 188-36 kyr BP and suggested that these laminae were deposited over a period of ca. 52 kyr BP. The estimated growth rates of Sannur's stalactite are variable and range from 0.12 to 9.30 μm/year. The stalactite began to grow with deposition rate of 3.7 μm/year (between 188 and 175 kyr BP), with non-deposition phase between 175 and 160 kyr BP, and increase rapidly around 145.35 kyr BP, (9.3 μm/year). By the end of the growth period it has decreased by about 4.1 μm/year.

(2) **Paleontogical "Nimir" Cave**

Nimir Cave is a large solution cave on the northern slope of the southern Galala plateau, ca. 40 km southwest of St. Anthony monastery. The main chamber is 36 m long, 18 m wide and 11 m high. The floor consists of aeolian sand and limestone talus. A large stalagmitic column dominates the far end of the main chamber (Halliday 2003). This cave is especially important for paleoecological studies, which revealed a radically different Holocene ecology (Goodman et al. 1992). Excavation of the cave revealed numerous finds representing remains of at least 29 individuals of leopards (Goodman et al. 1992). These materials seem derived from animals that visited, lived and died in the cave throughout the Holocene; radiocarbon dates of leopard tissue indicate that the species was present in the Epi-Paleolithic, Neolithic, Predynastic and Second Intermediate period (ca. 7–3.65 cal kyr BP). The cave has archaeological significance; rock art is represented by a group of leopards being chased by several men armed with spears (Hobbs and Goodman 1995).

(3) **Caves with archaeological significance**

Obeiyid and Sodmein caves are examples. Obeiyid Cave, with rock art, is located in Wadi Obeiyid, Farafra Depression (Hamdan et al. 2014). The cave is located about 50 m above the floor of the wadi and can be entered through a 2 × 2 m square opening extended in a N-S direction (Fig. 12.12a). The walls are sharp and straight and run parallel to the dominant joint trends. The opening has an unusual appearance and does not resemble other fracture bounded cavities. It may have been artificially enlarged and consists of three adjoining circular chambers connected to form an elongated cavity (Fig. 12.12b). They were termed Front (southwestern), middle and Back (northeastern) Galleries. The wall of the front and back galleries shows four big and five small solution hollows (niches), of diameters range from 5 to

50 cm. The ceilings are rounded off and in some places show dripstone stalactite and stalagmite deposits. The cavern is about 13 m in length, while its height varies from 1.5 m at the opening to 6 m in the back Gallery (Fig. 12.12c).

The Southern chamber attains 5.5 m, 4.5 m and 3.5 m in length, width and height, respectively. The middle chamber is 2.8 m in length and width and 2.4 m in height. The Northern chamber attains 3.5 m in length and width and 6 m in height. There are allogenic clastics in the floor of the eastern chamber, flow-stones in the floor of western chamber; rimestones and dripstones occur along the walls. Small stalagmites exist outside the cave. Two spleothem samples from Wadi Obeyed Cave were dated using U/Th dating to 45 ± 2 and 287 ± 67 kyr BP corresponding to flowstone and dripstone samples, respectively (Hamdan et al. 2014c).

The cave is very important for its wealth of rock art, displayed at various heights on the limestone walls. The lack of archaeological materials in the cave may, however, be due to its use as a ritual place. Paintings and engravings are located on two 'registers' (or levels) on the walls of the three rooms. Rock art in the Obeyed Cave is represented by carbonized negative human hand prints, depictions of animals (goats, giraffes), boats and lion paws; all are dated to middle Holocene occupation (Barich 2014).

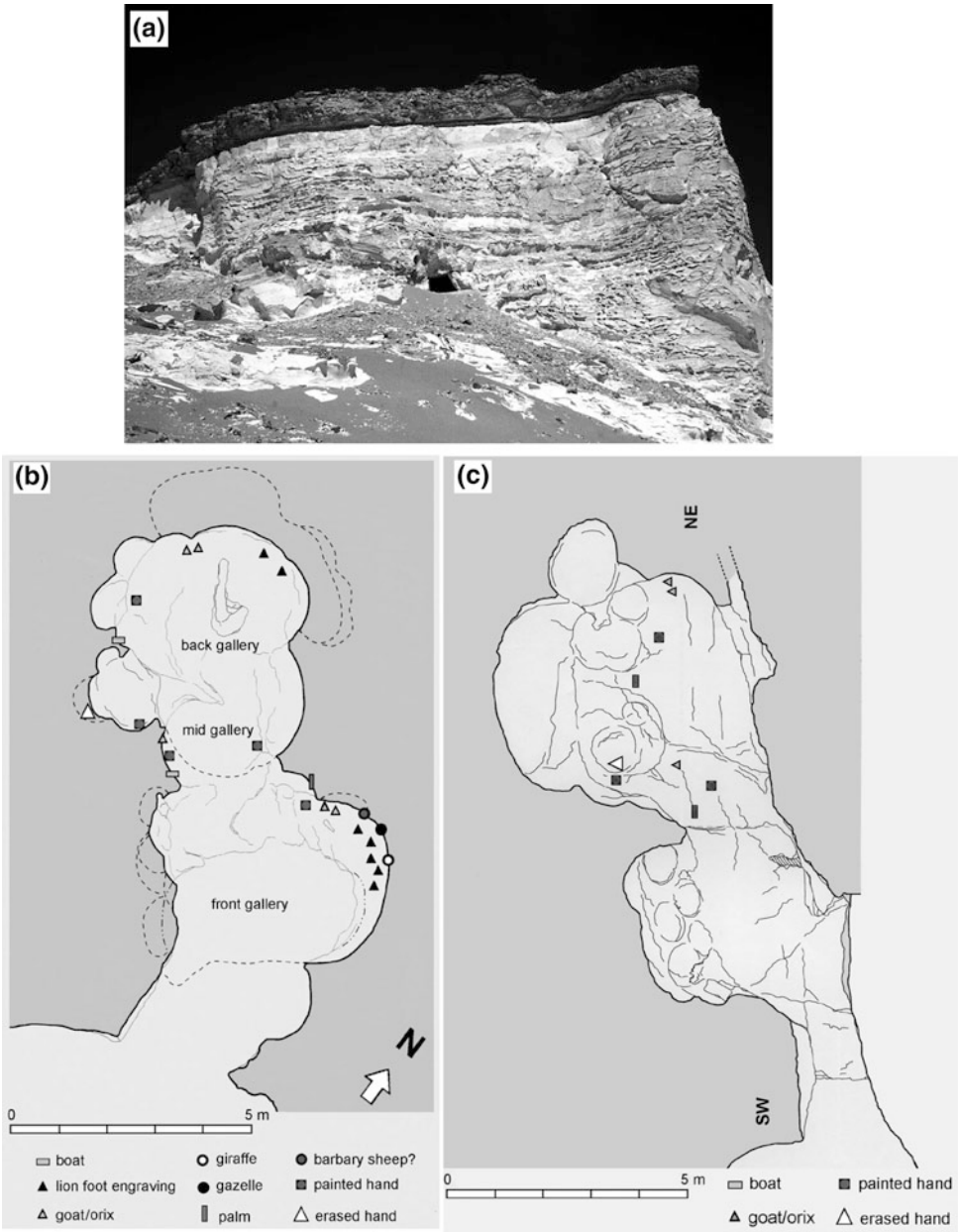

Fig. 12.12 **a** Farafra, Wadi Obeiyid. Cave 1, view of the cave which opens onto the southern slope of the Northern Plateau; **b** planimetry of the cave showing the three adjoining chambers which form the elongated cavity. Symbols indicate the position of rock art works; **b** planimetry of the cave showing the three adjoining chambers which form the elongated cavity. Symbols indicate the position of the rock art works; **c** cross-section of the cave along the NE-SW axis (*Source* Barich 2014)

Sodmein is a large but quite shallow cave standing at the base of a limestone cliff. It is developed within a system of microfaults on the Thebes Formation of Wadi Sodmein, 40 km NNW of the seaport of Quseir, Red Sea (Vermeersch et al. 1994). It was formed by both karstic and physical breakdown processes of the limestone bedrock (Moeyersons et al. 2002). Sodmein Cave has very important geologic and archaeological features. Geological importance of the cave is represented by ca. 4 m of stratified cave sediment dated to the late Quaternary. These sediments contain cryptotephra in two ca.50 cm layers at 25–30 cm and 150–155 cm (Barton et al. 2015). The upper cryptotephra is dated to late Pleistocene/early Holocene with a homogeneous calc-alkaline composition, most likely derived from central Anatolian volcanism. The lower cryptotephra has a dominant Na-rich trachyte component and dates to the late Pleistocene and an unknown volcanic eruption (Barton et al. 2015). Paleontologically, the cave sediments yield several organic units, containing herbivore dung, mammal (sometimes carnivore) coprolites and guano, items of great paleoecological importance during late Quaternary. Archaeologically, Sodmein Cave is one of the rare occupied in late Pleistocene sites in Northeast Africa. Its outstanding cave stratigraphy spans more than 4 m of stratified human occupation debris from the middle Paleolithic up to the Neolithic, with a stratigraphic hiatus between around 25 to 7.5 kyr BP (see Vermeersch 2008; Vermeersch et al. 1994, 1996, 2002). Moreover, the earliest domesticated sheep/goats in Egypt were found in Sodmein Cave and were dated to 7.5 cal kyr BP. The domesticated sheep/goats were diffused to the Western Desert immediately after their first arrival in the Sodmein Cave region during the constant movements of people between the Red Sea coast and the Western Desert.

(4) Collapsed caves of Sheikh Abdalla

Sheikh Abdalla is an oval depression in the Bahariya-Farafra Plateau and includes an extensive unroofed palaeocave system over a distance of 5 km, exposing an extensive network of galleries, separated by chalk walls and hills (Wanas et al. 2009). These ancient galleries contain vast quantities of speleothem and spelean breccias. There is a widespread, but discontinuous, horizon of dark grey epikarst breccia capping all the chalk hills and ridges in the area. The cave infilling at Sheikh Abdalla is represented by four facies of spelean deposition, (1) a coarse basal solution breccia comprising blocks of white chalk, limestone and some chert cemented by red terra rossa, (2) black carbonate-rich sediments and broken speleothem layers rich in organic matter or manganese, (3) laminated, red, fossiliferous sandstone breccias with thin layers of white to pink flowstone deposits and cave pearls, and (4) coarsely crystalline grey calcite speleothem, occasionally forming masses up to 4 m tall, 5 m wide and many meters long.

(5) Pseudokarsts

The term pseudokarst is used to describe a variety of non-dissolutional processes, forms and terrains similar to certain types of karst (Halliday (2007). Pseudokarst shares a considerable range of features, resources and values with karst; these commonly including caves and rock shelters. Unlike karst, integrated subsurface drainage may not be present in pseudokarst. Pseudokarst in rocks with calcareous cement, the major volume of rock not removed by solution but by wind deflation. According to Halliday (2007), the most important types of pseudokarst are rheogenic (developed in basalt flow), badland and piping (in soft clastic sediments), talus, crevice (sea caves), compaction and consequent pseudokarsts.

In Egypt, pseudokarst features are well developed along the exposed Nubian sandstone in southern Egypt, and are represented by columnar caves along the edges of vertical joints and sandstone towers (El-Gammal 2010). Most likely, these pseudokarst features are formed by wind erosion. In Gilf Kebir, pseudokarst features are represented by the Wadi Sura caves. These rock shelters are of special interest as potential analogues of cavernous features on Mars (e.g., El-Baz and Maxwell 1982) and yield important rock art pictures. These pseudokarst caves are formed by wind erosion along curved joints and mass wasting.

In the Eastern Desert, the Tree Shelter, near Quseir, is excavated in sandstone and most likely formed by undermining by fluvial action and mass wasting. It is one of the rare stratified sites (Marinova et al. 2008) which began around 8 cal kyr BP and continued until about 5 cal kyr BP. The archaeological finds show clear connections with the Nile Valley and the Western Desert during the African humid Period. The lower level (ca. 8.1–7.8 kyr BP) contained lithic tools of nomadic hunters. The higher level has numerous hearths (ca. 6.6–5 cal kyr BP) with animal and fish bones and Red Sea mollusks.

Another pseudokarst cave in the Eastern Desert named Wadi Bili Cave. The cave is cut into the calcareous sandstone plateau west of El Gouna (Vermeersch et al. 2005). It is situated at upstream of the northern bank of Wadi Bili gorge (27°23.154′ N and 32°33.451′ E). The cave measures about 20, 12, 3 m in width, depth and height, respectively. At the inner edge, the roof and floor join together i.e. by a curved roof. The cave floor is covered with fine sandstone debris and aeolian sand. The topographic plan assumes an elevation of the wadi floor in front of the cave of 95 m ASL. The frequently collapsed roof creates scree of large boulders

below the cave entrance. It seems that the cave was formed by water action of a fossil water-fall which eroded the horizontal sandstone layers easily and apparently also by salt wedging. Paleolithic remains are very rare. Only a single, possibly middle Paleolithic notched flake was found at depth of 80 cm near the cave entrance (Vermeersch et al. 2005).

In Moghra Depression (North Western Desert), a piping cave attains 250, 50, 10 m, in length, depth and height, respectively. It was excavated in soft sandstone and the ceiling remains being made of hard mudstone. It seems that the structure was formed by horizontal, graded grain-by grain removal of particles by channelized ground-waterflow and to a small extent by mass wasting. Crevice pseudokarst is well developed along the Mediterranean and Red Sea coasts. Bir Masoud in Alexandria is a good example of crevice pseudokarst formed by hydraulic wedging by waves and other forms of marine erosion. It forms tabular fractures extending hundreds of meters inland and these are readily traceable on the surface.

12.3.3.3 Tufa Deposits

The first scientific mention of the tufas of the Kharga Oasis region was made by Zittel (1883). Ball (1900) was the first to describe the tufas as Pleistocene in age and Beadnell (1909) originally recognized the tufas as fossil-spring deposits. The first systematic work on these deposits was carried out by Caton-Thompson (1952). Tufa is freshwater terrestrial carbonate rocks were deposited at positions along alkaline springs, seeps and streams, particularly at rapids and waterfalls (Nicoll et al. 1999). Tufas are derived from the dissolution and re-precipitation of calcium carbonate rocks. They were deposited from supersaturated water as it degassed CO_2 via turbulence and/or biogenic mediation of microbes and plants (Nicoll and Sallam 2017). There are different facies in spring tufas ranging from stepped, cascading waterfalls separated by small pools, to possibly ephemerally flowing small wadis, to marshy floodplains, to occasionally slightly larger lakes (Smith et al. 2004). Tufas always unconformably overlay older bedrock limestone in the Western Desert (Sultan et al. 1997) or Precambrian rocks in the Eastern Desert and Sinai (Hamdan and Brook 2015).

Tufas of the Western Desert are concentrated principally along escarpments and depressions of the Sinn el-Kaddab plateau at Kharga-Dakhla in the north to Kurkur-Dungle in the south. Tufas are absent north and south of these areas; however, a remnant of early Holocene tufas has been recorded at Gebel Uweinat (Marinova et al. 2014). Geologic setting play an important role in the formation of the tufas, where the thickness of the Nubian Sandstone Aquifer in tufa areas extends below 1000 m, while a deep fault system may allow water to rapidly reach the surface (Abotalib et al. 2016). Two types of tufa units have been recorded in the Western Desert, plateau and wadi tufas (Caton-Thompson 1952; Sultan et al. 1997; Smith et al. 2006).

Plateau tufa is the oldest and the topographically highest of the tufas, is typically heavily wind-fluted with a steel blue to black patina and densely recrystallized outer surface. Fresh surfaces of the tufa are white to buff, often resembling limestone. The plateau Tufa was formed by shallow sheets of lime-charged water flowing in undefined channels. It lack of primary structure is a result of diagenesis; however, a few reed casts often exist indicating an arcuate barrage dam (Smith 2004). The date of the plateau tufas is >400 kyr BP (Smith 2006) or >450 kyr BP (Sultan et al. 1997). Crombie et al. (1997) gave dates for the plateau tufas of Kurkur as about 300-450 kyr BP. No absolute dating is available for Dungle plateau tufas but Caton-Thompson (1952) suggested that the plateau tufa may all be Plio-Pleistocene in age.

Wadi Tufa occurs along the escarpment of the Sinn el Kaddab plateau and could be sub-divided into discrete sub-units but which may not be temporally correlated amongst localities (Smith 2004). It generally attains a thickness of 1–2 m and is represented by inclined sheets that follow the old slope of the escarpment or as a thick horizontal strata similar to Plateau Tufa. The color of weathered surfaces of Wadi tufas, range from black to brown to blue-gray; fresh surfaces are generally white to light tan. Much of the tufa is highly porous, with porosity principally resulting from the decay of incorporated plant material (e.g., Crombie et al. 1997; Nicoll et al. 1999). In Kharga Depression, Wadi tufas are subdivided into three units: Wadi Tufas 1, 2, and 3 (oldest to youngest), based on topographic and textural criteria (Smith et al. 2004, 2006). Younger tufa units may either overlie or be incised into older tufa units. Preservation of structure within the Wadi Tufa is usually excellent. Several facies within the Wadi Tufa were recorded, (1) a laminated to thinly bedded clastic tufa, with well preserved fragments of plant stem or leaf casts, (2) cascaded tufa barrage dams, as a combination of organically mediated deposits and flowstone-like, inorganically-precipitated deposits, (3) un-cemented oncoids (2–4 cm in diameter), ranging from roughly spherical to elongate in shape, which accumulated upstream of the dam and (4) inclined escarpment-veneer tufa, precipitated from the waters of springs that emerged relatively high up on the escarpment or from the base of the Thebes Group chalks. In Kharga, Wadi tufas contain middle Stone Age artifacts within a thin (50 cm) silt lens (Caton-Thompson 1952); an isolated, probable Acheulean implement, was found on the surface of an adjacent ridge (Smith et al. 2004). They exhibit dates of 260–219 and 160 kyr BP in Kurkur Oasis (Crombie et al. 1997) with only one more recent date for wadi tufas of Dungle, 22.900 ± 600 BP. In Dakhla they are dated to 220 ± 20, 125 ± 16 and 40 ± 10 kyr BP (Churcher et al. 1999). U/Th dates published for wadi tufas of Kharga as 272,

255, 190-175 and 45 kyr BP (Sultan et al. 1997; Hamdan 2003b). At Matana, east Kharga, two ESR dates on freshwater gastropods yield dates 65.1 ± 4.1 and 27.7 ± 1.9 kyr BP (Blackwell et al. 2012).

Hamdan and Brook (2015) studied the petrography, isotope geochemistry and AMS radiocarbon ages of eight tufas in the Eastern Desert and three tufas in Sinai. The tufas unconformably overly Precambrian basic igneous rocks (basalt, diabase and gabbros).

The ^{14}C ages of carbonate and organic residue in tufas from the Eastern Desert and Sinai suggest three phases of deposition associated with increased rainfall:

~62,000–56,000 cal yr BP; ~31,234–22,474 cal yr BP and ~12,058–6678 cal yr BP. Late Pleistocene tufas (mean $\delta\ ^{18}O$ = 7.74‰ and 7.66‰ VPDB) were deposited by spring waters initially similar in $\delta^{18}O$ to the Sinai Pleistocene ground waters (mean = 8.06‰; maximum = 6.53‰ VSMOW; Abouelmagd et al. 2012, 2014). Pleistocene tufas imply a temperature at deposition of 14.3–21.1 °C for the Sinai tufas and 14.0–20.8 °C for the Eastern Desert tufas (Hamdan and Brook 2015). The Holocene tufas (mean $\delta^{18}O$ = 6.59‰ and 6.63‰ VPDB) were deposited by spring waters initially similar in $\delta^{18}O$ to the Sinai Holocene ground waters (mean = 5.36‰; maximum to 4.84‰ VSMOW; Abouelmagd et al. 2012) and implies a deposition temperature of 21.22 ± 23.7 °C for the Sinai tufas and 21.41 ± 23.89° for the Eastern Desert tufas.

12.3.4 Quaternary Marine Sediments

The Quaternary witnessed a series of low and high sea level fluctuations corresponding to glacial/interglacial climatic cycles, respectively. Marine sediments related to these cycles are represented by raised coral reefs in the Red Sea coast, calcareous coast ridges along the Mediterranean coastal and placer deposits (black sands) on the northern coast of Nile Delta.

12.3.4.1 Quaternary Coral Reefs

The Pleistocene Red Sea reefs were among the first worldwide references concerning raised reefs (Sandford and Arkell 1939). The very limited uplift of the Egyptian coastal plain (at least during late Pleistocene) suggests that the respective altitudes of the late Quaternary marine terraces indicate their respective derived sea-level altitudes. From at least earliest Pleistocene times, the Egyptian coast of the Red Sea has been characterized by the development of fringing and barrier reefs. Owing to glacial-interglacial cycles, the Red Sea appears to have favored reef development during every interglacial high stand of sea-level. The Pleistocene sequences show at least five reefal units above the present sea level (Plaziat et al. 1990). The earlier, undated Pleistocene fringing reefs have been raised moderately, up to 50 m ASL (Plaziat et al. 1990), middle Pleistocene (>290–300 kyr BP) is found at +10 to +15 m ASL. A 200 kyr BP high-sea stand is recorded by a relic terrace at +17 m ASL. The late Pleistocene system (125–138 kyr BP) is very well represented with terraces at about +6 to +8 m ASL. The latest Pleistocene reef terrace (60 kyr BP) has remained near its original altitude (averaging 4 m ASL; Plaziat et al. 1990). The sedimentary facies are similar in modern and Pleistocene reefs, with silciclastic beach facies at the base and carbonate reefal facies at the top (Mansour and Madkour 2015). Reef sequences exhibit different degrees of diagenetic alteration which are reflected by a gradual change of skeletal particles and early-formed cement from aragonite and high Mg-calcite to low Mg-calcite.

12.3.4.2 Mediterranean Coastal Ridges

Quaternary deposits in northern Egypt are represented by elevated offshore bars, lagoonal beds, evaporites and marls (Butzer 1960; Said 1990). The Mediterranean coastal plain west of Alexandria, is characterized by the presence of a number of elongated ridges, also called Kurkar ridges, which run parallel to the coast, separated by longitudinal depressions. The lower three ridges to the shore, the 10, 25, 5 m high ridges (named the coastal, Abu Sir and Maryut bars) can be traced for long distance along the coast. The succeeding ridges, the 60, 80, 90 and 110 m high ridges (Khashm el Eish, Alam el Khadem, Miheirta, Raqaet el Halif and Alam Shaltut), are less conspicuous and do not form continuous ridges (Said 1990).

The ridges are composed of oolitic limestone (Shukri and Philip 1956; Butzer 1960), and they seem to represent successive fossil off shore bars that were formed in the receding Mediterranean during the Pleistocene. However, some literatures interpret these ridges as aeolinite deposits (Butzer 1960; El-Asmar 1994). The depressions between the ridges contain lagoonal deposits, such as evaporites and marls. Three calcareous oolitic ridges with two intervening lagoonal depressions have been recognized in the coastal plain in the Salum area (Selim 1974). They range in age from late Monasterian to Tyrrhenian. The ooids in the oldest (Tyrrhenian) ridges have developed micritic envelopes and are probably recycled detrital grains. The younger deposits (late Monasterian and main Monasterian) have a well-developed oolitic texture and were probably deposited in shallow, agitated marine waters. Oolites dominate the deposits of the first and second ridges, whereas bio-clastics with abundant coralline algae, benthonic foraminifera, mollusks, echinoderms and intra-clasts prevail in the deposits of the third and fourth ridges (Wali et al. 1994). Diagenetic alterations and cementation are concentrated below exposure surfaces (pedogenic calcrete horizons). Wali et al. (1994) believe that the ridges were initiated by the accumulation of

carbonate ooids as marine bars and then lithofied by early diagenetic processes under marine subaqueous conditions. Modification by aeolian processes followed after a phase of sub-aerial exposure and marine regression.

The lack of reliable absolute dating of the Mediterranean coastal ridges makes them of poor scientific importance for global sea level and climatic variation. However, a few absolute dates, using U/Th, OSL and ESR, have been published (El-Asmar 1994; El-Asmar and Wood 2000). The coastal ridge yield OSL dates of 0.6 ± 0.1 and 1.5 ± 0.2 cal kyr BP and ^{14}C dates of 3680 ± 40, 4100 ± 120 and 4355 ± 40 cal BP from top to bottom (El-Asmar and Wood 2000). The oolitic limestone of El-Max-Abu Sir (second ridge) yield U/Th ages of 90 ± 15 kyr BP, 110 ± 5 kyr BP and an OSLage of 104 ± 17 kyr BP. One *Helix* sp. sample collected from the paleosols at the northern flank of the second ridge yielded an OSL date of 67 ± 31 kyr BP. Three samples of the aeolinite of the third ridge gave OSL ages of 191 ± 42, 416 ± 255 and 454 ± 151 kyr BP (El-Asmar 1994). Four samples were studied from the marine beds of the third ridge gave ages of 423 ± 153, 546 ± 352 and 208 ± 59 kyr BP, respectively. One ESR determination on the *Cardium* limestone gave an age of 292 ± 48 kyr BP. The paleosols (Pink limestone) at the top of the Khashm El-Ish (fourth) ridge show a wide range of ages, giving age estimates between 360 ± 140 and 584 ± 317 kyr BP indicating a middle Pleistocene age.

12.3.4.3 Placer Deposits (Black Sands)

Egyptian black sands are beach placers deposited from the Nile stream during flood seasons reaching the Mediterranean Sea at the river mouth. They are heavy, glossy, partly magnetic mixtures of usually fine sand (El-Kammar et al. 2011). The River Nile transports heavy minerals from two sources, mainly from eastern and Equatorial Africa- in the south to the Mediterranean Sea in the North (Shukri 1950). The mineral composition of the Egyptian black sands is represented by six main minerals accompanied by minor minerals. According to their relative frequencies and economic importance, the six main minerals are: ilmenite, magnetite, zircon, monazite, garnet and rutile. Traces of cassiterite and gold as well as some rare earth elements (El-Kammar et al. 2011) in some minerals are also present. Elemental concentrations in Egyptian black sands show an average concentration of natural radionuclides (U and Th) higher than the average world level. However, exposure to natural radionuclides (U and Th) is still within the acceptable limits due to low exposure. However,, the black sands from north of Nile Delta are not recommended for use in building constructions due to the potenmtial for high radioactive doses. Kaiser et al. (2014) used high-resolution airborne gamma ray spectrometry to estimate radioactive elements spatial abundance along the Rosetta coastal zone area. They noticed that both Uranium and Thorium are concentrated in the black sand deposits along the beach. In addition, the areas with the highest concentrations of Uranium and Thorium show the highest level of radiogenic heat production.

Egyptian black sand deposits also occur along the Egyptian northern Mediterranean coast from Rosetta to Rafah. Their contents vary from place to place but beach area of Rosetta contains most of the economic heavy mineral reserves of black sand in Egypt owing to their great extension and high grade (Dabbour 1995). Rosetta black sands contain about 3% of some important economic minerals. The ore shows lateral variations with high concentrations in the West; these decrease gradually to the East. Heavy concentrations of black sands are deposited in a thin mantle near and parallel to the shoreline and thay also existed as naturally formed concentrated lenses. The thickness of the deposited layer range from 0.5 m to more than 40 m (Naim et al. 1993).

The formation of black sand facies comprises several steps: (1) deposition of fluvial Nile sediments rich in heavy minerals along the shore of the Mediterranean-during periods of high interglacial high sea level, (2) sorting of the sediments under the effect of waves and waves induced longshore currents, where the heavier and more stable minerals (opaque, garnet, zircon, tourmaline, rutile and monazite) are concentrated in the surf zone and the lighter and less stable minerals (hornblende, augite and epidote) are transported offshore, (3) during last glacial maximum (LGM) when sea level dropped abruptly and the delta sediments were exposed, wind action led to the formation of coastal dunes. Wind deflation also concentrated heavy minerals in the deflated sediments and in the newly formed coastal dunes. Therefore, the Egyptian black sands are now present either as beach sands or coastal sand dunes. The coastal sand dunes of El Burullus-Baltim area contain economic mineral reserves. These sand dunes extend for about 16 km and have an average with of 700 m. Using the individual mineralogical composition data of the evaluated four zones of this sand dune area, the calculated average economic mineral grade equals 4.87%. The estimated average total economic minerals content is 4.66% and this is distributed as follows: different ilmenite varieties, 3.41%; magnetite, 0.27%; garnet, 0.52%; zircon, 0.31%; rutile, 0.14% and monazite, 0.01% (Moustafa 2007).

El Kammar et al. (2011) compared heavy minerals in source areas (Shukri 1950s samples housed in the geology Museum, Cairo University) and those of black sand from the Rosetta area. They found several changes in morphology and composition of the heavy minerals during the long transportation. Brittle and meta-stable minerals (e.g., barite and pyrite and mica) are entirely lost and never reached to the Nile Delta. Abrasion polishes the surface of the heavy minerals and dissolution of these minerals takes place along

cleavage planes. Grains consisting of polycrystalline mineral clusters such as zircon from the White Nile and titano-magnetite from Atbara usually disintegrate into individual crystals during long transportation. The ultra-stable minerals as zircon and monazite experienced changes in their composition. Heterogeneity in zircon covers all aspects including; color, morphology, size, elongation index, radioactivity and composition. However, radioactivity discriminates the uraniferous zircon of the White Nile from the non-radioactive variety from the Ethiopian province.

12.4 Quaternary Sediments and Landforms Related to Arid Climate

12.4.1 Aeolian Deposits

Aeolian sands occupy a significant position in the geologic history of Egypt in general and in the Quaternary in particular. Generally, aeolian deposits cover about 160,000 km^2 of the Egyptian land representing about 16% of the total surface area of the country. Based on the total area of the dune coverage, the aeolian deposits are represented by six sand seas with >50% sand cover and total area >5000 km^2 (e.g. Great Sand Sea, Abu Moharik, North Sinai) and 10 dune fields with dune coverage less than 50% (e.g. West Delta, South Rayan, Embabi 2017).

The Great Sand Sea attains an area of more than 100 000 km^2 (Besler 2008). It is situated in westernmost Egypt, where its northwestern edge extends across the border into Libya. The sand sea does not lie in a distinct depression, but covers weakly sculptured ground sloping from more than 500 m ASL, in the south to less than 100 m ASL, near Siwa Depression in the north. The dunes of Great Sand Sea are represented by three dune types; linear, transverse and star. Linear dunes are the most common and are represented by two forms; sharp-crested recent linear "seif" ridges (Silk; Besler 2008) and the broad-crested dunes (whalebacks; Bagnold 1931, 1933 or Dra'a Besler 2008). Currently, the former is active while the latter are stabilized. The whalebacks had been active dunes from the end of the middle Paleolithic pluvial to the beginning of the African Humid Period at ca. 10 cal kyr BP (Haynes 1982). They stabilized by combined action of bioturbation, human occupation, pedogenesis, and slope wash vegetation under a semiarid climate from 10 to 6.5 cal kyr BP. The transverse dune type is represented by barchans and barchanoids and is found below the recent still active dunes in the northern part of the Great Sand Sea.

At 800 km long and 50 km width, Ghard Abu Moharik is most outstanding linear sand dune belt in the Western Desert of Egypt, with various dune density and dune types. Only recently, Ghard Abu Moharik was ranked as sand sea (Embabi 2017). The northern and middle parts comprise mainly linear dunes, whereas the southern section in Kharga Depression contains mostly barchans (Hamdan et al. 2016b). From south of Qattara to the Bahariya Depressions, it composed of isolated small-to-large linear dunes consisting of two dune chains: (1) a western chain represented by Ghard Williams and Ghard Ghorabi, at 32 and 71 km long, respectively and heights 30–45 m, and (2) an eastern group of relatively small dunes, called "Abu Moharik Dunes" (Embabi 2017), with lengths 1.5–8.5 km, and heights 5–16 m. In north Kharga plateau, the Ghard predominate with high-density linear dunes in one main chain with a secondary discontinuous belt to the east. The main chain also contains barchans and barchanoid belts, as well as mega-ripples. Inter-dune areas are occupied by transverse dunes, sometimes barchanoid, appearing as sand giant waves. The southern part (Kharga Depression to Egyptian Sudanese border) is characterized by low dune density and the predominance of barchan and barchanoid chains as well as sand sheets. Based on a ratio of the length/width ratio, most of the barchans in the southern part of Ghard Abu Moharik are fat (54%) or pudgy (24%) with length/width ratios of ≥ 1 and 0.75, respectively (Hamdan et al. 2016b).

An extensive dune field extends for about 185 km from the southern part of Wadi El-Rayan to the latitude of the city of Dairut in the Nile floodplain. It seems that the pre-dune topography of the southern part of Wadi El-Rayan controlled the development of this dune field into linear dunes in the northern part, then into barchans on the plateau surface in the southern part (Embabi 2017). Said (1981) named this stretch of aeolian sand dune remains as El Khafoug Formation; inter-fingering with both the Pre-Nile deposits of the middle Pleistocene and the Neo-Nile sediments of the late Pleistocene sediments. The Landsat ETM images and aerial photography both show that the barchan sand dunes are present in the western part of this dune belt extending over a rugged area with a relatively higher relief than the area covered by longitudinal sand dunes (El-Gammal and El-Gammal 2010). Longitudinal sand dunes are located in the eastern part of the dune field covering and surrounded by low land. These dunes are striking in a NW–SE direction (parallel to the prevailing NE wind) and are often composed of barchan dunes. The eastern horns of the barchan dunes are longer than their western ones. Sometimes these horns are coalescing with each other to constitute longitudinal sand dunes (El-Gammal and El-Gammal 2010).

The North Sinai landscape is dominated by the most complex dune system among Egyptian dunes (ca. 13,600 km^2). They are composed of ancient vegetated fixed dunes, overtopped by recent active dunes (see Misak and Attia 1983). Inland, the former are represented by less vegetated fixed dunes and coastal fixed dunes sank in the water of Bardawil lagoon and coastal sabkhas formed during LGM low sea level and were fixed during early Holocene

humid phase. Active dunes are represented by linear, crescent, and transverse dunes. Sand and dune movement represents a major hazard to development projects in the region of Sinai.

In northeast Cairo, the Khanka sand dune belt cover ca. 20% of the area, with numerous linear, transverse and star dunes, reflecting variable wind directions, e.g. NW, W, NE and S (Misak and Draz 1997). Linear and transverse dunes dominate the western and north-western fringes of the dune system. The longitudinal dunes range from 200 to 2000 m long and up to 150 m in width. Aerial photos (1955 and 1977) show annual rate of dune movement of ca. 30 m in the NE. The present annual rate of dune migration is relatively low due to intensive agricultural activities (Misak and Draz 1997).

Coastal dunes spread along the plains of the northern Mediterranean coast. The largest area covered by dunes with highest density extends from El-Borg to Gamasa. Dune types in this field vary between simple barchans with horns pointing southward, most notably in the Mid-Delta sector, to complex and deformed barchans and to small linear dunes. Maximum height is about 20 m in the vicinity of Rosetta and to the east of El-Borg but the most common height is 2–3 m (Embabi 2017).

There are two generations of coastal dunes, stabilized and active dune. Stabilized dunes are characterized by low elevation (4–7 m ASL), and conspicuous cross stratification and dense vegetation cover. They are also characterized by their relatively higher content of fine grain constituents (silt and clay). Optical Simulating Luminescence (OSL) dating for the stabilized dunes yield 2.6 ± 0.6–1.9 ± 0.4 cal Kyr BP (El-Asmar 2000). Remains of former Islamic settlements are found on these ancient dunes at Kom Mastero and El-Borg (Embabi 2017). Active dunes are higher and sharper than the ancient stabilized ones. They are represented by two dune types; longitudinal and barchans. The former are elongate in shape, more or less straight with continuous serratic crest without breaks with two steep sides 1–1.5 km long and 15–30 m height. Barchan dunes occur in two patterns, isolated and complex. Both have axes nearly normal to the wind regime of WNW and NW directions and reach 30 m in height and 50–300 m in length. Inter-dune areas in these recent dunes appear as innumerable small depressions with flat floors, some of which are occupied by temporary or permanent ponds. The ponds are fed by rainwater stored in dune sands that percolates into the inter-dune areas. Most of the area covered by coastal dunes has undergone reclamation since at laest Pharaonic times for a variety of purposes. However, the dunes are now gradually disappearing due to cultivation and urbanization (Embabi 2017).

The first attempt to estimate the rate of movement of Egyptian desert dunes was done by Cornish (1900), who measured a rate of 4.5 m/year for dune crests east of the Nile Delta. Many areas in the Western Desert were the subject of evaluation of sand dune movements by different authors (e.g., Ashri 1973; El-Gammal and Cherif 2006; Hamdan et al. 2016b); they assigned diverse dune rates ranging from 0.5 m/year to as high as 100 m/year. More recently, the mean movement of barchan dunes in the Toshka area varied from about 4 to 7.67 m/year, averaging 6 m/year along a SSW direction (Hamdan et al. 2016b).

The source of aeolian sand in Egypt is explained by three main hypotheses. The aeolian sands have been derived from arenaceous formations (i.e. Moghra Formation) in northern Egypt (Beadnell 1910; Ball 1927) and Nubian sandstone in the south (e.g. El-Baz 1988; El-Baz and Wolfe 1982). Several arguments face the latter source because in Nubian sand exposed in southern Egypt most dunes migrate in a north-to-south direction parallel to the prevailing winds. Said (1998) believed that dune fields of the Egyptian Western Deserts started to accumulate during the last glacial period when northern Africa was arid and the sea-level lower by at least 120 m. The exposed continental shelf which probably extended into the Mediterranean Sea at places for more than 40 km made a ready source for all the sand needed to build the huge dunes of the eastern Sahara. Recent studies, using textural, mineralogical and geochemical proxies (e.g. Hamdan et al. 2015) indicated that the formation of aeolian dunes was a complex multicasual process formed in several alluvial, lacustrine and aeolian environments throughout the Tertiary-Quaternary. The sands were reworked from arenaceous bedrock formations by alluvial processes extending from a south to north direction through radar rivers and inverted wadis (see above), before they were distributed by wind action during arid periods in the early-late Pleistocene and by alluvial and lacustrine processes during the middle Pleistocene and early Holocene. Indeed, aeolian dune sand of Egypt were formed in three cycles (Hamdan et al. 2015; Embabi 2017, with references therein). The first cycle (700–300 kyr BP) occurred during the arid phase of the middle Pleistocene, where Acheulean artifacts at the surfaces of inter-dune areas indicated that the dunes are older than Acheulean time (Haynes 1982). The second cycle (35–10 kyr BP), is without evidence of human occupation (Wendorf et al. 1993) and is characterized by the formation of whaleback dunes in different parts of the Western Desert in different wind regimes during the late Pleistocene glacial period where the winds were strong enough for dra'a formation (Besler 2008). The third and last cycle of dune development of the Great Sand Sea extended from the middle Holocene to the present time.

12.4.2 Wind Erosive Landforms (Yardangs)

In the Western Desert, large-scale aeolian erosional features include: (1) pits and hollows (blowouts), formed by deflation or removal of loose particles, (2) wind gaps, or wind-eroded notches in ridges, (3) wind-sculptured hills such as yardangs.

Yardangs (a Turkmenistan word for an inverted boat) are well developed on the surface of playa sediments due to the intensive hyperaridity that predominate allover Egypt during the late Holocene (Hamdan 2014b). These streamlined erosional ridges have long been known, not only in the Western Desert of Egypt, but also in most of the major deserts of the world (Embabi 2017) where they typically occur in large fields. Synonymy of yardangs in early studies Kharga Depression included "mud lions" or "sitting sphinxes" or simply hummocks (Beadnell 1909). Morphometric studies show that they averaged 2.5 ± 1.3 m in height, 16.9 ± 12.4 m in length, and 4.8 ± 1 m in width. There is no significant correlation ($R = -0.41$) between width and height but the length to width ratio is about 3:1 (Hamdan 1987, 2014a). These positive relationships between length/width indicate that yardangs pass through a cycle of development, whereby their size becomes smaller by time (Embabi 2017). The shape of playa yardangs is as asymmetric streamline or linear with a steep windward face and a gentle lee slope. Irregular or dome-like shapes are common in some fields of playa yardangs in Farafra Depression (Hamdan 2014a). Linear shapes are found in environments with a unidirectional wind regime such as in Kharga and Dakhla (Hamdan 1987). The windward face of many large yardangs is very steep and very rarely, some linear yardangs might acquire certain shapes like the sphinx.. The leeward ends of many yardangs are tapered and are lower in general than the windward side.

The formation of yardangs is apparently a stage in the denudation of playa deposits and may in fact explain the reduction of a playa surface through time. Hamdan (2014a), related the formation of the yardang to an interaction between internal (lithology, sedimentary structures and joints and fractures) and external factors (uni-directional winds, flow system around the yardangs and water action). These factors vary in different areas which in turn produce different yardang shapes. An evolutionary model of different yardang types in Farafra Depression (Hamdan 2014a) where after the main episode of playa formation, it is likely that the playa undergoa sequence of erosional events. The development of yardangs requires strong wind (highly charged with sand) and selective incision of the substrate in order to isolate positive forms between erosional grooves which become troughs, then corridors, as they deepen and widen (Fig. 12.13). Incision progressively focuses air flow, which exploitslithological/structural weaknesses to erode transversely and attack an upwind facing prow. The early development of yardangs produes irregular shapes as well as ambiguous axial trends inherited from relict fluvial dissection or giant desiccation cracks. During subsequent stages, wind blowing parallel to the irregular shaped yardangs, deepen grooves between them by deflation resulting linear ridges. Simultaneously, the ridges are streamlined, primarily by wind abrasion. The winds also rise above the ridges and subsequently descend forming eddies in a leeward direction. This process often creates depressions on the top of the ridges as well as abrading the top in a downwind direction. Deeping of the depressions at the top of the ridges leads to dissection into smaller flat topped yardangs with different shapes (Fig. 12.13). Flat topped domal yardangs are formed in the centre of the playa basin where the lithology is dominated by thick massive playa silt. Continuous wind erosion of the homogenous playa lithology leads to the formation of curved-top yardangs. A perfect domal yardang shape indicates that the erosion proceeded simultaneously on all surfaces by fine particles abrasion and vortices within a complex system of subsidiary air flow. Due to geologic structures, such as joints and calcified root casts, asymmetric domal yardangs are also formed. When wind approaches asymmetric domal yardangs, eddies are generated, with accelerates velocities along flanks of the yardangs. The wind eddies scour the sides of the yardang facing the wind. Since eddies are formed close to the ground surface and to height of ca. 1 m, erosion preceded much faster near the ground. This leads to lowering of the ground around the yardangs and exposes softer playa sand to further wind erosion (Fig. 12.13). As erosion proceeds, the upper hard playa silt becomes overhanging as a result of undermining of the lower softer layer and the yardang changes to a conical shape. At the edge of the playa basin, asymmetric domal yardangs are changed to a sphinx shapeby unidirectional wind and the effects of thin hard massive playa silt.

In a final stage, the yardangs lose their streamline shape and mushroomand cylindrical shapes are developed. Some yardangs may then split into several collapsed blocks while others are separated completely from their base and lean over or a reduced to form small pedestals (stack yardang) as the only indictor of a former yardang. All such remnants are eroded by time and flat surface is formed with residual and coarse sand often with abundant lithic artifacts.

Other yardangs occur on bedrock surfaces in the Dakhla and Kharga plateau and are also known as Kharafish (Brookes 1993). Bedrock yardangs develop in Tertiary limestone that does not contain a large content of chert. The ridges attain few hundred meters wide and few kilometers long and the furrows are shallow and broad. The floor of the furrows is occupied by late Holocene playa sediments associated with an indigenous late Neolithic-Old Kingdom archaeological culture (Sheikh Muftah), at the top of the plateau in front of Dakhla Oasis.

12.4.3 Evaporite Deposits

Arid climatic conditions prevailed in Egypt during the Quaternary as represented by thick evaporite deposits in the Qattara Depression, continental sabkhas in south western

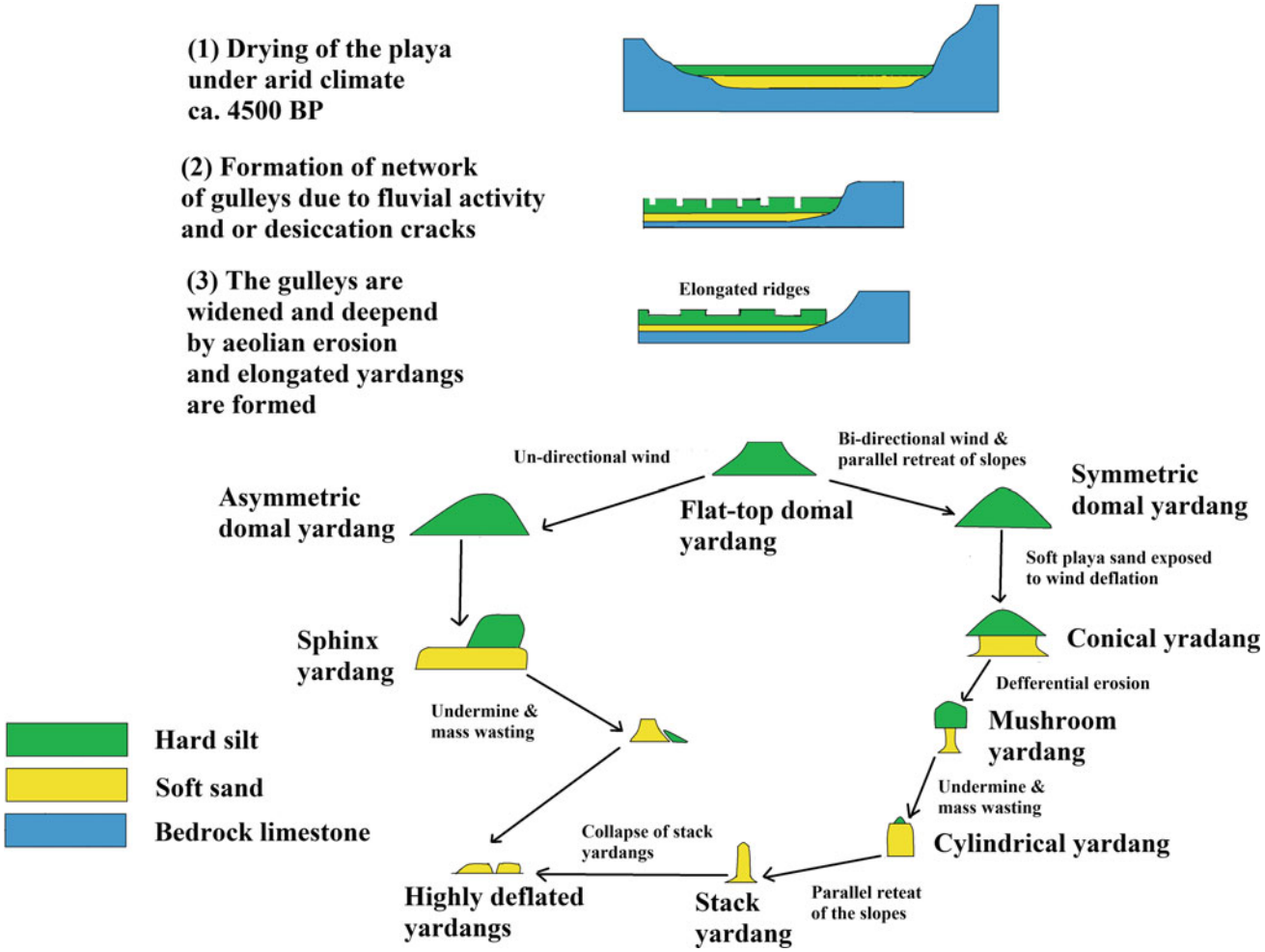

Fig. 12.13 An evolutionary model of yardang formation in the of Farafra Depression (*Source* Hamdan 2014a)

Desert and by hypersaline lakes in Wadi Natrun (El-Bassyony 1995; Attia and Hussein 2015; Taher and Abdel-Motelib 2015). The evaporite sediments of the Qattara Depression are represented by three types (Aref et al. 2002, Aref and Hamdan 2003). Type 1 evaporite sediments are the oldest and represent the earliest record of Quaternary aridity in the depression. They are present as random, isolated or dense, evaporite nodules within the top part of the Moghra clastics and form a dense crust capping a mesa-like plateau (called a salt plateau Ball 1933) at 100 m BSL. Type 2 evaporite sediments are comprise a dry, indurate rough sabkha surface that extends for hundreds of meters around type 1 terraces. It represents a previous stage of groundwater lowering since the sabkha surface has no connection with the present groundwater table. It consists of gypsum/anhydrite or halite crusts, 7–20 cm thick that forms a tepee polygonal structure with margins warped upwards to about 50 cm in height (Aref and Hamdan 2003). Type 3 evaporite sediment is recorded at levels lower than types 1 and 2 sediments, as wet, rough sabkha surface that also extends for hundreds of meters. It represents the last stage of a lowering groundwater table.

Salt weathering was one of the agents responsible for excavation of the Qattara Depression (Aref et al. 2002). Crystallization of halite and/or gypsum generates increased pressure that leads to mechanical disintegration of the bedrock into fine-grained debris. Features related to disintegration include blistering of the rock surface, splitting, spalling and/or granular disintegration. Salt weathering provides fine-grained debris that is easily removed by deflation, which accounts for the topographically lower level of the western part of the depression (134 m below sea level). The disintegration by salt weathering has been in effect since the onset of aridity in northern Egypt in Quaternary time. Howver, initial excavation of the depression started in late Miocene or Pliocene time by fluvial erosion, karstic processes, and mass-wasting and by wind deflation (Aref et al. 2002).

Quaternary continental sabkhas are existed also in Bir El Shab area, south Western Desert, where four sabkha units are recorded (Attia and Hussein 2015). Sabkha 1 consists of sand

and silt with an alum salt crust. Sabkha 2 includes wet silt and sands at its base and an alum and gypsum crust at the top. Sabkha 3 is composed of mudstone intercalated with ferruginous laminae and capped with alum and gypsum crusts associated with black crenulated microbial laminae. Sabkha 4 includes a gypsum crust which usually displays a polygonal fracture and tepee structure. Mineralogically, Bir El-Shab salt complex includes gypsum, natroalunite, tamarugite, nitratine and halite. These minerals indicate evaporation of non-alkaline water (Attia and Hussein 2015). No absolute dating is given to these sabkhas but their geomorphic and stratigraphic settings most likely refer to the Quaternary age.

In Wadi El Natrun, there are seven large alkaline, hypersaline lakes in addition to numerous small ephemeral pools (Taher and Abdel-Motelib 2015). Lake waters have extremely high salt concentrations of 91.0–393.9 g/l, and pH values of 8.5–11 (Taher 1999). Most lakes reach maximum levels in winter between December and March, with lowest levels in summer. Their depths range between 0.5 and 2 m, regulated by seasonal changes in influx seepage and evaporation (Mesbah et al. 2007). The mineral composition is represented by three main types of sodium salt; chlorides, carbonates and sulphates. Sodium chloride (halite, Na Cl), is the most abundant mineral present within these lakes (Shortland 2004). Halite occurs as a crust or found within the layer structure of the mineralogical deposits. Although Wadi Natrun is named after the mineral natron ($Na_2CO_3.10H_2O$), natrun is scarce in the mineralogical record but trona ($NaHCO_3.Na_2CO_3.2H_2O$) is the most common carbonate. Nahcolite ($NaHCO_3$) is also occasionally found within Lake Ruzunia (Attia et al. 1970). Sodium sulphates mineral is also represented by the double crystal salt, burkeite ($Na_2CO_3.2Na_2SO_4$).

The origin of the lakes water remains unclear. Pavlov (1962) suggested a radial inflow of underground waters towards the lakes. Underground flow from the Rosetta branch of the Nile could be another source (Shata and El-Fayoumi 1967; Attia et al. 1970). Chemical and isotopic data of the lake waters hower suggests the source is rainwater that occasionally infiltrates from the shallow alluvial and Eocene limestone aquifers (Sturchio et al. 1998). The Wadi Natrun has been identified as a potential source of both natron and salt from the middle Kingdoms onward and resources from within the wadi are believed to have been utilized in medicine, mummification and in the glass making industry.

12.4.4 Quaternary Paleoclimate, Paleoenvironmental and Archeology of Egypt

Quaternary paleoclimate of Egypt is related to the glacial-interglacial cycles well established in Europe and North America. These cycles are expressed in Egypt as alternating dry (interpluvials) and relatively humid intervals (pluvials) (e.g. Said 1981, 1990, 1993; Hamdan and Brook 2015 and many others). Currently, it is now accepted that there are seven pluvials corresponding to global eustatic events and warm humid phases (Said 1981). The oldest two pluvials (the Edfu and Armant pluvials) are assigned as the early Pleistocene. The position of these two pluvials in the early Pleistocene stratigraphic scheme is not well established, because of the lack of reliable dating and absence of interpluvial sediments (Wysocka et al. 2016). The five subsequent pluvials; Abbasia I, Abbasia II, Sahara I, Sahara II and the Nabata pluvials, are assigned to the middle–late Pleistocene and the early Holocene, respectively (cf. Said 1990).

Generally, the climate of Egypt during early Pleistocene (from ca. 2.84 Ma) was arid and Egyptian lands were proper desert (Said 1981). During this long arid episode, wind was active and modeled the fluvial sediments that had accumulated mainly in basins, e.g. the basin of the Great Sand Sea (Embabi 2017). This period was interrupted with a short pluvial (the Idfu Pluvial), during which a highly competent river (the Protonile) flowed in the Nile Valley (Said 1990). By the end of the early Pleistocene, another short pluvial period occurred, whitnessed by the Armant conglomerate Formation. This Armant Pluvial is separated from the Protonile Pluvial by a short arid phase (Said 1990). Unfortunately, few dates are available for the two early Pleistocene short wet periods; however, there is one early Pleistocene date of 2288 kyr BP from a snail-bearing horizon at Lazy Beach 1, Kharga Depression. This may indicate that the Kharga climate was relatively wet or its water table sat high enough to host hominins during the Matuyama Chron, MIS 87 (Blackwell et al. 2017).

Owing to the extensive tufa and spring deposits in the Western and Eastern Desert, the climate of Egypt during middle Pleistocene is well known (see Smith 2004, 2006; Sultan et al. 1997). Figure 12.13 shows a comparison of the uranium-series ages of lacustrine carbonates accumulated at Western Desert during the middle-late Pleistocene pluvial periods together with the glacial/interglacial curve (Imbrie et al. 1984). The distribution of dates demonstrate the clustering of carbonate deposition not only during most interglacial periods (e.g., during stages 5a, 5c, 5e, 7a, 7c, 7e), but also during glacial stages 6 and 8 (Fig. 12.14). Szabo et al. (1995) cited five pluvial periods: at 320–250, 240–190, 155–120, 90–65 and 10–5 kyr BP, corresponding to interglacial Oxygen Isotope Stages (OIS) 9, 7, 5e, 5c, 5a and 1, respectively. These pluvial periods correlate well with tufa and spring deposits exposed at Kharga (Smith 2004, 2006; Sultan et al. 1997), Dakhla (Blackwell et al. 2017), Kurkur (Crombie et al. 1997; Hamdan 2003b) and in the Eastern Desert (Hamdan 2000b; Hamdan and Brook 2015) as well as with lacustrine deposits (McKenzie 1993). More recently, ESR dates published by Blackwell et al. (2017)

show flourishing ecosystems in Dakhla and Kharga during MIS 5 (74–133 kyr BP), 7 (188–244 kyr BP), 9 (285–338 kyr BP), 11 (364–426 kyr BP), and 17 (659–712 kyr BP), and in shorter episodes in MIS 1 (0–12kyr BP), 2 (12–26 kyr BP), 3 (26–59 kyr BP), 6 (133–188 kyr BP), and 12 (426–475 kyr BP). Indeed, these dates associated with prehistoric sites confirm that enough water existed in the Western Desert to support animal and plant life including herbivoresand likely hominins during much of the mid and late Pleistocene (Blackwell et al. 2017). Generally, most dates of Western Desert tufas and spring deposits fall within the warm, odd numbered MIS periods that correlate with interglacial periods in the Northern Hemisphere (Sultan et al. 1997). Interestingly, wetter conditions also existing from colder periods (e.g. Hamdan and Brook 2015).

In Egypt, the oldest prehistoric sites materials are mainly represented by late Lower Paleolithic occupations on the margins of the Nile Valley and in the Western Desert (Fig. 12.14a). The sites include upper Acheulean Complex (later early Stone Age) artifacts, probably dated to >400 kyr BP, and terminal early Stone Age lithics, probably dated at >300 kyr BP (Brookes 1989, 1993; Kleindienst et al. 2009, 2016). In middle Pleistocene pluvial events, the Western Desert may have received as much precipitation as 50–85 cm/y (Kieniewicz and Smith 2007, 2009). Stable isotopic analysis of tufa sediments indicate that rain water-was delivered from the Atlantic by strong westerlies (e.g. Sultan et al. 1997; Abouelmagd et al. 2012). The existence of fossil freshwater mollusks in palustrine and/or lacustrine sediments may indicate permanent water bodies and even large lakes (Blackwell 2017). During wet periods of the middle Pleistocene, savanna and savanna-woodland environments were common in Egypt (Churcher et al. 1999). Vertebrate and mollusk fossils have been recovered from deposits dated to the Pleistocene and Holocene in the Western Desert (Churcher et al. 1999, 2008; Gautier 1980, 1981, 1984). Middle Pleistocene vertebrate taxa at Dakhla Oasis included African elephant, camel, hippopotamus,

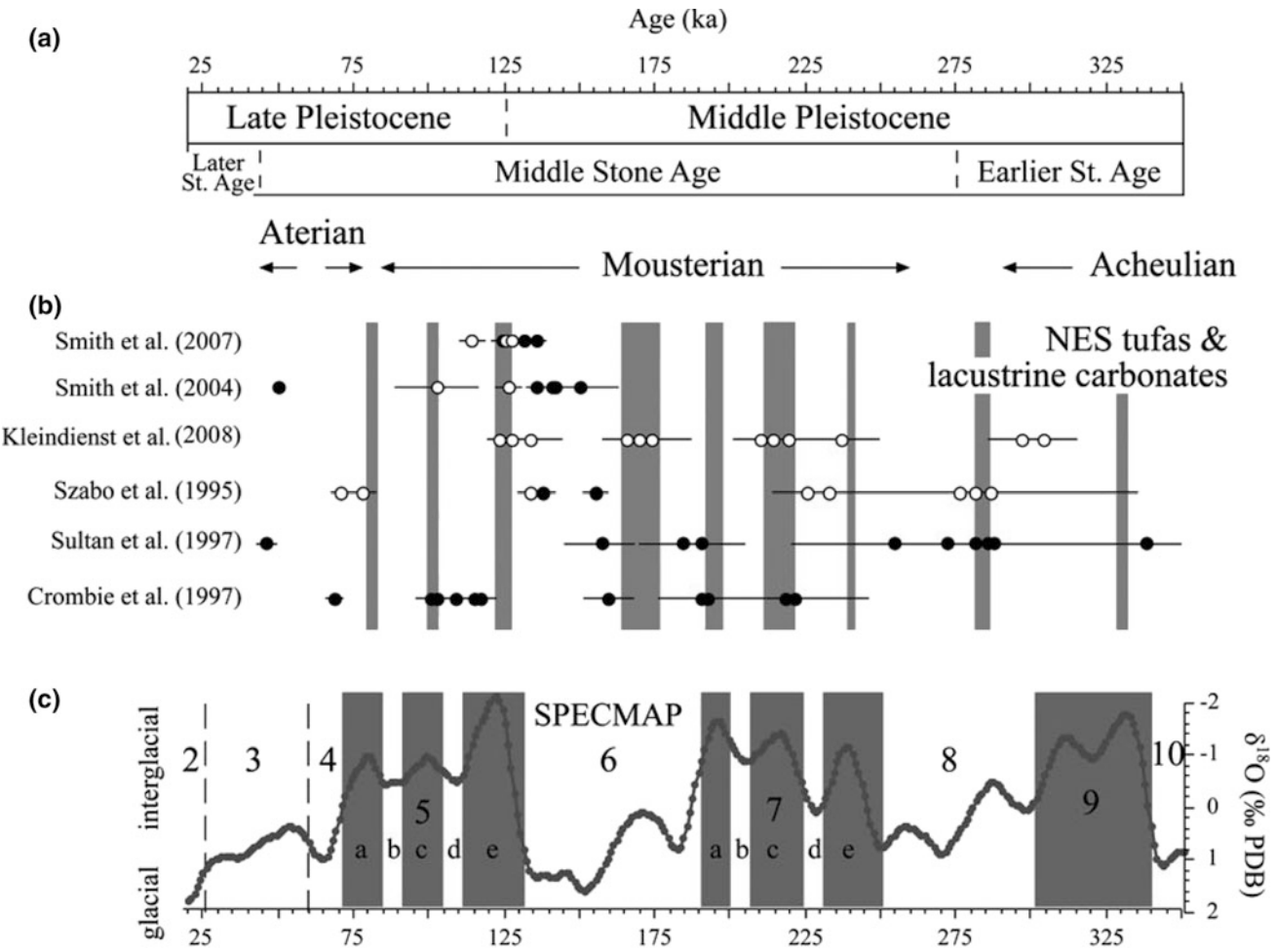

Fig. 12.14 **a** Age range of archaeological industries found in the northeastern Sahara (see text); **b** Uranium-series ages of lacustrine and spring carbonates from the northeastern Sahara. White (black) symbols indicate carbonates with (without) associated archaeological remains; **c** SPECMAP curve (Imbrie et al. 1984) (*Source* Larrasoana, 2012)

warthog, African buffalo, hartebeest, antelope, gazelle, small buck, extinct Cape zebra, wading birds, water fowl a small thrush-sized bird and small catfish (Churcher et al. 1999). The existence of freshwater snails and catfish in areas now proper desert indicate that the water was permanent and fresh which correlates with the presence of hippo, buffalo and zebra species that cannot exist far from potable water. The fauna and flora suggest a lake-shore environment with nearby savannah-woodland similar to the modern East African Valley.

In the Nile Valley, forty vertebrate taxa associated with archaeological sites dated to ca. 15,000 to 10,500 B.C. are known. Fish taxa are represented by Nile catfish, African barbel and Nile perch. The avian fauna includes twenty two species of shore, wading, and divingbirds. The mammalian fauna includes a canid, striped hyaena, *Lepus capensis*, Egyptian bandicoot or pest rat, wild ass, hippopotamus, wild cattle, bubal hartebeest, Dorcas gazelle, rhim or white gazelle and Barbary sheep (Gautier 1981). The remains of these animals collected from prehistoric sites of the Nile Valley are useful in constructing the ancient landscape and environment that prevailed during late Pleistocene. The fauna of the Nile River indicate that woodlands along the river banks and tree savannas and grasslands on the low hills and plains were widespread in the Nile Valley.

In the Eastern Desert, Pleistocene sediments in the Sodmein cave contain an extensive layer of humic material rich in plant micro-remains and Chironomidaeinsects (Marinova et al. 2008). In fact, the immature stages of these insect occur only in aquatic or wet habitats. The plant remains include, *Acacia tortilis* (a tree frequently used to make fire), *Clematis*sp., *Balanites* cf. *aegyptiaca* and Brassicaceae. The plant assemblage confirms conditions much wetter than the actual desert. Faunal analysis shows some remains of dorcas gazelle, rock dassie, a large bovid (buffalo), kudu and an elephantid which also indicate wetter environments in Eastern Desert during late Pleistocene (Marinova et al. 2008).

Between ca. 250–220 kyr BP, the middle Paleolithic began in Egypt with flakes made by the Levallois method (Bard 2007). Middle Paleolithic tools have been found in the Nile Valley, in Egypt and Nubia, but the best preserved sites are in the Western Desert (Fig. 12.14b). In Bir Sahara East and Bir Tarfawi, middle Paleolithic artifacts were found on the beaches of permanent lakes during wet intervals between 175 and 70 kyr BP (Wendorf and Schild 1993). After ca. 70 kyr BP the Western Desert was dry and cool and human habitation was no longer possible except in the oases. In Upper Egypt near Qena, evidence of a late middle Paleolithic culture dating to ca. 70–50 kyr BP has been identified (Van Peer et al. 2010). At the site of Taramsa-1, near the Ptolemaic temple of Hathor at Dendera, the oldest known human skeleton in Egypt has been excavated (Van Peer et al. 2010). From 70 to 12 kyr BP, dry conditions prevailed in Egypt and Saharan hyperarid environmental conditions expanded southward (Swezey 2001). Nile flow was also diminished (Lamb et al. 2007) and lakes dotting the Western and Eastern deserts during the Pleistocene interglacials dried out as dunes became active (e.g., Besler 2008). However, more humid conditions persisted especially around the Kharga and Dakhla Oases where water was available and these served as refuges for both hominins and other fauna (Blackwell et al. 2017).

During the hyperarid phase of the late Pleistocene, when the Sahara dried out, the Nile Valley also turned into a refuge for people and animals. The Western Desert remained largely uninhabitable until after ca. 10 kyr BP, creating a gap in the archaeological evidence of human cultures until after the upper and late Paleolithic. Upper Paleolithic sites in the Nile Valley are also rare (Bard 2007). The oldest known flint mine in the world (ca. 35–30 kyr BP), a source of stone for tools, is located at the site of Nazlet Khater-4 in middle Egypt (Vermeersch et al. 2002) where a grave of a robust *Homo sapiens sapiens* was found with a stone axe placed next to the skull (Vermeersch et al. 2002). Many more sites are known for the late Paleolithic ca. 21–12 kyr BP), than for the Upper Paleolithic (Bard 2007). Late Paleolithic sites are found in Lower Nubia and Upper Egypt, but not further north, where contemporary sites are probably buried under later river alluvium. Archaeological evidence suggests that the subsistence of late Plaeolithic peoples was based on hunting large mammals such as wild cattle and hartebeest, small dorcas gazelle, waterfowl, shellfish, and fish.

After a long late glacial hyperarid period, the entire Sahara, including Egypt, became wetter as tropical rainfall belts shifted northwards (Nicholson and Flohn 1980). Several palaeoclimatic data show that the early to mid-Holocene (10–5 BP) was a relatively humid period in Northern Africa, however, ITCZ effects didn't get further North than about 25° N (e.g. Shanahan et al. 2015). During this phase, often called the African Humid Period (AHP), grasslands covered the Sahara/Sahel region, with many lakes and wetlands (DeMenocal et al. 2000). During the AHP, summer heating of the Northern Hemisphere was maximized, with values of 8% more insolation than today due tocycles in the Earth's orbital parameters. More intense summer insolation deepened the East Saharan atmospheric low which in turn strengthened the summer African Southwest monsoon and brought Atlantic-derived moisture much further north than today (DeMenocal et al. 2000). The sequence of early Holocene playa development of Western Desert begins with an initial episode of wind deflation corresponding to the aeolian sand unit at the base of the early Holocene playa.

The sedimentological characteristics of the lacustrine sediments show an abundance of coarse clasts probably reflecting sedimentation by slope wash and sheet flow as a result of thundershower monsoon rains. Evidence for early

Holocene wet phases in the Eastern Sahara has been adequately documented in many of the modern oases and around the ancient, ephemeral playas in Southern Egypt (Wendorf and Schild 1980; Kröpelein 1987; Hassan et al. 2001). Haynes (1987) suggested that the mountains and surrounding plains in SW Egypt and NW Sudan received from 400 to 600 mm rainfall annually when occupied by Saharan Pastoral Neolithic communities. These poeple depicted their pastoral activities (particularly cattle) in the rock art of the area (Kuper and Kröpelein 2006). The most ancient playa sediments at Gilf Kebir were deposited between ca. 9300 cal. BP and 8200 cal. BP (Linstädter and Kröpelein 2004).

Moreover, stable isotope studies of carbon and oxygen, coupled with paleontological studies of mollusks and microfossils, confirm the widespread occurrence of stable freshwater lakes up to a few tens of meters deep in Dakhla Depression (Kieniewicz and Smith 2009). Also, higher precipitation and intensified monsoonal activity in the African Nile Headwaters led to higher Nile discharge and flooding of the Faiyum Depression (Hassan 1986; Hassan et al. 2012). Early Holocene river activity and surface groundwater recharge are recorded also in western desert of Egypt and northern Sudan (Pachur and Röper 1984; Pachur and Hoelzmann 2000).

The early Holocene humid period was interrupted by colder episodes of increased aridity, as shown by low Nile discharges: the most severe was around 8.2 cal kyr BP which is inferred from a widespread drying and increase in the oxygen isotope signal between 8400 and 8000 BP (Hassan et al. 2012; Hamdan et al. 2016a) and desiccation of the early Holocene play as associated with deposition of thermoclastic rubbles in Farafra Depression (Hassan et al. 2001; Hamdan and Lucarini 2013). The radiocarbon dates in the Bir Kiseiba region may indicate an arid period from 8.2 to 8.1 cal kyr BP (Close 1984), while a hyper-arid interval in the Nabta region occurred around 8.5 cal kyr BP (Nicoll 2004). There is no evidence of occupation in the southern Egyptian Western Desert (Wendorf and Schild 2001). Occupation is instead concentrated in Western oases and the Red Sea Mountains (Moyersons et al. 1999). Along the Nile, human occupation is consistently reported, and for the middle Nile region there is clear evidence of the population clustering along the river and moving south of the Third Cataract (Gatto and Zerboni 2015).

General, after the 8.2 cal kyr BP cooling event, moisture in Egypt generally decreased (Nicoll 2004), the northern playas began to dry as early as 7.7 cal kyr BP (Brookfield 2010). Also, most rainwater-fed playas began to wane around 7 cal kyr BP and became desiccated by 5.5 cal kyr BP. Vegetation diminished, decreasing the number of taxa, and sand was mobilized, forming dunes and sand sheets (Nicoll 2004). Botanical evidence from Egypt indicates that the savannah environment progressively disappearied in the middle Holocene as desert species substituted for more water-dependent plants. Savannah elements but persist but only in isolated ecological niches manly in the Western Desert Oases (Neumann 1989). At Siwa, the interfingering of playa layers with longitudinal dunes suggests a trend of seasonal variability in water availability (Haynes 1982). In south western Egypt around Selima, the level of lakes fluctuated and suffered profound evaporation after 8.9 cal kyr BP (Haynes et al. 1989).

In the middle Holocene, Sahelian vegetation zones were only 300–400 km north of their present range compared to 500–600 km during the early Holocene (Brookfield 2010). With increasing desiccation from 6 cal kyr BP onwards, savannah formations retreated to the south until their present position was reached by about 3.8 cal kyr BP (Neumann 1989). Some climate modeling results and paleoclimate data have indicated that the change from a semi-arid climate with about 250 mm/yr of rainfall to a hyperarid climate with less than 50 mm/year of rainfall occurred over a relatively short period of time, on the order of hundreds of years (DeMenocal et al. 2000).

During late Holocene, aridification started rapidly as the Western Desert lakes dried out and the level of Lake Qarun in the Faiyum dropped by ca. 15 m after 4.5 cal kyr BP (Hamdan and Lucarini 2013; Hamdan et al. 2016a, Hassan et al. 2012); sedimentation turned from freshwater into evaporitic/saline in Lake Qarun (Hamdan et al. 2016a); isotopic data on sediments and mollusks indicate a progressive decrease in the precipitation/evaporation balance (Hassan et al. 2012). These data indicate that the Nile flow diminished significantly (Hassan et al. 2017; Hamdan et al. 2018). In the wider region, pollen data illustrate that many tropical taxa disappeared or were confined to a few refuges (Nicoll 2004). Freshwater was available only in the Nile Valley and those Western Desert oases which inherited water from reservoirs formed in the AHP and occasionally from residual precipitations. According to most evidence, aridification continued up to the onset of present-day environmental conditions

Human occupation of the western Desert of Egypt indicates four distinct phases (Kuper and Kröpelein 2006): the Reoccupation phase (10.5–9 cal kyr BP); the Formation phase (9–7 cal kyr BP) ending abruptly in areas without permanent water; the Regionalization phase (7.3–5.5 cal kyr BP) featuring retreat to highland and Nile refuges; and the Marginalization phase (5.5–3.5 cal kyr BP). All these phases reflect the changing Holocene paleoclimatic and paleoenvironmental conditions in the Western Desert of Egypt. During the Reoccupation phase (10.5–9 cal kyr BP); the northward advance of monsoon rains at 10.5 cal kyr BP transformed the Sahara into a savannah, allowed hunter gatherers to migrateduring northwards into the present desert. During the Formation phase (9–7.3 cal kyr BP), human populations

adapted to multi-resources with domestic livestock of sheep and goats introduced from the Middle East and cattle probably from local domestication. Nabta playa has the earliest documented domestic cattle and goats, and these animals dominate rock art in the Western Desert. Recent studies in the Western Desert, Nile Valley and Faiyum show increase winter rainfall in Egypt during early and middle Holocene (Kröpelein 1987; Hassan et al. 2012; Hamdan and Lucarini 2013).

During the Regionalization phase (7300–5500 BP), populations retreated from increasing desertified land into refuges like the Gilf Kebir and plains further south, where rainfall was still sufficient and increase groundwater sources. By the time of the marginalization phase (5.5–3.5 cal kyr BP), permanent occupation of the desert was restricted to northern Sudan. The Gilf Kebir occupation ceased and a great migration to the Nile Valley occurred (Kuper and Kröpelein (2006). By the beginning of the early Predynastic Period, around 5.2 cal kyr BP, the inhabitants of Upper Egypt depended little on hunting for survival, having adopted an agricultural way of life.

The Pharaonic Empire became well-established along the Nile after 5 cal kyr BP; the western-most desert andoases, such as Abu Ballas in the western desert and Laqiya and Wadi Howar in the Sudan, then played only marginal roles except for mineral exploration and sporadic trade routes to more fertile areas in the west, south and east. Thus, by the beginning of the First Dynasty of Egypt (5.05 cal kyr BP), a united state had formed, with Memphis as probably its largest urban center, judging from the extent of the nearby cemetery fields on both sides of the Nile, at Saqqara (West Bank) and Helwan (East Bank). The development, however, of the requisite social specialization processes and hierarchies had begun much earlier, during the increasing aridity of the predynastic Naqada period at the latest.

Aknowledgments The authors greatly thank Roger Flower (UCL), Georg Brook (Georgia University, USA) and Juergen Wunderlich (Frankfurt Unversity, Germany) for their valuble comments and corrections that help in enhancement very much of the current chapter. They also wish to thank the following authores for their kind permissions to use some illustrations from their publications in this chapter; Barbara Barich (Roma University), Eman Ghoneim (University of North Carolina, USA), B.T. Pennington (University of Southampton, UK), A. Zaki (Ain Shams University, Egypt).

References

Abdelkareem M, El-Baz F (2015) Evidence of drainage reversal in the NE Sahara revealed by space-borne remote sensing data. J Afr Earth Sc 110:245–257

Abdelkareem M, Ghoneim E, El-Baz F, Askalany M (2012) New insight on palaeoriver development in the Nile Basin of the eastern Sahara. J Afr Earth Sc 62:35–40

Abotalib ZA, Mohamed RSA (2013) Surface evidences supporting a probable new concept for the river systems evolution in Egypt: a remote sensing overview. Environ Earth Sci 69:1621–1635

Abotalib AZ, Sultan M, Elkadiri R (2016) Groundwater processes in Saharan Africa: implications for landscape evolution in arid environments. Earth Sci Rev 156:108–136

Abouelmagd A, Sultan M, Milewski A, Kehew AE, Sturchio NC, Soliman F, Krishnamurthy RV, Cutrim E (2012) Toward a better understanding of palaeoclimatic regimes that recharged the fossil aquifers in North Africa: inferences from stable isotope and remote sensing data. Palaeogeogr Palaeoclimatol Palaeoecol 329–330: 137–149

Abouelmagd A, Sultan M, Sturchio NC, Soliman F, Rashed M, Ahmed M, Kehew AE, Milewski A, Chouinard K (2014) Paleoclimate record in the Nubian Sandstone aquifer, Sinai Peninsula, Egypt. Q Res 81:158–167

Abu-Bakr M, Ghoneim E, El-Baz F, Zeneldin M, Zeid S (2013) Use of radar data to unveil the paleolakes and the ancestral course of Wadi El-Arish, Sinai Peninsula, Egypt. Geomorphology 194:34–45

Adamson DA (1982) The integrated Nile. In MAJ Williams, DA Adamson (eds) A land between two niles: quaternary geology and biology in Central Sudan. A.A. Balkema, Rotterdam, pp 221–234

Ahmed S (1993) Collapse and solution red breccia of the Issawia Sharq locality, Nile Valley, Upper Egypt. Egypt J Geol 37(2):187–194

Aigner T (1983) A Pliocene cliff-line around the Giza pyramids plateau, Egypt. Palaeogeogr Palaeoclimatol Palaeoecol 42(3–4):313–322

Aly M, Zebker H, Giardino J, Klein A (2009) Permanent scatterer investigation of land subsidence in Greater Cairo, Egypt. Geophys J Int 178(3):1238–1245

Aly MH, Klein AG, Zebker HA, Giardino JR (2012) Land subsidence in the Nile Delta of Egypt observed by persistent scatterer interferometry. Remote Sens Lett 3(7):621–630

Andres W, Wunderlich J (1992) Environmental conditions for early settlement at Minshat Abu Omar, eastern Nile Delta, Egypt. In: van den Brink ECM (ed) The Nile delta in transition: 4th–3rd Millennium BC. IES, Tel Aviv, pp 157–166

Arduino G (1760) Sopra varie sue Osservazioni fatte in diverse parti del Territorio di Vicenza, ed altrove, appartenenti alla Teoria Terrestre, ed alla Mineralogia. Letter to Prof. Antonio Vallisnieri, dated 30th March, 1759. Nuova Raccolta di Opuscoli Scientifici e Filologici (Venice), v. 6 (1760)

Aref M, El-Khoriby E, Hamdan MA (2002) The role of salt weathering in the origin of Qattara Depression, Western Desert, Egypt. Geomorphology 45:181–195

Aref M, Hamdan MA (2003) Sedimentology and environmental interpretation of the evaporite deposits in the Qattara Depression, Western Desert, Egypt. Sedimentol Egypt 10:193–213

Ashour MM, Embabi NS, Donner J, Abu Zeid KA (2005) Geomorphology and quaternary geology of Abu El-Egl a playa, Western Desert of Egypt. Bull Egypt Geogr Soc 78:1–26

Ashri AH (1973) Themovement of the Sand Dune at Kharga Oasis, Egypt. J Geol 17:37–46

Attia AKM, Hilmy ME, Hegab OA (1970) Mineralogy of the sediments of Wadi el-Natrun lakes. Desert Inst Bull 2:327–357

Attia OE, Hussien KH (2015) Sedimentological characteristics of continental sabkha, south Western Desert, Egypt. Arab J Geosci 8:7973–7991

Bagnold R (1931) Journeys in the Libyan Desert 1929 and 1930. Geogr J 78:13–39

Bagnold R (1933) A further journey through the Libyan Desert. Geogr J 82:103–129

Ball J (1900) Kharga Oasis: its topography and geology. Survey Department, Public Works Ministry, Cairo

Ball J (1927) Problems of the Libyan Desert. Geogr J 70: 21–83, 105–128, 209–224, 512

Ball J (1933) The Qattara depression of the Libyan Desert and the possibility of its utilization for power production. Geogr J 82:289–314
Ball J (1939) Contributions to the geography of Egypt. Survey and Mines Department, Cairo, p 308
Bard KA (2007) Introduction to the archaeology of Ancient Egypt. Blackwell Publishing Ltd. 400 pp
Barich BE (2014) The Wadi Obeiyid Cave 1: the rock art archive. In: Barich BE, Lucarini G, Hamdan AM, Hassan FA (eds) From lake to sand, the archaeology of Farafra Oasis, Western Desert, Egypt. All'Insegna del Giglio, Firenze, pp 385–405
Barich BE, Hassan FA (1987) The Farafra Oasis archaeological project (Western Desert, Egypt). 1987 field campaign, Origini XIII:117–191
Barton RNE, Lane CS, Albert PG, White D, Collcutt SN, Bouzouggar A, Ditchfield P, Farr L, Oh A, Ottolini L, Smith VC, Van Peer P, Kindermann K (2015) The role of cryptotephra in refining the chronology of late Pleistocene human evolution and cultural change in North Africa. Q Sci Rev 118:151–169
Beadnell HJL (1909) An Egyptian Oasis: an account of the Oasis of Kharga in the Libyan Desert, with special reference to its history, physical geography, and water supply. John Murray, London
Beadnell L (1910) The sand dunes of the Libyan Desert. Geogr J 35:379–395
Becker RH, Sultan M (2009) Land subsidence in the Nile Delta: inferences from radar interferometry. Holocene 19(6):949–954
Besler H (2008) The great sand sea in Egypt: formation, dynamics and environmental change—a sediment analytical approach. Elsevier, Amsterdam
Blackwell BAB, Skinner AR, Smith JR, Hill CL, Churcher CS, Kieniewicz JM, Adelsberger KA, Blickstein JIB, Florentin JA, Deely AE, Spillar KV (2017) ESR analyses for herbivore teeth and molluscs from Kharga, Dakhleh, and Bir Tarfawi Oases: Constraining water availability and hominin Paleolithic activity in the Western Desert, Egypt. J Afr Earth Sci 136:216–238
Blackwell BAB, Skinner AR, Mashriqi F, Deely AE, Long RA, Gong JJJ, Kleindienst MR, Smith JR (2012) Challenges in constraining pluvial events and hominin activity: examples of ESR dating molluscs from the Western Desert, Egypt. Q Geochronol 10:430–435
Blankenhorn M (1900) Neues zur Geologie and palaeontologie Aegyptens. II: Das palaeogen (Eozaen und Oligozaen). Z Deutsch Geol Ges 52:403–479
Briere PR (2000) Playa, playa lake, sabkha: proposed definitions for old terms. J Arid Environ 45(1):1–7
Brown RH (1892) The Faiyum and Lake Moeris. Edward Stanford, London, p 110
Brookfield M (2010) The desertification of the Egyptian Sahara during the Holocene (the Last 10,000 years) and its influence on the rise of Egyptian Civilization In: Martini IP, Chesworth W (eds) Landscapes and societies. Springer Science & Business Media B.V. https://doi.org/10.1007/978-90-481-9413-1_6
Brook G, Embabi N, Ashour M, Edwards R, Cheng H, Cowart J, Dabous A (2002) Djara Cave in the Western Desert of Egypt: morphology and evidence of quaternary climatic change. Cave Karst Sci 29:57–66
Brookes IA (1989) Early Holocene basinal sediments of the Dakhla Oasis region, south-central Egypt. Quatern Res 32:139–152
Brookes IA (1993) Geomorphology and quaternary geology of the Dakhla Oasis region, Egypt. Q Sci Rev 12:529–552
Brookes IA (2001) Possible Miocene catastrophic flooding in Egypt's Western Desert. J Afr Earth Sci 32:325–333
Brookes IA (2003) Palaeofluvial estimates from exhumed meander scrolls, Taref Formation (Turonian), Dakhla Region, Western Desert, Egypt. Cretac Res 24(2):97–104
Bubenzer O, Hilgers A (2003) Luminescence dating of Holocene playa sediments of the Egyptian southern plateau Western Desert, Egypt. Q Sci Rev 22(10–13):1077–1084
Bubenzer O, Besler H, Hilgers A (2007) Filling the gap: OSL data expanding 14C chronology of late quaternary environmental change in the Libyan Desert. Q Int 175:41–52
Bunbury J, Jeffreys D (2011) Real and literary landscapes in Ancient Egypt. Camb Archaeol J 21(1), 65bri
Bunbury JM, Graham A, Hunter MA (2008) Stratigraphic landscape analysis: chartering the Holocene movements of the Nile at Karnak through ancient Egyptian times. Geoarchaeology 23:351–373
Bunbury JM, Tavares A, Pennington BT, Gonçalves P (2017) Development of the Memphite floodplain—landscape and settlement symbiosis in the Egyptian capital zone. In: Willems H, Dahms JM (eds) The Nile: natural and cultural landscape in Egypt. Proceedings of the international symposium held at the Johannes Gutenberg-Universität Mainz, 22 and 23 February 2013. Bielefeld: Transcript Verlag, pp 71–96
Butzer KW (1960) On the Pleistocene shorelines of Arab's Gulf. Egypt J Geol 68:626–637
Butzer KW (1964) Environment and archeology: an introduction to Pleistocene geography. Aldine Publishing Company, Chicago
Butzer KW (1980) Pleistocene history of the Nile valley in Egypt and lower Nubia. Sahara Nile 253:280
Butzer KW (1982) Archaeology as human ecology: method and theory for a contextual approach. Cambridge University Press
Butzer KW (1997) Late quaternary problems of the Egyptian Nile: stratigraphy, environments, prehistory. Paléorient 23(2):151–173
Butzer KW, Hansen CL (1968) Desert and river in Nubia. University of Wisconsin Press, 256 pp
Caton-Thompson G (1952) Kharga Oasis in prehistory. Athelon Press, London
Caton-Thompson G, Gardner EW (1929) Recent work on the problem of LakeMoeris'. Geogr J 73:20–60
Caton-Thompson G, Gardner EW (1934) The Desert Faiyum. The Royal Anthropological Institute of Great Britain and Ireland, London
Chen Z, Warne AG, Stanley DJ (1992) Late Quaternary evolution of the northwest Nile Delta between Rosetta and Alexandria. Egypt. J. Coast. Res. 8(3):527–561
Churcher CS, Kleindienst MR, Schwarcz HP (1999) Faunal remains from a middle Pleistocene lacustrine marl in Dakhla oasis, Egypt: palaeoenvironmental reconstructions. Palaeogeogr Palaeoclimatol Palaeoecol 154(4):301–312
Churcher CS, Kleindienst MR, Wiseman MF, McDonald MMA (2008) The quaternary faunas of Dakhla oasis, western desert of Egypt. In: Wiseman MF (ed) The Oasis papers 2: the 2nd international conference of the Dakhla Oasis project. Oxbow Books, Oxford, pp 1–24
Campmas E (2017) Integrating human-animal relationships into new data on aterian complexity: a paradigm shift for the North African middle stone age. Afr Archaeol Rev 34(4):469–491
Close AE (ed) (1984) Cattle-keepers of the Eastern Sahara: the Neolithic of Bır Kiseiba. Southern Methodist University, Dallas, p 452
Coutellier V, Stanley DJ (1987) Late Quaternary stratigraphy and paleogeography of the eastern Nile Delta, Egypt. Mar Geol 77(3–4):257–275
Crombie MK, Arvidson RE, Sturchio NC, Alfy ZE, Zeid KA (1997) Age and isotopic constraints on Pleistocene pluvial episodes in the Western Desert, Egypt. Palaeogeogr Palaeoclimatol Palaeoecol 130:337–355
Cornish V (1900) On desert sand dunes bordering the Nile Delta. Geogr J 43:1–32

Dabbour GA (1995) Estimation of the economic minerals reserves in Rosetta beach sands. Egypt Min 7:153–166
Dabous AA, Osmond JK (2000) U/TH study of speleothems from the Wadi Sannur Cavern Eastern Desert of Egypt. Carbonates Evaporites 15:1–16
DeHeinzelin J (1968) Geological history of the Nile Valley in Nubia. In: Wendorf IF (ed) The Prehistory of Nubia, Southern Methodist University, Dallas, Texas, pp 19–55
Deino AL, Behrensmeyer AK, Brooks AS, Yellen JE, Sharp WD, Potts R (2018) Chronology of the acheulean to middle stone age transition in eastern Africa. Science 360(6384):95–98
DeMenocal P, Ortiz J, Guilderson T et al (2000) Abrupt onset and termination of the African humid period: rapid climate responses to gradual insolation forcing. Q Sci Rev 19:347–361
De Wit HE (1993) The evolution of the Eastern Nile Delta as a factor in the development of human culture. In: Krzyzaniak L, Kobusiewicz M, Alexander J (eds) Environmental change and human culture in the Nile Basin and Northern Africa until the 2nd Millennium B.C. Poznan Archaeological Museum, Poznan, pp 305–320
De Wit HE, Van Stralen L (1988) Preliminary results of the 1987 palaeogeographical survey. In: van den Brink ECM (ed) The Archaeology of the Nile Delta: problems and priorities. Netherlands Foundation for Archaeological Research in Egypt, Amsterdam, pp 135–139
Donner J, Ashour MM, Brook GA, Embabi NS (2015) The quaternary history of the Western Desert of Egypt as recorded in the Abu El-Egl playa. Bull Soc Geog d'Egypte 88:1–18
Ebinger C (2005) Continental break-up: the East African perspective. Astron Geophys 46:2.16–12.21
El-Aref MM (1993) Paleokkarst surfaces in the Neogene succession of Wadi Essel-Wadi Sharm El ahari area, Egyptian Red Sea coast as indication of uplifting and expouse. Geol Soc Egypt Spec. Publ. no. 1:205–231
El-Aref MM, Lotfy Z (1985) Genetic karst significance of the iron ore deposits of El Bahariya Oasis, western Desert. Egypt. Ann Geol Surv Egypt 15:1–30
El-Aref MM, Refai E (1987) Paleokarst processes in the Eocene limestones of the Pyramids Plateau, Giza, Egypt. J Afr Earth Sci 6:367–377
El-Aref MM, Awadalah F, Ahmed S (1986) Karst landforms development and related sediments in the Miocene rocks of the Red Sea coastal zone, Egypt. Geologische Rundschau 75(3):781–790
El-Aref MM, Abou Khadrah A, Lotfi Z (1987) Karst topography and karstification processes in the Eocene limestone plateau of El Bahariya Oasis, Western Desert, Egypt. Z Geomorph N F 31:45–64
El-Aref MM, Saleh MH, Salama AM (2017a) Geomorphological classification and zonation of the exposed karst landforms in Bahariya—Farafra region, Western Desert Egypt. Int J Sci Res (IJSR) 6(5):956–965
El-Aref MM, Hammed MS, Salama AM (2017b) Inventory and assessment of the geomorphosites of Bahariya—Farafra territory, Western Desert, Egypt. Int J Sci Basic Appl Res 128–143
El-Asmar HM (1994) Aeolianite sedimentation along the northwestern coast of Egypt; Evidence for middle to late Quaternary aridity. Q Sci Rev 13:699–708
El-Asmar HA (2000) Geoenvironmental studies on the coastal area between Gamasa and Baltim, North of the Nile Delta. Z Geomorph N F, 44(1):59–73
El-Asmar HM, Wood P (2000) Quaternary shoreline development: the northwestern coast of Egypt. Q Sci Rev 19:1137–1149
El-Awady HMS (2009) Application of the geophysical survey for environmental and archaeological purposes, Central Western Part of the Nile Delta, Egypt. Unpublished MSc Thesis. University of Mansoura
El-Bassyony AA (1995) Sabkhas of Qattara Depression, Western Desert, Egypt—a survey. Sedimentol Egypt 3:13–26
El-Baz F (1988) Origin and evolution of the desert. Interdisc Sci Rev 13:331–347
El-Baz F, Maxwell T (eds) (1982) Desert landforms of Southwest Egypt: a basis for comparison with Mars. NASA, Washington, DC
El-Baz F, Wolfe RW (1982) Wind patterns in the Western Desert. In: El-Baz F, Maxwell TA (eds) Desert landforms of Southeast Egypt: a basis for comparison with Mars. NASA, CR-3611, pp 119–139
El-Baz F, Robinson C, Maxwell TA, Hemida IH (1998) Palao-channels of the great selima sand sheet in the Eastern Sahara and implications to ground water. Palaoecol Afr 26
El-Gammal EA (2010) New findings on the Karst in Nubia sandstone Southern Egypt. Nat Sci 8(8):125–129
El-Gammal EA, Cherif OH (2006) Use of remote sensing for the study of the hazards of Ghard Abu Muharik Sand Dune Field, Western Desert, Egypt. In: The 2nd international conference on water resources and arid environment. NARS, Cairo, pp 1–20
El-Gammal EA, El-Gammal AA (2010) Hazard impact and genetic development of sand dunes west of Samalut, Egypt. Egypt J Remote Sens Space Sci 13:137–151
El-Kammar AA, Ragab AA, Moustafa MI (2011) Geochemistry of economic heavy minerals from Rosetta Black Sand of Egypt. JAKU Earth Sci 22(2):69–97
El-Shahat A, Ayyad SN, Abdalla MA (1997) Pliocene facies and fossil contents of Qaret El-Muluk formation at Wadi El-Natrun Depression, western desert, Egypt. Facies 37(1):211–223
El-Shahat A, Ghazala H, Wilson P, Belal Z (2005) Lithofacies of the upper quaternary sequence of San el-Hagar area, Gharbiya Governorate, Nile Delta, Egypt. Mansoura J Geol Geophys 32:97–120
El-Sharkawi MA, El-Aref MM, Abdel Motelib A (1990) Manganese deposits in a Carboniferous palaeokarst profile, Um Bogmaregion, west-central Sinai, Egypt. Mineral Deposita 25:34–43
Embabi NS (2017) Landscapes and landforms of Egypt: landforms and evolution. World Geomorphol Landsc 336 pp. https://doi.org/10.1007/978-3-319-65661-8
Embabi NS (1999) Playas of the Western Desert, Egypt. Ann Acad Sci Fennicae, Geologica-Geographica 160:5–47
Fairbanks RG (1989) A 17,000-year glacio-eustatic sea level record: influence of glacial melting rates on the Younger Dryas event and deep-ocean circulation. Nature 342:637–642
Fielding L, Najman Y, Millar I, Butterworth P, Ando S, Padoan M, Barfod D, Kneller B (2017) A detrital record of the Nile River and its catchment. J Geol Soc 174:301–317
Fielding L, Najman Y, Millar I, Butterworth P, Garzanti E, Vezzoli G, Barfod D, Kneller B (2018) The initiation and evolution of the River Nile. Earth Planet Sci Lett 489:166–178
Flower RJ, Stickley C, Rose NL, Peglar S, Fathi AA, Appleby PG (2006). Environmental change at the desert margin: an assessment of recent paleolimnological records in Lake Qarun, middle Egypt. J Paleolimnol 35(1):1–24
Flower RJ, Keatings K, Hamdan M, Hassan FA, Boyle JF, Yamada K, Yasuda Y (2012) The structure and significance of early Holocene laminated sediments in the Faiyum Depression (Egypt) with special reference to diatoms. Diatom Res 27:127–140
Flower RJ, Keatings K, Hamdan M, Hassan FA (2013) StephanodiscusEhr. Speciesfrom holocene sediments in the Faiyum Depression (middle Egypt). Phytotaxa 127(1):66–80
Gatto MC, Zerboni A (2015) Holocene supra-regional environmental changes as trigger for major socio-cultural processes in Northeastern Africa and the Sahara. Afr Archaeol Rev 32:301–333
Gautier A (1980) Contributions to the archeozoology of Egypt. In: Wendorf F, Schild R (eds) Prehistory of the Eastern Sahara. Academic Press, New York, pp 317–344

Gautier A (1981) Non-marine molluscs and vertebrate remains from Upper Pleistocene deposits and middle Paleolithic sites at Bir Sahara and Bir Tarfawi, Western Desert, Egypt. In: Schild R, Wendorf F (eds) The prehistory of an Egyptian Oasis: a report of the combined prehistoric expedition to Bir Sahara and Bir Tarfawi, Western Desert, Egypt. Polska Academia Nauk, Warsaw, pp 126–145

Gautier A (1984) Quaternary mammals and archaeozoology of Egypt and the Sudan: a survey. In: Krzyzaniak L, Kobusiewicz M (eds) Origin and early development of food producing cultures in north-eastern Africa. Poznan Archaeological Museum, Poznan, pp 43–56

Ghoneim E, Robinson C, El-Baz F (2007) Radar topography data reveal drainage relics in the Eastern Sahara. Inter J Remote Sens 28:1759–1772

Giegengack RF (1968) Late Pleistocene history of the Nile Valley in Egyptian Nubia. Unpublished PhD thesis. Yale University

Giegengack R, Zaki A (2017). Inverted topographic features, now submerged beneath the water of Lake Nasser, document a morphostratigraphic sequence of high amplitude late-Pleistocene climate oscillation in Egyptian Nubia. J Afr Earth Sci 1–12

Gladfelter BG (1977) Geoarchaeology: the geomorphologist andarchaeology. Am Antiq 42(4):519–538

Gladfelter BG (1988) Late Pleistocene lakes within the mountains of southern Sinai: observations at the Tarfat Oasis. Bull Societe de Gtographie d'Egypte Tomes LXI/LXII, 29–49

Gladfelter BG (1990) The geomorphic situation of upper paleolithic sites in Wadi El Sheikh, Southern Sinai. Geoarchaeol Int J 127–141

Gladfelter BG (1992) Soil properties of sediments in Wadi Feiran, Sinai: a geoarchaeological interpretation. In Holliday VT (ed) Soil in archaeology, Smithonian Univ. Press 169–192

Goldberg P (1984) Late Quaternary history of Qadesh Barnea, northeastern Sinai. Zeit Geomorph 28:193–217

Goodman S, Hobbs J, Brewer D (1992) Nimir Cave: morphology and fauna of a cave in the Egyptian Eastern Desert. Paleoecol Afr 23:73–90

Goudie AS (2005) The drainage of Africa since the Cretaceous. Geomorphology 67:437–456

Gunn J (ed) (2004) Encyclopedia of Caves and Karst Science. Taylor and Francis Books, Inc. 1940 pp

Gunnell GF, Winkler AJ, Miller ER, Head JJ, Abdel El-Barkooky AN, Gawad M, Sanders WJ, Gingerich PD (2016) Small vertebrates from Khasm El-Raqaba, late middle Miocene, Eastern Desert, Egypt. Hist Biol 28(1–2):159–171

Günay G, Ekmekci M, Bayari CS, Kurttaş T, El-Bedewy F (1997) Sannur Cave: a crescent shaped cave in Egypt. In: Günay G, Johnson AI (eds) Karst: waters and environmental impacts. Balkema, Rotterdam

Halliday WR (2003) Caves and karsts of Northeast Africa. Int J Speleol 32(1/4):19–32

Halliday WR (2007) Pseudokarst in the 21st century. J Cave Karst Stud 69(1):103–113

Hamdan MA (1987) Geomorphology and quaternary geology of Umm El-Dabadib Area, Kharga Oasis. Dissertation, Ms thesis, Cairo University

Hamdan MA (1993) Pliocene and quaternary sediments and their relationship to the geological evolution of River Nile at lower Egypt. PhD thesis, Cairo University

Hamdan MA (2000a) Subsurface late Pleistocene Nile floodplain sediments of Saqqara area: palaeoenvironmental interpretations. J Sedimentol Egypt 8:243–254

Hamdan MA (2000b) Quaternary travertines of Wadis Abu Had-dib area Eastern Desert, Egypt: Paleoenvironment through field, sedimentology, age, and isotopic study. Sedimentol Egypt 8:49–62

Hamdan MA (2003a) Late quaternary geology and geoarchaeology of Kafr Hassan Dawood, east delta. In: Hawass Z, Pinch Brock L (eds) Egyptology at the Dawn of the twenty-first century: proceedings of the eighth international congress of Egyptologists, Cairo, 2000, vol 1. The American University in Cairo Press, Cairo, pp 221–228

Hamdan MA (2003b) Stable isotope and geochemistry of some travertine deposits of southern Egypt and their paleoclimatic and paleoenvironmental implications: sedimentology of Egypt 11:43–61

Hamdan MA, Lucarini G (2013) Holocene paleoenvironmental, paleoclimatic and geoarchaeological significance of the Sheikh El-Obeiyid area (Farafra Oasis, Egypt). Q Int 302:154–168

Hamdan MA (2014a) Sedimentological characteristics and geomorphic evolution of the Holocene playa of Wadi Obeiyid. In: Barich BE, Lucarini G, Hamdan AM, Hassan FA (eds) From lake to sand, the archaeology of Farafra Oasis, Western Desert, Egypt. All'Insegna del Giglio, Firenze, pp 81–91

Hamdan MA (2014b) Geology of the Holocene playa sediments of Hidden Valley, Wadi Obeiyid, Farafra. In: Barich BE, Lucarini G, Hamdan AM, Hassan FA (eds) From lake to sand, the archaeology of Farafra Oasis, Western Desert, Egypt. All'Insegna del Giglio, Firenze, pp 151–166

Hamdan MA, Hassan FA, Mahmoud A (2014c) The Wadi Obeiyid Cave 1—geological features. In: Barich BE, Lucarini G, Hamdan AM, Hassan FA (eds) From lake to sand, the archaeology of Farafra Oasis, Western Desert, Egypt. All'Insegna del Giglio, Firenze, pp 377–384

Hamdan MA, Brook GA (2015) Timing and characteristics of Late Pleistocene and Holocene wetter periods in the Eastern Desert and Sinai of Egypt, based on 14C dating and stable isotope analysis of spring tufa deposits. Quatern Sci Rev, 130:168–188

Hamdan MA, Abu Refaat AA, Anwar E, Shallaly NA (2015) Source of the aeolian dune sand of Toshka area, southeastern Western Desert, Egypt. Aeolian Res 17:275–289

Hamdan A, Ibrahim MIA, Shiha MA, Flower RJ, Hassan FA, Eltelet SAM (2016a) An exploratory early and middle Holocene sedimentary record with palynoforms and diatoms from Faiyum lake, Egypt. Q Int 410:30–42

Hamdan MA, Refaat AA, Abdel Wahed M (2016b) Morphologic characteristics and migration rate assessment of barchans dunes in the Southeastern Western Desert of Egypt. Geomorphology 257:57–74

Hamdan MA, Hassan FA, Flower RJ, Leroy SAG, Shallaly NA, Flynn A (2019) Source of Nile sediments in the floodplain at Saqqara inferred from mineralogical, geochemical, and pollen data, and their palaeoclimatic and geoarchaeological significance. Q Int. 501, 272-288

Hassan FA (1976) Prehistoric studies of the Siwa Oasis Region, 1975 season. Nyame Akuma 9:18–34

Hassan FA (1979a) Geoarchaeology: the geologist and archaeology. Am Antiq 44(2):267–270

Hassan FA (1979b) Archaeological explorations at Baharriya Oasis and the West Delta, Egypt. Curr Anthropol 20:806

Hassan FA (1986) Holocene lakes and prehistoric settlements of the Western Faiyum, Egypt. J Archaeol Sci 13:483–501

Hassan FA (1997) The dynamics of a riverine civilization: a geoarchaeological perspective on the Nile Valley. World Archaeol 29(2):51–74

Hassan FA (2007a) Extreme Nile floods and famines in Medieval Egypt (AD 930-1500) and their climatic implications. Q Int 173–174:101–112

Hassan FA (2007b) Droughts, famine and the collapse of the Old Kingdom: Rereading lpuwer. In: Hawass Z, Richards J (eds) The archaeology and art of ancient Egypt: essays in honor of David B.

O'Connor. Annales du Service des Antiquit_es de L'Egypte Cahier, vol 36, pp 357–377
Hassan FA (2010) Climate change, Nile floods and riparia. In: Hermon E (ed) Riparia dans l'empire romain pour la d_efinition du concept. BAR International S2066, Oxford, pp 131–152
Hassan FA, Hamdan MA (2008). The Faiyum Oasis—climate change and water management in ancient Egypt. In: Hassan (ed) Traditional water techniques: cultural heritage for a sustainable future. 6th Framework Programme, ShadufProject, pp 117–147
Hassan FA, Barich B, Mahmoud M, Hamdan MA (2001) Holocene playa deposits of Farafra Oasis, Egypt, and their palaeoclimatic and geoarchaeological significance. Geoarchaeol Int J 16(1): 29–44
Hassan FA, Hamdan MA, Flower RJ, Keatings K (2012) The oxygen and carbon isotopic records in Holocene freshwater mollusc shells from the Faiyum palaeolakes, Egypt: their palaeoenvironmental and palaeoclimatic implications. Q Int 266:175–187
Hassan FA, Hamdan MA, Mahmoud A (2014) Desert and Oasis: geomorphology and geomorphic evolution. In: Barich BE, Lucarini G, Hamdan AM, Hassan, FA (eds) From lake to sand, the archaeology of Farafra Oasis, Western Desert, Egypt. All'Insegna del Giglio, Firenze, pp 63–78
Hassan FA, Hamdan MA, Flower RJ, Shallely NA, Ebrahem E (2017) Holocene alluvial history and archaeological significance of the Nile floodplain in the Saqqara-Memphis region, Egypt. Q Sci Rev 176:51–70
Haynes CV (1980) Geological evidence of pluvial climates in the Nabta area of the Western Desert, Egypt. In: Wendorf F, Schild R (eds) Prehistory of the Eastern Sahara. Academic Press, New York, pp 353–371
Haynes CV (1982) Great Sand Sea and Selima sand sheet. Geomorphol Desertification Sci 217:629–632
Haynes CV (1987) Holocene migrations of the Sudano-Sahelian wetting front, Arba'in Desert, Eastern Sahara. In: Close A (ed) Prehistory of arid North Africa. Essays in honour of Fred Wendorf. Southern Methodist University Press, Dallas, pp 69–84
Haynes CV, Eyles CH, Pavlish LA, Ritchie JUC, Rybak M (1989) Holocene palaeoecology of the eastern Sahara: Selima oasis. Q Sci Rev 8:109–136
Hawass Z (1997) The discovery of the harbors of Khufu and Khafre at Giza. In: Berger C, Mathieu B (eds) Etudes sur l'Ancien Empire et la nécropole de Saqqara dédiées a Jean-Philippe Lauer. Orientalia Monspeliensia IX, Montpellier, pp 245–256
Hill CL, Schild R (2017) Pleistocene deposits in the southern Egyptian Sahara: lithostratigraphic relationships of sediments and landscape dynamics at Bir Tarfawi. Stud Q 34:23–38
Hillier JK, Bunbury JM, Graham A (2006) Monuments on a migrating Nile. J Archaeol Sci 34(7):1011–1015
Hobbs JJ, Goodman SM (1995) Leopard-hunting scenes in dated Rock Art from the Northern Eastern Desert of Egypt. Sahara 7: 7–16, réponses de Béatrix Midant-Reynes, idem: 124–126 et d'Alfred Muzzolini, idem: 126–127
Hoelzmann P (2002) Lacustrine sediments as key indicators of climate change during the late quaternary in Western Nubia (Eastern Sahara). Geo-Sciences in Northern Africa 375–388
Hsu KJ, Ryan WBF, Cita MB (1973) Late Miocene desiccation of the Mediterranean. Nature 242:239–243
Imbrie J, Hays JD, Martinson DG, Mclntyre A, Mix AC, Morley JJ (1984) The orbital theory of Pleistocene climate: Su pport from a revised chronology of the marine 6180 record. In Berger A, Imbrie J, Hays J, Kukla G, Saltzman B (eds) Milankovitch and climate, part 1. Plenum Reidel, Dordrecht, pp 269–305
Issar KS, Bruins S (1983) Some climatological conditions in the deserts of Sinai and the Negv during the latest Pleistocene. Paleogeogr Paleoclimatol Paleoecol 44:63–77
Issawi B (1971) Geology of Darb El-Arbain, Western Desert. Ann Geol Surv Egypt 1:53–92
Issawi B, McCauley JF (1992) The Cenozoic rivers of Egypt: the Nile problem. In: Adams B, Friedman R (eds) The followers of Horus. Oxbow Press, Oxford, pp 1–18
Issawi B, McCauley J (1993) The Cenozoic landscape of Egypt and its river systems. Ann Geol Surv Egypt 19:357–384
Issawi B, Osman R (2008) Egypt during the Cenozoic: geological history of the Nile river. Bull Tethys Geol Soc Cairo 3:43–62
Jeffreys DG (2008) Archaeological implications of the moving Nile. Egypt Archaeol 32:6–7
Jeffreys DG, Tavares A (1994) The historic landscape of early Dynastic Memphis. Mitteilungen des Deutschen Archäologischen Instituts, Abteilung Kairo 50:143–173
Jelínek R, Eckert S, Zeug G, Krausmann E (2009) Tsunami vulnerability and risk analysis applied to the City of Alexandria, Egypt. EUR—Scientific and Technical Research series, 40 pp
Kaiser MF, Aziz AM, Ghieth BM (2014) Environmental hazards and distribution of radioactive black sand along the Rosetta coastal zone in Egypt using airborne spectrometric and remote sensing data. J Environ Radioact 137:71–78
Kieniewicz JM, Smith JR (2007) Hydrologic and climatic implications of stable isotope and minor element analyses of authigenic calcite silts and gastropod shells from a mid-Pleistocene pluvial lake, Western Desert, Egypt. Q Res 68:341–344
Kieniewicz JM, Smith JR (2009) Paleoenvironmental reconstruction and water balance of a mid-Pleistocene pluvial lake, Dakhleh Oasis, Egypt. Bull Geol Soc Am 121:1154–1171
Kindermann K, Van Peer P, Henselowsky F (2018) At the lakeshore—An early Nubian Complex site linked with lacustrine sediments (Eastern Desert, Egypt). Q Int 485:131–139
Kindermann K, Bubenzer O, Nussbaum S, Riemer H, Darius F, Pöllath N, Smettan U (2006) Palaeoenvironment and Holocene land-use of Djara, Western Desert of Egypt. Q Sci Rev 25:1619–1637
Kleindienst MR, Smith JR, Adelsberger KA (2009) The Kharga oasis prehistory project (KOPP), 2008 field season: Part I geoarchaeology and pleistocene prehistory. Nyame Akuma 71:18–30
Kleindienst MR, Blackwell BAB, Skinner AR, Churcher CS, Kieniewicz JM, Smith JR, Wise NL, Long RA, Deely AE, Blickstein JIB, Chen KKL, Huang A, Kim MKD (2016) Assessing long-term habitability at an eastern Sahara oasis: ESR dating of molluscs and herbivore teeth at Dakhleh Oasis, Egypt. Q Int 408:106–120
Knetsch G (1954) Allgemein-geologische Beobachtungen aus Ägypten 1951–1953. Neues Jb Geol u Paläontol Abh 99:287–297
Kozlowski JK (ed) (1983) Qasr el-Sagha 1980. Contributions to the Holocene Geology, the predynastic and dynastic settlements in the Northern Fayum Desert Warschau-Krakow: UniversitasIagellonica
Kröpelein S (1987) Palaeoclimatic evidence from early to mid-Holocene playas in the Gilf—Kebir, southwest Egypt. Palaeoecol Afr 18:189–208
Kröpelein S (1993) Geomorphology, landscape evolution and paleoclimates of Southwest Egypt. Catena Suppl 26:31–65
Krom MD, Stanley DJ, Cliff RA, Woodward JC (2002) Nile River sediment fluctuations over the past 7000 yr and their key role in sapropel development. Geology 30(1):71–74
Kuper, R. 1996. Between the oases and the Nile—Djara: Rohlfs' Cave in the Western Desert. Interregional Contacts in the later Prehistory of Northeastern Africa. Poznan Archaeological Museum, Poznan, pp 81–91
Kuper R, Kröpelein S (2006) Climate-controlled Holocene occupation in the Sahara: motor of African evolution. Science 313:803–807
Kusky T, El-Baz F (2000) Neotectonics and fluvial geomorphology of the northern Sinai Peninsula. J Afr Earth Sci 31:213–235

Lamb HF, Bates CR, Coombes PV, Marshall MH, Umer M, Davies SJ, Dejen E (2007) Late Pleistocene desiccation of Lake Tana, source of the Blue Nile. Q Sci Rev 26:287–299

Larrasoan JC (2012) A Northeast Saharan perspective on environmental variability in North Africa and its implications for modern human origins. In: Hublin J-J, McPherron SP (eds) Modern origins: a North African perspective, vertebrate paleobiology and paleoanthropology. Springer Science + Business Media B.V., pp 19–34

Little OH (1936) Recent geological workin the Fayum and in the adjoining portion of the Nile Valley. Bull Institut d'Egypte 18:201–240

Linstädter J, Kröpelein S (2004) Wadi Bakht revisited: Holocene climate change and prehistoric occupation in the Gilf Kebir region of the Eastern Sahara, SW Egypt. Geoarchaeology 19:753–778

Lutley KL, Bunbury J (2008) The Nile on the move. Egypt Archaeol 35:261–292

Macgregor DS (2012) The development of the Nile drainage system: integration of onshore and offshore evidence. Petrol Geosci 18 (4):417–431

Mansour AM, Madkour HA (2015) Raised coral reefs and sediments in the coastal area of the Red Sea. In: Rasul NMA, Stewart ICF (eds) The Red Sea, Springer earth system sciences. Springer, Berlin, Heidelberg

Marks L, Salem A, Welc F, Nitychoruk J, Chen Z, Blaauw M, Zalat A, Majecka A, Szymanek M, Chodyka M, Tołoczko-Pasek A, Sun Q, Zhao X, Jiang J (2018) Holocene lake sediments from the Faiyum Oasis in Egypt: a record of environmental and climate change. Boreas 47(1):62–79

Marinova E, Linseele V, Vermeersch PM (2008) Holocene environment and subsistence patterns near the Tree Shelter, Red Sea Mountains, Egypt. Q Res 70:392–397

Marinova M Nele, Meckler A, McKay CP (2014) Holocene freshwater carbonate structures in the hyper-arid Gebel Uweinat region of the Sahara Desert (Southwestern Egypt). J Afr Earth Sci 89:50–55

Marriner N, Flaux C, Morhange C, Kaniewski D (2012) Nile Delta's sinking past: quantifiable links with Holocene compaction and climate-driven changes in sediment supply. Geology 40(12):1083–1086

Mourik A, Bijkerk J, Cascella A, Hüsing S, Hilgen F, Lourens L, Turco E (2010) Astronomical tuning of the La Vedova High Cliff Section (Ancona, Italy)—implications of the middle Miocene climate transition for Mediterranean sapro-pel formation. Earth Planet Sci Lett 297:249–261

Maxwell T (1980) Geomorphology of the Gilf Kebir. In: El-Baz et al (eds) Journey to the Gilf Kebir and Uwienat, Southwest Egypt (1978). Geogr J 146:76–83

Maxwell TA, Issawi B, Haynes CV (2010) Evidences for Pleistocene lakes in the Toshkka region, south Egypt. Geology 38:1135–1138

McCauley J, Schaber G, Breed C, Grolier M, Haynes C, Issawi B, Elachi C, Blom R (1982) Subsurface valleys and geoarcheology of the Eastern Sahara revealed by shuttle radar. Science 218:1004–1020

McCauley J, Breed M, Schaber G, Haynes V, Issawi B, El-Kilani A (1986) Palaeodrainages of the Eastern Sahara, The radar rivers revisited (SIR-A/B Implications for a Mid-Tertiary Trans-African Drainage System). IEE Trans Geo Sci Remote Sens GE 24:624–648

McHugh W, McCauley J, Haynes C, Breed C, Schaber G (1988) Paleorivers and geoarchaeology in the Southern Egyptian Sahara. Geoarchaeology 3:1–40

McKenzie J (1993) Pluvial conditions in the eastern Sahara following the penultimate deglaciation: implications for changes in atmospheric circulation patterns with global warming. Palaeogeogr Palaeoclimatol Palaeoecol 103:95–105

McDougall I, Morton WH, Williams MAJ (1975) Age and rates of denudation of Trap Series basalts at Blue Nile gorge, Ethiopia. Nature 254:207–209

Mein P, Pickford M (2010) Vallesian rodents from Sheikh Abdallah, Western Desert, Egypt. Hist Biol 22(1–3):224–259

Mesbah NM, Abou-El-Ela SH, Wiegel J (2007) Novel and unexpected prokaryptic diversity in water and sediments of the alkaline, Hypersaline Lakes of the Wadi An Natrun, Egypt. MicrobialEcology 55(2):369

Moustafa MI (2007) Separation flowsheet for high-purity concentrates of some economic minerals from El Burullus-Baltim sand dunes area, North Coast, Egypt. In: The 5th international conference on the geology of Africa, vol 1, pp 107–124

Motts WS (1969) Geology and hydrology of selected playas in Western United States. Air Force Cambridge Research Lab Report AFCRL-69–0214, 286 pp

Naim G, El Melegy ET,. El Azab A (1993) Black sand assessment. The Egyptian Geological Survey, 67 pp

Neumann K (1989) Holocene vegetation of the Eastern Sahara: charcoal from prehistoric sites. Afr Archaeol Rev 7:97–116

Nicholson SE, Flohn H (1980) African environmental and climatic changes and the general atmospheric circulation in late Pleistocene and Holocene. Clim Change 2:313–348

Nicoll K (2004) Recent environmental change and prehistorichuman activity in Egypt and northern Sudan. Q Sci Rev 23:561–580

Nicoll K, Sallam ES (2017) Paleospring tufa deposition in the Kurkur Oasis region and implications for tributary integration with the River Nile in southern Egypt. J Afr Earth Sc 136:239–251

Nicoll K, Giegengack R, Kleindienst M (1999) Petrogenesis of artifact-bearing fossil-spring tufa deposits from Kharga Oasis, Egypt. Geoarchaeol Int J 14:849–863

Misak RF, Attia S (1983) On the sand dunes of in Sinai Peninsula. Egypt J Geol 27:115–131

Misak RF, Draz MY (1997) Sand drift control of selected coastal and desert dunes in Egypt: case studies. J Arid Environ 35:17–28

Moeyersons J, Vermeersch PM, van Peer P, Thomas DSG, Singhvi AK (2002) Dry cave deposits and their palaeoenvironmental significance during the last 115 Ka, Sodmein Cave, Red Sea Mountains, Egypt. Q Sci Rev 21(7):837–851

Mostafa A (2013) Paleokarst shafts in the Western Desert of Egypt: a unique landscape. Acta Carsologica 42(1):49–60

Osinski GR, Schwarcz HP, Smith JR, Kleindienst MR, Haldemann AFC, Churcher CS (2007) Evidence for a ~200–100 ka meteorite impact in the Western Desert of Egypt. Earth Planet Sci Lett 253:378–388

Osinski GR, Kieniewicz J, Smith JR, Boslough MB, Eccleston M, Schwarcz HP, Kleindienst MR, Haldeman AFC, Churcher CS (2008) The Dakhleh glass: product of an impact airburst or cratering event in the western desert of Egypt. Meteorit Planet Sci 43 (12):2089–2107

Pachur H, Röper H (1984) The Libyan "Western Desert" and Northern Sudan during the late Pleistocene and Holocene. In: Klitzsch E, Said R, Schrank E (eds) Research in Egypt and Sudan, Band 50, Results of the Special Research Project in Arid Areas, Period 1981–1984, Berliner geowissenschaftlicheAbhandlungen, Reihe A, Band, vol 50, pp 249–284

Pachur H-J, Hoelzmann P (2000) Late Quaternary palaeoecology and palaeoclimates of the eastern Sahara. J Afr Earth Sci 30:929–939

Pavlov M (1962) Preliminary report on the ground water beneath the Wadi El-Natrun and adjacent areas. Report to General Desert Development Organization of U.A.R. Desert Institute, Cairo

Pik R, Marty B, Carignan J, Lave J (2003) Stability of the Upper Nile drainage net-work (Ethiopia) deduced from (U–Th)/He thermochronometry: implications for uplift and erosion of the Afar plume dome. Earth Planet Sci Lett 215:73–88

Rapp GR, Hill CL (2006) Geoarchaeology: the earth-science approach to archaeological interpretation. Yale University Press

Pennington BT, Bunbury J, Hovius N (2016) Emergence of civilization, changes in fluvio-deltaic style, and nutrient redistribution forced by Holocene sea-level rise. Geoarchaeol Int J 31(3):194–210
Pennington BT, Sturt F, Wilson P, Rowland J, Brown AG (2017) The fluvial evolution of the Holocene Nile Delta. Q Sci Rev 170:212–231
Philip G, El-Aref MM, Darwish M, Ewais E (1991) Paleoerosion surfaces and karst manifestations including " Egyptian Alabaster" in Gabal Homret Schaibun- Gabal Sannur area, east of the Nile valley, Egypt. Egypt J Geol 34:41–79
Pickford M, Wanas H, Soliman H (2006) Indications for a humid climate in the Western Desert of Egypt 11–10 Myr ago: evidence from Galagidae (Primates, Mammalia). Palaeoecology 5:935–943
Plaziat JC, Montenat C, Orszag-Sperber F, Philobbos E, Purser BH (1990) Geodynamic significance of continental sedimentation during initiation of the NW Sea rift (Egypt). In: Kogbe S, Lang J (eds) Continental sediments in Africa. J Afr Earth Sci, Oxford, 10 (1–2):355–360
Raboul H (1833) Géologie de la Période Quaternaire et Introduction à l'Histoire Ancienne. F.G. Levrault, Paris 222 pp
Rifai RI (2007) Reconstruction of the middle pleistocene climate of South Mediterranean using the Wadi Sannur speleothem, Eastern Desert, Egypt. Carbonates Evaporites 22(1):73–85
Rizzini A, Vezzani F, Cococcetta V, Milad G (1978) Stratigraphy and sedimentation of a Neogene-Quaternary section in the Nile Delta area. Mar Geol 27(3–4):327–348
Renne PR, Schwarcz HP, Kleindienst MR, Osinski GR, Donovan JJ (2010) Age of the Dakhleh impact event and implications for middle stone age archeology in the western desert of Egypt. Earth Planet Sci Lett 291:201–206
Rohling EJ, Marino G, Grant KM (2015) Mediterranean climate and oceanography, and the periodic development of anoxic events (sapropels). Earth-Sci Rev 143:62–97
Rowland JM, Hamdan MA (2012) The Holocene evolution of the Quesna turtleback: geological evolution and archaeological relationships within the Nile Delta. In: Kabacinski J, Chłodnicki M, Kobusiewicz M (eds) Prehistory of Northeastern Africa: new ideas and discoveries. Poznan Archaeological Museum, Poznan, pp 11–24
Said R (1981) The geological evolution of the River Nile. Springer, New York, p 151
Said R (1990) Quaternary. In: Said R (ed) The geology of Egypt, Chapter 25. A A Balkema, Rotterdam
Said R (1993) The River Nile: geology, hydrology and utilization. Pergamon Press, Oxford, p 320
Said R (1998) Sand accumulation and groundwater in the eastern Sahara: A rebuttal to El-Baz F (Episodes, vol 21, no 3). Episodes 21, 287–289
Schweinfurth G (1886) Reise in das Depressions-gebietimUmkreise des FajumimJanuar 1886'. Zeitschrifr der GesellschuftfirErdkundezu Berlin 21:96–149
Selim AA (1974) Origin and lithification of the Pleistocene carbonates of the Salum area, western coastal plain of Egypt. J Sediment Petrol 44:70–78
Sandford KS (1934) Paleolithic man and the Nile Valley in upper and middle Egypt. Chicago University Press, Oriental Publication, vol 3, pp 1–131
Sandford KS, Arkell J (1929) Paleolithic man and the Nile-Fayum Divide. Chicago University Press, Oriental Institute Publication, 1
Sandford KS, Arkell WJ (1939) Paleolithic man and the Nile Valley in Lower Egypt with some notes upon a part of the Red Sea Littoral: a study of the regions during Pliocene and Pleistocene Times. University of Chicago Press, Chicago
Schaber G, McCauley J, Breed C (1997) The use of maltifrequency and polarimetric SIR-C/X-SAR data in the geologic studies of Bir Safsaf. Egypt Remote Sens Environ 59:337–363
Schild R, Wendorf F (1989) The late Pleistocene Nile in Wadi Kubbaniya. In: Wendorf F, Schild R, Close AE (eds) The prehistory of Wadi Kubbaniya, vol 2. Southern Methodist University Press, Dallas, pp 15–100
Shahin M (1985) Hydrology of the Nile Basin. Elsevier, Amsterdam, p 575
Shanahan TM, McKyry KA, Hughen JT, Overpeck B, Otto-Bliesner CW, Heil J King, Scholz CA, Peck J (2015) The time-transgressive termination of the African Humid period. Nat Geosci 8(2):140–144
Shata A, El-Fayoumy I (1967) Geomorphological and morphopedological aspects of the region west of the Nile Delta with special reference to Wadi el Natrun area. Bull Desert Inst 17:1–28
Shortland AJ (2004) Evaporites of the Wadi Natrun: seasonal and annual variation and its implication for Ancient exploitation. Archaeometry 46:497–516
Shukri NM (1950) The mineralogy of some Nile sediments. Q J Geol Soc 105:511–534; 106:466–467
Shukri NM, Philip G, Said R (1956) The geology of the Mediterranean coast between Rosetta and Bardia, part II: Pleistocene sediments Geomorphology and Microfacies. lnst Egypt Bull 37:395–433
Smith JR (2012) Spatial and temporal variation in the nature of Pleistocene pluvial phase environments across North Africa. In: Hublin JJ, McPherron SP (eds) Modern origins: a North African perspective. Springer, New York, pp 35–48
Smith JR, Giegengack R, Schwarcz HP, McDonald MMA, Kleindienst MR, Hawkins AL, Churcher CS (2004) Reconstructing pluvial environments and human occupation through study of the stratigraphy and geochronology of fossil-spring tufas, Kharga Oasis, Egypt. Geoarchaeol Int J (Toronto, Ontario), 19(5):407–439
Smith JR, Kieniewicz JM, Adelsberger KA, HeilChapdelaine V (2006) Reconstructing Pleistocene pluvial phase environments, Western Desert, Egypt, from the geochemistry of authigenic water-lain deposits. Geochimica et Cosmochimica Acta, 70(18), supplement 1, p. A599
Sneh A (1982) Drainage systems of the quaternary in Northern Sinai with emphasis on Wadi El-Arish. Z Geomorph 26:129–185
Sneh A, Weissbrod T, Ehrlich E, Horowitz A, Moshkovitz S, Rosenfeld A (1986) Holocene evolution of the northeast corner of the Nile Delta. Q Res 26:194–206
Stanley DJ (1988) Subsidence in the northeastern Nile Delta: rapid rates, possible causes, and consequences. Science 240:497–500
Stanley DJ (1990) Recent subsidence and northeast tilting of the Nile Delta. Mar Geol 94(1–2):147–154
Stanley JD (2012) New geoarchaeological approaches to assess relative sea-level rise on recently submerged Egyptian and Italian coastal margins. Società Geologica d'Italia
Stanley DJ, Maldonado A (1977) Nile Cone: late quaternary stratigraphy and sediment dispersal. Nature 266:129–135
Stanley JD, Toscano MA (2009) Ancient archaeological sites buried and submerged along Egypt's Nile Delta Coast: Gauges of Holocene delta margin subsidence. J Coastal Res 25(1):158–170; 83
Stanley DJ, Warne AG (1993a) Nile Delta: recent geological evolution and human impact. Science 260(5108):628–634
Stanley DJ, Warne AG (1993b) Sea level and initiation of Predynastic culture in the Nile Delta. Nature 363(6428):435–438
Stanley DJ, Warne AG (1994) Worldwide initiation of Holocene marine deltas by deceleration of sea-level rise. Science 265 (5169):228–231
Stanley DJ, Warne AG, Davis HR, Bernasconi MP, Chen Z (1992) Nile Delta: the late Quaternary north-central Nile Delta from Manzala to Burullus Lagoons. Egypt Natl Geogr Res Explor 8(1):22–51
Sturchio N, Sultan M, El-Alfy Z, Taher AG, El-Maghraby A, El-Anabaawy M (1998) Geochemistry and origin of ground water in the newly reclaimed agricultural lands, western Nile Delta, Egypt: preliminary isotopic results. In: Proceedings 4th international conference geology of the Arab World. Cairo University, Egypt

Sultan M, Sturchio N, Hassan FA, Hamdan MAR, Mahmood AM, Alfy ZE, Stein T (1997) Precipitation source inferred from stable isotopic composition of Pleistocene groundwater and carbonate deposits in the Western Desert of Egypt. Q Res 48:29–37

Swezey C (2001) Eolian sediment responses to late Quaternary climate changes: temporal and spatial patterns in the Sahara. Palaeogeogr Palaeoclim Palaeoecol 167:119–155

Szabo BJ, Haynes CV, Maxwell TA (1995) Ages of quaternary pluvials episodes determined by Uranium-Series and radiocarbon dating of lacustrine deposits of Eastern Sahara. Palaeogeogr Palaeoclimatol Palaeoecol 113:227–242

Taher AG (1999) Inland saline lakes of Wadi El Natrun Depression, Egypt. Int J Salt Lake Res 8:149–169

Taher AG, Abdel-Motelib A (2015) New insights into microbially induced sedimentary structures in alkaline hypersaline El Beida Lake, Wadi El Natrun, Egypt. Geo-Mar Lett 35(5):341–353

Timmermann A, Friedrich T (2016) Late Pleistocene climate drivers of early human migration. Nature 538(7623):92

Tousson O (1922) Mémoire sur les ancienne branches du Nil. Memoire Institut d'Égypte 4:212

Van Neer W (1993) Fish remains from the Last Interglacial at Bir Tarfawi(Eastern Sahara, Egypt). In: Wendorf F, Schild R, Close A (eds) Egypt during the last interglacial, Plenum New York, pp 144–154

Van Peer P, Vermeersch PM, Paulissen E (2010) Taramsa 1: Chert quarrying, lithic technology and human burial at the Palaeolithic site of Taramsa 1, Upper Egypt. Leuven University Press, Leuven

Vermeersch PM (2008) A holocene prehistoric sequence in the Egyptian Red Sea area: the tree shelter. Egyptian Prehistory Monographs, 4

Vermeersch PM, Van Neer W (2015) Nile behaviour and late Palaeolithic humans in Upper Egypt during the late Pleistocene. Q Sci Rev 130:155–167

Vermeersch PM, Van Peer P, Moeyersons J, Van Neer W (1994) Sodmein Cave Site, Red Mountains (Egypt). Sahara 6:32–40

Vermeersch PM, Van Peer P, Moeyersons J, Van Neer W (1996) Neolithic occupation of the Sodmein Area, Red Sea Mountains, Egypt. In: Pwiti G, Soper R (eds) Aspects of African archaeology, papers from the 10th congress of the PanAfrican Association for prehistory and related studies. University of Zimbabwe publications, Harare, pp 411–419

Vermeersch PM, Paulissen E, Vanderbeken T (2002) Nazlet Khater 4. An Upper Palaeolithic underground chert mine. In PM Vermeersch (ed) Paleolithic quarrying sites in Upper and Middle Egypt. Egyptian Prehistoy Monograph, Leuvenm, vol 4, pp 211–271

Vermeersch PM, Van Peer P, Rots V, Paulussen R (2005) A survey of the Bili cave and its surroundings in the Red Sea mountains, El Gouna, Egypt. J Afr Archaeol 3:267–276

Vignard E (1923) Une nouvelle industrie lithique: le "S_ebilien". Bull Inst Fr Archeol Orient 22:1–76

Underwood CJ, King C, Steurbaut E (2013) Eocene initiation of Nile drainage due to East African uplift. Palaeogeogr Palaeoclimatol Palaeoecol 392:138–145

Wali AM, Brookfield ME, Schreiber BC (1994) The depositional and diagenetic evolution of the coastal ridges of northwestern Egypt. Sed Geol 90:113–136

Wanas HA, Pickford Mein MP, Soliman H, Segalen L (2009) Late Miocene karst system at Sheikh Abdallah, between Bahariya and Farafra, Western Desert, Egypt: implications for palaeoclimate and geomorphology. Geologica Acta 7(4):475–487

Warne AG, Stanley DJ (1993) Archaeology to refine Holocene subsidence rates along the Nile Delta margin, Egypt. Geology 21:715–718

Waters CN, Zalasiewicz J, Smmerhayes C (2016) The Anthropocene is functionally and stratigraphically distinct from the Holocene. Science 351:6269

Wendorf F, Schild R (1976) Prehistory of the Nile Valley. Academic Press, New York

Wendorf F, Schild R (1980) Prehistory of the Eastern Sahara. Academic Press, 414 pp

Wendorf F, Schild R (eds) (2001) Holocene settlements of the Egyptian Sahara, vol 1. The archaeology of Nabta playa. Kluwer Academic/Plenum, New York

Wendorf F, Schild R (1986) The geological setting. In: Close AE (ed) The prehistory of Wadi Kubbaniya, volume I: The Wadi Kubbaniya skeleton: a late Paleolithic Burial from Southern Egypt, Southern Methodist University Press, Dallas, Texas, pp 7–32

Wendorf F, Schild R (Assemblers), Close AE (eds) (1989) Prehistory of Wadi Kubbaniya III, Southern Methodist University Press, Dallas, Texas

Wendorf F, Schild R, Close A (eds) (1993) Egypt during the late interglacial. Plenum, New York, p 596

Williams MAJ, Williams FM, Duller GAT, Munro RN, El Tom OAM, Barrows TT, Macklin MG, Woodward JC, Talbot MR, Haberlah D, Fluin J (2010) Late Quaternary floods and droughts in the Nile valley, Sudan: new evidence from optically stimulated luminescence and AMS radiocarbon dating. Q Sci Rev 29:1116–1137

Williams MAJ, Duller GAT, Williams FM, Woodward JC, Macklin MG, El Tom OAM, Munro RN, El Hajaz Y, Barrows TT (2015) Causal links between Nile floods and eastern Mediterranean sapropel formation during the past 250 kyr confirmed by OSL and radiocarbon dating of Blue and White Nile sediments. Q Sci Rev 130:89–108

Woodward JC, Macklin MG, Krom MD, Williams MAJ (2007) The Nile: evolution, quaternary river environments and material fluxes. In: Gupta A (ed) Large rivers: geomorphology and management. Wiley and Sons, Ltd

Wysocka A, Welc F, Czarniecka U (2016) Sedimentary environment of the early Pleistocene gravels of the edfu formation from the Saqqara archaeological site (Egypt)—preliminary results. Studia Quat 33 (1):69–78

Youssef AM, El-Shater A, El-Khashab MH, El-Haddad BA (2018) Karst induced geo-hazards in Egypt: case study slope stability problems along some selected desert highways. In Wasowski J et al (eds) Engineering geology and geological engineering for sustainable use of the earth's resources, urbanization and infrastructure protection from geohazards, sustainable civil infrastructures. Springer International Publishing AG, pp 149–164

Zaki A, Giegengack R (2016) Inverted topography in the southeastern part of the Western Desert of Egypt. J Afr Earth Sci 121:56–61

Zaki AS, Pain CF, Edgett KS, Giegengack R (2018) Inverted stream channels in the Western Desert of Egypt: synergistic remote, field observations and laboratory analysis on Earth with applications to Mars. Icarus 309:105–124

Zittel K (1883) Beitrae zur Geologie und Palaeontologie der Libyschen Wuste. Fischer, Cassel

Fossil Flora of Egypt

13

Wagieh E. El-Saadawi, Samar Nour-El-Deen, Zainab M. El-Noamani, Mona H. Darwish and Marwah M. Kamal El-Din

Contents

Abstract

This work summarizes the results of two centuries of laborious investigations of the plant fossil remains in Egypt. As far as possible, emphasis was placed on fossil remains as elements of the biota in the geologic history of Egypt and as indicators of paleoclimate, paleoenvironment and their significance with respect to biostratigraphy and dating. The explored paleoflora of Egypt is very rich and diverse consisted of a mixture of the major plant groups extended from the Devonian to the Quaternary. The discovered fossil plant remains include algae, pteridophytes, gymnosperms, angiosperms (monocots and dicots) and palynomorphs of all groups. Very little is known about fossil fungi in scattered reports. Fossil

W. E. El-Saadawi · S. Nour-El-Deen (✉) · Z. M. El-Noamani · M. M. Kamal El-Din
Faculty of Science, Botany Department, Ain Shams University, Cairo, Egypt
e-mail: samarnour11@hotmail.com

M. H. Darwish
Faculty of Women for Arts, Science and Education, Botany Department, Ain Shams University, Cairo, Egypt

Z. Hamimi et al. (eds.), *The Geology of Egypt*, Regional Geology Reviews,
https://doi.org/10.1007/978-3-030-15265-9_13

evidence of bacteria and bryophytes (except their spores) is generally lacking. The Devonian assemblages are dominated by pteridophytes. The macro- and microfloral assemblages in Lower Carboniferous strata are restricted to pteridophytes, while the first gymnosperm plant appeared in the uppermost Carboniferous. Remains of petridophytes and gymnosperms were common in Early Permian. The plant micro- and macrofossils are extremely scarce in Triassic strata, with only few pteridophytes and gymnosperms. Ferns, cycadophytes and petrified woods of arborescent gymnosperms were recorded from Jurassic-Lower Cretaceous strata with microflora dominated by pteridophytic spores. Fossil coniferopsids first appear was in Early Cretaceous along with angiosperms and microalgae; whereas microflora was dominated by gymnospermic pollen. The richest paleoflora in Egypt, both macro- and microfossil, has been recovered from Cretaceous strata. Ferns, gymnosperms and angiosperms are abundantly preserved in most Egyptian middle and Upper Cretaceous plant-bearing sediments. Fossil plants known to be mangrove or mangrove associates are recorded from Upper Cretaceous strata, in addition to a rich flora of calcareous algae. Fossil plants in the Paleogene and Neogene strata have been extensively studied and documented. Fossil fruits were reported from the Paleocene with a few calcareous green and red algae. The Eocene, Oligocene and lower Miocene strata yielded a diverse and large number of fossil plant remains, especially fossil woods. No such petrified woods were reported in the middle Miocene, upper Miocene or Pliocene strata. Calcareous algae are common components in lower Eocene carbonate sediments. The Eocene strata include the mangrove plant beds of Wadi Hitan, which is a "Natural World Heritage site" reflecting the importance of its plant and animal remains. The Oligocene strata likewise include two very important and renowned fossiliferous sites, viz. Cairo Petrified Forest at Qattamiya (a protected area) and Gebel Qatrani in north Fayum. The latter yielded a diverse and large number of fossil plants particularly fossil wood, leaves, fruits, seeds, a few fungi, macroalgae, besides the first evidence for the occurrence of fossil Trachycarpeae (Palmae) in Africa. Records of palynomorphs of bryophytes, pteridophytes and spermatophytes as well as macroremains of angiosperms were reported from the Quaternary. Paleoclimatic inferences are given. Representatives of some micro- and macrofossil types are illustrated and a map showing some of the main fossiliferous sites in Egypt is provided.

13.1 Introduction

The fossil flora of Egypt includes remains of plants discovered as fossils in strata belonging to past geologic ages in various parts of the country. The plant-bearing strata (see Fig. 13.1 for some of the main fossiliferous localities) cover most geologic ages from the Devonian to the Quaternary and include many commonly recognized types of macro- and microfossils (Figs. 13.2, 13.3, 13.4, 13.5, 13.6).

Until the early 19th century, very little was known about Egyptian fossil flora. Generally, fossil wood of Egypt attracted the attention of a number of devoted European researchers and travelers more than any other kind of fossil plants. The first record of petrified stems is traced back to the 18th century, during the expedition of the French army to Egypt headed by Napoléon Bonaparte (1798–1801 A.D.). Rozière (1813–1824) reported on Egyptian fossil woods; however, under "Mineralogy", which is part of the famous book "*Description de l'Égypte*". Rozière (op. cit.) provided perfect hand-drawings of four fossil wood fragments, two from Wadi Natrun similar to sycamore wood and to aloe and one representative specimen for seyal or genus *Acacia* Miller, which still grows in Egypt, while the fourth fragment is a piece of petrified palm trunk collected from near Aswan. However, the identification of these fragments is not confirmed (except perhaps for palm wood) as determination of petrified wood at that time (i.e., about 200 years ago) was based only on the inspection of the external features.

As far as can be gleaned from the available literature, the first fossil land plants described from Egypt were *Nicolia aegyptiaca* (=*Detarioxylon aegyptiacum* (Unger) Louvet) and *Dadoxylon aegyptiacum* Unger (Unger 1858). This was followed by numerous publications on different kinds of plant fossil remains from different localities by European and later by Egyptian authors.

No fossil bacteria and no megafossil bryophytes (only their spores) had been reported from Egypt. There is reference, however, to a limited number of fossil fungi and a considerable number of fossil algae. Fossil vascular plants (i.e., pteridophytes, gymnosperms and angiosperms) reported from Egypt count several hundreds; these plants usually possess hard tissues and many are arborescent. Plant microfossils reported from Egypt include palynomorphs of all groups.

Fungi and algae are unicellular, filamentous, colonial or thalloid (i.e., not differentiated into organs). Thalli of some macroalgae may take the form of stems, branches and leaves, however, this is only a superficial resemblance. Bryophytes are nonvascular seedless plants, pteridophytes are vascular

Fig. 13.1 Map showing some of the main sites where plant fossil remains occur in Egypt. 1. Gebel El-Khashab, 'Qattamiya', Cairo; 2. Gebel Mokattam; 3. Gebel El-Khashab, southwest of Giza pyramids; 4. Qaret El-Raml; 5. Gebel Ruzza; 6. Wadi Natrun; 7. Cairo-Bahariya Desert Road; 8. Road between Esna and Wadi Halfa. Names of other main sites are indicated on the map

seedless plants, gymnosperms are vascular seed plants and finally angiosperms are vascular flowering seed plants.

The study of floras of past ages or paleofloras encroaches on and contributes to subjects as paleogeography, paleobiogeography, geology, biostratigraphy, paleoecology, paleoenvironment, paleoclimatology and coevolution. Fossil plants are important in dating sediments particularly in the absence of fossil fauna and geological evidence. They are also important in the reconstruction of paleoclimate. Most fossil plants, including leaves, seeds, fruits, pollen are transported, whereas trunks (see, e.g., Fig. 13.2) may sometimes be in situ in original growth position, thus indicating the paleoclimate of their growth site.

The literature dealing with fossil plants belonging to different geologic ages in Egypt is now quite extensive. It is to be found (particularly old publications) in journals of different disciplines including geology and geography. Dealing with such comprehensive literature in rather a limited space of a textbook requires critical priority choices because we need to cover a long history including hundreds of reported plant species belonging to different groups in the plant kingdom and to different geologic ages from the Late Devonian to the Holocene. It is impossible and it is not our intention to give abstracts of all publications on fossil plants of Egypt, however, we are going to concentrate on plants as components of the biota in the geological history of Egypt and as indicators of past climates, past environments and their importance in biostratigraphy and age determination.

The following is, therefore, a brief presentation of the progress of paleobotany in Egypt from its start about two centuries ago until the present day with particular stress on recent activities during the past four or five decades. For a comprehensive information about papers dealing with fossil plants of Egypt and published before 1980 but not mentioned in the text, see the bibliography published by El-Saadawi (1979). The presentation starts with fossils from Devonian strata in the Paleozoic era to fossils from Holocene strata at the end of the Cenozoic era.

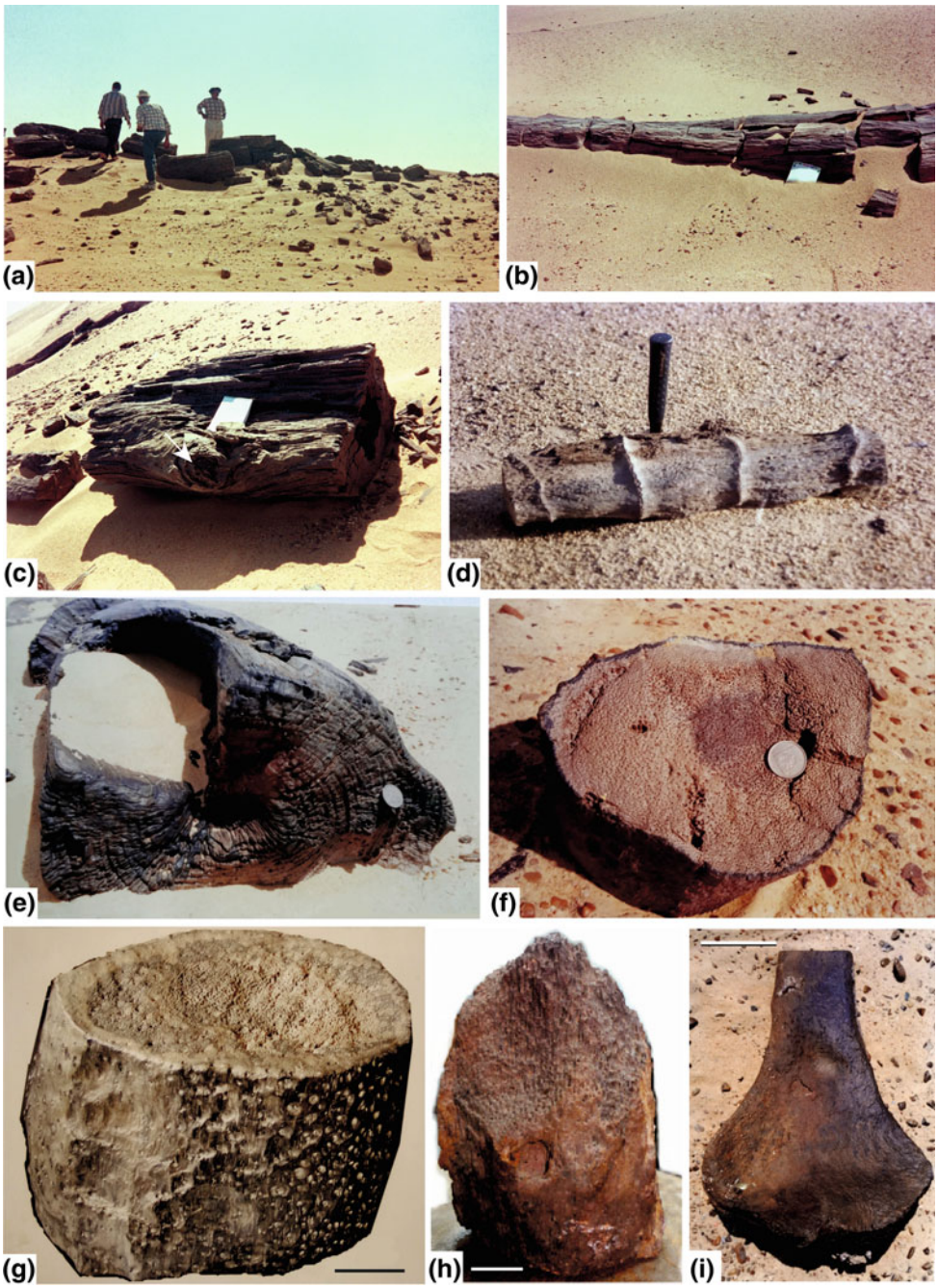

Fig. 13.2 **a**, **b** Large petrified logs exposed on desert surface and break across into fragments of variable lengths; **c** wood fragment showing a branch (arrow); **d** a petrified log showing nodes and internodes with clearly marked nodal lines; **e** a wood log showing growth rings; **f–h** petrified palm logs in the field; **i** a petrified palm sheathing leaf base and lower part of petiole; scales: g, h = 5 cm; i = 10 cm

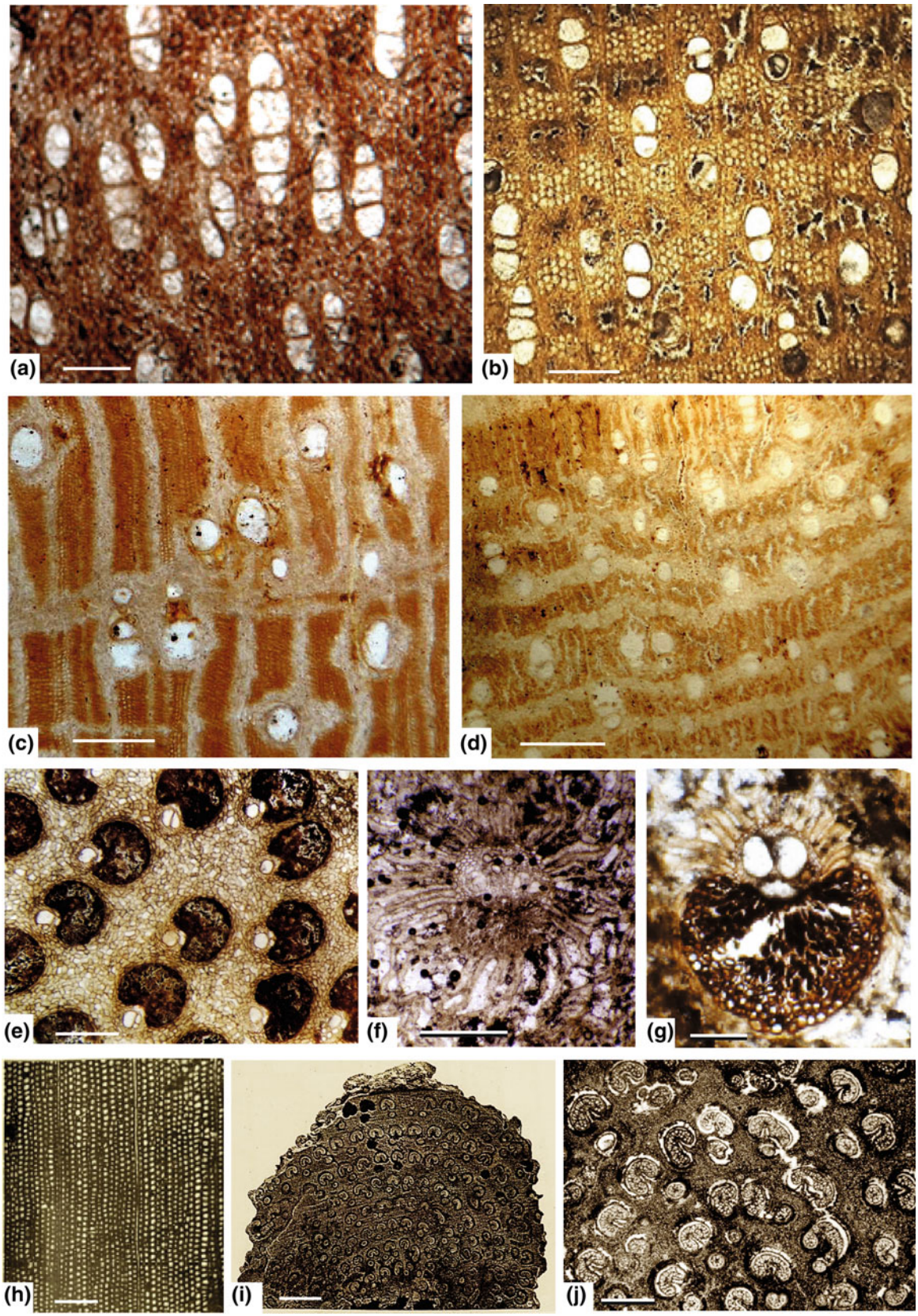

Fig. 13.3 Transverse thin sections of fossil wood. **a** *Bombacoxylon owenii,* early Miocene, Gebel El-Khashab Formation, Cairo-Bahariya desert road; scale = 500 μm; **b–d** petrified dicot woods from Oligocene CPF, **b** *Andiroxylon aegyptiacum,* scale = 200 μm; **c** *Detarioxylon aegyptiacum*, scale = 500 μm; **d** *Cynometroxylon tunesense*, scale = 500 μm. **e–g** Petrified palm woods: **e** *Palmoxylon compactum*, early Miocene, Gebel Ruzza, scale = 1.5 mm; **f, g** *Palmoxylon araneus* and *P. elsaadawii*, respectively, Oligocene Gebel Qatrani Formation, Fayum; scale = 500 μm. **h** Gymnosperm wood *Protophyllocladoxylon leuchsii,* Cretaceous, (reproduced from Kräusel 1939), scale = 200 μm. **i, j** Extinct fern *Weichselia reticulata*, Early Cretaceous, Bahariya Oasis (reproduced from Hirmer 1925, as *Osmundites* (?) *stromeri*; see Kräusel 1939); scales: i = 20 mm; j = 3 mm

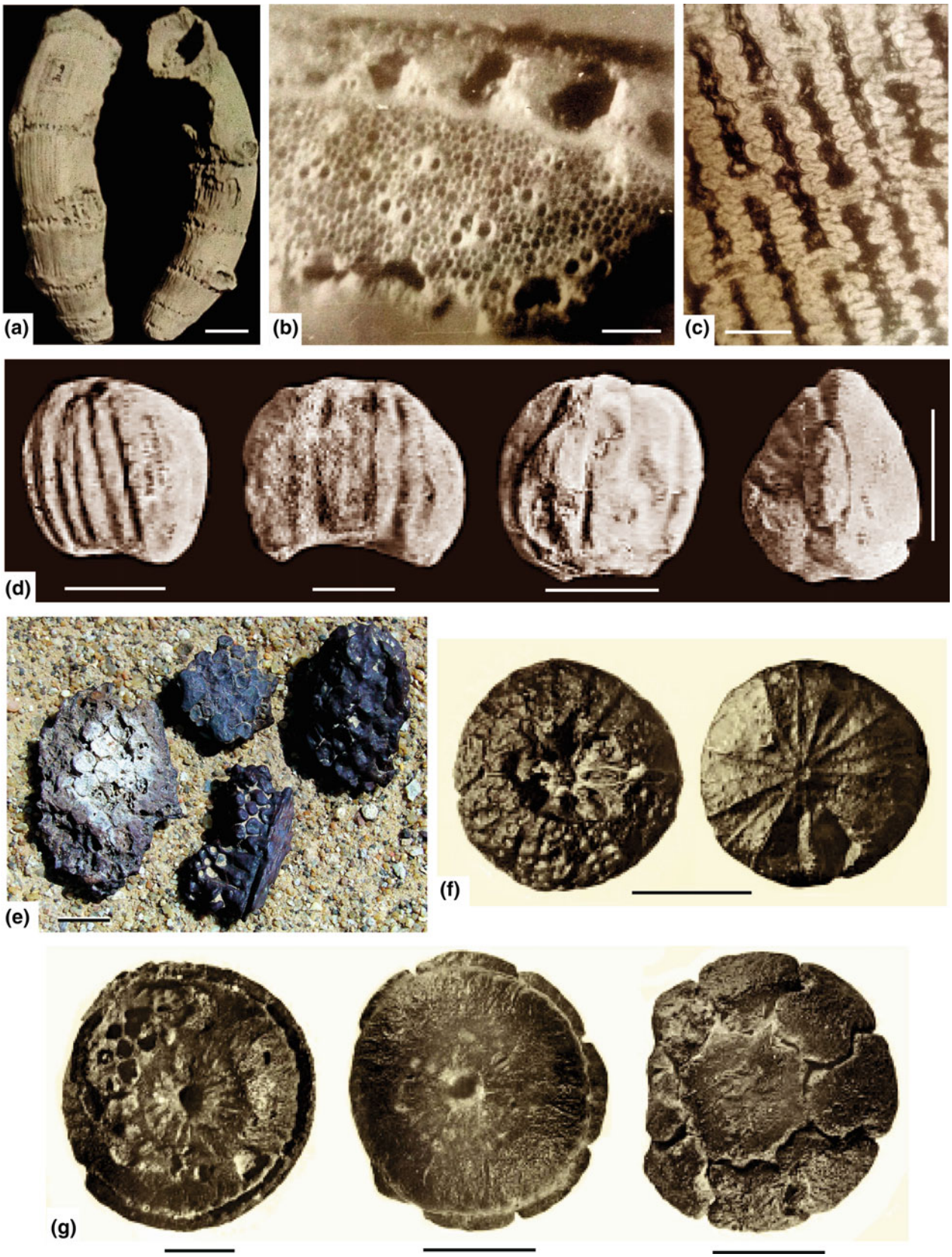

Fig. 13.4 **a–c** *Phragmites australis*, Pleistocene, Fayum (El-Saadawi et al. 1975, as *P. communis*), **a** Two different views of a fossil culm-base, scale = 1 cm; **b** a cut surface of an internode showing internal structure, scale = 0.5 mm; **c** a peel showing ripples of walls of epidermal cells, scale = 20 μm. **d** Fruits of *Nypa burtini*, Gebel Giuchi, Mokattam, middle Eocene (reproduced from Kräusel 1939, as *Nipadites sickenbergeri*), scale = 5 cm. **e** *Epipremnum* sp. (whole infructescences), early Oligocene Gebel Qatrani Formation, Fayum (Nour-El-Deen 2015), scale = 2 cm; **f** fruits of *Palaeowetherellia schweinfurthii*, Farafra, Late Cretaceous, scale = 1 cm (reproduced from Kräusel 1939, as *Diospyros schweinfurthi*); **g** fruits of *Nymphaeopsis bachmanni* Kräusel, Nymphaeaceae, Mokattam, early Oligocene, scale = 1 cm (reproduced from Kräusel 1939)

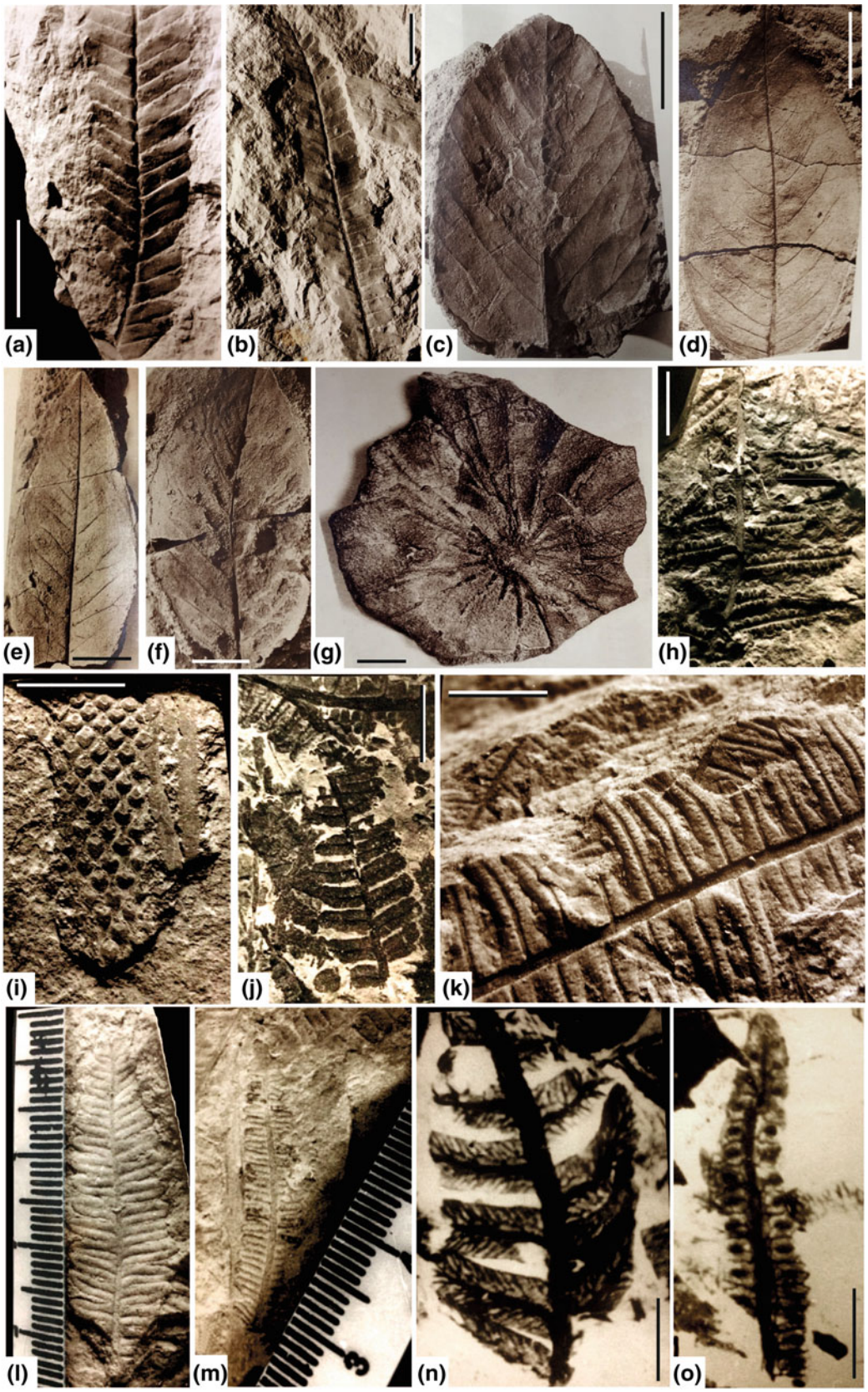
(a)
(b)
(c)
(d)
(e)
(f)
(g)
(h)
(i)
(j)
(k)
(l)
(m)
(n)
(o)

◀ **Fig. 13.5** **a, b** Fossil cycad leaves of *Otozamites daragii*, Lower Cretaceous beds, western side of Gulf of Suez; a) impression of the lower half of a frond, scale = 3 cm, **b** impression of the upper half of the same frond, scale = 2 cm; **c–g** Reproduced from Seward 1935, Early Cretaceous to Senonian, Nubian Sandstone; **c** *Dipterocarpophyllum humei*, scale = 5 cm; **d** *Dicotylophyllum balli* Seward, scale = 2 cm; **e** *Dicotylophyllum egyptiacum* Seward, scale = 3 cm; **f** *Dipterocarpophyllum zeraibense*, scale = 2 cm; **g** *Nelumbium* (corrected to *Nelumbites shweinfurthi* in Kräusel 1939), scale = 1 cm; **h** *Pecopteris unita*, Carboniferous, Abu Darag, scale = 5 mm; **i** *Lepidodendron mosaicum*, Early Carboniferous, Magharet El-Maiah, west-central Sinai, scale = 20 mm. **j–o** All from Late Jurassic to Early Cretaceous, Abu Darag, western side of Gulf of Suez: **j** *Cladophlebis gallatinensis*, scale = 10 mm; **k** *Phlebopteris smithii*, scale = 10 mm; **l** *Cladophlebis* sp.; **m** *Asplenium whitbyense*; **n** *Todites williamsonia*; scale = 3 mm; **o** *Laccopteris pulchella*, scale = 5 mm (**h–o** from Darwish 1990)

13.2 Paleozoic Era

13.2.1 Devonian Strata

Fourteen taxa of pteridophytes were reported from Devonian strata in south Egypt and north Sudan by Lejal-Nicol (1990) including one species of each of the genera cf. *Amadokia* Zalessky, *Archaeosigillaria* Kidston, cf. *Archaeosigillaria*, *Heleniella* Zalessky, *Lepidosigillaria* Kräusel and Weyland and cf. *Lepidosigillaria*; two species of each of cf. *Cyclostigma* Haught. and *Precyclostigma* Lejal-Nicol and four species of *Lepidodendropsis* Lutz.

13.2.2 Devonian-Carboniferous Strata

Six species of pteridophytes were reported from Upper Devonian-Tournaisian (=lowermost Carboniferous) strata in Wadi Malik area (in southwest Egypt) by Lejal-Nicol (1990) belonging to the genera *Archaeosigillaria*, cf. *Heleniella*, *Lepidodendron* Sternberg, *Lepidodendropsis*, *Pseudolepidodendropsis* Schweitzer and *Sublepidodendron* Nathorst ex Hirmer.

13.2.3 Lower Carboniferous Strata

Macro- and microfossil plant remains in Lower Carboniferous strata in Egypt belong to only pteridophytes. From Tournaisian-Visean age in Wadi Malik area Lejal-Nicol (1990) reported two species of *Prelepidodendron* Danzé-Corsin and one species of each of *Rhacopteris* Schimper and *Triphyllopteris* Schimper.

From Visean strata in Wadi Malik Lejal-Nicol (1981, 1987) and Klitzsch and Lejal-Nicol (1984) reported four species of *Lepidodendropsis* and one species of *Caenodendron* Zalessky, *Eskdalia* Kidston, *Lepidodendron*, *Lepidosigillaria* and *Nothorhacopteris* Archangelsky.

A pteridophyte species *Eremopteris whitei* Berry was reported from west of Abu Ras plateau (in Wadi Malik Formation), which resembles a species named *Sphenopteris whitei* (Berry) Jongmans (Jongmans and van der Heide 1955) from Lower Carboniferous rocks of Gulf of Suez (after Lejal-Nicol 1990).

The species *Noeggerathia dickeri* Horowitz of an extinct genus of noeggerathialean plant that lived during the Late Carboniferous and Early Permian periods was reported by Horowitz (1973) from the Lower Carboniferous of the upper Sandstone Formation of southwestern Sinai.

From Early Carboniferous age of Gebel Uweinat (in Wadi Malik Formation), Lejal-Nicol (1990) reported on one species of each of the genera *Cyclostigma*, *Lepidodendropsis*, cf. *Lepidodendropsis* and *Precyclostigma*.

From Early to mid-Carboniferous age (mostly Visean age) on the western side of Gulf of Suez in Wadi Dakhal area, Lejal-Nicol (1990) reported one species of each of the genera *Eskdalia*, *Lepidodendron*, *Lepidodendropsis*, *Protasolanus* Hörich, *Rhacopteris* and *Sublepidodendron*.

From Abu-Thora Formation in southwest Sinai (Early Carboniferous Visean age), Darwish and El-Kelani (2001) reported on the following taxa: *Heleniella costulata* Lejal, *Lepidodendron veltheimii* Sternberg, *Lepidodendropsis hirmeri* Lutz, *L. schuermanni* Jongmans and *Lepidophloios* (*Lepidofloyos*) *laricinum* Sternberg. The Early Carboniferous macrofossil flora of Egypt had many features in common with floras of other parts of the world as South America, Siberia, Mongolia and Himalaya (Lejal-Nicol 1990).

Many authors described microfossil floras from coal seams intercalating the sandstones of the Abu-Thora Formation exposed in west-central Sinai (e.g., Synelnikov and Kollerov 1959; Saad 1965; Kora and Schultz 1987). Saad (1965) described the spore assemblage obtained from two coal samples from Um Bogma district, west-central Sinai. The first sample was taken from Wadi Thora and yielded a rich spore assemblage including *Calamospora* Schopf, Wilson and Bentall, *Convolutispora* Hoffmeister, Staplin and Malloy, *Densosporites* (Berry) Schopf, Wilson and Bentall, *Lycospora* (Schopf, Wilson and Bentall) Potonié and Kremp, *Punctatisporites* (Ibrahim) Potonié and Kremp and *Raistrickia* (Schopf, Wilson and Bentall) Potonié and Kremp, and a middle Carboniferous age was proposed for this sample. The second sample was taken from Wadi Abu Zorab and the recovered palynoassemblage was dominated by *Calamospora*, *Convolutispora*, *Densosporites*, *Planisporites* (Knox) Potonié, *Punctatisporites*, *Verrucosisporites* (Ibrahim) Smith and Butterworth and *Verrucososporites* Knox. A Westphalian age (Late Carboniferous) was suggested for this sample.

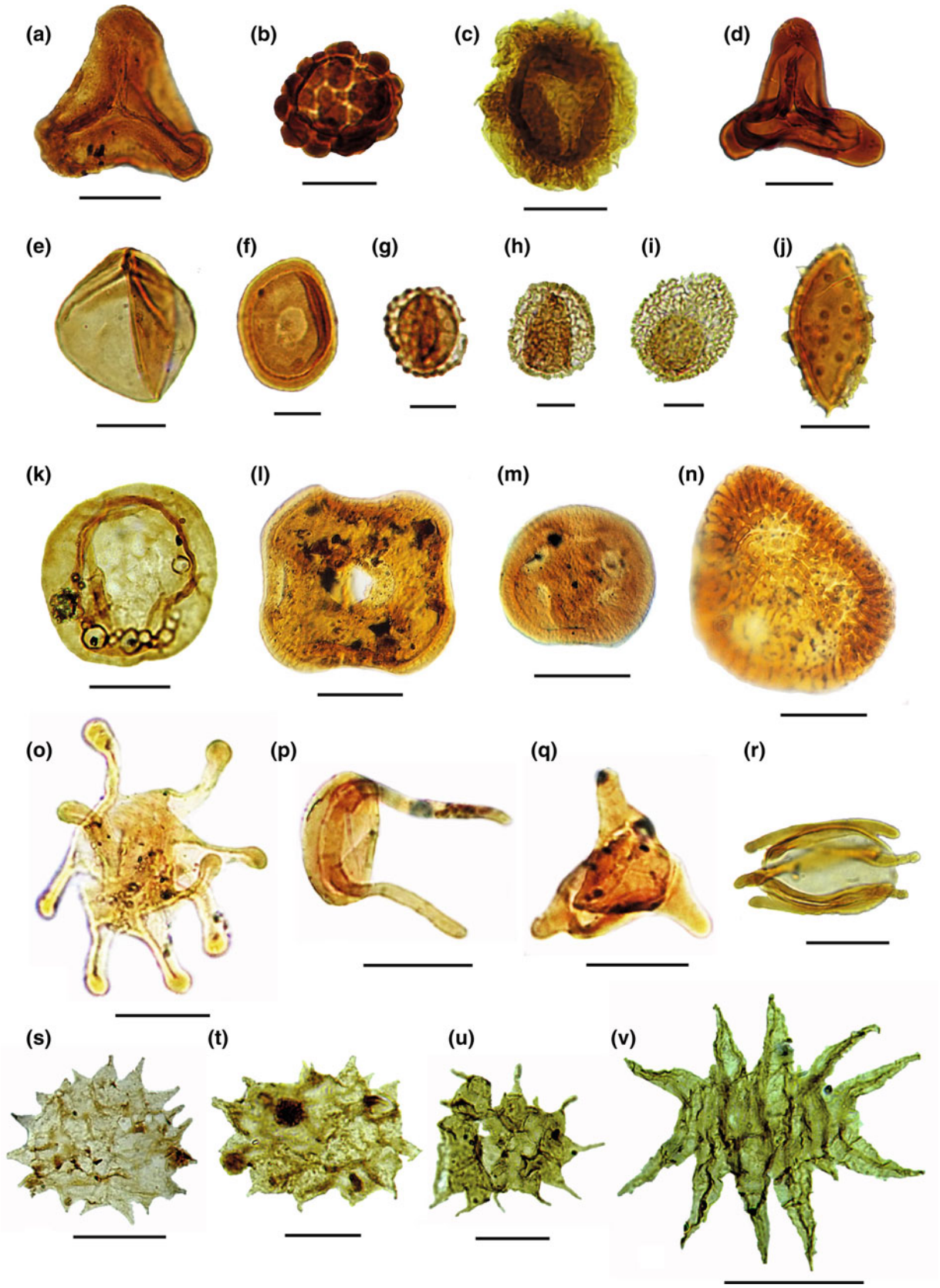
(a)
(b)
(c)
(d)
(e)
(f)
(g)
(h)
(i)
(j)
(k)
(l)
(m)
(n)
(o)
(p)
(q)
(r)
(s)
(t)
(u)
(v)

◀ **Fig. 13.6** Microfossils from subsurface Cretaceous strata in the northern part of Egypt. Figures **a–k**, **r–v** from northeast Sinai and Figs **l–q** from northern part of Western Desert; all from El-Noamani (2015, 2018), Ibrahim et al. (2017), El-Noamani and Saleh (2018). **a–e Pteridophytic spores**. **a** *Gleicheniidites senonicus* Ross, scale = 30 μm; **b** *Leptolepidites psarosus* Norris, scale = 20 μm; **c** *Crybelosporites pannuceus*, scale = 30 μm; **d** *Trilobosporites laevigatus* El Beialy, scale = 30 μm; **e** *Triplanosporites* sp., scale = 20 μm. **f, k, o–r Gymnosperm pollen**. **f** *Classopollis torosus* (Reissinger) Couper, scale = 10 μm; **k** *Araucariacites australis* Cookson ex Couper, scale = 30 μm; **o** *Elaterocolpites castelainii*, scale = 30 μm; **p** *Elateroplicites africaensis*, scale = 30 μm; **q** *Sofrepites legouxae* Jardiné, scale = 30 μm; **r** *Elaterosporites klaszii*, scale = 20 μm. **g–j, l–n Angiosperm pollen**. **g** *Brenneripollis reticulatus* (Brenner) Juhász and Góczán, scale = 10 μm; **h** *Afropollis operculatus* Doyle, Jardiné and Doerenkamp, scale = 10 μm; **i** *Afropollis jardinus*, scale = 10 μm; **j** *Echinomonocolpites* sp., scale = 20 μm; **l** *Cretacaeiporites densimurus*, scale = 30 μm; **m** *C. scabratus*, scale = 30 μm; **n** *C. aegyptiaca*, scale = 30 μm. **s–v Fossil microalgae**. **s** *Pediastrum boryanum* (Turpin) Meneghini, scale = 30 μm; **t** *P. kawraiskyi*, scale = 20 μm; **u** *P. simplex* Meyen, scale = 30 μm; **v** *Scenedesmus acuminatus*, scale = 30 μm

From subsurface core samples of Abu-Thora Formation in Um Bogma area, Kora (1993) identified late Visean to early Westphalian miospore assemblage including 72 species of pteridophyte spores related to Sphenopsida (e.g., *Calamospora*), Filicopsida (e.g., *Cyclogranisporites* Potonié and Kremp, *Punctatisporites* and *Verrucosisporites*) and Lycopsida (e.g., *Cirratriradites* Wilson and Coe, *Densosporites*, *Lycospora* and *Raistrickia*). The relative high representation of spores produced by herbaceous lycopods like *Densosporites* in the recorded assemblage indicates a partly-forested condition, marginal to swamps (Kora 1993).

13.2.4 Lower-Upper Carboniferous Strata

Sixteen species of pteridophytes were reported from Visean to Namurian age in Wadi Mukattab area in Sinai by Lejal-Nicol (1990) including one species of each of the genera cf. *Archaeocalamites* Stur, *Bothrodendron* Lindley and Hutton, *Caenodendron*, *Eskdalia*, *Lepidophloios* Sternberg, cf. *Tomiodendron* Radczenko and cf. *Triphyllopteris*; two species of each of *Lepidodendron*, *Lepidodendropsis* and *Nothorhacopteris*; and three species of *Rhacopteris*. This assemblage suggests a warm climate with varying degrees of humidity. It is possible to distinguish three areas, each having its own characteristic species: lowlands (swamps) with only Lycophyta, midlands (floodplains) with Lycophyta and fragile Pterophyta and uplands (sunny areas) with Lycophyta and Pterophyta with resistant leaf lamina (Lejal-Nicol 1990).

Three species of pteridophytes were reported from Namurian age (Early/Late Carboniferous) at Gebel Uweinat by Lejal-Nicol (1990), viz. cf. *Artisia* Sternberg (1 sp.) and *Rhodea* Sternberg (2 spp.). The occurrence of *Cordaites angulostriatus* Grand'Eury (gymnosperms) at higher levels seems to indicate a Stephanian age (Late Carboniferous).

13.2.5 Upper Carboniferous Strata

Four species of pteridophytes were reported from Sinai from lowermost part of Upper Carboniferous by Seward (1932) (he says Lower Carboniferous not ruled out), viz. *Halonia* Lindley and Hutton (1 sp.) and *Lepidodendron* (3 spp. or one of which is *Lepidostrobus* Brongniart).

Six species of pteridophytes (four Lycophyta and two Sphenophyta) and one species of gymnosperms (Coniferophyta) were reported from near Bir Quseib in the Gulf of Suez in strata of Stephanian age (Upper Carboniferous) by Lejal-Nicol (1990) under the genera *Equisetites* Sternberg, *Lepidodendron*, *Sigillaria* Brongniart, *Sphenopteris* (Brongniart) Sternberg, *Syringodendron* Sternberg, cf. *Tunguskadendron* Thomas and Meyen (of pteridophytes) and *Lebachia* Florin (now *Walchia* Sternberg) (of gymnosperms).

Six species of pteridophytes and four of gymnosperms were reported from Upper Carboniferous strata of Rod El-Hamal Formation in Wadi Araba on the western side of Gulf of Suez by Darwish and El-Safori (2016), viz. *Bothrodendron* (1 sp.), *Calamites* Brongniart (2 spp.), *Lepidodendron* (3 spp.) of pteridophytes and *Artisia* (2 spp.), *Callipteridium* Weiss (1 sp.) and *Cordaites* Unger (1 sp.) of gymnosperms.

Before the Permian, i.e., from Namurian to Westphalian, the paleoflora was poor in Egypt and there are even no records of macrofossil flora from the Westphalian (Lejal-Nicol 1990), however, as mentioned earlier, Saad (1965) reported on microfossil flora from Westphalian strata in west-central Sinai.

13.2.6 Permian Strata

Fragments of stem and leaf impressions of pteridophytes (Sphenophyta and Pterophyta) and gymnosperms (Cordaitophyta) were reported from Early Permian of Wadi El-Dome, on the western side of the Gulf of Suez by El-Saadawi et al. (2003). Permian plant remains were reported earlier (Schuermann et al. 1963; Lejal-Nicol 1987, 1990) from two other sites also on the western side of the Gulf of Suez, viz. Wadi Araba and Suez area. The plant remains belong to pteridophytes (Sphenophyta and Pterophyta) and gymnosperms (Pteridospermatophyta, Cordaitophyta and Coniferophyta).

The Permian flora in the three mentioned sites includes the following taxa:

1. Wadi El-Dome. Pteridophytes-Sphenophyta: *Annularia* Sternberg (1 sp.), *Asterophyllites* Brongniart (1 sp.), *Calamites* (2 spp.) and *Equisetites* (1 sp.); Pteridophytes-Pterophyta: *Pecopteris* (Brongniart) Sternberg (1 sp.); Gymnosperms-Cordaitophyta: *Cordaites* (2 spp.).

2. Wadi Araba. One species of each of the following taxa: Pteridophytes-Sphenophyta: *Lobatannularia* Kawasaki, cf. *Lobatannularia*, *Sphenophyllum* Brongniart and cf. *Sphenophyllum*; Pteridophytes-Pterophyta: *Asterotheca* Presl ex Corda; Gymnosperms-Pteridospermatophyta: *Gangamopteris* McCoy, *Callipteris* Brongniart (now *Autunia* Krasser) and *Thinnfeldia* Ettingshausen; Gymnosperms-Cordaitophyta: *Cordaites*, *Cordaitanthus* Feistmantel and *Dorycordaites* Zeiller; Gymnosperms-Coniferophyta: *Walchia*.

3. Suez Area. One species of each of the following taxa: Pteridophytes-Sphenophyta: cf. *Lobatannularia*, *Sphenophyllum*; Pteridophytes-Pterophyta: *Asterotheca*; Gymnosperms-Pteridospermatophyta: *Autunia*, cf. *Gangamopteris* and *Thinnfeldia*; Gymnosperms-Cordaitophyta: *Cordaitanthus*; Gymnosperms-Coniferophyta: *Walchia*.

The occurrence of *Autunia*, *Lobotannularia*, *Thinnfeldia* associated together in Egypt during the Permian suggests that Egypt during that time was intermediate in position between the paleofloristic provinces of the world (Euramerica, Gondwana, etc.) since these taxa were not known before from North Africa. The climate in the Permian became less warm than in the Carboniferous, Sphenophyta and Cordaitophyta grew in the lowlands, Pterophyta inhabited the flood plains, while the highlands were occupied by conifers (Lejal-Nicol 1990).

From the Permian-Triassic of Wadi Wahedia (Red Beds) in southwestern Egypt, Dupéron-Laudoueneix and Lejal-Nicol (1981) reported on the occurrence of the gymnosperm wood *Dadoxylon sudanense* Dupéron-Laudoueneix and Lejal-Nicol.

13.3 Mesozoic Era

13.3.1 Triassic Strata

A continental flora was reported by Carpentier and Farag (1948) from the Rhaetic (uppermost Triassic) strata of El-Galala El-Bahariya on the western side of the Gulf of Suez, including pteridophytes and gymnosperms:

Pteridophytes-Sphenophyta: *Equisetites laevis* Halle and *E. scanicus* (Sternb.) Halle;

Pteridophytes-Pterophyta: *Cladophlebis* sp., *Phlebopteris* aff. *muensteri* (Schenk) Hirmer and Hörhammer, *Todites williamsoni* (Brongniart) Seward;

Gymnosperms-Cycadophyta: *Zamites gigas* (Lindley and Hutton) Morris and *Z. schmiedellii* Sternberg.

Palynological data dealing with Triassic palynofloras of Egypt are almost lacking; this may be partly due to the uplift and erosion which prevailed during that time in vast areas of the country (Schrank 1991).

13.3.2 Jurassic Strata

Abd El-Shafy and El-Saadawi (1982) reported on Bathonian (Middle Jurassic) paleoflora from Ras El-Abd area south of Khashm El-Galala on the western side of the Gulf of Suez. The fossiliferous bed is rich with fragmentary plant impressions and marine fauna. Plant impressions consist of Cycadophyta (gymnosperms) foliage (*Otozamites galalaensis* El-Saadawi and *O. laceii* El-Saadawi), fern leaves and small branches but no conifers recorded. The rock composition of the plant-bearing bed with the presence of benthonic foraminifera and holothuroid sclerites in addition to the absence of large stems and roots indicate the transportation of the plant fragments from terrestrial biotope to a nearby shallow marine biotope; rapid biodegradation of organic matter took place in a warm paleoclimate. The two species of *Otozamites* of Ras El-Abd resemble *O. falsus* Harris and *O. mimetes* Harris of the Middle Jurassic of Yorkshire (Harris 1949) and *Otozamites* sp. of the Middle Jurassic of India (Bose 1974).

Ash (1972) reported on leaves of the fern (pteridophytes) *Piazopteris branneri* (White) Lorch from Lower Jurassic strata of Egypt. Webber (1961) reported on fern leaves from the Jurassic of Egypt. Lorch (1967) recorded fern fronds (leaves) and a few gymnosperms from the Jurassic of El-Maghara (=Al-Maghara) in north-central Sinai.

Al-Far (1966) reported on Jurassic coal deposits, plant and algal remains in many beds of Gabal El-Maghara in northern Sinai. He mentioned many sites, such as Wadi El-Mahl, Bir El-Maghara, Wadi Gohr El-Dabaa, Wadi Safa, Shusht El-Maghara, Wadi Sadd-el-Mashabba (Mashabba Formation).

Al-Far (1966) said that Shusha Formation at Bir Eshaish probably includes the following plant remains: *Eboracia* Thomas, *Marattiopsis* Schimper and *Stachypteris* Pomel (pteridophytes); *Baiera* Braun, *Pterophyllum* Brongniart and *Thinnfeldia* (gymnosperms); and Safa Formation (in the upper coal-bearing horizons) probably includes: *Cycadites* Buckland, *Otozamites* Braun, *Ptilophyllum* Morris and *Zamites* Brongniart (all gymnosperms); for more details on plant remains see Barthoux (1922) and Edwards (1932).

Al-Far (1966) concluded that the pre-Cretaceous rocks of El-Maghara region include three continental formations and cross-bedded quartzose sandstones and three marine formations. The three continental formations (viz. Mashabba, Shusha and Safa) are nonmarine or continental as they

proved to be fossil plant and/or coal-bearing and the main bulk of their strata is of deltaic, lagoonal, swampy, estuarine character.

The coal-bearing Safa Formation is of Bathonian age (Middle Jurassic). Al-Far (1966) mentioned that there is no proof as yet that indicates a drift or allochthonous origin for the Maghara coals. He also mentioned that the coal-bearing zone at Ayun Musa (southwest of Maghara), as revealed by spore analysis, does not correlate with the Safa Formation, however, Ayun Musa coals are of an early Bajocian age.

In Egypt there are reports on microfossil floras of Middle and Late Jurassic. The Middle Jurassic microfossil floras were described briefly by many authors (e.g., Saad 1963; Al-Far et al. 1965; Komarova et al. 1973; Sultan and Soliman 1978). These consist predominantly of pteridophytic spores such as *Concavisporites* Pflug, *Gleicheniidites* Ross ex Delcourt and Sprumont, *Ischyosporites* Balme, *Matonisporites* Couper and *Punctatisporites* Ibrahim (=*Todisporites* Couper) and gymnosperm pollen such as *Araucariacites* Cookson ex Couper, *Callialasporites* Dev, *Eucommiidites* Erdtman and *Inaperturopollenites* Pflug ex Pflug and Thomson. The diagnostic spore-pollen association for the Late Jurassic includes *Callialasporites*, *Cicatricosisporites* Potonié and Gelletich, *Concavissimisporites* Delcourt and Sprumont, *Ischyosporites* and *Spheripollenites* Couper (Schrank 1991).

13.3.3 Upper Jurassic-Lower Cretaceous Strata

Fossil plants found in the type locality of the Gilf Kebir Formation at Akaba pass show the presence of many pteridophyte and gymnosperm taxa in the Upper Jurassic and Lower Cretaceous strata, however, the absence of angiosperms indicates that the strata belong more probably to the Jurassic (Lejal-Nicol 1990).

Pteridophytes include *Cladophlebis* Brongniart (1 sp.), *Phlebopteris* Brongniart (3 spp.) and *Weichselia reticulata* (Stokes and Webb) Fontaine.

Gymnosperms include one species of each of the genera: *Dadoxylon* (*Araucarioxylon*), *Ginkgoites* Seward, *Podozamites* Braun, *Pterophyllum* and Cycadophyta fructifications.

A similar flora is present in the south of Gilf Kebir and the northeastern foothills of Gebel Uweinat with further species belonging to genera *Cladophlebis*, *Cyclopteris* Brongniart, *Pagiophyllum* Heer, *Phlebopteris* and *Podozamites* indicating a rather warm climate with short rainy seasons (Lejal-Nicol 1990).

Petrified gymnosperm wood of *Metapodocarpoxylon libanoticum* (Edwards) Dupéron-Laudoueneix and Pons from Late Jurassic-Early Cretaceous of Gebel Kamil in southwestern Egypt was described by Youssef (2002) erroneously under *Xenoxylon* Gothan. Many silicified gymnosperm trees identified as *Dadoxylon* (*Araucarioxylon*) *dallonii* were reported from the Jurassic of Wadi Wahedia (Lower Clastics) by Dupéron-Laudoueneix and Lejal-Nicol (1981).

The exact position of the Jurassic-Cretaceous boundary in Egypt is difficult to determine palynologically, because most of the recorded palynomorphs (whether marine or terrestrial) are stratigraphically long-ranging forms (Schrank 1991).

13.3.4 Lower Cretaceous Strata

An Early Cretaceous (Aptian-Albian) flora was recorded by Lejal-Nicol (1981) from the type locality of Abu Ballas Formation including angiosperms and ferns (*Weichselia reticulata*). From Wadi Shait, north of Aswan, she reported angiosperm leaves (*Araliaephyllum* Fontaine, *Ficophyllum* Fontaine, etc.). And from west of Kharga, in the southeastern foreland of Abu Tartur plateau, in the basal part of Maghrabi Formation she recorded angiosperms as *Cornophyllum* Newberry, *Magnoliaephyllum* Krasser and others (Lejal-Nicol 1990).

El-Saadawi and Farag (1972), Aboul Ela et al. (1989) and El-Saadawi and Kedves (1991) described megafossil plants and palynomorphs from kaolinitic layers of Early Cretaceous age exploitable from Abu Darag area on the western side of the Gulf of Suez. The macrofossil flora includes the following:

Pteridophytes: fern leaves;

Gymnosperms: Cycadopsida foliage: *Otozamites daragii* El-Saadawi and Kedves and *O. major* El-Saadawi and Kedves (Fig. 13.5a, b);

Cycadopsida reproductive organs: *Williamsonia aegyptiaca* El-Saadawi and Kedves;

Coniferopsida: *Pinus* L. stem, *Araucaria* Jussieu twigs, cones and seeds of conifers.

The microfossil flora identified by Aboul Ela et al. (1989) includes 25 palynomorphs and characterizes a Berriasian-Barremian (Early Cretaceous) age but a Late Jurassic-Early Cretaceous age cannot be excluded, and the recovered palynomorphs point to a terrestrial freshwater habitat. El-Saadawi and Kedves (1991) have confirmed an Early Cretaceous age and stated that they have not observed hystrichosphaerids or such kind of microremnants which indicate saltwater or brackish water conditions.

13.3.5 Middle to Upper Cretaceous Strata

From the middle Cretaceous of Aswan area Barthoux and Fritel (1925) reported on many species belonging to ferns, gymnosperms and angiosperms (*Cinnamomum* Schaeffer,

Laurus L., *Magnolia* L., *Nelumbium* Jussieu, *Sabalites* Saporta, *Weichselia* Stiehler, *Zosterites* Brongniart and many others).

From Wadi Zeriab, south of Quseir, Seward (1935) reported leaves of several angiosperms as *Dicotylophyllum* Saporta, *Dipterocarpophyllum* Edwards and *Nelumbium* which he dated Cretaceous to Tertiary (Fig. 13.5c–g).

Kräusel (1939) identified a large number of ferns, gymnosperms and angiosperms (monocots and dicots) from middle to Late Cretaceous age of different localities; he reported *Weichselia* (Matoniaceae) and *Nelumbites* (Nymphaeaceae) from Wadi Araba and Bahariya; *Dadoxylon* (Araucariaceae) from Gebel Hefhuf; and taxa belonging to families Dipterocarpaceae and Nymphaeaceae from between Esna and Wadi Halfa; Proteaceae, Sterculiaceae (or Malvaceae s.l.) and Ebenaceae from between Kharga and Dakhla Oases.

The beds overlying the Abu Aggag Formation, on the west bank of the Nile, yielded an association of fruits and leaves of angiosperms confirming the middle Cretaceous age given to these beds by Barthoux and Fritel (1925) as mentioned by Lejal-Nicol (1990).

Lejal-Nicol (1990) mentioned that the basal part of the Kiseiba Formation, northeast of Wadi Halfa includes a rich flora of Cenomanian to Maastrichtian age (Late Cretaceous) with species of *Dipterocarpophyllum*, *Magnoliaephyllum*, *Rogersia* Fontaine and others.

13.3.6 Upper Cretaceous Strata

Kedves et al. (2004a) reported on silicified coniferous gymnosperm woods collected from southwest of Aswan city on the western side of Lake Nasser at two localities, viz. Sinn-El-Khaddab and Garf Hussein which are of Late Cretaceous age.

Fossil woods of gymnosperms had been reported earlier (e.g., Unger 1858; Kräusel 1939; Youssef et al. 2000) from localities not far away from Aswan area, viz. the road between Esna and Wadi Halfa, Gebel Garra and Kharga Oasis. Kedves et al. (2004a) stated that the wood anatomical characteristic features of the specimens of Sinn-El-Khaddab and Garf Hussein refer to a tropical gymnosperm taxon (cf. *Podocarpoxylon* sp.).

Youssef and El-Saadawi (2004) spotted 60 large silicified trunks of arborescent gymnosperms in the desert area between Kharga and Dakhla Oases (of Late Cretaceous age); the only well-preserved trunk proved to be of *Metapodocarpoxylon libanoticum* which means that the vertical range of this species, in Egypt, extended from the end of the Jurassic till the Late Cretaceous.

Silicified tree trunks of gymnosperms (12 of them counted) and many scattered wood fragments were reported by Youssef et al. (2000) from an Upper Cretaceous desert site, about 12 km northwest of Kharga Oasis. One of the trees proved to represent a new to science conifer (araucarioid type of wood) which they named *Agathoxylon lifiyii* Youssef et al. Youssef et al. (2000) mentioned that the road between Kharga and Dakhla Oases (of Late Cretaceous age) yielded, until then, three gymnospermous woods, viz. *Agathoxylon lifiyii*, *Dadoxylon aegyptiacum* and *Protophyllocladoxylon leuchsii* Kräusel (Fig. 13.3h) in addition to nine species of angiospermous woods, viz. *Celastrinoxylon celastroides* (Schenk) Kräusel (Celastraceae), *Detarioxylon aegyptiacum* (Fabaceae=Leguminosae), *Ebenoxylon ebenoides* (Schenk) Edwards (Ebenaceae), *Ficoxylon* sp. (Moraceae), *Hibiscoxylon niloticum* Kräusel (Malvaceae), *Proteoxylon chargeense* Kräusel (Proteaceae), *Terminalioxylon intermedium* (Kräusel) Mädel-Angeliewa and Müller-Stoll (Combretaceae), *Ternstroemioxylon dachelense* Kräusel (Ternstroemiaceae or Theaceae s.l.) and *Palmoxylon zittelii* Schenk (Arecaceae). Kedves et al. (2004b) described another well-preserved specimen of silicified gymnosperm wood from the Upper Cretaceous site lying a short distance to the northwest of Kharga Oasis, and mentioned that it is similar but not identical with *Agathoxylon lifiyii*. They mentioned that the well-preserved specimen is of tropical gymnospermous origin and that its distinct annual rings indicate periodicity of the climate.

This association of *Agathoxylon* species, *Metapodocarpoxylon* Dupéron-Laudoueneix and Pons together with the other gymnosperm and angiosperm arborescent plants indicate that the climate in the Cretaceous time of this area was warm and wet (tropical or subtropical) with dry and rainy seasons deduced from the presence of annual rings in *Agathoxylon lifiyii*, *Agathoxylon* sp. and *Metapodocarpoxylon* sp. (Greguss 1967; Youssef et al. 2000; Philippe et al. 2003; Kedves et al. 2004b; Youssef and El-Saadawi 2004).

Kamal El-Din (2003) reported and described petrified wood logs from Campanian age (Upper Cretaceous, Hefhuf Formation) of Farafra Oasis. She referred the logs to angiosperms; three specimens to *Celastrinoxylon celastroides* (Celastraceae), two specimens to *Ficoxylon cretaceum* Schenk (Moraceae) and two specimens were left for further study. Kamal El-Din et al. (2006) studied the two leftover specimens and mentioned that one of them has characteristics seen in families: Lauraceae, Moraceae and Anacardiaceae while the second specimen has affinities that could not allow assigning it to any family. Kamal El-Din et al. (2006) concluded that in the Late Cretaceous there existed woods with combinations of characters not found in any extant wood. They added that three of the four woods they reported from the Campanian Hefhuf Formation of Farafra had banded and aliform parenchyma which is not a characteristic of Late Cretaceous dicot woods from higher latitudes (e.g., Wheeler and Bass 1991). It is not surprising

that woods of Farafra, i.e., from near equator, should differ from those growing at higher latitudes. The absence of distinct growth rings in the Farafra woods suggests that the climate was not markedly seasonal.

The paleoclimate of the Late Cretaceous in nearby localities south of the Farafra Oasis (Kharga Oasis and road between Kharga and Dakhla Oases) is suggested to be tropical or subtropical as deduced from the study of fossil wood features by Kedves et al. (2004b) and Youssef and El-Saadawi (2004); observations on wood anatomy of Farafra Oasis (Kamal El-Din et al. 2006) confirmed this interpretation of those authors. The Hefhuf Formation consists primarily of dolomitized limestone with varying amounts of fine-grained terrigenous-clastic influx, preserving a variety of plant and animal remains. It unconformably overlies the fluvial to marginal marine sandstones and claystones of the Quseir Formation, and is succeeded by a sequence of offshore carbonates and clastics (Geological Survey of Egypt 1982) representing a return to marine conditions after the onset of the major Campanian transgression (Hermina 1990). At that time the Farafra area lay in low paleolatitude north of a developing bay (see Reynolds et al. 1997), from which fossils may have been transported. The Hefhuf Formation is considered to be regionally correlative with the upper Campanian Duwi Formation and may be synonymous with it (Tawadros 2001). The fossil woods reported from the Farafra Oasis (Kamal El-Din 2003; Kamal El-Din et al. 2006) may, therefore, be slightly younger than specimens of Schenk (1883) and Kräusel (1939) from other Nubian Sandstone localities (mentioned also in Kamal El-Din 2003).

El-Saadawi et al. (2002) mentioned that the literature shows that two species of *Palmoxylon* Schenk (Arecaceae) are known from Upper Cretaceous strata of Egypt; *Palmoxylon stromeri* Kräusel from the Eastern Desert and *P. zittelii* from the Western Desert; both from the southern part of the country. Many other species of *Palmoxylon* are known from younger strata (Cenozoic era) and from localities in the northern part of the country.

Weichselia reticulata (Fig. 13.3i, j) associated with angiosperms of Cenomanian age (early-Late Cretaceous) including: *Cornophyllum*, *Laurophyllum* Göppert, *Liriophyllum* Lesquereux, *Rogersia*, *Typhaephyllum* Prakash and Boureau and *Vitiphyllum* Fontaine were reported from Bahariya Oasis (Lejal-Nicol and Dominik 1987).

Darwish and Attia (2007) worked on the rich flora (over 50 spp.) of the early-late Cenomanian age (Late Cretaceous) of Gebel Dist Member of Bahariya Formation, at the mangrove-dinosaur unit which lies about 14 km northwest of Gebel Dist in Bahariya Oasis. Earlier works on this mangrove area by Smith et al. (2001) and Schweitzer et al. (2003) reported the presence of fossil remains of crabs, fishes, turtles, crocodiles and bones of giant dinosaurs associated with plant remains.

Darwish and Attia (2007) recorded a few pteridophyte leaves (e.g., *Equisetum*, *Weichselia reticulata*); several gymnosperm foliage (Araucariaceae, Cycadaceae, Ginkgoaceae, Podozamitaceae, Taxodiaceae); leaves of a large number of dicots (e.g., *Aquatifolia* Wang and Dilcher, *Avicennia* L., *Celtis* L., *Ficus* L., *Laurophyllum*, *Magnoliaephyllum*, *Nelumbites* Berry, *Nelumbo* Adanson, *Nymphaea* L., *Populus* L., *Rogersia*, *Salix* L., *Vitiphyllum*) and leaves and fruits of monocots belonging to Arecaceae and Poaceae (formerly Gramineae), in addition to other fossil plants known to be mangrove or mangrove associates. Lyon et al. (2001) mentioned that plant remains in the Cenomanian Bahariya Formation existed in lagoonal and intertidal deposits and that some of the remains suggest long transport from inland forests while others indicate very little transport. They added that the occurrence of freshwater taxa such as *Nelumbites* and floating aquatic ferns in saltwater-influenced depositional environments suggests that freshwater ponds existed in the paralic environment. They also added that the form genera in Bahariya are similar to those in North American Cenomanian megafloras (e.g., Dakota Group Flora) and that leaf physiognomy indicates that the area was relatively dry and warm in the Cenomanian. Many plant species recorded by Darwish and Attia (2007) from the mangrove of Bahariya strata are also known to occur in the Cenomanian to Maastrichtian of the basal part of the Kiseiba Formation, northeast of Wadi Halfa (e.g., *Magnoliaephyllum*, *Nelumbites*, *Rogersia*) indicating that the climate was warm with rainy and dry seasons (Lejal-Nicol 1990).

From the mangrove sites of Gebel Ghorabi and Gebel Dist (early-late Cenomanian age) El-Saadawi et al. (2016b) described a petrified fern stem probably representing the rhizomes (underground stems) of *Weichselia reticulata* (fronds) and *Paradoxopteris stromeri* Hirmer (rachii) which were described a long time ago from the Cenomanian Bahariya Formation (see references given in El-Saadawi et al. 2016b). Gebel Dist Member is an estuarine sequence strongly affected by tides with some intercalations of lagoonal origin.

Gebel Hefhuf Formation in Bahariya Oasis is of late Campanian age (Late Cretaceous) from which petrified woods of two gymnosperms (*Cupressinoxylon* sp. and *Dadoxylon aegyptiacum*), two dicots (?*Celastrinoxylon* sp. and *Terminalioxylon intermedium*) and one monocot leaf impression (*Cyperites* sp.) had been reported (see Darwish and Attia 2007; El-Saadawi et al. 2016b). El-Saadawi et al. (2016b) described haloed axes or mottles which occur parallel to one another and exist in large numbers in the upper Campanian site of Gebel Hefhuf. These mottles may be indicators of the ancient Neotethys sea level and shoreline and most likely represent organic matter buried in soil below or near the water table much as characterized nowadays by the large numbers of pneumatophores (respiratory roots) of

mangrove plants as *Avicennia marina* (Forssk.) Vierh. or by the large numbers of stems and roots of mangrove associates as the rushes (e.g., sea rush or *Juncus maritimus* Lam.).

Coiffard and Mohr (2016) reported on a new tropical member of Araceae, i.e., *Afrocasia kahlertiana* Coiffard and Mohr. These monocotyledonous fossil leaves were found in the Campanian (Upper Cretaceous) of the Quseir Formation of Kharga Oasis.

In the last few decades a great deal of palynological investigations has been conducted on the subsurface Cretaceous deposits of Egypt, notably: Saad and Ghazaly (1976), Saad (1978), Sultan (1978, 1986), Penny (1986), Schrank and Ibrahim (1995), Ibrahim et al. (1995), Ibrahim (1996), Schrank and Mahmoud (2002), Ibrahim et al. (2009, 2017), El-Noamani (2018) among others. The following paragraphs give a generalized picture of the most characteristic guide miospore taxa that prevailed in the different ages of the Cretaceous period in Egypt.

The Neocomian microfossil flora is characterized by long-ranging miospore forms where gymnosperms dominate over pteridophytes (e.g., Saad and Ghazaly 1976). It is distinguished palynologically by the first appearance of the two marker species *Impardecispora apiverrucata* (Couper) Venkatachala et al. and *Pilosisporites trichopapillosus* (Thierg.) Delcourt and Sprumont (Ibrahim et al. 1995). The late Neocomian (Hauterivian) is characterized by the first appearance of the *Cicatricosisporites orbiculatus* Singh, which extends to the early Cenomanian (Schrank and Mahmoud 1998) and the first appearance of ephedralean pollen grains (e.g., *Ephedripites* Bolkhovitina ex Potonié) (Abdel Malik et al. 1981; Schrank 1992; Ibrahim and El-Beialy 1995; Ibrahim and Schrank 1996; Schrank and Mahmoud 1998). The gymnosperm pollen species *Dicheiropollis etruscus* Trevisan is a characteristic late Neocomian to Barremian guide pollen in northern Gondwana (Doyle et al. 1977; Schrank 1991; Ibrahim et al. 1995).

Barremian palynoflora is characterized by a rise in the abundance of ephedralean pollen grains along with minor appearance of primitive angiosperm pollen like *Asteropollis* Hedlund and Norris, *Clavatipollenites* Couper, *Liliacidites* Couper and *Retimonocolpites* Pierce (Ibrahim et al. 1995). During the Aptian, the percentage and diversity of angiosperm pollen increased especially the reticulate monocolpate genera such as *Afropollis* Doyle, Jardiné and Doerenkamp and *Brenneripollis* Juhász and Góczán (Fig. 13.6g–i). Early Aptian is also characterized by the first appearance of tricolpate pollen (Ibrahim et al. 1995). Albian palynoflora shows general similarities with the Aptian one, but it can be delimited by the first appearance of the pteridophyte spores *Balmeisporites holodictyus* Cookson and Dettmann and *Crybelosporites pannuceus* (Brenner) Srivastava (Fig. 13.6 c). *Afropollis jardinus* Doyle, Jardiné and Doerenkamp is one of the marker forms which is taken to mark the early Albian (Sultan 1987; Schrank and Ibrahim 1995; Mahmoud and Moawad 1999). Elaterate pollen (*Elaterocolpites* Jardiné and Magloire, *Elaterosporites* Jardiné and *Sofrepites* Jardiné) (Fig. 13.6o, q, r) are unique stratigraphic markers for the middle Albian to middle Cenomanian rocks in Egypt (Sultan and Aly 1986; Sultan 1987; El-Beialy et al. 1990; Aboul Ela and Mahrous 1992; Schrank and Ibrahim 1995; Mahmoud and Moawad 1999).

Galeacornea causea Stover, *Elateroplicites africaensis* Herngreen and *Elaterosporites verrucatus* (Jardiné and Magloire) Jardiné are late Albian-early Cenomanian markers, they appeared in a level above *Elaterocolpites castelainii* Jardiné and Magloire and *Elaterosporites klaszii* (Jardiné and Magloire) Jardiné (Sultan and Aly 1986; El-Beialy 1994; Schrank and Ibrahim 1995). This interval is also characterized by the occurrence of periporate angiosperm pollen *Cretacaeiporites polygonalis* Herngreen and *C. scabratus* Herngreen (Sultan and Aly 1986; Schrank and Ibrahim 1995).

The periporate pollen species *Cretacaeiporites densimurus* Schrank and Ibrahim (Fig. 13.6l) is accepted in Egypt to be an early Cenomanian stratigraphic marker (Schrank and Ibrahim 1995). This species in addition to its short vertical stratigraphical extension has limited geographical range (mainly recorded from the northern part of Egypt, north Western Desert and northeast Sinai) (Ibrahim et al. 2017; El-Noamani 2018). Another new *Cretacaeiporites* Herngreen species, viz. *C. aegyptiaca* El-Noamani et al. (Fig. 13.6n) has been described in Ibrahim et al. (2017) from the subsurface early Cenomanian of northwest Egypt. *Classopollis brasiliensis* Herngreen is possibly another early Cenomanian marker (Aboul Ela and Mahrous 1992; Schrank and Ibrahim 1995). The triporate pollen *Triporopollenites* Pflug and Thomson and *Proteacidites* Cookson ex Couper characterize the late Cenomanian of the Western Desert of Egypt. These two pollen taxa are similar to the early Cenomanian marker triporate pollen species *Triorites africaensis* Jardiné and Magloire of northern Gondwana (Ibrahim et al. 1995).

The spinose pollen tetrad of *Droseridites senonicus* Jardiné and Magloire is considered an index species in the Coniacian-Santonian sediments of Egypt (Sultan 1985; Ibrahim et al. 1995). In addition, the tricolpate angiosperm pollen *Foveotricolpites giganteus* (Jardiné and Magloire) Chêne et al. and *F. gigantoreticulatus* (Jardiné and Magloire) Schrank are the most characteristic members of the Coniacian microfossil flora in Egypt. The Campanian-Maastrichtian microfossil flora in Egypt can be easily recognized by the typical African-South American pollen types such as *Crassitricolporites* Herngreen, *Echimonocolpites* Hammen and Mutis, *Periretisyncolpites* Kieser and Chêne, *Spinizonocolpites* Muller and *Syncolporites* Hammen (Schrank 1991; Ibrahim et al. 1995).

Spinizonocolpites seems to be related to the mangrove palm *Nypa* Steck (*Nipa* Thunberg), its fossil fruit has been recorded from the Maastrichtian-Danian sediments of Bir Abu Munqar, south Western Desert (Gregor and Hagn 1982; Schrank 1991; El-Soughier et al. 2011).

The Cretaceous microalgal content has been studied by El-Noamani and Saleh (2018) from four subsurface samples recovered from Bougaz-1 well in northeast Sinai. Seven algal species related to four genera, viz. *Chomotriletes* Naumova, *Pediastrum* Meyen, *Scenedesmus* Meyen (Chlorophyta, green algae) and *Pterospermella* Eisenack (Prasinophyta, the oldest group of green algae) were identified. Of these, two species, viz. *Pediastrum kawraiskyi* Schmidle and *Scenedesmus acuminatus* (Lagerheim) Chodat, were recorded for the first time from the Cretaceous of Egypt (Fig. 13.6s–v).

Fossil calcareous algae are common components in carbonate sediments (shallow-marine limestones). They are significant in biostratigraphy and paleoenvironment reconstructions as most calcareous marine algae are good indicators of warm shallow water. Kräusel and Stromer (1924) reported on the corallinacean red alga "*Lithothamnium aschersoni* Schwager" from Cretaceous, north of Dakhla, which was changed later to *Sporolithon aschersonii* (Schwag.) Mouss. and Kuss (see Moussavian and Kuss 1990).

Kuss (1986) reported on the following taxa of calcareous marine algae from the Upper Cretaceous rocks of Wadi Qena and Wadi Araba:

1. **Wadi Qena**. Upper Cenomanian/lower Turonian strata. The green algae include: *Acicularia* d'Archiac (two indet. species), *Boueina pygmaea* Pia, *Dissocladella undulata* Raineri, indet. sp. of *Griphoporella* Pia, *Neomeris cretacea* Steinmann, *Pycnoporidium sinosum* Johnson and Konishi, *Trinocladus tripolitanus* Raineri and *Trinoclades* sp.
2. **Wadi Araba**. The green algae include: *Boueina pygmaea*, from Campanian-Maastrichtian of the southern Wadi Araba. The red algae include: *Pseudolithothamnium album* Pfender, *Parachaetetes asvapatii* Pia, and indet. sp. of the genera *Amphiroa* Lamouroux, *Archaeolithothamnium* Rothpletz and *Lithothamnium* Phillippi, all are common in Campanian-Maastrichtian; except an indet. sp. of *Pseudochaetetes* Haug from late Cenomanian-early Turonian.

Kuss and Conrad (1991) and Kuss (1994) reported on the following calcareous green and red algae from Cretaceous strata:

The green algae include: *Acicularia magnapora* Kuss, upper Turonian "Flint Series", Abu Roash/Hassana Dome, Giza;

Acroporella hamata Kuss, upper Cenomanian Hazera Formation, Gebel Hallal/Sinai;

Arabicodium Elliott (indet. sp.), upper Albian, Gebel Maghara/Sinai;

Boueina pygmaea, Cenomanian, Gebel El Minshera/northern Sinai;

Boueina cf. *hochstetteri* Toula, Cenomanian, Gebel Hallal/Sinai;

Clypeina Michelin (indet. sp.), upper Albian-?lower Cenomanian, Gebel Maghara/Sinai;

Cylindroporella aff. *barnesii* Johnson, upper Albian Araif el Naqa/Sinai;

C. parva Radoičić, Cenomanian, northern Galala;

C. sugdeni Elliott, upper Aptian-lower Albian, Sinai, lower-upper Albian limestones of the Gebel Maghara, and ? Albian-lower Cenomanian, Gebel Hallal/Sinai;

C. taurica Conrad and Varol and *C.* cf. *kochanskyae* Radoičić, ?upper Albian-Cenomanian, Gebel Hallal/Sinai;

Dissocladella undulata (Raineri) Pia, middle Coniacian, Eastern Desert;

Halimeda Lamouroux (indet. sp.), upper Cenomanian and Turonian northern Galala and the Sinai;

Heteroporella lepina Praturlon, middle Turonian limestones of the Acteonella Series underlying the Abu Roash outcrop near Cairo;

Likanella hammudai Radoičić, upper Cenomanian Hazera Formation, Gebel Hallal/Sinai; *L. sinaica* Kuss, ?upper Albian-Cenomanian, Gebel Hallal/Sinai;

Neomeris cretacea, upper Cenomanian-lower Turonian, within Albian, Sinai and Cenomanian of the Galala mountains;

Praturlonella hammudai Kuss and Conrad, numerous ill-preserved specimens, Cenomanian grainstones, Eastern Desert;

Salpingoporella dinarica Radoičić, Albian-Cenomanian, southern Sinai;

Suppiluliumaella aff. *schroederi* Brarattolo, Cenomanian, Sinai;

Trinocladus tripolitanus, Cenomanian-Turonian, Wadi Qena.

The red algae include: *Marinella lugeoni* Pfender, Cenomanian and Turonian, Gebel El Minshera/Sinai and Abu Roash;

Parachaetetes asvapatii, middle-upper Maastrichtian limestones, Eastern Desert;

P. cf. *hadhramautensis* Elliott, middle Albian, Sinai and upper Albian, Gebel Maghara;

Permocalculus budaensis Johnson, Turonian strata, Sinai;

P. irenae Elliott, Albian limestones, Sinai and northeastern Egypt;

?*Permocalculus* Elliott (indet. sp.), Cenomanian, Gebel El Minshera/northern Sinai;

Pseudochaetetes (indet. sp.), Cenomanian, Wadi Qena;

Pseudolithothamnium album, middle-upper Maastrichtian limestones, Eastern Desert.

Bucur et al. (2010) reported the following calcareous algae from upper Cenomanian-lower Turonian of the Eastern Desert: *Neomeris mokragorensis* Radoičić and Schlagintweit, *Trinocladus divnae* Radoičić, *T.* cf. *radoicicae* Elliott, *Dissocladella* sp.; along with *Salpingoporella milovanovici* Radoičić from lower-upper Cenomanian, Galala Formation and *Halimeda* cf. *elliotti* Conrad and Rioult from upper-lower Turonian of the Maghra el Hadida Formation.

13.3.7 Upper Cretaceous-Paleocene Strata

Gregor and Hagn (1982) reported on the following fruits from the Cretaceous-Paleocene boundary (or Danian) of Bir Abu Munqar above the Farafra-Dakhla road: cf. *Coryphoicarpus globoides* Koch, *Cupulopsis klitzschii* Gregor, *Munqaria kraeuseli* Gregor, *Nypa* (*Nipa*) *burtini* (Brongniart) Ettinghausen (=*Nipadites sickenbergeri* Bonnet) and *Stizocaryopsis bartheli* Gregor.

13.4 Cenozoic Era

13.4.1 Paleocene Strata

Chandler (1954) described fossil fruits from the Paleocene of Farafra and Quseir, viz. *Palaeowetherellia schweinfurthii* ('*schweinfurthi*') (Heer) Chandler from Farafra and *Anonaspermum* (Ball) Reid and Chandler, *Icacinicarya* Reid and Chandler and *Nypa* from Quseir.

Kuss and Conrad (1991) mentioned that both calcareous algae *Pseudolithothamnium album* (green algae) and *Parachaetetes asvapatii* (red algae) that occur within the middle-late Maastrichtian limestones of Eastern Desert were also found in similar facies in the overlying Paleocene limestones.

13.4.2 Eocene Strata

Lejal-Nicol (1990) recorded an Eocene dicot leaf flora from the Gulf of Suez area including: cf. *Anonaephyllum* sp., *Cassiaephyllum aegyptiacum* Lejal-Nicol, *Dicotylophyllum panandhroensis* Lakhanpal and Guleria, *Ficophyllum* sp., cf. *Hirtella* sp., cf. *Platanophyllum* sp., cf. *Sparganiophyllum* sp., *Terminaliphyllum africanum* Lejal-Nicol and cf. *Tiliaephyllum* sp. She stated that this Eocene flora is an association of Cretaceous forms with younger ones. It has to be mentioned that petrified dicot wood genera related to some of these leaf genera had been reported from many Paleogene and Neogene sites in Egypt and will be discussed later.

Wadi Al-Hitan is part of Wadi Al-Rayan Protected Area. El-Saadawi et al. (2018) mentioned that Wadi Al-Hitan (Whale Valley) is the first site in Egypt to be inscribed by UNESCO on the "Natural World Heritage List", which reflects the importance of fossil animals and plants reported from this wadi. Wadi Al-Hitan mangrove plant bed lies in late middle Eocene (Bartonian) at the top of Birket Qarun Formation, underlying Qasr El-Sagha Formation (Priabonian). El-Saadawi et al. (2018) reported casts, moulds and directly preserved hard parts of fossil plants and animals from this mangrove plant bed in Wadi Hitan area. The described fossil plants include casts and moulds of massive rhizomes (horizontal usually underground stems) comparable to those of the extant mangrove-associate palm *Nypa fruticans* Wurmb. The extended horizontal growth, dichotomous branching at wide intervals, that reached 7 m in Wadi Hitan, and the occurrence in levels separated from one another, vertically, by layers of sediments, all compare well with modern *Nypa fruticans*. The absence of aerial roots in *Nypa* and its vegetative growth from an underground rhizome (Tomlinson 1994) gives it the ability to relocate to a higher level in conditions of rapid sedimentation which explains its existence in several vertically superimposed beds (as in the middle member of Birket Qarun Formation) in Wadi Hitan.

El-Saadawi et al. (2018) mentioned that the mangrove-like root casts (vertical pneumatophores and prop roots and horizontal cable roots) are plentiful in the three members of Birket Qarun Formation. Field work (El-Saadawi et al. 2018) showed that the *Nypa*-like rhizomes and the cable-like roots extend horizontally in the beds whereas the pneumatophore and prop-like roots are oriented vertically perpendicular to them and to the lignite beds and as such are considered an evidence of their in situ occurrence. The overall morphological features and size of the fossil mangrove-like roots compare well with those of the extant mangrove trees as *Avicennia marina*, *Rhizophora mangle* L. and *R. mucronata* Lam. even in the presence of lenticels on the surface of pneumatophores. The fossil object described in the geological literature (see El-Saadawi 2005; El-Saadawi et al. 2018) as an entirely worm-bored, 18 m long tree trunk proved to be closely-spaced, elestite-filled siphons and borings of bivalvia which lived, more probably, on soft rock substrate and not on wood of trees. The other animal fossils represent most probably spines of Echinodermata.

The presence of *Nypa* fossils indicate proximity to land and tropical to subtropical environmental conditions. *Nypa*'s mangroves flourish in warm humid swamps, estuarines and tidal shores, not uncommonly associated with *Avicennia* L. and *Rhizophora* L. in area where the water is calm enough

to allow their growth (Nunn et al. 1993; Agrawala et al. 2003; Bkhat 2012). In this regard, it has to be mentioned that fruits of *Nypa burtini* had been reported from the Eocene of Gebel Mokattam in Cairo (Chandler 1954). Furthermore, *Nypa* was present on all continents during the Eocene (Bkhat 2012). Remains of *Avicennia*, *Bruguiera* Savigny and *Rhizophora* were also panatropic by the Eocene (Graham 1995; Plaziat et al. 2001). At present, however, *Nypa* exists only in the Indo-Malaysian region (Bkhat 2012) but species of *Avicennia*, *Bruguiera* and *Rhizophora* still grow on the Red Sea shores in south Egypt (Zahran 1977; Mandura 1997).

The fossil flora of the Late Cretaceous mangroves of Bahariya Oasis (Darwish and Attia 2007; El-Saadawi et al. 2016b) was quite different from that of Wadi Hitan including numerous pteridophytes, gymnosperms and angiosperms among which some leaves were assigned to the mangrove genus *Avicennia*. The oldest record of *Nypa* from Egypt was also from Late Cretaceous (Schrank 1987) and also other parts of the world (Muller 1981). The fossil mangrove plants and their associated animals particularly the whales (Hitan) encouraged international ecotourism, since the declaration by UNESCO in 2005 the site of Wadi Hitan as a "Natural World Heritage site".

El-Saadawi (2006) gave a summary of earlier publications on fossil plants of Fayum area, he mentioned a large number of fossils among which the following were from upper Eocene of north Dimé: **leaves** of *Ficus stromeri* Engelhardt (Moraceae), *Litsea engelhardti* Kräusel (Lauraceae), *Maesa zitteli* Engelhardt (Myrsinaceae), ?*Nymphaeites* sp. (Nymphaeaceae), and **a fruit** of *Securidaca tertiaria* Engelhardt (Polygalaceae).

The fossil calcareous algae reported from Egypt by Schwager (1883) have been briefly reviewed by Kräusel (in Kräusel and Stromer 1924). Kräusel listed the green calcareous algae: *Ovulites pyriformis* Schwager and *O. elongata* Lamarck from gray diatomaceous earth of lower Eocene, Miniya and *Dactylopora* sp. from lower Eocene diatomaceous earth between Assiut and Farafra, however, he suspected that this specimen is more closely related to the genus *Thyrsoporella* Gümbel.

Dragastan and Soliman (2002) reported the following calcareous algae from lower Eocene limestones of the Drunka Formation cropping out on both banks of Nile between Sohag and Quena: *Acicularia robusta* Dragastan and Soliman, *A. valeti* Segonzac, *Clypeina occidentalis* (Johnson and Kaska) Segonzac, *Clypeina* cf. *rotella* Yu-Jing, *Halicoryne* sp., *Halimeda tuna* (Ellis and Solander) Lamouroux, *H. fragilis* Taylor, *H. opuntia* (Linnaeus) Lamouroux, *Niloporella subglobosa* Dragastan and Soliman, *Ovulites arabica* (Pfender) Massieux, *O. elongata*, *O. margaritula* (Lamarck) Lamarck, *O. pyriformis* Schwager and *Terquemella bellovacensis* Munier-Chalmas.

13.4.3 Oligocene Strata

Darwish et al. (2000) described leaf impressions of Dipterocarpaceae (dicots), Cyperaceae and Poaceae (both monocots) in addition to a pod-like fruit enclosing seeds from sediments younger than the Paleocene or the basal Eocene and probably represent lower Oligocene of Farafra Oasis. Earlier records of fossil plants from Farafra Oasis area (e.g., Kräusel 1939; Chandler 1954; Gregor and Hagn 1982) are confined to the interval straddling the Cretaceous-Tertiary boundary. These angiosperm remains came from stromatolitic limestones, a carbonate-sandstone package crowning a group of three hillocks known collectively as the northern Gunna (or Gunna El-Bahariya), lying some 15 km to the north of Qasr Farafra. They all indicate a humid climate. Species of Dipterocarpaceae constitute forest trees of the humid tropics or subtropics, and the species of Cyperaceae are known to be chiefly marsh plants. Poaceae taxa (e.g., *Arundo* L., *Phragmites* Adanson and similar plants) also grow in swamps or at swamp margins. The locality, therefore, might have been occupied by large dipterocarpaceous trees under which grew the smaller herbs and grasses of the Cyperaceae and Poaceae, while stromatolites covered mainly mud flats.

The Oligocene strata in Egypt yielded a large number of fossil plants particularly fossil wood. Two sites are most important, viz. the Cairo Petrified Forest (CPF) at Qattamiya in New Cairo city (Oligocene Gebel Ahmar Formation) and Gebel Qatrani area in northern Fayum (Oligocene Gebel Qatrani Formation).

Large silicified tree and palm trunks occupy a wide area in the desert, about 20 km east of old Cairo city. Dicot trees count hundreds and extend a long distance in the Eastern Desert towards Suez. The nature and origin of these silicified trees attracted the attention of researchers and amateurs for almost 200 years (see El-Saadawi 1979; El-Saadawi et al. 2004, 2011). An area dense with wood logs, about 6 km^2, was chosen, declared a "Protected Area" by a decree in 1989, and named "The Cairo Petrified Forest, Protected Area".

El-Saadawi et al. (2011, 2013) summed up almost all earlier works on the CPF (e.g., Rüssegger 1836; Unger 1858; Kräusel 1939) and recorded and described new forms. Further, El-Saadawi et al. (2017) resumed the study of the CPF adding many new records to it, several to Egypt and one to science, bringing the number of species known from the CPF protected area and its vicinity to 30 wood taxa (27 dicots and 3 monocots) as given below:

Combretaceae: *Terminalioxylon edwardsii* (Kräusel) Mädel-Angeliewa and Müller-Stoll, *T. geinitzii* (Schenk) Mädel-Angeliewa and Müller-Stoll, *T. intermedium*, *T. primigenium* (Schenk) Mädel-Angeliewa and Müller-Stoll,

Ebenaceae: *Ebenoxylon aegyptiacum* Kräusel,

Fabaceae-Caesalpinioideae: *Afzelioxylon kiliani* Louvet,

A. welkitii (Lemoigne and Beauchamp) Lemoigne,
Copaiferoxylon matanzensis Cevallos-Ferriz and Barajas-Morales,
C. migiurtinum (Chiarugi) Müller-Stoll and Mädel,
Cynometroxylon tunesense Delteil-Desneux (Fig. 13.3d),
Detarioxylon aegyptiacum (Fig. 13.3c),
Fabaceae-Faboideae: *Andiroxylon aegyptiacum* Ziada (Fig. 13.3b),
Dalbergioxylon dicorynioides Müller-Stoll and Mädel,
Fabaceae-Mimosoideae: *Acacioxylon vegae* Schenk,
Dichrostachyoxylon palaeonyassanum Lakhanpal and Prakash,
D. royaderum Privé,
D. zirkelii (Felix) Müller-Stoll and Mädel,
Mimosoxylon calpocalycoides Lemoigne,
M. tenax (Felix) Müller-Stoll and Mädel,
Tetrapleuroxylon acaciae (Kräusel) Müller-Stoll and Mädel,
T. zaccarinii (Chiarugi) Müller-Stoll and Mädel,
Fagaceae: *Quercoxylon retzianum* Kräusel,
Malvaceae s.l.: *Bombacoxylon owenii* (Carruthers) Gottwald, *Sterculioxylon giarabubense* (Chiarugi) Kräusel,
Monimiaceae: *Atherospermoxylon aegyptiacum* (Schenk) Kräusel,
Moraceae: *Ficoxylon blanckenhorni* Kräusel, *F. cretaceum* Schenk,
Arecaceae: *Palmoxylon aschersonii* (‘*aschersoni*’) Schenk, *P. libycum* (Stenzel)
Kräusel, *P. pyriforme* Sahni.

Five of the 27 dicot wood species reported from CPF also occur in Wadi Ankebieh (or Anqabiya) which is also an Oligocene (Gebel Ahmar Formation) site lying about 20 km northeast of the CPF (Darwish et al. 2016). One of these five species (viz. *Bombacoxylon owenii*) was reported by Kamal El-Din (2002) from Gebel Shabraweet, which is also an Oligocene site, lying about 100 km to the east of the CPF (5 km to the south of Fayed city).

The occurrence of *Copaiferoxylon matanzensis* and *Mimosoxylon tenax* in the Oligocene Egyptian CPF and the Oligocene of Mexican deposits provides evidence of phytogeographic relationships between Africa and tropical America (see Lavin and Luckow 1993; Brea et al. 2012).

El-Saadawi et al. (2017) gave evidence that the extinction of family Combretaceae from Egypt wild flora for at least two million years now, although its fossil genus *Terminalioxylon* Schönfeld (representing extant *Terminalia* L.) was the largest genus in the Oligocene CPF (being represented by four species) was due to long periods of drought and low rainfall and not to temperature changes. Furthermore, El-Saadawi et al. (2017) mentioned that during the period of the CPF the majority of Fabaceae taxa found were either arborescent Mimosoideae or Caesalpinioideae with a few Faboideae while today, herbaceous annual Faboideae are the majority. It is a well-known fact that the annual herbaceous forms in any angiosperm family are a recent adaptation to overcome water stress. Cretaceous and early Cenozoic angiosperms were mostly perennial trees (Strickberger 2005). Thus, the current distribution of the three subfamilies (Mimosoideae, Caesalpinioideae and Faboideae) of the Fabaceae in our present day flora of Egypt is another evidence that the progressive water stress and lack of heavy rainfall was the main change that affected the climate of Egypt. The Nearest Living Relatives “NLRs” of the CPF 27-dicot taxa are mostly distributed in a range of tropical and/or subtropical forest types, including savannas in almost all continents of the world. The main physiognomic features of the dicot woods of the CPF also prove that the paleoclimate of their growth environment was subtropical to tropical with well-defined seasons and rainfall seasonality.

Gebel Qatrani is part of Qarun Protected Area in El-Fayum. Hundreds of intact massive petrified tree trunks lie on sand covering desert surface in groups. Fossil plants and animals reported from Gebel Qatrani (Rupelian, Fayum) are so numerous and have raised national and international interest (see, e.g., Bowen 1970; Bowen and Vondra 1974; Bown 1982; Bown et al. 1982; Wing and Tiffney 1982; Tiffney 1991; Dolson et al. 2002; El-Saadawi et al. 2002; El-Saadawi and Kamal El-Din 2004; El-Saadawi 2006; Nour-El-Deen 2015; Nour-El-Deen et al. 2018).

El-Saadawi and Kamal El-Din (2004) described two species of *Terminalioxylon* (i.e., *T. intermedium* and *T. primigenium*) from Gebel Qatrani at Widan el-Faras (the type locality of Gebel Qatrani Formation) in Fayum area. The two species belong to family Combretaceae (dicots) which is the second largest family after Fabaceae regarding the number of reported fossil wood species.

Fossil plants reported by many workers from El-Fayum and Gebel Qatrani Formation were summed up by El-Saadawi (2006) as follows:

Petrified wood logs: *Bombacoxylon owenii*, *Sterculioxylon giarabubense* (Malvaceae s.l.), *Ficoxylon blanckenhorni* (Moraceae), *Palmoxylon geometricum*, *P. pondicherriense* (Arecaceae), *Sapindoxylon stromeri* Kräusel (Sapindaceae), *Terminalioxylon intermedium*, *T. primigenium* (Combretaceae).

Leaves: a fan-palm leaf (Arecaceae), *Cynometra* (Fabaceae), *Nelumbo* (Nelumbonaceae), one leaf type (Ochnaceae), water fern *Salvinia* (Salviniaceae), one leaf type (Sapotaceae), *Triplochiton* Schumann (Malvaceae s.l.), *Typha*-like leaf (Typhaceae);

and **fruits/seeds**: *Anonaspermum* (Anonaceae, two species), *Canarium* (Burseraceae), *Epipremnum* Schott (Arecaceae, monocots), *Eohyperpa* (Menispermaceae), *Icacinicarya* (Icacinaceae). Also reported are fossil thalloid

macroalgae of the genus *Chara*. Charophytes are known to inhabit shallow freshwater bodies.

Nour-El-Deen et al. (2014) confirmed the presence of only two species of *Palmoxylon* from Gebel Qatrani Formation, viz. *P. geometricum* and *P. pondicherriense*. Four years later Nour-El-Deen et al. (2018) added the following three *Palmoxylon* species collected and described recently from the Oligocene (Rupelian) Gebel Qatrani Formation:

Palmoxylon araneus Nour-El-Deen, El-Saadawi and Thomas (Fig. 13.3f),

P. elsaadawii Nour-El-Deen and Thomas (Fig. 13.3g),

P. qatraniense Nour-El-Deen, El-Saadawi and Thomas.

These three species of palms are the first representatives of tribe Trachycarpeae on the African continent.

Nour-El-Deen (2015) described the following fossil dicot wood species from Rupelian Gebel Qatrani Formation:

Combretaceae: ?*Lumnitzeroxylon* Kramer (indet. sp.),
Terminalioxylon (4 spp.),

Fabaceae-Caesalpinioideae: *Caesalpinioxylon mogadaense* Boureau,
Cassinium prefistulai Prakash,
Hopeoxylon indicum Navale emend Awasthi,
Pahudioxylon Chowdhury, Ghosh and Kazmi (indet. sp.),

Fabaceae-Mimosoideae: *Albizinium pondicherriensis* Awasthi,
Tetrapleuroxylon cf. *acaciae* (Kräusel) Müller-Stoll and Mädel,

Malvaceae s.l.: *Bombacoxylon owenii*.

Vast literature (see El-Saadawi 2006; Nour-El-Deen et al. 2018) suggests that in the Oligocene, the Fayum area was coastal and subtropical to tropical in climate regime. The climate showed alternating wet and dry periods and might have been monsoonal. The macrofossil flora (wood, leaves, fruits and seeds) of Gebel Qatrani Formation indicate a tropical forest vegetation and mangrove swamps.

The closest analogue of the Qatrani fruit and seed flora is the Eocene London Clay of England (Chandler 1954) and modern tropical floras of Indo-Malaysia (Wing and Tiffney 1982). The abundance of *Epipremnum* in Gebel Qatrani indicates a local well-developed forest. The paleofloral assemblage of Gebel Qatrani Formation includes plants of mainly three diversified habitats: (1) brackish and marine mangrove nearshore habitat, (2) freshwater-terrestrial habitat, and (3) freshwater aquatic habitat. The first is indicated by the presence of *Cynometra* which today includes several tropical mangrove tree and shrub species, *Acrostichum* which is, today, restricted to the lowland side of mangrove forests and tropical coasts and Arecaceae are usually tropical or subtropical and some of them are mangrove associates. Shallow freshwater swamps or river sides hosted charophytes (algae) and aquatic floating plants as *Nelumbo* and *Salvinia*. The monsoon climate with alternating wet and dry periods has also supporting evidence from the wood microstructure.

There are few unquestionable records of fossil fungi from Egypt. Unger (1841–1847) described fungal hyphae of *Nyctomyces entoxylinus* Unger in the vessel elements of fossil woods of *Nicolia aegyptiaca* (synonymized later (Louvet 1973) with *Detarioxylon aegyptiacum*), collected from Asserak in the vicinity of Cairo in Egypt probably of Oligocene Gebel Ahmar Formation (see Kräusel and Stromer 1924; Kräusel 1939). More than half a century later, Julien (1904) reported (in an abstract only) on the presence of a new fossil fungus in a specimen of silicified wood from a petrified forest near Cairo with no mention of fungus or wood names.

Recently, Nour-El-Deen (2015) reported on the presence of fossil fungal hyphae in the vessel elements of a leguminous wood type from Oligocene Gebel Qatrani Formation. El-Saadawi et al. (2016a) reported the same in the vessels of rubiaceous wood type from Miocene of Gebel El-Khashab Formation in the west of Giza Pyramids.

13.4.4 Miocene Strata

The four species of *Terminalioxylon* (Combretaceae wood) reported earlier (see El-Saadawi et al. 2017) from the Oligocene CPF also occur in many Miocene sites in the northern half of Egypt. They are *T. edwardsii*, *T. geinitzii*, *T. intermedium* and *T. primigenium* (El-Saadawi and Kamal El-Din 2004). The geological age of *T. intermedium* goes as far back as the Cretaceous (in the southern part of Egypt) (El-Saadawi and Kamal El-Din 2004). El-Saadawi et al. (2002) mentioned that *Palmoxylon aschersonii* occurs in the early Miocene of Qaret El-Raml, Gebel Ruzza and the Miocene of Wadi Natrun while *Palmoxylon libycum* occurs in the Miocene of Wadi Natrun and Gebel El-Khashab.

El-Saadawi et al. (2010) reported on *Palmoxylon aschersonii* and *P. wadiai* from Cairo-Bahariya desert road, which is a lower Miocene site of Gebel El-Khashab Formation. Kamal El-Din et al. (2015) described *Bombacoxylon owenii* (Malvaceae), *Cynometroxylon* sp. cf. *holdenii* (Gupta) Prakash and Bande (Fabaceae) and *Dipterocarpoxylon africanum* Bancroft (Dipterocarpaceae) from the lower Miocene Moghra Formation exposed at certain sites in Siwa Oasis and from which Kamal El-Din et al. (2013) reported and described seven *Palmoxylon* species, viz. *Palmoxylon deccanense* Sahni, *P. edwardsi* Sahni, *P. geometricum* Sahni, *P. pondicherriense* Sahni, *P. prismaticum* Sahni, *P. pyriforme* and *P. sagari* Sahni. These silicified trunks of dicots and palms (monocots) occur in Moghra Formation which is a clastic fluviomarine delta-front sequence. This delta (called Siwa delta) was built by the south-north Gilf River flowing between Gilf Kebir plateau

(in the southwest of Egypt) and the Mediterranean (Issawi et al. 1999). The fossil wood taxa of Siwa Oasis (based on the NLRs and certain wood anatomical features as diffuse porosity, simple perforation plates, secretory canals, abundant axial parenchyma, banded parenchyma, in addition to growth rings in one species) indicate warm tropical climate with minor seasonality in precipitation (Kamal El-Din et al. 2015). The absence of growth rings in two of the species described from Siwa possibly implies that these species were able to tolerate slight changes in precipitation and/or temperature.

Kamal El-Din and Refaat (2001) described *Detarioxylon aegyptiacum* (Fabaceae) from lower Miocene sediments in southern Sinai (Gebel Hadahid, Rudeis Formation)—these sediments also contain plant imprints (not studied so far). This species is known from about 20 sites in Egypt spanning the Eocene, Miocene and probably extends to the Quaternary (see Kamal El-Din and Refaat 2001). The anatomical features of *Detarioxylon aegyptiacum* indicate tropical lowland habitats accompanied by seasonal climatic variations (Kamal El-Din and Refaat 2001 and references therein). The presence of the trunk in fine-grained sediments rich in planktonic foraminifera that were deposited in a relatively deep marine environment indicates most probably that *D. aegyptiacum* trees were growing on elevated lands at relatively high altitude in the proximity of the lower Miocene sea and then drifted away and deposited by a fluvial regime or otherwise in submarine fan environment in deeper parts of the basin. The habitat at the relatively high altitude must have been seasonally drier as indicated by the distinct growth rings of the wood.

Kamal El-Din and El-Saadawi (2004) described petrified wood of *Cynometroxylon schlangintweitii* Müller-Stoll and Mädel and *Afzelioxylon welkitii* (both Fabaceae) from lower Miocene strata of Gebel Ruzza, south of Wadi Faregh in north of the Western Desert of Egypt. El-Saadawi et al. (2014) gave a list of all Miocene petrified wood known until 2014 from Egypt including 21 dicot species and 14 monocots (all are *Palmoxylon* species) as mentioned below:

Anacardiaceae: *Glutoxylon symphonioides* (Bancroft) Lemoigne;

Clusiaceae (Guttiferae): *Guttiferoxylon fareghense* Kräusel;

Combretaceae: *Combretoxylon* sp., *Terminalioxylon geinitzii*, *T. intermedium*, *T. primigenium*, *Terminalioxylon* sp.;

Fabaceae-Caesalpinioideae: *Afzelioxylon welkitii*, *Cynometroxylon schlagintweitii*, *C. tunesense* Delteil-Desneux, *Cynometroxylon* sp., *Detarioxylon aegyptiacum*;

Fabaceae-Mimosoideae: *Leguminoxylon albizziae* Kräusel, *Mimosoxylon tenax*, *Tetrapleuroxylon acaciae*, *T. ingaeforme* (Felix) Müller-Stoll and Mädel;

Malvaceae s.l.: *Bombacoxylon langstoni* Wheeler and Lehman, *B. owenii* (Fig. 13.3a), *Sterculioxylon giarabubense*;

Moraceae: *Ficoxylon blanckenhornii*, *F. cretaceum*;

Arecaceae: *Palmoxylon aschersonii*, *P. compactum* Sahni (Fig. 13.3e), *P. deccanense*, *P. edwardsi*, *P. geometricum*, *P. indicum* Sahni, *P. lacunosum* (Unger) Felix, *P. libycum*, *P. pondicherriense*, *P. prismaticum* Sahni, *P. pyriforme*, *P. rewahense* Sahni, *P. sagari* and *P. wadiai* Sahni.

The paleoclimate depicted by the anatomical features of fossil wood having a few wide vessels is consistent with the warm, humid climate suggested for the early Miocene of the collection sites and the region in general. It is suggested (Salard-Cheboaldaeff 1979; Morley and Richards 1993) that the climate of the early Miocene of North Africa was followed by drier and more seasonal climate in the middle Miocene and until Pleistocene.

The only record of petrified wood of family Rubiaceae (dicots) in Egypt came from a lower Miocene site of Gebel El-Khashab Formation in the west of Giza Pyramids (El-Saadawi et al. 2016a). The anatomical features of this Rubiaceae wood specimen indicate nonseasonal cool temperate or more probably high montane tropical paleoclimate because most of the other fossil wood species known from the study site have features that are common in tropical nonseasonal climates (El-Saadawi et al. 2016a and references therein).

El-Beialy et al. (2005) studied the pollen palynoflora from the subsurface Miocene Rudeis and Kareem formations encountered in the GS-78-1 well drilled in the offshore Gulf of Suez area. They recorded numerous pollen taxa belonging to the families Chenopodiaceae, Compositae, Fabaceae, Malvaceae, Onagraceae, Poaceae and other conifer genera such as *Pinuspollenites* Raatz ex Potonié. The recorded palynofloras suggested that during the Miocene the Gulf of Suez was occupied by a mixed vegetation which fluctuated from dry (cool) grassland savanna, as deduced from the dominance of Poaceae and Chenopodiaceae, with few forest elements to a humid (warm) shrubland forest dominated by *Pinus* and other conifers. Regarding the paleoclimate, a subtropical to warm temperate climate is inferred, although palynomorphs belonging to Fabaceae (subfamilies Caesalpinioideae and Mimosoideae) are also represented and indicate tropical to subtropical climate, which is concordant with the recorded fossil woods from the Miocene strata in the northern part of Egypt.

13.4.5 Quaternary Strata

Gardner (1935) reported on the following angiosperms from Quaternary strata of Kharga Oasis: *Arundo* sp. (stems), *Celtis* sp. (fruit), *Ficus ingens* (Miq.) Miq. (leaves and fruits), *F.* cf. *salicifolia* Vahl (leaves), *F. sycomorus* L. (leaves, fruits and ?bracts), ?*Phoenix* sp. (leaves) and *Pteris vittata* L. (leaf pinnules). From Quaternary tufa deposits of

Kharga Oasis, Darwish and Awad (2002) described the following angiosperm leaves: *Acer tricuspidatum* Braun and Agassiz, *A.* cf. *tricuspidatum*, *Cyperus* L., *Dicotylophyllum* sp., *Ficus salicifolia*, *Ficus* sp. and *Salix* sp. From Quaternary tufa deposits at Bir Dungal, southwestern Desert of Egypt, Darwish (2003) described leaves of angiosperms (dicots and monocots): *Cornaephyllum* (1 sp.), *Ficus* (2 spp.), *Saliciphyllum* Conwentz (1 sp.) and a monocot leaf.

The freshwater green alga ?*Chara* sp. was reported from middle Pliocene of Wadi Natrun and from ?Quaternary (Pleistocene) of Kurkur Oasis in the Western Desert (Kräusel and Stromer 1924).

El-Saadawi et al. (1975, 1987) described silicified rhizomes of *Phragmites australis* (Cavanilles) Trinius ex Steudel (=*P. communis* Trinius) (Fig. 13.4a–c) and silicified roots of *Tamarix* sp. from Pleistocene, old Moeris lake deposits at Dimé. These plants grew in swamps around the old Pleistocene lake. From the same deposits, El-Saadawi et al. (1978) studied fossil diatoms (microalgae) reporting 41 species, the majority of which were freshwater forms particularly the centric forms. Earlier, Aleem (1958a, b) recorded 89 species of fossil diatoms from Pleistocene deposits at Bacchias. Most of the species were also freshwater forms indicating that the old Pleistocene lake was a freshwater lake, it is now almost a marine lake (see El-Saadawi et al. 1978).

Kholeif (2004) recorded *Lycopodium* L., *Polypodium* L. and *Sphagnum* L. spores from late Quaternary sediments of the southern Suez Isthmus.

Ziada et al. (2018) described Holocene palynomorphs from Fayum area including spores of some bryophytes, viz. *Phaeoceros* Proskauer, *Riccia* L. and *Sphagnum*, and many pteridophytes, viz. *Adiantum* L., *Ananthacorus* Underwood and Maxon ex Maxon, *Asplenium* L., *Blechnum* L., *Cyathea* Smith, *Danaea* Smith, *Dennstaedtia* Bernhardi, *Lycopodium*, *Ophioglossum* L., *Polypodium*, *Pteridium* Gleditsch ex Scopoli and *Selaginella* Beauvois. Leroy (1992) described spores of *Azolla nilotica* Decne. ex Mett. (an aquatic fern) from Holocene sediments in the eastern Nile Delta. Freshwater swamps no longer exist in Nile Delta and Egypt in general, and certain branches of the Nile had completely dried up inhibiting the flow of freshwater to the plant habitats hence most of the mentioned bryophytes and pteridophytes are now extinct from Egypt (Nicholson and Shaw 2000; Ziada et al. 2018).

It may be said in conclusion regarding paleoclimate of the early Miocene in Egypt that the predominance of wood with a few wide vessels is consistent with the warm, humid climate suggested for the early Miocene wood collection sites (17 of which are known from Egypt) and the region in general. It is suggested (Salard-Cheboaldaeff 1979; Morley and Richards 1993) that the climate of the early Miocene of North Africa was tropical and predominantly everwet followed by drier and high seasonality climate in the middle Miocene and until Pleistocene. Water stress due to climatic changes that lead to the region of Egypt suffering from long periods of drought and low rainfall but not temperature changes was most probably the primary reason for the extinction or disappearance of the luxurious Oligocene and early Miocene forests (dicot and palms) since almost none were reported in Egypt from middle Miocene, upper Miocene and Pliocene strata. However, the early part of the Quaternary was relatively wet with lakes, swamps and marshes and records indicate the occurrence of remains of angiosperms; mainly leaves and fruits of trees and stems and leaves of smaller herbaceous plants. There are also reports on microalgae and spores of bryophytes, pteridophytes and pollen grains of seed plants in the early part of the Holocene (see Ziada et al. 2018 and references therein). In the later part of the Holocene, swamps disappeared and the climate became dry and the flora in Egypt changed to its present form.

It has to be mentioned, however, that although research work on the fossil flora of Egypt is already over 150 years old, yet much work remains to be done. There are references especially in geological publications to the occurrence of plant remains in strata belonging to different geologic ages. These remains need to be explored in order to throw more light on the fossil flora of the country.

Acknowledgements The authors are grateful to Dr. Rifaat Osman, Prof. of Geology, Benha University, being their guide on many excursions which resulted in a great deal of paleobotanical published knowledge. They are also grateful to the reviewers Prof. Steven Manchester and Prof. Rakesh Mehrotra for the careful and insightful review of the mamuscript.

References

Abd El-Shafy E, El-Saadawi W (1982) Macroflora from the Jurassic of Ras El-Abd, Gulf of Suez, Egypt. Bull Fac Sci Zagazig Univ 4:33–40

Abdel Malik WM, Aboul Ela NM, El-Shamma AE (1981) Upper Jurassic-Lower Cretaceous microflora from the North-Western Desert, Egypt. N Jb Geol Paläont Abh 62:244–263

Aboul Ela NM, Mahrous HAR (1992) Albian-Cenomanian miospores from the subsurface of the north Western Desert, Egypt. N Jb Geol Paläont Mh 10:595–613

Aboul Ela NM, El-Saadawi WE, Darwish MH (1989) Some Lower Cretaceous microfloras from Abu Darag area, Western Side of the Gulf of Suez. Egypt J Geol 33(1,2):347–361

Agrawala S, Ota T, Risbey J, Hagenstad M, Smith J, Aalst M, Koshy K, Prasad B (2003) Development and climate change in Fiji: focus on coastal mangroves. Environment Directorate, Organisation for Economic Cooperation and Development OECD, Paris (France), 56 pp

Aleem AA (1958a) A taxonomic and paleoecological investigation of the diatom-flora of the extinct Fayoum lake (Upper Egypt). I. Systematic part. Bull Fac Sci Alex Univ Egypt 2:99–138

Aleem AA (1958b) A taxonomic and paleoecological investigation of the diatom-flora of the extinct Fayoum lake (Upper Egypt). II. Distribution and ecology. Bull Fac Sci Alex Univ Egypt 2:217–244

Al-Far DM (1966) Geology and coal deposits of Gebel El Maghara (north Sinai). Geological Survey and Mineral Research of Egypt, Cairo, Paper no. 37, 59 pp

Al-Far DM, Hagemann HW, Omara S (1965) Beitrage zur Geologie des kohle-fuhrend Gebietes von El Maghara, Nord-Sinai (Ägypten). Geol Mitt 4(4):397–429

Ash SR (1972) *Piazopteris branneri* from the Lower Jurassic, Egypt. Rev Palaeobot Palynol 13:147–154

Barthoux JC (1922) Chronologie et description des roches ignéss du désert Arabique. Mem Inst D Egypte le Caire 5:1–262

Barthoux JC, Fritel PH (I925) Flore crétacée du grès de Nubie. Mém Inst Ég 7(2):65–119. (Reviewed by Lorin H (1925). In: Bibliogr. Géogr., Paris, Année 35, pp 434)

Bkhat H (2012) Studies on the fossil mangroves of the Western Desert of Egypt. Unpublished PhD Dissertation, Ain Shams University, Cairo, Egypt

Bose MN (1974) The genus *Otozamites* Braun from the Mesozoic rocks of India. Palaeontographica Abt B 147(4–6):100–106

Bowen BE (1970) The stratigraphy of the Jebel el-Qatrani formation in the Fayum Deperssion, Egypt. UAR PhD Dissertation, IOWA State University (cited in Bown et al. 1982)

Bowen BE, Vondra CF (1974) Paleoenvironmental interpretations of the Oligocene Gabal el Qatrani Formation, Fayum Depression, Egypt. Ann Geol Surv Egypt 4:115–138

Bown TM (1982) Ichnofossils and rhizoliths of the nearshore fluvial Jebel Qatrani Formation (Oligocene), Fayum Province, Egypt. Palaeogeogr Palaeoclim Palaeoecol 40:255–309

Bown TM, Kraus M, Wing S, Fleagle J, Tiffney BH, Simons E, Vondra CF (1982) The Fayum Forest revisited. J Hum Evol 11:603–632

Brea M, Franco MJ, Lutz A (2012) Redescription and reassignment of *Entrerrioxylon victoriensis* from the upper Miocene, Paraná formation, South America. Rev Palaeobot Palynol 185:13–25

Bucur II, Nagm E, Wilmsen M (2010) Upper Cenomanian-Lower Turonian (Cretaceous) calcareous algae from the Eastern Desert of Egypt: taxonomy and significance. Stud Univ Babeş-Bolyai, Geol 55(1):29–36

Carpentier A, Farag IAM (1948) Sur une flore problment Rhetienne à El Galala El-Bahariya, Egypt. CR Acad Sci Paris 226:686–688

Chandler MEJ (1954) Some Upper Cretaceous and Eocene fruits from Egypt (with appendices by MY Hassan and MI Youssef). Bull British Museum (Nat Hist) Geol Ser 2:149–187

Coiffard C, Mohr BAR (2016) *Afrocasia kahlertiana* gen. et sp. nov., a new tropical member of Araceae from Late Cretaceous strata of northern Gondwana (Baris, Egypt). Taxon 65(6):1374–1384

Darwish MH (1990) Studies on some Egyptian fossil plants. Unpublished PhD Dissertation, Ain Shams University

Darwish MH (2003) Plant fragments from Quaternary Tufa deposits at Bir Dungul, Southwestern Desert, Egypt. Egypt J Biotechnol 15:277–284

Darwish MH, Attia Y (2007) Plant impressions from the mangrove-dinosaur Unit of the Upper Cretaceous Bahariya Formation of Egypt. Taeckholmia 27:105–125

Darwish MH, Awad SA (2002) Plant Fragments from Tufa Deposits (Quaternary), Kharga Oasis, Egypt. Pakistan J Biol Sci 5(11):2002

Darwish MH, El-Kelani A (2001) Lower Carboniferous plants from Abu-Thora Formation in Southwest Sinai. Taeckholmia 21(1):27–34

Darwish MH, El-Safori YA (2016) Late Carboniferous Macroflora from Rod El-Hamal Formation Wadi Araba, North Eastern Desert, Egypt. Taeckholmia 36(1):45–57

Darwish MH, Kamal El-Din MM, El-Saadawi WE (2016) On the Fossil Wood Flora of Wadi Ankebieh, Egypt, with Two New Records. Egypt J Bot 56(3) (Part 1):679–692

Darwish MH, Strougo A, El-Saadawi W (2000) Fossil plant remains from Oligocene (?) of Farafra Oasis, Egypt. Taeckholmia 20 (2):147–157

Dolson I, El-Barkooky A, Wehr F, Gingerich PD, Prochazka N, Shann M (2002) The Eocene and Oligocene Paleo-Geography of Whale Valley and the Fayoum Basins: implications for hyrocarbon Exploration in the Nile Delta and Eco-Tourism in the Greater Fayoum Basin. Cairo-AAPG/EPEX/SEG/EAGE Field Trip-no. 7:1–71

Doyle JA, Biens P, Doerenkamp A, Jardiné S (1977) Angiosperm pollen from the pre-Albian Lower Cretaceous of Equatorial Africa. Bull Centres Recherches Explor Produc El Aquitaine 1:451–473

Dragastan ON, Soliman HA (2002) Paleogene Calcareous Algae from Egypt. Micropaleontology 48(1):1–30

Dupéron-Laudoueneix M, Lejal-Nicol A (1981) Sur deux bois homoxylés du Sud-Quest de l'Egypte C.R. 160e Congr. Nat. Soc. Sav., Perpignan, Sci. I:29–40

Edwards WN (1932) Some Mesozoic plants from Africa. Ann Mag Nat Hist 10:406–411

El-Beialy SY (1994) Palynological investigations of Cretaceous sediments in the Abu El Gharadiq Oil Field, Western Desert, Egypt. Newsl Stratigr 31:71–84

El-Beialy SY, Ayyad SN, Kholeif SE (1990) Mesozoic-Tertiary palynomorphs and planktonic foraminifera of the subsurface section of the Sindy-1 well, eastern Nile Delta, Egypt. Newsl Stratiger 22:71–85

El-Beialy SY, Mahmoud MS, Ali AS (2005) Insight on the age, climate and depositional environments of the the Rudeis and Kareem formations, GS-78-1 well, Gulf of Suez Egypt: a palynological approach. Rev Esp Micropaleontol 37(2):273–289

El-Noamani ZM (2015) Palynological study on the subsurface Cretaceous in the Western Desert of Egypt. Unpublished PhD Dissertation, Ain Shams University, Cairo, Egypt

El-Noamani ZM (2018) Reconstruction of paleovegetation and paleoecology from the Early Cretaceous sporomorphs of Bougaz-1 well, northeast Sinai, Egypt. Egypt J Bot 58(3):397–409

El-Noamani ZM, Saleh AI (2018) Cretaceous Algal Palynomorphs from Northeast Sinai, Egypt: systematics and Paleoenvironmental Implications. Egypt J Bot 58(1):63–72

El-Saadawi WE (1979) A bibliography concerning fossil plants of Egypt. Phytologia 43:253–269

El-Saadawi W (2005) A fossil rhizome at the mangrove site of Wadi Hitan, Egypt. Taeckholmia 25:129–136

El-Saadawi W (2006) On the fossil flora of Jebel Qatrani area, Fayum, Egypt. Taeckholmia 26:131–140

El-Saadawi W, Farag E (1972) Some Mesozoic plants from Abu-Darag, Western side of Gulf of Suez. Egypt J Bot UAR 15(1):121–130

El-Saadawi W, Kamal-El-Din MM (2004) *Terminalioxylon* species from Gebel Qatrani Formation at Widan-el-Faras, Fayum, Egypt. Taeckholmia 24(1):63–78

El-Saadawi WE, Kedves M (1991) Palaeobotanical investigation on plant impressions and sporomorphs from Egypt. Plant Cell Biol Develop (Szeged) 2:8–33

El-Saadawi WE, Badawi AA, El-Awamri AA (1975) On silicified rhizome fragments of *Phragmites communis* Trin from the Pleistocene of El-Fayum, Egypt. Palaeontographica Abt B 154:172–178

El-Saadawi W, Badawi A, El-Awamri A (1987) Silicified root fragments of *Tamarix* L. from the Pleistocene of El-Fayum. Ann Rev Univ College for Women, Ain Shams Univ 12:321–335

El-Saadawi W, Badawi A, Shabaan A, El-Awamri A (1978) Pleistocene diatoms from El-Fayum. Proc Egypt Acad Sci 31:257–263

El-Saadawi W, Darwish MH, Abd-El-Azeam S (2003) Permian plant remains from Wadi El-Dome, western side of the Gulf of Suez, Egypt. Taeckholmia 23(1):83–96

El-Saadawi W, Darwish MH, Kamal-El-Din M, Youssef SG (2016a) The first record of Fossil Rubiaceae Wood from Egypt. Egypt J Bot 56(3):723–732

El-Saadawi W, Kamal-El-Din MM, Attia Y, El-Faramawi M (2011) The wood flora of the Cairo Petrified Forest, with five Paleogene new legume records for Egypt. Rev Palaeobot Palynol 167:184–195

El-Saadawi WE, Kamal-El-Din MM, El-Faramawi M, El-Noamani ZM (2010) Fossil palm woods of Egypt. III. A new site for *Palmoxylon aschersoni* Schenk and *P. wadiai* Sahni. Taeckholmia 30:145–159

El-Saadawi W, Kamal-El-Din M, El-Faramawi M, Ziada NA (2013) *Terminalioxylon edwardsii* from the Oligocene of Egypt, with a review of the genus in Africa. Taeckholmia 33(4):47–63

El-Saadawi W, Kamal-El-Din M, Wheeler E, Osman R, El-Faramawi M, El-Noamani ZM (2014) Early Miocene woods of Egypt. IAWA J 35(1):35–50

El-Saadawi WE, Osman R, El-Faramawi M, Bkhat H, Kamal El-Din MM (2016b) On the Cretaceous mangroves of Bahariya Oasis, Egypt. Taeckholmia 36:10–25

El-Saadawi WE, Osman R, El-Faramawi M, Bkhat H, Kamal El-Din MM, Ziada N (2018) On the Eocene mangroves of Wadi Al-Hitan World Heritage site, Fayum, Egypt. Egypt J Exp Biol (Bot) 14 (1):197–209

El-Saadawi W, Youssef SGM, Kamal-El-Din M (2002) Fossil palm woods of Egypt. I. *Palmoxylon aschersoni* Schenk and *P. libycum* (Stenzel) Krausel. Taeckholmia 22(1,2):143–153

El-Saadawi W, Youssef SGM, Kamal-El-Din MM (2004) Fossil palm woods of Egypt. II. Seven Tertiary *Palmoxylon* species new to the country. Rev Palaeobot Palynol 129(4):199–211

El-Saadawi W, Ziada NA, El-Faramawi M, Kamal-El-Din M, Loutfy MHA (2017) The Cairo Petrified Forest revisited. RevPalaeobot Palynol 238:34–42

El-Soughier MI, Mehrotra RC, Zhou Z, Shi G (2011) Nypa fruits and seeds from the Maastrichtian-Danian sediments of Bir Abu Minqar, South Western Desert, Egypt. Palaeoworld 20:75–83

Gardner EW (1935) The Pleistocene Fauna and Flora of Kharga Oasis, Egypt. Quart J Geol Soc Lond 91:479–518

Geological Survey of Egypt (1982) Sheet N-G-35, scale 1:1000000

Graham A (1995) Diversification of Gula/Caribbean mangrove communities through Cenozoic time. Biotropica 27:20–27

Gregor H, Hagn H (1982) Fossil fructifications from the Cretaceous-Palaeocene Boundary of SW-Egypt (Danian, Bir Abu Munqar). Tertiary Res 4:121–147

Greguss P (1967) Fossil Gymnosperm Woods in Hungary from the Permian to the Pliocene. Akadémiai Kiadó, Budapest, p 136

Harris TM (1949) Notes on the Jurassic flora of Yorkshire, 40–42, 41: the narrow-leaved *Otozamites* species. Ann Mag Nat Hist Lond Ser 12(2):275–299

Hermina M (1990) The surroundings of Kharga, Dakhla and Farafra oases. In: Said R (ed) Geology of Egypt. A.A. Balkema, Rotterdam, pp 259–292

Hirmer M (1925) 3. Die fossilen Pflanzen Ägyptens, D. Filicales. Ergebnisse der Forschungsreisen Prof. E. Stromers in den Wüsten Ägyptens, IV. Die fossilen Floren Ägyptens. Abh. Bayer. Akad. Wiss., München, Bd. 30, Abt. 3, I8 pp

Horowitz A (1973) *Noeggerathia dickeri* n.sp. from the carboniferous of Sinai. Rev Palaeobot Palynol 15(1):51–56

Ibrahim MIA (1996) Aptian-Turonian palynology of the Ghazalat-1 Well (GTX–1), Qattara Depression, Egypt. Rev Palaeobot Palynol 94:137–168

Ibrahim MIA, El-Beialy SY (1995) Kimmeridgian-Barremian palynostartigraphy of the Malha-1 well, Northern Sinai, Egypt. Sci Geol Bull 48(4):187–209

Ibrahim MIA, Dilcher D, Kholeif S (2009) Palynomorph succession and paleoenvironment in the Upper Cretaceous Abu Gharadig Oil Field, Northwestern Desert, Egypt. Micropaleontology 55(6):525–558

Ibrahim MIA, Schrank E (1996) Palynological studies on the Late Jurassic-Early Cretaceous of the Kahraman-1 well, norther Western Desert, Egypt. Geol. de l`Afriq. et de l`Atlantiq. sud: Actes Colloques Angers, pp 611–629

Ibrahim MIA, Schrank E, Abdel-Kireem MR (1995) Cretaceous biostratigraphy and palaeogeography of North Egypt and northeast Libya. 1st Symp. Geol Sirt Basin Petrol Res J 7:75–93

Ibrahim MIA, Zobaa MK, El-Noamani ZM, Tahoun SS (2017) A review of the angiosperm pollen genus *Cretacaeiporites* Herngreen, with one new species from the Upper Cretaceous of Egypt. Palynology 41(1):101–116

Issawi B, El Hinnawi M, Francis M, Mazhar A (1999) The Phanerozoic geology of Egypt a geodynamic approach. Egypt Geol Surv Spec Publ 76:1–462

Jongmans WJ, van der Heide S (1955) Flore et faune du Carbonifère inférieur de l'Egypte. Nether Geol Stich Meded Nieuwe Ser 8:57–59

Julien AA (1904) Fossil water fungus in petrified wood from Egypt. Bull Geol Soc Am Rochester (NY) I5:550

Kamal El-Din MM (2002) *Bombacoxylon owenii* (Carr.) Gottwald woods from Gebel Shabraweet, Eastern Desert, Egypt. Taeckholmia 22(1):91–99

Kamal El-Din MM (2003) Petrified wood from the Farafra Oasis, Egypt. IAWA J. 24(2):163–172

Kamal El-Din MM, Darwish MH, El-Saadawi W (2013) Fossil palm woods of Egypt: IV. New *Palmoxylon* records with a summary on macrofossil African Arecaceae. Palaeontographica Abt B 290(1–3):41–61

Kamal El-Din MM, Darwish MH, El-Saadawi W (2015) Novelties on Miocene woods from Egypt with a summary on African fossil woods of Fabaceae, Malvaceae and Dipterocarpaceae. Palaeontographica Abt B 292(4–6):173–199

Kamal El-Din MM, El-Saadawi W (2004) Two Leguminosae woods from the Miocene of Gebel Ruzza, Egypt. IAWA J 25(4):471–483

Kamal El-Din MM, Refaat AA (2001) *Detarioxylon aegyptiacum* (Leguminosae) from Lower Miocene marine sediments in Southern Sinai. Taeckholmia 21(1):103–114

Kamal El-Din MM, Wheeler EA, Bartlett JA (2006) Cretaceous woods from the Farafra Oasis, Egypt. IAWA J 27(2):137–143

Kedves M, El-Saadawi W, Youssef SGM (2004a) Fossil gymnosperm wood from Aswan Area. Plant Cell Biol Develop 16:23–28

Kedves M, Youssef SGM, El-Saadawi W, Mostafa RM (2004b) A new *Agathoxylon* data from the Late Cretaceous of Kharga Oasis, Egypt, investigated with combined methods. Taeckholmia 24(1):43–49

Kholeif SEA (2004) Palynology and palaeovegetation reconstruction in late Quaternary sediments of the southern Suez Isthmus: Egypt. J Afr Earth Sci 40(1–2):31–47

Klitzsch E, Lejal-Nicol A (1984) Flora and fauna from strata in southern Egypt and northern Sudan (Nubia and surrounding areas). Berliner Geowiss Abh (A) 50:47–79

Komarova NI, Kruchinina NV, Iskander NR (1973) Mezozojskie sporovo-pyl'cevye Kompleksy nekotorych rajonov Egipta [Mesozoic spore-pollen complexes of some regions of Egypt]. In: Palinologija Mezofita [Palynology of the Mesozoic], Proc. 3rd. Int. Palyn. Conf. Novosibirsk 1971, Nauka, Moscow. pp 124–127

Kora M (1993) Carboniferous miospores assemblages from the Abu Rodeiyim boreholes, west central Sinai, Egypt. Rev Micropalaeont 36(3):235–255

Kora M, Schultz G (1987) Lower Carboniferous Palynomorphs from Um Bogma, Sinai (Egypt). Grana 26:53–66

Kräusel R (1939) Ergebnisse der Forschungsreisen Prof. E. Stromers in den Wüsten Ägyptens, IV. Die fossilen Floren Ägyptens 3. Die fossilen Pflanzen Ägyptens, E-1. Abh. Bayer. Akad. Wiss., München N. F., 47, pp 1–140

Kräusel R, Stromer E (1924) Ergebnisse der Forschungsreisen Prof. E. Stromers in den Wüsten Ägyptens, IV. Die fossilen Floren

Ägyptens 1–3. A–C. Abh Bayer Akad Wiss Math-Nat Abt 30(2):1–48
Kuss J (1986) Upper Cretaceous calcareous algae from the Eastern Desert of Egypt. N Jb Geol Paläont Mh (4):223–238
Kuss J (1994) Cretaceous (Albian-Turonian) Calcareous Algae from Egypt and Jordan-Systematics, Stratigraphy and Paleogeography. Abh Geol B A 50S:295–317
Kuss J, Conrad M-A (1991) Calcareous Algae from Cretaceous Carbonates of Egypt, Sinai, and Southern Jordan. J Paleontol 65 (5):869–882
Lavin M, Luckow M (1993) Origins and Relationships of Tropical North America in the Context of the Boreotropics Hypothesis. Am J Bot 80(1):1–14
Lejal-Nicol A (1981) Nouvelles empreintes de la (Lingula Shale Unit) dans la région d'Abu Ballas (Égypte). CR 106è Cong Nat Soc Sav Perpignan Sci (1):15–27
Lejal-Nicol A (1987) Flores nouvelles du Paleozoiqueet du Mesozoique de L'Egypte et du Soudan septentrional. Berliner Geowiss Abh 75(A):151–248
Lejal-Nicol A (1990) Fossil flora. In: Said R (ed) The Geology of Egypt. Balkema, Rotterdam, Brookfield, pp 615–625
Lejal-Nicol A, Dominik W (1987). Plant cover and Paleoenvironment during the Cenomanian in Bahariya basin (Egypt). In: 14th International Botaical Congress, Berlin (Abstr.), p 402
Leory SAG (1992) Palynological evidence of *Azolla nilotica* Dec. in recent Holocene of the eastern Nile Delta and palaeoenvironment. Veg Hist Archaeobotany 1:43–52
Lorch J (1967) A Jurassic florule from Sinai. Israel J Bot 16:29–37
Louvet P (1973) Sur les affinités des flores tropicales ligneuses africaines tertiaire et actuelle. Bull Soc Bot Fr 120(9):385–395
Lyon MA, Johnson K, Wing SL, Nichols DJ, Lacovara KJ, Smith JB (2001) Late Cretaceous equatorial coastal vegetation: new megaflora associated with dinosaur finds in the Bahariya oasis, Egypt. In: Geological Society of America, Annual Meeting, November, 5–8, paper no. 82
Mahmoud MS, Moawad AMM (1999) Miospore and dinocyst biostratigraphy and palaeoecology of the Middle Cretaceous (Albian-early Cenomanian) sequence of the Ghoroud 1-X borehole, northern Western Desert, Egypt. 1st Int. Conf. Geol. Africa, Assiut, Egypt, v 1, pp 1–13
Mandura AS (1997) A mangrove stand under sewage pollution stress: Red Sea. Mangroves Salt Marshes 1(4):255–262
Morley RJ, Richards K (1993) Gramineae cuticle, a key indicator of Late Cenozoic climatic change in the Niger Delta. Rev Palaeobot Palynol 77:119–127
Moussavian E, Kuss H-J (1990) Typification and status of *Lithothamnium aschersoni* Schwager, 1883 (Corallinaceae, Rhodophyta) from Paleocene limestones of Egypt. A contribution to the synonymy and priority of the genera *Archaeolithothamnium* Rothpletz and *Sporolithon* Heydrich. Berliner Geowiss Abh (A) 120(2):929–942
Muller J (1981) Fossil pollen records of extant angiosperms. Bot Rev 47(1):1–142
Nicholson PT, Shaw I (2000) Ancient Egyptian materials and technology. Cambridge University Press, Cambridge, p 724
Nour-El-Deen S (2015) Studies on the fossil flora of Gebel Qatrani Formation, Fayum, Egypt. Unpublished PhD Dissertation, Ain Shams University, Cairo, Egypt
Nour-El-Deen S, Osman R, El-Saadawi W (2014) Some doubtful locality records for *Palmoxylon* from Gebel Qatrani Formation, Fayum, Egypt. Taeckholmia 34:67–76
Nour-El-Deen S, Thomas R, El-Saadawi W (2018) First record of fossil Trachycarpeae in Africa: three new species of *Palmoxylon* from the Oligocene (Rupelian) Gebel Qatrani Formation, Fayum, Egypt. J Syst Palaeontol 16(9):741–766
Nunn PD, Ravuvu AD, Kay R, Yamada K (1993) Assessment of coastal vulnerability and resilience to sea-level rise and climate change, case study: Viti Levu Island, Fiji, phase I: concept and approach. In: South Pacific Regional Environment Programme, Apia, and Environment Agency of Japan, Tokyo, pp 188
Penny JHJ (1986) An Early Cretaceous angiosperm pollen assemblages from Egypt. Spec. Pap. Palaeont. v. 35, pp 119–132
Philippe M, Cuny G, Bamford M, Jaillard E, Barale G, Gomez B, Ouaja M, Thévenard F, Thiebaut M, Von Sengbusch P (2003) *Metapodocarpoxylon libanoticum* (Edwards) Dupéron-Laudoueneix et Pons and Late Jurassic-Early Cretaceous continental biogeography. J Biogeogr 30:389–400
Plaziat JC, Cavagnetto C, Koeniguer JC, Baltzer F (2001) History and biogeography of the mangrove ecosystem based on a critical reassessment of the paleontological record. Wetlands Ecol Manag 9 (3):161–179
Reynolds PO, Schandelmeier H, Pudlo D (1997) The Late Cretaceous (Campanian-Maastrichtian, ca. 74 Ma). In: Schandelmeier H, Reynolds PO (eds) Paleogeography-paleotectonic Atlas of North-Eastern Africa, Arabia and Adjacent Areas, Late Neoproterozoic to Holocene. Balkema, Rotterdam, pp 81–88
Rozière FM (1813–1824) De la constitution physique de l'Égypte et de ses rapports avec les anciennes institutions de cette contrée, dans *Description de l'Égypte. Histoire naturelle*, vol II, pp 407–682; Part six, Chapter V. Bois fossiles, pp 658–660, 702
Rüssegger J (1836) Geognostische Beschaffenheit um Kairo. N. Jahrb. F. Min, Stuttgart, pp 687–691
Saad SI (1963) Pollen and Spores recently discovered in the coals of Sinai regionI. Euone Moussa district. Palaeontographica B 113:117–125
Saad SI (I965) Pollen and spores recently discovered in the coals of Sinai region 2. Um Bogma district. Palaeontographica B II5:139–149
Saad SI (1978) Palynological studies in the Egyptian Western Desert, Umbarka 1X borehole. Pollen Spores 20(2):261–301
Saad SI, Ghazaly G (1976) Palynological studies in Nubia sandstones form Kharga Oasis. Pollen Spores 18:407–470
Salard-Cheboldaeff M (1979) Palynologie Maestrichtienne et Tertiare du Cameroun. Etude qualitative et repartition vertical des principales espèces. Rev Palaeobot Palynol 28:365–388
Schenk A (1883) Fossile Hölzer. Palaeontographica 30(2):1–19
Schrank E (1987) Paleozoic and Mesozoic palynomorphs from northeast Africa (Egypt and Sudan) with special reference to Late Cretaceous pollen and dinoflagellates. Berl Geowiss Abh A 75 (1):249–310
Schrank E (1991) Mesozoic palynology and continental sediments in NE Africa (Egypt and Sudan) - a review. J Afr Earth Sci 12 (1/2):363–373
Schrank E (1992) Nonmarine Cretaceous correlations in Egypt and northern Sudan: palynological and palaeobotanical evidence. Cretac Res 13:351–368
Schrank E, Ibrahim MIA (1995) Cretaceous (Aptian-Maastrichtian) palynology of foraminifera-dated wells (KRM-1, AG-18) in northwestern, Egypt. Berl Geowiss AbhRh A 177:1–44
Schrank E, Mahmoud MS (1998) Palynology (pollen, spores and dinoflagellates) and Cretaceous stratigraphy of the Dakhla Oasis, Cetral Egypt. J Afr Earth Sci 26:167–193
Schrank E, Mahmoud MS (2002) Barremian angiosperm pollen and associated palynomorphs from Dakhla Oasis area, Egypt. Palaeontology 45(1):33–56
Schuermann HME, Burger D, Dijkstra SJ (I963) Permian near Wadi Araba eastern desert of Egypt. Geologie en Mijnbouw 42(10):329–336
Schwager C (1883) Die Foraminiferen aus den Eocaenablagerungen der libyschen Wüste und Aegyptens. Palaeontographica 30:79–153

Schweitzer CE, Lacovara KJ, Smith JB, Lamanna M, Lyon MA, Attia Y (2003) Mangrove-dwelling crabs (Decapoda: Brachyura: Necrocarcinidae) associated with dinosaurs from the Upper Cretaceous (Cenomanian) of Egypt. J Paleontol 77:888–894

Seward AC (1932) Carboniferous plants from Sinai. QJGS Lond 88:350–357

Seward AC (1935) Leaves of dicotyledons from the Nubian Sandstone of Egypt. Government Press, Bulaq, Geological Survey of Egypt, p 20

Smith JB, Lamanna MC, Lacovara KJ, Dadson P, Smith JR, Poole JC, Giegeng R, Attia Y (2001) A giant Sauropod Dinosaur from an Upper Cretaceous mangrove deposit in Egypt. Science 292 (5522):1704–1706

Strickberger MW (2005) Evolution, 3rd edn. Jones and Bartlett Publishers, 722 pp

Sultan IZ (1978) Mid-Cretaceous plant microfossils from the northern part of the Western Desert of Egypt. Rev Paleobot Palynol 25:259–267

Sultan IZ (1985) Maastrichtian plant microfossils from the el Mahamid area, Nile Valley, southern Egypt. Rev Micropaléont 28:213–222

Sultan IZ (1986) Palynostratigraphy of the Lower Cretaceous sediments in the Nile Delta region. Rev Esp Micropaleont 18:55–70

Sultan IZ (1987) Palynology of the Albian-Cenomanian strata in Mersa Matruh well, Western Desert, Egypt. J Afr Earth Sci 6:665–675

Sultan IZ, Aly SM (1986) Palyological zonation of Albian-Cenomanian sediments in the northern part of the Western Desert, Egypt. Bull Fac Sci Alex Univ 26(3):80–101

Sultan IZ, Soliman HA (1978) Palynostratigraphi du Bathenien-Callovien du puites no. 3 de Ba, Sinai Nord, Egypte. Rev Micropaleont, pp 108–111

Synelnikov AS, Kollerov DK (1959) Palynologic analysis and age of coal samples from El-Bedáa-Thora district, west-central Sinai. Geol. Surv. Egypt, no. 4, pp 1,2

Tawadros EE (2001) Geology of Egypt and Libya. A. A. Balkema, Rotterdam, Brookfield, p 468

Tiffney BH (1991) Paleoenvironment of the Oligocene Jebel Qatrani Formation, Fayum Depression, northern Egypt, based on floral remains. Geol Soc Am Abstracts 23:456

Tomlinson PB (1994) Botany of mangroves. Cambridge University Press, Cambridge, p 419

Unger F (1841–1847) Chloris protogaea. Beiträge zur Flora der Vorwelt. Leipzig

Unger F (1858) Der versteinerte Wald bei Cairo und einige andere Lager verkieselten Holzes in Ägypten. Sber. Akad. Wiss. Wien, Math.-Nat. Kl. 33:209–233

Webber PJ (1961) *Phlebopteris branneri* from the Western Desert of Egypt. Ann Mag Nat Hist Ser 13:4–7

Wheeler EA, Baas P (1991) A survey of the fossil record for dicotyledonous wood and its significance for evolutionary and ecological wood anatomy. IAWA Bull n.s. 12:275–332

Wing SL, Tiffney BH (1982) A paleotropical flora from the Oligocene Jebel Qatrani Formation of northern Egypt: a preliminary report. Botanical Society of America, Miscellaneous Series Publication, 162, 67

Youssef SGM (2002) *Xenoxylon* wood from Late Jurassic-Early Cretaceous of Gebel Kamil, Egypt. IAWA J 23(1):69–76

Youssef SGM, El-Saadawi W (2004) Fossil wood from the Nubian Sandstone of Kharga Oasis, Egypt. Taeckholmia 24(1):51–61

Youssef SGM, El-Saadawi W, Kedves M, Mostafa RM (2000) Wood anatomy of a silicified trunk from the Kharga Oasis, Egypt. Plant Cell Biol Develop 12:30–39

Zahran MA (1977) Africa A. Wet formations of the African Red Sea coast. In: Chapman VG (ed) Wet coastal ecosystem. Elsevier Scientific Publishing Company, Amsterdam, pp 215–231

Ziada NA, Ibrahim MIA, Abdel-Hameed UK, El-Saadawi W (2018) Bryophyte and pteridophyte spores in Holocene sediments from Fayoum Depression, Egypt: Core F1-08, Egypt. J Exp Biol (Bot) 14 (2):279–286

Mineral Resources in Egypt (I): Metallic Ores

14

Mortada El Aref, Yasser Abd El-Rahman, Basem Zoheir, Adel Surour, Hassan M. Helmy, Amr Abdelnasser, Ahmed Hassan Ahmed, and Mohamed El-Ahmadi Ibrahim

Contents

M. El Aref · Y. Abd El-Rahman (✉) · A. Surour
Geology Department, Faculty of Science, Cairo University, iza, 12613, Egypt
e-mail: yassermedhat@yahoo.com

M. El Aref
e-mail: elarefmortada@yahoo.com; elaref@sci.cu.edu.eg

A. Surour
e-mail: adelsurour@hotmail.com

B. Zoheir · A. Abdelnasser
Faculty of Science, Department of Geology, Benha University, 13518 Benha, Egypt
e-mail: basem.zoheir@gmail.com

A. Abdelnasser
e-mail: amr.khalil@fsc.bu.edu.eg; abdelnasser82@gmail.com

B. Zoheir
Institute of Geosciences, University of Kiel, Ludewig-Meyn Str. 10, 24118 Kiel, Germany

H. M. Helmy
Faculty of Science, Department of Geology, Minia University, Minya, Egypt
e-mail: hmhelmy@yahoo.com

A. H. Ahmed
Faculty of Earth Sciences, King Abdulaziz University, Jeddah, Saudi Arabia
e-mail: ahmohammed@kau.edu.sa

Faculty of Science, Department of Geology, Helwan University, Cairo, Egypt

M. El-Ahmadi Ibrahim
Nuclear Materials Authority, New Cairo, Egypt
e-mail: dr_mahmadi@yahoo.com

Z. Hamimi et al. (eds.), *The Geology of Egypt*, Regional Geology Reviews,
https://doi.org/10.1007/978-3-030-15265-9_14

Abstract

Mineral resources in Egypt are diverse. This chapter deals with the metallic ores. The chapter starts with the iron ores in Egypt and special emphasis is given to the origin of Egyptian banded iron-formations. In addition to iron, the chapter covers many types of ore deposits in Egypt including orogenic gold, Ti-rich, sulfide and precious metal, chromite, industrial metal oxides (Sn, W, Ta, Nb, and Mo) deposits as well as U occurrences in the basement rocks of Egypt and Egyptian manganese deposits.

14.1 Iron Ores of Egypt

Mortada El Aref

The Egyptian iron ores are of stratabound/stratiform type of near surface shallow marine and subarial environment, ranging in age from early Proterozoic to Paleogene and can be chronologically categorized into: (a) Pre-Cambrian Banded Iron Formation (BIF); (b) Mesozoic-Tertiary oolitic (oncolitic ironstones), and (c) Oligocene (?) Pre-rift iron laterite (Fig. 14.1). In this article, the geologic setting, geometry, mode of formation, mineral paragenesis, reserves (quality and quantity) of the iron ores are addressed. The opportunities and challenges for the imperative economic investments of these easy minable ores are also clarified.

14.1.1 Pre-cambrian Banded Iron Formation (BIF)

The Pre-Cambrian BIF successions are confined within the Pan-African (Proterozoic) thrust sheets incorporated with ophiolitic mélange complex and cropping out in separated locations in the Central Eastern Desert (Fig. 14.1). Early Proterozoic BIF is represented by the Umm Nar occurrence (El Aref et al. 1993a, b) which includes three tectono-stratigraphic units (Shaetian sheared granites (Pre-Pan African infrastructure); metasediments hosting BIF of shallow shelf environment and Pan-African ophiolitic mélange, separated by two main thrust faults and intruded by granites and younger gabbros (Fig. 14.2). During the Pan-African episode (late Proterozoic), mélange rocks thrust over the BIF and the host metasediments which together folded and thrust

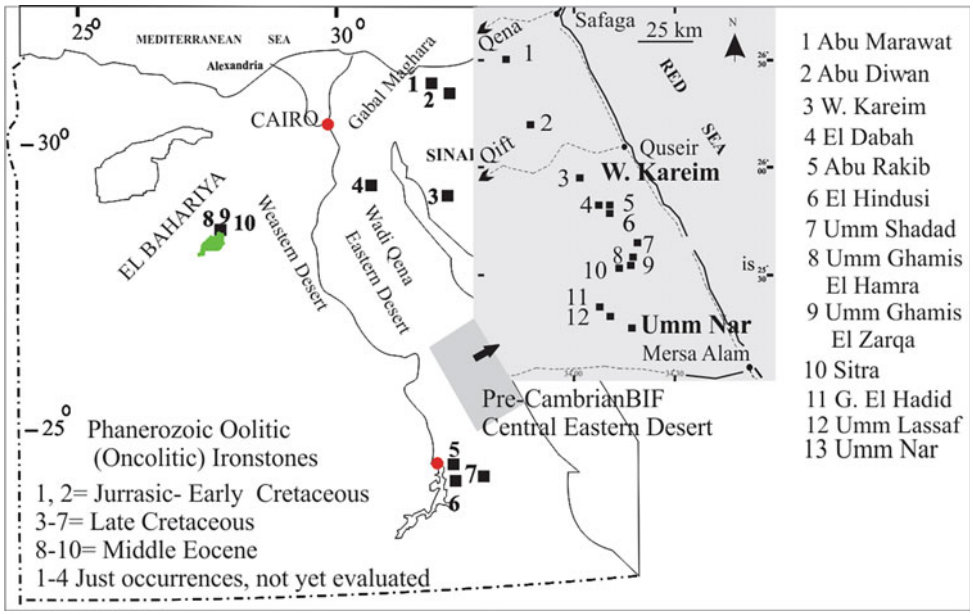

Fig. 14.1 Location map, the Egyptian Precambrian and Phanerozoic Fe ore deposits

over the sheared infrastructure. The metasediments comprise two successive zones, a lower zone of amphibolite schist and marble free of BIF, and an upper zone (~300 m thick) entirely formed of BIF rhythmic bands intercalated with mica schist (13.7 mt iron reserve of 41.8–45.3 Fe% and producing ore concentrates of 61 Fe%). Geometrically, the iron bands exhibit all scales of bedding from macro- to micro-banding (varved, wavy and stromatolitic), internally showing syn-sedimentary structures and rootless of intrafolial folds. The BIF succession is subjected to two folding phases resulted in the development of bedding parallel schistosity, intersected by axial plane foliations and strain-slip cleavage. Mineral paragenesis suggests that the original materials are ferruginous/calcareous muds, silica gel, silt, Fe clays and organic matters. These materials are converted into subsequent generations of magnetite, hematite, stilpnomelane and greenatite with minor abundant epidote, garnet, calcite, muscovite, biotite and graphite during different stages of crystallization, replacement, recrystallization and porphyroblast overgrowths under depositional, diagenetic and metamorphic (regional and deformational) conditions. The other BIF occurrences (Fig. 14.1) are considered to be of late Proterozoic Pan-African volcanogenic origin of island arc environment. In Wadi Kareim, a BIF sequence is confined within the middle part of thick metavolcaniclastics (up to 500 m thick), overlying and underlying submarine pillowed metavolcanics of basaltic, dacitic and andesitic composition interbedded with less abundant pyroclastic-epiclastic thin layers (Fig. 14.3). The two sequences are intruded by grey granites and truncated by molasse conglomerates of the Hammamat group and also dissected by trachyte plugs. The BIF bands are obviously intertongue with and laterally change into pyroclastics free of iron bands. Geometrically, they exhibit all scales of banding from macrobands down to micro-varved and sromatolitic laminations rhythmically alternating with metadust tuffs, marble and jasper bands and lamina. The most common internal fabrics and components are cross laminations, ripple marks, falser bedding and granular fabrics (ooids and oncoids) together with pronounced proportion of organic carbonaceous matter and palynomorphs (El Habaak 1992). According to El Habaak (1992), the original precipitates are ferruginous and Fe-rich calcareous mud, Fe-rich silica gel, organic materials, mineral detritals and ashes. The iron-rich bands are formed of magnetite, hematite, siderite, greenalite, stipnomelane, minnestotite, pyrite and goethite with gangue of quartz, calcite, dolomite, chlorite and lithic and crystal fragments, comprising granular carbonate, silicate and oxide-rich facies assemblages. Mineral paragenesis and textural relationships indicate sequential mineral formation, cementation, recrystallization and overgrowths under diagenetic to very low metamorphic conditions with subsequent martitization. The geometry, textures and the mineral paragenesis indicate deposition in a restricted shallow marine environment along the margins of island arc (calc-alkaline volcanic and volcaniclasts). The calculated ore reserves (after Abu El Saadat 2009) are: W. Kareim (17.7 mt, 41–44.6 Fe%), Abu Mrawat (6.5 mt, 44.4 Fe%), Um Ghamis Elzarqa (5, 6 mt, 42.1–44.6 Fe%), G. El Hadid (6.3 mt, 45.7 Fe%), producing Fe concentrates of up to 56.4–69 Fe%. More recent results are shown in Table 14.1. Additional ore reserves are very much expected in similar sites in the partially un-surveyed southern part of the Eastern Desert.

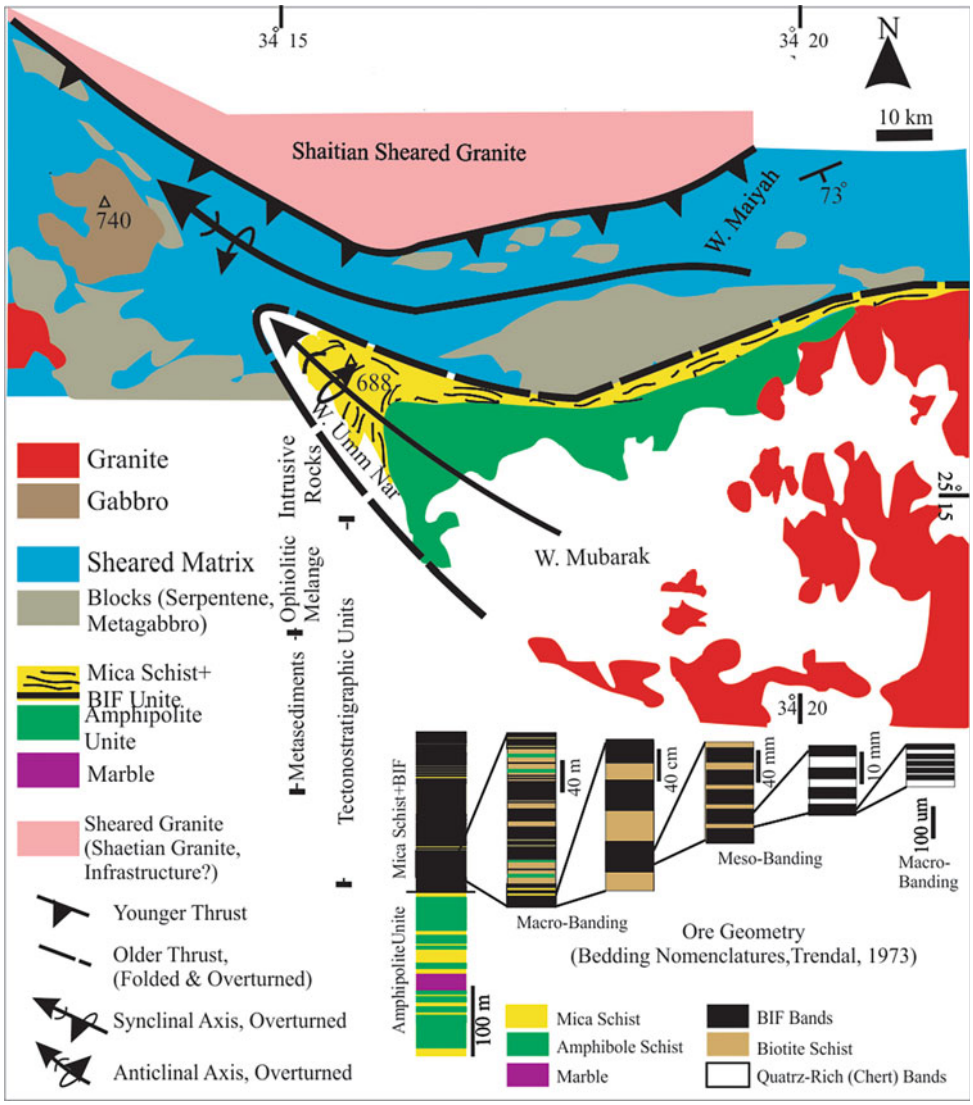

Fig. 14.2 Geology and geometry of Umm Nar BIF (El Aref et al., 1993a)

14.1.2 Mesozoic-Tertiary Oolitic-Oncolitic Ironstones

This ore type is coincided well with the southward transgression and northward regression of the Tethyan paleoshoreline during the Jurassic-Early Tertiary time spam, associated with continental sedimentation and lateritization on the adjacent hinterlands (El Aref 1996; Fig. 14.1). The Jurassic-Early Tertiary and late Cretaceous oolitic ironstones are recorded in north Sinai and Wadi Qena (El Sharkawi et al. 1989; Helba et al. 2003) and not yet evaluated. In the vicinity of Aswan (upper Egypt, Figs. 14.1 and 14.4), oolitic ironstone bands build up the Coniacian- Santonian upper storm-dominated segment (agitated medium) of the third shallowing coarsening upward cycle, that accompanied acceleration to current and wave activities during gradual progradation of linear tidal sand/Fe ooid bars on a basal shallow shelf mud (Fig. 14.4; El Sharkawi et al. 1999). The oolitic ironstone horizons range in thickness from 1 to 3 m. Each horizon consists of true and poorly or lean oolitic bands, ironstone conglomerates with mud-ironstone inter-beds of variable Fe contents (Fig. 14.5). It is composed of a microfacies assemblage of ferruginous mud, chamosite-hematite ooidal wackestone, hematite ooidal pack-ironstone, hematite ooidal grain-ironstone/ooidal sandy ironstones. Mechanically accreted Fe ooids are the essential framework components of the ironstone varieties and are formed of well- or ill-defined concentric lamina of hematite, chamosite, goethite and Fe oxyhydroxides, kaolinite, calcite and ultra-fine fluorapatite having variable Fe and P_2O_5

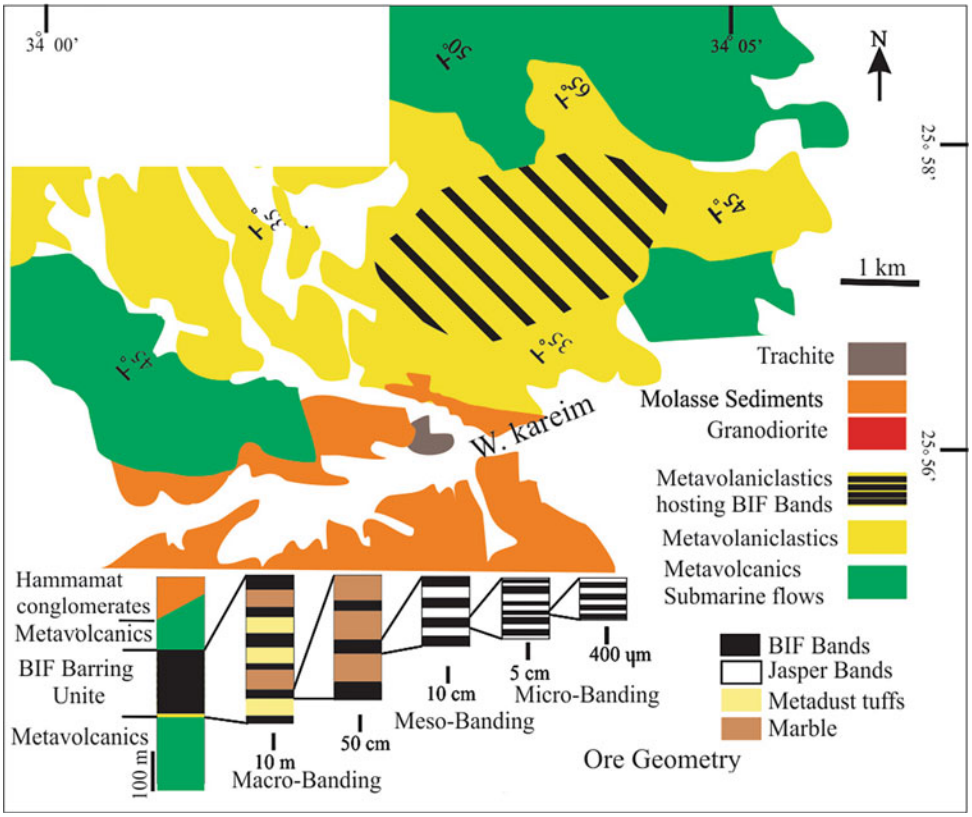

Fig. 14.3 Geology and geometry of Wadi Karim BIF (El Habaak 1992)

Table 14.1 BIF ore concentrates (El Midany and Abdel Khalek 2007)

Sample	Assay		Recovery	
	Fe (%)	I.R (%)	Fe (%)	I.R (%)
Wadi-Kareem	64.35	5.10	68.91	9.60
Gabal El-Hadid	62.72	10.12	66.52	20.03
Um-Nar	68.56	2.9	67.96	4.54
Abu-Marawat(1)	60.0	11.86	14.86	4.53
Abu-Marawat(2)	60.15	11.6	27.50	4.90
Abu-Marawat(3)	58.76	12.63	47.85	13.20

contents. The total measured proved ore reserve of the evaluated promising and accessible outcrops, east and south Aswan, is about 183,765 mt (Table 14.2; El Aref 1999) of average 43% Fe, 1.1% P_2O_5 and 18% SiO_2 having thin overburden of very much acceptable stripping ratio or even insignificant in some instances. The regional southward and south-eastward extensions of the discovered ore occurrences, particularly along Wadi Garrara-Gabal Abraq graben and Aswan Allaqi sector (until lat. 22°) are considered as a promising area, recommended for further exploration and prospection and evaluation (El Aref 1999). The low Fe and high phosphorous contents of this ore are not suitable for the requirements of steel production by the present Blast Furnace technology of the national ISCo, although, promising upgrading results are now available (e.g., Yahiya 2007). Also, successful phosphorous removal by combined microwave and ultrasound treatments are recently recorded (Omran et al. 2014, 2015).

14.1.3 El Bahariya Middle Eocene Iron Ore

With the beginning of Lutetian time, northward retreat of the Tethyan paleoshoreline took place and sea drowns the Bahariya paleohigh (Fig. 14.6), Western Desert that had stood as positive blocks subjected to denudation and pedogenesis since Late Cretaceous time (El Aref et al. 2001). Consequently, a general N to NE gentle sloping ramp developed, but with isolated submarine swells and islands. Along the ramp, a succession of fossiliferous carbonates facies (Lutetian sequence) onlapped

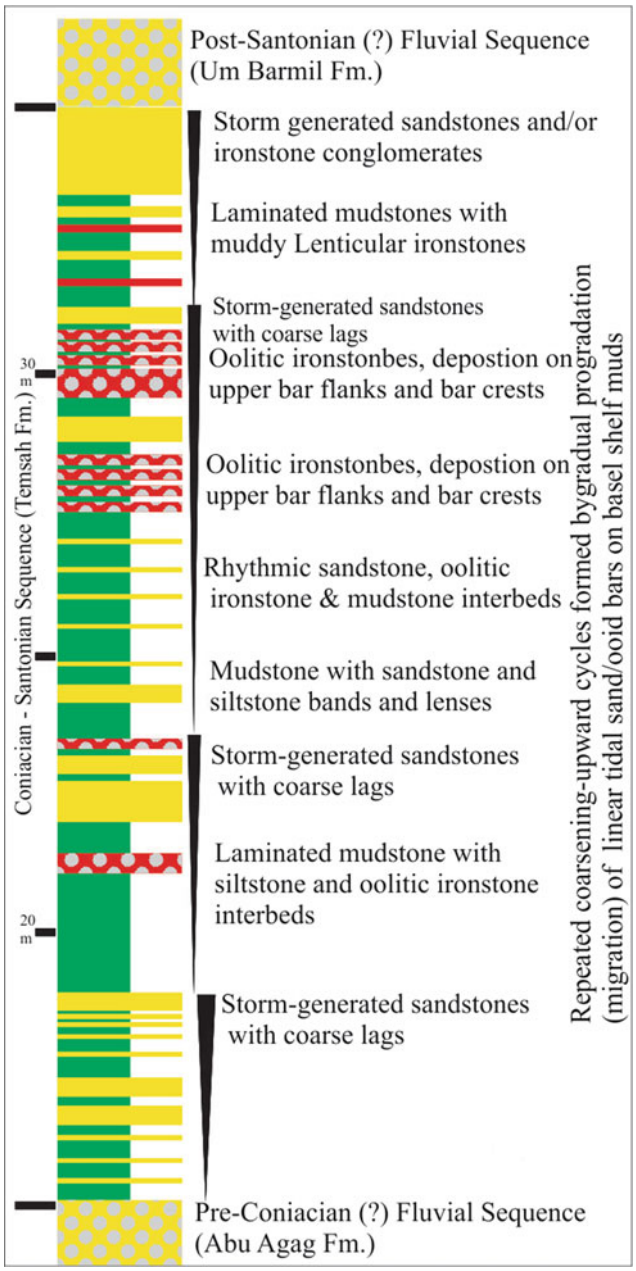

Fig. 14.4 Fine stratigraphy and environment of Aswan oolitic Fe ore

different Cretaceous rock units. Lateritic iron deposits are well developed on the exposed Cenomanian-Eocene unconformity surface. The facies assemblages of the ramp carbonate succession are accreted in back-bank/peritidal, bank/shoaland fore-bank/open marine environments. The vertical stacking of these facies constitutes shallowing–upward cycles, some of which terminated by paleokarst surfaces with paleosols. In local areas, upon the submarine swells of the northeastern plateau of the Bahariy Depression (e.g., El Gedida, El Harra, and Ghorabi mine areas), the Lutetian carbonate sequence changes entirely into a condensed section of oncolitic-oolitic and nummulitic ironstone facies (iron ores) punctuated by several depositional breaks and unconformities (Fig. 14.6). The ore stratigraphic profile represents an unconformity bounded reduced section underlain by the Cenomanian clastics and overlain by the Lutetian-Bartonian glauconitic sequence and/or Oligocene fluvial sediments. The ironstone succession is composed mainly autochtonous/para-autochthonous facies rich in ferriferous ooids, oncoids and various ferruginized skeletal particles (Fig. 14.6). The facies assemblage is organized in two main sequences separated by intra–Lutetian unconformity (paleokarst). The iron ore sequences represent the only Palaeogene economic ooidal ironstone record of the Southern Tethys associated with major marine transgressive–regressive megacycles that separated by subaerial exposure and lateritic weathering. Each facies sequence starts with tidal flat/lagoonal mud-ironstones with minor siliciclastic mudstones, displaying deposition from suspension in low energy water condition. These pass upward to shoals/megarippled grain- to pack-ironstone facies reflecting deposition during general shoaling-upward tendency and sea level fall (Salama et al. 2014). Biogenic accretion is the main mechanism which was responsible for the precipitation and diagenesis of the original precursor materials, i.e., amorphous Fe-oxyhydroxides and formation of various microbial structures, e.g., Fe stromatolites, oncoids and ooids among other forms (Helba et al. 2001). The ore mineral components and ore reserves and chemical contents are shown in Tables 14.3 and 14.4. The ore outcrops are accessible often with no considerable overburden (e.g., Ghorabi and the southern sector of El Harra mines and the central sector of El Gedida mine) or with suitable stripping ratio.

Since the discovery and evaluation of El Bahariya Fe ores in the seventies of the last century, only El Gedida mine are under active operation, delivering Fe ores to the National Iron Steel Company (ISCo) near Cairo as an essential iron supply with suitable quality for the present day Blast Furnace technological processes of the Company. The present reserves of this mine are insufficient for safety and continuous steel production in the near future. Until recently, all the beneficiation treatments of Ghorabi and El Harra Fe ores are unsuccessful; the resulted concentrates are of unreasonable recovery without considerable depletion of the harmful impurities, e.g., sulfur, phosphorous, arsenic and zinc. Thus, the ore of these occurrences by its present quality is not capable to be the future strategic ore reserves for the present technology of the ISCo. Accordingly, a serious attention must be payed for improving these reserves by either blending with high grade ore or Fe pellets, or by using suitable steel technology or other industrial investments secured by feasibility studies.

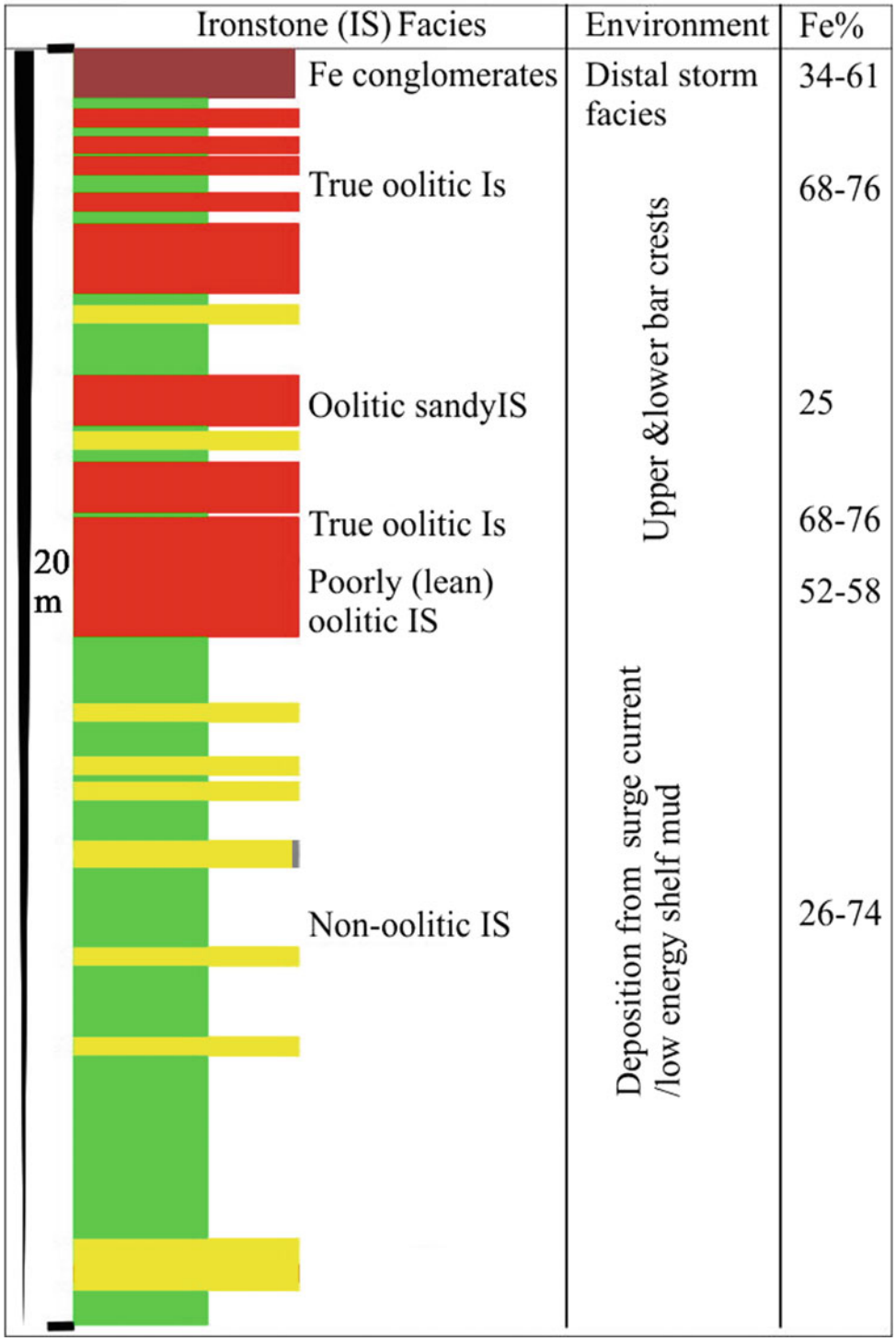

Fig. 14.5 Environment and Fe content of the different ironstone facies (shallowing upward cycle 3 of Fig. 14.4)

Table 14.2 Ore reserves of Aswan oolitic iron ore (El Aref 1999)

Recorded and Documented Reserves (Before 1976)				IEP, Re-evaluated Reserves and New Discoveries (1993-1997)							
				Exploration phases	EGSMA			Geology Department Cairo University			
Locality		Reserve (in tonnage)			Locality		Re-evaluated Reserve (in tonnage)	Locality		New estimated reserve (in tonnage)	Total Reserve in Phases
1	Nile Valley	11.418.750		Phase II (1995-1996)	1	North Aweirsha	15.596.822	9c	Rod El Kabash	32.917.500	
2	North Wadi Abu Shubeira	1.068.813			2	South Aweirsha	11.953.689				
3	South Wadi Abu Shubeira	8.032.500			3	U Huqban	12.784.750				
4	Um Barmil	1.419.000			4	Allawi	34.430.119				
5	Eadi Abu Aggag	5.159.700				Total Proved Reserve	74.765.380	Total Geological Reserve		32.917.500	107.682.880 Phase II
6	Um Esh	3.899.700		Phase III (1996-1997)	5	Aswan- K.21	30.000.000	9b	Dabaa East	65.289.261	
7	Ras Aqaba	9.129.925			6	Allaqi K.23	12.000.000				
8	Gabal Timsah	21.490.000			7	Road K.29	9.000.000				
9	Wadi um Udi	1.270.500			8	East Um Hebal	100.000.000				
10	Wadi Aweirsha	26.592.843	56.996.468		9	North and Central Wadi Arab	10.000.000	9a	Dabaa West	12.558.000	
11	Beida Um Huqban	8.378.825			10	East Wadi Arab	88.000.000				
12	West Allawi	15.951.250			11	End Khor Rahma	11.000.000				
13	East Allawi	6.073.550			12	Barqat Tukham	7.000.000				
14	Gabal El Diheisa	1.803.813				Total Geological Reserve	240.000.000	Total Geological Reserve		77.847.261	317.843.000 Phase III
	Total Reserve	121.688.907		Phase II & III	Estimated geological reserve= 240.000.000+77.847.261+32.917.500=350.764.761 m.t. Proved geological reserve of Um Hebal= 64.000.000 m.t. Additional proved reserve (Phase II)= 74.765.380-56.996.468= 17.768.912 m.t. Total proved reserve= 74.765.380+64.000.000= 138.765.380 m.t.						

Re-evaluated in Phase II

14.1.4 Pre-rift (Oligocene?) Um Ghrifat Iron Laterite, Red Sea Coastal Zone

Um Ghrifat mine (Fig. 14.7) is a site of red rooty and nodular ochre and earthy Al rich bauxite, representing alumino-ferroginous laterite (paleosol) developed along Pre-Cambrian–Miocene paleoerosion surface under tropical to subtropical paleoclimate. The pedogenic processes comprised lateritization and secondary bauxitization under active weathering followed by natroalunitization (El Aref 1993). Such ore setting and mode of formation may guide further intensive exploration allover the Pre-Cambrian-Phanerozoic unconformity of the Eastern Desert and south Sinai, as a very much promising site for similar products.

14.1.5 General Recommendation

To contribute in improvement of the economic return of the geological resources and to secure the national industries as well as raising the overall income, the investment and marketing of these Fe ores must have the priority during the design the imperative short and long-term mining investment strategy, within the frame of the Egyptian sustainable development strategy.

14.2 Egyptian BIF: Glaciogenic Versus Hydrothermal Origin?

Yasser Abd El-Rahman

Banded Iron Formations (BIF) occurrences are a restricted to the central segment of the Eastern Desert (CED) of Egypt between latitudes 25°15′ N and 26°55′ N. The BIF deposits in the CED shares common features, which were summarized by Hussein (1990). They occur as sharply defined stratigraphic units within layered volcanic-volcaniclastic successions of generally andesitic composition. The volcanogenic rocks were metamorphosed regionally under greenschist facies conditions, which locally reached amphibolite facies conditions. Iron-formation bands range in thickness from few centimeters to one or two meters and are commonly show signed of syn-depositional deformation such as faulting, folding, brecciation and slump structures. Many of the iron-formation bands consist of iron oxide

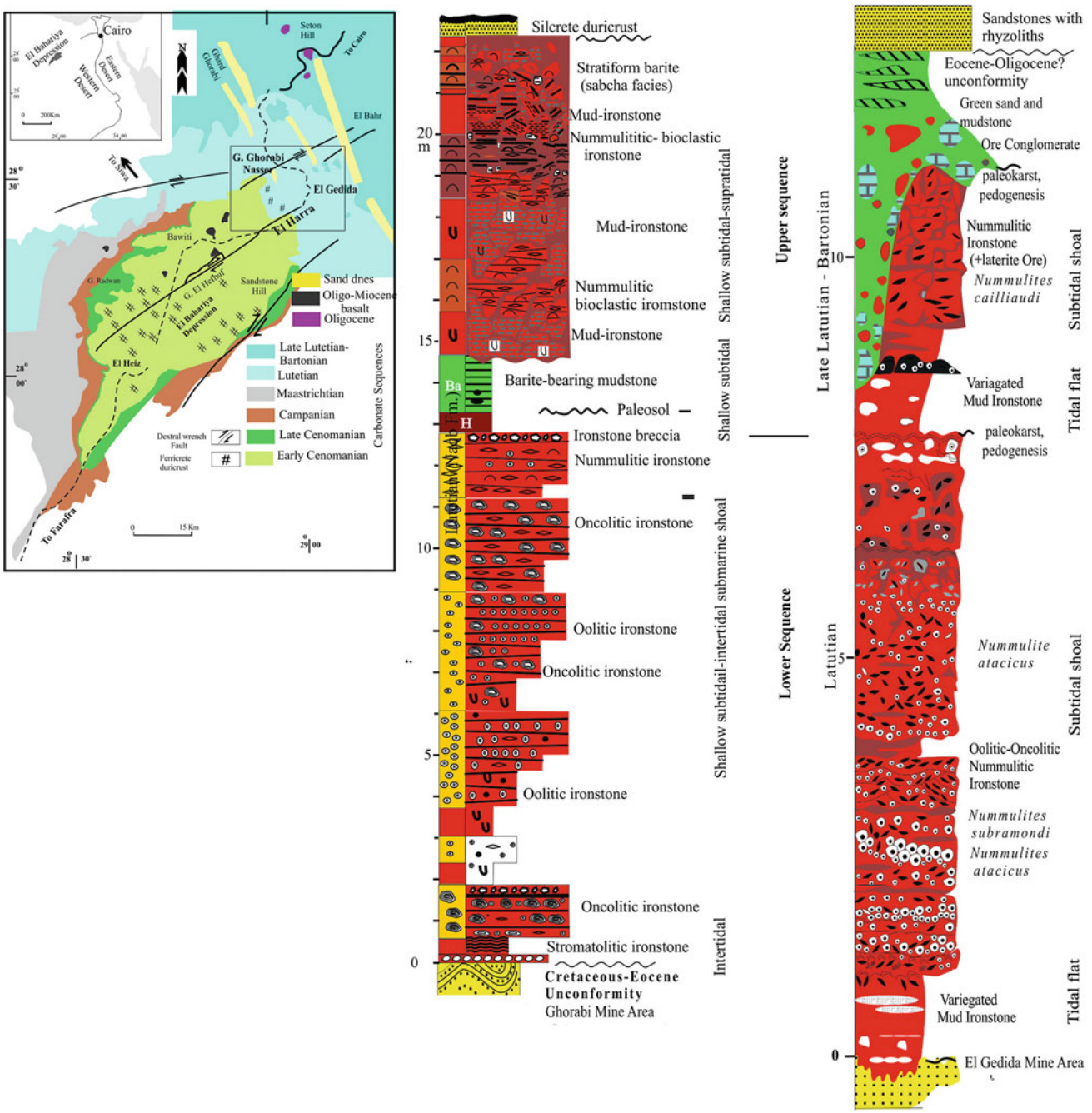

Fig. 14.6 Simplified geological map of the Bahariya region and fine stratigraphy, facies and environment of representative profiles of El Gedida (Salama et al. 2014) and Ghorabi (Helba et al. 2001) mines

(hematite and magnetite) meso- and micro-bands alternating commonly with chert, jasper along with silicates and rarely with carbonates.

The intimate association between the late Proterozoic volcanogenic rocks and the BIF in the CED of Egypt justify its similarity with the Algoma-type deposits. Sims and James (1984) considered such deposits as chemical precipitates that were deposited in an intra-oceanic island arc environment during the lulls in subaqueous calc-alkaline volcanic activities. El Aref (1993) interpreted the Um Nar BIF in the CED to be formed in a sedimentary environment that lacks any relics of volcanic or volcaniclastic intervals. Thus, the association of this BIF with pre-Pan-African metamorphosed shelf sediments (El Aref 1993) affiliated the Um Nar BIF with the Lake Superior-type BIF. El-Shazly and Khalil (2014) studied the schist, which is intercalated with the Um Nar BIF and revealed the presence of andesitic and dacitic tuffs and lapilli tuffs. Moreover, El-Shazly and Khalil (2016) obtained

Table 14.3 Mineral paragenesis of El Bahariya iron ore

Precursor materials (land derived)	Amorphous iron oxyhydroxide, ferrihydrite (iron rich colloidal/gel, Si, Al, Mg, CI, Na, P, Ca), quartz grains, glauconite			
Marine diagenesis and supergenisis (karest laleritizalion)				
Ore minerals	Gangue			
Goethite Hematite Amorphous Fe Oxyhydroxide	Quartz (cement, grains earthy, amor thious) Chert (concretion) Kaolinite lllite Alunite Jarosite Glauconite Apatite	Gypsum Halite Calcite Dolomite Siderite Barite Pyrite Phosphoric clays	Mn. Minerals Todorokite Psilomelane Hollandite Romanechite Pyrolusite Manjiroite	Tracing organic matter carbohydrates Organic Pigments Lipids Glycogen Proteins Cardioids

Table 14.4 Total workable proven reserves of Ghorabi, El Harra and El Gedida mine areas. Qebli (Abdel Motelib 1996)

Total workable (proved) reserves										
Area		Ore reserve	Fe	CL	SiO_2	MnO	BaO	AI_2O_3	Na_2O	K_2O
Ghorabi		55.5	48.50	0.97	9.9	3.92	1.78	1.13	0.39	0.22
Nsser	l	30.3	47.15	0.94	8.42	5.19	0.69	1.54	0.81	0.34
	2	7.5	44.76	0.60	11.27	2.94				
Elharra	l	57.1	44.06	0.74	13.09	3.48			0.40	0.25
	2	4.2								
Total		154.6								
El Gedida		59.2	52.14	0.46	7.69	2.45	1.35	1.45	0.34	

Note Additional Geological Reserves = 22.5 mt

LA-ICP-MS U–Pb zircon age of 725 ± 9 Ma for these volcaniclastic rocks, which refutes the suggested Pre-Pan African age that was suggested by El Aref (1993) for the Um Nar BIF. It is not just the Um Nar BIF, but all the volcaniclastic rocks intercalated with BIF in the Eastern Desert have Neoproterozoic ages (El-Sahzly and Khalil 2016), which include Wadi Karim (766 ± 9 Ma), Um Ghamis (857 ± 8 Ma), and Gebel El Hadid (717.9 ± 1 Ma).

The Neoproterozoic iron-formations are commonly intercalated with glaciogenic rocks worldwide (Young 1976). The intimate association between the Cryogenian glacial marine deposits and the iron-formations was a key aspect to support the Snowball Earth hypothesis that was suggested by Kirschvink (1992). Stern et al. (2006) and Ali et al. (2010) suggested that the association between the BIF and diamictite, represented by the Atud conglomerate, records the evidence for the Sturtian (~700 Ma) Snowball Earth event in the Eastern Desert of Egypt. On contrary, El-Shazly and Khalil (2016) rejected such evidence and identified the "block-in-matrix" outcrop in the Wadi Karim, which was identified as Atud diamictites by Ali et al. (2010), as volcanogenic agglomerates and lapilli tuffs.

Rare earth elements (REE) chemistry of BIF is commonly used to understand the redox conditions of the depositional basin (Cox et al. 2013). Most of the Neoproterozoic iron-formations show no true Ce anomaly, which make them similar to the Archean-early Paleoproterozoic BIF (Field B of Fig. 14.8) that was deposited in dominantly anoxic basins (Halverson et al. 2011). The widespread Sturtian glaciation resulted in isolating the basins from the oxygenated atmosphere and so creating such anoxic conditions. Melting the ice allowed re-oxygenating the basin and the deposition of the iron-formations (Kirschvink 1992). The redox-stratified basin model was adopted to interpret the formation of the BIF in Eastern Desert of Egypt (Basta et al. 2011; Khalil et al. 2015) in which the iron-formations was deposited across the redoxcline separating shallow oxic water from deeper anoxic water. Iron-formations deposited in redox-stratified basins, such as late Paleoproterozoic BIF (Field A of Fig. 14.8), are characterized by a wide range of Ce anomalies (Planavsky et al. 2010). On contrary modern seawater is characterized by pronounced negative Ce anomaly (Elderfield and Greaves 1982).

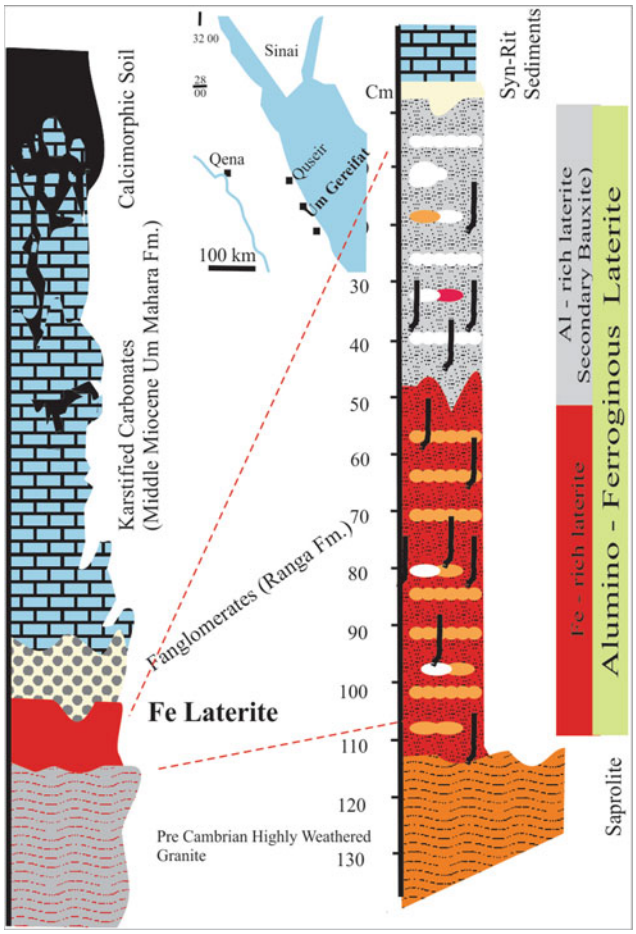

Fig. 14.7 Pre-rift Um Gereifat Fe laterite profile, Red Sea coastal zone (El Aref 1993)

The studies concerned with the REE geochemistry on the BIF from the Eastern Desert of Egypt are limited. The first study covers the Wadi Karim and the Anab BIF (Basta et al. 2011), while the second one covers the Gebel El Hadid BIF (Khalil et al. 2015). The Wadi Karim BIF is characterized by a negative Ce anomaly (Fig. 14.8). Assuming a minor effect of detrital components on the REE signature, such anomaly may indicate deposition in an oxygenated basin. The Anab BIF and the Gebel El Hadid BIF do not show a distinct Ce anomaly and plot in the Archean-Paleoproterozoic field (Fig. 14.8). Although such signature is in harmony with the Sturtian glaciation model, many examples of modern hydrothermal iron-rich deposits show no Ce anomaly, such as Ambitle Island (Pichler and Veizer 1999), Pitcairn and Macdonald volcanoes (Stoffers et al. 1993) and Loihi Seamount (Rouxel et al. 2018). Thus, the Wadi Karim BIF, Gebel El Hadid BIF and the Anab BIF might have deposited due to hydrothermal activities in dominantly oxic basins.

Positive Eu anomaly is a characteristic feature for the hydrothermal component in BIF deposits (Danielson et al. 1992). Using the approach of Planavsky et al. (2010) to calculate the Eu anomaly ((Eu/Eu* = Eusn/(0.67Smsn + 0.33 Tbsn), low positive Eu anomalies (1.24 ± 0.13 for Anab BIF, 1.26 ± 0.1 for Wadi Karim BIF, 1.2 ± 0.19 for Gebel El Hadid BIF) supports the low-temperature hydrothermal contribution to the formation of these BIF deposits. These values that were compiled from Basta et al. (2011) and Khalil et al. (2015) are higher than the Eu anomalies (0.49–0.86) recorded in other Neoproterozoic glaciogenic iron-formations that were mentioned by Cox et al. (2013).

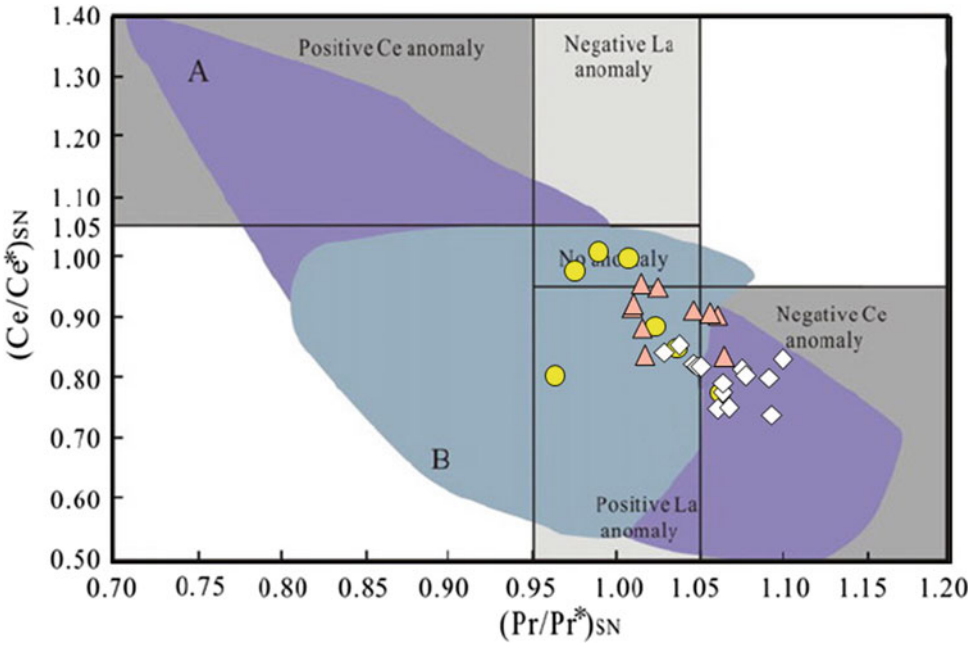

Fig. 14.8 Plot of Ce and Pr anomalies normalized to PAAS (after Bau and Dulski 1996) for the Wadi Karim BIF (white diamond) and the Anab BIF (pink triangle) from Basta et al. (2011) and the Gebel El Hadid BIF (yellow circles) from Khalil et al. (2015). Compilation of middle and late Paleoproterozoic (field A) and Archean-early Paleoproterozoic (field b) are from Wang et al. (2017) (PAAS normalization values are from McLennan 1989)

14.3 Orogenic Gold in the Eastern Desert, Egypt

Basem Zoheir

14.3.1 Introduction

In the Eastern Desert of Egypt, no strong indication supports the presence of intrusion-related and iron oxide copper–gold (IOCG) deposits. The classic low-sulfidation gold and Carlin-type gold deposits are completely absent. Accidental gold concentrations (a few ppm) in some of the volcanogenic massive and semi-massive sulfide (VMS) ores from the Eastern Desert are related to shear and silicification zones, that commonly represent overlapping transpressional and transcurrent structures (e.g., Um Samiuki and Darhieb deposits). Signs of volcanic activity-associated (epithermal) gold mineralization in the North Eastern Desert including extensive sulfidation and potassic alteration are consistent with the recent discovery of Au-bearing gossans and semi massive Zn–Cu sulfide ores associated with BIF-hosting metavolcanic rocks at Hamama prospect (Aton Resource Inc), best interpreted as a VMS-epithermal transition deposit. Similarly, poorly-constrained porphyry and associated high-sulfidation Au–Cu–Mo mineralization is described in terranes of cordilleran-type, high-K calc-alkaline volcanic and subvolcanic rocks (i.e., ~630–592 Ma Dokhan Volcanics), though no significant mining for copper, molybdenum or even gold from such occurrences has been reported.

Orogenic gold occurrences are, on the other hand, widespread, and are particularly confined to fault/shear zones in greenschist ophiolitic and island arc terranes. There are several lines of evidence suggest that gold mineralization was concurrent with late-orogenic convergence/transpression tectonics that were active in the Central Eastern Desert (CED) during the period of 620–585 Ma. Temporally coeval calc-alkaline magmatism during and subsequent to the peak metamorphic conditions could have contributed to the metal and volatile budget of the ore fluids, and aided convection of mainly metamorphic, low salinity aqueous-carbonic fluids at the greenschist-amphibolite facies interface.

Fluid inclusion studies show nearly consistent fluid composition and comparable pressure-temperature conditions for most deposits, despite the variable host lithologies and controlling structures. A careful eye will only see gradual steepening in the geothermal gradient (~100 °C/km) in gold deposits in the NED compared to those in the CED and SED (25–50 °C/km). This may imply mesothermal-to-epithermal transition, consistent with the different erosional levels. The stable isotope signature of hydrothermal carbonate associate with mineralized quartz suggests plausible derivation from dissolution of mainly continental carbonate ± multiphase mantle fluids. The sulfur isotope composition of hydrothermal pyrite from most deposits perfectly overlaps with sulfur isotope values of basaltic rocks, suggesting extensive regional dehydration and devolatilization of fertile mafic metavolcanic/volcanosedimentary rocks in mid-crustal levels. Supralithostatic retrograde fluids migrated upward to the infrastructure-suprastructure boundary would have then focused into D_2 or D_3 dilatant zones and were the underlying main generic factor in gold metallogeny of the Eastern Desert.

14.3.2 Typography, Setting and Main Characteristics

Orogenic gold deposits are represented by systems of quartz and quartz–carbonate veins in variably deformed granitoid-metamorphic terranes in almost all orogenic belts over the world, particularly in spatial association with major crustal structures (e.g., Groves et al. 1998, 2003; Goldfarb et al. 2001, 2005). A combination of dynamic stress changes and fluid pressure variations is generally invoked to explain the geometry of the vein systems and their strong structural control (e.g., Stüwe 1998; Ramsay et al. 1998; Goldfarb and Santosh 2014). Orogenic gold deposits are most commonly located in second- or third-order structures of trans-crustal fault zones at convergent margins (e.g., Bierlein and Crowe 2000; Kerrich et al. 2000; Groves et al. 1998, 2003; Bierlein et al. 2006; Goldfarb et al. 2005; Craw et al. 2009; Goldfarb and Groves 2015; Groves and Santosh 2016). Craw et al. (2009) suggested that alteration and gold mineralization is focused in shear zones where slow-moving fluid (mm/yr) is controlled by micro fractures and grain boundary permeability.

In the Eastern Desert, orogenic gold occurs in tracts of highly deformed island-arc metavolcanic-metavolcaniclastic ± ophiolitic rocks, with or without granitoid intrusions (e.g., Zoheir et al. 2011). Intrusions associated with orogenic gold in the CED are mostly calc-alkaline monzodiorite to syenogranite (e.g., El-Gaby et al. 1988), with geochemical characteristics of volcanic arc granites, formed in collisional to post-collisional environment (Zoheir et al. 2011, 2018a). Gold-bearing quartz veins hosted by shear/fault zones that cut granitoid intrusions or occur at their contacts are referred to as **granitoid-hosted gold** mineralization. The latter are consider by far the most important among all types of gold mineralization in the CED. Another significant sub-group of orogenic gold comprises gold in or close to sheared and altered lenses of K-metasomatized ophiolitic serpentinite (listvenite), commonly in association with other metal commodities, i.e., Cr, As, and Sb, and are referred to as **listvenite-lode gold associations** (Zoheir and Lehmann 2011). Auriferous quartz and quartz-carbonate veins hosted by variably deformed and

carbonatized island arc metavolcanic and metavolcaniclastic rocks represent a less significant sub-group of orogenic gold in the Eastern Desert. These deposits occur commonly at the closures of antiformal structures particularly where intersected by faults in greenschist facies metamorphosed meta-andesite, metagraywacke and meta-tuffs. These deposits are grouped as **greenstone-hosted lode gold** mineralization (Zoheir and Weihed 2014). Poorly constrained gold concentrations in banded iron formations (BIF) in the CED are only reported in quartz veins along shear zones.

The key geological characteristics of orogenic gold deposits in the Eastern Desert which have a bearing on their genesis can be summarized as follows:

(i) Almost all of these deposits occurs in the supracrustal, low or medium grade metamorphosed rocks, proximal to the major accretionary boundaries (Allaqi-Heiani suture, Barramiya-Um Salatit thrust zone), particularly where overprinted by post-collisional transcurrent structures (e.g., Hamisana shear zone, W. Hodein-W. Kharit zone, Atalla shear zone).

(ii) There is no association with specific lithologies, but no occurrences are reported in terranes dominated by the gneissic rocks (e.g., Hafafit culmination). In the CED, gold deposits are located some tens of kilometers apart from the supracrustal-infracrustal interface boundary.

(iii) In deposits hosted by the island arc metavolcanic and metsedimentary rocks, the mineralized quartz veins are folded, boudinaged and show abundant criteria of recrystallization, while deposits hosted by granitoid intrusions are characterized by quartz veins displaying multiple growth stages and brecciation, classic epithermal-like textures and preservation of open-space structures.

(iv) A preferential spatial association of gold-bearing quartz veins is observed with steeply dipping fault and shear zones, overprinting older basal thrust and low angle faults. Iron-rich host rocks are more commonly associated with mineralized quartz veins, while sulfide-rich and semi massive sulfides are rarely associated with gold occurrences.

(v) Quartz textures in the mineralized quartz veins indicate variable strain and confining pressure for each mineralization type. Brittle deformation and brecciation characterize deposits that are spatially associated with granitic intrusions. On the other hand, gold-bearing quartz veins hosted by foliated metavolcanic or metasedimentary rocks or associated with carbonatized serpentinite show abundant signs of dynamic recrystallization, bulging of grain boundaries, and subgrain development (e.g., Zoheir and Lehmann 2011; Zoheir and Moritz 2014).

(vi) The mineralogy comprises quartz-sericite-chlorite-dolomite-calcite with minor sulfides, and rare visible gold. Gold grain composition is either free-milling Au or Au–Ag alloy (electrum) with traces of Te, Hg, Cu, and Sb (e.g., Zoheir 2008a; Zoheir and Weihed 2014).

(vii) Fluid-inclusion studies indicate that many deposits formed mainly by fluid unmixing due to pressure fluctuation (lithostatic vs. hydrostatic), mixing of moderate and low salinity fluids, or due to partitioning of H_2S into the vapor phase and loss in O and S fugacities by hydration or sulfidation of the host rocks at depths of 2–11 km, assuming a pure lithostatic pressure (e.g., Harraz 2000; El-Tokhi and El-Muslem 2002; Zoheir 2008a; Zoheir et al. 2008a). A much shallower crustal level is assumed for gold deposition if hydrostatic pressure is considered.

14.3.3 Ore Fluids and Stable Isotope Characteristics

Fluid inclusion studies indicate a consistently low- to moderate-salinity ($\sim$1–13 wt% $NaCl_{eq.}$), H_2O-CO_2±CH_4 hydrothermal fluid. A variety of different geochemical mechanisms for gold deposition have been proposed, including wall-rock sulfidation and carbonation, boiling and phase separation and wall-rock, and mixing of fluids with different redox states and composition (aqueous +5 − 77 mol% CO_2). The mineralized lodes formed over a broad upper- to mid-crustal *P-T* conditions; $\leq$200–3000 bar and $\sim$200–370 °C (El-Kazzaz 1996; Loizenbauer and Neumayr 1996; Murr 1999; Klemm et al. 2001; Harraz 2000, 2002; El-Tokhi and El-Muslem 2002; Helmy et al. 2004; Zoheir 2008a, b; Zoheir and Mortiz 2014; Zoheir et al. 2018a). Conditions of gold deposition as defined by isochores for primary and pseudosecondary aqueous-carbonic inclusions indicate a clockwise pressure-temperature path (Fig. 14.9). This path can be extrapolated to the peak metamorphic conditions in metasedimentary rocks that represent intermediate conditions between suprastructure and infrastructure rocks in the Eastern Desert (Zoheir 2008b).

The clockwise P-T paths of mid-crustal (infrastructure) basement in the CED and SED indicate a common cooling path after collision and thrust-sheet and nappe formation. In similar settings pressures increase substantially before rocks begin to equilibrate thermally by relaxation of isotherms (England and Thompson 1984). Fritz et al. (2013) suggested that the clockwise P-T path of the CED infrastructures reflect advective heat flow by granite emplacement together with exhumation. The superstructure rocks, including the ophiolitic rocks in the CED experienced metamorphic conditions peaked at $\sim$4 kbar and $\sim$450 °C (Fritz et al. 2002). This

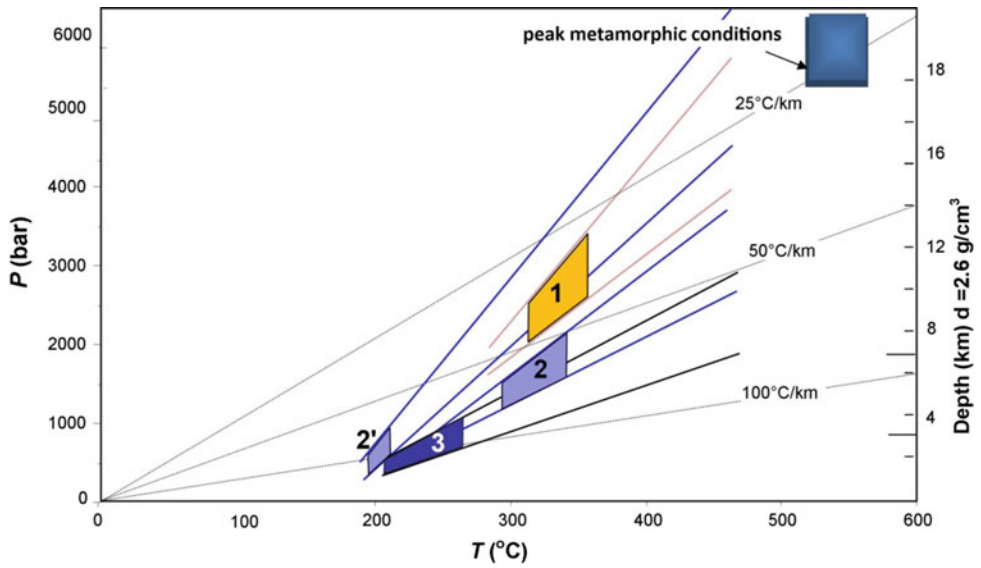

Fig. 14.9 P-T conditions of gold deposition based on isochores for aqueous-carbonic inclusions in (1) Betam deposit, (2, 2′) El-Sid deposit, and (3) Semna deposit. The peak metamorphic conditions in the SED and CED (Neumayr et al. 1998; Abd El-Naby et al. 2000; Abd El-Naby and Frisch 2002; Zoheir 2004). Geothermal gradients of 25, 50 and 100 °C/km (dotted lines), and depth of overburden in km are based on crustal rock density of 2.6 g/cm^{3}and assuming a lithostatic pressure. Notice that a late genetic gold-base metal mineralization (2′) in the El-Sid deposit is linked to a different, relatively saline aqueous fluid

metamorphic history reflects a variable, but consistently clockwise pressure-temperature path analogous with those of orogenic gold deposits.

An interesting feature commonly reported in gold mineralization confined to brittle-dominated shear zones in rigid host rocks is a gold-base metal mineral association late in the paragenesis. The latter replaces the early genetic sulfides and is associated with quartz veins showing no signs of ductile deformation. El-Sid deposit provides a good example where distinct mineralization event under epithermal conditions different from conditions during the early mineralization event. In the case of gold deposits hosted in foliated metavolcanic or metasedimentary rocks, the *P-T* path is continuous from early to late mineralization assemblages (see Zoheir 2008a, b).

The $\delta^{13}C$ values of carbonate disseminated in gold-bearing quartz veins from several orogenic gold deposits in the Eastern Desert are distinct from the carbon isotope range of marine carbonate or sedimentary organic carbonate (Fig. 14.10), but are consistent with C-isotope values of magmatic carbonate (−5 ± 3‰, Burrows et al. 1986) and/or mantle carbonate (−6 ± 2‰, Ohmoto 1986). The combined $\delta^{13}C_{V\text{-}PDB}$ and $\delta^{18}O_{V\text{-}SMOW}$ values of gold-associated carbonate in several Egyptian gold deposits show a narrow range (−2 to −10‰). In Fig. 14.10, the data are featured by roughly constant $\delta^{13}C_{V\text{-}PDB}$ over relatively wider ranges of $\delta^{18}O_{V\text{-}SMOW}$. The data partially overlap with the continental carbonate field, slightly with multiphase mantle fluids, which may suggest carbonate dissolution as main source ± mantle-derived fluids. Zhou et al. (2014) concluded that dissolution/decarbonation reactions during metamorphism of continental carbonate/carbonated rocks produce CO_2 with $\delta^{13}C$ values similar to or more enriched than parent rocks. The restricted variation in the carbon isotope in most studied deposits combined with the dilute, aqueous-carbonic, $\pm CH_4$ $\pm N_2$-bearing fluids is consistent with well-mixed mid-crustal (metamorphic) and sub-crustal (mantle-derived) fluids (e.g., Goldfarb and Groves 2015; Boskabadi et al. 2017).

The available $\delta^{34}S$ values of gold-related pyrites from some gold deposits in the Eastern Desert, reveal some apparent trends in the distribution of variations in $\delta^{34}S$(py):

(1) The total range of $\delta^{34}S$(py) values from the combined dataset (n ≈ 100) is −5‰ to +6‰ (Fig. 14.11), with no obvious consistent spatial relationship between lithologies, structures and means and ranges of $\delta^{34}S$ (py),

(2) Most deposits have gold-related pyrites with $\delta^{34}S$ values between 0 and +5‰, while a few deposits (here exemplified by the Barramiya deposit), have mean $\delta^{34}S$ values between −5 and +5‰, commonly related to recrystallized pyrite with much lighter $\delta^{34}S$ values. Another good example is the Um Garayat deposit, but distinction between hydrothermal and recrystallized pyrite is much easier because of the abundant recrystallization textures.

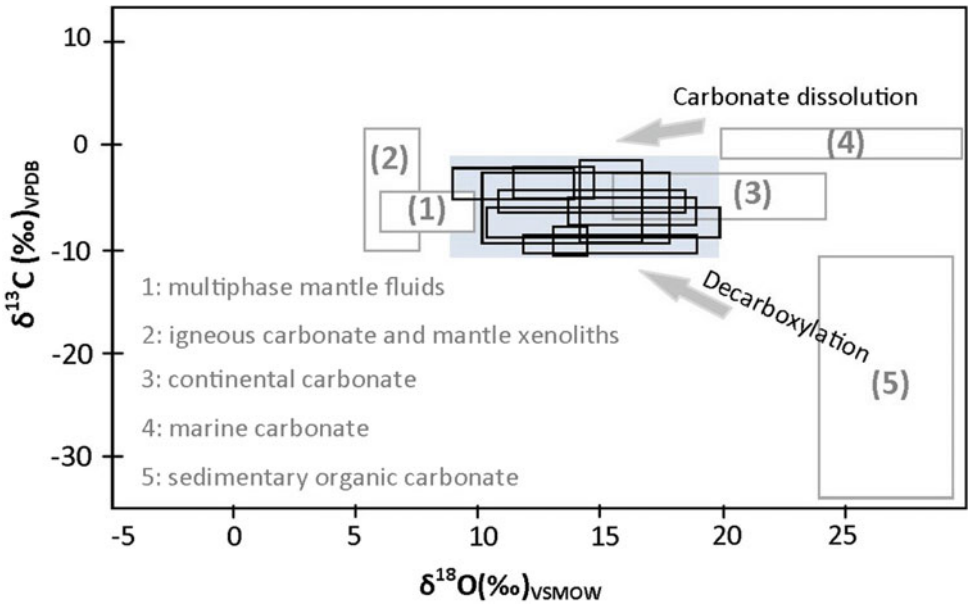

Fig. 14.10 Carbon and Oxygen isotope data of hydrothermal carbonate in gold-bearing quartz veins from different orogenic gold deposits in the Eastern Desert of Egypt (data source: El-Kazzaz 1996; Harraz 2000; Zoheir and Qaoud 2008; Zoheir 2012a, b, 2018a; Zoheir and Weihed 2014; Abdelnasser and Kumral 2016). Range of values for mantle-derived and igneous carbonate, sedimentary organic carbonate, marine carbonate and mantle carbonate are reported for comparison (data from Hoefs 2009)

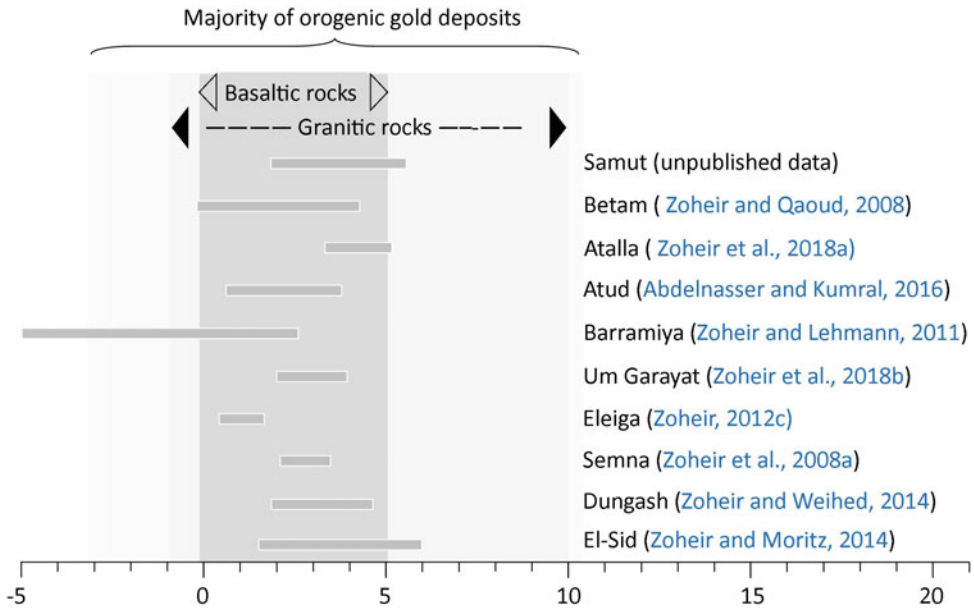

Fig. 14.11 Representative $\delta^{34}S$ data from several gold deposits in the Eastern Desert. Notice that the metamorphic rocks bracketing −20 to 20. The data source for basaltic and granitic rocks is Hoefs (2009), and the range for orogenic gold after Hodkiewicz et al. (2009)

(3) The $\delta^{34}S$(py) values precisely overlap with fields of sulfur isotope composition of basaltic rocks (Fig. 14.11; Schneider 1970; Alt 1994), suggesting reduced hydrothermal fluids, with near-homogeneous sulfur isotope compositions. The proposed source of sulfur is dissolution and/or desulfidation of primary magmatic sulfide minerals or average crustal sulfur (e.g., Ohmoto and Rye 1979; Hodkiewicz et al. 2009). Similarly, Saravanan and Mishra (2009) and Mishra et al. (2018) described consistently uniformity S-isotope compositions for gold deposits in the Dharwar Craton (India), and suggested a near-homogenous crustal reduced ore fluid. Ore fluid oxidation by partitioning of the reduced sulfur gas phases due to pressure fluctuation during fault open-seal-reopen (valve) system can explain the restricted limit of variation in sulfur isotope values of ore-related pyrites (e.g., Hodkiewicz et al. 2009).

14.3.4 Genetic Aspects

14.3.4.1 Ore Fluids: Metamorphic Versus Magmatic Sources

Typically, low-bulk salinity aqueous-carbonic fluids with traces of CH_4 and less commonly N_2 and H_2S are ascribed for ore fluids in several orogenic gold deposits worldwide. Ridley and Diamond (2000) summarized the results of many fluid inclusion studies of orogenic gold of different ages and geographic locations as indicating a commonly consistently ore-forming aqueous-carbonic fluid, with XCO_2 of 0.1–0.25, minor or trace $H_2S \pm CH_4 \pm N_2$, and salinities of 3–7 wt% $NaCl_{eq}$. The reduced sulfur species enhance the volatility of the ore fluid and facilitate Au transportation in the form of stable hydrosulfide and sulfide complexes (e.g., Seward 1991; Pokrovski et al. 2009), whereas CO_2 buffers the ore-bearing fluid to near-neutral pH values, promoting high gold solubility (Phillips and Evans 2004). The carbon dioxide also exerts an impact on extending the vapor-liquid immiscibility in the ore fluids to higher temperatures and pressures (Kokh et al. 2017).

The source of ore fluids in orogenic gold is widely considered to have been mainly metamorphic (e.g., Garofalo et al. 2014). Large volumes of aqueous-carbonic fluid are generated during the greenschist-to-amphibolite transition during high-temperature, low-pressure metamorphism of mafic volcanic or carbonaceous sedimentary rocks (e.g., Powell et al. 1991; Phillips and Powell 2009, 2010; Tomkins 2010; Fu et al. 2012; Wilson et al. 2013; Gaboury 2013; Tomkins 2013). Significant flux of carbon form dissolution of continental carbonate to the lithosphere and atmosphere is indicated by the heavy C isotope composition of mean global arc volcanic gas (−3.8 to −4.6‰) (Mason et al. 2017).

In the Eastern Desert, most fluid inclusion studies describe aqueous-carbonic ore fluids with variable contents of CO_2 (2–77 mol.%) $\pm CH_4 \pm N_2$ (≤ 5 mol.%), nearly consistent salinities (1.5 to 12.3 wt% $NaCl_{eq}$.) and total homogenization temperatures ranging from <180 to ~420 °C (Harraz and El-Dahhar 1993; El-Kazzaz 1996; Loizenbauer and Neumayr 1996; Shazly et al. 1998; Murr 1999; Sharara 1999; Harraz 2000, 2002; El Tokhi and El Muslem 2002; Helmy et al. 2004; Zoheir 2008a, b; Zoheir et al. 2008b, 2018a; Zoheir and Akaway 2010; Zoheir 2012a; Zoheir and Moritz 2014). Helmy and Zoheir (2015) suggested that the considerable amounts of CH_4 and CO_2 in the ore-related fluids in the El-Sid deposit could have generated by serpentinization of the ophiolitic ultramafic rocks and/or by hydration of graphite-bearing mélange matrix common in the area. A similar scenario is also suggested for the Barramiya deposit (Zoheir and Lehmann 2011), although in a different setting and lithologies. The calculated $\delta^{18}O_{H2O}$ and $\delta^{13}C_{CO2}$ values of the ore fluids based on $\delta^{18}O$ values of quartz and $\delta^{13}C$ and $\delta^{18}O$ values of carbonate in the main lodes of the Romite deposit indicate a metamorphic or mixed metamorphic-magmatic source (Zoheir 2012b). A nearly pure magmatic source for the ore fluids is deduced from the near zero carbon and sulfur isotope values of the Um Eleiga gold deposit (Zoheir 2012c). Similarly, Boskabadi et al. (2017) used the carbonate isotope composition to suggest that influx of mantle-derived CO_2-rich fluids led caused widespread carbonation in the CED and contributed to the breakdown of Au-bearing minerals in the ophiolitic serpentinite.

14.3.4.2 Metal Source: Metasomatized Peridotite Versus Mantle-Derived Magmatism

Based on mass-balance calculations, liberation of Au by metamorphism of back-arc basaltic to andesitic volcanic rocks (containing a few ppb Au) can result in sufficient amounts of the element to form giant deposits (Phillips et al. 1987; Hronsky et al. 2012). In a closed-system metamorphic event, recrystallization of volcanogenic massive sulfide ores in ophiolite or island-arc sections will internally mobilize Au from the lattice of the host sulfides (e.g., Wagner et al. 2007). The temporal correlation between mantle-sourced magmatism and giant orogenic gold deposits in central Asia region and in the Hercynian belt points towards an important role of magmatic underplating and melting of the lower crust by mantle upwelling in generation or pseudo-metamorphic ore fluids for orogenic gold (de Boorder 2012). Combining regional metamorphism in accretionary orogens and mantle-derived magmatism and crustal thickening is in agreement with the coincidence of major periods of orogenic gold in the Earth's history with periods of continental growth (Goldfarb et al. 2001).

In the Eastern Desert, the association of Ni, Co, Cr, As, and Au in the granitoid-hosted and greenstone- or listvenite-associated gold deposits led several authors to advocate that decarbonation by metamorphism of ophiolites in depth added these elements to CO_2-rich fluids introduced to the serpentinite-granite contact (e.g., Takla and Surour 1996; Harraz 2000, 2002; Klemm and Klemm 2013; Helmy and Zoheir 2015). Zoheir et al. (2018b) constrained on the mafic metavolcanic rocks as a possible fertile source for the Um Garayat gold deposit based on the sulfide-S and carbonate-O, C isotope values.

Takla et al. (1990, 1995) suggested a spatial association between gold mineralization in the Eastern Desert and sulfide-bearing gabbroic rocks intruded by granitic bodies. These gabbroic rocks commonly form small intrusions with troctolites, olivine gabbro, hornblende gabbro and anorthosite composition, and are referred to as post-collisional younger gabbros (Takla et al. 1981, 1997). These rocks have

geochemical characteristics of calc-alkaline, mantle-derived magmas (e.g., Abu El-Ela 1996), formed at the late Cordilleran stage (~655–570 Ma; El-Gaby et al. 1988). Concentrically zoned, mafic-ultramafic intrusions pertain to the younger gabbros in the Eastern Desert, and are commonly characterized by accessory PGE-bearing Cu–Ni–Fe-sulfide (e.g., Garson and Shalaby 1976; Helmy and Mogessie 2001; Helmy and El Mahallawi 2003; Helmy 2004). The bulk-rock trace element composition and EPMA data of the clinopyroxene point towards crystallization from a mantle-derived hydrous tholeiitic magma (Abdallah et al. 2018).

The post-collisional tectonic setting suggested for the younger gabbros, their mantle-derived genesis and the concentric mafic-ultramafic complex (Alaskan-type) nature of

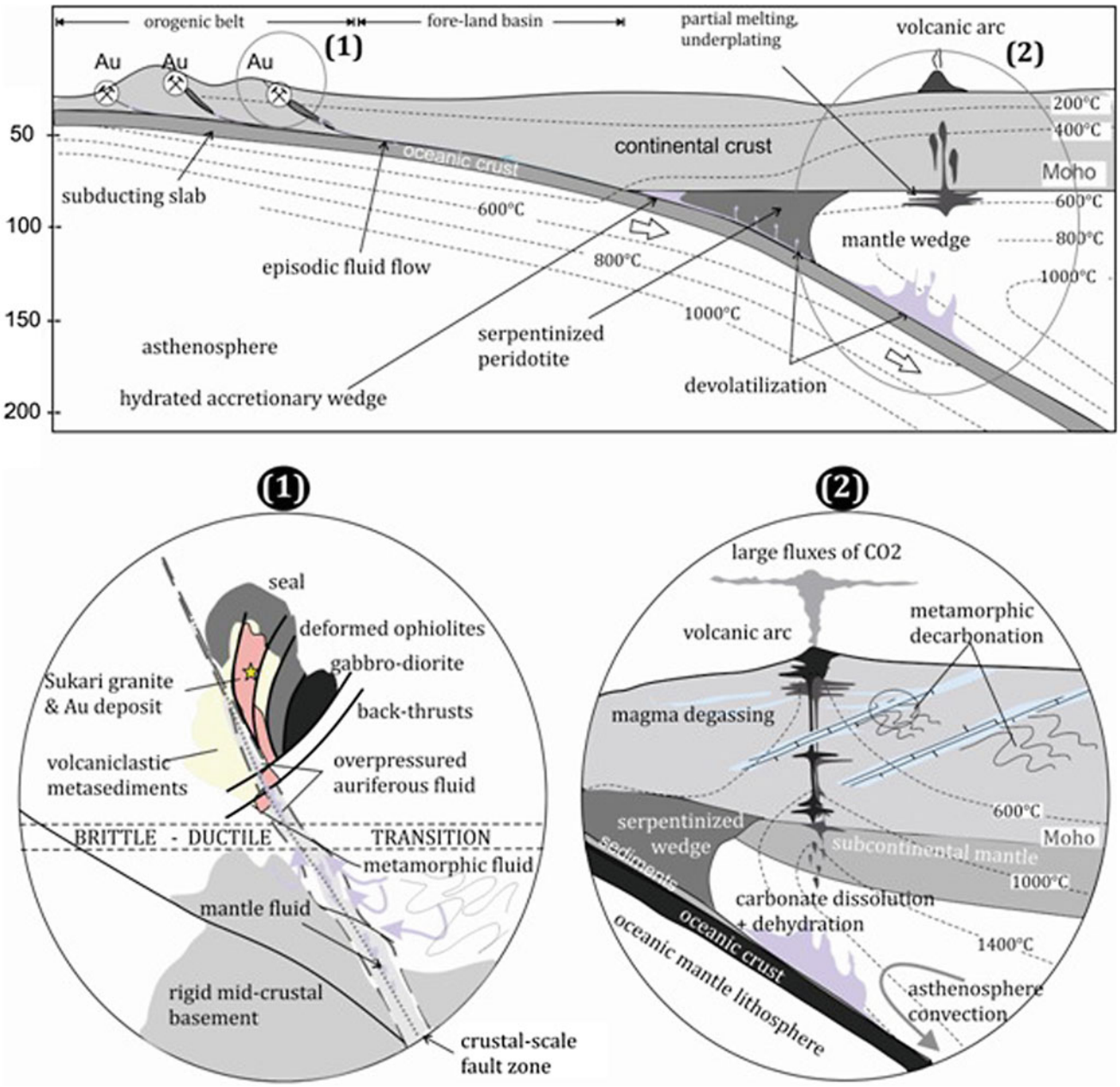

Fig. 14.12 Proposed schematic model of orogenic gold in the Eastern Desert of Egypt. (1) Schematic section through a continental arc, showing crustal-modified and crustal-derived (by prograde metamorphism) ore fluids infiltrate into pervasive mid-crustal structures and deposit gold in suitable structural and lithological seals. The crustal-modified fluids released during devolatilization of the subducting slab and traveled up-dip along the subducting slab-overlying mantle wedge interface (example is Sukari deposit; see Abd El-Wahed et al. 2016), (2) development of a hot zone at the base of the crust where hydrous basaltic arc magmas pool at their level of neutral buoyancy, differentiate, and interact with crustal rocks and melts (Richards 2011). Evolved, less dense, andesitic magmas rise into the mid-to-upper crust where they pool at their new level of neutral buoyancy to form batholithic complexes. In their path upwards, mantle-derived CO2-rich fluids are degassed from the ascending magma and mix with fluids by continental carbonate dissolution in the mid-crustal levels (crustal-modified fluids; see Mason et al. 2017). A good example in the Eastern Desert is Um Eleiga deposit (Zoheir 2012a)

some of them reflect multiple magmatic intrusions during the late-orogenic evolution of the Eastern Desert. This could reflect heating up of the lower crust causing metamorphism and anataxis, and attendant uplift and extension in shallower crustal levels (e.g., Henk et al. 1997). The melt source of these intrusions is considered to be a subcontinental-lithospheric mantle and their emplacement occurred during a regional rifting event (e.g., Eyuboglu et al. 2010). This reflects the role of magmatic underplating in introducing mantle-derived heat and components to the continental crust (Fig. 14.12).

14.3.4.3 Geodynamic Model and Timing of Orogenic Gold in the Eastern Desert

Goldfarb and Groves (2015) proposed a genetic model for orogenic gold in the Precambrian terranes, in which a devolatilized, subducted, relatively flat slab and its overlying sediment, or a fertilized tip of the mantle wedge releases aqueous-volatile fluids during a thermal event (Fig. 14.12). The pressure-temperature paths of the subducted slab and underplated rocks may follow a trajectory that allows for gold liberation at depth after peak collisional metamorphism of overlying rocks (e.g., Fyfe and Kerrich 1985). The role of the nature and thickness of the subcontinental mantle lithosphere (SCLM) in the formation of orogenic gold is discussed by Bierlein et al. (2006), who noticed that giant gold deposits are much more likely to develop in orogens with thin SCLM, and experienced a short pre-mineralization crustal history. Segments of orogens with back-arc basalts, transitional basalts and basanites are more likely associated with world-class and giant gold deposits if come in conjunction with a giant-scale fluid flux. Hydrothermal fluids by subduction-related crustal underplating and deep, late metamorphism, are released along crustal-scale faults and their splays during times of regional uplift (e.g., Kerrich and Wyman 1990). Fyfe (1992) suggested that where dense magmas occur beneath a continental crust, the lower crust starts to melt and degasses, producing high-temperature fluids rich in H_2O–CO_2–CO and S-halogen species.

In the Eastern Desert, the difference in the estimated pressure-temperature environments for the infrastructure and superstructure rocks led Stern (2018) to suggest that the rheological boundary between them is marked by a telescoped thermal gradient. The high grade metamorphism in the infrastructure was probably due to arc-related basaltic magmas underplating (~630 Ma: Stern 1994). Post-collisional, within-plate basaltic underplates, on the other hand, resulted in formation of <630 Ma crustal melts. Similarly, adakitic magmatism in the Arabian Shield, i.e., in the forearc Ad Dawadimi Basin, has been dated at 633 ± 9 Ma (Nettle et al. 2014). The timing of orogenic gold in the Eastern Desert is not fully established, but recent trails by Zoheir et al. (2015, 2018b) indicate that gold mineralization in the CED was concurrent with regional cooling and terrane uplift at ~600 Ma. Strong evidence exists for a N-S extension tectonic regime in the CED during that time, supported by the ~600 Ma bimodal E-W and NE-SW dike swarms (Stern 2018) and silica rich ignimbrites (630–592 Ma; Breitkreuz et al. 2010), almost concomitant with the course of the Najd fault system in the Eastern Desert (Stern et al. 1984).

A principal role in the geodynamic evolution, as well as gold metallogeny of the Eastern Desert is attributed to the subduction-dominated crustal growth history, the thin SCLM and the protracted terrane accretion terminated by East and West Gondwana collision. The later promoted transient remobilization events of the SCLM and development of plumbing structures (regional seals). Orogenic gold mineralization by crustal-derived (metamorphic) or crustal-modified (mantle-sourced) fluids was evidently linked with the major mantle processes during the crustal evolution of the Eastern Desert.

14.4 Titanium-Rich Deposits

Adel Surour

14.4.1 Titaniferous Iron Ore Deposits

14.4.1.1 Ore Type and Distribution

Host rocks for the titaniferous Fe ores in the Eastern Desert of Egypt are gabbroic rocks that are mostly fresh with limited metamorphism. They comprise olivine gabbro, melanorite, in addition to anorthosite. Ilmenite ore deposits are concentrated in the southern part of the Eastern Desert (Fig. 14.13) at Abu Ghalaga (the most economic one), Umm Effein, Umm Ginud, Kolmnab, Wadi Rahaba, Abu Dahr, Hamra Dome and Wadi El-Miyah (Amin 1954; El-Shazly 1959; Basta and Takla 1968a). The ore at Abu Ghalaga may attain up to 150 thick layer(s) trending NW-SE and dips 30°–45° with an extension up to 350 m. A unique titanomagnetite deposit is located at Korabkanci where a considerable reserve is estimated (Nasr et al. 2000; Makhlouf et al. 2008) as. These workers measured a titanomagnetite NNE-SSW layered body (2500 m long and 50–80 m wide) that is steeply dip to the east (80°–90°). The ilmenite and magnetite ores form by crystal settling, filter pressing and segregation of massive ores and syngenetic bands in a mafic

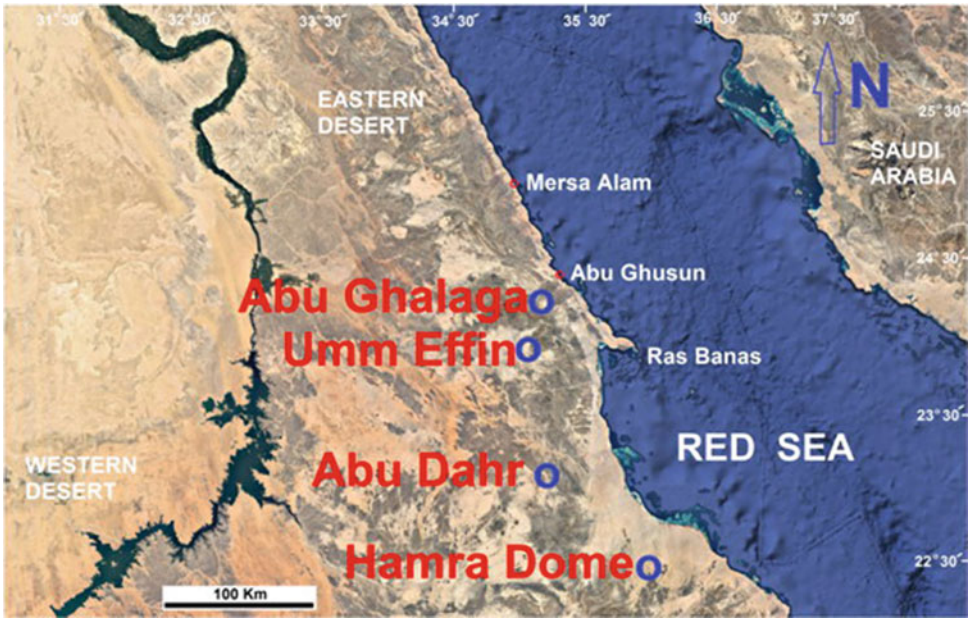

Fig. 14.13 The four major titaniferous iron ore deposits in the Eastern Desert of Egypt on a Google Satellite Image taken in 14 December 2015

magma chamber (Basta and Takla 1968a, b). At Abu Dahr, the ore occurs as a NE-SW discordant dyke-like body in altered gabbro that is hosted by serpentinites. The Abu Dahr ore bears considerable amount of apatite that becomes a nelsonite ore (apatite-Fe–Ti oxide ore) at Kolmnab in anorthosite (Basta and Girgis 1969). The nelsonite at Kolmenab (in the Nubian Shield), as well as at Wadi Khamal in Saudi Arabia (Arabian Shield) described by Harbi (2008), by in situ fractional crystallization of Fe, Ti, P and volatiles-rich gabbroic magma followed by injection into the anorthosite at high f_{O2}. Also, a liquid immiscibility model can be considered according to the recent approaches by Duchesne and Liégeois (2015).

14.4.1.2 Mineralogy, Geochemistry and Ore Reserves

Basta and Takla (1968b) distinguished three categories of the Abu Ghalaga ilmenite ore namely; massive black ore with 20–25% gangue and up to 71% ilmenite, disseminated ore with 40–45% gangue and up to 62% ilmenite and a red ore at the surface with remarkable oxidation products mainly as hematite. The Abu Ghalaga massive ore is dominated by ilmenite (averaging ~67%) in the massive ore, in addition to subordinate amount of titanomagnetite (4–17%), hematite (13–18%) and up to ~2% sulphides (Khalil 2001; Hawa 2014). The most common ore fabric is the hematite-ilmenite or hemo-ilmenite intergrowth texture (Fig. 14.14). The figure

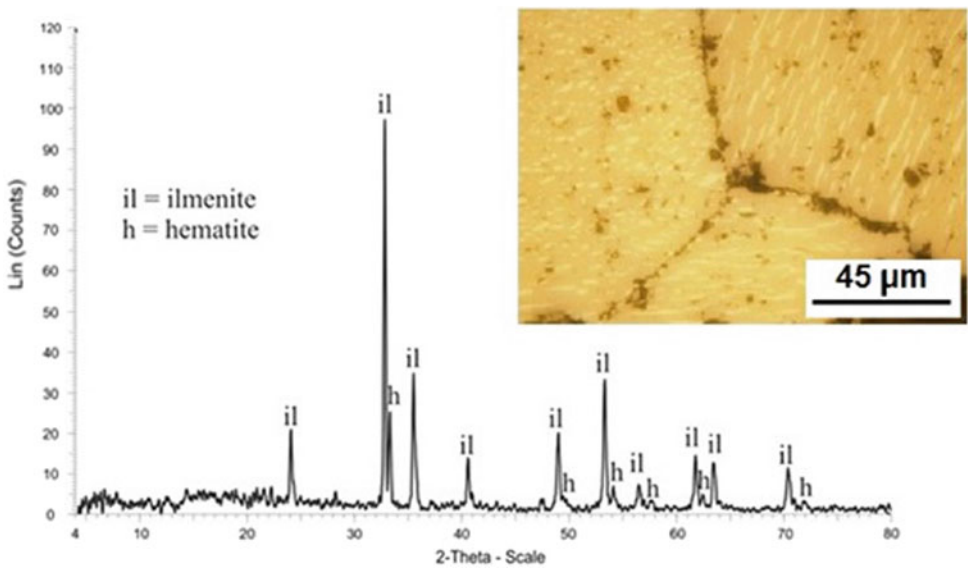

Fig. 14.14 XRD analysis and a reflected light microscope microphotograph showing the hemo-ilmenite composition of the Abu Ghalaga ilmenite ore (Shahien et al. 2015)

Table 14.5 Chemical composition of Abu Ghalaga ilmenite ore (Shahien et al. 2015)

Oxide	SiO_2	TiO_2	Al_2O_3	Fe_2O_3	MgO	CaO	Na_2O	K_2O	P_2O_5	MnO	Cr_2O_3
Wt%	1.97	40.91	1.10	51.90	3.38	0.33	0.07	<0.01	0.05	0.25	0.071

shows distinct polygonal contacts as an evidence of annealing. ICP-MS analysis of the Abu Ghalaga ore yields a TiO_2 average of 40.91 wt% in addition to considerable amounts of impurities such as with 1.97% SiO_2, 1.10 Al_2O_3, 0.05% P_2O_5, 0.25, % MnO and 3.38% MgO (Table 14.5). The ilmenite itself is Mn-rich (5–6% MnO) whereas MgO never exceeds 2%. The 3.38% MgO in the bulk ore sample is attributed to the presence of hornblende. The annealing fabrics (Fig. 14.14), deformation of hematite intergrowth lamellae in ilmenite and formation of metamorphic hornblende suggest ore remobilization during metamorphism at a 650 °C peak (Hawa 2014). Ore reserves of titaniferous iron ores in the Eastern Desert are much lower than in the black sand deposits on the Mediterranean amounting 40 and 606 Mt (Naim et al. 1993; Abouzeid and El Wgeeh 2008; Abouzeid and Khaled 2011).

14.4.1.3 Economic Potentiality and Extraction

The titanifrous iron ores in the Egyptian Precambrian shield rocks are still not well exploited but new hopes arise especially in the recent times with the advance in technology of mining and metallurgical processes. TiO_2 extracted from the Abu Ghalaga ilmenite ore can be used to produce pigments, welding-rod coatings, ceramics, papers and other chemical industries. According to Mahmoud et al. (2004), the produced white titanium dioxide pigments are produced either by the sulfate process or the dry chlorination process. Helal (2007) presented a method for ore beneficiation and ore upgrading in order to encourage new investments for the Abu Ghalaga by increasing TiO_2 from 16–22% to ~42% TiO_2 that classifies the ore as a medium-grade one.

During the last five years, there were some trials to synthesize rutile nanoparticles (10 to 100 nm) that contain about 95.92% TiO_2 and only 0.8% iron as Fe_2O_3 with the absence of coloring metals (Shahien et al. 2015). The workers recommended the successful usage of the synthesized rutile from the Abu Ghalaga ore for the production of white pigments and other industrial applications. The metallurgical scheme to produce such a synthesized rutile is a combined one consisting of mechanical activation followed by reduction, leaching with HCl and calcination. Shahien et al. (2015) believed that the impurities in the Abu Ghalaga ilmenite ore can be removed by carbothermic reduction and acid leaching. Nelsonite at Kolmnab is a peculiar ore that still needs extensive mineralogical and beneficiation studies because it would represent a potential source of rare-earth elements (REE) in addition to Fe and Ti. A technological sample of its counterpart in the Arabian Shield yielded 23.5% apatite concentrate with an overall 40.23% P_2O_5, and the extraction of the REEs from the phosphoric acid liquor using oxalic acid and sodium carbonate-bicarbonate mixture (1:10 w/w) yielded a 1.2% (w/w) rare-earth oxide cake (Harbi et al. 2011).

14.4.2 Black Sands

14.4.2.1 Background and Distribution

Floods associated with the pluvial periods which prevailed in Egypt during the Pleistocene were the cause of eroding the source rocks and liberate heavy minerals including monazite (Dawood and Abd El-Naby 2007). The mineral grains were transported through several wadis and tributaries to the main channel of the River Nile. The higher-density minerals are concentrated in areas of beach erosion, accounting for the formation of black-sand placers where the ultimate erosion is recorded (Fig. 14.15a). The heavy mineral concentrations of the Nile Delta in black sands and some sand dunes (Fig. 14.15b) are distinguished into two groups (Frihy et al. 1995; Frihy 2007), who paid attention to the spatial variation in heavy mineral content and its connection to sorting. The first group includes heavy minerals of lower density and coarser size (augite, hornblende and epidote). Heavy minerals in this group increase from west to east along the delta as they are easily to entrain and transport the coastal sediments toward the east by wave currents. In contrast, the second group includes heavy minerals of higher-density (opaques, garnet, zircon, rutile, tourmaline and monazite), which are relatively more difficult to entrain and transport by wave-current actions. Hence, minerals in this group form a lag deposit within the delta and beach sand. El-Askary and Frihy (1987) pointed out that the mineralogy of the sub-surface sediments at Rosetta and Damietta promontories is greatly controlled by the bulk mineralogy of the surface heavy minerals.

The black sands on the northern beach between Lake El-Bardawil (west) and El-Arish (east) in the northern Sinai Peninsula with very distinct geomorphological features of beach deposits are periodically modified with the shoreline changes (Frihy and Lotfy 1997). Dawood and Abdel-Naby (2007) studied the monazite from the black sands in the northern Sinai Peninsula that have been originated by eastward sea currents from the Nile Delta beaches, and concluded that without a comparison between the age and composition of monazite in the proposed source rocks and

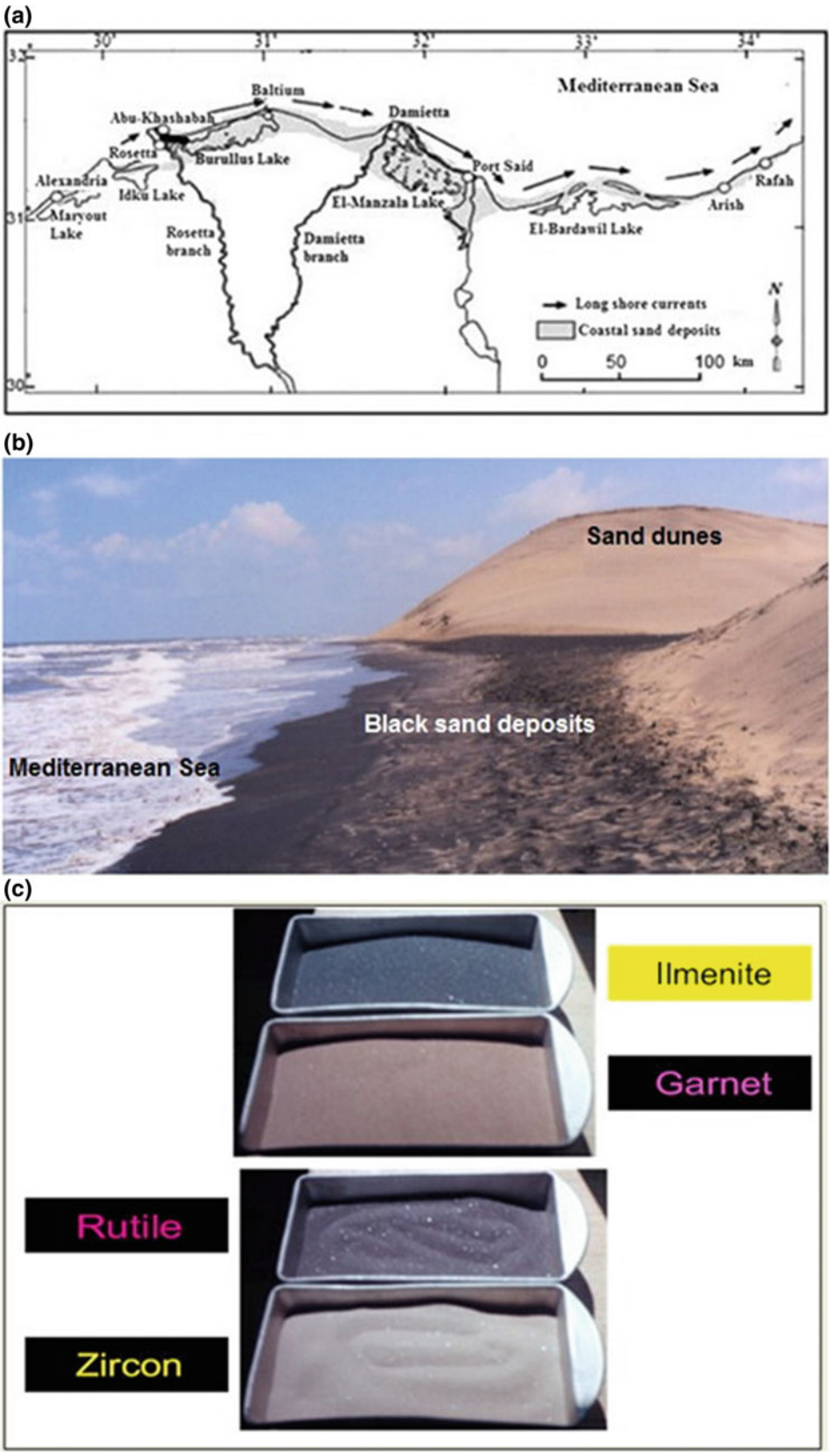

Fig. 14.15 **a** Extension of black sand and beach deposits on the Mediterranean coast in northern Egypt. **b** Field photo of the deposits, courtesy of the Egyptian Black Sand Company, National Service Projects Organization (NSPO). **c** Heavy minerals separated by the Egyptian company for Black Sands (ECBS) that belongs to the NSPO

beach sediments, the possibility that the monazite may have more than one provenance cannot be ruled out. These authors focused their study on monazite [(Ce,La,Nd,Th)PO_4] as a potential resource of very significant rare-earth metals. In addition to the black sand in Sinai, the stream sediments there are rich monazite that can be considered as a source of Ce and La, alongside with placer gold, Fe–Ti oxides and zircon (Surour et al. 2003). Recent geophysical studies (e.g., El-Sadek et al. 2012) help to locate the hidden horizons of black sands on the Mediterranean northern coast of Egypt. Their study enabled to determine high values of calculated metal factor that coincides with high electric IP chargeability and low electric resistivity values. The deep-seated magnetic response was interpreted to lie at an average depth of 239.6 m, while the near-surface magnetic responses were interpreted to lie at average depths of 9.1 m, 57.9 m, and 81.8 m, respectively.

14.4.2.2 Mineralogy and Geochemistry

Essential placers minerals that are concentrated in the Egyptian black sand deposits are Fe–Ti oxides (mainly magnetite, hematite, ilmenite and rutile). The main mineralogical bulk also includes the alteration products of the Fe–Ti oxides that are represented mainly by "leucoxene", anatase and brookite. Depending on the source rocks, the deposits include zircon, thorite, monazite and REE-bearing minerals (if the source is felsic, mostly igneous) or chromite (if the source is mafic-ultramafic rocks). In some instances, the deposits bear some other economic placers such as gold and cassiterite (El Gemmizi 1985). There are minor gold and traces of ferrotapiolite, cinnabar, native lead, chromite, and chevkinite in the cassiterite concentrate from the Rosetta black sands (Abdel-Karim and El-Shafey 2012). The first detailed microscopical, X-ray, chemical and spectrographic analyses of the Egyptian black sands were given by El-Hinnawi (1964). Sometimes, garnet is recorded in the Egyptian black sand and it is derived from regionally metamorphic politic rocks along the main course of the River Nile from the upstream in Ethiopia. The garnet modal percentage amounts 1.83% (Nakhla 1958) and has the composition $Pyr_{49}Alm_{42}Gros_5Sp_2And_1$ and with very characteristic Sc > Y as a common feature of Mg–Fe garnets (El-Hinnawi 1964) with high pyrope content that might have been brought from a high-pressure metamorphic terrain. The first insights on the microfabrics and microanalyses of exsolved ilmenite in the titanomagnetite of the Rosetta black sands were determined by the electron microprobe for the first time by El-Hinnawi (1969) who concluded that the common alterations are products of oxidation.

The average concentrations of Ti, V, Cr, Mn, Fe, Zn, As, Zr, Cd and Hf based on an accurate ICP-MS technique are 435.06 ppm, 322.32 ppm, 2515.03 ppm, 596.45 ppm, 185,894 ppm, 249.95 ppm, 309.32 ppm, 1077.26 ppm, 33.56 ppm and 3520.32 ppm, respectively for 18 black sand samples from the Mediterranean coast at the Abu Khashaba, Rosetta area (Mahmoud et al. 2013). Magnetite concentrate contains high concentrations of heavy metals such as V (1841 ppm), Ni (112) ppm, Zn (341 ppm) and Cu (62 ppm), in addition to appreciable amounts of 3.9 ppm Au and 1037 ppm Zr (El-Kammar et al. 2011). The latter workers stressed on the enrichments of the investigated black sands in Y (especially in the garnet-rich fractions) and high REEs content (particularly in the monazite).

As to the radionuclides, El-Gamal and Saleh (2012) studied the natural radioactivity of the coastal sediments, their heavy mineral distribution and grain size information to differentiate between the eroding and accreting areas of the Nile Delta coast off the Nile Delta up to 800 m. Their study on the distribution of primordial radionuclides allows good understanding of the radiological implication of these elements due to coastal processing. Results obtained from the study document the relatively high concentrations of ^{238}U and ^{232}Th series members, which were found in coincident at sites having higher heavy minerals percentages and detected at erosional beach than the accretion one. Numerically, El-Gamal and Saleh (2012) determined the offshore high concentrations off the Nile Delta at the Buruls Lake and Abu Quir Bay as follows: averages of ^{226}Ra, ^{214}Pb, ^{214}Bi and ^{210}Pb (as ^{238}U series) were 104.37 ± 84.66, 45.60 ± 37.83, 38.43 ± 32.49 and 35.69 ± 24.86 Bq/kg, respectively and ^{228}Ra and ^{212}Pb (as ^{232}Th series) were 54.26 ± 56.66 and 42.18 ± 44.66 Bq/kg, respectively. The highest average value of ^{40}K concentration (404.49 ± 125.81 Bq/kg) was detected in ae profile located at 2000.1 m west of the Rashid estuary. At the Rosetta beach itself, the concentrations of ^{238}U, ^{232}Th and ^{40}K ranged from 5.39 to 134.2, 6.6 to 160.8 and 57.6 to 492 $Bqkg^{-1}$, respectively. The range of activity concentrations of ^{137}Cs is between 0.05 and 0.91 $Bqkg^{-1}$ (Nada et al. 2012).

14.4.2.3 Economic Potentialities and Extraction

The economics of extracting the minerals ilmenite, magnetite, hematite, zircon, rutile and monazite from the black sands in northern Egypt between Alexandria and Rosetta (Fig. 14.15c) were given by Hedrick and Waked (1989) within the context of the investment climate in Egypt during the 1980s. Nano-sized TiO_2 as rutile for pigments can be prepared from titanyl sulfate and titanyl chloride produced from the acid attack of the Rosetta black sands at Abu Khashaba (Fouda et al. 2010). Size of the obtained nano-sized rutile varies from 22–46 nm in case of using H_2SO_4 to 29–59 nm in case of using HCl. In some spots (e.g., El-Burullus Lake), magnetite amounts 31.6% of the black sand volume and some experiments were carried out recently to produce iron for iron and steel industry

(Abdel-Karim and Barakat 2017). The tonnage of magnetite is 182,850 t and 98.26% recovery. The chemical composition of that magnetite suggests derivation from mafic volcanic rocks at the Blue Nile provenance and can be considered as a good indicator for the volcanic source of the Ethiopian plateau. Such a tonnage at El-Burullus is much lower than the 1,437,000 t for reserves of placer magnetite at the Rosetta beach (Naim et al. 1993).

The radioactive black sands are usually concentrated in the eroded areas like the Rosetta case at Abu Khashaba (Kaiser et al. 2014). Owing to their content of radioactive minerals (e.g., zircon, uranothorite and relatively monazite) the Egyptian black sands in the north are subject of extensive studies by the Nuclear Materials Authority of Egypt for the extraction of uranium that is needed to produce a "yellow cake". Specific accounts on the radioactive potentiality of the Egyptian black sands were presented as early as the late 1950s and early 1960s (e.g., Gindy 1961). During the last three decades, different flow sheets were presented for radioactive and REE-bearing heavy mineral separation from the Egyptian black sands, e.g., Ibrahim (1995), Moustafa (2007), Hussein (2011). The latter defined a successive scheme for adsorption of radioactive elements (U and Th) from monazite as the main target. It is highly recommended to investigate Fe–Ti oxide concentrates as well. According to Moustafa (2007), magnetite, ilmenite, zircon and rutile high-purity concentrates can be obtained in assays equals 99.6%, 99.55%, ≈100% and ≈100% and recoveries of 95.3%, 75.5%, 77.8% and 77.3%, respectively. Such information stress that the Egyptian black sands are potential sources of radionuclides, rare-earth elements, Fe and Ti so they are worth of international and local tenders in the atmosphere of new mining and investment laws of the state that have been formulated in 2016–2017. Finally, gold can be extracted as a bi-product. Fertility of gold in the Egyptian black sands have been documented, e.g., Hammoud and Khazback (1984), El Gemmizi (1985). Environmental aspects should be taken in consideration in order to avoid harmful impacts of extraction process both for the soil and water.

14.5 Sulfide and Precious Metal Deposits in Egypt

Hassan M. Helmy

Since the summary given by Hussein (1990) in the second edition of the Geology of Egypt book, many advances have been made on the sulfide mineral deposits of Egypt; few localities have been discovered and detailed information on ore mineralogy and chemistry have been added by many authors. Applying new analytical techniques and new geological concepts on these mineralizations led to new discoveries and ideas. Updated description of sulfide and precious metal deposits is given hereafter; the sulfide mineralizations are classified into five types:

(a) Copper-nickel-platinum group elements (PGE)
(b) Volcanogenic massive Zn–Cu–Pb–Ag sulfides
(c) Skarn-type Zn–Cu–Pb–Ag sulfides
(d) Porphyry-type Au–Cu sulfides
(e) Hydrothermal Au-bearing sulfides.

The following paragraphs summarize the advances made on the first four deposits during the last three decades.

14.5.1 Cu–Ni–PGE Sulfide Mineralizations

Sub-economic Cu–Ni–PGE mineralizations occur as small massive pockets and disseminations in the ultramafic portions of the layered complexes (e.g., Abu Swayel, Gabbro Akarem and Genina Gharbia) in the Eastern Desert (Helmy et al. 1995; Helmy and Mogessie 2001; Helmy 2004, 2005; Jedwab 1992). The study of these mineralizations using the electron microprobe allowed many researchers to locate micron-size platinum group minerals (PGM).

14.5.1.1 Abu Swayel

The Abu Swayel area is located 185 km southeast of Aswan and is covered by metasedimentary and metamorphosed mafic-ultramafric rocks. The metasedimentary rocks are represented by hornblende and biotite schists, gneisses and marble. The ultramafic rocks form large lens-like bodies (500 m long and up to 30 m thick) conformably interlayered in the metasedimentary rocks. All lithologies underwent amphibolite facies metamorphism (4–5 kbars and 650 °C, Helmy et al. 1995), 636 ± 10 Ma ago (Finger and Helmy 1998). The sulfide mineralizations occur as dissemination, small massive lenses and micro-veinlets in the ultramafic rocks. Sulfide minerals comprise chalcopyrite, violarite, cubanite and bornite; no primary magmatic textures of sulfide minerals are documented. Six platinum group minerals (PGM) were identified (Helmy et al. 1995). These PGM form micron-size inclusions in chalcopyrite and comprise michenerite (PdBiTe), froodite ($PbBi_2$), merenskyite (PdTe2), Palladian bismuthian melonite $(PdNi)(TeBi)_2$, sudburyite (PdSb) and geversite (PtSb). They occur in intimate association with hessite (Ag_2Te), Te-rich electrum (AuAg) and altaite (PbTe). High Pd and Pt contents (13 and 2 ppm, respectively) were determined by inductively coupled plasma mass spectrometry (***ICP-MS***) in massive sulfide samples (Helmy 1996). The Cu–Ni–PGE ore is of magmatic origin and was remobilized and recrystallized during the amphibolite facies metamorphism. The mode of occurrence

of the mineralized ultramafic lens and the regional geologic setting of the Abu Swayel area suggests that other hidden mineralized ultramafic lenses are present in the area.

14.5.1.2 Zabargad Island

There is a small occurrence of Ni-rich hydrothermaly altered peridotite in the Zabargad Island of the Red Sea. The reserves of this occurrence are not known. Jedwab (1992) described various platinum-group minerals (laurite RuS_2, moncheite $PtTe_2$, platinum, potarite PdHg), which were deposited during the successive magmatic differentiation of the parent mafic magma and hydrothermal alteration stages. The presence of laurite in Zabargad ore may suggest that the mineralization is ophiolite-related, the other low-temperature PGM are due to hydrothermal-oxidation processes.

14.5.1.3 Gabbro Akarem and Genina Gharbia

The Gabbro Akarem and Genina Gharbia mafic-ultramafic intrusions are Precambrian analogues of Alaskan-type complexes (Helmy and El Mahallawi 2003; Helmy et al. 2014). Both intrusions are concentrically zoned with dunite core enveloped by pyroxenites and gabbros. The ultramafic cores of the two complexes host disseminated and massive sulfide bodies. The ore reserves at Gabbro Akarem were estimated at 700,000 ton containing 0.95 wt% combined Ni and Cu (Carter 1975) and <1.0 ppm Pd + Pt (Helmy and Mogessie 2001). Pyrrhotite, pentlandite, chalcopyrite and pyrite are the common sulfides that show typical magmatic textures. Chrome spinel is a common oxide. Meresnkyite, michenerite and Pd-bearing bismuthian melonite (NiPd) $(TeBi)_2$ form micron-size inclusions in pyrrhotite and along cracks in sulfides. The Cu–PGE mineralization at Gabbro Akarem (Fig. 14.16) is typical magmatic; the low PGE content of the ore is due to formation in a dynamic environment (Helmy and Mogessie 2001). The compositional range of Palladian melonite (Helmy 2005) and the presence of native Te led Helmy (2004) to suggest that the Genina Gharbia deposit was formed in the late magmatic stage of the mafic magma crystallization.

14.5.1.4 Volcanogenic Massive Zn–Cu–Pb–Ag Sulfide Mineralizations

The Late Neoproterozoic (712 ± 24 Ma from Rb–Sr whole-rock isochron; Stern et al. 1991) Shadli Metavolcanic Belt of the south Eastern Desert (Fig. 14.17) hosts several polymetallic massive sulfide mineralizations. The occurrences present in the western part of the Shadli Metavolcanic Belt (Um Samiuki, Helgate, Maaqal) show common

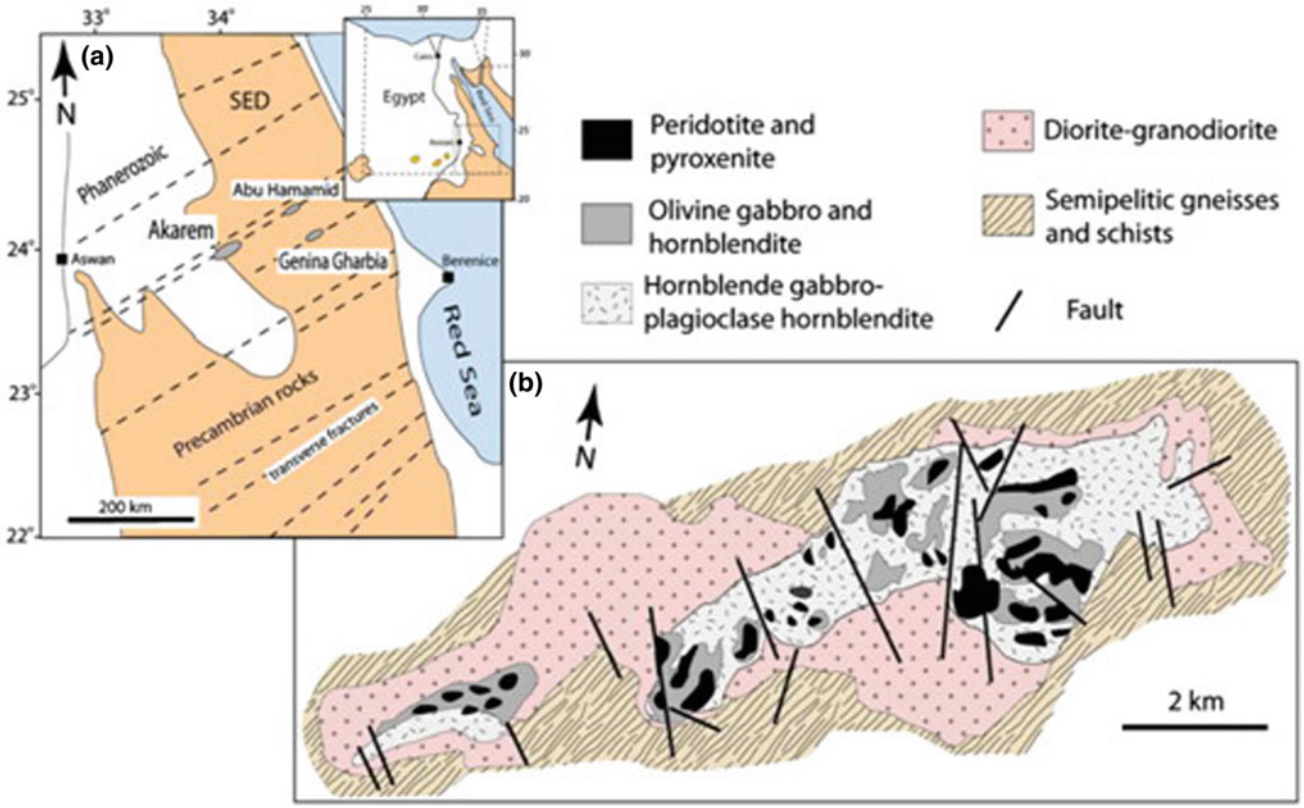

Fig. 14.16 **a** Location map of the concentrically-zoned (Alaskan-type) complexes in the Eastern Desert including Gabbro Akarem and Genina Gharbia. **b** A geologic map of Gabbro Akarem intrusion

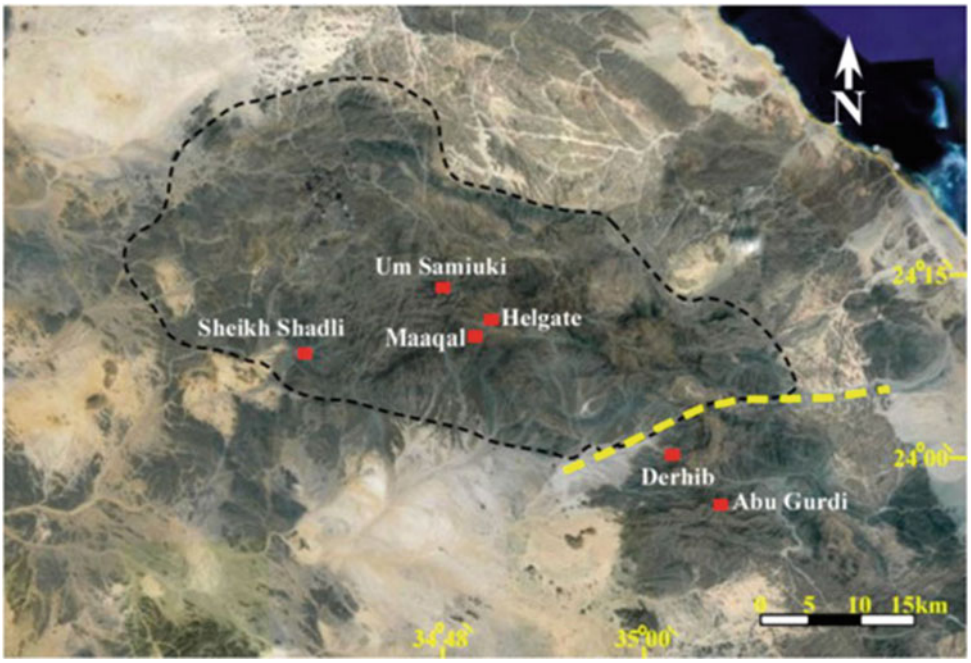

Fig. 14.17 Distribution of polymetallic massive sulfide deposits in the Shadli Metavolcanic Belt

geological, mineralogical and geochemical features different from the occurrences present in the eastern extension of the belt (Egat, Abu Gurdi, Derhib).

14.5.1.5 Um Samiuki, Helgate and Maaqal

The three mineralizations are stratigraphically controlled where they form lenses in the banded tuff and chert of the Hamamid Group (Searle et al. 1978) on top of metabasalts. The three occurrences show primary depositional features, like micro layering, and the same gangue mineral assemblage (chlorite, calcite, quartz) (Helmy 1996). The Zn–Cu–Pb–Ag mineralization at Um Samiuki, which is the largest among these deposits. Two lenticular bodies of massive sulfide ores (the Western and Eastern mines) occur conformably at the top of a thick series of felsic rocks. Ancient Egyptians and Romans worked these deposits for malachite. Searle et al. (1978) reported the results of detailed geological mapping and geochemical prospecting, and described the logs of six boreholes drilled in the area (with a total of 806 m). Ore reserves were estimated to slightly less than 300,000 tons, containing 11.5% Zn, 1.15% Cu, 1.1% Pb and 0.01% Ag (Searle 1975). Shalaby et al. (2004) analyzed various sulfide minerals for the precious metal content and noted that bornite is a major host of Ag. In addition to electrum (AuAg), hessite (Ag_2Te), and cervelleite (Ag_4TeS) are common silver tellurides in the Um Samiuki ores (Helmy 1999).

Helgate and Maaqal prospects are small in size. The mineralized zone in Helgate trends 300° with a 75° dips to the south and does not exceed 1 m in the form of veins concordant with the banded tuff and chert. The ore reserves are 13,000 ton of massive ore. At Helgate prospect, the massive sulfides occur as lenses in talc within 6-m-wide mineralized zone, which is contorted and disturbed due to post-depositional deformation. Searle et al. (1978) concluded that the Um Samiuki Zn–Cu–Pb mineralisation is of volcanogenic massive sulfide type, associated with acid volcanism. They stated that the base metal sulfide mineralisation is stratigraphically and tectonically controlled.

14.5.1.6 Derhib, Abu Gurdi and Egat Prospects

The Derhib, Abu Gurdi and Egat prospects are known for their talc mines. The talc ore developed along shear zones separating the Shadli Metavolcanics and ophiolitic mélange comprising metasediments and fragments of serpentinites and metagabbros. The Derhib and Abu Gurdi polymetallic sulfide mineralizations occur either as disseminations or small massive lenses and veins along the shear zones in talc-tremolite rocks. The sulfide ore at Derhib talc mine is confined to the lower levels, where it is rarely exposed on the surface. Pyrite, sphalerite, chalcopyrite, and galena are the major sulfide minerals while pyrrhotite, molybdenite and cubanite are common accessories. Magnetite is a major oxide mineral. Gangue minerals comprise tremolite, talc and

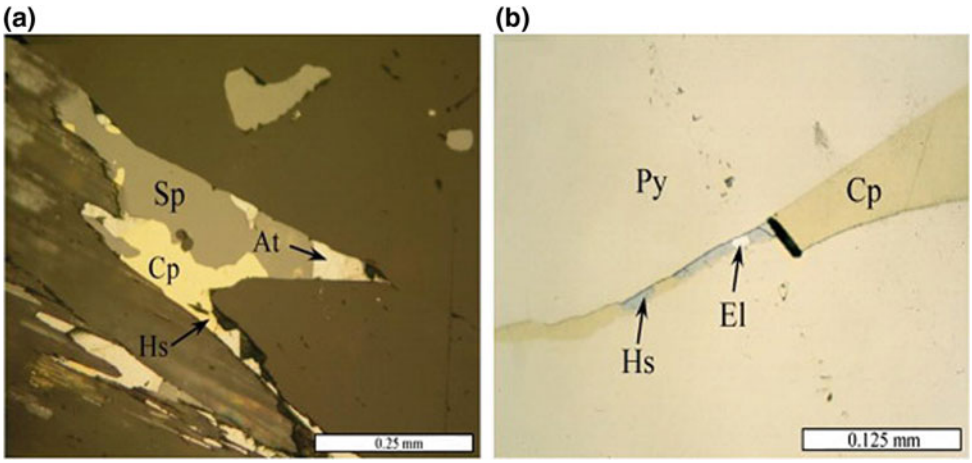

Fig. 14.18 **a** Remobilized sulfides (sphalerite Sp, chalcopyrite Cp, hessite Hs, altaite At) in a matrix of metamorphic amphibole (dark gray), Derhib area. **b** Recrystallized pyrite porphyroblasts (Py) and chalcopyrite (Cp), hessite (Hs) and electrum (El) interstitial to pyrite, Abu Gurdi area

chlorite. At Abu Gurdi, the sulfide mineralization is not exposed on surface. It was encountered in only one place, where massive and disseminated sulfides are hosted in talc. Sulfide zone occurs at depth 50 m below the surface associated with talc. Unlike the Um Samiuki, Maaqal and Helgate mineralizations, Derhib and Abu Gurdi sulfide minerals show pure metamorphic features like recrystallization, retexturing and remobilization (Fig. 14.18). The FeS content in sphalerite ranges from 1.4 to 19.4 mol percent. High Cd (0.1–5.1 wt%) and low Mn (0.1−0.8) contents are characteristic for sphalerite from Derhib mine area, while sphalerite from Abu Gurdi contain no Cd and Mn. High Se (up to 8.4 wt%) and traces of Ag (up to 0.2 wt%) are detected in galena from both areas. Pyrite from Derhib and Abu Gurdi contains traces of As (0.1 and 0.16 wt% respectively) and Co (0.1 and 0.12 wt% resp.).

Helmy (unpublished data) documented three silver-minerals from these prospects; hessite (Ag_2Te), electrum (Ag, Au) andvolynskyite ($AgBiTe_2$). Hessite is closely associated with galena while electrum occurs at pyrite and chalcopyrite surfaces. Silver minerals occur in intimate association with altaite (PbTe) and hedleyite (Bi_4Te_2S).

High Cu contents (up to 15 wt% and 3.3 wt% at Derhib and Abu Gurdi, respectively) have been detected in massive sulfides (Helmy, unpublished data). Abu Gurdi massive ore is rich in Zn (up to 38 wt%) and Pb (up to 3.3 wt%) than those of Derhib (up to 15 wt% Zn and 0.6 wt% Pb). High Ag and Au contents are recorded in Derhib (218 ppm and 2.4 ppm

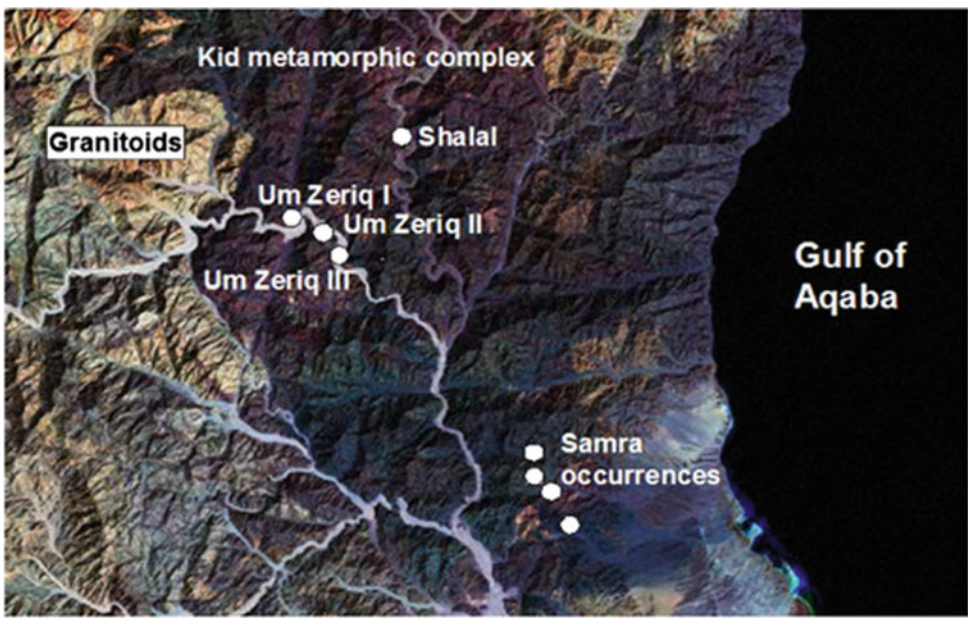

Fig. 14.19 Location of sulfide mineralizations in the Kid area, southeast Sinai, Egypt

Ag and Au, respectively) and Abu Gurdi (341 ppm and 2.2 ppm Ag and Au, respectively) The geologic, petrologic and geochemical (Zn/Cu and Ag/Au ratios) criteria suggest genetic relationship with the ophiolitic rocks in the area.

14.5.2 Skarn-Type Zn–Pb–Ag Mineralizations

A Precambrian skarn-type mineralization was recently discovered in the Wadi Kid area in southeast Sinai, Egypt (Fig. 14.19, Helmy et al. 2014c). The Kid metamorphic complex is a 4.5 km thick volcanosedimentary succession deposited in an active continental margin back-arc, remnant arc and intra-arc settings (Fowler et al. 2010 and references there in). The skarn-type Zn–Pb–As–Ag mineralization occurs in the Um Zeriq area that forms the lowest stratigraphic unit of the Kid group (Helmy et al. 2014c). The Um Zeriq Formation (>1500 m) consists of schists and phyllites derived from quartz-rich graphitic aluminous pelites and psammites, and feldspathic lithic greywackes. Carbonate and impure dolomites form minor components of pelites at a lower stratigraphic level. These lithologies are interbedded with lavas, pyroclastics and volcanogenic sediments. Abu El-Enen et al. (2003) showed that Um Zeriq pelites have similar compositions to those of active continental margin shales. Dating using the chemical Th–U-total Pb isochrone method yields a Th–Pb isochrone age of 660 ± 25 Ma for metamorphic monazite from metapelites (Helmy et al. 2014c).

The sulfide mineralization is located along shear zones and at the intersections of faults in three localities along Wadi Um Zeriq. The mineralizations are marked on surface by gossans, one of them (Um Zeriq 2) was traced in one drillhole (100 m depth) drilled by the Geological Survey of Egypt.

Two sulfide ore types define large-scale metal zoning; Cu–Zn–Co in calc-silicate rocks and Zn–Pb–As–Ag in metapelites (Fig. 14.19). The host rocks and the individual sulfide ore minerals have been intensely affected by amphibolite facies metamorphism (2.1–4.2 kbar and 500–620 °C) and deformational events, resulting in total obliteration of primary textures and the formation of textural and mineralogical modifications typical of metamorphosed base metal sulfide deposits. The metamorphic pressures and temperatures estimated from the sulfide mineral assemblage suggest that the sulfides underwent the peak-metamorphic conditions and later equilibrated during retrograde conditions (Helmy et al. 2014c).

Disseminated and massive sulfide occurrences consist of sphalerite, arsenopyrite, pyrite, löllingite, galena, and pyrrhotite, with variable modal proportions. Sphalerite geobarometry and arsenopyrite geothermometry, suggest peak metamorphic pressures of 3–3.6 kbar and temperatures of 540 ± 40 °C. Four silver-minerals are identified, i.e. freibergite "(Ag, Zn, Fe)$_{12}Sb_4S_{13}$", zoubekite ($AgPb_4Sb_4S_{10}$), miargyrite ($AgSbS_2$) and pyrargyrite (Ag_3SbS_3) in addition to another sulfosalt; boulangerite ($Sb_2Pb_2S_5$). Extensive involvement of metamorphic fluids is suggested by the complete transformation of the silicate mineral assemblage, in the vicinity of the sulfide mineral phases, to chlorite and the reconcentration of the original disseminated mineralization to massive sulfide bodies suggest. The preserved fabric is of a retrograde character, and the overall structural and textural relationships favor syntectonic formation during the main phase of deformation. Silver minerals suggest formation at low temperatures during retrograde cooling.

The Um Zeriq sulfide mineralization is structurally controlled and metamorphosed together with the host pelites at lower amphibolite facies conditions. Structural and textural modifications include deformation and re-equilibration of sulfide and host rock minerals, as well as redistribution of sulfide species. Silver-minerals are formed during retrograde cooling of the sulfide ore. Large metal and mineralogical zoning at Um Zeriq-Kid area are characteristic features of skarn deposits. The large-scale metal zoning reflects variable distances from the causative granitoid pluton(s). This area is highly prospective for Cu, Zn, Pb and Ag mineralization. For future exploration programs, emphasis should be placed on highly tectonized areas. The ore potentiality probably increases at depth (closer to the source).

14.5.3 Porphyry-Type Cu–Au Mineralizations

Since the early statement of Hussein (1990) on porphyry-type mineralizations in the Eastern Desert, few authors have investigated this type of mineralizations (Helmy and Kaindl 1999; Ahmed and Gharib 2016). These authors used field relations, petrographic observations and fluid inclusion data to characterize the mineralizing fluids of gold-copper bearing quartz veins, which are spatially associated with a granite-porphyry. Other important geologic features noted by later studies (Ahmed and Gharib 2016) include association with island-arc granite porphyry and volcanics, extensive deformation, zoned alteration zones and frequent abundance of gossans and copper staining along fault planes and joints.

Helmy and Kaindl (1999) noted four generations of genetically related quartz veins in the Hamash mine area. Two types of alteration are developed in vicinity of quartz veins; i.e., sericite-quartz-pyrite and chlorite-epidote-pyrite-sericite alteration. Pyrite is the major constituent while chalcopyrite, bornite, chalcocite and covellite are minor sulfides. Gold is present as inclusions in, or interstitial to, pyrite grains and as free-gold in quartz veins (Fig. 14.20).

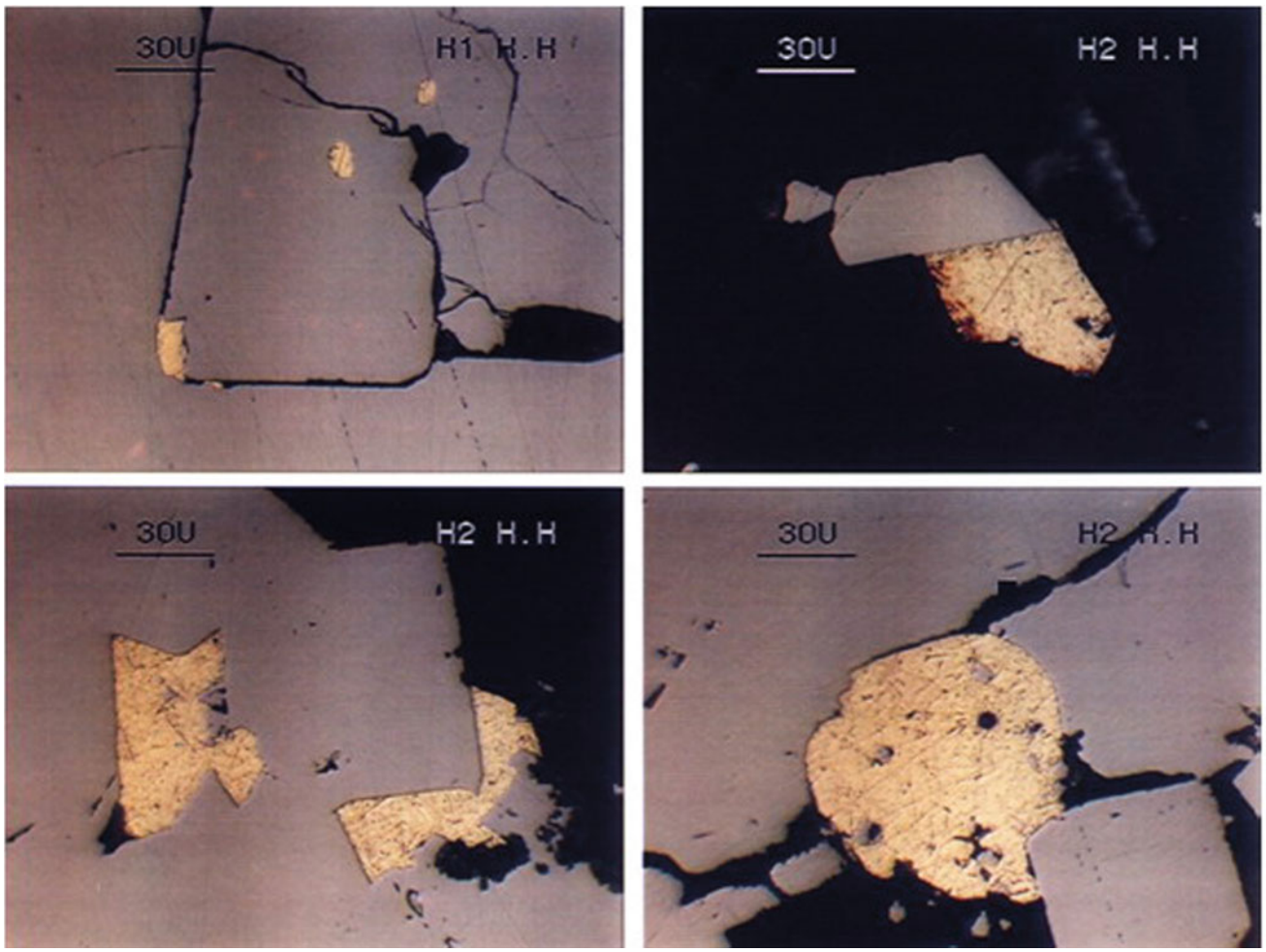

Fig. 14.20 Gold (yellow) textures in Hamash Cu–Au porphyry

Two types of fluid inclusions are distinguished: (1) primary H_2O–CO_2–CH_4–NaCl inclusions and (2) primary and secondary aqueous inclusions. Type I inclusions entrapped the end members of an unmixed fluid which consists of an aqueous phase and a CO_2-rich gas phase, respectively. Entrapment conditions of approximately 250 °C and 200 bars were estimated (Helmy and Kaindl 1999). Type II inclusions show low salinity (<9 wt% $NaCl_{eq}$) and a wide-range of homogenization temperatures (102° and 284 °C). Based on geological, mineralogical and fluid inclusion evidence, Helmy and Kaindl (1999) conclude that the Hamash Au–Cu mineralization shows a combination of porphyry- and epithermal-deposits characteristics. The metals including gold were probably transported as bisulfide complexes and precipitated due to wall-rock sulfidation, fluid mixing and phase separation.

At Hamata area, the Cu-porphyry mineralization occurs partly in a porphyritic granite intrusion and the surrounding altered arc mafic volcanics (Fig. 14.21). The mineralized rocks display simple ore mineral assemblages consisting of pyrite and chalcopyrite, with minor amounts of pyrrhotite, covellite, and sphalerite. Zoned alteration comprises: (1) propylitic alteration in the mafic volcanics; (2) phyllic-argillic alteration with extensive silisification of mafic volcanics; and (3) silica-potassic alteration, overprinted by phyllic-argillic ones. The mineralized outcrops have goethitic–hematitic capping with anomalous Cu values (up to 321 ppm). Ahmed and Gharib (2016) stated that the area is potential for a porphyry copper mineralization and recommended detailed exploration and further petrologic studies.

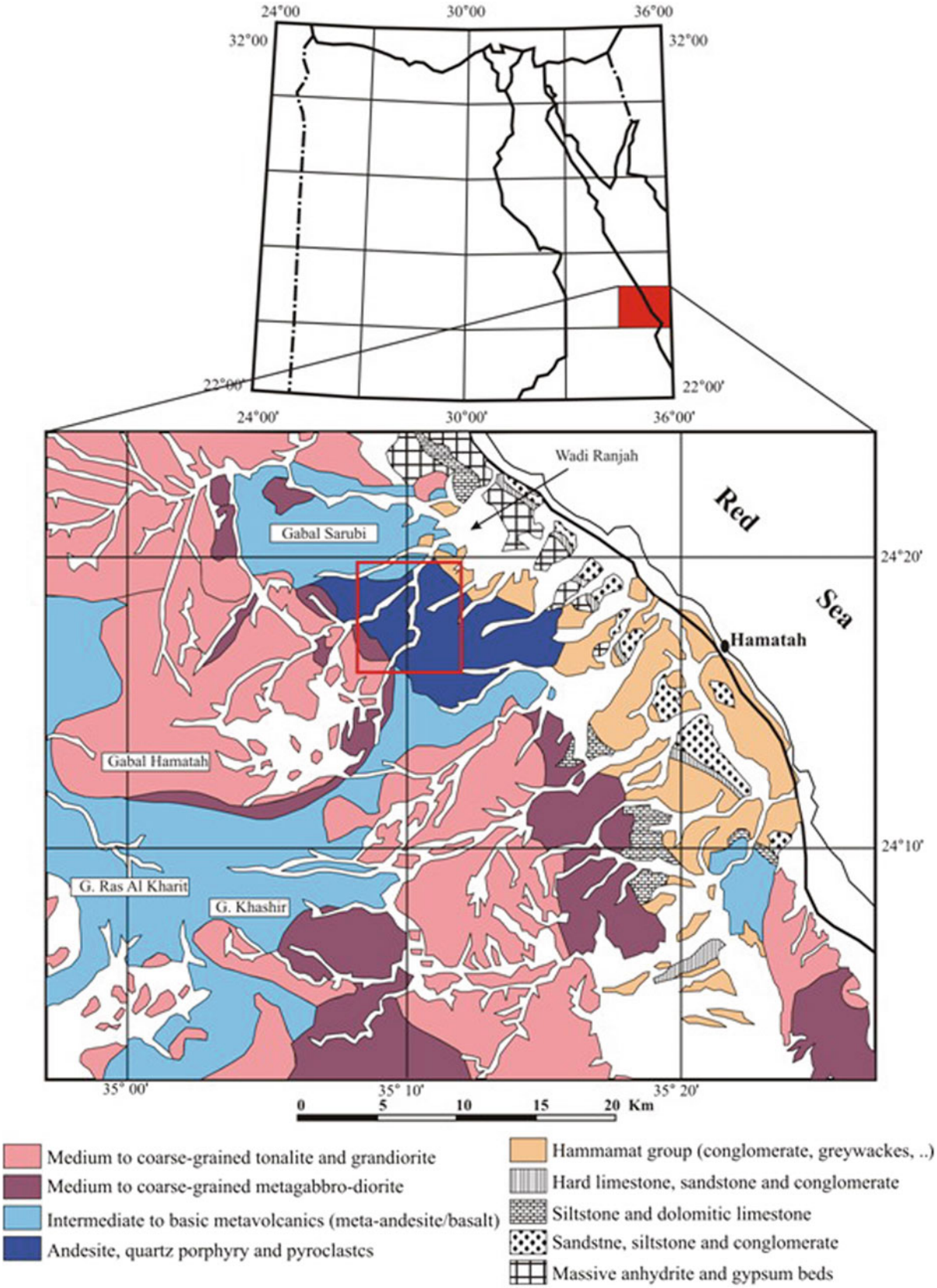

Fig. 14.21 Geological map of the Hamata area with the location of potential Cu-porphyry mineralization (red rectangular) from Ahmed and Gharib (2016)

14.6 Industrial Metal Oxides (Sn, W, Ta, Nb, and Mo)

Amr Abdelnasser

14.6.1 General Statement

Several huge mines in all over the world represent the main source of Tin (Sn), tantalum (Ta), niobium (Nb), tungsten (W), and molybdenum (Mo) metals are associated with pegmatite bodies as well as the rare-element granites (González et al. 2017). Examples of these mines are Yichun and Nanping in China (Huang et al. 2002; Rao et al. 2009), Greenbushes and Wodgina, in Australia (Partington et al. 1995; Sweetapple 2000; Fetherston 2004), Tanco, in Canada (Černý et al. 1996), Central Africa (Melcher et al. 2008, 2015, 2017), KolaPeninsula, in Russia (Pekov 2000), or Finland and French Central Massif (Boyd 2012).

In Egypt, these deposits are classified as mineralization related to plutonic rocks by Pohl (1984) either as albite-muscovite granites of calc-alkaline to peralkaline affinity having disseminated Ta–Nb–Sn in Abu Dabbab area, as pegmatites related to late granites having Sn, Be, Mo, U, Th, Nb, REE mineralization, or as quartz-carbonate veins related to granite cupolas having Au, Sn, W, Mo, Be and F in Igla area. Tin (Sn)-tungsten (W) deposits were first exploited in 1940 (Amin 1947). Their high potentialities are in the Central Eastern Desert (CED) of Egypt related to the younger albite granites (Abdel Meguid et al. 2003). They are associated with other rare metals e.g., Nb, Ta, Y, Zr, U, and rare earth elements (REEs) (Abdel Meguid et al. 2003). Sabet (1976) firstly described that these rare metals (Sn–W–Nb–Ta) were formed in association with albite granitoid plutons in CED of Egypt. These plutons (15 plutons) are characterized by small outcrops (<1 to 3 km^2) having domal-shaped (e.g., Nuweibi, Muelha, Zabara, Qash Amir), lensoid-shaped (e.g., HumrWaggat, Ineigi, Um Naggat), or stock-like (e.g., Igla, Abu-Dabab).

Genetically, this rare metal mineralization is related to the last stage of the granitic intrusions formed either by magmatic, post-magmatic or metasomatic processes (Schwartz 1992; Mohamed 1993, 2013b; Abdalla et al. 1998; Abdalla and Mohamed 1999). Černý (1989), Pollard (1989), and Fetherston (2004) divided the rare metal deposits into 4 types based on the host rock compositions: (1) peraluminous rare-element granitic pegmatites having Ta, Li, and Cs with Be, Sn, and Nb mineralization, (2) peraluminous rare-metal granites (known as; Li–mica albite granite, Li-F granites, or apogranites) having Ta and Sn with Be, Li, and Nb mineralization, (3) peralkaline granites and quartz syenites having Zr, rare earth element (REE), and Nb with Ta, Sn, U, and Th mineralization, and (4) Carbonatites and nepheline syenites having Nb, REE, P, and Zr with Ta mineralization. In Egypt, Hussein et al. (1982) who classified the Egyptian granites into G1, G2, and G3 granites stated that the Sn, W, Mo, Nb-Ta, REE, Be, and F deposits are mostly associated with the G3 granites, but some of them may also be associated with G2 granite masses. Moreover, Sabet et al. (1973) mentioned that the Sn–Nb–Ta–W–REEs mineralization is related to the albite granite (apogranite) exposed in Igla, Nuweibi, Abu Dabbab, and Humr Waggat areas. Some authors (e.g., El-Tabal 1979; Riad 1979; Asran 1985; Jahn et al. 1993; Helba et al. 1997) deduced that the rare-metal deposits are formed by the processes of the metasomatic alteration which affected the host granites (apogranites). Abdalla et al. (2008) determined two cassiterite types based on the types of host rock associations; magmatic and metasomatic albite granites. The metasomatized albite granite (apogranite)-related cassiterites have enhanced to moderate Nb, Ta, (with Nb/Ta ratios > 1), Ti, and FeO^{tot} and lower Ga_2O_3 (<0.01%). On the other hand, the magmatic albite granite-related cassiterites have a high concentration of Ta, Nb, (with Nb/Ta < 1 ratios), Ti, FeO^{tot}, and Ga_2O_3 (0.01–0.04%). However, the Sn–W deposits were mineralized at an estimated temperature about 320 °C and between 260–340 °C, and pressure up to 2.2 Kb and between 1.2–2.2 Kbar at Igla and Mueilha area, respectively (Mohamed and Bishara 1998; Mohamed 2013a). In the following paragraphs, the mineral deposits are dealt with are; Sn–W deposits, Nb–Ta deposits, and Mo deposits.

14.6.2 Tin (Sn)–Tungsten (W) Deposits

The tin-tungsten deposits have several mineralization styles (pegmatitic, hypothermal, and mesothermal) within different mineral facies (Amin 1947). Their lodes are mostly confined to the metamorphic rocks or at their contacts with granite. While the other veins mostly formed in diorites and granites. In these lodes, the paragenetic relationships between ore and gangue minerals suggest the sequence of mineralization started with feldspars, topaz, yellow mica, tourmaline, cassiterite, wolframite, fluorite, sericite, chlorite, and carbonate with more or less quartz (Amin 1947). These minerals (ore, alteration, and gangue) assumed the magmatic sourced-fluid have an alkaline affinity. These fluids, while the temperature-pressure relation was not in balance, were boiled along with the fractures leading to change their alkalinity. The changes in an alkaline state led to a temperature-pressure balance in which the metals deposited and therefore classified as xenothermal deposits (Amin 1947).

Tin (Sn) was used to produce bronze firstly by the ancient Egyptians who extracted it primarily from the Muelha mine. Tungsten (W) represents the secondary metal in the

importance occurring together with Sn. In CED, they occurred as vein-type mineralization in which cassiterite and wolframite formed in quartz veins with beryl, chalcopyrite, chalcocite, scheelite, huebnerite, malachite, covellite, azurite, chrysocolla, monazite, magnetite, galenite, sphalerite, tantalite-columbite, pyrochlore as ore minerals with alteration minerals e.g., albite, calcite, chlorite, fluorite, kaolinite, microcline, muscovite, orthoclase, rutile, sericite, tourmaline, topaz, zinnwaldite, and zircon (Hussein 1990; Abouzeid and Khaled 2011). The greisen alteration is the main post-magmatic alteration type which changed at the granitic contacts with metamorphic rocks into flakes and aggregates of mica, quartz, some fluorite, and topaz. It is associated with quartz veins in most deposits and monomineralic beryl and/or fluorite veins in other (Igla mines) which are distinct fracture-fillings mostly directed NE-SW steeply dip to SW, and genetically related muscovite granite masses (El-Ramly et al. 1970). The well-known Sn–W deposits in CED are Abu Dabbab, Igla, Nuweibi, and Muelha (Fig. 14.22) with particular occurrences such as Abu Hammad, Abu Kharif, El Dob, Fatira El-Beida, Maghrabiya, and Umm Bissilla. At these deposits, the cassiterite associated with B, Nb–Ta, W, and other lithophile elements which occurred as disseminated mineralization within the greisenization zone of the altered apogranites (Bugrov et al. 1973). Therefore, the Sn–W deposits in Egypt are vein-type and disseminated mineralization type.

Abu-Dabbab deposit is located at about 30 km north Marsa Alam in the CED of Egypt (25°20′ 27″ N, 34°32′20″ E) (Fig. 14.22). It has three main wadis; Wadi Mubarak, Wadi Abu-Dabbab, and Wadi Dabr. This area made up of ophiolitic mélange intruded by syn-orogenic metagabbro-diorite complexes and granitoids, that later intruded by late to post-orogenic granitoid intrusions (Fig. 14.23a). Also, this area contains post-accretionary volcanic and molasses-type sedimentary rocks (Helba et al. 1997; Abdalla et al. 1998; Ali 2003; Gaafar and Ali 2015). Abu Dabbab area represents mainly vein-type Sn deposits with Nb-Ta associations. The tin-bearing granitoid is the post-orogenic granitoid which is lithium albite granite (apogranite). It characterized by small stocks (ranging from 0.2 to 4 km^2 in area), with circular to dike-like outcrops.

It composed mainly of snowball quartz with albite inclusions in a white matrix of fine-grained and randomly oriented albite, K-feldspar, Li-mica, topaz and quartz with some accessory minerals e.g., columbite-tantalite, cassiterite, wolframite, beryl and traces of minute zircon crystals (Gaafar and Ali 2015). The cassiterite-bearing quartz vein and veinlets (ranging from 10 to 50 cm thick and 50 to 600 m length) traverse the contact between the metamorphosed rocks and the aplitic intrusion. This lode of mineralization is slightly deformed and locally dislocated by faults having displacements of 3–4 m (Amin 1947). Many authors (e.g., Sabet et al. 1973, 1976; Sabet 1976; Abouzeid and Khaled 2011) and projects e.g., (Gippsland) estimated the ore reserve in Abu Dabbab tin with Nb and Ta mineralization. They estimated 16,000 tons of ore in the veins and 500,000 tons of alluvium at 0.1% Sn in the wadis. Also, 0.027% Ta_2O_5, 0.020% Nb_2O_5, and 0.017% Sn are determined in 7.3 million tons of ore according to Gippsland report 2005.

The Igla Mine is located at 22 km from the Red Sea coast (40 km byroad), in CED at Lat. 25°06′ N and Long. 34°38′ 40″ E (Fig. 14.22). This area is made up of acid to intermediate volcanic and tuffs intruded by a small mass of apogranite (mostly tin-bearing lithium albite granite) (Fig. 14.23b). Its Sn–W mineralization was prospected and exploited during the 1940s with Abu Dabbab area. It is similar to Abu Dabbab deposit in the mode of occurrence in which the mineralized veins traverse the contact of gray-granite-diorite mass with the metamorphic rocks consisting of intercalation of greenstones, chloritic or pure mudstones and diabase (Amin 1947). These mineralized quartz veins related to this apogranite, contain cassiterite and wolframite with beryl directed mostly NE-SW dipping to SE. The related alteration is greisenization containing zinnwaldite, tourmaline, and fluorite. The ore mineralogy includes cassiterite crystals (occurred at vein contacts with the altered zone) and wolframite (occurred inside the veins) with some chalcopyrite, secondary malachite, tantalite-columbite, thorianite, and monazite (Kochine and Bassyuni 1968). The estimated ore reserve is about 1700 tons as a proven one having 7 tons of metallic tin, while 60 ton Sn as a probable reserve (Hussein 1990).

The Muelha area is located also in the CED at 24°52′ N, 34° 00′ E (Fig. 14.22), in which a tin-bearing stock is represented by biotite granite which intruded in the metasediments (Abdalla et al. 2008). At the southwestern contact of this granite with the metasediment, it was affected by alteration especially albitization and greisenization with subordinate silicification, and Li-muscovitization (Hussein 1990). The greisen zones are structurally-controlled associated with fractures at the intersection of NE- and NW-trending faults containing mica-bearing quartz veins and lenses having cassiterite, wolframite, fluorite, columbite, scheelite, and chalcopyrite. The geochemical analyses revealed that Sn values range from 0.1 to 0.3%. Other elements present are Nb (up to 300 ppm) and Be (100–1000 ppm). Anomalous values of W were sporadically spread, and high values of Bi (100–1000 ppm) were found only in quartz veins with sulfide mineralization. The zone of mineralization was checked with three shallow holes (45 m each) and Sn was found to average 0.1%. This mine is considered uneconomic because of the limited reserve and the low grade of ore, therefore wadi deposits (alluvium) were tested around Gabal Muelha and concluded that the panned samples contain cassiterite with magnetite, zircon, columbite, garnet, and ilmenite (El-Ramly et al. 1970; Hussein 1990). The cassiterite

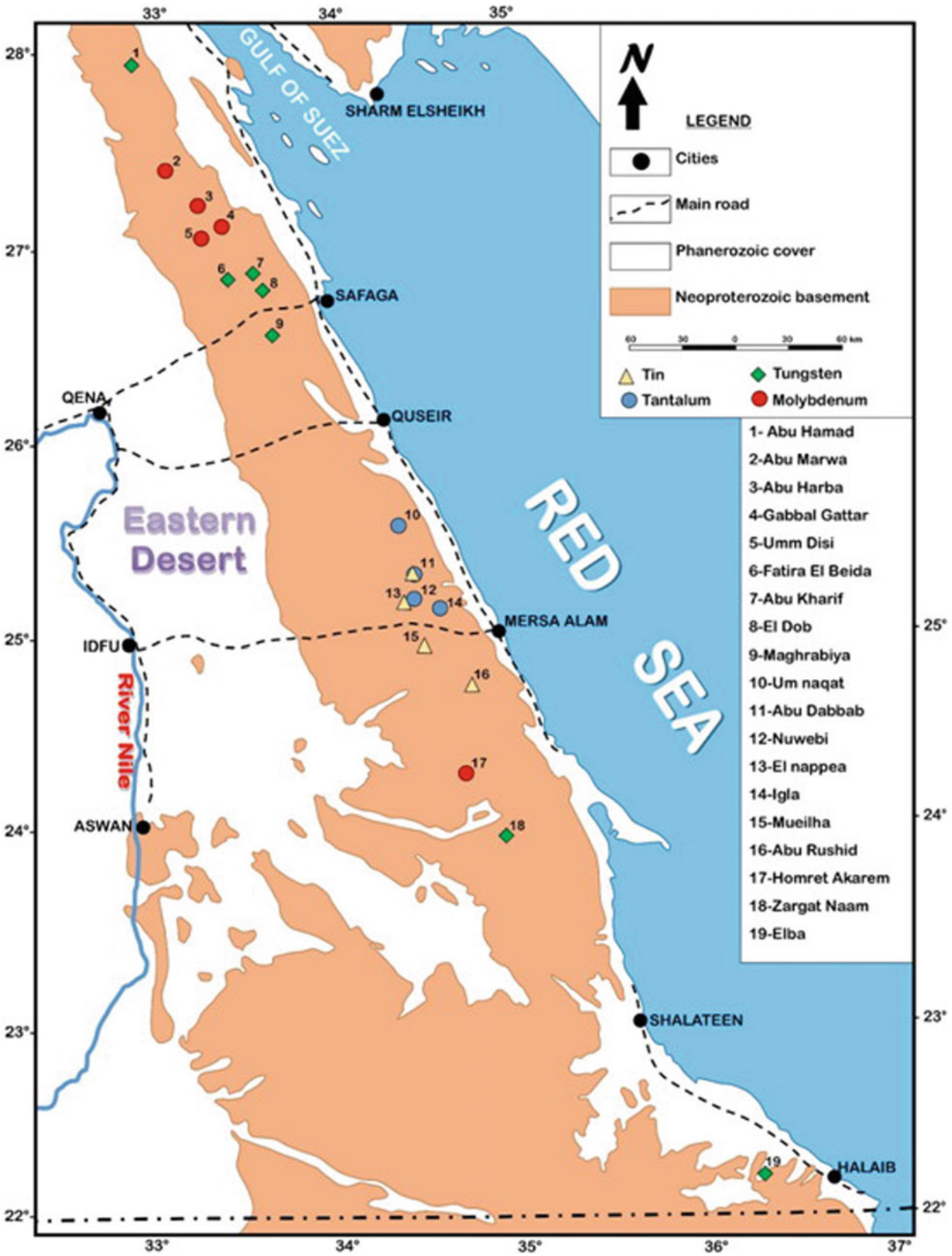

Fig. 14.22 Occurrences of tin, tungsten, tantalum, and molybdenum deposits in the Eastern Desert of Egypt, compiled from EGSMA (1998)

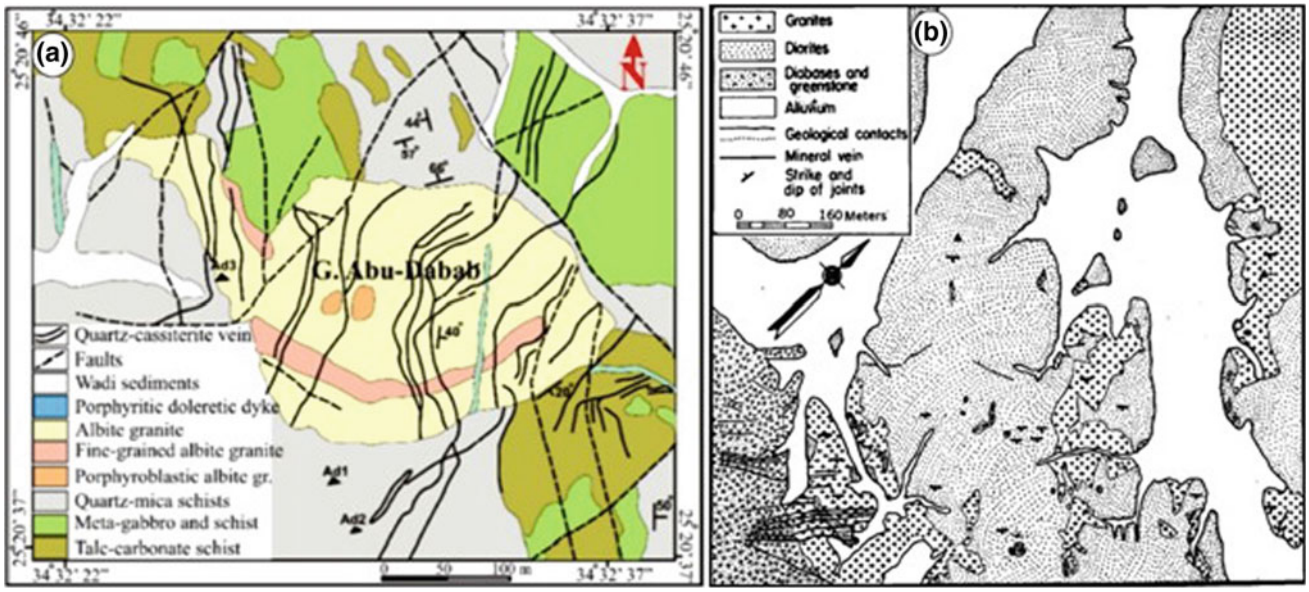

Fig. 14.23 Geologic map of **a** Abu Dabab area, CED, Egypt, modified from Sabet et al. (1976), **b** Igla Mine after Amin (1947)

content is about 500 gm/m^3 in a total volume of alluvium about 100,000 m^3, therefore the alluvial cassiterite is about 500 tons (Hussein 1990).

The above-mentioned areas are mainly tin mineralization with subordinate tungsten, while the tungsten mineralization is mainly in some area e.g.: Abu Hammad, Fatira El Beida, Abu Kharif, El Dob, Maghrabiya, Um Bisilla, Zargat Naam, Gash Amer, and Gabal Atud. Tungsten mineralization in these areas has mostly occurred as vein-type mineralization.

The veins in the Abu Hammad area (27°31′ N, 33°20′ E) (Fig. 14.22) are 14 veins associated with red granite that cut by dolerite dikes. They are nearly vertical ranging from 2–30 cm thick consisting mainly of quartz with feldspar and mica as well as wolframite and subordinate scheelite as ore minerals. The WO_3 content in the wolframite ranges from 46.4 to 69.05% without any reserve estimation (Dardir and Abu Zeid 1972).

While in the Fatira El Beida area (26°48′ N, 33°20′ E) (Fig. 14.22), the quartz veins are characterized by 10–30 cm thick and up to 500 m long trending NE-SW dipping 30° toward NW, which contain less amount of wolframite and associated with granite that cut by basic dikes (Hussein 1990).

On the other hand, the Abu Kharif area (26°48′ N, 33°25′ E) (Fig. 14.22) has two sets of wolframite-bearing quartz veins; the older one directed E-W dipping 30° toward N ranging from 20 to 150 cm thick and up to 150 m long consisting of quartz with irregularly distributed wolframite pockets. The younger one is directed NE-SW dipping nearly vertical to the NW consisting of quartz with orthoclase, fluorite, mica, and less amount of wolframite (Hussein 1990).

In the El Dob area (26°27′ N, 33°28′ E) (Fig. 14.22), the wolframite-bearing quartz veins are locally associate with the greisenized granite directed NE-SW dipping toward the SE ranging from 20 to 45 cm thick up to 1 km long. They composed mainly of milky quartz with orthoclase, mica, and irregularly distributed pockets of wolframite.

The Maghrabiya area, which is located at lat. 26°22′ N, and long. 33°27′ E (Fig. 14.22) contains three wolframite-bearing quartz veins cut through locally greisenized and kaolinized granite, trending N-S and/or NE-SW dipping nearly vertical to the west and extending up to 150 m long and 30 cm thick. Wolframite represents the only ore mineral irregularly distributed in these veins and has 52% WO_3 content (Hussein 1990).

The Um Bisilla area (25°21′ N, 34°01′ E) (Fig. 14.22) is made up of mineralized small quartz veins cut through muscovite-albite apogranite which intruded into the Hammamat sediments and volcanics. These veins directed NW-SE dipping toward NE composed essentially of quartz with subordinate calcite, chlorite, muscovite and barite. The ore mineralogy includes wolframite with subordinate magnetite, pyrite, chalcopyrite and malachite. El-Ramly et al. (1970) revealed that these veins have 0.006 to 0.01% W with very limited reserves.

The Zargat Naam (23°46′ N, 34°41′ E) and Gash Amer (22°18′ N, 36°12′ E) areas (Fig. 14.22) are limited in tungsten mineralization in which small wolframite-bearing formed either in the marginal contact of the granitic masses in the Zargat Naam area or along the fissure in younger granite in the Gash Amer area (Hussein 1990).

In the Atud area (Fig. 14.22), the wolframite is associated at the base of the Gabal Atud with auriferous quartz veins which are characterized by 30 cm thick and 20 m long directed NW-SE in the altered gabbro-diorite mass

(Saleeb-Roufaiel and Fasfous 1970). The ore mineralogy includes arsenopyrite, pyrite, pyrrhotite, goethite, and native gold with wolframite, tungstinite, scheelite, and rutile (Saleeb-Roufaiel and Fasfous 1970).

14.6.3 Niobium (Nb)–Tantalum (Ta) Mineralization

Niobium (Nb) and tantalum (Ta) mineralogy include economically important species of oxide minerals. These oxide species formed in widespread different genetic classes of deposits, while the silicate Nb and Ta species formed exclusively in the metasomatic suites of anorogenic rock type as well as in the peralkaline igneous suites (Černý and Ercit 1989). On the other hand, the phosphate and borate species of Nb and Ta are extremely rare. In Egypt, the Nb–Ta species are mostly oxides that are locally associated with the Sn–W deposits. In the 1960s, in the Abu Rusheid area, the Nb–Ta mineralization was first detected during the ground verification giving radiometric anomalies (Krs et al. 1973). Beside the Abu Rusheid area, this type of mineralization was also detected in the Abu Dabbab, the Nuweibi, and the Um Naggat areas in the CED of Egypt (Fig. 14.22).

The Abu Rusheid area (24°37′09″ N, 34°46′04″ E) (Fig. 14.23) is one of the high potential area in rare-metal mineralization including Nb, Ta, Sn, U, Th, and Zr metals hosted in the peralkaline granitic rocks. These mineralized granitic rocks were previously named psammmatic gneisses by Hassan (1964), El-Gemmizi (1984), Hilmy et al. (1990), Saleh (1997). These authors considered the Abu Rusheid area to have radioactive potentiality in addition to Nb–Ta mineralization. The Abu Rusheid area (Fig. 14.24a) is located at the NE of the Nugrus shear zone which belongs to the huge Sikait-Nugrus fault systems separating the high-temperature metamorphic rocks of the Hafafit complex from the low-grade ophiolitic and arc volcanic assemblages (Bennett and Mosley 1987; Greiling et al. 1988). Ali et al. (2011) stated that the Nb, Ta-, Sn-, U-, Th-, and Zr(Hf)-bearing mineralized zone that hosted in the granitic rock occurred in the Abu Rushied shear brittle-ductile zone area trending SSE. They reported two shear zone; the northern and southern ones, which cut through the peralkalic granitic gneisses and cataclastic to mylonitic rocks, and locally have least altered lamprophyre as well as sheared granitic aplite-pegmatite dykes. The mineralizing event was magmatic (629 ± 5 Ma, CHIME monazite) and later hydrothermal alteration which precipitates the Nb–Ta-bearing cassiterite with the REEs and radioactive elements (Ali et al. 2011). While, Raslan and Ali (2011) revealed that the Nb–Ta multi-oxide minerals (e.g., fergusonite, ishikawaite, and uranopyrochlore) occurred with uraninite, thorite and cassiterite as abundant inclusions in the recorded Hf-zircon and ferrocolumbite minerals that were formed in the Abu Rusheid pegmatites. The mineralization event started with the magmatic processes then followed by hydrothermal processes causing the precipitation of Nb-Ta multi-oxide minerals (Raslan and Ali 2011). The analyzed ore samples from the Abu Rusheid area have 0.3% Nb_2O_5 with a reserve of

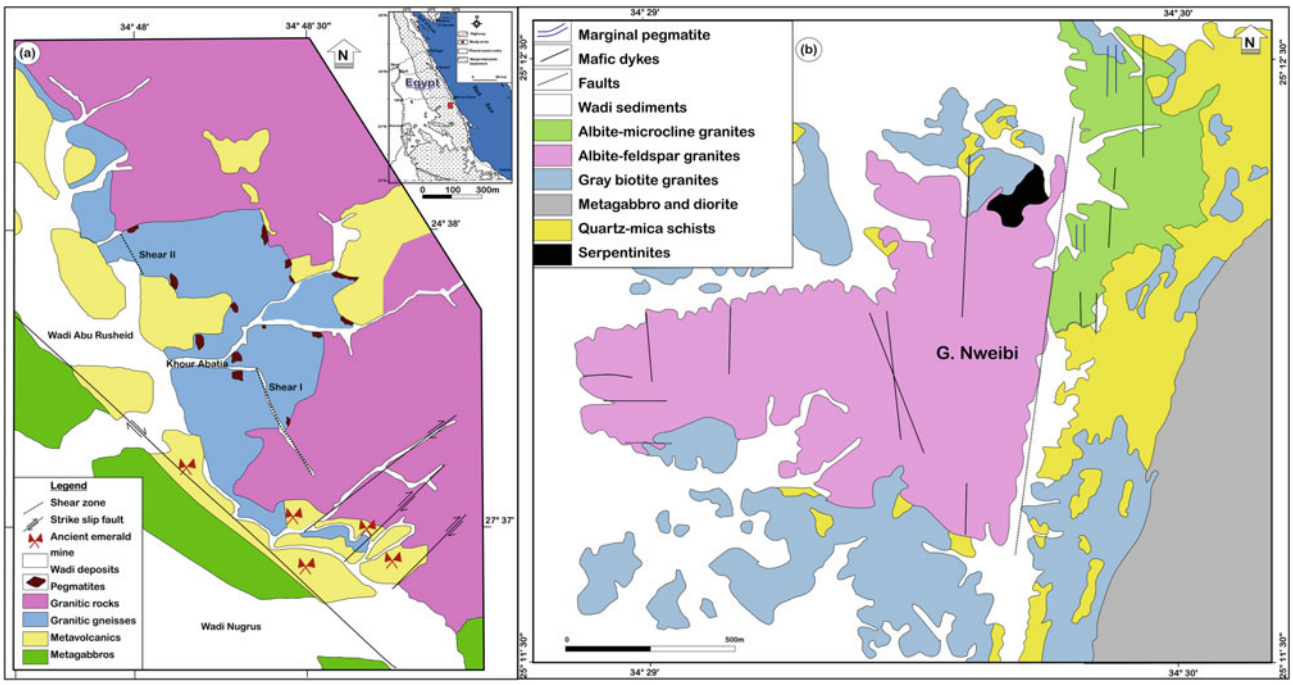

Fig. 14.24 Geological map of **a** Abu Rushied area, modified after Ibrahim et al. (2004a, b), **b** Nuweibi area, modified after Gaafar (2014)

90,000 tons of Nb_2O_5 and 0.033% Ta_2O_5 with 13,000 tons of Ta_2O_5 as a reserve estimation (Hussein 1990; Abouzeid and Khaled 2011).

The Abu Dabbab area is the most important Nb–Ta–Sn mineralization hosted in the apogranite stock which intruded in the quartz-biotite and quartz-chlorite schists with intercalated beds of tuffs and agglomerate (Hussein 1990). The ore reserve in Abu Dabbab area is previously mentioned in the last section according to Gippsland report 2005.

The Nuweibi area (25°12′ N, 34°30′ E) (Fig. 14.22) is in the CED in Egypt, 30 km north of the Marsa Alam and about 33 km west of the Red Sea coast. This area is made up of metasediments, serpentinites, metagabbros, grey granites, albite granites, post and pre-albite granite dykes (Fig. 14.24b) (El-Tabal 1979). The Nb–Ta mineralization in the Nuweibi area is mainly disseminated in the apogranite rocks as well as within quartz-cassiterite veins and greisenization alteration (Abouzeid and Khaled 2011). Therefore, the ore mineralogy includes columbite and tantalite with less amount of cassiterite, magnetite, ilmenite, zircon, topaz, and barite, and rarely apatite, rutile and monazite disseminated in the intensively albitized and mineralized zones in apogranite rocks (Hussein 1990; Abouzeid and Khaled 2011). Moreover, Gaafar (2014) studied the radioactive minerals in Nuweibi area that include uranothorite, thorite, zircon, and monazite associated with the Nb–Ta bearing minerals represented by columbite and tantalite having a Ta content up to 65.4 wt% Ta_2O_5 and a Nb content up to 60 wt% Nb_2O_5 based on the microprobe analyses. Naim et al. (1996) estimated the ore reserve in Nuweibi area of 114.7 million tons of low-grade ore with 0.022% Ta_2O_5, and 0.2% Nb_2O_5 (Abouzeid and Khaled 2011).

14.6.4 Molybdenum (Mo) Mineralization

The granites associated with the molybdenum mineralization were likely formed by partial melting of the earlier igneous rocks (Öhlander 1985). The molybdenite with chalcopyrite and galena deposited with columbite, wolframite, cassiterite, and sphalerite and associated with mainly K-metasomatism and greisenization and subordinate silica metasomatism (Kinnaird et al. 1985). Accordingly, these ore metals and granite magma were likely originated from the Pan-African continental crust with contributions from the mantle (Kinnaird et al. 1985). The molybdenum mineralization is also formed at a higher temperature ranging from 530 to 210 °C and related to veins filled with quartz + fluorite formed mostly in the porphyry system (Carten 1988; Carten et al. 1988; Seedorff and Einaudi 2004). In Egypt, the occurrences of molybdenite-bearing quartz veins which cut through the 'Pink granite' distributed in the NED in six localities; Gabal Gattar, AbuHarba, Wadi Dib, Abu Marwa, Umm Disi, and Homret Akarem (Fig. 14.22) (Hume and Greaves 1937; Dardir and Gadalla 1969).

Gabal Gattar area (27°05′29″ N, 33°16′10″ E) (Fig. 14.22) represents the largest Mo mineralization in Egypt, in which mineralized quartz veins ranging from 1 mm to 10 cm thick cut through the pink granites of the Gabal Gattar form a zone with 25 m wide and 500 m long. These veins are affected by pinch and swell and bifurcation striking N 10° E dipping 80° to the east (Hussein 1990). The molybdenite occurred either in the quartz veins or in the enclosing granite as disseminated coarse crystals ranging from 1 to 3 cm in size referring to the mineralized fluids shortly followed the intrusion of quartz veins (Dardir and Gadalla 1969). Helmy et al. (2014a, b) studied the Mo–Bi–Ag and U–F mineralization in Gabal Gattar area and concluded that they are hosted in fractionated and hydrothermally altered A-type granites and are genetically related, but they have different direction; Mo–Bi–Ag ore hosted in NS quartz veins, while batches and micro-veinlets of U–F mineralization controlled by NNE to NW trending structures. Helmy et al. (2014a, b) stated also that the precipitation of Mo, Bi and Ag is earlier from the saline fluids due to cooling, fluid mixing and wallrock sulfidation, while the precipitation of the U–F minerals is from the low salinity fluids after high input of meteoric water. The mineralized (F-rich) fluid originated from the last stage of granite crystallization, and the deposition of ore metals occurred in a shallow hydrothermal system (Helmy et al. 2014a, b). The ore reserve estimated ranged from 0.27 to 2.25% Mo with about 4500 tons (Hussein 1990).

The Abu Harba (27°18′20″ N, 33°12′45″ E), the Abu Marwa (27°20′20″ N, 33°05′45″ E), the Umm Disi (27°00′ N, 33°31′ E), and the Wadi Hafia (24°56′40″ N, 34°07′46″ E) areas are smaller Mo occurrences in which Mo-bearing quartz veins cut through greisenized granite ranging from 5 to 10 cm thick (Dardir and Gadalla 1969). There is no grade and ore reserve estimated.

The Homret Akarem area (24°11′08″ N, 34°04′39″ E) (Fig. 14.22) is located in the CED and is made up of metasediments intruded by granitic rocks dissected by lots of cassiterite-bearing quartz veins having high concentrations and anomalies of Mo, Bi, Cu, and Nb with Sn (Bugrov 1968). At this area, the mineralization style is vein-type in a zone of 1100 × 800 m in the granitic mass. These veins range from 1 cm to 2 m thick bordered by greisenization alteration zones. The textural and mineralogical studied revealed that Mo occurred in the mineralized core surrounded by a zone of cassiterite mineralization then Cu-mineralization in the outer side (Hussein 1990). The ore reserve and grade were estimated from the geological, geochemical, and geophysical studied from five drill holes (totally 1357 m) detected the high potential and promising

anomalies (Searle 1974). Accordingly, molybdenite is the most common mineral of economic importance with an average ore grade 0.031 Mo, and the reserves at about 8,000,000 tons (Searle 1974).

14.7 Chromite Deposits in Egypt

Ahmed Hassan Ahmed

14.7.1 Introduction

Chromite deposits are the solely primary source of chromium metal. The mineral chromite, used hereafter as "chromian spinel", is one of end members of the spinel group. The ideal formula for spinel is AB_2O_4, where "A" site filled by divalent cations, and "B" site filled by trivalent cations. Most common constituents in spinels are; Mg^{2+}, Fe^{2+}, Cr^{3+}, Fe^{3+} and Al^{3+}, while less common and usually minor cations are Mn^{2+}, Ti^{4+}, V^{3+}, Ni^{2+}, Co^{2+} and Zn^{2+}. The chromite ore occasionally named as "chromitite" ore, where two principal economic deposit types of chromitite exist: (i) Stratiform chromite deposits are typically located in stable continental shield environments. This type of chromitite hosted in layered igneous intrusions such as those of the Bushveld Igneous Complex, South Africa (Barnes and Maier 2002). (ii) Podiform chromite deposits that occur in the upper mantle peridotites and crustal rocks of ophiolites. The ophiolitic chromitites are present either as layers at the base of the magmatic cumulates or, more typically, as dykes, disc shaped lenses and pods in upper mantle peridotites (Stowe 1994; Arai and Ahmed 2018). In the Arabian-Nubian Shield, in general, and in the Egyptian basement complex, in particular, chromite deposits are of the latter type (podiform or ophiolitic chromitite). Ophiolites are occasionally found as dismembered sequences in the Arabian–Nubian Shield, which are now found in many cases as tectonic mélanges. The mineralogical and geochemical characteristics of the dismembered mantle sections (e.g., chromitites and peridotites) are helpful to predict the tectonic environments in which the ophiolitic complexes were formed. The podiform chromitite is now widely interpreted as a product of interaction between mantle harzburgite and uprising exotic basaltic melt (e.g., Arai and Yurimoto 1994; Zhou et al. 1994; Arai 1997). The genesis of podiform chromitite is one of the important igneous processes within the upper man-tle, and the mode of its formation will give constraints on the physico-chemical conditions as well as on the style of melt migration in the upper mantle (e.g., Lago et al. 1982; Leblanc and Ceuleneer 1992). In this section, I summarize the distribution of chromitite deposits and their ultramafic host rocks in the Egyptian ophiolite complexes. The petrological characteristics, including mineral chemistry and platinum-group elements (PGE) distribution and mineralogy, of the chromitite deposits and their host peridotites are discussed in detail to constrain their tectonic settings of formation.

14.7.2 Distribution of Chromitite Deposits and Host Rocks

The ophiolite and ophiolitic mélange rocks are distributed mainly in the central (CED) and southern (SED) parts of the Eastern Desert (Fig. 14.25). The late Proterozoic ophiolite complexes of Egypt consist of highly dismembered mafic-ultramafic association which is located mainly to the south of latitude 26° N and their distribution is very irregular along the Red Sea coast. The main outcrops of the ultramafic complexes in the CED and SED display several forms and sizes; as huge continuous masses like those of Gerf and Abu Dahr areas, as lensoidal masses in many areas, and as elongated thrust slices of many others (Fig. 14.25). In addition to the main ultramafic outcrops, small squeezed ultramafic lenses and irregular bodies can be also observed incorporated within the neighboring immature metasediments of the ophiolitic mélange. Chromitite pods of sub-economic value are common in almost all the serpentinized ultramafic rocks in the CED and SED of Egypt (e.g., Ahmed et al. 2001; Ahmed 2013). They occur mainly as small and irregular bodies of variable sizes and shapes (Fig. 14.26a, b) that in most cases are hosted by fully serpentinized peridotites, mainly harzburgite and subordinate dunite envelopes. The size of chromitite pods varies from few centimeters up to few tens of meters in many localities; the largest pods are found in the Abu Dahr area up to 50 m across, located at the top of Gebel Abu Dahr, which is already mined out for the last 50 years by the Egyptian Refractory Company. Continuous and discontinuous boudinaged chromitite lenses (Fig. 14.26b), up to several meters thick and few tens of meters long, are located at many places within talc-carbonate and serpentinized ultramafic rocks of the CED and SED of Egyptian Proterozoic ophiolites. The SED chromitite pods, in most cases, are larger in size than the CED examples. Many of the known chromitite pods have been worked out, but some others are still intact. More details about the distribution of chromitite deposits and their host ultramafic rocks can be found in the literature (e.g., Hussein 1990; Ahmed et al. 2001; Ahmed 2013; Khedr and Arai 2013, 2016).

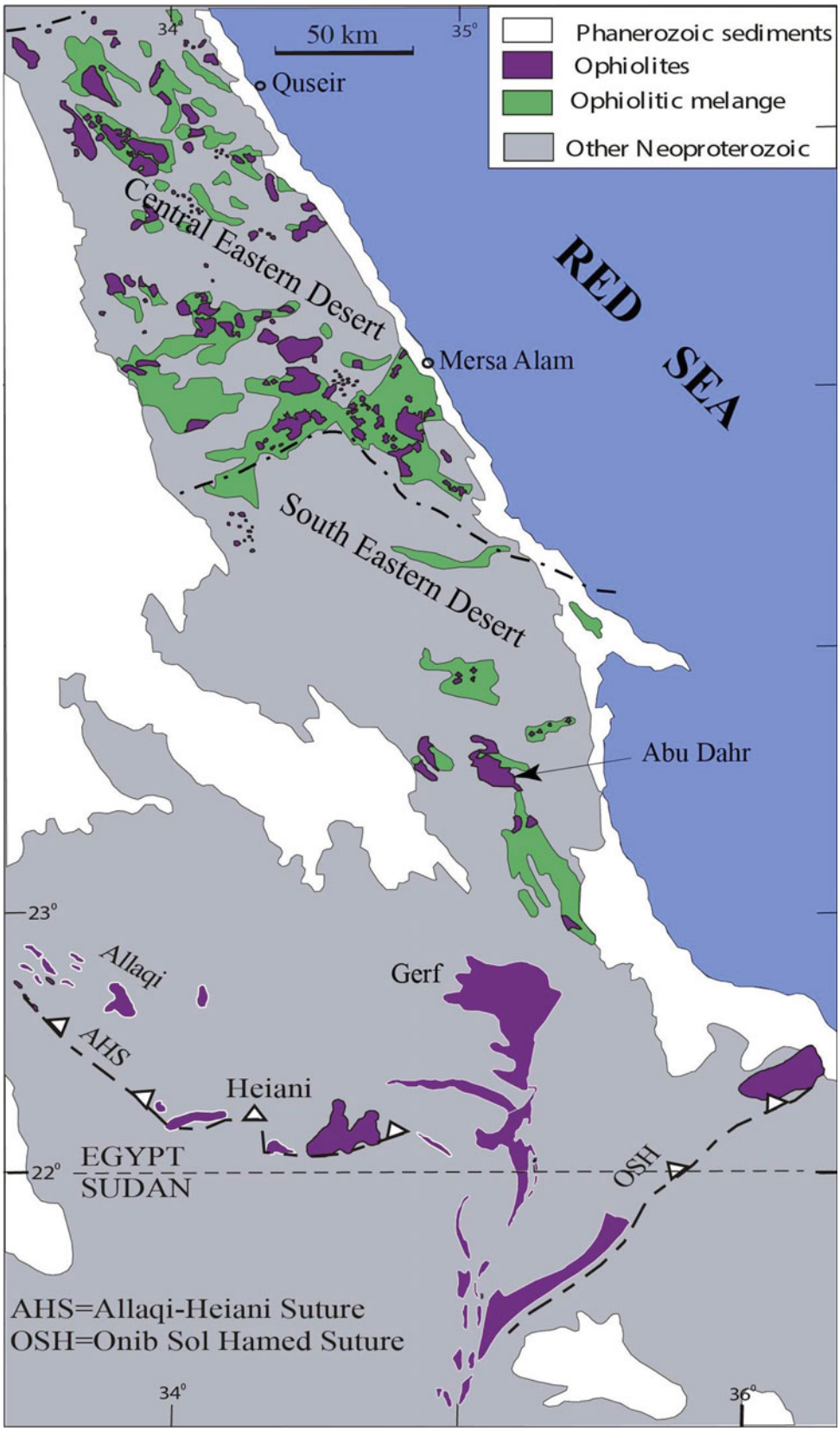

Fig. 14.25 Geologic map of the Eastern Desert of Egypt showing the distribution of ophiolites and ophiolitic mélange where podiform chromitites are located (modified from Azer and Stern 2007)

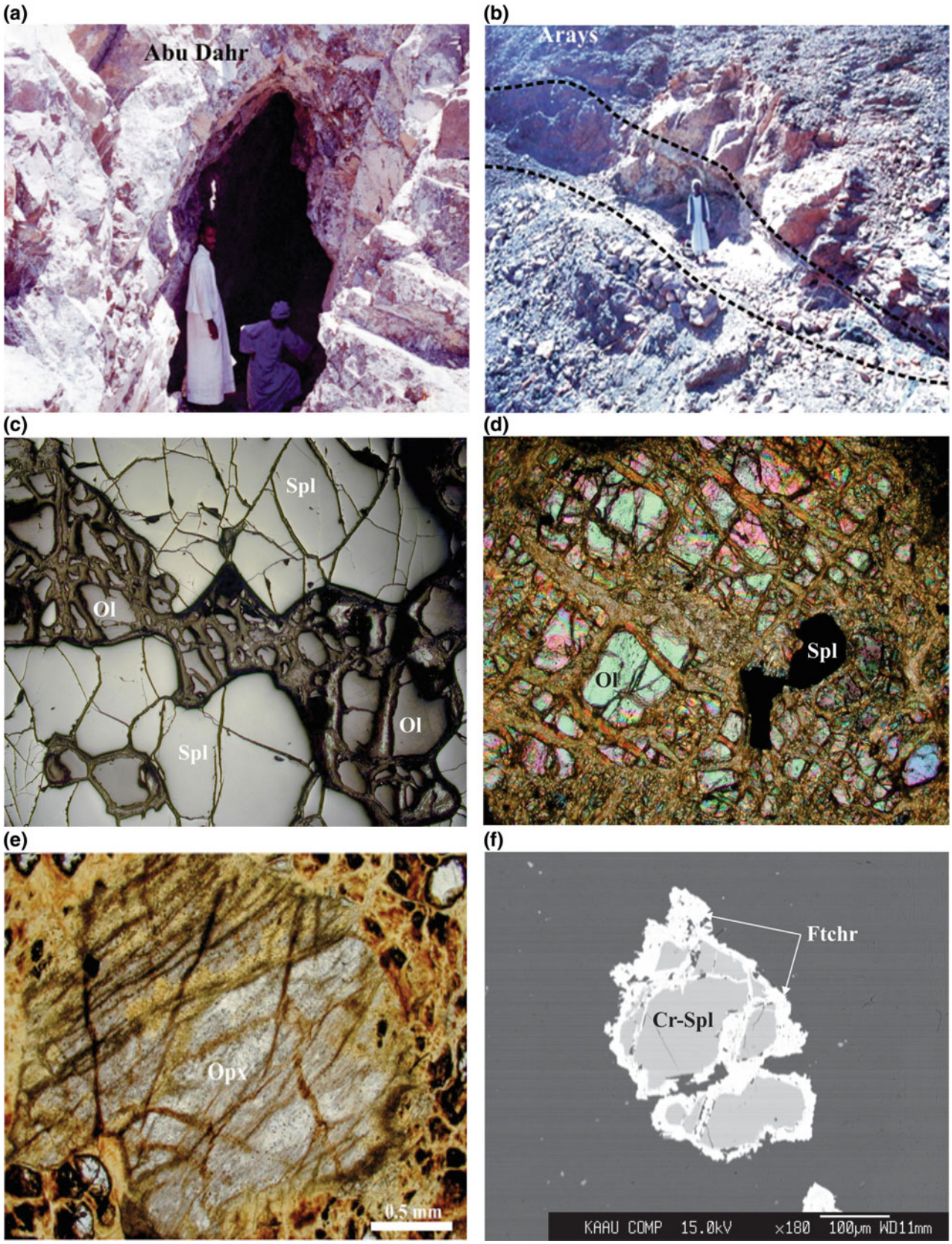

Fig. 14.26 **a**, **b** Field photographs of worked-out podiform chromitites from the Eastern Desert of Egypt. **c** Fresh olivine (Ol) in the interstitial matrix of Abu Dahr chromitite chromian spinel (Spl), reflected light. **d** Relatively fresh peridotite of Abu Siayil, SED, crossed Nicole. **e** Fresh orthopyroxene (Opx) of Arays peridotite, SED, polarized light. **f** Back-scattered image of chromian spinel (Cr-Spl) altered to ferritchromite (Ftchr) from harzburgite of Abu Dahr area, SED, Egypt

14.7.3 Petrography and Geochemistry of Chromitites and Ultramafic Host Rocks

Chromitite pods of both CED and SED localities display different types including massive, disseminated, nodular and anti-nodular tex-tured ores. The massive chromitite contains >90 volume% chromian spinel, the semi-massive and disseminated chromitites contain about 20–90 volume% chromian spinel, which is more euhedral in shape and smaller in size than in the massive one. Chromian spinels of both massive and disseminated types are generally highly fractured and sometimes mylonitised with gangue minerals of serpen-tine and chlorite. In most cases, chromian spinel grains of massive chromitite show either no or slight zonation of ferritchromite and Cr-rich magnetite. In the CED localities, silicate minerals (olivine and/or pyroxenes) in the interstitial matrix are almost altered to secondary minerals (serpentine and chlorite), while in some places of the SED chromitites (Abu Dahr, Abu Siayil, and Arays), the primary silicate minerals are still preserved (Fig. 14.26c) in the interstitial matrix (e.g., Ahmed et al. 2001; Ahmed 2013; Khedr and Arai 2013, 2016). Dunite envelopes and harzburgite host of the chromitite lenses are in most cases fully serpentinized as in the CED localities, while they are relatively fresh with remnants of primary olivine and orthopyroxene in the SED localities (Fig. 14.26d, e). The dunite envelopes and harzburgite host contain about 2 volume% chromian spinels, which display euhedral to anhedral crystals. In relatively fresh rocks, the chromian spinels are less altered whereas in the highly serpentinized peridotites the ferritchromite and Cr-rich magnetite are much abundant in chromian spinel rims and along the cracks (Fig. 14.26f).

Chromian spinel, in most cases, survives metamorphism and is frequently the only reliable indicator of the primary mantle lithology. In terms of the location and chromian spinel chemistry, there are two distinct types of chromitite in the Eastern Desert of Egypt; the CED chromitites and the SED ones. The earlier chromitite types (CED) have a wide compositional range of chromian spinel chemistry; ranges from high-Al to high-Cr types (Cr# = Cr/(Cr + AL) varies between 0.5 up to 0.9), whilst the latter chromitites (SED) consist of very refractory high-Cr chromian spinels, Cr# > 0.8 (Fig. 14.27a, b). Almost all the chromitite pods from the CED and SED localities are closely located to the Cr–Al join of the Cr–Al–Fe ternary diagram and they display wide range of Al–Cr contents in the CED case, but high Cr variety in the SED case, and both of them show low Fe^{3+} contents (Fig. 14.27a). They are all entirely plotted within the ophiolitic chromitites (Fig. 14.27a). The TiO_2 content is very low in all chromitites chromian spinels of all localities (<0.15 wt%), which is a common feature of ophiolitic chromitites (e.g., Arai and Yurimoto 1994; Zhou et al. 1994, 1996). The Mg# (=Mg/(Mg + Fe^{+2}) atomic ratio) of chromian spinel in the chromitites has an average ratio around 0.7, displaying a negative correlation with Cr# (e.g., Ahmed et al. 2001; Ahmed 2013). Chromian spinels in dunite envelopes of the CED and SED localities usually have similar Cr contents com-pared with those from chromitite pods, while those in harzburgites are compositionally dis-tinct, being have intermediate Cr# (around 0.5) in the CED and relatively higher Cr# (around 0.7) in the SED ones.

Primary silicate minerals (olivine and pyroxenes) are only observed in the SED complexes from both chromitite interstitial matrix and from dunites and harzburgite host rocks. Olivine exists in two modes of occurrence either as interstitial silicate matrix or as discrete inclusions within chromian spinels. The olivine inclusions within chromian spinels are highly forsteritic, the forsterite (Fo) content (=Mg# * 100) ranges from Fo_{96} to Fo_{98}, with an average of Fo_{97}, which is very similar to those in the interstitial matrix of podiform chromitites. The NiO contents of olivine inclusions and those in the interstitial matrix of chromitites are also very high, reached up to 1.4 wt%. On the other hand, olivines in the dunites and harzburgites also have high Fo content, but still lower than those included in and interstitial to chromitites chromian spinel. The Fo content of olivines in the dunite envelopes averages Fo_{93}, while itis slightly lower in harzburgites, averages Fo_{92}. The average NiO content of olivine in the dunites and harzburgites is about 0.40wt%, which is consistent with the primary mantle olivine. The analyzed orthopyroxenes and clinopyroxenes are mainly enstatite and diopside, respectively with high Mg# and compositions that are closely similar to those in the residual depleted mantle harzburgites.

14.7.4 PGE and PGM in Egyptian Chromitites

The platinum-group elements (PGE) contents of chromitites are distinctly higher than those of the associated dunites and harzburgites in all of the Eastern Desert chromitite localities. Consistent with chromian spinel chemistry, the SED chromitites show uniform chondrite-normalized PGE patterns with general negative slope from Ru to Pt as the ophiolitic chromitites (Fig. 14.28a). The total PGE contents of the SED chromitites range from 140 up to 320 ppb with restricted uniform patterns, where all chromitite pods show strong negative Pt anomalies. The $(Ru/Pt)_N$ ratio is very high and ranges from 11 up to 61 indicating strong decoupling of the IPGE (Os, Ir and Ru) and PPGE (Rh, Pt and Pd) (Fig. 14.28a). The $(Pd/Ir)_N$ ratio, one of the best indicator for fractionation, is very low in chromitites of all SED chromitites; the ratio ranges from 0.04 up to 0.19. The dunites and harzburgites host of the SED chromitites have

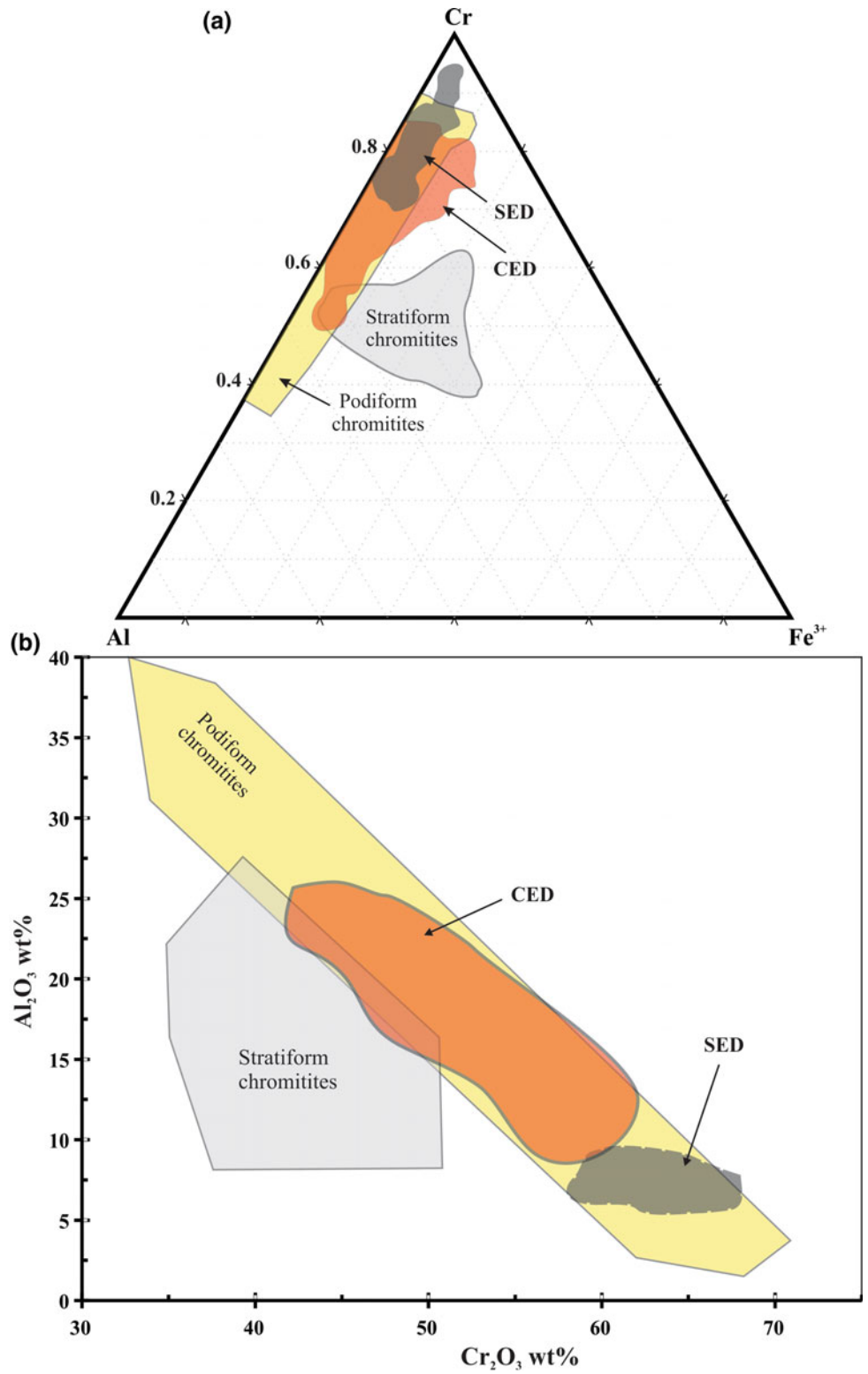

Fig. 14.27 **a** Triangular Cr–Al–Fe^{3+} variation (atomic ratios) and **b** Cr_2O_3 versus Al_2O_3 wt% variation diagrams of chromian spinels in the chromitite deposits of central Eastern Desert (CED) and southern Eastern Desert (SED) of Egypt. Compositional fields of ophiolitic and stratiform chromitites are shown for comparison

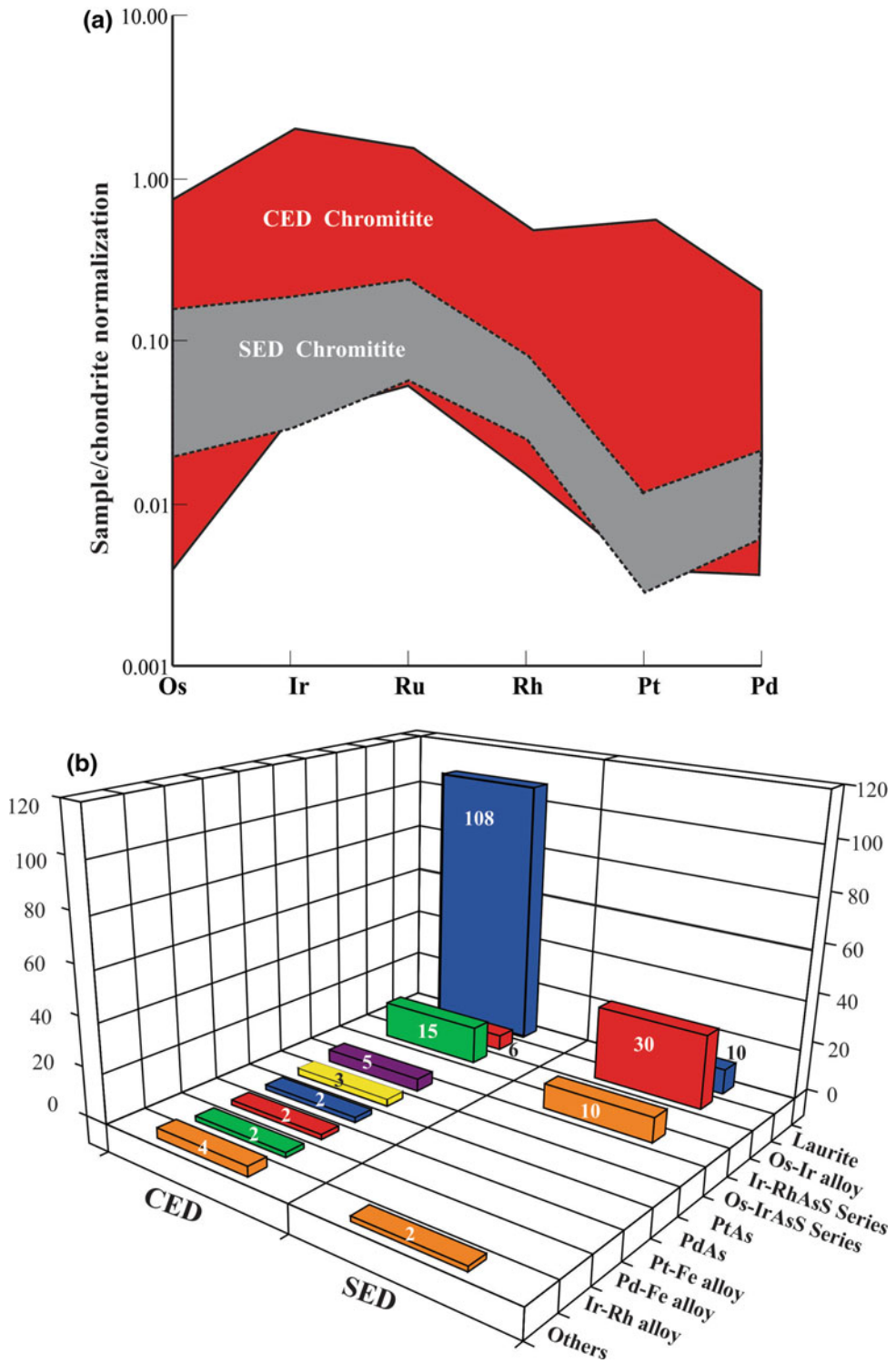

Fig. 14.28 **a** Chondrite-normalized PGE patterns of CED and SED chromitites of Egypt. **b** Frequency distribution histograms of PGM in the CED and SED chromitites

low PGE, mostly <50 ppb; being display relatively unfractionated chondrite-normalized PGE patterns. The CED chromitites, on the other hand, exhibit variable PGE contents and distribution patterns from locality to locality. Some chromitite pods in the CED show unusually high PGE content reached up to 3200 ppb and their dunite envelopes also have unexpectedly high PGE content up to 2300 ppb. The PGE-rich chromitites of the CED usually show gentle negative slope of PGE patterns (Fig. 14.28a), being enriched in both IPGE and PPGE, while the associated dunites exhibit U-shaped patterns showing enrichment in Os, Pt and Pd. The PGE-poor chromitites from other CED localities show low to intermediate PGE contents ranging from 58 to 365 ppb and generally display negative slopes (Fig. 14.28a) as in almost all ophiolitic chromitites. Dunite envelopes of the PGE-poor chromitites from CED show negatively-sloped PGE patterns at which PGE contents vary from 18 up to 76 ppb. Harzburgites in all of the CED and SED localities show nearly flat unfractionated PGE patterns; exhibiting restricted PGE contents vary from 27 up to 89 ppb (Ahmed and Arai 2002; Ahmed 2007, 2013).

Platinum-group minerals (PGM) of the Egyptian chromitite deposits have been rarely studied; there were very few studies documented PGM in podiform chromitites (El Haddad 1996; Styles et al. 1996). However, recently the PGM mineralogy and chemistry as well as in situ Os isotope geochemistry of Os-rich PGM were thoroughly studied in the Egyptian podiform chromitites (Ahmed et al. 2006; Ahmed 2007). Almost all chromitite deposits investigated in the CED and SED of Egypt were found to contain PGM grains, however the Wadi El-Lawi PGE-rich chromitite pods (Ahmed 2007), CED of Egypt, are the most enriched ones in PGE and PGM of all the pods investigated. Numerous PGM grains were petrographically and geochemically examined in both CED and SED chromitites. Os-rich laurite is the most popular PGM species in the CED chromitites, while Os–Ir alloys are the dominant PGM in the SED chromitites (Fig. 14.28b). Laurite (RuS_2) counts about 54% of the total PGM grains found in all areas investigated, whereas the least abundant PGM are (Pt–Pd)–Fe alloys (Fig. 14.28b). In general, three PGM groups have been found in the podiform chromitites from the Proterozoic ophiolite of the Eastern Desert of Egypt: sulfides, alloys and sulfarsenides–arsenides, in decreasing order of abundance. In most cases, the PGM grains are predominantly monophase and subordinately show polyphase PGM associations. The most common associations are laurite + osarsite and Os–Iralloy + laurite (Ahmed 2007). PGE-sulfides (mainly laurite and erlishmanite) form the main PGM in the CED chromitites, comprising about 77% (Figs. 14.28b and 14.29a) of the total PGM found in the CED chromitites. The grain size of PGE sulfides occasionally exceeds 5 μm, up to 40 μm across, which in most cases found exclusively as solitary euhedral crystals embedded within chemically fresh, but commonly cracked, chromian spinel (Fig. 14.29b). Upon weathering, Os-rich laurite has been altered to porous and ragged Os-poor laurite or to heterogeneous composite grains of Os-rich and Os-poor laurite surrounded by osarsite (OsAsS) (Fig. 14.29c). Pt–Fe, Pd–Fe alloys and native Pd are the main Pt and Pd phases found as small aggregates, of composite grains in the altered chromian spinels of the CED chromitites (Fig. 14.29d). Irarsite (IrAsS) and hollingworthite (RhAsS), with wide range ofsolid solution between them, are the main PGE sulfarsenides in the CED chromitites of Egypt. On the other hand, the PGE mineralogy in the SED chromitites is much simpler than those of the CED examples, comprising mainly Os–Ir alloy (Fig. 14.29e), few small grains of Os-poor, Os-free, and Os-rich laurite (Fig. 14.29f), and osarsite–irarsite sulfarsenides (Fig. 14.29 h). Os–Ir alloys are accounting for 75% of the total PGM grains found in the SED chromitites (Figs. 14.28b and 14.29a). For more details about PGM distribution and mineralogy in the Egyptian chromitites, audience is invited to refer to Ahmed (2007).

The Re–Os isotopic system has been directly applied to the study of PGE mineralization and related ore deposits. The ultimate source of Os can be definitely inferred from the large differences between the Os isotopic compositions of the crust and the mantle. Osmium isotopic systematics, therefore, in combination with other geochemical characteristics, can provide unique information about the geological settings at which this PGE mineralization has been formed, as well as about the crustal recycling process in subduction zones. The Os-rich PGMs encapsulated within fresh chromian spinel are likely the best materials to constrain the initial $^{187}Os/^{188}Os$ isotope values. Being consistent with the chromian spinel compositions, there is a clear difference in Os isotope ratios between the CED and SED chromitites of Egypt (Ahmed et al. 2006). The Os-rich PGMs from the CED chromitites have a sub-chondritic average $^{187}Os/^{188}Os$ of 0.12261 and $\gamma Os_{(t)=0}$ (−4.68), while those from the SED chromitites have asupra-chondritic $^{187}Os/^{188}Os$ of 0.12928 and $\gamma Os_{(t)=0}$ (+0.51). The isotopic heterogeneity of mantle rocks was attributed to at least two factors; (1) addition or subtraction of Re, and (2) addition of Os with different isotope ratios to the depleted mantle source (Walker et al. 1996). The least radiogenic values are most probably characteristic of the primary magmatic mantle system (Walker et al. 1996), whereas the more radiogenic ones are attributed to the assimilation of crustal materials.

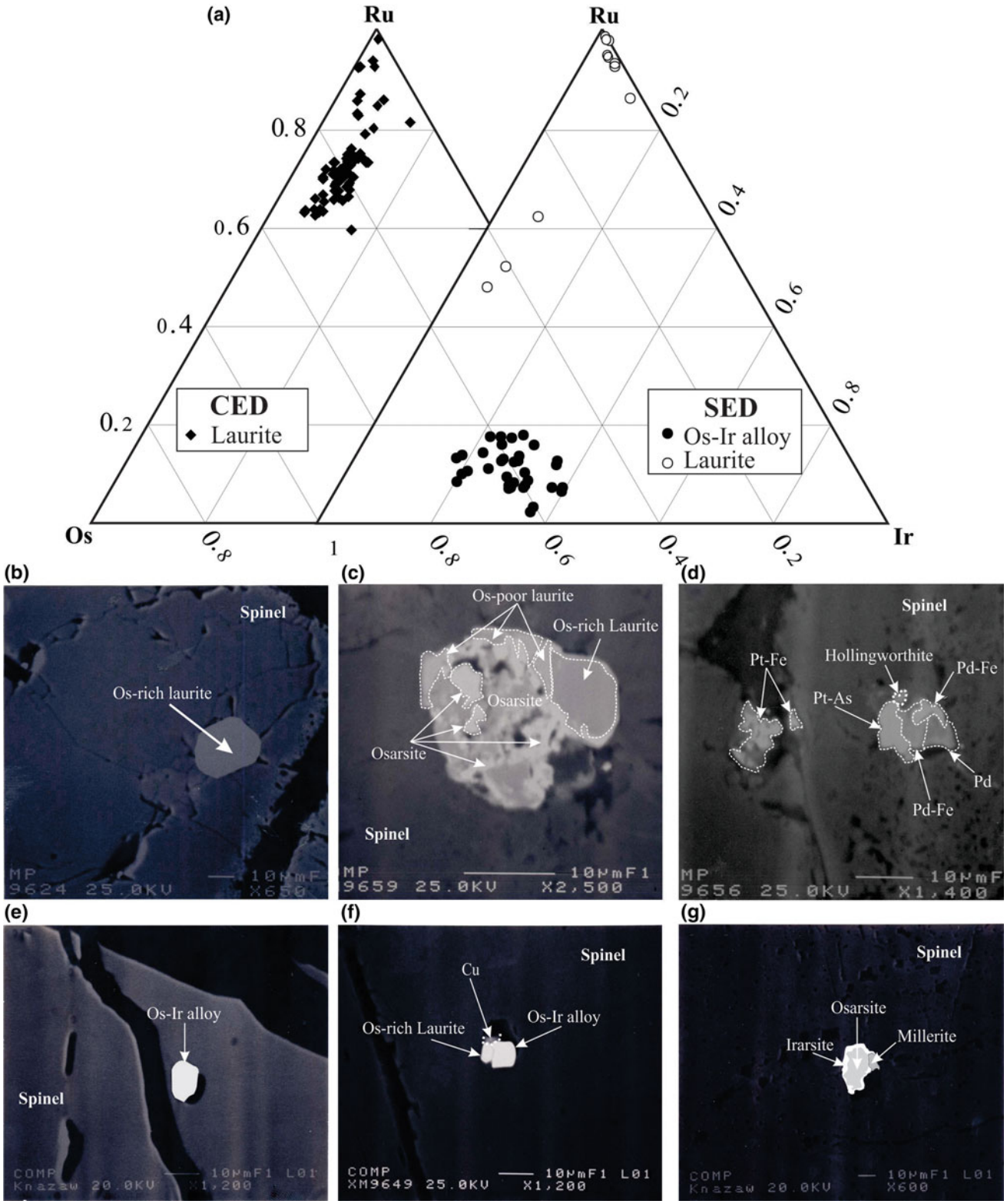

Fig. 14.29 **a** Compositional variation of laurite and Os–Ir alloys in terms of Ru–Os–Ir composition in the CED and SED of the Egyptian chromitites. **b–g** Back-scattered electron images of PGM grains included within chromian spinel of the Egyptian CED **b–d** and SED **e–g** chromitites. **b** Solitary perfect euhedral Os-rich laurite, **c** Os-rich and Os-poor laurites surrounded by osarsite within altered chromian spinel, **d** composite PGM grains containing Pt–Fe, Pd–Fe alloys, sperrylite (Pt–As), native Pd and hollingworthite, within altered chromian spinel. **e** Solitary perfect euhedral Os–Ir alloy, **f** Os–Ir alloy associated with small Os-rich laurite and native Cu, **g** osarsite–irarsite solid solution series associated with millerite within altered chromian spinel

14.7.5 Genetic Implications

There is a general consensus that, the podiform chromitite is essentially formed by melt–rock reaction model in the upper mantle, where chromite crystallization results from reaction between an upwelling primitive melt and the mantle peridotite through which it percolates (Kelemen 1990; Arai and Yurimoto 1994; Zhou et al. 1996; Arai 1997; Zhou and Robinson 1997; Ahmed 2013). The composition of chromitites is therefore controlled by the chemistry of both mantle peridotites and the uprising melt. The chemistry of the wall peridotite, especially its orthopyroxene and clinopyroxene (Al_2O_3 + Cr_2O_3 wt%) contents, may control the size and composition of podiform chromitites, because these components are significant in chromian spinel precipitation (Arai and Abe 1995; Ahmed et al. 2016). Chromitites with Al-rich spinel form where tholiitic (Al-rich) melt react with more fertile mantle peridotites (clinopyroxene-bearing harzburgite), while Cr-rich chromitite pods form by reaction between harzburgite and boninitic (Cr-rich) melt (Zhou et al. 1996; Arai 1997). Subsequently, the size and distribution of podiform chromitite, if any, will be very small and limited if highly depleted harzburgite is involved in the interaction, due to the low contents of (Al_2O_3 + Cr_2O_3 wt%) in the harzburgite wall. In contrast, if fertile peridotite (i.e., lherzolite) is involved in the interaction, spinel saturation in the produced mixed melt will not be reached and, in turn, podiform chromitite will not be formed (e.g., Arai 1997; Ahmed 2013; Ahmed et al. 2016). Instead, moderately refractory harzburgite is the most reliable candidate for podiform chromitite formation. This type of harzburgite is commonly abundant in arc and related settings (fore-arc and back-arc basins), where large size podiform chromitites with high Cr# (>0.7) are predominant.

The PGEs chemistry and mineralogy of podiform chromitites are useful indicators of degree of partial melting and the saturation of sulfur in the primary melt. The distinctive decoupling of the two PGEs subgroups (IPGE and PPGE) together with the high Cr# of chromian spinels (>0.70), strongly implies that the SED chromitites most probably formed as a result of interaction between tholeiitic melt and depleted mantle harzburgite. This is most easily formed by hydrous melting at a supra-subduction zone setting, where the downgoing slab is the source of water which, in turn, promotes the removal of PGEs from their mantle source. This can also be deduced from the presence of perfect euhedral Os–Ir alloys and the absence of well crystallized Os-rich laurite as inclusions in the SED chromitites, which suggests a melt with high temperature and very low $f(S_2)$ conditions was involved in the SED chromitite formation. Such high temperature and low $f(S_2)$ conditions might be obtained in high-degree partial melts which may be linked to a supra-subduction zone environment. The super-chondritic Os-isotope ratio of Os-rich PGM also supports this hypothesis for the SED chromitites. In contrast, the mainly presence of Os-rich laurite as the primary PGM inclusions in the CED chromitites is consistent with the narrow range of slightly high $f(S_2)$ in the mantle melt. The degree of partial melting in the CED localities might be not so high compared with the SED ones allowing a relatively higher $f(S_2)$ in the parental magma. This is also consistent with the wide compositional range of chromian spinel and the sub-chondritic Os-isotope ratio of PGM in the CED chromitites.

Therefore, it can be concluded that if the CED chromitites with primary Os-rich laurite inclusions and sub-chondritic Os-isotope ratios represent the primary composition of the mantle in the late Proterozoic ophiolite of Egypt, the chromitites in the SED with the primary Os–Ir alloy inclusions and super-chondritic Os-isotope ratios might be representative subduction components along the subduction zone setting. The diversity of primary PGM inclusions in chromian spinel from the CED to the SED chromitites, the sub-chondritic and supra-chondritic Os isotope ratios of Os-rich PGM in the CED and SED chromitites, respectively, combined with their petrological characteristics suggest that the mantle rocks of the late Proterozoic ophiolite of Egypt are representative of late Proterozoic equivalent to the depleted mantle lithosphere initially formed in mid-ocean ridge setting and then extensively modified in a supra-subduction zone setting.

14.8 Low Grade Uranium Occurrences in the Basement Rocks of Egypt

Mohamed El-Ahmadi Ibrahim

Nuclear Materials Authority (NMA), Cairo, Egypt started an ambitious program to re-evaluate the different types of the basement rocks in the Eastern Desert (ED) of Egypt and to define the suitable types that can bear U-mineralization in comparison with the U-environs in the world. These programs led to the discovery of some U-mineralization in the ED between the Red Sea and the Nil Valley. The principal types of uranium occurrences in the ED can be subdivided according to IAEA classification (1990 and 2003) into: 1-Metamorphic hosted deposits (metamorphosed sandstone deposits, metamorphosed high P-T mylonite and associated mafic lamprophyre dikes) and **2**-Vein types at Gabal (G.) Gattar, El-Missikat-El-Erediya, Um Samra-Um Bakra and El-Sella granites (Fig. 14.30).

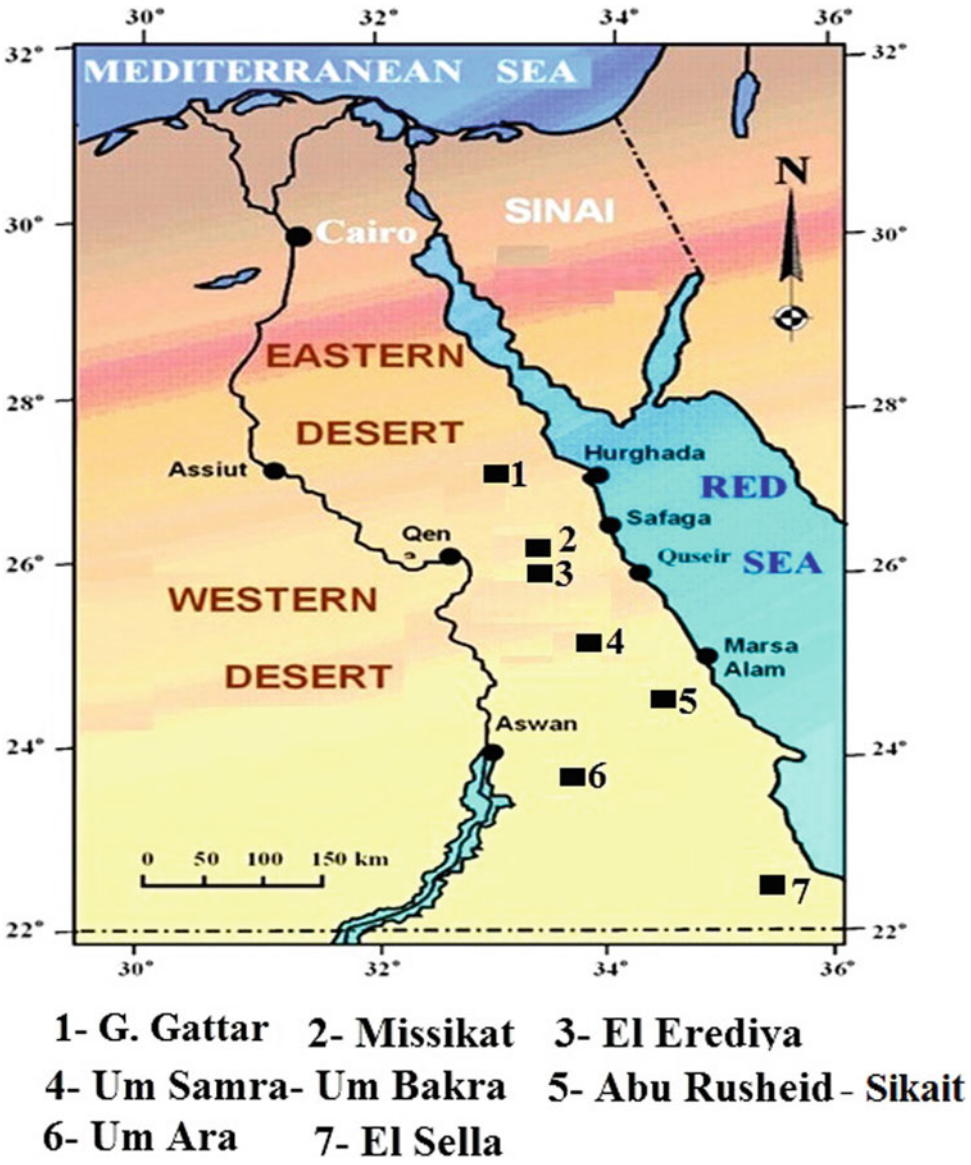

Fig. 14.30 Location of uranium occurrences in Egypt

14.8.1 Metamorphosed Sandstone-Type U Deposit

Wadi Sikait, which is located about 95 km SW of Marsa Alam town, can be considered as a respectable case study in the south Eastern Desert of Egypt. It strikes WNW-ESE and is 1.5 km far from Wadi (W.) Abu Rusheid (NW-SE trend). Ophiolitic mélange, metamorphosed sandstones (MSS), isotropic gabbro and porphyritic granite are the main exposed rocks. The MSS are highly tectonized and are elongated in the NW-SE (2 km in length and 150–500 m in width). They form float boat-like shape (Fig. 14.31a) and intruded by fertile porphyritic granite (20 ppm eU) and NE-SW lamprophyre dikes (Ibrahim et al. 2008, 2010).

The MSS are fine to medium-grained, whitish grey color arkoses to greywackes. The greywackes are composed mainly of quartz, plagioclase and k-feldspar. Garnet, fluorite, zircon and allanite are accessories, while chlorite and sericite are secondary products. The arkoses are composed mainly of quartz (80 vol%) and k-feldspars (18 vol%). Accessory minerals are represented by opaques, zircon and allanite, while sericite and clay minerals are the secondary minerals. The U contents (40–480 ppm) are five times higher than the U contents (15–85 ppm) recorded in the recent rock equivalents (less than million years). The U mineralization is represented by uranophane, β-uranophane, kasolite and autunite, which are associated with galena. The low eTh/eU ratio (0.5–2) indicates strong uranium mobility. The hydrothermal solutions played a major role in dissolution, transportation and deposition of the uranium along the open fractures associated with shearing, faults and bedding, which acted as good pathways for the solutions. The mobilization

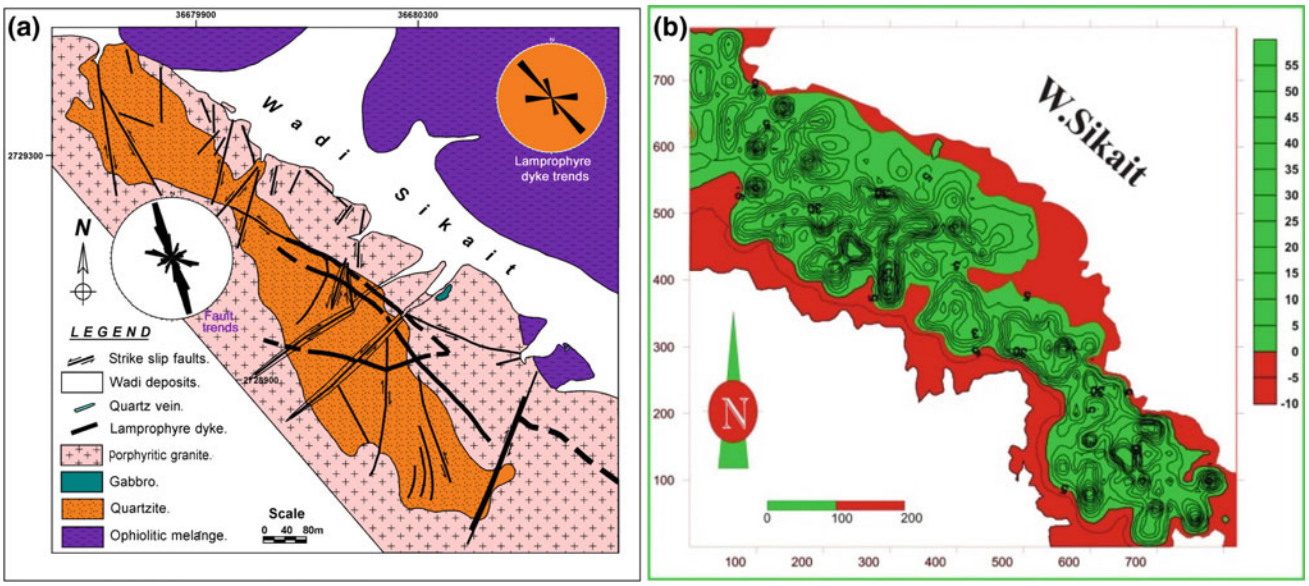

Fig. 14.31 **a** Mobility contour map for Sikait quartzite (after Ibrahim et al. 2010). **b** Geologic map of Sikait (after Ibrahim et al. 2010)

of uranium from the hot porphyritic granite towards the MSS (Fig. 14.31b) is due to the heat gradients maintained by metamorphism, emplacement of lamprophyre dikes in addition to the effect of post-depositional (diagenesis) and alteration processes (Na- and K-metasomatism, kaolinization and fluoritization) (Ibrahim et al. 2014).

14.8.2 Abu Rusheid High P-T Mylonite

The Abu Rusheid area is located 93 km south of Marsa Alam City on the Red Sea coast at the southern part of the Eastern Desert of Egypt and 2 km far from west Sikait. The cataclastic rocks in Abu Rusheid (3 km^2) intruded by syn- to post-tectonic granites, as well as, hot and depleted granites (peraluminous granites and highly fractionated calc-alkaline granites respectively). The cataclastic rocks are subdivided into: (a) protomylonite, (b) mylonite, (c) ultramylonite, and (d) quartzite with gradational contacts. They are highly sheared and characterized by banding (N-S) and dissected by two perpendicular shear zones generally trending N-S and E-W. The shear zones were emplaced by lamprophyre dikes. The latter are enriched in poly-mineralization. The N-S shear zone (up to 1.5 km in length and ranges from 2 to 10 m in width) is discontinuous, brecciated, highly tectonized and rich in Zn, REEs, U, Y Cu, Ag in a decreasing order of relative abundance. The E-W shear zone (600 m in length) is enriched in Nb–Ta, U, and Zn (Ibrahim et al. 2007a, b, c). Abu Rusheid area is traversed by good channel-ways represented by strike-slip faults (ENE-WSW, NNW-SSE, N-S and NNE–SSW) and later lamprophyre dikes, pegmatite and quartz veins. The mylonite covers a large area representing 65 vol% of the cataclastic rocks with low to medium relief (Ibrahim et al. 2002). They are fine to medium grained and well banded (striking NNW-SSE and dips 10° SW). These rocks are intercalated with protomylonite and are variably weathered producing red to yellow colors due to the alteration of sulfides to iron oxy-hydroxides (hematite-limonite). The mylonite is composed mainly of quartz, plagioclases, K-feldspars and micas (biotite, phologopite, muscovite and zinnwaldite). Kyanite, sillimanite, zircon, monazite and opaques are accessories. The precious metals were recorded as gold (2–3 g/ton) and nickel. Uranium content in cataclastic rocks ranges from 50 to 1500 ppm with an average of 300 ppm, while Th content ranges from 100 to 7000 ppm with an average of 600 ppm. In these rocks, Nb content ranges from 200 to 1500 ppm with an average of 500 ppm and Zr content ranges from 1400 to 20,000 ppm with an average of 2000 ppm. Metazeunerite $Cu(UO_2)2(AsO_4)2{\cdot}8H_2O$, kasolite $[Pb(UO_2)SiO_3{\cdot}(OH)_2]$, curite $[3PbO{\cdot}8UO_3{\cdot}4H_2O]$, boltwoodite $[K_2(UO_2)2(SiO_3OH)_2{\cdot}5H_2O]$, autunite $[Ca(UO_2)2(PO_4)2.8H_2O)]$, soddyite $[U(SiO_4)(OH)]$, carnotite $[K_2(UO_2)(VO_4)2.3H_2O]$, uranophane and β–uranophane $[CaO{\cdot}2(UO_3){\cdot}2(SiO_2){\cdot}6(H_2O)]$ and torbernite $[Cu(UO_2)2(PO_4)2.8\text{-}12(H_2O)]$ are the U minerals recorded in mylonite and protomylonite rocks (Ibrahim et al. 2004). Thorium minerals are represented by uranothorite $[(Th,U,Ce)\ SiO_4]$, thorite $[ThSiO_4]$ and thorianite. Nb–Ta minerals include Ishikawaite $[(U,Fe,Y)\ (Nb,Ta)_2O_6]$ and columbite-tantalite. Base metal minerals comprise arsenopyrite, pyrite, chalcopyrite, bunsenite, ilsemanite and galena (Ibrahim et al. 2004). More than 50 trenches were excavating in the area.

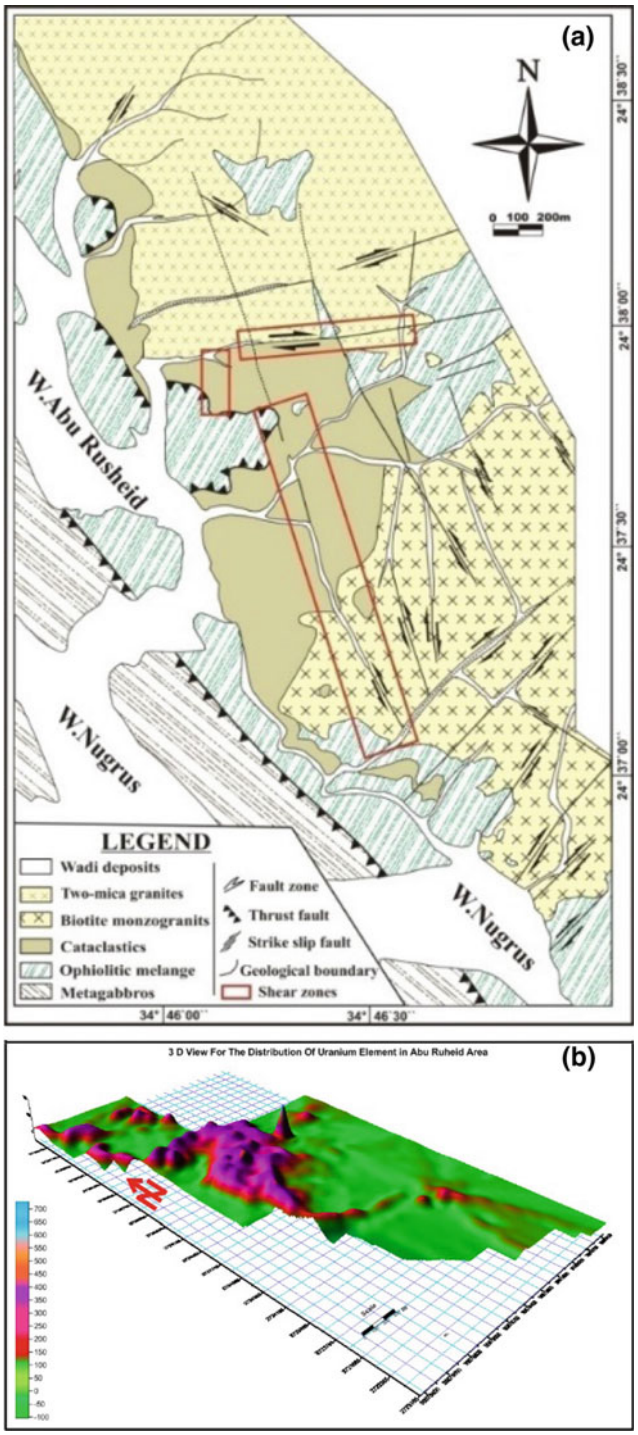

Fig. 14.32 **a** Semi-detailed geologic map of Abu Rusheid block, Southeastern Desert, Egypt (after Ibrahim et al. 2004a, b). **b** 3D view for uranium content in Abu Rusheid area, south Eastern Desert (after Ibrahim et al. 2002)

14.8.3 Mafic Lamprophyre Dikes

Three lamprophyre dikes (L_1–L_3) intruded Abu Rusheid rocks (cataclastics and monzogranite) in the south Eastern Desert of Egypt along shear zones trending NNW-SSE and E-W (Fig. 14.32). The lamprophyre dikes range from 1500 m to 500 m in length and 1.0 to 0.5 m in width, dipping 40°–80° towards the south. Microscopically, L_1 and L_2 dikes are mainly composed of plagioclases, amphiboles, phologopite, and relics of pyroxenes phenocrysts embedded in a fine-grained groundmass. Xenotime, fluorite, chlorite, and opaques are accessories. Kaolinite, illite, quartz, jarosite, epidote and clay minerals are secondary minerals. L_3 dikes are mainly composed of coarse-grained crenulated phologopite flakes assoaited with fine-grained K-feldspars and quartz forming augen structures. Opaques and fluorite are common. The two sets of dikes differ in age, mineralization, and geochemical aspect (Ibrahim et al. 2015). The NNW-SSE trending dikes (L_1 and L_2) are poly-mineralized and dislocate the E-W (L_3) trending dike. These dikes underwent multistage hydrothermal processes (ferrugination, fluoritization, kaolinitization, and calcification). They are characterized by common box works (physical trap) filled by incoming mineralization, and their feldspars and micas are relatively altered to clay minerals (chemical trap, Fig. 14.33).

From the mineralogical point of view, L_1 and L_2 lamprophyre dikes contain U minerals (uranophane, kasolite, autunite, and torbernite), Mn-franklinite, woodruffite, xenotime, fluorite, silver, copper, and scheelite. L_3 dikes contain Nb–Ta, Zn and U-minerals. The uranium content in lamprophyre dikes range from 550 to 2000 ppm. The source magma producing lamprophyre dikes are peralkaline to alkaline that was generated from the mantle and formed in a post-collisional tectonic setting with extensive Ti-rich metasomatism. The average ΣREE + Y content in lamprophyres (L_1 and L_2) is 1.2% ppm and HREE are more enriched than LREE (Ibrahim et al. 2015).

14.8.4 Um Samra-Um Bakra Vein-Type

Um Samra-Um Bakra area is located in the southern part of the Central Eastern Desert of Egypt and covered by; (1) ultramafic rocks and volcanogenic sediments, (2) syn-orogenic granites, isotropic gabbro, post-orogenic granites and (3) post-granitic dykes (basic and intermediate) and veins (black-, red-jasper and milky quartz). Um Samra-Um Bakra shear zone strikes N70° W–S70° E and dipping 45°/SSW and ranges from 10 to 500 m in thickness and extends 10 km in length.

Three generations of silica veins with different colors, mineralization and ages intruded the shear zone (Fig. 14.34). The milky quartz veins (2–5 km in length, 0.25–3 m in width) is the youngest generation; they are barren and runs WNW and dipping 70°/SSW. The red jasper veins (second generation) have a N65° W trend, dipping 45°/SSW (7 km

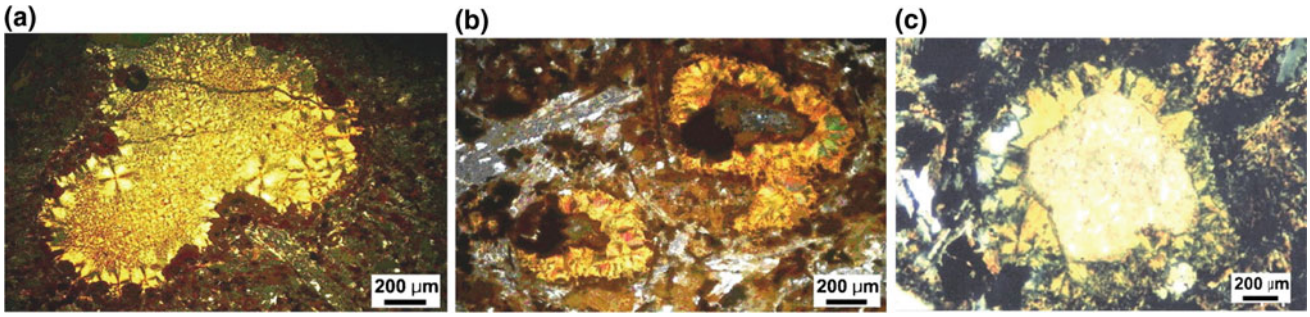

Fig. 14.33 Microphotographs showing box works filled with a radial secondary U mineral in corona texture (after Ibrahim et al. 2015)

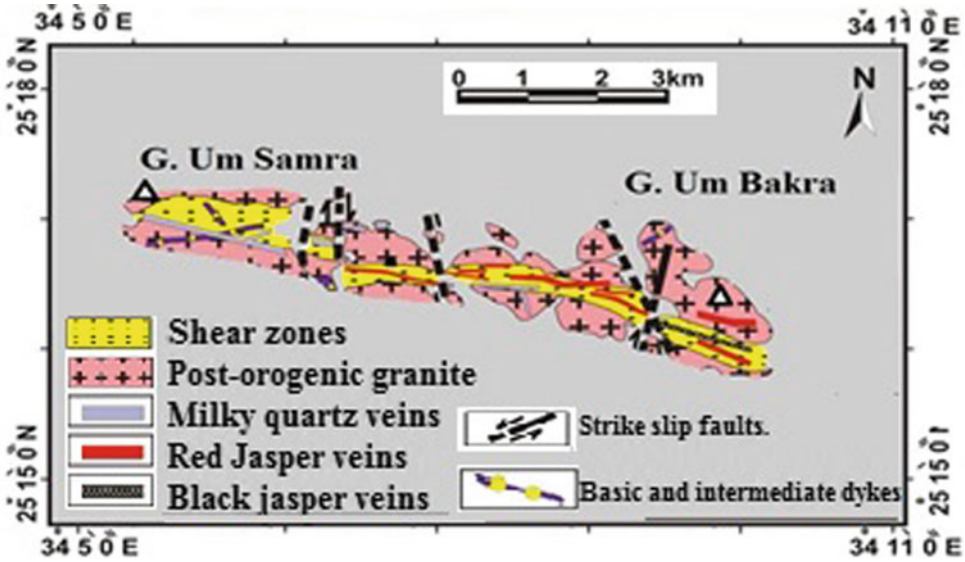

Fig. 14.34 Um Samra-Um Bakra uranium vein type (after Ibrahim et al. 2017)

in length, 0.30–3.0 m in width). The oldest generations are represented by black jasper veins (1.8 km in length, 0.5–10 m in width) trending N75° W and dipping 55°/SSW. The black jasper veins are more enriched in Ni, Cr, Zn, Cu, Au and Y than red ones (Ibrahim et al. 2017).

The mineralogical study at the Um Samra-Um Bakra shear zone confirms the presence of three mineralization stages through hydrothermal solutions. The first high-temperature stage is distinguished by the formation of native Au associated with hypogene primary sulfide minerals such as pyrite, galena, sphalerite and nickel. The second lower-temperature stage is illustrated by the formation of secondary minerals; uranium, copper minerals (atacamite, paratacamite, chrysocolla and cuprite), zincite, cassiterite, wolframite, Ni-chromite and Cr-spinel. The third stage is related to carbonate facies (calcification, fluoritization) formed after the oxidation (supergene alteration) (Ibrahim et al. 2017). The Uranium content in sheared granites ranges between 32 and 8600 ppm with an average of 2185 ppm and represented by: (a) meta-autunite [$Ca(UO_2)_2(PO_4)_2{\cdot}3H_2O$] (b) phurcalite [$Ca_2(UO_2)_3(PO_4)_2(OH)_4{\cdot}4H_2O$] and kasolite [$Pb(UO_2)SiO_4(H_2O)$]. The Thorium content ranges from 11 to 242 ppm with an average of 96 ppm and represented by uranothorite [$(Th,U)SiO_4$]. Uranium migrated from high topographic shear zone in the west to the east (low relief) by lateral solutions, transported through channel ways and redeposited on the surface and fissures of altered granites, and fixed by hematitization and kaolinitization. The presence of milky quartz veins on both sides of the shear zone prevents U migration (Ibrahim et al. 2017).

14.8.5 El-Sela Vein-Type

The El Sela area is bounded by latitudes 22°13′30″–22°19′00″ N and longitudes 36°10′00″–36°19′00″ E (Fig. 14.35). The El-Sela shear zone extends for 1.5 km in ENE-WSW direction and ranges from 2 to 30 m in width and steeply dipping from 75° to 85° to the south. Two main granitic intrusions at exposed in the El-Sela shear zone, are chronologically arranged from the oldest to the youngest by biotite granite (minor) and two-mica granite (major) (Ibrahim et al. 2003; Abdel Meguid et al. 2003). The two-mica granite is mainly leucocratic, peraluminous, syn-collisional

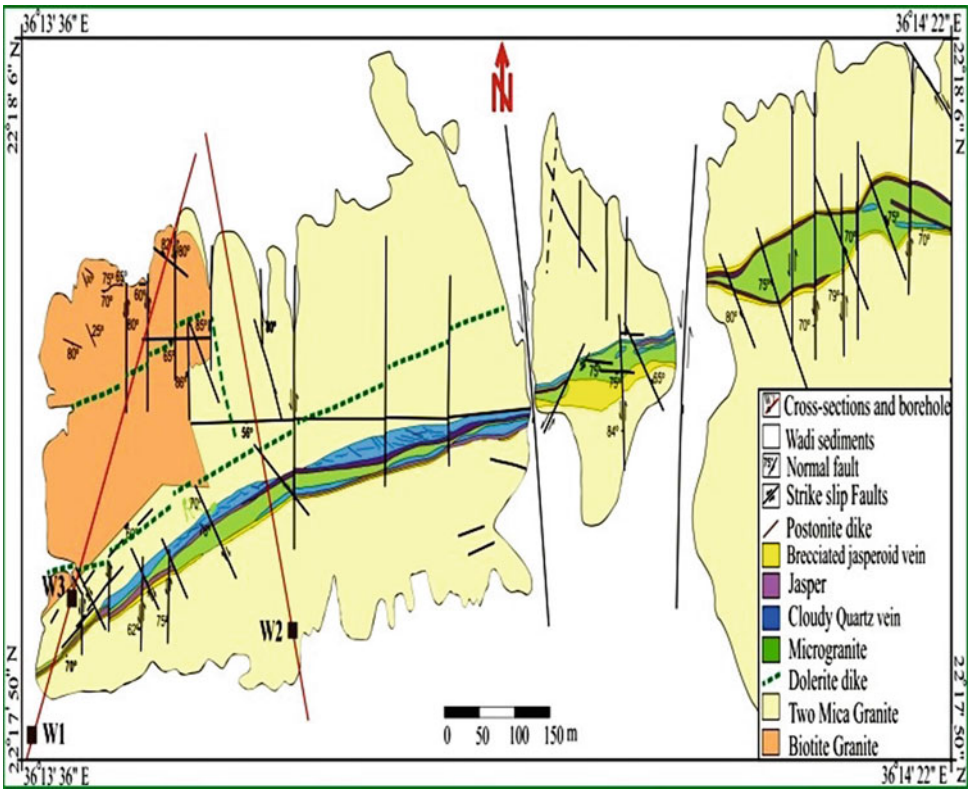

Fig. 14.35 El-Sela shear zone (ENE-WSW) cuts two mica granites, Eastern Desert, Egypt (after Abdel Meguid et al. 2003)

and composed essentially of K-feldspar, quartz, plagioclase, biotite and muscovite. Monazite, pyrite, zircon, galena, sphalerite, Nb-rutile, columbite, titanite, apatite and fluorite are accessories, while sericite, chlorite, epidote and kaolinite are alteration minerals. Two sets of structures are observed in the El Sela granite; a major E-W to ENE-WSW shear zone and N-S to NNE-SSW set of fault associated with different types of contemporaneous magmatic injections. These granites are dissected by three different types of dikes arranged as microgranite, dolerite and bostonite in order of decreasing abundance. They are mostly injected along ENE-WSW and/or NNW-SSE to N-S trends which represent the most important tectonic trends for U occurrences in the study area. The El-Sela shear zone is characterized by the existence of three generations of quartz and jasperoid veins invade the two-mica granite existed along the ENE-WSW major trend (Fig. 14.36). The barren milky quartz veins are the youngest one extending along the shear margins. They are highly brecciated and range in thickness between 1 and 4 m. The mineralized eed and grey to black jasper veins are the oldest and occur commonly parallel to the shear zone and the milky quartz veins. They are fragmented, brecciated and range in thickness between 0.5 and 1 m. They contain visible pyrite and uranophane minerals. Several types of alteration (argillization, fluoritization, silicification, calcification and ferrugination) are common in deep trenches and their uranium contents are up to 10,000 ppm. Uranophane, autunite and beta-uranophane are the main uranium minerals

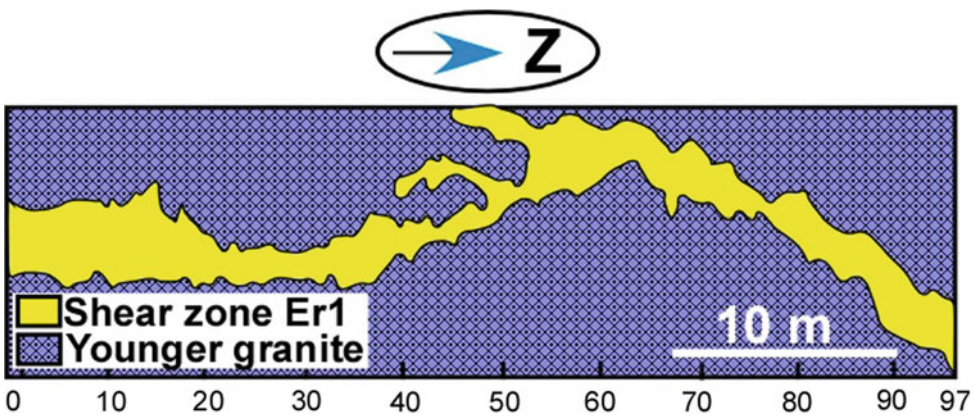

Fig. 14.36 Geological map of El-Arediya shear zone Er1 (after Hussein et al. 1986 and Abu-Deif et al. 2001)

identified in El-Sela and occur either as disseminated or as cavity filling (Abdel Meguid et al. 2003; Ibrahim et al. 2003; El-Kammar et al. 2007; Hassan 2014).

14.8.6 El Erediya Vein-Type

The EI-Erediya area is located in the central Eastern Desert covering about 25 km^2 bounded between latitudes 26°18′ 36″–26°21′36″ N and longitudes 33°27′18″–33°30″ E. EI-Erediya syenogranite has an oval shape, which is elongated in the NW-SE direction with a length of 6.5 km and width of 2.5 km. The syenogranite is dissected by dikes (aplites, pegmatite and basalt) and veins (jaspers). Hydrothermal alterations are common (silicification, kaolinization, hematitization, limonitization, sericitization and argillitiztion). The shear zones range in thickness from less than 0.5 m to more than 2 m and extend in NE-SW, NNE-SSW, ENE-WSW, and N-S trends. The jasperoid veins were intruded along the shear zones trending NE-SW and occupy their central parts filling closely parallel fractures at the center and surrounded along their extensions by zones of highly silicified and mylonitized granite, followed by wider zone of kaolinized granite, and the original syenogranite (Hussein et al. 1986). Jasperoid veins vary in thickness from few centimeters to 20 cm and in lengths from few meters to more than 100 m. Jasperoid veins host sulfide mineralization (mainly chalcopyrite, pyrite, and galena). Exploratory tunneling works were completed in early 1980 by the NMA at the southern part of the El-Erediya granitic pluton. A main adit was driven N50° W, perpendicular to the main trend of the shear zones. At the points of intersection, a number of drifts were driven after the extension of nine shear zones (Hussein et al. 1986; Abu-Deif 1991; Abu-Deif et al. 2001).

Uranium content in the jasperoid veins ranges from 200 to 600 ppm with an average of 462 ppm, whereas Th content ranges from 13 to 16 ppm with an average of 15 ppm. Massive and disseminated pitchblende, as well as other secondary uranium minerals such as uranophane, kasolite, and renardite were detected in shear zones (Hussein et al. 1986). Petscheckite, uranpyrochlore and the unidentified hydrated uranium niobate mineral are recognized by Abdel Naby (2008). These uranium minerals are accompanied by pyrite, galena, magnetite–titanomagnetite, ilmenite, hematite, rutile, titanite, fluorite, zircon, monazite, apatite, and tourmaline (El-Kammar et al. 1997). Based upon the U–Pb isochron method, the estimated age of the pitchblende varies from 130 to 160 Ma (Abu-Deif 1991). This age is related to the Late Jurassic–Early Cretaceous phase of the final Pan-African tectono-thermal event in Egypt.

14.9 Egyptian Manganese Deposits

Mortada El Aref

Manganese is an essential alloying element in nearly all types of steel and is used to increase strength, toughness, hardness and hardenability. Manganese is used for deoxidation and desulphurisation of ferrous metals and alloys and the production of ferromanganese and silicomanganese alloys for iron and steel manufacture and cast iron. Pure manganese (produced electrolytically) is utilized mostly in the preparation of nonferrous alloys of copper, aluminum, magnesium, and nickel and in the production of high-purity chemicals. Manganese oxide, is also used in the production of manganous salts or as an additive in fertilizers, a reagent in textile printing, chemical oxidant in organic synthesis, and as the cathode material in dry-cell batteries.

Concentration of Mn oxides of different geologic settings and variable economic values are recorded in several localities in Egypt (Fig. 14.37), including:

I. Sinai (Um Bogma region; Sharm El Sheikh),
II. Eastern Desert (Wadi Araba, East Ras-Zafarana; Wadi Bali, Gabal Abu Shaar, Ech Elmalaha; Wadi Meialeik; Halaib-El Ba region), and
III. Western Desert (El Bahariya Mn-rich Fe ore).

In this article, the geologic setting, ore types (facies), mode of formation and main characteristics of the functioning Um Bogma mine area are dealt with in some details. The other important and promising ore types are shortly reviewed.

14.9.1 Sinai Mn Ore Deposits (Um Bogma Region and Sharm El Sheikh)

14.9.1.1 Intra-carboniferous Stratabound/Stratiform Mn Ores (Um Bogma Region)

The estimated Mn ore reserves of Um Bogma region (Fig. 14.37) is about 30 million tons of average 27.45% Mn and 26.28% Fe (National Sinai Manganese Company, Dr A. Yahiya, personal communication). The average ore production is 35.000 tons per year used in the production of ferro-alloys, dry batteries and anti-acid blue bricks.

During the Early Carboniferous, the northeastern corner of Egypt was transgressed by shallow sea, whiles the southeastern and eastern sectors remained positive land under erosion (Fig. 14.38). The Um Bogma region is located along the Carboniferous paleoshoeline, where carbonate

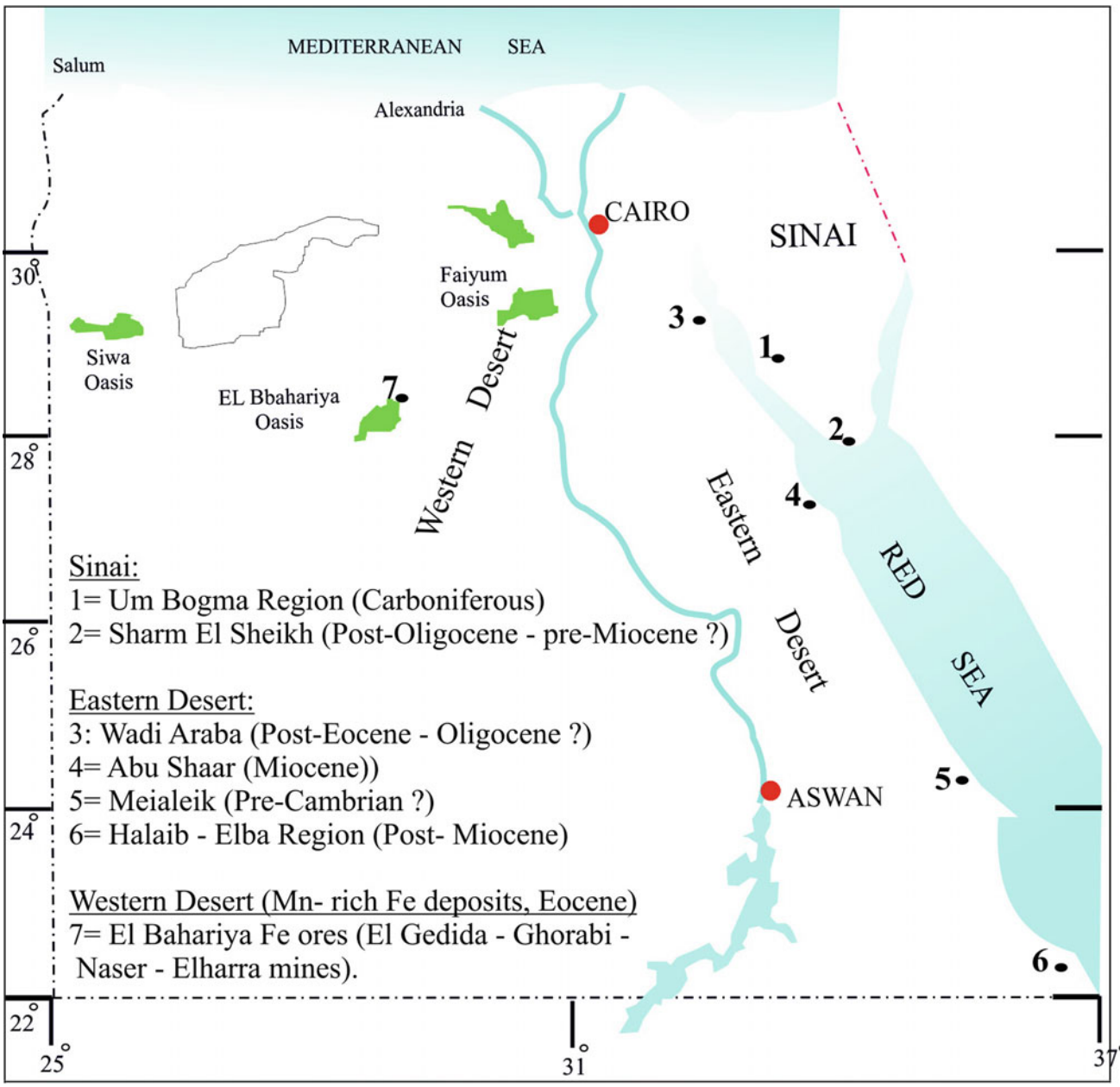

Fig. 14.37 Location map of the main Egyptian Manganese deposits and Mn-rich Fe deposits

sequences hosting Mn deposits have been deposited. The Carboniferous sequences and the related sequence boundaries (mainly paleo-karst surfaces) and the Mn intervals are shown in Fig. 14.39. The Early Carboniferous Um Bogma carbonate sequence (up to 45 m thick) rests directly above the Pre-Cambrian basement rocks in the northwestern part of the region at W. Khaboba and G. Nuhkl (Fig. 14.39). Towards east and south, carbonate rock association of this sequence is highly attenuated and truncates different stratigraphic horizons of the underlying Paleozoic clastic sequences and consists of two distinguished members. The lower one is formed by stratabound/stratiform Mn facies association bounded by two major unconformities (sequence boundaries), that manifested by the underlying Cambrian-Carboniferous truncated surface and an intra-formational (intra-Um Bogma) paleo-karst surface, along which karst profile is well developed and drowned by the onlapped carbonate facies association of the overlying transgressed Upper Member of the Um Bogma sequence (Figs. 14.39 and 14.40). Rapid fluvial progradation and near surface sedimentation followed the deposition of the Upper Um Bogma carbonates, truncating different stratigraphic horizons of the different carbonate and Mn facies (Fig. 14.40). Outside the Um Bogma region towards south,

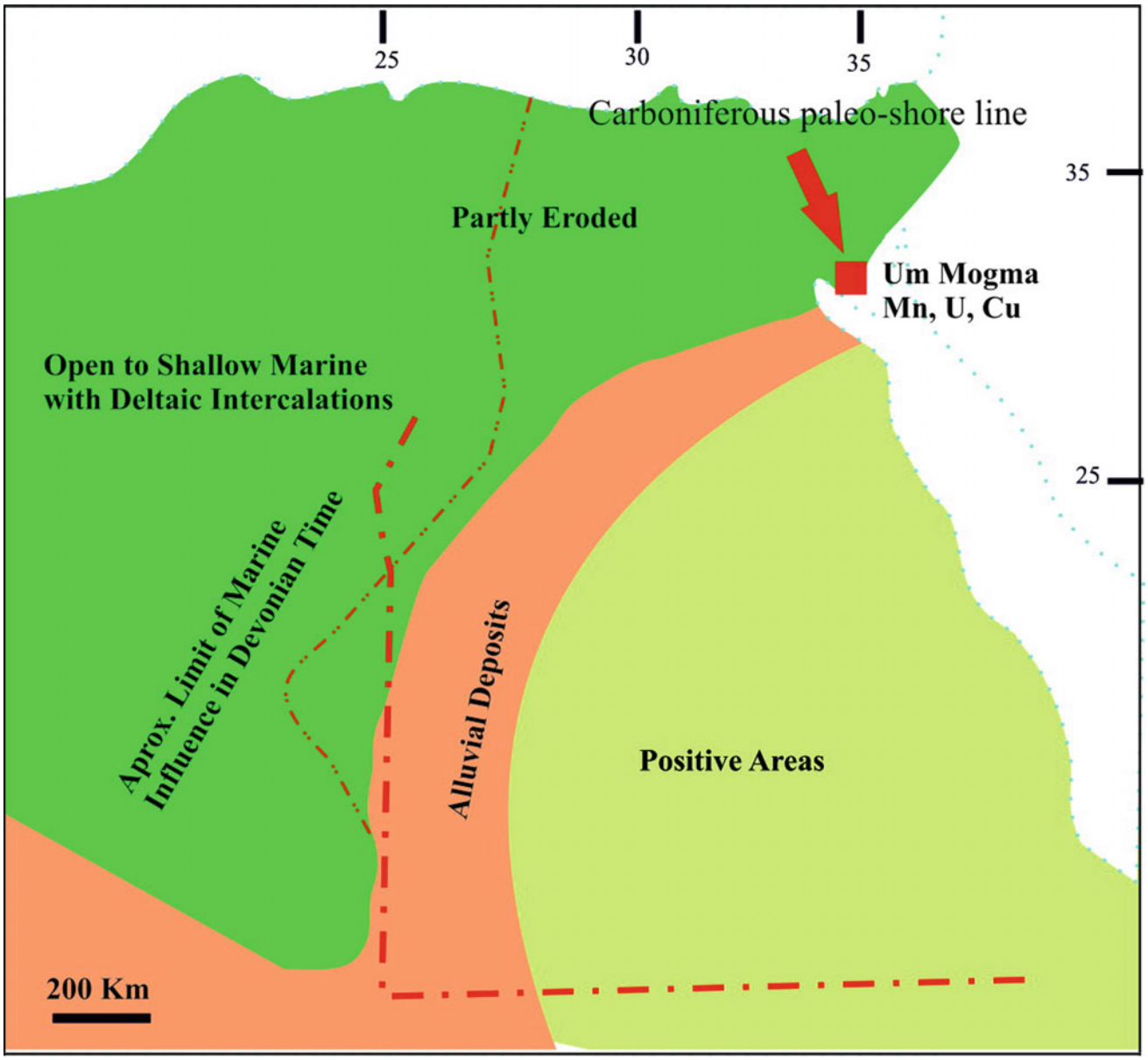

Fig. 14.38 Paleogeography of the Lower Carboniferous shore-line (After Klitzsgh and Wycsik 1987)

the Um Bogma sequence and the associated carbonates and Mn facies are completely missing and the overlying Abu thora clastic sequence rests directly on the Cambrian sequences. The stratabound Mn interval of the Lower Um Bogma sequence is formed of three general Mn ore facies which inter-tongue form east to west and changes westward into open marine carbonate facies (Fig. 14.40, zones A–D and Fig. 14.41). The recorded Mn facies include:

1. Stratiform continental Mn conglomerates, sandstones and mudstones, representing proximal facies of braided streams, well represented in the extreme eastern part of the Um Bogma region (Figs. 14.40, zone D and 14.41).
2. Stratiform lagoonal to swampy intercalated manganiferous mudstones and dolostones, prevailing in in the central part of the Um Bogma region (Figs. 14.40, zone C and 14.41). This facies was highly subjected to intensive paleo-karstificatiom inducing post-diagenetic telogenetic processes (supergenesis) and pedogenesis that resulted into the formation of well-preserved paleokarst profile (Fig. 14.41). The paleokarst telogenetic processes led to the concentration and redeposition of high grade Mn ore in the solution openings of the karstified rocks of the lower part of the paleo-karst profile and concentration of the more mobile elements including Cu and U in the subsoil and topsoil horizons (Figs. 14.39 and 14.41), and

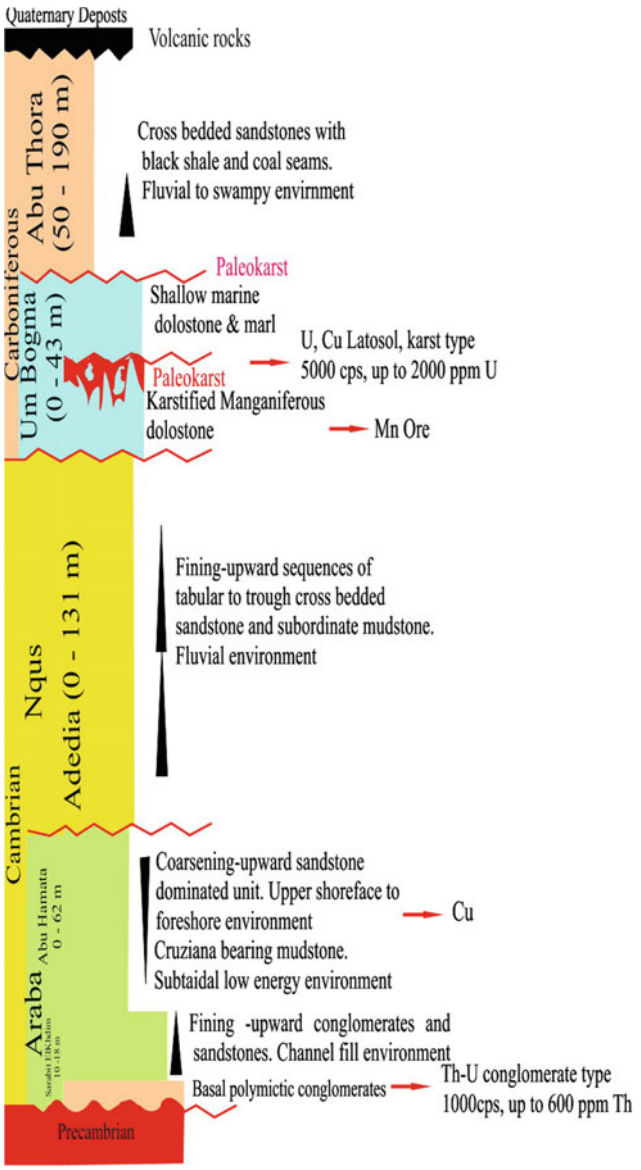

Fig. 14.39 Paleozoic rock units, unconformities and the related Mn ore and mineral concentration (El Sharkawi et al. 1990a; El Aref 1996; Abdel Motelib 1987, 1996; El Aref et al. 1998)

3. Near-shore shallowing pisolitic (oncolitic) Mn para-sequences of high energy depositional environment (Figs. 14.40, zone B and 14.41).

The main characteristic sedimentary structures, ore fabrics, ore lithology's paragenesis and paleo-environments of the recognized ore facies and also the superimposed paleokarst facies are compiled and summarized in Table 14.6. Chemical analyses of representative ore samples of different ore types or facies are represented in Table 14.7. The paleo-stratigraphic setting, paleo-geographic distribution, and lateral changes of the different Mn facies and the host marine carbonates from east to west, elucidate that Mn and Fe components were derived from the hinterlands as clasts and suspensions, and deposited in channels along the Carboniferous coastal zone forming the continental fluvial facies and debauched into the Carboniferous sea, depositing lagoon to shallow marine manganiferous facies in the central part and the marine carbonates in the extreme western part. Subsequent phase of uplifting and sea regression accompanied with paleo-karstificatiom processes under paleo-humid condition led to the development of the enriched Mn karst facies and paleosol products. The resultant Mn facies and the equivalent carbonates of the lower Um Bogma sequence were fossilized by the following younger carbonate transgression of the upper Um Bogma carbonates (Abdel Motelib 1996; El Aref 1996, 2001).

14.9.1.2 Oligo-Miocene? Flinty Conglomeritic Mn Ore (Sharm El Sheikh)

Small reserves of Mn ores are recorded north of Sharm (Bay) El Sheikh, southern Sinai (Fig. 14.37). According to Omara (1959) the ores are mainly breccia filling deposits of post-Oligocene/pre-Pleistocene age developed along fault lines by mineralized solutions of unknown sources and directions. However, the diagrammatic section of the deposits (Omara 1959) elucidates that the flinty conglomeritic Mn deposits constitute the basal conglomerates demarcating the contact between the Pre-Cambrian granites and the overlying clastic sequence of the Miocene Abu Gerfan of El Azabi and Eweda (1996). Further advanced geological investigations and ore evaluation are highly recommended in order to estimate the economic value of this ore type.

14.9.2 Eastern Desert

14.9.2.1 Post-Miocene-Recent (?) Surficial Conglomeritic Mn Deposits (Wadi Araba)

Small occurrences of Mn–Fe deposits of medium quality (~35%) are generally clarified by Abdallah (1961) in Wadi Araba, Gulf of Suez. According to Abdallah (1961), the deposits are found among the low Wadi terraces in the northern foothills of the southern Galala escarpments, 8 km SW of the Zafarana lighthouse (Fig. 14.37), rising conspicuously above the surrounding Wadi level. The deposits are subsequent to the host sediments and fractures. They consist mainly of psilomilane, hematite, limonite, and calcite

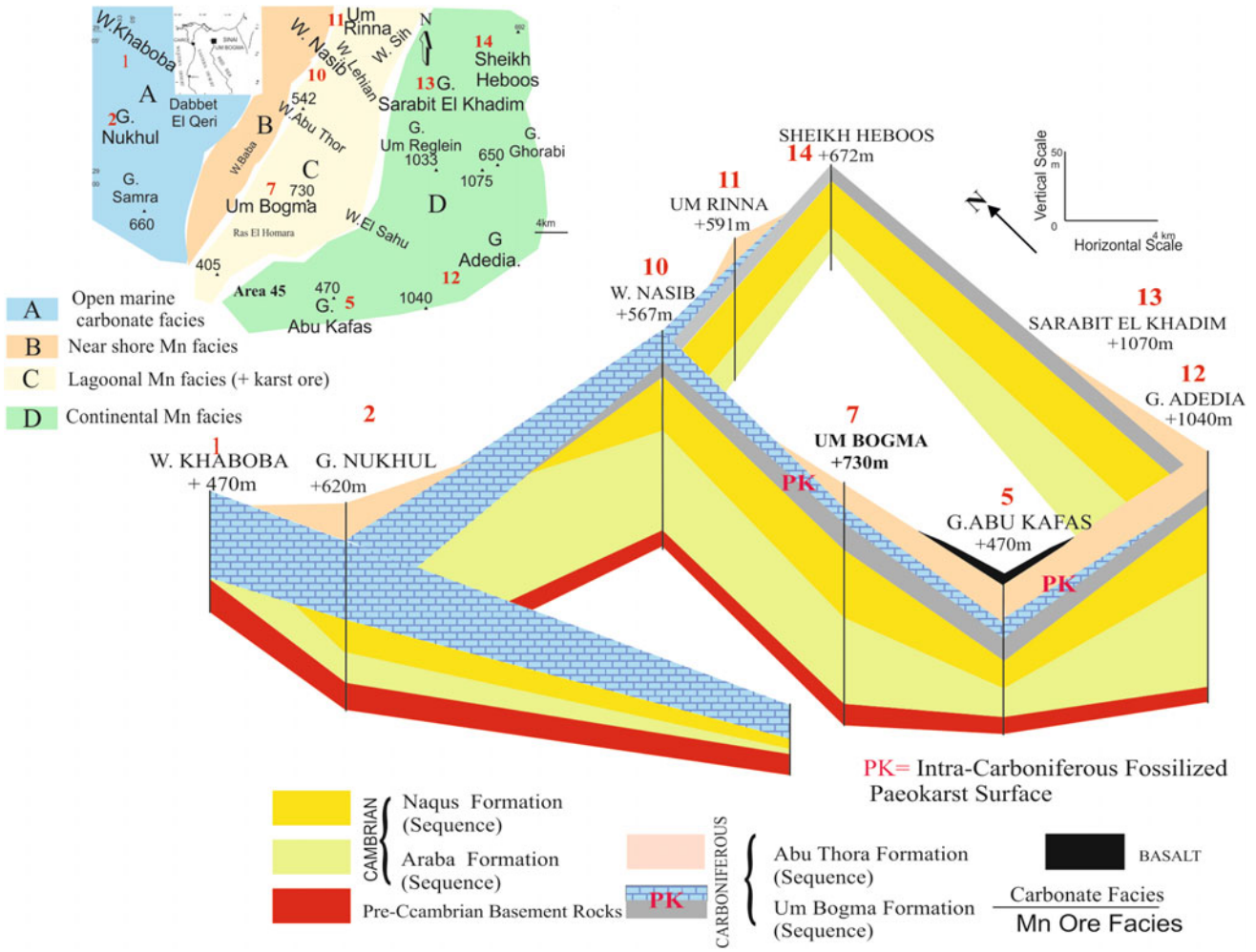

Fig. 14.40 Isometric panel diagram of the different Paleozoic rock units of Um Bogma region, west-central Sinai, Egypt and geographic distribution of the related intra-carboniferous Mn facies (Abdel Motelib 1996; El Aref and Abdel Motelib 2001)

cemented by hard siliceous iron oxides with general 20.81 to 55.35% Mn, 1.49 to 16.8% Fe and 1,78 to 33.7% Si. The total estimated reserves are ~4000 tons with 20–65 MnO% (Mineral Map of Egypt, EGSMA, 1979). Abdallah (1961) suggested that the Mn–Fe bearing rocks are of post-Middle Eocene (Oligocene) age formed by Mn–Fe solutions of volcanic origin. Personal investigations revealed that the Mn-rich deposits form a hard dark cap of variable thickness, unconformably overlying isolated small residual hills and ridges of Cretaceous clastics and/or Eocene carbonates with characteristic erosive lower surfaces. Such small hills and ridges are of very low relief and represent remains of the dissected low pediment segment of the retreated main scarps of El Galala plateau. The deposits are of conglomeritic nature of finning-upward tendance, forming small-scale lenticular bodies and elongated pockets enclosed within conglomeritic and coarse–grained ferruginous sandstones and limonitic and kaolinitic clays as well as thin ochreous palosols rich in carbonaceous plant remains and rhizocretions. This morphologic setting and sedimentological characteristics argue for fluvial origin of such deposits during the senile stage and terraces formation of Wadi Araba progression.

14.9.2.2 Syn-Rift (Miocene) Stratiform Oolitic-Oncolitic (Pisolitic) Mn Ore (Wadi Bali, Gabal Abu Shaar, Ech Elmalaha, Red Sea Coastal Zone)

Syn-rift (Miocene) stratiform oolitic-oncolitic (pisolitic) Mn ores of limited thickness and small reserves (with up to 35.8–45.14 MnO%), are well represented in Wadi Bali, Gabal Abu Shaar, Ech Elmalaha, Red Sea Coast (Fig. 14.37). The Mn bed

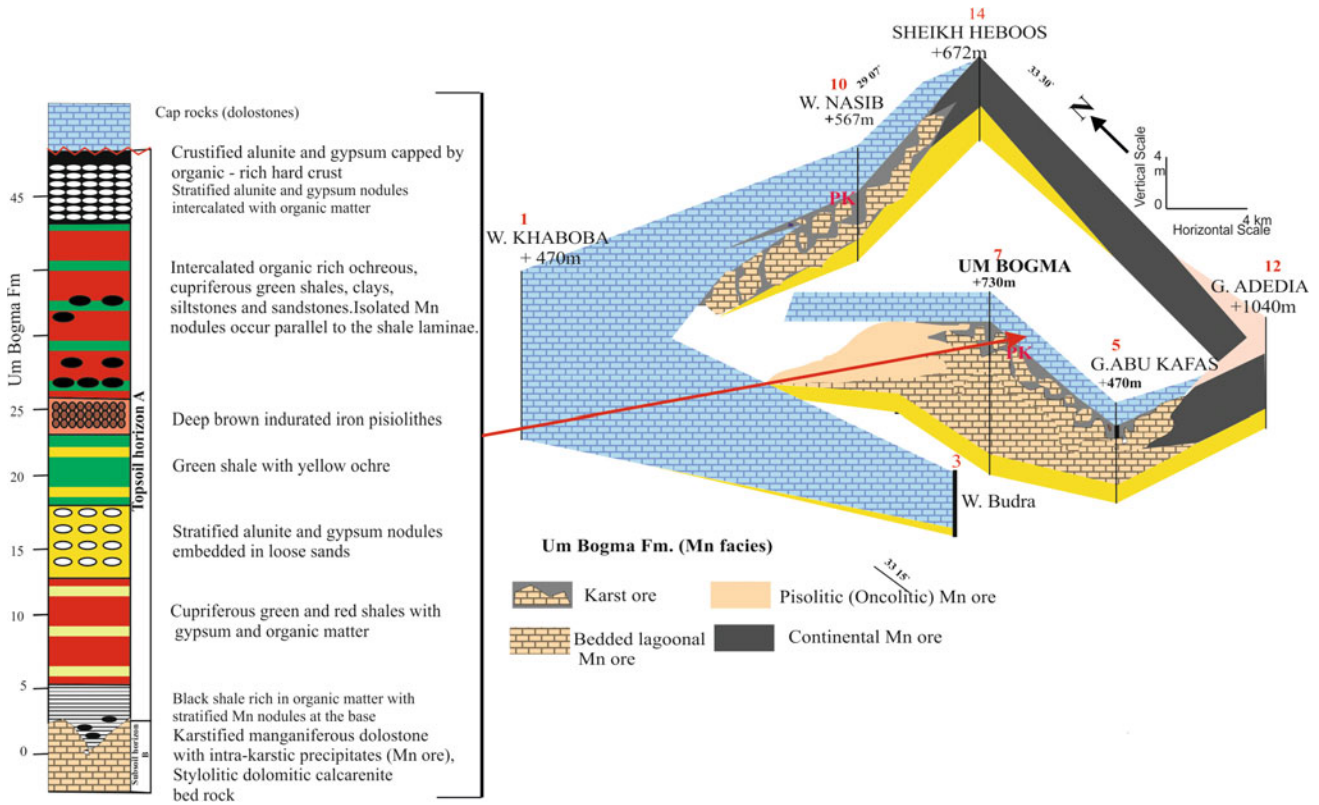

Fig. 14.41 Isometric diagram of Um Bogma Formation on the roght showing the stratigraphic set-up and geographic distribution of the different Mn ore facies (Abdel Motelib 1996; El Aref 1996, 2001; El Aref and Abdel Motelib 2001). Intra-Carboniferous paleokarest profile (PK) on the left (compiled and simplified after El Sharkawi et al. 1990a, b; Abdel Motelib 1996; El Aref et al. 1998)

extends laterally over a distance of about 3 Km^2 and is traceable on area of about 80 Km^2. Other small occurrences are also recorded in Wadi Um Deheiss El Bahari. The fine detailed geological, mineralogical and chemical integral data of this ore type appears in the Ph.D. Thesis of Dr. Abdel Motelib (1996). The ore forms a stratified bed, up to 80 cm thick, encountered within syn-rift Middle Miocene carbonate sequence of back-reef, fore-reef and lagoonal environments, interrupted by micro-unconformities. The Mn bed occurs within the upper algal lagoonal carbonate facies and is divisible into three zones (Fig. 14.42), an upper and lower red Fe-rich oolitic/oncolitic zones and a middle, much thicker black Mn-rich oolitic to oncolitic zone. These ore zones are made up of Mn and Fe ooids and oncoids of coarsening-upward arrangement, setting in earthy manganese and calcareous matrix. The essential Mn minerals are romanechit, manganite and pyrulosite, which are associated with hematite, goethite, calcite, dolomite, barite and anhydrite. The ore constituents show diverse varieties of megascopic and microscopic syn-depositional and syn-diagenetic textures. Abdel Motelib (1996) concluded that runoff carried Mn and Fe with other elements from weathered hinterlands to the site of oolite and oncolite formation where biogenic (microbial accretion) and physicochemical conditions, inducing differential mobility throughout marine digenesis are the essential parameters controlling the oolitization and oncolitization of the framework components and separation of the Mn and Fe rich zones. Biogenic accretion, compaction, oxidation-dehydration, corrosion, spastolith formation, brecciation, dolimitization and late calcite and barite cementation are the main diagenetic processes affecting the Mn bed.

The ore geometry, accessibility, extension, mineralogical and chemical characteristics support the necessity for further investigation and reserve estimation to evaluate its ability for at least small-scale mining project.

14.9.2.3 Pre-Cambrian? Mn Vein-Type (Wadi Meialeik)

Manganese–iron deposits occur in the Pre-Cambrian pink granites at Wadi Diieb and in the Pre-Cambrian amphibolite at Wadi Meialeik, west Marsa Wadi Lahmi, Red Sea coast (Fig. 14.37). The age relation of the Mn–Fe deposits was

Table 14.6 The main characteristics of Um Bogma Mn ore facies (compiled from El Sharkawi et al. 1990a, b; Abdel Motelib 1996; El Aref et al. 2001)

Ore types (facies) and environment				Sedimentary structures	Ore lithologies	Ore fabrics	Paragenesis
– Stratiform continental (channel fill) Mn conglomerate, sandstone and mudstone (Fig. 14.4, Zone D). – Surface slope deposits accumulated through mud flow of braided tributaries with derivation of framework components from nearby contiguous sources				Fining-upward cyclic sequences with erosive bases, lamination and cross lamination, desiccations, lenticular bedding, scouring and erosive sols	– Mn paraconglomerate – Mn sandstone, – Mn mudstone – Red ochers	Mn boulders, gravels, sands and silts; Mn-rich matrix, colloform encrustation and cockade structure, filamentous algae, dendritic leaf-like and cellular patterns	Pyrolusite, romanechite, Goethite, hematite, kaolinite, quartz, organic remains
Karstified manganiferous dolostone and mudstone (Drowned karst profile), Fig. 14.4, zone C	Soil horizons	Topsoil (eluvial)horizon	– Karst lateritization and bouxitization involving eluviation and illuviation processes (pedogenesis) and development of subsoil and topsoil horizons	Alternating multicolored layers of organic-rich alunitic, kaolinitic, gibssitic, cuprefrous, and ochreous shales, siltstones and sandstones with abundant Cu, U, and V minerals and organic and plant remains (polymorphs), Shrinkage cracks, nodular forms, rhizoliths and rhyzoctions			Mn and Fe oxides and hydroxides; Cu, U, V, carbonates, chlorides, silicates, sulphates, phosphates and vanadates; kaolinite, gibbsite, calcite, quartz, jarosite, dolomite, ankarite. illite, montomorilonite
		Subsoil (illuvial) horizon		Mn conglomerates in earthy matrix, Crackle breccia and Mn-rich speleothems, nodules and concretions, Collapse breccia, earthy Mn-rich precipitates and encrustation, Basal undulated surface of cuspate form dominated by solution sinkholes and small to large scale solution features (cavities) with collapse breccias and rotten stone fragments, Mn encrustations			
	(lower horizon) Parental (intact) rocks, (up to 9 m thick)		– Lagoonal to swampy manganiferous mudstones and dolostones, – Deposition in coastal low energy shallow lagoons, charged with Mn continental sediments, – Prevalence of splash meteoric water with continuous uplifting and subsequent karstification	– Stratified stylolitic manganiferous dolostones, – Cyclic alternating beds with ooids and peloids, Abundant marine fossils and bioclasts, – Thin lamination and desiccation cracks, Stratified gypsum and barite nodules, Crackle breccia, in sito brecciation, abundant in-filled solution openings (variable diameters) with collapse breccia and Mn-rich encrustation along cave walls, ceiling and floors, Pulverization, Mottling, Intensive karstification and brecciation towards the overlying horizon	– Laminated and crustified manganiferous mudstone, – Mottled ferruginous and manganiferous mudstone, – Manganiferous dolostone	– Bedding, lamination and desiccation, stylolitization, – In place brecciation and fracturing strata, – Mn concretions, pisoliths and glaebules, – Reddening, – Encrustation, filling cavities and solution opening, – Collapsing, cockade structure, boxwork and alveolar structures, – Dedolomitization, – Leaching and accumulation of Mn-rich earthy materials (soils), – Filamentous algal fabrics	Pyrolusite, manganite, romanechite, fearon dolomite, dedolomite goethite, hematite, Fe sesquioxides, calcite barite, gypsum, kaolinite
– Stratiform pisolitic (oncolitic) ore type (0–5 m thick), (Fig. 14.4, zone B) – Near shore (marginal marine environment, under shoaling storm-generated conditions				– Fairly bedded showing small-scale coarsening—upward arrangement, bioturation, abundant organic matter, pisolitths (oncoids), shrinkage fractures, ripple marks, flaser structure, matrix to grain—supported fabrics, skeletal fragments	Organic-rich bioturbated manganiferous and/ferruginousmudstones		Pyralusite, Geothite, calcite, barite, gypsum, anhydrite, Fe and Mn sesquioxides

Table 14.7 Chemical composition of representative Mn ore types (facies). 1 = Mn-rich conglomerate; 2 = Mn-rich pisolitic (oncolitic) Mn ore; 3 = Mn – rich mudstone (intact bedded ore, parent rock); 4 = Crustified Mn ore, cave filling 006Fr Karst ore (Abdel Motelib 1996)

	SiO	Al_2O_3	Fe_2O_3	Foe	MnO_2	MgO	CaO	CaO	K_2O	TiO_2	P_2O_5	H_2O^-	H_2O^+	CO_2	Org. Matt.	BaO	SO_3-	Total
1	28.94	0.46	15.90	1.62	36.96	0.33	3.64	0.32	0.06	0.02	0.38	0.92	2.96	0.77	5.61	0.86	–	9975
2	9.00	0.38	2.76	0.87	43.01	0.61	21.61	0.32	0.12	0.11	0.52	0.61	1.14	17.09	1.35	–	–	99.52
3	3.70	1.25	14.40	3.31	52.94	0.33	0.92	1.07	0.06	0.05	0.66	0.22	1.88	0.18	18.82	–	–	99.79
4	2.88	0.46	2.85	1.45	84.55	0.29	3.53	0.13	0.03	0.01	0.20	0.64	0.43	2.18	0.22	–	–	99.76

given by El Shazly (1957) who proposed that they were formed by weathering of Pre-Cambrian rocks and supergene deposition in fissures while replacement proceeded mainly along the walls of the fissures. The geological setting, mineralogy, geochemistry, ore characteristics and mode of formation of this occurrence are discussed in detail by Salem et al. (2010). The ore occurs as veins of up to 125 cm in thickness, cutting across Pre-Cambrian metagabbroic rocks. The ore minerals are represented by colloform pyrulosite, psilomelane and ramsdellite with variable abundance of goethite, hematite and jarosite related to hydrothermal open space filling processes (Salem et al. 2010). The gangue minerals are quartz, calcite and plagioclase. The ore is considered as Mn–Fe ore and classified by Salem et. al. (2010) into three distinguished types: (a) Mn-rich ore type of up to 39.9% MnO and 6.13% FeO, (b) Fe–Mn ore type of up to 33.31% MnO and 17.81% FeO, and (c) Fe-rich ore type of up to 37.08% FeO and 0.77% MnO.

Although the most high grade Mn ores are extracted, the geological setting of the present ore type encourages further exploration for similar vein type deposits as well as further re-evaluation, exploitation and marketing of the low grade ore types for any updated required and suitable uses, through small scale mining investment.

14.9.2.4 Post-Miocene Surficial Mn Deposits (Halaib-Alba Region)

Post-Miocene Mn and Ba deposits are long extracted from Halaib-Elba-Abu Ramad land stretch (Fig. 14.37). The ores of this region are now under reinvestigation, reserve estimation and exploitation by the Egyptian Shalaten mining Company. The Manganese ores (up to 45% Mn) occur as supergene surfacial deposits covering the low relief Miocene rocks of the Red Sea coastal zone or as fracture filling in the nearby granitic Pre-Cambrian basement rocks (El Shazly 1957; El Shazly and Saleeb 1959). These authors related the origin of these deposits to weathering of the Pre-Cambrian rocks and supergene deposition in fissures and fault fractures of the Miocene and granitic rocks with replacement along the walls of the fissures. Contradictory, epigenetic low temperature origin is suggested by Basta and Saleeb (1971). The ore is composed essentially of rhythmic encrustations of botryoidal pyrolusite, psilomelane, cryptomelane, ramsdellite, todorkite and nsutite with goethite, colloform chalcedony, quartz and late barite and blocky calcite cements (El Shazly and Saleeb 1959; Basta and Saleeb 1971). Balkhanov and Razvalyayev (1981) described the deposits as a product of deep-seated trans-magmatic ore-bearing solutions associated with the Cenozoic rifting of the Red Sea Zone. El Aref (1996) classified this ore type as Neogene surficial strata-bound deposits related to Plio-Pleistocene uplifting phase and weathering.

14.9.3 Western Desert (El Bahariya Mn–Rich Iron Ore)

Productive high Manganese Fe ore deposits selectively extracting from the El Bahariya iron ore of the Western Desert as a byproduct are of prime requirement and successfully usable in the Egyptian Cement industries. The remaining minable reserves of this ore type are about 50 million tons of 4–6.5% MnO and 40–47% Fe ready for marketing.

14.9.4 General Recommendations

Despite of the relatively low quantity and quality of most of the Mn deposits of the aforementioned small scale ore sites, their geographic distribution, accessibility and general characteristics encourage further detailed investigations and marketing in order to optimize their economic benefits. The investment of these deposits should be taken into account during the development planning of the surrounding domains.

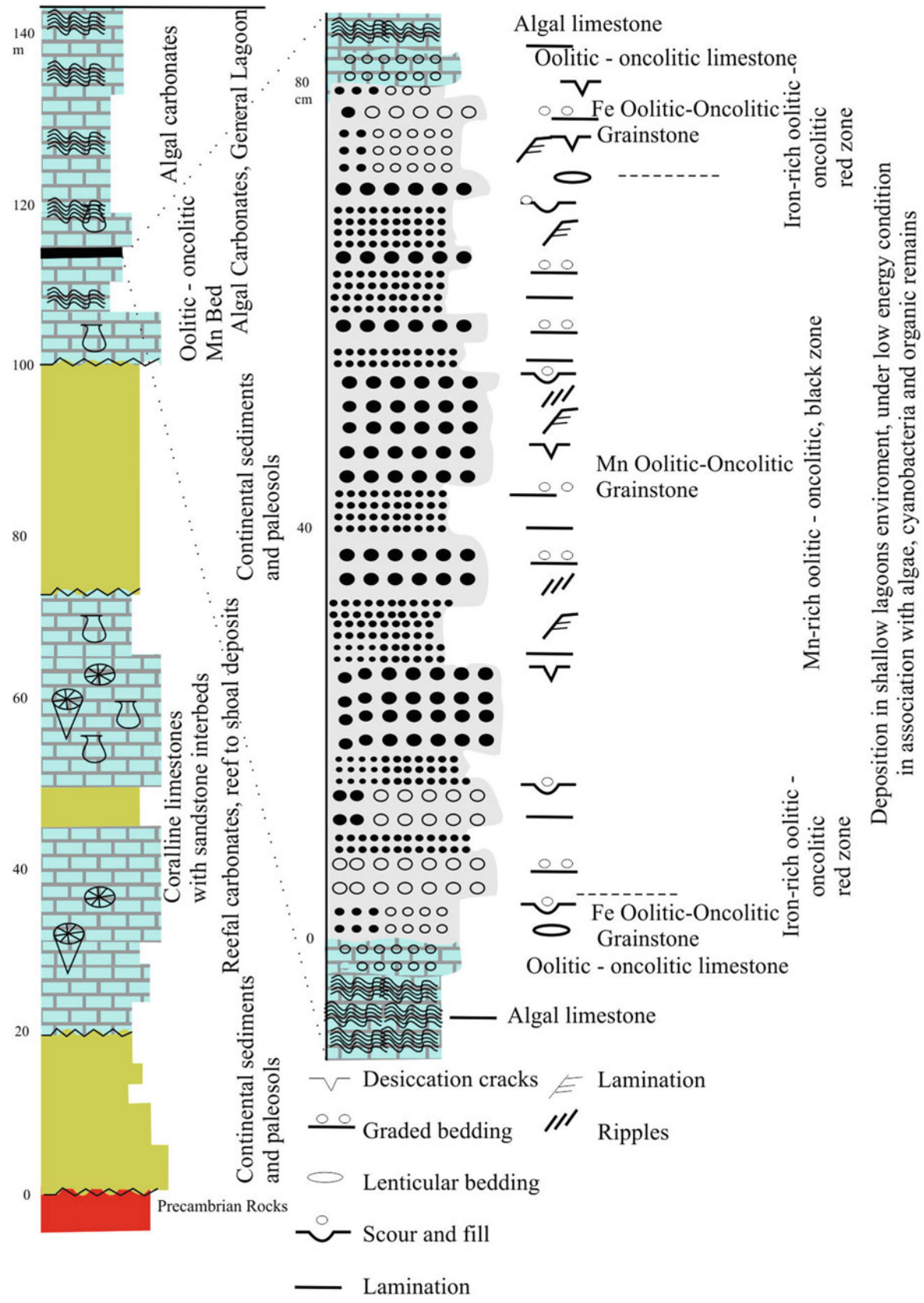

Fig. 14.42 Detailed lithostratigraphic log of the Mn bed of G. Abu Shaar El Qebli (Abdel Motelib 1996)

References

Abd El-Wahed M, Harraz H, El Behairy M (2016) Transpressional imbricate thrust zones controlling gold mineralization in the Central Eastern Desert of Egypt. Ore Geol Rev 78:424–446

Abdalla H, Helba H, Mohamed F (1998) Chemistry of columbite-tantalite minerals in rare metal granitoids, Eastern Desert, Egypt. Mineral Mag 62:821–836

Abdalla H, Mohamed F (1999) Mineralogical and geochemical investigation of emerald and beryl mineralisation, Pan-African Belt of Egypt: genetic and exploration aspects. J Afr Earth Sc 28:581–598

Abdalla HM, Matsueda H, Obeid MA, Takahashi R (2008) Chemistry of cassiterite in rare metal granitoids and the associated rocks in the Eastern Desert, Egypt. J Mineral Petrol Sci 103:318–326

Abdallah AM (1961) Note on the manganese-iron deposit in Wadi Araba, Gulf of Suez. J Geol U A R 5:77–79

Abdallah ShE, Ali Sh, Obeid MA (2018) Geochemistry of an Alaskan-type mafic-ultramafic complex in Eastern Desert, Egypt: new insights and constraints on the Neoproterozoic island arc magmatism. Geosci Front (in press). https://doi.org/10.1016/j.gsf.2018.04.009

Abdel Meguid A, Cuney M, Ammar S, Ibrahim T, Ali K, Shahin H, Omer S, Gaafar I, Masoud S, Khamis A (2003) Uranium potential of Eastern Desert granites. Egypt, Internal Research Reports, Nuclear Materials Authority, Egypt

Abdel Motelib A (1987) The cupriferous sediments in West Central Sinai, Egypt. Unpubl. MSc thesis, Cairo University, Faculty of Science, Egypt, 194 pp

Abdel Motelib A (1996) Geological and mineralogical studies of some manganese occurrences of Egypt. Unpubl. PhD thesis, Cairo University, Faculty of Science, Egypt, 304 pp

Abdel Naby H (2008) Genesis of secondary uranium minerals associated with jasperoid veins, El Erediya Area, Eastern Desert, Egypt. Mineral Depos 43:933–944

Abdel Naby H, Frisch W (2002) Origin of Wadi Haimur-AbuSwayel gneiss belt, south Eastern Desert, Egypt: petrological and geochronological constraints. Precambrian Res 113:307–332

Abdel Naby H, Frisch W, Hegner E (2000) Evolution of Pan-African Wadi Haimur metamorphic sole, Eastern Desert, Egypt. J Metamorph Geol 18:639–651

Abdel-Karim AM, Barakat MG (2017) Separation, upgrading, and mineralogy of placer magnetite in the black sands, northern coast of Egypt. Arab J Geosci 10:298. https://doi.org/10.1007/s12517-017-3075-0

Abdel-Karim AM, El-Shafey AM (2012) Mineralogy and chemical distribution study of placer cassiterite and some associated new recorded minerals, East Rosetta, Egypt. Arab J Geosci 5:807–816

Abdelnasser A, Kumral M (2016) Mineral chemistry and geochemical behavior of hydrothermal alterations associated with mafic intrusive-related Au deposits at the Atud area, Central Eastern Desert, Egypt. Ore Geol Rev 77:1–24

Abouzeid AM, El Wgeeh MA (2008) Mineral industry in Egypt—state of the art. In: Proceedings 11th international mineral processing symposium, Belek, Antalya, Turkey, pp 1–27

Abouzeid AM, Khaled AM (2011) Mineral industry in Egypt—Part I: metallic mineral commodities. Nat Res 2:35–53

Abu El Saadat MM (2009) Arab mining society, Special issue on the Egyptian Iron Ores, Cairo, pp 20–28

Abu El-Ela FF (1996) The petrology of the Abu Zawal gabbroic intrusion, Eastern Desert, Egypt: an example of an island-arc setting. J Afr Earth Sci 22:147–157

Abu El-Enen MM, Okrusch M, Will TM (2003) Metapelitic assemblages in the Umm Zeriq schists, central western Kid Belt, Sinai Peninsula, Egypt. NeuesJahrbuchfürMineralogie–Abhandlungen 178:277–306

Abu-Deif A (1991) The relation between the uranium mineralization and tectonics in some Pan-African granites, West of Safaga, Eastern Desert, Egypt. Unpublished PhD thesis, Assiut University, 216 pp

Abu-Deif A, Abouelnaga HS, Hassanein HI (2001) Distribution of radioelements and its relation to uranium migration, El Erediya exploratory tunnels, central Eastern Desert, Egypt. J King Abdul-Aziz Univ (Earth Science) 13:19–40

Ahmed AH (2007) Diversity of platinum-group minerals in podiform chromitites of the late Proterozoic ophiolite, Eastern Desert, Egypt: genetic implications. Ore Geol Rev 32:1–19

Ahmed AH (2013) Highly depleted harzburgite-dunite-chromitite complexes from the Neoproterozoic ophiolite, south Eastern Desert, Egypt: a possible recycled upper mantle lithosphere. Precambrian Res 233:173–192

Ahmed AH, Arai S (2002) Platinum-group element geochemistry in podiform chromitites and associated peridotites of the Precambrian ophiolite, Eastern Desert, Egypt. In: Proceedings, 9th international platinum symposium, Billings, Montana, pp. 1–4

Ahmed AH, Arai S, Attia AK (2001) Petrological characteristics of podiform chromitites and associated peridotites of the Pan African ophiolite complexes of Egypt. Miner Deposita 36:72–84

Ahmed AH, Gharib M (2016) Porphyry Cu mineralization in the eastern desert of Egypt: inference from geochemistry, alteration zones, and ore mineralogy. Arab J Geosci 9:179

Ahmed AH, Hanghøj K, Kelemen PB, Hart SR, Arai S (2006) Osmium isotope systematics of the Proterozoic and Phanerozoic ophiolitic chromitites: in-situ ion probe analysis of primary Os-rich PGM. Earth Planet Sci Lett 245:777–791

Ahmed AH, Moghazi AKM, Moufti MR, Dawood YH, Ali KA (2016) Nature of the lithospheric mantle beneath the Arabian Shield and genesis of Al-spinel micropods: evidence from the mantle xenoliths of Harrat Kishb, Western Saudi Arabia. Lithos 240–243:119–139

Ali KA, Stern RJ, Manton WI, Johnson PR, Mukherjee SK (2010) Neoproterozoic diamictite in the Eastern Desert of Egypt and Northern Saudi Arabia: evidence of ~750 Ma glaciation in the Arabian-Nubian Shield. Int J Earth Sci 99:705–726

Ali KG (2003) Geology and radioactivity of Naba-Nuweibi area, Central Eastern Desert, Egypt, Ain Shams Univ., Cairo, Egypt, 194 pp

Ali M, Lentz D, Hall D (2011) Mineralogy and geochemistry of Nb-, Ta-, Sn-, U-, Th-, and Zr-bearing granitic rocks from Abu Rusheid shear zones, South Eastern Desert, Egypt. Chin J Geochem 30:226–247

Alt JC (1994) A sulfur isotopic profile through the Troodos ophiolite, Cyprus: primary composition and the effects of seawater hydrothermal alteration. Geochim Cosmochim Acta 58:1825–1840

Amin MS (1947) A tin-tungsten deposit in Egypt. Econ Geol 42:637–671

Amin MS (1954) The ilmenite deposit of Abu Ghalqa, Egypt. Econ Geol Bull Soc Econ Geol 49:77–87

Arai S (1997) Control of wall-rock composition on the formation of podiform chromitites as a result of magma/peridotite interaction. Resour Geol 47:177–187

Arai S, Abe N (1995) Reaction of orthopyroxene in peridotite xenoliths withalkali–basalt melt and its implication for genesis of Alpine-type chromitite. Am Miner 80:1041–1047

Arai S, Ahmed AH (2018) Secular change of chromite concentration processes from the Archean to the Phanerozoic. In: Processes and ore deposits of ultramafic-mafic magmas through space and time. http://dx.doi.org/10.1016/B978-0-12-811159-8.00006-8

Arai S, Yurimoto H (1994) Podiform chromitites of the Tari-Misaka ultramafic complex, southwestern Japan, as mantle-melt interaction products. Econ Geol 89:1279–1288

Asran M (1985) Geology, petrography and geochemistry of the apogranites at Nuweibi and Abu Dabbab areas, Eastern desert, Egypt, M Sc thesis, Assiut University, Egypt

Azer MK, Stern R (2007) Neoproterozoic (835–720 Ma) serpentinites in the Eastern Desert, Egypt: fragments of forearc mantle. J Geol 115:457–472

Balkhanov VV, Razvalyayev V (1981) The origin of the manganese deposits of the western shore of the Red Sea (in association with rifting). Int Geol Rev 23:162–166

Barnes SJ, Maier WD (2002) Platinum-group elements and microstructures from Impala Platinum Mines, Bushveld Complex. J Petrol 43:171–198

Basta EZ, Girgis MH (1969) Petrological, mineralogical, and geochemical studies of the magnetite-ilmenite-apatite ore (nelsonite) from Kolmnab, south Eastern Desert, U.A.R. Egypt Acad Sci 22:47–157

Basta EZ, Saleeb GR (1971) Elba manganese ores and their origin, South Eastern Desert. U A R Mineral Mag 38:235–244

Basta EZ, Takla MA (1968a) Petrological studies on Abu Ghalaga ilmenite occurrence, Eastern Desert. Egypt J Geol 12:43–72

Basta EZ, Takla MA (1968b) Mineralogy and origin of Abu Ghalaga ilmenite occurrence, Eastern Desert. Egypt J Geol 12:87–124

Basta FF, Maurice AE, Fontboté L, Favarger PY (2011) Petrology and geochemistry of the banded iron formation (BIF) of Wadi Karim and Um Anab, Eastern Desert, Egypt: implications for the origin of Neoproterozoic BIF. Precambrian Res 187:277–292

Bau M, Dulski P (1996) Distribution of yttrium and rare-earth elements in the Penge and Kuruman iron-formations, Transvaal Supergroup, South Africa. Precambrian Res 79:37–55

Bennett J, Mosley P (1987) Current research in African earth sciences

Bierlein FP, Crowe DE (2000) Phanerozoic orogenic lode gold deposits. In: Hagemann SG, Brown PE (eds) Gold in 2000: reviews in economic geology, vol 13, pp 103–139

Bierlein FP, Groves DI, Goldfarb RJ, Dube B (2006) Lithospheric controls on the formation of provinces hosting giant orogenic gold deposits. Miner Deposita 40:874–886

Boskabadi A, Pitcairn IK, Broman C, Boyce A, Teagle DAH, Cooper MJ, Azer MK, Stern J, Mohamed FH, Majka J (2017) Carbonate alteration of ophiolitic rocks in the Arabian-Nubian Shield of Egypt: sources and compositions of the carbonating fluid and implications for the formation of Au deposits. Int Geol Rev 59:391–419

Boyd R (2012) The EU potential critical minerals resource. Critical minerals for the clean energy and high technology industries

Breitkreuz C, Eliwa H, Khalaf I, El Gameel K, Bühler B, Sergeev S, Larinov A, Murata M (2010) Neoproterozoic SHRIMP UePb zircon ages of silica-rich Dokhan Volcanics in the North Eastern Desert, Egypt. Precambrian Res 182:163–174

Bugrov V (1968) In UNDP technical report no. 3, Mineral potential of the Aswan region. Geochemical operations, pp 31–33

Bugrov V, Abu El-Gadael A, Soliman M (1973) Rare-metallic albitities as a new type of ore-mineralization in Egypt. Ann Geol Surv Egypt III:185–206

Burrows DR, Wood PC, Spooner ET (1986) Carbon isotope evidence for an magmatic origin for Archaen Au-quartz vein ore deposits. Nature 321:851–854

Carten R (1988) Comparison of field-based studies of the Henderson porphyry molybdenum deposit, Colorado, with experimental, and theoretical models of porphyry systems. In: Recent advances in the geology of granite-related mineral deposits, vol 39, pp 1-12

Carten RB, Geraghty EP, Walker BM, Shannon JR (1988) Cyclic development of igneous features and their relationship to high-temperature hydrothermal features in the Henderson porphyry molybdenum deposit, Colorado. Econ Geol 83:266–296

Carter GS (1975) Final report on the investigation of copper ± nickel sulphide mineralization at Gabbro Akarem. Internal Rep, As-wan Mineral Survey Project, Geol Surv Egypt, Cairo

Černý P (1989) Characteristics of pegmatite deposits of tantalum, Lanthanides, Tantalum and Niobium. Springer, pp 195–239

Černý P, Ercit T (1989) Mineralogy of niobium and tantalum: crystal chemical relationships, paragenetic aspects and their economic implications, Lanthanides, tantalum and niobium. Springer, pp 27–79

Černý P, Ercit T, Vanstone P (1996) Petrology and mineralization of the Tanco Rare-Element Pegmatite Southeastern Manitoba–Field trip Guidebook A4; Geological Association of Canada/Mineralogical Association of Canada, Annual Meeting, Winnipeg, Manitoba, p 72

Cox GM, Halverson GP, Minarik WG, Le Heron DP, Macdonald FA, Bellefroid EJ, Strauss JV (2013) Neoproterozoic iron formation: an evaluation of its temporal, environmental and tectonic significance. Chem Geol 362:232–249

Craw D, Upton P, MacKenzie DJ (2009) Hydrothermal alteration styles in ancient and modern orogenic gold deposits, New Zealand. NZ J Geol Geophys 52:11–26

Danielson A, Möller P, Dulski P (1992) The europium anomalies in banded iron formations and the thermal history of the oceanic crust. Chem Geol 97:89–100

Dardir A, Gadalla S (1969) Geology of molybdenite deposits between Lat. 27 00 and 27 30′ N (Eastern Desert of Egypt), Internal report

Dardir AA, Abu Zeid KM (1972) Geology of the basement rocks between latitudes 27 00′ and 27 30′ N, Eastern Desert. Ann. Geol. Surv. Egypt 2:129–159

Dawood YH, Abdel-Naby HH (2007) Mineral chemistry of monazite from the black sand deposits, northern Sinai, Egypt: a provenance perspective. Min Mag 71:389–406

de Boorder H (2012) Spatial and temporal distribution of the orogenic gold deposits in the Late Palaeozoic Variscides and Southern Tianshan—how orogenic are they? Ore Geol Rev 46:1–31

Duchesne J-C, Liégeois J-P (2015) The origin of nelsonite and high-Zr ferrodiorite associated with Proterozoic anorthosite. Ore Geol Rev 71:40–56

EGSMA (1998) Metallogenic map—Arab Republic of Egypt, Meatllic ores and non-metallic deposits, Scale 1:1,000,000. Egyptian geological survey and mining authority, pp Exploration Sheet

El Aref MM (1993) Pedogenesis and related gibbsite and natroalunite formation in Um Gereifat Area, Red Sea coastal zone, Egypt. Egypt J Geol 37(1):307–333

El Aref MM (1996) Phanerozoic stratiform and stratabound deposits of Egypt; their stratigraphic, paleo-geographic, topographic and environmental controls. In: Proceedings of the 2nd international conference on geology of the Arab world (1994), pp 97–124

El Aref MM (1999) Achievements of the Egyptian iron exploration project (IEP, 1993–1997). In: Proceedings of the fourth international conference on geology of the Arab world (1998), pp 10–22

El Aref MM (2001) Ores in the sedimentary cover. Phanerozoic stratabound ore deposits. Metallogenic map-Arab Republic of Egypt

El Aref MM, Abdel Wahed M, El Dougdoug A, El Manawi AW (1993a) Geological setting and deformational history of Umm Nar BIF and associated rocks, Eastern Desert, Egypt. Egypt J Geol 73:205–230

El Aref MM, Adel Motelib A (2001) Geology, facies distribution and environments of the Carboniferous stratabound Mn deposits of Um Bogma region, Sinai, Egypt. In: Proceedings of the second international conference on the geology of Africa, Assiut University, 2001, IA, pp 61–77

El Aref MM, El Dougdoug A, Abdel Wahed M, El Manawi AW (1993b) Diagenetic and metamorphic history of the Umm Nar BIF, Eastern Desert, Egypt. Mineral Deposita 28:264–278

El Aref MM, Helba AA, Saad F (2001) Lutetian ramp carbonate facies, hierarchy and environments, northeast El Bahariya depression. In:

Proceedings of the second international conference on the geology of Africa, Assiut University, 2001, IB, pp 385–403
El Aref MM, Hussein HA, El Aassy IE, Aita SK (1998) Mineralogy and geochemistry of the Carboniferous stratabound U karst latosol of Um Bogma region, west central Sinai, Egypt. In: Fourth international conference on geology of the Arab World (GAW4), Cairo University, abstract
El Gemmizi MA (1985) Note on the occurrence of gold and cassiterite in the Egyptian beach placer deposits. Econ Geol 85:769–772
El Habaak GH (1992) Geology of banded iron formation and associated metavolcanics at Wadi Kareim Area, Eastern Desert, Egypt. PhD thesis, Faculty of Science, Assiut University, 338 pp
El Haddad MA (1996) The first occurrence of platinum group minerals (PGM) in a chromitite deposit in the Eastern Desert, Egypt. Mineral Deposita 31:439–445
El Midany A, Abdel Khalek N (2007) Beneficiation of Eastern Desert iron ores: ore complexity and processing limitations. In: Iron symposium (2007), Central Metallurgical Research and Development Institute, Cairo, Egypt
El Sharkawi M, El Aref MM, El Manawi AW (1989) Paleoenvironments, classification and diagenetic aspects of ironstones in the Mesozoic sediments of El Maghara area, Egypt. Egypt Mineral 1:1–25
El Sharkawi MA, El Aref MM, Abdel Motelib A (1990a) Manganese deposits in Carboniferous paleokarst profile, Um Bogma region, West Central Sinai, Egypt. Mineral Deposita 25:34–43
El Sharkawi MA, El Aref MM, Abdel Motelib A (1990b) Syngeneic and paleo-karstic copper mineralization in the Paleozoic platform sediments of West Central Sinai, Egypt. In: Parnell J (ed) Special publication number 11 of the international association of sedimentologists, sediment-hosted mineral deposits. Black Well Scientific Publications, pp 159–172
El Sharkawi MA, El Aref MM, Mesaed A (1999) Stratigraphic setting and paleoenvironment of the Coniacian-Santonian ironstones of Aswan, South Egypt. Geol Soc Egypt Spec. Publ. 2:243–278
El Shazly EM (1957) Classification of Egyptian mineral deposits. Egypt J Egypt 1:1–21
El Shazly EM, Saleeb GR (1959) Contribution to the mineralogy of Egyptian manganese deposits. Econ Geol 54:59–71
El-Askary MA, Frihy OE (1987) Mineralogy of the subsurface sediments at Rosetta and Damietta promontories. Egypt Bull Inst Ocean Fish 13:111–120
El-Azabi M, Eweda Sh (1996) Clastic-carbonate sequence of Gabal El Sara, Sharm El Sheikh Area, southern Sinai, Egypt. Egypt J Geol 40:805–844
Elderfield H, Greaves MJ (1982) The rare earth elements in seawater. Science 296:214–219
El-Gaby S, List FK, Tehrani R (1988) Geology, evolution and metallogenesis of the Pan-African belt in Egypt. In: El Gaby S, Greiling RO (eds) The Pan-African belt of Northeast Africa and adjacent areas. Vieweg and Sohn, Weisbaden, pp 17–68
El-Gamal AA, Saleh IH (2012) Radiological and mineralogical investigation of accretion and erosion coastal sediments in Nile Delta Region, Egypt. J Ocean Marine Sci 3:41–55
El-Gemmizi MA (1984) On the occurrence and genesis of mud zircon in the radioactive psammitic gneisses of Wadi Nugrus, Eastern Desert, Egypt. J Univ Kawait, pp 285–294
El-Hinnawi EE (1964) Mineralogical and geochemical studies on Egyptian (U.A.R.) black sands. Beit zur Mineral Petrogr 9:519–532
El-Hinnawi EE (1969) Electron-probe investigation of some intergrowths in iron titanium minerals from Rosetta black sands. Contrib Mineral Petrol 21:332–337
El-Kammar AA, Ragab AA, Moustafa MI (2011) Geochemistry of economic heavy minerals from Rosetta black sand of Egypt. J King Abdulaziz Univ, Earth Sci Sec 22:69–97
El-Kammar AM, El-Hazik N, Mahdi M, Aly N (1997) Geochemistry of accessory minerals associated with radioactive mineralization in the central Eastern Desert, Egypt. J Afr Earth Sci 25:237–252
El-Kammar AM, Ibrahim ME, Amer TE, Abu Khoziem HA (2007) Aspects of alteration in two mica granites from Halaib area, south Eastern Desert, Egypt. In: The 10th international mining petroleum metallurgical engineering conference, Assuit University, 6–8 March
El-Kazzaz Y (1996) Shear zone-hosted gold mineralization in South Eastern Desert, Egypt. Proc Geol Surv Egypt Cent Conf, pp 185–204
El-Ramly M, Ivanov S, Kochin G (1970) Tin-tungsten mineralization in the Eastern Desert of Egypt. In: Studies on some mineral deposits of Egypt. The Egyptian geological survey, Cairo, pp 43–52
El-Sadek MA, Ammar AA, Elkhateeb SA (2012) Analysis and interpretation of the field and laboratory geophysical measurements of black-sand beach deposits, East Rosetta, Egypt. Intern J Geophys 1:1–10
El-Shazly AK, Khalil KI (2014) Banded iron formations of Um Nar, Eastern Desert of Egypt: P-T-X conditions of metamorphism and tectonic implications. Lithos 196–197:356–375
El-Shazly AK, Khalil KI (2016) Metamorphic and geochronologic constraints on the tectonic evolution of the Central Eastern Desert of Egypt. Precambrian Res 283:144–168
El-Shazly EM (1959) Report on the ilmenite ore at Abu Ghalaga, Eastern Desert. Unpubl Rep, Geol Surv Mineral Res Dept, Cairo
El-Tabal H (1979) Mineralogical studies on some rare metal apogranites from Nuweibi and Abu Dabbab areas, Eastern Desert, Egypt. MSc thesis, Al-Azhar Universiti, Cairo
El-Tokhi M, El-Muslem A (2002) Fluid inclusions in the gold-bearing quartz veins at Um Rus area, Eastern Desert, Egypt. Chin J Geochem 21:131–139
England PC, Thompson AB (1984) Pressure temperature time paths of regional metamorphism I. Heat transfer during the evolution of regions of thickened continental crust. J Petrol 25:894–928
Eyuboglu Y, Dudas FO, Santosh M, Yi K, Kwo S, Akaryali E (2010) Petrogenesis and U–Pb zircon chronology of adakitic porphyries within the Kop ultramafic massif (Eastern Pontides Orogenic Belt, NE Turkey). Gondwana Res 24:742–766
Fetherston JM (2004) Tantalum in Western Australia. Geological Survey of Western Australia
Finger F, Helmy HM (1998) Compositions and total-Pb model ages of monazite from high grade paragneises in the Abu Swayel area, southern Eastern Desert, Egypt. Mineral Petrol 62:269–289
Fouda MFR, Amin RS, Saleh HI, Labib AA, Mousa HA (2010) Preparation and characterization of nanosized titania prepared from beach black sands broad on the Mediterranean Sea coast in Egypt via reaction with acids. Aus J Basic Appl Sci 4:4540–4553
Fowler A, Hassen IS, Osman AF (2010) Neoproterozoic structural evolution of SE Sinai, Egypt: II. Convergent tectonic history of the continental arc Kid Group. J Afr Earth Sci 58:526–546
Frihy OE (2007) The Nile Delta: processes of heavy mineral sorting and depositional patterns. In: Mange MA, Wright DT (eds) Heavy minerals in use, Develop Sed, vol 58. Elsevier, Amsterdam, pp. 49–74
Frihy OE, Lotfy MF (1997) Shoreline changes and beach-sand sorting along the northern Sinai coast of Egypt. Geo-Marine Lett 17:140–146
Frihy OE, Lotfy MF, Komar PD (1995) Spatial variations in heavy minerals and patterns of sediment sorting along the Nile Delta, Egypt. Sed Geol 97:33–41
Fritz H, Abdelsalam M, Ali K, Bingen B, Collins AS, Fowler AR, Ghebreab W, Hauzenberger CA, Johnson P, Kusky T, Macey P, Muhongo S, Stern RJ, Viola G (2013) Orogen styles in the east African orogens: a review of the Neoproterozoic to Cambrian tectonic evolution. J Afr Earth Sci 86:65–106

Fritz H, Dallmeyer DR, Wallbrecher E, Loizenbauer J, Hoinkes G, Neumayr P, Khudeir AA (2002) Neoproterozoic tectonothermal evolution of the Central Eastern Desert, Egypt: a slow velocity tectonic process of core complex exhumation. J Afr Earth Sci 34:137–155

Fu B, Kendrick MA, Fairmaid AM, Phillips D, Wilson CJL, Mernagh TP (2012) New constraints on fluid sources in orogenic gold deposits, Victoria, Australia. Contrib Miner Petrol 163: 427–447

Fyfe WS (1992) Magma underplating of continental crust. J Volcanol Geoth Res 50:33–40

Fyfe WS, Kerrich R (1985) Fluids and thrusting. Chem Geol 49:353–362

Gaafar I (2014) Geophysical mapping, geochemical evidence and mineralogy for Nuweibi rare metal albite granite, Eastern Desert, Egypt. Open J Geol 4:108–136

Gaafar IM, Ali KG (2015) Geophysical and geochemical signature of rare metal granites, Central Eastern Desert, Egypt: implications for tectonic environment. Earth 4:161–179

Gaboury D (2013) Does gold in orogenic deposits come from pyrite in deeply buried carbon-rich sediments?: Insight from volatiles in fluid inclusions. Geology 41:1207–1210

Garofalo PS, Fricker PS, Gunther MB, Bersani D, Lotticci PP (2014) Physical–chemical properties and metal budget of gold-transporting hydrothermal fluids in orogenic deposits. In: Garofalo PS, Ridley JR (eds) Gold-transporting hydrothermal fluids in the earth's crust, vol 402. Geological Society Special Publication, pp 71–102

Garson MS, Shalaby IM (1976) Precambrian-Lower Paleozoic plate tectonics and metallogenesis in the Red Sea region. Geological Association of Canada, Special paper no 14

Gindy AR (1961) Radioactivity in monazite, zircon and "radioactive black" grains in black sands of Rosetta, Egypt. Econ Geol 56: 436–441

Goldfarb RJ, Baker T, Dube B, Groves DI, Hart CJR, Gosselin P (2005) Distribution, character, and genesis of gold deposits in metamorphic terranes. Econ Geol, 100th Anniversary volume, pp 407–450

Goldfarb RJ, Groves DI (2015) Orogenic gold: common or evolving fluid and metal sources through time. Lithos 233:2–26

Goldfarb RJ, Groves DI, Gardoll S (2001) Orogenic gold and geologic time: a global synthesis. Ore Geol Rev 18:1–75

Goldfarb RJ, Santosh M (2014) The dilemma of the Jiaodong gold deposits: are they unique? Geosci Front 5:139–153

González TL, Polonio FG, Moro FJL, Fernández AF, Contreras JLS, Benito MCM (2017) Tin-tantalum-niobium mineralization in the Penouta deposit (NW Spain): textural features and mineral chemistry to unravel the genesis and evolution of cassiterite and columbite group minerals in a peraluminous system. Ore Geol Rev 81:79–95

Greiling R, Kröner A, El-Ramly M, Rashwan A (1988) Structural relationships between the southern and central parts of the Eastern Desert of Egypt: details of a fold and thrust belt. The Pan-African belt of Northeast Africa and adjacent areas, 121146

Groves DI, Goldfarb RJ, Gebre-Mariam M, Hagemann SG, Robert F (1998) Orogenic gold deposits: a proposed classification in the context of their crustal distribution and relationship to other gold deposits. Ore Geol Rev 13:7–27

Groves DI, Goldfarb RJ, Robert F, Hart CJR (2003) Gold deposits in metamorphic belts: overview of current understanding, outstanding problems, future research, and exploration significance. Econ Geol 98:1–29

Groves DI, Santosh M (2016) The giant Jiaodong gold province: the key to a unified model for orogenic gold deposits? Geosci Front 7:409–417

Halverson GP, Poitrasson F, Hoffman PF, Nedelec A, Montel J-M, Kirby J (2011) Fe isotope and trace element geochemistry of the Neoproterozoic syn-glacial Rapitan iron formation. Earth Planet Sci Lett 309:100–112

Hammoud NS, Khazback AE (1984) Traces of native gold particles in Egyptian northern beach heavy minerals deposits. Egypt J Geol 28:79–82

Harbi HM (2008) Geology and lithostratigraphy of the ultramafic-mafic rocks and associated mineralizations, Wadi Khamal area, West-Central Arabian Shield. J King Abdulaziz Univ, Earth Sci Sec 19:119–157

Harbi HM, El-Shamawi MSE, Eldougdoug AA (2011) Mineral processing and extraction of rare-earth elements from the Wadi Khamal Nelsonite ore, Northwestern Saudi Arabia. Arab J Geosci 4:353–363

Harraz HZ (2000) A genetic model for a mesothermal Au deposit: evidence from fluid inclusions and stable isotopic studies at El-Sid Gold Mine, Eastern Desert. J Afr Earth Sc 30:267–282

Harraz HZ (2002) Fluid inclusions in the mesozonal gold deposit at Atud mine, Eastern Desert, Egypt. J Afr Earth Sci 35:347–363

Harraz HZ, Dahhar MA (1993) Nature and composition of gold-forming fluids at Umm Rus area, Eastern Desert, Egypt: evidence from fluid inclusions in vein materials. J Afr Earth Sci 16:341–353

Hassan AS (2014) Zr-Y-Nb-REE mineralization associated with microgranite and basic dykes at EL Sella shear zone, South Eastern Desert, Egypt. SpringerOpen Journals

Hassan M (1964) Geology and petrographical studies of the radioactive minerals and rocks in Wadi Sikait-Wadi El-Gemal area Eastern Desert. UAR M Sc thesis, Faculty of Science, Cairo University, p 165

Hawa YMA (2014) Mineral chemistry of extraordinary ilmenite from the Gabbroic rocks of Abu Ghalaga area, Eastern Desert, Egypt: evidence to metamorphic modification. In: The 6th international conference on geological sciences and engineering (ICGSE), 28–29 August, 2014, Paris 1(8), p 68 (Abstract). www.waset.org/abstracts/7253

Hedrick JB, Waked L (1989) Heavy minerals, including monazite, in Egypt's black sand deposits. J Less Common Metals 148:79–84

Helal A (2007) Proposed beneficiation and upgrading of Abu Ghalaga ilmenite ore. MinProcess Extr Metal Rev 28:1–58

Helba AA, El Aref MM, Saad F (2001) Lutetian oncoidal and ooidal ironstones sequences; depositional setting and origin; northeast El Bahariya Depression, Western Desert, Egypt. Egypt J Geol 45:235–351

Helba AA, El Manawy AW, El Aref MM (2003) Syndepositional lateritic alteration and clastics starvation as pathways in the formation of the oolitic ironstones of north Wadi Qena, Eastern Desert, Egypt. Egyptian Journal of Geology 47:255–274

Helba H, Trumbull R, Morteani G, Khalil S, Arslan A (1997) Geochemical and petrographic studies of Ta mineralization in the Nuweibi albite granite complex, Eastern Desert, Egypt. Mineral Deposita 32:164–179

Helmy HM (1996) Precious metal and base metal sulphide mineralization at Abu Swayel and Um Samiuki, Eastern Desert, Egypt. PhD Thesis, Minia University, Egypt

Helmy HM (1999) Um Samiuki Precambrian volcanogenic Zn–Cu–Pb deposit, South Eastern Desert, Egypt: a possible new occurrence of cervelleite. Can Mineral 37:143–154

Helmy HM (2004) Cu-Ni-PGE mineralization in the GeninaGharbia mafic-ultramafic intrusion, Eastern Desert, Egypt. Can Mineral 42:351–370

Helmy HM (2005) Melonite group minerals from three Cu–Ni–PGE prospects, Eastern Desert, Egypt. Ore Geol Rev 26:305–324

Helmy HM, Abd El-Rahman Y, Yoshikawa M, Shibata M, Arai S, Tamura A, Kagami H (2014a) Petrology and Sm-Nd dating of the Genina Gharbia Alaskan-type complex (Egypt): insights into deep levels of Neoproterozoic island arcs. Lithos 198–199:263–280

Helmy HM, El Mahallawi MM (2003) Gabbro Akarem mafic–ultramafic complex, Eastern Desert, Egypt: a Late Precambrian analogue of Alaskan-type complexes. Mineral Petrol 77:85–108

Helmy HM, Kaindl R (1999) Mineralogy and fluid inclusion studies of the Au–Cu quartz veins, Hamash area, South Eastern Desert, Egypt. Mineral Petrol 65:69–86

Helmy HM, Kaindl R, Fritz H, Loizenbauer J (2004) The Sukari gold mine, Eastern Desert-Egypt: structural setting, mineralogy and fluid inclusion study. Mineral Deposita 39:495–511

Helmy HM, Kaindl R, Shibata T (2014b) Genetically related Mo–Bi–Ag and U-F mineralization in A-type granite, Gabal Gattar, Eastern Desert, Egypt. Ore Geol Rev 62:181–190

Helmy HM, Mogessie A (2001) Gabbro Akarem, Eastern Desert Egypt: Cu–Ni–PGE mineralization in a concentrically zoned mafic-ultramafic complex. Mineral Deposita 36:58–71

Helmy HM, Shalaby I, Abdelrahman H (2014c) Large-scale metal zoning in a late-Precambrian skarn-type mineralization, SE Sinai, Egypt. J Afr Earth Sci 90:77–86

Helmy HM, Stumpfl EF, Kamel OA (1995) Platinum group minerals from the metamorphosed Abu Swayel Cu–Ni–PGE mineralization, South Eastern Desert, Egypt. Econ Geol 90:2350–2360

Helmy HM, Zoheir B (2015) Metal and fluid sources in a potential world-class gold deposit: El-Sid mine, Egypt. Int J Earth Sci 104:645–661

Henk A, Leander F, Teufel S, Oncken O (1997) Magmatic underplating, extension, and crustal reequilibration: Insights from a cross-section through the Ivrea Zone and the Strona-Ceneri Zone, Northern Italy. J Geol 105:367–378

Hilmy M, El-Bayoumi R, Eid A (1990) Geology, geochemistry and mineralization of the psammitic gneiss of Wadi Abu-Rusheid, Eastern Desert, Egypt. J Afr Earth Sci 11:197–205

Hodkiewicz PF, Groves DI, Davidson GJ, Weinberg RF, Hagemann SG (2009) Influence of structural setting on sulphur isotopes in Archean orogenic gold deposits, Eastern Goldfields province, Yilgarn, Western Australia. Mineral Deposita 44:129–150

Hoefs J (2009) Stable isotope geochemistry, 6th edn. Springer, Berlin, Heidelberg, 286 pp

Hronsky JMA, Groves DI, Loucks RR, Begg GC (2012) A unified model for gold mineralisation in accretionary orogens and implications for regional-scale exploration targeting methods. Mineral Deposita 47:339–358

Huang XL, Wang RC, Chen XM, Hu H, Liu CS (2002) Vertical variations in the mineralogy of the Yichun topaz–lepidolite granite, Jiangxi Province, southern China. Can Mineral 40:1047–1068

Hume WF, Greaves RH (1937) Geology of Egypt, 2. Government Press

Hussein AA (1990) Mineral deposits. In: Said R (ed) The geology of Egypt. Balkema, Rotterdam, pp 511–566

Hussein AAA, Ali MM, El Ramly M (1982) A proposed new classification of the granites of Egypt. J Volcanol Geoth Res 14:187–198

Hussein AEM (2011) Successive uranium and thorium adsorption from Egyptian monazite by solvent impregnated foam. J Radioanaly Nuc Chem 289:321–329

Hussein HA, Hassan MA, El Tahir MA, Abu-Deif A (1986) Uranium bearing siliceous veins in younger granites, Eastern Desert, Egypt. In: Report of the working group on uranium geology, IAEA, Vienna, TECDOC, vol 361, pp 143–157

Ibrahim I, Saleh G, Amer T, Mahmoud F, Abu El Hassan A, Ali M, Azab M, Rashed M, Khaleal F, Mahmoud M (2004a) Uranium and associated rare metals potentialities of Abu Rusheid Brecciated Shear Zone II, South Eastern Desert, Egypt. Nuclear Materials Authority, Cairo, Int. Rep: 182

Ibrahim ME, Abd El-Wahed AA, Rashed MA, Khaleal FM, Mansour GM, Watanabe K (2007a) Comparative study between alkaline and calc-alkaline lamprophyres, Abu Rusheid area, south Eastern Desert, Egypt. The 10th international mining petroleum metallurgical engineering conference, Assuit University, 99–115 pp

Ibrahim ME, El-Kalioby BA, Kamar MS, Abu Zeid EK, Ismail AM (2017) Um Samra-Um Bakra Shear Zone, Central Eastern Desert, Egypt: example of vein-type base metal mineralization. Int J Mining Sci 3:1–17.

Ibrahim ME, Saleh GM, Amer T, Mahmoud FO, Abu El Hassan AA, Ibrahim IH, Aly MA, Azab MS, Rashed MA, Khaleal FM, Mahmoud MA (2002) Uranium and associated rare metals potentialities of Abu Rusheid brecciated shear zones, south Eastern Desert, Egypt (Internal Report), 130 pp

Ibrahim ME, Saleh GM, Amer T, Mahmoud FO, Abu El Hassan AA, Ibrahim IH, Aly MA, Azab MS, Rashed MA, Khaleal FM, Mahmoud MA (2004b) Uranium and associated rare metals potentialities of Abu Rusheid brecciated shear zone II, south Eastern Desert, Egypt (Internal Report), 141 pp

Ibrahim ME, Saleh GM, El-Ghazalawi WS (2010) Low grade metamorphosed sandstone-type uranium deposit, Wadi Sikait, South Eastern Desert, Egypt. J Geol Mining Res 2:129–141

Ibrahim ME, Saleh GM, Falhm O, Abu El Hassan AA, Azab MS (2008) Low grade metamorphosed sandstone type—uranium deposit at Wadi Sikait South Eastern Desert of Egypt south Eastern Desert, Egypt (Internal Report), 111 pp

Ibrahim ME, Saleh GM, Hassan MA, El-Tokhi MM, Rashed MA (2007b) Geochemistry of lamprophyres bearing uranium mineralization, Abu Rusheid area, south Eastern Desert, Egypt. In: The 10th international mining petroleum metallurgical engineering conference, Assuit University, 41–55 pp

Ibrahim ME, Saleh GM, Rashed M, Watanabe K (2007c) Base metal mineralization in lamprophyre dykes at Abu Rusheid area, south Eastern Desert, Egypt. In: The 10th international mining petroleum metallurgical engineering conference, Assuit University, pp 31–40

Ibrahim ME, Watanabe K, Saleh GM, Ibrahim WS (2015) Abu Rusheid lamprophyre dikes, South Eastern Desert, Egypt: as physical-chemical traps for REEs, Zn, Y, U, Cu, W, and Ag. Int Res J Geol Mining (IRJGM) (2276-6618) vol 3, 3 pp

Ibrahim ME, Zalata MA, Ibrahim IH, Rashed MA (2003) El Sella Shear Zone, Southeastern Desert, Egypt; an example of vein-type uranium deposit. Egypt J Geol 47:689–704

Ibrahim MIM (1995) Investigation of some physical properties of zircon and rutile to prepare high purity mineral concentrates from black sand deposits. Unpub MSc Thesis, Mansoura Univ, Mansoura, Egypt

Ibrahim WS, Mostafa MS, Ibrahim ME, Watanabe K, Soliman FA (2014) Deformation history of Nugrus—Sikiat, South Eastern Desert; implication for tectonic environment. Int Res J Geol Mining 4:84–100

International Atomic Energy Agency "IAEA" (1990) The use of gamma-ray data to define the natural radiation environment, Vienna, Austria, Technical Report Series No.566, IAEA, p 48

International Atomic Energy Agency "IAEA" (2003) Guidelines for radioelement mapping using gamma ray spectrometry dataIAEA-TECDOC-1363, Vienna

Jahn S, Matheis G, Mohamed F, Tamish M, Shalaby I (1993) Rare-metal province Central Eastern Desert, Egypt, III. Geochemical indicators of rare-metal potentials (a contribution to IGCP 282 'Rare-metal Mineralization'). Geoscientific research in Northeast Africa. Balkema, Rotterdam, pp 489–494

Jedwab J (1992) Platinum group minerals in ultrabasic rocks and nickeliferous veins from Zabargad Island (Egypt). Compt Rendu Acad Sci, Paris', 314, Sr. II, 157 63

Kaiser MF, Aziz AM, Ghieth BM (2014) Environmental hazards and distribution of radioactive black sand along the Rosetta coastal zone in Egypt using airborne spectrometric and remote sensing data. J Environ Radioact 137:71–78

Kelemen PB (1990) Reaction between ultramafic rock and fractionating basalticmagma. I. Phase relations, the origin of calc-alkaline magma series, and the formation of discordant dunite. J Petrol 31:51–98

Kerrich R, Goldfarb R, Groves D, Garvin S (2000) The geodynamics of world-class gold deposits—characteristics, space–time distribution, and origins. Rev Econ Geol 13:501–544

Kerrich R, Wyman D (1990) Geodynamic setting of mesothermal gold deposits: an association with accretionary tectonic regimes. Geology 18:882–885

Khalil KI (2001) Mineralogical and Mineralogcal studies on the origin of the Abu Ghalaga ilmenite ore, southeastern Desert, Egypt. MERC Ain Shams Univ 15:94–118

Khalil KI, El–Shazly AE, Lehmann B (2015) Late Neoproterozoic banded iron formation (BIF) in the central Eastern Desert of Egypt: Mineralogical and geochemical implications for the origin of the Gebel El Hadid iron ore deposit. Ore Geol Rev 69:380–399

Khedr MZ, Arai S (2013) Origin of Neoproterozoic ophiolitic peridotites in south Eastern Desert, Egypt, constrained from primary mantle mineral chemistry. Mineral Petrol 107:807–828

Khedr MZ, Arai S (2016) Chemical variations of mineral inclusions in Neoproterozoic high-Cr chromitites from Egypt: evidence of fluids during chromitite genesis. Lithos 240–243:309–326

Kinnaird J, Bowden P, Ixer R, Odling N (1985) Mineralogy, geochemistry and mineralization of the Ririwai complex, northern Nigeria. J Afr Earth Sci 3:185–222

Kirschvink JL (1992) Late Proterozoic low-latitude global glaciation: the snowball earth. In: Schopf JW, Klein C (eds) The proterozoic biosphere. Cambridge University Press, Cambridge, pp 51–52

Klemm D, Klemm R, Murr A (2001) Gold of Pharaohs-6000 years of gold mining in Egypt and Nubia. J Afr Earth Sci 33:643–659

Klemm R, Klemm DD (2013) Gold and gold mining in Ancient Egypt and Nubia. Geoarchaeology of the ancient gold mining in the Egyptian and Sudanese Eastern Deserts. Springer, Berlin, Heidelberg, 649 pp

Klitzsh E, Wycisk P (1987) Geology of the sedimentary basins of northern Sudan and bordering areas. Berliner Geowis. Abh. 75: 97–136

Kochine G, Bassyuni F (1968) Mineral resources of the UAR, Part I, Metallic minerals. Internal Report, Geological Survey of Egypt

Kokh MA, Akinfiev NN, Pokrovski GS, Salvi S, Guillaume D (2017) The role of carbon dioxide in the transport and fractionation of metals by geological fluids. Geochim Cosmochim Acta 197: 433–466

Krs M, Soliman A, Amin A (1973) Geophysical phenomena over deep-seated tectonic zones in southern part of Eastern Desert of Egypt. Ann Geol Surv Egypt 3:125–138

Lago BL, Rabinowicz M, Nicolas A (1982) Podiform chromite ore bodies: a genetic model. J Petrol 23:103–125

Leblanc M, Ceuleneer G (1992) Chromite crystallization in a multicellular magma flow: evidence from a chromitite dike in the Oman ophiolite. Lithos 27:231–257

Loizenbauer J, Neumayr P (1996) Structural controls on the formation of the Fawakhir gold mine, El Sid-Eastern Desert, Egypt: tectonic and fluid inclusion evidence. In: Proceedings of the geological survey of Egypt centennial conference, pp 477–488

Mahmoud HH, Abdel-Lateef AM, Attiah AM (2013) Distribution of some elements in the Egyptian black sands from Abu Khashaba beach area. J Analy Sci, Methods Instr 3:62–66

Mahmoud M, Afifi A, Ibrahim I (2004) Reductive leaching of ilmenite ore in hydrochloric acid for preparation of synthetic rutile. J Hydrometal 73:99–109

Makhlouf A, Beniamin NY, Mansour MM, Mansour SA, El Sherbini H (2008) Mafic-ultramafic intrusion of south Korabkanci area with emphasis on titanomagnetite ores, south Eastern Desert, Egypt. Annals Geol Surv Egypt 30:1–20

Mason E, Edmonds M, Turchyn AV (2017) Remobilization of crustal carbon may dominate volcanic arc emissions. Science 357:290–294

Mclennan SM (1989) Rare Earth elements in sedimentary rocks; influence of provenance and sedimentary processes. Rev Mineral 21:169–200

Melcher F, Graupner T, Gäbler H-E, Sitnikova M, Henjes-Kunst F, Oberthür T, Gerdes A, Dewaele S (2015) Tantalum–(niobium–tin) mineralisation in African pegmatites and rare metal granites: Constraints from Ta–Nb oxide mineralogy, geochemistry and U–Pb geochronology. Ore Geol Rev 64:667–719

Melcher F, Graupner T, Gäbler H-E, Sitnikova M, Oberthür T, Gerdes A, Badanina E, Chudy T (2017) Mineralogical and chemical evolution of tantalum–(niobium–tin) mineralisation in pegmatites and granites. Part 2: Worldwide examples (excluding Africa) and an overview of global metallogenetic patterns. Ore Geol Rev 89: 946–987

Melcher F, Graupner T, Henjes-Kunst F, Oberthür T, Sitnikova M, Gäbler E, Gerdes A, Brätz H, Davis D, Dewaele S (2008) Analytical fingerprint of columbite-tantalite (coltan) mineralization in pegmatites: focus on Africa. In: Proceedings, ninth international congress for applied mineralogy (ICAM), pp 615–624

Mishra B, Pruseth KL, Hazarika P, Saravanan C (2018) Nature and source of the ore-forming fluids associated with orogenic gold deposits in the Dharwar Craton. Geosci Front 9:715–726

Mohamed F (1993) Rare metal-bearing and barren granites, Eastern Desert of Egypt: geochemical characterization and metallogenetic aspects. J Afr Earth Sci 17:525–539

Mohamed M, Bishara W (1998) Fluid inclusions study of Sn-W mineralization at Igla area central Eastern Desert, Egypt. Geol Soc Egypt Cairo 42:207–220

Mohamed MA-M (2013a) Evolution of mineralizing fluids of cassiterite–wolframite and fluorite deposits from Mueilha tin mine area, Eastern Desert of Egypt, evidence from fluid inclusion. Arab J Geosci 6:775–782

Mohamed MA-M (2013b) Immiscibilty between silicate magma and aqueous fluids in Egyptian rare-metal granites: melt and fluid inclusions study. Arab J Geosci 6:4021–4033

Moustafa MI (2007) Separation flowsheet for high-purity concentrate of economic minerals from El Burullus-Baltim sand dune area, north coast, Egypt. In: Proceedings of 5th international conferece geology, Africa 1, pp III-(107–124)

Murr A (1999) Genesis of gold mineralization of Fatria, Gidami, Atalla and Hangaliya, Eastern Desert of Egypt. (in German): Münchner Geological Hefte A, v 27, p 202

Nada A, Abd EL-Maksoud TM, Abu Zeid H, El-Asy IE, Mostafa SMI, Abd El-Azeem SA (2012) Correlation between radionuclides associated with zircon and monazite in beach sand of Rosetta, Egypt. J Radioanaly Nuc Chem 291:601–610

Naim G, El-Melegy A, Soliman K (1996) Tantalum-Niobium-Tin mineralization in Central Eastern De-sert, Egypt, a Review. In: Proceedings of geological survey, pp 599–622

Naim G, El-Melegy ET, El Azab A (1993) Black sand assessment. Intern Rep, Egypt Geolo Surv Mining Auth, 67 pp

Nakhla FM (1958) Mineralogy of the Egyptian black sands and its application. Egypt J Geol 2:1–8

Nasr BB, Sadek MF, Masoud MS (2000) Some new occurrences of titanomagnetite, Eastern Desert, Egypt. Annals Geol Surv Egypt 23:679–690

Nettle D, Halverson GP, Cox GM, Collins AS, Schmitz M, Gehling J, Johnson PR, Kadi Kh (2014) A middle–late Ediacaran volcano-sedimentary record from the eastern Arabian-Nubian shield. Terra Nova 26:120–129

Neumayr P, Hoinkes G, Puhl J, Mogessie A, Khudeir AA (1998) The Meatiq dome (Eastern Desert, Egypt) a Precambrian metamorphic core complex: petrological and geological evidence. J Metamorph Geol 16:259–279

Öhlander B (1985) Geochemical characteristics of granites associated with Proterozoic molybdenite mineralization in northern Sweden. Chem Geol 51:247–263

Ohmoto H (1986) Stable isotope geochemistry of ore deposits. Rev Mineral 16:491–559

Ohmoto H, Rye RO (1979) Isotopes of sulfur and carbon. In: Barnes HL (ed) Geochemistry of hydrothermal ore deposits, 2nd edn. Wiley, New York, pp 509–567

Omara S (1959) The geology of Sharm El Sheikh Sandstone, Sinai. Egypt J Geol III:107–120

Omran M, Fabritius T, Abdel-Khalek A, El-Aref M, Elmanawi A, Nasr M, Elmahdy A (2014) Microwave assisted liberation of high phosphorus oolitic iron ore. J Mineral Mater Charact Eng 2: 414–427

Omran M, Fabritius T, Elmahdy A, Abdel-Khalek A, El-Aref M, Elmanawi A (2015) XPS and FTIR spectroscopic study on microwave treated high phosphorus iron ore. Appl Surf Sci 345:127–140

Partington G, McNaughton N, Williams I (1995) A review of the geology, mineralization, and geochronology of the Greenbushes pegmatite, Western Australia. Econ Geol 90:616–635

Pekov IV (2000) Lovozero massif: history, pegmatites, minerals. Ocean Pictures Ltd

Philips GN, Evans KA (2004) Role of CO_2 in the formation of gold deposits. Lett Nat 429:860–863

Phillips GN, Groves DI, Brown IJ (1987) Source requirements for the Golden Mile, Kalgoolie: Significance to the metamorphic replacement model for Archean gold deposits. Can J Earth Sci 24: 1643–1651

Phillips GN, Powell R (2009) Formation of gold deposits—review and evaluation of the continuum model. Earth-Sci Rev 94:1–21

Phillips GN, Powell R (2010) Formation of gold deposits—a metamorphic devolatilization model. J Metamorph Geol 28: 689–718

Pichler T, Veizer J (1999) Precipitation of Fe(III) oxyhydroxides deposits from shallow-water hydrothermal fluids in Tutum Bay, Ambitle Island, Papua New Guinea. Chem Geol 162:15–31

Planavsky N, Bekker A, Rouxel OJ, Kamber B, Hofmann A, Knudsen A, Lyons TW (2010) Rare earth element and yttrium compositions of Archean and Paleoproterozoic Fe formations revisited: new perspectives on the significance and mechanisms of deposition. Geochim Cosmochim Acta 74:6387–6405

Pohl W (1984) Large scale metallogenic features of Pan African in east Africa, Nubia and Arabia. Bull Fac Earth Sci, King Abdul Aziz Univ, Jeddah 6:592–601

Pokrovski GS, Tagirov BR, Schott J, Hazemann J-L, Proux O (2009) A new view on gold speciation in sulfur-bearing hydrothermal fluids from in situ X-ray absorption spectroscopy and quantum-chemical modeling. Geochim Cosmochim Acta 73:5406–5427

Pollard P (1989) Geologic characteristics and genetic problems associated with the development of granite-hosted deposits of tantalum and niobium, Lanthanides, Tantalum and Niobium. Springer, pp 240–256

Powell R, Will TM, Phillips GN (1991) Metamorphism in Archaean greenstone belts. Calculated fluid compositions and implications for gold mineralization. J Metamorph Geol 9:141–150

Ramsay WRH, Bierlein FP, Arne DC (1998) Mesothermal gold mineralisation in space and time. Ore Geol. Rev Special Issue 13:1–406

Rao C, Wang RC, Hu H, Zhang WL (2009) Complex internal textures in oxide minerals from the Nanping No. 31 dyke of granitic pegmatite, Fujian Province, southeastern China. Can Mineral 47:1195–1212

Raslan MF, Ali MA (2011) Mineralogy and mineral chemistry of rare-metal pegmatites at Abu Rusheid granitic gneisses, South Eastern Desert. Egypt. Geologija 54:205–222

Riad A (1979) Geology and petrology on some apogranite occurrence, Nuweibi area, Eastern Desert, Egypt, MSc thesis, Al-Azhar University of Cairo

Richards JP (2011) Magmatic to hydrothermal metal fluxes in convergent and collided margins. Ore Geol Rev 40:1–26

Ridley JR, Diamond LW (2000) Fluid chemistry of orogenic lode gold deposits and implications for genetic models. Rev Econ Geol 13:141–162

Rouxel O, Toner B, German Y, Glazer B (2018) Geochemical and iron isotopic insights into hydrothermal iron oxyhydroxides deposit formation at Loihi Seamount. Geochim Cosmochim Acta 220:449–482

Sabet A (1976) Tin-tantalum deposit of Abu Dabbab. Annal Geol Survey Egypt 6:180–190

Sabet A, Chabanenco V, Tsogev V (1973) Tin-tungsten and rare metal mineralization in the Central Eastern Desert of Egypt. Annal Geol Survey Egypt 3:75–86

Sabet A, Tsogoev V, Baburin L, Raid A, Zakhari A, Armanius L (1976) Geologic structure and laws of localization of tantalum mineral zonation at the Nuweibi deposit. Ann Geol Surv Egypt VI:119–156

Salama W, El Aref M, Gaupp R (2014) Facies analysis and palaeoclimatic significance of ironstones formed during the Eocene greenhouse. Sedimentology 61:1594–1624

Saleeb-Roufaiel G, Fasfous B (1970) A note on a gold-bearing quartz-wolframite vein at Atud, Eastern Desert. J Geol U A R 14:35

Saleh G (1997) The potentiality of uranium occurrences in Wadi Nugrus area, south Eastern Desert. Manisora University, Egypt

Salem IA, Ibrahim ME, Abd El Monsef M (2010) Mineralogy, geochemistry, and origin of hydrothermal manganese veins at Wadi Maliek, Southern Eastern Desert, Egypt. Arab J Geosci. https://doi.org/10.1007/s12517-010-0195-1

Saravanan CS, Mishra B (2009) Uniformity in sulfur isotope composition in the orogenic gold deposits from the Dharwar Craton, southern India. Mineral Deposita 44:597–605

Schneider GB (1970) Cenozoic geology of the Madison Bluffs area, Gallatin County, Montana: Bozeman, Montana State University, MSc thesis, 56 pp

Schwartz M (1992) Geochemical criteria for distinguishing magmatic and metasomatic albite-enrichment in granitoids-examples from the Ta–Li granite Yichun (China) and the Sn–W deposit Tikus (Indonesia). Mineral Deposita 27:101–108

Searle D (1974) Final report on the geology and assessment of the Mo prospect of Homr Akarem. Internal Report, Geological Survey of Egypt

Searle DL (1975) Final report on the geology and mineralization at the Zn-Cu deposits of Um Samiuki, Eastern Desert. Aswan Mineral Survey Project, Geol Surv Egypt Internal Rep

Searle DL, Carter GS, Shalaby IM (1978) Mineral exploration at Umm Samiuki. UN Tech Rep Egypt 72-008/3

Seedorff E, Einaudi MT (2004) Henderson porphyry molybdenum system, Colorado: II. Decoupling of introduction and deposition of metals during geochemical evolution of hydrothermal fluids. Econ Geol 99:39–72

Seward TM (1991) The hydrothermal geochemistry of gold. In: Foster RP (ed) Gold metallogeny and exploration. Blackie, London, pp 37–62

Shahien MG, Khedr MH, Maurice AE, Farghali AA, Ali RAM (2015) Synthesis of high purity rutile nanoparticles from medium-grade Egyptian natural ilmenite. Beni-Suef Univ J Basic Appl Sci 4: 207–213

Shalaby IM, Stumpfl EF, Helmy HM, El Mahallawi OA, Kamel OA (2004) Silver and silver-bearing minerals at the Um Samiuki volcanogenic massive sulphide deposit, Eastern Desert, Egypt. Mineral Deposita 39:608–629

Sharara NA (1999) Stable isotopes and fluid inclusions of the gold mineralization at El Sukari District, central Eastern Desert, Egypt: genetic constraints. In: Proceedings of the 4th conference on geochemistry, Alexandria University, Alexandria, Egypt, pp 317–339

Shazly AG, Salem IA, Abdel Monem AA, El Shibiny NH (1998) Ore mineralogy, geochemistry and fluid inclusions of some gold bearing quartz veins in the Central Eastern Desert of Egypt. Egypt Mineral 10:51–74

Sims PK, James HL (1984) Banded iron-formation of late Proterozoic age in the central Eastern Desert, Egypt: Geology and tectonic setting. Econ Geol 79:1777–1784

Stern RJ (1994) Arc assembly and continental collision in the neoproterozoic East African Orogen: implications for the consolidation of Gondwanaland. Ann Rev Earth Planet Sci 22:319–351

Stern RJ (2018) Neoproterozoic formation and evolution of Eastern Desert continental crust: the importance of the infrastructure-superstructure transition. J Afr Earth Sci 146:15–27

Stern RJ, Avigad D, Miller NR, Beyth M (2006) Evidence for the Snowball earth hypothesis in the Arabian-Nubian shield and the East African Orogen. J Afr Earth Sci 44:1–20

Stern RJ, Gottfried D, Hedge CE (1984) Late Precambrian rifting and crustal evolution in the Northeastern Desert of Egypt. Geology 12:168–171

Stern RJ, Kröner A, Rashwan AA (1991) A late Precambrian (710 Ma) high volcanicity rift in the Southern Eastern Desert of Egypt. Geol Rundsch 80:155–170

Stoffers P, Glasby GP, Stuben D, Renner RM, Pierre TG, Webb J, Cardile CM (1993) Comparative mineralogy and geochemistry of hydrothermal iron-rich crusts from the Pitcairn, Teahitia-mehetia, and Macdonald hot spot areas of the S. W. pacific. Marine Georesour Geotechnol 11:45–86

Stowe CW (1994) Compositions and tectonic settings of chromite deposits through time. Econ Geol 89:528–546

Stüwe K (1998) Tectonic constraints on the timing relationships of metamorphism, fluid production, and gold-bearing quartz vein emplacement. Ore Geol Rev 13:219–228

Styles MT, Nasr BB, Connor EAO (1996) Several occurrences of platinum group minerals in the Nubian Shield of Eastern Egypt. Internal Report, Geological Survey of Egypt, pp 793–808

Surour AA, El-Kammar AA, Arafa EH, Korany HM (2003) Dahab stream sediments, southeastern Sinai, Egypt: a potential source of gold, magnetite and zircon. J Geochem Explor 77:25–43

Sweetapple MT (2000) Characteristics of Sn–Ta–Be–Li-industrial mineral deposits of the Archaean Pilbara Craton. Australian Geological Survey Organisation, Western Australia

Takla MA, Abdel Monem AA, Assaf HS, Basta FF, El Mansi MM (1997) The basement rocks of Samut–Atud area, central Eastern Desert, Egypt. In: 35th annual meeting, geological society., Egypt (Abstract)

Takla MA, Basta EZ, Fawzi E (1981) Characterization of the older and younger gabbros of Egypt. Delta J Sci 5:279–314

Takla MA, El Dougdoug AA, Gad MA, Rasmay AH, El Tabbal HK (1995) Gold-bearing quartz veins in mafic and ultramafic rocks, Hutite and Um Tenedba, South Eastern Desert, Egypt. Ann Geol Surv Egypt 20:411–432

Takla MA, El Dougdoug AA, Rasmay AH, Gad AA, El Tabbal HK (1990) Origin of Um Eleiga gold mineralization, south Eastern Desert, Egypt. Egypt Mineral 2:3–20

Takla MA, Surour AA (1996) On the occurrence of Ni-sulphides and arsenides in some Egyptian serpentinites. Egypt Mineral 8:1–18

Tomkins AG (2010) Windows of metamorphic sulfur liberation in the crust: implications for gold deposit genesis. Geochim Cosmochim Acta 74:3246–3259

Tomkins AG (2013) A biogeochemical influence on the secular distribution of orogenic gold. Econ Geol 108:193–197

Wagner T, Klemd R, Wenzel T, Mattsson B (2007) Gold upgrading in metamorphosed massive sulfide ore deposits: direct evidence from laser-ablation–inductively coupled plasma—mass spectrometry analysis of invisible gold. Geology 35:775–778

Walker RJ, Hanski E, Vuollo J, Liipo J (1996) The Os isotopic composition of Proterozoic upper mantle: evidence for chondritic upper mantle from the Outokumpu ophiolite, Finland. Earth Planet Sci Lett 141:161–173

Wang C, Wu H, Li W, Peng Z, Zhang L, Zhai M (2017) Changes of Ge/Si, REE + Y and Sm–Nd isotopes in alternating Fe- and Si-rich mesobands reveal source heterogeneity of the ~2.54 Ga Sijiaying banded iron formation in Eastern Hebei, China. Ore Geol Rev 80:363–376

Wilson CJL, Schaubs PM, Leader LD (2013) Mineral precipitation in the quartz reefs of the Bendigo gold deposit, Victoria, Australia. Econ Geol 108:259–278

Yahiya A (2007) Beneficiation of Aswan iron ores. In: Iron Symposium (2007), Central Metallurgical Research and Development Institute, Cairo, Egypt

Young GM (1976) Iron-formation and glaciogenic rocks of the Rapitan Group, Northwest Territories, Canada. Precambrian Res 3:137–158

Zhou M-F, Robinson PT (1997) Origin and tectonic environment of podiform chromite deposits. Econ Geol 92:259–262

Zhou MF, Robinson PT, Bai WJ (1994) Formation of podiform chromites by melt/rock interaction in the upper mantle. Miner Deposita 29:98–101

Zhou MF, Robinson PT, Malpas J, Li Z (1996) Podiform chromitites in the Luobusa ophiolite (southern Tibet): Implications for melt/rock interaction and chromite segregation in the upper mantle. J Petrol 37:3–21

Zhou ZJ, Chen YJ, Jiang SY, Zhao HX, Qin Y, Hu CJ (2014) Geology, geochemistry and ore genesis of the Wenyu gold deposit, Xiaoqinling gold field, Qinling Orogen, southern margin of North China Craton. Ore Geol Rev 59:1–20

Zoheir BA (2004) Gold mineralization in the Um El Tuyor Area, South Eastern Desert, Egypt: Geologic Context, Characteristics and Genesis. PhD Thesis. Ludwig-Maximilians-Universität München

Zoheir BA (2008a) Structural controls, temperature–pressure conditions and fluid evolution of orogenic gold mineralisation at the Betam mine, south Eastern Desert, Egypt. Mineral Deposita 43:79–95

Zoheir BA (2008b) Characteristics and genesis of shear zone-related gold mineralization in Egypt: a case study from the Um El Tuyor mine, south Eastern Desert. Ore Geol Rev 34:445–470

Zoheir BA (2012a) Lode-gold mineralization in convergent wrench structures: Examples from South Eastern Desert, Egypt. J Geochem Explor 114:82–97

Zoheir BA (2012b) Controls on lode gold mineralization, Romite deposit, South Eastern Desert, Egypt. Geosci Frontiers 3:571–585

Zoheir BA (2012c) Microchemistry and stable isotope systematics of gold mineralization in a gabbro–diorite complex, SE Egypt. Microchem J 103:148–157

Zoheir BA, Akawy A (2010) Genesis of the Abu Marawat gold deposit, central Eastern Desert of Egypt. J Afr Earth Sci 57:306–320

Zoheir BA, Akawy A, Hassan I (2008a) Role of fluid mixing and wallrock sulfidation in gold mineralization at the Semna mine area, central Eastern Desert of Egypt: evidence from hydrothermal alteration, fluid inclusions and stable isotope data. Ore Geol Rev 34:580–596

Zoheir BA, Creaser R, Lehmann B (2015) Re-Os geochronology of gold mineralization in the Fawakhir area, Eastern Desert, Egypt. Int Geol Rev 57:1418–1432

Zoheir BA, Deshesh F, Broman C, Pitcairn IK, El-Metwally A, Mashaal S (2018a) Granitoid-associated gold mineralization in Egypt: a case study from the Atalla mine. Mineral Deposita 53:701–720

Zoheir BA, Emam A, Pitcairn IK, Boskabadi A, Lehaye Y, Cooper MJ (2018b) Trace elements and isotope data of the Um Garayat gold deposit, Wadi Allaqi district, Egypt Mineralium Deposita (in press) https://doi.org/10.1007/s00126-018-0807-3

Zoheir BA, Feigenson M, Zi JW, Turrin B, Deshesh F, El-Metwally A (2018b) Ediacaran (~600 Ma) orogenic gold in Egypt: age of the Atalla gold mineralization and its geological significance. Int Geol Rev. https://doi.org/10.1080/00206814.2018.1463180

Zoheir BA, Goldfarb RJ, Weihed P (2011) Granitoid-associated lode gold deposits in the central Eastern Desert of Egypt. In: Geological Society of America (GSA) annual meeting: Minneapolis, MN, 470 pp

Zoheir BA, Lehmann B (2011) Listvenite–lode association at the Barramiya gold mine, Eastern Desert, Egypt. Ore Geol Rev 39:101–115

Zoheir BA, Moritz R (2014) Fluid evolution in the El-Sid gold deposit, Eastern Desert, Egypt. Geological Society, London, Special Publications 402, SP402. 3. https://doi.org/10.1144/SP402.3

Zoheir BA, Qaoud NN (2008) Hydrothermal alteration geochemistry of the Betam gold deposit, south Eastern Desert, Egypt: mass-volume-mineralogical changes and stable isotope systematics. Appl Earth Sci 117:55–76

Zoheir BA, Weihed P (2014) Greenstone-hosted lode-gold mineralization at Dungash mine, Eastern Desert, Egypt. J Afr Earth Sci 99:165–187

Zoheir BA, El-Shazly AK, Helba H, Khalil KI, Bodnar RJ (2008b) Origin and evolution of the Um Egat and Dungash orogenic gold deposits, Egyptian Eastern Desert: evidence from fluid inclusions in quartz. Econ Geol 103:405–424

Mineral Resources in Egypt (II): Non-metallic Ore Deposits

15

Ahmed El-Kammar, Adel Surour, Mohamed El-Sharkawi, and Hassan Khozyem

Contents

A. El-Kammar · A. Surour · M. El-Sharkawi
Faculty of Science, Department of Geology, Cairo University, Giza, Egypt
e-mail: amkammar@hotmail.com

H. Khozyem (✉)
Faculty of Science, Department of Geology, Aswan University, Aswan, Egypt
e-mail: hkhozyem@gmail.com

Z. Hamimi et al. (eds.), *The Geology of Egypt*, Regional Geology Reviews,
https://doi.org/10.1007/978-3-030-15265-9_15

Abstract

This chapter reviews four types of non-metallic ore deposits in Egypt. These deposits are phosphate, white sand (glass sand or silica sand), argillic and evaporite deposits.

15.1 Phosphate Deposits of Egypt: Composition, Origin, and Utilization

Ahmed El-Kammar

15.1.1 Introduction

Phosphate deposits are stratified shallow marine sedimentary rocks usually associated with black shale, limestone, glauconite, chert, and siltstone. They have different ages from Paleozoic to Quaternary; however, in Egypt, they belong to the Late Cretaceous-Paleogene time interval where stratigraphic boundaries are strongly time-transgressive. They belong to the Late Cretaceous Tethyan phosphogenic province that has regional extension in the Middle East and North Africa. The German traveler Zittel, discovered phosphate first time in Qift near Qena in 1888 but recorded in the same occurrence by Barron in 1897. Conversely, exploitation started about two decades later by European phosphate companies in both Nile Valley, and Red Sea regions. As a result, the high-grade ores are continuously been depleted, and beneficiation of lower grades seems to be an urgent commitment.

In this script, the term commercial phosphorite designate those containing above 27% P_2O_5 and it is medium-grade if containing <27 and >20% P_2O_5. The low-grade phosphate rocks are those containing <20 and >10% P_2O_5. They have value and can be adopted for several applications, even without beneficiation. Most of the worldwide phosphorite production utilized for production of phosphoric acid. About 90% of the produced acid is used to manufacture phosphate fertilizers such as the triple-superphosphate (TSP), and mono- and di-amonium phosphate (MAP and DAP). The price of one-ton of phosphoric acid is about 12 fold the price of one-ton commercial phosphorite ore. The conventional byproducts of the phosphoric acid industry are fluorine, uranium and rare earth elements.

15.1.2 Geologic Setting and Distribution

From the stratigraphic point of view, the Duwi (phosphate) Formation conformably underlays the Dakhla Formation strata and assigned as Upper Campanian to Early Maastrichtian age (Hermina 1972). On basis of palynological studies, Schrank and Perch-Nielsen (1985) assigned it as a Late Campanian to Early Maastrichtian age for the upper portion of the Duwi Formation (Fig. 15.1). Richardson (1982) and Dominik and Shaal (1984) reached a similar conclusion, based on vertebrate fauna. Glenn (1990) correlated the Duwi lithofacies along the central belt and concluded that it attains maximum thickness in the central part that extends from the Dakhla and Kharga oases in the west to the Red Sea from Quseir to Safaga in the east.

The name Duwi (phosphate) Formation was given by Youssef (1965), where the formation reaches maximum thickness (>70 m) in Gebel Duwi, W. Quseir and its minimum thickness (20 m) in Dakhla. However, Baioumy and Tada (2005) measured about 170 m thickness for Duwi (divided into three members) in the Red Sea region (Fig. 15.1) and the writer measured much less thickness of 12 m for the Duwi Fm in the Mawhoob area, N.W. Dakhla.

However, the spatial distribution of phosphorites in Egypt can be divided into seven domains (Fig. 15.2). The **first** represents the phosphorite occurrence in the Red Sea region, from Safaga due north to Hammadat and Zug El-Bohar south of Quseir. The phosphorite of this domain operated along half a century through underground mining. The structural instability, tilting of the phosphate beds (15–20°) and recharging the galleries by groundwater led to closing the mining activity for about 30 years. The proved huge geological reserves (billions scale) in this domain requires innovated technology for mining operation (Elwageeh et al. 2017). The **second** domain represents the Nile Valley occurrence where phosphorite operated since about 100 years from Qena due north to Edfu due south. El-Kammar et al. (1984) recorded first-time thick phosphate bed (2 m) in the lower Quseir (Variegated Shale) Formation in Gebel Zabara, 5 km SE Edfu. This phosphate is medium grade (20.2% P_2O_5, in average), poorly sorted mostly composed of collophane grains and pellets (>80%, by volume). The ongoing activities concentrate on the northern side of this domain, especially between Gebel Abu Had and Higaza. The **third** domain represents the unexplored plateau at the western side of the Nile Valley, between Qena and

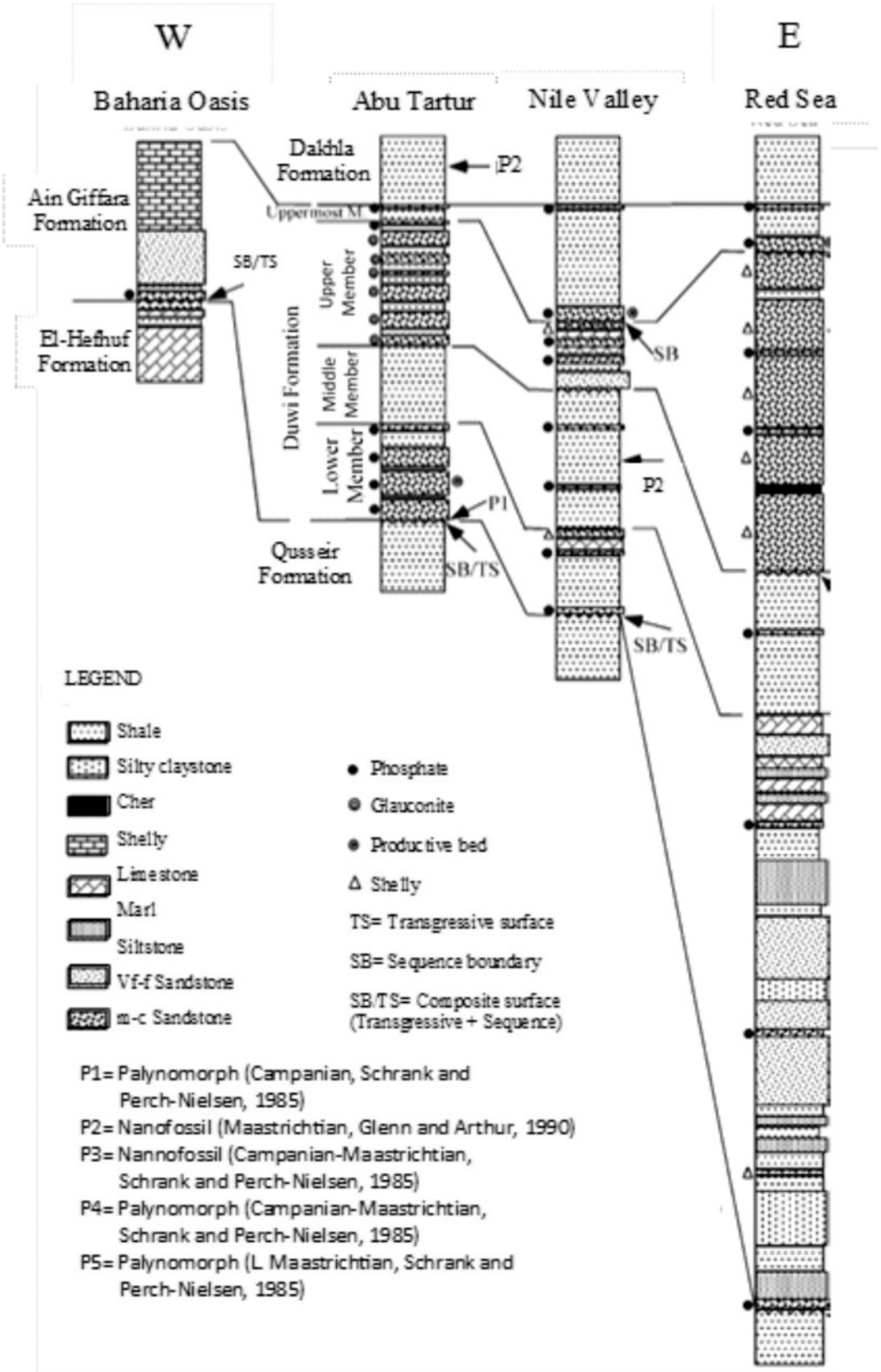

Fig. 15.1 Stratigraphic correlation of the Duwi (phosphate) Formation in Egypt (After Baioumy and Tada 2005)

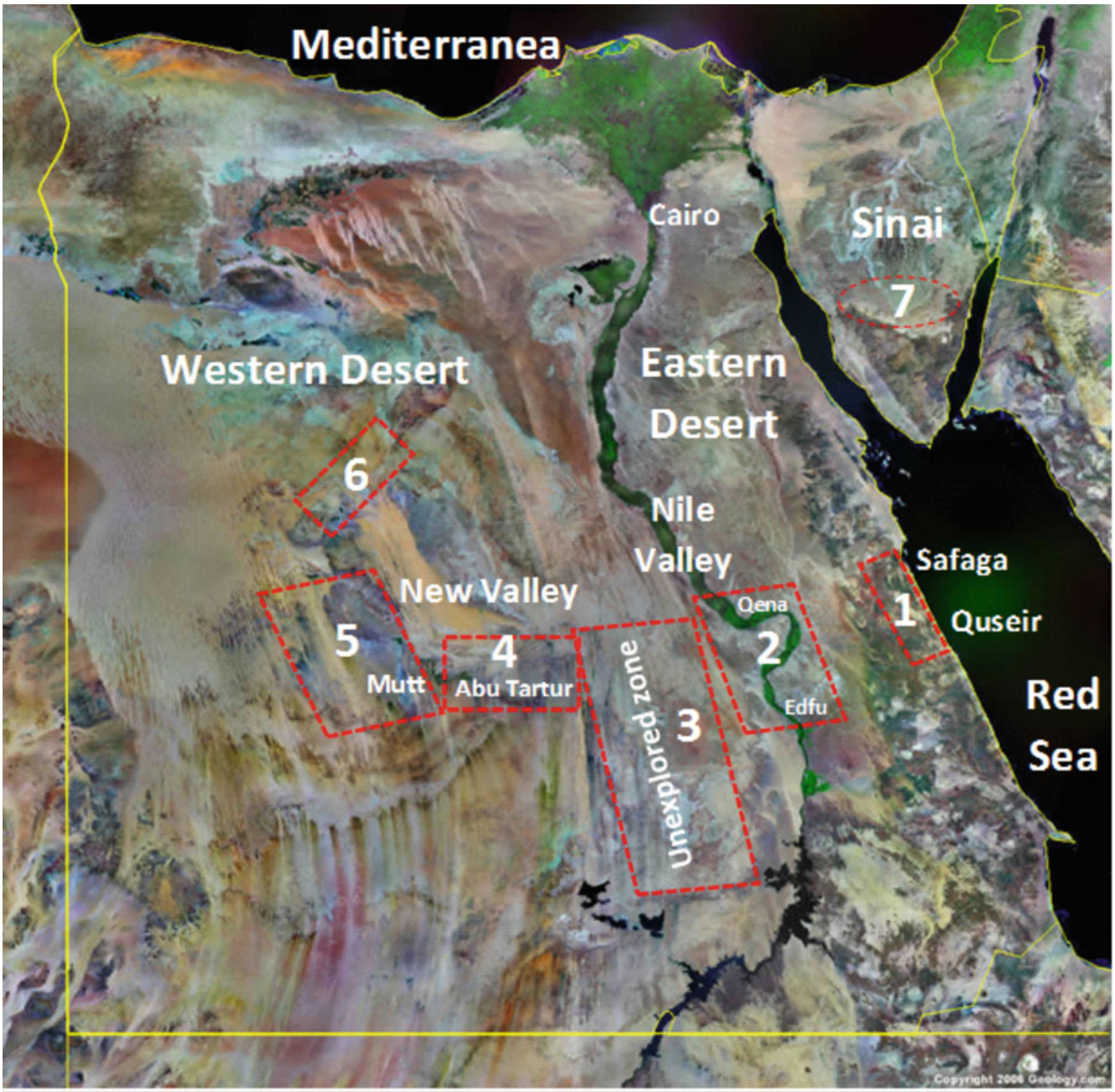

Fig. 15.2 Satellite image of Egypt illustrating the main occurrences of the phosphate rocks

Edfu and extending to the New Valley, where the discovery of optimistic potential resources is conceivable. The **fourth** domain represents Abu Tartur plateau where underground mining in the Maghrabi-Liffiya sector was not a rewarding experience. Excavation of the surface exposures and the low plateau supplies 2–3 million tons of commercial phosphorite per year. The available reserves grant consistent supply for the coming few decades. The **fifth** domain represents the near surface medium grade phosphate rock in the Dakhla Oasis, from Asmant village to north Mawhoob. The average thickness varies between 1.5 and 3 m. However, the thickness of the individual bed ranges, in most cases, between 30 and 90 cm. The grade of the ore ranges between 18 and 29% P_2O_5, averaging about 22%. Although the estimated reserves are in hundred millions of tons, the main challenges of operating this phosphate are its medium grade, scarcity of water and long distance of transportation (El-Kammar 2014). The **sixth** domain represents the phosphatic rocks exposed in Bahariya and Farafra Oasis, The main exposure occurs at the step-faulted syncline of Gebel El-Hehfhuf in the Bahariya Oasis. The phosphate is cemented mainly by dolomite and its grade is low to medium (8.5–17.4% P_2O_5) but it is abnormally uraniferous (180 ppm, U). El-Kammar (1977) attributed the high radioactivity to the thermal gradient accompanied the volcanic eruption in the Bahariya Oasis. The **seventh** domain represents the low- to medium

grade phosphate rocks belonging to Suder Formation (equivalent to Duwi Formation and of Campanian-Maastrichtian age). They occur in Sinai north of latitude 27°20′N in Gebel Qabeliat, Taba, Aref El-Naga, and Wadi El-Sabha.

Hamza and Osman (1986) reported two thin (25–30 cm) phosphate layers (23 and 9% P_2O_5) in the Upper Eocene of G. Mokattam, near Cairo. These phosphate layers represent the eastern termination of the Eocene Tethyan phosphogenic province that deposited the huge reserves of North Africa, especially in Morocco and Tunisia. The writer believes that similar U. Eocene unfeasible phosphate layers can further be encountered in other occurrences in North Egypt.

15.1.3 Mineral Composition

Philobbos (1964, 1969), have exclusively studied the petrography of the Red Sea and Nile Valley phosphorites. He classified the ore based on the textural relationships, and paragenesis, type, and composition of the cementing materials. Many others then followed this approach. However, the mineralogical and geochemical characterization of apatite as the only constituent of the phosphatic quotient was not effectively tackled.

Apatite occurs in four main end members, namely: hydroxyl-, chlor-, carbonate- and fluor-apatites. The main apatite variety in the marine sedimentary phosphorites is the carbonate fluorapatite, which assigned by McConnell (1973) as "*francolite*". The francolite of the phosphate deposits in Egypt contains 3–5% F, with F/P_2O_5 ratio of about 0.12 in average, while F in the bones of the living vertebrates is measured in tens of ppm (El-Kammar 1974). There is an eminent tendency for the secondary uptake of F ion during the apatitization process. The increase in F seems to be at the expenses of CO_2. Dabous (1982) reported changes in the lattice parameters, especially the length of a and c dimensions, and the lattice volume with respect to the contents of F and CO_2 in the francolite lattice.

Under the microscope, francolite occurs as submicron-sized crystals displaying two main forms. The low birefringence form appears like amorphous, customarily known as "collophane". Ferrugination obscure the optical properties of collophane, which enhances its isotropic-like appearance. The other form displays 1st order interference colors with extinction largely controlled by the biological structure of the bone skeletons. The strongest *d*-spacing characterizing the X-ray diffraction pattern of francolite; 2.79 ± 0.01 Å/100, 2.73 ± 0.01 Å/60 and ±2.63 ± 0.01 Å/30, are the counterpart of other end members and solid solutions of apatite. The precise identification of francolite requires crystal chemical analysis besides the X-ray diffraction analysis. El-Kammar and Saad-Eldin (1992) calculated the lattice dimensions of francolite to be 9.335 ± 0.028 Å and 6.899 ± 0,018 Å for a_o and c_o dimensions, respectively, whereas the lattice volume is 520 ± 4 $Å^3$. The lattice volume of francolite composing collophane is always smaller than that forming the bone carcasses. The color of bones or collophane has no influence on the lattice parameters. El-Kammar and Basta (1983) calculated the chemical formula of the francolite composing both the weathered and non-weathered phosphorites of Abu Tartur. They concluded that although the prevailing weathering activity imparted the phosphorites brownish hues due to mineral changes and staining, the chemical formula of apatite experienced minor change. The calculated empirical formulae are; $Ca_{9.22}(Sr,La,..)_{0.63}(OH)_{0.15}P_{5.12}(C,S,..)_{0.88}(F_{1.46}O_{22.71})OH_{0.83}$ and $Ca_{9.21}(Sr,La,..)_{0.75}(OH)_{0.04}P_{5.05}(C,S,..)_{0.95}(F_{1.52}O_{22.72})OH_{0.76}$ for weathered and non-weathered francolite, respectively.

The non-apatite components of phosphorites can be syn-depositional or diagenetic. The former is always represented by detrital components such as quartz, clays and accessory minerals. Since phosphorites are porous and permeable sediments, calcite, dolomite, ankerite, quartz, chalcedonic-quartz, gypsum, ferruginous materials and rarely collophane cement them. Sometimes, the cementing materials classify phosphorite being a decisive factor for the ore-grade, hardness, and the appropriate approach for beneficiation. Framboidal pyrite witnesses the anoxic conditions that prevailed during and after deposition of phosphorite. This pyrite fills void spaces of the francolite form, fossil chambers, and cementing materials as well. Upon weathering, hematite—"limonite" and gypsum—anhydrite are formed at the expenses of pyrite and epidiagenetic calcite cement. Moreover, illite, authigenic silica, and halite are enriched at the expenses of smectite-chlorite mixed layer clays and carbonate, together with total volume loss (El-Kammar and Basta 1983).

15.1.4 Geochemical Composition

The results of the descriptive statistic of about 500 analyses mostly collected from unpublished dissertations awarded from Egyptian and foreign universities on the Egyptian phosphorites are given in Table 15.1. The data provided by the unpublished dissertations of El-Kammar (1974), Dabous (1982), Tamish (1988), Saad EL-Din (1990), Ali (1995), and Sadek (2009), in addition to the published work of El-Hadad and Ahmed (1987) and Germann et al. (1984), are the core of the adopted database.

The geochemistry of the major ingredients is a precise translation of the mineral composition. The constituents that exist only in the francolite structure are P_2O_5 and F. In average, the F/P_2O_5 ratio in the Egyptian phosphorites is about 1.12. According to McConnell (1973), the introduction of F into the

Table 15.1 Descriptive statistic data of major components (%) and trace elements (ppm) of the three main occurrences of phosphorites in Egypt

Locality	Nile valley (n = 271)				Red Sea (n = 166)				Abu Tartur (n = 93)			
Parameter	Min.	Max.	Mean	δ*	Min.	Max.	Mean	δ*	Min.	Max.	Mean	δ*
SiO_2	0.01	52.68	11.94	10.4	0.41	52.27	8.86	8.47	2.66	27	6.63	4.64
Al_2O_3	0.04	3.48	0.61	0.52	BL**	2.99	0.51	0.5	0.27	2.34	1.03	0.53
TiO_2	0.001	0.52	0.03	0.05	BL	0.167	0.04	0.04	0.01	0.2	0.04	0.04
FeO	0.01	0.99	0.24	0.24	0.01	3.79	0.27	0.5	0.01	3.15	1.26	1.23
Fe_2O_3	0.06	20.51	2.08	1.56	BL	8.56	1.41	0.99	0.47	20.1	3.67	2.25
CaO	14.25	54.27	41.73	6.16	25.21	53.34	42.51	4.81	30.03	53.28	42.49	3.89
MgO	0.00	2.60	0.48	0.45	0.00	8.56	1.76	1.61	0.14	6.42	1.02	1.14
Na_2O	0.021	8.37	0.67	0.67	0.25	12.07	1.25	1.28	0.067	2.17	0.79	0.22
K_2O	0.01	1.8	0.12	0.21	0.01	2.56	0.12	0.24	0.05	0.8	0.14	0.11
MnO	0.005	8.47	0.18	0.56	BL	0.26	0.09	0.07	0.02	0.9	0.12	0.1
P_2O_5	18.45	37.83	25.75	3.85	19.05	34.51	25.81	3.48	19.96	36.81	27.95	3.22
F	0.41	3.44	2.45	0.51	1.48	3.73	2.55	0.46	1.59	3.05	2.74	0.29
Cl	0.02	7.65	0.4	0.78	0.18	4.76	1.2	1.05	0.1	1.89	0.36	0.59
SO_3	0.01	10.33	1.32	1.68	0.32	5.41	1.88	1.23	2.93	10.57	5.2	2.57
Sulfide	0.01	4.13	0.93	1.08	0.01	3.41	0.84	1.02	0.01	5.89	3.26	1.27
CO_2	0.10	21.18	6.46	3.23	1.90	16.37	10.18	2.82	0.10	10.45	2.72	2.22
Org.C.	0.00	1.77	0.32	0.27	0.01	5.84	1.70	1.59	0.06	1.22	0.47	0.23
H_2O^+	0.24	3.1	1.37	0.69	0.22	5.35	1.08	0.83	3.23	4.00	3.69	0.25
H_2O^-	0.16	4.52	1.04	0.78	0.47	4.80	2.01	0.83	0.76	4.18	1.88	0.83
L.O.I.	4.85	22.60	9.66	3.91	6.18	10.08	7.70	0.92	6.53	14.33	9.48	1.71
Be	0.3	6	2.64	1.51	1	10	1.78	1.46	1	8.7	3.07	2.01
B	3	55	18	11	6	150	32	58	3	90	40	31
Sc	1	29	8.73	5.34	1	11	4.2	2.9	2	99	17	17
V	4	276	67	52	3	1000	80	103	29	115	53	13
Cr	6	300	80	43	28	1185	130	110	15	148	55	17
Co	0	195	11	20	0	426	14	41	0	195	26	26
Ni	1	99	26	19	2	99	45	23	3	190	34	21
Cu	1	64	15	9	1	300	27	39	1	31	13	6
Zn	1	409	171	61	15	621	159	104	13	255	91	50
Ga	0.3	1.5	0.6	0.37	0.3	0.7	0.38	0.16	0.4	3	1.38	0.92
As	5.2	16	9	2	8	62	16	16	10	30	18	6
Sr	233	3000	1183	473	329	2568	945	466	110	2210	1155	550
Y	4	337	71	42	30	393	103	56	30	890	281	142
Zr	2	544	49	91	3	65	22	16	4	37	14	6
Mo	0	26	6.12	5.94	2	61	11.4	11.2	3	29.5	6.9	6.22
Ag	0.3	1	0.34	0.14	0.3	0.6	0.38	0.13	0.3	1.5	0.47	0.39
Cd	0	40	6.86	5.94	0.4	47.5	11.7	13.3	0.8	6.5	3.28	1.32
Sn	0	4	0.42	0.67	0.3	0.3	0.3	0	0.3	5	2.19	2.3
Ba	60	7065	512	658	17	521	129	103	8	980	77	119
Hf	0.1	1.9	0.58	0.49	0.06	3.74	1.13	1.29	0.11	6.3	1.28	1.58
Pb	1	109	30	42	0	187	33	54	2	116	58	48
Th	0.44	6.6	2.28	1.44	0.5	6.24	2.78	1.6	1.1	10.9	3.99	2.52
U	9	302	65	32	15	241	61.3	40	7	199	54	28

(continued)

Table 15.1 (continued)

Locality	Nile valley (n = 271)				Red Sea (n = 166)				Abu Tartur (n = 93)			
Parameter	Min.	Max.	Mean	δ*	Min.	Max.	Mean	δ*	Min.	Max.	Mean	δ*
REE	28	864	202	145	38	639	241	103	84	1768	704	340
LREE/HREE	1.79	3.46	2.42	1.98	8.62	6.65	6.1	4.59	5.38	5.28	5.91	4.63
Ce/Ce′	0.33	0.82	0.72	0.79	0.87	0.86	0.78	0.65	1.04	0.59	0.75	0.71

δ* means standard deviation, BL** means below detection, H_2O^+ means crystal water

apatite structure has several important consequences where it decreases solubility, improves its crystallinity, reduces lattice defect and accelerates crystal growth in the precipitating medium. However, most of the major constituent participate in more than one mineral phase. For example, CaO is a main component of francolite but also occurs as calcite, dolomite, gypsum/anhydrite and clay minerals. The CaO/P_2O_5 ratio in pure francolite is 1.42 (McConnell 1973). Higher values indicate additional non-francolite CaO, such as carbonate cementation. The ratio is 1.62, 1.65 and 1.52 for the average composition of Nile Valley, Red Sea, and Abu Tartur phosphorites, respectively. This implies that Abu Tartur phosphorites are the least calcareous. Silicate, sulfate, and carbonate groups are principally outside the francolite lattice, but they may occasionally substitute for phosphate group. Upon extensive weathering, pyrite framboids oxidize and produces sulfate group that substitutes for the phosphate group and deteriorates the quality of the ore.

The sedimentary marine phosphate deposits are generally good accumulator of trace elements by different mechanisms and under different controls. The terrestrial-proper elements, such as Ti, Th, Sc, and REE (especially the light ones) accumulate mostly during sedimentation, and their content increases distinctly at the beginning of the transgression where the detrital input is active. Sinking organic particulates scavenge metals from oceanic water (Balistrieri et al. 1981). However, phosphorites being permeable organic-rich system can store multivalent metals whom their lower oxidation state immobile such as U, V, Cu, Cr, Mo, Pb, and As. Contact time at the water sediments interface, the initial concentration of elements in water, pH, and temperature are controlling factors of trace elements accumulation. The francolite crystal structure allows simple and coupled atomic substitution in all sites (McConnell 1973). The abundance of the trace elements in phosphorites modifies during diagenesis and upon weathering (El-Kammar and Basta 1983).

In average, the abundance of the heavy metals in the Egyptian phosphorites follow the order; Zn > V > Co > Cu > Pb > Mo > Cd > Sn. However, the phosphorites of the Red Sea region accumulate higher quotient of the heavy metals compared with those of the Nile Valley and Abu Tartur. The later occurrence is a better accumulator of the terrestrial elements such as Th, Sc, Zr, Hf, Nb, Ta, and LREE. Consideration should be given to the peculiarities of the single beds in each geographic occurrence. The following are details on the rare earth elements (REE) and the naturally occurring radioactive metals (NORM) being important profitable byproducts and help better understanding of the paleoenvironments.

15.1.5 Rare Earth Elements (REE)

The REE in phosphorites have a dual importance, first to assess better understanding of the depositional environments and second to utilize as a potential byproduct of the phosphoric acid industry. Often, they are used proxies to reconstruct the sea level fluctuation, water chemistry and particulars of the depositional environments. Although phosphorites were discovered more than a century in Egypt, the geochemistry and economic importance of the REE was studied first time by El-Kammar (1974). This study documented an abnormal concentration of REE in Abu Tartur phosphorites and interpreted the REE configuration to depositional controls. Basta et al. (1974), Basta and El-Kammar (1976), and Hassan and El-Kammar (1975) later published the same work. Dardir and Kobtan (1980), Germann et al. (1984), and Tamish (1988) further confirmed the high content of REE in Abu Tartur phosphorites. The distribution of the REE in phosphorites is heterogeneous where collophane accumulates less REE than bone fragments of the same rock (El-Kammar et al. 1979). They also reported slight enhancement of the heavy rare earth elements (HREE) with increasing total REE.

Emsbo et al. (2015) concluded that the consistency of REE abundances within individual time horizons may identify time periods, like the Late Mississippian, Devonian, and Ordovician, that were favorable for the formation of phosphorites with high-REE abundances. They also added that the REE content of the U.S. phosphorites is entirely hosted in francolite. Auer et al. (2017) further supported the dependence of the REE concentration in phosphorites on seawater composition. They quoted that the wide range of REE enrichment patterns found in ancient marine phosphates lead to the proposition that water chemistry has been very different in the Earth's past. However, they added that both early and late diagenesis affect the REE signatures in phosphates altering primary marine signals. However, based

Table 15.2 Descriptive statistics of REE content of 43 core phosphorite samples from Abu Tartur, Safaga and Quseir

Variable	*La*	*Ce*	*Pr*	*Nd*	*Sm*	*Eu*	*Gd*	*Tb*	*Dy*	*Ho*	*Er*	*Tm*	*Yb*	*Lu*	*REE*	Δ Ce	Δ Eu	LRE/HRE
Mean (n = 43)	46.50	67.03	10.36	46.10	8.21	2.29	9.56	1.38	9.28	2.02	5.86	0.83	5.41	0.83	215.68	0.71	5.46	1.6
Minimum	5.10	3.75	0.70	3.40	0.60	0.10	0.90	0.10	0.90	0.20	0.70	0.10	0.60	0.10	17.75	0.42	6.00	1.3
Maximum	166.20	257.10	40.10	171.20	30.70	9.60	35.00	5.30	32.90	7.00	19.80	2.90	17.80	2.90	797.40	0.74	5.35	1.7
Standard deviation	42.22	70.53	10.67	45.88	8.43	2.58	9.50	1.41	8.69	1.86	5.22	0.76	4.61	0.73	211.69			

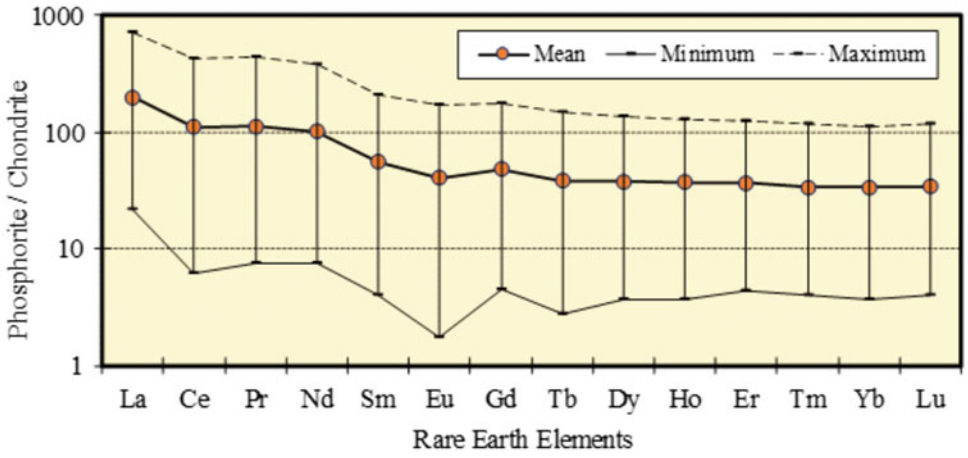

Fig. 15.3 Chondrite normalized REE patterns of mean, minimum and maximum concentrations of REE in 43 core phosphorite samples from Abu Tartur, Safaga and Quseir

on published data and ICP-MS analysis data of 43 phosphate core samples from Abu Tartur, Safaga, and Quseir (Table 15.2, Fig. 15.3), the following remarks can drown:

1. In average, the light REE (i.e., La, Ce, Pr, Nd, Sm, and Eu) represent about 84% of the total REE content. The chondrite-normalized pattern reflects a monazite signature.
2. In spite of the fact that the Ce-anomaly values reflect proper marine environments, it shows significant fluctuation from 0.42 to 0.74, suggesting variation in the sea level and depositional controls, especially the redox potential.
3. The REE content of phosphorites correlates intimately with Sc and Th, which are terrestrial indicator proper (Fig. 15.4). This possibly indicates that at least a foremost share of the REE has a terrestrial origin.
4. The REE budget varies in the phosphorites of the same age from one locality to another. This is, in fact, because they have a different stratigraphic position with respect to the Tethyan transgression event.
5. The phosphorites that deposited at the beginning of the Late Cretaceous transgression event occur at the base of the Duwi Formation, or even intercalated within the uppermost Quseir (Variegated Shale) Formation. These beds represent the shallowest basin forming the southern limits of the Tethyan phosphogenic belt and can be encountered in Hammadat south Quseir, south Edfu (e.g., in Fawaza and Silwa villages), and the lower bed of Abu Tartur plateau. All these phosphate beds are remarkably rich in REE + Y (about 1000 ppm). In the same occurrences, the upper phosphate beds contain less than half the REE + Y budget of the lowest bed. The REE-rich phosphorites are not only those of Abu Tartur but also all phosphorites of the southern borders of the phosphate belt across the country (Fig. 15.5). As transgression proceeds, the basin becomes deeper, and the REE budget decreases with relative enhancement of the HREE.

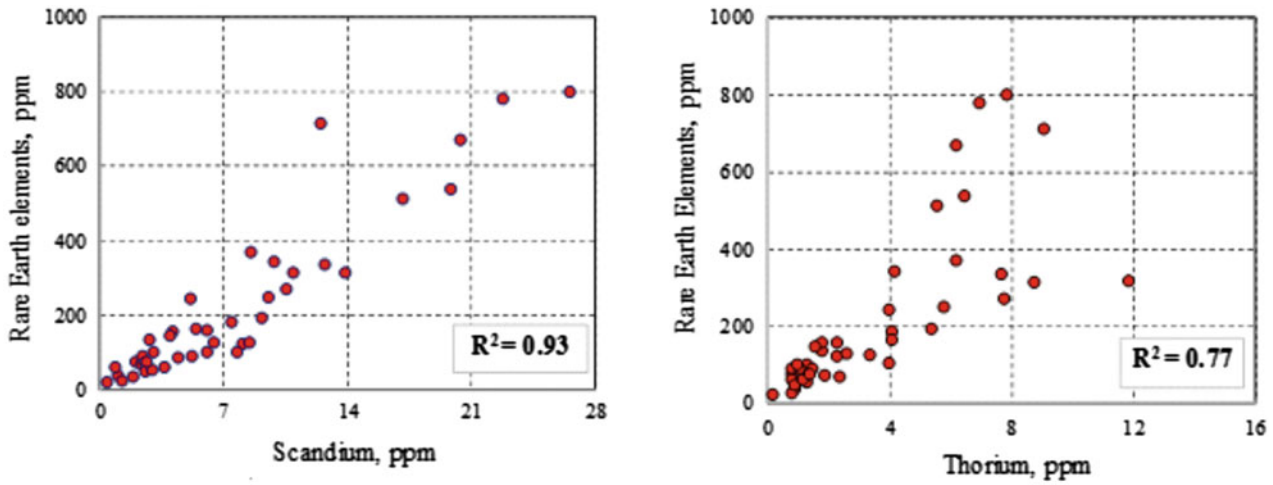

Fig. 15.4 Correlations between REE and the terrestrial-proper indicator (Sc and Th) in Egyptian phosphorites

Kechiched et al. (2016), records similar observation for Algerian phosphorites. They reported that phosphates from the southern basin show ∑REE content (623 ppm, in average), more than double that of the northern phosphorites accompanied with relative HREE enrichment (266 ppm, in average).

6. The phosphate bearing sediments of G. Hefhuf (Bahariya Oasis) are markedly enriched in the MREE due to diagenetic uptake from water that washed older rocks under the influence of the thermal gradients prevailed during the Oligo-Miocene time (El-Kammar 1977).

15.1.6 Natural Radioactivity

The naturally occurring radioactive metals (NORM) in phosphorites are U, Th and, K, with a marked predominance of the former. The main radionuclides (U and Th) accumulate into phosphorites during deposition but the main quotient of U accumulates through reduction of the soluble U^{6+} in the seawater to the immobile U^{4+}, at the water-sediment interface or during diagenesis. In general, the physicochemical controls during deposition, fabric characteristics of the rocks, diagenetic modifications and weathering activity, especially during

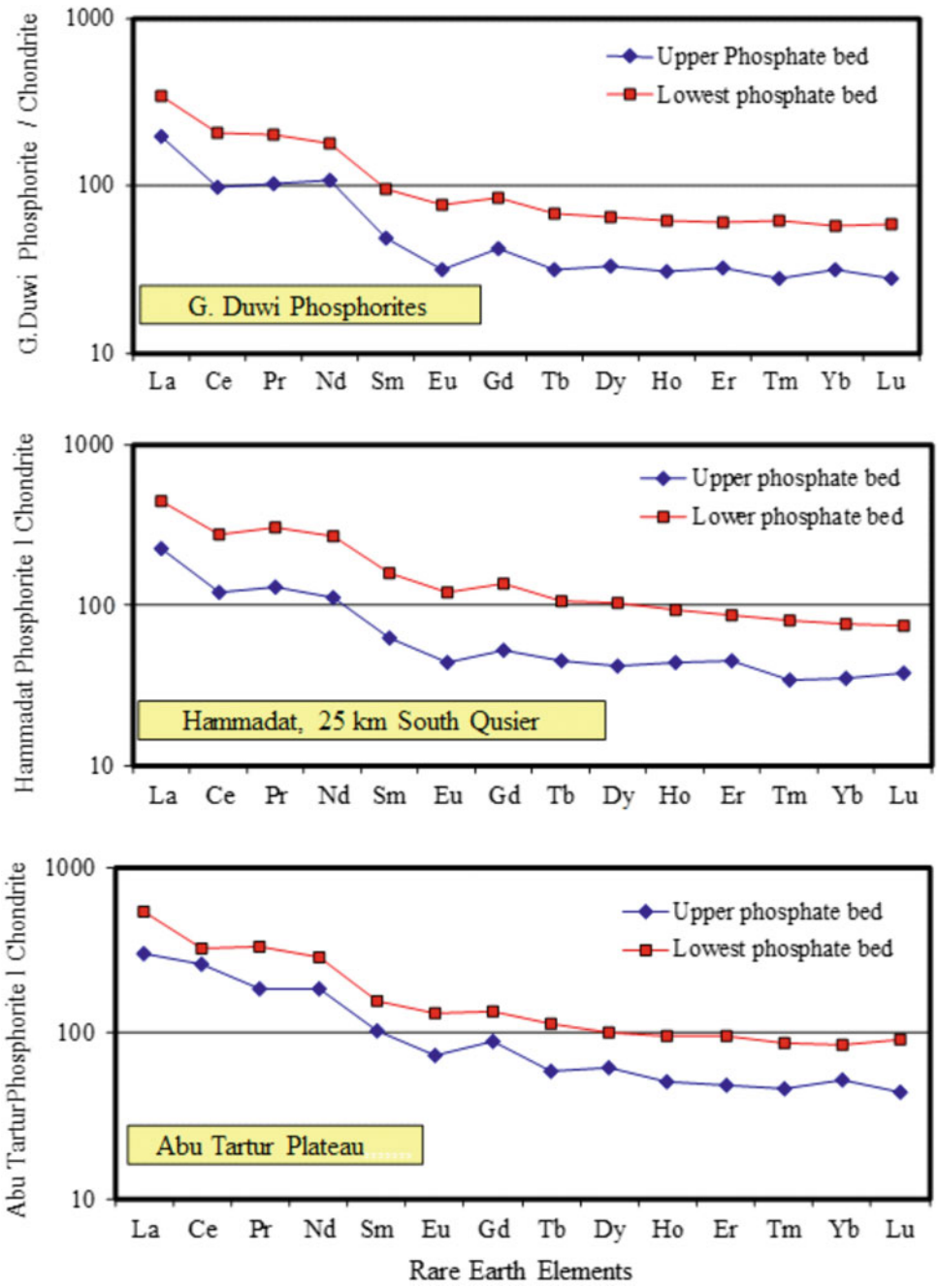

Fig. 15.5 Chondrite-normalized REE patterns of upper and lowermost phosphate beds of some occurrences in Egypt

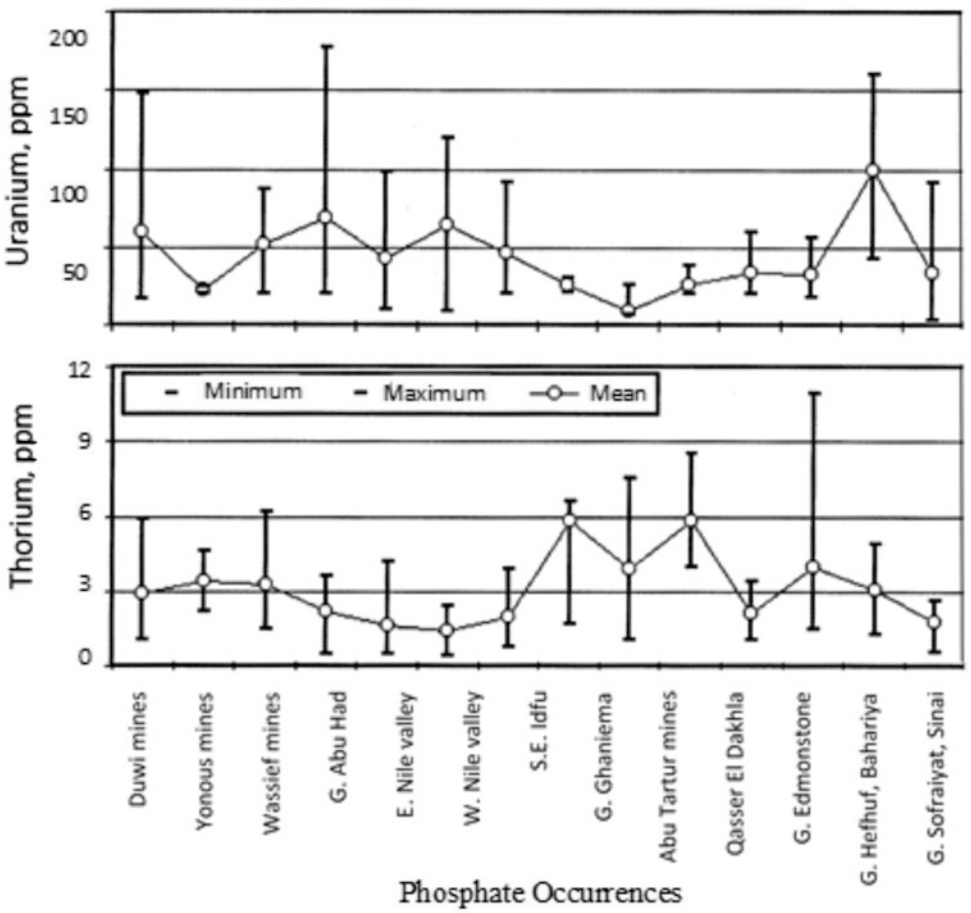

Fig. 15.6 Mutual abundance distribution of Th and U in phosphorites from different occurrences in Egypt (after El-Kammar and El-Kammar 2002)

the pluvial periods share together the abundance and distribution of uranium in phosphorites. Nevertheless, phosphorite horizons become enriched or depleted in uranium through its secondary migration in or out, so that an analysis of the relative content of uranium is never exactly the same, even for similar rocks taken from different locations (Fig. 15.6).

Numerous publications, as well as unpublished dissertations and reports, done on the NORM of the Egyptian phosphorites during the last seven decades. The following is recapitalization of the main conclusions: (1) Radioactivity is essentially related to uranium decay series and not thorium series, where the former exists in both U^{4+} and the easily leachable U^{6+} (Hussien 1954). (2) The depth of the depositional basin controls the relative abundance of U, Th and REE in the Egyptian phosphorites, where the shallowest sedimentation (e.g., the lowest phosphate bed in Abu Tartur) accumulates the least U and highest Th and REE (Hassan and El-Kammar 1975). (3) There is a substantial redistribution of U in phosphorites as well as other facies like glauconite in the weathering profile (El-Kammar and El-Reedy 1984). (4) The U content in the Egyptian phosphorites ranges between 20 and 180 ppm, averaging 58 ppm, whereas Th ranges between 0.5 and 11 ppm (El-Kammar and El-Kammar 2002). (5) As derived with the terrestrial input to the depositional basin, Th has a mutual abundance with the REE and the pseudo-lanthanides (Y and Sc). (6) U is mostly of marine origin, although limited quotient derives with detrital minerals such as zircon and monazite (Hussien 1954). (7) Disequilibrium state of uranium radioactivity dominates all phosphorites of Egypt because of the secondary mobilization of U (El Shazly 1984). (8) Exploration for phosphorite succeeded through the airborne survey of U radioactivity (El Shazly et al. 1979). (9) U is a potential benefit during phosphoric acid industry in Egypt (El-Kammar 2012).

During exploration program for oil shale in Egypt, El-Kammar (2010) noted that U is mutual with, although does not mirror, the total organic carbon content (Fig. 15.7). Generally, phosphorites are a better accumulator of U than oil shale and there is a prominent increase of U content (relative to TOC) at the upper part of the Dakhla Formation. Such peculiar enhancement of U cannot only be interpreted to the reduction of the soluble U^{6+} to the immobile U^{4+} under the prevailing anoxic conditions or to longer contact with seawater. It seems more eligible to believe that seawater was abnormally rich in U at this particular time interval.

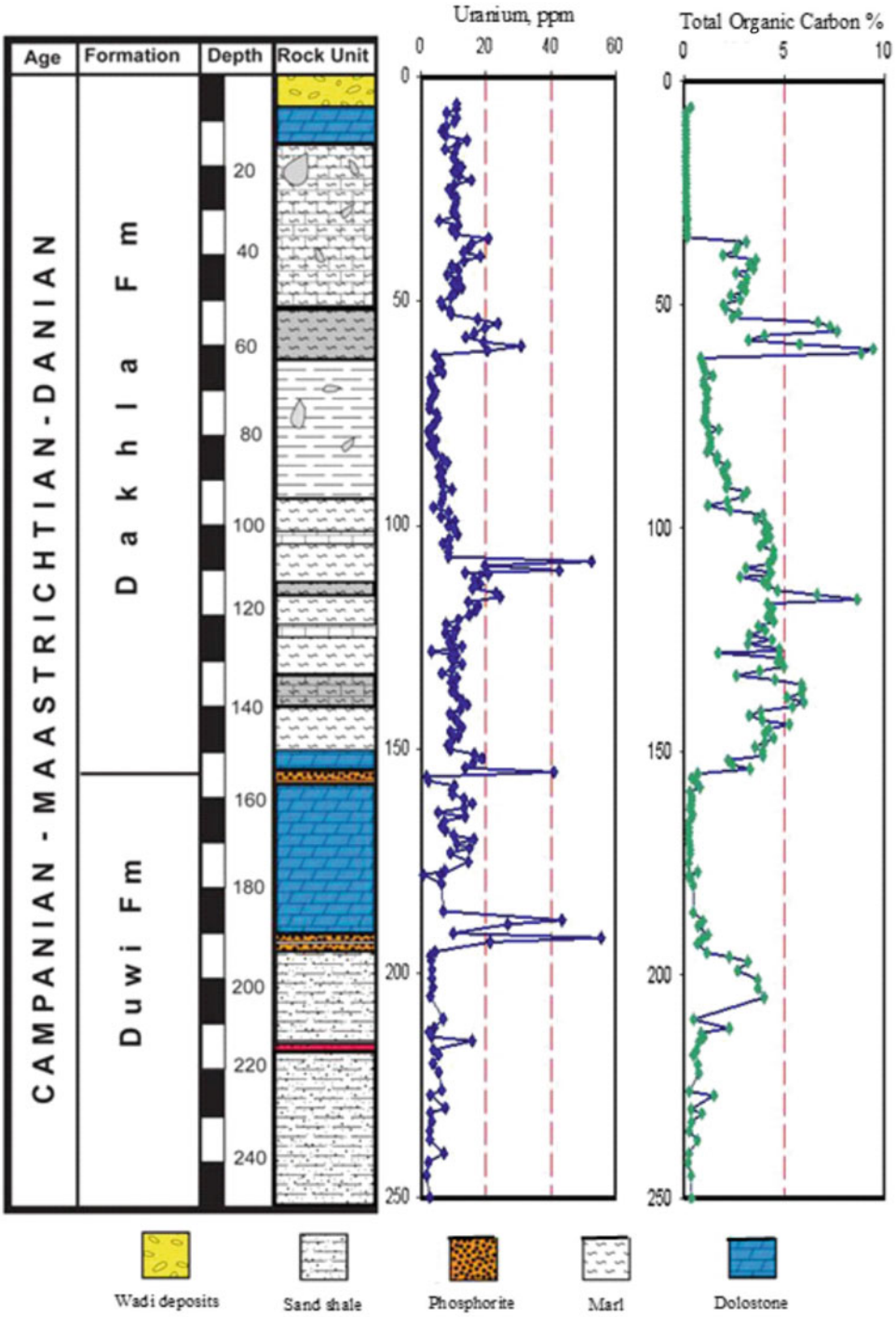

Fig. 15.7 Mutual distribution of U and TOC along the U. Cretaceous Paleogene section of Quseir area, Red Sea

15.1.7 Phosphogenesis

The enigma of the phosphate origin seems to be a result of debate and dispute of many authors. The suggestions and theories postulated for the origin appear sometimes in extreme contradiction, particularly when discussing the deposition system, which is the core of the problem.

The first model of phosphogenesis proposed by Kazakov (1939) who believed that phosphorite resulted from purely chemical precipitation. He further verified the model to include strong upwelling and high biological productivity. The upwelling currents derive the soluble phosphate salts resulting from the decay of the soft tissues of marine organisms at the minimum oxygen zone to the shallow zone.

Shallow restricted basins enhance higher quotient of soluble salts that leads to flourishment and diversity of marine life. A catastrophic destruction of marine life resulting from the mixing of cold-water mass with a warm water mass as might occasionally occur along the border of great ocean currents (Kazakov's upwelling). Hence, phosphorites and their associated sediments are intimately linked to upwelling and were formed along continental margins. However, Ahmed et al. (2014) reported that the main component of phosphate rocks is pellets in situ and common reworked biogenic debris, especially in the upper phosphate beds (e.g. fish teeth and bones), which along with abundant Thalassinoides burrows suggests that the skeletal material was the main source for phosphates in Egypt.

During late Campanian to early Maastrichtian in Egypt, transgression and sea-level oscillation were controlled by the regional tectonics, which in turn, systematized the sedimentation regime (Philobbos 1969) and developed broad continental shelves (Baioumy and Tada 2005) which developed high productivity upwelling and sedimentation of phosphorites, glauconite and organic-rich sediments (Schneider-Mor et al. 2012). Baioumy and Tada (2005) consider the deposition of the Duwi Formation as an initial stage of the Late Cretaceous marine transgression in Egypt. However, the recognition of thick phosphate bed (2 m) in the lower Quseir Formation in Gebel Zabara, 5 km SE Edfu (El-Kammar et al. 1984), proposes that the Tethyan transgression in Egypt started much before the Duwi Formation.

Glenn and Arthur (1990) suggest two depositional realms to interpret the common coexistence of glauconites and phosphorites in the Late Cretaceous of Egypt. The first is a shallow hemipelagic environment accompanying initial stages of marine transgression for deposition of black shale and phosphate, and the second is high energy depositional regime accompanying sea-level fall with delta advances for deposition of glauconites. The studies by Bock (1987a, b) concluded that the most likely phosphogentic model for Egyptian phosphorites to be one that visualizes the existence of a Tethys south coast upwelling area on the North African shelf, which provided nutrient-rich waters leading to the formation of primary organic and phosphate-rich sediments.

Many publications, especially during the last two decades, advocate for the crucial role of bacteria in the phosphogenesis. Hiatt et al. (2015) described preserved fossil bacteria in phosphate crusts and grains from the ca. 1850 million-year-old, near the end of the Earth's initial phosphogenic episode, in Michigan, which provides insight into the longevity and nature of this relationship. Caird et al. (2017) interpreted the phosphorite accumulation to biostromes, where francolite concentrates in microbial laminae. Phosphogenesis was restricted to the nearshore because biostromes that colonized intertidal flats created the necessary redox and sedimentologic conditions for the authigenic precipitation of francolite. Using spectromicroscopy techniques, Cosmidis et al. (2013) and Salama et al. (2015) identified submicrometer-scale traces of bacterial precipitation of francolite coupled with sulfate reduction in phosphorite of different countries. The observation of such fossil bacteria supports different non-exclusive phosphogenesis mechanisms.

The presence of a high quotient of francolite skeletal proposes extraordinary flourishment of marine animals followed by sudden mortality (Kazakov's upwelling theory), reworking, and good preservation. The upwelling and the configuration of the Tethyan continental shelf maintained the flourishment of the marine life. The presence of the chemically formed collophane grains and pellets together with skeletal and, the higher thickness in troughs support the reworking. This agrees with Obaidalla (2013), who concluded that the Paleocene sediments deposited more or less in a stable depositional basin with respect to the sediments of the upper Cretaceous, which deposited in an unstable one. However, there is no one common theory to convey the many phosphate assumptions and consequently no easy way to develop a common "language" for phosphogenesis.

15.1.8 Utilization and Its Challenges

The worldwide production of phosphate rocks goes mostly (>85%) for the production of phosphoric acid and fertilizers. This explains the intimate coherence between phosphorite prices in the international market and the "Food Price Index" as issued by FAO. The total world production of phosphorites in 2015 was 225 million tons, where the share of Egypt is about 2.5%. At present, only 20% out of this share is manufactured. Certainly, manufacturing of phosphorite in Egypt is a crucial commitment, where production of phosphoric acid, hence fertilizers, should be doubled in the coming decade to avoid food crises and to have sustainable agriculture development. As far as the author is aware, 10 new projects for production of phosphate fertilizers approved currently by the Industrial Development Authority (IDA), two of them, in the industrial zone of Suez and in Abu Tartur, have already taken substantial implementation steps.

In Egypt, the annual production of phosphates increased from 0.581 m tons in 1977, to about 2 m tons in 2010, but reached 5.5 m tons in three years. The supply price of the Egyptian phosphorites in 2015 was \$60/ton for the 30% P_2O_5 grade and it was \$35 for the grade 28% P_2O_5. The marked increase in production is essentially due to the excavation of phosphorite outcrops in Abu Tartur. In spite of the fact that the Arab countries produce only 52.5 million tons/year, which represents about 20.5 of the total world production in 2015, they own the largest reserves (Fig. 15.8). Applying new mining methods especially in the

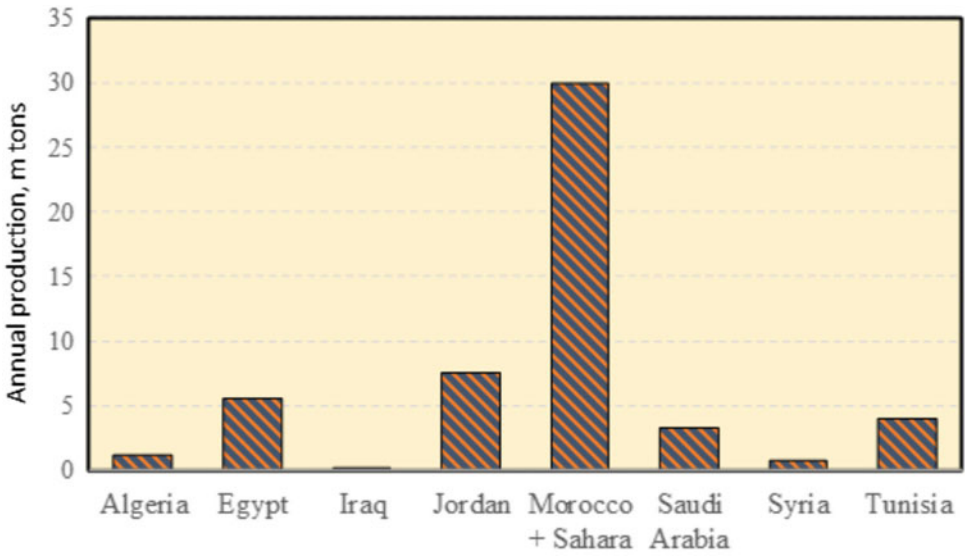

Fig. 15.8 Phosphate annual production of the Arab countries in 2015

Red Sea and Abu Tartur, exploration, and beneficiation of the medium and low-grade ore may drive the present 5.5 m tons annual production of Egypt to a prosperous frontier.

The theoretical P_2O_5 value for an ultrapure francolite is 41%, but marine phosphate deposits may contain up to 34% P_2O_5. However, most of the available commercial phosphate resources in Egypt are below 27% P_2O_5, where the highest grade and easily accessible resources exploited during the last 80 years. At present, the easy accessible commercial phosphates estimated to be 1.2 billion tons (U.S. Geological Survey, Mineral Commodity Summaries 2016), whereas much higher resources of the medium and low grades (10–25% P_2O_5) are available, especially in the Western Desert. It seems that the era of cheap high-grade phosphorites is over. Many phosphate deposits have not needed beneficiation but it is now changing. The conventionally applied methods for beneficiation of phosphorites includes; size reduction and screening, attrition scrubbing and classification, electrostatic separation, magnetic separation, chemical dissolution of carbonates, flotation, and calcination the composition. The beneficiation technique depends mainly on the composition and abundance of the non-phosphate minerals (usually called gangues). However, the published data refer to innovations to suit the ore to be beneficiated. For example, a Rotary Triboelectrostatic Separator applied by Tao and Al-Hwaiti (2010) to the beneficiate phosphorite from Jordan and advocated for the importance of desliming for effective beneficiation. Reverse scheme of wet flotation column designed to beneficiate Saudi calcareous phosphorites (25% P_2O_5) where a high purity ore of 35% P_2O_5 obtained at 95% recovery value (Al-Fariss et al. 2013). Shariati et al. (2015) used an integrated method of calcination and shaking table for concentrating the low-grade phosphate ore (9–10% P_2O_5) from Iran, the results show promise at producing grades of 30.77% P_2O_5 with 60.7–63.2% recovery. Column flotation technology adopted for successful beneficiation of low-grade phosphorites in different countries during the last three decades (El-Shall et al. 2004). Kawatra and Carlson (2013) give more details on beneficiation of low-grade phosphorites.

15.1.9 Environmental Hazards

The hazards caused by mining construction and operation, as well as the relevant diseases such as silicosis will not be considered herein. The present work is concerned with hazards related to the long-continued application of phosphate fertilizers to soils. In India, Hameed et al. (2014) measured the radioactivity of ^{238}U in the pristine soil, cultivated soil, single superphosphate, and triple superphosphate fertilizers to be 165, 182, 396 and 284 Bq/kg, respectively. The measured radioactivity is well below the permissible limit (370 Bq/kg) and hence cultivated soils do not pose any radiological risk. Similar conclusion reported by Hassan et al. (2016) for most phosphorites and fertilizers collected from Egypt, where the annual effective dose was in the range of the worldwide average value (480 Sv y-1). On contrary, El-Bahi et al. (2017) measured the radiological parameters in phosphate rocks and their products (phosphogypsum and fertilizers) and concluded that the total excess lifetime cancer risk (ELCR) is high in all samples, and represent a radiological risk for the health of the population. Cd is another potentially toxic metal where its maximum permissible limit in soil is 0.2 ppm. In spite of the fact that the phosphates of the Red Sea are the highest (11.7 ppm) and Abu Tartur is the least (3.3 ppm), the Egyptian phosphorites are generally less cadmiferous than those of Tunisia

(53 ppm), Morocco (21.4 ppm), and Jordan (23 ppm). According to da Conceicao and Bonotto (2006), the long application of phosphate fertilizers can redistribute and elevate toxic heavy metals for instance Cd, As and Pb in soil profiles (especially in acid soil) and consequently their transfer to the food chain and also raise the concentration of these elements in irrigation drainage waters.

15.2 White Sand (Glass Sand or Silica Sand)

Adel Surour

15.2.1 Definitions and Historical Background

Silicon constitutes almost 28% of the earth's crust. Silica sand is also known as quartz sand and industrial sand, and is largely used in several construction applications. According to the factsheet of the British Geological Survey (2009), silica sand is equivalent to industrial sand with more than 95% SiO_2 (in a narrow range grain size, mostly 0.5–1 mm), and are used for applications other than as construction aggregates. They are produced from both loosely consolidated sand deposits and by crushing weakly cemented sandstones. Generally, silica sands command higher prices than construction sands. The first industrial uses of crystalline silica were related to metallurgical and glass making activities some thousand years B.C. At least 4000 years ago, long before iron was smelted; glass-making was already a known craft. The oldest known specimens of glass were obtained from Babylon (2600 B.C.) and from Egypt (2500 B.C.). It could be conclusively proved that the glass-making was well established in these countries by around 1500 B.C. It has continued to support human development throughout history, being a key raw material in the industrial revolution especially in the glass, foundry and ceramics industries. Silica sand may also be known as silica sand abrasive when used for abrasive blasting. Owing to its snow-white colour, some of the silica sands are termed as "white sand deposits" either loose or compact. The term "glass sand" is preferably used for silica sands to manufacture glass since Antiquity and up to now.

Silica contributes to today's information technology revolution being used in the plastics of computer mouses and providing the raw material for silicon chips. The chemical, physical and mineralogical specifications of many industrial sand products differ from an application to another (MacLaws 1971). Most of specifications concerning high purity silica sand are connected to its uses as a raw material for the manufacture of glass, silicon carbide, and soluble silicates for the chemical industry, and for moulding sand, hydraulic fracturing sand, and filter sand. The presence of silica sand on metal materials can be a source of crevice corrosion on those metals. Quality requirements for sand of lesser purity used for special purposes such as sandblasting, abrasives, and building products also are different.

15.2.2 Formation, Mineralogy, Distribution and Testing Techniques

Silica occurs in three main crystalline forms principally quartz but it also occurs in other rarer mineral forms known as tridymite and cristobalite. chalcedony, agate, flint and jasper (crptocrystalline), and opal (hydrous form); sandstone (sedimentary deposit composed of small grains of quartz); quartzite (metamorphosed derivative of sandstone) and silica sand (weathered sandstone or quartzite enriched in silica) (Sundararajan et al. 2009). Silica phases are very durable that are resistant to heat and chemical attack and it is these properties that have made it industrially interesting to man and humanity. It is a granular material, and in addition to high percentage of silica minerals, silica sand may contain low levels of deleterious impurities such as clay, iron oxides, titania and refractory minerals.

According to Ladoo and Myers (1951), silica sands are classified on the basis of its industrial applications that can be listed as follows: (1) as an abrasive in blasting and scouring sand, and certain types of grinding and polishing materials, (2) for various types of building products, (3) in glassmaking, (4) in hydraulic fracturing of oil-well reservoirs, and (5) as a refractory agent in various types of foundry and modeling sands and to manufacture refractory bricks.

The silica sand is an assemblage of individual silica grains in the size range up to 2 mm. Sand can be formed in nature by natural weathering of sandstone and quartzite or mechanically by crushing a sandstone/quartzite or by a process of flotation whereby the various constituents in a pegmatite or kaolin mixture are separated. Also, silica sand occurs in association with clays and quite often as admixture with siliceous or lignitic overburden like in the Indian Peninsula. The occurrence of silica sand in world is widespread and extensive. Good quality silica sand reserves are situated in the UK, Germany, Belgium, France, Brazil etc. In Asia, silica sand is available almost in all the states of India (Sundararajan et al. 2009). In Egypt, silica sand is very common and the white sand deposits from different Egyptian localities are demanded by glass makers all over the worlds especially in Turkey and China. The major Egyptian silica deposits are represented by white sands from the northern Eastern Desert along the Gulf of Suez coast at Za'afrana and in the Sinai Peninsula. The raw white sands from the Egyptian deserts were exported extensively during the last

Table 15.3 Major white sand deposits in Egypt, with reserves and chemical ranges (Ezz-El Din et al. 2016)

Location	Reserves, M (ton)	Sio_{2f} (%)	Fe_2O_{3f} (%)	Al_2O_{3f} (%)	$CaO+MgO_2$ (%)
Western desert					
Wadi El-Natron	1.7	92.4–95.4	0.3–0.54	1.24–2.6	1.4–2.1
New Valley 1	ND	93.9–96.0	0.23–1.02	0.01–2.01	0.6–1.2
New Valley *2*	ND	93.9–96.1	0.30–1.3	0.01–2.1	0.8–1.2
North Fayoum	Unlimiited	90.5–98.0	0.25–2.24	0.03–2.24	0.71
Eastern desert					
Wadi Qena	258	94.8	0.33	4.0	–
Wadi El-Dakl	10	98.5–99.6	0.01–0.02	0.036–0.19	0.03–0.2
East Edfu	Unlimiited	ND	ND	ND	ND
East Maadi	Medium	95.0–97.0	0.27–0.42	0.6–1.44	0.12–0.2
Sinai					
Abu EI-Darag	4.1	97.2–98.6	0.03–0.07	0.23–1.43	0.22–1.07
Gabal El-Mensheieh	3	98.1	0.08–0.093	0.026–0.32	0.06–0.28
Wadi Filly	1.3	91.4–99.6	0.027–0.26	0.016–0.37	0.1–1.23
Abu Zneima	1.25	97.5–99.7	0.01–1.34	021–1.35	0.004–0.2
El-Gunna	2,500	90.3–96.5	0.026–0.08	1.85–6.0	0.01–0.35
Wadi Watir	ND	ND	ND	ND	ND
Kathrine-Newbie Road	ND	ND	ND	ND	ND

two decades to other markets other than Turkey and China, e.g. UAE, Cyprus, Greece, Albania, Italy, Georgia, Croatia, Syria, Lebanon, Malta, Kuwait, Qatar, Algeria and Libya. There are almost 17 authorized Egyptian companies in trading white sands under the new laws of mining and quarrying in Egypt as by 2018. Table 15.3 presents the reserves and chemical characteristics of Egyptian white sand deposits all over the territory.

Ezz-El Din et al. (2016) summarized the distribution of white sand deposits in Egypt, and stated that there are a large number of high-quality quartz deposits. All of them are spread in the Eastern Desert along the Red Sea Coast. Their modes of occurrence are as quartz caps of plutons formed as a result of magmatic differentiation and after granitic pluton cooled and solidified. Quartz veins were formed from the residual solutions after forming the caps, and these solutions penetrated through the cracks and along fissures to form veins and/or lensoidal bodies. Quartzite is present in both sedimentary and metamorphic rocks. It is originated from the metamorphism of sandstone. The quartz reserves in Egypt exceed 20 million tons in more than 30 localities. The white sands in Egypt exist in Sinai, North part of Eastern Desert, and in the Western Desert. The most important sandstone deposits in Egypt, quantity and quality, are in Wadi Qena in the Eastern Desert and Gebel El-Gunna in Sinai. The white sand in Wadi Qena constitutes most of the early lower Paleozoic Naqus Formation, North-East of Qena. The Northern part of Wadi Qena consists of the exposed lower Paleozoic rock units which are represented by Araba and Naqus Formation. At the Saint Katherine-Neuwiba, the Naqus Formation consists mainly of a thick sandstone sequence. Generally, the lower 30 m are white massive sandstone beds with minor ferruginous clayey and kaolinitic interbeds. Gebel El-Gunnah has the largest sand stone reserves in Sinai. There are more than 3 billion tons of high quality silica sands in 16 localities in Egypt. The most important locations are Wadi Qena and Wadi El-Dakhl (commercially known as El-Za'afrana) in the Eastern Desert, in addition to Gebel El-Gunnah (south Sinai) and El-Maadi, which is located in the Cairo suburbs (Ismaiel et al. 2017). They (op. cit.) concluded that two specific deposits at Wadi Qena and Somr El-Qaa have a very minor iron content (Fe_2O_3 from 0.01 to 0.09%) and hence they are suitable for the specifications of many industries such as glassmaking, abrasive, hydraulic fracturing, water filtration, building products, chemicals and semiconductors; as dug or with some essential beneficiation processes such as sizing and classification to produce the required size gradation, attrition scrubbing to iron oxide-clay coating removal and flotation to heavy mineral elimination.

The largest deposit of white sand in the Eastern Desert lies at Wadi Qena. The white sand in Wadi Qena constitutes most of the lower Paleozoic Naqus Formation (450 km^2) North-East of Qena (see sections (A) and (B), Fig. 15.9). The Northern part of Wadi Qena consists of the exposed lower Paleozoic rock units which are represented by the

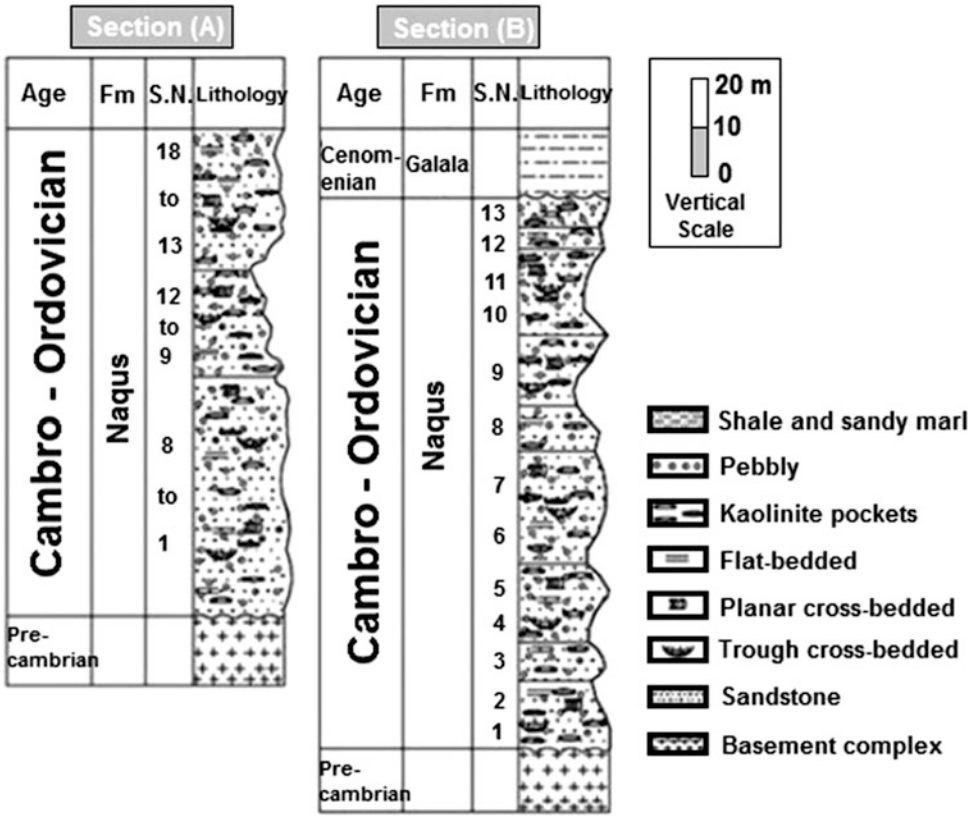

Fig. 15.9 Two stratigraphic sections containing white sand deposits of the Naqus Formation in the northern Eastern Desert (from Abou Al-Anwar and Al-Wekeil 2013)

Araba and Naqus formations (Wanas 2011). The Naqus Formation rests unconformably on the peneplained Precambrian crystalline rocks of Araba-Nubian shield and form scattered outcrops in a series of hills and mesas. The thickness of the Naqus Formation ranges from 22 to 120 m (Abou El-Anwar and El-Wekeil 2013). The upper boundary of the Naqus sandstones is absent in section (A), while in section (B) it is unconformably overlain by the shallow marine sediments of the Cenomanian Galala Formation.

In the Sinai Peninsula, white sands of the Neuwiba area, southeastern Sinai was considered by Khalid (1993) as a potential source of high-grade silica. El Fawal (1994) and Kamel et al. (1997) shed some light on the economic accumulations of these sands within the Carboniferous Abu Thora Formation, west-central Sinai. Abu Shabana (1998) estimated the reserve of the glass sands at Abu Rodeiyim and Abu Heish localities, west-central Sinai to about 8 million tons. Kamel et al. (1997) mentioned that the preliminary estimation of silica sands for the glass industry from such localities are about 1500 ton/year. The silica sand deposits occur within the Naqus Formation of Early Paleozoic age (Hassan 1967; Said 1971; Issawi and Jux 1982) as a thick siliciclastic sequence attaining 250 m thick that unconformably overlies the Araba Formation and is overlain by the Malha Formation. Abdel-Rahman (2002) investigated typical white sands of the Naqus Formation at the Wadi Watir area (particularly at Wadi Ghazala) in southeastern Sinai, and stated that the sand deposits there are characterized by the typical Fenstra or "Mashrabia" structure (Fig. 15.10), quartz pebbles and ferruginated laminations. Abdel-Rahman (2002) concluded that most of the silica sand deposits of the Wadi Watir region are of second and third grade that are not suitable to make high-quality container glass but they can be utilized for domestic art purposes. This deposit is very well-sorted and contains more than 90% of coarse to fine sand-sized gains that are sub-rounded to angular quartz grains, in association with some minor heavy minerals mostly Fe-oxides, rutile, zircon, tourmaline and andalusite. More recently, Ramadan (2014) studied the physicochemical properties of the white sandstone deposits along the Nuweiba-Saint Katherine road, and reported similar measurements of fine to medium in size, well-sorted, and about 90% of the grains fall in the range of 1.0–0.125 mm,. More than 85% are quartz-arenite that has the following chemical ranges 0.55–1.67% (Al_2O_3), 0.41–1.66% (Fe_2O_3) and 91.17–95.99% (SiO_2). In terms of purity, the quality is compatible with grades (E, F and G) on the British Standards and Serial Numbers (S/N) 7 to 9 according to U.S specifications.

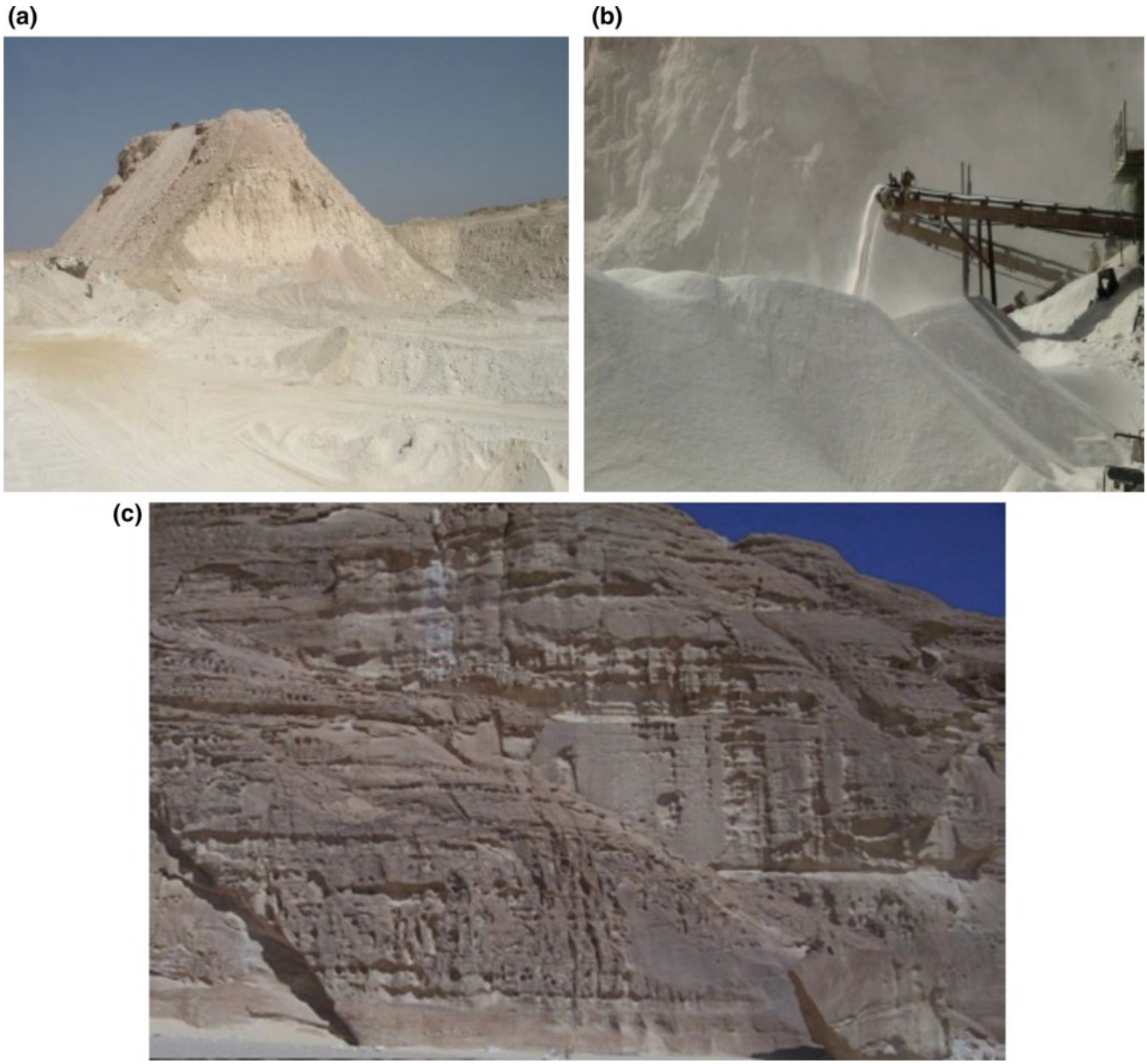

Fig. 15.10 **a** and **b** White sand deposits from the Eastern desert of Egypt and their extraction at Wadi El-Dakhl (from Ibrahim 2016). **c** White sand as quartz-arenite showing Fenstra or "Mashrabia" structure of the Naqus formation along the Nuweiba road in the Sinai Peninsula (from Ramadan 2014)

Impurities usually present in the silica sand are free and coated iron oxides, clay, titania and smaller amounts of sodium, potassium and calcium minerals. The iron, being the most detrimental impurity, can be reduced by a number of physical, physicochemical or chemical methods; the most appropriate method depends on the mineralogical forms and distribution of iron in the ore. Upgrading of silica sand requires partial removal of iron, and other minerals which are detrimental to its end use. While much of the liberated impurities can be reduced or removed by physical operations such as size separation (screening), gravity separation (spiral concentration), magnetic separation etc., sometimes, physico-chemical (flotation) or even chemical methods (leaching etc.) are to be adopted for effective removal of iron which may be in intimate association with the mineral quite often superficially. All producers of white sand or silica sands in general need to adopt simple, cost effective as well as environment-friendly processes and operations for value addition of the sand so that even a small/medium level entrepreneur can set up a beneficiation plant without much capital investment. In addition, there is also a need to employ sieving (screening) and other physical

operations as far as possible without any need for chemical processing.

There are some standard wet chemical methods supported by instrumental analysis in order to determine the chemical constituents. In most cases, the silica sand sample is analyzed for silica, alumina, and oxides of iron, titanium, calcium, sodium and potassium and loss on ignition (LOI). If XRF or ICP-MS techniques are not available, silica can be estimated gravimetrically by volatilizing with hydrofluoric acid, alumina by complexometric (indirect EDTA) titration, iron and titanium by spectrophotometry and calcium, sodium and potassium by flame photometry. X-ray diffraction (XRD) of the powder sample provides one of the easiest and semi quantitative methods for the identification of silica and clay minerals. Quartz and other silica minerals are observed using scanning electron microscope (SEM) for the morphological studies. The grains are mounted on a SEM brass stub. The mounted quartz grains are coated with gold in a vacuum evaporator. The relative densities and relevant bulk densities of the feed and various intermediates and final products are determined by standard methods.

15.2.3 Extraction, Beneficiation and Modern Applications in Egypt

Silica sand deposits are most commonly surface mined in open pit operations, but dredging and underground mining are also employed. Extracted ore undergoes considerable processing to increase the silica content by reducing impurities. It is then dried and sized to produce the optimum particle size distribution for the intended application. In Egypt, surface mining is usually used for mining of silica sands as a result of the presence of little or no overburden, about 1–15 m, in almost all the white sand deposits. The boreholes are drilled using pits of 3 inch diameter to a depth of 10–12 m, and then the broken material is transported to a size reduction and screening section, to be prepared for washing and processing.

Abu Khadra (2015) studied several natural silica resources in Egypt and concluded that many of the white sand deposits contain impurities that have a strong influence on the chemical quality and in turn the technical qualification of the silica raw materials. For example, the common iron oxide impurities might cause the highest damage by both their colour and properties. Such iron impurities are prohibitive to some advanced applications such as optical fibers, silicon for solar cells, semiconductors, microelectronics and refractories. Therefore, the majority of Egyptian white sand deposits need several beneficiation and upgrading techniques to match the technical specifications modern or high-tech industrial applications. Physical and chemical beneficiation methods such as gravity and magnetic separation, attrition, flotation and acid or alkaline leaching are used to remove iron impurities from quartz sands. Chemical processing to remove the iron oxide contaminants appear to be highly efficient as compared to physical beneficiation. Shaban and Abu Khadra (2016) summarized that leaching of iron bearing impurities can be performed using H_2SO_4, HCl, HF, phosphoric acid and oxalic acid, in which a mixture of 10% HF acid and 90% H_2SO_4, HCl and HNO_3 for 3–12 h is very effective. Also, phosphoric acid is considered as one of the best leaching agents in the purification of iron impurities from the quartz. It has advantages of a high leaching rate, low cost of production, simplified flow sheet, and less harmful to the target product. Shaban and Abu Khadra (2016) carried out some laboratory experiments to upgrade the Egyptian white sands and concluded that the best removal process (82%) can be achieved at 8 g/t oxalic acid concentration, 95 °C temperature and 120 min leaching time. The pilot sample has low silica content (99.441%) and considerable impurities of iron (0.112%). The final product exhibits high silica content (99.683% SiO_2) and lower iron content of (0.017%) as shown in Table 15.4 that match the requirements of ceramic, silicon carbide, silicon metal and the production of silicon for solar cells.

Gaber (2012) stated that the fine sand from the Za'afrana area is considered as an additive material to ochre and graphite for the production of paints and pigments. They can be utilized as extender and colored pigments to produce paint. The estimated reserves of the used ores give an indication of presence the sufficient quantities for stream production of the some paint and pigments needed for the Egyptian market. Extender pigments include those based on silicates and barite. Each of these types of pigments is somewhat

Table 15.4 Upgraded pilot sample of Egyptian white sand after beneficiation using oxalic acid method (Shaban and Abu Khadra 2016)

Oxides	(%)
Na_2O	0.035
K_2O	0.038
CaO	0.041
MgO	0.022
Al_2O_3	0.059
Fe_2O_3	0.017
TiO_2	0.010
P_20_5	0.032
so_3	0.010
Cl	0.020
Cr_2O_3	0.010
ZrO_2	0.013
MnO_2	0.012
SiO_2	99.683

different, but they all are relatively low cost materials that can be added in finely divided form to a paint to aid in its rheological properties (viscosity and flow control) an d to reinforce the dry film strength. The white sand of the Za'afrana area results indicate that the powder used with 7% of anticorrosive primer and non skid materials, iron oxide with 12%, graphite with 12% and barite with 25% of paint components.

As to modern applications of white sands, Ibrahim et al. (2016) believed that there are some new industrial applications of the Egyptian white sands such as protection coating for steel surfaces exposed to aggressive weathering conditions. Preparation and manufacturing of special type of sodium silicates to be used as a corrosion and abrasion resistance coating by using of white sands collected from Wadi El-Dakhl area related to Malha Formation-Early Cretaceous, successfully used as protective coating. The high stability and hardness of the produced sodium silicate offer a good protective coating when it's applied over the steel surfaces. The use of pure SiO_2 reaches 99.8% of some white sands help us to produce high quality special type of sodium silicate suitable to use as good mechanical protection coating. Hafez et al. (2016) showed that the white sands from north Sinai have a high concentration of SiO_2 (97.96%), and the XRD data show presence of large amount of high crystalline quartz in form of silica that exhibit thermoluminescence. Therefore, Hafez et al. (2016) did some experimental work and reached the conclusion that these sands can be used for high-doses dosimetry in several areas of applications of ionizing radiation. Finally, Boulos et al. (2017) succeeded to produce fused silica using either an arc or an electrical resistance heating Tamman furnace based on white sand samples from the north Eastern Desert. There is a need for the beneficiation of the used white sand samples to improve its SiO_2 content prior the fusion process. Hafez et al. (2017) followed a scheme of attrition scrubbing followed by a combined flotation-magnetic separation circuit, in order to obtain a sand concentrate assaying 0.0059% Fe_2O_3 and 0.015% Al_2O_3 with an overall recovery of 70%. Chemical leaching of this concentrate, by using HCl and stannous chloride at 50–60 °C leads to the production of ultra-pure sand concentrate that contains 0.0043% Fe_2O_3.

15.3 Argillic Deposits

Mohamed El-Sharkawi

Argillic deposits mean mostly the clay deposits. Many types of clays are known in the literature. The most common are:

Kaolin: A soft, fine, earthy, non plastic, usually white or nearly white clay (rock) composed essentially of clay minerals of the kaolin group, principally kaolinite, derived mainly from in situ decomposition of feldspars in granitic rocks. It remains white or nearly white on firing and known also as porcelain clay, white clay or China clay. it is used in the manufacture of ceramics, refractories and paper.

Montmorillonite: A group of expanding-lattice clay minerals generally derived from alteration of ferromagnesian minerals, calcic feldspars and volcanic glasses. Montmorillonite is the chief constituent of bentonite and fuller's earth. Also known as smectite.

Bentonite: A soft, plastic, porous, light coloured rock composed essentially of montmorillonite (smectite) group + colloidal silica, and produced by devitrification and accompanying chemical alteration of a glassy igneous material usually a tuff or volcanic ash. Colour ranges from white to light green and light blue when fresh, becoming light cream on exposure and gradually changing to yellow, red or brown. The rock is greasy and soap-like to the touch and commonly has the ability to absorb large quantities of water accompanied by an increase in volume 8 times. Also known as volcanic clay, soap clay and mineral soap.

Ball Clay: A highly plastic, sometimes refractory clay, commonly characterized by the presence of organic matter, colour ranges from light buff to various shades of grey. Used as a bonding constituent of ceramic wares. It has high wet and dry strength, long vitrification range and high firing shrinkage.

Origin of the name dates back to the early English practice of rolling the clay into balls weighing 13–22 kg and having diameters of about 25 cm.

Fireclay: A siliceous clay rich in hydrous aluminium silicates, capable of withstanding high temperatures without deforming (either disintegrating or becoming soft and pasty), and useful for the manufacture of refractory ceramic products such as crucibles and firebrick. It is deficient in iron, calcium and alkalis and approaches kaolin in composition, the better grades containing at least 35% alumina when fired.

Fuller's Earth: A very fine-grained, naturally occurring clay or clay-like material possessing a high adsorptive capacity, consisting largely of hydrated aluminium silicates (chiefly montmorillonite and palygorskite). It is used in whitening, degreasing or fulling (shrinking and thickening by application of moisture) woollen fabrics. Currently it is used as an adsorbent in refining and decolourizing oils and fats since it is a natural bleaching agent. Its colour ranges from light brown through yellow and white to light and dark green and it differs from ordinary clay by having a higher percentage of water and little or no plasticity, tending to break down into muddy sediment in water. Fuller's earth probably forms as a

residual deposit by decomposition of rock in place, as by devitrification of mafic volcanic glass.

In Egypt, the common argillic deposits are, kaolin, bentonite, ball clay, brick clay and fire clay. These will be treated in details in the following:

15.3.1 Kaolin

The kaolinite rich clays are mainly exposed in Aswan as well as Gulf of Suez provinces and generally characterized by a slow rate of slaking in water, low plasticity, high Al_2O_3 as well as a high and long vitrification range (1100–1500 °C). Hence, they are used in the production of shaped and unshaped refractories as well as vitreous china and white Portland cement. However, they are not suitable for the production of white wares due to their high colouring iron and titanium oxides content.

The main source of kaolin in Egypt is Southern Sinai and specifically the area east of Abu Zenima. Other source is upper Egypt south of Aswan, at Kalabsha.

15.3.1.1 Sinai Kaolin

The main kaolin mines belong to Sinai Manganese Company (SMC) which supplied the market with acceptable kaolin deposits. The main use was directed toward the ceramic and porcelain companies. The grades of the kaolin produced by SMC is shown in Table 15.5. Some of the old kaolin

Table 15.5 Specifications of kaolin types of Sinai Manganese company (Run of mine or crushed to 0 and 30 cm maximum)

Constituents	Type 1	Type 2	Type 3	Type 4
SiO_2	Max 52	50–56	55–62	58–68
Al_2O_3	Min 34	30–34	25–30	20–25
Fe_2O_3	0.90–1.20	0.90–1.20	0.90–1.10	0.80–1.20
TiO_2	1.50–2.30	1.50–2.30	1.40–2.00	1.30–1.80
CaO	0.10–0.15	0.10–0.15	0.30–0.60	0.20–0.30
MgO	0.05–0.10	0.05–0.10	0.20–0.40	0.10–0.20
Na_2O	0.10–0.20	0.10–0.02	0.10–0.20	0.10–0.02
K_2O	0.02–0.07	0.02–0.07	0.02–0.07	0.02–0.07
Cl	0.05	0.05	0.05	0.05
L.O.I. (105–1000)	12–14	11–12	9–11	7–9

Fig. 15.11 Open adits in the lower homogenous kaolin deposit. Issila East (Ibn Sokar) mine

Fig. 15.12 Entrance in the kaolin level with extensive iron staining at the contact with the overlying ferruginous sandstone. Tieh Ibn Sokar mine

quarries and mines are now abandoned. The company concentrate their mining operations on East Issila (Ibn Sokar) and Tieh Ibn Sokar (Figs. 15.11 and 15.12). The colour varies between grey, creamy, reddish and black. Chemical analysis of the various kaolin colours is shown in Table 15.6.

Geologically, the kaolin deposits pertain to the Cambrian and Cretaceous ages. The presence of impurities such as Ti and Fe lower the grade of the voluminous kaolin deposits. The deposits were subjected to pilot plant processing and the major problem facing the Sinai manganese Company is lowering the iron percentages of the kaolin. Brown to red iron staining in the microscopic cracks affects the workability of the kaolin deposit of Tieh Ibn Sokar deposits. Petrographically, the Sinian kaolin of Abu Zenima is characterized by the presence of silt-sized quartz grains (Figs. 15.13 and 15.4) which contribute to the high silica content. It is difficult to separate this quartz from the kaolin. It is interesting to note here that the early study on Egyptian clays by Gad and Barrett (1949) revealed that the percentages of free quartz in some clays from Aswan and Sinai are as follows: Sinai Kaolin 8%, Aswan Kaolin 47%. While the red Aswan clay is 18%, the white Aswan clay is 20% and siliceous Aswan clay is 56%. They proved also the presence of alunite in the Sinian kaolin. Chemically, the titanium oxide content ranges between 2.48 and 3.89% (Table 15.6). Processing of the Sinian kaolin resulted in lowering the TiO_2 content. The degree of whiteness of the kaolin is important to direct the raw kaolin to specific use. China clay is a marketable term to kaolin with high order of whiteness. The main use is in the porcelain industry and high quality paper filling (Refaei et al. 2016).

The white sandstone of Gunna area, east of Abu Zenima, South Sinai is in some places admixed with high grade kaolin (China clay). Feasibility studies conducted by private companies proved to to be feasible to process the kaolinitic white sand for the production of China clay. The door is still open to find a suitable and profitable solution to add value to the now ignored voluminous Sinian kaolinitic white sand deposits.

Table 15.6 Chemical composition of vari-coloured kaolin deposit of Ibn Sokar mine, South Sinai, after El Sharkawi et al. (2017)

Compound formula	Concentration (wt%)		
	Sample No. S11 (blackish)	Sample No. S12 (Reddish)	Sample No. S13 (Creamy)
Na_2O	0.46	0.10	0.16
MgO	0.18	–	–
Al_2O_3	26.70	34.08	33.70
SiO_2	42.12	45.48	46.57
P_2O_5	0.10	0.10	0.09
SO_3	0.37	0.15	0.12
K_2O	0.15	0.12	0.05
CaO	0.28	0.28	0.19
TiO_2	3.01	3.33	3.89
Cr_2O_3	0.09	0.06	0.05
MnO	0.31	–	0.10
$Fe_2O_3^{tot}$	11.39	2.98	1.76
NiO	0.44	0.01	0.01
CuO	0.03	0.01	0.01
ZnO	0.02	0.16	0.01
SrO	0.04	0.03	–
ZrO_2	0.26	0.16	0.18
Nb_2O_3	–	0.02	0.03
PbO	0.01	0.01	0.01
Cl	0.24	0.08	0.13
L.O.I	10.50	12.76	12.93

15.3.1.2 Aswan Kaolin (Kalabsha Kaolin)

About 105 km to the southwest of Aswan, in Wadi Kalabsha kaolin occurs in association with the Nubian sandstone. It is also known in Abu Agag, to the north of Aswan. The lithostratigraphic succession of kaolins in the Kalabsha area (Fig. 15.15) that starts with nodular and pisolitic kaolins and changes upwards to plastic (non-pisolitic) kaolins is typically the inverted succession of laterite profiles (Baioumy and Gilg 2011). Aswan kaolin is inferior quality when compared with the Sinian kaolin.

15.3.2 Bentonite

Bentonites consist essentially of clay minerals of the smectite group and has a wide range of industrial applications. The major problems facing the utilization of the Egyptian bentonites are their low concentration of smectite, high level of impurities, and inconsistent composition. Montmorillonite is the variety to which the swelling property is induced. The swelling property is not endless. The change of sonic montmorillonite to calcic montmorillonite means loosing the swelling property. The consumed montmorillonite needs to be activated through the cation exchange of Na for Ca. On the other hand, smectite-rich clays cover most of the Eastern as well as Western Deserts and have low Al_2O_3 content with variable amounts of quartz, calcite, gypsum and iron minerals as well as alkali water-soluble salts. They show high plasticity, drying and firing shrinkage as well as a low and short vitrification range (850–1000 °C). Therefore, they are applied for the production of ordinary Portland cement and building bricks. Also, they are recommended for the manufacture of light-weight clay aggregate due to their bloating on firing up to 1250 °C.

The only place which produce bentonite is the north coast hosted in the Cenozoic sediments. The chemical properties of the bentonite in the Egyptian market is shown in Table 15.7. It was reputed that geologically bentonite is tied to the weathered basaltic volcaniclastics. In Taiba area, north

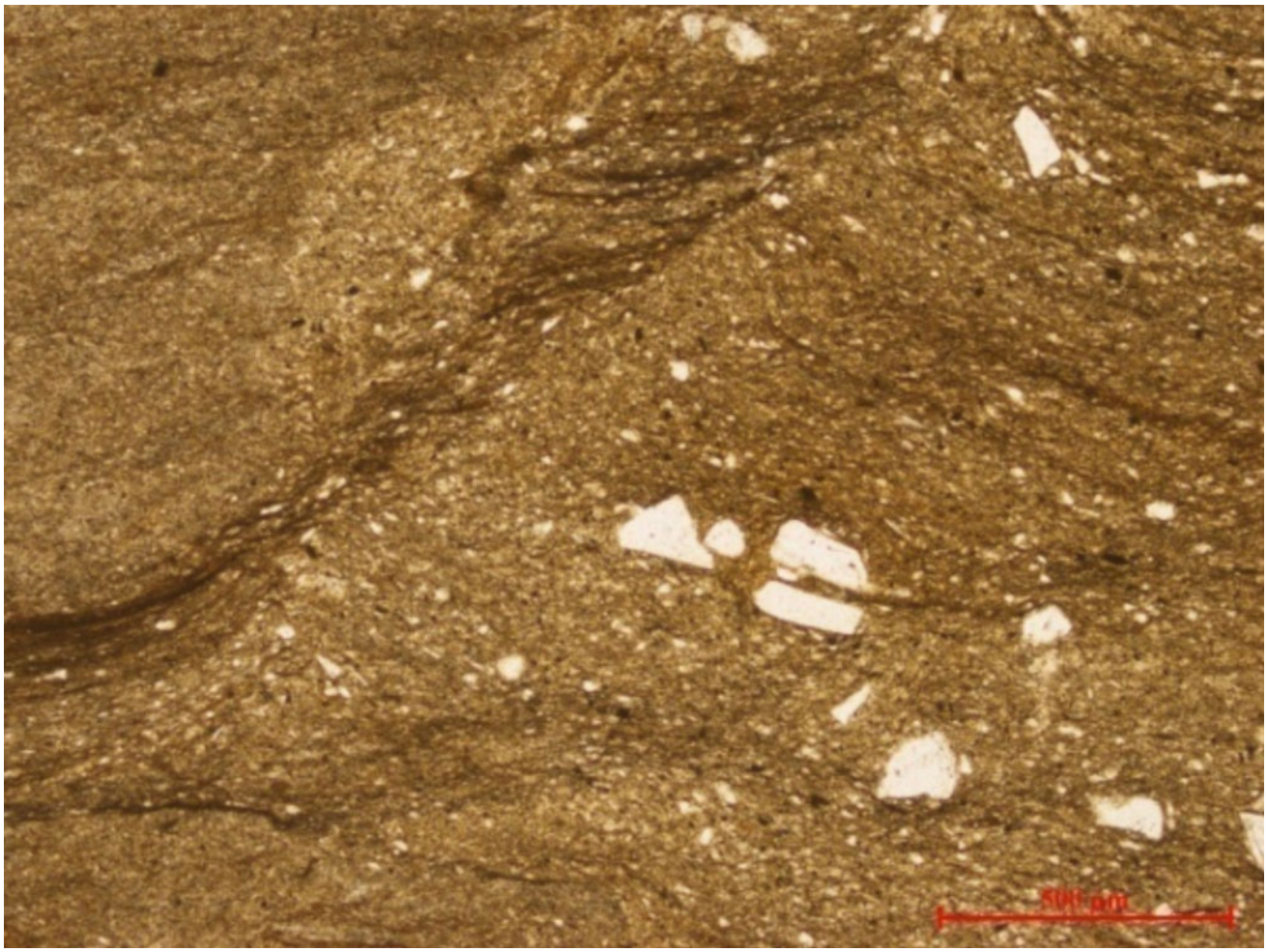

Fig. 15.13 Kaolinite littered with sand-sized and silt-sized quartz grains. PPL

of Abu Zenima, South Sinai, basaltic volcaniclastics occur underlying the thick basaltic flow. Bentonite is actually present but as low grade admixed with altered basaltic fragments. It is difficult to extract such bentonite, since it lies under a thick overburden and should be mined and not quarried. High plasticity of the "brown clay" is taken as a good sign for ranking the clay as bentonite. But in fact the brown colour could be deceiving. Kaolin could be also brown colour and could display plastic properties. The differential is attained through the XRD analysis of the clay. Kaolinite display the 7 angstrom peak while montmorillonite of the bentonite display the 14 angstrom peak.

Previous studies on some Egyptian bentonites such as Qasr El-Sagha, Kom-Osheim, Maadi, Aun-Musa, etc. suggested that, without beneficiation, they were unsuitable for most industrial applications drilling mud, foundry, refining and bleaching, etc. Response of these bentonitic clays to Na-exchange was poor and their hydration, plastic and rheological properties were inferior to those of standard commercial bentonites. Several attempts were made to upgrade these low grade bentonites to meet OCMArAPI specifications for drilling fluid and other industrial uses.

Samples of Egyptian bentonitic sediments (Table 15.7, no. 5), representing Gabal Hamdal of Abu-Zeneima locality (Hassan and Abdel Khalek 1998), were evaluated by different techniques for some applications such as bleaching, refining of oils and drilling mud. Utilization of these clays, after their upgrading and activation, can represent a value-added to the Egyptian economy by preventing the importation of high quality activated clays. Moreover the utilization of bentonite in pharmaceutical appilications is treated by Abdel-Motelib et al. (2011).

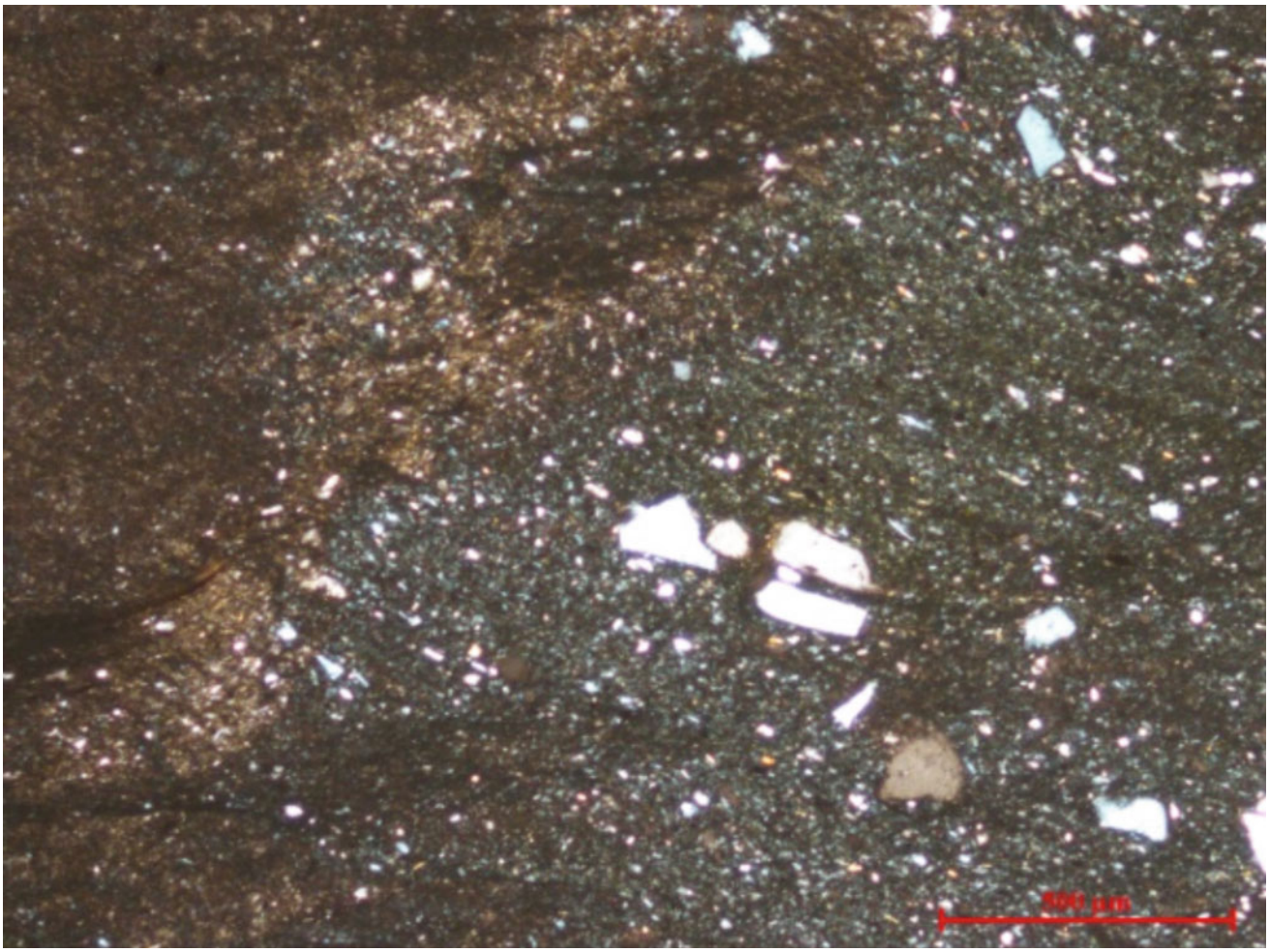

Fig. 15.14 The same as Fig. 15.13 but under crossed polarizers. Local enrichment in quartz in kaolinite. XPL

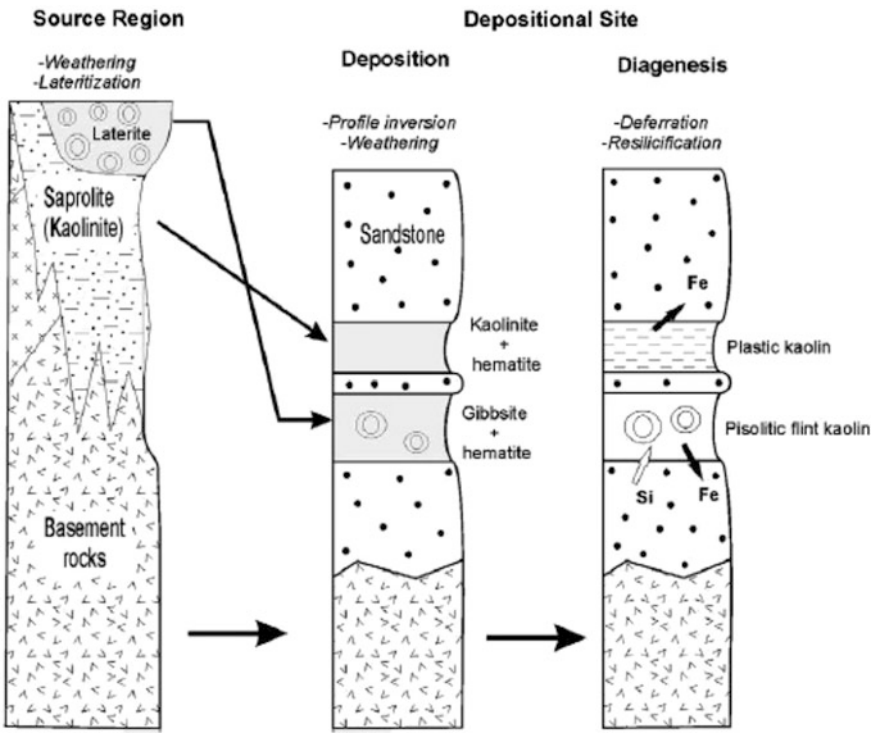

Fig. 15.15 Schematic diagram showing the possible sources and formational mechanisms of the pisolitic and plastic kaolins at Kalabsha area (After Baioumy and Gilg 2011)

Table 15.7 Chemical analyses of bentonites from Egypt

Element	1		2		3		4	5
SiO_2	50.62	50.11	52.67	49.70	53.23	49.93	51.04	42.40
Al_2O_3	21.77	19.64	20.10	19.39	22.71	18.86	20.41	11.62
Fe_2O_3	9.83	7.89	8.33	8.14	9.85	7.06	8.52	7.06
MgO	2.09	1.02	2.36	2.09	2.52	1.72	1.97	1.89
CaO	2.50	2.13	1.71	0.44	0.82	0.30	1.32	10.50
Na_2O	2.09	1.43	2.64	2.26	2.73	1.72	2.14	1.59
K_2O	1.98	1.82	2.61	2.04	2.96	2.44	2.31	0.98
SO_3^-	0.17	0.00	0.50	0.00	0.34	0.00	0.22	–
Cl^-	1.62	1.06	1.59	1.05	1.76	0.75	1.30	–
TiO_2	–	–	–	–	–	–	–	0.83
LOI	11.22	10.01	10.18	8.86	10.09	7.25	9.60	24.00

Code; 1 = North Qaret Shamekh, 2 = Deir El Gamel, 3 = Qur El Malik, 4 = Average of West and Southwest El Qattara Depression bentonite, 5 = Gebel Hamdal (Miocene), Abu Zenima, S.Sinai

15.3.3 Ball Clay

Ball clays are kaolinitic sedimentary clays that commonly consist of 20–80% kaolinite, 10–25% mica, 6–65% quartz. They are fine-grained and plastic in nature, and, unlike most earthenware clays, produce a fine quality white-coloured pottery body when fired, which is the key to their popularity with potters.

Aswan ball clays show abundance of clay fractions, low-order kaolinite, and illite. Chemically, it consists of SiO_2 44–77%, Al_2O_3 15–38%, TiO_2 1.1–3.7%, Fe_2O_3 0.3–15%, LOI 5–14.5%. The contents of fluxing agents, alkaline oxides, S and Cl, and toxic elements are low. Aswan ball clays were sourced from a mixture of more than rock types. They are environment-friendly and suitable for ceramic and refractory industries. Quarries and even mines are opened in Aswan to supply the market with ball clay. Other occurrences were accidentally discovered by Sinai Manganese Company while quarrying white sand east of Abu Zenima, South Sinai. The ndustrial use of ball clay is studied by Baioumy and Ismael (2014).

15.3.4 Brick Clay

Feverish search in the geologic column sediments for clays suitable to produce the red bricks since the 1960s following the ban to excavate the Nile sediments for the production of the red bricks. Prior to this date all red bricks were produced from the fertile Nile sediments. The Eocene grey clays are the most suitable for the production of red bricks. This clay is handicapped by the presence gypsum and halite. These harmful ingredients induce corrosion to the machinery and cracking of the produced red bricks.

15.3.5 Fire Clay

Frequently, other types of clay are known in the market, quarried and mined by private firms on small scales. These clays are known as fire clay based on their laboratory properties. The distribution and reserves of clays of volcanic origin is the least known in Upper Egypt, i.e., those tied to the Mesozoic Timsah Formation.

The field examination of the horizons hosting the volcanic rocks in the east of Aswan and traced in a westward direction.

Whenever facies change from proper volcanics to volcanic glass or tuffs and ashes, detailed stratigraphic and mineralogical studies should be carried out to find important clay deposits of considerable dimensions to be quarried with minimum overburden. Those with thick overburden will be also demarcated as a potential future targets.

15.4 Review on Some Evaporite Deposits in Egypt

Hassan Khozyem

15.4.1 Introduction

The word *brines* and *evaporites* is designed to express the chemical salt deposits that have been precipitated and concentrated during evaporation of natural solutions on the Earth's surface. At the beginning of the last century, these types of deposits were referred to as '*salt deposits*' and also, rarely, as '*evaporates*' (Goldschmidt 1937; Grabau 1920),

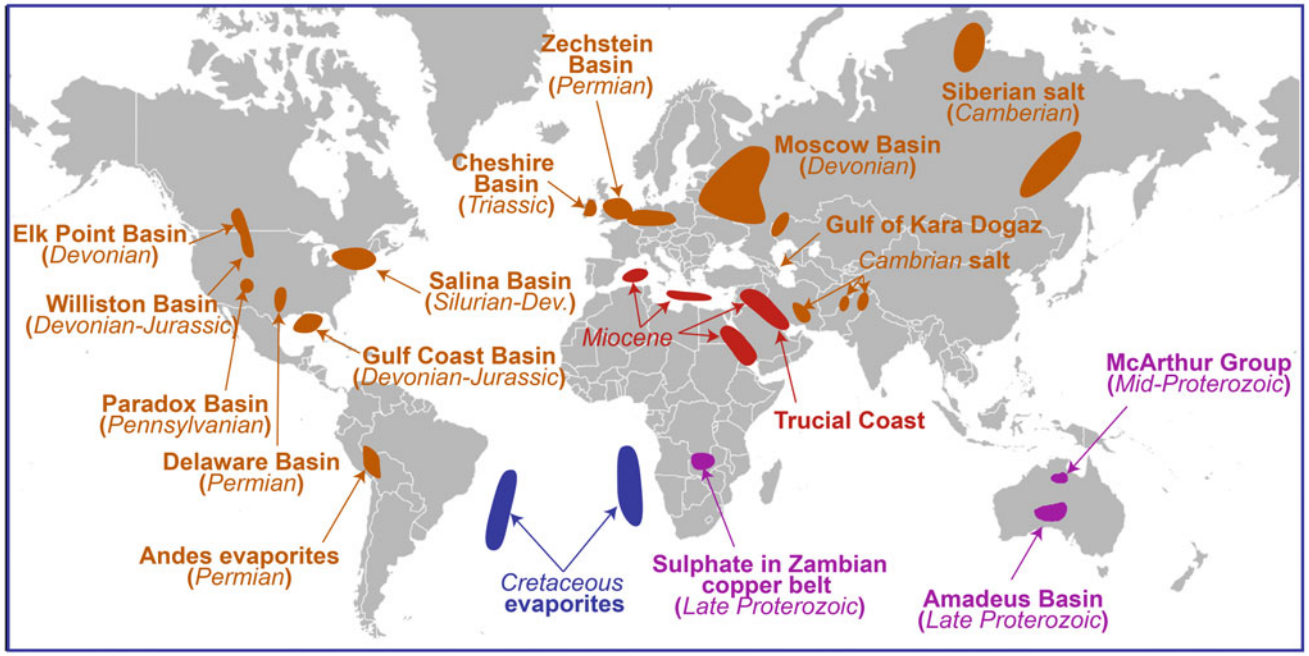

Fig. 15.16 Generalized Map showing the global distribution of major evaporites and its age

but due to the wide variety of their composition the term evaporite became more acceptable (Berkey 1922). Twenhofel (1950) stated that evaporite are a sedimentary group of deposits whose origin is due to evaporation, but some evaporite salts are formed by replacement or freezing of concentrated solutions, in some cases it subjected to heat and pressure, therefore, then evaporite form a new combinations and other evaporites can develop through metamorphism. The formal definition of evaporite deposits as stated in the GSL glossary "it is type of deposits formed by Evaporation and/or drying out of sea water (usually) in warm, dry climates, leaving behind deposits of crystallized mineral salts." Throughout the geologic history, evaporite occurs in both non-marine and marine-derived (thalassic) systems (Fig. 15.16). The non-marine, such as Polar Regions where cold temperatures promote the freezing-out of salts, continental lakes, sub-terranean aquifers, and sub-tropical oceanic environments. Whereas in marine environments, strong brines and evaporite formation can occur in coastal intertidal zones, supratidal zones (sabkhas), lagoons fed by direct flow from the sea, and the sea-marginal lakes (Fig. 15.17). Each of these environments characterized by its own basic physicochemical features and parameters that can control the formation of certain types of evaporite, these characteristics include: temperature, pH, salinity and type of dissolved major ions in sea water (Babel and Schreiber 2014). The formation of evaporite may be interpreted by three different hypotheses:

(1) Evaporation of a shallow restricted epicontinental sea or lagoon which receives inflows from the open ocean,

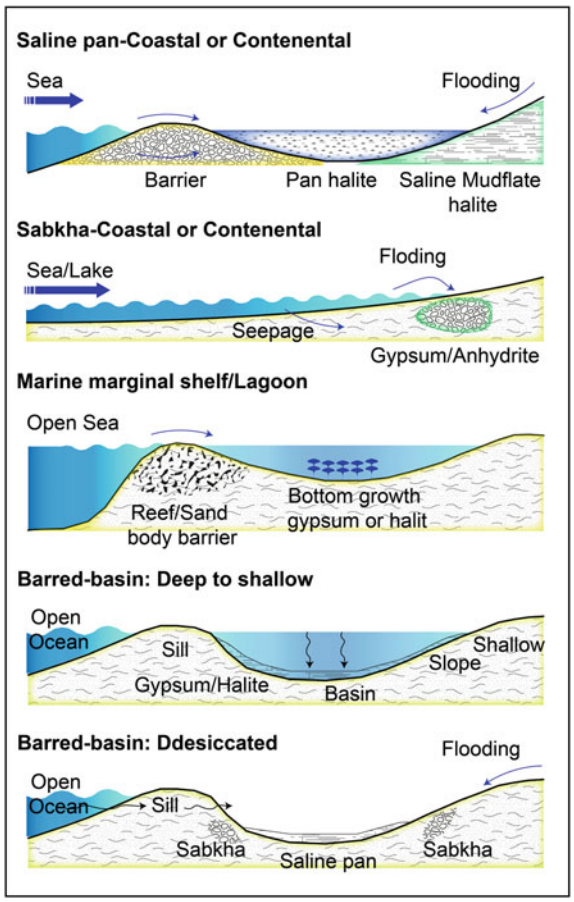

Fig. 15.17 Diagram illustrating the principal depositional environments of evaporites

(2) Evaporation of a deep-water basin which is separated from the open sea by a shallow sill (Schmalz 1969), and (3) Evaporation of playas or salt lakes which are situated in desiccated deep basins isolated from the open ocean (Hsü et al. 1973).

Mineralogically, most bedded ancient evaporites are varying combinations of (1) alkaline earth carbonates, (2) gypsum or anhydrite and (3) halite, with or without (4) the potash-entraining salts or bitterns (Warren 2010). These four groups of minerals forming more than 95% of the world's Phanerozoic and Neoproterozoic evaporites. Anhydrite and halite are the two dominant evaporite minerals. Varying combinations of sodium carbonate (soda-ash), sodium sulfate (salt-cake), and sodium borate salts are rarely deposited and therefore they are all economically exploited. Based on these characteristics and the formation environments, the common evaporite minerals are given in Table 15.8.

Table 15.8 The most common evaporite salts and minerals (after Eugster et al. 1980; Usdowski and Dietzel 1998; Babel and Schreiber 2014)

Sulfate	
Simple salts	
Anhydrite	$CaSO_4$
Gypsum	$CaSO_4.2H_2O$
Kieserite	$MgSO_4.H_2O$
Epsomite (reichardtite, bitter salt)	$MgSO_4.7H_2O$
Thenardite	Na_2SO_4
Mirabilite (Glauber's salt)	$Na_2SO_4.10H_2O$
Celestite	$SrSO_4$
Double salts	
Bloedite, blödite (astrakhanite)	$Na_2SO_4.MgSO_4.4H_2O$
Langbeinite	$K_2SO_4.2MgSO_4$
Glauberite	$Na_2SO_4.CaSO_4$
Polyhalite	$K_2SO_4.MgSO_4.2CaSO_4.2H_2O$
Carbonate	
Simple salts	
Aragonite, calcite	$CaCO_3$
Thermonatrite	$Na_2CO_3.H_2O$
Natron (natural Soda)	$Na_2CO_3.10H_2O$
Nahcolite	$NaHCO_3$
Double salts	
Dolomite	$CaCO_3.MgCO_3$
Trona	$NaHCO_3.Na_2CO_3.2H_2O$
Shortite	$2CaCO_3.Na_2CO_3$
Pierssonite	$CaCO_3.Na_2CO_3.2H_2O$
Gaylussite (natrocalcite)	$CaCO_3.Na_2CO_3.5H_2O$
Chloride	
Simple salts	
Halite	NaCl
Sylvite	KCl
Double salts	
Carnalite	$KCl.MgCl_2.6H_2O$
Complex salts	
Kainite	$4KCl.4MgSO_4.11H_2O$

15.4.2 Evaporite Deposits in Egypt

The economic evaporite deposits in Egypt is restricted to Miocene sediments. Miocene sediments are widely distributed, covering about 12% of the total area of the exposed sedimentary rocks in Egypt (Fig. 15.18). The Miocene sediments have great variations in their facies and exhibit a vast number of unconformity surfaces, indicating the tectonic nature of their depositional environments (Said 1990). In the following discussion we attempt to review the occurrence of the Miocene evaporites exposures in the Egyptian territory and their economic potentialities.

In Egypt, three major types of evaporite are present, 1. Massive evaporite deposits restricted to Miocene syn-rift deposits, 2. Messinian salinity crises and 3. The evaporite salts developed during Plio-Pleistocene and recent (Sabkha) (Fig. 15.18).

In general, the Egyptian economic massive evaporite deposits are restricted to four regions 1. Red sea 2. Gulf of Suez deposits, 3. Sinai evaporite deposits, 4. Northwestern desert (Northern Coast), whereas the post Miocene evaporite are distributed along the previous four regions in addition to the Wadi Nutron salt deposits.

15.4.3 Genetic Classification of Evaporite Deposits

The sedimentary succession of the Gulf of Suez and the northwestern part of the Red Sea ranges in age from the Upper Cretaceous to Lower Eocene (pre-rift sediments). The pre-rift sediments are overlain unconformably by the proto-rift that formed of lacustrine red mudstones, sandstone, breccias and conglomerates of the Nakheil Formation (Fig. 15.19). The Nakheil Formation is late Oligocene in age (Akkad and Dardir 1966; Said 1990) and is locally preserved in small hanging wall synclines formed along the Border Fault system. The Nakheil Fm. is overlain by the late Oligocene massive mafic volcanics. The Ranga Fm. unconformably overlies the late Oligocene volcanic and composed of coarse-grained sandstones and conglomerates of the Aquitanian–Burdigalian age (El Bassyony 1982).

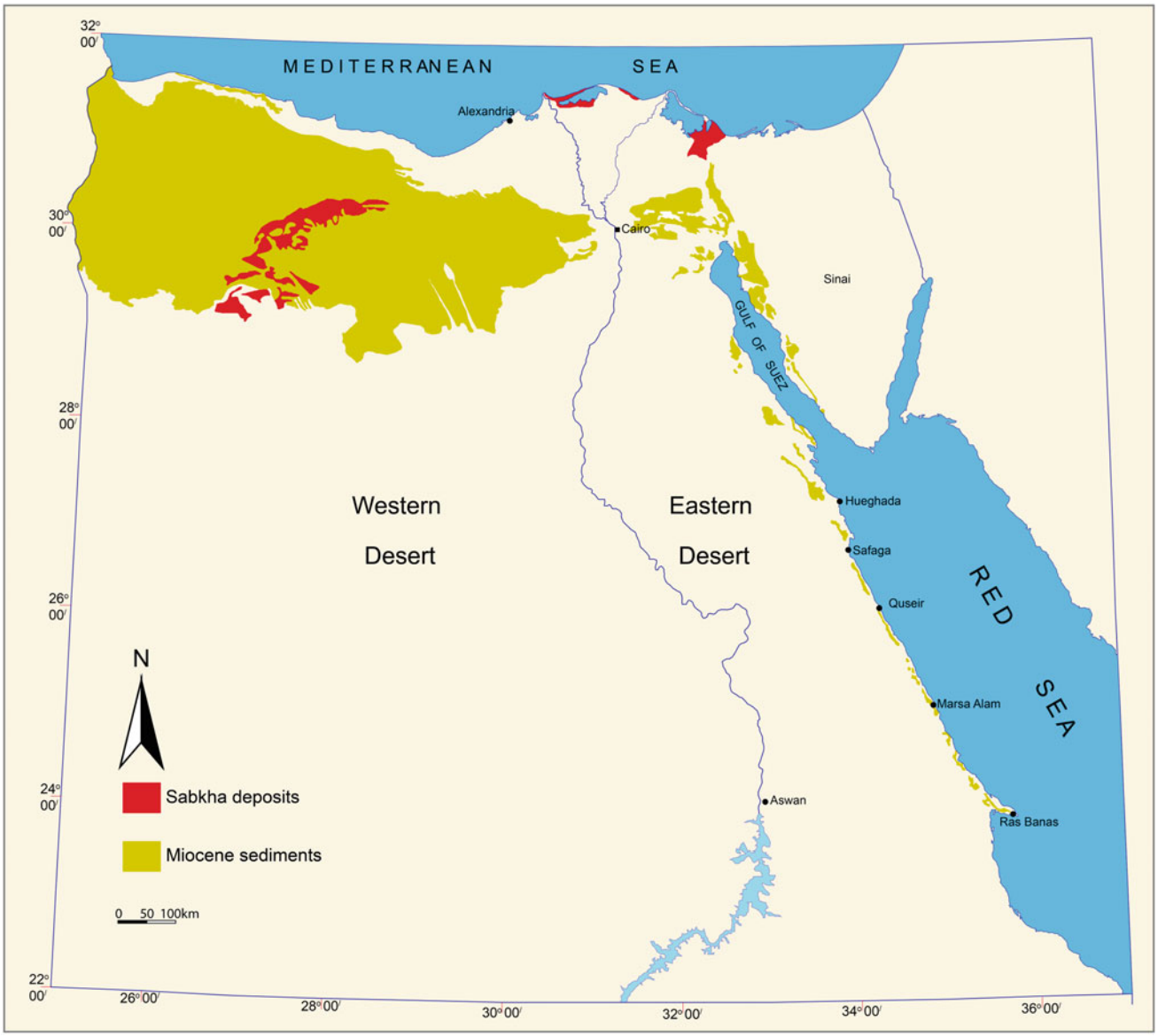

Fig. 15.18 Simplified geologic map showing the general distribution of Miocene sediment in Egypt together with Sabkha distributions

The lower part formed of continental red sandstones and conglomerates locally interbedded with few gypsum thin beds and marls (Philobbos and El-Hadded 1983). The upper part of the Ranga Fm. consists of shallow marine conglomerates and fossiliferous sandstones and patch reefs and locally named as Sayateen Fm. (Khalil and McClay 2002, 2004, 2009). Um Mahara Fm. is unconformably overlay the Ranga Fm. and formed of conglomerates are reefal limestones and shallow marine fine-grained clastics of the late Burdigalian-Langhian (El Bassyony 1982; Said 1990). The middle-late Miocene evaporite sequence of the Abu Dabbab Formation unconformably overlies the older syn-rift and pre-rift strata. The sedimentary succession in both Gulf of Suez and the Egyptian Red Sea coast can be correlated as follows (Fig. 15.19): the late Oligocene clastics of the Nakhil Fm., unconformably overlain by early Miocene clastics of the Ranga and carbonates of the Um Mahara Formations in the Red Sea Coast, are correlated to the Thayiba, Nukhul, and Rudeis Formations in the Gulf of Suez subsurface, respectively. The middle to late Miocene succession in the Red Sea are include intercalations of evaporite and clastics of the Abu Dabbab and Marsa Alam formations (Montenat et al. 1988; Issawi et al. 1971). These formations are correlated to the Kareem, Belayim, South Gharib, and Zeit in the Gulf of Suez subsurface, respectively. The middle to late Miocene succession is overlain by post-rift sediments that include undifferentiated Pliocene to Recent clastic sediments and raised beaches (Al Sharhan 2003).

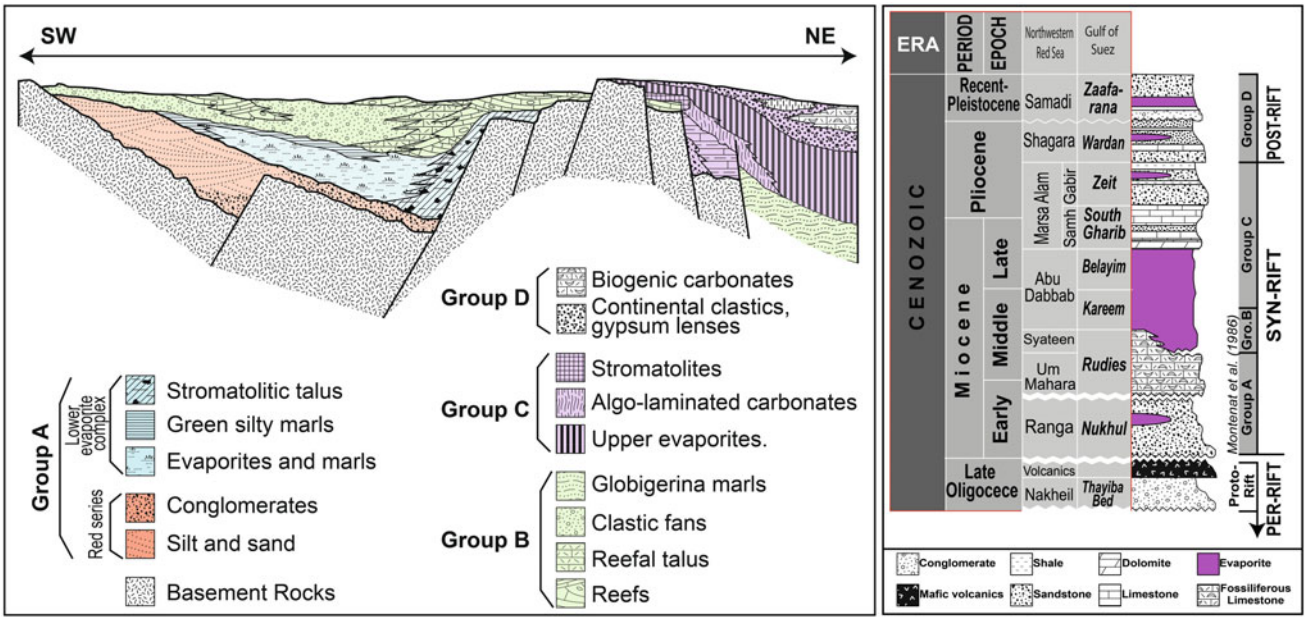

Fig. 15.19 Cross section represent the spatial relationships between the syn-rift sediments of the northwestern Red Sea coast-the Gulf of Suez. Syn-rift units: Group A: continental alluvial fans-playa deposit with interbedded basalt flows; Abu Ghusun Fm; marine marls with gypsum beds of the Ranga Fm, Group B: coarse terrigenous fan-deltas with local intercalated and capping reefs; shelf-edge reefs and associated mixed marine sediments, finer terrigenous deposits with widespread stromatolitic episodes and marginal coral biostromes, and Group C: dolomitic microbial laminites encrusting the platform and peripheral slope; onlapping bedded gypsum with fine terrigenous intercalations (modified after Montenat et al. 1986, 1988; Issawi et al. 1971; Said 1990). and Generalized stratigraphic section of the proto-rift syn-rift and post rift deposits in northwestern Red Sea and Gulf of Suez

The Syn-rift sedimentary succession is divided into four major distinct groups separated by unconformity surfaces (Montenat et al. 1988; Fig. 15.19) and divided as follows: (1) continental to restricted Subaquatic deposits of Oligocene to Early Burdigalian age (Group A), (2) open marine sediments of Burdigalian to middle Miocene (Group B), (3) major evaporite episode of middle Miocene to Messinian (Group C), and (4) open marine sediments of Plio-Pleistocene age (Group D) (Montenat et al. 1988; Issawi et al. 1971; Said 1990). The middle to late Miocene evaporite deposits in the Gulf of Suez cannot be separated from those of the Red Sea because of their genetic relationships, and there stratigraphic classification is similar to that of south western Sinai evaporite.

The evaporite deposits are of wide spatial distribution in the Egyptian Neogene sediments. They extend from Jabal El Zeit (south Suez) to Ras Banas (south Marsa Alam). The middle Miocene evaporite represents the main evaporite unit in the Gulf of Suez and the Egyptian Red Sea coast. The Miocene evaporite deposits of the Gulf of Suez and the northwestern Red Sea coast are linked to the rift system that started at late Oligocene and continued up to late Miocene. The evaporite occurs at several stages during the rift evolution and can be distinguished into three levels as follow:

15.4.3.1 Early Miocene Evaporites

The older evaporite, are thinner sequence of gypsum (locally anhydritic) deposited during the early Miocene deposited within relatively shallow proto-rift depressions (Orszag-Sperber and Plaziat 1990). The evaporite are overlain by Burdigalian marine sediments (Montenat et al. 1986; Thiriet 1987) that can be give this evaporite age of Aquitanian-early Burdigalian. This evaporite are croups out locally along the Red Sea coast overlying the continental sediments (Group A, Montenat et al. 1986, 1990, 1998; Orszag-Sperber and Plaziat 1990). Although this old evaporite are presence also within the Nukhul Fm. in the Gulf of Suez but, it's neglected due to its low economic values (Richardson and Arthur 1988; Hughes et al. 1992). Whereas the mid–late Miocene (syn-to post rift) evaporate are more important and economically valuable. It could reach to 2500 m thick, and it linked to the major phase of rifting subsidence (Orszag-Sperber et al. 1998).

In several localities on the Egyptian Red Sea coast (i.e. Ras Honkorab; Wadi Gasus), a sequence of gypsum and marl intercalations of 10–20 m. Thick croups out and overlies the Precambrian basement rocks and deposited with in a well-defined grabben.

Lithologically, these evaporite deposits are highly weathered with presence of laminations and traces of subvertically elongate selenite crystals. They comprise three individual beds of gypsum separated by marls with marine microfaunas and diatomites (Hughes et al. 1992). At Wadi Gasus (close to Safaga) it is composed of laminated gypsum detritus with erosional basal contacts suggesting a detrital

slope sedimentation. Marl intercalations include reworked blocks of gypsum suggesting the reworking of these evaporite on a slope (Hughes et al. 1992; Orszag-Sperber et al. 1998).

15.4.3.2 Mid to Late Miocene Evaporites

A long the Gulf of Suez, Northwestern Red Sea, and Sinai, the principal economic evaporite deposits are linked to the initial stage of syn-rift deposits (Group C) in which the marine is toward increasing restriction conditions. *In the Gulf of Suez*, the main evaposite unite is Kareem Fm. that represents the upper part of the early Miocene age (Langhian-Serravallian) and continues through the Belayim and lower south Gharib and Gebel Zeit Fms. of middle-late Miocene age (the Langhian to pre-Messinian). In the Gebel Zeit and Gemsa areas, the evaporite succession has been uplifted locally, evaporite beds of both Belayim and South Gharib Formations crops out along the Gebel Zeit and Gemsa highs several tens of meters thick as observed in Ras Dib north Gebel Zeit, west central Gebel Zeit, Ras El-Ush and occurs in Gemsa bensula (Fig. 15.20). The evaporite sequence is interbedded with marine marls associated with the diatomitic deposits (Rouchy et al. 1983, 1985; Gaudant and Rouchy 1986; Monty et al. 1987). These beds are composed of a mixture of gypsum and anhydrite in varying amounts. Gypsum occurs as isolated nodules, thin laminae and disseminated crystals within the interbedded biosilica-rich siltstones and marlstones as well as in the carbonates. Variable amounts of halite are recorded (Rouchy et al. 1995). Generally, the Gulf of Suez evaporite are dominated essentially of gypsum/anhydrite and halite. The upper parts of the Belayim Formation are composed mainly of anhydrite while the upper parts (South Gharib Formation) are dominated by halite (Hassan and EI Dashlouti 1970).

In the northwestern Red Sea, The evaporite associated with Group C is restricted to the mid-late Miocene Abu Dabbab Formation (alternatively; Abu Dabbab evaporite) in the northwestern Red Sea the lower part of this evaporite is

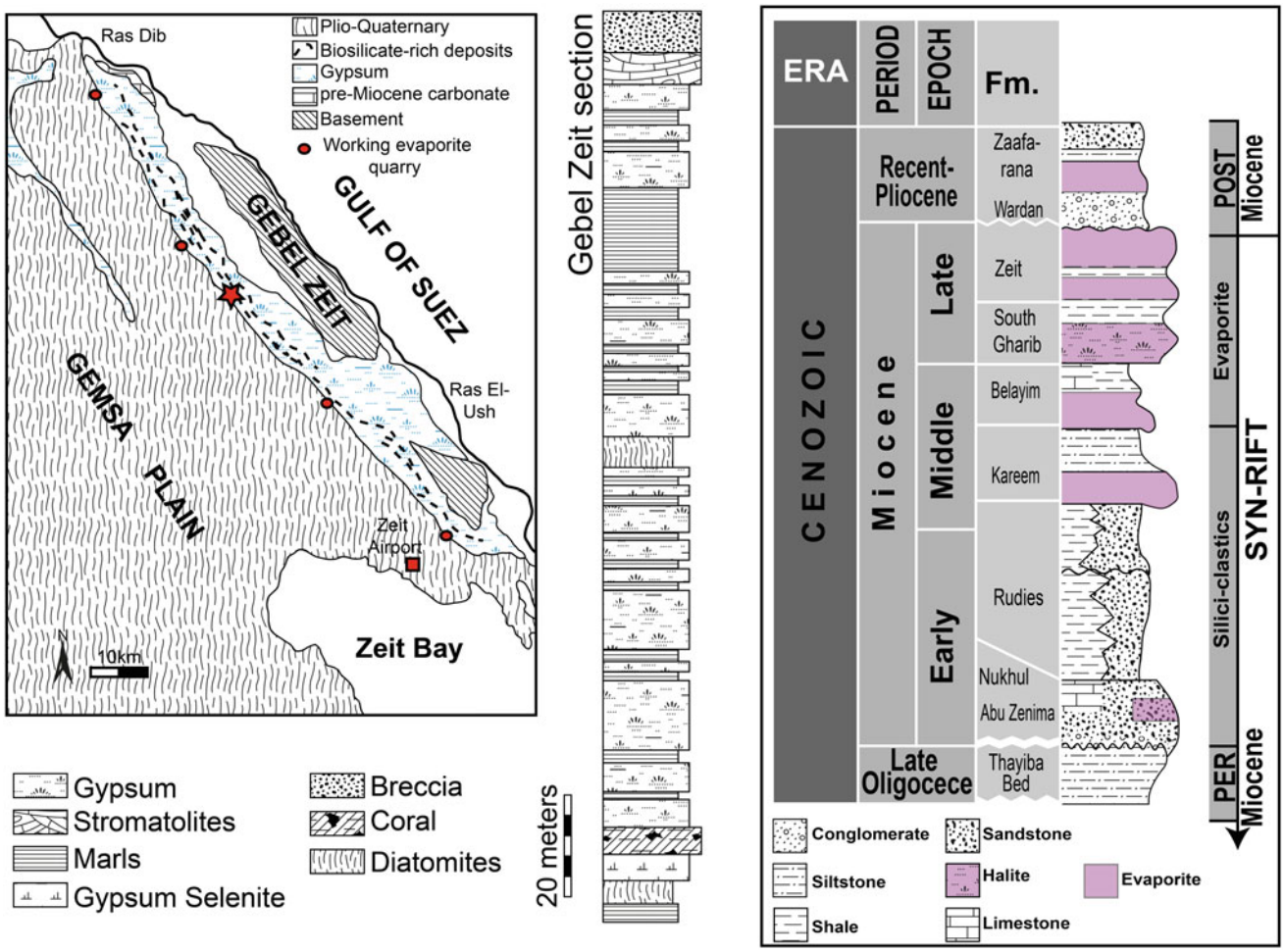

Fig. 15.20 Geologic map of the Gebel Zeit area, together with lithologic log of Gebel Zeit showing the different interval of evaporite deposits and the generalized chrono-, litho- and tectono-stratigraphy of the Gulf of Suez rift basin (After Bosworth et al. 2014)

correlatable to the Kareem formation in the Gulf of Suez (Orszag-Sperber et al. 1998), it is characterized by yellowish white to dark grey color and is easily identified in both field and satellite images. The Abu Dabbab evaporite is widespread and their outcrops can be found close to the present Red Sea Shoreline (i.e Wadi Ranga, south and north Qusier city, south safaga and Gebel Zeit; Fig. 15.21). The Abu Dabbab evaporite are massive to poorly bedded gypsum and anhydrite outcropping along the coastal plain, and it is up to 3 km in the offshore area (Tewfik and Ayyad 1982; Said 1990). In some areas such as north of Quseir city the Abu Dabbab evaporite exhibit thinly laminated, bedded and nodular anhydrite with microcrystalline gypsum at the basal part. Several intercalations of inter-bedded clay, dolomite and stromatolite layers were recorded within the evaporite succession (Abu Seif 2014).

Abu Dabbab Evaporite and its equivalent are the most famous evaporite formations in the northwestern Red Sea. The importance of this interval is due to the grade of gypsum and anhydrite that associated with these formations is

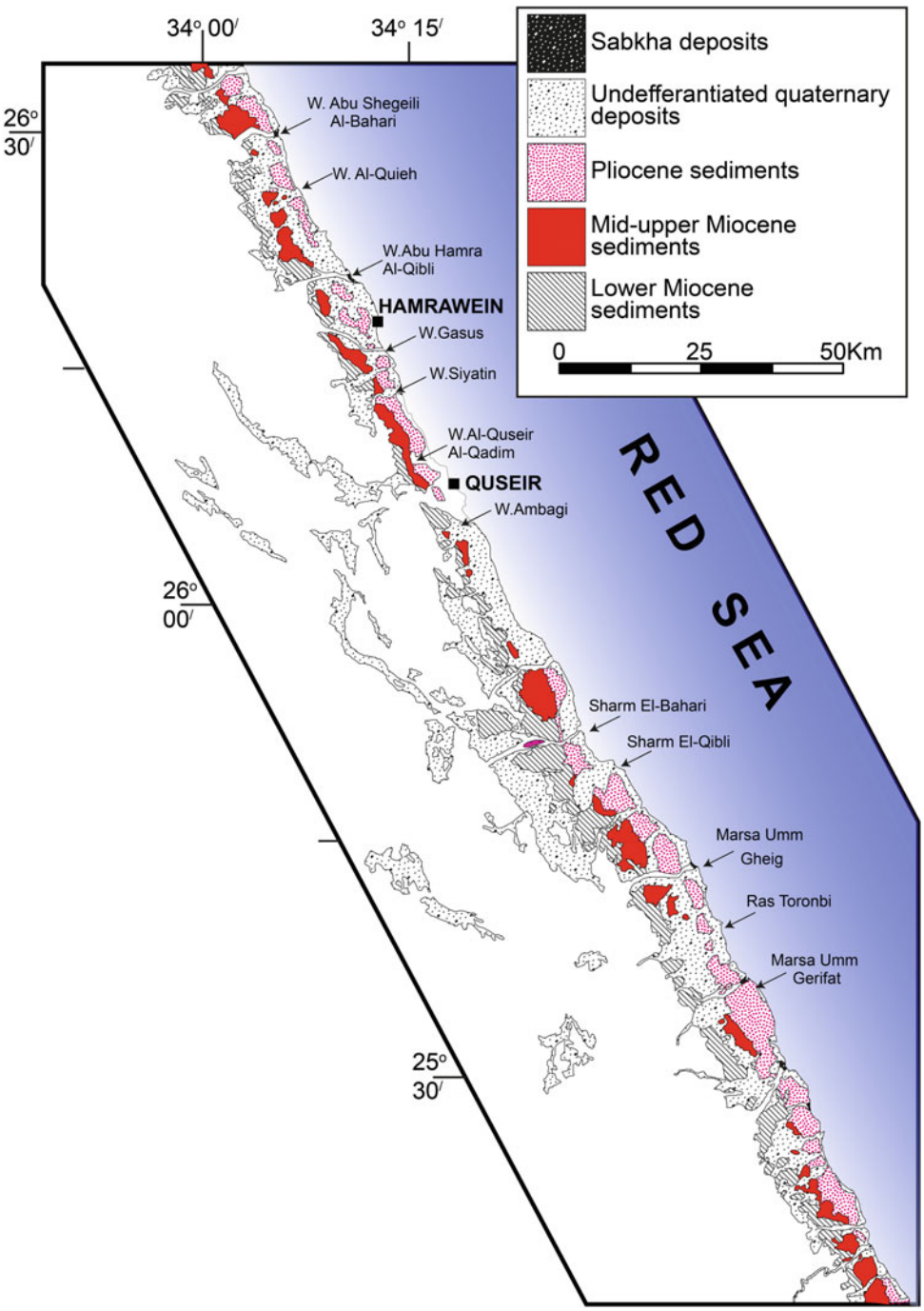

Fig. 15.21 Distribution of the Miocene syn-rift sediments along the northwestern Red Sea margin (Modified from Conoco 1987)

between medium to high grade that can be easily emerged in the cement industry, not only the grade but also the wide distribution along the Red Sea margin. For example, the thickness of Abu Dabbab evaporite in the area Northern El Quseir is about 45 m at Wadi Al-Quieh, 55 m at Wadi Abu Hamra Al-Qibli, 110 m at Wadi Siyateen and 85 m Wadi Al-Qusier Al Qadim with some new investigations were carried out at El Quseir-Qift entrance with thickness about 67 m of bedded gypsum (Fig. 15.22). Field investigations indicated that the Abu Dabbab Evaporite consists mainly of bedded and thinly laminated and nodular evaporite which are capped by anhydrite and changing downward into gypsum (Abu Seif 2014), with the presence of several thin dolomite layers. Mineralogically, The Abu Dabbab Evaporite are mainly composed of anhydrite (88–97%) with gypsum (3–12%). Downwardly in the section the gypsum content increased to (87–89%) and in favor of anhydrite (11–13%). Technically, the technical properties of the Abu Dabbab evaporite are summarizing the possibilities to integrate this type of anhydrite/gypsum in different industries. The water contents of the anhydrite cap is ranging between 8.8 and 9.8% in anhydrite, increased to be between 40.2 to 42.3% in gypsum. Specific gravity is decreasing downward the section and/or with increasing gypsum content, anhydrite (from 2.64 to 2.74 gm/cm^3), gypsum (from 2.34 to 2.37 gm/cm^3). Both anhydrite and gypsum of Abu Dabbab evaporite has low plasticity index the plasticity increased with decreasing water contents. The swelling index is linked to the relative percent of anhydrite, with increasing anhydrite content the swelling index is increased. In general, the geotechnical properties of the Abu Dabbab evaporite indicates that this type of evaporite is medium to low grade and only can be used for domestic uses such as fertilizers, and it still need more integrations.

Sinai evaporite deposits, the Miocene sediments in Sinai Peninsula are restricted to the west central Sinai (Fig. 15.23). The fluid inclusion, sulfur isotope and oxygen isotope values of the middle Miocene gypsum deposits (Attia et al. 1995) indicates that the west central Sinai is a northern extension of the Red sea rift. The evaporite are deposited with in

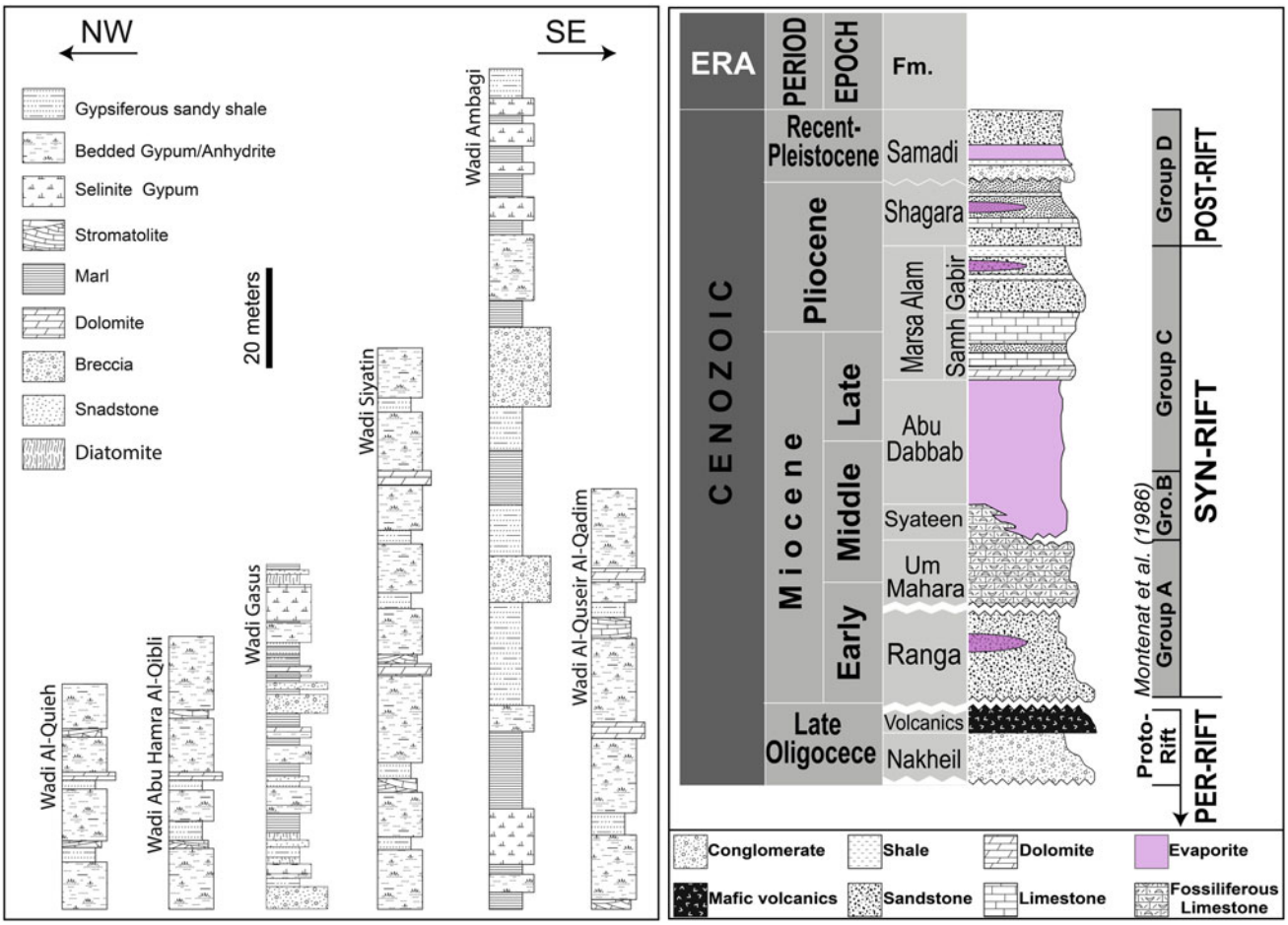

Fig. 15.22 Columnar sections represent the exposures of Abu Dabbab Evaporites in the northwestern Red Sea (After Abu Seif 2014; Orszag-Sperber et al. 1998) together with the generalized stratigraphic section of the syn-rift deposits along the Red Sea margin

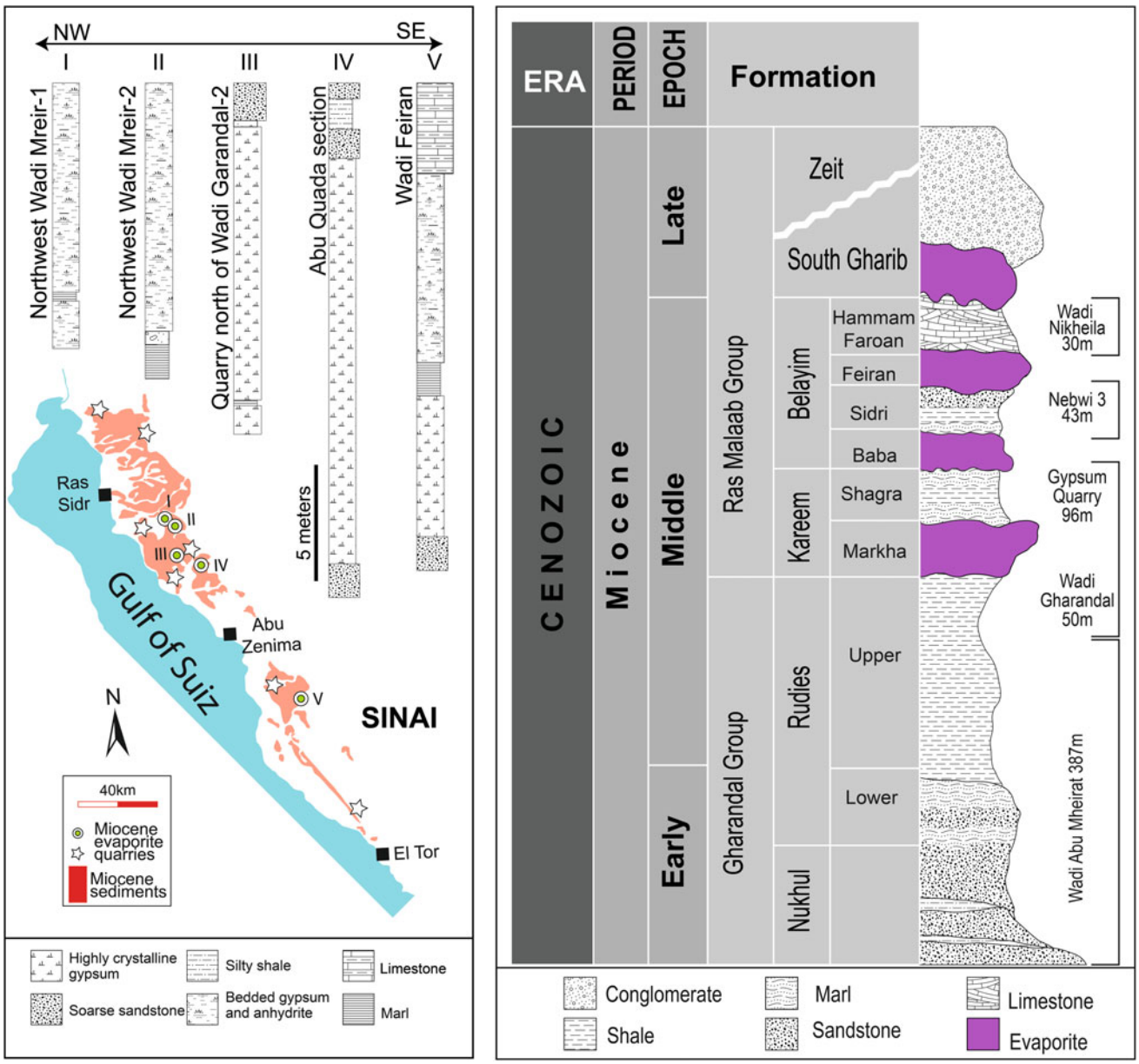

Fig. 15.23 Simplified lithological sections of exposed Ras Malaab evaporite in the west central Sinai (after Phillip et al. 1997; Attia et al. 1995) togeather with the generalized stratigraphic section of the Miocene syn-rift deposits exposed in west central Sinai (after Abdel-Monem et al. 2006)

subsidiary closed basin developed during the rifting period, and may separate from the main Gulf of Suez trough during the middle Eocene. During the high sea level stand the basin may be reconnected to the Gulf of Suez and would have been flooded by sea water to become a marine-fed lagoon (Attia 1993). Therefore, the west central Sinai evaporite is correctable to the mid-late Miocene evaporite of the Red sea and Gulf of Suez. Based on the classification of the National Committee of Geological Science (1976), the Miocene sediments in the west-central Sinai are commonly subdivided into two major rock units. The lower unit is Gharandal Group of Lower to Middle Miocene and the upper unit is the Ras Malaab Group of the middle to late Miocene. The lower clastic Gharandal Group is differentiated into three formal units, the Nukhul, Rudies and Kareem Fms, from base to top.

This Ras Malaab Group (El-Gezeery and Marzoukis 1974) is synonymous with the evaporitic Group (Said and El Heiny 1967). However, more recent work (Ouda and Masoud 1993; Burser and Philobbos 1993), considered the evaporite facies have deposited during the Serravallian (mid-late Miocene). The geologic age assignment of the Ras Malaab group dominated by evaporitic gypsum is middle to late Miocene. This is based on the fact that it overlies the Kareem Fm of the Gharandal Group and it

underlies directly the Pliocene clastics. The Ras Malaab Group consists of four major cycles of evaporite, shale, and limestone (Ghorab et al. 1964; Hassan and E1-Dashlouty 1970). The Miocene deposits are well developed in the west central Sinai, where the gypsum deposits (Ras Malaab group) are complete and uniform sequence is represented (Abdel-Monem et al. 2006).

The evaporite from the Ras Malaab and adjacent area are varied laterally from the southwest to the northeast direction (Fig. 15.23). In the north of Wadi Gharandal, the middle Miocene evaporite (Seravalian in age) are ranging in thickness between 15 and 30 m of massive well crystalline gypsum with vertically oriented crystals and termed massive selenite (Attia et al. 1995). Further to the north, at northwest Wadi Mreir, two open quarries producing gypsum from the middle Miocene evaporite and characterize by thick succession of well-defined bedded gypsum, each bed is formed of vertically oriented gypsum crystals and separated by carbonate mud bands. This features of the middle Miocen evaporite of Ras Malaab recommended that the deposition of this gypsum is formed in-situe crystallization from standing water body. In the Abu Qada depression south central Sinai, the evaporite deposits are exposed and restricted to the upper-middle Miocen (Serravalian) Kareem Fm (Zalat 2013). It is composed mainly of 35 m of white to light grey massive anhydrite interbeds in the lower part and followed by grey, highly calcareous shales, grading to marl, with occasional grey argillaceous limestone intercalations in the upper part of (Shagar Member). Along Gebel Qabeliat, in the area between Gebel Ekma and Gebel Abu Huswa, the Miocene sediments have been affected by faulting. Near Wadi Feiran, Miocene gypsum is found overlying the Eocene beds; whereas to the west of Gebel Ekma, the gypsum is found in faulted contact against the Nubia Sandstones (Allam and Khalil 1989). The sedimentary section in this area is well developed and represents by the two main rock units (Fig. 15.23), the Lower Miocene clastics (Gharandal Group) and the middle-upper Miocene evaporite (Ras Malaab Group). The evaporite in this area are mainly fibrous gypsum deposits intercalated with a small amount of argillaceous matter and carbonates, and is recorded in several intervals starting from the upper rock unit (Kareem Fm.) which is composed mainly of sandstones and shales with thin evaporitic beds at the base, That followed by the Ras Malaab Group consists mainly of: a) interbedded shales and sandstones with anhydrite and salt in the lower part (Belayim Fm); b) thick salt deposits in the middle part (South Gharib Fm.); and c) interbedded shales and anhydrite in the upper part (Zeit Fm.). In Wadi Fieran, a condensed massive evaporite sequence of 30 m thick croups out (Phillip et al. 1997). The lower part is composed mainly of highly crystalline gypsum (Kareen Fm?), where the upper evaporite sequence is partially transformed to anhydrite (Belayim Fm?). This massive evaporite sequence is determined to be middle to late Miocene but further assessment of age is needed.

Economically, the gypsum associated with Ras Malaab group, is vary in thickness from 5 to 40 m thick and is categorized as high grade gypsum based on its technical and chemical characteristics, where it possesses calcium sulphate ranging between 93 and 98%, pH (7.65), and soluble matter less than 0.65, with brightness reaching to 98%. It has colorless and fibrous structure. The fibrous grain shape is suitable for the paint film after application on substrate.

Northwestern desert, The Messinian Salinity Crisis (MSC) is known throughout the entire Mediterranean Sea as a prominent series of events which occurred less than 6 Ma (Hsu et al. 1973, 1977) and led to modifing the Mediterranean basin within a relatively limited time span (~650 kyr; Krijgsman et al. 1999; Manzi et al. 2013), and resulted from the disconnection between the Mediterranean Sea from the Red Sea and the Atlantic Ocean (Ryan et al. 1973; Ryan 2011). During the MSC a thick evaporite sequence was deposited throughout the Mediterranean basin that are presently located both on land and offshore (Hsu et al. 1973; Lofi et al. 2011; Manzi et al. 2014; Roveri et al. 2014a; Bache et al. 2015; Gorini et al. 2015). A sequence of about 2500 m of salts and gypsum were deposited in the deep basin of both Mediterranean Sea from the Red Sea. This evaporitic phase is recorded in many late Miocene sequences cropping out in the Mediterranean area (Youssef 1988; Hüsing et al. 2009; Gladstone et al. 2007; Köhler et al. 2008; Mansour 2015). Their outcrops extends for some tens of kilometers parallel to the coast of the Mediterranean Sea and reaches to 15 m thick (Aref 2003; Melegy and Ismael 2012; Wali 1993; Youssef 1988).

The northwestern Egypt evaporite deposits characterized by primary gypsum deposits and the sequence is represented mostly of gypsum interbedded with carbonates. The alternative deposition of gypsum and carbonates is controlled by sea level variations, climatic changes and local tectonic activities (Friedman and Krumbein 1985; James and Kendall 1992). The precipitation of this sequence of evaporite—carbonate seems to be deposited in supratidal area, shallow water lagoon and brine pond (Friedman and Krumbein 1985; James and Kendall 1992) and the precipitation may occur within microbial active medium (Arenas and Pomar 2010; Deng et al. 2010; Noffke et al. 2003; Wright and Oren 2005). In northwestern Egypt (e.g. Dir E1-Biraqat, southeast El Alamein, and Gebel E1-Hagif, E1-Ghorbaniat, El-Hammam and E1-Omayed and Alamein area gypsum quarries; Youssif 1988; Fig. 15.24), the middle Miocene carbonates (Marmarica Fm.) are overlain by early Messinian evaporite, El-Hagif Fm. (Omara and Sanad 1975; Aref 2003; Youssef and Kamel 1985; Youssef 1988). The Messinian evaporite sequence is formed of three gypsum horizons separated by

gypsiferous limestones, sandy gypsiferous marl, and clay layer. The lower gypsum layer is composed of stromatolite gypsum intercalated with microbial laminae, followed upward by skeletal gypsum with grass like gypsum capped by the upper one is between 9 and 11 m thick (Fig. 15.24). The upper gypsum layer is composed of overlained by large crystalline swallow-tail selenite gypsum. This evaporite *sequence* described as coastal lagoon deposits (Youssef and Kamel 1985; Aref 2003).

15.4.3.3 Post-Miocene Evaporite

The evaporite deposits in both Red Sea (Northern Safaga), Gulf of Suez (Gebel Zeita and Ras Gemsa) and Sinai (Ayun Mosa and Sharm El-Sheikh) is extended through Pliocene, Pleistocene and Holocene. These post-Miocene evaporite have different structural and environmental settings (Friedman et al. 1973; Kushnir 1981; El Haddad et al. 1984, 1993; Purser et al. 1987; Plaziat et al. 1995a; Aref 2003). This group of evaporite are deposited in shallow marine

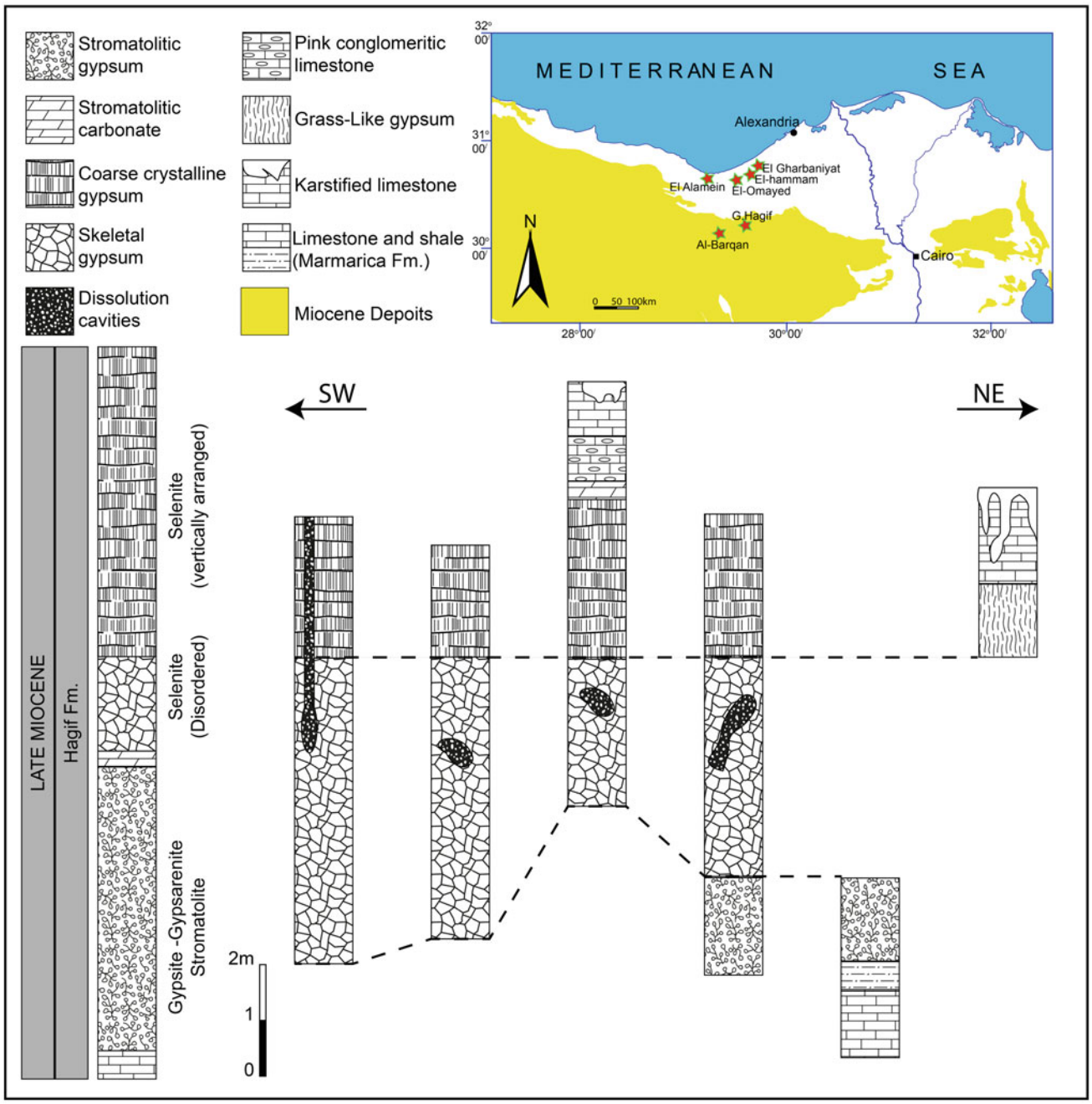

Fig. 15.24 Location map of well-known evaporite mines in the northwestern desert together with simplified lithological sections of exposed post Miocene evaporite in the northwesterndesert (after Youssef 1988; Mansour 2015)

environments with locally emerged sabkha, and evaporite crusts. Several tens of meter thick sediments of alternative gypsum, oolitic carbonates and sandy marls with dwarfed mega fossils are recorded (Orszag-Sperber et al. 1998).

The last evaporite group deposited in the both northwestern Red Sea and Gulf of Suez are thin evaporite beds (2–8 m thick) belongs to Quaternary and is deposited in shallow coastal lagoons (Plaziat et al. 1995, 1998). Gypsum occurs in the swallow form of (1–5 cm crystals of selenite) which have grown on the sediment water interface. These facies are underlain by stromatolites that cover the underlying open marine sediments. The evaporitic in this lagoons has been dated as 123 ± 10 k.y. (Plaziat et al. 1996). The economic value of this gypsum deposits are very low.

15.4.4 Natural Salt Deposits

The most important natural salt deposits in Egypt are located at Wadi Natrun area. Wadi Natrun is the most prominent geomorphological features in the North-Western Desert of Egypt. It located at latitudes 30°17′ to 30°19′N and longitudes 30°10′ to 30°25′E and its deepest point is situated at 24 m below sea level. The floor of the depression is occupied by several salt lakes trending NW-SE (El-Fazda, Umm Risha, Ruzounia, Zug-Hamra, El Beida, and El Gar lakes from SE to NW; Fig. 15.25) with a total length of 50 km and with an average width of 10 km (Salem and El Gammal 2017). Together, The Wadi El Natrun saline lakes in Egypt and the Florida saline lakes in the USA are the only two cases of Soda lakes in the world for natural salt production.

Wadi El Natrun area comprises many rock units. The basal part is Mamura Fm, it consists of interbedded fossiliferous shale, gypsiferous claystone, sandstone and lower Miocene limestone. It is followed upward by the Mikheimen Fm., which is composed of grey to conglomerates and conglomeratic sandstones of Miocene-Pliocene age. This section is overlain by a grayish to dark grey claystone with grey to greenish grey sandstones and few beds of yellowish white fossiliferous limestone of the Gar El Muluk Fm. that assigned to the lower Pliocene age. Upwardly The Gar El Muluk Fm. is followed by Solymanya Fm. of lower Pliocene age and consisting of greenish grey sandstones intercalated with fossiliferous limestone at the top. The Kalakh Fm., which is a pink cross-bedded calcarenite with the karstified columnar structure at the top, it is documented and depicts the Pliocene–Pleistocene age is overlying the Gar El Muluk Fm. The section is covered by Hamzi Fm, which is covalent the Wadi El Natrun facies that composed of white porcelaneous and pink limestones that are underlain by conglomerates (UNESCO 2006).

The lacustrine deposits of Wadi El Natrun lakes are classified into three groups (El Fayoumi 1964): (a) Freshwater marshes in the northern part, the surface deposits include a complex of dark clayey material from weathering of the gypsiferous clays, aeolian sand and degraded organic matter. (b) Salt deposits, are mostly underneath the shallow water of the salt lakes, such deposits are rich in natrun, thenardite and halite. (c) Wet salt marshes, occupies the areas east of the lakes, the areas affected by seasonal fluctuations in groundwater level. The surface deposits of these salt marshes are essentially sand cemented by salt material resulting from evaporation of the lake water. Nine salts are forming the most of the evaporite deposits in the Wadi Natrun, and are composed of the carbonates, sulphates and chlorides of sodium (Table 15.9).

Salt deposit at Lake Fazda are Halite and Burkeite covered by a massive pinkish white layer mostly composed of Natron with traces of Halite and Trona (Fig. 15.25). In Umm Risha Lake, the saline water is examined to produce salts. Brown and pink colored halite is formed within the lake during the brine formation within the lake. The bottom of Lake Ruzounia salt deposits are dominated by sulphate and carbonate salt minerals and halite is restricted to the upper interval and it was worked for salt production. The two small lakes Zug and Hamra are connected and always refers to as Zug-Hamra, the evaporite deposits in this lakes are represented by Halite and Torona, across the entire lake the sabkha deposit is formed mainly of thick evaporite deposit formed of Halite and Thenardite enveloped by Natron. The evaporite deposits of El Beida Lake is formed of varicolored salts deposited within the sabkha. Halite and Thenardite are under production in this site. El Gaar Lake is the largest lake in Wadi El Natrun halite is the abundant salt in the water of this lake, with mixture of both Trona and Burkeite (Fig. 15.25; Table 15.10).

In General, the evaporite salt deposits of Wadi El Natrun saline lakes are made up of, halite, thenardite and natron deposited on the bottom of the Lakes and surrounding sabkhas (Salem and El Gammal 2017; Shortland 2004, 2011). The lakes of El Raizonia, Umm Risha, El Fasda, El Beida and El Gaar have a strong economic potential for producing halite salts, whereas the mixed with halite, and El Beida, Umm Risha and El Fasda lakes have and economic values of natron salt and that should subjected to further evaluations.

15.4.5 Economic Value of Evaporite in Egypt

The Egyptian Gypsum and Anhydrite are present at sufficient grade to have strong effect on the economy of an excavation projects. Egypt is one of the world's largest gypsum producers participating by 1.24% of world production in 1994 and decreased in 2017 to 0.9% and it occupies the place 16th between the world gypsum producers, producing approximately 1.2Mmt/yr of gypsum. Much of this gypsum is found

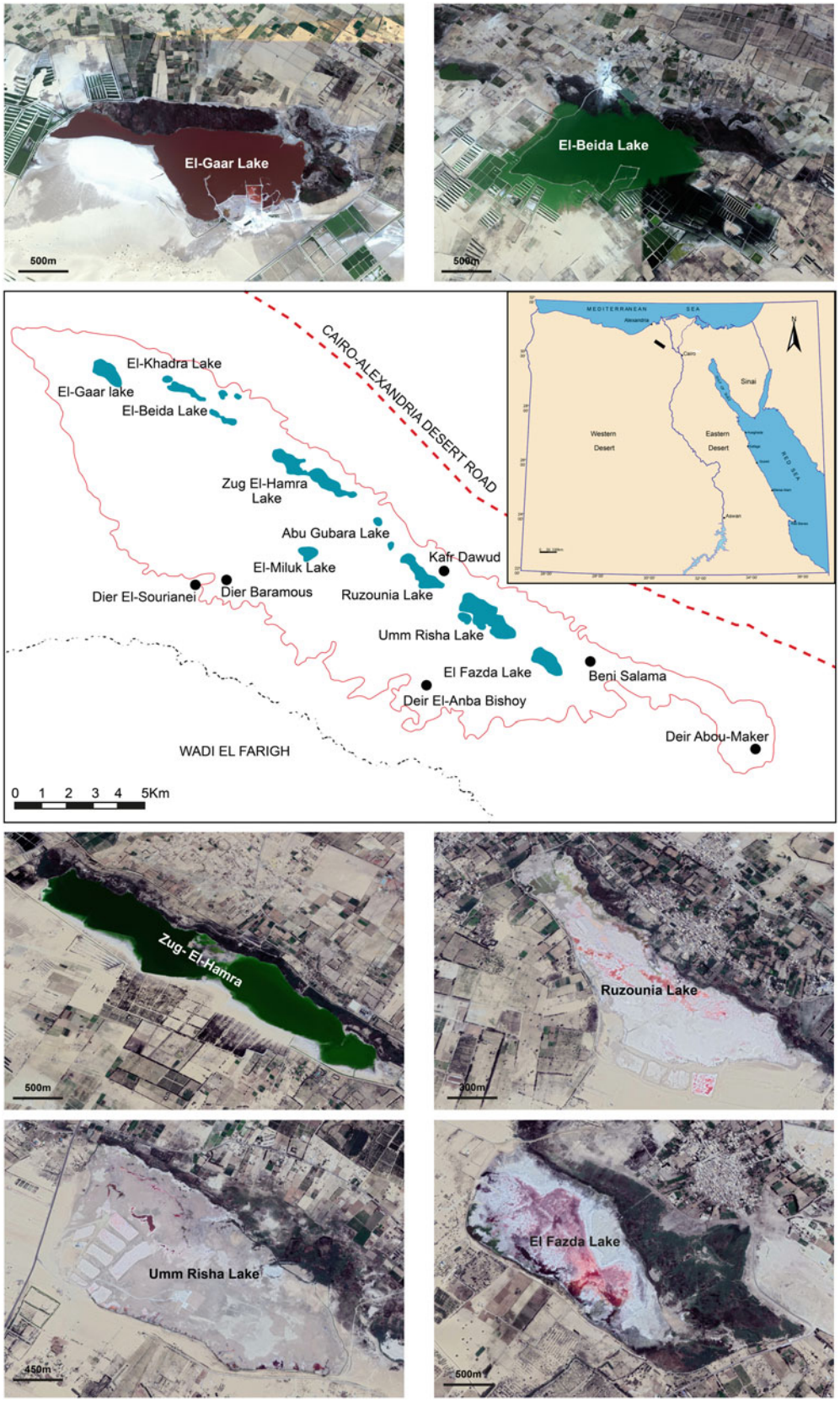

Fig. 15.25 Location map of the Wadi Natrun and its associated saline lakes (pictures from google earth)

Table 15.9 List of evaporite minerals observed in the Wadi Nartun area

Mineral name	Chemical composition
Natron	$Na_2CO_3 \cdot 10H_2O$
Thermonatrite	$Na_2CO_3 \cdot H_2O$
Trona	$Na_2CO_3 \cdot NaHCO_3 \cdot 2H_2O$
Nahcolite	$NaHCO_3$
Burkeite	$Na_6CO_3 \cdot 2SO_4$
Thenardite	Na_2SO_4
Mirabilite	$Na_2SO_4 \cdot 10H_2O$
Halite	NaCl
Pirsonnite	$Na_2CO_3 \cdot CaCO_3 \cdot 2H_2O$

in deposits on the Sinai Peninsula and the Mediterranean coast area of Egypt (Fig. 15.26; Table 15.11). High grade gypsum for exportation comes from Sinai. Gypsum for domestic consumption in construction materials, as an additive in agriculture, and in the cement industry comes from several small quarries west of Alexandria and from Gerza. The chemical and technical properties of some major gypsum and evaporite deposits are given below:

1. *El Ballah gypsum quarry* (Table 15.11), $CaSO_4$ = 90% combined with H_2O = 5.8%, NaCl = 0.24%, clay = 0.08%, silt and sand = 1.76%.
2. *El Hammam gypsum quarry*, $CaSO_4.2H_2O$ = 86.33%, Si = 0.25%, Al_2O_3 = 1.18%, Fe_2O_3 = 0.12%, $CaCO_3$ = 11.10%, chloride = 0.14% and Moisture = 0.18%.
3. *El Omayid gypsum quarry*, $CaSO_4.2H_2O$ = range from 66.44 to 89.15% the calculated average gypsum Content in the whole area is 79.18%.
4. *Gebel El Hagif gypsum quarry*, loss on ignition = 20.2%, Fe_2O_3 = 0.48%, $CaCO_3$ = 2.0%, NaCl = 0.3%, CaO = 33.5%, SO_3 = 46.4%.
5. *Gerza gypsum quarry*, H_2O = 0.34%, $CaCO_3$ = 9.38%, CaO = 30.48%, $CaSO_4$ = 77.52%, sulfate = 26.05%, SiO_2 = 6.58%, Fe = 0.90%, FeO = 1.2%, Al_2O_3 = 3.47%, Mn = 0.29%, MnO_2 = 0.31%, MgO = trace, chloride = 0.2%, CO_2 = 0.13%, organic materials = 0.92% and water of crystallization = 16.23%.
6. *Helwan locality* H_2O = 0.45%, L.O.I = 15.15%, CO_2 = 9.93%, Si = 4.41%, Fe = 0.34%, Mg = 0.11%, MgO = 0.12%, Al_2O_3 = 2.58%, CaO = 34.39%, sulfate = 33.6%, Mg = trace, chloride = 0.35%, $CaSO_4$ = 72.24%, and $CaCO_3$ = 19.41%.
7. *Manzallah lake gypsum quarry*, reserves are estimated to be 500,000.
8. *Ras Malaab gypsum*, reserves are estimated to be, sure = 21 million tons, probable = 40 Million tons, possible = 200 million tons. $CaSO_4$ = 81.31%, H_2O = 7.67%, oxides = 0.04%, $CaCO_3$ = 1.2%, $CaCl_2$ = 0.09%, and MgO = trace.
9. *Wadi El Rayan gypsum*, reserves are estimated to be 16 million tons.

It is clearly that the Egyptian gypsum and anhydrite ranges between medium to high grade based on its technical properties. The evaluation of economic values of the gypsum and

Table 15.10 Summary of evaporite minerals observed by various studies in Wadi Natrun Lakes

Lake	Lucas (1912)	Wenigswieser (1988)	Wenigswieser (1989)	Ouede (2002)	Salem and El Gammal (2017)
El Fazda	Salt at bottom, very little natrun; surrounded by natrun	Halite and thenardite at edge	Halite and burkeite [trona]	–	Halite and burkeite. Covered by Natron with traces of Halite and Trona
Umm Risha	Salt at bottom, very little natrun	Halite and thenardite at edge	Halite and traces of trona, etc. at edge; halite and dolomite in centre	Halite at edge; halite and traces of pirssonite in centre	Brown and pink colored halite
Ruzounia	Salt at bottom, very little natrun	–	–	Halite and burkeite	Sulphate and carbonate salt minerals and halite is restricted to the upper interval
Zug-Hamra	Large amount of natrun in bottom.	Halite and thenardite at edge	–	Halite and burkeite	Halite and torona
El Beida	Much salt, very little natrun; surrounded by natrun	Trona and thenardite	Halite and thenardite	Halite at edge; halite, thenardite and burkeite	Halite and thenardite
El Gaar	Very little natrun	Trona and thenardite	Halite in centre; halite and thenardite at edge	–	Halite, trona and burkeite

Fig. 15.26 Location map of the evaporite mines in Egypt (Wflburn et al. 1996 and Mineral Resources Data System USGS W029152, Metalogenic Map, EGSMA 1998)

anhydrite in Egypt is based on the published report of the US. Geological survey 2017 can be summarized as follows:

The evaporite production are remained steady in comparison to the previous year. Where as the production is determined for 2.2 million ton/year. In the last 18 years the Egypt rises of 64.42% in gypsum production. Its average production was around 1.8 million tons from 1998 to 2015 and it reached its maximum production of 3 million tons in 2010 and record lowest (178 thousand tons) in 2007. Regarding to the national income and according to statistics published by United Nations Statistical Office (2017), the indicator grew greatly by 41.33% compared with the previous year. The overall changes for the last 24 years show a rise of 420.2%. Besides, it has attained the compound average annual growth rate of 0.15% during the last 5 years with a marginal overall raise since the start of observations. It averaged 2.24 million US Dollar from 1994 to 2017 and it reached its all-time high of 6.9 million US Dollar in 2009 and record low of 0.2 million US Dollar in 2000. With increasing local demand due to the growth in Egyptian industry based on the gypsum and anhydrite (e.g. cement), in 2017, the gypsum importation rate increased by 8.29%. Whereas Egypt show a general decrease of 48.54% in importing gypsum is noted over the last 24 years.

The Common salt is extracted from several evaporite basins along the Mediterranean coast near Alexandria, Port Said and Damietta. Additional production comes from small operations at Marsa Matruh, Idku and Rosetta. Three grades of salt are produced: industrial (85% NaCl), washed (98% NaCl) and refined NaCl. Natural rock salt deposits about 300 m thick occur at Gebel al Zeit, Ras Gharib and Ras Gemsa on the Gulf of Suez and Wadi Natron. The upper layers often are rich in potassium salts, containing 4–6% K_2O. Salt production is currently used domestically.

Table 15.11 Locations of working and prospecting evaporite mines (Gypsum, Anhydrite and salts) in Egypt. The data collected from U.S. Geological Survey Golden (1996) and Mineral Resources Data System USGS W029152, Metalogenic Map, EGSMA, 1998

Mines producing minerals gypsum and salts			
Location	Latitude	Longitude	Ore deposit
Manzala	31	32	Salt
Matariys	31	31.91666667	Salts
Ras Shukeir	28.08333333	33.3	Salts
Idku	31.25	30.25	Salts
Harrara	30.88333333	30.31666667	Salt, Natron
Rosetta	31.41666667	30.38333333	Salt
Wadi Natrun	30.35	30.3	Salt, natrun
Ballah	30.71666667	32.33333333	Gypsum
Porl Said	31.21666667	32.36666667	Salt,
Marsa Matruh	31.35	27.28333333	Salt
Damiatta	30.21666667	30.8	Salt, black sand
Baltim	31.55	31.08333333	Salt
Beni Suef	29.01666667	31.15	Gypsum
El Alamein	30.83333	28.91667	Gypsum
El Ballah	30.73333	32.21667	Gypsum
El Bogirate	29.33333	30.45	Gypsum
El Hammam Gypsum	30.83333	29.41667	Gypsum
El Omayid	30.78333	29.16667	Gypsum
Gabel El Hagif	30.53333	29.43333	Gypsum
Gerza Gypsum	28.81	31.06	Gypsum
Gharbanyat	30.83333	29.5	Gypsum
Helwan	30.08333	31.16667	Gypsum
Maadi, Katamia	30.00001	31.11667	Gypsum
Manzallah Lake	31.16667	32.00001	Gypsum
Ras Malaab	29.16667	32.95	Gypsum
Wadi El Rayan	29.83333	32.75	Gypsum
Past producing mines			
Ras Gemsa	27.7	33.5	K-salt
Dimishqin	29.23333333	30.96666667	Gypsum
Gebel el Mudi	28.9	31	Gypsum
Byad el Nasara	29.06666667	31.13333333	Gypsum
Abu Sk	29.88333333	31.21666667	Gypsum
Ismallia	30.58333333	32.26666667	Gypsum
Gharbaniat	30.88333333	29.5	Gypsum
Omayid	30.78333333	29.2	Gypsum
Hammam	30.8	29.38333333	Gypsum
Quarret El farass	29.58333333	30.96666667	Gypsum
Burqan	30.6	29.5	Gypsum
Giza	29.45	31.2	Gypsum
Ras Malaab	29.21666667	32.93333333	Gypsum, Anhydrite
El Shatt	29.95	32.7	Gypsum
W. Rayian	29.85	32.86666667	Gypsum
Gharandal	29.41666667	33.1	Gypsum
Wadi Sidri	28.85	33.21666667	Gypsum
Ranga	24.41666667	35.16666667	Gypsum
Prospect and producing mines			
Bardawell	31.16666667	33.16666667	Gypsum
Alamein	30.83333333	28.95	Gypsum
Marsa Matruh	31.2	27.2	Gypsum
Buquirat	29.38333333	30.36666667	Gypsum
Ayun Musa	29.83333333	32.75	Gypsum
Ismallia	30.46666667	32.31666667	Gypsum
Ras Malaab	29.5	32.83333333	Gypsum
Abu Sweira	28.33333333	33.61666667	Gypsum
Gerza	29.4	31.11666667	Gypsum
Koraimat	29.31666667	31.45	Gypsum
Gebel El zeit	27.9	33.5	K-salt
Wadi El-Ahmar El Qadim	26	34.03333333	Gypsum
Abu Ghsun	24.5	35.15	Gypsum
Gebel El Hagi	30.53333333	29.46666667	Gypsum
El Alamein	30.83333333	28.91666667	Gypsum

References

Abdel-Monem AA, Abdel-Razek YA, Hassan GM, Eissa HM, Rasheed NM, and M Morsy (2006) ESR studies and dating of Egyptian Gypsum at Ras Malaab, Sinai, Egypt. In: VIII radiation physics & protection conference, 13–15 Nov 2006, Beni Sueif-Fayoum, Egypt

Abdel-Motelib A, Kader ZA, Ragab YA, Mosalamy M (2011) Suitability of a Miocene bentonite from North Western Desert of Egypt for pharmaceutical use. Appl Clay Sci 52:140–144

Abdel-Rahman IF (2002) Physical and chemical characteristics of silica sand deposits (white sand) of Wadi Watir region, Sinai. Acta Min Petrogr Szeged 43:79–83

Abou El-Anwar EA, El-Wekeil SS (2013) Contribution to the provenance and paleoclimate of the Lower Paleozoic sandstones of Naqus Formation, Wadi Qena, Northern Eastern Desert; integration of support petrography, mineralogy and geochemistry. J App Sci Res 9(10):6529–6546

Abu Seif ESS (2014) Geotechnical characteristics of anhydrite/Gypsum transformation in the Middle Miocene Evaporites, Red Sea Coast, Egypt. Arab J Sci Eng 39:247–260 (2014). https://doi.org/10.1007/s13369-013-0857-x

Abu Shabana M (1998) Glass sands of Abu-Thora formation west-central Sinai: lithostratigraphy, geochemistry, suitability, and reserve estimation. In: The 5th conference on the geology of Sinai for development, Oct 27–30, Saint Catherine, South Sinai, Egypt (abstract)

Abukhadra MR (2015) Study on qualifications of some Egyptian Quartz deposits for high technology applications. Master thesis, Geology Department, Faculty of Science, Beni Suef University, Egypt

Ahmed F, Farouk S, Abd El-Moghny M (2014) A regional stratigraphic correlation for the upper Campanian phosphorites and associated rocks in Egypt and Jordan. Proc Geol Assoc. http://dx.doi.org/10.1016/jpgeola.2014.06.002

Akkad S, Dardir AA (1966) Geology and phosphate deposits of Wasif, Safaga area. Geol Surv Egypt 36:35

Al Sharhan A (2003) Petroleum geology and potential hydro-carbon plays in the Gulf of Suez Rift Basin, Egypt. AAPG Bull 87(1):143–180

Al-Fariss T, Abd El-Aleem F, El-Nagdy K (2013) Beneficiation of Saudi phosphate ores by column flotation technology. J King Saud Univ Eng Sci 25:113–117

Ali MM (1995) Geochemistry of Gabal Qabeliat phosphate south-west Sinai, Egypt. M. E. R. C. Ain Shams Univ Earth Sci 9:134–144

Allam A, Khalil H (1989) Geology and stratigraphy of Gebel Qabeliat area, Southwestern Sinai, Egypt. J Afr Earth Sci 9(1):59–67

Aref MA (2003) Lithofacies characteristics, depositional environment and karstification of the Late Miocene (Messinian) gypsum deposits in the Northern Western Desert, Egypt. Sedimentol Egypt 11:9–27

Arenas C, Pomar L (2010) Microbial deposits in upper Miocene carbonates, Mallorca, Spain. Palaeogeog Palaeoclim Palaeoecol 297:465–485

Attia OEA (1993) Sedimentological and Petrological Studies of the Middle Miocene Evaporites on the Eastern Side of the Gulf of Suez, Sinai, Egypt. PhD in geology, University of Cairo, Cairo, 159 pp

Attia OEA, Lowenstein TK, Wail AM (1995) Middle Miocene gypsum, gulf of Syez: marine or non-marin. J Sed Res A65 (4):614–626

Auer G, Reuter M, Hauzenberger CA, Piller WE (2017) The impact of transport processes on rare earth element patterns in marine authigenic and biogenic phosphates. Geochimica et Cosmochimica Acta 203:140–156

Babel M, Schreiber BC (2014) Geochemistry of evaporites and evolution of Seawater. In: Fred M (ed) Treatise on geochemistry, sediments, diagenesis, and sedimentary rocks edition, 2nd edn, vol 9. 2nd Chapter: Chapter 9.18. Elsevier. https://doi.org/10.1016/B978-0-08-095975-7.00718-X

Bache F, Gargani J, Suc J-P, Gorini C, Rabineau M, Olivet J-L, Rubino J-L, Jouannic G, Clauzon G, Dos Reis T (2015) Constraining the Messinian salinity crisis. Mar Pet Geol 66:262–277

Baioumy H, Tada R (2005) Origin of Late Cretaceous phosphorites in Egypt. Cretac Res 26:261–275

Baioumy HM, Ismael SI (2014) Composition, origin and industrial suitability of the Aswan ball clays, Egypt. https://doi.org/10.1016/j.clay.2014.09.041

Baioumy HM, Gilg HA (2011) Pisolitic flint kaolin from Kalabsha, Egypt: a laterite-derived facies. Sed Geol 236(1):141–152

Balistrieri LS, Brewer PG, Murray JW (1981) Scavenging residence times of trace metals and surface chemistry of sinking particles in the deep ocean. Deep Sea Res 28:101–121

Basta E, El-Kammar AM, Schroll E (1974) Rare earth elements distribution in some Egyptian phosphorites. In: Proceedings of the 2nd Arab conference on mineral resources, Jeddah, Saudi Arabia, Nov 1974, vol 9, pp 150–174

Basta E, El-Kammar AM (1976) Mineralogy and geochemistry of the phosphorites of Abu Tartur, Western Desert, Egypt. In: The 25th international geological congress, Sydney, Australia, vol 2, Section 14, p 555

Berkey CP (1922) The new petrology. Bull Geol Soc China 1:12–31

Bock WD (1987a) Geochemie und genese der oberkretozischen phosphorite Agyptens. Berl Geowiss Abh 82:136p

Bock WD (1987b) Geochemie und genese der Oberkretazischen phosphorite Agypten. PhD thesis, Berliner Geowiss. Abh, vol 82, 138 pp

Bosworth W, Khalil S, Clare A, Comisky J, Abdelal H, Reed T, Kokkoros G (2014) Integration of outcrop and subsurface data during the development of a naturally fractured Eocene carbonate reservoir at the East Ras Budran concession, Gulf of Suez, Egypt. In: Spence GH, Redfern J, Aguilera R, Bevan TG, Cosgrove JW, Couples GD, Daniel J-M (eds) Advances in the study of fractured reservoirs. Geological Society, London. Special Publications, vol 374, pp 333–359

Boulos TR, Yehia A, Morsi MB, Ibrahim SS (2017) High quality fused silica from Egyptian silica sand concentrate. Inter J Sci Engin Invest 6:160–166

Burser B, Philobbos E (1993) The sedimentary expression of rifting in the NW Red Sea, Egypt. Geol Soc Egypt, Sepc Publ 1:1

Caird RA, Pufahl PK, Hiatt EE, Abram MB, Rocha AJD, Kyser TK (2017) Ediacaran stromatolites and intertidal phosphorite of the salitre formation, Brazil: phosphogenesis during the neoproterozoic oxygenation event. Sed Geol 350:55–71

Cosmidis J, Benzerara K, Menguy N, Arning E (2013) Microscopy evidence of bacterial microfossils in phosphorite crusts of the Peruvian shelf: implications for phosphogenesis mechanisms. Chem Geol 359:10–22

da Conceicao FT, Bonotto DM (2006) Radionuclides, heavy metals and fluorine incidence at Tapira phosphate rocks, Brazil, and their industrial (by) products. Environ Pollut 139:232–243

Dabous AA (1982) Mineralogy, geochemistry, and radioactivity of some Egyptian phosphorites. PhD thesis, Florida State University 201 pp

Dardir AA, Koptan SM (1980) Preliminary evaluation of the rare earth elements in sector Abu Tartur phosphorites. Ann Geol Surv Egypt 10:909–921

Deng S, Dong H, Lu G, Jiang H, Yu B, Bishop ME (2010) Microbial dolomite precipitation using sulfate reducing and halophilic bacteria: results from Qinghai Lake, Tibetan Plateau, NW China. Chem Geol 278:151–159

Dominik W, Shaal S (1984) Notes on the stratigraphy of Cretaceous phosphorites (Campanian) of the Western Desert, Egypt. Berliner Geowiss Abh 50:153–175

El Bassyony AA (1982) Stratigraphical studies on Miocene and younger exposures between Quseir and Berenice, Red Sea Coast, Egypt. PhD thesis, Ain Shams University, Cairo

El Fayoumi I F (1964) Geology of ground water supplies in Wadi El Natrun area, M.Sc. thesis, Faculty of Sciences, Cairo University

El Haddad A, Aissaoui DM, Soliman MA (1984) Mixed carbonate-siliciclastic sedimentation on a Miocene fault block, Gulf of Suez. Sed Geol 37:185–202

El Haddad A, Philobbos E, Mahran T (1993) Facies and sedimentary development of dominantly siliciclasticlate Neogene sediments, Hamata area, Red Sea coast, Egypt. In: Philobbos E, Purser BH (eds) Geodynamics and sedimentation of the Red Sea Gulf of Aden Rift System. Geological Society of Egypt, Special publication, vol 1, pp 253–276

El Sharkawi MA, Abdel Khalek N, Riad S, El Alfy Z, Mahmoud A, Darwesh M, Abdel Motelib A, Abdel Halim A, Abdel Monem A, Farghali M, Anass I, Ibrahim M (2017) Mineral resources and renewable energy for Abu Zenima Industrial Center, Sinai, Egypt. In: First international conference on oil shale and unconventional energy resources for sustainable development in Africa. Assist University, Quseir, 5–9 March, Abstract

El-Bahi S, Sroor A, Mohamed G, El-Gendy N (2017) Radiological impact of natural radioactivity in Egyptian phosphate rocks, phosphogypsum and phosphate fertilizers. Appl Radiat Isot 123:121–127

El-Fawal FM (1994) Abu Thora formation, west-central Sinai, facies analysis and depositional environment. Egypt J Geol 38

El-Gezeery MN, Marzouk IM (eds) (1974) The stratigraphic sub-committee of the National Committee of Geological Sciences (NCGS): Miocene rock stratigraphy of Egypt. J Geol 18:1

El-Hadad MA, Ahmed EA (1987) Distribution of REE and other elements in some Egyptian phosphorites. In: Symposium on phanerozoic and development in Egypt, Cairo

El-Kammar AM, El-Kammar MM (2002) On the trace elements composition of the Egyptian phosphorites: a new approach. In: Proceedings of the 6th international conference on the geology of the Arab world, Cairo University, Giza Egypt, 21–24 Feb 2002, pp 227–244

El-Kammar A, El-Amin H, Saadeldin M (1984) Mineralogical and geochemical studies of the phosphate-bearing sediments of South East Edfu, Upper Egypt. Aswan Sci Technol Bull 5:333–352

El-Kammar AM (1974) Comparative geochemical and mineralogical studies on Egyptian phosphorites. PhD dissertation, Geology Department, Faculty of Science, Cairo University, Giza, Egypt, 169 pp

El-Kammar AM (1977) Mineralogical characteristics of Gebel Hufhuf phosphate-bearing rocks, Bahariya Oases, Western Desert, Egypt. The IV Colluq. Aegean Region, Athens, Greece, Sept 1977. Proceedings, vol III, pp 997–1014

El-Kammar AM (2010) Oil shale in Egypt: country update. regional cooperation for clean utilization of oil shale, MED-EMIP Euro-Mediterranean Energy Market Integration Project, 24–25 Feb 2010, Sharm El Sheikh, Egypt

El-Kammar AM (2012) Uranium and thorium resources in the Egyptian phosphorites and their associating black shale. Expert Invited Talk. IAEA Regional workshop on uranium resources assessment and recovery from phosphate and rare earth elements ores, Cairo, 17–21 June 2012

El-Kammar AM (2014) Phosphorites: a visible target for optimistic prosperity. In: Invited talk, conference on phosphorites as national resources, APET (Association of Pioneer of Engineering and Technology), Leaders Development Center, Cairo, 8 May 2014

El-Kammar AM, Basta E (1983) Chemical weathering of the economic phosphates of Abu Tartur, Western Desert, Egypt. Chem Geol 38:321–328

El-Kammar AM, El Reedy W (1984) Geochemistry of uranium and some rare earth elements in the Cretaceous-Tertiary sediments of Abu Tartur, Western Desert, Egypt. Ann Geol Surv Egypt, XIV, pp 75–86

El-Kammar AM, Saad-Eldin M (1992) Mineralogy and crystal chemistry of the Egyptian sedimentary apatites. Abstracted and presented in the IGCP 325, Assiut University, Feb 1992

El-Kammar AM, Zayed MA, Amer SA (1979) Rare earths of the Nile Valley phosphorites, Upper Egypt. Chem Geol 24(1–2):69–81

El-Shall H, Zhang P, Abdel-Khalek NA, ElMofty SE (2004) Beneficiation technology of phosphates: challenges and solutions. Min Metall Proc 21(1):17–26

El-Shazly EM (1984) Factors influencing the distribution of uranium in phosphates in Egypt. In: Symposium on phosphates in the Arab World, Rabat, July 1984

El-Shazly EM, Salman AB, El Assay IE, El Rakaiby (1979) Discovery of phosphates in the northern Eastern Desert, Egypt. Ann Geol Surv Egypt 551–563

Elwageeh M, El-Kammar M, Mohamed Z (2017) Mining proposal for exploitation of tilted oil shale and phosphorite beds in Quseir-Safaga region, Red Sea. In: Invited talk at the first conference on "Oil shale and unconventional energy resources for sustainable development in Africa", 5–9 Mar 2017, Flamenco Beach and Resort, Quseir, Red Sea, Egypt

Emsbo P, McLaughlin P, Breit G, du Bray E, Koenig A (2015) Rare earth elements in sedimentary phosphate deposits: solution to the global REE crisis? Gondwana Res 27:776–785

Ezz-El Din M, Abouzeid AM, El Maadawy Kh, Khalid AM, El Sherif RE (2016) Mineral industry in Egypt—Part II non-metallic commodities—silica ores. J Min World Exp 5:9–27

Friedman GM, Abraham JA, Braun M, Miller DS (1973) Generations of carbonate particles and laminites in algal mats example from sea marginal hypersaline pool, Gulf of Aqaba, Red Sea. Am Assoc Pet Geol Bull 57:218–251

Friedman GM, Krumbein WE (1985) Hypersaline ecosystems: the Gavish Sabkha ecological studies, vol 53. Springer, Berlin

Gaber MAW (2012) Evaluation of some natural ores from Egyptian Eastern Desert to be utilized in producing of paint materials. J Pet Gas Expl Res 2(1):017–026

Gad GM, Barrett LR (1949) The composition of some Egyptian clays. Mineral Mag 28(206):587–597

Gaudant J, Rouchy JM (1986) Ras Dib: un nouveau gisement de Poissons fossiles du Miocene moyen du Gebel Zeit (Golfe de Suez, Egypte). Bulletin du Museum National d'Histoire Naturelle, Paris, 4° serie, 8, section C; vol 4, pp 463–481

Germann K, Bock WD, Schroter T (1984) Facies development of Upper Cretaceous phosphorites in Egypt: sedimentological and geochemical aspects. Berliner Gewiss Abh 50:345–361

Ghorab MA et al (1964) Oligocene and miocene rock stratigraphy of the Gulf of Suez region. Egyptian General Petroleum Corporation, Cairo

Gladstone R, Flecker R, Valdes P, Lunt D, Markwick P (2007) The Mediterranean hydrological budget from a Late Miocene global climate simulation. Palaeogeog Palaeoclimat Palaeoecol 251:254–267

Glenn CR (1990) Depositional sequences of the Duwi, Sibaiya and phosphate formations Egypt: phosphogenesis and glauconitization in a Late Cretaceous epeiric sea. In: Notholt AJ, Jarvis I (eds) Phosphorite research and development. Geological Society, London, Special Publication, vol 52, pp 205–222

Glenn CR, Arthur MA (1990) Anatomy and origin of a Cretaceous phosphorite-greensand giant, Egypt. Sedimentology 37(1):123

Goldschmidt VM (1937) The principles of distribution of chemical elements in minerals and rocks. J Chem Soc 1937:655–673

Gorini C, Montadert L, Rabineau M (2015) New imaging of the salinity crisis: dual Messinian lowstand megasequences in the deep basin of the eastern and western Mediterranean: a combined conceptual model. Mar Pet Geol 66:278–294

Grabau AW (1920) Geology of the non-metallic mineral deposits other than silicates. Principles of salt deposition, vol 1. McGraw-Hill, New York, pp 1–435

GSL glossary. https://www.geolsoc.org.uk/ks3/gsl/education/resources/rockcycle/page3451.html

Hafez HS, Abd-Elmageed KE, Sheha ER, El-Kolaly MA, Sayed MS (2016) Thermoluminescence studies of Egyptian white sand after gamma ray exposure and its usability for radiation measurements. Arab J Nucl Sci Appl 94(1):1–9

Hameed P, Pillai G, Mathiyarasu R (2014) A study on the impact of phosphate fertilizers on the radioactivity profile of cultivated soils in Srirangam (Tamil Nadu, India). J Radiat Res Appl Sci 7:463–471

Hamza F, Osman A (1986) An upper eocene phosphate occurrence: origin and paleoenvironment. Med East Res Cent Ain Shams Univ 6:115–123

Hassan AA (1967) A new Carboniferous occurrence in the Abu Durba, Sinai, Egypt. In: The 6th Arabian petroleum conference, Baghdad, Iraq, p 8

Hassan F, El Dashlouti S (1970) Miocene evaporites of Gulf of Suez region and their significance. Am Assoc Pet Geol Bull 54:1686–1696

Hassan N, Mansour N, Fayez-Hassan M, Sedqy E (2016) Assessment of natural radioactivity in fertilizers and phosphate ores in Egypt. J Taibah Univ Sci 10:296–306

Hassan F, El Kammar AM (1975) Environmental conditions affecting the accumulation of uranium and rare earth's in Egyptian phosphorites, Egypt. J Geol 19(2):169–178

Hassan MS, Abdel-Khalek NA (1998) Beneficiation and applications of an Egyptian bentonite. Appl Clay Sci 13:99–115

Hermina MH (1972) Review on the phosphate deposits of Egypt. In: Proceedings of the second Arab conference of mineral resources, pp 109–149

Hiatt EE, Pufahl PK, Edwards CT (2015) Sedimentary phosphate and associated fossil bacteria in a Paleoproterozoic tidal flat in the 1.85 Ga Michigamme formation, Michigan, USA. Sed Geol 319:24–39

Hsü KJ, Cita MB, Ryan WBF (1973) The origin of the Mediterranean evaporites. In Ryan WBF, Hsü KJ et al (eds) Initial reports of the deep sea drilling project, vol XIII, Washington (U. S. Government Printing Office)

Hsu KJ, Montadert L, Bernoulli D, Biancacita M, Erickson A, Garrison RE et al (1977) History of Mediterranean salinity crisis. Nature 267(5610):399–403

Hsu KJ, Ryan WBF, Cita MB (1973) Late Miocene desiccation of Mediterranean. Nature 242(5395):240–244

Hughes GW, Abdine S, Girgis MH (1992) Miocene biofacies development and geological history of the Gulf of Suez, Egypt. Mar Pet Geol 9(1):2–28

Hüsing SK, Dekkers MJ, Franke C, Krijgsman W (2009) The Tortonian reference section at Monte dei Corvi (Italy): evidence for early remanence acquisition in greigite-bearing sediments. Geophys J Int 179:125–143

Hussein H (1954) Studies on some Egyptian phosphates with special reference to their radioactivity. M.Sc. thesis, Alexandria University, Egypt

Ibrahim GEA, Mousa AS, El-Hariri TYM, Hassnien IM, Zakzouk NI (2016) New industrial use of Egyptian white sands from Wadi El-Dakhl Area, Eastern Desert, Egypt. Int J Innov Sci Eng Technol 3(1):216–525

Ismaiel HAH, Askalany MM, Ali AI (2017) Evaluation of white silica sands in North Eastern Desert, Egypt. Int J Sci Eng Res 8(5):1713–1722

Issawi B, Francis M, El Hinnawy M, Mehanna A, El Deftar T (1971) Geology of the Safaga-Quseir Coastal plain and of Mohamed Rabah area. Ann Geol Surv Egypt 1(1971):1–19

Issawi B, Jux U (1982) Contribution on the stratigraphy of the Paleozoic rocks in Egypt. Geol Surv Egypt 64:28 pp

James NP, Kendall AC (1992) Introduction to carbonate and evaporite facies models. In: Walker RG, James NP (eds) Facies models, response to sea level changes. Geological Association *of* Canada, Slittsville, pp 265–275

Kamel OA, Abdou-Soliman FH, Abd El-Maaboud MHM (1997) Sinai Carboniferous white sands: their heavy mineral assemblages, fabric, geochemistry, and suitability for glass industry. In: The 3rd international conference on geochemistry, Alexandria, Egypt (abstract)

Kawatra SK, Carlson JT (2013) Beneficiation of phosphate ore. Society for Mining, Metallurgy, and Exploration

Kazakov AV (1939) The phosphate facies: origin of phosphorites and the geologic factors of formation of the deposits. Trans Sci Inst Fert Insect-Fungicides Moscow 145:1–106

Kechicheda R, Laouara R, Bruguierc O, Laouar-Salmia S, Ameur-Zaimecheb O, Foufou A (2016) Preliminary data of REE in Algerian phosphorites: a comparative study and paleo-redox insights. Proc Eng 138:19–29

Khalid AM (1993) Geology and geochemistry of Nuweiba area, South Sinai, Egypt. PhD thesis, Suez Canal University, Ismailia, Egypt

Khalil S, McClay KR (2002) Extensional fault-related folding, northwestern Red Sea, Egypt. J Struct Geol (Special Volume) 24:743–762

Khalil S, McClay KR (2004) Structural control on Miocene sediment input sites, northwestern Red Sea, Egypt. In: Proceedings of the seventh conference of geology of Sinai for development, Suez Canal University, Ismailia, pp 297–315

Khalil S, McClay KR (2009) Structural control on synrift sedimentation, northwestern Red Sea margin, Egypt. J Struct Geol 26:1018–1034

Köhler CM, Heslop D, Dekkers MJ, Krijgsman W, van Hinsbergen DJ, von Dobeneck T (2008) Tracking provenance changes during the late Miocene in the Eastern Mediterranean Metochia section using geochemical and environmental magnetic proxies. Geochem Geophys Geosyst 9:Q12018. https://doi.org/10.1029/2008GC002127

Krijgsman W, Hilgen FJ, Raffi I, Sierro FJ, Wilson DS (1999) Chronology, causes and progression of the Messinian salinity crisis. Nature 400(6745):652–655

Kushnir (1981) Formation and early diagenesis of varved evaporite sediment in a coastal hypersaline pool. J Sediment Petrol 51:193–1203

Ladoo RB, Myers WM (1951) Nonmetallic minerals, 2nd edn. McGraw-Hill, New York, 473 pp

Lofi J, Déverchère J, Gaullet V, Gillet H, Gorini C, Guennoc P, Loncke L, Maillard A, Sage F, Thinon I (2011) Seismic atlas: the "Messinian Salinity Crisis" markers in the Mediterranean and Black Seas. Commission for the Geological Map of the World, 77, rue Claude-Bernard, 75055 Paris, France, 73 pp

Mansour AS (2015) Sedimentology and environmental interpretation of carbonate deposits associating the evaporites-bearing Miocene succession, northern Western Desert, Egypt. Carbonates Evaporites 30:167–179. https://doi.org/10.1007/s13146-014-0200-y.

Manzi V, Gennari R, Hilgen F, Krijgsman W, Lugli S, Roveri M et al (2013) Age refinement of the Messinian salinity crisis onset in the Mediterranean. Terra Nova 25(4):315–322

Manzi V, Lugli S, Roveri M, Dela Pierre F, Gennari F, Lozar F, Natalicchio M, Schreiber BC, Taviani M, Turco E (2014) The Messinian salinity crisis in Cyprus: a further step towards a new stratigraphic framework for Eastern Mediterranean. Basin Res 1–30

McConnell D (1973) Apatite—its crystal chemistry, mineralogy, utilization and geologic and biological occurrences. Springer, Wien, New York, 111 pp

McLaws IJ (1971) Uses and specifications of silica sand. Research Council of Alberta. RCA/AGS Earth sciences report 1971-04, 67 pp

Melegy A, Ismael IS (2012) Sulfur isotope geochemistry of Messinian gypsum deposits from the northern coast Egypt: paleoenvironmental implications. Earth Sci India 5:122–138

Montenat C, Angelier J, Beaudouin B, Bolze J, Burollet PF (eds) (1990) Gulf of Suez and Red Sea—special conference of the Société Géologique de France, Paris, 7 Dec 1987. Bulletin de la Société Géologique de France 6(3):U 371

Montenat C, D'estevou P, Purser B, Burollet P, Jar-rige J, Sperber F, Philobbos E, Plaziat J, Part P, Richert J, Roussel N, Thiriet J (1988) Tectonic and sedimentary evolution of the Gulf of Suez and the Northwestern Red Sea. Tectophysics 153(1–4):161–177. https://doi.org/10.1016/0040-1951(88)90013-3

Montenat C, Orszag-Sperber F, Ott D'estevou P, Purser BH, Richert JP (1986) Étude d'une transversale de la marge occidentale de la Mer Rouge: le secteur de Ras Honkorab Abu Ghusun, Égypte [Study of a transverse on the western margin of the Red Sea; Ras Honkorab Abu Ghusun sector, Egypt.] Documents et Travaux, Institut Géologique Albert de Lapparent, 10, 145–170 (In French)

Montenat C, Orszag-Sperber F, Plaziat JC, Purser BH (1998) The sedimentary record of the initial stage of Oligo-Miocene rifting in the Gulf of Suez and northern Red Sea. In: Purser BH, Bosence DWJ (eds) Sedimentation and tectonics in rift basins: Red Sea-Gulf of Aden. Chapman & Hall, London, pp 146–161

Monty C, Rouchy JM, Maurin A, Bernet-Rollande MC, Perthuisot JP (1987) Reef-stromatolites-evaporites facies relationships from the Middle Miocene: examples from the Gulf of Suez and the Red Sea. Lecture Notes Earth Sci (Evaporite Basins) 13:75–86

National Committee of Geological Sciences (N. C. G. S.) (1976) Miocene rock stratigraphy of Egypt. Egypt J Geol 18:1–69

Noffke N, Gerdesb G, Klenkec T (2003) Benthic cyanobacteria and their influence on the sedimentary dynamics of peritidal depositional systems (siliciclastic, evaporitic salty, and evaporitic carbonatic). Earth Sci Rev 62:163–176

Obaidalla N (2013) Planktonic foraminiferal biostratigraphy of the Upper Cretaceous to mid-Paleocene of the Dababiya Quarry Corehole, Upper Nile Valley, Egypt. Stratigraphy 9(3–4):229–240

Omara SM, Sanad S (1975) Rock stratigraphy and structural features of the area between Wadi E1 Natrun and the Moghra depression (Western Desert, Egypt). Geol Jahrb Beih 16:45–73

Orszag-Sperber F, Plaziat JC (1990) La sédimentation continentale (Oligo-Miocène) des fossés du proto-rift du NW de la Mer Rouge. Continental sedimentation (Oligo-Miocene) in depressions of the proto-rift of the north-western Red Sea, Egypt. Bulletin de la Société Géologique de France, Série VIII 6(3):385–396 (In French)

Orszag-Sperber F, Harwood G, Kendall A, Purser BH (1998) A review of the evaporites of the Red Sea-Gulf of Suez rift. In: Purser BH, Bosence DWJ (eds) Sedimentation and tectonics in rift basins: Red Sea-Gulf of Aden. Chapman & Hall, London, pp 409–428

Ouda KH, Masoud (1993) Sedimentation history and geological evolution of the Gulf of Suez during the late Oligocene-Miocene. Geol Soc Egypt Sepc Publ 1:47

Phillip G, Imam MM, Abdel Gawad GI (1997) Planktonic foraminiferal biostratigraphy of the Miocene sequence in the area between Wadi El-Tayiba and Wadi Sidri, west central Sinai, Egypt. J Afr Earth Sci 25(3):435–451

Philobbos ER, El-Hadded AA (1983) Contribution to the lithostratigraphy of Miocene and Pliocene sediments of the Red Sea coastal zone (abstract). Geol Soc Egypt

Philobbos ER (1964) Geology, and petrography of the phosphates of the Safaga–Quseir region. M.Sc. thesis, Assiut University

Philobbos ER (1969) Geology of the phosphorites of the Nile Valley. PhD thesis, Assiut University, Egypt

Plaziat JC, Baltzer F, Choukri A, Conchon O, Freytet P, Orszag-Sperber F, Purser B, Raguideau A, Reyss JL (1995a) Quaternary changes in the Egyptian shoreline of the northwestern Red Sea and Gulf of Suez. Quatern Int 29(30):11–22

Plaziat JC, Montenat C, Barrier P, Janin MC, Orszag-Sperber F, Philobbos E (1998) Stratigraphy of the Egyptian syn-rift deposits; correlations between axial and peripheral sequences of the NW Red Sea and Gulf of Suez and their tectonic and eustatic controls. In: Purser BH, Bosence DWJ (eds) Sedimentation and tectonics in rift basins: Red Sea-Gulf of Aden. Chapman & Hall, London, pp 211–222

Plaziat JC, Baltzer F, Choukri A, Conchon O, Freytet P, Orszag-Sperber F, Purser B, Raguideau A, Reyss JL (1995b) Quaternary changes in the Egyptian shoreline of the northwestern Red Sea and Gulf of Suez. Quatern Int 29(30):11–22

Plaziat JC, Reyss JL, Choukri A, Orszag-Sperber F, Purser B, Baltzer F (1996) U/Th chronology of the reef deposits of the Egyptian Red Sea and Gulf of Suez. In: Proceedings of the 17th regional international association of sedimentologists meetings, pp 213–214

Purser B, Aissaoui DM, Orszag-Sperber F (1987) Diagenèse et rifting; évolution postsédimentaire des sédiments carbonatés Miocènes sur la bordure NW de la Mer Rouge. (Diagenesis and rifting: post-sedimentary evolution of Miocene carbonate

Ramadan MS (2014) Characteristics of white sand deposits in southern Sinai region, Egypt. Middle East J Appl Sci 4(1):100–108

Refaei DA, Abdelrahman MK, Ibrahim IA, Eldears F, Kandil AT (2016) Improvement the quality of Egyptian kaolin for industrial applications. Int J Adv Technol 8:174. https://doi.org/10.4172/0976-4860.1000174

Richardson M, Arthur MA (1988) The Gulf of Suez–northern Red Sea Neogene rift: a quantitative basin analysis. Mar Pet Geol 5(3):247

Richardson M (1982) A depositional model for the Cretaceous Duwi (Phosphate) formation, South of Quseir, Red Sea coast, Egypt. M. Sc. thesis, University South Carolina

Rouchy JM, Bernet-Rollande M, Maurin AF, Monty E (1983) Sedimentolugical and palaeogeographic significance of various bioconstructed carbonates associated with Middle Miocene evaporites ncar Gebel Esh Mellaha, Egypt. Comptes Rendues de IAcademie des Sciences (Series 2) 6:457 –462

Rouchy JM, Monty C, Pierre C, Bernetrollande MC, Maurin AF, Perthuisot JP (1985) Genèse des corps carbonatés diagénétiques par réduction de sulfates dans le Miocène évaporitique du Golfe de Suez et de la Mer Rouge (Sulphate reduction and formation of diagenetic carbonate bodies in the evaporitic Miocene of the Gulf of Suez and of the Red Sea.). Comptes Rendus de l'Académie des Sciences, Série II 301(16):1193–1198 (In French)

Rouchy JM, Nod D, Wali AMA, Aref MAM (1995) Evaporitic and biosiliceous cyclic sedimentation in the Miocene of the Gulf of Suez-depositional and diagenetic aspects. Sed Geol 94(1995):277–297

Roveri M, Flecker R, Krijgsman W, Lofi J, Lugli S, Manzi V, Sierro FJ, Bertini A, Camerlenghi A, De Lange GJ, Govers R, Hilgen FJ, Hübscher C, Meijer PTH, Stoica M (2014) The Messinian salinity crisis: past and future of a great challenge for marine sciences. Mar Geol 352:25–58

Ryan WBF (2011) Geodynamic responses to a two-step model of the Messinian salinity crisis. Bull Soc Geol Fr 182(2):73–78

Ryan WBF, Cita MB, Hsu JK (1973) Initial report of deep sea drilling project. U.S. Govt. Printing Office, Washington DC

Saad EL-Din M (1990) Comparative geochemical studies on the Egyptian phosphorites and the crystal chemistry of their apatite. PhD thesis, Assiut University, 161 pp

Sadek AF (2009) Comparative geochemical studies on phosphorites of North Africa. Unpublished M.Sc. thesis, Department of Natural Resources, Institute of African Research and Studies, Cairo University, 124 pp

Said R (1971) Explanatory notes to accompany the geological map of Egypt. Geol Surv Egypt

Said R (ed) (1990) The geology of Egypt. Balkema, Rotterdam, 734 pp

Said R, El Heiny I (1967) Planktonic foraminifera from the Miocene rocks of the Gulf of Suez region. Contr Cushman Found Foram Res 18:14

Salama W, El-Kammar A, Saunders M, Morsy R, Kong C (2015) Microbial pathways and palaeoenvironmental conditions involved in the formation of phosphorite grains, Safaga District, Egypt. Sediment Geol 325:41–58

Salem SA, El Gammal EA (2017) Salt minerals at Wadi El Natrun saline lakes, Egypt. New implications from remote sensing data. Eur Chem Bull 7(2):72–80. https://doi.org/10.17628/ecb.2018.7.72-80

Schmalz RF (1969) Deep-water evaporite deposition: a genetic model. Am Assoc Pet Geol Bull 53:758

Schneider-Mor AS, Yam R, Bianchi C, Kunz-Pirrung M, Gersonde R, Shemesh A (2012) Variable sequence of events during the past seven terminations in two deep-sea cores from the Southern Ocean. Quatern Res 77:317–325

Schrank E, Perch-Nielsen K (1985) Late Cretaceous palynostratigraphy in Egypt with comments on Maastrichtian and Early Tertiary calcareous nannofossils. News1 Stratigr 15:81–99

Sediments on the NW margin of the Red Sea. Notes et Mémoires TOTAL, Compagnie Française des Pétroles, vol 21, pp 145–166 (In French)

Shaban M, Abu Khadra MR (2016) Enhancing the technical qualifications of Egyptian white sand using acid leaching; response surface analysis and optimization. Intern J Mineral Proc Extr Metal 1(4):33–40

Shariati S, Ramadi A, Salsani A (2015) Beneficiation of low-grade phosphate deposits by a combination of calcination and shaking tables: Southwest Iran. Minerals 5:367–379. https://doi.org/10.3390/min5030367

Shortland AJ (2004) Evaporites of the Wadi Natrun: seasonal and annual variation and its implication for ancient exploitation. Archaeometry 46:497–516

Shortland AJ, Degryse P, Walton M, Geer M, Lauwers V, Salou L (2011) The evaporitic deposits of Lake Fazda (Wadi Natrun, Egypt) and their use in roman glass production. Archaeometry 53(5)916–929

Sundararajan M, Ramaswamy S, Raghavan P (2009) Evaluation for the beneficiability of white silica sands from the overburden of lignite mine situated in Rajpardi district of Gujarat, India. J Min Mater Character Eng 8(9):701–713

Tamish M (1988) Geomathmatical and geochemical studies on Egyptian phosphorite deposits; PhD thesis, Berlin

Tao D, Al-Hwaiti M (2010) Beneficiation study of Eshidiya phosphorites using a rotary triboelectrostatic separator. Min Sci Technol 20:0357–0364

Tewfik N, Ayyad M (1982) Petroleum exploration in the Red Sea Shelf of Egypt. In: Sixth exploration seminar. Egyptian General Petroleum Corporation, Cairo

Thiriet JP (1987) Evolution tectonique et sedimentaire de la marge occidentale de la Mer Rouge au Neogene, region de Port Safaga (Egypte). These, Universite Claude Bernard, Lyon

Twenhofel WH (1950) Principles of sedimentation, 2nd edn. McGraw-Hill, New York, pp 1–673

U.S. Geological Survey, Mineral Commodity Summaries (2016) U.S. Department of the Interior. U.S. Geological Survey. https://minerals.usgs.gov/minerals/pubs/mcs/index.html

UNESCO (2006) The geological map of Egypt. Project capacity building for the Egyptian geological survey and national authority for remote sensing and space sciences, Egypt

United Nations Statistical Office (2017) Published report

Usdowski E, Dietzel M (1998) Atlas and data of solid-solution equilibria of marine evaporites. Springer, Berlin, Heidelberg, pp 1–316

Wali AM (1993) Gharbaniyat stromatolitic gypsum (west Alexandria): a clue for hypersaline syndepositional feature. Bull Fac Sci Zagazig Univ 15:399–422

Wanas HA (2011) The lower paleozoic rock units in Egypt: an overview. Geosci Front 2(4):491–507

Warren JK (2010) Evaporites through time: tectonic, climatic and eustatic controls in marine and nonmarine deposits. Earth Sci Rev 98:217–268

Wflburn DR, Di Francesco C, Bleiwas DI (1996) Estimated use of explosives in the mining industries of Egypt, Jordan, Syria, Tunisia, and Turkey. U.S. Geological Survey Golden, CO this report was prepared for the US Department of Energy's Office of Non-Proliferation and National Security

Wright DT, Oren A (2005) Nonphotosynthetic bacteria and the formation of carbonates and evaporites through time. Geomicrobiol J 22:27–53

Youssef EA (1988) Sedimentological studies of Neogene evaporites in the northern Western Desert, Egypt. Sed Geol 59:261–273

Youssef EA, Kamel AA (1985) Depositional environment of Dir El Biraqat evaporites, north Western Desert, Egypt. Bull Fac Sci Cairo Univ 53:377–396

Youssef MI (1965) Genesis of bedded phosphorites. Econ Geol 60:590–600

Zalat AA (2013) Palaeoenvironmental reconstruction of the early to Middle Miocene sequence in West Central Sinai, Egypt, as revealed from fossil diatoms. Acta Geol Sin 92(1):354–366

The Petroleum Geology of Egypt and History of Exploration

16

John Dolson

Contents

Abstract

Egypt has proven gas reserves as of the end of 2016 of 16.9 BBOE (98 TCF) and oil and condensate reserves of 18.5 BBO, with an estimated yet-to-find that may exceed 224 TCF (38.6 BBOE). Exploration activity, particularly in the offshore Nile Delta and Mediterranean, continues to add new giant field discoveries which extend eastward into the Levant Basin. Egypt's geological history is complex, with multiple phases of basin formation resulting in working petroleum systems from Paleozoic through Pliocene strata. The Gulf of Suez, Western Desert and Nile Delta are the most prolific provinces. Upper Egypt and the Red Sea offer additional potential, as do poorly understood basins across Upper Egypt. The oldest proven potential source rocks are in the poorly imaged Carboniferous basins in the Western Desert, hidden beneath the Hercynian unconformity and are thus poorly understood. Their contribution to proven production is unknown and much of the deeper production is attributed to charge from Jurassic or Cretaceous shales via fault juxtaposition with the Paleozoic. Fundamental basement architecture was not understood regionally until country-wide gravity, magnetic and seismic studies were completed in 2001. Deep basin geometries are still being unraveled and modified with thousands of additional wells, new age dating and imaging techniques, most of which remains in proprietary studies in individual companies. Shallower structural trends, however, are certainly strongly controlled these older basement, Paleozoic, and Jurassic and Cretaceous fault systems. Many of the deep structures run oblique to shallower Middle and Upper Cretaceous fabrics, causing the deeper, poorly imaged traps to be missed. Better 2D and 3D seismic has revealed many of the deeper structures, particularly in the Western Desert, opening up new plays. Tertiary trends frequently run perpendicular to the older structures, but have fault transfer zones or other anomalies controlled by the older

J. Dolson (✉)
DSP Geosciences and Associates, London, 4205, UK
e-mail: John.Dolson@Delonexenergy.com; jcdolson@aol.com; johndolson@dspgeosciences.comcastbiz.net

Delonex Energy, London, 4205, UK

Lennox Drive, Coconut Grove, Florida, UK

Z. Hamimi et al. (eds.), *The Geology of Egypt*, Regional Geology Reviews,
https://doi.org/10.1007/978-3-030-15265-9_16

faults. Pliocene plays are almost exclusively confined to the Nile Delta. Substantial deep reserves have been found in Oligo-Miocene turbidites in the Nile Delta, with high porosity and permeability as deep as 7 km in high pressure-high temperature traps. Upper Egypt Lower Cretaceous rifts are lightly explored, and not extensively covered by either 2D or 3D seismic. Successful Red Sea exploration has been elusive, with only oil and gas shows and recoveries and no commercial fields, but remains an area of high promise. Since 2015, a new play in Miocene and Cretaceous carbonate reefs has developed in the offshore Mediterranean in the Egyptian side of the Exclusive Economic Zone (EEZ) deep water between Egypt and Cyprus and has unlocked the largest gas field in Egypt's history. This play, long overlooked, is currently the most active and promising exploration frontier in the country and surrounding Mediterranean basins. This chapter provides an overview of Egypt's petroleum geology, in part by examining the past exploration history, play concepts, changing paradigms and advances in technology which have more almost tripled the country's reserves in the last 17 years.

16.1 Introduction

The last comprehensive book dealing with the overall geology of Egypt was that of Said (1990). Since that time, an enormous amount of new subsurface data from wells, gravity, magnetics and seismic have dramatically altered our understanding of the petroleum potential of this region. A comprehensive look at the petroleum systems of Egypt using much of these data (Dolson et al. 2001) was expanded upon with a focus on the Nile Delta (Dolson et al. 2002b). An updated look at petroleum potential was covered in (Dolson et al. 2014).

Egypt's primary basins and provinces are shown on Fig. 16.1. The basin shapes are shown with three map overlays on Fig. 16.1. The background image is a relief map on economic basement (SEEBASE-Structurally Enhanced view of Economic Basement) produced in a multi-company funded effort in 2001 and 2002 by the Frogtech Company in Australia. The first published maps of this effort, which dramatically refined the deep basin structures, was that of Dolson et al. (2004) and Loutit et al. (2001). The faults shown, particularly those in the offshore Mediterranean, are deep seated crustal features discussed in Bentham (2011). The second overlay is a modified structure map on basement (area A on Fig. 16.1) completed in projects funded by El Paso Energy from 2009 to 2010 and published with their permission (Dolson et al. 2014; Wescott et al. 2011). The third overlay is a Gulf of Suez top of Eocene structure map (Area B on Fig. 16.1) which approximates the overall shape at depth of Precambrian basement. A basement map for the Gulf of Suez is illustrated from high resolution gravity and magnetics in Peijs et al. (2012). The Gulf of Suez Eocene structure map is also discussed in more detail in (Dolson et al. 2001, 2014; Wescott et al. 2016).

Over 10,600 exploratory wells have been drilled and over 1300 fields discovered. The Western Desert Basin shapes, in particular, have undergone extensive re-thinking as substantially better deep seismic imaging became available with new 2 and 3D seismic in the early 2000s. Both the Gulf of Suez and Western Desert provinces have suffered for years from poor deep imaging, limiting the ability to explore the deepest petroleum systems. While incremental improvements have been made in the Gulf of Suez, dramatic advances were made in the Western Desert, resulting in an explosion of wells and new field discoveries, dominated by Apache Egypt, which has found over 3 billion barrels of new oil and gas since 2001. However, the biggest reserve adds have been in the Nile Delta (Fig. 16.2).

In 2001, Egypt had a reserve base of 15.7 BBOE, which, as of this writing has tripled to 35.9 BBOE, with most of those new reserves in the Nile Delta and Western Desert. In Dolson et al. (2001) statistical yet-to-find analysis predicted 85–100 TCF (14.6–58 BBOE) of future gas reserves, a number which was deemed excessive high by many. The database in this chapter (primarily from IHS Energy EDIN data) is complete to early 2016, and shows that the minimum reserve growth predicted in 2001 has already been reached and exceeded. Dolson et al. (2014) provided a revised yet-to-find of 218 TCF (37.6 BBOE), in line with recent publications by the USGS (Kirschbaum et al. 2010; Schenk et al. 2012). We provide a third update later in this chapter, based on the new Zohr carbonate gas discovery in the Mediterranean (Cozzi et al. 2017; Esestime et al. 2016; Nikolaou 2016). Estimates for Western Desert reserves shown on Fig. 16.2, may be low, as some industry experts estimate as high as 5.6 BBOE recoverable discovered to date, with a yet-to-find that may reach 7 BBOE.

This chapter explores the petroleum geology of Egypt through the eyes of the explorers who have unlocked many of its trends, as well as the fundamental basin structure and stratigraphy. Figure 16.2 shows that exploration successes have proceeded in five phases, discussed in detail in the next section. Jumps in volumes of hydrocarbons found in any basin can be attributed to (1) changes in concepts and/or technology (2) changing business terms making some trends finally worth the effort to explore (3) rarely, by blind luck. The jumps in the creaming curve shown on Fig. 16.2 reflect evolving concepts of basin evolution and potential followed by increasingly better seismic and deep imaging and finally,

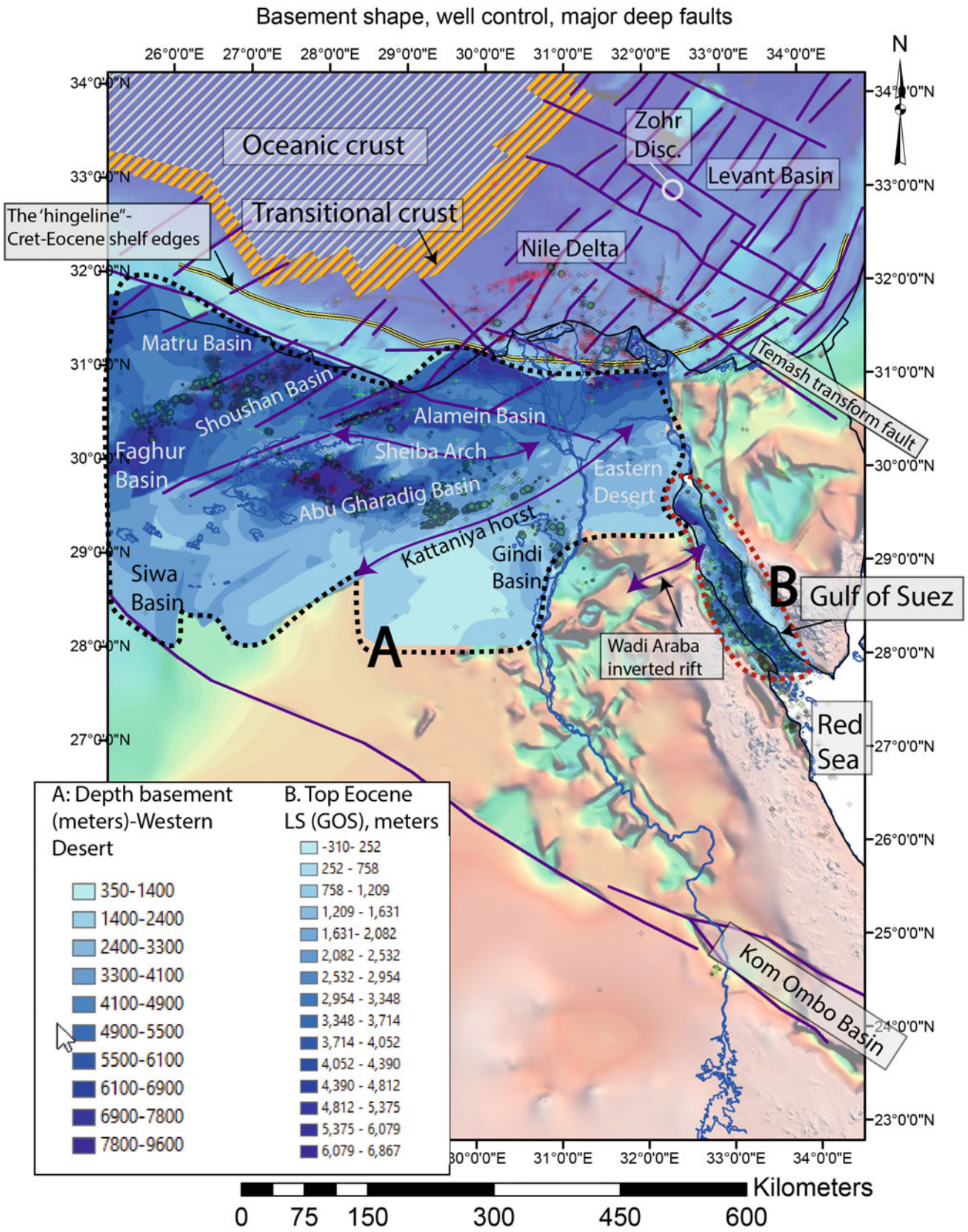

Fig. 16.1 Basin shaped map, well control and major provinces. Faults shown are major crustal lineaments. The background image is a shaded SEEBASE basement relief map. Area A is a structure map on basement (Western and Eastern Desert) and B, structural relief on the top of Eocene Limestone in the Gulf of Suez

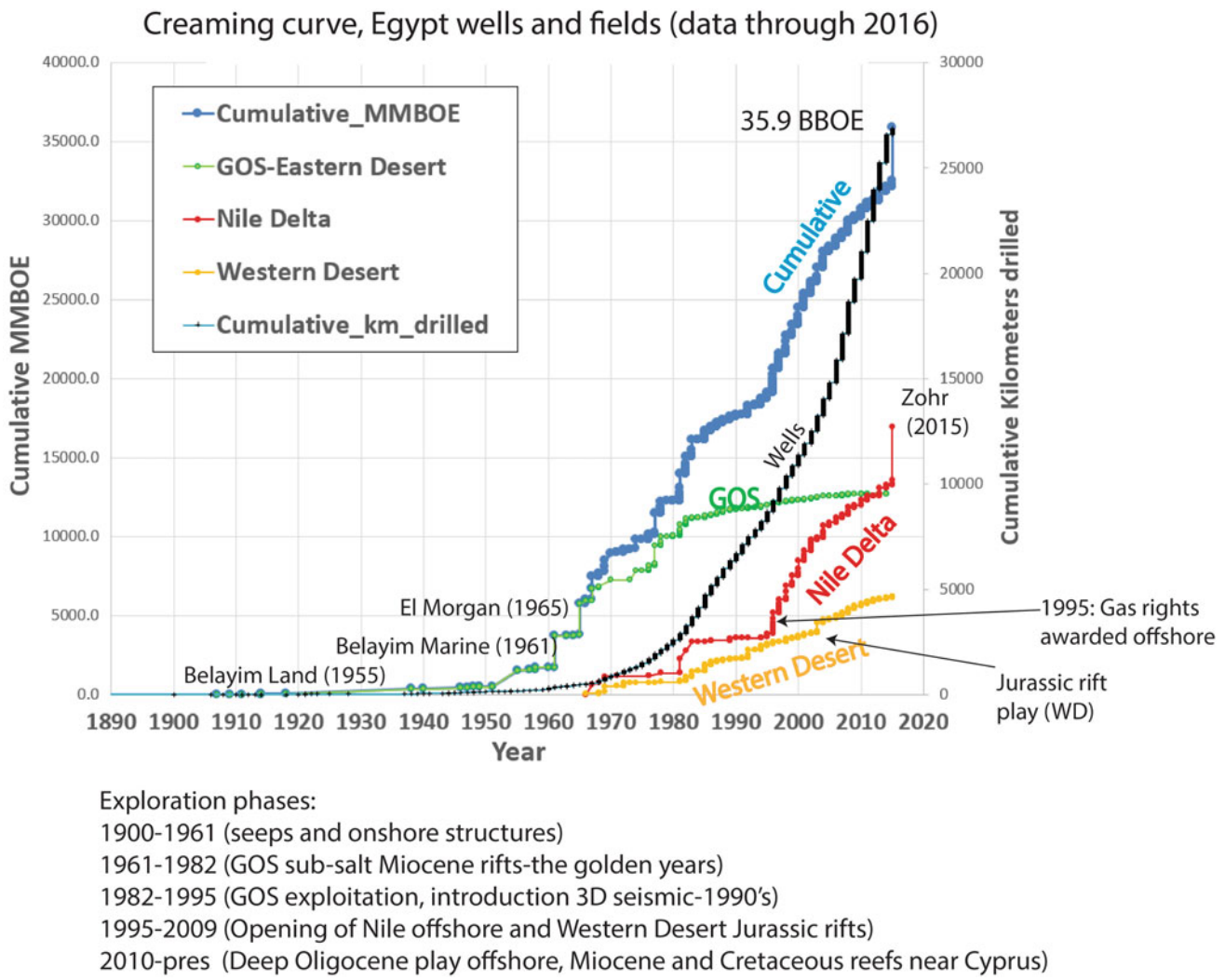

Fig. 16.2 Creaming curve showing cumulative MMBOE reserves versus time and reserve growth by province

the awarding of gas rights in the offshore Mediterranean deep water. Luck has played only a minor role in this reserve growth.

16.2 Overview of Field Sizes and Fluids

Figure 16.3 shows the distribution of oil and gas fields by fluid ratios. The Gulf of Suez (GOS) is primarily an oil province, with some larger gas fields in the SE corner. GOS fields produce from pre-rift Eocene through Paleozoic strata on large fault blocks and syn-rift Miocene strata on both structural highs and flank traps. Western Desert basins are mixed oil and gas, mostly in fault-related closures. By far the deepest basin is the Abu Gharadig, which has deep, untested traps below established Mid-Cretaceous reservoirs. Pay zones range from the Upper Cretaceous Khoman Formation through Jurassic and Paleozoic strata, mostly in fault-related closures, including flower structures and inverted basins. The Nile Delta, in contrast, is a Tertiary gas province and contains some of the largest fields in Egypt. Not shown are the productive gas fields in the Levant Basin, which have largely been discovered within the last decade, and provide a NE extension of the Nile Delta petroleum system (Belopolsky et al. 2012; Bentham 2011; Cunningham 2011; Gardosh 2011; Gardosh et al. 2009; Roberts and Peace 2007; Schenk et al. 2012). The productive limit of the petroleum system is presumed to be west and north of the transitional crust line and south of the Troodos Ophiolite in Cyprus. Considerable 'running room' remains outboard of the major Nile Delta clastic play fairways.

Upper Egypt has established pays in Lower Cretaceous rifted sandstones of the poorly defined Kom Ombo Basin. The Red Sea has yet to be found productive, but good shows of recoverable oil typed to Miocene source rocks have been tested by Amerada Hess. These trends are described in more

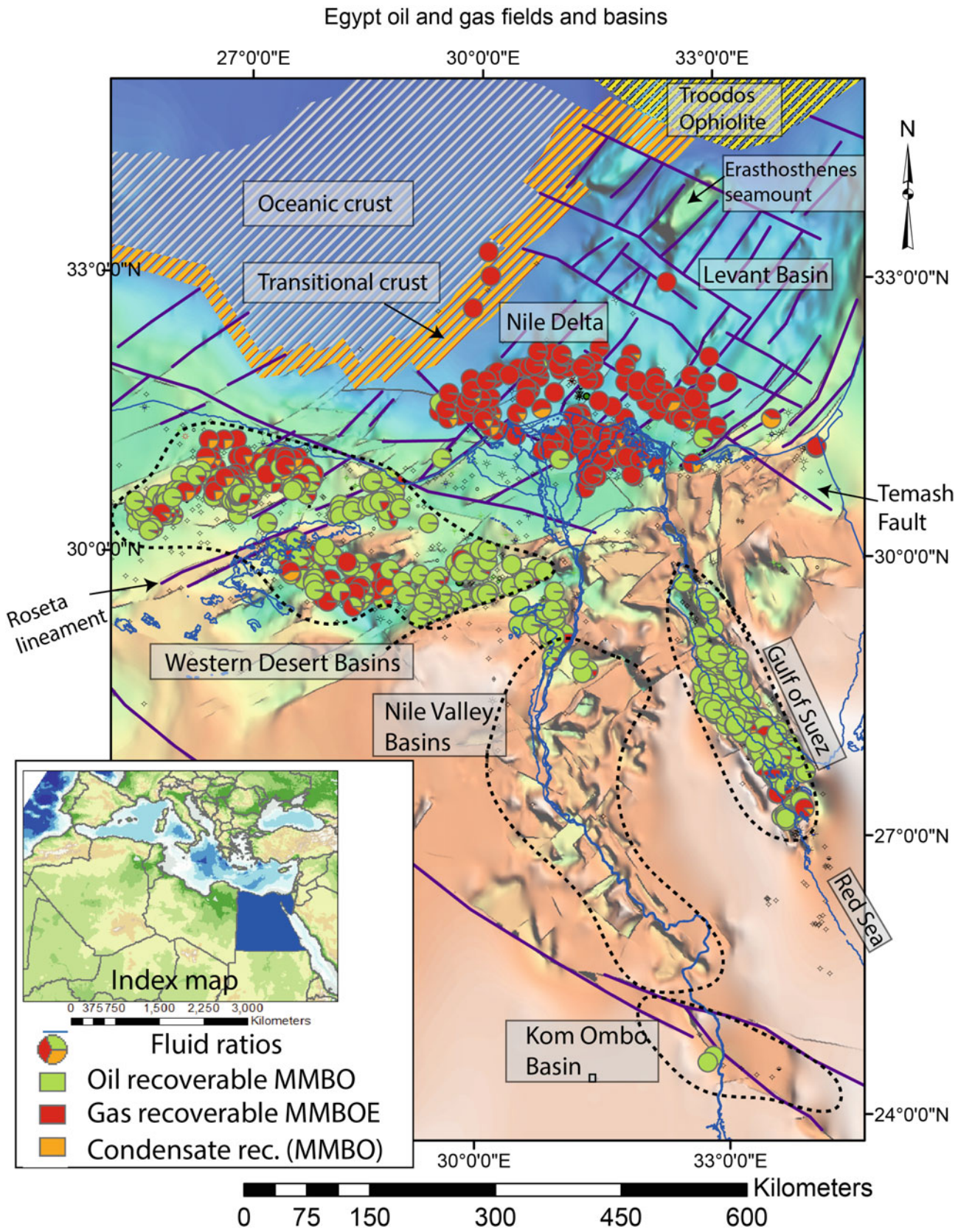

Fig. 16.3 Fields by fluid phase ratios and regional crustal features

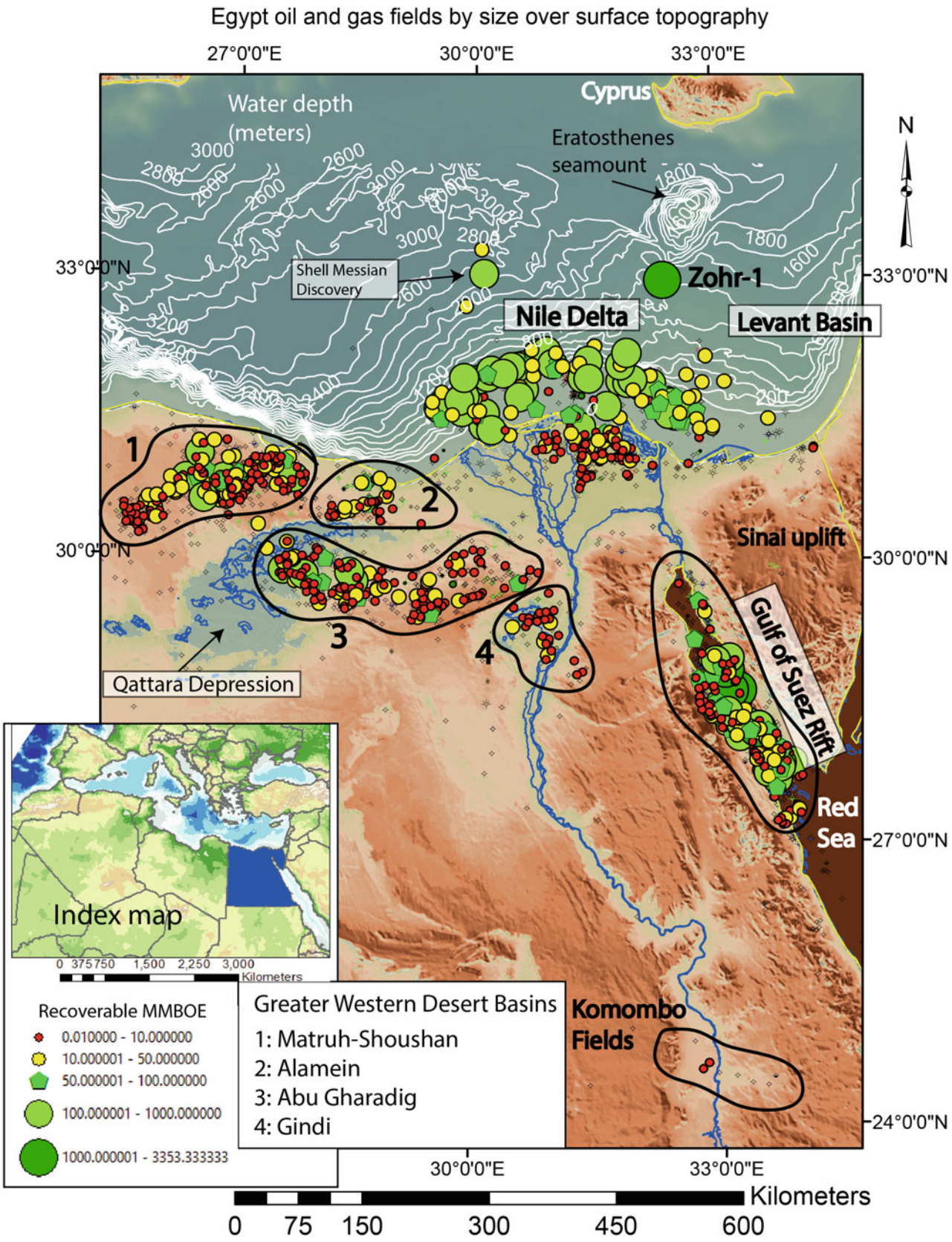

Fig. 16.4 Fields classified by recoverable MMOE overlying surface topography

detail in Dolson et al. (2014), Gordon (2012), Gordon et al. (2011) and Wood et al. (2012). The Kom Ombo Basin remains intriguing, but land-locked with no pipeline and struggling on reservoir quality and lateral seal (Dolson et al. 2014) and (Editors 2012). The nearest Cretaceous age rift with a similar orientation and fill is far to the south in the Muglad Basin of Sudan (Mohamed and Mohammed 2008; Mustafa and Tyson 2002; Salama 1997).

There are efforts to explore the red sea, including the acquisition of about 10,000 km of 2D seismic and gravity and magnetic data, done as a multiclient project. Also, the ministry is going to announce the first bid round in December of 2018. This should help realizing the potential of the Red Sea region. Upper Egypt and Red Sea trends are not further elaborated on.

Figure 16.4 shows field distribution by recoverable MMBOE. Also shown is a shaded relief map of the surface digital elevation model and offshore bathymetry of the Nile Delta. Clusters of Western Desert production are located within the greater Matruh, Shoushan (1), Alamein (2), Abu Gharadig (3) and Gindi (4) basins. The giant Zohr discovery (30 TCF) is located far outboard of the Nile Delta clastic fairway and is a new play opener, consisting of large stacked Miocene and Cretaceous isolated carbonate platform reefs fringing the Eratosthenes seamount. The northwest extension of the Nile Delta petroleum system is marked by a large sub-economic Messinian gas discovery near to or overlying transitional ocean crust. The gap between the southerly Nile Delta clastic trend and these northern fields is thus an untested petroleum fair way in water depths from 1200 to 2600 m. Egypt's largest and oldest oil fields are located in the Gulf of Suez rift, have had only small fields added in the last decade.

Exploration efforts onshore, particularly in the Western Desert, have been hampered both by its large aerial extent, a lack of high quality and extensive 2D seismic coverage and desert dune topography. In addition, much of the Western Desert is covered with mines and unexploded ordinance from the battle of El Alamein in WWII. These hazards require extensive surface studies and hazard removal before acquiring seismic or drilling wells. Some areas, such as the Qattara Depression, have difficult, muddy and swampy terrain making seismic data difficult to obtain or even traverse in 4-wheel drive vehicles. Prior to 2000, very little seismic data existed in the Gindi Basin, which is now a proven productive Cretaceous petroleum system. In addition, no pipelines exist in Upper Egypt to transport oil from the Kom Ombo Basin, which has to be trucked out. All the surface basins in Egypt have gentle dune or desert topography overlying deeper structures with no surface expression. Dune fields often make seismic acquisition difficult.

16.3 Stratigraphic Organization of the Petroleum System

Figure 16.5 shows the chronostratigraphic settings of the major basins of Egypt. Egypt's tectonic history can largely be defined by 14 major events. The deepest viable reservoirs are Cambro-Ordovician glacial deposits largely deposited

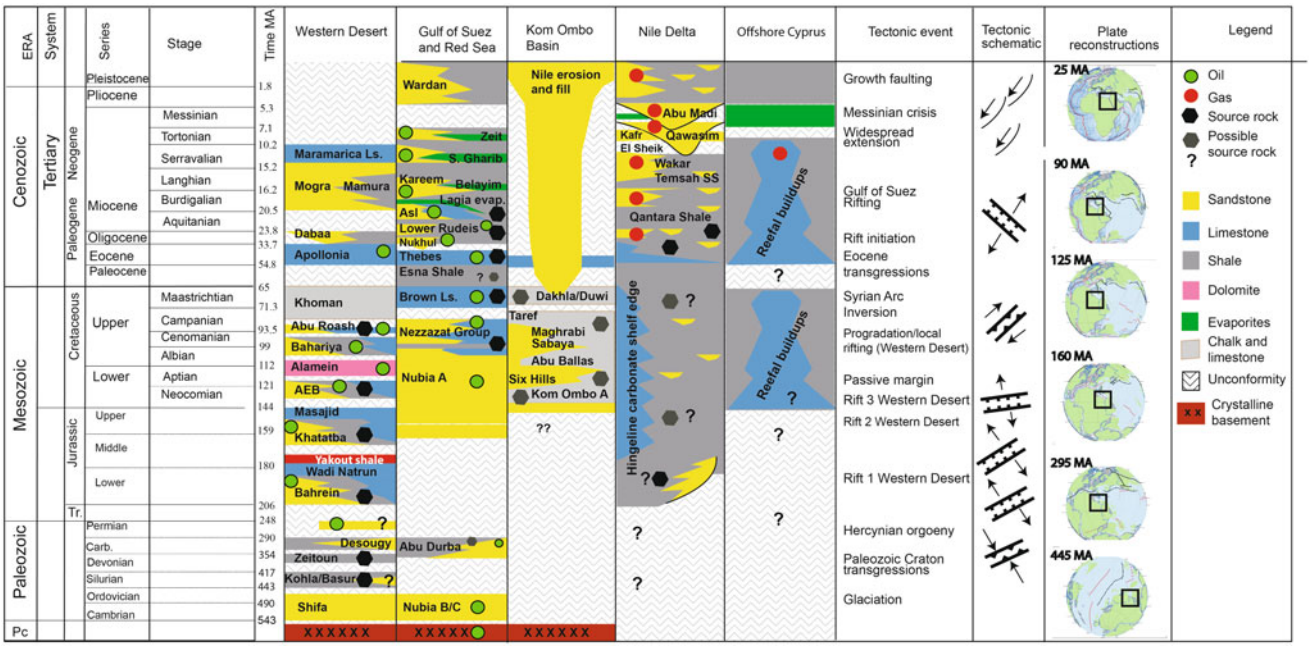

Fig. 16.5 Nomenclature and petroleum systems of major basins in Egypt

across a broad craton which was subsequently repeatedly buried and exposed during multiple transgressions in the Carboniferous. In early Permian time, regional compression and uplift associated with the Hercynian orogeny and formation of Pangea, created widespread unconformities which eroded and buried these earlier features. To the west, in Libya and Algeria, sub-Hercynian traps consist of structural and stratigraphic closures often sourced by large glacially scoured valleys that were subsequently infilled with Silurian and Devonian source rocks (Boote et al. 1998; Dauphin et al. 2007; Dixon et al. 2018; Dupouy et al. 2017; Heron 2009; Klett 2000; Traut et al. 1998). Similar stratigraphic settings must surely exist across northern Egypt, but have not been detailed yet from unpublished recent seismic and well control.

Apache Egypt has reported (Joe Versfelt, personal communication) new Paleozoic pay zones and 'surprises' in the complexity of the burial history and distribution of sub-Hercynian stratigraphic and structural features in the Western Desert. To date, the charge of the Paleozoic reservoirs appears to largely from fault juxtaposition with mature Jurassic source rocks. Versfelt also reports that basement type is highly variable and older depth to basement maps need updating, with at least two older volcanic events and basement variability complicating gravity and magnetic signatures.

Some of the new 3D seismic showing deep, unexplored plays was published, along with a discussion on the potential in (Dolson et al. 2014). Although the source of the oils in the Paleozoic reservoirs remains unpublished and speculated as Jurassic, Paleozoic source rocks are proven and discussed in Dolson et al. (2014), but the timing of potential expulsion and migration is poorly understood. Significant changes in ages and Paleozoic tectonic features from new age dating and seismic are suggested in Bosworth and Stockli (2017). Understanding and mapping these changes will require release of a lot of the new subsurface data to re-write the story of Paleozoic evolution across Egypt. Further Paleozoic geology will not be explored in this chapter, and certainly, when proprietary company data are released, substantial advances will be made in our understanding of the geology of the deepest viable reservoirs in the Western Desert.

In Early Jurassic time, rifting, associated with the breakup of Pangea, created the deep NE-SW and some E-W trending basins shown on Fig. 16.1. At least 3 phases of rifting are documented across the Western Desert. The first two rifting events responded to an overall NW-SE extension direction which was also influenced to an unknown degree by underlying Paleozoic tectonic fabrics and older fault systems. As shown on Fig. 16.5, Rift 3 in the Western Desert was from a more north-south extension, with resulting rift geometries trending in a more east-west orientation, often oblique to the underlying Cretaceous rifts. These rifts, particular the Rift 2 event, filled with coaly and shaley estuarine source rocks of the Khatatba Formation, a major contributor to the oil and gas recovered in the Western Desert. A more extensive treatment of the distribution of these rifts, source rock and maturation is given in Dolson et al. (2014) and Wescott et al. (2011).

Importantly, these deep rift trends extend northeastward under the Nile Delta and into the Levant Basin, where they set up deep structural traps formed by overlying drape of Oligocene and Miocene strata. It is uncertain what contribution, if any, their deep Jurassic and Cretaceous source rocks might have on fluids in the Nile Delta or how deep the petroleum system extends beneath the delta, although Miocene and Pliocene oils on shore in the Nile Delta have been attributed to Cretaceous and Jurassic source rocks in two fields (Leila and Moscariello 2017). Some of the largest fields in the delta, like the Temsah-Akhen field, lie over transform faults formed as part of the Jurassic rifting events (see Temsah fault trend, Fig. 16.1). These structures end up oriented NW-SE over the deeper lineaments.

During lower through upper Cretaceous time, widespread transgressions buried many of the older structures as a result of regional transgressions accompany periods of global sea level rise caused by a 'hot house' climate, when polar ice caps ceased to exist. These cratonic transgressions deposited source rocks associated with the AEB, Alamein, Bahariya and Abu Roash formations. Most of these source rocks are only mature in the Abu Gharadig Basin, but provide a substantial contribution to Bahariya and Abu Roash reservoirs in that basin.

By Upper Cretaceous time, northward movement of the Egyptian plate created a north-south compressional stress creating widespread dextral shearing and basin inversion across northern Egypt. Large inverted rift grabens like the Kattaniya Horst and Wadi Araba uplift (Fig. 16.1) were subsequently developed.

During these inversions, the Khoman chalks were deposited across structural lows, forming a regional seal to the Western Desert petroleum system. The time-equivalent Upper Cretaceous Brown Limestone and Esna Shale form important source rocks in the Gulf of Suez.

Periods of widespread exposure, karsting and erosion followed in the Paleocene until another 'hot house' event in the Eocene deposited widespread carbonates across Egypt. The regional carbonate shelf edges at both Mid-Upper Cretaceous and Eocene time are located near the 'hingeline' shown on Fig. 16.1. North of this feature, only deep-water shales and condensed section were deposited. The 'hingeline' is an important structural and stratigraphic shelf edge,

as it marks the abrupt transition to deep water Oligo-Miocene turbidites to the north with more continental facies or equivalent unconformities to the south.

Eocene source rocks of the Thebes Formation are significant in the Gulf of Suez and form rich, but thermally immature source rocks of the Apollonia Formation in parts of the Western Desert. They are heavily entrenched by Oligocene canyons across the 'hingeline', and these canyons provide major sediment input points for Oligo-Miocene clastics into the Nile Delta (Dolson et al. 2014).

Early Oligocene time was dominated by NE-SW extension, creating the opening of the Gulf of Suez and Red Sea rifts. Miocene source rocks were deposited in syn-rift lows and provide additional source rocks to the Miocene reservoirs of the Gulf of Suez. Regionally, Egypt was tilted northward and large volumes of clastics began to move north through paleo-Nile valleys, translating large amounts of coarse sediment offshore. Major unconformities in outcrop strata (Dolson et al. 2002a) reflect these periods of uplift and erosion. The gross paleogeography of Eocene and Oligocene strata is illustrated in Dolson et al. (2002a) and Dolson et al. (2014).

Commencing about 8 MA, regional sea level drawdown, thought to be due a tectonic closure of the Straits of Gibraltar, created the Messinian crisis, during which as much as 550 m of sea level lowering occurred. Widespread salts and evaporites were subsequently deposited across the barren Mediterranean Basin. Around the Mediterranean flanks, huge subaerially carved canyons developed. During subsequent episodic transgressions, these canyons filled with fluvial, estuarine and marine sediments. These valleys were not fully buried until about 3.3 MA, when a major Pliocene flooding event transgressed within the paleo-Nile valley as far southward as Aswan. The resultant complexes of stacked incised valley deposits form stratigraphic and structural traps in the Abu Madi and Qawasim formations (Dalla et al. 1997; Palmieri et al. 1996). An interesting global discussion of the Messinian crisis is given in Pigott et al. (2014) and Leila and Moscariello (2018).

Pliocene growth faulting and progradation set up the youngest reservoirs and traps in the Nile delta. Most of the reservoirs are in turbidite slope channels and growth faults, with a few structural traps onshore in shallow marine strata. Excellent summaries of the play types and traps include (Boucher et al. 2004; Cross et al. 2009; Kellner et al. 2018; Samuel et al. 2003). A good summary of some of the deeper, older structural grains beneath these Pliocene fields is that of Monir and Shenkar (2016).

Until recently, however, the distal carbonate trends in the Exclusive Economic Zone between Egypt and Cyprus were disregarded as having potential, despite their obvious signature on seismic. In 2015, ENI successfully tested these carbonates with the Zohr-1 discovery (Figs. 16.1 and 16.4), opening a new play fairway which is active as of this writing.

16.4 Exploration History

Perhaps one of the most famous quotes of the explorer is that of Wallace Pratt: "Where oil is first found is, in the final analysis, in the minds of men." This is certainly true in Egypt, where exploration has had several periods of spectacular growth owing to new concepts and acquisition of data. In addition, changing business terms also spurred discovery, like awarding gas rights in the offshore deep-water Nile Delta in 1995 (Fig. 16.2).

The earliest exploration efforts (Fig. 16.6a) were localized near surface seeps long used for centuries by Egyptians for lamps, grease and other products. Three seminal publications detail the history of early exploration in Egypt (Hegazy 1992; Matbouly and Sabbagh 1996; Moussa and Matbouly 1994). The Gulf of Suez exploration history is further briefly summarized in Wescott et al. (2016). These seeps are along the flanks of the Gulf of Suez. The first true exploration success was an accident in 1868, made by a French mining company digging for sulfur. Commercial oil was discovered at Gemsa Field in 1908.

Opening a new basin is a difficult thing to do, particularly in countries like Egypt where scant drilling had been done since the first well was spudded in 1886. By the end of 1961, only about 290 wells had been drilled anywhere in Egypt. However, the discovery of the Ras Gharib Field (1938 by Anglo-Egyptian Oil), Belayim Land by IEOC (1955), as well as Belayim Marine (1961, IEOC), had put Egypt 'on the radar screen' of other operators. All these traps are on tilted Miocene rifted fault blocks.

In the early 1960s Amoco Production Co. (now BP) established an office in Cairo under the leadership of a young geologist, Jim Vanderbeek (1926–1993). The author once asked Vanderbeek why he selected Egypt for one of the company's only international venture. At this point in time, Amoco was largely only a USA based organization. His response was simple. "There was big oil in Libya to the west and big oil in Saud Arabia to the east, so I figured there had to be big oil in the middle, in Egypt". Amoco's senior management remained skeptical, however, and only gave Vanderbeek permission to drill a few wells. Gravity and magnetics, plus sea floor topography, were the primary tools used for offshore exploration. Critically, large salt domes overlie the deep rift blocks and wells drilled at the crest of the salt closures frequently missed the deeper tilted fault blocks. Amoco's first wells, spudded in June and September of 1964, were dry holes but with significant oil and gas

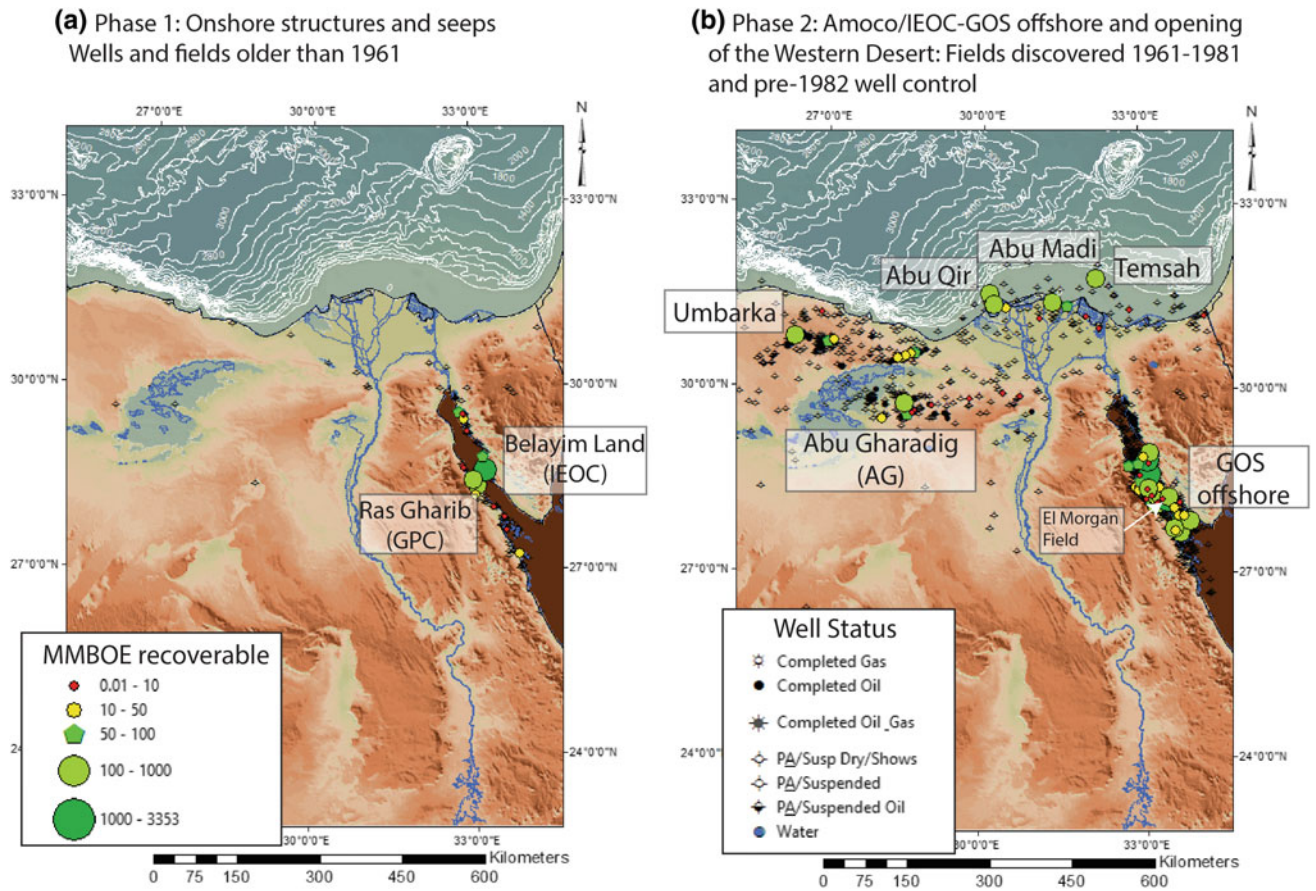

Fig. 16.6 Phase 1 and 2 of exploration history based on Creaming curves (Fig. 16.2)

shows. Chicago management ostensibly decided to 'pull the plug' and abandon the country, but Vanderbeek insisted he still had a commitment well to drill for water if he was not able to find oil. So, in January of 1965, the discovery well of the giant El Morgan Field was staked as a 'exploratory water well'. It logged over 2000 ft. (609 m of oil pay) with over 1.5 BBO reserves!

Vanderbeek then flew to Chicago to tell the board that his "little water well encountered 4–5 feet of pay". He then laid an electric log out on the floor at a scale of 1 ft = 500 ft of well log and paced the log off with his feet. "Here's one foot of pay, now another, now 4–5 feet of pay". His request for pipeline money was not immediately granted, but he used local Egyptian labor to put a line in overland. When the money was approved, he informed the board that he had already gotten the field onstream and pipeline built.

His challenges were not behind him, however. In 1967, during the Arab-Israeli war, Israeli gunboats seized the El Morgan Field. Vanderbeek refused to evacuate during the war and continued to look for ways to develop the Gulf of Suez and explore elsewhere in Egypt, particularly the Western Desert. It took enormous work and diplomacy to keep the Giant El Morgan Field online during this time period, regardless of war conditions, completing negotiations between President Nasser, Vanderbeek and the Israeli government. In contrast, IEOC lost 220,000 BOPD production from 1967 to 1973 when Israel seized its Abu Rudeis and Belayim fields (Sayed Matbouly, personal communication). In recognition for his service and leadership in the Energy sector, he was awarded Egypt's highest civilian honor, the Order of the Republic (Work 1994).

In the mid 1970s he returned to head up exploration in Amoco's Denver Region, where the author had a chance to work with him before his death in 1993. He was an extraordinary leader and oil finder, who opened up the Wyoming/Utah overthrust belt giant fields, thrust belt fields in the Arkoma Basin and developed the first large giant coal gas field in the San Juan Basin. He epitomized the aggressive, creative leader and thinker that is a rarity in any oil company, but a necessary ingredient to success.

A period of extensive exploration offshore followed with 2D seismic data from 1962 to 1981, with the bulk of the major oil fields found during this period (Fig. 16.6). During this same period, the Western Desert saw an explosion of

activity, but also many dry holes. Exploration commenced with widespread aeromagnetic surveys and CDP (common depth point) seismic of low fold and quality. From 1963 to 1973, Amoco, Phillips and GPC drilled over 125 wells, discovering the Alamein oil field (1966), Abu Gharadig oil field (1969), and Umbarka Field (1969) all of which produced from Lower and Middle Cretaceous reservoirs. Seismic quality remained the obstacle to successful deep exploration, plus a focus on the Cretaceous based on oil shows and established pays. Structure maps on the Alamein Dolomite became the primary means of exploring, as this horizon was reasonably imaged with seismic. Dolson et al. (2001) illustrate a typical Western Desert seismic line showing poor imaging below the Alamein dolomite, in direct contrast to images from 3D seismic in Dolson et al. (2014).

During this same period, active exploration discovered the Abu Qir, Abu Madi and Temsah fields in the Nile delta. Abu Qir Field proved up the Pliocene and Messinian potential and Abu Madi Field opened up incised valley plays in a major Messinian canyon. The Temsah Field, however was not recognized for the 4–7 TCF (690–1200 MMBOE) reserve base it has today. The discovery well (1977) was staked as an oil well and tested a huge closure (Dolson 2016a, b). The well encountered over-pressured gas, condensate and water in Serravallian (Miocene) sandstones. The presence of water was discouraging, as the closure far exceeded the column in the well, suggesting either compartmentalized reservoirs or and underfilled structure. A subsequent offset (Temsah-2) was drilled to test up-dip of the poorly imaged Temsah-1 well, but came in at a similar elevation to Temsah-1 but with no water leg. As Mobil did not have the gas rights, the lease was abandoned and not picked up again until 1992 by IEOC and Amoco, who shot a 3D survey and drilled an additional discovery, with pays at both the Serravallian 'Temsah Sandstone' and overlying 'Wakar Sandstone'. Additional drilling by IEOC and Amoco established deeper and deeper gas to the northeast on the structure, with variable levels of water-bearing sands, usual at the base of the reservoirs.

Earlier interpretations considered these water zones 'perched' as pressure versus depth plots showed the gas columns were in pressure continuity, but the water legs were slightly over-pressured. Perched analogs are covered in a number of publications (Cade et al. 1999; Cross et al. 2009; Marcou et al. 2004; Shang et al. 2009). Methods of detection of perched versus tilted hydrocarbon/water contacts are summarized in Chapter 4 of Dolson (2016b).

It was not recognized by BP (formerly Amoco) until the mid-2000s that deep basin hydrodynamic flow was responsible for developing a tilted gas/water contact, pushing the major gas accumulation off the flank to the northeast. Hence, it took over 25 years to recognize the true size of the giant Temsah-Akhen complex. A Temsah hydrodynamic model is discussed later in this chapter.

Phase 3 (Fig. 16.7a) shown generally reflects a relatively slow expansion of the Western Desert and Nile Delta fields and a genuine 'slow down' in the finding rates and field sizes in the Gulf of Suez. During this time, most exploration continued to be carried out with 2D seismic of variable quality, with extremely difficult sub-salt imaging in the Gulf of Suez. Commencing in the early 1990s, broader 3D surveys came into existence in all the basins. In the Western Desert, Phoenix and Shell discovered Jurassic reservoirs in the Salam and giant Obaiyed Field. However, the trap is (and remains) difficult to image and the reservoirs are generally tight and largely impermeable. Obaiyed did, however, prove that a Jurassic petroleum system existed. In the Nile Delta, Wakar and Port Fouad fields confirmed more Miocene pay zones in deeper structures.

The Gulf of Suez discovery rates had dropped considerably by the early 1990s. Hundreds of wells had tested the best structural anomalies. Amoco, which had undergone extraordinary success until 1989, drilled 32 dry holes in a row by the end of 1993. Production had dropped to about 400,000 BOPD (down from a peak of 600,000) and fields were undergoing steep declines. The author arrived in Egypt as Senior Geologist to GUPCO in 1994, with the ominous warning to all staff that "you have 3 years to turn exploration around, halt the production decline, or go home."

GUPCO staff completely reorganized their work processes and technology, moving from paper maps and cross sections to workstations and 3D seismic. A super computer (primitive by today's standards) helped accelerate seismic processing and use of innovative techniques to try to remove the ubiquitous multiples created by as many as 28 layers of salts and sandstones in the shallow section. Data integration of all disciplines was instituted, along with extensive additional training, outcrop analog field work, rigorous peer reviews and a formal prospect risk assessment. Quantitative dipmeter assessment and visualization of dip directions on seismic helped find new, hard to visualize, fault traps.

The change in work processes, fortunately, worked. In the field development teams, the value of working in integrated teams was documented by Hughes et al. (1997). Exploration results jumped to a 70+% success rate and a reversal of a 20% decline rate in the giant October Field. Collectively, teams held production rates at 360,000 BOPD for 18 months with no decline, a significant accomplishment despite a natural decline rate of 20% without intervention. Numerous company awards flowed to both the exploration and production teams, including Amoco's First Place, World Wide Exploration Excellence award in 1997. The exploration story

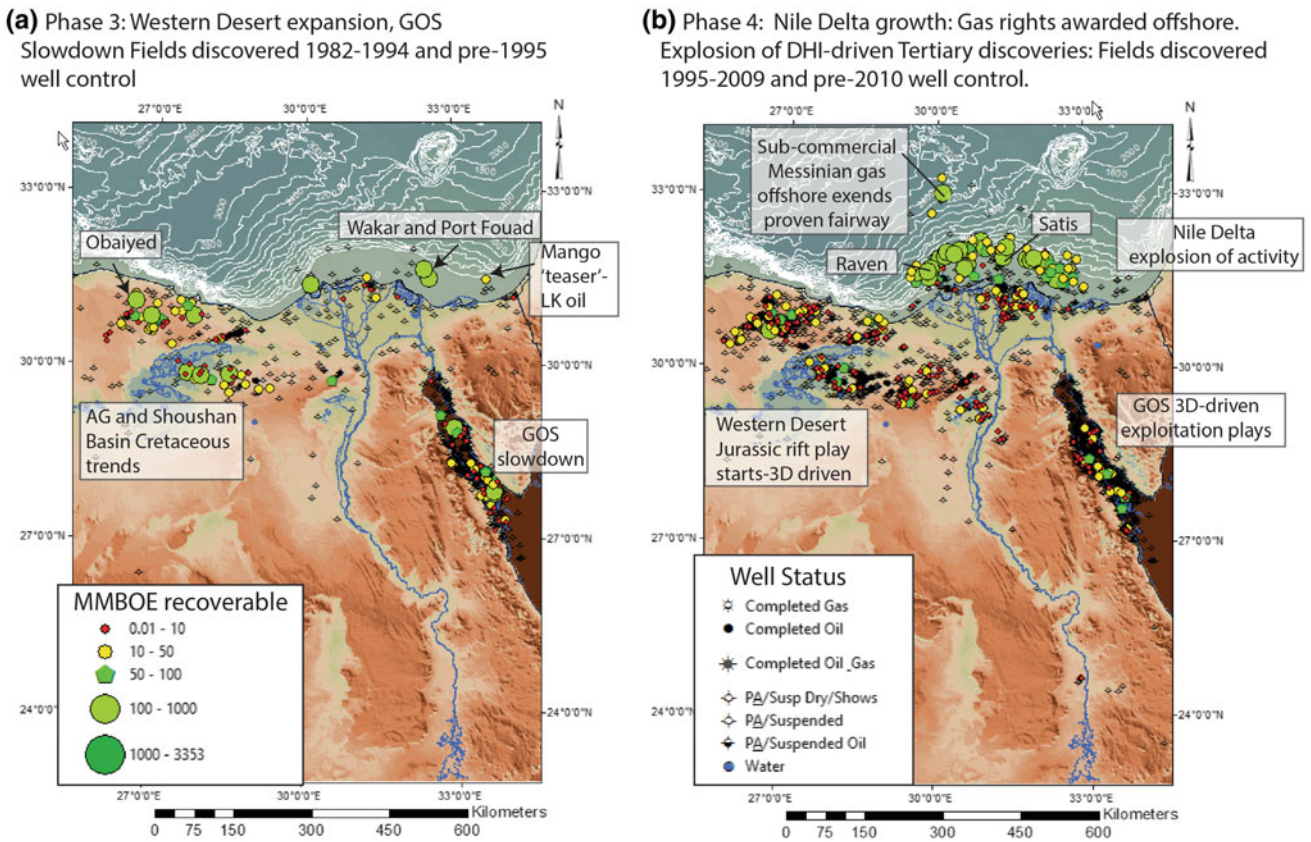

Fig. 16.7 Phases 3 and 4 of Egypt exploration history

is documented in more detail in Dolson et al. (1997). The methods used to successful exploit smaller reserves in a mature basin are typical of things all companies in the Gulf of Suez have had to do to find new reserves in this complex basin, where poor seismic imaging is the norm, not the exception. The downside to our success was losing our top Egyptian staff to other companies eager to capitalize on their skills and unique training!

Phase 4 (Fig. 16.7b) illustrates the explosion of activity in the deep-water Nile Delta after deep water gas rights were awarded and DHI driven 'bright spot' exploration commenced in Pliocene trends turbidite channels. BP opened up the deeper Miocene-Oligocene trends in 2003 with the discovery of the Raven Field followed by Satis Field in 2008 (Dolson et al. 2014). The Satis-1 well is particularly important as it proved darcy permeability Oligocene at 6.5 km depth in turbidite sandstones in high temperature, high pressure reservoirs. In addition, source rock and oil-to source correlations from the Satis-1 well have shown that the gas fields of the eastern Nile Delta are sourced from Oligocene shales with low HI values which yield dominantly gas with a low GOR content. The source of the western Nile Delta fluids remains unknown.

During Phase 4, Apache dramatically expanded discoveries in the Western Desert. Apache entered Egypt in the early 1990s, purchasing Qarun Field in the Gindi Basin from Phoenix Exploration. With no history of exploration in Egypt, they aggressively acquired 2D seismic in many locations, including a broader survey of the Gindi Basin. Additionally, they entered into partnership with other companies in the Shoushan Basin and purchased Repsol's fields in 2001. Their first 30+ wells were dry holes, drilled entirely on 2D data and with limited fundamental understanding of the deep basin potential, a common theme with all companies operating in the Western Desert. Apache management called a 'time out' and initiated a country-wide synthesis of deep basement architecture from merged gravity, magnetic and key seismic surveys from 5 participating companies, including the Amoco teams I was part of. The resulting product (SEEBASE, EARS phase 1 study), developed by the Frogtech company in Australia (then SRK consulting) established the first real delineation of the deeper Jurassic

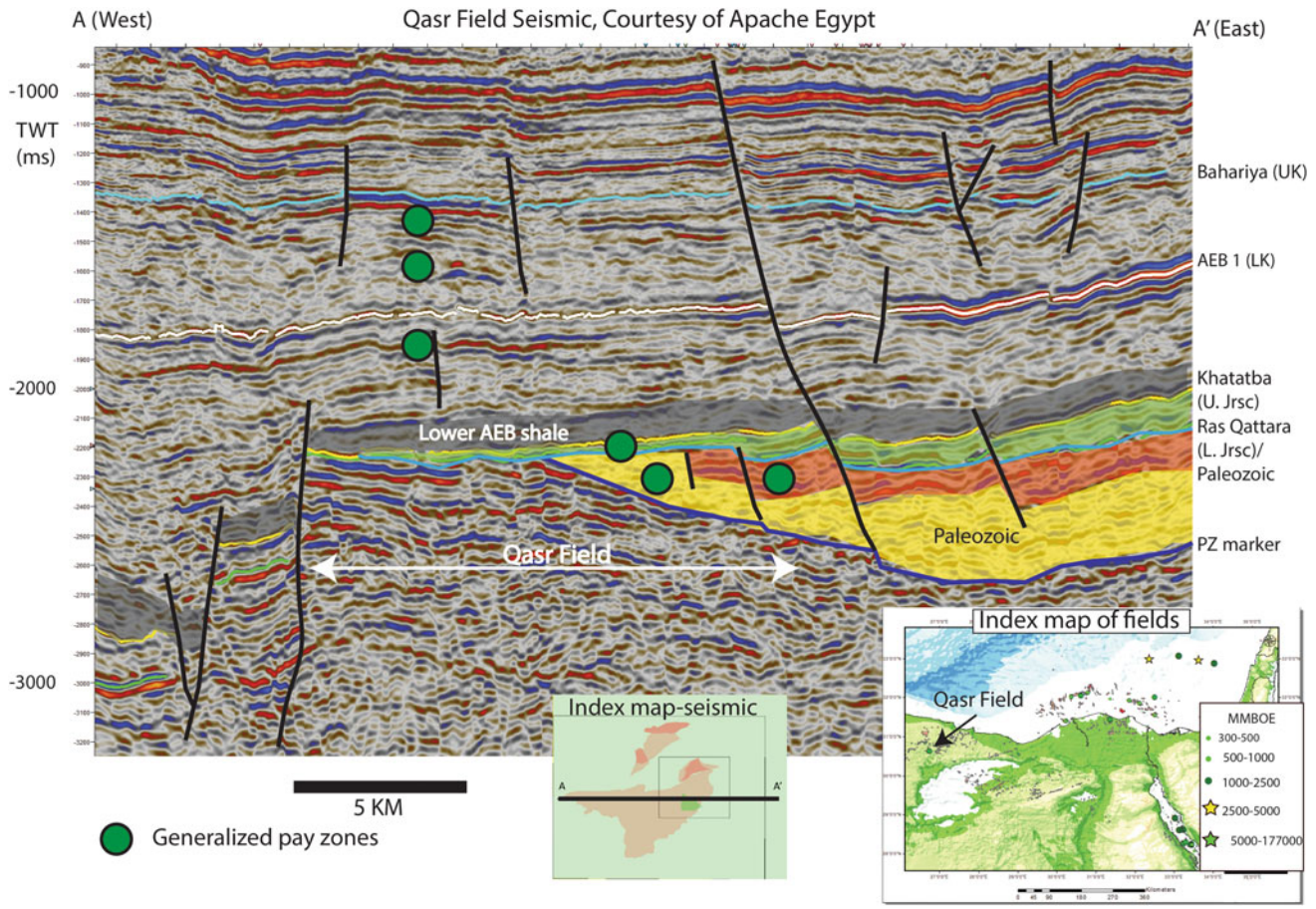

Fig. 16.8 Qasr Field seismic and giant combination trap

rifts. A second study, completed in 2002 (MARS, Phase II) extended the basement mapping across the offshore Nile Delta. In the last decade, drilling has confirmed some of these trends and also resulted in substantial changes in some areas, but with data not yet released by private companies. Despite this, the deeper play was well enough defined to spur activity.

Apache aggressively pursued acreage acquisition, seismic and the purchase of smaller fields across the province based on this work. Interestingly, the other 4 companies participating in the studies failed to capitalize on the concepts of deeper trends oblique to shallower structures. This included BP, during the transition from Amoco to BP staffing, with serious internal disagreement over the full potential of the basin. The 'conventional thinkers' won the day at BP and other companies, and Apache was left with little opposition to expand its position.

Apache's acquisition of large 3D seismic surveys paid off, when they successfully recognized the deep Jurassic rifts running oblique to the shallow Cretaceous structures. In 2003, those other companies that failed to capitalize on the SEEBASE study, watched, chagrined, as Apache tested a deep combination trap and discovered the giant QASR field (3 TCF, 130 MMBO oil and condensate), the largest onshore gas field in Egypt (Fig. 16.8).

Figure 16.8 seismic (courtesy of Apache Egypt and KPC) shows a complex erosional trap over an inverted Jurassic and Paleozoic section that produces at multiple levels, including the shallow Bahariya reservoirs that drape over the deeper structure. The Lower AEB shales form the top seal and the faults and juxtaposition to these shales the lateral seals. More significantly, this deeper structure was not imaged on 2D data, where historically, resolution at the Bahariya level and below were poor at best. In speaking with the first staff to drill this feature their general comment was "we couldn't believe it; the deep trends were nearly perpendicular to the shallow trends."

While other companies continued to use Alamein level structure maps to drill deeper targets on poor dated, Apache had making the leap by trying something different and

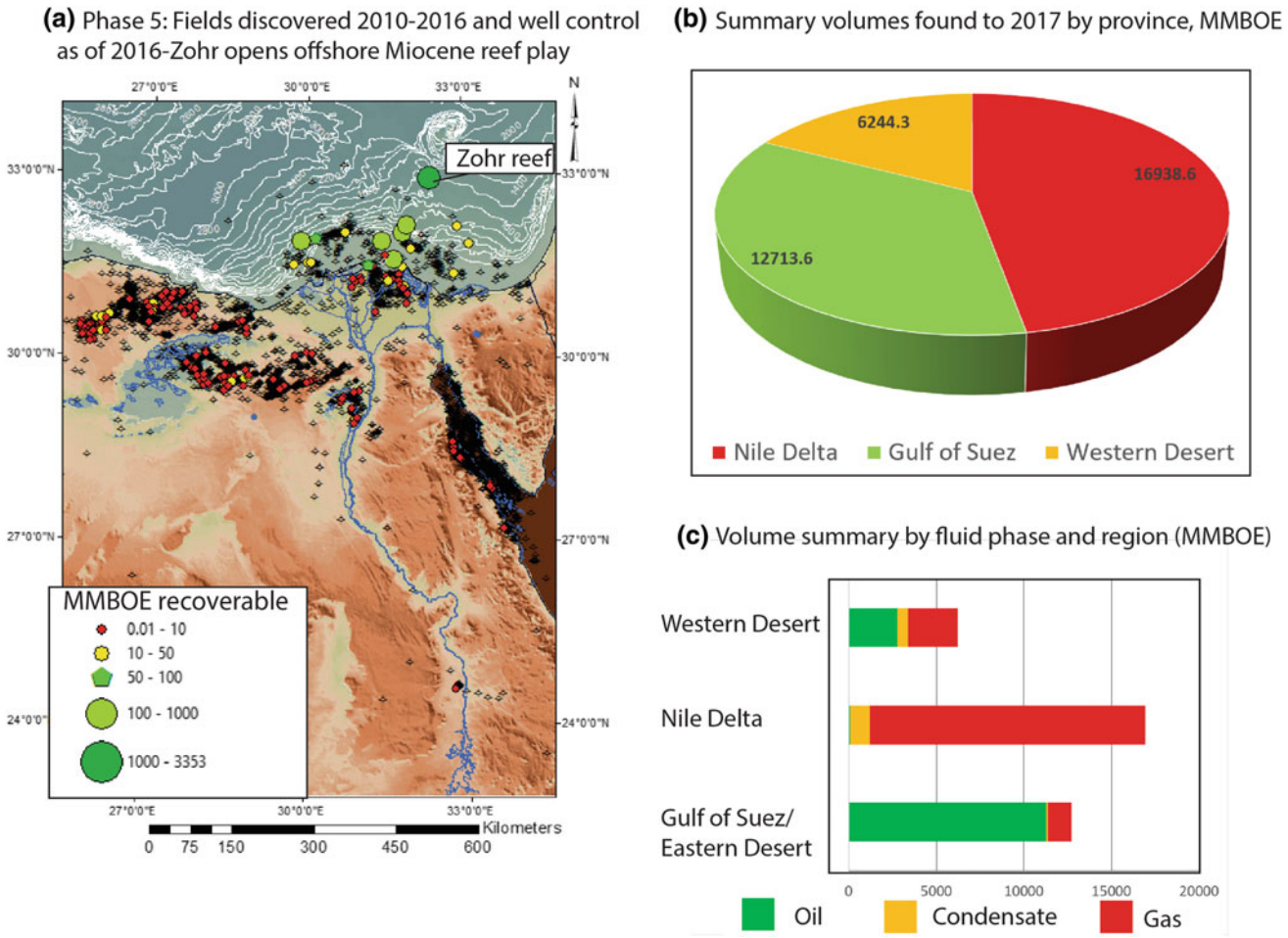

Fig. 16.9 Phase 5 exploration and summary of discovered volumes

thinking 'out of the box' with new data. Old methods of simply adding a hand-contoured, well-based isopach map of the Alamein to top of Jurassic to a seismically constrained Alamein structure map to map Jurassic structure kept most of the other companies in the Western Desert from finding the deep reserves. These kinds of maps had little hope of getting the Jurassic and deeper structural features correct. Some of this success is detailed in Oldani et al. (2013). Apache estimates they have discovered 3 BBOE hydrocarbons in the Western Desert since their first entry in this area in the late 1990s.

During this fourth phase of exploration, oil was also first discovered in the Nile Delta in the Tamad and West Dikirnis Fields. Merlon made the discovery as a result of extensive 3D seismic in their Mansoura Concession. Source and oil studies suggest these Miocene Qawasim and Pliocene Kafr El Sheik reservoirs in the West Dikirnis Field are charged from Upper Cretaceous to Lower Tertiary terrigenous clay-rich source rocks. Messinian reservoirs at El-Tamad Field are sourced from Jurassic source rocks, with migration from much deeper, thermally mature strata (Leila and Moscariello 2017; Rigzone 2006). The Messinian section in the Nile Delta consists of complexly layered incised valley fills with a variety of facies forming the reservoirs and seals. Some of that complexity is demonstrated by (Leila and Moscariello 2018). High quality 3D seismic is essential to unravel new traps and develop discoveries.

Phase 5 (Fig. 16.9) illustrates that the giant fields continue to be found largely in the Nile Delta. As of this writing, Egypt has 35.89 BBOE of reserves (Fig. 16.9b), with gas by far dominant in the Nile Delta (Fig. 16.9c).

By far the most significant recent development is the discovery of the 30 TCF Zohr Reef trend (Figs. 16.9 and 16.10).

Understanding of the Nile Delta has advanced considerably since the deep exploration potential was recognized and

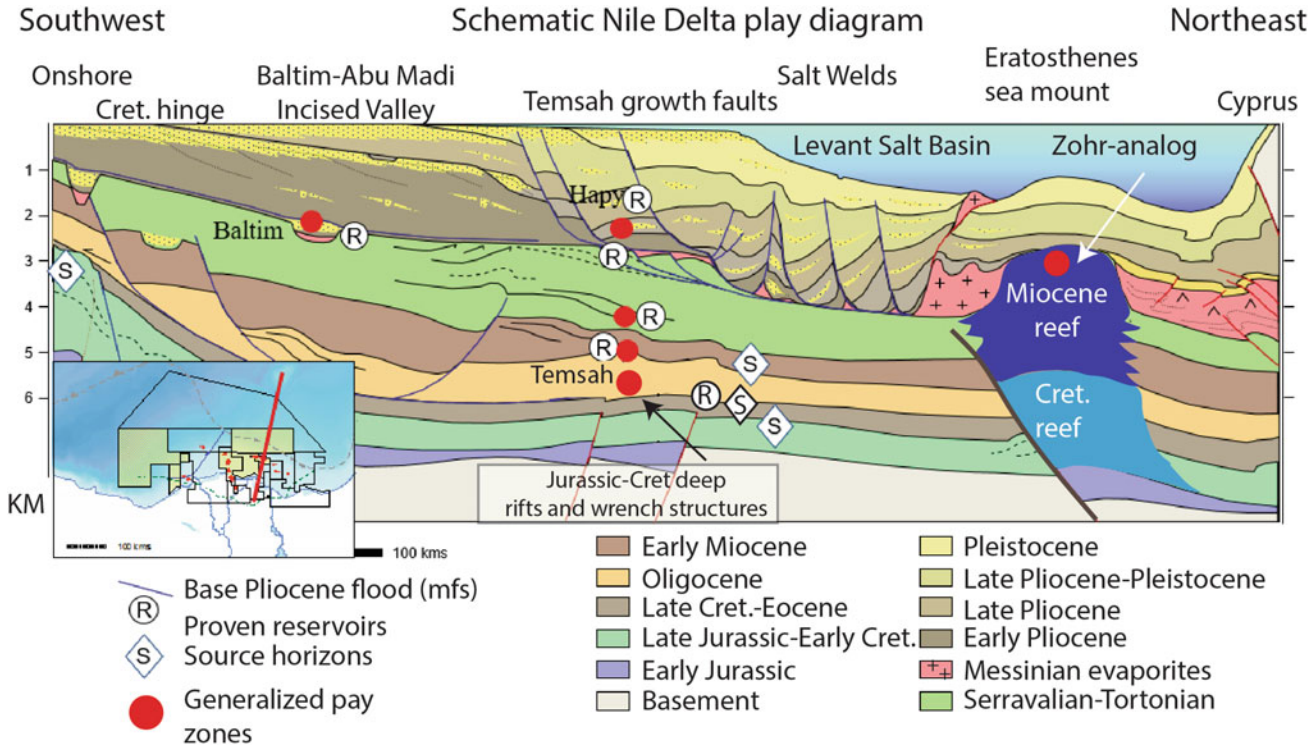

Fig. 16.10 Play schematic of the Nile Delta. Modified from Dolson et al. 2001

discussed (Boucher et al. 2004; Dolson et al. 2004; Dolson 2005) and Nashaat (1998) and Nashaat et al. (1996). Most significantly, the large carbonate build-ups of the Eratosthenes seamount in the EEZ (Figs. 16.3 and 16.4) were overlooked in flanking areas. Shell Egypt, in particular, held the deep water NEMED blocks for over a decade, testing traditional Pliocene amplitudes and some Messinian closures, with initial targets looking for oil out-board of gas. After many years of economic failure, they dropped the future Zohr block, which was acquired by ENI. The Zohr analog shown on Fig. 16.10 at the Eratosthenes seamount, was identified as a significant play by ENI (Cozzi et al. 2017; ENI 2015; Esestime et al. 2016; Nikolaou 2016). Towards the Nile to the southwest, the plays are Miocene clastics in turbidite fans and channels, at drilling depths that frequently exceed 6 km. The feature labeled 'Cretaceous reef' may well be an accreted basement high and is speculative at best on the schematic, but ENI reports Cretaceous age carbonates within this feature, which is flanked by deep-water turbidites. The exact age of the feature apparently remains in debate (Sayed Matbouly, personal communication) with some local staff believing the entire buildup is Cretaceous. Published references cited show, however, stacked Miocene carbonates over Cretaceous carbonates.

Multiple companies had an opportunity to 'farm in' to the Zohr prospect, which was only defined with reprocessed 2D seismic data and later confirmed by 3D seismic data. However, the feature was so large as to be able to easily locate a well on the reef. Concerns existed by other companies of seal capacity at shallow depth and charge, since basin modeling indicated mature source rocks were much deeper. ENI took the chance on a biogenic charge, and were proven correct. The discovery (Fig. 16.11) is the largest gas field in the offshore Mediterranean and largest in Egypt's history. The spike in the creaming curve (Fig. 16.2) shows just how significant this discovery is. In February, 2018, ENI announced that it had found a significant new gas discovery in a 'look-alike to Zohr' in offshore Cyprus (Reuters 2018).

With a gas column exceeding 600 m, seal capacity of the overlying evaporites is no longer a question. The dry gas has been confirmed as biogenic in origin. The shallow drill depths significantly offset the cost of development in deep water. Substantial opportunities exist for new discoveries in this new play.

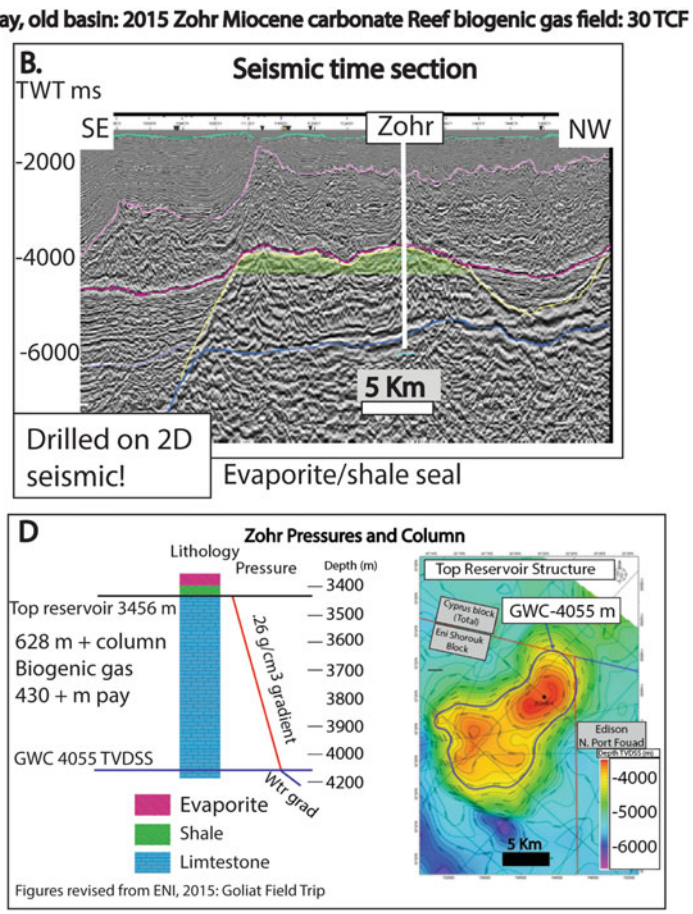

Fig. 16.11 Zohr discovery. Modified from ENI 2015 and (Dolson et al. 2017)

16.5 Nile Delta Pressures and Hydrodynamics

Pressure analysis in the Nile Delta may continue to unlock new reserves in tilted gas/water fields, many of which may be under-evaluated. Figure 16.12 shows schematics of the pressure systems the impact on migration and charge. The area underlying the thick progradation packages of Pliocene deltaic sandstones is highly over-pressured. The pressures cross stratigraphic and structural boundaries and set up deep basin hydrodynamic flow vertically and laterally (Fig. 16.12a). The deeply incised Abu Madi valley canyon, however, is normally pressured and provides a conduit for fluids to enter and migrate southward up the valley networks (Fig. 16.12b). These kinds of 'pressure relief' systems provide important pressure regressions which can enhance seal capacity in traps and lower the risk of migration into a carrier bed. Both the Raven and Satis discovery were made after extensive work modeling pressure regressions in the delta. The Satis well was drilled into an Oligocene turbidite channel complex that was in continuity up-dip with a dry hole (Habbar-1) well (Fig. 16.7b) which contained residual gas and a sharp pressure regression caused by the beveling of the normally pressured Abu Madi valley system with the underlying Oligocene shale seals (Dolson et al. 2014).

In addition, hydrodynamically trapped hydrocarbons may exist off-structure throughout the deep basins. The quantification of hydrodynamic tilting was first covered by (Hubbert 1953) but most global exploration focus has only considered this important around shallow basin flanks. Over-pressures in deep basins, however, create flow from elevated hydraulic head created by differences in excess pressure. Tilted contacts from deep basin water flow have recently been recognized in a number of basins (Dennis et al. 2005; Ferrero et al. 2012; Muggeridge and Mahmode 2012; Riley 2009; Robertson et al. 2013; Swarbrick and O'Connor 2010).

As mentioned earlier, the giant Temsah-Akhen complex has a tilted contact (Fig. 16.13). The Temsah-Akhen closure exceeds 500 m and the structure itself is over 60 km long. Crestal wells, however, failed to find the large reserves, which were tilted off the flank to the northeast. The hydrodynamic model shown below was created from regional over-pressure maps as defined by mud-weight mapping (Fig. 16.12b), converted to hydraulic head. The hydrodynamic maps, when used in a migration model, correctly

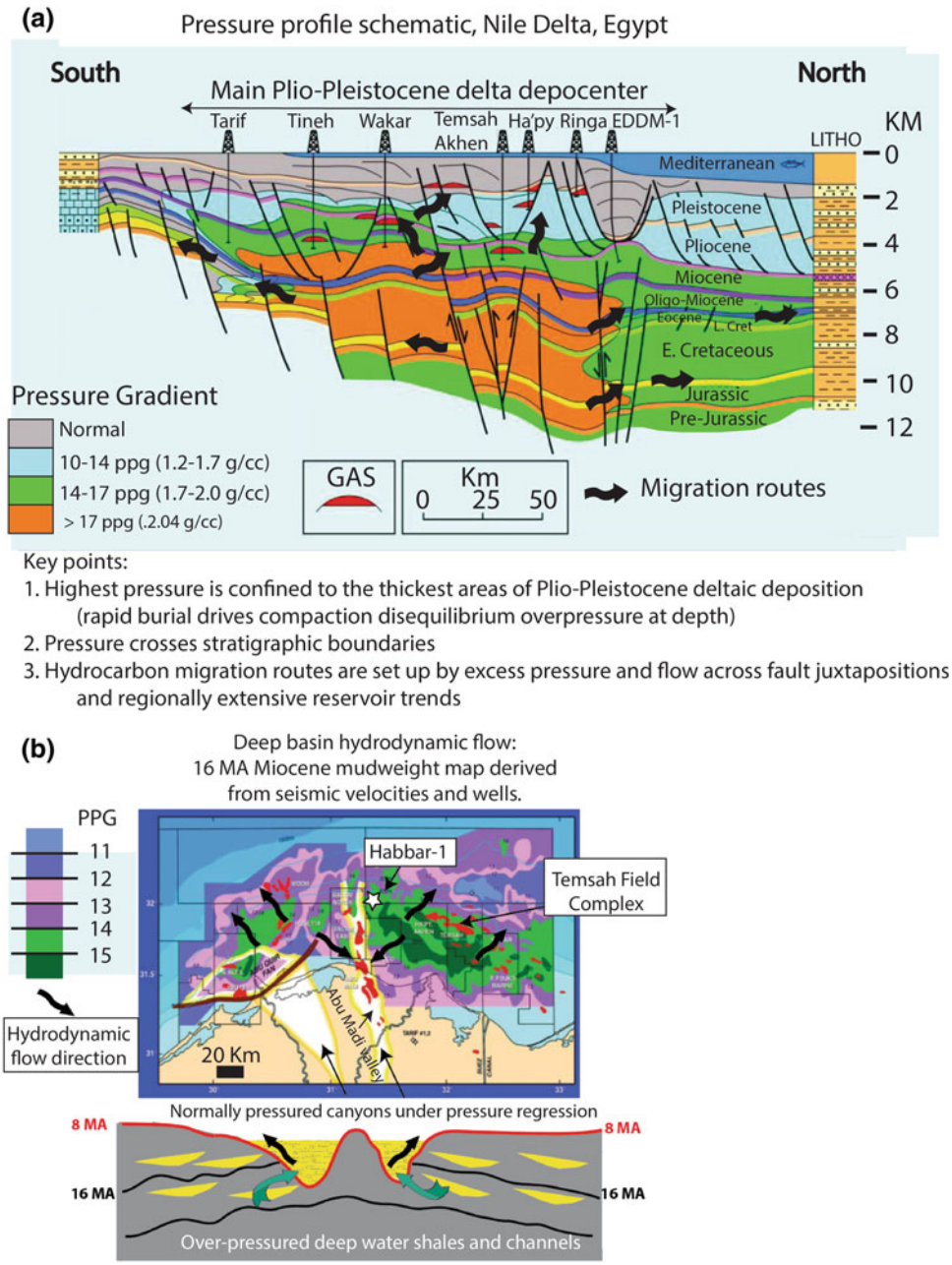

Fig. 16.12 Pressure systems of the Nile Delta and complex vertical and lateral migration. Arrows indicate fluid flow direction. Modified from (Heppard and Albertin 1998; Heppard et al. 2000)

predict the northeastward tilt of the field. The process and more detailed analysis of this trap is described in Chapter 4 of (Dolson 2016b) with applications to the Nile Delta in Dolson (2016a).

16.6 Gulf of Suez Potential

The Gulf of Suez remains enigmatic. The basin is very mature statistically, with only small fields found in the last 20 years, a classic result of companies focused on doing the same thing over and over again and expecting a different result. The basin needs breakthrough imaging and new thinking. The potential exists, when economics become favorable, to develop unconventional source rocks throughout this basin and it its basin centers (Dolson 2016c). Figure 16.14b shows the generalized location of the major 'kitchens' across the basin and the distribution of both syn-rift and pre-rift reservoirs (Fig. 16.14a). Until new plays are tried and seismic imaging improved, exploration in this basin may remain limited to small additional pools, with an occasional large discovery. In understanding the GOS

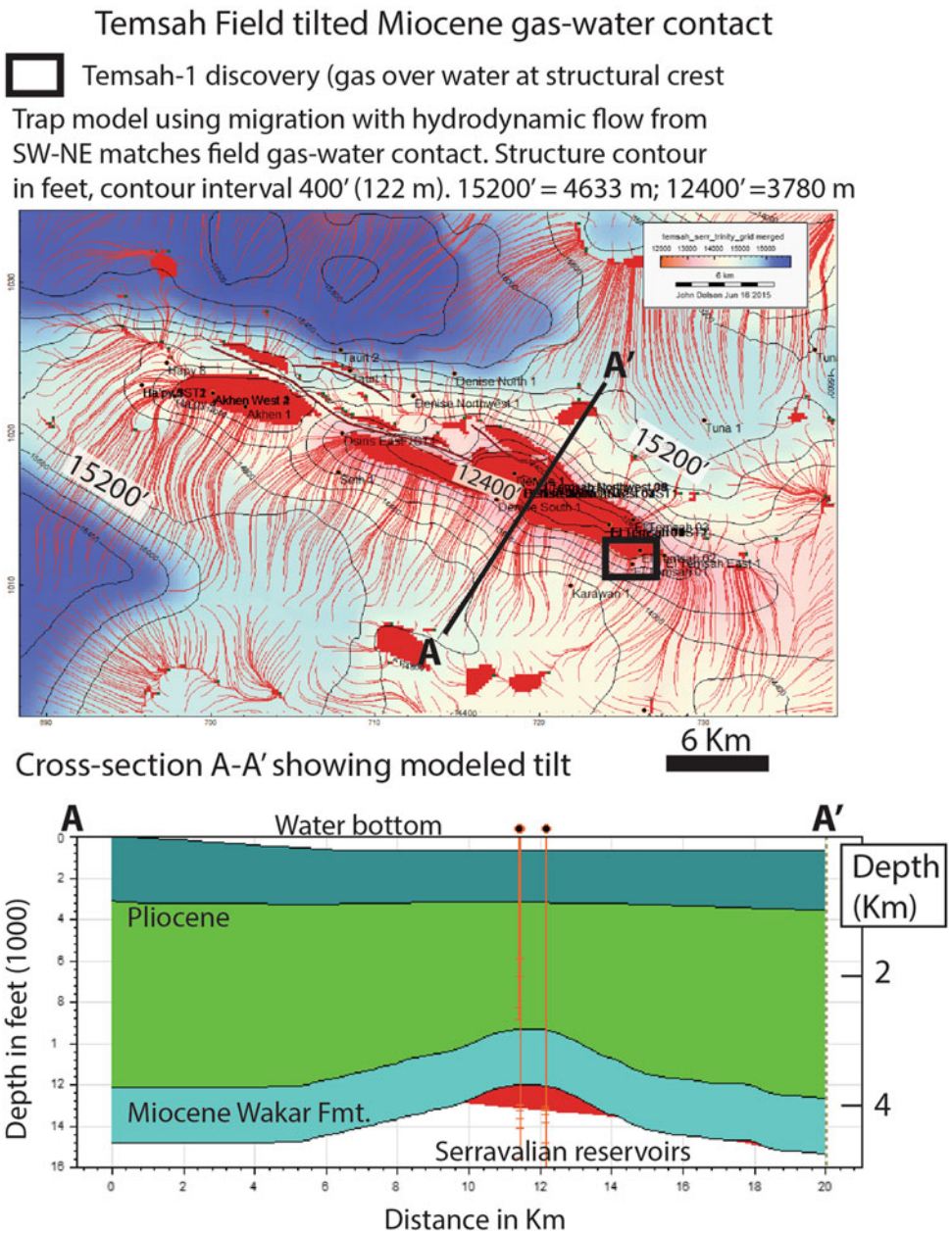

Fig. 16.13 Modeling in Trinity software (www.zetaware.com) of the hydrodynamic trap at the Temsah-Akhen complex, Nile Delta

petroleum system, the reader is also encouraged to read Alsharhan (2003) and Shagar (2006).

One example of the integrated technology required to unlock the deeper structural trends is shown in Fig. 16.15. The Erdma Field is a shallow southwest plunging faulted nose with a combination hydrodynamic and stratigraphic trap component at the shallow S40 Miocene sandstone level. The area was first tested by BP in the early 1980s but found gas-condensate deemed non-commercial in the Erdma-1 and 4 wells. In the mid 1990s, Amoco acquired the acreage and re-interpreted the S40 sand levels as perched or tilted gas/water contacts in pressure continuity over a broad area, suggesting a 150 + BCF gas accumulation.

A twin to the ERDMA-1 well (ESM-1, also known as the Ras El Deeb Marine East-1) was drilled in 1997 and flowed high rates of gas and condensate over 18 months with no production decline, proving that the abandoned BP wells had actually drilled into a significant gas/condensate pool. Intriguing deeper shows, however, pointed to additional potential. The LL87-4 well had been abandoned as non-commercial gas, but had strong oil shows and calculated but untested pay in the Miocene Nukhul Formation. The

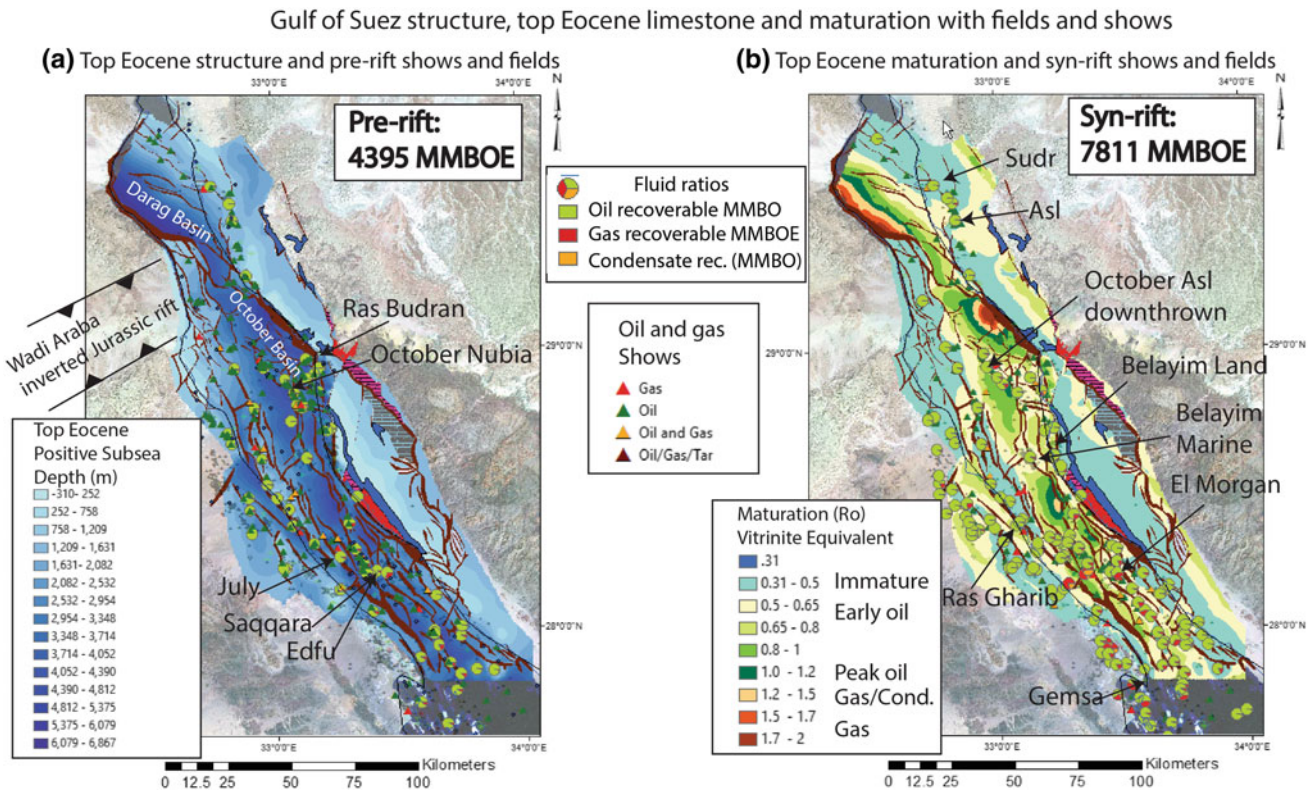

Fig. 16.14 Gulf of Suez structure **a** and maturation **b** at the top Eocene Thebes carbonate. Pre-rift reservoirs shown on **a** consist of Eocene Thebes and older strata. Syn-rift reservoir **b** are Oligo-Miocene in age

Nukhul Formation is a rift initiation deposit which is commonly only present on the downside of active rift faults (Dolson et al. 1996; Jackson et al. 2006; Ramzy et al. 1996; Winn et al. 2001; Wescott et al. 1996; Young et al. 2002). The LL87-SE1 well, in addition, had tested oil and gas from the Lower Cretaceous Matulla Formation. Dipmeters on this well indicated there was room to move structurally high to the northeast. Seismic reprocessing and a fully developed 3D structural model were completed by the early 2000s. The Saqqarra discovery well was drilled in 2003, followed quickly by the Edfu discovery on another deep block (Fig. 16.14 A for location). The two Nubia fields together contain an estimated 30–105 MMBO recoverable reserves. The key to these deep discoveries was a careful integration of oil show and test data with dipmeters, and sound depositional models of syn-rift geometries and reprocesses seismic showing a better image of the deep structure.

16.7 Future Growth and Yet-to-Find

The Nile Delta will continue to be the growth engine for Egypt's large reserves. The bottom of the petroleum system has not been determined, despite wells drilling over 7 km of section. Multiple plays exist and the petroleum system is now proven to work all the way to Cyprus and as far northwest, at a minimum, as the Shell Messinian discovery shown on Fig. 16.4. Non-commercial discoveries with gas over water should be re-examined as part of a possible up-dip tilted accumulation. Additional refinement of fluid to source rock studies may also unlock additional plays not even recognized to date.

The Mango-1 well (Fig. 16.3a) has long shown that Cretaceous pays extend offshore and potentially underneath the deeper Nile Delta. The deep structures remain unmapped and unexplored in many areas, particularly the poorly imaged sub-salt plays in ultra-deep water.

In the Western Desert, at the time of this writing, ENI discovered a new Paleozoic oil field in the promising Faghur Basin (Energy Egypt 2018). The South Faghur Field is located in Southwest Meleiha area located almost 100 km north of the Siwa Oasis and tested light oil from the Paleozoic Desouky Formation of Carboniferous age. Although the source of the oil is not known, this discovery will open up new opportunities for deeper Paleozoic targets in the Western Desert. Success rates for companies that hold the bulk of the well and area-wide 3D surveys continue to find exploration success and growth in the Western Desert.

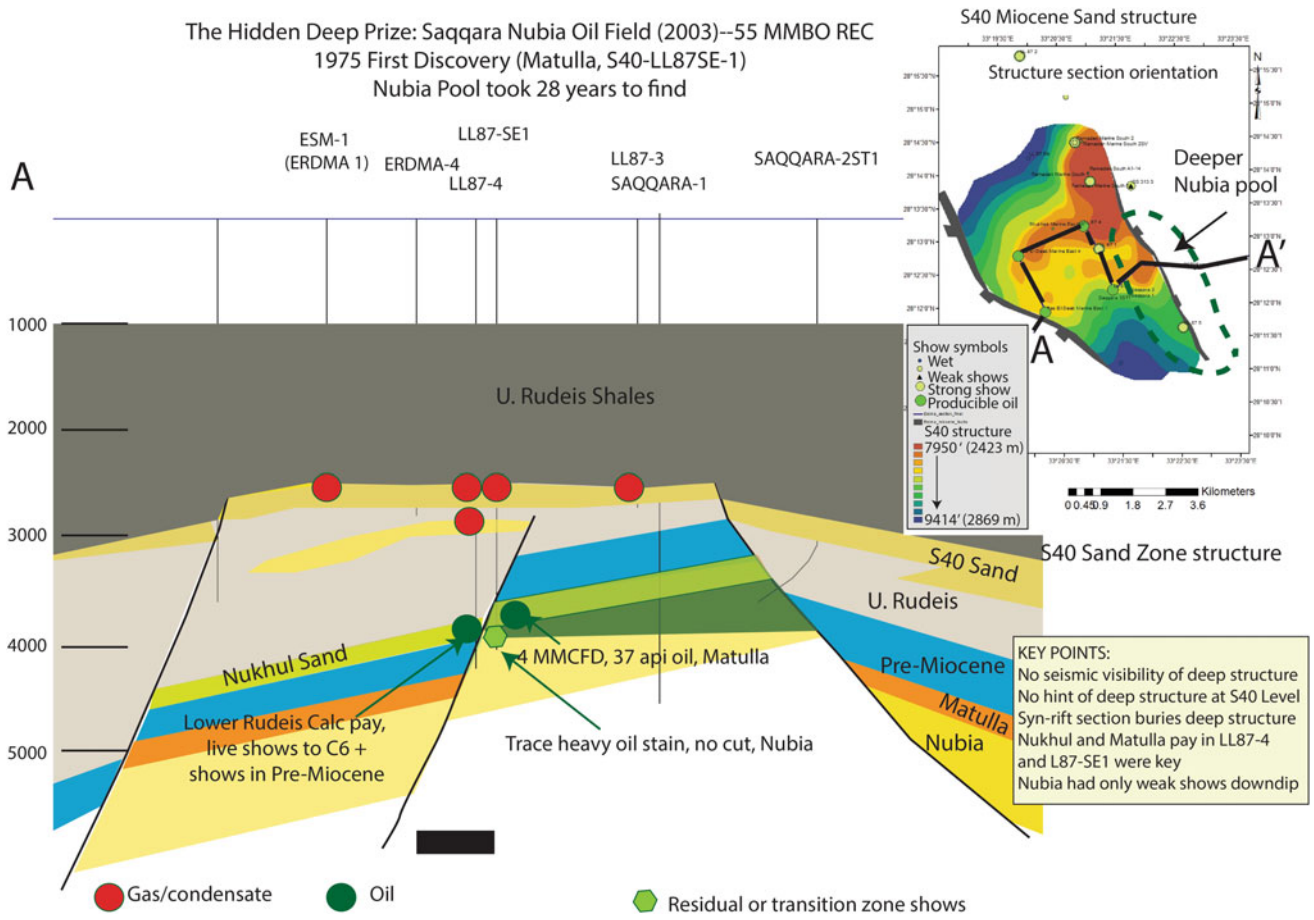

Fig. 16.15 Schematic of the 2003 discovery of the 30–80 MMBO Saqqara Field deeper pool trap, Erdma area, southern Gulf of Suez. See Fig. 16.14a for location

Progressively better seismic programs are constantly being developed and implemented, like Broadband 3D seismic followed by Prestack seismic inversion.

Yet-to-find analysis from statistics remains, at best, an elusive 'best guess', but post Zohr discovery statistics suggest substantial room exists for new fields (Fig. 16.16). Method A yields the least biased solution and B yields a much larger number. A yet to find of 38.6 BBOE (224 TCF) is similar to other estimates for the region (Kirschbaum et al. 2010; Schenk et al. 2012). Especially given the new Zohr play it is not unreasonable, however, to expect to see the large reserve growth speculated eventually become a reality.

Hunting for oil and gas is an exciting and difficult task. Advances in seismic imaging are making huge differences. For example, globally, 50% of new fields found since 2000 have been in stratigraphic and combination traps, up from 10 to 15% in prior decades (Dolson et al. 2017). Much of this success is due to improved reservoir and seal imaging from 3D seismic, as well as better ways to model petroleum systems and charge and migration.

One thing is certain. Reserve growth in old fields and new field discoveries will continue. Some significant lessons can be learned from understanding the history of exploration, particularly some of the bold moves made by explorers like Jim Vanderbeek and others at the earliest days of the Gulf of Suez, and by ENI recognizing a huge new carbonate play offshore in 2015. Big reserve advancements take creative thinking and creative, bold management. Egypt's future petroleum potential is significant and only awaits the creativity of future explorers. Conventional wisdom will add reserves, but new ideas, technical and business changes not even thought of today will make the big differences.

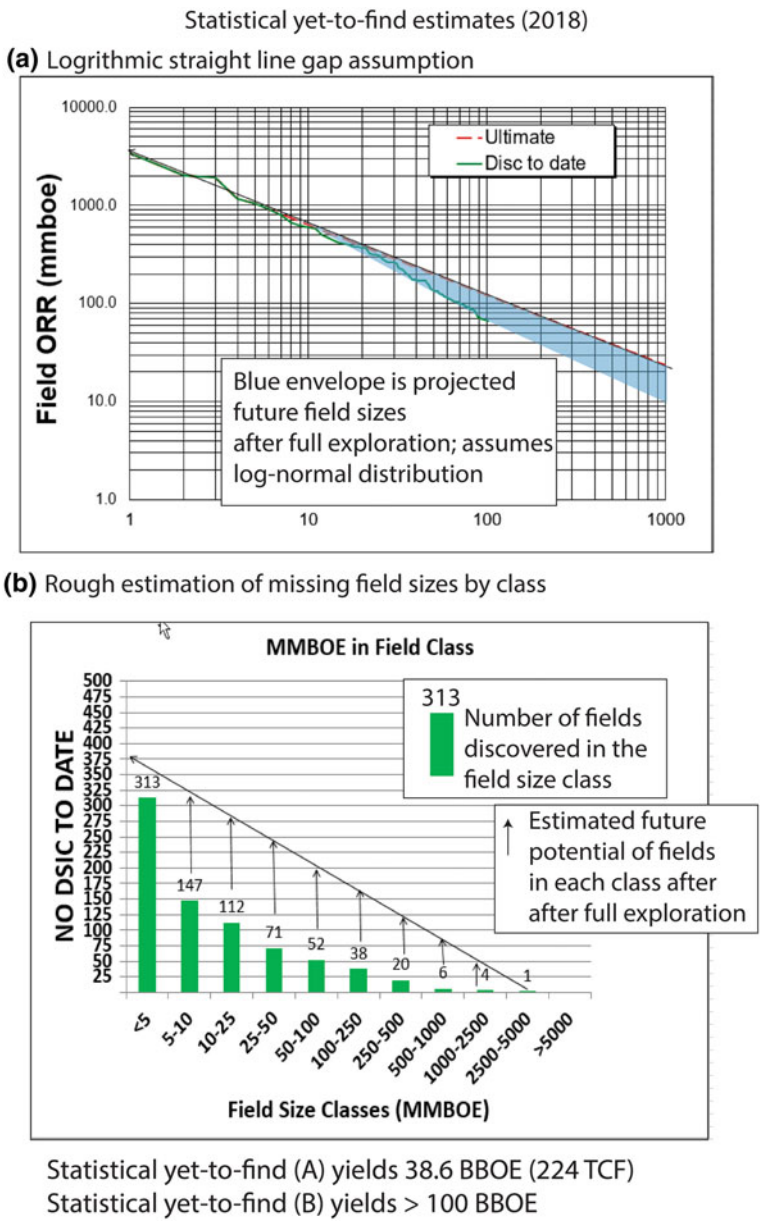

Fig. 16.16 Predicted yet-to-find from current field size distributions

Acknowledgements Sayed Matbouly, Samir Abdelmoaty, Joe Versfelt and Frank Ethridge have reviewed this chapter and made many useful suggestions, for which the author is very grateful.The author's 8 ½ years working in Egypt for Amoco and BP was a marvelous learning experience. The author is indebted to his many GUPCO and Amoco/BP Egypt peers, and many other geoscientists from other companies, who made working and learning there such an enjoyable experience, including be able to see our kids graduate from Cairo American College at the foot of the Sphynx and Pyramids in 2000 and 2002. In particular, Dave Blanchard, Sayed Matbouly, the late Adel Sehim, Mahmoud Atta, Samir Abdelmoaty, Larry McVay, Chuck Pittman, Jay Thorseth, John Garing, Bill Wescott, Eleanor Rowley, Paul Boucher, Jennifer Villinski, and many others all played a big role in advancing our understanding of the exploration potential of Egypt. The 128 Egyptian staff I worked with at GUPCO were an extraordinary team, as were my colleagues in Amoco Egypt, many of whom remain close friends. EGPC conferences and guidebooks have also been fundamental to helping all explorers understand old discoveries, old biases and to unlock new ideas.I'd like also to thank Zakaria Hamimi and Ahmed El Barkooky for their invitation to contribute this chapter to their upcoming Springer-Verlag publication on the Geology of Egypt. My wife, as usual, I thank repeatedly for helping proof some of the grammar and tolerating the work of putting this chapter together.

References

Alsharhan AS (2003) Petroleum geology and potential hydrocarbon plays in the Gulf of Suez rift basin, Egypt. Am Assoc Pet Geol Bull 87:143–180

Belopolsky A, Tari G, Craig J, Illife J (eds) (2012) New and emerging plays in the eastern Mediterranean: an introduction vol 18. Petroleum Geoscience, The Geological Society of London, London, United Kingdom

Bentham P (2011) Understanding crustal structure and the early opening history of the Eastern Mediterranean Basin, offshore Northern Egypt and the Levant. In: New and emerging plays in the Eastern Mediterranean, London, England, February, 2011. The Geological Society of London, pp 67–68

Boote DRD, Clark-Lowes DD, Traut MW (1998) Paleozoic petroleum systems of North Africa. In: MacGregor DS, Moody RTJ, Clark-Lowes DD (eds) Petroleum Geology of North Africa. Special Publication No. 132. Geological Society, London, United Kingdom, pp 7–68

Bosworth W, Stockli DF (2017) A new chronostratigraphic framework for the Paleozoic strata of Sinai, Egypt, based on geochronologic and thermochronologic constraints (abs.). Paper presented at the AAPG Africa Regional GTW, Paleozoic Hydrocarbon Potential of North Africa, Marrakech, Morocco, November 1–4, 2017

Boucher PJ, Dolson JC, Boucher PJ, Siok J, Heppard PD (2004) Key challenges to realizing full potential in an emerging giant gas province: Nile Delta/Mediterranean Offshore, Deep water, Egypt. Houston Geological Society, pp 25–27

Cade CA, Grant SM, Witt CJ (1999) Integrated petrographic and petrophysical analysis for risk reduction, Ormen Lange area, Norway. In: European association of geologists and engineers 61st conference and technical exhibition, Helsinki, Finland, June 7–11, 1999. EAGE, p 4

Cozzi A et al (2017) Zohr giant gas discovery: a paradigm shift in the Nile Delta and East Mediterranean exploration. In: Paper presented at the AAPG/SEG 2017 international conference and exhibition, London, England, October 15–18, 2017

Cross NE, Cuningham A, Cook RJ, Taha A, Esmaie E, Swidan NE (2009) Three-dimensional seismic geomorphology of a deep-water slope-channel system: the Sequoia field, offshore west Nile Delta, Egypt. Am Assoc Pet Geol Bull 93:1063–1086

Cunningham S (2011) Tamar-the opening of a frontier basin in the Eastern Mediterranean. In: Paper presented at the AAPG annual conventional and exhibition, Houston, Texas, April 10–13, 2011

Dalla S, Harby H, Serazzi M (1997) Hydrocarbon exploration in a complex incised valley fill: an example from the late Messinian Abu Madi Formation (Nile Delta basin, Egypt). Lead Edge 16:1819–1824

Dauphin L, Martin A, Desaubliaux G (2007) 3D field modeling of Algerian Glacial Ordovician Reservoirs. In: Paper presented at the AAPG international convention and exhibition, Long Beach, California, April 1–4, 2007

Dennis H, Bergmo P, Holt T Tilted oil-water contacts: modelling the effects of aquifer heterogeneity. In: Petroleum Geology conference series 2005, London, United Kingdom, 2005. Geological Society of London, pp 145–158

Dixon RJ, Patton TL, Hirst JPP, Diggens J (2018) Transition from subglacial to proglacial depositional systems: implications for reservoir architecture, Illizi Basin, Algeria. In: Paper presented at the AAPG international conference and exhibition, San Antonio, Texas, April 20–23, 2008

Dolson J (2016a) Understanding Nile Delta pressures and hydrodynamics: are these keys to unlocking new reserves? In: Bosworth B, Fattah AA (eds) AAPG geosciences technology workshop 2016: hydrocarbon potential of the Sinai micro-plate and surrounding basins, Alexandria, Egypt, March 18–19, 2016. American Association of Petroleum Geologists and Egyptian Petroleum Exploration Society

Dolson J (2016b) Understanding oil and gas shows and seals in the search for hydrocarbons. Springer International Publishing Switzerland, Switzerland. https://doi.org/10.1007/978-3-319-29710-1

Dolson J (2016c) What will it take to bring a renaissance to Gulf of Suez exploration: has the time arrived to try some unconventional exploration? In: Bosworth B, Fattah AA (eds) AAPG geosciences technology workshop 2016: hydrocarbon potential of the Sinai micro-plate and surrounding basins, Alexandria, Egypt, March 18–19, 2016. American Association of Petroleum Geologists and Egyptian Petroleum Exploration Society

Dolson J, El-Gendi O, Sharmy H, Fathalla M, Gaafar I (1996) Gulf of Suez rift basin sequence models–Part A. Miocene sequence stratigraphy and exploration significance in the greater October Field area, Northern Gulf of Suez. In: Youssef M (ed) Proceedings of the 13th petroleum conference, vol 2. The Egyptian General Petroleum Corporation, Cairo, Egypt, pp 227–241

Dolson JC, Steer B, Garing J, Osborne G, Gad A, Amr H (1997) 3D seismic and workstation technology brings technical revolution to the Gulf of Suez Petroleum Company. Lead Edge 16:1809–1817

Dolson JC, Shann MV, Matbouly S, Harwood C, Rashed R, Hammouda H (2001) The petroleum potential of Egypt. In: Downey MW, Threet JC, Morgan WA (eds) Petroleum provinces of the 21st Century, vol Memoir 74. American Association of Petroleum Geologists, Tulsa, Oklahoma, pp 453–482

Dolson J, Barkooky AE, Wehr F, Gingerich P, Prochazka N, Shann M (2002a) The eocene and oligocene paleo-ecology and paleo-geography of whale valley and the Fayoum basins: implications for hydrocarbon exploration in the Nile Delta and eco-tourism in the greater Fayoum basin. American Association of Petroleum Geologists, Search and Discovery Article #10030 (2002). http://www.searchanddiscovery.net/documents/cairo/index.htm

Dolson JC, Boucher PJ, Dodd T, Ismail J (2002b) The petroleum potential of the emerging Mediterranean offshore gas plays, Egypt. Oil Gas J 32–37

Dolson JC, Boucher PJ, Siok J, Heppard PD (2004) Key challenges to realizing full potential in an emerging giant gas province: Nile Delta/Mediterranean offshore, deep water, Egypt. In: Burley S (ed) Petroleum geology: North-West Europe and global perspectives—proceedings of the 6th petroleum geology conference, London, United Kingdom. Geological Society of London, pp 607–624

Dolson JC, Boucher, PJ, Siok J, Heppard PD (2005) Key challenges to realizing full potential in an emerging giant gas province: Nile Delta/Mediterranean offshore, deep water, Egypt. In: Dore AG, Vining BA (ed) 6th Petroleum geology conference, London, United Kingdom. The Geological Society of London, pp 607–624

Dolson JC, Atta M, Blanchard D, Sehim A, Villinski J, Loutit T, Romine K (2014) Egypt's future petroleum resources: a revised look in the 21st Century. In: Marlow L, Kendall C, Yose L (eds) Petroleum systems of the Tethyan region, vol Memoir 106. American Association of Petroleum Geologists, Tulsa, Oklahoma, pp 143–178

Dolson J, He Z, Horn BW (2017) Advances and perspectives on stratigraphic trap exploration-making the subtle trap obvious. In: Paper presented at the AAPG 2017 Middle East region geosciences technology workshop, stratigraphic traps of the Middle East, Muscat, Oman

Dupouy M, Desabliaus G, Nosjean N, Lloyd A, Cherif R (2017) Integrated sedimentological case study of glacial Ordovician reservoirs in the Illizi Basin, Algeria. In: Paper presented at the 79th EAGE conference and exhibition 2017, Paris, France, June, 2017

Editors (2012) Sea Dragon taps deeper oil pay in Egypt's Kom Ombo. Oil Gas J

Energy Egypt (2018) Eni announces second oil discovery at Faghur Basin in Egypt's Western Desert. Energy Egypt Newsletter. https://energyegypt.net/eni-announces-second-oil-discovery-at-faghur-basin-in-egypts-western-desert/:1

Esestime P, Hewitt A, Hodgson N (2016) Zohr—a newborn carbonate play in the Levantine Basin, East-Mediterranean. First Break 34:7

Ferrero MB, Price S, Hognestad J (2012) Predicting water in the crest of a giant gas field: Ormen Lange hydrodynamic aquifer model Society of Petroleum Engineers SPE 153507:1–13
Gardosh M (2011) Stratigraphic and structural framework of gas discoveries in the Late Tertiary section offshore Israel. In: New and emerging plays in the Eastern Mediterranean, London, England, February, 2011. The Geological Society of London, pp 25–26
Gardosh M, Druckman Y, Buchbiner B (2009) The Late Tertiary deep-water siliciclastic system of the Levant margin—an emerging play offshore Israel
Goliat Field Trip (2015) ENI.com
Gordon G (2012) Prospectivity in the north Red Sea, Egypt: new data, new challenges, new opportunities. In: Paper presented at the The challenges of sub-salt exploration and development in deep sea Middle East and North Africa, Amman, Jordon, June 11–13, 2012
Gordon G et al (2011) The hydrocarbon prospectivity of the Egyptian North Red Sea Basin. In: Vining BA, Pickering SC (eds) Petroleum geology: from mature basins to new frontiers, London, United Kingdom, January, 2011. Proceedings of the 7th petroleum geology conference. Geological Society of London, pp 783–789
Hegazy A (ed) (1992) Western Desert, oil and gas fields (a comprehensive overview) vol 1. The Egyptian General Petroleum Corporation, Cairo, Egypt
Heppard PD, Albertin ML (1998) Abnormal pressure evaluation of the recent Pliocene and Miocene gas discoveries from the Eastern Nile Delta, Egypt, Using 2D and 3D seismic lines. Am Assoc Pet Geol Bull 82:1–6
Heppard PD, Dolson JC, Allegar NC, Scholtz SM (2000) Overpressure evaluation and hydrocarbon systems of offshore Nile Delta, Egypt. In: Mediterranean offshore conference, Alexandria, Egypt. Egyptian General Petroleum Corporation, p CD
Heron DPL (2009) Interpretation of Late Ordoviian galciogenic reservoirs from 3-D seismic data: an example from the Murzuq Basin, Libya. Geol Mag 147:28–41
Hubbert MK (1953) Entrapment of petroleum under hydrodynamic conditions. Am Assoc Petrol Geol Bull 37:1954–2026
Hughes SC, Ahmed H, Raheem TA (1997) Exploiting the mature South El Morgan Kareem reservoir for yet more oil: a case study on multi-discipline reservoir management. In: Paper presented at the Middle East oil show and conference, Bahrain, 15–18 March
Jackson CAL, Gawthorpe RL, Leppard CW, Sharp IR (2006) Rift-initiation development of normal fault blocks: insights from the Hammam Faraun fault block, Suez Rift, Egypt. J Geol Soc Lond 164:165–183. https://doi.org/10.1144/0016-764904-164
Kellner A, Brink GJ, Khawaga HE (2018) Depositional history of the western Nle Delta, Egypt: Late Rupelian to Pleistocene. Am Assoc Pet Geol Bull 102:1841–1865
Kirschbaum MA et al (2010) Assessment of undiscovered oil and gas resources of the Nile Delta Basin Province, Eastern Mediterranean: vol U.S. Geological Survey Fact Sheet 2010–3027. United States Geological Survey, Reston, Virginia
Leila M, Moscariello A (2017) Organic geochemistry of oil and natural gas in the West Dikirnis and El-Tamad fields, onshore Nile Delta, Egypt: Interpretation of potential source rocks. J Pet Geol 40:37–58. First published: 19 December 2016. https://doi.org/10.1111/jpg.12663
Leila M, Moscariello A (2018) Depositional and petrophysical controls on the volumes of hydrocarbons trapped in the Messinian reservoirs, onshore Nile Delta, Egypt. Pet Afr 4:250–267
Loutit T, Allard D, Dolson JC, Schruers J, Laura S (2001) A new view of Egypt's hydrocarbon potential (abs). In: Ibrahim M (ed) Middle East and North Africa conference, London, UK
Marcou JA, Samsu D, Kasim A, Meizarwin, Davis N (2004) Tangguh LNG's gas resource: discovery, appraisal and certification. In: Paper presented at the IPA-AAPG deepwater and frontier exploration in Asia and Australasia symposium
Matbouly S, Sabbagh ME (eds) (1996) Gulf of Suez oil fields (a comprehensive overview) vol 1. The Egyptian General Petroleum Corporation, Cairo, Egypt
Mohamed AE, Mohammed AS (2008) Stratigraphy and tectonic evolution of the oil producing horizons of Muglad Basin, Sudan. J Sci Technol 9:8
Monir M, Shenkar O (2016) Pre-Messinian petroleum system and trapping style, offshore western Nile Delta, Egypt. In: Paper presented at the AAPG/SPE Africa energy and technology conference, Nairobi City, Kenya
Moussa DS, Matbouly DS (eds) (1994) Nile Delta and North Sinai: fields, discoveries and hydrocarbon potentials (a comprehensive overview). The Egyptian General Petroleum Corporation, Cairo, Egypt
Muggeridge A, Mahmode H (2012) Hydrodynamic aquifer or reservoir compartmentalization? Am Assoc Pet Geol Bull 96:315–336
Mustafa AA, Tyson RV (2002) Organic facies of Early Cretaceous synrift lacustrine source rocks from the Muglad Basin, Sudan. J Pet Geol 25:351–366
Nashaat M (1998) Seals assessment in the Nile Delta, Western Desert and Gulf of Suez, Egypt. In: Eloui M (ed) 14th petroleum conference, vol 1. The Egyptian General Petroleum Corporation. Cairo, Egypt, pp 492–510
Nashaat M, Carlin S, Bagnoli G, Moussa A (1996) The pre-Messinian overpressure study in the Nile Delta area: a supporting methodology for understanding hydrocarbon accumulation. In: Youssef M (ed) 13th Petroleum conference, vol 1. The Egyptian General Petroleum Corporation. Cairo, Egypt, pp 193–202
Nikolaou KA (2016) The discovery of Zohr Gas Field in Egypt "A game changer": impacts-opportunities. In: Paper presented at the 9th SE Europe energy dialogue: the quest for a new energy balance, Cyprus, June 29–30, 2016
Oldani MJ, Maher TM, Versfelt J, Eichler RJ, Monk D (2013) The Apache Egypt story: 18 years of success and growth in Egypt's Western Desert, 1994–2012. In: Paper presented at the HGS international dinner meeting, Houston, Texas
Palmieri G, Harby H, Marini JA, Hashem F, Dalla S, Shash M (1996) Baltim fields complex: an outstanding example of hydrocarbon accumulations in a fluvial Messinian incised valley. In: Youssef M (ed) Proceedings of the 13th petroleum conference, vol 1. The Egyptian General Petroleum Corporation, Cairo, Egypt, pp 256–269
Peijs JAMM, Bevan TG, Piombino JT (2012) The Gulf of Suez rift basin. In: Roberts DG, Bally AW (eds) Regional geology and tectonics: phanerozoic rift systems and sedimentary basins, vol 1B. Geological Society of London, London, UK, pp 165–194
Pigott JD, Williams MT, Abdel-Fattah M, Pigott KL (2014) The Messinian Mediterranean crisis: a model for the Permian Delaware Basin? In: Paper presented at the AAPG international conference and exhibition, Istanbul, Turkey
Klett RR (2000) Tanezzuft-Sbaa structural/stratigraphic assessment Unit 20580301 vol USGS World Petroleum Assessment 2000. United States Geological Survey, Reston, Virginia
Ramzy M, Steer B, Abu-Shadi F, Schlorholtz M, Mika J, Dolson J, Zinger M (1996) Gulf of Suez rift basin sequence models–Part B. Miocene sequence stratigraphy and exploration significance in the central and southern Gulf of Suez. In: Youssef M (ed) Proceedings of the 13th petroleum conference, vol 2. The Egyptian General Petroleum Corporation, Cairo, Egypt, pp 242–256
Reuters (2018) Eni/Total find natgas off Cyprus in field close to Zohr Reuters. https://www.reuters.com/article/us-cyprus-natgas/eni-total-find-natgas-off-cyprus-in-field-close-to-zohr-idUSKBN1FS1G3

Rigzone (2006) Melrose reports Egyptian Discovery RIGZONE. https://www.rigzone.com/news/oil_gas/a/39012/melrose_reports_egyptian_discovery/:1

Riley G (2009) Supergiant fields in an overpressured lacustrine petroleum system: the South Caspian Basin. In: Paper presented at the AAPG 2009 distinguished lecture series, Tulsa, Oklahoma

Roberts G, Peace D (2007) Hydrocarbon plays and prospectively of the Levantine Basin, offshore Lebanon and Syria from modern seismic data. GeoArabia 12:99–124

Robertson J, Goulty NR, Swarbrick RE (2013) Overpressure distributions in palaeogene reservoirs of the UK Central North Sea and implications for lateral and vertical fluid flow. Pet Geosci 19: 223–236

Said R (ed) (1990) The geology of Egypt vol 1. A. A. Balkema Publishers, Rotterdam, The Netherlands

Salama RB (1997) Chapter 6 Rift Basins of the Sudan. In: Miall AD (ed) Sedimentary basins of the world, vol 3. Elsevier, pp 105–149

Samuel A, Kneller B, Raslan S, Sharp A, Parsons C (2003) Prolific deep-marine slope channels of the Nile Delta, Egypt. Am Assoc Pet Geol Bull 87:541–560

Schenk CJ et al (2012) Assessment of undiscovered oil and gas resources of the Levant Basin Province, Eastern Mediterranean vol Fact Sheet 2010–3014. World Petroleum Resources Project United States Geological Survey, Reston, Virginia

Shagar A (2006) Source rock evaluation of some intervals in the Gulf of Suez area, Egypt. Egypt J Aquat Res 32:70–87

Shang BZ, Casabianca D, Pelissier M (2009) Model for multiple fluid contacts in a connected reservoir and its applications. In: Paper presented at the 71st EAGE conference and exhibition, Amsterdam, The Netherlands, June 8–11, 2009

Swarbrick R, O'Connor S (2010) Low pressure to high pressures–how regional overpressure mapping helps find trapped hydrocarbons. In: Paper presented at the finding petroleum, Inmarsat Conference Center, London, United Kingdom

Traut MW, Boote DRD, Clark-Lowes DD (1998) Exploration history of the Paleozoic petroleum systems of North Africa. In: MacGregor DS, Moody RTJ, Clark-Lowes DD (eds) Petroleum geology of North Africa. Special Publication No. 132. Geological Society, London, United Kingdom, pp 69–78

Winn Jr RD, Crevello PD, Bosworth W (2001) Lower Miocene Nukhul formation, Gebel el Zeit, Egypt: model for structural control on early synrift strata and reservoirs, Gulf of Suez. Am Assoc Pet Geol Bull 85:1871–1890

Wescott WA et al. (2011) Jurassic rift architecture in the northeastern Western Desert, Egypt. In: Paper presented at the AAPG international conference and exhibition, Milan, Italy

Wescott WA, Atta M, Dolson JC (2016) A brief history of the exploration history of the Gulf of Suez, Egypt. In: Paper presented at the AAPG international conference and exhibition, Cancun, Mexico

Wescott WA, Nummedal D, Krebs WN, Karamat SA (1996) Depositional facies of the early synrift strata on the Sinai margin of the Gulf of Suez. In: Matbouli S (ed) Proceedings of the 13th petroleum conference, vol 1. The Egyptian General Petroleum Corporation, Cairo, Egypt, pp 297–312

Wood B, Zakariya A, Hady AA (2012) Resetting the geological framework of the Al Baraka field, Komombo Concession, Upper Egypt. In: Paper presented at the GEO-2012, 10th Middle East Geosciences Conference and Exhibition, Manama, Bahrain

Work DF (1994) Memorial, James Wilson Vanderbeek (1926–1993). Am Assoc Pet Geol Bull 78:1

Young MJ, Gawthorpe RL, Sharp IR (2002) Architecture and evolution of the syn-rift clastic depositional systems towards the tip of a major fault segment, Suez Rift, Egypt. Basin Res 14:1–23

Other Fuel Resources

17

Ahmed El-Kammar and Nader A. A. Edress

Contents

Abstract

This chapter reviews fuel resources other than petroleum. The first part describes the oil shale of Egypt, which is considered as an overlooked future energy resource. The second part describes coal resource in Sinai.

17.1 Oil Shale of Egypt: The Overlooked Future Energy Resources

Ahmed El-Kammar

A. El-Kammar (✉)
Faculty of Science, Department of Geology, Cairo University, Giza, Egypt
e-mail: amkammar@hotmail.com

N. A. A. Edress
Faculty of Science, Department of Geology, Helwan University, Ain Helwan, Egypt
e-mail: nedress@outlook.com

17.1.1 Introduction

Certainly, oil is the driving force behind most achievements of the 20th and 21st Centuries. The annual world consumption of oil in 2016 was 35 billion barrel. The USA, European Union, and China consume half of this great amount. In spite of the modern energy-efficient and diverse fuel technologies, the world consumption of oil is still continuously growing, and possibly the conventional resources cannot fulfill the oil demand in the foreseeable future. However, there is no straightforward consensus has emerged concerning the lifetime of the conventional oil as a main non-renewable resource and the impact of the shale oil production on the oil price nexus. Conversely, the unprecedented increase in oil prices between 2007 and 2009 triggered eagerness of oil shale companies to invest and develop technologies of shale oil production. This production in the USA steered the marked drop in oil prices in the current decade. It is evident that the price, at which shale oil produced, controls the price of the conventional oil largely and possibly vice versa.

Z. Hamimi et al. (eds.), *The Geology of Egypt*, Regional Geology Reviews,
https://doi.org/10.1007/978-3-030-15265-9_17

In spite of their well-defined meaning, some terms are erratically used as a synonym or in a wrong sense. The following is brief definitions of the currently used terms in the field of oil shale business. (1) The term "oil shale" describes fine-grained, laminated immature organic-rich (>5%, TOC) sedimentary rock, ranging in lithology from calcareous shale to limestone, of different colors, ages, and geological settings. It can produce shale oil upon artificial retorting or natural catagenic maturation. Sometimes, the produced shale oil needs costly refinement. Oil shale is an excellent source rock did not reach maturation level mostly because of inadequate burial. This does not necessarily mean that the oil-producing countries are those having remarkable oil shale reserves. For example, Morocco is not an oil-producing country but it has important reserves of oil shale. (2) Shale oil is the retorted yield from oil shale upon artificial pyrolysis. (3) The term "hot shale" describes the abnormally radioactive organic-rich sediments (including oil shale). Its radioactivity is mostly related to uranium decay series rather than thorium. Production of yellowcake from such shale is sustainable. (4) The "carbonaceous shale" is dark colored sediment rich in humic (non-sapropelic) organic matter mostly of terrestrial origin. It is more gas-prone. By definition, if carbonaceous shale contains less than 40% mineral fraction and more than 60% organic fraction, it classifies as coal. (5) The name "black shale" is abroad term describing the dark-colored thinly laminated organic-rich sediments, must not necessarily reach the oil shale grade. They are of different ages, lithology, and environment of deposition. (6) The term bituminous shale describes oil shale that reached a level of maturation, where the generated bitumen could not migrate. The source rock becomes oil impregnated, and as such will act as a reservoir. (7) The term "oil shale reserves" describes the proven geological resources that are viable for commercial utilization. The main difficulties challenging an accurate evaluation of these reserves are their rapid vertical and horizontal change in technical parameters and thickness. Additional challenges are the depth of the resources and the structural framework of the hosting sedimentary sequence.

Despite the fact that oil shale resources are huge and worldwide spread, the proved economic reserves are still limited. Vast areas, especially in the underdeveloped countries, still not yet explored. In literature, the term "resources" means different perceptions, which leads to the erroneous calculation of the oil shale potential. The term "proved resources" designates the mineable deposits that are ready to produce shale oil and gas upon retorting. The economic assessment of such proved resources depends on the cost of exploitation, operation, refinement and the current price of conventional oil and gas. The term "geological or in-place resources" is ambiguous because it does not consider the retorting feasibility and operation economics. Frequently, the geological reserves are huge but the proved economic resources are limited, at the present circumstances. The term "technical properties" of oil shale is a vector of multiple parameters, including; thickness, extension, depth, quality, structural framework, accessibility, and moisture content, in addition to the logistics and political stability of the working site. The term "barrels-equivalent" of shale oil means yield calculated on basis of detailed Fischer assay and Rock-Eval data on proved resources. If the estimation of the resources is geological or in-place, the term becomes barrels-equivalent of shale oil in-place.

However, the objective of this chapter is to draw attention to the critical importance of the indigenous oil shale resources as a genuine replacement for the continuously depleting conventional resources. It is important to endorse environmentally friendly development and utilization of oil shale as a part of our energy security strategy. Detailed exploration of predictable prolific oil shale resources in Egypt is required.

17.1.2 Global Distribution of Oil Shale

Several hundred geographic locations of potential oil shale reserves (>1 billion metric tons) are recorded in all continents, but the largest are those of the Green River Formation in the USA. However, according to Dyni (2010), the global in-place shale oil resources are about 4.8 trillion barrels at end-2008. Nevertheless, the writer believes that these reserves are rudimentary, and the actual reserves must be higher. Exploration and drilling are still required in many places, but it is a crucial commitment to Africa. The following is a brief note on the world largest oil shale occurrences.

The Eocene Green River Formation in Colorado, Wyoming, Utah and other states in the USA host vast oil shale geological reserves, of about six trillion barrels-equivalent of shale oil in-place, in three intermountain separated basins. At present, about one-third of these reserves are of high grade and can produce shale oil at a compatible price with conventional oil. In Russia, the Early Cretaceous prolific organic-rich siliceous shales of the Bazhenov Formation cover about million km^2 in West Siberian deposited under anoxic deep marine condition. According to Chazan (2013), this formation is the world's largest oil source rock that contains substantial reserves of tight oil of about two trillion barrels in-place shale oil. Russia, as the second world reserves, is followed by D.R. Congo, Brazil, Italy, Morocco, Israel, Jordan, Australia, Estonia, China, Canada, France, and Egypt, arranged in a descending order of their reserves (Fig. 17.1). The following

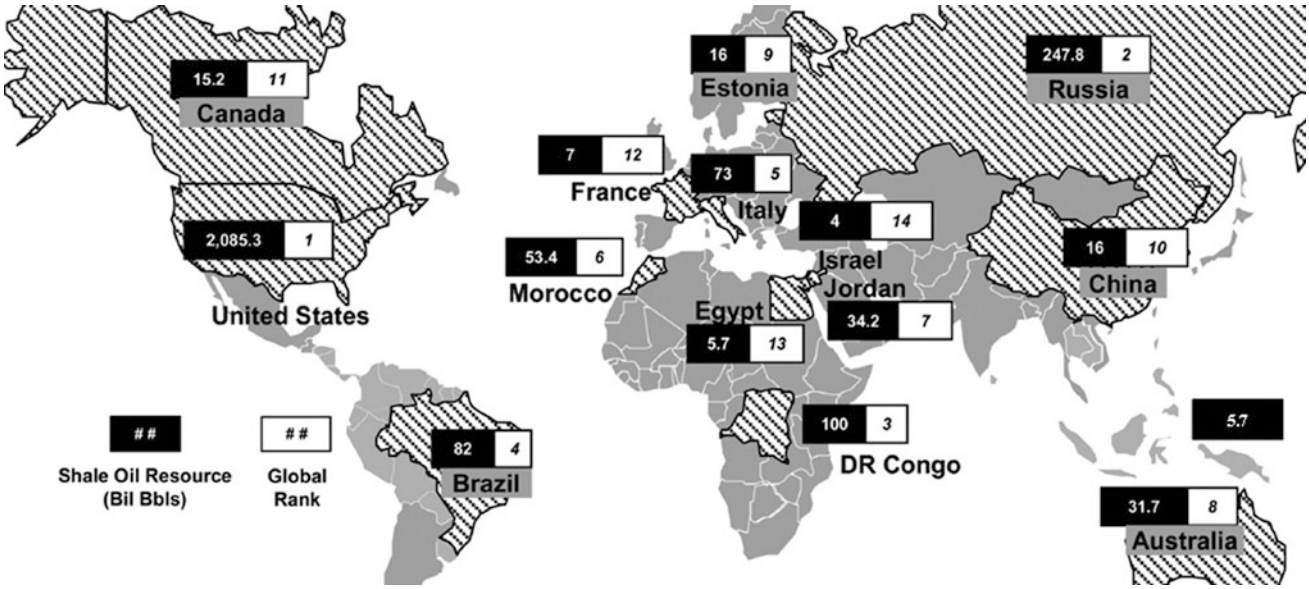

Fig. 17.1 World resources of oil shale in billion tons, after Knaus et al. (2010)

are short notes on some potential worldwide oil shale resources.

In the Democratic Republic of the Congo, multiple deposits of tar sands occur in the Tanganyika Graben region, while vast Cretaceous oil shale deposits, possibly double the size of the in-place reserves of Morocco, occur in Congo basin (mostly offshore). Despite the huge tar sand and oil shale resources, detailed exploration and utilization cannot proceed because of the political instability and civil war. According to Dyni (2010), the land of DR Congo contains 100 billion barrels in-place shale oil resources, which represents about 60% of total Africa.

In China, about 720 billion tons of Mesozoic-Tertiary oil shales occur in different occurrences, but those of Fushun (Liaoning), is the most important. However, the proven reserves are only 36 billion tons. Despite the limited shale oil yield of the lacustrine Fushun oil shale (6.3%), production of oil is commercial, being mined as a byproduct of the Eocene coal. In Brazil, the oil shale occurs in two stratigraphic horizons. The first is Tertiary lacustrine oil shale in Paraiba Valley with total reserves of 840 million barrels of in situ shale oil. The elder is of Permian age, spread in the southern part of the country, and it has the greatest commercial value where the reserves are 600 million barrels of shale-oil equivalent (the yield ranges between 2 and 7%).

17.1.3 Oil Shale in the Arab World

The Arab world holds 49.6% of the worlds substantiated oil reserves, about 29.1% of the world's natural gas and, about 43% of the world's total proven oil reserve of 713.6 billion barrels (House of Commons 2012). The global oil market is unlikely to change in the near future. There have been many recent discoveries of oil reserves outside the GCC region such as shale oil in the USA, deep offshore in Brazil and oil sands in Canada (Al-Maamary et al. 2017). Despite the considerable production and reserves of the conventional oil and gas, the land of the Arabs holds huge possibilities of unconventional non-renewable energy resources in general and oil shale in particular. The international oil shale corporations signed several memoranda of understanding with the governments of Morocco and Jordan to produce shale oil from their indigenous resources. Despite the memoranda and the fact that oil shale was discovered in some Arab states such as Morocco, Tunisia, Jordan, and Egypt several decades, shale oil is not yet produced! This is possibly due to the instability after the Arab spring and the perceptible drop in prices of conventional oil. Important oil shale resources in some other Arab Counties, such as Algeria, Syria, Saudi Arabia, Iraq, and Yemen, have recently been reported.

17.1.4 Oil Shale in Egypt

The phosphorite producing companies in Quseir and Safaga areas, Red Sea, Egypt, dumped huge tonnage of oil shale near their operating mines. This oil shale caps the mined phosphorites, which caused hazards for miners such as collapses and self-ignition. These dumped resources triggered researchers to study the oil shale of the Quseir-Safaga region for the last half-century. The oil shale, being organic-rich, can possibly deteriorate upon exposure to atmospheric conditions and, therefore, cannot be sampled

from the outcropping exposures. The pioneer study was that by Mustafa and Ghaly (1964). They estimated the oil and gas content in the dumped oil shale of some mines such as Tundoub and Nekheil, near Quseir. Malak et al. (1977) studied the origin and the organic composition of the same deposits. In 1983–1987, the German team of the Berlin Technical University guided by Prof. E. Kleitsch contributed much to the stratigraphy, origin, extension and potentiality of the oil shale resources in Quseir-Safaga region (Robison and Tröger 1983; Ganz 1984; Tröger 1984; Schrank 1984; Germann et al. 1987). El-Kammar (1987, 1993) gave a comprehensive study on the oil shale of the Red Sea and Kharga-Dakhla oases. He gave more details on the oil-yield, biomarker content, organic geochemistry and organic petrography of the oil shale of the Red Sea region and Abu Tartur mines. Hisdata on the Kharga-Dakhla oases, except Abu Tartur mines, were based on surface exposed samples where organic matter is highly degraded.

Geographically, the U. Cretaceous-L. Paleogene oil shale occupies the middle latitudes of Egypt. It is well studied and characterized in the Red Sea region and Abu Tartur mine area (Fig. 17.2). However, its extension westward o the Red Sea region as far as the New Valley is poorly studied and the relevant data are sparse and fragmented. The Carboniferous black carbonaceous shale of Um Bogma, SW Sinai and those recorded by Said (1962) in Rod El-Hammal of Wadi Araba have limited extension and their kerogen belongs to type III with relatively low TOC. They are insignificant gas prone resources and cannot be classified as oil shale. The same is valid for the minor resources of the Middle Eocene in the west of Gharaq and Wadi Maela, in Fayoum area.

The detailed exploration of oil shale in the Red Sea region (2006–2010) was directed at the delineation of potential resources and provided genuine data on the available in-place reserves, mining, utilization, and benefits. The stratigraphic and gamma logging correlations besides the electric profiles confirmed the wide extension of high-grade immature source rock at shallow depths. The kerogen is mostly of type I (liptinite) and mixed type I + II (exinite), i.e., oil-prone and derived essentially from marine sources (El-Kammar 2017). The dry basis Fischer assay data suggest that the oil shale in Quseir-Safaga produces oil yield ranges between 35 and 110 L per ton. In Quseir area, the in-place geological reserves of oil shale of the >800-kcal/kg quality

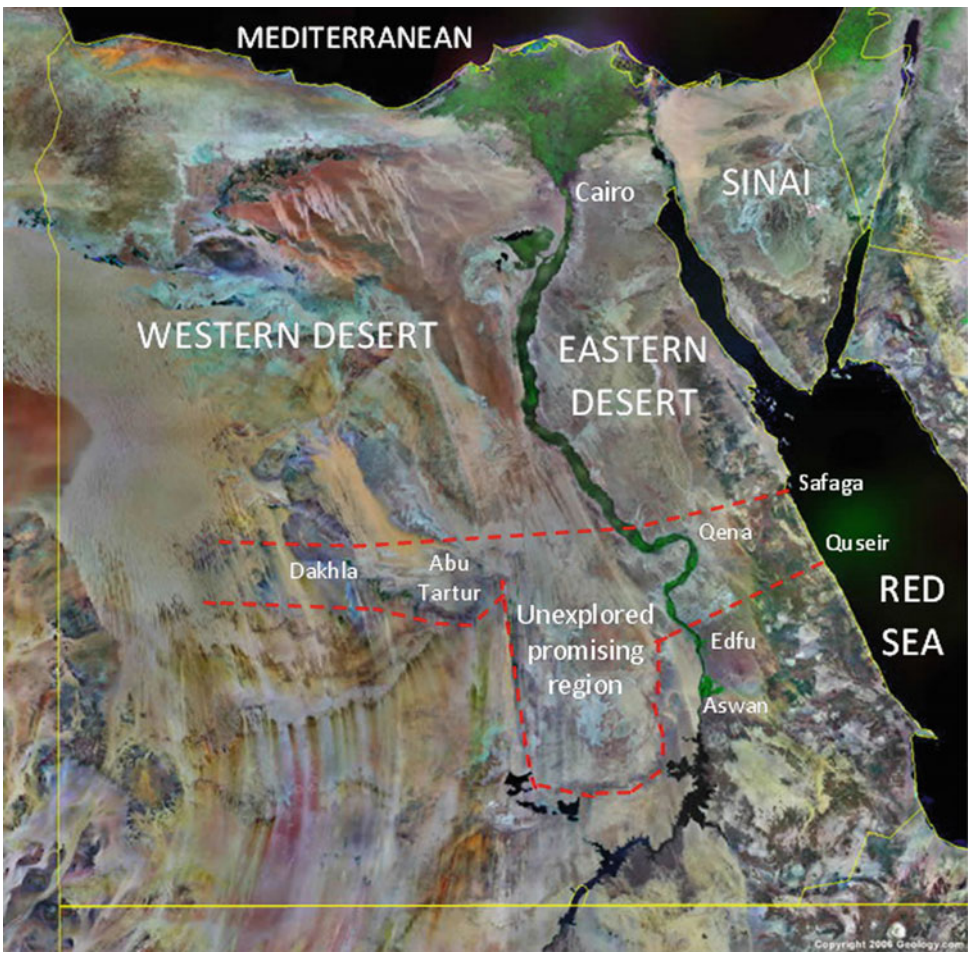

Fig. 17.2 Satellite image of Egypt showing the possible geographic distribution of oil shale resources

are more than 9 billion tons in-place that can produce about 87 L per ton, upon pyrolysis. These values suggest that the explored oil shale is suitable for surface retorting, direct combustion, and production of electricity at a competitive price (El-Kammar 2017). The writer is backing the development of innovative mining techniques to exploit both oil shale and phosphorites (billion-ton scale) from G. Duwi (Quseir-Safaga region), to overcome the serious structural challenge.

17.1.5 Geologic Setting and Genesis

The near-surface organic-rich sediments that meet the technical specification of oil shale in Egypt are those of the U. Cretaceous-L. Paleogene that occupies a belt extending from Safaga-Quseir in the east to Kharga-Dakhla in the west, passing through Qena-Edfu at the Nile Valley. This belt outcrops out along a distance of about 600 km with a width varying between tens of km in the Red Sea region to about 300 km in the Nile Valley region (Fig. 17.2). It is a part of a worldwide potential oil shale belt of a major marine transgression event. The sedimentary association of that event consists of a black (including oil) shale, limestone, phosphorite, chert, glauconite, and dolostone. That sedimentary succession gained its interest, a century ago, when the commercial phosphorites were discovered and exploited. During the last two decades, oil shale experienced renewed global interest as a potential future unconventional fuel especially during the boom on the price of conventional oil.

The sea-level transgression reached its maximum in the early Turonian, as observed in shallow water sections from Egypt to Morocco (El-Sabbagh et al. 2011). The organic richness of the Late Cretaceous sediments indicates that the continental shelve maintained a high productivity upwelling regime. Anoxic-dyoxic, and sometimes euxinic, conditions conserved the accumulated organic matter whether of marine or terrestrial origin. These organic-rich sediments were deposited in two main conformable geological formations, namely; Duwi Formation (below) and Dakhla Formation (above). According to Abdel-Malik (1982) and Schrank (1984), the former is mostly Campanian to early Maastrichtian in age whereas the Dakhla Formation was deposited in nearshore to deep marine environments during Maastrichtian to Early Paleogene as indicated by the presence of dinoflagellates, nanoplanktons, planktonic foraminifera and from palynology. The Campanian Quseir Formation, which underlies the Duwi Formation, consists of multicolored claystone, siltstone, and sandstone. It is non-fossiliferous except badly preserved plant remains and it is mostly pre-transgression. According to El-Shafeiy et al. (2017), the transgression event was associated with highly negative Ce-anomalies, high hydrogen index values, and photic zone anoxia was prominent. However, during the periods of enhanced input of terrigenous material, indicated by high Al contents and type III kerogen, water-column stratification ceased and bottom waters became oxic.

The boundary between the Dakhla Formation (the main host of oil shale) and its overlying Esna Formation represents an abrupt impressive environmental change marked by the total absence of the fauna, or presence of dwarf foraminifera, as well as the presence of dolomite crystals and the dominance of framboidal pyrite. These characters indicate a regressive sea level with euxinic evaporative environments that led to inadequate conditions for life. This points toward the restricted environment of the inner ramp and related to tidal flats and arid evaporitic coasts (Abu Ali et al. 2017). In many instances, the Esna Formation is entirely eroded and the contacts occurring between Dakhla Formation and either Tarawan or Theses formations are unconformable.

Oil shale can be deposited under a wide diversity of conditions, from freshwater to marine water. Anoxic to dyoxic conditions are described for the deposition of oil shale in shallow ponds, lakes, estuarine, and epicontinental marine basins. Euxinic conditions can be designated for specific sulfide-rich horizons, e.g., the Dakhla Formation of Abu Tartur plateau. The spatial and sequential changes in the depositional environments explain the heterogeneity in the technical properties of oil shale.

17.1.6 Organic Composition

The quality of oil shale is controlled by many factors, out of which organic richness and type of kerogen are most important. The present discussion is based on TOC and Rock-Eval data of 423-core samples containing above 4% TOC and representing the three geological formations, namely; Quseir, Duwi, and Dakhla, from bottom to top. The descriptive statistics of the data illustrates that the average TOC is about 5.25% with a maximum content of 14.62% (Table 17.1). TOC and S2 (labile fraction) are strongly correlated (Fig. 17.3). This together with T-max of 424 °C, on average, suggest immature nature and the oil shale shall be potential upon pyrolysis. The S2 value reaches 127 and averages 36.5 mgHC/g rock. The low values belong to the Quseir Formation whereas the high values go to the Dakhla Formation and specific horizons of the Duwi Formation, particularly above the commercial phosphate beds. The obtained data suggest also that the generated quotient of kerogen (S1) does not exceed 11% and the degraded organic

Table 17.1 Descriptive statistics of organic component of Red Sea and Abu Tartur oil shale

Variables	Minimum	Maximum	Mean	Std. Dev.
TOC	4.00	14.62	5.25	1.47
S1	0.06	8.53	0.72	0.74
S2	3.80	127.13	36.53	15.68
S3	0.23	3.96	1.04	0.53
Tmax	405	445	424	5.65
HI	89	1177	685	158.44
OI	3.08	70.74	20.81	11.48
S1/TOC	1.31	70.92	12.85	10.15
PI	0.00	0.09	0.02	0.02

matter (S3) is insignificant, except some horizons of the Quseir Formation where oxygen index (OI) reaches 70 $mgCO_2/gTOC$. The very high hydrogen index (HI) and low OI support an adequate preservation condition of organic matter during the deposition of the prolific horizons of both Dakhla and Duwi formations.

The plots of HI versus T-max and OI indicate that the kerogen content of about one-fourth of the Dakhla Formation samples and 10% of the Duwi Formation samples belong to type I, mostly of marine liptinite. The kerogen of the majority of samples of these two formations belongs to type I–II suggesting marine source with a terrestrial contribution. Kerogen type III is determined for 92% of the Quseir Formation samples, suggesting a main terrestrial origin of organic matter (Figs. 17.4 and 17.5). Few samples of the Quseir Formation contain kerogen type I or I + II. These samples represent the intermittent transgression periods before the major U. Cretaceous transgressive event.

The correlation matrix among data of TOC, Rock-Eval and some inorganic components (Table 17.2) suggests an intimate coherence between TOC and the multivalent redox-sensitive elements such as Cd, Mo, V, Zn and U. This implies that the anoxic conditions maintained during the sedimentation of organic matter are responsible for the accumulation of these metals.

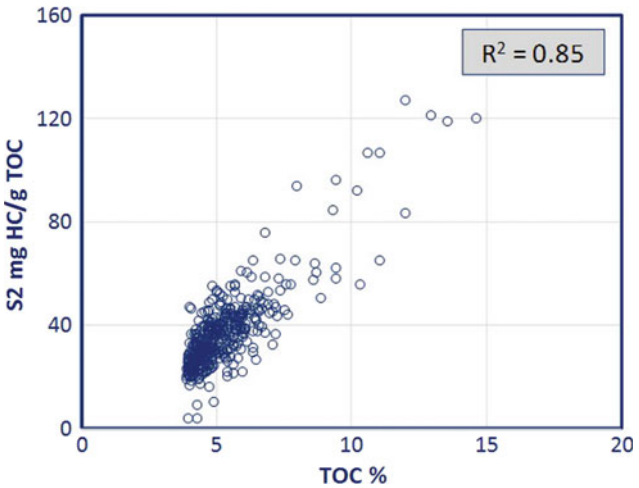

Fig. 17.3 Relationship between TOC and S2

17.1.7 Biomarkers and Maturity Indicators

By definition, oil shale is an immature kerogen-rich sediment where biomarkers (geochemical fossils) are eventually preserved. Customarily, the biomarkers are used to synthesize the maturation level of kerogen and the depositional environments. El-Kammar (1993), documented that the distribution of n-alkanes is unimodal with maximum abundance betweenn-C17 and n-C20 inferring common autochthonous marine organic matter of Safaga-Quseir area. However, some samples, especially from Abu Tartur, show evidence of mixed autochthonous (marine) and allochthonous (terrigenous) organic matter. The high phytane oil shale of Egypt indicates the high population of archaebacteria and reducing conditions during sedimentation. The predominance of hetero-compounds and asphaltenes, the naphthene bulge between C25 and C30 (resulting from steranes and triterpenes), and the high phytane abundance support the immaturity of the oil shale of Egypt.

El-Shafeiy et al. (2014) confirmed the assumption of Sepúlveda et al. (2009) concerning the drastic deterioration of all steroids at the Maastrichtian/Danian boundary because the eukaryotic algae were affected by the extinction of phytoplanktonic communities and the diminished productivity at the boundary, whereas bacteria and cyanobacteria were not affected in the same manner. They concluded that the kerogen in the Abu Tartur section is of type III except at the Duwi/Dakhla transition. Low T-max, high Carbon Preference Index, good preservation of carboxylic acids and abundant 17b, 21b-hopanes and—hopanoic acids indicate immaturity. Although thermal maturation was only low, the preponderance of rearranged steranes (diasterenes) over regular steranes indicates enhanced clay catalysis. Significant allochthonous input typifies the Abu Tartur section deposits, which are characterized by high contents of long-chain n-alkanes and low carbonate contents. The high content of desmethyl steranes and diasterenes suggests that marine algae were the main marine primary producers. The presence of different isomers of hopanes (C27, C29–C31) and hopanoic acids (C31–C33) reveals input from various bacteria. The observed variation in the abundance of biomarkers corresponds to changes in planktic algal assemblages associated with sea level change and episodic photic zone anoxia as indicated by the occurrence of aryl isoprenoids, biomarkers of green sulfur bacteria.

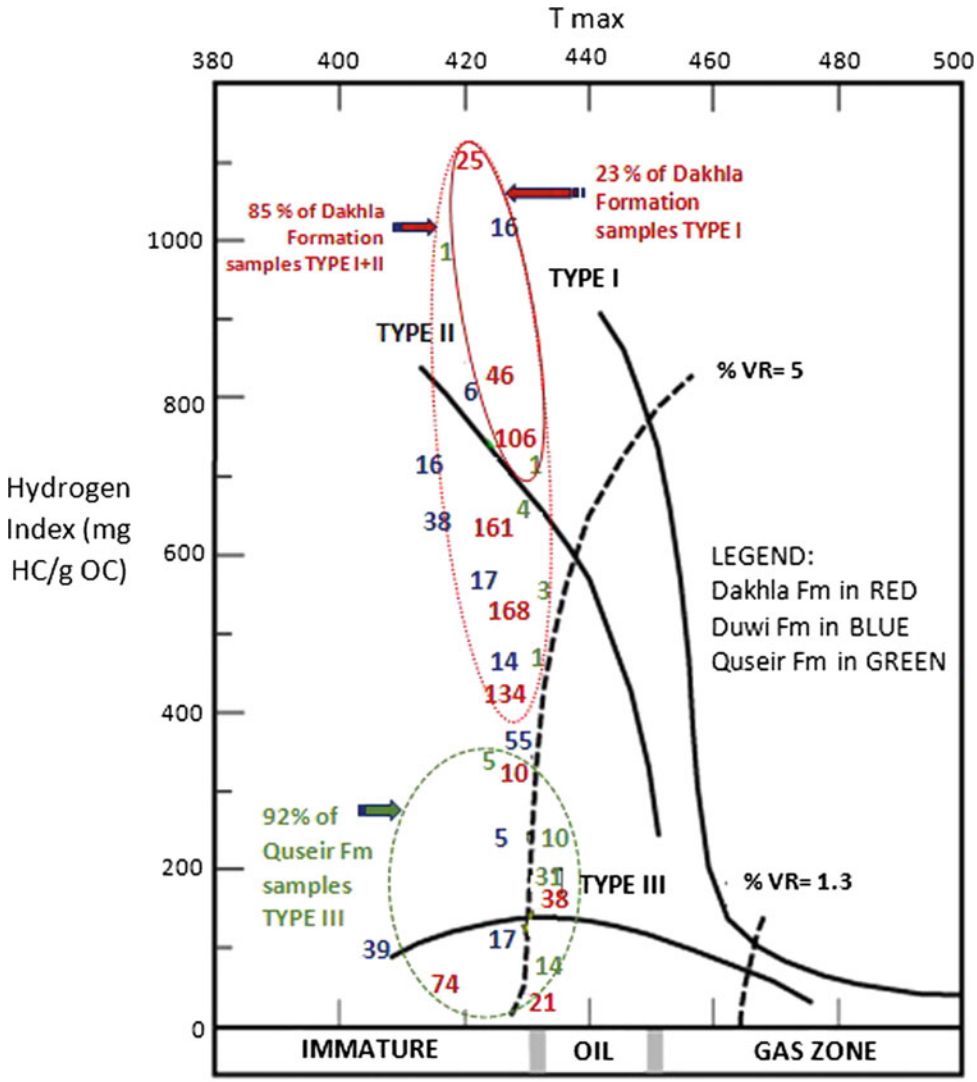

Fig. 17.4 Relationship between hydrogen index (HI) and maximum rate of hydrocarbon generation (T-max)

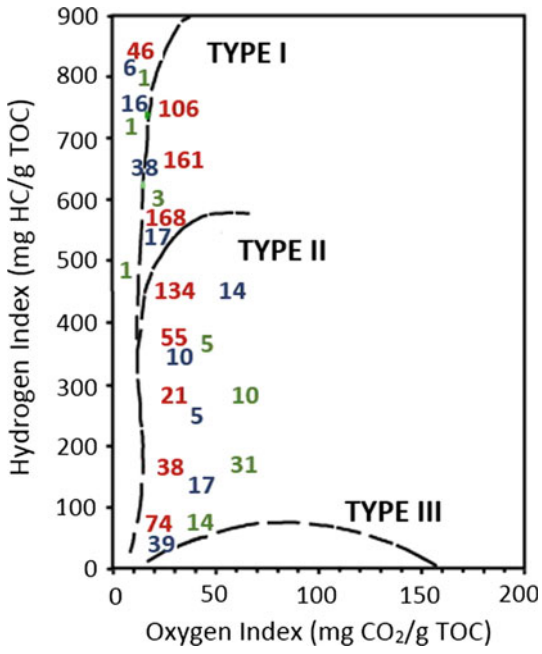

Fig. 17.5 Hydrogen index (HI) versus oxygen index (OI)

17.1.8 Inorganic Composition

Table 17.3 summarizes the descriptive statistics of the chemical analysis data of 54 major and trace elements of 423 core oil shale samples containing more than 4% TOC. The data reduction produces four main factor simitating the role of the transgression-regression event during the deposition of the oil shale (Table 17.4). The first two factors correspond to the terrestrial and marine demands with loading >50% of total variables. The other two factors signify the anoxic and oxic influence with prevailing of the former. The terrestrial factor loads for the major oxides: Al_2O_3, TiO_2, Fe_2O_3, and K_2O (Fig. 17.6), as well as their substituting trace elements, such as Li, Rb, and Cs for K, Ga for Al and Sn for Fe. This factor loads also for other terrestrial-proper indicators such as Th, Zr, Hf, Nb, Ta, and LREE. The marine factor loads for Ca and P together with the relevant trace elements such as Y and HREE. The anoxia factor loads for a group of redox-sensitive elements such as Cd, Cu, Mo, Sb, V, Zn and Ag (in addition to S, TOC, and S2). The fourth and the weakest factor expresses the impact of the oxic conditions

Table 17.2 Correlation matrix among data of TOC, Rock-Eval and some inorganic components

Variable	Al	Fe^{total}	Ca	P	S	Cd	Mo	V	Zn	U	Th	REE + Y	TOC	S1	S2	S3	Tmax	HI
TOC	–0.17	–0.11	0.00	0.19	0.16	**0.75**	**0.67**	**0.59**	**0.64**	**0.40**	−0.16	−0.13						
S1	–0.18	–0.08	–0.04	0.02	0.12	**0.45**	**0.46**	**0.42**	**0.42**	0.17	–0.12	–0.22	**0.57**					
S2	–0.30	–0.27	0.17	0.24	0.05	**0.64**	**0.55**	**0.46**	**0.58**	**0.40**	–0.32	–0.21	**0.85**	**0.45**				
S3	0.01	–0.04	0.07	–0.11	–0.14	0.17	0.21	0.21	0.07	0.01	0.10	0.16	0.08	–0.12	0.04			
Tmax	0.32	0.28	–0.34	–0.38	0.06	–0.16	–0.12	–0.05	–0.12	**–0.44**	0.34	0.06	–2.3	0.11	–0.28	0.02		
HI	–0.38	**–0.40**	**0.40**	0.20	–0.14	0.15	0.10	0.04	0.18	0.24	**–0.44**	–0.24	0.24	0.10	**0.69**	0.02	–0.23	
OI	0.08	0.00	0.05	–0.20	–0.19	–0.12	–0.08	–0.05	–0.13	–0.18	–0.15	0.20	–0.31	–0.30	–0.25	**0.88**	0.13	–0.05

and it loads only for Na and Sr (in addition to S3). In this case, the loading for Na must not necessarily indicate salinity because it is not mutual with Sr and Ca. The above four factors define the link between chemical composition and the depositional environments in a practical manner. However, the afterwards text focuses on some specific geochemical associations, namely: the terrestrial/marine indicators, the redox-sensitive elements, the rare earth elements and the radioelements.

1. Terrestrial/marine indicators: The elements, Al, Fe, Ti, and K have a thalassophobe nature and they are common constituents of clay minerals, which dominate during the regression periods and vice versa. They can be used to proxy for the terrestrial input to the depositional basin. They have mutual distribution with the other terrestrial-indicators such as Zr, Hf, Nb, Ta, Th, and LREE. In turn, they have negative distribution with the marine indicators such as Ca, P, U and Y, HREE and negative Ce-anomaly. Therefore, ratios between Al and Ca, Al and Fe, Th and U, or LREE and HREE may help the reconstruction of the sea-level oscillation (Fig. 17.7).
2. Redox-sensitive elements: The correlation matrix of the redox-sensitive elements (Table 17.5) specifies their different speciation. It is evident that Fe and S as partners of pyrite, and other sulfides as well, are responsible for the accumulation of As and Sn. The correlation indicates that the elements; Cd, Cu, Mo, Ni, Sb, V, Zn, and U are organic matter-bound. However, reduction maintained by organic matter seems to be most effective for Cd and Mo (Fig. 17.8). Pb and Sb show no clear dependence on neither organic matter nor sulfide.
3. Rare earth elements: The REE distribution in oil shale expresses both marine and terrestrial contribution to the depositional basin. The factor analysis symbolizes the terrestrial influence by the LREE and the marine by the HREE (Fig. 17.9). The LREE contribution bears a clear signature of monazite pattern whereas the HREE replicates a xenotime-like pattern. In each case, the contribution of the LREE to the total REE budget is much

Table 17.3 Summary of descriptive statistics of chemical analysis data. Data are given in ppm, unless otherwise stated

Variable	Minimum	Maximum	Mean (n = 423)	Standard deviation
Al_2O_3%	0.55	16.23	8.34	3.53
TiO_2%	0.03	1.03	0.31	0.15
Fe_2O_3%	0.21	6.81	3.12	1.36
MgO%	0.26	13.11	1.37	1.60
CaO%	0.74	47.85	29.70	9.31
Na_2O%	0.06	1.09	0.31	0.19
K_2O%	0.10	1.47	0.48	0.24
P2O5%	0.09	11.45	1.86	1.95
S%	0.10	4.15	1.76	0.70
Li	5.2	100.2	39.6	20.8
Rb	2.6	50.2	18.9	9.3
Cs	0.30	8.60	1.58	0.86
Ga	1.17	23.03	10.59	4.63
Sr	92	1504	820	265
Ba	15	297	66	34
As	0.10	30.60	8.60	6.82
Cd	0.07	240.9	6.2	20.8
Co	0.4	157.2	11.7	18.5
Cr	77	787	324	88
Cu	13	111	34	12
Mn	19	648	91	61
Mo	1	601	21	51
Ni	28	366	92	31
Sb	0.12	27.7	1.42	1.83
Sn	0.06	8.00	1.06	0.62
Pb	0.10	372.2	9.11	18.34
V	33	2256	139	193
Zn	25	1865	173	197
Ag ppb	0.11	8087	230	545
Zr	2.7	94	34	13
Hf	0.05	2.53	0.91	0.38

(continued)

Table 17.3 (continued)

Variable	Minimum	Maximum	Mean (n = 423)	Standard deviation
Nb	0.78	17.89	6.77	2.96
Ta	0.00	0.80	0.33	0.16
U	2.5	60.2	15.0	8.4
Th	0.6	10.0	4.3	1.8
Sc	1.1	14.8	7.9	2.9
Y	7.9	84.1	26.1	10.3
La	7.10	45.50	22.87	6.71
Ce	5.17	83.10	34.40	12.53
Pr	1.50	9.10	4.97	1.56
Nd	6.50	43.70	20.29	6.50
Sm	0.90	7.70	3.49	1.11
Eu	0.10	1.70	0.85	0.28
Gd	1.00	8.00	3.59	1.11
Tb	0.05	1.10	0.51	0.16
Dy	0.90	7.80	3.42	1.06
Ho	0.05	1.80	0.70	0.25
Er	0.50	5.20	2.02	0.66
Tm	0.05	0.70	0.27	0.10
Yb	0.60	4.90	1.90	0.63
Lu	0.05	0.80	0.29	0.11
ΣREE + Y	39.67	257.18	125.65	36.47

Table 17.4 Summary of data reduction of 423 chemical analyses

Eigenvalue	20.25	10.73	7.89	4.29
Variance %	33.19	17.59	12.94	7.04
Factor	Terrestrial	Marine	Anoxic	Oxic
AI_2O_3	**0.84**	−0.46	0.08	0.02
TiO_2	**0.79**	−0.46	0.09	−0.08
Fe_2O_3	**0.76**	−0.43	0.13	−0.10
MgO	−0.19	−0.07	0.09	−0.55
CaO	−0.72	**0.45**	−0.29	0.16
Na_2O	0.30	−0.07	0.04	**0.72**
K_2O	**0.70**	−0.23	0.26	−0.06
P_2O_5	−0.11	**0.79**	−0.16	−0.26
S	0.46	−0.25	0.25	−0.20
Li	**0.65**	−0.37	0.00	−0.05
Rb	**0.70**	−0.23	0.23	0.00
Cs	**0.66**	−0.23	0.32	−0.20
Ga	**0.86**	−0.45	0.10	0.00

(continued)

Table 17.4 (continued)

Eigenvalue	20.25	10.73	7.89	4.29
Variance %	33.19	17.59	12.94	7.04
Factor	Terrestrial	Marine	Anoxic	Oxic
Sr	−0.41	0.29	−0.20	**0.70**
Ba	**0.53**	0.05	0.12	0.33
As	0.10	−0.25	−0.06	0.33
Cd	−0.01	0.38	**0.85**	0.07
Co	0.12	0.25	−0.07	0.03
Cr	0.31	0.42	0.35	0.05
Cu	0.31	0.33	**0.67**	0.23
Mn	0.19	−0.07	0.01	−0.50
Mo	0.05	0.37	**0.84**	0.08
Ni	0.18	0.40	0.71	0.26
Sb	0.10	0.32	**0.82**	0.15
Sn	**0.68**	−0.20	0.15	0.04
Pb	0.10	0.13	0.00	−0.15
V	0.19	0.22	**0.87**	0.09
Zn	0.02	0.32	**0.72**	−0.01
Ag	0.08	**0.41**	**0.71**	0.12
Zr	**0.82**	−0.35	0.18	0.14
Hf	**0.84**	−0.37	0.20	0.13
Nb	**0.85**	−0.44	0.08	0.12
Ta	**0.82**	−0.42	0.11	0.10
U	−0.14	**0.84**	0.10	−0.17
Th	**0.92**	−0.28	0.05	0.00
Sc	**0.86**	−0.25	−0.02	−0.05
Y	0.27	**0.90**	−0.25	−0.06
La	**0.90**	0.31	−0.17	0.03
Ce	**0.92**	−0.07	−0.09	−0.01
Pr	**0.96**	0.11	−0.15	−0.01
Nd	**0.91**	0.23	−0.16	−0.02
Sm	**0.92**	0.26	−0.17	−0.06
Eu	**0.92**	0.23	−0.18	−0.09
Gd	**0.77**	**0.54**	−0.24	−0.06
Tb	**0.78**	**0.51**	−0.21	−0.07
Dy	**0.70**	**0.63**	−0.24	−0.07
Ho	**0.59**	**0.73**	−0.21	−0.09
Er	**0.51**	**0.79**	−0.25	−0.07
Tm	**0.47**	**0.75**	−0.21	−0.18
Yb	**0.44**	**0.82**	−0.25	−0.08
Lu	**0.41**	**0.81**	−0.22	−0.11
REE Y	**0.87**	0.42	−0.20	−0.03

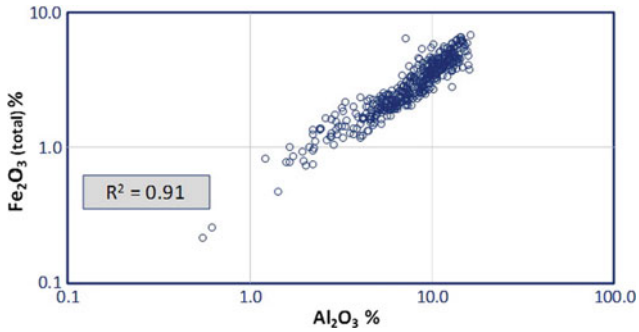

Fig. 17.6 Correlation between Al_2O_3 and Fe_2O_3 as terrestrial indicators

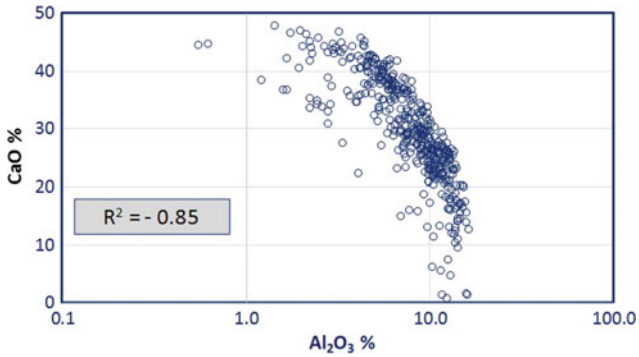

Fig. 17.7 Correlation between Al_2O_3 as a terrestrial indicator and CaO as a marine indicator

higher than the HREE. Auer et al. (2017) documented that modern ocean REEs exhibit a distinct pattern with enrichment of heavy REEs and strong depletion in cerium. Under marine environments, negative Ce anomaly, resulting from oxidation of Ce^{III} into the immobile Ce^{IV}, provides a potentially useful redox proxy in

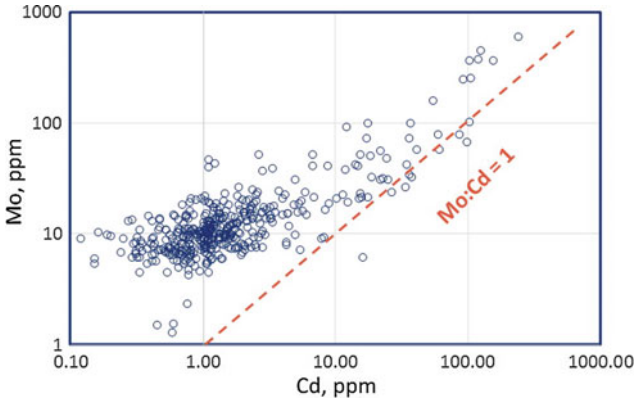

Fig. 17.8 Correlation between the two redox-sensitive elements; Cd and Mo

carbonate-dominated marine settings (Tostevin et al. 2016). The oil shale of Quseir-Safaga region displays a perfect negative correlation Ce anomaly and the LREE/HREE ratio (Fig. 17.10). Based on a plot of Ce anomaly versus alumina, Abu Ali (2013) could recognize the sea level oscillation during the deposition of the U. Cretaceous-L. Paleogene organic-rich sediments of Wassief area, Red Sea (Fig. 17.11). The plot suggests that Quseir Formation was deposited almost before the transgression, except limited intermittent intervals, whereas Duwi and Dakhla formation were deposited under marine-proper environments with oscillating sea level. The sedimentation of the Esna Formation took place under nearshore environments. According to Birdwell (2012), when REE concentrations in spent shale were normalized to an original rock basis, concentrations were comparable to those of the raw shale, indicating that REE are conserved in processed oil shales.

Table 17.5 Correlation matrix of the redox-sensitive elements

Variables	Fe_2O_3	S	As	Cd	Cr	Cu	Mo	Ni	Sb	Sn	Pb	V	Zn	U
S	**0.82**													
As	0.30	**0.40**												
Cd	−0.04	0.12	−0.09											
Cr	0.15	0.28	−0.04	0.36										
Cu	0.09	0.06	−0.15	**0.65**	0.48									
Mo	0.01	0.15	−0.09	**0.92**	0.33	0.63								
Ni	0.01	0.08	−0.17	**0.68**	0.64	0.84	0.71							
Sb	0.06	0.15	−0.04	**0.85**	0.38	0.60	0.93	0.75						
Sn	**0.60**	0.37	0.14	0.05	0.23	0.26	0.08	0.15	0.17					
Pb	0.07	0.07	−0.02	0.02	0.04	0.02	0.04	0.02	0.02	0.06				
V	0.18	0.22	−0.06	**0.85**	0.31	**0.66**	**0.93**	**0.73**	**0.94**	0.21	0.04			
Zn	0.00	0.13	−0.13	**0.81**	0.29	**0.63**	**0.70**	**0.57**	**0.60**	0.03	0.08	**0.65**		
U	−0.35	−0.09	−0.15	**0.40**	0.35	0.18	0.41	0.31	0.34	−0.23	0.20	0.28	0.33	
TOC	−0.11	0.16	−0.03	**0.75**	**0.41**	**0.54**	**0.67**	**0.57**	**0.59**	−0.10	0.01	**0.59**	**0.64**	**0.40**

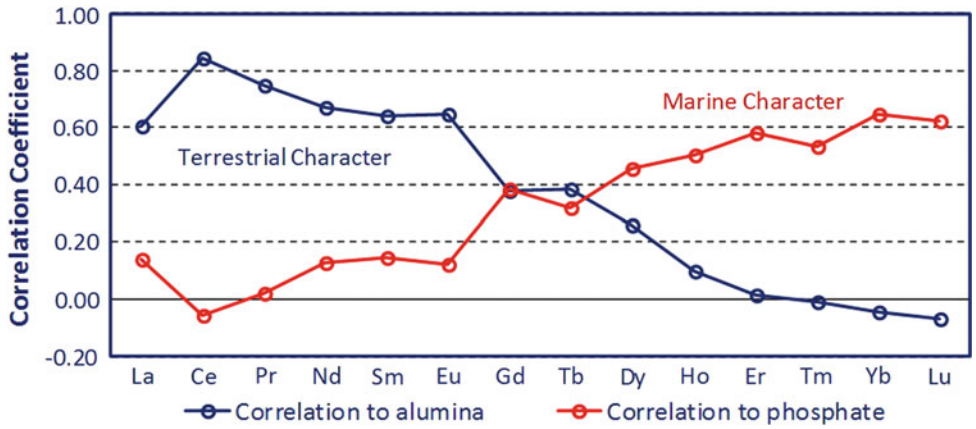

Fig. 17.9 REE loading for terrestrial and marine indicators

4. Radioelements: The reducing conditions sustained at the water-organic rich sediments interface reduce the soluble U^{VI} into the insoluble U^{IV}. The strong gamma-spectrometric signature of oil shale is principally related to U-decay series. The average concentration of U in the studied oil shale is 15 ppm but exceeds 60 ppm as a maximum value. The average content of Th is 4.3 ppm and increases with increasing detrital input (Fig. 17.12). Despite the fact that organic matter is directly responsible for the reduction of U to its immobile tetravalent state, U shows a better correlation with P_2O_5 rather than with TOC (Figs. 17.13 and 17.14). It seems that U is eventually phosphate bound rather than organic matter bound in the oil shale. Leaching experiments indicated that dilute oxidant acid can recover more than 95% of the U content in the oil shale. According to Galindo et al. (2006), the ^{238}U decay series has a radioactive equilibrium state, owing to minimal weathering processes of the Moroccan oil shale.

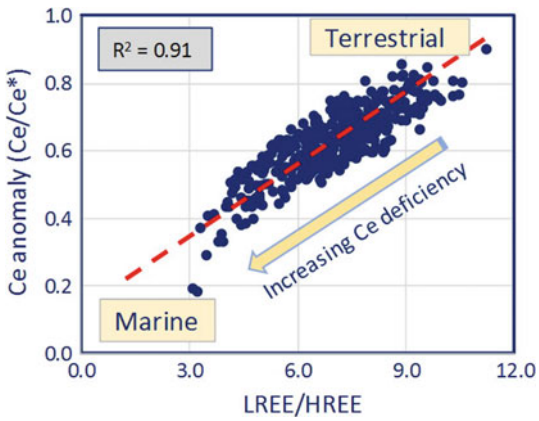

Fig. 17.10 Plot of Ce anomaly versus LREE/HREE ratio

The broad logic of the above statements agrees with the conclusion quoted by Fu et al. (2011), who classified the trace element content of oil shale from China into three affinity groups, the important of the group are the inorganic (terrestrial) and organic (marine) groups.

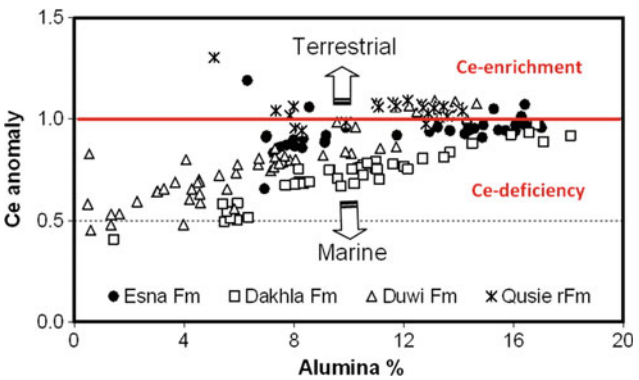

Fig. 17.11 Recognition of the depositional environment from plot of Ce anomaly versus Al_2O_3

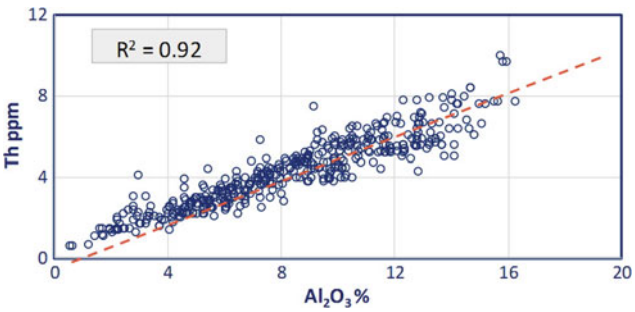

Fig. 17.12 Plot of Al_2O_3 versus Th, as two reliable terrestrial indicators

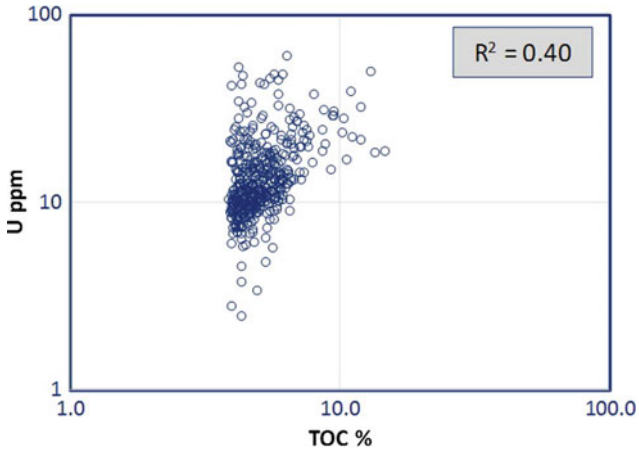

Fig. 17.13 Correlation between U and TOC

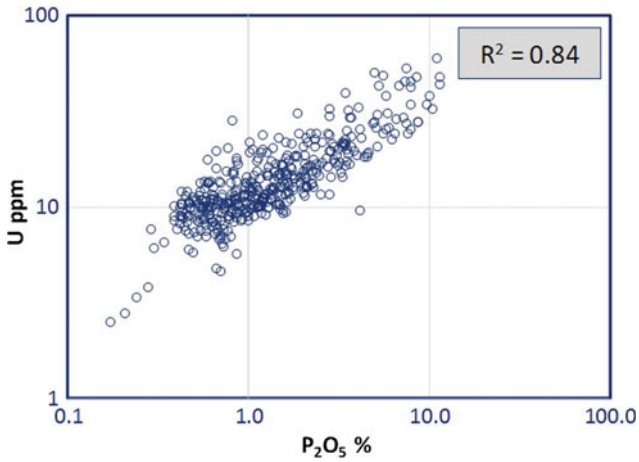

Fig. 17.14 Correlation between U and P_2O_5

17.1.9 Effect of Weathering

The dry air causes the rock to decay only very slowly, as is attested by the marvellous preservation of carved inscriptions dating from three and four thousand years ago in the arid climate of Egypt (Krauskopf 1979). This statement is undoubtedly true when colors are made of ultrastable minerals such as hematite, "limonite", goethite, pyrolusite, malachite and gypsum that were customarily used by ancient Egyptians. The statement becomes misleading when a system of organic matter rich-sediment is considered. Acids generated from the breakdown of organic matter and sulfides enhance weathering even by dew, but mostly during the pluvial periods. Oil shale, in particular, is readily vulnerable to chemical weathering. The destruction of organic matter and sulfides is accompanied with marked modifications of both organic and mineral constituents. The study of the weathering profiles developed on organic carbon-rich black shales by Petsch et al. (2000) focused only on the changes occurring in the organic compounds. They documented loss between 60 and nearly 100% of total organic carbon because of weathering. Pyrite loss coincides with or precedes organic carbon loss. They noted also that weathering causes a relative abundance of C=C and C=O bonds relative to alkyl C–H bonds accompanied with depletion of branched alkyl or long-chain n-alkyl moieties.

In oil shale, smectite shows a strong tendency to form complexes with a remarkable variety of organic molecules, which occupy the interlayer space and give rise to well-defined interlayer d spacing by XRD. This variety is known as organophilic-smectite where its interlayer organic molecules are less liable to weathering. The multivalent redox-sensitive metals such as V, Mo, Cd, and U are significantly leached out in the weathering profile (El-Kammar 2017).

The expression of extensive chemical weathering on the surface exposed oil shale is a reduction of color to pale grey with brownish patches, the dominance of gypsiferous streaks and veinlets, fissile with slippery nature and its occurrence as slope-maker (Fig. 17.15). El-Kammar and El-Kammar (1996) quantified the changes in composition due to the prolonged exposure to chemical weathering as follows: (1) Mass destruction of organic matter, even those interstratified within phyllosilicates, and pseudomorphic breakdown of framboidal pyrite (Fig. 17.16). (2) Marked breakdown of carbonate minerals (ankerite, dolomite, and-calcite) due to reaction with acids developed from weathering of sulfides and organic compounds. (3) The remarkable transformation of smectite into illite, passing through smectite/illite mixed layer. The mass breakdown of the carbonate minerals enhances the clay content in the weathering profile of the oil shale. This is accompanied by the removal of interlayer cations and increases of alumina in the silica tetrahedral layer. The total mass loss of black shales upon chemical weathering under arid environments is estimated to be about 45%, on average.

It is important to note that soil derived from the oil shale of Egypt, or elsewhere, represents a weathering product enriched in Cd, Cu, Mo, and U, which are classified as potentially toxic metals relative to the Nile and Delta soils. The soil originated from oil shale is environmentally unfriendly and special consideration should be given to the speciation of the mentioned toxic metals.

17.1.10 Utilization

The first record of production of shale oil through thermal distillation (retorting) of oil shale was by the Arab physician Yahya Ibn Masawaih Al-Mardini, in Upper Mesopotamia (North Iraq), about a thousand year ago. Long before that date, the people of North Iraq used the outcropping Jurassic

Fig. 17.15 (Left) Weathering appearance of oil shale, (right) Oil shale is slope maker on outcropping exposures

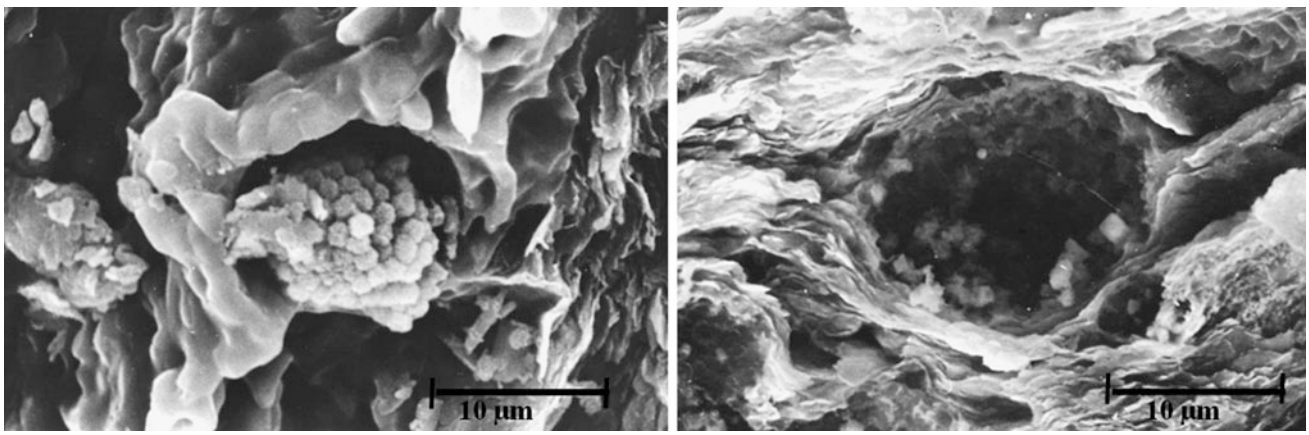

Fig. 17.16 Effect of chemical weathering on framboidal pyrite in oil shale

high-grade oil shale for cooking, medical treatments, road construction and decorative purposes. Several attempts for the distillation of oil shale were done in Austria (Tyrol), Russia (Volga), Germany (Baltic), Australia (Newnes deposit), among others, from the 14th to the 19th Centuries. The modern retorting approach of shale oil started in France in 1837. Many European scientists and enterprises developed different retorting techniques until the end of the 19th Century. Despite the huge resources of oil shale, at present, the shale oil is commercially produced only in China, Estonia, and Brazil, in addition to the USA on an experimental basis.

During oil shale pyrolysis, kerogen decomposes thermally to bitumen at low temperatures (300–700 °C), in the absence of oxygen. The decomposition rate increases with increasing pyrolysis temperature. Temperatures over 700 °C may cause endothermic breakdown of carbonates, which consumes heat and, in turn, increases heating expenses. High moisture content of the oil shale (>10%) does the same. A large number of patented retorting technologies have been introduced during the last few decades. According to Yefimov and Li (2009), oil shale retorting is a very simple process because it involves only the application of heat to break down the kerogen followed by removal and quenching of the volatile products. However, these technologies follow two main approaches, namely: in situ and ex situ. The former technologies apply pyrolysis on underground resources whereas the second requires transportation of the oil shale to the retorting facility

on the ground surface. The ex situ methods have been realized commercially since the early 20th Century. The pyrolysis products are oil, gas and spent shale. However, the produced shale oil is different from the conventional oil in composition and impurities. The shale oil is customarily heavier and richer in olefins and heteroatoms like oxygen, nitrogen, and sulfur. Moreover, it needs costly purification from suspended impurities. Some ex situ technologies depend on the direct combustion to operate power plants.

There are two main technologies of the ex situ retort, namely: (a) directly and indirectly heated gas-fired retort, and (b) direct solid heat carrier retort. The direct gas retort uses hot gas from different sources (can be recycled) in a vertical shaft kiln. Fushun, Paraho, and Kiviter have industrialized this technology of retort. In the indirect gas heat retort, oil shale is heated through a barrier wall, which reduces the heat transfer efficiency and, in turn, increases the expenses. The directly solid heated retort depends on direct contact between oil shale and hot solid surface. This technology has the advantage of high yield, and it is applied by different marked methods, e.g., Lurgi–Ruhrgas, Tosco, Taciuk and Galoter retorts. The capsule method was introduced by RedLeaf© in 2010 as a green technology for production of shale oil and gas besides heavy condensate and spent shale. Currently, the company has abandoned this approach for an alternative technology.

Oil shale spent shale (ash) is a byproduct of retorting and it may cause a serious environmental hazard if not properly utilized. The shale oil producing countries produce millions of tons of spent shale annually. It is mainly applied as road mortar and to improve the stabilization of constructions. It is also used as additives for the Portland cement industry. The modern application of spent shale includes the production of polymers and remediation of polluted and acid soil. Spent shale can be a potential source of heavy metals especially V, Zn, and Cd, in addition to U. The spent shale produced from the oil shale of the Nekheil mines (Quseir area) contains more than 1% V + Zn, as well as 60 ppm U. More than 95% of U in this spent shale can easily be recovered by dilute oxidant acid leaching (El-Kammar 2017).

The Fischer Assay analysis provides crucial data on the technical properties of the oil shale resources of the Quseir-Safaga region. The obtained data of 40 samples suggest that this oil shale produces between 30 and 120 L, averaging 45 L of shale oil per ton. A high yield averaging about 100 L (25 gallons) per ton is confirmed for 2 m thick oil shale in Nekheil (Quseir) and Mohamed Rabah area (Safaga). This yield represents up to 11.5% of the rock mass. Additional gas yield is determined to be up to 5% of the rock mass. Both oil and gas yields are strongly correlated. The relatively low moisture content (about 3% in average) is a very positive technical character, and the loss of energy because of the endothermic dehydration reaction is very low. The spent shale ranges between 80 and 90% for the prolific horizons and it is inversely related to oil and gas yields.

17.2 Coal Resources in Sinai, Egypt

Nader A. A. Edress

The famous outcrops of coal deposits in Egypt are located in Sinai Peninsula with different ages and localities. They reflect the suitable circumstances of paleogeography, diversity and evolved flora, and sedimentary paleo-environment capable of developing and accumulating peat-forming mire systems within those places. Maghara and Thora coal seams are examples of the most appropriate sites for accumulation of coal-bearing strata in Sinai, Egypt.

17.2.1 Maghara Coal Seams

The Maghara coal deposit is located in the north central part of Sinai Peninsula about 50 km south of the Mediterranean coast and 250 km northeast of Cairo. It is situated between 30°35′ and 30°50′ north latitude and 33°10′ and 33°40′ east longitude (Fig. 17.17). Coal-bearing strata are part of a sedimentary succession of the East Maghara Basin exposed in a narrow belt in the Gebel Maghara anticline structure of north-central Sinai while elsewhere they are concealed under younger Cretaceous to Eocene sediments permeability.

17.2.1.1 Stratigraphy

The origin of the Maghara coal seams has a close relationship to the divergent and extensional deformations between the African and Eurasian plates responsible for opening the Neotethys Ocean in the Eastern Mediterranean and development of several basins in north and central Sinai in the Early Jurassic time (Jenkins 1990; Zaghloul and Khidr 1992; Aal and Lelek 1994; Veevers 2004). The beginning and ending of deposition in these basins considerably varied. In the east, Maghara Basin has ≈2000 m thick Jurassic sequence, which unconformably overlies Middle Triassic rocks (Eyal et al. 1980). However, the entire fill of the basin ranging from Jurassic through Cretaceous to early Cenozoic (Eocene) reaches 3150 m. During Jurassic to Cretaceous times, this basin together with other central Sinai sub- basins were situated between the Arabian Nubian Shield highland in the south and the deep-water Neotethys Ocean in the north. Sedimentary record in the basin grades northwards from terrestrial and coastal plain to shallow marine carbonate

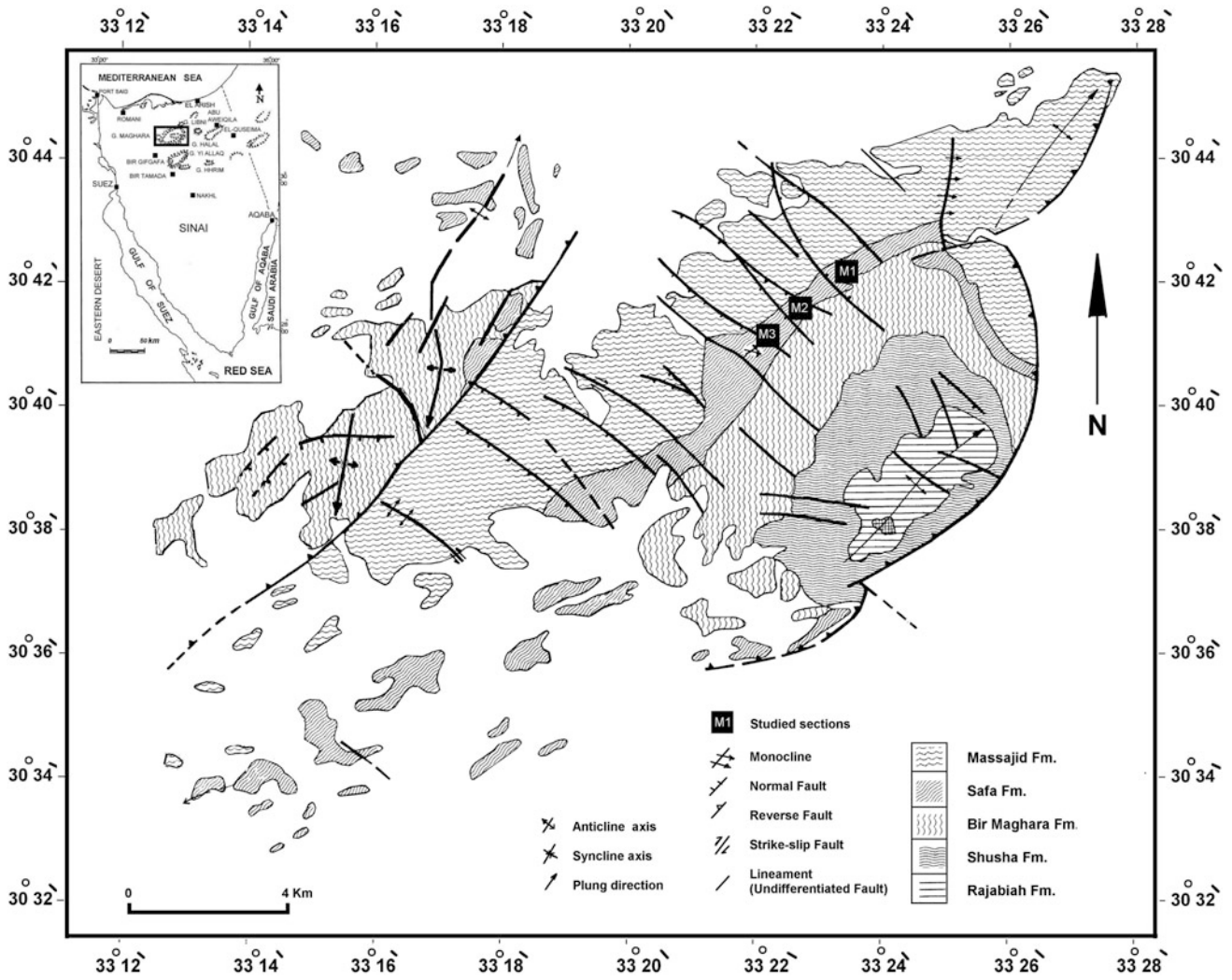

Fig. 17.17 Geologic map of the Maghara area (After EGS 1992)

platform (Jenkins 1990; Abed et al. 1996; Osamn et al. 2000; Moustafa and Salama 2005; Kuss and Boukhary 2008). These environments alternate also vertically, thus suggesting prominent relative sea-level changes during deposition (Fig. 17.18).

The Jurassic strata in the North Central Sinai area are subdivided into six lithostratigraphic units in the rank of formations that together form the Maghara Group (Said 1990; Issawi et al. 1999) (Fig. 17.18). The Lower Jurassic formations comprise fluvial to nearshore marine sandstones with subordinate coal- bearing clay and silty beds. The coarse facies of the Mashabba and Rajabian formations are interpreted as deposits of the braided fluvial system running from the southern hinterland area to the north. They alternate with shallow marine sandstone and carbonate particularly in upper parts of the formations. Individual formations, therefore, record transgressive-regressive cycles. The Middle Jurassic Safa Formation includes coal seams of the Maghara coal deposit. The Upper Jurassic Masajid Formation records a widespread marine transgression and deposition of shallow marine coral limestone following glauconitic marls at the base and shale interbed at the top.

17.2.1.2 Geological Setting

In the Maghara area, the outcropping Jurassic succession reaches a thickness of approximately 2200 m and includes coal-bearing strata of the Safa Formation of Bathonian age (Kelley and Wallis 1991; Tawdros 2001). Sinai Coal Company (1994) recorded five coal seams numbered from top to bottom (Fig. 17.18). Their thicknesses vary between 10 and 135 cm. Economic thickness (over 1 m) and quality reach only the lowermost coal seam No 5, which was exploited in the Maghara mine. This coal is underlain and overlain by 10–50 cm black shale beds rich in plant remains. Palynological data from Maghara coal-bearing interval show alternation of pteridophyte-/gymnosperm (Mohsen 1990),

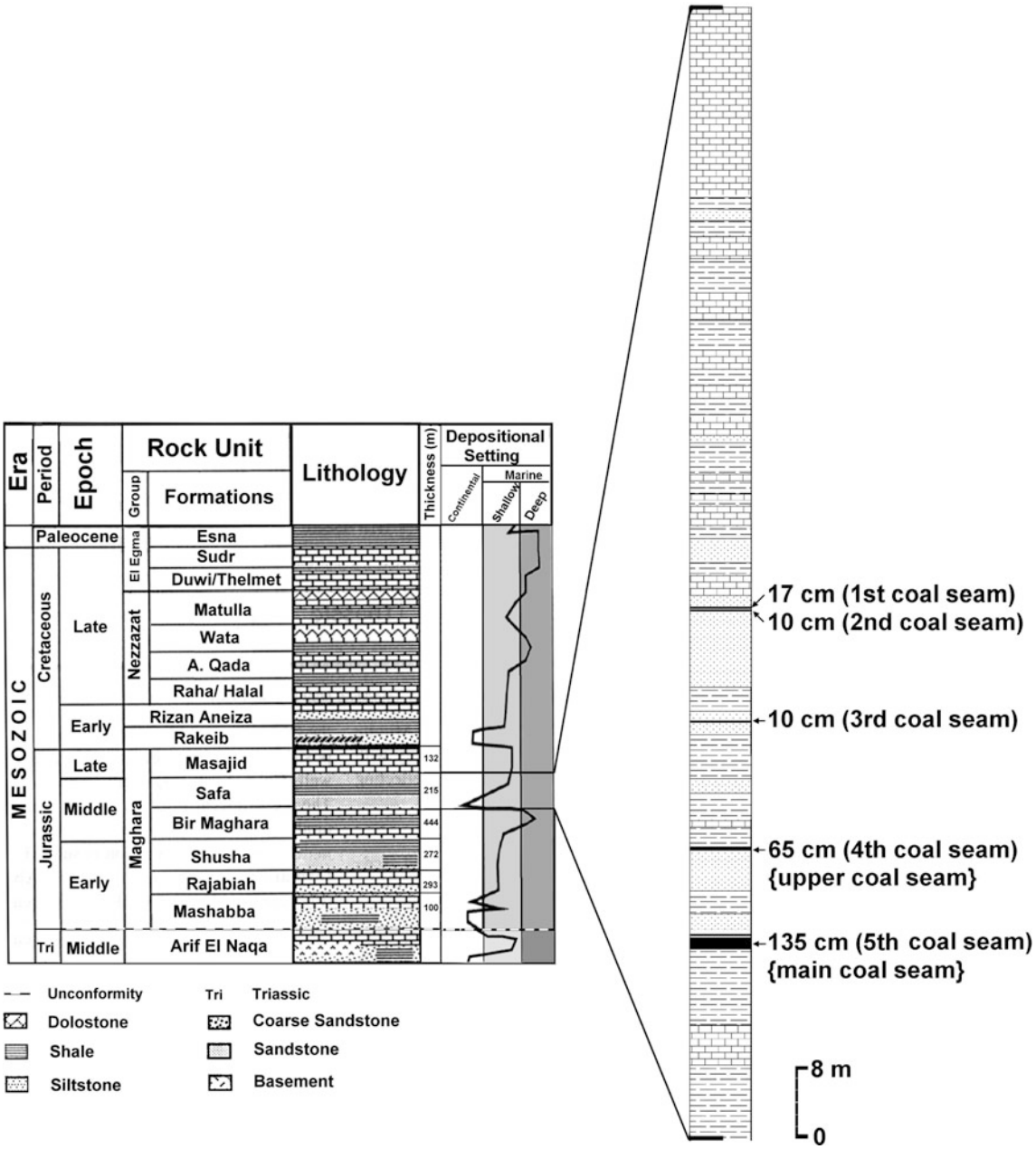

Fig. 17.18 Generalized lithostratigraphic subdivision of strata in basins of the Northern Sinai area (Said 1962; Al-Far 1966; Jenkins 1990; EGPC 1994). The right column shows a section of the Safa Formation exposed at Wadi Safa (Sinai Coal Company 1994)

dominated vegetation with marine elements, including dinoflagellates and acritarchs that indicates oscillation between non-marine swamp and coastal marine nearshore environments. The Maghara coal is a part of the Assemblage Zone No. III of Mohsen (1990) that is dominated by pteridophytic spores (59.7%), whereas the rest consists of gymnosperms pollens. Marine microflora is missing. The recorded spores represent mostly ferns and lycopsids (Balme 1995). Structurally, the Maghara coal-bearing strata in Gebel El-Maghara is a plunging anticline fold trending SW–NE with a dip of NW flank of ≈25 o and steeper SE flank dipping at 80–90° (Said 1990).

The Maghara coal seams are a part of the terrestrial succession evolved by a shallowing-upward of the marine limestone succession of the Bir Maghara Formation. It is overlain by shale with drifting plant remains as evidence of inundation of the mire precursor. It suggests that coal was developed from coastal mire established during relative sea level drop and its formation terminated subsequent relative sea level rise (Fig. 17.18).

17.2.1.3 Lithotypes and Maceral Analysis

Lithotypes

The macroscopic examination of coal sections along Maghra mine proved the presence of all the main seven lithotypes of Diessel (1992, Fig. 17.19). In a descending order, they are represented by clarain (23%), duroclarain (19%), clarodurain (15%), durain (15%), shaly coal (15%), vitrain (12%), and fusian (1%). The distribution of lithotypes in the 5th coal seam of Maghara is not random, but, in all three sections, displays a pattern of dull lithotypes at the base to bright lithotypes in two-thirds of three-fourths of the coal seam sections where bright (vitrain) coal dominates. Above this level, an opposite trend is observed up to the top of the coal (Fig. 17.19).

Macerals Analysis

The Maghara coal mine is characterized by the predominance of vitrinite macerals followed by liptinite and inertinite (Figs. 17.20, 17.21 and 17.22). An average content of vitrinite group on mmf bases is 71.1%. Telovitrinite, represented dominantly by collotelinite, is the most abundant vitrinite subgroup of the average 34% (Fig. 17.22). It is characterized by poorly defined structure and occurs as thin bands or isolated fragments of variable thickness/size within mostly liptodetrinite and collodetrinite groundmass. Threat-like resine ornamentation is the dominant features of collotelinite impregnation with resinite maceral (Figs. 17.20a–d).

Liptinite is the second most abundant maceral group. Its content varies between 12.5 and 72.4%, averaging 25.2%. The most common liptinite maceral is sporinite, 8% in average (Fig. 17.21a–c, and e). Sporangia or pollen organs filled with spores/pollens have been also found (Fig. 17.21 c). Resinite is the second most important maceral (6.8% on average). Inertinite in the studied coal samples is present in very low values between 1.2 and 13% (~4% on average). The identified types were all the macerals of the group (Figs. 17.20c, f–h; 17.21 a–f). Micrinite is the dominant maceral of the group. It commonly occurs as aggregate within vitrinite. Fusinite is present in arc-shaped fragments of former cell tissues (Bogen structure, Fig. 17.20g). Semi-fusinite is rare. The content of dispersed mineral

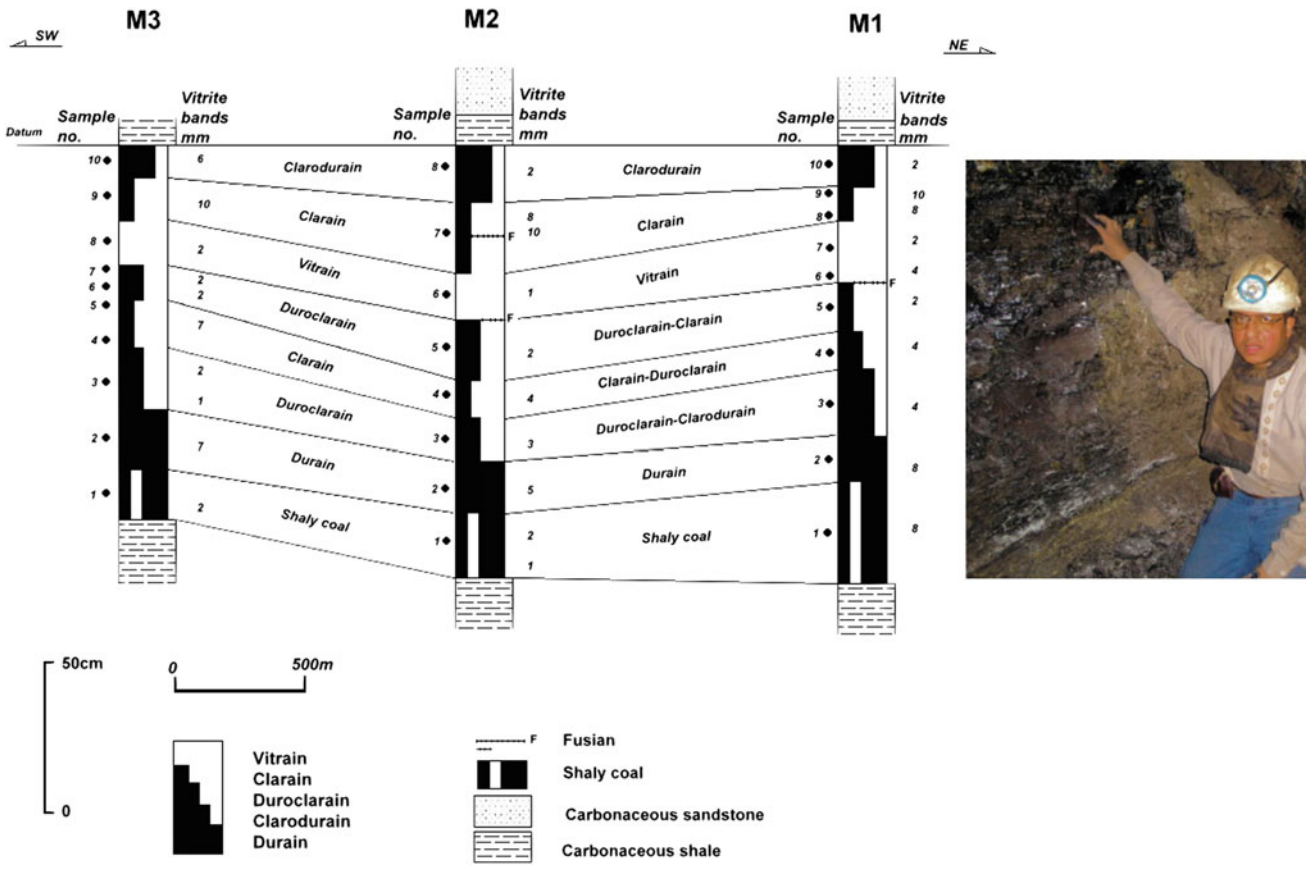

Fig. 17.19 Samples and lithotypes of M1, M2, and M3 sections along the main gallery of Maghara mine (Edress et al. 2018)

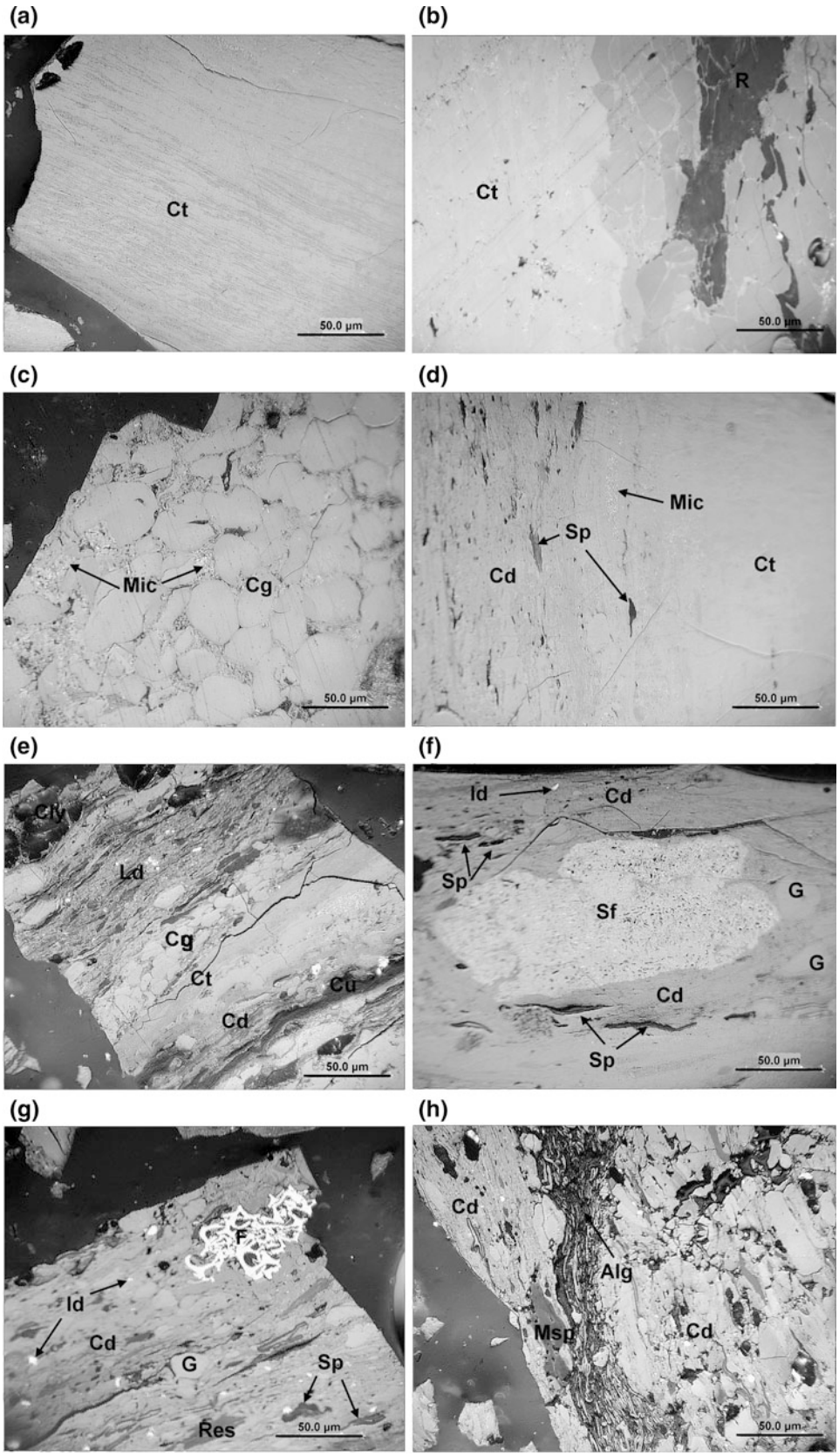

Fig. 17.20 Typical macerals of the Maghara coal seam (Edress et al. 2018). **a** Collotelinite with dark threat-like resinite impregnation (M3-4), **b** Collotelinite impregnation by resinite that gives a dark tone of impregnated cell lumen (M3-5), **c** Micrinite occurs within a void space of corpogelinite (M1-4), **d** Collotelinite (at right) transformed into collodetrinite at left with micrinite, sporinite and resinite (M1-5), **e** Rapidly change bands of macerals from collodetrinite with cutinite at base forward to collotelinite, then corpogelinite, liptodetrinite and finally clay minerals at the top (M1-4), **f** Semifusinite enclosed within collodetrinite groundmass with sporinite, inertodetrinite, resinite and gelinite (M3-4), **g** Fusinite embedded within collodetrinite groundmass with sporinite, inertodetrinite, resinite and gelinite (M1-10), **h** Very dark lamalginite sandwiched between collodetrinite-rich gelinite at right and collodetrinite-rich sporinite, megasporinite and resinite at left, Inertodetrinite dispersed within both collodetrinite groundmass (M1-10). Bar scale: 50 µm

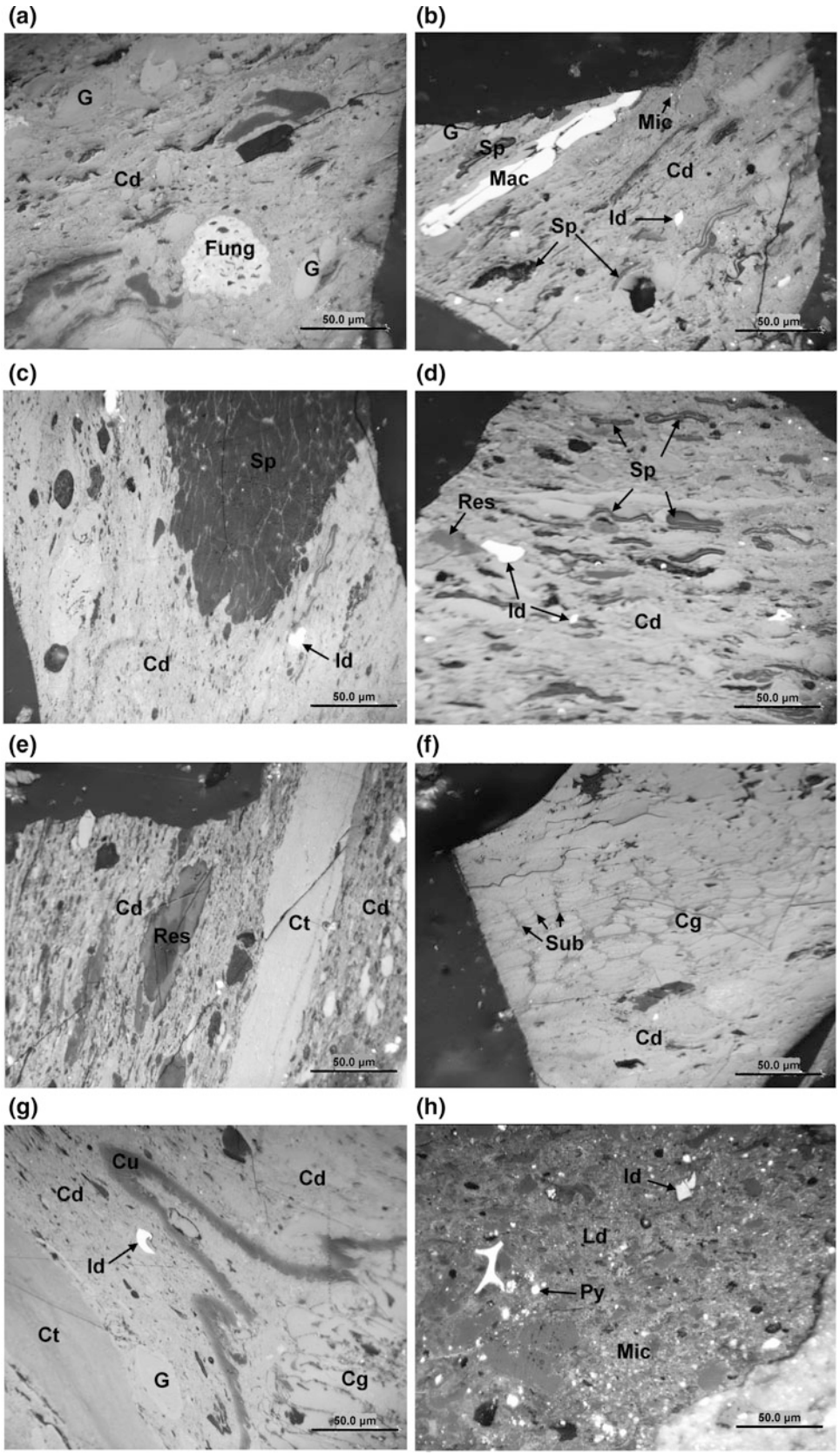

Fig. 17.21 Typical macerals of the Maghara coal seam (Edress et al. 2018), **a** Collodetrinite matrix associated with multicellular funginite, sporinite, resinite, and gelinite (M3-8), **b** Collodetrinite ground mass encompass macrinite, sporinite, resinite, inertodetrinite (M3-1), **c** Mega-sporangium associated with colldetrinite, inertodetrinite, and resinite (M1-2), **d** Collodetrinite rich sporinite, with intertodetrinite, micrinite, and resinite (M1-10), **e** Thin Collotelinite bands between two bands of collodetrinite. Resinite shows a light zonation. Sporinite, resinite and alginate are present too (M3-2), **f** Thin suberinte cell walls of corpogelinite and collodetrinite, inertodetrinite and resinite association (M1-8), **g** Collodetrinite matrix embedded cutinite, inertodetrinite, gelinite, and micrinite, with corpogelinite and collotelinite association (M3-4), **h** Dark Liptodetrinite groundmass with inertodetrinite, micrinite and mineral pyrite (M1-1). Bar scale: 50 µm

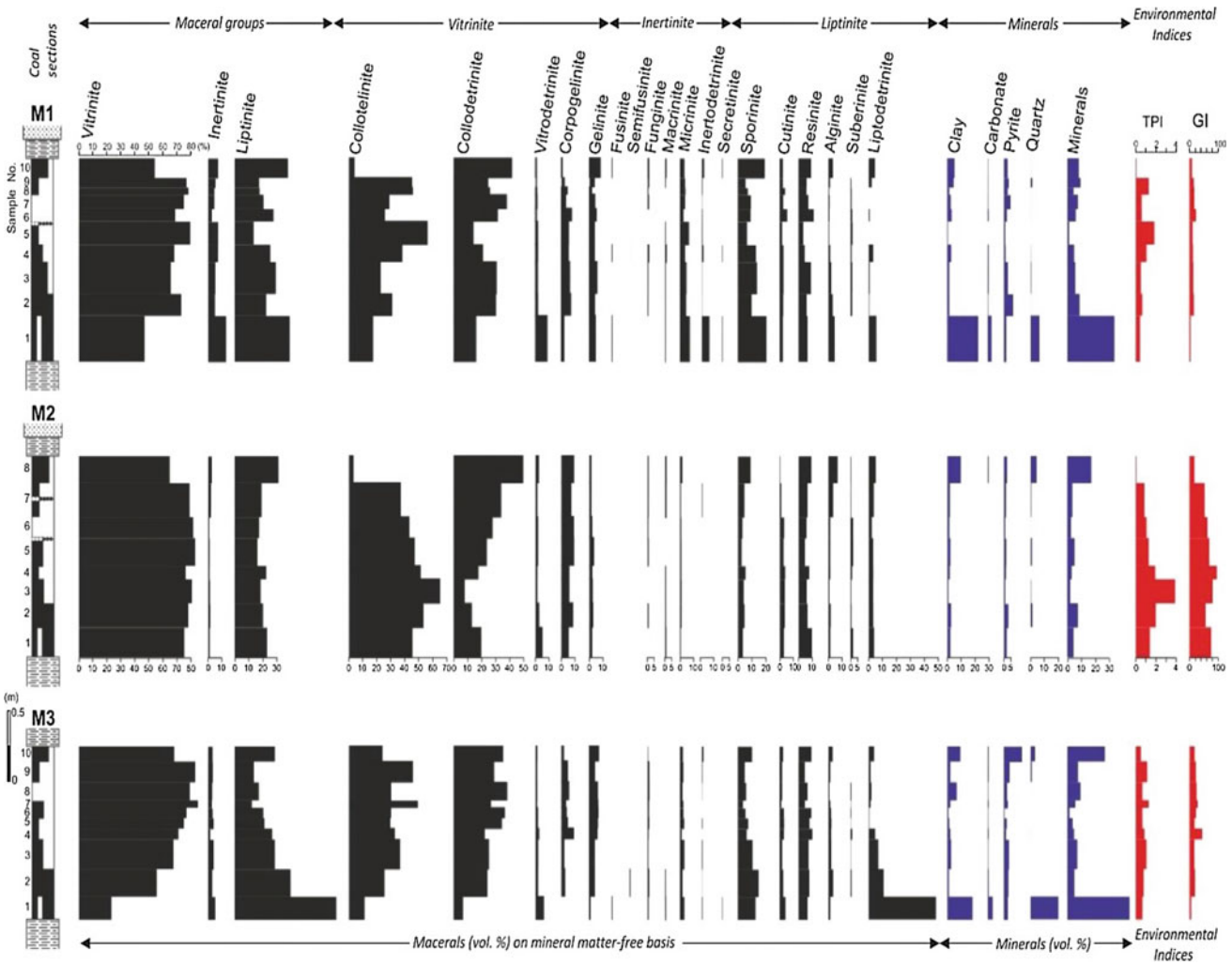

Fig. 17.22 Maceral distribution and values of Gelification Index (GI) and Tissue Preservation Index (TPI) indices in the sections of the Maghara mine (Edress et al. 2018)

matter is generally low (9.9% on average), except the lowest and uppermost samples in most sections.

Maceral Indices and Facies Diagrams *GI (Gelification Index) versus TPI (Tissue Preservation Index)*

The GI of the Maghara coal mine varying between 3.7 and 95.6 is 30.8 on average. The TPI values of coal lie between 0.1 and 3.8, averaging 1. Plotting of Mahgara coal samples on Diesel's (1982 & 1992) Facies diagram (Fig. 17.23) indicates their position mostly in the area of limno-telmatic (46%) and telmatic (43%) zones. Only three samples with high ash content at the base of coal Sects. (11%) fall within limnic conditions.

17.2.1.4 Hydrological Model of Mire Systems

The basal few tens of centimeters of the Maghara coal starting with carbonaceous/argillaceous coal is rich in clay minerals and quartz grains (Fig. 17.19). The organic matter shows low vitrinite and increased liptinite contents (Fig. 17.22). This combination together with common alginite suggests a high groundwater table, irregularly dense vegetation cover with areas of open water and scarce vegetation. Such an environment supports the undisturbed deposition of mud suspension (Mach et al. 2013; Opluštil et al. 2013).

The middle part of the coal sections with brightening uptrend is marked by an increase of vitrinite content compensated by the decrease of liptinite and mineral matter. Generally, the increasing content of collotelinite, up the section together with the TPI (Fig. 17.22) suggests a rising potential for preservation of plant tissues. It probably reflexes an increasing proportion of arborescent vegetation and acidity of the peat swamp water due to humic acid production and low clay content. Such conditions inhibited bacterial decomposition and preservation of plant tissues (Diessel 1992; Calder 1993). Palynological data suggest that

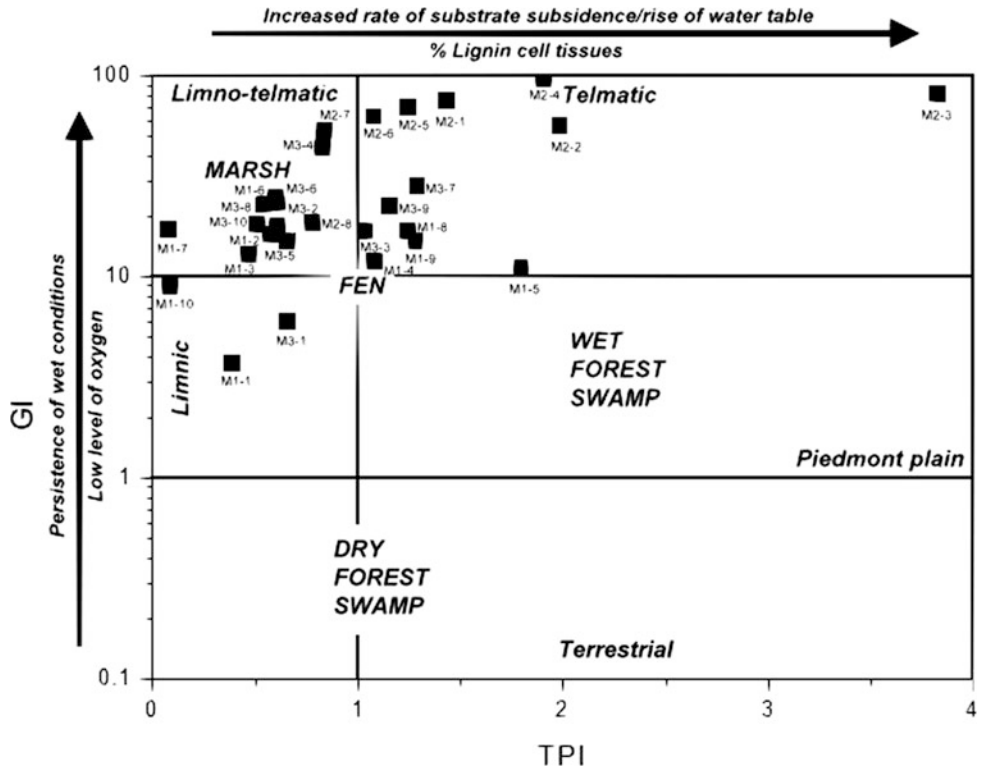

Fig. 17.23 The GI versus TPI diagram for coal facies types of Maghara coal (Edress et al. 2018)

peat-forming forest was dominated by podocarpacean and araucarian conifer trees (Mohsen 1990). In this stage of development, the precursor of the Maghara main coal was probably a rheotrophic forest peat swamp with anoxic waterlogged conditions supporting severe gelification. The increase of arborescent vegetation proportion and overall density of vegetation cover suggests upward decreasing accommodation/peat accumulation ratio typical of the process of terrestrialization (Diessel et al. 2000, Petersen and Ratanashien 2011).

The upper part of coal with dulling uptrend is interpreted as a record of increasing of accommodation/peat accumulation ratio that is typical of paludification process (Diessel et al. 2000) resulting in mire inundation, cessation of peat formation and its replacement by clastic deposition (Fig. 17.19). Facies indices show a decrease in the potential for preservation of plant tissues and overall transition to limno-telmatic and finally to limnic conditions similar to those in the basal part of coal.

The hydrological and depositional model of the Maghara coal mine shows that changes in water table controlled the petrographic composition of the resulting coal seam. In the coastal position, like in the case of the precursor of the Maghara main coal, the groundwater and seawater are hydrologically connected. It implies that the relative sea level rise will cause also the groundwater table in the mire to rise. This, in turn, results in the creation of accommodation space for peat and/or siliciclastics (Bohacs and Suter 1997; Diessel et al. 2000; Diessel 2007; Holz et al. 2002; Petersen and Ratanshien 2011). Peat formation is thus, controlled by sea-level changes and is considered in the sequence stratigraphic context (e.g. Bohacs and Suter 1997; Diessel 2007).

Consequently, the part of coal seam sections with upward brightening trend indicates cessation of relative sea level rise and terrestrialization of the environment. Similarly, the remaining dulling upward part of coal represents a paludification process related to sea-level rise. This is also supported by the increased pyrite content in the roof of coal. It is assumed that the vertical succession of environments recorded in the sections of the Maghara main coal is lateral shifts resulting from the same environments that coexisted as zones between the dry terrestrial (fluvial) habitats further south and littoral conditions of the Neotethys Ocean to the north (Fig. 17.24).

17.2.1.5 Fuel Analysis and Rank Determination

A comprehensive study of proximate and ultimate analysis performed by Edress and Abdel-Fatah (2018) for twenty eight coal samples of Maghara coal indicated that the main coal seam (MCS) is classified as high grade coal, medium

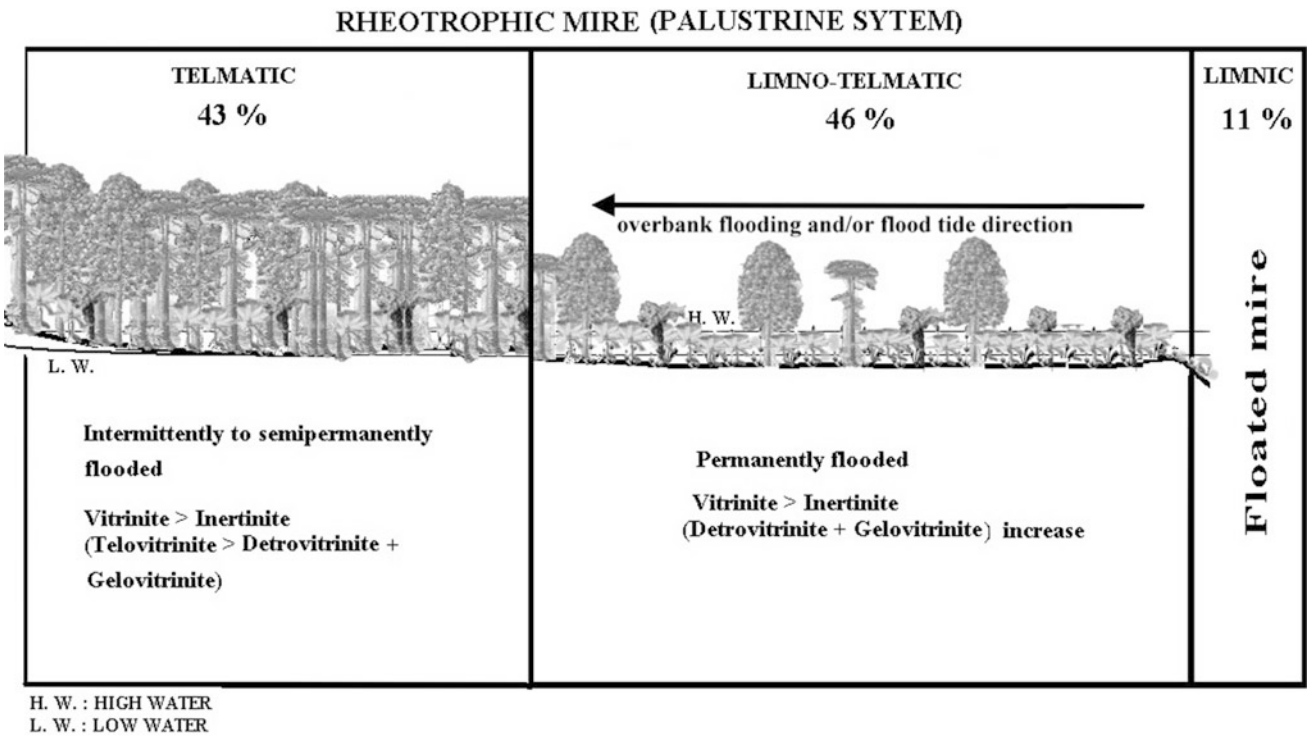

Fig. 17.24 No-scale proposal hydrogeological model of Maghara coal forming mire; percentage taken as average data values from macerals, indices and facies diagrams (Edress et al. 2018)

rank (D) of Para-bituminous class based on its average values of ash content 7.1% (dry-base; d.b), gross calorific value 29 Mj/kg, moist ash free, and random vitrinite reflectance 0.43% (Fig. 17.25). Synonym nomenclature of the studied Maghara coal-based to ASTM classification is high volatile (C) class of bituminous group with agglomerating character attributed to their values of gross calorific value 30 Mj/kg-(moist-mineral-matter-free; mmmf), fixed carbon 45% (dry-mineral-matter- free; dmmf) and volatile matter 54.8% dmmf.

Elemental ratio of H/C versus O/C indicates that the majority of the Maghara coal occupies the area of vitrinite genesis pathway on van Krevelen diagram and within the area of per-hydrous in Seyler chart of the dominated anoxic condition. The Maghara coal is a type III kerogen, corresponding to the humic characteristic, within the immature and mature zones of coalification (Durand and Monin 1980, Fig. 17.26).

17.2.2 Thora Coal Seam

17.2.2.1 Stratigraphy

In the study area, the Paleozoic strata appear to be perfectly horizontal representing, structurally, the eastern shoulder of the Gulf of Suez Basin. Stratigraphically, the area of study contains clearly obvious outcrops of Paleozoic age. The Paleozoic strata unconformably overlie the Precambrian pink granitic rocks which are highly affected by basic dykes. They are differentiated into five formations from base to top; Araba Formation (Lower Cambrian) consisting mainly of vary-colored sandstone which is composed of quartz arenite of 98 m. It is overlain by cross-bedding white color sandstone of Naqus Formation (Upper Cambrian) attaining 40 m. A distinctive 43 m dolomitic limestone of the Um Bogma Formation of Lower Carboniferous unconformably overlies Naqus Formation. The Abu Thora Formation (Visean) conformably overlies Um Bogma limestone (Said 1990; Kora et al. 1994; Issawi et al. 1999). It is composed of three rock units of lower and upper sandstone sandwiches coal-bearing shale with a maximum thickness of about 227 m. The topped strata are of a Permian age, which is characterized by red beds of coarse-grained sandstone and shale of Qiseib Formation unconformably overlying Abu Thora Formation. Jurassic sill occasionally caps the Abu Thora Formation, especially in the area west of Gebel Hazbar.

The coal-bearing strata within the Abu Thora Formation attain 12 m in thickness. They are composed mainly of shale. Lithologically, they are differentiated from top to base into; 2.5 m of kaolinitic shale at the top, 3 m of coaly shale and carbonaceous shale, 55 cm of coal seam which overlains 7 m of coaly shale and carbonaceous shale at the bottom

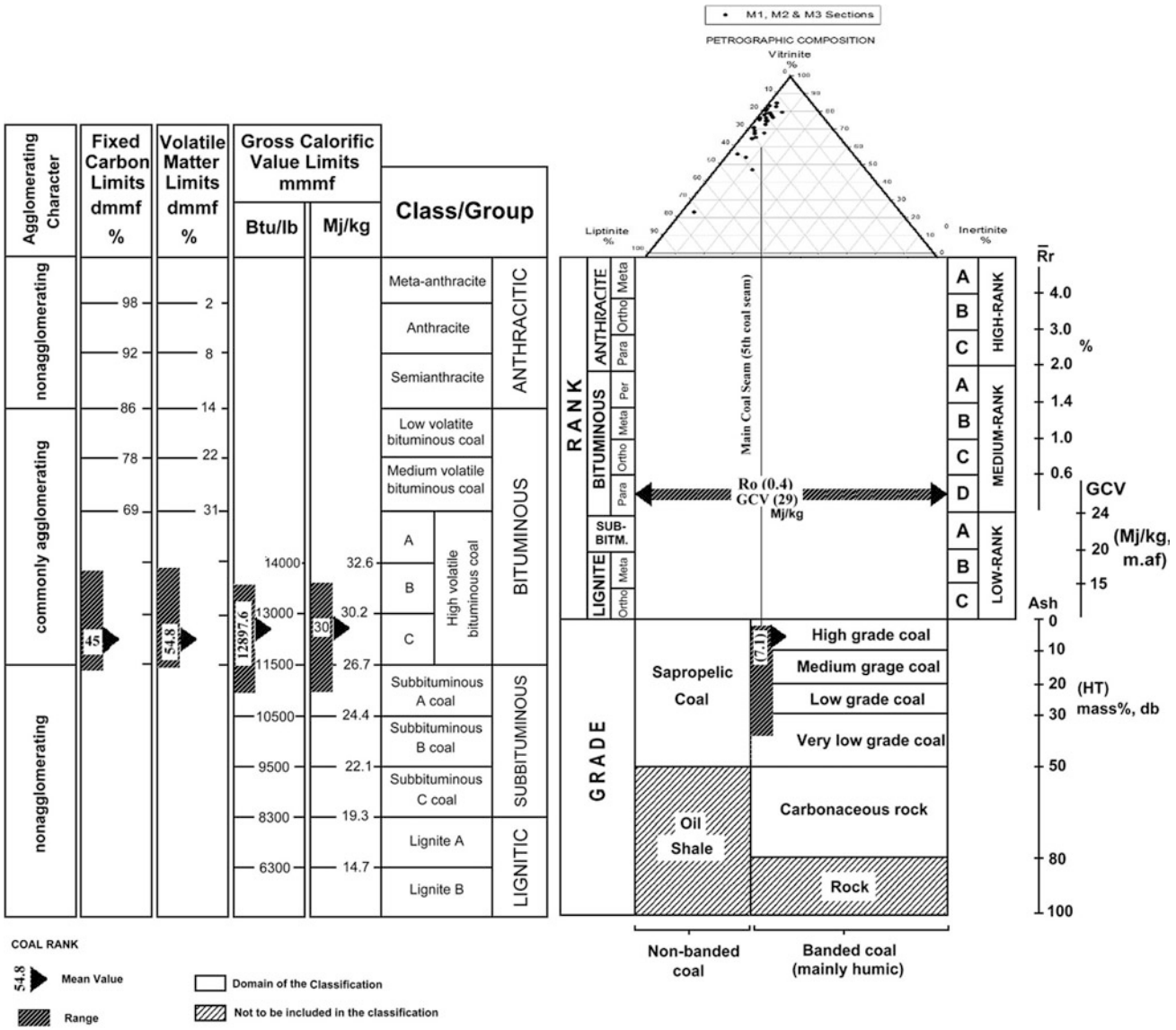

Fig. 17.25 Rank of the Maghara coal on the basis of the different rank parameters according to the international classification of in situ coal; 1998 (right side) and standard classification of coal by rank (ASTM: D 388-99 2016) on the left side (Edress and Abdel Fatah 2018)

(Fig. 17.18). They extend in the study area for about 15 km along the NE–SW trend with a sedimentary cover of sandstone, which does not exceed 29 m thickness.

Edress and Khalid (2018) conclude that the Carboniferous coal seam within Abu Thora (Ataqa) Formation is a combination of coal and shaly coal facies. The abundance of shaly coal facies is three times more than coal facies. The pure coal samples concentrate in the area situated at the west of Gebel Hazbar. Coal seam ranges in thickness between 20 cm in the west to 72 cm toward the northeast with an average thickness of 55 cm.

17.2.2.2 Geological Setting

The Early Carboniferous (Visean) time was characterized by few diversities of flora like sphenopsides and pteridosperms/fern, which much dominated along the global worldwide carbonate ramps. In addition, the first evidence of mangal (mangrove) flora extended along and near the shoreline (Greb et al. 2006). At the Late Carboniferous, the entire primitive flora were well developed and were replaced by extensive accumulation of lycopsids which covers the widespread mire system of peat swamps in earth history (Walker 2000; Scotese 2001; Thomas 2002).

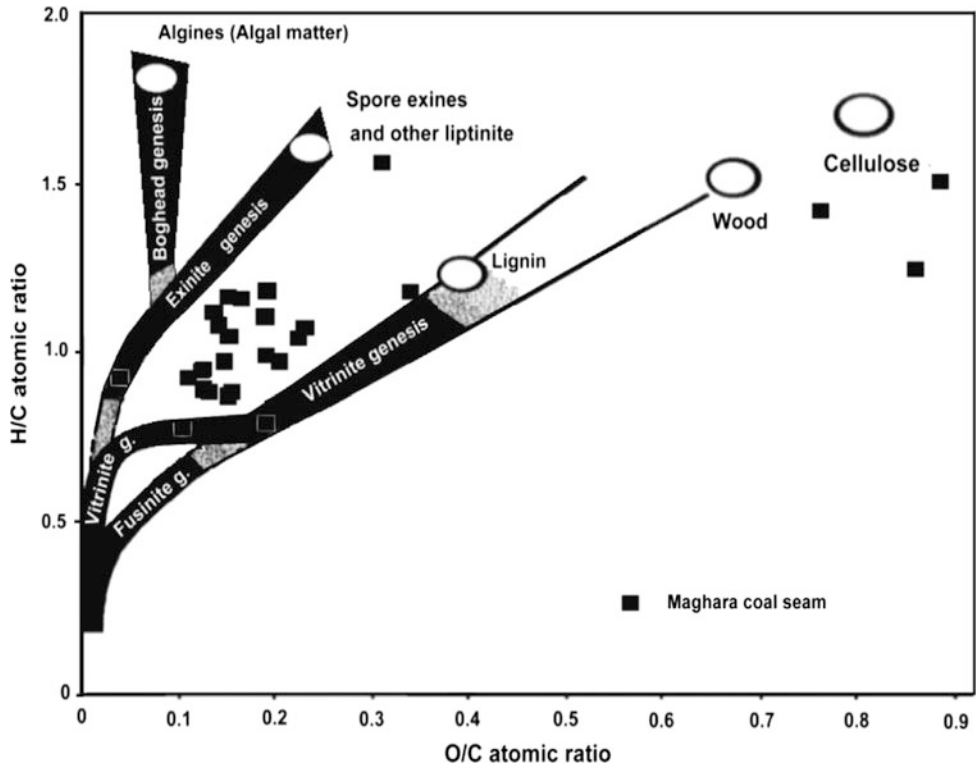

Fig. 17.26 Position of the Maghara coal on the van Krevelen Diagram using H/C versus O/C atomic ratios (Edress and Abdel Fatah 2018)

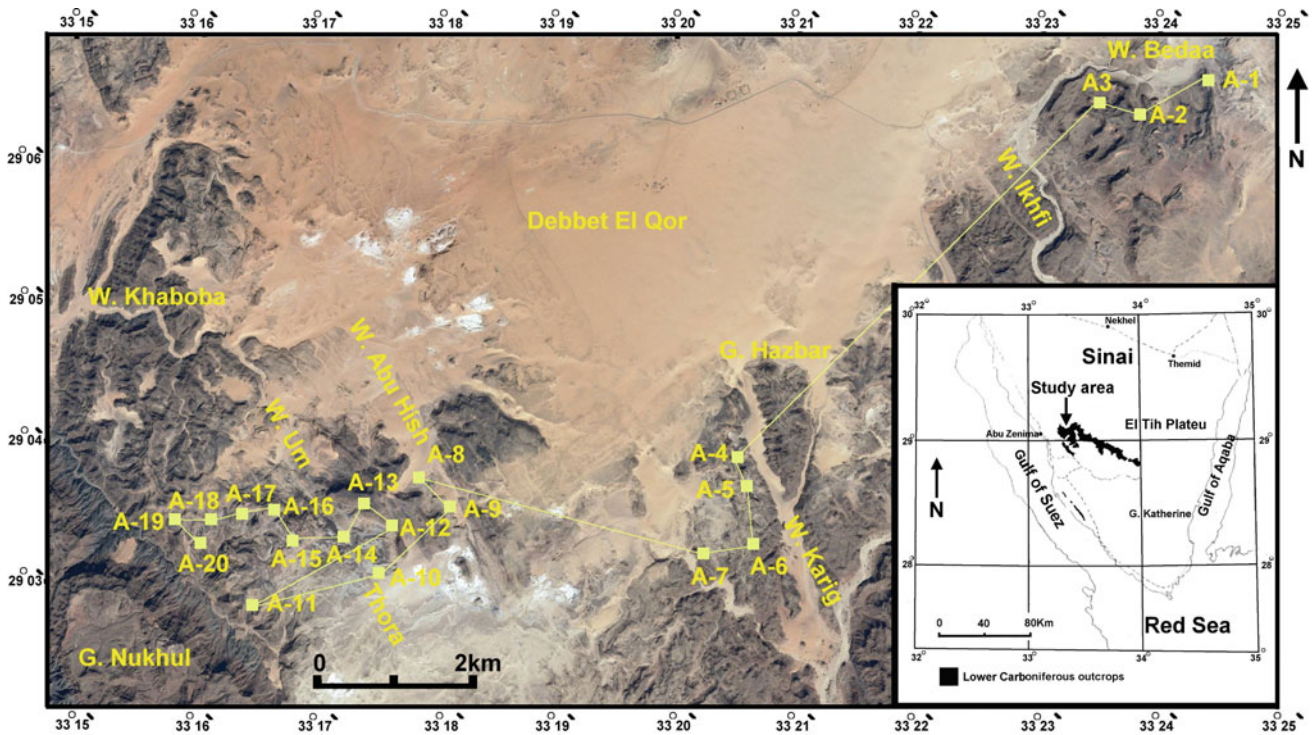

Fig. 17.27 Location map of the Thora area minimized at right corner, and the position of the collected channel coal samples along the exposures of Abu Thora Formation (Edress and Khalid 2018)

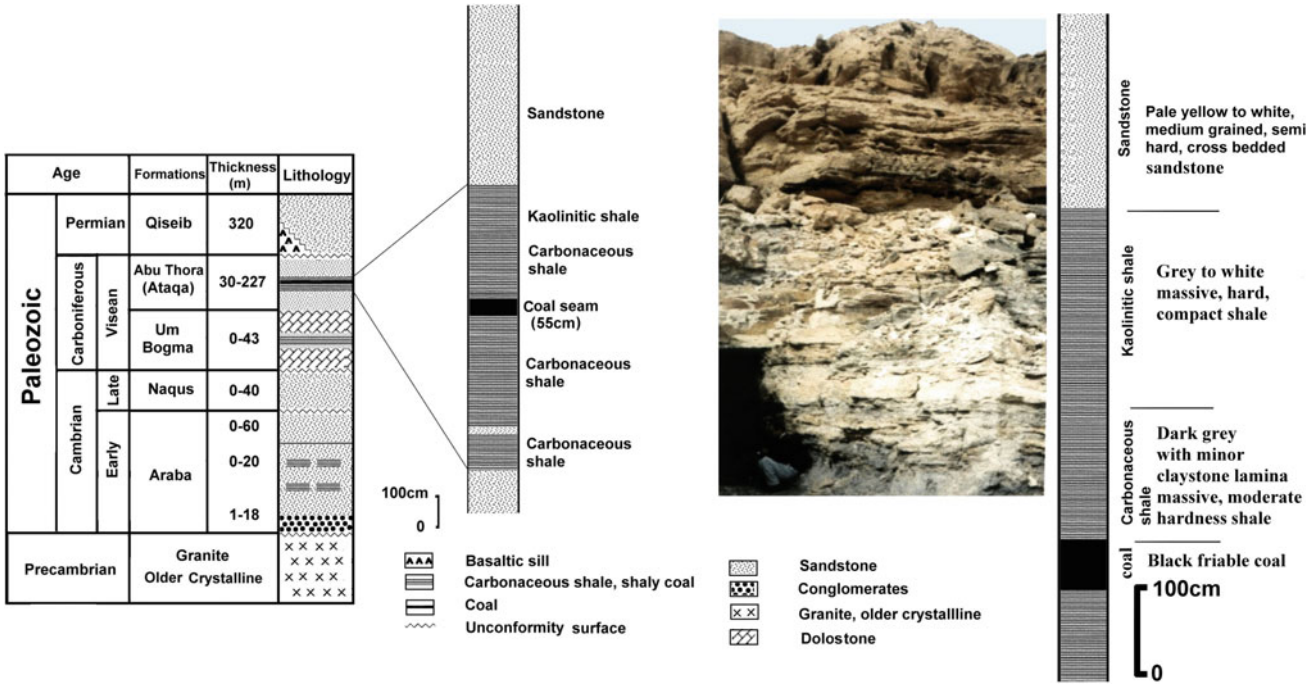

Fig. 17.28 Generalized stratigraphic succession at the study area indicated by the column of the coal bearing horizon of Abu Thora Fm and an old shaft following the outcrop of the coal seam (after Said 1990; Kora et al. 1994; Tawdros 2001; Baioumy 2013)

The Lower Carboniferous outcrops in the Egyptian Sinai Peninsula represent an elongated belt of NW–SE direction extending for about 80 km in length and approximately 25 km in width. They occupy an area lying between longitudes 33°12′–34°00′E and latitudes of 28°17′–29°10′N (Fig. 17.27). The Lower Carboniferous (Visean Age) in Sinai is represented by two distinctive formations; the dolomitic Um Bogma Formation at the bottom, which is overlain by clastic sandstone with the middle coaly shale of the coal-bearing horizon of Abu Thora (Ataqa) Formation at the top (Fig. 17.28). The Wadi Bedaa-Gebel Hazbar-Gebel Nukhul District, is located about 140 km to the southeast of Suez City and 25 km east of Abu Zenima City and between latitudes 29°02′ and 29°07′N and longitudes 33°15′ and 33° 25′E.

17.2.2.3 Fuel Analysis and Coalification Paleo-Temperature

According to Edress and Khalid (2018) fuel analysis classifies the Thora coal seam as a bituminous high volatile (b) class. The synonym classification of the Thora coal is a medium rank ortho-bituminous (c) with low-grade to shaly coal facies based on ash content and vitrinite reflectance values according to the international classification of in situ coal (Fig. 17.29). Vitrinite reflectance of average 0.72 characterizes the studied coal samples as mature within the catagenesis stage of maturation. Coalification paleo-temperature, estimated according to vitrinite reflectance, ranges between 97–113 °C. The exceeding paleo-temperature within the study area may be attributed to the Jurassic sill that capped the Abu Thora Formation, especially in the area situated west of Gebel Hazbar.

Van Krevelen diagram illustrates the studied coal seam laying between vitrinite genesis pathway and exinite genesis pathway that emphasizes the good preservation of coal components of lignin and spore exines under anoxic dominated waterlogged swamp environment (Fig. 17.30). In addition, the high hydrogen content of the average 7.74% of almost Thora coal greater than 5.5% (dmmf) emphasizes the per-hydrous coal types that accumulate under anoxic high water level within concave to the planner shaped mire system. The arborescent plants of vascular tissues are dominant during the accumulation of peat-forming mire according to the high values of the average 198.9 C/N atomic ratios.

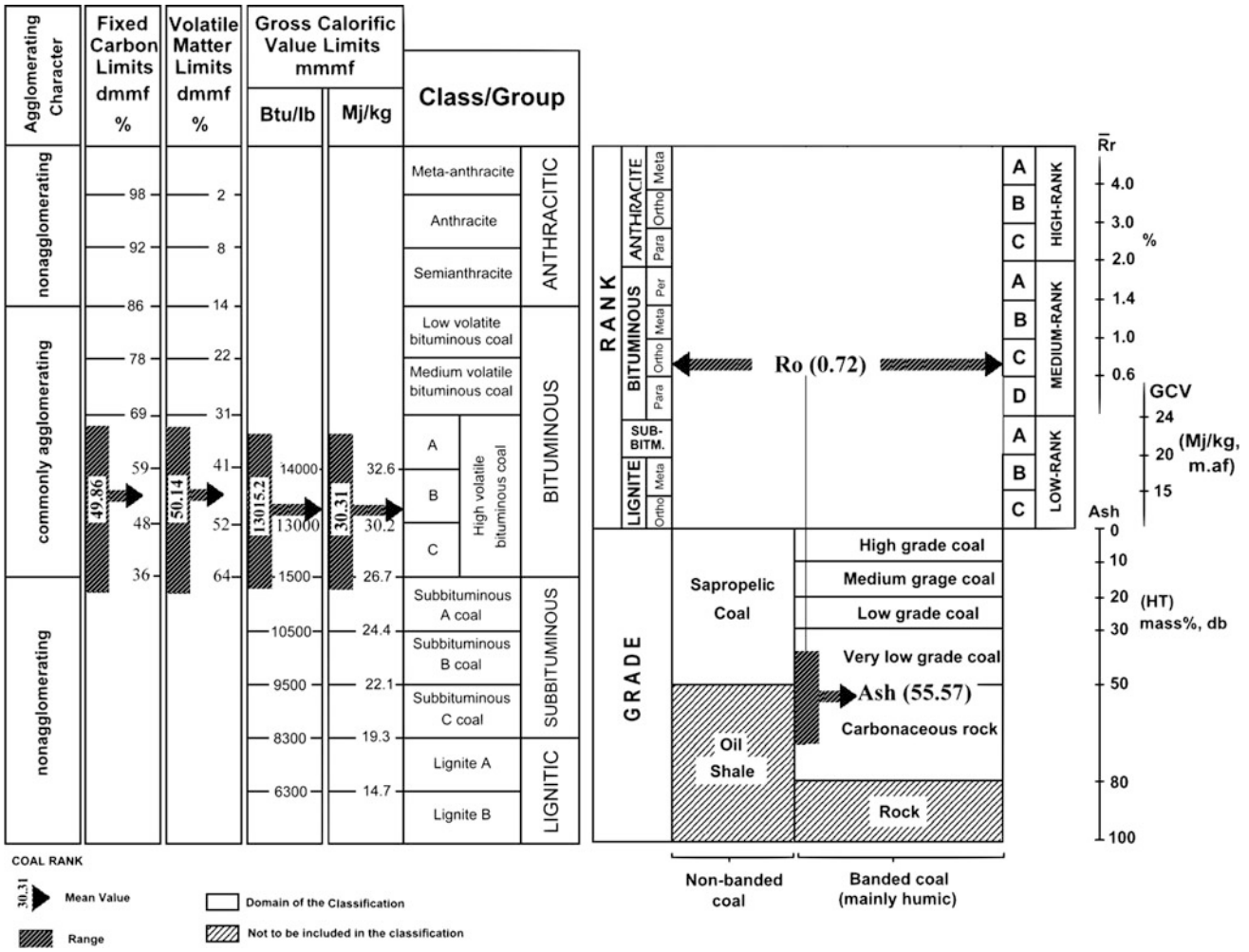

Fig. 17.29 Coal-Rank of the Thora coal seam on the basis of the different rank parameters according to the international classification of in situ coal; 1998 (right side) and standard classification of coal by rank (ASTM: D-388-99, 2016) on the left side (Edress and Khalid 2018)

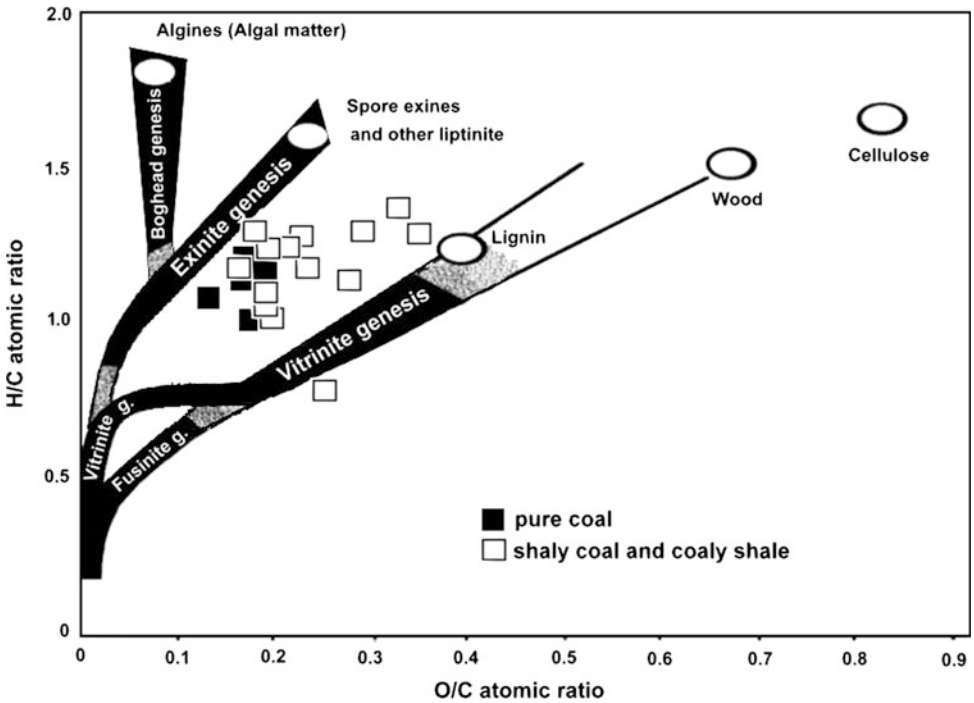

Fig. 17.30 Plotting of Thora coal on the van Krevelen diagram using H/C versus O/C

References

Aal A, Lelek JJ (1994) Structural development of the north Sinai, Egypt and its implications on the hydrocarbon prospectivity of the Mesozoic. In: Proceedings of the Middle East petrol geoscience conference GEO-94, vol 1, pp 15–30

Abdel-Malik WM (1982) Calcareous nannoplankton from the sequence between Dakhla and Esna Shale formations (Upper Cretaceous-Lower Eocene) in Quseir area, Egypt: Revista Española de Micropaleontol 14:73–84

Abed MM, Ayyad SN, Abu-Zeid RH (1996) Stratigraphic classification of Triassic-Cretaceous rocks of Gebel Arif El-Naga, Northeastern Sinai, Egypt. Newslett Strat 33:117–131

Abu Ali RS (2013) Mineralogical, geochemical and biostratigraphical studies on the Cretaceous/Tertiary (k/t) boundary in the Safaga region, Eastern Desert, Egypt. Unpublished MSc thesis, Faculty of Science, Cairo University, 120 pp

Abu-Ali R, El-Kammar A, Kuss J (2017) Paleo-environmental reconstructions of the Late Cretaceous–Paleogene black shale, Safaga, Egypt, GeoBremen 24.9.17–29.9.17

Al-Far DM (1966) Geology and coal deposits of Gebel Maghara, north Sinai. Egypt. Geol Surv 37–59

Al-Maamary H, Kazem H, Chaichan M (2017) The impact of oil price fluctuations on common renewable energies in GCC countries. Renew Sustain Energy Rev 75:989–1007

ASTM-D-388-99 (2016) Standard classification of coal by rank. The American Society for Testing and Materials, 100 Barr Harbor Drive, PO Box C700, West Conshohocken, United States, pp 1–6

Auer G, Reuter M, Hauzenberger CA, Piller WE (2017) The impact of transport processes on rare earth element patterns in marine authigenic and biogenic phosphates. Geochim Cosmochim Acta 203:140–156

Baioumy H (2013) Hydrogen and oxygen isotopic compositions of sedimentary kaolin deposits, Egypt, Paleoclimatic implications. Appl Geochem 29:182–188

Balme BE (1995) Fossil in situ spores and pollen grains: an annotated catalogue. Rev Palaeobot Palynol 87:81–324

Birdwell JE (2012) Review of rare earth element concentrations in oil shales of the Eocene Green River Formation, U.S. Geological Survey Open-File Report 2012–1016, 20 pp

Bohacs K, Suter J (1997) Sequence stratigraphic distribution of coaly rocks: fundamental controls and paralic examples. AAPG Bull 81:1612–1639

Calder JH (1993) The evolution of a ground-water-influenced (Westphalian B) peat-forming ecosystem in a piedmont setting: The No. 3 seam, Springhill coalfield, Cumberland Basin, Nova Scotia. In: Cobb JC, Cecil CB (eds) Modern and ancient coal-forming environments. Boulder, Colorado, Geological Society of America S. P., vol 286, pp 140–153. Diessel CFK (1982) An appraisal of coal facies based on maceral characteristics. In: Mallett CW (ed) Australian Coal Geol., vol 4, pp 474–484

Chazan G (2013) Russia gears up for shale boom. The Financial Times. Retrieved March 31, 2013

Diessel CFK (1992) Coal-bearing depositional systems. Springer, Berlin

Diessel CFK (2007) Utility of coal petrology for sequence-stratigraphic analysis. Int J Coal Geol 70:3–34

Diessel CFK, Boyd R, Wadsworth J, Leckie D, Chalmers G (2000) On balanced and unbalanced accommodation/peat accumulation ratios in the Cretaceous coals from Gates Formation, Western Canada, and their sequence-stratigraphic significance. Int J Coal Geol 43:143–186

Durand B, Monin JC (1980) Elemental analysis of kerogen (C, H, O, N, S, Fe). In: Durand B (ed) Kerogen. Technip Paris

Dyni JR (2010) Oil shale, in 2010 survey of energy resources. World Energy Council, London, www.worldenergy.org

Edress NAA, Abd El-Fatah AR (2018) Fuel analyses and rank determination of the Egyptian Maghara main coal seam, north-central Sinai, Egypt. Egypt J Petrol (In press)

Edress NAA, Khalid AK (2018) Coalification and fuel analysis of the Lower Carboniferous Thora coal seam in Bedaa-Gebel Hazbar-Gebel Nukhul district, Sinai, Egypt. J Afr Earth Sci 144:76–82

Edress NAA, Opluštil S, Sýkorová I (2018) Depositional environments of the Jurassic Maghara main coal seam in north-central Sinai, Egypt. J Afr Earth Sci 140:241–255

EGS (1992) Geological map of Sinai, Arab Republic of Egypt (Sheet No. 5), Scale 1:250 000

El Kammar MM (1987) Stratigraphical and mineralogical studies on the black shale at Quseir area, Red Sea coast, Egypt. MSc thesis, Cairo University 140 pp

El-Kammar MM (1993) Organic and inorganic composition of the Upper Cretaceous-Lower Tertiary black shales from Egypt and their hydrocarbon potentialities. PhD thesis, Faculty of Sciences, Cairo University, 227 pp

El-Kammar AM, El Kammar MM (1996) Potentiality of chemical weathering under arid conditions of black shales from Egypt. J Arid Environ 33(2):179–199

El-Kammar AM (2017) Oil shale resources in Egypt: the present status and future vision. Arab J Geosci 10:439. https://doi.org/10.1007/s12517-017-3152-4

El-Sabbagh A, Tantawy A, Keller G, Khozyem H, Spangenberg J, Adatte T, Gertsch B (2011) Stratigraphy of the Cenomanian-Turonian Oceanic Anoxic Event OAE2 in shallow shelf sequences of NE Egypt. Cretac Res 32:705–722

El-Shafeiy M, Birgel D, El-Kammar A, El-Barkooky A, Wagreich M, Mohamed M, Peckmann J (2014) Palaeoecological and post-depositional changes recorded in Campanian-Maastrichtian black shales, Abu Tartur plateau, Egypt. Cretac Res 50:38–51

El-Shafeiy M, Birgel D, El-Kammar A, El-Barkooky A, Wagreich M, Tahoun S, Peckmann J (2017) Integrated palaeo-environmental proxies of the Campanian to Danian organic-rich Quseir section, Egypt. Mar Pet Geology 86:771–786

Eyal M, Bartov Y, Shimron AE, Bentor YK (1980) Sinai geological map, scale 1:500 000. Geo Surv Israel

Fu X, Wang J, Zeng Y, Tan F, Feng X (2011) Concentration and mode of occurrence of trace elements in marine oil shale from the Bilong Co area, northern Tibet, China. Int J Coal Geol 85:112–122

Galindo C, Mougin I, Nourreddine A, Fakhri S (2006) Study of the partitioning of uranium and thorium in Moroccan black shale. Czech J Phys 56(Suppl):D49–D54

Ganz H (1984) Organic geochemical and palynological studies of a Dakhla Shale profile in Southeast Egypt. Part B. Origin of the organic matter and its relation to phosphorites formation. Berl Geowiss Abh A 50:363–374

Germann K, Bock WD, Ganz H, Schröter T, Tröger U (1987) Depositional conditions of Late Cretaceous phosphorites and black shales in Egypt. Berl Geowiss Abh A, 629–668

Greb S, Dimichele W, Gastaldo RA (2006) Evolution and importance of wetlands in earth history. Geol Soc Am Spec Pap 399:1–40. https://doi.org/10.1130/2006.2399(01)

Holz M, Kalkreuth W, Banerjee I (2002) Sequence stratigraphy of paralic coal-bearing strata: an overview. Int J Coal Geol 48:147–179

House of Commons (HC) (2012) Foreign affairs committee–second report British foreign policy and the "Arab Spring". Parliament, London

International Classification of in-seam Coals (1998) United Nations, New York and Geneva

Issawi B, El Hinnawi M, Francis M, Mazhar A (1999) The phanerozoic geology of Egypt: a geodynamic approach. Egypt Geol SurvS. 76:1–462

Jenkins DA (1990) North and central Sinai. In: Said R (ed) The geology of Egypt, Chapter 19. Balkema, pp 361–380
Keely ML, Wallis RJ (1991) The Jurassic system in northern Egypt: depositional and tectonic regimes. J Petrol Geol 14:49–64
Knaus E, Killen J, Biglarbigi Kh, Crawford P (2010) An overview of oil shale resources, In Ogunsola et al. (eds) Oil shale: a solution to the liquid fuel dilemma ACS symposium series. American Chemical Society, Washington, DC
Kora M, El-Shahat A, Abu-Shabana M (1994) Lithostratigraphy of the manganese-bearing Um Bogma Formation, West Central Sinai, Egypt. J Afr Earth Sci 18:151–162
Krauskopf KB (1979) Introduction to geochemistry: McGraw Hill, New York, 721 pp
Kuss J, Boukhary M (2008) A new upper Oligocene marine record from northern Sinai (Egypt) and its paleogeographic context. Geo Arab 13:59–84
Mach K, Sýkorová I, Konzalová M, Opluštil S (2013) Effect of relative lake-level changes in mire–lake system on the petrographic and floristic compositions of a coal seam, in the Most Basin (Miocene), Czech Republic. Int J Coal Geol 105:120–136
Malak EK, Philobbos ER, Abdou IK, Ashry MM (1977) Some petrographical, mineralogical and organic geochemical characteristics of black shales from Quseir and Safaga, Red Sea area, Egypt. Bull Inst De'sert Egypt 27:1–15
Mohsen SA (1990) The middle Jurassic microflora from El Maghara N 4 borehole, northern Sinai, Egypt. J Afr Earth Sci 11:207–216
Mostafa AR, Salama ME (2005) The Sinai Hinge Zone: a major crustal boundary in northern Sinai, abstract. In: 43rd Annual meeting of the Egypt. Geol Soci, Cairo, December 2005
Mustafa A, Ghaly EL (1964) Survey of Quseir shales and other carbonaceous shales in Egypt. J Chem Eng Data 9(4):557–567
Opluštil S, Edress NA, Sýkorová I (2013) Climatic vs. tectonic controls on peat accretion in non-marine setting; an example from the Žacléř Formation (Yeadonian–Bolsovian) in the Intra-Sudetic Basin (Czech Republic). Int J Coal Geol 116–117:135–157
Osman RA, Ahmed SM, Mahmoud NI (2000) Cretaceous-Lower Tertiary rocks at Gebel Halal area, Northern Sinai, Egypt; a stratigraphy and sedimentary history. In: Proceeding of 5th international conference on the geology of the Arab World, Cairo, pp 1309–1332
Petersen HI, Ratanasthien B (2011) Coal facies in a Cenozoic paralic lignite bed, Krabi Basin, southern Thailand: Changing peat-forming conditions related to relative sea-level controlled watertable variations. Int J Coal Geol 87:2–12
Petsch ST, Berner RA, Eglinton TI (2000) A field study of the chemical weathering of ancient sedimentary organic matter. Org Geochem 31:475–487
Robison VD, Tröger U (1983) Geology and organic geochemistry of Dakhla Shale, Egypt. Abstr AAPG Bull 67:542
Said R (1962) The geology of Egypt. Elsevier, Amsterdam, p 177p
Said R (1990) The geology of Egypt. Balkema, Rotterdam Brookfield
Schrank E (1984) Organic geochemical and palynological studies of a Dakhla Shale (Late Cretaceous) in southeast Egypt. Part A—succession of microflora and depositional environment. Berliner Geowiss Abh 50:189–207
Scotese CR (2001) Atlas of Earth history, V. 1. Paleogeography, Paleo-Map project, Arlington, Texas. www.scotese.com/earth.html
Sepúlveda J, Wendler J, Leider A, Kuss J, Summons R, Hinrichs KU (2009) Molecular isotopic evidence of environmental and ecological changes across the Cenomanian-Turonian boundary in the Levant Platform of central Jordan. Org Geochem 40:553–568
Sinai Coal Co. (1994) Stratigraphic correlation of upper and main coal seams, v. scale 1:100, H. Scale, 1:2000, Maghara coal project sheet
Tawdros EE (2001) Geology of Egypt and Lybia. Balkema Publishers, USA
Thomas L (2002) Coal geology. Wiley, England
Tostevin R, Shields G, Tarbuck G, He T, Clarkson M, Wood R (2016) Effective use of cerium anomalies as a redox proxy in carbonate-dominated marine settings. Chem Geol 438:146–162
Tröger U (1984) The oil shale potential of Egypt. Berliner Geowissenschaftliche Abhandlungen (A) 50:375–380
Veevers JJ (2004) Gondwanaland from 650–500 Ma assembly through 320 Ma merger in Pangea to 185–100 Ma breakup: supercontinental tectonics via stratigraphy and radiometric dating. Earth-Sci Rev 68:1–132
Walker S (2000) Major coalfields of the world. International Energy Agency, Coal Research, London
Yefimov V, Li S (2009) Coal, oil shale, natural bitumen, heavy oil and peat, vol. II, extraction of oil shale: surface and in situ retorting. Encyclopedia of Life Support Systems (EOLSS)
Zaghloul Z, Khidr I (1992) Subsurface geological setting of the Mesozoic-Cenozoic formations and hydrocarbon potentials, North Sinai. In: 11th EGPC exploration seminar, Egypt, vol 1, pp 563–577

Water Resources in Egypt

18

Mustafa El-Rawy, Fathy Abdalla, and Mohamed El Alfy

Contents

M. El-Rawy
Civil Engineering Department, Faculty of Engineering,
Minia University, Minia, 61111, Egypt
e-mail: mustafa.elrawy@mu.edu.eg

Civil Engineering Department, College of Engineering,
Shaqra University, Dawadmi, Ar Riyadh, 11911, Saudi Arabia
e-mail: mustafa.elrawy@su.edu.sa

F. Abdalla (✉)
Geology Department, Faculty of Science,
South Valley University, Qena, 83523, Egypt
e-mail: fathy.abdallah@sci.svu.edu.eg

Deanship of Scientific Research, King Saud University,
Riyadh, Saudi Arabia
e-mail: fabdalla@ksu.edu.sa

M. El Alfy
Faculty of Science, Geology Department, Mansoura University,
Mansoura, 35516, Egypt
e-mail: alfy@mans.edu.eg

Abstract

From the late Eocene up to the late Middle Pleistocene, Egypt was a wet country due to the rainfall and rivers running through it. Out of the 1660 BCM/y of water that falls within the Nile basin, Egypt receives only 55.5 BCM/y representing about 97% of the renewable water resources in Egypt. This is in addition to the groundwater, domestic wastewater, rainfall, and desalinated water. The Blue Nile, the Atbara and the Sobat, all of which rise in Ethiopia, contribute approximately 85% of the Nile waters that reach the Aswan High Dam (AHD). The White Nile, which obtains its water from Lake Victoria and its tributaries, constitutes 15% of the Nile waters. The annual average flow of the Nile waters is 84 BCM/y, as measured at the AHD. Lake Nasser with a storage capacity of 168.9 BCM was created 5 km upstream of Aswan city in Upper Egypt, after the construction of the

Z. Hamimi et al. (eds.), *The Geology of Egypt*, Regional Geology Reviews,
https://doi.org/10.1007/978-3-030-15265-9_18

AHD. In addition, several barrages were erected to control the water level and discharges into the river. Serious efforts must be made by authorities in the Nile basin countries to develop strategies and plans for mitigation and adaptation as the threat of the expected climatic changes might adversely affect the amount of water resources in the Nile basin.

18.1 Surface Water Resources in Egypt

Mustafa El-Rawy
Fathy Abdalla

18.1.1 Introduction

The surface water resources in Egypt include the River Nile, precipitation, and flash floods. The River Nile, which originates outside the country, is considered to be the lifeblood of Egypt contributing about 97% of the renewable water resources and is the main source of fresh water in Egypt. The river, of a length measuring almost 6650 km, runs through eleven countries viz., Tanzania, Democratic Republic of Congo, Uganda, Kenya, Burundi, Rwanda, Ethiopia, Eritrea, South Sudan, Sudan, and Egypt. It flows to the Mediterranean Sea with a length of 1520 km within Egypt and branches into Rosetta and Damietta in the Delta. The Nile water in Egypt is controlled by the High Aswan Dam (AHD), the old Aswan Dam (AD), and some of the downstream barrages (Fig. 18.1). The AD has a storage volume of 5 billion cubic meters per year (BCM/y). The AHD is located upstream of the AD with a storage reservoir (Lake Nasser) having a live storage (operational storage) of 90 BCM/y (MWRI 2005a). Lake Nasser extends up to 350 km in Egypt and 150 km in Sudan and has a width of 12 km on an average.

The water of the Nile is becoming increasingly insufficient for the requirement in Egypt due to population growth, traditional irrigation systems (flash irrigation), water contamination, irregular distribution of water resources, and frequent droughts caused by extreme global weather patterns. Since 2000, Egypt is below the water poverty limit and new water resources are sought to cover the shortage by the year 2050 (MWRI 2014). In addition to the water from the Nile, the amount of drainage water that was reused in 2011 was about 7 BCM/y (MWRI 2005a; Omar 2011; CEDARE 2014). Egypt produces between 5.5 and 6.5 BCM/y of domestic wastewater, out of which about 2.97 BCM/y undergoes primary or secondary treatment and only 0.7 BCM/y is reused for agriculture (Abdelwahab and Omar 2011; CEDARE 2014). The total amount of desalinated water in Egypt in 2012 was assessed to be 60 MCM/y (Moawad 2012; MWRI water strategy for 2050 (MWRI 2010)), when the total effective rainfall was about 1.3 BCM/y (MWRI 2005a).

18.1.2 Nile Basin Countries and Climate

The Nile (Fig. 18.1) runs from the south to the north towards its estuary in the Mediterranean Sea in the northeastern part of the continent of Africa. It extends from 4° south to 32° north and the Nile basin covers an area of 3.4 million km^2 in eleven African countries (Dumont 2009) spread over different topographical, geographical and climatological regions. The river originates from two main sources that meet in Khartoum to form the Nile (Kendie 1999; Collins 2002; Fig. 18.2). These are (i) the plateau of the tropical lakes through the White Nile including Lakes Victoria, Kyoga, Edward, George, and Albert, which contributes about 15 BCM and constitutes 15% of the revenue of the River Nile at the AHD, and (ii) the Ethiopian plateau, which is the main source and contributes about 79.5 BCM at the AHD, and accounts for 85% of the revenue of the Nile at the AHD through three main rivers viz., the Blue Nile from Lake Tana (54 BCM), the Sobat River (13.5 BCM), and the Atbara River (12 BCM) (Noaman and El Quosy 2017). The amount of water lost in the Sudd, (swampy lowland regions in South Sudan, formed by the White Nile) by evaporation from the lakes and swamps and through evapotranspiration from vegetated cover, is about 31 BCM (Noaman and El Quosy 2017).

The total flow of the Nile at the AHD is 94.5 BCM, and due to evaporation from the surface and seepage along the Nile from Khartoum to Aswan, about 10.5 BCM of the total Nile flow is lost (Fig. 18.2), therefore, the net average natural flow at Aswan is about 84 BCM/y. According to the water agreement between Sudan and Egypt in 1959, 18.5 BCM was apportioned to Sudan, and 55.5 BCM to Egypt (MWRI 2005b; Abdin and Gaafar 2009; FAO 2013a, b). This allotment was based on the net yield of water, after taking into account the Aswan reservoir and other storage and regulations (Noaman and El Quosy 2017). The White Nile moves along a mild slope northward to form a junction with the Blue Nile at Khartoum, where the Atbara River links the main course of the Nile about 300 km north of Khartoum and the Nile downstream of Khartoum is called the river Nile (Fig. 18.1).

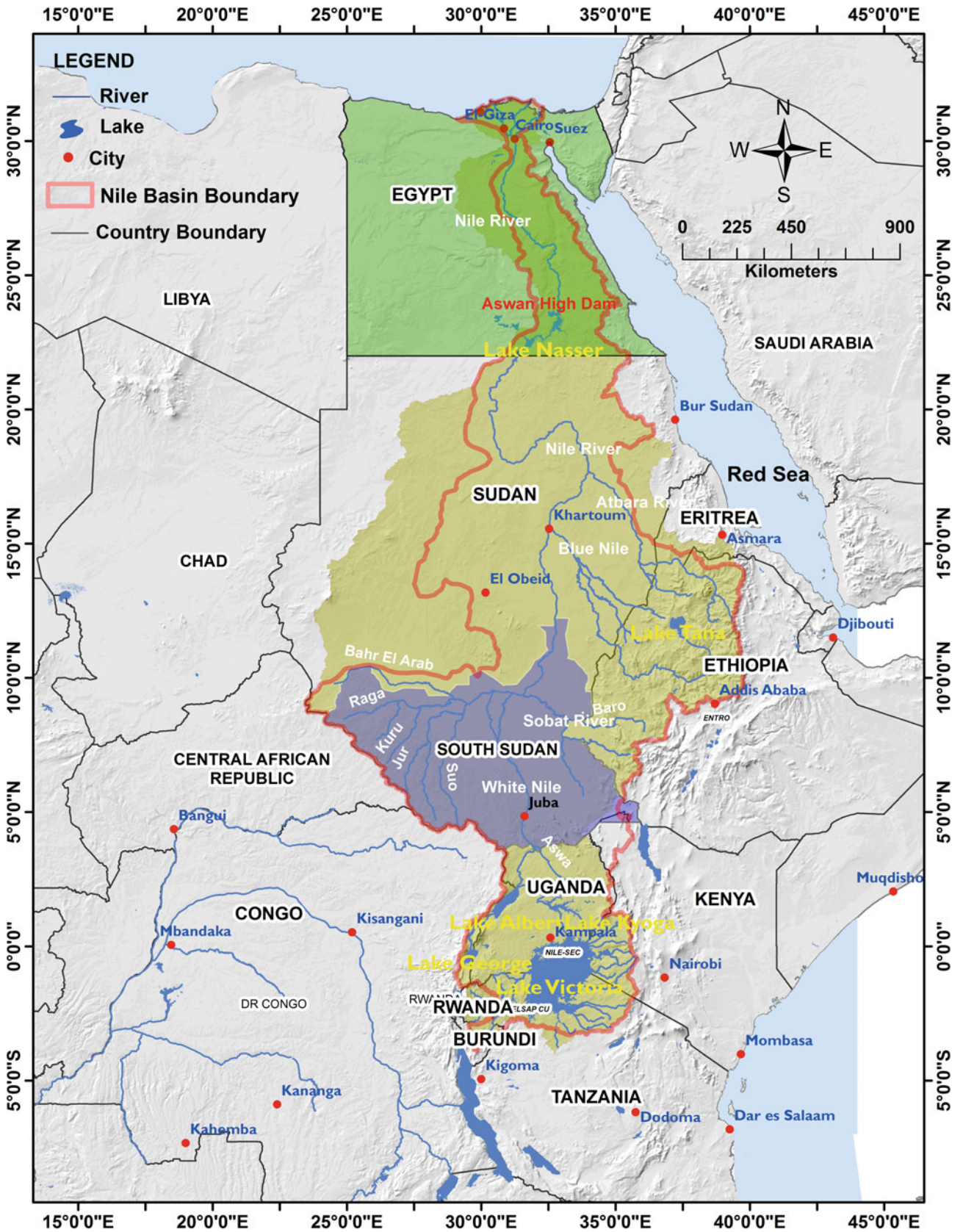

Fig. 18.1 Basin of the river Nile and its water resources

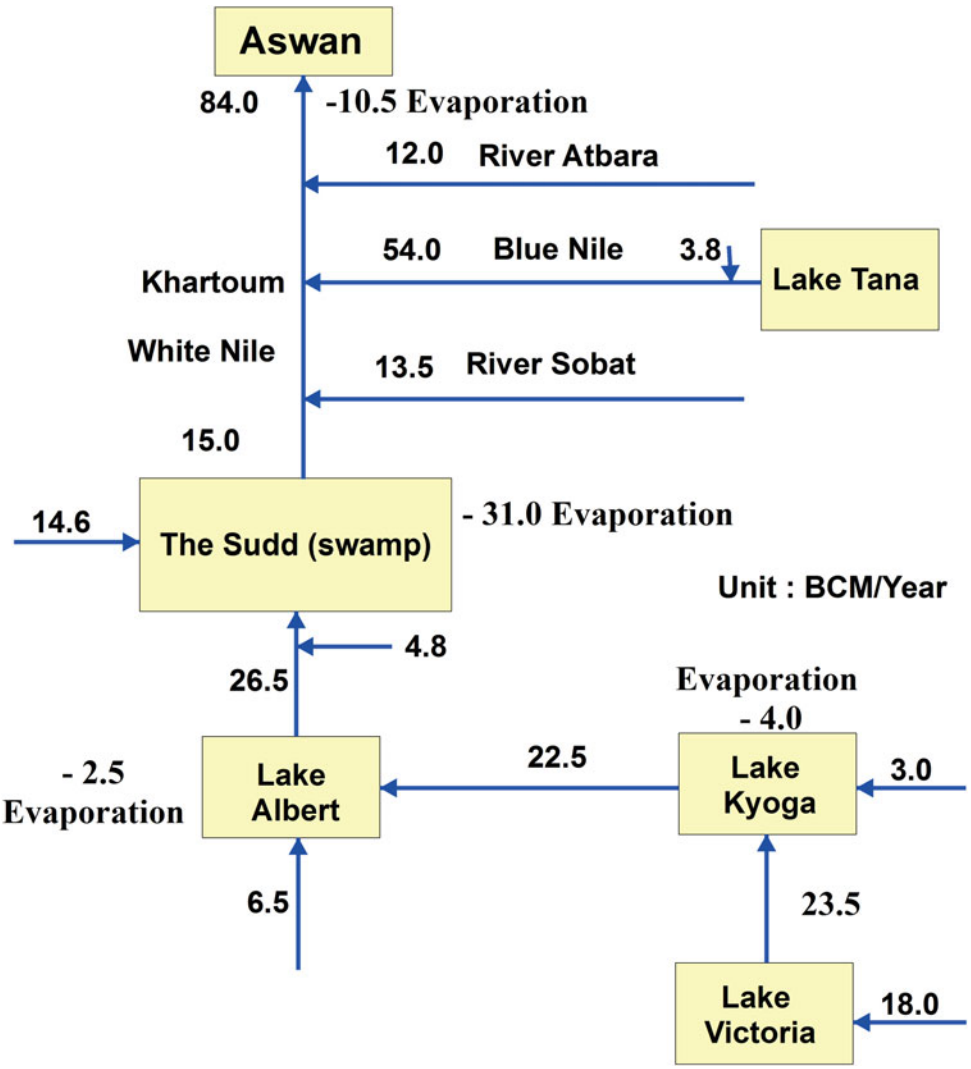

Fig. 18.2 Mean natural flow of the Nile

More than half of the region of the Nile basin is arid and semi-arid where precipitation is limited and evaporation and seepage losses are extremely high. The total amount of precipitation over the Nile basin countries is about 7000 BCM/y, of which 1660 BCM/y lies in the Nile basin. The mean precipitation in the entire Nile basin is 615 mm/y (Ribbe and Ahmed 2006). About 28% of the basin receives <100 mm of rainfall annually and its northern parts are characterized by hyper-arid conditions. About 34% of the basin receives between 700 and 1300 mm rainfall and is characterized by sub-humid conditions. Only the southwestern part of South Sudan, the region of the Lake Victoria basin, and the Ethiopian highlands receive rainfall of over 1000 mm/y (Camberlin 2009). Figure 18.3 shows the rainfall distribution in the Nile Basin, which varies from 800 to more than 1800 mm/y in parts of the Upper Nile area to less than 300 mm/y in the northern parts of Sudan and less than 100 mm/y in the whole of Egypt (Noaman and El Quosy 2017). The expected climate changes due to the effects of global warming will raise the average global surface temperature with continued rise in the sea level and amount of precipitation, and precipitation patterns will be adversely affected and change.

18.1.3 Main International Agreements of the Water of the River Nile

The most important international water agreements between Egypt and the Nile basin countries are the agreement between Egypt and Anglo-Egyptian Sudan on May 7, 1929, and the 1959 Nile agreement between Sudan and Egypt for full utilization of the Nile waters.

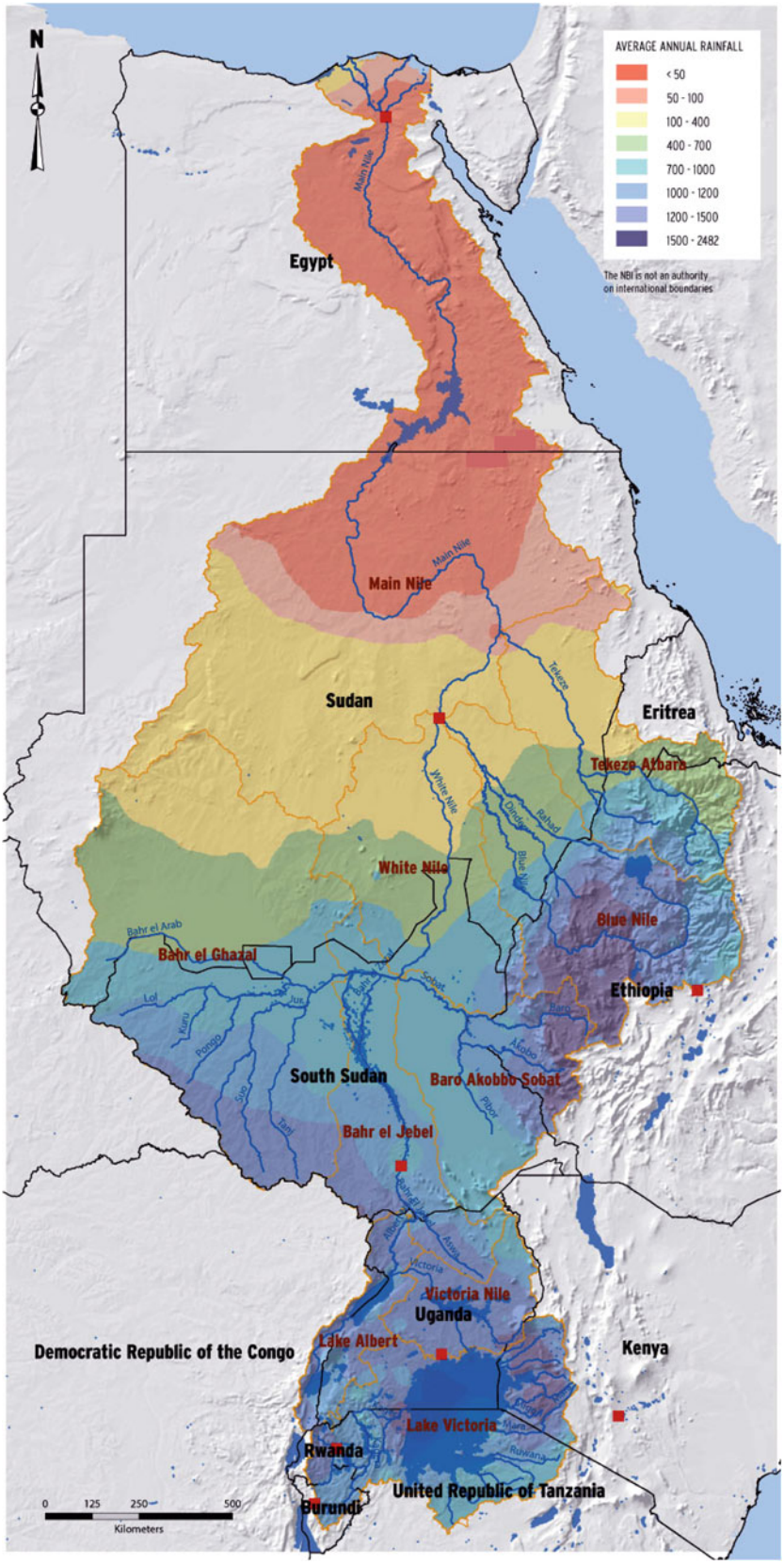

Fig. 18.3 The distribution of rainfall in the Nile basin (*Source* The Nile Basin water resource atlas home page http://atlas.nilebasin.org/treatise/average-annual-rainfall/)

- The Agreement between Egypt and Anglo-Egyptian Sudan (May 7, 1929) states that "Egypt reserves the right to monitor the Nile flow in the upstream countries. Egypt assumes the right to undertake River Nile related projects without the consent of upper riparian states and to veto any construction projects that would affect her interests adversely" (Demin 2015).
- The objective of the 1959 agreement was to gain full control and utilization of the annual Nile flow. Finally, in 1959, the agreement for the Full Utilization of the Nile Waters was signed between Sudan and Egypt without inviting them to join the agreement or obtaining the consensus of other riparian countries. The agreement contained the following main points (Demin 2015):
  - The controversy on the quantity of average annual Nile flow was settled and it was agreed to be about 84 BCM, as measured at the AHD.
  - The agreement allowed the entire average annual flow of the Nile to be shared between Sudan and Egypt at 18.5 and 55.5 BCM, respectively.
  - The annual water loss due to evaporation and other factors estimated to be 10 BCM. This quantity would be deducted from the Nile yield before the share was assigned to Egypt and Sudan.
  - Sudan, in agreement with Egypt, would construct projects that would enhance the Nile flow by preventing evaporation losses in the Sudd swamps of the White Nile located in southern Sudan. The cost and benefit of the same was to be divided equally between the two countries.

18.1.4 Lake Nasser and Aswan High Dam

Lake Nasser is one of the greatest man-made lakes in the world located on the border between Egypt and Sudan, between longitudes 30°07′ and 33°15′E and latitudes 20°27′ N and 23°58′N. It was created after the construction of the AHD in 1971 on the river Nile, 5 km upstream of Aswan city in Upper Egypt (Fig. 18.4). Two-thirds of its part in the north is located in Egypt and is called Lake Nasser, while the rest of it is located in Sudan and is known as Lake Nubia (El Kobtan et al. 2016). The lake in Egypt is located between latitudes 22°00′N and 24°00′N and longitudes 31°00′E and 34°00′E (El Gammal et al. 2010). Lake Nasser is 550 km in length and 35 km in width with a surface area of 5250 km^2. The maximum depth of the water in the lake is 180 m, the normal elevation is 183 m, and it holds 132 km^3 of water.

The AHD is a rockfill dam with a grout curtain and clay core (Abu-Zeid and El-Shibini 1997). The dam is of 4000 m length, 980 m width at the base, 40 m width at the crest, and 111 m height. The maximum water discharge that can pass through the AHD is 11,000 m^3/s. When the water level reaches an elevation between 178 and 183 m, an extra 5000 m^3/s can pass through emergency spillways to the Toshka Canal links and then to the Toshka Depression (Mobasher 2010). There are 12 turbines with a capacity of 175 MW each and the installed capacity hydropower of the dam is 2100 MW. The annual generation of hydropower in 2004 was 10,042 GWh (CARMA 2015). The main objective of creating the AHD and Lake Nasser was to manage the Nile water and save the Nile Delta and flood plains, supporting agriculture in the vicinity, from flooding. Egypt was dependent on the annual floodwaters of the Nile for irrigation of the agricultural land before the construction of the AHD and water level gauges were used to measure the flood level. The foreseeable annual flood of the Nile was useful for providing fertile sediments and water for irrigation of agriculture. However, low floods meant that less land would receive water for irrigation, whereas high floods meant that crops would be washed away. In addition, the AHD increased the share of Egyptian water from the Nile by 7.5 BCM by avoiding discharge of fresh water into the sea (Conniff et al. 2012).

Before the construction of the dam, the flooding of the Nile occurred annually and about 50% of the water drained into the Mediterranean Sea uneconomically. The AHD controlled the floods by regulating the flow of the river and supplying water for irrigation during the year, which resulted in an almost two-fold increase in the agricultural yield (Abu-Zeid and El-Shibini 1997; El Gamal and Zaki 2017).

The water levels and storage capacity of Lake Nasser for different operation zones of the AHD reservoir are presented in Table 18.1 and Fig. 18.5. The lake is divided into four storage zones based on the water levels viz., the lake water capacity of 168.9 BCM, of which 31.6 BCM serves as dead storage for sediment, 89.7 BCM as live storage, 16.2 BCM as food control storage, and 31.4 BCM as maximum surcharge storage. The lake is located in a very hot, dry climate, therefore, about 25% of the Nile waters into Lake Nasser (55.5 km^3/year) are lost through evaporation and seepage (Muala et al. 2014). The amount of water evaporating from the lake ranges from 8 to 12 BCM/y with an average of 10 BCM/y (Ebaid and Ismail 2010), while the annual rainfall over the lake is negligible (Elsawwaf et al. 2010).

The variation in the water level of Lake Nasser during the period 1964 to 2008 is shown in Fig. 18.6a, b. During the

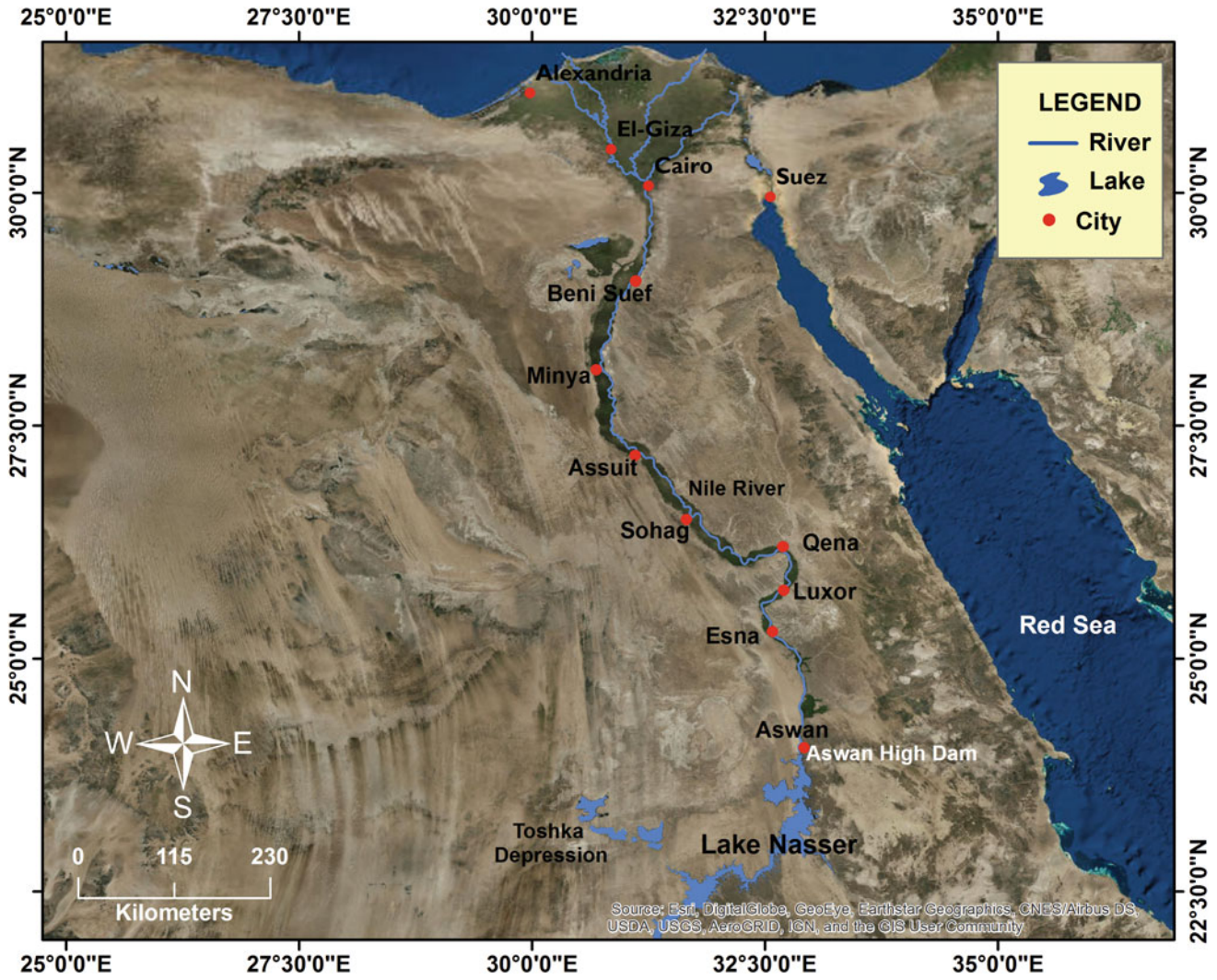

Fig. 18.4 Lake Nasser and Aswan High Dam and River Nile in Egypt

Table 18.1 Storage capacity of Lake Nasser

Storage zone	Level (m.asl)	Volume (BCM)	Cumulative volume (BCM)
Dead storage	<147	31.6	31.6
Active storage	147–175	89.7	121.3
Food control storage	175–178	16.2	137.5
Maximum surcharge storage	178–183	31.4	168.9

period from 1964 to 1972, the lake was in an early initiation stage, from 1984 to 1992, it was in a low water support stage and from 2000 to 2008 the lake was in a good water support stage with water from the river Nile between drought cycles. The maximum water level in the lake during the period from 1964 to 2008 was 181.8 m in the year 1999 (Fig. 18.6a). The difference between the maximum (180 m) and minimum (160 m) water levels is constant (20 m) after 1968 (Fig. 18.6a, b). This indicates that the lake water discharges were more or less stable from 1968 till the present date (El Gammal et al. 2010).

18.1.5 The River Nile and Its Branches

After the construction of the AHD, in an attempt to achieve continuous irrigation, barrages were built to control the water level and discharges into the river. The Delta Barrage

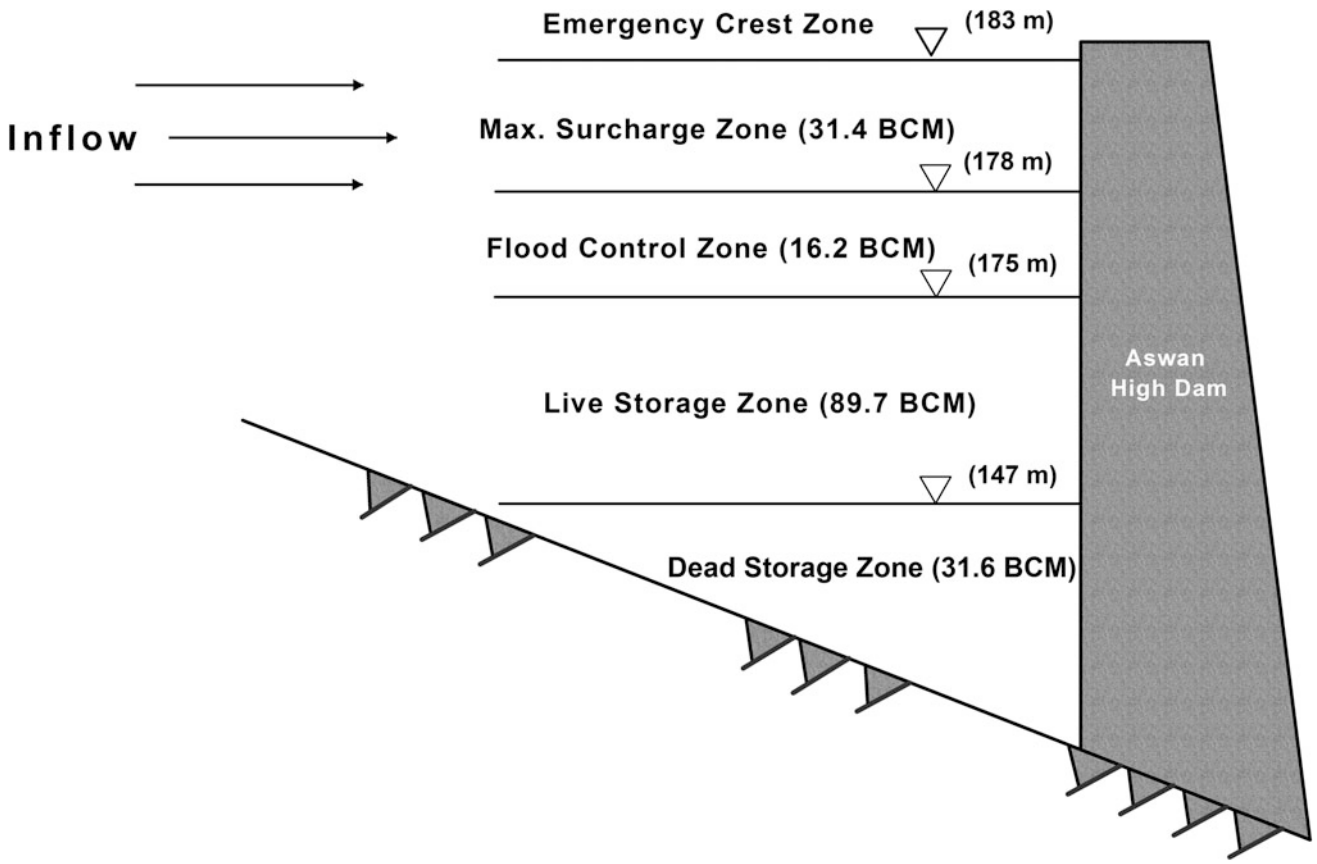

Fig. 18.5 Water levels and storage capacity of Lake Nasser for different operation zones of AHD reservoir (modified after El-Shafie et al. 2007)

was constructed in 1861 at the point where the river divides into the Damietta and Rosetta branches at the top of the Nile delta. Other barrages (Esna, Nag-Hammadi, and Assiut) were constructed between Aswan and the delta to control the water level for agricultural and navigational purposes (Locks). These barrages are situated at 167, 359, and 544 km below the AHD, respectively, as shown in Fig. 18.7 (MWRI 2005a).

The River Nile in Egypt, along the 946 km stretch from the Aswan to the Delta Barrage reach is divided into four major reaches between two hydraulic structures (Fig. 18.7) (NRI 1992). The description of these four reaches is as follows: Reach 1 is located between downstream of Old Aswan Dam and upstream of Esna Barrages with a length of 167 km. Reach 2 is located between downstream of Esna Barrage and upstream of Naga Hammadi Barrage with a length of 193 km. Reach 3 is located between downstream of Naga Hammadi Barrage and upstream of Assiut Barrage with a length of 185 km, whereas Reach 4 is located between downstream of Assiut Barrage and upstream of Delta Barrage with a length of 409 km (NRI 1992).

The construction of the old Esna Barrage started in 1906 and ended in 1909. The main purpose of the Esna Barrage was to improve the irrigation system in the Qena Province. The barrage was used to raise the water levels of the Kalabia and Asfoun canals on both sides of the Nile, which are located on the upstream of the Esna Barrage. The old Esna Barrage consists of 120 vents, each 5 m wide, designed for the heading up of a maximum of 2.5 m between the upstream and downstream water levels. The area served by the Esna Barrage is 68,000 ha (28,000 ha on the eastern side of the river through the Kalabia canal and 40,000 ha to the west through the Asfoun canal), in addition to the area served in the Qena province (El-Fakharany and Fekry 2014). The construction of the new Esna Barrage replaced the old Esna Barrage on the Nile in 1994.

The old Naga Hammadi Barrage, constructed on the river Nile between 1927 and 1930, is situated 359 km downstream of the AHD and was completed in 1963. The aim of this barrage was to raise the water level in the upstream part to provide the necessary head for two main irrigation canals supplying water to the cultivation areas in the downstream

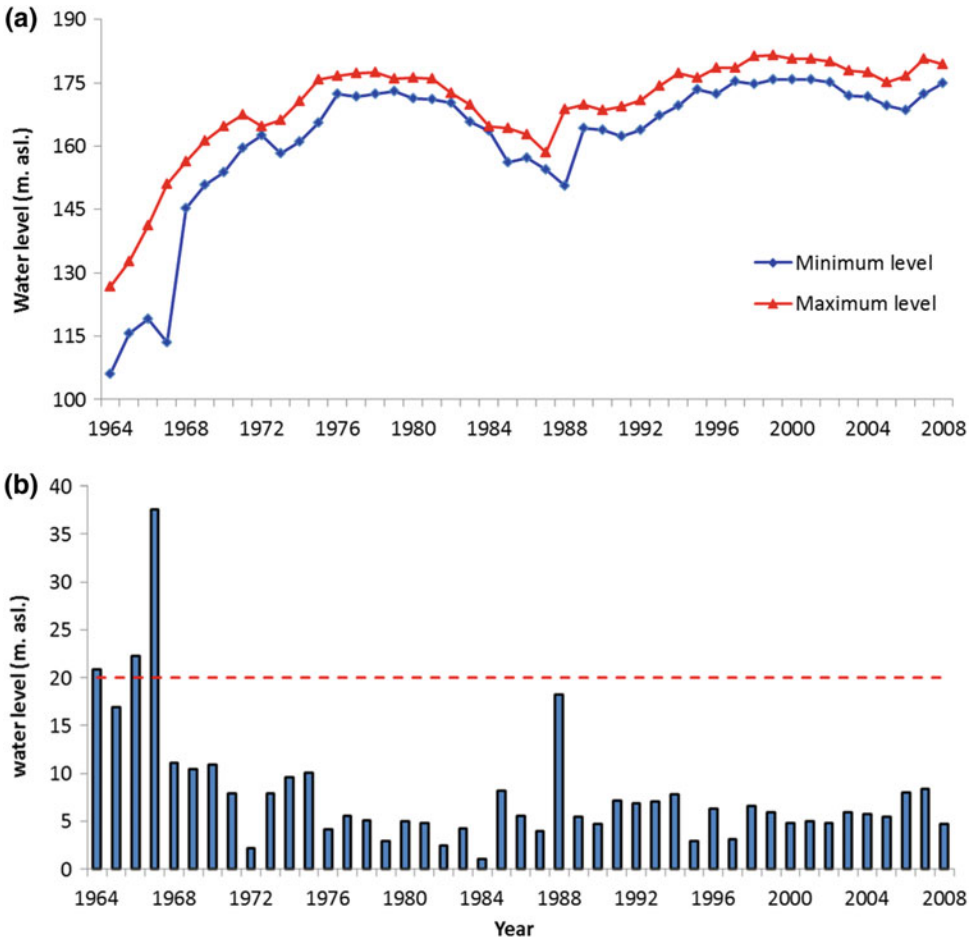

Fig. 18.6 **a** The variation in water level (maximum and minimum) recorded at Lake Nasser during the years from 1964 to 2008, **b** the difference between maximum and minimum water levels (collected from Water Resources and Irrigation Ministry and Agriculture Ministry of Egypt and El Gammal et al. 2010)

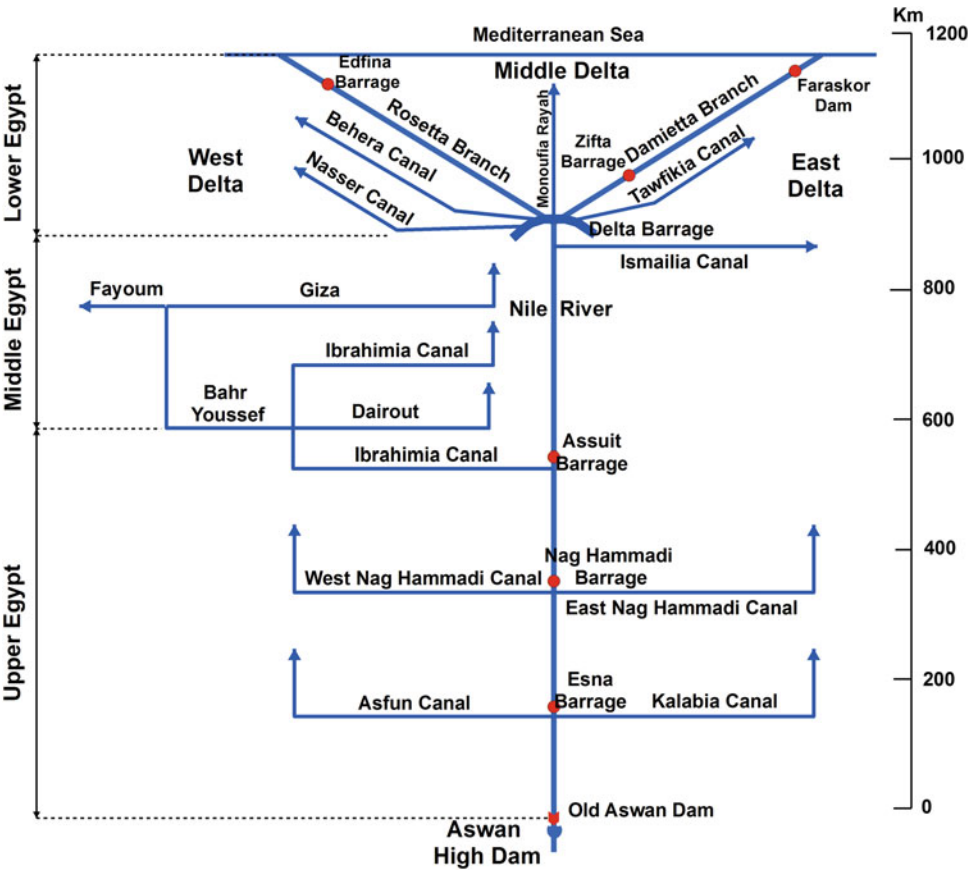

Fig. 18.7 Water hydraulic structures on the Nile in Egypt (modified after Abu Zeid 1995)

reach of 180 km. The two canals are the West Naga Hammadi and East Naga Hammadi that supply water to irrigated lands, totaling approximately 49,980 and 184,380 ha, respectively. The barrage consists of 100 vents, each 6 m wide with a lock 16 m long and 8 m wide (Sattar and Raslan 2014 and Said et al. 2014). It was decided to build a new barrage weir 3.5 km downstream from the old Naga Hammadi Barrage to make it possible to safely withstand the expected differential head resulting from head pond levels required for irrigation purposes and to incorporate a hydropower plant to generate 460 GWh of electricity per year. The barrage would also enhance the navigation with the construction of two navigable locks, large enough to accommodate two of the largest ships operating on the Nile at the same time in each chamber. The construction work on the new barrage project started in 2002 and was completed in the spring of 2008 (Dawoud and Allam 2004; Sattar and Raslan 2014 and Said et al. 2014).

The Assiut Barrage was built on the Nile, 544 km downstream of the AHD, during the period from 1898 to 1902 to serve 432,000 ha in Middle Egypt and Fayoum, in addition to 68,000 ha of basin-irrigated lands (El Quosy and Khalifa 2017). At the same time, the Ibrahimia Canal was constructed. The Assiut Barrage was used to regulate the flow to the Ibrahimia canal so that only the designated discharge is allowed, even during high-flood seasons. The off-take of Ibrahimia canal consists of nine vents, 5 m wide each, and a lock chamber of width 8.5 m and length 50 m. In 2011, the Egyptian government started to replace the existing barrage with a new structure incorporating a hydropower plant. The new Assiut barrage is located on the Nile 400 m downstream of the existing barrage. The main goals of the new barrage are to ensure the water supply for irrigation, to generate hydropower, and to increase the navigation capacity in the Nile. The new barrage started operating in 2018 (Batisha 2012; Mohamed and Abo-Elwafa 2014). It includes a hydropower plant providing 32 MW power with four 8 MW turbines and a bridge crossing the Nile with two navigation locks on the right side. The new barrage was designed to maintain an upstream water level of 4 m required for feeding the Ibrahimia canal with a minimum discharge of 445 m^3/s flow into the Ibrahimia canal to irrigate about 70,000 ha of the agriculture areas between the new barrage and Cairo (Assiut Barrage Project and MWRI).

The Ibrahimia Canal is one of the largest artificial canals in the world. It was constructed to irrigate the royal sugar cane farms in the El-Minya Governorate during the summer. The Canal procures its water from the Nile near the city of Assiut, and water flows north for a distance of 60.60 km to the Dairut city. Its branches feed the agricultural areas between Assiut and El-Minya, the Beni-suef governorate and Giza governorate, and the Fayoum governorate through the Bahr Youssef canal. The canal is used to irrigate about 276,000 ha in summer in addition to 168,000 ha of basin irrigation (El Quosy and Khalifa 2017). Bahr Youssef canal is considered one of the main branches of the Ibrahimia canal, which obtains its water near Dairut at 60.60 km on the Ibrahimia canal. This canal passes from Dairut through El-Minia until it reaches the Beni-Suef governorate and then ends in El-Fayoum with a total length of about 316 km (El Quosy and Khalif 2017). The Ismailia Canal is fed by the river Nile at Boulak in the center of Cairo flowing northeast to connect to Lake Temsah. The canal was designed to irrigate 40,000 ha during the floods (El Quosy and Khalifa 2017).

The Delta Barrages were constructed between the years 1936 and 1939 and designed to raise the upstream water level during floods. The benefit of the Delta Barrages is the perennial irrigation of the lands upstream from the barrages, and about 1.5 million ha downstream of the barrages even during low floods. After the construction of the Delta Barrages and the raising of the upstream water levels in the Delta, it was necessary to construct principal canals to feed the areas in the downstream in the Delta (El Quosy and Khalif 2017). Therefore, Rayah Tawfiki in the Delta, Rayah Menonfi in the Middle Delta, and Rayah Behieri in the Western Delta were constructed. These three structures were built in the period between 1850 and 1887. Rayah Tawfiki was designed to serve about 180,000 ha with a maximum discharge of 19 MCM/day. The Zifta Barrage regulator was constructed between 1901 and 1902 on the Dammietta Branch to help the Delta Barrages to serve extra areas on both sides of the Dammietta Branch. The canals in the upstream of the Zifta Barrage irrigate about 173,000 ha in the Ghanbia Governorate (El Quosy and Khalif 2017). The flow of water in the various irrigation canals in upper and middle Egypt was 18.2 BCM/y during 1998 and 1999, based on the water allocation. The annual flow to the branches upstream of the Delta Barrages is 27.4 BCM, of the Rosetta Branch is 12.0 BCM, and 13.8 BCM in the Damietta Branch (El Gamal and Zaki 2017).

18.1.6 Nile-Groundwater Interaction

In Egypt, the Nile acts as a drain for the Quaternary aquifer in the Nile Valley as the groundwater levels are higher than those of the river, except at the upstream part of the barrages. However, the construction of several barrages along the course of the Nile leads to an increase in its water level. Therefore, the river water recharges the aquifer due to the direct hydraulic conductivity between the Nile and the aquifer adjacent to the banks. This raises the groundwater level and the amount of water flowing from the river to the aquifer depends on the difference in water head between them as well as the hydraulic conductance of the base layer sediments of the river. These sites are considered to be the

proposed locations for riverbank filtration (RBF) as drinking water supplies. Many large cities, all over the world, rely on RBF water due to the natural filtration of the river banks (Abdalla and Shamrukh 2010, 2011; Abdalla and Shamrukh 2016; Ghodeif et al. 2018; Paufler et al. 2018). Nowadays, Egypt strongly supports the RBF technology as a source of drinking water, especially along the Nile Valley towns, instead of direct surface water intake.

18.1.7 Major Water Users in Egypt

The major users of water are the agricultural, domestic, and industrial consumers. The agricultural sector is the largest consumer of water in Egypt with about 85% of the total demand for water (MWRI 2005b). The total irrigated area in 2011 was 3.612 million ha with a water demand of 60.9 BCM/y (CAPMAS 2012). This signifies that the average consumption of water is about 3150 m^3/ha/y (CEDARE 2014). The water requirement for the industrial sector estimated to be 7.5 BCM/y in 2011, most of which was returned back to agricultural drains and sanitary sewer systems. According to CAPMAS (2012), the net industrial demand for water was about 1.2 BCM/y in 2011 (CEDARE 2014). The total municipal water use was estimated to be 8.9 BMC/y in 2011 (HCWW 2013; EWRA 2011). This water is mostly consumed and the rest either returns back to the sewage collection system or seeps into the ground (CEDARE 2014). The Nile and some of the irrigation canals are used for navigation. There is, at least, an amount of about 75 Mm^3/day of water in the form of discharges from the AHD, which is also required for the drinking water plants along the river (CEDARE 2014). The causes for water losses include preparing land for cultivation (0.2 BCM/y); evaporation from empty lands (0.6 BCM/y), water surfaces (2.4 BCM/y) and fish ponds (0.4 BCM/y); drainage water to Fayoum (0.7 BCM/y), the desert (1.0 BCM/y), and to the sea (15.7 BCM/y). The sum total of the losses was 21.1 BCM in 2010 (MWRI 2013).

18.1.8 Nile Water Quality

Generally, rivers and other surface water bodies, all over the world, are more vulnerable to pollution as compared to groundwater, due to discharge of untreated industrial, agricultural, and domestic wastewater into them. In Egypt, from Aswan to Cairo, the Nile receives wastewater discharge from more than 124 point sources (Fig. 18.8) amounting to more than 5,000,000 m^3/y of water along its banks. This water is untreated or partially treated wastewater (Abdalla and Shamrukh 2011, 2016), accordingly various pollutants are recorded in the river water. Excessive amounts of faecal coliform bacteria such as *Escherichia coli (E. coli)* in untreated sewage disease causing pathogens produce diseases in humans (diarrhea, abdominal cramps, vomiting due to salmonella, and cholera). Organic contaminants may move into the Nile water from the surrounding cultivated lands and wastewater discharge from villages and towns. Also, the discharge of untreated wastewater, agricultural runoff and raw sewage into the Nile can lead to the deterioration of groundwater in the adjacent Quaternary aquifer.

According to Abdalla and Shamrukh (2010, 2011), Abdalla and Scheytt (2012), Abdalla and Shamrukh (2016), the results from the Assiut and Helwan areas showed that the average water temperature was 27 °C and pH value was within the permissible limit of 6.5–8.5, as prescribed for drinking water by the EHCW guidelines and WHO standards. The turbidity, which is a measure of the cloudiness of water indicating the presence of suspended particles and disease-causing organisms such as bacteria, viruses, and parasites, was 11 NTU, which was much above the permissible limit of 1.0 NTU for drinking water, but is in the typical range for surface water. The TDS and TH values were 122 and 186 mg/l, respectively, which were far below the permissible limits of 500 mg/l. Chloride and sulfate concentrations were 10.5 and 10.7 mg/l, respectively, which were less than the permissible limits recommended by the EHCW and WHO. Copper, nickel, lead, chromium and cadmium were detected, however, their concentration was

Fig. 18.8 Main sources of contamination to the River Nile

lower than the permissible limit of 0.005 mg/l. The concentrations of iron, manganese and zinc in the Nile water were 0.08, 0.01, and 0.01 mg/l, respectively, which were below the acceptable limits specified by WHO (0.3, 0.4, and 5 mg/l for Fe, Mn, and Zn, respectively). Similarly, the nitrate concentration was found to be within the permissible limits specified by EHCW and WHO. The maximum total organic carbon (TOC) content that was recorded was about 4.43 mg/l, which was relatively high, suggesting an additional source of TOC, most probably from sewage discharge by agricultural drainage from nearby villages and towns.

A microbiological analysis of the Nile water in the Assiut area showed that the number of the total and faecal coliforms (cfu/100 ml) as well as total algal in the Nile water was higher than that prescribed by the EHCW and WHO standards. Drinking water supplies must be free from microorganisms or the counts must be less than 1 colony forming unit per 100 ml water (cfu/100 ml). Higher bacterial counts clearly indicate that the Nile water is polluted by sewage faecal contamination. The presence of *E. coli* in water bodies indicates recent faecal contamination. Based on the water quality index (WQI) value, the Nile water is classified as unsuitable with grade E (>100) or poor water quality with grade C (>56), which is due to the high level of turbidity, total coliform and *E. coli* bacteria that exceed the safety limit of drinking water standards.

18.1.9 Conclusions

The Nile, as the main water resource in Egypt with 55.5 BCM/y, represents about 97% of the renewable water resources in Egypt. It has two main tributaries, the White Nile and the Blue Nile which meet in Khartoum to form the river Nile. At the AHD in Egypt, the annual average flow of the Nile is 84 BCM/y, out of which the share of Egypt is 55.5 BCM, that of Sudan and South Sudan is 18.5 BCM, and the rest, which is about 10 BCM, is lost by evaporation. After the construction of the AHD, several barrages were designed to control the water level and discharges into the river. Climatic changes affecting the various components of the hydrological cycle are expected to adversely affect the water resources in the Nile basin. WQI values showed that the Nile water is unsuitable for direct human consumption, due to the high level of turbidity, *E. coli* bacteria and total coliform and algae, that exceed the safety limit of drinking water standards. The source of the high load of bacteria in the Nile water is caused by the domestic raw sewage from agricultural runoff. Consequently, numerous efforts must be made to reduce the contamination load and improve the quality of the water of the Nile.

18.2 Groundwater Resources in Egypt

Mohamed El Alfy
Fathy Abdalla

Abstract
Egypt is experiencing a severe water shortage that is expected to worsen because of the increasing demand for water for domestic, agricultural, and industrial use. The main water resources include the River Nile and renewable and non-renewable groundwater. Groundwater is a vital source for domestic and irrigation purposes, especially in the desert areas. Groundwater forms a moderate part of the total water supply in Egypt, however, the demand for groundwater resources is expected to increase in the near future 2020 to be ≈110 billion cubic meters per year (BCM/y). The main groundwater resources in Egypt are the Nile Valley and Nile Delta and Nubian Sandstone aquifers in the Western Desert and Sinai Peninsula. Various minor aquifers are available locally in the coastal areas, and the eastern and western Nile Delta, however, new strategies for the development of these water resources must be implemented. Advanced and more effective techniques such as tracing techniques, Remote Sensing (RS), Geographic Information System (GIS), and modeling are noteworthy to open new areas for further research in the future with unique and accurate information, especially about groundwater mapping, recharge and pollution processes. Due to the current overexploitation of groundwater in some areas, the water quality is deteriorating rapidly. Therefore, the use of groundwater must be monitored by measures such as user inventories and strengthening of the license system for its abstraction, to reduce the environmental effects.

18.2.1 Introduction

Egypt is a desert country and only 4% of its area inhabited. Groundwater is, therefore, a vital factor for economic growth and sustainable development. The country experiences severe water shortage, as the available surface water resources have not increased since the 1950s, while population growth has been enormous. The water share for each person in Egypt is continuously declining, as the population has

increased from 24 to 104 million in 52 years (1955–2017) and is expected to grow to 153 million by 2050 (Worldometers 2017). In addition to the growing population, a significantly larger amount of water is being used for industrial, agricultural, and other purposes, consequently, the already limited fresh water resources are under severe stress. Moreover, the quality of the surface water and groundwater is deteriorating rapidly. The main water resources include the Nile River, precipitation, and groundwater (renewable and non-renewable). Groundwater is a vital source for domestic and other use and irrigation, especially in the desert areas. Other local water resources include the harvested water from rainfall and flash floods and the reused drainage water and treated wastewater. Desalination provides domestic water to various tourist areas on the coasts of the Mediterranean and Red Seas, and the Gulfs of Suez and Aqaba. The estimated total annual water demand in Egypt for all sectors is 76–78 BCM/y, with the agricultural sector consuming 82–86% of this volume (MWRI 2005b; FAO 2016). In 1959, the Nile Waters Agreement was signed between Egypt and Sudan, for full control utilization of the Nile waters reaching the Nasser Lake. The agreement allowed the entire average annual flow of the Nile to be shared between Sudan and Egypt, the amount of water allocated being 18.5 and 55.5 BCM/y, respectively, however, Egypt depends mainly on the surface water of the Nile River. An estimated 1.3 BCM/y of water is harvested from rainfall and flash floods, ≈1 BCM/y of water from desalination processes and the rest of the demand for water is abstracted from groundwater (7–8 BCM/y). Currently, the gap between the water demands and water supply is about 14 BCM/y, which is compensated by increasing the rate of wastewater recycling, rainwater harvesting and desalination processes. In addition, Egypt imports ≈30 BCM/y virtual water (water embedded in the products exchanged internationally) mostly agricultural products. Subsurface geological and climatic conditions are the principal factors controlling the spatial and temporal distribution and availability of groundwater. Climatic change is expected to place significant pressure on the already scarce water resources because of rising temperatures, changes in precipitation patterns, inland evaporation, and salinization (Elsaeed 2011). Therefore, sustained efforts, using different approaches, must be directed towards finding and conserving water resources for which basic hydrogeological data, such as aquifer geometry, hydraulic characteristics, water level, and historic extraction records would be required.

18.2.2 Climate

Numerous Quaternary climate changes have occurred because of the alternating north–south shifts of the present-day climatic belts (Horowitz 1979). The climate of Egypt and the Middle East up to the Upper Pleistocene was humid, as proven by the existence of the wide, dry tributaries of the major wadis. There were three general paleoclimatic patterns during the Pleistocene period (Issar and Gilead 1986). The first prevailed during the Early Pleistocene (savannah climate), with springs flowing through limestone outcrops while the second was characterized by extensive alluviation processes, with a relatively high quantity of silt being mixed with gravel deposits. This indicates humid conditions, albeit at lower levels than those of the Early Pleistocene (Middle to early Upper Pleistocene [500,000–60,000 years ago]). The third pattern prevailed in the Upper Pleistocene (60,000–10,000 years ago) and was characterized by the deposition of loess layers in the lacustrine deposits (Issar and Bruins 1983). The present-day Egypt is located in an arid to semiarid zone in the coastal areas, where the average temperature ranges from 14 to 30 °C. In the inland desert zone, the temperature ranges from 7 to 43 °C in summer, and 0–18 °C in winter. The narrow Mediterranean coastal zone receives the maximum precipitation, with rainfall around Alexandria being approximately 200 mm/y, and that in Rafah exceeding 250 mm/y (Fig. 18.9). The intensity of precipitation decreases quickly in regions away from the coastal areas with the long-term average at Cairo about 25.7 mm/y, becoming very rare in Upper Egypt (<2 mm/y to zero). Some areas in the Western and Eastern deserts and the Sinai Peninsula can be completely dry for several years, but occasional and sudden high-intensity rainstorms could create catastrophic flash floods. However, along the Mediterranean coast, with no access to the Nile river water and only limited groundwater resources, rainfall harvesting as a low-cost technique is important for intercepting surface water for irrigation. Drilling of shallow recharge wells could enhance the groundwater recharge process to some extent (Alataway and El Alfy 2019).

18.2.3 Groundwater Resources

The current water shortage in Egypt is expected to worsen due to the population growth and the attendant increasing demands for water for agricultural and other use. Although the contribution of groundwater to the total water supply in Egypt is moderate, groundwater essentially supports life in the desert areas. Across the Egyptian territories, regional hydrogeological systems are heterogeneous, with both shallow and deep aquifers in different hydrogeological settings, with different recharge rates, hydraulic parameters, water quality, and water age. The shallow aquifers are located in the coastal areas and replenished by rainfall and surface water. Groundwater, accessed via hand-dug wells,

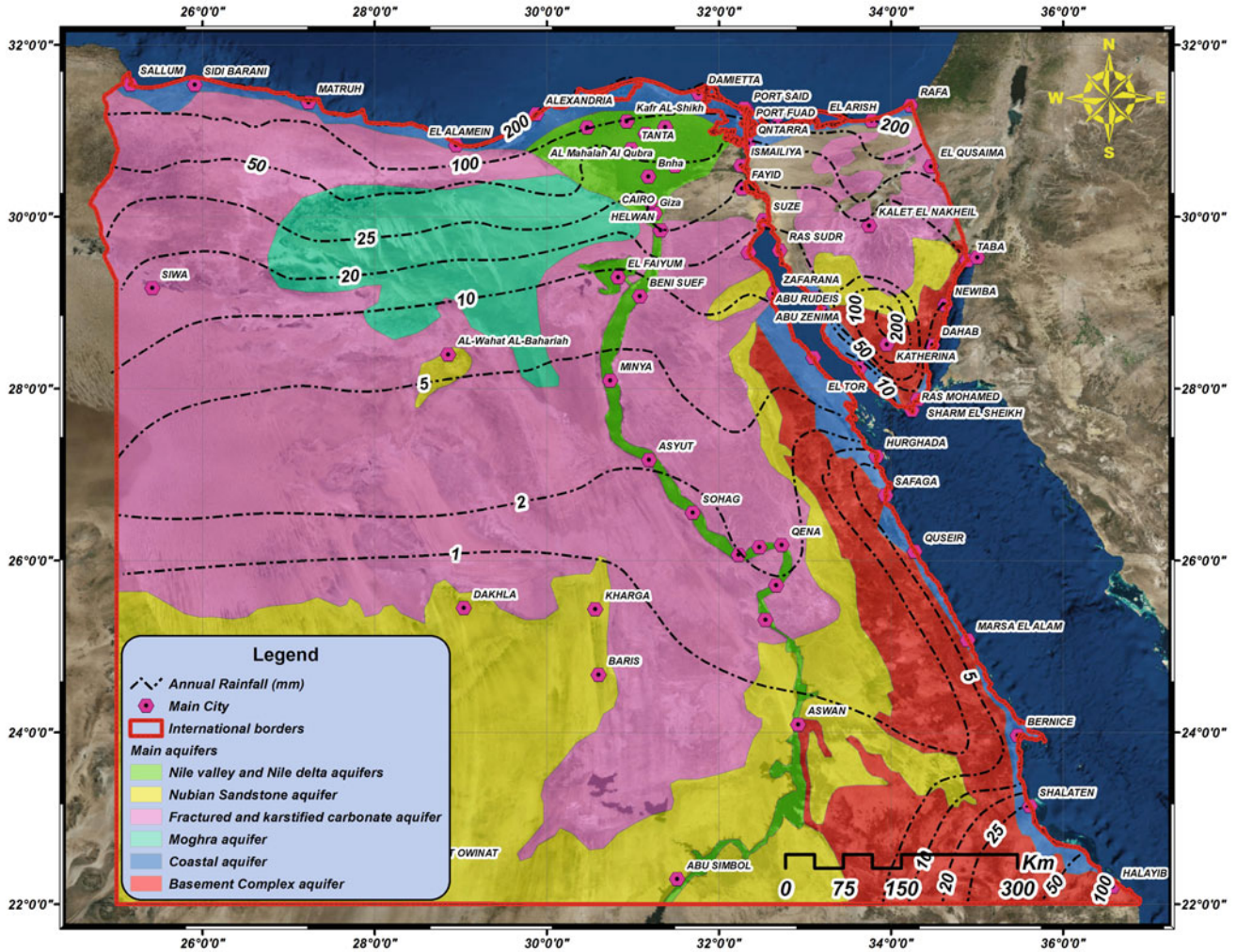

Fig. 18.9 Spatial distribution of the average annual rainfall and major aquifers systems (compiled from different sources)

provides water for domestic and irrigation use. The deep regional aquifer systems in the Western Desert and Sinai Peninsula contain fossil water (non-renewable) which is obtained on a large scale via boreholes with mechanized pumps. In Egypt, two main aquifer systems are prevalent, namely, (i) the granular system, represented by aquifers such as the Nile Valley and Delta systems, Nubian sandstone system, and the coastal and Moghra systems (Fig. 18.9) and (ii) the fissured and karstified aquifer systems, composed of limestone, and hard igneous and metamorphic rocks (Hefny and Shata 2004). These aquifer systems cover five diverse hydrogeological zones, namely, the Nile Valley and Delta, Western Desert, Eastern Desert, Mediterranean or Coastal region, and the Sinai Peninsula and have been referred to by many authors (RIGW 1980, 1992, 1993, 1995, 2002, 2003; MPWWR 1988; RIGW-IWACO 1988; Abdel Moneim 2009). The most important groundwater resources in Egypt are the Nile Valley and Nile Delta aquifers, and the Nubian Sandstone Aquifer in the Western Desert and Sinai Peninsula. The others are minor aquifers used locally in the coastal areas, the eastern and western Nile Delta, and others.

18.2.3.1 The Nile Valley and Nile Delta Aquifer Systems

The Nile Valley and Delta aquifer systems, representing approximately 87% of the exploited groundwater (MWRI 2005a), are the most important aquifers in Egypt according to the abstraction rates and aquifer accessibility. In 2010, the amount of exploited groundwater was assessed to be 6.2 BCM/y, but the annual yield of the aquifer was less than 8.4 BCM/y (MWRI 2012). These aquifers are recharged mainly by infiltrated water from the Nile River, its branches and channels, and excess irrigation water.

The Nile Valley aquifer composed mainly of fluvial sand, silt, and clay, is restricted to the flood plain of the Nile River (Figs. 18.9 and 18.10). This aquifer is represented by two hydrogeological units (Abdalla et al. 2009; Abdalla and Khalil 2018), namely, permeable sands and gravels of the

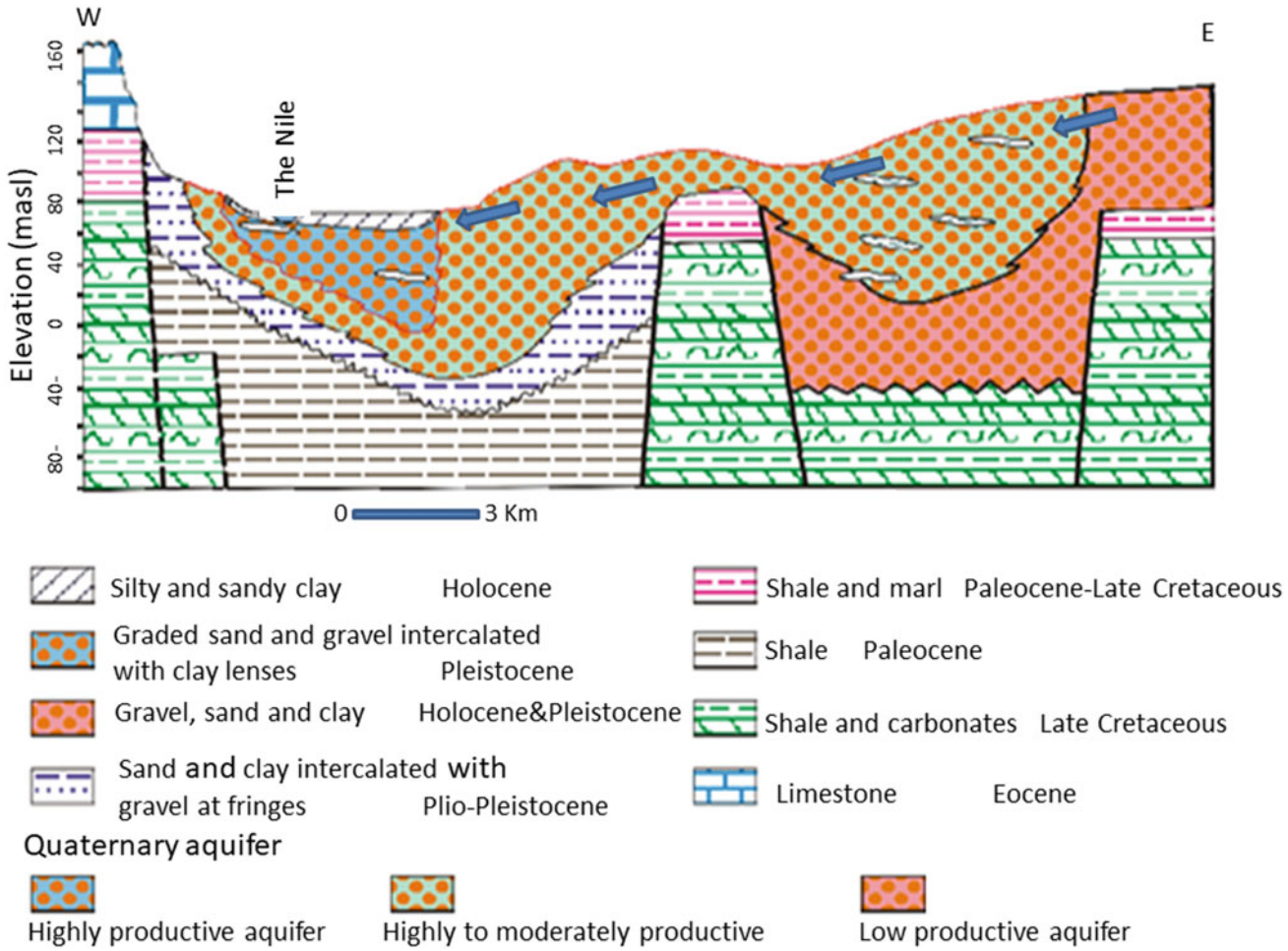

Fig. 18.10 E-W hydrogeological cross section in the Nile Valley in the Qena area (Abdalla et al. 2009)

Pleistocene age at the base, and semi-permeable clay–silt layers of the Holocene age at the top. The aquifer is thickest in the central part of the valley, decreasing gradually (by <40 m) away from the center. The saturation thickness declines from 300 m at Sohag to less than tens of meters at Luxor (Kamel 2004). The Holocene clay cap varies in thickness from 10 to 14 m at Helwan, south of Cairo, vanishing at the eastern and western boundaries of the flood plain. The Pleistocene layer varies in thickness between 50 and 80 m close to Helwan (Sadek and Abd El-Samie 2001; Abdalla and Scheyt 2012). The recharge rate is estimated to be about >3.5 BCM/y and the total groundwater storage is approximately 200 BCM/y. There is no hydraulic connection between the Nile Valley and the Nubian Sandstone aquifers owing to the existence of thick clay deposits (Pliocene) at the base of the former, except in places of major flaws. There are lateral losses into the Nile, however, the boundary on both sides of the valley is pervious. During the flood period before 1960, an increase in the level of the Nile caused lateral water seepage to the graded sand member, with reverse flows during periods of low river levels. After the building of the Aswan High Dam, the river channel acted as a drainage line, capturing the groundwater. The depth to the water table ranges between 3 and 20 m in the valley flood plain, increasing in depth to more than 80 m far towards the east (Abdalla et al. 2009; Abdalla and Shamrukh 2016). The hydraulic conductivity of the clay–silt layer at the top is low, varying between 0.4 and 1.0 m/day, but increases downwards. The lower sand and gravel layers have high hydraulic conductivity, varying between 60 and 100 m/day, with the transmissivity varying between 2000 and 20,000 m^2/day (Abd El-Bassier 1997).

The Nile Delta aquifer is composed of sand and gravel, with intercalated clay lenses and is protected by an impervious clay layer of thickness varying from a few meters to 50 m. The saturated thickness of the aquifer varies between 190 m in the southern part of the Nile Delta to 350 m at Tanta (Al-Agha et al. 2015). The groundwater is extremely shallow, with the depth to the groundwater varying between 1 and 2 m in the northern part, 3 and 4 m in the central part,

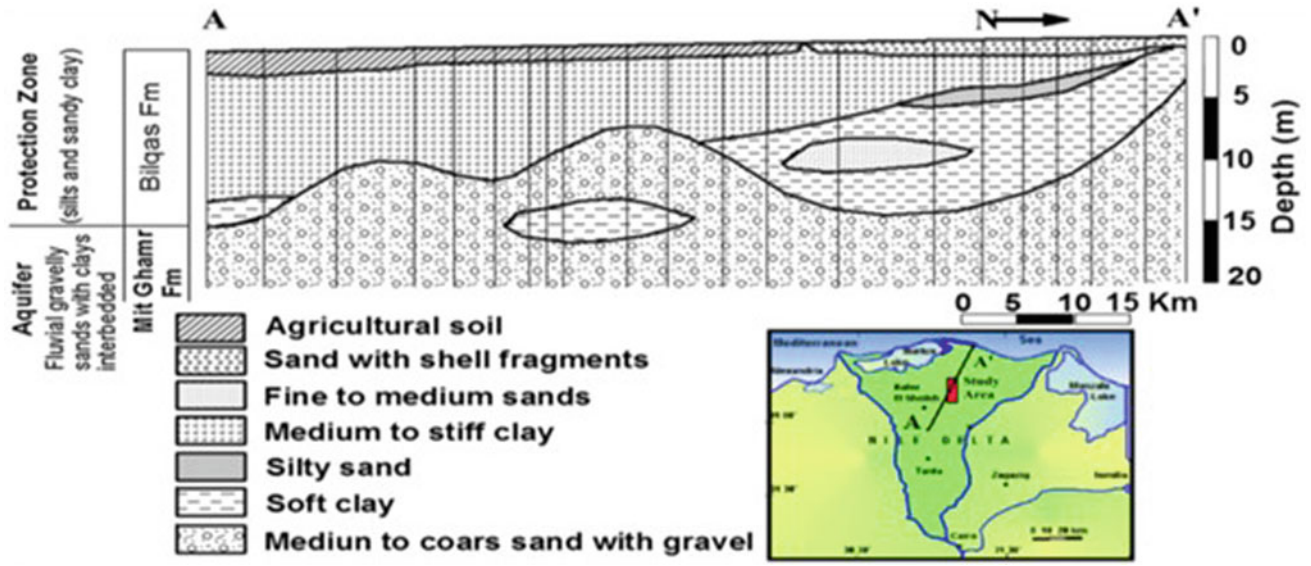

Fig. 18.11 Hydrogeological cross section in the northern part of the Nile Delta (Fergany and Claudet 2009)

and 5 m in the southern part (Mabrouk et al. 2013). The aquifer storage is estimated to be 500 BCM/y (Sherif 1999). The shallow depths to the groundwater table and high production rate of the drilled wells (100–300 m^3/h) allow the abstraction of large volumes of groundwater at a relatively low cost. Recharges from surface water, estimated to be 6.78 BCM/y (FAO 2013a, b) to this aquifer, occur by seepage of Nile River water, canals, drains, and irrigated areas. The aquifer outflow to surface water is through well abstractions (4.6 BCM/y), the drainage system, and, in some areas in the north, to the Nile River (El Arabi 2012). The aquifer has excellent hydraulic parameters, with the transmissivity reaching 25,000 m^2/day (El Tahlawi et al. 2008). Plans to increase groundwater exploitation must be revised wisely to avoid seawater intrusion.

From the south to the north along the Nile Delta, the groundwater quality varies significantly and influenced by the hydrogeological setting, water source, and anthropogenic influences. In the Nile Valley area, groundwater quality is superior at TDS < 1500 mg/l, but at the valley margins (east and west), where groundwater is a significant source for domestic, irrigation, and other uses, the salinity tends to be high (Hefny et al. 1992). High nitrate concentrations are observed in many areas (Abdalla et al. 2009; Abdalla and Khalil 2018; El Alfy et al. 2019) due to contamination from irrigation return flows and untreated sewage infiltration. The quality of the groundwater in the Nile Delta system, especially in the southern part, is good (TDS < 1000 mg/l), but it has high manganese concentration in particular under reducing conditions. To the north of Mansoura and close to the Mediterranean Sea, there is higher salinity because of seawater intrusion and the leaching of lagoon deposits (Gemail et al. 2011, 2017). Fresh groundwater is dominant in the upper zone of the aquifer, while brackish groundwater is found in the lower zone. In the coastal area close to the sea, there are indications of brackish water (TDS 2500 mg/l) at a depth of 100–150 m below the shallow saline–hypersaline groundwater. The groundwater is highly vulnerable to pollution where the protective clay cap is extremely thin or missing (RIGW 1995; El-Rawy et al. 2019; Ismail and El-Rawy 2018), and such vulnerable areas need additional protection measures (Fig. 18.11).

18.2.3.2 Nubian Sandstone Aquifer

The transboundary Nubian Sandstone Aquifer is a vital groundwater resource in Egypt and North Africa that extends from Egypt into Libya, Chad, and Sudan. It covers an area of 2 million km^2, and dates from the Paleozoic–Mesozoic eras (Nashed et al. 2014). The aquifer is composed of three major sub-basins separated by basement uplifts, viz., Dakhla in Egypt, Northern Sudan Platform and Kufra in Libya, with a maximum thickness of about 3, 4, and 0.5 km respectively. It is bounded on the east, south, and west by basement outcrops and on the north by the fresh–salt water line (Mohamed et al. 2016). This aquifer, with vast volumes of groundwater, is undoubtedly the most significant source of fresh water outside the Nile system. It consists of sandstone, with shale and clay interactions. The sandstone overlies the basement rock that is crosscut by an E–W fault system in the southern part of Egypt (Issawi 1978). In Egypt, the northern boundary of the aquifer points toward the fresh–salt water line that follows a fault north of Siwa, stretching through the Nile Valley between Minya and Beni Suef, and bending northeast into the Sinai Peninsula (Fig. 18.12). From the

southwestern to the northern parts of the Western Desert, the hyrdrogeological conditions of the Nubian Sandstone Aquifer are unconfined, semi-confined, confined, and artesian. It is in the unconfined condition, with thick marine shale and clay layers, south of latitude 25°N. The saturated thickness of the fresh part of the aquifer ranges between 200 m in East Oweinat and 3500 m in Farafra (Mohamed et al. 2016). The hydraulic coefficients of the aquifer are adequate, with high bulk porosity (20%), and the fracture system can induce secondary porosity. The transmissivity values range between 1000 and 4000 m^2/day, and the storativity of the semi-confined part is approximately 10^{-3} (El Sayed et al. 2004). The groundwater is non-renewable (fossil water) and the rainfall recharge is extremely low under the present climatic conditions. The aquifer was recharged during the humid Pleistocene, with various climatic changes (Issar 2003). The groundwater age is deemed to vary between 14,000 and 40,000 years (Schneider and Sonntag 1985), however, isotopic studies indicate an age of 0.2–1.0 × 10^6 years (Sturchio et al. 2004). Aquifer discharge occurs in the Western Desert through artesian and pumping wells and natural springs. The total stored fresh water volume probably exceeds 150,000 BCM/y (Thorweihe and Heinl 1996).

In Egypt, the total storage is approximately 40,000 BCM/y, however, exploiting this resource depends on the cost of pumping and economic returns over a fixed period. The total potential pumping withdrawal of groundwater in the Western Desert (East Oweinat, and the Farafra and Dakhla oases) is approximately 3.5 BCM/y (El Arabi 2012; El Alfy 2014). In Sinai, the aquifer has potential for further groundwater development (200–300 × 10^6 m^3/y), (JICA 1999) and in the Eastern Desert, the potential is 50–100 × 10^6 m^3/y. If constant large-scale depletion in the Western Desert continues, the aquifer will come under stress and the water level will decline (Fig. 18.13). In different areas in the Western Desert and Sinai Peninsula, superior quality water is pumped in from the Nubian Aquifer,

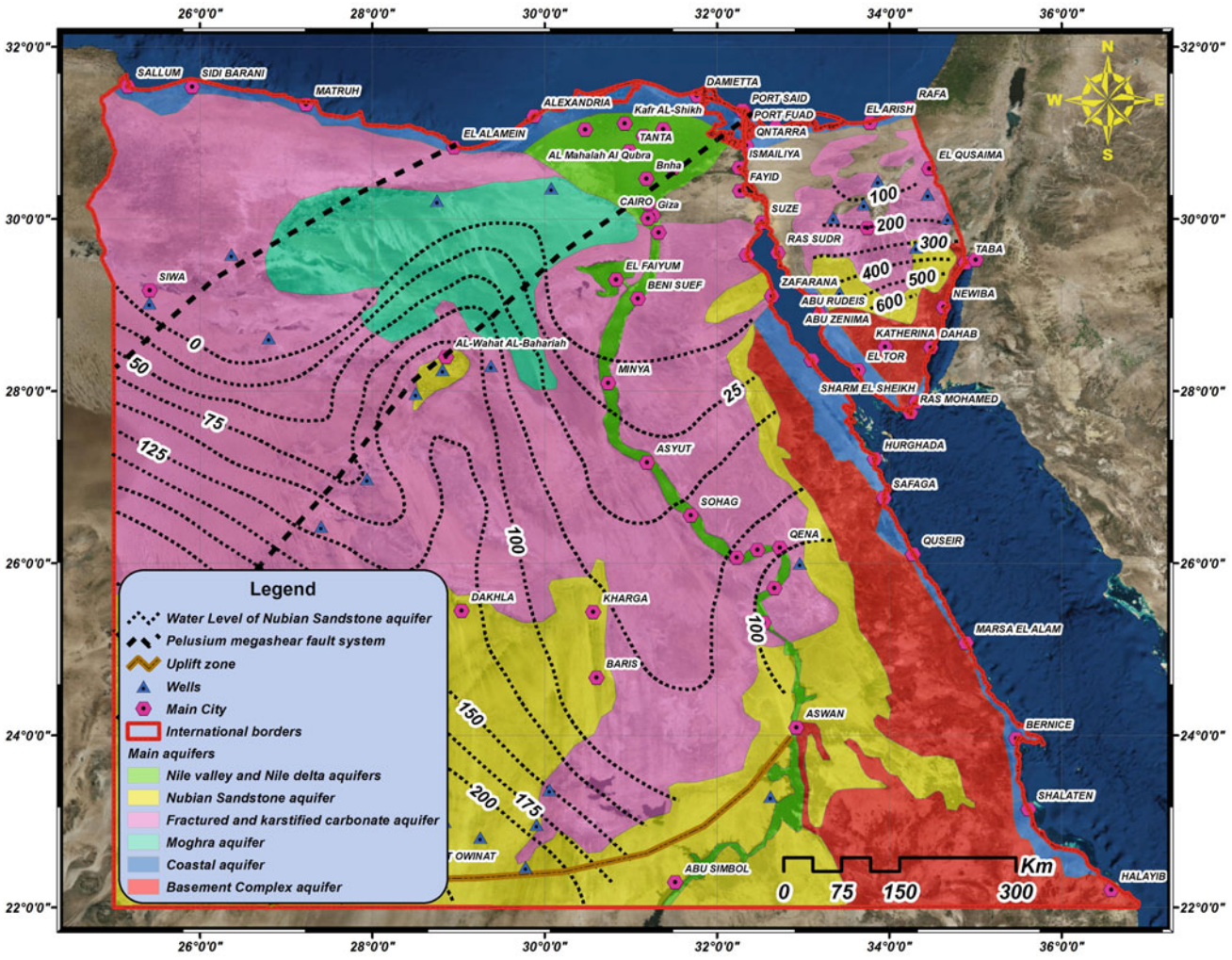

Fig. 18.12 Water level, exposure, and structure elements of the Nubian Sandstone Aquifer (compiled from different sources)

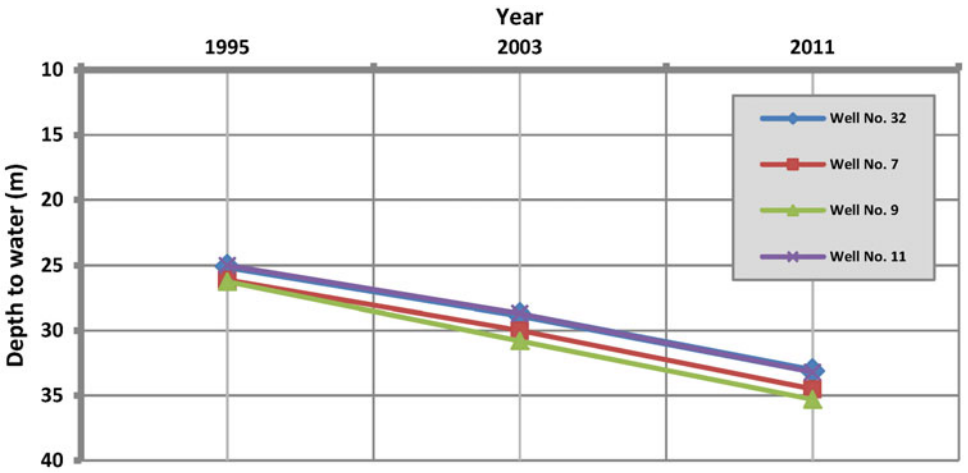

Fig. 18.13 Depth to water in some wells of East Oweinat area (El Alfy 2014)

however, the iron and manganese concentrations are relatively high. Groundwater salinity varies vertically and horizontally. In the El Bahariya Oasis, groundwater exists with a high potentiality in four water-bearing horizons separated by interbedded shale and clay beds with good water quality and the flow patterns are from SW to NE (Khaled and Abdalla 2013). In the Kharga and Dakhla oases, TDS decreases in depth from >1000 mg/l in the upper horizons to 200 mg/l in the lower horizons. In the Siwa area, near the salt–water interface, the upper horizon has fresh water (200–400 mg/l), whereas the deeper horizon has hypersaline water (up to 100,000 mg/l). This groundwater is highly corrosive because of the free CO_2 and H_2S content and low redox potential. The high iron and manganese concentrations (2–20 mg/l) recorded in Farafra, Baharia, and other areas cause clogging of the well screens (Korany 1995).

18.2.3.3 Fractured and Karstified Carbonate Aquifer

Fissured carbonate aquifers occur in the Upper Cretaceous and Eocene limestone rock that occupies more than 50% of the surface area of Egypt. They are found in the northern and central parts of the Western Desert, locally in the Eastern Desert, and in the central and northern Sinai Peninsula (Abdalla and Scheytt 2012). In central Sinai, the Upper Cretaceous aquifer is characterized by a thick section, exceeding 800–1000 m, composed mainly of chalk, chalky limestone, marl, dolomite, dolomitic limestone, and shale. The Eocene rock comprises limestone, marl limestone, and marl of different formations. The thickness of these units decreases gradually southward to approximately 200 m near the outcrop at the El Egma and El Tih plateaus. In the central part of the Western Desert, the fissured limestone outcrops are dotted with more than 200 springs, with a total flow of 200,000 m^3/day. Various wells tap into this aquifer, where the water levels are 62–80 m amsl at Gebel Augilla and the EI-Farafra Oasis (Joint Venture Qattara 1979). The aquifer is recharged mainly by upward groundwater leakage from the underlying Nubia Sandstone Aquifer through existing deep faults, and irregularly from direct rainfall and surface runoff (EI-Ramly 1967; II Nouva Castoro 1986). In the Sinai Peninsula, the annual recharge is estimated to be 76 MCM (JICA 1999). Here, the Upper Cretaceous aquifer extends from the central part to the north of the Maghara and EI-Halal areas, where a down-faulted block of tertiary-age rock forms its northern boundary. The conditions of this aquifer system are free to semi-confined in central Sinai, with low discharge rates through many shallow wells and natural contact springs. The direction of the regional flow is mainly from the highlands towards the lowlands. There is a general SE–NW flow, with a hydraulic gradient of 0.0035 (Fig. 18.14).

Owing to low porosity and permeability, the groundwater occurrence and flow are limited to karstified sedimentary deposits, fissures, and fault systems, which could improve the groundwater potential of the aquifer. The estimated hydraulic conductivity varies from 6.4×10^{-5} to 2.1×10^{-3} m/s (Wagdy et al. 2008). In the Helwan area, the transmissivity varies between 4.6×10^{-3} and 9.3×10^{-3} m^2/s. Well productivity differs from one location to another, depending on the intensity and continuity of fractures (Abdalla and Scheytt 2012). In the Siwa Oasis, the well production rate varies significantly from 5 to >300 m^3/h. In central Sinai, the hydraulic conductivity is 18.4 m/day and transmissivity is 663.7 m^2/day (JICA 1992).

Salinity varies due to the location of the recharge area, in addition to the type of rock of the water-bearing rocks. The outcropping carbonate aquifers contain brackish water, and fresh water occurs only in areas where relatively fresh water recharges the aquifer through infiltration from wadi deposits or upward leakage from the Nubian Aquifer. Groundwater quality in the Farafra Oasis is relatively fresh, with salinity <1000 mg/l. In the southern part of the northern plateau, the TDS value varies from 2000 to 5000 mg/l and in the north,

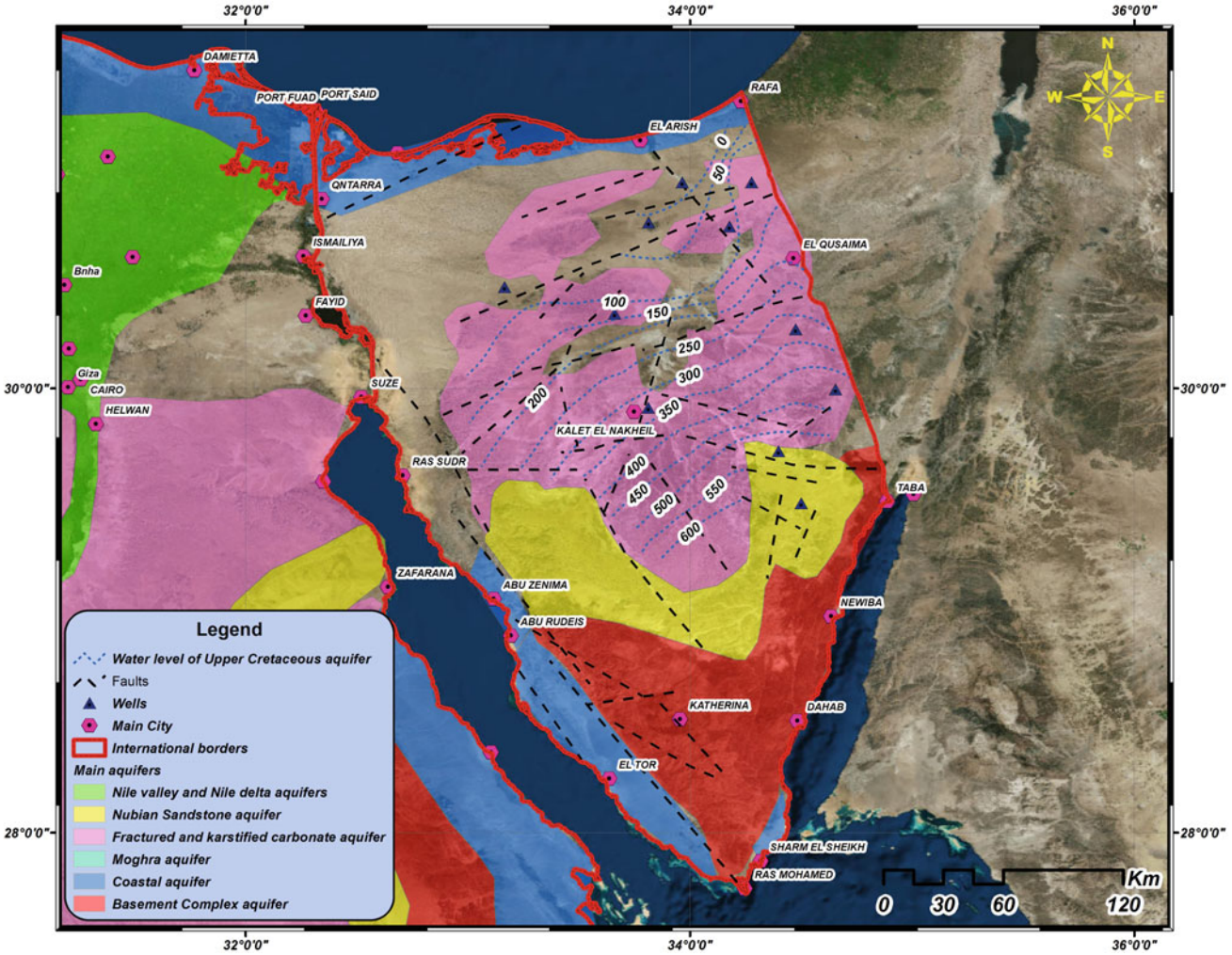

Fig. 18.14 Water level of the fractured aquifer (modified after JICA 1992, 1999)

where the aquifer is capped by the Dabaa shales, the TDS increases to >10,000 mg/l (Joint Venture Qattara 1979). In the Helwan area, fissured limestone shows some karstic features with groundwater flow through several warm springs and the TDS values increase to >5000 mg/l (Abdalla and Scheytt 2012). In central and north Sinai, the salinity increases towards the north, ranging from 3800 to 5000 mg/l (JICA 1992).

18.2.3.4 Moghra Aquifer

The Moghra Aquifer is exposed at the surface, northwest of the Nile Delta, covering an area of 50,000 km^2 and extending from Wadi Farigh to the Qattara Depression. The thickness varies between 75 and 700 m, and the aquifer dips beneath younger formations to the north (RIGW 1993). It consists of sand, gravel, and sandy shale of the Moghra Formation (Fig. 18.15). Dabaa shale and basaltic sheets occur at the base of the Moghra Aquifer, with overlying limestone to shaly limestone and marl of the Marmarica Formation (Said 1962). In the southern part unconfined conditions exist, but they become confined in the north. The annual yield exceeds 1 BCM, and the current annual discharge is estimated at 200 MCM. The groundwater flow is directed westward towards the Qattara Depression, with a hydraulic gradient of <0.2 m/km (Fig. 18.16). The permeability decreases northwards from 25 m/day at Wadi El-Farig to < 1 m/day near the coast, and transmissivity varies from 500 to 5000 m^2/day (Dawoud et al. 2005; El Tahlawi et al. 2008). Groundwater recharge of this aquifer is a combination of meteoric and fossil water, with a small rainfall input, lateral recharge from the Nile Delta, and upward leakage from the underlying Nubian Sandstone Aquifer (MacAlister et al. 2012). The annual leakage from the Nile Delta Aquifer is assessed to be 50–100 × 10^6 m^3 (RIGW-IWACO 1992). Aquifer discharge occurs by lateral seepage into carbonate rocks west of the Qattara Depression, with significant evaporation in the Qattara and Wadi EI Natron depressions. Numerous springs occur at the

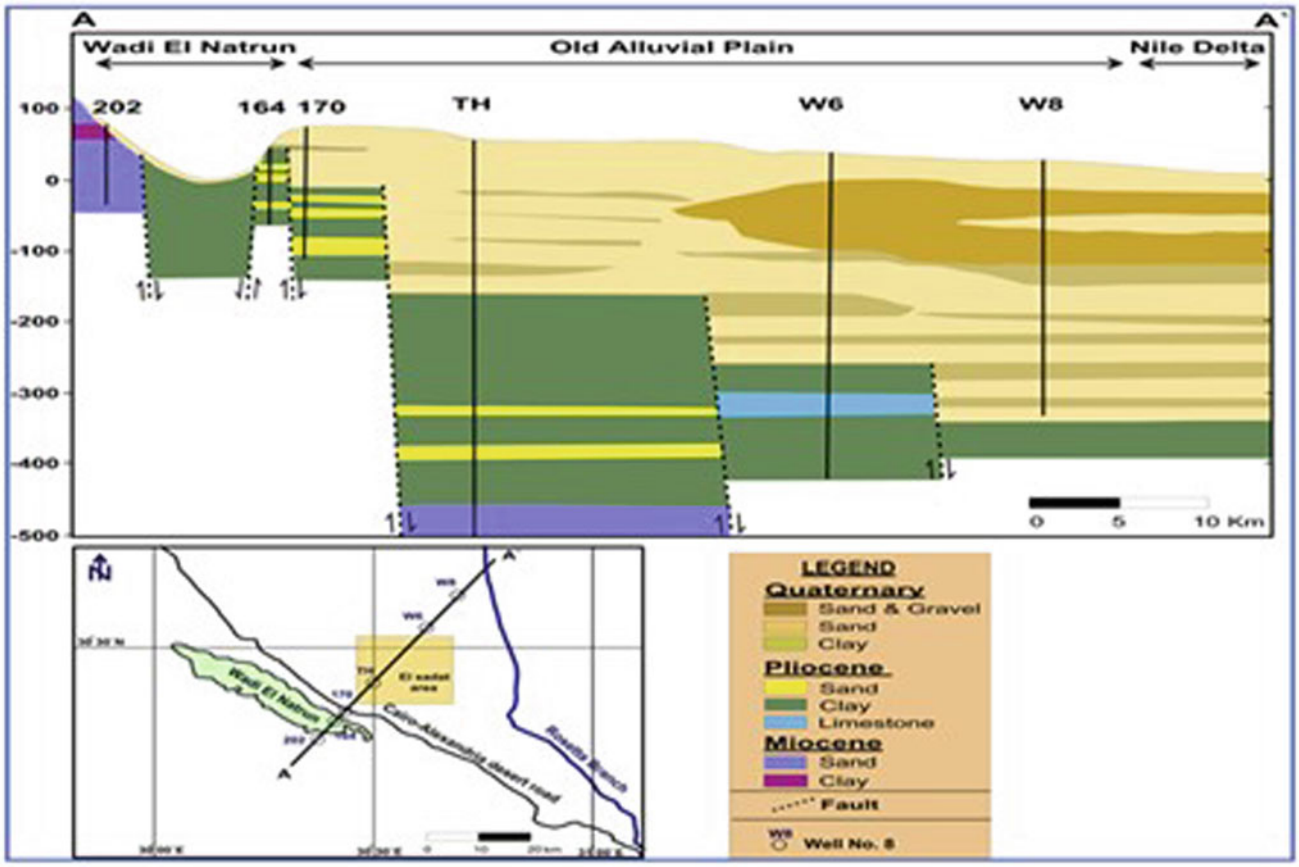

Fig. 18.15 Hydrogeological cross section of the shallow aquifers between the Rosetta branch and Wadi El Natrun (modified after El-Abd 2005; Massoud et al. 2014)

water-table/ground-surface intersection. Discharge at >200 × 10^6 m^3/y occurs through irrigation wells, and in Wadi El-Farigh, 60,000 feddan (252 × 10^6 m^2) is irrigated by groundwater (Youssef et al. 2012).

The aquifer only contains fresh groundwater near its eastern border at Wadi El-Farigh (500–1000 mg/l), and salinity increases north and westward, reaching >5000 mg/l (El Tahlawi et al. 2008). The quality and sustainability of this water are at risk, as the water levels are declining, and salinization and nitrate pollution affect the water quality. In the study area, the hydraulic head decreases by approximately 0.5 m/y. Remedial measures such as decreasing the number of pumping wells, reducing the initial and running times, and applying a discrete irrigation system are required for sustainable development of this aquifer (Youssef et al. 2012).

18.2.3.5 Coastal Aquifer

Small-scale exploitation of shallow wells at abstraction rates of <100 MCM/y provides water to various coastal areas in the Sinai Peninsula and Western Desert. The coastal aquifers are recharged by meteoric water, upward leakage, or cross flow from the underlying and adjacent aquifers depending on their location and hydrological setting. Quaternary and Late Tertiary coastal aquifer systems are located along the Mediterranean and Red Seas, and Suez and Aqaba coasts. In the northern coast, the aquifer system consists of oolitic limestone, 40 m thick, and in North Sinai it comprises calcareous sandstone, 70 m thick. In the Al-Arish area, the aquifer system is formed by connected minor aquifers, namely, the sandy (sand dune), gravelly (old beach), and calcareous sandstone (Kurkar) aquifers. In the Red Sea and gulf coastal areas, the aquifer system includes fluviatile sediments settled at the deltaic areas of the main wadis. In southwestern Sinai, the El Qa'a plain hosts the Miocene and Oligo-Miocene sand aquifer, that is recharged by direct meteoric water, seepage from the Quaternary aquifer, and upward leakage from the deeper aquifer. The groundwater of these aquifers is generally under phreatic conditions, however, rainfall, excessive pumping, and evapotranspiration cause groundwater fluctuations. Thin fresh water lenses float over the highly saline water, allowing the abstraction of only small volumes to avoid the seawater intrusion (El Alfy and Merkel 2011). Coastal aquifers generally have fresh to

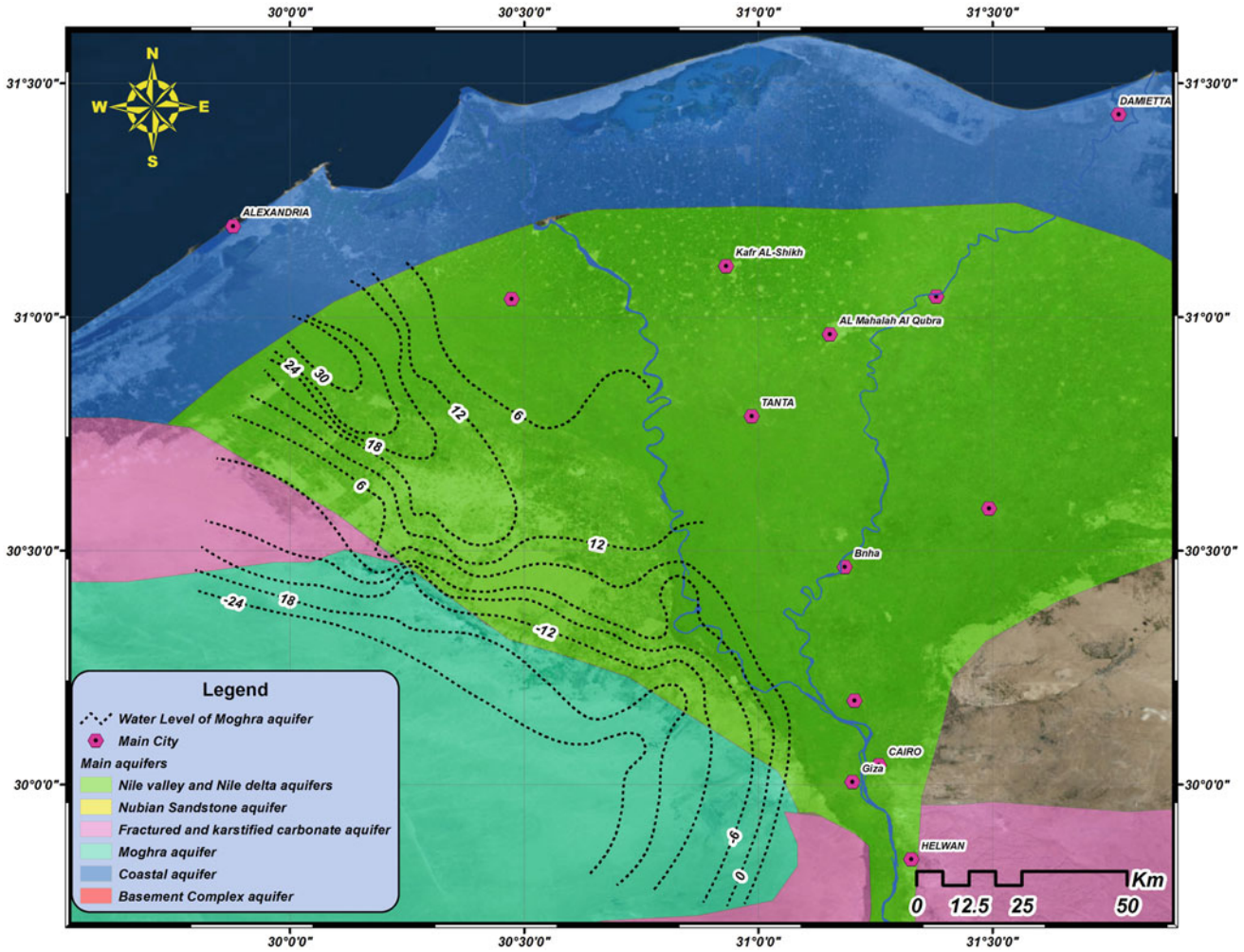

Fig. 18.16 Groundwater levels of the Moghra Aquifer, west of the Nile Delta (compiled from different sources)

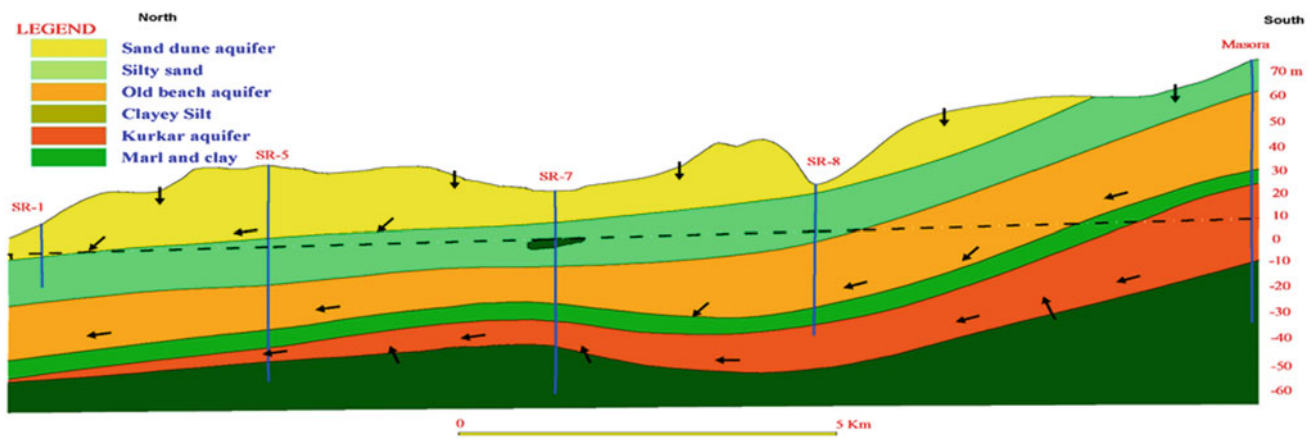

Fig. 18.17 Hydrogeological SE-NW cross-section in Rafah coastal area (El Alfy 2003)

brackish water, in the El Qa'a plain and groundwater salinity reaches >1500 mg/l, (El Tahlawi et al. 2008). In such coastal areas, the pollution risk is high, as the depth to the groundwater is shallow and the ability of aquifer to attenuate water pollution is poor (Fig. 18.17). The water levels show a declining trend with time because the discharge rates exceed the recharge, causing upward leakage from the deeper aquifer and saltwater intrusion (El Alfy 2012, 2013).

18.2.3.6 Basement Complex Aquifers

The Pre-Cambrian basement complex aquifer predominates in the Eastern Desert and the southern part of the Sinai Peninsula. Generally, this rock is impermeable, however, aquifers could occur where weathered rock and extensive fracturing systems exist. Filled fractures and dykes in the form of subsurface dams could deter the flow of groundwater and some natural springs could be formed (Wadi Feran and Wadi Baba, southwestern Sinai). In the Barramiya gold mining area (Eastern Desert), faults and dykes influence the movement of groundwater significantly (El Tahlawi et al. 2008). This aquifer is recharged mainly by small quantities of infiltrating rainwater and flash flood water. A more productive zone is located at the contact between the weathered rock and the bedrock. The higher aquifer transmissivity and yielding zones are characterized by highly fractured and hydraulically connected systems. Unconfined conditions prevail in the weathered aquifer, but the fractured aquifer is leaky. Occasionally, alluvial deposits are found in shallow wadis above or adjacent to the basement rock, however, wadi tributaries drain the watershed area of the basement rock. The alluvium deposits form a local aquifer, with shallow to moderate depths of 0–30 m and 30–100 m, respectively. The aquifers are connected hydraulically and depending on the elevation and hydraulic conditions, they could recharge or discharge each other. In 1984, the abstraction of groundwater was assessed at 5×10^6 m^3/y, but in 2008 reached $>8 \times 10^6$ m^3/y. The groundwater is relatively saline, except for local spots in the upper watershed areas. High-salinity water, unsuitable for domestic use, is pumped from shallow wells in the Quaternary and the connected fissured hard rock aquifer.

18.2.4 Conclusions

Egypt is a desert country and therefore, groundwater is a vital factor for economic growth and sustainable development. The main water resources include the Nile River, precipitation, and groundwater (renewable and non-renewable). Groundwater forms a moderate part of the total water supply in Egypt, however, the demand for groundwater resources is expected to increase in the near future. Across the Egyptian territories regional hydrogeological systems are heterogeneous, with both shallow and deep aquifers in different hydrogeological settings, with different recharge rates, hydraulic parameters, water quality, and water age. The shallow aquifers are located in the coastal areas and are replenished by rainfall and surface water. The deep regional aquifer systems in the Western Desert and Sinai Peninsula contain fossil water (non-renewable) that is exploited on a large scale via boreholes with submersible pumps. The main groundwater resources in Egypt are the Nile Valley and Nile Delta aquifer and the Nubian Sandstone Aquifer in the Western Desert and Sinai Peninsula. Various minor aquifers are available locally in the coastal areas, the eastern and western Nile Delta, and other areas. Other local water resources include the harvested water from rainfall and flash floods, the reused drainage water and treated wastewater and desalination on the coasts of the Mediterranean and Red Seas. Climatic changes are expected to place significant pressure on the already scarce water resources because of rising temperatures, changes in precipitation patterns, inland evaporation, and salinization. Due to the current groundwater overexploitation in some areas, the water quality is deteriorating rapidly. New strategies using different approaches especially modeling, tracing and GIS techniques for water resource development must be implemented. Moreover, feasibility studies must be conducted to locate the water harvesting sites and flood protection zones, and small reservoirs behind retardation dams could be developed for storage and subsequent infiltration to recharge the shallow groundwater. As a reservoir could fill rapidly with sediment, drilling of shallow recharge wells could enhance the recharge process to some extent.

References

Abd El-Bassier M (1997) Hydrogeological and hydrochemical studies of the Quaternary aquifer in Qena Governorate. Unpublished MSc thesis, Faculty of Science, Assiut University

Abdalla F, Scheytt T (2012) Hydrochemistry of surface water and groundwater from a fractured carbonate aquifer in the Helwan area, Egypt. J Earth Syst Sci 121(1):109–124

Abdalla F, Ahmed A, Omr A (2009) Degradation of groundwater quality of Quaternary aquifer at Qena, Egypt. J Environ Stud 1:19–32

Abdalla F, Khalil R (2018) Potential effects of groundwater and surface water contamination in an urban area, Qus City, Upper Egypt. J Afr Earth Sci 141C:164–178

Abdalla F, Shamrukh M (2011) Riverbank filtration as an alternative treatment technology: Abu Tieg Case Study, Egypt. In Ray C, Shamrukh M (eds) Riverbank filtration for water security in desert countries. NATO science for peace and security series C: environmental security, pp 255–268

Abdalla F, Shamrukh M (2010) Riverbank filtration: developing countries choice for water supply treatment, Egypt Case. In: 1st International Water Association IWA Malaysia Young Water Professionals Conference (IWAYWP2010), 2–4 Mar 2010, Kuala Lumpur, Malaysia. ISBN 983-9805-86-4

Abdalla F, Shamrukh M (2016) Quantification of River Nile/Quaternary Aquifer exchanges via riverbank filtration by hydrochemical and biological indicators, Assuit, Egypt. J Earth Syst Sci 125–8:1697–1711

Abdel Moneim A (2009) Overview of water resources and requirements in Egypt; the factors controlling its management and development. J Environ Stud 2:85–97

Abdelwahab R, Omar M (2011) Wastewater reuse in Egypt: opportunities and challenges. Arab World. Arab Water Council Report

Abdin E, Gaafar I (2009) Rational water use in Egypt. In: El Moujabber M, Mandi L, TrisorioLiuzzi G, Martín I, Rabi A, Rodríguez R (eds) Technological perspectives for rational use of water resources in the Mediterranean region. Bari: CIHEAM, 11–27 (Options Méditerranéennes: Série A. Séminaires Méditerranéens; n. 88). http://om.ciheam.org/om/pdf/a88/00801177.pdf

Abu-Zeid M (1995) Major policies and programs for irrigation, drainage and water resources development in Egypt. In: Abdel Hakim T (ed) Egyptian agriculture profile. CIHEAM, Montpellier, pp 33–49

Abu-Zeid A, El-Shibini Z (1997) Egypt's High Aswan Dam. Int J Water Resour Dev 13(2):209–218. https://doi.org/10.1080/07900629749836

Al-Agha D, Closas A, Molle F (2015) Survey of groundwater use in the central part of the Nile Delta. Activity Report, Australian Centre for International Agricultural Research

Alataway A, El Alfy M (2019) Rainwater harvesting and artificial groundwater recharge in arid areas: case study in Wadi Al-Alb, Saudi Arabia. J Water Resour Plan Manag 145(1). https://doi.org/10.1061/(ASCE)WR.1943-5452.0001009

Batisha AF (2012) Assiut Barrage in Egypt: past, present and future. Irrig Drain Syst Eng 1:1. https://doi.org/10.4172/2168-9768.1000e104

CAPMAS (2012) Central Agency for public mobilization and statistics 2011 statistics year book. http://www.capmas.gov.eg/

Camberlin P (2009) Nile Basin climates. In: Dumont HJ (ed) The Nile: origin, environments, limnology and human use, Monographiae Biologicae, vol 89. Springer, Dordrecht, pp 307–333

Carbon Monitoring for Action (CARMA). Aswan High Dam. http://carma.org/plant/detail/2398

CEDARE (2014) Egypt Water Sector M&E Rapid Assessment Report. Monitoring & Evaluation for Water in North Africa (MEWINA) Project. Water Resources Management Program, CEDARE

Collins R (2002) The Nile. Yale University Press/New Haven and London

Conniff K, Molden D, Peden D, Awulachew SB (2012) Nile water and agriculture: past present and future. In Awulachew SB, Smakhtin V, Molden D, Peden D (eds) The Nile River Basin: water, agriculture, governance and livelihoods. Abingdon, UK: Routledge – Earthscan, pp 5–29

Dawoud M, Allam R (2004) Effect of New Nag Hammadi Barrage on groundwater and drainage conditions and suggestion of mitigation measures. Water Resour Manage 18:321–337

Dawoud M, Darwish M, El-Kady M (2005) GIS-based groundwater management model for western Nile Delta. Water Resour Manage 19:585–605

Demin AP (2015) Distribution of water resources: a case study of the transboundary Nile River. Geogr Nat Resour 36(2):198–205

Dumont HJ (ed) (2009) The Nile: origin, environments, limnology and human use. Springer, Dordrecht, Heidelberg. https://doi.org/10.1007/978-1-4020-9726-3

Ebaid I, Ismail S (2010) Lake Nasser evaporation reduction study. J Adv Res 1(4):315–322. https://doi.org/10.1016/j.jare.2010.09.002

Egyptian Higher Committee of Water (EHCW) (2007) Egyptian Standards for drinking and domestic water according to the Act 27/1978 in regulating of the public water supplies. Egyptian Governmental Press, Egypt

El Alfy M (2003) Environmental impact of the geomorphological and hydrogeological aspects of Rafah area, North Sinai, Egypt. PhD thesis, Fac. Sci. Mansoura Univ., 216 p

El-Abd E (2005) The geological impact on the water bearing formations on the Area Southwest Nile Delta, Egypt. PhD thesis, Fac. Sci. Minufiya Univ., Egypt

El Alfy M (2012) Integrated geostatistics and GIS techniques for assessing groundwater contamination in Al-Arish area, Sinai, Egypt. Arab J Geosci 5(2):197–215

El Alfy M (2013) Hydrochemical modelling and assessment of groundwater contamination in Northwest Sinai, Egypt. Water Environ Res 85(3):211–223

El Alfy M (2014) Numerical groundwater modelling as an effective tool for management of water resources in arid areas. Hydrol Sci J 59 (6):1259–1274

El Alfy M, Merkel B (2011) Assessment of human impact on quaternary aquifers of Rafah Area, NE Sinai, Egypt. Int J Econ Environ Geol 1:1–9

El Alfy M, Abdalla F, Moubark K, Alharbi T (2019) Hydrochemical equilibrium and statistical approaches as effective tools for identifying groundwater evolution and pollution sources in arid areas. Geosci J 23(2):299–314. https://doi.org/10.1007/s12303-018-0039-7

El Arabi N (2012) Environmental management of groundwater in Egypt via artificial recharge extending the practice to soil aquifer treatment (SAT). Int J Environ Sustain 1(3):66–82

El Fakharany Z, Fekry A (2014) Assessment of New Esna barrage impacts on groundwater and proposed measures. Water Sci 28:65–73. https://doi.org/10.1016/j.wsj.2014.09.003

El Gamal T, Zaki N (2017) Egyptian irrigation after the Aswan High Dam. In: Satoh M, Aboulroos S (eds) Irrigated agriculture in Egypt. Springer, Cham. https://doi.org/10.1007/978-3-319-30216-4_4

El Gammal A, Salem S, El Gammal A (2010) Change detection studies on the world's biggest artificial lake (Lake Nasser, Egypt). Egypt J Remote Sens Space Sci 13:89–99. https://doi.org/10.1016/j.ejrs.2010.08.001

El Kobtan H, Salem M, Attia K, Ahmed S, Abou El-Magd I (2016) Sedimentological study of Lake Nasser; Egypt, using integrated improved techniques of core sampling, X ray diffraction and GIS platform. Cogent Geosci 2:1168069

El Quosy D, Khalifa H (2017) Control of the Nile's flow: the introduction of perennial irrigation for modern agriculture. In: Satoh M, Aboulroos S (eds) Irrigated agriculture in Egypt. Springer, Cham. https://doi.org/10.1007/978-3-319-30216-4_3

EI-Ramly I (1967) Contribution to the hydrogeological study of limestone terrains in UAR, Actes du Colloques de Dubrovnik, Octobre 1965, Hydrologie des Roches Fissures, vol 1, Publ No 73, AIRS—UNESCO

El-Rawy M, Ismail E, Abdalla O (2019) Assessment of groundwater quality assessment using GIS, hydrogeochemsitry, and factor analysis in Qena governorate, Egypt. Desalin Water Treat 1–16. https://doi.org/10.5004/dwt.2019.24423

Elsaeed G (2011) Effects of climate change on Egypt's water supply. The NATO advanced research workshop on climate change, vol 30. Human Health and National Security, Dubrovnik, Croatia: Dubrovnik, pp 337–347

El-Shafie M, Taha MR, Noureldin A (2007) A neuro-fuzzy model for inflow forecasting of the Nile River at Aswan high dam. Water Resour Manag 21(3):533–556. https://doi.org/10.1007/s11269-006-9027-1

El Sayed E, Dahab K, Ebraheem A (2004) Hydrogeological and hydrogeochemical aspects of the Nubian Sandstone Aquifer in East Oweinat area, SW Egypt. Neues Jahrbuch für Geologie und Palaontologie, Abhandlungen 233(1):121–152

Elsawwaf M, Willems P, Pagano A, Berlamont J (2010) Evaporation estimates from Nasser Lake, Egypt, based on three floating station data and Bowen ratio energy budget. Theoret Appl Climatol 100(3–4):439–465. https://doi.org/10.1007/s00704-009-0168-z

El Tahlawi M, Farrag A, Ahmed S (2008) Groundwater of Egypt: "An environmental overview". Environ Geol 55(3):639–652

EWRA (2011) Egyptian Water Regulatory Agency fourth water and wastewater report

FAO (2013a) AQUASTAT database. Food and Agriculture Organization of the United Nations (FAO)

FAO (2013b) Monitoring of climate change risk impacts of sea level rise on groundwater and agriculture in the Nile Delta. TCP/EGY/3301

FAO (2016) Egypt, regional report. AQUASTAT website. Food and Agriculture Organization of the United Nations. http://www.fao.org/nr/water/aquastat/water_res/index.stm

Fergany EA, Claudet SB (2009) Microtremor measurements in the Nile Delta basin: response of the topmost sedimentary layers. Seismol Res Lett 80(4):591–598

Gemail Kh, El-Shishtawy A, El Alfy M, Ghoneim M, Abd El-Bary M (2011) Assessment of aquifer vulnerability to industrial waste water using resistivity measurements. A case study, along El-Gharbyia main drain, Nile Delta, Egypt. J Appl Geophys 75(1):140–150

Gemail K, El Alfy M, Ghoneim M, Shishtawy A, Abd El-Bary M (2017) Comparison of DRASTIC and DC resistivity modeling for assessing aquifer vulnerability in the central Nile Delta, Egypt. Environ Earth Sci 76(9):350

Ghodeif K, Paufler S, Grischek T, Wahaab R, Souaya E, Bakr M, Abogabal A (2018) Riverbank filtration in Cairo, Egypt—Part I: Installation of a new riverbank filtration site and first monitoring results. Environ Earth Sci 77(7):270. https://doi.org/10.1007/s12665-018-7450-2

HCWW, Moawad A, Fahmy K, Afifi M, Mahmoud R (2013) Responses to Misr Consult questionnaire

Hefny K, Shata A (2004) Underground water in Egypt. Cairo, Egypt, Ministry of Water Supplies and Irrigation, unpublished report

Hefny K, Farid M, Hussein M (1992) Groundwater assessment in Egypt. Int J Water Resour Dev 8(2):126–134

Horowitz A (1979) The quaternary of Israel. Academic Press, New York/London, p 394

II Nouva Castoro (1986) Techno-economical feasibility study for the reclamation of 50,000 feddans in Farafra Oasis, Part 1—Geohydrogeology: Unpublished report to the general authority for land reclamation, Cairo

Issar A (2003) Climate changes during the Holocene and their impact on hydrological systems. Cambridge University Press, Cambridge

Issawi B (1978) Geology of Nubia west area, Western Desert, Egypt. Ann Geol Surv Egypt 237–253

Ismail E, El-Rawy M (2018) Assessment of groundwater quality in West Sohag, Egypt. Desalin Water Treat 123:101–108. https://doi.org/10.5004/dwt.2018.22687

Issar A, Bruins H (1983) Special climatic conditions in the Sinai and Negev during the Most Upper Pleistocene. Paleogeoq Paleoclimat Paleoeco 42:63–72

Issar A, Gilead I (1986) Pleistocene climates and hydrology of the Negev (Israel) and Sinai (Egypt) deserts. Berliner Geowissenschaftliche Abhandlungen, Reihe A 72:17–25

JICA (1992) North Sinai groundwater resources study in the Arab Republic of Egypt. Final report. Submitted to the Research Institute for Water Resources. Ministry of Public Works and Water Resources, Cairo, Egypt

JICA (1999) South Sinai groundwater resources study in the Arab Republic of Egypt. Main report to the Research Institute for Water Resources. Ministry of Public Works and Water Resources, Cairo, Egypt

Joint Venture Qattara (1979) "Study Qattara Depression", Vol III, Part 1 Topography, regional geology and hydrogeology. Lahmeyer International, Salzgitter Consult and Deutsche Project, Union GmbH, German Federal Republic

Kamel E (2004) Geology of Luxor Area and its relationship to groundwater uprising under the Pharaoh Temples. Unpublished MSc thesis, Aswan Faculty of Science, South Valley University, Egypt

Kendie D (1999) Egypt and the hydro-politics of the Blue Nile River. Northeast Afr Stud 6(1–2):141–169. https://doi.org/10.1353/nas.2002.0002

Khaled M, Abdalla F (2013) Hydrogeophysical study for additional groundwater supplies in El Heiz Area, Southern part of El Bahariya Oasis, Western Desert, Egypt. Arab J Geosci 6:761–774

Korany E (1995) Hydrogeologic evaluation of the deeper aquifer in Bahariya mines area, Egypt. In: Symposium of Nubia sandstone rocks, Bengazy, Libya, pp 1–38

Mabrouk B, Jonoski A, Solomatine D, Uhlenbrook S (2013) A review of seawater intrusion in the Nile Delta groundwater system—the basis for assessing impacts due to climate changes and water resources development. https://doi.org/10.5194/hessd-10-10873-2013

MacAlister C, Pavelic P, Tindimugaya C, Ayenew T, Ibrahim M, Abdel Meguid M (2012) Overview of groundwater in the Nile River Basin. AGRIS, pp 186–211

Massoud U, Kenawy A, Ragab E, Abbas A, El-Kosery H (2014) Characterization of the groundwater aquifers at El Sadat City by joint inversion of VES and TEM data. NRIAG J Astron Geophys 3:137–149

Moawad A (2012) Water and sanitation status in Egypt. Presentation. National Launching Workshop on Water Sector M&E in Egypt

Mobasher MA (2010) Adaptive reservoir operation strategies under changing boundary conditions—the case of Aswan high Dam Reservoir. PhD thesis, TU Darmstadt, Darmstadt, Germany

Mohamed A, Sultan M, Ahmed M, Yan E, Ahmed E (2016) Aquifer recharge, depletion, and connectivity: Inferences from GRACE, land surface models, and geochemical and geophysical data. Geol Soc Am Bull 129(5/6):534–546

Mohamed TA, Abo-Elwafa A (2014) Characterization of water quality around the New Assiut Barrage and its hydropower plant. Assiut J Agric Sci 45(5):39–52

MPWWR (1988) Rehabilitation and improvement of water delivery systems in old lands. Proj. No. EGY/85/012. Final report

Muala E, Mohamed YA, Duan Z, Van der Zaag P (2014) Estimation of reservoir discharges from Lake Nasser and Roseires Reservoir in the Nile Basin using satellite altimetry and imagery data. Remote Sens 6:7522–7545. https://doi.org/10.3390/rs6087522

MWRI (Ministry of Water Resources and Irrigation) (2005a) National Water Resources Plan 2017. Ministry of Water Resources and Irrigation Planning Sector

MWRI (Ministry of Water Resources and Irrigation) (2005b) National Water Resources Plan for Egypt 2017. Ministry of Water Resources and Irrigation

MWRI (Ministry of Water Resources and Irrigation) (2010) The draft of the development and management of water resources strategy 2050. Ministry of Irrigation and Water Resources (MWRI), Cairo, Egypt

MWRI (Ministry of Water Resources and Irrigation) (2012) Strategy of Water Resources of Egypt till 2050. Ministry of Water Resources and Irrigation

MWRI (Ministry of Water Resources and Irrigation) (2013) Redeveloping the National Plan of Water Resources Water Strategy until 2017. Ministry of Water Resources and Irrigation, Cairo

MWRI (Ministry of Water Resources and Irrigation Egypt) (2014) Water scarcity in Egypt: the urgent need for regional cooperation among the Nile Basin Countries, p 5

MWRI (Ministry of Water Resources and Irrigation). New Assiut Barrage. In Arabic. https://www.mwri.gov.eg/index.php/ministry-2/ministry

Nashed A, Sproul A, Leslie G (2014) Water resources and the potential of brackish groundwater extraction in Egypt: a review. J Water Supply: Res Technol—AQUA 63(6):399–428

Noaman M, El Quosy D (2017) Hydrology of the Nile and ancient agriculture. In: Satoh M, Aboulroos S (eds) Irrigated agriculture in Egypt. Springer, Cham, pp 9–28. https://doi.org/10.1007/978-3-319-30216-4_2

NRI (1992) River regime of the Nile in Egypt. Nile Research Institute, Egypt

Omar M (2011) Agricultural drainage water in Egypt. Session on wastewater management on the Arab World. Arab Water Council, Dubai, UAI

Paufler S, Grischek T, Bartak R, Ghodeif K, Wahaab R, Boernick R (2018) Riverbank filtration in Cairo, Egypt: Part II—Detailed investigation of a new riverbank filtration site with a focus on manganese. Environ Earth Sci 77(8):318. https://doi.org/10.1007/s12665-018-7500-9

Ribbe L, Ahmed S (2006) Transboundary water management in the River Nile Basin. Technol Resour Manag Dev 4:13–27

RIGW (1980) Project of safe yield study for groundwater aquifers in the Nile Delta and Upper Egypt. Part 1. Ministry of Irrigation, Academy of Scientific Research and Technology, and Organization of Atomic Energy, Egypt, Cairo (In Arabic)

RIGW (1992) Groundwater resources and projection of groundwater development. Water security project (WSP), Cairo

RIGW (1993) The Possibility of the Reclamation of 60,000 Feddan in Wadi EI-Faregh Area. Report submitted to the General Company for Research and Groundwater, Cairo

RIGW (1995) Regional prospective of the fissured carbonate aquifer system in Egypt. First technical report

RIGW (2002) Environmental management of groundwater resources in Egypt. Final report, Egypt

RIGW (2003) Impacts of future surface water development on groundwater aquifer system in the West Nile Delta Region, Cairo

RIGW-IWACO (1988) Research Institute for Groundwater (1988–1993), Hydrogeological map of Egypt, scale 1:2,000,000. Cairo

RIGW-IWACO (1992) Hydrogeological map of the Nile Delta, scale 1:500,000

Sadek M, Abd El-Samie S (2001) Pollution vulnerability of the Quaternary aquifer near Cairo, Egypt, as indicated by isotopes and hydrochemistry. Hydrogeol J 9:273–281

Said E, Moussa AMA, El-Din MN, Hassan N (2014) Morphological changes of reach two of the Nile River. In: Lehfeldt, Kopmann (eds) ICHE 2014, Hamburg. © 2014 Bundesanstalt für Wasserbau ISBN 978-3-939230-32-8

Said R (1962) The geology of Egypt. Elsevier, Amsterdam, p 377

Sattar A, Raslan M (2014) Predicting morphological changes DS New Naga-Hammadi Barrage for extreme Nile flood flows: a Monte Carlo analysis. J Adv Res 5(1):197–207. https://doi.org/10.1016/j.jare.2012.12.004

Schneider M, Sonntag C (1985) Hydrogeology of the Gebel Uweinat-Aswan uplift system, Eastern Sahara. International congress on hydrogeology of rocks of low permeability, Tucson

Sherif M (1999) The Nile Delta Aquifer in Egypt, Chapter 17. In: Bear J, Cheng A, Sorek S, Ouazar D, Herrera A (eds) Seawater intrusion in coastal aquifers, concepts methods and practices. Theory and application of transport in Porous Media, vol 14. Kluwer Academic Publishers, The Netherlands, pp 559–590

Sturchio N, Du X, Purtschert R, Lehmann B, Sultan M, Patterson L, Lu Z, Müller P, Bigler T, Bailey K, O'Connor T, Young L, Lorenzo R, Becker R (2004) One million year old groundwater in the Sahara revealed by krypton-81 and chlorine-36. Geophys Res Lett 31:1–4

Thorweihe U, Heinl M (1996) Groundwater resources of the Nubian aquifer system. Technical University of Berlin, Germany, p 95

Wagdy A, El Adway H, El-Gamal M (2008) Vegetation dynamics assisted hydrological analysis for Wady Degla. UNDP/GEF/Cairo University, Egypt

Worldometers (2017). www.worldometers.info. Accessed Oct 2017

World Health Organization (WHO) (2008) Guidelines for drinking-water quality, 3rd edn, incorporating the first and second Addenda, vol 1, Geneva, Switzerland

Youssef T, Gad M, Ali M (2012) Assessment of groundwater resources management in Wadi El-Farigh Area using MODFLOW. IOSR J Eng 2(10):69–78